

CODEN: JASMAN

ISSN: 0001-4966

The Journal of the Acoustical Society of America

Vol. 113, No. 1

January 2003

ACOUSTICAL NEWS—USA	1
USA Meetings Calendar	2
ACOUSTICAL STANDARDS NEWS	5
Standards Meetings Calendar	5
ABSTRACTS FROM ACOUSTICS RESEARCH LETTERS ONLINE	13
BOOK REVIEWS	14
REVIEWS OF ACOUSTICAL PATENTS	16
FORUM	32

LETTERS TO THE EDITOR

Virtual error sensing for active noise control in a one-dimensional waveguide: Performance prediction versus measurement (L)	Jacqueline M. Munn, Ben S. Cazzolato, Colin D. Kestell, Colin H. Hansen	35
Laboratory measurements of sound scattering from a buried sphere above and below the critical angle (L)	Harry J. Simpson, Brian H. Houston, Raymond Lin	39
Comment on “Development of panel loudspeaker system: Design, evaluation and enhancement” [J. Acoust Soc. Am. 106, 2751–2761 (2001)] (L)	Frank Fahy	43
Acoustic and vibration background noise in the collapsed structure of the World Trade Center (L)	Thomas B. Gabrielson, Matthew E. Poese, Anthony A. Atchley	45
The role of envelope beat cues in the detection and discrimination of second-order amplitude modulation (L)	Christian Füllgrabe, Christian Lorenzi	49
Central locus for nonspeech context effects on phonetic identification (L)	Andrew J. Lotto, Sarah C. Sullivan, Lori L. Holt	53
Sounds produced by individual white whales, <i>Delphinapterus leucas</i> , from Svalbard during capture (L)	Sofie M. Van Parijs, Christian Lydersen, Kit M. Kovacs	57

GENERAL LINEAR ACOUSTICS [20]

Direct and inverse scattering of transient acoustic waves by a slab of rigid porous material	Z. E. A. Fellah, M. Fellah, W. Lauriks, C. Depollier	61
The reflection of bounded inhomogeneous waves on a liquid/solid interface	S. Vanaverbeke, F. Windels, O. Leroy	73

(Continued)

CONTENTS—Continued from preceding page

Experimental demonstration of noninvasive transskull adaptive focusing based on prior computed tomography scans	J.-F. Aubry, M. Tanter, M. Pernot, J.-L. Thomas, M. Fink	84
Scattering from a single bubble near a roughened air–water interface: Laboratory measurements and modeling	Peter H. Dahl, George Kapodistrias	94
Circumferential resonance modes of solid elastic cylinders excited by obliquely incident acoustic waves	Ying Fan, Farhang Honarvar, Anthony N. Sinclair, Mohammad-Reza Jafari	102
Sound source reconstruction using inverse boundary element calculations	Andreas Schuhmacher, Jørgen Hald, Karsten Bo Rasmussen, Per Christian Hansen	114
Inverse estimation of the acoustic impedance of a porous woven hose from measured transmission coefficients	Chul-Min Park, Jeong-Guon Ih, Yoshio Nakayama, Hideo Takao	128
NONLINEAR ACOUSTICS [25]		
Modeling of nonlinear ultrasound propagation in tissue from array transducers	Roger J. Zemp, Jahangir Tavakkoli, Richard S. C. Cobbold	139
Acoustic streaming generated by standing waves in two-dimensional channels of arbitrary width	Mark F. Hamilton, Yuri A. Ilinskii, Evgenia A. Zabolotskaya	153
AEROACOUSTICS, ATMOSPHERIC SOUND [28]		
Reynolds number effects on flow/acoustic mechanisms in spherical windscreens	Z. Charlie Zheng, Bee K. Tan	161
Acoustic near-field characteristics of a conical, premixed flame	Doh-Hyoung Lee, Tim C. Lieuwen	167
Application of an acoustic noise removal method to aircraft-based atmospheric temperature measurements	Ronald J. Hugo, Scott R. Nowlin, Ila L. Hahn, Frank D. Eaton, Kim A. McCrae	178
Active stereo sound localization	Greg L. Reid, Evangelos Milios	185
UNDERWATER SOUND [30]		
A method of images for a penetrable acoustic waveguide	John A. Fawcett	194
Broadband sound propagation in shallow water and geoaoustic inversion	D. P. Knobles, R. A. Koch, L. A. Thompson, K. C. Focke, P. E. Eisman	205
Spectral and modal formulations for the Doppler-shifted field scattered by an object moving in a stratified medium	Yi-san Lai, Nicholas C. Makris	223
Motion compensation for adaptive horizontal line array processing	T. C. Yang	245
ULTRASONICS, QUANTUM ACOUSTICS, AND PHYSICAL EFFECTS OF SOUND [35]		
Narrow band laser-generated surface acoustic waves using a formed source in the ablative regime	Shant Kenderian, B. Boro Djordjevic, Robert E. Green, Jr.	261
TRANSDUCTION [38]		
Derivation of an optimal directivity pattern for sweet spot widening in stereo sound reproduction	Josep A. Ródenas, Ronald M. Aarts, A. J. E. M. Janssen	267
Electromechanical coupling factor of capacitive micromachined ultrasonic transducers	Alessandro Caronti, Riccardo Carotenuto, Massimo Pappalardo	279
A directional acoustic array using silicon micromachined piezoresistive microphones	David P. Arnold, Toshikazu Nishida, Louis N. Cattafesta, Mark Sheplak	289
Acoustic scattering by a cylindrical shell with symmetric line constraints in the heavy fluid-loading limit	E. A. Skelton	299

CONTENTS—Continued from preceding page

STRUCTURAL ACOUSTICS AND VIBRATION [40]

- | | | |
|--|--|-----|
| Leaky helical flexural wave backscattering contributions from tilted water-filled cylindrical shells | Florian J. Blonigen, Philip L. Marston | 309 |
| Application of Padé via Lanczos approximations for efficient multifrequency solution of Helmholtz problems | Marcus M. Wagner, Peter M. Pinsky, Manish Malhotra | 313 |

NOISE: ITS EFFECTS AND CONTROL [50]

- | | | |
|---|---|-----|
| A passive means for cancellation of structurally radiated tones | Jeffrey A. Zapfe, Eric E. Ungar | 320 |
| Lattice form adaptive infinite impulse response filtering algorithm for active noise control | Jing Lu, Chunhua Shen, Xiaojun Qiu, Boling Xu | 327 |
| A- and C-weighted sound levels as predictors of the annoyance caused by shooting sounds, for various façade attenuation types | Joos Vos | 336 |

ACOUSTIC SIGNAL PROCESSING [60]

- | | | |
|--|---|-----|
| Investigation of phase coupling phenomena in sustained portion of musical instruments sound | Shlomo Dubnov, Xavier Rodet | 348 |
| Compensation for source nonstationarity in multireference, scan-based near-field acoustical holography | Hyu-Sang Kwon, Yong-Joe Kim, J. Stuart Bolton | 360 |

PHYSIOLOGICAL ACOUSTICS [64]

- | | | |
|--|---|-----|
| An auditory-periphery model of the effects of acoustic trauma on auditory nerve responses | Ian C. Bruce, Murray B. Sachs, Eric D. Young | 369 |
| Ear-canal acoustic admittance and reflectance effects in human neonates. I. Predictions of otoacoustic emission and auditory brainstem responses | Douglas H. Keefe, Fei Zhao, Stephen T. Neely, Michael P. Gorga, Betty R. Vohr | 389 |
| Ear-canal acoustic admittance and reflectance measurements in human neonates. II. Predictions of middle-ear dysfunction and sensorineural hearing loss | Douglas H. Keefe, Michael P. Gorga, Stephen T. Neely, Fei Zhao, Betty R. Vohr | 407 |
| Objective estimates of cochlear tuning by otoacoustic emission analysis | Arturo Moleti, Renata Sisto | 423 |
| Physiopathological significance of distortion-product otoacoustic emissions at $2f_1-f_2$ produced by high- versus low-level stimuli | Paul Avan, Pierre Bonfils, Laurent Gilain, Thierry Mom | 430 |
| Effect of current stimulus on <i>in vivo</i> cochlear mechanics | Anand A. Parthasarathi, Karl Grosh, Jiefu Zheng, Alfred L. Nuttall | 442 |
| Effect of outer hair cell piezoelectricity on high-frequency receptor potentials | Alexander A. Spector, William E. Brownell, Aleksander S. Popel | 453 |

PSYCHOLOGICAL ACOUSTICS [66]

- | | | |
|---|---|-----|
| Effect of amplitude modulation coherence for masked speech signals filtered into narrow bands | Emily Buss, Joseph W. Wall III, John H. Grose | 462 |
| Detection and direction-discrimination of diotic and dichotic ramp modulations in amplitude and phase | Caroline Witton, Michael I. G. Simpson, G. Bruce Henning, Adrian Rees, G. G. R. Green | 468 |

SPEECH PRODUCTION [70]

- | | | |
|--|---|-----|
| Analysis of the three-dimensional tongue shape using a three-index factor analysis model | Yanli Zheng, Mark Hasegawa-Johnson, Shamala Pizza | 478 |
| Flow visualization and pressure distributions in a model of the glottis with a symmetric and oblique divergent angle of 10 degrees | Daoud Shinwari, Ronald C. Scherer, Kenneth J. DeWitt, Abdollah A. Afjeh | 487 |
| The synergy between speech production and perception | Powen Ru, Taishih Chi, Shihab Shamma | 498 |

CONTENTS—Continued from preceding page

Effects of prosodic boundary on /aC/ sequences: Acoustic results	Marija Tabain	516
Learning to produce speech with an altered vocal tract: The role of auditory feedback	Jeffery A. Jones, K. G. Munhall	532
Individual talker differences in voice-onset-time	J. Sean Allen, Joanne L. Miller, David DeSteno	544
Spectral models of additive and modulation noise in speech and phonatory excitation signals	Jean Schoentgen	553
SPEECH PERCEPTION [71]		
Unfolding of phonetic information over time: A database of Dutch diphone perception	Roel Smits, Natasha Warner, James M. McQueen, Anne Cutler	563
MUSIC AND MUSICAL INSTRUMENTS [75]		
Discrete-time modeling of woodwind instrument bores using wave variables	Maarten van Walstijn, Murray Campbell	575
BIOACOUSTICS [80]		
Suppression of large intraluminal bubble expansion in shock wave lithotripsy without compromising stone comminution: Refinement of reflector geometry	Yufeng Zhou, Pei Zhong	586
Echolocation signals of wild Atlantic spotted dolphin (<i>Stenella frontalis</i>)	Whitlow W. L. Au, Denise L. Herzing	598
Echolocation in the Risso's dolphin, <i>Grampus griseus</i>	Jennifer D. Philips, Paul E. Nachtigall, Whitlow W. L. Au, Jeffrey L. Pawloski, Herbert L. Roitblat	605
The influence of flight speed on the ranging performance of bats using frequency modulated echolocation pulses	Arjan M. Boonman, Stuart Parsons, Gareth Jones	617
Measuring hearing in the harbor seal (<i>Phoca vitulina</i>): Comparison of behavioral and auditory brainstem response techniques	Lawrence F. Wolski, Rindy C. Anderson, Ann E. Bowles, Pamela K. Yochem	629
High intensity anthropogenic sound damages fish ears	Robert D. McCauley, Jane Fewtrell, Arthur N. Popper	638
A comparison of the fragmentation thresholds and inertial cavitation doses of different ultrasound contrast agents	Wen-Shiang Chen, Thomas J. Matula, Andrew A. Brayman, Lawrence A. Crum	643
Microparticle column geometry in acoustic stationary fields	Andrew Hancock, Michael F. Insana, John S. Allen	652
ERRATA		
Erratum: "Analysis of the time-reversal operator for scatterers of finite size" [J. Acoust. Soc. Am. 112, 411–419 (2002)]	David Chambers	660

ACOUSTICAL NEWS—USA

Elaine Moran

Acoustical Society of America, Suite 1N01, 2 Huntington Quadrangle, Melville, NY 11747-4502

Editor's Note: Readers of this Journal are encouraged to submit news items on awards, appointments, and other activities about themselves or their colleagues. Deadline dates for news items and notices are 2 months prior to publication.

New Fellows of the Acoustical Society of America



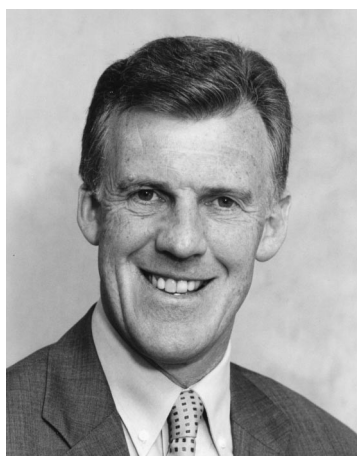
George E. Ioup—For contributions to signal processing in underwater acoustics.



Hugh McDermott—For signal processing that improves speech recognition with cochlear implants.



Colette M. McKay—For contributions to measurement and improvement of speech recognition with cochlear implants.



Philip A. Nelson—For contributions to active control and auralization.



Jack Randorff—For contributions to education in the practical applications of architectural acoustics and noise control.

ASA members receive awards from ASME International

Jan D. Achenbach was named an honorary member of the American Society of Mechanical Engineers (ASME International). The award citation read: "For research and teaching excellence and more than 350 scholarly publications highlighting new analytical and experimental work in quantita-

tive nondestructive evaluation, wave propagation in elastic solids, and fracture mechanics, among other areas."

Dr. Achenbach is Walter P. Murphy and Distinguished McCormick School Professor, Department of Civil and Environmental Engineering and Director, Center for Quality Engineering and Failure Prevention at Northwestern University in Evanston, Illinois.

Ira Dyer has been named the 2002 recipient of the Per Bruel Gold Medal for Noise Control and Acoustics. The award citation reads as follows:

"For establishing research and educational programs in ocean engineering and original contributions to the understanding of underwater acoustics, flow-generated noise, ocean ambient noise, and structural acoustics."

Dr. Dyer is retired Professor of Ocean Engineering, Massachusetts Institute of Technology. He received the ASA R. Bruce Lindsay Award (formerly Biennial Award) in 1960 and the Gold Medal of the Acoustical Society of America in 1996. Professor Dyer also served as ASA Vice President (1973–74) and President (1986–87) and is currently the Chair of the Committee on Investments.

Advanced-degree dissertations in acoustics

Editor's note: Abstracts of Doctoral and Master's theses will be welcomed at all times. Please note that they must be limited to 200 words, must include the appropriate PACS classification numbers, and formatted as shown below. If sent by postal mail, note that they must be double-spaced. The address for obtaining a copy of the thesis is helpful. Submit abstracts to: Acoustical Society of America, Thesis Abstracts, Suite 1NO1, 2 Huntington Quadrangle, Melville, NY 11747-4502, E-mail: asa@aip.org

Acoustic scattering from fluid-loaded finite cylindrical shells. Helical waves: Time-domain analysis and resonance complete identification [43.20.Ks, 43.40.Ey, 43.40.Fz, 43.20.Fn]—Lionel Haumesser, *Laboratoire d'Acoustique Ultrasonore et d'Electronique, Université du Havre, Le Havre, France, December 2001 (Doctoral Thesis)*. Acoustic pressure scattered from fluid-loaded finite cylindrical shells is experimentally and theoretically investigated. Spectral and time-domain signatures of such objects are interpreted in terms of resonances and propagations of surface waves. The scatterers are made of stainless steel, with inner to outer radii ratio equal to 0.83 and 0.97. They are excited under the far-field conditions by broadband ultrasonic signals ($10 < k_1 a < 60$), for incidence angles between 0° (normal incidence to the shell main axis) and 50° . Resonance vibration modes are experimentally determined by using two bistatic experimental setups: the first leads to the identification of circumferential modes (n) and the second yields the identification of axial modes (m). The results are in agreement with those obtained with a hybrid modal theoretical approach combining elasticity theory and Kirchhoff diffraction integral. Resonances present in backscattered spectral responses, associated with S_0 and T_0 helical waves, are completely identified (nature of the wave, frequency, n , m). Time-domain responses are analyzed by a geometrical model linking wave helical travel paths on the shell to echo arrival times of the T_0 wave. This geometrical approach also enables the consideration of effects due to the presence of an internal plate bulkhead.

Thesis advisor: Professor Gérard Maze.

Copies of this thesis written in French can be obtained from Professor G. Maze, LAUE, Université du Havre, BP4006 Pl. R. Schuman, 76610 Le Havre, France. E-mail address: maze@iut.univ-lehavre.fr

USA Meetings Calendar

Listed below is a summary of meetings related to acoustics to be held in the U.S. in the near future. The month/year notation refers to the issue in which a complete meeting announcement appeared.

2003

- | | |
|----------------|--|
| 13–15 March | American Auditory Society Annual meeting, Scottsdale, AZ [American Auditory Society, 352 Sundial Ridge Cir., Dammeron Valley, UT 84783; Tel.: 435-574-0062; Fax: 435-574-0063; E-mail: amaudsoc@aol.com; WWW: www.amauditorysoc.org]. |
| 28 April–2 May | 145th Meeting of the Acoustical Society of America, Nashville, TN [Acoustical Society of America, Suite 1NO1, 2 Huntington Quadrangle, Melville, NY 11747-4502; Tel.: 516-576-2360; Fax: 516-576-2377; E-mail: asa@aip.org; WWW: asa.aip.org]. |
| 5–8 May | SAE Noise & Vibration Conference & Exhibition, |

23–25 June

5–8 Oct.

10–14 Nov.

Traverse City, MI [P. Kreh, SAE International, 755 W. Big Beaver Rd., Suite 1600, Troy, MI 48084; Fax: 724-776-1830; WWW: <http://www.sae.org>].

NOISE-CON 2003, Cleveland, OH [INCE Business Office, Iowa State University, 212 Marston Hall, Ames, IA 50011-2153; Fax: 515-294-3528; E-mail: ibo@ince.org].

IEEE International Ultrasonics Symposium, Honolulu, HI [W. D. O'Brien, Jr., Bioacoustics Research Lab., University of Illinois, Urbana, IL 61801-2991; Fax: 217-244-0105; WWW: www.ieee-uffc.org].

146th Meeting of the Acoustical Society of America, Austin, TX [Acoustical Society of America, Suite 1NO1, 2 Huntington Quadrangle, Melville, NY 11747-4502; Tel.: 516-576-2360; Fax: 516-576-2377; E-mail: asa@aip.org; WWW: asa.aip.org].

2004

24–28 May

75th Anniversary Meeting (147th Meeting) of the Acoustical Society of America, New York, NY [Acoustical Society of America, Suite 1NO1, 2 Huntington Quadrangle, Melville, NY 11747-4502; Tel.: 516-576-2360; Fax: 516-576-2377; E-mail: asa@aip.org; WWW: asa.aip.org].

3–7 Aug.

8th International Conference of Music Perception and Cognition, Evanston, IL [School of Music, Northwestern University, Evanston, IL 60201; WWW: www.icmpc.org/conferences.html].

15–19 Nov.

148th Meeting of the Acoustical Society of America, San Diego, CA [Acoustical Society of America, Suite 1NO1, 2 Huntington Quadrangle, Melville, NY 11747-4502; Tel.: 516-576-2360; Fax: 516-576-2377; E-mail: asa@aip.org; WWW: asa.aip.org].

Cumulative Indexes to the *Journal of the Acoustical Society of America*

Ordering information: Orders must be paid by check or money order in U.S. funds drawn on a U.S. bank or by Mastercard, Visa, or American Express credit cards. Send orders to Circulation and Fulfillment Division, American Institute of Physics, Suite 1NO1, 2 Huntington Quadrangle, Melville, NY 11747-4502; Tel.: 516-576-2270. Non-U.S. orders add \$11 per index.

Some indexes are out of print as noted below.

Volumes 1–10, 1929–1938: JASA and Contemporary Literature, 1937–1939. Classified by subject and indexed by author. Pp. 131. Price: ASA members \$5; nonmembers \$10.

Volumes 11–20, 1939–1948: JASA, Contemporary Literature, and Patents. Classified by subject and indexed by author and inventor. Pp. 395. Out of print.

Volumes 21–30, 1949–1958: JASA, Contemporary Literature, and Patents. Classified by subject and indexed by author and inventor. Pp. 952. Price: ASA members \$20; nonmembers \$75.

Volumes 31–35, 1959–1963: JASA, Contemporary Literature, and Patents. Classified by subject and indexed by author and inventor. Pp. 1140. Price: ASA members \$20; nonmembers \$90.

Volumes 36–44, 1964–1968: JASA and Patents. Classified by subject and indexed by author and inventor. Pp. 485. Out of print.

Volumes 36–44, 1964–1968: Contemporary Literature. Classified by subject and indexed by author. Pp. 1060. Out of print.

Volumes 45–54, 1969–1973: JASA and Patents. Classified by subject and indexed by author and inventor. Pp. 540. Price: \$20 (paperbound); ASA members \$25 (clothbound); nonmembers \$60 (clothbound).

Volumes 55–64, 1974–1978: JASA and Patents. Classified by subject and indexed by author and inventor. Pp. 816. Price: \$20 (paperbound); ASA members \$25 (clothbound); nonmembers \$60 (clothbound).

Volumes 65–74, 1979–1983: JASA and Patents. Classified by subject and indexed by author and inventor. Pp. 624. Price: ASA members \$25 (paperbound); nonmembers \$75 (clothbound). **Volumes 75–84, 1984–1988:** JASA and Patents. Classified by subject and indexed by author and inventor. Pp. 625. Price: ASA members \$30 (paperbound); nonmembers \$80 (clothbound).

Volumes 85–94, 1989–1993: JASA and Patents. Classified by subject and indexed by author and inventor. Pp. 736. Price: ASA members \$30 (paperbound); nonmembers \$80 (clothbound).

Volumes 95–104, 1994–1998: JASA and Patents. Classified by subject and indexed by author and inventor. Pp. 632. Price: ASA members \$40 (paperbound); nonmembers \$90 (clothbound).

BOOK REVIEWS

P. L. Marston

Physics Department, Washington State University, Pullman, Washington 99164

These reviews of books and other forms of information express the opinions of the individual reviewers and are not necessarily endorsed by the Editorial Board of this Journal.

Editorial Policy: *If there is a negative review, the author of the book will be given a chance to respond to the review in this section of the Journal and the reviewer will be allowed to respond to the author's comments. [See "Book Reviews Editor's Note," J. Acoust. Soc. Am. 81, 1651 (May 1987).]*

Seismic Ray Theory

Vlastislav Cerveny

Cambridge University Press, New York, 2001.

vii + 713 pp. Price: \$130.00 (hardcover) ISBN: 0521366712.

The book *Seismic Ray Theory* by V. Cerveny is concerned with the theory of high-frequency body wave propagation in an inhomogeneous, anisotropic elastic solid. The book is the most complete description of this topic that is currently available. The author is exceptionally well qualified to write such a book as he has made many fundamental contributions to the material covered.

The book is comprised of six chapters. The first provides a brief overview of the book. In Chap. 2 the elastodynamic equations of motion in an inhomogeneous, anisotropic 3-d elastic medium are introduced. Elementary plane wave solutions and Green's function solutions are discussed, and the equations governing high-frequency asymptotic wave motion are systematically developed. Anisotropy, first introduced here, remains a central theme throughout the book. Chapter 3 is concerned with the solution to the coupled ray and travel time equations in 3-d environments. Chapter 4 develops dynamic ray tracing wherein the evolution of ray variational quantities following ray trajectories is described. The propagator matrix is introduced. Chapter 5 is concerned with the calculation of ray amplitudes. Included are discussion of Gaussian beam summation methods and the Maslov–Chapman integral. Chapter 6 is concerned with the time domain—the construction of the transient response, a synthetic seismogram, to transient forcing.

All of the material presented is developed from basic concepts, so the reader need not have any a priori knowledge of ray methods or waves in elastic solids. A moderately strong mathematical background (familiarity with complex variables, integral transforms, and vector and tensor calculus) and some knowledge of basic continuum mechanics is assumed, however. While some mathematical skill is required, Cerveny does a good job of keeping the focus on the physics, not allowing the mathematics to become a distraction. The focus of the book is clearly and consistently on the theory of ray methods in seismic wave propagation. The theory behind some numerical methods is discussed, but numerical methods are themselves not a focus. Practical issues relating to seismic data interpretation are not considered. The choice of material covered is fairly traditional with an emphasis on results that are needed to solve seismic body wave problems. Some less traditional topics such as ray chaos, the catastrophe classification of caustics, and the use of space–time rays to model surface (Rayleigh and Love) wave propagation problems are discussed, but only very briefly.

Two clear strengths of the book are its treatment of elastic media, including anisotropy and dissipative effects, and its treatment of the time domain, i.e., the construction of synthetic seismograms. The strong focus on transient wavefields is not surprising, as in seismic applications fixed frequency wavefields are of interest only insofar as they can be used to construct transient wavefields. Sadly, the time domain is poorly treated in many books on acoustics, and is poorly understood by many acousticians.

Readers interested primarily in the application of ray methods to sound propagation in fluids might be frustrated by the strong focus of the book on elastic media. The acoustic problem is, of course, a special case, but some fluid-specific problems such as sound propagation in the presence of background flow are not treated. Also, there is no treatment of wave propagation

in fluid-saturated porous elastic media; marine sediments are often treated using models of this type. The scattering of sound by discrete elastic objects is also not considered in the book; ray methods are very useful in this context as well.

The comments above about omitted topics should not be interpreted as a criticism of the book; rather, they should be interpreted as a warning to potential readers and purchasers of the book not to expect an encyclopedic survey of ray methods. Overall, I think that Cerveny's choice of topics covered is quite sensible in that it allowed him to maintain a clear focus throughout the book.

The style of the book is simultaneously that of textbook and monograph: textbook because all results presented are derived from basic principles; and monograph because the results presented are current and the bibliography extensive. There are no exercises, however, so the utility of the book as a textbook is limited.

Cerveny is a distinguished scholar who has made many fundamental contributions to the study of seismic body wave propagation, especially in the area of Gaussian beam summation methods. Because of his stature and considerable experience, I would have welcomed a more critical discussion—even if it were biased—of different ray-based methods, and ray methods generally. For instance, the Maslov–Chapman wavefield representation is described and its connection to a Gaussian beam sum is noted, but there is no discussion of the relative advantages and disadvantages of each representation.

Seismic Ray Theory is ideally suited to researchers, including graduate students, whose work involves the interpretation of body wave seismograms. Indeed, for this group, I think that *Seismic Ray Theory* would be an indispensable reference. I expect that even experienced body wave seismologists would likely learn a great deal from reading the book. The book is also well suited to researchers in other fields who want to learn about how ray methods are applied in seismic applications. The book could be used as a textbook in an advanced graduate level course on seismic ray methods, or portions of the book could be assigned as supplementary reading in an introductory graduate level course on theoretical seismology. Its utility as a textbook is somewhat limited, however, by the lack of exercises.

MICHAEL G. BROWN

Rosenstiel School of Marine and Atmospheric Science

University of Miami

4600 Rickenbacker Cswy.

Miami, Florida 33149

Fundamentals and Applications of Ultrasonic Waves

David Cheeke

CRC Press, Boca Raton, 2002.

360 pp. Price: \$99.95 (hardcover) ISBN: 0849301300.

We learn from the Preface that Cheeke has written this book as a text for senior undergraduate and graduate students in a one semester course in ultrasonics. He starts with a chapter giving an overview of ultrasonics covering the history of the subject and outlining its principal divisions. This should be useful to beginning students and specialists in other fields. The *second chapter* takes us into the basics of vibrations, including a brief sur-

vey of Fourier theory. Wave motion is introduced using the string in vibration, not usually regarded as an ultrasonic phenomenon. We then move onto three-dimensional waves, dispersion, group velocity, and wave packets. *Chapter 3* examines bulk waves in fluids starting with a derivation of the one-dimensional wave equation. There are discussions of the velocity in gases and liquids based on physical theories, and then impedance, energy density, and intensity are introduced. Poynting vector, attenuation due to viscosity, and attenuation are discussed finishing with the concept of relaxation. *Chapter 4* brings us to the theory of elasticity. Starting with a review of tensor analysis we proceed through the strain and stress tensors and then the generalized form of Hooke's law, finishing by determining equivalencies between different forms of elastic constants. Advanced mathematical presentations such as this are not usually found in ultrasonic texts. *Chapter 5* takes us into the elastodynamics of bulk acoustic waves in solids. The presentation starts with one-dimensional waves and then an extension of the argument to three dimensions using analogies from electromagnetic theory. There is a useful discussion of material properties including a descriptive treatment of attenuation theory from solid state physics. *Chapter 6* covers radiation theory with an emphasis on problems related to ultrasonic beams. It begins with the spherical source, and continues into a discussion of the circular piston radiator. There are descriptive treatments of scattering, focussed acoustic waves, radiation pressure, and the Doppler effect. A rather unusual feature of the book is its unified treatment of reflection and transmission at interfaces which is presented in *Chap. 7*. Most of the subtopics here are to be found in standard texts with the exception of the solid-fluid interface which is covered in some detail, and provides a good prelude to the discussion of surface waves. The concept of slowness is introduced. *Chapter 8* is devoted to surface (Rayleigh) waves. Rayleigh's basic theory is reviewed, showing that waves can propagate with energy confined to a solid-vacuum interface. For a fluid-loaded surface there are various possibilities including a pure lossless mode, called a Stoneley Wave, and various "leaky" Rayleigh waves. The topic of displacement of beams of finite widths, when being reflected, is discussed. Other waves known as Schmidt head waves are summarized. *Chapter 9* covers Lamb waves which propagate in plates. The same potential method is used as for reflection of bulk waves and Rayleigh waves, but in this case the presence of the second boundary leads to symmetric and antisymmetric solutions. Fluid-loading effects are discussed and then fluid-loaded cylinders with mention of creeping waves. In *Chap. 10* Cheeke introduces partial wave analysis as a technique for analysis of acoustic waveguides which can be used more generally than the potential method. He starts with horizontal shear (SH) modes and rederives results for Lamb and Rayleigh waves. We then move on to layered substrates as a case first studied in seismology but also of interest in nondestructive evaluation (NDE) of multilayered electronics. Love waves are modified SH waves which propagate in a thin crust on a half-space. Conditions for trapping or leakage are examined. There are similar analyses for Lamb and Stoneley waves. There is a brief review of guided waves in multilayered structures. The cylinder as a waveguide is a classical problem which Cheeke simply summarizes. The chapter is concluded with a discussion of general considerations in the design of acoustic waveguides. *Chapter 11* covers crystal acoustics. Cheeke derives the Christoffel equation which is the basis for finding the phase velocities of the three waves which can propagate in an anisotropic medium. The cubic crystal is taken as a specific example. The Poynting vector does not necessarily coincide with the phase velocity direction. The thermodynamic theory of piezoelectricity is also included in this chapter as also the concept of piezoelectric coupling factor. This leads us on to *Chap. 12* where we encounter piezoelectric transducers, delay lines, and analog signal processing. An equivalent circuit for a bulk acoustic wave (BAW) transducer was first proposed by Mason. The BAW and later the surface acoustic wave (SAW) transducer led to the development of the delay line which was of importance during World War II because the velocity of acoustic waves is 10^{-5} times that of light so that the dimensions of the devices became practicable. SAW devices are compatible with microelectronic technology and have become the basis of a whole signal processing technology. The discussion here follows G. S. Kino's "Acoustic Waves:

Devices, Imaging, and Analog Signal Processing." *Chapter 13* is perhaps the most original in the book in that it contains more of Cheeke's research interests on acoustic microsensors. He starts by describing the action of the thickness-shear mode (TSM) resonator whose resonance frequency is altered by an absorbed thin film. TSM resonators may be used in liquids. SAW sensors are very sensitive to surface environment changes and a number of examples are given. SH type sensors are described as also flexural plate wave (FPW) sensors and thin rod sensors. These devices can be used for gravimetric measurements of deposits, and density and viscosity of liquids. Other applications include temperature, flow, and level sensing. Chemical gas sensors detect, identify, and measure the concentration of chemical species in a gaseous environment. Gas chromatography with acoustic detection and biosensing are discussed. *Chapter 14* covers acoustic microscopy. The scanning acoustic microscope (SAM) was developed by Lemons and Quate in 1973 and is now used in NDE of microelectronics and imaging of biological samples. The SAM does not have the problems of optical microscopes. Topics such as resolution, lens design, contrast mechanisms, and measurements are covered in some detail. Finally, details of some applications are given, including the imaging of biological samples, films and substrates, and NDE of materials and devices. The chapter finishes with an assessment of the subject in which Cheeke opines that the future lies with the application of atomic force microscopy to acoustic imaging. *Chapter 15* is a review of NDE of materials covering some modern developments having application in microelectronics. The material here shows how the theory of Chaps. 7-9 can be applied in practice. The emphasis is on Rayleigh wave NDE, critical angle reflectivity, Lamb waves, and inversion techniques for layered structures, especially the modal frequency spacing method. There are sections on measurements of thickness, adhesion, and cladding. *Chapter 16* comprises some special topics which Cheeke believes to be of future potential importance in ultrasonics. He starts with multiple scattering, a topic of concern in several areas, with emphasis on Biot's theory of multiple scattering by solid particles in liquids. This is followed by a discussion of time reversal, a technique with the potential to improve signals received in situations with multiple scattering. Picosecond ultrasonics, or the use of extremely short pulses, generated by lasers, for example, is discussed as also air-coupled ultrasonics. The chapter concludes with a section on resonant ultrasonic spectroscopy, a variant of acoustic signature analysis. *Chapter 17*, which concludes the volume, is on cavitation and sonoluminescence (SL). It begins with a review of bubble dynamics drawing on T. G. Leighton's "The Acoustic Bubble." The reader becomes acquainted with such concepts as cavitation threshold, cavitation noise, subharmonics, etc. Older work using sound fields containing many bubbles and the features of SL under such conditions is summarized. The opening up of the subject that occurred after the perfection of techniques for studying SL from single bubbles is then described. The interesting recent work which points to a dissociation mechanism as the explanation of SL is summarized well. However, practical applications of cavitation, such as cleaning and processing are not mentioned.

The book would be suitable for physicists and mechanical and electrical engineers. Previous books on ultrasonics are not referred to, perhaps because they are heavily technological, although Cheeke stresses in the Preface that applications are to receive emphasis in the volume. In comparison with earlier books, the approach is quite mathematical and the work could in fact pass for a treatise on physical acoustics. Another similar indication is the omission of any discussion of systems theory and digital signal processing, on which some of the most important developments in medical ultrasonics and NDE depend. With these exceptions the book is a good addition to the ultrasonics literature in general and should be invaluable to workers in the NDE of microelectronics in particular.

ROBERT D. FINCH

Department of Mechanical Engineering
University of Houston
Houston, Texas 77204

REVIEWS OF ACOUSTICAL PATENTS

Lloyd Rice

11222 Flatiron Drive, Lafayette, Colorado 80026

The purpose of these acoustical patent reviews is to provide enough information for a Journal reader to decide whether to seek more information from the patent itself. Any opinions expressed here are those of reviewers as individuals and are not legal opinions. Printed copies of United States Patents may be ordered at \$3.00 each from the Commissioner of Patents and Trademarks, Washington, DC 20231. Patents are available via the Internet at <http://www.uspto.gov>.

Reviewers for this issue:

GEORGE L. AUGSPURGER, *Perception, Incorporated, Box 39536, Los Angeles, California 90039*

MARK KAHRS, *Department of Electrical Engineering, University of Pittsburgh, Pittsburgh, Pennsylvania 15261*

HASSAN NAMARVAR, *Department of BioMed Engineering, University of Southern California, Los Angeles, California 90089*

DAVID PREVES, *Micro-Tech Hearing Instruments, 3500 Holly Lane No., Suite 10, Plymouth, Minnesota 55447*

DANIEL R. RAICHEL, *2727 Moore Lane, Fort Collins, Colorado 80526*

CARL J. ROSENBERG, *Acentech, Incorporated, 33 Moulton Street, Cambridge, Massachusetts 02138*

WILLIAM THOMPSON, JR., *Pennsylvania State University, University Park, Pennsylvania 16802*

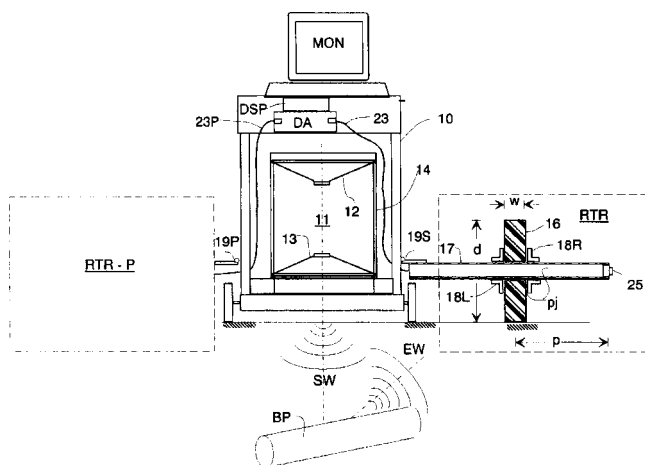
ROBERT C. WAAG, *Department of Electrical and Computer Engineering, Univ. of Rochester, Rochester, New York 14627*

5,802,013

43.28.En MOBILE SENSOR FOR GROUND PENETRATING SONAR

Ronald Lee Earp, assignor to Lucent Technologies Incorporated
1 September 1998 (Class 367/178); filed 9 June 1997

A system for searching for buried objects in the ground, such as pipes, consists of a mobile transmitter unit **10** containing two loudspeakers **12** and **13** mounted in a tube **14** which is aimed at the ground. The two loudspeakers are driven 180 degrees out-of-phase and separated so as to maximize the energy into the ground. Unit **RTR** consists of a hollow PVC tube **17** supported by a silicon rubber wheel **16** that rolls along the ground in concert



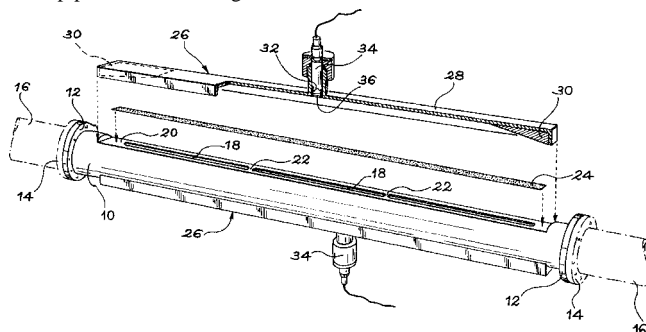
with the transmitter unit **10**. Inside, and in intimate contact with tube **17** is a sensor unit that receives echoes from any buried object **BP**. Monitor **MON** is shown mounted on the transmitter unit. A second identical unit **RTR** could be deployed on the left of the transmitter and the outputs of the two sensors could be differenced to increase discrimination against false returns when there are no actual targets.—WT

5,925,821

43.28.Ra DEVICE FOR MEASURING NOISE IN A PIPE TRAVERSED BY A FLUID

Philippe Bousquet, assignor to Societe National Industrielle
20 July 1999 (Class 73/592); filed in France 17 June 1997

A pipe section **10** is inserted into some fluid-conducting pipe system (air is the only fluid discussed in this patent) for the purpose of making noise measurements. The pipe section **10**, of the same cross-sectional size as the initial pipe **16**, has an elongated slot **18** covered with a resistive material **24**



which is transparent to the noise but which confines the fluid. The slot is capped by structure **26** which creates a rigid-walled, shallow, rectangular, parallelepiped-shaped cavity. Two wedge-shaped shims **30** define the ends of the cavity and are said to permit good impedance matching of the device with the pipe and to limit the influence of evanescent waves. One or more microphones **34** are mounted in holes **32** spaced along the cavity such that their diaphragms **36** are flush with the inner face of the cavity.—WT

5,787,048

43.30.Nb SHIP WAKE SIGNATURE SUPPRESSION

Matthew J. Sanford, assignor to the United States of America as represented by the Secretary of the Navy
28 July 1998 (Class 367/1); filed 6 May 1997

By injecting ultrasonic energy (frequency range from 0.5 to 2.5 MHz) into a ship's wake, by means of a transducer towed by the ship, for example, microbubbles of the size 1000 microns or less are caused to coalesce into bigger bubbles which rapidly rise to the surface and disperse into the atmosphere. This has the effect of altering the ship's signature and reducing its detectability.—WT

5,796,679

43.30.Xm DOPPLER VELOCIMETER FOR MONITORING GROUNDWATER FLOW

Norbert E. Yankielun, assignor to the United States of America as represented by the Secretary of the Army
18 August 1998 (Class 367/99); filed 14 June 1995

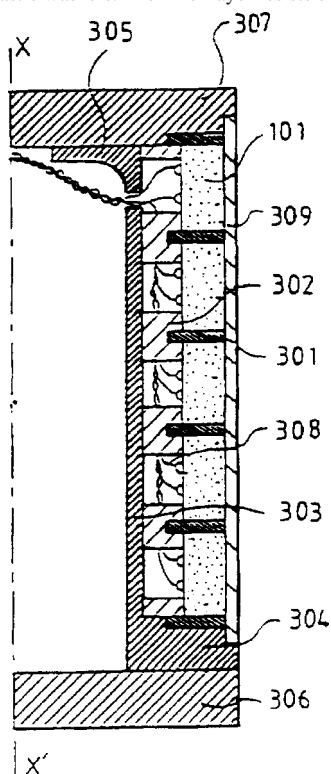
The direction and velocity of groundwater flow are determined by inserting a source and a number of separated sensors, whose positions are known relative to that of the source, into a bore hole below the water table level and observing the Doppler shift in various directions. The resulting velocity components are then added vectorially.—WT

5,784,341

43.30.Yj UNDERWATER ACOUSTIC TRANSMITTER FOR LARGE SUBMERSION

Eric Sernit *et al.*, assignors to Thomson-CSF
21 July 1998 (Class 367/155); filed in France 14 October 1994

A sonar transducer consists of a stack of coaxial, equi-sized, concentric, piezoceramic cylinders (only the top one, 101, is tagged). In this embodiment, the piezoceramic is tangentially polarized. The cylinders are isolated from one another and from the housing cylinder 303 by a series of three-layer washer shaped decouplers 301 (again, only one of them is tagged). The three layers consist of a hard rigid washer sandwiched between two flexible and elastic washers. The inner layer resists crushing due to large



hydrostatic pressures while the outer layers allow relatively free movement of the piezoceramic cylinders with respect to one another. A series of centering annuli 302 position the stack of piezoceramic cylinders on the housing cylinder 303 and also provide vibration decoupling. End caps 306 and 307 and an acoustically transparent sleeve 309 complete the assembly. Flanges 304 and 305 of cylinder 303 support the hydrostatic force exerted on the end caps 306 and 307.—WT

6,418,082

43.30.Yj BOTTOM MOORED AND TETHERED SENSORS FOR SENSING AMPLITUDE AND DIRECTION OF PRESSURE WAVES

Warren C. Hollis and Mildred H. Hollis, assignors to Lockheed Martin Corporation
9 July 2002 (Class 367/118); filed 22 June 2000

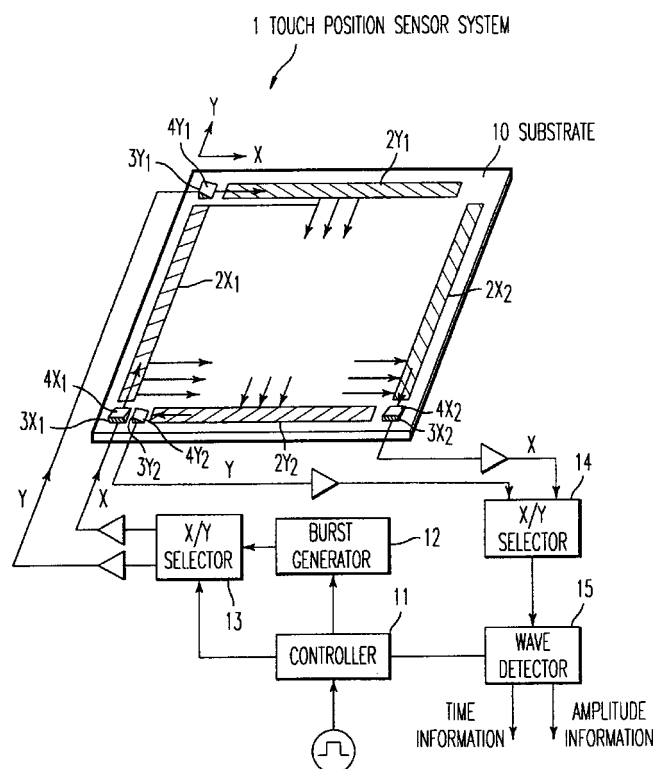
A bottom-moored and tethered sensor system consists of a pair of orthogonally oriented directional hydrophones, e.g., DIFAR sensors, housed in a buoyant chamber which is tethered a fixed distance from the ocean's bottom. The tether also orients the plane, defined by the principal response axes of the pair of hydrophones, so that it is parallel to the surface of the ocean. The chamber also houses a compass to provide a directional magnetic-reference signal. By determining the angle between the directional magnetic-reference signal and the output signals of the hydrophones, the sensor system is able to compute heading information about a detected target. A transmitter within the chamber communicates this information either over a signal cable to a shore-based receiver or via radio. The system is potentially a low cost, reusable, surveillance system, deployable in a wide range of water depths, and featuring a long operating life since it can be powered from a shore-based site via the signal/power cable.—WT

6,392,167

43.35.Pt ACOUSTIC TOUCH POSITION SENSING SYSTEM WITH LARGE TOUCH SENSING SURFACE

Yoshikatsu Nakagawa, assignor to Ricoh Company, Limited
21 May 2002 (Class 178/18.04); filed in Japan 7 May 1998

Touch screen technology includes more than the mouseless computer screens found in warehouse operations and retail stores. A demand exists for much larger displays as well. A typical touch screen may use an acoustic-positioning system in which an array of transmitters 2X1 generates parallel acoustic waves that travel across a substrate to an array of receivers 2X2 on



the opposite edge. A second pair of arrays **2Y1**, **2Y2** is oriented at appropriate angles to the first pair. This arrangement has proved successful for screen widths up to 1.25 m. The described invention is similar, but generates and detects a Barker sequence of pseudo-random noise. Because the detecting means includes amplitude and phase rather than relying on amplitude alone, the signal-to-noise ratio is substantially increased and screen size can be increased accordingly.—GLA

6,411,748

43.35.Sx WIDE TUNING RANGE ACOUSTO-OPTICAL FIBER BRAGG GRATING FILTER (FBGF)

Lawrence E. Foltzer, assignor to Alcatel USA Sourcing, L.P.
25 June 2002 (Class 385/7); filed 17 July 2000

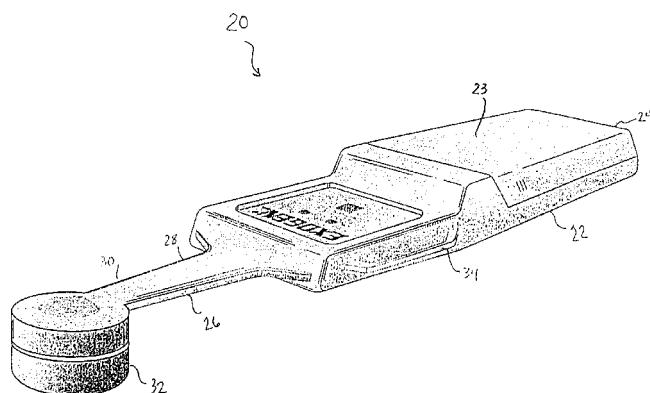
This patent describes an acousto-optical filter having a wide tuning range and also the method of constructing the device. An acoustic transducer is provided to generate an acoustic pressure wave at a specific frequency that is propagated longitudinally along an optical fiber member. The pressure wave generates alternating localized compressions and rarefactions in the optical fiber in such a manner that a grating (i.e., periodic changes in the fiber's refractive index) is created therein. The grating reflects optical signals of a particular wavelength depending on its period or pitch (i.e., Bragg resonance wavelength). The acoustic transducer modulates the frequency so that a variable grating pitch is obtained, causing a corresponding change in the Bragg resonance of the grating. In response, a reflected optical signal selected from the incoming multiplexed optical signals tunes to a different wavelength. A close-looped controller is provided for controlling input signals to the acoustic transducer/actuator so as to modulate the tuning of the reflected optical signals.—DRR

6,406,443

43.35.Wa SELF-CONTAINED ULTRASOUND APPLICATOR

Roger J. Talish, assignor to Exogen, Incorporated
18 June 2002 (Class 601/2); filed 13 June 2000

This self-contained ultrasound applicator is designed for treating injuries. It consists of a cantilever connected to a mounting structure and an ultrasonic transducer positioned adjacent to a distal portion of the cantilever



for abutment with a treatment site. The applicator also includes a means for attaching it to a treatment site. For mounting, the cantilever is configured to essentially bias the ultrasonic transducer toward a treatment area.—DRR

6,406,429

43.35.Yb DETECTION OF CYSTIC STRUCTURES USING PULSED ULTRASONICALLY INDUCED RESONANT CAVITATION

Yoseph Bar-Cohen and John S. Kovach, assignors to City of Hope; California Institute of Technology
18 June 2002 (Class 600/438); filed 23 August 2000

This patent covers an apparatus and method for early detection of cystic structures indicative of ovarian and breast cancers. Ultrasonic wave energy at a unique resonant frequency is used to induce cavitation in the cystic fluid which is characteristic of the cystic structures in the ovaries associated with ovarian cancer and in the breast associated with breast cancer. Cavitation bubbles in the cystic fluid implode, generating implosion waves that are detected by ultrasonic receiving transducers attached to the patient's abdomen. Moving the transducers allows the detected signals to be processed and analyzed to identify the location and the structure of the cysts.—DRR

6,409,669

43.35.Yb ULTRASOUND TRANSDUCER ASSEMBLY INCORPORATING ACOUSTIC MIRROR

Richard A. Hager and David W. Clark, assignors to Koninklijke Philips Electronics N.V.
25 June 2002 (Class 600/447); filed 24 February 1999

The subject ultrasonic transducer assembly contains an acoustic mirror, an ultrasound transducer positioned to direct a scanned ultrasound beam at the acoustic mirror, and an actuating device for moving the mirror relative to the scanned ultrasonic beam so that the reflected beam scans a three-dimensional volume. An ultrasonic impedance matching fluid may be deployed between the transducer and the mirror. The actuating device may configure the mirror by translation or by rotation and translation. The mirror may either have a single acoustically reflective surface or it may be a polygon having many acoustically reflective surfaces.—DRR

6,409,670

43.35.Yb HIGH SAMPLE RATE DOPPLER ULTRASOUND SYSTEM

Lin Xin Yao and Gan Yao, assignors to Siemens Medical Solutions USA, Incorporated
25 June 2002 (Class 600/453); filed 27 April 2000

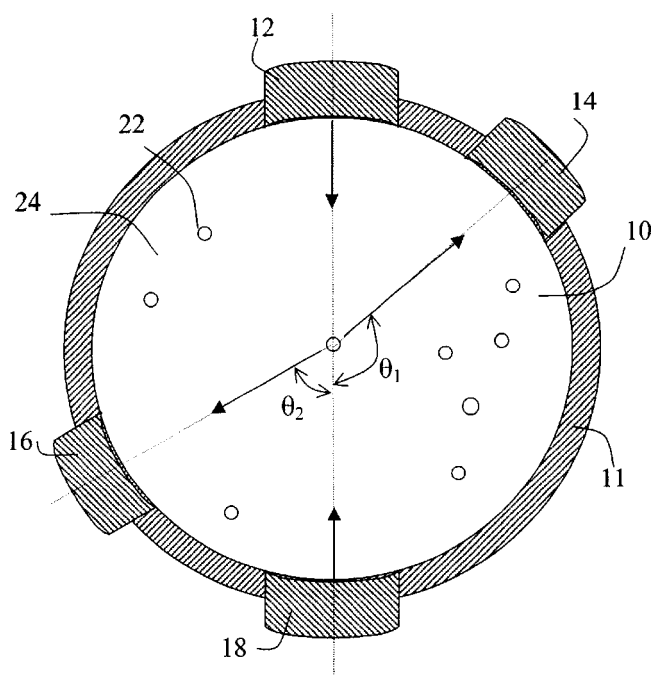
This method entails receiving Doppler ultrasound signals at a high sample rate, at greater depths, and from a large range gate size by increasing the length of time during which echoes can be received with respect to the time required to transmit the Doppler pulses from which the echo signals are generated. In one embodiment, a Doppler pulse is transmitted for a time equal to the time required for an ultrasonic sound wave to travel from a transducer to a top of a range gate and back. Echo signals created in response to the long Doppler pulse are received for a time equal to the transmit time plus the time required for an ultrasonic wave to travel from the top of the range gate to the bottom of the range gate. In another embodiment, each transducer element transmits a phase-shifted Doppler pulse in which the phase-shift is selected on the basis of the time required for an ultrasonic sound wave to travel from the transducer to a desired focal point. Being transmitted simultaneously, the pulse arrive at different times at the focal point and constructively add up. Echo signals created in response to the sum of the pulses can be sampled at substantially any rate to analyze the moving blood flow in the area of tissue defined by a range gate.—DRR

6,417,857

43.35.Yb SYSTEM ARCHITECTURE AND METHOD FOR OPERATING A MEDICAL DIAGNOSTIC ULTRASOUND SYSTEM

David J. Finger *et al.*, assignors to Acuson Corporation
9 July 2002 (Class 345/505); filed 21 June 2001

A method and system are described for processing, transferring, and storing ultrasound data and other information. The apparatus includes a memory, a programmable single-instruction multiple-data (SIMD) processor (or two symmetric processors), a source of acoustic data (such as a data bus), and a system bus. A number of embodiments are described. One embodiment includes an interface driver that translates logical addresses associated with ultrasound data to physical addresses for storage in a memory. Another embodiment features a programmable SIMD processor that processes ultrasound image data.—DRR



6,391,653

43.35.Zc ACOUSTIC STANDING-WAVE ENHANCEMENT OF A FIBER-OPTIC SALMONELLA BIOSENSOR

Stephen V. Letcher *et al.*, assignors to The Board of Governors for Higher Education, State of Rhode Island and Providence Plantations
21 May 2002 (Class 436/518); filed 19 July 2000

The patent explains that detection of fluorescence or luminescence from biological reactions *in vivo* is used in many biosensor applications. The process requires that dye molecules find their way to the optically active region of a fiberoptic sensor. One technique for concentrating microparticles into the desired area utilizes the force field generated by a stationary ultrasonic wave. The patent describes a further improvement in which a biosensor test chamber serves as an ultrasonic standing-wave cell, allowing microspheres or cells to be concentrated in parallel layers or in a column along the axis of the chamber. The entire complex is manipulated acoustically.—GLA

calculate a parameter related to scattering angles. "By comparing the calculated parameter with known values in a database, the sample can be characterized."—GLA

6,401,540

43.35.Zc METHOD AND APPARATUS FOR DETECTING INTERNAL STRUCTURES OF BULK OBJECTS USING ACOUSTIC IMAGING

Vance A. Deason and Kenneth L. Telschow, assignors to Bechtel BWXT Idaho, LLC
11 June 2002 (Class 73/657); filed 29 February 2000

"Acoustic imaging" captures the phase and amplitude of an acoustic wave after it has passed through an object, then uses wave reconstruction techniques to produce an optical image for study and analysis. In some systems an array of microphones picks up a secondary airborne acoustic signal. In other systems the object is immersed in water and an optical hologram is produced at the surface of the liquid. This invention attempts to achieve greater resolution by optically sensing the surface displacement of the object itself. Although the patent is more concerned with optics than acoustics, those interested in this field will find it easy to follow.—GLA

6,401,538

43.35.Zc METHOD AND APPARATUS FOR ACOUSTIC FLUID ANALYSIS

Wei Han *et al.*, assignors to Halliburton Energy Services, Incorporated
11 June 2002 (Class 73/599); filed 6 September 2000

The invention is concerned with downhole testing in oil and gas wells. In a preferred embodiment ultrasonic transducers 12 and 18 alternately emit tone bursts and the resulting scattered signals are picked up by receivers 14 and 16. Relative amplitudes of the received signals can then be used to

5,870,482

43.38.Bs MINIATURE SILICON CONDENSER MICROPHONE

Peter V. Loeppert and David E. Schafer, assignors to Knowles Electronics, Incorporated
9 February 1999 (Class 381/174); filed 25 February 1997

An alternate configuration of the moveable diaphragm of a miniature capacitor microphone consists of making this diaphragm the free end portion of a thin cantilevered beam. The fixed back plate of the capacitor is the portion of a frame structure that lies beneath this free end. It is alleged that

this configuration reduces inherent material stress in the diaphragm while at the same time resulting in a much more compliant structure than if it were an edge-clamped diaphragm. Several embodiments of the diaphragm, the back plate, associated circuitry, and methods of venting the air gap to minimize mechanical damping are discussed.—WT

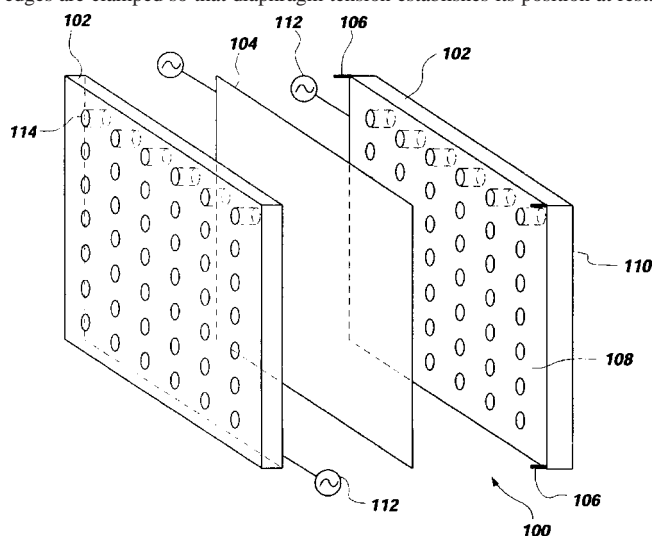
6,393,129

43.38.Bs PAPER STRUCTURES FOR SPEAKER TRANSDUCERS

Terry J. Conrad *et al.*, assignors to American Technology Corporation

21 May 2002 (Class 381/191); filed 16 August 1999

This patent is a continuation-in-part of four earlier patent applications, all filed in 1998. In a conventional push-pull electrostatic loudspeaker, diaphragm 104 is centered between perforated stators 102. At least two of its edges are clamped so that diaphragm tension establishes its position at rest.



In a separate patent application the inventors describe an alternate arrangement using a nontensioned, nonplanar diaphragm. In either case, the stators, the diaphragm, or both can be made of coated paper or cardboard to create an inexpensive, "disposable" loudspeaker.—GLA

5,888,845

43.38.Bs METHOD OF MAKING HIGH SENSITIVITY MICRO-MACHINED PRESSURE SENSORS AND ACOUSTIC TRANSDUCERS

Rashid Bashir and Abul Kabir, assignors to National Semiconductor Corporation

30 March 1999 (Class 438/53); filed 2 May 1996

A high-sensitivity micro-sized pressure sensor is achieved as a result of creating a very thin sensing diaphragm by growing a single crystal highly doped silicon layer on a substrate via a chemical vapor deposition (CVD) process. The diaphragm then constitutes the movable plate of a parallel plate capacitor and pressure variations are conventionally detected because of changes in capacitance, hence voltage, due to the motion of the movable plate. Because very thin diaphragms (less than one micron) can be created via the CVD method, highly sensitive transducers can be realized.—WT

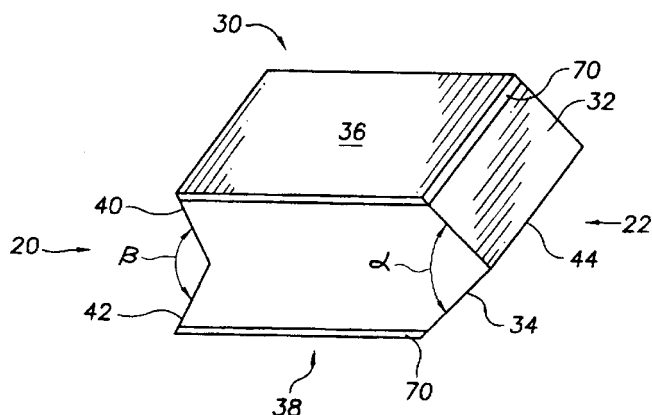
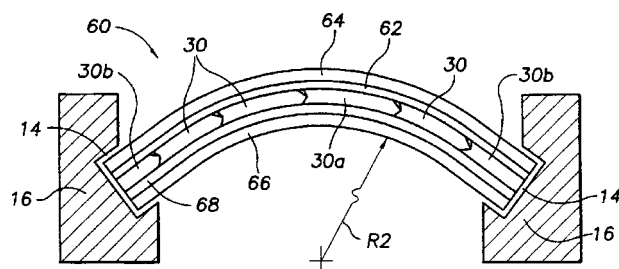
5,781,646

43.38.Fx MULTI-SEGMENTED HIGH DEFORMATION PIEZOELECTRIC ARRAY

Samuel A. Face, Norfolk, Virginia

14 July 1998 (Class 381/190); filed 9 May 1997

A multi-segmented, flextensional transducer consists of a number of piezoelectric elements 30 each of which has a convex surface 22 at one end and a concave surface 20 at the opposite end. These elements are arranged end-to-end such that the convex end of one engages, or nests in, the concave end of the next one. The extreme left and right ends of the chain are supported by suitable frames 16. Items 62 and 68 are electrically conductive



layers while items 64 and 66 are water-proof acoustically transparent layers. The structure is assembled with a curved profile (radius R2) as shown. When energized, the array of piezoelectric elements experiences large deformations in the up-down directions, especially central element 30a. The largest deformation exceeds that which could be realized with a thin, monolithic, curved piezoelectric motor section of the same size. Piezoelectric elements 30 with curved rather than pointed ends are also discussed.—WT

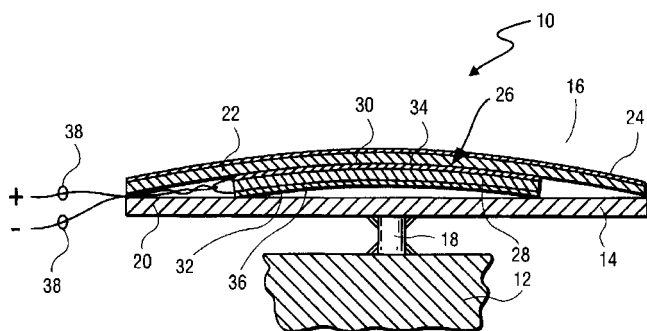
6,396,197

43.38.Fx PIEZOELECTRIC SPEAKER

Andrei Szilagyi and Michael Strugach, assignors to Speaker Acquisition Sub

28 May 2002 (Class 310/330); filed 6 April 1998

The device is a piezoelectric driver that might be attached to a table top or a TV cabinet. Energy from bending element 26 is supposed to be coupled to a relatively flexible mounting surface via rigid post 18. However,



since no additional inertia mass is shown or mentioned, one suspects that the actual mode of operation would be more like a lightweight vibrating shell spaced apart from a more massive supporting structure.—GLA

6,416,478

43.38.Hz EXTENDED BANDWIDTH ULTRASONIC TRANSDUCER AND METHOD

John A. Hossack, assignor to Acuson Corporation
9 July 2002 (Class 600/459); filed 20 December 1999

The patent defines a transducer structure that can be optimized to transmit pressure waves at one frequency and receive energy at another frequency. This is done by arranging transducer elements in an array formed by multiple layers of transducer material. A transceiver provides an excitation signal to the transducer and receives energy from the transducer. All of the layers are coupled to the transceiver during transmission so that all of the layers are activated. Some of the layers are decoupled from the transceiver during reception so that not all of the layers contribute to the received signal. A filter circuit is also responsive to the coupling, providing additional low-, high-, or band-pass filtering appropriate for either transmit or receive. The pressure waves at the second frequency are responsive to tissue and/or contrast agents.—DRR

6,389,935

43.38.Ja ACOUSTIC DISPLAY SCREEN

Henry Azima *et al.*, assignors to New Transducers Limited
21 May 2002 (Class 81/388); filed 8 July 1998

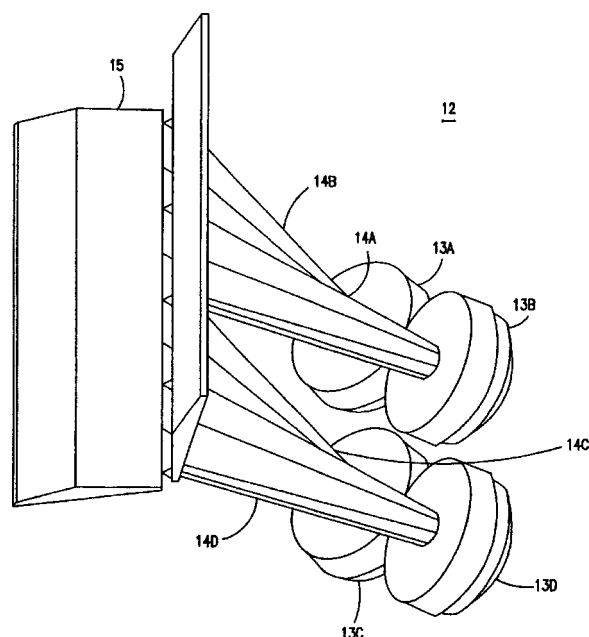
Using a distributed mode (panel type) loudspeaker as a projection screen is hardly a new idea. However, the patent includes useful information about various ways to fabricate such a dual-purpose screen.—GLA

6,394,223

43.38.Ja LOUDSPEAKER WITH DIFFERENTIAL ENERGY DISTRIBUTION IN VERTICAL AND HORIZONTAL PLANES

Richard W. Lehman, assignor to Clair Brothers Audio Enterprises, Incorporated
28 May 2002 (Class 181/152); filed 23 June 2000

During the past two years there has been a frenzy of activity devoted to finding ways of transforming the acoustical output of a conventional high-frequency driver into a coherent line source that can drive a wedge-shaped horn. Those outside the concert sound industry may justifiably wonder why, but an explanation is outside the scope of this patent review. One



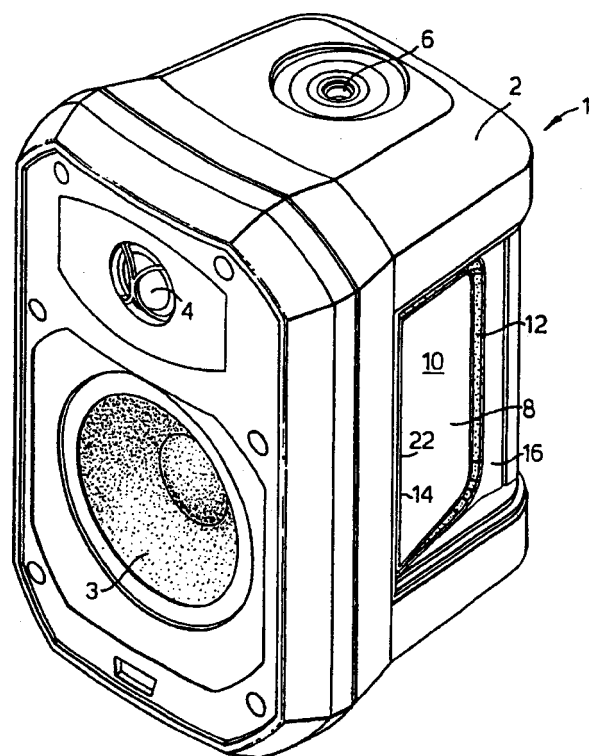
approach is to design a simple round-to-rectangular waveguide 14A, 14D and then stack a number of these to make a seamless line array. The patent departs from prior art by arguing that the array should form a shallow arc rather than a straight line.—GLA

6,396,936

43.38.Ja AUXILIARY BASS RADIATOR UNITS

Stuart Michael Nevill, assignor to B&W Loudspeaker Limited
28 May 2002 (Class 381/349); filed in the United Kingdom 24 November 1998

Vibrating side panel 10 operates as a passive radiator, performing the same function as a tuned vent but occupying less space. Because the panel is



hinged rather than being flexibly suspended, unwanted rocking modes are said to be substantially avoided.—GLA

6,397,972

43.38.Ja LOUDSPEAKERS

Graham Bank and Julian Fordham, assignors to New Transducers Limited
4 June 2002 (Class 181/148); filed in the United Kingdom 14 May 1999

Resilient, open-cell foam fills the cavity between the diaphragm of a panel-type loudspeaker and the rear surface of its enclosure. The foam absorbs rear radiation and also provides a compliant suspension for the panel.—GLA

6,404,894

43.38.Ja PACKAGING

Henry Azima *et al.*, assignors to New Transducers Limited
11 June 2002 (Class 381/152); filed in the United Kingdom 2 September 1995

Can the lid of a box serve as the diaphragm of a panel-type loudspeaker? Of course. But to qualify for protection under the claims of this patent it must be a very special lid "...having selected values of certain physical parameters which enable the member to sustain and propagate input vibrational energy in a predetermined frequency range by a plurality of resonant bending wave modes in at least one operative area extending transversely of thickness such that..." etc., etc., etc. The actual sentence goes on for another 110 words!—GLA

6,377,679

43.38.Si SPEAKERPHONE

Hiroshi Hashimoto *et al.*, assignors to Kabushiki Kaisha Kobe Seiko Sho
23 April 2002 (Class 379/388.05); filed in Japan 26 December 1996

Prior art speakerphone systems experience problems due to unwanted interactions between the room adaptation and echo canceler operations. The method presented here combines the two functions, using the integral of the received line signal to estimate the echo residual and comparing the transmitted line power to the past microphone signal. The result is said to be a speakerphone with high-quality, full-duplex operation.—DLR

6,381,224

43.38.Si METHOD AND APPARATUS FOR CONTROLLING A FULL-DUPLEX COMMUNICATION SYSTEM

John Eugene Lane *et al.*, assignors to Motorola, Incorporated
30 April 2002 (Class 370/286); filed 31 March 1999

This combination speakerphone and echo canceler includes a gain control on the microphone signal and applies the inverse of the microphone gain to the speaker output signal. This is said to effectively isolate the echo canceler operation from variations in the acoustic environment.—DLR

6,381,309

43.38.Si PERSONAL COMPUTER HAVING A SOUND CARD

Jacques Tremblay, assignor to Auristar Technologies, Incorporated
30 April 2002 (Class 379/52); filed 17 March 2000

The patent describes an extension device for use with a computer sound card. The device decodes signals used by the Telephone Device for the Deaf (TDD) system, allowing a deaf person to use the computer as a TDD interface on the telephone line.—DLR

6,393,902

43.40.Yq NOISE TESTING SYSTEM WITH TEMPERATURE RESPONSIVE SENSITIVITY

James C. Juranitch, assignor to Veri-Tek Incorporated
28 May 2002 (Class 73/116); filed 29 June 1998

A fairly straightforward system for testing gear noise includes a driving means, an acoustic sensor, and a temperature sensor. The test bench is supported by isolation pads to minimize extraneous mechanical vibrations. The testing sequence, noise analysis, and pass-fail determination are all controlled by a computer program. Numerous practical variants are described but, since the patent is written in pure legalese, the descriptions are not all that easy to understand.—GLA

6,411,925

43.50.Fe SPEECH PROCESSING APPARATUS AND METHOD FOR NOISE MASKING

Robert Alexander Keiller, assignor to Canon Kabushiki Kaisha
25 June 2002 (Class 704/200); filed in the United Kingdom 20 October 1998

This invention provides a method for noise masking of speech signals to check that training examples of an automatic speech recognizer are consistent in order to reduce mismatches during use. The distribution of energy level within each frame of speech is determined and energy levels less than a masking level are set to the masking level.—HHN

6,413,180

43.50.Gf POWER TRANSMITTING MECHANISM WITH SILENT CHAIN AND SPROCKETS

Makoto Kanehira *et al.*, assignors to Tsubakimoto Chain Company
2 July 2002 (Class 474/164); filed in Japan 6 July 1999

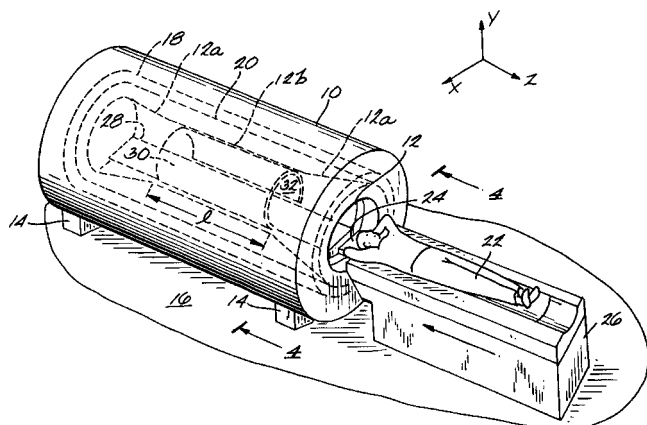
A power transmitting system includes a silent chain trained around the teeth of driving and driven sprockets and a second silent chain trained around the teeth of a second pair of sprockets. The two driving sprockets are mounted in a parallel relationship on a single drive shaft with the teeth of the first offset by one half pitch from the teeth of the other. The pitch of the driving sprockets varies randomly along the circumference of the sprockets. The silent chains have a single pitch. By phasing the two driving sprockets, periodic meshing impact sounds emitted from the respective silent chains are cancelled out or offset each other. The periodicity of the meshing impact noise is agitated by the random tooth pitch of the driving sprockets to such an extent that the resonant sound is sufficiently reduced.—DRR

6,414,489

43.50.Gf APPARATUS FOR REDUCING ACOUSTIC NOISE IN AN MR IMAGING SYSTEM

David E. Dean *et al.*, assignors to General Electric Company
2 July 2002 (Class 324/318); filed 18 December 1999

The apparatus is said to substantially reduce the acoustic noise or disturbance that is experienced by patients, users, or others in the vicinity of a magnetic resonance imaging (MRI) system. The apparatus consists of a



bridge fixed within the MRI system's bore to support the patient during the data acquisition and a curved frame, usually of fiberglass, which is removable/insertable in the bore for placement upon the bridge. The frame, when in place upon the bridge, encloses a space within the bore that is disposed to receive the imaging subject. A layer of material, such as open cell foam, covers the frame. The material is capable of absorbing substantial amounts of acoustic energy present in the bore. The material is also highly transmissive to rf signals required for MRI data acquisition and avoids spurious rf signal generation that would add noise to the data.—DRR

6,401,028

43.50.Vt POSITION GUIDING METHOD AND SYSTEM USING SOUND CHANGES

Tsuyoshi Kamiya *et al.*, assignors to Yamaha Hatsudoki Kabushiki Kaisha
4 June 2002 (Class 701/200); filed in Japan 27 October 2000

Suppose that you are driving a luxury vehicle (car or motorcycle) fitted with a fancy positional guidance system. Existing systems can sound an alarm when you are within a short range of a selected target location but something less crude is obviously desirable. One might design a voice guidance system for example—"You're getting warmer, now you're getting cooler." Yamaha has come up with an even more sophisticated scheme that starts out with an imaginary sound source at the target location. A real-time virtual reality program then calculates what you would hear at your present location if the source actually existed.—GLA

6,413,141

43.50.Yw NOISE ACTIVATED MOBILE

Sharon M. Putney, Raymond, Ohio
2 July 2002 (Class 446/227); filed 11 August 2000

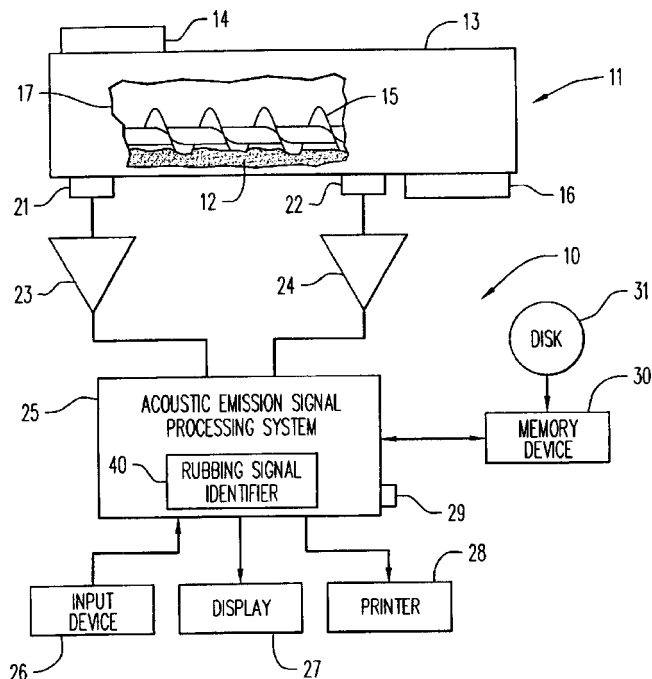
The mobile covered by this patent is similar to conventional mobiles for babies' cribs except that it responds to loud noises by activating a motor. A control circuit tracks elapsed time, senses relatively loud noises, and actuates the motor.—DRR

6,418,384

43.50.Yw ACOUSTIC EMISSION MONITOR, METHOD AND MEMORY MEDIA FOR SOLID MATERIAL PROCESSING MACHINERY

Remi Rothea and Etienne Foucher, assignors to Rhodia, Incorporated
9 July 2002 (Class 702/56); filed 11 May 1999

An apparatus is provided to identify rubbing sounds in the acoustic emissions produced by a machine that processes solid materials (such as aspirin). The apparatus includes an acoustic signal processing system having a computer, a software filter, and a rubbing signal identifier that configures the computer to set filter conditions to detect a rubbing sound. The filter



conditions remove some operating noise having a bit rate higher than the operating rate of the rotating part of the machinery by excluding amplitudes less than a front end filter duration. The rubbing sounds are detected by an intensity greater than a predetermined intensity, acoustic emission activity greater than the operating rate of the rotating part, and signal length greater than a predetermined value.—DRR

6,416,852

43.55.Ev CERAMICS SOUND ABSORPTION MATERIAL

Hidenao Kawasaki and Osamu Kawasaki, assignors to Isolite Insulating Products Company, Limited
9 July 2002 (Class 428/304.4); filed in Japan 17 November 1999

When the ceramic block of this invention is fired, the combustible pore-forming material that was mixed in burns out, leaving a porous block with sound-absorbing properties and excellent weatherability. Grooves on the outer surface of the block are glazed and hence easy to clean and less likely to stain. Because the glaze is only on the surface, it does not block the sound absorptive properties of the ceramic.—CJR

6,412,852

43.55.Ti WATER, DUST AND SOUND ATTENUATING BARRIER AND TRIM PANEL MODULE AND METHOD FOR ASSEMBLING WITHIN A VEHICLE DOOR

Chi Hong Koa *et al.*, assignors to Foamade Industries, Incorporated; General Motors Corporation
2 July 2002 (Class 296/146.7); filed 25 July 2000

This patent describes a modular trim panel for a car door that is assembled and installed as a combined unit.—CJR

6,411,289

43.58.Kr MUSIC VISUALIZATION SYSTEM UTILIZING THREE DIMENSIONAL GRAPHICAL REPRESENTATIONS OF MUSICAL CHARACTERISTICS

Franklin B. Zimmerman, Philadelphia, Pennsylvania
25 June 2002 (Class 345/302); filed 7 August 1997

A color waterfall plot (i.e., graphical output of the short time Fourier transform) falls into the obvious category, even as long ago as 1997.—MK

6,415,584

43.58.Vb TUNING MEANS FOR TUNING STRINGED INSTRUMENTS, A GUITAR COMPRISING TUNING MEANS AND A METHOD OF TUNING STRINGED INSTRUMENTS

Richard John Whittall *et al.*, assignors to Automatic Tuning Developments Limited
9 July 2002 (Class 54/312 R); filed in the United Kingdom 10 March 1998

Imagine a guitar tuner with robotic control. Starting with the lowest E string, the tuner turns the pegs one by one until the guitar is in tune (according to the controller).—MK

6,412,594

43.58.Wc WATER GUN WITH SOUND EFFECTS MODULE

David Small and Paul S. Rago, assignors to Shoot the Moon Products II, LLC
2 July 2002 (Class 181/149); filed 4 October 2000

Water guns need sounds claim the inventors. The solution is to add yet another sound chip that is activated when the trigger is pulled. A large fraction of the patent is devoted to describing the means to waterproof the electronics.—MK

6,416,021

43.58.Wc LOCOMOTIVE WHISTLE CONTROLLED RAILROAD GRADE CROSSING WARNING SYSTEM

George Jefferson Greene, Jr., LaRue, Texas
9 July 2002 (Class 246/294); filed 29 May 2001

Many railroad crossings are still unguarded, resulting in fatalities every year. The patent describes a train horn activated crossing that could be solar powered. The inventor prefers this method over track sensors and doesn't say how the train horns are discriminated from other sounds.—MK

6,416,381

43.58.Wc MOTION INDUCED SOUND AND LIGHT GENERATING SYSTEM

Christopher G. Walter and Matt Fuligni, assignors to The Little Tikes Company
9 July 2002 (Class 446/397); filed 15 August 2000

Rocking toys are great for toddlers and other small children. Add a now ubiquitous sound chip and a simple finite state machine and you've got more sounds to drive parents crazy.—MK

6,414,620

43.60.Qv SOUND PROCESSING SYSTEM

Kengo Maeda and Tomoyuki Kawai, assignors to Sharp Kabushiki Kaisha
2 July 2002 (Class 341/155); filed in Japan 28 November 2000

This sound processing system includes a digital signal processing section with A/D and D/A converters, a control section, two data memory sections, and two program memory sections. The program memory areas are connected together through a first bus and the data memory areas are connected through a second bus. The system can serve as a voice processor for voice recognition purposes or voice synthesis that is required to be performed in real-time in mobile electronic devices such as cell phones.—DRR

6,415,255

43.60.Qv APPARATUS AND METHOD FOR AN ARRAY PROCESSING ACCELERATOR FOR A DIGITAL SIGNAL PROCESSOR

Paul E. Cohen and Ioannis S. Dedes, assignors to NEC Electronics, Incorporated
2 July 2002 (Class 704/223); filed 10 June 1999

The device entails processing of information, and more particularly, to systematic searches involving selected locations in arrays of information. The device follows algebraic code excited linear prediction (ACELP) speech encoding techniques. It includes a search accelerator unit (SAU) to assist a digital processor in accessing a sequence of regularly (i.e., incrementally) spaced nonneighboring locations of an array. The SAU, being external to the digital signal processor, supplements the addressing capability of a digital signal processor so that references to a sequence of entries in the array can be performed more efficiently.—DRR

6,406,439

**43.64.Ri PHASE LOCK EVOKED RESPONSE
AUDIOMETER**

Lawrence Thomas Cohen *et al.*, assignors to The University of Melbourne

18 June 2002 (Class 600/559); filed 1 December 2000

This is a device intended primarily for testing the hearing of children or other people who are unable, due to mental illness or disability, to participate in conventional behavioral deafness testing. The device includes an evoked response audiometer that supplies to a patient an auditory stimulus signal consisting of a carrier frequency that is modulated by at least two different forms of modulation such that the stimulus is substantially frequency specific. The signal is presented for a sufficiently long period of time to enable phase-locked steady-state potentials to be evoked in the brain of the patient. The brain potentials are analyzed to establish whether they are phase locked to the modulated auditory signal. Provision is made to selectively delay or advance one modulation with respect to the other in order to enhance the response evoked by the auditory stimulus.—DRR

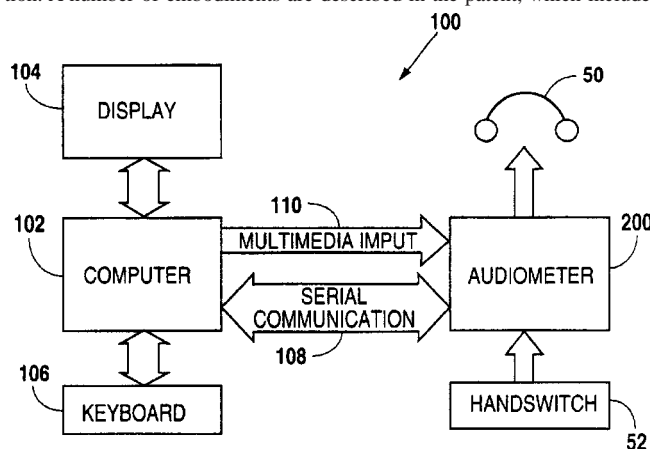
6,416,482

**43.66.Sr MULTIMEDIA FEATURE FOR DIAGNOSTIC
INSTRUMENTATION**

Leroy Braun, Austin and Jack Foreman, Pflugerville, both of Texas

9 July 2002 (Class 600/559); filed 25 August 1998

This is a system for automating the administration of audiometric testing by selectively switching the audiometric output between test tones generated by the audiometer and sound signals generated from digital information. A number of embodiments are described in the patent, which includes



means of switching between a computer and tone generator, a processor with memory for storing digital data, means of outputting between the audiometric system and the subject, etc.—DRR

6,408,273

**43.66.Ts METHOD AND DEVICE FOR THE
PROCESSING OF SOUNDS FOR AUDITORY
CORRECTION FOR HEARING IMPAIRED
INDIVIDUALS**

Gilles Quagliaro *et al.*, assignors to Thomson-CSF

18 June 2002 (Class 704/271); filed in France 4 December 1998

The processing method described in this patent is said to provide auditory correction for a hearing-impaired person, including extracting pitch, voicing, energy, and spectrum characteristics of an input speech signal. In this method, the pitch characteristic is multiplied by a pitch factor, the voic-

ing characteristic is modified by a voicing factor, the energy characteristic is compressed, and the spectrum is modified by applying a homothetical compression function. A speech signal is reconstituted to be perceptible to the hearing-impaired person on the basis of the modified pitch, voicing, energy, and spectrum characteristics.—DRR

6,408,468

43.66.Ts PILLOW TO FACILITATE HEARING

Kristen Comfort, Johnson City, New York

25 June 2002 (Class 5/636); filed 19 July 2001

If a person happens to be hard of hearing in one ear and tends to lie on a pillow with his/her good ear against the pillow, sound is fairly precluded from reaching that ear. This pillow contains a hole for receiving the user's ear. The ear hole is channeled to one or more external holes so as to receive sounds external to the pillow. The remainder of the pillow is filled with conventional materials and a pillowcase has holes corresponding to the holes in the pillow. Nothing is said about accommodating a person who tosses and turns in his/her sleep.—DRR

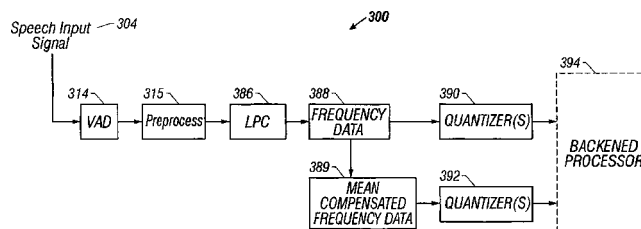
6,418,412

**43.72.Bs QUANTIZATION USING FREQUENCY AND
MEAN COMPENSATED FREQUENCY INPUT
DATA FOR ROBUST SPEECH RECOGNITION**

Safdar M. Asghar and Lin Cong, assignors to Legerity, Incorporated

9 July 2002 (Class 704/256); filed 28 August 2000

Noisy listening environments, such as inside automobiles or airplanes, degrade speech recognition accuracy. However, noise is generally constant in these settings and compensation may therefore be applied before frequency parameter coefficients are sent to an input signal speech classifier. Splitting the signal into spectral subbands may be used to enhance processing in selected frequency bands more affected by noise. To improve performance, neural nets may be used for classification of the mixer input data and for network postprocessing. Matrix quantizers are used with vector quantiz-



ers to reduce errors when operating on short duration input signals. The system also may use fuzzy associations to develop observation sequence data and reduce quantization error. Additional backend speech classifiers such as hidden Markov models (HMMs) may be used for determining initial state and state transition probabilities, derived from vector and matrix quantizers representing both time and frequency domain information, respectively. Such HMMs may be consolidated to improve system performance and efficiency.—DAP

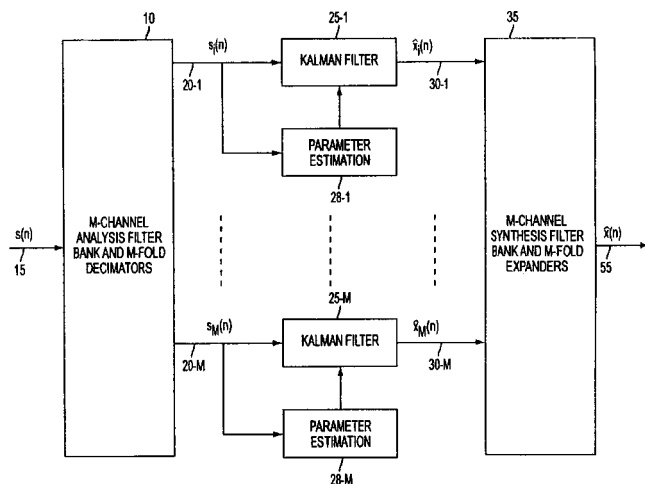
6,408,269

43.72.Ew FRAME-BASED SUBBAND KALMAN FILTERING METHOD AND APPARATUS FOR SPEECH ENHANCEMENT

Wen-Rong Wu *et al.*, assignors to Industrial Technology Research Institute

18 June 2002 (Class 704/228); filed 3 March 1999

This invention describes a frame-based subband Kalman filtering method to enhance speech. The aim is to apply low-order Kalman filters to reduce the complexity of computation while maintaining a comparable performance relative to the conventional Kalman-EM technique. A multi-channel filter bank and decimator decompose noisy speech 15 into subband



speech signals. The autoregression (AR) parameters of each subband for each frame are estimated 28 using Yule-Walker equations. A bank of low-order Kalman filters 25 is applied to estimate the noise variance of each subband. Filtered signals 30 are then expanded and synthesized by a multi-channel synthesis filter bank 35.—HHN

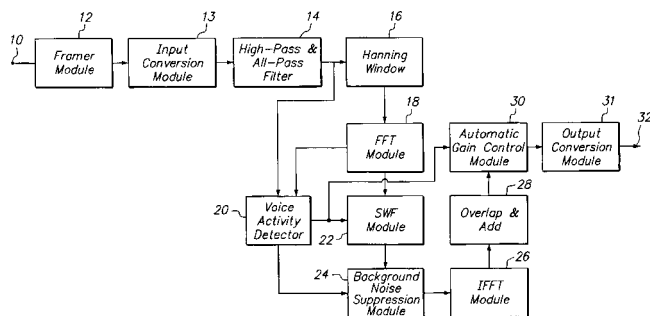
6,415,253

43.72.Ew METHOD AND APPARATUS FOR ENHANCING NOISE-CORRUPTED SPEECH

Steven A. Johnson, assignor to Meta-C Corporation

2 July 2002 (Class 704/210); filed 19 February 1999

The purpose of this patent is to enhance noisy speech 10 using a spectrum subtraction technique 24. After dividing speech into frames and removing a dc component and the minimum phase aspect of noisy speech, power spectrum 18 of the prefiltered signal is estimated. A voice activity detector (VAD) 20 determines the state of speech as silence, speech, primary



detection, or hangover state. Based on classified states of VAD, a smoothed Wiener filter 22 filters the data frames and an automatic gain control unit 30 calculates the proper gain to produce noise-reduced speech 32 at the desired output level.—HHN

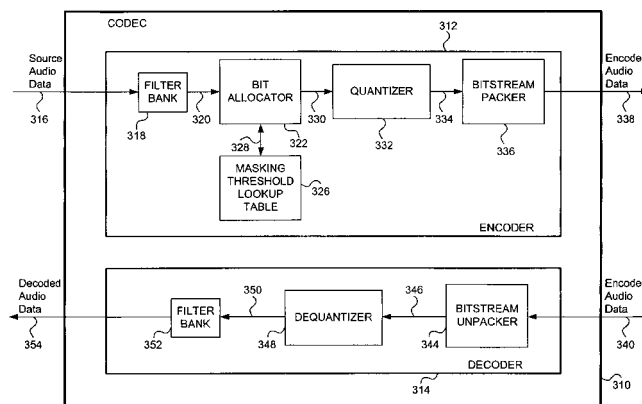
6,418,404

43.72.Gy SYSTEM AND METHOD FOR EFFECTIVELY IMPLEMENTING FIXED MASKING THRESHOLDS IN AN AUDIO ENCODER DEVICE

Lin Yin, assignor to Sony Corporation; Sony Electronics Incorporated

9 July 2002 (Class 704/200.1); filed 28 December 1998

A masking threshold lookup table is created based upon empirical data from normal or hearing impaired persons. A filter bank encoder receives and filters audio data into frequency subbands. The output of the filters is compared to the masking threshold lookup table by the bit allocator which separates the filtered audio data into categories falling above and below the



masking thresholds. Audio data falling below the masking thresholds is discarded to reduce the amount of audio data processed by the encoder. The supra-threshold audio data is quantized and sent to a bitstream packer.—DAP

6,377,928

43.72.Ja VOICE RECOGNITION FOR ANIMATED AGENT-BASED NAVIGATION

Parichay Saxena *et al.*, assignors to Sony Corporation; Sony Electronics, Incorporated

23 April 2002 (Class 704/275); filed 31 March 1999

This web page navigation system combines an HTML reader/parser, the controls necessary to operate the display, and speech input and output functions. The goal is full browsing capability in a hands-free situation or for a blind person.—DLR

6,377,931

43.72.Ja SPEECH MANIPULATION FOR CONTINUOUS SPEECH PLAYBACK OVER A PACKET NETWORK

Eyal Shlomot, assignor to Mindspeed Technologies
23 April 2002 (Class 704/503); filed 28 September 1999

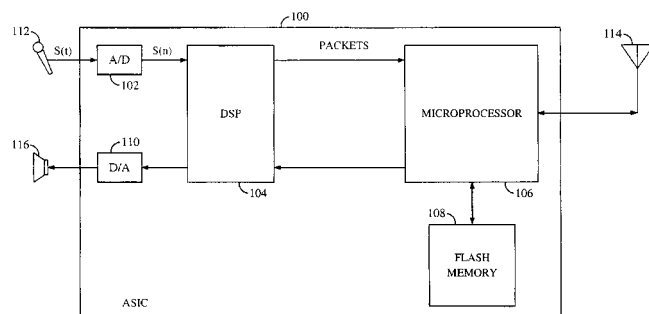
The patent describes a system for achieving continuous speech output under conditions of variable packet arrival rates. A jitter buffer receives incoming packets. Either compression or stretching of the audio output adjusts the rate of speech output from the buffer depending on how full the buffer is.—DLR

6,411,926

43.72.Ne DISTRIBUTED VOICE RECOGNITION SYSTEM

Chienchung Chang, assignor to QUALCOMM, Incorporated
25 June 2002 (Class 704/221); filed 8 February 1999

Both a DSP and a microprocessor are used in a digital cellular telephone. For hands-free operation, speech recognition is accomplished without the DSP using the relatively low computational power of the microprocessor to slowly extract and decode relevant parameters and compare them to words or templates stored in a vocabulary contained in a nonvolatile



memory. When greater speed is required, the DSP is configured to extract the relevant parameters. A microprocessor interposed between the DSP and memory compares the extracted parameters to the speech templates stored in the vocabulary and makes decisions on which template is the closest match.—DAP

6,411,927

43.72.Ne ROBUST PREPROCESSING SIGNAL EQUALIZATION SYSTEM AND METHOD FOR NORMALIZING TO A TARGET ENVIRONMENT

Philippe Morin *et al.*, assignors to Matsushita Electric Corporation of America
25 June 2002 (Class 704/224); filed 4 September 1998

Speaker variability, unstable channel effects, and environmental background noise variability often degrade the performance of speech recognition systems. To improve accuracy by minimizing the effects of the above variables, a preprocessing system normalizes an audio source in real time to one or more predetermined targets. An equalization of the audio source, as affected by its environment, is performed first by filtering to match a pre-

determined target channel such as a standard microphone response. Next, the signal level of the audio source is adjusted without speech present to a level that matches a predetermined target background noise level. Finally, with speech present, the system mixes noise with the audio source so as to achieve a target signal-to-noise ratio.—DAP

6,411,928

43.72.Ne APPARATUS AND METHOD FOR RECOGNIZING VOICE WITH REDUCED SENSITIVITY TO AMBIENT NOISE

Shin-ichi Tsurufuji *et al.*, assignors to Sanyo Electric
25 June 2002 (Class 704/233); filed in Japan 9 February 1990

The accuracy of speech recognition systems is frequently reduced by the presence of environmental noise as is the case, for example, in moving automobiles. To improve performance by reducing the influence of ambient noise, the front end of a speech recognition system includes a microphone whose output is utilized only if it exceeds a stored threshold value. The threshold value is changed as the level of ambient noise varies. A multi-band bank of band-pass filters is used so that feature parameters are derived only for microphone signals exceeding frequency-specific threshold values.—DAP

6,418,411

43.72.Ne METHOD AND SYSTEM FOR ADAPTIVE SPEECH RECOGNITION IN A NOISY ENVIRONMENT

Yifan Gong, assignor to Texas Instruments Incorporated
9 July 2002 (Class 704/256); filed 10 February 2000

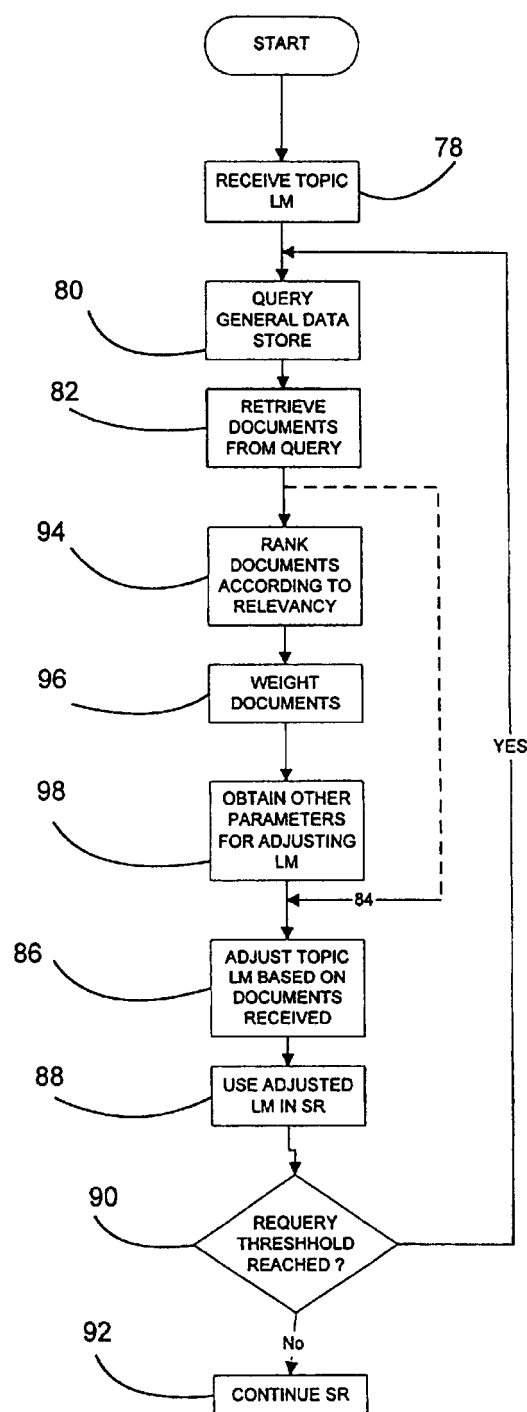
For hands-free operation of a cell phone with a remotely located microphone, in an automobile, for example, environmental noise often makes communication difficult. To facilitate speaker-independent speech recognition with a noise reduction feature in a variety of listening environments, a one-time adaptation of hidden Markov models (HMMs) is first performed without the noise source (e.g., engine off). Cepstral mean normalization is then used with a large amount of data for further training of the initial HMMs to compensate for the environment and microphone characteristics. Thereafter, with a few additional known utterances, the gender of the speaker is determined and adaptation to a particular speaker is performed to further narrow the selection of which HMMs to use.—DAP

6,418,431

43.72.Ne INFORMATION RETRIEVAL AND SPEECH RECOGNITION BASED ON LANGUAGE MODELS

Milind V. Mahajan and Xuedong D. Huang, assignors to Microsoft Corporation
9 July 2002 (Class 707/4); filed 30 March 1998

As in conventional speech recognition systems, a small storage area is used to store the relatively sparse, user- or task-specific topic information for language modeling. To speed up formulation of a language model and to improve its accuracy, the system also queries general databases such as



those accessible on the Internet. Probability estimates of the most likely N words or word sequences are thus adjusted by multiple information stores, providing a much larger database from which to adapt the language model to the actual user.—DAP

6,417,440

43.75.Mn DAMPER FORMED OF POWDER-CONTAINING SYNTHETIC RESIN AND KEYBOARD MUSICAL INSTRUMENT EQUIPPED WITH THE SAME

Fumiyoshi Furuki, assignor to Yamaha Corporation
9 July 2002 (Class 84/719); filed in Japan 1 May 2000

A piano mechanism is proposed that uses synthetic resin instead of lead weights, thereby making the instrument “free from environmental pollution.” If only the Romans had known.—MK

6,417,435

43.75.St AUDIO-ACOUSTIC PROFICIENCY TESTING DEVICE

Constantin B. Chantzis, Glen Rock, New Jersey and Daniel I. Rosen, Stateline, Nevada
9 July 2002 (Class 84/477 R); filed 28 February 2001

This devious patent, conspicuously absent of implementation detail, attempts to argue that musical performance can be measured via comparison against a reference together with a laundry list of statistical methods. No results are shown or discussed.—MK

6,406,348

43.75.Tv MUSICAL DRINKS VESSELS

Walter Pearce, assignor to Textformat Limited
18 June 2002 (Class 446/81); filed in the United Kingdom 3 February 1999

Like United States Patent 6,335,691 [reviewed in J. Acoust. Soc. Am. 112(1), 23 (2002)], the inventor here proposes adding a light-activated sound chip to the end of a bottle. The output transducer is also at the end of the bottle. Such an invention can not only be used to tell the drinker to buy more, but also to sing lullabies to babies.—MK

6,416,411

43.75.Wx GAME MACHINE WITH RANDOM SOUND EFFECTS

Nakayasu Tsukahara, assignor to Aruze Corporation
9 July 2002 (Class 463/35); filed in Japan 28 October 1998

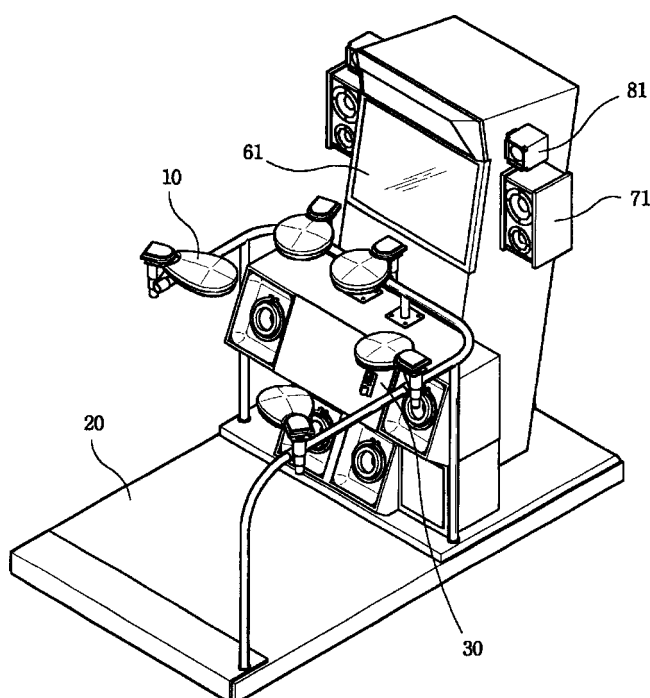
Playing the same arcade game becomes boring so state the inventors. The solution is to use a random sequence generator to change the soundeffects thereby enabling the players to “fully enjoy the pleasure of gaming.”—MK

6,417,436

43.75.Wx HAND-OPERATED DANCING MACHINE

Kim Beyoung-Wook, assignor to Interzone 21 Company, Limited
9 July 2002 (Class 84/600); filed in the Republic of Korea 22 August 2000

It's a short step from automatic music arcade game machines to automatic dance game machines. Basically, the dancer is a percussionist and



uses the drum sensors to match the machine's dance rhythm. Naturally, how the scoring works is anyone's guess.—MK

6,418,406

43.75.Wx SYNTHESIS OF HIGH-PITCHED SOUNDS

Vishu R. Viswanathan and Wai-Ming Lai, assignors to Texas Instruments Incorporated

9 July 2002 (Class 704/207); filed 14 August 1996

Upsampling and downsampling is a well-known technique (Crochiere and Rabiner) for performing rational sampling rate conversion. This can be used to pitch shift voices as well. The inventors have combined pitch shifting with LPC coding but, unfortunately, the authors have ignored the effect of shifting formants; these defects were well known in 1996 when this patent was filed. They have also conveniently forgotten that pitch shifting in western scales often demands irrational factors.—MK

6,409,720

43.80.Sh METHODS OF TONGUE REDUCTION USING HIGH INTENSITY FOCUSED ULTRASOUND TO FORM AN ABLATED TISSUE AREA CONTAINING A PLURALITY OF LESIONS

James B. Hissong and Fred B. Dinger III, assignors to Medtronic Xomed, Incorporated

25 June 2002 (Class 606/27); filed 31 July 2000

A method of tongue reduction by thermal ablation uses high-intensity focused ultrasound. An ultrasound emitting transducer is introduced into the patient's mouth and positioned near the external surface of the tongue. Sound is emitted from the transducer and focused into the tissue of the tongue, ablating the tissue in a lesioned area below the surface. The lesions are permitted to be absorbed by the patient's body and/or remain as altered tissue such that the tongue is reduced in size to correspondingly increase the size of the patient's airway and/or is stiffened to resist vibration (e.g., from snoring).—DRR

6,413,216

43.80.Sh METHOD AND ASSEMBLY FOR PERFORMING ULTRASOUND SURGERY USING CAVITATION

Charles A. Cain and J. Brian Fowlkes, assignors to The Regents of the University of Michigan

2 July 2002 (Class 600/439); filed 22 December 1999

A method and assembly are described to apply an ultrasonic beam to generate cavitation and create a controlled surgical lesion in a selected treatment volume inside a patient. Numerous cavitation bubbles are generated in the treatment volume. Ideally, the threshold for cavitation in the treatment volume is lowered below that of the surrounding tissues. The expected location of the surgical lesion within the treatment volume may be previewed and then the microbubbles in the treatment volume are cavitated with the ultrasonic beam to create the controlled surgical lesion. In addition, substances can be associated with the microbubbles so that the cavitation of the microbubbles delivers the substances to the treatment volume. The creation of the surgical lesion can then also be verified.—DRR

6,413,254

43.80.Sh METHOD OF TONGUE REDUCTION BY THERMAL ABLATION USING HIGH INTENSITY FOCUSED ULTRASOUND

James B. Hissong and Fred B. Dinger, assignors to Medtronic Xomed, Incorporated

2 July 2002 (Class 606/27); filed 19 January 2000

This patent is similar to the above patent 6,409,720 by the same inventors and assigned to the same company. The configurations of the respective devices differ slightly, with the earlier patent emphasizing the treatment of multiple lesions.—DRR

6,416,486

43.80.Sh ULTRASONIC SURGICAL DEVICE HAVING AN EMBEDDING SURFACE AND A COAGULATING SURFACE

Scott D. Wampler, assignor to Ethicon Endo-Surgery, Incorporated

9 July 2002 (Class 601/2); filed 31 March 1999

This ultrasonic surgical device may be useful for repairing a defect in tissue, such as inguinal hernia, through the use of a prosthetic and the application of ultrasonic energy. The device contains an acoustic assembly having a solid core waveguide. The waveguide extends from the housing and has an end effector at the distal end for the conduction of ultrasonic energy. Two versions of end effectors are described here, each having an embedding surface at the distal end and a coagulating surface extending from the embedding surface. One end effector has a cylindrical shaft, an embedding surface, and an angled coagulating surface. The other end effector has a truncated cone having a circumferential coagulating surface and a distal embedding surface.—DRR

6,416,492

43.80.Sh RADIATION DELIVERY SYSTEM UTILIZING INTRAVASCULAR ULTRASOUND

Eric D. Nielson, assignor to SciMed Life Systems, Incorporated

9 July 2002 (Class 604/22); filed 28 September 2000

This device is a radiation delivery system that fully integrates intravascular ultrasound (IVUS) technology. The radiation system includes a catheter having a distal head. A fixed or removable radiation source is located in or adjacent to the distal head. The head includes an ultrasonic

transducer and a radiation shield with a window. The transducer facilitates placement of the window such that only a portion of the treatment site is exposed to radiation. The transducer provides a signal indicating relative position, tissue geometry, and/or tissue characteristics that may be used to determine the appropriate placement of the window. This helps to control the dosage to target different areas of the treatment site.—DRR

6,406,430

43.80.Vj ULTRASOUND IMAGE DISPLAY BY COMBINING ENHANCED FLOW IMAGING IN B-MODE AND COLOR FLOW MODE

Syed O. Ishrak *et al.*, assignors to GE Medical Systems Global Technology Company, LLC
18 June 2002 (Class 600/441); filed 24 April 2000

Gray scale data, e.g., blood flow or contrast, that represent movement, and color flow data, e.g., power or velocity, that also represent movement are processed together and displayed so that movement is shown in a colored gray scale image.—RCW

6,406,431

43.80.Vj SYSTEM FOR IMAGING THE BLADDER DURING VOIDING

William L. Barnard *et al.*, assignors to Diagnostic Ultrasound Corporation
18 June 2002 (Class 600/443); filed 17 February 2000

This system uses successive ultrasonic images of a bladder during the voiding process. The images are processed to form a continuous moving image that spans the entire voiding event. The acquisition of data is initiated by the user. Processing is used to compensate for movement of the subject or device during the voiding process.—RCW

6,406,484

43.80.Vj REMOVAL APPARATUS FOR USE IN THE REMOVAL OF IMPACTED CERUMEN FROM THE AUDITORY CANAL

Eric L. Lang, Philadelphia, Pennsylvania
18 June 2002 (Class 606/162); filed 1 November 2000

This device may be basically described as a vacuum cleaner for removing cerumen from within an auditory canal. The hand-held instrument contains an auditory canal plug that seals over the auditory canal when manually pressed against the canal. The plug contains an aperture that leads to a vacuum chamber within the hand-held instrument. A manually operated control valve monitors the flow of air through the auditory canal plug and into the vacuum chamber. Since the hand-held instrument merely contains the vacuum chamber, it must be placed on a base that contains a vacuum pump connected pneumatically to the vacuum chamber. The vacuum pump generates a negative pressure in the vacuum chamber that is maintained even after the hand-held instrument is removed from the base.—DRR

6,406,486

43.80.Vj APPARATUS AND METHOD FOR VASODILATION

Ralph De La Torre and Kenton W. Gregory, assignors to The General Hospital Corporation
18 June 2002 (Class 607/89); filed 15 December 1999

A method and apparatus are described here for dilating blood vessels in vasospasm through the use of high-frequency acoustic waves. The apparatus contains a catheter having a fluid-filled lumen. A wave generator located within the catheter lumen generates a wave front that propagates

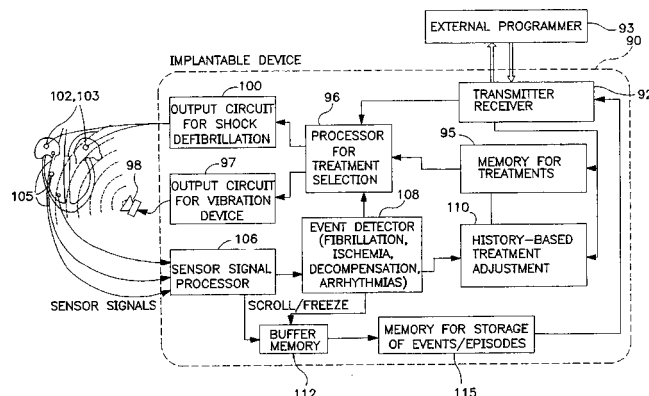
through the fluid in the lumen and is transmitted from the distal end of the catheter to propagate through the fluid in the blood vessel. An energy source connected to the wave generator provides energy for producing the wave front.—DRR

6,408,205

43.80.Vj SYSTEM FOR DELIVERING MECHANICAL WAVES

Alexis Renirie *et al.*, assignors to Medtronic, Incorporated
18 June 2002 (Class 607/5); filed 6 December 1999

An implanted system delivers mechanical waves to one or more selected patient areas, e.g., the heart and/or lungs. The mechanical waves are delivered to treat fibrillation or like arrhythmias, enhance lung gas exchange, enhance cardiac muscle relaxation, or increase coronary perfusion. Mechanical waves are generated preferably in the frequency range of 1–50 000 Hz. The waves may be delivered continuously for short or long time periods or they may be controlled timewise either with respect to detected portions of a patient's heartbeat signal or in response to a detected event such as fibrillation. In one embodiment, the implantable system in-



cludes a defibrillation shock generator and control for responding to a defibrillation event by first delivering a sequence of mechanical waves and then delivering an electrical defibrillation shock. In another embodiment, the system and method treat incipient fibrillation or arrhythmia by delivering mechanical waves of predetermined timing to the patient's heart and/or lungs. In a third embodiment, mechanical waves are delivered through an array of transducers to the patient's atrial wall to treat atrial fibrillation.—DRR

6,413,218

43.80.Vj MEDICAL DIAGNOSTIC ULTRASOUND IMAGING SYSTEM AND METHOD FOR DETERMINING AN ACOUSTIC OUTPUT PARAMETER OF A TRANSMITTED ULTRASONIC BEAM

John W. Allison *et al.*, assignors to Acuson Corporation
2 July 2002 (Class 600/443); filed 10 February 2000

This system and method determine an acoustic output parameter of a transmitted ultrasonic beam. The region of the parameter determination is either user selected or automatically chosen by an adjustment in the imaging system and may be where the output is not peak. An indication of the output parameter is provided.—RCW

6,409,667

43.80.Vj MEDICAL DIAGNOSTIC ULTRASOUND TRANSDUCER SYSTEM AND METHOD FOR HARMONIC IMAGING

John A. Hossack, assignor to Acuson Corporation
25 June 2002 (Class 600/443); filed 23 February 2000

The transducer in this system is comprised of two stacked piezoelectric layers. Information from each of the layers is independently processed during transmission or reception or both. A filter then isolates harmonic information for imaging. The multilayer construction and independent processing result in a wide bandwidth as well as providing information at the second harmonic to which many transducers are insensitive.—RCW

6,409,671

43.80.Vj ULTRASONOGRAPHY

Morten Eriksen and Sigmund Frigstad, assignors to Nycomed Imaging AS
25 June 2002 (Class 600/458); filed in the United Kingdom 18 December 1997

Local aberrations in perfusion or compliance of vascular tissue are detected in images. Waveforms representative of arterial pulsatility are produced. The waveforms are analyzed for variations such as phase distortion that is characteristic of the aberrations in perfusion or compliance.—RCW

6,409,673

43.80.Vj METHOD AND APPARATUS FOR INTRAVASCULAR TWO-DIMENSIONAL ULTRASONOGRAPHY

Paul G. Yock, assignor to Cardiovascular Imaging Systems, Incorporated
25 June 2002 (Class 600/463); filed 23 March 2001

Ultrasonic images of a vessel wall are produced using a catheter that is inserted into the vessel. The catheter includes a drive cable to obtain a circumferential scan around the catheter. The size and flexibility of the catheter permit introduction into a vessel and subsequent passage through the vessel to an imaging position.—RCW

6,413,215

43.80.Vj IMPLANT WEAR DEBRIS DETECTION APPARATUS AND METHOD

Junru Wu *et al.*, assignors to The University of Vermont
2 July 2002 (Class 600/437); filed 13 September 2000

This is a system for detecting wear debris particulates from a medical implant within the body of a living animal. An acoustic transmitter sends acoustic energy from outside the body to a soft tissue region near the implant. An acoustic receiver, also located outside the body, detects resultant acoustic energy generated by the debris particles and produces a received signal indicative thereof. A processor evaluates at least one parameter associated with the debris particles.—DRR

6,413,217

43.80.Vj ULTRASOUND ENLARGED IMAGE DISPLAY TECHNIQUES

Larry Y. L. Mo, assignor to GE Medical Systems Global Technology Company, LLC
2 July 2002 (Class 600/440); filed 30 March 2000

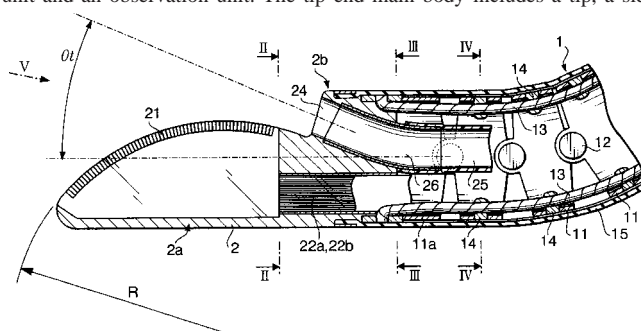
A reference b-mode image is displayed and data are processed to produce as well as also display along with the reference image an enlarged image of a region of interest in the reference image.—RCW

6,409,666

43.80.Vj TIP END OF ULTRASONIC ENDOSCOPE

Keiji Ito, assignor to Asahi Kogaku Kogyo Kabushiki Kaisha
25 June 2002 (Class 600/439); filed in Japan 15 April 1999

A flexible insertion tube of an endoscope includes a bendable portion that is formed at its tip end. The bendable portion may be flexed in any arbitrary direction. A tip end main body is connected at the tip end of the bendable portion, and the former is provided with an ultrasonic scanning unit and an observation unit. The tip end main body includes a tip, a side



section, and a rear side section. The tip end section is provided with a convex type ultrasonic probe and the rear end side section contains an instrument outlet that allows a treatment instrument to protrude, an observation window that is directed to a forward side with respect to the scanning direction of the ultrasonic probe, and an illumination window to permit light to illuminate an area to be observed through the observation window.—DRR

6,413,219

43.80.Vj THREE-DIMENSIONAL ULTRASOUND DATA DISPLAY USING MULTIPLE CUT PLANES

Ricardo Scott Avila *et al.*, assignors to General Electric Company
2 July 2002 (Class 600/443); filed 14 March 2000

A three-dimensional projection image is used to depict a volume. Three mutually orthogonal planar images are also shown. A graphical representation of the volume and the planes is displayed using color. Any one of the four images can be reconstructed in real time using a trackball.—RCW

6,413,221

43.80.Vj ULTRASONIC SYSTEM AND METHOD EMPLOYING VARIABLE FILTERING OF ECHO RETURN SIGNALS

George A. Brock-Fisher, Andover, Massachusetts
2 July 2002 (Class 600/458); filed 11 February 2000

An ultrasonic system is controlled to image a microbubble contrast agent in a region of fluid flow. The transmitter emits signals at various power levels. The receiver extracts echo signal components that fall within a determined bandwidth and is controlled to alter the bandwidth or center frequency according to the transmitted power.—RCW

FORUM

Forum is intended for communications that raise acoustical concerns, express acoustical viewpoints, or stimulate acoustical research and applications without necessarily including new findings. Publication will occur on a selective basis when such communications have particular relevance, importance, or interest to the acoustical community or the Society. Submit such items to the JASA Editorial Office, and specify that they are intended for the FORUM. Condensation or other editorial changes may be requested of the author.

Opinions expressed are those of the individual authors and are not necessarily endorsed by the Acoustical Society of America.

ETHICAL TREATMENT OF ANIMALS IN RESEARCH

[DOI: 10.1121/1.1523391]

To the Editor:

As members of the Acoustical Society of America (ASA), we write this letter as acoustics professionals who feel that the use of animals in research is neither beneficial nor ethical. Furthermore, we feel the ASA policy towards animals in research, which follows the "Guide for the Care and Use of Laboratory Animals" published by the National Institutes of Health (NIH),¹ fails to provide even the most fundamental comfort for laboratory animals.

We are always horrified by the clinical descriptions of experiments performed on dogs, monkeys, chinchillas, cats, and mice for publication in the *Journal of the Acoustical Society of America*. They have even created a new language to mitigate any pangs of moral repulsion that might surface. Dogs are not dogs; they are "canine subjects" (implying that they have some choice in the matter). Electric shocks are "stimulation." Finally, when the experiment is finished, instead of saying they are killing an animal, they say they "sacrifice" the subject.

Healthy, social, intelligent mammals like dogs, cats, and monkeys have holes cut in their heads and mechanical devices attached to their skulls. They are intentionally given collapsed lungs, have their eyes sewn shut, are shocked in order to produce vocalizations, and are subjected to a myriad of other procedures that would be considered nothing short of torture if done to a human animal. To make matters worse, all too often this so-called "research" never seems to arrive at a conclusion.

Many people would say that the current guidelines are sufficient to safeguard the animals' comfort, yet strangely if one would suggest that someone donate his or her cat or dog for research, it would elicit looks of disgust and concern. It would be safe to assume that few members of the ASA have bothered to flip to the last few pages of our journal to read the guidelines for animal and human research.² Suffice it to say that the guidelines for animals comprise a total of six short, vague paragraphs, while the guidelines for human research are lengthy and thorough. As an example, the animal use guidelines read, "Consideration should be given to the appropriateness of experimental procedures..." Notice the word "consideration," which falls far short of in-depth thought, much less research into alternative methods. Also, the word "should" is used instead of "must," which makes the entire sentence a suggestion rather than a requirement, and therefore unenforceable. Note also the conspicuous absence of the word "ethical." In contrast, the guidelines for human research read, "In planning a study, the investigator has the responsibility to make a careful evaluation of its ethical acceptability." There is nothing left to doubt here. There is ethical responsibility and careful evaluation. What would be so difficult in protecting animals at least to this degree?

Many would say that this is as it should be, because animals are... well... animals after all and humans are somehow special. As scientists, we should be able to quantifiably identify this difference between human and nonhuman animals that gives us the ethical right to torture them for our doctoral dissertations. Is it the ability to reason? An adult dog has a greater ability to reason than a human infant. Are infants, then, subject to scientific research? Is it the ability to use language? Many primates have been taught sign language, and many humans such as infants and the severely mentally disabled are not able to use language. Should we then be able to experiment

on the mentally disabled? Upon analysis, it can easily be shown that there is no quantifiable difference between human and nonhuman animals that would give us the right to experiment on them.

In the lab animal circuit it takes only the cry from the experimenters that they are saving human lives to remove the humanity within most of us. They argue that people are worth more than animals, and with animals, anything goes, in spite of the ASA code, in the name of saving lives. So the issues are two: does the research help and if it does or doesn't, is it right to experiment on unwilling subjects (human or animal)? Evidence shows that the answer is no on both counts.

Animals are not people, either mentally or physiologically. Their differences are significant. Systems differ, effects of drugs on each are different, yet there is some similarity. Both species feel pain, both have somewhat similar organs, all know fear, and both know the feeling of confinement. If they differ, how effective is the research? If they are similar, how can we dare subject them to these horrors? Animal testing isn't a panacea: thalidomide and Raxar,³ both tested on animals, nevertheless caused fatalities, deformation, or both in people. Aspirin will kill a cat, yet we use it. Tobacco companies used dogs in experiments to perform reliable tests. Asbestos passed animal tests, too. Maybe half of all drugs on the market are pulled because they produce death or sickness in people. Do we need chinchillas to be exposed to 140 dB blasts?

The debate over the use of animals in scientific study has become highly charged in recent years. In the interest of replacing animals in classrooms and laboratories, many researchers and physicians have developed state-of-the-art alternatives that work superbly, often greatly surpassing the effectiveness of animals models used before. It is time that more effort is put into developing alternative methods in the field of bioacoustics as well.

In 1993, the NIH Revitalization Act mandated the inclusion of women and minorities in clinical research supported by NIH, based on the concern that observations on men may not apply to women. Children were later added based on the same notion. If men are different enough from women to require separate tests, surely similar principles should be applied with regard to animal studies. Nonhuman animals must be more different from humans than men are from women or children are from adults, yet animal experimentation continues. Today, many health care organizations are proposing that similar principles be applied with regard to animal studies. This makes good sense both ethically and scientifically. New guidelines are needed to put concerns about species differences on a par with those related to gender and age differences. The goals of such principles would be twofold: First, they would encourage the pursuit of research methods that have maximal applicability to humans. Second, they would serve to reduce animal use, an important mandate of animal stewardship, and one of its basic "3 Rs": reduction, replacement, and refinement.

By removing animals from the equation, we remove those very variables that make animal tests unreliable, namely, their individual reactions to stress, manipulation, pain, and even sheer boredom and their extreme differences as species. As UC-Davis scientist Joseph Garner *et al.*⁴ discovered, the obsessive, repetitive movements seen in caged animals, once thought insignificant, are now believed to be signs of brain damage, a variable that alters if not invalidates resultant findings. Computer models respond only to the procedure being tested, allowing researchers to zero in on cause and effect much more rapidly.

By removing animals from often-cruel confinement, tests, and even death, we reintroduce a respect for life that has been sorely missing. Even

grade school administrators are utilizing better ways to teach biology and other life sciences. Many of us may remember dissecting earthworms, frogs, or even pigs in biology class. Today, new technology allows youngsters to “dissect” frogs via digital scalpel on their computers through innovative CD-ROM programs. Children can investigate the structure and function of anatomy at their own pace, repeating the lessons as many times as necessary, all the while leaving natural ecosystems in place. With products like the NIH Visible Human project and the NASA iAnatomy project, similar changes are taking place in the nation’s medical schools, in research labs, and virtually all areas of science. Technology may finally remove animals—and all the related controversy—from research.

Currently, the Public Health Service Policy on Humane Care and Use of Laboratory Animals (Health Research Extension Act of 1985, Public Law 99-158) requires that scientists conducting animal studies have available to them instruction or training on “the concept, availability, and use of research or testing methods that limit the use of animals or limit animal distress.” Again, this language is far too vague to be effective. Investigators would benefit from more specific language.

Recommendations

The following principles would be a significant move toward these goals:

- (1) Strong priority in funding and publication must be given to human studies.
- (2) Investigators proposing studies on animals must be required in the application process to describe the possibilities for meeting the goals of their research, broadly defined, (a) through human clinical or epidemio-

logical research, and (b) through other methods, such as cell culture methods or computer modeling. In so doing, they must focus on the overall goals of the research, not on their own specific model. If, in the investigator’s judgment, such methods are not yet available, they must describe what factors limit their availability.

- (3) Investigators must be required in the application process to describe the applicability of the proposed animal model to humans. If using a pharmacologic compound, they must address similarities and differences in biochemical pathways involved in its absorption, distribution, metabolism, excretion, and biochemical action to the extent they are known.
- (4) If successful, these principles will reduce animal use, as is required by basic animal welfare mandates, and will increase the applicability of research results to human clinical problems.

Sincerely,

Clifford Kaminsky, LAacoustics

Richard J. Peppin, Scantek, Inc.

¹DHEW Publication No. (NIH) 80-23, Office of Science and Health Reports, DRR/NIH, Bethesda, MD 20205.

²See, for example, “Guiding Principals for Research Involving Human or Animal Subjects,” *J. Acoust. Soc. Am.* **108**, No. 2 (2000) (no page number).

³Glaxo Wellcome press release, 27 October 1999.

⁴J. P. Garner, C. L. Meehan, and J. A. Mench, “Stereotypic parrots fail the same psychiatric task as stereotypic autists and schizophrenics,” in *Proceedings of the 35th International Congress of the ISAE*, Davis, CA, Center For Animal Welfare, UC Davis (2001).

Virtual error sensing for active noise control in a one-dimensional waveguide: Performance prediction versus measurement (L)

Jacqueline M. Munn, Ben S. Cazzolato, Colin D. Kestell, and Colin H. Hansen
Department of Mechanical Engineering, Adelaide University, SA, 5005, Australia

(Received 15 March 2002; revised 13 September 2002; accepted 23 September 2002)

Virtual error sensing is a novel active noise control technique, which is designed to produce a zone of attenuation remote from the physical error sensors. In this letter virtual sensing is investigated for tonal noise (both on and off resonance) in a long narrow duct. The performance of the virtual error sensors using real-time control is compared to the performance determined from an analytical model and the performance determined through the postprocessing of experimental data. Two examples of control using postprocessed experimental transfer function data are presented; the first relied on transfer functions measured using broadband noise and the second relied on transfer functions measured at discrete frequencies. The results highlight the significant errors encountered as a result of using broadband transfer functions in lightly damped enclosures. © 2003 Acoustical Society of America. [DOI: 10.1121/1.1523386]

PACS numbers: 43.50.Ki [MRS]

I. INTRODUCTION

The use of a local active noise control system within a highly damped and modally dense enclosure can result in small “zones of quiet” around the error sensor. Therefore, for an observer to perceive any reduction in noise level, the error sensor must be placed in very close proximity to the observer’s head, which in many cases is impractical. The concept of “virtual” sensing, an active noise control technique where a local zone of quiet is created at a location remote from the error sensor was first introduced by Garcia-Bonito *et al.*¹ Cazzolato² introduced a novel forward-difference extrapolation virtual sensing technique designed to adapt to any physical system changes. Two virtual error sensing algorithms were developed to predict the sound pressure at the observer location. The techniques were applied to control tonal noise in a long narrow duct model and the results were validated with experimental data.³ However, in both cases, control performance was evaluated by quadratic optimization of the postprocessed transfer function data. Here, the results of real-time active noise control using a feedforward controller with hard-wired virtual error sensors are compared to results obtained using transfer function data. It will be shown that the reason for the poor experimental performance observed by Kestell *et al.*³ was almost entirely due to the errors inherent in broadband transfer function measurements in a lightly damped enclosure.

II. THEORY

At low frequencies, when the distance between the transducers making up the virtual sensor is much less than a wavelength, the spatial rate of change of sound pressure is low and therefore predictable.⁴ Hence, by fitting a straight or curved line between the pressures p_1 , p_2 , and p_3 measured at fixed locations, the pressure p_v at a remote location can be estimated (Fig. 1). The two forward-difference virtual microphone algorithms are summarized below.

(1) Two-microphone, linear prediction:

$$p_v = \begin{bmatrix} \frac{x}{h} & 1 \end{bmatrix} \begin{bmatrix} 0.5 & -0.5 \\ 1.0 & 0 \end{bmatrix} \begin{bmatrix} p_2 \\ p_1 \end{bmatrix}. \quad (1)$$

(2) Three-microphone, quadratic prediction:

$$p_v = \begin{bmatrix} \left(\frac{x}{h}\right)^2 & \frac{x}{h} & 1 \end{bmatrix} \begin{bmatrix} 0.5 & -1.0 & 0.5 \\ 1.5 & -2.0 & 0.5 \\ 1.0 & 0 & 0 \end{bmatrix} \begin{bmatrix} p_3 \\ p_2 \\ p_1 \end{bmatrix}, \quad (2)$$

where p_v is the pressure at the observer location, x is the distance between the observer and the nearest sensor, p_1 , p_2 , and p_3 are the measured pressures, and h is the separation distance between the transducers for the quadratic prediction and is equal to 25 mm. The separation distance between the two microphones in the linear prediction is $2h$. For a full derivation of the prediction equations see Ref. 4.

III. EXPERIMENT

The results for real-time control in the duct were compared to the results obtained using both the analytical model and postprocessed experimental data. A primary noise source was positioned at one end of the duct with a control source located 0.5 m from the opposite end (Fig. 2). The sound pressure profile around the virtual sensors was observed over

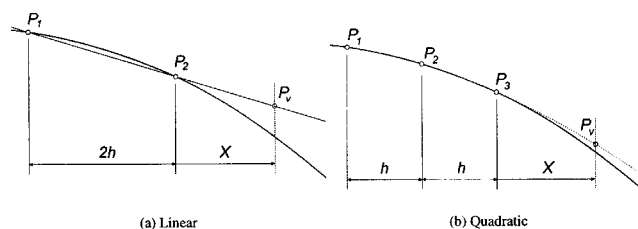


FIG. 1. Forward-difference extrapolation.

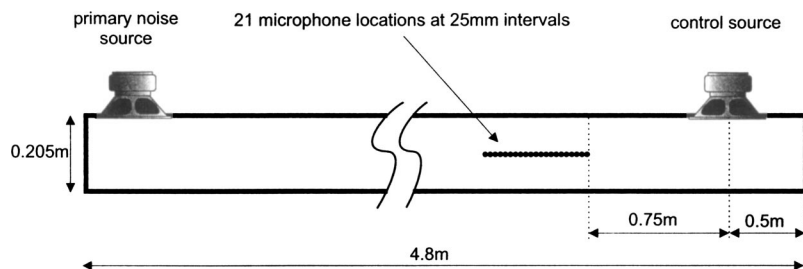


FIG. 2. Schematic system representation of the long narrow duct.

a 0.5-m length with 21 equally spaced measurement locations. The duct was rigidly terminated and had a resonance quality factor, Q , of approximately 50.

The analytical model of the duct was evaluated using MATLAB. Transfer functions between the primary and secondary source and the 21 measurement locations were calculated using classical theory⁵ in which the first 25 modes were considered.

For the postprocessed results, transfer functions were measured between the two sources and the 21 measurement locations. Two types of postprocessed results are presented here: calculations based on broadband transfer functions measured using random noise and calculations based on discrete frequency transfer functions measured using discrete tones corresponding to a specific resonance frequency. The broadband transfer functions were measured from 0 to 400 Hz with a sampling frequency of 1024 Hz and a bandwidth of 0.5 Hz.

The data (measured and simulated) were then postpro-

cessed and the cost function minimized using quadratic optimization, which incorporated a 1% error (40-dB control limit) to simulate the errors expected in a real-time controller.

The real-time experiments discussed here were conducted using the Causal Systems EZ-ANCII feedforward controller.

IV. RESULTS FOR RIGIDLY TERMINATED DUCT

Figure 3 shows the results obtained when controlling an acoustic resonance in a long, narrow, rigidly terminated duct. The vertical lines represent the sensor locations and the solid circle represents the observer location. The top curve without any circles represents the uncontrolled primary field. The other curves represent the controlled sound field at increasing separation distances between the observer and the sensors. The distance between the observer and the sensors is indicated by the distance between the right-most vertical line

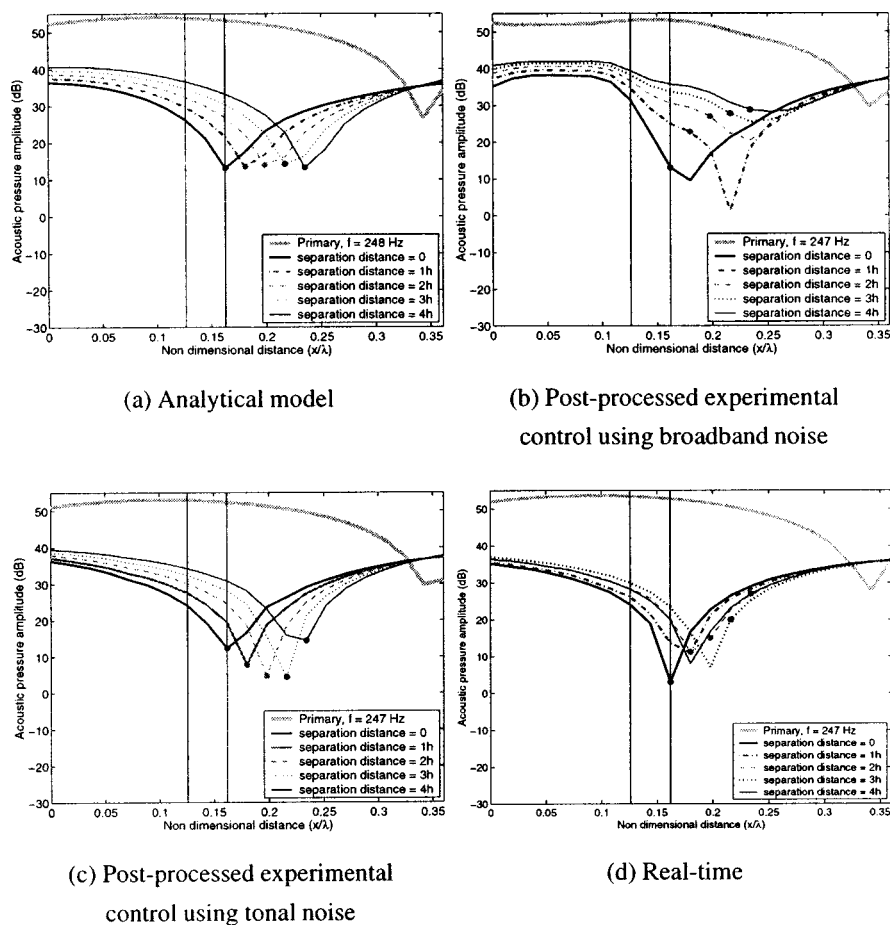


FIG. 3. Uncontrolled and controlled sound pressure amplitudes along a rigidly terminated duct at an acoustic resonance using linear virtual microphones.

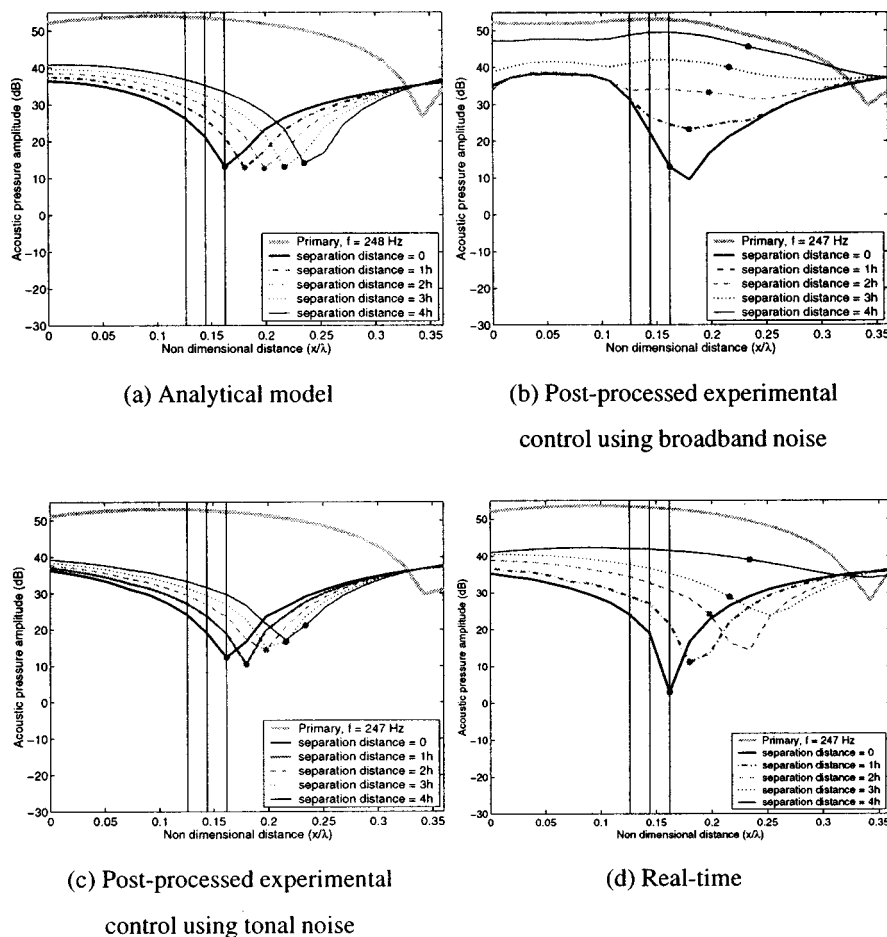


FIG. 4. Uncontrolled and controlled sound pressure amplitudes along a rigidly terminated duct at an acoustic resonance using quadratic virtual microphones.

and the solid circle located on the curve. Figures 3(a)–(d) show a comparison of the performance of the four control evaluation methods using the linear virtual microphone. Analytical control shows an attenuation of approximately 40 dB at all separation distances due to the artificial 1% error applied to the calculated optimal control source strengths. The postprocessed tonal, broadband control and the real-time control all show a decrease in attenuation as the separation distance between the transducers and the observer location is increased to $4h$. Control using the tonal experimental transfer function compares more favorably to the theory than the other experimental examples with 37 dB attenuation at an observer/sensor separation distance of $4h$. The postprocessed control using broadband transfer function data performed the worst with 19 dB of attenuation at $4h$, while the real-time control achieved an attenuation of 25 dB at $4h$.

It can therefore be concluded that the performance of the control obtained using postprocessed transfer function measurements obtained with broadband noise in a lightly damped enclosure is affected by errors associated with the use of the fast Fourier transform used to calculate the frequency response functions. These errors are greatest when the coherence is low, occurring at resonances and antiresonances. The poor coherence at the antiresonances is a result of low signal-to-noise ratio. The coherence is lowest at resonance which is due to spectral leakage, even though this was minimized by using a Hanning window and a large number of points in the FFT (2048). In heavily damped enclosures

leakage is generally not a problem when measuring broadband transfer functions since the resonant peaks are broader (than in a lightly damped enclosure). Using tonal noise to measure the transfer functions eliminates the low coherence caused by leakage in a lightly damped enclosure, consequently resulting in higher levels of predicted attenuation as a result of active noise control, for all separation distances.

Unlike the postprocessed data, which used a single microphone, the real-time measurements used a minimum of two microphones. Sensitivity and phase mismatch between the sensors used in real-time experiments limited the performance.

Figure 4 shows the performance of the quadratic virtual microphone for the four different control strategies. The analytical model shows an attenuation of 40 dB for all separation distances. Note that this is an artificial limit imposed to simulate the expected limitations of a real-time controller. Similar to the linear virtual microphone, the real-time control example also achieves greater attenuation than the postprocessed control using broadband transfer function data for all separation distances. Control using postprocessed tonal transfer function data was much better than that achieved by the other two experimental control examples with 33 dB attenuation at $4h$.

Comparing the quadratic virtual microphone control examples with the corresponding linear control examples shows that the linear algorithm outperforms the quadratic algorithm with the exception of the analytical models. This is

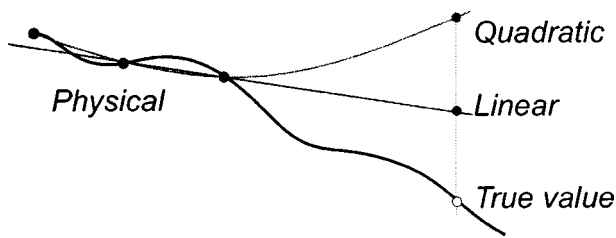


FIG. 5. Prediction errors in the presence of short wavelength spatial pressure variations.

due to the presence of short wavelength spatial variations in the experimental data (see Fig. 5) as suggested by Kestell *et al.*³ Consequently, quadratic predictions are less accurate than the linear estimates when using physical data. The real-time experiment used three microphones and matching both phase and magnitude sensitivities was very difficult and, consequently, the pressure estimate at the virtual location was degraded.

The experiments presented here were also repeated at an acoustic antiresonance. Conclusions drawn from the results of those experiments agreed with all of the conclusions presented here. These results can be found in Ref. 6.

V. CONCLUSIONS

The performance of two forward-difference prediction virtual algorithms using real-time control in a long, narrow, rigid-walled duct has been evaluated. The results are in agreement with those of Kestell *et al.*³ and suggest that these forward-difference virtual microphones can be successfully implemented in a real-time feedforward control situation.

Results obtained using postprocessed transfer function data with random noise excitation in a lightly damped enclosure were significantly affected by inherent FFT errors. This implies that tonal excitation should be used to obtain transfer

function data for use in predicting the expected performance of an ideal real-time controller. Alternatively, the FFT bin width needs to be larger than the inverse of the decay time.

In practice, the performance of real-time control is influenced by phase and sensitivity mismatch between the prediction transducers. Thus accurate system calibration and transducer selection is important. The linear prediction algorithm outperformed the quadratic prediction algorithm, which confirms that the quadratic algorithm is more sensitive to short wavelength spatial variations.

In the reactive environment in which these experiments were conducted, the spatial distribution of the sound field at resonance is determined by the mode shape or eigenfunction. This is, in fact, a sinusoid and therefore in this environment the possible prediction method could be a sinusoidal extrapolation. This could form the basis for future work.

Work to improve the prediction algorithm and reduce the effect of short wavelength extraneous noise has begun and involves using higher-order microphone arrays, containing redundant microphones.

¹J. Garcia-Bonito, S. J. Elliott, and C. C. Boucher, "A virtual microphone arrangement in a practical active headrest," in *Proceedings of Inter-noise 96* (1996), pp. 1115–1120.

²B. S. Cazzolato, "Sensing systems for active control of sound transmission into cavities," Ph.D. thesis, The University of Adelaide, Adelaide, South Australia, April 1999.

³C. D. Kestell, B. S. Cazzolato, and C. H. Hansen, "Active noise control with virtual sensors in a long narrow duct," *Int. J. Acoust. Vibration* **5**(2), 63–76 (2000).

⁴C. D. Kestell, "Active control of sound in a light aircraft cabin with virtual sensors," Ph.D. thesis, The University of Adelaide, Adelaide, South Australia, 2000.

⁵P. A. Nelson and S. J. Elliott, *Active Control of Sound* (Academic, London, 1992).

⁶J. M. Munn, C. D. Kestell, B. S. Cazzolato, and C. H. Hansen, "Real-time feedforward active control using virtual sensors in a long narrow duct," in *The Australian Acoustical Society Annual Conference, Canberra, Canberra, Australia* (2001).

Laboratory measurements of sound scattering from a buried sphere above and below the critical angle (L)

Harry J. Simpson^{a)} and Brian H. Houston

Naval Research Laboratory, Code 7136, 4555 Overlook Avenue SW, Washington, DC 20375

Raymond Lin

Coastal Systems Station/Dahlgren Division, Naval Surface Warfare Center, Code R21,
6703 West Highway 98, Panama City, Florida 32407-7001

(Received 12 June 2001; revised 28 May 2002; accepted 23 September 2002)

Laboratory measurements of low frequency (1–10 kHz) evanescent wave field scattering from a sphere buried in water-saturated sand was examined. A 60 cm stainless steel sphere was buried just below a sand–water interface and the acoustic backscattering cross section was measured for above and below critical angle geometries. The below critical angle insonification results clearly show significant levels of backscatter from the buried sphere due to evanescent wave insonification at the lower end of the spectrum (1–3.5 kHz). These measurements compare favorably with first principle estimates of the backscattered target strength and with a T-matrix-based numerical model. © 2003 Acoustical Society of America. [DOI: 10.1121/1.1523310]

PACS numbers: 43.30.Gv, 43.20.Fn [DLB]

I. INTRODUCTION

Long-range detection and classification of objects buried in the sea-floor continues to be a challenging problem. It is well known that lower frequency acoustical systems (1–10 kHz) have several potential advantages over their high frequency counterparts. The longer wavelengths at these frequencies are less affected by small-scale interface topography, attenuation, and inhomogeneities.^{1–6} Moreover, because the evanescent field decay is order λ , a resulting deeper penetration is found at these longer wavelengths.^{5–8} In order to fully explore these differences, particularly for long ranges and shallow grazing conditions, it is important to understand the physics of the interactions between the acoustic energy, the interface, and the scattering from buried structures. Towards this end, we report direct experimental evidence of high levels of scattering from a buried sphere that is due to excitation by evanescent wave energy.

These studies were conducted at the NRL shallow water laboratory where control and care were taken to ensure a homogeneous sandy bottom and a smooth interface. With these parameters under control, the scattering from inhomogeneities in the bottom and from interface roughness is eliminated in the experimental results. The scattering measurements reported here are only as a result of the evanescent field interacting with a single buried object in the bottom. This highly controlled data set is useful for comparison to various models reported in the literature, including those of Lim *et al.*,¹ Williams and Thorsos,² Maguer *et al.*,⁵ and Schmidt and Lee.⁴ For the work reported here, the experimental results are compared to the T-matrix-based numerical model described in Ref. 1, though modified for the physical parameters of the present measurement.

II. MEASUREMENT LABORATORY

The laboratory employed for these measurements is detailed by Simpson,⁷ and we briefly review them here. The pool physical boundaries are 8 m wide, 10 m long, and 7 m deep. It has a 3.8 m de-ionized water column over a 3.0-m-deep sandy bottom that is filtered, washed, and well characterized. Further, it forms a nearly uniform bed of material, in a volumetric sense, with a mean grain diameter of 240 μm and the interface can be smoothed and leveled to less than 0.5 mm of rms roughness. Both of these conditions eliminate scattering due to inhomogeneities and a roughened interface and enable the direct investigation of evanescent wave interactions with buried structures.

A diagram of the measurement configuration is shown in Fig. 1. For the work presented here, a robotic scanner is used to position a Brüel and Kjaer model 8103 omnidirectional hydrophone. Care is taken to produce a plane-wave-like field in the vertical plane of the measurement in order to eliminate above critical wave vector components from a diverging source. To accomplish this, a 3 m line array source is used to produce a constant phase front at the ranges used in these experiments. It is suspended so that the wave field excites the sand–water interface at either a 30° or 20° angle-of-incidence (Fig. 1). A computer is used to control the robotics system and to acquire the data via CAMAC (Computer Automated Measurement and Control) instrumentation.

The incident acoustic pulse is designed to be flat over a band from 1 to 20 kHz. Briefly, this is done by solving for a wave form that inverts the response of the entire system: i.e., the source electronics, line array, hydrophone, and receiver electronics. With the line array and receiver hydrophone in a free-field condition, a 4 μs digital pulse is delivered to the source electronics which, in turn, results in a broadband impulsive wave form being generated in the water. This response is measured using the hydrophone at the intended target range. For these measurements, a four-pole Butter-

^{a)}Electronic mail: harry.simpson.nrl.navy.mil

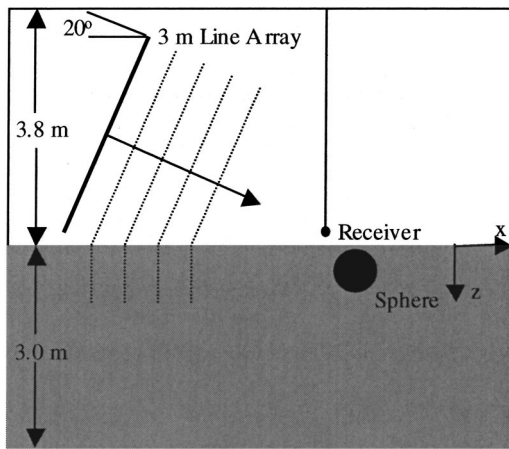


FIG. 1. The in-water portion of the measurement apparatus employed in these experiments. A 3 m line-array source is used to insonify the interface at a 30° (above critical) and 20° (below critical) angle of incidence. The pool facility is 10 m long, 8 m wide, and 7 m deep, the sand and water are 3.0 and 3.8 m deep, respectively.

worth filter is selected as a desired wave form to invert to. The measured impulse response at the hydrophone is then processed using a Wiener filter deconvolution to solve for a voltage time history that is subsequently down-loaded into an arbitrary wave form generator. Therefore, a pressure pulse is delivered by the source that has the temporal and spectral characteristics of a Butterworth filter. This response, a direct measure of the free-field incident pressure, is used to normalize the scattered returns. The peak source pressure level for these measurements is 159 dB (*re* 1 μ Pa at 1 m).

III. MEASUREMENTS

Previous measurements reported by Simpson⁷ have shown that the sediment and de-ionized water in this laboratory have compressional wave speeds of 1680 and 1482 m/s, respectively, resulting in a critical angle of 28° . A 60-cm-diam stainless steel sphere was buried (Fig. 1) to within approximately 3 cm of the fluid–water interface by use of a water-jet system. The sphere is hollow, air filled, and has a wall thickness of 1.5 cm. After each burial and extraction, the interface is smoothed to less than 0.5 mm of rms roughness. In the effort reported here, scattering measurements were made for two insonification angles.

For the first measurement, the source was set at a 30° insonification angle. This angle is measured up from the interface to the normal of the wave fronts, as shown in Fig. 1. The source is 2.5 m from the insertion point of the sphere measured along the normal to the wave fronts. The hydrophone is positioned 0.6 m from the insertion point, again, along the normal to the wave fronts to 0.3 m above the sand–water interface. After the scattering data are acquired, the sphere is extracted, the hole in the sandy bottom is filled and the interface is smoothed and leveled. Following this, a background measurement is taken that is used off-line to coherently remove the part of the direct and bottom acoustic paths that overlap the scattered return from the target. After performing this subtraction, the data are windowed in the time domain to include only the direct scattering from the

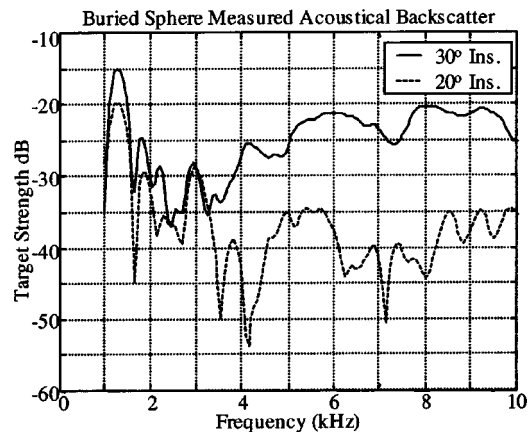


FIG. 2. The 30° insonification backscattered measurement from a buried sphere is shown as the solid line. The 20° insonification backscattered measurement from a buried sphere is shown with a dashed line.

buried sphere. This target return is then Fourier transformed and normalized using the free-field measurement of the incident pulse described previously.

A second buried sphere scattering measurement was made with the source set at a 20° insonification angle. Again, this angle is measured up from the interface to the normal of the wave fronts. The measurement configuration for the 20° measurement was nearly identical to the 30° measurement, except the source was rotated to 20° and the hydrophone was 0.9 m along the normal wave fronts but remaining 0.3 m above the bottom. The measured data are processed in an identical fashion to the previous measurements. The data from both measurements are shown in Fig. 2 where they have been normalized to the free-field measurement of the source response and presented as target strength *re* 1 m.

IV. MODEL

The model used to predict the scattering from this buried stainless steel sphere is described by Lim *et al.*¹ Only a brief overview of the model will be discussed along with the detailed parameters used in the model. The scattering from the buried elastic sphere is formulated using a T-matrix-based solution to the Helmholtz equation that was then applied to a bounded region. For the case considered here, a smooth interface between the sandy bottom and the water column is assumed, and the poro-elastic effects of the sandy bottom are ignored by modeling the bottom as a fluid. The calculation is further simplified by assuming an infinite half space for both the sandy bottom and the water column. This is accomplished experimentally by windowing the temporal data to eliminate the reverberations from the facility boundaries.

The insonifying wave was modeled as a plane-wave and the scattering from the buried sphere was calculated for the same backscattered locations as in the measurements. The parameters used for the T-matrix-based numerical model are detailed in Table I. Due to the temporal windowing necessitated by the finite boundaries of the measurement facility, the resulting numerical prediction was processed in a similar manner for direct comparison to the experimental results. The scattered amplitude of the numerical prediction was normalized to a unit insonification amplitude. The calculated

TABLE I. Physical parameter used in T-matrix-based calculation.

Sediment velocity	(1680- <i>i</i> 15.39) m/s
Sediment attenuation	5.95 dB/m at 20 kHz or 0.5 dB/wavelength
Water velocity	1482 m/s
Steel velocity	5790 m/s
Sediment density	1966 kg/m ³
Water density	1000 kg/m ³
Steel density	7900 kg/m ³

scattered frequency response was zero padded with additional frequency bins to obtain the same temporal resolution as the experiment. The frequency response was then inverse Fourier transformed and the temporal response was truncated to have the same vector length as the experiment. The temporal data were then convolved with the free field system response of the measurement and then the results were windowed using the same temporal window as the experimental data. This time domain prediction then followed the same remaining processing as the experimental data.

V. DISCUSSION

A comparison between the above and below critical angle experiments reveals a dramatic difference. For frequencies below 3.5 kHz, the target strength for the below critical angle case is only slightly below that of the above critical angle insonification measurement of 30° (Fig. 2). This is an expected result if scattering due to evanescent wave penetration is playing a dominant role. The approximate 5 dB of reduction in the below versus above critical angle scattering target strengths for the sphere resonance feature at 1.2 kHz is consistent with our estimates of losses due to evanescent decay of the incident field and attenuation within the sediment.

This is arrived at by a straightforward application of a two fluid-layer model (e.g., Officer⁹ or Brekhovskikh¹⁰) where the evanescent acoustic pressure decays exponentially into the sediment (*z* direction, Fig. 1), but is allowed to propagate along the sediment interface (*x* direction, Fig. 1). We have $P = P_0 \exp(-\mu z + ikx \cos \theta)$ and $\mu = k \sqrt{\cos^2 \theta - n^2}$, where P_0 is the peak or rms pressure at the interface, μ and k are the wave numbers in the water and sediment, respectively, θ is the angle of incidence of the plane wave measured up from the interface, and n is the index. The acoustic properties of our lab are well characterized,⁷ the sediment and water phase velocities are 1680 and 1482 m/s, respectively ($n = 1482/1680$). For the purposes of our estimate we need only calculate the differences in the insonifying pressures for the two experiments ($\theta = 30^\circ$ and $\theta = 20^\circ$) at the sphere mid-depth, 30 cm. Here, we assume that the differences in the net scattered signals due to sediment attenuation and differing refractive paths are minor. For the 30° case (nonevanescent case) we compute a relative amplitude of $0.96 P_0$ (−0.35 dB) and for the 20° case (evanescent component) we compute a relative amplitude of $0.61 P_0$ (−4.29 dB). We therefore anticipate a difference in excitation pressure on the buried sphere to be ~4 dB.

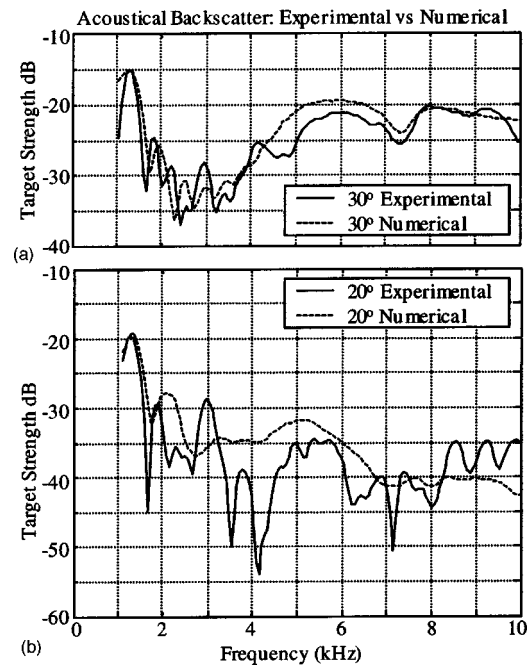


FIG. 3. Comparison of the experimental data with a T-matrix-based numerical solution. (a) Comparison for a 30° insonification of the buried sphere. (b) Comparison for a 20° insonification of the buried sphere. For both comparisons, the experimental data are shown with the solid line and the numerical prediction is shown with a dashed line.

We also compare these experimental results directly with predicted target strengths from T-matrix calculations. Figure 3(a) is a comparison of the numerical and experimental backscattered target strengths for an insonification angle of 30°. We get reasonable agreement over the entire band of the measurement, 1–10 kHz. Figure 3(b) is the comparison of the numerical and experimental backscattered target strengths for the 20° (below critical) insonification. Here again we get reasonable agreement between the predicted and measured target strengths below 3.5 kHz. However, we see a greater divergence of the comparison for frequencies above 3.5 kHz.

This divergence at higher frequencies for the 20° insonification is a result of the minimum detectable target strength for this measurement configuration. The measured acousto-electronic noise floor was below a −50 dB target strength for frequencies above 3 kHz; this should provide enough signal to noise to resolve features at the −40 dB target strength level. However, the compact range processing techniques that were incorporated for these measurements are a more limiting factor. An assessment of the quality of the coherent subtraction process indicates a nominal 35 dB common-mode-rejection of the background field across the band. For frequencies above 5 kHz, this result defines a measurement floor at approximately −40 dB target strength that is the threshold sensitivity of the experiments. Thus at the low levels of the 20 insonification measurements above 5 kHz, we would expect only marginal agreement with the numerical predictions [Fig. 3(b)].

The most important result to consider from these measurements is the data below 3.5 kHz. Here, the backscattered energy for the 20° and 30° insonification angles are directly

comparable, are well above the subtraction floor, and agree well with the T-matrix-based numerical model. These measurements clearly demonstrate how evanescent wave penetration can give rise to significant backscatter levels for large, ~ 0.5 m, buried objects at frequencies below 3.5 kHz.

ACKNOWLEDGMENTS

This work was supported by the Office of Naval Research. We wish to thank Dr. Carl K. Frederickson, Steve W. Liskey, Roger Volk, and Timothy J. Yoder for their participation in the experimental measurements.

- ¹R. Lim, J. L. Lopes, R. H. Hackman, and D. G. Todoroff, "Scattering by objects buried in underwater sediments: Theory and experiment," *J. Acoust. Soc. Am.* **93**, 1762–1783 (1993).
- ²R. Lim, K. L. Williams, and E. I. Thorsos, "Acoustic scattering by a three-dimensional elastic object near a rough surface," *J. Acoust. Soc. Am.* **107**, 1246–1262 (2000).
- ³R. Lim, "Acoustic scattering by a partially buried three-dimensional elas-

tic obstacle," *J. Acoust. Soc. Am.* **104**, 769–782 (1998).

- ⁴H. Schmidt and J. Lee, "Physics of 3-D scattering from rippled seabeds and buried targets in shallow water," *J. Acoust. Soc. Am.* **105**, 1605–1617 (1999).
- ⁵A. Maguer, W. L. J. Fox, H. Schmidt, E. Pouliquen, and E. Bovio, "Mechanisms for subcritical penetration into a sandy bottom: Experimental and modeling results," *J. Acoust. Soc. Am.* **107**, 1215–1225 (2000).
- ⁶W. L. J. Fox and A. Maguer, "Detection of buried objects at low grazing angles: Preliminary experimental results," SACLANTCEN Report No. SN: SR-293, 1998.
- ⁷H. J. Simpson and B. H. Houston, "Synthetic array measurements of acoustical waves propagating into a water-saturated sandy bottom for a smoothed and a roughened interface," *J. Acoust. Soc. Am.* **107**, 2329–2337 (2000).
- ⁸R. Lim, K. L. Williams, and E. I. Thorsos, "Acoustic scattering by a three-dimensional elastic object near a rough surface," *J. Acoust. Soc. Am.* **107**, 1246–1262 (2000), Fig. 4.
- ⁹C. B. Officer, *Introduction to the Theory of Sound Transmission* (McGraw-Hill, New York, 1958), Chap. 5, p. 188.
- ¹⁰L. M. Brekovskikh and O. A. Godin, *Acoustics of Layered Media*, Springer Series on Wave Phenomena, Vol. 5, edited by L. B. Felson (Springer, New York, 1990), Chap. 2, p. 23.

Comment on “Development of panel loudspeaker system: Design, evaluation and enhancement” [J. Acoust. Soc. Am. 106, 2751–2761 (2001)] (L)

Frank Fahy^{a)}

University of Southampton, Southampton SO17 1BJ, United Kingdom

(Received 11 January 2002; accepted for publication 4 October 2002)

This letter concerns the paper “Development of panel loudspeaker system: Design, evaluation and enhancement” [M. R. Bai and T. Huang, J. Acoust. Soc. Am. **109**, 2751–2761 (2001)]. It is suggested that the radiation field generated by the near vibration field induced by a point force acting on the plate has been neglected. It is pointed out that its relative contribution is crucially dependent upon the mechanical loss factor of the panel, for which no data are presented. The conclusion that the radiated power per unit mean square force is independent of frequency neglects the radiation efficiency factor. Other perceived shortcomings of the paper are noted. © 2003 Acoustical Society of America. [DOI: 10.1121/1.1526495]

PACS numbers: 43.38.Ja [SLE]

In a recent paper by Bai and Huang, the authors state that “The ‘coupled’ electrical-mechanical-acoustical system should be solved simultaneously. For the present, this is somewhat impractical from the engineering standpoint.” I am surprised by this statement, since the computational tools for solving fully coupled vibroacoustic problems involving flat, baffled panels coupled to semi-infinite fluid volumes has been commercially available for a number of years. When the calculation has to cover the full audio-frequency range, this is, admittedly, a large computational problem, but it would have been useful to readers to learn the reasons for the authors’ contention of impracticability.

It is stated that “Resonance of flexural motion is encouraged such that the panel vibrates as randomly as possible.” I feel that clarification of this statement is necessary, since the vibration field of a linear elastic structure excited by a single point force is everywhere fully coherent, irrespective of the time history of the force. Perhaps the authors mean that the spatial correlation of the field, evaluated in frequency bands sufficiently large to encompass the resonant response of a number of modes, tends to that of an ideal, two-dimensional diffuse field. It should also be pointed out that, contrary to the implication at the end of Sec. II, the evanescent components of panel vibration associated with other than simply supported boundaries do contribute to panel radiation since they contain supersonic wave number components.

It is surprising that the discussion of radiation is confined to the reverberant component of the vibration field and that no explicit mention is made of the radiation associated with the near vibration field generated by a point force acting on a plate. Interestingly, at frequencies well below the critical frequency (10 214 Hz for the experimental DML), the far field so generated is omni-directional and the associated sound power per unit mean square force is independent of frequency and plate stiffness and inversely dependent on the square of the panel mass per unit area. The contribution of

this source of sound, relative to that of the reverberant vibration field in the plate, increases with the plate loss factor. Control of the panel mechanical loss factor is vital, because the proportion of input power radiated by the reverberant component of panel vibration is crucially dependent upon the ratio of mechanical to radiation loss factor. Unfortunately, the paper informs us of neither the value of panel loss factor employed in the calculations nor that of the experimental plate.

The authors admit that a more rigorous analysis of the problem demands that the frequency dependence of the driving point impedance of a reverberant panel should be taken into account. However, it is likely that the assumption of a frequency-independent, real impedance is reasonable, on two grounds. First, the average of the driving point impedance of a finite plate over a frequency band containing a number of resonance frequencies equals that of the infinite plate. Second, the effects of the back emf in the coil, which reduces the current from a constant voltage amplifier at plate resonances, together with its inertial impedance, which may become comparable with that of the plate at resonances, tend to smooth out the effect of resonant peaks in plate admittance.

The statement below Eq. (23), that either small bending stiffness *or* small mass per unit area should be selected for small panels, is rather puzzling. It would have been useful to point out at this stage that the asymptotic density of flexural modes is proportional to the inverse of the expression for f_0 given by Eq. (23), which is another reason for keeping f_0 as small as possible.

As a matter of good scientific practice, the value of the ratio of bending stiffness to mass per unit area should not be quoted to five significant figures. We are not told how the material properties of the polyurethane panel were estimated (and we should be), but even the most highly refined experimental estimates cannot produce such precision.

It is stated in Sec. II that the radiated power per unit force should be “constant” (presumably meaning “independent of frequency”), because the point impedance is independent of frequency, and so therefore is the driving point

^{a)}Electronic mail: frank.fahy@care4free.net

velocity. Even if the space-averaged mean square reverberant field velocity were consequently independent of frequency (which is the case only for frequency-independent loss factor), the sound power is proportional to the product of the space-average mean square velocity and the radiation efficiency, and the latter is certainly not independent of frequency below the critical frequency.

The results presented in Fig. 12 are somewhat worrisome. The DML radiation spectrum in Fig. 12(a) shows a “peak” at just below 20 kHz, which is higher than substantial portions of the curve *within* the stated bandwidth of excitation (0–16 kHz). Is this an indication of nonlinearity of response? In Fig. 12(b), the experimental curves for both forms of loudspeaker exhibit a sharp minimum at about 530 Hz. Is this an artifact of the test conditions—interference from a floor reflection perhaps? If so, the claim to have minimized the effect of room response cannot be upheld. The authors make no comment about the broad radiation peak in the vicinity of 9 kHz, but the proximity of the estimated critical frequency is surely significant.

The paper contains a number of mathematical errors.

The factor 2π is missing from the denominator of Eq. (9) and the leading sign should not be negative. The exponents in both Eqs. (9) and (10) lack a negative sign [the authors use $+j$ in the time exponent in Eq. (3)]. The panel mobility quoted in Table I has the units inverted.

Irrespective of the foregoing comments, I suggest that the claim made in the abstract that “Panel speakers are investigated...” is too sweeping, since only one particular form of DML was studied. The enigmatic conclusion that “To further improve the efficiency of panel speakers, planar radiators without resort to the mechanism of flexural waves should be sought in future” appears to conflict with the authors’ comments that the generation of many flexural modes produces the beneficial effects of suppression of beaming through “diffuse” radiation. Elaboration of this intriguing proposal is eagerly awaited.

¹M. R. Bai and T. Huang, “Development of panel loudspeaker system: Design, evaluation and enhancement,” *J. Acoust. Soc. Am.* **109**, 2751–2761 (2001).

Acoustic and vibration background noise in the collapsed structure of the World Trade Center (L)

Thomas B. Gabrielson,^{a)} Matthew E. Poese, and Anthony A. Atchley
The Pennsylvania State University, P.O. Box 30, State College, Pennsylvania 16804

(Received 12 April 2002; revised 13 August 2002; accepted 23 August 2002)

Measurements of acoustic and vibration background noise were made on 18 September 2001 at the southern edge of the World Trade Center collapse. Sensors were deployed in a configuration reasonable for survivor search and near an on-going recovery operation and heavy debris removal. Geophones were placed on steel beams that extended into a deep void and a microphone was lowered below ground level into a pocket in the rubble. Even in what appeared at ground level to be a high-noise environment, weak or distant taps and bangs generated either by the authors or by recovery personnel produced distinct signals from the microphone and geophones. © 2003 Acoustical Society of America. [DOI: 10.1121/1.1513799]

PACS numbers: 43.50.Rq, 43.50.Yw [SLE]

In structure collapses caused by severe storms, earthquakes, floods, or explosions, one of the primary goals of Urban Search and Rescue¹ (USAR) teams is the detection and location of survivors. Detection of acoustic and vibration signals provides two plausible techniques for this mission either through passive “listening” or through active signaling and listening for a response. However, does the high ambient noise level typical of a collapsed structure with an on-going search/rescue/recovery operation prevent the use of acoustic or vibration sensors for detection of survivors? Without some understanding of the level and character of the background acoustic and vibration noise, it is difficult to develop effective systems² for detection and localization.

This letter presents measurements of the acoustic and vibration background at the World Trade Center collapse site. Because of severe access limitations, only one microphone and three geophones were deployed and their signals recorded at a single location. However, the measurements were taken with sensors deployed in a configuration reasonable for survivor search near on-going recovery operations and heavy debris removal. There were at least 50 USAR/FDNY/NYPD³ personnel working within 50 m of the measurement site and at least three heavy-lift cranes were operating continuously.

During the recording period from 11:30 to 13:00 EST on 18 September 2001, there were significant changes in both the acoustic and vibration background noise levels. Shoring timbers were being cut with a gasoline-powered saw 8 m away to support an active recovery operation 20 m away. At the recovery location, 30 to 40 rescue personnel were pounding the shoring material into place, running an air-hammer, and moving material around the site. The nearest heavy-lift crane (50 m away) repositioned several times and extracted several loads of steel beams. Figure 1 shows the location of the measurement site (near the northwest corner of the heavily damaged Bankers Trust building) and the local noise sources.

The bare microphone cartridge was soldered directly to one end of a length of RG174 coaxial cable with power

supplied by battery from the other end. The microphone element was lowered 2 to 3 m below ground level into a pocket in the rubble through an opening about 1 m by 0.5 m. The geophones were placed on steel box beams (formerly vertical structural-support members from the load-bearing exterior walls of the South Tower) that extended into a deep void loosely filled with rubble (see Fig. 2).

The microphone was a Panasonic WM62A electret capsule (6 mm diameter, 2.7 mm long) with a nominal response of 5 mV/Pa. The microphone response was determined by comparison with a reference microphone (B&K 4136) in a plane-wave tube with sinusoidal excitation swept from 25 to 10 000 Hz. Because the directional characteristics of the acoustic field in the rubble cavity were unknown, no attempt was made to correct the higher frequency response of the microphone for its orientation with respect to the field.

The vibration sensors were Geospace Corporation GS14L3 geophones with 28 Hz resonance and a nominal above-resonance velocity response of 11 V/(m/s). The individual on-axis acceleration responses of the geophones were determined by comparison with a reference accelerometer (Kistler 8630B5) on a shaker table with sinusoidal excitation swept from 10 to 1100 Hz. The responses were fit with single-degree-of-freedom response functions and subsequently applied to convert the measured voltage to acceleration.

The data were recorded using a Sony TCD-D8 DAT recorder and all of the response functions were applied to the entire sensor/recorder/playback system. The DAT set the noise floor for the geophones (at about 0.5 nm/s rms per root hertz noise-equivalent velocity above resonance—about 0.3 μ g rms per root hertz at 1000 Hz). The electret cartridge self-noise set the noise floor for the microphone measurements at about 8 μ Pa rms per root hertz above 1000 Hz.

Figure 3 illustrates the range of acoustic noise measured with the below-ground microphone. The lower curve is an averaged⁴ 16-s sample of the quietest period and the upper curve is an averaged 16-s sample of the noisiest period. At the higher frequencies, the pressure spectral density of the quiet noise curve reached the microphone noise floor (shown

^{a)}Electronic mail: tbg3@psu.edu

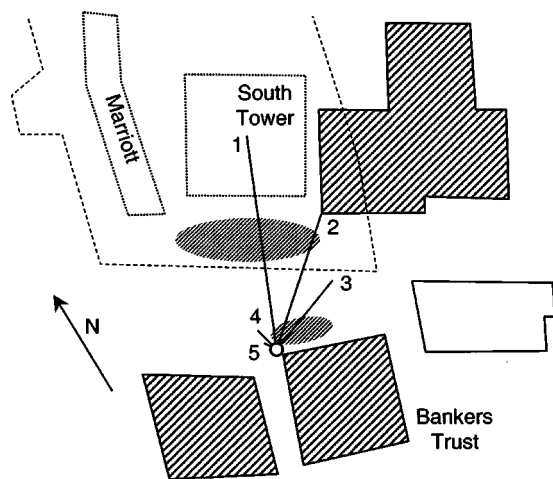


FIG. 1. Location of the measurement site (open circle) near the northwest corner of the Bankers Trust building. The shaded ellipses are deep collapse cavities. Reference distances are indicated by numbers: (1) 120 m to the center of the South Tower, (2) 80 m to the southwest corner of World Trade Center Four, (3) 50 m to the nearest (operating) heavy crane, (4) 20 m to an active recovery operation, and (5) 8 m to a gasoline-powered wood saw in intermittent operation. The dashed line shows the location of the slurry wall that surrounds the foundation area for the two towers; dotted lines outline completely collapsed structures; and shading indicates structures with major damage.



FIG. 2. Orientation of the steel box beams at the measurement location with a view to the north-northeast toward the South Tower. Two 12 by 14 in. beams are prominent in the foreground. These beams extend diagonally downward into a deep collapse cavity. Just beyond these beams are many smaller box beams. The microphone was lowered into the cavity on the far side of the larger beams in the foreground.

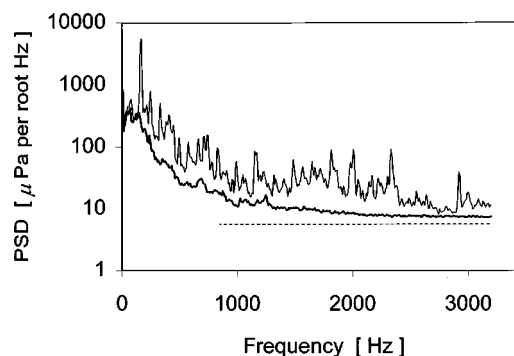


FIG. 3. Pressure spectral density (PSD—expressed in μPa rms per root hertz) measured with the microphone. The upper curve represents measurements taken during the period of highest noise while the lower (darker) curve represents the lowest-noise period. The low-noise curve reaches the self-noise level (dashed line) of the microphone above 2000 Hz.

by the dashed line). Although the acquisition system recorded frequency components of the signals to 20 kHz, the results are shown to 3.2 kHz for two reasons: (1) audible detection is the most important for emergency-response personnel, and (2) the spectra of tapping and banging sounds⁵ contain very little energy above 3 kHz in large structures.

Figure 4 shows the range of vibration noise measured with one of the geophones. As in Fig. 3, the upper and lower curves are averaged 16-s samples of the highest and lowest noise levels recorded. At the highest frequencies, the acquisition system noise (shown by the dashed line) limited the measurement.

Figure 5 shows a typical spectrogram from one of the noisier periods at the WTC site. Several features are of special note. There is a persistent pattern of horizontal lines through the lower section of the geophone spectrogram (lower spectrogram in Fig. 5). While the segment shown in Fig. 5 is only 4 s long, this pattern persisted throughout the measurement period. In principle, this stable pattern of background noise could be removed in real time; however, it did not seem to inhibit aural identification of impulsive events (like banging, tapping, or hammering). There were also transient but repeated events. One transient event in Fig. 5 that starts at 2 s was the result of nearby operation of a gasoline-

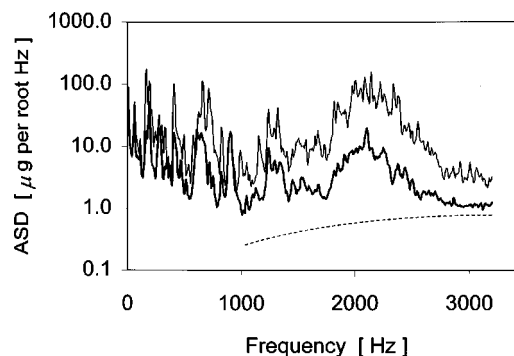


FIG. 4. Acceleration spectral density (ASD—expressed in μg rms per root hertz) measured with a geophone on one of the 12 by 14 in. steel box beams. The upper curve represents the highest-noise period and the lower (darker) curve represents the lowest-noise period. Above 3000 Hz, the low-noise curve reaches the noise floor of the data acquisition system (shown by the dashed line).

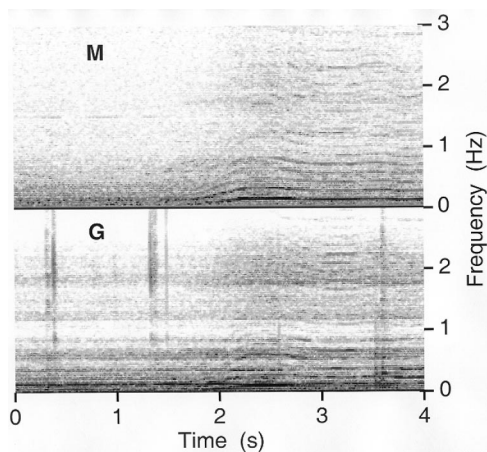


FIG. 5. Spectrograms from the microphone (M) and one geophone (G) for a period of high background noise. Frequency (from a few Hz to 3000 Hz) is shown on the vertical scale and time is shown on the horizontal scale. The vertical lines on the geophone spectrogram are impulselike events—bangs and taps—at 0.4, 1.3, and 3.6 s. During this period, a gasoline-powered saw was started. The harmonic structure of the noise from the saw is clearly seen in the microphone spectrogram between 2 and 4 s. The impulselike events are rarely seen in the microphone spectrograms.

powered saw being used to cut shoring timbers. This event is particularly evident on the microphone spectrogram (upper spectrogram in Fig. 5). The harmonic pattern of the spectrum of the sound from the saw is clear. Furthermore, the fundamental and harmonics shifted up as the speed of the blade was increased, then the frequencies shifted down as the blade slowed entering the wood. Impulsive events that sound like banging or tapping appear as vertical lines in the spectrogram and several of these are seen in the geophone spectrogram.

Even in what appeared at ground level to be a high-noise environment, the microphone lowered into a cavity and the geophones placed on solid structural elements showed relatively low background noise signals above a few hundred hertz. The rms background sound indicated by the microphone was well below $100 \mu\text{Pa}$ per root hertz above 1000 Hz even through high-noise periods; the rms low-noise-period background sound approached $10 \mu\text{Pa}$ per root hertz. These results support the strategy of lowering microphones into collapsed structures in addition to listening for survivor signals from the surface.⁶ Placing the microphone in voids in the collapsed structure reduces much of the surface-produced airborne noise.

At frequencies greater than a few hundred hertz, the rms acceleration spectral density of the background noise signal from the geophone was between 2 and $20 \mu\text{g}$ per root hertz during the low-noise periods. Rejection of airborne noise by the geophone along with good propagation through solid structural elements resulted in audibly distinct signals (listening with headphones) from weak and distant taps and bangs. Consequently, well-placed geophones may be useful for detection of survivors in large-building collapses beyond the ranges expected for present systems.⁷

Gentle tapping on nearby beams was clearly audible when listening to the geophone signals even when difficult to see from a time-series or spectrum display. Prior to making measurements at the World Trade Center site, the geophones

were tested in a six-story parking structure near Times Square in Manhattan. The parking structure is a simple, steel beam structure with reinforced concrete floors. Vertical columns (8 by 8 in. steel I-beams⁸) on a grid with spacing that varied from 5 to 7 m supported horizontal beams (5 by 14 in. steel I-beams) at each floor with the reinforced concrete slabs poured on corrugated steel on the horizontal-beam grid work. With the geophones on vertical beams at ground level, other beams and floor areas were tapped with a small piece of concrete rubble. This tapping was clearly audible throughout the structure as far as the sixth floor vertically (the uppermost floor—15 m up) and displaced 30 m horizontally from the geophone location on the ground floor. The acceleration spectral density of the background noise at the parking garage was similar to the lower spectral density (the background noise) shown in Fig. 4 with frequent, impulsive signals that protruded above the quiet background noise.

Some of the tonal pattern in the spectra of the background noise was the result of characteristics of the source mechanisms but an important contributor to the apparent spectral structure from the geophones was the natural filtering of the steel-beam network to which the geophones were attached. This observation was evident in that spectra of stronger bangs and impulse-like sounds were shaped in a manner similar to the spectrum of the persistent background noise. A transient event would produce greater background noise at the frequencies of the background “lines.” In effect, the background noise provides a crude diagnostic of the filtering characteristics of the structure to which the sensor is attached.

ACKNOWLEDGMENTS

D’Arcy Morgen and Chris Tillery (National Institute of Justice, Department of Justice) arranged for access to the site and liaison with search-and-rescue teams on site. Geospace Corporation (Houston, TX) donated and expedited shipment of geophones. James McConnell (Acoustech Corporation, State College, PA) provided sensors and cables. Ray Wakeland (Graduate Program in Acoustics) worked with other members of the team overnight to construct equipment. On short notice, Radio Shack (State College and Times Square stores) located and delivered numerous items of electronics. The State College office of Trailways expedited a no-cost shipment of material to New York City. The Pennsylvania Urban Search and Rescue team (PA Task Force 1) provided valuable information regarding search and rescue procedures and operation of standard USAR equipment. Various NYPD, FDNY, and USAR personnel expedited access and assisted in many ways. The Office of Naval Research has provided continued support for development of acoustic systems and the resulting infrastructure that made fast reaction possible.

¹ As of this writing, there are 28 USAR teams in the United States. These teams are coordinated nationally by the Federal Emergency Management Agency (FEMA) but each team has a home state. The teams must be able to mobilize within 6 h and function autonomously for 72 h.

² There is a commercial acoustic and vibration detection system that is part of the standard equipment list for USAR teams. This letter does not address the current performance of any commercial system; rather, the intent

is to provide basic design data for improvements in employment of existing systems or for development of alternative systems.

³Fire Department of New York (FDNY) and New York Police Department (NYPD).

⁴All data shown in Figs. 3 and 4 are rms averages of 64 samples of 0.25-s duration.

⁵Throughout this paper, banging or tapping refers either to test sounds made by us or to similar noises produced by the on-site recovery teams.

⁶The observation is often made that survivors trapped in collapsed structures hear the rescuers well before the rescuers hear the survivors. See

FEMA National US&R Response System Rescue Specialist Training Manual, SM Appendix A.

⁷Reference 6, p. 11, cites useable ranges of 25 ft for acoustic detection and 75 ft for vibration detection for conventional systems. This does not imply that conventional systems are deficient; this manual assumes deployment in more common small-to-medium structure collapses. It is certainly possible that a change in employment tactics is more important than a change in the detection system itself.

⁸Commercial structural elements are sized in inches and this convention is followed herein.

The role of envelope beat cues in the detection and discrimination of second-order amplitude modulation (L)

Christian Füllgrabe^{a)}

Laboratoire de Psychologie Expérimentale—UMR CNRS 8581, Institut de Psychologie, Université René Descartes—Paris 5, 71, Av. Edouard Vaillant, 92774 Boulogne-Billancourt, France

Christian Lorenzi

Laboratoire de Psychologie Expérimentale—UMR CNRS 8581, Institut de Psychologie, Université René Descartes—Paris 5, 71, Av. Edouard Vaillant, 92774 Boulogne-Billancourt, France
and Institut Universitaire de France

(Received 3 January 2002; revised 7 September 2002; accepted 23 September 2002)

The present study extends previous work from Lorenzi *et al.* [J. Acoust. Soc. Am. **110**, 2470–2478 (2001)] by investigating the respective contribution of two temporal cues (fast modulation sideband and slow envelope beat cues) to the detection and discrimination of “second-order” sinusoidal amplitude modulation (SAM). Second-order SAM detection and rate discrimination abilities were measured at low beat rates ($f'_m \leq 128$ Hz) with a “carrier” modulation rate fixed at a high value ($f_m = 256$ Hz). The second-order SAM data were compared with first-order SAM detection and rate discrimination thresholds measured in similar conditions at rates f_m between 1 and 256 Hz. The results showed that (1) through 64 Hz, first- and second-order SAM detection thresholds increased similarly when stimulus duration decreased from 2 s to 250 ms, whereas first-order SAM detection thresholds remained unaffected by changes in duration when $f_m \geq 128$ Hz, and (2) through 32 Hz, first- and second-order SAM rate discrimination thresholds were similar and substantially lower than first-order SAM rate discrimination thresholds measured at $f_m \geq 128$ Hz. These data demonstrate that the perception of second-order SAM is mainly based on the slow envelope beat cues. They also suggest a substantial contribution of the slow envelope beat cues appearing at the output of modulation filters tuned to or near f_m to the perception of second-order SAM. © 2003 Acoustical Society of America. [DOI: 10.1121/1.1523383]

PACS numbers: 43.66.Ba, 43.66.Dc, 43.66.Mk [NPV]

I. RATIONALE

In a recent study (Lorenzi *et al.*, 2001a), sensitivity to multicomponent temporal envelopes was assessed by measuring detection thresholds for “second-order” SAM, that is sinusoidal modulation applied to the *modulation depth* of a SAM noise. The SAM noise (or “first-order” SAM) acted as a “carrier” stimulus of rate f_m , and the sinusoidal modulation of the SAM-noise modulation depth (of rate f'_m) generated (i) two sidebands in the stimulus’ modulation spectrum at rates $f_m - f'_m$ and $f_m + f'_m$, and (ii) a beat at a rate f'_m in the stimulus’ temporal envelope. “Second-order” TMTFs relating second-order modulation detection thresholds to f'_m were lowpass in shape, and parallel measurements of masked modulation detection thresholds revealed that second-order SAM detection probably depended on the detection of the beat in the envelope at rate f'_m . There was no spectral energy at the beat rate in the modulation spectrum of the “physical” stimulus. Still, the modulation filterbank (MFB) model—which assumes that a bank of broadly tuned filters decomposes the envelope (e.g., Dau *et al.*, 1997)—accounted for these second-order SAM detection data provided that auditory nonlinearities introduce an audible distortion product in the internal representation of the sound’s envelope at the beat rate f'_m (Sheft and Yost, 1996; Shofner *et al.*, 1996; Moore

et al., 1999). An additional set of studies (Lorenzi *et al.*, 2001b) further investigated the role of envelope beat cues in second-order SAM detection by measuring second-order SAM detection thresholds with a 2-Hz-wide narrow-band noise carrier. The results showed that, when $f_m = 256$ Hz, the masking effect produced by the intrinsic statistical fluctuations of the narrow-band noise carrier (≤ 2 Hz) was mostly restricted to the lowest second-order modulation rates ($f'_m \leq 16$ Hz). In agreement with the distortion hypothesis, this indicated that detection of spectral energy at f'_m contributed to second-order modulation detection. Nevertheless, these slow fluctuations did *not* abolish the ability to detect second-order modulation: whereas they nearly abolished the ability to detect first-order modulation at similar rates. This was consistent with previous data suggesting that the distortion product at the beat rate was relatively weak (Moore *et al.*, 1999), but also revealed that *additional* envelope cues contributed to second-order SAM detection. The present study aimed at determining which cues are actually used by listeners in second-order SAM perception.

Fast modulation sideband cues (near f_m) might have been involved in these tasks. However, given the poor modulation frequency selectivity assumed by the MFB model (e.g., Lorenzi *et al.*, 2001a), sidebands would not be resolved at most second-order modulation rates. On the other hand, slow envelope beat cues might also have appeared at the output of modulation filters tuned to or near the carrier rate

^{a)}Electronic mail: christian.fullgrabe@psycho.univ-paris5.fr

f_m , due to the interaction of the carrier and sideband components in these broadly tuned filters. The purpose of the present study was to extend previous work from Lorenzi *et al.* (2001b) by determining the respective contribution of those (slow) envelope beat cues (at f'_m) and (fast) modulation sideband cues (near f_m) to second-order SAM perception. To address this issue, second-order SAM detection and rate discrimination thresholds were measured at low beat rates ($1 \leq f'_m \leq 128$ Hz and $4 \leq f'_m \leq 32$ Hz in the detection and discrimination experiments, respectively) with a carrier rate (in the modulation domain) fixed at a high value, $f_m = 256$ Hz. A 9-kHz pure-tone carrier was used in all experiments. As shown previously by Viemeister (1979) and Sheft and Yost (1990) for gated noise carriers, a decrease in stimulus duration does not affect first-order SAM detection thresholds for $f_m > 125$ Hz. By contrast, a substantial increase in first-order SAM detection thresholds is observed at the lowest rates ($f_m \leq 16$ Hz) for the shortest duration tested. Thus, a decrease in stimulus duration should yield an increase in second-order SAM detection thresholds if listeners do use slow envelope beat cues (wherever they might originate from), but should not affect second-order SAM detection thresholds if listeners do use (fast) modulation sideband cues (near f_m). Previous studies (e.g., Lee, 1994) also showed that the just-noticeable change in the modulation rate of first-order SAM increases with the reference modulation rate. Thus, second-order SAM rate discrimination thresholds measured at low beat rates ($4 \leq f'_m \leq 32$ Hz) should be (i) similar to those measured with first-order SAM at common rates, and (ii) lower than first-order SAM rate discrimination thresholds measured at high rates (e.g., $f_m \geq 128$ Hz) if listeners do use slow envelope beat cues. On the other hand, second-order SAM rate discrimination thresholds measured at low beat rates should be similar to those measured with first-order SAM at high rates if listeners do use (fast) modulation sideband cues (near f_m). The present paper reports these two detection and discrimination experiments.

II. LISTENERS, STIMULI, AND METHODS

Four normal-hearing listeners (ages ranged from 22 to 27 years), participated in the experiments. Modulation was applied over the full duration of a 9-kHz pure-tone carrier. All stimuli were equivalent in energy (rms) and delivered binaurally via Sennheiser HD 565 earphones at 75 dB SPL. In the detection tasks, stimulus duration was fixed at 2000, 500, or 250 ms including 50-ms rise/fall times shaped using a raised-cosine function. In the discrimination tasks, the duration of each stimulus (standard and target) was chosen at random from an interval ranging from 2 to 2.5 s, including 50-ms rise/fall times. The randomization of the duration of the stimuli, carrying always an integer number of first-order modulation cycles (for first-order SAM discrimination task) or second-order modulation cycles (for second-order SAM discrimination task), was used to prevent listeners from performing the task by counting the number of cycles. In all experiments, the interstimulus interval was fixed at 1 s.

The reader is referred to a previous publication (Lorenzi *et al.*, 2001b) for details of the stimulus generation and pro-

cedures used in the detection tasks. Briefly, first- and second-order SAM detection thresholds were obtained using a two-interval, two-alternative forced choice (2I, 2AFC), two-down, one-up adaptive procedure with feedback. In the first-order SAM detection task, the starting phase of the modulation was randomized on each interval, and modulation depth m at threshold was measured at rates f_m of 1, 2, 4, 8, 16, 32, 64, 128, and 256 Hz. In the second-order SAM detection task, the starting phases of first- and second-order modulations were identical and randomized on each interval. Modulation depth m' at threshold was measured with the carrier modulation depth m fixed at 0.5, and the carrier modulation rate f_m fixed at 256 Hz; the second-order modulation rate f'_m was fixed at 1, 2, 4, 8, 16, 32, 64, or 128 Hz. For each listener and for each rate, thresholds presented here are based upon three estimates.

First-order modulation rate discrimination thresholds were also obtained using a 2I, 2AFC procedure. In a typical block, the listeners' task was to discriminate a standard stimulus having a fixed rate (referred to as the reference first-order modulation rate f_m , fixed at either 4, 8, 16, 32, 128, or 256 Hz) from a target stimulus having a variable rate of $f_m + \Delta f_m$, by indicating the interval with the higher rate. In both stimuli, the starting phase of the modulation was randomized on each interval. In each trial, the standard and target stimuli were successively presented in random order to the listener. Over a given block, the SAM depth m was held constant at +6, +12, or +24 dB above individual SAM detection thresholds (assessed in the detection tasks at the same rate f_m for a stimulus duration of 2 s). For the target stimulus, the modulation rate was varied using a two-down, one-up stepping rule that estimates the difference limen Δf_m necessary for 70.7% correct discrimination. Feedback about the correct interval was given after each trial. The step size of the variation corresponded initially to a factor of 1.26, and was reduced to 1.12 after the first two reversals. The mean of the last 10 reversals in a series of 16 reversals was taken as the threshold estimate for that block (in Hz). For each listener and each reference modulation rate, thresholds presented here are based upon three estimates.

Difference limens for rates of second-order sine modulators were obtained using an identical procedure to that used to gain difference limens for rates of first-order sine modulators. All stimuli were modulated at a rate f_m fixed at 256 Hz (with $m = 0.5$) and modulation depth was sinusoidally modulated at a given second-order modulation rate (with $m' = 0.5$). In each trial of a typical block, the listeners' task was to discriminate a standard stimulus having a fixed second-order modulation rate (referred to as the reference modulation rate f'_m , fixed at either 4, 8, 16, or 32 Hz) from a target stimulus having a variable second-order modulation rate of $f'_m + \Delta f'_m$, by indicating the interval with the higher rate. Consequently, the target could be discriminated from the standard as soon as *any* change in modulation rate was heard. In both stimuli, the starting phases of first- and second-order modulations were identical and randomized on each interval.

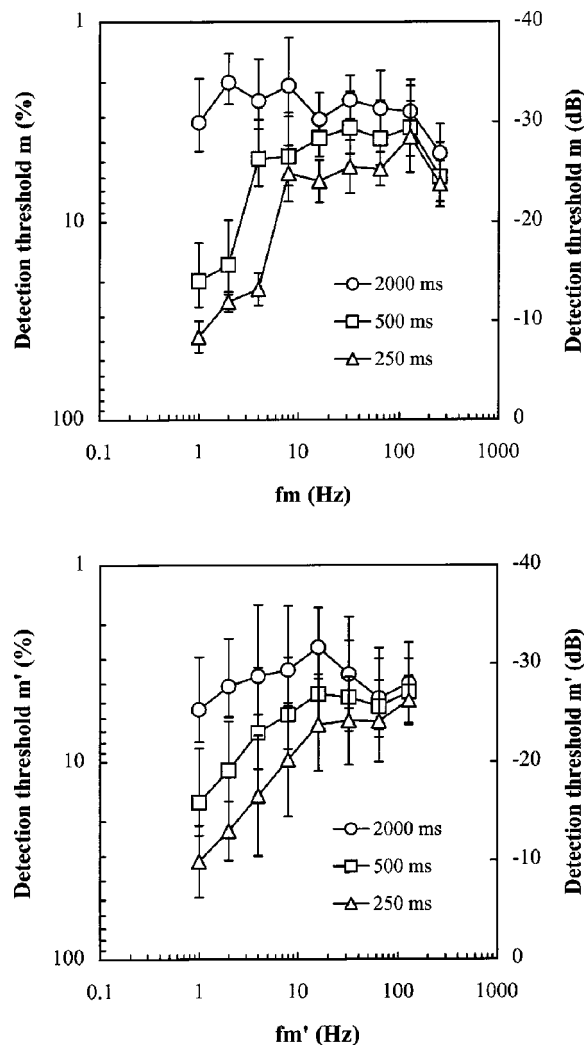


FIG. 1. Mean first- and second-order temporal modulation transfer functions (TMTFs) for four normal-hearing listeners using a 9-kHz pure-tone carrier with stimulus durations of 250 (triangles), 500 (squares), and 2000 ms (circles). The upper panel shows first-order modulation depth at threshold [m , in % (left ordinate) and in dB (right ordinate)] as a function of first-order modulation rate f_m . The lower panel shows second-order modulation depth at threshold [m' , in % (left ordinate) and in dB (right ordinate)] as a function of second-order modulation rate f'_m .

III. RESULTS

Since the pattern of results for each stimulus duration are similar across listeners, mean first- and second-order TMTFs are shown in Fig. 1. In agreement with previous studies using high-frequency sine carriers (e.g., Lorenzi *et al.*, 2001b), first-order modulation detection thresholds measured with a duration of 2 s are roughly constant up to $f_m = 256$ Hz. As shown previously by Viemeister (1979) and Sheft and Yost (1990), a decrease in duration from 2 s to 250 ms does not affect the present first-order modulation detection thresholds for $f_m \geq 128$ Hz, but yields an abrupt and substantial increase in first-order modulation detection thresholds at the lowest rates tested ($f_m \leq 8$ Hz). This results in high-pass TMTF shapes for duration of 500 and 250 ms. The constant thresholds obtained below 8 Hz and for the shortest durations are probably due to the fact that less than a full modulation cycle is presented to the listeners. At such low rates, the drop in sensitivity is important. For instance, at

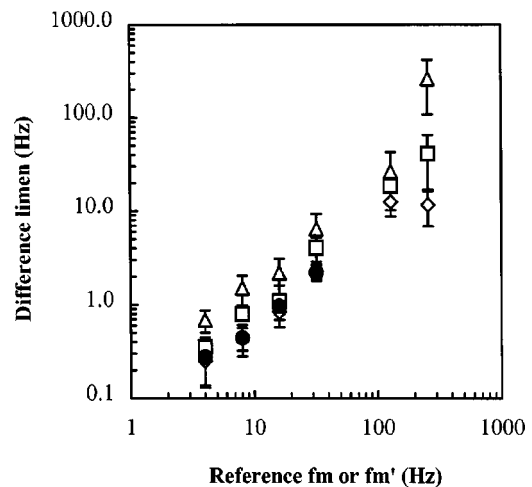


FIG. 2. Mean first- and second-order AM rate discrimination data for four normal-hearing listeners, using a 2–2.5-s-long 9-kHz pure-tone carrier. First-order AM rate difference limens Δf_m (in Hz) measured for modulation depths of +6 (triangles), +12 (squares), and +24 dB (diamonds) above detection threshold are plotted along with second-order AM rate difference limen $\Delta f'_m$ (filled circles) as a function of reference first- and second-order modulation rate f_m and f'_m , respectively.

$f_m = 1$ Hz, a decrease in duration from 2 s to 250 ms yields a threshold increase by a factor of 11, compared to an increase by only a factor of 3 at $f_m = 8$ Hz. A similar trend is observed in the second-order modulation detection data. Figure 1 shows that second-order modulation detection thresholds measured for a duration of 2 s are roughly constant up to $f'_m = 128$ Hz. As for first-order modulation detection thresholds, second-order modulation detection thresholds measured at the lowest second-order modulation rates ($f'_m \leq 16$ Hz) increase when duration decreases from 2 s to 250 ms, resulting in high-pass second-order TMTF shapes for the shortest durations. Unlike first-order modulation detection data, the decrease in duration yields a progressive increase in second-order modulation detection thresholds instead of an abrupt one. Moreover, the effect of duration appears less important for second-order modulation than for first-order SAM: At $f'_m = 1$ Hz, a decrease in duration from 2 s to 250 ms yields an increase in second-order modulation detection threshold by a factor of 6. Although the ability to detect second-order modulation is not completely abolished at $f'_m = 1$ Hz for a duration of 250 ms, mean thresholds drop to about 32% (individual thresholds ranging from 16% to 42%), getting close to the worst threshold that can be measured for second-order modulation (i.e., $m' = 50\%$). This suggests that the weaker effect of duration on second-order modulation detection thresholds may be due to a floor effect.

Mean first- and second-order modulation rate discrimination thresholds (Δf_m and $\Delta f'_m$) are plotted as a function of the reference first- or second-order modulation rate (f_m or f'_m) in Fig. 2. Overall, mean first-order modulation rate discrimination thresholds (Δf_m) increase when modulation depth m decreases. This effect is relatively small up to $f_m = 128$ Hz, but becomes stronger at $f_m = 256$ Hz. For each SAM depth, the mean first-order modulation rate discrimination thresholds increase with increasing reference first-order modulation rate f_m . Overall, first-order modulation rate dis-

crimination thresholds are lower than 3 Hz when f_m is below 32 Hz, but range from 10 to 200 Hz when f_m is 128 or 256 Hz. For the highest SAM depth tested (24 dB above detection threshold), our results are in agreement with the study by Lee (1994) on discrimination of SAM rate with tonal carriers. Figure 2 also shows that, as for first-order modulation, the mean second-order modulation rate discrimination thresholds ($\Delta f'_m$) increase with increasing reference second-order modulation rate f'_m . In agreement with Lee (1994), Weber's law holds for the discrimination rate of both first- and second-order modulation rate when f_m and f'_m are strictly below 128 Hz: $\Delta f'_m/f'_m$ and $\Delta f'_m/f'_m$ range approximately between 0.05 and 0.07 for both first-order SAM presented at +24 dB above detection threshold and second-order SAM. Figure 2 finally shows that (i) second-order modulation rate discrimination thresholds are similar to first-order modulation rate discrimination thresholds measured at common modulation rates through 32 Hz with a SAM depth of +24 dB above threshold, and (ii) second-order modulation rate discrimination thresholds are substantially lower than first-order modulation rate discrimination thresholds measured at $f_m \geq 128$ Hz at each SAM depth.

IV. DISCUSSION AND CONCLUSIONS

The first set of experiments assessed the effects of stimulus duration on first- and second-order SAM detection. Through 64 Hz, first- and second-order modulation detection thresholds increased similarly when duration decreased from 2 s to 250 ms, whereas first-order modulation detection thresholds at $f_m \geq 128$ Hz remained unaffected by changes in duration. The second set of experiments assessed modulation rate discrimination thresholds for first- and second-order SAM. For each SAM depth tested, first-order modulation rate discrimination thresholds increased with increasing reference first-order modulation rate f_m . A similar trend was observed in the second-order modulation data: Discrimination thresholds increased with increasing reference second-order modulation rate f'_m . The data also showed that, through 32 Hz, first- and second-order modulation rate discrimination thresholds were similar and substantially lower than first-order modulation rate discrimination thresholds measured at $f_m \geq 128$ Hz.

These results therefore demonstrate that in the study of Lorenzi *et al.* (2001b): (i) Slow envelope beat cues contributed mainly to the detection of second-order SAM, and (ii) consistent with recent estimates of modulation frequency selectivity, fast sideband cues did not play any role in the de-

tection of second-order SAM. The present results reveal that these conclusions also hold for second-order SAM rate discrimination. It is important to note that, at the lower second-order modulation rates tested, a decrease in duration yielded a substantial increase in second-order SAM detection thresholds (the highest mean threshold being about 32%). This contrasts with the detection data obtained by Lorenzi *et al.* (2001b) using a masking paradigm. In this study, the slow fluctuations of the narrow-band noise carrier yielded a much smaller increase in second-order SAM detection thresholds (the highest masked thresholds being about 10% for $f_m = 256$ Hz). These data, however, remain compatible with the MFB model if (i) the amplitude of the distortion product at the envelope beat rate f'_m is weak (as suggested by Moore *et al.*, 1999), and (ii) salient envelope beat cues also appear at the output of modulation filters tuned to or near the carrier rate f_m . In Lorenzi *et al.* (2001b), the slow fluctuations of the noise carrier *only* masked the weak distortion product at f'_m , but left intact the envelope beat cues appearing in the high-frequency region of the internal modulation spectrum (near f_m). In the present study, a decrease in stimulus duration affected *any* envelope beat cues appearing in the internal modulation spectrum, causing therefore a greater drop in second-order SAM sensitivity.

ACKNOWLEDGMENT

This work was supported by the Cognitique program (MENRT).

- Dau, T., Kollmeier, B., and Kohlrausch, A. (1997). "Modeling auditory processing of amplitude modulation: I. Modulation detection and masking with narrow-band carriers," *J. Acoust. Soc. Am.* **102**, 2892–2905.
- Lee, J. (1994). "Amplitude modulation rate discrimination with sinusoidal carriers," *J. Acoust. Soc. Am.* **96**, 2140–2147.
- Lorenzi, C., Soares, C., and Vonner, T. (2001a). "Second-order temporal modulation transfer functions," *J. Acoust. Soc. Am.* **110**, 1030–1038.
- Lorenzi, C., Simpson, M. I. G., Millman, R. E., Griffiths, T. D., Woods, W. P., Rees, A., and Green, G. G. R. (2001b). "Second-order modulation detection thresholds for pure-tone and narrow-band noise carriers," *J. Acoust. Soc. Am.* **110**, 2470–2478.
- Moore, B. C. J., Sek, A., and Glasberg, B. R. (1999). "Modulation masking produced by beating modulators," *J. Acoust. Soc. Am.* **106**, 908–918.
- Sheft, S., and Yost, W. A. (1990). "Temporal integration in amplitude modulation detection," *J. Acoust. Soc. Am.* **88**, 796–805.
- Sheft, S., and Yost, W. A. (1996). "Modulation detection interference with two-component masker modulators," *J. Acoust. Soc. Am.* **102**, 1106–1112.
- Shofner, W. P., Sheft, S., and Guzman, S. J. (1996). "Responses of ventral cochlear nucleus units in the chinchilla to amplitude modulation by low-frequency, two-tone complexes," *J. Acoust. Soc. Am.* **99**, 3592–3605.
- Viemeister, N. F. (1979). "Temporal modulation transfer functions based upon modulation thresholds," *J. Acoust. Soc. Am.* **66**, 1364–1380.

Central locus for nonspeech context effects on phonetic identification (L)

Andrew J. Lotto^{a)} and Sarah C. Sullivan^{b)}

Department of Psychology, Washington State University, P.O. Box 644820, Pullman, Washington 99164

Lori L. Holt

Department of Psychology and Center for the Neural Basis of Cognition, Carnegie Mellon University, Pittsburgh, Pennsylvania 15213

(Received 29 May 2002; revised 9 October 2002; accepted 14 October 2002)

Recently, Holt and Lotto [Hear. Res. **167**, 156–169 (2002)] reported that preceding speech sounds can influence phonetic identification of a target syllable even when the context sounds are presented to the opposite ear or when there is a long intervening silence. These results led them to conclude that phonetic context effects are mostly due to nonperipheral auditory interactions. In the present paper, similar presentation manipulations were made with nonspeech context sounds. The results agree qualitatively with the results for speech contexts. Taken together, these findings suggest that the same nonperipheral mechanisms may be responsible for effects of both speech and nonspeech context on phonetic identification. © 2003 Acoustical Society of America.
[DOI: 10.1121/1.1527959]

PACS numbers: 43.71.An, 43.71.Pc, 43.66.Lj [CWT]

I. INTRODUCTION

There exists a class of perceptual phenomena known as *phonetic context effects* in which the perceived phonemic identity of a speech sound is moderated by the identity of neighboring speech sounds. That is, identical acoustics can lead to different identifications depending on the identity of precursor speech sounds. For example, the reported identification of a syllable-initial stop can be changed from /g/ to /d/ by changing the preceding context syllable from /a/ to /ar/ (Mann, 1980).

Holt and Lotto (2002) attempted to ascertain the level of the auditory system at which the stimulus interactions underlying phonetic context effects occur. In one experiment, they presented context syllables (e.g., /a/ or /ar/) and target syllables (/da/–/ga/ series members) to opposite ears. The identity of the context syllable affected identifications of the target syllable even in this dichotic presentation condition. However, the size of the identification boundary shift was slightly smaller than for diotic presentation conditions. In a second experiment the duration of the silent gap between the context and target syllable was varied from 25 to 400 ms (this gap was typically 50 ms in previous experiments). A significant effect of context was evident even when context offset and target onset were separated by as much as 275 ms. Holt and Lotto (2002) argue that these results suggest that context effects are partially mediated by nonperipheral mechanisms. That is, it is unlikely that they are due to masking or interactions at the level of the auditory nerve or perhaps even cochlear nucleus. In agreement with these conclusions, Holt and Rhode (2000) failed to find evidence for

appropriate speech-sound stimulus interactions in recordings from chinchilla VIIIth nerve.

Recently, there have been a number of demonstrations of shifts in phonetic identification caused by nonspeech context sounds such as sine-wave tones (Lotto and Kluender, 1998; Holt *et al.*, 2000). Lotto and Kluender (1998) presented listeners consonant–vowel (CV) syllables preceded by sine-wave tones that modeled the frequency trajectory of the third formant (F_3) of /a/ or /ar/. Listeners identified the CVs more often as /ga/ following the sine-wave modeling /a/ and more often as /da/ following the sine-wave modeling /ar/. Because these nonspeech context sounds had no perceived phonetic content, the authors proposed that the spectral content of the context sounds moderates the shift in identity of the target speech sounds. In this case, high-frequency spectral energy (F_3 offset of /a/ or high-frequency sine wave) leads to more /ga/ responses (/g/ has a low-frequency F_3 onset) and low-frequency spectral energy (F_3 offset of /ar/ or low-frequency sine wave) results in more /da/ responses (/d/ has a high-frequency F_3 onset). This pattern of results has been referred to as *spectral contrast* (Holt *et al.*, 2000).

The question that is immediately raised is whether the processes responsible for nonspeech context effects are the same as those underlying speech context effects. Fowler *et al.* (2000) suggest that nonspeech context effects are primarily due to masking. On the other hand, they propose that speech context effects are due specifically to perception of speech gestures.

In addition to a masking account, it is possible that nonspeech context effects are complex demonstrations of *auditory enhancement* (Viemeister, 1980; Viemeister and Bacon, 1982; Summerfield *et al.*, 1984). Auditory enhancement refers, generally, to a class of effects in which energy in a frequency region is perceptually enhanced if it is preceded by a sound that lacks energy in that region.

Holt and Lotto (2002) argue that their results are incom-

^{a)}Electronic mail: alotto@wsu.edu

^{b)}Sarah Sullivan is currently in the Department of Psychology, University of Texas-Austin.

patible with an auditory enhancement or peripheral masking account of *speech* context effects. In particular, the time course of auditory enhancement appears to differ from the speech context effects. Holt and Lotto demonstrated that speech context effects are present out to at least 275 ms of intervening silent gap. Viemeister and Bacon (1982) found no appreciable auditory enhancement in a masking study beyond about 100 ms of intervening silence. In addition, auditory enhancement appears to be a strictly monaural phenomenon. Summerfield and Assmann (1989) failed to find effects of a precursor stimulus in auditory enhancement vowel experiments when the context was presented to the contralateral ear. In contrast, Holt and Lotto demonstrated robust effects of speech contexts presented to the opposite ear of the target syllables.

The purpose of the two experiments presented here is to determine whether auditory enhancement or peripheral masking can completely account for nonspeech context effects. The manipulations utilized by Holt and Lotto (2002) have been replicated here with nonspeech contextual sounds. Experiment 1 examines the effect of dichotic versus diotic presentation on nonspeech context effects. In experiment 2, subjects are presented context and target syllables with varying durations of intervening silence. The question is whether these manipulations will moderate nonspeech context effects in a qualitatively different manner than witnessed for speech context effects. If not, then it may be reasonable to suggest that similar mechanisms are culpable for both speech and nonspeech context effects.

II. EXPERIMENT 1 (DICHOTIC VERSUS DIOTIC PRESENTATION)

A. Methods

1. Subjects

Twenty-four undergraduate students at Washington State University participated in the experiment for course credit. All were native English speakers that reported no hearing deficits or disorders.

2. Stimuli

A ten-member series of synthetic speech varying acoustically in *F3* onset frequency and varying perceptually from

/ga/ to /da/ was created using the cascade branch of the Klatt (1980) synthesizer. For these stimuli, *F3* onset frequency varied from 1800 to 2700 Hz in 100-Hz steps. From onset, *F3* frequency changed linearly to a steady-state value of 2450 Hz across 80 ms. All other synthesis parameters were constant across series members. The first formant frequency (*F1*) increased linearly from 300 to 750 Hz and the second formant (*F2*) frequency declined from 1650 to 1200 Hz across 80 ms. The fourth formant (*F4*) had a steady-state value of 2850 Hz. Fundamental frequency (*f0*) was 110 Hz over the first 200 ms and decreased to 95 Hz over the last 50 ms. Total stimulus duration was 250 ms. This CV series is identical to that used by Holt and Lotto (2002) in experiments 1b and 2b.

The nonspeech context stimuli were based on the speech precursors used in Holt and Lotto (2002). An analog of /al/ and /ar/ was created by using the synthesis parameters from Holt and Lotto in the parallel branch of the Klatt (1980) synthesizer. Amplitudes for all formants other than *F3* were set to zero. This resulted in a 250-ms harmonic complex (*f0* equals 110 Hz) with a single frequency-varying amplitude peak. In terms of synthesis parameters, the frequency of this single formant was set at 2450 Hz for the first 100 ms for both contexts. The two contexts differed in the formant frequency trajectory over the final 150 ms. For the context modeling /al/ (referred to as *highfreq*), the formant increased linearly in frequency to 2700 Hz. For the context modeling /ar/ (*lowfreq*), the formant decreased linearly to 1600 Hz. These context sounds are not perceived as speech and certainly contain no identifiable phonemic content.

All stimuli were synthesized with 16-bit resolution at a 20-kHz sampling rate and stored on a computer disk following synthesis. Stimulus presentation was under the control of a microcomputer and Tucker Davis Technologies (TDT) hardware. Context sounds and target syllables were appended online with a 50-ms intervening silent interval. Following D/A conversion (TDT, DD1), stimuli were low-pass filtered at a 9.8-kHz cutoff frequency (TDT, FTG2), attenuated (TDT, PA4), and presented over headphones (Sennheiser HD 285) at 75 dB SPL (A).

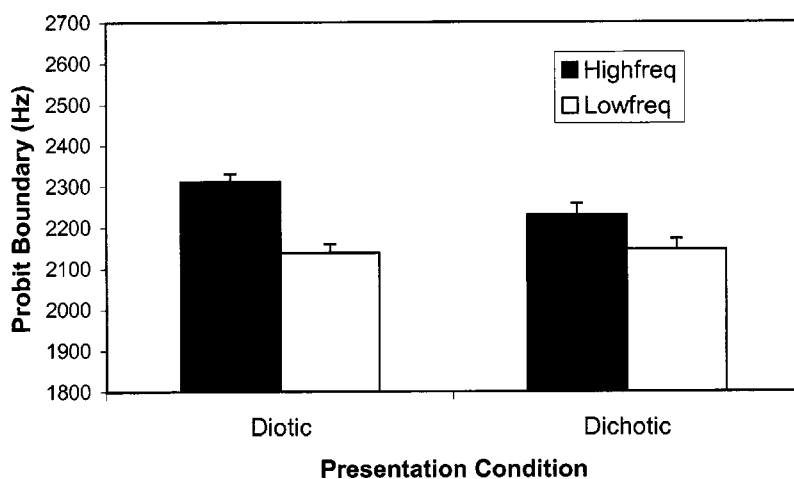


FIG. 1. Boundaries for identification of /ga-/da/ syllables preceded by *highfreq* (dark bars) and *lowfreq* (light bars) for diotic and dichotic presentation conditions. Taller bars (higher-frequency boundaries) indicate more "ga" responses. A difference in bar height reflects an influence of preceding context on consonant identification.

TABLE I. Means and standard deviations (in parentheses) of identification boundaries as a function of context and silent interval duration from experiment 2. Differences between contexts were tested with paired-sample t-tests.

Context	25 ms	50 ms	100 ms	175 ms	275 ms	400 ms
Highfreq	2451.4 (101.8)	2403.7 (102.8)	2322.9 (124.1)	2311.4 (64.7)	2268.7 (141.7)	2296.1 (98.2)
Lowfreq	2300.4 (146.3)	2307.6 (140.5)	2232.8 (109.7)	2256.2 (87.2)	2257.7 (101.3)	2291.7 (109.2)
t-test df=16	3.64	2.74	2.92	2.33	0.36	0.14
p-value	0.0022	0.014	0.0099	0.033	0.72	0.89

3. Procedure

One to three subjects were tested concurrently in a sound-attenuated booth during a single experimental session. During each trial, listeners heard the appended stimuli (context followed by target syllable) over headphones. The listeners' task was to identify the target syllable as "da" or "ga" by pressing a labeled button on an electronic response box. Intertrial interval was approximately 3 s.

The experiment was divided into two blocks corresponding to diotic and dichotic presentation. Each subject completed both blocks and order of block presentation was counterbalanced across subjects. In the dichotic block, context and target were presented to opposite ears, with ear of context presentation randomized across trials. In the diotic block, both context and target were presented to *both* ears on each trial. In each block, listeners responded to 10 repetitions of each of the context/target combinations (2 contexts \times 10 target CVs \times 10 repetitions=200 trials per block). In all, the experiment lasted approximately 45 min.

B. Results and discussion

Previous context effect experiments (e.g., Lotto and Kluender, 1998) have used a performance criterion for inclusion of data in analyses. For the current two experiments, data were withheld from analyses for subjects who failed to correctly identify the two endpoint CVs (the best /da/ and /ga/) at least 80% of the time across conditions. In experiment 1, this led to the exclusion of data from two subjects. Identification boundaries were computed on the percentage of "ga" responses through probit analysis. These boundaries (in terms of F_3 frequency of the CV series) are presented in Fig. 1. In the diotic presentation condition, identification boundaries significantly shifted from *highfreq* (2310.4 Hz) compared to *lowfreq* (2138.1 Hz) contexts [$t(21)=6.74$, $p<0.0001$]. An identification shift was also present for the dichotic presentation condition [from 2229.7 to 2145.7 Hz; $t(21)=2.24$, $p<0.05$]. A 2 (presentation condition) \times 2 (context) repeated measures ANOVA revealed that the effect of context was significantly greater in the diotic presentation condition [$F(1,21)=4.665$, $p<0.05$].

The results of experiment 1 are consistent with the results of experiment 1b of Holt and Lotto (2002). In the latter study, speech context effects were present for both diotic and dichotic presentation, but the effect of context was numerically smaller in the dichotic condition. A 2 (speech versus nonspeech) \times 2 (presentation condition) \times 2 (context) mixed-

model ANOVA confirmed the agreement of the results from the two experiments. There were no significant interactions including the speech versus nonspeech variable ($p>0.10$). This agreement of results suggests that similar mechanisms may underlie both speech and nonspeech context effects on phonemic identification. In both cases, it is unlikely that the identification shifts are caused solely by peripheral masking or auditory enhancement, as these mechanisms are monaural in nature. It is still possible that these peripheral mechanisms play some role in both speech and nonspeech context effects since both effects are smaller when context and target cannot interact in the periphery.

III. EXPERIMENT 2 (SILENT GAP DURATION)

A. Methods

1. Subjects

Twenty undergraduates at Washington State University participated for course credit. All were native speakers of English that reported no hearing deficits or disorders. None of the subjects participated in experiment 1.

2. Stimuli

Stimuli were identical to those used in experiment 1. Only the duration of the intervening silent interval differed. The six intervening silent intervals were 25, 50, 100, 175, 275, and 400 ms. These duration intervals are identical to those used in experiment 2b of Holt and Lotto (2002).

3. Procedure

The task for the subjects was the same as in experiment 1. Each subject participated in three blocks of 120 trials (2 contexts \times 6 gap durations \times 10 CV target stimuli). Within each block, presentation order of stimuli was randomized. The context and target stimuli were presented to both ears.

B. Results and discussion

Data from three subjects who failed to identify 80% of endpoint stimuli were excluded from further analysis. Probit boundaries for each gap duration \times context condition are presented in Table I.

Planned paired-sample t-tests were used to examine the context effect at each duration of intervening silence. The spectral content of the contextual sound caused a significant shift in identification boundaries for all silent gap durations up to and including 175 ms ($p<0.05$; see Table I). No

effect of context was present for the 275- and 400-ms gap conditions ($p_s > 0.72$). Qualitatively equivalent results were obtained for tests computed on the mean percent of “ga” responses.

This pattern of results is quite similar to that obtained by Holt and Lotto (2002) in experiment 2b. They found an effect of speech context on CV identification out to 275 ms of intervening silence. No effect was present for a 400-ms silent gap. In both the nonspeech and speech context experiments, the size of the context effect decreases monotonically with increasing gap duration.

IV. GENERAL DISCUSSION

The pattern of results from both experiments described here matches the pattern obtained by Holt and Lotto (2002) with speech contexts. A significant context effect on CV identification remains when context is presented contralaterally to target. In both cases, the dichotic context effect is robust though smaller than for diotic presentation conditions. Effects of context also remain for substantial durations of intervening silent gaps. For speech contexts, this gap can extend to at least 275 ms. For nonspeech contexts, significant shifts were demonstrated out to 175 ms.

Fowler *et al.* (2000) propose that speech and nonspeech context effects are different in kind. However, the agreement of the current results with those of Holt and Lotto (2002) implicates similar mechanisms in both kinds of context effects. This agreement can be added to the mounting evidence for a general auditory role in speech context effects. Several previous studies have demonstrated nonspeech context effects that are equivalent in size of boundary shift to corresponding speech context effects (Lotto and Kluender, 1998; Holt *et al.*, 2000). The current studies extend these similarities across a series of presentation manipulations.

The results of these experiments support the contention of Lotto and Kluender (1998; Lotto *et al.*, 1997) that general mechanisms of the auditory system are at least partially responsible for the kinds of speech context effects examined here. The result of these general mechanisms is the perceptual emphasis of energy in frequency regions that are less represented in context sounds. That is, changes in the pattern of spectral energy are enhanced. The behavioral input-output function can be described as *spectral contrast* and it appears to be a general property of auditory systems. Lotto *et al.* (1997) demonstrated that birds (Japanese quail, *Coturnix japonica*) trained to respond to /da/ and /ga/ stimuli also show contrastive response shifts with /al/ and /ar/ contexts. Lotto and Kluender’s description of the pattern of con-

trastive output does not implicate any particular mechanism. However, the results of the current set of experiments provide evidence against some proposed mechanisms.

Given the monaural nature of peripheral masking and auditory enhancement, it is unlikely that either of these mechanisms is solely responsible for context effects. The fact that dichotic context effects were smaller suggests that it is possible that peripheral mechanisms play *some* role. However, a complete explanation will require a description of more central processes that take input from both ears. The relative temporal robustness of the context effects described in experiment 2 is also consistent with a central mechanism. In general, as one observes effects of interactions at more central levels of the auditory system, there is a longer temporal window over which auditory events interact and influence one another (Popper and Fay, 1992). These results are in agreement with neurophysiological investigations of speech context effects that found little evidence for contrast at the auditory nerve (Holt and Rhode, 2000).

- Fowler, C. A., Brown, J. M., and Mann, V. A. (2000). “Contrast effects do not underlie effects of preceding liquids on stop-consonant identification by humans,” *J. Exp. Psychol.* **26**, 877–888.
- Holt, L. L., and Lotto, A. J. (2002). “Behavioral examinations of the neural mechanisms of speech context effects,” *Hear. Res.* **167**, 156–169.
- Holt, L. L., Lotto, A. J., and Kluender, K. R. (2000). “Neighboring spectral content influences vowel identification,” *J. Acoust. Soc. Am.* **108**, 710–722.
- Holt, L. L., and Rhode, W. S. (2000). “Examining context-dependent speech perception in the chinchilla cochlear nucleus.” Paper presented at the 2000 Midwinter Meeting of Association for Research in Otolaryngology, St. Petersburg Beach, FL.
- Klatt, D. H. (1980). “Software for a cascade/parallel formant synthesizer,” *J. Acoust. Soc. Am.* **67**, 971–990.
- Lotto, A. J., and Kluender, K. R. (1998). “General contrast effects of speech perception: Effect of preceding liquid on stop consonant identification,” *Percept. Psychophys.* **60**, 602–619.
- Lotto, A. J., Kluender, K. R., and Holt, L. L. (1997). “Perceptual compensation for coarticulation by Japanese quail (*Coturnix coturnix japonica*),” *J. Acoust. Soc. Am.* **102**, 1134–1140.
- Mann, V. A. (1980). “Influence of preceding liquid on stop-consonant perception,” *Percept. Psychophys.* **28**, 407–412.
- Popper, A. N., and Fay, R. R. (1992). *The Mammalian Auditory Pathway: Neurophysiology* (Springer, New York).
- Summerfield, Q., and Assmann, P. F. (1989). “Auditory enhancement and the perception of concurrent vowels,” *Percept. Psychophys.* **45**, 529–536.
- Summerfield, Q., Haggard, M., Foster, J., and Gray, S. (1984). “Perceiving vowels from uniform spectra: Phonetic exploration of an auditory after effect,” *Percept. Psychophys.* **35**, 203–213.
- Viemeister, N. F. (1980). “Adaptation of masking,” in *Psychophysical, Physiological, and Behavioral Studies in Hearing*, edited by G. van den Brink and F. S. Bilsen (Delft University Press, Delft, The Netherlands), pp. 190–199.
- Viemeister, N. F., and Bacon, S. P. (1982). “Forward masking by enhanced components in harmonic complexes,” *J. Acoust. Soc. Am.* **71**, 1502–1507.

Sounds produced by individual white whales, *Delphinapterus leucas*, from Svalbard during capture (L)

Sofie M. Van Parijs,^{a)} Christian Lydersen, and Kit M. Kovacs
Norwegian Polar Institute, N-9296 Tromsø, Norway

(Received 28 February 2002; revised 2 May 2002; accepted 1 October 2002)

Recordings were made of the sounds produced by white whales during capture events in Storfjorden, Svalbard, in the late autumn. Only four of eight captured individuals produced sounds. Four subadults, one female and three males, between 330 and 375 cm long, did not produce sounds during handling. The four animals that produced sounds were as follows: a female subadult of 280 cm produced repetitive broadband clicks; a solitary calf produced harmonic sounds, which we suggest may serve as mother–calf “contact calls,” and a mother–calf pair were the two animals that produced the most sounds in the study. The mother produced “crooning” broadband clicks and frequently moved her head toward her calf while producing underwater sounds. The calf produced three types of frequency-modulated sounds interspersed within broadband click trains. No sounds were heard from any of the animals once they were free-swimming, or during *ad lib* recording sessions in the study area, even though groups of white whales were sighted on several occasions away from the capture net. © 2003 Acoustical Society of America. [DOI: 10.1121/1.1528931]

PACS numbers: 43.80.Ka, 43.40.Dx, 43.70.Bk [WA]

I. INTRODUCTION

White whales, *Delphinapterus leucas*, produce a wide range of variable underwater sounds (e.g., Sjøre and Smith, 1986a, b; Bel'kovich and Sh'ekotov, 1992, 1993). These sounds have been shown to vary according to behavioral context (e.g., Sjøre and Smith, 1986a, b; Bel'kovich and Sh'ekotov, 1992, 1993); a variety of studies have linked individual signals with specific behaviors and group contexts (Morgan, 1979; Bel'kovich and Sh'ekotov, 1992, 1993). However, few studies have studied the sounds produced by individual whales (e.g., Au and Nachtigall, 1997). Given the complexity of white whale sounds, further investigations of this kind are necessary to improve our understanding of sound usage in this species. White whales are thought to alter their calling behavior in response to the presence of vessels (Finley *et al.*, 1990; Lesage *et al.*, 1999) and a variety of cetacean species have been shown to produce “contact calls” during stressful situations (Caldwell *et al.*, 1990). The aim of this study was to investigate the sounds produced by individual white whales during capture.

II. METHODS

This study was carried out between 17 and 23 October 2001 at Wichebukta in Storfjorden (78°31'N, 18°55'E), eastern Spitsbergen. White whales were captured using a net set from the beach and the sex and age of all individuals were determined [see Lydersen *et al.* (2001) for more details]. The whales were captured for the purpose of deploying satellite transmitters. During the handling process continuous recordings were made of the sounds of each captured whale. A hydrophone was placed 0.5 m deep in the water in front of

the head of each individual and recordings were made of any sounds that were produced during handling and upon release. Recordings of the sounds were made using a High Tech Inc. hydrophone (model HTI-96-MIN, sensitivity: –170 dB, flat frequency response: 5 Hz to 30 kHz; add ± 1.0 dB) and a digital audio tape recorder, Sony TCD-D8 (frequency response 5 Hz to 22 kHz ± 1.0 dB). The recordings were digitized and displayed as spectrograms (fast Fourier transforms, *dt*: 10 ms, *df*: 102 Hz, FFT size: 512) using the BatSound analysis PC software program (Pettersson Elektronik A.B., 1996).

Sounds were divided into two broad categories, broadband clicks and narrow-band frequency-modulated sounds. Frequency-modulated sound types were defined according to variations in their spectral contours. Only high-quality records, where all sound contours were distinctly measurable on the spectrograms, were used for these analyses. Two sound parameters were measured for burst pulses and narrow-band frequency modulated sounds: (1) total duration (s) and (2) frequency with the greatest energy, *F*_{max} (kHz). For broadband clicks four measurements were made: (1) the duration of the click train (s); (2) the interclick interval ICI (s), (3) number of clicks per seconds, and (4) the interval between one click train and the next, BCI (s). Measurements were restricted by the upper limit (22 kHz) of the recording equipment.

Ad lib recordings were made each day during the study period, from a zodiac that was adrift several hundred meters offshore in the bay in which the net was set.

III. RESULTS

Eight whales were captured during the study period: five were subadults, one mother–calf pair was captured, and one solitary calf. Four of the five subadults (one female and three males) did not produce any sounds. These animals were all

^{a)} Author to whom correspondence should be addressed. Sofie Van Parijs, Norwegian College of Fisheries Science, University of Tromsø, 9037 Tromsø, Norway. Electronic mail: sofievp@nfh.uit.no

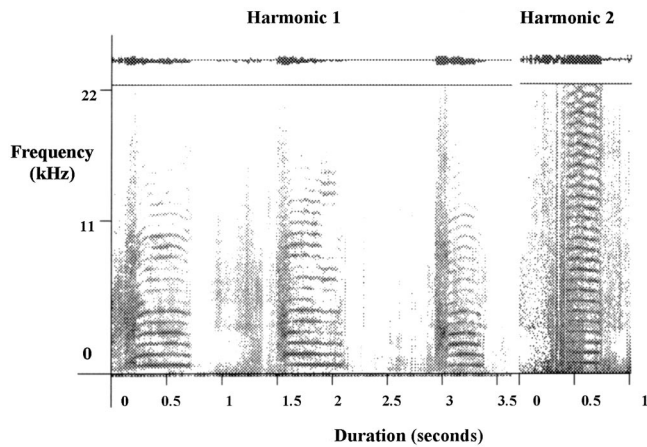


FIG. 1. Spectrograms of the harmonic sounds 1 and 2 produced by the solitary female calf (fast Fourier transforms, dt : 10 ms, df : 102 Hz, FFT size: 512). The gaps in the time scale on the x axis represent the start and end of each spectrogram.

more than 320 cm in length. A mother–calf pair, a solitary calf and, a subadult that was 280 cm long each produced sounds. All of these whales were females.

Sounds produced by the solitary calf were distinct from all other sounds recorded in this study, in that they contained frequency-modulated calls. There were two distinct sounds, harmonic 1 and 2 (Fig. 1). The calf produced sounds for 66% of the handling time ($n=24$ min). Harmonic 1 ($n=108$) had a mean duration of 0.7 ± 0.01 SE s, with a mean Fmax of 3.3 ± 0.07 SE kHz. Harmonic 2 ($n=39$) had a mean duration of 0.4 ± 0.01 SE s and a mean Fmax of 1.5 ± 0.2 SE. During production of this sound air was expelled by the calf through its blowhole.

The mother–calf pair were kept in close contact with one another throughout their handling time. The mother produced sounds 79% of the time and the calf produced sounds 43% of the time ($n=35$ min). The sounds produced by the mother were composed of repetitive click trains that varied greatly in duration (mean 1.9 ± 1.3 SE s, $n=339$) (Fig. 2). ICI varied from 0.46 to 0.012 s in duration with a mean of 27 clicks produced per second ($n=241$). The mean BCI was 1.5 ± 1.1 SE s ($n=235$). The click trains produced by the mother had a distinct audible “crooning” sound. The female frequently moved her head toward the calf while producing underwater sounds. The calf from the mother–calf pair produced click trains ($n=206$) and occasional frequency-modulated sounds within the click trains ($n=32$) (Fig. 3). The calf’s click trains had a mean duration of 0.6 ± 0.5 SE s. ICI varied from 0.5 to 0.09 s in duration, with a mean of 18 clicks per second. The mean BCI was 6.5 ± 1.3 SE s ($n=153$). This calf produced three types of frequency-modulated sounds, all of which occurred with either one or no harmonics (Fig. 3): a flat contour ($n=18$), an upsweep ($n=9$), and a variable contour ($n=5$). The mean duration of the flat contour whistle was 0.4 ± 0.05 SE s, with the mean frequency of the first harmonic at 7.6 ± 0.3 SE kHz and the second harmonic of 15.1 ± 0.1 SE kHz. Upsweep whistles were 0.3 ± 0.03 SE s in duration and 7.9 ± 0.02 SE kHz in the

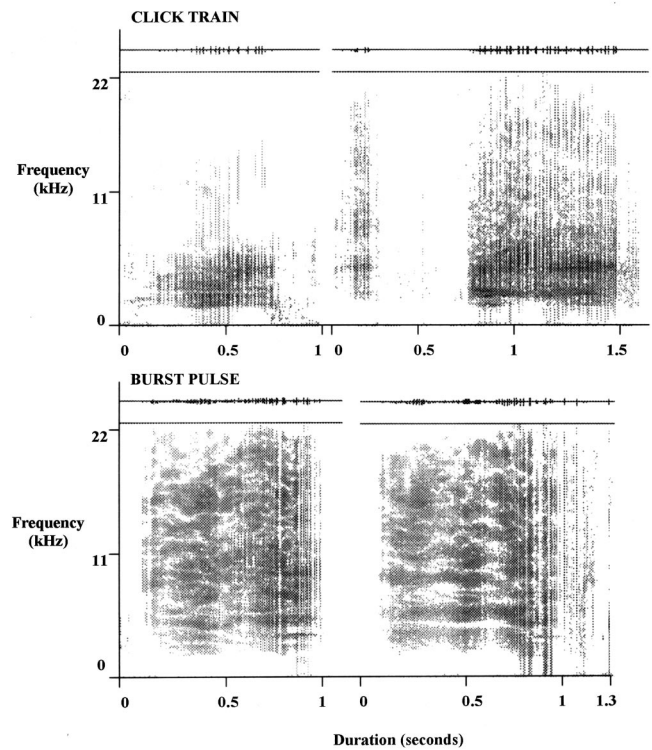


FIG. 2. Spectrograms of the broadband clicks and burst pulsed sounds produced by the adult female from the mother–calf pair (fast Fourier transforms, dt : 10 ms, df : 102 Hz, FFT size: 512). The gaps in the time scale on the x axis represent the start and end of each spectrogram.

first harmonic and 15.0 ± 0.08 SE kHz in the second harmonic. Variable contour whistles were considerably longer in duration (mean of 1.2 ± 0.9 SE s), but had a comparable Fmax of 7.7 ± 0.3 SE kHz in the first harmonic and 15.1 ± 0.3 SE kHz in the second harmonic. The subadult female produced only click trains (Fig. 4). A total of 37 min were recorded for this animal, during which the subadult produced sounds 28% of the time. The click trains had a mean duration of 0.3 ± 0.08 SE s ($n=89$). ICI varied from 0.41 to 0.03 s in duration with a mean of 22 clicks per second. The mean BCI was 11.5 ± 2.7 SE s ($n=153$).

A total of 7 h of *ad lib* recordings were made from a drifting zodiac. Even though whales passed close to the boat on several occasions, no white whale sounds were recorded from any free-swimming individuals.

IV. DISCUSSION

This study has shown that individual white whales produce a variety of different sounds during a similar, stressful situation. Surprisingly, subadults of more than 320 cm in length did not produce any sounds under 22 kHz, while being held in a net and manipulated. Although it is possible that subadults produced ultrasonic sounds, during this and in other studies, the majority of sounds produced by white whales have either a part or the whole component that occurs below 22 kHz (e.g., Sjare and Smith, 1986a, b; Bel’kovich and Sh’ekotov, 1992, 1993). Among the subadults that did

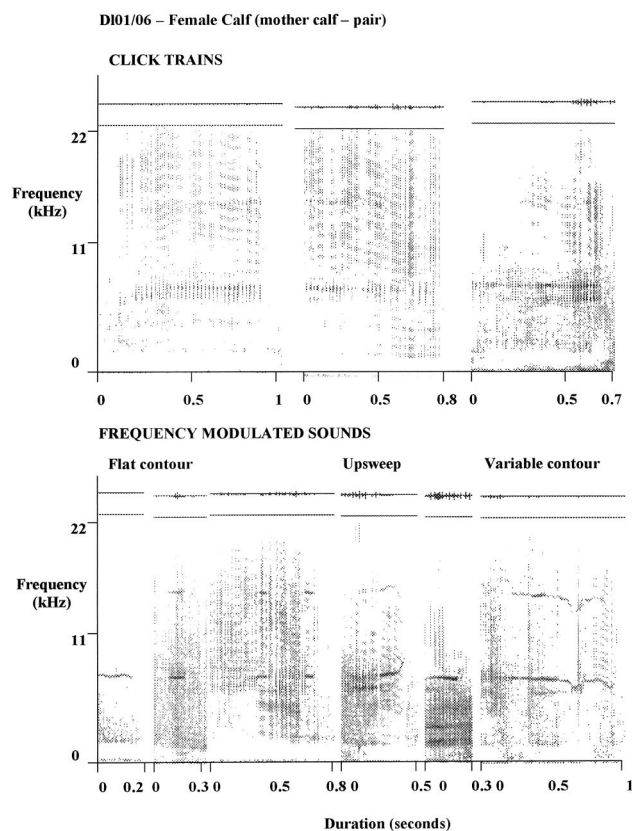


FIG. 3. Spectrograms of the broadband clicks and the flat, upsweep and variable contour frequency modulated sounds produced by the female calf from the mother-calf pair (fast Fourier transforms, dt : 10 ms, df : 102 Hz, FFT size: 512). The gaps in the time scale on the x axis represent the start and end of each spectrogram.

not produce sounds, there were one female and three males, therefore it is unlikely that this result is related to variation in sex. It is more likely that it is related to age. The single subadult that did produce sounds was 280 cm in length, suggesting it was between three and four years of age (Heide-Jørgensen and Teilmann, 1994). The sounds that it produced were solely broadband clicks. Click series, as defined by

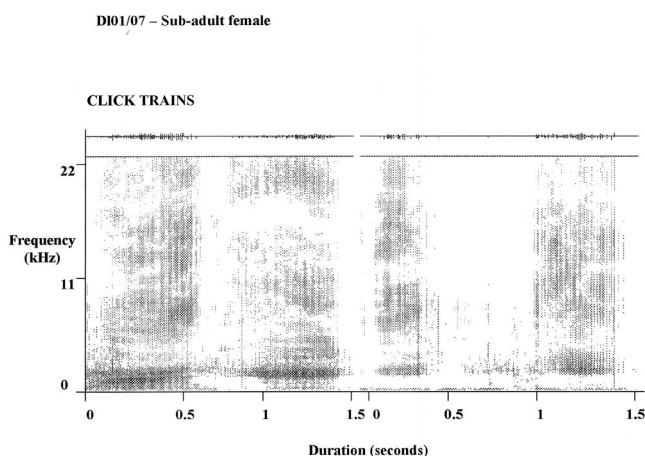


FIG. 4. Spectrograms of the broadband clicks produced by the subadult female (fast Fourier transforms, dt : 10 ms, df : 102 Hz, FFT size: 512). The gaps in the time scale on the x axis represent the start and end of each spectrogram.

Sjare and Smith (1986a), are used most frequently during “socially interactive” or “alarm situations.” The click series produced by this individual in this study resembled the broadband clicks observed in Sjare and Smith (1986a).

The solitary calf produced sounds that were different from those recorded for other individuals. Similar sounds to this harmonic call have been documented in the repertoires of wild ranging white whales (Sjare and Smith, 1986a; Bel’kovich and Sh’ekotov, 1992, 1993). The size of this individual suggests that it was one to two years old and therefore still likely to have been dependent on its mother. Mother-calf whistles are produced in *Tursiops sp.* and have been shown to facilitate reunions between mother-calf pairs (e.g., Smolker *et al.*, 1993). It is possible that the sounds produced by the calf were a mother-calf contact call produced during separation. The behavior of the mother suggested that these sounds were directed toward her calf. Bel’kovich and Sh’ekotov (1992) show spectrographs of sounds produced by mother-calf pairs, some of which resemble those produced in this study. However, the sounds used by the mother-calf pair in this study differ significantly from the whistles reported in many delphinid mother-calf contact behaviors (Smolker *et al.*, 1993).

The fact that only young animals and members of a mother-calf pair produced sounds during capture suggests that previously described “alarm calls” (Finley *et al.*, 1990; Lesage *et al.*, 1999) may actually be contact calls between mothers and dependent young. No sounds were recorded from free-swimming whales, although groups were sighted in the area where boats were operating. Additionally, no sounds were produced from males or large juveniles that were captured, presumably in a “stressful” situation. Unlike many delphinid species (Caldwell *et al.*, 1990), the white whales in this study did not produce a standard “contact call.” The sounds produced by individual animals during handling were variable, but the age/status of animals emitting calls and their structure suggest that it is likely that they all served as “contact calls.”

ACKNOWLEDGMENTS

We thank Magnus Andersen, Guttorm Christensen, Colin Hunter, Øle Anders Nøst, Morten Tryland, Masa Tet-suka, and Hans Wolkers for their assistance in capturing the whales. This study was supported by funds from the Norwegian Polar Institute (NPI). SVP was funded via a European Union Marie Curie Postdoctoral Fellowship. Ethical approval was obtained from the Norwegian Animal Care Authority, and the Environmental Office of the Governor of Svalbard issued permits for this work.

- Au, W. W. L., and Nachtigall, P. E. (1997). “Acoustics of echolocating dolphins and small whales.” *Mar. Fresh. Behav. Physiol.* **29**, 127–162.
- Bel’kovich, V. M., and Sh’ekotov, M. N. (1992). “Individual signals of belugas associated with hunting behavior in the white sea,” in *Marine Mammal Sensory Systems*, edited by J. Thomas, R. A. Kastelein, and A. Y. Supin (Plenum, New York), pp. 439–449.
- Bel’kovich, V. M., and Sh’ekotov, M. N. (1993). “The Belukha whale: natural behavior and bioacoustics,” USSR Academy of Sciences, Shirshov

- Institute of Oceanology, translated by Marina A. Svanidze, edited by J. C. Haney and C. Recchia (Woods Hole Oceanographic Institution, Woods Hole, MA).
- Caldwell, M. C., Caldwell, D. K., and Tyack, P. L. (1990). "Review of the signature whistles hypothesis for the Atlantic bottlenose dolphin," in *The Bottlenose Dolphin*, edited by S. Leatherwood and R. R. Reeves (Academic, San Diego, CA), pp. 199–234.
- Finley, K. J., Miller, G. W., Davis, R. A., and Greene C. R. (1990). "Reactions of belugas, *Delphinapterus leucas*, and narwhals, *Monodon monoceros*, to ice-breaking ships in the Canadian high Arctic," in *Advances in Research on the Beluga Whale, Delphinapterus leucas*, edited by T. G. Smith, D. J. St. Aubin, and J. R. Geraci (Department of Fisheries and Oceans, Canada), pp. 97–118.
- Heide-Jørgensen, M. P., and Teilmann, J. (1994). "Growth, reproduction, age structure and feeding habits of white whales (*Delphinapterus leucas*) in west Greenland waters," *Bioscience* **39**, 195–212.
- Lesage, V., Barrette, C., Kingsley, M. C. S., and Sjøre, B. (1999). "The effect of vessel noise on the sound production behavior of belugas in the St. Lawrence estuary, Canada," *Marine Mammal Sci.* **15**, 64–84.
- Lydersen, C., Martin, A. R., Kovacs, K. M., and Gjertz, I. (2001). "Summer and autumn movements of white whales, *Delphinapterus leucas*, in Svalbard, Norway," *Mar. Ecol.: Prog. Ser.* **219**, 265–274.
- Morgan, D. W. (1979). "The vocal and behavioral reactions of beluga, *Delphinapterus leucas*, to playback of its sounds," in *Behavior of Marine Animals: Current Perspectives in Research*, edited by H. E. Winn and B. L. Olla (Plenum, New York), pp. 391–423.
- Pettersson Elektronik A. B. (1996). "Batsound," Tallbacksvägen 51, S-75645 Uppsala, Sweden.
- Sjøre, B. L., and Smith, T. G. (1986a). "The relationship between behavioral activity and underwater sounds of the white whale, *Delphinapterus leucas*," *Can. J. Zool.* **64**, 2824–2831.
- Sjøre, B. L., and Smith, T. G. (1986b). "The vocal repertoire of white whales, *Delphinapterus leucas*, summering in Cunningham Inlet, Northwest Territories," *Can. J. Zool.* **64**, 407–415.
- Smolker, R. A., Mann, J., and Smuts, B. B. (1993). "Use of signature whistles during separation and reunions by wild bottle-nosed-dolphin mothers and infants," *Behav. Ecol. Sociobiol.* **33**, 393–402.

Direct and inverse scattering of transient acoustic waves by a slab of rigid porous material

Z. E. A. Fellah

Laboratorium voor Akoestiek en Thermische Fysica, Katholieke Universiteit Leuven, Celestijnenlaan 200 D, B-3001 Heverlee, Belgium

M. Fellah

Laboratoire de Physique Théorique, Institut de Physique, USTHB, BP 32 El Alia, Bab Ezzouar 16111, Algérie

W. Lauriks

Laboratorium voor Akoestiek en Thermische Fysica, Katholieke Universiteit Leuven, Celestijnenlaan 200 D, B-3001 Heverlee, Belgium

C. Depollier

Laboratoire d'Acoustique de l'Université du Maine, UMR-CNRS 6613, Université du Maine, Avenue Olivier Messiaen 72085 Le Mans Cedex 09, France

(Received 23 May 2002; revised 9 October 2002; accepted 21 October 2002)

This paper provides a temporal model of the direct and inverse scattering problem for the propagation of transient ultrasonic waves in a homogeneous isotropic slab of porous material having a rigid frame. This new time domain model of wave propagation takes into account the viscous and thermal losses of the medium as described by the model of Johnson *et al.* [D. L. Johnson, J. Koplik, and R. Dashen, *J. Fluid. Mech.* **176**, 379 (1987)] and Allard [J. F. Allard (Chapman and Hall, London, 1993)] modified by a fractional calculus based method applied in the time domain. This paper is devoted to the analytical calculus of acoustic field in a slab of porous material. The main result is the derivation of the expression of the scattering operators (reflection and transmission) which are the responses of the medium to an incident acoustic pulse. In this model the reflection operator is the sum of two contributions: the first interface and the bulk of the medium. Experimental and numerical results are given as a validation of our model. © 2003 Acoustical Society of America. [DOI: 10.1121/1.1528592]

PACS numbers: 43.20.Bi, 43.20.Hq [ANN]

I. INTRODUCTION

The ultrasonic characterization of porous materials saturated by air is of a great interest for a large class of industrial applications. These materials are frequently used in the automotive and aeronautics industries or in the building trade. The determination of the properties of a medium from waves that have been reflected by or transmitted through the medium is a classical inverse scattering problem. Such problems are often approached by taking a physical model of the scattering process, generating a synthetic response for some assumed values of the parameters, adjusting these parameters until reasonable agreement is obtained between the synthetic response and the observed data. Some of the recent progresses in this area are reviewed in Allard¹ and Lafarge.² Many applications like medical imaging or inverse scattering problems require the study of the behavior of pulses traveling into porous media,³ it is only recently that the response of these media to such excitations has been fully addressed in Fellah *et al.*^{4–7} for some elementary configurations in porous media. To efficiently cope with the specific problems appearing in the transient acoustic field propagation, new approaches are required.⁸ At present most analysis of signal propagation are carried out in the frequency domain using the Fourier transform to translate the results in the time domain and vice versa. This, however, has several limitations.

The first is that the transformation is difficult to compute numerically with sufficient accuracy for non analytical functions. For example, using Fourier transform to obtain time domain results for a lossy material is a more complicated approach than using a true time domain analysis, and the numerical results are less accurate. The second disadvantage is that by working in the frequency domain some numerical information is lost or hard to recover. For example, in case of noisy data it may be difficult to reconstruct the chronological events of a signal by phase unwrapping. Consequently, it is difficult to obtain a deep understanding to transient signal propagation using frequency domain method.

The time domain response of the material is described by an instantaneous response and a “susceptibility” kernel responsible of the memory effects. A time domain approach differs from the frequency analysis in that the susceptibility functions of the problem are convolution operators acting on the velocity and pressure fields, and therefore a different algebraic formalism has to be applied to solve the wave equation. In the past, many authors have used the fractional calculus as an empirical method to describe the properties of viscoelastic materials, e.g., in Caputo⁹ and Bagley.¹⁰ The observation that the asymptotic expressions of stiffness and damping in porous materials are proportional to fractional powers of frequency suggests the fact that time derivatives of

fractional order might describe the behavior of sound waves in this kind of materials, including relaxation and frequency dependence.

The core of this paper is the analytical calculus in time domain of the acoustic field inside the porous material and the derivation of the expression of the scattering operators (reflection and transmission) which are the responses of the medium to an incident acoustic pulse.

The outline of this paper is as follows. In Sec. II, a time domain model is given, the connection between the fractional derivatives and wave propagation in rigid porous media in high frequency range is established, the basic equations are written in the time domain. Section III is devoted to the direct problem and to the general solution of the propagation wave in this domain. Section IV contains the expressions of the reflection and transmission kernels in the time domain. In Sec. V, a validation via ultrasonic measurements for the direct problem is treated and finally in Sec. VI an approach to inverse problem given the physical parameters describing the propagation of ultrasonic waves in porous materials is given.

II. MODEL

In the acoustics of porous materials, one distinguishes two situations according to whether the frame is moving or not. In the first case, the dynamics of the waves due to the coupling between the solid skeleton and the fluid is well described by the Biot theory.^{11,12} In air-saturated porous media the structure is generally motionless and the waves propagate only in the fluid. This case is described by the model of equivalent fluid which is a particular case of the Biot model, in which the interactions between the fluid and the structure are taken into account in two frequency response factors: the dynamic tortuosity of the medium $\alpha(\omega)$ given by Johnson *et al.*¹³ and the dynamic compressibility of the air included in the porous material $\beta(\omega)$ given by Allard.¹ In the frequency domain, these factors multiply the density of the fluid and its compressibility respectively and represent the deviation from the behavior of the fluid in free space as the frequency increases. In the time domain, they act as operators and in the high frequency approximation their expressions are given by Fellah and Depollier^{4,5} and Fellah *et al.*^{6,7} as

$$\tilde{\alpha}(t) = \alpha_\infty \left(\delta(t) + \frac{2}{\Lambda} \left(\frac{\eta}{\pi \rho_f} \right)^{1/2} t^{-1/2} \right), \quad (1)$$

$$\tilde{\beta}(t) = \left(\delta(t) + \frac{2(\gamma-1)}{\Lambda'} \left(\frac{\eta}{\pi \text{Pr} \rho_f} \right)^{1/2} t^{-1/2} \right), \quad (2)$$

in these equations, $\delta(t)$ is the Dirac function, Pr is the Prandtl number, η and ρ_f are, respectively, the fluid viscosity and the fluid density and γ is the adiabatic constant. The relevant physical parameters of the model are the tortuosity of the medium α_∞ initially introduced by Zwikker and Kosten,¹⁴ the viscous and thermal characteristic lengths Λ and Λ' introduced by Johnson *et al.*¹³ and Allard.¹ In this model the time convolution of $t^{-1/2}$ with a function is interpreted as a semi derivative operator following the definition

of the fractional derivative of order ν given in Samko and colleagues¹⁵

$$D^\nu[x(t)] = \frac{1}{\Gamma(-\nu)} \int_0^t (t-u)^{-\nu-1} x(u) du, \quad (3)$$

where $\Gamma(x)$ is the gamma function.

In this framework, the basic equations of our model can be written as

$$\rho_f \tilde{\alpha}(t) * \frac{\partial v_i}{\partial t} = -\nabla_{ip} \quad \text{and} \quad \frac{\tilde{\beta}(t)}{K_a} * \frac{\partial p}{\partial t} = -\nabla \cdot v, \quad (4)$$

where $*$ denotes the time convolution operation, p is the acoustic pressure, v is the particle velocity, and K_a is the bulk modulus of the air. The first equation is the Euler equation, the second one is a constitutive equation obtained from the equation of mass conservation associated with the behavior (or adiabatic) equation.

For a wave propagating along the x -axis, these equations become:

$$\rho_f \alpha_\infty \frac{\partial v}{\partial t} + 2 \frac{\rho_f \alpha_\infty}{\Lambda} \left(\frac{\eta}{\pi \rho_f} \right)^{1/2} \int_0^t \frac{\partial v / \partial t'}{\sqrt{t-t'}} dt' = -\frac{\partial p}{\partial x}, \quad (5)$$

$$\frac{1}{K_a} \frac{\partial p}{\partial t} + 2 \frac{\gamma-1}{K_a \Lambda'} \left(\frac{\eta}{\pi \text{Pr} \rho_f} \right)^{1/2} \int_0^t \frac{\partial p / \partial t'}{\sqrt{t-t'}} dt' = -\frac{\partial v}{\partial x}, \quad (6)$$

in these equations the convolutions express the dispersive nature of the porous material. They take into account the memory effects due the fact that the response of the medium to the wave excitation is not instantaneous but needs more time to become effective. The retarding force is no longer proportional to the time derivative of the acoustic velocity but is found to be proportional to the fractional derivative of order 1/2 of this quantity. This occurs because the volume of fluid participating to the motion is not the same during the whole length of the signal as it is in the case of a fully developed steady flow. The phenomena may be understood by considering such a volume of fluid in a pore to be in harmonic motion. At high frequencies, only a thin layer of fluid is excited: the average shear stress is high. At a lower frequency, the same amplitude of fluid motion allows a thicker layer of fluid to participate in the motion and consequently the shear stress is less. The penetration distance of the viscous forces and therefore the excitation of the fluid depends on frequency. In the time domain, such a dependence is associated with a fractional derivative.

III. DIRECT PROBLEM

The direct scattering problem is that of determining the scattered field as well as the internal field, that arises when a known incident field impinges on the porous material with known physical properties. To compute the solution of the direct problem one need to know the Green's function⁶ of the modified wave equation in the porous medium. In that case, the internal field is given by the time convolution of the

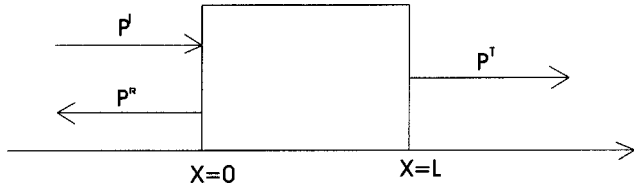


FIG. 1. Geometry of the problem.

Green's function with the incident wave and the reflected and transmitted fields are deduced from the internal field and the boundary conditions.

The generalized lossy wave equation in the time domain is derived from the basic equations (4) by elementary calculation in the following form:

$$\frac{\partial^2 p}{\partial x^2} - A \frac{\partial^2 p}{\partial t^2} - B \int_0^t \frac{\partial^2 p / \partial t'^2}{\sqrt{t-t'}} dt' - C \frac{\partial p}{\partial t} = 0, \quad (7)$$

where the coefficients A , B and C are constants, respectively, given by;

$$A = \frac{\rho_f \alpha_\infty}{K_a}, \quad B = \frac{2\alpha_\infty}{K_a} \sqrt{\frac{\rho_f \eta}{\pi}} \left(\frac{1}{\Lambda} + \frac{\gamma-1}{\sqrt{\text{Pr} \Lambda'}} \right), \quad (8)$$

$$C = \frac{4\alpha_\infty(\gamma-1)\eta}{K_a \Lambda \Lambda' \sqrt{\text{Pr}}},$$

the first one is related to the velocity $c = 1/\sqrt{\rho_f \alpha_\infty / K_a}$ of the wave in the air included in the porous material. α_∞ appears as the refractive index of the medium which changes the wave velocity from $c_0 = \sqrt{K_a / \rho_f}$ in free space to $c = c_0 / \sqrt{\alpha_\infty}$ in the porous medium. The other coefficients are essentially dependent of the characteristic lengths Λ and Λ' and express the viscous and thermal interactions between the fluid and the structure. The constant B governs the spreading of the signal while C is responsible of the attenuation of the wave. Obviously, a knowledge of these three coefficients allows the determination of the parameters α_∞ , Λ and Λ' . One way to solve Eq. (7) with suitable initial and boundary conditions is by using the Laplace transform. The approach is quite simple although the inverse Laplace transform require tedious calculus.¹⁶ A suitable setting for the introduction of the time domain solution of the modified wave propagation equation (7) is provided by the following model.

A. General solution of the propagation equation

In this section some notation is introduced. The geometry of the problem is shown in Fig. 1. An homogeneous porous material occupies the region $0 \leq x \leq L$. This medium is assumed to be isotropic and to have a rigid frame. A short sound pulse impinges normally on the medium from the left. It gives rise to an acoustic pressure field $p(x, t)$ and an acoustic velocity field $v(x, t)$ within the material, which satisfying the propagation equation (7) written also as:

$$\frac{\partial^2 p(x, t)}{\partial x^2} - \left(\frac{1}{c^2} \delta(t) + CH(t) + \frac{\beta}{\sqrt{t}} \right) * \frac{\partial^2 p(x, t)}{\partial t^2} = 0, \quad (9)$$

where $H(t)$ is the Heaviside function:¹⁷ $H(t) = 0$ for $t < 0$, $H(0) = 1/2$ and $H(t) = 1$, for $t > 0$.

It is assumed that the pressure field is continuous at the boundary of the material

$$p(0^+, t) = p(0^-, t), \quad p(L^-, t) = p(L^+, t), \quad (10)$$

(where \pm superscript denotes the limit from the left and the right, respectively) and to the initial conditions

$$p(x, t)|_{t=0} = 0 \quad \frac{\partial p}{\partial t} \Big|_{t=0} = 0, \quad (11)$$

which means that the medium is idle for $t = 0$.

If the incident sound wave is launched in the region $x \leq 0$, then the general solution of Eq. (9) in the region to the left of the material is the sum of the incident and reflected fields

$$p_1(x, t) = p^i \left(t - \frac{x}{c_0} \right) + p^r \left(t + \frac{x}{c_0} \right), \quad x < 0, \quad (12)$$

here, $p_1(x, t)$ is the field in the region $x < 0$, p^i and p^r denote the incident and the reflected field, respectively. In addition, a transmitted field is produced in the region at the right of the material. This has the form

$$p_3(x, t) = p^t \left(t - \frac{L}{c} - \frac{(x-L)}{c_0} \right), \quad x > L. \quad (13)$$

[$p_3(x, t)$ is the field in the region $x > L$ and p^t is the transmitted field.]

The incident and scattered fields are related by the scattering operators (i.e., reflection and transmission operators) for the material. These are integral operators represented by

$$p^r(x, t) = \int_0^t \tilde{R}(\tau) p^i \left(t - \tau + \frac{x}{c_0} \right) d\tau$$

$$= \tilde{R}(t) * p^i(t) * \delta \left(t + \frac{x}{c_0} \right), \quad (14)$$

$$p^t(x, t) = \int_0^t \tilde{T}(\tau) p^i \left(t - \tau - \frac{L}{c} - \frac{(x-L)}{c_0} \right) d\tau$$

$$= \tilde{T}(t) * p^i(t) * \delta \left(t - \frac{L}{c} - \frac{(x-L)}{c_0} \right). \quad (15)$$

In Eqs. (14) and (15) the functions \tilde{R} and \tilde{T} are the reflection and the transmission kernels, respectively, for incidence from the left. Note that the lower limit of integration in Eqs. (14), (15) is chosen to be 0, which is equivalent to assuming that the incident wave front first impinges on the material at $t = 0$.

The scattering operators given in Eqs. (14) and (15) are independent of the incident field used in scattering experiment and depend only on the properties of the materials. In the region $x \leq 0$, the field $p_1(x, t)$ is given by:

$$p_1(x, t) = \left[\delta \left(t - \frac{x}{c_0} \right) + \tilde{R}(t) * \delta \left(t + \frac{x}{c_0} \right) \right] * p^i(t). \quad (16)$$

Equation (9) are solved by the Laplace transform method by taking into account to the conditions (10) and (11). We note $P(x, z)$ the Laplace transform of $p(x, t)$ defined by

$$P(x,z) = \mathcal{L}[p(x,t)] = \int_0^\infty \exp(-zt) p(x,t) dt. \quad (17)$$

Using the following relations

$$\mathcal{L}[\delta(t)] = 1, \quad \mathcal{L}[H(t)] = \frac{1}{z}, \quad \text{and} \quad \mathcal{L}\left[\frac{1}{\sqrt{t}}\right] = \sqrt{\frac{\pi}{z}}, \quad (18)$$

the Laplace transform of the wave equation (9) satisfying the initials conditions (11) becomes:

$$\frac{\partial^2 P_2(x,z)}{\partial x^2} - \frac{f(z)}{c^2} P_2(x,z) = 0, \quad (19)$$

where $P_2(x,z)$ is the Laplace transform of the acoustic pressure $p_2(x,t)$ inside the porous material for $0 \leq x \leq L$ and $f(z) = z^2 + b'z\sqrt{z} + c'z$, $b' = B \cdot c^2 \sqrt{\pi}$, $c' = C \cdot c^2$.

The Laplace transform of the field outside the materials is given by

$$P_1(x,z) = \left[\exp\left(-z \frac{x}{c_0}\right) + R(z) \exp\left(z \frac{x}{c_0}\right) \right] \varphi(z), \quad x \leq 0, \quad (20)$$

$$P_3(x,z) = T(z) \exp\left[-\left(\frac{L}{c} + \frac{(x-L)}{c_0}\right)z\right] \varphi(z), \quad x \geq L. \quad (21)$$

Here $P_1(x,z)$ and $P_3(x,z)$ are, respectively, the Laplace transform of the field at the left and the right of the material, $\varphi(z)$ denotes the Laplace transform of the incident field $p^i(t)$ and finally $R(z)$ and $T(z)$ are the Laplace transform of the reflection and transmission kernels respectively. The Laplace transform of the continuous conditions (10) are written as

$$P_2(0^+, z) = P_1(0^-, z) \quad \text{and} \quad P_2(L^-, z) = P_3(L^+, z), \quad (22)$$

where $P_1(0^-, z)$ and $P_3(L^+, z)$ are the Laplace transform of $p_1(x,t)$ and $p_3(x,t)$, respectively, given by

$$P_1(0^-, z) = (1 + R(z)) \varphi(z), \quad (23)$$

$$P_3(L^-, z) = T(z) \exp\left(-\frac{L}{c}\right) z \varphi(z) \quad (24)$$

from Eqs. (19) and (22), we deduce the expression of the field inside the material $P_2(x,z)$

$$P_2(x,z) = P_1(0^-, z) \frac{\sinh\left(\frac{L-x}{c} \sqrt{f(z)}\right)}{\sinh\left(\frac{L}{c} \sqrt{f(z)}\right)} + P_3(L^+, z) \frac{\sinh\left(\frac{x}{c} \sqrt{f(z)}\right)}{\sinh\left(\frac{L}{c} \sqrt{f(z)}\right)}, \quad (25)$$

where \sinh is the hyperbolic sine function.

The inverse Laplace transform of $\exp(-k\sqrt{f(z)})$, where k is a positive constant, gives the Green function of the medium:⁶

$$F(t,k) = \begin{cases} 0 & \text{if } 0 \leq t \leq k \\ \Xi(t) + \Delta \int_0^{t-k} h(t,\xi) d\xi & \text{if } t \geq k \end{cases} \quad (26)$$

with

$$\Xi(t) = \frac{b'}{4\sqrt{\pi}} \frac{k}{(t-k)^{3/2}} \exp\left(-\frac{b'^2 k^2}{16(t-k)}\right), \quad (27)$$

where $h(\tau, \xi)$ has the following form:

$$h(\xi, \tau) = -\frac{1}{4\pi^{3/2}} \frac{1}{\sqrt{(\tau-\xi)^2 - k^2}} \frac{1}{\xi^{3/2}} \times \int_{-1}^1 \exp\left(-\frac{\chi(\mu, \tau, \xi)}{2}\right) \times (\chi(\mu, \tau, \xi) - 1) \frac{\mu d\mu}{\sqrt{1-\mu^2}}, \quad (28)$$

and where $\chi(\mu, \tau, \xi) = (\Delta\mu\sqrt{(\tau-\xi)^2 - k^2} + b'(\tau-\xi))^2/8\xi$, $b' = Bc_0^2\sqrt{\pi}$, $c' = Cc_0^2$, and $\Delta = b'^2 - 4c'$. The inverse Laplace transform of $P_2(x,z)$ gives the complete solution of the wave equation in time domain in the porous material taking into account the multiple reflections at the interfaces $x=0$ and $x=L$. (Appendix A).

$$p_2(x,t) = \sum_{n \geq 0} \left[F\left(t, 2n \frac{L}{c} + \frac{x}{c}\right) - F\left(t, (2n+2) \frac{L}{c} - \frac{x}{c}\right) \right] * p_1(0,t) + \sum_{n \geq 0} \left[F\left(t, (2n+1) \frac{L}{c} - \frac{x}{c}\right) - F\left(t, (2n+1) \frac{L}{c} + \frac{x}{c}\right) \right] * p_3(L,t), \quad (29)$$

which can be written as:

$$\begin{aligned}
p_2(x,t) = & \sum_{n \geq 0} \int_{2nL/c+x/c}^t F\left(\tau, 2n \frac{L}{c} + \frac{x}{c}\right) p_1(0, t-\tau) d\tau - \sum_{n \geq 0} \int_{(2n+2)L/c-x/c}^t F\left(\tau, (2n+2) \frac{L}{c} - \frac{x}{c}\right) p_1(0, t-\tau) d\tau \\
& + \sum_{n \geq 0} \int_{(2n+1)L/c-x/c}^t F\left(\tau, (2n+1) \frac{L}{c} - \frac{x}{c}\right) p_3(L, t-\tau) d\tau \\
& - \sum_{n \geq 0} \int_{(2n+1)L/c+x/c}^t F\left(\tau, (2n+1) \frac{L}{c} + \frac{x}{c}\right) p_3(L, t-\tau) d\tau.
\end{aligned} \tag{30}$$

IV. REFLECTION AND TRANSMISSION SCATTERING OPERATORS

To derive the reflection and transmission coefficients the boundary conditions flow velocity at the interfaces $x=0$ and $x=L$ are needed. The Euler equation is written in the regions (1) ($x \leq 0$) and (2) ($0 \leq x \leq L$) as:

$$\rho_f \frac{\partial v_1(x,t)}{\partial t} \Big|_{x=0} = - \frac{\partial p_1(x,t)}{\partial x} \Big|_{x=0}, \quad x \leq 0, \tag{31}$$

$$\rho_f \tilde{\alpha}(t) * \frac{\partial v_2(x,t)}{\partial t} \Big|_{x=0} = - \frac{\partial p_2(x,t)}{\partial x} \Big|_{x=0}, \quad 0 \leq x \leq L, \tag{32}$$

where $v_1(x,t)$ and $v_2(x,t)$ are the acoustic velocity field in the regions (1) and (2), respectively. In the free space [region (1)], the tortuosity operator is equal to 1.

The equation of the flow continuity at $x=0$ is written as:

$$v_1(x,t) = \phi v_2(x,t), \tag{33}$$

where ϕ is the porosity of the medium. From Eqs. (31), (32), and (33) it is easy to write:

$$\tilde{\alpha}(t) * \frac{\partial p_1(x,t)}{\partial x} \Big|_{x=0} = \phi \frac{\partial p_2(x,t)}{\partial x} \Big|_{x=0}, \tag{34}$$

with

$$\frac{\partial p_1(x,t)}{\partial x} \Big|_{x=0} = \frac{1}{c_0} (-\delta(t) + \tilde{R}(t)) * \frac{\partial p^i(t)}{\partial t}. \tag{35}$$

The Laplace transform of Eq. (34) gives a relation between the reflection and transmission coefficient

$$\begin{aligned}
(R(z)-1) \sinh\left(\frac{L}{c} \sqrt{f(z)}\right) &= \frac{\phi c_0}{c} \frac{\sqrt{f(z)}}{z \alpha(z)} \left[T(z) \exp\left(\frac{-Lz}{c}\right) \right. \\
&\quad \left. - (1+R(z)) \cosh\left(\frac{L}{c} \sqrt{f(z)}\right) \right],
\end{aligned} \tag{36}$$

where $\alpha(z)$ is the Laplace transform of $\tilde{\alpha}(t)$.

At the interface $x=L$, the Euler equation is written in the two regions (2) and (3) ($x \geq L$) as:

$$\rho_f \tilde{\alpha}(t) * \frac{\partial v_2(x,t)}{\partial t} \Big|_{x=L^-} = - \frac{\partial p_2(x,t)}{\partial x} \Big|_{x=L^-}, \tag{37}$$

$$\rho_f \frac{\partial v_3(x,t)}{\partial t} \Big|_{x=L^+} = - \frac{\partial p_3(x,t)}{\partial x} \Big|_{x=L^+}.$$

At $x=L$, the continuity of the flow velocity leads to the relation

$$v_3(L^+, t) = \phi v_2(L^-, t). \tag{38}$$

From Eqs. (37)–(38), we have:

$$\tilde{\alpha}(t) * \frac{\partial p_3(x,t)}{\partial x} \Big|_{x=L^+} = \phi \frac{\partial p_2(x,t)}{\partial x} \Big|_{x=L^-}, \tag{39}$$

with

$$\frac{\partial p_3(x,t)}{\partial x} \Big|_{x=L^+} = - \frac{1}{c_0} \tilde{T}(t) * \frac{\partial p^i}{\partial t} \Big|_{t=L/c}, \tag{40}$$

the Laplace transform of Eq. (39) gives:

$$\begin{aligned}
T(z) \exp\left(-\frac{L}{c} z\right) \sinh\left(\frac{L}{c} \sqrt{f(z)}\right) \\
= \frac{\phi c_0}{c} \frac{\sqrt{f(z)}}{z \alpha(z)} \left[-T(z) \exp\left(-\frac{L}{c} z\right) \right. \\
\left. \times \cosh\left(\frac{L}{c} \sqrt{f(z)}\right) + 1 + R(z) \right].
\end{aligned} \tag{41}$$

The functions $R(z)$ and $T(z)$ following from Eqs. (36) and (41) are the reflection coefficient $[R(z)]$ and the transmission coefficient $(T(z))$ given by:

$$R(z) = \frac{\left(-\frac{\phi^2}{\alpha_\infty} + 1\right) \sinh\left(\frac{L}{c} \sqrt{f(z)}\right)}{2 \frac{\phi}{\sqrt{\alpha_\infty}} \cosh\left(\frac{L}{c} \sqrt{f(z)}\right) + \left(\frac{\phi^2}{\alpha_\infty} + 1\right) \sinh\left(\frac{L}{c} \sqrt{f(z)}\right)}, \tag{42}$$

$$T(z) = \frac{2 \frac{\phi}{\sqrt{\alpha_\infty}} \exp\left(\frac{L}{c} z\right)}{2 \frac{\phi}{\sqrt{\alpha_\infty}} \cosh\left(\frac{L}{c} \sqrt{f(z)}\right) + \left(\frac{\phi^2}{\alpha_\infty} + 1\right) \sinh\left(\frac{L}{c} \sqrt{f(z)}\right)}. \tag{43}$$

The development of these expressions in exponential series (Appendix B) and the inverse Laplace transform lead to the reflection and transmission scattering kernels

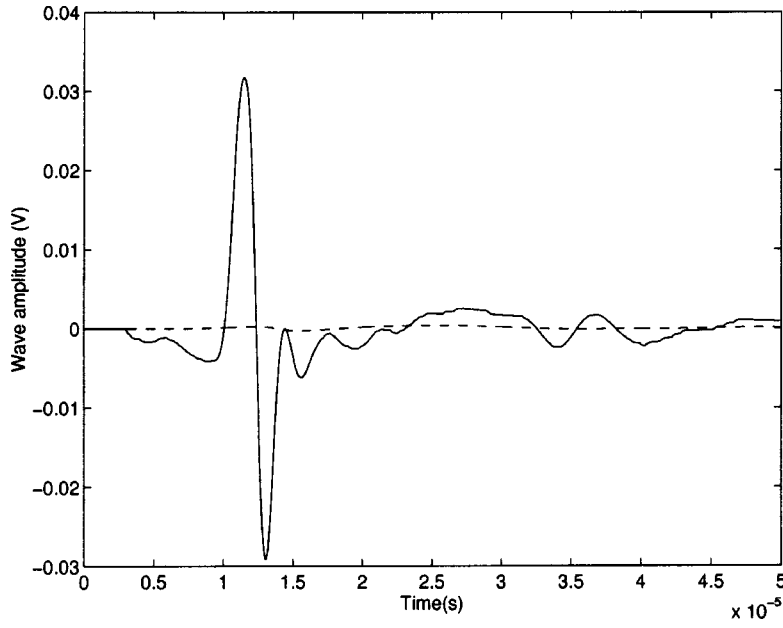


FIG. 2. Simulated contributions of the interface $x=0$ (solid line) and of the bulk material (dashed line) to the reflected wave.

$$\tilde{R}(t) = \left(\frac{-\phi + \sqrt{\alpha_\infty}}{\phi + \sqrt{\alpha_\infty}} \right) \sum_{n \geq 0} \left(\frac{\phi - \sqrt{\alpha_\infty}}{\phi + \sqrt{\alpha_\infty}} \right)^{2n} \times \left[F\left(t, 2n \frac{L}{c}\right) - F\left(t, (2n+2) \frac{L}{c}\right) \right], \quad (44)$$

These expressions takes into account the n -multiple reflections in the material. In most cases, in porous materials saturated by air, the multiply reflection effects are negligible because of the high attenuation of sound waves in these media. So, by taking into account only the first reflections at the interfaces $x=0$ and $x=L$, the pressure $p_2(x,t)$ in the material becomes

$$\tilde{T}(t) = \frac{4\phi\sqrt{\alpha_\infty}}{(\sqrt{\alpha_\infty} + \phi)^2} \sum_{n \geq 0} \left(\frac{\phi - \sqrt{\alpha_\infty}}{\phi + \sqrt{\alpha_\infty}} \right)^{2n} \times F\left(t + \frac{L}{c_0}, (2n+1) \frac{L}{c}\right). \quad (45)$$

$$p_2(x,t) = \left[F\left(t, \frac{x}{c}\right) - F\left(t, \frac{2L}{c} - \frac{x}{c}\right) \right] * p_1(0,t) + \left[F\left(t, \frac{L}{c} - \frac{x}{c}\right) - F\left(t, \frac{L}{c} + \frac{x}{c}\right) \right] * p_3(L,t), \quad (46)$$

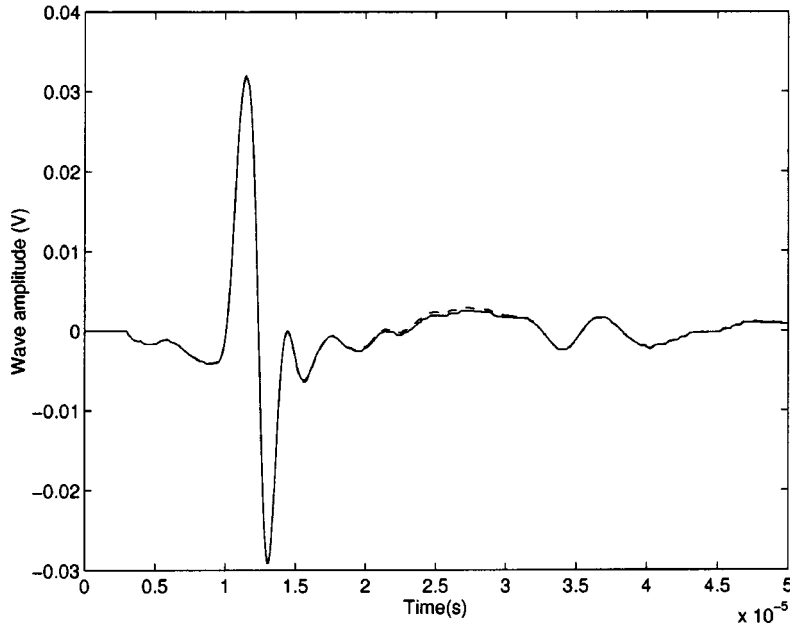


FIG. 3. Reflected wave at the interface $x=0$ (solid line) and the total reflected wave (dashed line).

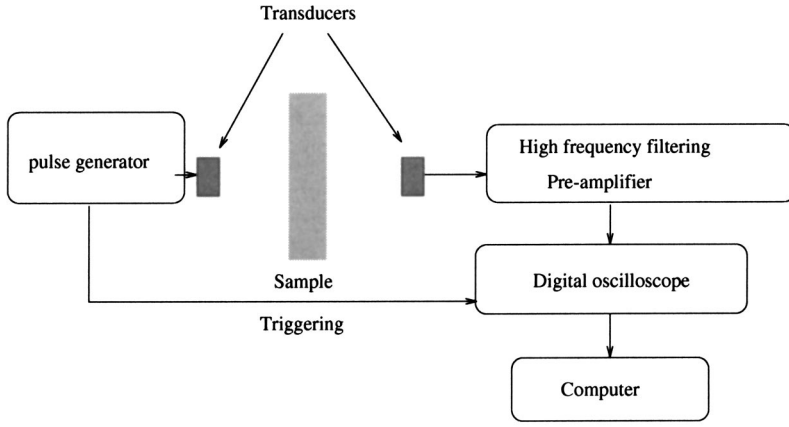


FIG. 4. Experimental setup of the ultrasonic measurements in transmitted mode.

and can also be written as

$$\begin{aligned}
 p_2(x, t) = & \int_{x/c}^t F\left(\tau, \frac{x}{c}\right) p_1(0, t - \tau) d\tau \\
 & - \int_{2L/c - x/c}^t F\left(\tau, \frac{2L}{c} - \frac{x}{c}\right) \\
 & \times p_1(0, t - \tau) d\tau + \int_{L/c - x/c}^t F\left(\tau, \frac{L}{c} - \frac{x}{c}\right) \\
 & \times p_3(L, t - \tau) d\tau - \int_{L/c + x/c}^t F\left(\tau, \frac{L}{c} + \frac{x}{c}\right) \\
 & \times p_3(L, t - \tau) d\tau.
 \end{aligned} \quad (47)$$

So, the kernels of reflection and transmission operators are given by

$$\tilde{R}(t) = \frac{\sqrt{\alpha_\infty} - \phi}{\sqrt{\alpha_\infty} + \phi} \delta(t) - \frac{4\phi\sqrt{\alpha_\infty}(\sqrt{\alpha_\infty} - \phi)}{(\sqrt{\alpha_\infty} + \phi)^3} F\left(t, \frac{2L}{c}\right), \quad (48)$$

$$\tilde{T}(t) = \frac{4\phi\sqrt{\alpha_\infty}}{(\phi + \sqrt{\alpha_\infty})^2} F\left(t + \frac{L}{c}, \frac{L}{c}\right). \quad (49)$$

In Eq. (48) the first term is equivalent to the reflection at the interface $x=0$. The part of the wave corresponding to this term is not subjected to the dispersion but it is just multiplied by the factor $(\sqrt{\alpha_\infty} - \phi)/(\sqrt{\alpha_\infty} + \phi)$. This shows that although the tortuosity is a bulk parameter, it may be evaluated from the wave reflected at the first interface when the porosity is known. The second term: $-[4\phi\sqrt{\alpha_\infty}(\sqrt{\alpha_\infty} - \phi)/(\sqrt{\alpha_\infty} + \phi)^3]F(t, 2L/c)$ in Eq. (48) is the bulk contribution to the reflection. Figure 2 shows each contribution to the reflected wave simulated from the expression (48) for a plastic foam M1. The solid line curve corresponds to the reflection at the first interface $x=0$ and the dashed line curve corresponds to the reflected wave (bulk contribution) at the second interface $x=L$. The parameters used in the simulation namely thickness: 5 cm, $\phi=0.98$, $\alpha_\infty=1.04$, $\Lambda=200 \mu\text{m}$, and $\Lambda'=600 \mu\text{m}$ have been determined by classical methods.¹⁸⁻²⁰ As we can see, the bulk contribution to the reflected wave is negligible when it is compared to the first interface contribution. In Fig. 3 we show by numerical simulation the difference between the reflected wave at the first interface [due to the term: $(\sqrt{\alpha_\infty} - \phi)/(\sqrt{\alpha_\infty} + \phi)$ in Eq. (48)] and the total reflected wave [all terms in Eq. (48)]. The difference between the two curves is weak and the reflected wave by the porous material may be approximated by the reflected wave by the first interface with a good accuracy.

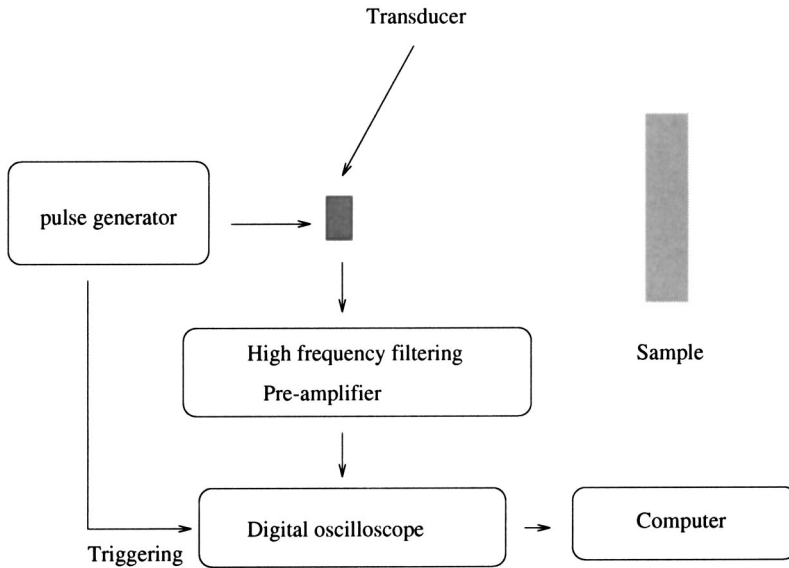


FIG. 5. Experimental setup of the ultrasonic measurements in reflected mode.

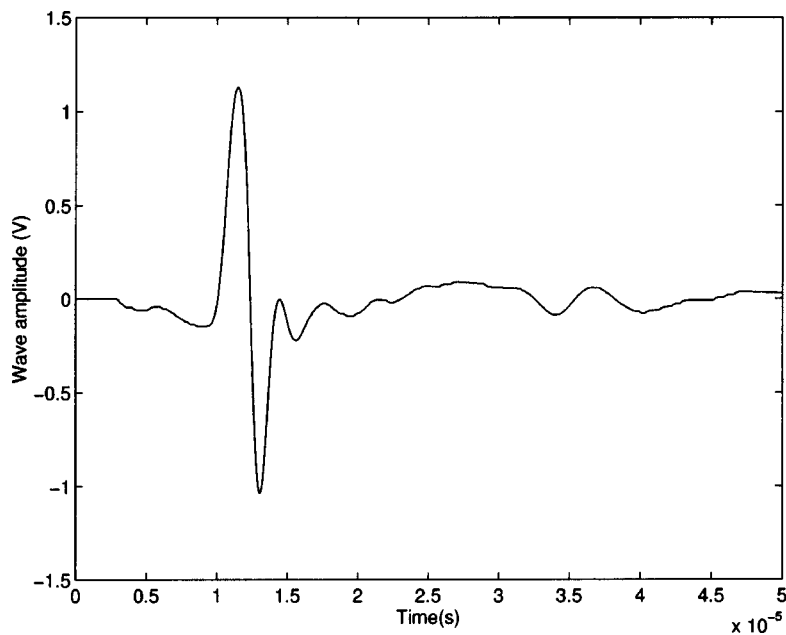


FIG. 6. Incident signal given out by the transducer.

V. ULTRASONIC MEASUREMENTS

As an application of this model, some numerical simulations are compared to experimental results. Experiments are done in air with two broadband Panametrics V389 piezoelectric transducers having a 250 kHz central frequency in air and a bandwidth at 6 dB extending from 60 kHz to 420 kHz. Pulses of 900 V are provided by a 5058 PR Panametrics pulser/receiver. The received signals are amplified up to 90 dB and filtered above 1 MHz to avoid high frequency noise (energy is totally filtered by the sample in this upper frequency domain). Electronics perturbations are removed by 1000 acquisition averages. The experimental setup is shown in Fig. 4.

Reflected waves are processed by an other experimental set up given in Fig. 5. One transducer is used alternatively as a transmitter and receiver in order to detect the reflected wave.

Measurements have been performed on plastic foam M1. Figure 6 shows the incident signal generated by the transducer. Numerical simulation and experimental results (transmitted signal) are presented in Fig. 7. The numerical results are obtained from the convolution of the transmission operator with the signal generated by the transducer shown in Fig. 6. A good agreement between experimental data and theory is observed, which allows the validation of our model and the expression of the kernel of the transmission operator.

VI. INVERSE PROBLEM

A slab of porous material is characterized by four parameters, namely, the porosity ϕ , the tortuosity α_∞ , the viscous characteristic length Λ , and the thermal characteristic length Λ' , the values of which are crucial for the behavior of the sound waves in such materials. So, it is of some importance to work out new experimental methods and efficient

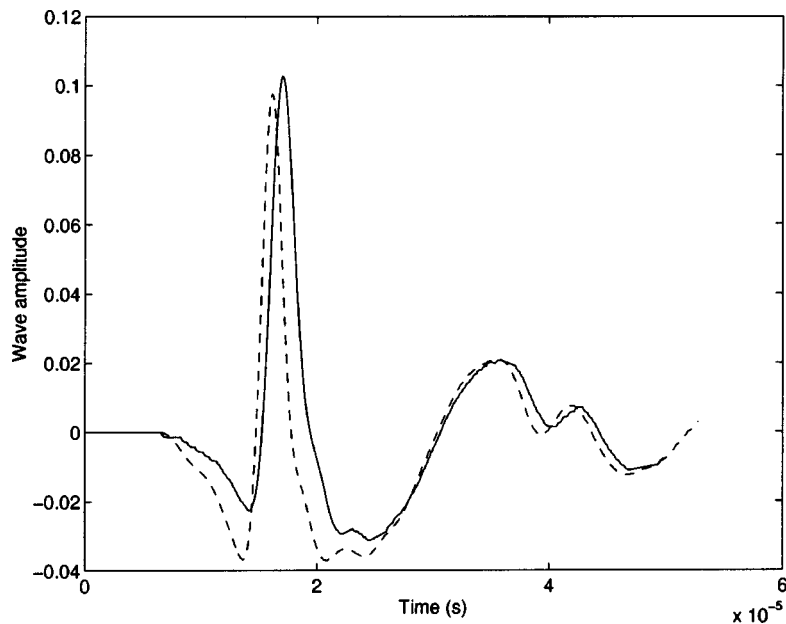


FIG. 7. Direct problem: experimental (solid line) and simulated transmitted signals (dashed line).

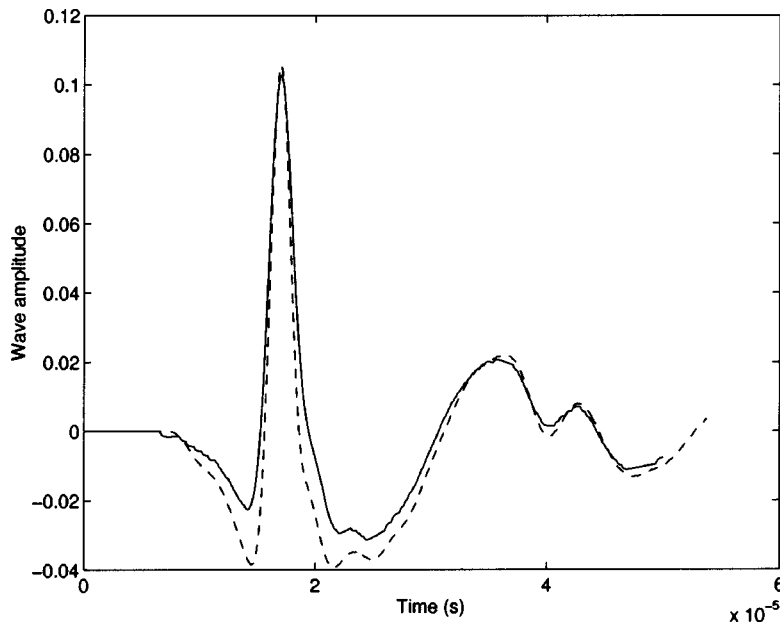


FIG. 8. Inverse problem: experimental (solid line) and simulated transmitted signals (dashed line).

tools for their estimation. Therefore, a basic inverse problem associated with the slab may be stated as follows: from the measurements of the transmitted and/or reflected signals outside the slab, find the values of the parameters of the medium. As shown in Sec. III, the solution of the direct problem is the system of two operators expressed as functions on ϕ , α_∞ , Λ and Λ' . The inversion algorithm for finding the values of the parameters of the slab is based on a fitting procedure: find the values of the parameters ϕ , α_∞ , Λ and Λ' such that the transmitted and reflected signal describes the scattering problem in the best possible way (e.g., in the least-squares sense). The inverse problem is to find values of parameters ϕ , α_∞ , Λ and Λ' which minimize the functions

$$U_1(\phi, \alpha_\infty, \Lambda, \Lambda') = \int_0^t (r(t) - p^r(x, t))^2 dt,$$

$$U_2(\phi, \alpha_\infty, \Lambda, \Lambda') = \int_0^t (s(t) - p^t(x, t))^2 dt,$$

where $r(t)$ is the experimentally determined reflected signal, $p^r(x, t)$ is reflected wave predicted from Eq. (14), $s(t)$ is the experimentally determined transmitted signal and $p^t(x, t)$ is the transmitted wave predicted from Eq. (15). However, because of the nonlinearity of the equations, the analytical solution of the inverse problem by the conventional least-squares methods is tedious. In our case, one can seek the numerical solution of the least-square method which minimize the $U_{1,2}(\phi, \alpha_\infty, \Lambda, \Lambda')$ defined by

$$U_1(\phi, \alpha_\infty, \Lambda, \Lambda') = \sum_{i=1}^{i=N} (r_i - p^r(x, t_i))^2,$$

$$U_2(\phi, \alpha_\infty, \Lambda, \Lambda') = \sum_{i=1}^{i=N} (s_i - p^t(x, t_i))^2,$$

where $r_i = r(t_i)_{i=1,2,\dots,N}$ [resp. $s_i = s(t_i)_{i=1,2,\dots,N}$] represents the discrete set of values of the reflected (resp. transmitted) experimental signal and $p^r(x, t_i)_{i=1,2,\dots,N}$ (resp. $p^t(x, t_i)_{i=1,2,\dots,N}$) is the discrete set of values of the simulated

reflected (resp. transmitted) signal. Figure 8 shows a comparison between experimental transmitted signal and simulated signal obtained by optimization from the inverse problem. The optimized parameters are $\alpha_\infty = 1.05$, $\Lambda = 208 \mu\text{m}$, and $\Lambda' = 624 \mu\text{m}$. The comparison between Figs. 7 and 8 shows that the values of the acoustic parameters obtained by solving the inverse problem in the time-domain method leads to better results than those given by classical methods.¹⁸⁻²²

Now, we will try to estimate the porosity via the measurement of reflected waves knowing the value of the tortu-

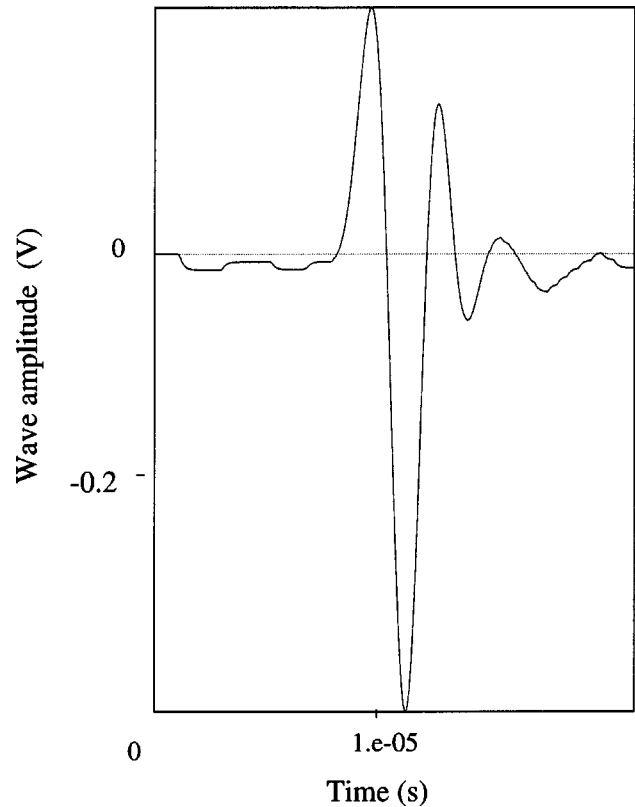


FIG. 9. Incident signal in reflected mode.

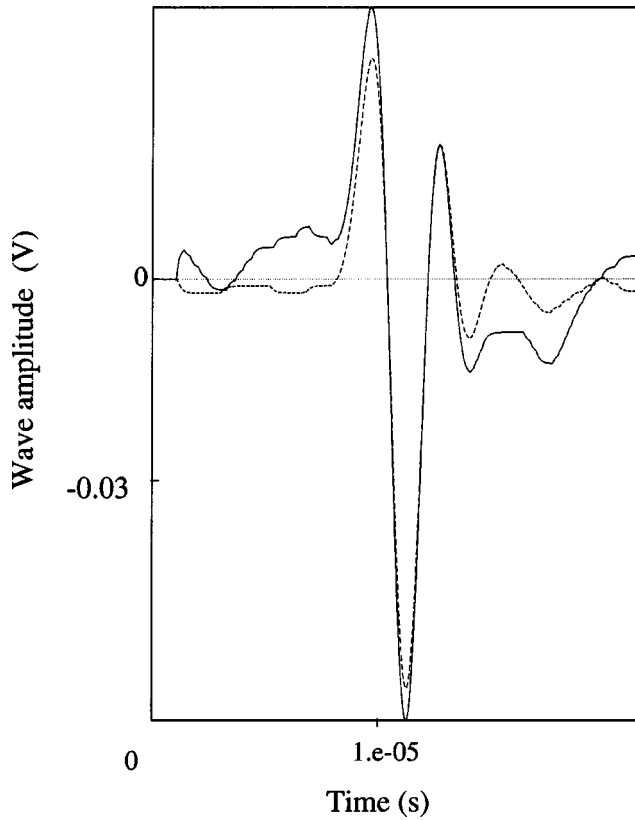


FIG. 10. Experimental reflected signal (solid line) and simulated reflected signal (dashed line).

osity (optimized by solving the inverse problem for the transmitted wave) and using the fact that the measured reflected wave is essentially due to the reflected wave at the first interface. The experimental setup using is shown in Fig. 5.

Figure 9 shows the incident signal generated by the transducer and Fig. 10 shows the comparison between experimental reflected signal by the foam M1 and simulated signal obtained by optimization of the inverse problem, the optimized value of the porosity is $\phi=0.97$.

In the future, one hopes to use this new method to measure the tortuosity and the porosity of plastic foams which are at the moment measured by a classical static methods.^{20–22}

VII. CONCLUSION

In this paper the propagation equation in time domain in a slab of porous material having a rigid frame is considered in the high frequency range. A time domain model of wave propagation in such material is worked out from the concept of fractional calculus. The analytical general solution of the wave propagation in the time domain is established for a slab of porous medium. The kernels of the reflection and transmission scattering operators are derived giving simple relations between these operators and the parameters of the medium. It is shown that the reflection scattering operator is equal to the sum of two contributions: the first interface and the bulk of the porous medium.

An experimental validation of the theoretical expressions of the scattering operators illustrates the good agree-

ment between numerical and experimental results and shows that this time domain model is well suited for the characterization of porous media via acoustic wave propagation. To progress in this area, coming works will must improve experimental methods and inversion algorithms.

APPENDIX A: EXPRESSION OF THE ACOUSTIC FIELD INSIDE THE POROUS MATERIAL

The expression of the acoustic field inside the porous material taking into account the multiple reflection at the interfaces $x=0$ and $x=L$ is given from the Eq. (25)

$$P_2(x,z) = P_1(0^-, z) \frac{\sinh(\alpha\sqrt{f(z)})}{\sinh(\beta\sqrt{f(z)})} + P_3(L^+, z) \frac{\sinh(\theta\sqrt{f(z)})}{\sinh(\beta\sqrt{f(z)})},$$

with $\alpha=L-x/c$, $\beta=L/c$ and $\theta=x/c$ by the following development in series:

$$\begin{aligned} \frac{\sinh(\alpha\sqrt{f(z)})}{\sinh(\beta\sqrt{f(z)})} &= \frac{\exp(\alpha\sqrt{f(z)}) - \exp(-\alpha\sqrt{f(z)})}{\exp(\beta\sqrt{f(z)}) - \exp(-\beta\sqrt{f(z)})} \\ &= \frac{\exp(\alpha\sqrt{f(z)}) - \exp(-\alpha\sqrt{f(z)})}{\exp(\beta\sqrt{f(z)})[1 - \exp(-2\beta\sqrt{f(z)})]} \\ &= \frac{\exp(\alpha\sqrt{f(z)}) - \exp(-\alpha\sqrt{f(z)})}{\exp(\beta\sqrt{f(z)})} \\ &\quad \times \sum_{n \geq 0} \exp(-2n\beta\sqrt{f(z)}) \\ &= [\exp(\alpha\sqrt{f(z)}) - \exp(-\alpha\sqrt{f(z)})] \\ &\quad \times \sum_{n \geq 0} \exp(-(2n+1)\beta\sqrt{f(z)}) \\ &= \sum_{n \geq 0} [\exp(-[(2n+1)\beta - \alpha]\sqrt{f(z)}) \\ &\quad - \exp(-[(2n+1)\beta + \alpha]\sqrt{f(z)})], \end{aligned}$$

and the inverse Laplace transform of $P_2(x,z)$:

$$\begin{aligned} p_2(x,t) &= \mathcal{L}^{-1} P_2(x,z) \\ &= p_1(0,t) * \mathcal{L}^{-1} \left[\frac{\sinh(\alpha\sqrt{f(z)})}{\sinh(\beta\sqrt{f(z)})} \right] \\ &\quad + p_3(L,t) * \mathcal{L}^{-1} \left[\frac{\sinh(\theta\sqrt{f(z)})}{\sinh(\beta\sqrt{f(z)})} \right], \end{aligned}$$

where

$$\mathcal{L}^{-1} \left[\frac{\sinh(\alpha\sqrt{f(z)})}{\sinh(\beta\sqrt{f(z)})} \right] = \sum_{n \geq 0} [F(t, (2n+1)\beta - \alpha) - F(t, (2n+1)\beta + \alpha)]$$

and

$$F(t, k) = \mathcal{L}^{-1}[\exp(-k\sqrt{f(z)})]$$

is given by Eq. (26). The field $p_2(x, t)$ inside the porous medium is then given by:

$$p_2(x, t) = p_1(0, t) * \sum_{n \geq 0} [F(t, (2n+1)\beta - \alpha) - F(t, (2n+1)\beta + \alpha)] + p_3(L, t) * \sum_{n \geq 0} [F(t, (2n+1)\beta - \theta) - F(t, (2n+1)\beta + \theta)].$$

By substituting α , β and θ by their values, we find the expression (29).

APPENDIX B: EXPRESSION OF THE REFLECTION AND TRANSMISSION OPERATORS

To write the time domain expressions of the reflection and transmission kernels we consider their Laplace transforms. In the domain of validity of this model,⁴ $(c/\phi c_0) \times [z\alpha(z)/\sqrt{f(z)}] \approx (\sqrt{\alpha_\infty}/\phi)$. Putting $a = (\sqrt{\alpha_\infty}/\phi)$, from Eq. (36) and Eq. (41), we get the system:

$$a(-1 + R(z)) \sinh\left(\frac{L}{c} \sqrt{f(z)}\right) = T(z) \exp\left(-\frac{L}{c} z\right) - (1 + R(z)) \cosh\left(\frac{L}{c} \sqrt{f(z)}\right),$$

$$aT(z) \exp\left(-\frac{L}{c} z\right) \sinh\left(\frac{L}{c} \sqrt{f(z)}\right) = -T(z) \exp\left(-\frac{L}{c} z\right) + R(z) + 1,$$

the solution of which is given by:

$$R(z) = \frac{(a^2 - 1) \sinh\left(\frac{L}{c} \sqrt{f(z)}\right)}{2a \cosh\left(\frac{L}{c} \sqrt{f(z)}\right) + (a^2 + 1) \sinh\left(\frac{L}{c} \sqrt{f(z)}\right)},$$

$$T(z) = \frac{2a \exp\left(\frac{L}{c} z\right)}{2a \cosh\left(\frac{L}{c} \sqrt{f(z)}\right) + (2 + 1) \sinh\left(\frac{L}{c} \sqrt{f(z)}\right)},$$

which corresponds to the expressions given in Eq. (42) and Eq. (43). The reflection coefficient $R(z)$ can be written as

$$R(z) = \frac{(a^2 - 1) \left[\exp\left(\frac{L}{c} \sqrt{f(z)}\right) - \exp\left(-\frac{L}{c} \sqrt{f(z)}\right) \right]}{2a \left[\exp\left(\frac{L}{c} \sqrt{f(z)}\right) + \exp\left(-\frac{L}{c} \sqrt{f(z)}\right) \right] + (a^2 + 1) \left[\exp\left(\frac{L}{c} \sqrt{f(z)}\right) - \exp\left(-\frac{L}{c} \sqrt{f(z)}\right) \right]}$$

and is equivalent to

$$R(z) = \left[\frac{a^2 - 1}{(a + 1)^2} \right] \frac{1 - \exp\left(-2 \frac{L}{c} \sqrt{f(z)}\right)}{1 - \left(\frac{a - 1}{a + 1}\right)^2 \exp\left(-2 \frac{L}{c} \sqrt{f(z)}\right)}.$$

From the identity

$$\frac{1}{1 - \left(\frac{a - 1}{a + 1}\right)^2 \exp\left(-2 \frac{L}{c} \sqrt{f(z)}\right)} = \sum_{n \geq 0} \left(\frac{a - 1}{a + 1}\right)^{2n} \exp\left(-2n \frac{L}{c} \sqrt{f(z)}\right)$$

$R(z)$ has the following form:

$$R(z) = \left(\frac{a - 1}{a + 1}\right) \sum_{n \geq 0} \left(\frac{a - 1}{a + 1}\right)^{2n} \left[\exp\left(-2n \frac{L}{c} \sqrt{f(z)}\right) - \exp\left(-2(n + 1) \frac{L}{c} \sqrt{f(z)}\right) \right]. \quad (50)$$

The kernel of the reflection scattering operator $\tilde{R}(t)$ is given by the inverse Laplace transform of this equation

$$\tilde{R}(t) = \left(\frac{a - 1}{a + 1}\right) \sum_{n \geq 0} \left(\frac{a - 1}{a + 1}\right)^{2n} \left[F\left(t, 2n \frac{L}{c}\right) - F\left(t, 2(n + 1) \frac{L}{c}\right) \right], \quad (51)$$

where $F(t, k)$ is given by Eq. (26). In the same manner, the transmission coefficient is given by:

$$T(z) = \frac{4a \exp\left(\frac{L}{c}z\right)}{2a \left[\exp\left(\frac{L}{c}\sqrt{f(z)}\right) + \exp\left(-\frac{L}{c}\sqrt{f(z)}\right) \right] + (a^2 + 1) \left[\exp\left(\frac{L}{c}\sqrt{f(z)}\right) - \exp\left(-\frac{L}{c}\sqrt{f(z)}\right) \right]},$$

which can be written as:

$$T(z) = \frac{4a \exp\left(\frac{L}{c}z\right) \exp\left(-\frac{L}{c}\sqrt{f(z)}\right)}{(a+1)^2 - (a-1)^2 \exp\left(-2\frac{L}{c}\sqrt{f(z)}\right)}.$$

Expanding this relation in series, one gets

$$T(z) = \frac{4a}{(a+1)^2} \exp\left(\frac{L}{c}z\right) \sum_{n \geq 0} \left(\frac{a-1}{a+1}\right)^{2n} \times \exp\left(-(2n+1)\frac{L}{c}\sqrt{f(z)}\right),$$

which by inverse Laplace transform leads to the kernel of the transmission scattering operator:

$$\tilde{T}(t) = \frac{4a}{(a+1)^2} \sum_{n \geq 0} \left(\frac{a-1}{a+1}\right)^{2n} F\left(t + \frac{L}{c}, (2n+1)\frac{L}{c}\right). \quad (52)$$

The reflection operator is obtained with $n=0$ and $x=L$ in Eq. (51):

$$\tilde{R}(t) = \left(\frac{a-1}{a+1}\right) \left[\delta(t) - \frac{4a}{(a+1)^2} F\left(t, 2\frac{L}{c}\right) \right].$$

The transmission operator is obtained with $n=0$ and $x=L$ in Eq. (52):

$$\tilde{T}(t) = \frac{4a}{(a+1)^2} F\left(t + \frac{L}{c}, \frac{L}{c}\right).$$

¹J. F. Allard, *Propagation of Sound in Porous Media: Modeling Sound Absorbing Materials* (Chapman and Hall, London, 1993).

²D. Lafarge, "Sound propagation in porous materials having a rigid frame saturated by gas" (in French), Ph.D. Dissertation, Université du Maine (1993).

³L. Päiväranta and E. Somersalo, Eds., *Inverse Problems in Mathematical Physics* (Springer, Berlin, 1993).

⁴Z. E. A. Fellah and C. Depollier, "Transient acoustic wave propagation in rigid porous media: A time-domain approach," *J. Acoust. Soc. Am.* **107**, 683–688 (2000).

⁵Z. E. A. Fellah and C. Depollier, "On the propagation of acoustic pulses in

porous rigid media: A time domain approach," *J. Comput. Acoust.* **9**, 1163–1173 (2001).

⁶Z. E. A. Fellah, C. Depollier, and M. Fellah, "An approach to direct and inverse time-domain scattering of acoustic waves from rigid porous materials by a fractional calculus based method," *J. Sound Vib.* **244**, 359–366 (2001).

⁷Z. E. A. Fellah, C. Depollier, and M. Fellah, "Application of fractional calculus to the sound waves propagation in rigid porous materials: Validation via ultrasonic measurements," *Acta Acust. (Beijing)* **88**, 34–39 (2002).

⁸T. L. Szabo, "Time domain wave equations for lossy media obeying a frequency power law," *J. Acoust. Soc. Am.* **96**, 491–500 (1994).

⁹M. Caputo, "Vibrations of an infinite plate with a frequency independent Q," *J. Acoust. Soc. Am.* **60**, 634–639 (1976).

¹⁰R. L. Bagley and P. J. Torvik, "On the fractional calculus Model of Viscoelastic Behavior," *J. Rheol.* **30**, 133–155 (1983).

¹¹M. A. Biot, "The theory of propagation of elastic waves in fluid-saturated porous solid. I. Low frequency range," *J. Acoust. Soc. Am.* **28**, 168–178 (1956).

¹²M. A. Biot, "The theory of propagation of elastic waves in fluid-saturated porous solid. I. Higher frequency range," *J. Acoust. Soc. Am.* **28**, 179–191 (1956).

¹³D. L. Johnson, J. Koplik, and R. Dashen, "Theory of dynamic permeability and tortuosity in fluid-saturated porous media," *J. Fluid Mech.* **176**, 379–402 (1987).

¹⁴C. Zwikker and C. W. Kosten, *Sound Absorbing Materials* (Elsevier, New York, 1949).

¹⁵S. G. Samko, A. A. Kilbas, and O. I. Marichev, *Fractional Integrals and Derivatives: Theory and Applications* (Gordon and Breach Science, Amsterdam, 1993).

¹⁶Z. E. A. Fellah, "Propagation of acoustics waves in porous media: Temporal approach," Ph.D. Dissertation, Université du Maine, France (2000).

¹⁷E. W. Weisstein, *Concise Encyclopedia of Mathematics* (Chapman and Hall, Boca Raton, 1999).

¹⁸P. Leclaire, L. Kelders, W. Lauriks, N. R. Brown, M. Melon, and B. Castagnède, "Determination of the viscous and thermal characteristics lengths of plastic foams by ultrasonic measurements in helium and air," *J. Appl. Phys.* **80**, 2009–2012 (1996).

¹⁹N. Brown, M. Melon, V. Montembault, B. Castagnède, W. Lauriks, and P. Leclaire, "Evaluation of viscous characteristic length of air-saturated porous materials from the ultrasonic dispersion curve," *C. R. Acad. Sci. Paris II* **322**, 121–127 (1996).

²⁰M. Henry, "Measurement of porous media parameters. Experimental study of acoustic behavior of plastic foams at low frequency range," Ph.D. Dissertation, Université du Maine (1997).

²¹L. L. Beranek, "Acoustic impedance of porous materials," *J. Acoust. Soc. Am.* **13**, 248 (1942).

²²Y. Champoux, M. R. Stinson, and G. A. Daigle, "Air-based system for the measurements of the porosity," *J. Acoust. Soc. Am.* **89**, 910 (1991).

The reflection of bounded inhomogeneous waves on a liquid/solid interface

S. Vanaverbeke,^{a)} F. Windels,^{b)} and O. Leroy

Interdisciplinary Research Center (IRC), E. Sabbelaan 53, B-8500 Kortrijk, Belgium

(Received 18 May 2001; revised 28 August 2002; accepted 20 September 2002)

Fourier analysis and normal mode theory are used to describe the reflection of bounded inhomogeneous waves on a liquid/solid interface. Nonspecular reflection phenomena in the Rayleigh angle are studied in detail. In this way, an explanation is given for the Rayleigh dip phenomenon for positive inhomogeneity factors and the related result of a reflection coefficient larger than unity when the sign of the inhomogeneity factor is reversed. In the limit of large beamwidths, the reflection coefficient predicted by the infinite plane inhomogeneous wave theory is obtained. These results are entirely consistent with the experimental work published by Deschamps [J. Acoust. Soc. Am. **96**, 2841–2848 (1994)]. The energy efficiency of Rayleigh wave excitation is investigated as well. It is shown that for large beamwidths, the energy efficiency for bounded inhomogeneous waves is considerably higher in comparison with Gaussian and square-profiled beams. © 2003 Acoustical Society of America. [DOI: 10.1121/1.1523081]

PACS numbers: 43.20.El, 43.40.Fz, 43.20.Ks [DEC]

I. INTRODUCTION

Recent advances in linear acoustics have shown that the most general solutions of the wave equations in an homogeneous, isotropic and linearly viscoelastic medium are given by complex harmonic waves. Good reviews of this subject can be found in the works of Poirée,¹ Deschamps² and Van Den Abeele and Leroy.³ However, the notion of these kind of wave phenomena first appeared in electromagnetism.⁴ Complex harmonic waves are characterized by a complex wave vector, where the real and imaginary parts in general do not have the same orientation, corresponding to an exponential damping of the wave amplitude both in the direction of propagation and orthogonal to it. Recently, the effect of introducing a complex frequency was studied by Poncelet⁵ and allows the investigation of transient phenomena. When the media are assumed lossless, only complex harmonic waves with exponential damping orthogonal to the direction of propagation can exist, and these particular waves are then called inhomogeneous waves, but the term evanescent waves is also used by some authors.^{6–8} The study of complex harmonic waves is important because they are immediately generated when wave interaction with absorbing media is studied⁹ and the structure of interface waves, such as Rayleigh waves and Stoneley waves, which are important for ultrasonic ndt-applications, cannot be described by means of plane homogeneous waves.^{10,11} When considering bounded acoustic beams in ideal media, Claeys and Leroy¹² were the first to use bulk inhomogeneous plane waves as a fundamental tool in the modeling of the scattering of Gaussian ultrasonic beams on liquid/solid interfaces and on plates. This work was reviewed in detail by Leroy.¹³ Van Den Abeele and Leroy³ subsequently showed the large sensitivity of the

reflection/transmission coefficients of inhomogeneous plane waves on the physical properties of the media on which scattering takes place. By means of the transmission of a plane homogeneous wave through an absorbing PVC-prism,¹⁴ Deschamps¹⁵ was able to generate bulk inhomogeneous waves in water and measured the reflection coefficient on aluminum plates, but some results, notably the appearance of a reflection coefficient larger than one, could not be explained satisfactorily by theory. Moreover, all previous theoretical studies were based on infinite plane wave theory, but from the point of view of a comparison between theory and experiment, it should be recognized that inhomogeneous waves can only be approximated by bounded acoustic beams. Therefore, our purpose in this paper is to consider inhomogeneous waves as a special kind of bounded acoustic beams, and to develop a model for the scattering of bounded inhomogeneous waves on a liquid/solid interface.

In Sec. I, we model bounded inhomogeneous waves as well as bounded Gaussian beams and square profiled beams. We then use normal mode theory^{16–18} and the well known Fourier method^{19–21} to derive expressions for the reflected sound field on a liquid/solid interface. In Sec. II, we use the results of Sec. I to calculate the reflected profiles on water/steel and water/aluminum interfaces for various beam parameters and investigate the reflection coefficient as a function of the incidence angle. We compare the results of the Fourier model and normal mode theory and examine the Rayleigh dip phenomenon in detail. In Sec. III, we calculate the energy efficiency of surface wave excitation in the Rayleigh angle on a liquid/solid interface and compare bounded inhomogeneous waves, Gaussian beams and square profiled beams. Finally, in Sec. IV we end up with some conclusions.

II. THEORY

A. The Fourier model

A scheme of the coordinate system that will be used in this paper is given in Fig. 1. We consider a two-dimensional

^{a)}Research Assistant for the Flemish Institute for the Encouragement of the Scientific and Technological Research in Industry (IWT). Electronic mail: sigfried.vanaverbeke@kula.ac.be

^{b)}Research assistant for the National Fund for Scientific Research Flanders (FWO).

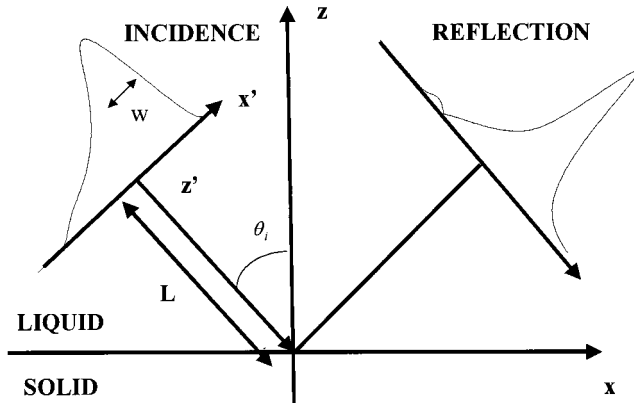


FIG. 1. Reflection of a bounded inhomogeneous wave on a liquid/solid interface

bounded ultrasonic beam incident under an angle θ_i on a liquid/solid interface. In an intrinsic coordinate system (x', z') with the z' -axis pointing in the direction of propagation, we propose the following expression for the magnitude of the acoustic displacement in the plane $z'=0$:

$$U_i(x', 0) = NU_0 \exp(\beta x' - (|x'|/w)^p/p). \quad (1)$$

In this expression, w is the half beamwidth, β is the inhomogeneity parameter and $|\cdot|$ stands for the absolute value of a real quantity. We still need a parameter describing the behavior at the edges of the profile. From the known generalization of the Gaussian function which is used in the context of the study of inverse problems,²² we decided to introduce an exponent and a denominator p . We assume a time dependence equal to $\exp(-i\omega t)$ with angular frequency $\omega = 2\pi f$ and f the sound frequency in Hz, but we will suppress this factor for reasons of brevity. The normalization constant N is given by

$$N = \exp(-(x_m/L)^p/p + |\beta|x_m), \quad (2)$$

with

$$x_m = (|\beta|L^p)^{1/(p-1)}. \quad (3)$$

By taking different values for the parameters β , L and p , we can model incident Gaussian beams, square profiles and spatially bounded inhomogeneous waves. In Fig. 2 we illustrate this by taking $w=20$ mm and plotting expression (1) versus the normalized distance x'/w for 3 choices of the parameters β and p : $\beta=0$ m⁻¹, $p=2$ (a Gaussian profile), $\beta=0$ m⁻¹, $p=10$ (a square profile) and $\beta=50$ m⁻¹, $p=10$ (a bounded inhomogeneous wave). By increasing the value of p , we can increase the steepness of the edges of the profile. In practice, expression (1) can, for example, be fitted to a set of experimental data in a plane parallel to the transducer surface. In the plane $z'=0$, we can now take the Fourier transform of Eq. (1):

$$V(k_{x'}) = \int_{-\infty}^{+\infty} U_i(x', 0) \exp(-ik_{x'}x') dx'. \quad (4)$$

The bounded acoustic beam described by Eq. (1) will then propagate as

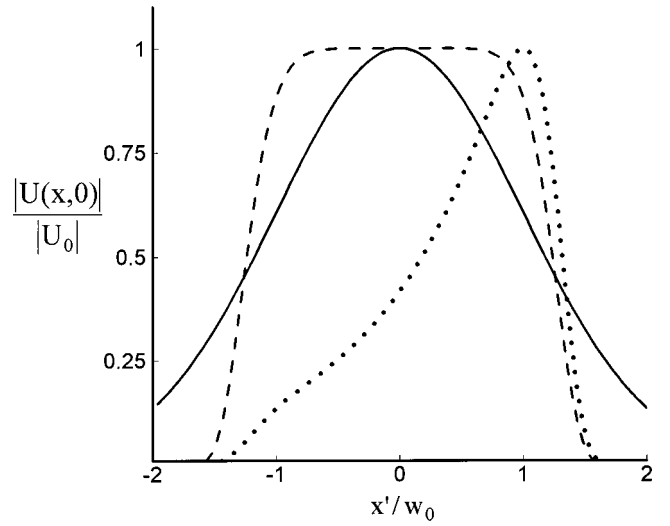


FIG. 2. Incident profiles for $w=20$ mm: a Gaussian beam; $\beta=0$ m⁻¹, $p=2$ (solid line); a square profile; $\beta=0$ m⁻¹, $p=8$ (dashed line); a bounded inhomogeneous wave; $\beta=50$ m⁻¹, $p=8$ (dotted line).

$$U_i(x', z') = \frac{1}{2\pi} \int_{-\infty}^{+\infty} V(k_{x'}) \exp(I(k_{x'}x' + k_{z'}z')) dk_{x'}, \quad (5)$$

where $k_{z'} = \sqrt{k^2 - k_{x'}^2}$, with $k = \omega/v$ the wave number of longitudinal sound waves in the liquid and v the longitudinal wave speed. If the width of the ultrasonic beam is large compared with the sound wavelength and the propagation path is not too long, we can use the paraxial approximation and write the z' -component of the wave vector as a Taylor series to first order in $k_{x'}^2$:

$$k_{z'} = k - \frac{k_{x'}^2}{2k}. \quad (6)$$

When we restrict the Taylor series to the first term, the effects of propagation diffraction are neglected and the sound profile described by Eq. (1) will propagate without distortion, because the z' -dependence in the Fourier integral (5) now becomes independent of $k_{x'}$ and leads to a propagation factor in front of the integral. This approximation was in fact also used by Bertoni and Tamir¹⁹ and Ngoc and Mayer.²⁰ Using expressions (1) and (4), we can then write

$$U_i(x', z') = NU_0 \exp(Ikz') \exp(-(|x'|/w)^p/p + \beta x'). \quad (7)$$

In the (x', z') coordinate system, the interface is described by

$$z' = L + \tan(\theta_i)x', \quad (8)$$

where L is the main propagation distance of the incident sound beam as shown in Fig. 1. From Eq. (7), we then obtain for the acoustic field at the interface,

$$\begin{aligned} U_i(x', z' = L + \tan(\theta_i)x') \\ = NU_0 \exp(Ik(L + \tan(\theta_i)x')) \\ \times \exp(-(|x'|/w)^p/p + \beta x'). \end{aligned} \quad (9)$$

Considering the (x, z) coordinate system with the z -axis pointing upwards into the liquid, we have the following relation:

$$x' = x \cos(\theta_i). \quad (10)$$

Using the foregoing expressions, we can rewrite expression (9) in the (x, z) coordinate system,

$$U_i(x, z=0) = \exp(ikL) U_0 \exp(ik_i x) \times \exp(-(|x|/w_0)^p / p + \beta_i x), \quad (11)$$

where $w_0 = w/\cos(\theta_i)$ is the projected beamwidth on the interface, $\beta_i = \beta \cos(\theta_i)$ is the projected inhomogeneity parameter and $k_i = k \sin(\theta_i)$ is the x -component of the central wavevector. For the case of a Gaussian beam ($p=2$, $\beta_i = 0 \text{ m}^{-1}$), expression (11) describes exactly the same amplitude distribution as adopted by Bertoni and Tamir¹⁹ and Ngoc and Mayer,²⁰ except for the constant propagation factor $\exp(ikL)$, which we will omit further. We now have the following Fourier transform pair for the sound field on the interface:

$$V(k_x) = \int_{-\infty}^{+\infty} U_i(x, 0) \exp(-ik_x x) dx, \quad (12)$$

and

$$U_i(x, 0) = \int_{-\infty}^{+\infty} V(k_x) \exp(ik_x x) dk_x. \quad (13)$$

To calculate the reflected sound beam, we multiply every component in the plane wave spectrum of the incident beam by the reflection coefficient $R(k_x)$ at a liquid/solid interface and obtain

$$U_R(x, 0) = \frac{1}{2\pi} \int_{-\infty}^{+\infty} R(k_x) V(k_x) \exp(ik_x x) dk_x. \quad (14)$$

The reflection coefficient $R(k_x)$ is given by¹²

$$R(k_x) = \frac{(k_s^2 - 2k_x^2)^2 + 4k_x^2 k_{lz} k_{sz} - \rho k_s^4 k_{lz}/k_z}{(k_s^2 - 2k_x^2)^2 + 4k_x^2 k_{lz} k_{sz} + \rho k_s^4 k_{lz}/k_z}, \quad (15)$$

where

$$k_{lz} = \sqrt{k_l^2 - k_x^2}, \quad (16)$$

$$k_{sz} = \sqrt{k_s^2 - k_x^2}, \quad (17)$$

$$\rho = \frac{\rho_1}{\rho_2}, \quad (18)$$

$$k_l = \frac{\omega}{v_l}, \quad (19)$$

$$k_s = \frac{\omega}{v_s}. \quad (20)$$

In these expressions, ρ_1 and ρ_2 are the densities of the liquid and the solid and v_s and v_l are the shear wave speed and the longitudinal wave speed in the solid medium. To compute the profile of the reflected sound beam on the interface, the integral (14) must be calculated numerically.

B. Normal mode theory

An alternative method to describe the interaction of bounded ultrasonic beams with a liquid/solid interface was formulated by Jia^{16,17} and subsequently extended by Windels, Vanaverbeke and Leroy¹⁸ to derive analytical expressions for the reflection of a Gaussian ultrasonic beam on a liquid/coating/solid structure. This model describes the reflection of bounded ultrasonic beams on layered elastic media by considering the excitation of the normal modes of the medium by the incident sound field. The amplitude $a_n(x)$ of the n -th normal mode excited in the solid medium is given by the normal mode equation,

$$\frac{da_n(x)}{dx} - Ik_n a_n(x) = f_n(x)/4P_n, \quad (21)$$

where k_n is the wave number of the n -th propagating mode, P_n is the associated average power flow per unit length orthogonal to the plane of incidence, and $f_n(x)$ is the loading applied on the interface between the liquid and the solid medium. The derivation of this equation is based on the orthogonality relations satisfied by the normal modes of a waveguide and can be found in the book of Auld.²³ If the liquid is nonviscous, the loading can be expressed as

$$f_n(x) = I\omega u_{nz}^*(0) T_{zz}(x, 0), \quad (22)$$

where $u_{nz}^*(0)$ is the complex conjugate of the normal displacement component of the n -th normal mode of the medium at the interface and T_{zz} is the normal stress. It should be emphasized that the normal modes considered here are found by solving the dispersion equation of a stress-free medium. If liquid loading is present, these modes will become leaky waves. However, if the density of the liquid is small compared to the density of the solid, we can approximate the displacement fields of the leaky modes as those of the corresponding normal modes. This approach, which is based on perturbation theory, is valid for most ultrasonic immersion techniques. If the incident and reflected sound fields are denoted by U_i and U_R as before, the boundary conditions to be fulfilled at $z=0$ are

$$-U_i(x, 0) \cos(\theta_i) + U_R(x, 0) \cos(\theta_i) = u_{nz}^*(0) a_n(x), \quad (23)$$

$$I\omega Z \cos(\theta_i) U_i(x, 0) + I\omega Z U_R(x, 0) \cos(\theta_i) = T_{zz}(x, 0), \quad (24)$$

where Z is the acoustic impedance of the liquid. After eliminating U_R in Eqs. (23) and (24) and using (22), the mode amplitude equation (21) becomes¹⁶

$$\frac{da_n(x)}{dx} + (-Ik_n + \alpha_n) a_n(x) = -\beta_n U_i(x, 0), \quad (25)$$

where α_n corresponds to the attenuation per unit length due to reradiation at the interface and β_n is given by

$$\beta_n = \frac{\omega^2 Z \cos(\theta_i) u_{nz}^*(0)}{2P_n}. \quad (26)$$

The leaking rate α_n can be expressed as

TABLE I. The values of the material parameters used in the numerical calculations.

Material	Density (kg/m ³)	Shear velocity (m/s)	Longitudinal velocity (m/s)
Water	1000	-	1480
Steel	7900	3100	5790
Brass	8600	2260	4660

$$\alpha_n = \frac{\omega^2 Z |u_{nz}(0)|^2}{4 P_n}, \quad (27)$$

and depends on the normal component of the displacement field of the n -th normal mode at the li-liquid/solid interface. After integrating the mode amplitude equation (21), we again use the boundary conditions (23) and (24) and the form of the incident sound field (11) to derive the following expression for the reflected sound beam:

$$U_R(x, 0) = U_i(x, 0) - 2\alpha_n U_0 \exp(ik_n x - \alpha_n x) F(x), \quad (28)$$

with

$$F(x) = \int_{-\infty}^x dx' \exp(-(|x'|/w_0)^p/p + \beta_i x') + (k_i - k_n)x' + \alpha_n x'). \quad (29)$$

The physical interpretation of expressions (28) and (29) is that the modal amplitude is cumulatively excited due to the overlap of the incident sound beam with the exponentially decaying modal field in the region of insonification, but there is a phase mismatch $k_i - k_n$ that prevents this energy transfer. Expressions (28) and (29) lead to analytical results for a Gaussian beam,¹⁶ but for bounded inhomogeneous

waves one has to calculate them numerically. It is important to remark that the normal mode theory described above is only a good approximation when we consider Rayleigh angle phenomena.

III. SIMULATIONS

We now use the theory developed in the preceding section to investigate the reflection of bounded inhomogeneous waves on a liquid–solid interface. In the subsequent simulations, we will consider water/aluminum and water/steel interfaces. The density and the longitudinal wave speed for water are taken to be $\rho_1 = 1000 \text{ kg/m}^3$ and $v = 1480 \text{ m/s}$. The material parameters for aluminum and stainless steel can be found in Table I. In Fig. 3, we consider the reflection of bounded inhomogeneous waves in the Rayleigh angle on a water/steel interface at a frequency of 4 MHz. The corresponding incidence angle is equal to 30.968° . The reflected beam profiles are plotted on the interface for $\beta = 50 \text{ m}^{-1}$ and -50 m^{-1} and $w = 10$ and 30 mm , respectively, together with the incident sound fields. The bounds of the incident exponential profile were modeled using $p = 8$ in expression (11). The results were calculated using both Fourier analysis and normal mode theory and are shown to be in perfect agreement.

Several important conclusions can be drawn from these figures. The reflected beam profiles consist of a specular lobe, which is in general small, and a large nonspecular lobe with an exponentially decaying trailing field along the interface. Due to the phase reversal between these two components of the reflected sound field, a null zone is created. This is a consequence of the redistribution of energy due to the excitation of a leaky Rayleigh wave and was described theo-

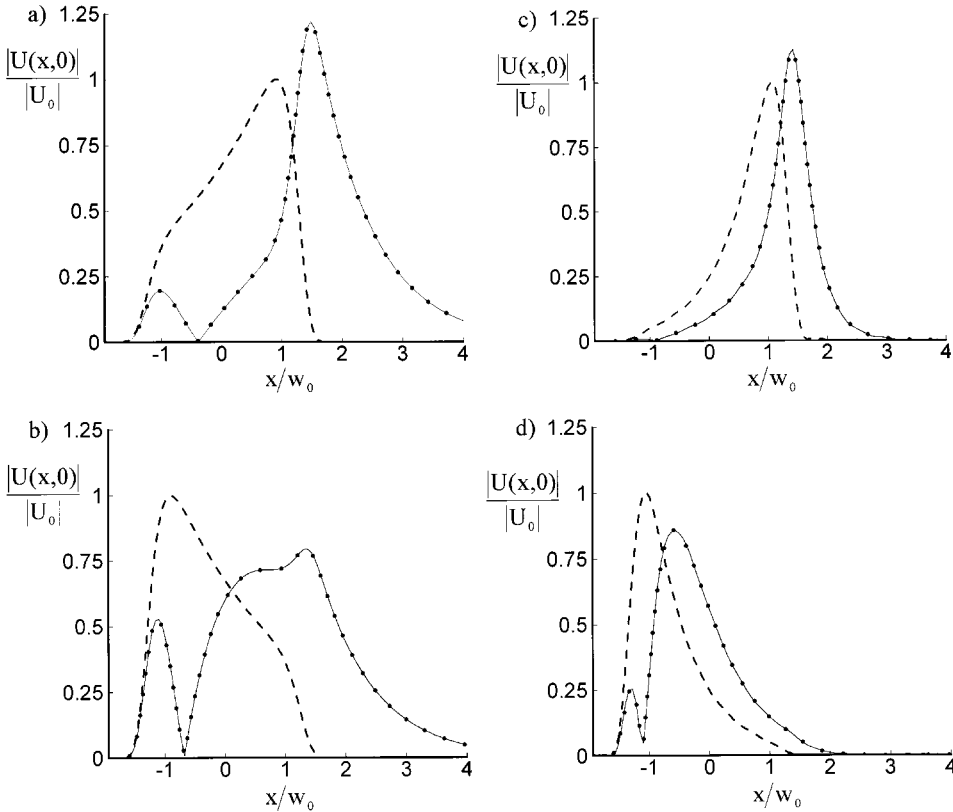


FIG. 3. Reflected beam profiles in the Rayleigh angle on a water/steel interface with $f = 4 \text{ MHz}$ and $p = 8$: (a) $w = 10 \text{ mm}$, $\beta = 50 \text{ m}^{-1}$; (b) $w = 10 \text{ mm}$, $\beta = -50 \text{ m}^{-1}$; (c) $w = 30 \text{ mm}$, $\beta = 50 \text{ m}^{-1}$; (d) $w = 30 \text{ mm}$, $\beta = -50 \text{ m}^{-1}$. The reflected profiles were calculated using Fourier analysis (full lines) and normal mode theory (dotted lines) and are shown together with the incident profiles (dashed lines).

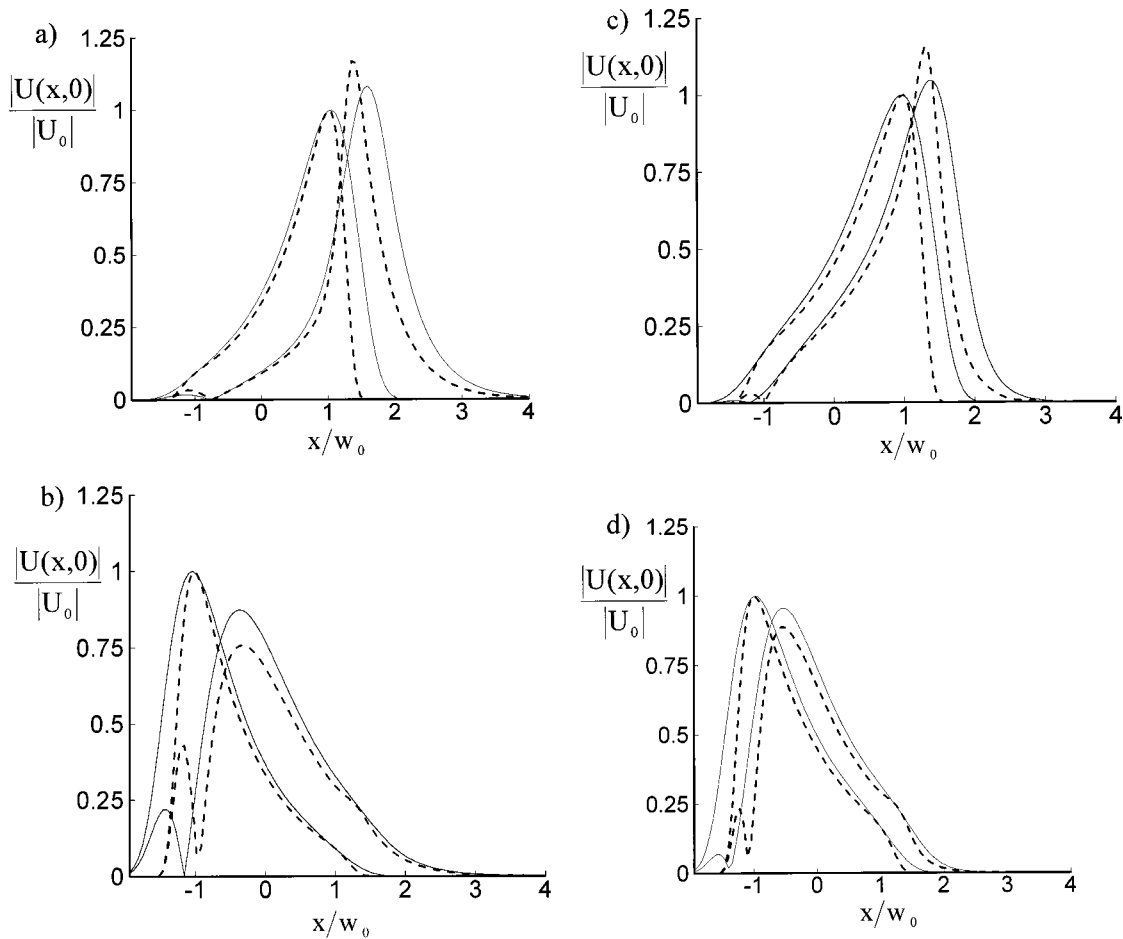


FIG. 4. Influence of the parameter p on the reflected beam profiles in the Rayleigh angle of a water/steel interface: (a) $f=4$ MHz, $w=20$ mm, $\beta=60$ m $^{-1}$; (b) $f=4$ MHz, $w=20$ mm, $\beta=-60$ m $^{-1}$; and in the Rayleigh angle of a water/aluminum interface: (c) $f=3$ MHz, $w=20$ mm, $\beta=45$ m $^{-1}$; (d) $f=3$ MHz, $w=20$ mm, $\beta=-45$ m $^{-1}$. The incident and reflected profiles are plotted for $p=5$ (full lines) and $p=10$ (dashed lines).

retically by Bertoni and Tamir¹⁹ for the case of Gaussian beams. However, these authors never extended their theory to bounded ultrasonic beams with a general profile. For small beamwidths, the reflected profiles are in general quite distorted, but when the beamwidth increases, the specular lobe starts to disappear and the reflected profiles consist almost entirely of the nonspecular lobe, as shown in Figs. 3(c) and 3(d). Figure 4 shows the influence of the edges of the incident profile on the reflected sound beam in the Rayleigh angle of a water/steel interface with $f=4$ MHz and $\beta=60$ and -60 m $^{-1}$ [Figs. 4(a) and (b) and in the Rayleigh angle of a water/aluminum interface with $f=3$ MHz and $\beta=45$ and -45 m $^{-1}$ [Figs. 4(c) and (d)]. The Rayleigh angle of the water/aluminum interface is approximately 30.2° . In all figures, the incident profiles are plotted for $p=5$ and $p=10$ with a half beamwidth of 20 mm. The resulting reflected sound fields were calculated using Fourier analysis. If the edges of the incident profile are steep, the reflected beam can have a maximum amplitude that is larger than that of the incident sound field if the inhomogeneity factor is positive. When considering negative inhomogeneity factors, the effect is mainly to recreate the specular lobe. Due to the conservation of energy, the maximum in the nonspecular lobe correspondingly diminishes. We may conclude that if the steepness of the edges is not too large, the reflected sound beam

may behave almost as a displaced copy of the incident sound beam with a phase reversal of 180° . This phenomenon is analogous to the lateral displacement of Gaussian ultrasonic beams observed by Schoch.²⁴ The parameters used to calculate the reflected profiles for the water/aluminum interface correspond almost exactly to the experimental arrangement of Deschamps,¹⁵ who indeed observed a lateral displacement of the reflected profile in the Rayleigh angle. The physical mechanism for this lateral displacement is revealed to be a consequence of the nonspecular reflection. Furthermore, let us consider the mean direction of propagation of the plane wave components in the Fourier model, which corresponds to $x'=0$ in Fig. 1. In the reflected sound field, there is an associated specular direction. We can define a local reflection coefficient as the ratio between the amplitude of the reflected and the incident sound field at these points. In this way, a reflection coefficient smaller than unity is obtained for positive inhomogeneity factors. This result corresponds to the Rayleigh dip phenomenon, discussed by Leroy, Poirée, Sebbag and Quentin.²⁵ For the negative inhomogeneity factors, the lateral displacement of the reflected profile to the right will correspond to a reflection coefficient larger than unity, as found by Deschamps.¹⁵

In Figs. 5 and 6, we have used the Fourier model to calculate the modulus of the reflection coefficient defined

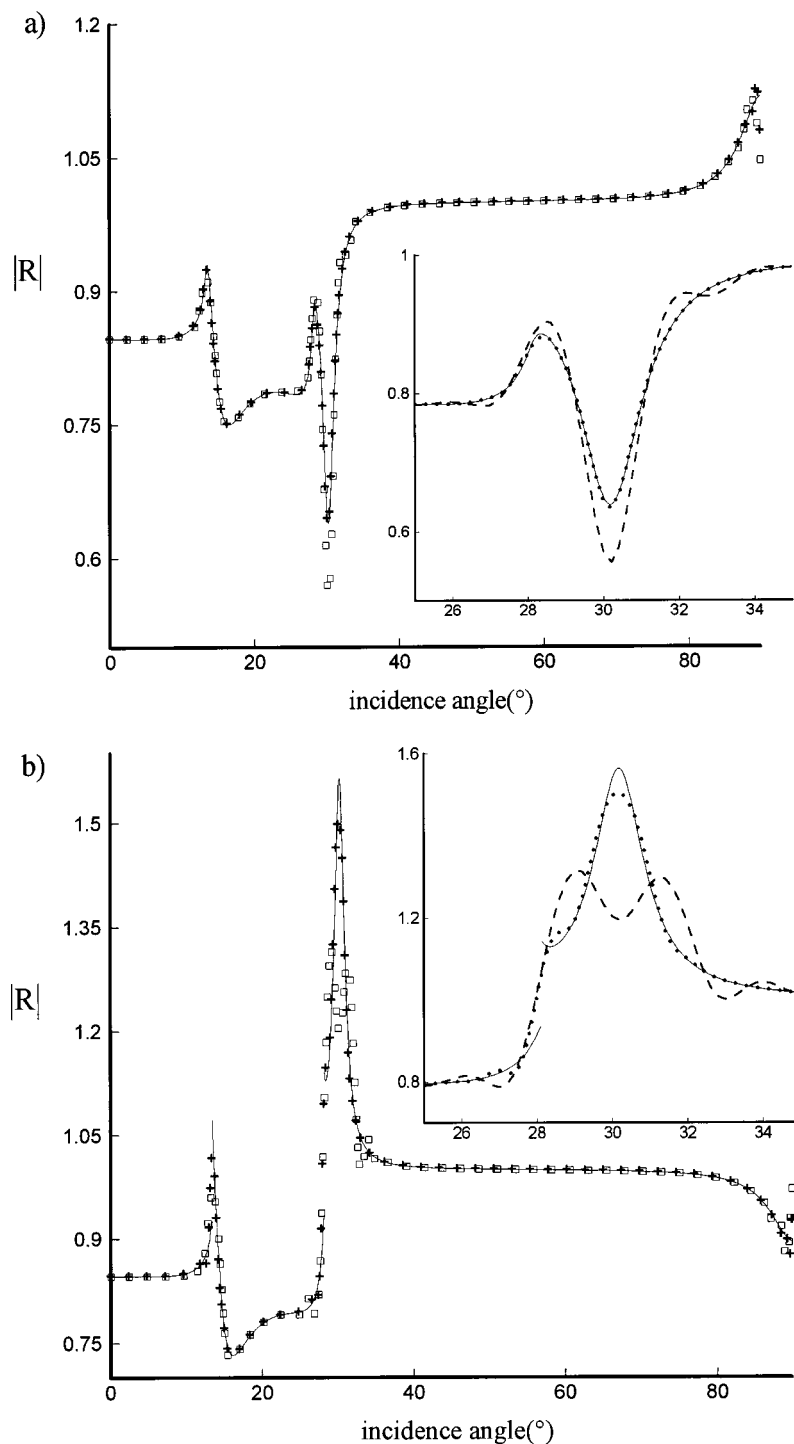


FIG. 5. The modulus of the reflection coefficient as a function of the angle of incidence on a water/aluminum interface with $f=3 \text{ MHz}$ and $p=8$: (a) $\beta=45 \text{ m}^{-1}$ and (b) $\beta=-45 \text{ m}^{-1}$. Results are shown for $w=10 \text{ mm}$ (\square) and $w=20 \text{ mm}$ (+), together with the modulus of the reflection coefficient for infinite plane inhomogeneous waves (full line). The insets show the region around the Rayleigh angle with $w=10 \text{ mm}$ (dashed line) and $w=20 \text{ mm}$ (dotted line).

above as a function of the angle of incidence on a water/aluminum interface at a frequency of 3 MHz with $\beta=45$ and -45 m^{-1} and on a water/steel interface at a frequency of 4 MHz with $\beta=50$ and -50 m^{-1} . Results are shown for w equal to 10 and 20 mm, together with the modulus of the reflection coefficient for infinite plane inhomogeneous waves as given by expression (15), where the component k_x of the wavevector along the interface can be written as

$$k_x = k \sin(\theta_i) - I \beta \cos(\theta_i). \quad (30)$$

With increasing beamwidth, the region of the incident sound field around $x'=0$ is found to behave as if it were an infinite plane wave and the local reflection coefficient ap-

proaches the reflection coefficient for infinite plane inhomogeneous waves. This can be intuitively understood since the presence of the spatial edges of the exponential profile does not have a large influence on the central part when the beamwidth is sufficiently large. For $w=20 \text{ mm}$, the agreement is almost exact for the water/aluminum interface, with only a small difference at the Rayleigh angle for the negative value of the inhomogeneity factor. For the water/steel interface, the convergence is slower and a value of approximately 1.8 for the reflection coefficient is found at the Rayleigh angle for $\beta=-50 \text{ m}^{-1}$. It is important to notice that in infinite plane inhomogeneous wave theory, there is an inherent degree of

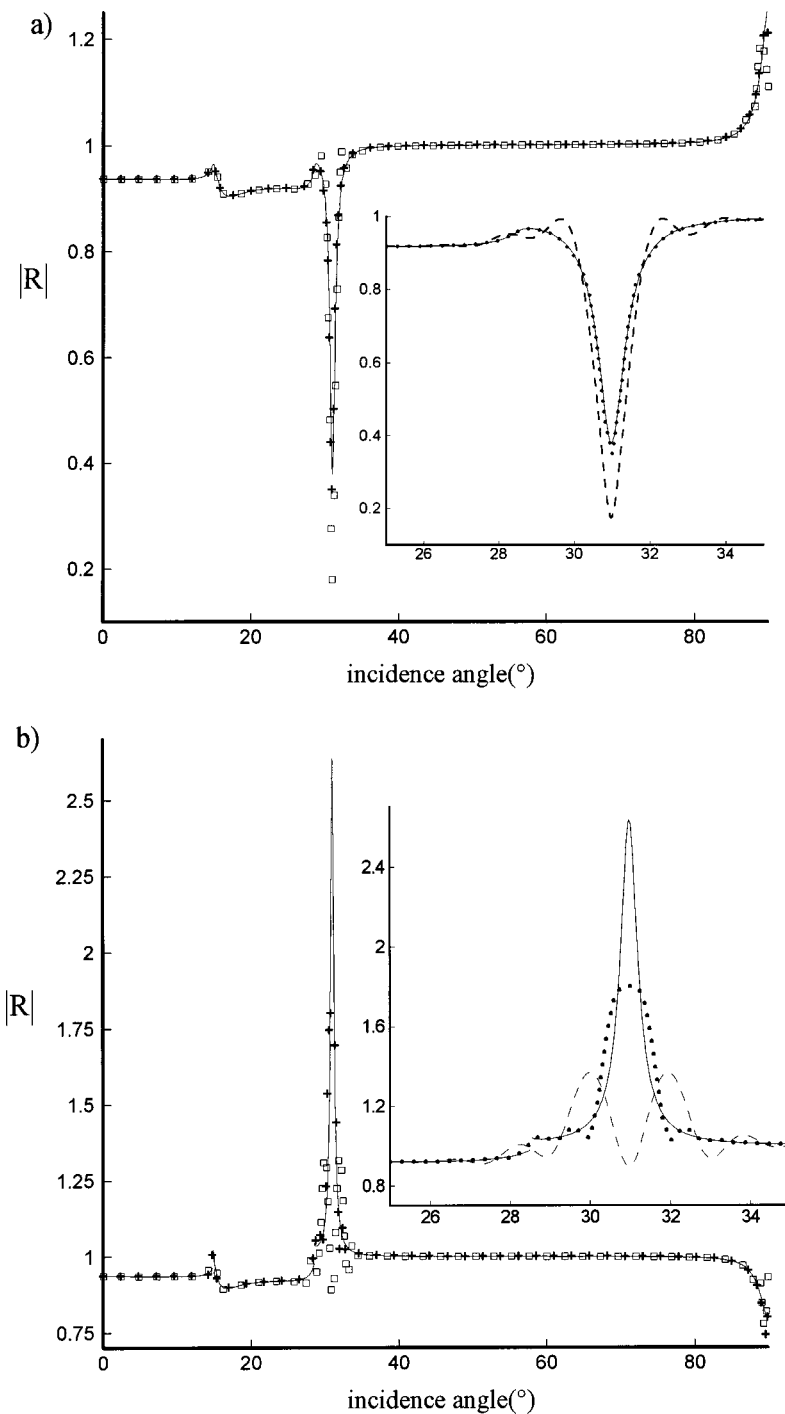


FIG. 6. The same as Fig. 5, but for a water/steel interface with $f=4$ Mhz, $p=8$ and (a) $\beta=50 \text{ m}^{-1}$; (b) $\beta=-50 \text{ m}^{-1}$.

freedom in the generalized laws of Snell that corresponds to the choice of sign for the z -component of the wave vector of the longitudinal and transverse waves in the reflection coefficient. To obtain a reflection coefficient consistent with experiment, these choices have to be made according to the angle of incidence and can be found in Deschamps,¹⁵ but a clear physical motivation is missing. Moreover, discontinuities are present at the longitudinal and shear critical angles for negative values of the inhomogeneity factor. The model we present here does not suffer from these difficulties and sheds more light on the physics of the reflection process. Interestingly, the local reflection coefficient shows oscillating behavior near the Rayleigh angle for smaller beamwidths. In

general, this phenomenon is connected with the presence of the sharp edges of the sound profile and should be verified experimentally.

We now consider the Rayleigh dip phenomenon in more detail. In Fig. 7, the reflected beam profiles in the Rayleigh angle of the water/steel interface are shown for a half beam-width of 30 mm, a frequency of 2 MHz and $\beta=20, 35, 55$ and 85 m^{-1} . If β is smaller than 55 m^{-1} , a specular lobe is present and the point $x=0$ lies in the nonspecular lobe of the reflected field. For $\beta=55 \text{ m}^{-1}$, the specular lobe is almost absent and all incident energy is shifted in the nonspecular lobe. The reflection coefficient is zero for this value of β . For larger values of β there is again a specular lobe, but now x

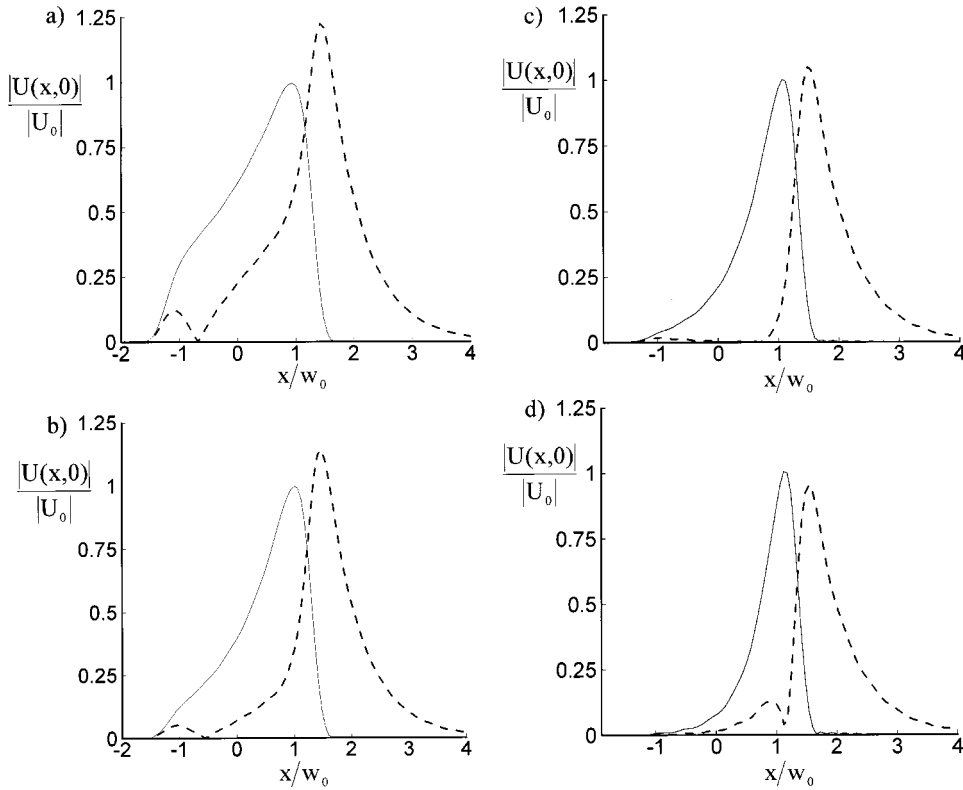


FIG. 7. Reflected beam profiles in the Rayleigh angle on a water/steel interface with $f=2$ MHz, $p=8$, $w=30$ mm: (a) $\beta=20 \text{ m}^{-1}$; (b) $\beta=35 \text{ m}^{-1}$; (c) $\beta=55 \text{ m}^{-1}$; (d) $\beta=85 \text{ m}^{-1}$. Full line: incident field; dashed line: reflected field.

$=0$ is inside this lobe. In Fig. 8 the modulus and phase of the local reflection coefficient are plotted as a function of β . We conclude that the zero of the reflection coefficient and the associated phase reversal must be interpreted as local phenomena, since bounded inhomogeneous waves only locally behave as infinite plane waves. However, a reflection coefficient which is locally defined contains of course only limited information on the reflected sound field and we could consider a reflection coefficient for bounded acoustic beams based on optical diffraction methods, as considered by Leroy and Claeys.²⁶ We would then find a minimum in the Rayleigh angle for both positive and negative inhomogeneity factors, the amplitude of which depends on the degree of distortion of the reflected sound field.

IV. ENERGY CONSIDERATIONS

To compute the energy efficiency of surface wave generation in the Rayleigh angle on a liquid/solid interface, we start from the normal component of the energy flux vector in the liquid:²⁷

$$I_z = -\text{Re}(\sigma_{iz})\text{Re}(u_i), \quad (31)$$

where σ_{iz} are the relevant components of the Cauchy stress tensor, u_i are the components of the particle velocity and $\text{Re}(\cdot)$ is the real part of a complex quantity. If the liquid is nonviscous and p denotes the acoustic pressure, we have

$$\sigma_{ij} = -p \delta_{ij}, \quad (32)$$

with

$$p = -\rho v^2 \nabla \cdot \vec{u}. \quad (33)$$

Working out expression (31) using (32) and (33) and integrating over one period of the ultrasonic wave, we obtain for

the normal component of the mean energy flux of the incident and reflected sound fields at the interface $z=0$:

$$\bar{I}_{iz}(x,0) = \frac{\rho v^2 \omega}{2} \text{Im}(\nabla \cdot \vec{u}_i u_{iz}^*), \quad (34)$$

and

$$\bar{I}_{rz}(x,0) = \frac{\rho v^2 \omega}{2} \text{Im}(\nabla \cdot \vec{u}_r u_{rz}^*), \quad (35)$$

with $\text{Im}(\cdot)$ the imaginary part of the quantity in brackets. The energy efficiency $\eta(x)$ of Rayleigh wave excitation is defined in analogy with Tamir *et al.*²⁸ and can be written as

$$\eta(x) = \frac{\int_{-\infty}^x dx' (|\bar{I}_{iz}| - |\bar{I}_{rz}|)}{\int_{-\infty}^{+\infty} dx' |\bar{I}_{iz}|}. \quad (36)$$

Expression (36) can be interpreted as follows. When the incidence angle is equal to the Rayleigh angle, a part of the incident energy penetrates into the solid medium and propagates as a Rayleigh wave, which subsequently reradiates into the liquid and appears as a nonspecular lobe in the reflected beam. As a consequence, at a given position along the interface, a horizontal energy flux exists which can be found by calculating the energy incident in the interval $(-\infty, x)$ and subtracting the energy reflected away in that same interval. The energy efficiency is then calculated by normalizing this energy flux with the total energy of the incident sound beam. Due to the two competing physical processes at work, on the one hand excitation of the Rayleigh wave by the incident sound field and on the other hand reradiation into the liquid, the energy efficiency will go through a maximum at position x_m when plotted versus the horizontal distance x on the interface. The height of this maximum as a function of the

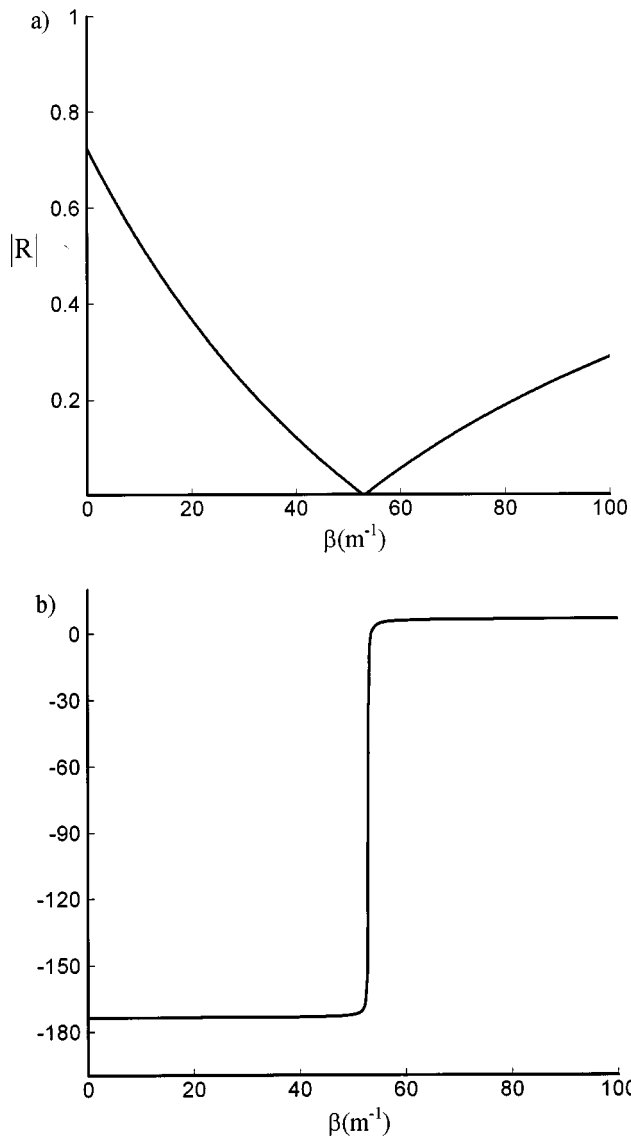


FIG. 8. The modulus (a) and phase (b) of the reflection coefficient as a function of β with $f=2$ MHz, $p=8$ and $w=30$ mm.

beam parameters is interesting. With the help of the representation (11), we can work out expression (34) and derive an analytical expression for the normal component of the time averaged energy flux of the incident sound wave:

$$\bar{I}_{iz}(x,0) = -\frac{1}{2} \rho c \omega^2 \cos(\theta_i) \exp\left(-2\left(\frac{|x|}{w_0}\right)^p \Big/ p + 2\beta_i x\right). \quad (37)$$

The mean energy flux in the reflected sound beam can be computed numerically as a function of x , starting from the integral representation (14) for the reflected field or the expressions (28) and (29). The energy efficiency is then found by numerically computing the integrals in (36). Since this procedure yields identical results for both Fourier analysis and normal mode theory, only the results of Fourier analysis will be shown further.

In Fig. 9, we have used the method described above to compute the maximum energy efficiency $\eta(x_m)$ as a function of the half beamwidth w on a water/steel interface at a frequency of 4 MHz. We compare Gaussian beams, square-

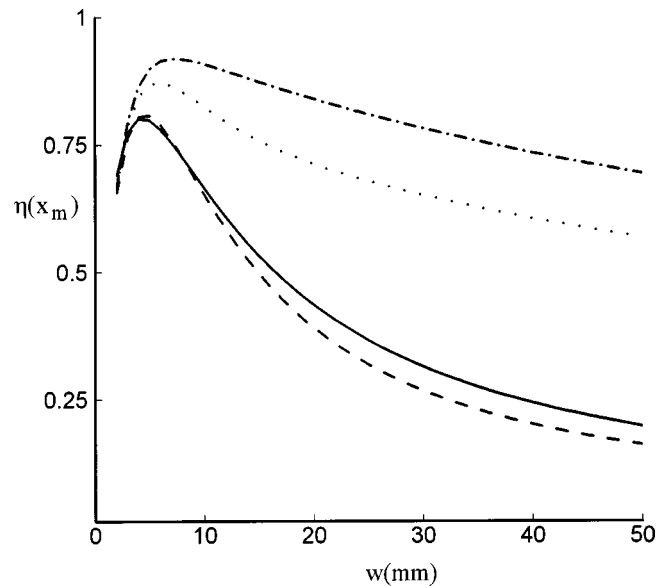


FIG. 9. The maximum energy efficiency of surface wave generation in the Rayleigh angle on a water/steel interface as a function of the half beamwidth w at a frequency of 4 MHz. Full line: Gaussian beams ($p=2, \beta=0 \text{ m}^{-1}$); dashed line: square-profiled beams ($p=8, \beta=0 \text{ m}^{-1}$); dotted line and dash-dotted line: bounded inhomogeneous waves with $p=8$ and $\beta=50 \text{ m}^{-1}$ and 100 m^{-1} .

profiled beams and bounded inhomogeneous waves. Since Fourier analysis and normal mode theory are entirely consistent in the Rayleigh angle, we only show the curves calculated using Fourier analysis. The energy efficiency for Gaussian beams and square-profiled beams attains a maximum of about 80% at $w=5$ mm but diminishes significantly for larger beamwidths. If the half beamwidth is more than 10 mm, the energy efficiency for Gaussian beams turns out to be slightly higher in comparison with square-profiled beams. However, the introduction of a nonzero inhomogeneity factor has a much more drastic effect. With increasing values of β , the maximum rises to 90% and the decay of the curves becomes progressively slower. Figure 9 shows that the difference between $\beta=100 \text{ m}^{-1}$ and the Gaussian or square-profiled beams can reach 40%. This result may be useful in the construction of wedge transducers if inhomogeneous waves could be generated using a more efficient method. In Fig. 10, the effect of reversing the sign of β is examined. For negative values of β , the energy efficiency is found to be lower. This can be intuitively understood from the fact that an incident profile with negative β excites the Rayleigh wave strongly at its maximum, but for further places on the interface less energy is arriving. On the contrary, for positive β the excitation is amplified at further points on the interface. In Fig. 11, the influence of the ultrasonic frequency on the energy efficiency is illustrated. We again show the curves for a Gaussian beam and a bounded inhomogeneous wave with $\beta=100 \text{ m}^{-1}$ at a frequency of 4 MHz, together with the corresponding curves at 10 MHz. The introduction of a higher frequency mainly causes a shift of the maximum of the curves towards smaller beamwidths and lower energy efficiencies at higher beamwidths, but the behavior of bounded inhomogeneous waves is largely unaffected in comparison with Gaussian beams.

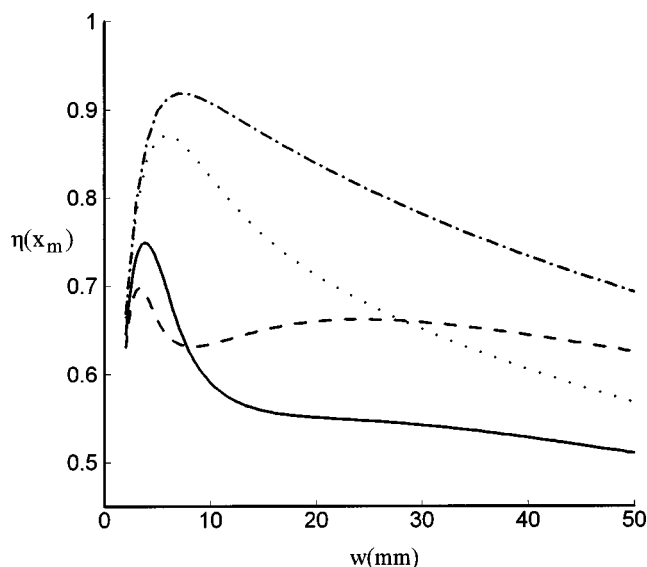


FIG. 10. The influence of the sign of the inhomogeneity factor on the maximum energy efficiency at a frequency of 4 MHz: full line: $p=8$, $\beta = -50 \text{ m}^{-1}$; dashed line: $p=8$, $\beta = -100 \text{ m}^{-1}$; dotted line: $p=8$, $\beta = 50 \text{ m}^{-1}$; dash-dotted line: $p=8$, $\beta = 100 \text{ m}^{-1}$.

V. CONCLUSIONS

In studying the reflection of infinite plane inhomogeneous waves on a liquid/solid interface, difficulties were found when trying to explain results like $|R|=0$ or $|R|>1$. We have shown that by considering bounded inhomogeneous plane waves, the interpretation of the locally defined reflection coefficient becomes much clearer. Using Fourier analysis and normal mode theory to describe inhomogeneous waves as bounded acoustic beams, significant nonspecular effects are found in the Rayleigh angle. Moreover, if these models are used to compute the local reflection coefficient, we obtain complete consistency with published data and we develop a better understanding of the correspondence be-

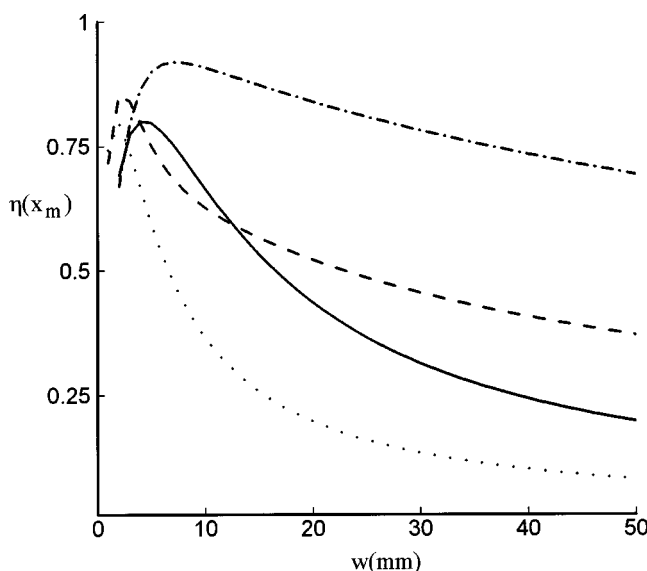


FIG. 11. The influence of the frequency on the maximum energy efficiency: full line: $p=2$, $\beta=0 \text{ m}^{-1}$, $f=4 \text{ MHz}$; dashed line: $p=8$, $\beta=100 \text{ m}^{-1}$, $f=10 \text{ MHz}$; dotted line: $p=2$, $\beta=0 \text{ m}^{-1}$, $f=10 \text{ MHz}$; dash-dotted line: $p=8$, $\beta=100 \text{ m}^{-1}$, $f=4 \text{ MHz}$.

tween infinite plane inhomogeneous wave theory and the theory of bounded acoustic beams. The calculation of the energy efficiency of surface wave excitation reveals that bounded inhomogeneous waves may be useful in the construction of wedge transducers.

ACKNOWLEDGMENTS

The first two authors would like to thank the Flemish Institute for the Encouragement of the Scientific and Technological Research in Industry (IWT) and the National Fund for Scientific Research Flanders (FWO) for the financial support that made this research possible.

- ¹B. Poirée, "Complex harmonic plane waves," in *Physical Acoustics*, edited by O. Leroy and M. Breazeale (Plenum, New York, 1991).
- ²M. Deschamps, "L'onde plane hétérogène et ses applications en acoustique linéaire," *J. Acoust.* **4**, 269–305 (1991).
- ³K. Van Den Abeele and O. Leroy, "Complex harmonic wave scattering as the framework for investigation of bounded beam reflection and transmission at plane interfaces and its importance in the study of vibrational modes," *J. Acoust. Soc. Am.* **93**, 308–323 (1993).
- ⁴M. Lefèvre and M. Montel, "Influence de l'absorption sur les propriétés optiques des solides: propagation des ondes électromagnétiques hétérogènes, planes et uniformes, dans les milieux homogènes et isotropes," *Opt. Acta* **20**, 97–128 (1973).
- ⁵O. Poncelet, Ph.D. thesis, University of Bordeaux, France, 1996.
- ⁶B. Poirée, "Les ondes planes évanescences dans les fluides parfaits et les solides élastiques," *J. Acoust.* **2**, 205–216 (1989).
- ⁷M. Hayes, "Inhomogeneous plane waves," *Arch. Ration. Mech. Anal.* **85**, 41–79 (1984).
- ⁸B. Poirée and L. Sebbag, "Les lois de la réflexion-réfraction des ondes planes harmoniques évanescences. I. Mise en équations," *J. Acoust.* **4**, 21–46 (1991).
- ⁹M. Deschamps and C. Changlin, "Réflexion-réfraction de l'onde plane hétérogène: lois de Snell-Descartes et continuité de l'énergie," *J. Acoust.* **2**, 229–240 (1989).
- ¹⁰G. Quentin, A. Derem, and B. Poirée, "The formalism of evanescent plane waves and its importance in the study of the generalized Rayleigh wave," *J. Acoust.* **3**, 321–336 (1990).
- ¹¹B. Poirée and F. Luppé, "Evanescent plane waves and the Scholte-Stoneley interface wave," *J. Acoust.* **4**, 575–588 (1991).
- ¹²J. M. Claeys and O. Leroy, "Reflection and transmission of bounded sound beams on half-spaces and through plates," *J. Acoust. Soc. Am.* **72**, 585–590 (1982).
- ¹³O. Leroy, "Non-specular reflection-transmission phenomena of bounded beams described by inhomogeneous plane waves," in *Acoustic Interactions with Submerged Elastic Structures*, edited by A. Guran, J. Ripoché, and F. Ziegler (World Scientific, Singapore, 1996), Part I.
- ¹⁴M. Deschamps and B. Hosten, "Génération de l'onde hétérogène de volume dans un liquide non absorbant," *Acustica* **68**, 92–95 (1989).
- ¹⁵M. Deschamps, "Reflection and refraction of the evanescent plane wave on plane interfaces," *J. Acoust. Soc. Am.* **96**, 2841–2848 (1994).
- ¹⁶X. Jia, "Normal-mode theory of nonspecular phenomena for a finite-aperture ultrasonic beam reflected from layered media," *Appl. Phys. Lett.* **70**, 1–4 (1997).
- ¹⁷X. Jia, "Modal analysis of Lamb wave generation in elastic plates by liquid wedge transducers," *J. Acoust. Soc. Am.* **101**, 1–9 (1997).
- ¹⁸F. Windels, S. Vanaverbeke, and O. Leroy, "Thin coating characterization by Rayleigh waves: An analytical model based on normal mode theory," *J. Acoust. Soc. Am.* **110**, 1349–1359 (2001).
- ¹⁹H. L. Bertoni and T. Tamir, "Unified theory of Rayleigh-Angle phenomena for acoustic beams at liquid-solid interfaces," *Appl. Phys.* **2**, 157–172 (1973).
- ²⁰T. Ngoc and W. Mayer, "Numerical method for reflected beam profiles near Rayleigh angle," *J. Acoust. Soc. Am.* **67**, 1149–1152 (1980).
- ²¹M. A. Breazeale, L. Adler, and G. Scott, "Interaction of ultrasonic waves incident at the Rayleigh angle onto a liquid-solid interface," *J. Appl. Phys.* **48**, 530–537 (1977).
- ²²A. Tarantola, *Inverse Problem Theory: Methods for Data Fitting and Model Parameter Estimation* (Elsevier, Amsterdam, 1987), p. 26.

- ²³B. A. Auld, *Acoustic Fields and Waves in Solids* (Wiley, New York, 1973), Vol. 2, Chap. 10.
- ²⁴A. Schoch, "Schallreflexion, Schallbrechung und Schallbeugung," *Ergeb. Exakten Naturwiss.* **23**, 127–234 (1950).
- ²⁵O. Leroy, B. Poirée, L. Sebbag, and G. Quentin, "On the reflection coefficient of acoustic beams," *Acustica* **66**, 84–89 (1988).
- ²⁶O. Leroy and J. M. Claeys, "Optical measurement of the reflection coefficient for bounded acoustic waves," *J. Acoust. Soc. Am.* **75**, 1346–1351 (1984).
- ²⁷O. Leroy, G. Quentin, and J. M. Claeys, "Energy conservation for inhomogeneous plane waves," *J. Acoust. Soc. Am.* **84**, 374–378 (1988).
- ²⁸T. Tamir and H. L. Bertoni, "Lateral displacement of optical beams at multilayered and periodic structures," *J. Opt. Soc. Am.* **61**, 1397–1413 (1971).

Experimental demonstration of noninvasive transskull adaptive focusing based on prior computed tomography scans

J.-F. Aubry,^{a)} M. Tanter, M. Pernot, J.-L. Thomas, and M. Fink
*Laboratoire Ondes et Acoustique, ESPCI, Université Paris VII, U.M.R. C.N.R.S. 7587,
10 rue Vauquelin, 75005 Paris, France*

(Received 30 October 2001; revised 24 August 2002; accepted 28 October 2002)

Developing minimally invasive brain surgery by high-intensity focused ultrasound beams is of great interest in cancer therapy. However, the skull induces strong aberrations both in phase and amplitude, resulting in a severe degradation of the beam shape. Thus, an efficient brain tumor therapy would require an adaptive focusing, taking into account the effects of the skull. In this paper, we will show that the acoustic properties of the skull can be deduced from high resolution CT scans and used to achieve a noninvasive adaptive focusing. Simulations have been performed with a full 3-D finite differences code, taking into account all the heterogeneities inside the skull. The set of signals to be emitted in order to focus through the skull can thus be computed. The complete adaptive focusing procedure based on prior CT scans has been experimentally validated. This could have promising applications in brain tumor hyperthermia but also in transcranial ultrasonic imaging. © 2003 Acoustical Society of America. [DOI: 10.1121/1.1529663]

PACS numbers: 43.20.-f, 43.20.Ei, 43.20.Jr, 43.35.Cg [AJS]

I. INTRODUCTION

Extracorporeal ablation of human tumors using High-Intensity Focused Ultrasound (HIFU) has been intensively investigated during the past decades.¹⁻⁴ Prostate cancer is certainly the most suitable application:^{5,6} the target is reached via an endorectal probe close to the prostate tissue. It is much more difficult to cure tumors located deeply in the tissues: in this case, parts of the emitted wave front will encounter regions with different acoustic velocities, and different absorption coefficients, so that the heating beam pattern will be degraded. The worst medium to focus through is certainly the skull, as it was first shown by White *et al.*⁷ during investigations into echographic brain imaging, and Fry *et al.*^{8,9} during investigations into brain hyperthermia: a large discrepancy between high acoustic velocity of the skull (about 3000 m s⁻¹) and the low velocity of brain tissues (about 1540 m s⁻¹) combined with a severe attenuation of ultrasound in the bone strongly degrade the beam shape.

Several methods have been developed to precisely focus through the skull. The most invasive method consists in removing the piece of the skull in regard of the emitting array of transducers. Such a method has been experimentally used on living rats and cats in the early 1970s.¹⁰ More recently, thermally induced lesions in rabbit brains were also studied by using a craniotomy.¹¹ One can also correct the aberrations induced by the skull either by using a Time Reversal Mirror¹² or by time shifting.^{13,14} In the case of Time Reversal Mirrors, prior to the treatment and taking advantage of the biopsy, which ensures that the tumor is malignant, a hydrophone could be inserted in the neighborhood of the tumor and used as a beacon. Once the diagnostic would be confirmed and the hydrophone removed, the time-reversed signals with amplitude compensation could be emitted in order

to correct both phase and amplitude aberrations induced by the skull. Then, steering the signals¹⁵ would enable one to precisely heat the whole tumor spot by spot. A refined extension of this method is the use of a spatiotemporal inverse filter:¹⁶ taking advantage of the biopsy, one could put a set of transducers along the path followed by the physician. Then, after recording the whole set of impulse responses coming from the set of transducers, one could perform a very accurate focusing: it has been shown experimentally at low power¹⁷ that it was possible to reach the same focusing quality through a human skull as the one obtained in water: phase distortion and attenuation induced by the skull can be corrected.

Recently, the possibility to deduce the acoustic properties of the skull from MRI and CT images raised new hopes for noninvasive brain therapy. Hynynen *et al.*^{18,19} proposed to use MRI images for extracting the skull profile, without information on the internal heterogeneities. Then, using a three-layer model (water outside the skull, skull, and brain inside the skull), they numerically highlighted the necessity to perform the phase correction to focus through the skull. They proposed to perform this correction by deducing the phase aberrations induced by the skull thanks to simulations with the three-layer model.²⁰ In this work, they highlighted that the model would be enhanced by taking into account the heterogeneities of the skull. As CT images can give the internal structure of the skull, it is definitely more suited for modeling the ultrasonic properties of the skull.²⁰⁻²² In order to take into account all the information of the CT images, we propose here to use a three-dimensional (3-D) finite differences numerical simulation of the complete wave equation. By taking into account the internal heterogeneities in density, speed, and absorption, this finite differences simulation tries to model all the defocusing effects highlighted by White *et al.*⁷

It will first be explained how the acoustic velocity, the

^{a)}Electronic mail: jf.aubry@espci.fr

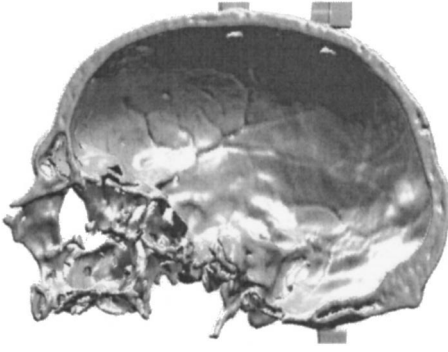


FIG. 1. CT scan of the entire skull.

density, and the absorption coefficient of the skull can be deduced from CT images. In Sec. II, comparisons between computed and experimental wave fronts passing through the same area of the same skull fully validate this model. Then, it will be shown in Sec. III that these results lead to noninvasive focusing through the skull. The focusing pattern obtained with a conventional time-reversal experiment is indeed close to the one experimentally obtained with our method based on simulations. Thus, by using CT images of the skull, it is possible to noninvasively correct both the phase and the amplitude aberrations induced by the skull. Beyond its interest for noninvasive brain therapy, full 3-D finite differences simulations are an interesting tool for modeling and understanding the complex acoustic wave propagation through bones.

II. ACOUSTIC PROPERTIES OF THE SKULL DEDUCED FROM CT IMAGES

It is known that cortical bones give no signal on Magnetic Resonance Imaging (MRI), whatever their density, but MRI is capable to provide the thickness of the skull. In this case, one can only model the acoustical properties of the skull with a uniform density, sound speed, and absorption. CT images can measure the internal density of the skull, enabling us to use more accurate models of the acoustical properties of the skull, taking into account the heterogeneities of density, sound speed, and absorption inside the skull.

A. CT images

High-resolution CT images have been performed at the Institut Français du Pétrole (IFP), on a General Electric FXi model with a 0.2 mm in-plane spatial resolution. With transducers working at a central frequency of 1.5 MHz, it corresponds to a $\lambda/7$ precision in the skull, which is of great importance when trying to precisely simulate the wave propagation. The entire CT scan of the skull is given in Fig. 1. The scan parameters were set to 120 kV, 60 mA. Slices were 1 mm thick with a 0.5 mm pitch so that each slice was overlapping the previous one.

A dried human skull was midsagittally cut into two halves. In order to reproduce *in vivo* conditions as closely as possible, the skull is immersed in water and degassed so that no air bubble is trapped in porous zones. Instead of being filled with marrow, the porous parts of the skull are thus filled with water. However, it is important that those porous

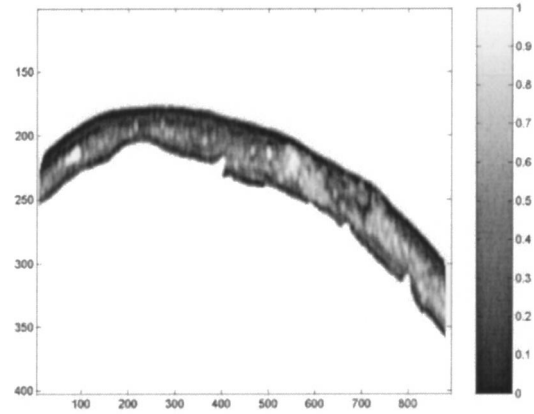


FIG. 2. Porosity map of a slice of the 3-D CT data.

parts are not filled with air bubbles that would introduce artifacts in the CT scans. Raw CT values were given into Hounsfield Units (H), defined by

$$H = 1000 \frac{\mu_x - \mu_{\text{water}}}{\mu_{\text{bone}} - \mu_{\text{water}}}, \quad (1)$$

with μ_x , μ_{bone} , and μ_{water} , respectively, denoting the photoelectric linear attenuation coefficient of the explored tissue, bone, and water.

As the skull was placed in water and degassed, it is exclusively made of water and bone with a varying density. Consequently, Φ being the bone porosity, we propose here a linear relationship between the photoelectric linear attenuation coefficient of the explored tissue, and the attenuation coefficients of bone and water:

$$\mu_x = \Phi \mu_{\text{water}} + (1 - \Phi) \mu_{\text{bone}}. \quad (2)$$

In that case, the porosity map is directly linked to the Hounsfield map:

$$\Phi = 1 - \frac{H}{1000}. \quad (3)$$

Finally, all the acoustic properties (density, speed, and absorption coefficient) of the skull were deduced from the porosity maps. The porosity map of a slice is given in Fig. 2. Basically, the skull presents a three-layered structure, with a porous zone, called the diploe, stacked between two dense layers, respectively, the outer and inner tables. We can see that the diploe is very inhomogeneous and that it is sometimes hard to differentiate it from the tables.

B. Acoustic properties of the skull deduced from CT imaging

All the experiments were made with a plane linear array of 128 transducers working at a central frequency of 1.5 MHz, so that frequency ranges from 0.8 to 2 MHz. The elevation of the array (VERMON) is 1 cm, with a 0.5 mm pitch.

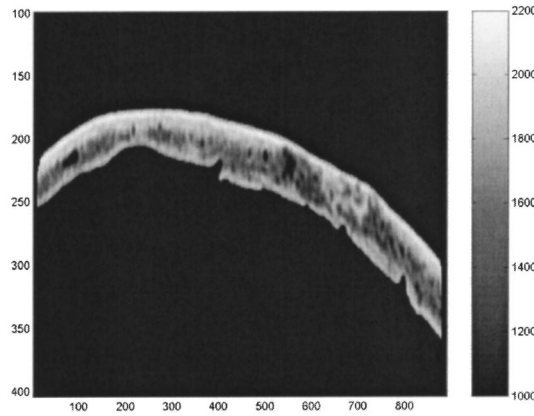


FIG. 3. Slice of the 3-D mass density map deduced from CT scans.

1. Density

Mass density maps are easily deduced from the bone porosity:

$$d = \Phi \times d_{\text{water}} + (1 - \Phi) \times d_{\text{bone}}. \quad (4)$$

d_{water} is the mass density of water and has been set to 1000 kg m^{-3} ; d_{bone} is the maximum mass density in the cortical bone. One can see that our simple model [Eq. (2) and Eq. (4)] implies a linear relationship between the bone density and the Hounsfield units, as observed experimentally by Rho *et al.*²³ and Ploeg *et al.*²⁴

Fry *et al.*²⁵ statistically studied the acoustical properties of human skulls. They found an average mass density of 1900 kg m^{-3} in the inner table. Taking into account the heterogeneities inside the inner table, the maximum mass density of the cortical bone (d_{bone}) has thus been set to 2100 kg m^{-3} in order to obtain the same average mass density in the inner table as the one given by Fry *et al.* A slice of the 3-D mass density map is given in Fig. 3.

2. Speed of sound

The speed of sound is harder to deduce from the skull porosity. The diploe and the inner and outer tables have different mechanical properties.²⁵ Acoustic waves propagating in the fluid and the solid media are coupled, which is correctly described by the Biot theory if the wavelength is negligible compared to the size of the heterogeneities. At 1.5 MHz, the wavelength is unfortunately of the order of magnitude of the heterogeneities. However, Carter and Hayes²⁶ showed that the elastic modulus of bone is proportional to the apparent density cubed, which suggests a linear relationship between velocity and porosity:

$$c = c_{\text{min}} + (c_{\text{max}} - c_{\text{min}}) \times (1 - \Phi). \quad (5)$$

As porous parts are filled with water, c_{min} has been set to $1.5 \text{ mm } \mu\text{s}^{-1}$. Fry *et al.*²⁵ measured the same value in the inner and the outer table for the speed of sound: $2.9 \text{ mm } \mu\text{s}^{-1}$. According to this, c_{max} has been set to $2.9 \text{ mm } \mu\text{s}^{-1}$. A slice of the 3-D velocity map is given in Fig. 4. In order to give an idea of the entire 3-D velocity mesh used in the simulation, a representation is given in Fig. 5.

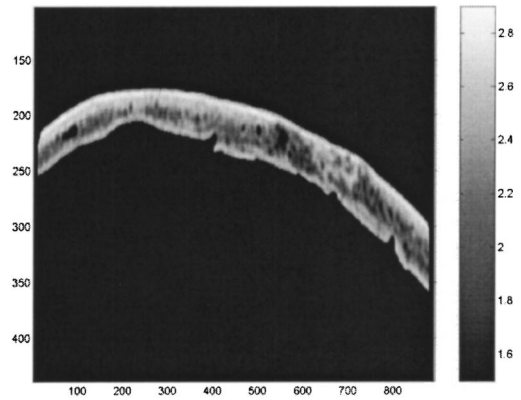


FIG. 4. Slice of the 3-D acoustic speed map deduced from CT scans.

3. Absorption

As ultrasonic absorption is known to occur mainly in the diploe,²⁵ the absorption coefficient is expected to be a growing function of porosity. The following power law model was experimentally adjusted:

$$\text{abs} = \text{abs}_{\text{min}} + (\text{abs}_{\text{max}} - \text{abs}_{\text{min}}) \times (\Phi)^\beta. \quad (6)$$

Evaluating the mean absorption of wave fronts propagating through different parts of the skull showed that β could vary between 0.3 and 0.7. The best comparison between simulation and experiments were obtained with $\beta = 0.5$; $\text{abs}_{\text{min}} = 0.2 \text{ dB mm}^{-1}$; $\text{abs}_{\text{max}} = 8 \text{ dB mm}^{-1}$. This definitely sets the absorption coefficients for all the experiments performed through this skull. A slice of the 3-D absorption map is given in Fig. 6.

C. Numerical simulations

Simulations were performed with a finite differences program called ACEL developed in our lab. For 3-D simulations through the skull, a 20 h computational time is needed to compute a $70 \text{ mm} \times 10 \text{ mm} \times 30 \text{ mm}$ box at an ultrasonic frequency of 1.5 MHz with a 500 MHz computer. Basically, the program is based on a discretization of the linear acoustic wave equation in heterogeneous absorbing media (7):

$$\left(1 + \tau_0(\mathbf{r}) \frac{\partial}{\partial t}\right) \left[\rho_0(\mathbf{r}) \nabla \cdot \left(\frac{1}{\rho_0(\mathbf{r})} \nabla p(\mathbf{r}, t) \right) \right] - \frac{1}{c_0(\mathbf{r})^2} \frac{\partial^2 p(\mathbf{r}, t)}{\partial t^2} = S_0(\mathbf{r}, t). \quad (7)$$

This equation accurately models fluids with sound speed, density, and absorption heterogeneities. Mode conversions and shear waves are not taken into account. Nevertheless, they can be neglected in a first approximation²⁵ as the wave front incidence angle on the skull's interface remains close to normal incidence. As the wavelength in the skull is larger than the inclusions, microstructures in the diploe are averaged by introducing an effective medium. In the bandwidth of the transducers, insertion loss increases as the second power of the frequency.²⁵ A second power frequency dependence of the insertion loss corresponds to a constant relaxation time,²⁸ as set in the simulation. In order to ensure a

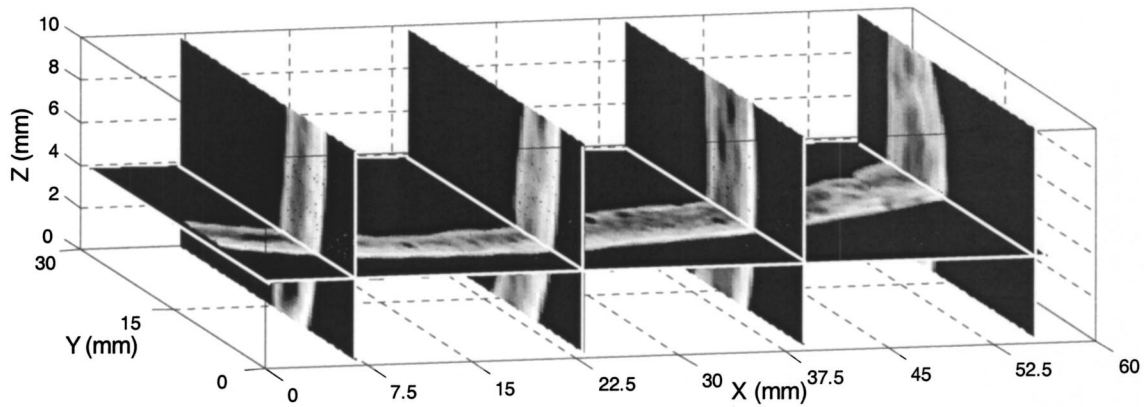


FIG. 5. A 3-D spatial representation of the sound speed distribution deduced from CT scans and used as input data in the full 3-D finite differences simulation (the box is 60 mm×30 mm×12.5 mm).

precise simulation, taking into account density, sound speed, and absorption heterogeneities, the spatial pitch is set to less than one-tenth of a wavelength and the time step is automatically set to ensure the von Neumann stability criteria.²⁹ Strongly absorbing boundary conditions based on a fourth-order approximation of Higdon conditions³⁰ are used at the sides and edges of the mesh to avoid unphysical reflections. Sets of receivers and emitters can be easily defined thanks to an intuitive graphic interface, as well as the velocity, density, and absorption maps [Eqs. (4), (5), and (6)] respectively, $c_0(\mathbf{r})$, $\rho_0(\mathbf{r})$, and $\tau_0(\mathbf{r})$. Then the numerical code propagates the wave front from the set of emitters to the set of receivers. The maps presented in Sec. II B were interpolated to one-tenth of a wavelength.

The position of the set of transducers on the simulation mesh is critical. It is indeed of great importance to carefully place the transducers at the same location in the simulations and in the experiment. Basically, the exact positions of three markers on the skull were recorded and the experimental configuration was reproduced with a one-millimeter precision in each direction. We did not notice significant degradation of the experimental focusing patterns based on simulations due to this variance in the estimation of the markers location. Further investigations could quantitatively estimate the effect of positioning errors.

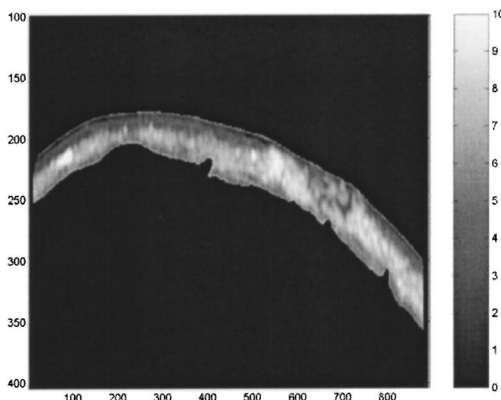


FIG. 6. Slice of the 3-D absorption map deduced from CT scans.

III. EXPERIMENTAL VALIDATION: COMPARISON BETWEEN COMPUTED AND EXPERIMENTAL WAVE FRONTS

The midsagittally cut human skull was placed between our linear array of 128 transducers and a needle hydrophone (Fig. 7). The whole experiment was immersed in water. In the general case, out of plane refractions have to be taken into account, explaining why a 3-D simulation code had to be computed. Nevertheless, we first tried to achieve a 2-D experiment by placing the needle hydrophone close to the skull. The surface of the skull has been aligned with the surface of our active elements in order to minimize refraction out of the simulation and experimental plane. Thus, first simulations could be performed in two dimensions, which is much more rapid. The hydrophone has a one millimeter external diameter housing and 0.5 mm diameter active surface ($\lambda/2$), so that one can assume that the experiment takes place in one slice of the CT scan (each slice is indeed 1 mm thick). A plane wave was emitted by the array of a transducer, and the hydrophone was translated along the x axis in order to record the wave front after passing through the skull. The plane wave front before passing the skull has also been recorded and is plotted in Fig. 8.

As expected, after propagation through the skull, the plane wave is strongly distorted, suffering both phase and amplitude distortions. The experimental wave front is presented in Fig. 9(a) and can be compared to the simulated one displayed in Fig. 9(b). At first glance, the simulation remarkably reproduces the influence of the skull. In Fig. 9(c) is reproduced the corresponding porosity map of the skull in

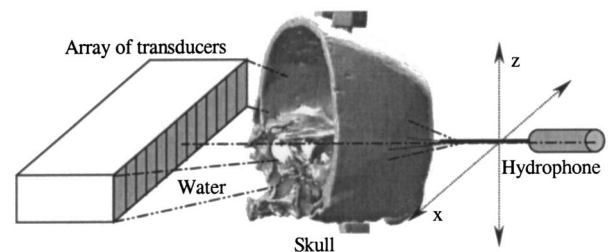


FIG. 7. Experimental setup.

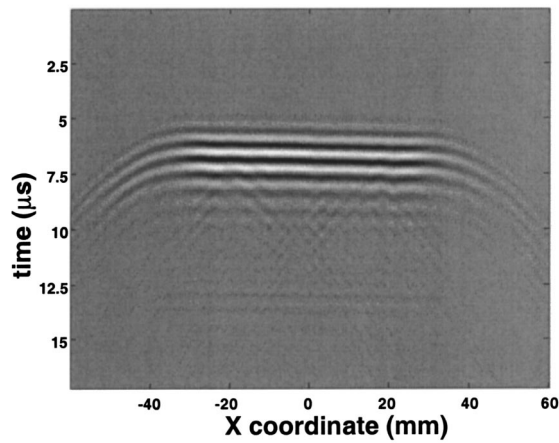


FIG. 8. Plane wave before passing through the skull (experiment).

order to explain the influence of the skull. Two different zones have been highlighted. The zone one corresponds to a dense part of the skull with a relatively uniform absorption, so that the wave front is mainly distorted by the varying thickness of the skull, which is well reproduced on simulations. At position 40 mm on both experimental and simulated wave fronts, a dislocation can be seen: this is due to a notch [white arrow No. 2 in Fig. 9(c)] that acts like an acoustic lens.

A quantitative comparison between simulated and experimental wave fronts can be done. In Fig. 10(a) is plotted the relative time shifts between simulation and experiment. Time shifts have been evaluated by cross-correlating the signals of Figs. 9(a) and 8(b). In order to obtain a good focusing, Goodman³¹ showed that the precision on the phase of the emitted signal should be less than $T/8$, where T is the period of the signal. One can see in Fig. 10(a) that this cri-

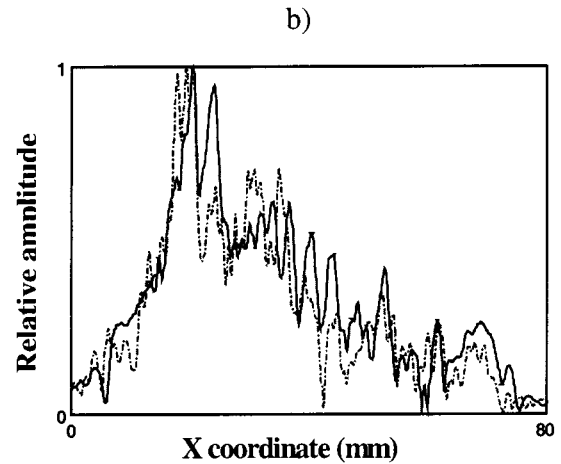
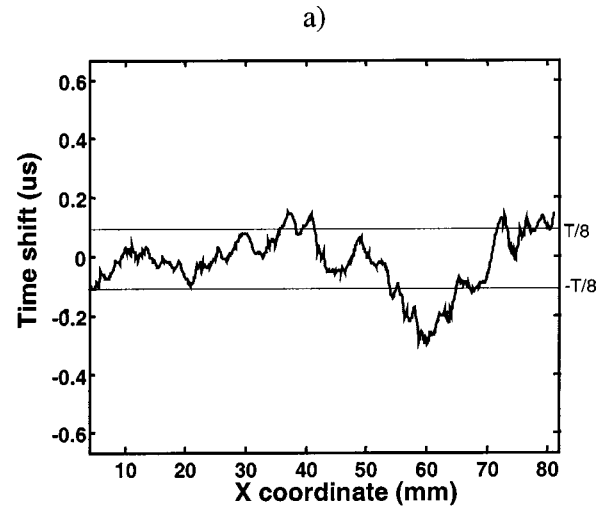


FIG. 10. (a) Relative phase shift between the experimental and simulated plane wave propagating through the skull. (b) A comparison between experimental (dotted line) and simulated (solid line) normalized amplitude.

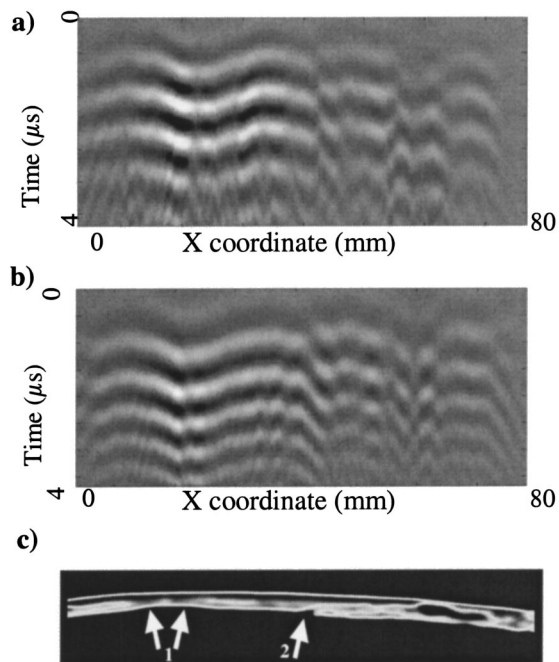


FIG. 9. Wave front after propagating through the skull: (a) Experiment; (b) simulation; (c) corresponding porosity map of the skull.

teria is well respected, except in one zone around position 60 corresponding to very low signal amplitude [see Fig. 9(a)]. Respective normalized amplitude at central frequency recorded or simulated at each location of the hydrophone are also plotted in Fig. 10(b) and are quite similar.

Studying the propagation of a plane wave through a human skull enabled us to validate the whole simulation process. In the following section, we will apply this process to perform noninvasive focusing through the skull.

IV. APPLICATION TO NONINVASIVE FOCUSING THROUGH THE SKULL

A. Experimental setup

The experimental setup, presented in Fig. 11, slightly differs from the one presented in Sec. II. Our aim is to determine the set of signals that have to be emitted on the array of transducers in order to obtain a sharp focusing. The quality of the focusing is experimentally checked by translating the hydrophone along the x axis and recording the maximum of pressure amplitude. In this section, as out of plane refrac-

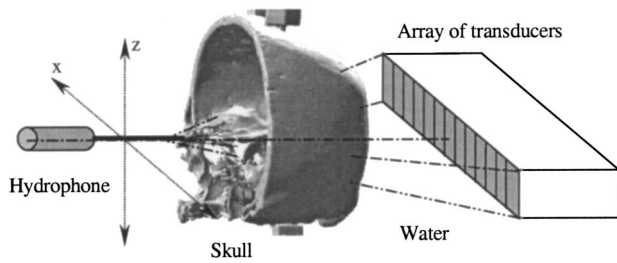


FIG. 11. Experimental setup.

tion effects have to be taken into account, all the simulations were performed with our full 3-D finite differences code. (See Fig. 12.)

B. Noninvasive time reversal

As seen in Sec. II, when focusing through the skull, parts of the wave front encounter regions with strongly different acoustic velocity and different absorption coefficient. This induces a severe spreading in the main lobe and an increase of the side lobes level, as one can see later in Fig. 14, showing the experimental directivity pattern obtained when focusing through the skull by emitting a cylindrical law with the array of transducers (dash-dotted line). This directivity pattern was obtained by plotting in a linear scale the square of the maximum of pressure amplitude recorded by the needle hydrophone at each location along the x axis. Such a focal spot is definitely not suited for brain hyperthermia: the maximum of pressure amplitude is not on the target (target at center) and the focusing quality is so poor that necrosis would also be induced in surrounding tissues.

Time reversal enables to correct the phase aberrations induced by the skull.¹² Basically, a pulse emitted by an acoustic source placed at the desired focus is recorded by an array of transducers after propagation through the medium. Then the recorded signals are time reversed and reemitted, so that the wave front propagates back to the source as if the

experiment was played backward. The experimental wave front coming from the central location of the hydrophone was recorded on the array of transducers and is presented in Fig. 13(a) after the time reversal operation. These time-reversed signals were experimentally reemitted by the array. We obtained the corresponding directivity pattern plotted in Fig. 14 (dotted line).

Thanks to simulations, it is possible to avoid the need of an ultrasonic source at focus by using a virtual source. An acoustic source was indeed placed on our CT images at the location of the desired focus. A pulse emitted by this virtual source was numerically propagated by the 3-D finite differences code through the skull to the array of transducers. This wave front numerically recorded on the array is presented after the time reversal operation in Fig. 13(b) and is very close to the one experimentally acquired [Fig. 13(a)]. The time-reversed simulated wave front was then experimentally emitted by the array of transducers. Finally, the experimental directivity pattern obtained by emitting the simulated set of signals is plotted in Fig. 14 (gray solid line). These experiments support the feasibility of totally noninvasive brain hyperthermia, since the focusing based on CT images (solid line) is close to the one obtained with a real acoustic source placed at the desired focus (dotted line): the focusing patterns are very similar, excluding an increase of the secondary lobe located at +10 mm from the center when using the simulated wave front. The strong defocusing effect observed when using a cylindrical law (dash-dotted line) is now well compensated for hyperthermia applications. Ebbini *et al.*²⁷ proposed an 8 dB side lobes amplitude as a threshold in order to avoid burning surrounding tissues. This is the case here.

In previous work, Thomas *et al.*¹² showed that at high frequencies (1.5 MHz) the focusing pattern could be strongly enhanced by combining time reversal with amplitude compensation. We will show in the following section that this can also be performed noninvasively.

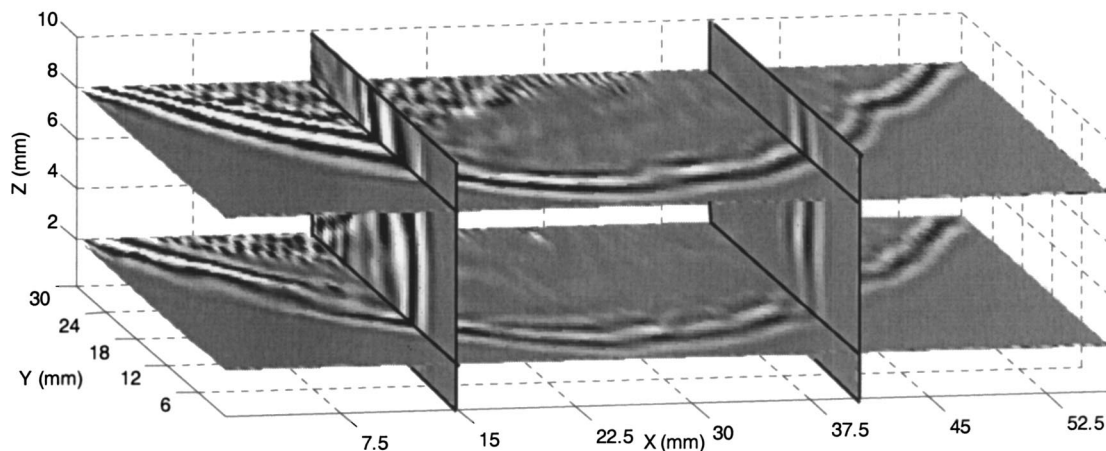


FIG. 12. Full 3-D finite differences simulation: 3-D spatial representation at a given time of the acoustic field passing through the skull (in a linear scale). The wave front is coming from a point-like source inside the brain. The calculation box (60 mm×30 mm×12.5 mm) corresponds to the 3-D volume presented in Fig. 5. One can notice some field variations along the elevation axis.

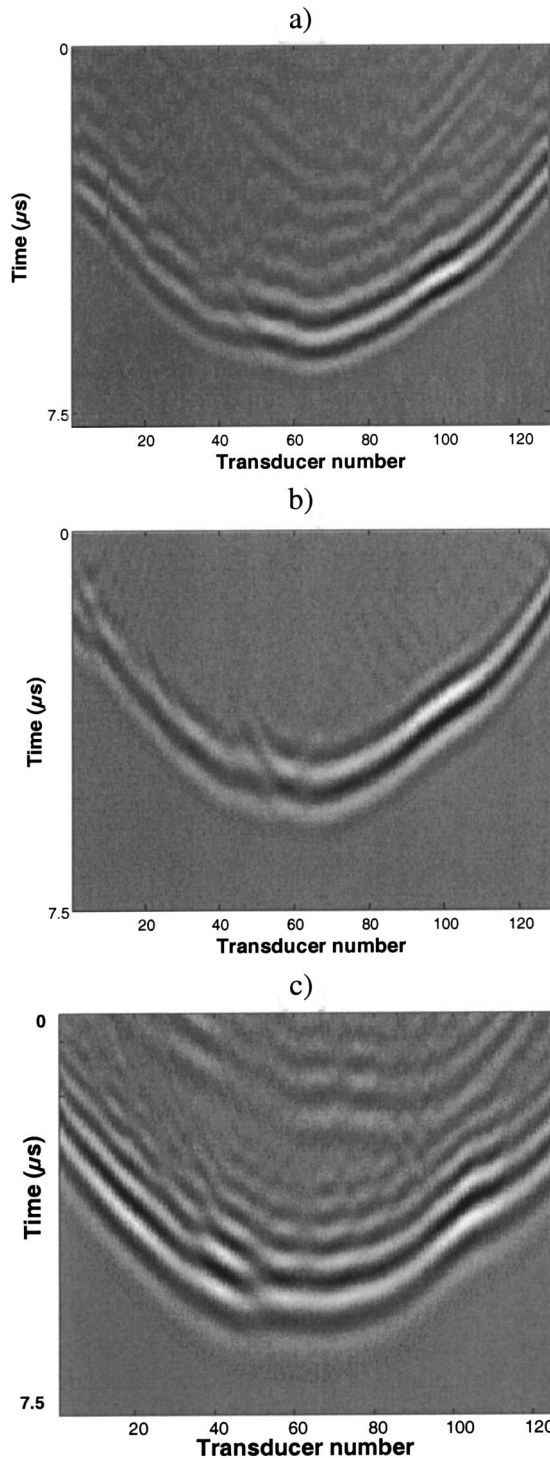


FIG. 13. Time-reversed signals emitted by the array of transducers: (a) From experimental signals; (b) from the computed wave front (heterogeneous model); and (c) from a computed wave front (homogeneous model).

C. Noninvasive time reversal with amplitude compensation

Time reversal corrects phase aberrations induced by the propagating medium but does not correct amplitude aberrations. When focusing through a strongly absorbing medium like a human skull, the focusing can be improved by correcting the amplitude of the recorded signals.¹² This is particularly important when working at central frequencies above 1

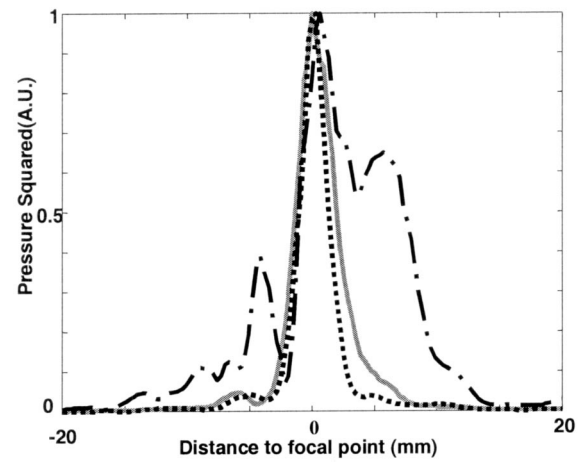


FIG. 14. Directivity pattern through the skull: energy (pressure squared) is plotted in a linear scale after emission of the time reversal of signals experimentally acquired (dotted line), of simulated signals (gray solid line), and of cylindrical law (dash-dotted line).

MHz. The skull absorption is indeed increasing with the frequency, suggesting to work at low frequency. But decreasing the frequency also means decreasing the resolution and decreasing the heating of soft tissues, as their absorption coefficient is also increasing with the frequency. A compromise has to be determined. Hynynen *et al.* decided to work at low frequency to optimize the Specific Absorption Rate,¹⁹ which is a good choice in order to avoid wasting energy in the skull. In that case, compensating the amplitude would only slightly improve the focusing, and a correct focusing can be achieved without amplitude correction. Another concern is the combination of HIFU and cavitation that may induce hemorrhages in the brain. As the cavitation threshold decreases with the frequency, hemorrhages are more likely to occur at low frequency. Our lab chose to work in a higher-frequency range (from 800 kHz to 1.5 MHz) for therapy, but also imaging. In that case, absorption effects become more important and an amplitude correction has been proposed.

Basically, assuming that the skull is an infinitely thin layer close to the emitting array of transducers, one can apply a gain on parts of the wave front that suffered a loss while passing through the skull. This so-called amplitude compensation is fully described in Ref. 12. The time-reversed signals obtained, respectively, by experiment and simulation presented in Fig. 13 were amplitude compensated (Fig. 15) and then were both experimentally emitted by the array of transducers. The corresponding focusing patterns are plotted in Fig. 16.

The focusing pattern obtained with a conventional time-reversal experiment with amplitude compensation is slightly better than the one based on simulations. More precisely, the right side has a lower level. Further work could show whether a better positioning system or a more precise adjustment of the parameters of the inhomogeneous model presented here could enhance the noninvasive process.

Either experimentally acquired or deduced from simulations, the focusing patterns obtained using time-reversal combined with amplitude compensation are much sharper since the effective aperture of the emitting array is enhanced.

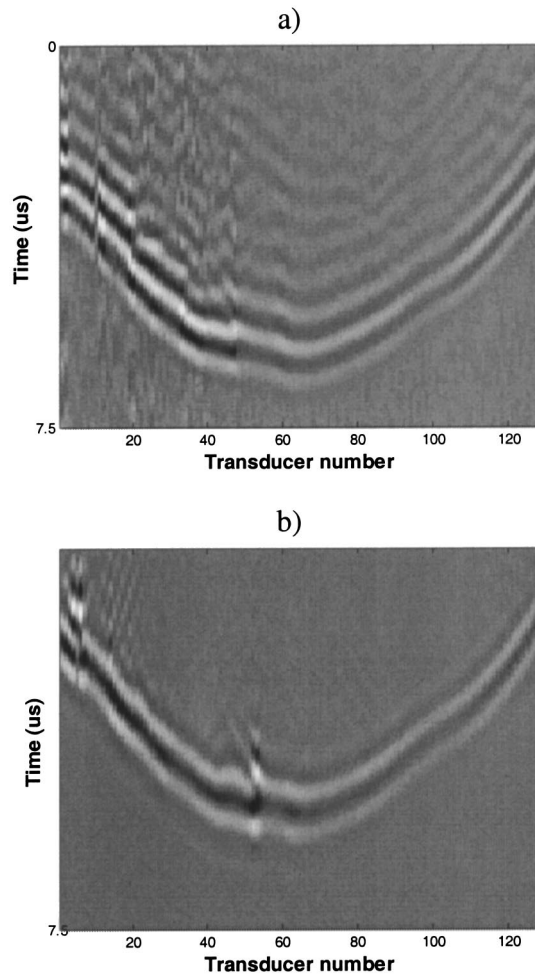


FIG. 15. Time-reversed signals with amplitude compensation emitted by the array of transducers: (a) From experimental acquisition and (b) from a computed wave front (heterogeneous model).

Moreover, the side lobe level is lower. Thus, the therapy will be more precise and tissues located in the near-field will be homogeneously insonified. Adding the amplitude compensation protects the brain tissues to the detriment of an overheating in the most absorbing parts of the skull. This overheating will be studied in further works.

D. Comparison with a homogeneous model

The full 3-D finite differences codes developed in this article take into account all the internal heterogeneities in density, speed, and absorption of the human skull detected on prior CT scans. A homogeneous model of the skull can also be proposed.^{18,20} In a first approximation, one can indeed consider that the main effect of the skull results in its varying thickness, as the acoustic velocity and the density of the skull are about twice the velocity and the density of water and of the brain. In that case a fast simulation code can be used, based on ray tracing theory. In order to determine the advantage of taking into account the internal heterogeneities, other noninvasive focus have been conducted on other parts of the human skull. Two simulations of the wave front coming from a virtual source placed on the target were conducted: one with the previously presented heterogeneous model and one

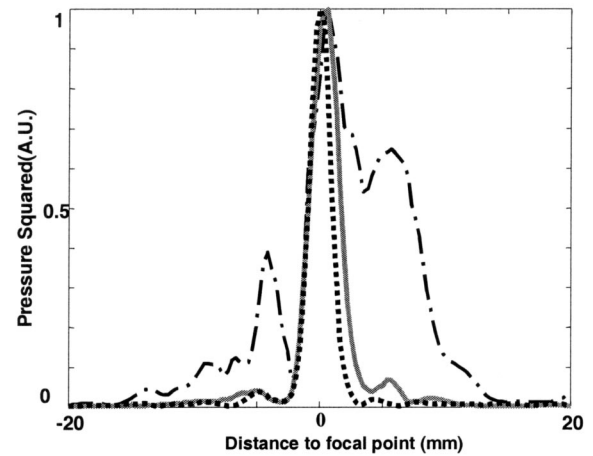


FIG. 16. The directivity pattern through the skull: energy (pressure squared) is plotted in a linear scale after the emission of time reversal with amplitude compensation of signals experimentally acquired (dotted line) and simulated signals (gray solid line) and of cylindrical law (dash-dotted line).

with a homogeneous model. In the homogeneous model, according to the value deduced by Hynynen²⁰ from Fry *et al.*,²⁵ a mean velocity of $2.65 \text{ mm } \mu\text{s}^{-1}$ has been taken, and a mean density of 1800 kg m^{-3} .

The emitted wave front was either not corrected or corrected thanks to the homogeneous or the heterogeneous model. They were emitted with the linear array of 128 transducers. The corresponding energy distributions are plotted in a linear scale in Fig. 17. One can clearly see that the homogeneous model (dotted line) improves the focusing compared to a noncorrected wave front (dash-dotted line). The side lobes are significantly reduced, with a 10 dB gain. One can notice that the directivity pattern obtained with the homogeneous model is more symmetric and globally centered on the target, even if the maximum of pressure amplitude is not on the target: on this area of the skull, destructive interferences occur at the center. But the heterogeneous model developed in this article reaches a better focusing: the directivity pattern

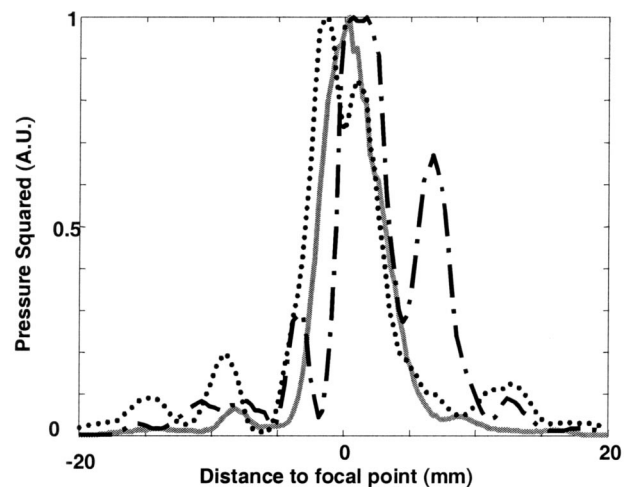


FIG. 17. Directivity pattern through the skull: energy (pressure squared) is plotted in a linear scale after the emission of cylindrical law (dash-dotted line), time reversal of simulated signals with heterogeneous model (gray solid line), and with a homogeneous model (dotted line).

is quite symmetric, the maximum of pressure amplitude is close to the target and the side lobes level are very low. Over 90 experiments conducted with various focusing techniques on various areas of the skull, the focusing capabilities were compared. Using a noncorrected wave front, a mean 1.5 mm absolute deviation from the target was observed, with a 0.2 mm standard deviation. With a noninvasive correction deduced from a homogeneous medium, the mean deviation decreased to 1.15 mm with a 0.2 mm standard deviation. The mean gain on the first side lobe was 6.2 dB, and 3 dB on the second side lobe. With a noninvasive correction deduced from a heterogeneous medium, the mean deviation decreased to 0.63 mm with a 0.3 mm standard deviation. Compared to noncorrected wave front, the mean gain on the first side lobe was 9.4, and 8.7 dB on the second side lobe. Thus, the heterogeneous model presented here shows a significant improvement, even if the homogeneous model shows good results compared to a noncorrected focusing. One also has to notice that the homogeneous model was solved here by using a finite differences code, taking into account higher refraction angles than codes derived from ray tracing theory. Moreover, the wave front coming from the virtual source has been simulated with the homogeneous model in the same configuration used in Secs. III B and III C. This wave front is presented in Fig. 13(c), and can be compared to the experimental one [Fig. 13(a)] and the one obtained with the heterogeneous model [Fig. 13(b)]. One can see that the amplitude of the wave front is not well reproduced. This means that such a model only allows performing time shifting or time reversal. With a more complex model like the heterogeneous one presented here, one can try to perform more complex focusing by changing the phase and the amplitude of the signals. Even if time shifting is necessary and has to be taken into account to perform brain hyperthermia,¹⁹ new developments can be envisioned with a more accurate model, such as amplitude compensation.¹²

Of course, this first study has to be extended on other human skulls that the laboratory is currently looking for. The different models also have to be compared at lower frequencies, where the distortions induced by the skull are less important.

V. CONCLUSION

Based on prior CT scans, a 3-D finite differences numerical simulation of the complete wave equation has been proposed. This 3-D code takes into account the internal heterogeneities in density, speed, and absorption of the human skull. Thanks to this model, simulated wave fronts passing through the modeled skull are very close to the corresponding experimental wave fronts propagating through the same part of the skull. Moreover, the propagation through the skull of a wave front coming from a virtual point-like source located inside the brain can be simulated and recorded by a set of receivers. The same geometry is experimentally reproduced and the simulated wave front is time reversed and experimentally emitted by a real array of transducers. This enables us to achieve a complete time reversal experiment combined with amplitude compensation without the need of a physical source inside the brain, as the finite differences

code guided by CT scans allows us to create virtual sources inside the brain. As both phase and amplitude aberration induced by the skull can be noninvasively corrected, this technique could show encouraging promise in brain hyperthermia. A time reversal mirror made of 200 high-power transducers is under construction to bring into play this noninvasive hyperthermia protocol. Beyond its interest for noninvasive brain therapy, full 3-D finite differences simulations are an interesting tool for modeling and understanding the complex acoustic wave propagation through the skull.

ACKNOWLEDGMENTS

CT images were performed at the Laboratoire de Tomographie X of the Institut Français du Pétrole. We wish to thank Corinne Fichen and Camille Schlitter for both technical assistance and support.

- ¹G. ter Haar, "Acoustic surgery," *Phys. Today* **54**, 29–32 (2001).
- ²K. Hynynen, O. Pomeroy, D. N. Smith, P. E. Huber, N. J. McDannold, J. Kettenbach, J. Baum, S. Singer, and F. A. Jolesz, "MRI imaging-guided focused ultrasound surgery of fibroadenomas in the breast: a feasibility study," *Radiology* **219**, 176–185 (2001).
- ³Feng Wu, W. Z. Chen, J. Bai, J. Z. Zou, Z. L. Wang, H. Zhu, and Z. B. Wang, "Pathological changes in human malignant carcinoma treated with high-intensity ultrasound," *Ultrasound Med. Biol.* **27**, 1099–1106 (2001).
- ⁴S. Vaezy, M. Andrew, P. Kaczkowski, and L. Crum, "Image-guided acoustic therapy," *Annu. Rev. Bioeng.* **3**, 375–390 (2001).
- ⁵T. Uchida, N. Sanghvi *et al.*, "Transrectal high-intensity focused ultrasound for treatment of patients with localized prostate cancer: a preliminary report," *Urology* **59**(3) 394–399 (2002).
- ⁶A. Gelet, J. Y. Chapelon, R. Bouvier, R. Souchon, C. Pangaud, A. F. Abdelrahim, D. Cathignol, and J. M. Dubernard, "Treatment of prostate cancer with transrectal focused ultrasound: early clinical experience," *Eur. Urol.* **29**, 174–183 (1996).
- ⁷D. N. White, J. M. Clark, J. N. Chesebrough, M. N. White, and J. K. Campbell, "Effect of skull in degrading the display of echoencephalographic B and C scans," *J. Acoust. Soc. Am.* **44**, 1339–1345 (1968).
- ⁸F. J. Fry, "Transskull transmission of an intense focused ultrasonic beam," *Ultrasound Med. Biol.* **3**, 179–184 (1977).
- ⁹F. J. Fry and S. A. Goss, "Further studies of the transskull transmission of an intense focused ultrasonic beam: lesion production at 500 kHz," *Ultrasound Med. Biol.* **6**, 33–38 (1980).
- ¹⁰F. J. Fry, G. Kossof, R. C. Eggleton, and F. Dunn, "Threshold Ultrasonic dosages for structural changes in the mammalian brain," *J. Acoust. Soc. Am.* **48**, 1413–1417 (1970).
- ¹¹N. I. Vykhodtseva, K. Hynynen, and C. Damianou, "Pulse duration and peak intensity during focused ultrasound surgery: theoretical and experimental effects in rabbit brain *in vivo*," *Ultrasound Med. Biol.* **20**, 987–1000 (1994).
- ¹²J.-L. Thomas and M. Fink, "Ultrasonic beam focusing through tissue inhomogeneities with a time reversal mirror: application to transskull therapy," *IEEE Trans. Ultrason. Ferroelectr. Freq. Control* **43**, 1122–1129 (1996).
- ¹³G. T. Clement, J. Sun, T. Giesecke, and K. Hynynen, "A hemisphere array for non invasive ultrasound surgery and therapy," *Phys. Med. Biol.* **45**, 3707–3719 (2000).
- ¹⁴G. T. Clement, J. P. White, and K. Hynynen, "Investigation of a large area phased array for focused ultrasound surgery through the skull," *Phys. Med. Biol.* **45**, 1071–1083 (2000).
- ¹⁵M. Tanter, J.-L. Thomas, and M. Fink, "Focusing and steering through absorbing and aberrating layers: Application to ultrasonic propagation through the skull," *J. Acoust. Soc. Am.* **103**, 2403–2410 (1998).
- ¹⁶M. Tanter, J.-F. Aubry, J. Gerber, J.-L. Thomas, and M. Fink, "Optimal focusing by spatio-temporal inverse filter. I. Basic principles," *J. Acoust. Soc. Am.* **110**, 37–47 (2001).
- ¹⁷J.-F. Aubry, M. Tanter, J. Gerber, J.-L. Thomas, and M. Fink, "Optimal focusing by spatio-temporal inverse filter. II. Application to focusing through absorbing and reverberating media," *J. Acoust. Soc. Am.* **110**, 48–58 (2001).

- ¹⁸J. Sun and K. Hynynen, "Focusing of therapeutic ultrasound through a human skull: A numerical study," *J. Acoust. Soc. Am.* **104**, 1705–1715 (1998).
- ¹⁹J. Sun and K. Hynynen, "The potential of transskull ultrasound therapy and surgery using the maximum available surface area," *J. Acoust. Soc. Am.* **105**, 2519–2527 (1999).
- ²⁰K. Hynynen and J. Sun, "Transskull ultrasound therapy: The feasibility of using image derived skull thickness information to correct the phase distortion," *IEEE Trans. Ultrason. Ferroelectr. Freq. Control* **46**, 752–755 (1999).
- ²¹G. T. Clement, C. Connor, and K. Hynynen, "Treatment planning for transskull focused ultrasound surgery and therapy," *Proceedings of the 17th International Congress on Acoustics*, 2001.
- ²²M. Pernot, J.-F. Aubry, M. Tanter, J.-L. Thomas, and M. Fink, "Experimental validation of finite differences simulations of the ultrasonic wave propagation through skull," *Proc. IEEE Ultrason. Symp.* **2**, 1547–1550 (2001).
- ²³J. Y. Rho, M. C. Hobato, and R. B. Ashman, "Relations of mechanical properties to density and CT numbers in human bone," *Med. Eng. Phys.* **17**, 347–355 (1995).
- ²⁴H. Ploeg, W. Taylor, M. Warner, D. Hertig, and S. Clift, "FEA and bone remodelling after total hip replacement," awarded Best Paper Award, *Proceedings of the NAFEMS World Congress*, 2001, pp. 13–17. A version of this article is available online at (<http://www.nafems.org/publications/downloads/Bone%20Remodeling.pdf>).
- ²⁵F. J. Fry and J. E. Barger, "Acoustical properties of the human skull," *J. Acoust. Soc. Am.* **65**, 1576–1590 (1978).
- ²⁶D. R. Carter and W. C. Hayes, "The compressive behavior of bone as a two-phase porous structure," *J. Bone Jt. Surg.* **59A**, 954–962 (1977).
- ²⁷E. S. Ebbini and C. A. Cain, "A spherical-section ultrasound phased-array applicator for deep localized hyperthermia," *IEEE Trans. Biomed. Eng.* **38**, 634–643 (1991).
- ²⁸L. E. Kinsler, A. R. Frey, A. B. Coppens, and J. V. Sanders, *Fundamentals of Acoustics* (Wiley, New York, 1982), ISBN 0-471-02933-5, pp. 142–145.
- ²⁹W. H. Press, S. A. Teukolsky, W. T. Vetterling, and B. P. Flannery, *Numerical Recipes in C* (Cambridge University Press, Cambridge, 1992), ISBN 0-521-43108-5, pp. 836–849.
- ³⁰R. L. Higdon, "Absorbing boundary conditions for elastic waves," *Geophys. Soc. Expl. Geophys.* **56**, 231–241 (1991).
- ³¹J. W. Goodman, *Statistical Optics* (Wiley, New York, 1985).

Scattering from a single bubble near a roughened air–water interface: Laboratory measurements and modeling

Peter H. Dahl and George Kapodistrias

Applied Physics Laboratory, University of Washington, Seattle, Washington 98105

(Received 23 April 2001; revised 12 February 2002; accepted 12 September 2002)

The problem of scattering from a single bubble located close to a slightly roughened, air–water interface is studied both theoretically and experimentally. Two well-controlled laboratory experiments were performed to investigate the effects of surface roughness on the scattering response of the bubble. In the first experiment, a bubble of radius $1200\ \mu\text{m}$ was placed on a fine thread at a variable distance, d , from the mean-still-water level of the surface, which was roughened using a wind source. In the second experiment, a bubble of radius $800\ \mu\text{m}$ was utilized, while the water surface was roughened using a plunger wave-making source. The waveheights and important characteristic length scales associated with each experiment were quantified using digital photography. The wind source produced waveheights that were represented by a Gaussian distribution, while the plunger source produced waveheights that were represented by a bimodal distribution. To model the acoustic measurements, an expression describing the four scattering paths, from source to bubble to receiver, was used. A random phase shift due to the surface roughness was added to the paths that interacted with the surface, and expectations of this phase shift were computed based on the analytical representations for the waveheight distribution. The data show good agreement with the simulations and the sensitivity of scattering from a subsurface bubble to small changes in waveheight is illustrated. The experiments highlight important parametric dependencies, which are summarized here, and the relation between monostatic and bistatic scattering is also discussed. © 2003 Acoustical Society of America.

[DOI: 10.1121/1.1519543]

PACS numbers: 43.20.Fn, 43.30.Cq, 43.40.Ga, 43.30.Zk [DLB]

I. INTRODUCTION

In an earlier, related paper¹ a model for acoustic scattering from a single bubble located close to a flat, air–water interface was presented along with verifying experimental measurements. The model consists of two multiplicative factors: one accounts for the coherent combination of four major paths by which scattering can occur (two of which are reciprocal in the monostatic case), and the other accounts for multiple scattering between the bubble and the air–water interface. It was demonstrated that multiple scattering can play a substantial role for bubble depths, d , such that $kd < 1$, where k is the acoustic wavenumber, but the essential features of scattering from a single bubble located close to a flat, air–water interface are produced by the coherent combination of the four paths.

In this paper the effects of a slightly roughened, air–water interface on the coherent combination of the four major paths are studied, and the model from Ref. 1 is modified to include these effects. We also present verifying laboratory measurements of monostatic scattering from a single bubble (performed at a frequency of 120 kHz) located close to a slightly roughened air–water interface, that was characterized using digital photography.

In the following section a model for backscattering from a single bubble located below a roughened air–water interface is described. In Sec. III we describe our experimental procedure and measurements, starting with the measurements of surface roughness, and how these are incorporated into the model, followed by the acoustic measurements and

comparisons of these data with predictions based on our model. A discussion is presented in Sec. IV; here, important parametric dependencies are summarized and the relation between monostatic and bistatic scattering is discussed.

II. MODEL FOR BACKSCATTERING FROM A SINGLE BUBBLE LOCATED CLOSE TO A ROUGHENED AIR–WATER INTERFACE

The backscattered pressure, P_s , from a single bubble located a distance d below mean-still-water level of a roughened air–water interface, and range r from the transducer (with $d/r \ll 1$) is expressed as

$$P_s = \frac{e^{2ikr}}{r^2} [f_{180} e^{2ik\beta} - 2f_\theta e^{2ik(\alpha+\beta)+i\phi} + f_{180} e^{2ik\alpha+2i\phi}], \quad (1)$$

where α and β are the distances shown in Fig. 1 (II), and ϕ is a phase factor (discussed below). For $d/r \ll 1$, one grazing angle, θ , applies to all values of d , and ultimately the variables α and β are expressed in terms of d and θ . Four paths (labeled I–IV in Fig. 1) are associated with Eq. (1), two of which (II and III) are reciprocal and add coherently, thus giving rise to the three terms shown.

Equation (1) originates from Eq. (16) of Ref. 1, but contains two changes. The first is that here f_{180} and f_θ represent the complex scattering amplitude of a bubble at scattering angles of 180 degrees and at $180 \text{ degrees} \pm 2\theta$ degrees, respectively (Fig. 1). In this work we find these amplitudes from the first two terms (monopole and dipole) of Ander-

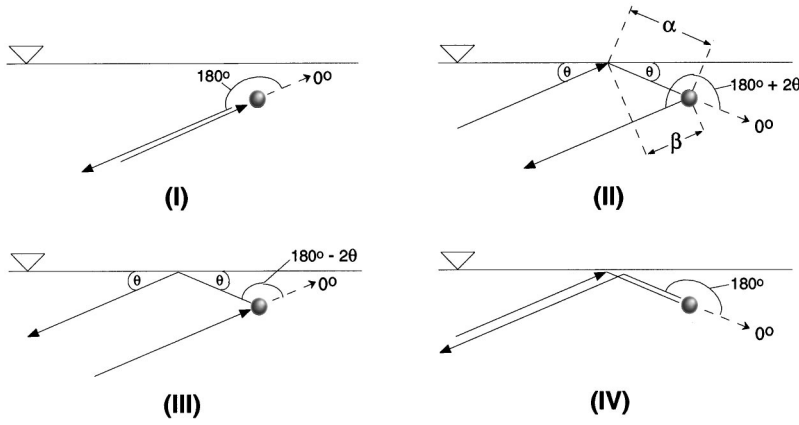


FIG. 1. Geometry describing monostatic scattering from a bubble located a distance d below mean-still-water level, for $d/r \ll 1$ where r is range to source and receiver. Four paths, labeled (I)–(IV), are identified.

son's solution² for scattering from a fluid-filled sphere of arbitrary size. The manner by which Anderson's solution is expressed in the form of a complex scattering amplitude is discussed in Ref. 3. In Eq. (16) of Ref. 1, a single variable, f_B , was used to represent the bubble's complex scattering amplitude associated with its monopole response. In this study, however, larger bubbles of radius a equal to 800 and 1200 μm were used, putting ka at about 0.41 and 0.61, respectively, for our frequency of 120 kHz and necessitating the use of an angle-dependent complex scattering amplitude.

The second change is that the influence of the roughened air–water interface is accounted for by factors $e^{i\phi}$ and $e^{2i\phi}$, representing the added phase shift ϕ and 2ϕ , imparted by one and two reflections, respectively, from the roughened air–water interface. Setting $\phi=0$ and $f_{180}=f_\theta$, we recover an equation for an ideal flat, pressure-release boundary as obtained in Ref. 1. We invoke the Kirchhoff approximation (e.g., see Ref. 4), for which the added phase shift relative to the phase shift upon reflection from the mean surface equals $2k\Delta \sin \theta$, where Δ is the surface displacement and θ is the grazing angle. Justification for use of the Kirchhoff approximation is given in the next section.

The backscattering cross section, σ_{bs} , is defined as $\langle P_s P_s^* \rangle r^2 / |P_{inc}|^2$, where the incident field P_{inc} is by convention equal to e^{ikr}/r and $\langle P_s P_s^* \rangle$ is the mean-square backscattered pressure. Here σ_{bs} (our experimental observable) is reported in terms of target strength, $TS = 10 \log_{10} \sigma_{bs}$, in dB re 1 m^2 .

To model σ_{bs} we take the ensemble average of $P_s P_s^*$ in Eq. (1) multiplied by r^4 , giving

$$\sigma_{bs}(d) = 2|f_{180}|^2 + 4|f_\theta|^2 + 2|f_{180}|^2 \mathcal{R}_2 \cos(4kd \sin \theta) - 4\mathcal{R}_1 \cos(2kd \sin \theta)(f_\theta f_{180}^* + f_{180} f_\theta^*), \quad (2)$$

where

$$\mathcal{R}_1 = \langle e^{\pm i2k\Delta \sin \theta} \rangle, \quad (3)$$

and

$$\mathcal{R}_2 = \langle e^{\pm i4k\Delta \sin \theta} \rangle. \quad (4)$$

The factors \mathcal{R}_1 and \mathcal{R}_2 can be determined given a suitable representation of the probability density function (PDF) for the surface elevation variable Δ and both become 1 in the limit of a perfectly flat surface.

III. EXPERIMENTS ON BACKSCATTERING FROM A SINGLE BUBBLE LOCATED CLOSE TO A ROUGHENED AIR–WATER INTERFACE

Two sets of experiments were performed using the system shown in Fig. 2. Since the experimental apparatus and procedure (for all but surface wave generation) are described in detail in Refs. 1 and 3, we give only a brief description here. The basic apparatus consists of a plexiglass tank and a transducer that was rotated an angle θ from the horizontal axis. The transducer's (two-way) beamwidth was 9.9 degrees, defined as the full angle between points 3 dB down from the maximum response axis. The input signal to the transducer was a five-cycle tone burst with a center frequency of 120 kHz. The received signal from each transmitted ping was amplified, band-pass filtered between 100 and 140 kHz, and digitized at a sample rate of 1 MHz. The mean-square voltage was taken within a time gate corresponding to the bubble's range, based on a 30-ping average, and the quantity $\langle P_s P_s^* \rangle$ computed, based on the calibration of the system as described in Refs. 1 and 3.

In the first experiment, a roughened surface was created by wind using a fan positioned approximately 15 cm above

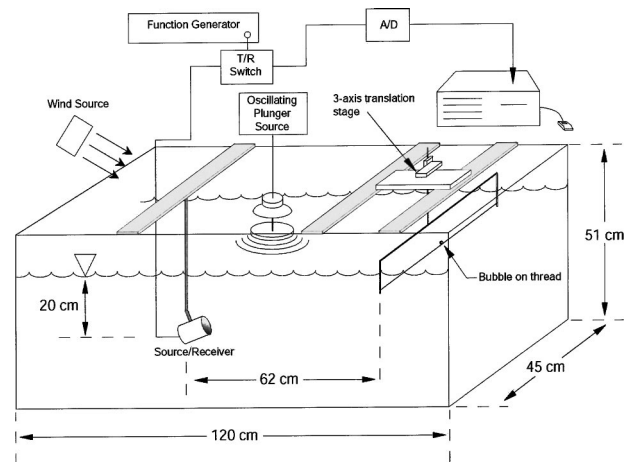


FIG. 2. Experimental apparatus for measuring backscattering from a bubble beneath a roughened air–water interface. Two wave generation mechanisms were used: a wind source (fan) and an oscillating plunger source. (Plunger source was not in the water while the fan was operating.) A small bubble target is depicted on a thread, which is 62 cm to the right of the acoustic source/receiver. The drawing is not to scale.

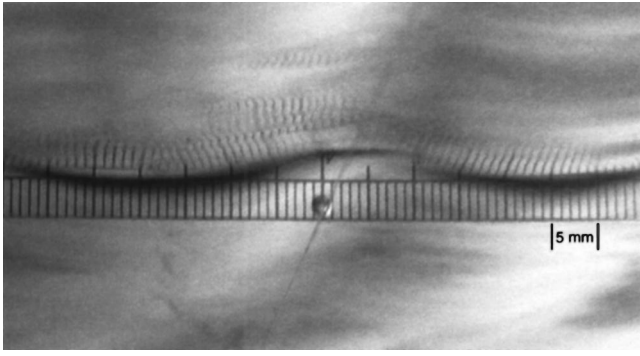


FIG. 3. Photograph of a single bubble below the slightly roughened air–water interface and scaled ruler (1 mm graduation). This photograph was taken immediately after the acoustic measurements for the wind-source experiment were completed. The size of the bubble is $1200\ \mu\text{m}$. The long wavelength of the surface wave is about $45\ \text{mm}$, and the diameter of the thread is $100\ \mu\text{m}$.

the water and tilted slightly downward (Fig. 2), producing a surface with rms waveheight of about $1\ \text{mm}$. The fan-generated wind speed was $3.5\ \text{m/s}$, measured $5\ \text{cm}$ above the water using a portable anemometer. Although the relation between wind speed and waveheight in this case is a very unnatural one owing to restricted fetch and air flow within the confines of the tank, the wind speed does have significance because of the important assertion made here that no bubbles were created in association with the roughened surface. For example, Kolaini *et al.*⁵ studied the creation of bubbles by encapsulating wind-generated capillary waves. Their study was conducted in a similar-sized tank, and they determined a wind speed threshold of about $8\ \text{m/s}$ for bubble creation via an encapsulation mechanism.

In the second experiment, a roughened surface was created using a plunging-type wave maker consisting of a shallow, plastic bowl ($25\ \text{cm}$ diam) set into gentle oscillation while never breaking contact with the water. Here, too, care was taken to avoid creating bubbles. This process launched a wave crest at frequency between 5 and $6\ \text{Hz}$ (estimated by analyzing video records of the plunger and flow play-back speed) and created a surface with rms waveheight of about $0.6\ \text{mm}$.

A. Measurements of the roughened air–water interface and their use in acoustic modeling

The artificially roughened, air–water interface was quantified using a digital camera and a scaled ruler placed in the field of view. Digital photographs (e.g., Fig. 3) were quantified using NIH image, a public domain image processing software package, with a horizontal sampling interval of $1\ \text{mm}$. The surface characterization photographs were made immediately following completion of the acoustic measurements. An ensemble of ten photographs, each covering approximately $70\ \text{mm}$ of surface, were taken for each surface type.

Sample autocorrelation (acf) functions for the wind and plunger surfaces based on the ten-member ensemble are shown in Fig. 4. Although the acf estimates have a high variance, they do satisfy their main purpose of characterizing important length scales of surface roughness. For example,

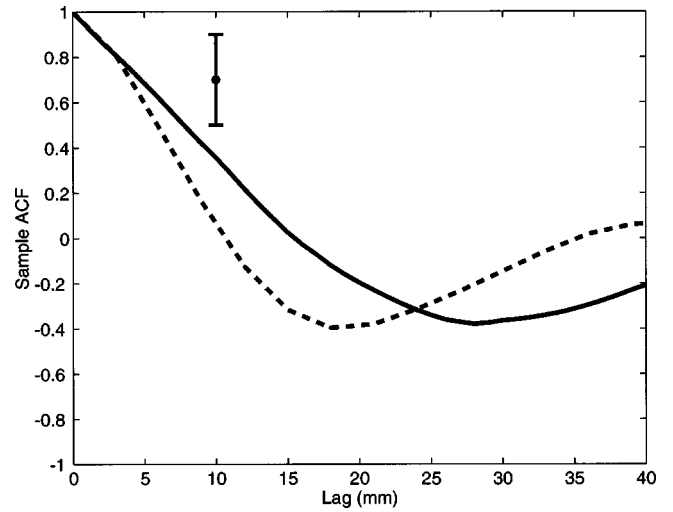


FIG. 4. Sample autocorrelation functions for the wind (dashed line) and plunger (solid line) surfaces. The vertical bar (offset from results) represents uncertainty in results for spatial lags $\geq 10\ \text{mm}$.

the first zero-crossing for the plunger data is approximately $15\ \text{mm}$, which is consistent with a long wavelength scale of about $60\ \text{mm}$ were the acf to be modeled as a damped cosine of this wavelength. Using the dispersion relation

$$(2\pi F)^2 = gK + g\tau K^3/\rho, \quad (5)$$

where K is the capillary wavenumber, g is the gravitational constant, ρ is water density, and τ is surface tension ($0.074\ \text{N/m}$), a capillary wave of about $60\ \text{mm}$ will have a frequency $F=5.4\ \text{Hz}$, which is consistent with our video estimates. Similarly, the first zero-crossing for the wind data is approximately $11\ \text{mm}$, putting the long wavelength for wind surface at about $44\ \text{mm}$. Both sample acf estimates are reasonably described by a simple model of the form $c(x) = e^{-|x|/\lambda_0} \cos(K_0 x)$, where x is the lag variable in the primary direction of the waves (i.e., along the ruler shown in Fig. 3) and K_0 is the wavenumber corresponding to the long wavelength. The length scale λ_0 is about $20\ \text{mm}$ for the wind data and about $27\ \text{mm}$ for the plunger data.

For a nominal estimate of the surface radius of curvature, r_c , we use $r_c \sim 0.3\lambda_0^2/\sigma$ (see Ref. 6, p. 23), where σ is the rms waveheight, which puts r_c at about $120\ \text{mm}$ when using (λ_0, σ) from the wind surface. Using $k=506\ \text{m}^{-1}$ (based on tank water sound speed $c=1490\ \text{m/s}$), and the nominal grazing angle for the experiments, $\theta \approx 17.5$ degrees, then the less restrictive inequality for validity of Kirchhoff theory is satisfied, namely that $kr_c \sin \theta \gg 1$ (see Ref. 6, p. 104).

Figure 5 shows empirical probability density functions (or PDFs) of measurements of surface elevation for the wind and plunger surfaces with each based on the elevation data originating from a ten-member ensemble of digital photographs. The empirical PDF for the wind surface is reasonably well approximated by a Gaussian PDF with zero mean and standard deviation, σ , equal to $1\ \text{mm}$. Thus, for modeling purposes, we represent the PDF for wind surface elevation, $p_w(\Delta)$, using

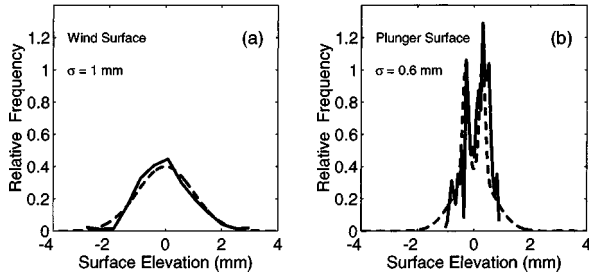


FIG. 5. Empirical probability density function (solid, black line) for wind surface (a), and plunger surface (b) data. The dashed curves represent modeled probability density functions, which are Eq. (6) for the wind data and Eq. (7) for the plunger data.

$$p_w(\Delta) = \frac{1}{\sqrt{2\pi}\sigma} e^{-\Delta^2/2\sigma^2}, \quad (6)$$

which is plotted along with the data in Fig. 5(a).

Regarding the plunger surface data, first the quality of the surface amplitude measurements is somewhat reduced by a small but apparent saturation effect that occurs when $|\Delta|$ exceeds about 1 mm, as evidenced by the slight rise in empirical PDF amplitudes near ± 1 mm. We proceed to construct a model PDF for the empirical PDF based on a reasonable assumption that the uncensored probability of wave amplitude greater than 1 mm is small. Second, the empirical PDF is bimodal, a consequence that likely arises from the addition of two wave contributions, and therefore a convolution of their respective PDFs, one contribution being a sine-like wave originating from the plunger source and the other being a more complicated wave pattern originating from reflections from all four walls. Rather than proceed with convolution to obtain a model PDF, it is sufficient to represent the empirical PDF with a simple combination of three Gaussians, two of which are centered at a wave amplitude $a=0.3$ mm, with standard deviation $\sigma_1=0.1$ mm; both of these functions are given a weight n_1 . The third Gaussian has a zero mean amplitude with standard deviation $\sigma_2=0.7$ mm and this function is given a weight n_2 . The weights n_1 and n_2 are 0.175 and 0.65, respectively, with $2n_1+n_2=1$. The PDF for the plunger surface elevation, $p_p(\Delta)$, is thus represented using

$$p_p(\Delta) = \frac{n_1}{\sqrt{2\pi}\sigma_1} e^{-(\Delta-a)^2/2\sigma_1^2} + \frac{n_1}{\sqrt{2\pi}\sigma_1} e^{-(\Delta+a)^2/2\sigma_1^2} + \frac{n_2}{\sqrt{2\pi}\sigma_2} e^{-\Delta^2/2\sigma_2^2}, \quad (7)$$

which is plotted along with the data in Fig. 5(b). The probability of $|\Delta| > 1$ mm based on Eq. (7) is 0.1, which is consistent with our claim that the saturation effect is small.

A note regarding the above PDFs: we do not claim that Eqs. (6) and (7) are genuine statistical models for the random variable Δ as it was generated by wind and plunger mechanisms. That is, the empirical PDF from the wind data does not represent, in a rigorous statistical sense, a true random sample from a population described by Eq. (6), insofar as the probability of the chi-squared statistic⁷ is less than 5%. The

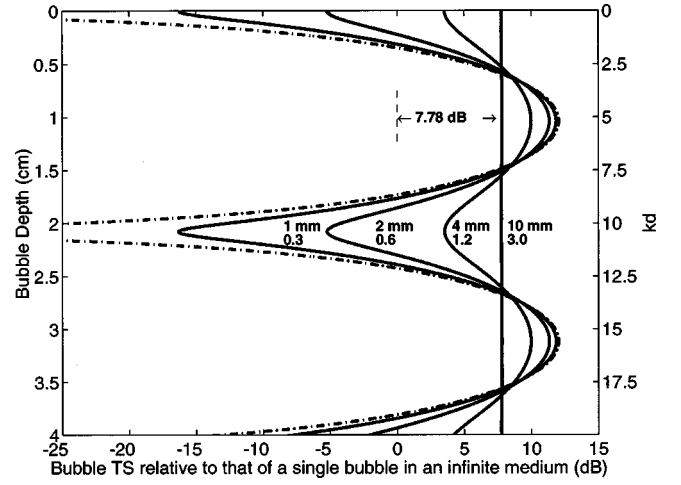


FIG. 6. Model prediction of the TS of a single bubble versus depth d below roughened air-water interface, relative to that of a single bubble in an infinite medium, which here is set to 0 dB. The model predictions are based on an acoustic frequency of 120 kHz and grazing angle $\theta=17.5$ degrees, and assumes a monopole scattering response of the bubble. The five curves represent five rms waveheights (σ) used in the calculations. Listed below each nonzero waveheight is the corresponding value for the parameter $\chi = 2k\sigma \sin \theta$. The case of zero waveheight (perfectly flat) is plotted as a dotted-dashed line.

same is true for the plunger data. However, a genuine statistical model for the Δ measurements, the quality of which is marginal, is not needed here. Instead, a reasonable approximation for the surface elevation PDF is required, and Eqs. (6) and (7) fulfill this requirement.

The constants \mathcal{R}_1 and \mathcal{R}_2 for the wind surface are computed by

$$\mathcal{R}_1 = \int_{-\infty}^{+\infty} p_w(\Delta) \cos(2k\Delta \sin \theta) d\Delta = e^{-2(k\sigma \sin \theta)^2}, \quad (8)$$

and, similarly,

$$\mathcal{R}_2 = e^{-8(k\sigma \sin \theta)^2}. \quad (9)$$

Using $\sigma=0.001$ m puts $\mathcal{R}_1=0.9487$ and $\mathcal{R}_2=0.8100$ at a frequency of 120 kHz and $\theta=17.5$ degrees. For the plunger surface, the same analysis using $p_p(\Delta)$ gives

$$\mathcal{R}_1 = 2n_1 e^{-8(k\sigma_1 \sin \theta)^2} \cos(4ka \sin \theta) + n_2 e^{-8(k\sigma_2 \sin \theta)^2}, \quad (10)$$

and

$$\mathcal{R}_2 = 2n_1 e^{-2(k\sigma_1 \sin \theta)^2} \cos(2ka \sin \theta) + n_2 e^{-2(k\sigma_2 \sin \theta)^2}. \quad (11)$$

Using σ_1 , σ_2 , and a expressed in m puts $\mathcal{R}_1=0.9840$ and $\mathcal{R}_2=0.9379$.

B. Measurements of acoustic scattering, and model/data comparisons

Before discussing the acoustic scattering measurements it is instructive to first examine the theoretical dependence of bubble TS on bubble depth and interface roughness (shown in Fig. 6). Here the interface is characterized by zero-mean

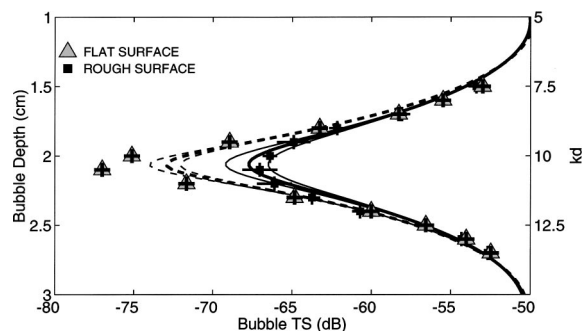


FIG. 7. Theoretical curves for scattering from a single bubble of radius 1200 μm located close to a flat (dashed lines) and wind-roughened (black lines) air–water interface at 120 kHz, compared with experimental data plotted with same color code. The horizontal and vertical lines through each data point represent experimental uncertainty in the measurement. Three model curves are shown for both the flat and roughened cases. These are based on the incoherent addition of three estimates of the equivalent background TS (high, low, and average) as discussed in the text, with the thicker curves based on the average background.

Gaussian PDF and the effect of differing values of the rms waveheight σ ranging from 0 to 10 mm is shown for a frequency of 120 kHz and grazing angle of 17.5 degrees. This is equivalent to a range of the parameter $\chi = 2k\sigma \sin \theta$ of 0 to nearly π . The figure is for illustrative purposes only, and it is important to note the following: (1) The bubble is assumed to be a monopole scatterer in the absence of the air–water boundary and thus $f_\theta = f_{180}$; here both f_θ and f_{180} are artificially set to unity, which puts the TS of the bubble in an infinite medium equal to 0 dB. (2) Effects associated with the finite bandwidth of the pulse are not included. For example, the deep null near depth 2 cm for the perfectly flat case would be filled in somewhat if bandwidth effects were included. (3) Background noise is not included, which would also fill in nulls but would have little effect near peaks such as near depth 1 cm. The key points of Fig. 6 are the strong sensitivity to mm changes in rms waveheight (this sensitivity being frequency dependent), and that an asymptotic rough-surface value is quickly reached. When the rms waveheight reaches 10 mm, the bubble TS becomes constant with depth and is 7.78 dB greater than the TS of a single bubble in free space. This value, equal to $10 \log_{10} 6$, is based on the incoherent combination of two of the aforementioned four paths and coherent combination of the other two paths. Finally, in Ref. 1 it is shown that σ_{bs} goes as $\sin^4(kd \sin \theta)$ for a perfectly flat surface, and thus the first null for nonzero depth occurs at $d = \pi/(k \sin \theta)$, or 20.6 mm for a frequency of 120 kHz and grazing angle of 17.5 degrees. According to the model, near this key depth scattering will exhibit the greatest sensitivity to changes in surface roughness. We thus concentrated our measurement effort near this region, because a reduction in bubble radius due to dissolution necessarily limited the experimental duration to about 25 min.

Figure 7 shows the results of the wind-surface experiment, for which the bubble radius was 1200 μm , and Fig. 8 shows the results from the plunger-surface experiment, for which the bubble radius was 800 μm . Both rough and flat surface measurements were made at each depth according to the following sequence: (1) A set of 30 backscattered intensities (using five-cycle pulse) were collected while the fan or

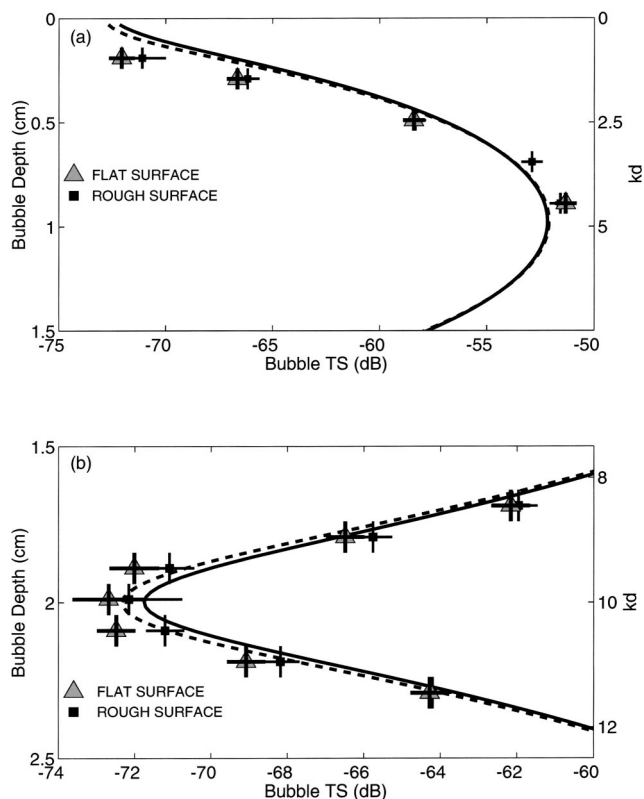


FIG. 8. Theoretical curves for scattering from a single bubble of radius 800 μm located close to a flat (dashed lines) and plunger-roughened (black lines) air–water interface at 120 kHz, compared with experimental data plotted with same color code. Results are shown in two plots, (a) and (b), that require different dynamic ranges for display. The horizontal and vertical lines through each data point represent experimental uncertainty in the measurement. The model curves incorporate an equivalent background TS as discussed in the text.

plunger source was operating, and a steady-state rough surface was in effect. (2) The fan or plunger source was turned off, and the surface returned to nearly a perfectly flat state within a few seconds. (3) Scattering measurements were repeated for the flat surface condition.

The backscattered intensities were ensemble averaged yielding an estimate of σ_{bs} upon applying calibration constants. The sequence was typically repeated four or five times, each time producing an estimate of σ_{bs} , then the bubble's vertical position was changed and measurements continued. This process lasted approximately 20 min. Each data point represents the linear average of σ_{bs} , expressed in dB, i.e., TS. Error bars about each data point are intended to represent the uncertainty in vertical position (vertical bars) and the statistical variation in the acoustic measurements (horizontal bars). For the latter, the difference between the minimum and maximum TS estimate within each set of estimates is taken to represent the probable range in the acoustic measurements.

Three arguments must be made in order to produce the model curves in Figs. 7 and 8 for comparison with the acoustic observations. First, the finite bandwidth of the pulse of length $T = 5/120\,000$ s is accounted for by computing Eq. (2) at 21 discrete frequencies, f_i , separated by 1 kHz and bracketing the center frequency, $f_o = 120$ kHz. This frequency spread of ± 10 kHz represents the nominal 3-dB bandwidth

of the rectangular pulse. The 21 values of σ_{bs} for a given depth are weighted according to $((\sin W)/W)^2$, where $W = \pi(f_i - f_o)T$, to reflect the spectrum of the pulse, and the weighted values are then averaged to produce a (noise-free) model estimate of σ_{bs} at a given depth d .

Second, the fluctuating background interference level, expressed in terms of an equivalent background or bubble-free TS, plays an important role in the model-data comparison, particularly in the vicinity of $d=2$ cm where backscattered levels approach a minimum. We frequently measured the background level using the same aforementioned measurement protocol, but without a bubble in the acoustic field. During the time frame of the wind-surface experiment, the equivalent background TS for when the fan was off ranged from -80 to -75 dB, with an average of -77 dB. The equivalent background TS for when the fan was on ranged from -74 to -68 dB, with an average of -70 dB. We postulate that the higher background level while the fan was on was due to Bragg scattering from capillary waves of wavelength close to 6.5 mm.

Because of the orientation of the transducer with respect to the direction of wind-generated waves (Fig. 2), it is likely that scattering from parasitic capillary waves riding on the leeward face of the primary wind-generated waves (see Ref. 8) contributed to the background level. Given this condition, it thus would have been possible to lower the background level somewhat by using the opposite orientation *vis-à-vis* the transducer look direction and wind direction. This would have required, however, a tank about twice as long as ours in order to place the transducer and fan at opposite ends of the tank while placing the bubble target in the middle, with sufficient separation from both transducer and fan.

In Fig. 7, the three different model curves shown for both flat and rough surface cases incorporate the three estimates for equivalent background TS (high, low, and average) measured in each case. Background TS is incorporated into the model by the incoherent addition of an equivalent background σ_{bs} . The thicker lines are based on the average background value of σ_{bs} and the two thinner lines are based on the high- and low-background values of σ_{bs} .

During the time frame of the plunger-surface experiment (performed about one month after the wind surface measurements), repeated measurements of equivalent background TS for when the plunger source was either on or off averaged -73 dB with a tight distribution (± 0.5 dB). Use of the plunger source clearly knocked down the background level associated with Bragg scattering that we observed with the wind surface. However, the flat-surface, or quiescent, background level also increased during this period by about 4 dB. In Fig. 8, only one model curve is shown for each of the flat and rough-surface cases, both of which incorporate an equivalent background TS equal to -73 dB.

The third argument pertains to bubble sizing. The two bubble radii, 1200 and 800 μm , were determined acoustically because these radii were too large to be sized by the auxiliary optical procedure used on smaller bubbles.^{1,3} We have confidence in these bubble-size estimates based on the following: (a) We conclusively verified the scattering response of a single bubble versus depth d beneath a flat,

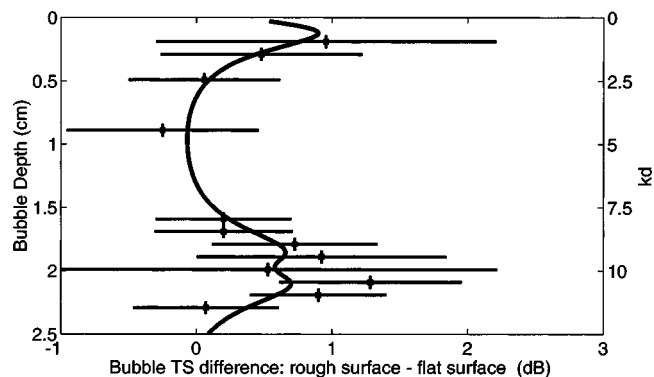


FIG. 9. Difference in measured TS, defined as the measured TS for plunger-roughened surface minus that for the flat surface (circles), compared with equivalent values obtained from the model. The horizontal and vertical lines through each data point represent experimental uncertainty in the measurement. The model curve represents the decibel difference between plunger-roughened and flat surface models, based on the best estimate of the equivalent background TS.

pressure-release surface.¹ (b) Our system was reliably calibrated using a reference sphere.^{1,3} (c) In this work, sizing was achieved by adjusting the flat-surface model to agree with flat-surface measurements made in regions of expected high backscattering. These regions were in the vicinity of $d=1.5$ and 2.5 cm for wind surface data in Fig. 7, and $d=0.5$ to 1.0 cm for the plunger surface data in Fig. 8.

The results of the wind-surface experiment (Fig. 7) show the significant effect on the scattering due to a change in rms surface roughness of only 1 mm. Our model curves also agree with the data, with the expectation of the two flat-surface measurements made at a depth close to 2 cm. It is quite possible that here the fluctuating background level is responsible. For example, using an equivalent background TS of -86 dB would have produced a much better agreement with these two data points without changing model-data agreement for the other flat-surface data points. Such a background value, although not measured during the experiment, is quite plausible. (For example, in the related paper¹ involving similar experiments using flat surfaces conducted a few months prior to these, the equivalent background TS was measured to be -84 dB.)

For the plunger surface experiment, about the same number of measurements were taken. But instead of allocating the entire measurement effort to depths close to 2 cm, a few measurements were also made at shallower depths. The results are shown in two plots, Figs. 8(a) and (b), that require different dynamic ranges for display. In the case of the plunger surface with its even smaller rms waveheight of 0.6 mm, less than 1 dB separates the models for flat and rough surfaces. Here, too, however, the data appear to be consistent with the model results. This can perhaps be better seen by computing the difference in measured TS for the flat and rough surface cases, and comparing these with an equivalent value obtained from the model. Results are displayed in Fig. 9 where the solid line represents the decibel difference between rough and flat surface models.

IV. DISCUSSION

Of the two surfaces and their corresponding PDFs [given by Eqs. (6) and (7)] investigated here, the Gaussian

PDF from the wind surface is much more representative of natural sea surfaces.⁹ From the simple expressions for \mathcal{R}_1 and \mathcal{R}_2 associated with the Gaussian PDF, it is clear that the rms waveheight σ , combined with grazing angle and frequency, establishes a critical parameter, $\chi = 2k\sigma \sin \theta$, that governs the behavior of the field backscattered from a bubble located beneath a roughened air–water interface. The parameter χ is well known from the study of reflection and scattering from rough surfaces. As Fig. 6 shows, the range over which χ has influence in this process is $0 \leq \chi < \pi$; for $\chi > \pi$, there is no change in the scattering versus depth behavior for increasing roughness. To be sure, the model developed for this laboratory-scale work using a single bubble has little applicability to field data. Yet, the model's general agreement with our laboratory data does lend credence to field models based on the same ideas, which are themselves difficult to explicitly verify in a field setting. Specifically, we refer to a monostatic form,¹⁰ and bistatic form,¹¹ of such a model; both model forms embody the same mechanism of four paths by which scattering can occur but assume the surface roughness is large with $\chi > \pi$.

In this study, our exploration of the χ parameter space involved only small values; these being 0 (flat surface), 0.18 (plunger surface), and 0.30 (wind surface). There were practical limitations (set by our small tank facility and equipment) that limited us to these small values, and we intend to explore larger values of χ in future studies. In terms of ka , our measurements were near $ka = O(1)$. However, our results are expected to apply for the case $ka \ll 1$, upon using the more simple angle-independent complex scattering response in Eq. (1).

It is interesting, though, to relate the response for $\chi = 0$, which we have thoroughly measured both here and previously,¹ to the response for $\chi \geq \pi$ (e.g., as shown in the model demonstration curves displayed in Fig. 6). For this, we revert (without loss of generality) to the scattering response of a bubble of radius a with $ka \ll 1$ beneath a flat air–water interface (modeled as a pressure-release interface). This response, without its factor accounting for multiple scattering between bubble and air–water interface discussed in Ref. 1, reduced to the compact expression

$$\sigma_{bs}(d) = 16|f_B|^2 \sin^4(kd \sin \theta). \quad (12)$$

With f_B set artificially to unity, Eq. (12) describes the $\chi = 0$ response shown in the model demonstration curves of Fig. 6. As previously noted, the equation is periodic with a depth cycle equal to $\pi/(k \sin \theta)$. Upon taking a depth average of $\sigma_{bs}(d)$ over one cycle, the result is exactly $6|f_B|^2$, or 7.78 dB greater than the TS of a single bubble in the infinite-medium case. The amplification factor of 6 is the same result for $\chi \geq \pi$, as one would expect on the basis of energy conservation. Taking a depth average of $\sigma_{bs}(d)$ over an arbitrary depth, say the characteristic depth of bubbles beneath the air–water interface, z^* , with $z^* \gg \pi/(k \sin \theta)$, will also yield a value very close to 6. Inclusion of the factor that accounts for multiple scattering does not change this result.

This analysis can be repeated using the equivalent ($\chi = 0$) bistatic response, also derived and evaluated experi-

mentally in Ref. 1. The bistatic response (again excluding the multiple scattering factor) is

$$\sigma_{bi}(d) = 4|f_B|^2 \left[\cos \left(kA \frac{d}{r} \cos \theta \right) - \cos(2kd \sin \theta) \right]^2, \quad (13)$$

where A , for aperture length, is the separation between the centers of source and receiver. (A line originating from the mean-still-water level at grazing angle θ would intersect the aperture at its midpoint.) Note that Eq. (13) is not valid for a widely separated source and receiver, e.g., as in bistatic forward scattering from the sea surface. [Further discussion on the geometric approximations inherent in Eq. (13) can be found in Ref. 1.] The equation does, however, provide the basis to proceed with the argument that taking a depth average of $\sigma_{bi}(d)$ over the depth z^* , gives

$$\frac{\langle \sigma_{bi} \rangle}{|f_B|^2} = 4 + 2 \frac{\sin \Gamma}{\Gamma} + O \left(\frac{1}{kz^* \sin \theta} \right), \quad (14)$$

which is governed by the parameter Γ , where

$$\Gamma = \frac{2kAz^* \cos \theta}{r}. \quad (15)$$

For $\Gamma \geq \pi$, depth averaging of the bistatic response yields an amplification factor of 4, representing the incoherent addition of the four paths, as must be the case. For $\Gamma = 0$, two of the four paths become reciprocal, and the amplification factor of 6 results. As a practical matter, depth averages for the two quantities, σ_{bs} in Eq. (12) and σ_{bi} in Eq. (13), merge for $\Gamma < \pi$.

Importantly, we expect the result concerning the parameter Γ to apply also to the monostatic¹⁰ and bistatic¹¹ field models for the contribution of near-surface bubbles to the apparent backscattering cross section per unit area of sea surface. The contribution from bubbles in this case represents a depth integration of their combined scattering. Both of these field models are parametrized by β_I , defined as the depth-integrated extinction cross section per unit volume associated with bubble scattering and absorption. But in the low-bubble-density limit ($\beta_I \ll 1$), the bistatic model, evaluated in the limit of source and receiver co-location, is a factor of $\frac{2}{3}$ that of the monostatic model. Strictly speaking, if such a limit is to be taken, then the result should be multiplied by the factor $1 + (\sin \Gamma)/2\Gamma$, which itself becomes $\frac{3}{2}$ in the limit of source and receiver co-location.

¹G. Kapodistrias and P. H. Dahl, "On scattering from a bubble located near a flat air–water interface: Laboratory measurements and modeling," *J. Acoust. Soc. Am.* **110**, 1271–1281 (2001).

²V. C. Anderson, "Sound scattering from a fluid sphere," *J. Acoust. Soc. Am.* **22**, 426–431 (1950).

³G. Kapodistrias and P. H. Dahl, "Effects of interaction between two bubble scatterers," *J. Acoust. Soc. Am.* **107**, 3006–3017 (2000).

⁴H. Medwin and C. S. Clay, *Fundamentals of Acoustical Oceanography* (Academic, San Diego, 1998), pp. 594–595.

⁵A. R. Kolaini, L. A. Crum, and R. A. Roy, "Bubble production by capillary waves," *J. Acoust. Soc. Am.* **95**, 1913–1921 (1994).

⁶J. A. Ogilvy, *Theory of Wave Scattering from Random Surfaces* (IOP, London, 1991).

⁷J. H. Zar, *Biostatistical Analysis* (Prentice Hall, Englewood Cliffs, NJ, 1974).

- ⁸W. J. Plant, P. H. Dahl, and W. Keller, "Microwave and acoustic scattering from parasitic capillary waves," J. Geophys. Res. **104**(C11), 25853–25865 (1999).
- ⁹B. Kinsman, *Wind Waves, Their Generation and Propagation on the Ocean Surface* (Prentice Hall, Englewood Cliffs, NJ, 1965).
- ¹⁰P. H. Dahl, W. J. Plant, B. Nützel, A. Schmidt, H. Herwig, and E. A. Terray, "Simultaneous acoustic and microwave backscattering from the sea surface," J. Acoust. Soc. Am. **101**, 2583–2595 (1997).
- ¹¹P. H. Dahl, "On bistatic sea surface scattering: Field measurements and modeling," J. Acoust. Soc. Am. **105**, 2155–2169 (1999).

Circumferential resonance modes of solid elastic cylinders excited by obliquely incident acoustic waves

Ying Fan

Department of Mechanical and Industrial Engineering, University of Toronto, 5 King's College Road, Toronto, Ontario M5S 3G8, Canada

Farhang Honarvar

Department of Mechanical Engineering, K. N. Toosi University of Technology, P.O. Box 16765-3381, Tehran, Iran

Anthony N. Sinclair^{a)}

Department of Mechanical and Industrial Engineering, University of Toronto, 5 King's College Road, Toronto, Ontario M5S 3G8, Canada

Mohammad-Reza Jafari

Department of Mechanical Engineering, K. N. Toosi University of Technology, P.O. Box 16765-3381, Tehran, Iran

(Received 21 March 2002; revised 5 October 2002; accepted 7 October 2002)

When an immersed solid elastic cylinder is insonified by an obliquely incident plane acoustic wave, some of the resonance modes of the cylinder are excited. These modes are directly related to the incidence angle of the insonifying wave. In this paper, the circumferential resonance modes of such immersed elastic cylinders are studied over a large range of incidence angles and frequencies and physical explanations are presented for singular features of the frequency-incidence angle plots. These features include the pairing of one axially guided mode with each transverse whispering gallery mode, the appearance of an anomalous pseudo-Rayleigh in the cylinder at incidence angles greater than the Rayleigh angle, and distortional effects of the longitudinal whispering gallery modes on the entire resonance spectrum of the cylinder. The physical explanations are derived from Resonance Scattering Theory (RST), which is employed to determine the interior displacement field of the cylinder and its dependence on insonification angle. © 2003 Acoustical Society of America. [DOI: 10.1121/1.1525289]

PACS numbers: 43.20.Fn, 43.40.Ks [ANN]

I. INTRODUCTION

An analysis of the ultrasonic scattering characteristics of a cylinder may be used to determine its geometric and elastic properties, or the boundary conditions between the cylinder and the surrounding medium.^{1,2} The scattered pressure field from a submerged cylinder contains valuable information about the resonance modes of the cylinder. The resonance modes of the cylinder serve as its signatures, therefore, it is necessary to have a thorough understanding of the characteristics of these resonance modes in order to study the properties of the cylinder. In this paper, the dependence of the scattering spectrum and resonance modes of an immersed solid elastic cylinder insonified by a plane acoustic wave is explored as a function of the incidence angle of the insonifying wave. Physical explanations for the dependence of the resonance frequencies on the angle of incidence are given. The dependence of the resonance frequencies on the angle of incidence has never been studied to this extent before.

Earliest studies of wave scattering from cylinders, conducted by Faran, dealt with normally incident compressional waves on a submerged elastic, isotropic, and homogeneous

rod.³ A normal mode expansion technique was used; this technique has now become relatively straightforward with the advent of high-powered desktop computers and mathematical libraries such as IMSL⁴ and MATLAB.⁵ The scattering spectrum consists of a number of sharp resonances, superimposed on a relatively flat background. A physical explanation for this general form of response was provided by Resonance Scattering Theory (RST), according to which each resonance can be linked to the constructive interference of a single surface wave making multiple encirclements of the cylinder.⁶⁻⁸

Several researchers have explored extensions of RST to more general cases than those studied by Faran. These include investigations on the effects of obliquely incident plane waves,⁹⁻¹¹ absorptive materials,^{12,13} multi-layered cylinders,^{2,13} encasement in a solid matrix,^{14,15} and material anisotropy.^{16,17} In each case, the method of solution follows the same format: the wave equation is solved in cylindrical coordinates in each medium, yielding a normal mode expansion with several unknown coefficients. Boundary conditions expressed in terms of stresses and displacements at each cylindrical interface are then used to solve for the coefficients. Extensive bibliographies and reviews of these topics can be found in the works by Uberall,⁸ Gaunaurd,¹⁸ and Addison and Sinclair.¹⁴

^{a)} Author to whom correspondence should be addressed. Electronic mail: sinclair@mie.utoronto.ca

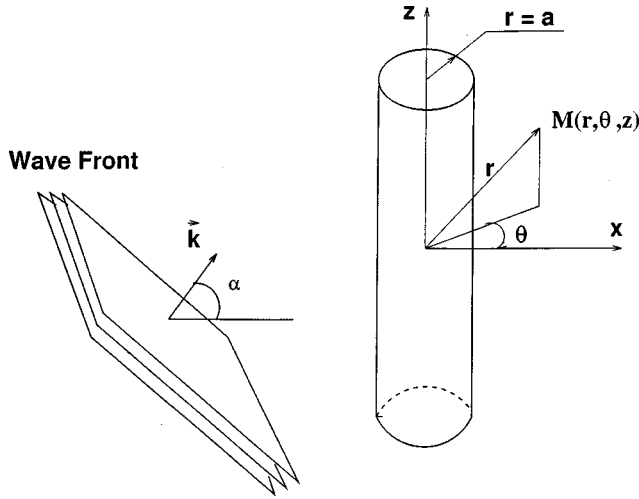


FIG. 1. Geometry used for formulating the problem.

The case of obliquely incident waves holds particular interest for a certain class of nondestructive evaluation (NDE) problems. Fibers used in reinforced composite materials typically possess transverse isotropy. Ultrasonic characterization of the axial properties of the fiber and fiber/matrix interface requires that the incident wave impinge on the cylinder at an oblique angle of $\alpha \neq 0$; see Fig. 1. Similar reasoning applies to the characterization of transversely isotropic rods such as those used in the telecommunications industry;¹⁹ the anisotropic grain structure and stiffness properties of these rods are closely linked to their low-noise signal transmission capabilities.²⁰

To date, a number of RST studies have been conducted that focus on the issue of plane waves incident at oblique angles. White's formulation for wave scattering from an embedded rod provided solutions for nonzero values of α , however, the lack of computing power available at that time restricted his numerical solutions to cases with $\alpha = 0$.²¹ Many other researchers including Flax *et al.*,⁹ Veksler,¹¹ Nagl *et al.*,²² and Maze *et al.*²³ pursued this topic and demonstrated that beside the two classes of surface waves observed at normal incidence, i.e., *Rayleigh* and *whispering gallery* waves, an entirely new set of surface waves, termed *axially guided* waves, are introduced when the incident wave vector has a nonzero component along the axis of the cylinder. These waves travel along helical paths with the helix angle dependent on the phase velocity of the wave, and generate a new set of resonant modes. Such modes are significant even in experimental studies designed to feature normally incident waves because a wave with a finite wave front does have components with nonzero projection along the axis of the cylinder. This causes guided modes to exist in almost all practical applications. Conoir *et al.*²⁴ demonstrated that the resonance frequencies of these vibration modes generally shift to the right as the incidence angle α is increased. Lecroq *et al.* studied the scattering of waves from air-filled finite cylindrical shells.²⁵ They plotted the resonance curves for a steel cylindrical shell for different resonance modes.

More recent works by Fan *et al.*¹⁵ and Honarvar and Sinclair¹⁶ deal with transversely isotropic rods and relatively small incident angles. Experimental verification of numerical

results with $\alpha > 10^\circ$ are difficult, as such experiments require plane waves with a very broad wavefront. However, if one is to assess accurately the extent of transverse isotropy in rods designed to have enhanced axial properties, then such studies with appreciable α values are essential. To learn more about the nature of surface waves and resonance modes at higher angles of incidence, one has to first consider the case of isotropic cylinders. The focus of the current work is to investigate the resonance modes of an isotropic immersed elastic cylinder over a large range of incident angles, including values beyond critical angles.

II. THEORY

In this section, the mathematical model for the scattering of a plane acoustic wave from an immersed elastic cylinder is briefly reviewed. Details of this mathematical model were already published by the authors.¹⁶ Although the model can be used for both isotropic and transversely isotropic cylinders, only isotropic materials are considered here.

Figure 1 shows an infinite monochromatic plane acoustic wave of frequency $\omega/2\pi$ incident at an angle α on a submerged cylinder of infinite length and radius a .

A cylindrical coordinate system (r, θ, z) is chosen with the z -direction coincident with the axis of the cylinder. The pressure p_i of the incident plane compressional wave can be written as

$$p_i = \sum_{n=0}^{\infty} \varepsilon_n i^n J_n(k_{\perp} r) \cos(n\theta), \quad (1)$$

where ε_n is the Neumann factor ($\varepsilon_0 = 1$ and $\varepsilon_n = 2$ for $n \geq 1$) and J_n are the Bessel functions of the first kind of order n , $k_{\perp} = k \cos \alpha$, $k = \omega/c$ and c is the compressional wave velocity in the surrounding fluid medium. The time dependence is suppressed.

The scattered pressure field is given by

$$p_s = \sum_{n=0}^{\infty} \varepsilon_n i^n A_n H_n^{(1)}(k_{\perp} r) \cos(n\theta), \quad (2)$$

where $H_n^{(1)}$ are the Hankel functions of the first kind of order n and A_n are the unknown scattering coefficients.

The displacement vector inside the cylinder is written in terms of three scalar potential functions ϕ , χ , and ψ ,

$$\mathbf{u} = \nabla \phi + \nabla \times (\chi \hat{e}_z) + a \nabla \times \nabla \times (\psi \hat{e}_z). \quad (3)$$

In order to satisfy the equations of motion, these potential functions must be of the form,

$$\phi = \sum_{n=0}^{\infty} B_n J_n(k_L r) \cos n\theta, \quad (4)$$

$$\psi = \sum_{n=0}^{\infty} C_n J_n(k_T r) \cos n\theta, \quad (5)$$

$$\chi = \sum_{n=0}^{\infty} D_n J_n(k_T r) \sin n\theta, \quad (6)$$

where B_n , C_n , and D_n are unknown coefficients and

$$k_L = \left(\frac{\omega^2}{c_L^2} - k_z^2 \right)^{1/2}; \quad k_T = \left(\frac{\omega^2}{c_T^2} - k_z^2 \right)^{1/2}. \quad (7)$$

c_L and c_T are, respectively, the bulk compressional and bulk shear wave velocities of the material and $k_z = k \sin \alpha$. The four unknown coefficients A_n , B_n , C_n and D_n can be determined by applying the four boundary conditions at the water/cylinder interface, i.e., continuity of normal displacement and normal stress as well as nullity of the shear stresses. This will result in the following system of algebraic equations:

$$\begin{pmatrix} a_{11} & a_{12} & a_{13} & a_{14} \\ a_{21} & a_{22} & a_{23} & a_{24} \\ 0 & a_{32} & a_{33} & a_{34} \\ 0 & a_{42} & a_{43} & a_{44} \end{pmatrix} \begin{pmatrix} A_n \\ B_n \\ C_n \\ D_n \end{pmatrix} = \begin{pmatrix} b_1 \\ b_2 \\ 0 \\ 0 \end{pmatrix}. \quad (8)$$

Expressions for elements a_{ij} and b_i can be found in Ref. 16. Equation (8) can be solved for any of the unknown coefficients using Cramer's rule. By solving Eq. (8) for A_n , the scattered pressure field can be completely determined.

Resonance peaks occur at frequencies where the matrix of Eq. (8) becomes singular, i.e., its determinant becomes equal to zero. The roots of this determinant are the circumferential resonance frequencies of the cylinder.

The scattered pressure field is usually evaluated in the far-field ($r \gg a$) at a fixed angle θ for a range of frequencies. The resulting far-field amplitude spectrum, which is called the *form function* is obtained from the following equation⁷

$$f_\infty(\theta, ka) = \left(\frac{2r}{a} \right)^{1/2} p_s e^{-ik_\perp r}, \quad (9)$$

where ka , the product of wave number and cylinder radius, is the normalized frequency. The form function can be written as the sum of individual normal modes,

$$f_\infty(\theta, ka) = \sum_{n=0}^{\infty} f_n(\theta, ka) = \sum_{n=0}^{\infty} \frac{2}{\sqrt{i\pi k_\perp a}} \epsilon_n A_n \cos(n\theta). \quad (10)$$

Resonance scattering theory (RST) states that the spectrum of the returned echo consists of two distinct parts: the first part varies smoothly with frequency and would be present even if the cylinder were impenetrable (nonresonant background), and the other part is the resonance spectrum which consists of a number of resonance peaks which coincide with the eigenfrequencies of the circumferential vibrations of the cylinder.

For a cylindrical geometry, the nonresonant background scattering component (rigid background in case of metal cylinders) can be separated from the resonance scattering part. For a rigid cylinder the scattering coefficients $A_n^{(\text{rigid})}$ are⁷

$$A_n^{(\text{rigid})}(ka) = - \frac{J'_n(ka)}{H_n^{(1)'}(ka)}. \quad (11)$$

The resonance spectrum of each mode can be obtained by removing the rigid background,²⁶

$$f_n^{(\text{res})}(\theta, ka) = \frac{2}{\sqrt{i\pi k_\perp a}} \epsilon_n \frac{A_n - A_n^{(\text{rigid})}}{1 + 2A_n^{(\text{rigid})}} \cos(n\theta). \quad (12)$$

The displacement field inside the cylinder can also be determined by solving Eq. (8) for B_n , C_n and D_n and substituting these values in Eq. (3).

III. EFFECT OF ANGLE OF INCIDENCE ON RESONANCE MODES

As mentioned earlier, for a solid elastic cylinder, the form function consists of resonance spectra superimposed on a smooth background corresponding to a rigid cylinder. The resonance modes in the spectrum are linked to the standing surface waves which are formed around the cylinder. The surface waves are divided into three major types: pseudo-Rayleigh waves, whispering gallery waves and axially guided waves. The axially guided waves only appear when the incident wave angle is nonzero, i.e., $\alpha \neq 0$.

Figure 2 shows the form function of an aluminum cylinder insonified by an obliquely incident plane acoustic wave at $\alpha = 5^\circ$. Each dip in Fig. 2 is due to a certain resonance frequency identified by the integers (n, l) . The first of these two integers defines the mode number and the second one indicates the eigenfrequency label for that mode; $l = 1$ corresponds to a pseudo-Rayleigh wave and $l = 2, 3, \dots$ to whispering gallery waves. Resonances associated with axially guided waves are designated by $\langle n, p \rangle$ where, n is the mode number and p is the eigenfrequency label.

Figure 3 shows the resonance frequencies of an immersed aluminum cylinder insonified by a plane acoustic wave for $0^\circ \leq \alpha \leq 40^\circ$. These resonances correspond to frequencies for which the real part of the determinant of the coefficient matrix in Eq. (8) goes to zero.⁷ (Typical ratios of imaginary to real components of the wave number are less than 10^{-4} . Considering this small ratio, it is an acceptable approximation to ignore the imaginary component when calculating the resonance frequencies.) Figures 3(a)–3(d) show the variation of frequencies of resonance modes with changes in the incidence angle for different resonance modes. Key resonance modes are labeled according to their (n, l) or $\langle n, l \rangle$ designation in Fig. 3(a).

An extension to the information conveyed by Fig. 3 can be displayed by plotting the resonance curves using Eq. (12). Figure 4 shows the resonance spectrum of the aluminum cylinder corresponding to $\alpha = 5^\circ$. The advantage of using Eq. (12) is that both the center frequency and bandwidth (all information contained in the complex frequency) of each resonance mode are shown in Fig. 4; hence enabling the comparison of their attenuations. In Fig. 5, we have used the resonance spectra obtained from Eq. (12) at different incidence angles for plotting the resonance curves. Figure 5 is a top view of resonance curves plotted at different incident angles and placed next to one another. The bandwidth of the resonance frequencies is indicated by the thickness of the dark lines describing the curves. It can be observed that although different approaches are used for plotting Figs. 3(a) and 5(a), they both show the same characteristic behavior of the resonance curves.

A. Shift of the resonance frequencies

Figures 3 and 5 show the changes in frequencies of specific resonance modes of an aluminum cylinder with increase

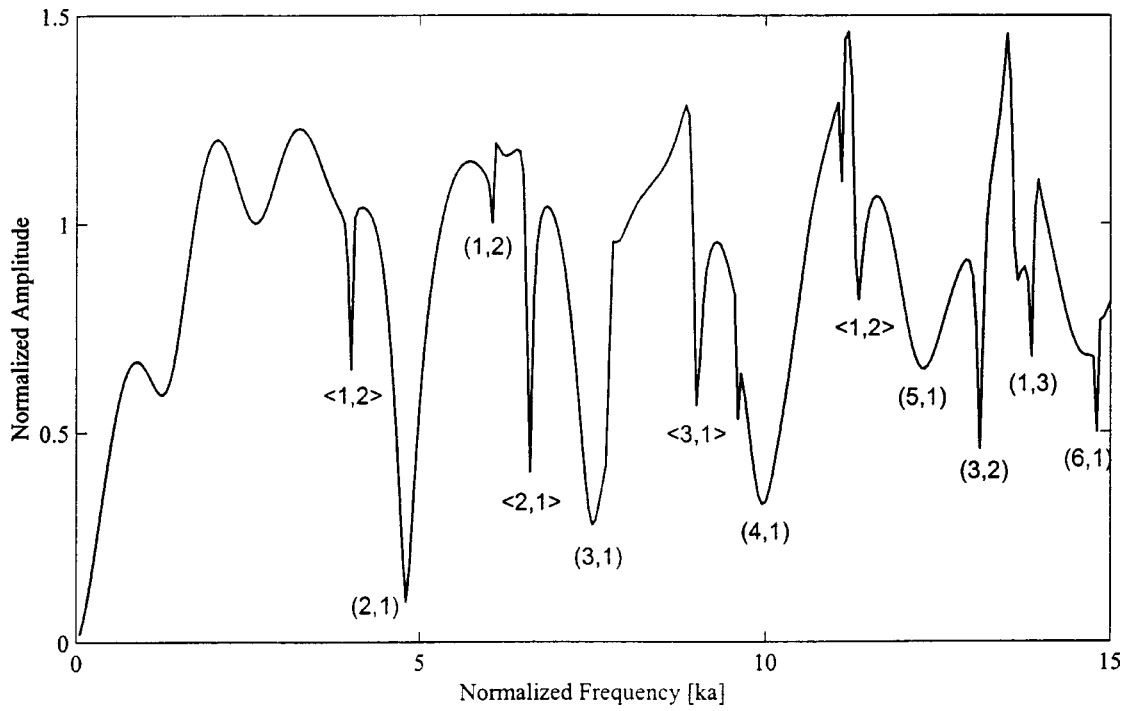


FIG. 2. Form function for an aluminum cylinder at $\alpha = 5^\circ$.

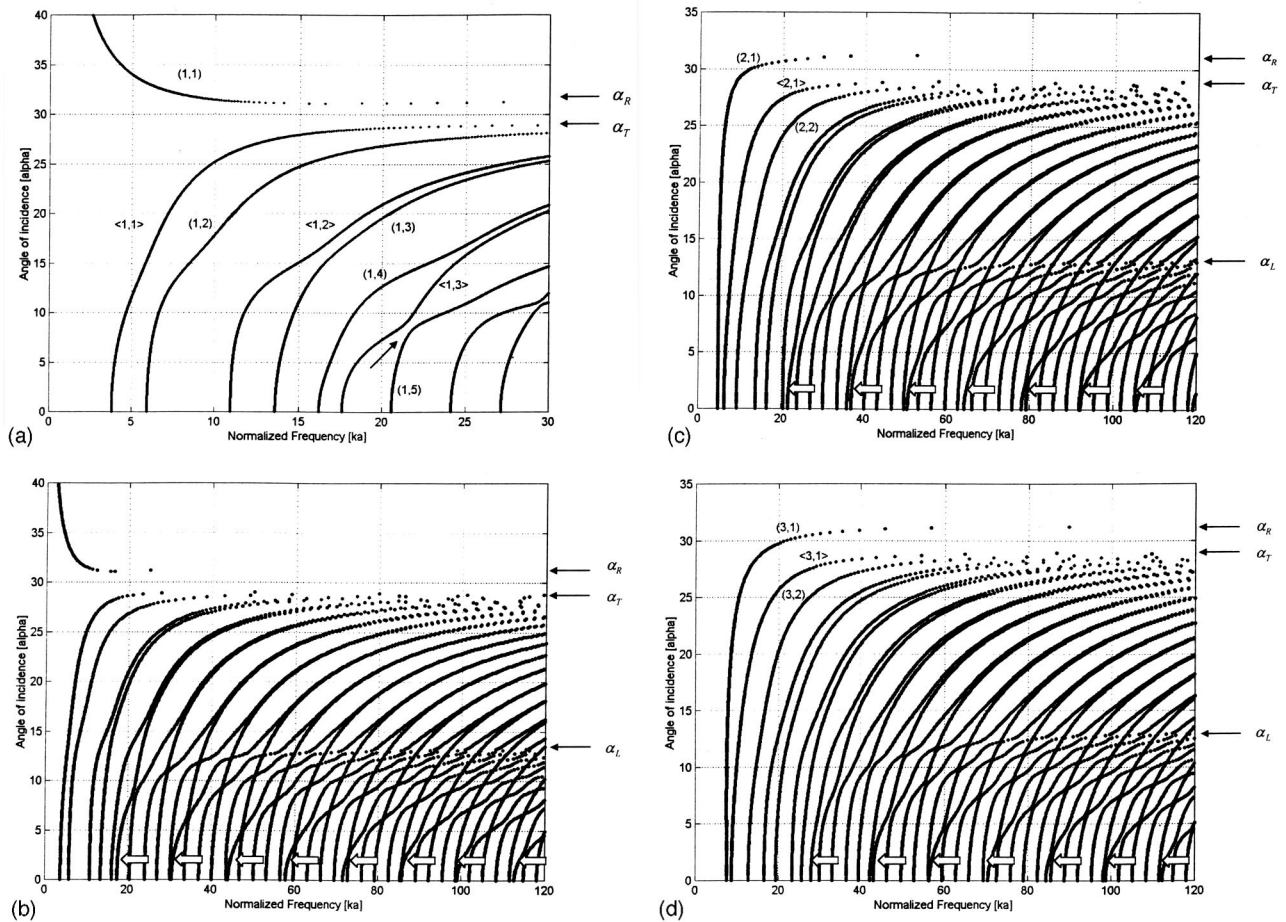


FIG. 3. Resonance curves of an aluminum cylinder. The resonance frequencies are the roots of the real part of the coefficient matrix of Eq. (8). (a) $n = 1$ and $0 \leq ka \leq 30$, (b) $n = 1$ and $0 \leq ka \leq 120$, (c) $n = 2$, (d) $n = 3$.

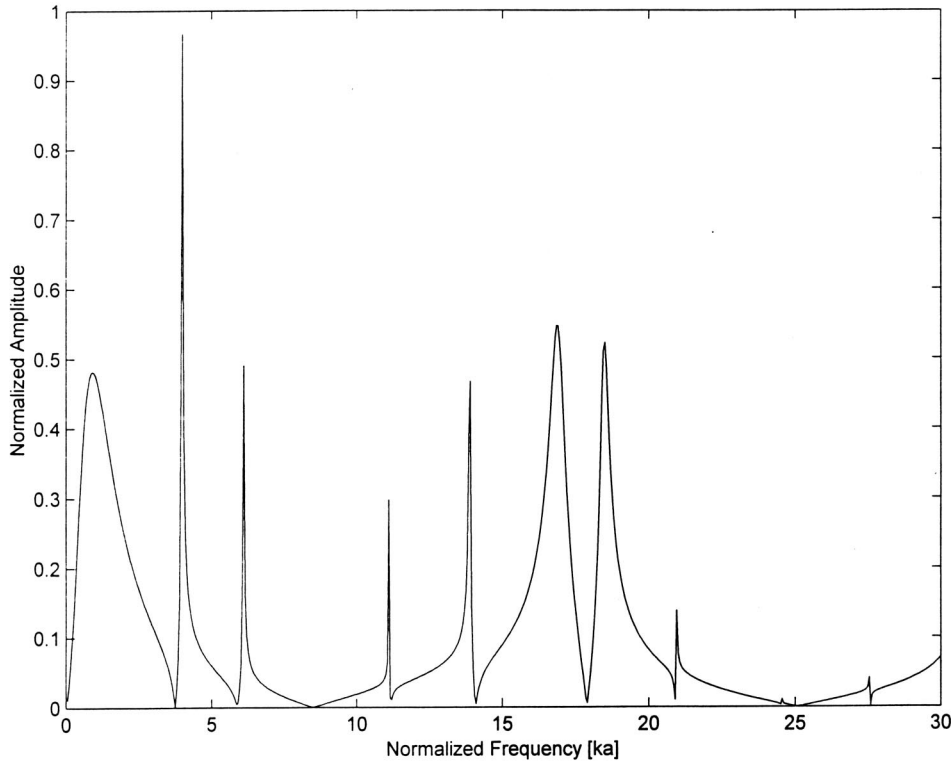


FIG. 4. Resonance spectrum of an aluminum cylinder at $\alpha = 5^\circ$.

of the angle of incidence. It is observed that below the second critical angle, α_T , all the resonance frequencies corresponding to whispering gallery and axially guided waves increase monotonically with the increase of α , and tend to infinity as α approaches the second critical angle, α_T . A similar behavior is observed for pseudo-Rayleigh waves with higher mode numbers ($n \geq 2$, and $l = 1$); see Figs. 3(c) and (d). The pseudo-Rayleigh mode corresponding to $n = 1$ in Figs. 3(a) and (b) is special and will be considered in the next section. With increase of the angle of incidence, pseudo-Rayleigh waves approach the true Rayleigh wave (on a submerged plate) and the corresponding resonance frequencies approach the Rayleigh angle, $\alpha_R \approx 31^\circ$.

A similar observation was reported by Conoir *et al.*,²⁴ who explained the shift of resonance frequencies using the connection between the propagation of helical surface waves around the cylinder and formation of resonance modes.

Following the approach of Ref. 24, a physical explanation for the rightward shift of all resonance frequencies with an increase in the angle of incidence can be presented as follows. In physical terms, a resonance indicates a standing wave pattern. For the case of a normally incident wave, an integral number n of wavelengths of the corresponding wave pattern are distributed around the circumference of the cylinder such that,

$$\lambda_n = 2\pi a/n \quad \text{and} \quad k_n = 2\pi/\lambda_n, \quad (13)$$

where λ_n and k_n are the wave number and the projection of the total wave vector in the θ direction, respectively. For an obliquely incident wave, k_n can be related to the total wave vector k_γ by (see Fig. 6),

$$k_n = k_\gamma \cos \gamma = 2\pi \cos \gamma / \lambda_\gamma, \quad (14)$$

where γ is the refraction angle and λ_γ is the wavelength. Substituting Eq. (13) into Eq. (14), λ_n can be related to the helical wavelength λ_γ by

$$\lambda_\gamma = \lambda_n \cos \gamma. \quad (15)$$

The resonance frequency is

$$f_{\text{res}} = c_{ph} / \lambda_\gamma, \quad (16)$$

where c_{ph} is the phase velocity of the corresponding surface wave. Substituting Eqs. (13) and (15) into Eq. (16) gives

$$f_{\text{res}} = (nc_{ph}) / (2\pi a \cos \gamma). \quad (17)$$

Equation (17) shows that the resonance frequency is inversely proportional to $\cos \gamma$. For the case of immersed elastic cylinders, an increase in α causes an increase of the refraction angle γ and consequently a decrease in $\cos \gamma$. Therefore, the resonance frequency f increases with the increase of the angle of incidence, α . When γ reaches $\pi/2$ (i.e., critical angle), the resonance frequency tends to infinity.

B. Resonance mode (1,1)

A single pseudo-Rayleigh wave corresponding to mode $(n,1)$ is present at $\alpha \leq \alpha_R$ when $n > 1$. The corresponding $(2,1)$ and $(3,1)$ modes for an immersed aluminum cylinder are shown in Figs. 3(c) and (d), respectively.

The $(1,1)$ resonance mode, shown in Figs. 3(a) and 5(a) is anomalous. Curiously, this pseudo-Rayleigh mode for $n = 1$ appears only for incident angles greater or equal to α_R , such that one would expect that penetration of energy into the cylinder would be impossible. The existence of resonances above Rayleigh angle is reported in the literature,²⁷ however, no physical explanation is provided. To confirm the

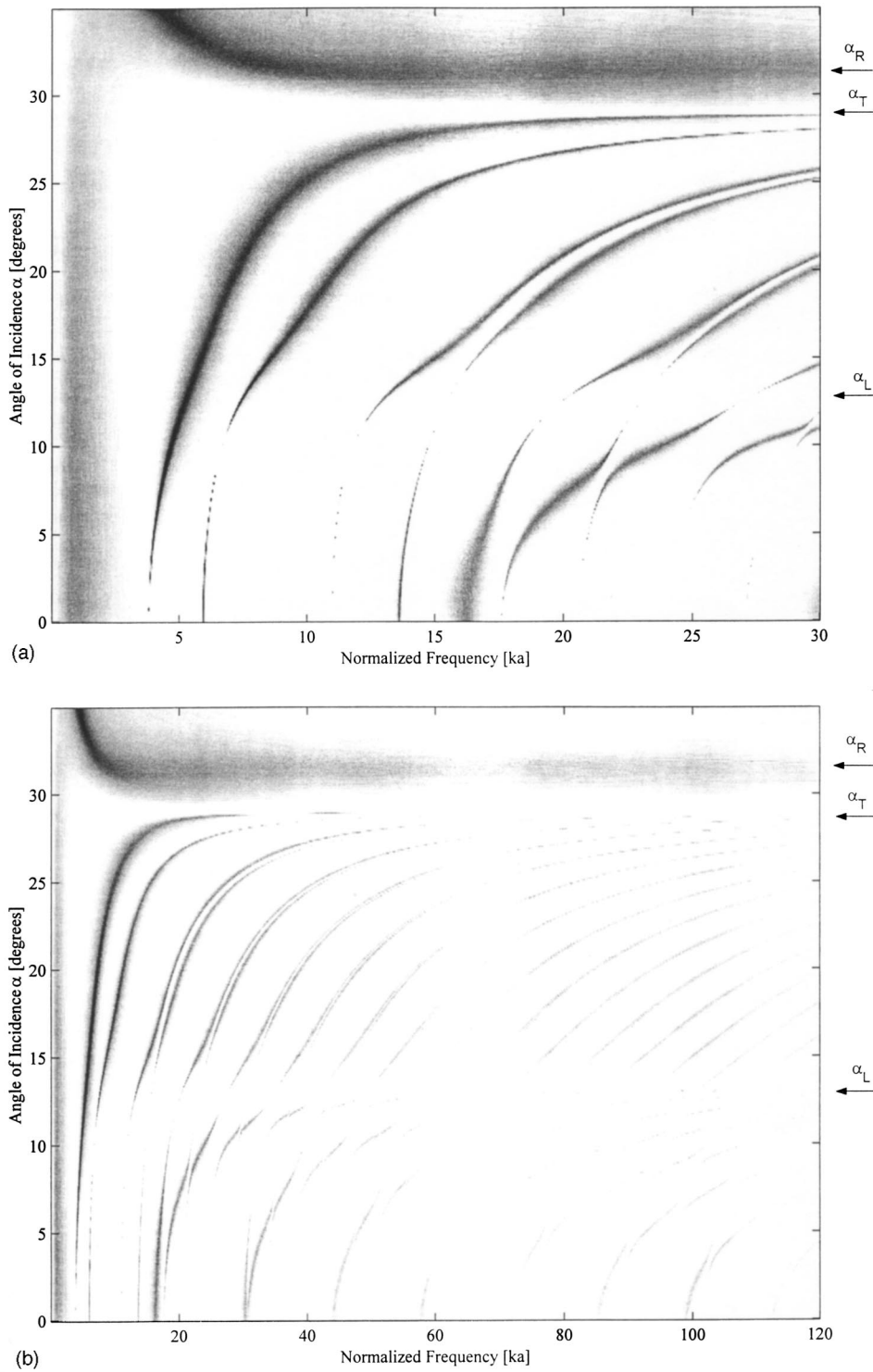


FIG. 5. Resonance curves of an aluminum cylinder. This is the top view of a three dimensional graph obtained by plotting the resonance spectra for different incident angles using Eq. (12). (a) $n=1$ and $0 \leq ka \leq 30$, (b) $n=1$ and $0 \leq ka \leq 120$.

existence of this resonance mode, plots showing the amplitude and phase changes at resonance frequencies corresponding to various incident angles are plotted in Fig. 7 based on Eq. (12) for $\alpha=30^\circ$ and $\alpha=35^\circ$. The existence of a resonant mode beyond the second critical angle is indicated in the phase diagram by a sudden phase shift; see Fig. 7(d).

The pseudo-Rayleigh mode (1, 1) is alternatively referred to as the rigid-body translation mode, i.e., the cylinder moves vertically back and forth without distortion. Figure 8(a) shows the displacement field at a cross-section of the

cylinder for the (1, 1) mode at $\alpha=33^\circ$. It is observed that the true motion is made up primarily of a common translational component. Figure 8(b) shows the displacement field for the same mode at $ka \approx 67$ and $\alpha=31.24^\circ$. The corresponding displacement field for higher order pseudo-Rayleigh modes, e.g., (2, 1) and (3, 1), at comparable ka values showed a similar displacement field, hence, indicating that all pseudo-Rayleigh modes approach the true Rayleigh mode at high frequencies. The reason for the upward curving of (1, 1) mode with the increase of α is not completely understood yet

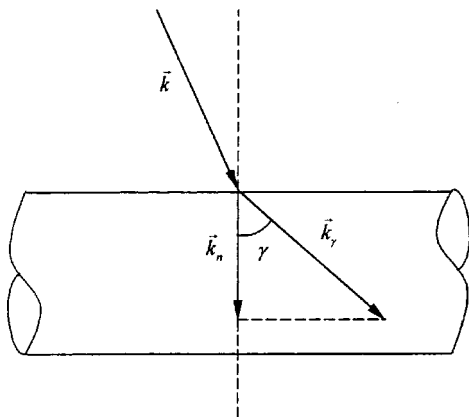


FIG. 6. Refracted surface wave on the cylinder.

but it can be correlated to corresponding decrease in the radial component of the wave vector. In other words, if the wavelength is larger than a certain value, this mode cannot be directly generated.

The pressure amplitude, σ_{rr} , at the boundary of the cylinder is plotted for mode (1, 1) in Fig. 9. As shown in Fig. 9, σ_{rr} is zero at $\theta=90^\circ$ and $\theta=270^\circ$ and it reaches its maximum value at $\theta=0^\circ$ and $\theta=180^\circ$, which indicates that an external force acts in a horizontal direction on the cylinder and causes a translational motion, see the arrows next to the cylinder in Fig. 9.

C. Compressional whispering gallery waves

There exist two types of whispering gallery waves. The waves in the first category are called transverse whispering gallery waves, which feature predominantly shearing stresses. A qualitative description of the ray paths for these waves was presented by Uberall.²⁸ The wave vectors point along chords that link two points on the boundary of the cylinder. The number of wavelengths within each chord, determines the resonance mode number. A detailed mathematical analysis was given by Brekhovskikh,²⁹ and by Dickey *et al.*³⁰ In the limit of large values of ka , the wave speed approaches the bulk shear wave velocity.

The second category of whispering gallery waves features predominantly normal stresses. Unlike their shearing counterparts, the imaginary parts of these compressional whispering gallery resonances are quite dominant and consequently they are significantly attenuated. For this reason, such resonances are not observed experimentally.³⁰

All of the surface waves corresponding to resonance modes shown in Figs. 3 and 5 feature predominantly shearing actions. The imaginary parts of their frequencies are small giving them very small attenuations. For example, for the resonance frequencies shown in Fig. 3(a), the maximum ratio of the imaginary to real part is in the range of 10^{-4} . Considering the transverse nature of these resonance modes, one would expect that the first critical angle would not play a major role in the values of resonance frequencies shown in Fig. 3. Examination of Fig. 3, however, shows that some curious features are observed at incident angles $0 \leq \alpha \leq \alpha_L$. These features are:

- (1) Severe serpentine distortions are noted in the $ka - \alpha$ plots for both the transverse whispering gallery modes as well as the guided modes within this range of low α values. These distortions are not random; in several locations, there is a marked deviation of two different modes towards a specific point. A typical example is indicated by the solid arrow in Fig. 3(a), where both the $\langle 1, 3 \rangle$ and $\langle 1, 5 \rangle$ modes deviate toward the point $(\alpha = 8.6^\circ, ka = 22)$.
- (2) The distortions described in item (1) form distinct patterns that are clearly visible in Figs. 3 and 5. The patterns consist of arcs rising vertically from the horizontal axis, then curving to the right, and then asymptotically approaching the line $\alpha = \alpha_L$ at high frequencies. Some of the intercepts of these arcs with the horizontal axis are indicated by block arrows in Figs. 3(b), (c), and (d).

The origin of *arc* patterns mentioned above was numerically determined to be the leaky compressional whispering gallery modes. At the complex frequencies corresponding to these modes, the determinant of the real part of the coefficient matrix in Eq. (8) goes to zero. However, previous work by Dickey *et al.*³⁰ showed that it is extremely difficult to find these particular complex roots corresponding to oblique incidence because a large number of roots are clustered close together. Despite the fact that these modes are not explicitly featured in Fig. 3, their influence is still present, i.e., resonance frequencies of guided and transverse whispering gallery modes are significantly distorted when they are located close to one of the leaky compressional whispering gallery modes. As a result, the locus of resonances corresponding to each compressional whispering gallery mode appears as an arcing *shadow* in Figs. 3(b), (c), and (d).

To verify this conclusion, based on the shadow arcs, dispersion curves for the first three compressional whispering gallery modes are plotted corresponding to normal incidence ($\alpha=0$). For this purpose, we use the relation $c_{ph} = (2\pi af)/n$, where f is the resonance frequency in Hz and is derived from the ka values observed in Figs. 3(b), (c), and (d). These ka values are the normalized frequencies corresponding to the first three shadow arcs at $\alpha=0^\circ$ in each figure. Figure 10 shows these dispersion curves, which agree with the results reported by Dickey *et al.*³⁰ In the limit of high radius-to-wavelength ratio, the speed of longitudinal whispering gallery waves approaches the speed of the longitudinal lateral waves. As a result, the *shadow arcs* in Fig. 3 are strongly dependent on the axial stiffness of the rod; their shapes could therefore be used to help assess the extent of anisotropy in transversely isotropic cylinders.

It is noteworthy that an analogous behavior has been observed by Uberall *et al.* in the study of the dispersion curves of Lamb waves propagating in elastic plates.³¹ The dispersion curves corresponding to symmetric and antisymmetric modes of Lamb waves show very similar serpentine distortions. This behavior, which is very similar to that observed in our study is referred to as “repulsion of the curves” in Ref. 31. This similarity is consistent with the dispersive nature of guided waves in solid cylinders and plates.³²

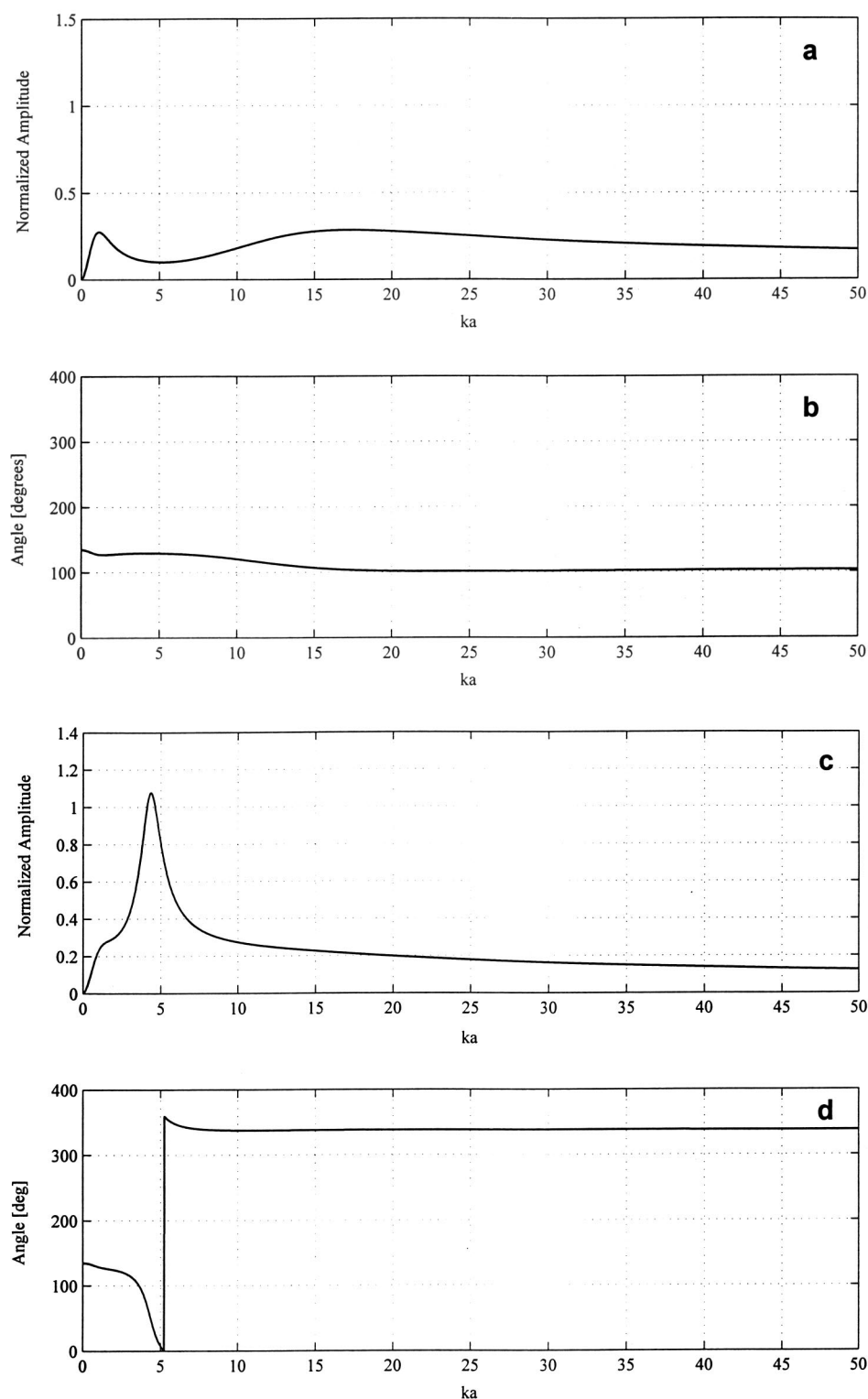


FIG. 7. Resonance mode (1, 1): (a) amplitude spectrum at $\alpha=30^\circ$, (b) phase diagram at $\alpha=30^\circ$, (c) amplitude spectrum at $\alpha=35^\circ$, (d) phase diagram at $\alpha=35^\circ$.

D. Wave pairs

As seen in Fig. 3, each transverse whispering gallery mode is paired with a single guided wave mode, such that the two modes become indistinguishable as α approaches α_T . For small values of α , each mode pair splits in two. When $\alpha=0$, the guided mode disappears completely, leaving only the transverse whispering gallery component of each pair.

The merging of these two modes at large incident angles

can be explained by considering the physics of transverse whispering gallery and axially guided modes. Both modes feature primarily shear action. The axially guided waves propagate in a helical path along the axial direction of the cylinder. The angle of each helix depends on the incidence angle and phase velocity of the corresponding surface wave. It has been shown by Dickey *et al.*³⁰ that in the limit when the cylinder radius tends to infinity, the displacement fields of the transverse/longitudinal whispering gallery modes be-

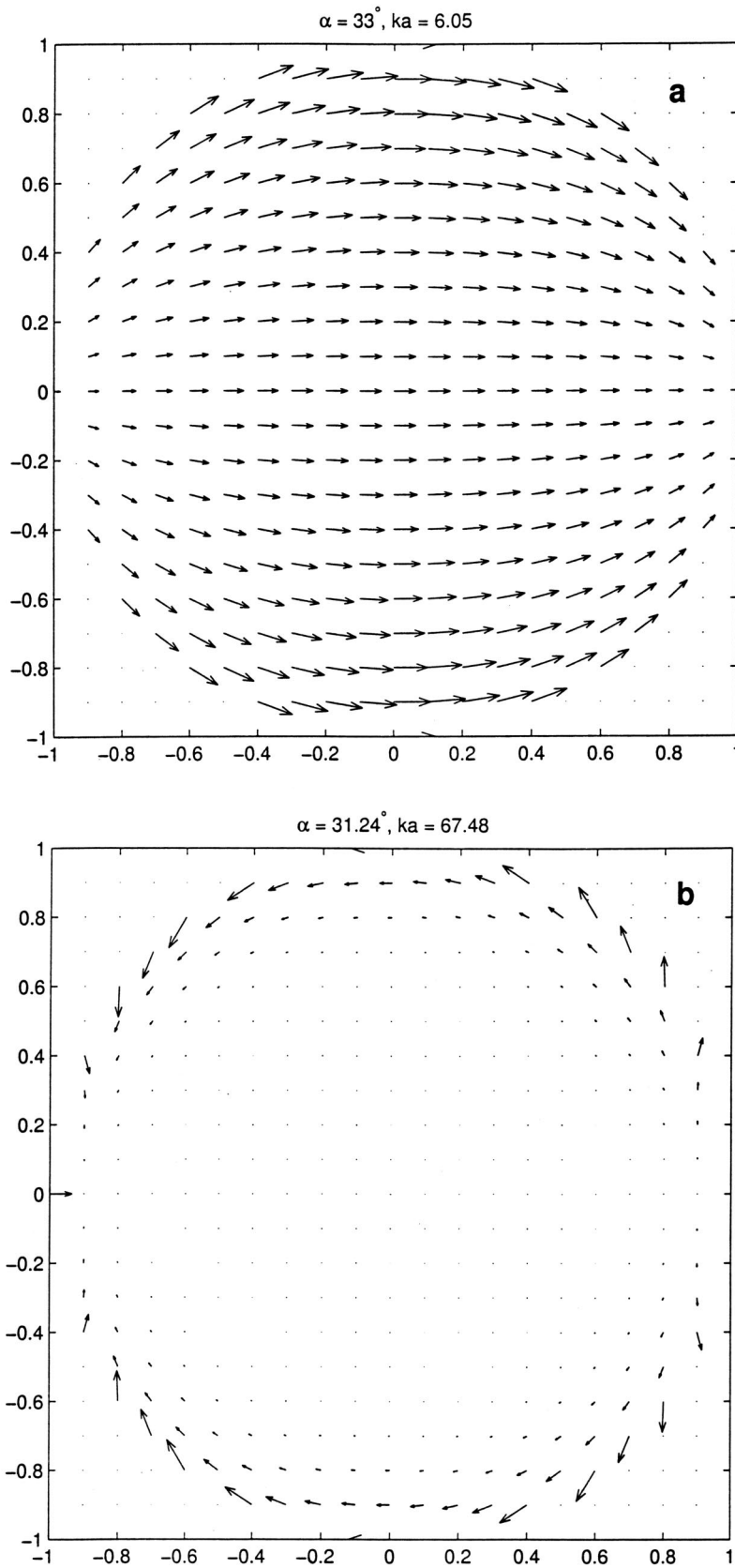


FIG. 8. (a) Displacement field at a cross section of the aluminum cylinder for the (1, 1) mode at $\alpha=33^\circ$ and $ka=6.05$. The length of the arrow is proportional to the amplitude of the displacement. (b) Displacement field at a cross section of the aluminum cylinder for the (1, 1) mode at $\alpha=\alpha_R$ and $ka\approx 67$.

come the expressions for the transverse/longitudinal lateral waves on a flat elastic half-space bounded by a fluid. As the incident angle increases, the whispering gallery waves tend to propagate close to the surface and along the axial direction

of the cylinder, in a manner very similar to an axially guided wave. These two types of modes merge into one as the incident angle approaches the second critical angle. To confirm this point, two sets of resonance modes corresponding to

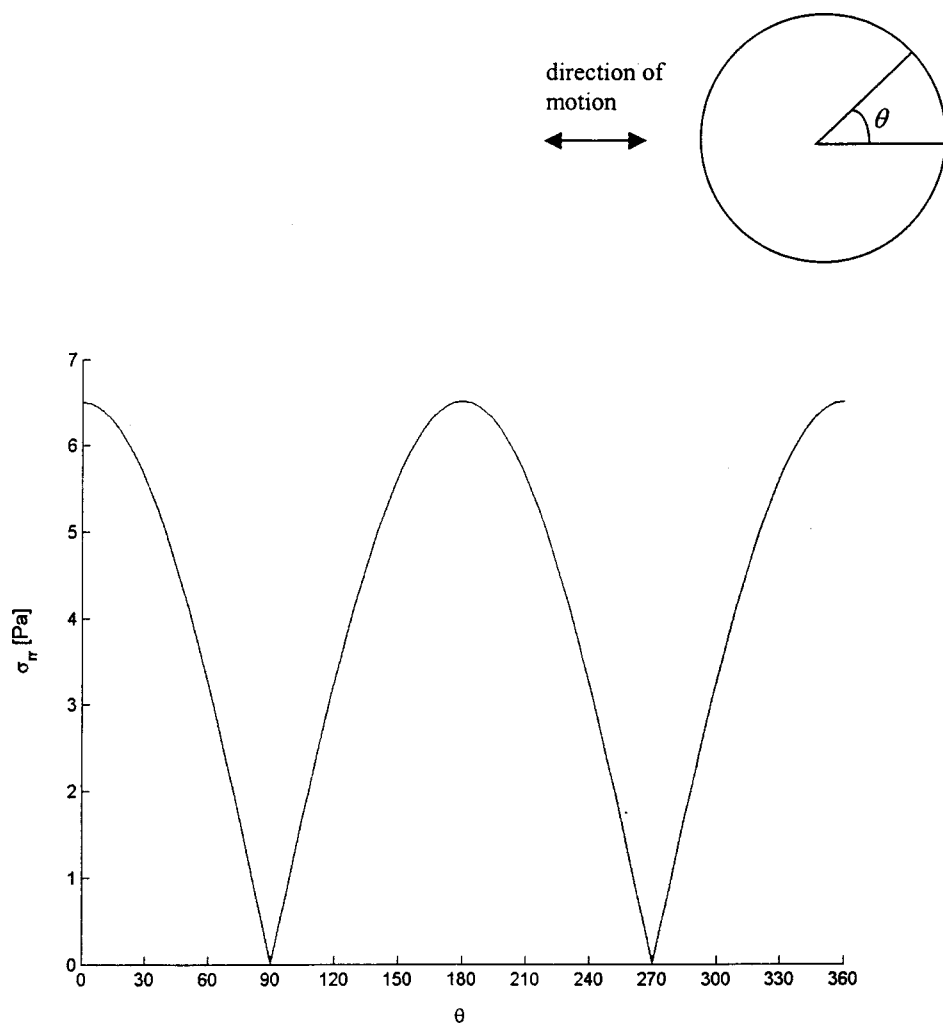


FIG. 9. Stress σ_{rr} at the boundary of the cylinder for mode (1, 1), the transmitter is located at $\theta=180^\circ$.

different incidence angles are selected in Fig. 3(a) and the displacement field of each mode is plotted in Fig. 11. Within each pair of modes, one corresponds to the axially guided mode $\langle 1, 2 \rangle$ and the other to the whispering gallery mode (1,

3). At the small incidence angle of $\alpha=5^\circ$, as shown in Fig. 11(a), these two modes have different displacement fields. As the incidence angle approaches α_T , the corresponding displacement fields u_z and u_θ of the two modes become identi-

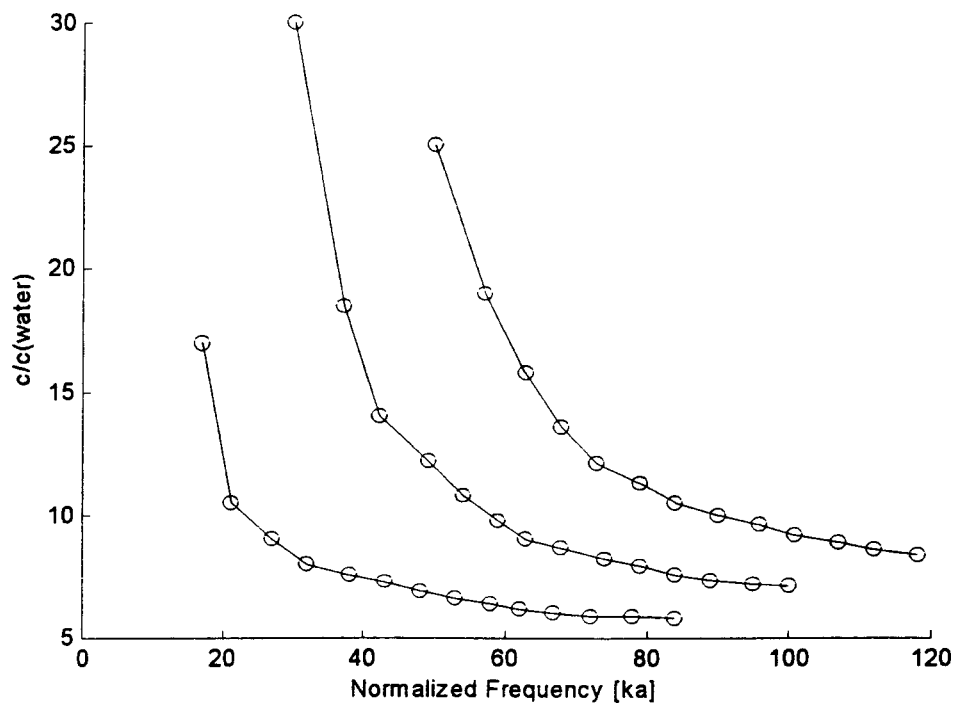


FIG. 10. Dispersion curves for the first three groups of longitudinal whispering gallery waves.

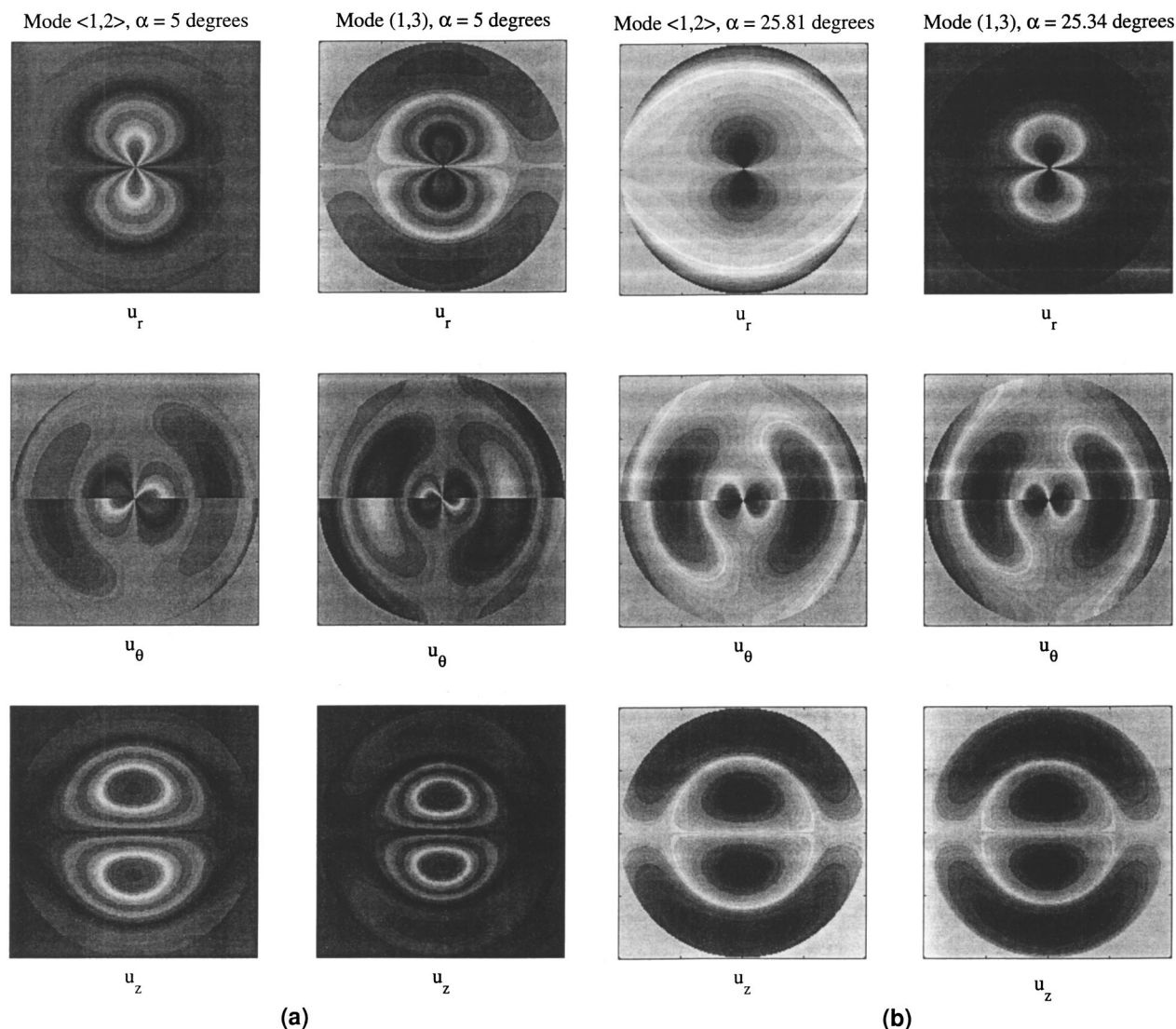


FIG. 11. (a) Displacement fields for mode $\langle 1, 2 \rangle$ and $(1, 3)$ at $\alpha = 5^\circ$. (b) Displacement fields for mode $\langle 1, 2 \rangle$ and $(1, 3)$ at $\alpha \approx 25^\circ$.

cal, see Fig. 11(b), while u_r fields, although equal in magnitude, show opposite directions. Consequently, at large incidence angles, radial displacement fields of these two waves cancel each other. Therefore, the merging of a whispering gallery wave and its adjacent axially guided wave, at large incidence angles, results in a guided wave propagating along the axis of the cylinder without any radial components.

IV. CONCLUSIONS

Using Resonance Scattering Theory (RST), the resonance modes of an immersed aluminum cylinder were studied over a large range of incidence angles. With the increase of the incidence angle, it was observed that the resonance frequencies shift to higher frequencies in a nonuniform manner. The distortion of the $ka - \alpha$ curves at incidence angles below the first critical angle can be attributed to modes associated with leaky compressional whispering gallery waves. As the angle of incidence approaches the second critical angle, resonance frequencies of both whispering gallery and axially guided modes tend to infinity, while resonance frequencies of pseudo-Rayleigh modes do not tend to infinity,

until incidence angle is close to the Rayleigh angle. The $(1, 1)$ pseudo-Rayleigh mode behave differently and only appears at or above the Rayleigh angle. The motion of this resonance mode is made up primarily of a common translational component and resembles the true Rayleigh wave on a submerged cylinder. The whispering gallery and axially guided modes observed in the $ka - \alpha$ plots feature predominantly shear action. At large incidence angles, a whispering gallery mode and its neighboring axially guided mode merge together and produce similar but opposite radial displacement fields such that the resultant wave does not have any radial components.

¹F. Honarvar and A. N. Sinclair, "Nondestructive evaluation of cylindrical components by resonance acoustic spectroscopy," *Ultrasonics* **36**, 845–854 (1998).

²F. Honarvar and A. N. Sinclair, "Scattering of an obliquely incident plane wave from a circular clad rod," *J. Acoust. Soc. Am.* **102**, 1–8 (1997).

³J. J. Faran, Jr., "Sound Scattering by solid cylinders and spheres," *J. Acoust. Soc. Am.* **23**, 405–418 (1951).

⁴Visual Numerics, Inc., *IMSL C Numerical Library*, 1991.

⁵The Mathworks, Inc., *Using Matlab*, 2000.

⁶L. Flax, L. R. Dragonette, and H. Überall, "Theory of resonance excita-

- tion by sound scattering," J. Acoust. Soc. Am. **63**, 723–731 (1978).
- ⁷L. Flax, G. C. Gaunaurd, and H. Überall, *Theory of Resonance Scattering*, Vol. 15 of *Physical Acoustics* (Academic, New York, 1981), pp. 191–294, Chap. 3.
 - ⁸H. Überall, *Acoustic Resonance Scattering* (Gordon and Breach Science, Philadelphia, PA, 1992).
 - ⁹L. Flax, V. K. Varadan, and V. V. Varadan, "Scattering of an obliquely incident acoustic wave by an infinite cylinder," J. Acoust. Soc. Am. **68**, 1832–1835 (1980).
 - ¹⁰T. Li and M. Ueda, "Sound scattering of a plane wave obliquely incident on a cylinder," J. Acoust. Soc. Am. **86**, 2363–2367 (1989).
 - ¹¹N. D. Veksler, *Resonance Acoustic Spectroscopy*, Springer Series on Wave Phenomena (Springer-Verlag, New York, 1993).
 - ¹²G. V. Frisk, J. W. Dickey, and H. Überall, "Surface wave modes on elastic cylinders," J. Acoust. Soc. Am. **58**, 996–1008 (1975).
 - ¹³L. Flax and W. G. Neubauer, "Acoustic reflection from layered absorptive cylinders," J. Acoust. Soc. Am. **61**, 307–312 (1977).
 - ¹⁴R. C. Addison, Jr. and A. N. Sinclair, "Calculated and Measured Ultrasonic Response of an Elastic Cylinder Embedded in an Elastic Medium," in *Review of Progress in Quantitative Nondestructive Evaluation*, edited by D. O. Thompson and D. E. Chimenti (Brunswick, Maine, 1991).
 - ¹⁵Y. Fan, A. N. Sinclair, and F. Honarvar, "Scattering of a plane acoustic wave from a transversely isotropic cylinder encased in a solid elastic medium," J. Acoust. Soc. Am. **106**, 1229–1236 (1999).
 - ¹⁶F. Honarvar and A. N. Sinclair, "Acoustic wave scattering from transversely isotropic cylinders," J. Acoust. Soc. Am. **100**, 57–63 (1996).
 - ¹⁷F. Ahmad and A. Rahman, "Acoustic scattering by transversely isotropic cylinder," Int. J. Eng. Sci. **38**, 325–335 (2000).
 - ¹⁸G. C. Gaunaurd, "Elastic and acoustic resonance wave scattering," Appl. Mech. Rev. **42**, 143–192 (1989).
 - ¹⁹A. Ohno, "Continuous-casting of single-crystal ingots by the OCC process," J. Met. **38**, 14–16 (1986).
 - ²⁰A. Sinclair, Y. Fan, and F. Honarvar, Ultrasonic Characterization of Continuously Cast Rod by Resonance Acoustic Spectroscopy, Nondestructive Testing and Evaluation (Taylor and Francis, accepted).
 - ²¹R. M. White, "Elastic wave scattering at a cylindrical discontinuity in a solid," J. Acoust. Soc. Am. **30**, 771–785 (1958).
 - ²²A. Nagl, H. Überall, P. P. Delsanto, J. D. Almar, and E. Rosario, "Refraction effects in the generation of helical surface waves on a cylindrical obstacle," Wave Motion **5**, 235–247 (1983).
 - ²³G. Maze, J. L. Izbicki, and J. Ripoché, "Resonances of plates and cylinders: Guided waves," J. Acoust. Soc. Am. **77**, 1352–1357 (1985).
 - ²⁴J. M. Conoir, P. Rembert, O. Lenoir, and J. L. Izbicki, "Relation between surface helical waves and elastic cylinder resonances," J. Acoust. Soc. Am. **93**, 1300–1307 (1993).
 - ²⁵F. Lecroq, G. Maze, D. Decultot, and J. Ripoché, "Acoustic scattering from an air-filled cylindrical shell with welded flat plate endcaps: Experimental and theoretical study," J. Acoust. Soc. Am. **95**, 762–769 (1994).
 - ²⁶H. Rhee and Y. Park, "Novel acoustic wave resonance scattering formalism," J. Acoust. Soc. Am. **102**, 3401–3412 (1997).
 - ²⁷J. M. Conoir, "Resonance scattering theory for oblique incidence: Scattering by an elastic infinite cylinder," in *Electromagnetic and Acoustic Scattering: Detection and Inverse Problem Conference Proc.* (Marseille, 1988), pp. 96–108.
 - ²⁸H. Überall, *Surface Waves in Acoustics*, Vol. 10 of *Physical Acoustics* (Academic, New York, 1973), Chap. 1.
 - ²⁹L. M. Brekhovskikh, "Surface waves confined to the curvature of the boundary in solids," Sov. Phys. Acoust. **13**, 462–472 (1968).
 - ³⁰J. W. Dickey, G. V. Frisk, and H. Überall, "Whispering gallery wave modes on elastic cylinders," J. Acoust. Soc. Am. **59**, 1339–1346 (1976).
 - ³¹H. Überall, B. Hosten, M. Deschamps, and A. Gerard, "Repulsion of phase-velocity dispersion curves and the nature of plate vibrations," J. Acoust. Soc. Am. **96**, 908–917 (1994).
 - ³²J. L. Rose, *Ultrasonic Waves in Solid Media* (Cambridge University Press, New York, 1999).

Sound source reconstruction using inverse boundary element calculations

Andreas Schuhmacher^{a)} and Jørgen Hald
Brüel & Kjær A/S, Skodsborgvej 307, DK-2850 Nærum, Denmark

Karsten Bo Rasmussen^{b)}
*Ørsted-DTU, Section of Acoustic Technology, Building 352, Technical University of Denmark,
DK-2800 Kgs. Lyngby, Denmark*

Per Christian Hansen
*Informatics and Mathematical Modelling, Building 321, Technical University of Denmark,
DK-2800 Kgs. Lyngby, Denmark*

(Received 8 February 2002; revised 28 September 2002; accepted 22 October 2002)

Whereas standard boundary element calculations focus on the forward problem of computing the radiated acoustic field from a vibrating structure, the aim in this work is to reverse the process, i.e., to determine vibration from acoustic field data. This inverse problem is brought on a form suited for solution by means of an inverse boundary element method. Since the numerical treatment of the inverse source reconstruction results in a discrete ill-posed problem, regularization is imposed to avoid unstable solutions dominated by errors. In the present work the emphasis is on Tikhonov regularization and parameter-choice methods not requiring an error-norm estimate for choosing the right amount of regularization. Several parameter-choice strategies have been presented lately, but it still remains to be seen how well these can handle industrial applications with real measurement data. In the present work it is demonstrated that the L-curve criterion is robust with respect to the errors in a real measurement situation. In particular, it is shown that the L-curve criterion is superior to the more conventional generalized cross-validation (GCV) approach for the present tire noise studies. © 2003 Acoustical Society of America. [DOI: 10.1121/1.1529668]

PACS numbers: 43.20.Fn, 43.35.Sx, 43.60.Cg [MO]

I. INTRODUCTION

Our objective in this work is to compute the unknown surface velocity distribution on a complex acoustic source from measured acoustic field data. Hence, we are faced with an inverse source problem to be solved, which involves forming a transfer matrix relating the pressure at every field point to the normal component of the surface velocity. In the present work this forward modeling is done by means of a boundary element method (BEM). Several developments in the area of source reconstruction involving arbitrarily shaped geometries have been presented in the past.¹ Earlier work presented the basic concept of using BEM (mainly the direct formulation) in reconstruction problems for setting up a transfer matrix, while the singular value decomposition (SVD) routine is part of the matrix inversion.²⁻⁴ More recent work also deals with the reconstruction process based on indirect BEM for selecting optimum field points from a set of candidates.⁵ Applications involving inverse source problems based on BEM can be found, for example, within the automotive and aerospace industry. Both interior and exterior noise problems have been studied.⁶⁻⁹

Some parts of the sound field radiated by a vibrating structure die out very quickly away from the source and therefore contribute very little at the field microphone posi-

tions; these sound field components are often referred to as the evanescent waves. The reconstruction of the particular vibration patterns that create the evanescent waves will involve a strong amplification of very small signal components, and as a consequence, the inverse problem is very sensitive to the noise and errors in the measured data. The inverse problem is therefore said to be ill-posed.

As a consequence of the inverse problem being ill-posed, the transfer matrix computed by the BEM is ill-conditioned, thus requiring special treatment. In that respect, the SVD is the preferred tool toward regularizing the ill-posed problem. Whereas setting up the transfer matrix and making use of its SVD is well documented, the final step of choosing the correct amount of regularization is not fully understood. The discrepancy principle, which uses *a priori* knowledge of the measurement errors, has been used in connection with Tikhonov regularization⁷ and Landweber iteration.¹⁰ The generalized cross-validation (GCV) method has also been used by several researchers in conjunction with Tikhonov regularization, and it has been shown to produce useful results for cases where spatially white noise contaminates the field data.^{11,12} Recent work compares several iterative and direct inverse methods for near-field acoustic holography,¹³ and among these we find a modified Tikhonov approach with the discrepancy principle and the GCV used as the parameter-choice method.

In the present work we describe an approach to the inverse problem based upon an indirect BEM formulation in

^{a)}Electronic mail: schuhmache@bksv.com

^{b)}Present address: Oticon A/S, Strandvejen 58, DK-2900 Hellerup, Denmark.

conjunction with Tikhonov regularization, and using the SVD as an analysis tool. The influence of the regularization parameter and the filtering process associated with Tikhonov regularization is investigated by means of the L-curve, which is a log-log plot of the solution's norm versus the norm of the residual vector. The L-curve,¹⁴ which is not used too often in connection with sound source reconstruction, seeks to determine the optimal amount of regularization, and this method is compared to the more popular GCV method. A practical case using a car tire and real test data demonstrates the performance of both parameter-choice methods. In addition, a comparison with planar near-field acoustic holography is made in order to compare the different source reconstructions.

Since the setup of the inverse acoustic source problem uses the BEM as a workhorse, some general boundary element issues will be discussed in Sec. II. In Sec. III we introduce inverse methods based on SVD and Tikhonov regularization, and different parameter-choice methods will be introduced. Implementation issues are discussed in Sec. IV, including how to set up the discrete ill-posed problem and bring it on Tikhonov form. In Sec. V we demonstrate the performance of the GCV and L-curve methods for a couple of inverse problems involving measurement data. Two different applications are studied; a stationary tire structure excited by a shaker and a tire rolling at constant speed.

II. BOUNDARY INTEGRAL FORMULATIONS OF THE FORWARD PROBLEM

An exterior acoustic forward problem is considered, that is, only the fluid outside a vibrating source surface having an arbitrary shape is addressed. No secondary sound sources or obstacles exist in the exterior region. The acoustic pressure in the fluid must satisfy the Helmholtz equation, and when subject to the Sommerfeld radiation condition and a Neumann boundary condition on the source surface, boundary integral formulations can be found. These express the acoustic pressure at field points in terms of the source surface velocity. Boundary integral equations provide a complete formulation of the acoustic problem, thus making these equations an obvious choice in connection with radiation and/or scattering problems involving arbitrarily shaped structures. Moreover, they have the advantage that the infinite nature of the exterior region is implicit in the surface representation.

The formulations are often classified as either direct or indirect—where the direct formulation corresponds to a Helmholtz integral equation and the numerous indirect formulations are based on layer potentials. The direct formulation is used more often, but it has some built-in limitations. A serious shortcoming is the failure when it is applied to bodies of thin shape or regular bodies with thin appendages. This thin-shape breakdown of the direct formulation was investigated extensively by Martinez¹⁵ and recently by Cutanda *et al.*,¹⁶ and remedies ensuring a meaningful formulation for thin shapes were proposed.

In this work we focus on the indirect formulations, where the exterior acoustic field is expressed in terms of single layers, double layers, or combined single and double

layers^{17–19} on the source boundary S . For a point P lying strictly in the exterior region, we can express the pressure p_f by the single-layer formulation,

$$p_f(P) = - \int_S \sigma(Q) G(P, Q) dS(Q), \quad (1)$$

where $\sigma(Q)$ is the source strength at Q on S , and subscript f denotes a field quantity. $G(P, Q)$ is the free-space Green's function satisfying the Sommerfeld radiation condition, i.e., $G(P, Q) = e^{-jkR}/4\pi R$, where R is the distance between P and Q , and k is the acoustic wave number. This formulation can be viewed as a distribution of simple sources (monopoles) on the surface. The only remaining issue when solving the exterior Neumann problem is to determine the unknown source strengths $\sigma(Q)$ by matching them to the prescribed normal surface velocity ν_n . While the surface pressure is a continuous function across S , the surface velocity ν_n exhibits a jump property and thus we can write the unknown source densities as

$$\sigma(Q) = -j\omega\rho(\nu_n^+(Q) - \nu_n^-(Q)), \quad (2)$$

where $\nu_n^+(Q)$ and $\nu_n^-(Q)$ are the velocities on the two sides of the surface at the point Q . Once the source strengths $\sigma(Q)$ are known, we are able to find the pressure on the surface or in the exterior by means of surface integration.

Another possibility is to express the field pressure by a double-layer formulation,

$$p_f(P) = \int_S \mu(Q) \frac{\partial G(P, Q)}{\partial n_Q} dS(Q), \quad (3)$$

where $\mu(Q)$ is the source density. This representation of the exterior field can be viewed as a distribution of double sources (dipoles) over S . In the double-layer representation, the source density represents a pressure jump across S with a continuous surface velocity, and the density function μ is written for P on S as

$$\mu(Q) = p_s^+(Q) - p_s^-(Q), \quad (4)$$

where $p_s^+(Q)$ and $p_s^-(Q)$ are the pressures on the two sides of the surface at the point Q .

A third alternative is to make use of a combined approach by mixing the two layers, ending up with a general jump formulation that is able to model both a pressure jump and a surface velocity jump. This jump formulation is described in the literature as an alternative to formulations based on the Helmholtz integral equation, and it is applicable to thin structures frequently appearing in studies of real structures.^{20,21} We can consider the mixed layer formulation as based on vibrating thin shells with general impedance boundary conditions on both sides of the shells.²² The versatility of this general jump formulation, with the ability to handle complex structures, has led to the implementation in many commercial BEM codes, and it is used to study real industrial applications. Furthermore, this formulation is attractive because it can overcome the serious difficulty associated with irregular frequencies, where the equations fail to

provide correct and meaningful results. However, the implementation is not as straightforward as one based on the Helmholtz integral equation.

In the present work we have chosen to work with a hard thin-shell formulation, i.e., the same normal velocity on each side of the surface. We thus end up with the double-layer formulation in Eq. (3). In order to establish the forward modeling problem, we must derive a complete procedure for computing the field pressure in the exterior region, given the normal surface velocities everywhere on the surface. This is done in two stages; first, the necessary “intermediate” source density μ must be determined from the known normal surface velocity, and then the acoustic field exterior to the surface is determined from straightforward integration. In this work we use a variational approach²³ to provide the link between the surface parameters. This link between normal surface velocities and jump pressures is provided by considering the normal derivative of p_f on the surface. This derivative, in turn, is equal to $-j\omega\rho\bar{v}_n(P)$, and we obtain

$$-j\omega\rho\bar{v}_n(P) = \int_S \mu(Q) \frac{\partial^2 G(P, Q)}{\partial n_P \partial n_Q} dS(Q), \quad (5)$$

where the surface velocity \bar{v}_n is known. Using the variational approach, the unknown pressure jump can be evaluated from²³

$$\begin{aligned} -j\omega\rho \int_S \delta\mu(P) \bar{v}_n(P) dS(P) \\ = \int_S \int_S \delta\mu(P) \mu(Q) \frac{\partial^2 G(P, Q)}{\partial n_P \partial n_Q} dS(P) dS(Q), \end{aligned} \quad (6)$$

where $\delta\mu(P)$ denotes a variation in the pressure jump. Here the hypersingularity associated with Green’s function must be reduced to a weak singularity before the numerical integration.

Another problem occurring with BEM techniques in practice is the mathematical breakdown of the formulation at specific so-called critical or irregular frequencies. These special frequencies are related to eigenfrequencies of the interior region and will be present if an interior BEM problem is analyzed, but they will also affect the results of an exterior BEM analysis if no effort is made to remove their influence. Since meaningless results can occur at the irregular frequencies, we assume throughout this work that such frequencies are avoided. A modified formulation²⁴ based on both jump terms, which incorporates impedance boundary conditions on the inner surface, can be used to avoid the problems with irregular frequencies; this feature is not included in the present work.

III. THE INVERSE PROBLEM

Whenever a sound source reconstruction problem is discretized—by means of BEM or other discretization methods—a so-called discrete ill-posed problem arises. In this section we describe how to deal with such problems.

The discretized problem can be written in general matrix–vector form as

$$\mathbf{A}\mathbf{x} = \mathbf{b}, \quad (7)$$

where \mathbf{A} is a complex transfer matrix of dimension $m \times n$, i.e., m rows and n columns. Hence, the complex vectors \mathbf{x} and \mathbf{b} are of dimension n and m , respectively. In the following we assume that the system is either square or overdetermined, i.e., $m \geq n$. The matrix \mathbf{A} represents a model of the system under investigation while \mathbf{b} is a data vector of known measured values. In our work the system under study is the radiation process from a source to a number of receivers, \mathbf{b} represents the response at the position of the receivers, and the model represented by \mathbf{A} should be “inverted” in order to deduce the source descriptors in \mathbf{x} . We will only consider errors \mathbf{e} on the right-hand side, while errors in \mathbf{A} are neglected. When Eq. (7) arises from discretization of an inverse problem, \mathbf{A} will be very ill conditioned. Consequently, a straightforward solution of the discrete inverse problem is not satisfactory, and special regularization techniques should be employed in order to solve Eq. (7) in a nearby sense.

A. Singular value decomposition

Solving discrete ill-posed problems via a direct solution approach should preferably be combined with tools that provide some kind of analysis of the specific problem at hand. Such tools do not solve the problem itself, but will often provide the necessary information before any next step toward a useful solution of the problem is taken. When it comes to ill-conditioned matrices, the ultimate analysis tool seems to be the singular value decomposition (SVD). Given the transfer matrix \mathbf{A} , we can write the SVD of this matrix as²⁵

$$\mathbf{A} = \mathbf{U}\mathbf{\Sigma}\mathbf{V}^H, \quad (8)$$

where \mathbf{U} is a matrix of dimension $m \times n$, \mathbf{V} is $n \times n$ and $\mathbf{\Sigma}$ is a diagonal matrix containing n non-negative singular values σ_i in nonincreasing order. The superscript H in Eq. (8) denotes the complex conjugate transposed.

The two matrices \mathbf{U} and \mathbf{V} are written in the form

$$\mathbf{U} = (\mathbf{u}_1 \cdots \mathbf{u}_n), \quad \mathbf{V} = (\mathbf{v}_1 \cdots \mathbf{v}_n), \quad (9)$$

where \mathbf{u}_i (dimension m) and \mathbf{v}_i (dimension n) are called the left and right singular vectors. An important property of these vectors is their orthonormality, i.e., $\mathbf{U}^H\mathbf{U} = \mathbf{V}^H\mathbf{V} = \mathbf{I}_n$, with \mathbf{I}_n the identity matrix of order n .

The condition number (based on the 2-norm) of \mathbf{A} can be expressed as the ratio of the largest and the smallest singular value,²⁵ i.e., $\text{cond}(\mathbf{A}) = \sigma_1 / \sigma_n$. This quantity measures a solution’s sensitivity to perturbations in the matrix itself as well as on the right-hand side. When we are dealing with ill-conditioned matrices, the range of singular values span many orders of magnitude and \mathbf{A} is very ill conditioned. Some kind of filtering of the singular values must be added to the original problem before any solution step makes sense.

The behavior of the left and right singular vectors deserves special attention, because any filtering relies on this behavior. Hansen *et al.*²⁶ demonstrate that the left and right singular vectors tend to have more oscillations as the index i increases when the transfer matrix arises from discretization of an inverse problem. Thus, we will assume that high-frequency spatial information is linked to left- and right-singular vectors having high index i . Likewise, the vectors

with a small index represent slowly varying functions having few sign changes over the source surface. These considerations have not been proven, but for practical problems derived from integral equations they appear to be valid.

B. Tikhonov regularization

If all SVD components are taken into account, a very oscillating solution with a huge norm is obtained due to the error component \mathbf{e} of the right-hand side \mathbf{b} . One way of suppressing the disastrous influence of these errors is to solve the initial ill-conditioned problem in a nearby sense with a constraint on the size of the sought solution. The solution size is linked to the solution smoothness, because ignoring components with a high index will lead to a smooth solution with reasonable size as measured by an appropriate norm.

In mathematical form, we can write this as a minimization problem, where the functional to be minimized involves a residual norm and a discrete smoothing norm $\|\mathbf{L}\mathbf{x}\|_2$ acting on the solution vector:

$$\min_{\mathbf{x}} \{ \|\mathbf{A}\mathbf{x} - \mathbf{b}\|_2^2 + \lambda^2 \|\mathbf{L}\mathbf{x}\|_2^2 \}. \quad (10)$$

This form of regularization is known as Tikhonov regularization, which is discussed at length, e.g., in Hansen.²⁷ The regularization parameter λ is the only input when a suitable smoothing norm has been defined. A possible implementation is described in Sec. IV B. If $\lambda = 0$ we obtain the least-squares problem and the unregularized solution is computed. A large λ favors a small solution size at the cost of a large residual norm. Hence, λ controls the degree to which the sought regularized solution should fit to the measured data in \mathbf{b} or have a small solution size. Clearly, solving Eq. (10) involves a trade-off between the residual norm and the solution size, and this is determined by the single parameter λ . We return to our choice of \mathbf{L} later.

For the choice of $\mathbf{L} = \mathbf{I}_n$, the Tikhonov regularized solution can be written conveniently in terms of the SVD of \mathbf{A} as²⁷

$$\mathbf{x}_\lambda = \sum_{i=1}^n \frac{\sigma_i^2}{\sigma_i^2 + \lambda^2} \frac{\mathbf{u}_i^H \mathbf{b}}{\sigma_i} \mathbf{v}_i. \quad (11)$$

The filtering is described by the filter factors $f_i = \sigma_i^2 / (\sigma_i^2 + \lambda^2)$. In practice, the regularization parameter is chosen to lie between the highest and smallest singular value. Hence, the filter gradually dampens singular values smaller than λ .

C. Parameter-choice methods

The main difficulty with regularization methods is that a proper choice of the amount of regularization is not easily found. Choosing the continuous parameter λ in Tikhonov regularization is not straightforward. Ideally, we would like to determine the optimal regularization parameter such that the computed regularized solution provides the best possible estimate of the exact solution. The difficulty is that the exact solution is not available. Regularization parameters that are good approximations to the optimal ones can, however, be estimated by means of parameter-choice methods. Williams¹³

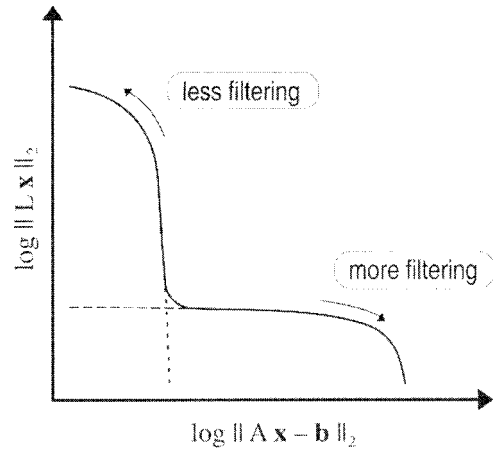


FIG. 1. The generic L-curve form; a plot in the log–log scale of the discrete smoothing norm versus the residual norm as a function of regularization parameter λ . From Ref. 27.

used the discrepancy principle and its compensated version, which require estimating the error norm $\|\mathbf{e}\|_2$ to determine the regularization parameter. The error norm can be estimated from the measurement data using the left-singular vectors, however, a very good estimate of the error norm is usually needed in order for the discrepancy principle to be robust, cf. Sec. 7.7 in Ref. 27.

Hence, there is a need for parameter-choice methods that do not require information about the error norm $\|\mathbf{e}\|_2$. Here we consider two $\|\mathbf{e}\|_2$ -free methods for extracting an optimal regularization parameter. The first method, which is very popular, is called generalized cross-validation (GCV). It is based on the philosophy that an arbitrary element b_i of the right-hand side should be predicted well by the regularized solution, when this element is left out of the inverse problem. This method works well if the noise is spatially white, i.e., if the elements of the noise vector are unbiased and have the same variance. Useful reconstructions were obtained by Nelson^{11,12} for a couple of inverse source problems with random errors representing measurement noise and using, among other techniques, the GCV as a parameter-choice method.

Another $\|\mathbf{e}\|_2$ -free approach to estimating the regularization parameter in Tikhonov regularization is the so-called L-curve criterion.¹⁴ The idea behind the L-curve is to plot the discrete smoothing norm of the regularized solution versus the residual norm in log–log scale, for all valid regularization parameters. The generic form of the L-curve is plotted in Fig. 1. The smoothing norm here is $\|\mathbf{L}\mathbf{x}_\lambda\|_2$ and the residual norm is $\|\mathbf{A}\mathbf{x}_\lambda - \mathbf{b}\|_2$, i.e., the two terms occurring in the functional to be minimized in Tikhonov regularization. The shape of the L curve can be explained by considering its different sections. The horizontal part of the curve is characterized by solutions that have been smoothed too much (over-regularized), whereas the vertical part is characterized by solutions dominated by the effects of errors (under-regularized). In between these parts, we find solutions representing a balance between fitting the solution to data and keeping the solution's smoothing norm small. The optimum

value of the regularization parameter defined by the L-curve criterion is at the corner of the curve, where we find a solution that has a reasonably small residual as well as a reasonably limited smoothing norm. We note that this is only possible in a plot in log–log scale.²⁸ A number of simulated case studies²⁹ dealing with simulated noise/error sources revealed that the L-curve criterion is more robust than the GCV method, especially when the added noise is non-white. This is an important finding before studying real applications, where the noise component of the field data cannot be considered to be white.

IV. IMPLEMENTATION OF THE INVERSE SOURCE PROBLEM

Integral formulations are usually implemented numerically by a boundary element method where the surface of the boundary is replaced by a number of interconnected elements. These surface elements can typically be either triangles or squares, and the associated interpolation functions for the source values are typically linear or quadratic. In the present study triangular linear elements are used for describing the geometry as well as the acoustic variables on the surface. Hence, linear interpolation is used throughout for the geometry as well as the acoustic parameters, and the elements are therefore isoparametric, i.e., the same order of shape function is used in both cases. We note the general rule of thumb that the element size should not exceed one-fourth of the shortest wavelength for the linear elements.

First we derive the set of matrix equations needed to formulate the inverse problem, and we define the transfer matrix associated with the problem. The matrices are easily computed by means of the developed indirect BEM implementation. Subsequently, we will establish a functional amenable to Tikhonov regularization that will be the type of regularization imposed on the problem. Since the modeling of the inverse problem is linked to the BEM in acoustics, we will use the term Inverse Boundary Element Method (IBEM) or inverse BEM.

A. Formation of the inverse BEM transfer matrix

We will consider the surface S of a closed or open structure, and normal vector on the surface S points into the exterior. We assume that m microphones are situated in the exterior region of the source. Basically these microphones can be located anywhere in this region, but some locations may be preferred over others.^{5,32} For every microphone position we will then measure an acoustic pressure.

The goal of the discretization of Eqs. (3) and (6) is to link the m measured field pressures to an acoustic quantity on the source surface. From the indirect formulation we first establish the relation between the field pressures p_f and the pressure jump μ on the source surface by discretization of the integral representation, Eq. (3). For each boundary element we introduce the vectors \mathbf{N}_i and $\boldsymbol{\mu}_i$, which represent the shape function for linear triangles and the nodal values of the pressure jump distribution, respectively. This leads to the discretized problem

$$p_f(P) = \sum_{i=1}^e \int_{S_i} \mathbf{N}_i^T(Q) \boldsymbol{\mu}_i \frac{\partial G(P, Q)}{\partial n_Q} dS_i(Q), \quad (12)$$

where e is the number of boundary elements.

For each measurement point we now use Eq. (12) to express the measured field p_f in terms of the nodal values of the pressure jumps. The integrals in Eq. (12) can be evaluated using standard Gauss quadrature, as long as the point P is not too close to the source surface. Otherwise, singularities involved in the integral formulation should be removed for P in the very close near-field. A modified boundary element formulation based on Helmholtz integral equation has been reported to overcome such problems.^{30,31} In our case the minimum distance between field points and source surface for BEM calculations is set to one-half an element length. Expressed in matrix-vector form, the discretized problem becomes

$$\mathbf{p}_f = \mathbf{G}\boldsymbol{\mu}, \quad (13)$$

where \mathbf{p}_f is a complex vector containing the m field pressure values at a specific frequency, and $\boldsymbol{\mu}$ is a vector with the pressure jump values on the discretized surface containing n nodes. The $m \times n$ transfer matrix \mathbf{G} is notoriously ill conditioned.

Rather than solving Eq. (13) for $\boldsymbol{\mu}$ given a known vector \mathbf{p}_f , we will relate the field pressure vector to the normal surface velocity vector \mathbf{v}_n . This is done by means of the relation between pressure jump and normal surface velocity from the indirect boundary element formulation Eq. (6) which, when discretized, takes the form

$$\begin{aligned} -j\omega\rho\boldsymbol{\delta}\boldsymbol{\mu}^T \left(\int_S \mathbf{N}\cdot\mathbf{N}^T dS(P) \right) \mathbf{v}_n \\ = \boldsymbol{\delta}\boldsymbol{\mu}^T \left(\int_S \int_S \mathbf{N} \frac{\partial^2 G(P, Q)}{\partial n_P \partial n_Q} \mathbf{N}^T dS(P) dS(Q) \right) \boldsymbol{\mu}, \end{aligned} \quad (14)$$

or in matrix–vector form,

$$-j\omega\rho\mathbf{B}\mathbf{v}_n = \mathbf{Q}\boldsymbol{\mu}. \quad (15)$$

The two matrices \mathbf{B} and \mathbf{Q} are symmetric, i.e., $\mathbf{B} = \mathbf{B}^T$ and $\mathbf{Q} = \mathbf{Q}^T$.

Combining Eqs. (13) and (15) we then obtain

$$\mathbf{p}_f = -j\omega\rho\mathbf{G}\mathbf{Q}^{-1}\mathbf{B}\mathbf{v}_n = \mathbf{H}\mathbf{v}_n. \quad (16)$$

Here, we have introduced the $m \times n$ rectangular transfer matrix, $\mathbf{H} = -j\omega\rho\mathbf{G}\mathbf{Q}^{-1}\mathbf{B}$, which is further analyzed in our IBEM problems. A similar way of assembling a transfer matrix using indirect BEM has been done by Zhang *et al.*^{5,32}

Since \mathbf{G} is ill-conditioned for measurement points lying strictly in the exterior, this property is carried over to the transfer matrix \mathbf{H} that relates the normal surface velocity at nodes to acoustic pressure at measurement points. Note that the assembly of \mathbf{H} necessitates the inverse of \mathbf{Q} , which will not cause trouble as long we avoid irregular frequencies (interior Neumann eigenfrequencies) for a closed structure. Consequently, Eq. (16) represents a discrete ill-posed problem of the form studied in Sec. III. Treating irregular frequencies in inverse BEM were discussed in Ref. 32 based on

the same considerations as in Sec. II. How to solve Eq. (16) in the nearby sense by formulating a Tikhonov problem is discussed next.

B. Tikhonov problem

The regularization imposed in this investigation is based on Tikhonov's method with a parameter-choice method to estimate the optimal regularization parameter. In general form, the minimisation problem for Tikhonov regularization is written as

$$\min_{\mathbf{v}_n} \{ \|\mathbf{H}\mathbf{v}_n - \mathbf{p}_f\|_2^2 + \lambda^2 \|\mathbf{L}\mathbf{v}_n\|_2^2 \}. \quad (17)$$

The discrete smoothing norm $\|\mathbf{L}\mathbf{v}_n\|_2$ must be chosen to preferably reflect some physical quantity to be penalized, that is, to have limited size. One such quantity could be some type of energy associated with a vibrating thin shell since the model is based upon shells. The equivalent kinetic energy of the entire shell structure makes sense, since the size of this quantity will increase dramatically if the nonradiating components have too large an influence on the regularized solution.

The “kinetic energy smoothing norm” is derived by considering the squared surface velocity over the shell surface. Since we only have access to the normal component of surface velocity, the equivalent total kinetic shell energy is written as

$$\int_S |\nu_n|^2 dS = \int_S \nu_n \nu_n^* dS, \quad (18)$$

where the asterisk denotes a “complex conjugate.” We can discretize this quantity using standard Gaussian quadrature and the discretization of Eq. (18) is written as

$$\int_S \mathbf{v}_n^H \mathbf{N} \mathbf{N}^T \mathbf{v}_n dS = \mathbf{v}_n^H \mathbf{B} \mathbf{v}_n, \quad (19)$$

with the shape function vector \mathbf{N} , and \mathbf{B} is similar to the one defined via Eq. (14).

To simplify the calculations in the Tikhonov regularization, we may approximate the total surface function $\nu_n \nu_n^*$ as a linear function. Consequently, we end up with a diagonal matrix \mathbf{D} that can be considered as an approximation to \mathbf{B} . Using this approach, the surface integral is written as

$$\mathbf{v}_n^H \left(\int_S \text{diag}(\mathbf{N}) dS \right) \mathbf{v}_n = \mathbf{v}_n^H \mathbf{D} \mathbf{v}_n. \quad (20)$$

Here the integrand is a sum of element areas weighted by the shape functions. Hence, only one Gauss point for each element integration is required. For each element integration over S_i , the value $\frac{1}{3}S_i$ is added on the diagonal of the area matrix for each node participating in element i . As a result, the diagonal element of \mathbf{D} corresponding to a node in the BEM model will contain one-third of the total area of all elements of which the node takes part. Thus, the kinetic energy smoothing norm simply introduces an area weighting of the nodal values. The discrete smoothing norm is now written as

$$\mathbf{v}_n^H \mathbf{D} \mathbf{v}_n = \|\mathbf{D}^{1/2} \mathbf{v}_n\|_2^2, \quad (21)$$

where the regularization matrix $\mathbf{D}^{1/2}$ is found by taking the square root of all the diagonal entries. Had our matrix not been diagonal, Cholesky factorization would have been necessary. Notice that if the element size is almost constant over the entire mesh surface, \mathbf{D} will be close to the identity matrix, except for a multiplication constant. In that case, the standard form ($\mathbf{L}=\mathbf{I}_n$) of Eq. (17) could just as well be used. However, for a general mesh $\mathbf{D}^{1/2}$ should be used instead of the identity matrix. Hence, the general form Tikhonov regularization is rewritten in standard form and solved.²⁹

V. CASE STUDIES

In order to demonstrate the capabilities of inverse BEM, some real-life applications have been studied.²⁹ The sound sources considered and modeled are based on a real tire structure mounted on a rim and loaded onto a drum surface. The tire is a standard tire for passenger cars and its characteristics as a source were studied as a stationary tire excited by a shaker as well as a rolling tire with a constant speed of 80 km/h on the dynamometer.

A. Tire measurements

The measurements were recorded using a planar microphone array for the side measurement, and a curved array for close-up measurements at the front and the rear of the tire. Moreover, four reference microphones were distributed around the tire in order to allow the use of a scan technique and to derive a principal component description of the sound field. In this way, the problem of limited coherence between individual sources is addressed. Two of these four reference microphones were placed on the ground in front of and behind the tire, while the other two microphones were located in the air above the tire. When dealing with cross-spectral holography techniques and sound radiation from tires, four reference microphones seem to be sufficient.³³ For the tire side, a 6×6 microphone array was scanned across a plane area with dimensions 1.7×0.9 m. The microphone spacing in the horizontal and vertical direction was 0.05 m, giving a total of 665 measurement points in the plane, which was located 0.07 m from the sidewall of the tire. In addition, a curved array of 12 microphones scanned the rear and front of the tire. The curved array was scanned across the curved surface in 13 steps with a step size of 0.05 m, thus giving 156 measurement points. The distance between the curved array and the curved part of the tire was about 0.07 m. The front of the tire was not measured during the standing tire measurement, as the shaker occupied part of the space there. In total, 821 measurement positions were made for the shaken tire and 977 for the rolling tire. In addition to the IBEM reconstructions, we processed the data recorded at the tire side using Near-field Acoustic Holography as implemented in the Brüel & Kjær STSF^{34,35} system. This allows for a comparison of the transformed sound fields obtained using IBEM and STSF. For example, we can compare the sound field reconstructions close to the tire side obtained by the two methods.

In order to model the acoustic environment, a boundary element mesh of the complete tire was made and the hard ground is taken into account via an infinite rigid plane located 0.05 m below the tire. The tire boundary element mesh consists of linear triangles of maximum length 0.05 m, resulting in 1052 elements and 526 nodes. The tire mesh including meshes of the side measurement and the rear measurement is shown in Fig. 2.

B. Stationary tire excited by a shaker

First, we study the inverse BEM problem for the shaken tire at a low frequency, 100 Hz, the cross-spectral measurement being made with a frequency bandwidth equal to 20 Hz. The field pressure information from the measured 821 points close to the tire surface will now be used to establish an inverse problem, where the normal surface velocity at the 526 boundary nodes is sought. The transfer matrix is thus overdetermined and of size 821×526 . As a result of the principal component description of the sound field, we can consider each principal hologram as a field pressure distribution and we can process the holograms individually, since they are mutually independent (incoherent). That is, for each principal hologram we determine a regularized surface velocity distribution by means of the SVD and Tikhonov regularization, where the optimum regularization parameter is chosen by either GCV or the L-curve criterion. The total surface velocity level is obtained by summing the principal component contributions on a power basis, subject to a Wiener filter

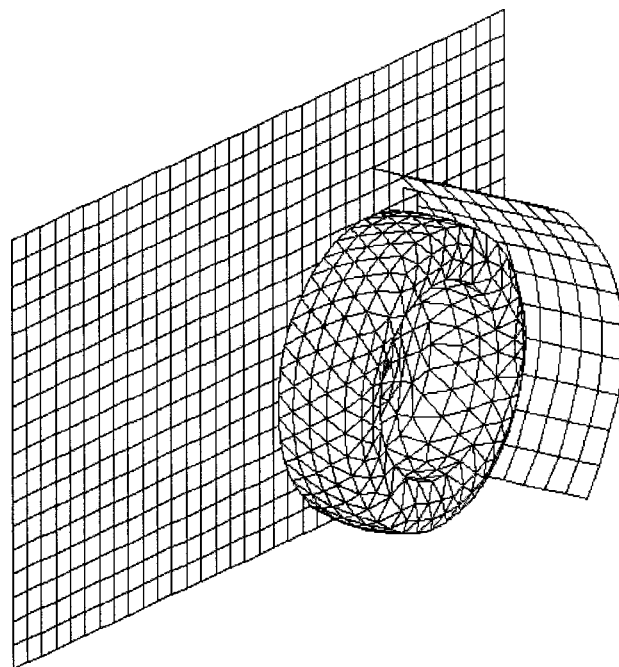


FIG. 2. Tire mesh (1052 elements, 526 nodes) and field point mesh (821 points) for stationary tire application.

controlled by the principal autopowers. In our case the filter has a dynamic range of 15 dB with a smooth cutoff, which means that the first and the second principal component are unaffected by the filter, whereas the third and the fourth prin-

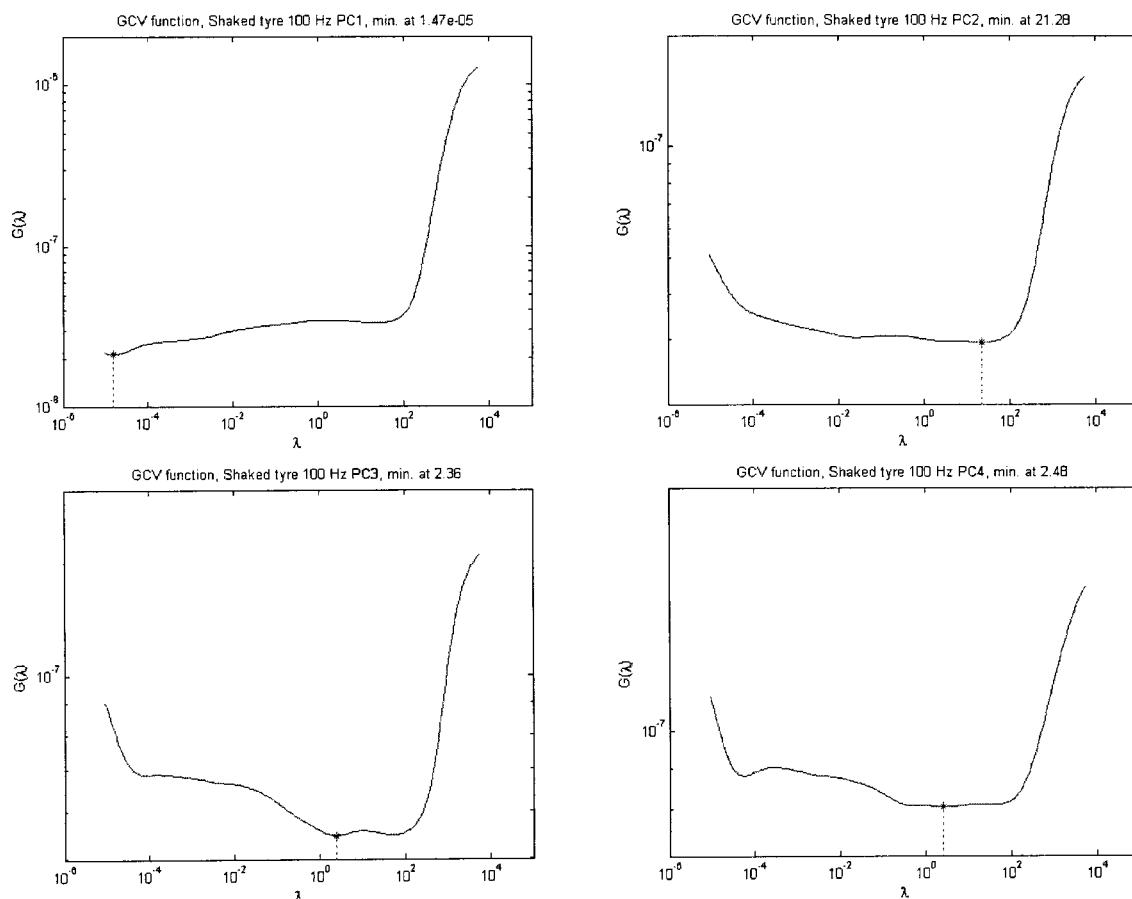


FIG. 3. GCV functions processed for each principal hologram for shaker excited tire at 100 Hz.

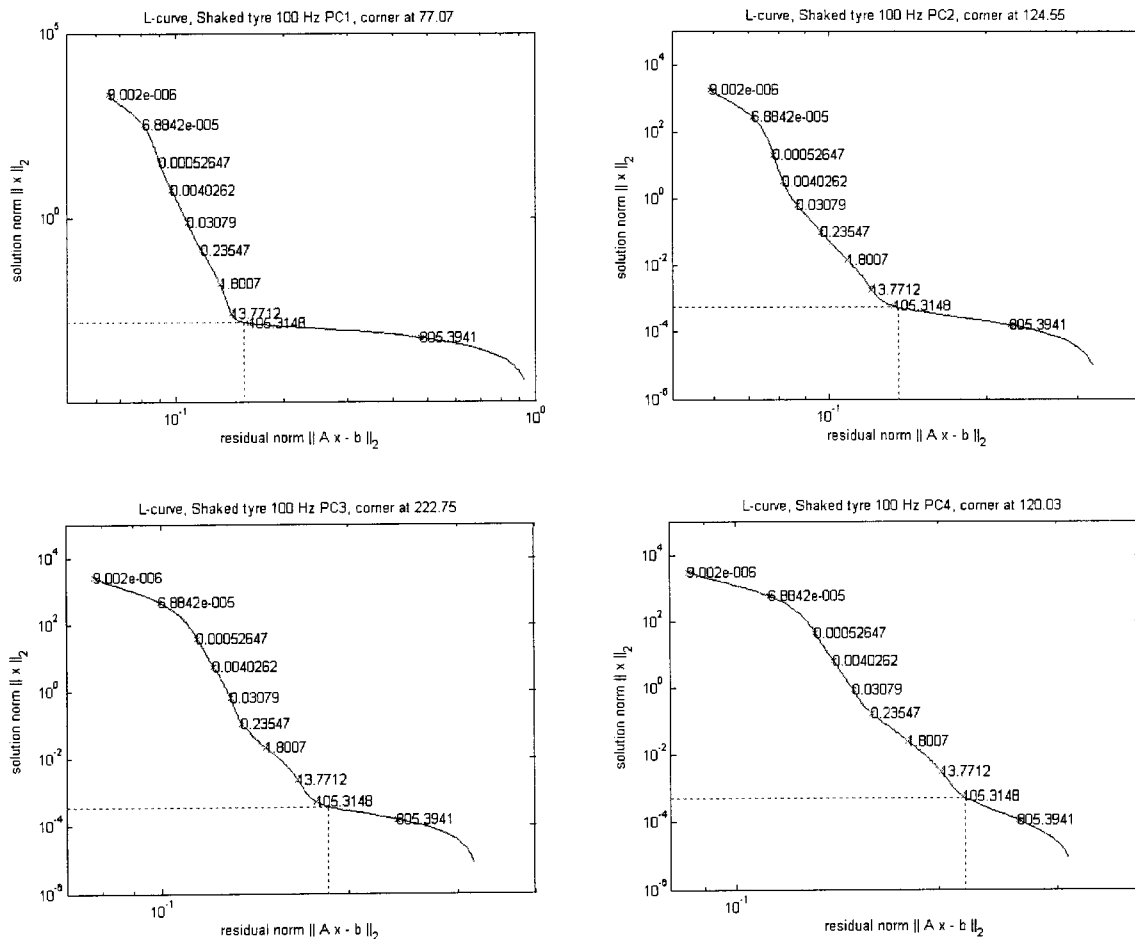


FIG. 4. L-curves corresponding to each principal hologram for a shaker excited tire at 100 Hz. The regularization parameter is marked on the curve.

cipal component are attenuated. In the chosen frequency band, the autopowers of the second, third, and fourth principal component were 10, 16, and 19 dB, respectively, below the autopower of the first principal component. Since there is only one source mechanism (the shaker), one would expect only a single dominating principal component. A major reason for this not happening is the rather large measurement bandwidth. If within the measurement bandwidth the source vibration pattern changes a lot as a function of frequency, the different patterns will be seen to some degree as independent sources. This could explain the existence of the principal component, which is only 10 dB below the highest one. Other reasons for nonzero principal components are finite-averaging time, nonstationarity and nonlinear dynamic behavior of structural components.

An inspection of the SVD components (not shown here) reveals that a regularization parameter λ of the order 100 is appropriate for each principal component. First the GCV method was used to determine the optimum λ for each principal component, and the GCV functions are shown in Fig. 3. It is clear that the estimated regularization parameters are too small, thus resulting in undersmoothed solutions completely dominated by measurement errors. Hence, the regularized surface velocity solution obtained by this method will be meaningless. This is surprising in the sense that the stationary tire excited by a shaker is the simpler one of the two applications. The probable cause is that the measurement er-

rors are not spatially white, as assumed by the GCV method. We mention two error types.

(1) Transducer mismatch. These errors “follow” the array transducers during the scanning, and the resulting errors in the measured sound pressure will therefore be correlated with the true sound pressure.

(2) Transducer position errors. The measurement positions are never exactly known in the coordinate system of the BEM model. The resulting errors in the measured pressure will also tend to be correlated with the true pressure.

Further errors may occur as a result of the drum and as a result of a large obstacle located close to the tire side, which was not scanned. This obstacle was mounted to the rim of the tire but just like the drum it is not part of the acoustic boundary element model for the inverse analysis.

When the same problem is analyzed using the L-curve, we get the four curves shown in Fig. 4. Especially the first L-curve exhibits the generic shape of Fig. 1 with a well-defined corner. Furthermore, the computed regularization parameters are all close to 100, which agrees very well with our SVD analysis. The dynamic range of the applied Tikhonov filters, i.e., $20 \log(\sigma_1/\lambda_L)$, is 37, 33, 28 and 33 dB for principal component one to four, respectively; here λ_L is the optimum regularization parameter computed by the L-curve criterion, and σ_1 is the largest singular value. The solutions obtained by the GCV are seen to be located on the upper of the ver-

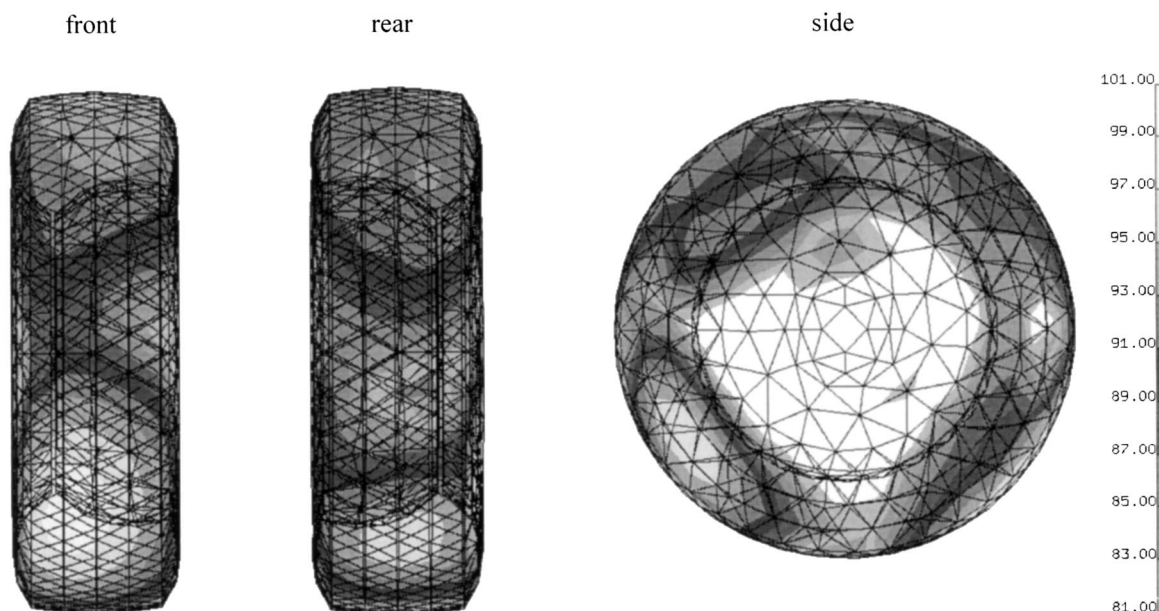


FIG. 5. Reconstructed surface velocity for shaker excited tire at 100 Hz.

tical part of each L-curve and thereby illustrating the differences obtained for this case.

The reason for the success of the L-curve criterion is that it does not rely on the noise being spatially white as GCV does; also colored/correlated noise gives rise to a distinct corner on the curve. The GCV function, on the other

hand, may fail to have a suited minimum when the noise is not spatially white.

The computed regularised surface velocity solution for each principal component represents a principal source related to the vibrating tire structure. This total surface velocity distribution is shown on the tire model in Fig. 5. Note that

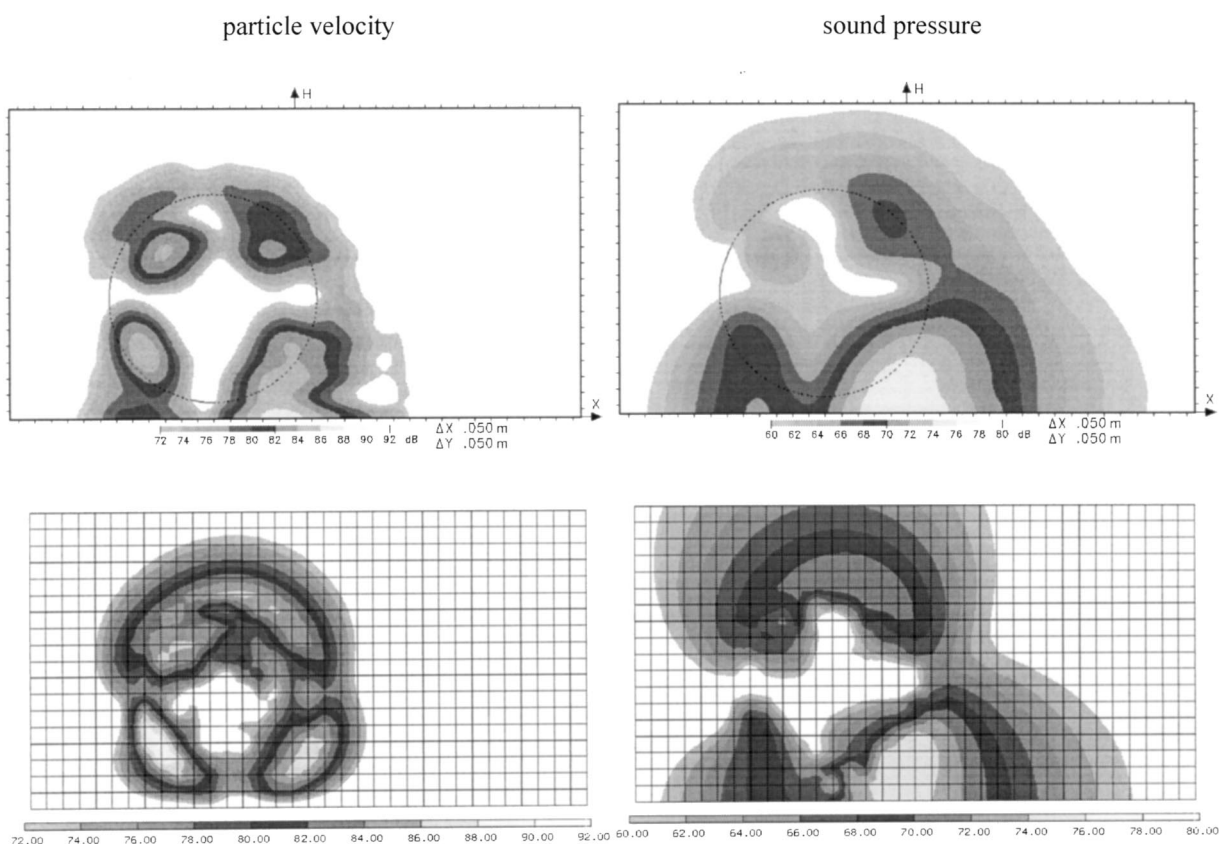


FIG. 6. Reconstructed normal particle velocity and sound pressure on a calculation plane 2 cm from the tire side of the shaker excited tire at 100 Hz. Results for STSF (top) and IBEM using L-curve criterion (bottom).

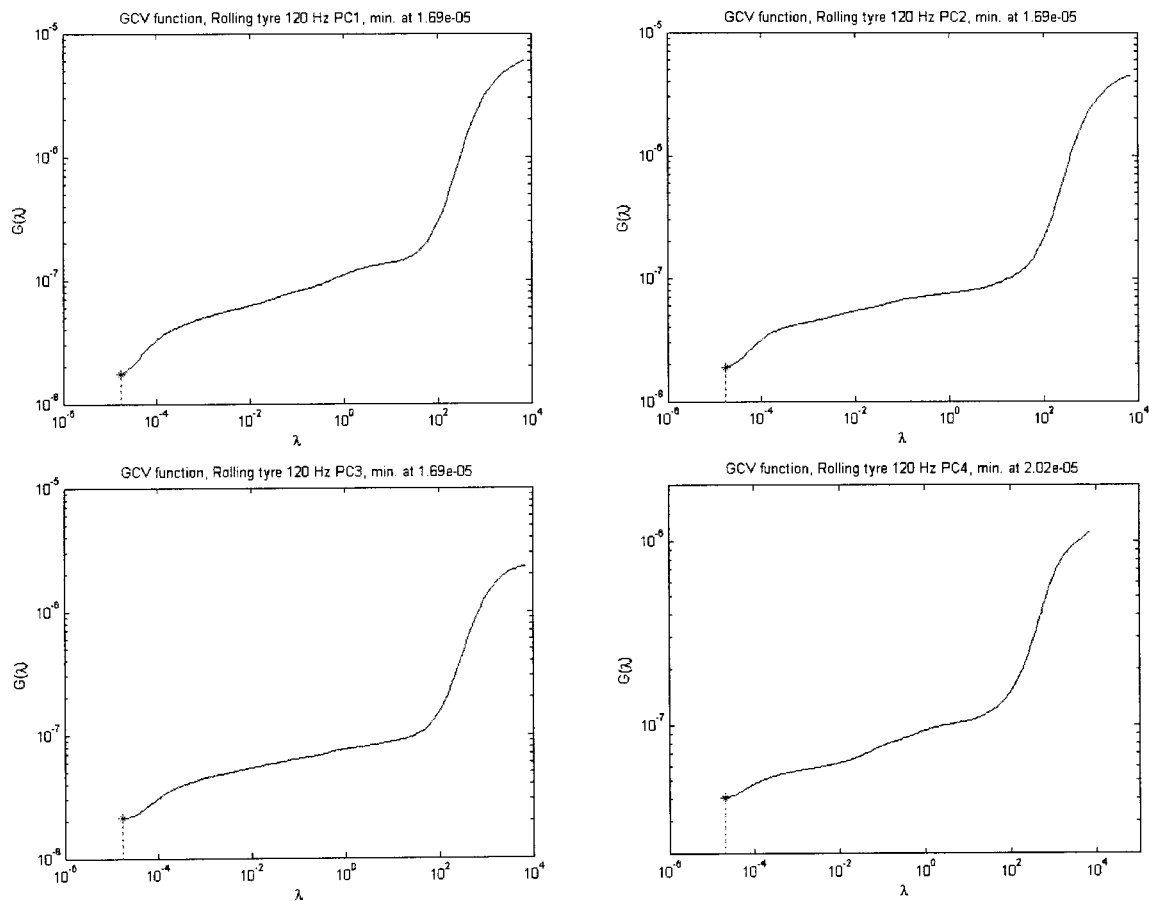


FIG. 7. GCV functions processed for each principal hologram for rolling tire at 120 Hz.

only the highest 20 dB of the available data are plotted. Since we can observe the tire from any position, we can look at the spot where the shaker excites the tire (front). This reveals a significant hot spot associated with a maximum vibration level. Further sources of vibration are found on the rear part of the tire close to the ground and on the tire sidewall. This surface velocity reconstruction will now be used as boundary condition in a forward BEM problem for computing the sound field close to the tire.

In order to compare the sound field reconstructions obtained by IBEM and STSF, the sound pressure and the particle velocity was computed on a plane close to the tire sidewall. Using STSF, this was done by processing the measurement data from the plane array measurement at the tire side, and then backward propagating the acoustic field 0.05 m onto a plane close to the tire side. A similar filtering (15 dB dynamic range, smooth cutoff) of the individual principal components was done, but for the regularization part a fixed dynamic range of 30 dB was used for every principal component. This is simply because no automatic detection of a useful dynamic range is implemented in the current STSF application and 30 dB is the maximum allowed range. When using IBEM with the L-curve criterion, the principal holograms were processed independently in order to obtain a set of principal sources. These sources were then processed as part of a forward BEM problem for computing the normal component of the particle velocity and the acoustic pressure over the same plane as in the STSF computation. The par-

ticle velocity and pressure distributions obtained are shown in Fig. 6 together with the result of the STSF calculation. Both the sound pressure level distributions and the particle velocity distributions obtained by STSF and by IBEM (L-curve), see Fig. 6, are in good agreement. The levels are almost identical and are shown using the same color bar with the same step size. Clearly, the L-curve criterion applied to each principal component leads to a useful reconstructed particle velocity distribution judged from the STSF calculations. However, it would be more convincing to have the actual measurement data for the calculation plane when doing comparisons.

As mentioned previously, the frequency bandwidth is probably the major reason that we do not see only a single nonzero principal component. Nonzero components arising because of the bandwidth represent real sound fields and real sources. The only error in our IBEM equations will be in the transfer matrix and arise from the fact that we have assumed all sound field components to be at the center frequency of the band. But beyond the frequency bandwidth, there are other causes for a nonzero principal component, which have no relation to real sources. The two components dominated by noise and errors represent a challenge to the applied regularization schemes. From the computed L-curves it is clear that the noisy principal components should be discarded since there is nearly only a vertical part, which can easily lead to very small regularization parameters and thus solutions with a significant norm. For that reason a lower limit on

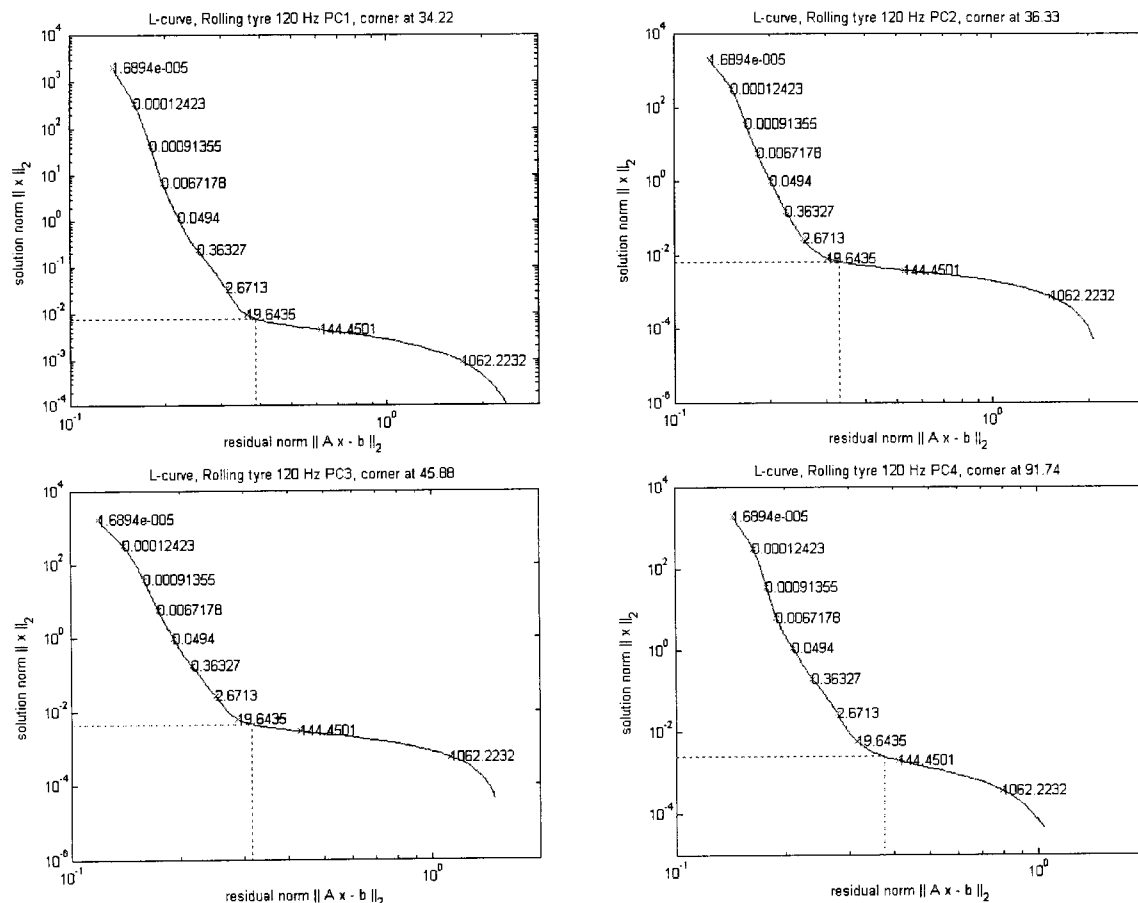


FIG. 8. L-curves corresponding to each principal hologram for rolling tire at 120 Hz. The regularization parameter is marked on the curve.

the regularization parameter could be imposed or a sharp principal component filter should be used. The solutions of Fig. 6 obtained by STSF and by IBEM are dominated by the first principal component with the highest principal auto-power.

C. Rolling tire

A similar analysis is carried out for the rolling tire case. One major difference between the two measurement cases is that the rolling tire measurement includes a curved array

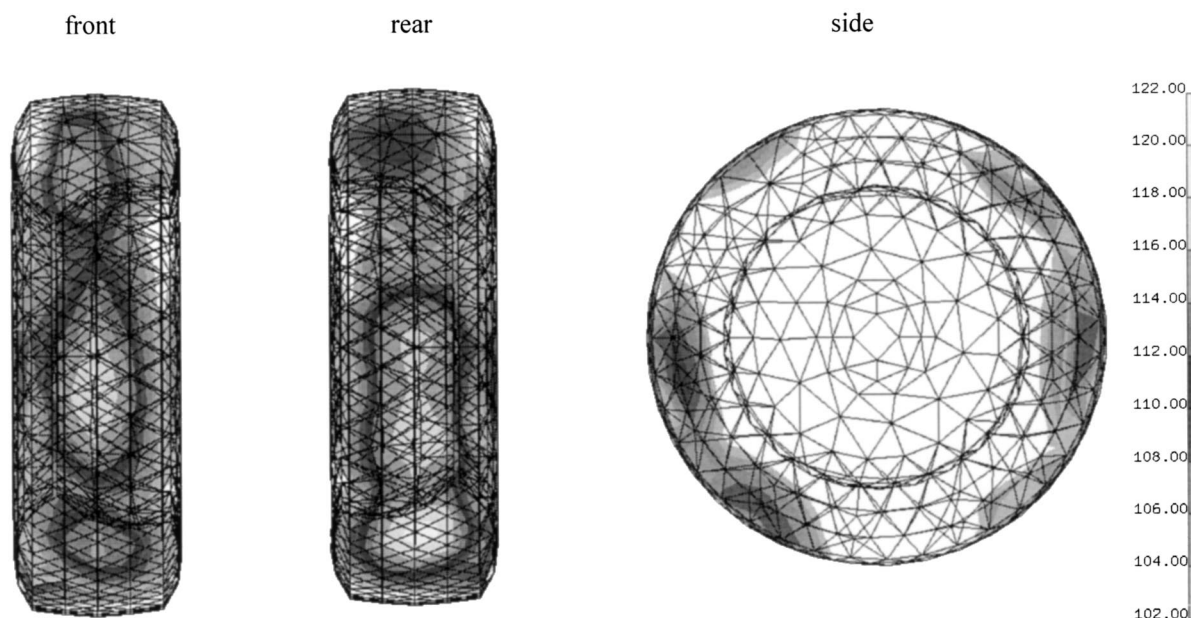


FIG. 9. Reconstructed surface velocity for rolling tire at 120 Hz.

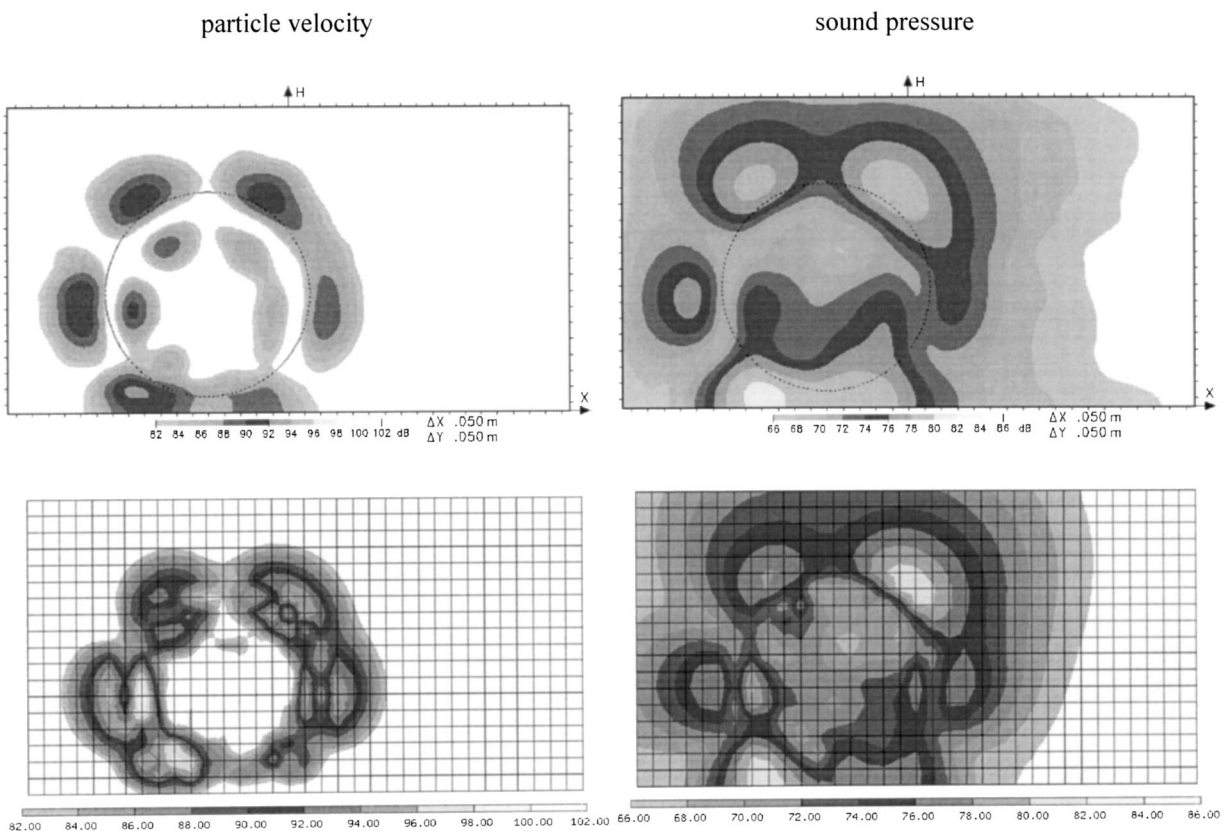


FIG. 10. Reconstructed normal particle velocity and sound pressure on calculation plane 2 cm from the tire side of the rolling tire at 120 Hz. Results for STSF (top) and IBEM using L-curve criterion (bottom).

scanning of the tire front, thus providing more information about the total sound field around the rolling tire. Again, this curved array was located 0.07 m from the tire and scanned with a step size of 0.05 m. By adding these front measurement positions to the plane and curved array measurement positions from the shaken tire setup, we end up with a total of 977 measurement points.

Using the same set of four reference microphones, a principal component description of the sound field was derived. Again, we use a low frequency, this time corresponding to a band of width 20 Hz centered at 120 Hz. For the analysis, this gives us a 977×526 transfer matrix for the rolling tire. Each of the four principal holograms at 120 Hz is again associated with an inverse problem. Compared to the shaken tire measurement, we will now for the rolling tire expect some additional errors arising from the rotating drum producing background noise, as well as wind noise induced in the microphones due to wind from the fast rotating tire. However, these additional error components will be rather uncorrelated with the noise radiated from the tire, so provided they are not too large they are not expected to cause major additional problems. A major difference from the case of the shaken tire measurement is that now we will have four significant principal components—all four containing information about the noise due to tire vibration. The autopowers of the second, third, and fourth principal component was 5, 10, and 15 dB, respectively, below the autopower of the first principal component.

Similar to before, a SVD analysis reveals that the regu-

larization parameters for this case should be about 50. The GCV function for each of the four right-hand sides is shown in Fig. 7 and the computed minimum is marked. Again, the GCV leads to severely undersmoothed solutions, as the estimated regularization parameters are all far too small. It is also noted that the GCV functions in this case start increasing slowly followed by a more rapid increase, which results in minimums on the left part of the curve. This is simply a consequence of the noise and errors in the measurement data and the resulting computed surface velocity distribution will also in this case be completely meaningless.

The L-curve analysis gives the four curves shown in Fig. 8, where each curve has a distinct corner, even for this complicated case. The vertical part of each curve is not strictly vertical, indicating that the errors are far from being spatially white. For small regularization parameters we see that the residual norm continues to decrease when regularization is turned further down, explaining why the GCV functions behave as in Fig. 7. Furthermore, the computed regularization parameters are all close to 50 in case of the L-curve criterion, which agrees very well with a SVD analysis. The dynamic range of the applied Tikhonov filters is in this case 46, 46, 44, and 38 dB for principal component one to four, respectively. The higher dynamic ranges for the rolling tire is because the surface velocity distribution is made up by more SVD components as long as they are not dominated by noise. The difference in solution between the two test cases can be seen from Fourier coefficients; for the shaker excited tire, the

Fourier coefficients $|\mathbf{u}_f^H \mathbf{p}_f|$ decay more rapidly than for the rolling tire case until they both hit a noise level.

The total surface velocity distribution on the tire model is shown in Fig. 9, where only the highest 20 dB of the available data are plotted. From the front and the rear of the tire we find the strongest vibration on the tire tread, especially close to the leading (front) and the trailing edge (rear) of the tire. Further vibration is associated with the tire side-wall.

As with the foregoing case, we compare with results from STSF. The reconstructed surface velocity data are fed into a forward BEM calculation for computing the sound field on the STSF calculation plane. The STSF calculations are again done with a fixed dynamic range of 30 dB for each principal component. The obtained results for particle velocity and pressure are shown in Fig. 10. In this case, there is a slight difference in level for the particle velocity calculation, which is due to higher dynamic ranges for the IBEM reconstructions. On the other hand, both methods show the same regions of maximum level. For the pressure distribution, we obtain comparable results from the two methods. This is because the pressure distribution does not require as many high spatial frequencies as the particle velocity distribution. The higher dynamic ranges therefore do not have the same impact. These considerations illustrate how useful is the automatic ($\|\mathbf{e}\|_2$ -free) detection of the applicable dynamic range.

VI. CONCLUSIONS

A model of an inverse acoustic source problem was made using the indirect variational BEM formulation described in the first part of the paper. A transfer matrix relating field pressures to surface velocities was formed to take part in a Tikhonov regularization problem. The crucial part associated with choosing the optimal amount of regularization was discussed in the context of error-free parameter-choice methods. The optimal amount of regularization was estimated using the L-curve criterion as well as the popular GCV method for two different tire applications. In both cases we compared reconstructed acoustic field quantities on a plane surface close to the tire side with data from near-field acoustic holography (STSF). In all our experiments, the L-curve criterion provided realistic source reconstructions. The reconstructed source distributions computed by means of GCV were incorrect as a result of the complicated error distributions contaminating the measured data. While the GCV method is well established for reconstruction in the presence of spatially white noise, the cases investigated in this work demonstrate that the L-curve method may be a better choice for practical measurements, where spatially correlated measurement errors such as transducer phase and position errors are present. As a consequence, the L-curve criterion seems to be more robust than the GCV for estimating the optimal amount of regularization.

¹F. Augusztinovicz and M. Tournour, "Reconstruction of source strength distribution by inverting the boundary element method," in *Boundary Elements in Acoustics*, edited by O. von Estorff (WIT Press, Southampton, 2000).

²M. R. Bai, "Application of BEM (boundary element method)-based

acoustic holography to radiation analysis of sound sources with arbitrarily shaped geometries," *J. Acoust. Soc. Am.* **92**, 533–549 (1992).

³G.-T. Kim and B.-H. Lee, "3-D sound source reconstruction and field prediction using the Helmholtz integral equation," *J. Acoust. Soc. Am.* **136**, 245–261 (1990).

⁴W. A. Veronesi and J. D. Maynard, "Digital holographic reconstruction of sources with arbitrarily shaped surfaces," *J. Acoust. Soc. Am.* **85**, 588–598 (1989).

⁵Z. Zhang, N. Vlahopoulos, S. T. Raveendra, T. Allen, and K. Y. Zhang, "A computational acoustic field reconstruction process based on an indirect boundary element formulation," *J. Acoust. Soc. Am.* **108**, 2167–2178 (2000).

⁶E. G. Williams, B. H. Houston, P. C. Herdic, S. T. Raveendra, and B. Gardner, "Interior near-field acoustical holography in flight," *J. Acoust. Soc. Am.* **108**, 1451–1463 (2000).

⁷B.-K. Kim and J.-G. Ih, "On the reconstruction of the vibro-acoustic field over the surface enclosing an interior space using the boundary element method," *J. Acoust. Soc. Am.* **100**, 3003–3016 (1996).

⁸A. Schuhmacher, J. Hald, and E.-U. Saemann, "A comparison of inverse boundary element method and near-field acoustical holography applied to sound radiation from a tire," *Proceedings of the Sixth International Congress on Sound and Vibration*, Copenhagen, 1999.

⁹A. Schuhmacher, "Practical application of inverse boundary element method to sound field studies of tires," *Proceedings of Internoise '99*, Ft. Lauderdale, 1999.

¹⁰B.-K. Kim and J.-G. Ih, "Design of an optimal wave-vector filter for enhancing the resolution of reconstructed source field by near-field acoustical holography (NAH)," *J. Acoust. Soc. Am.* **107**, 3289–3297 (2000).

¹¹P. A. Nelson, "Some inverse problems in acoustics," in Ref. 8.

¹²P. A. Nelson and S. H. Yoon, "Estimation of acoustic source strength by inverse methods: Part II: Methods for choosing regularisation parameters," ISVR Technical Report No. 279, University of Southampton, 1998.

¹³E. G. Williams, "Regularization methods for near-field acoustical holography," *J. Acoust. Soc. Am.* **110**, 1976–1988 (2001).

¹⁴P. C. Hansen, "Analysis of discrete ill-posed problems by means of the L-curve," *SIAM Rev.* **34**, 561–580 (1992).

¹⁵R. Martinez, "The thin-shape breakdown (TSB) of the Helmholtz integral equation," *J. Acoust. Soc. Am.* **90**, 2728–2738 (1991).

¹⁶V. Cutanda, P. M. Juhl, and F. Jacobsen, "On the modeling of narrow gaps using the standard BEM," *J. Acoust. Soc. Am.* **109**, 1296–1303 (2001).

¹⁷P. J. T. Filippi, "Layer potentials and acoustic diffraction," *J. Sound Vib.* **54**, 473–500 (1977).

¹⁸M. N. Sayhi, Y. Ousset, and G. Verchery, "Solution of radiation problems by collocation of integral formulations in terms of single and double layer potentials," *J. Sound Vib.* **74**, 187–204 (1981).

¹⁹X. Zeng, J. Bielak, and R. C. MacCamy, "Unified symmetric finite element and boundary integral variational coupling methods for linear fluid-structure interaction," *Numerical Methods for Partial Differential Equations* **8**, 451–467 (1992).

²⁰O. von Estorff, A. Homm, and F. Bartels, "Sound radiation of a cantilever plate—comparisons of BEM results with experimental data," *Betech* 91, Southampton, 1991.

²¹O. von Estorff, M. Fischer, and W. J. M. Keiper, "Sound radiation of a tuning-fork by boundary elements," *BEM* 14, Seville, 1992.

²²S. T. Raveendra, N. Vlahopoulos, and A. Graves, "An indirect boundary element formulation for multi-valued impedance simulation in structural acoustics," *Appl. Math. Model.* **22**, 379–393 (1998).

²³R. Jeans and I. C. Mathews, "A comparison of numerical collocation and variational procedures to the hypersingular acoustic integral operator," *Comput. Methods Appl. Mech. Eng.* **101**, 5–26 (1992).

²⁴S. T. Raveendra, "Analysis of periodic acoustic problems with double sided impedance condition," *Proceedings Noise-Con '97*, Pennsylvania, 1997.

²⁵G. H. Golub and C. F. van Loan, *Matrix Computations* (The Johns Hopkins University Press, Baltimore, MD, 1996).

²⁶P. C. Hansen, M. E. Kilmer, and R. H. Kjeldsen, "Exploiting residual information in the regularisation of discrete ill-posed problems," *SIAM J. Sci. Comput. (USA)* (submitted).

²⁷P. C. Hansen, *Rank-Deficient and Discrete Ill-Posed Problems* (SIAM, Philadelphia, 1998).

²⁸P. C. Hansen and D. P. O'Leary, "The use of the L-curve in the regularisation of discrete ill-posed problems," *SIAM J. Sci. Comput. (USA)* **14**, 1487–1503 (1993).

- ²⁹A. P. Schuhmacher, "Sound source reconstruction using inverse sound field calculations," Ph.D. thesis, Department of Acoustic Technology, Technical University of Denmark, Report 77, 2000.
- ³⁰S.-C. Kang and J.-G. Ih, "On the accuracy of nearfield pressure predicted by the acoustic boundary element method," *J. Sound Vib.* **233**, 353–358 (2000).
- ³¹S.-C. Kang and J.-G. Ih, "Use of nonsingular boundary integral formulation for reducing errors due to near-field measurements in the boundary element method based near-field acoustic holography," *J. Acoust. Soc. Am.* **109**, 1320–1328 (2001).
- ³²Z. Zhang, N. Vlahopoulos, T. Allen, and K. Y. Zhang, "A source reconstruction process based on an indirect variational boundary element formulation," *Eng. Anal. Boundary Elem.* **25**, 93–114 (2001).
- ³³H.-S. Kwon, J. S. Bolton, and D. L. Hallman, "Nearfield acoustical holography applied to sound radiation from tires," *Proceedings Noise-Con '98*, Ypsilanti, 1998.
- ³⁴J. Hald, "STSF—a unique technique for scan-based near-field acoustic holography without restrictions on coherence," Brüel & Kjær Technical Review No. 1, 1989.
- ³⁵J. Hald, "STSF—a unique technique for scan-based near-field acoustic holography without restrictions on coherence," Brüel & Kjær Technical Review No. 2, 1989.

Inverse estimation of the acoustic impedance of a porous woven hose from measured transmission coefficients

Chul-Min Park and Jeong-Guon Ih^{a)}

Center for Noise and Vibration Control, Department of Mechanical Engineering, Korea Advanced Institute of Science and Technology, Science Town, Taejeon 305-701, Korea

Yoshio Nakayama

Nihon Sekiso Ind. Co. Ltd., 1-3 Hinakita-cho, Okazaki, Aichi, Japan

Hideo Takao

Maruyasu Ind. Co. Ltd., 1 Kitayama, Hashime-cho, Okazaki, Aichi, Japan

(Received 11 March 2002; revised 7 September 2002; accepted 4 October 2002)

A porous tube, comprised of a resin-coated woven fabric has recently been used as an effective component for use in intake systems of internal combustion engines to reduce the intake noise. For the prediction of the acoustic performance of an engine intake system with a porous woven hose, the acoustic wall impedance of the hose must be known. However, the accurate measurement of the wall impedance of a porous woven hose is not easy because of its peculiar acoustical and structural characteristics. A new measurement technique is proposed herein, that is valid over the low to mid frequency ranges. The acoustics impedance is inversely estimated from an overdetermined set of measured pressure transmission coefficients for specimens of different lengths and the reflection coefficient of end termination. The method involves only one measurement setup, and, as a result, it is very simple. A variation of the proposed method, an inverse estimation method using one of the four-pole parameters is also proposed. An error sensitivity analysis was performed to investigate the effect of measurement error on the accuracy of the final result. The measured TL for samples with arbitrary lengths and arbitrary porous frequency are in reasonably good agreement with values predicted from curve-fitted impedance data. © 2003 Acoustical Society of America. [DOI: 10.1121/1.1526664]

PACS numbers: 43.20.Mv, 43.50.Gf, 43.58.Bh [LLT]

I. INTRODUCTION

It is known that the pipe resonance of an intake system is the major cause of intake noise in cars. Intake noise is one of important noise control targets for achieving interior acoustic comfort in cars, in particular, at low and major engine operating speeds. In order to suppress the resonances of the total and/or parts of the intake system, several Helmholtz resonators and/or quarter-wavelength tube resonators are frequently employed in the majority of modern engines. However, the problem in using resonators added on to the intake system is that it becomes quite difficult to find available vacant space in the engine compartment because of the very compact layout used for the engine, transmission, engine accessories, structural members, and the enclosure. The vacant spaces needed are usually larger than the other accessories in the engine compartment and it is desirable that they do not interact with other pipes, mechanisms, and harnesses. For example, some resonator volumes are in excess of 4 liters. Furthermore, often, such a tuning is required within a very limited, short period during the final development phase of a new car: one of the top priority issues of automotive companies is the shortening of development time for a new car. Recently, wire-reinforced porous tubes of woven fabric

coated with acrylic resin have been introduced into the intake systems of many internal combustion engines for purposes of reducing noise radiated from the snorkel opening. Resonators in an intake system, for suppressing acoustic resonances and adverse effects due to installing a resonator for a frequency, can be replaced by one section of a porous woven hose.¹ An added advantage of a porous woven hose is its flexibility, which permits the system layout and isolation of transmitted vibration to be readily achieved. It has also been reported that, in addition to the foregoing advantageous characteristics, many car manufacturers employ porous woven hoses in order to improve the sound quality as well.² Because of this, the porous woven hose is now considered to be a very promising and efficient silencing component in spite of its relatively high cost.

Although the porous woven hose has now been adopted in a number of engine intake systems, its acoustic performance has not previously been predicted well because of the difficulty in measuring the acoustic impedance. An accurate measurement of wall impedance has not been easy because of its peculiar acoustical and structural characteristics: flow resistance, thickness variation due to small corrugations, local inhomogeneities in material composition, local stiffness variation, interlacing roughness, coating uniformity, diameter, and length. Figure 1 shows a conceptual diagram of a typical structure of a commercially available porous woven hose.² The goal of this study was to develop an accurate

^{a)} Author to whom correspondence should be addressed. NOVIC, Dept. of Mechanical Engineering, KAIST, Science Town, Taejeon 305-701, Korea. Electronic mail: ihih@sorak.kaist.ac.kr

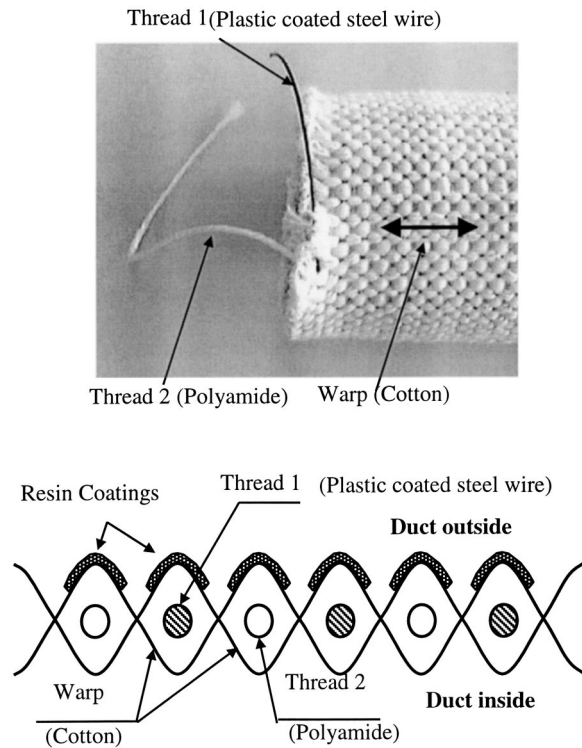


FIG. 1. Typical structure of a commercially available porous woven hose (Ref. 2).

technique for measuring the acoustic impedance of a porous woven hose, which can take into account its peculiar physical characteristics. When the impedance measurement is to be carried out using an impedance tube, the porous woven hose must be cut into the form of a circular flat specimen.^{3,4} In this case, structural characteristics of the wall will be altered because the base structure formed by 1 mm steel cords coated with plastics are cut and flattened: cord tension will be relieved and porosity will be changed. Various tests had been attempted on flat wall samples of porous woven hose, but no reproducible data have yet been reported. This indicates that acoustical impedance is dependent on permeability effects as well as structural effects. In order to take into account of all possible effects, the wall impedance should be measured under normal service conditions, viz., for a cylindrical specimen connected between two rigid ducts.

The two-step estimation method¹ is proposed for the measurement of acoustic impedance: First, the reactance is measured by means of a concentric measurement layout and second, the resistance is estimated from the measured transmission loss and reactance, which was measured in the first step. In the first step, a rigid concentric chamber and two microphones are required. In the second step, instrumentation to support on the two-microphone method⁵ or multiple microphone method⁶ is needed and an exhaustive numerical calculation is required following the measurements to obtain the value of the resistance. Thus, the above method is quite cumbersome because it involves two-stage measurements with the two different types of instrumentation and measurement layouts and the resistance estimation process. Furthermore, it cannot take the effect of mean flow into account. In this paper, a new measurement technique is presented, which

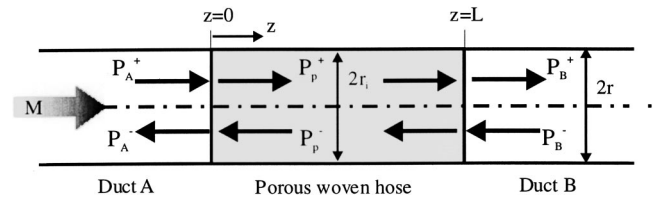


FIG. 2. Sound field in the porous duct system. Pressures designated with the superscript “+” denotes the positive-going (i.e., downstream) waves and those with “-” denotes the negative-going (i.e., upstream) waves. M denotes the Mach number.

utilizes only one measurement setup and, thus, it is relatively simple compared with the two-step estimation method.¹ In this new method, the acoustics impedance is inversely calculated from the measured pressure transmission coefficient of several specimens of equal porosity and the reflection coefficient of the end termination. Therefore, this method is referred to as the “inverse estimation method” in this paper. The other advantage of this measurement is that the apparatus can also be used for the direct measurement of transmission loss. The pressure transmission coefficient is expressed by the four-pole parameters of transfer matrix and the acoustic impedance is then obtained iteratively from the fitting model for the transmission coefficient. An error sensitivity analysis is performed to investigate the effect of measurement error on the accuracy of the final result. After the present method was experimentally applied to actual hoses, the empirical curve-fitted model of the measured impedance was used for calculating the acoustic impedance of a hose with an arbitrary porous frequency. A comparison between the predicted and measured TL is shown in order to demonstrate the accuracy and effectiveness of the proposed technique.

II. BACKGROUND THEORY OF INVERSE MEASUREMENT

A. Transfer matrix representation

Consider a sound field within a porous woven hose with a mean flow as depicted in Fig. 2. An acoustic source exists at one end of the duct and a linear passive termination is located at the opposite end. The walls of the duct A and B are assumed to be rigid and no active source is present inside the whole duct system except the source loudspeaker. The sound pressure, P , and particle velocity, u , of the plane wave propagating axially inside the ducts A and B , and those of the additional cross modes propagating inside the porous woven hose can be written as^{7,8}

$$P_A(z) = P_A^+ \exp(-jk^+z) + P_A^- \exp(jk^-z), \quad (1)$$

$$u_A(z) = \frac{1}{Z_c} \{P_A^+ \exp(-jk^+z) - P_A^- \exp(jk^-z)\}, \quad (2)$$

$$P_p(z) = P_p^+ \exp(-jk_z^+z) + P_p^- \exp(jk_z^-z), \quad (3)$$

$$u_p(z) = \frac{1}{\rho_0 c_0} \left\{ \frac{k_z^+}{(k_0 - M k_z^+)} P_p^+ \exp(-j k_z^+ z) - \frac{k_z^-}{(k_0 + M k_z^-)} P_p^- \exp(j k_z^- z) \right\}, \quad (4)$$

$$P_B(z) = P_B^+ \exp\{-j k^+(z-L)\} + P_B^- \exp\{j k^-(z-L)\}, \quad (5)$$

$$u_B(z) = \frac{1}{Z_c} [P_B^+ \exp\{-j k^+(z-L)\} - P_B^- \exp\{j k^-(z-L)\}], \quad (6)$$

where

$$\frac{Z_n}{\rho_0 c_0} = j \frac{2}{k_0 r_i} \frac{(k_0 \mp k_z^\pm M)^2}{(k_0 \mp k_z^\pm M)^2 - (k_z^\pm)^2}, \quad (7)$$

$$(k_0 \mp k_z^\pm M)^2 = (k_z^\pm)^2 + (k_r^\pm)^2, \quad (8)$$

$$k^\pm = \frac{k_0 + \delta - j\delta}{1 \pm M}, \quad (9)$$

$$Z_c = \rho_0 c_0 \left(1 - \frac{\delta}{k_0} + j \frac{\delta}{k_0} \right), \quad (10)$$

$$\delta = \delta_v + \delta_t = \frac{\sqrt{2}}{2r_i} \frac{\omega}{c_0} \left[\sqrt{\frac{\mu}{\rho_0 \omega}} + (\gamma - 1) \sqrt{\frac{\kappa}{\rho_0 C_p \omega}} \right] + \frac{\Psi M}{r_i} \left(1 + \frac{\text{Re}}{2\Psi} \frac{\partial \Psi}{\partial \text{Re}} \right). \quad (11)$$

Here, the subscripts A , B , p refer to duct A , duct B , the porous tube, respectively, the superscripts “+” and “-” denote the incident and reflected pressures, respectively, k_z^\pm and k_r^\pm denotes the forward and backward complex propagation constants in the axial and radial direction, respectively. $P(z)$ denotes the acoustic pressure at position z , $u(z)$ the

particle velocity at position z , k_0 the free-space wave number ($k_0 = \omega/c_0$), c_0 the speed of sound, ρ_0 the density of the fluid medium, ω the angular frequency, r_i the inner radius of porous woven hose, Z_n the normal impedance at $r = r_i$, i.e., at the inner wall of porous woven hose, M the mean flow Mach number, k^+ and k^- denote the forward and backward complex propagation constants in ducts A and B , respectively. μ is the shear viscosity coefficient, γ the specific heat ratio, κ the heat conduction coefficient, C_p the specific heat at constant pressure, Re the Reynolds number of the flow, Ψ the coefficient of friction for turbulent flow, and δ is attenuation constant. The origin of the attenuation constant is from the visco-thermal and turbulent effects. Continuity of acoustic pressure and volume velocity for the fundamental mode at the interfaces between the duct A/B and the porous woven hose gives matching conditions as follows:

$$\begin{bmatrix} P_A \\ u_A S \end{bmatrix}_{z=0} = \begin{bmatrix} P_p \\ u_p S_p \end{bmatrix}_{z=0}, \quad (12)$$

$$\begin{bmatrix} P_p \\ u_p S_p \end{bmatrix}_{z=L} = \begin{bmatrix} P_B \\ u_B S \end{bmatrix}_{z=L}. \quad (13)$$

Here, S ($= \pi r_A^2 = \pi r_B^2$, in the measurement setup) indicates the cross sectional area of the inlet (with radius r_A) or outlet (with radius r_B) duct, and S_p ($= \pi r_i^2$) means the sectional area of the porous woven hose. Additionally, by adopting the acoustic pressure and volume velocity as two state variables, the relation of acoustics variables between the inlet and outlet of the porous woven hose can be represented as follows:

$$\begin{bmatrix} P_p \\ u_p S_p \end{bmatrix}_{z=0} = \begin{bmatrix} T_{11} & T_{12} \\ T_{21} & T_{22} \end{bmatrix} \begin{bmatrix} P_p \\ u_p S_p \end{bmatrix}_{z=L}, \quad (14)$$

where the four-pole parameters⁷ in Eq. (14) can be expressed as

$$T_{11} = \frac{k_z^- (k_0 - M k_z^+) \exp(j k_z^+ L) + k_z^+ (k_0 + M k_z^-) \exp(-j k_z^- L)}{k_0 (k_z^+ + k_z^-)}, \quad (15a)$$

$$T_{12} = \frac{\rho_0 c_0}{S_p} \frac{(k_0 + M k_z^-) (k_0 - M k_z^+)}{(k_z^+ + k_z^-)} \frac{\exp(+j k_z^+ L) - \exp(-j k_z^- L)}{k_0}, \quad (15b)$$

$$T_{21} = \frac{S_p k_z^+ k_z^-}{\rho_0 c_0} \frac{\exp(+j k_z^+ L) - \exp(-j k_z^- L)}{k_0 (k_z^+ + k_z^-)}, \quad (15c)$$

$$T_{22} = \frac{k_z^+ (k_0 + M k_z^-) \exp(+j k_z^+ L) + k_z^- (k_0 - M k_z^+) \exp(-j k_z^- L)}{k_0 (k_z^+ + k_z^-)}. \quad (15d)$$

Consequently, the relation between the upstream and downstream parameters can be obtained from Eqs. (12)–(15) as follows:

$$\begin{bmatrix} P_A \\ u_A S \end{bmatrix}_{z=0} = \begin{bmatrix} T_{11} & T_{12} \\ T_{21} & T_{22} \end{bmatrix} \begin{bmatrix} P_B \\ u_B S \end{bmatrix}_{z=L}, \quad (16a)$$

$$\begin{bmatrix} P_A^+ + P_A^- \\ \frac{S}{Z_c}(P_A^+ - P_A^-) \end{bmatrix} = \begin{bmatrix} T_{11} & T_{12} \\ T_{21} & T_{22} \end{bmatrix} \begin{bmatrix} P_B^+ + P_B^- \\ \frac{S}{Z_c}(P_B^+ - P_B^-) \end{bmatrix}. \quad (16b)$$

B. Relation between four-pole parameters and pressure transmission coefficient

The pressure transmission coefficient τ is defined as the ratio between the incident and transmitted acoustic pressure.⁷ For a porous woven hose section with a mean flow, the pressure transmission coefficient τ can be derived from Eq. (16b) in terms of the foregoing four-pole parameters as

$$\frac{1}{\tau} \equiv \frac{P_A^+}{P_B^+} = F\left(k_z^\pm, L, k_0, M, \frac{P_B^-}{P_B^+}\right), \quad (17)$$

where

$$\begin{aligned} F\left(k_z^\pm, L, k_0, M, \frac{P_B^-}{P_B^+}\right) &= \frac{1}{2} \left(T_{11} + T_{12} \frac{S}{Z_c} + T_{21} \frac{Z_c}{S} + T_{22} \right) \\ &+ \frac{1}{2} \frac{P_B^-}{P_B^+} \left(T_{11} - T_{12} \frac{S}{Z_c} + T_{21} \frac{Z_c}{S} - T_{22} \right). \end{aligned} \quad (18)$$

If the downstream termination is anechoic, i.e., $P_B^-/P_B^+ = 0$, the TL of a porous woven hose specimen can be obtained from Eqs. (17) and (18) as

$$TL = 20 \log_{10} \left\{ \left| F\left(k_z^\pm, L, k_0, M, \frac{P_B^-}{P_B^+} = 0\right) \right| \right\}, \quad (19a)$$

where

$$F\left(k_z^\pm, L, k_0, M, \frac{P_B^-}{P_B^+} = 0\right) = \frac{1}{2} \left(T_{11} + T_{12} \frac{S}{Z_c} + T_{21} \frac{Z_c}{S} + T_{22} \right). \quad (19b)$$

The acoustic impedance of porous woven hose is defined as the ratio between the acoustic pressure difference across the wall and the average normal particle velocity of the outer and inner wall.⁹ The relation among normal impedance Z_n , impedance of porous woven hose Z_p , and radiation impedance Z_{rad} , can be written as^{1,9}

$$\begin{aligned} \frac{Z_n}{\rho_0 c_0} &= \frac{p_{int}}{\rho_0 c_0 u_{int}} \Big|_{r=r_i} \\ &= \frac{r_i}{r_o} \frac{p_{ext}}{\rho_0 c_0 u_{ext}} \Big|_{r=r_o} + \frac{r_i + r_o}{2r_o} \frac{Z_p}{\rho_0 c_0} \\ &= \frac{r_i}{r_o} \frac{Z_{rad}}{\rho_0 c_0} + \frac{r_i + r_o}{2r_o} \frac{Z_p}{\rho_0 c_0}, \end{aligned} \quad (20)$$

where the subscript “int” refers to the interior properties of the porous woven hose, the subscript “ext” its exterior properties, and r_o its outer radius. Ignoring the radiation impedance, Eq. (20) is reduced to¹

$$\beta \equiv \frac{Z_p}{\rho_0 c_0} \approx \frac{2r_o}{r_i + r_o} \frac{Z_n}{\rho_0 c_0}. \quad (21)$$

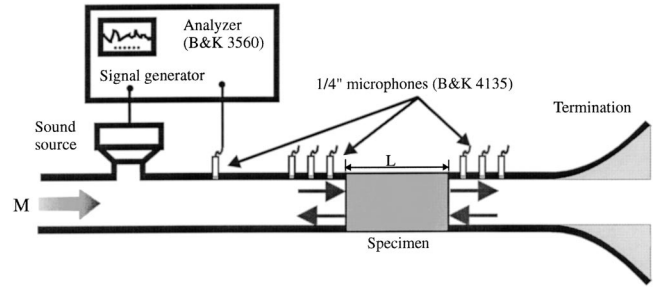


FIG. 3. Apparatus for the measurement of in-duct acoustic characteristics of a porous woven hose.

It should be noted that the radiation impedance can be ignored if the total length of the porous woven hose is less than about 0.65 m.^{1,9} Fortunately, in most practical service conditions using porous woven hose, short tube lengths of less than 0.65 m are used.

Note that the measured transfer function relating the sound pressures at two sides, A and B , can be written as

$$H_t = \frac{P_B^+ + P_B^-}{P_A^+ + P_A^-} = \frac{P_B^+}{P_A^+} \frac{1 + R_B}{1 + R_A}, \quad (22)$$

where the pressure reflection coefficients at the upstream and downstream side, respectively, are defined as

$$R_A = \frac{P_A^-}{P_A^+}, \quad (23a)$$

$$R_B = \frac{P_B^-}{P_B^+}. \quad (23b)$$

Consequently, one can easily express the pressure transmission coefficient τ by the measurable quantities such as R_A , R_B , H_t ,

$$\frac{1}{\tau} = \frac{P_A^+}{P_B^+} = \frac{1}{H_t} \frac{1 + R_B}{1 + R_A}. \quad (24)$$

C. Inverse estimation of acoustic impedance

Using the same experimental setup for the measurement of transmission loss, τ and R_B can be measured. Figure 3 shows the layout used in the measurement setup, performed for an overdetermined set of N porous woven hose samples, which differ in lengths but have the same porosity or weaving/coating structure. In this study, the multiple microphone method⁶ was adopted for the direct measurement of in-duct acoustic properties such as TL , τ , R_B . Substituting these measured in-duct acoustic properties into Eqs. (7), (8), (17), and (21), the acoustic impedance can be obtained by using the following least-square technique.¹⁰ It should be recalled that k_z is a function of β , i.e., τ is a function of the impedance of porous woven hose. If each of the N data can be expressed by the following data as

$$\left(\frac{1}{\tau_i}, k_0, M, L_i, R_B \right) \quad (i = 1, 2, \dots, N), \quad (25)$$

then the problem is to compute the estimated values of the parameters, required to minimize the following quantity:

$$\Phi_1 = \sum_{i=1}^N \left| \left(\frac{1}{\tau_i} - F_i(\beta; k_0, M, L_i, R_B|_i) \right) \right|^2. \quad (26)$$

Here, parameter β refers to the “population value” as defined in Eq. (26) and the value of $1/\tau_i = F_i(\beta; k_0, M, L_i, R_B|_i)$ of the i th specimen refers to the “expected value.”

By using the Taylor series expansion near $\beta = \beta_0$ and truncating to the linear terms, one can obtain

$$\begin{bmatrix} \frac{1}{\tau_1} \\ \vdots \\ \frac{1}{\tau_N} \end{bmatrix} = \begin{bmatrix} F_1(\beta_0 + \delta) \\ \vdots \\ F_N(\beta_0 + \delta) \end{bmatrix} \cong \begin{bmatrix} F_1(\beta_0) \\ \vdots \\ F_N(\beta_0) \end{bmatrix} + \delta \begin{bmatrix} \frac{\partial F_1}{\partial \beta} \\ \vdots \\ \frac{\partial F_N}{\partial \beta} \end{bmatrix}_{\beta=\beta_0}, \quad (27)$$

where $\delta = \beta - \beta_0$. Because the perturbation δ in Eq. (27) is a linear function in β , it can be determined from the standard least-square sense, viz., $\partial \Phi_1 / \partial \delta = 0$. This implies that δ can be obtained by solving

$$A \delta = Y, \quad (28)$$

where

$$A = \begin{bmatrix} \frac{\partial F_1}{\partial \beta} \\ \vdots \\ \frac{\partial F_N}{\partial \beta} \end{bmatrix}_{\beta=\beta_0}, \quad (29)$$

$$Y = \begin{bmatrix} \frac{1}{\tau_1} - F_1(\beta_0) \\ \vdots \\ \frac{1}{\tau_N} - F_N(\beta_0) \end{bmatrix}. \quad (30)$$

The least-square solution of Eq. (28) can be obtained by using the generalized inverse as

$$\delta = (A^H A)^{-1} A^H Y \quad (31a)$$

or

$$\delta = \frac{\sum_{i=1}^N \left(\frac{\partial F_i}{\partial \beta} \right)_{\beta=\beta_0}^* \left(\frac{1}{\tau_i} - F_i(\beta_0) \right)}{\sum_{i=1}^N \left(\frac{\partial F_i}{\partial \beta} \right)_{\beta=\beta_0}^* \left(\frac{\partial F_i}{\partial \beta} \right)_{\beta=\beta_0}}. \quad (31b)$$

Here, A^H denotes the Hermitian matrix of A and the superscript $*$ denotes the complex conjugate. The derivatives in Eq. (31b) are given in Appendix A.

The actual computation is carried out in the following manner: First, the initial estimate is assumed to be β_{01} . δ can then be obtained from Eq. (31) and the new estimate β_{02} can be obtained from the relation, $\beta_{02} = \beta_{01} + \delta$. Next, by using the new estimate β_{02} , the first step is repeated. This calculation loop is repeated until the error δ is smaller than the

preset criterion. From this simple numerical iteration, the population value $\beta = Z_p / \rho_0 c_0$, indicating the normalized acoustic impedance of porous woven hose, can be obtained.

D. Alternate method: inverse estimation of impedance from T_{11}

In the preceding section, the acoustic impedance was obtained by using the measured transmission coefficients of an over-determined set of porous woven hoses with the same weaving/coating texture but which are of different lengths. Alternatively, one can utilize the parameter T_{11} , which is one of the four-pole parameters in the transfer matrix of the porous woven hose, in a manner similar to that used in the preceding section. In this case, the data-fitting model can be set as

$$G(\beta; k_0, L) = \cos(k_z L), \quad (32)$$

in which each of the overdetermined N data can be expressed by

$$(T_{11}|_i, k_0, L_i) \quad (i = 1, 2, \dots, N). \quad (33)$$

Now, the problem is to estimate the involved parameters by minimizing the following equation:

$$\Phi_2 = \sum_{i=1}^N |(T_{11})_i - G_i(\beta; k_0, L_i)|^2. \quad (34)$$

The acoustic impedance can be estimated by solving Eq. (32) in the same manner as utilized in the preceding section.

Equation (32) implies that the precise measurement of T_{11} is crucial in the successful application of this technique. However, it may not be of great importance, because the measurement of four-pole parameters is one of the usual processes used in characterizing the acoustic performance of silencer elements. Various experimental techniques including the experimental transfer matrix method,⁷ the two-source method,¹¹ and the two-load method¹² have been widely employed in the measurement of the acoustical properties of silencer system components. It has recently been reported that the transfer matrix parameters can be used to evaluate the acoustical characteristics of typical homogeneous and isotropic porous materials.¹³ The acoustic reciprocity and the symmetrical nature of the transfer matrix are key features in the implementation of this technique in the absence of medium flow. Such a concept of using the basic nature of the transfer matrix of sound absorbing materials can be directly applicable to the case of a porous woven hose in the absence of mean flow. If symmetry conditions and reciprocity hold, it follows that

$$T_{11} = T_{22}, \quad (35)$$

$$T_{11} T_{22} - T_{12} T_{21} = 1. \quad (36)$$

By combining Eqs. (15), (35), and (36), T_{11} can be derived directly in terms of the pressure transmission coefficient τ and the reflection coefficients R_A and R_B as

$$T_{11} = \frac{1}{2} \frac{1 - R_A^2 + \tau^2(1 - R_B^2)}{\tau(1 - R_A R_B)}. \quad (37)$$

III. RESULTS AND DISCUSSION

A. Experimental results

It should be noted that the overall physical characteristics of a porous woven hose have been rated by a single-figure parameter, which is mainly affected by the length, radius, materials, weaving quality, and coating conditions. This parameter is referred to as the “porous frequency” by manufacturers as well as the NVH (noise, vibration, and harshness) engineers in major automotive companies around the world.¹⁴ The porous frequency representing the overall openness or porosity of the porous woven hose is given by

$$f_p = \frac{\gamma P_0}{2\pi} \frac{1}{VZ} = \frac{\gamma P_0}{2\pi} \frac{1}{\pi r_i^2 L} \frac{1}{\Delta P/Q}. \quad (38)$$

Here, P_0 denotes the ambient pressure, V the internal volume of hose, L the length of hose, ΔP the effective pressure drop at the hose inlet relative to the ambient pressure, Q the volume flow rate through the hose wall, and $Z = \Delta P/Q$. This parameter is typically determined at a given specific volume flow rate $Q = 0.026 \text{ m}^3/\text{s}$, which corresponds to 25–40% of the maximum flow rate of the actual intake systems of 1.5–2.5 liter engines. Because the dimension of porous frequency is the inverse of time, related field engineers have referred to this as the porous frequency in Hz. However, it should be noted that the porous frequency has no direct relation with the ordinary frequency. For this reason, the unit Hz is not used for the porous frequency, f_p , in this paper, in order to avoid any confusion that might occur. The interpretation of the physical meaning of porous frequency and its precise method of determination are described in Ref. 14.

Because the range of porous frequency typically used in an automotive intake system is from about 100 to 600, the experiments were performed with samples within this practical range. In the intake system of a typical engine, the mean flow Mach number is usually below 0.1 M .¹⁵ Therefore, the experiments were performed using $M = 0, 0.034$, and 0.081 in an anechoic chamber. Figure 3 shows the measurement setup. A signal analyzer (B&K3560) was used to feed the stationary random signal for the acoustic driver mounted at one end of the duct and to calculate the spectra from the measured signals. The acoustic transfer functions were measured with flush mounted 1/4-inch microphones (B&K 4135). The Reynolds number of the flow was of the order of 10^4 at the measurement conditions used and the correlation technique was adopted to suppress the flow-generated noise from the turbulent flow.⁶ The reference sound pressure, measured at the microphone position located 1.5 m upstream to the actual measurement sensors, was used as the reference signal, for use in the correlation technique.

Figure 4 shows the measured impedance using the above described method with mean flow conditions of $M = 0, 0.034$, and 0.081. These values were measured in the frequency range of 180–1500 Hz because the source power was not sufficient below 180 Hz. In this measurement, two specimens with different lengths of $L = 300, 393 \text{ mm}$ were used. In the estimation process, the sound reflection from the end termination was taken into account. As can be easily expected, the variation of impedance becomes large, with in-

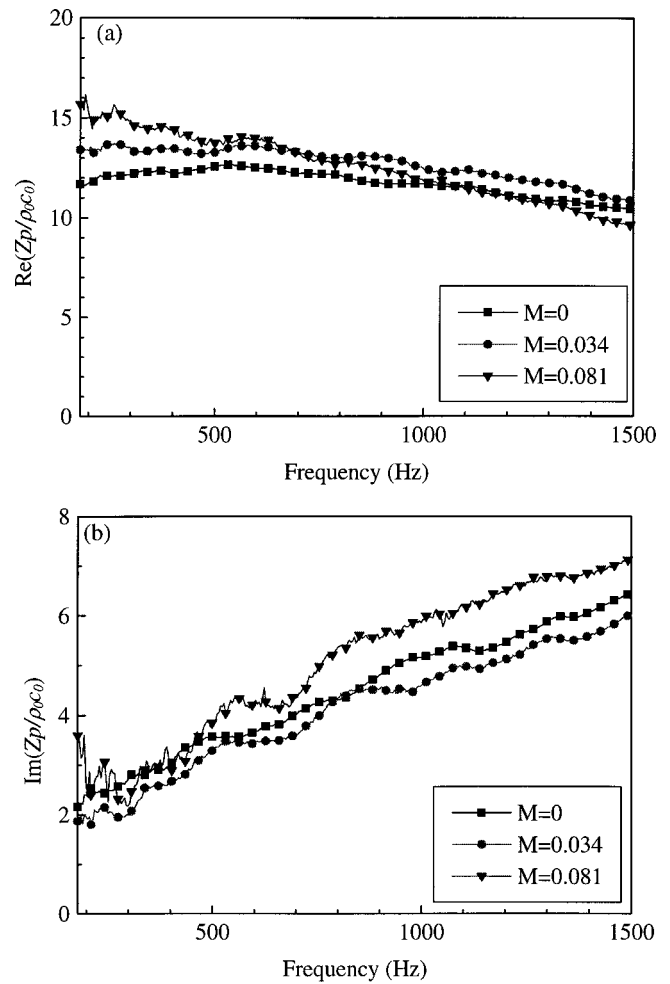


FIG. 4. An example of the measured acoustic impedance of porous ducts at varying mean flow conditions ($f_p = 300$). (a) Resistance, (b) reactance.

creasing mean flow velocity. The effect of mean flow on the resistance is significant, particularly in cases of low frequencies, a long tube, and a high flow velocity. The resistance becomes small as the frequency increases, whereas the resistance is nearly constant with a change in frequency in the absence of a mean flow. This corresponds to the fact that the TL in the presence of mean flow is lower in the low frequency range and higher in the high frequency range than the TL obtained in the absence of a mean flow.

It should be mentioned that only a single duct could be satisfactorily used in this inverse procedure because the number of unknown variables is equal to the number of equations in this case. However, because of the inevitable measurement error in almost all the measurement cases, the overdetermination technique is adopted for the purpose of reducing the random error, which is included in the measured data. Figure 5 shows the measured values and one can clearly find that the normalized root-mean-square error, ε_{RMS} , becomes small as the number of specimen ducts, which are different in length, increases. In this figure, the experimental impedance value by using the seven ducts was assumed as the reference value for the calculation of ε_{RMS} .

Figure 6 shows a comparison of the measured and predicted impedances under arbitrary conditions. The prediction was made using the curve-fitting model described in Appen-

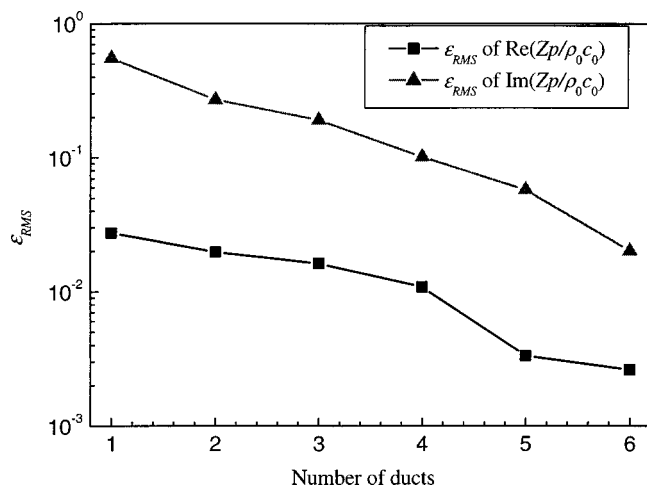


FIG. 5. Change of the normalized root-mean-square error (ϵ_{RMS}) by varying the employed number of ducts that are different in length ($f_p=400$; $M=0.03$; $L=300, 330, 360, 390, 420, 450$, and 480 mm).

dix B, which makes use of measured impedance data for the conditions of $M=0, 0.034$, and 0.081 , and $f_p=200, 400$, and 600 . A comparison between the predicted and measured TL is shown in Fig. 7 to demonstrate the effectiveness of the proposed technique. As can be seen in Fig. 7, the predicted

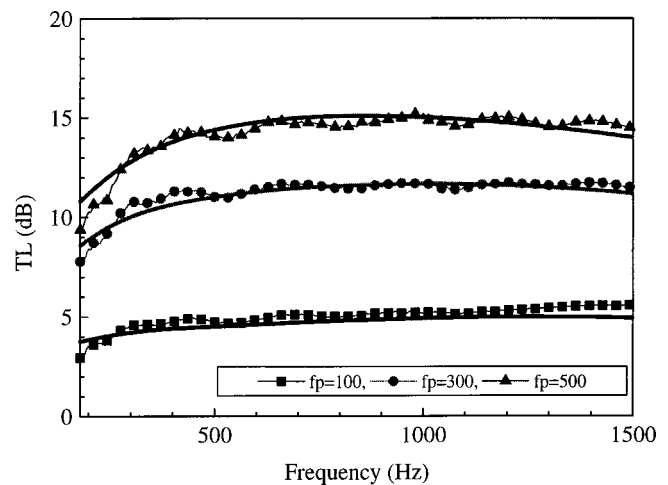


FIG. 7. A comparison of measured and predicted TL calculated from impedance by the use of a curve fitting model. Symbols, measured TL ; thick solid lines, predicted TL ($M=0.058$, $2r_i=55$ mm, $L=480$ mm).

TL agrees reasonably well with the measured TL , for porous woven hoses at arbitrarily given conditions of length ($L=480$ mm), porous frequencies ($f_p=100, 300, 500$), and Mach number ($M=0.058$). In summary, the actual computation is carried out in the following manner: First, the im-

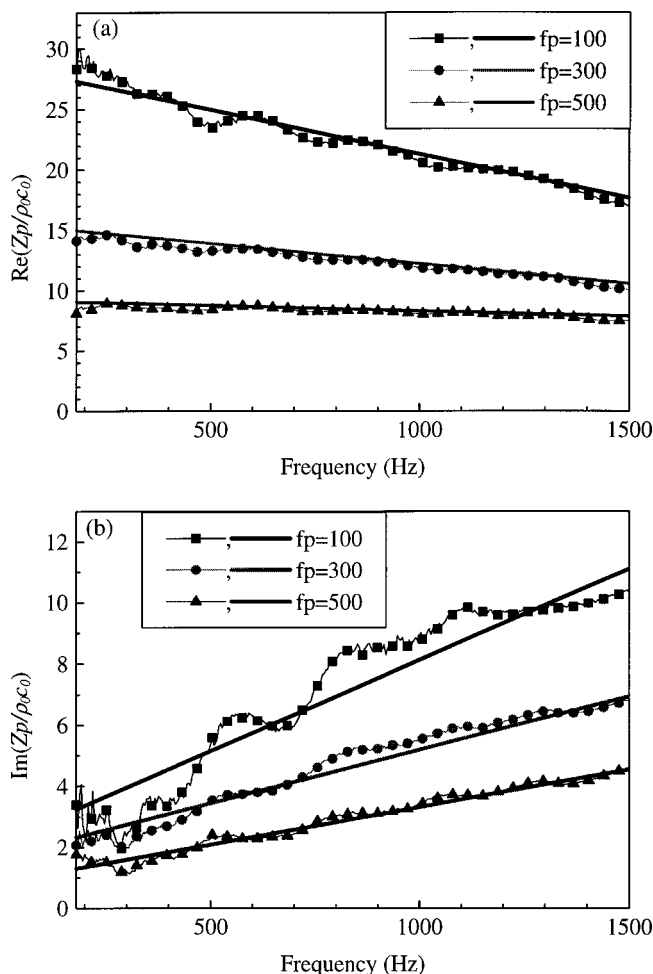


FIG. 6. Comparison of the measured and predicted impedance by the use of a curve fitting model. Symbol and thin line, measured impedance; thick line, predicted impedance for $M=0.058$. (a) Resistance, (b) reactance.

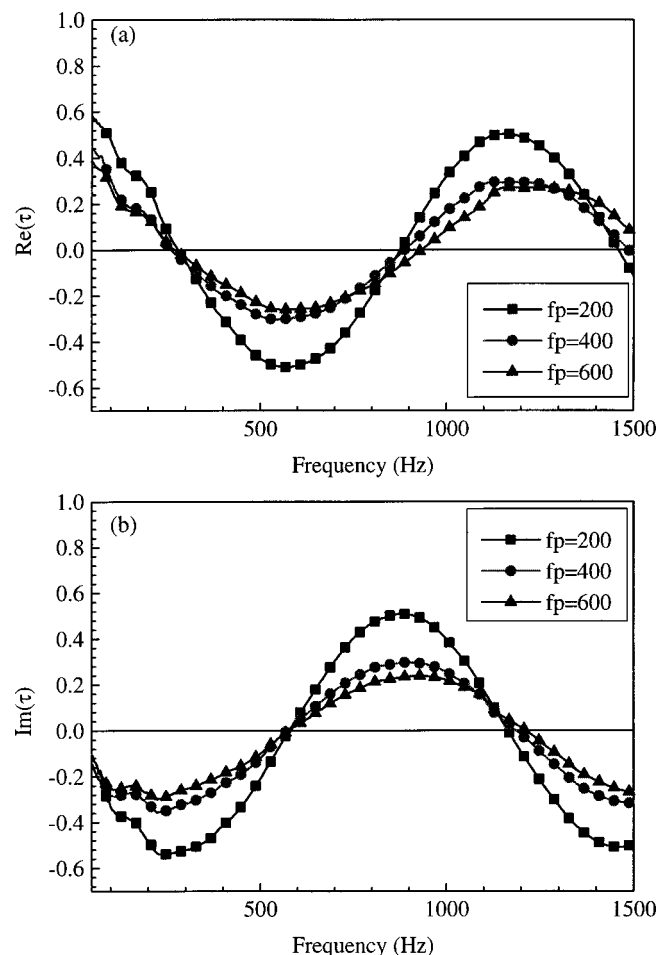


FIG. 8. Measured pressure transmission coefficient (τ) of porous ducts at varying porous frequencies ($M=0$, $2r_i=55$ mm, $L=300$ mm). (a) Real part of τ , (b) imaginary part of τ .

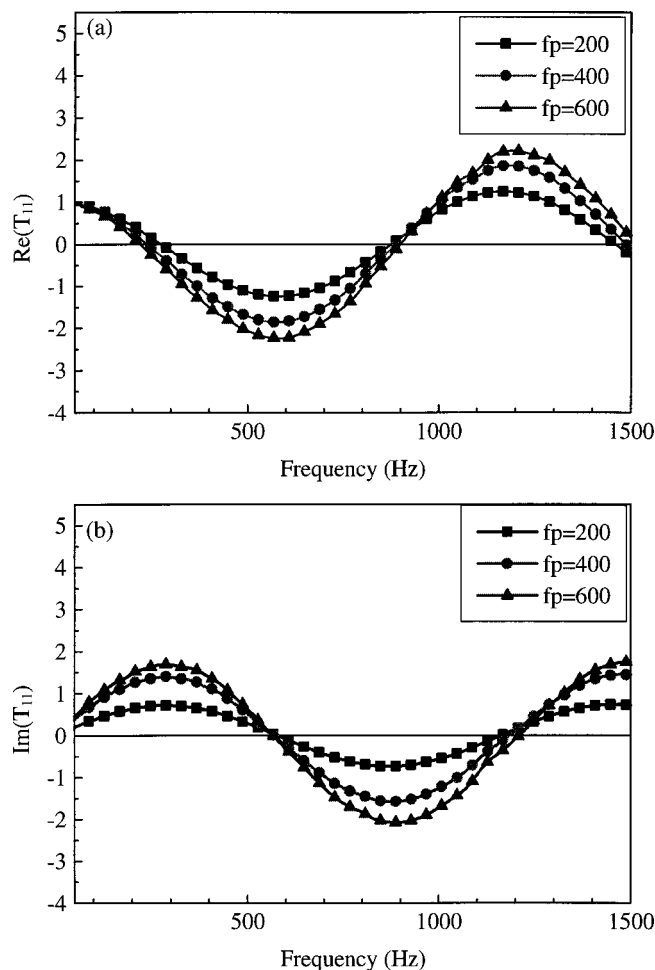


FIG. 9. Measured T_{11} of porous ducts at varying porous frequencies ($M=0$, $2r_i=55$ mm, $L=300$ mm). (a) Real part of T_{11} , (b) imaginary part of T_{11} .

pedances of several duct conditions are measured by using the proposed measurement technique. Second, the curve-fitting model is obtained from the impedances measured in the first step. Third, the impedance of a porous woven hose with an arbitrary condition is predicted by using the curve-fitting model obtained in the second step. Last, the TL of the porous woven hose with the arbitrary condition is predicted from the predicted impedance obtained in the previous step.

In the absence of mean flow, the acoustic impedance can be estimated from τ or T_{11} , which can be obtained from the same raw data, i.e., the transfer functions between microphones as shown in Fig. 3. Figure 8 shows an example of measured values of τ for a 300 mm tube specimen, at varying porous frequencies, f_p . As mentioned above, the measured transmission coefficient data for several different lengths of tubes are the basis of further calculations, from which the acoustic impedance can be inversely estimated. Alternatively, one can obtain T_{11} from Eq. (37), in which the parameters τ , R_A , and R_B are measured by using the same experimental technique and setup as shown in Fig. 3. Figure 9 shows an example of the measured T_{11} for a 300 mm tube specimen, at varying porous frequencies. A comparison of the acoustic impedance estimated from the two inverse estimation methods, in which the calculations are based on the

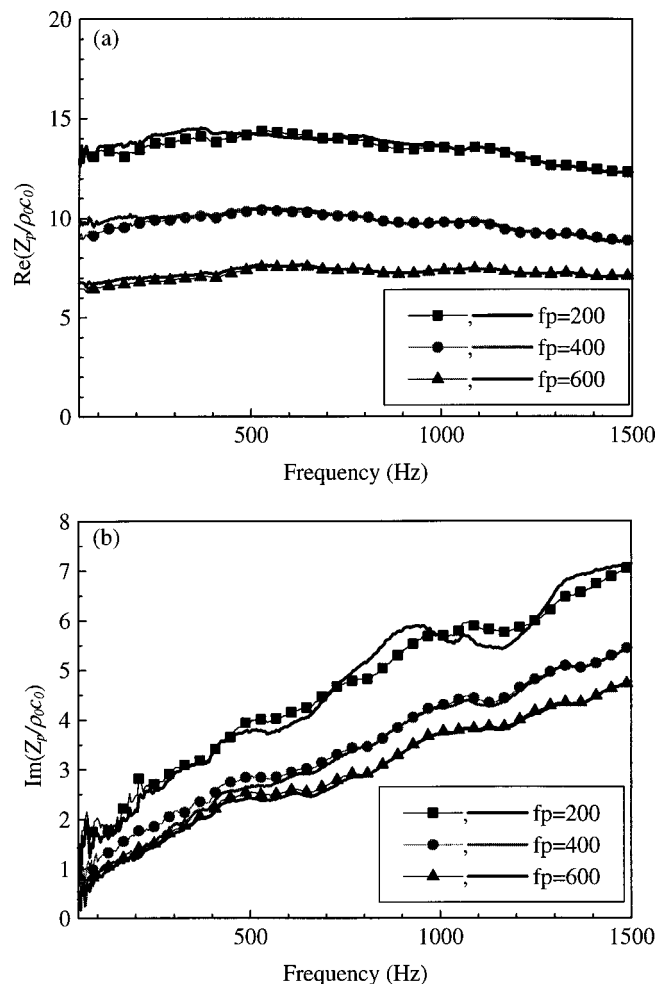


FIG. 10. A comparison of acoustic impedances of porous ducts estimated by the two inverse estimation methods ($M=0$). Symbols denote the impedance estimated from the measured τ ; thick solid lines denote the impedance estimated from the measured T_{11} . (a) Resistance, (b) reactance.

measured overdetermined data, is shown in Fig. 10. Although all measurement and calculation conditions for the two methods were maintained the same, the reactance obtained from T_{11} fluctuates to a greater extent than that for τ , which generally indicates that the inverse estimation method using τ is more robust. This tendency is especially prominent for samples with low porous frequencies.

B. Simulation of error sensitivity

Because the measurement error is always influential on the final result, the error sensitivity of the present method was investigated numerically. An impedance pattern, for which the trend is similar to the actual measured impedance,¹ is assumed as illustrated in Fig. 11. It is also assumed that the termination is anechoic, i.e., $R_B=0$. The transmission coefficient τ of a porous woven hose section 300 mm and 393 mm in length were calculated using Eq. (17). The simulation result reveals that the estimated impedance is in good agreement with the assumed impedance. Figure 12 shows the resulting error in the estimated impedance, when a measurement error of 1% is intentionally added to a τ value for the $L=393$ mm case. It can be seen that the reactance is relatively quite sensitive to input errors at low frequencies below

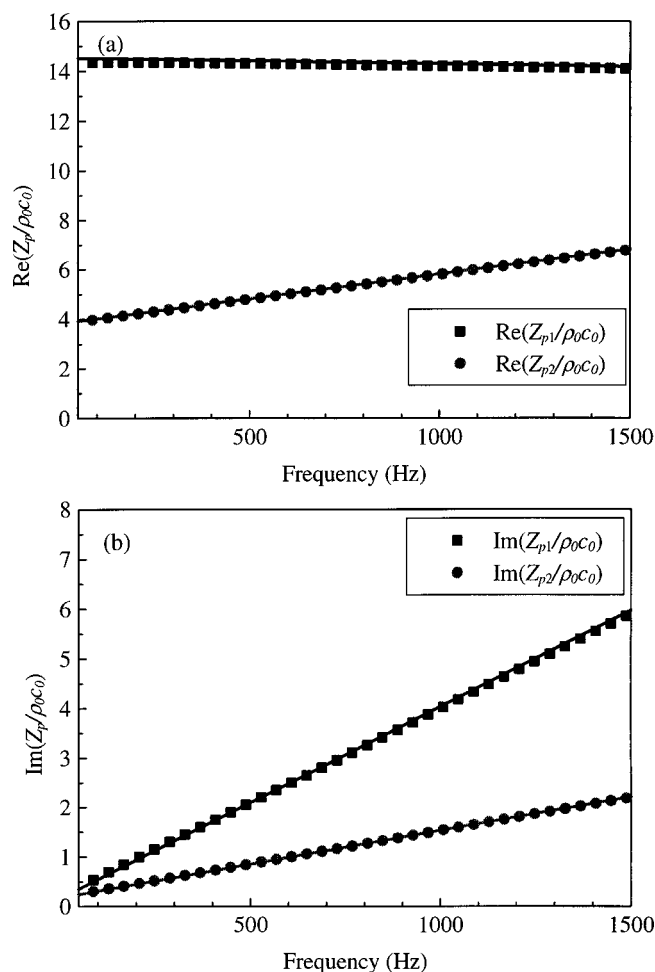


FIG. 11. Comparison of assumed and estimated impedances of porous ducts for two different porous frequencies. Symbols denote the assumed impedance and thick lines are estimated values from two pressure transmission coefficients for tubes with $L=300$ mm and $L=393$ mm. An input error of 1% is included in the transmission coefficients. (a) Resistance, (b) reactance.

about 300 Hz, in particular for the sample with a low porosity, whereas the resistance seems to be insensitive to the input error.

It should be noted that the two inverse estimation meth-

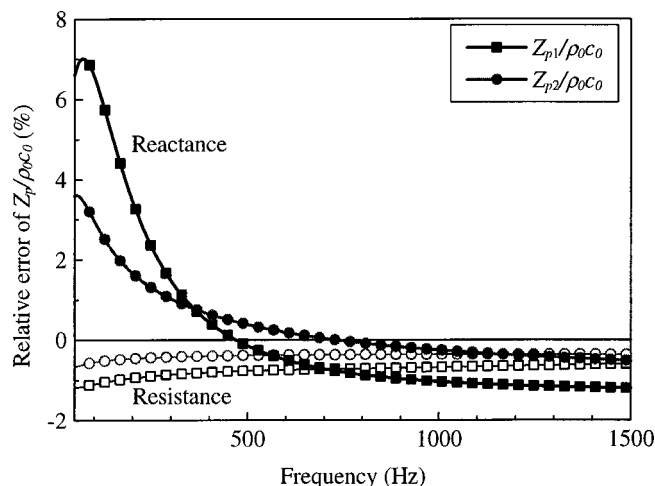


FIG. 12. Predicted impedance error due to a 1% measurement error in the pressure transmission coefficient, τ .

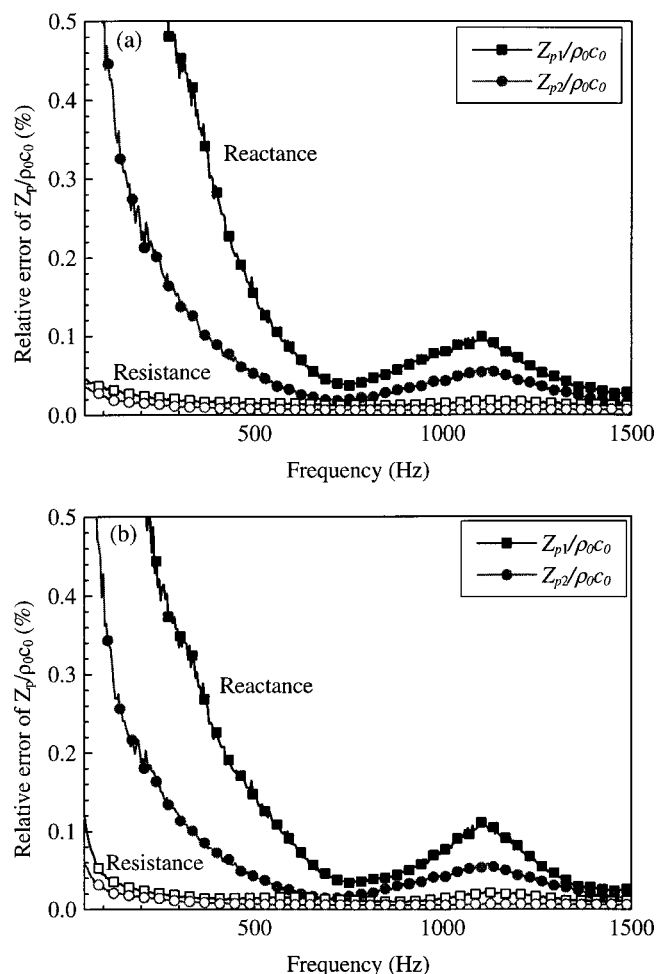


FIG. 13. A comparison of relative resultant errors due to a 1% random error included in the measured transfer function. (a) Relative error of impedance estimated from τ , (b) relative error of impedance estimated from T_{11} .

ods described herein are commonly based on the transfer function measurement method.^{5,6} Therefore, for the purpose of comparison of the error sensitivity of the two methods, a numerical simulation which takes into account the effect of measurement error in the transfer function (H_{il}) should be performed. To this end, the acoustic impedance, which has a similar trend with the actual measured impedance,¹ is shown in Fig. 11. When a random error of 1% is included in the measured transfer functions, the relative errors in the impedances, as estimated by two methods, turn out to be as in Fig. 13. The relative errors shown in Fig. 13 are obtained from the root-mean-squared values of results from 500 simulations. One can observe that both methods have very similar relative error sensitivity, but, in the low frequencies, the relative error in reactance is larger than that for resistance.

IV. CONCLUSIONS

This study focused on developing a measurement technique for the acoustic impedance of a porous woven hose: the technique overcomes the difficulties related to the peculiar physical characteristics of porous woven hoses and should permit the prediction of overall acoustic performance. To this end, the inverse estimation method was developed, which is valid within the frequency range of 50–1500 Hz

without flow and of 180–1500 Hz with flow. The inverse estimation method involved only one measurement setup, so that it was much simpler than the previous two-step estimation method.¹ In the inverse estimation method, the acoustics impedance was iteratively estimated in the least-square sense from the overdetermined set of the measured pressure transmission coefficients of the specimens and the reflection coefficient of termination. The other advantage of this measurement method is that the measurement setup could be also used for the direct measurement of transmission loss. A variation of the proposed method, an inverse estimation method using one of the four-pole parameters, T_{11} , is also proposed. An error sensitivity analysis was performed to investigate the effect of measurement error on the accuracy of the final result.

The experimental results show that the effect of mean flow on the resistance was significant, particularly at low frequencies, for a long tube, with a high flow velocity. The resistance becomes small as the frequency increases, whereas the resistance is nearly constant along the frequency in the absence of mean flow. The impedance for a sample with an arbitrary porous frequency was predicted by means of a curve-fitting method with measured impedance data at various conditions. From the curve-fitting model, if the information on mean flow, ordinary frequency, and porous frequency (or the effective flow resistivity) of the porous woven hose is specified, one can easily obtain the acoustic resistance and reactance of a given hose. It was noted that the predicted TL for porous woven hoses of an arbitrary length, arbitrary porous frequencies, and arbitrary mean flow conditions are in reasonably good agreement with the measured TL values. The present measurement technique could be very useful in the acoustic analysis and design of automotive intake systems that contain a porous woven hose section. In addition, the proposed measurement techniques can be generally applied to the acoustic duct system having a compliant wall or having a sound-absorbing wall.

ACKNOWLEDGMENTS

The authors wish to thank Nihon Sekiso Co., Japan, for financial and experimental supports. The authors also thank Dr. S.-H. Jang for useful comments. This work has been also partially funded by the BK21 Project and NRL.

APPENDIX A: DERIVATIVES IN EQ. (31b)

The derivatives in Eq. (31b) can be obtained as follows:

$$\begin{aligned} \frac{\partial F_i}{\partial \beta} = & \frac{1}{2} \left(\frac{\partial T_{11}}{\partial \beta} + \frac{S}{\rho_0 c_0} \frac{\partial T_{12}}{\partial \beta} + \frac{\rho_0 c_0}{S} \frac{\partial T_{21}}{\partial \beta} + \frac{\partial T_{22}}{\partial \beta} \right) \\ & + \frac{1}{2} R_B \left(\frac{\partial T_{11}}{\partial \beta} - \frac{S}{\rho_0 c_0} \frac{\partial T_{12}}{\partial \beta} + \frac{\rho_0 c_0}{S} \frac{\partial T_{21}}{\partial \beta} - \frac{\partial T_{22}}{\partial \beta} \right). \end{aligned} \quad (A1)$$

Here,

$$\frac{\partial T_{11}}{\partial \beta} = \frac{\partial T_{11}}{\partial k_z^+} \frac{\partial k_z^+}{\partial \beta} + \frac{\partial T_{11}}{\partial k_z^-} \frac{\partial k_z^-}{\partial \beta}, \quad (A2)$$

$$\frac{\partial T_{12}}{\partial \beta} = \frac{\partial T_{12}}{\partial k_z^+} \frac{\partial k_z^+}{\partial \beta} + \frac{\partial T_{12}}{\partial k_z^-} \frac{\partial k_z^-}{\partial \beta}, \quad (A3)$$

$$\frac{\partial T_{21}}{\partial \beta} = \frac{\partial T_{21}}{\partial k_z^+} \frac{\partial k_z^+}{\partial \beta} + \frac{\partial T_{21}}{\partial k_z^-} \frac{\partial k_z^-}{\partial \beta}, \quad (A4)$$

$$\frac{\partial T_{22}}{\partial \beta} = \frac{\partial T_{22}}{\partial k_z^+} \frac{\partial k_z^+}{\partial \beta} + \frac{\partial T_{22}}{\partial k_z^-} \frac{\partial k_z^-}{\partial \beta}, \quad (A5)$$

$$\begin{aligned} \frac{\partial T_{11}}{\partial k_z^+} = & -k_z^- (k_0 + M k_z^-) \frac{\exp(j k_z^+ L) - \exp(-j k_z^- L)}{k_0 (k_z^+ + k_z^-)^2} \\ & + j L \frac{k_z^- (k_0 - M k_z^+) \exp(j k_z^+ L)}{k_0 (k_z^+ + k_z^-)}, \end{aligned} \quad (A6)$$

$$\begin{aligned} \frac{\partial T_{11}}{\partial k_z^-} = & k_z^+ (k_0 - M k_z^+) \frac{\exp(j k_z^+ L) - \exp(-j k_z^- L)}{k_0 (k_z^+ + k_z^-)^2} \\ & - j L \frac{k_z^+ (k_0 + M k_z^-) \exp(-j k_z^- L)}{k_0 (k_z^+ + k_z^-)}, \end{aligned} \quad (A7)$$

$$\begin{aligned} \frac{\partial T_{12}}{\partial k_z^+} = & - \frac{\rho_0 c_0}{S_p} \frac{(k_0 + M k_z^-)(k_0 + M k_z^-)}{(k_z^+ + k_z^-)^2} \\ & \times \frac{\exp(+j k_z^+ L) - \exp(-j k_z^- L)}{k_0} \\ & + j L \frac{\rho_0 c_0}{S_p} \frac{(k_0 + M k_z^-)(k_0 - M k_z^+)}{(k_z^+ + k_z^-)} \frac{\exp(+j k_z^+ L)}{k_0}, \end{aligned} \quad (A8)$$

$$\begin{aligned} \frac{\partial T_{12}}{\partial k_z^-} = & - \frac{\rho_0 c_0}{S_p} \frac{(k_0 - M k_z^+)(k_0 - M k_z^+)}{(k_z^+ + k_z^-)^2} \\ & \times \frac{\exp(+j k_z^+ L) - \exp(-j k_z^- L)}{k_0} \\ & + j L \frac{\rho_0 c_0}{S_p} \frac{(k_0 + M k_z^-)(k_0 - M k_z^+)}{(k_z^+ + k_z^-)} \frac{\exp(-j k_z^- L)}{k_0}, \end{aligned} \quad (A9)$$

$$\begin{aligned} \frac{\partial T_{21}}{\partial k_z^+} = & \frac{S_p}{\rho_0 c_0} \left[k_z^- k_z^- \frac{\exp(+j k_z^+ L) - \exp(-j k_z^- L)}{k_0 (k_z^+ + k_z^-)^2} \right. \\ & \left. + j L k_z^+ k_z^- \frac{\exp(+j k_z^+ L)}{k_0 (k_z^+ + k_z^-)} \right], \end{aligned} \quad (A10)$$

$$\begin{aligned} \frac{\partial T_{21}}{\partial k_z^-} = & \frac{S_p}{\rho_0 c_0} \left[k_z^+ k_z^+ \frac{\exp(+j k_z^+ L) - \exp(-j k_z^- L)}{k_0 (k_z^+ + k_z^-)^2} \right. \\ & \left. + j L k_z^+ k_z^- \frac{\exp(-j k_z^- L)}{k_0 (k_z^+ + k_z^-)} \right], \end{aligned} \quad (A11)$$

$$\begin{aligned} \frac{\partial T_{22}}{\partial k_z^+} = & k_z^- (k_0 + M k_z^-) \frac{\exp(+j k_z^+ L) - \exp(-j k_z^- L)}{k_0 (k_z^+ + k_z^-)^2} \\ & + j L \frac{k_z^+ (k_0 + M k_z^-) \exp(+j k_z^+ L)}{k_0 (k_z^+ + k_z^-)}, \end{aligned} \quad (A12)$$

$$\frac{\partial T_{22}}{\partial k_z^-} = -k_z^+(k_0 - Mk_z^+) \frac{\exp(+jk_z^+L) - \exp(-jk_z^-L)}{k_0(k_z^+ + k_z^-)^2} - jL \frac{k_z^-(k_0 - Mk_z^+) \exp(-jk_z^-L)}{k_0(k_z^+ + k_z^-)}, \quad (A13)$$

$$\frac{\partial k_z^\pm}{\partial \beta} = \frac{r_i + r_o}{2r_o} \left[\frac{k_0 r_i}{jk_r^\pm} \left\{ \left(1 \mp \frac{Mk_z^\pm}{k_0} \right)^2 + \left(\frac{r_i + r_o}{2r_o} j\beta \frac{k_r^\pm r_i}{k_0 r_i} \left(1 \mp \frac{Mk_z^\pm}{k_0} \right)^{-1} \right)^2 \right\} \frac{\partial k_r^\pm}{\partial k_z^\pm} \right. \\ \left. + \frac{2M}{k_0} \frac{r_i + r_o}{2r_o} \beta \left(1 \mp \frac{Mk_z^\pm}{k_0} \right)^{-1} \right]^{-1}, \quad (A14)$$

$$\frac{\partial k_r^\pm}{\partial k_z^\pm} = \frac{\mp Mk_0 - k_z^\pm (1 - M^2)}{k_r^\pm}. \quad (A15)$$

APPENDIX B: ESTIMATION OF ACOUSTIC IMPEDANCE AT AN ARBITRARY POROUS FREQUENCY

The acoustic impedance of a porous woven hose must be known in order to predict the acoustic performance of such a hose with an arbitrary frequency or arbitrary weaving and coating conditions or arbitrary mean flow conditions or all of these variable conditions. The acoustic impedance for an arbitrary porous frequency can be estimated by using the curve-fitting method from the measured impedance spectra exists as a database.¹ The curve fitting model on porous frequency, frequency, and Mach number is proposed as

$$\operatorname{Re} \left(\frac{Z_p}{\rho_0 c_0} \right) = \{ (a_1 M + a_2) f_{p\text{REF}} + (a_3 M + a_4) \} f + (a_5 M + a_6) f_{p\text{REF}} + (a_7 M + a_8), \quad (B1)$$

$$\operatorname{Im} \left(\frac{Z_p}{\rho_0 c_0} \right) = \{ (b_1 M + b_2) f_{p\text{REF}} + (b_3 M + b_4) \} f + (b_5 M + b_6) f_{p\text{REF}} + (b_7 M + b_8). \quad (B2)$$

Here, $f_{p\text{REF}}$ denotes the reference porous frequency for a given specific length and radius, f is the ordinary frequency in Hz, M is the Mach number, and the coefficients a_1 – a_8 and b_1 – b_8 are constants. It should be noted that the porous frequencies of any two porous woven hoses having same wall properties are not the same, if their dimensions, i.e., length and/or diameter, are not the same.¹⁴ In this paper, the reference length and radius of the reference porous frequency

are set as $2r_{i\text{REF}} = 55$ mm, $L_{\text{REF}} = 1$ m, and $P_{0\text{REF}} = 101\,300$ Pa for purposes of demonstration. The coefficients a_1 – a_8 and b_1 – b_8 can be obtained by regression analysis on the measured impedance data within the practical service conditions.

From these curve-fitting models, if the mean flow, the ordinary frequency, and the porous frequency (or the effective flow resistivity) are specified, one can easily obtain the acoustic resistance and reactance of a specific porous woven hose.

¹C.-M. Park, J.-G. Ih, Y. Nakayama, and S. Kitahara, "Measurement of acoustic impedance and prediction of transmission loss of the porous woven hose in engine intake systems," *Appl. Acoust.* **63**, 775–794 (2002).

²H. Takao, S. Kitahara, S. Hatano, and T. Hashimoto, "Evaluation of sound quality of interior porous intake duct noise," *Proceedings of the Seminar on Sound Quality*, Tokyo, Japan, 2001, pp. 47–57.

³ASTM C384-95, Standard method for impedance and absorption of acoustical materials by the impedance tube method (American Society for Testing and Materials, Philadelphia, 1995).

⁴ASTM E1050-98, Standard test method for impedance and absorption of acoustical materials using a tube, two microphones, and a digital frequency analysis system (American Society for Testing and Materials, Philadelphia, 1998).

⁵J. Y. Chung and D. A. Blaser, "Transfer function method of measuring in-duct acoustic properties. I. Theory," *J. Acoust. Soc. Am.* **68**, 907–913 (1980).

⁶S.-H. Jang and J.-G. Ih, "On the multiple microphone method for measuring in-duct acoustics properties in the presence of mean flow," *J. Acoust. Soc. Am.* **103**, 1520–1526 (1998).

⁷M. L. Munjal, *Acoustics of Ducts and Mufflers* (Wiley, New York, 1987), Chaps. 1 and 5.

⁸V. L. Khitrik, "Propagation of sound in a cylindrical duct with porous walls," *Acoust. Phys.* **42**, 646–647 (1996).

⁹A. Cummings and R. Kirby, "Low-frequency sound transmission in ducts with permeable walls," *J. Sound Vib.* **226**, 237–2521 (1999).

¹⁰D. W. Marquardt, "An algorithm for least-squares estimation of nonlinear parameters," *J. Soc. Ind. Appl. Math.* **11**, 431–439 (1963).

¹¹M. L. Munjal, "Theory of a source-location method for direct experimental evaluation of the four-pole parameters of an aeroacoustic element," *J. Sound Vib.* **141**, 323–333 (1990).

¹²M. G. Parasad and M. J. Crocker, "Evaluation of four-pole parameters for a straight pipe with a mean flow and a linear temperature gradient," *J. Acoust. Soc. Am.* **69**, 916–921 (1981).

¹³B. H. Song and J. S. Bolton, "A transfer-matrix approach for estimating the characteristic impedance and wave numbers of limp and rigid porous materials," *J. Acoust. Soc. Am.* **107**, 1131–1152 (2000).

¹⁴C.-M. Park, J.-G. Ih, Y. Nakayama, and S. Kitahara, "Single-figure rating of porous woven hoses using a nonlinear flow resistance model," *J. Sound Vib.* **257**, 404–410 (2002).

¹⁵D. E. Baxa, *Noise Control in Internal Combustion Engines* (Wiley, New York, 1982), Chap. 5.

¹⁶E. Kreyszig, *Advanced Engineering Mathematics* (Wiley, New York, 1988), Chap. 24.

¹⁷M. Abom and H. Boden, "Error analysis of two-microphone measurements in ducts with flow," *J. Acoust. Soc. Am.* **83**, 2429–2438 (1988).

Modeling of nonlinear ultrasound propagation in tissue from array transducers

Roger J. Zemp

Department of Biomedical Engineering, University of California at Davis, 1026 Academic Surge, Davis, California 95616

Jahangir Tavakkoli

Focus Surgery, Inc., 3940 Pendleton Way, Indianapolis, Indiana 46226

Richard S. C. Cobbold^{a)}

Institute of Biomaterials and Biomedical Engineering, University of Toronto, Toronto, Ontario M5S 3G9, Canada

(Received 11 April 2002; revised 5 October 2002; accepted 14 October 2002)

A computationally efficient model capable of simulating finite-amplitude ultrasound beam propagation in water and in tissue from phased linear arrays and other transducers of arbitrary quasiplanar geometry is described. It is based on a second-order operator splitting approach [Tavakkoli *et al.*, *J. Acoust. Soc. Am.* **104**, 2061–2072 (1998)], with a fractional step-marching scheme, whereby the effects of diffraction, attenuation, and nonlinearity can be computed independently over incremental steps. This approach is an extension to that of Christopher and Parker [*J. Acoust. Soc. Am.* **90**, 507–521; **90**, 488–499 (1991)], wherein linear and nonlinear effects are propagated separately over incremental steps, and the computation of the diffractive substeps are based on an angular spectrum technique with a modified sampling scheme for accurate and efficient implementation of diffractive propagation from nonradially symmetric sources. Results of the model are compared with published data. Predicted field profiles for nonlinear propagation in tissue from realistic array transducers using the pulse inversion method are presented. © 2003 Acoustical Society of America. [DOI: 10.1121/1.1528926]

PACS numbers: 43.25.Jh, 43.80.Qf [MFH]

I. INTRODUCTION

Until recently, most medical ultrasonic devices were designed with the assumption that ultrasound beams propagate in a linear manner. The assumption of linearity, however, is only true in the small signal limit, and in fact, many diagnostic and therapeutic ultrasound systems use excitations for which the small signal approximation does not hold. Tissue harmonic imaging is an important application, which takes advantage of harmonics arising from tissue nonlinearity.^{1–6} By extracting harmonic information arising from nonlinear propagation, tissue harmonic imaging generates a smaller and less distributed effective sample volume, and thus offers improved resolution and clutter suppression. Moreover, it has been conjectured that because nonlinearities mostly culminate at the focal region of an ultrasound beam, near-field distortions such as aberration and reverberation artifacts may be significantly reduced.^{4,5} In recent years a number of clinical studies have convincingly demonstrated the advantages of tissue harmonic imaging over standard B-mode imaging.⁷

Central to the design and optimization of tissue harmonic imaging systems is a firm understanding of finite-amplitude acoustic beam propagation. Numerical modeling allows for both qualitative understanding and quantitative analysis of nonlinear effects in tissue. A significant obstacle to quantitative modeling of more complex sources such as linear arrays is the large computational burden of existing

nonlinear propagation algorithms. The primary purpose of this paper is to present a computationally efficient model of finite-amplitude ultrasound beam propagation in tissue from a realistic medical ultrasound scanner. With the ability to simulate nonlinear beam propagation from a phased array transducer, optimal design of diagnostic and therapeutic ultrasound systems may be facilitated.

Many of the approaches used to simulate nonlinear ultrasound beam propagation in dissipative media have been reviewed in Hamilton and Blackstock.⁸ Some of these are based on the widely used KZK equation that approximately characterizes nonlinear beam propagation in thermoviscous fluids.^{9–12} Notably, Cahill and Baker^{13,14} used the KZK approach to simulate the nonlinear field response from a phased array transducer in water. More recently, Li and Zagzebski¹⁵ described a KZK model for harmonic ultrasound imaging in tissue, for a circular (axisymmetric) transducer. The viscous loss model of the KZK equation gives rise to a quadratic dependence of the attenuation coefficient with frequency. However, most soft biological tissues exhibits a frequency dependence proportional to f^b , where b is typically close to unity. There are both time- and frequency-domain numerical models, which enable artificial adjustment of the frequency dependence of the medium attenuation to match the near-linear relationship of tissue.^{9,15} Unfortunately, the computational burden of such approaches is considerable, especially with nonaxisymmetric sources and pulsed excitation. Christopher and Parker^{16,17} have developed a phenomenological

^{a)}Electronic mail: cobbold@ecf.utoronto.ca

model, based on propagation of the effects of attenuation, nonlinearity, and diffraction separately over small incremental steps. Their approach is valid for arbitrary media, and has been applied to continuous wave (cw) and pulsed as well as axisymmetric¹⁷ and nonaxisymmetric^{4,18} sources. A similar operator-splitting approach has been used by Lee and Hamilton⁹ for time-domain modeling based on the KZK equation.

Tavakkoli *et al.*¹⁹ have simulated highly focused sources in both water and tissue using a time-domain second-order operator-splitting scheme with a fractional step algorithm. They, like Christopher and Parker, propagated the effects of diffraction, attenuation, and nonlinearity over incremental steps. But, because their operator-splitting scheme was of second-order accuracy, they were able to use relatively large steps compared to those used by Christopher and Parker. However, in order to have a full diffraction solution, their diffraction substep was calculated using a computationally burdensome Rayleigh integral approach that, even with axisymmetric sources, took approximately 90% of the overall computation time.

We have developed a new method for simulating nonlinear ultrasound beam propagation in tissue. In this model, finite-amplitude propagation from nonaxisymmetric sources may be simulated in a computationally efficient way. We use a second-order operator-splitting technique, similar to that of Tavakkoli *et al.*,¹⁹ and a much more efficient diffraction algorithm based on the angular spectrum approach, akin to that of Christopher and Parker.¹⁶

II. BASIC CONSIDERATIONS

A. Model equation and fractional step approach

In our operator-splitting scheme, the effects of diffraction, attenuation, and nonlinearity are propagated separately over incremental distances. This technique is based on a reduced evolution equation, valid for one-way propagation of quasi-plane waves, given by

$$\frac{\partial v}{\partial z} = L_A \cdot v + L_N \cdot v + L_D \cdot v, \quad (1)$$

where L_A , L_N , and L_D are operators representing absorption, nonlinearity, and diffraction, respectively, and v is the particle velocity. This equation assumes that the operators L_D , L_A , and L_N exist such that Eq. (1) accurately describes finite-amplitude beam propagation in tissue. Partial justification for its use is based on the fact that by integrating the KZK equation with respect to retarded time, a form equivalent to Eq. (1) is obtained. Both theoretical and experimental confirmation for the use of Eq. (1) stems from the efforts by Tavakkoli *et al.*,¹⁹ who used this equation as a basis for their nonlinear model and obtained reasonable agreement with experiments of finite-amplitude propagation from a highly focused source in a tissue-mimicking fluid. More recently, Remenieras *et al.*²⁰ successfully compared the theory of Tavakkoli *et al.*¹⁹ with experimental results for a plane piston transducer emitting short pulses. Moreover, Khokhlova *et al.*²¹ have reported good agreements with their KZK calculations for a cw circular piston. Finally, the approach used

by Christopher and Parker¹⁷ can be shown²² to be equivalent to a first-order operator splitting of an equation equivalent to Eq. (1). Thus, although our approach is intrinsically phenomenological, there is precedence for its applicability and validity.

B. Second-order operator-splitting approach

Over sufficiently small steps, the effects of diffraction, nonlinearity, and attenuation can be assumed to be independent. Consider first the effect of diffraction. Given the normal particle velocity field profile $v(x, y, z_1; t)$ across a plane $z = z_1$, we may represent the field profile across plane $z = z_2$ assuming diffractive propagation only (no nonlinearity or attenuation) by introducing a propagation operator $\Gamma_{D, \Delta z}$, such that $v(x, y, z_2; t) = \Gamma_{D, \Delta z} v(x, y, z_1; t)$ where $\Delta z = z_2 - z_1$ is the propagation distance between the two planes. The operator $\Gamma_{D, \Delta z} v(x, y, z_1; t)$ then represents a solution at $z = z_1 + \Delta z$ to the diffraction subequation

$$\frac{\partial v}{\partial z} = L_D \cdot v, \quad (2)$$

with the initial condition $v = v(x, y, z_1; t)$. Similarly, we may define propagation operators $\Gamma_{N, \Delta z}$ and $\Gamma_{A, \Delta z}$ for nonlinearity and absorption, respectively. Thus, $v(x, y, z_2; t) = \Gamma_{N, \Delta z} v(x, y, z_1; t)$ is a solution to the nonlinear subequation, and $v(x, y, z_2; t) = \Gamma_{A, \Delta z} v(x, y, z_1; t)$ is a solution to the absorption subequation given the initial condition $v = v(x, y, z_1; t)$ on plane $z = z_1$. The modeling methodology used by Christopher and Parker¹⁷ can be shown²² to be equivalent to a first-order operator-splitting scheme represented by

$$\begin{aligned} v(x, y, z_2; t) &\equiv \Gamma_{D+A+N, \Delta z} v(x, y, z_1; t) \\ &= \Gamma_{D+A, \Delta z} \Gamma_{N, \Delta z} v(x, y, z_1; t) + O(\Delta z^2), \end{aligned} \quad (3)$$

where $\Gamma_{D+A+N, \Delta z} v(x, y, z_1; t)$ represents a solution at $z = z_1 + \Delta z$ to Eq. (1), and $\Gamma_{D+A, \Delta z} v(x, y, z_1; t)$ represents a solution at $z = z_1 + \Delta z$ to the subequation

$$\frac{\partial v}{\partial z} = L_D \cdot v + L_A \cdot v, \quad (4)$$

given the initial condition $v = v(x, y, z_1; t)$. In fact, Eq. (3) states that the combined effects of diffraction, absorption, and nonlinearity can be approximated by a single incremental step of combined diffraction and attenuation, followed by one step of nonlinearity.

A second-order operator-splitting scheme given by

$$\begin{aligned} v(x, y, z_2; t) &\equiv \Gamma_{D+A+N, \Delta z} v(x, y, z_1; t) \\ &= \Gamma_{D, \Delta z/2} \Gamma_{N+A, \Delta z} \Gamma_{D, \Delta z/2} v(x, y, z_1; t) \\ &\quad + O(\Delta z^3), \end{aligned} \quad (5)$$

was introduced by Tavakkoli *et al.*¹⁹ for predicting the field produced by a highly focused lithotripsy transducer. They used adaptive step sizes—large steps in the near field and smaller steps in the focal region. Even for the highly nonlinear pressure amplitudes produced by this source, 23 planes out to the focal region sufficed to achieve very good agreement with experimental results. In contrast, Christopher's¹⁸

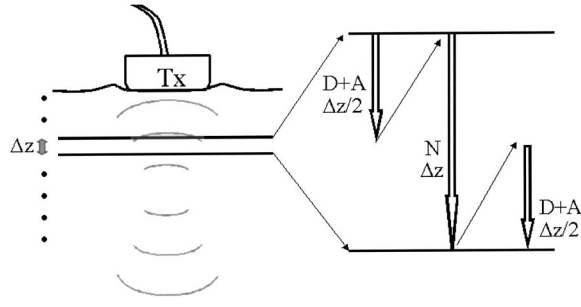


FIG. 1. Illustration of the fractional step-marching scheme and the operator-splitting approach described by Eq. (6). The acoustic field from the transducer (T_x) is propagated plane-by-plane in incremental steps. Each step involves the propagation of diffraction (D), attenuation (A), and nonlinearity (N).

first-order scheme required a large number of fractional steps (hundreds or thousands) out to the focal region. Similarly, the use of a finite difference technique to solve the KZK equation generally requires relatively fine axial meshing.

For the reasons associated with code stability, as detailed in Sec. II, the algorithm we developed for cw excitation of a linear array combined nonlinearity with the attenuation substeps in the manner described by Eq. (5). However, for the pulsed excitation described in Sec. III, we used a variation of this second-order operator-splitting method to enable the effects of diffraction and attenuation to be combined. This alternative second-order approach is expressed by

$$\begin{aligned} v(x, y, z_2; t) &\equiv \Gamma_{D+A+N, \Delta z} v(x, y, z_1; t) \\ &= \Gamma_{D+A, \Delta z/2} \Gamma_{N, \Delta z} \Gamma_{D+A, \Delta z/2} v(x, y, z_1; t) \\ &\quad + O(\Delta z^3), \end{aligned} \quad (6)$$

and is illustrated in Fig. 1. Here, attenuation is coupled with the diffraction half step rather than the nonlinear substep, as is the case in (5). It was anticipated that considerable computational savings could be obtained by taking advantage of the larger axial steps that these second-order operator-splitting schemes allow.

C. Diffraction algorithm

The choice of an efficient diffraction algorithm was of prime importance in our investigations. We sought a computationally efficient approach that would be valid for plane-to-plane propagations, where the source plane may not be axisymmetric and the field distribution may not be separable, i.e., it may not be represented as the product of temporal and spatial functions. In a fractional step-marching algorithm, the accuracy of each step is dependent on the previous computations. To minimize magnification of errors in the propagation procedure, a diffraction algorithm reasonably accurate in the near field is needed. Finally, the method should be able to accurately simulate the steady state and transient response of phased array transducers with dynamic focusing and beam steering.

We investigated diffraction algorithms based on the following three methods: (i) the impulse response; (ii) the Rayleigh integral; and (iii) the angular spectrum. Because the impulse response approach is only valid for separable

sources it was not considered further. Both the Rayleigh integral and angular spectrum methods provide full solutions but can differ by orders of magnitude in terms of their computation burden. If N_x , and N_y are the number of samples in the lateral x - and y directions, respectively, and N_t is the number of temporal samples, then the Rayleigh integral method can be shown to have a computation burden in the order of $N_t(N_x N_y)^2$. For the angular spectrum method (including a 2D FFT and a 2D IFFT), the computation burden is on the order of $N_x N_y N_t \log_2(N_x N_y/2)$. For example if $N_x = N_y = N_t = 512$, the angular spectrum method is on the order of 10^4 more efficient than the Rayleigh method. The computational efficiency was the primary reason that we chose the angular spectrum method.

Briefly, the angular spectrum method^{23,24} is a frequency-domain approach, in which the field $s(x, y, z_0; \omega)$ across a source plane z_0 for the spectral component ω may be described as a spatial frequency distribution $S(k_x, k_y, z_0; \omega) = \mathcal{F}_{2D}\{s(x, y, z_0; \omega)\}$. It can be shown that the field on a plane a distance Δz away from a source plane is given by

$$s(x, y, z_1; \omega) = \mathcal{F}_{2D}^{-1}\{S(k_x, k_y, z_0; \omega) \times H(k_x, k_y, \Delta z; \omega)\}, \quad (7a)$$

where H is a linear transfer function given by

$$H(k_x, k_y, \Delta z; \omega) = \begin{cases} e^{j\Delta z \sqrt{k^2 - (k_x^2 + k_y^2)}} & \text{for } (k_x^2 + k_y^2) \leq k^2 \\ e^{-\Delta z \sqrt{k_x^2 + k_y^2 - k^2}} & \text{for } (k_x^2 + k_y^2) > k^2 \end{cases}, \quad (7b)$$

and $k = 2\pi/\lambda$, where λ is the wavelength. Alternatively, the diffractive propagation may be done by convolving the source field distribution s with a point-spread function, $h(x, y, z, \Delta z; \omega)$, i.e.,

$$s(x, y, z_1; \omega) = h(x, y, \Delta z; \omega) * s(x, y, z_0; \omega), \quad (8a)$$

where

$$h(x, y, \Delta z; \omega) = -\frac{\Delta z e^{jkR}}{2\pi R^2} \left(jk - \frac{1}{R} \right), \quad (8b)$$

in which $R = \sqrt{x^2 + y^2 + \Delta z^2}$. Equations (7a) and (8a) suggest two different ways of numerically determining the field using the discrete Fourier transform. For Eq. (7a) both the source and transfer function are sampled in the spatial frequency domain, whereas for Eq. (8a) the impulse response and the source are sampled in the spatial domain.

Christopher and Parker¹⁶ and Wu *et al.*^{25,26} offer useful details concerning the numerical implementation of the angular spectrum approach for 1D or axisymmetric sources. Methods for nonaxisymmetric continuous-wave sources are detailed by Wu *et al.*²⁷ Related k -space algorithms have been used for simulating acoustic propagation in inhomogeneous media.^{28,29} To simulate pulse propagation and nonlinear effects, a multispectral algorithm is needed. In selecting a 2D multispectral diffraction algorithm, we must consider the propagation of each frequency component, and in doing so, may choose to sample either the point-spread function h , or the transfer function H . Following Christopher and Parker,¹⁶ the first approach is called the spatial sampled convolution

(SSC) algorithm, and the second the frequency sampled convolution (FSC) algorithm. These two approaches may have very different consequences.

D. Sampling and aliasing issues

Before further explanation is made regarding the above two methods, it should be noted that our approach to diffractive propagation of nonaxisymmetric sources differs somewhat from that of Christopher.¹⁸ He sampled the transfer function in the spatial frequency domain, using small axial increments, on the order of a wavelength or less. With small propagation distances, convolutional wraparound error is small. When we attempted to use larger steps, we found that aliasing artifacts were more severe. For radially symmetric sources, wraparound error can be greatly reduced using the ray theory truncation.^{16,30} Unfortunately, we found that the truncation scheme was not completely appropriate for nonaxisymmetric sources. Briefly, the ray theory truncation prescribes a radially symmetric upper bound on the spatial frequency information required to represent a field profile out to a given lateral extent. Spatial frequency truncation is numerically advantageous, since the transfer function H contains information beyond this bound that is difficult to sample. Inclusion of undersampled information beyond this bound leads to aliasing in the convolution. For radially symmetric sources, the convolution can be accomplished with the (discrete) Hankel transform, which has only a radial dependence. When nonaxisymmetric sources are considered the (discrete) 2D Fourier transform must be used. Thus, on attempting to apply the ray theory truncation, we attempt to impose a radially symmetric truncation bound on a rectangular spatial frequency domain. Aliasing and truncation errors thus come into play when considering nonaxisymmetric sources—and these errors are significant when using interplane step sizes larger than a wavelength. Since we would like to use large step sizes in order to reduce the computation burden, we focused on choosing a sampling scheme whereby convolutional wraparound errors are minimized, especially for large propagation distances.

Wu *et al.*^{25,26} offer a concise treatment of two different types of aliasing errors associated with numerical implementation of the (FSC) angular spectrum approach. One is the aliasing error in the spatial frequency domain due to the discrete Fourier transform (DFT) of a finite-sized source (discussed in Sec. E below), and the other is aliasing in the spatial domain due to inadequate representation of H . Paralleling their work, we sought a numerical angular spectrum algorithm that would minimize both types of errors.

A few crucial points should be noted in selecting an optimal sampling scheme for the key problem of propagating cw from a source plane to an observation plane, and in discussing these we shall denote the lateral sample spacings by Δx and Δy . First, except for very small propagation distances ($< \lambda$), the transfer function H is poorly behaved at loci on or near the radiation circle $k^2 = k_x^2 + k_y^2$. If the sampling scheme is such that the spatial frequency extent $k_{x \max} = 2\pi/\Delta x$, $k_{y \max} = 2\pi/\Delta y$ of the transform domain contains any portion of this radiation circle, H cannot be adequately

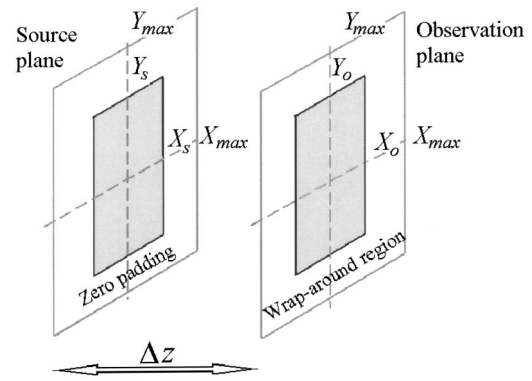


FIG. 2. Geometry of the source and observation planes.

sampled, no matter what spatial frequency sampling (or equivalently spatial extent) is used. Second, H tapers off exponentially to zero beyond the radiation circle. Third, except for very small propagation distances ($< \lambda$), the point-spread function h is well behaved, and may be adequately sampled by using the Nyquist spatial sampling interval of $\Delta x = \Delta y \leq \lambda/2$. This last point can be understood by noting that the spatial frequency spectrum of h will consist of a sampled version of H which is infinitely wrapped around itself with a “period” equal to or greater than the radius of the radiation circle, k . Thus, only the exponentially decaying evanescent tail of H is aliased back into the spectrum, and this contribution will be negligible. Fourth, for small (subwavelength) propagation distances, h approaches a delta function, and cannot be sampled adequately at the Nyquist interval. In this case, sampling H may be a better choice.

For large propagation steps, although we may sample h with the Nyquist interval to obtain accurate results, this may not always be advisable from a computational point of view. This is because $\lambda/2$ sampling is not always necessary for adequate representation of a harmonic field profile across a propagation plane. A smooth field profile, such as the far-field main-lobe region of a source, will have a narrow angular spectrum, and thus the highest spectral component may be much less than k . If the field profile can be sampled with intervals coarser than $\lambda/2$, computationally speaking, it would be better to find a way to also sample the propagator functions (either h or H) with this same coarser sampling rate for efficient evaluation of the convolution.

Sampling the point-spread function h coarser than $\lambda/2$ will not suffice, because the spatial frequency spectrum will have significant wraparound error. We may question whether sampling H would be a better alternative. With sampling coarser than $\lambda/2$, the radiation circle will be either exterior to the extent of the discrete spatial frequency domain ($k_{x \max} = 2\pi/\Delta x$, $k_{y \max} = 2\pi/\Delta y$), or partially contained within that domain. If the radiation circle is partially contained within the domain, sampling H will incur serious aliasing errors, and thus our only alternative is to sample h at $\Delta x = \Delta y \leq \lambda/2$. If the radiation circle is completely external to the transform domain, sampling H in the spatial frequency domain can be done only if the oscillations of H can be adequately sampled.

For the given spatial extents, $[X_{\max}, Y_{\max}]$ (see Fig. 2)

and the given spatial sampling intervals Δx , Δy , the question of whether or not to sample H then becomes a question of deciding whether the spatial frequency sampling intervals $\Delta k_x = 2\pi/X_{\max}$, $\Delta k_y = 2\pi/Y_{\max}$ are adequate. The answer comes from the Nyquist theorem, and is based on analysis of the highest frequency of oscillations of H contained within the transform domain. Because we know the oscillations increase close to the radiation circle, the highest frequency oscillations will occur at the corners $[k_{x\max}, k_{y\max}]$ of the transform domain. In order to determine the required sampling interval, we use Taylor series expansion to expand the argument of H in the neighborhood of $[k_{x\max}, k_{y\max}]$ to express it in the form

$$H(k_x, k_y) \approx e^{j(\beta_x k_x + \beta_y k_y + \text{constant})}, \quad (9)$$

where β_x and β_y provide a measure of the maximum frequency of oscillations in H .

To determine β_x and β_y , we note that the transfer function as given by Eq. (7) can be written as $H = \exp[jg(k_x, k_y)]$, where $g(k_x, k_y) = \Delta z \sqrt{k^2 - (k_x^2 + k_y^2)}$. By using a 2D Taylor expansion around $[k_{x\max}, k_{y\max}]$, the first-order expression for g is

$$g(k_x, k_y) \approx g(k_{x\max}, k_{y\max}) + (k_x - k_{x\max}) \left. \frac{\partial g}{\partial k_x} \right|_{k_{x\max}, k_{y\max}} + (k_y - k_{y\max}) \left. \frac{\partial g}{\partial k_y} \right|_{k_{x\max}, k_{y\max}}.$$

By substituting this into Eq. (7) and comparing with Eq. (9), we find an expression comparable to the 1D result given as Eq. (5) in Ref. 26, and extended to 2D nonaxisymmetric sources in Ref. 27, Eq. (7)

$$\begin{aligned} \beta_x &= \left. \frac{\partial g}{\partial k_x} \right|_{k_{x\max}, k_{y\max}} \\ &= - \left. \frac{\Delta z k_x}{\sqrt{k^2 - (k_x^2 + k_y^2)}} \right|_{k_{x\max}, k_{y\max}} \\ &= - \frac{\Delta z k_{x\max}}{\sqrt{k^2 - (k_{x\max}^2 + k_{y\max}^2)}}, \end{aligned} \quad (10)$$

with a similar result for β_y . Thus, according to the Nyquist theorem the spatial sampling interval $\Delta k_{x,\text{crit}}$ that adequately samples H is given by

$$\Delta k_{x,\text{crit}} \leq \frac{\pi}{2|\beta_x|} = \frac{\pi \sqrt{k^2 - (k_{x\max}^2 + k_{y\max}^2)}}{2\Delta z k_{x\max}}, \quad (11)$$

and a similar result is obtained for $\Delta k_{y,\text{crit}}$. If $\Delta k_x = 2\pi/X_{\max}$ and $\Delta k_y = 2\pi/Y_{\max}$ are smaller than $\Delta k_{x,\text{crit}}$ and $\Delta k_{y,\text{crit}}$, respectively, then H will be undersampled, requiring that we must sample h with a minimum interval of $\lambda/2$. Otherwise, sampling of the H is feasible and advisable, since this approach will be more computationally efficient than sampling h . Figure 3 provides a summary of our angular-spectrum sampling schemes.

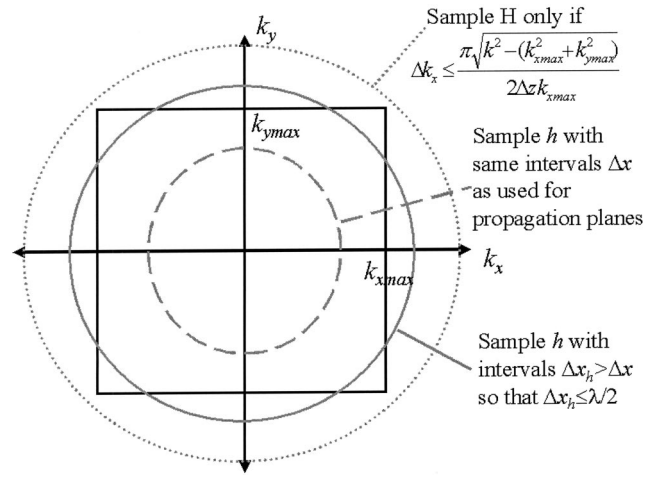


FIG. 3. Illustrating the geometry of the spatial frequency domain and the selection of schemes for the sampling diffraction propagator functions.

As illustrated in Fig. 2 the spatial extents X_{\max} and Y_{\max} are determined by (i) the desired spatial extent $[\pm X_s, \pm Y_s]$ of a potentially infinite extent source plane and (ii) the desired spatial extent $[\pm X_0, \pm Y_0]$ in the observation plane. The extent $[\pm X_s, \pm Y_s]$ should contain the bulk of the energy of the propagating beam, with negligible amounts exterior to this. To obtain the correct results of diffractive propagation out to the observation plane, the extent of the source plane must be zero padded out to at least $X_{\max} \geq X_s + X_0$, and $Y_{\max} \geq Y_s + Y_0$.

In the situations when spatial domain sampling of h is used (the SSC approach), h should be sampled out to $[\pm X_{\max}, \pm Y_{\max}]$, and then convolved with the zero padded source s by taking the 2D FFT of these 2D sequences, multiplying their transforms, and taking the inverse 2D FFT of the product. The core extent $[\pm X_0, \pm Y_0]$ will contain the desired results, and the rim exterior to this, out to $[\pm X_{\max}, \pm Y_{\max}]$, will contain the convolutional wraparound error.

E. Sampling of the transducer surface in the spatial frequency domain

Sampling the surface of a transducer can be troublesome because undersampling of abrupt edges will lead to aliasing errors in the spatial frequency domain. Spatial domain sampling may be a reasonable approach when the bulk of the energy in the source's angular spectrum is within the discrete spatial frequency domain $[\pm k_{x\max}, \pm k_{y\max}]$, as may be the case for large, apodized, directional sources, or when the observation plane is in the far field of each surface element.

An alternative approach³¹ that avoids the above problem assumes linear propagation from the transducer surface to a plane in close vicinity. The transient field on this plane can then be calculated by using, for example, the impulse response method.³² With this as the base source plane, the operator approach, incorporating the angular spectrum method, can then be used to account for nonlinear propagation. Wu *et al.*²⁵ present yet another alternative based on a discrete Sinc-Fourier transform that allows aliasing-free computation of spatially sampled sources in the spatial frequency domain.

A much simpler method can be used if an analytic form of the 2D Fourier transform of the source aperture can be obtained. The source can then be sampled in the spatial frequency domain. In doing so, the source needs only be sampled out to the radiation circle, or the spatial frequency extent of the transform domain, whichever is smaller. This approach has the advantage that aliasing artifacts from undersampling of the source can be eliminated. As an example of this approach, we consider a linear array transducer of the type often used in ultrasound scanners. For a linear array of N elements of height H_e , width W , and center-to-center spacing d , the array length is $D = (N-1)d + W$. If N is even, the 2D Fourier transform of the aperture function can readily be shown to be given by

$$S(k_x, k_y) = \mathcal{J}\{\xi(y) \text{rect}(y/H_e)\} \times \sum_{n=-N/2}^{N/2} A_n \frac{\sin(Wk_x)}{Wk_x} e^{-jndk_x} e^{j\phi_n}, \quad (12)$$

where, for the n th element, A_n is an apodization factor, $e^{j\phi_n}$ is a phase delay, ξ represents the complex phase delay and apodization of a lens used for elevation plane focusing, and $\text{rect}(x) \equiv 1$ for $|x| \leq 0.5$ and $\equiv 0$ for $|x| > 0.5$. Although the y component of the Fourier transform may be difficult to evaluate analytically, it can be numerically calculated. In the absence of a lens ($\xi=1$) it can be analytically determined as $\mathcal{J}\{\text{rect}(y/H_e)\} = \sin(H_e k_y)/(H_e k_y)$.

III. MODELING FINITE-AMPLITUDE PROPAGATION FROM CW SOURCES

A propagating finite-amplitude wave will undergo distortion due to convective and nonlinear effects.⁸ This distortion gives rise to harmonics not present in the initial spectrum and thus, in modeling nonlinear propagation, each of these harmonic components must be accounted for. Like Christopher and Parker¹⁷ we used a frequency-domain technique based on the angular spectrum method and Burger's equation to propagate the effects of diffraction and nonlinearity over incremental steps. The algorithm, which provides an iterative description of the propagating wave and incorporates the effects of attenuation, is based on that given by Haran and Cook.³³ Taking into account the effects of attenuation and nonlinearity, our algorithm for the particle velocity can be expressed as

$$v_n(z + \Delta z) = v_n(z) + j \frac{\beta 2 \pi f_0}{2c_0^2} \Delta z \left[\sum_{i=1}^{n-1} i v_i v_{n-i} + \sum_{i=n+1}^N n v_i v_{n-i}^* \right] - \alpha_0 (n f_0)^b v_n \Delta z, \quad (13)$$

where N is the number of harmonics to be retained in the computation process, β is the coefficient of nonlinearity, $n f_0$ is the n th harmonic frequency, and we have assumed that the frequency dependence of the attenuation coefficient can be written in the general form $\alpha(f) = \alpha_0 f^b$.

Although our model is similar to that of Christopher and Parker,¹⁷ it has the following important differences: (i) It uses a second-order operator splitting described by Eq. (5):

(ii) it uses bigger diffractive steps ($\gg \lambda$) between propagation planes: (iii) it uses a novel sampling scheme to handle propagation from nonradially symmetric sources: (iv) it samples the aperture in the spatial frequency domain: (v) it combines attenuation with the nonlinear substep, rather than combining attenuation with the diffraction substep. Additionally, we used several smaller nonlinear substeps for each diffractive substep. By including attenuation in the nonlinear algorithm and using smaller substeps, better stability was achieved—especially in light of the large diffractive substeps allowed by the second-order operator-splitting algorithm.

We now describe the multiharmonic diffractive propagation algorithm, which we developed. For simplicity, let us presume that each harmonic profile has an identical planar sampling scheme. Moreover, although it is possible to use an adaptive gridding scheme, we found it simpler to use a uniform gridding scheme for each plane along the direction of propagation.

Intuitively, one might presume that the sampling intervals Δx and Δy , which are needed to represent planar distributions in propagation of harmonics, would be at most $\lambda_N/2$, where λ_N is the wavelength of the highest harmonic present in the field. Although this is the interval needed to adequately sample the point-spread function h for step sizes $\Delta z > \lambda$, the harmonic profile itself may be much smoother than this Nyquist rate requires. The second harmonic profile in the far field of a piston source in a dissipative medium is one example of a smooth field profile that can be adequately sampled with intervals much less than $\lambda_N/2$ (e.g., Baker *et al.*¹¹).

In their investigations of axisymmetric sources, Christopher and Parker¹⁷ found that reasonable modeling results could be obtained with radial sampling at spatial frequencies far less than the Nyquist frequency of the highest harmonic. Specifically, for focused fields involving up to 50 harmonics, very good results were obtained using radial sampling at four times the Nyquist frequency of the fundamental. For unfocused fields, one or two times the Nyquist frequency of the fundamental worked very well. Although their studies were for axisymmetric sources, we found similar results for rectangular sources. If the minimum spatial sampling frequency that will yield a convergent solution is γ times the Nyquist frequency of the fundamental, then our results indicate that in a medium with moderate nonlinearity and dissipation characteristics typical of most tissues, γ is typically in the range 1 to 4, though they will vary for different scenarios.

Once the lateral sampling frequencies have been chosen, each harmonic profile must be propagated an incremental distance using either the FSC or the SSC algorithms. Based on the analysis in Sec. ID, a reliable way of choosing whether to sample h or to sample H can be specified. If the source plane harmonic profiles are sampled at γ times the Nyquist rate of the fundamental then, for harmonics $n > \gamma$, the discrete spatial frequency transform domain will be completely inside the radiation circles $k_n^2 = k_x^2 + k_y^2$, where k_n is the magnitude of the wave vector for the n th harmonic. Thus, if the lowest harmonic satisfying $n > \gamma$ is denoted by n_H , then for higher harmonics such that $n \geq n_H$ it will be possible to sample H at the same frequency as the angular spectrum

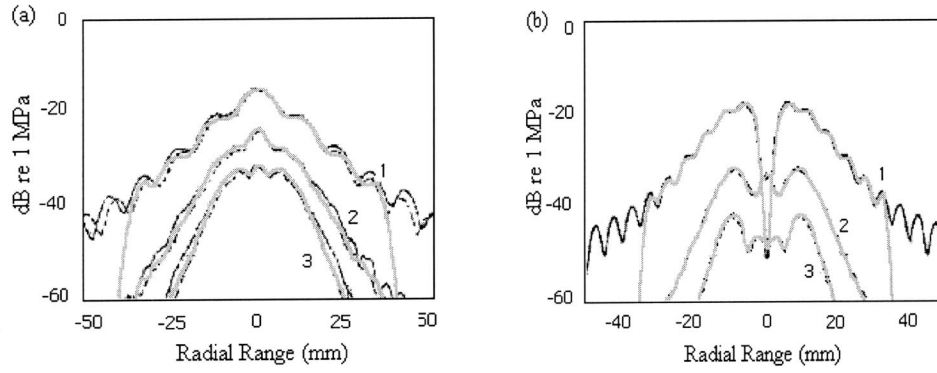


FIG. 4. Lateral profiles comparing the results of our model (thick gray lines) for the first three harmonics (1, 2, and 3) in water, from an unfocused 1.9-cm radius piston at 2.25 MHz and a source pressure amplitude of 100 kPa. The following additional parameters as given by Baker *et al.* (Ref. 11) were used: $\alpha = 25 \times 10^{-15} \text{ Np/(m} \times \text{Hz}^2)$, $c = 1486 \text{ m/s}$, and $\beta = 3.5$. (a) Comparison to the experimental (black solid lines) and the KZK model (black dashed lines) results of Baker *et al.* at an axial distance of 50 cm. (b) Predictions of Christopher and Parker (Ref. 17) (black solid lines) at an axial distance of 27.5 cm using the same set of parameters.

of the source. For lower harmonics satisfying $n \leq n_H - 1$, sampling H is not advisable since convolutional wraparound can occur, which may give erroneous results with the FSC algorithm. Exceptions to this hypothesis may occur when either the propagation distance is small compared to the harmonic wavelength, or when the angular spectrum of the source plane is very narrow. The minimum harmonic n_H for which sampling H is reliable can be obtained by first expressing Eq. (11) in terms of the n th wave number, k_n . This equation can then be used to find the minimum harmonic number, n_H , for which frequency domain sampling of H will give accurate results, given the chosen sampling extents and intervals. It is given by

$$n_H = \sqrt{(2\Delta z \gamma \Delta k_x / \pi)^2 + 2\gamma^2}, \quad (14)$$

where $\gamma = k_{x \text{ max}} / k_0$. By selectively using either the SSC or the FSC algorithms in this way, the accuracy of the diffractive substeps can be optimized while minimizing computational cost.

A. Comparison with published data for propagation in water

To verify that our algorithm accurately models nonlinear propagation, we compared our predictions to published theoretical and experimental results, examples of which will be shown. In Fig. 4(a) our lateral profile results for propagation from a plane piston in water are compared to the experimental and KZK simulation results of Baker *et al.*¹¹ Figure 4(b) provides a comparison with the predictions of Christopher and Parker.¹⁷ For our simulations just 20 propagation planes were used, which should be compared to that Baker *et al.* who used a smaller step size in their finite difference code corresponding to over 1000 planes. On the other hand, Christopher and Parker used small steps (about 20 per cm) which would correspond to 550 axial steps for the results shown in Fig. 4(b). For our model, both figures show that the fundamental drops off at around 35 mm on either side of the main lobe. This is because we applied a window taper between 35 and 40 mm to reduce errors associated with abrupt truncation of an infinite-extent field. Except for this, our results and the published data are in excellent agreement.

B. Comparison with the KZK for propagation in tissue

The attenuation of soft tissue is much greater than that for water, and as a result the computational burden should be much reduced. This is because increasing attenuation with frequency requires that fewer harmonics need be retained in order to maintain sufficient accuracy and stability. In order to assess our approach, we compared our results with the KZK results of Averkiou *et al.*³⁴ for a 2-MHz focused disk transducer propagating into a tissue-like medium, whose attenuation depends on frequency ($b = 1.1$). Other details are given in the caption for Fig. 5. For our simulations, we sampled the aperture in the spatial domain, and, like Averkiou *et al.*, modeled the focused disk as a plane piston with a complex spherical phase weighting function of $e^{jk\sqrt{F^2 + r^2}}$, where F is the focal distance. For the results shown in Figs. 5(a) and (b), only 5 harmonics were retained, and just 20 propagation planes were used with a lateral sampling of 2.1 times the Nyquist frequency of the fundamental. For Fig. 5(c), 100 propagation planes were used so as to capture the axial variations of the harmonics, especially in the near field. The deep nulls which are seen in the results of Averkiou *et al.*,³⁴ but not in ours, are due to their finer axial sampling intervals.

Our model avoids the parabolic approximation used in the KZK model for diffraction calculation. However, like the KZK model, we have used the plane impedance relation in order to relate the pressure on a plane (subsequent to the transducer surface) to the normal component of the particle velocity. This approximation is of the same order as the parabolic approximation. Consequently, the accuracy of our model should at least be comparable to that of the KZK model for both near- and far-field calculations not too far off-axis. However, far off-axis for focused sources, our technique may be more accurate than the KZK, since this is where the parabolic approximation fails. Evidence to support this can be obtained from Figs. 5(a) and (d). It should be noted that in Fig. 5(a) considerable differences exist off-axis between our model and that of Averkiou *et al.* In particular, the nulls in the fundamental sidelobes are not in the same location. Like Averkiou *et al.*, we used the same complex apodization function to simulate focusing, which is consis-

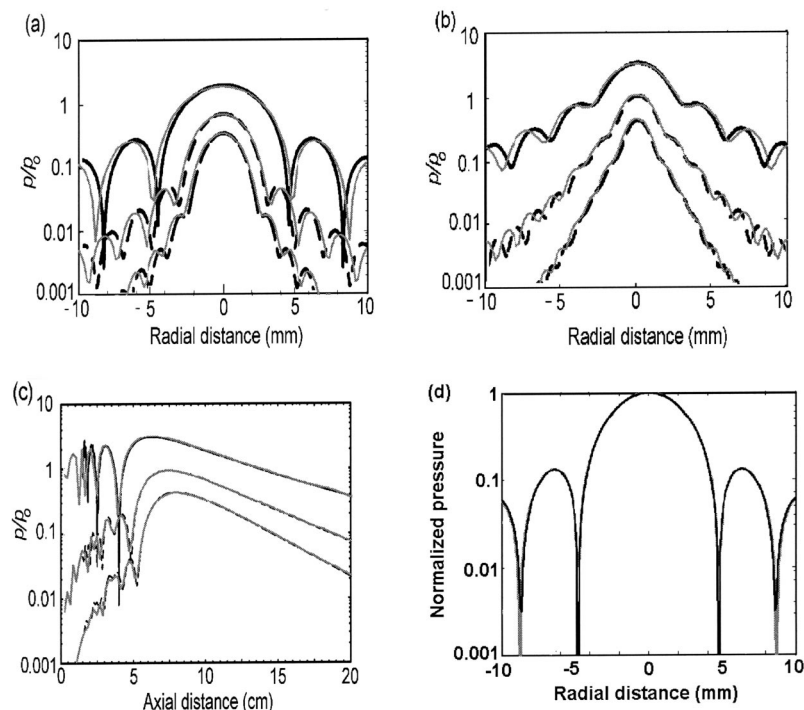


FIG. 5. Comparison of lateral (a)–(b) and axial (c) normalized pressure profiles for the first three harmonics calculated using our model (gray) with those reported by Averkiou *et al.* (Ref. 34) (black) using the KZK model. A circular disk transducer was assumed excited at 2.0 MHz using a source pressure of 372 kPa and having a radius of 1.0 cm with a 10-cm focal length lens. The propagating medium was taken to have the following properties: $\alpha=0.3$ dB/(cm \times MHz $^{1.1}$), $c=1550$ m/s, and $\beta=5.0$. (a) Lateral profiles at the focal distance 10 cm. (b) Lateral profiles at 7.0 cm. (c) Axial profiles. Note in (a) and (b) that off-axis, our results differ somewhat from the KZK results. Shown in (d) is the fundamental lateral profile at 10 cm of our diffraction algorithm compared with the analytical prediction with classic Bessel directivity.

tent with a Fresnel approximation. As shown in Fig. 5(d), we checked our results at low amplitudes with the well-known Fresnel approximation for a focused disk transducer, first obtained by O’Neil,³⁵ and found excellent agreement. Furthermore, the nulls in the sidelobes of Fig. 5(a) corresponded exactly with the location of zeros of the Bessel function used in the Fresnel approximation. Thus, our model, based on the second-order operator-splitting scheme, may offer a new way of improving the accuracy while maintaining or improving computational efficiency.

C. Nonlinear propagation in tissue from a cw linear phased array

We now consider a 64-element 2-MHz linear phased array with no beam steering, no apodization, but with an elevation plane lens ($F=4.0$ cm) and the following dimensions: $H=20$ mm, $W=\lambda/2$, $d=3\lambda/4$, $D=37$ mm. The spatial frequency-domain sampling approach as outlined in Sec. I D was used. Only five harmonics were retained in this cw simulation, where lateral sampling was done at 1.5 times the Nyquist rate of the fundamental, and 50 planes were used in the axial direction out to the focal region. Shown in Figs. 6 and 7 are the simulated azimuthal ($x-z$) and elevation ($y-z$) pressure profiles. As expected, the main-lobe region of the harmonics is much narrower than the fundamental. Moreover, the harmonic sidelobes drop off much faster compared with the fundamental. In phased array B-mode imaging, fundamental sidelobes have been known to be particularly troublesome, causing clutter artifacts. For harmonic sidelobes, however, it seems that attenuation dominates over nonlinearity, and thus, clutter artifacts may be reduced by using the harmonic signal. There is notable harmonic build-up off-axis before the focal region, which may be troublesome for imaging purposes. Moreover, as seen in Fig. 6(a), the last maximum in the focal region is slightly closer

to the transducer than the 4-cm mark. As previously noted for a piston transducer,^{10,36} this can occur if the fundamental band is donating energy to higher harmonics more quickly than it can be focused. A possible misconception concerning one of the advantages of harmonic imaging arises from the belief that the main lobe of the second harmonic beam profile is narrower than the main lobe of the profile generated by direct linear excitation at the second harmonic frequency. To illustrate this issue, we consider a linear array with the dimensions given in the caption to Fig. 8 excited nonlinearly at 2 MHz at a pressure amplitude of 347 kPa. At the focal depth of 10 cm the azimuth and elevation second harmonic lateral profiles are represented by black curves in Figs. 8(a) and (b), respectively. On the other hand, gray curves in the figures are fundamental profiles when the same array is excited at 4 MHz in the absence of any nonlinear propagation. The azimuthal main-lobe profile is narrower than the second harmonic profile; however, the sidelobes of the harmonic profile drop off much faster than the 4-MHz fundamental profile, since attenuation likely dominates over nonlinearity in this region. This characteristic would be of considerable importance in the performance of tissue harmonic imaging systems.

IV. NONLINEAR DISTORTION FOR PULSED EXCITATION

Our approach to modeling nonlinear pulse propagation differs from the cw method described above. Because a time-domain nonlinear algorithm was chosen, it was more efficient to combine diffraction and attenuation and to use the second-order operator-splitting scheme given by Eq. (6). In order to model pulsed propagation the operators in this equation will be time dependent, similar in principle to the time-domain KZK operator splitting technique of Lee and Hamilton.⁹

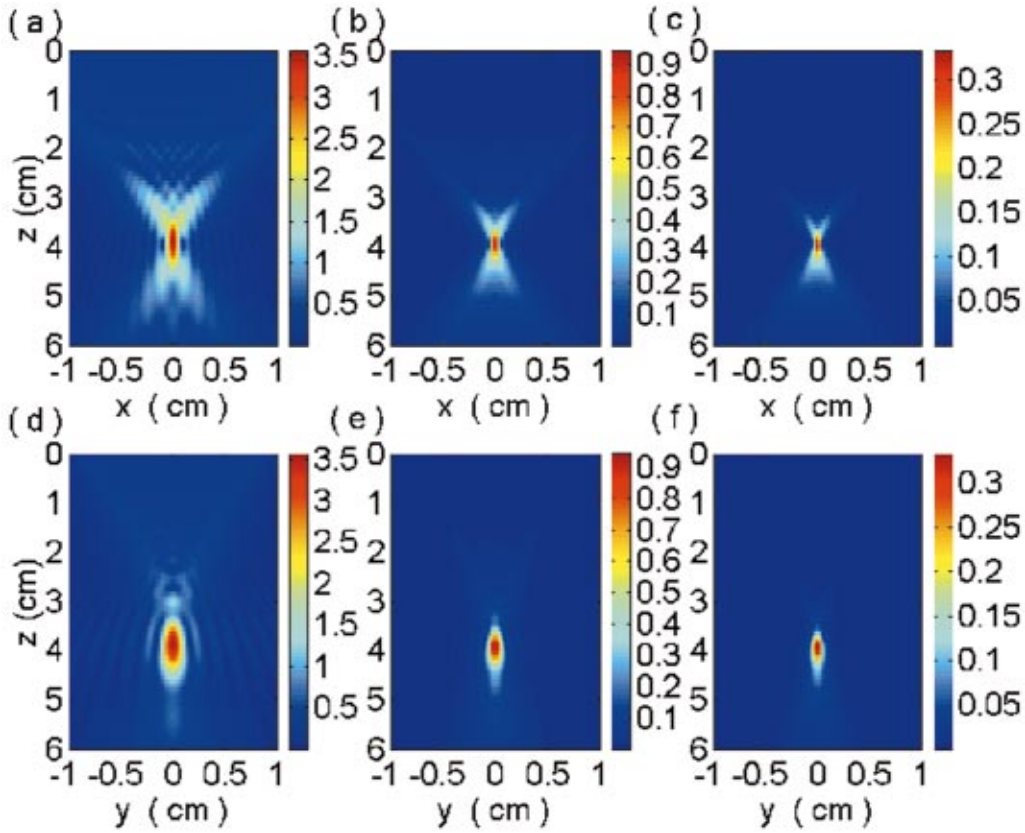


FIG. 6. Azimuthal and elevation profiles for a 64-element 2-MHz cw linear array ($H_e = 10$ mm, $W = \lambda/2$, $d = 3\lambda/4$, $D = 37$ mm) propagating in a soft tissue-like medium. (a) to (c) Azimuthal profiles. (d) to (f) Elevation profiles. (a) and (d) Fundamental, (b) and (e) Second harmonic, and (c) and (f) third harmonic. Focusing in both the azimuthal and elevation directions were at a depth of 4 cm. The tissue parameters used in these simulations were $c = 1550$ m/s, $\rho = 1050$ kg/m³, $\beta = 5$, $\alpha_0 = 3$ dB/(cmMHz^{1.1}), and $b = 1.1$. The source pressure amplitude was 347 kPa and the color scale gives the pressure in MPa.

A. Nonlinear algorithm

The nonlinear substeps were computed using the time-domain algorithm developed by Christopher.³⁷ For short

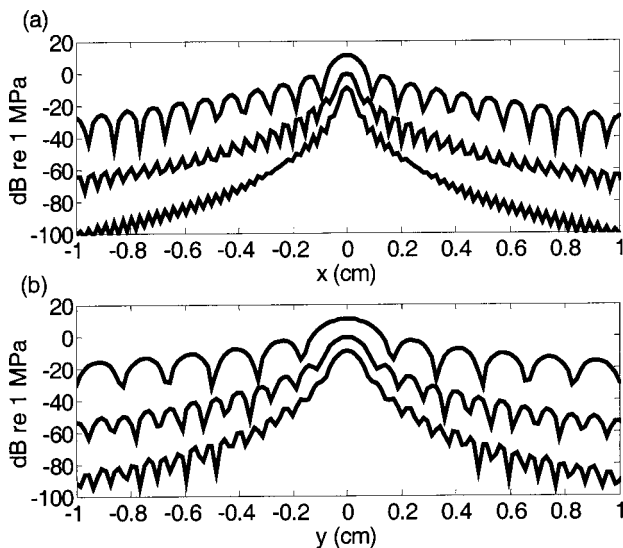


FIG. 7. Lateral cw harmonic pressure profiles from an array transducer in the focal plane along the azimuthal (a) and elevation (b) directions. The fundamental, second, and third harmonics are shown. The parameters are identical to those of Fig. 6.

pulses, an advantage of the time-domain algorithm over a frequency-domain algorithm [such as that expressed by Eq. (13)] is savings in computational cost. It can be shown that the frequency-domain algorithm has a computational complexity on the order of fifth power of the number of frequency components retained for calculations.⁸ For cw sources, just a few harmonics is sufficient to model most nonlinear phenomena in tissue. For pulsed sources, however, a large spectrum of frequency components is needed to model a linear pulse propagation and even more is needed for the harmonic components generated in the nonlinear propagation process. Moreover, as noted earlier, there are instabilities associated with the use of Eq. (13). Although the robust and efficient nature of Christopher's time-domain algorithm was a major asset, its use in combination with our angular spectrum diffraction approach requires the use of two 3D FFTs: an inverse and forward after and before each diffractive substep. While this time-frequency hybrid approach required careful memory management and a reasonably large random access memory, the resulting computational savings and stability outweighed this disadvantage. This time-frequency hybrid algorithm was verified by comparing the results obtained with the frequency-domain solution to Burger's equation for pulsed excitation.

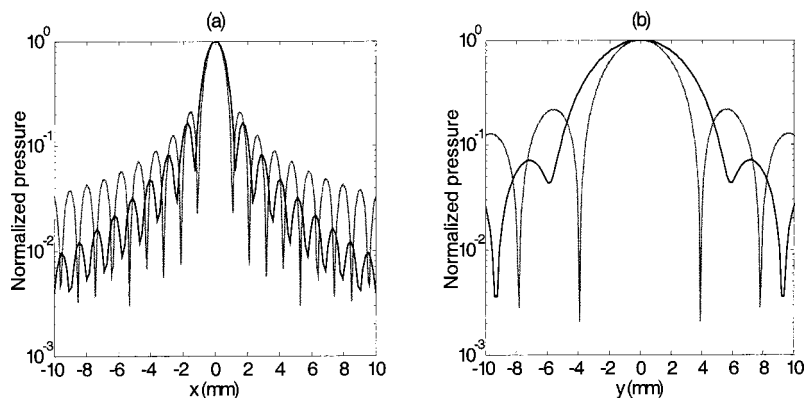


FIG. 8. Azimuthal (a) and elevation (b) lateral profiles at the focal depth of 10 cm of a cw excited 64-element phased array with no elevation lens ($H_e = 10$ mm, $W = \lambda/2$, $d = 3\lambda/4$, $D = 37$ mm). Black lines are nonlinear second harmonic profiles when excited at 2 MHz with a source pressure amplitude of 347 kPa. Gray curves are pressure profiles in the absence of any nonlinear propagation when excited at 4.0 MHz. Note that the harmonic profiles have a wider main lobe than that for the higher frequency source, but much lower sidelobes. The tissue parameters were the same as those used for Fig. 6.

B. Diffraction substep

The development of a diffraction algorithm for nonlinear pulse propagation required that we consider the following issues: (i) selection of temporal sampling; (ii) determining an adequate temporal extent to the signal; (iii) sampling of the propagation planes; and (iv) choosing between the FSC or SSC algorithms for each discrete spectral frequency. The first two are addressed in the next subsection.

C. Temporal sampling and windowing

For nonlinear propagation in tissue, the effect of frequency-dependent attenuation is to attenuate the higher harmonics generated by nonlinearity. Based on our experience with cw propagation in tissue, 5–30 harmonics of the center frequency f_c will often be sufficient, although the number of harmonics needed will vary for different source and excitation parameters. For simulating nonlinear propagation for diagnostic pulse–echo ultrasound systems, a sampling frequency of 5–30 times the Nyquist frequency of $(2f_c + \Delta f)$ of the initial spectrum was adopted for pulsed simulations, where Δf is the -6 -dB bandwidth. The adequacy or otherwise of the sampling rate can be assessed by increasing the sampling rate to see if there is a significant change in the results.

In our plane-to-plane fractional step-marching scheme, temporal aliasing of the signal can be avoided by choosing a sufficiently long temporal window, or pulse repetition interval in the initial signal. Let the pulse duration plus the difference between the shortest and the longest transit times from the transducer plane (for example) to a given location on an adjacent plane be denoted by T_p . Evidently, the temporal window used should be at least of duration T_p so as to avoid temporal wraparound error. To ensure that a pulse is adequately represented in the frequency domain, sampling at $\Delta f \leq (1/2T_p)$ would be needed. The closer the observation plane to the source, the greater the temporal window needed to prevent aliasing.

D. Lateral sampling of the propagation planes

The same considerations apply to the lateral sampling of the propagation planes as in our earlier discussion of cw excitation. The difference in the pulsed case is that such a sampling scheme must adequately propagate the spectrum of frequencies initially present in the source excitation.

E. Sampling of the propagator functions

For each frequency component $f_n = nf_s = n/T_p$, the choice of sampling either the spatial point-spread function h or the frequency-domain transfer function H once again hinges on whether the corresponding radiation circle for the given frequency is wholly or partly contained within the discrete spatial frequency domain. Defining $f_{\max} = f_c + \Delta f/2$ and $\gamma = \zeta f_{\max}/f_s$, the index n_H given in Eq. (14) can again be used to optimally select a sampling scheme as was done in Sec. III.

F. Verification of algorithm

Having verified the accuracy of the nonlinear plane-wave algorithm, and the diffraction algorithm, verification of the full nonlinear propagation algorithm was performed with a few key tests. In the limit as $\beta \rightarrow 0$, the nonlinear algorithm should behave in a linear way. For this test we compared our algorithm with the impulse response method for a plane piston transducer and obtained excellent agreement.

In a second test, the field for quasicontinuous wave pulse produced by a focused disk transducer on-axis was determined using the pulsed nonlinear algorithm and compared to the results from the cw algorithm described earlier. For the cw algorithm a 30-cycle pulse modulated by a cosine taper on the first and last five cycles was used with peak pressure of $p_0 = 250$ kPa. The other simulation parameters were the same as Fig. 5 and Averkiou *et al.*³⁴ The cw algorithm used 30 propagation steps and 25 harmonics. The pulsed algorithm used 45 propagation steps and 25 harmonics. A steady-state region of the resulting propagated pulse on-axis at 10 cm from the transducer was isolated, and one cycle extracted from this region. This cycle is compared with the results from the cw nonlinear propagation algorithm. The peak deviation was 2.5% and the mean-square error averaged over one cycle and normalized by the peak amplitude was 1.2%.

Last, we compared our pulsed algorithm with the frequency-domain solution to Burger's equation for the case of a plane wave in an attenuating medium. Figure 9 shows both the time- and frequency-domain comparisons.

G. Pulse inversion results

The idea of using two transmission pulses, the second being of opposite phase to the first, has been examined as a

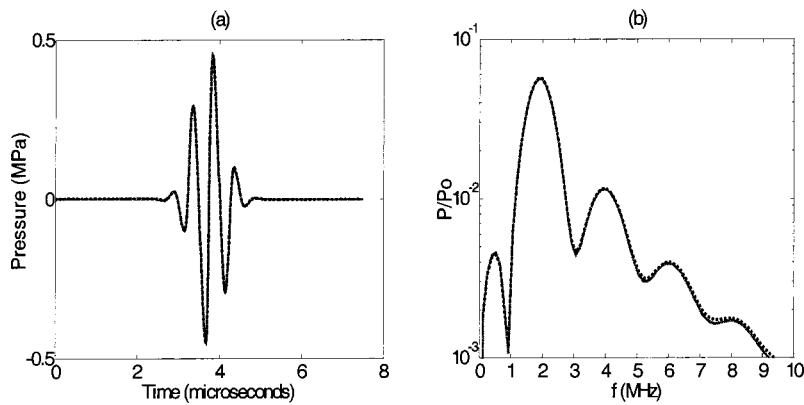


FIG. 9. Comparison between time-domain (gray solid line) and frequency-domain (black dotted line) algorithms for the case of a plane wave in an attenuating medium. The time-domain waveforms (a) differ by less than 1.5%. The frequency spectra (b) are also in good agreement. The initial pulse was given as $p_0 \exp[-(t-t_0)^2/(2\sigma^2)] \sin[2\pi f_0(t-t_0)]$, where $p_0=1$ MPa, $t_0=15/(2f_0)$, $\sigma=\pi/(\sqrt{2}f_0)$, and $f_0=2$ MHz. The waveform propagated a distance of 10 cm in a medium with parameters $c=1500$ m/s, $\rho=1000$ kg/m³, $\beta=3.5$, $b=1.0$, and $\alpha_0=3$ dB/(cm \times MHz^{1.0}).

means of reducing the problems that arise from spectral overlap between the fundamental and second harmonic scattered signals in both tissue harmonic imaging and contrast agent imaging.³⁸ Recently, Li and Zagzebski¹⁵ performed simulation studies of harmonic image formation for a focused disk transducer and demonstrated small improvements to the image quality by using the pulse inversion technique. We also have used this method but have applied it to the more realistic case of a phased linear array, using one-way propagation. Because scattering in tissue is generally weak, the process of reception can be treated as a linear process. Moreover, a composite signal can be formed from the sum of the normal and inverted transmissions. For a Gaussian modulated transmit pulse, the pressure pulse waveform at the focus of a phased array calculated using our nonlinear model together with its spectrum magnitude are shown in Fig.

10(a). The waveform due to transmission of the inverted pulse is shown in Fig. 10(b); it has a very similar though not identical spectrum magnitude. If the scattering process is assumed to be frequency independent over the incident signal bandwidth, then the composite (transmit–receive) signal obtained by adding the above two waveforms is illustrated in (c): it has a spectrum in which the even harmonics is approximately doubled and the odd harmonics as well as the fundamental are almost eliminated. Also seen in this waveform is a low-frequency response whose peak amplitude occurs below 1 MHz. This appears to be produced by a process known as self-demodulation region, a term originally used by Berkta³⁹ to describe low-frequency acoustic generation by nonlinear pulsed high-frequency sound, and which has been experimentally and theoretically investigated for a thermoviscous fluid by Averkiou *et al.*³

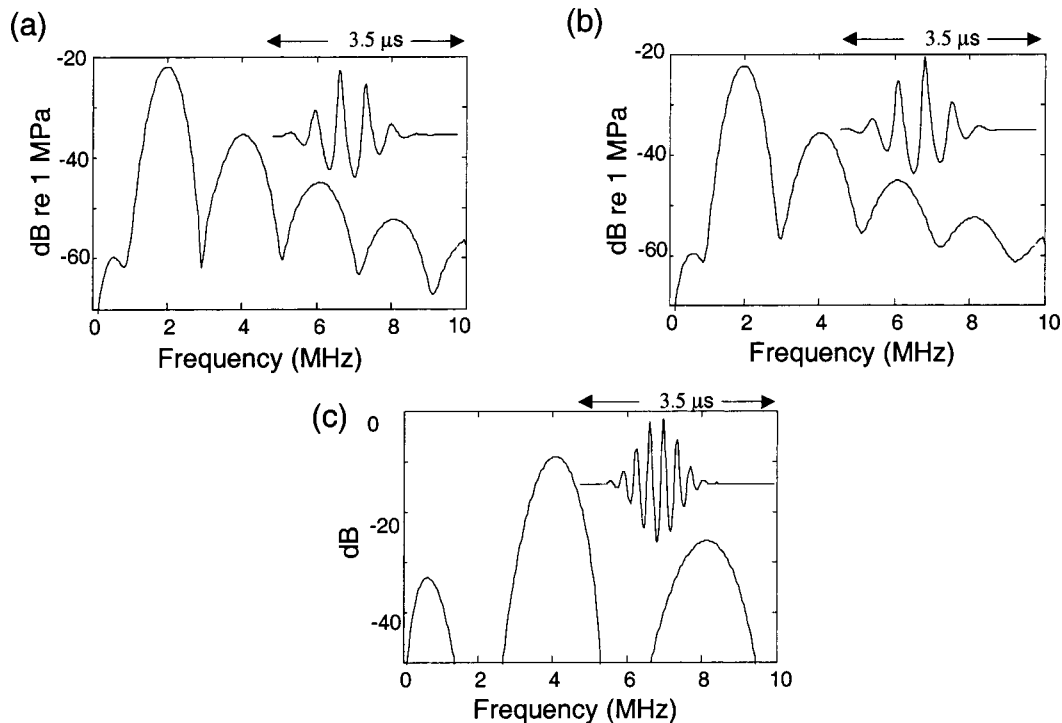


FIG. 10. Illustration of the use of pulse inversion for tissue harmonic imaging at the focal point of a 64-element linear array ($H_e=12$ mm, $W=\lambda_0/2$, $d=5\lambda_0/8$). Focusing in both the azimuthal and elevation directions was at a depth of 5.0 cm. The tissue parameters were the same as those used for Fig. 6. A Gaussian modulated sine wave was assumed as the transmit signal with a center frequency of 2.0 MHz, a 50% bandwidth, and a peak pressure of 400 kPa at the surface of the array. (a) Showing the pressure waveforms at the focal point for the normal and (b) inverted transmit waveforms and their spectra. The waveforms had peak positive values of ~ 2.5 MPa and negative values of ~ -1.5 MPa. (c) Showing the effective pulse inversion waveform, found by adding the two waveforms, and its spectrum. Only 30 propagation planes were used in this simulation, with each nonlinear step employing 4 propagation substeps.

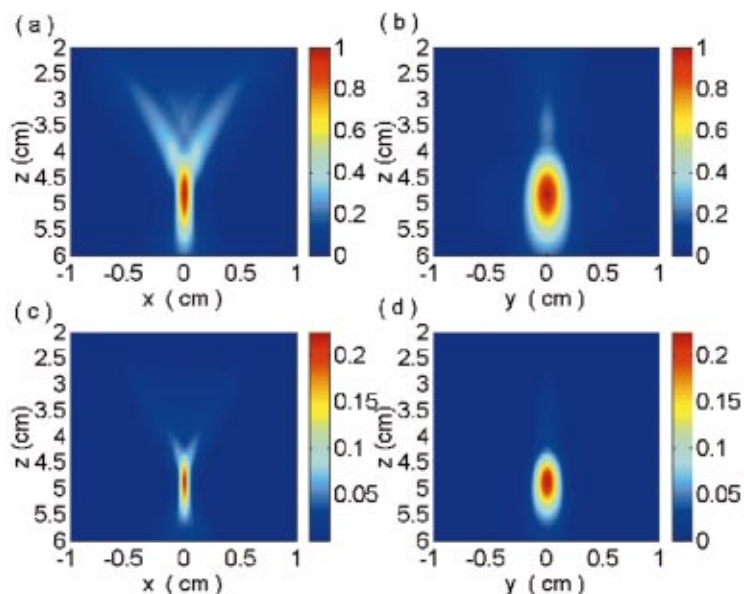


FIG. 11. Normalized second harmonic intensity profiles of a 64-element linear phased array ($H_e = 12$ mm, $W = \lambda_0/2$, $d = 5\lambda_0/8$) for a source waveform consisting of Gaussian modulated sine waves with maximal pressures of 400 kPa, a center frequency of 2 MHz, and a 80% bandwidth. (a) Azimuthal and (b) elevation planes. Effective pulse inversion intensity profiles in the azimuthal (c) and elevation planes (d). These were obtained from the waveform obtained by adding the pressure field distribution produced by an inverted pulse to that of the noninverted pulsed. Azimuthal and elevation focusing were used and both had a focal depth of 5.0 cm. The tissue parameters were the same as those used for Fig. 6. Only 30 propagation planes were used out to the focal region, with each nonlinear step employing 4 propagation substeps.

As a further illustration of the capabilities of the model, the transmitted field was simulated for a linear phased array excited by a Gaussian pulse and propagating into tissue. The field profile in the azimuthal and elevation directions are compared in Figs. 11 and 12 to the effective “pulse inversion field.” This effective field represents the result of two nonlinear transmissions: one with a normal pulse and the second with an inverted pulse. The effective field at each location was determined by adding the two waveforms at each location, thereby eliminating the energy due to linear propagation, leaving only energy due to nonlinear propagation. An alternative method to produce the similar results would have been to use two transmit waveform pulses with the same shape but differing amplitudes, the first having sufficient amplitude to produce nonlinear propagation and the second with a sufficiently small amplitude for linear propagation, and then subtracting the two transmit fields after appropriate normalization. Here again, we assume a frequency independent scatterer. As illustrated in Figs. 11 and 12 the energy distribution due to nonlinear propagation is narrower than the “one-pulse” field, where linear propagation dominates. Such methods for visualizing nonlinear propagation fields may prove useful in quantitative design simulations for tissue harmonic imaging applications.

V. COMPUTATIONAL ISSUES

Our model was developed using MATLAB 5.3 (MathWorks Inc.), and implemented on a PC with a 533-MHz Pentium III processor and 512 MB of random access memory. Full 4D (three dimensions of space and one of time) field simulations were performed for a linear phased array as a realistic nonaxisymmetric source for both the cw and pulsed excitations. For the cw case, calculations took only a few minutes to complete. To model pulsed sources, however, significant memory management was required, and to produce results such as presented in Fig. 11, the code took about 5 h to execute. It is anticipated that this runtime may be significantly shortened by using a larger random access memory and by using a compiled version of the code. Adaptive meshes and nonuniform step sizes may further reduce computational cost.

These results show that, while maintaining the same degree of accuracy, our numerical model for full 4D nonlinear field simulations has a great advantage over similar models in terms of computation burden and stability.

VI. CONCLUSIONS

A computational model of nonlinear propagation in tissue has been developed, which is capable of simulating

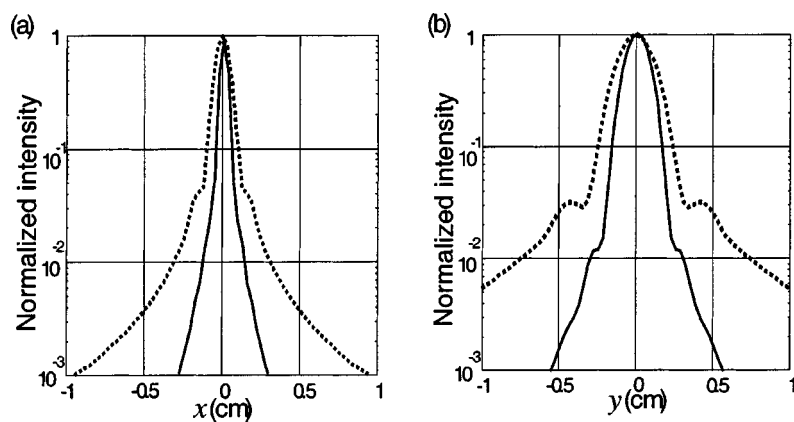


FIG. 12. The azimuthal and elevation focal plane ($z = 5$ cm) intensity profiles for the distributions shown in Fig. 11. (a) Azimuthal pulsed field (dotted) and effective pulse inversion profile (solid). (b) Elevation pulsed field (dotted) and effective pulse inversion profile (solid).

finite-amplitude acoustic fields of nonaxisymmetric sources, including linear phased arrays. Using the computational power of a regular PC desktop computer, the calculation times required for full 4D simulations are on the order of a few minutes for cw sources, and a few (3–5) hours for pulsed sources. Our model is based on a second-order operator-splitting scheme, whereby diffraction, attenuation, and nonlinearity can be computed independently over incremental steps. This scheme allows for larger axial propagation steps compared with first-order models, thus allowing computational savings, while maintaining accuracy.

A numerically implemented angular spectrum approach has been presented that has a modified sampling scheme for efficient computation of diffraction over larger propagation steps. This avoids wraparound errors and as a result has good accuracy even in the near-field region. Nonlinear substeps are computed using standard frequency- and time-domain algorithms for cw and pulsed excitations, respectively.

Comparing beam profiles for 4-MHz second harmonic imaging with 4-MHz fundamental imaging, we found that the 4-MHz fundamental beam was actually narrower than the 4-MHz second harmonic profile; however, the sidelobes of the harmonic profile dropped off much faster than those of the fundamental. Application of our nonlinear propagation model to the pulse inversion scheme was used as a unique way of visualizing nonlinear energy accumulation.

Our nonlinear propagation model compares well with published data for cw nonlinear propagation in both water and tissue. Evidence was given to show that our model may be more accurate than the KZK model off-axis for focused sources, since it avoids the parabolic approximation. Experimental confirmation of the pulsed nonlinear propagation in tissue-like media is planned for future research. The numerical model presented here has the capability to simulate nonlinear propagation from realistic medical ultrasound scanners, and hence may hold significant promise for the design and optimization of tissue harmonic imaging systems, as well as for therapeutic ultrasound systems where nonlinear effects would be prominent.

ACKNOWLEDGMENTS

We much appreciate the helpful comments and suggestions of Ted Christopher, and wish to thank the National Science and Engineering Research Council of Canada and the Canadian Institutes of Health Research for financial support.

- ¹T. G. Muir, "Nonlinear effects in acoustical imaging," in *Acoustical Imaging*, edited by K. Y. Wang, *Proceedings of the 9th International Symposium on Acoustical Imaging* (Plenum, New York, 1980), Vol. 9, pp. 93–109.
- ²B. Ward, A. C. Baker, and V. F. Humphrey, "Nonlinear propagation applied to the improvement of resolution in diagnostic medical imaging," *J. Acoust. Soc. Am.* **101**, 143–154 (1997).
- ³M. A. Averkiou, Y. S. Lee, and M. F. Hamilton, "Self-demodulation of amplitude- and frequency-modulated pulses in a thermoviscous fluid," *J. Acoust. Soc. Am.* **94**, 2876–2883 (1993).
- ⁴T. Christopher, "Finite amplitude distortion-based inhomogeneous pulse echo ultrasonic imaging," *IEEE Trans. Ultrason. Ferroelectr. Freq. Control* **44**, 125–139 (1997).
- ⁵T. Christopher, "Experimental investigation of finite amplitude distortion-

- based, second harmonic pulse echo ultrasonic imaging," *IEEE Trans. Ultrason. Ferroelectr. Freq. Control* **45**, 158–162 (1998).
- ⁶V. F. Humphrey, "Nonlinear propagation in ultrasonic fields: Measurements, modelling, and harmonic imaging," *Ultrasonics* **38**, 267–272 (2000).
- ⁷I. Puls, D. Berg, M. Maurer, M. Schliesser, G. Hetzel, and G. Becker, "Transcranial sonography of the brain parenchyma: comparison of B-mode imaging and tissue harmonic imaging," *Ultrasound Med. Biol.* **26**, 189–194 (2000); S. Tanaka, O. Oshikawa, T. Sasaki, T. Ioka, and H. Tsukuma, "Evaluation of tissue harmonic imaging for the diagnosis of focal liver lesions," *Ultrasound Med. Biol.* **26**, 183–187 (2000).
- ⁸*Nonlinear Acoustics*, edited by M. F. Hamilton and D. T. Blackstock (Academic, New York, 1998).
- ⁹Y. S. Lee and M. F. Hamilton, "Time domain modeling of pulsed finite-amplitude sound beams," *J. Acoust. Soc. Am.* **97**, 906–917 (1995).
- ¹⁰S. I. Aanosen, T. Barkve, J. Naze Tjøtta, and S. Tjøtta, "Distortion and harmonic generation in the near field of a finite amplitude sound beam," *J. Acoust. Soc. Am.* **75**, 749–768 (1984).
- ¹¹A. C. Baker, K. Anastasiadis, and V. F. Humphrey, "The nonlinear pressure field of a plane circular piston: Theory and experiment," *J. Acoust. Soc. Am.* **84**, 1483–1487 (1988).
- ¹²A. C. Baker and V. F. Humphrey, "Distortion and high frequency generation due to nonlinear propagation of short ultrasonic pulses from a plane circular piston," *J. Acoust. Soc. Am.* **92**, 1699–1705 (1992).
- ¹³M. D. Cahill and A. C. Baker, "Increased off-axis energy deposition due to diffraction and nonlinear propagation of ultrasound from rectangular sources," *J. Acoust. Soc. Am.* **102**, 199–203 (1997).
- ¹⁴M. D. Cahill and A. C. Baker, "Numerical simulation of the acoustic field of a phased-array medical ultrasound scanner," *J. Acoust. Soc. Am.* **104**, 1274–1284 (1998).
- ¹⁵Y. Li and J. A. Zagzebski, "Computer model for harmonic ultrasound imaging," *IEEE Trans. Ultrason. Ferroelectr. Freq. Control* **47**, 1000–1013 (2000).
- ¹⁶P. T. Christopher and K. J. Parker, "New approaches to the linear propagation of acoustic fields," *J. Acoust. Soc. Am.* **90**, 507–521 (1991).
- ¹⁷P. T. Christopher and K. J. Parker, "New approaches to nonlinear diffractive field propagation," *J. Acoust. Soc. Am.* **90**, 488–499 (1991).
- ¹⁸T. Christopher, "Modeling the Dornier HM3 lithotripter," *J. Acoust. Soc. Am.* **95**, 3088–3095 (1994).
- ¹⁹J. Tavakkoli, D. Cathignol, R. Souchon, and O. A. Sapozhnikov, "Modeling of pulsed finite-amplitude focused sound beams in time domain," *J. Acoust. Soc. Am.* **104**, 2061–2072 (1998).
- ²⁰J. P. Remenieras, O. Bou Matar, V. Labat, and F. Patat, "Time-domain modeling of nonlinear distortion of pulsed finite amplitude sound beams," *Ultrasonics* **38**, 305–311 (2000).
- ²¹V. A. Khokhlova, R. Souchon, J. Tavakkoli, O. A. Sapozhnikov, and D. Cathignol, "Numerical modeling of finite amplitude sound beams: Shock formation in the near field of a cw plane piston source," *J. Acoust. Soc. Am.* **110**, 95–108 (2001).
- ²²R. J. Zemp, "Modeling Nonlinear Ultrasound Propagation in Tissue," M.A.Sc. thesis, University of Toronto, 2000. (www.bme.ucdavis.edu/~rzemp/utoronto/rz_thesis2000.htm)
- ²³D. Gaskill, *Linear Systems, Fourier Transforms, and Optics* (Wiley, New York, 1978).
- ²⁴J. W. Goodman, *Introduction to Fourier Optics*, 2nd ed. (McGraw-Hill, New York, 1996).
- ²⁵P. Wu, R. Kazys, and T. Stepinski, "Analysis of the numerically implemented angular spectrum approach based on the evaluation of two-dimensional acoustic fields. I. Errors due to the discrete Fourier transform and discretization," *J. Acoust. Soc. Am.* **99**, 1339–1348 (1996).
- ²⁶P. Wu, R. Kazys, and T. Stepinski, "Analysis of the numerically implemented angular spectrum approach based on the evaluation of two-dimensional acoustic fields. II. Characteristics as a function of angular range," *J. Acoust. Soc. Am.* **99**, 1349–1359 (1996).
- ²⁷P. Wu, R. Kazys, and T. Stepinski, "Optimal selection of parameters for the angular spectrum approach to numerically evaluate acoustic fields," *J. Acoust. Soc. Am.* **101**, 125–134 (1997).
- ²⁸T. D. Mast, L. P. Souriau, D. Liu, M. Tabei, A. I. Nachman, and R. C. Waag, "A k-space method for large-scale models of wave propagation in tissue," *IEEE Trans. Ultrason. Ferroelectr. Freq. Control* **48**, 341–354 (2001).
- ²⁹Q. H. Liu, "The pseudospectral time-domain (PSTD) algorithm for acoustic waves in absorptive media," *IEEE Trans. Ultrason. Ferroelectr. Freq. Control* **45**, 1044–1055 (1998).

- ³⁰R. C. Waag, J. A. Campbell, J. Ridder, and P. R. Mesdag, "Cross-sectional measurements and extrapolations of ultrasonic fields," *IEEE Trans. Ultrason. Ferroelectr. Freq. Control* **32**, 26–35 (1985).
- ³¹P. Wu and T. Stepinski, "Extension of the angular spectrum approach to curved radiators," *J. Acoust. Soc. Am.* **105**, 2618–2627 (1999).
- ³²J. L. San Emeterio and L. G. Ullate, "Diffraction impulse response of rectangular transducers," *J. Acoust. Soc. Am.* **92**, 651–662 (1992).
- ³³M. E. Haran and B. D. Cook, "Distortion of finite amplitude ultrasound in lossy media," *J. Acoust. Soc. Am.* **73**, 774–779 (1983); D. H. Trivett and A. L. Van Buren, "Comments on 'Distortion of finite amplitude ultrasound in lossy media' [*J. Acoust. Soc. Am.* **73**, 774–779 (1983)]," *J. Acoust. Soc. Am.* **76**, 1257–1258 (1984).
- ³⁴M. A. Averkiou, D. N. Roundhill, and J. E. Powers, "A new imaging technique based on the nonlinear properties of tissue," 1997 IEEE Ultrasonics Symp. Proc., 1561–1566 (1997).
- ³⁵H. T. O'Neil, "Theory of focusing radiators," *J. Acoust. Soc. Am.* **21**, 516–526 (1949).
- ³⁶S. Nachev, D. Cathignol, J. N. Tjotta, A. M. Berg, and S. Tjotta, "Investigation of a high intensity sound beam from a plane transducer. Experimental and theoretical results," *J. Acoust. Soc. Am.* **98**, 2303–2323 (1995).
- ³⁷P. T. Christopher, "A nonlinear plane-wave algorithm for diffractive propagation involving shock waves," *J. Comput. Acoust.* **1**, 371–393 (1993).
- ³⁸D. H. Simpson, T. C. Chien, and P. N. Burns, "Pulse inversion Doppler: A new method for detecting nonlinear echoes from microbubble contrast agents," *IEEE Trans. Ultrason. Ferroelectr. Freq. Control* **46**, 372–381 (1999).
- ³⁹H. O. Berkta, "Possible exploitation of non-linear acoustics in underwater transmitting applications," *J. Sound Vib.* **2**, 435–461 (1965).

Acoustic streaming generated by standing waves in two-dimensional channels of arbitrary width

Mark F. Hamilton, Yurii A. Ilinskii, and Evgenia A. Zabolotskaya

Department of Mechanical Engineering, The University of Texas at Austin, Austin, Texas 78712-1063,
and Applied Research Laboratories, The University of Texas at Austin, Austin, Texas 78713-8029

(Received 18 June 2002; revised 5 October 2002; accepted 14 October 2002)

An analytic solution is derived for acoustic streaming generated by a standing wave in a viscous fluid that occupies a two-dimensional channel of arbitrary width. The main restriction is that the boundary layer thickness is a small fraction of the acoustic wavelength. Both the outer, Rayleigh streaming vortices and the inner, boundary layer vortices are accurately described. For wide channels and outside the boundary layer, the solution is in agreement with results obtained by others for Rayleigh streaming. As channel width is reduced, the inner vortices increase in size relative to the Rayleigh vortices. For channel widths less than about 10 times the boundary layer thickness, the Rayleigh vortices disappear and only the inner vortices exist. The obtained solution is compared with those derived by Rayleigh, Westervelt, Nyborg, and Zarembo. © 2003 Acoustical Society of America. [DOI: 10.1121/1.1528928]

PACS numbers: 43.25.Nm [RR]

I. INTRODUCTION

Acoustic streaming generated by a plane standing wave in a two-dimensional channel of arbitrary width is investigated analytically. The streaming is produced in a viscous fluid by shear forces in the boundary layer along the channel walls. The problem was solved initially by Rayleigh¹ for a wide channel, in which the boundary layer thickness is negligible in comparison with channel width. His solution describes the steady vortices outside the boundary layer, commonly referred to now as Rayleigh streaming. Various modifications of Rayleigh's solution have been proposed, most notably by Westervelt² and Nyborg,³ but until very recently the focus has been on streaming outside the boundary layer, and there was previously no need to remove the restriction to wide channels. See Nyborg^{3,4} for more detailed discussion of these and other relevant investigations.

It is well known that inside the boundary layer there exist streaming vortices whose directions of rotation are opposite those of the outer, Rayleigh streaming vortices.⁵ In the 1950s there began a series of investigations of a related phenomenon, the inner streaming vortices produced by oscillatory flow near cylinders. In these studies the inner vortices were comparable in thickness to the cylinder radii, and consequently they were easily observed in experiments. This series of investigations is also reviewed by Nyborg.^{3,4}

A theoretical analysis of the inner streaming vortices generated by a standing wave in grazing contact with a plane boundary in a semi-infinite fluid was conducted by Zarembo⁶ and discussed by Rudenko and Soluyan.⁷ In this case the effective channel width is infinite, and therefore application to narrow channels is automatically excluded. But more important, the solution for the standing wave was derived by assuming it to be divergence-free, and this approximation causes the solution for streaming in the boundary layer to deviate from the correct result.

During 2001 there appeared the first two investigations of streaming in which the restriction to narrow channels was removed. The first of these, by Waxler,⁸ presents a method for calculating the streaming in a thermoviscous gas confined

by parallel plates with arbitrary separation. The second, by Bailliet *et al.*,⁹ adds thermal conductivity and temperature dependence of the viscosity, and considers cylindrical tubes as well as parallel plates. Both investigations assume the existence of a mean temperature gradient along the channel walls, connected with their focus on thermoacoustic engine stacks, and therefore numerical integration is required to calculate the streaming velocity. The latter investigation⁹ reveals the prominence of the inner streaming vortices in narrow channels, but the analysis is based on the Eulerian streaming velocity, and proper interpretation requires analysis of the average mass transport velocity.

In the present paper, a completely analytic solution is derived for the average mass transport velocity generated by a standing wave confined by parallel plates. Temperature effects are not considered here. The solution is valid for channels of arbitrary width. For wide channels and outside the boundary layer, the solution is in agreement with classical results for Rayleigh streaming.¹⁻³ As channel width is reduced, the inner vortices increase in size relative to the Rayleigh vortices. For sufficiently narrow channels (widths less than about ten times the boundary layer thickness) the Rayleigh vortices disappear and only the inner vortices exist. The present work was motivated by observations of streaming patterns calculated numerically for the interior of thermoacoustic engine stacks,¹⁰ whose pore widths are on the order of the boundary layer thickness.

II. STANDING WAVE FIELD

We consider a two-dimensional rectangular resonator with rigid walls that occupies the volume defined by $-x_0 \leq x \leq x_0$, $-y_0 \leq y \leq y_0$, as shown in Fig. 1. The fluid is assumed to be viscous, but not heat conducting. Excitation of the sound field inside is assumed to be accomplished by shaking the resonator along the x axis with velocity $v(t)$. In an Eulerian coordinate system attached to the resonator, both the x and y components of the particle velocity vanish at the walls. From symmetry considerations, the x component u_x

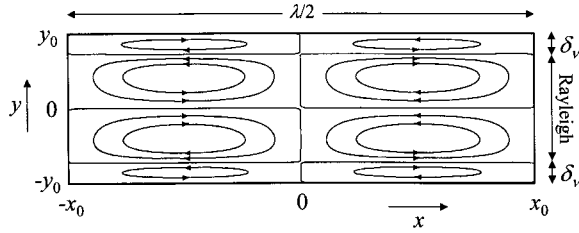


FIG. 1. Acoustic streaming patterns in a resonator with rigid ends, excited in its lowest mode.

must be an even function of y , such that $\partial u_x / \partial y = 0$ at $y = 0$. The y component u_y must be an odd function of y , such that it vanishes at $y = 0$.

The viscous penetration depth is assumed to be very small compared with the acoustic wavelength. For a resonator driven in its lowest mode this condition corresponds to $x_0 \gg \nu / c_0$, where ν is the kinematic viscosity and c_0 is the small-signal sound speed. This restriction is very weak in practice. Under this condition, the leading-order approximations of the linearized continuity, momentum, and state equations in the Eulerian coordinate system attached to the resonator are¹¹

$$\frac{1}{\rho_0} \frac{\partial \rho'}{\partial t} + \frac{\partial u_x}{\partial x} + \frac{\partial u_y}{\partial y} = 0, \quad (1)$$

$$\rho_0 \frac{\partial u_x}{\partial t} + \frac{\partial p}{\partial x} = \mu \frac{\partial^2 u_x}{\partial y^2} - \rho_0 \dot{v}(t), \quad (2)$$

$$\frac{\partial p}{\partial y} = 0, \quad (3)$$

$$p = c_0^2 \rho'. \quad (4)$$

In the continuity equation, Eq. (1), ρ_0 and ρ' are the ambient and excess densities, respectively. In the x component of the momentum equation, Eq. (2), μ is the shear viscosity ($\nu = \mu / \rho_0$), and the term $-\rho_0 \dot{v}(t)$ may be regarded as a body force per unit volume. The y component, Eq. (3), indicates that the acoustic pressure p is constant across the channel.

Now assume harmonic excitation of the resonator,

$$v(t) = \frac{1}{2} v_0 e^{i\omega t} + \text{c.c.}, \quad (5)$$

in which case

$$u_{x,y} = \frac{1}{2} \tilde{u}_{x,y}(x, y) e^{i\omega t} + \text{c.c.}, \quad p = \frac{1}{2} \tilde{p}(x) e^{i\omega t} + \text{c.c.}, \quad (6)$$

where the functional form of p follows from Eq. (3). Equations (1) and (2) thus become

$$\frac{i\omega}{\rho_0 c_0^2} \tilde{p} + \frac{\partial \tilde{u}_x}{\partial x} + \frac{\partial \tilde{u}_y}{\partial y} = 0, \quad (7)$$

$$\tilde{u}_x + \frac{1}{i\omega \rho_0} \frac{d\tilde{p}}{dx} = \frac{\nu}{i\omega} \frac{\partial^2 \tilde{u}_x}{\partial y^2} - v_0. \quad (8)$$

Since \tilde{p} is a function of x alone we introduce the quantity

$$\tilde{u}_{x0}(x) = -\frac{1}{i\omega \rho_0} \frac{d\tilde{p}}{dx} - v_0 \quad (9)$$

in Eq. (8). The general solution of Eq. (8), taking into account that $\partial \tilde{u}_x / \partial y = 0$ at $y = 0$, is

$$\tilde{u}_x = \tilde{u}_{x0}(x) + A(x) \cosh \beta y, \quad (10)$$

where

$$\beta = \frac{1+i}{\delta_\nu}, \quad \delta_\nu = \sqrt{\frac{2\nu}{\omega}}, \quad (11)$$

and δ_ν is the viscous penetration depth. Since the particle velocity vanishes at the wall we have $\tilde{u}_x = 0$ at $y = \pm y_0$, which yields $A = -\tilde{u}_{x0} / \cosh \beta y_0$ and thus

$$\tilde{u}_x = \tilde{u}_{x0}(x) \left(1 - \frac{\cosh \beta y}{\cosh \beta y_0} \right). \quad (12)$$

The x dependence of the particle velocity field is determined by averaging the continuity and momentum equations across the channel. To this end we introduce U_x , the average particle velocity (a normalized axial volume velocity) in the x direction:

$$U_x(x) = \frac{1}{2y_0} \int_{-y_0}^{y_0} \tilde{u}_x(x, y) dy. \quad (13)$$

Substitution of Eq. (12) yields

$$U_x = (1 - f_\nu) \tilde{u}_{x0}(x), \quad (14)$$

where

$$f_\nu = \frac{\tanh \beta y_0}{\beta y_0}, \quad (15)$$

and Eq. (12) becomes

$$\tilde{u}_x = \frac{U_x(x)}{1 - f_\nu} \left(1 - \frac{\cosh \beta y}{\cosh \beta y_0} \right). \quad (16)$$

The transverse velocity component is determined by integrating the terms in Eq. (7) with respect to y from 0 to y , noting that $\tilde{u}_y = 0$ at $y = 0$:

$$\tilde{u}_y = - \int_0^y \frac{\partial \tilde{u}_x}{\partial x} dy - \frac{i\omega y}{\rho_0 c_0^2} \tilde{p}(x). \quad (17)$$

Averaging the terms in Eq. (7) with respect to y , across the channel from $-y_0$ to y_0 , gives

$$\frac{dU_x}{dx} + \frac{i\omega}{\rho_0 c_0^2} \tilde{p}(x) = 0, \quad (18)$$

where the boundary conditions $\tilde{u}_y = 0$ at $y = \pm y_0$ were taken into account. Performing the same integral over the momentum equation, Eq. (8), yields

$$U_x(x) + \frac{1}{i\omega \rho_0} \frac{d\tilde{p}}{dx} = \frac{\nu}{i\omega y_0} \frac{\partial \tilde{u}_x}{\partial y} \bigg|_{y_0} - v_0, \quad (19)$$

where we have used the symmetry relation $\partial \tilde{u}_x / \partial y|_{-y_0}^{y_0} = 2(\partial \tilde{u}_x / \partial y)|_{y=y_0}$. From Eq. (16) one obtains

$$\frac{\nu}{i\omega y_0} \frac{\partial \tilde{u}_x}{\partial y} \bigg|_{y_0} = -\frac{f_\nu U_x}{1 - f_\nu}, \quad (20)$$

and Eq. (19) becomes

$$\frac{1}{i\omega\rho_0} \frac{d\tilde{p}}{dx} + \frac{U_x(x)}{1-f_\nu} = -v_0. \quad (21)$$

Combining Eqs. (18) and (21) to eliminate \tilde{p} yields

$$\frac{d^2 U_x}{dx^2} - \alpha^2 U_x = -\frac{\omega^2}{c_0^2} v_0, \quad (22)$$

where

$$\alpha = \frac{i\omega/c_0}{\sqrt{1-f_\nu}}. \quad (23)$$

The general solution of Eq. (22) is

$$U_x = A \cosh \alpha x + B \sinh \alpha x + C. \quad (24)$$

Substitution in Eq. (22) determines C , and the boundary conditions $U_x = 0$ at $x = \pm x_0$ determine A and B :

$$U_x = (1-f_\nu)v_0 \left(\frac{\cosh \alpha x}{\cosh \alpha x_0} - 1 \right). \quad (25)$$

From Eq. (14) we also have

$$\tilde{u}_{x0} = v_0 \left(\frac{\cosh \alpha x}{\cosh \alpha x_0} - 1 \right). \quad (26)$$

The acoustic pressure is obtained from Eq. (18),

$$\tilde{p} = -\rho_0 c_0 v_0 (1-f_\nu)^{1/2} \frac{\sinh \alpha x}{\cosh \alpha x_0}, \quad (27)$$

and the axial component of the particle velocity follows from Eqs. (12) and (26):

$$\tilde{u}_x = -v_0 \left(1 - \frac{\cosh \alpha x}{\cosh \alpha x_0} \right) \left(1 - \frac{\cosh \beta y}{\cosh \beta y_0} \right). \quad (28)$$

Substitution of Eqs. (27) and (28) in (17) yields

$$\tilde{u}_y = -v_0 y_0 \alpha f_\nu \frac{\sinh \alpha x}{\cosh \alpha x_0} \left(\frac{y}{y_0} - \frac{\sinh \beta y}{\sinh \beta y_0} \right). \quad (29)$$

Equations (27)–(29) are the complete linear solutions for the acoustic pressure and particle velocity in the resonator, and they are free of any restriction on channel width.

It may be noted that both \tilde{u}_x and \tilde{u}_y vanish along the side walls, at $y = \pm y_0$, but only \tilde{u}_x vanishes at the ends, $x = \pm x_0$. However, the ends of the resonator influence the sound field only within distance $\sim \delta_\nu$. Since the boundary layer thickness is negligible compared with resonator length, the boundary conditions on \tilde{u}_y at $x = \pm x_0$ have negligible influence on the field in the volume of the resonator.

Before displaying velocity profiles it is useful to consider limiting forms of the solution for wide and narrow channels. For wide channels (large y_0/δ_ν) one obtains, for the particle velocity field outside the boundary layer,

$$\tilde{u}_x \approx v_0 \left(\frac{\cos \tilde{k}x}{\cos \tilde{k}x_0} - 1 \right), \quad (30)$$

$$\tilde{u}_y \approx (1-i) \frac{v_0 \delta_\nu \omega}{2c_0} \frac{\sin \tilde{k}x}{\cos \tilde{k}x_0} \frac{y}{y_0}, \quad (31)$$

in which \tilde{k} is a complex wave number:

$$\tilde{k} = \frac{\omega/c_0}{\sqrt{1-f_\nu}} \approx \frac{\omega}{c_0} + (1-i) \frac{\sqrt{2\nu\omega}}{4y_0 c_0}. \quad (32)$$

The profile of \tilde{u}_x exhibits no y dependence, and the profile of \tilde{u}_y is linear in y . The last term in Eq. (32) is the classical result for attenuation and dispersion associated with a plane wave propagating in a wide channel formed by parallel plates separated by distance $2y_0$.¹²

For narrow channels (small y_0/δ_ν) one obtains

$$\tilde{u}_x \approx -i \frac{v_0 y_0^2}{\delta_\nu^2} \left(1 - \frac{\cosh \alpha x}{\cosh \alpha x_0} \right) \left(1 - \frac{y^2}{y_0^2} \right), \quad (33)$$

$$\tilde{u}_y \approx (1-i) \frac{v_0 y_0^2 \omega}{2\sqrt{3} \delta_\nu c_0} \frac{\sinh \alpha x}{\cosh \alpha x_0} \left(\frac{y}{y_0} - \frac{y^3}{y_0^3} \right). \quad (34)$$

In this limit the profile of \tilde{u}_x is parabolic in y and the profile of \tilde{u}_y is somewhat sinusoidal in appearance, with extrema at $y/y_0 = \pm 1/\sqrt{3} \approx \pm 0.58$.

We now return to the complete solution, Eqs. (28) and (29), in which the y dependence of $\tilde{u}_{x,y}$ is denoted $Y_{x,y}(y)$:

$$Y_x(y) = 1 - \frac{\cosh \beta y}{\cosh \beta y_0}, \quad Y_y(y) = \frac{y}{y_0} - \frac{\sinh \beta y}{\sinh \beta y_0}. \quad (35)$$

These functions are graphed in Fig. 2 for several values of the dimensionless channel width y_0/δ_ν , with solid lines for $|Y_x|$ and dashed lines for $|Y_y| \operatorname{sgn} y$ (the reason for including $\operatorname{sgn} y$ is to account for change in direction at the midplane). Figures 2(a) and (b) are examples of wide channels, for which the velocity field outside the boundary layer is approximated reasonably well by Eqs. (30) and (31). The value $y_0/\delta_\nu = 2$ in Fig. 2(d) is a nominal pore size for stacks in thermoacoustic engines,¹³ and the y dependencies are approaching those expressed in Eqs. (33) and (34).

Equations (28) and (29) may be compared with expressions used by others to describe a standing wave that drives acoustic streaming in a channel. Rayleigh's solution for a standing wave in a wide channel, Eqs. (23) and (24) in *The Theory of Sound*,¹ is virtually indistinguishable from the results in Figs. 2(a) and (b). Deviations become significant only for smaller values of y_0/δ_ν , such as those used in Figs. 2(c) and (d). Moreover, Rayleigh's solution is often presented^{2,3} with an approximation based on the assumption that $y/y_0 \approx 1$, because the sound field outside the boundary layer has negligible influence on acoustic streaming.

III. ACOUSTIC STREAMING

A. Basic equations

Here we include terms of second order in the acoustic variables to determine the acoustic streaming. The analysis begins with the x component of the momentum equation, approximated by assuming that the viscous penetration depth is a very small fraction of a wavelength:¹¹

$$\frac{\partial(\rho u_x)}{\partial t} + \frac{\partial(\rho u_x^2)}{\partial x} + \frac{\partial(\rho u_x u_y)}{\partial y} = -\frac{\partial p}{\partial x} + \mu \frac{\partial^2 u_x}{\partial y^2} - \rho \dot{v}(t), \quad (36)$$

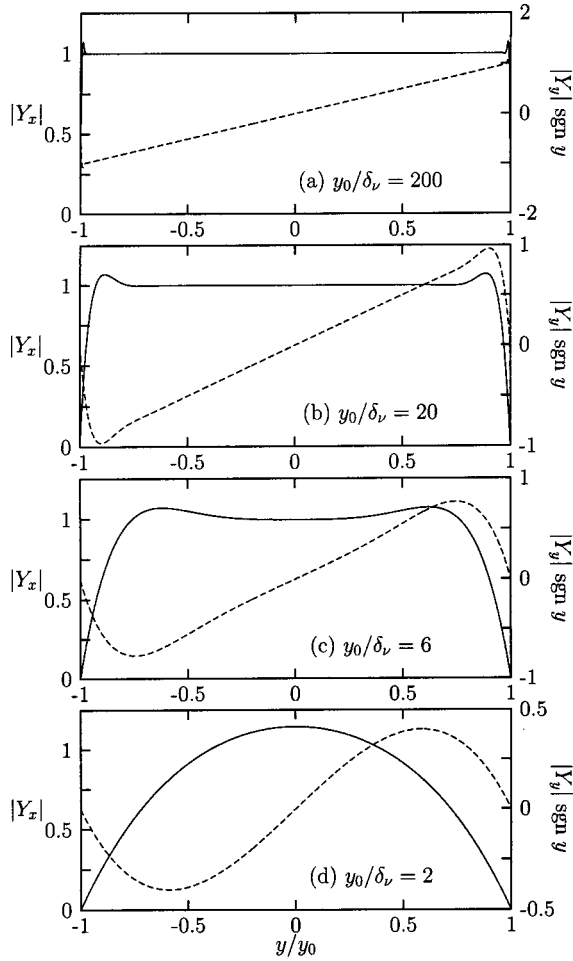


FIG. 2. Profiles of the x (solid lines) and y (dashed lines) components of the acoustic particle velocity for standing waves in channels of different widths.

where $\rho = \rho_0 + \rho'$ is the total density. Taking the time average of Eq. (36) yields

$$\mu \frac{\partial^2 \bar{u}_x}{\partial y^2} = K(x) - F(x, y), \quad (37)$$

where at second order

$$K(x) = \frac{d\bar{p}}{dx} + \frac{\langle p\dot{v} \rangle}{c_0^2}, \quad (38)$$

$$F(x, y) = -\rho_0 \frac{\partial \langle u_x^2 \rangle}{\partial x} - \rho_0 \frac{\partial \langle u_x u_y \rangle}{\partial y}, \quad (39)$$

in which Eq. (4) was used. The angular brackets $\langle \cdot \rangle$ indicate the time average of the quantity inside, and we define $\bar{u}_{x,y} = \langle u_{x,y} \rangle$ and $\bar{p} = \langle p \rangle$ for the acoustic streaming velocity components and dc pressure, respectively. Without the term corresponding to the source excitation $v(t)$, Eqs. (37)–(39) constitute a common starting point for investigating streaming in channels.³

The principal difference here is that Eqs. (27)–(29) for the sound field are for channels of arbitrary width, in contrast to classical analyses, which apply to only wide channels.^{1–3,6,7} In addition, previous analyses do not consider a specific source excitation, but instead just the existence of a standing wave in the channel. Here, a velocity source ap-

pears as the last term in Eqs. (36) and (38). With the source condition given by Eq. (5), the acoustic field is given in the first approximation by Eqs. (6), such that Eqs. (38) and (39) become

$$K(x) = \frac{d\bar{p}}{dx} + \frac{\omega \text{Im} \tilde{p} v_0^*}{2c_0^2}, \quad (40)$$

$$F(x, y) = -\frac{\rho_0}{2} \left(\frac{\partial |\tilde{u}_x|^2}{\partial x} + \text{Re} \frac{\partial (\tilde{u}_x \tilde{u}_y^*)}{\partial y} \right), \quad (41)$$

where the asterisk indicates the complex conjugate.

The solution procedure is as follows. Equation (37) is integrated twice with respect to y to solve for \bar{u}_x , the x component of the Eulerian streaming velocity vector $\bar{\mathbf{u}}$. The quantity ultimately of interest is the average mass transport velocity $\bar{\mathbf{u}}^M$ given by³

$$\bar{\mathbf{u}}^M = \bar{\mathbf{u}} + \langle \rho' \mathbf{u} \rangle / \rho_0, \quad (42)$$

where \mathbf{u} is the acoustic particle velocity. Making use of Eqs. (4) and (6) one obtains

$$\bar{\mathbf{u}}^M = \bar{\mathbf{u}} + \frac{\text{Re} \tilde{p} \tilde{\mathbf{u}}^*}{2\rho_0 c_0^2}. \quad (43)$$

Given \bar{u}_x , \bar{p} and \tilde{u}_x , the x component \bar{u}_x^M is determined. Since the mass transport velocity is by definition divergence-free, its y component \bar{u}_y^M is obtained by integrating

$$\nabla \cdot \bar{\mathbf{u}}^M = 0 \quad (44)$$

with respect to y . The streaming patterns presented in Sec. III C correspond to the vector field $\bar{\mathbf{u}}^M$.

A related quantity, considered by Rayleigh¹ and discussed in greater detail by Westervelt,² is the average Lagrangian streaming velocity $\bar{\mathbf{u}}^L$:

$$\bar{\mathbf{u}}^L = \bar{\mathbf{u}} + \langle \xi \cdot \nabla \mathbf{u} \rangle, \quad (45)$$

where $\xi = \int \mathbf{u} dt$ is the acoustic particle displacement. Like $\bar{\mathbf{u}}^M$, $\bar{\mathbf{u}}^L$ is also divergence-free at second order² (whereas $\bar{\mathbf{u}}$ is not). For all one-dimensional acoustic fields $\langle \rho' \mathbf{u} \rangle / \rho_0 = \langle \xi \cdot \nabla \mathbf{u} \rangle$ and therefore $\bar{\mathbf{u}}^M = \bar{\mathbf{u}}^L$. For plane standing waves, in which ρ' and \mathbf{u} differ in phase by 90 degrees, $\langle \rho' \mathbf{u} \rangle$ is zero and thus $\bar{\mathbf{u}} = \bar{\mathbf{u}}^M = \bar{\mathbf{u}}^L$. However, for sound waves in contact with surfaces, $\langle \rho' \mathbf{u} \rangle / \rho_0$ and $\langle \xi \cdot \nabla \mathbf{u} \rangle$ can differ significantly in the boundary layer, and consequently so too can $\bar{\mathbf{u}}$, $\bar{\mathbf{u}}^M$, and $\bar{\mathbf{u}}^L$. Care must therefore be taken when comparing solutions for the inner streaming vortices generated by standing waves in channels. In wide channels, the acoustic particle motion outside the boundary layer is close to one-dimensional, and thus $\bar{\mathbf{u}} \approx \bar{\mathbf{u}}^M \approx \bar{\mathbf{u}}^L$ for the outer (Rayleigh) streaming vortices.

B. Average mass transport velocity

We begin by expressing the acoustic field variables as follows:

$$\tilde{p} = -(1 - f_\nu) \frac{\rho_0 c_0^2}{i\omega} \frac{d\tilde{u}_{x0}}{dx}, \quad (46)$$

$$\tilde{u}_x = \tilde{u}_{x0}(x) Y_x(y), \quad (47)$$

$$\tilde{u}_y = -f_\nu y_0 \frac{d\tilde{u}_{x0}}{dx} Y_y(y), \quad (48)$$

where \tilde{u}_{x0} , Y_x , and Y_y are given in Eqs. (26) and (35). Two integrations of Eq. (37) with respect to y yield

$$\tilde{u}_x = V(x, y) + C_2(x)y^2 + C_0(x) \quad (49)$$

for the Eulerian streaming velocity, where the coefficients C_0 and C_2 will be determined by boundary conditions on the mass transport velocity. There can be no term that is linear in y because \tilde{u}_x must be an even function of y . The function V results from integration of Eq. (41):

$$V(x, y) = V_0 \operatorname{Re}\{G(x)[H_1(y) + iH_2(y)]\}, \quad (50)$$

where

$$V_0 = \frac{|v_0|^2 \delta_\nu^2}{x_0 \nu} = \frac{2|v_0|^2}{x_0 \omega} \quad (51)$$

is a characteristic velocity amplitude, and the x dependence is determined by

$$\begin{aligned} G(x) &= \frac{x_0}{|v_0|^2} \frac{d\tilde{u}_{x0}^*}{dx} \tilde{u}_{x0} \\ &= \alpha^* x_0 \frac{\sinh \alpha^* x}{\cosh \alpha^* x_0} \left(\frac{\cosh \alpha x}{\cosh \alpha x_0} - 1 \right). \end{aligned} \quad (52)$$

The y dependence is given by

$$H_1(y) = \frac{\cosh(2y/\delta_\nu) - \cos(2y/\delta_\nu)}{8|\cosh \beta y_0|^2} - \operatorname{Im} \frac{\cosh \beta y}{\cosh \beta y_0}, \quad (53)$$

$$\begin{aligned} H_2(y) &= f_\nu^* \frac{\cosh \beta y - \beta y \sinh \beta y}{4 \cosh \beta y_0} + \frac{1}{4} \frac{\cosh \beta^* y}{\cosh \beta^* y_0} \\ &\quad - \frac{\cosh(2y/\delta_\nu) + i \cos(2y/\delta_\nu)}{8\beta \delta_\nu |\cosh \beta y_0|^2}. \end{aligned} \quad (54)$$

H_1 results from two integrations of $|Y_x|^2 = Y_x Y_x^*$, and H_2 results from one integration of $Y_x Y_y^*$. Both integrals produce terms proportional to y^2 that are not included in Eqs. (53) and (54). Instead, these terms are taken into account by C_2 in Eq. (49). Formally one obtains

$$C_2(x) = \frac{1}{2\mu} \left[K(x) + \frac{\rho_0 |v_0|^2}{2x_0} \operatorname{Re}\{(2 - f_\nu^*)G(x)\} \right], \quad (55)$$

where K is given by Eq. (40). However, Eq. (55) is unnecessary unless one wishes to calculate the dc pressure \bar{p} after C_2 is determined by the boundary conditions.

From Eq. (43) for the mass transport velocity one obtains

$$\tilde{u}_x^M = \tilde{u}_x(x, y) + V_0 \operatorname{Re}\{\frac{1}{4}i(1 - f_\nu)G^*(x)Y_x^*(y)\}. \quad (56)$$

The stream function ψ is introduced on the basis of Eq. (44):

$$\tilde{u}_x^M = \partial\psi/\partial y, \quad \tilde{u}_y^M = -\partial\psi/\partial x. \quad (57)$$

Substitution of Eq. (56) into the first of Eqs. (57) and integration with respect to y yields

$$\psi = \Psi(x, y) + A_3(x) \frac{y^3}{y_0^3} + A_1(x) \frac{y}{y_0}. \quad (58)$$

Coefficients of even powers of y were set to zero because ψ must be an odd function of y , and

$$\begin{aligned} \Psi &= V_0 \delta_\nu \operatorname{Re}\{G(x)[H_3(y) + iH_4(y)] \\ &\quad + \frac{1}{4}i(1 - f_\nu)G^*(x)H_5(y)\}, \end{aligned} \quad (59)$$

where $H_{3,4} = \delta_\nu^{-1} \int H_{1,2} dy$ and $H_5 = \delta_\nu^{-1} \int Y_x^* dy$:

$$H_3(y) = \frac{\sinh(2y/\delta_\nu) - \sin(2y/\delta_\nu)}{16|\cosh \beta y_0|^2} - \operatorname{Im} \frac{\sinh \beta y}{\beta \delta_\nu \cosh \beta y_0}, \quad (60)$$

$$\begin{aligned} H_4(y) &= f_\nu^* \frac{2 \sinh \beta y - \beta y \cosh \beta y}{4\beta \delta_\nu \cosh \beta y_0} + \frac{i}{4\beta \delta_\nu} \frac{\sinh \beta^* y}{\cosh \beta^* y_0} \\ &\quad - \frac{\sinh(2y/\delta_\nu) + i \sin(2y/\delta_\nu)}{16\beta \delta_\nu |\cosh \beta y_0|^2}, \end{aligned} \quad (61)$$

$$H_5(y) = \frac{y}{\delta_\nu} - \frac{i}{\beta \delta_\nu} \frac{\sinh \beta^* y}{\cosh \beta^* y_0}. \quad (62)$$

From Eqs. (57) and (58), \tilde{u}_x^M is now expressed as

$$\tilde{u}_x^M = \tilde{u}_x^M(x, y) + \frac{1}{y_0} \left[3A_3(x) \frac{y^2}{y_0^2} + A_1(x) \right], \quad (63)$$

where

$$\begin{aligned} \tilde{u}_x^M &= V_0 \operatorname{Re}\{G(x)[H_1(y) + iH_2(y)] \\ &\quad + \frac{1}{4}i(1 - f_\nu)G^*(x)Y_x^*(y)\}. \end{aligned} \quad (64)$$

The unknown functions $A_1(x)$ and $A_3(x)$ are determined by the condition that the motion must vanish at the side walls, and thus

$$\tilde{u}_x^M(x, y_0) = V(x, y_0) + \frac{3}{y_0} A_3(x) + \frac{1}{y_0} A_1(x) = 0, \quad (65)$$

$$\psi(x, y_0) = \Psi(x, y_0) + A_3(x) + A_1(x) = 0, \quad (66)$$

where $\tilde{u}_x^M(x, y_0) = V(x, y_0)$ because $Y_x(y_0) = 0$. Equation (66) follows from the condition $\tilde{u}_y^M(x, y_0) = 0$. One therefore obtains

$$A_1(x) = -\frac{3}{2}\Psi(x, y_0) + \frac{1}{2}y_0 V(x, y_0), \quad (67)$$

$$A_3(x) = \frac{1}{2}\Psi(x, y_0) - \frac{1}{2}y_0 V(x, y_0). \quad (68)$$

All quantities are now determined in Eq. (58) for the stream function ψ , and in Eq. (63) for the longitudinal velocity \tilde{u}_x^M . Comparison of Eqs. (49) and (63) yields $C_2 = (3/y_0^3)A_3$, and the dc pressure \bar{p} can be determined directly from Eqs. (55) and (40), if desired.

The y component of the mass transport velocity is obtained by substituting Eq. (58) into the second of Eqs. (57):

$$\tilde{u}_y^M = -\frac{1}{x_0} \left[\hat{\Psi}(x, y) + \hat{A}_3(x) \frac{y^3}{y_0^3} + \hat{A}_1(x) \frac{y}{y_0} \right], \quad (69)$$

where the hats indicate use of the expressions for Ψ , A_3 , and A_1 but with G replaced everywhere by

$$\begin{aligned} \hat{G}(x) &= x_0 \frac{dG}{dx} = (\alpha^* x_0)^2 \frac{\cosh \alpha^* x}{\cosh \alpha^* x_0} \left(\frac{\cosh \alpha x}{\cosh \alpha x_0} - 1 \right) \\ &\quad + \left| \alpha x_0 \frac{\sinh \alpha x}{\cosh \alpha x_0} \right|^2. \end{aligned} \quad (70)$$

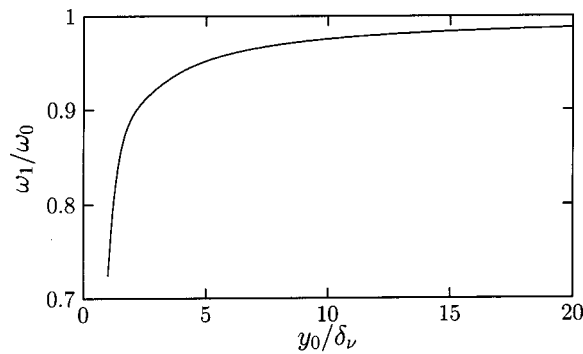


FIG. 3. Lowest resonance frequency ω_1 as a function of channel width, normalized by the natural frequency ω_0 when the resonator contains an inviscid fluid.

The complete average mass transport velocity field is thus determined explicitly by Eqs. (63) and (69).

C. Results

To interpret the solutions given by Eqs. (58), (63), and (69) for the average mass transport velocity is it convenient to recognize that with appropriate normalization they are functions of only four dimensionless parameters. Specifically, the dimensionless quantities

$$\frac{c_0}{|v_0|^2 y_0} \psi(x, y), \quad \frac{c_0}{|v_0|^2} \bar{u}_x^M(x, y), \quad \frac{c_0 x_0}{|v_0|^2 y_0} \bar{u}_y^M(x, y) \quad (71)$$

may be expressed as functions of the form

$$f\left(\frac{x}{x_0}, \frac{y}{y_0}; \frac{y_0}{\delta_\nu}, \frac{\omega}{\omega_0}\right), \quad (72)$$

where $\omega_0 = \pi c_0 / 2x_0$ is the fundamental natural frequency of the resonator in the absence of viscosity. Streaming patterns displayed in terms of the dimensionless coordinates x/x_0 and y/y_0 are thus determined completely by the dimensionless channel width y_0/δ_ν and drive frequency ω/ω_0 .

Although the drive frequency ω in the solution is arbitrary, it is common to consider excitation at the lowest resonance frequency of the system, which we label ω_1 . Our method for determining ω_1 as a function of y_0/δ_ν is to find the value of ω at which the longitudinal component of the acoustic particle velocity is maximized in the center of the resonator. Equation (28) was used to evaluate $|\tilde{u}_x(0,0)|$ for this purpose, which corresponds to maximizing the quantity $|1 - \text{sech } \alpha x_0|$ as a function of ω/ω_0 . Values of ω_1/ω_0 obtained in this way are shown in Fig. 3, and they are seen to differ from unity only slightly over the domain of interest (recall Fig. 2). With $\omega = \omega_1$, the solutions in Eq. (71) can be plotted as functions of x/x_0 and y/y_0 depending on the sole parameter y_0/δ_ν .

From Eqs. (71) it is seen that an appropriate velocity for normalizing the solutions is one that is proportional to $|v_0|^2/c_0$. We choose this velocity to be

$$u_R = \frac{3}{16} \frac{u_0^2}{c_0}, \quad (73)$$

where $u_0 = |\tilde{u}_x(0,0)|$, which is proportional to $|v_0|$, is the maximum longitudinal particle velocity amplitude in a standing wave driven at the lowest resonance frequency. Equation (73) is chosen because for standing waves in wide channels, i.e., in the limit $y_0/\delta_\nu \rightarrow \infty$, it is the peak streaming velocity obtained by Rayleigh¹ in the midplane of the channel.

Shown in Fig. 4 for $\omega = \omega_1$ and five values of y_0/δ_ν are streamlines $\psi(x, y) = \text{const}$ (left column) obtained from Eqs. (58) for the upper right quadrant of Fig. 1, the corresponding longitudinal velocity profiles $\bar{u}_x^M(y)$ at $x = x_0/2$ (middle column) obtained from Eq. (63), and the transverse velocity profiles $\bar{u}_y^M(y)$ at $x = 0$ (right column) obtained from Eq. (69). The upper row, with $y_0/\delta_\nu = 20$, reveals predominantly Rayleigh streaming, which circulates in the clockwise direction. For increasingly wider channels, the inner streaming vortex becomes negligible in comparison with the Rayleigh streaming, and $|\bar{u}_x^M|$ approaches u_R at $y = 0$. Simultaneously, the location where \bar{u}_x^M changes sign and where \bar{u}_y^M is a maximum approaches $y = y_0/\sqrt{3}$.¹

As channel width becomes narrow, the inner streaming vortex increases in size relative to the Rayleigh streaming vortex. Rayleigh streaming is nonexistent when \bar{u}_y^M does not change sign, and the transition to this situation occurs at $y_0/\delta_\nu = 5.7$ (fourth row). For $y_0/\delta_\nu < 5.7$ only the inner streaming vortex exists, and the flow is purely counterclockwise. The value $y_0/\delta_\nu = 2$ in the bottom row corresponds to channels within the stacks of thermoacoustic engines.

For low excitation levels, the results in Fig. 4 are indistinguishable from numerical solutions of the fully nonlinear equations of motion (specifically, obtained with the code described in Ref. 11) for the geometry in Fig. 1, where the mass transport velocity is determined by taking the time average of the momentum density. Conversely, the present analytical solution provides a benchmark for verifying the accuracy of the aforementioned code, in particular the ability to extract a small dc effect from a large-amplitude time waveform. The numerical results also show that the present analytical solution, derived for the ideal resonator depicted in Fig. 1, describes qualitatively the streaming patterns in the pores of thermoacoustic engine stacks.

D. Comparisons with previous work

The principal features of the present solution are that it describes streaming in channels of arbitrary width, and it is completely analytic. Outside the boundary layer in wide channels the solution is in agreement with previous results for Rayleigh streaming.¹⁻³ The salient characteristics of streaming in narrow channels are observed to be the prominence of the inner vortex, and the disappearance of the Rayleigh vortex in sufficiently narrow channels. Indeed, the solutions derived by Rayleigh,¹ Westervelt,² and Nyborg³ differ from each other and from the present solution only in the boundary layer region. Another solution, derived by Zarembo⁶ and discussed by Rudenko and Soluyan,⁷ differs also outside the boundary layer. The various analytic solutions are compared in Fig. 5 for $y_0/\delta_\nu = 20$. From Fig. 4 it is observed that for this width the inner streaming vortex occupies 10% of the channel. Figure 5(a) displays the x compo-

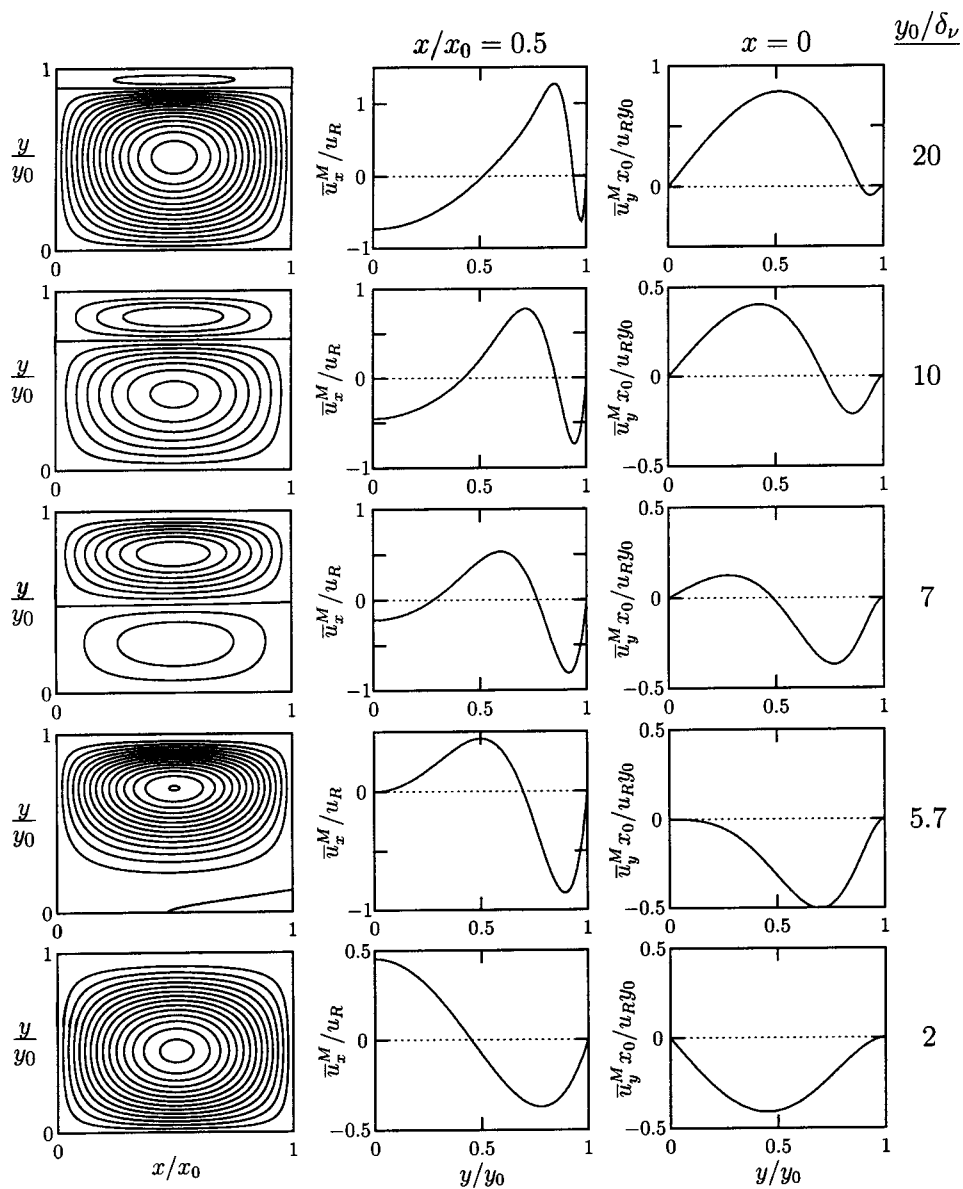


FIG. 4. Acoustic streaming patterns for the average mass transport velocity in a resonator with rigid ends, excited in its lowest mode, as a function of channel width. Left column: streamlines. Middle column: transverse distribution of x component at $x/x_0 = 0.5$. Right column: transverse distribution of y component at $x/x_0 = 0$.

ment of the streaming velocity for the entire half-width of the channel at $x/x_0 = 0.5$, and Fig. 5(b) zooms in on the boundary layer region.

R is Rayleigh's solution for the Eulerian streaming velocity in a wide channel.¹ The restriction to wide channels enters through approximations he employs when deriving the solution for the sound field.

W is Westervelt's solution for the Eulerian streaming velocity.² Westervelt begins with Rayleigh's solution for the sound field, but he avoids approximations introduced by Rayleigh in the forcing function of the streaming equation. Westervelt points out that the net effect of Rayleigh's approximations is to formally substitute the relation $\partial \tilde{u}_x / \partial x = -\partial \tilde{u}_y / \partial y$ in Eq. (41). However, it should be emphasized that Rayleigh's solution for the sound field does not satisfy relations for incompressible fluids.

W^L and W^M are the Lagrangian streaming velocity and mass transport velocity, respectively, obtained by substituting Westervelt's solution for the Eulerian velocity component \tilde{u}_x into Eqs. (45) and (42) to obtain the respective x components, and then using the divergence-free relation for the

transformed velocity to obtain the y components. W^L was presented by Westervelt,² and W^M is the solution presented by Nyborg.³ The difference between these two solutions is precisely the difference between the terms $\langle \xi \cdot \nabla \mathbf{u} \rangle$ and $\langle \rho' \mathbf{u} \rangle / \rho_0$. It is seen in Fig. 5 that R , W , W^L , and W^M differ significantly only within the boundary layer.

Z is Zarembo's solution for the Eulerian streaming velocity.⁶ The main difference in his approach is the solution used for the sound field. It is not derived for a wide channel, but rather for an infinite fluid in contact with a single wall. In addition, the relation $\partial \tilde{u}_x / \partial x = -\partial \tilde{u}_y / \partial y$ for an incompressible fluid is used to obtain \tilde{u}_y from \tilde{u}_x . In the end, \tilde{u}_x is the same as that obtained by Rayleigh, but \tilde{u}_y is different and grows linearly without bound away from the wall. Consequently, the solution for the Eulerian streaming velocity in the boundary layer differs from the results obtained by both Rayleigh and Westervelt. The outer streaming predicted by Zarembo is for a semi-infinite fluid and it is therefore entirely different from Rayleigh's solution for a wide channel.

We note that it is relatively straightforward to modify Zarembo's solution for the streaming such that it applies to a

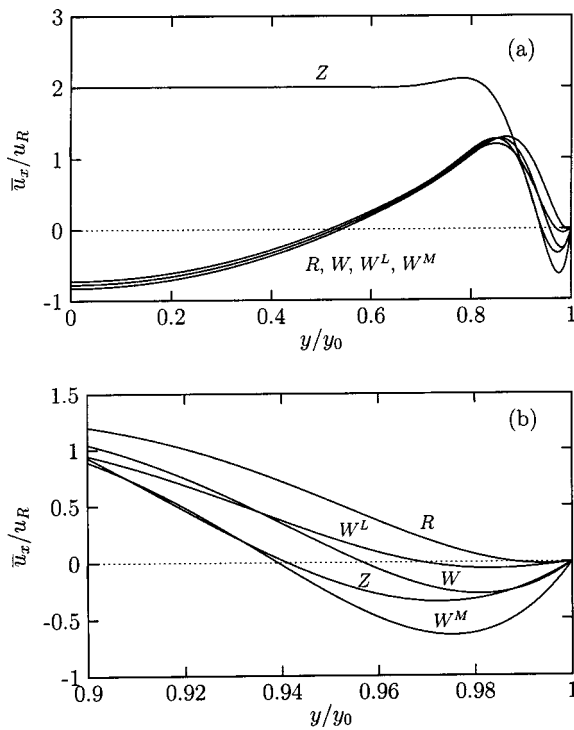


FIG. 5. Comparison of solutions obtained by others (see text) for the x component of the acoustic streaming velocity, corresponding to the conditions in the top row of Fig. 4.

wide but finite channel. Begin with the same solution for the sound field, and after integrating the forcing function in the streaming equation, evaluate the integration constants by setting the velocity to zero at the far wall (as well as at the near wall). This modification of Zaremba's solution provides a proper description of Rayleigh streaming outside the boundary layer. Inside the boundary layer, the solution still differs from those of Rayleigh and Westervelt.

The present solution, given by Eq. (63), is indistinguishable from W^M in Fig. 5. For widths on the order of the viscous penetration depth, however, Eq. (63) differs significantly from W^M throughout the channel.

IV. CONCLUSION

The solution derived in this paper for streaming produced by a standing wave in a channel is free of the restriction to wide channels that applies to earlier analytical studies of this problem. In particular, it describes the inner streaming vortex confined to the boundary layer, in addition to the outer Rayleigh streaming. Moreover, it shows that the Rayleigh streaming disappears when the channel is sufficiently narrow. The main restriction on the solution is that the boundary layer thickness is small in comparison with the acoustic wavelength.

Thermal effects were ignored in the present discussion, but these too may be included in the solution.¹⁴ One effect is heat conduction, which introduces a thermal boundary layer

in addition to the viscous boundary layer. The other is the temperature dependence of the viscosity coefficient. Inclusion of these effects reveals that the streaming patterns remain essentially the same, but that the velocity increases by about 10% for wide channels, and considerably more for some narrow channels.

It was noted that the original motivation for this work was to understand the steaming patterns within the pores of thermoacoustic stacks. Comparison with direct numerical simulations revealed that the analytical solution, which corresponds to the geometry in Fig. 1, does describe qualitatively the streaming patterns inside the pores, even though the stack length is a small fraction of the resonator length. Work is currently underway to describe the streaming pattern not only inside the stack, but through the transition region at the ends and out into the volume of the resonator.

ACKNOWLEDGMENTS

This work was supported by the Office of Naval Research, and by the Internal Research and Development Program at Applied Research Laboratories, The University of Texas at Austin.

- ¹Lord Rayleigh, "On the circulation of air observed in Kundt's tubes, and on some allied acoustical problems," *Philos. Trans. R. Soc. London* **175**, 1–21 (1884); Sec. 3. See also Lord Rayleigh (J. W. Strutt), *The Theory of Sound*, 2nd ed. (Dover, New York, 1945), Vol. 2, Sec. 352.
- ²P. J. Westervelt, "The theory of steady rotational flow generated by a sound field," *J. Acoust. Soc. Am.* **25**, 60–67 (1953); see Sec. V. See also errata on p. 799 of the same volume.
- ³W. L. Nyborg, "Acoustic streaming," in *Physical Acoustics*, edited by W. P. Mason (Academic, New York, 1965), Vol. 2B, Chap. 11, pp. 290–295.
- ⁴W. L. Nyborg, "Acoustic streaming," in *Nonlinear Acoustics*, edited by M. F. Hamilton and D. T. Blackstock (Academic, San Diego, 1998), Chap. 7, Sec. 3.3.
- ⁵We use the terminology "Rayleigh streaming" to describe only the outer vortices generated by standing waves in a channel, as Rayleigh provides no discussion of the inner vortices.
- ⁶L. K. Zaremba, "Acoustic streaming," in *High-Intensity Ultrasonic Fields*, edited by L. D. Rozenberg (Plenum, New York, 1971), Part III, pp. 156–164.
- ⁷O. V. Rudenko and S. I. Soluyan, *Theoretical Foundations of Nonlinear Acoustics* (Plenum, New York, 1977), pp. 206–210.
- ⁸R. Waxler, "Stationary velocity and pressure gradients in a thermoacoustic stack," *J. Acoust. Soc. Am.* **109**, 2739–2750 (2001).
- ⁹H. Bailliet, V. Gusev, R. Raspet, and R. A. Hiller, "Acoustic streaming in closed thermoacoustic devices," *J. Acoust. Soc. Am.* **110**, 1808–1821 (2001).
- ¹⁰M. F. Hamilton, Yu. A. Ilinskii, and E. A. Zabolotskaya, "Nonlinear two-dimensional model for a thermoacoustic engine," *1st International Workshop on Thermoacoustics*, 's-Hertogenbosch, The Netherlands, 23–25 April 2001.
- ¹¹M. F. Hamilton, Yu. A. Ilinskii, and E. A. Zabolotskaya, "Nonlinear two-dimensional model for thermoacoustic engines," *J. Acoust. Soc. Am.* **111**, 2076–2086 (2002).
- ¹²S. Temkin, *Elements of Acoustics* (Acoustical Society of America, New York, 2001), Eq. (6.8.36).
- ¹³G. W. Swift, "Thermoacoustic engines," *J. Acoust. Soc. Am.* **84**, 1145–1180 (1985).
- ¹⁴M. F. Hamilton, Yu. A. Ilinskii, and E. A. Zabolotskaya, "Effect of thermal conductivity on acoustic streaming in a narrow channel," *J. Acoust. Soc. Am.* **111**, 2418(A) (2002).

Reynolds number effects on flow/acoustic mechanisms in spherical windscreens^{a)}

Z. Charlie Zheng^{b)} and Bee K. Tan

Department of Mechanical and Nuclear Engineering, Kansas State University, Manhattan, Kansas 66506

(Received 5 April 2002; revised 12 September 2002; accepted 24 September 2002)

There is a practical need to fully understand the mechanisms involved in the flow/pressure fluctuations around a screened microphone. A stream of uniform flow with low-frequency turbulence encountering a rigid, impermeable spherical windscreen is considered in this study. Pressure distributions on the surface of the sphere are determined by the flow structure. Pressure fluctuations at the center of the sphere are then calculated based on the integration of surface pressure distributions. Because of the low-frequency assumption, results from steady-state laminar flows can be used to investigate the Reynolds number effects on wind noise reduction. Three types of flow have been studied in this paper: an inviscid case, a low-Reynolds-number Stokes flow, and intermediate- and high-Reynolds-number flows. A Reynolds-number/wind-noise-reduction correlation shows that the wind noise reduction increases with decreasing Reynolds number. © 2003 Acoustical Society of America. [DOI: 10.1121/1.1527927]

PACS numbers: 43.28.Gq, 43.28.Ra, 43.50.Gf, 43.28.Hr [MSH]

I. INTRODUCTION

Windscreens are widely used in outdoor microphone measurement; therefore, there is a practical need to fully understand the mechanisms involved in the flow/pressure fluctuations around a screened microphone. The understanding may lead to optimized design of the windscreen for measurement microphones. However, the wind noise sensed by a microphone inside a windscreen is a complicated aerodynamic noise problem. In low-turbulence flows, the dominant noise is produced by the interaction of the flow with the microphone as a result of pressure gradients across the microphone face due to wake shedding from the microphone. Strasberg (1988) performed dimensional analysis of windscreen noise for measurements made in low-turbulence conditions and showed that the one-third-octave sound pressure obeyed scaling laws involving the average speed of the flow, the air density, and the diameter of the screen. This suggests that windscreen-generated velocity fluctuations account for the wind noise in low-turbulence environments. Morgan and Raspet (1992) argued that under high-turbulence conditions, the dominant source of pressure fluctuations at the microphone outdoors was the intrinsic turbulence in the incoming flow. For flow through a porous windscreen or over a rough foam surface, the amplitude of the pressure fluctuation can possibly be reduced due to reduced wake fluctuations, as shown by Hosier and Donovan (1979) (although under the low-turbulence conditions in their study).

In this study, analytical methods have been used to investigate the flow/acoustic mechanisms assuming a high-turbulence scenario. Therefore, the vortex shedding effects

are not considered. A rigid surface, impermeable spherical windscreen model is used to study wind noise reductions at low frequencies. In this model, the impermeable surface of the windscreen transmits the pressure fluctuations to quiescent air media inside. Since the turbulence outdoors is highly weighted to low frequencies, the largest contributions to the overall wind noise level are at low frequencies. Therefore, the study is restricted to wind noise generation due to turbulence whose spatial scales are much larger than the windscreen diameter. The mean flow across the screen can be considered as a steady flow. The results of this model have given good agreement in comparison with experimental data in literature. The model could thus be adopted for investigating the theoretical calculation of wind noise reduction (WNR) in more complicated windscreens such as porous medium windscreens.

To justify the use of a steady-state flow model, two sets of measurement data by Morgan (1993) for WNR versus screen numbers are plotted in Fig. 1. The screen number (D/λ) is defined as the ratio between the windscreen diameter, D , and the wavelength, λ . The first set of data is for a windscreen of 90-mm diameter in a flow of 4.85 m/s, and the second set is for a windscreen of 180-mm diameter in a flow of 4.74 m/s. It can be seen that when the screen number is below 0.3, the WNR is almost constant. After that, the WNR increases rapidly with an increase in the screen number. This is because the scale of the turbulence becomes smaller and the steady-state assumption is no longer valid. Figure 1 also shows that the analysis presented in this paper only applies to the cases where the length scale of the turbulence is larger than the size of the windscreen.

The choice of a simple, steady-state system makes it possible to compare the calculated results to measurements of pressure coefficients on smooth rigid spheres and to other analytical models. The pressure fluctuations induced on the spherical windscreen surface can then be used to obtain the

^{a)}Portions of this work were presented in Z. C. Zheng, "A computational study of the flow/acoustic mechanisms in screened microphones," Proceedings of ASME FEDSM'01, FEDSM2001-18204, 2001 ASME Fluids Engineering Division Summer Meeting, 29 May–1 June 2001, New Orleans, LA.

^{b)}Electronic mail: zzheng@ksu.edu

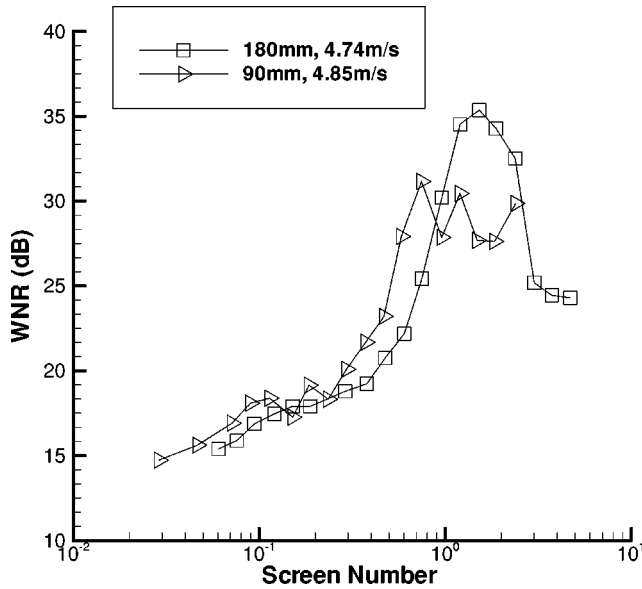


FIG. 1. Measured wind noise reduction by Morgan (1993), as a function of screen number (D/λ), where D is the diameter of the windscreen and λ is the wavelength. The data are extracted from Fig. 14 in Morgan (1993). The triangle-symbol line is for a windscreen with diameter of 90 mm and flow speed of 4.84 m/s. The square-symbol line is for a windscreen with diameter of 180 mm and flow speed of 4.85 m/s.

pressure levels which can be sensed by a microphone placed at the center of the windscreen.

In the following sections, the pressure fluctuation relationship inside and outside on the surfaces of the sphere is presented at first. The results are then used to study three types of flow: an inviscid case, a low-Reynolds-number Stokes flow, and intermediate- and high-Reynolds-number flows. The inviscid and Stokes flow cases are the two extreme cases in which analytical solutions can be pursued. The flow field of the third case can be calculated using computational fluid dynamics (CFD) techniques. A flow solver software, FLUENT, was used to provide flow field to determine the pressure distribution on the sphere surface. The wind noise reduction on the microphone can be determined from both the theoretical results and experimental data in literature, using the steady-state pressure distribution on the surface. Finally, a correlation between the WNR and Reynolds numbers is obtained.

II. PRESSURE FLUCTUATION RELATIONSHIPS

It is assumed that there is no flow inside the windscreen sphere. Therefore, the pressure fluctuations inside the sphere obey the Laplace equation under the incompressibility assumption. Theoretically, the pressure inside the sphere can thus be fully determined by the surface pressure. However, the validity and accuracy of using surface pressure integrations to estimate the center pressure for the windscreen noise reduction calculation, which is based on the solution of the Laplace equation, are unable to be fully addressed at this point. This requires that the results presented here be compared with those from the simulations with permeable boundaries on the sphere. The only indication of validity of the proposed idealized treatment is the results from Morgan's (1993) measurement, where the integration of measured sur-

face pressure coefficient, C_p , gave values close to the measured wind noise reduction levels at the center of the screen.

In a spherical coordinate system, (r, θ, ϕ) , where ϕ is the azimuthal angle, the average value property of the Laplace equation yields the following solution for the pressure at the center of the sphere:

$$p(0) = \frac{1}{4\pi} \int_0^{2\pi} d\phi \int_0^\pi p(a, \theta, \phi) \sin \theta d\theta. \quad (1)$$

This means that the wind noise detected at the center of the screen is the average of the surface pressure fluctuations.

If we assume azimuthal symmetry in this spherical problem, i.e., $p(a, \theta, \phi)$ independent of ϕ , Eq. (1) reduces to

$$p(0) = \frac{1}{2} \int_0^\pi p(a, \theta) \sin \theta d\theta. \quad (2)$$

Consequently, if we let

$$x = \cos \theta, \quad (3)$$

and

$$p(a, \theta) = f(x), \quad (4)$$

then we can have

$$p(0) = \frac{1}{2} \int_{-1}^1 f(x) dx. \quad (5)$$

It is worth noting that general solutions for pressure fluctuations at locations other than the center under nonaxisymmetric outside flow field can be obtained by using spherical harmonics following a similar procedure to that in Jackson (1963).

III. INVISCID CASE

For unsteady, inviscid incompressible flow over a sphere, the flow is irrotational if the incoming flow is uniform. A three-dimensional velocity potential exists for flow around a sphere (e.g., Currie, 1993), as follows:

$$\phi(r, \theta) = U \left(r + \frac{1}{2} \frac{a^3}{r^2} \right) \cos \theta, \quad (6)$$

where U is the incoming velocity. Using the unsteady Bernoulli equation, Phelps (1938) showed that on the surface of a sphere

$$p(a, \theta) = \frac{1}{8} \rho U^2 (9 \cos^2 \theta - 5) + \frac{3}{2} \rho a \left(\frac{\partial U}{\partial t} \right) \cos \theta + P, \quad (7)$$

where P is the pressure of the incoming flow. The velocity, U , can be expressed as

$$U = \bar{U} + u'. \quad (8)$$

The prime for the pressure fluctuations in this paper is omitted. If only the pressure fluctuations caused by flow are considered, and neglecting higher order terms, Eq. (7) yields

$$\frac{p(a, \theta)}{\rho \bar{U} u'} = \frac{1}{4} [9 \cos^2 \theta - 5] + \frac{3}{2} \frac{a}{\bar{U}} \frac{\partial u'}{\partial t} \cos \theta. \quad (9)$$

Once the surface pressure fluctuation is known, Eq. (5) can be used to obtain the pressure fluctuation at the sphere center. Since the integration of the odd function terms of x in $f(x)$ must be zero, the effects of the second term in Eq. (9) vanish. Therefore

$$\frac{p(0)}{\rho \bar{U} u'} = \frac{1}{2} \int_{-1}^{+1} g(x) dx = -\frac{1}{2}, \quad (10)$$

where

$$g(x) = \frac{1}{4}[9x^2 - 5].$$

The integral function, $g(x)$, is the same as the pressure distribution coefficient, C_p , on a sphere in steady flow. It should be noted that this pressure distribution coefficient, which is symmetric with respect to $x=0$, results in zero drag (D'Alembert paradox). However, the arithmetic average of it, Eq. (10), results in a net value of $-1/2$. Since the unscreened pressure fluctuation is $\rho \bar{U} u'$ in a uniform stream, the wind noise reduction of the spherical screen in decibels is

$$\text{WNR} = -10 \log_{10} \left(\frac{p(0)}{\rho \bar{U} u'} \right)^2 = 6.02 \text{ dB}. \quad (11)$$

According to the above procedure, the WNR of a spherical screen is determined by the integration of the surface C_p from a corresponding steady flow. This concept will be extended to finite Reynolds-number flows later in the paper, where experiment and CFD results from steady-state studies will be used to determine the wind noise reduction. Apparently, the wind noise reduction is independent of the velocity fluctuation frequency as well as the windscreen size. This is caused by two factors: the inviscid assumption and the microphone being at the center of the sphere. However, for low-frequency turbulence, the frequency of incoming velocity fluctuations is low (in comparison with \bar{U}/a); thus, the second term on the right-hand side of Eq. (9) can be neglected. The surface pressure fluctuation is then independent of the size of the screen. Therefore, under conditions of low-frequency turbulence, the wind noise reduction does not change with the size of the screen. Furthermore, this is true even when the microphone is not located at the center of the sphere, because the pressure inside the sphere is determined by the surface pressure only.

Thus far, the analysis presented in this section has been for an unsteady flow in which the fluctuation flow (u') was parallel to the mean flow (\bar{U}). During the review process associated with this article, it was brought to the attention of the authors that forcing the velocity fluctuation to be in parallel with the mean velocity was in fact nonphysical. Alternatively, it can be shown that, since the pressure fluctuation is related to the linear term in the square of velocity magnitude, the contributions from velocity fluctuations perpendicular to the mean flow are of higher order, according to the following expression:

$$\begin{aligned} |\mathbf{U}|^2 &= |\bar{U}\mathbf{i} + u'\mathbf{i} + v'\mathbf{j} + w'\mathbf{k}|^2 \\ &= \bar{U}^2 + 2\bar{U}u' + u'^2 + v'^2 + w'^2. \end{aligned} \quad (12)$$

Therefore, the results are still correct even with an arbitrary velocity fluctuation.

IV. LOW-REYNOLDS-NUMBER FLOW

The Stokes creeping-flow approximation is used in this case. Although this flow may not actually occur in practice for the problem discussed here, it is analyzed for the purpose of comparison. The pressure fluctuation on the surface is expressed as (e.g., Currie, 1993)

$$\frac{p(a, \theta)}{\rho \bar{U} u'} = -\frac{3}{2} \frac{\cos \theta}{\text{Re}}, \quad (13)$$

where

$$\text{Re} = \frac{\rho \bar{U} a}{\mu}. \quad (14)$$

Because of the antisymmetric pressure distribution with respect to $x=0$ in Eq. (13), the pressure fluctuation at the center, which is the arithmetic average of the distribution, is thus equal to zero. This means for a low-Reynolds-number flow, the wind noise due to flow fluctuation can be totally screened out if the microphone is placed at the center.

By comparing the cases in Secs. III and IV, it can be seen that the wind noise reduction is reduced from infinite for very low Reynolds-number flow to 6.02 dB for inviscid flow (with infinite Reynolds numbers). The surface pressure distribution changes from antisymmetric to symmetric with respect to $x=0$ ($\theta=\pi/2$) when the Reynolds number increases, with the lower bound of the wind noise reduction occurring in the symmetric pressure distribution case. In the next section, high but finite Reynolds number cases are considered which are more applicable in realistic situations. The wind noise reduction is expected to fall between infinity and 6.02 dB, and the pressure distributions on the surface of the sphere should be neither symmetric nor antisymmetric with respect to the x direction.

V. INTERMEDIATE- AND HIGH-REYNOLDS-NUMBER FLOW

For intermediate or high Reynolds numbers, analytical solutions do not exist and the analysis has to be based on experimental data or numerical solutions. In this study, computational fluid dynamics is used to compute the flow field, and comparisons are made with well-known experimental data. Because the typical turbulence eddy size is much larger than the screen radius, the computations are mostly based on a laminar flow model. Turbulent simulations are also performed for comparison purposes. A flow solver software, FLUENT, is used to solve the three-dimensional Navier-Stokes equations. The pressure distributions on the spherical surface can be obtained from the CFD solution. It has been discussed earlier that for low-frequency turbulence, the distribution function of the surface pressure fluctuations is the same as that of the steady pressure distribution. Therefore, a steady-state computation is used to determine the distribution

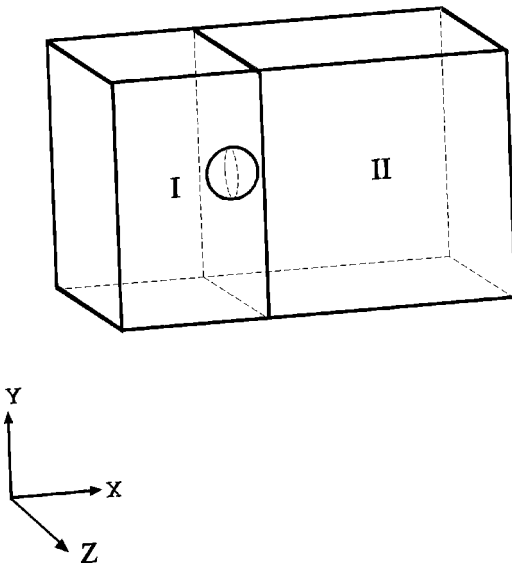


FIG. 2. The computational fluid dynamics model, where the incoming flow is in the positive x direction. Volumes I and II are the two volumes used to map the grid mesh.

function. The integration of the distribution function, as shown in Eq. (5), yields the pressure fluctuation at the sphere center.

The computational model is shown in Fig. 2. The computational domain is a $16a$ (in the x direction) $\times 10a \times 10a$ box, with a sphere of radius a inside. The center of the sphere is located a distance of $6a$ downstream from the inflow plane in the flow direction, which is also the x direction. The sphere is also centered in the computational domain with respect to the y - and z coordinates. A uniform velocity in the x direction is specified at the inflow plane. The error introduced by this can be estimated using Eq. (6), which shows that the influence of the sphere on the inflow velocity decays at $O(a^3/r^3)$. Hence, less than 0.5% [$O(1/6^3)$] velocity straining at the in-flow plane is introduced by placing a sphere centered a distance of $6a$ downstream from the inflow plane. Lee (2000) chose an upstream in-flow plane at $6a$ for lower Reynolds number cases, with Re in the range of $O(10^2)$. It was noticed that the influence of the sphere on the inflow was more significant at lower Reynolds numbers. From the velocity distribution in Stokes flow past a sphere, the influence of the sphere decays with distance according to $O(a/r)$. Therefore, the selection of the uniform inflow plane position for the given Reynolds number range is sufficiently upstream from the sphere. At the outflow plane, an outflow extrapolation boundary condition is specified. Free-stream boundary conditions are specified on the side boundaries of the computational box. Since the side walls are $5a$ away from the sphere center, the side-wall boundary effects on the flow field near the sphere surface can be neglected.

A grid generation package, GAMBIT, was used to generate the numerical grid. The domain was split into two subdomains, volume I and volume II, with a y - z junction plane at the center of the sphere (at $x=0$), as shown in Fig. 2, in order to create a source face in each subdomain for permissible Cooper meshing. A grid number of 50 was used on all the edges in each volume. A grid interval ratio of 0.3 was

used towards the junction plane of the two volumes in the x direction. In the y - and z directions, a grid interval ratio of 0.8 was used towards the centers of the edges (double ratio). The purpose of these interval ratios was to generate a fine grid mesh near the sphere surface. The Cooper algorithm was then used to generate a hex/wedge grid mesh. It projected or extruded the boundary face mesh from one end of a volume to the other and then divided up the extruded mesh to form the volume mesh. After the projection, the number of grids on the surface of the sphere was 376 in the flow direction (the x direction) and 32 in the azimuthal direction. The grid number was doubled to test the resolution requirement, and only minor differences in the results were found.

The grid mesh was then imported to FLUENT. Since only large-scale, low-frequency turbulence effects were considered, steady-state computations were performed, as discussed previously. A segregated steady-state 3D laminar solver was used with an implicitly iterative, second-order upwind scheme for momentum equations and the SIMPLE algorithm (Patankar, 1980) for pressure-velocity coupling. The convergence criteria were set at 10^{-4} for velocity residuals and 10^{-3} for continuity residual. Air was used as the simulation fluid, with $\rho = 1.225 \text{ kg/m}^3$ and $\mu = 1.789 \times 10^{-5} \text{ kg/m-s}$. Values of inlet velocity were specified based on the Reynolds number range.

For a 45-mm-radius screen with incoming flow at 9.5 m/s, the Reynolds number is approximately 3×10^4 . According to Achenbach's experiment (1972), the critical Reynolds number at which the drag coefficient reaches the minimum is 1.75×10^5 . In addition, a transition in the free shear layer from a laminar to a turbulent flow occurs near the critical Reynolds number. Therefore, most of the windscreens operate within the subcritical Reynolds number range where the flow remains laminar after the separation, again justifying the usage of laminar simulations.

Turbulent cases were also added in the simulations for comparison purposes, and to provide additional data points to be used for subsequent curve fitting, although the very high Reynolds number cases are rare in windscreen problems. We chose the Spalart-Allmaras model (1992) for the turbulence, which is a relatively simple one-equation model that solves a modeled transport equation for the kinematic eddy (turbulent) viscosity. The Spalart-Allmaras model, designed especially for applications involving wall-bounded flows, has been shown to give good results for boundary layers subjected to adverse pressure gradients. An additional advantage is that in FLUENT, the Spalart-Allmaras model has been implemented to use wall functions when the mesh resolution does not need to be very fine. This might make it the best choice for relatively coarse meshes. Furthermore, the near-wall gradients of the transport variables in the model are much smaller than the gradients of the transport variables in k - ϵ type models. This also might make the model less sensitive to numerical errors when nonlayered meshes are used near walls, as in current simulations. However, higher resolutions are still required for these cases than for the laminar cases, especially near the surface of the sphere. The number of points on each edge was doubled to 100, with grid interval ratios towards the junction plane of 0.25 in volume I

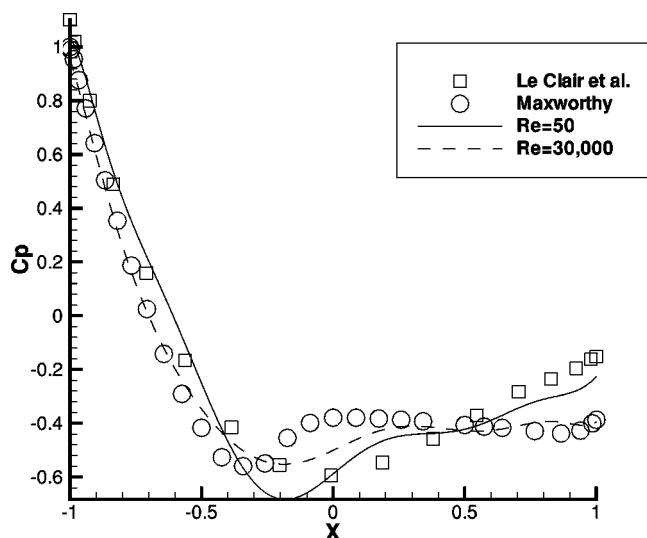


FIG. 3. Comparisons of computational C_p results with literature data for the laminar flow cases. The curves are the computational results and the symbols are the literature data.

and 0.125 in volume II in the x direction. In the y - and z directions, the same grid ratio was used as in the laminar cases. After the projection, the number of grid points on the surface of the sphere was increased to 3189 in the flow direction and 96 in the azimuthal direction. In addition to using the same velocity and continuity convergence criteria as in the laminar cases, a convergence residual for the turbulent viscosity was set at 10^{-3} .

In the following comparisons, for laminar cases a Reynolds number of 3×10^4 was selected since reputable experimental data at this Reynolds number can be found in Maxworthy (1969). A low Reynolds number case of $Re=50$ was also added to compare with literature data for low Reynolds number cases where vortex shedding does not exist in the wake. For turbulent cases, very high Reynolds number cases measured by Achenbach (1972) have been found at Reynolds numbers of 1.59×10^5 , 5.7×10^5 , and 2.5×10^6 .

Figures 3 and 4 show comparisons between the computational results and literature data for C_p versus x on the surface of a sphere. Two sets of data have been compared for the laminar cases in Fig. 3: one at $Re=50$ by Le Clair *et al.* (1970) and the other at $Re=3 \times 10^4$ by Maxworthy (1969). (It should be noted that the Reynolds number specified here was based on radius, while most of the published literature uses diameter.) Figure 3 shows that the agreement is good, particularly at the upstream half of the sphere before the adverse pressure gradients occur. Three turbulent cases are shown in Fig. 4 for comparison with Achenbach's experimental results. Again, good agreement at the upstream half of the sphere was achieved. For the two highest Reynolds number cases, the trough value and the rebound of the C_p were slightly underpredicted in the simulations. This may be attributed to the turbulence model used in the simulations, or the resolution issues near the solid boundary. However, it was not the intention of this paper to resolve the turbulent simulation issues and, as stated previously, the primary interest was within the laminar flow regime. Nevertheless, the good agreement between calculation and measurement pro-

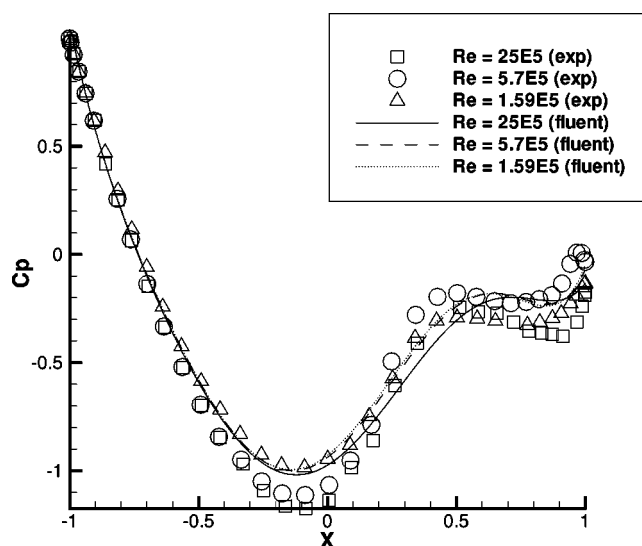


FIG. 4. Comparisons of computational C_p results with literature data for the turbulent flow cases. The curves are the computational results and the symbols are the literature data.

vides evidence that this computational tool could be used for further investigation, when experimental data associated with more complicated windscreen materials such as porous foams are difficult to obtain.

Figure 5 shows a plot of the WNR versus Reynolds number. The calculated WNR data results from the computational model are shown along with that from experimental measurements. A correlation relationship was obtained by curve-fitting these data. The restrictions on the behavior at the two extremities were also applied to the correlation; i.e., $WNR=\infty$ and 6.02 dB at $Re=0$ and ∞ , respectively. The resulting correlation was of the form

$$WNR = \alpha Re^{-\beta} + 6.02, \quad (15)$$

where $\alpha=18.057$ and $\beta=0.171$. This curve shows that when the Reynolds number decreases the wind noise reduction increases, until it reaches an extreme condition where reduc-

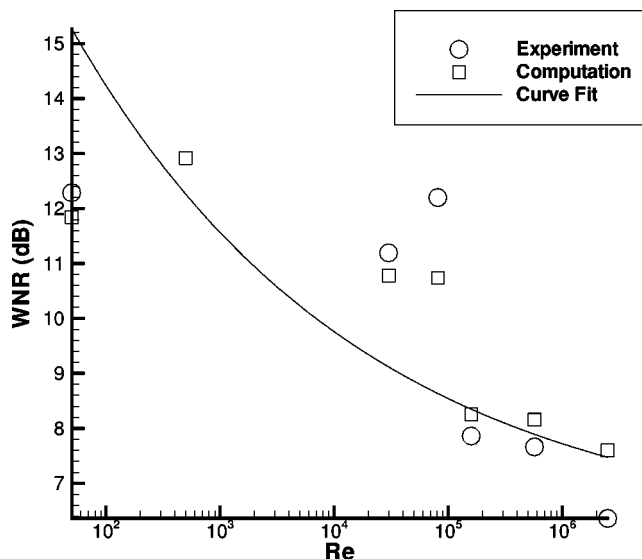


FIG. 5. Correlation between Re and WNR . The curve is from curve fitting of the literature experimental data and our computational data.

tion is sufficiently large such that the noise becomes zero at the center of the sphere at very low Reynolds number.

It should be noted that the experiments in Morgan (1993) used a Pitot tube embedded in 90-mm and 180-mm-diameter windscreens made of foam material. These windscreens were neither impermeable nor rigid. The corresponding Reynolds numbers for a free-stream velocity of 9.5 m/s associated with these measurements were 2.93×10^4 and 5.86×10^4 , respectively. The experimental data showed that the C_p value at the stagnation point was only 0.8 for each of the two cases. However, the integration of the C_p distribution data still gave the WNR values of 16.3 and 14.6 dB, respectively, for the 90-mm and 180-mm windscreens, which were close to the measured reductions. These WNR values are higher than those given from Fig. 5, which are approximately 9.2 and 8.8 dB, respectively, for these two Reynolds numbers. These differences are apparently due to the increased wind noise reduction capability offered by the foam materials used in the experimental tests. If one revisits Fig. 1, which contains the direct measurement data for WNR, the corresponding Reynolds numbers of the two cases in Fig. 1 are approximately 1.5×10^4 and 3.0×10^4 for the 90-mm and 180-mm windscreens, respectively. At these two Reynolds numbers, the WNR from Fig 5 is 9.5 dB for the 90-mm case and 9.2 dB for the 180-mm case. Such a small difference cannot be discerned in Fig. 1, where the slight increase of WNR with rising screen number is the dominant trend. For high Reynolds numbers ($Re > 10^4$), Fig. 5 shows that a Reynolds number increase of ten times causes only less than 1 dB WNR decrease. Therefore, WNR is not very sensitive to changes in Reynolds number at the high Reynolds number range. This correlation is only for low-frequency wind noise reduction, because this paper is only concerned with wind noise below 10 Hz where it is independent of the frequency (as shown in Fig. 1). Higher-frequency turbulence will require a more detailed study of the unsteady flow. Unsteady flow over a sphere has been investigated in recent literature such as Mei and Adrian (1992), Tomboulides and Orszag (2000), Howe *et al.* (2001), among others.

VI. CONCLUSIONS

The conclusions here only apply to the model wind-screen in this analysis, which is impermeable and rigid, yet of no impedance to pressure fluctuation transmission. This model has shown promising comparisons with experiments and has the potential of being adopted for more complicated windscreens. For low-frequency turbulence, wind noise reduction is independent of frequency; therefore, steady-state flow analysis can be used to determine wind noise reduction levels. It is shown in this paper that for a spherical wind-screen, the value of the noise reduction at the center can be calculated from integration of the surface pressure coefficient on the sphere in a corresponding steady-state flow. By using

computational fluid dynamic simulations, and reprocessing experimental measurement data in the literature in a wide range of Reynolds numbers, it has been found that, although it is independent of frequency, wind noise reduction is correlated with the Reynolds number defined by the wind speed and the windscreen radius. A power-fit type correlation shows that the wind noise reduction increases with decrease of the Reynolds number, with the lowest extreme of 6.02 dB in the inviscid flow case and a value of infinity in the creeping flow case.

ACKNOWLEDGMENTS

The authors are grateful for fruitful discussions with Dr. R. Raspet and Dr. J. Seiner of National Center for Physical Acoustics (NCPA) at University of Mississippi, and the partial financial support from NCPA. Special thanks go to Dr. Raspet for his comments on an earlier version of the manuscript. The authors would also like to thank the Associate Editor and the reviewers for a number of insightful comments.

- Achenbach, E. (1972). "Experiments on the flow past spheres at very high Reynolds numbers," *J. Fluid Mech.* **54**, 565–575.
- Currie, I. G. (1993). *Fundamental Mechanics of Fluids*, 2nd ed. (McGraw-Hill, New York).
- Hosier, R. N., and Donovan, P. R. (1979). "Microphone windscreen performance," National Bureau of Standards Report, NBSIR 79-1599.
- Howe, M. S., Lauchle, G. C., and Wang, J. (2001). "Aerodynamic lift and drag fluctuations of a sphere," *J. Fluid Mech.* **436**, 41–57.
- Jackson, J. D. (1963). *Classical Electrodynamics* (Wiley, New York).
- Le Clair, B. P., Hamielec, A. E., and Pruppacher, H. R. (1970). "A numerical study of the drag on a sphere at low and intermediate Reynolds numbers," *J. Atmos. Sci.* **27**, 308–315.
- Lee, S. (2000). "A numerical study of the unsteady wake behind a sphere in a uniform flow at moderate Reynolds numbers," *Comput. Fluids* **29**, 639–667.
- Maxworthy, T. (1969). "Experiments on the flow around a sphere at high Reynolds numbers," *J. Appl. Mech.* **E36**, 598–607.
- Mei, R., and Adrian, R. J. (1992). "Flow past a sphere with an oscillation in the free-stream velocity and unsteady drag at finite Reynolds number," *J. Fluid Mech.* **237**, 323–343.
- Morgan, M. S. (1993). "An investigation of the sources and attenuation of wind noise in measurement microphones," Ph.D. dissertation, Department of Physics and Astronomy, University of Mississippi. PARGUM Report 93-01.
- Morgan, S., and Raspet, R. (1992). "Investigation of the mechanisms of low-frequency wind noise generation outdoors," *J. Acoust. Soc. Am.* **92**, 1180–1183.
- Patankar, S. V. (1980). *Numerical Heat Transfer and Fluid Flow* (McGraw-Hill, New York).
- Phelps, W. D. (1938). "Microphone wind screening," in *RCA Review* 3 (Radio Corporation of America, New York), pp. 203–212.
- Spalart, P., and Allmaras, S. (1992). "A one-equation turbulence model for aerodynamic flows," AIAA Paper No. AIAA-92-0439, American Institute of Aeronautics and Astronautics, 1992.
- Strasberg, M. (1988). "Dimensional analysis of windscreen noise," *J. Acoust. Soc. Am.* **83**, 544–548.
- Tomboulides, A. G., and Orszag, S. A. (2000). "Numerical investigation of transitional and weak turbulent flow past a sphere," *J. Fluid Mech.* **416**, 45–74.

Acoustic near-field characteristics of a conical, premixed flame

Doh-Hyoung Lee and Tim C. Lieuwen^{a)}

School of Aerospace Engineering, Georgia Institute of Technology, 270 Ferst Drive, Atlanta, Georgia 30332-0150

(Received 23 June 2000; revised 20 August 2002; accepted 4 September 2002)

The occurrence of self-excited pressure oscillations routinely plagues the development of combustion systems. These oscillations are often driven by interactions between the flame and acoustic perturbations. This study was performed to characterize the structure of the acoustic field in the near field of the flame and the manner in which it is influenced by oscillation frequency, combustor geometry, flame length and temperature ratio. The results of these calculations indicate that the acoustic velocity has primarily one- and two-dimensional features near the flame tip and base, respectively. The magnitude of the radial velocity components increases with temperature ratio across the flame, while their axial extent increases with frequency. However, the acoustic pressure has primarily one-dimensional characteristics. They also show that the acoustic field structure exhibits only moderate dependencies upon area expansion and flame temperature ratio for values typical of practical systems. Finally, they show that the local characteristics of the acoustic field, as well as the overall plane-wave reflection coefficient, exhibit a decreasing dependence upon the flame length as the area expansion ratio increases. © 2003 Acoustical Society of America.
[DOI: 10.1121/1.1520547]

PACS numbers: 43.28.Kt [MSH]

I. INTRODUCTION

This paper describes results of an investigation of the interactions between a premixed flame front and plane acoustic waves. Such acoustic wave–flame interactions play important roles in the characteristic unsteadiness of turbulent combustion systems found in most processing, power generating, and propulsion applications. In particular, this work is motivated by the problem of combustion instabilities, which routinely plagues the development of combustion systems in industrial processing,¹ solid and liquid rockets,^{2,3} ramjets,⁴ afterburners, and land-based gas turbines.⁵ These oscillations lead to enhanced vibration, reduced part life, flame blowoff or flashback, and even complete system failure. They generally occur at frequencies associated with the combustor's natural longitudinal, radial, azimuthal, or bulk modes. They arise from interactions between oscillatory flow and heat release processes in the combustor and are manifested as large amplitude, organized oscillations of the combustor's flow fields. The unsteady heat release generated by the acoustic disturbance adds energy to the acoustic field when it is in phase with the pressure oscillations.⁶

Acoustic wave–flame interactions are complex and involve the simultaneous interactions between a number of flow and combustion processes.^{7–12} The specific processes which need to be considered depend upon whether the combustor is burning a solid (e.g., solid rockets), liquid (e.g., liquid rockets or aircraft engines), or gaseous fuel (e.g., land-based gas turbines), and in the manner of fuel and oxidizer preparation (e.g., premixed versus non-premixed). In this paper, we specifically focus on gaseous fueled, premixed systems. Thus, it is most relevant to low emissions, land-based gas turbines.²⁸ In such systems, oscillations are generally as-

sociated with bulk or longitudinal modes and occur in a frequency range from about 50–1000 Hz.⁷

A complete understanding of the overall acoustic wave–flame interaction problem necessarily requires a more basic understanding of several issues: First, because the flame's position and orientation depends upon the local burning rate and flow characteristics, acoustic velocity perturbations cause wrinkling and movement of the flame front. These disturbances have been visualized in several experimental investigations, such as those of DuCruix *et al.*¹³ in a simple Bunsen flame and Shih *et al.*¹⁴ in a more complex, swirling flow. In addition, calculations of the flame's dynamics and its resultant heat release disturbances have been reported by Boyer and Quinard,¹⁵ Fleifel *et al.*,¹² Marble and Candel,¹⁰ and Yang and Culick.¹⁶ These studies predict the dependence of the flame's unsteady heat release upon such parameters as the mean flame position, frequency of oscillations, and mean flow velocity.

Second, the flame's relative propagation speed into the unburned mixture (the mass burning rate) is sensitive to the perturbations in pressure, temperature, and strain rate that accompany the acoustic wave. McIntosh,^{17,18} Peters and Ludford,¹⁹ and Ledder and Kapila²⁰ have reported calculations of the unsteady flame structure and determined the transfer function relating the response of the unsteady mass burning rate to pressure fluctuations. The response of the mass burning rate to strain rate fluctuations has also been studied analytically by Joulin²¹ and computationally by Im and Chen.²²

Third, acoustic, entropy and vorticity modes become strongly coupled at the flame front, leading to energy transfer between these different disturbance modes and amplification or damping of acoustic waves. Calculations of this energy transfer have been reported by Lieuwen²³ and Markstein.²⁴

^{a)}Electronic mail: tim.lieuwen@aerospace.gatech.edu

Fourth, acoustic waves interact with intrinsic flame instabilities and/or cause parametric flame–acoustic instabilities. The parametric acoustic instability of planar flames is due to the periodic acceleration of the flame front by the unsteady flow field, which separates two regions of differing densities. Such instabilities are often observed in flames propagating from one end of a tube to another and have been investigated in several experimental^{24,25} and theoretical investigations.^{26,27} In addition, it has been shown that acoustic oscillations can stabilize the inherent Darrieus–Landau flame instability.²⁵

As can be inferred from the above discussion, many of the fundamental characteristics of premixed flame–acoustic wave interactions have been studied. It should be noted, however, that most of these studies have focused their attention on highly idealized geometries (such as flat flames) which have little resemblance to those encountered in practical devices; e.g., see Refs. 17, 18, 23, 24. This has been done in order to focus on the problem of relating acoustic oscillations and the resultant heat release perturbation.

The solution to the acoustic–flame interaction problem requires understanding of both the acoustic field–heat release transfer function and the local acoustic field at the flame that is disturbing it. This latter issue has been largely ignored in the literature. It has been circumvented in analyses that have considered more realistic flame geometries, such as those of Fleifel *et al.*,¹² Yang and Culick,¹⁶ and Marble and Candel,¹⁰ which assumed that the local acoustic oscillations that are disturbing the flame are one-dimensional.

Basic acoustic considerations suggest that such a description of the flame’s acoustic near field is unrealistic. A planar incident wave impinging upon a flame front generates not only planar reflected and transmitted waves, but also multidimensional disturbances that are generally evanescent for the frequencies of interest. Since the flame is disturbed by the local, multidimensional acoustic field, it seems clear that calculations of its interactions with the acoustic field must account for these multidimensional characteristics.

The objective of this paper is to provide some insight into the structure of the acoustic oscillations that are disturbing the flame. As such, this analysis restricts its attention to what is primarily an acoustic problem, as opposed to the majority of the above-cited studies which are primarily unsteady combustion analyses. Particularly, it seeks to clarify the characteristics of the flame’s acoustic near field, such as its dependence upon combustor geometry and flame characteristics; e.g., duct diameter, dump expansion ratio, flame length, or temperature ratio across the flame. These flame characteristics are more fundamentally affected by such parameters as fuel type, equivalence ratio, upstream reactants temperature, and mean flow velocity. In particular, the paper seeks to obtain “leading order” results which provide insight into these characteristics that have some general validity, regardless of the specific details of the fuel kinetics or the fillet radius of the rapid expansion piece. As such, certain “lower order” phenomenon which could be incorporated into the analysis, but would require specifying more geometrical or kinetic details, are not included so as not to compromise this generality.

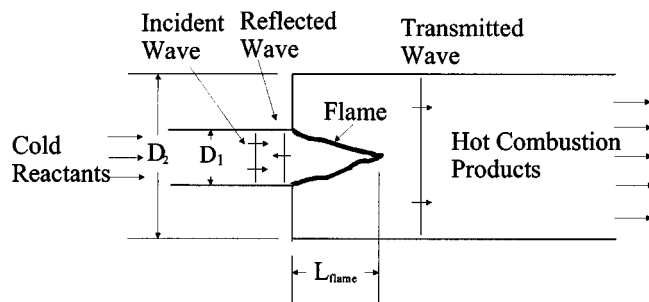


FIG. 1. Schematic of investigated configuration for case where disturbance originates from upstream.

The paper is organized in the following manner: In the following Analysis section, we discuss the modeled geometry, outline the basic assumptions and restrictions of the model, and present the numerical solution procedure. Then, the Results section discusses the characteristics of the acoustic field and the manner in which it is affected by flame and geometric parameters. The Concluding Remarks section summarizes the principal conclusions of the analysis and suggests an approach whereby these results can be coupled with more fundamental unsteady combustion studies to analyze flame–acoustic interactions in realistic geometries.

II. ANALYSIS

A. Geometry

The investigated geometry is shown in Fig. 1. It consists of an axisymmetric domain, where a premixed flame of length L_{flame} is located at the junction between two ducts of diameters D_1 and D_2 . Such a rapid expansion is often referred to as a “dump” in the combustion literature and is used to create a recirculation region for stabilizing the flame. This geometry closely resembles that found in a range of laboratory and industrial hardware, such as Bunsen burners, ramjets, and some furnace designs. In addition, it contains many of the dominant features of more complex hardware. For example, modern low emissions gas turbine combustors generally consist of either several smaller diameter ducts (called premixers) transitioning into a single, larger duct (the combustor), such as in “can-type combustors,” or a circumferential array of ducts (premixers) transitioning into an annular shaped combustor.²⁸

The flame’s mean position is assumed to be conical. This shape closely resembles that typically observed in this geometry in flows with low to moderate amounts of swirl in the mean flow (in highly swirling flows, the flame is generally more flattened because of the presence of a central recirculation region, due to vortex breakdown).²⁹ In reality, nonuniformities in mean flow profile and flame propagation speed cause some deviations in the flame from this conical shape. However, the differences in acoustic field structure are small, as long as these deviations in shape are small relative to the other characteristic lengths in the problem: the duct diameters, flame length, and acoustic wavelength. Such a restriction is well satisfied over a wide range of situations.

B. Jump conditions

The region of chemical reactions is generally confined to a front which has a complex inner structure consisting of several zones where the fuel is broken down, a radical pool is created and consumed, and heat is released. The thickness of this front is usually quite thin relative to other hydrodynamic and acoustic length scales. For example, the thickness of a stoichiometric methane–air flame is about 1 mm.²⁹ For reference, an acoustic disturbance with a 1-mm wavelength corresponds to disturbances with frequencies of 330 and 850 kHz at temperatures of 300 and 2000 K, respectively. In contrast, acoustic wavelengths for the frequencies of interest, say 50–1000 Hz, are substantially longer than 1 mm. Given this disparity in length scales between flame thickness and acoustic wavelength, we treat the flame front as a surface of temperature discontinuity and assume that no additional entropy production occurs outside of it. Such an approximation is routinely used in the combustion literature^{12,13,15,24,30} and is satisfied to a high degree of accuracy for the frequencies of interest here.

Using the mass, momentum, and energy conservation equations, the linearized jump conditions across the flame front have been derived in several studies.^{23,24,30–32} The following expressions are derived in Lieuwen,²³ where terms of the order of the mean flow Mach number squared and the ratio of the flame thickness to acoustic wavelength are neglected:

$$\text{Normal momentum: } \frac{p'_1}{\bar{p}} = \frac{p'_2}{\bar{p}}, \quad (1)$$

$$\text{Energy: } \frac{u'_{n,2}}{c_1} - \frac{u'_{n,1}}{c_1} = M_s \left(\frac{\bar{T}_2}{\bar{T}_1} - 1 \right) \left(-\frac{(\gamma-1)}{\gamma} \frac{p'_1}{\bar{p}} + \frac{S'_1}{\bar{S}_1} \right), \quad (2)$$

where the notation $()'$ and $\bar{()}$ is used to denote the mean and fluctuating component of the variable and the subscripts 1 and 2 denote the variable's value on the up- and downstream side of the flame. In addition, the variables u_n , p , M_s , c , γ , \bar{T}_2/\bar{T}_1 and S_1 denote the normal velocity, pressure, mean flame speed Mach number relative to the unburned gas, sound speed, specific heats ratio, temperature ratio across the flame, and flame speed, respectively. Note that the fluctuating flame speed is, in general, a function of the fluctuating pressure, temperature, and flow strain rate. It should also be noted that the unsteady terms consist not only of acoustic fluctuations, but the superposition of the acoustic, entropy, and vorticity modes. The mass and tangential momentum conditions are also derived in Ref. 23 but not considered here because, within the approximations of this analysis, are only needed to solve for the characteristics of the entropy and vorticity modes. See Refs. 23 and 24 for further discussion.

Although not needed for the calculations below, for completeness we present the kinematic equation relating the flame front position to the flow field and flame speed characteristics:²⁴

$$\frac{\partial \xi}{\partial t} = u - v \frac{\partial \xi}{\partial r} - S_1 \sqrt{\left(\frac{\partial \xi}{\partial r} \right)^2 + 1} \quad (3)$$

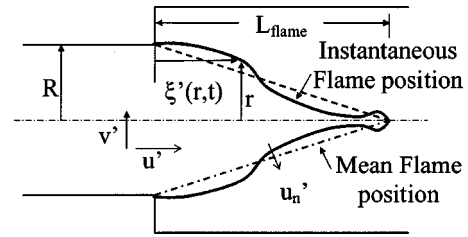


FIG. 2. Schematic illustrating variables used to characterize flame region.

where $\xi(r,t)$, u , and v denote the axial flame displacement, axial velocity, and radial velocity, respectively; see Fig. 2. Note that Eq. (3) assumes that $\xi(r,t)$ is a single-valued function of the radial coordinate, r . More general expressions are given in Markstein.²⁴

Consider the magnitudes of the terms on the right side of Eq. (2), which quantify the jump in normal velocity across the flame. The first term is of $O(M_s)$ relative to those on the left, assuming that $p' \sim \bar{p}cu'$. Assuming that the normalized flame speed and pressure perturbations are also of similar magnitude as McIntosh's analysis suggests,¹⁷ i.e., $S'_1/\bar{S}_1 \sim O(p'_1/\bar{p})$, then the second term on the right is also of $O(M_s)$. Typical values of M_s are very low; e.g., the flame speed of a stoichiometric methane–air mixture is about 40 cm/s.²⁹ Using an upstream temperature of 300 K, this corresponds to an M_s value of 0.001. As such, we neglect these terms in this analysis so that the jump conditions across the flame are

$$p'_1 = p'_2, \quad (4)$$

$$u'_{n,2} = u'_{n,1}. \quad (5)$$

A critical point regarding this assumption should be emphasized. The neglected terms are responsible for unsteady heat addition and, thus, amplification or damping of the acoustic field by the acoustic–flame interaction. At first glance, then, it may appear that their neglect completely removes the interesting physics from the problem. However, these unsteady heat release terms can be calculated to good accuracy using the solutions of Eqs. (4)–(5) and standard perturbation procedures. To illustrate, denote the terms on the right side of Eq. (2) as $M_s \psi(p', u', \dots)$, and expand the unsteady fields about their value in the limit of vanishing right-hand side of Eq. (2); e.g., $u' = u'_o + M_s u'_1 + \dots$. The unsteady heat release can then be expanded in a similar fashion as

$$M_s \psi(p', u', \dots) = M_s \psi(p'_o, u'_o, \dots) + M_s^2 \left(p'_1 \frac{\partial \psi}{\partial p'} \bigg|_{p'_o} + u'_1 \frac{\partial \psi}{\partial u'} \bigg|_{u'_o} \right) + \dots$$

This shows that the leading order heat release perturbations can be calculated using the approximations in this analysis. The approximation utilized by invoking Eq. (5) is useful because it allows us to generate general results that are independent of the details of the heat release model that is used.

It should also be noted that this approximation is well supported by experiments. For example, data presented by Lieuwen³³ and Poinot *et al.*³⁴ show that the pressure ampli-

tude during an instability grows by about 1 percent each cycle, implying that the real part of the right side of Eq. (2) is small. Also, measurements reported by Lovett and Uznanski³⁵ show that the frequency shift induced by the unsteady heat release (obtained by comparing instability frequencies during stable and unstable operation) is less than 10 percent, indicating that the imaginary part of the right side of Eq. (2) is also small.

Several other points should be noted: First, although the flame front is moving as a result of the acoustic perturbations [see Eq. (3)], for this linear analysis the matching conditions given by Eqs. (4)–(5) are applied at the mean flame location. Second, the velocity in Eqs. (2) and (5) refers, in general, to the sum of the acoustic and vortical components; i.e., these disturbance modes are coupled at the flame front where they have similar magnitudes. In this analysis, it is assumed that the normal vortical velocity component is small relative to that of the acoustic component and, thus, is neglected. Because of the substantially shorter wavelength of the vortical component and its solenoidal character, its normal component is of the order of the flame speed Mach number relative to that of the normal acoustic velocity.²³ The tangential components of the vortical and acoustic perturbations are of similar magnitude, however. Analysis that fully includes this vortical–acoustic coupling shows that it results in an acoustic damping term that is $O(M_s)$.²³

C. Acoustic field

As noted above, we assume that the acoustic field is divided into two isentropic regions (of differing mean properties) up- and downstream of the flame that are coupled across the flame front. As such, these wave motions are described by the classical, isentropic wave equation. We assume that the mean flow Mach number of the burned and unburned gases is low and, thus, neglect convection effects on these wave motions. With the exception of certain military applications, such as ramjets and afterburners, this approximation is well satisfied in the flame region of most combustion systems where the Mach number, M , is typically below 0.1. As such, the following Helmholtz equations describe the harmonic wave motions in the regions up- and downstream of the flame³⁶ at an angular frequency, ω :

$$\text{Upstream of flame: } \nabla^2 p' + k_1^2 p' = 0, \quad (6)$$

$$\text{Downstream of flame: } \nabla^2 p' + k_2^2 p' = 0, \quad (7)$$

where $k = \omega/c$ is the wave number. The equivalent integral form of Eqs. (6) or (7), the Helmholtz integral equation, is given by:³⁶

Upstream of flame

$$p'(\mathbf{x})C(\mathbf{x}) = - \int_S \int (i\omega\bar{\rho}_1 \mathbf{u}'(\mathbf{x}_s)G(\mathbf{x}_s, \mathbf{x}) - p'(\mathbf{x}_s)\nabla G(\mathbf{x}_s, \mathbf{x})) \cdot \mathbf{n}_1 dS, \quad (8)$$

Downstream of flame

$$p'(\mathbf{x})C(\mathbf{x}) = - \int_S \int (i\omega\bar{\rho}_2 \mathbf{u}'(\mathbf{x}_s)G(\mathbf{x}_s, \mathbf{x}) - p'(\mathbf{x}_s)\nabla G(\mathbf{x}_s, \mathbf{x})) \cdot \mathbf{n}_2 dS, \quad (9)$$

where \mathbf{x} , \mathbf{x}_s , \mathbf{u}' , and \mathbf{n} denote the measurement point, boundary surface point (consisting of the closed region demarcated by the flame front, combustor wall, and up- or downstream boundary), acoustic velocity vector, and unit normal vector pointing out of the respective domain, respectively. Also, G is the free-space Green's function, $G = e^{-ik|\mathbf{x}-\mathbf{x}_s|}/(4\pi|\mathbf{x}-\mathbf{x}_s|)$. For this choice of G , it can be shown that $C(x) = 1/2$, 1, and 0 for smooth boundary points, interior domain, and exterior domain points, respectively (the interior domain is defined as the region inside of the ducts).³⁷ Also, the time dependence of the harmonic oscillations is given by $e^{-i\omega t}$.

Similar to the acoustic–vortical coupling at the flame, the velocity disturbance modes are coupled at the rapid expansion point where their magnitudes are similar. This coupling can be handled analytically by imposing a Kutta condition at the rapid expansion; e.g., see Crighton³⁸ or Howe.³⁹ This vorticity generation results in an $O(M)$ modification to the acoustic field structure in the vicinity of this point and acoustic damping.⁴⁰ This effect is neglected in this analysis, consistent with our prior neglect of $O(M)$ terms. Note also that if the position of the flame base remains fixed (i.e., it doesn't move in response to oscillations), then even if this effect were retained it would not exert much impact on the dynamics of the flame because it is confined to the vicinity of the rapid expansion point. This flame base condition is likely satisfied in well-stabilized flames, but not in flames near the point of blowout, and has been suggested as a flame front boundary condition in prior studies.^{12,13} Assuming it is satisfied, the velocity field characteristics at the stabilization point are less important than at locations farther downstream.

Solution of Eqs. (8)–(9) requires specifying the value of the pressure or normal velocity over the surface of integration, i.e., $p'(\mathbf{x}_s)$ or $\mathbf{u}'(\mathbf{x}_s) \cdot \mathbf{n}$. The jump conditions derived in the prior section are used to couple the acoustic field across the flame, while the normal velocity at the combustor side walls was set to zero. Thus, this problem reduces to that of solving two coupled integral equations for the pressure. The velocity is then determined from the calculated pressure using the linearized Euler equation.

The boundary element method (BEM) was used to numerically solve the coupled integral equations. Except for points where $|\mathbf{x}-\mathbf{x}_s| \sim 0$, integrals were evaluated using a four-point Gaussian quadrature scheme. Integration in the vicinity of the singular point $|\mathbf{x}-\mathbf{x}_s| \sim 0$ was performed analytically using a Taylor series expansion of the Green's function. Details of implementation of the BEM are described in Refs. 7 and 37. Comparison of the numerical solutions with exact and approximate analytical solutions showed that errors in pressure magnitude were less than 1 percent when $k_1\Delta < 0.15$, where Δ is the boundary element width.⁷

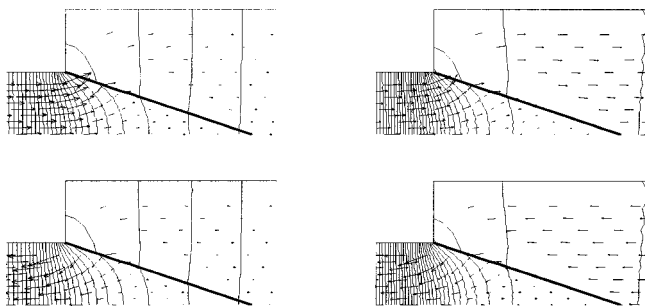


FIG. 3. Instantaneous pressure contours and velocity vectors (at 90-deg phase differences) for a case where the flame was excited from upstream at the dimensionless frequency $D_1/\lambda_1 = 0.2$. ($L_{\text{flame}}/D_1 = 1.59$, $D_2/D_1 = 2$, and $T_2/T_1 = 6.67$.)

III. RESULTS

This section presents the results of typical calculations with various geometries and conditions. To obtain these results, a plane disturbance is imposed upon the flame from up- or downstream. Upon reaching the flame, it is partially reflected and partially transmitted. A nonreflecting boundary condition (impedance, $Z = \rho c$) is imposed on the transmitted wave side. Although more complex boundary conditions apply in realistic situations, we use these conditions because they are canonical cases from which the wave field resulting from arbitrary, one-dimensional up- and downstream boundary conditions can be constructed. Calculations were performed for frequencies below the radial duct cutoff modes, so that only plane-wave modes propagate (calculations were performed at frequencies above the cutoff value of the first circumferential mode, but because the domain is axisymmetric, these modes are not excited). The computational domain was extended far enough up- and downstream such that the acoustic field was one-dimensional at the up- and downstream boundaries.

A. Qualitative structure of acoustic field

Figure 3 and Fig. 4 plot the spatial structure of the pressure and velocity field in the vicinity of the flame at four successive 90-deg phases of a cycle. The plots show the wave field at two dimensionless frequencies. Since the investigated geometry is axisymmetric, only the top half is shown. The mean flame location is indicated by the bold line. The upstream, unburned region is on the left. The figure clearly

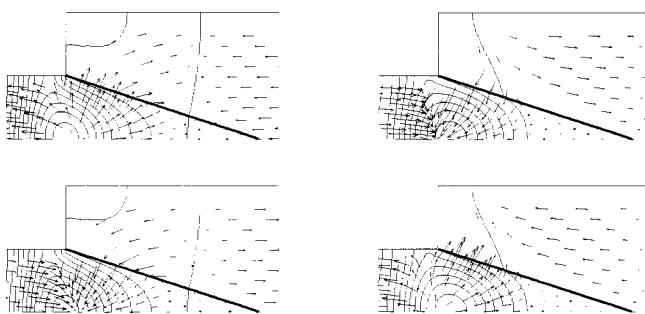


FIG. 4. Instantaneous pressure contours and velocity vectors (at 90-deg phase differences) for cases where the flame was excited from upstream at the dimensionless frequency $D_1/\lambda_1 = 1$. ($L_{\text{flame}}/D_1 = 1.59$, $D_2/D_1 = 2$, and $T_2/T_1 = 6.67$.)

shows the multidimensional nature of the acoustic velocity in the vicinity of the flame (while the acoustic pressure also appears to be strongly multidimensional, this is due to the scaling of the isobars and will be discussed below). Note that up- and downstream of the flame the acoustic field is one-dimensional. This occurs because the frequencies fall below the cutoff value so that evanescent, multidimensional disturbances excited in the vicinity of the flame and area expansion decay with increasing up- and downstream distance.

Examination of the velocity vectors in Fig. 3 shows that both the axial and radial components are in phase along the length of the flame; i.e., the fluid oscillates back and forth in a bulk motion. Figure 4 illustrates the results of a computation at a higher dimensionless frequency, showing that the phase of the velocity oscillations significantly changes along the flame surface; i.e., at some points in the cycle, the instantaneous velocity is positive and negative at the flame base and tip, respectively.

Several additional items should be noted from the figures. First, examination of the isobars shows the “bending” (i.e., refraction) of the wave as it passes through the flame. It is interesting to note the changes in the “degree of bending” as the wave progresses from the base of the flame towards its tip (particularly evident in Fig. 3). Second, the figures illustrate that successive isobars are spaced farther apart downstream of the flame than upstream. This difference in isobar spacing reflects the change in wavelength, λ , of the disturbance as the sound speed changes across the flame; i.e., since $\lambda = c/f$, the increase in temperature by a factor of 6.67 increases λ by a factor of ~ 2.6 . Note also that the isobar spacing increases along the centerline, even in the unburned gas region. This observation suggests that the acoustic field structure in the unburned region near the flame tip is dominated by the burned gas temperature. Finally, note the significantly smaller acoustic velocities near the flame tip than at the flame base. These lower velocities occur because of the lower pressure gradients in this region. The effects of the substantial density change across the flame can be seen by comparing the velocity vectors in the burned and unburned region near the flame tip. The velocity in the hotter, lower density burned gas is substantially higher than in the unburned gas, even though the pressure gradient is comparable.

We next consider the manner in which the structure of the acoustic field changes with area ratio of the rapid expansion. Figure 5 and Fig. 6 plot isocontours of the pressure magnitude for several expansion ratios for a case where the incident wave originates from upstream. Note that the acoustic field has a standing and traveling wave structure up- and downstream of the flame, respectively. Because the pressure-field amplitude is constant in the traveling wave region, the points in the figure downstream of the flame where no isobars are plotted can be approximately considered as defining this traveling wave regime. Comparison of the isobar structure in these figures illustrates a qualitative change in the acoustic field structure with increasing area ratio. In a straight duct, the region of highest pressure gradient (where the largest velocities occur) occurs at an axial location somewhere between the flame base and tip. This high-pressure gradient regime moves back toward the dump with increas-

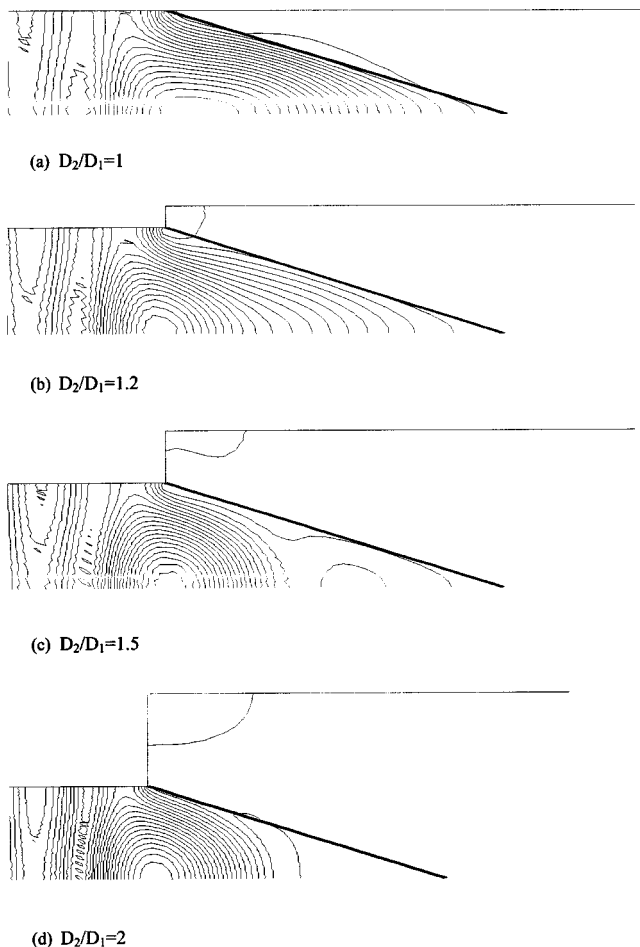


FIG. 5. Magnitude isobars at several area ratios. The flames were excited from upstream at the dimensionless frequency $D_1/\lambda_1 = 1$. ($L_{\text{flame}}/D_1 = 1.59$ and $T_2/T_1 = 6.67$.)

ing area ratio, indicating that the geometric features begin to exert a stronger influence on the structure of the acoustic field than the flame location. As will be discussed further below, similar behavior is observed in the flame reflection coefficient; i.e., the area ratio of the rapid expansion has a much stronger influence on the reflection coefficient than the flame location.

Figure 7 plots the magnitude of the isobars for a case where the flame is excited by a disturbance originating from downstream. Note that in this case, the downstream field has

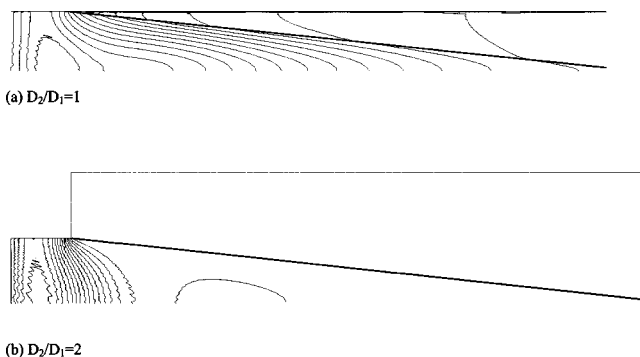


FIG. 6. Magnitude isobars at two area ratios for a longer flame length case than in Fig. 5. The flames were excited from downstream at the dimensionless frequency $D_1/\lambda_1 = 1$. ($L_{\text{flame}}/D_1 = 4.97$ and $T_2/T_1 = 6.67$.)

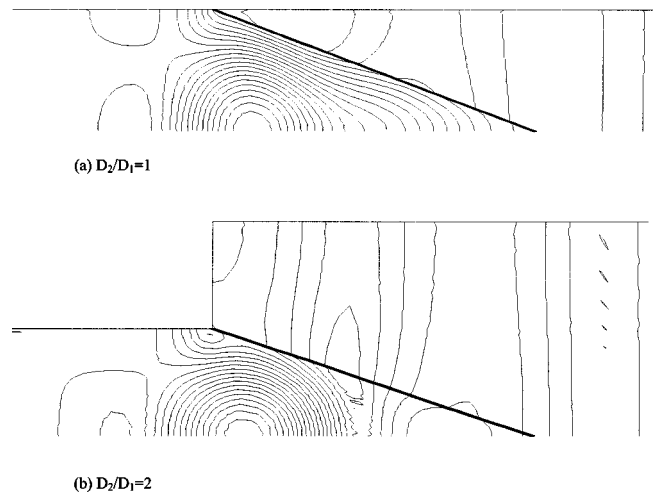


FIG. 7. Magnitude isobars at two area ratios. The flames were excited from downstream at the dimensionless frequency $D_1/\lambda_1 = 1$. ($L_{\text{flame}}/D_1 = 1.59$ and $T_2/T_1 = 6.67$.)

a standing wave structure, while the upstream field is a traveling wave. It can be seen that the pressure isobars exhibit near-radial uniformity over a significantly larger portion of the flame region in the larger D_2/D_1 case. Note also that the acoustic field has a standing wave structure over the majority of the flame's length, regardless of diameter ratio. These characteristics contrast with those shown in Fig. 5 and Fig. 6, which show that the acoustic field has a substantial traveling wave region in the larger diameter ratio cases. This result is significant because it shows that the pressure-velocity relationship at the flame depends upon the duct diameter ratio and the direction from which the incident wave originates. In turn, velocity perturbations exert a large role in disturbing the flame and generating heat release oscillations, while the relative phase between pressure and heat release determines whether the disturbance is amplified or damped.

B. Dimensionality of acoustic field

We next quantify the two-dimensional characteristics of the acoustic field in the vicinity of the flame. Understanding this issue is important for evaluating the accuracy of simplified, one-dimensional models; e.g., see Refs. 11, 12, 13, 16. Figure 8 and Fig. 9 compare the axial dependence of the acoustic pressure at the centerline, flame, and wall. Except near the flame base, these curves lie on top of each other. The pressure at the flame and wall is particularly similar, due to the longer acoustic wavelength in this higher temperature region.

Several of the observations made in the prior section can also be seen in these results. Examination of Fig. 8 (upstream wave incidence) shows that the pressure magnitude has a nearly constant value over the last 2/3 of the flame length, implying a traveling wave field structure. This can also be seen from the phase results, which have a linear phase roll that begins at roughly the same axial location ($x/L_{\text{flame}} \sim 0.3$). In contrast, Fig. 9 (downstream wave incidence) shows that, within the flame region, the pressure magnitude varies axially and the phase does not, implying a standing wave structure.

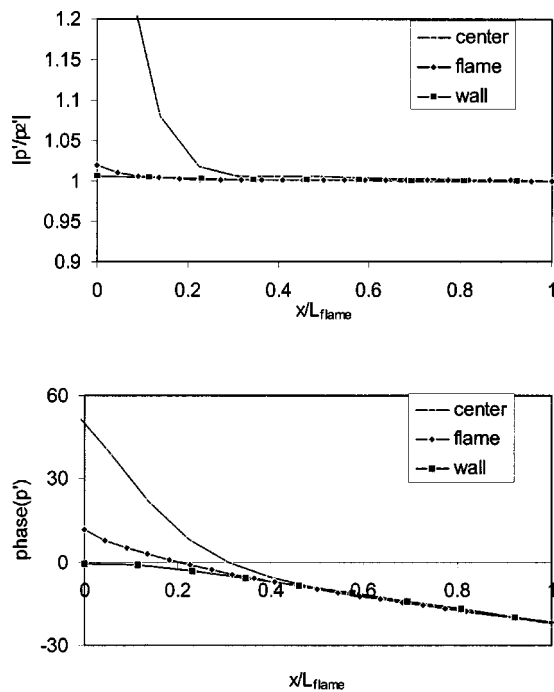


FIG. 8. Comparison of pressures at the flame, combustor wall, and centerline. The flame was excited from upstream. ($D_2/D_1=2$, $D_1/\lambda_1=0.1$, $L_{\text{flame}}/D_1=1.73$, and $T_2/T_1=6.67$.)

Figure 10 plots the maximum difference between wall and flame pressures upon the nondimensional frequency. As expected, the deviation between the wall and flame pressure increases with frequency (or decreasing wavelength). For example, the difference in $|p'|$ at the flame front and combustor wall increases from about 1 percent to 6 percent as D_1/λ_1 increases from 0.1 to 0.3. The corresponding maxi-

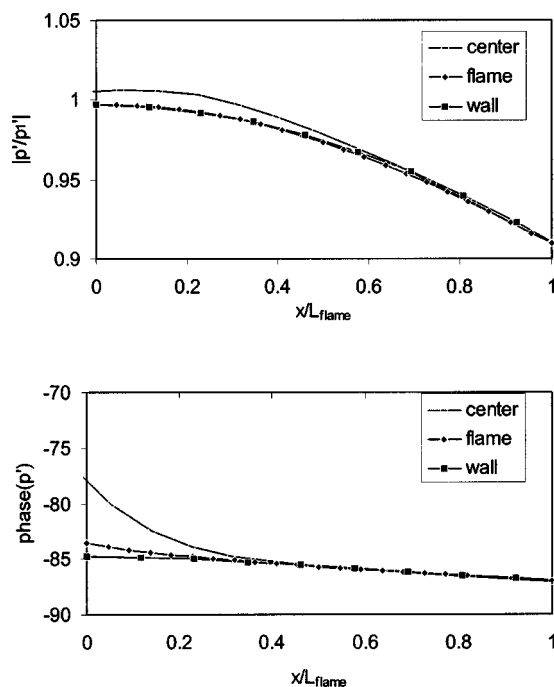


FIG. 9. Comparison of pressures at the flame, combustor wall, and centerline. The flame was excited from downstream. ($D_2/D_1=2$, $D_1/\lambda_1=0.1$, $L_{\text{flame}}/D_1=1.73$, and $T_2/T_1=6.67$.)

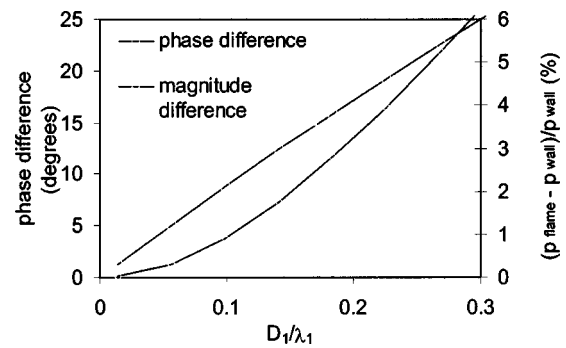


FIG. 10. Dependence of the maximum phase and magnitude difference between the wall and flame pressure upon the ratio of the duct diameter and wavelength. The flame was excited from upstream. ($D_2/D_1=2$, $L_{\text{flame}}/D_1=1.73$, and $T_2/T_1=6.67$.)

um phase difference between the two locations increases from 4 to 20 degrees. These results indicate that while there are differences between the wall and flame pressures, these differences are not substantial. In other words, the acoustic pressure remains nearly one-dimensional over the examined frequency range. Reference 41 provides additional discussion of the characteristics of the pressure field in premixed flame geometries and the implications of these results upon acoustic measurements in combustors.

In contrast, the acoustic velocity at the flame appears to have significant two-dimensional features, as might be expected from Fig. 3 and Fig. 4. The following paragraphs consider the departure of the acoustic velocity from quasi-one-dimensionality by plotting the ratio of the radial velocity component, v' , to the total velocity, v^* , where $v^* = v'/\sqrt{v'^2 + u'^2}$ and u' is the axial velocity component. Note that v^* values of 0 and 1 denote purely axial and radial velocity fields, respectively.

Figure 11 and Fig. 12 plot the dependence of v^* upon axial location along the flame front and temperature ratio across the flame for a case where the incident wave originates from upstream. The plots were obtained at two nondimensional frequency values. Analogous results for the downstream excitation case are shown in Fig. 13 and Fig. 14. The figures show that v^* values tend toward unity near the base

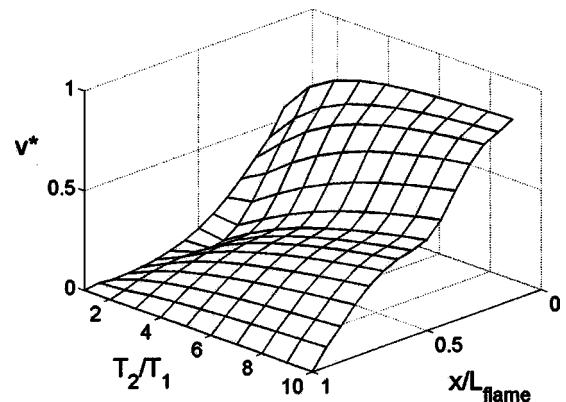


FIG. 11. Dependence of dimensionless ratio of radial to total velocity magnitude, v^* , upon axial location along the flame and temperature ratio. The flame was excited from upstream. ($L_{\text{flame}}/D_1=1.59$, $D_2/D_1=2$, and $D_1/\lambda_1=0.3$.)

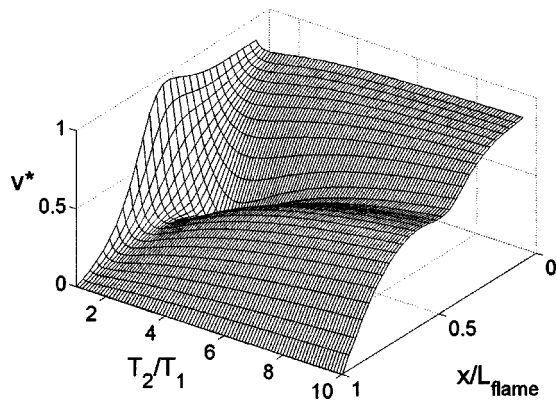


FIG. 12. Dependence of dimensionless ratio of radial to total velocity magnitude, v^* , upon axial location along the flame and temperature ratio. The flame was excited from upstream. ($L_{\text{flame}}/D_1=1.59$, $D_2/D_1=2$, and $D_1/\lambda_1=0.566$.)

of the flame but approach zero near the flame tip. These results imply that, in all calculated cases, the acoustic velocity is dominated by the radial and axial components at the flame base and tip, respectively, and emphasize the strong two-dimensionality of the acoustic velocity near the base of the flame.

As expected, the figures show that the acoustic field retains two-dimensional features over a larger axial extent of the flame at the higher frequency cases. In general, the figure also shows that the two-dimensionality of the acoustic field increases with temperature ratio across the flame. The primary exception to this occurs in the higher frequency cases; see Fig. 12 and Fig. 14, near $T_2/T_1 \sim 1$ values, which occurs because of an axial velocity node that occurs midway along the flame in this shorter wavelength case. Note also that, because of the rapid expansion at the dump plane, the acoustic velocity field retains its two-dimensional features even in the case where the temperature ratio has values of unity. However, the magnitude and axial extent of the two-dimensional velocity features increase with temperature ratio. Finally, note that the characteristics of v^* change very little, and in only a quantitative manner for the realistic temperature ratios of $T_2/T_1=3-7$. This implies that variations in temperature ratio, induced by fuel-air ratio or air preheat

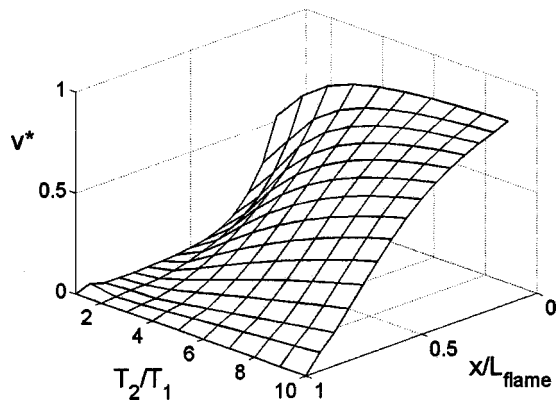


FIG. 13. Dependence of dimensionless ratio of radial to total velocity magnitude, v^* , upon axial location along the flame and temperature ratio. The flame was excited from downstream. ($L_{\text{flame}}/D_1=1.59$, $D_2/D_1=2$, and $D_1/\lambda_1=0.3$.)

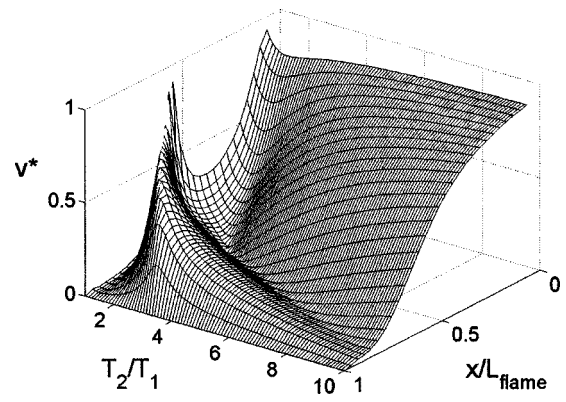


FIG. 14. Dependence of dimensionless ratio of radial to total velocity magnitude, v^* , upon axial location along the flame and temperature ratio. The flame was excited from downstream. ($L_{\text{flame}}/D_1=1.59$, $D_2/D_1=2$, and $D_1/\lambda_1=0.566$.)

temperature modifications, do not cause substantial changes in the structure of the acoustic field.

Figure 15 and Fig. 16 plot the axial dependence of v^* for several dimensionless frequency values at the fixed $T_2/T_1=6.67$ temperature ratio. As also mentioned above, the figure shows that v^* has non-negligible values over a longer axial extent of the flame with increasing frequency. This result is to be expected, because of the slower decay of two-dimensional, evanescent disturbances with increasing frequency. This effect is particularly prominent near the flame tip, $x/L_{\text{flame}} \sim 0.5-0.8$. Next, note that the qualitative characteristics of v^* remain essentially the same over $D_1/\lambda_1 \sim 0-1$ range in the downstream incidence case. In contrast, it exhibits qualitative differences in the $D_1/\lambda_1 \sim 0-0.4$ and $0.4-1$ ranges for the downstream incidence case. Practical combustion systems have a number of acoustic modes with their associated frequencies whose stability change with operating conditions and geometry. The above results suggest that the structure of the acoustic field oscillations associated with these different modes remains similar if D_1/λ_1 remains below about 0.4.

Figure 17 and Fig. 18 plot the axial dependence of v^* for different dump expansion ratios at the fixed $T_2/T_1=6.67$ temperature ratio. The figure shows that v^* is sensi-

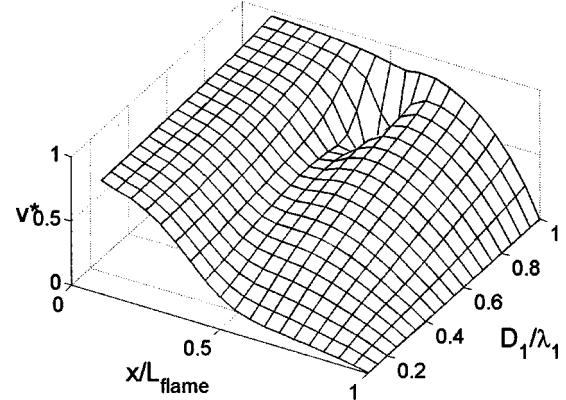


FIG. 15. Dependence of dimensionless ratio of radial to total velocity magnitude, v^* , upon axial location along the flame and dimensionless frequency. The flame was excited from upstream. ($D_2/D_1=2$, $L_{\text{flame}}/D_1=1.59$, and $T_2/T_1=6.67$.)

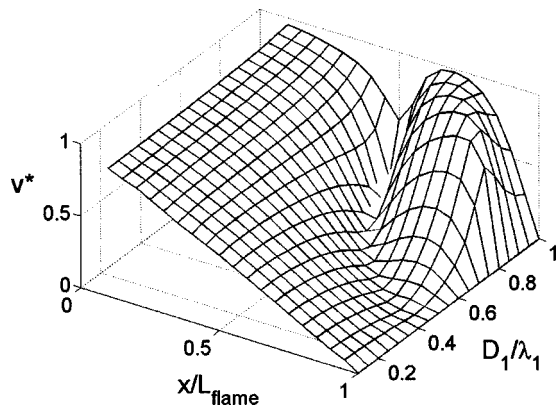


FIG. 16. Dependence of dimensionless ratio of radial to total velocity magnitude, v^* , upon axial location along the flame and dimensionless frequency. The flame was excited from downstream. ($D_2/D_1=2$, $L_{\text{flame}}/D_1=1.59$, and $T_2/T_1=6.67$.)

tive to changes in area ratio only when D_2/D_1 has near unity values. Little change in v^* occurs for higher D_2/D_1 values. Given that this area ratio is generally large in practical systems, these results imply that the characteristics of the acoustic field exhibits virtually no dependence upon moderate changes in this ratio.

C. Plane-wave reflection coefficient

The reflection coefficient is an important parameter that determines the relative magnitude of the plane-wave component of the pressure and velocity components that are forcing oscillations at the flame. We next consider how the pressure reflection coefficient varies with frequency and geometry and compare it to its quasi-one-dimensional value. This quasi-one-dimensional value can be obtained from momentum and energy conservation considerations

$$R_{1D} = \frac{1 - A_2/A_1 \sqrt{T_2/T_1}}{1 + A_2/A_1 \sqrt{T_2/T_1}}, \quad (10)$$

where A_2/A_1 denotes the area ratio between ducts. In order to determine the reflection coefficient from the computed results, the flame base was specified as the “origin” of the reflected wave. Note that this choice of origin affects the

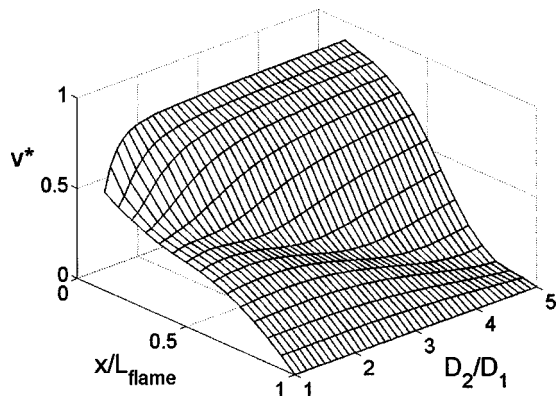


FIG. 17. Dependence of dimensionless ratio of radial to total velocity magnitude, v^* , upon axial location along the flame and dump expansion ratio. The flame was excited from upstream. ($D_1/\lambda_1=0.3$, $L_{\text{flame}}/D_1=1.59$, and $T_2/T_1=6.67$.)

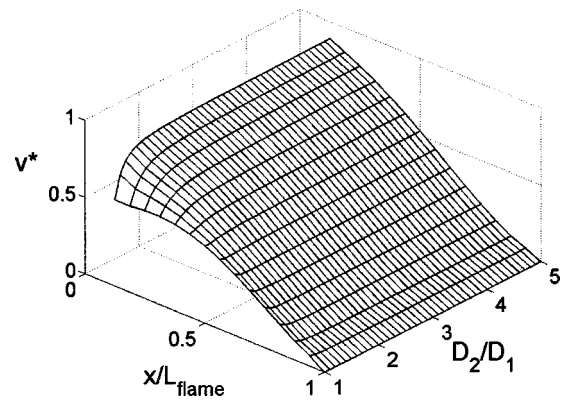


FIG. 18. Dependence of dimensionless ratio of radial to total velocity magnitude, v^* , upon axial location along the flame and dump expansion ratio. The flame was excited from downstream. ($D_1/\lambda_1=0.3$, $L_{\text{flame}}/D_1=1.59$, and $T_2/T_1=6.67$.)

phase, but not the amplitude of the reflection coefficient. Figure 19 plots the dependence of the reflection coefficient upon the dimensionless frequency for a straight duct case. The figure shows that the reflection coefficient magnitude, $|R|$, monotonically decreases with increasing D_1/λ_1 . This occurs because the change in gas temperature appears less “abrupt” as the acoustic wavelength decreases. For the same reasons, $|R|$ decreases more rapidly with increasing D_1/λ_1 in the longer flame case, $L_{\text{flame}}/D_1=2.46$, than the $L_{\text{flame}}/D_1=0.866$ case. Note also the linear phase dependence upon D_1/λ_1 . This result suggests that a more suitable location for the “origin” of the reflected wave is at an axial location downstream of the flame base.

Figure 20 and Fig. 21 plot similar results for a case where the diameter ratio, D_2/D_1 , is 2. The figures show that $|R|$ does not exhibit as strong a dependence upon L_{flame}/D_1

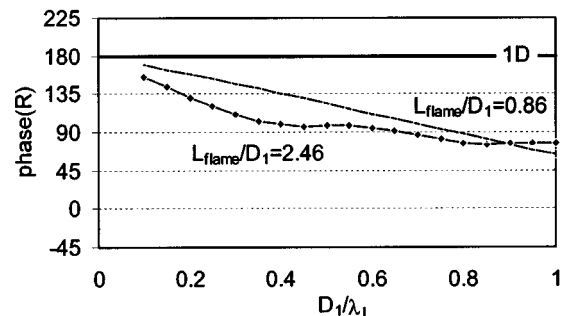
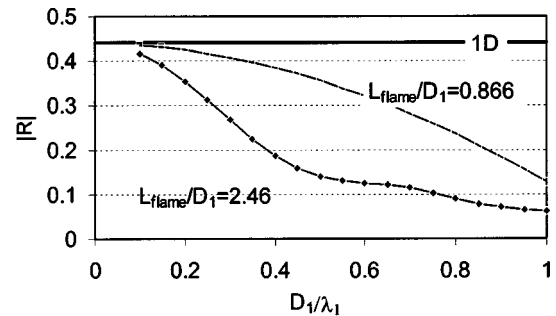


FIG. 19. Dependence of the plane-wave reflection coefficient upon D_1/λ_1 for a straight duct geometry. The flame was excited from upstream. ($T_2/T_1=6.67$, and $D_2/D_1=1$.)

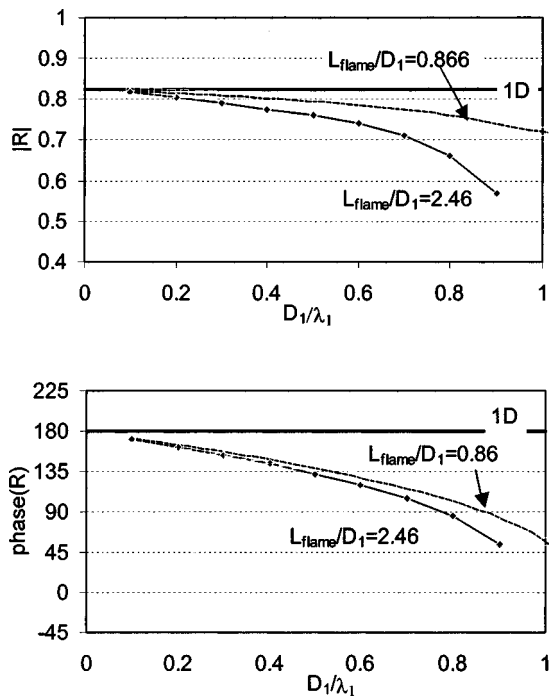


FIG. 20. Dependence of the plane-wave reflection coefficient upon D_1/λ_1 for duct with diameter expansion ratio of 2. The flame was excited from upstream. ($T_2/T_1 = 6.67$, and $D_2/D_1 = 2$.)

as in the straight duct case. This result is consistent with the above results and illustrates that the geometric characteristics of the area expansion exert a larger impact than those of the flame upon the acoustic field characteristics, unless $D_2/D_1 \sim 1$.

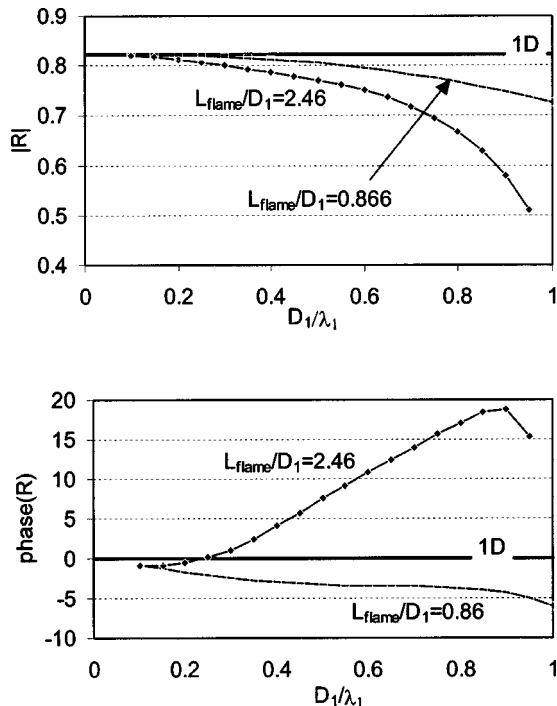


FIG. 21. Dependence of the reflection coefficient upon D_1/λ_1 for duct with diameter expansion ratio of 2. The flame was excited from downstream. ($T_2/T_1 = 6.67$, and $D_2/D_1 = 2$.)

IV. CONCLUDING REMARKS

This paper has presented an analysis of characteristics of the acoustic near field of a flame. Its principal results are: (1) the acoustic field structure exhibits primarily traveling and standing wave characteristics when the incident wave originates from up- and downstream of the flame, respectively; (2) the acoustic field is primarily controlled by the rapid area expansion, as opposed to the flame length, unless the expansion ratio $D_2/D_1 \sim 1$; (3) the magnitude and axial extent of the two-dimensional features of the velocity field increase with temperature ratio across the flame and frequency, respectively; and (4) the acoustic pressure has dominantly one-dimensional characteristics. These results provide increased understanding of the dependence of the structure of the acoustic field upon such key parameters as temperature ratio, area expansion ratio, flame length, and frequency. The logical extension of this work is to incorporate these results into a flame response model to determine the flame's heat release response to the imposed perturbations; i.e., given a model for the flame's response to local pressure, temperature, and velocity perturbations (such as derived in Refs. 12, 17, 19, 20, 21), the unsteady heat release may be determined from the acoustic field values that are calculated from analyses such as described in this paper.

- ¹A. Putnam, *Combustion Driven Oscillations in Industry* (American Elsevier, New York, 1971).
- ²E. W. Price, "Combustion Instability in Solid Propellant Rocket Motors, *Astronautica Acta* **5**, 63–72 (1959).
- ³L. Crocco and S. Cheng, *Theory of Combustion Instability in Liquid Propellant Rocket Motors* (Butterworths Scientific, London, 1956).
- ⁴U. G. Hegde, D. Reuter, B. R. Daniel, and B. T. Zinn, "Flame Driving of Longitudinal Instabilities in Dump Type Ramjet Combustors," *Combust. Sci. Technol.* **55**, 125–138 (1987).
- ⁵A. A. Peracchio and W. M. Proscia, "Nonlinear Heat Release/Acoustic Model for Thermo-Acoustic Instability in Lean Premixed Combustors," ASME Paper # 98-GT-269.
- ⁶J. S. W. Rayleigh, *The Theory of Sound* (New York, 1945), Vol. 2, p. 226.
- ⁷T. Lieuwen, "Investigation of Combustion Instability Mechanisms in Premixed Gas Turbines," Ph.D. thesis, Georgia Institute of Technology, Aug. 1999.
- ⁸T. J. Anderson and S. A. Morford, "Dynamic Flame Structure in a Low NOx Premixed Combustor," ASME Paper # 98-GT-568.
- ⁹B. T. Chu, "On the Generation of Pressure Waves at a Plane Flame Front," in *Fourth Symposium (International) on Combustion* (The Combustion Institute, Pittsburgh, 1953), pp. 603–612.
- ¹⁰F. E. Marble and S. M. Candel, "An Analytical Study of the Non-Steady Behavior of Large Combustors," in *Seventeenth International Symposium on Combustion* (The Combustion Institute, Pittsburgh, 1978), pp. 761–769.
- ¹¹A. Dowling, "Nonlinear Self-Excited Oscillations of a Ducted Flame," *J. Fluid Mech.* **346**, 271–290 (1997).
- ¹²M. Fleifel, A. M. Annaswamy, Z. A. Ghoniem, and A. F. Ghoniem, "Response of a Laminar Premixed Flame to Flow Oscillations: A Kinematic Model and Thermoacoustic Instability Results," *Combust. Flame* **106**, 487–510 (1996).
- ¹³S. Ducruix, D. Durox, and S. Candel, "Theoretical and Experimental Determinations of the Transfer Function of a Laminar Premixed Flame," *28th International Symposium on Combustion* (The Combustion Institute, Pittsburgh, 2000).
- ¹⁴W. P. Shih, J. Lee, and D. Santaviceca, "Stability and Emissions Characteristics of a Lean Premixed Gas Turbine Combustor," in *Twenty-Sixth Symposium (International) on Combustion* (The Combustion Institute, Pittsburgh, 1996), pp. 2771–2778.
- ¹⁵L. Boyer and J. Quinard, "On the Dynamics of Anchored Flames," *Combust. Flame* **82**, 51–65 (1990).
- ¹⁶V. Yang and F. E. C. Culick, "Linear Theory of Pressure Oscillations in

- Liquid-Fueled Ramjet Engines," AIAA Paper #83-0574.
- ¹⁷A. C. McIntosh, "Pressure Disturbances of Different Length Scales Interacting with Conventional Flames," *Combust. Sci. Technol.* **75**, 287–309 (1991).
 - ¹⁸A. C. McIntosh, "Deflagration Fronts and Compressibility," *Philos. Trans. R. Soc. London, Ser. A* **357**, 3523–3538 (1999).
 - ¹⁹N. Peters and G. S. S. Ludford, "The Effect of Pressure Variations on Premixed Flames," *Combust. Sci. Technol.* **34**, 331–344 (1983).
 - ²⁰G. Ledder and A. K. Kapila, "The Response of Premixed Flames to Pressure Perturbations," *Combust. Sci. Technol.* **76**, 21–44 (1991).
 - ²¹G. Joulin, "On the Response of Premixed Flames to Time Dependent Stretch and Curvature," *Combust. Sci. Technol.* **97**, 219–229 (1994).
 - ²²H. G. Im and J. H. Chen, "Effects of Flow Transients on the Burning Velocity of Laminar Hydrogen/Air Premixed Flames," *Proc. Comb. Inst.* **28**, 1833–1840 (2000).
 - ²³T. Liewen, "Theoretical Investigation of Unsteady Flow Interactions With a Premixed Planar Flame," *J. Fluid Mech.* **435**, 289–303 (2001).
 - ²⁴G. H. Markstein, in *Nonsteady Flame Propagation*, edited by G. H. Markstein (Pergamon, New York, 1964).
 - ²⁵G. Searby and D. Rochwerger, "A Parametric Acoustic Instability in Premixed Flames," *J. Fluid Mech.* **231**, 529–543 (1991).
 - ²⁶P. Pelce and D. Rochwerger, "Vibratory Instability of Cellular Flames Propagating in Tubes," *J. Fluid Mech.* **239**, 293–307 (1992).
 - ²⁷P. Clavin, P. Pelce, and L. He, "One-Dimensional Vibratory Instability of Planar Flames Propagating in Tubes," *J. Fluid Mech.* **216**, 299–322 (1990).
 - ²⁸S. M. Correa, "A Review of NO_x Formation Under Gas-Turbine Combustion Conditions," *Combust. Sci. Technol.* **87**, 329–362 (1992).
 - ²⁹S. Turns, *An Introduction to Combustion* (McGraw-Hill, New York, 2000).
 - ³⁰M. Matalon and B. J. Matkowsky, "Flames as Gas Dynamics Discontinuities," *J. Fluid Mech.* **124**, 239–259 (1982).
 - ³¹R. C. Aldredge and F. A. Williams, "Influence of Wrinkled Premixed Flame Dynamics on Large Scale, Low Intensity Turbulent Flow," *J. Fluid Mech.* **228**, 487–511 (1991).
 - ³²P. Clavin and F. A. Williams, "Effects of Molecular Diffusion and of Thermal Expansion on the Structure and Dynamics of Premixed Flames in Turbulent Flows of Large Scale and Low Intensity, Influence," *J. Fluid Mech.* **116**, 251–282 (1982).
 - ³³T. Liewen, "Experimental Investigation of Limit Cycle Oscillations in an Unstable Gas Turbine Combustor," *J. Propul. Power* **18**(1), 61–67 (2002).
 - ³⁴T. Poinso, D. Veynante, F. Bourienne, S. Candel, E. Esposito, and J. Surget, "Initiation and Suppression of Combustion Instabilities by Active Control," *Proc. Comb. Inst.* **22**, 1363–1370 (1988).
 - ³⁵J. Lovett and K. Uznanski, "Prediction of Combustion Dynamics in a Staged Premixed Combustor," ASME Paper #GT-2002-30646.
 - ³⁶A. D. Pierce, *Acoustics: An Introduction to its Physical Principles and Applications* (Acoustical Society of America, 1994).
 - ³⁷C. A. Brebbia, J. J. Silva, and P. W. Partridge, "Computational Formulation," in *Boundary Element Methods in Acoustics*, edited by R. D. Ciskowski and C. A. Brebbia (Computational Mechanics, Boston, 1994), pp. 13–60.
 - ³⁸D. G. Crighton, "The Kutta Condition in Unsteady Flow," *Annu. Rev. Fluid Mech.* **17**, 411–445 (1985).
 - ³⁹M. S. Howe, *Acoustics of Fluid-Structure Interactions* (Cambridge University Press, Cambridge, 1998).
 - ⁴⁰D. W. Bechert, "Sound Absorption Caused by Vorticity Shedding, Demonstrated with a Jet Flow," *J. Sound Vib.* **70**, 389–405 (1980).
 - ⁴¹T. Liewen and B. T. Zinn, "On the Experimental Determination of Combustion Process Driving in an Unstable Combustor," *Combust. Sci. Technol.* **157**, 111–127 (2000).

Application of an acoustic noise removal method to aircraft-based atmospheric temperature measurements

Ronald J. Hugo^{a)}

University of Calgary, Calgary, Alberta T2N 1N4, Canada

Scott R. Nowlin, Ila L. Hahn, Frank D. Eaton, and Kim A. McCrae

Air Force Research Laboratory/Directed Energy Directorate, Kirtland AFB, New Mexico 87117

(Received 16 August 2002; revised 8 October 2002; accepted 9 October 2002)

An acoustic noise removal method is used to reject engine acoustical disturbances from aircraft-based atmospheric temperature measurements. Removal of engine noise from atmospheric temperature measurements allows a larger wave number range to be fit while quantifying the magnitude of atmospheric temperature turbulence. The larger wave number range was found to result in a more statistically certain spectral slope estimate, with up to a 50% reduction in the standard deviation of measured spectral slopes. The noise removal technique was found to break down under conditions of weak atmospheric temperature turbulence where the engine acoustical disturbance can be several orders of magnitude larger than atmospheric temperature turbulence. © 2003 Acoustical Society of America. [DOI: 10.1121/1.1528591]

PACS numbers: 43.28.Ra, 43.28.Vd, 43.50.Ed [MSH]

I. INTRODUCTION

The goal of the atmospheric characterization group at the Air Force Research Laboratory (AFRL) has been to measure atmospheric temperature fluctuations in the troposphere and stratosphere using an aircraft-based sensor platform.^{1–3} Temperature fluctuation measurements are used in simulation programs to assess the performance of passive and active airborne optical systems. Temperature fluctuations at these altitudes and in the frequency range of interest are low (on the order of milliKelvins). Atmospheric temperature fluctuation measurements have been made using a 5 μm diameter constant current wire operating as a resistance thermometer in the low overheat mode.⁴

Conditions of strong atmospheric turbulence reveal the expected $-5/3$ decay for isotropic homogeneous turbulence,^{5,6} as shown in Fig. 1 where the temperature spectra is plotted in terms of wave number [$k = (2\pi f/U)$ where f is temporal frequency in Hz and U aircraft velocity]. The region of $-5/3$ decay is referred to as the inertial subrange of turbulence. It is characterized by a cascade of kinetic energy from large energy-producing structures at low wave number (outer scale of turbulence) to small energy dissipating structures at high wave number (inner scale of turbulence). The cascade from large to small structures is caused by nonlinear interactions in the fluid, and it ends at the inner scale of turbulence where viscous dissipation converts velocity shear into thermal energy. In the altitudes of interest, outer scale estimates are at a few tens of meters ($k \approx 0.02$) and inner scale estimates at a few centimeters ($k \approx 50$),⁷ placing the wave number range of interest ($0.5 < k < 5.0$) within the inertial subrange of turbulence.

Under weak turbulence conditions, a -3 spectral slope is seen and believed to be associated with either transitional

laminar free shear flows or with gravity wave activity.⁸ It is also under these weak turbulence conditions that other non-Kolmogorov features appear in the temperature spectra, and their nature depends on the aircraft flown and on the flight Mach number at which the data was collected. These non-Kolmogorov features can be seen in the temperature spectra in Fig. 2, collected from a Grumman Gulfstream II (GII) aircraft, where a “spike/bump” feature is noted along with what are labeled high Mach features. The high Mach features were examined in a separate paper⁹ and found to appear in the data only when the aircraft Mach number exceeded approximately 0.78. These high Mach features were attributed to shock formation and an associated flow separation instability which occurred once the critical Mach number¹⁰ on the probe-mount strut was reached.

The “spike/bump” feature appeared in the temperature spectra only while flying at altitudes above 28 000 ft (8530 m). The source of the “spike/bump” feature was discussed in an earlier article,¹¹ where by examining both constant-current-wire and microphone measurements, it was shown to be caused by a jet screech interaction. Jet screech involves a resonant interaction between the jet’s vortical structures and a quasi-periodic shock cell structure that develops in the jet’s exhaust stream.^{12–15} The vortical interaction results in a strong acoustical wave that propagates upstream from the engines and is sensed by the constant current wire as a temperature fluctuation.

A. Standard data processing routine

The standard data reduction methodology used by the atmospheric characterization group for determining the magnitude of temperature fluctuation strength has followed the “spectral method” described by Wyngaard *et al.*¹⁶ where a line is fit to the temperature fluctuation spectra when plotted versus wave number in log-log space (cf. Fig. 1). The line fit is performed over a wave number range that encompasses the inertial subrange of turbulence,^{5,6} and for isotropic and

^{a)} Author to whom correspondence should be addressed; electronic mail: hugo@ucalgary.ca

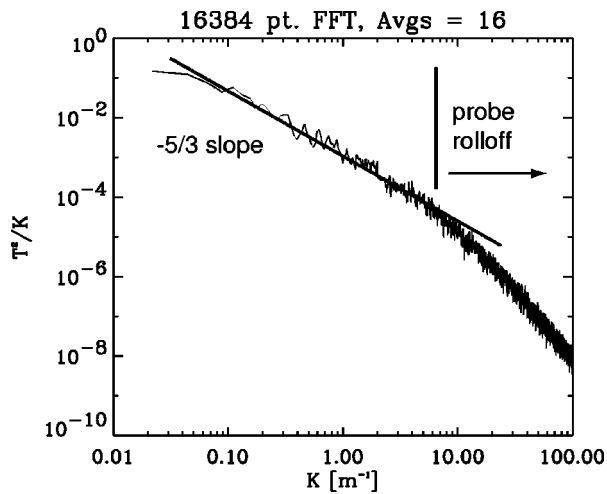


FIG. 1. Temperature spectra—Kolmogorov.

homogeneous turbulence the resulting fit normally has a slope of $-5/3$. When using the “spectral method,” the strength of turbulence at wave number $k=1$ then characterizes the magnitude of turbulence.

The presence of nonatmospheric sources in temperature fluctuation measurements can lead to erroneous estimates of atmospheric temperature fluctuation strength using the spectral method. This occurs when nonatmospheric sources contribute spectral energy over the wave number range where the spectral line fit is being made. The nonatmospheric sources are evident through both a visual inspection of spectra and by calculating spectral slopes, with slopes other than $-5/3$ or -3 indicative of nonatmospheric-source contamination. In order to improve the accuracy of atmospheric temperature fluctuation measurements, it is desirable to develop methods for removing nonatmospheric sources from the temperature fluctuation data.

A noise rejection technique developed by Chung¹⁷ was able to reject hydrodynamic pressure fluctuations (flow noise) from microphones placed on a moving vehicle, resulting in an improved estimate of the vehicle’s noise. Chung’s method was able to reject flow-noise interference from three (or more) microphones placed close to one another, provided

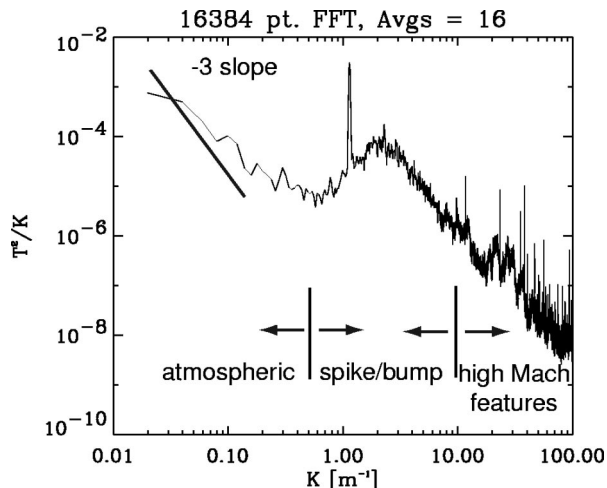


FIG. 2. Temperature spectra—“spike-bump” on GII aircraft.

that the flow noise at each microphone was mutually independent. This paper will evaluate the validity of applying Chung’s method to the atmospheric temperature fluctuation data using signals from two microphones and a constant current anemometer.

A number of basic differences exist between Chung’s original application and the current application. In Chung’s application, only microphone signals were used and the coherent signal was the desired signal (the vehicle noise). In the current application, a temperature sensor and two microphones are used and the coherent signal (the jet screech noise) is not the desired signal. The signal of interest is the uncorrelated atmospheric temperature fluctuation signal.

The success of the noise rejection method will be evaluated by examining the statistics of atmospheric temperature fluctuation spectral slopes. If the method is successful, the mean of the filtered spectral slopes should be closer to $-5/3$ than the mean of unfiltered spectral slopes and the standard deviation of the spectral slopes should be reduced.

The paper will begin by discussing the aircraft and associated hardware used to collect the atmospheric temperature fluctuation data. A section describing the noise removal process will then be given. This is followed by a section demonstrating the application of the noise removal process to the atmospheric temperature fluctuation data. The paper ends with a conclusions section.

II. EXPERIMENTAL HARDWARE

As mentioned in the Introduction, the goal of the atmospheric characterization program has been to collect atmospheric temperature fluctuation data in the troposphere and stratosphere. Temperature fluctuations at these altitudes and in the frequency range of interest are low and on the order of milliKelvins. The low signal levels have led to the development of a high-gain/low-electronic-noise constant current anemometer system.³

The normal constant current anemometer sensor suite was augmented while performing the noise identification experiments.¹¹ Much of the hardware used during these experiments¹¹ was used in the current investigation and consequently its description will be repeated.

A. Aircraft description

Data was collected with the constant current anemometer probe mount installed on the side of a Grumman Gulfstream II (GII) aircraft (S/N 023). The GII was equipped with the radome of a Gulfstream III; otherwise, the aircraft was a standard Gulfstream II. The probe mount was secured to an existing oval panel on the lower left side of the fuselage, parallel to the front landing gear and below the fuselage’s horizontal centerplane.

The GII was equipped with two Rolls-Royce Spey Mk 511-8 turbofan engines. The Spey Mk 511-8 has a two-spool type axial flow compressor, consisting of a 5 stage low pressure section and a 12 stage high pressure section. The engine’s jet exhaust was convergent and of the fixed-area type, 0.55 m in diameter, and was without noise suppression

equipment. The exhaust plane of each of the symmetrically opposed turbofan engines was 17.43 m aft of the radome nose, and 1.94 m off of the aircraft's centerline.

B. Anemometer/probe mount

The fragile nature of the 5 μm constant current probes led to the development of a protective probe mount by members of the AFRL atmospheric characterization group in the early 1990's. The probe mount protects the anemometer probes in a retracted state during ascent and then extends them into the flow once the aircraft is above the clouds. The probe mount consists of a strut extending perpendicular to the fuselage wall, with two probe arms extending forward from the strut. Heater strips mounted on either side of each probe arm prevent the formation of ice during ascent. Power to the heaters is turned off once the aircraft is above the cloud ceiling. A more detailed description of the probe mount geometry can be found in an earlier paper.⁹

The constant current wire probes were mounted at the upstream tip of each probe arm, in either an extended or retracted configuration. The probes used were DISA 55P52's which consist of two wires per probe. The two probe arms provide a degree of redundancy where if the extended set of wires should break due to a collision with an airborne particle, the other set of protected (retracted) wires are extended and used. In the extended state, the 55P52 sensor is located 2.08 m aft of the nose of the GII, and 0.81 m off of the aircraft's centerline.

In addition to the constant current wires, the probe mount had a PCB microphone (MIC #1), Model 103A03, flush mounted into the end plate of the probe-mount strut (2.74 m aft of nose). A second microphone (MIC #2) was flush mounted into the fuselage wall above and at the same streamwise position as the constant current wires, and a third (MIC #3) was mounted approximately four jet-nozzle diameters downstream of the engine-exhaust exit plane along the aircraft centerline (equidistant to both engine exhaust planes). Each microphone signal was fed through a battery powered signal conditioner, PCB Model 480E09. As mentioned earlier, all three microphone signals were used in a separate study¹¹ to monitor engine acoustics and correlate engine noise with the non-atmospheric sources found in the temperature spectra. Only signals from the two upstream microphones (MIC #1 and #2) were used for the results described here.

Data sets were typically 10 min in duration consisting of four channels of fluctuating temperature data and three channels of microphone data. The data were acquired at 12 kHz (per channel) with a TEAC RD-130TE DAT Data Recorder which provided internal anti-aliasing filters. The data were then transferred to an IBM RS/6000 and processed using IDL (Interactive Data Language) based analysis routines. All spectra presented in this paper were evaluated based on ensembles of 16 nonoverlapped Hanning-windowed 16384 point FFT's. While collecting atmospheric data, aircraft Mach number, pressure altitude, and atmospheric static temperature were recorded manually.

III. NOISE REMOVAL PROCESS

As mentioned in the Introduction, the noise removal process used in this paper is based on a technique^{17,18} that was originally developed to remove hydrodynamic pressure fluctuations (flow noise) from three or more microphone signals. The method uses coherence function relations between simultaneous measurements at three physically separate transducer locations and computes the coherent spectral energy between all three signals. The three signals used for the results reported in this paper are one of the constant current anemometer signals (Signal #1 denoted with a subscript 1), the signal from MIC #1 mounted in the end plate of the probe-strut housing (Signal #2 denoted with a subscript 2), and the signal from MIC #2 flush mounted into the GII's fuselage wall (Signal #3 denoted with a subscript 3). With these three input signals, the analysis procedure solves for the coherent portion of all three signals; the acoustical noise due to jet screech. As such, it treats the atmospheric temperature fluctuation data sensed by the constant current wire as an uncorrelated noise source. The *filtered* atmospheric temperature spectra is then computed by subtracting the coherent acoustical spectra from the *measured* temperature spectra.

Although not necessary for the noise removal process, the two pressure signals measured by the microphones were first converted into temperature fluctuations using the relation:¹⁹

$$\frac{T'}{T_{\text{ref}}} = \frac{\gamma - 1}{\gamma} \frac{P'}{P_{\text{ref}}}, \quad (1)$$

where P' and T' are the instantaneous static pressure and static temperature fluctuations, respectively, P_{ref} and T_{ref} are the local static pressure and local static temperature, respectively, and γ is the ratio of specific heats ($C_p/C_v = 1.4$ for air at 300 K).

The first step in the noise removal process is the computation of the coherence functions [$\gamma_{xy}^2(f)$] between every two-pair combination of the three signals:

$$\gamma_{12}^2 = \frac{|G_{12}|^2}{G_{11}G_{22}}, \quad (2)$$

$$\gamma_{23}^2 = \frac{|G_{23}|^2}{G_{22}G_{33}}, \quad (3)$$

$$\gamma_{31}^2 = \frac{|G_{31}|^2}{G_{33}G_{11}}, \quad (4)$$

where the G_{xy} 's represent cross-spectral density functions:

$$G_{12} = \frac{2}{N\Delta t} [X_1^* \times X_2], \quad (5)$$

$$G_{23} = \frac{2}{N\Delta t} [X_2^* \times X_3], \quad (6)$$

$$G_{31} = \frac{2}{N\Delta t} [X_3^* \times X_1]. \quad (7)$$

Here X_1 represents the complex Fourier Transform of Signal #1 and X_1^* its complex conjugate. The N in Eqs. (5), (6), and (7) represents the number of points used to compute the FFT

and Δt the time interval between consecutive data points. The other terms in Eqs. (2), (3), and (4) are the autospectral density functions and are given by:

$$G_{11} = \frac{2}{N\Delta t} [X_1^* \times X_1], \quad (8)$$

$$G_{22} = \frac{2}{N\Delta t} [X_2^* \times X_2], \quad (9)$$

$$G_{33} = \frac{2}{N\Delta t} [X_3^* \times X_3]. \quad (10)$$

Once all three coherence functions have been determined, the coherent portion of each of the three spectra can be computed using the following relations, with derivation given in Chung.¹⁷

$$G_{1'1'} = G_{11} \left(\frac{\gamma_{12} \times \gamma_{31}}{\gamma_{23}} \right), \quad (11)$$

$$G_{2'2'} = G_{22} \left(\frac{\gamma_{23} \times \gamma_{12}}{\gamma_{31}} \right), \quad (12)$$

$$G_{3'3'} = G_{33} \left(\frac{\gamma_{31} \times \gamma_{23}}{\gamma_{12}} \right). \quad (13)$$

The coherent portion of each spectra is the engine-acoustic noise that has been filtered of uncorrelated atmospheric temperature fluctuations in the case of $G_{1'1'}$, and uncorrelated hydrodynamic pressure fluctuations in the case of $G_{2'2'}$ and $G_{3'3'}$. The desired atmospheric temperature fluctuation spectra can then be solved for by subtracting the engine-noise-induced coherent portion ($G_{1'1'}$) from the *measured* constant-current anemometer temperature spectra (G_{11}), resulting in a final *filtered* spectra (G_{1f1f}). The *filtered* atmospheric temperature spectra can be expressed as

$$G_{1f1f} = G_{11} - G_{1'1'}, \quad (14)$$

from which atmospheric temperature fluctuation strength is determined using the spectral method.

As will be described in the next section, it was found useful to perform a smoothing operation on the term in brackets in each of Eqs. (11), (12), and (13) by combining the value at one frequency bin with values at adjacent frequency bins. This operation was found to produce smoother filtered spectra. Chung¹⁷ found a similar benefit while performing a spectral smoothing operation on the final filtered spectra (G_{1f1f}). Although both smoothing operations are equivalent, the operation performed here was the preferred method as it enabled one to observe where energy was being removed from the original unfiltered spectra (G_{11}) by examining the smoothed multiplicative factor in Eqs. (11), (12), and (13).

IV. RESULTS

In this section, a case study is made by applying the noise removal procedure to one 10 min segment of atmospheric temperature data. As will be shown, the overall success of the noise removal process depends on the relative signal-to-noise ratio between atmospheric temperature fluc-

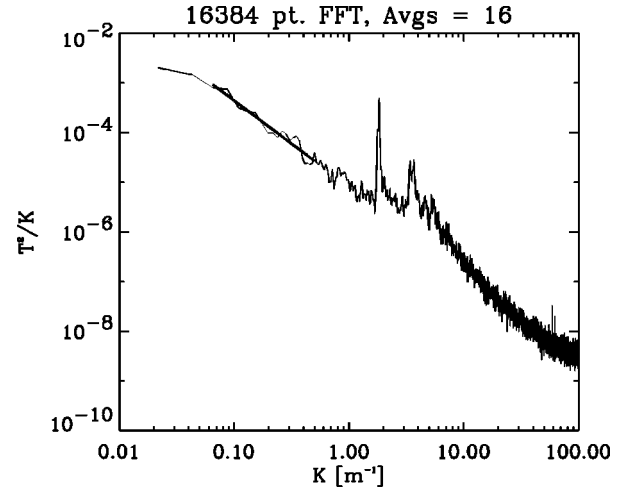


FIG. 3. Unfiltered PSD G_{11} .

tuations and engine-acoustic noise. The signal-to-noise ratio of this particular ten minute data set is typical of data collected during the atmospheric characterization experiments.

An unfiltered power spectral density function of the temperature fluctuation signal for the last 22 s of the data set is shown in Fig. 3. As can be seen, the jet screech spike, a harmonic, and evidence of a broader underlying bump are apparent from the temperature spectra.

The coherence function between the constant current anemometer signal and the probe-strut-mounted microphone is shown in Fig. 4. Comparing Fig. 4 with Fig. 3, the region of high coherence noted in Fig. 4 coincides with the location of the spike and bump in Fig. 3. The level of high coherence indicates that much of the energy in the temperature fluctuation spectra is due to engine-acoustic noise.

The multiplying factor ($\gamma_{12} \times \gamma_{31} / \gamma_{23}$) used in Eq. (11) to condition the original spectra is shown plotted in Fig. 5. As can be seen, wavenumbers encompassing the range $1 < k < 10$ have multiplying factors close to 1.0 where much of the temperature spectral energy is attributed to engine-acoustic noise. Wavenumbers below 1 and greater than 10 show multiplying factors on average around 0.3. It is known from the results of the noise identification studies¹¹ that the amplitude of the jet disturbance drops off for wave numbers less than 1.0. As such, the contribution of engine acoustical noise to atmospheric temperature spectral energy for wave numbers below 0.3 can be assumed negligible. Consequently,

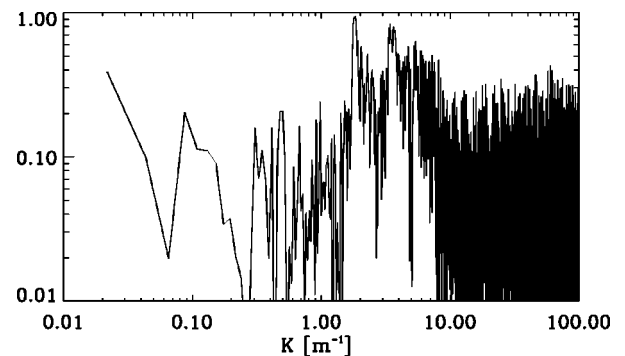


FIG. 4. Coherence function γ_{12}^2 between CCA and probe-strut microphone.

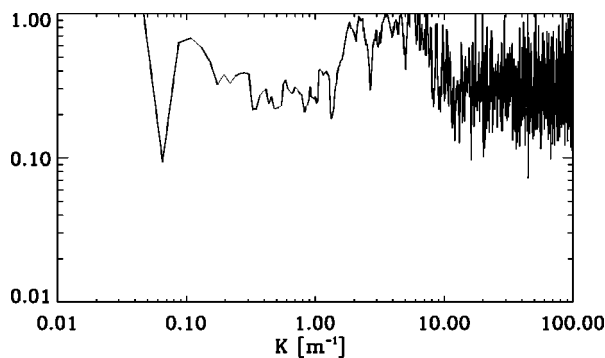


FIG. 5. Multiplying factor ($\gamma_{12} \times \gamma_{31} / \gamma_{23}$) from Eq. (11).

the noise removal process was applied only to a wave number range where engine noise contamination was expected, translating to wave numbers greater than 0.3 for the current application.

In an effort to produce a more continuous filtered spectra, frequency smoothing was applied to the coherency factor plotted in Fig. 5 (the data in this figure was produced by smoothing over 11 frequency bins). Examples of three filtered atmospheric temperature spectra ($G_{1,f,1_f}$) with increasing amounts of smoothing are shown in Figs. 6, 7, and 8. The effect of increased smoothing is seen to be a reduction in the number of discrete spectral spikes.

A. Turbulence strength quantification using the "spectral method"

A visual comparison between the three filtered spectra (Figs. 6, 7, and 8) and the unfiltered spectra (Fig. 3) shows that the noise removal process removes much of the energy that caused the unfiltered spectra to appear non-Kolmogorov (slope other than $-5/3$). The straight lines overlayed on each of the spectra in Figs. 3, 6, 7, and 8 represent the results of linear regression applied to the spectra in log-log space. The regression for the unfiltered spectra was performed over two wave number ranges, $0.05 < k < 0.5$ and $0.5 < k < 4.0$, resulting in two different spectral slopes. The wave number range with the slope closest to $-5/3$ was the one used to quantify the strength of atmospheric temperature turbulence. The re-

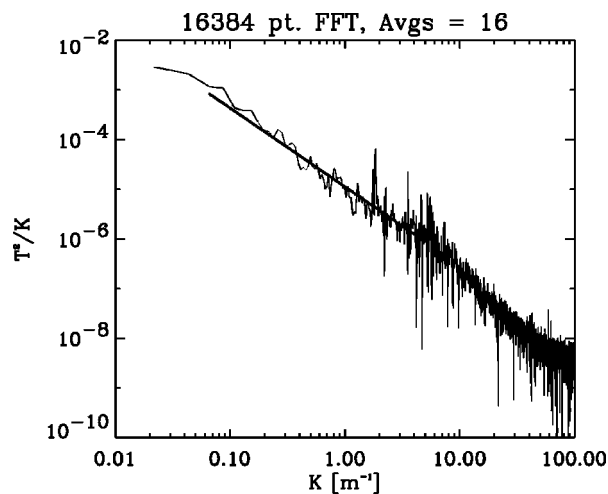


FIG. 7. Filtered PSD $G_{1,f,1_f}$ -7 point smoothing.

gression for the filtered spectra was performed over three wave number ranges: $0.01 < k < 0.3$, $0.2 < k < 4.0$ and $0.05 < k < 5.0$, again with the range resulting in the slope closest to $-5/3$ the one used to quantify the strength of atmospheric temperature turbulence. The $0.01 < k < 0.3$ range, encompassing wave numbers not affected by the noise removal process, was selected as a default condition should the noise removal process result in erroneous spectra. An example breakdown in the noise removal process will be given at the end of this section.

As mentioned in the Introduction, a slope of $-5/3$ is indicative of Kolmogorov turbulence in the inertial subrange while slopes of -3 can be anticipated for either transitional laminar free shear flows or for gravity wave activity. As such, examining the slopes of all of the unfiltered and filtered spectra in the ten minute data set considered in the case study provides a quantitative means of assessing the merits of the noise removal process. Table I lists the means and standard deviations for all of the unfiltered and filtered spectral slopes, with varying amounts of smoothing applied to the filtered spectra. Although the mean slope does not change significantly with the application of noise removal, the standard deviation of the spectral slopes is seen to change a great deal.

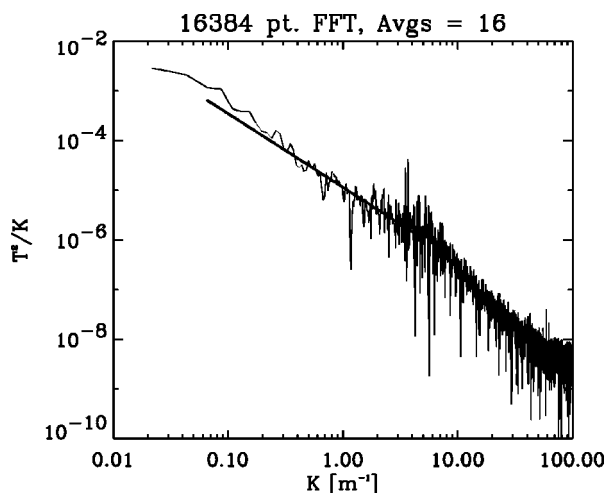


FIG. 6. Filtered PSD $G_{1,f,1_f}$ -3 point smoothing.

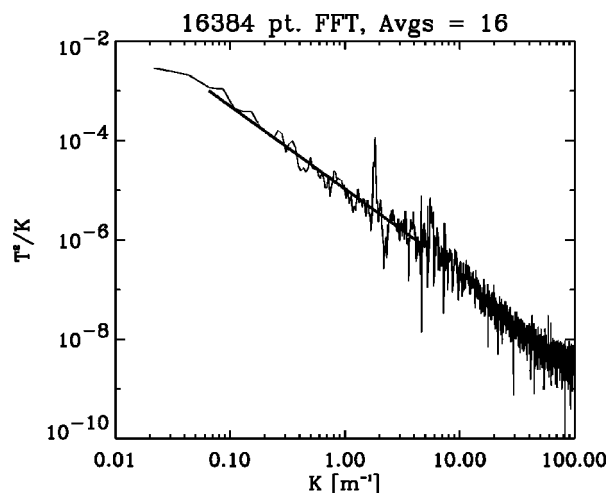


FIG. 8. Filtered PSD $G_{1,f,1_f}$ -11 point smoothing.

TABLE I. Spectral slopes and slope standard deviation.

# Points smoothed	μ_{slope}	σ_{slope}
Unfiltered	-1.55	0.254
3	-1.54	0.142
5	-1.55	0.139
7	-1.56	0.136
9	-1.57	0.134
11	-1.57	0.133

Reductions in standard deviation by as much as 50% are noted while comparing the results of the 11-point-smoothed filtered spectra with the unfiltered spectra.

The reduction in standard deviation of spectral slopes with application of the noise removal process can be made more evident by examining histograms of spectral slopes for the entire ten minute data set. Histograms of both unfiltered and filtered spectral slopes are shown in Figs. 9 and 10, respectively. The reduction in standard deviation of spectral slopes with application of the noise removal process is significant for it shows that turbulence that was originally interpreted as non-Kolmogorov (slopes other than $-5/3$) is actually very close to being Kolmogorov, only masked by nonatmospheric sources in the temperature fluctuation data.

B. Low signal-to-noise ratio case

Although the results presented thus far are encouraging, the effectiveness of the noise removal process is restricted by the relative signal-to-noise ratio between atmospheric temperature fluctuations and engine noise. This can be demonstrated by first considering the unfiltered spectra shown in Fig. 11, and then examining the results of the filtering process in Fig. 12. Although the filtering process is seen to have removed a significant amount of energy, the resulting filtered spectra still remains contaminated. As such, for cases of weak atmospheric temperature fluctuation strength the most reliable method of estimating spectral magnitude remains to examine only those portions of the spectra where engine noise is known not to contaminate ($k < 0.3$).

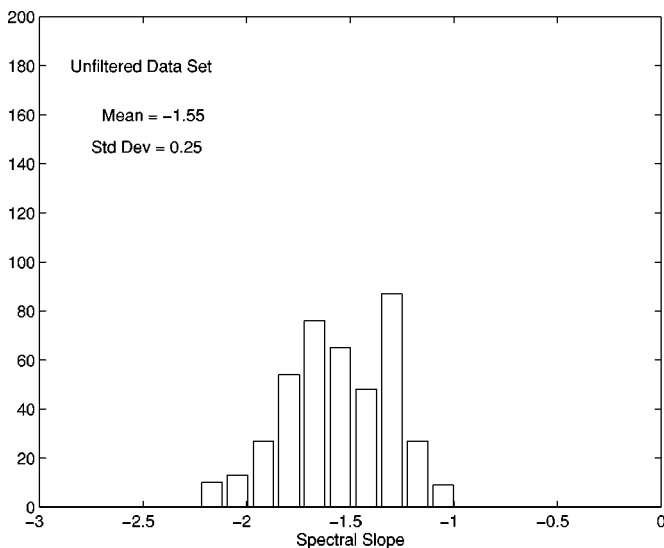


FIG. 9. Unfiltered spectral slopes.

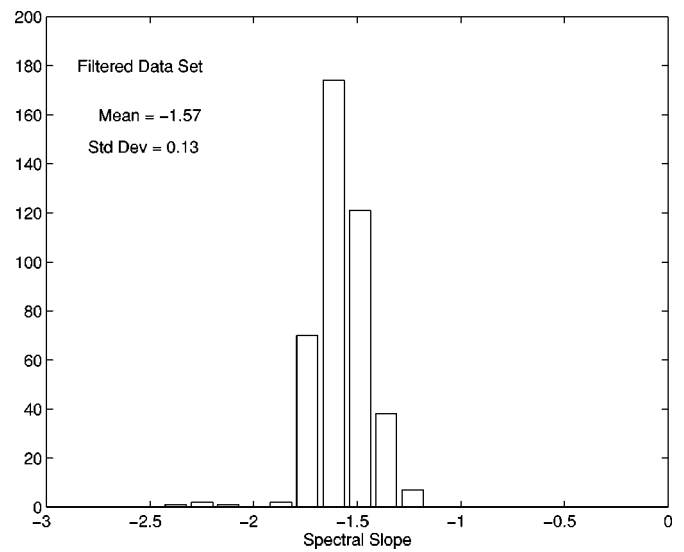
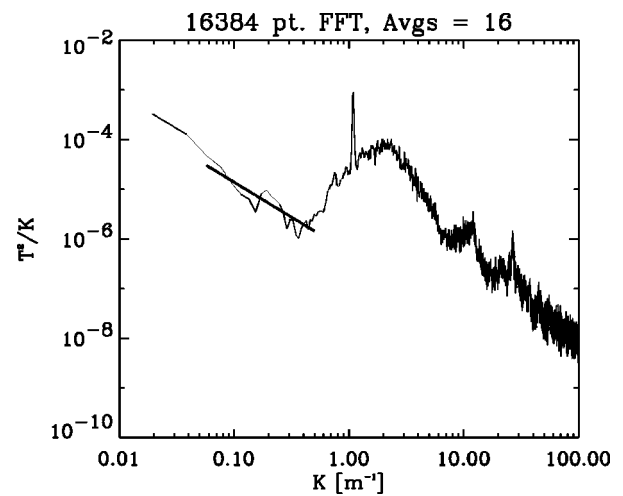
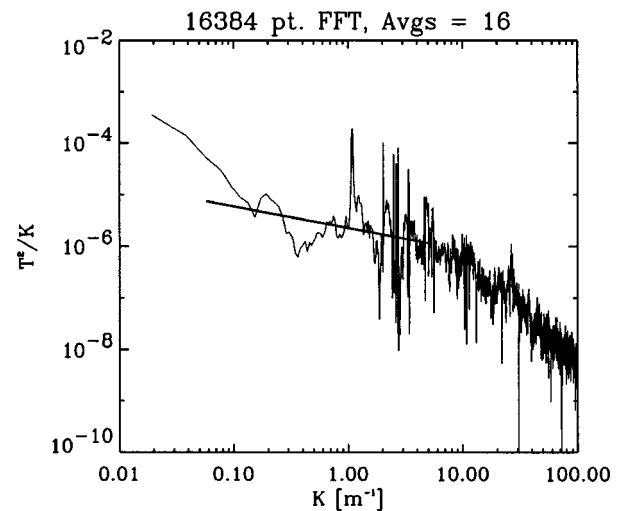


FIG. 10. Filtered spectral slopes.

FIG. 11. Unfiltered PSD G_{11} .FIG. 12. Filtered PSD G_{11} -11 point smoothing.

It should be mentioned that the data presented in Fig. 11 was collected at a high cruise velocity. These are the same conditions that result in engine acoustical energy at the lowest wave numbers and with the highest spectral magnitudes.¹¹ Consequently, engine noise is most detrimental to the measurement of atmospheric temperature turbulence strength while flying under these conditions. As a result, a second method that has been implemented in order to improve data quality has been to fly the aircraft at as low of a speed as possible while collecting data, moving the engine's acoustical disturbance to higher wave numbers with diminished magnitude.

V. CONCLUSIONS

The presence of jet-noise in atmospheric temperature fluctuation measurements forced spectral slopes to be fit over two different wave number ranges when processing unfiltered spectra. A case of strong atmospheric temperature fluctuation (Fig. 1) permitted spectral slopes to be fit over the relatively large wave number range $0.5 < k < 4.0$ as the strong atmospheric temperature signal masked the nonatmospheric engine noise. A case of intermediate atmospheric temperature fluctuation strength (Fig. 3) required spectral slopes to be fit over a wave number range ($0.05 < k < 0.5$) where acoustical energy was weaker and consequently did not contribute to the atmospheric temperature's spectral energy.

A noise removal technique, originally presented by Chung,¹⁷ was found to be successful at removing the effects of engine noise from aircraft-based atmospheric temperature fluctuation measurements. The addition of two microphones, located within the vicinity of the constant current anemometer wire, were the only hardware changes required to implement the noise removal method.

By removing spectral energy due to the engine-related acoustic source, the noise-removal process enabled linear regression to be performed over a larger wave number range ($0.05 < k < 5.0$) than was possible using unfiltered spectra. This larger range allowed the computation of spectral slopes based on an increased number of data points, resulting in more statistically certain slope estimates. The procedure described was found to reduce the standard deviation of atmospheric temperature spectral slopes by as much as 50%.

The noise removal process was shown to be successful as long as the magnitude of the atmospheric temperature fluctuations were on the same order as the acoustical signal. The noise removal process was found to break down under conditions of weak atmospheric temperature turbulence strength where engine noise can be up to several orders of magnitude greater than atmospheric temperature fluctuations.

It was found beneficial under these weak turbulence conditions to fit the temperature spectra over a low wave number range ($0.05 < k < 0.3$) where engine noise is known to contribute little to temperature fluctuations.

ACKNOWLEDGMENTS

The authors would like to thank Tom Straiton, Art Harris, Darren Paul, Danny Sutton, and Mike Saslawsky of MetroLaser, Inc. Albuquerque, NM for being adaptable while preparing for and performing the flight tests.

- ¹L.J. Otten, A.L. Pavel, W.E. Finley, and W.C. Rose, "A Survey of Recent Atmospheric Turbulence Measurements from a Subsonic Aircraft," AIAA Paper 81-0298.
- ²W.C. Rose and L.J. Otten, "Airborne Measurements of Atmospheric Turbulence," *AeroOptical Phenomena*, Progress in Astronautics and Aeronautics, Vol. 80 (American Institute of Aeronautics and Astronautics, Inc., New York, 1982), pp. 325–337.
- ³B. Masson, B. Scruggs, M. Hayes, J. Wissler, K. Bishop, and D. Kyrakis, "Airborne Measurement of Tropopausal Temperature Fluctuations," AIAA Paper 96-0265.
- ⁴H.H. Bruun, *Hot-Wire Anemometry, Principles and Signal Analysis* (Oxford University Press, New York, 1995), pp. 44–45.
- ⁵J.O. Hinze, *Turbulence*, 2nd ed. (McGraw-Hill, New York, 1975), pp. 228–229.
- ⁶U. Frisch, *Turbulence, The Legacy of A. N. Kolmogorov* (Cambridge University Press, Cambridge, 1995), pp. 61–67.
- ⁷F. D. Eaton and G. D. Nastrom, "Preliminary estimates of the vertical profiles of inner and outer scales from White Sands Missile Range, New Mexico, VHF radar observations," *Radio Sci.* **33**, 895–903 (1998).
- ⁸G.D. Nastrom and K.S. Gage, "A climatology of atmospheric wave number spectra of wind and temperature observed by a commercial aircraft," *J. Atmos. Sci.* **42**, 950–960 (1985).
- ⁹R.J. Hugo, S.R. Nowlin, K.A. McCrae, I.L. Hahn, and K.P. Bishop, "Shedding Characteristics of a Low Aspect Ratio Probe Mount in Subsonic Flow," AIAA Paper 98-2831.
- ¹⁰J.D. Anderson, *Fundamentals of Aerodynamics*, 3rd ed. (McGraw-Hill, New York, 2001), pp. 604–612.
- ¹¹R.J. Hugo, S.R. Nowlin, I.L. Hahn, F.D. Eaton, and K.A. McCrae, "Acoustic noise-source identification in aircraft-based atmospheric temperature measurements," *AIAA J.* **40**, 1382–1387 (2002).
- ¹²J.M. Seiner, "Advances in High Speed Jet Aeroacoustics," AIAA Paper 84-2275.
- ¹³T.D. Norum, "Screech suppression in supersonic jets," *AIAA J.* **21**, 235–240 (1983).
- ¹⁴C.K.W. Tam, J.M. Seiner, and J.C. Yu, "Proposed relationship between broadband shock associated noise and screech tones," *J. Sound Vib.* **110**, 309–321 (1986).
- ¹⁵A. Powell, Y. Umeda, and R. Ishii, "Observations of the oscillation modes of choked circular jets," *J. Acoust. Soc. Am.* **92**, 2823–2836 (1992).
- ¹⁶J.C. Wyngaard, Y. Isumi, and S.A. Collins, "Behavior of the refractive index structure parameter near the ground," *J. Opt. Soc. Am.* **61**, 1646–1650 (1971).
- ¹⁷J.Y. Chung, "Rejection of flow noise using a coherence function method," *J. Acoust. Soc. Am.* **62**, 388–395 (1977).
- ¹⁸J.S. Bendat and A.G. Piersol, *Random Data, Analysis and Measurement Procedures*, 2nd ed. (Wiley, New York, 1986), pp. 190–192.
- ¹⁹A.D. Pierce, *Acoustics, An Introduction to Its Physical Principles and Applications* (McGraw Hill, New York, 1981), pp. 28–30.

Active stereo sound localization

Greg L. Reid

Department of Computer Science, York University, Toronto M3J 1P3, Canada

Evangelos Milios^{a)}

Faculty of Computer Science, Dalhousie University, Halifax B3H 1W5, Canada

(Received 13 January 2000; revised 8 August 2002; accepted 28 August 2002)

Estimating the direction of arrival of sound in three-dimensional space is typically performed by generalized time-delay processing on a set of signals from a fixed array of omnidirectional microphones. This requires specialized multichannel A/D hardware, and careful arrangement of the microphones into an array. This work is motivated by the desire to instead only use standard two-channel audio A/D hardware and portable equipment. To estimate direction of arrival of persistent sound, the position of the microphones is made variable by mounting them on one or more computer-controlled pan-and-tilt units. In this paper, we describe the signal processing and control algorithm of a device with two omnidirectional microphones on a fixed baseline and two rotational degrees of freedom. Experimental results with real data are reported with both impulsive and speech sounds in an untreated, normally reverberant indoor environment. © 2003 Acoustical Society of America. [DOI: 10.1121/1.1518469]

PACS numbers: 43.28.Tc, 43.60.Gk [LCS]

I. INTRODUCTION

In human auditory perception, it is believed that there are three basic cues from which most sound localization is derived.^{1,2} Interaural time difference is the primary horizontal cue for humans at lower frequencies (below 1 KHz). Interaural intensity (or level) difference is the primary horizontal cue at higher frequencies (above 4 KHz), which correspond to wavelengths smaller than the size of the ear. Spectral cues are due to the fact that the spectral characteristics of a perceived sound are affected by the presence of one's outer ears, head and torso. Spectral cues extend our perception into the vertical plane.

Many existing implementations of sound source localization have used arrays of omnidirectional microphones with beam forming³ and generalized time-delay techniques.^{4,5} These approaches often require special purpose multichannel A/D hardware which generate significant amounts of signal data and require intensive computation. Large spatial separation between microphones and a larger number of microphones (16) are used^{4,5} to steer a camera towards a speaker in a normally reverberant conference room setting. This system performs speaker localization in three-dimensional space, not simply direction-of-arrival estimation. The system performs well in typical conference rooms with good accuracy in both sound direction and location. Rabinkin *et al.*⁴ report a 30 cm accuracy in the estimate of a sound source position in three-dimensional space for similar size and style rooms as used in our experiments. This corresponds to an angular resolution of 5.7° in the sound direction at an average 3 m distance which is comparable to that achieved in our work. Rabinkin *et al.* also performed tests in larger reverberant rooms like auditoriums and found that their errors increased significantly. However their system is

nonportable as it depends on the placement of the microphones within the room which can occupy a fair amount of space as the microphones are as much as 0.5 m apart.

Another approach using two microphones is reported by Zakarauskas and Cynader.⁶ The authors simulate the human auditory system by focusing on spectral cues for three-dimensional sound source localization and modeling the spectral characteristics from which humans derive directional information. This is done by means of a neural network where the system would learn its spectral cues to localize sounds. Simulation results show remarkably good accuracy of better than 1° for broadband sounds. However for tests involving human voice their results were relatively poor with 15°–30° error. This limits their approach to applications involving broad band sounds. In comparison, the work reported in this paper maintains nearly the same error bounds for both broad band and voice sources although more signal processing is required in the voice testing to maintain reliable time-delay values.

Estimating the direction of a sound source from signals received at two fixed directional microphones has been addressed and tested only in simulation mode by Datum *et al.*⁷ In their work, the microphones are fixed in space, both pointing forward with a slight difference in elevation. The central problem addressed is how to represent the nonlinear mapping from signal features to source direction, which is solved by an artificial neural network. The inputs to the neural network are estimates of both the time delay and the intensity difference at a number of distinct frequencies. The measure for the time delay is the phase difference at the two microphones. The measure for the intensity difference is the intensity ratio (in dB) at the two microphones at distinct frequencies. Datum *et al.* report on performance of their method in simulation. An average position error of less than 10 cm can be reasonably inferred from their figures. At distance of 1 m between source and sensors, this corresponds to an angular

^{a)}Electronic mail: eem@cs.dal.ca



FIG. 1. Left: A directional microphone mounted on a computer controlled pan-tilt unit (PTU). Right: A pair of omnidirectional microphones spatially separated also mounted on a PTU. The PTUs allow the microphones' position and orientation to be manipulated creating an active system.

error of 5.7° , and puts those results very close to both Rabinkin *et al.*⁴ and the errors achieved in our study. However it should be noted that their range of errors changes greatly by position and by the amount of noise added to the training sessions. Localization of sources near zero incidence angle can be estimated most accurately, but for other incidence angles the error is much worse than 5.7° . Our system, in a similar azimuth range, did not show the same degradation at larger angles, which was naturally expected due to our active approach that adapts the orientation of the microphone baseline to the direction of incidence of the incoming sound signal.

Our work intends to replace the functionality of an array of microphones with two microphones mounted on a computer-controlled pan-tilt unit, as shown in Fig. 1. The use of active microphones achieves with physical motion what microphone arrays must achieve with massive data collection and computation. We call our approach "Active Audition",⁸ the auditory equivalent of "Active Vision",⁹ where cameras are mounted on PTUs and verging stereo is used for tracking visual targets. Here we investigate the computational principles underlying the active audition approach. The objective is to develop and evaluate the performance of algorithms for source direction determination using an active audition system. Two more approaches, one using a directional microphone with two rotational degrees of freedom and another using a combination of a directional and an omnidirectional microphone are discussed in a technical report.¹⁰

Section II describes the proposed methodology and localization principle. Section III presents the signal processing required for estimating interaural time differences (time delays) from both impulsive and speech signal data. Section IV presents experimental results with both impulsive and speech sounds. Section V discusses the feasibility and properties of the proposed method.

II. ACTIVE SOUND SOURCE LOCALIZATION

The essence of the approach is to locate the direction of arrival of sound as the intersection of two cones sharing the same vertex. We first review the relation between direction of arrival and time delay estimated at two omnidirectional microphones. Then we describe the geometry of direction of arrival estimation in three-dimensional space when the position of the two microphones is computer controllable.

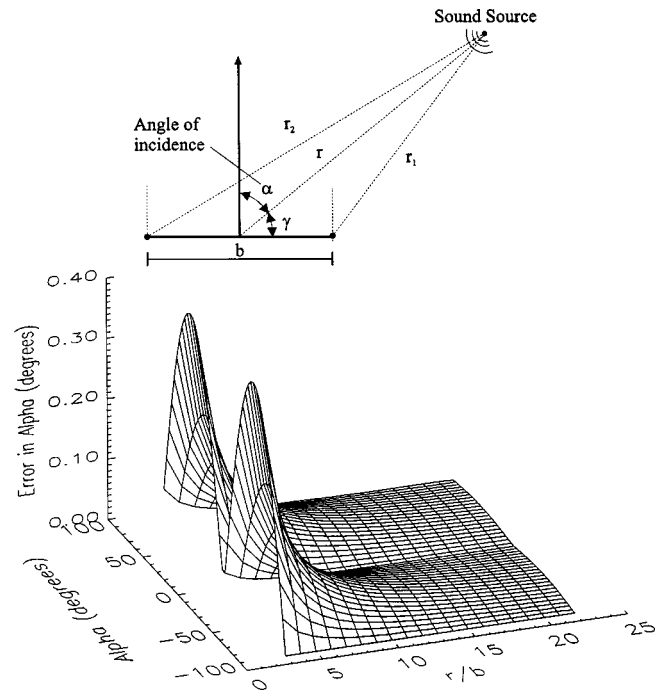


FIG. 2. The top figure illustrates the near-field situation with respect to two microphones listening to the same source. The bottom figure plots the error created as a result of using a far-field approximation in near-field cases. The error is a function of both the angle to the sound source and the ratio of the distance to the source and the distance separating the two microphones.

A. Time-delay estimation

In the two-dimensional version of the direction-of-arrival estimation, the time delay between the signals from two omnidirectional microphones is related to the angle of incidence α (Fig. 2) and is calculated by simple geometric constraints,

$$\sin(\alpha) = \frac{ct}{b} = \frac{cn}{fb}, \quad (1)$$

where c is the speed of sound, t is the time delay in seconds, n is the time delay in samples, f is the sampling frequency, and b is the length of the baseline between the microphones. To achieve subsample accuracy in the estimation of time delay t , it is possible to perform quadratic interpolation on the three correlation values at $n-1$, n , $n+1$ centered at the maximum of the correlation n , but this was not done in this work.

B. Far-field assumption

Equation (1) makes the assumption that the sound source is a large enough distance away so that the direction of arrival of the sound is approximately the same at both microphones. This is strictly true for a source at an infinite distance away.

The general case is given in Fig. 2. Time delay corresponds to the path length difference between r_1 and r_2 :

$$\text{Time Delay} = (r_2 - r_1)/c, \quad (2)$$

where r_1 and r_2 are related to the angle γ towards the sound source as taken from the center of the baseline by using the cosine law

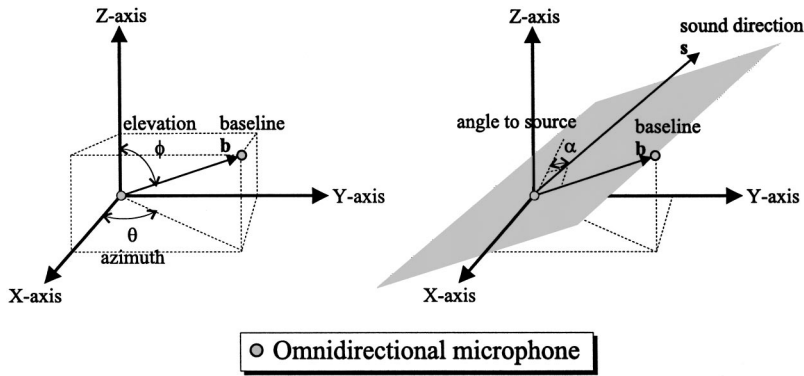


FIG. 3. Two microphones form a baseline, \mathbf{b} with an orientation (θ, ϕ) in 3D space. The direction to a sound event is given by \mathbf{s} . The simple two-dimensional solution yields the angle, α , between \mathbf{b} and \mathbf{s} on the plane that they form. This is the basis for the three-dimensional solution.

$$r_1 = \sqrt{r^2 + \left(\frac{b}{2}\right)^2 - 2r\left(\frac{b}{2}\right)\cos(\gamma)}$$

$$= \sqrt{r^2 + \frac{b^2}{4} - rb\cos(\gamma)}, \quad (3)$$

$$r_2 = \sqrt{r^2 + \left(\frac{b}{2}\right)^2 - 2r\left(\frac{b}{2}\right)\cos(\pi - \gamma)}$$

$$= \sqrt{r^2 + \frac{b^2}{4} + rb\cos(\gamma)}, \quad (4)$$

where $\alpha = (\pi/2) - \gamma$. The error between the actual angle α and its approximation using the far-field assumption is given by

$$\text{Error}\left(\alpha, \frac{r}{b}\right) = \left| \alpha - \alpha_{\text{approximate}} \right| = \left| \alpha - \arcsin\left(\frac{r_2 - r_1}{b}\right) \right|. \quad (5)$$

This error is a function of both the actual source direction, α , and the ratio of r/b . Figure 2 shows the effective error for a number of values of r/b over the full range of α . It is noted that for values of r/b greater than 3 this error is less than 0.1° .

C. Active omnidirectional microphone pair

This method uses two omnidirectional microphones forming a baseline and relies on time delay information to compute angles of incidence (directions of arrival) with respect to two different positions of the microphone pair.

The intuition behind this method is the following. A single angle of incidence measurement from a single orientation of the microphone baseline constrains the source direction to be on a right circular cone. This cone has its vertex at a fixed reference point (the midpoint of the baseline) and its axis of symmetry is the baseline itself. A single rotation of

the baseline about a horizontal or vertical axis through its midpoint yields another cone on which the source direction should lie. Figures 3 and 4 illustrate the concept.

For a single baseline position, the solution cone is defined as follows. Its vertex is the reference point (the midpoint of the baseline), its axis of symmetry is the unit vector along the baseline, and its angle α between the normal of the baseline and any line of the cone that contains its vertex is given by Eq. (1). Solving for the source direction is a geometric problem of finding the intersection between two cones. More generally, if time delay measurements from more than the minimum number of baselines required are obtained then we have an overdetermined problem and the solution is found by satisfying a least squares criterion.

Consider the unknown source direction as a unit vector \mathbf{s} with its start at the reference point and pointing towards the sound source. This vector is the unique solution and is independent of the orientation of the baseline. The following constraint on \mathbf{s} then applies for a particular orientation i of the baseline \mathbf{b}_i and a direction of arrival at angle γ_i with respect to baseline (unit) vector \mathbf{b}_i ,

$$\mathbf{s} \cdot \mathbf{b}_i = \cos \gamma_i \quad (6)$$

or equivalently,

$$s_x b_{ix} + s_y b_{iy} + s_z b_{iz} = \cos \gamma_i = \cos(\pi/2 - \alpha_i) = \sin \alpha_i, \quad (7)$$

where quantities b_{ix} , b_{iy} , b_{iz} are the Cartesian coordinates of a unit vector with azimuth and elevation given by (θ_i, ϕ_i) , respectively. Azimuth and elevation of the microphone baseline are controlled by the motors of the pan-and-tilt unit. Angle $\gamma_i = (\pi/2) - \alpha_i$ represents the direction of arrival with respect to the selected baseline position. Using Eq. (1), γ can be computed from the measured time delay of the microphones. Combining (1) and (7) becomes

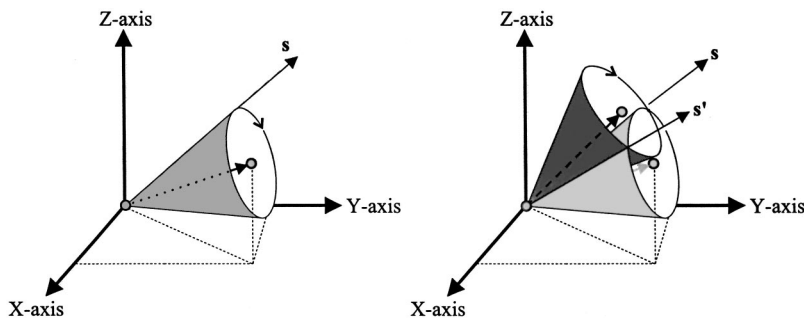


FIG. 4. Two different positions of the baseline yield two solution cones, which intersect at two lines denoted by \mathbf{s} and \mathbf{s}' , representing possible directions of arrival.

$$s_x \cos \theta \cos \phi + s_y \sin \theta \cos \phi + s_z \sin \phi$$

$$= \sin \alpha_i = \frac{cn}{fd} \quad (8)$$

which is a linear equation with three unknowns, s_x , s_y , s_z .

1. Linear solution

To find a unique solution for the sound source direction requires solving for the unknown variables s_x , s_y , and s_z . Since Eq. (8) is linear, this can be solved by obtaining three linear equations. Before solving this linear system of equations using one of the standard methods, it is necessary to ensure that the equations are consistent and yield a unique solution. Equivalently, we require that the three corresponding \mathbf{b} vectors not be coplanar. To ensure this, baseline control can alternate between changing the azimuth, θ , and elevation, ϕ components of the baseline orientation.

2. Nonlinear solution

For each orientation of the baseline there is a different instantiation of Eq. (7). There is also an implicit nonlinear constraint that $s_x^2 + s_y^2 + s_z^2 = 1$ since \mathbf{s} and \mathbf{b} are unit vectors. To compute \mathbf{s} , a least squares approach can be used.

Rewriting Eq. (7) gives

$$f_i(s_x, s_y, s_z) = s_x b_{ix} + s_y b_{iy} + s_z b_{iz} - c_i = 0, \quad (9)$$

where $c_i = \cos \gamma_i$ and

$$f_{\text{nonlinear}}(s_x, s_y, s_z) = s_x^2 + s_y^2 + s_z^2 - 1 = 0. \quad (10)$$

The solution can be obtained by solving the following minimization problem in s_x , s_y , and s_z ,

$$\min_{s_x, s_y, s_z} \left(f_{\text{nonlinear}}(s_x, s_y, s_z) + \lambda \sum_i f_i(s_x, s_y, s_z) \right). \quad (11)$$

Weight λ was chosen equal to 1. Iterative nonlinear optimization algorithms can then be used to solve this problem.¹¹ In order to assure convergence, an initial solution is required which is near the correct solution. The simplest way to ensure convergence is to first calculate the linear solution of a set of three linear equations obtained by instantiating Eq. (7) for three different orientations of the baseline, and then to refine the linear solution by using the nonlinear approach after inclusion of the nonlinear constraint $s_x^2 + s_y^2 + s_z^2 = 1$.

III. SIGNAL PROCESSING FOR TIME-DELAY ESTIMATION

We now describe the signal processing techniques for reliable time-delay estimation. A time delay is estimated by correlating the two channels of a window of stereo sound data from the two microphones, and looking for the peak of the correlation function. The location of the peak corresponds to the time-delay estimate (interpolation to achieve subsample accuracy was not used). Before correlation, filtering is carried out to reduce noise, and a signal level test is performed to check for the presence of a genuine sound event. The peak in the correlation function must be strong for

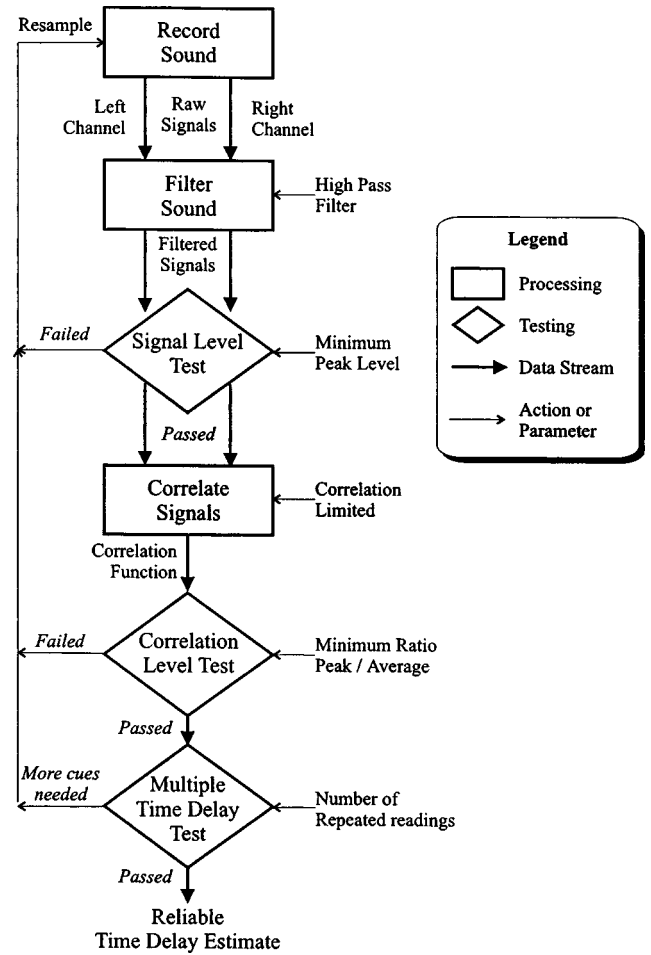


FIG. 5. Signal processing for time-delay estimation.

it to be used for time-delay estimation. The correlation level test is carried out for this purpose. A conservative threshold is chosen to reduce the likelihood of a false peak being used. The field of optimal time-delay estimation has a long history and it is fairly advanced.^{12,13} In this work we have followed a rather basic approach to the problem. In future work, we plan to use more sophisticated techniques from the literature. Figure 5 shows a summary of our approach.

The five steps are the following:

- (1) *Filtering.* This involves high pass filtering to eliminate low-frequency interference (for example due to ventilation fans). A high pass linear-phase FIR filter was designed using the McClellan–Parks algorithm¹⁴ with 185 taps. The upper and lower edges of the two bands as a fraction of the sampling frequency were band 1 [0.000, 0.005], and band 2 [0.015, 0.5], or, in terms of frequencies in Hz, band 1 [0 Hz, 110.25 Hz], band 2 [330.75 Hz, 11025 Hz]. Desired responses were 0 and 1 and weights were 10 and 1 for bands 1 and 2, respectively.
- (2) *Signal level test.* This involves a test to discriminate between the presence of a sound event to be located and “silence.” Only if the average signal level and absolute peak signal level within the recorded window is significantly larger than estimates of the same quantities for background sound will the window be used to estimate a time delay. Otherwise it will be discarded.

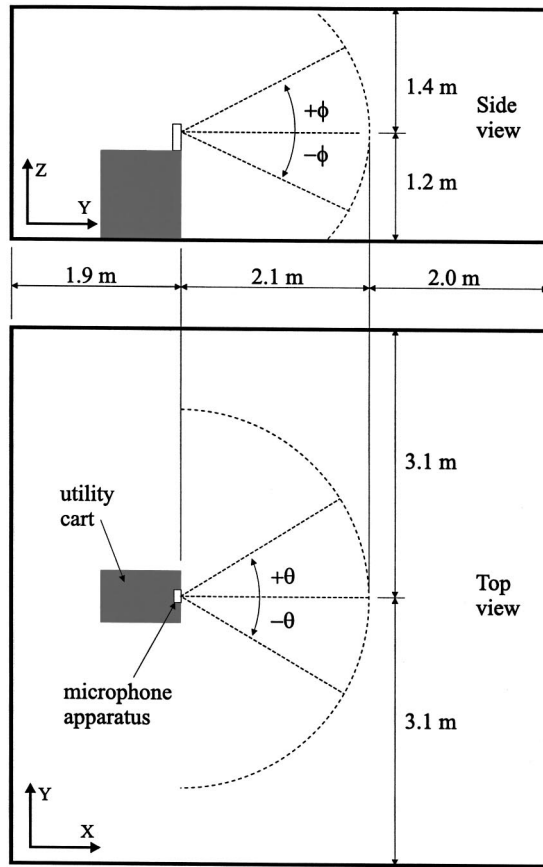


FIG. 6. The measurements for the experimental setup are shown above. The dotted arc represents possible positions of the sound source which are always kept at a constant distance from the microphone apparatus.

- (3) *Correlation domain limit.* The correlation function, c , is given by

$$c(i) = \sum_t s_r(t+i)s_l(t), \quad (12)$$

where s_r and s_l are the right and left signal channels, respectively, and t ranges over the time window of the input signals. Correlation index i is calculated over a much smaller range (± 20 samples) corresponding to the expected range of delays for the baseline of 30 cm, which corresponds to a propagation delay of 20 samples between the two microphones. The time window used contains 4000 samples, or 0.18 s. From Fig. 6 we see that reflections off the floor or ceiling travel over a path of about 3.4 m, reflections off side walls and wall behind the speaker travel over a path of about 6.5 m. Given that the direct path is 2.1 m, the above propagation paths correspond to delays of 3.8 ms (85 samples) and 13 ms (288 samples) for floor/ceiling and side/back wall reflections, respectively. This implies that the time window includes reflected signals. The strongest reflected signals are the ones off the floor and ceiling, which arrive from the same azimuth as the direct path signal, but from different elevations. As a result, we would expect higher repeatability and lower variance in the azimuth estimates. This is confirmed by the experimental results presented later. The value of i that maximizes $c(i)$ corresponds to the time-delay estimate for the direct path

signal. The interval over which i can vary for time-delay estimation is much smaller than the duration of the input signals. As a result, it is sufficient to use the direct formula above for computing the correlation function over the interval of interest. Limiting the interval over which $c(i)$ is computed has the effect of eliminating ghost peaks in the correlation function that are due to shifts equal to multiples of the period of a periodic signal.

- (4) *Correlation peak level test.* For reliable time-delay estimation, the correlation function should have strong positive peaks. To reduce the likelihood of false peaks, we require that the maximum peak be considerably greater than both the largest secondary peak as well as the average of the correlation function.
- (5) *Multiple time delay test.* A final check on the result is performed by clustering the time delay from a number of consecutive signal time windows (with fixed baseline orientation) and discarding the outliers.

Impulsive sounds are characterized by a sudden large intensity change which quickly decays into background noise. Examples include a hand clap or a slamming door. The frequency spectrum is broad band. Since these events are very short in time duration, the entire signal is often captured within one sampling window. The sudden large intensity peaks are easy to detect by the peak-based signal level test described earlier.

In the case of speech, the sound event will likely have occurred over several consecutive sampling windows. Speech is comprised of many different kinds of sounds, some or all of which could appear within a sampling window. Some of these sounds will be more difficult to estimate time delay from, for example, unvoiced sounds or whispering due to their low intensity. So in the case of speech it is desirable not only to eliminate sample data which does not contain sound, but also data which are less likely to produce reliable time-delay estimates. This is accomplished by the signal level test.

IV. EXPERIMENTAL RESULTS

Two sets of experiments are described in this section. The first uses an impulsive sound and the second experiment uses speech. The experiments apply a listening apparatus controlled by computer to locate the direction of arrival of sound in three dimensions. The sound source is a speaker, which is placed in a fixed position and the computer is asked to estimate its position 25 consecutive times, while the speaker plays back continuous speech. The experiment is repeated for impulsive sounds without changing the position of the speaker, while the speaker plays back repeated hand claps.

The source is then moved and the experiment is repeated for both speech and hand clap sound in the new position. For each source position, the difference between the estimates of azimuth and elevation obtained from the speech and hand clap sound, and the standard deviation of the multiple estimates give an indication of the consistency of the algorithm.

TABLE I. Discernible angles for time delays in integer units for our experimental setup. The maximum error due to angle quantization is also shown.

Time delay in integer units	Angle	Max error	Time delay in integer units	Angle	Max error
0	0.0°	1.48°	10	31.1°	1.76°
1	3.0°	1.49°	11	34.7°	1.84°
2	5.9°	1.49°	12	38.3°	1.94°
3	8.9°	1.51°	13	42.2°	2.07°
2	11.9°	1.52°	14	46.4°	2.24°
5	15.0°	1.55°	15	50.9°	2.48°
6	18.1°	1.57°	16	55.8°	2.85°
7	21.2°	1.61°	17	61.5°	3.41°
8	24.4°	1.65°	18	68.5°	5.34°
9	27.7°	1.70°	19	79.2°	5.34°

A. Experimental setting

The environment for the following experiments is an ordinary rectangular room about 6 m wide, 7 m long, and 3 m high. The center of the room has been cleared of furniture and the listening apparatus is placed on a cart at a distance of 2.1 m (7 ft) from the area where the sound source is located. The room is carpeted, has standard ceiling tiles, windows, a white board, wall-mounted book shelves and a small counter in one corner. No special treatment was made to the room, therefore the room exhibits reverberation qualities typical of a conference room. The room arrangement and positioning of apparatus and sound source are shown in Fig. 6.

The listening apparatus for these experiments consists of a pair of two Genexxa 3303003 electret condenser microphones (with diameter of approximately 8 mm) mounted at either end of a wooden rod forming a baseline b of length 0.3 m. The assembly is mounted on a Pan-Tilt Unit (PTU) allowing its orientation (b_θ, b_ϕ) to be controlled by computer.

In order for the far-field assumption to be applicable, the distance r to the sound source must be sufficiently larger than the length of b [Eq. (5)]. We selected a distance of $r = 2$ m which corresponds to $r/b = 6.7$.

Figure 2 shows the error introduced by making the far-field assumption with these parameters. It is less than 0.05° for the worst case, which is acceptable for this application.

Sound signal collection is done in stereo through a conventional A/D sound board on a Macintosh Powerbook 520 (upgraded to a PowerPC processor) at a sampling rate of $f = 22\,050$ Hz and using 16-bit resolution. Using Eq. (1) and setting the time delay value to the equivalent of $n = 1$ gives the best resolution that can be expected from this listening apparatus

$$\alpha_{\min} = \sin^{-1} \left(\frac{c}{fb} \right) \approx 3^\circ. \quad (13)$$

The number of discernible angles can then be calculated by determining the range of time-delay values for this setup. To find this, consider a sound source at $\alpha = 90^\circ$ to the baseline and apply Eq. (1),

$$\pm n = \pm \frac{fd}{b} \approx \pm 19. \quad (14)$$

The value of n must be an integer since it represents the time delay as a number of finite samples (assuming no interpolation to achieve subsample resolution in estimating n). The number of possible time delays is then the range of $[-19, 19]$ which is 39 discrete values. Equation (1) is used to map all the possible time delays in integer units to their corresponding angles. Table I shows the discernible angles for α which can be achieved for time-delay values of 0 to 19. The table is symmetric for the negative time-delay values.

Table I demonstrates that the theoretical resolution of approximately 3° or equivalent maximum error due to angle quantization of $\pm 1.5^\circ$ is accurate only at a time delay of 1 but remains reasonably close to that value up to about time delay of 14 (46.4°) where after the error begins to diverge. This is reflected in the values of maximum error due to angle quantization. Therefore, it would be desirable to orient the microphone baseline so as to obtain time-delay values inside the -14 to 14 range wherever possible. This is accomplished using a simple algorithm to steer the orientation of the microphones within this range. The ability of the active approach to adapt the geometry of the sensing apparatus to the direction of arrival is an important advantage over the fixed array approaches.

The algorithm used for orientation control is given in Table II. It uses the last time-delay measurement to determine how to change the orientation of the microphones and whether to make a relatively large or small change. A random factor is added so that the same set of orientations are not repeated in cycle. Movements are made in azimuth or elevation but not in both and alternate each time an orientation is changed. This is done to ensure that every three consecutive orientation vectors, \mathbf{b}_i , cannot be coplanar, which would create an underdetermined set of equations. In these experiments, the algorithm is applied to azimuth (pan) movements. This is due to the PTU elevation (tilt) range being too limited, so two specific elevations are alternated.

The need for mechanical steering of the microphone pair makes our method suitable in cases where the sound source is either stationary in space or moves much slower than the time constants involved in the mechanical movements of the pan-and-tilt unit. Fixed arrays have an advantage where rapid movement of the sound source is involved.

The experiment requires measurements to be taken with the sound source at different locations in three-dimensional

TABLE II. The orientation change algorithm. The term *random* refers to a function which would produce a uniformly distributed random number between 0 and 1.

```

// Choose next pan direction
if (timeDelay <= 14 && timeDelay >= -14)
    // Small move
    changeDirection = -1*(sign(timeDelay)*20.0+10*random);
else
    // Larger move
    changeDirection = -1*(sign(timeDelay)*30.0+20*random);
// Apply direction change alternately to pan or tilt
if (nextPan)
    panPos += changeDirection;
else
    // Alternate between two tilt values, -10 and -40 deg.
    if (tiltPos <= -30.0)
        tiltPos = -10.0;
    else
        tiltPos = -40.0;
}
nextPan = !nextPan;

```

space. To accomplish this, predetermined distances from the wall and heights from the floor are mapped out in a grid. These distances were calculated by considering source positions at azimuths from $\theta = -40^\circ$ to 40° in 10° increments at

elevation $\phi = 0^\circ$. Likewise, the heights were taken from $\phi = -30^\circ$ to 20° in 10° increments with $\theta = 0^\circ$. However in order to maintain equal signal levels throughout the experiment, the sound source must always be kept at a constant distance from the listening apparatus. The result is that the actual sound source azimuth θ will stretch with elevations off of zero. The sound source remained in the same position for both experiments (impulsive and speech) before being moved to the next position. In this way, the proximity between the direction estimates from the impulsive and speech sounds is an indication of the precision of these estimates.

B. Impulsive source

For the impulsive sound experiment a recording of a single hand clap was used and repeated at 1 s intervals. The sound event is the same to that used in Fig. 7. Using the rationale described in Sec. III, the following tests and thresholds are chosen.

- (1) *Filtering*: The filter used was described earlier in Sec. III. The cutoff frequency of 200 Hz is used to attenuate line noise and environmental noise such as overhead ventilation fans.

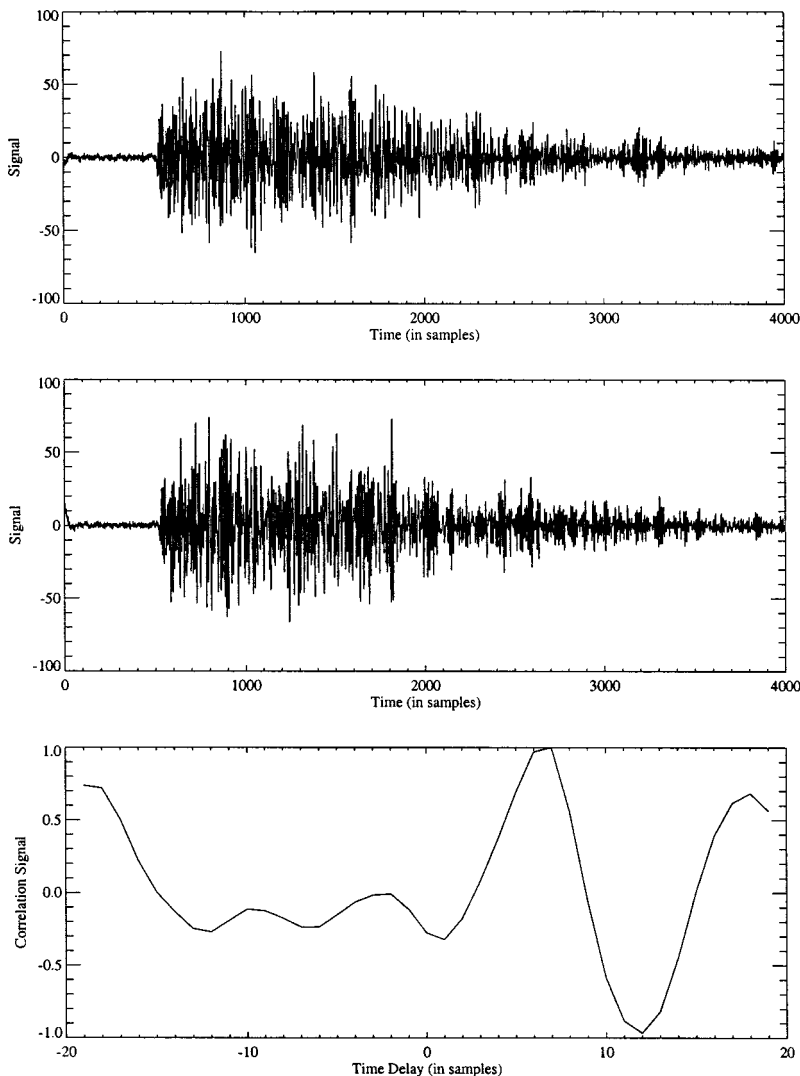


FIG. 7. The three plots show two channels of sampled data from the experimental setup (see Sec. IV) and their correlation. Time and time-delay unit is one sampling period. The sound recorded is of a single hand clap, a good example of an impulsive sound (high peaks and short duration). Due to reflections, the resulting correlation has several smaller peaks. The strongest peak represents the correct time delay for the given experimental setup (seven samples).

- (2) *Peak level*: A signal level threshold equal to 9.5 dB above background noise, while signal level peaks were often about 14 dB above background noise.
- (3) *Correlation domain*: The correlation domain is dependent upon the geometry of the apparatus and sampling rate used in audio collection. It is therefore independent of the nature of the sound source.
- (4) *Correlation signal level*: The primary peak in the correlation signal as a function of time delay must be above a specified multiple of the average of the correlation signal, for it to be acceptable towards estimating the time delay. It has been determined experimentally that a ratio of 20 succeeds in differentiating between correct and false peaks. If the correlation signal level is below 20 times the average, then the primary peak is considered unreliable and the time-delay estimate derived from it is rejected. Strong peaks due to reflected signals may lead to a high average, and therefore rejection of the primary peak.
- (5) *Multiple time-delay estimates*: While most often the above techniques produced the correct time-delay estimates, multiple readings were required to ensure good estimates were produced. Five consecutive time-delay estimates from five nonoverlapping time windows (of 4000 samples or 0.18 s each, with the next window starting after the processing of the previous window has finished) were obtained over a time interval of approximately 1 s and the median value was considered the final time-delay estimate.

C. Speech source

The speech sample was recorded from a female subject reading a short passage of text. The sound sample was then played back in a continuous loop. The same passage was also read by a male reader and similar results were obtained. Using the rationale described in Sec. III, the following tests and thresholds are chosen.

- (1) *Filtering*: Same as in the impulsive case.
- (2) *Peak level*: A signal level at 1.6 dB the background noise level was chosen. The reason such a low signal level was chosen is because, compared to the impulsive case, speech is considerably closer in both signal level and in frequency to the background noise level in the room.
- (3) *Correlation domain*: Same as in the impulsive case.
- (4) *Correlation signal level*: The primary peak of the correlation function is located and its value is considered as a multiple of the average correlation value. While speech tends to have fewer peaks than impulsive sounds, they are lower in magnitude and therefore result in a lower ratio of peak to average. A ratio of 5.0 was chosen for this test.
- (5) *Multiple time-delay estimates*: Even after the application of the previous tests, the system did not produce good time-delay estimates as often as in the impulsive case. In order to ensure good time-delay estimates, the median of seven consecutive time-delay estimates over a time interval of approximately 1.3 s was taken as the final estimate.

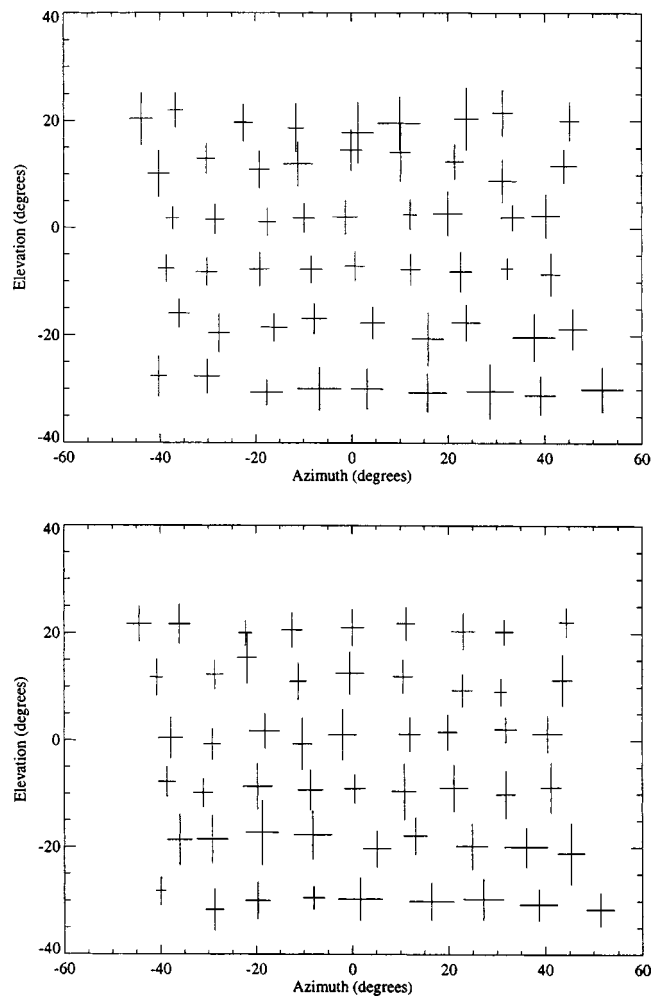


FIG. 8. The graphs show the estimated sound direction of arrival in both azimuth and elevation for an impulsive source (top) and a speech source (bottom). Each estimated position is computed from 25 estimates of the source in the same position. The size of the cross represents the standard deviation in azimuth and elevation, and the intersection of the standard deviation lines is at the estimated position.

D. Results

The results for both experiments are shown in Fig. 8. Each “cross” is the result of 25 measurements of the direction of arrival of the sound source in a fixed location. The cross is centered at the average position of those measurements with its width and height illustrating the standard deviation of the azimuth and elevation estimates, respectively. In general what is seen is a somewhat smaller standard deviation in azimuth than in elevation: the standard deviations of the azimuth and elevation estimates from the hand clap experiments are 2.55° and 3.61° , and from the speech experiments are 2.53° and 3.65° , respectively.

Figure 9 shows the average estimated positions for the impulsive and speech source experiments overlaid on top of each other. There is good agreement between the impulsive and speech source estimates: the average distances between the impulsive and speech source estimates are 0.85° and 1.43° along the azimuth and elevation dimension, respectively. The standard deviations of the distance between the impulsive and speech source estimates are 0.68° and 1.04° along the azimuth and elevation dimension, respectively.

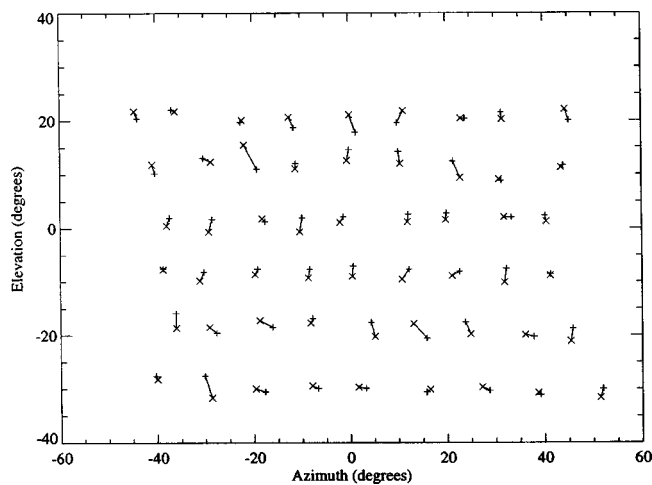


FIG. 9. The graph has the overlaid average estimated positions of the experimental data from Fig. 8. The estimated positions are + and × for hand clap and voice, respectively. Hand clap and voice estimates for the same source location are connected with a line.

V. DISCUSSION

We have presented techniques for estimating the direction of arrival of sound in three-dimensional space using only two omnidirectional microphones on a fixed baseline mounted on a pan-and-tilt unit, whose orientation is actively controlled to optimize the geometry of incidence of sound and collect multiple angle of incidence measurements that can be combined to adequately constrain the direction of arrival. Our approach is similar in spirit to active vision, whereby cameras are mounted on computer-controlled pan-and-tilt units and the geometry is adjusted to resolve computer vision problems that are under constrained in the fixed geometry case. Our approach does not require specialized multichannel A/D hardware, and can be implemented on off-the-shelf computing platforms that are equipped with the standard stereo sound input. In this paper, we describe a signal processing and control algorithm associated with our experimental design. Experimental results are reported with

both impulsive and speech sounds in an untreated, normally reverberant indoor environment, resulting in about 4° accuracy in both azimuth and elevation.

ACKNOWLEDGMENT

A condensed description of this work was presented at the European Signal Processing Conference, September 8–11, 1998, Vol. IV, pp. 2353–2356.

- ¹F. L. Wrightman and D. J. Kistler, "Factors affecting the relative salience of sound localization cues," in *Binaural and Spectral Hearing in Real and Virtual Environments*, edited by R. H. Gilkey and T. R. Anderson (Lawrence Erlbaum Associates, 1997).
- ²J. Blauert, *Spatial Hearing* (MIT Press, Cambridge, MA, 1997).
- ³J. Flanagan, J. Johnston, R. Zahn, and G. Elko, "Computer-steered microphone arrays for sound transduction in large rooms," *J. Acoust. Soc. Am.* **78**, 1508–1518 (1985).
- ⁴D. V. Rabinkin, R. J. Renomeron, A. Dahl, J. C. French, J. L. Flanagan, and M. H. Bianchi, "A DSP implementation of source location using microphone arrays," *J. Acoust. Soc. Am.* **99**, 2503 (1996).
- ⁵M. S. Brandstein, J. E. Adcock, and H. F. Silverman, "A closed-form location estimator for use with room environment microphone arrays," *IEEE Trans. Speech Audio Process.* **5**, 45–50 (1997).
- ⁶P. Zakarauskas and M. S. Cynader, "A computational theory of spectral cue localization," *J. Acoust. Soc. Am.* **94**, 1323–1331 (1993).
- ⁷M. S. Datum, F. Palmieri, and A. Moiseff, "An artificial neural network for sound localization using binaural cues," *J. Acoust. Soc. Am.* **100**, 372–383 (1996).
- ⁸G. Reid and E. Milios, "Active binaural sound localization," IX European Signal Processing Conference (EUSIPCO), 1998, Vol. IV, pp. 2353–2356.
- ⁹E. Milios, M. Jenkin, and J. Tsotsos, "Design and performance of TRISH, a binocular robot head with torsional eye movements," *Int. J. Pattern Recognit. Artif. Intell.* **7**, 51–68 (1993).
- ¹⁰G. Reid and E. Milios, Active stereo sound localization. Technical Report CS-1999-09, Department of Computer Science, York University, 1999.
- ¹¹W. Press, S. Teukolsky, W. Vetterling, and B. Flannery, *Numerical Recipes in C: The Art of Scientific Computing*, 2nd ed. (Cambridge University Press, Cambridge, UK, 1992).
- ¹²Jian Li and Renbiao Wu, "An efficient algorithm for time delay estimation," *IEEE Trans. Signal Process.* **46**, 2231–2235 (1988).
- ¹³R. J. Vaccaro, "The past, present, and the future of underwater acoustic signal processing," *IEEE Signal Process. Mag.* **15**, 21–51 (1998).
- ¹⁴P. Embree and B. Kimble, *C Language Algorithms for Digital Signal Processing* (Prentice-Hall, Englewood Cliffs, NJ, 1991).

A method of images for a penetrable acoustic waveguide

John A. Fawcett^{a)}

DRDC Atlantic, P.O. Box 1012, Dartmouth, NS B2Y 3Z7, Canada

(Received 16 November 2001; revised 7 August 2002; accepted 23 September 2002)

In this paper the complex-image approximation to the reflection coefficient for water over a seabed half-space is used to generate an image representation for a bounded acoustic waveguide with an underlying layered seabed. The images are true point sources; they have constant amplitudes which are raypath independent and, in the case of a Pekeris waveguide, frequency-independent. This image representation is ideal for constructing the Green's function kernel of the boundary integral equation method for target scattering in a waveguide. The singular behavior of the Green's function for an infinitesimal source/receiver separation, possibly with the target adjacent to one of the interfaces, is modeled correctly and the image expansion has a simple analytic form which can be analytically differentiated. The method is also accurate for significant source/receiver separations, which means that it can be used in the modeling of scattering from large-sized objects and can also be used as an efficient and accurate short-range propagation model for harmonic and broadband propagation in a penetrable waveguide. [DOI: 10.1121/1.1523082]

PACS numbers: 43.30.Gv, 43.20.El [DLB]

I. INTRODUCTION

For a perfect waveguide, it is well known^{1,2} that the field within the waveguide can be exactly expressed as an infinite series of point sources located above and below the top and bottom surfaces of the waveguide. This representation is useful for constructing the Green's function kernel for boundary integral equation methods (BIEM) for scattering problems (target and bathymetric) in a perfect waveguide.^{3,4} For this case, the advantage of the image approach over wave number integrals and modal methods is at very short ranges where the Green's function exhibits singular behavior (and this behavior is crucial in the BIEM). The singular terms consist of the direct term and an additional singular term, when the source and receiver point are close to one of the boundaries, due to one of the image sources approaching the boundary. The image method models this singular behavior very naturally. The modal and wave number methods must include a very large amount of evanescent energy to be accurate and in the case of modal sums, there may be convergence problems.⁵ The drawback of the image method for the perfect waveguide is that it exhibits poor convergence properties as the source/receiver horizontal range increases. In Ref. 3, Wu proposes a hybrid method for computing the waveguide Green's function for a boundary integral equation method, using the image solution for "short" ranges and the modal representation for "longer" ranges. Of course, if one is willing to compute many terms in the image series, it is possible to extend the validity and because of the simplicity of its terms, it may still be computationally advantageous to use it even if a large number of terms are required.³

For a waveguide with penetrable boundaries (i.e., not rigid or pressure release) the extension of the image method is not obvious. It is possible to think of images corresponding to the various orders of ray multipaths in the waveguide with amplitude terms which vary according to the angle of

reflection of the ray (i.e., ray theory thought of in terms of images). However, ray theory is a high-frequency theory and requires frequency-dependent corrections to be accurate for reflections off the seabed. A thorough discussion of these various corrections to classical ray theory can be found in Refs. 6 and 7. Reference 7 clearly shows that with careful asymptotic analysis of the wave number integral for a Pekeris waveguide, an accurate multipath ray theory can be developed. However, it is not clear that a ray-based method, even with corrections, is appropriate for accurately constructing the Green's function kernel on a scattering object (and recall it is the normal derivative of the Green's function that is used in a BIEM for a rigid object), particularly at low frequencies, very short ranges, and for the object very near an interface. In addition, the image method outlined in this paper is very simple: a set of true point sources is set up, based upon a representation of the half-space reflection coefficient, and any subsequent pressure field computations are very straightforward.

The method of complex images has been used often in the electromagnetics literature (Refs. 8–11 are examples of this work) and recently in underwater acoustics¹² as a means of efficiently computing the half-space Green's function. In this method the usual wave number integral is replaced by a small number of image terms with complex amplitudes and positions. This method has been used to efficiently compute the Green's function to solve scattering problems.^{10,11} References 8–12 also discuss the details of numerically determining the exponential fits and give examples of the efficiency and accuracy of the method, including layered media.¹¹ Our original motivation for the image method of this paper was to determine a set of complex images that could be used to accurately construct the Green's function kernel for a BIEM in a penetrable waveguide. Starting with the set of images determined for the bottom half-space, intuitively one can construct the image representation for the penetrable waveguide by iteratively reflecting the images above and below

^{a)}Electronic mail: john.fawcett@drdc-rddc.gc.ca

the waveguide's boundaries in a manner analogous to the perfect waveguide image solution (although as will be shown, it is a little more complicated than this). The images that are determined in this manner are true point sources with constant amplitudes (no receiver dependence). Once the positions and amplitude of these point sources are determined, the computation of the pressure field for any receiver position is straightforward—a simple evaluation of the distances, D_q , from the image locations and the evaluation of the corresponding exponentials $\exp(ikD_q)/(4\pi D_q)$. This set of point sources is ideal for computing the Green's function for scattering problems, either for boundary integral methods or wave field superposition methods¹³ in a waveguide, as it has the correct singular behavior for source/receiver points approaching each other as well as approaching the boundaries of the waveguides. However, as will be shown it is also accurate for significant source/receiver ranges. The other advantages of this method are that the simple analytic form of the point sources allows for the easy analytic computation of derivatives (for example, the normal derivative of the Green's function on a target surface) and, in fact, it is possible to analytically expand each point source in terms of spherical harmonics, which may have applications to T-matrix scattering methods.¹⁴ The method naturally handles a general layered seabed.

In the examples, we will illustrate the method as an effective short-range propagation model, at ranges where other methods such as modes (especially if leaky modes are included) or the wave number integral method are effective. However, for the perfect waveguide, at the very short ranges of interest in target scattering modeling (and possibly very close to one of the interfaces), these methods have to include a large amount of evanescent energy. It will be shown that for a homogeneous seabed the complex-image parameters need only be determined for a single frequency and the method does not become computationally more intensive as the frequency increases. This is in contrast to modal and wave number methods where the number of modes or the number of integration panels increases with frequency.

In summary, the method which is derived in this paper builds up a set of point sources. These sources are true point sources with the simple analytic form $a_q \exp(ikD_q)/(4\pi D_q)$. Once this set of points sources has been determined, any subsequent computations for a receiver anywhere in the waveguide are very straightforward (no need to monitor ray-paths, apply corrections, etc.) and applies for distances in the singular regime to significant source/receiver distances. The method will work for general layered seabeds, but it is particularly efficient for a Pekeris waveguide, where the set of sources need only be computed once for broadband or multifrequency computations. There are no low or high frequency restrictions on the usefulness of the method. It is an ideal method for BIEM computations but is also applicable to short-range propagation modeling.

II. THEORY

We start by a quick review of the method of complex images for an underlying half-space and discuss the frequency dependence of the parameters. Then we consider a

bounded waveguide and show how the set of complex images determined for the half-space can be used to construct a set of images for a bounded waveguide.

A. Complex images for a half-space

As discussed earlier, the method of complex images has been used frequently in the electromagnetics^{8–11} and the acoustics literature¹² for efficiently computing the Green's function for a homogeneous or layered half-space. This Green's function can then be used either for propagation or scattering modeling.

In the complex image method for a half-space, we start with wave number integral expression for the pressure field due to a point source above a half-space (see, for example, Ref. 2):

$$p(r, z, r=0, z_s) = \frac{e^{ikD}}{4\pi D} - \frac{1}{2\pi} \int_0^\infty J_0(hr) R(h) \frac{e^{i\gamma(z+z_s)}}{2i\gamma} h dh, \quad (1)$$

where $R(h)$ is the half-space reflection coefficient, D is the distance between the source and receiver, $\gamma(h)$ is the vertical wave number $\gamma(h) \equiv \sqrt{(\omega/c)^2 - h^2}$, c is the sound speed, ω is the circular frequency, and $k \equiv \omega/c$. The integral in Eq. (1) represents the reflected field. We also know that if we consider a point source at a depth z_q (and horizontal distance r away) we can write;

$$\frac{e^{ikD_q}}{4\pi D_q} = -\frac{1}{2\pi} \int_0^\infty J_0(hr) \frac{e^{i\gamma(z-z_q)}}{2i\gamma} h dh. \quad (2)$$

Let us consider $z_q = -z_s + i\alpha_q$ where z_s is the true source depth, then from Eq. (2) it follows that

$$\sum_{q=1}^Q a_q \frac{e^{ikD_q}}{4\pi D_q} = -\frac{1}{2\pi} \int_0^\infty J_0(hr) \frac{e^{i\gamma(z+z_s)}}{2i\gamma} \left[\sum_{q=1}^Q a_q e^{\gamma\alpha_q} \right] h dh. \quad (3)$$

From this and Eq. (1) it follows that if the coefficients (a_q, α_q) are determined so that in the horizontal wave number (h) domain

$$\sum_{q=1}^Q a_q \exp(\alpha_q \gamma(h)) \approx R(h), \quad (4)$$

then the reflected pressure field is given by

$$p_r(r, z) = \sum_{q=1}^Q a_q \frac{e^{ikD_q}}{4\pi D_q}, \quad (5)$$

where

$$D_q \equiv \sqrt{(x-x_s)^2 + (y-y_s)^2 + (z+z_s-i\alpha_q)^2}. \quad (6)$$

The parameters α_q are complex and γ is real for h real and $h < \omega/c_1$. Thus in this interval $\exp(\alpha_q \gamma)$ is a decaying or growing oscillatory exponential. For $h > \omega/c_1$ and along the real- h axis, γ is positive imaginary and thus this imposes the constraint that $\Im \alpha_q \geq 0$ in order that the exponential remains bounded. We find that in practice, that this constraint is satisfied by our exponential fits as long as one considers some range of h with $h > \omega/c_1$ —we often use $1.5\omega/c_1$ as our upper limit. However, it is also easy to include an extra point,

e.g., $h = 10\omega/c_1$, $R(h) = R_\infty$ in the fit to effectively impose the constraint on α_q .

In Eq. (6) the seabed/water interface is defined as $z = 0$; the coordinates with subscript s refer to the source coordinates. It can be shown that as $h \rightarrow \infty$, $R(h) \rightarrow R_\infty = (\rho_2 - \rho_1)/(\rho_1 + \rho_2)$. This means that the correct singular behavior of the Green's function for source and receiver points near the seabed is modeled by a source, reflected about the interface from the true source position, with strength R_∞ . Because of this we can choose this explicitly to be one of the sources in Eq. (4), thus ensuring the correct singular behavior of the Green's function near the seabed interface (e.g., take $a_1 = R_\infty$ and $\alpha_1 = 0$ and then determine the other coefficients to fit $R(h) - R_\infty$). In Ref. 12 a nonlinear least-squares fit was used to determine [using Eq. (4)] the parameters a_j and α_j . In this reference the bottom half-space was taken to be homogeneous. Three or four coefficients were found to be sufficient in the examples of that paper and a simple Gauss-Newton method of determining the fit to the reflection coefficient was found to be robust and efficient. Other approaches to determining these coefficients can be found in the references. There is no basic difference in the case that the bottom half-space is layered except that, in this case, $R(h)$ may be a more complicated function of h ; this means that more complex exponentials will have to be used to obtain an adequate fit.

In the case of a homogeneous bottom half-space, the reflection coefficient has the simple form:

$$R(h) = \frac{\rho_2 \gamma_1 - \rho_1 \gamma_2}{\rho_2 \gamma_1 + \rho_1 \gamma_2}, \quad (7)$$

where

$$p(r, z) = \frac{-i}{4\pi} \int_0^\infty \frac{e^{i\gamma|z-z_s|} + R_S(h)e^{i\gamma(z+z_s)} + R_B(h)e^{2i\gamma L}[e^{-i\gamma(z+z_s)} + R_S(h)e^{-i\gamma|z-z_s|}]}{\gamma(1 - R_S(h)R_B(h)e^{2i\gamma L})} J_0(hr) h dh, \quad (11)$$

where L is the depth of the waveguide, and R_B and R_S are the bottom and top reflection coefficients, respectively. One can now expand the denominator of the integrand to obtain²

$$\frac{1}{1 - R_S(h)R_B(h)e^{2i\gamma L}} = \sum_{n=0}^{\infty} (R_S R_B)^n e^{in2\gamma L}. \quad (12)$$

Using the complex-image representation for $R_B(h)$,

$$R_B(h) = \sum_{q=1}^Q a_q \exp(\gamma(h)\alpha_q), \quad (13)$$

then the n th term in this binomial expansion of Eq. (12) is given by

$$(R_B(h))^n = \left(\sum_{q=1}^Q a_q \exp(\gamma(h)\alpha_q) \right)^n. \quad (14)$$

From Ref. 15, the number of unique terms in the expansion of Eq. (14) is

$$\gamma_i \equiv \sqrt{\omega^2/c_i^2 - h^2}. \quad (8)$$

From Eqs. (7) and (8) it can be seen that if one considers the reflection coefficient as function of $\tilde{h} = h/\omega$ then the coefficient is, in fact, independent of frequency. In terms of \tilde{h} , Eq. (4) can be written

$$\sum_{q=1}^Q a_q \exp(|\omega| \gamma(\tilde{h}) \alpha_q) \approx R(\tilde{h}). \quad (9)$$

From Eq. (9) it can be seen that if a_q , α_q are determined for one frequency ω_1 then the results for any other frequency ω_2 are simply

$$\{a_q(\omega_2), \alpha_q(\omega_2)\} = \{a_q(\omega_1), (\omega_1/\omega_2)\alpha_q(\omega_1)\}, \quad \omega_1, \omega_2 > 0. \quad (10)$$

The expression of Eq. (10) is perhaps obvious, since there is no length scale in the problem other than the wavelength. However, it is an important concept because it means that for the half-space problem and for the bounded waveguide problem discussed in the following, once the set of complex parameters has been determined for one frequency, then the set of images has been determined for all frequencies.

B. Complex-image representation for propagation in a bounded waveguide

Let us now consider the waveguide with a bottom half-space at $z = L$ and a pressure-release surface at $z = 0$. For a penetrable waveguide, top and bottom, the expression for the pressure field, due to a point source at depth z_s , is given by the wave number integral,²

$$Q_n = \binom{n+Q-1}{n}. \quad (15)$$

One could in general expand R_S in terms of exponentials for a general upper bounding surface and obtain an image expansion for this combined case as well, but in this paper R_S is simply set to -1 . However, there are situations, such as a scatterer within a bounded sediment layer, where one could use this approach. Substituting Eqs. (14) and (12) into the wave number integral, Eq. (11), the various exponentials can be collected and each identified with a source position by using the formalism of the method of complex images.

As a more intuitive approach, let us consider the following iterative procedure (see Fig. 1). The physical source is reflected about the top-surface resulting in a negative image. These two sources each induce Q complex images in the seabed at locations: (1) $2L - z_s + i\alpha_q$ ($q = 1, \dots, Q$) with amplitudes a_q and (2) $2L + z_s + i\alpha_q$ with amplitudes $-a_q$. These coefficients are then all reflected about the upper in-

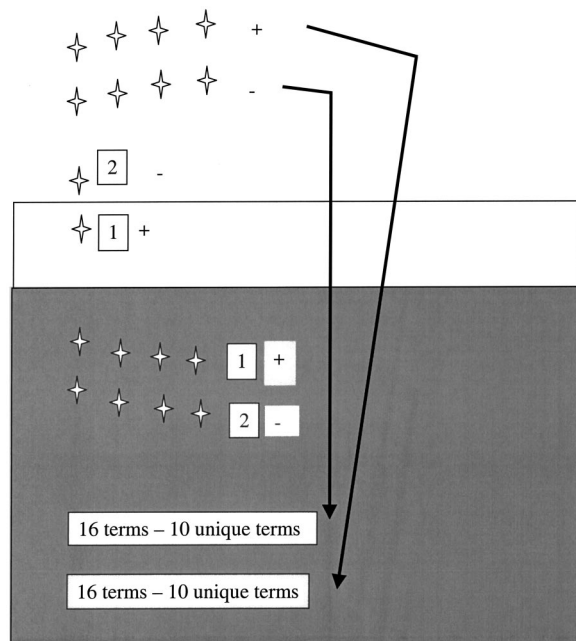


FIG. 1. Schematic of complex-image representation for a waveguide; the symbols 1 and 2 denote how the direct and surface reflected terms are represented in the seabed. These seabed terms then induce terms above the top surface; these terms then induce new complex images in the seabed and so on.

terface with the amplitudes multiplied by (-1) . In this process we have a representation which accounts for the direct energy and for the surface reflected, seabed reflected, surface/seabed reflected, seabed/surface reflected and surface/seabed/surface reflected paths. For many scattering problems, this is probably sufficient to approximate the Green's function for relatively short ranges.

To continue this procedure, each of the Q complex positions in the 2 sets of images above the top surface induces another Q position below the seabed. In other words, these 2 sets of Q parameters now induce 2 sets of Q^2 parameters in the bottom (although as shown from Eq. (15) the number of unique source positions is less than this). For example, if there are 4 original exponentials with complex depth parameters $(\alpha_1, \alpha_2, \alpha_3, \alpha_4)$ describing the half-space reflection coefficient, then there are sets of 10 source locations at $z = 4L - z_s + i\tilde{\alpha}_q$ and $z = 4L + z_s + i\tilde{\alpha}_q$, $q = 1, \dots, 10$ where the values of $\tilde{\alpha}_q$ are given by: $2\alpha_1, 2\alpha_2, 2\alpha_3, 2\alpha_4, \alpha_1 + \alpha_2, \alpha_1 + \alpha_3, \alpha_1 + \alpha_4, \alpha_2 + \alpha_3, \alpha_2 + \alpha_4, \alpha_3 + \alpha_4$.

Thus after a few seabed reflections, say 3 or 4, the number of terms begins to get unwieldy. For example, if $Q = 4$ and $n = 4$ the number of terms given by Eq. (15) is 35 (and the total number of images is larger than this). However, as will be seen in the numerical examples, this number of multipaths allows one to accurately model the waveguide's propagation out to significant ranges, while retaining the correct singular behavior of the Green's function near the source and near the boundaries. For target scattering problems, it may often be sufficient to keep just the first or second seabed reflection.

However, it is clear that it would be desirable to reduce the growing number of images at each additional order. Another approach is that instead of successively iterating on the

original set of complex images, a different set of exponentials can be fit to each power of the reflection coefficient. For example,

$$R^2(h) \approx \sum_{q=1}^Q b_q \exp(\gamma \tau_q) \quad (16)$$

and so on for higher powers. (In Ref. 7 an asymptotic analysis of the wave number integral for powers of the reflection coefficient is carried out.) In the numerical examples, we will show that a set of 6 parameter fits provide very good fits to all powers up to and including the fourth power of a reflection coefficient. This has the disadvantage that more exponential fits are required. However, we found these fits to be straightforward and accurate using the same least-squares algorithm as previously. It was straightforward to loop the algorithm over the powers of $R(h)$ using the previously determined parameters for $R^{n-1}(h)$, as the initial estimate for the parameters of $R^n(h)$. The disadvantage of doing more fits may be significantly offset in the reduction of the number of images.

It is also important to recall from the previous discussion that the parameters for the image series values for one frequency can be used to simply determine the values at all other frequencies in the case of a homogeneous seabed. For the case of a layered seabed this is not the case. Another type of exponential fit which can be employed is to directly fit a sum of exponentials to the terms,

$$t_1(h) \equiv \frac{1}{1 + R_B(h) \exp(2i\gamma L)} - 1, \quad (17)$$

$$t_2(h) \equiv \frac{R_B(h)}{1 + R_B(h) \exp(2i\gamma L)}.$$

These are the terms in Eq. (11) with $R_S(h) \equiv -1$; the first term has unity subtracted off so that we can explicitly extract the direct and top surface image sources. The images from these fits can then be used in conjunction with the terms in Eq. (11), $\exp(i\gamma|z - z_s|)$, $\exp(i\gamma(z + z_s))$, $\exp(2i\gamma L) \exp(-i\gamma|z - z_s|)$, $\exp(2i\gamma L) \exp(i\gamma(z + z_s))$ to produce a set of images. The advantage of this approach is that unlike the multipath expansion method, there is no real range restriction on the accuracy (although, ultimately the upper range does depend upon the accuracy of the integrand approximation). The disadvantages are that along the real- h axis the integrand will have singularities due to the modes (or the poles will be slightly displaced in the case of attenuation) and thus this will be a complicated integrand to fit, although the fit can be performed along a slightly displaced contour of integration. The integrand may become even more difficult to approximate for increasing frequency or waveguide depth. It also maybe that for short ranges, the multipath expansion method may require fewer terms than this more global approach. However, in the numerical examples, we will show a case where this approach is probably preferable, except possibly for ranges where only one or two bottom bounces are accurate.

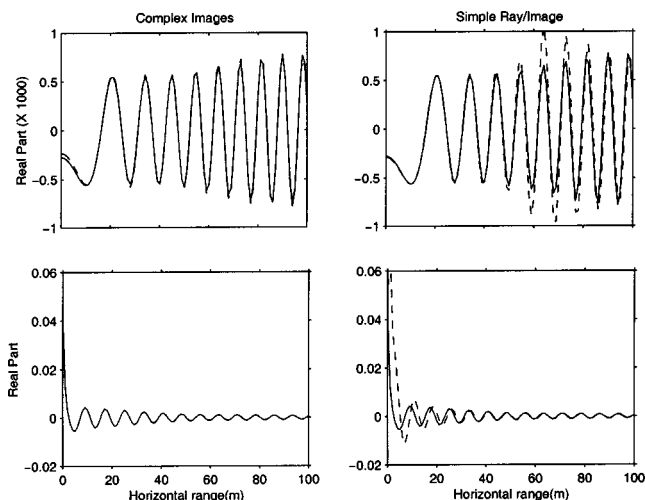


FIG. 2. The computed reflected field (real part) as a function of horizontal range as computed by the exact wave number integral (solid line) and column 1: complex image expression (dashed line) and column 2: simple ray/image expression (dashed line)—the top two panels are for the source and receiver located 20 m above the seabed and the bottom two panels, 0.2 m above the seabed.

III. NUMERICAL EXAMPLES

In this paper, only fluid-like bottom half-spaces will be considered. In Ref. 12 an elastic half-space was also considered; the only change to the approach for the fluid case is if one wishes to include the Scholte pole contribution.

First, a simple half-space problem (no upper surface) is considered. For this and all other examples of the paper, the water column will have a constant sound speed $c_w = 1500$ m/s and $\rho_w = 1$ g/cm³. The underlying half-space for this example has a sound speed $c_p = 1800$ m/s and density $\rho = 1.5$ g/cm³ and there is no attenuation. The frequency of the source is 200 Hz. The reflected fields (the real part is shown in Fig. 2) are computed for a line of receivers (starting horizontal range = 0.1 m) with: (top panel) source/receiver height (z_s and z_r) above seabed equal to 20 m and (bottom panel) source/receiver height above seabed equal to 0.2 m. The results are shown in Fig. 2 with the first column being the results using the complex-image (dashed line) method (four terms, one is the asymptotic term) along with the result from the wave number integral (solid line). The second column are the results using the simple ray/image (dashed) along with the results from the wave number integral. The expression for the ray-image method is given by

$$p_{\text{ray}} = \frac{1}{4\pi} \frac{e^{ikD}}{D} R(\theta), \quad (18)$$

where $D \equiv \sqrt{r^2 + (z_r + z_s)^2}$, $R(\theta)$ is the plane wave reflection coefficient, and $\theta \equiv \sin(r/D)$. The wave number and complex-image curves are very close, whereas noticeable differences with the simple ray expression can be seen. In particular, for $z_s/z_r = 20$ m, the differences occur at the longer ranges (possibly, due to the fact that these ranges correspond to the critical angle region) whereas for $z_s/z_r = 0.2$ m the differences are significant for approximately the first 30 m. This example serves to illustrate that using simple ray-image theory may not be sufficient for some propagation

or scattering geometries. Of course, as discussed in Sec. I, this ray theory result can be improved upon by using various corrections.

Let us now consider a complex-image computation for a waveguide 40 m deep. For our initial computations, $f = 200$ Hz and 2 source/receiver depths are considered: 30/20 and 3/37 m. The bottom half space is taken to be homogeneous and has the parameters: (1) 4000 m/s and $\rho = 4$ g/cm³, (2) 3000 m/s and $\rho = 3$ g/cm³ (3) 2400 m/s, and $\rho = 2.25$ g/cm³ and (4) 1800 m/s and $\rho = 1.5$ g/cm³. There is no attenuation in the half-space. There is no problem including attenuation in this method, but no attenuation is a more rigorous test of the image method because otherwise some of the higher-angle energy would be attenuated with respect to range. In terms of modes, the proper modes' wave numbers lie on the real wave number axis for these examples.

A four-parameter fit to the reflection coefficient is used. For the first exponential, $a_1 = R_\infty$ and $\alpha_1 = 0$. This term accounts for the asymptotic behavior of the reflection coefficient and means that the bottom image term will have exactly the correct singular behavior for a source/receiver pair approaching the bottom. The approach as outlined earlier is now used; the sources are flipped around the top and bottom boundaries to yield images which account for up to and including 3 seabed reflections. The total number of images, including the direct and all seabed and above free surface images is 138. If one just includes up to 2 seabed reflections this becomes 58. In Fig. 3 the transmission loss curve (please note that this is $20 \log_{10}(|p|)$, this number should be shifted by $20 \log_{10}(4\pi)$ to obtain the true transmission loss, i.e., we have not normalized these values by the amplitude at 1 m range) is shown as a function of range for an exact solution (using the integral of Eq. (11) (solid line) and for the image method (dash-dot)). As can be seen for the most rigid seabed, there is very good overall agreement between the 2 curves, for both source/receiver combinations, out to about 200 m range (or 5 waveguide depths), although there are small differences earlier than this, for example, a small peak at about 100 m which is not perfectly modelled. As the bottom becomes more penetrable the agreement becomes better, out to 400 m or more for the 1800 m/s bottom.

The explanation for the range of validity of these representations is likely connected with the critical angle of the waveguide. For a fixed range there will be a certain order of multipath, $n+1$ (this refers to the number of bottom bounces), whose angle of incidence at the seabed exceeds the critical angle, thus having a reflection coefficient at the seabed, R , whose amplitude is less than one; the total path will then have an amplitude proportional to $|R|^{(n+1)}$, which maybe considerably less than unity. If this is the case, then it is expected that n terms will give a good approximation to the true pressure field; in the time domain, this corresponds to simply saying that out to this range, the $n+1$ multipath arrivals and beyond are significantly weaker than the other arrivals. This is analogous to ray methods⁷ which monitor the relative importance of the various multipaths and decide numerically whether to include them or not in the computation. As the seabed becomes more penetrable and the critical angle decreases, this convergence will become more rapid

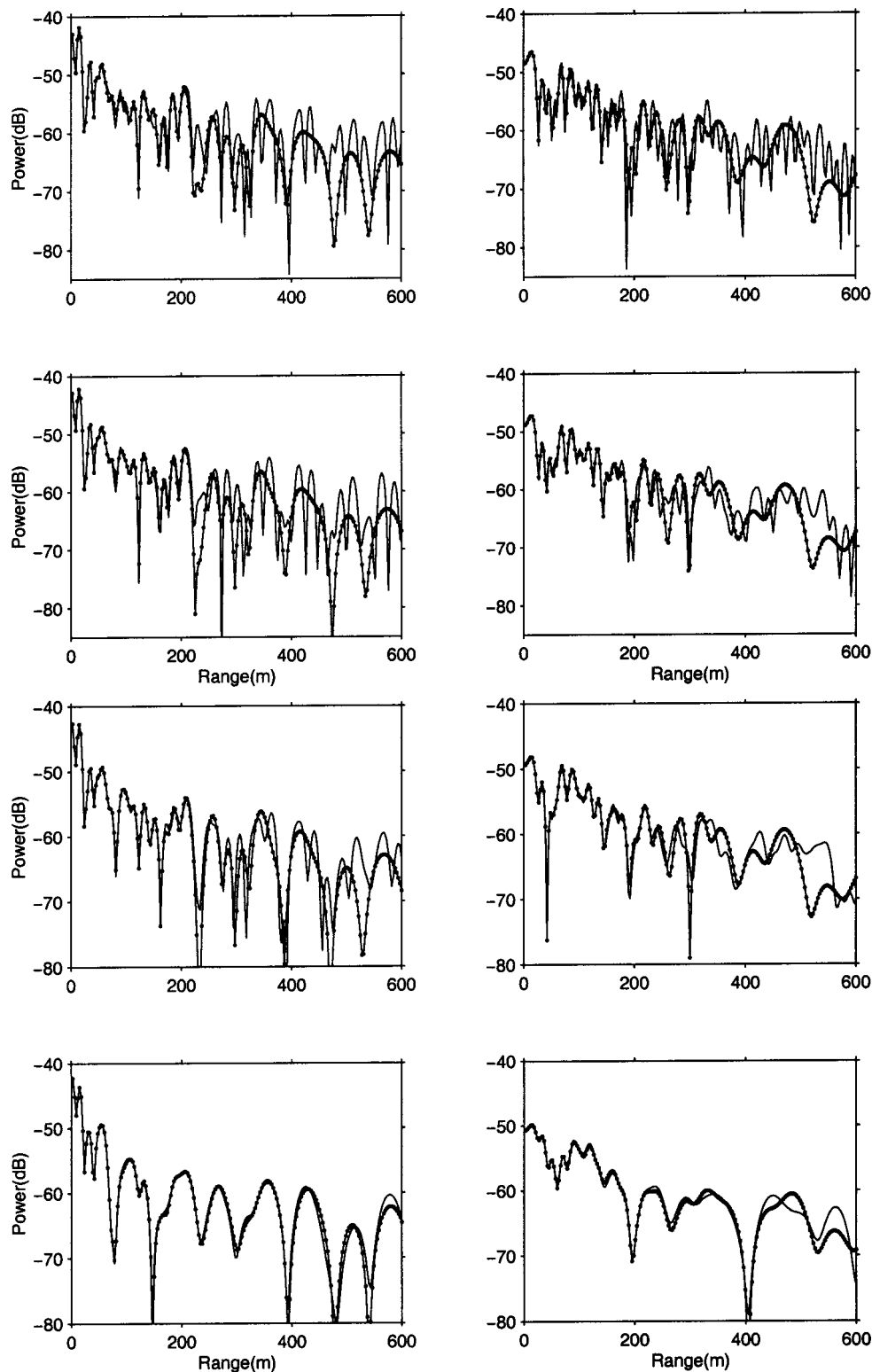


FIG. 3. The computed transmission loss curves for: (column one) $z_s = 30$ m and $z_r = 20$ m and (column 2) $z_s = 3$ and $z_r = 37$ m for the 4 different seabeds.

with range. This is in contrast to the perfect waveguide where all orders of multipaths are trapped within the waveguide and only geometrical spreading causes a decrease in amplitude. These concepts are only a guideline; there is not a sharp boundary between the relative amplitudes of the different multipath orders, rather a transition zone. Also, of course, even though an order of multipath is relatively weak in a certain area, they are still present and the agreement between

the exact and the finite image-method solution will not be perfect. In the time domain these multipaths will appear as small arrivals which the image method, with a finite number of orders, cannot model. It is difficult to give definite quantitative bounds on the range of validity of the complex image expression for a given number of seabed reflections; however, simple ray considerations indicate that the critical angle and the depth of the waveguide are important parameters.

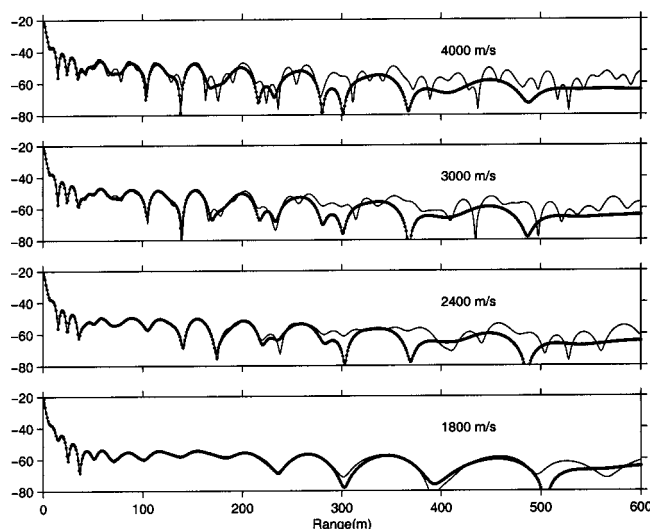


FIG. 4. The computed transmission loss curves for $z_s=39.99$ m and $z_r=39.5$ m and the 4 different seabeds—solid is exact, dotted is method of images.

The case of the source and receiver very close to the seabed is a situation of interest for modeling scattering from an object near or on the seabed. In Fig. 4 we show the results for the four seabed types for $z_s=39.99$ m and $z_r=39.5$ m; here some care had to be taken with the wave number integral (the length of integration had to be increased) to yield good results. As can be seen, the agreement is once again excellent. There is a small feature at about 80 m for the most rigid case which is not modeled correctly by the image method, but overall, it is difficult to deduce a significant difference in the accuracy of the image method from the results of the previous figure.

Let us consider the effect of waveguide depth. The source/receiver depths are fixed at 5 and 10 m, respectively, and we consider the third seabed type ($c=2400$ m/s and $\rho=2.25$ g/cm³). The exact and image curves are shown in Fig. 5 for waveguide depths of 20, 40, and 80 m. As might be expected the range of validity does depend upon the depth of

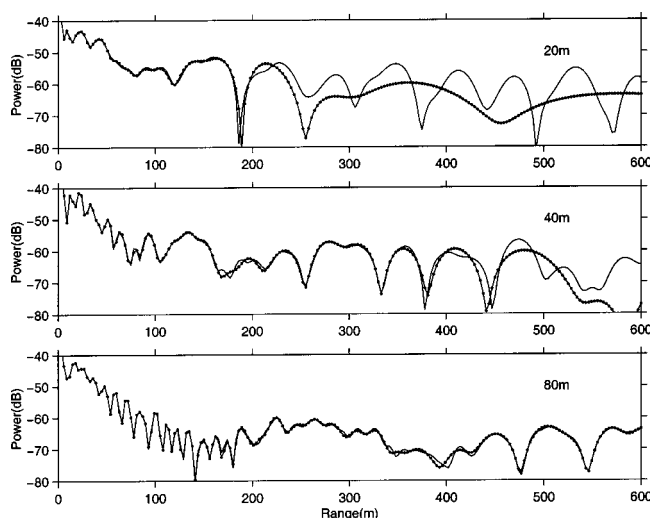


FIG. 5. The exact and image transmission loss curves for $z_s=5$ m and $z_r=10$ m for 200 Hz as a function of varying waveguide depths, 20, 40, and 80 m for the third bottom type $c=2400$ m/s, $\rho=2.25$ g/cm³.

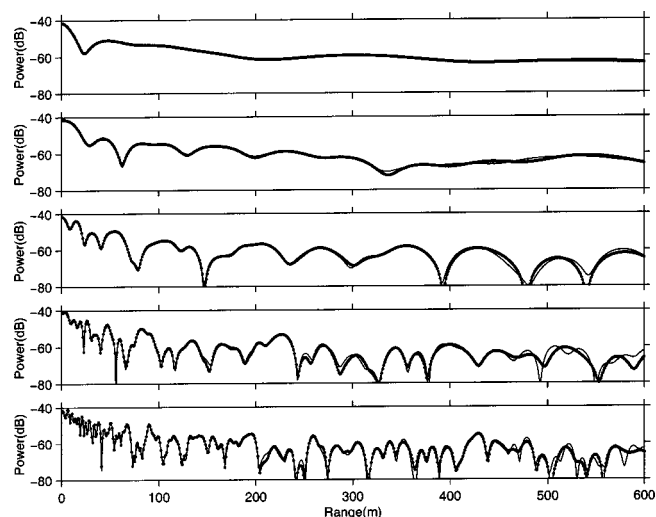


FIG. 6. The exact and image transmission loss curves for $z_s=30$ m, $z_r=20$ m for frequencies of 50, 100, 200, 400, and 800 Hz for the fourth seabed type $c=1800$ m/s, $\rho=1.5$ g/cm³ and waveguide depth=40 m.

the waveguide. At the 80 m depth, the image solution has excellent agreement with the exact solution all the way out to 600 m and beyond.

Fixing the waveguide depth at 40 m and considering the fourth seabed type, for which we know the image solution is good until about 450 m for the 200 Hz case, we examine the performance as a function of frequency. In Fig. 6 the exact solutions and the image solutions are shown for 50, 100, 200, 400, and 800 Hz for the source/receiver depths of 30/20 m. We emphasize the point that the complex parameters are only computed at a single frequency and reused at all the other frequencies using the scaling relationship of Eq. (10) with all the image positions shifted accordingly. As can be seen the agreement is excellent for all frequencies to a range of 450 m, where there are some differences.

Thus far, we have considered homogeneous bottoms; as mentioned previously, there is no conceptual difficulty to modeling a layered bottom (see, e.g., Ref. 11 in the electromagnetic literature). Now, the following layered seabed is considered. There are 2 sediment layers of 10 m thickness: layer 1, $c_p=1700$ m/s and $\rho=1.7$ g/cm³, layer 2: $c_p=1800$ m/s and $\rho=1.8$ g/cm³ and an underlying half-space with $c_p=2200$ m/s and $\rho=2.2$ g/cm³ and the entire seabed has an attenuation of 0.25 dB/λ. Numerically, the complex-image method for a layered seabed is somewhat more difficult because it will, in general, require more exponentials to model the more complicated behavior of the reflection coefficient as a function of horizontal wave number. However, for the cases we have considered it was found that the coefficients could still be determined straightforwardly with the Gauss–Newton least-squares algorithm.

We have shown that the number of images for a waveguide increases with expansion order as the binomial number given in Eq. (14). Thus it is advantageous to try to keep the basic number of coefficients approximating the reflection coefficient as small as possible. In Fig. 7, the real and imaginary parts of the exact reflection coefficient as a function of horizontal wave number are shown with the corresponding

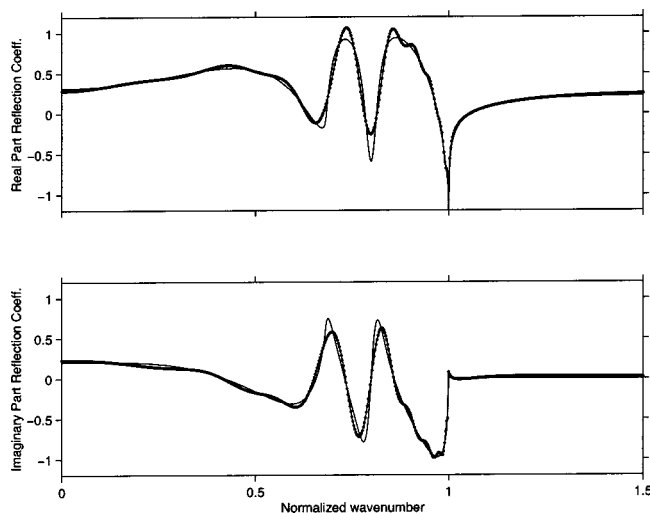


FIG. 7. Real and imaginary parts of the reflection coefficient for layered bottom for 7-exponential fit (6 plus asymptotic term), exact (solid) and exponential fit (dotted) at 100 Hz.

exponential fit with 7 terms (1 term is the asymptotic term—which can be shown to be $(\rho_2 - \rho_1)/(\rho_2 + \rho_1)$, where ρ_2 refers to the density of the upper sediment layer). As can be seen, it is a very good fit but differences can be seen. Using higher numbers of terms yields better fits, but this in turn leads to more source terms in the waveguide image expansion, so there is a trade-off of how many terms should be used to approximate the basic reflection coefficient. Computing the waveguide image solution up to and including 3 bottom bounces requires 478 images, when 7 terms are used for the reflection coefficient (two bottom bounces would require 142). The resulting transmission loss curves (exact and image solution) for a 40-m-deep waveguide at 100 Hz are shown in Fig. 8 ($z_s = 30$ m, $z_r = 20$ m). The agreement is excellent until about 300–350 m. This example illustrates that there is no difficulty in using the theory for a layered seabed. However, it is evident that more images will be required in the case that the layered half-space reflection coefficient has a more complicated behavior than the homoge-

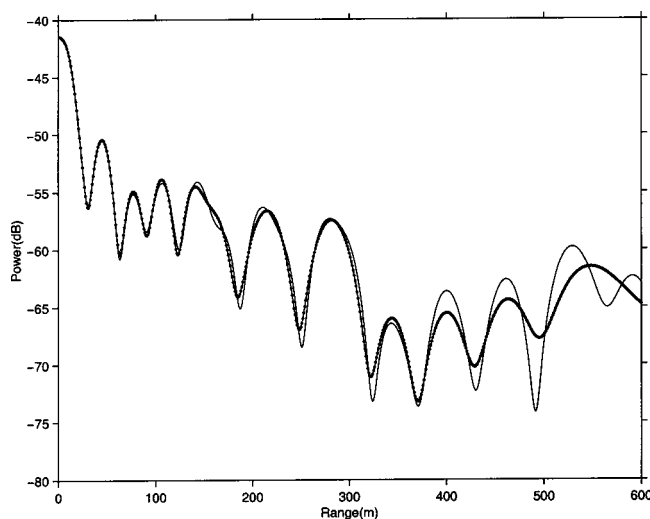


FIG. 8. Resulting transmission loss curves for point source, $z_s = 30$ m and $z_r = 20$ m exact and image solution for the layered seabed.

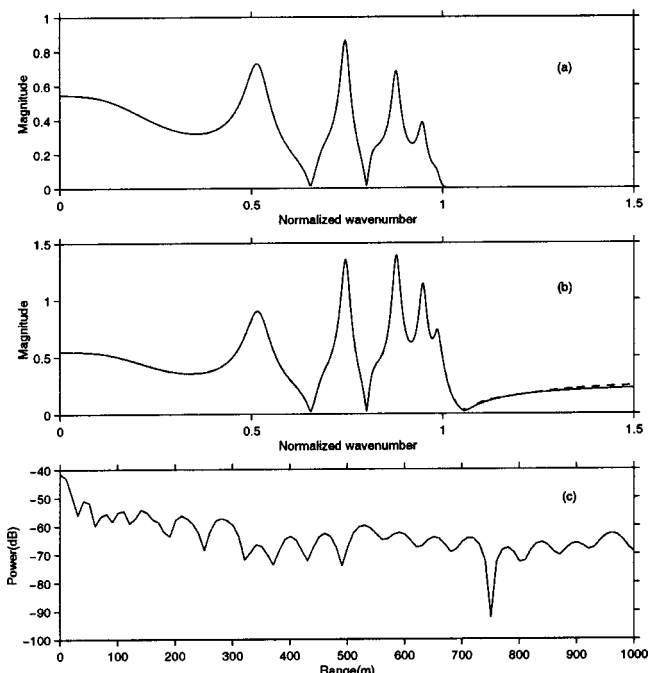


FIG. 9. Results of fitting 81 terms directly to $t_1(h)$ (a), $t_2(h)$ (solid is exact curves, dashed is fitted curve), (b), and the resulting transmission loss curves for point source, $z_s = 30$ m and $z_r = 20$ m exact and image solution for the layered seabed (c).

neous case [note, for sufficiently low frequencies or high frequencies (where only the upper layer is important) the layered-space reflection coefficient behavior may become “smoother” in nature]. Also, as mentioned previously, unlike the homogeneous half-space case, it is now necessary to perform a new exponential fit for each frequency.

Another possible approach for the layered seabed (particularly, since there is no simple frequency dependence of the complex images for the seabed reflection coefficient in this case) is to attempt to directly fit complex exponentials to the terms of Eq. (17), $t_1(h)$, and $t_2(h)$ (the same layered seabed as previously is considered at a frequency of 100 Hz). In Figs. 9(a) and (b), 81-term fits to $t_1(h)$ and $t_2(h)$ are shown (solid line is the exact curve and the dashed is the fit). In this case to determine the exponentials, we simply defined the coefficients α_q for $t_1(h)$,

$$\alpha_q = (80 + (q - 1) \times 10)i, \quad q = 1, \dots, 81 \quad (19)$$

and for $t_2(h)$,

$$\alpha_q = ((q - 1) \times 10)i, \quad q = 1, \dots, 81. \quad (20)$$

The corresponding amplitude coefficients were then simply determined by a linear least-squares fit of the sum of exponentials to $t_1(h)$ and $t_2(h)$ evaluated at 1001 different values of h . The first amplitude value for $t_2(h)$ was set to the asymptotic value of the reflection coefficient R_∞ to explicitly account for the singular term as the seabed is approached. The starting value of 80 in Eq. (19) was chosen as this is $2L$ (L is the waveguide depth) and the spacing of 10 corresponds to $L/4$. The total number of images used for this example is 326; this corresponds to the images of Eqs. (19) and (20) in conjunction with the exponentials of the numerator of the integrand in Eq. (11) and the direct and top surface images.

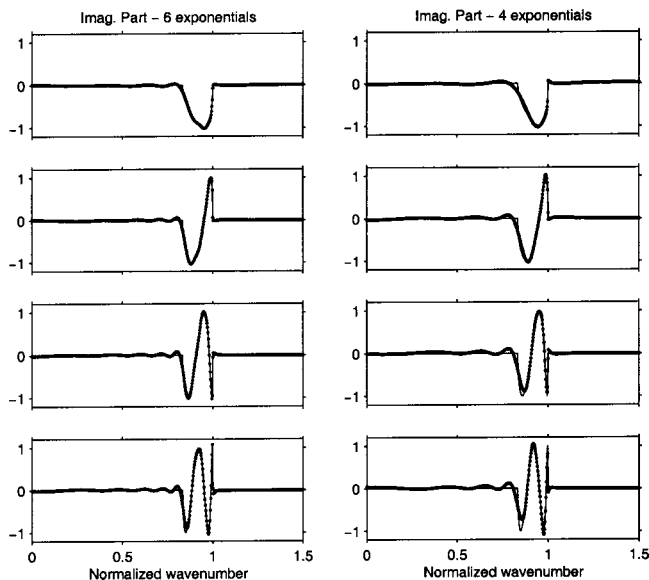


FIG. 10. Exponential fits to the powers of the reflection coefficient (imaginary part shown) for the seabed $c_p = 1800$ m/s and $\rho = 1.5$ g/cm³ using 6 exponential and 4 exponential fits.

This number is smaller than the number we used with the multipath approach for this seabed and the transmission loss curve [Fig. 9(c)] is very accurate to at least 1000 m.

It is clear from the previous examples and the theory, that if one uses the multipath approach, then the number of terms increases significantly as one increases the order of multipath in the image expansion. (and recall, that for the homogeneous seabed this is often the desired approach because of the simple frequency dependence of the images). A possible way to reduce the required number of images is to use the concept of Eq. (16). A different exponential fit is made for $R(h)$, $R^2(h)$, etc., using a fixed number of terms (although, in general, one could use a different number of terms for each power depending upon the desired accuracy). In Fig. 10 we show the exponential fits to the reflection coefficient for $c_p = 1800$ m/s and $\rho = 1.5$ g/cm³ (we show the imaginary part) for the first, second, third, and fourth powers using a 6-exponential fit and a 4-exponential fit; as can be seen, although the 4-exponent fit (a different set for each power) yields a good fit, the 6-exponent fit is better and has only a small amount of error at the fourth power of the reflection coefficient.

In Fig. 11 we show the resulting transmission loss curves, exact computation, and the results of using up to and including the fourth power of the reflection coefficient using the 6-exponential and 4-exponential fits. This is the case for the source at 3 m depth and the receiver at 37 m depth, where in Fig. 3 there was some disagreement between the exact and image-method curves at about 450 m. However, in that case only up to the third power of the reflection coefficient was computed. Here, we include the fourth power and indeed the agreement is now good until approximately 600 m. Although the 6-exponential fit may be a little better than the 4-exponential fit, the agreement is very good for both cases. For the 6-exponential fit, a total of 98 images were used and for the 4-exponential fit, a total of 66 images.

We saw from Fig. 11 that an extra set of coefficients for

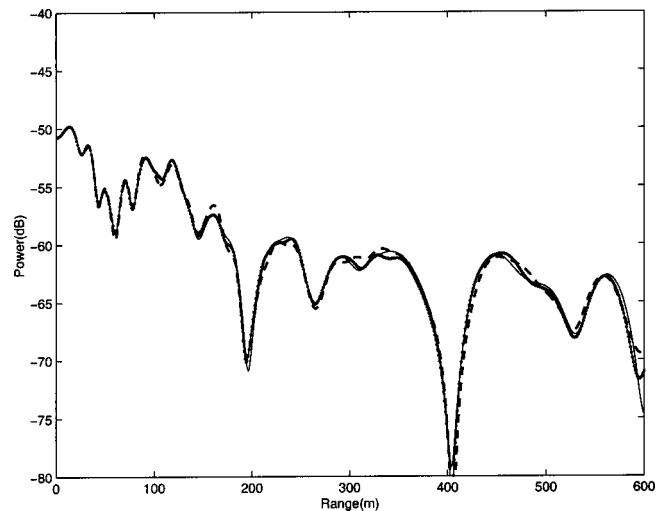


FIG. 11. Resulting transmission loss curves (exact (thin solid), using up to and including fourth powers of reflection coefficient: 6-exponential fit (thick dots) and 4-exponential fit (dashed) for $c_p = 1800$ m/s and $\rho = 1.5$ g/cm³ and $z_s = 3$ m and $z_r = 37$ m.

the fourth power of the reflection coefficient yielded a good fit in the transmission loss curves for approximately another 150 m from the case where only the third power was included. In Fig. 12 we show the results of including the fourth, third, second, and first order seabed reflections. As can be seen the curves' agreement with the exact solution does tend to decrease by about 150 m for each order of the reflection coefficient.

Finally, for the Pekeris waveguide case, it is very straightforward to perform broadband computations; here we use the method of fitting 6-exponentials to $R(h)$, $R^2(h)$, $R^3(h)$, $R^4(h)$ —the fit to $R(h)$ is constructed so that one of the terms is the exact asymptotic term. This is done at a single frequency and a set of $a_q(f_0)$, $\alpha_q(f_0)$ determined for each order. Computationally a loop over frequency is performed: at each frequency $\alpha_q(f) = \alpha_q(f_0)f_0/f$ and $a_q(f) = a_q(f_0)$ (for each order) and the pressure field is computed by simply summing over the images, using the distances for

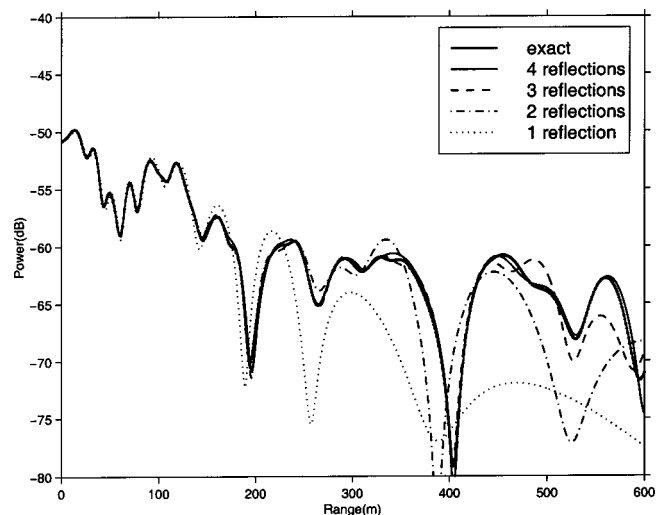


FIG. 12. The variation of the image solution with the number of seabed reflections for $c_p = 1800$ m/s and $\rho = 1.5$ g/cm³ and $z_s = 3$ m and $z_r = 37$ m.

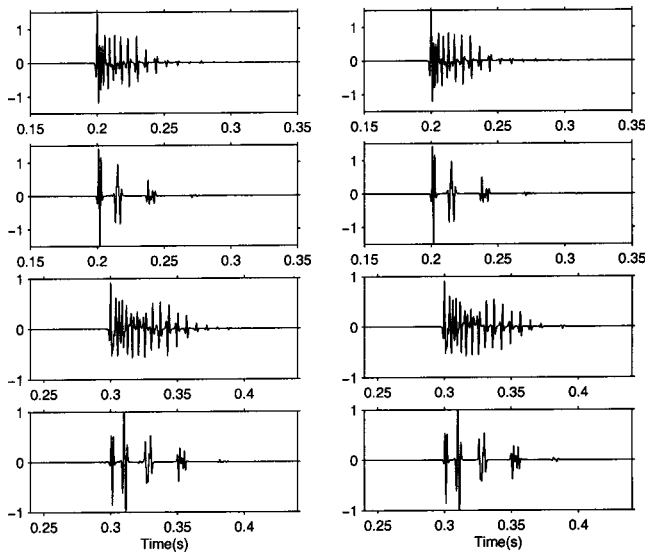


FIG. 13. Pulse computations for a 400 Hz Ricker wavelet; left column, exact solution and right column, image solution: (1) $z_s = 30$ m and $z_r = 20$ m, (2) $z_s = 3$ m and $z_r = 37$ m for 300 m range and then repeated at 450 m range. All for seabed $c_p = 1800$ m/s, $\rho = 1.5$ g/cm³.

a given receiver position. At the end of the computations, a pulse can be Fourier synthesized. In the example to follow a Ricker wavelet at center frequency 400 Hz was used. The complex pressure values for 1001 frequencies starting at 10 Hz and ending at 1010 Hz were computed and used in the Fourier synthesis of the time series. In Fig. 13 the exact time series (computed by looping over the wave number integral) and the image computations are shown for the 2 source/receiver combinations 30 m/20 m and 3 m/37 m and for 300 and 450 m ranges. There are some very small differences in details between the two sets of time series, but as can be seen the overall agreement is excellent.

IV. SUMMARY

In this paper we have extended the method of images used for a perfect waveguide to the penetrable case using the method of complex images as the basic building block. The resulting images in the expansion are true point sources with a simple analytic form which can be easily analytically differentiated. There is an analogy with ray theory in the sense that each power of the reflection coefficient used in the image expansion effectively models another order of multipaths in the waveguide. However, unlike a ray/image interpretation, the images used in this expansion have a constant amplitude which does not vary according to the angle of incidence and do not require any specific corrections to be accurate. In the case of a Pekeris waveguide, for multifrequency computations, the image parameters need only be computed at a single frequency (they can then be simply determined at all other frequencies). The theory is also applicable to general seabeds but in this case, the coefficients must be determined for each frequency (because, the seabed itself may now have a complicated frequency dependence). Because of their simple analytic form and the fact that the set of images has the correct singular behavior (including near or on the interfaces), they are ideal for constructing the

Green's function kernel in a BIEM. Compared to the image method for the perfect waveguide, this method is accurate to significant ranges. This is because steep angle energy dies out quickly in a penetrable waveguide and thus this method improves as the seabed becomes more penetrable. However, it provided good results even for the case of a seabed with $c_p = 4000$ m/s and $\rho = 4$ g/cm³.

We discussed three methods for computing the images. The first method uses a simple fit to the reflection coefficient for the seabed and then uses successive powers of that one expansion. The disadvantage of this approach is that after the third or fourth power of the reflection coefficient, the number of terms begins to increase rapidly. The second method consisted of performing a separate fit for each power of reflection coefficient, keeping the number of terms for each power small. The additional fits are numerically inexpensive as one can quickly loop the least-square program through the successive powers and, at least for the examples considered, would be the preferred approach for homogeneous seabeds. The third method that we employed for a layered seabed was to directly fit sums of exponentials to the integrand, without first expanding it binomially. This resulted in a representation that was very accurate for a long range (at least 1000 m). The fits for this approach are frequency-dependent, but since the complex-image fits to the seabed reflection coefficient are also frequency-dependent in this case, this is not a disadvantage.

It is difficult to quantify precisely the computational efficiency of the complex-image method relative to other methods. This depends on a large number of factors, such as frequency, source/receiver positions, etc. In this paper we used a wave number integral for the benchmark solution. Neither this method nor the complex-image method were greatly optimized, although the wave number integral technique was somewhat optimized for the case of constant depths and varying horizontal range. For most of the examples of this paper, the complex-image method computed the pressure field more rapidly than the wave number integral approach (once the complex image parameters had been determined). An exception was for the case of the layered seabed where 478 complex images were used in the computation of the pressure field. Here the wave number integral approach was somewhat faster for the computation of a single transmission loss curve. However, even for this example, if several different source/receiver depths are considered at a fixed range, then the complex image method became faster. However, in general, it is difficult to make a rigorous statement about the relative computational timings of the two methods. Ultimately, this will depend upon the particular scenario and frequency range being considered and the number of images required by the image method and the number of integration steps required by the wave number integral to obtain the desired accuracy. There is also a small overhead in the initial determination of the complex parameters associated with the complex image method. The situations where we expect the method of complex images to be particularly efficient are: (1) the computation of the pressure fields for a wide range of source/receiver positions (e.g., the computation of the Green's function for a BIEM computa-

tion and moving target/receiver scenarios), (2) the multifrequency computation of the pressure field for a Pekeris waveguide, (3) high frequencies. In these first two types of computation the initial overhead of computing the complex parameters once is relatively very small compared to the large number of subsequent computations. In multifrequency or high frequency computations, the wave number integral requires an increasing number of integration steps as a function of frequency (and modal methods will require a larger number of modes) whereas the image method does not require more terms.

The theory and numerical examples of this paper were concerned with a constant sound speed in the water column. This means, in practice, that the variation of the sound speed in the water has to be sufficiently small or the ranges of propagation small enough that the isovelocity approximation is accurate. It is an area of future research to determine whether the concepts of complex images, perhaps in conjunction with asymptotic theories, are generalizable and useful for a sound speed profile in the water column.

¹L. Brekhovskikh and Y. Lysanov, *Fundamentals of Ocean Acoustics* (Springer, Berlin, 1982).

²G. Frisk, *Ocean and Seabed Acoustics: A Theory of Wave Propagation* (PTR Prentice-Hall, New York, 1994).

³T. W. Wu, "On computational aspects of the boundary element method for acoustic radiation and scattering in a perfect waveguide," *J. Acoust. Soc. Am.* **96**, 3733–3743 (1994).

⁴J. Fawcett, "An efficient three-dimensional boundary integral equation method for solving azimuthally symmetric scattering problems in the oceanic waveguide," *J. Acoust. Soc. Am.* **94**, 2307–2314 (1993).

⁵T. W. Dawson and J. Fawcett, "A boundary integral method for acoustic scattering in a waveguide with non-planar surfaces," *J. Acoust. Soc. Am.* **87**, 1110–1125 (1990).

⁶L. Brekhovskikh and O. Godin, *Acoustics of Layered Media. II. Point Sources and Bounded Beams* (Springer, Berlin, 1992).

⁷E. K. Westwood, "Ray methods for flat and sloping shallow-water waveguides," *J. Acoust. Soc. Am.* **85**, 1885–1894 (1989).

⁸R. M. Shubair and Y. L. Chow, "A simple and accurate complex image interpretation of vertical antennas present in contiguous dielectric half spaces," *IEEE Trans. Antennas Propag.* **41**, 806–812 (1993).

⁹J. J. Yang, Y. L. Chow, and D. G. Fang, "Discrete complex images of a three-dimensional dipole above and within a lossy ground," *IEE Proc., Part H: Microwaves, Opt., and Antennas* **138**, 319–326 (1991).

¹⁰S. Vitebskiy, K. Sturges, and L. Carin, "Short-pulse plane-wave scattering from buried perfectly conducting bodies of revolution," *IEEE Trans. Antennas Propag.* **44**, 143–151 (1996).

¹¹N. Geng and L. Carin, "Wide-band electromagnetic scattering from a dielectric BOR buried in a layered lossy dispersive medium," *IEEE Trans. Antennas Propag.* **47**, 610–619 (1999).

¹²J. Fawcett, "Complex-image approximations to the half-space acousto-elastic Green's function," *J. Acoust. Soc. Am.* **108**, 2791–2795 (2000).

¹³A. Sarkissian, "Multiple scattering effects when scattering from a target in a bounded medium," *J. Acoust. Soc. Am.* **96**, 3137–3144 (1994).

¹⁴G. C. Gaunard and H. Huang, "Acoustic scattering by a spherical body near a plane boundary," *J. Acoust. Soc. Am.* **96**, 2526–2536 (1994).

¹⁵*CRC Standard Mathematical Tables and Formulae*, edited by D. Zwillinger (CRC Press, Boca Raton, FL, 1996), p. 169.

Broadband sound propagation in shallow water and geoacoustic inversion

D. P. Knobles, R. A. Koch, L. A. Thompson, K. C. Focke, and P. E. Eisman
Applied Research Laboratories, The University of Texas at Austin, Austin, Texas 78713

(Received 21 December 2000; revised 30 November 2001; accepted 26 June 2002)

Part of an experiment to test a measurement package in a shallow water region in the Gulf of Mexico was designed to gather broadband acoustic data suitable for inversion to estimate seabed geoacoustic parameters. Continuous wave tow acoustic signals at multiple frequencies and broadband impulsive source signals were recorded on a horizontal line array in a high-noise environment. Simulated annealing with a normal mode forward propagation model is utilized to invert for a geoacoustic representation of the seabed. Several inversions are made from different data samples of two light bulb implosions, the measured sound speed profiles at the HLA and at the positions of the light bulb deployments, and for two different cost functions. The different cost functions, measured sound speed profiles, and measured time series result in different inverted geoacoustic profiles from which transmission loss is generated for comparison with measurements. On the basis of physical consistency and from the comparison of the transmission loss and time series, a best estimate geoacoustic profile is selected and compared to those obtained from previously reported inversions. Uncertainties in the sound speed profile are shown to affect the uncertainties of the estimated seabed parameters. © 2003 Acoustical Society of America. [DOI: 10.1121/1.1521930]

PACS numbers: 43.30.Bp, 43.30.Wi [DLB]

I. INTRODUCTION

From a historical perspective inversion for environmental parameters has always played a role at some level in the application of propagation models to analyze acoustic data measured in ocean environments. The inverse problem is intimately associated with our general ability to predict, as part of propagation analyses, the measured acoustic data in the form of transmission loss (TL) from multitonal tow data, time series generated from impulsive sources, or broadband data created by moving sources such as surface ships. Geoacoustic inversion is a topic of current interest in the sonar and ocean acoustics communities since improvements in the accuracy of low-frequency sound propagation predictions for a shallow water ocean environment are contingent on knowledge of the seabed parameters.^{1–3} The accuracy of an inversion for shallow water seabed parameters using acoustic data depends on several factors. They include the quality of the experimental measurements, details of the data reduction and signal processing, the choice of data employed in the inversion, the choice of a cost function, the assumed seabed representation, *a priori* knowledge such as the sound speed structure in the water column and bathymetry, and the inversion method. In addition, a well-validated forward acoustic propagation model with a high level of accuracy is required.

In inversion problems it is important to take into consideration the uncertainties or standard deviations of the estimated parameters. Part of these uncertainties can be estimated on the basis of the statistics generated by all the forward calls made in an inversion. The uncertainties generally reflect the modeled field's sensitivity with respect to the parameters. In addition to uncertainties resulting from the nature of sound field sensitivity, uncertainties in the esti-

mated parameters result from the uncertainties in model parameters held constant in the inversion calculation. For example, in shallow water an especially difficult problem is that even though the depth-dependent sound speed profile (SSP) can in principle be measured during the collection of acoustic data, significant fluctuations often occur in azimuth, range, and time. In a geoacoustic inversion calculation, one usually selects measured SSPs that are nearest in space and time to the acoustic measurements. Errors in the assumed SSP are a source of errors in the estimated geoacoustic representation of the seabed. Furthermore, errors in the assumed bathymetry and source–receiver geometry are additional sources of errors. In principle, one can use multiple SSPs and acoustic measurements to gain insight into the nature of the uncertainty in the estimated geoacoustic parameters.

This paper describes an investigation of acoustic data collected in a shallow water environment in the Gulf of Mexico. The analysis takes an inversion approach to extract a geoacoustic representation of the seabed with parameter uncertainties. The experiment and analysis presented an excellent opportunity to address the issues raised above and to better comprehend the essential elements of geoacoustic inversion in shallow water. Concerning the choice of data in the inversion, the general approach is to take advantage of the sensitivity of the frequency and spatial dependence of the sound field to the seabed structure. Consistent with this approach is the use of broadband data collected on a horizontal line array (HLA). If the experiment is designed to collect data from approximately range-independent propagation paths, a normal mode model, such as that of Westwood *et al.*, is an appropriate selection to provide accurate forward solutions to the acoustic Helmholtz wave equation.⁴ In shallow

water the complex interaction of sound with the seabed causes the multidimensional cost function to contain, in addition to the global minimum, a large number of local minima. For this reason, it is assumed that a simulated annealing approach is an appropriate selection for the inversion method.

A basic premise of the experiment and analysis is that the signals received from light bulb implosions can be utilized to estimate the geoacoustic structure of the seabed. With this geoacoustic structure as input to the same forward propagation model used in the inversion, multifrequency TL versus range can be generated. A comparison of the modeled TL with the measured TL, supplemented by a comparison of our inversion results with the previous inversions and geo-physical descriptions reported in the literature, would demonstrate the validity of the broadband inversion approach.

Several aspects of the current work distinguish it from previous inversion studies. Most inversion studies are made using a few single-frequency measurements. However, the frequency dependence of the acoustic response is sensitive to the details of the geoacoustic structure of the seabed. For example, in cases where the acoustic field is composed of numerous multipaths that interact with the seabed, the magnitude of the field as a function of frequency can exhibit a complicated behavior. This frequency dependence generally has a high degree of sensitivity to the structure of the seabed physical properties. For this reason, the current study employs a large number of frequencies in a low-frequency band (75–500 Hz) in the inversion calculation. Knobles and Koch previously presented an inversion of broadband impulsive data using a normal mode approach.⁵ Their inversion approach, however, was based on physical intuition, as opposed to an automated optimization approach. Another important aspect of the current work is that the optimization does not depend on *a priori* information in the sense that the parameters are allowed to vary over the full range of physically possible values. Previously reported inversion studies invoked *a priori* information about the seabed to limit the size of the inverse problem. A risk in the latter approach is that the *a priori* information may be in error. On the other hand, it makes sense to constrain the search to parameter ranges that are self-consistent, e.g., low densities and attenuations for low-speed sediments. Finally, the research attempts to comprehend how environmental uncertainties, such as those in the SSP, can affect uncertainties in the inverted seabed parameters.

II. EXPERIMENT

A. General description of SWAMI

An experimental device was constructed to make low-frequency acoustic measurements in shallow water environments. The shallow water acoustic measurement instrument (SWAMI) consists of a bottom-mounted instrumentation package (IP), a temporary command telemetry buoy, and an acoustic array. SWAMI is well suited for making basic acoustic measurements for propagation analysis. Figure 1 is an illustration of the SWAMI system. In the experiment dis-

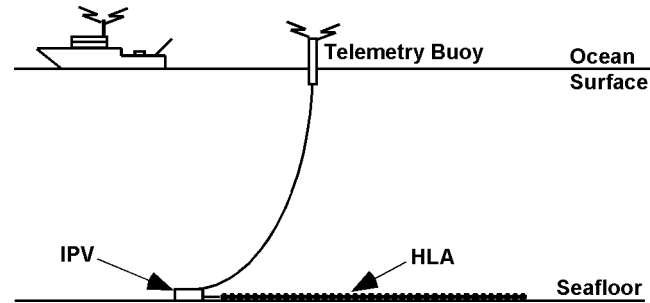


FIG. 1. Deployment of shallow water acoustic measurement instrument (SWAMI) in HLA configuration.

cussed in this paper, the SWAMI array was an unequally spaced 52-element HLA about 530 m in length. The IP contains an instrumentation pressure vessel (IPV) and two battery packs. After deployment, the command telemetry buoy provides a temporary link to the IP that allows the verification of array geometry, confirmation of electronics functionality, and modification of recorder parameters. After completing the initial deployment testing, an acoustic release disconnects the command telemetry buoy, and the umbilical is submerged with an anchor.

The SWAMI recording system consists of 52 data channels in a 1 kHz bandwidth. The phase tracking is ± 2 degrees from 0 to 700 Hz. The recorder dynamic range is 72 dB in 12 bits and can be placed anywhere within approximately 110 dB of available dynamic range by adjusting the input and A/D gains of the system. SWAMI can record for six days cumulative for a total storage capacity of 288 Gbytes. The hydrophones on the HLA have a dual sensitivity of -168 or -222 dB *re*: 1 V/ μ Pa. The maximum signal pressure level that can be recorded is $+168$ or $+222$ dB *re*: 1 μ Pa. The frequency response of the hydrophones is approximately flat

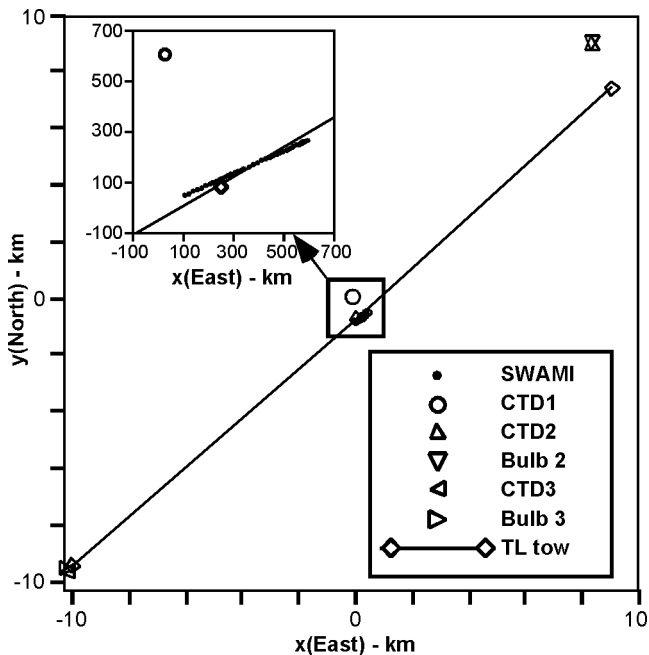


FIG. 2. Location of sources, receivers, and CTD measurements.

with a ± 1 -dB variation from 5 Hz to 2 kHz. The IP weight is about 900 kg and its volume is $1.7 \times 2.1 \times 1 \text{ m}^3$.

B. General description of experiment and acoustic measurements

During 23–26 February 1998, a SWAMI experiment was conducted in the Gulf of Mexico about 50 miles south of Port Aransas, TX. The location of the GPS antenna on the ship at the time SWAMI was deployed on the seabed was $27^\circ 31.96' \text{ N}$, $96^\circ 15.19' \text{ W}$. A corrected position of the SWAMI array was calculated on the basis of ship geometry, water depth, and the estimated shape of the deployment cable.

The experiment was designed to address the question of what acoustic data are required to perform a successful inversion to seabed parameters. The portion of the experiment analyzed in this paper is illustrated in Fig. 2. The SWAMI HLA was deployed along the 110 m bathymetric contour. Hydrophone 52 of the array is at a bearing of 66° true North relative to hydrophone 1 of the array and the IP. Environmental measurements included CTD and high-frequency sonar water depth measurements along acoustic transmission paths. In addition, differential GPS measurements allowed for precise localization of the receiver and sources. Acoustic measurements included signals received from light bulb implosions approximately positioned on both array endfires and from a J-15-1 multiple tonal source towed on a 10-km radial from the HLA. The water depth along the J-15-1 tow was approximately constant. A CTD measurement was made about 500 m from the HLA just after deployment. Also, CTD measurements were made near the positions of the light bulb implosions. In the subsequent discussions, the SWAMI location is Station 1 and the positions of the light bulb deployments are Stations 2 and 3. Station 2 is about 10.5 km to the northeast of Station 1, whereas Station 3 is about 11.1 km to the southwest of Station 1. The TL measurements in this analysis are obtained from an approximately straight-line J-15-1 tow about 5 degrees off the array endfire between Stations 2 and 1. Unfortunately, planned short-range light bulb deployments and additional CTD measurements were eliminated from the measurements because of the rapid approach of a storm.

Figures 3(a) and (b) show received time series of the light bulb implosion at Station 2 for hydrophone 52 and at Station 3 for hydrophone 1, respectively. The data sampling rate employed by SWAMI was 2457.6 Hz. The source depth was 30 m for both light bulb implosions. The time series at Station 2 is from the 75–500-Hz band, whereas the time series at Station 3 is from the 250–500-Hz band. The filtering eliminated noise from two seismic sources. Unfortunately, the noise was significant up to about 250 Hz in the time series generated by the Station 3 light bulb deployment. For the time series in Fig. 3(a), one observes a continuous set of arrivals with a total duration of about 200 ms. A similar signal duration is observed in the time series in Fig. 3(b). For both cases noise is still present in the selected bands, most likely because of reverberation from the two seismic sources. Figure 4 shows the source time series of the light bulb implosion at Station 2 on a monitoring hydrophone. One ob-

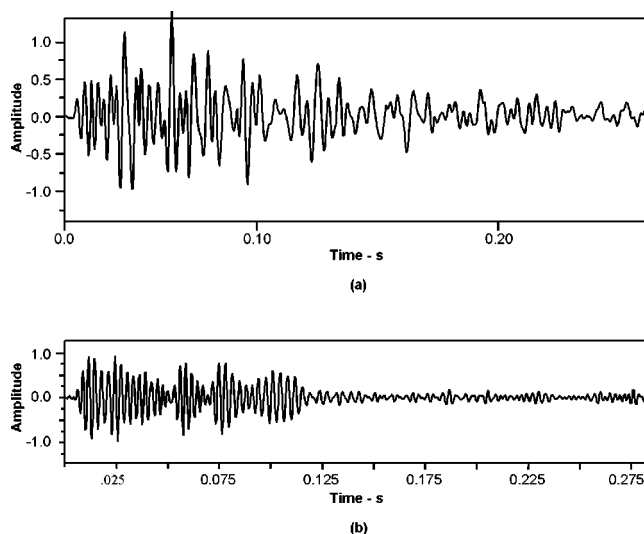


FIG. 3. (a) Measured time series generated by light bulb implosion at Station 2 approximately 10 km from HLA. Source depth is 30 m and the frequency band is 75–500 Hz. (b) Measured time series generated by light bulb implosion at Station 3 approximately 11 km from HLA. Source depth is 30 and the frequency band is 250–500 Hz.

serves the initial negative pressure pulse, the standard signature of an implosion, followed by about seven bubble pulses. It is of interest to note that the peak pressure is positive in the first bubble pulse. Light bulbs are an excellent acoustic source because of their wideband spectrum, consistency, and ease of deployment. The energy source level (ESL), which is the time integral of the intensity of the waveform is about $162.8 \text{ dB re: } 1 (\mu \text{ Pa})^2 \cdot \text{s} @ 1 \text{ m}$. The small ESL results partly from the signal's short 15-ms duration. A nearly identical source waveform was recorded at Station 3.

Figure 5 shows the measured TL at 53, 103, 153, and 503 Hz over a track that is almost identical to the propagation path between the light bulb position at Station 2 and the SWAMI array. The source depth for the tonal data was about 29.5 m. The TL measurements were initiated just after the light bulb deployment and CTD measurements at Station 2.

C. Existing and supporting data

The experimental site was chosen for several reasons, including accessibility, the temporal stability of the water

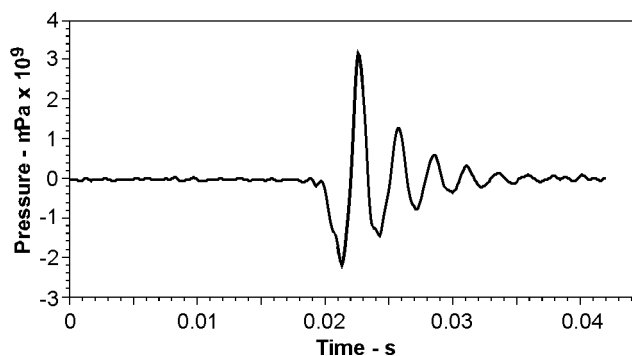


FIG. 4. Measured light bulb source waveform deployed at Station 2 in 75–500-Hz band. Source depth is 30 m.

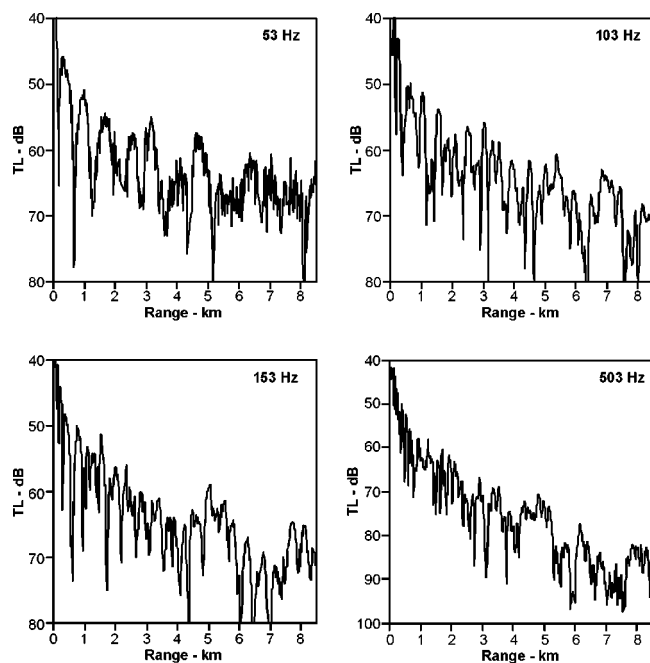


FIG. 5. Measured transmission loss at 53, 103, 153, and 503 Hz over a 10-km interval at an approximately constant water depth of 110 m. Depth of J-15-1 source is about 29.5 m.

column, small bathymetric slopes, and the prior geophysical measurements in the area.⁶ Further, the location is within a site where several acoustic measurements and seabed inversions previously have been reported.^{7–9} A specific seismic cross section about 17 km to the northeast from SWAMI was reported in Ref. 6, and showed approximately five sediment layers over the first 100 m of sediment. The top layer, deposited during the Holocene, has an average composition of clay and silt. A difference of the current experimental location from the site examined in Refs. 7–9 (commonly referred to as the GEMINI site) is that the late Wisconsin sediment layers are known to consist of sandlike sediments near the GEMINI site, whereas Berryhill reports that near the SWAMI location the late Wisconsin layers do not exhibit evidence of significant sand contributions.⁶ Another interesting aspect of the GEMINI site is that, in addition to the inversion conducted by Lynch *et al.*,⁸ an additional inversion was conducted by Collins, Kuperman, and Schmidt⁹ in one of the first tests of the simulated annealing approach for geoacoustic inversion.

Figure 6 shows the SSP derived from the CTD Measurements made at Stations 1–3. The CTD measurements at Stations 1 and 2 are separated by about 4 h, 13 min and by 10.56 km. The CTD measurements at Stations 1 and 3 are separated by about 8 h, 17 min and by 11.1 km. CTD measurements were terminated about 5 m above the seafloor to avoid damage to the CTD apparatus. The SSPs in Fig. 6 were extrapolated as isospeed to the seafloor from the terminal CTD depth based on a suggestion that the sound speed is constant near the bottom due to mixing by bottom currents.¹⁰ The three CTD measurements exhibit several features in qualitative agreement. An isospeed layer is present down to about 30 m, and from 30–50 m there is a small (2 m/s)

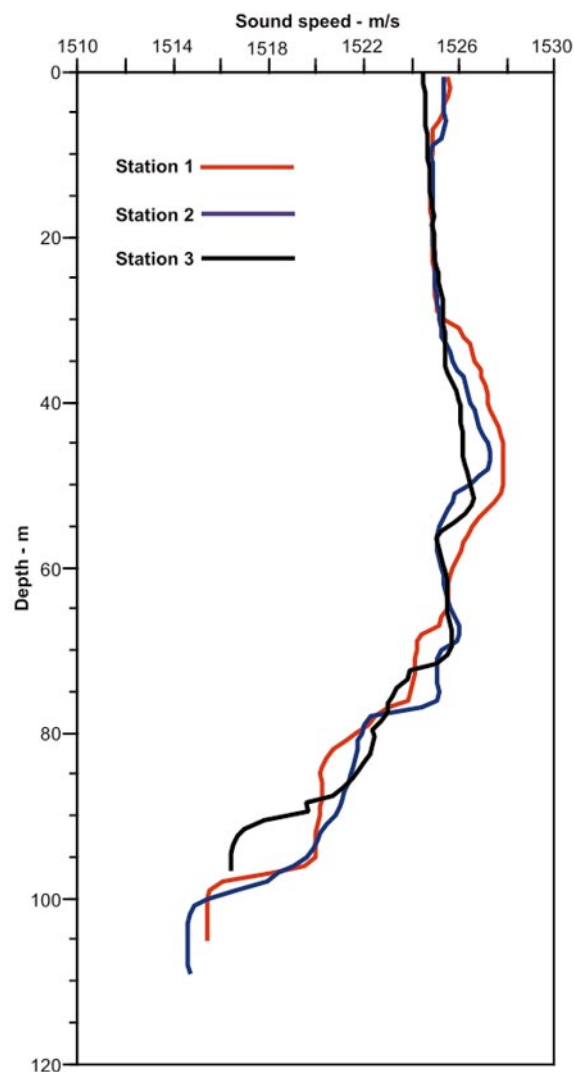


FIG. 6. Sound speed profiles derived from CTD measurements taken at Stations 1–3.

increase in the sound speed, followed by a thermocline to about 100 m. However, there are notable quantitative differences on the order of 1–2 m/s above 10 m and below about 30 m. The lower sound speed values at Station 3 over the first 10-m result from an early morning measurement after overnight surface cooling. Though the differences are small, there may result important perturbations in the geoacoustic parameters from inversions with the three SSPs. For example, a preliminary analysis comparing measured TL with modeled predictions from the SSPs measured at Stations 1 and 2 showed significant variations in the interference patterns, and these variations increased with increasing frequency and range. Thus, errors in the geoacoustic parameters may be expected when inversions from high frequency or long range data are performed with a SSP that is only approximate.

Figure 7 illustrates the measured bathymetry from Station 3 to Station 2 and the details along the HLA at Station 1. Near hydrophone 1 the water depth is approximately 109.5 m. The water depth increases to about 112 m of hydrophone 30 which is approximately 430 m from hydrophone 1. After

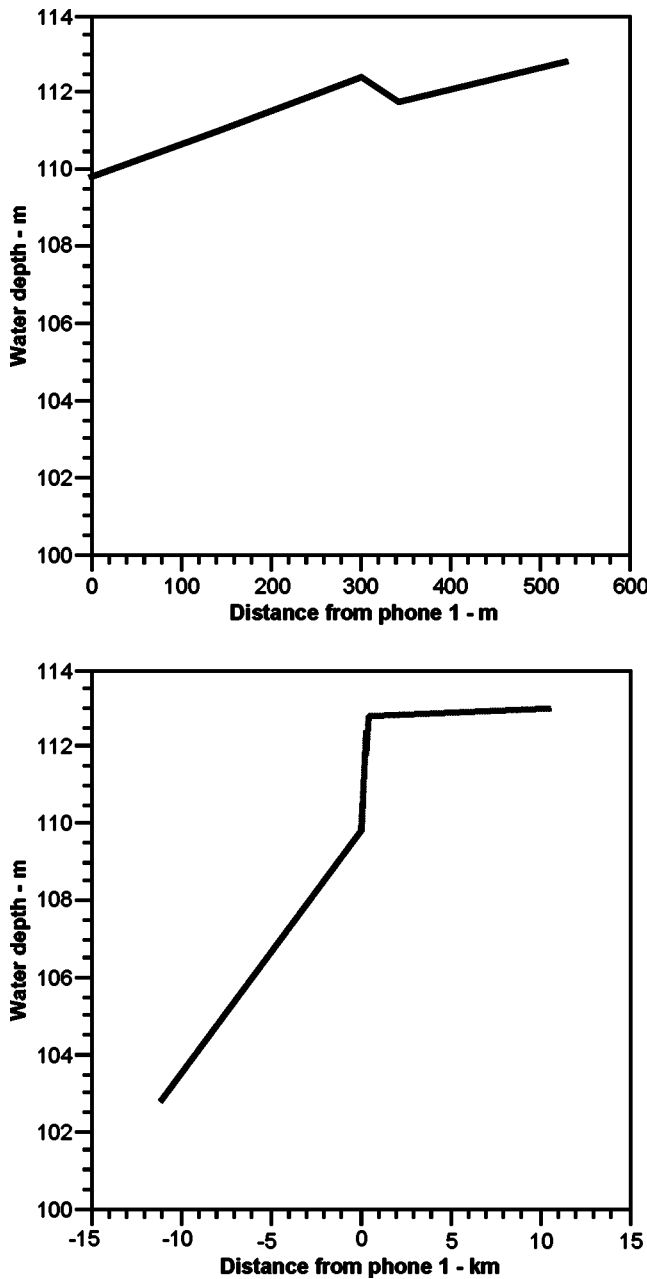


FIG. 7. Measured bathymetry over acoustic paths and HLA.

hydrophone 30, the water depth stays approximately constant. Thus, sound propagation from the light bulb position at Station 2 to hydrophones 30–52 approximately represents propagation over a flat bottom. The water depth decreased to about 102.8 m over an approximately constant slope between Station 1 and the light bulb position at Station 3.

III. INVERSION METHODOLOGY

We now describe several aspects of the broadband inversion methodology. Specifically, we discuss the selection of the forward acoustic model, the cost functions, the seabed representation, and the optimization approach.

The forward model for the propagation of sound in the ocean waveguide is the normal mode algorithm, ORCA, re-

ported by Westwood *et al.*⁴ A normal mode approach is well suited for the inversion problem in horizontal stratified environments when the predicted received pressure on an array of hydrophones is required at multiple frequencies. In general, ORCA has the capability to solve the normal mode eigenvalue problem in the complex plane. This general approach treats the modal attenuation in an exact manner, and the leaky modes give an approximate representation to the modal continuum. The full complex wavenumber solution, however, is computationally intensive. Further, for each seabed solution, one generally needs to carefully examine the horizontal wavenumber spectrum to verify its accuracy, because the complex eigenvalue search is not completely robust at some specific frequencies and sets of seabed parameters. In a typical application of a modern optimization approach to geoacoustic inversion, it is not uncommon for the number of forward calls to be on the order of 10^5 . An option was selected within ORCA to solve the eigenvalue problem on the real axis and then employ standard perturbation theory to estimate the imaginary part of the horizontal wavenumber eigenvalue that accounts for sediment attenuation. The real axis approximation also neglects continuum contributions associated with the final layer, usually assumed to be a homogeneous half-space. The real axis approximation can be one to two orders of magnitude faster than the full complex plane calculation. An argument can be made that the real axis approximation is reasonable for the problem at hand. First, the forward model computes the broadband field at a source-receiver range on the order of 100 water depths. Clearly, the continuum part of the acoustic field can be safely neglected. Second, if we allow our argument to be influenced by the *a priori* knowledge that at least the first 20 m of sediment has a soft low-loss character like that of a clayey silt, one can anticipate that the perturbative form of the modal attenuation will be reasonably good in the proximity of the true or global solution for the geoacoustic profile.

Two cost functions were considered in this analysis. The first cost function is a peak cross correlation of measured and modeled time series averaged over the individual hydrophones of the array:

$$E = 1 - \tilde{C}, \quad (3.1)$$

$$\tilde{C} = \frac{1}{N} \sum_i^N \left| \sum_j^K M_i(\omega_j, \mathbf{X}) D_i^*(\omega_j) \exp(i\omega_j \tau_{p_i}) \right|. \quad (3.2)$$

In Eq. (3.2), M_i and D_i are the modeled and measured complex pressures at the i th receiver, respectively, and $*$ represents complex conjugation. The modeled pressure is the product of the simulated response function and the measured source spectrum. The modeled pressure is a function of the solution vector \mathbf{X} , to be estimated with an inversion method such as simulated annealing. The product of the model and data are summed coherently over a total of K frequencies, where $\omega_j = 2\pi f_j$. The cross correlation is averaged over N hydrophones, where τ_{p_i} represents the time delay for the i th hydrophone that gives a peak in the cross correlation. Thus,

the cost function is an incoherent sum over hydrophones and a coherent sum over frequency. The second cost function considered in this work has the form of a coherent sum over frequency and a coherent sum over the product of model and data cross-spectral pairs,

$$E = 1 - \tilde{C}(\mathbf{X}), \quad (3.3)$$

where $C(\mathbf{X})$ is the correlation between data and model cross-spectra for the set of environmental parameters \mathbf{X} so that

$$\tilde{C}(\mathbf{X}) = \frac{1}{N} \left| \sum_f \sum_{i \neq j} \sum_j R_{ij}(f) M_i^*(f, \mathbf{X}) M_j(f, \mathbf{X}) \right|, \quad (3.4)$$

and N is the normalization that gives $-1 \leq C \leq 1$. $R_{ij}(f)$ is the normalized cross-spectrum of the measured signals on the i th and j th hydrophones at frequency f . The normalized data cross spectra are

$$R_{ij}(f) = D_i(f) D_j^*(f), \quad (3.5)$$

where $D_i(f)$ is normalized so that

$$\sqrt{\sum_i \sum_f |D_i(f)|^2} = 1. \quad (3.6)$$

The normalized modeled field $M_i(f, \mathbf{X})$ is propagated from the source to the i th hydrophone at frequency f for the environment \mathbf{X} . The modeled fields are normalized so that

$$\sqrt{\sum_i \sum_f |M_i(f, \mathbf{X})|^2} = 1. \quad (3.7)$$

Clearly Eq. (3.5) shows that knowledge of the details of the phase of the source function is not required. The fully coherent (over both space and frequency) matched-field processing correlation function in Eq. (3.4) was introduced by Westwood¹¹ in a broadband matched-field analysis for a deep-water waveguide and by Knobles and Mitchell¹² for a shallow water waveguide. It is important to note that the diagonal elements in Eq. (3.4) are not included in the coherent sum over hydrophone pairs. There are two reasons for the exclusion of the diagonal terms. First, the exclusion increases the coherence gain of the signal relative to assumed incoherent noise. Second, the exclusion reduces the severity of the side lobes in the ambiguity patterns of the cost function. In the absence of noise, both cost functions should lead to identical solutions.

The selection of a seabed representation requires careful consideration for a specific geoacoustic inverse problem. This selection should reflect an attempt to include with minimal complexity the important physical mechanisms of the acoustic interaction with the seabed. In this analysis the seabed is assumed to consist of fluid layers. This assumption is consistent with the choice of the real axis approximation in

ORCA, since the inclusion of shear effects in the normal mode approach requires the solution of the complex eigenvalue problem. While shear wave mechanisms become important for thin sediments over such materials as chalk or sandstone, there is no geophysical evidence here of such a seabed structure. It is further assumed that each sediment layer can be described by six parameters: the surface compressional sound speed and attenuation, the sediment layer thickness, a constant density, and constant gradients for the sound speed and attenuation. The neglect of a density gradient is consistent with the study by Rutherford and Hawker on the effect of density gradients on the bottom plane wave reflection coefficient.¹³ A seismic cross section measured about 17 km from SWAMI suggests that a realistic seabed representation would be six sediment layers over a homogeneous half-space.⁶ Such a representation would require 39 parameters. The sparse acoustic data considered in this analysis is insufficient for the unique determination of a seven-layer representation. Further, it is well known that the unique determination of specific parameters becomes more difficult as the number of parameters increase. A reasonable compromise was selected that considered a seabed with two sediment layers over a homogeneous basement. Such a representation allows for reflection and transmission at the three interfaces and refraction within the two sediment layers.

On the basis of experience gained using a Levenberg–Marquardt approach¹⁴ to perform geoacoustic inversion for simulated data, a simulated annealing method was selected as the optimization approach.^{15–18} The specific annealing approach used in this study is that reported by Goffe *et al.*¹⁶ Past experience demonstrated that success with a Levenberg–Marquardt approach requires a combination of grid search and multiple random starting positions to counteract the tendency for the solution to become entrapped in local minima. Directed Monte Carlo searches such as simulated annealing and the genetic algorithm are useful alternatives to troublesome local methods. Simulated annealing is a global optimization method that has the ability to find a global minimum within a multidimensional space containing numerous suboptimum minima. The employment of a simulated annealing method for the inversion of seabed parameters from low-frequency acoustic data is a fairly well-established method in the ocean acoustics community.^{9,17,18} Numerous tests were made with the Goffe algorithm, including the application to benchmark geoacoustic simulated data sets.¹⁴ A key aspect of this annealing approach is that, as the temperature decreases, the size of the random perturbation of a parameter is decreased by maintaining the number of accepted perturbations at 50%. This approach is to be compared to that employed by Fallat and Dosso.¹⁸

IV. APPLICATION TO EXPERIMENTAL DATA

Qualitatively, there is a fairly well-established geophysical description of the specific location where the acoustic measurements were made, but precise “ground truth” information does not exist, on parameters such as sound speeds and densities. At most, the existing geophysical information gives upper and lower bounds for certain geoacoustic param-

TABLE I. First sediment layer geoacoustic parameters and water depth with average peak cross-correlation cost function using data generated from a light bulb in 75–500-Hz band at Station 2.

	SSP at Station 2	SSP at Station 1	
	EA ₁	EA ₂	EA _{2m}
Water depth (m)	112.5	109.1	109.1
Top sound speed (m/s)	1472.4	1486.3	1476.3
Sound speed gradient (1/s)	2.21	1.54	1.74
Density (g/cm ³)	1.525	1.91	1.51
Top attenuation (dB/m-kHz)	0.017	0.013	0.01
Bottom attenuation (dB/m-kHz)	0.035	0.04	0.037
Thickness (m)	60.3	69.6	69.6
Cost function	0.33	0.39	0.51

eters. For example, one should expect the ratio of the top sediment to bottom water sound speed to have an upper limit near or below unity. The density should have an upper limit of about 1.6 g/cm³. The seismic profiles indicate a lower limit of about 20 m for the sediment thickness of the first layer. However, if Ref. 6 is correct, that the Wisconsin layers below the Holecene layer do not contain significant amounts of sand, the effective lower limit for a sediment thickness of the first layer may be greater than 20 m. It is significantly more difficult to establish upper and lower limits for the sound speed gradient and attenuation. Under these circumstances one must adopt another measure to establish the validity of an inversion. The basic scientific approach adopted in this analysis was to first make individual inversion calculations using selected combinations of the received time series from the light bulb implusions at Stations 1 and 3, the CTD measurements at the three stations, and the two cost functions in Eqs. (3.2) and (3.4). Assumed to be important for the analysis was comprehending how observed differences in the water column sound speed structure affected the seabed parameter estimates obtained from the optimization. From the separate geoacoustic solutions modeled TL is generated to be compared to the measured TL versus range of Fig. 5. Both the TL and time series comparisons aid in selecting a geoacoustic representation, along with parameter

uncertainties, that most closely represents the actual geoacoustic structure. We may think of this type of analysis as a self-consistent approach to inversion. Comparing these results to the geophysical description⁶ and the previous inversions at the GEMINI location^{7–9} further aids in judging the consistency of the results.

The geoacoustic parameters that the analysis attempted to extract from the experimental data were described in the previous section. With the inclusion of water depth as a parameter, the problem becomes 16-dimensional. However, an initial analysis indicated that it was reasonable to hold the basement parameters fixed at the nominal values of $C_B = 2000$ m/s, $p_B = 2.2$ g/cm³, and $\alpha_B = 0.1$ dB/m/kHz, thus further reducing the dimension of the problem to 13. Although the previous inversions and geophysical descriptions indicated a soft first sediment layer, this *a priori* information was not considered in the inversion. Parameters were generally allowed to vary within the bounds as described by Hamilton.¹⁹ The permitted range of the sound speeds at the top of each sediment layer is 1450–1750 m/s. The permitted range of the sediment density in each layer was 1.2–2.0 g/cm³. The permitted range of the attenuations at the top of each sediment layer was 0.005–0.30 dB/m/kHz. The permitted range of the sound speed and attenuation gradients in each layer were 0.7–3.0 s^{−1} and 0.0001–0.05 dB/m²/kHz, respectively. The permitted range of the sediment thickness of each sediment layer was 5–100 m.

A. Station 2 light bulb inversions and transmission loss comparisons

The bathymetry between hydrophones 30–52 and Station 2 is approximately flat. Thus the analysis became focused on an inversion of the Station 2 light bulb data measured on hydrophones 30–52. The experimental analysis using the combination of the cost function in Eq. (3.2) and the SSP measured at Station 2 will be referred to as EA₁. Likewise we will refer to the analysis with the combination of the SSP measured at Station 1 and the cost function in Eq. (3.2) as EA₂. Also, EA₃ and EA₄ refer to the analysis with

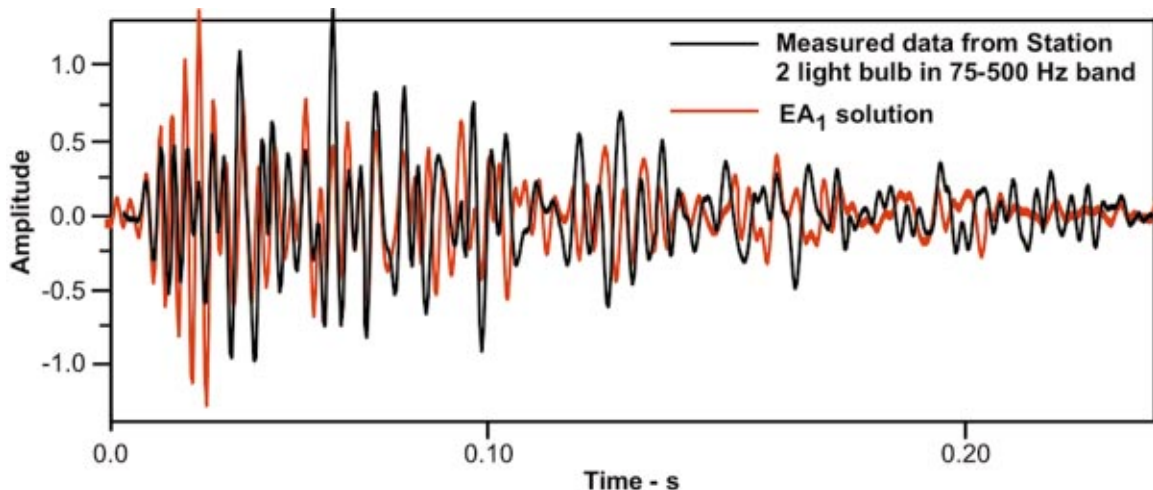


FIG. 8. Comparison of measured time series generated from Station 2 light bulb deployment with time series modeled using the EA₁ geoacoustic solution. Source depth is 30 m and bandwidth is 75–500 Hz.

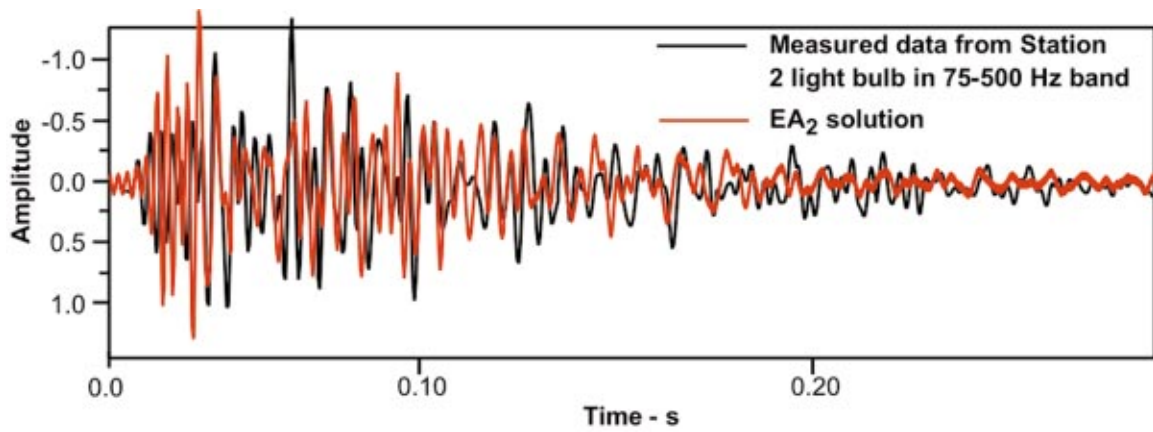


FIG. 9. Comparison of measured time series generated from Station 2 light bulb deployment with time series modeled using the EA₂ geoacoustic solution. Source depth is 30 m and bandwidth is 75–500 Hz.

the cost function in Eq. (3.4) with the SSP measured at Stations 2 and 1, respectively. The permitted range of the water depth was 109–114 m.

Though ORCA is efficient, it was still impractical for the 13-dimensional problem to allow the simulated annealing ap-

proach described above to converge to a degree where the parameter perturbations had become sufficiently small. An approximation was introduced that attempted to decouple the parameter space into two subspaces. One subspace contained the parameters in the first sediment layer plus the water

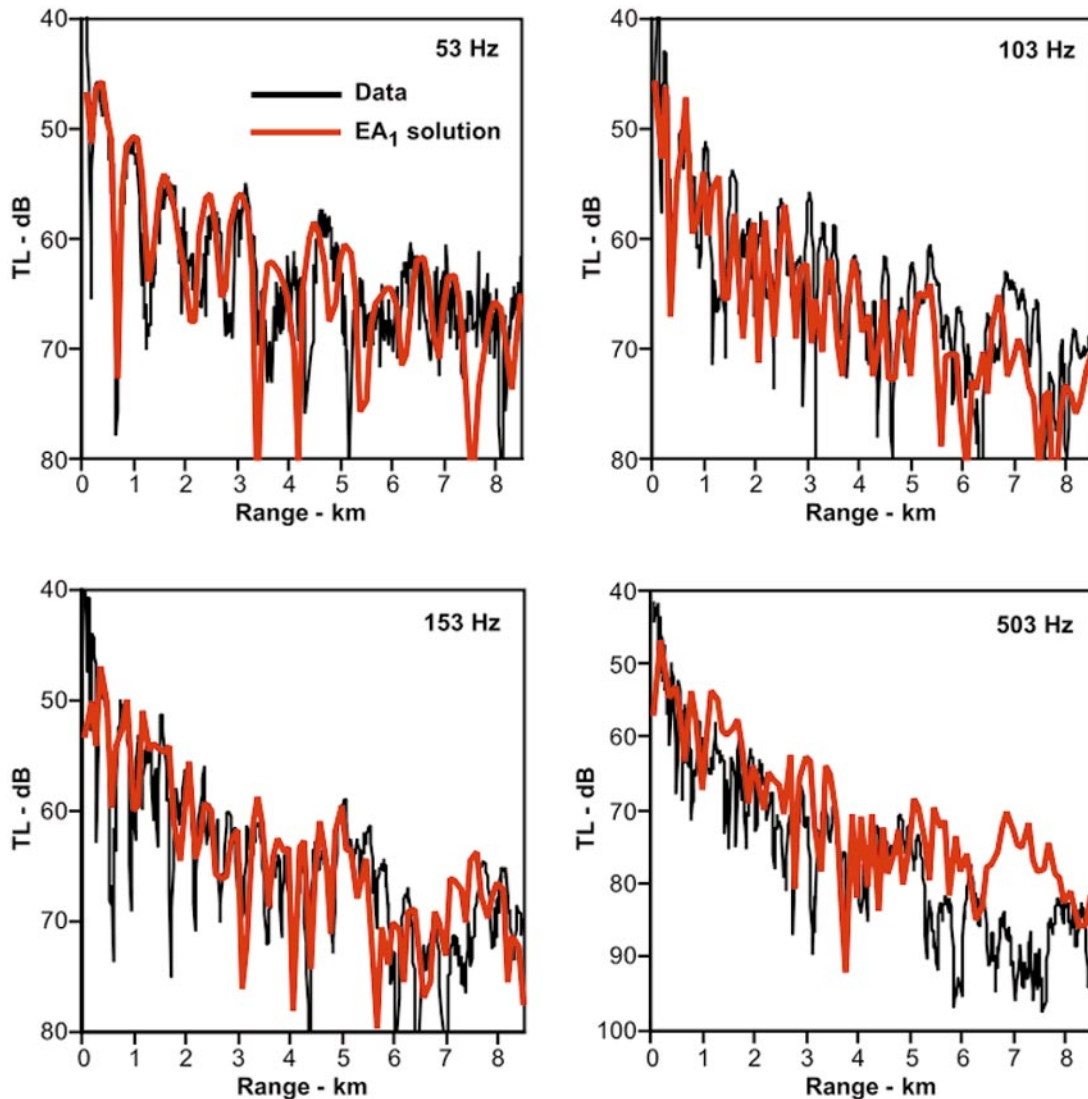


FIG. 10. Comparison of measured transmission loss with transmission loss modeled using the EA₁ geoacoustic solution. Source depth is 29.5 m.

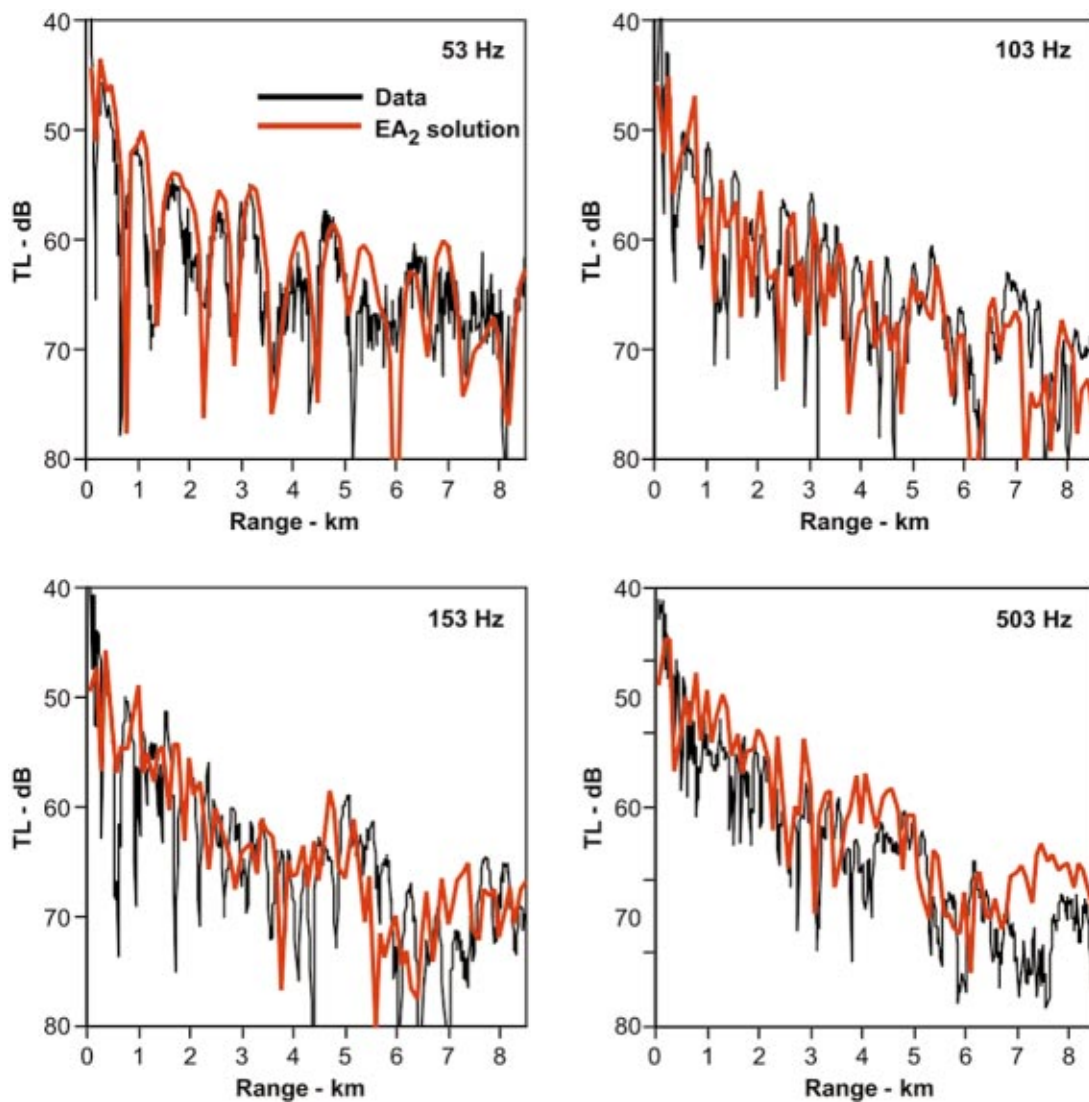


FIG. 11. Comparison of measured transmission loss with transmission loss modeled using the EA₂ geoacoustic solution. Source depth is 29.5 m.

depth, and the second subspace contained the parameters in the second sediment layer. The idea was first to hold the parameters in the second subspace at nominal values within the permitted search space, and to perform an inversion for the parameters in the first subspace in the 75–500-Hz band. The second step was to hold the parameters in the first

subspace fixed and then perform an inversion for the parameters in the second subspace in the 75–200-Hz band. In principle, this process would converge if the two spaces were adequately decoupled or if the acoustic field were insensitive to the second subspace parameters. We found the latter to be true.

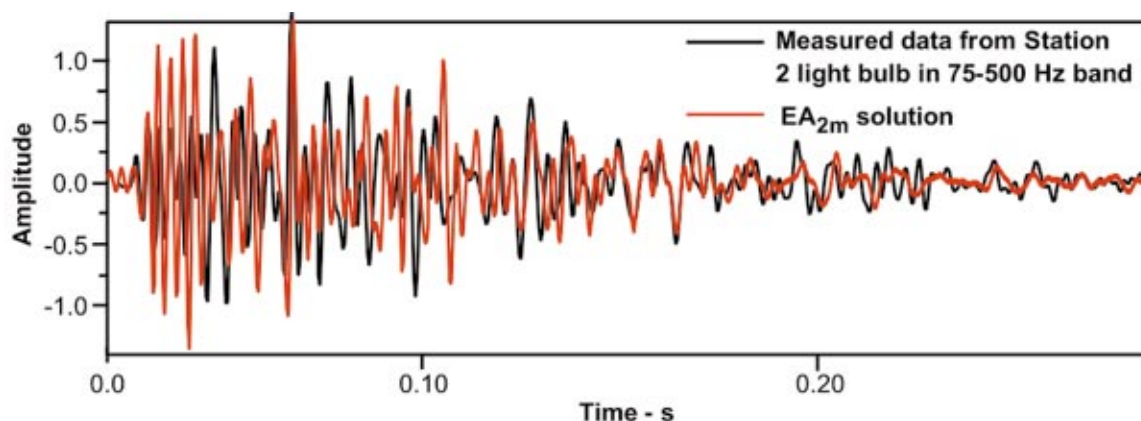


FIG. 12. Comparison of measured time series generated from Station 2 light bulb deployment with time series model using the EA_{2m} geoacoustic solution. Source depth is 30 m and bandwidth is 75–500 Hz.

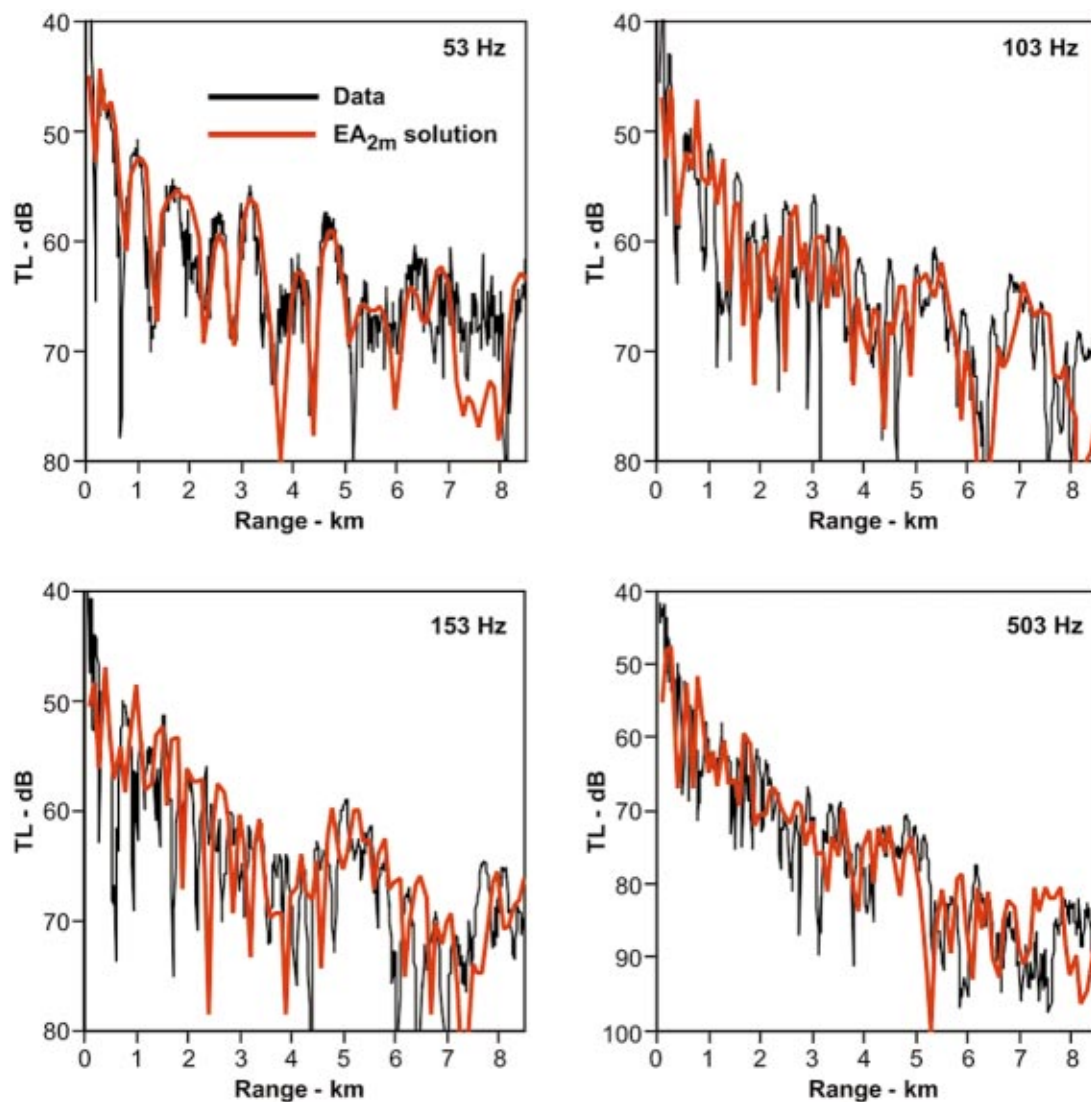


FIG. 13. Comparison of measured transmission loss with transmission loss modeled using the EA_{2m} geoacoustic solution. Source depth is 29.5 m.

For each individual inversion, the starting temperature of the simulated annealing algorithm was fixed in such a manner that approximately 5% of the uphill moves were initially rejected. The temperature was decreased by multiplying the previous temperature by a reduction factor less than unity. The reduction factor was set to 0.90 after examination of several test cases using simulated data. For each parameter change, the complex frequency response is computed and convolved with the measured source waveform shown in Fig. 4. One hundred perturbations were made for each parameter per temperature. Approximately 100 temperature reductions were made for each EA_n ; $n = 1, 2, 3$, and 4. All calculations were made using a single processor on a SUN 4000 computer. The starting vectors were varied to minimize the possibility that the simulated annealing process would settle into a local minimum instead of the global minimum. The total computation time for each inversion run was excessive, on the order of several weeks for each EA_n . While this approach is clearly not efficient, the focus on the research at this stage was finding the true global minimum for each EA_n .

From the start the inversions indicated a thick (≈ 50 – 70 m) first sediment layer. In a few cases, tests were made to determine if the parameters values assumed for the second layer were influencing this result. The optimization consistently rejected the possibility of a thin soft layer over a harder layer. For example, even though the overall time

TABLE II. First sediment layer geoacoustic parameters and water depth with coherent cross-spectra cost function using data generated from a light bulb in 75–500 Hz band at Station 2.

	SSP at Station 2	SSP at Station 1
	EA_3	EA_4
Water depth (m)	111.59	110.10
Top sound speed (m/s)	1510.8	1504.5
Sound speed gradient (1/s)	1.48	1.92
Density (g/cm^3)	1.50	1.24
Top attenuation (dB/m-kHz)	0.0079	0.011
Bottom attenuation (dB/m-kHz)	0.041	0.041
Thickness (m)	49.21	51.90
Cost function	0.41	0.35

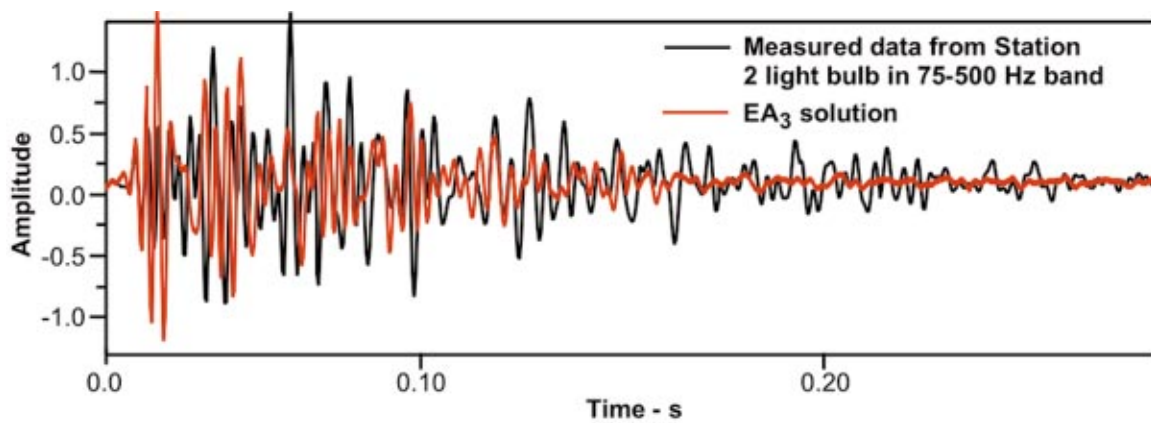


FIG. 14. Comparison of measured time series generated from Station 2 light bulb deployment with time series modeled using the EA₃ geoacoustic solution. Source depth is 30 m and bandwidth is 75–500 Hz.

spread of the impulse response could be reproduced by a hard layer near the water–sediment interface, the details of the arrivals were of a very different nature than those observed in the measured data. Although the simulated annealing was allowed to obtain parameters in the second layer using a subset of the lower frequency band, the sensitivity of the impulse response to changes in the second subspace was very small. It was determined that as a result of the large source–receiver range (≈ 100 water depths) accurate information for the second subspace could not be obtained. The result of the second layer inversions for EA₂ was the following. The ratio of the sound speed at the top of the second layer to the sound speed at the bottom of the first layer was 1.05. The density of the second layer was 1.59 g/cm³. The sediment thickness was 39.3 m and the sound speed gradient was 1.057 s⁻¹. The attenuation at the top of the second layer and the attenuation gradient were 0.3 and 0.034 dB/m/kHz/m, respectively. The parameters of the basement were those previously listed. Again, the numerical values for the second layer lack meaning because of the insensitivity of the sound field to the second layer parameters resulting from the large thickness estimated for the first layer. However, one may expect that for lower frequencies and shorter ranges,

such as those associated with the TL measurements, the details of the second layer may be important.

Presented in Table I are the broadband geoacoustic inversion solutions for EA₁ and EA₂ that utilize the cost function in Eq. (3.2). Both inversions give a description of the seabed as a single low-speed sediment layer with a thickness of 60–70 m. For a bottom water sound speed (C_{bw}) of about 1515.1 m/s, the sound speed ratio, $R = C_1/C_{bw}$, is 0.971 and 0.981 for EA₁ and EA₂, respectively. It is important to remember that the EA₁ and the EA₂ solutions differ only in the small differences in the water column sound speed structure measured at Stations 1 and 2. Thus, assuming that the optimization approach found the true global minimum for each case, one observes that the small 1–2-m/s sound speed differences between the two measured SSPs result in different values for the estimated seabed geoacoustic parameters, especially the density and sound speed gradient.

The EA₁ and EA₂ solutions indicate that refraction within the first layer is an important physical mechanism of the sound field interaction with the seabed. The details of the modal turning points within the sediment are governed by R and the sound speed gradient. Figures 8 and 9 show the comparisons for the measured and modeled time series using

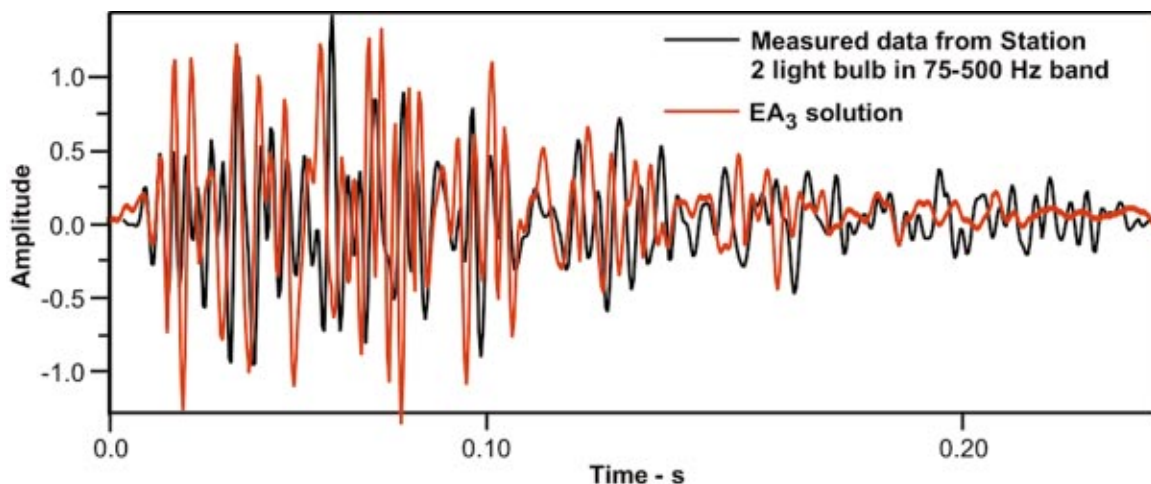


FIG. 15. Comparison of measured time series generated from Station 2 light bulb deployment with time series modeled using the EA₄ geoacoustic solution. Source depth is 30 m and bandwidth is 75–500 Hz.

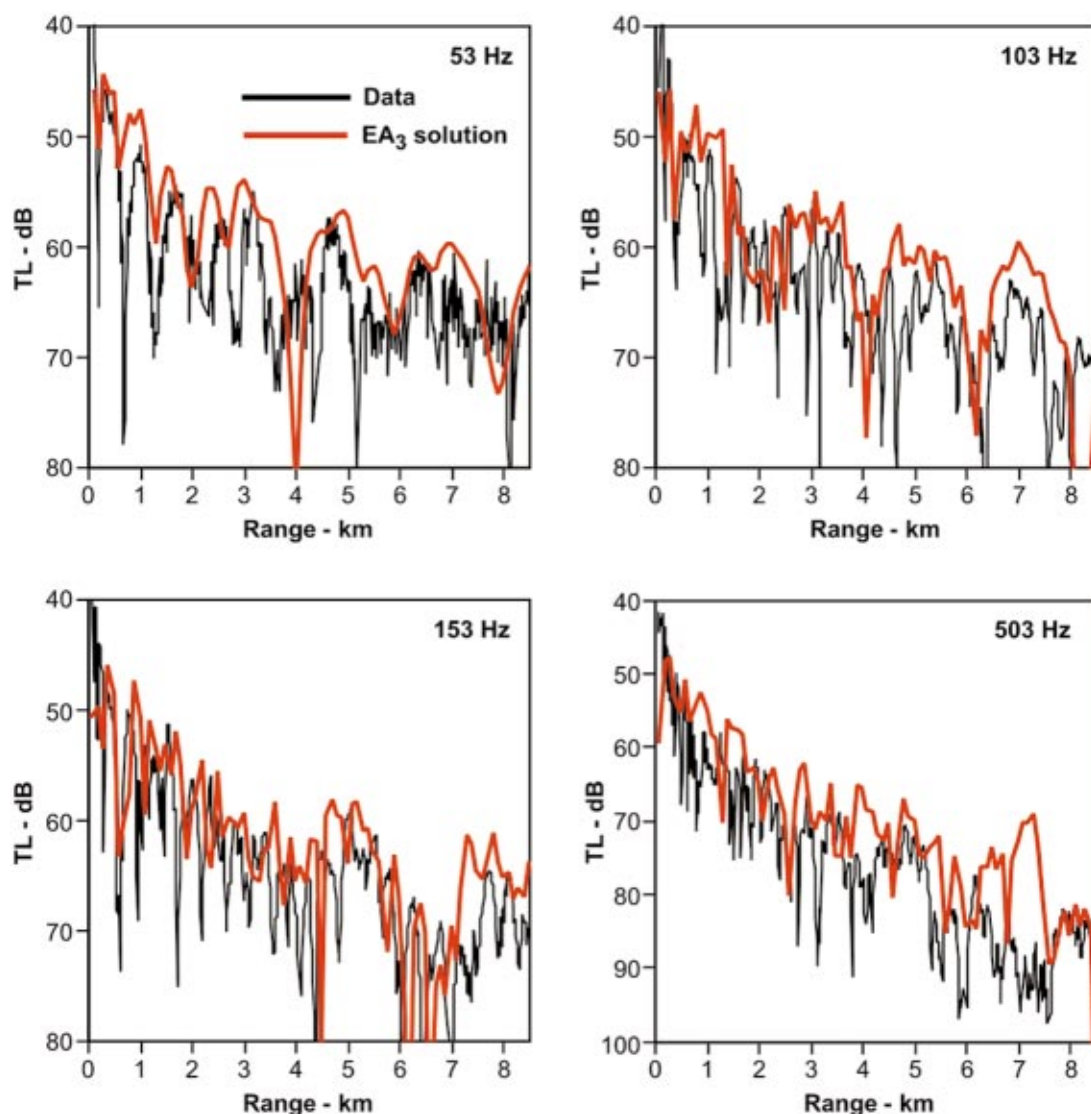


FIG. 16. Comparison of measured transmission loss with transmission loss modeled using the EA₃ geoacoustic solution. Source depth is 29.5 m.

the EA₁ and EA₂ solutions, respectively. Qualitatively, the comparisons are good. The peak cross-correlation value between the measured and modeled time series in the 75–500-Hz band is on the order of 0.7 for both EA₁ and EA₂. Figures 10 and 11 present a comparison of the measured and modeled TL using the EA₁ and EA₂ solutions, respectively. For both EA₁ and EA₂ the level of agreement with the measured data is good. For EA₁, one observes fairly good agreement at 53, 103, and 153 Hz. For 503 Hz the level of agreement is fairly good out to about 5 km where the model begins to underestimate the TL. For EA₂, the agreement at 53 Hz is better than that observed for EA₁. However, for 153 Hz the EA₂ solution does not compare as well to the data as does the EA₁ solution. As in the EA₁ case, the EA₂ solution at 503 Hz underestimates the TL starting at about 5 km. The complex interference pattern in the low-frequency TL as a function of range results from the presence of several low-order modes and is consistent with the large time spread of the impulse response.

While the solution obtained from the EA₂ light bulb in-

version results in reasonably good fits to the TL data, the geoacoustic profile is unphysical in the sense that the density of 1.91 g/cm³ is not consistent with the sediment's low sound speed and low loss structure. This can be expected in an unconstrained inversion, but postprocessing adjustments should be made to obtain a more physical seabed representation for which the modeled and measured broadband and narrow-band responses are still in reasonable agreement. Our approach in this case was first to lower the density to a more physical value of 1.51 g/cm³. This increased the penetration of the sound field into the sediment, thus increasing the loss because of attenuation. The sound speed gradient was then increased slightly and the attenuation lowered in order to decrease the loss resulting from the decrease in the density. Finally, the surface sound speed in the top sediment was lowered slightly to improve the TL fit at the lower frequencies. The resulting geoacoustic representation is listed in Table I as EA_{2m}. Figure 12 shows the comparison of the measured time series and the time series obtained using the EA_{2m} solution. The quality of fit is reasonably good. It ap-

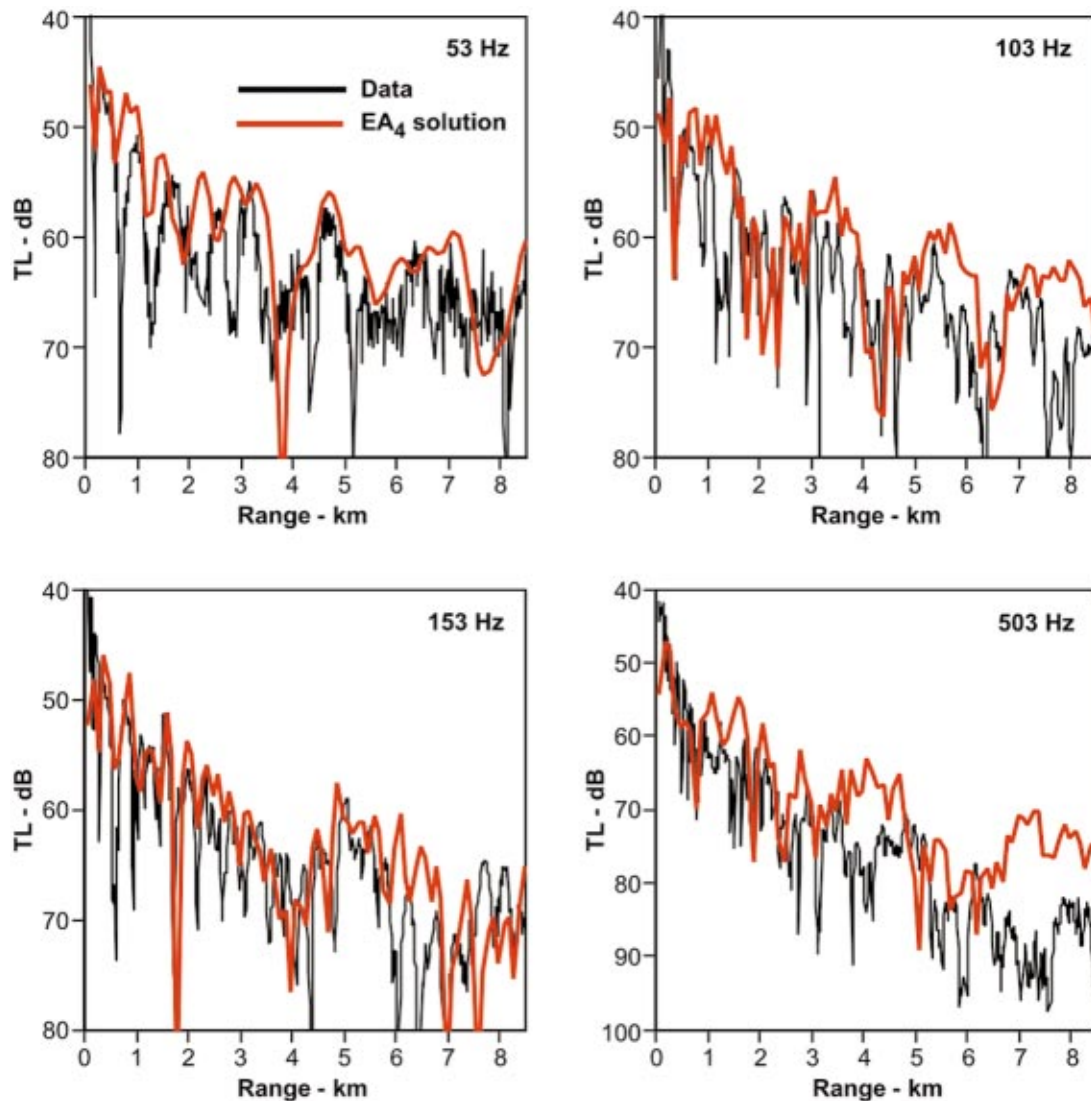


FIG. 17. Comparison of measured transmission loss with transmission loss modeled using the EA₄ geoacoustic solution. Source depth is 29.5 m.

pears that some of the later modeled arrivals give a better fit than those in Figs. 8 and 9. However, the significance of this observation is not clear since the cost function for the EA_{2m} solution is slightly higher as compared to those associated with the EA₁ and EA₂ solutions. Figure 13 presents the comparisons of the measured and modeled TL obtained using the EA_{2m} solution. The TL comparison are at least as good as those presented in Figs. 10 and 11. The TL at 503 Hz for the EA_{2m} solution gives a better fit to the data as compared to

the EA₁ and EA₂ solutions. In many aspects EA_{2m} solution is very similar to the EA₁ solution, the main difference being that the EA₁ solution has a larger sound speed gradient and a higher attenuation.

Presented in Table II are the broadband geoacoustic inversion solutions for EA₃ and EA₄ that utilize the cost function in Eq. (3.4). No attempt was made to optimize the second layer. The second layer parameters were held fixed to the EA₁ and EA₂ values. As in the case of the EA₁ and EA₂

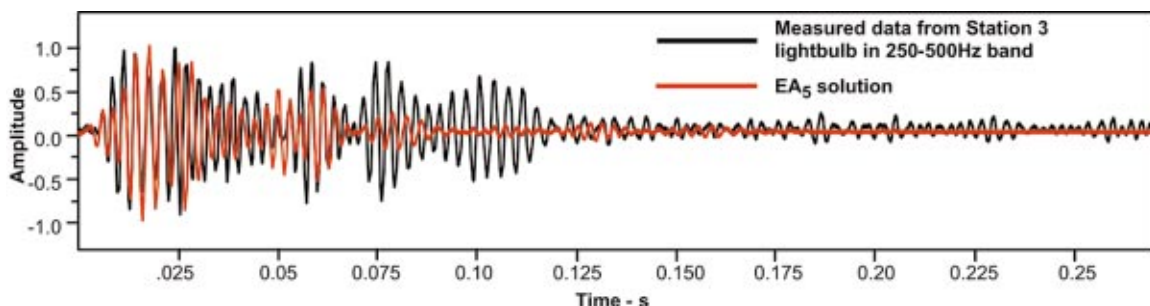


FIG. 18. Comparison of measured time series generated from Station 3 light bulb deployment with time series modeled using the EA₅ geoacoustic solution. Source depth is 30 m and bandwidth is 250–500 Hz.

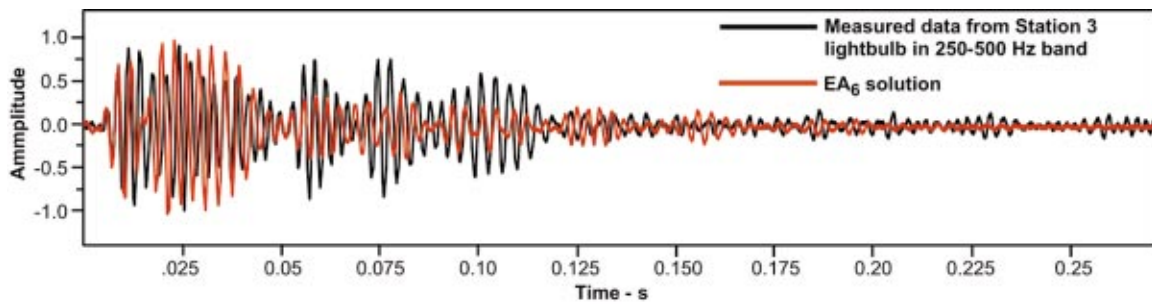


FIG. 19. Comparison of measured time series generated from Station 3 light bulb deployment with time series modeled using the EA₆ geoacoustic solution with a water depth of 106.35 m. Source depth is 30 m and bandwidth is 250–500 Hz.

solutions, the EA₃ and EA₄ solutions describe the seabed as a single soft sediment layer, but slightly thinner. The sound speed ratio is 0.993 and 0.997 for the EA₃ and EA₄ solutions, respectively. While these ratios are still less than unity, they are larger by a significant amount than those in the EA₁, EA₂, and EA_{2m} solutions. As with the EA₁, EA₂, and EA_{2m} solutions the main physical mechanism of the sound field interaction with the seabed is refraction within the first layer. Figures 14 and 15 show the comparisons for the measured time series and the time series modeled using the EA₃ and EA₄ solutions, respectively. Qualitatively, the comparison for the EA₂ solution is good, but not as good as for the EA₁, EA₂, and EA_{2m} solutions. The EA₃ solution gives too short a time spread compared to the measured data. The EA₄ solution gives a time series that compares about as well as those predicted by the EA₁, EA₂, and EA_{2m} solutions. Figures 16 and 17 present a comparison of the measured and modeled TL using the EA₃ and EA₄ solutions. Overall, the TL comparisons are not as good as those associated with the EA₁, EA₂, and EA_{2m} solutions. Specifically, one observes that the EA₃ and EA₄ solutions do not properly predict the details of the interference patterns at the lower frequencies and predict too low a loss at both 103 and 503 Hz past 3 km. As observed for the EA₁ and EA₂ solutions, the differences in the measured SSPs resulted in different estimates for the density and sound speed gradient for the EA₃ and EA₄ solutions. Also, not only can small differences in the assumed SSP lead to differences in the estimated parameters, the details of the assumed cost function can greatly affect the estimated values of the seabed parameters. On the basis of the TL comparisons, the solutions with the lower ratios (EA₁, EA₂, and EA_{2m}) appear to more accurately describe the true seabed geoacoustics as compared to the higher ratio EA₃ and EA₄ solutions.

B. Station 3 light bulb inversions and comparisons to transmission loss

Because of the limitations imposed by the high noise in the 0–250-Hz band and the range dependence of the bathymetry, a more limited analysis of the light bulb event at Station 3 was performed. Specifically, the measured SSP at Station 3 was chosen for an inversion using the two cost functions. EA₅ and EA₆ refer to the inversion solutions obtained using the cost functions in Eqs. (3.2) and (3.4), respectively. Unlike the case where the propagation paths between Station 2 and

hydrophones 30–52 are approximately range independent, the propagation paths from Station 3 to all the receivers are downslope since the water depth at Station 3 is approximately 103 m. Though maximizing the number of hydrophones in the cost function is important, only hydrophones 1–20 were employed, and the water depth was allowed to vary between 102 and 112 m. The hypothesis was that an average water depth would describe the frequency dependence of the acoustic response function to a reasonable degree of accuracy. The SSP at Station 3 was utilized because it more accurately reflected the cooler temperatures in the surface layer at the early morning hour when the Station 3 light bulb measurement was made.

Presented in Table III are the geoacoustic inversion solutions for EA₅ and EA₆. As in the case of the Station 2 inversions, the EA₅ and EA₆ solutions give a description of the seabed as a single thick low-speed sediment layer. The sound speed ratios are 0.998 and 0.978 for the EA₅ and EA₆ solutions, respectively. The difference in these two ratios are similar to the differences in the ratios obtained for the various cases in the Station 2 analyses described in Sec. IV A. Figures 18 and 19 compare measured and modeled time series from station 3 light bulb deployment using the EA₅ and EA₆ geoacoustic solutions, respectively. The time series predicted by the EA₅ solution has too short a duration as compared to the measured data. The time series predicted by the EA₆ solution is in good agreement with the measured data. Figure 20 compares the measured Station 3 time series to a model prediction that uses the geoacoustic profile in EA_{2m} with a water depth of 106.35 m and the SSP at Station 3. Qualitatively, one obtains good agreement. This is encouraging because it demonstrates a consistency check for the

TABLE III. First sediment layer geoacoustic parameters and water depth using acoustic data generated by a light bulb in 250–500-Hz band at Station 3.

	SSP at Station 3	
	EA ₅	EA ₆
Water depth (m)	106.35	102.9
Top sound speed (m/s)	1511.9	1482.2
Sound speed gradient (1/s)	2.62	3.0
Density (g/cm ³)	1.55	1.6
Top attenuation (dB/m-kHz)	0.01	0.0083
Bottom attenuation (dB/m-kHz)	0.072	0.069
Thickness (m)	62.0	51.9
Cost function	0.39	0.35

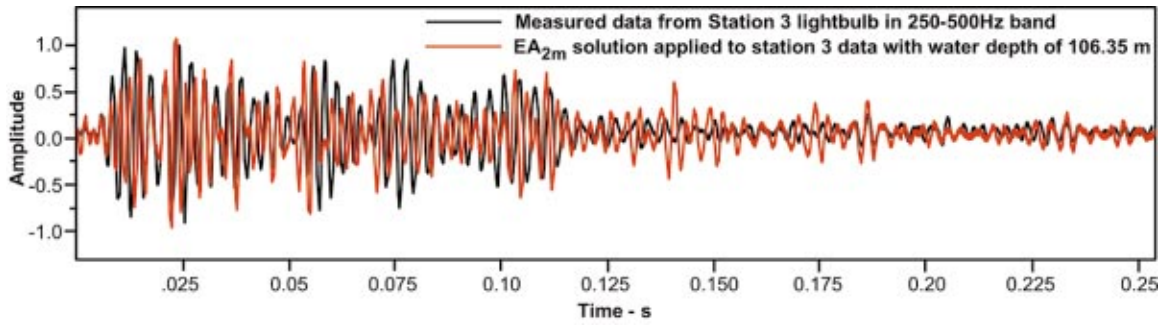


FIG. 20. Comparison of measured time series generated from Station 3 light bulb deployment with time series modeled using the EA_{2m} geoacoustic solution. Source depth is 30 m and bandwidth is 250–500 Hz.

EA_{2m} inversion applied to an independent measurement. Figures 21 and 22 compare the measured TL with that predicted by the EA_5 and EA_6 solutions, respectively. The EA_5 comparisons are not especially good because of the high sound speed ratio. The EA_6 comparisons are significantly better, reflecting the observations made in Sec. IV A with regard to the sound speed ratio at the water sediment-interface.

C. Discussion

On the basis of the six inversions plus the modification of the EA_2 result, EA_1 and EA_{2m} , which are approximately equivalent, appear to give the best fits to the experimental data and are physically consistent. One may argue that they represent the actual seabed more closely than the other solutions. Table IV compares selected parameters in EA_1 and

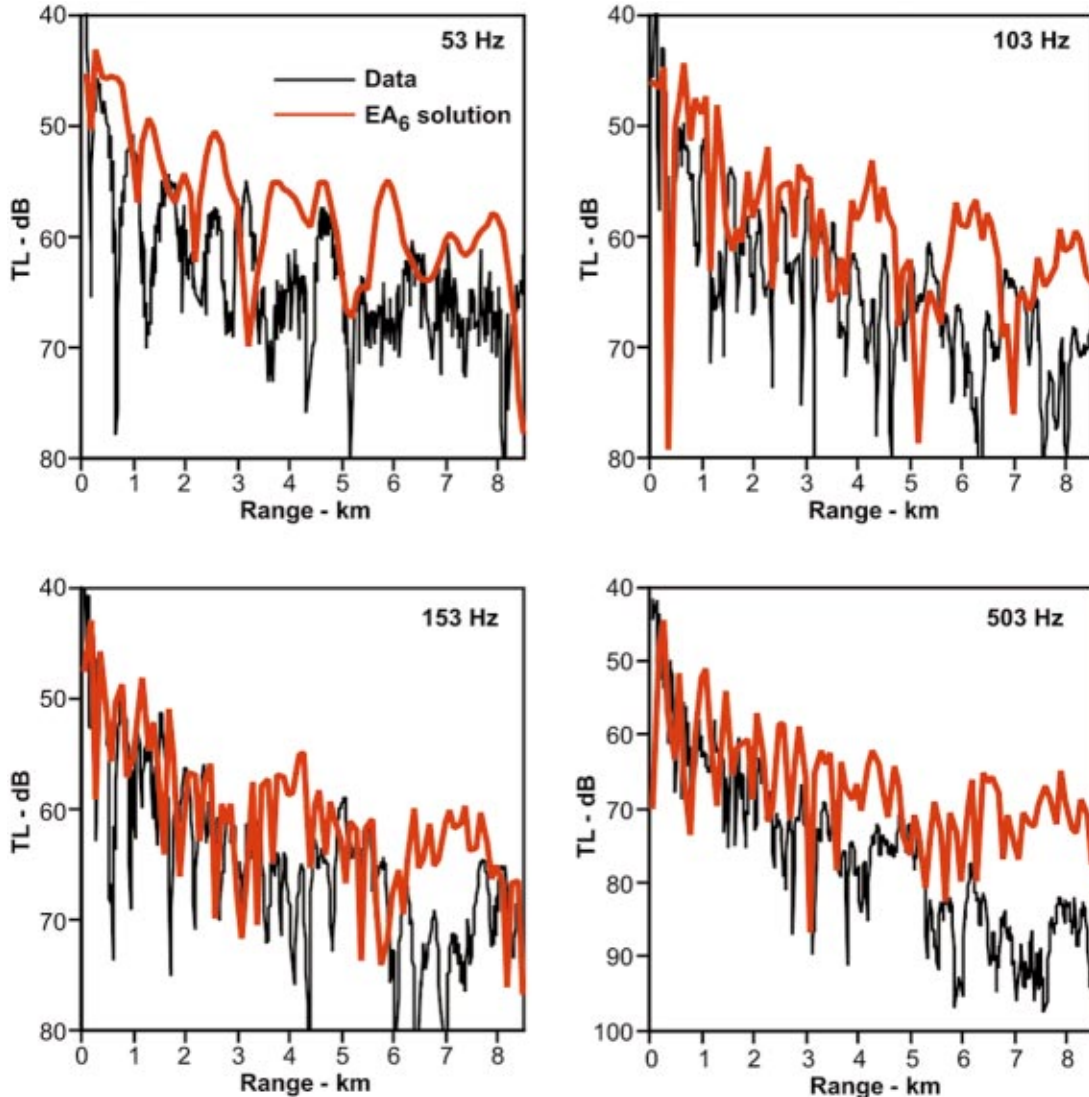


FIG. 21. Comparison of measured transmission loss with transmission loss modeled using the EA_5 geoacoustic solution. Source depth is 29.5 m.

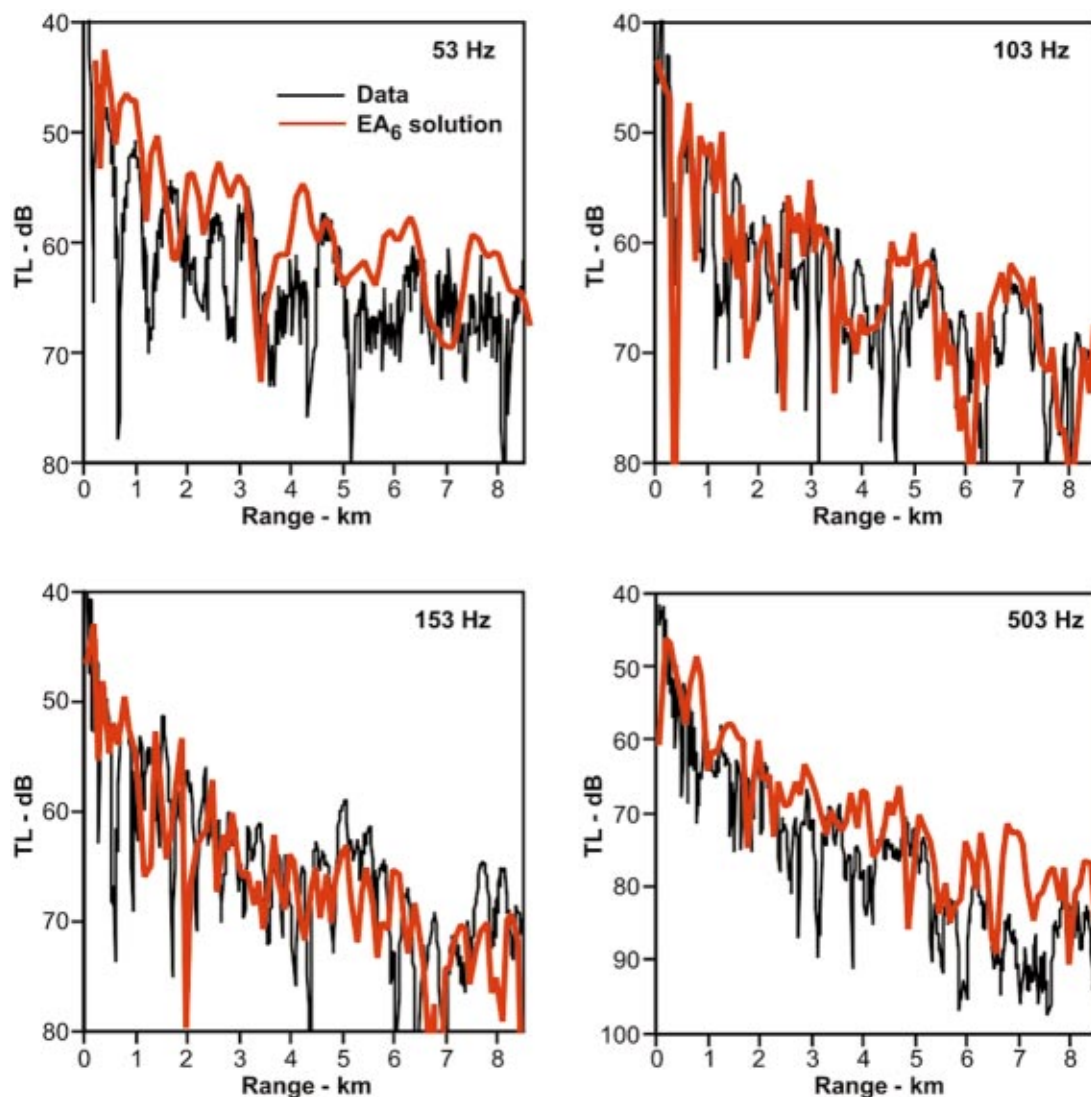


FIG. 22. Comparison of measured transmission loss with transmission loss modeled using the EA₆ geoacoustic solution. Source depth is 29.5 m.

EA_{2m} to previously published values at a nearby location.⁷⁻⁹ The EA₁ and EA_{2m} sound speed ratios are close to the value reported by Collins *et al.*⁹ The EA₁ sound speed gradient compares well with those reported in Refs. 8 and 9 while the gradient in EA_{2m} is smaller. The densities compare fairly well. The EA₁ value for the attenuation agrees well with that reported in Ref. 9; however, the EA_{2m} value is about half the value reported in Ref. 9.

Figures 23 and 24 show the cost function and parameter values for about 5000 forward calls in the EA₁ and EA₂ calculations, respectively. These cost function values were evaluated for a wide distribution of temperatures. Viewed in

this manner the cost function structure suggests the uncertainty of the estimated parameters. For both EA₁ and EA₂ the best determined parameter is clearly the top sediment sound speed. From these distributions, one may say that for EA₁ the estimated value of the top sediment sound speed is approximately 1470 m/s. For EA₂ the estimated value of the top sediment sound speed is approximately 1485 m/s. The cost functions for the sediment thickness supports the earlier observation that a thin sediment over a hard sediment did not give the correct arrival structure in the time series. One may interpret the distributions in Figs. 23(b) and 24(b) as placing a lower limit of about 45 m on the sediment thickness. In

TABLE IV. Comparisons of selected geoacoustic parameters from first sediment layer of EA₁ and EA_{2m} with reported values for GEMINI location.

	EA ₁	EA _{2m}	Rubano	Lynch <i>et al.</i>	Collins <i>et al.</i>
Sound speed ratio	0.9718	0.9744	0.9820	0.9840	0.9710
Sound speed gradient (1/s)	2.21	1.74	...	2.25	2.03
Density (g/cc)	1.52	1.51	1.40	1.56	1.66
Top attenuation (dB/m-kHz)	0.017	0.010	0.022

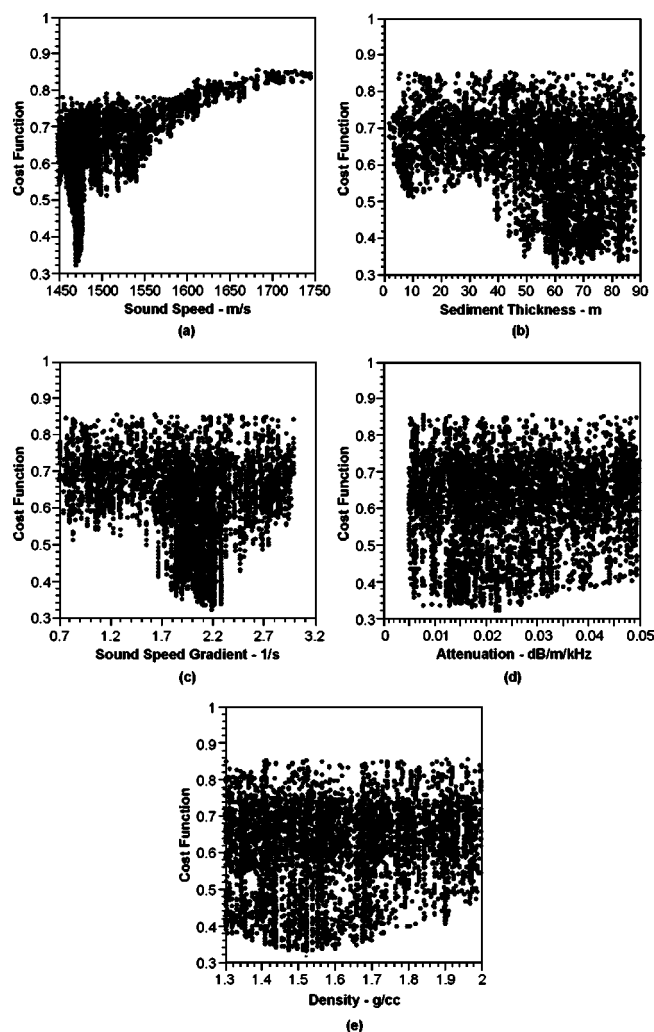


FIG. 23. Cost function distributions for selected parameters of first sediment layer in EA₁ solution.

Fig. 23(c) one observes that the EA₁ distribution for the sound speed gradient gives an estimated value of about 2.2 s^{-1} . In Fig. 24(c) one observes that the EA₂ distribution for the sound speed gradient suggests an estimated value of about 1.55 s^{-1} . Both Figs. 23(d) and 24(d) appear to suggest an upper limit of about 0.03 dB/m/kHz for the top sediment attenuation. In Fig. 23(e) one sees that the minimum value of the cost function occurs around 1.5 g/cm^3 . In Fig. 24(e), however, one sees that the minimum value of the cost function occurs around 1.9 g/cm^3 . Clearly the sound speed structure and sediment thickness have significantly less uncertainty than the density and attenuation. This is consistent with previous benchmark geoaoustic inversion studies for noise-free simulated data.^{14,20} Figures 23(b), 23(d), 24(b), and 24(d) quantify for this analysis the effect that small fluctuations in the assumed SSP can have on the estimated values and uncertainties of the sound speed gradient and density.

The TL modeling calculations provided a clear understanding of the seabed interaction mechanisms for the experimental location. The time scale of the impulse response in a shallow water waveguide with a soft seabed is dependent

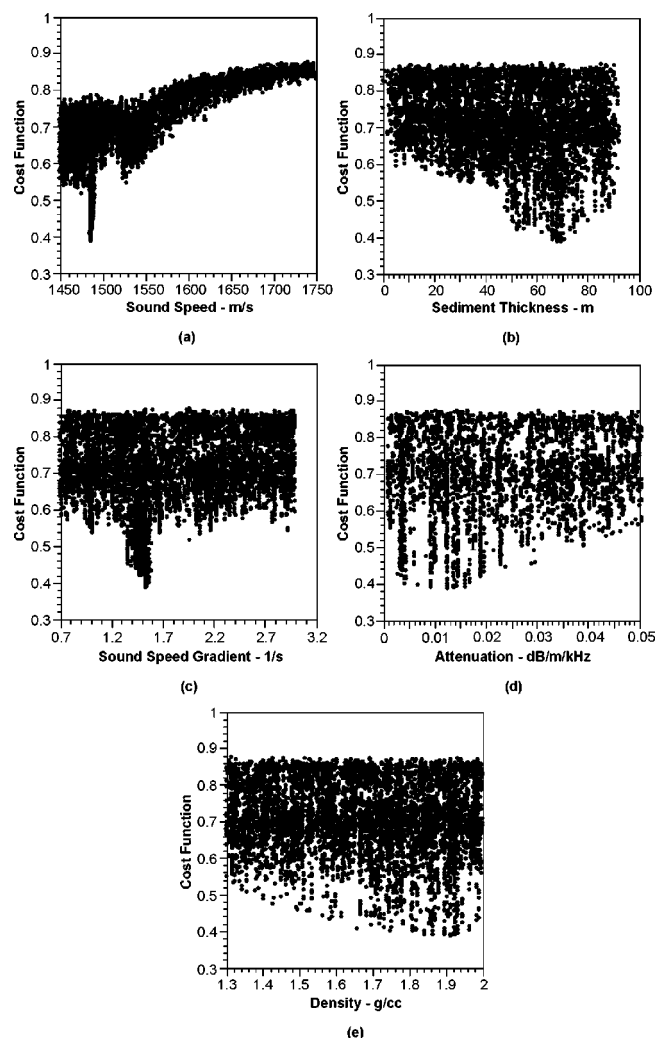


FIG. 24. Cost function distributions for selected parameters of first sediment layer in EA₂ solution.

in a complex manner on the details of the velocity and attenuation structure. The observed large time spread of the impulse response results from both the low velocity and low attenuation of the thick upper sediment, coupled with a fairly large upper layer sound speed gradient that produces and preserves a large number of multipath arrivals. From a normal mode point of view, the dispersion of the modal group velocities of the significant modes, their dispersion over the frequency bandwidth, and the details of the modal attenuations allows for a significant time spread of the modal arrivals. The presence of several low-order modes results in the complex interference pattern in the low-frequency transmission loss as a function of range, and is consistent with the large time spread of the impulse response.

V. SUMMARY

In summary, an acoustic propagation experiment was conducted in a shallow water environment in the Gulf of Mexico. Both broadband and narrow-band acoustic measurements were made on a horizontal line array with a length of about five water depth. An optimization analysis to estimate the geoaoustic structure of the seabed, using a simulated

annealing approach with uncalibrated light bulb sources, was demonstrated. The simulated annealing algorithm was linked to a broadband normal mode model. Several broadband cost functions, measured SSPs, and light bulb events were utilized in the inversions. Measured TL at multiple frequencies served as a basis to select an inversion solution considered to describe the actual seabed most accurately. For the same SSP and light bulb data, it was observed that the two cost functions led to differences in the inferred geoacoustic structure of the seabed, whose effects were easily quantified in the TL comparisons. Compared to the data-model cross-spectra cost function the average peak cross-correlation cost function produced a more accurate geoacoustic representation of the seabed. However, one cannot conclude from this single analysis that this is a general result. The cross-spectra cost function is sensitive to errors in the assumed hydrophone positions. Thus the difference in inversion results between the two cost functions may be associated with possible errors in the reconstruction of the array geometry. It was also observed that the small deviations in the measured SSPs had a significant effect on the uncertainties of the sound speed gradient and the density. However, the effect of the SSP deviations was smaller than the effect of varying the cost functions.

ACKNOWLEDGMENTS

The authors acknowledge the numerous helpful suggestions and comments made by the anonymous reviewers. This research was jointly supported by the Office of Naval Research and SPAWAR.

¹R. J. Cederberg, W. L. Siegmann, M. J. Jacobson, and W. M. Carey, "Predictability of acoustic intensity and horizontal wavenumbers in shallow water at low frequencies using parabolic approximations," *J. Acoust. Soc. Am.* **94**, 1034–1043 (1993).

²W. M. Carey, J. Doult, R. Evans, and L. Dillman, "Shallow water sound transmission measurements on the New Jersey Continental Shelf," *IEEE J. Ocean. Eng.* **20**, 321–336 (1995).

- ³D. P. Knobles, E. K. Westwood, and J. E. LeMond, "Modal time-series structure in a shallow water environment," *IEEE J. Ocean. Eng.* **23**, 188–202 (1998).
- ⁴E. K. Westwood, C. T. Tindle, and N. R. Chapman, "A normal mode model for acousto-elastic ocean environments," *J. Acoust. Soc. Am.* **100**, 3631–3645 (1996).
- ⁵D. P. Knobles and R. A. Koch, "A time series analysis of sound propagation in a strongly multipath shallow water environment with an adiabatic normal mode approach," *IEEE J. Ocean. Eng.* **21**, 1–13 (1996).
- ⁶H. L. Berryhill, Jr., *Late Quaternary Facies and Structure, Northern Gulf of Mexico*, AAPG Studies in Geology 23 (The American Association of Petroleum Geologists, 1986).
- ⁷L. A. Rubano, "Acoustic propagation in shallow water over a low-velocity bottom," *J. Acoust. Soc. Am.* **67**, 1608–1613 (1980).
- ⁸J. F. Lynch, S. D. Rajan, and G. V. Frisk, "A comparison of broadband and narrow-band inversions for bottom geoacoustic properties at a site near Corpus Christi, Texas," *J. Acoust. Soc. Am.* **89**, 648 (1988).
- ⁹M. D. Collins, W. A. Kuperman, and H. Schmidt, "Nonlinear inversion for ocean-bottom properties," *J. Acoust. Soc. Am.* **92**, 2770–2783 (1992).
- ¹⁰A. Anderson, private communication.
- ¹¹E. K. Westwood, "Broadband matched-field source localization," *J. Acoust. Soc. Am.* **91**, 2777–2798 (1992).
- ¹²D. P. Knobles and S. K. Mitchell, "Broadband localization by matched-fields in range and bearing in shallow water," *J. Acoust. Soc. Am.* **96**, 1813–1820 (1994).
- ¹³S. R. Rutherford and K. E. Hawker, "The effects of density gradients on bottom reflection loss for a class of marine sediments," *J. Acoust. Soc. Am.* **63**, 750–757 (1978).
- ¹⁴D. P. Knobles, R. A. Koch, E. K. Westwood, and T. Udagawa, "The inversion of ocean waveguide parameters using a nonlinear least squares approach," *J. Comput. Acoust.* **6**, 83–97 (1998).
- ¹⁵S. Kirkpatrick, C. D. Gelatt, and M. P. Vecchi, "Optimization by simulated annealing," *Science* **220**, 671–680 (1983).
- ¹⁶W. L. Goffe, G. D. Ferrier, and J. Rogers, "Global optimization of statistical functions with simulated annealing," *J. Econometr.* **60**, 65–99 (1994).
- ¹⁷N. R. Chapman and C. E. Lindsay, "Matched-field inversion for geoacoustic model parameters in shallow water," *IEEE J. Ocean. Eng.* **21**, 347 (1996).
- ¹⁸M. R. Fallat and S. E. Dosso, "Geoacoustic inversion for the Workshop 1997 Benchmark test cases using simulated annealing," *J. Comput. Acoust.* **6**, 29–43 (1998).
- ¹⁹E. L. Hamilton, "Geoacoustic modeling of the seafloor," *J. Acoust. Soc. Am.* **68**, 1313–1340 (1980).
- ²⁰"Benchmark geoacoustic inversion techniques for range-dependent environments," Gulfport, MI, May 2001.

Spectral and modal formulations for the Doppler-shifted field scattered by an object moving in a stratified medium

Yi-san Lai and Nicholas C. Makris^{a)}

Massachusetts Institute of Technology, Cambridge, Massachusetts 02139

(Received 5 April 2001; revised 13 March 2002; accepted 12 June 2002)

Spectral and normal mode formulations for the three-dimensional field scattered by an object moving in a stratified medium are derived using full-field wave theory. The derivations are based on Green's theorem for the time-domain scalar wave equation and account for Doppler effects induced by target motion as well as source and receiver motion. The formulations are valid when multiple scattering between the object and waveguide boundaries can be neglected, and the scattered field can be expressed as a linear function of the object's plane wave scattering function. The advantage of the spectral formulation is that it incorporates the entire wave number spectrum, including evanescent waves, and therefore can potentially be used at much closer ranges to the target than the modal formulation. The normal mode formulation is more computationally efficient but is limited to longer ranges. For a monochromatic source that excites N incident modes in the waveguide, there will be roughly N^2 distinct harmonic components in the scattered field. The Doppler shifts in the scattered field are highly dependent upon the waveguide environment, target shape, and measurement geometry. The Doppler effects are illustrated through a number of canonical examples. © 2003 Acoustical Society of America. [DOI: 10.1121/1.1499135]

PACS numbers: 43.30.Gv, 43.30.Vh, 43.30.Es [DLB]

I. INTRODUCTION

Standard active sonar and radar systems estimate the instantaneous velocity of a moving target in free space by resolving Doppler shifts in the frequency spectrum of scattered waves. To obtain all components of the velocity vector, a multistatic measurement geometry may be necessary. This type of active scenario is well suited to the velocity estimation of a distant body because the frequency spectrum of the source is known and controllable and so can be tailored to the resolution constraints of the problem at hand. In passive sonar and radar, however, velocity estimation by Doppler shift analysis is often less reliable because the distant object must itself radiate enough power to be detected. Additionally, the frequency spectrum of this radiation must be known, and have sufficiently narrow bandwidth and stability for Doppler shifts to be extracted robustly.

The problem of using active sonar to estimate the velocity of an underwater target moving in an ocean waveguide has complications not found in the free-space analogue. This is because propagation and scattering effects in a waveguide are typically not separable as they are in the far field free-space scenario. Also, multiple frequency components are typically present in the field scattered from an object moving in an ocean waveguide even if the active source of radiation is harmonic. An accurate physical model for the field scattered from an object moving in a stratified ocean waveguide must then be derived before techniques can be developed to estimate the submerged object's velocity. It is the goal of this paper to derive such a model and to investigate the Doppler effects induced by motion of a source, target, and receiver in a stratified ocean waveguide. Inclusion of source and re-

ceiver motion is also necessary because the source and receivers are typically mounted on research vessels that move with speeds similar to that of the target, and so induce their own Doppler effects that must be differentiated from those induced by the target.

Doppler effects induced by the motion of a radiating source that is passively measured at a moving receiver in free space have been extensively studied in acoustics.^{1,2} Doppler effects for the corresponding passive problem of a moving source and a moving receiver submerged in a stratified ocean waveguide have also been studied in the literature.^{3,4} Multimodal propagation and dispersion make the Doppler effects far more complicated in a waveguide than in free space. For example, the field radiated by a time harmonic source moving in an ocean waveguide can be received with multiple frequency components because of multimodal propagation.

A number of models exist for three-dimensional scattering from targets submerged in a stratified medium, as described in Ref. 5. A particularly convenient and widely used approach is the single-scatter theory developed in Refs. 5–8. The major advantage of this approach is that the scattered field is expressed in terms of the target's free-space plane wave scattering function. This theory is valid when (1) the propagation medium is horizontally stratified and range-independent; (2) the object is contained within an iso-velocity layer; (3) multiple scattering between the object and waveguide boundaries make negligible contribution at the receiver; and (4) the range from the object to source and receiver is sufficiently large that the scattered field can be expressed as a linear function of the object's plane wave scattering function. This theory, however, assumes that the source, receiver, and target are not moving so that Doppler effects must be negligible.

In this paper, the single scatter theory is generalized to

^{a)}Electronic mail: makris@mit.edu

include the effects of source, receiver, and target motion. Analytical expressions are obtained for the field scattered to a moving receiver from a moving target in a stratified ocean waveguide by a moving source. The formulations are fully bistatic, and all the motions are assumed to be horizontal with constant velocities. Both the expressions for a simple harmonic source and a source with arbitrary time dependence are derived in this paper. Spectral and modal representations of the scattered field are derived from first principles using the time-domain formulation of Green's theorem. The spectral representation makes fewer assumptions and is more accurate than the normal mode representation at closer ranges, but the normal mode formulation provides a compelling physical interpretation and can be used at longer ranges without significant loss of accuracy. The single scatter theory of Refs. 6 and 7 then becomes a special case of the present more general theory when the source, receiver, and target are at rest. The four listed restrictions of the stationary single scatter theory also apply to the generalized theory developed in this paper.

It is noteworthy that when the target, source, or receiver are moving, the scattered field no longer obeys reciprocity, as is evident in our present formulation. The concept of a time-reversal mirror⁹⁻¹¹ therefore is not directly applicable under motion of the target, source, or receiver. This is true in both free space and in a stratified medium.

A simple and intuitive technique for deriving the field radiated from a moving source measured at a moving receiver using delta functions is also presented for both spectral and modal formulations. The spectral representation is identical to the result of Ref. 4. The normal mode representation makes more accurate approximations than those used in Ref. 3. The resulting expressions are used in the scattering problem to describe the incident field from the moving source at the moving target.

II. ANALYTIC FORMULATION

Analytical expressions for the field scattered from a moving source by a moving object measured at a moving receiver are derived from first principles using the time-domain scalar wave equation and the corresponding time-domain formulation of Green's theorem.

Some of the basic approximations and techniques used in Refs. 6 and 7 to solve the stationary scattering problem are also applied here. The major difference, however, is that we must solve the problem with the time-domain scalar wave equation instead of the Helmholtz equation to account for motion of the source, receiver, and target.

The time-domain scalar wave equation for the total field Φ_T with a source function $q(\mathbf{r}_0, t_0)$ is

$$\nabla_0^2 \Phi_T(\mathbf{r}_0, t_0) - \frac{1}{c^2} \frac{\partial^2 \Phi_T(\mathbf{r}_0, t_0)}{\partial t_0^2} = -q(\mathbf{r}_0, t_0). \quad (1)$$

The Green function for the time-domain scalar wave equation satisfies

$$\nabla_0^2 G(\mathbf{r}, t | \mathbf{r}_0, t_0) - \frac{1}{c^2} \frac{\partial^2 G(\mathbf{r}, t | \mathbf{r}_0, t_0)}{\partial t_0^2} = -\delta(\mathbf{r} - \mathbf{r}_0) \delta(t - t_0). \quad (2)$$

By applying Green's theorem, the total field Φ_T can be expressed as¹²

$$\begin{aligned} \Phi_T(\mathbf{r}, t) = & \int_0^{t^+} dt_0 \int dV_0 G(\mathbf{r}, t | \mathbf{r}_0, t_0) q(\mathbf{r}_0, t_0) \\ & + \int_0^{t^+} dt_0 \oint d\mathbf{S}_0 \cdot \left(G(\mathbf{r}, t | \mathbf{r}_0, t_0) \nabla_0 \Phi_T \right. \\ & \left. - \Phi_T \nabla_0 G(\mathbf{r}, t | \mathbf{r}_0, t_0) \right) \\ & - \frac{1}{c^2} \int dV_0 \left[\frac{\partial G(\mathbf{r}, t | \mathbf{r}_0, t_0)}{\partial t_0} \Phi_T \right. \\ & \left. - G(\mathbf{r}, t | \mathbf{r}_0, t_0) \frac{\partial \Phi_T}{\partial t_0} \right]_{t_0=0}, \end{aligned} \quad (3)$$

which differs from Eq. (7.3.5) of Ref. 12 only by a 4π factor due to differing choices for the delta function normalization. The first integral represents the incident field Φ_i induced by the source, and the second integral represents the scattered field Φ_s . The third integral accounts for the transient response. For example, given a time harmonic source turned on at $t_0 = 0$, this integral vanishes after the source has been operating for a time duration t^+ large compared to the source period. The first two integrals then represent the steady state response, and the total field is the summation of the first two integrals

$$\Phi_T(\mathbf{r}, t) = \Phi_i(\mathbf{r}, t) + \Phi_s(\mathbf{r}, t) \quad (4)$$

with incident field

$$\Phi_i(\mathbf{r}, t) = \int_0^{t^+} dt_0 \int dV_0 G(\mathbf{r}, t | \mathbf{r}_0, t_0) q(\mathbf{r}_0, t_0) \quad (5)$$

and scattered field

$$\begin{aligned} \Phi_s(\mathbf{r}, t) = & \int_0^{t^+} dt_0 \oint d\mathbf{S}_0 \cdot \left(G(\mathbf{r}, t | \mathbf{r}_0, t_0) \nabla_0 \Phi_T \right. \\ & \left. - \Phi_T \nabla_0 G(\mathbf{r}, t | \mathbf{r}_0, t_0) \right). \end{aligned} \quad (6)$$

Following the type of abbreviating convention adopted in Refs. 6 and 7, we will drop the first term in Eq. (6) in the derivation to avoid cumbersome and uninformative algebra. The derivation with both terms proceeds in exactly the same manner and leads to exactly the same expression for the scattered field. This expression is in terms of the object's plane wave scattering function for an object with arbitrary boundary conditions.⁵⁻⁷

The scattered field from a rigid surface with unspecified shape is

$$\begin{aligned} \Phi_s(\mathbf{r}, t) = & - \int_0^{t^+} dt_0 \oint d\mathbf{S}_0 \cdot \left(\Phi_T(\mathbf{r}_0, t_0) \nabla_0 G(\mathbf{r}, t | \mathbf{r}_0, t_0) \right) \\ = & - \int_0^{t^+} dt_0 \oint d\mathbf{S}_0 \cdot \left([\Phi_i(\mathbf{r}_0, t_0) \right. \\ & \left. + \Phi_s(\mathbf{r}_0, t_0)] \nabla_0 G(\mathbf{r}, t | \mathbf{r}_0, t_0) \right). \end{aligned} \quad (7)$$

For a steady wave problem, this leads to Eq. (37) of Ref. 6 directly.

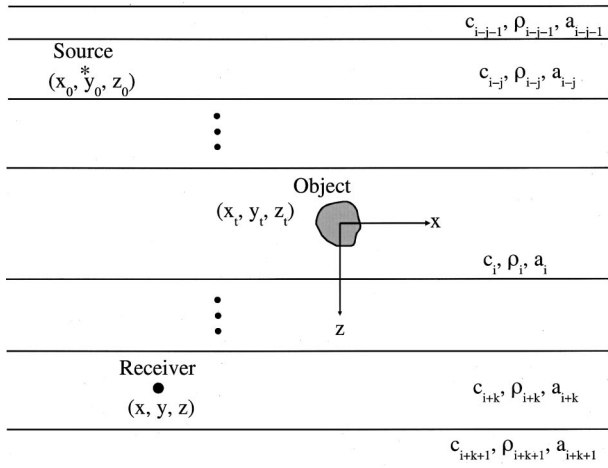


FIG. 1. Measurement geometry for a submerged object in a horizontally stratified waveguide ensounded by a point source. The coordinate system is centered at the centroid of the object with positive z pointing down. Each layer i is characterized by sound speed c_i , density ρ_i , and attenuation a_i .

For economy, the notation of Ref. 7 is used here and in the remainder of this article. Figure 2 of Ref. 7 shows the geometry of spatial and wave number coordinates. For example, the object centroid *at the initial location of the object* is at the center of all coordinate systems, as shown in Fig. 1. Source coordinates are denoted by (x_0, y_0, z_0) , receiver coordinates by (x, y, z) , and coordinates on the surface of the target by $(x_\sigma, y_\sigma, z_\sigma)$ where the positive z axis points downward and is normal to the interfaces between horizontal strata. Spatial cylindrical (ρ, θ, z) and spherical (r, θ, ϕ) systems are defined by $x = r \sin \theta \cos \phi$, $y = r \sin \theta \sin \phi$, $z = r \cos \theta$, and $\rho^2 = x^2 + y^2$. Wave number coordinates for the incident $(\xi_{ix}, \xi_{iy}, \gamma_i)$ and scattered field (ξ_x, ξ_y, γ) also originate at the target center and are related to polar and azimuthal propagation angles by $\xi^2 = \xi_x^2 + \xi_y^2$, where

$$\xi_x = k \sin \alpha \cos \beta, \quad (8)$$

$$\xi_y = k \sin \alpha \sin \beta, \quad (9)$$

$$\xi_z = k \cos \alpha, \quad (10)$$

$$k^2 = \left(\frac{\omega}{c} \right)^2 = \gamma^2 + \xi^2. \quad (11)$$

The superscript 0 is used to denote the initial positions of the source, target, and receiver, for example, $x(t)|_{t=0} = x^0$.

A. Spectral representation of the Doppler-shifted field scattered from a moving target by a simple-harmonic source in a stratified waveguide

A spectral representation for the field from a moving source, scattered by a moving target at a moving receiver, is now derived. The source is taken to be a simple-harmonic one with frequency Ω , and the motions of the source, target, and receiver are all horizontal with constant velocity.

In order to calculate the scattered field, Eq. (7) is applied where the incident field at a point \mathbf{r}_σ on the surface of the target depends on time t_σ . The scattered field at the receiver location \mathbf{r} at time t can then be calculated by

$$\Phi_s(\mathbf{r}, t) = - \int_0^{t^+} dt_\sigma \oint d\mathbf{S}_\sigma \cdot \left([\Phi_i(\mathbf{r}_\sigma, t_\sigma) + \Phi_s(\mathbf{r}_\sigma, t_\sigma)] \nabla_\sigma G(\mathbf{r}, t | \mathbf{r}_\sigma, t_\sigma) \right), \quad (12)$$

where the surface integral is carried out on the surface of the scatterer.

The incident field induced by a simple-harmonic source at frequency Ω moving with horizontal velocity \mathbf{v}_0 and received at a point \mathbf{r}_σ on the surface of an object moving with horizontal velocity \mathbf{v}_σ is obtained from Eq. (A10) as

$$\Phi_i(\mathbf{r}_\sigma, t) = \frac{1}{2\pi} \int_{-\infty}^{\infty} d^2 \xi_i g(z_\sigma, z_0; \Omega + \xi_i \cdot \mathbf{v}_0) \times e^{i \xi_i \cdot (\boldsymbol{\rho}_\sigma^0 - \boldsymbol{\rho}_0^0)} e^{-i(\Omega + \xi_i \cdot (\mathbf{v}_0 - \mathbf{v}_\sigma))t}. \quad (13)$$

With the decomposition proposed in Eq. (6) of Ref. 7, the depth-dependent Green function defined in Eq. (A7) becomes

$$g(z_\sigma, z_0; \omega_i) = A(z_0; \omega_i) e^{i \gamma_i(\omega_i) z_\sigma} + B(z_0; \omega_i) e^{-i \gamma_i(\omega_i) z_\sigma} \quad (14)$$

with the shifted frequency of the incident field

$$\omega_i = \Omega + \xi_i \cdot \mathbf{v}_0. \quad (15)$$

The location of a point on the surface of the target is

$$\mathbf{r}_\sigma = \mathbf{r}_\sigma^0 + \mathbf{v}_\sigma t_\sigma \quad (16)$$

with \mathbf{r}_σ^0 as its initial location at $t_\sigma = 0$ and \mathbf{v}_σ as its horizontal velocity. The incident field in Eq. (13) then becomes

$$\Phi_i(\mathbf{r}_\sigma, t_\sigma) = \frac{1}{2\pi} \int_{-\infty}^{\infty} d^2 \xi_i e^{-i \xi_i \cdot \boldsymbol{\rho}_\sigma^0} e^{-i(\Omega + \xi_i \cdot (\mathbf{v}_0 - \mathbf{v}_\sigma))t_\sigma} \times [A(z_0; \omega_i) e^{i(\xi_i \cdot \boldsymbol{\rho}_\sigma^0 + \gamma_i(\omega_i) z_\sigma)} + B(z_0; \omega_i) e^{i(\xi_i \cdot \boldsymbol{\rho}_\sigma^0 - \gamma_i(\omega_i) z_\sigma)}]. \quad (17)$$

The spectral representation of Green's function for the Helmholtz equation in a stratified waveguide is

$$G(\mathbf{r} | \mathbf{r}_\sigma; \omega) = \frac{1}{2\pi} \int_{-\infty}^{\infty} d^2 \xi g(z, z_\sigma; \omega) e^{i \xi \cdot (\boldsymbol{\rho} - \boldsymbol{\rho}_\sigma)}. \quad (18)$$

Similarly, the depth-dependent Green function in Eq. (18) is decomposed as

$$g(z, z_\sigma; \omega) = C(z; \omega) e^{i \gamma_i(\omega) z_\sigma} + D(z; \omega) e^{-i \gamma_i(\omega) z_\sigma}. \quad (19)$$

The motion of the receiver is expressed as

$$\mathbf{r} = \mathbf{r}^0 + \mathbf{v} t, \quad (20)$$

where \mathbf{r}^0 is its initial location at time $t = 0$ and \mathbf{v} is its horizontal velocity. The Green function for the time-domain scalar wave equation from the surface of the target \mathbf{r}_σ at time t_σ to the receiver location \mathbf{r} at time t then becomes

$$G(\mathbf{r}, t | \mathbf{r}_\sigma, t_\sigma) = \frac{1}{2\pi} \int_{-\infty}^{\infty} d\omega e^{-i\omega(t-t_\sigma)} \frac{1}{2\pi} \int_{-\infty}^{\infty} d^2\xi e^{i\xi \cdot \mathbf{r}_\sigma^0} e^{i\xi \cdot \mathbf{v} t} e^{-i\xi \cdot \mathbf{v}_\sigma t_\sigma} \times [C(z; \omega) e^{i(-\xi \cdot \mathbf{r}_\sigma^0 + \gamma_i(\omega) z_\sigma)} + D(z; \omega) e^{i(-\xi \cdot \mathbf{r}_\sigma^0 - \gamma_i(\omega) z_\sigma)}]. \quad (21)$$

Inserting Eqs. (17) and (21) into Eq. (12) leads to the scattered field

$$\Phi_s(\mathbf{r}, t) = -\frac{1}{2\pi} \int_0^{t^+} dt_\sigma \oint d\mathbf{S}_\sigma \cdot \left\{ \left[\frac{1}{2\pi} \int_{-\infty}^{\infty} d^2\xi e^{-i\xi \cdot \mathbf{r}_\sigma^0} e^{-i(\Omega + \xi_i \cdot (\mathbf{v}_0 - \mathbf{v}_\sigma)) t_\sigma} \times [A(z_0; \omega_i) e^{i(\xi_i \cdot \mathbf{r}_\sigma^0 + \gamma_i(\omega_i) z_\sigma)} + B(z_0; \omega_i) e^{i(\xi_i \cdot \mathbf{r}_\sigma^0 - \gamma_i(\omega_i) z_\sigma)}] + \Phi_s(\mathbf{r}_\sigma, t_\sigma) \right] \times \nabla_\sigma \left(\int_{-\infty}^{\infty} d\omega e^{-i\omega(t-t_\sigma)} \frac{1}{2\pi} \int_{-\infty}^{\infty} d^2\xi e^{i\xi \cdot \mathbf{r}_\sigma^0} e^{i\xi \cdot \mathbf{v} t} e^{-i\xi \cdot \mathbf{v}_\sigma t_\sigma} \times [C(z; \omega) e^{i(-\xi \cdot \mathbf{r}_\sigma^0 + \gamma_i(\omega) z_\sigma)} + D(z; \omega) e^{i(-\xi \cdot \mathbf{r}_\sigma^0 - \gamma_i(\omega) z_\sigma)}] \right) \right\}, \quad (22)$$

where $\xi \cdot \mathbf{r} + \gamma z = kr \eta(\alpha, \beta; \theta, \phi)$ and

$$\eta(\alpha, \beta; \theta, \phi) = \cos \alpha \cos \theta + \sin \alpha \sin \theta \cos(\beta - \phi) \quad (23)$$

is the cosine of the angle between the propagation direction (α, β) and field coordinate direction (θ, ϕ) where the angles α, β may be complex. Substituting this angular representation into Eq. (22) yields

$$\Phi_s(\mathbf{r}, t) = -\frac{1}{2\pi} \int_0^{t^+} dt_\sigma \oint d\mathbf{S}_\sigma \cdot \left\{ \left[\frac{1}{2\pi} \int_{-\infty}^{\infty} d^2\xi e^{-i\xi \cdot \mathbf{r}_\sigma^0} e^{-i(\Omega + \xi_i \cdot (\mathbf{v}_0 - \mathbf{v}_\sigma)) t_\sigma} \times [A(z_0; \omega_i) e^{ik(\omega_i) r_\sigma^0 \eta(\alpha_i(\omega_i), \beta_i; \theta_\sigma^0, \phi_\sigma^0)} + B(z_0; \omega_i) e^{ik(\omega_i) r_\sigma^0 \eta(\pi - \alpha_i(\omega_i), \beta_i; \theta_\sigma^0, \phi_\sigma^0)}] + \Phi_s(\mathbf{r}_\sigma, t_\sigma) \right] \times \nabla_\sigma \left(\int_{-\infty}^{\infty} d\omega e^{-i\omega(t-t_\sigma)} \frac{1}{2\pi} \int_{-\infty}^{\infty} d^2\xi e^{i\xi \cdot \mathbf{r}_\sigma^0} e^{i\xi \cdot \mathbf{v} t} e^{-i\xi \cdot \mathbf{v}_\sigma t_\sigma} \times [C(z; \omega) e^{-ik(\omega) r_\sigma^0 \eta(\pi - \alpha(\omega), \beta; \theta_\sigma^0, \phi_\sigma^0)} + D(z; \omega) e^{-ik(\omega) r_\sigma^0 \eta(\alpha(\omega), \beta; \theta_\sigma^0, \phi_\sigma^0)}] \right) \right\}, \quad (24)$$

where (α_i, β_i) is the propagation direction of the incident plane waves and $(\theta_\sigma^0, \phi_\sigma^0)$ is the direction of \mathbf{r}_σ^0 , the initial location of a point on the target with respect to the initial position of the target centroid which is the origin of all coordinates.

For low Mach number motion, the scattered field on the surface of the object in Eq. (24) is approximately

$$\hat{\Phi}_s(\mathbf{r}_\sigma, t_\sigma) \approx \hat{\Phi}_s(\mathbf{r}_\sigma; \omega_i) e^{-i\omega_i t_\sigma} \quad (25)$$

for a given incident plane wave. The wave number vectors for the downgoing and upgoing waves are defined as

$$\mathbf{k}_i^+ = \xi_i + \gamma_i \hat{\mathbf{i}}_z, \quad (26)$$

$$\mathbf{k}_i^- = \xi_i - \gamma_i \hat{\mathbf{i}}_z. \quad (27)$$

When the Mach number of the target motion is small, the scattered fields on the surface of the moving target $\hat{\Phi}_s(\mathbf{r}_\sigma, \mathbf{k}_i^+; \omega_i)$ and $\hat{\Phi}_s(\mathbf{r}_\sigma, \mathbf{k}_i^-; \omega_i)$, which are induced by downgoing and upgoing incident plane waves with unit amplitudes, can be approximated as the scattered fields at the initial locations of the target multiplied by a phase shift factor $e^{i\xi_i \cdot \mathbf{v}_\sigma t_\sigma}$ that accounts for the *rigid body translation of the centroid*. The scattered field on the object then becomes

$$\Phi_s(\mathbf{r}_\sigma, t_\sigma) = \frac{1}{2\pi} \int_{-\infty}^{\infty} d^2\xi e^{-i\xi \cdot \mathbf{r}_\sigma^0} e^{-i(\Omega + \xi_i \cdot (\mathbf{v}_0 - \mathbf{v}_\sigma)) t_\sigma} \times [A(z_0; \omega_i) \hat{\Phi}_s(\mathbf{r}_\sigma^0, \mathbf{k}_i^+; \omega_i) + B(z_0; \omega_i) \hat{\Phi}_s(\mathbf{r}_\sigma^0, \mathbf{k}_i^-; \omega_i)]. \quad (28)$$

Introducing Eq. (28) into Eq. (24), then leads to the scattered field

$$\begin{aligned}
\Phi_s(\mathbf{r}, t) = & -\frac{1}{2\pi} \int_0^{t^+} dt_\sigma \oint d\mathbf{S}_\sigma \cdot \left\{ \left[\frac{1}{2\pi} \int_{-\infty}^{\infty} d^2 \xi_i e^{-i \xi_i \cdot \mathbf{p}_0^0} e^{-i(\Omega + \xi_i \cdot (\mathbf{v}_0 - \mathbf{v}_\sigma)) t_\sigma} \right. \right. \\
& \times (A(z_0; \omega_i) \{e^{ik(\omega_i) r_\sigma^0} \eta(\alpha_i(\omega_i), \beta_i; \theta_\sigma^0, \phi_\sigma^0) + \hat{\Phi}_s(\mathbf{r}_\sigma^0, \mathbf{k}_i^+; \omega_i)\} \\
& + B(z_0; \omega_i) \{e^{ik(\omega_i) r_\sigma^0} \eta(\pi - \alpha_i(\omega_i), \beta_i; \theta_\sigma^0, \phi_\sigma^0) + \hat{\Phi}_s(\mathbf{r}_\sigma^0, \mathbf{k}_i^-; \omega_i)\}) \left. \right] \\
& \times \nabla_\sigma \left(\int_{-\infty}^{\infty} d\omega e^{-i\omega(t-t_\sigma)} \frac{1}{2\pi} \int_{-\infty}^{\infty} d^2 \xi e^{i \xi \cdot \mathbf{p}^0} e^{i \xi \cdot \mathbf{v} t} e^{-i \xi \cdot \mathbf{v}_\sigma t_\sigma} \right. \\
& \left. \left. \times [C(z; \omega) e^{-ik(\omega) r_\sigma^0} \eta(\pi - \alpha(\omega), \beta; \theta_\sigma^0, \phi_\sigma^0) + D(z; \omega) e^{-ik(\omega) r_\sigma^0} \eta(\alpha(\omega), \beta; \theta_\sigma^0, \phi_\sigma^0)] \right] \right\}. \quad (29)
\end{aligned}$$

For sufficiently long time duration t , the integral over t_σ introduces the delta function $\delta(\omega - \Omega - \xi_i \cdot (\mathbf{v}_0 - \mathbf{v}_\sigma) - \xi \cdot \mathbf{v}_\sigma)$ to the integrand. Integrating over ω then leads to

$$\begin{aligned}
\Phi_s(\mathbf{r}, t) = & -\frac{1}{2\pi} \int_{-\infty}^{\infty} d^2 \xi_i \int_{-\infty}^{\infty} d^2 \xi e^{i[\xi \cdot \mathbf{p}^0 - \xi_i \cdot \mathbf{p}_0^0]} e^{-i[\Omega + \xi_i \cdot (\mathbf{v}_0 - \mathbf{v}_\sigma) + \xi \cdot (\mathbf{v}_\sigma - \mathbf{v})] t} \\
& \times \oint d\mathbf{S}_\sigma \cdot \left\{ [A(z_0; \omega_i) \{e^{ik(\omega_i) r_\sigma^0} \eta(\alpha_i(\omega_i), \beta_i; \theta_\sigma^0, \phi_\sigma^0) + \hat{\Phi}_s(\mathbf{r}_\sigma^0, \mathbf{k}_i^+; \omega_i)\} \right. \\
& + B(z_0; \omega_i) \{e^{ik(\omega_i) r_\sigma^0} \eta(\pi - \alpha_i(\omega_i), \beta_i; \theta_\sigma^0, \phi_\sigma^0) + \hat{\Phi}_s(\mathbf{r}_\sigma^0, \mathbf{k}_i^-; \omega_i)\}] \\
& \left. \times \nabla_\sigma \left(C(z; \omega_s) e^{-ik(\omega_s) r_\sigma^0} \eta(\pi - \alpha(\omega_s), \beta; \theta_\sigma^0, \phi_\sigma^0) + D(z; \omega_s) e^{-ik(\omega_s) r_\sigma^0} \eta(\alpha(\omega_s), \beta; \theta_\sigma^0, \phi_\sigma^0) \right) \right\}, \quad (30)
\end{aligned}$$

where the Doppler shifted frequency of the scattered field is

$$\omega_s = \Omega + \xi_i \cdot (\mathbf{v}_0 - \mathbf{v}_\sigma) + \xi \cdot \mathbf{v}_\sigma. \quad (31)$$

It is important to note that the time dependence has been factored from the surface integral in going from Eq. (29) to Eq. (30) following our approximation for the assumed low Mach number motion. This means, for example, that the object's orientation with respect to the incoming and outgoing waves is not significantly altered for a time period large enough compared to the source period for the source to be considered harmonic. This is discussed in more detail, for example, in Sec. II C and Appendix B.

We can then express the scattered field in the waveguide in terms of the plane-wave scattering function $S(\alpha, \beta; \alpha_i, \beta_i; \omega)$ of the object. With the aid of Eq. (C19), Eq. (30) becomes

$$\begin{aligned}
\Phi_s(\mathbf{r}, t) = & \frac{1}{\pi} \int_{-\infty}^{\infty} \int_{-\infty}^{\infty} d^2 \xi d^2 \xi_i \frac{1}{k(\omega_s)} \\
& \times e^{i[\xi \cdot \mathbf{p}^0 - \xi_i \cdot \mathbf{p}_0^0]} e^{-i[\Omega + \xi_i \cdot (\mathbf{v}_0 - \mathbf{v}_\sigma) + \xi \cdot (\mathbf{v}_\sigma - \mathbf{v})] t} \\
& \times F(z, z_0; \xi, \xi_i; \omega_s, \omega_i), \quad (32)
\end{aligned}$$

which is an expression for the field scattered by a moving target with arbitrary shape, where

$$\begin{aligned}
F(z, z_0; \xi, \xi_i; \omega_s, \omega_i) = & \{A(z_0; \omega_i) C(z; \omega_s) S(\pi - \alpha(\omega_s), \beta; \alpha_i(\omega_i), \beta_i; \omega_s) \\
& + A(z_0; \omega_i) D(z; \omega_s) S(\alpha(\omega_s), \beta; \alpha_i(\omega_i), \beta_i; \omega_s) \\
& + B(z_0; \omega_i) C(z; \omega_s) S(\pi - \alpha(\omega_s), \beta; \pi - \alpha_i(\omega_i), \beta_i; \omega_s) \\
& + B(z_0; \omega_i) D(z; \omega_s) S(\alpha(\omega_s), \beta; \pi - \alpha_i(\omega_i), \beta_i; \omega_s)\}. \quad (33)
\end{aligned}$$

The formulation is fully bistatic and incorporates horizontal velocities of the source, target, and receiver. The source is assumed to be a simple-harmonic one radiating at frequency Ω , but the received time series will contain multiple frequency components due to Doppler effects. The Doppler frequency shifts are indicated in the argument of the complex exponential function of Eq. (32).

When the source, target, and receiver are at rest, all incident frequencies ω_i and scattered frequencies ω_s are equal to the source frequency Ω . In this case Eq. (32) reduces to Eq. (18) of Ref. 7 multiplied by $\exp(-i\Omega t)$ where reciprocity for harmonic waves

$$d_0 G(\mathbf{r}_\sigma | \mathbf{r}_0; \omega) = d_\sigma G(\mathbf{r}_0 | \mathbf{r}_\sigma; \omega) \quad (34)$$

was invoked for the incident field and the medium densities d_0 and d_σ in the layers of the source and target depth were assumed identical.

In Eq. (33), all coefficients (A 's and B 's) of the incident field are evaluated at the incident frequency ω_i , and all the coefficients of the scattered field (C 's and D 's) are evaluated at the scattered frequency ω_s . The wave number normalization k^{-1} and the plane-wave scatter function S are evaluated

at the scattered frequency ω_s as well. The equivalent elevation angles α_i of the incident plane waves are evaluated at the incident frequency ω_i , and the equivalent elevation angles α of the scattered plane waves are evaluated at the scattered frequency ω_s .

B. Spectral representation of the Doppler-shifted field scattered from a moving target by a source with arbitrary time dependence in a stratified waveguide

The Doppler-shifted scattered field induced by a source with arbitrary time dependence $q(t)$ and frequency spectrum $Q(\Omega)$ can be obtained in the receiver's frame of reference from Eq. (32) by Fourier synthesis as

$$\begin{aligned} \Psi_s(\mathbf{r}, t) = & \frac{1}{2\pi^2} \int_{-\infty}^{\infty} d\Omega Q(\Omega) \int_{-\infty}^{\infty} \int_{-\infty}^{\infty} d^2\xi d^2\xi_i \frac{1}{k(\omega_s)} \\ & \times e^{i[\xi \cdot \rho^0 - \xi_i \cdot \rho_0^0]} e^{-i[\Omega + \xi_i \cdot (\mathbf{v}_0 - \mathbf{v}_\sigma) + \xi \cdot (\mathbf{v}_\sigma - \mathbf{v})]t} \\ & \times F(z, z_0; \xi, \xi_i; \omega_s, \omega_i). \end{aligned} \quad (35)$$

A direct implementation of Eq. (35), however, will be inefficient because the four-dimensional wave number integrals are coupled with time in the argument of the complex exponential function and so need to be evaluated at each individual time instant. Similar difficulties for the passive problem of modeling propagation from a moving source to a moving receiver are discussed in Ref. 4 by Schmidt and Kuperman. They note that by transforming the Doppler-shifted field from the "source frequency" to a representation in terms of the "receiver frequency," the wave number and frequency integrations can be integrated independently.⁴

The frequency spectrum of the scattered field in the receiver's frame of reference is obtained by applying a Fourier transform to Eq. (35),

$$\Psi_s(\mathbf{r}, \omega') = \int_{-\infty}^{\infty} dt e^{i\omega' t} \Psi_s(\mathbf{r}, t) \quad (36)$$

where ω' is the frequency in the receiver's frame of reference. Integrating over t introduces the delta function $\delta(\omega' - \Omega - \xi_i \cdot (\mathbf{v}_0 - \mathbf{v}_\sigma) - \xi \cdot (\mathbf{v}_\sigma - \mathbf{v}))$ in the integrand. Upon integrating over Ω , the frequency spectrum of the Doppler-shifted scattered field in the receiver's frame of reference then becomes

$$\begin{aligned} \Psi_s(\mathbf{r}, \omega') = & \frac{1}{\pi} \int_{-\infty}^{\infty} \int_{-\infty}^{\infty} d^2\xi d^2\xi_i \frac{1}{k(\omega_s)} e^{i[\xi \cdot \rho^0 - \xi_i \cdot \rho_0^0]} \\ & \times Q(\omega' - \xi_i \cdot (\mathbf{v}_0 - \mathbf{v}_\sigma) - \xi \cdot (\mathbf{v}_\sigma - \mathbf{v})) \\ & \times F(z, z_0; \xi, \xi_i; \omega_s, \omega_i), \end{aligned} \quad (37)$$

where the shifted frequencies ω_i and ω_s in terms of ω' are equal to

$$\omega_i = \omega' + \xi \cdot (\mathbf{v} - \mathbf{v}_\sigma) + \xi_i \cdot \mathbf{v}_\sigma \quad (38)$$

and

$$\omega_s = \omega' + \xi \cdot \mathbf{v}. \quad (39)$$

Equation (37) can be implemented efficiently and directly without the need for time domain processing.

C. Normal mode representation of the Doppler-shifted field scattered from a moving target by a simple-harmonic source in a stratified waveguide

At sufficiently long source and receiver ranges from the target, the scattered field can be well represented as a sum of normal modes. The modal representation for the scattered field with a simple-harmonic source is derived in this section.

Green's function for the time-domain wave equation in a waveguide can be written as an inverse Fourier transform of the modal form of Green's function for the Helmholtz equation,

$$\begin{aligned} G(\mathbf{r}, t | \mathbf{r}_\sigma, t_\sigma) = & \frac{1}{2\pi} \int_{-\infty}^{\infty} d\omega G(\mathbf{r} | \mathbf{r}_\sigma; \omega) e^{-i\omega(t-t_\sigma)} \\ = & \frac{1}{2\pi} \int_{-\infty}^{\infty} d\omega e^{-i\omega(t-t_\sigma)} \\ & \times \frac{id}{4} \sum_m u_m(z; \omega) u_m(z_\sigma; \omega) \\ & \times H_0^{(1)}(\xi_m(\omega) |\boldsymbol{\rho} - \boldsymbol{\rho}_\sigma|), \end{aligned} \quad (40)$$

where $u_m(z; \omega)$ and $\xi_m(\omega)$ are the amplitude function and horizontal wave number of the m th mode at frequency ω . We assume $\xi_m(\omega) |\boldsymbol{\rho} - \boldsymbol{\rho}_\sigma| \gg 1$, and the asymptotic form of the zeroth-order Hankel function of the first kind is used

$$\begin{aligned} H_0^{(1)}(\xi_m(\omega) |\boldsymbol{\rho} - \boldsymbol{\rho}_\sigma|) \\ \approx \sqrt{\frac{2}{\pi \xi_m(\omega) |\boldsymbol{\rho} - \boldsymbol{\rho}_\sigma|}} e^{i(\xi_m(\omega) |\boldsymbol{\rho} - \boldsymbol{\rho}_\sigma| - \pi/4)}. \end{aligned} \quad (41)$$

For a moving target, the horizontal position vector $\boldsymbol{\rho}_\sigma$ is

$$\begin{aligned} \boldsymbol{\rho}_\sigma = & \boldsymbol{\rho}_\sigma^0 + \mathbf{v}_\sigma t_\sigma \\ = & (\rho_\sigma^0 \cos \phi_\sigma^0 \mathbf{i}_x + \rho_\sigma^0 \sin \phi_\sigma^0 \mathbf{i}_y) \\ & + (v_\sigma t_\sigma \cos \phi_\sigma \mathbf{i}_x + v_\sigma t_\sigma \sin \phi_\sigma \mathbf{i}_y), \end{aligned} \quad (42)$$

where $\boldsymbol{\rho}_\sigma^0$ is its initial position at $t_\sigma=0$ and \mathbf{v}_σ is its horizontal velocity. Similarly, the horizontal position vector of the receiver $\boldsymbol{\rho}$ is

$$\begin{aligned} \boldsymbol{\rho} = & \boldsymbol{\rho}^0 + \mathbf{v} t \\ = & (\rho^0 \cos \phi^0 \mathbf{i}_x + \rho^0 \sin \phi^0 \mathbf{i}_y) + (v t \cos \phi \mathbf{i}_x + v t \sin \phi \mathbf{i}_y), \end{aligned} \quad (43)$$

where $\boldsymbol{\rho}^0$ is its initial position at $t_\sigma=0$ and \mathbf{v} is its horizontal velocity.

For the bistatic configuration used in the scattering problem, the horizontal range to a point on the target is much smaller than the range to the receiver so that $|\boldsymbol{\rho}_\sigma| \ll |\boldsymbol{\rho}|$. For low Mach number motions of the target as in typical sonar scenarios, the displacements $|\mathbf{v}_\sigma t_\sigma|$ of a target point and $|\mathbf{v} t|$ of the receiver are also much smaller than $|\boldsymbol{\rho}|$ so that the azimuthal angle of the vector $\boldsymbol{\rho}^0 + \mathbf{v} t - \boldsymbol{\rho}_\sigma^0$ is approximately equal to the azimuthal angle ϕ^0 of the vector $\boldsymbol{\rho}^0$ even for a time duration t so much larger than the source period that the source can be considered harmonic. An approximation for $|\boldsymbol{\rho} - \boldsymbol{\rho}_\sigma|$ can then be made that

$$|\boldsymbol{\rho} - \boldsymbol{\rho}_\sigma| = |\boldsymbol{\rho}^0 + \mathbf{v}t - \boldsymbol{\rho}_\sigma^0 - \mathbf{v}_\sigma t_\sigma|$$

$$\approx |\boldsymbol{\rho}^0 + \mathbf{v}t - \boldsymbol{\rho}_\sigma^0| - v_\sigma t_\sigma \cos(\phi^0 - \varphi_\sigma). \quad (44a)$$

Similarly, the azimuthal angle of the vector $\boldsymbol{\rho}^0 - \boldsymbol{\rho}_\sigma^0$ is approximated as ϕ^0 because $|\boldsymbol{\rho}_\sigma| \ll |\boldsymbol{\rho}|$. This leads to

$$|\boldsymbol{\rho} - \boldsymbol{\rho}_\sigma| \approx |\boldsymbol{\rho}^0 - \boldsymbol{\rho}_\sigma^0| + vt \cos(\phi^0 - \varphi) - v_\sigma t_\sigma \cos(\phi^0 - \varphi_\sigma). \quad (44b)$$

Then since $|\boldsymbol{\rho}_\sigma^0| \ll |\boldsymbol{\rho}^0|$ we have

$$|\boldsymbol{\rho} - \boldsymbol{\rho}_\sigma| \approx \rho^0 - \rho_\sigma^0 \cos(\phi^0 - \phi_\sigma^0) + vt \cos(\phi^0 - \varphi) - v_\sigma t_\sigma \cos(\phi^0 - \varphi_\sigma). \quad (44c)$$

Green's function for the time-domain scalar wave equation from a point on the surface of the target \mathbf{r}_σ at retarded time t_σ to the receiver location \mathbf{r} at time t then can be approximated as

$$G(\mathbf{r}, t | \mathbf{r}_\sigma, t_\sigma) = \frac{1}{2\pi} \int_{-\infty}^{\infty} d\omega e^{-i\omega(t-t_\sigma)}$$

$$\times \frac{id}{\sqrt{8\pi}} e^{-i(\pi/4)} \sum_m \frac{u_m(z; \omega) u_m(z_\sigma; \omega)}{\sqrt{\xi_m(\omega)} \rho^0}$$

$$\times e^{i\xi_m(\omega)[\rho^0 - \rho_\sigma^0 \cos(\phi^0 - \phi_\sigma^0)]}$$

$$\times e^{i\xi_m(\omega)v \cos(\phi^0 - \varphi)t} e^{-i\xi_m(\omega)v_\sigma \cos(\phi^0 - \varphi_\sigma)t_\sigma}. \quad (45)$$

As in Eqs. (41) and (42) of Ref. 6, the Green function

and the incident field are now expressed as a linear superposition of equivalent plane waves in the layer of the target via

$$G(\mathbf{r}, t | \mathbf{r}_\sigma, t_\sigma) = \frac{1}{2\pi} \int_{-\infty}^{\infty} d\omega e^{-i\omega(t-t_\sigma)}$$

$$\times \sum_m [A_m(\mathbf{r}^0; \omega) e^{-ik(\omega)r_\sigma^0 \eta(\pi - \alpha_m, \phi^0; \theta_\sigma^0, \phi_\sigma^0)}$$

$$- B_m(\mathbf{r}^0; \omega) e^{-ik(\omega)r_\sigma^0 \eta(\alpha_m, \phi^0; \theta_\sigma^0, \phi_\sigma^0)}]$$

$$\times e^{i\xi_m(\omega)v \cos(\phi^0 - \varphi)t} e^{-i\xi_m(\omega)v_\sigma \cos(\phi^0 - \varphi_\sigma)t_\sigma} \quad (46)$$

and

$$\Phi_i(\mathbf{r}_\sigma, t_\sigma) = \sum_l \frac{1}{1 + \frac{v_0}{v_l^G(\Omega)} \cos(\phi_0^0 - \varphi_0)}$$

$$\times [A_l(\mathbf{r}_0^0; \omega_l) e^{ik(\omega_l)r_\sigma^0 \eta(\alpha_l, \pi - \phi_0^0; \theta_\sigma^0, \phi_\sigma^0)}$$

$$- B_l(\mathbf{r}_0^0; \omega_l) e^{ik(\omega_l)r_\sigma^0 \eta(\pi - \alpha_l, \pi - \phi_0^0; \theta_\sigma^0, \phi_\sigma^0)}]$$

$$\times e^{-i(\omega_l + \xi_l(\omega_l)v_\sigma \cos(\phi_0^0 - \varphi_\sigma))t_\sigma}, \quad (47)$$

where Eq. (47) is derived in from Eq. (B11), and ω_l is the Doppler-shifted frequency of the l th mode as defined in Eq. (B10). Substituting Eqs. (46) and (47) into Eq. (12) leads to

$$\Phi_s(\mathbf{r}, t) = -\frac{1}{2\pi} \int_0^{t^+} dt_\sigma \oint d\mathbf{S}_\sigma \cdot \left\{ \left[\sum_l \frac{1}{1 + [v_0/v_l^G(\Omega)] \cos(\phi_0^0 - \varphi_0)} [A_l(\mathbf{r}_0^0; \omega_l) e^{ik(\omega_l)r_\sigma^0 \eta(\alpha_l, \pi - \phi_0^0; \theta_\sigma^0, \phi_\sigma^0)} \right. \right.$$

$$\left. - B_l(\mathbf{r}_0^0; \omega_l) e^{ik(\omega_l)r_\sigma^0 \eta(\pi - \alpha_l, \pi - \phi_0^0; \theta_\sigma^0, \phi_\sigma^0)}] e^{-i(\omega_l + \xi_l(\omega_l)v_\sigma \cos(\phi_0^0 - \varphi_\sigma))t_\sigma} + \Phi_s(\mathbf{r}_\sigma, t_\sigma) \right]$$

$$\times \nabla_\sigma \left(\int_{-\infty}^{\infty} d\omega e^{-i\omega(t-t_\sigma)} \sum_m [A_m(\mathbf{r}^0; \omega) e^{-ik(\omega)r_\sigma^0 \eta(\pi - \alpha_m, \phi^0; \theta_\sigma^0, \phi_\sigma^0)} \right.$$

$$\left. - B_m(\mathbf{r}^0; \omega) e^{-ik(\omega)r_\sigma^0 \eta(\alpha_m, \phi^0; \theta_\sigma^0, \phi_\sigma^0)}] e^{i\xi_m(\omega)v \cos(\phi^0 - \varphi)t} e^{-i\xi_m(\omega)v_\sigma \cos(\phi^0 - \varphi_\sigma)t_\sigma} \right) \Bigg\}. \quad (48)$$

For low Mach number motion, the scattered field on the surface of the object in Eq. (48) is approximately $\hat{\Phi}_s(\mathbf{r}_\sigma, t_\sigma) \approx \hat{\Phi}_s(\mathbf{r}_\sigma; \omega_l) e^{-i\omega_l t_\sigma}$ for a given incident plane wave. We define the wave number vectors for the downgoing and upgoing waves for the l th mode as

$$\mathbf{k}_l^+ = \xi_l \hat{\mathbf{i}}_p + \gamma_l \hat{\mathbf{i}}_z, \quad (49)$$

$$\mathbf{k}_l^- = \xi_l \hat{\mathbf{i}}_p - \gamma_l \hat{\mathbf{i}}_z. \quad (50)$$

The scattered field on the surface of the target given in Eq. (48) can then be represented in terms of downgoing and upgoing plane incident waves with unit amplitudes $\hat{\Phi}_s(\mathbf{r}_\sigma, \mathbf{k}_l^+; \omega_l)$ and $\hat{\Phi}_s(\mathbf{r}_\sigma, \mathbf{k}_l^-; \omega_l)$, respectively, via

$$\Phi_s(\mathbf{r}_\sigma, t_\sigma) = \sum_l \frac{e^{-i\omega_l t_\sigma}}{1 + \frac{v_0}{v_l^G(\Omega)} \cos(\phi_0^0 - \varphi_0)} [A_l(\mathbf{r}_0^0; \omega_l) \hat{\Phi}_s(\mathbf{r}_\sigma, \mathbf{k}_l^+; \omega_l) - B_l(\mathbf{r}_0^0; \omega_l) \hat{\Phi}_s(\mathbf{r}_\sigma, \mathbf{k}_l^-; \omega_l)]. \quad (51)$$

Just as in the derivation for the spectral representation, in Sec. II A, approximations are made for $\hat{\Phi}_s(\mathbf{r}_\sigma, \mathbf{k}_l^+; \omega_l)$ and $\hat{\Phi}_s(\mathbf{r}_\sigma, \mathbf{k}_l^-; \omega_l)$ that account for rigid body translation. Equation (51) then becomes

$$\begin{aligned} \Phi_s(\mathbf{r}_\sigma, t_\sigma) = \sum_l \frac{1}{1 + \frac{v_0}{v_l^G(\Omega)} \cos(\phi_0^0 - \varphi_0)} e^{-i(\omega_l + \xi_l(\omega_l) v_\sigma \cos(\phi_0^0 - \varphi_\sigma)) t_\sigma} \\ \times [A_l(\mathbf{r}_0^0; \omega_l) \hat{\Phi}_s(\mathbf{r}_\sigma, \mathbf{k}_l^+; \omega_l) - B_l(\mathbf{r}_0^0; \omega_l) \hat{\Phi}_s(\mathbf{r}_\sigma, \mathbf{k}_l^-; \omega_l)]. \end{aligned} \quad (52)$$

When this is inserted into Eq. (48) the scattered field takes the form

$$\begin{aligned} \Phi_s(\mathbf{r}, t) = -\frac{1}{2\pi} \int_0^{t^+} dt_\sigma \oint d\mathbf{S}_\sigma \cdot \left\{ \sum_l \frac{1}{1 + [v_0/v_l^G(\Omega)] \cos(\phi_0^0 - \varphi_0)} e^{-i(\omega_l + \xi_l(\omega_l) v_\sigma \cos(\phi_0^0 - \varphi_\sigma)) t_\sigma} \right. \\ \times \left(A_l(\mathbf{r}_0^0; \omega_l) [e^{ik(\omega_l) r_\sigma^0 \eta(\alpha_l, \pi - \phi_0^0; \theta_\sigma^0, \phi_\sigma^0)} + \hat{\Phi}_s(\mathbf{r}_\sigma, \mathbf{k}_l^+; \omega_l)] \right. \\ \left. - B_l(\mathbf{r}_0^0; \omega_l) [e^{ik(\omega_l) r_\sigma^0 \eta(\pi - \alpha_l, \pi - \phi_0^0; \theta_\sigma^0, \phi_\sigma^0)} + \hat{\Phi}_s(\mathbf{r}_\sigma, \mathbf{k}_l^-; \omega_l)] \right) \\ \times \nabla_\sigma \left(\int_{-\infty}^{\infty} d\omega e^{-i\omega(t-t_\sigma)} \sum_m [A_m(\mathbf{r}^0; \omega) e^{-ik(\omega) r_\sigma^0 \eta(\pi - \alpha_m, \phi^0; \theta_\sigma^0, \phi_\sigma^0)} - B_m(\mathbf{r}^0; \omega) e^{-ik(\omega) r_\sigma^0 \eta(\alpha_m, \phi^0; \theta_\sigma^0, \phi_\sigma^0)}] \right. \\ \left. \times e^{i\xi_m(\omega) v_\sigma \cos(\phi^0 - \varphi)} e^{-i\xi_m(\omega) v_\sigma \cos(\phi^0 - \varphi_\sigma) t_\sigma} \right) \Bigg\}. \end{aligned} \quad (53)$$

For sufficiently long time duration t , integration over t_σ introduces the delta function $\delta(\omega - \omega_l - \xi_l(\omega_l) v_\sigma \cos(\phi_0^0 - \varphi_\sigma) - \xi_m(\omega) v_\sigma \cos(\phi^0 - \varphi_\sigma))$ to the integrand.

In order to integrate over ω , we need to solve the transcendental equation for the argument $h(\omega)$ of the δ function

$$\begin{aligned} h(\omega) = \omega - \omega_l - \xi_l(\omega_l) v_\sigma \cos(\phi_0^0 - \varphi_\sigma) \\ - \xi_m(\omega) v_\sigma \cos(\phi^0 - \varphi_\sigma) = 0. \end{aligned} \quad (54)$$

Equation (54) can be solved numerically. However, an approximation that can be evaluated analytically is desired. The derivative of $h(\omega)$ with respect to ω is

$$\begin{aligned} \frac{dh(\omega)}{d\omega} &= 1 - \frac{d\xi_m(\omega)}{d\omega} v_\sigma \cos(\phi^0 - \varphi_\sigma) \\ &= 1 - \frac{v_\sigma}{v_m^G(\omega)} \cos(\phi^0 - \varphi_\sigma), \end{aligned} \quad (55)$$

where $v_m^G(\omega)$ is the group velocity of the m th mode at frequency ω . For low Mach number motions, Eq. (55) is close to unity, so that $h(\omega)$ is nearly linear around the roots of Eq. (54). Using the Newton–Raphson method with the frequency ω_l as an initial guess, the first iteration yields a reasonably accurate solution of Eq. (54) as

$$\omega_{m,l} = \omega_l - \frac{h(\omega_l)}{h'(\omega_l)} = \omega_l + \frac{\xi_l(\omega_l) v_\sigma \cos(\phi_0^0 - \varphi_\sigma) + \xi_m(\omega_l) v_\sigma \cos(\phi^0 - \varphi_\sigma)}{1 - \frac{v_\sigma}{v_m^G(\omega_l)} \cos(\phi^0 - \varphi_\sigma)}, \quad (56)$$

where $v_m^G(\omega_l)$ is the group velocity of the m th mode at frequency ω_l . Here $\omega_{m,l}$ is the doubly Doppler-shifted frequency with respect to the l th incident mode and the m th outgoing mode. Using the property of the δ function for any functions f, h [Eq. (9.6) in Ref. 2] it must hold that

$$\int_{-\infty}^{\infty} f(\omega) \delta(h(\omega)) d\omega = \left[\frac{f(\omega)}{|dh/d\omega|} \right]_{\omega=\omega^*}, \quad (57)$$

where ω^* is a zero of h , i.e., $h(\omega^*)=0$. Integrating over ω gives

$$\begin{aligned} \Phi_s(\mathbf{r}, t) = & - \sum_l \sum_m \oint d\mathbf{S}_\sigma \cdot \left\{ \frac{1}{1 + [v_0/v_l^G(\Omega)] \cos(\phi_0^0 - \varphi_0)} \frac{1}{1 - [v_\sigma/v_m^G(\omega_{m,l})] \cos(\phi^0 - \varphi_\sigma)} \right. \\ & \times (A_l(\mathbf{r}_0^0; \omega_l) [e^{ik(\omega_l)r_\sigma^0 \eta(\alpha_l, \pi - \phi_0^0; \theta_\sigma^0, \phi_\sigma^0)} + \hat{\Phi}_s(\mathbf{r}_\sigma^0, \mathbf{k}_l^+; \omega_l)] \\ & - B_l(\mathbf{r}_0^0; \omega_l) [e^{ik(\omega_l)r_\sigma^0 \eta(\pi - \alpha_l, \pi - \phi_0^0; \theta_\sigma^0, \phi_\sigma^0)} + \hat{\Phi}_s(\mathbf{r}_\sigma^0, \mathbf{k}_l^-; \omega_l)]) \\ & \times \nabla_\sigma \left([A_m(\mathbf{r}^0; \omega_{m,l}) e^{-ik(\omega_{m,l})r_\sigma^0 \eta(\pi - \alpha_m, \phi^0; \theta_\sigma^0, \phi_\sigma^0)} - B_m(\mathbf{r}^0; \omega) e^{-ik(\omega_{m,l})r_\sigma^0 \eta(\alpha_m, \phi^0; \theta_\sigma^0, \phi_\sigma^0)}] \right. \\ & \left. \left. \times e^{-i(\omega_{m,l} - \xi_m(\omega_{m,l})v \cos(\phi^0 - \varphi))t} \right) \right\}. \end{aligned} \quad (58)$$

With the aid of Eq. (C19), the scattered field can finally be written in terms of the scattering function of the target as

$$\begin{aligned} \Phi_s(\mathbf{r}, t) = & 4\pi \sum_l \sum_m \frac{1}{1 + \frac{v_0}{v_l^G(\Omega)} \cos(\phi_0^0 - \varphi_0)} \frac{1}{1 - \frac{v_\sigma}{v_m^G(\omega_{m,l})} \cos(\phi^0 - \varphi_\sigma)} \frac{1}{k(\omega_{m,l})} \\ & \times [A_l(\mathbf{r}_0^0; \omega_l) A_m(\mathbf{r}^0; \omega_{m,l}) S(\pi - \alpha_m(\omega_{m,l}), \phi^0; \alpha_l(\omega_l), \pi - \phi_0^0; \omega_{m,l}) \\ & - A_l(\mathbf{r}_0^0; \omega_l) B_m(\mathbf{r}^0; \omega_{m,l}) S(\alpha_m(\omega_{m,l}), \phi^0; \alpha_l(\omega_l), \pi - \phi_0^0; \omega_{m,l}) \\ & - B_l(\mathbf{r}_0^0; \omega_l) A_m(\mathbf{r}^0; \omega_{m,l}) S(\pi - \alpha_m(\omega_{m,l}), \phi^0; \pi - \alpha_l(\omega_l), \pi - \phi_0^0; \omega_{m,l}) \\ & + B_l(\mathbf{r}_0^0; \omega_l) B_m(\mathbf{r}^0; \omega_{m,l}) S(\alpha_m(\omega_{m,l}), \phi^0; \pi - \alpha_l(\omega_l), \pi - \phi_0^0; \omega_{m,l})] e^{-i(\omega_{m,l} - \xi_m(\omega_{m,l})v \cos(\phi^0 - \varphi))t}. \end{aligned} \quad (59)$$

When there is no motion of the source, target, or receiver, all the incident and scattered frequencies are evaluated at the source frequency Ω , and Eq. (59) leads to the special case Eq. (51) of Ref. 6 multiplied by $\exp(-i\Omega t)$.

If the number of modes that truncates the modal summation excited at the source frequency Ω is N , this same number can be used to truncate the incident and outgoing modal summations for low Mach number motions. The total number of discrete frequency components will then be roughly N^2 due to the coupling between incident and scattered modes at the target.

D. Normal mode representation of the Doppler-shifted field scattered from a moving target by a source with arbitrary time dependence in a stratified waveguide

For a source with arbitrary time dependence $q(t)$ and frequency spectrum $Q(\Omega)$, the normal mode representation of the Doppler-shifted scattered field can be formulated by Fourier synthesis as

$$\Psi_s(\mathbf{r}, t) = \frac{1}{2\pi} \int_{-\infty}^{\infty} d\Omega Q(\Omega) \Phi_s(\mathbf{r}, t), \quad (60)$$

where $\Phi_s(\mathbf{r}, t)$ is given in Eq. (59).

Equation (60), however, is computationally inefficient because the modal summation needs to be evaluated at every time instant. Just as in the spectral representation of the scattered field from a source with arbitrary time dependence, transformation to the frequency spectrum in the receiver's frame of reference can speed up the computation significantly.

Applying a Fourier transform to Eq. (60) is not desired because both shifted frequencies ω_l and $\omega_{m,l}$ of the incident and scattered field are approximations obtained by the Newton–Raphson method in terms of the source frequency Ω . A derivation for the shifted frequencies in terms of the receiving frequency ω' based on those approximated values will give inaccurate and complicated results. Therefore, the frequency spectrum in the receiver's frame of reference needs to be derived from intermediate expressions for the incident field and scattered field before the approximations by the Newton–Raphson method are made. The derivation is lengthy and is given in Appendix D. With the aid of Eq. (C19), the scattered field of Eq. (D14) is expressed in terms of the scattering function of the target as

$$\begin{aligned}\Psi_s(\mathbf{r}, \omega') = & 4\pi \sum_l \sum_m \frac{Q(\Omega_{lm})}{k(\omega'_m)} \frac{1}{1 - \frac{v}{v_m^G(\omega'_m)} \cos(\phi^0 - \varphi)} \frac{1}{1 + \frac{v_\sigma}{v_l^G(\omega'_{l,m})} \cos(\phi_0^0 - \varphi_\sigma)} \\ & \times [A_l(\mathbf{r}_0^0; \omega'_{l,m}) A_m(\mathbf{r}^0; \omega'_m) S(\pi - \alpha_m(\omega'_m), \phi^0; \alpha_l(\omega'_{l,m}), \pi - \phi_0^0; \omega'_m) \\ & - A_l(\mathbf{r}_0^0; \omega'_{l,m}) B_m(\mathbf{r}^0; \omega'_m) S(\alpha_m(\omega'_m), \phi^0; \alpha_l(\omega'_{l,m}), \pi - \phi_0^0; \omega'_m) \\ & - B_l(\mathbf{r}_0^0; \omega'_{l,m}) A_m(\mathbf{r}^0; \omega'_m) S(\pi - \alpha_m(\omega'_m), \phi^0; \pi - \alpha_l(\omega'_{l,m}), \pi - \phi_0^0; \omega'_m) \\ & + B_l(\mathbf{r}_0^0; \omega'_{l,m}) B_m(\mathbf{r}^0; \omega'_m) S(\alpha_m(\omega'_m), \phi^0; \pi - \alpha_l(\omega'_{l,m}), \pi - \phi_0^0; \omega'_m)],\end{aligned}\quad (61)$$

where the frequency of the source spectrum is

$$\Omega_{lm} = \omega'_{l,m} + \xi_l(\omega'_{l,m}) v_0 \cos(\phi_0^0 - \varphi_0). \quad (62)$$

Equation (61) can be implemented efficiently and directly without the need for time domain processing.

III. ILLUSTRATIVE EXAMPLES

Equation (61) is implemented with a modified version of the normal mode code KRAKENC.¹³ The formulation is fully bistatic and incorporates the motion of source, target, and receiver. For simplicity, only monostatic configurations are illustrated. These have the strongest Doppler frequency shifts when only the target is in motion and the source and receiver are at rest.

The source function to be used in all examples is a Gaussian modulated wave form

$$q(t) = \frac{1}{\sqrt{2\pi}\sigma} e^{-(t-t_0)^2/2\sigma^2} e^{-i2\pi f_c(t-t_0)} \quad (63)$$

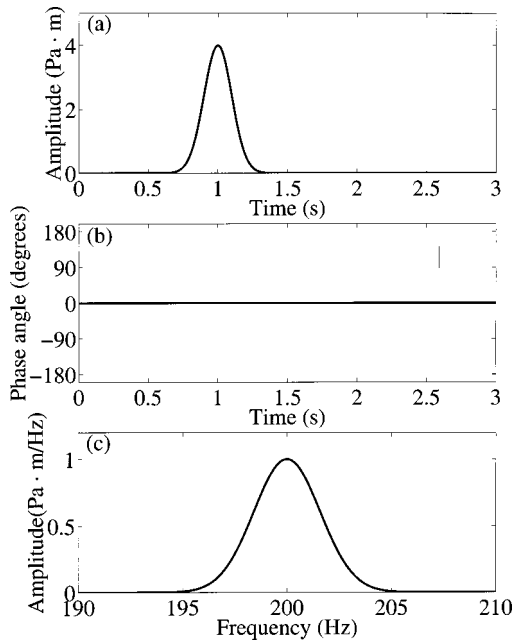


FIG. 2. Plot (a) and (b) show the amplitude and phase of the source function, demodulated by the 200 Hz carrier frequency, versus time. Plot (c) shows the magnitude of the frequency spectrum of the source.

with carrier frequency $f_c = 200$ Hz, $t_0 = 1$ s and $\sigma = 0.1$ s. Its frequency spectrum is

$$Q(f) = e^{-(1/2)\sigma^2[2\pi(f-f_c)]^2} e^{i2\pi f t_0}. \quad (64)$$

The amplitude and phase of the time series of the source demodulated by the carrier frequency $f_c = 200$ Hz is shown in Figs. 2(a) and 2(b). The frequency spectrum of the source is shown in Fig. 2(c).

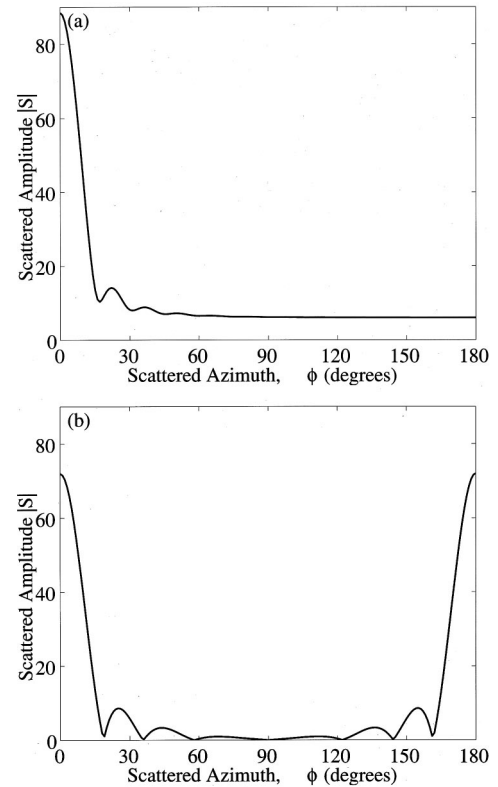


FIG. 3. The magnitude of the free space plane-wave scattering function $S(\theta = 90^\circ, \beta = \phi; \alpha_i = 90^\circ, \beta_i = 0^\circ)$ for (a) a pressure-release sphere with $ka = 12$ at 200 Hz and (b) a pressure-release circular disk with $ka = 12$ at 200 Hz. The incident wave is parallel to the disk's surface normal, i.e., at broadside to the disk.

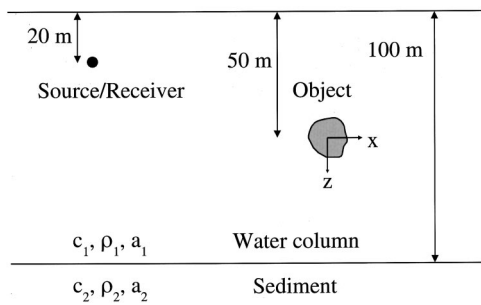


FIG. 4. Measurement geometry for object scattering in a Pekeris waveguide. The source and receiver are collocated at a depth of 20 m, and the centroid of the target is at a depth of 50 m.

All time series illustrations in this paper follow the same convention used in Figs. 2(a) and 2(b). They show the magnitude and phase of the signals demodulated by the carrier frequency at 200 Hz. The phase is only shown at times when the signal amplitude is not negligibly small. All horizontal axes of time series plots in this section are labeled with “reduced time,” which is the actual time minus the round-trip horizontal range divided by the sound speed.

Two types of targets are used as to illustrate scattering characteristics, including a pressure-release sphere and a perfectly reflecting circular disk which both have $ka = 12$ at 200

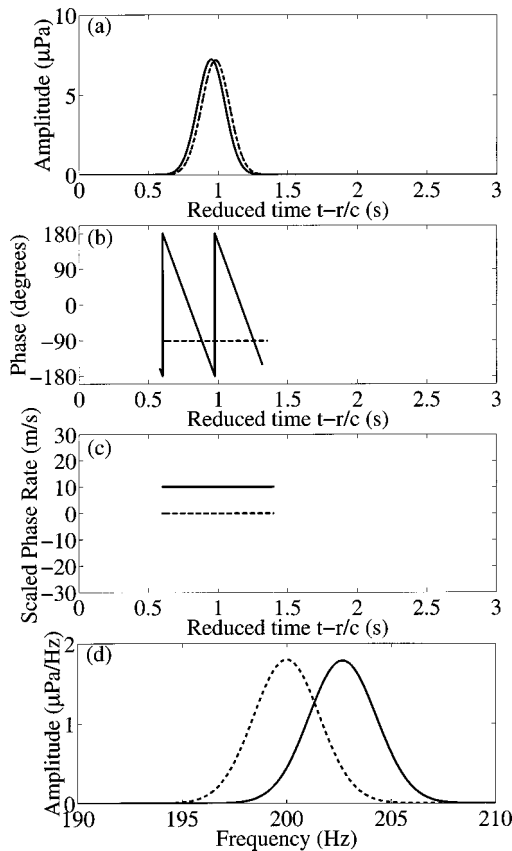


FIG. 5. The scattered field and its scaled phase rate for the Gaussian modulated source in free space. The object is a pressure-release sphere of $ka = 12$ at 200 Hz. The dashed curves are for a stationary target. The solid curves are for a target moving toward the source at 10 m/s. Plots (a) and (b) show the amplitude and phase of the time series demodulated by the 200 Hz carrier frequency. Plot (c) shows the scaled phase rate of the demodulated time series from Eq. (65). Plot (d) shows the frequency spectra.

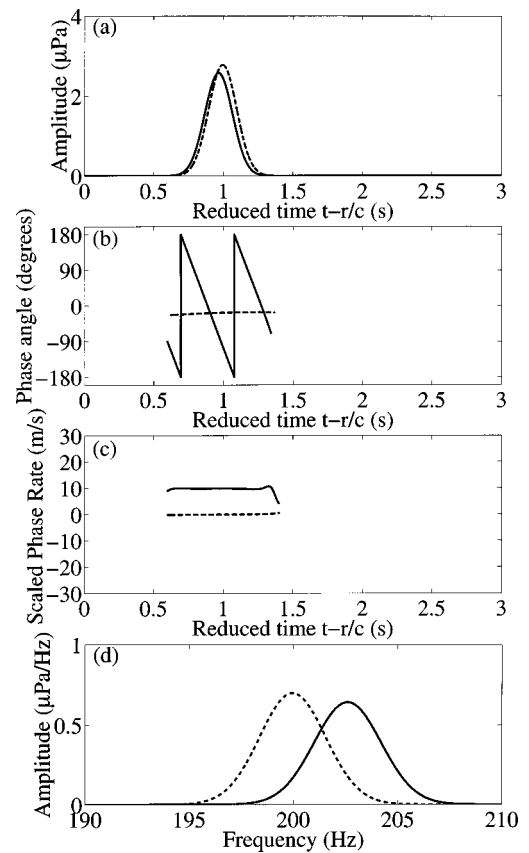


FIG. 6. The scattered field and its scaled phase rate for the Gaussian modulated source. The bottom type is silt. Source and receiver are collocated at 20-m depth with 50-m target depth. The horizontal range of the target is 2000 m from the source. The object is a pressure-release sphere of $ka = 12$ at 200 Hz. The dashed curves are for a stationary target. The solid curves are for a target moving toward the source at 10 m/s. Plots (a) and (b) show the amplitude and phase of the time series demodulated by the 200 Hz carrier frequency. Plot (c) shows the scaled phase rate of the demodulated time series Eq. (65). Plot (d) shows the frequency spectra.

Hz, where a is the radius of the sphere and disk. The free space plane wave scattering function of the sphere is given in Eq. (A2) of Ref. 7. The scatter function of the disk is given in Ref. 14. Figures 3(a) and (b) show the magnitude of the scatter functions versus scattering angle for the sphere and the disk, respectively. The incident wave is parallel to the disk’s surface normal, i.e., at broadside to the disk.

Before illustrating the problem in a waveguide, examples of object scattering in free space are shown for comparison. The measurement geometry is the same as that shown in Fig. 4 but without the waveguide boundaries.

A monostatic sonar with collocated point source and receiver senses a pressure-release sphere with $ka = 12$ at $f_c = 200$ Hz. The sonar and target are in water with a sound speed of 1500 m/s, and they are initially separated by 2000 m in the horizontal and 30 m in the vertical. Equation (C18) is used to perform the simulations. The dashed curves in Figs. 5(a) and 5(b) show the amplitude and phase of the demodulated time series of the scattered signals from a stationary target. The dashed curve in Fig. 5(d) shows its frequency spectrum. Since free space is nondispersive, and the scatter function is nearly constant over the frequency band of the source, the received wave form appears effectively as a

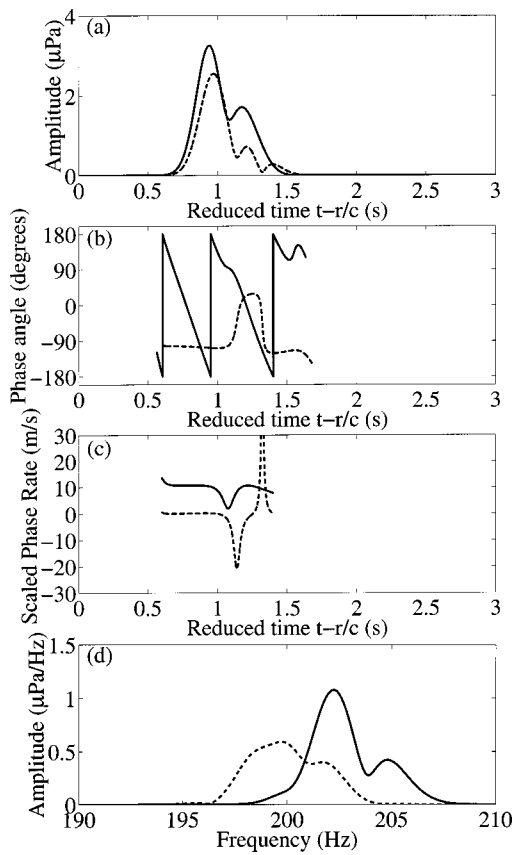


FIG. 7. Same as Fig. 6 except bottom type is sand.

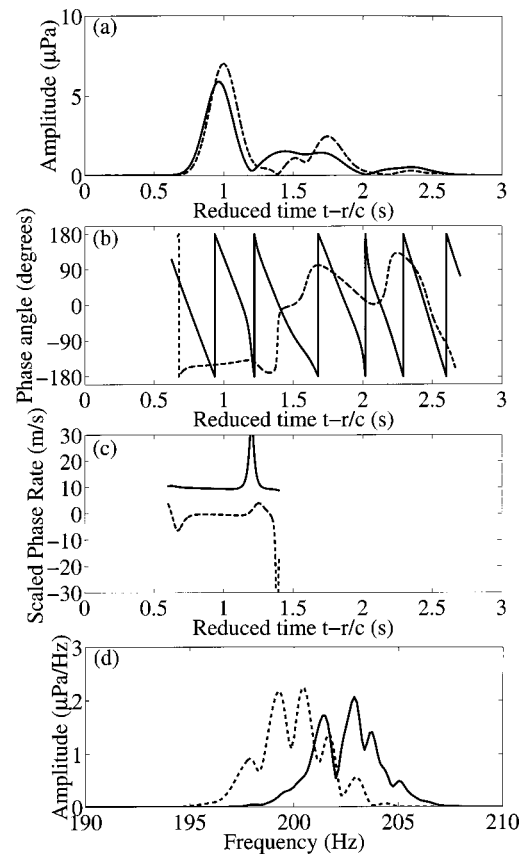


FIG. 8. Same as Fig. 6 except bottom type is limestone.

scaled and time-shifted version of the transmitted signal, with negligible spectral distortion. The time series after demodulation and the spectrum of the field scattered from a sphere moving at 10 m/s toward the source are shown as the solid curves in Figs. 5(a), 5(b) and 5(d). It can be seen that the free space Doppler-shifted spectrum can be very closely approximated by a translated version of the stationary spectrum since negligible distortion is introduced by the Doppler shift, dynamical factors described in Appendix C, and scatter function over the frequency band of the source. The phase angle versus time in Fig. 5(b) shows that the phase is nearly a constant versus time for a stationary object. For the moving target, the phase angle is decreasing with respect to time at a constant rate, which represents a single frequency shift induced by the target motion.

The frequency shift is linearly proportional to the radial component of target velocity in free space when the scattering function of the target does not vary significantly versus frequency within the band of the source. Active sonar and radar systems in free space typically take the scaled phase rate

$$\mu(t) = -\frac{c}{4\pi f_c} \frac{d\Theta(t)}{dt} \quad (65)$$

as an estimate of the target's radial velocity where $\Theta(t)$ is the phase angle of the sonar return after demodulation by the carrier frequency. The dashed curve and the solid curve in Fig. 5(c) show that the scaled phase rate $\mu(t)$ matches the

true value of the radial velocity of the targets, 0 m/s and 10 m/s for the examples shown.

In all illustrative examples of this section, a water column of 100 m depth is used to simulate a typical continental shelf environment. The density of the water is 1000 kg/m³, the sound speed is 1500 m/s, and the attenuation is 6.0×10^{-5} dB/λ. The simulations are performed over different seabed types to illustrate the dependence of the Doppler effects on bottom properties. All seabeds are modeled as half-spaces. The source and the receiver are collocated at a depth of 20 m without motion, and the centroid of the target is at a depth of 50 m.

First, we show how different bottom types affect the Doppler shifts. Sand, silt, and limestone are used as the homogeneous material of the bottom half-space. The density, sound speed, and attenuation are taken to be 1900 kg/m³, 1700 m/s, and 0.8 dB/λ for sand, 1400 kg/m³, 1520 m/s, and 0.3 dB/λ for silt. The density, compressional speed and shear speed of limestone are 2200 kg/m³, 2500 m/s, and 800 m/s, respectively. The attenuation coefficients are 0.1 and 0.2 dB/λ for compression and shear, respectively.

A silt bottom is used for the simulations in Fig. 6. A pressure-release sphere with $ka = 12$ at 200 Hz is used as the target. The dashed curves in Figs. 6(a) and 6(b) show the amplitude and phase of the demodulated time series of the scattered signals from a stationary target, and the dashed curve in Fig. 6(d) shows its frequency spectrum. Both the amplitude of the time series and frequency spectrum appear to be Gaussian, which indicates that the dispersion due to multipath effects in the waveguide is weak for this type of

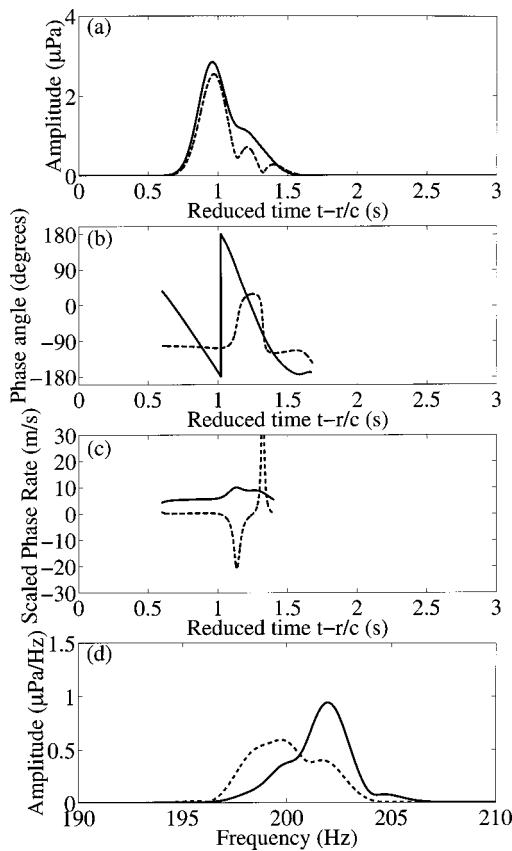


FIG. 9. Same as Fig. 6 except the bottom type is sand and target velocity is changed. The target is moving toward the source at 5 m/s.

bottom. The scattered field is dominated by the lowest order mode. The solid curves in Figs. 6(a) and 6(b) show the received time series scattered by a sphere moving toward the source at 10 m/s, and the solid curve in Fig. 6(d) shows its frequency spectrum. The shape of the time series still looks Gaussian, and the arrival time is slightly earlier than the stationary case due to the shortening of the horizontal distance. The frequency shifts due to Doppler effects can be observed in the solid curve in Fig. 6(d). The spectrum also looks Gaussian but is shifted with the frequency shift of the first mode, which is close to the frequency shift of the scattered field in free space. Similar to the examples for free space, the phase versus time shown in Fig. 6(b) is nearly a constant for the stationary target, and the phase is changing at nearly a constant rate for the moving target. Applying Eq. (65), the scaled phase rate $\mu(t)$ is calculated for both the stationary and the moving targets and is plotted as the dashed and the solid curves in Fig. 6(c), respectively. Because the sonar return is not significantly distorted by the multimodal dispersion and Doppler effects, the scaled phase rate is close to the target's true radial velocity for both the stationary and the moving target. This indicates that the scaled phase rate $\mu(t)$ in Eq. (65) can be used to estimate the radial velocity of targets for this particular scenario of a weakly dispersive waveguide.

Figure 7 shows demodulated time series and frequency spectra for a sand bottom. The same spherical scatterer is used as in Fig. 6. The dashed curves in Fig. 7(a) and 7(b) show the amplitude and phase of the demodulated time series

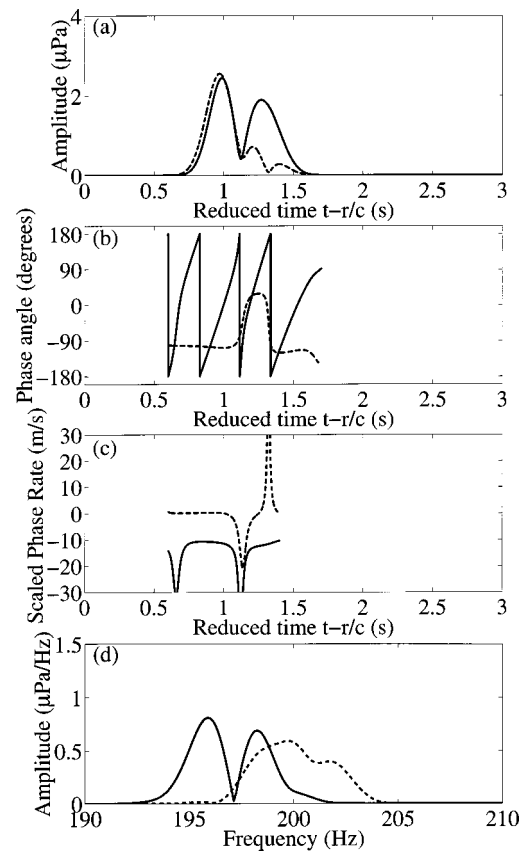


FIG. 10. Same as Fig. 6 except the bottom type is sand and target moves away from source at 10 m/s.

when the sphere is stationary. We see that the time series has not only the arrival from the first mode but also the late arrivals from the higher order modes with slower group velocities. This indicates that the dispersion is much stronger for a sand bottom than a silt bottom. The received signals from a moving sphere [solid curves in Fig. 7(a)] show that not only the first arrival is earlier than in the stationary case but the contributions of the higher order modes are also different. From Fig. 7(d), we can see that the spectrum of the stationary case (dashed curve) is distorted due to multimodal effects. The shifted spectrum (solid curve) is also distorted and is not simply a translated version of the stationary spectrum (dashed curve). This is because the lower order modes have larger frequency shifts than the higher order modes so that energy is nonuniformly shifted across frequency. The phase of the demodulated time series in Fig. 7(b) shows that the phase angle versus time for the stationary target (dashed curve) varies slowly but is no longer nearly a constant like in free space and for a silt bottom. This is because of the higher order modes introduce different phase changes. The phase change versus time (solid curve) is not changing at a constant rate as in free space or for a silt bottom. The higher order modes introduce multiple Doppler shifts and alter the rate of phase change. Figure 7(c) shows the scaled phase rate $\mu(t)$ of the demodulated time series calculated by Eq. (65). The dashed curve is for the stationary target and the solid curve is for the moving target. The strong late arrivals in the received field shown in Fig. 7(a) introduce significant distortion of the phase angle in Fig. 7(b) and make the scaled

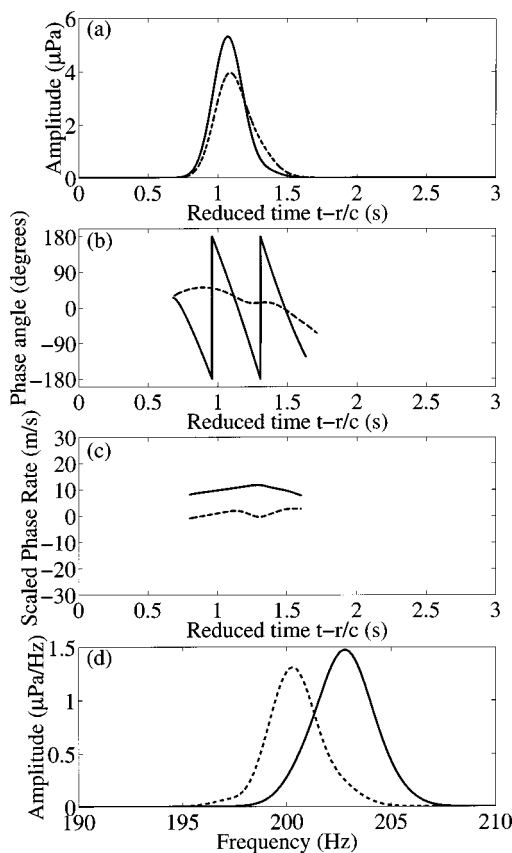


FIG. 11. Same as Fig. 6 except the bottom type is sand and the target is at 3000 m horizontal range from source/receiver.

phase rates in Fig. 7(c) inconsistent with the target's true radial velocities. Even if the target is not moving at all, a rapid change occurs in the scaled phase rate when a strong late arrival corresponding to a higher order mode with slower group velocity arrives. The difference between the scaled phase rate $\mu(t)$ and the target's true radial velocity can be greater than 10 m/s when a strong late arrival is received. This example shows that when the sonar return is significantly distorted by multimodal effects, the scaled phase rate $\mu(t)$ in Eq. (65) cannot be used to reliably estimate the target's radial component velocity.

Limestone bottoms typically have relatively low attenuation, support many higher order modes and so lead to highly dispersive shallow water propagation. As shown in the received field scattered by a stationary sphere (dashed curves) and by a sphere moving at 10 m/s toward the source (solid curves) in Fig. 8(a), several late arrivals are present with long time delays induced by the higher order modes. The highly distorted spectra for a stationary sphere and a sphere moving toward the source at 10 m/s are shown in Fig. 8(d). Again, the Doppler-shifted frequency spectrum (solid curve) is not simply a translated version of the stationary spectrum (dashed curve). Figure 8(b) shows that the phase changes significantly versus time due to the multimodal effects even if the target is not moving. While the target is moving, the phase change is complicated due to the multiple Doppler shifts. The scaled phase rate $\mu(t)$ of the demodulated time series in Eq. (65) for both the stationary and moving target are shown as the dashed curve and the solid curve in Fig.

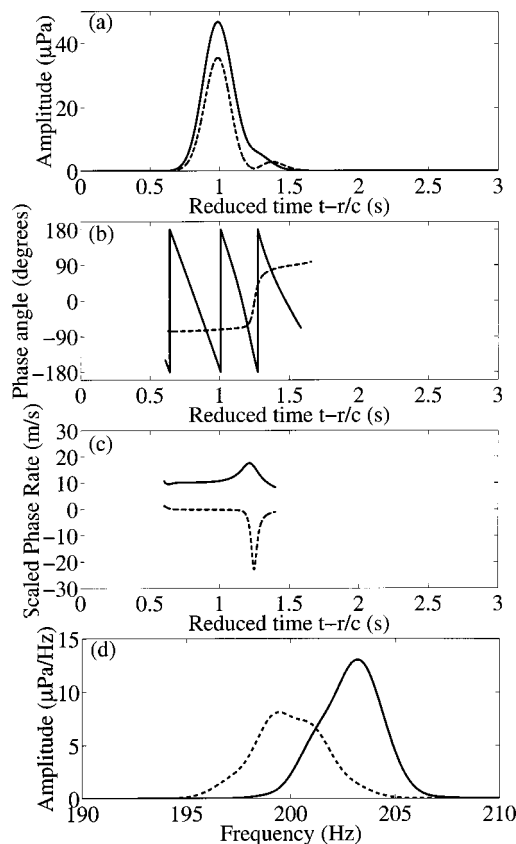


FIG. 12. Same as Fig. 6 except the bottom type is sand and the target is a perfectly reflective disk with $ka = 12$ at 200 Hz.

8(c). As in the waveguide with a sand bottom, rapid changes of scaled phase rate occur making it differ by more than 10 m/s from the true value of the target's radial velocity. All these results indicate that the Doppler shifts in the scattered field are highly dependent on the ocean environment.

Since Doppler effects are a function of target velocity, target velocity may be estimated by measurements of Doppler shifted fields given a known source function and waveguide environment. The sensitivity of the Doppler shifted field to variations in target velocity then becomes an important factor. To investigate this issue, consider again the case of a sand bottom with a spherical target as in Fig. 7, but now with the target moving toward the source at 5 m/s rather than 10 m/s. Figure 9 shows the time series and spectrum of the resulting scattered field, where the solid curve in Fig. 9(d) is the Doppler shifted spectrum. As expected, the dispersive effect in the time series and the frequency shift in the spectrum is smaller for reduced target speed. The phase of the demodulated time series for the target moving at 5 m/s also changes slower than when the target is moving at 10 m/s as shown in Fig. 9(b). These effects are significant since the reduction in time spread of the higher order modes is on the order of tenths of a second and the frequency spectrum is significantly altered over the entire bandwidth of the signal. When the target is moving away from the source, the Doppler frequency shifts are negative. To illustrate this, Fig. 10 shows the time series and spectra for the scattered field from a sphere moving away from the source at 10 m/s, where the bottom type is sand as in Fig. 7. The first arrival for the

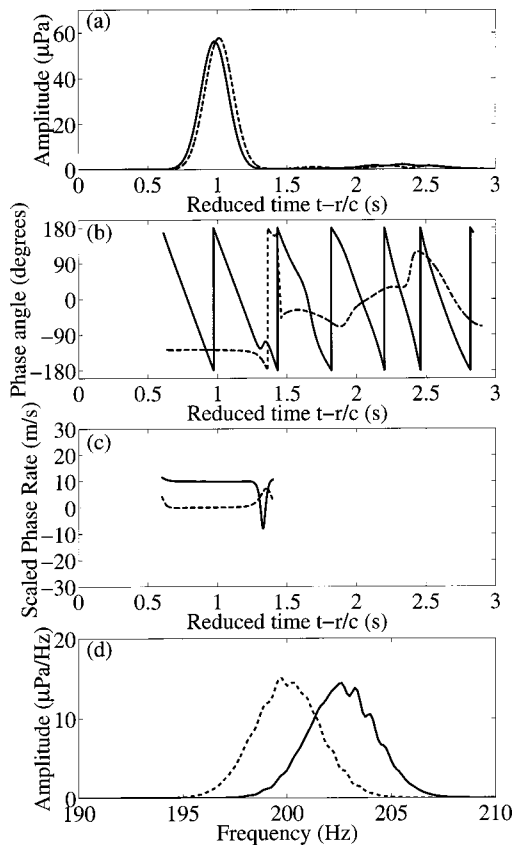


FIG. 13. Same as Fig. 12 except the bottom type is limestone.

moving target in Fig. 10(a) arrives slightly later than in the stationary case because the target is moving away from the source. The negative frequency shift is significant, and on the order of the signal bandwidth, as is evident in the spectrum in Fig. 10(d). The negative frequency shift is also shown as the positive rate of phase change of the solid curve in Fig. 10(b). On the other hand, the rate of phase change is negative for a target moving toward the source and receiver.

The next example illustrates Doppler effects at greater target ranges. Using sand as the bottom type and the sphere at 3000 m initial range from the source, the time series [dashed curves in Fig. 11(a)] is dispersed less than the dashed curves in Fig. 7(a) where the horizontal range is 2000 m. The scattered field from a target moving toward the source at 10 m/s [solid curves in Fig. 11(a)] is also dispersed less than those in Fig. 7(a). This indicates that Doppler effects are highly dependent on the measured geometry.

A perfectly reflecting circular disk facing the source with the same radius as the sphere of $ka=12$ at 200 Hz is used to illustrate variations in the scattered field for flat versus rounded targets. A sand bottom as used in Fig. 7 is also used in Fig. 12. Figures 12(a), 12(b), and 12(d) show the scattered field from a stationary disk and a disk moving toward the source at 10 m/s. With the same measurement geometry and 2000 m as the initial horizontal distance, the time series in Fig. 12(a) appear to be dispersed far less than the time series in Fig. 7(a). The unshifted and shifted frequency spectra of Fig. 12(d) also exhibit this phenomenon. The same measurement geometry and scatterer is used in Fig. 13 but with a limestone bottom. Figures 13(a) and 13(b) show the

scattered field from a stationary disk and a disk moving toward the source at 10 m/s. These time series are also much less dispersive than the scattered field from a spherical scatterer. The unshifted and shifted frequency spectra in Fig. 13(d) are both less distorted than the spectra with a spherical scatterer in Fig. 8(d). This is because scattering from the disk is much stronger in the specular direction than the other directions. Figure 3(b) shows the magnitude of the free-space plane-wave scattering function of the circular disk. Comparing Figs. 3(a) and (b), we can see that the scattering function of the sphere does not vary too much near the specular reflection direction. This leads to relatively uniform coupling between different modes of the incident and scattered field. On the other hand, the disk is highly directional near the specular reflection direction and gives strongest coupling between a given mode of the incident field and the same mode of the scattered field, i.e., diagonal terms of a coupling matrix. Since higher order modes attenuate more than lower order modes and the coupling term between a lower order mode and a higher order mode is weaker, the received signal is dominated by the lower order modes of both the incident and scattered field from the disk. Time-frequency spreading is also significantly weaker than for a spherical scatterer.

It is not always true that the scattered field is stronger when the target is moving toward the source than at rest in a waveguide. For a moving source in free space, the sound field in the forward direction is always more intense than that in the back direction because of the factor $[1 - M \cos \theta]^{-1}$ in pressure, which accounts for free-space dynamics, where M is the Mach number and θ is the angle between the direction of motion and the direction of the field point.² In a waveguide, although there are similar dynamical factors

$$\left[1 + \frac{v_0}{v_l^G(\Omega)} \cos(\phi_0^0 - \phi_0) \right]^{-1},$$

$$\left[1 - \frac{v_\sigma}{v_m^G(\omega_{m,l})} \cos(\phi^0 - \phi_\sigma) \right]^{-1}$$

in the modal expression of Eq. (59), they are so close to unity for low Mach number motions of the source and target, respectively, and are not the dominant factors for the changes of signal amplitudes. In a waveguide the field magnitude can fluctuate rapidly as a function of position, frequency, and waveguide environment due to modal interference. The observed fluctuations in field magnitude of the various examples given are dominated by such changes in modal interference as a function of frequency due to Doppler shifting. For example, Fig. 6(d) shows that with a silt bottom and a target moving toward the source, the scattered field is actually weaker than the scattered field from a stationary target because the modal interference with Doppler shifting is more destructive than without.

IV. CONCLUSION

Analytical expressions for the three-dimensional field scattered by a moving target from a moving source to a moving receiver in a general horizontally stratified ocean waveguide are derived from first principles using the time-domain

formulation of Green's theorem. Spectral and modal representations of the Doppler-shifted scattered field for a simple harmonic source and a source with arbitrary time dependence are obtained. The expressions are valid when the source and receiver are sufficiently far from the target that multiple scattering between the target and waveguide boundaries can be neglected and the scattered field can be expressed as a linear function of the target's plane wave scattering function. The source, target, and receiver are assumed to move horizontally with low Mach numbers, as is typical in many active sonar scenarios.

The modal representation has a compelling physical interpretation exhibited by the fact that a simple harmonic source that excites N modes in the waveguide, for example, will excite roughly N^2 distinct harmonic components in the scattered field due to coupling between the incident modes and the scattered modes. The spectral representation, however, is more general and can be used at closer ranges to the target.

Simulations show that Doppler shifts induced in the scattered field by target motion are highly dependent on the waveguide environment, target shape, and measurement geometry. For a highly dispersive waveguide that supports many trapped modes, the frequency spectrum of the field scattered by a moving target typically exhibits significant distortion compared to that of a stationary target or the same target moving in free space. Rounded scatterers with relatively omnidirectional scattering functions, such as spherical scatterers, have greater coupling between incident modes and scattered modes than flat objects that scatter strongest in the specular direction. The scattered field from an object in a multimodal waveguide tends to suffer greater dispersion as the target becomes more rounded and the scattering becomes more omnidirectional.

It is noteworthy that when the target, source, or receiver are moving, the scattered field no longer obeys reciprocity, as is evident in our present formulation. The concept of a time-reversal mirror⁹⁻¹¹ therefore is not directly applicable under motion of the target, source, or receiver. This is true in both free space and in a stratified medium.

A new derivation for the Doppler shifted field radiated to a moving receiver from a moving source in a stratified medium that proved advantageous in the present work is also presented. The new modal formulation is more accurate than previous formulations, since for example, it accounts for variation in mode shape due to Doppler shift.

APPENDIX A: SPECTRAL REPRESENTATION OF THE DOPPLER-SHIFTED FIELD RADIATED BY A MOVING SOURCE TO A MOVING RECEIVER IN A STRATIFIED WAVEGUIDE

A spectral representation for the wave field induced by a moving source and measured at a moving receiver has been presented in Ref. 4. An alternative derivation utilizing Eq. (5) is presented here to represent incident fields in the scattering problem. The result is consistent with prior research but is better suited to the problem at hand.

The location of a moving source is denoted by

$$\mathbf{r}_0 = \mathbf{r}_0^0 + \mathbf{v}_0 t_0, \quad (\text{A1})$$

where \mathbf{r}_0^0 is the initial location of the source at $t_0=0$ and \mathbf{v}_0 is its horizontal velocity. For simple-harmonic radiation at frequency Ω , the source function $q(\mathbf{r}_s, t_0)$ is

$$q(\mathbf{r}_s, t_0) = e^{-i\Omega t_0} \delta(\mathbf{r}_s - \mathbf{r}_0^0 - \mathbf{v}_0 t_0). \quad (\text{A2})$$

The location of a moving receiver is denoted by

$$\mathbf{r} = \mathbf{r}^0 + \mathbf{v} t, \quad (\text{A3})$$

where \mathbf{r}^0 is the initial location of the receiver at $t=0$ and \mathbf{v} is its horizontal velocity. After changing the variables of integration in Eq. (5) from \mathbf{r}_0 to \mathbf{r}_s and V_0 to V_s , and applying Eq. (A2), Eq. (5) becomes

$$\Phi_i(\mathbf{r}, t) = \int_0^{t^+} dt_0 G((\mathbf{r}^0 + \mathbf{v} t), t | (\mathbf{r}_0^0 + \mathbf{v}_0 t_0), t_0) e^{-i\Omega t_0}. \quad (\text{A4})$$

Green's function for the time-domain scalar wave equation of the waveguide can be obtained by applying an inverse Fourier transform to Green's function for the Helmholtz equation at frequency ω ,

$$G(\mathbf{r}, t | \mathbf{r}_0, t_0) = \frac{1}{2\pi} \int_{-\infty}^{\infty} G(\mathbf{r} | \mathbf{r}_0; \omega) e^{-i\omega(t-t_0)} d\omega, \quad (\text{A5})$$

where the spectral representation of Green's function for the Helmholtz equation of a stratified waveguide is given by

$$G(\mathbf{r} | \mathbf{r}_0; \omega) = \frac{1}{2\pi} \int_{-\infty}^{\infty} d^2 \xi_i g(z, z_0; \omega) e^{i\xi_i \cdot (\boldsymbol{\rho} - \boldsymbol{\rho}_0)}. \quad (\text{A6})$$

The depth dependent Green function $g(z, z_0; \omega)$ in Eq. (A6) is defined as

$$g(z, z_0; \omega) = \frac{1}{2\pi} \int_{-\infty}^{\infty} d^2 \boldsymbol{\rho}' G(\mathbf{r} | \mathbf{r}_0; \omega) e^{-i\xi_i \cdot \boldsymbol{\rho}'}, \quad (\text{A7})$$

where $\boldsymbol{\rho}' = \boldsymbol{\rho} - \boldsymbol{\rho}_0$. With this Eq. (A5) can be expressed as

$$G(\mathbf{r}, t | \mathbf{r}_0, t_0) = \frac{1}{2\pi} \int_{-\infty}^{\infty} d\omega e^{-i\omega(t-t_0)} \times \frac{1}{2\pi} \int_{-\infty}^{\infty} d^2 \xi_i g(z, z_0; \omega) e^{i\xi_i \cdot (\boldsymbol{\rho} - \boldsymbol{\rho}_0)}. \quad (\text{A8})$$

After inserting Eq. (A8) into Eq. (A4), the incident field becomes

$$\Phi_i(\mathbf{r}, t) = \frac{1}{2\pi} \int_0^{t^+} dt_0 \frac{1}{2\pi} \int_{-\infty}^{\infty} d\omega e^{-i\omega t} e^{i(\omega - \Omega)t_0} \times \int_{-\infty}^{\infty} d^2 \xi_i g(z, z_0; \omega) e^{i\xi_i \cdot (\boldsymbol{\rho}^0 + \mathbf{v} t - \boldsymbol{\rho}_0^0 - \mathbf{v}_0 t_0)}. \quad (\text{A9})$$

For sufficiently long duration t , integration over t_0 leads to

$$\begin{aligned}
\Phi_i(\mathbf{r}, t) &= \frac{1}{2\pi} \int_{-\infty}^{\infty} d\omega e^{-i\omega t} \int_{-\infty}^{\infty} d^2\xi_i \delta(\omega - \Omega - \xi_i \cdot \mathbf{v}_0) \\
&\quad \times g(z, z_0; \omega) e^{i\xi_i \cdot (\boldsymbol{\rho}^0 + \mathbf{v}t - \boldsymbol{\rho}_0^0)} \\
&= \frac{1}{2\pi} \int_{-\infty}^{\infty} d^2\xi_i g(z, z_0; \Omega + \xi_i \cdot \mathbf{v}_0) \\
&\quad \times e^{i\xi_i \cdot [\boldsymbol{\rho}^0 - \boldsymbol{\rho}_0^0]} e^{-i(\Omega + \xi_i \cdot (\mathbf{v}_0 - \mathbf{v}))t}, \tag{A10}
\end{aligned}$$

which is consistent with Eq. (14) of Ref. 4.

APPENDIX B: NORMAL MODE REPRESENTATION OF THE DOPPLER-SHIFTED FIELD RADIATED BY A MOVING SOURCE TO A MOVING RECEIVER IN A STRATIFIED WAVEGUIDE

The incident field from a moving source at a moving receiver is derived with an alternative modal method and compared with prior results of Ref. 3.

Green's function for the Helmholtz equation of the waveguide can be expressed in terms of normal modes by

$$\begin{aligned}
G(\mathbf{r}_\sigma | \mathbf{r}_0; \omega) &= \frac{id}{4} \sum_l u_l(z_\sigma; \omega) u_l(z_0; \omega) H_0^{(1)}(\xi_l(\omega) |\boldsymbol{\rho}_\sigma - \boldsymbol{\rho}_0|) \\
&\approx \frac{id}{\sqrt{8\pi}} e^{-i(\pi/4)} \sum_l \frac{u_l(z_\sigma; \omega) u_l(z_0; \omega)}{\sqrt{\xi_l(\omega) |\boldsymbol{\rho}_\sigma - \boldsymbol{\rho}_0|}} \\
&\quad \times e^{i\xi_l(\omega) |\boldsymbol{\rho}_0 - \boldsymbol{\rho}_\sigma|}. \tag{B1}
\end{aligned}$$

We take the receiver $\boldsymbol{\rho}_\sigma$ to be a point on the target for consistency with the derivation of the target scattering problem. For a moving target, the horizontal position vector $\boldsymbol{\rho}_\sigma$ of a point on the target is

$$\begin{aligned}
\boldsymbol{\rho}_\sigma &= \boldsymbol{\rho}_\sigma^0 + \mathbf{v}_\sigma t_\sigma \\
&= (\rho_\sigma^0 \cos \phi_\sigma^0 \mathbf{i}_x + \rho_\sigma^0 \sin \phi_\sigma^0 \mathbf{i}_y) \\
&\quad + (v_\sigma t_\sigma \cos \varphi_\sigma \mathbf{i}_x + v_\sigma t_\sigma \sin \varphi_\sigma \mathbf{i}_y), \tag{B2}
\end{aligned}$$

where $\boldsymbol{\rho}_\sigma^0$ is the initial horizontal position at $t_\sigma=0$ and \mathbf{v}_σ is the horizontal velocity of the target point. Similarly, the horizontal position vector of the moving source $\boldsymbol{\rho}_0$ is

$$\begin{aligned}
\boldsymbol{\rho}_0 &= \boldsymbol{\rho}_0^0 + \mathbf{v}_0 t_0 \\
&= (\rho_0^0 \cos \phi_0^0 \mathbf{i}_x + \rho_0^0 \sin \phi_0^0 \mathbf{i}_y) \\
&\quad + (v_0 t_0 \cos \varphi_0 \mathbf{i}_x + v_0 t_0 \sin \varphi_0 \mathbf{i}_y), \tag{B3}
\end{aligned}$$

where $\boldsymbol{\rho}^0$ is the initial horizontal position at $t_0=0$ and \mathbf{v}_0 is its horizontal velocity of the source.

We assume the horizontal range ρ_0 of the source is much larger than the range to the target point ρ_σ . In the present formulation, the displacements due to motion are assumed to be much smaller than ρ_0 . This is typically a good assumption for low Mach number motions of the source and target even after they have been operating after many periods of the simple-harmonic source, i.e., $t_0, t_\sigma \gg 2\pi/\Omega$. Therefore, the azimuthal angles of the vectors $\boldsymbol{\rho}_0^0 + \mathbf{v}_0 t_0 - \boldsymbol{\rho}_\sigma^0$ and $\boldsymbol{\rho}_0^0 - \boldsymbol{\rho}_\sigma^0$ are approximately the same. An approximation can then be made

$$\begin{aligned}
|\boldsymbol{\rho}_0 - \boldsymbol{\rho}_\sigma| &\approx \rho_0^0 - \rho_\sigma^0 \cos(\phi_0^0 - \phi_\sigma^0) + v_0 t_0 \cos(\phi_0^0 - \varphi_0) \\
&\quad - v_\sigma t_\sigma \cos(\phi_0^0 - \varphi_\sigma), \tag{B4}
\end{aligned}$$

as in Eq. (44c). After substituting these expressions in Eq. (A5), Green's function for the time domain wave equation of the waveguide becomes

$$\begin{aligned}
G(\mathbf{r}_\sigma, t_\sigma | \mathbf{r}_0, t_0) &= \frac{1}{2\pi} \int_{-\infty}^{\infty} d\omega e^{-i\omega(t_\sigma - t_0)} \frac{id}{\sqrt{8\pi}} e^{-i(\pi/4)} \\
&\quad \times \sum_l \frac{u_l(z_\sigma; \omega) u_l(z_0; \omega)}{\sqrt{\xi_l(\omega) \rho_0^0}} \\
&\quad \times e^{i\xi_l(\omega) [\rho_0^0 - \rho_\sigma^0 \cos(\phi_0^0 - \phi_\sigma^0)]} e^{i\xi_l(\omega) v_0 \cos(\phi_0^0 - \varphi_0) t_0} \\
&\quad \times e^{-i\xi_l(\omega) v_\sigma \cos(\phi_0^0 - \varphi_\sigma) t_\sigma}. \tag{B5}
\end{aligned}$$

Similarly, the incident field in Eq. (A4) becomes

$$\begin{aligned}
\Phi_i(\mathbf{r}_\sigma, t_\sigma) &= \frac{1}{2\pi} \int_0^{t_\sigma^+} dt_0 \int_{-\infty}^{\infty} d\omega e^{-i\omega t_\sigma} e^{i(\omega - \Omega) t_0} \\
&\quad \times \frac{id}{\sqrt{8\pi}} e^{-i(\pi/4)} \sum_l \frac{u_l(z_\sigma; \omega) u_l(z_0; \omega)}{\sqrt{\xi_l(\omega) \rho_0^0}} \\
&\quad \times e^{i\xi_l(\omega) [\rho_0^0 - \rho_\sigma^0 \cos(\phi_0^0 - \phi_\sigma^0)]} \\
&\quad \times e^{i\xi_l(\omega) v_0 \cos(\phi_0^0 - \varphi_0) t_0} \\
&\quad \times e^{-i\xi_l(\omega) v_\sigma \cos(\phi_0^0 - \varphi_\sigma) t_\sigma}. \tag{B6}
\end{aligned}$$

For sufficiently long time duration t_σ , the integral over t_0 can be approximated as

$$\begin{aligned}
\Phi_i(\mathbf{r}_\sigma, t_\sigma) &= \int_{-\infty}^{\infty} d\omega e^{-i\omega t_\sigma} \frac{id}{\sqrt{8\pi}} e^{-i(\pi/4)} \\
&\quad \times \sum_l \delta(\omega - \Omega + \xi_l(\omega) v_0 \cos(\phi_0^0 - \varphi_0)) \\
&\quad \times \frac{u_l(z_\sigma; \omega) u_l(z_0; \omega)}{\sqrt{\xi_l(\omega) \rho_0^0}} \\
&\quad \times e^{i\xi_l(\omega) [\rho_0^0 - \rho_\sigma^0 \cos(\phi_0^0 - \phi_\sigma^0)]} \\
&\quad \times e^{-i\xi_l(\omega) v_\sigma \cos(\phi_0^0 - \varphi_\sigma) t_\sigma}. \tag{B7}
\end{aligned}$$

In order to integrate over ω , we need to find the value of ω that makes the argument of the δ function zero. It is a transcendental equation in ω that cannot be solved analytically

$$h(\omega) = \omega - \Omega + \xi_l(\omega) v_0 \cos(\phi_0^0 - \varphi_0) = 0. \tag{B8}$$

Taking the derivative of $h(\omega)$ with respect to ω yields

$$\begin{aligned}
\frac{dh(\omega)}{d\omega} &= 1 + \frac{d\xi_l(\omega)}{d\omega} v_0 \cos(\phi_0^0 - \varphi_0) \\
&= 1 + \frac{v_0}{v_l^G(\omega)} \cos(\phi_0^0 - \varphi_0), \tag{B9}
\end{aligned}$$

where $v_l^G(\omega)$ is the group velocity of the l th mode at frequency ω . For low Mach number motion of the source, the term

$$\frac{v_0}{v_l^G(\omega)} \cos(\phi_0^0 - \varphi_0)$$

is much smaller than unity. Therefore, the change of slope of $h(\omega)$ is small for a small change of ω and the Newton–Raphson method with only a single iteration gives a reasonably accurate solution for Eq. (B8). Using the source frequency Ω as the initial guess, the first iteration of Newton–Raphson method yields

$$\omega_l = \Omega - \frac{h(\Omega)}{h'(\Omega)} = \Omega - \frac{\xi_l(\Omega) v_0 \cos(\phi_0^0 - \varphi_0)}{1 + \frac{v_0}{v_l^G(\Omega)} \cos(\phi_0^0 - \varphi_0)}. \quad (\text{B10})$$

The horizontal wave number ξ_l and the group velocity v_l^G of the l th mode are both easily evaluated at the source frequency Ω . With the property of the δ function in Eq. (57), the incident field in Eq. (B7) becomes

$$\begin{aligned} \Phi_i(\mathbf{r}_\sigma, t_\sigma) &= \frac{id}{\sqrt{8\pi}} e^{-i(\pi/4)} \sum_l \frac{1}{1 + \frac{v_0}{v_l^G(\Omega)} \cos(\phi_0^0 - \varphi_0)} \\ &\times \frac{u_l(z_\sigma; \omega_l) u_l(z_0; \omega_l)}{\sqrt{\xi_l(\omega_l) \rho_0^0}} \\ &\times e^{i\xi_l(\omega_l)[\rho_0^0 - \rho_\sigma^0 \cos(\phi_0^0 - \phi_\sigma^0)]} \\ &\times e^{-i[\omega_l + \xi_l(\omega_l) v_\sigma \cos(\phi_0^0 - \varphi_\sigma)] t_\sigma}. \end{aligned} \quad (\text{B11})$$

This expression accounts for the changes in mode shape due to Doppler shifts in frequency that were not considered in Ref. 3. An additional amplification factor

$$\left[1 + \frac{v_0}{v_l^G(\Omega)} \cos(\phi_0^0 - \varphi_0) \right]^{-1}$$

arises that is similar to the $[1 - (v_0/c) \cos \theta]^{-1}$ factor for the field induced by a moving source in free space as discussed in Refs. 1 and 2 and shown in Eq. (C18).

Our result is consistent with Eq. (35) of Ref. 3 to first order. The major difference is that all terms in the formulation of Ref. 3 are evaluated at the source frequency Ω , but several terms in our formulation are evaluated at the Doppler shifted frequencies. For example, changes in mode shape due to Doppler shifts in frequency are taken into account in our formulation but not in that of Ref. 3. The additional accuracy of the current formulation requires computation of normal modes at shifted frequency components.

APPENDIX C: DERIVATION OF THE PLANE-WAVE SCATTERING FUNCTION FOR A MOVING SCATTERER IN FREE SPACE FROM GREEN'S THEOREM

The purpose here is to derive a surface-integral expression for the plane-wave scattering function of an object moving in free space at low Mach number.

The scattering of plane incident waves from a target moving in free space can be formulated using Green's theorem for the time-domain scalar wave equation, described in Eq. (12).

The location of a point on the surface of the target is denoted by

$$\mathbf{r}_\sigma = \mathbf{r}_c + \mathbf{r}_\sigma^0, \quad (\text{C1})$$

where \mathbf{r}_c is the centroid of the object with elevation angle θ_c and azimuthal angle ϕ_c . The surface point \mathbf{r}_σ relative to \mathbf{r}_c is denoted by the relative position vector \mathbf{r}_σ^0 with elevation angle θ_σ^0 and azimuthal angle ϕ_σ^0 with respect to the object's centroid. Since the shape of the object does not change and the motion is assumed to be irrotational, \mathbf{r}_σ^0 , θ_σ^0 , and ϕ_σ^0 are all independent of time. By defining the cosine between directions (α, β) and (θ, ϕ) as

$$\eta(\alpha, \beta; \theta, \phi) = \cos \alpha \cos \theta + \sin \alpha \sin \theta \cos(\beta - \phi) \quad (\text{C2})$$

an incident plane wave with unit amplitude and frequency ω_i can be expressed as

$$\begin{aligned} \hat{\Phi}_i(\mathbf{r}_\sigma, t_\sigma) &= e^{i[\mathbf{k}_i \cdot \mathbf{r}_\sigma - \omega_i t_\sigma]} \\ &= e^{i[\mathbf{k}_i \cdot (\mathbf{r}_c + \mathbf{r}_\sigma^0) - \omega_i t_\sigma]} \\ &= e^{i\mathbf{k}_i \cdot \mathbf{r}_c} e^{ik_i r_\sigma^0 \eta(\alpha_i, \beta_i; \theta_\sigma^0, \phi_\sigma^0)} e^{-i\omega_i t_\sigma}, \end{aligned} \quad (\text{C3})$$

where $k_i = \omega_i/c$. Green's function in free space can be represented by an inverse Fourier transform of Green's function for the Helmholtz equation via

$$G(\mathbf{r}, t | \mathbf{r}_\sigma, t_\sigma) = \frac{1}{2\pi} \int_{-\infty}^{\infty} G(\mathbf{r} | \mathbf{r}_\sigma; \omega) e^{-i\omega(t-t_\sigma)} d\omega, \quad (\text{C4})$$

where Green's function for the Helmholtz equation is

$$G(\mathbf{r} | \mathbf{r}_\sigma; \omega) = \frac{1}{4\pi} \frac{e^{ik|\mathbf{r} - \mathbf{r}_\sigma|}}{|\mathbf{r} - \mathbf{r}_\sigma|} = \frac{1}{4\pi} \frac{e^{ik|\mathbf{r} - \mathbf{r}_c - \mathbf{r}_\sigma^0|}}{|\mathbf{r} - \mathbf{r}_c - \mathbf{r}_\sigma^0|}$$

with $k = \omega/c$. In the far field where $r \gg r_c$ and $r \gg r_\sigma^0$, Green's function for the Helmholtz equation can be approximated as

$$\begin{aligned} G(\mathbf{r} | \mathbf{r}_\sigma; \omega) &\approx \frac{1}{4\pi r} e^{ikr} e^{-ikr_c \eta(\theta, \phi; \theta_c, \phi_c)} \\ &\times e^{-ikr_\sigma^0 \eta(\theta, \phi; \theta_\sigma^0, \phi_\sigma^0)}. \end{aligned} \quad (\text{C5})$$

Inserting Eq. (C5) into Eq. (C4) yields

$$\begin{aligned} G(\mathbf{r}, t | \mathbf{r}_\sigma, t_\sigma) &= \frac{1}{2\pi} \frac{1}{4\pi r} \int_{-\infty}^{\infty} e^{ikr} e^{-ikr_c \eta(\theta, \phi; \theta_c, \phi_c)} \\ &\times e^{-ikr_\sigma^0 \eta(\theta, \phi; \theta_\sigma^0, \phi_\sigma^0)} e^{-i\omega(t-t_\sigma)} d\omega. \end{aligned} \quad (\text{C6})$$

Substituting Eq. (C6) into Eq. (12), the scattered field becomes

$$\begin{aligned}\hat{\Phi}_s(\mathbf{r}, t) = & -\frac{1}{4\pi} \int_0^{t^+} dt_\sigma \frac{1}{2\pi} \int_{-\infty}^{\infty} d\omega \frac{e^{ikr}}{r} e^{-i\omega(t-t_\sigma)} \\ & \times \oint d\mathbf{S}_\sigma \cdot \left([e^{i\mathbf{k}_i \cdot \mathbf{r}_c} e^{ik_i r_\sigma^0} \eta(\alpha_i, \beta_i; \theta_\sigma^0, \phi_\sigma^0)] \right. \\ & \times e^{-i\omega t_\sigma + \hat{\Phi}_s(\mathbf{r}_\sigma, t_\sigma)] \\ & \left. \times \nabla_\sigma [e^{-ikr_c \eta(\theta, \phi; \theta_c, \phi_c)} e^{-ikr_\sigma^0 \eta(\theta, \phi; \theta_\sigma^0, \phi_\sigma^0)}] \right),\end{aligned}\quad (C7)$$

where $\hat{\Phi}_s(\mathbf{r}_\sigma, t_\sigma)$ is the scattered field on the surface of the object induced by an incident plane wave with the wave number vector \mathbf{k}_i and unit amplitude. For low Mach number motions of the target, approximations can be made for the scattered field on the target such that $\hat{\Phi}_s(\mathbf{r}_\sigma, t_\sigma)$ is approximated as the scattered field at the initial location of the surface, with a phase shift factor $e^{i\mathbf{k}_i \cdot \mathbf{r}_c}$ due to rigid translation of the centroid, modulated by $\exp(-i\omega t_\sigma)$ so that

$$\hat{\Phi}_s(\mathbf{r}_\sigma, t_\sigma) \approx \hat{\Phi}_s(\mathbf{r}_\sigma^0, \mathbf{k}_i; \omega_i) e^{-i\omega_i t_\sigma} e^{i\mathbf{k}_i \cdot \mathbf{r}_c}. \quad (C8)$$

If the centroid of the scatterer is moving with constant velocity \mathbf{v}_σ then

$$\mathbf{r}_c = \mathbf{v}_\sigma t_\sigma, \quad (C9)$$

where the initial location of \mathbf{r}_c at $t_\sigma=0$ is the coordinate system's origin. Substituting Eqs. (C8) and (C9) into Eq. (C7) yields

$$\begin{aligned}\hat{\Phi}_s(\mathbf{r}, t) = & -\frac{1}{4\pi} \int_0^{t^+} dt_\sigma \frac{1}{2\pi} \int_{-\infty}^{\infty} d\omega \frac{e^{ikr}}{r} e^{-i\omega(t-t_\sigma)} \\ & \times \oint d\mathbf{S}_\sigma \cdot \left([e^{ik_i r_\sigma^0} \eta(\alpha_i, \beta_i; \theta_\sigma^0, \phi_\sigma^0)] \right. \\ & \times e^{-i(\omega_i - \mathbf{k}_i \cdot \mathbf{v}_\sigma) t_\sigma + \hat{\Phi}_s(\mathbf{r}_\sigma^0, \mathbf{k}_i; \omega_i) e^{-i(\omega_i - \mathbf{k}_i \cdot \mathbf{v}_\sigma) t_\sigma}} \\ & \left. \times \nabla_\sigma [e^{-ikv_\sigma t_\sigma \eta(\theta, \phi; \theta_c, \phi_c)} e^{-ikr_\sigma^0 \eta(\theta, \phi; \theta_\sigma^0, \phi_\sigma^0)}] \right).\end{aligned}\quad (C10)$$

For sufficiently long time duration t , the integral over t_σ introduces the delta function $\delta(\omega(1 - (v_\sigma/c)) \times \eta(\theta, \phi; \theta_c, \phi_c) - \omega_i + \mathbf{k}_i \cdot \mathbf{v}_\sigma)$ to the integrand. The property of the δ function described in Eq. (57) in this case leads to

$$\omega^* = \frac{\omega_i - \mathbf{k}_i \cdot \mathbf{v}_\sigma}{1 - \frac{v_\sigma}{c} \eta(\theta, \phi; \theta_c, \phi_c)}, \quad (C11)$$

where ω^* is the Doppler shifted frequency in the direction of propagation (θ, ϕ) . Integrating over ω then yields

$$\begin{aligned}\hat{\Phi}_s(\mathbf{r}, t) = & -\frac{1}{4\pi} \frac{1}{1 - \frac{v_\sigma}{c} \eta(\theta, \phi; \theta_c, \phi_c)} \frac{e^{i\omega^*((r/c)-t)}}{r} \\ & \times \oint d\mathbf{S}_\sigma \cdot \left([e^{ik_i r_\sigma^0} \eta(\alpha_i, \beta_i; \theta_\sigma^0, \phi_\sigma^0)] + \hat{\Phi}_s(\mathbf{r}_\sigma^0, \mathbf{k}_i; \omega_i) \right] \\ & \times \nabla_\sigma [e^{-i(\omega^*/c)r_\sigma^0} \eta(\theta, \phi; \theta_\sigma^0, \phi_\sigma^0)]).\end{aligned}\quad (C12)$$

In the far field, the scattered field can be approximated as a point source radiating with an angular weighting factor¹⁵ given by the object's plane-wave scattering function via

$$\Psi_s(\mathbf{r}|\mathbf{r}_c; \omega) \approx \frac{e^{ik|\mathbf{r}-\mathbf{r}_c|}}{k|\mathbf{r}-\mathbf{r}_c|} S(\theta, \phi; \alpha_i, \beta_i; \omega), \quad (C13)$$

which for $r \gg r_c$ reduces to

$$\begin{aligned}\Psi_s(\mathbf{r}|\mathbf{r}_c; \omega) \approx & \frac{1}{kr} e^{ikr} e^{-ikr_c \eta(\theta, \phi; \theta_c, \phi_c)} \\ & \times S(\theta, \phi; \alpha_i, \beta_i; \omega).\end{aligned}\quad (C14)$$

The field induced by a moving point source can be expressed as

$$\hat{\Phi}_s(\mathbf{r}, t) = \int_0^{t^+} dt_\sigma \int dV_c \Psi_s(\mathbf{r}, t|\mathbf{r}_c, t_\sigma) q(\mathbf{r}_c, t_\sigma) \quad (C15)$$

with source function

$$q(\mathbf{r}_c, t_\sigma) = e^{-i\omega_i t_\sigma} \delta(\mathbf{r}_c - \mathbf{v}_\sigma t_\sigma). \quad (C16)$$

Equation (C15) then becomes

$$\begin{aligned}\hat{\Phi}_s(\mathbf{r}, t) = & \int_0^{t^+} dt_\sigma \frac{1}{2\pi} \int_{-\infty}^{\infty} d\omega e^{-i\omega(t-t_\sigma)} \Psi_s(\mathbf{r}|\mathbf{v}_\sigma t_\sigma; \omega) e^{-i\omega_i t_\sigma} \\ \approx & \int_0^{t^+} dt_\sigma \frac{1}{2\pi} \int_{-\infty}^{\infty} d\omega \frac{e^{ikr}}{r} e^{-i\omega(t-t_\sigma)} \\ & \times \frac{1}{k} S(\theta, \phi; \alpha_i, \beta_i; \omega) e^{-i(\omega_i - \mathbf{k}_i \cdot \mathbf{v}_\sigma) t_\sigma} \\ & \times e^{-ikv_\sigma t_\sigma \eta(\theta, \phi; \theta_c, \phi_c)}.\end{aligned}\quad (C17)$$

Using similar techniques as before to integrate over t_σ and ω , the scattered field becomes

$$\begin{aligned}\hat{\Phi}_s(\mathbf{r}, t) = & \frac{1}{1 - \frac{v_\sigma}{c} \eta(\theta, \phi; \theta_c, \phi_c)} \frac{e^{i\omega^*((r/c)-t)}}{\frac{\omega^*}{c} r} \\ & \times S(\theta, \phi; \alpha_i, \beta_i; \omega^*),\end{aligned}\quad (C18)$$

where $[1 - (v_\sigma/c) \eta(\theta, \phi; \theta_c, \phi_c)]^{-1}$ is a dynamical factor due to the motion.² By equating Eq. (C12) with Eq. (C18), the plane-wave scattering function $S(\theta, \phi; \alpha_i, \beta_i; \omega^*)$ for an object moving at low Mach number in free space can be written in terms of a surface integral over the object by

$$\begin{aligned}S(\theta, \phi; \alpha_i, \beta_i; \omega^*) \approx & -\frac{\omega^*}{4\pi c} \oint d\mathbf{S}_\sigma \cdot ([e^{ik_i r_\sigma^0} \eta(\alpha_i, \beta_i; \theta_\sigma^0, \phi_\sigma^0)] \\ & + \hat{\Phi}_s(\mathbf{r}_\sigma^0, \mathbf{k}_i; \omega_i)] \nabla_\sigma [e^{-i(\omega^*/c)r_\sigma^0} \eta(\theta, \phi; \theta_\sigma^0, \phi_\sigma^0)]).\end{aligned}\quad (C19)$$

If the object is not moving, Eq. (C19) leads to the special case Eq. (C9) of Ref. 6 directly.

APPENDIX D: DERIVATION OF THE NORMAL MODE REPRESENTATION OF THE DOPPLER-SHIFTED FIELD SCATTERED FROM A MOVING TARGET BY A SOURCE WITH ARBITRARY TIME DEPENDENCE IN A STRATIFIED WAVEGUIDE

Using the incident field described in Eq. (B7) and decomposing the field into upgoing and downgoing plane waves yields

$$\begin{aligned} \Phi_i(\mathbf{r}_\sigma, t_\sigma) &= \int_{-\infty}^{\infty} d\omega_0 \sum_l \delta(\omega_0 - \Omega + \xi_l(\omega_0) v_0 \cos(\phi_0^0 - \varphi_0)) \\ &\times [A_l(\mathbf{r}_0^0; \omega_0) e^{ik(\omega_0) r_\sigma^0 \eta(\alpha_l, \pi - \phi_0^0; \theta_\sigma^0, \phi_\sigma^0)} \\ &- B_l(\mathbf{r}_0^0; \omega_0) e^{ik(\omega_0) r_\sigma^0 \eta(\pi - \alpha_l, \pi - \phi_0^0; \theta_\sigma^0, \phi_\sigma^0)}] \\ &\times e^{-i(\omega_0 + \xi_l(\omega_0) v_\sigma \cos(\phi_0^0 - \varphi_\sigma)) t_\sigma}. \end{aligned} \quad (D1)$$

As in Sec. II C the total scattered field on the surface of the target can be represented as

$$\begin{aligned} \Phi_s(\mathbf{r}_\sigma, t_\sigma) &= \int_{-\infty}^{\infty} d\omega_0 \sum_l \delta(\omega_0 - \Omega + \xi_l(\omega_0) v_0 \cos(\phi_0^0 - \varphi_0)) \\ &\times [A_l(\mathbf{r}_0^0; \omega_0) \hat{\Phi}_s(\mathbf{r}_\sigma, \mathbf{k}_l^+; \omega_0) \\ &- B_l(\mathbf{r}_0^0; \omega_0) \hat{\Phi}_s(\mathbf{r}_\sigma, \mathbf{k}_l^-; \omega_0)] \end{aligned}$$

$$-B_l(\mathbf{r}_0^0; \omega_0) \hat{\Phi}_s(\mathbf{r}_\sigma, \mathbf{k}_l^-; \omega_0)] e^{-i\omega_0 t_\sigma}. \quad (D2)$$

For low Mach number motion, $\hat{\Phi}_s(\mathbf{r}_\sigma, \mathbf{k}_l^+; \omega_0)$ and $\hat{\Phi}_s(\mathbf{r}_\sigma, \mathbf{k}_l^-; \omega_0)$ are approximated as the scattered fields at the initial location of the surface $\hat{\Phi}_s(\mathbf{r}_\sigma^0, \mathbf{k}_l^+; \omega_0)$ and $\hat{\Phi}_s(\mathbf{r}_\sigma^0, \mathbf{k}_l^-; \omega_0)$ multiplied by the phase shift $e^{-i\xi_l(\omega_0) v_\sigma \cos(\phi_0^0 - \varphi_\sigma) t_\sigma}$

Equation (D2) then becomes

$$\begin{aligned} \Phi_s(\mathbf{r}_\sigma, t) &= \int_{-\infty}^{\infty} d\omega_0 \sum_l \delta(\omega_0 - \Omega + \xi_l(\omega_0) v_0 \cos(\phi_0^0 - \varphi_0)) \\ &\times [A_l(\mathbf{r}_0^0; \omega_0) \hat{\Phi}_s(\mathbf{r}_\sigma^0, \mathbf{k}_l^+; \omega_0) \\ &- B_l(\mathbf{r}_0^0; \omega_0) \hat{\Phi}_s(\mathbf{r}_\sigma^0, \mathbf{k}_l^-; \omega_0)] \\ &\times e^{-i(\omega_0 + \xi_l(\omega_0) v_\sigma \cos(\phi_0^0 - \varphi_\sigma)) t_\sigma}. \end{aligned} \quad (D3)$$

Substituting Eqs. (46), (D1) and (D3) into Eq. (12), the scattered field induced by a simple-harmonic source with source frequency Ω is expressed as

$$\begin{aligned} \Phi_s(\mathbf{r}, t) &\approx -\frac{1}{2\pi} \int_0^{t^+} dt_\sigma \oint d\mathbf{S}_\sigma \cdot \left\{ \int_{-\infty}^{\infty} d\omega_0 \sum_l \delta(\omega_0 - \Omega + \xi_l(\omega_0) v_0 \cos(\phi_0^0 - \varphi_0)) e^{-i(\omega_0 + \xi_l(\omega_0) v_\sigma \cos(\phi_0^0 - \varphi_\sigma)) t_\sigma} \right. \\ &\times \left(A_l(\mathbf{r}_0^0; \omega_0) [e^{ik(\omega_0) r_\sigma^0 \eta(\alpha_l, \pi - \phi_0^0; \theta_\sigma^0, \phi_\sigma^0)} + \hat{\Phi}_s(\mathbf{r}_\sigma^0, \mathbf{k}_l^+; \omega_0)] \right. \\ &\left. - B_l(\mathbf{r}_0^0; \omega_0) [e^{ik(\omega_0) r_\sigma^0 \eta(\pi - \alpha_l, \pi - \phi_0^0; \theta_\sigma^0, \phi_\sigma^0)} + \hat{\Phi}_s(\mathbf{r}_\sigma^0, \mathbf{k}_l^-; \omega_0)] \right) \\ &\times \nabla_\sigma \left(\int_{-\infty}^{\infty} d\omega e^{-i\omega(t-t_\sigma)} \sum_m [A_m(\mathbf{r}^0; \omega) e^{-ik(\omega) r_\sigma^0 \eta(\pi - \alpha_m, \phi_0^0; \theta_\sigma^0, \phi_\sigma^0)} - B_m(\mathbf{r}^0; \omega) e^{-ik(\omega) r_\sigma^0 \eta(\alpha_m, \phi_0^0; \theta_\sigma^0, \phi_\sigma^0)}] \right. \\ &\left. \times e^{i\xi_m(\omega) v \cos(\phi_0^0 - \varphi) t} e^{-i\xi_m(\omega) v_\sigma \cos(\phi_0^0 - \varphi_\sigma) t_\sigma} \right) \left. \right\}. \end{aligned} \quad (D4)$$

For an arbitrary source with frequency spectrum $Q(\Omega)$, the normal mode representation of the Doppler-shifted scattered field is formulated by Fourier synthesis

$$\Psi_s(\mathbf{r}, t) = \frac{1}{2\pi} \int_{-\infty}^{\infty} d\Omega Q(\Omega) \Phi_s(\mathbf{r}, t). \quad (D5)$$

The frequency spectrum of the scattered field in the receiver's frame of reference is obtained by applying a Fourier transform to Eq. (D5),

$$\Psi_s(\mathbf{r}, \omega') = \int_{-\infty}^{\infty} dt e^{i\omega' t} \Psi_s(\mathbf{r}, t), \quad (D6)$$

where ω' is the frequency in the receiver frame of reference. Integrating over t leads to

$$\begin{aligned}
\Psi_s(\mathbf{r}, \omega') \approx & -\frac{1}{2\pi} \int_{-\infty}^{\infty} d\Omega \mathcal{Q}(\Omega) \int_0^{t^+} dt_\sigma \oint d\mathbf{S}_\sigma \cdot \left\{ \int_{-\infty}^{\infty} d\omega_0 \sum_l \delta(\omega_0 - \Omega + \xi_l(\omega_0)v_\sigma \cos(\phi_0^0 - \varphi_0)) \right. \\
& \times e^{-i(\omega_0 + \xi_l(\omega_0)v_\sigma \cos(\phi_0^0 - \varphi_0))t_\sigma} \\
& \times \left(A_l(\mathbf{r}_0^0; \omega_0) [e^{ik(\omega_0)r_\sigma^0} \eta(\alpha_l, \pi - \phi_0^0; \theta_\sigma^0, \phi_\sigma^0) + \hat{\Phi}_s(\mathbf{r}_\sigma^0, \mathbf{k}_l^+; \omega_0)] \right. \\
& \left. - B_l(\mathbf{r}_0^0; \omega_0) [e^{ik(\omega_0)r_\sigma^0} \eta(\pi - \alpha_l, \pi - \phi_0^0; \theta_\sigma^0, \phi_\sigma^0) + \hat{\Phi}_s(\mathbf{r}_\sigma^0, \mathbf{k}_l^-; \omega_0)] \right) \\
& \times \nabla_\sigma \left(\int_{-\infty}^{\infty} d\omega e^{i\omega t_\sigma} \sum_m [A_m(\mathbf{r}^0; \omega) e^{-ik(\omega)r_\sigma^0} \eta(\pi - \alpha_m, \phi^0; \theta_\sigma^0, \phi_\sigma^0) - B_m(\mathbf{r}^0; \omega) e^{-ik(\omega)r_\sigma^0} \eta(\alpha_m, \phi^0; \theta_\sigma^0, \phi_\sigma^0)] \right. \\
& \left. \times e^{-i\xi_m(\omega)v_\sigma \cos(\phi^0 - \varphi_\sigma)t_\sigma} \delta(\omega - \omega' - \xi_m(\omega)v_\sigma \cos(\phi^0 - \varphi)) \right) \Bigg\}. \tag{D7}
\end{aligned}$$

In order to integrate over ω , the roots of the transcendental equation of ω need to be computed

$$h(\omega) = \omega - \omega' - \xi_m(\omega)v_\sigma \cos(\phi^0 - \varphi) = 0. \tag{D8}$$

Newton–Raphson method is used to find the approximated solutions of Eq. (D8). First iteration with ω' as the initial guess gives

$$\omega'_m = \omega' - \frac{-\xi_m(\omega')v_\sigma \cos(\phi^0 - \varphi)}{1 - \frac{v}{v_m^G(\omega')} \cos(\phi^0 - \varphi)}, \tag{D9}$$

where $v_m^G(\omega')$ is the group velocity of the m th mode at frequency ω' .

Integrating over ω yields a δ function of ω_0 . Performing integration over Ω yields

$$\begin{aligned}
\Psi_s(\mathbf{r}, \omega') \approx & -\frac{1}{2\pi} \int_0^{t^+} dt_\sigma \oint d\mathbf{S}_\sigma \cdot \left\{ \int_{-\infty}^{\infty} d\omega_0 \sum_l \mathcal{Q}(\omega_0 + \xi_l(\omega_0)v_\sigma \cos(\phi_0^0 - \varphi_0)) e^{-i(\omega_0 + \xi_l(\omega_0)v_\sigma \cos(\phi_0^0 - \varphi_0))t_\sigma} \right. \\
& \times \left(A_l(\mathbf{r}_0^0; \omega_0) [e^{ik(\omega_0)r_\sigma^0} \eta(\alpha_l, \pi - \phi_0^0; \theta_\sigma^0, \phi_\sigma^0) + \hat{\Phi}_s(\mathbf{r}_\sigma^0, \mathbf{k}_l^+; \omega_0)] \right. \\
& \left. - B_l(\mathbf{r}_0^0; \omega_0) [e^{ik(\omega_0)r_\sigma^0} \eta(\pi - \alpha_l, \pi - \phi_0^0; \theta_\sigma^0, \phi_\sigma^0) + \hat{\Phi}_s(\mathbf{r}_\sigma^0, \mathbf{k}_l^-; \omega_0)] \right) \\
& \times \nabla_\sigma \left(\sum_m \frac{1}{1 - [v/v_m^G(\omega'_m)] \cos(\phi^0 - \varphi)} [A_m(\mathbf{r}^0; \omega'_m) e^{-ik(\omega'_m)r_\sigma^0} \eta(\pi - \alpha_m, \phi^0; \theta_\sigma^0, \phi_\sigma^0) \right. \\
& \left. - B_m(\mathbf{r}^0; \omega'_m) e^{-ik(\omega'_m)r_\sigma^0} \eta(\alpha_m, \phi^0; \theta_\sigma^0, \phi_\sigma^0)] e^{i[\omega'_m - \xi_m(\omega'_m)v_\sigma \cos(\phi^0 - \varphi)]t_\sigma} \right) \Bigg\}. \tag{D10}
\end{aligned}$$

For sufficiently long time duration t , the integration over t_σ introduces the delta function $\delta(\omega_0 - \omega'_m + \xi_l(\omega_0)v_\sigma \cos(\phi_0^0 - \varphi_0) + \xi_m(\omega'_m)v_\sigma \cos(\phi^0 - \varphi_\sigma))$ to the integrand. Once again, a transcendental equation in ω_0 for the argument of the delta function needs to be solved by means of Newton–Raphson method

$$h(\omega_0) = \omega_0 - \omega'_m + \xi_l(\omega_0)v_\sigma \cos(\phi_0^0 - \varphi_0) + \xi_m(\omega'_m)v_\sigma \cos(\phi^0 - \varphi_\sigma) = 0. \tag{D11}$$

The derivative of $h(\omega)$ with respect to ω_0 is

$$\frac{dh(\omega_0)}{d\omega_0} = 1 + \frac{v_\sigma}{v_l^G(\omega_0)} \cos(\phi_0^0 - \varphi_\sigma). \tag{D12}$$

First iteration of Newton–Raphson method with ω'_m as the initial guess is

$$\begin{aligned}\omega'_{l,m} &= \omega'_m - \frac{h(\omega'_m)}{h'(\omega'_m)} \\ &= \omega'_m - \frac{\xi_l(\omega'_m)v_\sigma \cos(\phi_0^0 - \varphi_\sigma) + \xi_m(\omega'_m)v_\sigma \cos(\phi_0^0 - \varphi_\sigma)}{1 + \frac{v_\sigma}{v_l^G(\omega'_m)} \cos(\phi_0^0 - \varphi_\sigma)}.\end{aligned}\quad (\text{D13})$$

Integrating over ω_0 finally yields

$$\begin{aligned}\Psi_s(\mathbf{r}, \omega') &\approx - \oint d\mathbf{S}_\sigma \cdot \left\{ \sum_l \sum_m \mathcal{Q}(\omega'_{l,m} + \xi_l(\omega'_{l,m})v_0 \cos(\phi_0^0 - \varphi_0)) \right. \\ &\quad \times \frac{1}{1 - [v/v_m^G(\omega'_m)] \cos(\phi_0^0 - \varphi)} \frac{1}{1 + [v_\sigma/v_l^G(\omega'_{l,m})] \cos(\phi_0^0 - \varphi_\sigma)} \\ &\quad \times (A_l(\mathbf{r}_0^0; \omega'_{l,m}) [e^{ik(\omega'_{l,m})r_\sigma^0 \eta(\alpha_l, \pi - \phi_0^0; \theta_\sigma^0, \phi_\sigma^0)} + \hat{\Phi}_s(\mathbf{r}_\sigma^0, \mathbf{k}_l^+; \omega'_{l,m})] \\ &\quad - B_l(\mathbf{r}_0^0; \omega'_{l,m}) [e^{ik(\omega'_{l,m})r_\sigma^0 \eta(\pi - \alpha_l, \pi - \phi_0^0; \theta_\sigma^0, \phi_\sigma^0)} + \hat{\Phi}_s(\mathbf{r}_\sigma^0, \mathbf{k}_l^-; \omega'_{l,m})]) \\ &\quad \times \nabla_\sigma (A_m(\mathbf{r}^0; \omega'_m) e^{-ik(\omega'_m)r_\sigma^0 \eta(\pi - \alpha_m, \phi_0^0; \theta_\sigma^0, \phi_\sigma^0)} - B_m(\mathbf{r}^0; \omega'_m) e^{-ik(\omega'_m)r_\sigma^0 \eta(\alpha_m, \phi_0^0; \theta_\sigma^0, \phi_\sigma^0)}) \Big\}.\end{aligned}\quad (\text{D14})$$

¹P. M. Morse and K. U. Ingard, *Theoretical Acoustics* (Princeton University Press, Princeton, NJ, 1968), pp. 721–724.

²A. P. Dowling and J. E. Ffowcs Williams, *Sound and Sources of Sound* (Horwood, Chichester, 1983), pp. 187–199.

³K. E. Hawker, “A normal mode theory of acoustic Doppler effects in the oceanic waveguide,” *J. Acoust. Soc. Am.* **65**, 675–681 (1979).

⁴H. Schmidt and W. A. Kuperman, “Spectral and modal representations of the Doppler-shifted field in ocean waveguides,” *J. Acoust. Soc. Am.* **96**, 386–395 (1994).

⁵N. C. Makris, “A spectral approach to 3-D object scattering in layered media applied to scattering from submerged spheres,” *J. Acoust. Soc. Am.* **104**, 2105–2113 (1998).

⁶F. Ingenito, “Scattering from an object in a stratified medium,” *J. Acoust. Soc. Am.* **82**, 2051–2059 (1987).

⁷N. C. Makris, F. Ingenito, and W. A. Kuperman, “Detection of a submerged object insonified by surface noise in an ocean waveguide,” *J. Acoust. Soc. Am.* **96**, 1703–1724 (1994).

⁸N. C. Makris and P. Ratilal, “A unified model for reverberation and sub-

merged object scattering in a stratified ocean waveguide,” *J. Acoust. Soc. Am.* **109**, 909–941 (2001).

⁹D. R. Jackson and D. R. Dowling, “Phase conjugation in underwater acoustics,” *J. Acoust. Soc. Am.* **89**, 171–181 (1991).

¹⁰M. Fink, “Time-reversed acoustics,” *Phys. Today* **50**, 34–40 (1997).

¹¹H. C. Song, W. A. Kuperman, W. S. Hodgkiss, T. Akal, and C. Ferla, “Interactive time reversal in the ocean,” *J. Acoust. Soc. Am.* **105**, 3176–3184 (1999).

¹²P. M. Morse and H. Feshbach, *Methods of Theoretical Physics* (McGraw–Hill, New York, 1953), Vol. 1, pp. 834–837.

¹³M. B. Porter, The KRAKEN normal mode program, SACLANT Undersea Research Centre, La Spezia, Italy, September, 1991.

¹⁴P. Ratilal, Y. Lai, and N. Makris, “Validity of the sonar equation and Babinet’s principle in a stratified medium,” *J. Acoust. Soc. Am.* **112**, 1797–1816 (2002).

¹⁵*Electromagnetic and Acoustic Scattering by Simple Shapes*, edited by J. J. Bowman, T. B. A. Senior, and P. L. E. Uslenghi (North-Holland, Amsterdam, 1969), p. I.2.

Motion compensation for adaptive horizontal line array processing

T. C. Yang^{a)}

Naval Research Laboratory, Washington, DC 20375

(Received 29 March 2002; revised 30 August 2002; accepted 21 October 2002)

Large aperture horizontal line arrays have small resolution cells and can be used to separate a target signal from an interference signal by array beamforming. High-resolution adaptive array processing can be used to place a null at the interference signal so that the array gain can be much higher than that of conventional beamforming. But these nice features are significantly degraded by the source motion, which reduces the time period under which the environment can be considered stationary from the array processing point of view. For adaptive array processing, a large number of data samples are generally required to minimize the variance of the cross-spectral density, or the covariance matrix, between the array elements. For a moving source and interference, the penalty of integrating over a large number of samples is the spread of signal and interference energy to more than one or two eigenvalues. The signal and interference are no longer clearly identified by the eigenvectors and, consequently, the ability to suppress the interference suffers. We show in this paper that the effect of source motion can be compensated for the (signal) beam covariance matrix, thus allowing integration over a large number of data samples without loss in the signal beam power. We employ an equivalent of a rotating coordinate frame to track the signal bearing change and use the waveguide invariant theory to compensate the signal range change by frequency shifting. © 2003 Acoustical Society of America. [DOI: 10.1121/1.1528929]

PACS numbers: 43.30.Wi, 43.60.Gk, 43.30.Bp [WMC]

I. INTRODUCTION

In an ocean environment, particularly in shallow water, many loud surface ships are present, interfering with the detection and directional finding of a target signal (henceforth, target=signal). Interference rejection usually requires a narrow beamwidth and an adaptive beamforming algorithm. A large aperture horizontal array (HLA) can be used to exclude many distributed interfering sources (long-range ships) outside the search beam. High-resolution adaptive beamforming produces a narrow beamwidth and suppresses the contribution of loud (nearby) interfering ships by placing nulls at the interference bearings (interference nulling).

Many adaptive beamforming approaches, such as the minimum variance distortionless response (MVDR) algorithm,¹ assume a well-conditioned covariance matrix.²⁻⁴ But in reality the true covariance matrix is not known and must be estimated from the data. A large number of data samples are normally required to reduce the variance of the estimated covariance matrix. When the target and interference sources are moving, as often is the case, the nonstationarity of the acoustic environment limits the number of data samples (snapshots) available for estimating the covariance matrix, resulting in a “snapshot-deficient” condition.^{5,6} Adaptive beam power estimates will be biased under the “snapshot-deficient” condition.²⁻⁶ The performance degradation is worse as the array aperture increases, thus defeating the purpose of a large aperture HLA. This is referred to as the source motion (degradation) effect on adaptive array processing. How to process the signal to compensate for the

motion effect is a research topic of great interest. In this paper a beam domain approach for motion compensation is presented.

Assuming that the target and interference signals are separated in the beam space, the effect of source motion on the signal covariance matrix can be estimated and compensated for, thus allowing the data to be integrated over a large number of data samples. The interference field is suppressed by the difference of the interferer motion from the target motion. The motion compensation method is intended for a large aperture HLA.

The focus of this paper is on adaptive beamforming for a moving target source in the presence of a loud interference source. One notes that for conventional (Bartlett) processing, there are other approaches for motion compensation, such as matched field processing methods that use a different replica field for a different data sample⁷ (for a hypothesized source track). This algorithm (referred to by some as “track-before-detect”) when generalized to the Capon (MVDR) processor will have the same “snapshot-deficient” problem discussed below involving the inverse of the covariance matrix. The beam domain approach for motion compensation, on the other hand, carries over directly to adaptive matched-beam processing.⁸ We confine ourselves to the use of a plane wave steering vector in this paper.

For adaptive beamforming, the question is the following: “What is the minimum number of data samples required for estimating the covariance matrix so that it is statistically unbiased?” Assuming that the data samples are independent and identically Gaussian distributed, previous work has suggested that the minimum number of data samples required for an adequate estimation of the covariance matrix is three

^{a)}Electronic mail: yang@wave.nrl.navy.mil

times the number of elements in the array.⁴ This condition is hardly met for a sonar array, particularly under the “snapshot-deficient” condition. Numerical examples (Fig. 1 of Ref. 5) have shown, for $M=N$, where M is the number of data samples and N is the number of sensors on the array, the MVDR beam power suffers a -6 to -12 dB loss for a HLA of 4 to 16 sensors. In contrast, for $M=3N$ the loss is ~ 1 dB.

A less than fully adaptive algorithm, based on dominant mode rejection, has been proposed for interference suppression.⁹ Assuming that the eigenvectors of the largest eigenvalues are associated with the interference sources, interference suppression can be achieved by removing these eigenvectors from the covariance matrix or the weighting factor. The advantage of this method is that it requires a shorter integration time than the fully adaptive MVDR, since the large eigenvalues can be estimated using a smaller number of data samples. Its performance has been studied and compared with the MVDR method.¹⁰

If, on the other hand, one uses a large number of data samples to estimate the covariance matrix, what is the penalty of ignoring the nonstationarity condition? For moving sources, the consequence is a spread of the signal energy, as measured by the eigenvalue spectrum of the covariance matrix from one to more eigenvalues. This was nicely illustrated in Ref. 6 as a function of the source bearing rate. The price paid is a loss of signal energy and a reduced ability to reject the interferers. A remedy is to limit the signal loss using the white noise constraint,¹¹ as discussed in Ref. 6.

In the beam domain, it will be shown below that when the signal and interference field occupy different beams, the motion will spread the beam covariance eigenvalue spectrum from one to two (or three) eigenvalues, but the eigenvalues and eigenvectors of the signal and interference remain in two separate beam subspaces centered on the signal and interference bearings. For a source changing bearing, the motion effect can be compensated by integrating over the signal beam covariance matrix (the beam covariance submatrix in the signal space) that synchronizes with the source bearing rate. For a source changing range, it is shown that elements of the signal beam covariance matrix have the same range and frequency dependence as predicted by the waveguide invariant theory. The source range change can be compensated by a frequency change (shift).^{12,13} Using the beam-domain motion compensation algorithm, it is shown that MVDR yields the same beam power and beamwidth for the moving source as the stationary source (for both the bearing and range change cases). The interference power is suppressed by the motion compensation algorithm when the interferer has a different motion than the signal source.

This paper is organized as follows: in Sec. II we give a tutorial review of the stationarity requirements for the estimation of the covariance matrix in the element space. We illustrate the eigenvalue spectrum spread due to the source motion, which makes the identification of the signal and interference eigenvectors difficult in the element space. Previous work has assumed a plane wave model for the signal and interference field. Here the signal and interference fields are modeled using a realistic ocean environment. In Sec. III, we analyze the motion effect on the beam domain covariance

matrix. The key point is that even with motion, the signal and interference eigenvectors still remain in two separate beam subspaces as long as they are resolved in bearing. In Sec. IV, we present a motion compensation algorithm for a fast bearing-rate signal in the presence of a loud interferer. In Sec. V, we present a motion compensation algorithm for a fast range-rate signal in the presence of a loud interferer. Both algorithms are carried out in the beam space. In Sec. VI we summarize the paper. Appendixes A and B are extended footnotes for materials covered in the text.

II. SOURCE MOTION EFFECT: ESTIMATION OF THE COVARIANCE MATRIX

In this section we review the basic issues regarding the estimation of a covariance matrix from the point of view of adaptive array beamforming. The spatial and temporal coherence of the acoustic field are limited in real data by sound scattering from the random ocean. They impose additional constraints on array processing,¹⁴ which we do not consider here.

We start with the well-known MVDR beamforming algorithm,¹ as given by

$$B^{\text{MVDR}}(\theta) = \frac{1}{\mathbf{p}^H \mathbf{R}^{-1} \mathbf{p}}, \quad (1)$$

where $\mathbf{R} = \langle \mathbf{p}_{\text{data}} \mathbf{p}_{\text{data}}^H \rangle$ is the covariance matrix obtained from the received pressure field; the superscript H denotes Hermitian conjugate. The variable \mathbf{p} (without a subscript) is the replica field or the steering vector. The boldface capital \mathbf{R} denotes a matrix, the boldface lowercase \mathbf{p} denotes a vector. For plane wave beamforming, the n th element of the steering vector \mathbf{p} is given by

$$p_n = \exp(-jk_0 x_n \sin \theta), \quad (2)$$

where θ is the steering vector measured from the broadside of the horizontal line array (HLA) and k_0 is the wave number. For a uniformly distributed line array, $x_n = nd$, where d is the phone spacing.

For an environment including a target signal, an interference signal and noise, the covariance matrix is given by

$$\mathbf{R} = \sigma_T \mathbf{p}_T \mathbf{p}_T^H + \sigma_I \mathbf{p}_I \mathbf{p}_I^H + \sigma_n \mathbf{R}_n, \quad (3)$$

where σ denotes the intensity of the received target (T) signal, interference (I) field, and noise (n). The basic assumptions of Eq. (3) are that the signal, the interference field, and noise are statistically independent and uncorrelated with each other so that the covariance matrix is a summation of the covariance matrices of the signal, interference, and noise.

The true covariance matrix is not known in practice and must be estimated from data. The popular approach is to average (or integrate) the cross-spectral matrix over data samples (under the ergodic assumption for a stationary condition):

$$\hat{\mathbf{R}} = \langle \mathbf{p} \mathbf{p}^H \rangle = \sum_{m=1}^M \mathbf{p}(m) \mathbf{p}(m)^H / M, \quad (4)$$

where

$$\mathbf{p}(m) = \sqrt{\sigma_T} \mathbf{p}_T + \sqrt{\sigma_I} \mathbf{p}_I + \sqrt{\sigma_n} \mathbf{p}_{\text{noise}}$$

is the pressure field at time m , and the summation is over M data samples. The estimation of the covariance matrix depends on the integration time, and the acoustic conditions. For moving sources (including the target and interferers), the integration time needs to be short enough so that the dynamic behavior of the signal field is captured and the noise covariance matrix can be considered stationary (the short-term stationarity condition). But for a short integration time, Eq. (4) may deviate significantly from Eq. (3), producing bias in the beam power estimate.^{2–5} A long integration time is required to minimize the variance of the covariance matrix, but then the details of the spatial structure of the moving signal field may be blurred. We consider two cases: a short integration ($M < N$) and long integration time ($M \geq N$), with N being the total number of elements on the HLA.

A. Short integration time

For a fast bearing-rate source, the available snapshots are limited by the stationary condition. Two conditions are used to calculate the available number of snapshots.^{6,10}

- (1) *Length of FFT.* For a given integration time, the number of snapshots is inversely proportional to the FFT size. The tradeoff is between a short FFT and a larger number of data samples versus a long FFT and a small number of data samples. For frequency domain processing, there is a lower limit on the FFT size given by the requirement that the signal received on all elements of the array be contained in the same FFT window. Since the delay time across the array for a given signal is the largest at the endfire direction, a lower limit of the FFT window is given by $\tau = L/c$, where L is the array aperture, and c is the sound speed. For the numerical example given below using an array of 100 sensors with $L = 594$ m and $c = 1500$ m/s, one finds $\tau \approx 0.4$ s, which yields a frequency bin of 2.5 Hz. Note that the beamforming steering vector is for the center of the frequency bin. To avoid the phase error across the array due to the finite frequency bin size, Ref. 6 suggests a more stringent requirement for the frequency bin size, which is eight times smaller than given above. The minimum FFT window increases to 3.2 s.
- (2) *The short-term stationarity limit.* Short-term stationarity implies the assumption that the ocean environment is considered “stationary” for a short term. For a HLA, the short time limit is determined by the duration the signal will stay in the same beam. For a beamwidth of, say, $\sim 2^\circ$ (for an array of ~ 40 wavelengths), and a signal at a range of $R = 5$ km, traveling at $\nu = 20$ knots (see the example below), the short time limit is $\tau = R\theta/\nu \approx 17$ s.

TABLE I. Properties of bearing-changing target and interference sources (Case 1).

	Depth (m)	Range (km)	Bearing span ($^\circ$)	Speed (knot)	Source level (dB)
Target source	50	5	–6–6	20	0
Interference source	5	10	30–33	5	26

Given a FFT window of 1 s, only 17 time frames are available before the stationary condition is violated.

We thus see that for a fast bearing-changing source, the numbers of data samples available without violating the stationarity condition are severely limited, i.e. $M < N$, the snapshot-deficient condition. This results in undersampling of the covariance matrix. The snapshot-deficient condition becomes worse as the array aperture increases.

B. Long integration time

For a moving source, by integrating the covariance matrix over a large number of data sample, one pays a price for violating the short-term stationarity condition. The consequence of source motion is a spread of the eigenvalue spectrum, which was nicely illustrated in Ref. 6 for a fast bearing-rate source, assuming a plane wave model. We will illustrate the same results using a realistic ocean environment with multipath arrivals. We shall also consider a source that changes range rapidly. For both cases, we add an (additional) interference field generated by a surface ship.

For numerical simulations, we shall consider a bottom-mounted HLA in the SWellEx-96 environment,¹⁵ where the water depth is 210 m, and the sound speed is close to 1490 m/s for the majority of the water column, except for the top 30 m, where the sound speeds increase to 1525 m/s at the surface. The HLA shall have 100 elements spaced at 6 m uniformly. We consider two cases. Case 1 involves a fast bearing-changing target and a slow bearing-changing interference source. The target has a speed of 20 knots moving from -6° to 6° in bearing (from the broadside of the HLA) in 100 time frames. The target range is 5 km and the target depth is 50 m. The interference source is a surface ship with a radiation source at a depth of 5 m. It is located at a range of 10 km, traveling with a speed of 5 knots. It changes bearing from 30° – 33° in the same time period. It has a source level 20 times stronger than the signal. Case 2 involves a fast range-changing target at the bearing of 0° with a depth, speed, and initial range the same as in Case 1. The surface interference is now at a range of 20 km with a source level 50 times of the signal. It has a fixed bearing of 30° with the same depth and speed as in Case 1. In both cases, we assume a white noise ~ 20 dB down from the signal at the element level. The properties of the moving source and interference are summarized in Tables I and II for Cases 1 and 2, respectively.

The pressure field is calculated using the KRAKEN normal mode code.¹⁶ The covariance matrix is integrated (averaged) over all 100 samples. Figure 1 shows the eigenvalue spectrum for Case 1 at three different frequencies (100, 110,

TABLE II. Properties of range-changing target and interference sources (Case 2).

	Depth (m)	Range span (km)	Bearing ($^\circ$)	Speed (knot)	Source level (dB)
Target source	50	5–6.03	0	20	0
Interference source	5	20–20.26	30	5	34

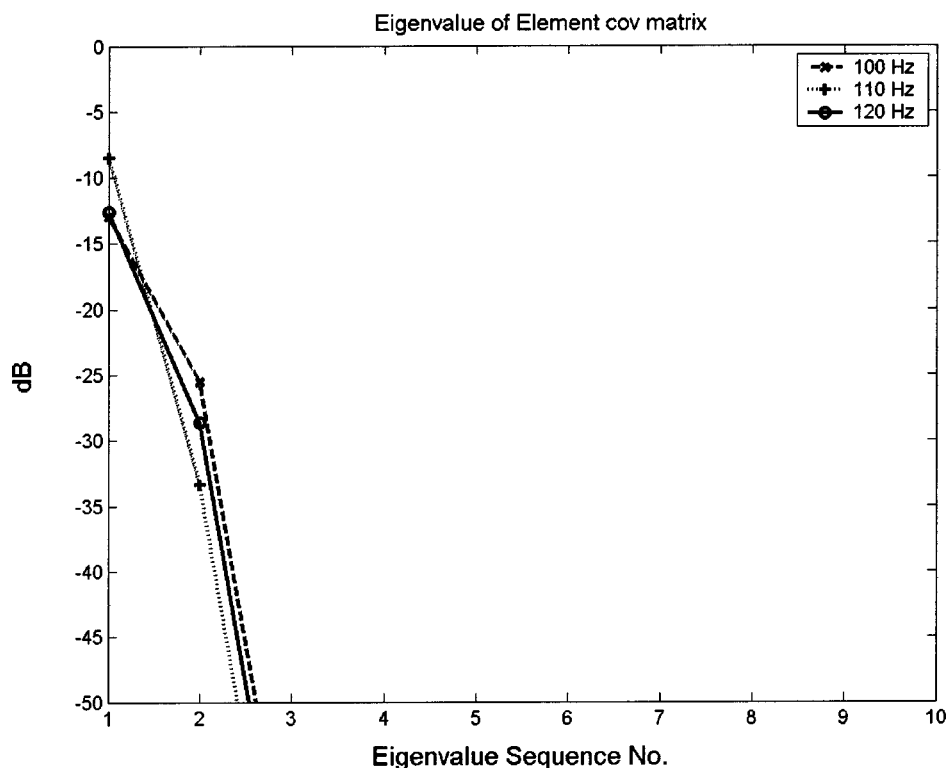


FIG. 1. Eigenvalue spectrum of the element-space covariance matrix for a stationary source and interference (Case 1) at three different (100, 110, and 120 Hz) frequencies. The first and second eigenvalues are associated with the interference and source, respectively. Eigenvalues are connected by lines to distinguish between different frequencies.

and 120 Hz), when the target and interference source are both stationary. It can be independently verified that the first (largest) eigenvalue and eigenvector are dominated by the surface ship, and the second eigenvalue and eigenvector are dominated by the target signal; the rest are associated with the noise. In this case, the interference field from the surface ship can be rejected by removing the first eigenvector from either the covariance matrix, or the MVDR weighting factor. Figure 2 shows the MVDR beam outputs using a white noise constraint¹¹ of 2 dB. (The white noise constraint determines the amount of diagonal loading for the rank deficient covariance matrix so that the normalized MVDR beam power for the white noise is equal to or less than the

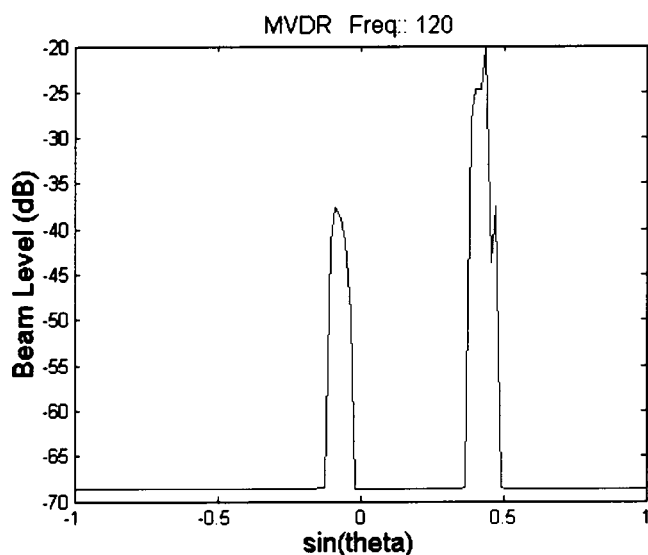


FIG. 2. The MVDR beam power for a stationary broadside source and interference at 30°.

white noise constraint. The white noise constraint is used here to minimize the signal loss due to the mismatch between the signal field and the plane wave steering vector.) Both the signal and surface interference beams have narrow beamwidths compared with conventional beamforming (not shown here).

Figures 3 and 4 show the eigenvalue spectrum at 100, 110, and 120 Hz for Cases 1 and 2, respectively. We note that because of the source motion, the signal energy has spread to more than two eigenvalues. The largest eigenvalue in Figs. 3 and 4 are predominantly associated with the surface interference source; they have different magnitudes because the surface interference source is at a different range and has a different source level between Cases 1 and 2. The second and higher eigenvalues are a mixture of signal and interference fields. Since the received level of the interference field is much (>10 dB) stronger than that of the signal field, its contribution (to the second and higher) eigenvalues is non-negligible compared with the signal contribution. In this regard, note that the second eigenvalues in Fig. 3 have much larger amplitudes than the second eigenvalues in Fig. 1. The mixture of the signal and interference eigenvalues and eigenvectors is known to degrade the performance of interference rejection algorithms for weak signal level cases. Figure 5 shows the MVDR beam outputs using the same white noise constraint. Note that the beam at the broadside direction has a much wider width than the corresponding beam in Fig. 2. This is because the signal has covered a bearing from -6° to 6° .

III. THE BEAM COVARIANCE MATRIX

In this section, we analyze the motion effect on the beam covariance matrix, i.e., the cross-spectral density between

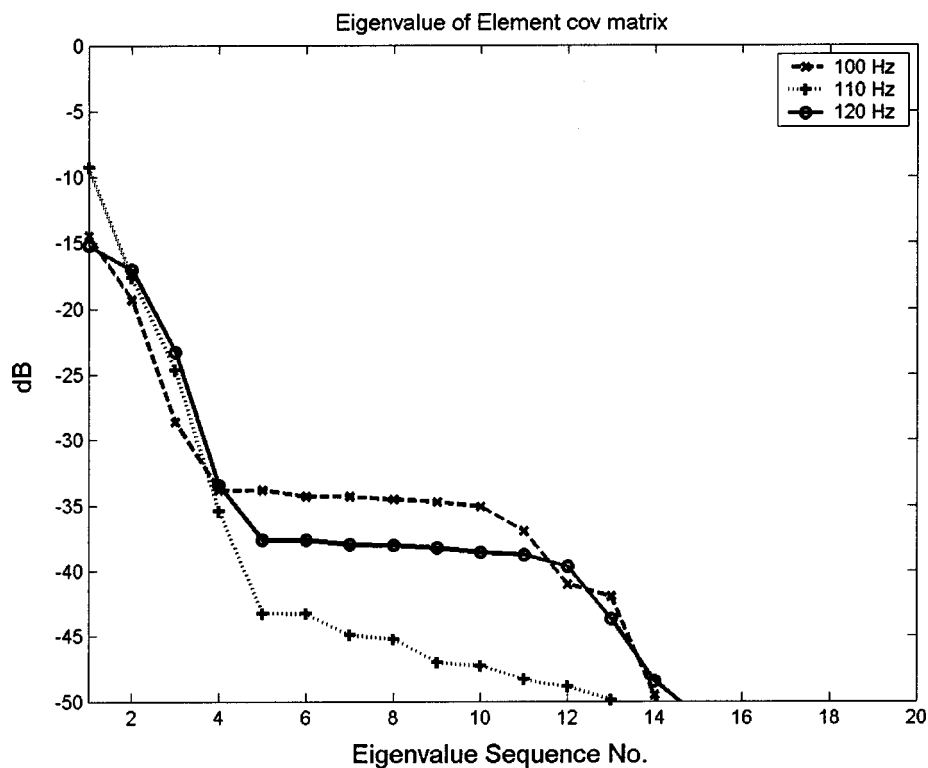


FIG. 3. The eigenvalue spectrum of the element-space covariance matrix at 100, 110, and 120 Hz, for a moving source and interference constantly changing bearing. See Case 1 in the text (Table I).

different beams. We show that the target signal and interference signal belong to two different beam subspaces as long as they are adequately resolved in bearing. The motion spreads the signal and interference energy over several eigenvalues in their respective beam subspaces. Since they are separated from each other, they can be processed coherently in their own beam space to recover the beam energy loss due to source-motion compensation (see Secs. III and IV be-

low). Motion compensation is difficult in the element space, as the eigenvectors of the signal and interference fields are mixed by the source motion effect, and are not *a priori* separable, as discussed above.

Recall the conventional beamforming algorithm, by which the pressure field for each element of the HLA is multiplied by a phase factor according to a plane wave arrival at the steered angle,

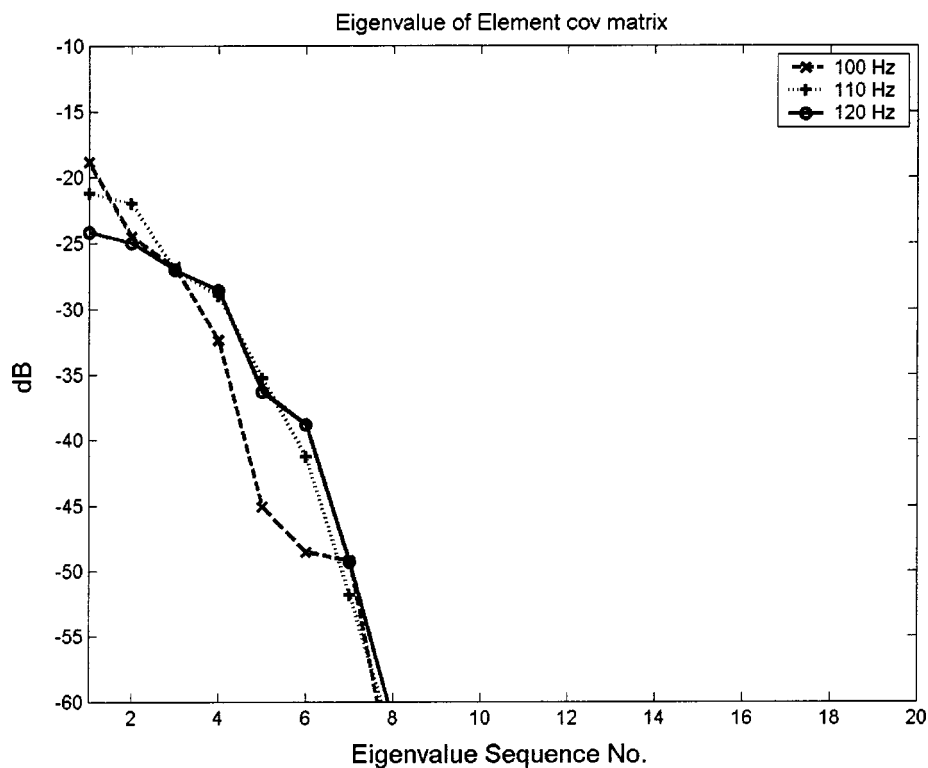


FIG. 4. The eigenvalue spectrum of the element-space covariance matrix for a moving source and interference constantly changing range at three different (100, 110, and 120 Hz) frequencies. See Case 2 in the text (Table II).

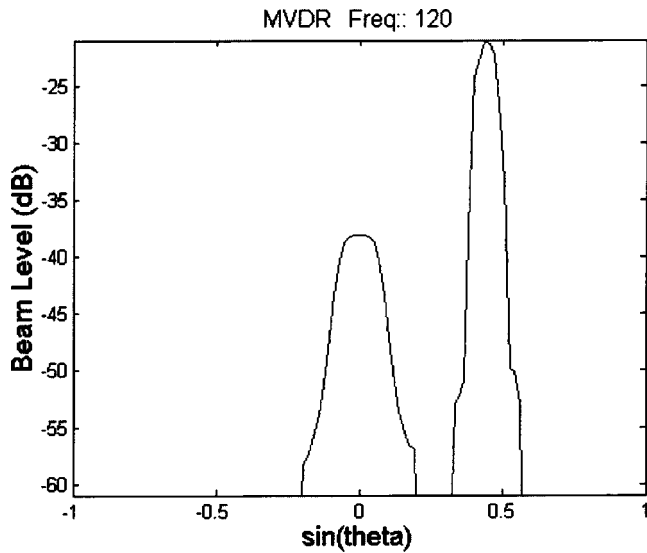


FIG. 5. The MVDR beam power for a bearing-changing broadside source and interference at 30° (Case I) using all 100 data samples.

$$a_i \equiv a(\vartheta_i) = \sum_n \exp(-jk_0 x_n \sin \vartheta_i) p_n \equiv \sum_n T_{in} p_n, \quad (5)$$

where k_0 is the wave number for sound speed $c_0 = 1500$ m/s, ϑ_i is the angle of the i th beam, and T_{in} is the i, n th element of a matrix \mathbf{T} . For a uniformly spaced HLA, $x_n = nd$, and $T_{in} = \exp(-jk_0 dn\kappa_i)$, where $\kappa_i \equiv \sin \vartheta_i$ and d is the element spacing. Assuming that beams are uniformly spaced in the κ_i space, with a total number of beams equaling the number of phones N , one notes that \mathbf{T} is an orthogonal matrix satisfying $\mathbf{T}\mathbf{T}^H = \mathbf{T}^H\mathbf{T} = \mathbf{NI}$. Equation (5) states that the beam vector \mathbf{a} is an orthogonal transformation of the pressure vector \mathbf{p} , expressed in vector-matrix notion as

$$\mathbf{a} = \mathbf{T}\mathbf{p}. \quad (6)$$

The beam covariance matrix is then given by

$$\mathbf{Q} = \langle \mathbf{a}_{\text{data}} \mathbf{a}_{\text{data}}^H \rangle = \mathbf{TRT}^H, \quad (7)$$

where \mathbf{a}_{data} is the conventional beam output for the received data, replacing \mathbf{p} by \mathbf{p}_{data} in Eq. (6). The beam space MVDR algorithm, denoted as MBDR for distinction, is given by

$$B^{\text{MBDR}}(\theta) = (\mathbf{a}^H \mathbf{Q}^{-1} \mathbf{a})^{-1}, \quad (8)$$

where the beam steering vector is given by Eq. (6) after substituting the plane wave steering vector \mathbf{p} from Eq. (2).

We shall denote θ_S as the steering/search angle and θ_T as the signal angle (bearing) and ϑ_i as the beam angle, index i , used in matrix multiplication. We note that the beam steering vector \mathbf{a} is the conventional beam output for a plane wave arriving at the angle θ_S . It has a beamwidth $\sin(\vartheta_i - \theta_S) \approx 1/N$, N being the number of sensors on the HLA. Thus, the elements of the beam steering vector \mathbf{a} are small except for the $\pm w$ beams adjacent to the signal-look beam. This is particularly so for a large aperture HLA, where the side lobe levels are low. We then find that in this approximation, only the $2w + 1$ beam subspace of the beam covariance matrix will contribute to the MBDR output at angle θ_S . Thus we can use a beam subspace processor,⁸

$$B^{\text{MBDR}}(\theta) = (\hat{\mathbf{a}}^H \hat{\mathbf{Q}}^{-1} \hat{\mathbf{a}})^{-1}, \quad (9)$$

where $\hat{\mathbf{a}}$ is a subvector of \mathbf{a} , of dimension $2w + 1$, and $\hat{\mathbf{Q}}$ is a submatrix of \mathbf{Q} , of dimension $(2w + 1) \times (2w + 1)$ indexed around the signal-look directions. The parameter w denotes the number of signal beams covered by the signal beamwidth. For example, if the beamwidth is 2° and we form a beam at each degree, then $w = 2$. For this case, the matrix inversion will be for a 5×5 matrix, which is much faster than the inversion of a matrix of dimension 100×100 in the element space. The relationship between the beam-space MVDR with the element-space MVDR is briefly discussed in Appendix A.

For this paper, we are going to oversample the beam space. In our numerical calculations, we shall use a 1° beam near the broadside directions. This leads to a beam increment of $\Delta = \sin(1^\circ) \sim 0.0174$, and hence a total of $2/\Delta \approx 115$ beams in the $\sin \theta$ space (versus $N = 100$). For the eigenvalue calculations, we shall use a beam submatrix of dimension larger than 5 to include the beam spread due to multipath arrivals and source bearing change. The eigenvalue spectrum is calculated for a submatrix \mathbf{Q} of dimension 11×11 centered on the signal or interference bearings.

Let us consider Case 2 first, where the target and interferer stay at a fixed bearing but are changing range. The beam eigenvalues are shown in Figs. 6(a) and (b) for the target and interference source, respectively, using their respective beam covariance submatrices. We see that the signal energy for the broadside target remains to a high degree in the first eigenvalue. The interference energy spreads over ~ 5 eigenvalues. The basic premise here is that the eigenvalues and eigenvectors of the target and interference are separable in the beam space (when the target and interferer are separated by at least w beams). In that case, it will be shown below in Sec. V that the signal energy can be integrated by analyzing the signal beam intensity striation. This processing suppresses the interference energy when the interferer has a different range or range rate than the target.

Figure 7(a) shows the signal eigenvalues for a broadside target changing bearing from -6° to 6° (Case 1). We see that the signal energy spreads from 1 (as for a stationary source) to 8 eigenvalues. Figure 7(b) shows the signal eigenvalues for the same target changing bearing from -6° to -5° . The eigenvalue spread is limited to ≤ 3 eigenvalues. We note that the beam covariance matrix for the signal changing bearing from -6° to 6° is the sum of signal beam covariance matrices for bearing change from -6° to -5° , -5° to -4° , -4° to -3° , etc. Consequently, the eigenvectors of the former covariance matrix is the sum of the eigenvectors of the latter covariance matrices. Indeed in Fig. 7(a), one finds that the eigenvalue spectra at 100 and 120 Hz consist of 6–8 eigenvalues of similar magnitudes, corresponding to 6–8 independent eigenvectors. At 110 Hz, the eigenvectors of the individual matrices add coherently into two dominant eigenvectors. Knowing the relationship between the beam covariance matrices, it is possible to integrate the beam covariance matrices coherently (by searching for the target bearing rate), so that it produces one large eigenvalue. (See Sec. IV.) Again, we assume that the signal and interference

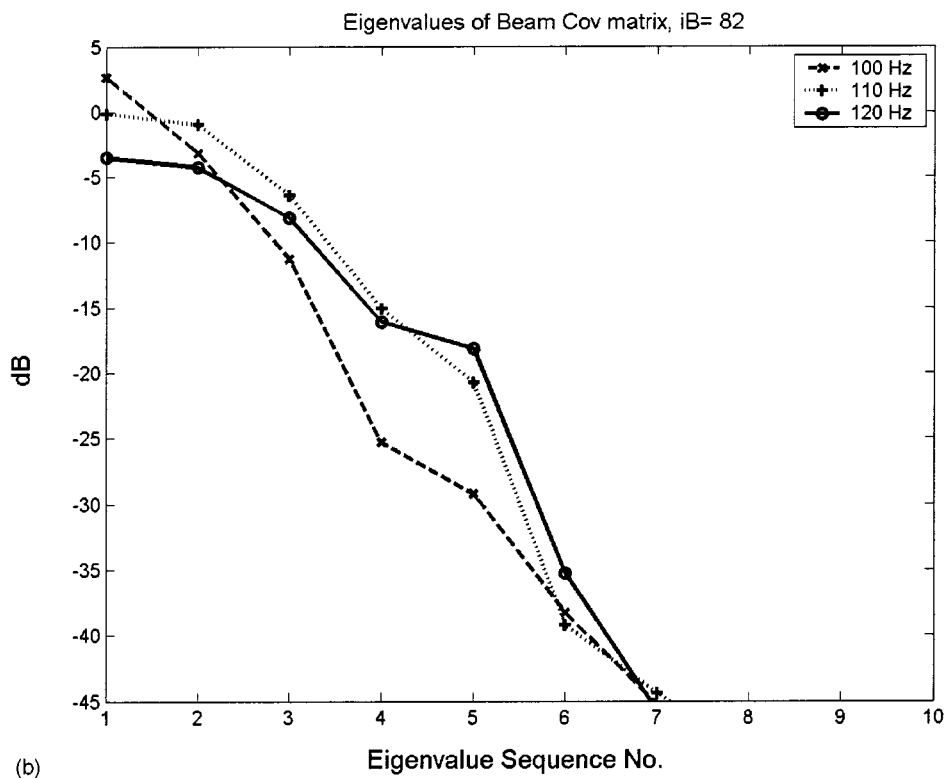
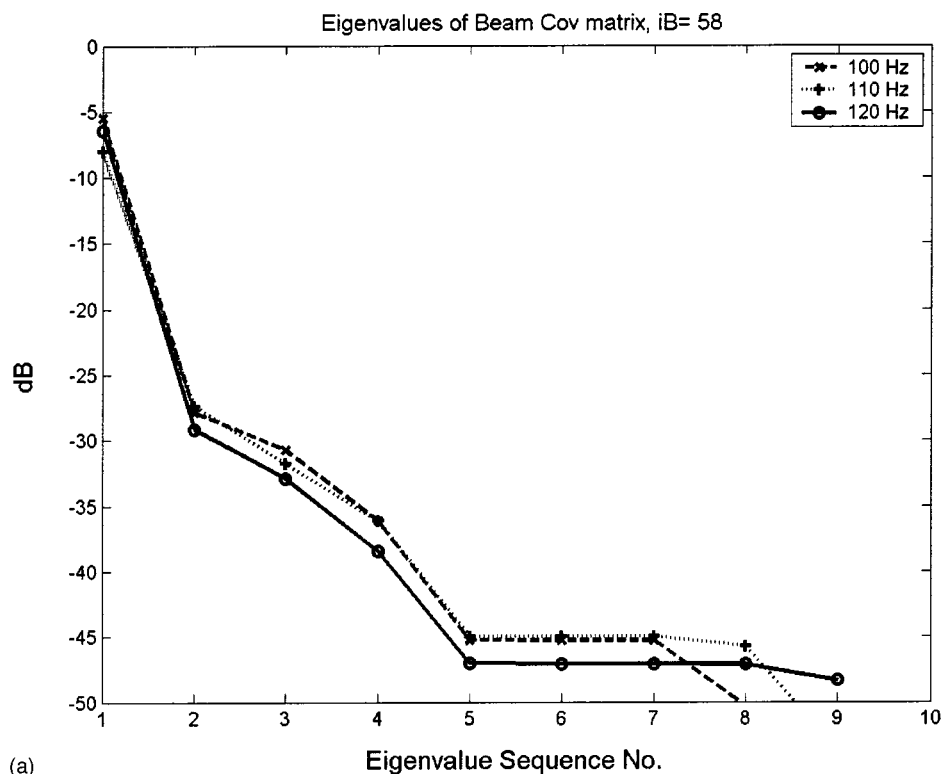


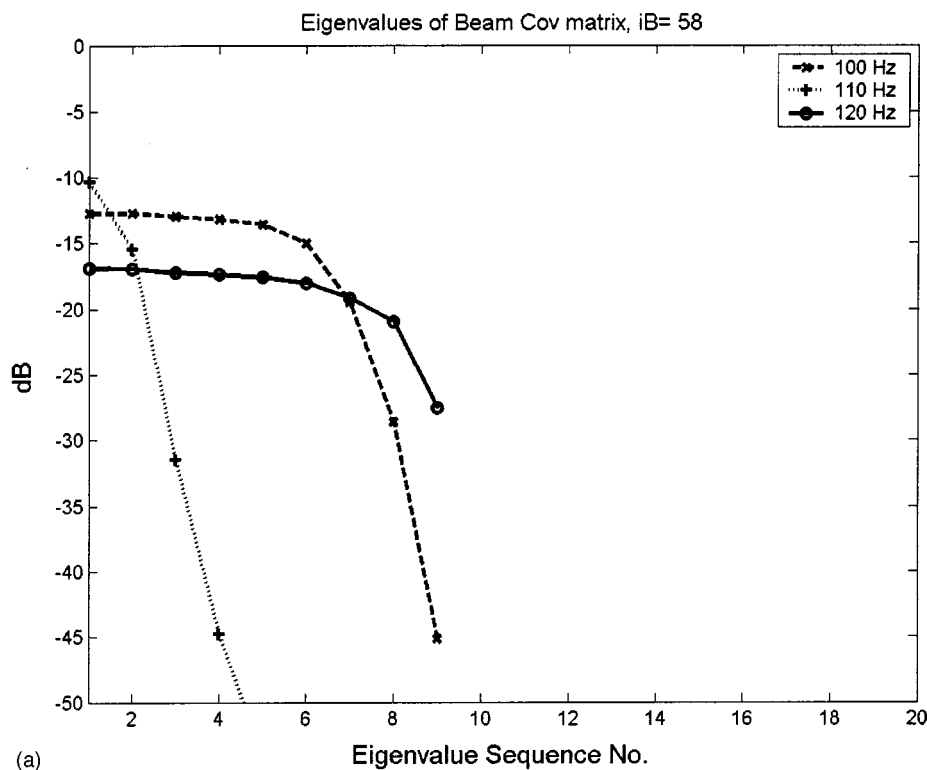
FIG. 6. The eigenvalue spectrum of the beam subspace covariance matrix for a target (a) and interference source (b), both changing range, at three different (100, 110, and 120 Hz) frequencies. (See Case 2.)

field are separated by at least w beams (at any instant of time).

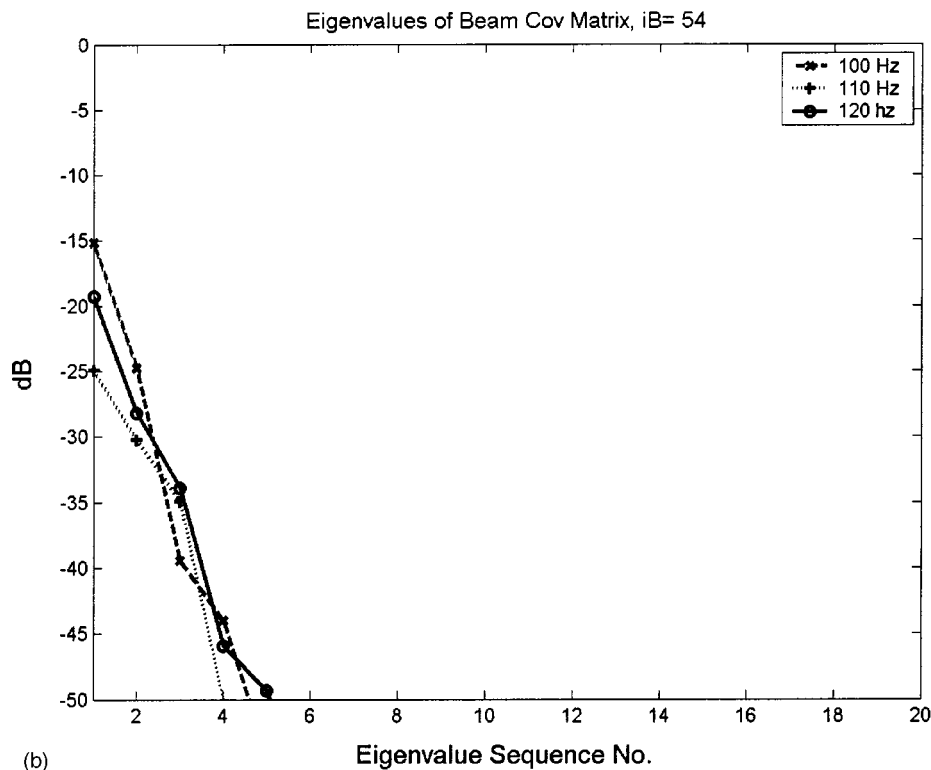
For a signal near the endfire direction, the multipath arrivals often spread the signal energy over more than one beam. For plane wave adaptive beamforming, the multipaths are processed incoherently as independent signal arrivals, despite the fact that they originate from the same

source. One may desire coherent processing of the multipath arrivals. A coherent multipath combination would require a beam domain matched-field processor, e.g., the adaptive matched-beam processor. That topic is outside the scope of this paper.

Although the focus of this paper is on motion compensation, we note that the beam domain approach presents an



(a)



(b)

FIG. 7. The eigenvalue spectrum of the beam sub-space covariance matrix for a moving source changing bearing (Case 1) at three different (100, 110, and 120 Hz) frequencies. In (a) the source bearing changes from -6° to 6° and in (b) the source bearing changes only by $\sim 1^\circ$.

advantage on interference rejection, even for a stationary signal and interference. In the element space, the largest eigenvalue is likely to be dominated by a loud interference. When the signal and interference fields are not orthogonal (as is often the case in reality), it is difficult to remove the eigenvector of the interference without losing the signal energy. The situation is different in the beam domain. Note that in

the signal beam (sub-)space, the largest eigenvalue will be dominated by the signal, since energy leakage from the interference source to the signal beam has been suppressed by the array beamforming peak-to-side lobe ratio (≥ 20 dB for the example given above). Removal of the interference eigenvalue/eigenvector has a lesser effect on the signal field. Likewise, note that in the beam (sub-)space pointing to the

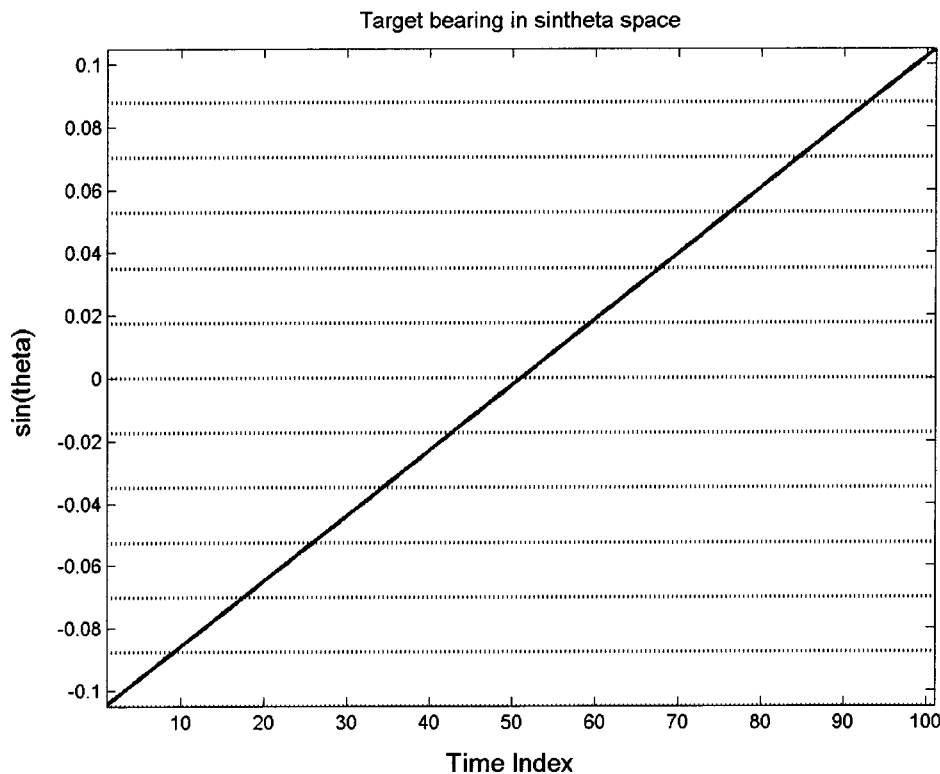


FIG. 8. Source track in bearing versus the beam angles, plotted in $\sin \theta$ space.

interference, the largest eigenvalue will be dominated by the interference field.

IV. MOTION COMPENSATION: A FAST BEARING-RATE SOURCE

For bearing-rate compensation the concept is best described by a rotating coordinate system focused on the target so that the signal retains a constant bearing in this coordinate, and its spectral energy are added up coherently across the HLA. The interference, having a different bearing rate than the signal, will appear to spread over a range of bearing and its energy will be smeared.

This idea is not new and is already implemented in the so-called scissogram. A scissogram is a beam spectrogram that follows a bearing-changing target. The rotating coordinate system is a mathematical framework for describing the scissogram.

Why work in the beam space? Note that to investigate the target spectral content, one uses the scissogram since the spectra of individual elements are dominated by the interference signal. For the same reason, to integrate the signal energy coherently across the array for a bearing-changing target, one should use the signal beam covariance matrix following the target. In contrast, the element space covariance matrix will be dominated by the interference field (as shown above). The beam covariance submatrix at the signal direction has a negligible contribution from the interference field.

The beam domain motion compensation algorithm works as follows. We assume that the signal has been detected by usual array processing, e.g., conventional beam-forming. Thus, we know the approximate bearing of the signal and the corresponding beam subspace for the signal. We

assume that the processor does not know the bearing rate and will search for the bearing rate that yields the highest beam power for the signal beam subspace, as determined by the value of its first eigenvalue. For a given bearing rate, we first construct a bearing track. As an example, Fig. 8 shows a bearing track in the $\sin \theta$ space for an initial bearing of -6° with a hypothesized bearing rate of $0.12^\circ/\text{unit time}$. (For Case 1, the signal moves from -6° to 6° in 100 units of time.) The horizontal line denotes the beam indices. Figure 9 shows the discrete version of the bearing track as only a finite number of beams are available.

We shall explain a procedure for implementing the rotating coordinate in the beam space. The rotating coordinate basically rennumbers the beam indices of the beam cross-spectral matrix $\mathbf{a}_{\text{data}} \mathbf{a}_{\text{data}}^H$ for each data sample according to a hypothesized bearing track (as depicted by Fig. 9) and then adds them up to produce a beam covariance matrix. The beam index is numbered from 1 to 115 with the beam at $\sin \theta = -1$ as No. 1. Use Fig. 9 as an example, there is no bearing change for the first four data frames (the signal stays in beam No. 52), thus the (complex) beam covariance matrices for time 1 to 4 are just added together. For the time frames 5–13, the signal bearing has changed by one beam. The beam cross-spectral matrix for these (5th–13th) time frames will be shifted up by one index and shifted left by one index with the topmost row and leftmost column wrapped around to the bottom-most row and rightmost column. The resulting (5th–13th) beam cross-spectral matrices will be added to the cross-spectral matrices of the previous four (1st–4th). For the next nine data frames, according to Fig. 9, the target bearing has changed by two beams. Hence, the beam cross-spectral matrices will be shifted up and shifted left by two indices and added to the previous beam cross-

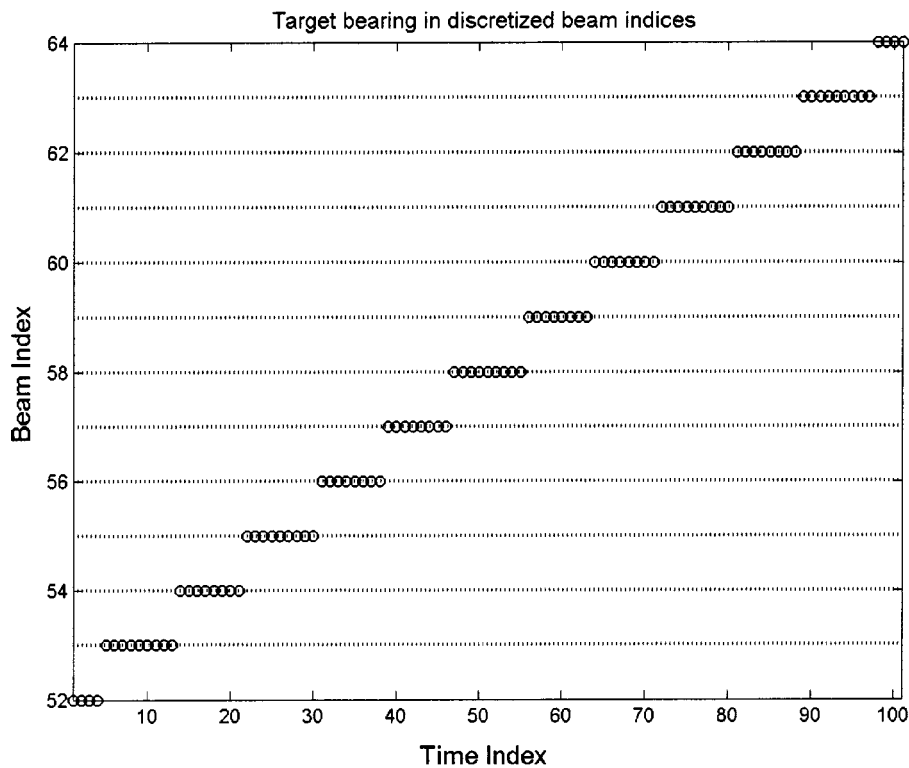


FIG. 9. Beam indices (in terms of $\sin \theta$) used for aligning the beam space covariance matrix based on the bearing track of Fig. 8.

spectral matrices. This process is continued for all 100 data frames for the hypothesized bearing track of Fig. 9. A final beam covariance matrix is obtained for the hypothesized bearing track. This beam covariance matrix will be, in principle, the same as that for a stationary source, since in the rotating coordinates, the source is stationary.

For each hypothesized target-bearing rate (bearing track) one finds the largest eigenvalue of the beam covariance submatrix in the signal beam space. After repeating the above

process for a given range of bearing rate (bearing track), one plots the level of the first eigenvalue as a function of the search bearing rate. The results for Case 1 are shown in Fig. 10. It shows a peak at a bearing rate of $\sim 0.1^\circ/\text{unit time}$, which is slightly lower than the true value of $0.12^\circ/\text{unit time}$. The estimation error is due to the discrete beams used for bearing rate compensation.

Using the (final) beam covariance matrix obtained at the bearing rate of $\sim 0.1^\circ/\text{unit time}$, we apply the beam domain

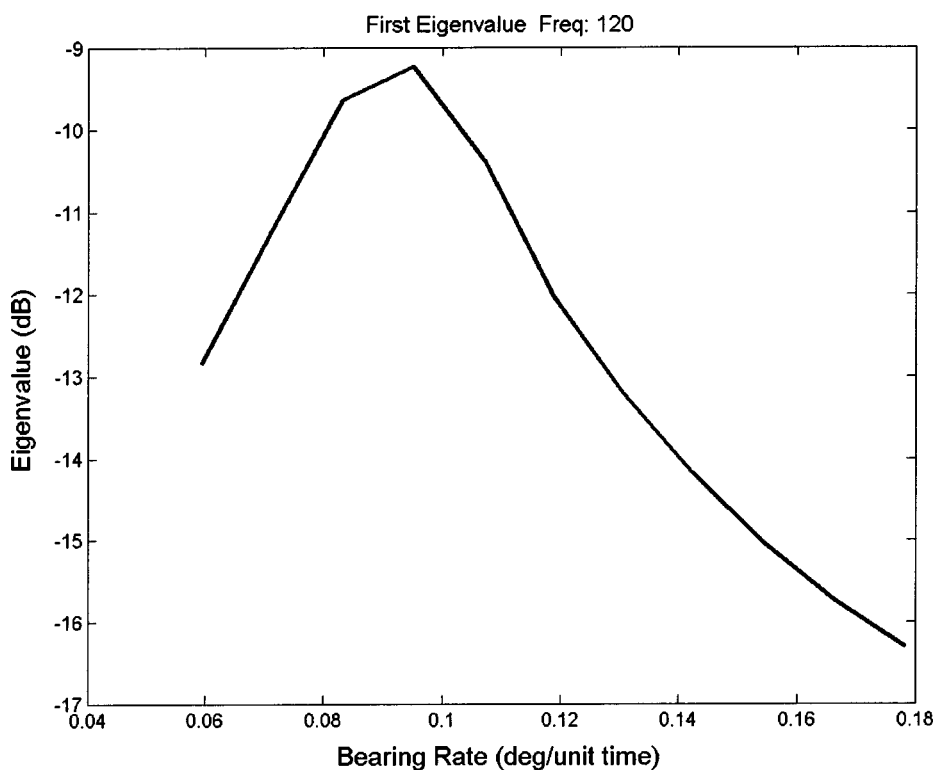


FIG. 10. Amplitude of the first (largest) eigenvalue of the beam-domain signal submatrix as a function of the bearing rate used to compensate for the source motion.

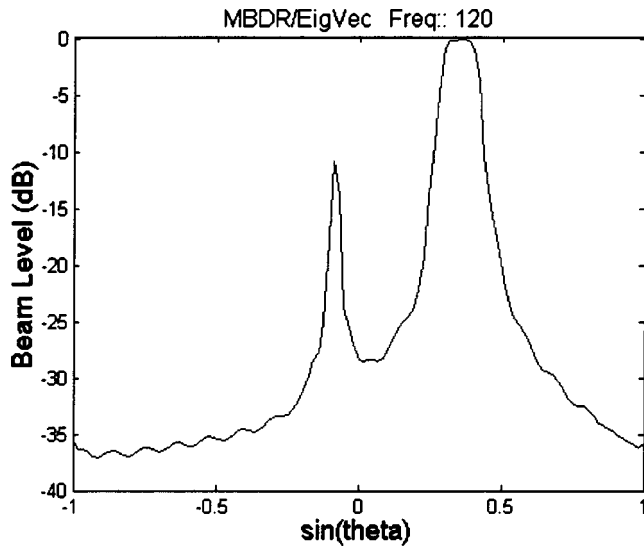


FIG. 11. The beam-domain MVDR beam power after motion compensation.

MVDR, Eq. (9), and plot the output beam power in Fig. 11. We see that the signal has a sharp peak, as expected for MVDR. The interference source shows up as a broadband peak since its motion was not compensated. The peak-to-interference ratio has improved by 6 dB over the element-space MVDR, as shown in Fig. 5; the latter was not compensated for motion.

V. MOTION COMPENSATION: A FAST RANGE-RATE SOURCE

For range-rate compensation, one needs a discriminator related to range that differentiates the target signal from the interference field. The discriminator to be used here is the frequency–range (scaling) relationship as predicted by the waveguide-invariant theory. It was shown previously for a time-reversal vertical line array (VLA), focusing the acoustic energy to a (slightly) different range than the original source location can be accomplished by frequency shifting.¹² Likewise, for matched-field processing on a VLA, source range change can be compensated for by frequency shift of the covariance matrix.¹³ However, the same approach does not work for a HLA, as the element space covariance matrix for a HLA does not have the same frequency and range dependence as for a VLA.¹³ The technical reason is that there is only one range parameter for a VLA, but there are many range parameters for a HLA.

We first show that the beam covariance matrix for a source changing range will exhibit the same frequency–range dependence as predicted by the waveguide-invariant theory. Equipped with this, source range change can be compensated by frequency shift. Consequently, a range compensation algorithm can be used to search for the target range rate and recover the signal loss due to motion. The interference field is suppressed when the interferer has a different range rate than the target source.

A. Beam striations

We have previously shown that the conventional beam output for a HLA also exhibits the same striation pattern as a

function of frequency and range as predicted by the waveguide-invariant theory.¹⁷ We will show that the same frequency–range dependence is also true for the beam covariance matrix for the signal. In Appendix B we show that the conventional beam output, for an array of N phones spaced at d , can be written as

$$b(\theta, \omega) = \sum_m A_m \exp(-jk_m r_C) \exp\left(-j \frac{(N-1)d}{2} k_0 \sin \theta\right) \times \text{sinc}(k_m \sin \theta_T - k_0 \sin \theta), \quad (10)$$

where r_C is the range to the source from the center of the array, k_m is the mode wave number, ω is the acoustic frequency,

$$\text{sinc}(X) \equiv \sin\left(\frac{Nd}{2} X\right) / \sin\left(\frac{d}{2} X\right), \quad (11)$$

and A_m is the mode amplitude,

$$A_m \approx \sqrt{2\pi} \psi_m(z) \psi_m(z_S) / \sqrt{k_m r_C},$$

where $\psi_m(z)$ is the mode depth function.

Let $X_m = k_m \sin \theta_T - k_0 \sin \theta$, the beam intensity spectrum can be written as

$$B(\theta, \omega) \equiv |b(\theta, \omega)|^2 = \sum_{m,n} A_m^* A_n e^{j(k_m - k_n) r_C} \text{sinc}(X_m) \text{sinc}(X_n). \quad (12)$$

We note that when the signal is at the broadside direction, $\text{sinc}(X_m) = N$ at the signal look direction. The beam intensity is N^2 times that of a single element. For a nonbroadside source, the angle of the beam containing the m th mode signal can be offset from the source bearing by many degrees, as the m th mode signal arrives at an angle determined by $\sin \theta_m = k_m \sin \theta_T / k_0 = \cos \phi_m \sin \theta_T$, where ϕ_m is the mode vertical arrival (depletion/elevation) angle. The beam is spread by the mode arrival angles θ_m , particularly for an endfire source. (For a numerical illustration, see Ref. 17.) For an endfire target, the signal beam is no longer peaked at the source bearing.

An individual m th mode arrival covers an angle span determined by $\text{sinc}(X_m)$ as

$$(\sin \theta - \sin \theta_m) < \frac{\pi}{Nd k_0} = \frac{1}{N}, \quad (13)$$

where d is set at a half-wavelength. The m th mode beam intensity at beam angle θ_m is proportional to that of a single element and has the same striation pattern as for a single element.¹⁷

From Eq. (10), one obtains the beam covariance matrix as

$$C(i, j) = e^{-j[(N-1)d/2]k_0(\sin \theta_i - \sin \theta_j)} \sum_{m,n} A_m^* A_n e^{j(k_m - k_n) r_C} \times \text{sinc}(X_{m,i}) \text{sinc}(X_{n,j}), \quad (14)$$

where i, j are beam indices associated with the bearing angle. The dominant elements of the beam covariance are those

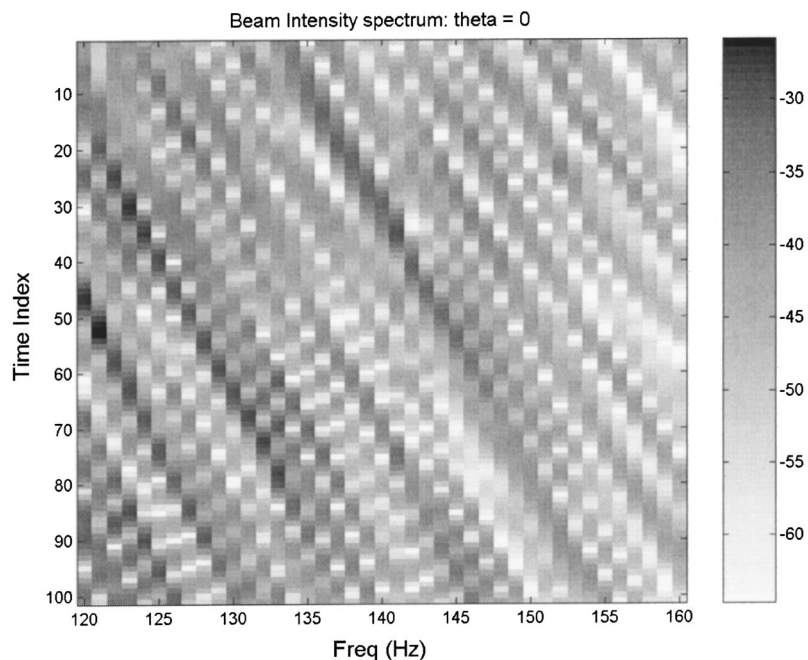


FIG. 12. Intensity striations as a function of time and frequency for the beam pointing to the source (Case 2).

beams for which $\sin b(X_{m,i}) \sim 1$, i.e., beams that satisfy Eq. (13). Compare Eq. (14) with Eq. (12); we note that the covariance matrix [Eq. (14)] has the same frequency–range dependence through the exponential term as the beam power [Eq. (12)].

The beam power at the signal direction (broadside to the array) is plotted in Fig. 12 as a function of frequency and time for Case 2. Recall that the signal travels 1.03 km during a time period of 100 units (Table II). We see that the beam intensity in Fig. 12 exhibits a striation pattern as a function of frequency and time. This pattern has been shown previously to be identical to that of a single element except that the level has been enhanced by the signal gain.¹⁷

(The slope of the striation pattern for a single element has previously been shown to agree between model and

measurement.¹⁸ This suggests that the modeled beam striation patterns should also agree with data, although the agreement has not been verified experimentally.)

In Fig. 13, we plot the intensity of the beam covariance matrix between a beam one index lower and another beam one index higher than the signal beam. We see that it shows the same striation pattern as the beam power, Fig. 12. (The beam power relates to the diagonal element of the beam covariance matrix.)

The slope of the above striation is related theoretically to the so-called waveguide invariant parameter, β .^{19–21} The waveguide-invariant theory says that the slope of the striation for the single-element acoustic intensity, plotted as a function of frequency and range, is given by

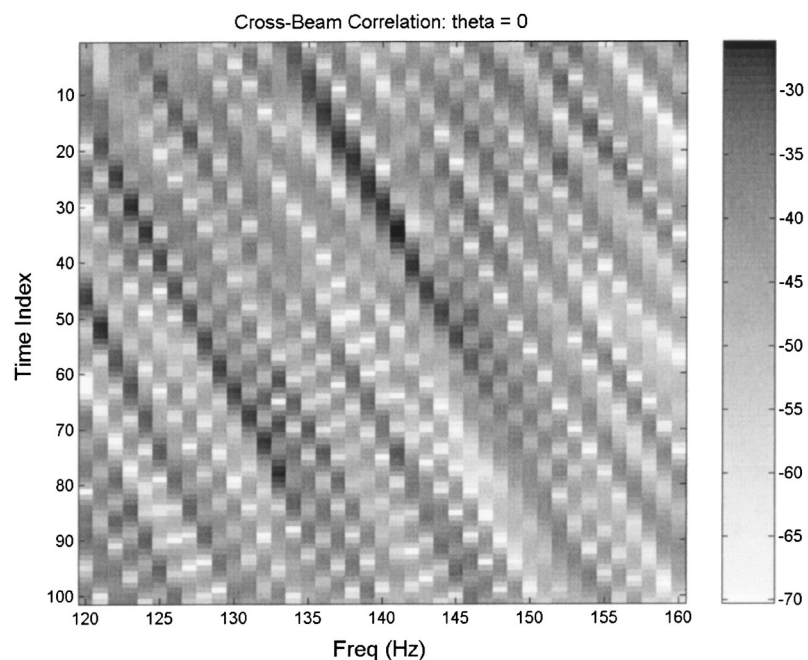


FIG. 13. Striation pattern of the beam correlation between two beams one index below and one index above the signal beam (Case 2).

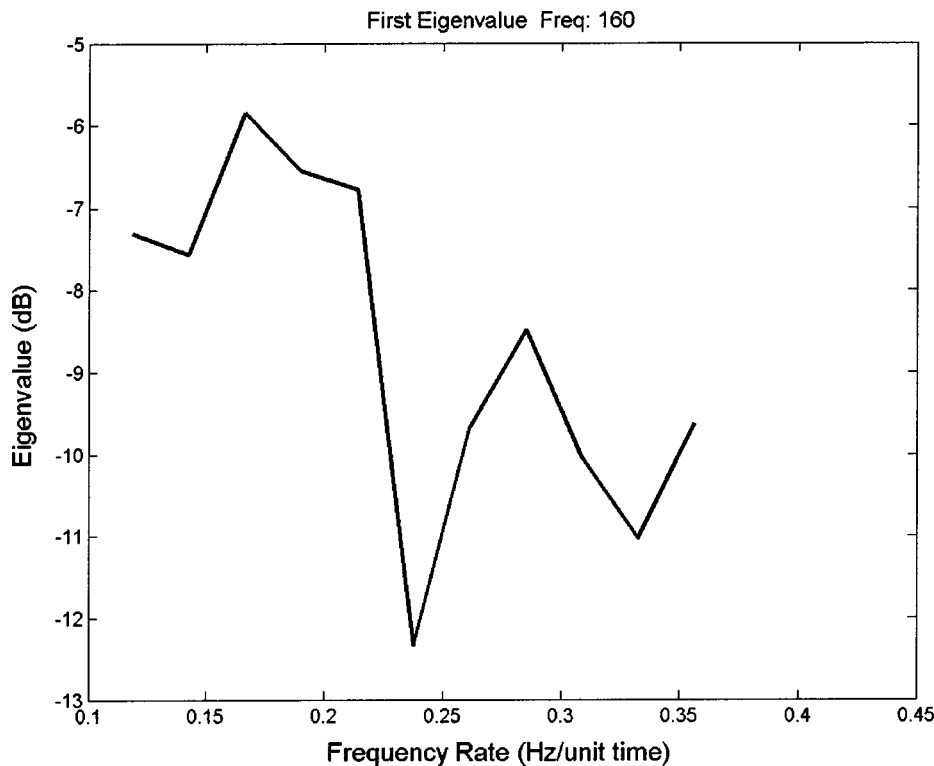


FIG. 14. Amplitude of the first (largest) eigenvalue of the beam-domain signal submatrix as a function of the frequency rate used to compensate for the source motion.

$$\frac{d\omega}{dr} = \beta \frac{\omega}{r}, \quad (15)$$

where β is given by the ratio of the difference of phase slowness between a pair of modes over that of the group slowness between the same pair of modes.^{19–21} The parameter β is called the waveguide invariant since it is a “universal” number for a group of modes. Assuming the source travels with a constant velocity v , the above equation can be rewritten as

$$\frac{d\omega}{dt} = \beta \frac{\omega v}{r} \equiv \gamma, \quad (16)$$

where γ is the slope of frequency striation with respect to time. Based on the analysis above, the waveguide invariants can be extended to the beam intensity, and the beam covariance matrix. The frequency striation slope γ can be directly measured from the beam intensity spectrum. We find that γ is approximately 0.2 Hz/unit time in Fig. 12.

Based on Eq. (16), the beam intensity [Eq. (10)] at the signal direction satisfies the following equation:

$$B(\omega, t + dt) = B(\omega + \gamma d\omega, t). \quad (17)$$

Thus, the signal range change can be compensated by a frequency shift between the adjacent data frames. The same is also true for the elements of the beam covariance matrix indexed around the signal directions. The side lobe beams (outside the signal arrival directions) normally have a different striation pattern.¹⁷

B. Range-rate compensation

Next, we address the beam domain adaptive processing for range-rate compensation assuming that the target signal

has been detected and its bearing is known. We do not assume that β is known in advance; it can be a function of the source–receiver geometry, and frequency. Nor do we assume that the source range is known. Although γ can be measured from the intensity spectrum of the signal beam when there is a sufficient signal-to-noise ratio, we shall assume that it is unknown (or known only approximately) and shall search for it during array processing. The parameter γ will be called the frequency-shift rate or frequency rate for short.

The algorithm for a frequency-rate search works as follows: For a given frequency rate, the beam covariance matrix for each data frame is shifted in frequency according to Eq. (17) for all of its elements. The beam covariance matrices are then summed (integrated). We then calculate the value of the first (largest) eigenvalue of the beam covariance submatrix at the signal arrival direction. The process is repeated for other anticipated frequency rates. The eigenvalue is then plotted as a function of the frequency-shift rate. Figure 14 shows the search result. It yields an estimation of the frequency rate at a value of 0.16 Hz/unit time. The entire beam covariance matrix will be summed using this frequency rate. The final beam covariance matrix will be used by the beam domain adaptive processor.

Figure 15 shows the beam power using the element space MVDR algorithm, with the covariance matrix integrated over the 100 data frames without motion compensation. (The beam pointing to the surface ship is somewhat skewed due to the spreading of mode arrival angles, as remarked above.) Figure 16 shows the beam power using the beam domain MVDR algorithm that includes range-rate compensation (via the above frequency-shift algorithm). Comparing Fig. 16 with 15, we see that the signal-to-interference ratio has improved by 10 dB by the range-rate compensation algorithm. While the signal power has been

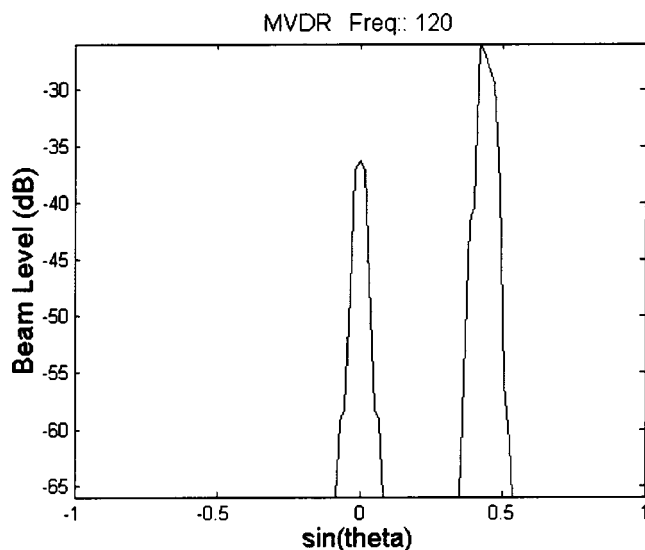


FIG. 15. The MVDR beam power for a range-changing broadside source and interference at 30° (Case 2) using all 100 data samples.

coherently added up following the frequency striation of the signal, the interference beam power has been suppressed since the interference field has a different frequency-shift rate than the signal. Note that the interferer is at a different range and has a different speed than the signal source.

Although the above simulation uses a signal at the broadside direction, the same approach can be applied to a signal at an endfire direction. It was shown in Ref. 17 that the signal arrival beams for a near endfire signal have the same beam striation pattern as the signal beam for a broadside signal. Each signal arrival beam may have a somewhat lower intensity due to signal energy spread over multiple beams.

C. Generalizations

The above discussions showed that the motion effect on the signal field could be compensated for in the beam do-

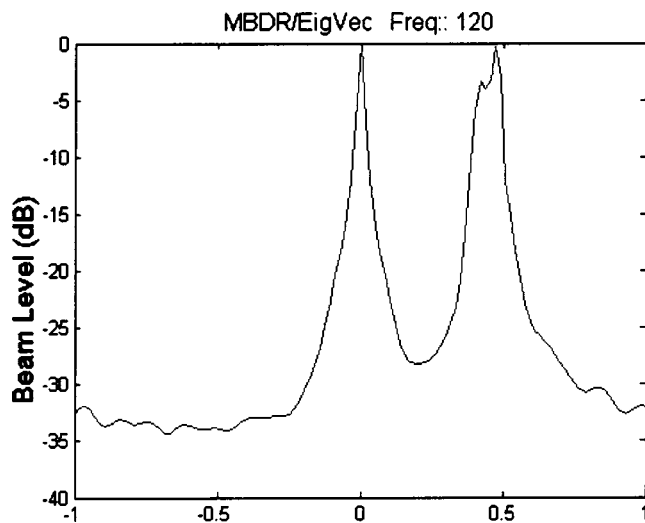


FIG. 16. The beam-domain MVDR beam power for a range-changing broadside source and interference at 30° (Case 2) after motion compensation.

main using the signal beam covariance matrix. This allows a “long” integration time for the (beam) covariance matrix. We showed that the MVDR signal beam retains the same beam power for the moving source as for a stationary source. The interferer is found suppressed when its motion does not match the signal source.

Although we addressed bearing-rate and range-rate compensations separately in the above sections (Secs. III and IV B), the algorithms can be generalized to a more general case when the target is changing bearing and range at the same time. The full development of the algorithms is beyond the scope of this paper, but the concept can be easily illustrated. The process involves a search of possible paths connecting an area of initial and an area of final source locations in the x - y or range-bearing coordinate. Assuming that the source travels with a constant velocity, the bearing and range rate can be calculated from a given hypothesized path of the source travel. For each bearing and range rate, an eigenvalue is obtained for the signal beam covariance matrix compensated for the range and bearing change by a frequency and beam shift. The path that produces the highest overall signal eigenvalue yields an estimate of the target bearing and range rate and hence the target track. (This search process is analogous to matched field tracking as discussed in Ref. 7, for which the search is carried in the range-depth domain.) A final beam covariance matrix is obtained for the entire beams by integrating the beam covariance matrix using the estimated bearing and range rate, based on the above motion compensation algorithm.

VI. SUMMARY AND CONCLUSIONS

In this paper we analyze the source motion effect on the estimation of the covariance matrix in both the element and beam space. The motion effect spreads the signal energy from one to several eigenvalues when integrated over many data samples. Consequently, when interference is present, the eigenvectors of the signal and interference are mixed with each other and are no longer easily separable in the element space. Eigenvalue spreading also occurs in the beam space but the signal and interference eigenvectors belong to different beam (sub-)spaces as long as the signal and interference field show up in different beams. It is then possible to process the signal (in the beam domain) without being affected by the interference field.

(The basic difference between beam and element space processing can be explained using the analogy of frequency and time domain processing. Assume that the signal and interference field have different spectral content and both have Doppler shift due to source motion. One finds that it is difficult to correct for the signal Doppler shift in the time domain since the time series data are dominated by the interference field. The natural thing is to process the data in the frequency domain where the signal and interference field are separated by their frequency contents. The conventional beams are in this context same as the wave number transform of the pressure fields. The signal and interference field occupy different beams.)

We propose two beam-space algorithms to compensate for the source motion so that the beam covariance matrix can

be integrated over a long time to produce one large eigenvalue for the signal field. The anticipated payoff is recovery of the signal loss due to source motion, less degradation (bias) in the MVDR beam power, and suppression of the interference power.

For a fast bearing-rate source, the beam covariance matrices are realigned in the beam space by searching/tracking the source bearing change. For a fast range-rate source, the beam covariance matrices are integrated by frequency shifting. The frequency-shifting rate is searched using the beam submatrix centered on the source. Using simulated data, we showed a significant improvement of the beam-domain MVDR performance, with motion compensation, over that of the element-space MVDR, without motion compensation. The signal beam width is narrow as for a stationary source. The interference power has been suppressed when the motion of the interference does not match that of the signal, resulting in a 6–10 dB improvement in the signal-to-interference ratio over the element-space MVDR.

ACKNOWLEDGMENTS

This work is supported by the Office of Naval Research. Thanks are due Y. P. Lee for useful discussions.

APPENDIX A: THE BEAM DOMAIN MVDR PROCESSOR

Using the orthogonal matrix \mathbf{T} , the MVDR beam power, Eq. (1), can be rewritten as

$$B^{\text{MVDR}}(\theta) = (\mathbf{p}^H \mathbf{R}^{-1} \mathbf{p})^{-1} = (\mathbf{p}^H \mathbf{T}^H \mathbf{T} \mathbf{R}^{-1} \mathbf{T}^H \mathbf{T} \mathbf{p})^{-1} \\ \equiv (\mathbf{a}^H \mathbf{X}^{-1} \mathbf{a})^{-1}, \quad (\text{A1})$$

where \mathbf{a} is given by Eq. (6), with \mathbf{p} in Eq. (6) being the steering vector for plane wave beamforming as given in Eq. (2), and

$$\mathbf{X}^{-1} \equiv \mathbf{T} \mathbf{R}^{-1} \mathbf{T}^H \quad (\text{A2})$$

is a beam domain matrix. Equation (A1) is the beam domain expression of the MVDR algorithm.²²

Equation (A1) is not very useful for a large aperture HLA. The MVDR algorithm requires the inverse of the covariance matrix \mathbf{R} , which involves a calculation of the order $\sim O(N^3)$ for N elements. The beam domain expression requires two additional matrix multiplications that involve a calculation of $\sim O(N^2)$. For a large aperture array, the matrix inversion is already computationally intensive and there is no incentive to go to the beam domain. For beam domain processing, one would like to calculate the beam covariance matrix directly from the conventional beam outputs as in Eq. (7). However, in practice, one notes that $\mathbf{Q}^{-1} \neq \mathbf{X}^{-1}$ when the number of beams does not equal the number of phones.

The alternative algorithm for the beam domain MVDR as given by Eq. (9) reduces the computations by >1–2 orders of magnitudes than the element space MVDR. As discussed in the text, the beam domain uses a beam submatrix of the order 3×3 . The inversion of a matrix of dimension 3 is several orders of magnitude faster than the inversion of a matrix of dimension 100. One notes that conventional beamforming is the first step of processing for many sonar array

systems, and in some systems the conventional beams are the only data available for post-processing. Given the fact that conventional beams have already been obtained, Eq. (9) is the preferred algorithm. The beam power of Eq. (9) has been checked to agree with the element space MVDR for a plane wave model.

Note that there are other ways to implement the beam subspace processors, but most of them yield a higher side lobe level compared with the element-space MVDR. For example, high side lobe levels are found if a submatrix of the inverse matrix \mathbf{Q}^{-1} [with \mathbf{Q} defined in Eq. (7)] is used instead of the inverse of $\hat{\mathbf{Q}}$, as described above. One could also zero out all elements in \mathbf{Q} except for the sub-matrix containing $\hat{\mathbf{Q}}$, add a small unit matrix (diagonal loading) and then take the matrix inverse. The results are not satisfactory and the processing is computationally intensive.

APPENDIX B: THE CONVENTIONAL BEAM OUTPUT

The conventional beam output of a horizontal line array is given below using a normal mode representation of the pressure field,

$$p_j(\omega) = \sum_m \sqrt{2\pi} \exp(-jk_m r_j) \psi_m(z) \psi_m(z_s) / \sqrt{k_m r_j} \\ \equiv \sum_m A_m \exp(-jk_m r_j), \quad (\text{B1})$$

where r_j is the range from the source to the j th element, and we shall assume that all the elements are at the same depth z . For an array of N elements, with spacing d , we form a conventional beam as follows:

$$b(\theta, \omega) = \sum_{n=1}^N e^{j(n-1)k_0 d \sin \theta} p_n(\omega), \quad (\text{B2})$$

where the angle θ is measured from the broadside of the HLA and $k_0 = \omega/c_0$, with c_0 being the sound speed at the HLA depth. For the analytical calculations below, we shall take a farfield expansion of the source–receiver range,

$$r_n \approx r_0 - (n-1)d \sin \theta_T, \quad (\text{B3})$$

where r_0 is the range to the first element of the array and θ_T is the source bearing. We then find that

$$b(\theta, \omega) = \sum_m A_m \exp(-jk_m r_0) \sum_{n=1}^N \exp(j(n-1) \\ \times d[k_m \sin \theta_T - k_0 \sin \theta]) \\ = \sum_m A_m \exp(-jk_m r_C) \\ \times \exp\left(-j \frac{(N-1)d}{2} k_0 \sin \theta\right) \\ \times \text{sinc}(k_m \sin \theta_T - k_0 \sin \theta), \quad (\text{B4})$$

where

$$r_C \equiv r_0 - \frac{(N-1)d}{2} \sin \theta_T$$

is the range to the source from the center of the array, and

$$\sin b(X) \equiv \sin\left(\frac{Nd}{2}X\right) / \sin\left(\frac{d}{2}X\right).$$

- ¹J. Capon, "High resolution wavenumber spectrum analysis," *Proc. IEEE* **57**, 1408–1418 (1969).
- ²N. R. Goodman, "Statistical analysis based on a certain multivariate complex Gaussian distribution," *Ann. Math. Stat.* **34**, 152–177 (1963).
- ³J. Capon and N. R. Goodman, "Probability distributions for estimates of the frequency–wavenumber spectrum," *Proc. IEEE* **58**, 1785–1786 (1970).
- ⁴S. Reed, J. D. Mallett, and L. E. Brennan, "Rapid convergence rate in adaptive arrays," *IEEE Trans. Aerosp. Electron. Syst.* **AES-10**, 853–863 (1974).
- ⁵D. E. Grant, J. H. Gross, and M. Z. Lawrence, "Cross-spectral matrix estimation effects on adaptive beamforming," *J. Acoust. Soc. Am.* **98**, 517–524 (1995).
- ⁶B. Baggeroer and H. Cox, "Passive sonar limits upon nulling multiple moving ships with large aperture arrays," *Proceedings of the 33rd Aslo-mar Conference on Signals, Systems & Computers* (Pacific Grove, CA, Nov. 1999), pp 103–108.
- ⁷See, for example, L. T. Fialkowski, J. S. Perkins, M. D. Collins, J. A. Fawcett, and W. A. Kuperman, "Matched-field source tracking by ambiguity surface averaging," *J. Acoust. Soc. Am.* **110**, 739–746 (2001) and references therein.
- ⁸T. C. Yang, "Adaptive matched-beam processing for a horizontal line array," unpublished.
- ⁹A. Abraham and N. L. Owsley, "Beamforming with dominant mode rejection," in *IEEE Oceans 1990 Conference Proceedings*, pp. 470–475.
- ¹⁰T. R. Messerschmitt and R. A. Gramann, "Evaluation of the dominant mode rejection beamformer using reduced integration times," *IEEE J. Ocean. Eng.* **22**, 385–392 (1997).
- ¹¹H. Cox, R. M. Zeskind, and M. M. Owen, "Robust adaptive beamforming," *IEEE Trans. Acoust., Speech, Signal Processing* **ASSP-35**, 1365–1376 (1987).
- ¹²H. C. Song, W. A. Kuperman, W. S. Hodgkiss, T. Akal, and C. Ferla, "A time-reversal mirror with variable range focusing," *J. Acoust. Soc. Am.* **103**, 3234–3240 (1998).
- ¹³L. M. Zurk, "Source motion compensation using wave guide invariant theory," *J. Acoust. Soc. Am.* **110**, 2717 (2001).
- ¹⁴For a discussion of these issues see, for example, W. M. Carey and W. B. Moseley, "Space–time processing, environmental-acoustic effects," *IEEE J. Ocean. Eng.* **16**, 285–301 (1991).
- ¹⁵N. O. Booth, A. T. Abawi, P. W. Schey, and W. S. Hodgkiss, "Detectability of low-level broad-band signals using adaptive matched-field processing with vertical aperture arrays," *IEEE J. Ocean. Eng.* **25**, 296–313 (2000).
- ¹⁶M. B. Porter, "The Kraken normal mode program", user's manual, SACLANT Undersea Research Centre, La Spezia, Italy, 1991.
- ¹⁷T. C. Yang, "Beam intensity striations and applications," *J. Acoust. Soc. Am.* (in press).
- ¹⁸G. L. D'Spain and W. A. Kuperman, "Application of waveguide invariants to analysis of spectrograms from shallow water environments that vary in range and azimuth," *J. Acoust. Soc. Am.* **106**, 2454–2468 (1999).
- ¹⁹L. M. Brekhovskikh and Y. P. Lysanov, *Fundamentals of Ocean Acoustics*, 2nd ed. (Springer-Verlag, New York, 1991), pp. 140–145, 148–152.
- ²⁰S. D. Chuprov, "Interference structure of a sound field in a layered ocean," *Acoustics of the Ocean: Current Status* (in Russian), edited by L. M. Brekhovskikh and I. B. Andreev (Nauka, Moscow, 1982), pp. 71–91.
- ²¹G. A. Grachev, "Theory of acoustic field invariants in layered waveguide," *Acoust. Phys.* **39**, 33–35 (1993).
- ²²K. Yoo and T. C. Yang, "Adaptive matched beam processing for source localization," *J. Acoust. Soc. Am.* **106**, 2127 (1999).

Narrow band laser-generated surface acoustic waves using a formed source in the ablative regime

Shant Kenderian^{a)} and B. Boro Djordjevic^{b)}

Center for Nondestructive Evaluation, The Johns Hopkins University, 810 Wyman Park Drive—Suite G010, Baltimore, Maryland 21211

Robert E. Green, Jr.

The Johns Hopkins University, 3400 North Charles Street, Maryland Hall 102, Baltimore, Maryland 21218

(Received 19 June 2002; revised 18 October 2002; accepted 28 October 2002)

A narrow band laser-generated acoustic signal was created using a 4-element lenticular array. This arrangement of the array produces an acoustical signal with frequency content that is compatible with the response of a noncontact and remote broadband receiver, such as a capacitive air-coupled transducer. To support the experimental observations, a simplified concept is presented to explain the effect of a line array source on the frequency content of a surface acoustic wave. The analytical model solution for the wave front shape is derived from the point load solution of Lamb's problem that represents the displacement of a surface acoustic wave generated by an ablative line array. The distribution function, which was used for the model to represent the laser light energy, was tailored to depict the actual energy distribution that illuminates the lenticular array. Filtering functions are applied to the resultant surface displacement function to retain frequencies similar to those detected by the broadband 50 kHz–2.25 MHz receiver. The theoretical model showed good agreement with experimental results. © 2003 Acoustical Society of America. [DOI: 10.1121/1.1529664]

PACS numbers: 43.35.Sx, 43.38.Yn, 43.20.Rz [YHB]

I. INTRODUCTION

In recent years, a growing number of researchers have combined air-coupled detection with laser generation of acoustic signals.^{1–4} This hybrid technique provides a very flexible and simple method for a noncontact and remote generation and detection of ultrasound. While the frequencies of remote air-coupled detectors are limited to less than 3 MHz, those of a laser-generated acoustic signal are inversely proportional to the laser pulse width and can extend beyond 100 MHz. To obtain a laser-generated signal with a narrow band range of frequencies, investigators have used spatial arrays illumination sources produced by several means, including the use of lenticular arrays,⁵ optical diffraction gratings,⁶ multiple lasers,⁷ interference patterns,^{8–11} and shadow mask.^{12,13} While the use of a shadow mask has been shown to be effective and easy to use, a substantial amount of the laser light energy is masked out, leaving less than 50% to deposit on the surface of the material.¹⁴ In this paper, a lenticular array was used to illuminate the surface of an aluminum specimen with a multiple line light array. This was achieved by trimming high-power cylindrical lenses to the appropriate size in order to produce the desired laser source geometry. The advantage of this technique is that, except for minor losses associated with the optical properties of the lenses, all of the laser light energy is available for the generation of the acoustic signal. A simplified concept is presented first, followed by the experimental results, and then the theoretical solution. To the best of our knowledge, no theoretical model has been presented in the past, which de-

scribes the effect of “ablative” laser source multiplane illumination geometry on the frequency content of the resultant surface acoustic wave.

II. SIMPLIFIED CONCEPT

Consider a laser light line array shown in Fig. 1, where w and $2h$ are the width and length of each line, respectively, and d is the spacing between lines. A surface acoustic wave generated with a laser light focused to a single point may be represented by a simplified triangular wave, as shown in Fig. 2(a). The frequency of the generated signal is the reciprocal of Δt_1 , which is a function of the laser pulse width, shape, and the physical properties of the material. For light pulse geometry of a finite width and length, such as a line, there is an infinitesimal delay between the elements that comprise the illuminated region. A continuous train of signals will arrive between the first and last arrivals, which propagate a distance of R_0 and R_1 , respectively, as shown in Fig. 1. Each element generates a signal similar to that in Fig. 2(a) so that the sum of the signals of these elements is shown in Fig. 2(b). The frequency content of the signal in Fig. 2(b) is different from that in Fig. 2(a), as a result of the difference between Δt_1 and Δt_2 . This difference, in the time domain, may be calculated from $(R_1 - R_0)/C_R$, where C_R is the velocity of the Rayleigh or surface acoustic wave. In the case of a line array, the signal shown in Fig. 2(b) is repeated at intervals corresponding to the spacing between lines (d) and the number of lines (N). Three fundamental frequencies emerge from this arrangement, which are the reciprocals of Δt_2 , Δt_3 , and Δt_4 , as shown in Fig. 2(c). A line array of only two elements was considered in Fig. 2(c) to avoid redundancy. The difference between Δt_4 and Δt_2 is directly

^{a)}Electronic mail: shant@jhu.edu

^{b)}Electronic mail: boro@jhu.edu

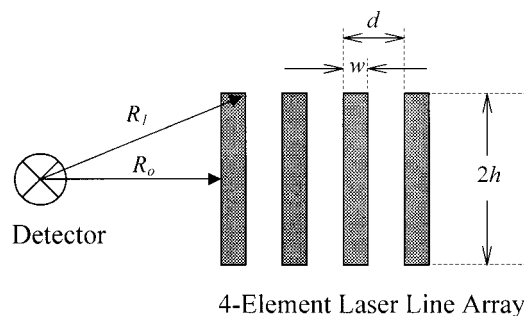


FIG. 1. Schematic representation of a laser line array illuminated region with respect to a detector.

related to the separation distance between the lines (d). Further enhancement of the frequency may be obtained upon increasing the width of the lines (w) while maintaining a constant d . When $w = d/2$ the peaks and troughs of the generated acoustic signal are equally spaced and $\Delta t_3 = \Delta t_2$.

During an actual experiment, by reason of the thermal and optical absorption properties of the material, the resultant surface acoustic wave generated by a laser pulse is not symmetric. Therefore, complete cancellation between the positive and negative surface displacement components, as shown in Fig. 2(b), does not occur. Furthermore, the energy distribution of the laser light across the four elements of the line array is not uniform. It is usually approximated with a Gaussian distribution. In addition, the illumination of the four rectangular lenses covered by the circular cross section of the laser beam is not identical in surface area or intensity.

III. EXPERIMENT

A cylindrical lens with 38 mm focal length was trimmed to 3 mm width and cut to four pieces to produce a four-element lenticular array with spacing of $d = 3$ mm. Increasing the number of elements in a line array narrows the bandwidth of a laser-generated signal. Distributing light over more elements reduces the intensity of the laser pulse per line. Lanza di Scalea *et al.*¹⁴ have shown that the optimum

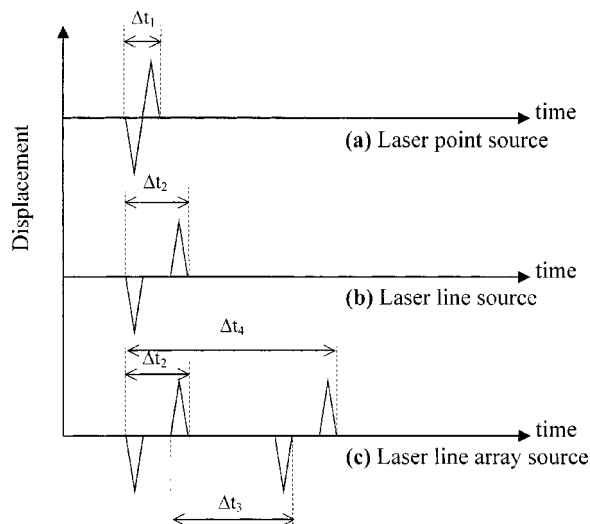


FIG. 2. Simplified graphic representation of a surface acoustic waveform signal obtained from (a) a laser point source (b) laser line source, and (c) laser line array source.

number of lines, to maintain a strong narrow band signal, was four. Very little reduction in the bandwidth is obtained for an array with more than four lines, while the intensity of the signal continues to decrease. With a Rayleigh velocity of 2.91 mm/ μ s in aluminum, the 3 mm separation between lines corresponds to an approximate frequency of 1 MHz.

A Q-switch Nd:YAG infrared (IR) pulsed laser was used to generate the surface acoustic wave signals. The laser operates at a wavelength of 1064 nm providing a pulse width of 4–7 ns and 6 mm beam diameter. Laser light energy is adjustable between 40 and 400 mJ. The laser light was delivered through a set of mirrors, a diverging lens, and then impinged on the surface of the specimen through the four-element lenticular array. The length and width of each element in the laser light line array depends on the focal length of the array elements and the standoff distance between the array and the specimen.

A capacitive air-coupled receiver,¹⁵ capable of detecting frequencies between 50 kHz and 2.25 MHz, was positioned such that the signal propagated a total distance of 70 mm along the surface of the aluminum specimen and 5 mm in air before reaching the detector.

The width of the illumination line on the surface of the specimen depends on the focal point of the lenticular array and the distance between the specimen and the array. To obtain different ratios between the surface areas of the illuminated and dark regions, the specimen was brought in and out of focus with respect to the focal point of the lenticular array. The resultant signal will be referred to as *in focus*, for narrow illumination lines, and *out of focus*, for broad lines. Figure 3 shows the photo image of the laser pulse, the acoustic waveforms, and the frequency content of the detected signal for both *in-focus* and *out-of-focus* conditions. The photo image of the illuminated region was recorded by applying the laser pulse to a laser alignment paper. These image imprints give a good indication of the illuminated region but do not provide the intensity or energy distribution of the laser pulse. Each narrow line projected by the *in-focus* four-element array produced an acoustic signal waveform similar to that shown in the simplified representation in Fig. 2(b). As shown in Fig. 3, the frequency of the *in-focus* signal is distributed between three peaks, as anticipated earlier from the condition described in Fig. 2(c). These peaks were centered near 0.8, 1.3, and 2.0 MHz, corresponding to Δt_2 , Δt_3 , and Δt_4 of 0.5, 0.75, and 1.3 μ s, respectively. As the lenticular array was brought out of focus, the lines became wider and the spacing between them became smaller. An optimum frequency was attained when the illumination line width was approximately half the spacing between lines. The ultrasonic frequency generated by the *out-of-focus* illumination array source was centered along one frequency peak, near 0.8 MHz, which corresponds to $\Delta t_3 = \Delta t_2 = 1.25 \mu$ s.

IV. THEORETICAL APPROACH

In 1989, McKie *et al.*⁵ developed a model in order to help predict the nature of a generated acoustic signal, which would arise as a result of varying the pulse duration of a laser-generated line array. Although the model was applied to both thermoelastic and ablative regimes, the model was built

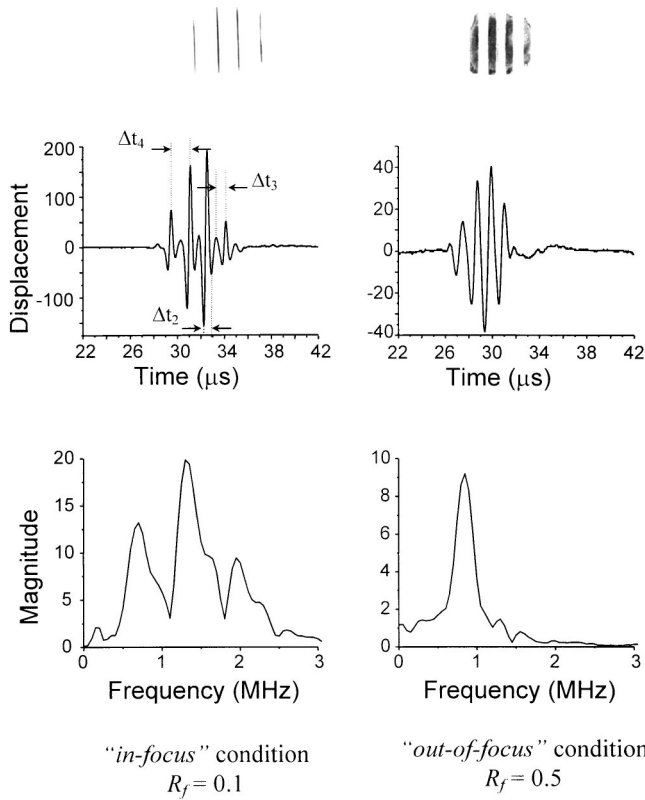


FIG. 3. Laser pulse illumination image (top), resultant waveforms (middle), and frequency content (bottom) of a four-element laser line array incident on an aluminum specimen. Narrow illumination lines (left) represent *in-focus* condition. Broad lines (right) represent *out-of-focus* condition.

based on equations developed by Rose¹⁶ for a point source in the thermoelastic regime. Nevertheless, the model was concerned with bulk modes rather than surface waves. In 1992, Huang *et al.*⁶ provided a brief theoretical principle of narrow-band signal generation using a laser line array source in the thermoelastic regime. They demonstrated that the generation of narrow-band surface waves can be controlled by adjusting the line array parameters. In 1996, Mourad *et al.*¹⁷ provides a solution for an acoustic wave generated by a transient line source in an anisotropic cubic system of symmetry. Doyle *et al.* in 1996,¹⁸ and Royer *et al.* in 2000,¹⁹ developed displacement relationships of a Rayleigh wave generated from a laser line source in the thermoelastic regime.

In the present work, the generation of a surface acoustic wave using an ablative laser line array source is modeled from Achenbach's solutions to Lamb's problem.²⁰ Achenbach²¹ presents a solution for a normal point load on a half-space and derives a time-distance-dependent relationship between the magnitude of the applied load and the surface displacement of the longitudinal, transverse, and Rayleigh waves. For a given load magnitude and a fixed separation distance between the source and the detector, this relationship becomes a function of only time, and will be denoted with $w(t)$ in this text. This relationship is plotted in Fig. 4 for an arbitrary load magnitude and 70 mm propagation distance in aluminum.

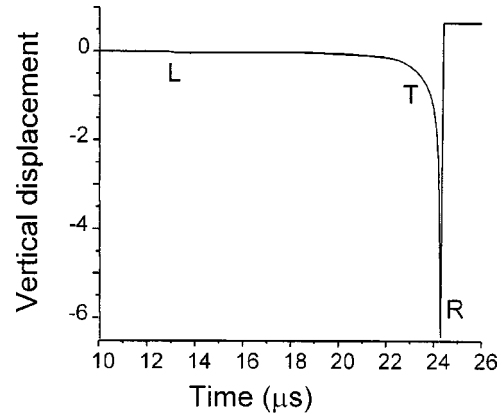


FIG. 4. Vertical displacement at the free surface for a normal point load on a half-space according to Achenbach (Ref. 21). L denotes the arrival time of the longitudinal wave, T of the transverse wave, and R of the Rayleigh wave.

A. Pulse energy distribution function

As mentioned earlier, the laser beam intensity profile is usually approximated with a Gaussian distribution, given in Eq. (1), where σ_x and μ_x are the standard deviation and mean of the intensity distribution along the x direction and are given the values $D/6$ and $D/2$, respectively,

$$F(x) = \frac{1}{\sigma_x \sqrt{2\pi}} \exp\left(-\frac{1}{2\sigma_x^2}(x - \mu_x)^2\right), \quad (1)$$

where D is the width of the lenticular array, which is equal to Nd . D is also considered to be the diameter of the laser beam that illuminates the surface of the lenticular array, as shown in Fig. 5. The lenses then focus the laser light to N distinct lines on the surface of the specimen. The width of these lines w is directly related to the ratio between the specimen-to-lens standoff distance and the focal length of the lens. This ratio will be referred to as the focal factor R_f , where R_f is assumed to be 0 at the focal point and 1 when the lenses are in direct contact with the illuminated surface. For the cylindrical lenses used in this experiment, the minimum line width

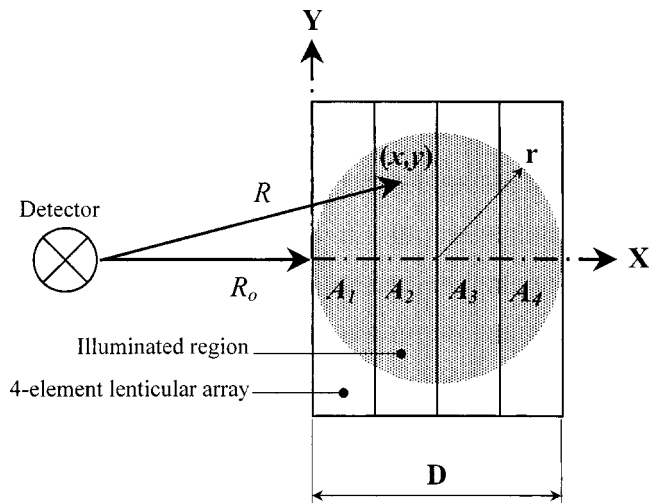


FIG. 5. Geometry of a four-element lenticular array with respect to the illuminated region showing the coordinate system and nomenclature used in this paper.

of the laser light measured at the focal point was one-tenth that of the original source. Therefore, a focal factor of $R_f = 0.1$ is assumed for the *in-focus* condition. If N was the number of lenses in the lenticular array and D was the total width of the array then w is expressed by Eq. (2).

$$w = \frac{DR_f}{N} = dR_f. \quad (2)$$

Using a Heaviside step function, the distribution function $F(x)$ is spatially divided among N lenses. The distribution function for each element i , where $i = 1 \cdots N$, is represented by $F_i(x)$ in Eq. (3). Here $F(x)$ is given by Eq. (1) and H is the Heaviside step function, such that

$$H(x-a) = \begin{cases} 0, & \text{if } x < a, \\ 1 & \text{if } x > a. \end{cases} \quad (3)$$

Equation (3) is an expression of a Gaussian distribution, along the x direction, divided into N elements to represent the distribution of the energy of a laser light illuminating N ,

$$F_i(x) = F(x)H(x - (i-1)w)H(iw - x) \quad (4)$$

elements of the lenticular array. Upon projecting the light from the array onto the surface of the specimen, the width of the illuminated region is reduced by a factor equal to R_f . This factor was introduced into Eq. (3) through w , which is a function of R_f , as shown by Eq. (2). However, these elements have not yet been separated by a distance d , as shown in Fig. 1, so that they may truly represent an N -element line source illuminating the surface of the specimen. To do so, the lines need to be shifted by a value of δx , along the x direction. The value of δx is given by Eq. (5). The resultant distribution function for each line $G_i(x)$ is given by Eq. (6) and for the whole array $G(x)$ by Eq. (7), where A_i is a factor representing the surface area fraction of laser light illuminating the i th lens:

$$\delta x_i = \frac{D}{2N} (2i - 1 - R_f), \quad (5)$$

$$G_i(x) = F_i(x - \delta x_i), \quad (6)$$

$$G(x) = \sum_i^N G_i(x) A_i. \quad (7)$$

A second distribution function $G(x, y)$ needs to be considered to represent the distribution of the laser pulse energy along the y direction. Equation (8) gives the expression of a Gaussian distribution function, where σ_y and μ_y are the standard deviation and mean of the laser light intensity distribution along the y direction, respectively. In this case, while the mean is always zero, Eq. (9), the standard deviation has a value of one-third the height of the illuminated region in the y direction for any given value of x , Eq. (10). The resultant function for a four-element line array along the $y=0$ direction and for $R_f=0.1$ is shown in Fig. 6:

$$G(x, y) = \frac{1}{\sigma_y \sqrt{2\pi}} \exp\left(-\frac{1}{2\sigma_y^2} (y - \mu_y)^2\right), \quad (8)$$

$$\mu = 0, \quad (9)$$

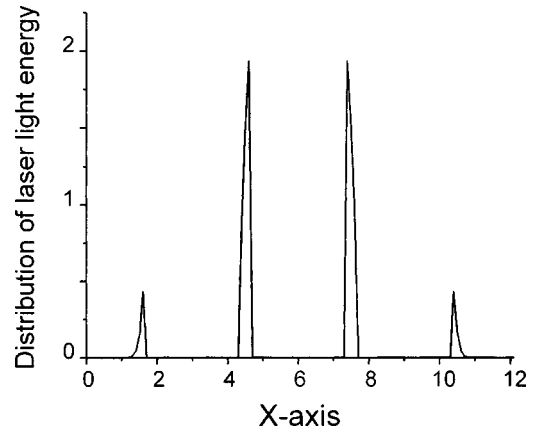


FIG. 6. Laser energy distribution function on the surface of the specimen along the $y=0$ direction, for focal factor $R_f=0.1$, and $N=4$.

$$\sigma_y = \frac{\sqrt{2rx - x^2}}{3}. \quad (10)$$

B. Point pulse solution

As mentioned earlier, Achenbach's point load surface vertical displacement relationship will be treated as a function of only time $z(t)$. To obtain the equivalent vertical surface displacement relationship for a point pulse instead of a point load, the time derivative of $z(t)$ needs to be taken. This is carried out under the assumption that the duration of a laser pulse is infinitesimal, which is a reasonable assumption considering the 4–7 ns pulse duration of a Q-switch laser in contrast with a permanently applied load considered by $z(t)$. However, a mathematical artificial singularity is encountered upon the arrival of the Rayleigh wave as a result of the $-\infty$ to $+\infty$ slope change shown in Fig. 4. This is explained by the fact that only first-order elastic constants were considered in Achenbach's solution to the vertical surface displacement caused by a point load. Therefore, to take the time derivative of $z(t)$, a Fourier transform is taken, Eq. (11), and the derivation is carried out in the frequency domain, Eq. (12), where \mathfrak{F} is the Fourier transform function and Re and Im are the real and imaginary components, respectively. Before inverse Fourier transforming the signal back to the time domain, the output of Eq. (12) is multiplied by the frequency content of the generating laser pulse $L(f)$, as shown in Eq. (13). Therefore, $L(f)$ serves as a bandpass function that retains only the frequencies generated by the laser pulse. All frequencies higher than those generated by the ablating laser, including those responsible for the singularity, are eliminated and a realistic waveform is obtained:

$$Z(f) = \mathfrak{F}[z(t)], \quad (11)$$

$$Z'(f) = [\text{Re}(Z(f)) + i \text{Im}(Z(f))] * 2\pi f, \quad (12)$$

$$U_p(t) = z'(t) = \mathfrak{F}^{-1}[Z'(f) * L(f)]. \quad (13)$$

In the preceding equations, the prime superscripts are to indicate time derivatives. The resultant vertical displacement is given a new symbol $U(t)$ with a subscript “p” to indicate that the displacement is that of a point load. The frequency content of the resultant displacement, shown in Fig. 7, is

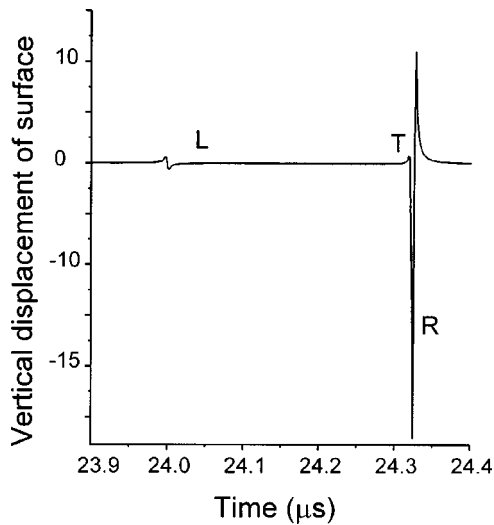


FIG. 7. Vertical displacement at the free surface for a normal point pulse load on a half-space. L denotes the arrival time of the longitudinal wave, T of the transverse wave, and R of the Rayleigh wave.

very high, as it pertains to an infinitesimal point pulse. In experiment, however, the ablated region has a finite dimension and the frequency of the generated signals is lowered as a result. Further filtering will be necessary, to match the detector characteristics, before the final signal is obtained.

C. Line array pulse

Consider the (x, y) coordinate system shown in Fig. 5 and the distance R_0 shown in Fig. 1. The surface vertical displacement generated by a line array pulse is computed by simple superposition of the vertical displacements $U_p(t)$, shown in Fig. 7, arising from all the points comprising the line array. Each displacement component is multiplied by the laser light intensity distribution functions in the x and y directions, given by Eqs. (7) and (8), to represent the strength of the signal generated at each point in the line array. The result is given by Eq. (14). The subscript “la” is used to indicate that the displacement is that of a line array. Because of the symmetry along the $y=0$ line, the signals generated from $(x, +y)$ and $(x, -y)$ are identical to the detector. Therefore, only the $+y$ direction was considered in the equations leading to Eq. (14) and a factor of 2 was introduced to compensate for the $-y$ direction. The distance R an acoustic signal propagates from any point to the detector is expressed as a function of R_0 and the (x, y) coordinates within the illuminated region, as shown in Fig. 5, where R_0 is distance between the array and the detector, as shown in Fig. 1. The relationship is given by Eq. (15). The arrival time of the signal is expressed in terms of the propagation distance R and the Rayleigh wave velocity C_R , Eq. (16), which would effectively make the vertical displacements $U_{la}(t)$, given by Eq. (14), a function of R .

V. RESULTS

Equation (14) yields the surface displacement of an acoustic wave generated by an N -element laser line array source operating in the ablative regime. Here, the variable N is built-in within the distribution function $G(x)$. The results

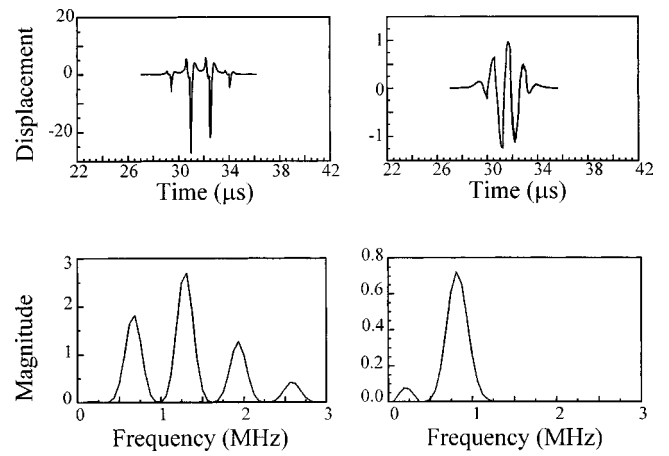


FIG. 8. Waveforms (top) and frequency content (bottom) of a four-element line array based on the model presented by Eq. (13). Two values of the focal factor R_f were considered, $R_f=0.1$ (left) for the in-focus condition and $R_f=0.5$ (right) for the out-of-focus condition.

for a four-element line array are shown in Fig. 8. Two focal factor R_f values were considered, 0.1 for an *in-focus* (narrow) and 0.5 for an *out-of-focus* (broad) line array source, as shown in Fig. 3. Although the frequency content shown in Fig. 8 agree very well with that shown in Fig. 3, the waveforms agreed to a lesser extent. This may be attributed to two factors. The first is that the frequency of the detected signal was bound between a 0.3 MHz lower limit set by

$$U_{la}(t) = \sum_x \sum_y 2U_p(t)G(x)G(y), \quad (14)$$

$$R = \sqrt{(R_0 + x)^2 + y^2}, \quad (15)$$

$$t = \frac{R}{C_R}, \quad (16)$$

the high-pass filter and 2.25 MHz upper limit corresponding to the detection limit of the capacitive air-coupled transducer. A bandpass filter is applied to the waveforms shown in Fig. 8 accordingly and the results are shown in Fig. 9. The second factor is that the model considered a laser beam of a Gaussian energy distribution with a diameter equal to the width of the lenticular array, $2r=D$, as shown in Fig. 5. The energy distribution at the extremities of the Gaussian distribution is very low. At these low-energy levels, below the threshold of ablation, the generation condition transitions to the thermoelastic regime and produces a very weak acoustic signal.

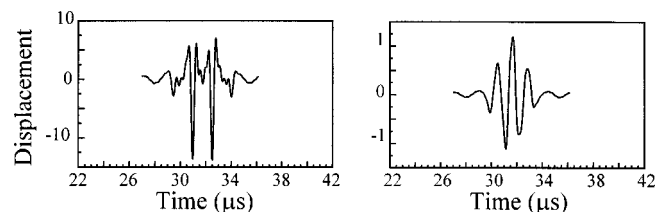


FIG. 9. Resultant waveforms upon applying a bandpass filter to waveforms shown in Fig. 8 retaining frequencies between 0.3 and 2.25 MHz.

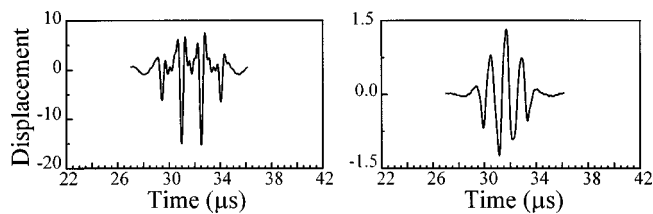


FIG. 10. Resultant waveforms upon applying a 14 mm laser beam to a 12 mm lenticular array to waveforms shown in Fig. 9.

The signal is further weakened at the extreme ends of the distribution. To produce a viable signal, such as that shown in Fig. 3, the 12 mm lenticular array is illuminated with a 14 mm laser beam diameter. This affects not only the energy distribution along the four-element lenticular array but also the surface area fraction of laser light illuminating each lens, A_i . Figure 10 shows the waveforms obtained upon applying a 14 mm laser beam to a 12 mm lenticular array to emulate the conditions of the experimental results shown in Fig. 3.

VI. CONCLUSION

A mathematical model was constructed to represent the surface displacement of a laser line array as an acoustic source, working in the ablative regime. The model was tested on a four-element lenticular array, each lens 3 mm wide, illuminated by a laser pulse 14 mm in diameter. Good agreement was found between the frequency content of the acoustic signal obtained experimentally, Fig. 3, and that produced by the model, Fig. 8. The relative magnitudes and the centers of the frequency peaks agree very well for both “*in-focus*” and “*out-of-focus*” conditions. After applying a bandpass filter to the model and retaining only the frequencies within the detection range of the receiver, the resultant waveforms, Fig. 10, showed reasonable agreement with experiment, Fig. 3. In the “*out-of-focus*” condition, the waveforms agreed in their time of flight (TOF) and sinusoidal shape of the wave. However, the waveforms of the “*in-focus*” condition agreed to a lesser extent. Although they agreed in their TOF and pulse-like shape of these waves, the amplitudes of the positive half of the waveforms differed between model and experiment. The actual signal shape is influenced by a number of factors. Although the energy distribution of a 14 mm diameter pulse to a 12 mm lenticular array was compensated for, the actual distribution of the laser energy is not necessarily Gaussian. Slight misalignments in the optical components can affect the laser illumination of each lens and have a noticeable effect on the ultrasonic signal. The model did not take into account the thermoelastic signal because it is very weak when compared to the ablative signal. Filtering functions were found to have a great influence on the resultant waveform. A Gaussian function was assumed for this model, as it most closely represents the response of the detector.

ACKNOWLEDGMENTS

The authors would like to thank Joseph Dickey and James B. Spicer at the Center for Nondestructive Evaluation and the Materials Science and Engineering Department at the Johns Hopkins University for technical discussions and insights.

- ¹H. E. Kautz, “Noncontact determination of antisymmetric plate wave velocities in ceramic matrix composites,” *Res. Nondestruct. Eval.* **9**, 137–146 (1997).
- ²K. C. Baldwin, T. P. Brendt, and M. J. Ehrlich, “Narrowband laser generation/air-coupled detection ultrasonic system for online process control of composites,” *Ultrasonics* **37**, 329–334 (1999).
- ³S. Kenderian, B. B. Djordjevic, and R. E. Green, Jr., “Laser based and air-coupled ultrasound as noncontact and remote techniques for testing of railroad track,” *Mater. Eval.* **60**, 65–70 (2002).
- ⁴S. Kenderian, B. B. Djordjevic, and R. E. Green, Jr., “Point and line source laser generation of ultrasound for inspection of internal and surface flaws in rail and structural materials,” *Res. Nondestruct. Eval.* **13**, 189–200 (2001).
- ⁵A. D. W. McKie, J. W. Wagner, J. B. Spicer, and C. M. Penny, “Laser generation of narrow-band and directed ultrasound,” *Ultrasonics* **27**, 323–330 (1989).
- ⁶J. Huang, S. Krishnaswamy, and J. D. Achenbach, “Laser generation of narrow-band surface waves,” *J. Acoust. Soc. Am.* **92**, 2527–2531 (1992).
- ⁷T. W. Murray, J. B. Deaton, Jr., and J. W. Wagner, “Experimental evaluation of enhanced generation of ultrasonic waves using an array of laser sources,” *Ultrasonics* **34**, 69–77 (1996).
- ⁸A. Harata, N. Nishimura, and T. Sawada, “Laser-induced surface acoustic-waves and photothermal surface gratings generated by crossing 2 pulsed laser-beams,” *Appl. Phys. Lett.* **57**, 132–134 (1990).
- ⁹H. Nishino, Y. Tsukahara, Y. Nagata, T. Koda, and K. Yamanaka, “Excitation of high-frequency surface acoustic-waves by phase-velocity scanning of a laser interference fringe,” *Appl. Phys. Lett.* **62**, 2036–2038 (1993).
- ¹⁰H. Nakano and S. Nagai, “Laser generation of antisymmetric Lamb waves in thin plates,” *Ultrasonics* **29**, 230–234 (1991).
- ¹¹K. A. Nelson, R. J. D. Miller, D. R. Lutz, and M. D. Fayer, “Optical-generation of tunable ultrasonic-waves,” *J. Appl. Phys.* **53**, 1144–1149 (1982).
- ¹²D. Royer and E. Dieulesaint, “Analysis of thermal generation of Rayleigh waves,” *J. Appl. Phys.* **56**, 2507–2511 (1984).
- ¹³E. A. Ash, E. Dieulesaint, and H. Rakouth, “Generation of surface acoustic waves by means of a CW laser,” *Electron. Lett.* **16**, 470–472 (1980).
- ¹⁴F. Lanza di Scalea, T. P. Brendt, J. B. Spicer, and B. B. Djordjevic, “Remote laser generation of narrow-band surface wave through optical fibers,” *IEEE Trans. Ultrason. Ferroelectr. Freq. Control* **46**, 1551–1557 (1999).
- ¹⁵W. M. D. Wright, D. W. Schindel, and D. A. Hutchins, “Studies of laser generated ultrasound using micromachined silicon electrostatic transducer in air,” *J. Acoust. Soc. Am.* **95**, 2567–2575 (1994).
- ¹⁶L. R. F. Rose, “Point source representation for laser generated ultrasound,” *J. Acoust. Soc. Am.* **75**, 723–732 (1984).
- ¹⁷A. Mourad and M. Deschamps, “Acoustic waves generated by a transient line source in an anisotropic half-space,” *Acustica-Acta Acustica* **82**, 839–851 (1996).
- ¹⁸P. A. Doyle and C. M. Scala, “Near-field ultrasonic Rayleigh waves from a laser line source,” *Ultrasonics* **34**, 1–8 (1996).
- ¹⁹D. Royer and C. Chenu, “Experimental and theoretical waveforms of Rayleigh waves generated by a thermoelastic laser line source,” *Ultrasonics* **38**, 891–895 (2000).
- ²⁰H. Lamb, “On the propagation of tremors over the surface of an elastic solid,” *Philos. Trans. R. Soc. London, Ser. A* **203**, 1–42 (1904).
- ²¹J. D. Achenbach, “Wave propagation in elastic solids,” in *Applied Mathematics and Mechanics*, edited by H. A. Lauwerier and W. T. Koiter (American Elsevier, Inc., New York, 1973), Chap. 7, Sec. 7.12, pp. 310–318.

Derivation of an optimal directivity pattern for sweet spot widening in stereo sound reproduction

Josep A. Ródenas,^{a)} Ronald M. Aarts,^{b)} and A. J. E. M. Janssen

Philips Research Laboratories Eindhoven, Professor Holstlaan 4, NL-5656 AA Eindhoven, The Netherlands

(Received 12 March 2002; accepted for publication 27 September 2002)

In this paper the correction of the degradation of the stereophonic illusion during sound reproduction due to off-center listening is investigated. The main idea is that the directivity pattern of a loudspeaker array should have a well-defined shape such that a good stereo reproduction is achieved in a large listening area. Therefore, a mathematical description to derive an optimal directivity pattern ℓ_{opt} that achieves sweet spot widening in a large listening area for stereophonic sound applications is described. This optimal directivity pattern is based on parametrized time/intensity trading data coming from psycho-acoustic experiments within a wide listening area. After the study, the required digital FIR filters are determined by means of a least-squares optimization method for a given stereo base setup (two pair of drivers for the loudspeaker arrays and 2.5-m distance between loudspeakers), which radiate sound in a broad range of listening positions in accordance with the derived ℓ_{opt} . Informal listening tests have shown that the ℓ_{opt} worked as predicted by the theoretical simulations. They also demonstrated the correct central sound localization for speech and music for a number of listening positions. This application is referred to as “*Position-Independent (PI) stereo*.” © 2003 Acoustical Society of America. [DOI: 10.1121/1.1527928]

PACS numbers: 43.38.Ar, 43.38.Hz, 43.38.Vk [SLE]

I. INTRODUCTION

This paper presents a mathematical derivation of a loudspeaker array to achieve correct localization for stereophonic sound reproduction in a wide listening area. An ideal stereophonic sound reproduction system is one which is capable of reconstructing the wavefront from a given sound scene in an exact form over a region in space occupied by the head of a listener. The use of two spatially separated loudspeakers imposes restrictions on the ability of stereophony to reconstruct the correct acoustic field so that a sharp image can be perceived. Such a system can provide a well-defined image for a centrally located listener mainly at low frequencies, depending on the geometrical displacement of the speakers relative to the listener (Blumlein, 1958).

The basis of stereophony is the ability to create *phantom sources*. It is known that the brain locates a monophonic signal originated from a single source by comparing the differences in the arrival time and intensity of that signal at each ear. If the same monophonic signal is played through two loudspeakers on either side of the listener, then the sound seems to appear from midway between the two loudspeakers since the traveling time of the signal arriving at each ear is the same. This is called a phantom (or virtual) source (Blumlein, 1958; Makita, 1962; Blauert, 1983). In the present work we will discuss how to enlarge the region within which the image remains reasonably free (Bauer, 1960; Crabbe, 1979). We consider only image localization in the horizontal plane since we are primarily interested in stereo sound reproduction.

In general, it can be stated that correct localization within a wide listening area is beneficial for all applications where a good stereophonic sound is required: audio, video, or car stereo. The idea of achieving an increase in the sweet spot area in a stereophonic setup has been recently introduced and studied at the Philips Research Labs in Eindhoven and the stereo sound system has been called “*Position-Independent (PI) stereo*” (Ródenas and Aarts, 2001a, b; Aarts, 1992). The main idea is that the directivity pattern of a loudspeaker array should have a well-defined shape such that a good stereo sound reproduction is achieved in a large listening area. Optimal digital filters are then designed and applied to individual drivers of linear loudspeaker arrays in order to obtain a directivity pattern of a specific shape. This shape has to be adapted to the time/intensity trading mechanism of the human auditory system via psycho-acoustic experiments within a wide listening area (Aarts, 1992).

The goal here is to derive an optimal directivity pattern ℓ_{opt} for the PI-stereo system, which is based on parametrized time/intensity trading data, and then to find, by means of an optimization process, the corresponding FIR filter coefficients that achieve this optimal directivity pattern. It has been proved that an optimal directivity pattern for a loudspeaker can be realized by using an array of drivers positioned at a specific distance from each other (Bauer, 1960; Kates, 1980; Davis, 1987). In our case we used the parametrized time/intensity trading data. Hence, achieving a practical design for PI-stereo sound reproduction, which is a pair of loudspeaker cabinets each equipped with a pair of drivers, which are separated at a given distance to achieve two frequency ranges (high and mid), so as to obtain the desired optimal directivity pattern.

We start first, in Sec. II, describing the limitation of having a sweet spot and the need to improve the stereo-

^{a)}Currently with Hewlett-Packard, Avda. Graells 501, 08190 Sant Cugat, Spain. Electronic mail: josep_rodenas@hp.com

^{b)}Author to whom correspondence should be addressed. Electronic mail: ronald.m.aarts@philips.com

phonic sound reproduction system. Section III describes the human auditory localization, since it is the sound field as perceived by the listener that determines the apparent phantom source. In Sec. IV we introduce briefly the PI-stereo system. Then, in Sec. V, we present the mathematical description to obtain the optimal directivity pattern that gives the best localization performance. We also describe the optimization method to derive the required FIR filter coefficients to drive the loudspeaker cabinets. Later, in Sec. VI, we present the time, frequency, and polar responses of the optimal FIR filters for a practical implementation of two drivers for the loudspeaker arrays. In Sec. VII we present the measured directivity patterns in an anechoic room. Some preliminary listening tests and discussion on the performance of the implemented PI-stereo system will be described in Sec. VIII. Finally, the main conclusions will be summarized in Sec. IX.

II. SWEET SPOT LIMITATION

Generally it is considered as a serious artifact of the traditional stereo system that the stereophonic illusion works only in a limited region. Optimum stereo perception only occurs if the listener is placed exactly in the median plane between the two loudspeakers (*sweet spot*).

One reason that there is a sweet spot is that in two-loudspeaker reproduction, the signals at the listener's ears are formed by the interference of acoustic waves emanating from the loudspeakers. With two loudspeakers, the field can be controlled precisely at only two points (unless unusual acoustical conditions exist, such as the presence of resonant structures). For the present application, those points are at the listener's ears. If the listener moves his head so that the ears are no longer at the designated positions, sound image distortion will appear, caused by unintended signals created by unanticipated interference. Primary causes of the changing interference are differing times of arrival due to differing loudspeaker listener distances, amplitude variations of the impinging waves due to these same varying distances (aggravated by the listener sitting close to the loudspeakers), and uncompensated secondary reflections (improved by the listener sitting close to the loudspeakers) (Leakey, 1960; Jordan, 1971; Lipshitz, 1986).

These problems are illustrated with one example as shown in Fig. 1. The localization performance of a listener using a conventional stereo setup can be quite poor for a listener positioned off-center. Consider a center-front soloist, or, equivalently, assume that the two loudspeakers are radiating exactly the same sound pressure precisely in phase. When the listener is equidistant from the two loudspeakers, the apparent phantom source is perceived to be centered between the loudspeakers. This is illustrated in the figure, where L_0 is the centered listener and I_0 is the intended centered image. As the listener moves to the right, the perceived image also moves to the right. This is shown by the succession of perceived images I_1 through I_4 , which correspond to listener positions L_1 through L_4 . Finally, at listener position L_4 , what is intended to be a centered image is perceived instead as coming from the right loudspeaker.

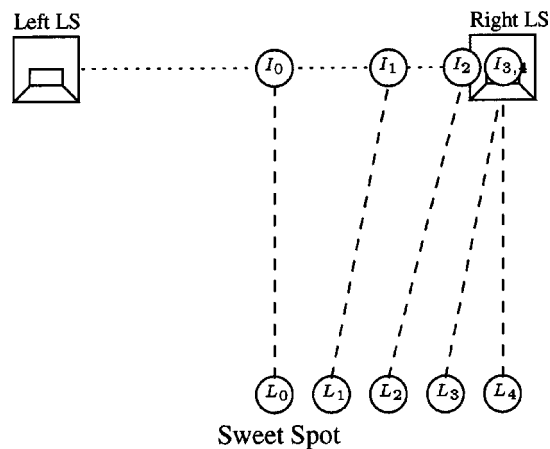


FIG. 1. Conventional arrangement of loudspeakers exhibiting the apparent motion of the phantom sound image I_n for several listener positions L_n .

Thus, if the head is moved laterally, the sound rapidly seems to come from the nearest loudspeaker only. As pointed out, this is mainly because of two additional effects: the intensity of the nearest loudspeaker at the listener's head is highest, and its wavefront arrives earlier (law of the first wavefront or *precedence effect*) (Blauert, 1983).

III. AUDITORY LOCALIZATION

By comparing the signals at the ears, the brain is thought to derive two primary psycho-acoustic cues that determine the perceived horizontal position of a sound source. These broad mechanisms involve the detection of timing or phase differences between the ears (*interaural time differences* or ITDs), and of amplitude or spectral differences between the ears (*interaural intensity difference* or IIDs), which explains all major phenomena of frequency-dependent localization (Stevens and Newman, 1936; Leakey, 1959; Franssen, 1960). They are caused by the wave propagation time difference (primarily below 1.5 kHz) and the shadowing effect of the head (primarily above 1.5 kHz), respectively.

The binaural system is mainly sensitive to IID cues for frequencies above about 500 Hz. IID cues become large and reliable for frequencies above 3000 Hz, making IID cues most effective at high frequencies. In contrast, the binaural system is capable of using ITD cues only at low frequencies, below about 1500 Hz (Kates, 1980).

We will use these binaural differences by employing the phenomena of *time-intensity trading* (the ability to compensate for a left or right bias in the time of arrival by introducing a counterbias in amplitude) (Franssen, 1960; Blauert, 1983; Aarts, 1992). As the listener gets closer to one loudspeaker and sounds arrives sooner, sound from the far loudspeaker should become louder by a certain amount. This means that the loudspeaker should radiate more loudly in some directions than in others. In theory, if the pattern of level as a function of angle is chosen properly, the imaging will be rendered stable for listening positions in a wide listening area. This is actually the goal of the PI-stereo system, and therefore we are now in a position to introduce the basis of the PI-stereo sound system.

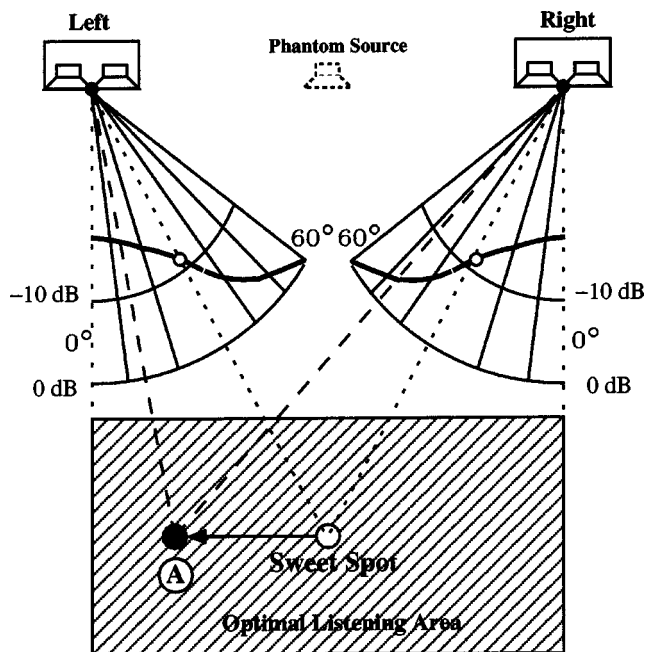


FIG. 2. Optimal listening area for PI-stereo sound reproduction.

IV. THE POSITION-INDEPENDENT STEREO SYSTEM

The current PI-stereo system is basically composed of two loudspeaker arrays, each fitted into a single cabinet, together with an optimal directivity pattern which has been designed such that a good stereo sound reproduction is achieved in a large listening area (Ródenas and Aarts, 2001a, b). A standard listening setup for PI-stereo sound reproduction is shown in Fig. 2.

The main idea here is the following: if the listener moves to the left position (A), the sound intensity from the right loudspeaker increases at the listener's position, while that of the left loudspeaker decreases in such a way that this intensity difference compensates the time arrival difference from both loudspeakers. Thus, the phantom source remains in the middle. This can also be seen as a sort of automatic balance control depending on the position of the listener. However, the PI-stereo system we propose here is passive and does not depend on the position of the listener.

In order to calculate the required directivity pattern, that is the amount of intensity level compensation required for the loudspeakers, listening tests in an anechoic room were conducted (Aarts, 1992). During these tests, the differences in intensity levels between right and left loudspeakers needed to obtain a central sound image for several listening positions were measured (see Fig. 3). From these experiments, which were done by using broadband signals, the required differences for the sound-pressure values at different angles for the loudspeakers were determined and thus the time/intensity trading data.

In the next section, we will introduce the approach consisting of a mathematical derivation, which is based on parametrized time/intensity trading plots, to derive an optimal directivity pattern ℓ_{opt} for the loudspeaker array and, consequently, to obtain the optimal FIR filter coefficients for a specific stereo sound reproduction setup consisting of two

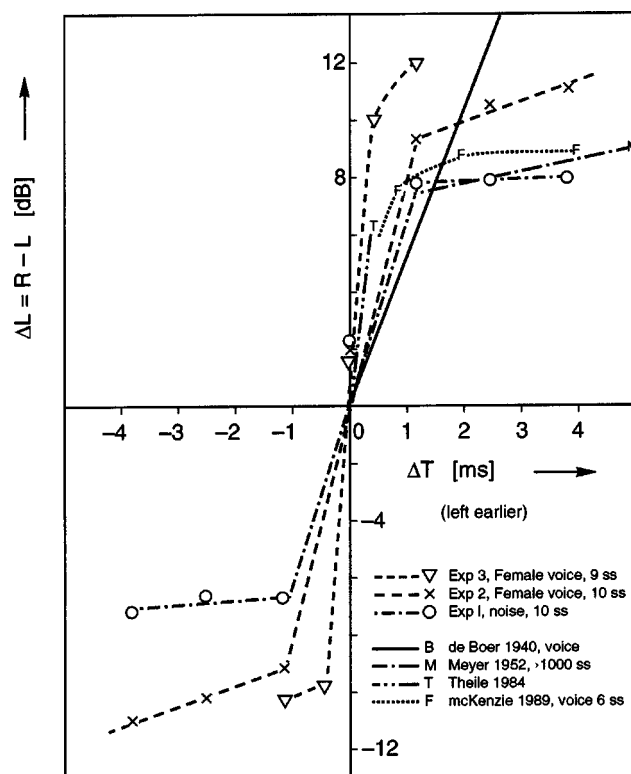


FIG. 3. Time/intensity trading results from the experiments in comparison with other experiments from the literature [after Aarts (1992)].

drivers for each of the loudspeaker arrays that are separated by a distance of 2.5 m.

V. MATHEMATICAL DERIVATION

A. Definition of the problem

We wish to find the optimal directivity pattern ℓ_{opt} that achieves a correct sound localization (robust PI-stereo effect) in a wide listening area for a specific stereo base distance. The PI-stereo problem is considered to be symmetrical and it can be described in the setup shown in Fig. 4.

The sound pressures p_L and p_R at a given point $s = (r, \theta)$ due to the left and right loudspeaker arrays, respectively, are given by

$$p_L(\Omega_L, \theta, r_L) = \frac{e^{-i\omega r_L/c}}{r_L} \sum_{m=-M}^M x_{L,m} e^{im\Omega_L}, \quad (1)$$

$$p_R(\Omega_R, \theta, r_R) = \frac{e^{-i\omega r_R/c}}{r_R} \sum_{m=-M}^M x_{R,m} e^{im\Omega_R}, \quad (2)$$

where θ is the angle of observation, d is the distance between the drivers in each loudspeaker array ($1 \text{ cm} < d < 10 \text{ cm}$), D is the distance between the centers of the two loudspeaker arrays ($1 \text{ m} < D < 5 \text{ m}$), $\Omega_L = \omega d \sin \varphi_L / c$ with $0 < \varphi_L < \pi/4$ and $\Omega_R = \omega d \sin \varphi_R / c$ with $0 < \varphi_R < \pi/4$, ω is the angular frequency of the sound with $\pi c/10d \leq \omega \leq \pi c/d$, r is the distance from the origin to the observation point $s = (r, \theta)$, r_L is the distance from the center of the left loudspeaker array to s and r_R is the distance from the center of the right loudspeaker array to s , c is the velocity of sound ($c = 343 \text{ m/s}$), $x_{L,m}$ is the complex coefficient for the m th

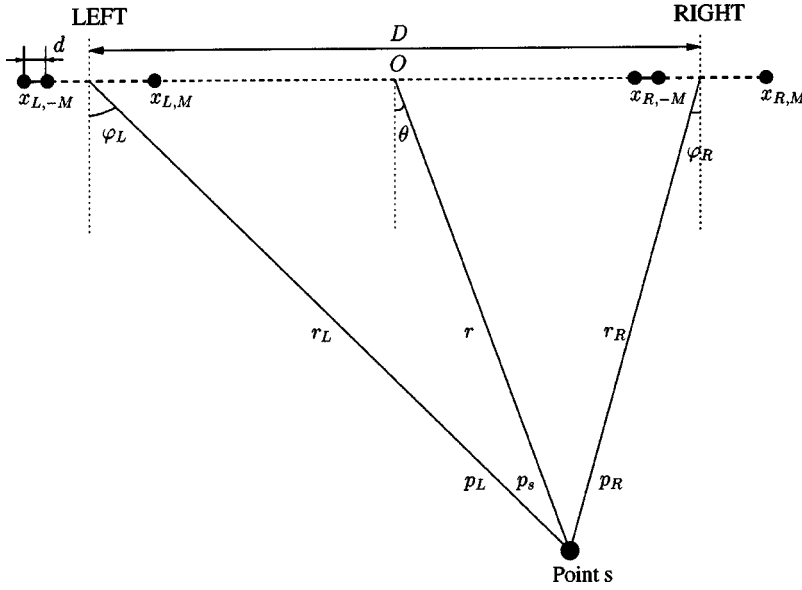


FIG. 4. Setup for the mathematical derivation of robust PI-stereo.

driver of the left loudspeaker array and $x_{R,m}$ is the complex coefficient for the m th driver of the right loudspeaker array with $|x_{R,m}^L| \leq 1$, $x \in \mathbb{C}$, and $N=2M+1$ is the number of drivers in each loudspeaker array, with the constraints $d \ll r$ and $d \ll D$. In this case N is odd; however, for the case N is even we arrive at similar formulas and we will use $N=2$ as an example in Sec. VII.

The sound pressure at point s due to both loudspeaker arrays is

$$p_s = p_L + p_R. \quad (3)$$

We want to determine $x_{R,m}^L(\omega)$ such that

$$\int_A \epsilon^2(r, \theta, x_L, x_R) w(r, \theta) dA \quad (4)$$

is minimal, where A is the listening area, $w(r, \theta)$ is a weight function, the error

$$\epsilon = \Delta L - f(\Delta T), \quad (5)$$

and $\Delta L = 20 \log |p_R/p_L|$. The parametrized function $f(\Delta L)$ is depicted in Fig. 5 and it is based on time/intensity trading

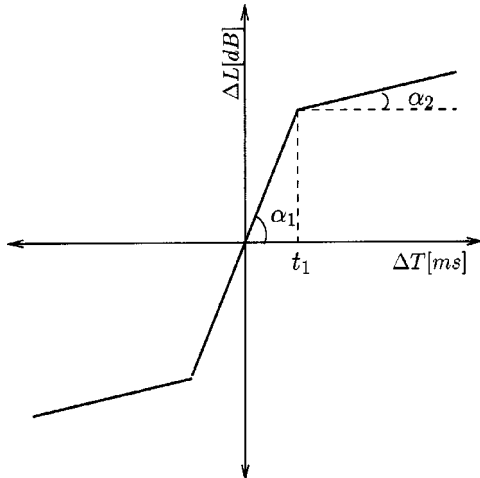


FIG. 5. Parametrization of the time/intensity trading data.

experiments as given in Fig. 3. This function has the following form:

$$f(\Delta T) = \begin{cases} \alpha_1 \Delta T & \text{for } 0 \leq \Delta T \leq t_1 \\ \alpha_2 (\Delta T - t_1) + f(t_1) & \text{for } \Delta T > t_1 \end{cases}, \quad (6)$$

where $f(-\Delta T) = -f(\Delta T)$, $\Delta T = (r_R - r_L)/c$, and t_1 is in ms, α_1 and α_2 are in dB/ms.

B. Solution of the problem

We fix $\omega \in [\pi c/10d, \pi c/d]$. When solving the described problem we consider the geometrical description shown in Fig. 6. We should then deal with the symmetrical setup, in which a given sound pressure F is

$$F(r_L, \varphi_L) = p_L(\Omega, \theta, r) \quad \text{and} \quad F(r_R, \varphi_R) = p_R(\Omega, \theta, r), \quad (7)$$

where

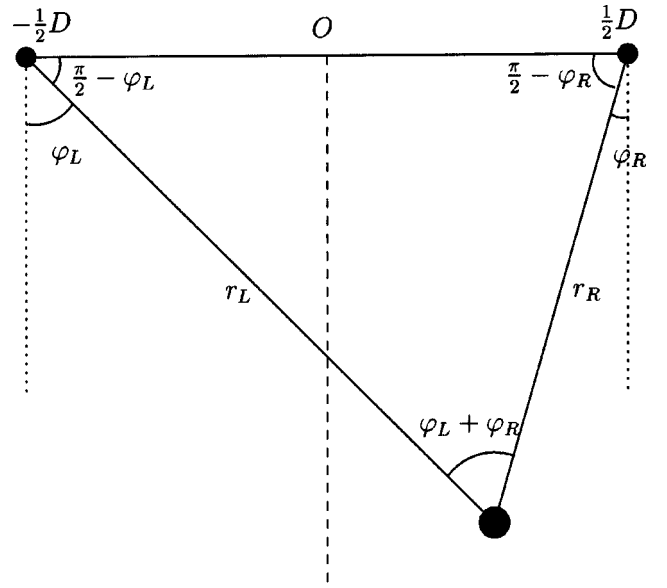


FIG. 6. Trigonometrical geometry for solving the mathematical derivation.

$$F(r, \varphi) = \frac{e^{-i\omega r/c}}{r} \sum_m x_m e^{(im\omega d \sin \varphi)/c}. \quad (8)$$

We set

$$G(z) = \left| \sum_m x_m e^{(imzd)/c} \right|, \quad (9)$$

so that

$$|F(r, \varphi)| = \frac{G(\omega \sin \varphi)}{r}. \quad (10)$$

The distance term r in Eq. (10) compensates for the intensity difference caused by the corresponding pathlength to the observation point s . These distances are already incorporated in the experimental data on the time/intensity trading. Since we are interested in finding only the optimal directivity pattern at the left and right loudspeaker arrays, we should not now include this term in the derivation. Then, Eq. (10) becomes:

$$|F(\varphi)| = G(\omega \sin \varphi). \quad (11)$$

Therefore, as previously described in Eq. (5), our objective is to minimize the average value of

$$\epsilon^2(\varphi_L, \varphi_R) = \left| 20 \log \left| \frac{F(\varphi_R)}{F(\varphi_L)} \right| - f \left(\frac{r_R - r_L}{c} \right) \right|^2, \quad (12)$$

while maximizing the total average power. Note that the right-hand side of Eq. (12) is invariant with respect to multiplication of F by a constant. Hence, one should aim to find an F that minimizes Eq. (12) such that $\max_m |x_m| = 1$ in order to maximize power.

We note that the error ϵ in Eq. (12) is just a function of φ_L , φ_R , and the distances r_R and r_L being determined by φ_L and φ_R . We can eliminate r_R and r_L by expressing them in terms of φ_L and φ_R by using the *sine rule* as follows (see also Fig. 6):

$$\frac{\sin(\pi/2 - \varphi_L)}{r_R} = \frac{\sin(\pi/2 - \varphi_R)}{r_L} = \frac{\sin(\varphi_L + \varphi_R)}{D}, \quad (13)$$

so that

$$r_L = \frac{D \cos \varphi_R}{\sin(\varphi_L + \varphi_R)}; \quad r_R = \frac{D \cos \varphi_L}{\sin(\varphi_L + \varphi_R)}. \quad (14)$$

Consequently, we have

$$r_R - r_L = \frac{D(\cos \varphi_L - \cos \varphi_R)}{\sin(\varphi_L + \varphi_R)} = \frac{D \sin 1/2(\varphi_R - \varphi_L)}{\cos 1/2(\varphi_R + \varphi_L)}. \quad (15)$$

Hence, the error ϵ is given by

$$\epsilon^2(\varphi_L, \varphi_R) = \left| 20 \log G(\omega \sin \varphi_R) - 20 \log G(\omega \sin \varphi_L) - f \left(\frac{D \sin 1/2(\varphi_R - \varphi_L)}{c \cos 1/2(\varphi_R + \varphi_L)} \right) \right|^2. \quad (16)$$

We now let

$$\ell(\varphi) = 20 \log G(\omega \sin \varphi), \quad (17)$$

and

$$h(\varphi, \psi) = f \left(\frac{D \sin 1/2(\varphi - \psi)}{c \cos 1/2(\varphi + \psi)} \right) \quad (18)$$

for $0 \leq \varphi, \psi \leq \pi/2$. Since f is odd, we have

$$h(\varphi, \psi) = -h(\psi, \varphi). \quad (19)$$

We then seek to minimize the average value of

$$|\ell(\varphi) - \ell(\psi) - h(\varphi, \psi)|^2, \quad \text{with } \varphi = \varphi_R, \psi = \varphi_L \quad (20)$$

over all square integrable functions ℓ (with respect to the weight function w). Having found this ℓ_{opt} , we must find the coefficients x_m as in Eq. (9) such that the average value of

$$|\ell(\varphi) - 20 \log G(\omega \sin \varphi)|^2 \quad (21)$$

is minimal.

In order to minimize the average value of Eq. (20), we introduce a weight function of the form

$$W(\varphi, \psi) = w(\varphi)w(\psi), \quad 0 \leq \varphi, \psi \leq \pi/2 \quad (22)$$

with $w(\varphi)$ a bounded, non-negative function of $\varphi \in [0, \pi/2]$, and we seek to minimize

$$\int_0^{\pi/2} \int_0^{\pi/2} |\ell(\varphi) - \ell(\psi) - h(\varphi, \psi)|^2 W(\varphi, \psi) d\varphi d\psi \quad (23)$$

over all square integrable functions ℓ . The restriction to W of the particular form in Eq. (22) is made to facilitate the developments in the Appendix. Since the functional, as given by Eq. (23), depends on ℓ through the difference $\ell(\varphi) - \ell(\psi)$, so that adding a constant to ℓ yields the same value, we require that

$$\int_0^{\pi/2} \ell(\varphi) w(\varphi) d\varphi = 0. \quad (24)$$

In the Appendix we show that the minimizing $\ell = \ell_{\text{opt}}$ is given by

$$\ell_{\text{opt}}(\varphi) = \frac{1}{C} \int_0^{\pi/2} h(\varphi, \psi) w(\psi) d\psi, \quad (25)$$

where

$$C = \int_0^{\pi/2} w(\varphi) d\varphi. \quad (26)$$

Furthermore, we show in the Appendix that the evaluation of the integral on the right-hand side of Eq. (25) with h given in Eq. (18) can be done according to

$$\begin{aligned} & \int_0^{\pi/2} h(\varphi, \psi) w(\psi) d\psi \\ &= 2 \cos \varphi \int_{-1}^{\tan 1/2 \varphi} f \left(\frac{D}{c} x \right) \\ & \quad \times \frac{w(\varphi - \arctan(x \cos \varphi / (1 - x \sin \varphi)))}{1 - 2x \sin \varphi + x^2} dx, \end{aligned} \quad (27)$$

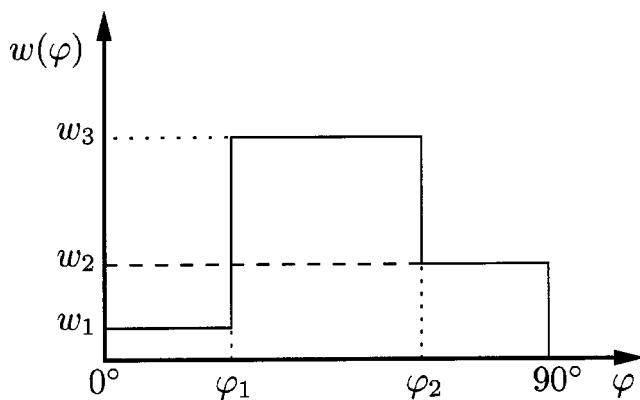


FIG. 7. Weight function to emphasize the region over which the optimization is carried out.

where $0 \leq \varphi \leq \pi/2$. With f a piecewise linear function as in Eq. (6) and w a piecewise constant function as, for instance, in Fig. 7, the evaluation of ℓ_{opt} reduces to applying the appropriate analytic formulas for integrals involving low-degree rational integrands.

The function ℓ_{opt} found above is, in general, not of the special form as in Eq. (17) with a G as given in Eq. (9) where we use the coefficients x_m . Hence, we describe the approach to derive the x_m used in Eq. (9) in the next section.

C. Optimization to find the optimal filter coefficients x_m

To find the required FIR filter coefficients x_m we use a *least-squares optimization* method (Marquardt, 1963; Dennis, 1977) such that

$$2C \int_0^{\pi/2} \left| 20 \log \left| \sum_m \hat{x}_m(\omega) e^{(im\omega \sin \varphi)/c} \right| - \ell_{\text{opt}}(\varphi) \right|^2 w(\varphi) d\varphi \quad (28)$$

is minimal. Note here that the coefficients $\hat{x}_m(\omega)$ depend on the frequency ω . The optimal x_m are then found as

$$x_m = S \hat{x}_m, \quad (29)$$

where m is the driver index and the scaling constant S is such that $\max_{m \in \mathbf{R}} |x_{m,\text{opt}}| = 1$.

D. Simulation results

We show here some simulations for the optimal directivity pattern ℓ_{opt} obtained from the computation of Eq. (25). Figure 7 shows the type of weight function used in this study. This function depends on three weights (w_1 , w_2 , and w_3) at given angles (φ_1 and φ_2). In this case we chose: $w_1 = w_2 = 0$ and $w_3 = 1$ at angles $\varphi_1 = 24.35^\circ$ and $\varphi_2 = 37.25^\circ$. This choice emphasizes the middle angles (in relation to the working region 0° – 60°) over the extreme angles.

Figure 8 shows the results from the simulations for ℓ_{opt} for several stereo base distances going from 1 to 2.5 m for angles in the working region (0° – 60°) for PI-stereo. The parametrized time/intensity trading parameters have been obtained from the data plots (for stereo base distances of 2.5 and 1 m) coming from Aarts (1992), and for the remaining

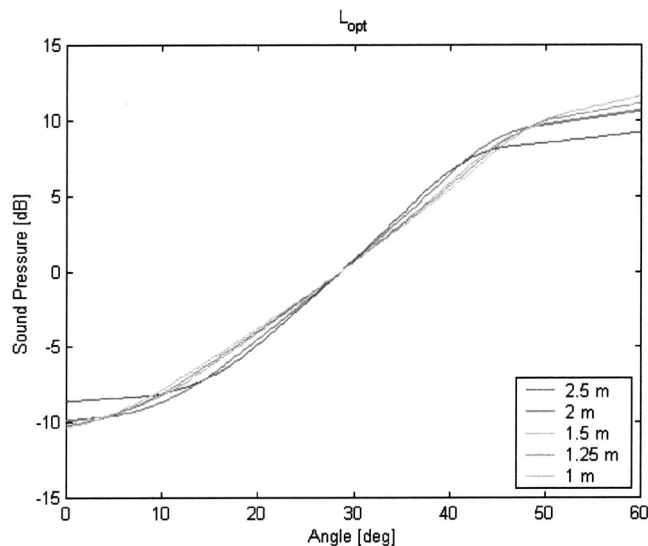


FIG. 8. ℓ_{opt} 's in the working region (0° – 60°) for several stereo base distances.

distances, some approximation curves were derived to estimate the parameters. The stereo base distances used for the simulations are presented in Table I.

Figure 9 shows the resulting time/intensity trading plots obtained from the estimated ℓ_{opt} 's for the two stereo base distances (1 and 2.5 m) compared with the time/intensity trading plots given by Aarts (1992). It can be seen that for very small time differences (that is, for middle angles) the approximation is quite good; however, for larger time differences the approximation becomes slightly worse. The reason for these approximation errors in the time/intensity trading data comes basically from the fact that we are trying to achieve an optimal directivity pattern for a wide area, thus giving an approximate optimal directivity pattern at all positions in the listening area. Since we have applied the weight function at the intermediate angles, the approximation in this region is better.

VI. OPTIMAL FIR FILTER RESPONSES

We have used the optimization method described in Sec. V C to obtain the optimal FIR filters x_m which achieve the derived optimal directivity pattern ℓ_{opt} using MATLAB. We used the ℓ_{opt} previously found for a 2.5-m stereo base distance. We also used $N=2$ as a number of drivers for the left and right loudspeaker arrays (we will refer to these drivers from now on as A and B). It is important to note here that

TABLE I. Stereo base distances D and parametrized time/intensity trading parameters (α_1 , α_2 , and t_1) for the function given in Eq. (6) used in the simulation of ℓ_{opt} .

Distance (m)	Parametrized $f(\Delta T)$		t_1 (ms)
	α_1 (dB/ms)	α_2 (dB/ms)	
1	15.62	3.54	0.64
1.25	13	2.27	0.75
1.5	11.17	1.55	0.85
2	9.25	1.16	1
2.5	8	0.7	1

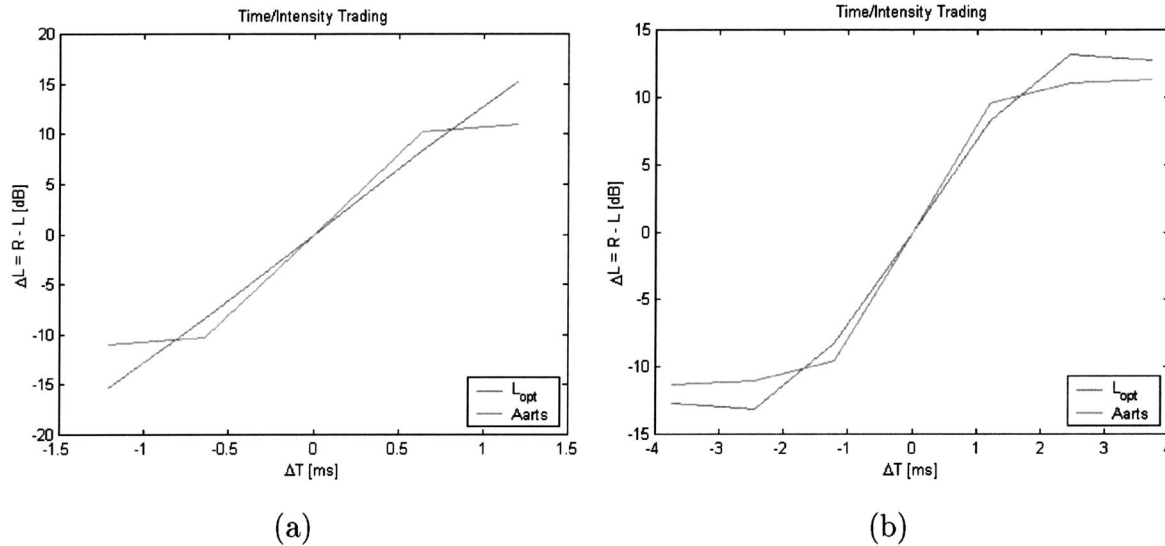


FIG. 9. Time/intensity trading approximations for the parametrized time/intensity trading plot coming from the ℓ_{opt} compared with the time/intensity trading plot given by Aarts (1992). (a) Stereo base of 1 m. (b) Stereo base of 2.5 m.

since the processing of PI-stereo is split into two frequency bands (200–2000 Hz for midrange and 2000–12 000 Hz for high range), the optimization has been computed for these two frequency ranges (see Fig. 10).

Figure 11 shows the results for the estimated FIR filters for 40 coefficients. Figure 11(a) shows the impulse and frequency responses of the *A* and *B* drivers for the midrange filters, and Fig. 11(b) shows the responses of the *A* and *B* drivers for the high-range filters. We can see that the impulse responses of filters *A* and *B* are odd-symmetric; thus, the magnitudes of the transfer functions are the same, only the phase differs. This can be observed from the frequency responses of the filters. We notice that the filters generally have a low-pass behavior.

Figure 12 presents the theoretical sound pressures and the obtained polar plots when using the estimated FIR filter coefficients. Figure 12(a) shows the plots for the midrange and Fig. 12(b) for the high range. It can be easily observed that the final approximation error to the desired optimal di-

rectivity pattern ℓ_{opt} is quite large. This is due to the fact that in our case we are limited to the use of only two drivers to achieve the desired ℓ_{opt} which is obviously not good enough. Indeed, the more drivers (thus filters) we use in the optimization method, the better the approximation we get to the ℓ_{opt} in the directivity pattern simulation (see Fig. 13).

VII. MEASUREMENT RESULTS OF THE DIRECTIVITY PATTERNS

We have measured the impulse responses at stated angles of the PI-stereo system using the computed FIR filters. The impulse response measurements were done with a system for acoustical measurements which is based on a turntable for loudspeaker rotation and on a maximum-length sequence (MLS) measurement system.

The PI-stereo cabinet to be measured was placed on the turntable facing a microphone (1/2-in. 4133 free-field B&K). Impulse response measurements were done every 5° so that a total of 72 measurements was realized in one revolution.

Figure 14 shows the measured directivity patterns normalized at half of the working regions for PI-stereo (i.e., 30°) for the right response PI-stereo cabinet in an anechoic room at different frequencies. For comparison purposes, we should focus our attention on the working region for PI-stereo for angles going from 0° to 60°. Although the intent of the PI-stereo implementation of this paper is to generate frequency-independent directivity patterns, it is clear that there are significant deviations at higher frequencies.

VIII. INFORMAL LISTENING TESTS AND DISCUSSION

We have tested the PI-stereo system for a distance of around 2.5-m separation between the left and right PI-stereo cabinets. A listening room was used to study the influence of room boundaries, and despite room reflections, the PI-stereo effect remained.

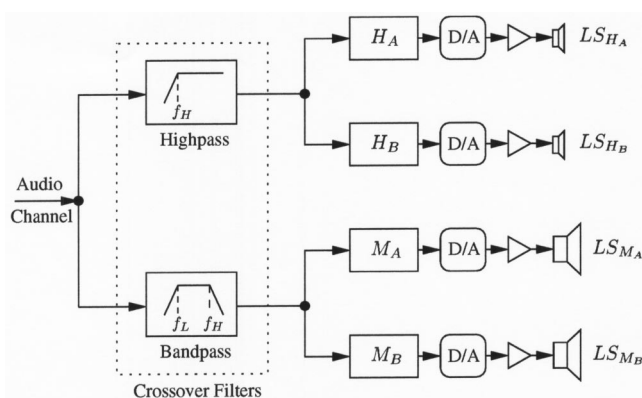


FIG. 10. A schematic block diagram of one array for the processing of one of the audio channels. The frequency range splitting is achieved by means of crossover filters. Filters H_A and H_B for the high-frequency range and filters M_A and M_B for the midfrequency range are obtained by the proposed method. These filters drive the two arrays of loudspeakers, LS_{H_A} , LS_{H_B} and LS_{M_A} , LS_{M_B} .

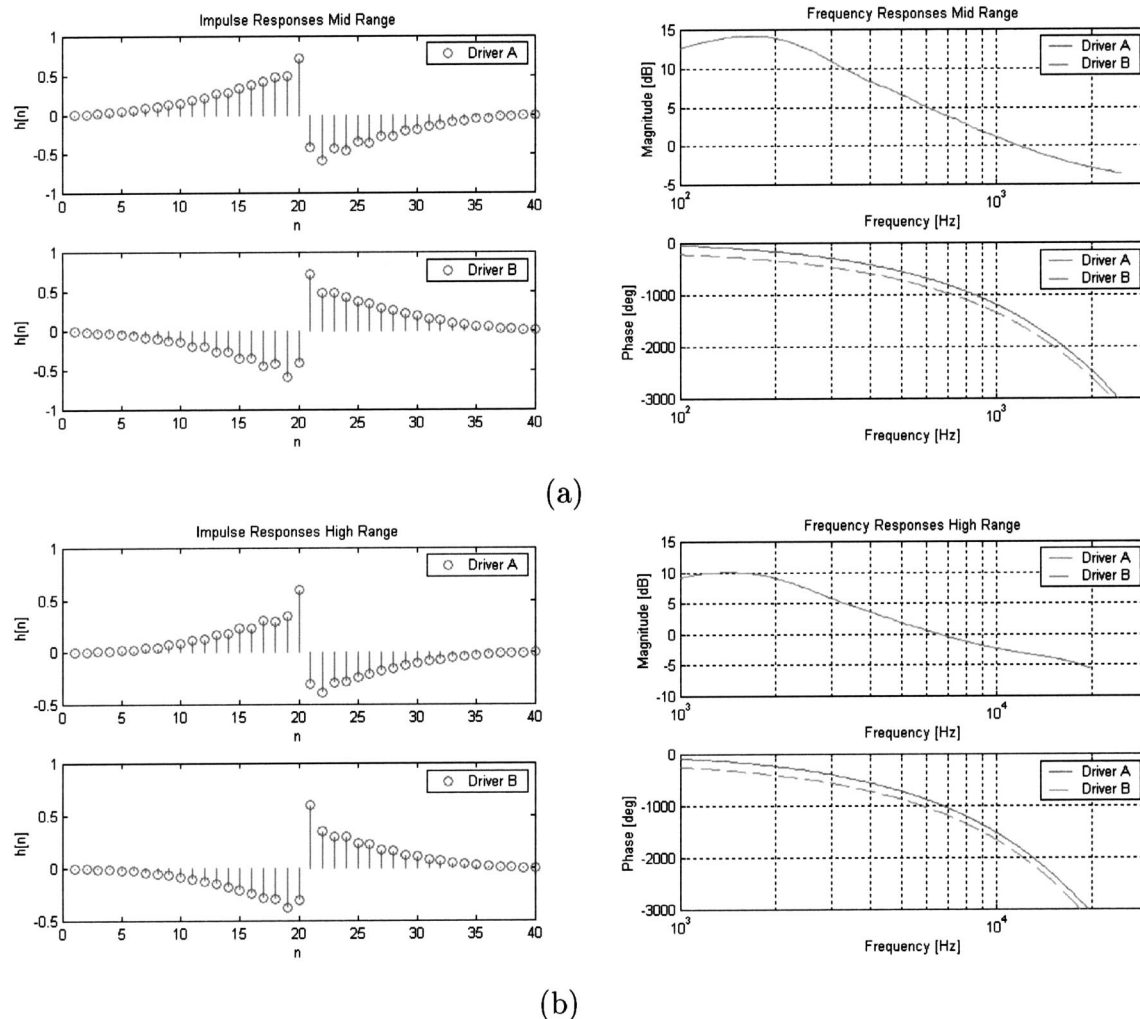


FIG. 11. Impulse and frequency responses of the 40-tap FIR filters. (a) Midrange. (b) High range.

A group of experienced listeners (7 subjects) tested the PI-stereo system in comparison with normal stereo at different on- and off-axis listening positions. Some of the parameters considered for comparison were: sound localization, apparent source width (ASW), coloration, and loudness.

Both normal stereo and PI-stereo were reproduced by the same loudspeaker cabinets, so there was no shift in the stereo image at the sweet spot. Some informal listening tests were undertaken to investigate the sound localization performance and robustness of the obtained optimal directivity pattern ℓ_{opt} and the associated FIR filters. From the experiments, it was observed that the influence of the stereo base distance was not critical to notice the PI-stereo effect (it only became slightly overdone, for narrower distances, or underdone for wider distances).

The listener's observations showed that the PI-stereo system worked as predicted by the simulation plots (see Sec. VI). Correct central sound localization for speech and music was demonstrated for a number of on- and off-axis listening positions. The difference between normal stereo and PI-stereo at the sweet spot was very modest. The stereo sound sensation, in particular the placement of central voices, was independent of the listening position within a large area. This

central placement of voices was specially appreciated when listening to the PI-stereo system for a TV setup. When listening to normal stereo at lateral positions, listeners experienced an annoying spatial distortion in that the sound did not come from the same position as the TV image. The differences between normal stereo and PI-stereo depends somewhat on the type of the music recording; however, for PI-stereo the sound was well localized, coming from the same location as the TV image.

In conclusion, we can summarize the main results obtained from the listening tests

- (i) Robust sound image in terms of sound localization;
- (ii) Well-localized and clear centered phantom source; and
- (iii) Better spatial images at lateral positions.

IX. CONCLUSIONS

We have introduced a new position-independent system for stereophonic sound reproduction ensuring correct sound localization in a large listening area. A mathematical derivation to achieve an optimal directivity pattern which offers a more robust and natural high-quality stereo sound in a large

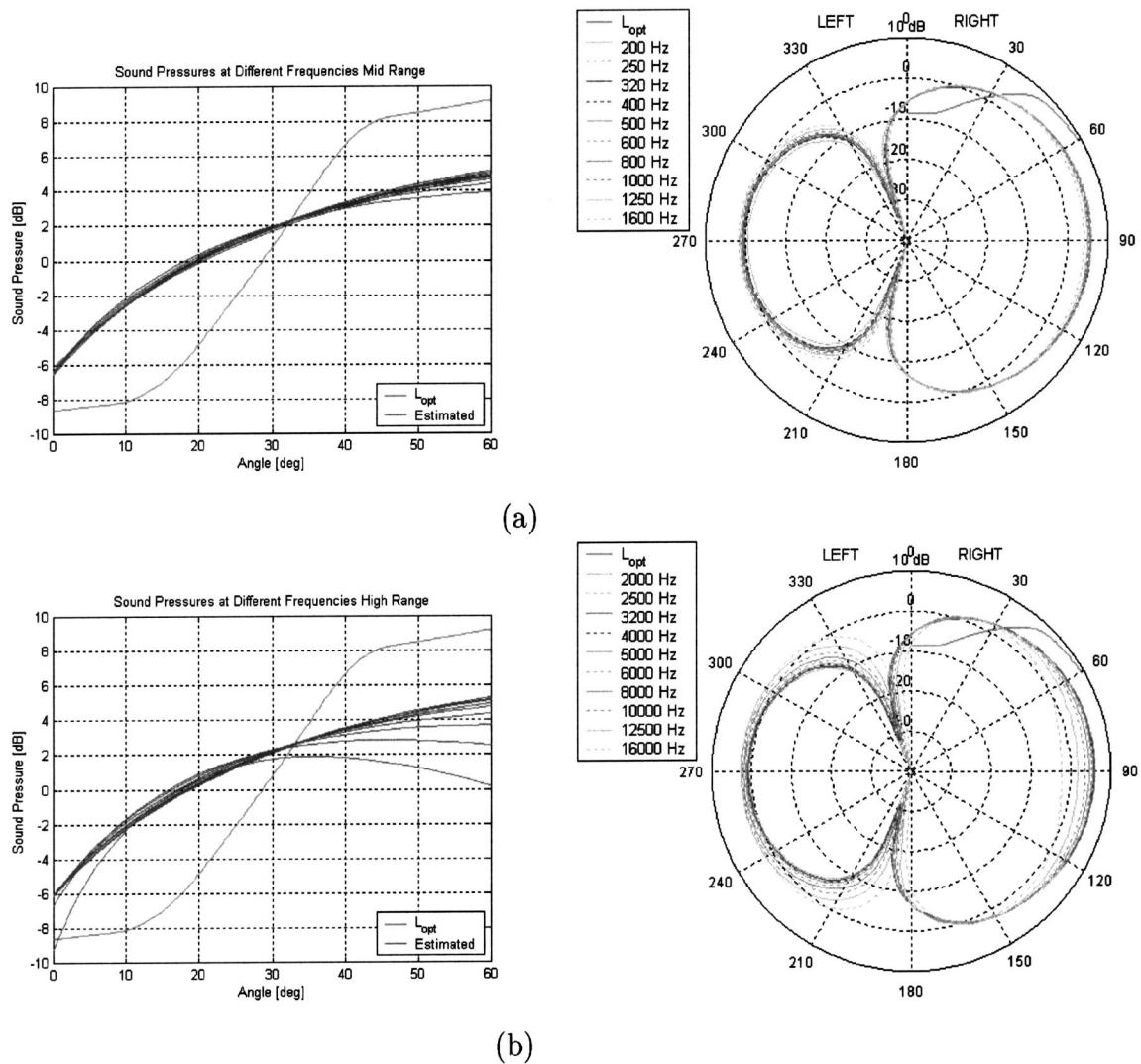


FIG. 12. Sound pressures and polar plots at different frequencies in the working region for the required FIR filters. (a) Midrange. (b) High range.

listening area has been presented. This optimal directivity pattern has been adapted to parametrized time/intensity trading data for enlarging the sweet spot area.

It has also been illustrated that imaging in the traditional stereophonic system is restricted to an extremely narrow listening area. Outside this area, spatial distortion of the sound image occurs.

A digital filtering technique for PI-stereo has been designed and applied to the individual drivers of loudspeaker arrays in a cabinet in order to achieve the optimal frequency-independent directivity pattern.

Preliminary listening tests have shown that the PI-stereo system, based on the optimal directivity pattern ℓ_{opt} , worked as predicted by the theoretical simulations. The system also demonstrated correct central sound localization for speech and music for a large listening area. PI-stereo images appear to be more robust with lateral movement than images in normal stereo. The stereo sound sensation was listening-position independent, thus enlarging the sweet spot area.

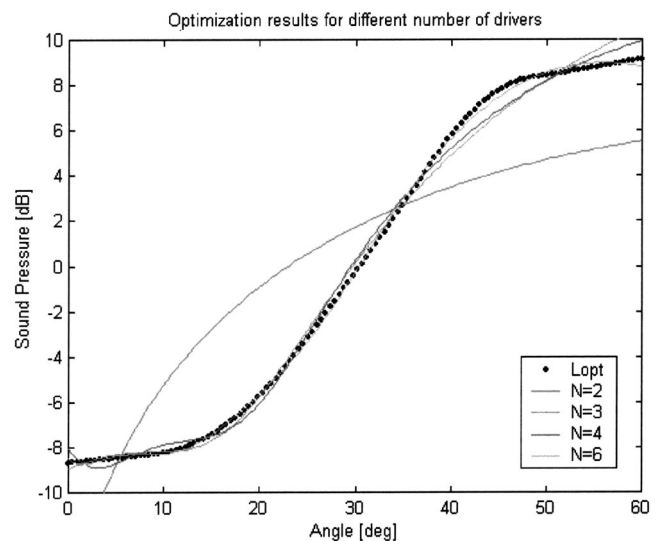


FIG. 13. Optimization results for the approximation of the ℓ_{opt} for different number of drivers N in the loudspeaker array.

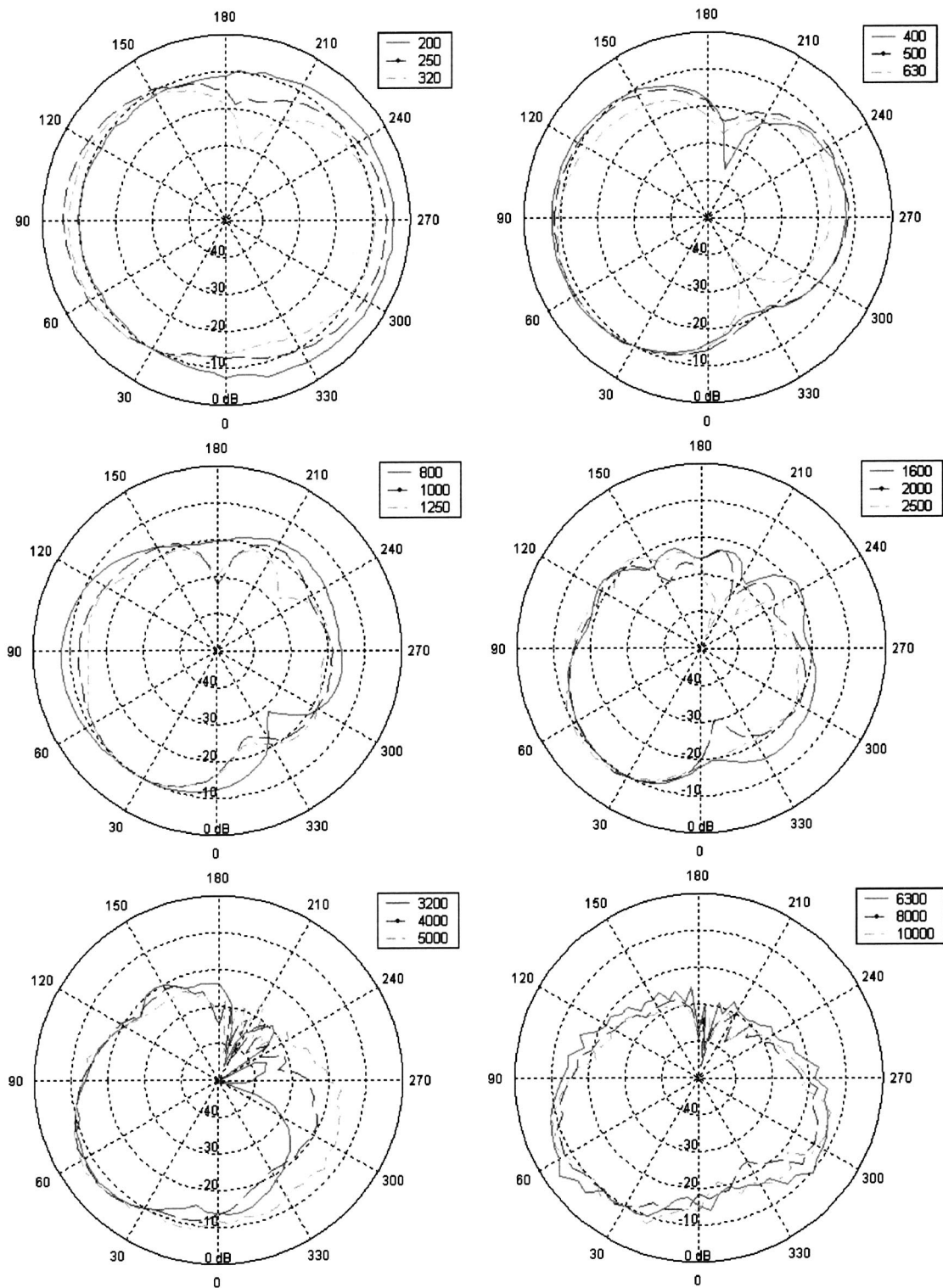


FIG. 14. Measured directivity pattern plots at different frequencies normalized at 30° for the right PI-stereo cabinet.

The outcome of this work has shown that an optimal directivity pattern for loudspeaker arrays in stereophonic applications can be very useful for sweet spot widening.

ACKNOWLEDGMENTS

The authors would like to thank Professor John Vanderkooy for his very valuable comments and suggestions for improving the final manuscript.

APPENDIX: OPTIMAL DIRECTIVITY PATTERN ℓ_{opt}

Given a function $h(\varphi, \psi)$ with $\varphi, \psi \in [0, \pi/2]$, satisfying Eq. (19), we seek to minimize

$$d_w^2(\ell(\varphi) - \ell(\psi) - h(\varphi, \psi)):$$

$$= \int_0^{\pi/2} \int_0^{\pi/2} |\ell(\varphi) - \ell(\psi) - h(\varphi, \psi)|^2 w(\varphi) w(\psi) d\varphi d\psi, \quad (\text{A1})$$

over all square integrable functions $\ell(\varphi)$ (with respect to the weight $w(\varphi)$ with $\varphi \in [0, \pi/2]$), satisfying Eq. (24). In Eq. (A1) the weight function w is bounded and non-negative.

We consider the linear subspace M of all square integrable functions [with respect to the weight $w(\varphi)w(\psi)$ as in Eq. (A1)] of the form:

$$k(\varphi, \psi) = \ell(\varphi) - \ell(\psi), \quad \varphi, \psi \in \left[0, \frac{\pi}{2}\right] \quad (\text{A2})$$

with ℓ satisfying Eq. (24). Furthermore, we let P_M be the orthogonal projection operator of the space of all square integrable functions $h(\varphi, \psi)$ satisfying $h(\psi, \varphi) = -h(\varphi, \psi)$ as in Eq. (19) onto the space M . Then, minimizing the functional in Eq. (A1) amounts to finding the orthogonal projection $P_M h$ of h as

$$(P_M h)(\varphi, \psi) = \ell_{\text{opt}}(\varphi) - \ell_{\text{opt}}(\psi), \quad \varphi, \psi \in \left[0, \frac{\pi}{2}\right], \quad (\text{A3})$$

where $\ell = \ell_{\text{opt}}$ is square integrable [with respect to the weight $w(\varphi)$], satisfies Eq. (24), and minimizes Eq. (A1).

We compute for an ℓ as above

$$\begin{aligned} d_w^2(\ell(\varphi) - \ell(\psi) - h(\varphi, \psi)) &= \int_0^{\pi/2} \int_0^{\pi/2} (|\ell(\varphi)|^2 + |\ell(\psi)|^2 \\ &\quad - 2\ell(\varphi)\ell(\psi))w(\varphi)w(\psi)d\varphi d\psi \\ &\quad - 2 \int_0^{\pi/2} \int_0^{\pi/2} h(\varphi, \psi)\ell(\varphi)w(\varphi)w(\psi)d\varphi d\psi \\ &\quad + 2 \int_0^{\pi/2} \int_0^{\pi/2} h(\varphi, \psi)\ell(\psi)w(\varphi)w(\psi)d\varphi d\psi \\ &\quad + \int_0^{\pi/2} \int_0^{\pi/2} |h(\varphi, \psi)|^2 w(\varphi)w(\psi)d\varphi d\psi. \end{aligned} \quad (\text{A4})$$

Now we have

$$\begin{aligned} &\int_0^{\pi/2} \int_0^{\pi/2} |\ell(\varphi)|^2 w(\varphi)w(\psi)d\varphi d\psi \\ &= \int_0^{\pi/2} \int_0^{\pi/2} |\ell(\psi)|^2 w(\varphi)w(\psi)d\varphi d\psi \\ &= C \int_0^{\pi/2} |\ell(\varphi)|^2 w(\varphi)d\varphi, \end{aligned} \quad (\text{A5})$$

where C is given by Eq. (26), and

$$\begin{aligned} &\int_0^{\pi/2} \int_0^{\pi/2} \ell(\varphi)\ell(\psi)w(\varphi)w(\psi)d\varphi d\psi \\ &= \left(\int_0^{\pi/2} \ell(\varphi)w(\varphi)d\varphi \right)^2 = 0 \end{aligned} \quad (\text{A6})$$

by Eq. (24). Also, using Eqs. (19) and (24), we have

$$\begin{aligned} &\int_0^{\pi/2} \int_0^{\pi/2} h(\varphi, \psi)\ell(\varphi)w(\varphi)w(\psi)d\varphi d\psi \\ &= - \int_0^{\pi/2} \int_0^{\pi/2} h(\varphi, \psi)\ell(\psi)w(\varphi)w(\psi)d\varphi d\psi \\ &= \int_0^{\pi/2} \ell(\varphi)m_w(\varphi)d\varphi, \end{aligned} \quad (\text{A7})$$

where we have set

$$m_w(\varphi) = \int_0^{\pi/2} h(\varphi, \psi)w(\psi)d\psi, \quad \varphi \in \left[0, \frac{\pi}{2}\right]. \quad (\text{A8})$$

It follows that

$$\begin{aligned} &d_w^2(\ell(\varphi) - \ell(\psi) - h(\varphi, \psi)) \\ &= 2C \int_0^{\pi/2} \left(\ell(\varphi) - \frac{1}{C}m_w(\varphi) \right)^2 w(\varphi)d\varphi \\ &\quad + \int_0^{\pi/2} \int_0^{\pi/2} |h(\varphi, \psi)|^2 w(\varphi)w(\psi)d\varphi d\psi \\ &\quad - \frac{2}{C} \int_0^{\pi/2} m_w^2(\varphi)d\varphi. \end{aligned} \quad (\text{A9})$$

Hence, the minimal value of the functional occurs for

$$\ell_{\text{opt}}(\varphi) = \frac{1}{C}m_w(\varphi), \quad \varphi \in \left[0, \frac{\pi}{2}\right], \quad (\text{A10})$$

where C and m_w are given by Eqs. (26) and (A8). The function ℓ_{opt} is unique on the set of all φ with $w(\varphi) > 0$.

In Sec. V B [Eq. (18)] we have h of the form

$$h(\varphi, \psi) = f\left(\frac{D \sin 1/2(\varphi - \psi)}{c \cos 1/2(\varphi + \psi)}\right), \quad \varphi, \psi \in \left[0, \frac{\pi}{2}\right] \quad (\text{A11})$$

with $f(x)$ an odd, piecewise linear function of $x \in \mathbf{R}$. Such an h indeed satisfies Eq. (19). Furthermore, the integral representation of $m_w(\varphi)$, as needed in Eq. (A10) for ℓ_{opt} , can be rewritten by introducing for any $\varphi \in [0, \pi/2]$ the new variable

$$\begin{aligned} x &= \frac{\sin 1/2(\varphi - \psi)}{\cos 1/2(\varphi + \psi)} \\ &= \sin \varphi - \cos \varphi \tan \frac{1}{2}(\varphi + \psi) \in [-1, \tan \frac{1}{2}\varphi]. \end{aligned} \quad (\text{A12})$$

Solving ψ from Eq. (A12) [which is most easily done by using the second right-hand side member in Eq. (A12)], we find

$$\psi = \varphi - 2 \arctan\left(\frac{x \cos \varphi}{1 - x \sin \varphi}\right), \quad (\text{A13})$$

and

$$d\psi = \frac{-2 \cos \varphi}{1 - 2x \sin \varphi + x^2} dx. \quad (\text{A14})$$

This then yields Eq. (27).

- Aarts, R. M. (1992). "Time/intensity trading stereophony for (HD)TV and audio applications," in *14th International Congress on Acoustics* (Beijing, China) (session L8-3).
- Bauer, B. B. (1960). "Broadening the area of stereophonic perception," *J. Audio Eng. Soc.* **8**, 91–94.
- Blauert, J. (1983). *Spatial Hearing* (MIT Press, Cambridge, MA).
- Blumlein, A. D. (1958). "Improvements in and relating to sound-transmission, sound-recording, and sound-reproducing systems," *J. Audio Eng. Soc.* **6**, 91–98.
- Crabbe, J. (1979). "Broadening the stereo seat," *HI-FI News Record Rev.* **24**, 64–68.
- Davis, M. F. (1987). "Loudspeaker systems with optimized wide-listening area imaging," *J. Audio Eng. Soc.* **35**, 888–896.
- Dennis, J. E. (1977). *Nonlinear Least Squares: State of the Art in Numerical Analysis* (Academic, New York).
- Franssen, N. V. (1960). "Some Considerations on the Mechanism of Directional Hearing," Ph.D. thesis, Technical University of Delft, The Netherlands.
- Jordan, E. J. (1971). "Loudspeaker stereo techniques: How to combine left and right signals and get the message from the medium," *Wireless World*, 67–70.
- Kates, J. (1980). "Optimum loudspeaker directional patterns," *J. Audio Eng. Soc.* **28**, 787–794.
- Leakey, D. M. (1959). "Some measurements on the effects of interchannel intensity and time differences in two channel sound systems," *J. Acoust. Soc. Am.* **31**, 977–986.
- Leakey, D. M. (1960). "Further thoughts on stereophonic sound systems," *Wireless World*, 154–160.
- Lipshitz, S. P. (1986). "Stereo microphone techniques," *J. Audio Eng. Soc.* **34**, 716–744.
- Makita, Y. (1962). "The directional localization of sound in the stereophonic sound field," *E.B.U. Review* **73**, 102–108.
- Marquardt, D. (1963). "An algorithm for least-squares estimation of non-linear parameters," *SIAM (Soc. Ind. Appl. Math.) J. Appl. Math.* **11**, 431–441.
- Rodenas, J. A., and Aarts, R. M. (2001a). "Position independent stereophonic sound reproduction," *Nederlands Akoestisch Genootschap NAG Journal*, 37–47.
- Rodenas, J. A., and Aarts, R. M. (2001b). "Sweet spot widening for stereophonic sound reproduction," in *IEEE WASPAA*, New Paltz, NY, 21–24 October, pp. 191–194.
- Stevens, S. S., and Newman, E. B. (1936). "The localization of actual sources of sound," *Am. J. Psychol.* **48**, 297–306.

Electromechanical coupling factor of capacitive micromachined ultrasonic transducers

Alessandro Caronti,^{a)} Riccardo Carotenuto, and Massimo Pappalardo
*Dipartimento di Ingegneria Elettronica, Università Roma Tre, Via della Vasca Navale 84,
00146 Roma, Italy*

(Received 15 February 2002; revised 15 May 2002; accepted 14 October 2002)

Recently, a linear, analytical distributed model for capacitive micromachined ultrasonic transducers (CMUTs) was presented, and an electromechanical equivalent circuit based on the theory reported was used to describe the behavior of the transducer [IEEE Trans. Ultrason. Ferroelectr. Freq. Control **49**, 159–168 (2002)]. The distributed model is applied here to calculate the dynamic coupling factor k_w of a lossless CMUT, based on a definition that involves the energies stored in a dynamic vibration cycle, and the results are compared with those obtained with a lumped model. A strong discrepancy is found between the two models as the bias voltage increases. The lumped model predicts an increasing dynamic k factor up to unity, whereas the distributed model predicts a more realistic saturation of this parameter to values substantially lower. It is demonstrated that the maximum value of k_w , corresponding to an operating point close to the diaphragm collapse, is 0.4 for a CMUT single cell with a circular membrane diaphragm and no parasitic capacitance (0.36 for a cell with a circular plate diaphragm). This means that the dynamic coupling factor of a CMUT is comparable to that of a piezoceramic plate oscillating in the thickness mode. Parasitic capacitance decreases the value of k_w , because it does not contribute to the energy conversion. The effective coupling factor k_{eff} is also investigated, showing that this parameter coincides with k_w within the lumped model approximation, but a quite different result is obtained if a computation is made with the more accurate distributed model. As a consequence, k_{eff} , which can be measured from the transducer electrical impedance, does not give a reliable value of the actual dynamic coupling factor. © 2003 Acoustical Society of America. [DOI: 10.1121/1.1527958]

PACS numbers: 43.38.Bs, 43.38.Ar [SLE]

I. INTRODUCTION

Historically, the concept of the coupling factor of an electromechanical transducer, usually called a k factor, was introduced to characterize its ability to convert electrical energy into mechanical energy, and *vice versa*. Following the early work by Mason concerned with piezoelectric crystals,^{2,3} the designers of transducers started to use the coupling factor both to characterize different piezomaterials and as an index of performance of transducers under practical configurations.

Actually, coupling coefficients not only depend on the type of material, but also on the stress distribution, electric field, and geometry of the piezoelement. Indeed, the coefficients known as material coupling factors k_{mat} (e.g., k_t , k_p , k_{ij}), refer to a one-dimensional geometry and to a static or quasistatic energy transformation cycle, and can be easily computed as a combination of appropriate elastic, dielectric, and piezoelectric constants. In recent years, capacitive micromachined ultrasonic transducers have shown to be a promising alternative to piezoelectric transducers, especially in ultrasound imaging and nondestructive testing.^{4,5} The ease of fabrication, integration with custom electronics, wide bandwidth in immersion operation, and large dynamic range of the CMUT have indicated that this technology is poten-

tially better than piezoelectric technology for the realization of two-dimensional (2-D) phased arrays for 3-D imaging.^{6,7}

For electrostatic transducers, including CMUTs, only a k factor has to be defined if the geometry of the membrane is assumed, as usual, to be circular; further, it is common use to refer to a dynamic energy transformation cycle rather than to a static one. Basic references for the dynamic coupling factor of electrostatic transducers are the book by Kinsler *et al.*⁸ and the book by Hunt.⁹ In Ref. 8, the coupling factor is defined in a general way as a ratio of energies, in Ref. 9 it is explicitly defined as a combination of parameters. The two approaches substantially give the same result, except for a small discrepancy that will be discussed in detail in the present work.

Also relevant to the present work are recent papers reporting calculation of quasistatic coupling coefficients for electrostrictive ceramics.^{10–12} In Ref. 10 the method of computing the coupling coefficient for an electrostrictor is based on a generalization of the IEEE Standard on Piezoelectricity,¹³ while the definition proposed in Ref. 12 generalizes that advanced by Berlincourt *et al.*¹⁴ in a way that produces a zero value of the coupling coefficient for an unbiased electrostrictive material. Significantly, a “universal” equivalent circuit that is applicable to electrostrictive, piezoelectric and electrostatic transducers, based on the linearized 3-D theory of lead magnesium niobate (PMN), is derived in Ref. 11, and the theoretical coupling coefficients for piezoelectric and electrostatic transducers are recovered

^{a)}Telephone: +39 06 55177081; fax: +39 06 5579078; electronic mail: caronti@uniroma3.it

as special cases. In particular, the expression of the coupling factor of a single-sided electrostatic transducer given by Hunt is obtained with an appropriate correspondence of parameters. Although the lumped equivalent circuit given in Ref. 11, as well as Hunt's theory, can describe the first-order behavior of the electrostatic transducer, the flexural bending of the diaphragm is not adequately taken into account for coupling factor evaluation.

In this paper, starting from a definition based on converted and stored energies involved in a vibration cycle, the dynamic coupling factor k_w of a lossless CMUT is calculated by using both lumped and distributed parameter models. The use of a distributed model is essential to account for the flexural vibration of the membrane in the electrostatic cell. Actually, it is found that k_w approaches a peak value of about 0.4 as the bias voltage increases, unlike the lumped model prediction of an increasing k factor up to unity.

The classical effective coupling factor k_{eff} , which can be easily measured from the transducer electrical impedance, is also investigated. It is demonstrated that k_{eff} computed with the lumped model coincides with k_w , but this identity drops if a more realistic calculation is performed by using the distributed model.

II. COUPLING FACTOR DEFINITIONS

As mentioned in the Introduction, Kinsler *et al.*⁸ define the k factor of an electrostatic transducer as the square root of the ratio of stored mechanical energy to total energy stored in a lossless vibration cycle, and derive a simple expression of k_w using a lumped parameter model. Hunt⁹ explicitly defines the coupling factor as a combination of parameters resulting in a slightly different expression, as will be discussed later.

According to the latest IEEE Standard on Piezoelectricity,¹³ the coupling factors are nondimensional coefficients that are useful to characterize a piezoelectric material under a particular stress and electric field configuration in the conversion of stored energy into mechanical or electric work. A graphic illustration of the electromechanical conversion is reported, showing that the static piezoelectric coupling factor, denoted here as k_{mat} , can be defined, with reference to a static or quasistatic lossless transformation cycle of a piezoelectric specimen, as the square root of the ratio of the converted energy W_c to the total stored energy per unit volume W ,

$$k_{\text{mat}} = \sqrt{\frac{W_c}{W}}. \quad (1)$$

In dynamic conditions, that is, when the element is in oscillation, it is still possible to define the k factor as a ratio of energies,¹⁵

$$k_w = \sqrt{\frac{E_c}{E_{\text{tot}}}}, \quad (2)$$

where E_c is the converted energy and E_{tot} is the total energy involved in a vibration cycle. A very common k factor, the only one that can be easily measured from the electrical impedance, is the effective coupling factor,¹³

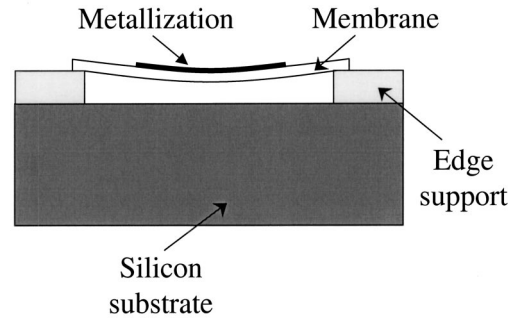


FIG. 1. Schematic cross section of a CMUT cell.

$$k_{\text{eff}} = \sqrt{\frac{f_p^2 - f_s^2}{f_p^2}}, \quad (3)$$

where f_s and f_p are the frequencies of maximum and minimum conductance, respectively. As demonstrated by Lamberti *et al.*,¹⁵ the piezoelectric coupling factor computed according to Eq. (2) coincides, for a lossless specimen, with the effective coupling factor given by Eq. (3), so that the same physical meaning can be attributed to k_{eff} . In addition, k_w is proportional to k_{mat} according to the following relation:

$$k_w^2 = \frac{8}{\pi^2} k_{\text{mat}}^2. \quad (4)$$

These results are also important for CMUTs for two reasons: first, by means of Eq. (2) the coupling factor k_w can also be computed for this kind of transducer, and a comparison with the piezoelectric coupling factor based on the same definition is then possible; second, k_w can be calculated by using both lumped and distributed models, and it will be shown that more realistic results are obtained with the latter.

Calculations of electromechanical coupling coefficients for CMUTs according to definitions (2) and (3) will be presented in the next section.

III. COUPLING FACTOR OF CMUTS

A schematic of a CMUT single cell, consisting of a metallized diaphragm (top electrode) stretched over a heavily doped silicon substrate (bottom electrode), is shown in Fig. 1. Many such elements are electrically connected in parallel to make the transducer, as can be seen from the portion of a CMUT shown in Fig. 2. The details of the fabrication process from different research groups can be found in Refs. 16–18.

The dynamic coupling factor can be computed by considering an idealized vibration cycle in which the energy is converted either to electric or mechanical work, the result being the same as demonstrated in Ref. 13 for a static transformation cycle of a piezoelectric specimen.

In the following subsections, a lossless dynamic cycle in which the conversion of energy is from mechanical to electrical work is considered. With reference to the equivalent circuit of a CMUT driven in transmission shown in Fig. 3,¹ this type of conversion takes place when the transducer does not radiate energy, i.e., $\mathbf{Z}_r = 0$, and it is disconnected from the electrical source (e.g., $\mathbf{Z}_s \rightarrow \infty$). In these conditions, the

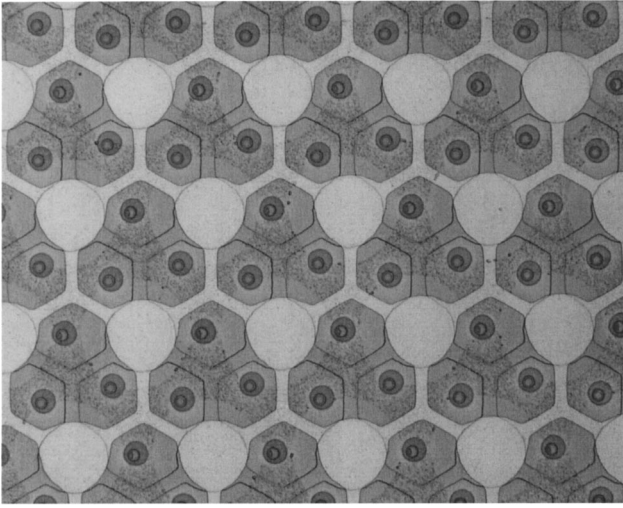


FIG. 2. Top view of a CMUT, consisting of a 2-D array of circular membranes. The regions in light gray are membrane electrodes and upper interconnections, the holes around each membrane are used to form the cavity below by selective etching of a sacrificial material.

CMUT is in free oscillation and part of the energy of vibration, in each lossless cycle, is converted into electrostatic energy and stored in the transducer capacitance.

The dynamic coupling factor will be computed for a single electrostatic cell by using both lumped and distributed parameter models; the calculation for an ideal CMUT with all identical elements, including parasitic capacitance, is also reported.

A. Lumped parameter model

Consider a CMUT single cell with no internal losses, driven by a sinusoidal voltage $\mathbf{V} = V_{ac}e^{j\omega t}$ and working in vacuum, so that no acoustic energy is radiated.

In order to calculate the electromechanical coupling factor we make use of the equivalent circuit of Fig. 4, which is obtained from the circuit of Fig. 3 by setting $\mathbf{Z}_s \rightarrow \infty$ and $\mathbf{Z}_r = 0$, and using lumped parameters in place of \mathbf{Z}_{Eb} and \mathbf{Z}_m , whose real parts are vanishing in the absence of losses. In the circuit of Fig. 4, C_{01} is the static capacitance of the cell, L_e is the electrical inductance corresponding to the mass of the diaphragm, and C_e is the electrical capacitance associated to the mechanical compliance. These parameters can be obtained by expanding the expression for the mechanical impedance around the fundamental resonance frequency of the diaphragm,¹⁹ that is, around the point where the device is

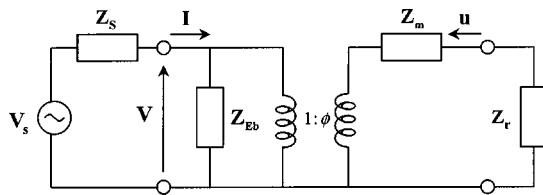


FIG. 3. Electromechanical equivalent circuit of a transmitting CMUT. \mathbf{Z}_s is the source impedance, \mathbf{Z}_{Eb} is the blocked electrical impedance, \mathbf{Z}_m is the mechanical impedance, and \mathbf{Z}_r is the radiation impedance. According to phasor notation, boldface is used to represent quantities in the frequency domain.

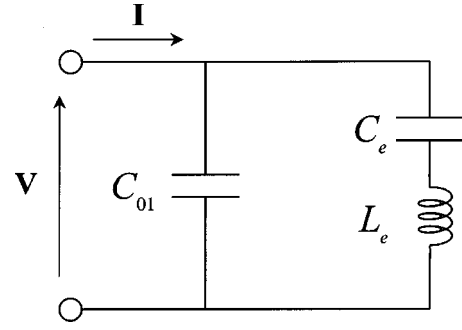


FIG. 4. Lumped equivalent circuit of a single cell for the coupling factor calculation.

intended to operate. Depending on the structural model used for the diaphragm, analytical expressions for the mechanical impedance are reported in Ref. 1. If the diaphragm is modeled as a membrane, the lumped inductance, and capacitance are found to be

$$L_e^{(m)} = \frac{m}{\phi_1^2} = \frac{1.446\rho_s S_1}{\phi_1^2}, \quad (5)$$

$$C_e^{(m)} = \phi_1^2 c_m = \phi_1^2 \frac{0.9568}{8\pi\tau}, \quad (6)$$

where m and c_m are the effective mass and compliance of the membrane around the resonance frequency, ϕ_1 is the transformation factor of the cell, ρ_s is the surface mass density, τ is the membrane tension per unit length, and S_1 is the area of the diaphragm. If the diaphragm is modeled as a plate, the lumped parameters are

$$L_e^{(p)} = \frac{1.883\rho_s S_1}{\phi_1^2} \quad (7)$$

$$C_e^{(p)} = \phi_1^2 \frac{0.977S_1}{192\pi^2 D}, \quad (8)$$

where D is the flexural rigidity of the plate. The transformation factor is defined as¹

$$\phi_1 = \frac{C_{01}V_{DC}}{d_0}, \quad (9)$$

where V_{DC} is the bias voltage and d_0 is the effective distance between the electrodes, including the static displacement of the diaphragm.

Suppose now that the diaphragm is in free oscillation with a velocity $v(t)$, the electrical source being disconnected from the transducer. The coupling factor can be easily computed by setting in the inductor an initial current I_0 at $t=0$, representing the amplitude of the transverse velocity, and calculating the transient of the circuit of Fig. 4. The electrical current in the loop results,

$$i(t) = I_0 \cos(\omega_0 t), \quad (10)$$

where ω_0 is the natural frequency,

$$\omega_0 = \frac{1}{\sqrt{L_e C_s}}, \quad (11)$$

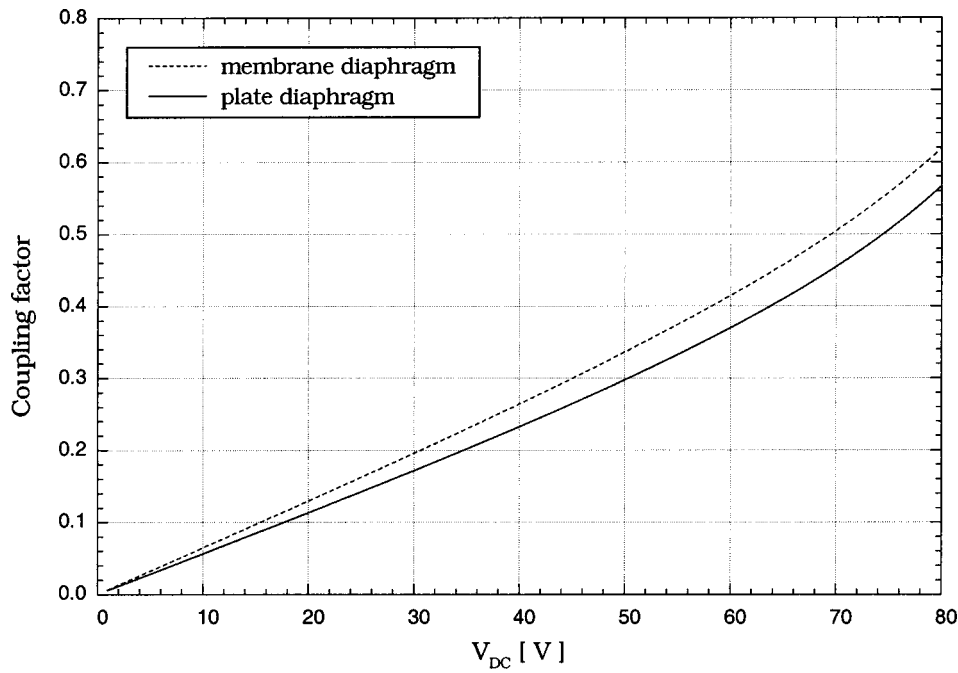


FIG. 5. Dynamic coupling factor of a CMUT single cell with membrane and plate diaphragm, computed in the lumped parameter approximation.

and C_s is the series capacitance of C_e and C_{01} . The kinetic energy is given by

$$KE(t) = \frac{1}{2} L_e I_0^2 \cos^2(\omega_0 t), \quad (12)$$

and the voltage across the capacitance C_{01} is

$$v_{C_0}(t) = \frac{I_0}{\omega_0 C_{01}} \sin(\omega_0 t). \quad (13)$$

When the diaphragm passes through the position of static deflection, the strain energy variation with respect to the bias point is zero and all the energy is in kinetic form. In this situation, the total energy involved in a vibration cycle can be calculated from Eq. (12) as

$$E_{\text{tot}} = (KE)_{\text{max}} = \frac{1}{2} L_e I_0^2. \quad (14)$$

On the other hand, when the diaphragm has its maximum displacement, the kinetic energy is zero and the electrostatic energy stored in C_{01} , representing the energy converted from mechanical into electrical form, is given by [see Eq. (13)]

$$EE = \frac{1}{2} C_{01} \left(\frac{I_0}{\omega_0 C_{01}} \right)^2 = \left(\frac{C_s}{C_{01}} \right) \frac{1}{2} L_e I_0^2. \quad (15)$$

According to Eq. (2), the dynamic coupling factor is

$$k_w = \sqrt{\frac{EE}{E_{\text{tot}}}} = \sqrt{\frac{C_s}{C_{01}}} = \sqrt{\frac{C_e}{C_e + C_{01}}}. \quad (16)$$

A plot of k_w is shown in Fig. 5 as a function of the bias voltage V_{DC} for a membrane and a plate diaphragm. The physical parameters of the CMUT element used for simulation are listed in Table I (CMUT III). The spring-softening effect,²⁰ that is, the increasing compliance of the diaphragm with increasing bias voltage, has not been taken into account.

As can be seen, the coupling factor of a membrane is higher than that of a plate, owing to the fact that a clamped membrane has a higher average displacement. The difference gets lower as the bias voltage, hence the displacement, decreases.

The electrostatic spring-softening can be included in the lumped model by roughly decreasing the stiffness of the diaphragm by the quantity ϕ_1^2/C_{01} ,^{8,9,20} so that the mechanical compliance changes from c_m to

TABLE I. Parameters of the CMUTs used for coupling factor calculations.

Parameters	CMUT I ^a	CMUT II ^b	CMUT III ^c	CMUT IV ^d
Membrane radius a (μm)	52.5	20.0	20.0	25.0
Membrane thickness d_m (μm)	0.5	0.6	0.45	0.6
Membrane collapse voltage V_{cr} (V)	155	112	82	74
Gap height d_g (μm)	1.0	0.35	0.40	0.35
Resonance frequency f_R (MHz)	2.3	6.9	5.2	4.4
Number of elements	9510	1510	1510	930
Total surface area (mm^2)	100.0	3.24	3.24	3.24

^aData from Ref. 16.

^bUnpublished data.

^cData from Ref. 17.

^dUnpublished data.

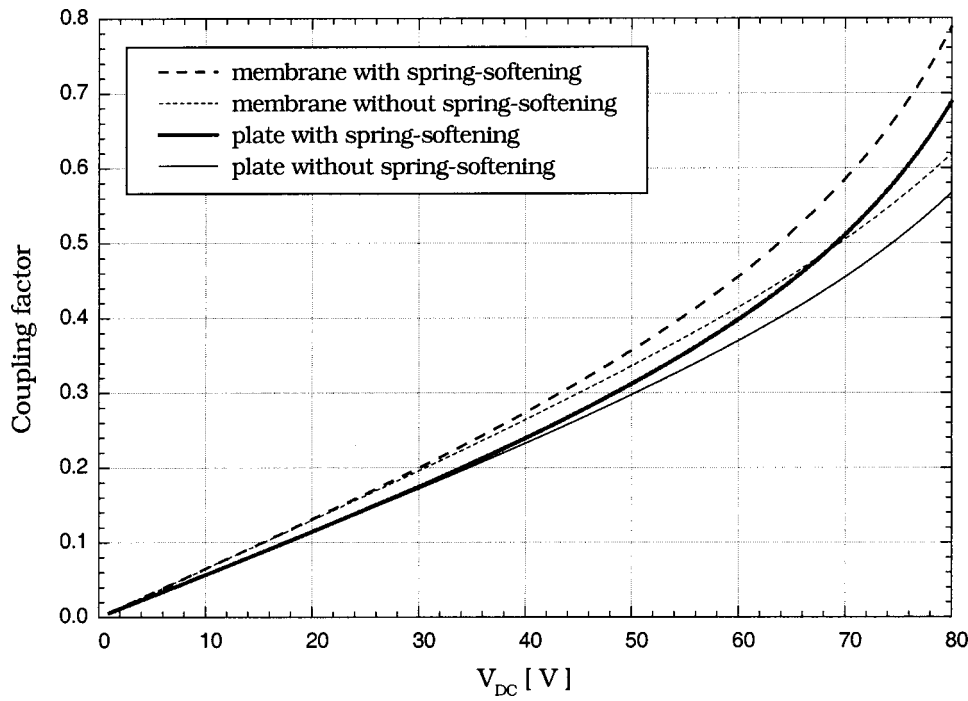


FIG. 6. Dynamic coupling factor of a CMUT single cell including or not the electrostatic spring softening. A lumped parameter approximation is used for computation.

$$c'_m = \frac{c_m}{\left(1 - \frac{\phi_1^2 c_m}{C_{01}}\right)}, \quad (17)$$

and the coupling factor given by Eq. (16) becomes

$$k_w = \sqrt{\frac{\phi_1^2 c'_m}{\phi_1^2 c'_m + C_{01}}} = \sqrt{\frac{\phi_1^2 c_m}{C_{01}}} = \sqrt{\frac{C_e}{C_{01}}}. \quad (18)$$

This relation, that was derived according to Eq. (2), coincides with the electromechanical coupling coefficient of a single electrostatic unit as explicitly defined by Hunt (Ref. 9, p. 181). An ambiguity exists in the literature between Refs. 9 and 8, because in Ref. 8, p. 351 the reported expression of the coupling factor is the same as Eq. (16), which does not include the spring-softening effect. A comparison between coupling factors including or not this effect is shown in Fig. 6. Note that the discrepancy becomes important as the bias voltage increases.

As far as effective coupling factor is concerned, according to Eq. (3) the frequencies f_s and f_p , in the absence of losses, coincide with the frequencies f_r and f_a of infinite and zero admittance, respectively. The input electrical admittance of the circuit of Fig. 4 is

$$\mathbf{Y}_{\text{Ei}} = j \left\{ \omega C_{01} - \frac{1}{(\omega L_e - 1/(\omega C_e))} \right\}. \quad (19)$$

Setting $\mathbf{Y}_{\text{Ei}} = \infty$ and $\mathbf{Y}_{\text{Ei}} = 0$, the resonance and antiresonance frequencies turn out to be $f_r = 1/(2\pi\sqrt{L_e C_e})$ and $f_a = 1/(2\pi\sqrt{L_e C_s})$, respectively. The substitution into Eq. (3) yields

$$k_{\text{eff}} = \sqrt{\frac{f_a^2 - f_r^2}{f_a^2}} = \sqrt{\frac{C_e}{C_e + C_{01}}}. \quad (20)$$

Thus, as anticipated in the Introduction, the effective coupling factor k_{eff} , within the validity of the lumped approxi-

mation, has the same value as the dynamic coupling factor k_w without spring softening [see Eq. (16)]. It is interesting to note that if k_{eff} is computed as $\sqrt{(f_a^2 - f_r^2)/f_r^2}$, the result coincides with k_w as given by Eq. (18), including the spring-softening effect.

A better evaluation of the variation of the coupling coefficients with the polarizing voltage is provided by the distributed model, as discussed in the next section.

B. Distributed parameter model

In the previous section we computed the dynamic coupling factor of a single electrostatic cell by using a lumped parameter circuit. In this section we calculate the coupling factor by using a more accurate distributed model of CMUTs,¹ including parasitic capacitance and the spring-softening effect.

Consider a CMUT with no losses, consisting of n identical microelements electrically connected in parallel, and driven by a sinusoidal voltage $\mathbf{V} = V_{\text{ac}} e^{j\omega t}$.

With reference to the equivalent circuit of Fig. 3, the input electrical admittance can be expressed by the sum of two contributions:

$$\mathbf{Y}_{\text{Ei}} = \frac{\mathbf{I}}{\mathbf{V}} = \mathbf{Y}_{\text{Eb}} + \mathbf{Y}_{\text{Em}}, \quad (21)$$

where \mathbf{Y}_{Eb} is the blocked admittance and \mathbf{Y}_{Em} is the motional admittance.⁸

At each antiresonance frequency, $\mathbf{Y}_{\text{Ei}} = 0$ and the charge on the electrodes remains unchanged while the diaphragm is oscillating, because the signal source is electrically insulated from the transducer. This condition permits us to evaluate the dynamic coupling factor, as done in the previous section.

Again, the total energy involved in a vibration cycle is the kinetic energy at its maximum value that can be obtained by multiplying by n the kinetic energy of a single membrane,

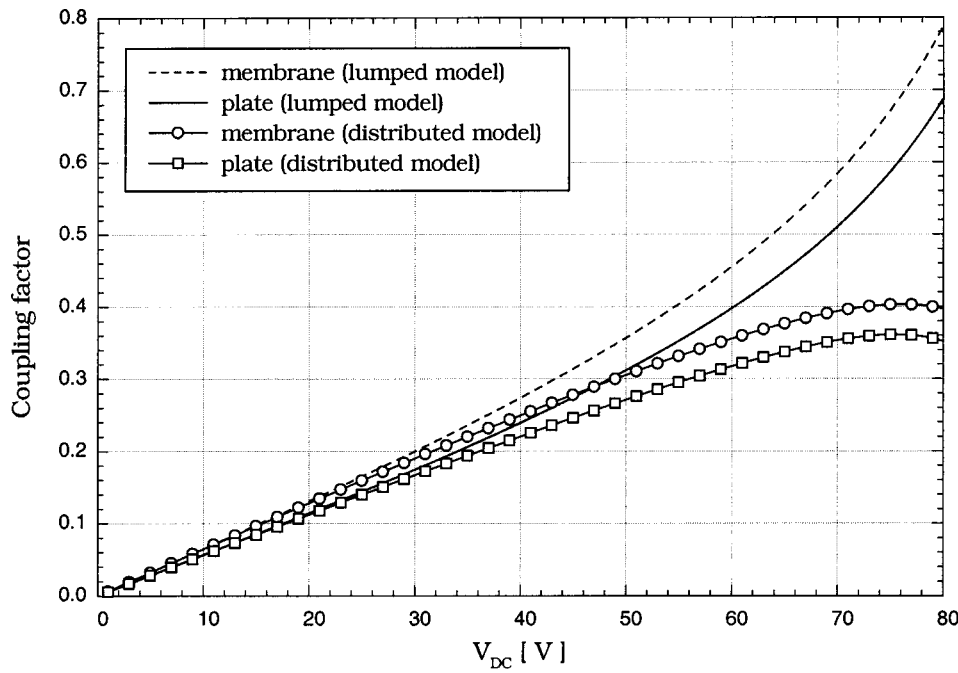


FIG. 7. Dynamic coupling factor of a CMUT single cell with a membrane and plate diaphragm and no parasitic capacitance. Simulations based on lumped and distributed models are shown.

$$(KE)_{\max} = n \times \frac{1}{2} \rho_s \iint_{S_1} \left(\frac{\partial \psi}{\partial t} \right)_{\max}^2 dS_1, \quad (22)$$

where $\psi = \psi(r, t)$ is the symmetric transverse displacement, whose analytical expression depends on the diaphragm model. For a clamped circular membrane without any interaction with the surroundings, the transverse displacement in frequency domain is¹

$$\Psi(r, \omega) = -\frac{\phi_1 \mathbf{V}}{\pi \tau} \frac{[J_0(k_s r) - J_0(k_s a)]}{(k_s a)^2 J_0(k_s a)}, \quad (23)$$

where a is the radius and k_s is the wave number of the membrane,

$$k_s = \frac{\omega}{\sqrt{\tau/\rho_s}} \sqrt{1 + \frac{\epsilon_0 V_{DC}^2}{\rho_s d_0^3 \omega^2}}. \quad (24)$$

For a clamped circular plate, the transverse displacement has the expression¹

$$\Psi(r, \omega) = -\phi_1 \mathbf{V} \frac{S_1}{\pi^2 D} \left\{ \frac{[J_0(K_s r) - J_0(K_s a)]I_1(K_s a) + [I_0(K_s r) - I_0(K_s a)]J_1(K_s a)}{(K_s a)^4 [J_0(K_s a)I_1(K_s a) + I_0(K_s a)J_1(K_s a)]} \right\}, \quad (25)$$

where the parameter K_s is given by

$$K_s^4 = \frac{\omega^2 \rho_s}{D} + \frac{\epsilon_0 V_{DC}^2}{D d_0^3}. \quad (26)$$

The integral in (22) has been computed numerically for both membrane and plate models. The electrical energy stored in a vibration cycle is

$$EE = \frac{1}{2} (C_{0a} + C_p) V_{ac}^2, \quad (27)$$

where $C_{0a} = n C_{01}$ is the active capacitance of the transducer and C_p is the parasitic capacitance. The active capacitance of a single cell has been evaluated numerically, including the static deformation produced by the polarizing voltage and neglecting the fringing field. Thus, also the value of C_{0a} slightly depends on the bias voltage.

Antiresonance frequencies can be calculated from Eq. (21) setting $\mathbf{I} = d\mathbf{Q}/dt = 0$. If mechanical and electrical

losses, as well as radiation in the surrounding medium, are neglected, the blocked admittance is given by¹

$$\mathbf{Y}_{Eb} = j\omega(C_{0a} + C_p), \quad (28)$$

and the motional admittance is

$$\mathbf{Y}_{Em} = \frac{\phi^2}{\text{Im}\{\mathbf{Z}_m\}}, \quad (29)$$

where $\phi = (C_{0a} V_{DC})/d_0$ is the transformation factor of the CMUT, and $\mathbf{Z}_m = n \mathbf{Z}_{m1}$ is the mechanical impedance of the totality of membranes. Numerical solutions of Eq. (21) with $\mathbf{I} = 0$ have been obtained for several values of the bias voltage, and the corresponding antiresonance frequencies have been used to evaluate the total energy; see Eqs. (22)–(26). Finally, k_w has been computed according to Eq. (2) with E_c given by Eq. (27).

Figure 7 shows a comparison between the lumped and

distributed model calculations of the dynamic coupling factor of a single cell ($n=1$) with no parasitic capacitance ($C_p=0$), both including the spring-softening effect. For low values of the bias voltage, the lumped model prediction approximates to that of the distributed model. For higher values, the coupling factor yielded by the distributed model is lower, because the piston-like motion of the diaphragm in the lumped model is more effective in the energy conversion than the actual flexural motion. In other words, because of the actual nonuniform energy distribution over the membrane area, a greater kinetic energy must be supplied in a vibration cycle to convert the same electrical energy as the piston motion does in the lumped model.

As can be seen, a quite different prediction results from distributed model as the bias voltage reaches its critical value; indeed, the coupling factor has a saturation-like behavior with a peak value in proximity of the collapse voltage, in contrast with the increase nearly up to unity predicted by the lumped model.

Since the CMUT performance improves with increasing bias voltage, the transducer is frequently biased near the collapse, and an investigation of this operating condition is then required. This will be done in the next section.

IV. ANALYSIS OF THE COLLAPSE POINT

A. Lumped parameter model

When a polarizing voltage is applied to the diaphragm of an electrostatic cell, the displacement can be found by solving the static equilibrium equation, which is obtained by equating the restoring force to the electrostatic force.

If the cell is represented as a parallel plate capacitor and the restoring force is assumed to be linear, the equilibrium equation can be written as

$$-\frac{1}{c_{m0}}x_{DC} = \frac{\epsilon_0 S_1 V_{DC}^2}{2d_0^2} = \frac{\epsilon_0 S_1 V_{DC}^2}{2\left(\frac{d_m}{\epsilon_r} + d_g + x_{DC}\right)^2}, \quad (30)$$

where d_m is the thickness, ϵ_r is the relative permittivity and c_{m0} is the low-frequency mechanical compliance of the diaphragm, d_g is the gap height and x_{DC} is the static displacement.

When the bias voltage reaches a critical value, the parabolic curve of the electrostatic force, given by the right-hand side of Eq. (30), becomes tangent to the straight line representing the elastic restoring force, given by the left-hand member. In this situation, the slope of the two curves must be the same at the point of tangency, and derivative of Eq. (30) with respect to x_{DC} yields

$$\frac{1}{c_{m0}} = \frac{\epsilon_0 S_1 V_{DC}^2}{d_0^3}. \quad (31)$$

Equations (30) and (31) define the collapse point of the diaphragm;^{9,21} beyond the critical voltage, the electrostatic force overwhelms the restoring force and the diaphragm collapses over the fixed electrode. Solving Eqs. (30), (31) for x_{DC} and V_{DC} , the maximum equilibrium displacement is found to be

$$x_{cr} = -\frac{d_e}{3}, \quad (32)$$

and the corresponding collapse voltage is

$$V_{cr} = \sqrt{\frac{8}{27} \frac{d_e^3}{c_{m0} \epsilon_0 S_1}}, \quad (33)$$

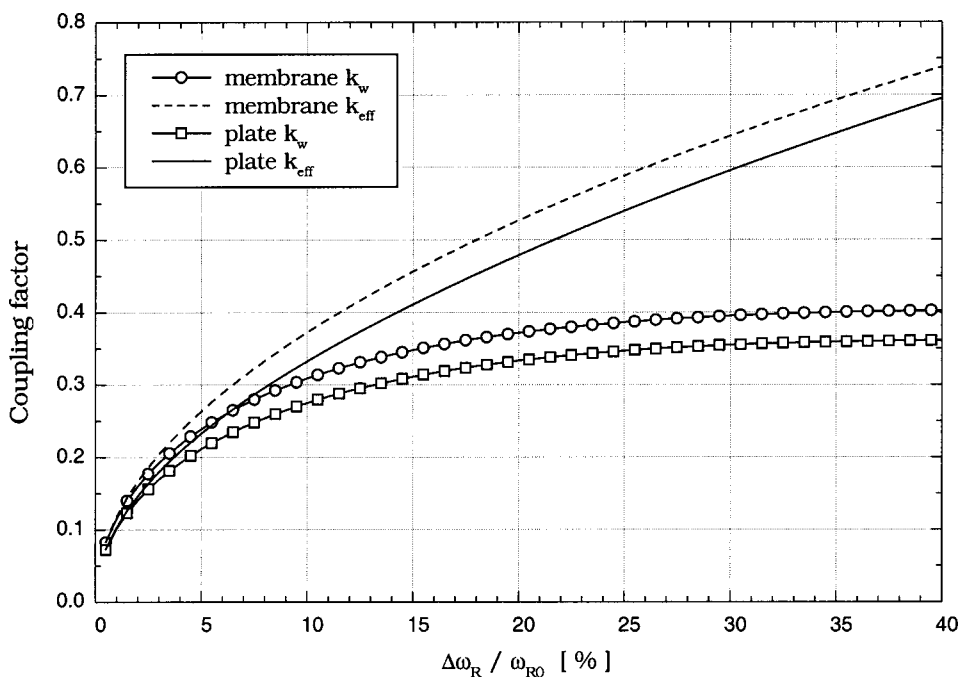


FIG. 8. Dynamic coupling factor of a CMUT, computed with the distributed model, as a function of the resonance frequency shift normalized to the fundamental frequency ω_{R0} without bias effects.

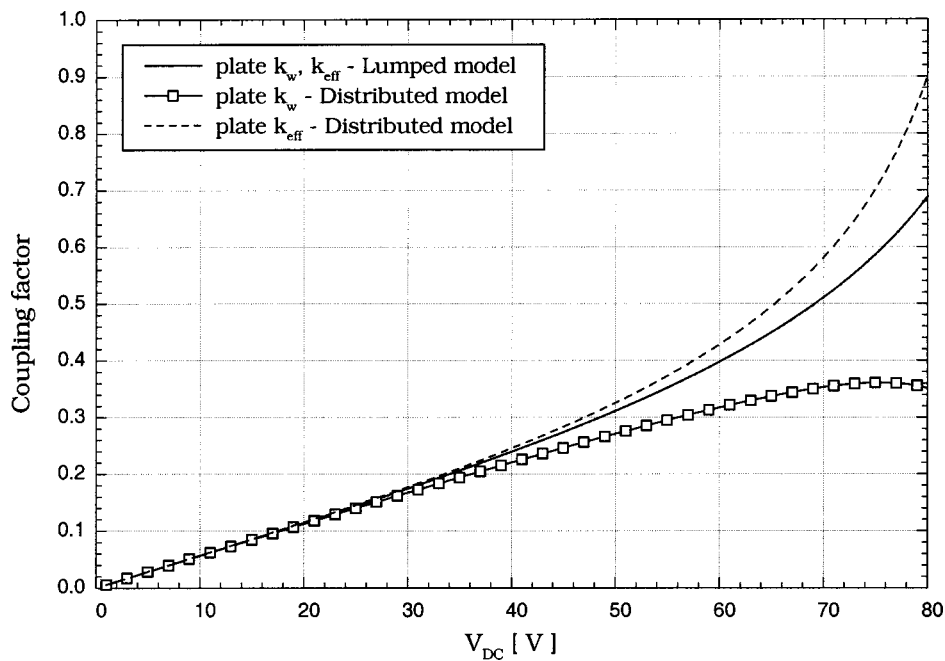


FIG. 9. Coupling coefficients of a CMUT single cell with a plate diaphragm.

where $d_e = d_m / \epsilon_r + d_g$ is the effective distance between the electrodes without polarization. Using these relations in Eq. (9) and substituting in Eqs. (6) and (8) with $c_m = 0.9568 c_{m0}$ for a membrane ($c_m = 0.977 c_{m0}$ for a plate), the parameters $C_e^{(m)}$, $C_e^{(p)}$ turn out to be approximately equal to the static capacitance of the cell. For a membrane we have

$$C_e^{(m)} = \left(\frac{C_{01}^{(cr)} V_{cr}}{d_e + x_{cr}} \right)^2 0.9568 c_{m0} = 0.9568 C_{01}^{(cr)}, \quad (34)$$

while for a plate $C_e^{(p)} = 0.977 C_{01}^{(cr)}$, where $C_{01}^{(cr)} = \epsilon_0 S_1 / (d_e + x_{cr})$ is the critical value of C_{01} . Thus, the coupling factor given by Eq. (18) approaches unity.

Actually, as reported in Ref. 9, pp. 184–185, membrane collapse usually occurs at values of the normalized displacement $-x_{cr}/d_e$ substantially less than the theoretical limit

given by Eq. (32). For example, in Ref. 9 was found, for an electrostatic device experimentally tested, that fall-in occurred at a value of $-x_{cr}/d_e$ around 0.22. As noted, this premature collapse was likely to be caused by the fact that the central portion of the diaphragm reaches the critical spacing while the average static displacement x_{DC} is still lower than its critical value. With this value of x_{cr} , the critical parameter C_e is found to be about 0.55 both for membrane and plate diaphragms, and the resulting maximum value of the coupling factor is 0.74.

The validity of these results is, however, limited to the lumped parameter approximation. In the next paragraph, the coupling factor will be investigated near the critical point by using the distributed parameter model.

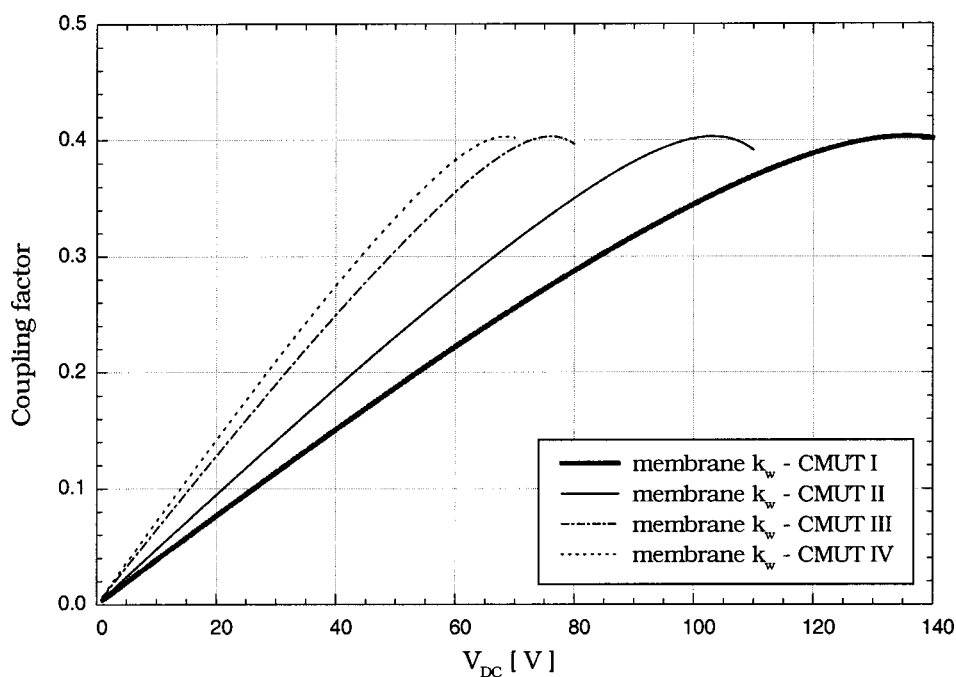


FIG. 10. Coupling factor of several CMUTs with membrane diaphragm cells. Parasitic capacitance has not been considered in the simulations.

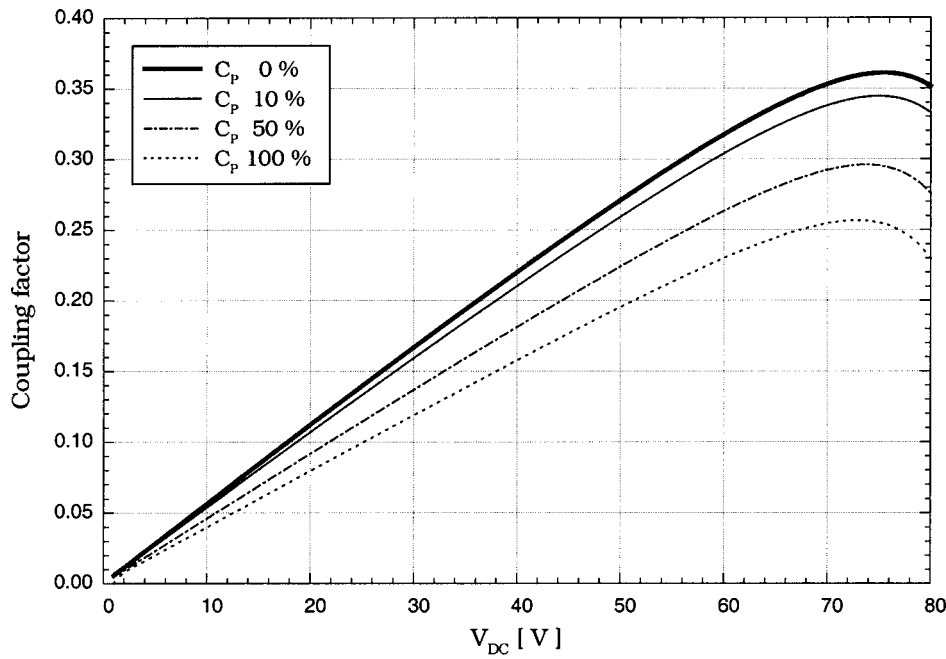


FIG. 11. Coupling factor of a CMUT with plate diaphragm cells for several values of the parasitic capacitance in percent of the active capacitance.

B. Distributed parameter model

As it is known, the condition for the fundamental resonance frequency ω_R of a clamped circular membrane is $ka = 2.405$,⁸ which substituted into Eq. (24) for an electrostatically excited membrane yields

$$\left(\frac{\omega_R a}{\sqrt{\tau/\rho_s}} \right)^2 = (2.405)^2 - \frac{\epsilon_0 V_{DC}^2 a^2}{\tau d_0^3}. \quad (35)$$

Note that, according to the spring-softening behavior, the resonance frequency decreases as the polarizing voltage increases. The absolute maximum value of V_{DC} is the one that makes the right-hand side of Eq. (35) equal to zero and the collapse voltage must be proportional to this value, i.e.,

$$V_{cr} = \mu \sqrt{\frac{\tau d_e^3}{\epsilon_0 a^2}} = \mu \sqrt{\frac{d_e^3}{8 c_{m0} \epsilon_0 S_1}}, \quad (36)$$

where $0 < \mu < 1$ is a numerical coefficient. As can be noted, Eq. (36) exhibits the same functional dependence as Eq. (33), which is derived according to the lumped model. If the coupling factor k_w is calculated, in the way illustrated in the previous section, as a function of the relative amount $\Delta\omega_R/\omega_{R0}$ by which the fundamental frequency drops because of the bias voltage, as given by Eq. (35), the resulting plot is shown in Fig. 8. The effective coupling factor, computed according to Eq. (20) with f_a and f_r numerically evaluated, is also shown.

As it is possible to see, unlike the lumped model predictions, for the distributed model the effective coupling factor k_{eff} does not coincide with k_w , so that a measure of k_{eff} from the CMUT electrical impedance does not represent a reliable value of k_w . Also note that, as soon as ω_R changes of 15% of its nominal value, the coupling factor k_w is at 85% of its maximum value.

Figure 9 shows the behavior of k_w and k_{eff} of a single cell with a plate diaphragm as a function of V_{DC} , both com-

puted with lumped and distributed models. It is notable that all the k factors draw together for low values of the bias voltage.

A result worthy of note is the one shown in Fig. 10, where k_w is plotted for several CMUTs with circular membranes having different dimensions, stress, fundamental frequency, and collapse voltage, as reported in Table I. As one can see, the maximum value of the coupling factor yielded by the distributed model is about 0.4, regardless of the transducer design. This value seems to be reasonably a bounding value of the coupling factor k_w of an electrostatic cell with a circular membrane.

For a piezoceramic plate oscillating in thickness mode, the dynamic k factor is a reduced value of the thickness material coupling factor k_t , which usually takes values in the range 0.45–0.50. If this range is used into Eq. (4), the corresponding range of k_w turns out to be 0.40–0.45. Thus, the coupling factor of a CMUT with circular membranes is very close to that of a piezoceramic oscillating in the thickness direction.

Finally, the coupling coefficient of a CMUT is worsened by the parasitic capacitance, for it does not contribute to the energy conversion. A plot of k_w for several values of C_p in percent of the active capacitance C_{0a} is shown in Fig. 11.

V. CONCLUSIONS

In this paper, a definition of the electromechanical coupling coefficient, involving the energies stored in a dynamic vibration cycle, has been used to calculate the dynamic coupling factor k_w for lossless CMUTs by using both lumped and distributed parameter models. A strong discrepancy exists between the lumped and distributed model predictions of k_w as the bias voltage reaches its critical value. The maximum value of k_w , corresponding to membrane collapse, is close to unity for the lumped model, whereas a quite lower value of about 0.40 for a cell with membrane diaphragm

(0.36 for plate diaphragm), which is approached with a saturation-like behavior, is predicted by the distributed model. Further, calculations of k_w for several CMUTs with circular membranes, having different geometry and stress, have shown that the peak value, which is reached at different critical voltages, is always 0.40. This result permits us to state that the coupling factor of a CMUT is very close to that of a piezoceramic plate oscillating in thickness direction, for which the dynamic k factor has typically values between 0.40 and 0.45.

The effective coupling coefficient k_{eff} has also been investigated, showing that this parameter is a good estimation of the device coupling factor only for low values of the bias voltage, far from the critical point. Actually, k_{eff} coincides with k_w within the lumped model approximation, but when it is computed using a more accurate distributed model this coincidence drops and, for practical higher voltages, k_{eff} must be abandoned as a reliable measure of the CMUT coupling factor.

- ¹A. Caronti, G. Caliano, A. Iula, and M. Pappalardo, "An accurate model for capacitive micromachined ultrasonic transducers," *IEEE Trans. Ultrason. Ferroelectr. Freq. Control* **49**, 159–168 (2002).
- ²W. P. Mason, "An electromechanical representation of a piezoelectric crystal used as a transducer," *Proc. IRE* **23**, 1252–1263 (1935).
- ³W. P. Mason, *Piezoelectric Crystals and Their Applications to Ultrasonics* (Van Nostrand, New York, 1950).
- ⁴M. I. Haller and B. T. Khuri-Yakub, "A surface micromachined ultrasonic air transducer," *IEEE Trans. Ultrason. Ferroelectr. Freq. Control* **43**, 1–6 (1996).
- ⁵X. C. Jin, I. Ladabaum, F. L. Degertekin, S. Calmes, and B. T. Khuri-Yakub, "Fabrication and characterization of surface micromachined capacitive ultrasonic immersion transducers," *IEEE/ASME J. Microelectromech. Syst.* **8**, 100–114 (1999).
- ⁶O. Oralkan, X. C. Jin, K. Kaviani, A. S. Ergun, F. L. Degertekin, M. Karaman, and B. T. Khuri-Yakub, "Initial pulse-echo imaging results with one-dimensional capacitive micromachined ultrasonic transducer arrays," *IEEE Ultrasonics Symposium* (IEEE, New York, 2000), pp. 959–962.
- ⁷U. Demirci, O. Oralkan, J. A. Johnson, A. S. Ergun, M. Karaman, and B.

- T. Khuri-Yakub, "Capacitive micromachined ultrasonic transducer arrays for medical imaging: experimental results," *IEEE Ultrasonics Symposium* (IEEE, New York, 2001), pp. 957–960.
- ⁸L. E. Kinsler, A. R. Frey, A. B. Coppens, and J. V. Sanders, *Fundamentals of Acoustics* (Wiley, New York, 1982).
- ⁹F. V. Hunt, *Electroacoustics. The Analysis of Transduction, and Its Historical Background* (American Institute of Physics, Woodbury, NY, 1982).
- ¹⁰C. L. Hom, S. M. Pilgrim, N. Shankar, K. Bridger, M. Massuda, and S. R. Winzer, "Calculation of quasi-static electromechanical coupling coefficients for electrostrictive ceramic materials," *IEEE Trans. Ultrason. Ferroelectr. Freq. Control* **41**, 542–551 (1994).
- ¹¹J. C. Piquette and S. E. Forsythe, "Generalized material model for lead magnesium niobate (PMN) and an associated electromechanical equivalent circuit," *J. Acoust. Soc. Am.* **104**, 2763–2772 (1998).
- ¹²J. C. Piquette, "Quasistatic coupling coefficients for electrostrictive ceramics," *J. Acoust. Soc. Am.* **110**, 197–207 (2001).
- ¹³ANSI/IEEE Std. 176/1987, "IEEE Standard on Piezoelectricity" (IEEE, New York, 1987).
- ¹⁴D. A. Berlincourt, D. R. Curran, and H. Jaffe, "Piezoelectric and piezomagnetic materials and their function in transducers," in *Physical Acoustics*, edited by W. P. Mason (Academic, New York, 1964), Vol. IA, pp. 169–270.
- ¹⁵N. Lamberti, A. Iula, and M. Pappalardo, "The electromechanical coupling factor in static and dynamic conditions," *Acustica* **85**, 39–46 (1999).
- ¹⁶X. C. Jin, I. Ladabaum, and B. T. Khuri-Yakub, "The microfabrication of capacitive ultrasonic transducers," *IEEE/ASME J. Microelectromech. Syst.* **7**, 295–302 (1998).
- ¹⁷A. Caronti, H. Majjad, S. Ballandras, G. Caliano, R. Carotenuto, A. Iula, V. Foglietti, and M. Pappalardo, "Vibration maps of capacitive micromachined ultrasonic transducers by laser interferometry," *IEEE Trans. Ultrason. Ferroelectr. Freq. Control* **49**, 289–292 (2002).
- ¹⁸O. Ahrens, D. Hohlfeld, A. Buhrdorf, O. Glitza, and J. Binder, "A new class of capacitive micromachined ultrasonic transducers," in Ref. 6, pp. 939–942.
- ¹⁹W. P. Mason, *Electromechanical Transducers and Wave Filters* (Van Nostrand, New York, 1943).
- ²⁰I. Ladabaum, X. C. Jin, H. T. Soh, A. Atalar, and B. T. Khuri-Yakub, "Surface micromachined capacitive ultrasonic transducers," *IEEE Trans. Ultrason. Ferroelectr. Freq. Control* **45**, 678–690 (1998).
- ²¹A. Bozkurt, I. Ladabaum, A. Atalar, and B. T. Khuri-Yakub, "Theory and analysis of electrode size optimization for capacitive microfabricated ultrasonic transducers," *IEEE Trans. Ultrason. Ferroelectr. Freq. Control* **46**, 1364–1374 (1999).

A directional acoustic array using silicon micromachined piezoresistive microphones^{a)}

David P. Arnold^{b)} and Toshikazu Nishida

*Department of Electrical and Computer Engineering, Interdisciplinary Microsystems Group,
University of Florida, Gainesville, Florida 32611-6130*

Louis N. Cattafesta and Mark Sheplak^{c)}

*Department of Mechanical and Aerospace Engineering, Interdisciplinary Microsystems Group,
University of Florida, Gainesville, Florida 32611-6250*

(Received 14 March 2002; revised 26 September 2002; accepted 13 October 2002)

The need for noise source localization and characterization has driven the development of advanced sound field measurement techniques using microphone arrays. Unfortunately, the cost and complexity of these systems currently limit their widespread use. Directional acoustic arrays are commonly used in wind tunnel studies of aeroacoustic sources and may consist of hundreds of condenser microphones. A microelectromechanical system (MEMS)-based directional acoustic array system is presented to demonstrate key technologies to reduce the cost, increase the mobility, and improve the data processing efficiency versus conventional systems. The system uses 16 hybrid-packaged MEMS silicon piezoresistive microphones that are mounted to a printed circuit board. In addition, a high-speed signal processing system was employed to generate the array response in near real time. Dynamic calibrations of the microphone sensor modules indicate an average sensitivity of $831 \mu\text{V}/\text{Pa}$ with matched magnitude ($\pm 0.6 \text{ dB}$) and phase ($\pm 1^\circ$) responses between devices. The array system was characterized in an anechoic chamber using a monopole source as a function of frequency, sound pressure level, and source location. The performance of the MEMS-based array is comparable to conventional array systems and also benefits from significant cost savings. © 2003 Acoustical Society of America. [DOI: 10.1121/1.1527960]

PACS numbers: 43.38.Hz, 43.38.Gy [SLE]

I. INTRODUCTION

As aircraft noise regulations become more stringent, the need for modeling and measuring aircraft noise becomes more important. In order to design quieter aircraft, the physical mechanisms of noise generation must be understood and any theoretical model or computational simulation must be experimentally validated. One validation method is the comparison of the farfield acoustic pressures. Typically, single microphone measurements of aeroacoustic sources in wind tunnels are hampered by poor signal-to-noise ratios that arise from microphone wind self-noise, tunnel system drive noise, reverberation, and electromagnetic interference.¹ In addition, a single microphone cannot distinguish between pressure contributions from different source locations. The need for more precise noise source characterization and localization has driven the development of advanced sound field measurement techniques. In particular, the development and application of directional microphone arrays has been documented as a means to localize and characterize aeroacoustic sources in the presence of high background noise.^{1–12}

Although knowledge of the acoustic farfield does not uniquely define the noise source,¹³ the qualitative localization of a source and analyses of the spatial and temporal characteristics of its farfield radiation can provide insight into noise generation mechanisms. Modern acoustic arrays used in wind tunnel studies of airframe noise are typically constructed of large numbers (tens or hundreds) of instrumentation grade condenser microphones, and range in aperture size from several inches to several feet.^{6–12} Data collection, followed by extensive post-processing, has been used to implement various beamforming processes, including conventional beamforming, array shading, and shear-layer corrections.^{6–12} The resulting data files can exceed 500 GB in size and require significant post-processing time per dataset.⁷

A greater number of microphones in an array can improve its ability to characterize a sound field. In particular, an increase in the number of microphones enhances the signal to noise ratio of an array, defined as the *array gain*, given (in dB) by $10 \log(M)$, where M is the number of microphones.¹⁴ In addition, a large number of microphones may be used to improve the spatial resolution and extend the frequency range of an array. The spatial resolution of an array is inversely related to the product kD , where $k = \omega/c$ is the acoustic wave number, ω is the radian frequency, c is the speed of sound, and D is the aperture size. Thus, a larger aperture may be needed to maintain sufficient spatial resolution at low frequencies. In contrast, the intersensor spacing must be less than one-half of the smallest wavelength of

^{a)}Portions of this work were presented in "Technology development for directional acoustic arrays," at the *142nd Meeting of the Acoustical Society of America*, Ft. Lauderdale, FL, December 2001 and "MEMS-based acoustic array technology," at the *40th AIAA Aerospace Sciences Meeting & Exhibit*, Reno, NV, January 2002.

^{b)}Now affiliated with School of Electrical and Computer Engineering, Georgia Institute of Technology, Atlanta, GA 30332-0250.

^{c)}Electronic mail: ms@mae.ufl.edu

interest to avoid spatial aliasing.¹⁴ The feasibility of scaling the current technology to multiple arrays with larger numbers (hundreds or thousands) of microphones is limited by the cost per channel (microphone, amplifier, data acquisition), data handling efficiency (acquisition capabilities, signal processing complexity, storage requirements), and array mobility (size, weight, cabling). In addition, experiments performed in large wind tunnels are costly and require extensive setup.¹⁵ Therefore, an array system that provides near real-time output in a cost-effective manner would be advantageous.

Our goal in this paper is to present the design and initial results of a high-speed, reduced-cost acoustic array system designed for aeroacoustic measurements. To address these scaling issues, MEMS microphones and novel packaging techniques were used to build a compact, modular printed circuit board (PCB) array. Batch-fabricated MEMS microphones offer a substantial cost reduction and the potential for improved amplitude and phase matching relative to the commercial condenser microphones used in conventional acoustic arrays. Implementation of the microphone array on the PCB allows for signal conditioning and amplification to be collocated at the array. It also offers the potential of using on-board digital signal processing (DSP) hardware to execute beamforming algorithms without having to transfer the data to remote processors. However, a separate high-speed data acquisition and signal processing system was used in this study.

II. BACKGROUND

An acoustic array is a collection of spatially distributed microphones used to measure an acoustic field. The signals from each microphone are selectively weighted and phase shifted through a signal processing technique known as beamforming in order to focus the array at a region in space. This provides the array with an electronically steerable, directional response. In this section we review the conventional beamforming equations used to generate the array output. An in-depth treatment of spatial arrays and beamforming theory can be found in Johnson and Dudgeon.¹⁴

Consider a collection of M omnidirectional microphones in unbounded free space with the origin of a coordinate system located at the array center. Let \vec{x}_m denote the location of the m th microphone and consider a point monopole at position \vec{x}' as shown in Fig. 1. Let $y_m(t)$ denote the continuous time signal detected by the m th microphone. The classical continuous time, “delay-and-sum” beamforming equation is given as a weighted linear sum of time shifted signals,

$$z(t) \equiv \sum_{m=1}^M w_m y_m(t - \Delta_m), \quad (1)$$

where w_m is a weighting factor and Δ_m is a time shift applied to the m th microphone.¹⁴ By selecting appropriate delays, the acoustic signals from a chosen finite region in the field are coherently amplified while signals emanating from other areas are attenuated.

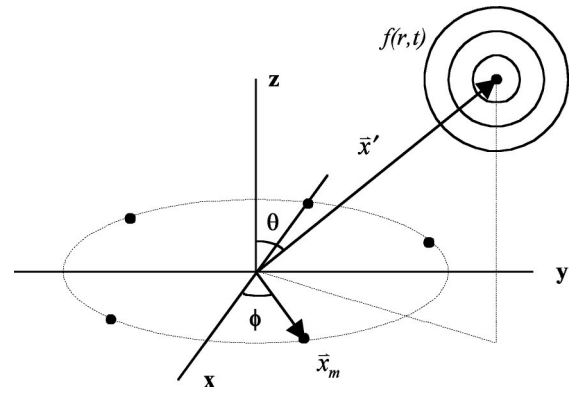


FIG. 1. Array configuration depicting a point monopole source and an array of five microphones.

Assuming an ideal point monopole source at an arbitrary array focus location, \vec{x} , the time shift and weight for the m th microphone are

$$\Delta_m = \frac{r - r_m}{c} \quad (2)$$

and

$$w_m = \frac{r_m}{r}, \quad (3)$$

where r and r_m are the radial distances from the focus location to the array center and the m th microphone, respectively. The time shift synchronizes each of the measured signals to the signal at the array center. The weight is assigned to compensate for the geometric attenuation of spherically spreading waves. Modification of these coefficients is the basis of more advanced beamforming techniques such as shading and shear layer corrections.⁷ If the focus location coincides with the actual location of the source, the signals from the microphones are coherently summed and the beamformer output is maximized.

This beamforming process is premised on the assumption that ideal pressure measurements are made in the farfield of a distribution of compact, spatially distinct, mutually independent point monopoles. The presence of coherent, closely spaced, or continuously distributed sources, as well as higher order dipoles or quadrupoles, all limit the accuracy of the array measurement.¹⁶ Thus, the results obtained from an acoustic array must be interpreted within the assumptions made of the sources, which are not usually known *a priori*. Additionally, the measurement of the farfield does not uniquely define the source.¹³ For these reasons, array measurements can only be considered qualitative with regards to source characterization.

Frequency-domain beamforming offers several benefits over time-domain methods. These include techniques for reducing side lobes and narrowing the main lobe in the array pattern, as well as reducing noise and reflection effects.⁵ Using standard Fourier transform pairs, the beamforming expression from Eq. (1) can be transformed into the frequency domain,

$$Z(\omega) = \sum_{m=1}^M w_m Y_m(\omega) e^{-j\omega\Delta_m}, \quad (4)$$

where $Y_m(\omega)$ and $Z(\omega)$ are the Fourier transforms of $y_m(t)$ and $z(t)$, respectively. Equations (2) and (3) still hold, but Δ_m now represents a phase shift.

A data acquisition system is used to discretely sample data from the microphones at a fixed sampling frequency, f_s . The time record for each channel, denoted $y_m[n]$, is divided into L blocks, each block consisting of N points, and an N -point fast Fourier transform¹⁷ (FFT) is applied to each block of data. Equation (4) can be rewritten to define the discrete frequency-domain *array response* at the k th frequency bin as

$$Z_k = \sum_{m=1}^M w_m Y_{mk} e^{-j\omega_k\Delta_m}, \quad (5)$$

where Y_{mk} represents the k th FFT coefficient of the m th channel and $\omega_k = k2\pi f_s/N$ is the corresponding radian frequency. This can be expressed in matrix form as

$$Z_k = \mathbf{e}_k^H \mathbf{Y}_k, \quad (6)$$

where $(\cdot)^H$ denotes the Hermitian transpose. The *steering vector*, \mathbf{e}_k , contains the weights and phase shifts to be applied to the system and is given by

$$\mathbf{e}_k = \begin{bmatrix} w_1 e^{j\omega_k\Delta_1} \\ \vdots \\ w_M e^{j\omega_k\Delta_M} \end{bmatrix}. \quad (7)$$

The term \mathbf{Y}_k contains the k th FFT coefficients for all M channels,

$$\mathbf{Y}_k = \begin{bmatrix} Y_{1k} \\ \vdots \\ Y_{Mk} \end{bmatrix}. \quad (8)$$

The N discrete terms of Z represent the discrete frequency spectrum of the beamformer output. If desired, an inverse Fourier transform could be used to convert back to a time-domain representation.

More commonly, the *array power response* is used, representing a time-averaged power spectrum.¹⁴ The array power response at the k th frequency bin is given by

$$P_k = \mathbf{e}_k^H E[\mathbf{Y}_k \mathbf{Y}_k^H] \mathbf{e}_k, \quad (9)$$

where $E[\cdot]$ denotes the expected value. The term P_k is a real-valued scalar having units of power (Pa^2). The inner term,

$$\mathbf{R}_k \equiv E[\mathbf{Y}_k \mathbf{Y}_k^H] = \begin{bmatrix} G_{11k} & G_{12k} & \cdots & G_{1Mk} \\ G_{21k} & G_{22k} & & \vdots \\ \vdots & & \ddots & \\ G_{M1k} & \cdots & & G_{MMk} \end{bmatrix}, \quad (10)$$

is known as the *spatial correlation matrix* or *cross-spectral matrix* and forms the basis of more advanced beamforming algorithms.¹⁴ Each term in the matrix represents a complex valued cross-spectral coefficient given by

$$G_{ij_k} = E[Y_{i_k} Y_{j_k}^*], \quad (11)$$

where $(\cdot)^*$ denotes the complex conjugate. The $M \times M$ cross-spectral matrix contains the relative magnitude and phase relations between all pairs of microphones and therefore captures all of the information needed to compute the signal location.¹⁴

For stationary data, averaging is used to reduce random noise in the measurements.¹⁷ Averaging the cross-spectral matrix yields a robust measurement because the relative phase information between microphones is assumed to be precisely known.¹⁴ An estimate for the expected value of the cross spectral matrix is given as an average over L blocks of data,

$$\hat{\mathbf{R}}_k = \frac{1}{L} \sum_{l=1}^L \mathbf{Y}_{kl} \mathbf{Y}_{kl}^H, \quad (12)$$

and thus the estimated array power response is given by

$$\hat{P}_k = \mathbf{e}_k^H \hat{\mathbf{R}}_k \mathbf{e}_k. \quad (13)$$

If desired, a corresponding value known as the *array pressure response* (having units of Pa) can be computed by taking the square root of the array power response.

From Eqs. (12) and (13), it is noted that the time-averaged cross-spectral matrix needs only to be computed once; only the steering vector changes in the computation of the array response at various focus locations. This leads to a computational efficiency when the array response is desired over a region of space, as is the case for spatial mapping applications. In addition, since the cross-spectral matrix contains all of the relevant field information, it can be saved rather than the raw time signals if the spectral analysis parameters (block size, number of averages, etc.) are fixed. This can offer significant reductions in the data storage requirements.

In the same manner that linear time-invariant systems are characterized by examining the frequency response, the array pattern corresponds to the wave number-frequency response of a spatiotemporal filter.¹⁴ Physically, it represents the array response to an acoustic point source in the same way that the impulse response function represents the response of a linear system to an impulse function. The array pattern is a function of frequency, array focus location, and actual source location, and is given by¹⁴

$$W(\omega, \vec{x}, \vec{x}') = \sum_{m=1}^M \frac{r_m}{r} \frac{r'}{r'_m} \exp \left\{ j\omega \left[\frac{(r' - r) - (r'_m - r_m)}{c} \right] \right\}. \quad (14)$$

The focus location, \vec{x} , determines r and r_m , the radial distances from the focus location to the array center and m th microphone, respectively. The source location, \vec{x}' , determines r' and r'_m , the radial distances from the source to the array center and m th microphone, respectively. The array pattern is generally plotted at a particular frequency for a fixed source location.

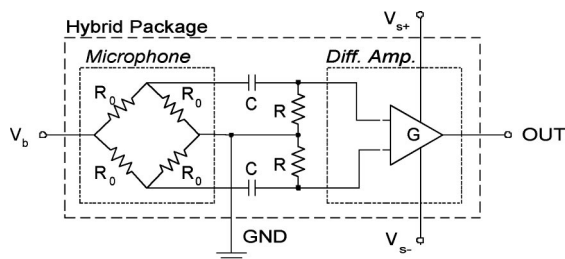


FIG. 2. Circuit schematic of hybrid package. $R_0 \approx 600 \, \Omega$, $R = 147 \, \text{k}\Omega$, $C = 0.68 \, \mu\text{F}$, $G = 500$, $V_b = 3 \, \text{V}$, $V_s = \pm 10 \, \text{V}$.

III. ARRAY SYSTEM DESIGN AND CONSTRUCTION

The design and fabrication of the MEMS-based array system are presented in this section. Details of the construction of the hybrid package and printed circuit board array are included. This is followed by a discussion of the data acquisition and signal processing system used to generate the array pressure response. Full details of the array system are reported by Arnold.¹⁸

A. Hybrid microphone-amplifier packages

The hybrid microphone-amplifier package combines a micromachined piezoresistive silicon microphone¹⁹ and an Analog Devices AD624 low-noise differential amplifier²⁰ into a 16-pin, 1.5 cm diameter TO-8 semiconductor package. The differential outputs of the microphone Wheatstone bridge are AC-coupled to the inputs of the amplifier via two resistor-capacitor (RC) pairs, as shown in Fig. 2, with a corner frequency given by $f_c = 1/(2\pi RC) = 1.6 \, \text{Hz}$. This hybrid package provides a small, self-contained microphone module with an amplified, low-impedance output. The sensor packages are fitted into sockets on a printed circuit board array, permitting external calibration and interchangeability.

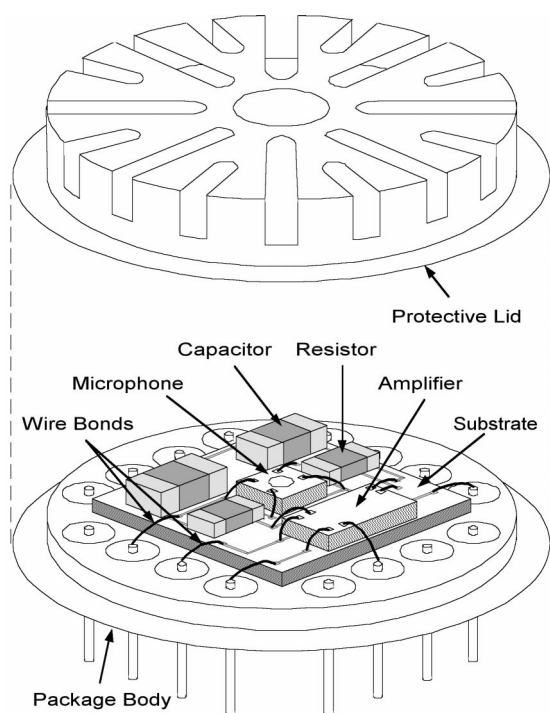


FIG. 3. Diagram of the hybrid microphone-amplifier packaging scheme.

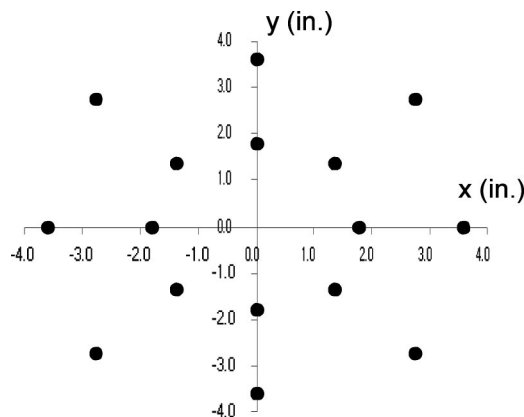


FIG. 4. Plot of array layout (inches).

The construction of the hybrid package consists of four layers, as shown in Fig. 3: the package body or “header,” a silicon substrate, the component layer, and a protective lid. A TO-8 package serves as the primary structural element. A silicon substrate is bonded to the header using conductive silver epoxy. The substrate, passivated with silicon dioxide, provides metal bond pads and interconnecting traces for the devices. The components are bonded to the exposed bond pads of the silicon substrate using conductive silver epoxy. Gold wire bonds are used to make additional electrical connections between the chip bond pads and package pins. A slotted lid provides protection against physical damage while permitting acoustic waves to pass. The TO-8 header and lid are connected to the circuit ground for additional electromagnetic shielding.

B. Printed circuit board array

The performance of an array (spatial selectivity, influence of sidelobes, array gain, etc.) is directly influenced by the quantity and geometry of the sensors. Our goal in the research was to validate the concept of a MEMS-based array, not to optimize a particular array geometry. Thus, a layout similar to Cluster 3 in NASA’s small aperture directional array (SADA)⁷ was selected, allowing for a comparison to previously published results. The configuration is identical with the exception that the center microphone has been omitted due to the limitation of 16 channels in the data acquisition system used for testing. As shown in Fig. 4, the planar layout consists of four concentric rings with radii 1.80, 1.94, 3.60, and 3.89 in., each having four microphones.

The array is constructed from a double-sided copper clad PCB that serves as the electrical interface and mechanical structure. The top surface of the PCB contains the 16 microphone packages and a laser diode to permit accurate aiming of the array. The bottom surface contains small (SMB-type) connectors for the coaxial cabling. Four layers of Garolite are milled and throughbolted to the circuit board array to provide additional rigidity, as shown in Fig. 5. The theoretical array patterns, obtained using Eq. (14), are shown in Figs. 6–8 at 2, 6, and 10 kHz for a 48 in. \times 48 in. scan plane that is parallel to the array face and centered on the z axis for a source at a distance of 36 in. These plots indicate

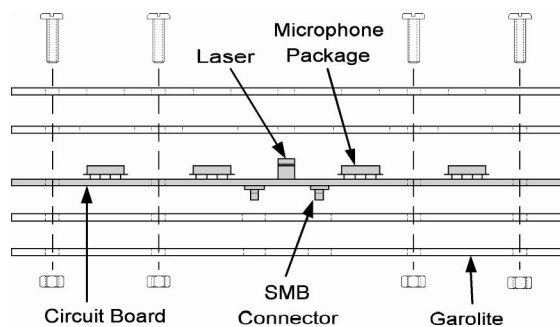


FIG. 5. Diagram of array construction depicting circuit board array and Garolite stiffening layers.

the spatial selectivity of the array, illustrating a narrowing primary lobe (improved spatial resolution) and increasing side lobes with increasing frequency.

C. Signal processing

The signal processing consists of continuously sampling data from the array, computing the fast Fourier transform (FFT) on blocks of data, and using conventional frequency-domain beamforming methods as outlined in Sec. II to obtain the array pressure response over a scanned region in space.

An Agilent E1432A VXI-based digitizer is used to acquire the signals from the array. The digitizer is interfaced to a host computer (866 MHz Pentium III, 256 MB RAM) via a National Instruments MXI-2 interface bus. The host controls

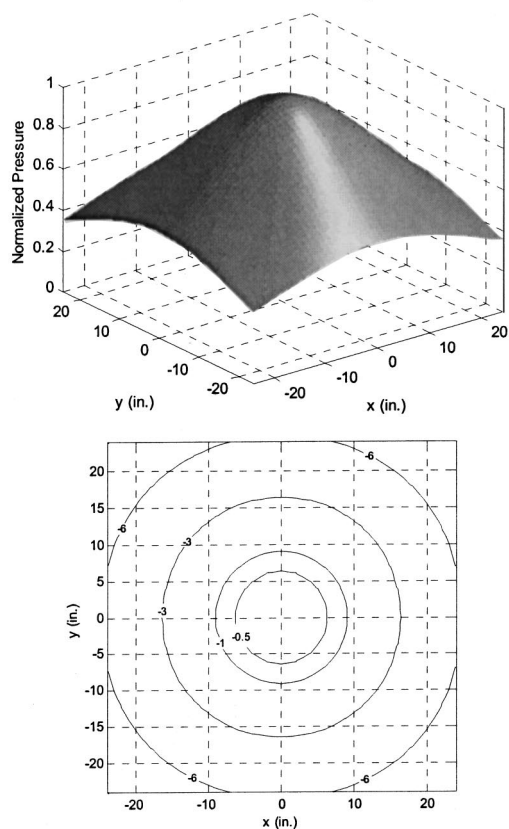


FIG. 6. Theoretical array pattern and contour plot (0.5, 1, 3, 6, and 9 dB) at 2 kHz for 48 in.×48 in. scan plane at 36 in.

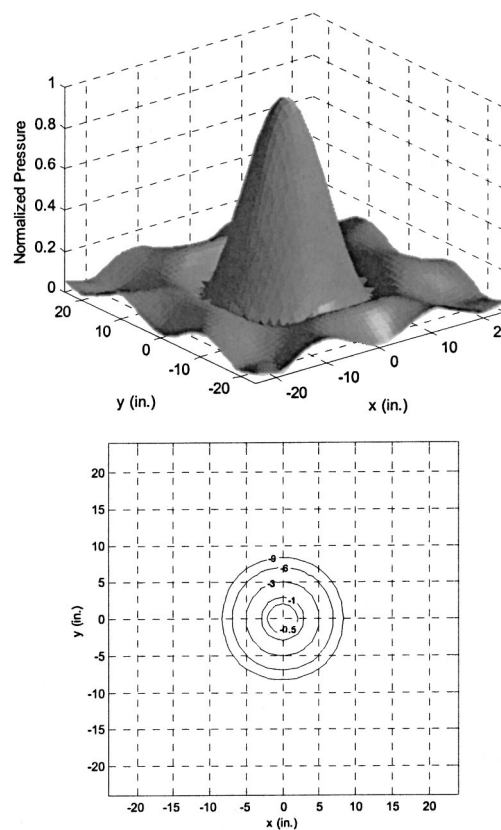


FIG. 7. Theoretical array pattern and contour plot (0.5, 1, 3, 6, and 9 dB) at 6 kHz for 48 in.×48 in. scan plane at 36 in.

the operation of the digitizer, runs the beamforming algorithms, and displays and saves the results using MATLAB v.6.0. In operation, the digitizer samples all 16 channels with 16-bit resolution at a sampling rate of 25.6 kHz. The Agilent E1432A provides the capability to perform real-time fast Fourier transforms (FFTs) on the incoming data, significantly reducing the computational load on the host computer. A Hanning window is used in computing 1024-point FFTs, yielding a frequency resolution of 25 Hz. The digitizer internally compensates for the power lost in the windowing operation by scaling the output by the Hanning window weighting factor of $\sqrt{8/3}$.¹⁷ Typically, 400 nonoverlapping blocks are used, corresponding to 16 s of time data.

The cross-spectral matrices for all 512 bin frequencies are computed in real time for each successive block of FFT data that is transferred to the PC host. The time-averaged cross-spectral matrices are obtained by Eq. (12) and the data is converted to units of pressure squared (Pa^2) by dividing by the square of the microphone sensitivity. The array power response is obtained using Eqs. (2), (3), (7), and (13) and then dividing by the number of microphones squared (M^2) to normalize the array output to that of a single microphone. The pressure response is given by the square root of this result. For most of the measurements made in calibrating the array, a 48 in.×48 in. grid of regularly spaced (1 in. increments) focal locations are used in a scan plane parallel to the array face at a distance of 36 in. along the z axis. The computation time required to obtain the pressure response over the scan plane for a single frequency bin is under 4 s. If

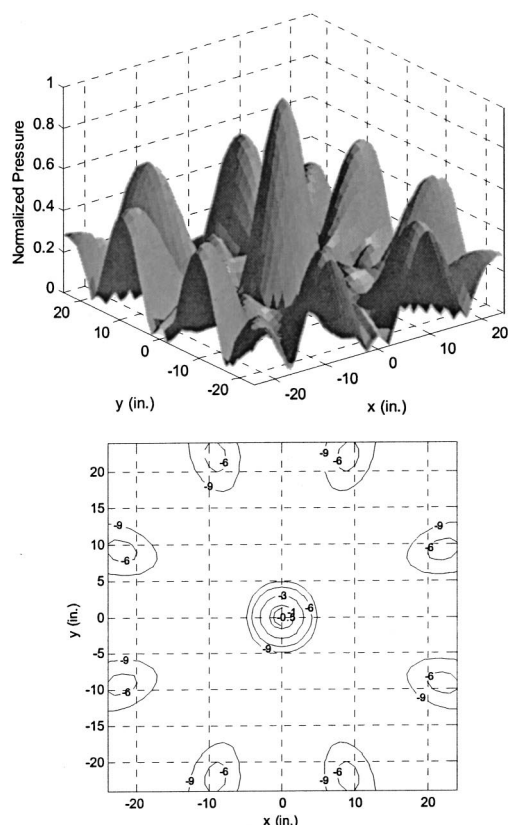


FIG. 8. Theoretical array pattern and contour plot (0.5, 1, 3, 6, and 9 dB) at 10 kHz for 48 in. \times 48 in. scan plane at 36 in.

needed, the power responses from multiple bins can be summed to obtain the power over a wider frequency bin (e.g., octave analysis). The required computation time is increased by approximately 4 s for each additional frequency bin included in the power response analysis. The time-averaged cross-spectral matrices for all 512 frequency bins are stored to disk, resulting in a file size of 2 MB.

IV. EXPERIMENTAL RESULTS

The experimental methodologies and results for calibrations of the hybrid package and array system are discussed in this section. The frequency responses of the hybrid microphone packages are obtained using a plane wave tube (PWT) acoustic calibrator. The characterization of the array system is performed using an acoustic point source in the University of Florida's Anechoic Aeroacoustic Test Facility.

A. Hybrid package characterization

Each hybrid microphone package is tested individually for amplitude and phase using a 2.54 cm \times 2.54 cm square cross section, normal incidence PWT designed to support plane waves up to 6.7 kHz.^{18,19} The microphone package and a 1/8 in. Brüel and Kjær (B&K) 4138 reference microphone are flush mounted at the terminating end of the tube and subjected to normally incident plane waves. The frequency response of the hybrid package is determined with respect to the B&K microphone.

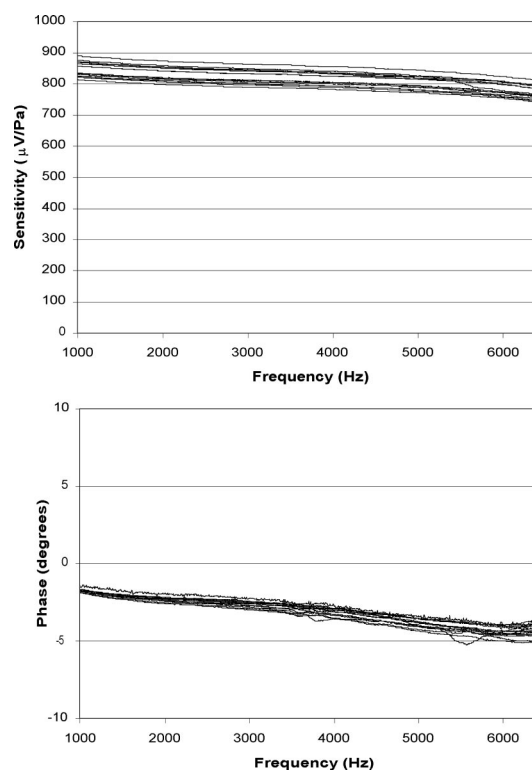


FIG. 9. Magnitude and phase response of 16 hybrid packages at \sim 110 dB.

The measured responses of the 16 hybrid packages are shown in Fig. 9 over the frequency range of 1–6.5 kHz at sound pressure levels of approximately 110 dB (Ref. 20 μ Pa). The average sensitivity of each hybrid package is seen to vary from 780 to 855 μ V/Pa with a mean of 831 μ V/Pa over the range tested. A linear trend is noted in the phase response, which could be a phase variation, but may be attributed to a mounting misalignment in the PWT calibration.¹⁹ An offset in the axial location of the reference and test microphones will result in a linear bias in the phase measurement. An offset of only 1 mm would result in a phase bias error of 6.25° at 6 kHz. Although the PWT is limited to a maximum frequency of 6.7 kHz, the microphones have demonstrated a flat response to 20 kHz and possess a predicted resonant frequency of 131 kHz.¹⁹

For the purposes of array signal processing, as can be seen from Eqs. (2) and (3), matching of the magnitudes and phases between sensor packages is important to minimize uncertainty. The frequency response data are reformatted and shown in Fig. 10 as a relative sensitivity and phase with respect to microphone number one. The magnitude responses of all microphones are shown to match within ± 0.6 dB, and the phase responses are matched within $\pm 1^\circ$ over the frequency range tested. Mosher *et al.*²¹ states that phase matching within $\pm 10^\circ$ is sufficient for obtaining reasonable results without the need for phase corrections. Therefore, the hybrid microphone packages are considered acceptable for use in the array and all the presented data are from uncorrected, raw measurements.

B. Array characterization

A method for extensively characterizing an acoustic array has been reported by Mosher *et al.*²¹ However, for this

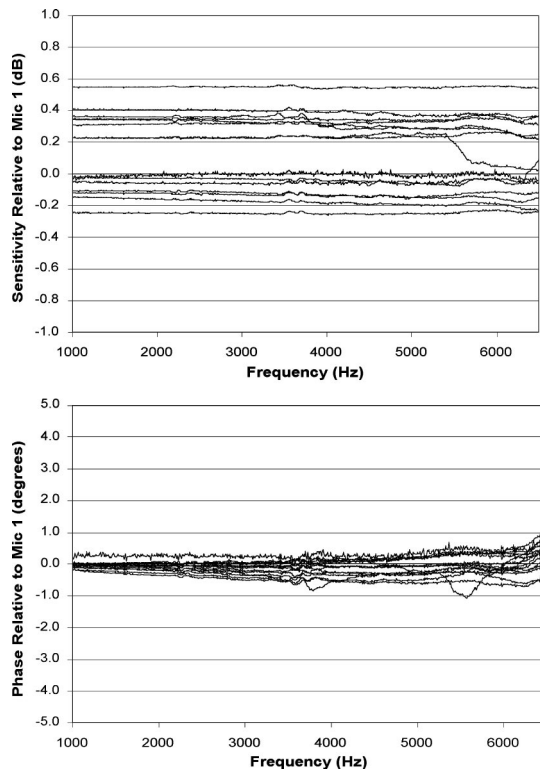


FIG. 10. Relative magnitude and phase of 16 hybrid packages with respect to microphone number one.

paper, only a preliminary characterization was performed in order to verify proper operation of the MEMS-based system. The array response to an acoustic point source was measured in an anechoic chamber, having a 100 Hz cutoff frequency, as a function of source frequency, source amplitude, and source location. Each measured response was compared to the theoretical response (array pattern) given by Eq. (14). The acoustic point source consists of a JBL 2426J-compression driver mated to a 53 cm long, 1.9 cm diameter metal pipe. The pressure field generated by the device is modeled as a piston at the end of a pipe and performs suitably as a point monopole for frequencies below 11.5 kHz.¹⁸

Several metrics were used to quantify the differences between the measured and theoretical responses. For this analysis, the measured array response is normalized by its peak value for a direct comparison to the normalized array pattern. The first metric is a comparison of the beamwidths of the mainlobe at 0.5, 1, 3, 6, and 9 dB down from the peak values.⁷ Because the main lobe does not have perfect cylindrical symmetry, an equivalent beamwidth is used. It is obtained by computing the diameter of a circle having the same area as enclosed by the respective contour curve. The second metric is to compute a weighted root mean squared (rms) error for the measured response. It provides an estimate of the total relative error over J scan locations and is expressed as

$$\text{weighted_error}_{\text{rms}} = \sqrt{\frac{\sum_{j=1}^J M_j (T_j - M_j)^2}{J}}, \quad (15)$$

where T_j and M_j represent the normalized theoretical and measured responses at the j th scan location, respectively. The

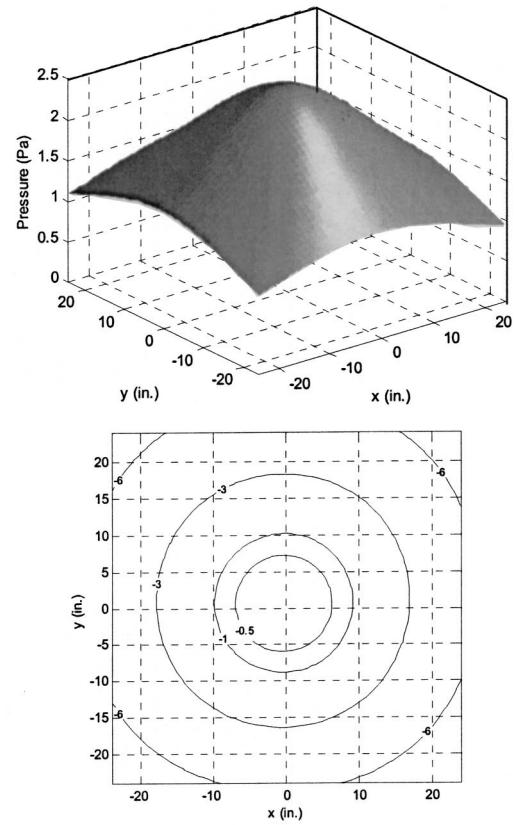


FIG. 11. Measured array pressure response and contour plot (0.5, 1, 3, 6, and 9 dB) at 2 kHz and ~ 100 dB for a 48 in. \times 48 in. scan plane at 36 in.

error is weighted by the measured response M_j to account for the relative effect the errors would have in the total measured response. A third metric is a comparison of the location of the measured peak response to the actual source location.

1. Array response versus frequency

The array response was first examined as a function of frequency for a point source positioned at a distance of 36 in. on the z axis of the array. Discrete tones were used to achieve an average sound pressure level of approximately 100 dB at the array microphones. The measured array pressure responses are shown at 2, 6, and 10 kHz in Figs. 11–13. These measured responses closely match the corresponding theoretical array patterns, shown in Figs. 6–8.

The equivalent 3 dB main lobe beamwidth is shown in Fig. 14 for frequencies from 1 to 10 kHz. This data is representative of the results obtained for the equivalent 0.5, 1, 6, and 9 dB beamwidths. The measured beamwidths are shown to closely match the theoretical values for frequencies of 3 kHz and higher. Due to the relatively small aperture size, errors are expected at the lower frequencies. Verification of the main lobe beamwidth is important from a spatial resolution standpoint, but it does not validate the total response, particularly the effect of side lobes. A measure of the total error is given by the weighted rms errors as shown in Fig. 15. It is important to note that unlike the theoretical response, the acoustic array interacts with the incident sound field, resulting in scattering. Thus, the measured response includes these scattering effects, which are unaccounted for

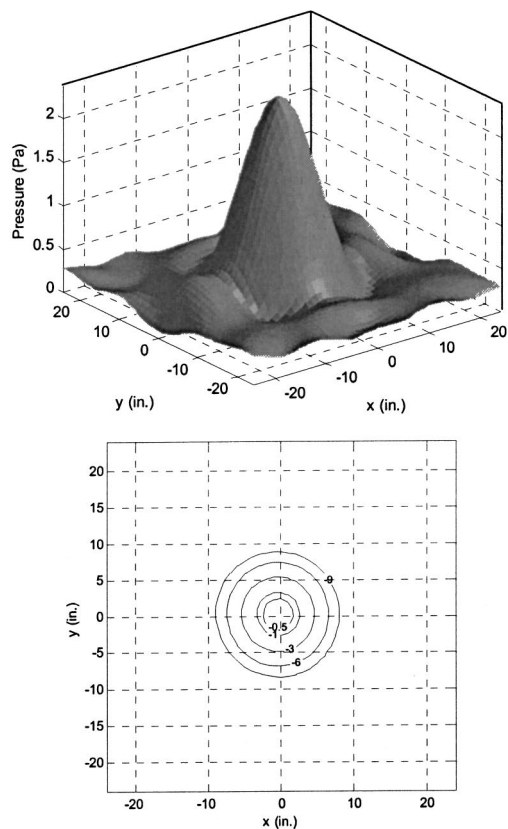


FIG. 12. Measured array pressure response and contour plot (0.5, 1, 3, 6, and 9 dB) at 6 kHz and ~ 100 dB for a 48 in. \times 48 in. scan plane at 36 in.

in the theoretical response. The error remains below 5% up to 8 kHz before increasing to a maximum of 9% at 10 kHz. One possible explanation is that diffraction effects from the microphone package may become important at higher frequencies. If the package is crudely modeled as the end of a rigid cylinder, it is known that diffraction effects become significant for values of kd larger than 2, where k is the acoustic wave number and d is the radius of the cylinder.¹³ It is noted that for the 1.5 cm package, $kd=2$ at approximately 7.2 kHz.

2. Array response versus sound pressure

One benefit of an acoustic array is its improvement in the signal to noise ratio of the measured signal, referred to as the array gain. The use of multiple microphones enables the measurement of source signals that are below the noise floor of any one particular microphone. Thus, an important characteristic of an array is its performance as a function of incident sound pressure, or equivalently the signal-to-noise ratio of the microphones. For this experiment, the point source is fixed along the z axis of the array at a distance of 36 in. and the array response to a 6 kHz tone is measured at various sound pressure levels. As a reference, the array was removed and a single B&K 4138 microphone was used to measure the free-field sound pressure level at the location of the array origin for several sinusoidal voltage amplitudes supplied to the speaker. The array was then reinstalled and the responses were measured using the calibrated speaker voltage inputs.

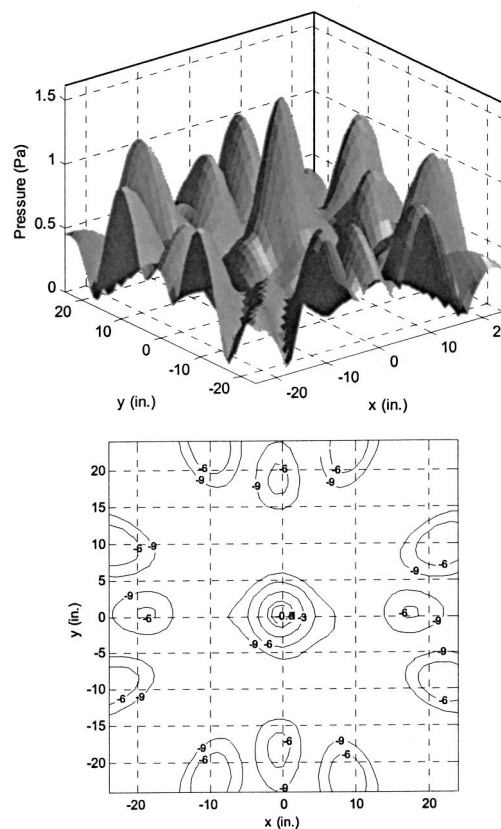


FIG. 13. Measured array pressure response and contour plot (0.5, 1, 3, 6, and 9 dB) at 10 kHz and ~ 100 dB for a 48 in. \times 48 in. scan plane at 36 in.

Figure 16 shows the average microphone pressure and the peak array pressure versus the free-field pressure measured by the single B&K microphone. For a strong, tonal point source, the free-field pressure, the average microphone pressure, and the peak array pressure should all be equal. At higher sound pressure levels, the average microphone pressure and peak array pressure converge to within 1 dB, but there is an offset of approximately 5 dB between these values and the free-field value. A 3 dB increase could be explained as a pressure doubling due to a sound hard boundary condition at the face of the array. The additional amplification may be due to diffraction effects. Regardless of the absolute levels, the lower end of the curve illustrates the existence of the array gain. As the incident sound pressure level decreases, the average microphone response asymptotes to 69.1 dB

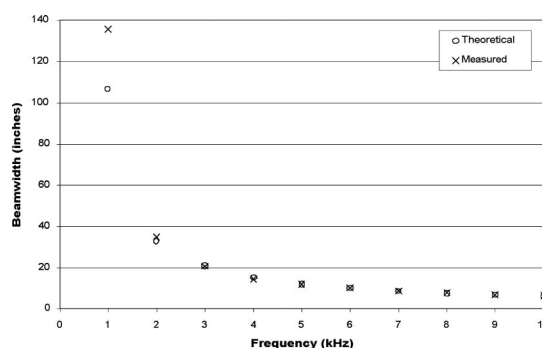


FIG. 14. Theoretical and measured 3 dB beamwidths as a function of frequency at ~ 100 dB for source at 36 in.

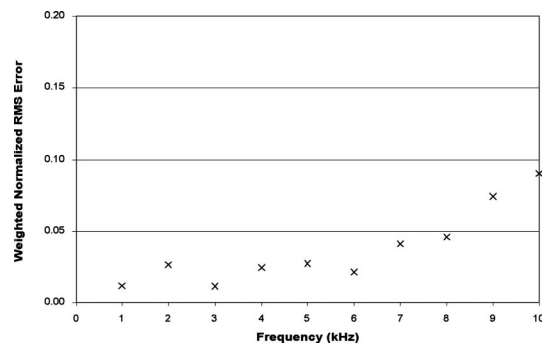


FIG. 15. Weighted rms error as a function of frequency at ~ 100 dB for a 48 in. \times 48 in. scan plane at 36 in.

while the peak array response asymptotes to 57.5 dB. Thus, the array can effectively detect a source that is 11.6 dB below the noise floor of the individual microphones. The asymptotic values represent the minimum detectable signals for a 25 Hz bin at 6 kHz. The estimated noise floors for a 1 Hz bin at 6 kHz are 55.1 dB for the hybrid packages and 43.5 dB for the array. The microphones possess a linear response to sound pressure levels of at least 160 dB.¹⁹

3. Array response versus location

Perhaps the most useful aspect of a directional array is its capability for source localization. As a one-dimensional verification, a 6 kHz source at a distance of 36 in. is translated in the x direction in 3 in. increments to a distance of 24 in., and the performance of the array was examined. Ideally, the array response should be calibrated over a broad range of locations in space.²¹ Figure 17 shows the weighted rms error for the array response as a function of the x location. The error remains constant at approximately 2.5% over the range tested.

Of greater importance is the ability of the array to accurately locate a source in space. Figure 18 shows the absolute spatial error of the peak array response plotted vs the x location of the source. It should be noted that a finer mesh, using a grid of 0.1 in. in the array response, was used to obtain the measures of spatial error. The error is seen to randomly fluctuate as a function of position, with a mean value of 0.3 in. These values are reasonable considering the accuracy in distance measurements in setting up the experi-

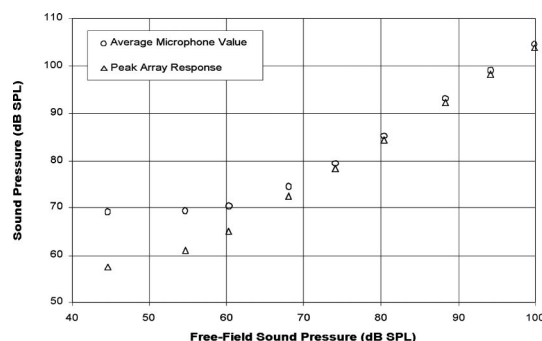


FIG. 16. Average array microphone pressure and peak array response pressure versus free-field pressure at 6 kHz.

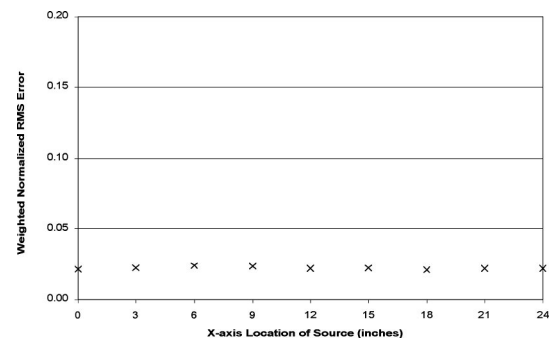


FIG. 17. Absolute spatial error (in inches) in the peak response of the array at 6 kHz and ~ 100 dB.

ment was ± 0.25 in. Thus, the performance at 6 kHz appears to be independent of the source location.

V. CONCLUSIONS AND FUTURE WORK

A directional acoustic array has been developed using a MEMS piezoresistive microphone, a hybrid sensor packaging scheme, printed circuit board construction technique, and a VXI-based signal processing system to produce a high-speed, cost-effective, modular, array measurement system. In addition to reducing the cost, the use of a printed circuit board as the array structure allows for the potential integration of the signal conditioning, data acquisition, and/or signal processing hardware. The estimated total cost of the 16-channel array, excluding labor and the cost of the data acquisition and signal processing system, is significantly less than a conventional array. The hybrid packages can be interchanged between low-cost printed circuit boards of various geometries, further reducing the costs. The use of high-speed data acquisition and digital signal processors has enabled near real-time computation of the time-averaged cross-spectral matrices. This provides the user with almost instant access to array response results and eliminates the need to save large amounts of time-series data. The resulting time savings can reduce the experimental costs, particularly for large wind tunnel studies.

The results from calibrations of the hybrid package and array verify the functionality of the system. From plane wave tube calibrations, the hybrid microphone packages show an average sensitivity of $831 \mu\text{V}/\text{Pa}$ with matched magnitude (± 0.6 dB) and phase ($\pm 1^\circ$) responses. From tests conducted

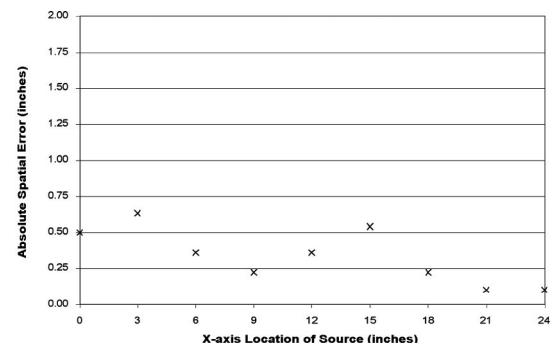


FIG. 18. Weighted rms error at 6 kHz and ~ 100 dB as a function of the source x location.

in an anechoic chamber, the array shows accurate source localization capabilities of ± 0.3 in. It has a minimum detectable signal of 47.8 dB for a 1 Hz bin at 6 kHz and a maximum input of 160 dB. For the small-aperture array presented, the usable frequency range is limited to 3–8 kHz. A larger number of sensors can broaden the frequency range by increasing the overall array size while maintaining small intersensor spacings. The array noise floor was experimentally verified to be 11.6 dB below the noise floor of the individual microphones, as predicted by the theoretical array gain.

For this array system, an extensive calibration is needed to quantify the response over a larger parameter space. The calibration should include *in situ* calibrations of the microphones and a complete analysis of the directivity and accuracy of the array over a broad frequency range.²¹ An analysis of the scattering effects could provide insight for improvements in accuracy. Additional efforts are aimed at reducing the size and increasing the physical robustness of the hybrid packages, improving the construction techniques used for the array, and integrating the signal conditioning and amplification circuitry at the array. The integration of DSP hardware with the PCB microphone array is currently being undertaken to further increase the system performance.

ACKNOWLEDGMENTS

Financial support for this work is provided by a NASA–Langley Research Center Grant #NAG-1-2133, monitored by Dr. William H. Humphreys, Jr. Integration of the DSP hardware with the microphone array for real-time monitoring is supported by National Science Foundation (NSF) Grant No. ECS-0097636. Also, David P. Arnold is supported by a National Science Foundation Graduate Research Fellowship. The authors would also like to thank Dr. Mark Allen at the Georgia Institute of Technology for support in the fabrication of the silicon substrates used in the hybrid package. Appreciation is also extended to David Martin and Dr. Jian Li at the University of Florida.

¹P. T. Soderman and S. C. Noble, “Directional microphone array for acoustic studies of wind tunnel models,” *J. Aircr.* **12**, 168–173 (1975).

²J. Billingsley and R. Kinns, “The acoustic telescope,” *J. Sound Vib.* **48**, 485–510 (1976).

- ³T. F. Brooks, M. A. Marcolini, and D. S. Pope, “A directional array approach for the measurement of rotor noise source distributions with controlled spatial resolution,” *J. Sound Vib.* **112**, 192–197 (1987).
- ⁴J. R. Underbrink and R. P. Dougherty, “Array design for non-intrusive measurement of noise sources,” *Noise-Con 96 Proceedings*, Seattle, Washington, September 1996, pp. 757–762.
- ⁵M. Mosher, “Phased arrays for aeroacoustic testing: theoretical development,” *2nd AIAA/CEAS Aeroacoustics Conference*, AIAA Paper 96-1713, State College, PA, May 1996.
- ⁶M. E. Watts, M. Mosher, and M. Barnes, “The microphone array phased processing system (MAPPS),” in Ref. 5, AIAA Paper 96-1714, May 1996.
- ⁷W. H. Humphreys, T. F. Brooks, W. W. Hunter, and K. R. Meadows, “Design and use of microphone directional arrays for aeroacoustic measurements,” *36th Aerospace Sciences Meeting & Exhibit*, Reno, NV, AIAA Paper 98-0471, January 1998.
- ⁸W. H. Herkes and W. H. Stoker, “Wind tunnel measurements of airframe noise of a high-speed civil transport,” in Ref. 7, AIAA Paper 98-0472.
- ⁹R. W. Stoker and R. Sen, “An experimental investigation of airframe noise using a model-scale Boeing 777,” *39th AIAA Aerospace Sciences Meeting & Exhibit*, Reno, NV, AIAA Paper 2001-0987, January 2001.
- ¹⁰J. F. Piet and G. Elias, “Airframe noise source localization using a microphone array,” *3rd AIAA/CEAS Aeroacoustics Conference*, Atlanta, GA, AIAA Paper 97-1643, May 1997.
- ¹¹R. Davy and H. Remy, “Airframe noise characteristics of a 1/11 scale Airbus model,” *4th AIAA/CEAS Aeroacoustics Conference*, Toulouse, France, AIAA Paper 98-2335, June 1998.
- ¹²P. Sijtsma and H. Holthuisen, “Source location by phased array measurements in closed wind tunnel test sections,” *5th AIAA/CEAS Aeroacoustics Conference*, Bellevue, WA, AIAA Paper 99-1814, May 1999.
- ¹³A. P. Dowling and J. E. Ffowcs Williams, *Sound and Sources of Sound* (Ellis Horwood Limited, Chichester, England, 1983), Chap. 7.
- ¹⁴D. H. Johnson and D. E. Dudgeon, *Array Signal Processing* (Prentice-Hall, Englewood Cliffs, NJ, 1993), Chaps. 1–4.
- ¹⁵J. Kegelman, “Accelerating ground-test cycle time: the six-minute model change and other visions for the 21st century,” in Ref. 7, AIAA Paper 98-0142.
- ¹⁶T. F. Brooks and W. M. Humphreys, “Effect of directional array size on the measurement of airframe noise components,” in Ref. 12, AIAA Paper 99-1958.
- ¹⁷J. S. Bendat and A. G. Piersol, *Random Data Analysis and Measurement Procedures*, 3rd ed. (Wiley, New York, 2000), Chaps. 1, 11.
- ¹⁸D. P. Arnold, “A MEMS-based directional acoustic array for aeroacoustic measurements,” Master’s thesis, University of Florida, Gainesville, FL, 2001.
- ¹⁹D. P. Arnold, S. Bhardwaj, S. Gururaj, T. Nishida, and M. Sheplak, “A piezoresistive microphone for aeroacoustic measurements,” *Proceedings of ASME IMECE 2001*, New York, NY, November 2001.
- ²⁰“AD624 precision instrumentation amplifier,” Product Data Sheet, Rev. C, Analog Devices, May 2001.
- ²¹M. Mosher, M. E. Watts, S. M. Jaeger, and S. Jovic, “Calibration of microphone arrays for phased array processing,” in Ref. 10, AIAA Paper 97-1678.

Acoustic scattering by a cylindrical shell with symmetric line constraints in the heavy fluid-loading limit

E. A. Skelton

Mathematics Department, Imperial College of Science, Technology & Medicine, London SW7 2BZ, England

(Received 13 February 2002; accepted for publication 22 August 2002)

A cylindrical shell, modelled using Donnell–Mushtari thin shell theory, is reinforced by two internal rigid plates attached to the shell along lines parallel to the shell axis. A circumferential mode expansion is used to obtain numerical results for the scattered sound field due to the presence of the reaction forces along the attachment lines. In the heavy fluid-loading limit, which is appropriate for low and mid-frequency ranges for practical underwater structures, asymptotic analysis is presented which allows the peak frequencies in the scattered field due to the reaction forces to be expressed (to leading order) in terms of the geometry and the shell and fluid parameters. These predictions agree well with results obtained by numerically evaluating the infinite sums needed to calculate the reaction forces and hence the scattered field. © 2003 Acoustical Society of America.

[DOI: 10.1121/1.1521427]

PACS numbers: 43.40.Ey, 43.40.Fz, 43.20.Fn, 43.20.Bi [ANN]

I. INTRODUCTION

The acoustic properties of an infinitely long circular cylindrical elastic shell have been widely studied, both because this geometry permits an exact solution of the linear equations of motion, and because it provides a good model for many structures of practical importance, such as aircraft or submarines. However, these vehicles also contain much internal structure connected to the shell and this may have a large effect on the sound scattered or radiated by the body. In order to devise quiet systems it is important to understand how the presence of internal structure may lead to peaks in the sound field. An active area of research is therefore the investigation of the scattering of sound by an infinitely long elastic cylindrical shell to which internal structure is attached along lines parallel to the shell axis.

Early work on this problem includes that of Reddy and Mallik,¹ who considered the effect of axial stiffeners equally spaced around a layered cylinder, and of Mead and Bardell,² who investigated an *in vacuo* shell with similar stiffeners. Bjarnason, Achenbach, and Igusa³ investigated a shell with an internal plate and external fluid loading using a Lagrange equation formulation. Theoretical prediction of the scattered sound in each of these papers involves the numerical evaluation of various infinite summations resulting from a circumferential modes expansion. Papers by Felsen and Guo,^{4,5} addressing the problem, use a combination of ray fields in the fluid with mode fields in the structure, which, at high frequencies, is better computationally than using only a circumferential mode expansion. A series of papers by Klauson and Metsaveer and others^{6–9} has used the circumferential mode expansion to model the scattering by a shell with internal plates or stiffening ribs attached parallel to the axis of the shell. The Timoshenko–Mindlin theory of plates and shells is used⁶ to obtain numerical predictions, which are compared with results observed experimentally,⁷ and seen to correlate well. They concluded⁸ that resonances in the spectrum of scattering from a stiffened shell may be attributed to flexural waves generated by the reaction forces of the stiffener acting

on the shell, and that every component of the reaction force plays a role in the vibration of the stiffened shell, but in the far-field the radial reaction force produces the dominant contribution to the scattered field in their frequency range of interest. More recently⁹ they have incorporated linear elasticity theory to model the shell into their numerical work, and have again shown good agreement with experimental results. Guo¹⁰ also used a circumferential mode expansion to obtain numerical results for the scattered field when the internal structure is modelled as a mass-spring system, concluding that at low frequencies the scattering is determined by the joints between the internal structure and the shell, rather than the details of the internal structure. The mass-spring system was then replaced^{11–13} by an internal plate and the numerical results indicated that in the low and mid frequency ranges whether the plate was pinned or clamped to the shell made little difference to the far-field scattered sound, and that the waves in the shell are strongly affected by geometric constraints imposed by the location of the attachment points, rather than the dynamic response of the plate. Bondaryk and Schmidt¹⁴ presented an analysis of experimental scattering data, noting that there is interest in the mid-frequency range where numerical methods tend to encounter large computational burdens, leaving a gap in the understanding of the structure. Loftman and Bliss¹⁵ proposed a method to improve computational efficiency of problems involving structural inhomogeneity and fluid-loading, and demonstrated it by applying the method to a shell with lengthwise constraints.

These authors have thus used a variety of numerical techniques to obtain scattering results for the various cylindrical geometries with lengthwise constraints. Their work presents numerical results of the calculated far-field scattered pressure over various frequency ranges, or of the numerical efficiency of their method. Here, a model for the scattering over a range of low frequencies by an elastic cylindrical shell with simple lengthwise constraints is investigated, firstly using the circumferential mode expansion in order to generate some numerical results, but then it is investigated further

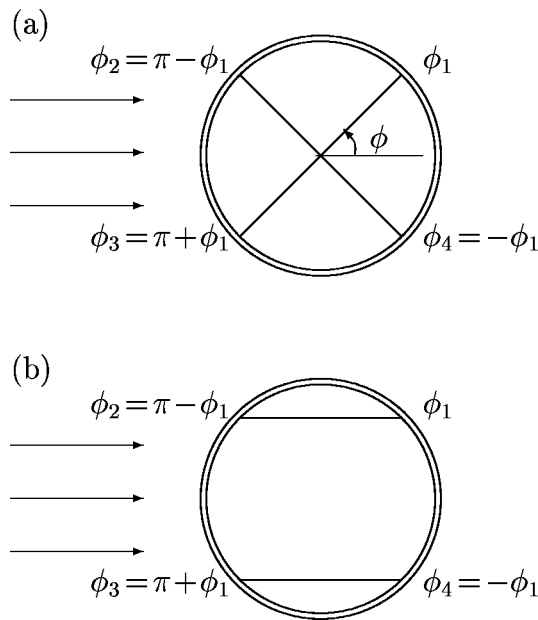


FIG. 1. Cross-sectional geometry of the problem, (a) elastic cylindrical shell with rigid reinforcing plates, (b) elastic cylindrical shell with rigid decking.

analytically in the asymptotic limit of heavy exterior fluid-loading on the shell. This limit is appropriate to many practical underwater structures at low and mid frequencies, and has been successfully applied to various plate^{16–18} and axially symmetric shell^{19,20} configurations. The shell stiffening in this simple model is provided by intersecting internal plates pinned to the shell, but neglects the dynamics of the internal plates as previous work^{11–13} has indicated that this will be of less importance than the geometrical configuration of the attachment lines and the shell properties. Thus, as only the attachment geometry is of interest it may also be considered as a model for other internal structures consisting of non-intersecting plates or decking, for example. It is expected that this asymptotic analysis may be developed further in order to include the dynamics of the internal structure and/or other attachment methods, but for clarity of presentation these details are omitted here. Similarly, for simplicity of exposition a symmetric geometry only is considered here, although with some modification the asymptotic analysis may also be applied to the case of non-symmetric angles of incidence. The leading order asymptotic analysis presented here allows the frequencies of peaks occurring in the scattered sound field to be predicted approximately in terms of the shell parameters and the geometry of the attachment lines. The analysis presented here is not intended to replace detailed numerical results, but to aid their interpretation in terms of wave propagation in the fluid-loaded shell.

II. PROBLEM FORMULATION

In the problem under consideration an infinitely long thin elastic cylindrical shell of radius a , thickness h , Young's modulus E , Poisson's ratio σ , and density ρ_s , is immersed in fluid of density ρ in which the sound speed is c . The shell is empty except for two infinitely long rigid reinforcing plates, representing either structural support or decking, as shown in Fig. 1. A time-harmonic acoustic plane wave of

angular frequency ω ,

$$p_i(r, z, \phi) = e^{i\alpha z} \sum_{n=0}^{\infty} e_n i^n \cos n\phi J_n(\gamma r), \quad (1)$$

in which the time-harmonic factor $\exp(-i\omega t)$ is suppressed, $\alpha = -k \cos \theta_f$, $k = \omega/c$, $\gamma = \sqrt{(k^2 - \alpha^2)} = k \sin \theta_f$, $e_0 = 1$, $e_n = 2$ otherwise, and J_n is the Bessel function of the first kind of order n , is incident on the shell such that the direction of propagation is symmetric with respect to the rigid plates, but is oblique with respect to the axis of the shell, being at angle θ_f to the axis.

The total acoustic pressure in the fluid may be decomposed as

$$p = p_i + p_r + p_e, \quad (2)$$

where

$$p_r = -e^{i\alpha z} \sum_{n=0}^{\infty} e_n i^n \cos n\phi H_n(\gamma r) J'_n(\gamma a) / H'_n(\gamma a), \quad (3)$$

in which H_n is the Hankel function of order n and $'$ denotes differentiation with respect to argument, is the scattered sound field due to a rigid boundary at $r = a$, and

$$p_e(r, z, \phi) = \frac{\rho \omega^2 e^{i\alpha z}}{k \sin \theta_f} \sum_{n=0}^{\infty} u_{rn} \cos n\phi H_n(\gamma r) / H'_n(\gamma a) \quad (4)$$

is the scattered sound associated with radial motion of the shell surface, where the components of the shell displacement have the Fourier series

$$\begin{pmatrix} u_r(z, \phi) \\ u_z(z, \phi) \\ u_\phi(z, \phi) \end{pmatrix} = e^{i\alpha z} \sum_{n=0}^{\infty} \begin{pmatrix} u_{rn} \cos n\phi \\ u_{zn} \cos n\phi \\ u_{\phi n} \sin n\phi \end{pmatrix}. \quad (5)$$

The rigid plates are assumed to be hinged to the shell, hence at the lines where they are attached no moments are transmitted when the shell vibrates, but the total reaction force exerted on the shell may be expressed as

$$\begin{pmatrix} F_r(z, \phi) \\ F_z(z, \phi) \\ F_\phi(z, \phi) \end{pmatrix} = e^{i\alpha z} \sum_{m=1}^4 \begin{pmatrix} F_{rm} \delta(\phi - \phi_m) \\ F_{zm} \delta(\phi - \phi_m) \\ F_{\phi m} \delta(\phi - \phi_m) \end{pmatrix}, \quad (6)$$

where δ denotes the delta function, F_{rm} , F_{zm} , $F_{\phi m}$ denote the radial, axial, and tangential components of the reaction force at $\phi = \phi_m$ and ϕ_m , $m = 1, 2, 3, 4$ are the angular coordinates of the four attachment lines. By using the Fourier series expansion for the δ -function, and noting that in this symmetric problem $F_{r1} = F_{r4}$, $F_{r2} = F_{r3}$, $F_{z1} = F_{z4}$, $F_{z2} = F_{z3}$, $F_{\phi 1} = -F_{\phi 4}$, and $F_{\phi 2} = -F_{\phi 3}$ this may be written

$$\begin{pmatrix} F_r(z, \phi) \\ F_z(z, \phi) \\ F_\phi(z, \phi) \end{pmatrix} = \frac{e^{i\alpha z}}{\pi} \sum_{n=0}^{\infty} e_n \sum_{m=1}^2 \begin{pmatrix} F_{rm} \cos n\phi_m \cos n\phi \\ F_{zm} \cos n\phi_m \cos n\phi \\ F_{\phi m} \sin n\phi_m \sin n\phi \end{pmatrix}. \quad (7)$$

Using the Donnell–Muskhvishvili equations to describe the motion of the shell with the forces driving the motion given by Eqs. (1)–(4) and (7), the equation governing the n th harmonic of the shell displacement is found to be

$$\mathbf{S}(\alpha, n) \begin{pmatrix} u_{rn} \\ u_{zn} \\ u_{\phi n} \end{pmatrix} = \begin{pmatrix} -2ie_n i^n / \pi \gamma a H'_n(\gamma a) \\ 0 \\ 0 \end{pmatrix} + \frac{e_n}{\pi} \sum_{m=1}^2 \begin{pmatrix} F_{rm} \cos n \phi_m \\ F_{zm} \cos n \phi_m \\ F_{\phi m} \sin n \phi_m \end{pmatrix}, \quad (8)$$

where the elements of the dynamic stiffness matrix $\mathbf{S}(\alpha, n)$ for the shell with exterior fluid loading are

$$S_{11} = E_1 [1/a^2 + \beta^2 (a^2 \alpha^4 + 2n^2 \alpha^2 + n^4/a^2)] - \rho_s \omega^2 h + \rho \omega^2 H_n(\gamma a) / \gamma H'_n(\gamma a), \quad (9a)$$

$$S_{12} = E_1 i \alpha \sigma / a, \quad (9b)$$

$$S_{13} = E_1 n / a^2, \quad (9c)$$

$$S_{21} = -S_{12}, \quad (9d)$$

$$S_{22} = E_1 [\alpha^2 + n^2 (1 - \sigma) / 2a^2] - \rho_s \omega^2 h, \quad (9e)$$

$$S_{23} = -E_1 i \alpha n (1 + \sigma) / 2a, \quad (9f)$$

$$S_{31} = S_{13}, \quad (9g)$$

$$S_{32} = -S_{23}, \quad (9h)$$

$$S_{33} = E_1 [\alpha^2 (1 - \sigma) / 2 + n^2 / a^2] - \rho_s \omega^2 h, \quad (9i)$$

where $E_1 = Eh / (1 - \sigma^2)$ and $\beta^2 = h^2 / 12a^2$.

Thus, once the reaction forces are known $(u_{rn}, u_{zn}, u_{\phi n})^T$ is obtained from Eq. (8), and hence the acoustic pressure due to the motion of the shell is calculated from Eq. (4). The unknown reaction forces are determined by considering the motion of the rigid plates.

A. Oblique incidence, $\theta_i \neq 90^\circ$

Along the lines where the shell is attached to the plates the shell displacement is equal to the plate displacement, which may only be that of rigid body motion. Equation (5) shows that the displacement of the shell is everywhere proportional to $\exp(i\alpha z)$. Hence, along the lines $\phi = \phi_1$ and $\phi = \phi_2$ the only possible rigid body motion is zero motion, i.e.,

$$\sum_{n=0}^{\infty} \begin{pmatrix} u_{rn} \cos n \phi_1 \\ u_{zn} \cos n \phi_1 \\ u_{\phi n} \sin n \phi_1 \end{pmatrix} = \sum_{n=0}^{\infty} \begin{pmatrix} u_{rn} \cos n \phi_2 \\ u_{zn} \cos n \phi_2 \\ u_{\phi n} \sin n \phi_2 \end{pmatrix} = \begin{pmatrix} 0 \\ 0 \\ 0 \end{pmatrix}. \quad (10)$$

Equation (8) allows the terms in this summation to be written

$$\begin{pmatrix} u_{rn} \cos n \phi \\ u_{zn} \cos n \phi \\ u_{\phi n} \sin n \phi \end{pmatrix} = \frac{-2ie_n i^n}{\pi \gamma a H'_n(\gamma a)} \begin{pmatrix} S^{-1}(\alpha, n)_{11} \cos n \phi \\ S^{-1}(\alpha, n)_{21} \cos n \phi \\ S^{-1}(\alpha, n)_{31} \sin n \phi \end{pmatrix} + \frac{e_n}{\pi} \sum_{m=1}^2 \mathbf{M}(\alpha, n, m, \phi) \begin{pmatrix} F_{rm} \\ F_{zm} \\ F_{\phi m} \end{pmatrix}, \quad (11)$$

where

$$\mathbf{M}(\alpha, n, m, \phi) = \begin{pmatrix} S^{-1}(\alpha, n)_{11} \cos n \phi_m \cos n \phi & S^{-1}(\alpha, n)_{12} \cos n \phi_m \cos n \phi & S^{-1}(\alpha, n)_{13} \sin n \phi_m \cos n \phi \\ S^{-1}(\alpha, n)_{21} \cos n \phi_m \cos n \phi & S^{-1}(\alpha, n)_{22} \cos n \phi_m \cos n \phi & S^{-1}(\alpha, n)_{23} \sin n \phi_m \cos n \phi \\ S^{-1}(\alpha, n)_{31} \cos n \phi_m \sin n \phi & S^{-1}(\alpha, n)_{32} \cos n \phi_m \sin n \phi & S^{-1}(\alpha, n)_{33} \sin n \phi_m \sin n \phi \end{pmatrix}. \quad (12)$$

Hence, evaluating Eq. (11) at $\phi = \phi_1$ and $\phi = \phi_2$ in turn and performing the infinite summation of Eq. (10) leads to the matrix equation for the reaction forces

$$\mathbf{B} \begin{pmatrix} F_{r1} \\ F_{z1} \\ F_{\phi 1} \\ F_{r2} \\ F_{z2} \\ F_{\phi 2} \end{pmatrix} = \frac{2i}{\gamma a} \sum_{n=0}^{\infty} \frac{e_n i^n}{H'_n(\gamma a)} \begin{pmatrix} S^{-1}(\alpha, n)_{11} \cos n \phi_1 \\ S^{-1}(\alpha, n)_{21} \cos n \phi_1 \\ S^{-1}(\alpha, n)_{31} \sin n \phi_1 \\ S^{-1}(\alpha, n)_{11} \cos n \phi_2 \\ S^{-1}(\alpha, n)_{21} \cos n \phi_2 \\ S^{-1}(\alpha, n)_{31} \sin n \phi_2 \end{pmatrix}, \quad (13)$$

where

$$B_{ij} = \begin{cases} \sum_{n=0}^{\infty} e_n M(\alpha, n, 1, \phi_1)_{ij} & \text{if } i = 1, 2, 3, j = 1, 2, 3 \\ \sum_{n=0}^{\infty} e_n M(\alpha, n, 2, \phi_1)_{i(j-3)} & \text{if } i = 1, 2, 3, j = 4, 5, 6 \\ \sum_{n=0}^{\infty} e_n M(\alpha, n, 1, \phi_2)_{(i-3)j} & \text{if } i = 4, 5, 6, j = 1, 2, 3 \\ \sum_{n=0}^{\infty} e_n M(\alpha, n, 2, \phi_2)_{(i-3)(j-3)} & \text{if } i = 4, 5, 6, j = 4, 5, 6 \end{cases}. \quad (14)$$

Thus the reaction forces, and hence the scattered pressure, may be evaluated by truncating the infinite sums after a suitably large finite number of terms to evaluate the matrix elements and then inverting the resulting matrix equation.

B. Normal incidence, $\theta_f = 90^\circ$

For normal incidence $\alpha = 0$ and the problem becomes independent of the axial coordinate z , and in particular $u_{zn} = 0$ and $F_{zm} = 0$. This permits rigid body motion of the internal plate structure in the propagation direction of the incident wave. Thus in this case the boundary condition (10) at $\phi = \phi_1$ and $\phi = \phi_2$ is modified to

$$\sum_{n=0}^{\infty} \begin{pmatrix} u_{rn} \cos n\phi \\ u_{\phi n} \sin n\phi \end{pmatrix} = U \begin{pmatrix} \cos \phi \\ -\sin \phi \end{pmatrix}, \quad (15)$$

where U is the displacement of the rigid plate structure in the propagation direction of the incident wave, together with another equation obtained by considering the equation of motion of the plates,

$$2 \sum_{m=1}^2 (F_{rm} \cos \phi_m - F_{\phi m} \sin \phi_m) = M \omega^2 U, \quad (16)$$

where M is the mass per unit axial length of the rigid plates. Hence, the equation for determining the reaction forces for normal incidence is

$$\begin{pmatrix} B_{11} & B_{13} & B_{14} & B_{16} & -\cos \phi_1 \\ B_{31} & B_{33} & B_{34} & B_{36} & \sin \phi_1 \\ B_{41} & B_{43} & B_{44} & B_{46} & -\cos \phi_2 \\ B_{61} & B_{63} & B_{64} & B_{66} & \sin \phi_2 \\ -\cos \phi_1 & \sin \phi_1 & -\cos \phi_2 & \sin \phi_2 & \frac{M \omega^2}{2\pi} \end{pmatrix} \times \begin{pmatrix} F_{r1} \\ F_{\phi 1} \\ F_{r2} \\ F_{\phi 2} \\ \pi U \end{pmatrix} = \frac{2i}{\gamma a} \sum_{n=0}^{\infty} \frac{e_n i^n}{H'_n(\gamma a)} \begin{pmatrix} S^{-1}(\alpha, n)_{11} \cos n\phi_1 \\ S^{-1}(\alpha, n)_{31} \sin n\phi_1 \\ S^{-1}(\alpha, n)_{11} \cos n\phi_2 \\ S^{-1}(\alpha, n)_{31} \sin n\phi_2 \\ 0 \end{pmatrix}. \quad (17)$$

This somewhat artificial mathematical distinction between normal and oblique incidence arises from the idealized concept of a completely rigid internal structure. In practice the internal structure will not be completely rigid and the behavior of the system will be continuous as θ_f passes through 90° . However, the analysis and interpretation of the behavior of the idealized structure should provide a reasonable approximation to that of a very stiff structure.

III. HEAVY FLUID LOADING ASYMPTOTIC ANALYSIS

Sums of the type needed to calculate the elements of the matrix \mathbf{B} have been evaluated asymptotically in the limit of heavy fluid loading. Heavy fluid loading means that $\alpha_1 \gg \alpha_0$ and $\alpha_1 \gg k$, where

$$\alpha_1 = (\rho \omega^2 / D)^{1/5}, \quad (18)$$

$$\alpha_0 = (\rho_s \omega^2 h / D)^{1/4}, \quad (19)$$

$$D = E_1 \beta^2 a^2, \quad (20)$$

and D is the bending stiffness of an equivalent elastic plate with the same thickness as the shell, α_1 is the free wave number of such a plate with fluid loading and α_0 is the free wave number of the plate *in vacuo*. The heavy fluid loading conditions are therefore satisfied, for example, over a range of low frequencies for steel shells of practical thicknesses in water. Skelton²¹ has shown that for \mathbf{A} defined as

$$\mathbf{A}(\alpha, \phi) = \sum_{n=0}^{\infty} e_n \times \begin{pmatrix} S_{11}^{-1} \cos n\phi & S_{12}^{-1} \cos n\phi & -S_{13}^{-1} \sin n\phi \\ S_{21}^{-1} \cos n\phi & S_{22}^{-1} \cos n\phi & -S_{23}^{-1} \sin n\phi \\ S_{31}^{-1} \sin n\phi & S_{32}^{-1} \sin n\phi & S_{33}^{-1} \cos n\phi \end{pmatrix} \quad (21)$$

the leading order terms in the asymptotic expansion of the elements of \mathbf{A} in the heavy fluid-loading limit are

$$A_{11}(\alpha, \phi) \sim \begin{cases} -\frac{2\pi a}{5D\alpha_2^3} \left\{ \cot\left(\frac{2\pi}{5}\right) + \cot(\pi\alpha_2 a) \right\} & \text{if } |\phi| = 0, 2\pi, 4\pi, \dots, \\ -\frac{2\pi a}{5D\alpha_2^3} \frac{\cos((\pi - |\phi|)\alpha_2 a)}{\sin(\pi\alpha_2 a)} & \text{if } |\phi| < 2\pi, \phi \neq 0, \end{cases} \quad \text{as } \alpha_1 a \rightarrow \infty, \quad (22)$$

$$A_{12}(\alpha, \phi) \sim O\left(\frac{\ln(\alpha_1 a)}{(\alpha_1 a)^5}\right) \sim A_{21}(\alpha, \phi) \quad \text{as } \alpha_1 a \rightarrow \infty. \quad (23)$$

$$A_{13}(\alpha, \phi) = -A_{31}(\alpha, \phi) \begin{cases} \equiv 0 & \text{if } |\phi| = 0, 2\pi, 4\pi, \dots, \\ \sim \frac{2\pi}{5D\alpha_2^4} \text{sign}(\phi) \frac{\sin((\pi - |\phi|)\alpha_2 a)}{\sin(\pi\alpha_2 a)} & \text{if } |\phi| < 2\pi, \phi \neq 0, \end{cases} \quad \text{as } \alpha_1 a \rightarrow \infty, \quad (24)$$

$$A_{22}(\alpha, \phi) \begin{cases} \sim \frac{\pi/(1+\sigma)}{\rho_s \omega^2 h} \left\{ \frac{(2P^2 - (1-\sigma)Q^2)}{P} \frac{\cos P_2(\pi - |\phi|)}{\sin \pi P_2} - Q(1+\sigma) \frac{\cos Q_2(\pi - |\phi|)}{\sin \pi Q_2} \right\}, & |\phi| \leq 2\pi, \\ \alpha \neq 0 \text{ as } \alpha_1 a \rightarrow \infty, \\ \equiv -\frac{\pi Q \cos Q(\pi - |\phi|)}{\rho_s \omega^2 h \sin \pi Q}, & \alpha = 0, \end{cases} \quad (25)$$

$$A_{23}(\alpha, \phi) = A_{32}(\alpha, \phi) \begin{cases} \equiv 0 & \text{if } |\phi| = 0, 2\pi, \dots, \\ \sim \frac{i\alpha a \pi \operatorname{sign}(\phi)}{\rho_s \omega^2 h} \left\{ \frac{\sin P_2(\pi - |\phi|)}{\sin P_2 \pi} - \frac{\sin Q_2(\pi - |\phi|)}{\sin Q_2 \pi} \right\} & \text{if } |\phi| < 2\pi, \quad \phi \neq 0, \end{cases} \quad \text{as } \alpha_1 a \rightarrow \infty, \quad (26)$$

$$A_{33}(\alpha, \phi) \sim \frac{\pi}{\rho_s \omega^2 h} \frac{1 - \sigma}{1 + \sigma} \left\{ \frac{(R^2 - Q^2) \cos Q_2(\pi - |\phi|)}{Q \sin \pi Q_2} + \frac{(P^2 - R^2) \cos P_2(\pi - |\phi|)}{P \sin \pi P_2} \right\}, \quad |\phi| \leq 2\pi \quad \text{as } \alpha_1 a \rightarrow \infty, \quad (27)$$

where α_2 is a more accurate value for the component in the “tangential” direction of the free wave number in the fluid-loaded plate and $x = \alpha_2 a$ is the positive real root of the quintic polynomial

$$x((x^2 + \alpha^2 a^2)^2 - (\alpha_0 a)^4) - (\alpha_1 a)^5 = 0, \quad (28)$$

$$P^2 = a^2(\rho_s \omega^2 h / E_1 - \alpha^2), \quad (29)$$

$$Q^2 = a^2(2\rho_s \omega^2 h / E_1(1 - \sigma) - \alpha^2), \quad (30)$$

$$R^2 = a^2(2\rho_s \omega^2 h / E_1 - 2\alpha^2) / (1 - \sigma), \quad (31)$$

and P_2 and Q_2 are more accurate values for the poles of S_{22}^{-1} , which include $O(1/\rho)$ corrections to the first order approximations, P and Q ,

$$P_2 \sim P - F(\alpha, P) / 2PE_1^2(1 - \sigma)(P^2 - Q^2)S_{11}(\alpha, P), \quad (32)$$

$$Q_2 \sim Q + F(\alpha, Q) / 2QE_1^2(1 - \sigma)(P^2 - Q^2)S_{11}(\alpha, Q), \quad (33)$$

where

$$F(\alpha, n) = S_{13}(S_{21}S_{32} - S_{22}S_{33}) - S_{12}(S_{21}S_{33} - S_{23}S_{31}). \quad (34)$$

It is straightforward to express the elements of the matrix \mathbf{B} in terms of the elements of \mathbf{A} . Thus, taking into account the symmetries of this problem and retaining only terms of order up to $(1/\alpha_1 a)^3$, the matrix \mathbf{B} may be approximated in the heavy fluid-loading limit as

$$\mathbf{B} = \frac{1}{2} \begin{pmatrix} B_{11} & 0 & 0 & B_{14} & 0 & 0 \\ 0 & B_{22} & B_{23} & 0 & B_{25} & B_{26} \\ 0 & -B_{23} & B_{33} & 0 & B_{26} & B_{36} \\ B_{14} & 0 & 0 & B_{11} & 0 & 0 \\ 0 & B_{25} & -B_{26} & 0 & B_{22} & -B_{23} \\ 0 & -B_{26} & B_{36} & 0 & B_{23} & B_{33} \end{pmatrix} + O\left(\frac{1}{(\alpha_1 a)^4}\right) \quad (35)$$

in which

$$B_{11} = A_{11}(\alpha, 0) + A_{11}(\alpha, 2\phi_1), \quad (36)$$

$$B_{14} = A_{11}(\alpha, 2\phi_1 - \pi) + A_{11}(\alpha, \pi), \quad (37)$$

$$B_{22} = A_{22}(\alpha, 0) + A_{22}(\alpha, 2\phi_1), \quad (38)$$

$$B_{23} = -A_{23}(\alpha, 2\phi_1), \quad (39)$$

$$B_{25} = A_{22}(\alpha, 2\phi_1 - \pi) + A_{22}(\alpha, \pi), \quad (40)$$

$$B_{26} = A_{23}(\alpha, 2\phi_1 - \pi), \quad (41)$$

$$B_{33} = A_{33}(\alpha, 0) - A_{33}(\alpha, 2\phi_1), \quad (42)$$

$$B_{36} = A_{33}(\alpha, 2\phi_1 - \pi) - A_{33}(\alpha, \pi), \quad (43)$$

in which the heavy fluid-loading approximations to the elements of \mathbf{A} given by Eqs. (22)–(27) are now to be used. Hence, in the heavy fluid-loading limit, Eq. (13) may be rearranged as

$$\begin{pmatrix} B_{11} & B_{14} \\ B_{14} & B_{11} \end{pmatrix} \begin{pmatrix} F_{r1} \\ F_{r2} \end{pmatrix} = \frac{4i}{\gamma a} \sum_{n=0}^{\infty} \frac{e_n i^n \cos n \phi_1 S^{-1}(\alpha, n)_{11}}{H'_n(\gamma a)} \times \begin{pmatrix} 1 \\ (-1)^n \end{pmatrix} = \begin{pmatrix} X_1 \\ X_2 \end{pmatrix}, \quad (44)$$

together with

$$\begin{pmatrix} B_{22} & B_{23} & B_{25} & B_{26} \\ -B_{23} & B_{33} & B_{26} & B_{36} \\ B_{25} & -B_{26} & B_{22} & -B_{23} \\ -B_{26} & B_{36} & B_{23} & B_{33} \end{pmatrix} \begin{pmatrix} F_{z1} \\ F_{\phi1} \\ F_{z2} \\ F_{\phi2} \end{pmatrix} = \frac{4i}{\gamma a} \sum_{n=0}^{\infty} \frac{e_n i^n}{H'_n(\gamma a)} \begin{pmatrix} S^{-1}(\alpha, n)_{21} \cos n \phi_1 \\ S^{-1}(\alpha, n)_{31} \sin n \phi_1 \\ S^{-1}(\alpha, n)_{21} (-1)^n \cos n \phi_1 \\ -S^{-1}(\alpha, n)_{31} (-1)^n \sin n \phi_1 \end{pmatrix}, \quad (45)$$

in which the equations for the radial forces have been decoupled from those for the axial and tangential forces to leading order. The elements B_{13} , B_{16} , B_{31} , B_{34} , B_{43} , B_{46} , B_{61} , and B_{64} , which are $O(1/(\alpha_1 a)^4)$ and have been neglected in obtaining Eqs. (44) and (45), are in general nonzero and hence provide a small amount of coupling between the radial and the axial and circumferential equations.

Since in the heavy fluid-loading limit the terms in the matrices on the right-hand side of Eqs. (44) and (45) are all of order $O(1/(\alpha_1 a)^5)$ as $\alpha_1 a \rightarrow \infty$ and the elements X_1 and X_2 in Eq. (44) are of order $O(1/(\alpha_1 a)^3)$ and the elements of the vector on the left-hand side of Eq. (45) are $O(1)$ it is clear that, unless the matrices are singular, the radial forces exhibit $O(1/(\alpha_1 a)^2)$ behavior, and the tangential and axial forces exhibit $O(1/(\alpha_1 a)^5)$ behavior. In addition, since A_{11} is $O(1/(\alpha_1 a)^3)$, A_{12} is $O(\ln(\alpha_1 a)/(\alpha_1 a)^5)$, and A_{13} is $O(1/(\alpha_1 a)^4)$ the component of the radial displacement due to these radial reaction forces is $O(1/(\alpha_1 a)^5)$, that due to the axial reaction forces is $O(\ln(\alpha_1 a)/(\alpha_1 a)^{10})$, and that due to the tangential reaction forces is $O(1/(\alpha_1 a)^9)$. Hence, unless the matrices on the left-hand side of Eq. (44) and (45) are

singular the dominant contribution to the radial displacement of the shell, and the scattered pressure attributable to the presence of the rigid plates, is that from the radial reaction forces. Thus, some very narrow peaks in the scattered field may be expected when the determinant of the matrix in Eq. (45) is zero, i.e., when

$$[(B_{25}-B_{22})(B_{36}+B_{33})-(B_{23}+B_{26})^2] \times [(B_{25}+B_{22})(B_{36}-B_{33})-(B_{23}-B_{26})^2]=0, \quad (46)$$

but with even a very small amount of damping included in the problem the level of such peaks will be small compared to the scattering due to the radial reaction forces and not many such peaks may be expected to be observed. This equation will not be investigated further here. As the main contribution to the scattered sound due to the plates is expected to be due to the radial reaction forces, Eq. (44) is investigated further. Thus it is found that to leading order

$$F_{r1}+F_{r2}=(X_1+X_2)/(B_{11}+B_{14}), \quad (47)$$

$$F_{r1}-F_{r2}=(X_1-X_2)/(B_{11}-B_{14}). \quad (48)$$

The combination of radial reaction forces in Eq. (47) is that which occurs as the forcing term in Eq. (8) for even harmonics, and the combination in Eq. (48) is that which occurs for odd harmonics. Hence, for even harmonics peaks will occur in the scattered sound field due to the rigid plates at frequencies whose leading order approximation is obtained from

$$B_{11}+B_{14}=0, \quad (49)$$

and for odd harmonics the frequencies are obtained from

$$B_{11}-B_{14}=0. \quad (50)$$

The conditions for peaks in the scattered sound field, Eqs. (49) and (50) may be interpreted in terms of the receptance of the fluid-loaded cylindrical shell in the heavy fluid-loading limit.²¹ The asymptotic approximations Eqs. (22)–(24) for the receptance indicate that when a radial line force with $e^{i\alpha z}$ variation is applied to the shell at $\phi=0$ it excites, to leading order, radial motion in the shell in the form of a disturbance which decays with distance from the application line together with flexural waves which propagate helically around the shell with the same wavenumber as in an elastic plate of the same thickness with heavy fluid loading, and

whose propagation direction makes the angle $\tan^{-1}(\alpha_2/\alpha)$ to the axis of the shell. As the fluid loading is heavy the decaying disturbance is only significant very close to the application line. Interference between the two propagating helical waves leads to a circumferential standing wave pattern with nodes when $|\phi|a$ is an odd number of $\frac{1}{4}$ circumferential wavelengths, and to large displacement amplitudes elsewhere when a whole number of half circumferential wavelengths fit around the shell circumference.

By considering radial line forces \tilde{F}_{r1} and \tilde{F}_{r2} acting on the shell, as in this scattering problem, it is clear that if these forces *alone* are such that they produce no radial displacement at ϕ_1 and ϕ_2 then neither will their multiples and hence large amplitude reaction forces are possible which can excite large amplitude shell vibrations at other circumferential locations and hence large scattering amplitudes. The conditions for this to occur are

$$\begin{aligned} \tilde{F}_{r1}A_{11}(\alpha,0)+\tilde{F}_{r1}A_{11}(\alpha,2\phi_1) \\ +\tilde{F}_{r2}A_{11}(\alpha,\pi-2\phi_1)+\tilde{F}_{r2}A_{11}(\alpha,\pi)=0, \end{aligned} \quad (51)$$

$$\tilde{F}_{r1}A_{11}(\alpha,\pi-2\phi_1)+\tilde{F}_{r1}A_{11}(\alpha,\pi)$$

$$+\tilde{F}_{r2}A_{11}(\alpha,0)+\tilde{F}_{r2}A_{11}(\alpha,2\phi_1)=0.$$

Adding and subtracting these equations leads to the equivalent formulation

$$\begin{aligned} (\tilde{F}_{r1}+\tilde{F}_{r2})\{A_{11}(\alpha,0)+A_{11}(\alpha,2\phi_1) \\ +A_{11}(\alpha,\pi-2\phi_1)+A_{11}(\alpha,\pi)\}=0, \\ (\tilde{F}_{r1}-\tilde{F}_{r2})\{A_{11}(\alpha,0)+A_{11}(\alpha,2\phi_1) \\ -A_{11}(\alpha,\pi-2\phi_1)-A_{11}(\alpha,\pi)\}=0, \end{aligned} \quad (52)$$

from which it may be deduced that for even harmonics, for which $\tilde{F}_{r1}+\tilde{F}_{r2}$ is nonzero, the condition for peaks in the scattered field is $B_{11}+B_{14}=0$, while for odd harmonics for which $\tilde{F}_{r1}-\tilde{F}_{r2}$ is nonzero, the condition for peaks in the scattered field is $B_{11}-B_{14}=0$.

A. Even harmonics

Equations (36), (37), and (22) allow $B_{11}+B_{14}$ to be written, after some algebraic manipulation, as

$$B_{11}+B_{14}=\frac{-2\pi a\left\{\sin\left(\frac{\pi\alpha_2 a}{2}+\frac{2\pi}{5}\right)+\sin\left(\frac{2\pi}{5}\right)\cos\left((\pi-4\phi_1)\frac{\alpha_2 a}{2}\right)\right\}}{5D\alpha_2^3\sin\left(\frac{\pi\alpha_2 a}{2}\right)\sin\left(\frac{2\pi}{5}\right)}. \quad (53)$$

Hence, for the even harmonics peaks occur when

$$\sin(\lambda+2\pi/5)=-\sin(2\pi/5)\cos((1-4\phi_1/\pi)\lambda) \quad (54)$$

provided that

$$\sin\lambda\neq 0, \quad (55)$$

where $\lambda=\pi\alpha_2 a/2$. For a given value of ϕ_1 values for λ and thus for $\alpha_2 a$ may be found by solving this equation. Some examples of the solutions for λ for particular values of ϕ_1 are given below. The leading order approximation for the frequencies for the peaks are determined by substituting these particular values for $\alpha_2 a$ into Eq. (28), regarding it as

a quadratic equation for ω^2 , whose solution is therefore known explicitly.

1. Solutions for λ when $\phi_1=45^\circ$, perpendicular plates

For perpendicular plates $\phi_1 = \pi/4$ and Eq. (54) reduces to

$$\sin(\lambda + 2\pi/5) = -\sin(2\pi/5), \quad (56)$$

whose solutions are thus known exactly. Those for which $\sin \lambda \neq 0$ are

$$\lambda = (2m+1)\pi + \pi/5, \quad m=0,1,2,\dots \quad (57)$$

2. Solutions for λ when $\phi_1=30^\circ$

When $\phi_1 = \pi/6$ Eq. (54) reduces to

$$\sin(3\psi + 2\pi/5) = -\sin(2\pi/5)\cos(\psi), \quad (58)$$

where $\lambda = 3\psi$, which may be expanded, making use of trigonometric identities, to a cubic equation for $\tan \psi$.

$$B_{11} - B_{14} = \frac{-2\pi a \left\{ \cos\left(\frac{\pi\alpha_2 a}{2} + \frac{2\pi}{5}\right) - \sin\left(\frac{2\pi}{5}\right) \sin\left((\pi - 4\phi_1) \frac{\alpha_2 a}{2}\right) \right\}}{5D\alpha_2^3 \cos\left(\frac{\pi\alpha_2 a}{2}\right) \sin\left(\frac{2\pi}{5}\right)}. \quad (61)$$

Hence, for the odd harmonics peaks occur when

$$\cos(\lambda + 2\pi/5) = \sin(2\pi/5)\sin((1 - 4\phi_1/\pi)\lambda) \quad (62)$$

provided that

$$\cos \lambda \neq 0. \quad (63)$$

1. Solutions for λ when $\phi_1=45^\circ$, perpendicular plates

For perpendicular plates $\phi_1 = \pi/4$ and Eq. (62) reduces to

$$\cos(\lambda + 2\pi/5) = 0, \quad (64)$$

whose solutions are thus known exactly as

$$\lambda = m\pi + \pi/10, \quad m=0,1,2,\dots \quad (65)$$

2. Solutions for λ when $\phi_1=30^\circ$

When $\phi_1 = \pi/6$ Eq. (62) reduces to

$$\cos(3\psi + 2\pi/5) = \sin(2\pi/5)\sin(\psi), \quad (66)$$

which, after making use of trigonometric identities and noting that the required solutions must have nonzero values for $\cos \psi$ in order to satisfy Eq. (63), is equivalent to the equation

$$\cos(2\pi/5)(1 - 3\tan^2\psi) = 4\sin(2\pi/5)\tan\psi. \quad (67)$$

Equation (67) is a quadratic equation for $\tan \psi$, whose two solutions, $\tan \psi_4$ and $\tan \psi_5$ are

$$\tan \psi_{4,5} = (-2\tan(2\pi/5) \pm \sqrt{4\tan^2(2\pi/5) + 3})/3. \quad (68)$$

Hence the solutions for λ in this case are

$$\tan \psi(3 - \tan^2 \psi)\cos(2\pi/5) = -2\sin(2\pi/5)(1 - \tan^2 \psi). \quad (59)$$

This has three real roots, $\tan \psi_1$, $\tan \psi_2$, $\tan \psi_3$, say, and hence, writing $\lambda_j = 3\psi_j$, the solutions for λ are

$$\lambda = \lambda_j + 3m\pi, \quad j=1,2,3, \quad m=0,1,2,\dots \quad (60)$$

3. Solutions for λ when $\phi_1=60^\circ$

When $\phi_1 = \pi/3$ Eq. (54) again reduces to Eq. (58) and hence the solutions for λ are also given by Eq. (60) in this case.

B. Odd harmonics

Equations (36), (37), and (22) allow $B_{11}-B_{14}$ to be written, after some algebraic manipulation, as

$$\lambda = \begin{cases} 3m\pi + \lambda_4, \\ 3m\pi + \lambda_5, \end{cases} \quad m=0,1,2,\dots \quad (69)$$

3. Solutions for λ when $\phi_1=60^\circ$

When $\phi_1 = \pi/3$ Eq. (62) reduces to

$$\cos(3\psi + 2\pi/5) = -\sin(2\pi/5)\sin(\psi), \quad (70)$$

which, reduces to a cubic equation for $\tan \psi$

$$1 - 3\tan^2 \psi = 2\tan(2\pi/5)\tan \psi(1 - \tan^2 \psi). \quad (71)$$

The substitution $\psi = \pi/2 + \psi'$ allows this equation to be rewritten as

$$\tan \psi'(3 - \tan^2 \psi')\cos(2\pi/5) = -2\sin(2\pi/5)(1 - \tan^2 \psi'), \quad (72)$$

which is Eq. (59) rewritten with variable ψ' . Hence the solutions for λ in this case are related to those obtained for the even harmonics for $\phi_1 = \pi/6$:

$$\lambda = \lambda_j + 3\pi/2 + 3m\pi, \quad j=1,2,3, \quad m=0,1,2,\dots \quad (73)$$

IV. NUMERICAL RESULTS

Fortran computer programs have been written to calculate the reaction forces from Eq. (13) and the total far-field scattered pressure from Eqs. (3), (4), (8), and the large argument asymptotic form of the Hankel function. Figures 2 and 3 show results obtained for a steel cylindrical shell, $E = 19.5 \times 10^{10}$, $\sigma = 0.29$, $\rho_s = 7700$, of radius $a = 5$, and thickness $h = 0.05$, immersed in water, $\rho = 1000$, $c = 1500$. In

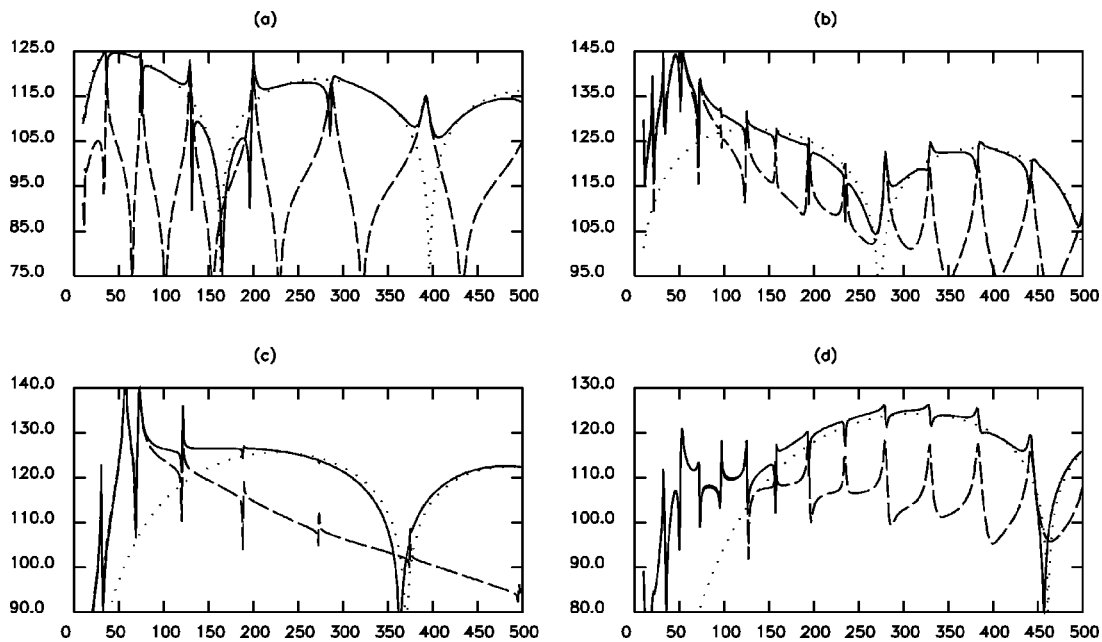


FIG. 2. Far-field scattered pressure (dB) as a function of frequency (Hz) for a plane wave incident at 45° to steel cylindrical shell of radius 5 m, thickness 0.05 m with perpendicular internal plates, $\phi_1=45^\circ$, in water. (a) $n=0$ harmonic, (b) $n=1$ harmonic, (c) $n=2$ harmonic, (d) $n=3$ harmonic. —, total scattered field; ---, scattering due to reaction forces only, ···, scattering by unstiffened shell.

each graph shown the incident plane wave propagates at 45° to the axis of the shell, $\theta_f = \pi/4$. These figures show the total scattered field in particular circumferential harmonics, n , using a dB scale, where the quantity plotted as a solid line is

$$20 \log_{10} \left[\lim_{r \rightarrow \infty} |r^{1/2} (p_{rn} + p_{en})| \right] + 120,$$

and on the same scale the component of the scattered field attributable to the presence of the internal rigid plates is shown as a broken line and that attributable to scattering by the unstiffened shell is shown as a dotted line. In all of the

calculations, the infinite summation which occurs in Eq. (13) is approximated by its first 200 terms. The frequency range shown in each of the figures is 10–500 Hz, with results calculated at intervals of 1 Hz. This is contained within the frequency range for which the heavy fluid-loading asymptotic results (22)–(27) are appropriate.²¹

Figure 2 shows results for (a) $n=0$ harmonic, (b) $n=1$ harmonic, (c) $n=2$ harmonic, and (d) $n=3$ harmonic for perpendicular internal plates, $\phi_1=45^\circ$. In Figs. 2(a), (b), and (d) the field due to the internal plates consists of several

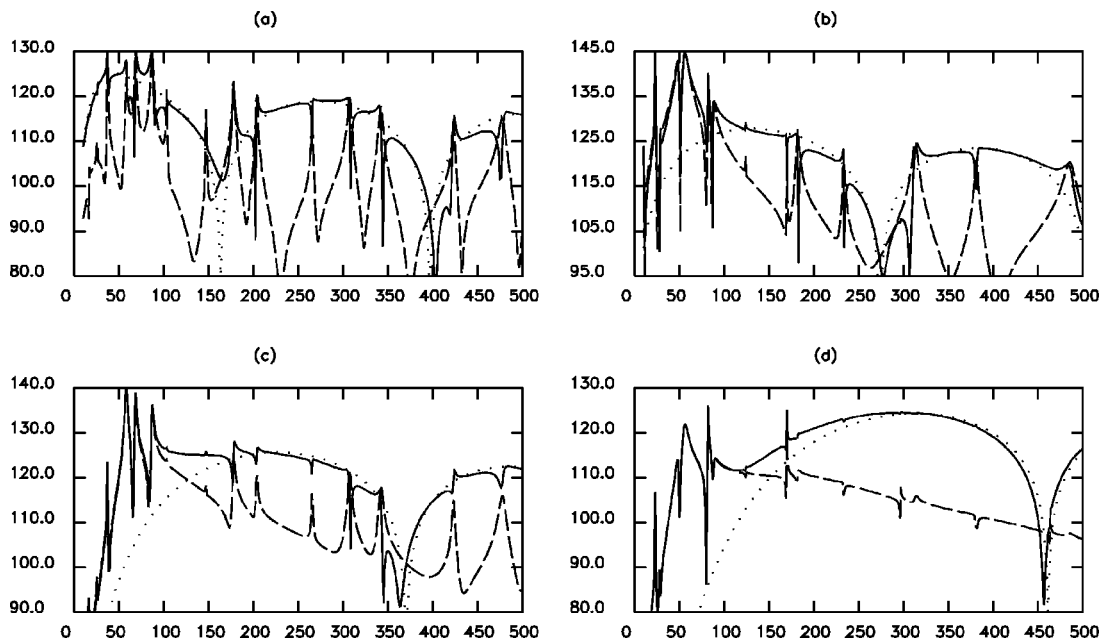


FIG. 3. Far-field scattered pressure (dB) as a function of frequency (Hz) for a plane wave incident at 45° to steel cylindrical shell of radius 5 m, thickness 0.05 m with internal plates, $\phi_1=30^\circ$, in water. (a) $n=0$ harmonic, (b) $n=1$ harmonic, (c) $n=2$ harmonic, (d) $n=3$ harmonic. —, total scattered field, ---, scattering due to reaction forces only, ···, scattering by unstiffened shell.

wide peaks whose effects can also be observed when combined with the scattered field due to a rigid surface and an unconstrained elastic surface in the total field. The frequencies of the peaks for the $n=1$ harmonic coincide with those for the $n=3$ harmonic, but not those of the $n=0$ harmonic. There are twice as many peaks for the $n=1$ or $n=3$ harmonics as there are for the $n=0$ harmonic. Similar wide peaks are however absent from the $n=2$ harmonic. The scattering due to the internal plates is much less than that of the unconstrained shell at frequencies above about 100 Hz. There are a few very narrow peaks but their magnitude does not greatly affect the total scattered field. From Eq. (8) it is clear that only the circumferential reaction forces contribute to the shell displacement for the $n=2$ harmonic. These are known to have a smaller effect on the sound field than the radial forces, and have not been further investigated here. The features of Fig. 2 noted above are thus in qualitative agreement with the results (57) and (65) obtained by asymptotic analysis for the heavy fluid-loading limit. From the leading order theory, Eq. (57) predicts peaks for the $n=0$ harmonic at 35, 73, 127, 196, 283, and 387 Hz when $\theta_f = \pi/4$. For the odd harmonics when $\theta_f = \pi/4$, Eq. (65) predicts peaks at 20, 33, 50, 71, 95, 123, 156, 192, 233, 278, 327, 381, and 440 Hz. There is thus also good qualitative agreement with the numerical results presented in Fig. 2, with most predicted frequencies within 2 Hz of the values obtained numerically. Including extra terms in Eq. (28) to determine α_2 more accurately or including a correction term to take account of the small amount of coupling between the equations for the radial forces and the axial and circumferential forces, noted after Eq. (45), may reduce this discrepancy further.

Figure 3 shows corresponding results for the same cylindrical shell when the internal plates are no longer perpendicular, but have $\phi_1 = 30^\circ$. In Figs. 3(a), (b), and (c) the field attributable to the internal plates consists of several fairly wide peaks whose presence can be observed in the plots of the total scattered field. The frequencies of the peaks for the $n=0$ harmonic coincide with those of the $n=2$ harmonic, but not those of the $n=1$ harmonic. In a frequency interval with approximately two wide peaks for the $n=1$ harmonic, the $n=0$ and $n=2$ harmonics each exhibit approximately three wide peaks. The number of peaks for the $n=0$ or $n=2$ harmonics when $\phi_1 = \pi/6$ is approximately twice the number for the $n=0$ harmonic when $\phi_1 = \pi/4$. The number of peaks for the $n=1$ harmonic when $\phi_1 = \pi/6$ is approximately $2/3$ of the number of peaks for the $n=1$ or $n=3$ harmonics when $\phi_1 = \pi/4$. For the $n=3$ harmonic significant wide peaks are absent. From Eq. (8) it is clear that when $\phi_1 = \pi/6$, only the circumferential component of the reaction forces contributes to the shell excitation for the $n=3$ harmonic. These are expected to have a smaller effect than the radial forces and have not been investigated here. However, some peaks of relatively small magnitude can be observed in Fig. 3(d), at the same frequencies as those observed for the $n=1$ harmonic in Fig. 3(b). This is due to the small amount of coupling, noted after Eq. (45), between the equations for the radial forces and the axial and circumferential forces, which was neglected in the analysis above, but if included may lead to a peak of small magnitude in the axial and cir-

cumferential forces at frequencies primarily associated with peaks of the radial forces. The features noted above are thus in qualitative agreement with Eqs. (60) and (69) for $\phi_1 = \pi/6$ and Eqs. (57) and (65) for $\phi_1 = \pi/4$. When $\phi_1 = \pi/6$ and $\theta_f = \pi/4$ Eq. (60) predicts peaks for the $n=0$ and $n=2$ harmonics at 17, 27, 37, 65, 84, 102, 146, 175, 202, 265, 304, 340, 423, and 474 Hz. Equation (69) predicts peaks for the $n=1$ harmonic at 28, 50, 86, 123, 178, 232, 308, 380, and 479 Hz. Thus there is good qualitative agreement between the asymptotic results for heavy fluid-loading and the numerical results presented in Fig. 3.

V. CONCLUDING REMARKS

The presence of internal rigid stiffening plates or decking in an elastic cylindrical shell results in constraints at the attachment points, and has a significant effect on the scattered sound field. Numerical results from the formulation presented here show that this results in a number of peaks in the scattered sound field as a function of frequency. Asymptotic analysis in the heavy fluid-loading limit, which is appropriate to many practical underwater structures over a significant range of low frequencies allows these peak frequencies to be predicted. In this range of parameters the most significant scattering due to the constraints is that due to the radial reaction forces. For a particular stiffened elastic shell peaks in the scattered field occur, to leading order, at the same frequencies for all the even circumferential harmonics. Similarly, to leading order, for all the odd circumferential harmonics the peaks in the scattered field occur at the same frequencies, but different from those for the even harmonics.

- ¹E. S. Reddy and A. K. Mallik, "Response of and sound radiation from a layered cylinder with regular axial stiffeners," *J. Sound Vib.* **103**, 519–531 (1985).
- ²D. J. Mead and N. S. Bardell, "Free vibration of a thin cylindrical shell with discrete axial stiffeners," *J. Sound Vib.* **111**, 229–250 (1986).
- ³J. Bjarnason, J. D. Achenbach, and T. Igusa, "Acoustic radiation from a cylindrical shell with an internal plate," *Wave Motion* **15**, 23–41 (1992).
- ⁴L. B. Felsen and Y. P. Guo, "Hybrid ray-mode parameterization of acoustic scattering from submerged thin elastic shells with interior loading," *J. Acoust. Soc. Am.* **94**, 888–895 (1993).
- ⁵Y. P. Guo and L. B. Felsen, "Wave-number spectrum and normal-mode solutions for sound-scattering from internally loaded cylindrical shells," *J. Acoust. Soc. Am.* **94**, 896–899 (1993).
- ⁶A. Klauson and J. Metsaveer, "Sound scattering by a cylindrical shell reinforced by lengthwise ribs and walls," *J. Acoust. Soc. Am.* **91**, 1834–1843 (1992).
- ⁷A. Klauson, G. Maze, and J. Metsaveer, "Acoustic scattering by submerged cylindrical shell stiffened by an internal lengthwise rib," *J. Acoust. Soc. Am.* **96**, 1575–1581 (1994).
- ⁸A. Klauson, J. Metsaveer, D. Décultot, G. Maze, and J. Ripoché, "Identification of the resonances of a cylindrical shell stiffened by an internal lengthwise rib," *J. Acoust. Soc. Am.* **100**, 3135–3143 (1996).
- ⁹A. Baillard, J. M. Conoir, D. Décultot, G. Maze, A. Klauson, and J. Metsaveer, "Acoustic scattering from fluid-loaded stiffened cylindrical shell: Analysis using elasticity theory," *J. Acoust. Soc. Am.* **107**, 3208–3216 (2000).
- ¹⁰Y. P. Guo, "Sound scattering from an internally loaded cylindrical shell," *J. Acoust. Soc. Am.* **91**, 926–938 (1992).
- ¹¹Y. P. Guo, "Sound scattering from cylindrical shells with internal elastic plates," *J. Acoust. Soc. Am.* **93**, 1936–1946 (1993).
- ¹²Y. P. Guo, "Acoustic radiation from cylindrical shells due to internal forcing," *J. Acoust. Soc. Am.* **99**, 1495–1505 (1996).
- ¹³Y. P. Guo, "Acoustic scattering from cylindrical shells with deck-type internal plate at oblique incidence," *J. Acoust. Soc. Am.* **99**, 2701–2713 (1996).

- ¹⁴J. E. Bondaryk and H. Schmidt, "Array processing for the analysis of stiffened, fluid-loaded cylindrical shells," *J. Acoust. Soc. Am.* **97**, 1067–1077 (1995).
- ¹⁵R. C. Loftman and D. B. Bliss, "Analytical/numerical matching for efficient calculation of scattering from cylindrical shells with lengthwise constraints," *J. Acoust. Soc. Am.* **103**, 1885–1896 (1998).
- ¹⁶F. G. Leppington, "Acoustic scattering by membranes and plates with line constraints," *J. Sound Vib.* **58**, 319–332 (1978).
- ¹⁷I. D. Abrahams, "Scattering of sound by a heavily fluid-loaded finite elastic plate," *Proc. R. Soc. London, Ser. A* **378**, 89–117 (1981).
- ¹⁸S. G. L. Smith and R. V. Craster, "Numerical and asymptotic approaches to scattering problems involving finite elastic plates in structural acoustics," *Wave Motion* **30**, 17–41 (1999).
- ¹⁹J. B. Lawrie, "Vibrations of a heavily fluid-loaded semi-infinite cylindrical elastic shell II," *Proc. R. Soc. London, Ser. A* **414**, 371–387 (1987).
- ²⁰E. A. Skelton, "Acoustic scattering by a disk or annulus linking two concentric cylindrical shells, part II: results for heavy exterior fluid-loading on both shells," *J. Sound Vib.* **154**, 221–248 (1992).
- ²¹E. A. Skelton, "Line force receptance of an elastic cylindrical shell with heavy exterior fluid-loading," *J. Sound Vib.* **256**, 131–153 (2002).

Leaky helical flexural wave backscattering contributions from tilted water-filled cylindrical shells

Florian J. Blonigen^{a)} and Philip L. Marston^{b)}

Department of Physics, Washington State University, Pullman, Washington 99164-2814

(Received 11 July 2002; revised 24 September 2002; accepted 7 October 2002)

Helical flexural waves on a bluntly truncated tilted water-filled cylindrical steel shell in water are found to give large contributions to the backscattering above the coincidence frequency. The presence of the water inside the shell increases the damping of the leaky wave when short tone bursts are used. The magnitude of the scattering is found by modifying a ray analysis developed for empty shells. When longer bursts are used, some of the internally radiated energy (corresponding to the case of one internal chord) is superposed on the ordinary helical ray backscattering. This occurs as a consequence of the internal excitation of helical rays. © 2003 Acoustical Society of America. [DOI: 10.1121/1.1526471]

PACS numbers: 43.40.Fz, 43.30.Gv, 43.20.Fn [ANN]

I. INTRODUCTION

Simple approximations to the scattering by penetrable truncated cylinders have long been of general interest.¹ Recent work has shown that leaky helical flexural waves contribute significantly to the high-frequency backscattering by tilted empty cylindrical truncated shells in water.²⁻⁵ In this letter, we report observations of related backscattering contributions from *water-filled* cylindrical shells where the helical wave scattering mechanisms and amplitudes are modified by the presence of the fluid interior. A simple approximation is presented for estimating important contributions to the scattering amplitudes above the coincidence frequency. In contrast to the empty cylinder case, helical waves leak energy into the inner fluid of the cylindrical shell as well as the outer fluid. Thus, the damping rate of leaky helical waves is increased and their resulting backscattering contributions are decreased as compared to the case of an evacuated (or air-filled) interior. However, sound rays crossing the interior may excite additional helical waves on the shell (see Fig. 1), yielding backscattering returns not present in the empty shell case. These returns, when superposed with the regular returns, yield larger backscattering magnitudes than those obtained from considering the regular returns alone. The example considered is the case of a moderately thick steel shell. The scattering considered significantly exceeds the diffraction from flat the ends of rigid cylinder having the same size as the shell.

Blonigen³ derived the leaky helical ray contribution to the backscattering form function of empty tilted cylinders that is restated here to within an overall phase factor:

$$f_n = - \left(\frac{8\alpha}{\sin \psi} \right) B d_n \exp(ik_p \sigma_n - ik d_n \sin \gamma). \quad (1)$$

The form function is defined such that its magnitude is unity for the case of geometric reflection from a sphere having the

same radius as the cylinder.^{2,6} The geometry is shown in Fig. 2 of Ref. 3. The subscript n denotes the order of helical ray contributing to the backscattering, where the quantity $n+1$ is equal to the number of complete circumnavigations of the cylinder by the helical ray. On the right-hand side of Eq. (1), α is the damping rate of leaky rays on the cylinder and $k_p = k_l + i\alpha$ is the complex leaky wave number computed as described in Ref. 5. Here, $k_l = k(c/c_l)$ is the real part of the leaky wave number where k is the wave number in water, c_l is the phase velocity ($c_l > c$) of the leaky wave of type l , and c is the speed of sound in water. The phase factors depend on the geometry of the helical ray path, where σ_n is the path length of the helical ray on the cylinder and d_n is an effective aperture length of the target as explained in Sec. II of Ref. 3. The factor B is the reflection coefficient for the reflection of helical waves off the far cylinder truncation; such a reflection process is necessary before the helical rays will reradiate in the backscattering direction. Finally, ψ is the pitch angle of the helical ray path and γ is the tilt angle of the cylinder measured from broadside incidence.⁵ The approximation $|B| = 1$ is used because the frequency is far below the threshold for propagation of higher-order antisymmetric Lamb waves on a plate having the same thickness as the cylinder.⁴ The open-cylinder geometry considered below avoids some of the complications resulting from end-caps.

Equation (1) must be modified in the case of a water-filled interior. The leaky wave damping parameter α increases in going to the water-filled case. Calculations for the supersonic flexural a_0 Lamb wave on metal plates in water give $\alpha_2 \approx 2\alpha$ for the damping parameter α_2 in the two-sided symmetric fluid loading case where the damping parameter is α in the case of fluid loading on one side of the plate only.⁷ The same damping relationship should also hold to a good approximation between the filled and empty shell cases. Thus, Eq. (1) may be modified to give the result

$$f_n = - \left(\frac{8\alpha}{\sin \psi} \right) B d_n \exp(ik_l \sigma_n - 2\alpha \sigma_n - ik d_n \sin \gamma) \quad (2)$$

for the backscattering form function of the n th order helical wave contribution for a water-filled shell. Note that the sub-

^{a)}Present address: Center for Subsurface Sensing and Imaging Systems, Northeastern University, Boston, MA 02115.

^{b)}Electronic mail: marston@wsu.edu

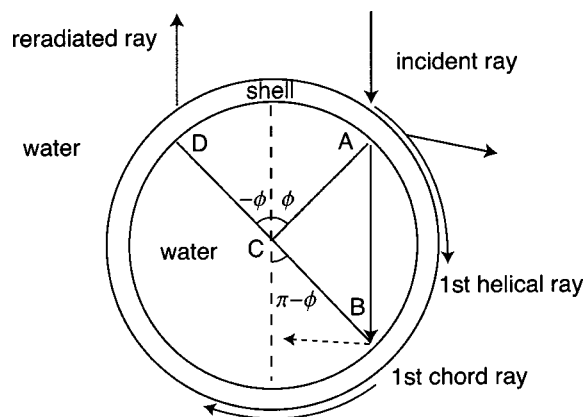


FIG. 1. Rays for helical wave backscattering contributions for the water-filled cylindrical shell as projected onto the base plane. Helical waves are launched by incident rays at point A and reradiate into the inner and outer fluid. The first helical wave is launched at point A and reradiates in the backscattering direction at point D as in the air-filled case. A crossing ray in the shell interior is reradiated at point A and launches another helical ray at point B, which also reradiates in the backscattering direction at point D. This is referred to as the first chord contribution. The dashed chord shown from point B causes a weaker second chord contribution that is as not investigated.

stitution $\alpha_2 = 2\alpha$ is not made in the prefactor of this expression. This is because the prefactor, when expressed in terms of α_2 , contains an extra factor of $1/2$ for the case of a shell fluid loaded on both sides.⁸ Note that Eq. (2) is to be evaluated using the leaky wave parameters k_l and α for the case of an *evacuated* cylindrical shell since the effect of fluid loading on k_l is small. Physically, this doubling of the damping parameter in the factor $\exp(-2\alpha\sigma_n)$ of Eq. (2) takes into account the fact that leaky waves reradiate on both sides of the shell in the water-filled case. The prescription for doubling the leaky wave damping is evident for the case of a plate fluid loaded on both sides since energy is lost to the surrounding fluid at the same rate on both sides of the plate. In the case of a shell that wraps around on itself, the energy reradiated to the interior of the shell may re-excite more leaky rays on the shell from within.

The relevant ray paths for the water-filled shell experiments are shown in the diagram in Fig. 1. Only helical rays of the *first class* are shown, that is, rays which travel only once around the backside of the cylinder (these correspond to helical wave order $n=0$). Figure 1 gives a diagram of the water-filled shell as seen in the base plane. The leaky helical waves are excited by an incident ray at point A at some azimuthal angle ϕ as measured from the meridian. This angle is determined from a wave-vector matching coupling condition. The resulting leaky ray, labeled as the *first helical ray* in the figure, reradiates into the interior fluid of the shell as well as into the outer fluid. It travels once around the backside of the shell and reradiates into the backscattering direction (assuming it has reflected once off the cylinder truncation) at azimuthal angle $-\phi$ (point D). This is a regular helical wave contribution that was also observed in the air-filled shell experiments of previous work.³ Starting at point A, the first helical ray reradiates into both the inner and outer fluids. One ray crosses the interior of the shell from point A to point B as shown in Fig. 1. This ray path is referred to as the *first chord*

ray since it has one internal chord in its ray path. At point B, which is at azimuthal angle $\pi-\phi$, the first chord ray excites a leaky helical ray from the interior of the shell, as the coupling condition is also satisfied there. This helical ray also travels once around the backside of the cylinder and can contribute to the backscattering as the leaky ray reaches point D at azimuthal angle $-\phi$. There are other first chord rays where the internal ray is generated at other points along the ray path for azimuthal angles $>\phi$, yet the backscattering contributions produced by such rays all have the same arrival time. Both the first helical and first chord rays are grouped under the heading of helical rays belonging to the first class since the ray path goes around the backside of the cylinder only once.

II. BACKSCATTERING EXPERIMENTS: WATER-FILLED SHELLS

The backscattering contributions of the first helical ray and the first chord ray were investigated in experiments with a water-filled cylindrical shell target. The same cylinder used in the air-filled shell experiments of Ref. 3 was employed as a target. (This is the thicker of the two shells previously considered^{2,3,5} with outer radius $a=21$ mm, thickness=3.4 mm, and length=245 mm.) The endcaps were removed, allowing the interior of the cylinder to be freely flooded. The cylinder was suspended by fishing line passed through the interior of the shell. In the experiment, five cycle tone bursts were used with a center frequency of 225 kHz, which corresponds to $ka=20$. Backscattered records were recorded at every 0.5° of tilt angle from $\gamma=10^\circ$ to $\gamma=30^\circ$. The records are displayed in Fig. 2, cascaded as a function of the tilt angle. Also shown in Fig. 2 are the predicted arrival times for various scattering contributions due to flexural (a_0) helical leaky waves. The two solid curves give the leading-edge arrival times for the first helical and first chord rays. The earlier arrival corresponds to that of the first helical ray. The dashed curve gives the arrival times for the second helical wave ($n=1$). The contribution due to the first helical ray is weaker than in the air-filled shell experiments^{2,3} because the damping is larger in the water-filled shell case. With the arrival of the first chord contribution, however, the magnitude of the backscattered signal rises abruptly in Fig. 2. Thus, it is important to consider the contributions from ray paths with internal chords for water-filled shells. Inspection of Fig. 2 suggests that with $\gamma<17^\circ$ the chord signal arrives close to the build up of the first helical signal visible on the left of the second curve.

The experimental form function magnitude of the first helical wave contribution alone was determined from the maximum of the envelope of the backscattered signal in the time interval between the arrival of the first helical ray and the arrival of the first chord ray. This was evaluated by constructing the analytic signal. The amplitude calibration procedure described in Appendix B of Ref. 6 was used. For tilt angles greater than 27° , the relevant time window lies between the arrival of the first helical wave and the second helical wave, since there the second helical wave arrives before the first chord ray contribution. The objective was to gate out all contributions except that of the first helical wave

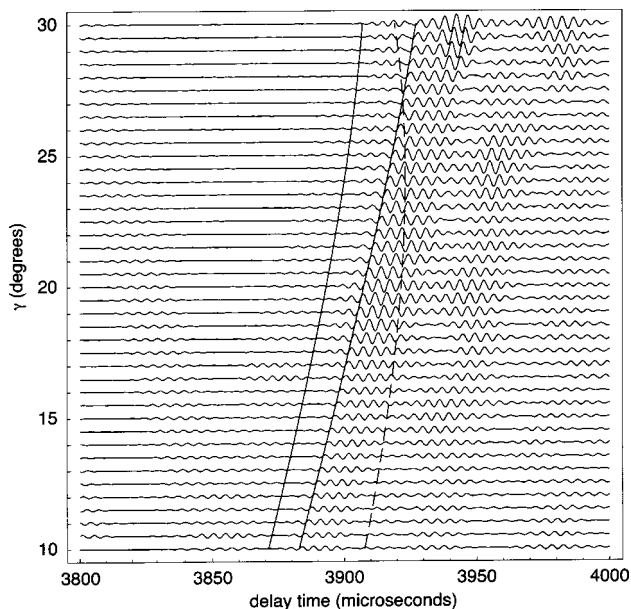


FIG. 2. Time records of backscattered five-cycle tone bursts from the water-filled cylindrical shell target cascaded as a function of tilt angle at $ka=20$ (frequency 225 kHz). The delay time is referenced to the time that the incident burst was sent from the transducer and the relationship between the timing and the geometry was determined by recording the echo for broad-side illumination. The two solid curves are the theoretical leading-edge arrival times of the first helical ray and first chord ray. The helical ray arrives before the chord ray. The arrival time for the second helical ray is given by the dashed curve. These curves were computed by using the leaky wave phase velocity to determine the coupling locations and the group velocity to determine the helical ray contribution to the delay.

arrival and consider that contribution alone. The lower set of solid circles in Fig. 3 gives experimental values for the first helical wave arrival for the water-filled shell plotted as a function of the tilt angle. The solid curve is the steady state form function magnitude for the first helical wave return, $|f_n(ka, \gamma)|$, where $f_n(ka, \gamma)$ is given by Eq. (2) for a water-filled cylindrical shell, $n=0$ for the first helical wave arrival, and $ka=20$. Though the general magnitudes are in agreement with Eq. (2), there is extra structure to the experimental form function. Inspection of Fig. 2 suggests that the first helical wave contribution was not always isolated from other contributions. The other contributions may affect the observed structure.

An additional experiment was done with the water-filled shell at the same frequency ($ka=20$) and over the same tilt angle range ($10^\circ < \gamma < 30^\circ$) but using longer tone bursts of 12 cycles. Such bursts are sufficiently long to enable the first helical ray and first chord ray contributions to interfere. An experimental form function value was calculated using the maximum of the envelope of the backscattered signal in the time window where the first helical and first chord contributions interfere. This time window lies between the arrival of the first chord ray and the second helical ray, which was purposely gated out. The time window was also modified in order to exclude possible interference from edge diffracted returns. These values for the experimental form function are plotted as open circles in Fig. 3. The theoretical form function magnitude of the first helical wave contribution for the air-filled shell, Eq. (1), is shown as the dashed line in Fig. 3.

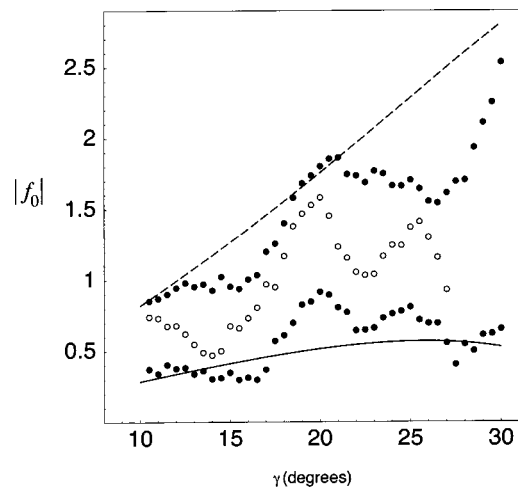


FIG. 3. The magnitude of the backscattering form function as a function of the tilt angle for the water-filled cylindrical shell target due to the first helical wave arrival at $ka=20$. The solid curve is the ray theory given by Eq. (2) for $n=0$. The lower set of solid points give the experimental results. The open circles give the experimental form function magnitude for the superposition of the first helical and first chord arrivals. The dashed curve is the theoretical form function of the first helical wave contribution for the air-filled shell target given by Eq. (1) for $n=0$ and the upper set of solid points give the empty-shell data from Fig. 6 of Ref. 3.

The results of the air-filled shell experiments, Fig. 6 of Ref. 3, are also replotted here as the upper set of solid circles. Comparing those plots with the open circles suggests the superposition of the first helical and first chord contribution is similar in general magnitude and structure to the form function for the first helical wave alone for the air-filled target. The open circles lie in between the solid and dashed curves in Fig. 3.

III. DISCUSSION

The backscattering experiment for a tilted water-filled cylindrical shell shows that the modified theoretical form function for leaky helical flexural wave backscattering contributions, given by Eq. (2), is in moderate agreement with the experimental data for nearly isolated helical rays that have traveled once around the backside of the cylinder. It was also demonstrated that the experimental form function increases when the contribution of the ray with one internal chord is superposed on the regular contribution for $ka=20$. The experimental values are bounded by the theoretical value for the regular helical ray contribution alone for the case of an empty cylindrical shell target [Eq. (1)]. This can be understood physically in that a reduced fraction of energy remains in the interior of the water-filled shell target, so that to a certain extent, the target responds as if it were empty. Leaky waves leak energy into both the inner and outer fluids for the water-filled case, but the waves in the shell interior may re-excite leaky waves on the shell, e.g., through the first chord ray mechanism shown in Fig. 1, which can also contribute to the backscattering. The results in Fig. 3 show that much of the energy lost to the interior can be recovered through this mechanism.

Similar experiments were done at ka of 25 and 30 and compared with predictions analogous to those shown in Fig. 3. While the quasi-isolated helical contributions had com-

parisons with Eq. (2) that are similar to Fig. 3, for the cases where the first chord contributions are superposed, a larger percentage of the energy was lost. Some energy may be lost when internal chords do not re-excite helical rays from the interior but simply leave the *tilted* cylinder through its open end. When internal modes are reflected from the open end of a tube, radiative losses of energy generally increase with increasing ka . This radiation is accentuated geometrically at larger tilt angles, which could explain why the experimental amplitudes given by the open circles in Fig. 3 are suppressed in comparison to the dashed line for tilt angles greater than 20° . The reduction in backscattering for ka of 25 and 30 may also be influenced by the particular way the first helical and first chord rays interfere.

The experiments show that taking into account the ray contributions having internal chords significantly modifies helical-ray backscattering by water-filled tilted cylinders. This was previously demonstrated for meridional rays.⁹ Unlike the case of broadside illumination,¹⁰ for open tilted shells the leaky ray portion of the path is important to chord contributions that are backscattered. That is because at high frequencies it is the leaky rays (not the chords) that are primarily reflected by the truncation. For some tilted cylinders, such as solid plastic cylinders,¹¹ however, the internal reflection of chords by the end may be significant. Contributions to scattering by chords radiated by surface waves have also been investigated for dielectric spheres.^{12,13}

ACKNOWLEDGMENT

This work is supported by the Office of Naval Research.

¹T. K. Stanton, "Sound scattering by cylinders of finite length. I. Fluid cylinders," *J. Acoust. Soc. Am.* **83**, 55–63 (1988).

- ²S. F. Morse, P. L. Marston, and G. Kaduchak, "High frequency back-scattering enhancements by thick finite cylindrical shells in water at oblique incidence: experiments, interpretation and calculations," *J. Acoust. Soc. Am.* **103**, 785–794 (1998).
- ³F. J. Blonigen and P. L. Marston, "Leaky helical flexural wave back-scattering contributions from tilted cylindrical shells in water: Observations and modeling," *J. Acoust. Soc. Am.* **112**, 528–536 (2002).
- ⁴S. F. Morse and P. L. Marston, "Meridional ray backscattering enhancements for empty truncated tilted cylindrical shells: Measurements, ray model and effects of a mode threshold," *J. Acoust. Soc. Am.* **112**, 1318–1326 (2002).
- ⁵F. J. Blonigen and P. L. Marston, "Leaky helical flexural wave scattering contributions from tilted cylindrical shells: Ray theory and wave-vector anisotropy," *J. Acoust. Soc. Am.* **110**, 1764–1769 (2001).
- ⁶K. Gipson and P. L. Marston, "Backscattering enhancements due to reflection of meridional leaky Rayleigh waves at the blunt truncation of a tilted solid cylinder in water: Observations and theory," *J. Acoust. Soc. Am.* **106**, 1673–1680 (1999).
- ⁷X. L. Bao, H. Franklin, P. K. Raju, H. Uberall, and O. Poncelet, "Fluid-borne and Lamb-type waves on elastic plates in contact with two different fluids," *Acustica* **84**, 823–829 (1998).
- ⁸P. L. Marston, "Leaky waves on weakly-curved scatterers: II. Convolution formulation for two-dimensional high-frequency scattering," *J. Acoust. Soc. Am.* **97**, 34–41 (1995).
- ⁹G. Kaduchak, C. M. Wassmuth, and C. M. Loeffler, "Elastic wave contributions in high-resolution acoustic images of fluid-filled, finite cylindrical shells in water," *J. Acoust. Soc. Am.* **100**, 64–71 (1996).
- ¹⁰J. P. Sessarego, J. Sagéoli, C. Gazanhes, and H. Überall, "Two Scholte–Stoneley waves on doubly fluid-loaded plates and shells," *J. Acoust. Soc. Am.* **101**, 135–142 (1997).
- ¹¹F. J. Blonigen and P. L. Marston, "Backscattering enhancements for tilted solid plastic cylinders in water due to the caustic merging transition: Observations and theory," *J. Acoust. Soc. Am.* **107**, 689–698 (2000).
- ¹²H. M. Nussenzweig, "High-frequency scattering by a transparent sphere. 2. Theory of the rainbow and the glory," *J. Math. Phys.* **10**, 125–176 (1969).
- ¹³P. L. Marston, "A time-resolved glimpse of the tetrahertz glory," *Nature (London)* **391**, 841–842 (1998).

Application of Padé via Lanczos approximations for efficient multifrequency solution of Helmholtz problems

Marcus M. Wagner and Peter M. Pinsky

Division of Mechanics and Computation, Stanford University, Stanford, California 94305

Manish Malhotra

Sun Microsystems, 901 San Antonio Road, Palo Alto, California 94303

(Received 28 January 2002; revised 29 January 2002; accepted 1 August 2002)

This paper addresses the efficient solution of acoustic problems in which the primary interest is obtaining the solution only on restricted portions of the domain but over a wide range of frequencies. The exterior acoustics boundary value problem is approximated using the finite element method in combination with the Dirichlet-to-Neumann (DtN) map. The restriction domain problem is formally posed in transfer function form based on the finite element solution. In order to obtain the solution over a range of frequencies, a matrix-valued Padé approximation of the transfer function is employed, using a two-sided block Lanczos algorithm. This approach provides a stable and efficient representation of the Padé approximation. In order to apply the algorithm, it is necessary to reformulate the transfer function due to the frequency dependency in the nonreflecting boundary condition. This is illustrated for the case of the DtN boundary condition, but there is no restriction on the approach which can also be applied to other radiation boundary conditions. Numerical tests confirm that the approach offers significant computational speed-up. © 2003 Acoustical Society of America. [DOI: 10.1121/1.1514932]

PACS numbers: 43.40.Rj, 43.20.-f, 02.70.Dh, 02.60.Dc [LLT]

I. INTRODUCTION

The acoustic design of an engineering structure typically requires the computation of the acoustic field over a range of frequencies, necessitating computation of the full solution for each frequency of interest. Furthermore, although the complete acoustic field is usually computed at each frequency, for many design applications the acoustic field is of interest only over restricted regions of the problem domain. An example is the pressure at selected locations in the near field or on a spherical surface. The latter case can be used for evaluation of the acoustic far field since it is only necessary to compute the pressure field and its normal gradient on a closed surface containing the acoustic sources and scatterers. Similarly, computations may be used only for the evaluation of bilinear forms, such as the average acoustic power. Such integral forms arise as objective functionals in optimization and inverse problems, or may be of direct interest in computing spatial averages of the solution field. In the sequel, the restriction of the acoustic field to a specified subdomain is referred to as a partial field. In this paper, an efficient computational approach for solution of partial fields obtained simultaneously for all frequencies of interest in a window is described.

An algorithm for the computation of a particular partial field simultaneously over multiple frequencies for exterior acoustics based on Padé approximants obtained via the Lanczos algorithm has been presented by Malhotra and Pinsky.¹ In that approach, the computational domain is truncated by use of the Dirichlet-to-Neumann (DtN) map,² and the special case of a partial field corresponding to the Fourier coefficients of the pressure on the truncation boundary was considered. In this paper, the treatment of more general partial

fields and the extension of the algorithm to the case of unsymmetric systems is considered.

The proposed algorithm employs the Galerkin finite element method for discretization of the exterior Helmholtz problem. The infinite fluid domain is truncated on a separable surface, such as a circle or sphere, on which the DtN map is used as a boundary condition to enforce the asymptotic behavior of the solution at infinity. The DtN boundary condition is an exact boundary condition in the sense that the error can be made arbitrarily small by the use of additional terms in its expansion.³ The resulting system matrix for the acoustic problem has a highly complex frequency dependence resulting from the DtN boundary condition. However, an examination of the DtN kernel makes it clear that its matrix contribution may be interpreted as a low-rank update of the system matrix, allowing its inverse to be obtained explicitly by using the Sherman–Morrison–Woodbury formula.⁴ This step facilitates a reorganization of the frequency dependence of the inverse operator, and in turn allows the partial field operator to be obtained from an auxiliary problem which is in so-called standard shifted form. The standard shifted form, in which the shift parameter measures the difference between the current frequency and a reference frequency, is commonly employed in linear dynamical systems, for example, in electrical circuit simulation.⁵

One well-established methodology to circumvent the direct inversion of the system operator at each frequency for linear dynamical systems uses matrix-valued Padé approximations. This approach has been used in electrical circuit analysis.⁶ This approximation is a rational function that exactly coincides, in a specified number of terms, with the Taylor-series expansion of the transfer function. The evaluation of the coefficients of the series is usually carried out by direct computation, which gives rise to the so-called

asymptotic waveform evaluation (AWE) algorithm.^{7,8} This algorithm has recently also been used in the simulation of electromagnetic field problems^{9,10} in combination with finite element discretization. In these electromagnetic applications, local but nonexact boundary conditions have been employed because they exhibit a simple frequency dependence. No attempt to use an exact boundary condition, such as the DtN condition, has been reported.

A second and significant limitation of the AWE algorithm is that it is limited to a small number of series terms, since the computation of the entries involves inversion of a highly ill-conditioned matrix.¹¹ A recently introduced alternative approach uses the Padé-via-Lanczos (PVL) connection,^{12,13} which bases the computation of the approximation function on a two-sided Lanczos algorithm¹⁴ without explicit evaluation of the series entries. This approach has been used successfully in the simulation of electrical circuits^{5,15} and has been extended to the case of multiple input vectors by Freund.¹⁶ The approximation is obtained by applying an unsymmetric block Lanczos algorithm¹⁷ on the standard shifted form and exploiting the matrix-valued Padé-via-Lanczos (MPVL) connection.¹⁶ The first reported application of this algorithm for the simulation of electromagnetic field problems¹⁸ employed nonexact, local, absorbing boundary conditions. The first application to exterior acoustics described by Malhotra and Pinsky¹ employs the exact, nonlocal, DtN boundary condition.

II. EXTERIOR ACOUSTIC PROBLEM

Consider an inviscid compressible fluid occupying an infinite domain denoted Ω_∞ and containing a rigid scatterer with boundary Γ . A complex description $p \in \mathbb{C}$ with a time dependency of $e^{i\omega t}$ is assumed, where ω is the angular frequency. In order to make the boundary-value problem amenable to approximate solution by the finite element method, the infinite-domain problem is transformed into an equivalent statement over a bounded domain. To accomplish this, the infinite domain is truncated on a surface Γ_{DtN} . The general form of the boundary-value problem of radiation and scattering from a rigid obstacle can then be stated as follows: Find the acoustic pressure p satisfying

$$-\nabla^2 p - \kappa^2 p = f \quad \text{in } \Omega, \quad (1)$$

$$p = g \quad \text{on } \Gamma_g, \quad (2)$$

$$\nabla p \cdot \mathbf{n} = h \quad \text{on } \Gamma_h, \quad (3)$$

$$\nabla p \cdot \mathbf{n} = -\mathcal{B}_{\text{DtN}}(p) \quad \text{on } \Gamma_{\text{DtN}}. \quad (4)$$

Equation (1) is the Helmholtz equation with a source term f on the right-hand side. The acoustic wave number κ is defined as $\kappa = \omega/c$, where c is the speed of sound. Dirichlet and Neumann boundary conditions are given by Eqs. (2) and (3), respectively, where the regions Γ_g and Γ_h constitute a disjunct nonoverlapping partition of Γ , i.e., $\Gamma = \Gamma_g \cup \Gamma_h$. Finally, Eq. (4) imposes the Dirichlet-to-Neumann (DtN) map² as an exact nonreflecting boundary condition for time-harmonic acoustics. Explicit forms of the DtN operator can be obtained for separable surfaces such as a circle and a sphere of radius R . In a computation, the infinite series is

truncated after N_{DtN} terms. It can be shown¹⁹ that this truncation may lead to a singular system matrix. For this reason, the DtN condition is modified by adding and subtracting a local $B_1(p)(\mathbf{x})$ condition of Bayliss *et al.*²⁰ The DtN operator is then given as

$$\begin{aligned} \tilde{\mathcal{B}}^h(p) = & \sum_{n=0}^{N_{\text{DtN}}} \frac{\alpha_n}{2\pi R} \underbrace{\left(\frac{\kappa H'_n(\kappa R)}{H_n(\kappa R)} - i\kappa + \frac{D-1}{2R} \right)}_{=: \tilde{z}_n} \\ & \times \int_{\Gamma_{\text{DtN}}} s_n(\mathbf{x}, \boldsymbol{\xi}) p(\boldsymbol{\xi}) d\Gamma_{\boldsymbol{\xi}}, \end{aligned} \quad (5)$$

where the DtN kernels $s_n(\mathbf{x}, \boldsymbol{\xi})$ in 2D are the *surface harmonics*

$$s_n = \alpha_n \cos n(\theta - \theta'), \quad \alpha_n = \begin{cases} 1 & \text{if } n=0 \\ 2 & \text{if } n>0 \end{cases} \quad (6)$$

on Γ_{DtN} and $z_n(\kappa R)$ can be identified as *radial-impedance coefficients*. $H_n(\cdot)$ are Hankel functions of the first kind and order n , and the prime on $H'_n(\cdot)$ indicates differentiation with respect to the argument.

III. FINITE ELEMENT DISCRETIZATION

Discretization of the weak form of Eqs. (1)–(4) in the computational domain Ω into E subdomains Ω^e , $e = 1, \dots, E$ and introduction of finite element approximations of the form

$$p^h(\mathbf{x}) = \mathbf{N}^e \mathbf{p}^e \quad \text{and} \quad \hat{p}^h(\mathbf{x}) = \mathbf{N}^e \hat{\mathbf{p}}^e, \quad \mathbf{x} \in \Omega^e \quad (7)$$

results in the matrix form of the problem (see Hughes²¹)

$$[\mathbf{K} - \kappa^2 \mathbf{M} + \mathbf{B}_1(\kappa) + \tilde{\mathbf{K}}_{\text{DtN}}(\kappa)] \mathbf{p} = \mathbf{f}. \quad (8)$$

For details on the DtN matrices $\tilde{\mathbf{K}}_{\text{DtN}}$ and \mathbf{B}_1 , see Malhotra.²² Let N denote the total number of unknowns in the matrix problem, so that the solution vector \mathbf{p} and load vector \mathbf{f} are both of dimension N , $\mathbf{K} \in \mathbb{R}^{N \times N}$ is a symmetric positive semidefinite stiffness matrix, and $\mathbf{M} \in \mathbb{R}^{N \times N}$ is a symmetric positive definite mass matrix. The DtN operators $\tilde{\mathbf{K}}_{\text{DtN}} \in \mathbb{C}^{N_{\text{DtN}} \times N_{\text{DtN}}}$ and $\mathbf{B}_1 \in \mathbb{C}^{N_{\text{DtN}} \times N_{\text{DtN}}}$ are complex matrices whose dimensions correspond to the number of nodes on the DtN boundary. Moreover, due to the nonlocal character of the DtN operator, $\tilde{\mathbf{K}}_{\text{DtN}}$ is a dense matrix. Both matrices depend on the wave number κ . To formulate Eq. (8) in a dimensionally correct way, the $N_{\text{DtN}} \times N_{\text{DtN}}$ -dimensional matrices are written in a block matrix form of expanded dimension $N \times N$, which is always possible upon proper numbering of the DtN modes.

An important step in the derivation of the proposed algorithm is the reformulation of the DtN matrix $\tilde{\mathbf{K}}_{\text{DtN}}$ and its treatment as a low-rank update of the system matrix. From an investigation of the integral expression of the operator in Eq. (5), it can be shown²² that $\text{rank}(\tilde{\mathbf{K}}_{\text{DtN}}) = N_{\text{mod}}$, $N_{\text{mod}} \ll N$, where, in 2D, $N_{\text{mod}} = 2N_{\text{DtN}} + 1$ is the number of unknown *modal coefficients* in the truncated DtN series of Eq. (5). The matrix expression for this operator on a circular boundary in two dimensions has the form

$$\tilde{\mathbf{K}}_{\text{DtN}} = \sum_{n=0}^{N_{\text{DtN}}} \tilde{z}_n (\mathbf{c}_n \mathbf{c}_n^T + \mathbf{s}_n \mathbf{s}_n^T), \quad (9)$$

with the modified impedance coefficient $\bar{z}_n = \tilde{z}_n \alpha_n R^2$ and the discretized surface harmonics^{22,23}

$$\mathbf{c}_n = \int_0^{2\pi} \mathbf{N}(\theta) \cos n\theta \, d\theta \in \mathbb{R}^{N \times 1}$$

and (10)

$$\mathbf{s}_n = \int_0^{2\pi} \mathbf{N}(\theta) \sin n\theta \, d\theta \in \mathbb{R}^{N \times 1}.$$

This representation is further developed by introducing the matrices

$$\mathbf{F} = [\mathbf{c}_0, \mathbf{c}_1, \dots, \mathbf{c}_{N_{\text{DtN}}}, \mathbf{s}_1, \dots, \mathbf{s}_{N_{\text{DtN}}}] \in \mathbb{R}^{N \times N_{\text{mod}}}, \quad (11)$$

and

$$\mathbf{\Lambda} = \text{diag}\{\bar{z}_0, \bar{z}_1, \dots, \bar{z}_{N_{\text{DtN}}}, \bar{z}_1, \dots, \bar{z}_{N_{\text{DtN}}}\} \in \mathbb{C}^{N_{\text{mod}} \times N_{\text{mod}}}. \quad (12)$$

Hence, a factorization of $\tilde{\mathbf{K}}_{\text{DtN}}$ is given as

$$\tilde{\mathbf{K}}_{\text{DtN}} = \mathbf{F} \mathbf{\Lambda} \mathbf{F}^T. \quad (13)$$

Clearly, the nonzero elements in each column of \mathbf{F} represent the discretized surface harmonics of Eq. (6) defined on the DtN surface Γ_{DtN} . The matrix \mathbf{F} has full column rank. It is important to note that N_{mod} is *generally very small compared to N* , $N_{\text{mod}} \ll N$, and $\mathbf{\Lambda}$ is a diagonal $N_{\text{mod}} \times N_{\text{mod}}$ -dimensional matrix containing the impedance coefficients z_n , $n = 1, \dots, N_{\text{mod}}$ of Eq. (5). It follows that the elements of $\mathbf{\Lambda}$ depend on the wave number κ , while \mathbf{F} is frequency independent. A more detailed description of the structure of those matrices is given by Malhotra.²²

IV. DERIVATION OF TRANSFER FUNCTION

In Sec. VI an algorithm for multifrequency analysis in a frequency window is introduced. Generally speaking, the algorithm is based on a Taylor series expansion of the inverse operator of Eq. (8). To enable an arbitrary choice of the frequency window an expansion point κ_0 of the Taylor series is introduced here by introducing a *frequency-shift* parameter

$$\sigma_i = \kappa_i^2 - \kappa_0^2, \quad i = 1, \dots, N_f. \quad (14)$$

This yields for Eq. (8)

$$\underbrace{[\mathbf{K} - \kappa_0^2 \mathbf{M} + \mathbf{B}_1(\kappa_0) - \sigma_i \mathbf{M} + \mathbf{F} \mathbf{\Lambda} \mathbf{F}^T]}_{\mathbf{A}_0(\kappa_0)} \mathbf{p} = \mathbf{f}. \quad (15)$$

Note that the local boundary condition B_1 is evaluated at the reference frequency κ_0 in Eq. (15). Defining the matrix \mathbf{A}_0

that incorporates all terms in Eq. (15) that are either frequency independent or evaluated at κ_0 and introducing the matrix \mathbf{A}_{σ_i} , which contains all terms except the DtN matrix, the system in Eq. (15) can be expressed in the form

$$[\mathbf{A}_{\sigma_i} + \mathbf{F} \mathbf{\Lambda} \mathbf{F}^T] \mathbf{p} = \mathbf{f}. \quad (16)$$

In the following, the two partial fields considered in this paper are defined. The first involves far-field solutions. Expressing the pressure field on Γ_{DtN} in terms of discretized surface harmonics

$$p(R, \theta) = \sum_{n=0}^{N_{\text{DtN}}} (a_n \cos n\theta + b_n \sin n\theta), \quad (17)$$

reduces the problem of far-field computations to one where only the modal coefficients a_n and b_n need to be computed. The pressure field on Γ_{DtN} is expanded using the first N_{mod} surface harmonics that emanates from N_{DtN} terms in the kernels of Eq. (17). The resulting modal coefficients can then be written as a complex-valued function

$$\mathbf{H}_1 = [a_0, a_1, \dots, a_{N_{\text{DtN}}}, b_1, \dots, b_{N_{\text{DtN}}}] = \mathbf{D} \mathbf{F}^T \mathbf{p} \in \mathbb{C}^{N_{\text{mod}} \times 1}, \quad (18)$$

where \mathbf{F} is defined in Eq. (11) and $\mathbf{D} \in \mathbb{R}^{N_{\text{mod}} \times N_{\text{mod}}}$ contains orthonormalization constants.

The second part of the partial-field computations involves solutions at N_{nf} selected points in the near field. Filtering these points out of the nodal vector \mathbf{p} with the Boolean matrix $\mathbf{E} \in \mathbb{R}^{N \times N_{\text{nf}}}$ yields a second function

$$\mathbf{H}_2 = \mathbf{E}^T \mathbf{p} \in \mathbb{R}^{N_{\text{nf}} \times 1}. \quad (19)$$

The unknown nodal pressure vector \mathbf{p} appearing in the expressions for \mathbf{H}_1 and \mathbf{H}_2 can be formally expressed with use of the inverse of Eq. (16).

The evaluation of the complete pressure vector may be computationally too expensive to carry out over several frequencies. In order to arrive at an efficient algorithm for the computation of the partial fields over multiple frequencies, the partial field transfer functions Eq. (18) and Eq. (19) are reformulated into a standard shifted form. To start, the frequency dependence is simplified by first applying the Sherman–Morrison–Woodbury formula⁴ to express the matrix inverse in terms of $\mathbf{A}_{\sigma_i}^{-1}$

$$[\mathbf{A}_{\sigma_i} + \mathbf{F} \mathbf{\Lambda} \mathbf{F}^T]^{-1} = \mathbf{A}_{\sigma_i}^{-1} - \mathbf{A}_{\sigma_i}^{-1} \mathbf{F} (\mathbf{\Lambda}^{-1} + \mathbf{F}^T \mathbf{A}_{\sigma_i}^{-1} \mathbf{F})^{-1} \mathbf{F}^T \mathbf{A}_{\sigma_i}^{-1}. \quad (20)$$

Sorting \mathbf{H}_1 and \mathbf{H}_2 together in one vector $\mathbf{H}(\sigma_i)$ yields

$$\mathbf{H}(\sigma_i) = \begin{bmatrix} \mathbf{H}_1 \\ \mathbf{H}_2 \end{bmatrix} = \begin{bmatrix} \underbrace{\mathbf{D} \mathbf{F}^T \mathbf{A}_{\sigma_i}^{-1} \mathbf{f}}_{\mathbf{w}_F} - \underbrace{\mathbf{D} \mathbf{F}^T \mathbf{A}_{\sigma_i}^{-1} \mathbf{F}}_{\mathbf{w}_F} \underbrace{(\mathbf{\Lambda}^{-1} + \mathbf{F}^T \mathbf{A}_{\sigma_i}^{-1} \mathbf{F})^{-1}}_{\mathbf{w}_F} \underbrace{\mathbf{F}^T \mathbf{A}_{\sigma_i}^{-1} \mathbf{f}}_{\mathbf{w}_F} \\ \underbrace{\mathbf{E}^T \mathbf{A}_{\sigma_i}^{-1} \mathbf{f}}_{\mathbf{w}_E} - \underbrace{\mathbf{E}^T \mathbf{A}_{\sigma_i}^{-1} \mathbf{F}}_{\mathbf{w}_E} \underbrace{(\mathbf{\Lambda}^{-1} + \mathbf{F}^T \mathbf{A}_{\sigma_i}^{-1} \mathbf{F})^{-1}}_{\mathbf{w}_F} \underbrace{\mathbf{F}^T \mathbf{A}_{\sigma_i}^{-1} \mathbf{f}}_{\mathbf{w}_F} \end{bmatrix}. \quad (21)$$

However, Eq. (21) does not yet exhibit the desired standard shifted structure necessary to apply the approximation outlined in Sec. V. To further develop the expression, observe that several repeated terms can be identified. Rearranging these terms in a new $(N_{\text{nf}} + N_{\text{mod}}) \times (N_{\text{mod}} + 1)$ -dimensional matrix $\mathbf{W}(\sigma_i)$ yields

$$\mathbf{W}(\sigma_i) = \begin{bmatrix} \mathbf{w}_F & \mathbf{W}_F \\ \mathbf{w}_E & \mathbf{W}_E \end{bmatrix} = \begin{bmatrix} \mathbf{F}^T \\ \mathbf{E}^T \end{bmatrix} [\mathbf{I} - \sigma_i \mathbf{A}_0^{-1} \mathbf{M}]^{-1} \mathbf{A}_0^{-1} [\mathbf{f} \quad \mathbf{F}]. \quad (22)$$

Definition of the matrices $\mathbf{L} = [\mathbf{F}\mathbf{E}] \in \mathbb{R}^{N \times (N_{\text{nf}} + N_{\text{mod}})}$, $\mathbf{R} = \mathbf{A}_0^{-1} [\mathbf{f}\mathbf{F}] \in \mathbb{R}^{N \times (N_{\text{mod}} + 1)}$, and $\mathbf{A} = \mathbf{A}_0^{-1} \mathbf{M} \in \mathbb{R}^{N \times N}$ leads to the transfer function

$$\mathbf{W}(\sigma_i) = \mathbf{L}^T [\mathbf{I} - \sigma_i \mathbf{A}]^{-1} \mathbf{R} \in \mathbb{C}^{p \times m}, \quad (23)$$

where $p = N_{\text{nf}} + N_{\text{mod}}$ and $m = N_{\text{mod}} + 1$ for brevity. This equation has the form required to apply the banded unsymmetric Lanczos process detailed in the following section. Such representations can be derived for many practical applications,^{1,16} such as electrical circuits, electromagnetic field problems, and acoustics.

V. THE PADÉ-VIA-LANCZOS CONNECTION

This section introduces an approximation of Eq. (23) which enables a computationally efficient solution for a frequency band. The approximation takes advantage of the transfer function form developed in the previous section. A spectral representation of Eq. (23) shows that \mathbf{W} is a matrix rational function. For this reason, Eq. (23) is approximated by a *matrix-valued Padé approximation*.²⁴ A matrix-valued Padé approximation $[n-1/n]_{\mathbf{W}}(\sigma_i) \in \mathbb{C}^{p \times m}$ is a rational function $[n-1/n]_{\mathbf{W}}: \mathbb{R} \rightarrow (\mathbb{C} \cup \{\infty\})^{p \times m}$ that coincides with the matrix function $\mathbf{W}(\sigma)$ in the first $2n$ terms in its Taylor-series expansion.

The well-known asymptotic waveform evaluation (AWE) technique^{7,8} for the computation of Padé approximations involves the inversion of a Hankel matrix which is known to be ill-conditioned even for small system sizes. This fact limits this approach to orders of N typically ≤ 10 (see Ref. 5).

To circumvent this drawback, another way to obtain matrix Padé approximants is employed by projecting the matrix system in Eq. (23) onto a block Krylov subspace. The subspace bases and the projection itself are computed via an unsymmetric block Lanczos algorithm derived by Aliaga *et al.*¹⁷ This connection between the matrix Padé approximation and the unsymmetric Lanczos algorithm has been observed by Feldmann and Freund⁵ and is referred to in the literature as the *matrix Padé-via-Lanczos algorithm* (MPVL). By computing the Taylor coefficients of Eq. (23), it can be shown¹⁶ that $[n-1/n]_{\mathbf{W}}(\sigma_i)$ can be obtained as

$$[n-1/n]_{\mathbf{W}}(\sigma_i) = \begin{bmatrix} \boldsymbol{\eta}_n \\ \mathbf{O}_{(n-p) \times p} \end{bmatrix}^T \boldsymbol{\Delta}_n [\mathbf{I}_n - \sigma_i \mathbf{T}_n] \times \begin{bmatrix} \boldsymbol{\rho}_n \\ \mathbf{O}_{(n-m) \times m} \end{bmatrix}, \quad (24)$$

where $\boldsymbol{\eta}_n \in \mathbb{C}^{p \times p}$, $\boldsymbol{\Delta}_n \in \mathbb{C}^{n \times n}$, $\mathbf{T}_n \in \mathbb{C}^{n \times n}$, and $\boldsymbol{\rho}_n \in \mathbb{C}^{m \times m}$ are obtained by applying an unsymmetric block Lanczos

algorithm¹⁷ with \mathbf{L} , \mathbf{A} , and \mathbf{R} as starting block matrices. By doing so, \mathbf{A} is projected on the right Krylov subspace $\mathcal{K}(\mathbf{A}, \mathbf{R})$ of dimension n . The projected matrix is \mathbf{T}_n . Matrices $\boldsymbol{\eta}_n$ and $\boldsymbol{\rho}_n$ contain normalization factors of \mathbf{L} and \mathbf{R} , respectively, and $\boldsymbol{\Delta}_n$ contains biorthogonalization factors of the underlying Lanczos algorithm.

By applying MPVL, the N -dimensional matrix problem in Eq. (23) is replaced by an approximation of dimension n , $n \ll N$. This feature will be exploited for the acoustic problem to obtain simultaneous solutions at multiple frequencies.

VI. ACOUSTIC MULTIFREQUENCY ANALYSIS

The reformulated transfer function in Eq. (22) is approximated with MPVL and solved for all frequency points of interest. The obtained results are inserted into Eq. (21), which yields formally an n th matrix Padé approximant of \mathbf{H} . This final result is computationally inexpensive, since the evaluation of the vector \mathbf{q} involves only the solution of a dense $N_{\text{mod}} \times N_{\text{mod}}$ system; see Eq. (21). The pressure values at particular points in the domain are directly contained in $[n-1/n]_{\mathbf{H}}$, while the pressure values on the DtN boundary have to be computed from the obtained modal parameters via Eq. (17). The complete procedure is outlined in the algorithm below.

A. Algorithm 1

Input: N_{mod} , N_{DtN} , N_f , N_{nf} , κ_0 , n , and σ_i .

Output: Approximants $[n-1/n]_{\mathbf{H}}(\sigma_i)$ to $\mathbf{H}(\sigma_i)$ for each σ_i .

- (1) Compute \mathbf{K} , \mathbf{M} , $\mathbf{B}_1(\kappa_0)$, \mathbf{F} .
- (2) Set up $\mathbf{A}_0 := \mathbf{K} - k_0^2 \mathbf{M} + \mathbf{B}_1$.
- (3) Execute n block iterations of the unsymmetric banded Lanczos process with \mathbf{L} , \mathbf{A} , \mathbf{R} defined in Eq. (22). Obtain \mathbf{T}_n , $\boldsymbol{\Delta}_n$, and $\boldsymbol{\rho}_n$, $\boldsymbol{\eta}_n$ as defined in Eq. (24).
- (4) **for** σ_i , $i = 0, 1, 2, \dots, N_f$
 - (a) Evaluate the Padé approximation in Eq. (24) for each σ_i . This involves the solution of a banded tridiagonal system in \mathbf{T}_n .
 - (b) Solve the dense $N_{\text{mod}} \times N_{\text{mod}}$ system for \mathbf{q} . Note that \mathbf{A} is a frequency-dependent diagonal matrix.
 - (c) Finally, evaluate Eq. (21) to obtain the modal parameters of the ansatz in Eq. (17) and with this the pressures on the DtN boundary. Moreover, the second row in Eq. (21) yields the pressure values at any desired point in the interior of the computational domain.

end for

VII. NUMERICAL EXAMPLES

To assess the numerical properties of the proposed method, the problem of radiation of sound from a source on a circle is investigated. With respect to Eq. (17), Neumann boundary conditions in the form

$$\nabla p \cdot \mathbf{n}|_{r=a, \theta} = \sum_{k=1}^{N_{\text{DtN}}} q_k(a) \cos(k\theta) \quad (25)$$

are prescribed at $r = a$, with radius $a = 0.01$ m. For the numerical tests a randomly distributed amplification vector q_k ,

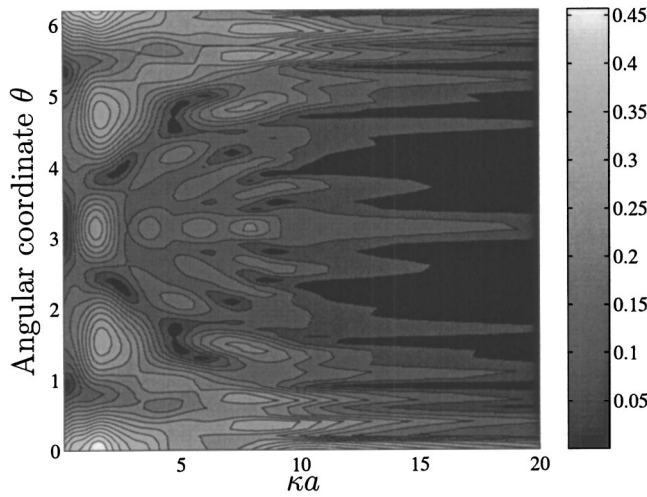


FIG. 1. Pressure amplitude over the Helmholtz number range $\kappa a = [0, 20]$ of the analytic solution of the DtN boundary described with angular coordinate $\theta = [0, 2\pi]$. Parameters are $n = 105$ and $\kappa_0 a = 10$.

$k = 1, \dots, N_{\text{DtN}}$, $0 < q_k < 1$ is chosen. The DtN boundary is concentric with the circle and has radius $R = 0.015$ m.

Figure 1 depicts the analytic solution. The x axis displays the range of the nondimensional wave number κa , which is chosen for the example to be $\kappa a \in [0, 20]$. The y axis denotes the angular coordinate $\theta \in [0, 2\pi]$ parametrizing the points of the DtN boundary.

The finite element discretization employs a mesh size $h/a = 0.0125$, providing a minimum of 25 elements per wavelength and thus minimizing effects of discretization errors. The total number of degrees of freedom is $N = 30\,914$. The mesh consists of 30 160 bilinear quadrilateral elements in the domain and 753 linear 1D elements on the DtN boundary. The DtN series is truncated at $N_{\text{DtN}} = 10$ terms. The quality of the proposed method is illustrated by Fig. 2, which shows the solution for the described mesh for a combination of parameters $n = 105$, and $\kappa_0 a = 10$. The results compared to Fig. 1 are indistinguishable over the computed frequency range.

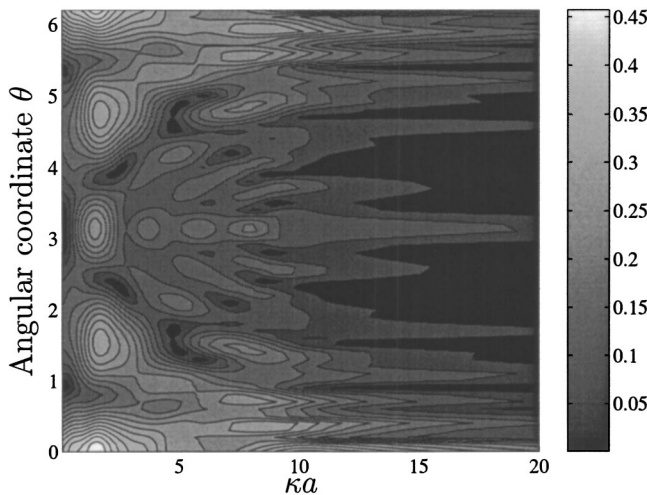


FIG. 2. Pressure amplitude over the Helmholtz number range $\kappa a = [0, 20]$ of the computed solution of the DtN boundary described with angular coordinate $\theta = [0, 2\pi]$. Parameters are $n = 105$ and $\kappa_0 a = 10$.

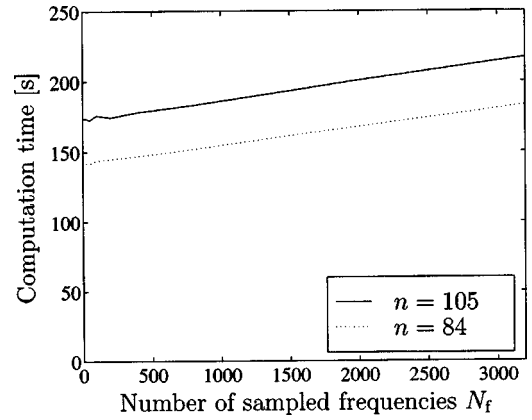


FIG. 3. Computation time for the multifrequency method versus the number of sampled frequencies in the frequency window $\kappa a = [0, 20]$, $\kappa_0 a = 10$, for two different numbers of Lanczos iterations $n = [84, 105]$.

The essential question regarding the proposed method is the reduction in solution time. All computations are performed here with a single-processor 850-MHz Pentium III PC with 256 MB RAM. In Fig. 3 the computation time of the MFPF algorithm in seconds in the chosen frequency window is depicted versus the number of sampled frequencies for two different numbers of Lanczos iterations. The figure shows clearly that a large amount of time is spent in the computation of the Krylov subspace projection, described in step 3 in Algorithm 1. The linear increase in computation time with regard to the number of sampled frequencies is due to the loop in step 4 in Algorithm 1 to set up the final Padé approximation. This behavior is the same for different numbers of Lanczos iterations, as Fig. 3 shows. In Fig. 4 the percentage of the time spent in the loop over all frequencies as compared to the fixed overhead of computing the Krylov projection with the block Lanczos algorithm is shown. Even for the largest number of sampled frequencies, the percentage is only 21%, substantiating the statement that the proposed method provides solutions simultaneously for as many frequency points as desired.

To compare the multifrequency solver developed here, a highly efficient QMR solution algorithm is used²² that employs an SSOR preconditioner of Oberai *et al.*²³ tailored spe-

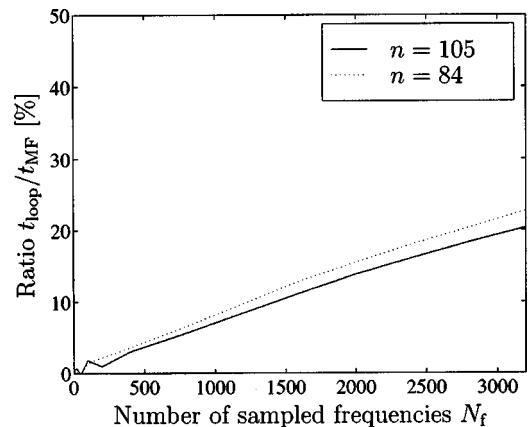


FIG. 4. Ratio of the computation time spent in the block Lanczos algorithm and the computation time spent in the loop t_{loop} of Algorithm 1 versus the number of sampled frequencies.

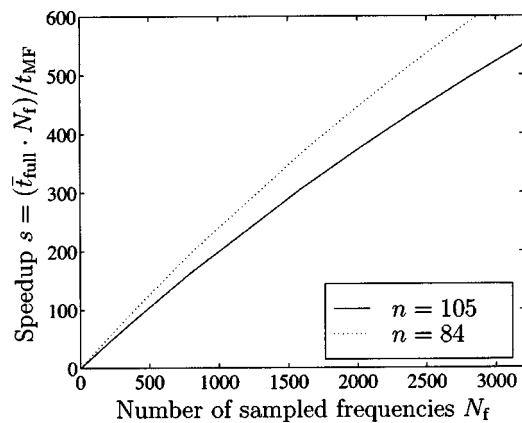


FIG. 5. Speedup of the proposed method for several numbers of Lanczos iterations in comparison to an iterative QMR solver versus the number of sampled frequencies in the fixed frequency window $\kappa a = [0, 20]$, $\kappa_0 a = 10$, for two different numbers of Lanczos iterations $n = [84, 105]$.

cifically for the case of exterior acoustics. The residual tolerance is set to 10^{-6} and convergence is obtained in this example typically after several hundred iterations, depending on the frequency point of solution. In Fig. 5 a speedup s is plotted, where this number is defined as

$$s = \frac{\bar{t}_{\text{full}} \cdot N_f}{t_{\text{MF}}}, \quad (26)$$

where \bar{t}_{full} is the mean full time of a full solution in the given frequency range. The mean value is necessary, since depending on the frequency point of evaluation, the iterative solver converges differently. The time t_{MF} is the total time spent by the multifrequency partial field (MFPF) algorithm for a given number of frequencies N_f . The method is capable of providing speedups of several orders of magnitude for this example if compared to an iterative QMR solver. This effect grows with the system size. Moreover, if a comparison with a direct solver is carried out, the speedup grows even faster.

Besides the computation time, the accuracy of the methodology is of central interest. To quantify this, the relative error on the DtN boundary measured in the L_2 norm

$$e = \frac{\|\mathbf{p} - \mathbf{p}^h\|_{L_2}}{\|\mathbf{p}\|_{L_2}} \cdot 100, \quad (27)$$

is used. In the following, the influence of the two main parameters, the expansion point $\kappa_0 a$ and the number of Lanczos iterations n of the proposed method, is investigated. The algorithm computes the modal coefficients a_n and b_n from Eq. (17) and, with the same equation, the pressure distribution on the DtN boundary is obtained.

In Fig. 6 the relative error in the L_2 norm as defined in Eq. (27) is plotted versus the frequency range, where curves for different expansion points $\kappa_0 a \in [1, 5, 10]$ are shown. The range of convergence of the approximation is expected to be clustered around the expansion point. This fact is substantiated in Fig. 6. This is most easily seen by examining the curve for expansion point $\kappa_0 a = 10$. The error remains under 1% in a range $1 < \kappa a < 16$. Similar results are obtained for the two other expansion points.

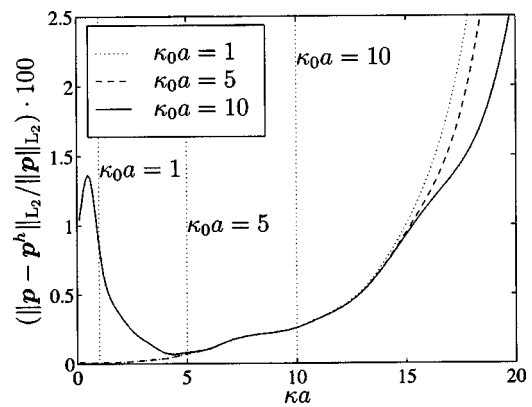


FIG. 6. Exact relative error between the analytic and computed pressure measured in the L_2 norm for $n = 105$, $\kappa a = [0, 20]$ and several expansion points $\kappa_0 a = [1, 5, 10]$.

Moreover, Fig. 6 shows the excellent overall accuracy that can be achieved with the methodology over the complete frequency range. Errors for the whole frequency window are well under 3%. The growth of the error in the higher frequency range is due to the pollution effect^{24,25} and not due to a loss of accuracy in the Padé approximation. This can be shown by comparing the results to other computed results and not to the exact analytical solution. The error properties of the proposed method are under investigation and will be discussed in more detail elsewhere.

Figure 7 shows the dependence of the solution on the number of Lanczos iterations. The number of Lanczos iterations defines implicitly the order of the Padé approximation. For this investigation, the solution is considered at a certain point $\theta = \pi$ on the DtN boundary. With 42 and 63 iterations, the solution is converging only in a small window around the chosen expansion point $\kappa_0 = 10$. For 84 iterations, the convergence radius is already extensively larger, and for 105 and 210 iterations the results basically coincide with the analytic solution in the chosen frequency window. An extension of the frequency window will show that convergence is lost at some point, but since the mesh size has to be adapted to the enlarged frequency range, this is not shown here.

Note for all these examples the differences in system sizes to be solved. The dimension of the original system is

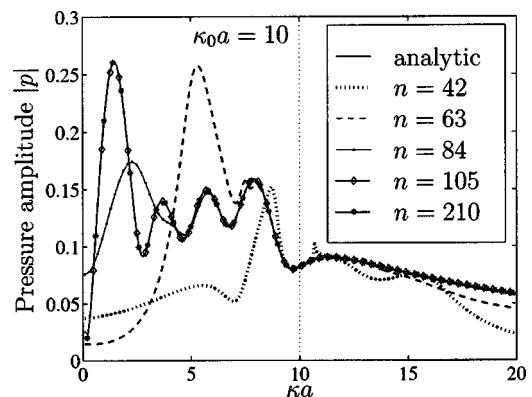


FIG. 7. Convergence of the solution with respect to the number of Lanczos iterations. Solution over $\kappa a = [0, 20]$ for several iteration numbers at the point $\theta = \pi$ on the DtN boundary.

$N = 30\,914$, whereas the proposed methodology provides accurate results over the whole frequency range for a minimum of 105 Lanczos iterations. Hence, the solution of a system of 30 914 equations is effectively replaced by the solution of a banded system with 105 equations and a dense system with $N_{\text{mod}} = 21$ equations.

VIII. CONCLUSION

The analysis of multifrequency problems of exterior acoustics in partial fields of the computational domain is extended in this paper to the unsymmetric case. The N -dimensional partial field function in Eq. (21) is effectively projected onto a Krylov subspace of much lower dimension, allowing for the simultaneous solution over a complete frequency range. The main costs of the algorithm are the factorization of \mathbf{A}_0 and the evaluation of matrix–vector products with this matrix in the Lanczos algorithm. In view of the full system size, the extra cost for the solutions of the banded block system of dimension $n \times n$ arising in Eq. (24) and the dense block system of dimensions $N_{\text{mod}} \times N_{\text{mod}}$ at each desired frequency is negligible. The unsymmetric case is of particular interest also in fluid–structure interaction problems, since the coupled equations—in the form suitable for our method—are unsymmetric by construction.

In the numerical examples presented, the computational cost for the solution over a frequency band is reduced by an order of magnitude, and this advantage grows as larger systems are considered. Moreover, the approximation properties of the Padé approximant show excellent performance over a wide frequency range.

ACKNOWLEDGMENTS

This work is supported by the ONR under Contract No. N00014-99-1-0121 with Stanford University. This support is gratefully acknowledged. The first author is grateful for the support by the German Academic Exchange Office (DAAD) under Contract No. D/00/30328.

¹M. Malhotra and P. M. Pinsky, “Efficient computation of multifrequency far-field solutions of the Helmholtz equation using Padé approximation,” *J. Comput. Acoust.* **8**, 223–240 (2000).

²J. Keller and D. Givoli, “Exact nonreflecting boundary conditions,” *J. Comput. Phys.* **82**, 172–192 (1989).

³D. Givoli, *Numerical Methods for Problems in Infinite Domains* (Elsevier Science, Amsterdam, 1992).

⁴G. H. Golub and C. F. Van Loan, *Matrix Computations* (Johns Hopkins University Press, Baltimore, 1983).

⁵P. Feldmann and R. Freund, “Efficient linear circuit analysis by Padé approximation via the Lanczos process,” *IEEE Trans. Comput.-Aided Des. Int. Circuits Systems* **14**, 639–649 (1995).

⁶G. Baker, Jr. and P. Graves-Morris, *Padé Approximants*, 2nd ed. (Cambridge University Press, New York, 1996).

⁷L. T. Pillage and R. A. Rohrer, “Asymptotic waveform evaluation for timing analysis,” *IEEE Trans. Comput.-Aided Des. Int. Circuits Systems* **9**, 352–366 (1990).

⁸V. Raghavan, R. A. Rohrer, L. T. Pillage, J. Y. Lee, J. E. Bracken, and M. M. Alaybeyi, “AWE-Inspired,” in *Proceedings of the IEEE Conference on Custom Integrated Circuits*, pp. 18.1.1–18.1.8 (1993).

⁹J. Gong and J. Volakis, “AWE implementation for electromagnetic FEM analysis,” *Electron. Lett.* **32**, 2216–2217 (1996).

¹⁰M. Kuzuoglu and R. Mittra, “Finite element solution of electromagnetic problems over a wide frequency range via the Padé approximation,” *Comput. Methods Appl. Mech. Eng.* **169**, 263–277 (1999).

¹¹R. Freund, “Krylov-subspace methods for reduced-order modeling in circuit simulation,” *J. Comput. Appl. Math.* **123**, 395–421 (2000).

¹²W. Gragg, “Matrix interpretations and applications of the continued fraction algorithm,” *Rocky Mt. J. Math.* **4**, 213–225 (1974).

¹³W. Gragg and A. Lindquist, “On the partial realization problem,” *Linear Algebr. Appl.* **50**, 277–319 (1983).

¹⁴C. Lanczos, “An iteration method for the solution of the eigenvalue problem of linear differential and integral operators,” *J. Res. Natl. Bur. Stand.* **45**, 255–282 (1950).

¹⁵K. Gallivan, E. Grimme, and P. Van Dooren, “Asymptotic wave-form evaluation via a Lanczos method,” *Appl. Math. Lett.* **7**, 75–80 (1994).

¹⁶R. W. Freund, “Computation of matrix Padé approximations of transfer functions via a Lanczos-type process,” in *Approximation Theory VIII, Vol. 1: Approximation and Interpolation*, edited by C. K. Chiu and L. L. Schumaker (World Scientific, Singapore, 1995), pp. 215–222.

¹⁷J. I. Aliaga, D. L. Boley, R. W. Freund, and V. Hernandez, “A Lanczos-type method for multiple starting vectors,” *Math. Comput.* **69**, 1577–1601 (2000).

¹⁸R. Slone and R. Lee, “Applying Padé via Lanczos to the finite element method for electromagnetic radiation problems,” *Radio Sci.* **35**, 331–340 (2000).

¹⁹M. J. Grote and J. Keller, “On nonreflecting boundary conditions,” *J. Comput. Phys.* **122**, 231–243 (1995).

²⁰A. Bayliss, M. Gunzburger, and E. Turkel, “Boundary conditions for the numerical solution of elliptic equations in exterior domains,” *SIAM (Soc. Ind. Appl. Math.) J. Appl. Math.* **42**, 430–451 (1982).

²¹T. J. R. Hughes, *The Finite Element Method* (Prentice-Hall, Englewood Cliffs, NJ, 1987).

²²M. Malhotra, Ph.D. thesis, Stanford University, 1996.

²³A. A. Oberai, M. Malhotra, and P. M. Pinsky, “On the implementation of the Dirichlet-to-Neumann radiation condition for iterative solution of the Helmholtz equation,” *Appl. Numer. Math.* **27**, 443–464 (1998).

²⁴G. Xu and A. Bultheel, “Matrix Padé approximation: definitions and properties,” *Linear Algebr. Appl.* **137–138**, 67–136 (1990).

²⁵F. Ihlenburg, *Finite-Element Analysis of Acoustic Scattering, Applied Mathematical Sciences* (Springer, Berlin, Heidelberg, New York, 1998), Vol. 132.

A passive means for cancellation of structurally radiated tones^{a)}

Jeffrey A. Zapfe^{b)} and Eric E. Ungar

Acentech, Incorporated, Cambridge, Massachusetts 02138-1118

(Received 26 February 2002; revised 29 July 2002; accepted 7 October 2002)

The concept of cancellation of constant-frequency sound radiated from a vibrating surface by means of an attached mechanical oscillator is discussed. It is observed that the mass of a mechanical oscillator whose spring is attached to the vibrating surface will vibrate at comparatively large amplitudes and out of phase with that surface, provided that the surface vibrates at a frequency that is slightly higher than the oscillator's natural frequency. From this observation it is concluded that an oscillator's mass with a relatively small surface area can produce a volume velocity that is equal and opposite to that of the vibrating surface, resulting in cancellation of the sound radiated from the surface. Practical considerations in the design of such an oscillator are discussed, and the canceling performance from oscillators consisting of edge-supported circular disks is analyzed. An experimental canceling oscillator consisting of an edge-supported disk is described, and measurements made with this disk attached to a piston are shown to be in good agreement with analytical predictions. A tonal noise reduction exceeding 20 dB was demonstrated experimentally.

© 2003 Acoustical Society of America. [DOI: 10.1121/1.1526490]

PACS numbers: 43.50.Gf, 43.40.Rj, 43.50.Ki [JHG]

I. INTRODUCTION

It has long been known that two sound waves of opposite phase interfere with each other destructively, so that the intensity of the combined wave is less than that of either of the separate waves. Recent years have seen much work on active systems for generating sound that interferes with unwanted sound and thus results in noise reduction. Such systems typically consist of microphones and loudspeakers whose outputs are determined by control processors; they require a source of power and tend to be relatively complex. The present paper, in contrast, deals with a simple passive system for the attenuation of structurally radiated tonal noise, such as occurs, for example in electrical transformers, constant-speed machinery, and screeching train wheels.

The basic idea of a tone canceler using an opposed-phase mechanical oscillator was presented by the authors in June 2001, together with some preliminary proof-of-concept experimental data.¹ A canceler based on the same idea, but consisting of a different mechanical arrangement (a disk supported on a flexible bellows) was described in a December 2001 note by Eatwell²—however, without theoretical analysis or test data. The present paper builds upon the authors' previously presented information by discussing the underlying theory, indicating design considerations, and displaying the results of experimental measurements.

II. TONE CANCELER CONCEPT

A. Undamped spring-mass oscillator

Review of the rather well-known behavior of a simple undamped linear spring-mass system like that sketched in

Fig. 1 permits one to readily visualize how a similar system may be employed for canceling structurally radiated constant-frequency sound. If the base of the spring is made to oscillate at a given frequency ω with velocity amplitude V_0 , then the mass vibrates at the same frequency with amplitude V , which is given by the well-known relation

$$\frac{V}{V_0} = \frac{1}{1-b}, \quad (1)$$

where

$$b = (\omega/\omega_n)^2 \quad (2)$$

and where ω_n denotes the radian natural frequency of the spring-mass system and is given by

$$\omega_n = \sqrt{K/M}, \quad (3)$$

with K and M representing the spring constant and the mass, respectively. From Eq. (1), which is plotted in Fig. 1, one may observe that V and V_0 are of opposite sign if the excitation frequency ω is greater than the natural frequency ω_n . This implies that the phase of the sound radiated from the top surface of the mass will be essentially opposite to the phase of the sound radiated from the oscillating base, provided that the distance between the two radiating surfaces is much smaller than an acoustic wavelength. Consequently the sound radiated from the mass will interfere destructively with that radiated from the base.

Furthermore, if ω is only slightly greater than ω_n , then the magnitude of V is considerably greater than that of V_0 . Recalling that the sound pressure radiated from a vibrating surface is proportional to the product of the surface's area and its normal velocity, one may realize that in this frequency regime a mass with a relatively small area may generate sound that cancels that which is radiated from a much larger base area.

^{a)}A part of this paper was presented at the 141st meeting of the Acoustical Society of America, 4–8 June 1981, Chicago, Illinois.

^{b)}Author to whom correspondence should be addressed. Electronic mail: jzapfe@acentech.com

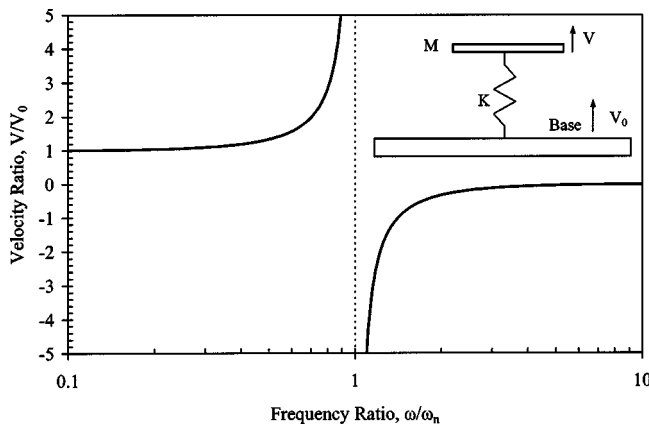


FIG. 1. Velocity ratio (—) of a single degree of freedom mechanical oscillator driven by harmonic base motion.

B. Effect of damping

If one takes damping into account by introducing phasor notation and replacing the spring constant K by the complex spring constant $K^* = K(1 + j\eta)$, where η represents the system's loss factor and $j = \sqrt{-1}$, one finds that

$$\left| \frac{V}{V_0} \right|^2 = \frac{1 + \eta^2}{(1 - b)^2 + \eta^2} \quad (4)$$

and

$$\tan \varphi = - \frac{\eta b}{1 - b + \eta^2}, \quad (5)$$

where φ represents the phase angle between V and V_0 . One may note that the phase angle changes from negative to positive as b becomes greater than $1 + \eta^2$. Thus, a tone canceler with a small surface area should operate at a frequency ratio given by $b = 1 + \eta^2 + \varepsilon^2$, where $\varepsilon^2 \ll 1$. With this frequency ratio, Eq. (4) becomes

$$\left| \frac{V}{V_0} \right|^2 = \frac{1 + \eta^2}{(\eta^2 + \varepsilon^2)^2 + \eta^2}, \quad (6)$$

from which one may conclude that both η and ε need to be small if $|V/V_0|$ is to be large. Note that if $\eta^2 \ll 1$ and $\varepsilon^2 \ll 1$, then $|V/V_0| \approx 1/\eta$.

III. PRACTICAL CONSIDERATIONS

In a mass-spring arrangement consisting of an essentially rigid disk supported at its midpoint on a spring, sound radiation from the underside of the disk would negate at least partially the radiation from its upper surface. In order to avoid this undesirable situation, one might consider enclosing the volume under the disk with a circumferential baffle. For efficient sound radiation, the gap between the disk's circumference and the baffle would need to be made very small or be provided with a seal. Small gaps require careful construction and can potentially result in friction between the disk and baffle, thus increasing the damping of the system and thereby reducing its cancellation effectiveness.

If a rigid disk were supported on an elastomeric pad that extends over the entire area of the disk, then no baffle would be needed. However, because the stiffness and damping of

elastomers typically change significantly with changes in frequency and temperature, it would be difficult to design such a canceler to operate at a given frequency and the canceler's performance likely would be affected considerably by temperature changes.

One might also consider supporting a rigid disk at its circumference on a thin cylindrical resilient element. Elastomeric elements are again undesirable here for the reasons mentioned above and metallic bellows constructions tend to be complex and costly. Any of these arrangements would need to be sealed to the base structure to minimize radiation from the underside of the disk and to avoid damping that would result from air pumping through small openings.

The foregoing considerations lead one to consider employing a circular disk that is supported rigidly at its circumference, so that the disk serves as both the mass and spring elements of the canceler. The circumferential support may consist of a short section of a stiff cylindrical shell, sealed at the disk and at the base to avoid air leaks. When sealed, the disk and shell entrap a volume of air whose stiffness affects the disk's dynamics. Appendix A provides a method for evaluating the effect of the entrapped air.

IV. SOUND RADIATION FROM A DISK DRIVEN AT ITS CIRCUMFERENCE

A. Relation of radiated sound pressure to surface velocity

The magnitude, P , of the far field pressure that results in a fluid at a distance, R , from a circular disk located in an infinite baffle and vibrating at the radian frequency ω is given³ by

$$P = \frac{\omega \rho_a}{R} \int_0^a V_n(r) J_0[k_a r \sin \theta] r dr, \quad (7)$$

where ρ_a is the density of the fluid, R is the distance from the center of the disk to the observation point, $V_n(r)$ represents the normal velocity phasor of the piston surface at the radial coordinate r along the disk surface, and a denotes the radius of the disk. J_0 is the zero order Bessel function of the first kind; k_a denotes the wave number in the fluid and θ is the angle between R and the surface normal through the center of the disk. Figure 2 shows a cross-sectional cut along a diameter through a circular piston in a rigid baffle and indicates the coordinate system and key parameters. The radiating surface is depicted as that of a flexible disk attached to a larger rigid piston.

B. Disk mode shapes

It is reasonable to assume that the normal velocity distribution of a disk that is vibrating at or near its fundamental resonance can be approximated by the mode shape corresponding to that resonance. The fundamental flexural mode shape of a uniform circular plate that is supported at its circumference may be written⁴ as

$$\Phi = A J_0(kr) + B I_0(kr), \quad (8)$$

where I_0 denotes the modified zero-order Bessel function of the first kind, k represents the wave number of the flexural

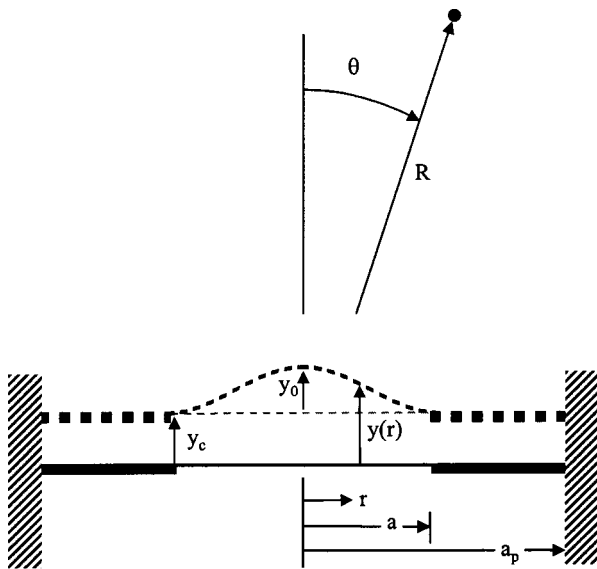


FIG. 2. Coordinate system and key parameters used for the calculation of the far-field pressure radiated from a circular disk in a rigid baffle. Equilibrium position (—) and deflected position (---).

vibrations on the plate, and A and B are constants that depend on the boundary conditions. The values of these constants, normalized to unity at the center of the disk ($r=0$), are given in Table I, together with the related values of ka and of other parameters that are discussed later.

It should be noted that the mode shape and natural frequency of a simply supported plate depend on the value of the plate material's Poisson's ratio. The tabulated values pertain to a Poisson's ratio of 0.3, which is typical for most metals.

C. Response of a disk supported and driven at its circumference

Consider a disk that is supported at its circumference, and that this circumference is displaced in the direction perpendicular to the plane of the disk by an amount $y_c(t)$. If the displacement distribution on the disk itself corresponds to its fundamental mode shape, then the displacement of any point on the disk may be written as

$$y(t) = y_c(t) + y_0(t)\Phi(r), \quad (9)$$

where y_0 denotes the displacement at the center of the disk with respect to the edge and where $\Phi(r)$ represents the mode shape, normalized to unit deflection at the disk center.

If one takes y_c and y_0 as generalized coordinates, one may use the Euler–Lagrange equation to obtain the equation of motion for the base-driven case as

$$\frac{d}{dt} \left(\frac{\partial T}{\partial \dot{y}_0} \right) + \frac{\partial U}{\partial y_0} = 0, \quad (10)$$

where T denotes the kinetic energy and U the potential energy of the system. The kinetic energy is given by

$$\begin{aligned} T &= \int_S \frac{m}{2} \dot{y}^2 dS \\ &= \pi m \int_0^a (\dot{y}_c + \dot{y}_0 \Phi)^2 r dr \\ &= \frac{M_1}{2} \dot{y}_c^2 + M_2 \dot{y}_c \dot{y}_0 + \frac{M_3}{2} \dot{y}_0^2, \end{aligned} \quad (11)$$

where m denotes the mass per unit area, S is the area of the disk, and where

$$M_1 = \pi a^2 m, \quad (12a)$$

$$M_2 = 2\pi m \int_0^a \Phi r dr = 2M_1 \Omega_2, \quad (12b)$$

$$M_3 = 2\pi m \int_0^a \Phi^2 r dr = 2M_1 \Omega_3. \quad (12c)$$

Ω_2 and Ω_3 are integrals of the mode shape which are defined as

$$\Omega_2 = \int_0^1 x \Phi(x) dx, \quad (12d)$$

$$\Omega_3 = \int_0^1 x \Phi^2(x) dx, \quad (12e)$$

where x represents the nondimensional radial coordinate r/a .

One may recognize M_1 as the actual mass of the disk and M_3 as its modal mass. If one expresses the potential energy U in terms of the modal stiffness K as

$$U = \frac{K}{2} y_0^2, \quad (13)$$

substitutes the foregoing results into Eq. (10) and lets $y_c = Y_c e^{j\omega t}$ and $y_0 = Y_0 e^{j\omega t}$, where $j = \sqrt{-1}$, one obtains

$$-M_2 Y_c \omega^2 - M_3 Y_0 \omega^2 + K Y_0 = 0. \quad (14)$$

Noting that the radian natural frequency of the disk may be expressed in terms of its modal stiffness and modal mass as

$$\omega_n = \sqrt{K/M_3}, \quad (15)$$

one finds by substitution into Eq. (14), that the ratio of the displacement at the center of the disk to the displacement at the circumference is given by

$$\frac{Y_0}{Y_c} = \frac{M_2}{M_3} \frac{b}{1-b} = \frac{\Omega_2}{\Omega_3} \frac{b}{1-b}, \quad (16a)$$

TABLE I. Parameters for the fundamental modes of edge-supported disks.

Circumference	A	B	ka	Ω_2	Ω_3	Ω_2/Ω_3	β
Simply supported	1.0383	-0.038 27	2.2215	0.2247	0.1425	1.5768	0.7087
Clamped	0.9472	0.0528	3.1962	0.1558	0.0914	1.7043	0.5311

which applies in the absence of damping. The parameter b is defined as in Eq. (2). If damping is considered by way of the modal loss factor η , Eq. (16a) becomes

$$\frac{Y_0}{Y_c} = \frac{\Omega_2}{\Omega_3} \frac{b(1-b) - b\eta j}{(1-b)^2 + \eta^2}. \quad (16b)$$

Values of Ω_2/Ω_3 , obtained by numerical integration, are given in Table I.

D. Surface velocity on a circular piston with a central canceler disk

Consider a piston of radius a_p that has a disk with a smaller radius a at its center, with the disk's circumferential edge attached to the piston. The normal velocity distribution over the combined surface of the piston and disk may be written as

$$V_n(r) = V_c \left[1 + \frac{Y_0}{Y_c} \Phi \right], \quad \text{for } 0 < r < a, \quad (17a)$$

$$V_n(r) = V_c, \quad \text{for } a < r < a_p. \quad (17b)$$

One may calculate the sound radiation from this arrangement by substitution of Eq. (17) into Eq. (7). The required integration generally needs to be done numerically.

E. On-axis cancellation

Along the normal to the surface at the center of the piston, the Bessel function in Eq. (7) has unity value. Substitution of Eq. (17) into that equation may be found to yield

$$\begin{aligned} P &= \frac{\omega \rho_a V_c}{R} \left[\frac{a_p^2}{2} + \frac{Y_0}{Y_c} \int_0^a \Phi r dr \right] \\ &= \frac{\omega \rho_a V_c}{R} \left[\frac{a_p^2}{2} + \frac{Y_0}{Y_c} a^2 \Omega_2 \right]. \end{aligned} \quad (18)$$

Using the undamped form of the amplification ratio, Y_0/Y_c , given by Eq. (16a), one may rewrite Eq. (18) as

$$P = \frac{\omega \rho_a V_c a_p^2}{2R} \left[1 + A\beta \frac{b}{1-b} \right], \quad (19)$$

where $A = a^2/a_p^2$ is equal to the ratio of the canceler disk area to the piston area, and the dimensionless parameter β is given by

$$\beta = 2\Omega_2 \frac{M_2}{M_3} = 2 \frac{\Omega_2^2}{\Omega_3}. \quad (20)$$

Values of this parameter are listed in Table I. Perfect cancellation occurs in the undamped case when $P=0$ in Eq. (19), that is, when the bracketed term vanishes. One finds that this happens at frequencies ω_c that obey

$$b_c = \left(\frac{\omega_c}{\omega_n} \right)^2 = \frac{1}{1 - A\beta}. \quad (21)$$

If damping is considered, the on-axis pressure is given by

$$P = \frac{\omega \rho_a V_c a_p^2}{2R} \left[1 + A\beta \frac{b(1-b) - b\eta j}{(1-b)^2 + \eta^2} \right], \quad (22)$$

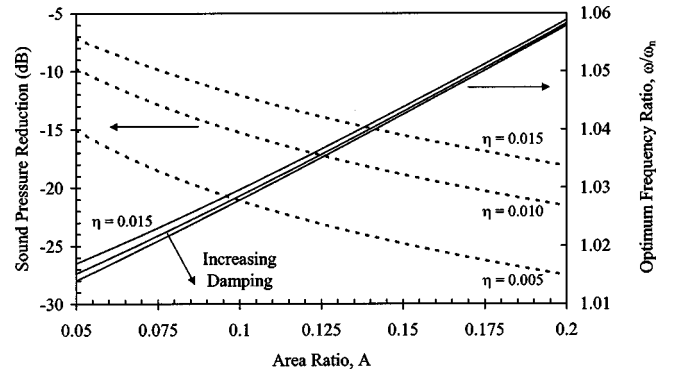


FIG. 3. Optimum on-axis cancellation frequency (—) and sound pressure reduction (---) as a function of canceler to piston area ratio and canceler loss factor, assuming clamped circumferential boundary.

from which expression one may determine the frequency for minimum radiated sound pressure.

Figure 3 shows the numerically calculated values of the optimum cancellation frequency ratio ω_c/ω_n at which the minimum sound pressure (greatest sound reduction) occurs for various area ratios and damping values. It is evident that, for a given area ratio, damping has only a minor influence on the frequency ratio required for maximum noise reduction. However, at a given operating point (area ratio and frequency ratio) damping has a significant influence on the achievable attenuation. Note also that the attenuation increases with increasing area ratio and frequency ratio. This suggests that a canceler with a large radiating area and moderate amplification, operating with a phase shift near 180° , will produce more attenuation than a smaller canceler operating less out-of-phase, but at a higher amplitude ratio.

V. EXPERIMENTAL AND THEORETICAL RESULTS

A. Experimental setup

The relatively simple test arrangement shown schematically in Fig. 4 was assembled and placed in an anechoic chamber for measurement of the performance of an experimental canceler. A 12.1 cm diameter piston, made of 5 cm thick high-density fiberboard, faced with a 1 mm thick steel plate, served as the primary sound radiator. The piston was mounted in a close-fitting opening in a heavy wooden box with 7.6 cm thick sides. A B&K model 4804 mechanical

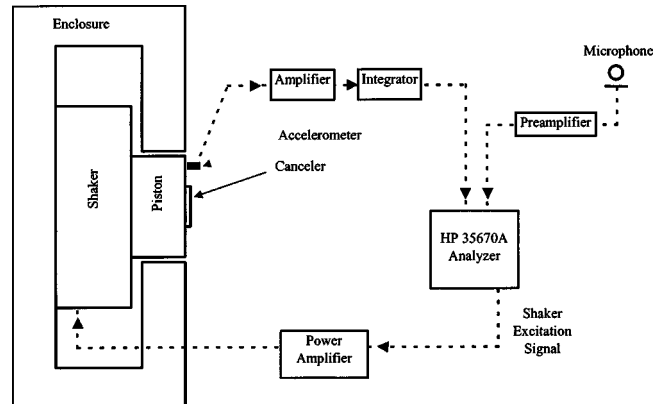


FIG. 4. Test apparatus.

shaker, which was used to actuate the piston, was located inside the box. The gap around the piston's circumference was filled with flexible silicone caulk.

The piston's vibration velocity was measured by means of a BBN model 501 accelerometer, whose output was fed via an EPAC model 60/10 low-noise amplifier to a BBN integration module and from there to a Hewlett-Packard 35670A spectrum analyzer. The sound pressure was measured by use of a B&K 1962-9610 microphone (1.27 cm diameter), connected to a General Radio P42 pre-amplifier, whose output was fed to the second channel of the HP analyzer. The analyzer's controllable source output was fed to a B&K model 2712 power amplifier which was used to drive the shaker.

In a typical test the sound at a selected location was measured while the piston was driven with a random noise signal. The signal analyzer was used to determine the transfer function between the radiated noise and the piston velocity.

B. Experimental canceler

The experimental canceler consisted of a conveniently available copper pipe cap, shaped like a shallow, flat-bottomed cup with a 41 mm diameter. The open end of the cup was attached to the piston using an epoxy adhesive. The bottom of the cup played the role of the canceler disk. The cup's side was 7 mm high and its wall thickness was 0.25 mm. This configuration was chosen on the basis of preliminary measurements to demonstrate cancellation at approximately 1000 Hz. No attempt was made to tune its frequency precisely, although this could readily have been done by adding mass to the disk and/or modifying its thickness. Auxiliary measurements showed that the fundamental natural frequency of the device was 1036 Hz and that its loss factor was about 0.005. The radiating area of the disk was about 12% of the piston area.

C. On-axis results

Figure 5 shows the on-axis sound pressure level measured at a distance of 292 cm from the face of the piston, as a function of the driving frequency. Data are shown for the bare piston and for the piston with the canceler attached. In order to facilitate the interpretation of the results, all of the sound pressure data presented in this figure have been scaled to correspond to a constant piston velocity of 1 cm/s, although during the experiment the piston velocity varied slightly from this value.

At the disk's natural frequency of 1036 Hz, the canceler increased the sound pressure level by about 24 dB beyond that measured for the bare piston. This increase in sound pressure occurs when the disk is driven near and below its natural frequency. In this frequency region, the disk vibrates near resonance with a vibration amplitude much greater than that of the piston. At frequencies slightly below the natural frequency, the motion of the disk is in phase with that of the piston and the total sound pressure greatly exceeds that produced by the piston alone. At frequencies that are slightly above the 1036 Hz natural frequency, the disk's motion is out

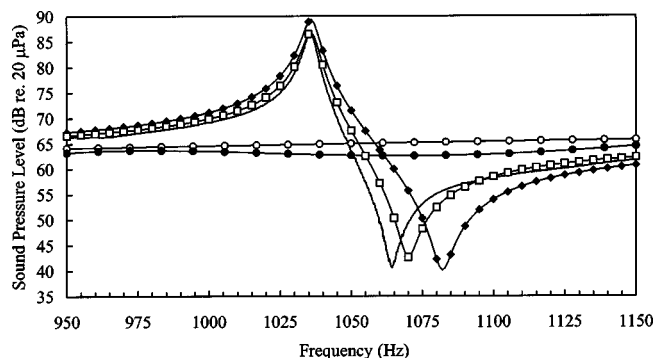


FIG. 5. Predicted on-axis sound pressure at a distance of 292 cm for (—○—) piston alone, (---□---) piston with canceler (clamped edges) and (---◆---) piston with canceler (simply-supported edges); compared to measured sound pressure, (—●—) piston alone and (—) piston with canceler.

of phase with that of the piston, but is so much greater than that of the piston that its sound radiation predominates. As the driving frequency is increased further, the disk's motion continues to be out of phase with that of the piston, but decreases in amplitude. At approximately 1065 Hz a point is reached where the disk's volume velocity nearly cancels the piston's volume velocity, resulting in a decrease in the sound pressure level that amounts to about 22 dB. At yet higher driving frequencies the disk still vibrates out of phase with the piston, but at smaller amplitudes, resulting in less cancellation.

Also shown in Fig. 5 are the theoretically predicted sound pressure levels, calculated for (a) the bare piston, (b) a disk with a simply supported circumferential boundary, and (c) a disk with a clamped circumference. In each of these cases the disk's fundamental resonant frequency was taken to be 1036 Hz and its loss factor was assumed to be equal to 0.005, so as to match the parameters of the experimental device. The calculated optimum reduction in the sound pressure level due to the device is 22.5 dB for the clamped disk and 25 dB for the simply supported disk. Note that the predicted sound pressure radiated from the bare piston exceeds the measured sound pressure by up to 2.7 dB at some frequencies. The authors attribute this discrepancy to out-of-phase sound that was radiated from the baffle at frequencies between 1050 Hz and 1080 Hz.

For a piston and canceler disk arrangement with the dimensions and fundamental natural frequency of the experimental setup one finds from Eq. (21) that the theoretical frequencies for total cancellation in the absence of damping are 1082 Hz and 1070 Hz for disks with simply supported and with clamped edges, respectively. These frequencies may be seen to be very nearly the same as the predicted frequencies at which sound pressure level minima occur for disks with damping, as evident from Fig. 5.

A disk with a simply supported circumference produces cancellation at a higher frequency than a similar disk with a clamped circumference because the former is a more efficient radiator—that is, it produces a greater volume velocity and more sound radiation for a given deflection at the center. A more efficient radiator can generate a given volume velocity with less amplification and can therefore operate further off resonance than a less efficient radiator.

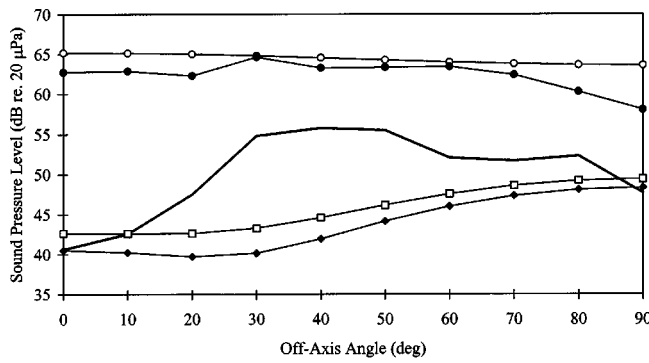


FIG. 6. Predicted off-axis sound pressure at a distance of 292 cm at optimum cancellation frequency for (—○—) piston alone, (—□—) piston with canceller (clamped edges) and (—◇—) piston with canceller (simply-supported edges); compared to measured sound pressure, (—●—) piston alone and (—) piston with canceller.

It appears from Fig. 5 that the measured cancellation frequency of the experimental device is lower than the cancellation frequencies calculated for the two idealized disks. In view of the discussion in the foregoing paragraph, this implies that the experimental disk is a less efficient radiator than the idealized disks—a condition that may occur due to nonuniform thickness of the experimental disk or to nonlinearities associated with large deflections which are not considered in the theoretical analysis.

D. Off-axis results

Figure 6 shows how the measured and predicted sound pressures vary with the angle measured from the normal to the piston surface. The predicted values were obtained by numerical integration based on Eq. (7); the development is not presented here. Each set of data shown corresponds to the optimum on-axis cancellation frequency, namely, 1065 Hz for the experimental data, 1070 Hz for the canceler disk with clamped edges, and 1083 Hz for the canceler disk with simply supported edges. Again, all data are normalized to a piston velocity of 1 cm/s.

Figure 6 indicates that the sound pressure radiated from the piston alone is reasonably constant over a considerable range of angles, whereas the pressure radiated by the piston with the attached canceler varies considerably. The off-axis cancellation performance predicted for the two theoretical cancelers differs little from their on-axis performance for angles up to perhaps 30°, but the predicted performance then decreases with increasing angle. It should be noted, however, that due to the increasing difference between the directivities of the piston and the disk, optimum cancellation at larger angles occurs at higher frequencies than for the 0° case. For example, at an off-axis angle of 70°, optimum cancellation for a clamped disk occurs at 1077 Hz compared to 1070 Hz at 0°.

The measured attenuation shown in Fig. 6 for angles between 20° and 60° is significantly less than that predicted for disks with either of the two boundary conditions. The reason for this discrepancy remains to be investigated.

VI. CONCLUSIONS

It has been shown that steady tonal noise radiated from a vibrating surface can be cancelled effectively by a passive system consisting of a simple mechanical oscillator attached to the vibrating surface. The oscillator's natural frequency is selected to lie slightly below the frequency of the tone being radiated, so that the phase of oscillator's motion is opposite to that of the surface. Optimum cancellation occurs at the frequency where the volume velocity produced by the oscillator is equal and opposite to that produced by the radiating surface.

Cancellation of a tone radiated from a circular piston by means of a centrally attached circular disk, supported from the piston at its circumference, was investigated analytically and experimentally with generally good agreement. Substantial noise reductions were demonstrated experimentally; a reduction of about 22 dB was measured on-axis, with smaller reductions observed off-axis. Although this study was confined to circular geometries, the major facets of its results are expected to apply also to radiating areas and cancelers of other shapes.

APPENDIX A: EFFECT OF ENCLOSED AIR VOLUME

From the relation for adiabatic compression of a gas one finds that the pressure increase p_i that results in a gas volume u when this volume is reduced by an amount u_d obeys

$$\frac{p_i}{p_0} = \frac{\gamma u_d}{u}, \quad (\text{A1})$$

where γ represents the ratio of specific heats of the confined gas and p_0 denotes the pressure of the gas in the initial volume.

The volume change associated with a disk deflection $y(r) = y_0 \Phi(r)$ may be found by integration of this deflection over the disk area, yielding a result that may be written by use of Eq. (12d) as

$$u_d = 2\pi a^2 \Omega_2 y_0. \quad (\text{A2})$$

One may find the work done on the disk as the pressure increases from 0 to p_i by use of the two foregoing equations and integrating over the area of the disk. This work is equal to the potential energy contribution ΔU due to the pressure in the confined volume and may be found to obey

$$\Delta U = \frac{\gamma p_0}{u_0} (2\pi a^2 \Omega_2)^2 \frac{y_0^2}{2} = \Delta K \frac{y_0^2}{2}, \quad (\text{A3})$$

where ΔK denotes the increase in the disk's modal stiffness due to the pressure in the confined volume. In view of Eqs. (15) and (12c) one may write

$$K = M_3 \omega_n^2 = \frac{2\pi}{a^2} \Omega_3 D N^2, \quad (\text{A4})$$

where

$$N \equiv \omega_n a^2 \sqrt{m/D} \quad (\text{A5})$$

is a nondimensional natural frequency parameter.⁴ For a disk whose edges are clamped, $N = 10.2158$; for a disk whose edges are simply supported and of a material with $\nu = 0.3$,

$N=4.9359$. The symbol D denotes the disk's flexural rigidity, which obeys

$$D = \frac{Eh^3}{12(1-\nu^2)}, \quad (\text{A6})$$

where E and ν represent the modulus of elasticity and Poisson's ratio of the disk material, respectively. The total modal stiffness in presence of entrapped air is $K + \Delta K$, and one thus may find that the natural frequency ω_{na} of the disk, including the effect of the entrapped air, is related to the natural frequency ω_n in absence of entrapped air as

$$\frac{\omega_{na}}{\omega_n} = \sqrt{1 + \frac{\Delta K}{K}} = \sqrt{1 + \frac{(1-\nu^2)p_0}{E} \frac{a^4}{h^3 l}} R, \quad (\text{A7})$$

where l denotes the height of the cylindrical air volume and

$$R \equiv \frac{24\gamma\Omega_2^2}{N^2\Omega_3}. \quad (\text{A8})$$

From the previously cited values one finds that $R=0.0855$ for disks with clamped edges and $R=0.489$ for disks with simply supported edges and Poisson's ratio 0.3.

Consider the previously described experimental canceller, for example. It has a 0.25 mm thick disk of copper (with $E=110$ GPa) with a 20.5 mm radius and a cylindrical confined air space that is 7 mm high. If the confined air initially is at atmospheric pressure ($p_0=100$ kPa), one finds that ω_{na}/ω_n amounts to 1.06 if the disk's edges are taken as clamped and to 1.29 if its edges are taken as simply supported.

¹J. A. Zapfe and E. E. Ungar, "A passive means for cancellation of structurally radiated tones," *J. Acoust. Soc. Am.* **109**, 2352 (2001).

²G. P. Eatwell, "SoundSpring—A vibration excited sound absorber," *Sound Vib.* **35**, 12–15 (2001).

³F. Fahy, *Sound and Structural Vibration* (Academic, London, 1985), pp. 58–59.

⁴A. W. Leissa, *Vibration of Plates*, NASA SP-160 (National Aeronautics and Space Administration, Washington, DC, 1969), pp. 7–10.

Lattice form adaptive infinite impulse response filtering algorithm for active noise control

Jing Lu,^{a)} Chunhua Shen, Xiaojun Qiu, and Boling Xu

State Key Laboratory of Modern Acoustics and Institute of Acoustics, Nanjing University, Nanjing 210093, China

(Received 24 May 2002; revised 18 October 2002; accepted 23 October 2002)

In some situations of active noise control, infinite impulse response (IIR) filters are more suitable than finite impulse response (FIR) filters owing to the poles in the transfer function. A number of algorithms have been derived for applying IIR filters in active noise control; however, most of them use the direct form IIR filter structure, which faces the difficulties of checking stability and relatively slow convergence speed for noise composed of narrow-band components with large power disparity. To overcome these difficulties along with using the direct form IIR filters, a new adaptive algorithm is proposed in this paper, which uses and updates the lattice form adaptive IIR filter in an active noise control system. Full mathematical derivations of the proposed algorithm are presented, and the comparison between the proposed algorithm and the commonly used filtered-u LMS and filtered-v LMS algorithms shows the superiority of the proposed algorithm. © 2003 Acoustical Society of America. [DOI: 10.1121/1.1529665]

PACS numbers: 43.50.Ki [KAC]

I. INTRODUCTION

Most active noise control systems (ANC) use adaptive FIR filters and filtered-x LMS algorithm (FXLMS) due to their simplicity and inherent stability.¹ However, there are some situations where adaptive IIR filters may be more suitable.^{1–3} For example, when there are poles in the primary plant transfer function, or when there is feedback from the control output to the reference sensor, if an FIR filter is used in such a system, very long taps are needed. However, with an IIR filter, much fewer taps can be used, resulting in less computation load. In general, an IIR filter with sufficient order can exactly match poles as well as zeros of the physical system, resulting in a lower residual mean squared error.

Although the algorithms using adaptive IIR filters for active noise control have been proposed for many years, they still have not been widely used in the application of the active noise control system due to the following disadvantages.^{1–6} First, IIR filters are not unconditionally stable due to the possibility that some poles of the filters might move outside of the unit circle during the weights update. Second, the existing adaptive algorithms have a lower convergence speed and may converge to a local minimum. Therefore, it is recommended that whenever possible, adaptive FIR filters should be used.⁷

The adaptive IIR filters used in active noise control are usually in the direct form, for example, the filtered-u LMS (FULMS) algorithm,⁴ filtered-v LMS (FVLMS) algorithm,⁵ and the “correct algorithm” proposed by Snyder.³ All these adaptive algorithms use the direct form IIR filter, hence having the same problems of possible instability and slow convergence. The lattice structure is an alternative form of a digital filter, which possesses the advantages of inherent stability and greatly reduced sensitivity to the eigenvalue spread

of the reference signal.^{8,9} Many algorithms have been proposed to make the lattice form adaptive IIR filter.^{9–13} This paper will propose a new adaptive algorithm for using the lattice form adaptive IIR filter in active noise control. Full mathematical derivations of the lattice gradient descent algorithm and a simplified gradient lattice algorithm will be presented, and the performance of the proposed algorithm will be compared with the FUVLMS and FVLMS algorithm.

The idea of using lattice filters in active noise control is not new. However, it is usually used as a preprocessor followed by an FIR filter.^{14–20} The preprocessor (lattice filter) decorrelates the reference signal to produce uncorrelated backward prediction error signals based on the Gram–Schmidt orthogonalization process.²¹ Then, the FIR filter operates on these uncorrelated signals; thus, the convergence of the adaptive filter does not suffer from eigenvalue disparity problems. It was shown that this form of the active noise control system converges significantly faster than the traditional transversal filter when the primary noise consists of sinusoidal components with widely differing power. Recent application of lattice filters can be found in Ref. 22, where an active noise control algorithm based on multivariable gradient lattice filters was proposed. However, the authors still treated the lattice structure and FIR filter separately by just using the decorrelation property of lattice filters. The primary difference of our proposed lattice algorithm is that the lattice filter is used as the control filter, not just as a preprocessor; thus, not only the benefits of adaptive IIR filter are held, but also the problem of slow convergence and possibility of instability is avoided.

II. THE LATTICE GRADIENT DESCENT ALGORITHM FOR ANC

Figure 1 shows the flowgraph of the tapped state normalized lattice form IIR filter for active noise control for the case in which the filter order M is set to 3. In this figure, the

^{a)}Electronic mail: lujing@nju.edu.cn

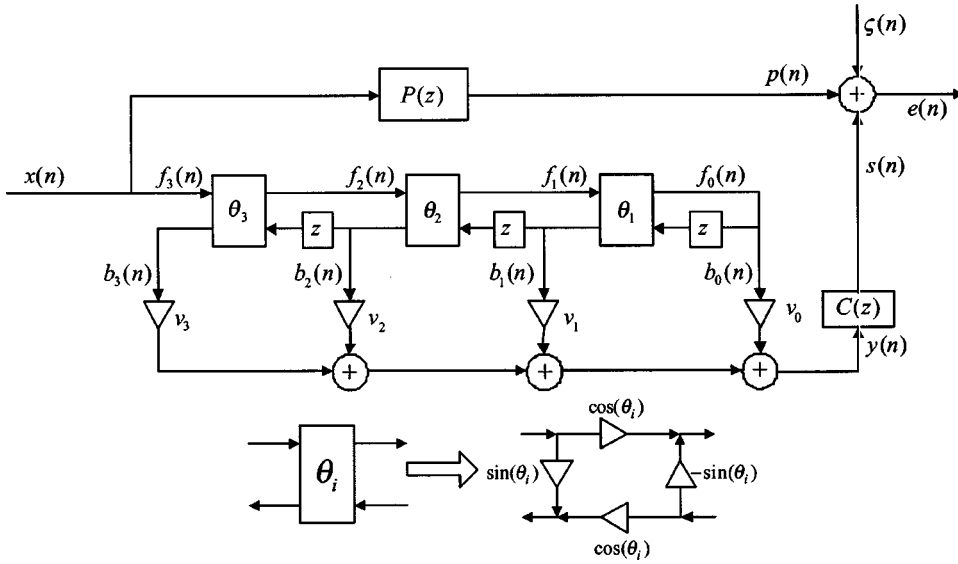


FIG. 1. Tapped state normalized lattice filter for active noise control for $M=3$.

primary path transfer function $P(z)$ represents the transfer function from the noise source (reference signal is assumed to be picked there) to the error sensor; the cancellation path transfer function $C(z)$ represents the acoustic path from the secondary source to the error sensor. $\{\zeta(\cdot)\}$ is some kind of noise which is statistically independent of the reference signal $\{x(\cdot)\}$. Driven by the reference signal $\{x(\cdot)\}$ with $x(n)$ the most recent input sample, the output of the lattice filter $y(n)$ at time n passes through the cancellation path $C(z)$ and produces the control signal $s(n)$ at the location of the error sensor. The error sensor, which is the sum of the primary noise $p(n)$, uncorrelated noise $\zeta(n)$, and control signal $s(n)$, will be picked up by the error sensor and be used by the adaptive algorithm to update the lattice filter parameters.

The filter parameters are the rotation angles $\{\theta_1, \dots, \theta_M\}$ plus the tap parameters $\{v_0, \dots, v_M\}$, which are related to the direct form filter parameters in a nonlinear manner, and may be converted to the direct form filter parameters and vice versa.^{8,21} As shown in Fig. 1, the cascade structure in the lattice filter propagates a forward signal $f_k(n)$ and a backward signal $b_k(n)$ at time n and section number k . By adapting $\{\theta_k\}$ in such a way that $|\sin \theta_k| < 1$, the stability of the lattice filter is ensured.⁹

The output of the lattice filter is

$$y(n) = \sum_{k=0}^M b_k(n) v_k, \quad (1)$$

$\{b_k(n)\}$ for $k=M, M-1, \dots, 1$ are obtained by the Schur recursion⁹

$$\begin{bmatrix} f_{k-1}(n) \\ b_k(n) \end{bmatrix} = \begin{bmatrix} \cos \theta_k & -\sin \theta_k \\ \sin \theta_k & \cos \theta_k \end{bmatrix} \begin{bmatrix} f_k(n) \\ b_{k-1}(n-1) \end{bmatrix}, \quad (2)$$

where $f_M(n) = x(n)$ and $b_0(n) = f_0(n)$.

Development of the lattice version of the gradient descent algorithm for active noise control follows the same methodology as for the direct form: the output error is differentiated with respect to the filter parameters to obtain negative gradient signals.⁹ The convergence properties of the direct form and lattice algorithms are theoretically equivalent:

both algorithms seek the minimum points of the cost function $E[e^2(n)]$, but in different parameter spaces. The key advantage of the lattice over the direct form concerns filter stability: the lattice filter is inherently stable in time-varying environments while the direct form is not.^{8,9} The following mathematical derivations are similar to those in Ref. 9, except where in Ref. 9, the algorithm is derived for normal adaptive filtering without taking into the account of the cancellation path.

Set z as the unit delay operator, that means for any input sequence $\{u(n)\}$, $zu(n) = u(n-1)$; therefore, the transfer function that will be used in the following derivations can be regarded as the rational model of the unit delay operator.

As with the direct form algorithm, the output error signal is

$$e(n) = p(n) + s(n) + \zeta(n) = [P(z) + W(z)C(z)]x(n) + \zeta(n), \quad (3)$$

where $W(z)$ is the transfer function of the lattice filter. The parametric derivatives of this error signal are given by

$$\frac{\partial e(n)}{\partial v_k} = \frac{\partial s(n)}{\partial v_k} = \frac{\partial W(z)}{\partial v_k} C(z)x(n) \quad (4)$$

$$\frac{\partial e(n)}{\partial \theta_k} = \frac{\partial s(n)}{\partial \theta_k} = \frac{\partial W(z)}{\partial \theta_k} C(z)x(n).$$

The derivative with respect to the tap parameters $\{v_k\}$ is straightforward. In the lattice form, there is

$$W(z) = \sum_{k=0}^M v_k B_k(z), \quad (5)$$

so that

$$\frac{\partial e(n)}{\partial v_k} = B_k(z)C(z)x(n), \quad (6)$$

where $B_k(z)$ is the transfer function of the lattice filter corresponding to the k th backward signal. The signals obtained from Eq. (6) are called filtered regressor signals, as they are formed by filtering the input with the cancellation path trans-

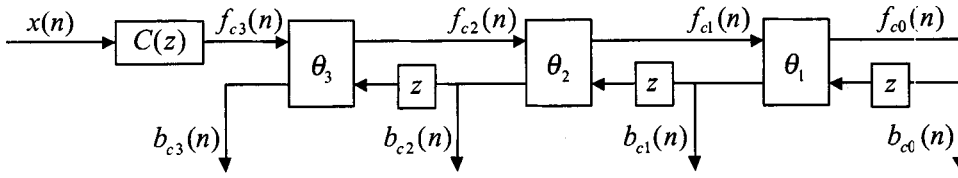


FIG. 2. Filtered regressor signals for the tap parameters.

fer function and the lattice filter. The signals can be obtained with an auxiliary lattice filter, as shown in Fig. 2 for the case $M=3$, where the filtered regressor signal for the tap parameters $\{\nu_k\}$ is $\{b_{ck}(n)\}$. The instantaneous estimate of the gradient signal of the cost function $E[e^2(n)]$ corresponding to the tap parameter ν_k is

$$\nabla_{\nu_k}(n) = 2e(n) \frac{\partial e(n)}{\partial \nu_k} = 2e(n)b_{ck}(n). \quad (7)$$

With the negative gradient direction $-\nabla \nu_k(n)$, the corresponding gradient descent form algorithm can be easily constructed as shown in Appendix A. For the case of $C(z) = 1$ where the cancellation path is ideal, the algorithm is simplified to the case of normal lattice form adaptive filtering; the filtered regressor signals for the tap parameters become $\{b_k(n)\}$ in Fig. 1. In this case, it is not necessary to use a separate auxiliary lattice filter to obtain the filtered regressor signals.

Obtaining derivative signals with respect to the rotation angles $\{\theta_k\}$ is more complicated. Via Eqs. (3) and (5), there is

$$\frac{\partial e(n)}{\partial \theta_k} = \frac{\partial W(z)}{\partial \theta_k} C(z)x(n) = \sum_{l=0}^M v_l \frac{\partial B_l(z)}{\partial \theta_k} C(z)x(n), \quad (8)$$

which requires obtaining the sensitivity function $\partial B_l(z)/\partial \theta_k$.

Set now

$$\frac{\partial B_l(z)}{\partial \theta_k} \triangleq B_{\theta k, l}(z), \quad \frac{\partial F_l(z)}{\partial \theta_k} \triangleq F_{\theta k, l}(z).$$

By applying differential operator $\partial/\partial \theta_k$ to the z transform of Eq. (2), there are

$$\begin{bmatrix} F_{\theta k, l-1}(z) \\ B_{\theta k, l}(z) \end{bmatrix} = \begin{bmatrix} \cos \theta_l & -\sin \theta_l \\ \sin \theta_l & \cos \theta_l \end{bmatrix} \begin{bmatrix} F_{\theta k, l}(z) \\ zB_{\theta k, l-1}(z) \end{bmatrix}, \quad \text{if } k \neq l \quad (9)$$

and

$$\begin{bmatrix} F_{\theta k, l-1}(z) \\ B_{\theta k, l}(z) \end{bmatrix} = \begin{bmatrix} \cos \theta_l & -\sin \theta_l \\ \sin \theta_l & \cos \theta_l \end{bmatrix} \begin{bmatrix} F_{\theta k, l}(z) \\ zB_{\theta k, l-1}(z) \end{bmatrix} + \begin{bmatrix} -\sin \theta_l & -\cos \theta_l \\ \cos \theta_l & -\sin \theta_l \end{bmatrix} \begin{bmatrix} F_l(z) \\ zB_{l-1}(z) \end{bmatrix}, \quad \text{if } k = l \quad (10)$$

by using

$$\begin{aligned} F_{l-1}(z) &= \cos \theta_l \cdot F_l(z) - \sin \theta_l \cdot zB_{l-1}(z) \\ B_l(z) &= \sin \theta_l \cdot F_l(z) + \cos \theta_l \cdot zB_{l-1}(z). \end{aligned} \quad (11)$$

For $k=l$, there is

$$\begin{bmatrix} F_{\theta k, l-1}(z) \\ B_{\theta k, l}(z) \end{bmatrix} = \begin{bmatrix} \cos \theta_l & -\sin \theta_l \\ \sin \theta_l & \cos \theta_l \end{bmatrix} \begin{bmatrix} F_{\theta k, l}(z) \\ zB_{\theta k, l-1}(z) \end{bmatrix} + \begin{bmatrix} -B_l(z) \\ F_{l-1}(z) \end{bmatrix}. \quad (12)$$

Because $F_M(z) = 1$ and $B_0(z) = F_0(z)$ for all $\{\theta_k\}$, the boundary conditions for completing the recursion are

$$F_{\theta k, M}(z) = 0, \quad B_{\theta k, 0}(z) = F_{\theta k, 0}(z). \quad (13)$$

For illustration purposes, Fig. 3 shows the filtered regressor signal corresponding to the rotation parameter θ_2 for the filter order of $M=3$.

The instantaneous estimate of the gradient signal of the cost function $E[e^2(n)]$ corresponding to the rotation parameter θ_k is

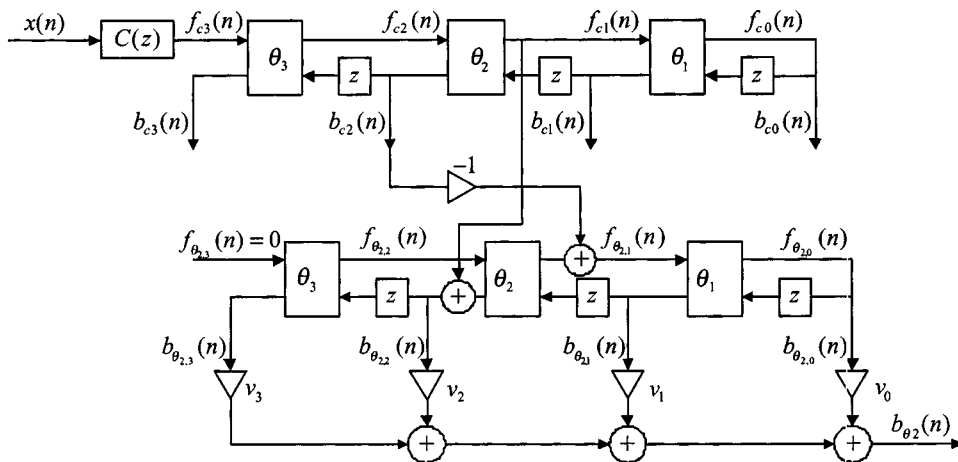


FIG. 3. Filtered regressor signal for the rotation parameter.

$$\nabla_{\theta_k}(n) = 2e(n) \frac{\partial e(n)}{\partial \theta_k} = 2e(n)b_{\theta_k}(n). \quad (14)$$

An overall algorithm list is given in Appendix A. Note that the “Test” step in the algorithm not only guarantees the stability of the adaptive process but also ensures the uniqueness of the mapping from the transfer function space to the parameter space.⁹

It should be noted that M additional lattice filters are required to obtain the filtered regressor signals $\{-\nabla \theta_k(n)\}$ corresponding to the rotation parameters. Thus, the complexity is of the order M^2 , both for computation and storage. Considering that the normally used direct form IIR filters such as filtered-u⁴ algorithm and simplified filtered-v algorithm⁵ required only order M computation and storage, the increased complexity of the lattice form is an obvious disadvantage. A simplified gradient lattice algorithm with a computation complexity order of M is described below.

III. THE SIMPLIFIED GRADIENT LATTICE ALGORITHM FOR ANC

After examining the behavior of the filtered regressor signals $\{\nabla \theta_k\}$ corresponding to the rotation parameters along the reduced error surface with the tap parameters $\{\nu_k\}$ being optimized, a partial gradient algorithm of order M complexity can be derived. The derivation is quite complex, and the details are omitted for brevity. However, a similar deviation of adaptive lattice algorithm that used in system identification can be found in Ref. 9, which does not take into account the cancellation path as in an ANC system.

Consider the ideal update formula

$$\begin{aligned} v_k(n+1) &= v_k(n) - \frac{\mu}{2} \frac{\partial E[e^2(n)]}{\partial v_k}, \\ \theta_k(n+1) &= \theta_k(n) - \frac{\mu}{2} \frac{\partial E[e^2(n)]}{\partial \theta_k}, \end{aligned} \quad (15)$$

where the final correction terms may be written as the inner product

$$\begin{aligned} -\frac{\mu}{2} \frac{\partial E[e^2(n)]}{\partial v_k} &= -\mu \left\langle \frac{\partial W(z)}{\partial v_k} C(z), S_x(z) \right\rangle \\ &\quad \times [P(z) + W(z)C(z)], \\ -\frac{\mu}{2} \frac{\partial E[e^2(n)]}{\partial \theta_k} &= -\mu \left\langle \frac{\partial W(z)}{\partial \theta_k} C(z), S_x(z) \right\rangle \\ &\quad \times [P(z) + W(z)C(z)], \end{aligned} \quad (16)$$

where $S_x(z)$ is the spectral density function associated with the reference signal $\{x(\cdot)\}$ and the inner product is defined as $\langle F(z), G(z) \rangle = (1/2\pi j) \oint_{|z|=1} F(z)G(z^{-1})(dz/z)$.

With tap parameters $\{\nu_k\}$ being optimized, there is

$$\left\langle \frac{\partial W(z)}{\partial v_k} C(z), S_x(z) [P(z) + W(z)C(z)] \right\rangle = 0. \quad (17)$$

Using the above condition, it can be shown that if the parameters are held stationary, the following equation can be obtained:

$$\begin{aligned} &-\mu \left\langle \frac{\partial W(z)}{\partial \theta_k} C(z), S_x(z) [P(z) + W(z)C(z)] \right\rangle \\ &= \mu \left\langle \frac{\partial D_M(z)}{\partial \theta_k} \frac{1}{D_M(z)} W(z)C(z), S_x(z) \right. \\ &\quad \left. \times [P(z) + W(z)C(z)] \right\rangle. \end{aligned}$$

Thus

$$\theta_k(n+1) = \theta_k(n) + \mu \frac{\partial D_M(z)}{\partial \theta_k} \frac{1}{D_M(z)} W(z)C(z)x(n), \quad (18)$$

where $D_M(z)$ is equal to $H(z)$ of the corresponding equivalent direct form IIR filter with a transfer function of $G(z)/H(z)$. After further deviation and approximation, it can be shown

$$\frac{\partial D_M(z)}{\partial \theta_k} \frac{1}{D_M(z)} \approx \gamma_k z B_{k-1}(z), \quad (19)$$

where

$$\gamma_k = \prod_{l=k+1}^M \cos \theta_l, \quad \gamma_M = 1. \quad (20)$$

The resulting algorithm would appear as

$$\begin{aligned} v_k(n+1) &= v_k(n) - \mu e(n) \cdot B_k(z)C(z)x(n), \\ k &= 0, 1, \dots, M, \\ \theta_k(n+1) &= \theta_k(n) + \mu e(n) \cdot \gamma_k z B_{k-1}(z)W(z)C(z)x(n), \\ k &= 1, 2, \dots, M. \end{aligned} \quad (21)$$

Figure 4 shows the flowgraph for generating the necessary filtered regressor signals. The algorithm listing appears in Appendix B. Note that the technique used to determine the values of $\{\sin \theta_k(n+1)\}$ and $\{\cos \theta_k(n+1)\}$ is called “annihilation operations,”⁹ where the need for computing trigonometric functions in every step is avoided and thus the efficiency for the algorithm’s implementation is improved. Accordingly the “Test” step in the algorithm has been modified and appears different from that in Appendix A.

It can be found that the complexity of the algorithm is reduced to the order of M . Note, although it can be shown that the stationary points of the above simplified algorithm are indeed the stationary points of the cost function $E[e^2(n)]$,⁹ the possibility that the convergence points are the saddle points cannot be excluded because the expected value of the update term concerning the rotation angles $\{\theta_k\}$ is not indeed a negative gradient vector of the cost function. However, the following simulations suggest that this algorithm tends towards a local minimum.

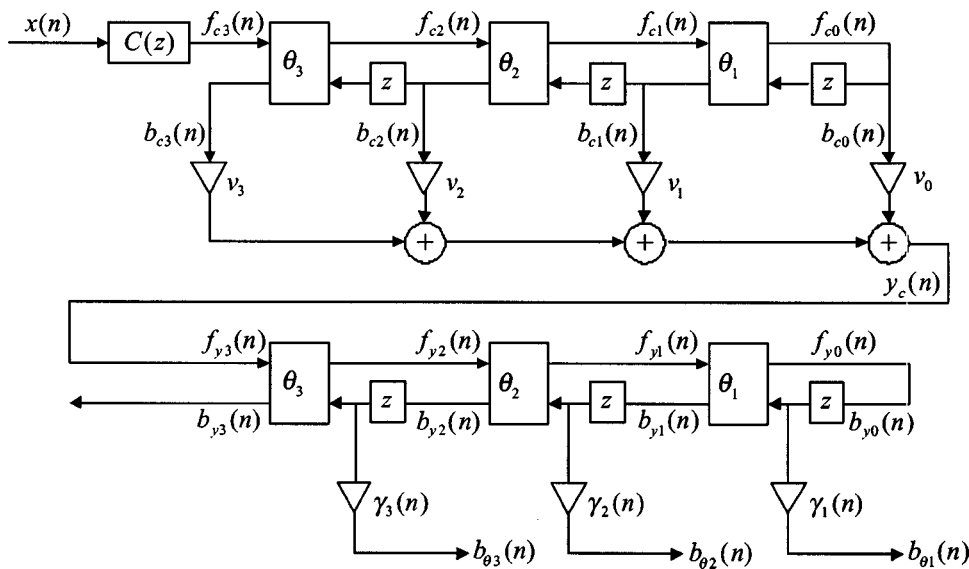


FIG. 4. Generation of filtered regressor signals in simplified gradient algorithm.

IV. SIMULATION RESULTS

A. Description of the simulations

In this section, several illustrative results are presented on comparisons between the proposed algorithm and commonly used FULMS algorithm⁴ and FVLMS algorithm.⁵ Only the simplified gradient lattice algorithm described in Sec. III will be used for simulations, which will be called LFRLMS (lattice filtered reference LMS) algorithm in the following context. All the simulations were conducted using the acoustic transfer functions of a single input and output active noise control system measured in the anechoic room with a sampling rate of 8000 Hz. Figure 5 shows a schematic diagram of the system, where two identical loudspeakers were placed 20 cm from each other, one acted as the noise source and the other acted as the control source. An error microphone was placed 1.3 m away from the center of two loudspeakers. The impulse responses corresponding to the primary path and the cancellation path are shown in Fig. 6. Note, the optimum filter form for ANC is somewhat like $-P(z)/C(z)$ and the filter order of the adaptive controller should be equal to or higher than that of $-P(z)/C(z)$ (which is 128 in our simulation) to yield optimum control as far as ANC for wideband noise is concerned. However, in most realistic ANC systems, it is not possible to make the adaptive filter order satisfy the above condition, so the order of the IIR filter was set to 64 for all the algorithms to make the simulations more realistic while still holding quite good performance. The step size parameters of the adaptive algo-

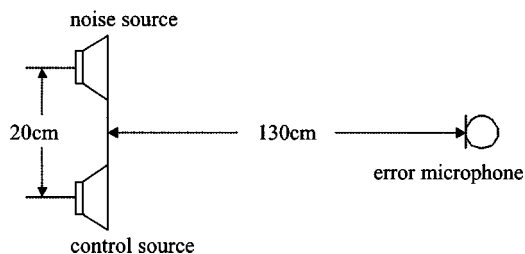


FIG. 5. Schematic diagram of the simulation system.

rithms were adjusted to the extent that any increase to the parameter would cause the control process to be unstable.

B. Convergence speed

The white Gaussian noise with 4000-Hz bandwidth generated by the computer was used as the noise source first, and the convergence speeds of the three algorithms are shown in Fig. 7. It can be seen that there is no dramatic difference among these three algorithms as far as for attenuating white noise. FVLMS algorithm and FULMS algorithm perform almost the same and the proposed LFRLMS algorithm gives slightly better performance than the other two algorithms. Theoretically the convergence performance of the lattice form and direct form IIR filters should be similar for the noise signal with quite flat power spectrum. However, because lattice form adaptive IIR filters are more stable, the convergence coefficient may be set a little larger, resulting in faster convergence speed.

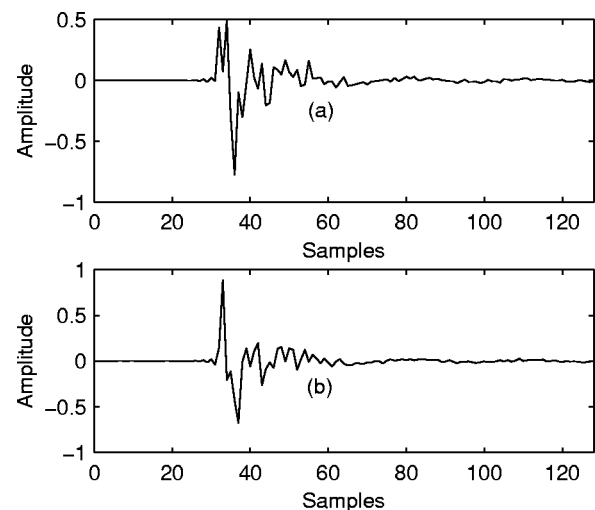


FIG. 6. Impulse responses used for primary path and secondary path with (a) primary path and (b) secondary path.

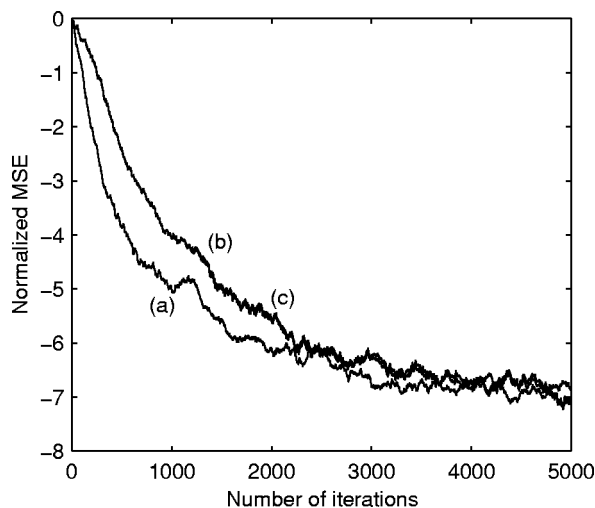


FIG. 7. Convergence comparisons between different algorithms with (a) LFRMS algorithm; (b) FULMS algorithm; and (c) FVLMS algorithm.

C. Robustness to cancellation path model errors

As the most often used FXLMS algorithm in ANC, all three of these algorithms use the model of the cancellation path transfer function. In convergence comparison, the simulation results were calculated with models that were exactly the same as the plant, which may not be the case in practical situations. In order to evaluate the effect of the model errors on the performance of the algorithms, simulations of the same ANC system with noisy cancellation path models were performed. Note that if the errors in the cancellation path model are too large, none of the algorithms will converge.

The performance of all these algorithms using exact and noisy plant models are shown in Figs. 8–10, respectively. It can be seen that even when the cancellation model error becomes quite large (with SNR 0 dB), the proposed LFRMS algorithm still gives quite good performance while the FVLMS algorithm and the FULMS both deteriorate greatly. This can partly be explained by the following reasons: the lattice structure bears the ability of orthogonalizing the input

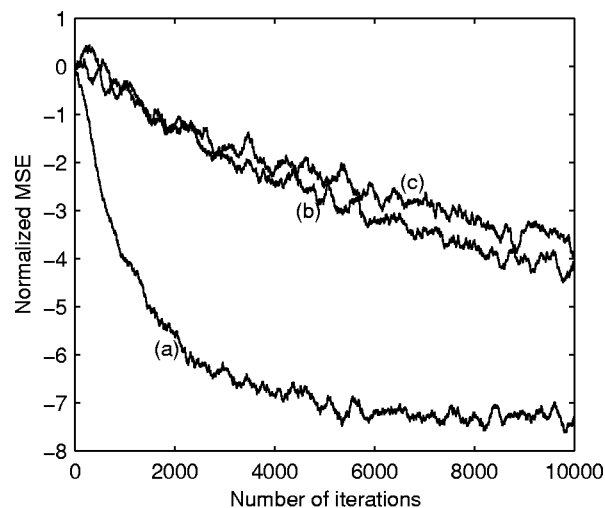


FIG. 9. Learning curves for the FVLMS algorithm with (a) perfect model of the secondary path; (b) secondary path model with a SNR of 5 dB; and (c) secondary path model with a SNR of 0 dB.

signal^{8,21} and this ability compensates the influence of the cancellation path model error partly and makes the lattice form adaptive IIR filtering algorithm more robust. It also can be seen that FVLMS algorithm deteriorates most when cancellation path model error was added. This is probably caused by the fact that the complex calculation of gradient vector corresponding to the parameters of direct form IIR filter used in FVLMS algorithm makes it more sensitive to the model error. Although simulations here provide some indications for the different robustness of the three algorithms, further theoretical work is ongoing to fully characterize the behavior of all the adaptive IIR filters used in ANC. Another important property that should be noted is that with the addition of cancellation path model error, there is almost no necessity to modify the step size of the proposed LFRMS algorithm, which makes this algorithm more attractive in practice. This is also owed to the superiority of stability of the proposed algorithm.

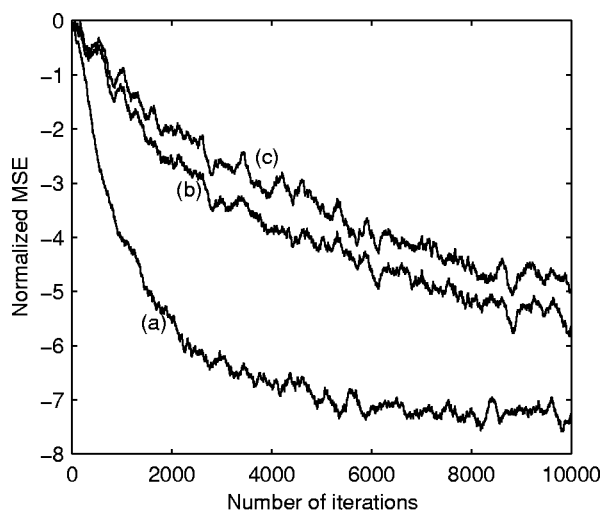


FIG. 8. Learning curves for the FULMS algorithm with (a) perfect model of the secondary path; (b) secondary path model with a SNR of 5 dB; and (c) secondary path model with a SNR of 0 dB.

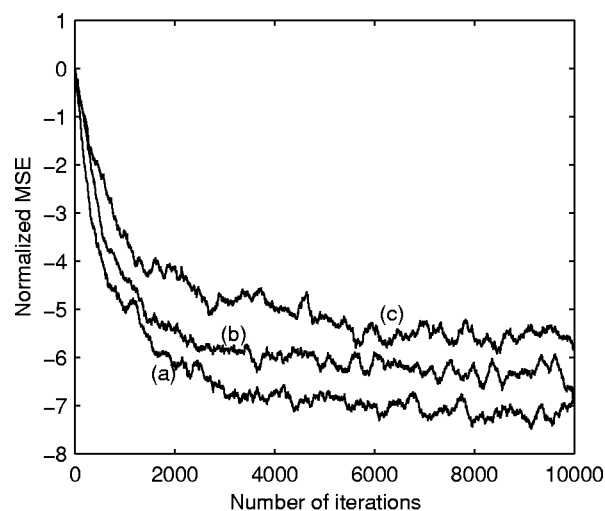


FIG. 10. Learning curves for the LFRMS algorithm with (a) perfect model of the secondary path; (b) secondary path model with a SNR of 5 dB; and (c) secondary path model with a SNR of 0 dB.

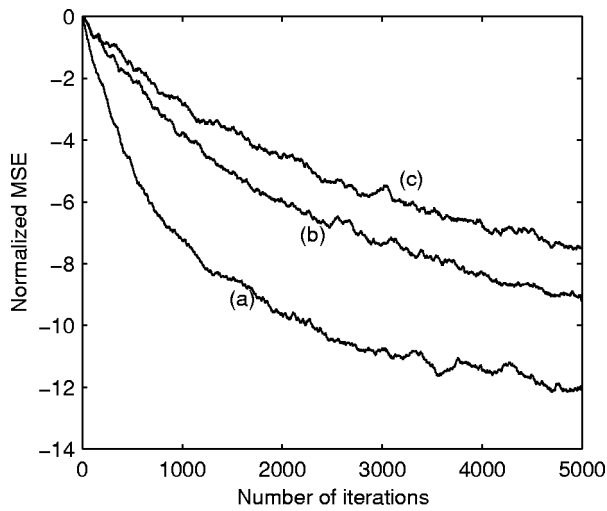


FIG. 11. Learning curves for different algorithms of 5000 iterations with noise source of large power disparity. (a) LFRLMS algorithm; (b) FULMS algorithm; and (c) FVLMS algorithm.

D. Test for noise with large power disparity

In an actual ANC system, the noise signal to be controlled sometimes contains narrow-band components with large power disparity such as fan noise and babble noise. This results in a large eigenvalue spread of the input autocorrelation matrix and will cause the convergence rate of normal LMS algorithm decrease significantly.^{1,8} To test the efficiency of different algorithms for the controlling of more “real” noise, the summation of 100 sinusoid signals with random frequency between 0 and 3000 Hz were used as the noise for the simulations and all the sinusoid components have random amplitudes between 0 and 0.5 and random initialization phases between 0 and 360 deg. The learning curves shown in Figs. 11 and 12 were obtained from an ensemble of 20 trials. Comparing Fig. 11 with Fig. 7, it can be seen that the convergence rate of LFRLMS algorithms only decreases slightly while both FVLMS and FULMS algorithms converge much slower than that for controlling

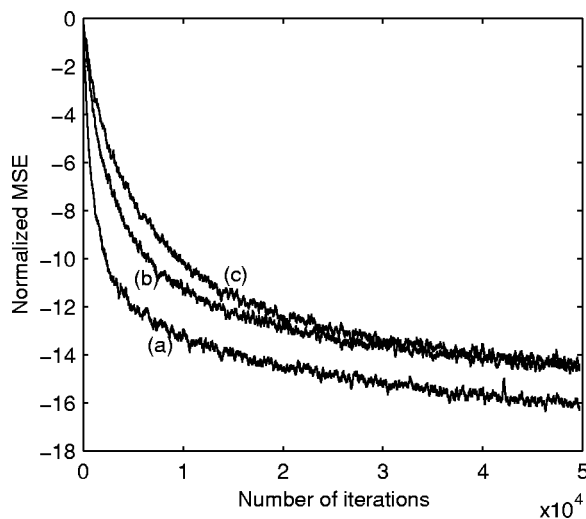


FIG. 12. Learning curves for different algorithms of 50 000 iterations with noise source of large power disparity. (a) LFRLMS algorithm; (b) FULMS algorithm; and (c) FVLMS algorithm.

white-noise signal; and from the learning curve of 50 000 iterations in Fig. 12, it can be seen that LFRLMS algorithm converges on a level approximately 2 dB below the other two algorithms. It should also be noted that the FVLMS algorithm suffers most from the change of noise source probably also due to the complex calculation of gradient vector corresponding to the parameters of direct form IIR filter.

Although all the above simulations are based on the impulse responses measured in the anechoic room, similar results can be obtained by using the impulses responses measured in a normal room with room dynamics. The main differences are the longer filter length and heavier computation burden.

V. CONCLUSIONS

In this paper, the full and simplified gradient IIR lattice algorithms for ANC were mathematically derived. Then, the simplified gradient IIR lattice algorithm was tested by using the measured transfer functions from an active noise control system. The simulation results demonstrated that the proposed lattice form adaptive IIR filtering algorithm not only converges faster than the commonly used FULMS and FVLMS algorithms when the noise source consists of sinusoid components with wide power disparity, but also converges to a smaller mean squared error. It also showed that the proposed algorithm is far less sensitive to the cancellation path modeling error, which possibly results in a more robust system in practice. Theoretical analysis of the stability of the proposed algorithm and the implementation of the algorithm in a real-time DSP ANC system are ongoing.

ACKNOWLEDGMENTS

The authors are sincerely grateful to Professor P.A. Regalia (Institut National des Télécommunications, France) and Professor Martin Bouchard (School of Information Technology and Engineering, University of Ottawa) for their helpful advice on using the adaptive IIR filters and some calculations concerning simulations. This work was supported by National Natural Science Foundation No. 60272037.

APPENDIX A: THE GRADIENT LATTICE ALGORITHM

Initialization:

Set the order of the lattice filter M and stepsize μ

All the filter coefficients and states are set to 0.

Lattice filter computation:

- Let $f_M(n) = x(n)$.
- for $k = M, M-1, \dots, 1$ do

$$\begin{bmatrix} f_{k-1}(n) \\ b_k(n) \end{bmatrix} = \begin{bmatrix} \cos \theta_k(n) & -\sin \theta_k(n) \\ \sin \theta_k(n) & \cos \theta_k(n) \end{bmatrix} \begin{bmatrix} f_k(n) \\ b_{k-1}(n-1) \end{bmatrix}$$

end for

- $b_0(n) = f_0(n)$.

- Lattice filter output:

$$y(n) = \sum_{k=0}^M b_k(n) v_k(n).$$

Post filter computation:

- **Let** $f_{cM}(n) = c(n)$, where

$$c(n) = \sum_{i=0}^N c_{wi}(i)x(n-i).$$

($c_{wi}(n)$ ($i=0, \dots, n$) are the estimated cancellation path impulse response with order $n+1$.)

- **for** $k=M, M-1, \dots, 1$ **do**

$$\begin{bmatrix} f_{ck-1}(n) \\ b_{ck}(n) \end{bmatrix} = \begin{bmatrix} \cos \theta_k(n) & -\sin \theta_k(n) \\ \sin \theta_k(n) & \cos \theta_k(n) \end{bmatrix} \begin{bmatrix} f_{ck}(n) \\ b_{ck-1}(n-1) \end{bmatrix}$$

end for

- $b_{c0}(n) = f_{c0}(n)$. (Filtered regressor signal corresponding to v_k is $b_{ck}(n)$.)
- **for** $k=1, \dots, M$ **do**
Let $f_{\theta_{k,M}} = 0$.
for $l=M, M-1, \dots, 1$ **do**
if $l=k$

$$\begin{bmatrix} f_{\theta_{k,l-1}}(n) \\ b_{\theta_{k,l}}(n) \end{bmatrix} = \begin{bmatrix} \cos \theta_l(n) & -\sin \theta_l(n) \\ \sin \theta_l(n) & \cos \theta_l(n) \end{bmatrix} \begin{bmatrix} f_{\theta_{k,l}}(n) \\ b_{\theta_{k,l-1}}(n-1) \end{bmatrix} + \begin{bmatrix} -b_{cl}(n) \\ f_{cl-1}(n) \end{bmatrix}$$

else

$$\begin{bmatrix} f_{\theta_{k,l-1}}(n) \\ b_{\theta_{k,l}}(n) \end{bmatrix} = \begin{bmatrix} \cos \theta_l(n) & -\sin \theta_l(n) \\ \sin \theta_l(n) & \cos \theta_l(n) \end{bmatrix} \begin{bmatrix} f_{\theta_{k,l}}(n) \\ b_{\theta_{k,l-1}}(n-1) \end{bmatrix}$$

end if

$$b_{\theta_{k,0}}(n) = f_{\theta_{k,0}}(n).$$

end l loop.

Filtered regressor signal corresponding to θ_k :

$$b_{\theta k}(n) = \sum_{l=0}^M v_l b_{\theta_{k,l}}(n).$$

end k loop.

Filter coefficient updates:

$$v_k(n+1) = v_k(n) + \mu e(n) b_{ck}(n)$$

$$\theta_k(n+1) = \theta_k(n) + \mu e(n) b_{\theta k}(n)$$

Test:

for $k=1, \dots, M$ **do**

$$\text{if } |\theta_k(n+1)| > \pi/2 \quad \text{set } \theta_k(n+1) = \theta_k(n).$$

end for

APPENDIX B: THE SIMPLIFIED GRADIENT LATTICE ALGORITHM

Initialization:

Set the order of the lattice filter M and stepsize μ

All the filter coefficients and states are set to 0.

Lattice filter computation:

- **Let** $f_M(n) = x(n)$.
- **for** $k=M, M-1, \dots, 1$ **do**

$$\begin{bmatrix} f_{k-1}(n) \\ b_k(n) \end{bmatrix} = \begin{bmatrix} \cos \theta_k(n) & -\sin \theta_k(n) \\ \sin \theta_k(n) & \cos \theta_k(n) \end{bmatrix} \begin{bmatrix} f_k(n) \\ b_{k-1}(n-1) \end{bmatrix}$$

end for

- $b_0(n) = f_0(n)$.
- Lattice filter output:

$$y(n) = \sum_{k=0}^M b_k(n) v_k(n)$$

Post filter computation:

- **Let** $f_{cM}(n) = c(n)$, where

$$c(n) = \sum_{i=0}^N c_{wi}(i)x(n-i).$$

($c_{wi}(n)$ ($i=0, \dots, n$) are the estimated cancellation path impulse response with order $n+1$.)

- **for** $k=M, M-1, \dots, 1$ **do**

$$\begin{bmatrix} f_{ck-1}(n) \\ b_{ck}(n) \end{bmatrix} = \begin{bmatrix} \cos \theta_k(n) & -\sin \theta_k(n) \\ \sin \theta_k(n) & \cos \theta_k(n) \end{bmatrix} \begin{bmatrix} f_{ck}(n) \\ b_{ck-1}(n-1) \end{bmatrix}$$

end for

- $b_{c0}(n) = f_{c0}(n)$. (Filtered regressor signal corresponding to v_k is $b_{ck}(n)$.)

Filter regressor:

- **Let** $\gamma_M = 1$.

- **for** $k=M, M-1, \dots, 1$ **do**

Filtered regressor signal corresponding to θ_k :

$$b_{\theta k}(n) = -\gamma_k b_{yk-1}(n)$$

$$\gamma_{k-1} = \gamma_k \cos \theta_k(n)$$

end for

Filter coefficient updates:

$$v_k(n+1) = v_k(n) - \mu e(n) b_{ck}(n)$$

- **Let** $g_M = 1$

- **For** $k=M, M-1, \dots, 1$ **do**

$$\begin{bmatrix} g_{k-1} \\ q_k \end{bmatrix} = \begin{bmatrix} \cos \theta_k(n) & -\sin \theta_k(n) \\ \sin \theta_k(n) & \cos \theta_k(n) \end{bmatrix} \begin{bmatrix} g_k \\ \mu e(n) b_{\theta k}(n) \end{bmatrix}$$

Test:

$$\text{if } g_{k-1} < 0, \text{ set } g_{k-1} = g_k \cos \theta_k(n)$$

end for

- **Let** $\alpha_0 = g_0$
- **For** $k = 1, 2, \dots, M$ **do**

$$\begin{bmatrix} \alpha_k \\ 0 \end{bmatrix} = \begin{bmatrix} \cos \theta_k(n+1) & \sin \theta_k(n+1) \\ -\sin \theta_k(n+1) & \cos \theta_k(n+1) \end{bmatrix} \begin{bmatrix} \alpha_{k-1} \\ q_k \end{bmatrix}$$

end for

Post filter computation:

- $y_c(n) = \sum_{k=0}^M b_{ck}(n) v_k(n)$
- **Let** $f_{yM}(n) = y_c(n)$
- **for** $k = M, M-1, \dots, 1$ **do**

$$\begin{bmatrix} f_{yk-1}(n+1) \\ b_{yk}(n+1) \end{bmatrix} = \begin{bmatrix} \cos \theta_k(n+1) & -\sin \theta_k(n+1) \\ \sin \theta_k(n+1) & \cos \theta_k(n+1) \end{bmatrix} \begin{bmatrix} f_{yk}(n) \\ b_{yk-1}(n) \end{bmatrix}$$

end for

- $b_{y0}(n) = f_{y0}(n)$.

¹S. M. Kuo and D. R. Morgan, *Active Noise Control Systems—Algorithms and DSP Implementations* (Wiley, New York, 1996).

²B. L. Olsen, R. W. Jones, B. R. Mace and C. R. Halkyard, "Increasing the Convergence Rate of Adaptive Feedforward ANC," in Proceedings of International Symposium on *Active Control of Sound and Vibration*, Fort Lauderdale, FL, December 1999.

³C. H. Hansen and S. D. Snyder, *Active Control of Noise and Vibration* (E&FN SPON, 1997).

⁴L. J. Eriksson, "Development of the Filtered-U Algorithm for Active Noise Control," *J. Acoust. Soc. Am.* **89**, 257–265 (1991).

⁵D. H. Crawford and R. W. Stewart, "Adaptive IIR Filtered-v Algorithms for Active Noise Control," *J. Acoust. Soc. Am.* **101**, 2097–2103 (1997).

⁶L. J. Eriksson, T. A. Laak, and M. C. Allie, "On-line Secondary Path Modeling for FIR and IIR Adaptive Control in the Presence of Acoustic Feedback," in Proceedings of International Symposium on *Active Control of Sound and Vibration*, Fort Lauderdale, FL, December 1999.

⁷A. P. Liavas and P. A. Regalia, "Acoustic Echo Cancellation: Do IIR Models Offer Better Modeling Capabilities Than Their FIR Counterparts?" *IEEE Trans. Signal Process.* **46**(9), 2499–2504 (1998).

⁸S. Haykin, *Adaptive Filter Theory* (Prentice-Hall, Englewood Cliffs, NJ, 1991).

⁹P. A. Regalia, *Adaptive IIR Filtering in Signal Processing and Control* (Dekker, New York, 1995).

¹⁰S. Horvath, Jr., "Lattice Form Adaptive Recursive Digital Filters: Algorithms and Applications," in Proceedings of IEEE Int. Symp. Circuits Syst., pp. 128–33 (1980).

¹¹P. A. Regalia, "Stable and Efficient Lattice Algorithms for Adaptive IIR Filtering," *IEEE Trans. Signal Process.* **40**(2), 375–388 (1992).

¹²K. X. Miao, H. Fan, and M. Doroslovaeki, "Cascade Lattice IIR Adaptive Filters," *IEEE Trans. Signal Process.* **42**(4), 721–741 (1994).

¹³R. Lopez-Valcarce and F. Perez-Gonzalez, "Adaptive Lattice IIR Filtering Revisited: Convergence Issue and New Algorithms with Improved Stability Properties," *IEEE Trans. Signal Process.* **49**(4), 811–821 (2001).

¹⁴D. C. Swanson, "Lattice Filter Embedding Techniques for Active Noise Control," in Proceedings of International Congress and Exposition on Noise Control Engineering, pp. 165–168 (1991).

¹⁵N. C. Mackenzie and C. H. Hansen, "The Use of an Alternative Adaptive Algorithm with a Lattice Structured Filter for a Multi-channel Active Noise or Vibration Control System," in Proceedings of International Congress and Exposition on Noise Control Engineering, pp. 177–180 (1991).

¹⁶K. Char and S. M. Kuo, "Performance Evaluation of Various Active Noise Control Algorithm," in Proceedings of International Congress and Exposition on Noise Control Engineering, pp. 331–336 (1994).

¹⁷S. M. Kuo and J. Luan, "Cross-coupled Filtered-X LMS Algorithm and Lattice Structure for Active Noise Control Systems," in Proceedings of IEEE Int. Symp. Circuits Syst., pp. 459–462 (1993).

¹⁸H. J. Lee, Y.-C. Park, C. Lee, and D. H. Youn, "Fast Active Noise Control Algorithm for Car Exhaust Noise Control," *IEE Electron. Lett.* **36**(14), 1250–1251 (2000).

¹⁹Y. C. Park and S. D. Sommerfeldt, "A Fast Adaptive Noise Control Algorithm Based on the Lattice Structure," *Appl. Acoust.* **47**(1), 1–25 (1996).

²⁰Y. Tu and C. R. Fuller, "Multiple Reference Feedforward Active Noise Control. II. Reference Preprocessing and Experimental Results," *J. Sound Vib.* **233**(5), 761–774 (2000).

²¹C. F. N. Cowan and P. M. Grant, *Adaptive Filters* (Prentice-Hall, Englewood Cliffs, NJ, 1985).

²²S. J. Chen and J. S. Gibson, "Feedforward Adaptive Noise Control with Multivariable Gradient Lattice Filters," *IEEE Trans. Signal Process.* **49**(3), 511–520 (2001).

A- and C-weighted sound levels as predictors of the annoyance caused by shooting sounds, for various façade attenuation types

Joos Vos

TNO Human Factors, P.O. Box 23, 3769 ZG Soesterberg, The Netherlands

(Received 4 March 2002; revised 9 October 2002; accepted 10 October 2002)

In a previous study on the annoyance caused by a great variety of shooting sounds [J. Acoust. Soc. Am. **109**, 244–253 (2001)], it was shown that the annoyance, as rated indoors with the windows closed, could be adequately predicted from the outdoor A-weighted and C-weighted sound-exposure levels [ASEL (L_{AE}) and CSEL (L_{CE})] of the impulse sounds. The explained variance in the mean ratings by (outdoor) ASEL was significantly increased by adding the product $(L_{CE} - L_{AE})(L_{AE})$ as a second variable. In the present study it was investigated to which extent the additional contribution of the second predictor is also relevant for façade attenuation types with lower and higher degrees of sound isolation than applied previously. Twenty subjects rated the indoor annoyance caused by 11 different impulse types produced by firearms ranging in caliber from 7.62 to 155 mm, at various levels and for five façade attenuation conditions. The effect of façade attenuation on the ratings was large and consistent. In all conditions, an optimal prediction of the annoyance was obtained with outdoor ASEL as the first, and $(L_{CE} - L_{AE})(L_{AE})$ as the second predictor. The benefit of the second predictor, expressed as the increase in the explained variance, ranged from 2.5 to 55 percent points, and strongly increased with the degree of façade attenuation. It was concluded that for the determination of the rating sound level, the acoustic parameters ASEL and CSEL are very powerful. In addition, the results showed that for the whole set of impulses included, the annoyance could also be predicted very well by the weighted sum of indoor ASEL and the product $(L_{CE} - L_{AE})(L_{AE})$.
© 2003 Acoustical Society of America. [DOI: 10.1121/1.1527957]

PACS numbers: 43.50.Pn, 43.50.Ba, 43.50.Qp, 43.66.Lj [MRS]

I. INTRODUCTION

In studies on the annoyance caused by impulse sounds produced by small firearms, it has become quite common to express the dose of a single event as the A-weighted sound-exposure level or the dose of a series of events as the A-weighted equivalent sound level (e.g., see Buchta, 1990; Schomer *et al.*, 1994; Schomer and Wagner, 1995; Vos, 1990, 2001; Vos and Geurtsen, 1987). For shooting sounds produced by medium-large and large firearms, however, there have been various discussions about which frequency weighting would be more appropriate, A or C (Buchta, 1996; Bullen *et al.*, 1991; Meloni and Rosenheck, 1995; Schomer, 1977; Schomer and Sias, 1998; Vos, 1995a).

In a previous study on the annoyance caused by impulse sounds produced by small, medium-large, and large firearms (Vos, 2001), it was shown that an almost perfect prediction of the annoyance, as rated indoors with the windows closed, was obtained on the basis of the outdoor A-weighted sound-exposure level (ASEL; L_{AE}) and the C-weighted sound-exposure level (CSEL; L_{CE}) of the sounds. With ASEL as the primary predictor, the explained variance, r^2 , in the mean ratings was already as high as 0.87. With the product $(L_{CE} - L_{AE})(L_{AE})$ as a second predictor, (multiple) r^2 further increased to about 0.97.

Inclusion of the term $(L_{CE} - L_{AE})(L_{AE})$ implies that (1) the annoyance increases with the “heaviness” of the sound [$(L_{CE} - L_{AE})$ is small for sounds with relatively little energy in the low-frequency bands, such as those produced by pis-

tols and rifles, and $(L_{CE} - L_{AE})$ is high for sounds with relatively more energy in the low-frequency bands, such as those produced by mortars and howitzers], and (2) the additional annoyance due to the heaviness of the sound increases with ASEL.

The benefit of using both A-weighted and C-weighted sound levels (either measured with the time constant of 125 ms [rms fast], or expressed as sound exposure levels) has also been shown by Buchta (1996) for explaining differences in the annoyance caused by the impulses produced by rifles, 20–35-mm cannons, and various detonations, and by Schomer and Sias (1998) for explaining differences in the annoyance caused by sonic booms and blast sounds.

In the previous study, the simulated frequency-dependent façade attenuation represented the average of noise reduction characteristics that is frequently found for Dutch dwellings with the windows closed (Vos, 2001). It is of interest to verify the relevance of the second predictor both for lower and for higher façade attenuation types. Lower outdoor-to-indoor noise reductions are relevant to residents who prefer their bedroom windows to be slightly open for the major part of the year, and who prefer their living room windows slightly open in the summer. Higher noise reductions are relevant to countries where special window glazing is generally applied for improving thermal isolation.

The results from secondary analyses of the data sets of over ten social surveys on the effect of outdoor-to-indoor

noise reduction suggest that residents who are relatively well insulated from noise exposure at home are less annoyed (Fields, 1993). If the combined use of ASEL and CSEL would lead to a high predictability of the annoyance for various degrees of façade attenuation, this method might be a potential tool for reducing the variation in individual reactions to shooting sounds.

In the present experiment, 20 subjects rated the indoor annoyance caused by a great variety of shooting sounds for five conditions in which the façade attenuation varied from low to very high.

In practice, residents may be subject to various degrees of insulation during the day, and especially in the summer, may spend a significant portion of their time outdoors in the garden, at the balcony, or on the terrace. It is understood that the overall annoyance is in some way determined by the annoyance experienced in these different conditions (for references, e.g., see Vos, 2001). A study on the way in which the annoyance in the various insulation conditions contributes to the overall annoyance, however, is beyond the scope of the present article.

II. METHODS

A. Stimuli

In addition to muzzle bangs produced by small (impulse types 1–4 in Table I), medium-large (impulse types 5 and 8), and large firearms (impulse type 11), the experiment also included combinations of muzzle and projectile bangs (impulse types 6 and 7), a spectral modification of the 155-mm howitzer muzzle bang (impulse type 9), and the sound from a detonating hand grenade (impulse type 10). With the exception of impulse type 2, these stimuli have also been used in a previous study (Vos, 2001).

For the relevant impulse types, free-field digital recordings were made at source–receiver distances ranging from 100–200 m for the small firearms to 800–900 m for the medium-large and large firearms. From each recording various versions of the impulse sound were prepared, yielding bangs with different sound-exposure levels. Detailed information about the recordings and subsequent (spectral) processing is given in Vos (2001). Briefly, in the preparation of bangs with levels lower than that of the originally recorded bang, both additional broadband attenuation (geometric spreading) and additional attenuation of (mainly) the high-frequency components (air absorption) was applied. For example, assume the availability of an original recording at a distance of 800 m, and the need for a new bang at a sound level corresponding to a simulated distance of 3200 m. The additional broadband attenuation then equals $20 \log(3200/800) = 12$ dB. The additional attenuation due to air absorption in the various frequency bands is calculated for a distance of $3200 - 800 = 2400$ m. The calculations were performed for a meteorological condition with a temperature of 10 °C and a relative humidity of 80% (ISO, 1978).

To simulate the various frequency-dependent outdoor-to-indoor noise reductions, further spectral filtering of the impulses was applied. For each façade attenuation type, the level reduction is shown in Fig. 1. In the condition which

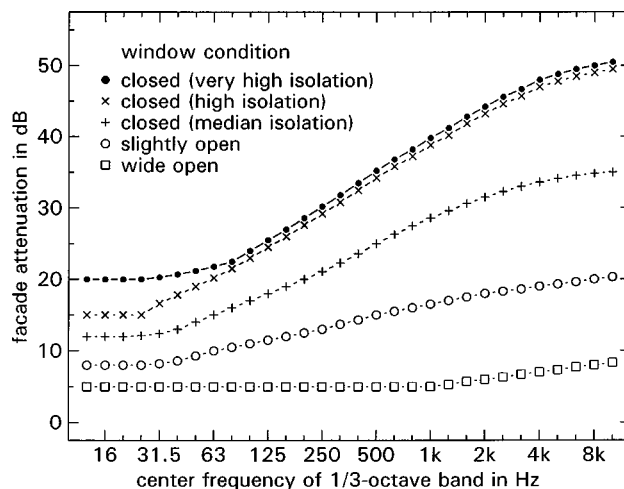


FIG. 1. Frequency-dependent outdoor-to-indoor sound reduction for five conditions.

simulated wide-open windows, an attenuation of 5 dB was assumed for frequencies between 12.5 and 1000 Hz. For higher frequencies the attenuation was 8 dB at most. With the windows slightly open, the attenuation ranged from 8 dB up to 20 dB. There were three conditions which simulated closed windows. With a median degree of isolation the façade attenuation increased from 12 dB for the 16-Hz and 31.5-Hz octave bands up to 35 dB for the 8-kHz octave band. Within 1 dB, this latter façade attenuation type was equal to the outdoor-to-indoor noise reduction applied in Vos (2001). With the high degree of isolation in the windows-closed condition, the attenuation ranged from 15 dB up to 50 dB. By using a specific type of double glazing, such a high airborne noise reduction can be realized (Gerretsen, 1996). To explore the effects of a very high degree of isolation, a façade attenuation type was included in which the reduction in sound level for the frequencies in the two lower octave bands was as high as 20 dB.

As in Vos (2001), a finite impulse response (FIR) filter on a DSP card was used to attenuate the signals, and to compensate as much as possible for the resonances due to room dimensions and for the nonflat frequency characteristics of the audio equipment.

In the two façade attenuation conditions with relatively small reductions in sound level, there were five versions per impulse type, yielding 55 (11 types \times 5 levels) different impulses. The (outdoor) ASELs ranged from 47 to 75 dB, in steps of 7 dB. Outdoor CSEL ranged from 48 to 97 dB. In the other three façade attenuation conditions, the total number of impulses presented was lower: as a result of the simulated façade attenuation, several impulses were inaudible or hardly audible.

Figure 2 shows the linear sound exposure level (SEL) in the various $\frac{1}{3}$ -octave bands for the five versions of the muzzle bang from a 9-mm pistol, a 0.5-in. machine gun, and a 35-mm cannon, and the sound of a detonating hand grenade. In all cases the levels were determined at the position of the heads of the subjects in the conditions with the windows wide open.

For the pistol bangs [Fig. 2(a)] the spectral content is

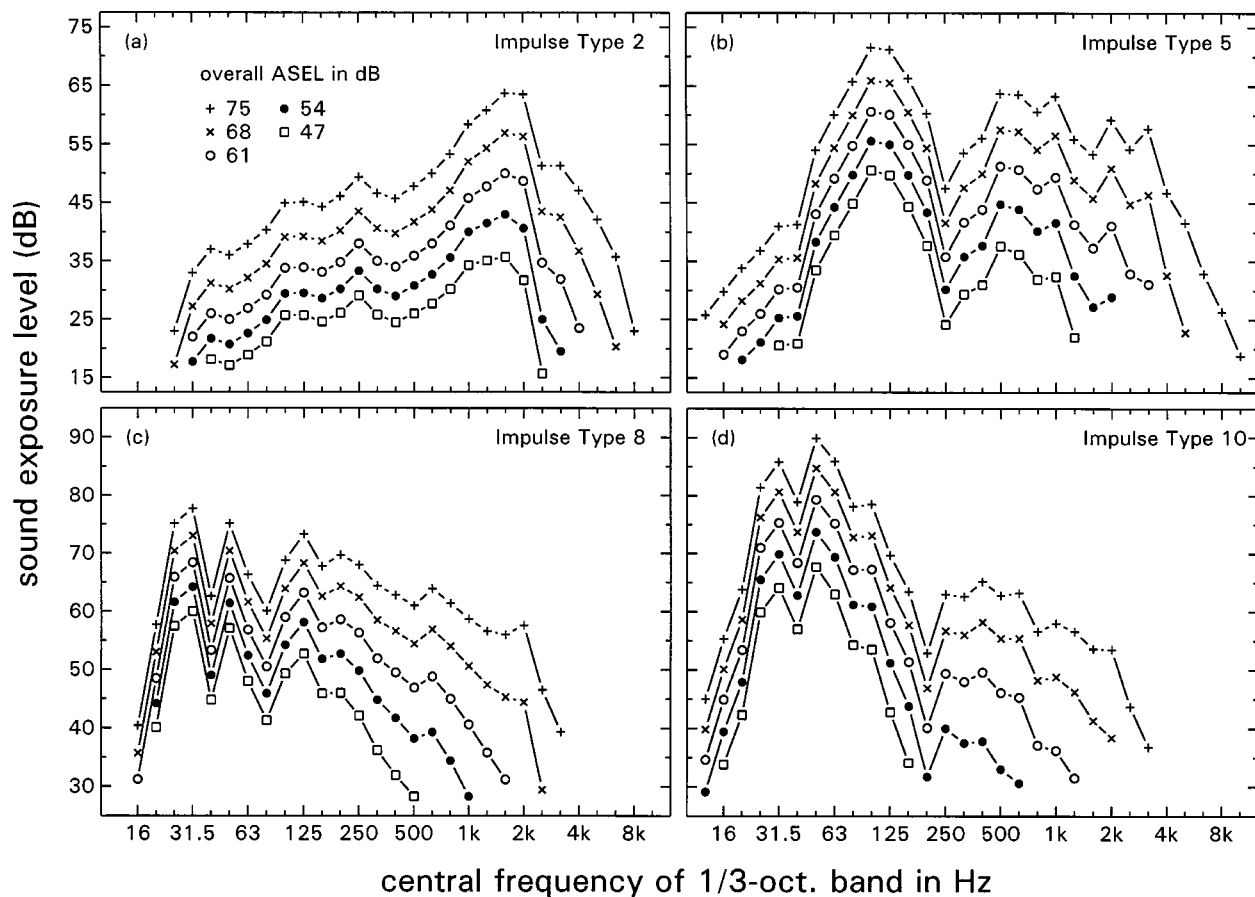


FIG. 2. Sound-exposure levels in the various $\frac{1}{3}$ -octave bands for five versions of the bang from (a) a 9-mm pistol; (b) a 0.5-in. machine gun; (c) a 35-mm cannon; and (d) a detonating hand grenade, as determined at the ears of the subjects in the simulated conditions with the windows wide open. For each impulse type, the five spectra correspond to overall outdoor ASELs of 47, 54, 61, 68, or 75 dB.

dominated by the energy in the frequency bands between about 800 and 2500 Hz, whereas for the bangs from the detonating hand grenade [Fig. 2(d)], the spectral content is dominated by the energy in frequency bands between about 20 and 125 Hz.

For frequencies lower than 25 Hz, the sound levels of the howitzer bangs drop by about 35 dB/octave. Results from outdoor measurements reported in Kerry *et al.* (1996) show that for a similar bang produced by a 155-mm howitzer, the sound level in this low-frequency band drops by about 6 dB/octave. The discrepancy between our spectra and those reported by Kerry *et al.* (1996) might for a relevant part be explained by the limitations of our audio system noted above.

For the machine gun [Fig. 2(b)] and the 35-mm cannon [Fig. 2(c)], the spectrum contains both lower and higher frequency components at a significant sound level. For all impulse types, Fig. 2 also shows that due to the simulated air absorption, the relative contribution of the higher frequency components decreases with overall level. For information about the rise time and the duration of the impulse sounds, the reader is referred to Vos (2001).

Various experts confirmed that the bangs sounded realistic. This held true also for the heavy bangs produced by the hand grenade and the 155-mm howitzer. Given that for frequencies higher than 25 Hz the frequency response was flat, it is not *a priori* evident that our experimental results would

have been different if we had been able to reproduce the sound levels in Kerry *et al.* (1996) for frequencies lower than 25 Hz.

In order to make the acoustic environment more realistic as well, a soft, spectrally modified pink noise was continuously present throughout the experiment at an A-weighted average level of 35 dB. The spectral content was dominated by energy in the frequency range between 25 and 125 Hz. For higher frequencies, the spectral envelope slope was -6 dB/octave.

B. Apparatus

The experiment was entirely computer controlled. The sounds were reproduced in the listening room ($w \times l \times h = 3.5 \times 5.9 \times 3.3$ m) by means of two amplifier/speaker sets, one set for frequencies lower than, and one set for frequencies higher than 150 Hz. The speakers were positioned in the doorway of an adjacent room and were hidden behind a curtain. The reverberation time of the room corresponded to that of a normal living room. Hearing thresholds were determined with the help of a Madsen memory threshold audiometer (MTA 86).

C. Subjects

Twenty subjects, ten males and ten females, between 19 and 30 years of age, participated in the experiment. Before

the experimental sessions, their hearing thresholds were determined with pure tones between 250 and 8000 Hz. Nineteen subjects had hearing levels ≤ 15 dB in any part of the audiogram (best ears). One subject with hearing levels ≤ 5 dB for frequencies up to 4 kHz had a local hearing loss of 25 dB at 6 kHz. Since frequencies higher than 4 kHz were considered to be irrelevant to the present study, this subject was regarded as a suitable participant as well. For obtaining information about the hearing levels at frequencies lower than 250 Hz, the individual hearing thresholds at 500 and 250 Hz were extrapolated. It was concluded that for all 20 subjects, their hearing levels at frequencies between 30 and 125 Hz must have been ≤ 15 dB as well. The subjects were paid for their services.

D. Experimental design

The independent variables were: (1) façade attenuation (five types, from very low to very high degrees of reduction in sound level; see Fig. 1); (2) impulse type (11 types produced by firearms ranging in caliber from 7.62 to 155 mm; see Table I); sound level (outdoor ASELs of 47, 54, 61, 68, or 75 dB). In Sec. II A, it was explained that with respect to sound level there was an incomplete factorial design. All three factors were varied within subjects. Each condition (189 bangs in total) was presented twice for rating.

E. Procedure

After each trial, in which a specific stimulus was presented twice within about 8 s, the subjects responded to the question “How annoying would you find the sound if you heard it at home in the living room (or study) on a regular basis?” They were told that the bangs were presented in various ways to simulate indoor listening conditions with the windows partly or completely closed. The subjects were encouraged to use the whole range of the rating scale with values from 1 (“not annoying at all”) to 10 (“extremely annoying”). Each subject was tested separately.

For obtaining mutually comparable ratings for the annoyance in the various façade attenuation conditions, it was decided to vary façade attenuation within blocks. The 189 bangs were assigned to five blocks of 37 or 38 stimuli each. Both for the first and for the second ratings, presentation order of these blocks was balanced by means of Latin squares. Presentation order of the stimuli within the blocks was randomized. Before the experimental sessions, the subjects received nine practice trials. The total duration of the experimental session was about 4 h, including various breaks in between. The background noise was continuously present without interruption.

III. RESULTS

Since in noise zoning it is mandatory to express the noise dose as levels measured outdoors, it was decided to design the experiments in such a way that the outdoor levels were varied systematically. This implies that in Sec. III A the statistical significance of the effects of the outdoor sound level and the other stimulus variables could be efficiently tested with the help of analyses of variance.

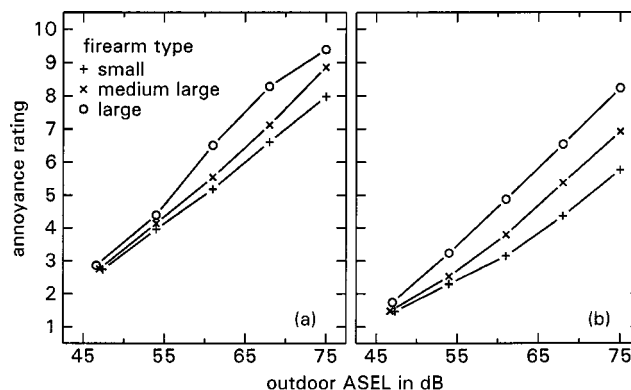


FIG. 3. Mean annoyance ratings as a function of outdoor ASEL, for three categories of firearm caliber and two types of façade attenuation simulating listening conditions with the windows (a) wide open; and (b) slightly open.

In Sec. III B, the ratings are related to indoor levels. Here, the effects will be analyzed by means of linear regression only.

A. Indoor ratings as a function of outdoor levels

The results are presented for each façade attenuation type separately. Analyses of variance were performed on the various sets of annoyance ratings. For all sets, the main effect of subjects was highly significant ($p < 0.000\,001$). The difference between the mean ratings from the subjects with the highest and the lowest scores was typically about 2 scale units.

For the larger data sets (Secs. III A 1–3) the variance explained by the stimulus variables was more than 4–7 times as large, and for the smaller data sets (Secs. III A 4–5) it was about 2 times as large as the variance explained by individual differences.

In general, the analyses of variance showed that the ratings determined in the first measurements were not significantly different from those determined in the second measurements, and that there were no significant first- and second-order interaction effects of replication and the stimulus variables. In the more detailed presentation of the results below, it was therefore decided to average across replication.

1. Windows wide open

The annoyance ratings obtained in the condition with the windows wide open were subjected to an analysis of variance [20 (subjects) \times 11 (impulse type) \times 5 (outdoor sound level) \times 2 (replication), all repeated measures]. The ratings significantly increased with increasing ASEL [$F(4,76) = 410$, $p < 0.000\,001$] and were significantly affected by impulse type [$F(10,190) = 16.0$, $p < 0.000\,001$]. A *post hoc* Tukey test (Winer, 1970) showed that averaged across sound level, the bangs from impulse types 1–8 were all less annoying than the bangs from impulse types 9–11 ($p \leq 0.05$). Moreover, there was a significant interaction effect between impulse type and sound level [$F(40,760) = 3.72$, $p < 0.000\,001$].

The interaction effect is shown in Fig. 3(a) for a number of bangs produced by small firearms (impulse types 1 and 2), medium-large firearms (impulse types 5 and 8), and large firearms (impulse types 10 and 11). Figure 3(a) illustrates

TABLE I. Annoyance ratings, averaged across subjects and replications, for the 11 impulse types and the outdoor measured ASELs (dB) in two listening conditions.

No.	Firearm/ammunition	ASEL:	Windows wide open					Windows slightly open				
			47	54	61	68	75	47	54	61	68	75
1	Pistol	2.9	4.1	5.2	6.6	8.0	1.4	2.2	3.1	4.3	5.8	
2	Pistol Glock 9 mm	2.6	3.9	5.2	6.6	7.9	1.5	2.4	3.2	4.4	5.7	
3	Rifle 7.62 mm	2.7	3.9	5.6	6.9	8.6	1.6	2.3	3.3	5.1	6.3	
4	Rifle 0.30 in.	3.1	4.2	5.5	7.1	8.4	1.7	2.5	3.5	4.8	6.4	
5	Machine gun 0.5 in.	2.9	4.1	5.4	7.1	8.9	1.5	2.5	3.4	5.1	6.7	
6	Cannon 25 mm DST 127	2.5	4.0	5.1	6.6	8.4	1.3	2.6	3.6	4.6	6.1	
7	Cannon 35 mm	2.7	3.8	5.2	7.1	8.2	1.5	2.4	3.6	4.7	6.5	
8	Cannon 35 mm	2.7	4.1	5.7	7.2	8.8	1.5	2.6	4.2	5.6	7.2	
9	Howitzer 155 mm, charge 5M4 ^a	3.2	4.9	6.5	7.7	8.9	1.9	3.0	4.6	5.9	7.4	
10	Hand grenade	2.6	4.1	6.3	8.2	9.5	1.6	2.9	4.7	6.7	8.3	
11	Howitzer 155 mm, charge 5M4	3.1	4.7	6.7	8.3	9.3	1.9	3.6	5.0	6.4	8.2	

^aAdditional spectral modification: 63 Hz high pass.

that at low outdoor ASELs all bangs were about equally annoying, whereas at higher ASELs the bangs from the medium-large firearms were less annoying than the bangs from the large firearms, and that they were more annoying than the bangs from the small firearms.

On the basis of the mean annoyance ratings given in columns 3–7 of Table I, it can be verified that the nature of the interaction effect described above also holds for the impulse types that were not included in Fig. 3(a).

The 55 mean annoyance ratings (y) from Table I were subjected to a (forward stepwise) multiple linear regression analysis in which the independent variables are individually added to the model at each step of the regression, until the best regression model is obtained. The potential predictors were outdoor ASEL, CSEL, $L_{CE}-L_{AE}$, and $(L_{CE}-L_{AE})(L_{AE})$. ASEL was selected as the first predictor ($y = -7.1 + 0.21L_{AE}$) and the explained variance, r^2 , in the mean ratings was equal to 95.4%. Apparently, none of the other (single) variables could predict the mean ratings more accurately than ASEL did. The product $(L_{CE}-L_{AE})(L_{AE})$ was selected as the second predictor [$y = -7.7 + 0.21L_{AE} + 0.0007(L_{CE}-L_{AE})(L_{AE})$, (multiple) $r^2 = 97.9\%$]. The constants and regression weights for the two linear functions, as well as the corresponding r^2 values, are given also in Table II. Statistically, the increase of 2.5 percent points in the explained variance was highly significant ($p < 0.000001$). The variable $L_{CE}-L_{AE}$ was not selected as the second predictor, because addition of this variable would have yielded a smaller increase in the explained variance (2.1 instead of 2.5 percent points). A further small (half a percent point) but significant ($p < 0.0005$) increase in the explained variance

was obtained by the selection of $L_{CE}-L_{AE}$ as the third predictor.

Table III shows the difference between the outdoor CSEL and ASEL for the various outdoor ASELs at which the bangs were presented. The differences increase with increasing weapon caliber and decreasing ASEL (a decrease in the sound level in front of the façade corresponds to an increase in the distance between the source and the receiver). As in the previous study (see Table III in Vos, 2001), $L_{CE}-L_{AE}$ ranges from about -1 to 30 dB.

2. Windows slightly open

The annoyance ratings obtained in the condition with the windows slightly open were subjected to an analysis of variance with exactly the same design that was used in Sec. III A 1. The ratings significantly increased with increasing ASEL [$F(4,76) = 288$, $p < 0.000001$] and were significantly affected by impulse type [$F(10,190) = 21.6$, $p < 0.000001$]. A *post hoc* Tukey test showed that averaged across sound level, the bangs from impulse types 1–7 were all less annoying than the bangs from impulse types 9–11 ($p \leq 0.01$). Moreover, there was a significant interaction effect between impulse type and sound level [$F(40,760) = 6.24$, $p < 0.000001$].

The interaction effect is shown in Fig. 3(b) for the same impulse types that were depicted in Fig. 3(a). Figure 3(b) illustrates that at the lowest outdoor ASEL all bangs were about equally annoying, whereas at higher ASELs the bangs from the medium-large firearms were less annoying than the

TABLE II. Constants, regression weights, and r^2 values for analyses with one or two predictors, for five façade attenuation types.

Window condition	$y = \gamma + \alpha L_{AE}$			$y = \gamma + \alpha L_{AE} + \beta (L_{CE} - L_{AE})(L_{AE})$				Increase in r^2
	γ	α	r^2	γ	α	β	r^2	
Wide open	-7.1	0.21	0.954	-7.7	0.21	0.0007	0.979	0.025
Slightly open	-7.3	0.19	0.896	-8.2	0.19	0.0011	0.968	0.072
Closed (median isolation)	-6.5	0.15	0.705	-9.2	0.17	0.0015	0.970	0.265
Closed (high isolation)	-4.9	0.11	0.402	-9.4	0.16	0.0014	0.949	0.547
Closed (very high isolation)	-6.5	0.14	0.864	-8.4	0.14	0.0011	0.967	0.103

TABLE III. Difference between the outdoor CSEL and ASEL for the various outdoor ASELs at which the bangs were presented.

Impulse type no.	Outdoor ASEL				
	47	54	61	68	75
1	0.6	-0.2	-0.6	-0.9	-1.1
2	0.5	0.0	-0.3	-0.5	-0.6
3	5.8	4.2	3.3	2.7	2.3
4	8.5	6.9	5.7	4.9	4.4
5	12.0	10.0	8.4	7.2	6.2
6	16.3	12.7	9.6	7.1	5.2
7	17.5	14.1	11.3	9.1	7.4
8	19.2	16.7	14.3	12.1	10.3
9	23.4	20.7	17.6	14.8	12.4
10	27.1	26.3	25.0	23.3	21.6
11	28.7	26.2	23.1	20.2	17.6

bangs from the large firearms, and that they were more annoying than the bangs from the small firearms.

On the basis of the mean annoyance ratings given in columns 8–12 of Table I, it can be verified that the nature of the interaction effect described above also holds for the impulse types that were not included in Fig. 3(b).

Again, the 55 mean annoyance ratings (y) from Table I were subjected to a multiple linear regression analysis with the same potential predictors used in Sec. III A 1. ASEL was selected as the first predictor, with $r^2=89.6\%$. The product $(L_{CE}-L_{AE})(L_{AE})$ was selected as the second predictor, with (multiple) $r^2=96.8\%$ (see Table II). Statistically, the increase of 7.2 percent points in the explained variance was highly significant ($p<0.000001$). A further small but significant increase in the explained variance of 1 percent point was obtained by the selection of $L_{CE}-L_{AE}$ as the third predictor.

3. Median isolation with windows closed

Figure 4(a) shows the mean annoyance ratings in the condition in which a median isolation with the windows closed was simulated, as a function of outdoor ASEL and with firearm caliber as a parameter. Again, the bangs from the medium-large firearms [Fig. 4(a) shows the results from impulse types 5 and 8] were more annoying than the bangs from the small firearms (impulse types 1 and 2), and the

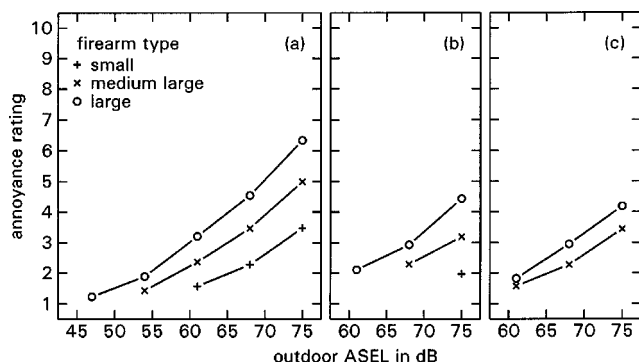


FIG. 4. Mean annoyance ratings as a function of outdoor ASEL, for three categories of firearm caliber and for three simulated listening conditions with the windows closed, resulting in (a) a median; (b) a high; and (c) a very high degree of façade attenuation.

bangs from the large firearms (impulse types 10 and 11) were more annoying than those of the medium-large firearms. Moreover, the growth in the annoyance with increasing ASEL was greater for the bangs from the medium-large and large firearms than it was for the bangs from the small firearms.

The mean annoyance ratings are given in columns 2–6 of Table IV. Fourteen conditions were excluded because the impulses were not or were only faintly audible. To test the significance of the effects described above, two analyses of variance were performed. In the first analysis, the ratings for four versions of impulse types 5–11, with ASELs of 54, 61, 68, or 75 dB were included. The second analysis included the ratings for three versions of all 11 impulse types, with ASELs of 61, 68, or 75 dB.

The first analysis showed that the ratings significantly increased with increasing ASEL [$F(3,57)=220$, $p<0.000001$] and were significantly affected by impulse type [$F(6,114)=31.4$, $p<0.000001$]. Moreover, there was a significant interaction effect between impulse type and sound level [$F(18,342)=3.0$, $p<0.0001$]. The results of the second analysis led to essentially the same conclusions.

The 41 mean annoyance ratings (y) from Table IV were subjected to a multiple linear regression analysis with ASEL, $L_{CE}-L_{AE}$, and $(L_{CE}-L_{AE})(L_{AE})$ as the potential predictors.² ASEL was selected as the first predictor, with $r^2=70.5\%$. The product $(L_{CE}-L_{AE})(L_{AE})$ was selected as the second predictor, with (multiple) $r^2=97.0\%$ (Table II). The increase of 26.5 percent points in the explained variance was highly significant. The third predictor did not allow a further significant improvement of r^2 .

4. High isolation with windows closed

Figure 4(b) shows the mean annoyance ratings in the condition in which a high isolation with the windows closed was simulated. Again, the bangs from the medium-large firearms were more annoying than the bangs from the small firearms, and the bangs from the large firearms were more annoying than those of the medium-large firearms. The growth in the annoyance with increasing ASEL was slightly greater for the bangs from the large firearms than it was for the bangs from the medium-large firearms.

The mean annoyance ratings are given in columns 7–9 of Table IV. Thirty conditions were excluded because the impulses were inaudible or only faintly audible. To test the significance of the effects described above, two analyses of variance were performed. In the first analysis, the ratings for three versions of impulse types 6 and 8–11, with ASELs of 61, 68, or 75 dB were included. The second analysis included the ratings for two versions of impulse types 3–11, with ASELs of 68 or 75 dB.

The first analysis showed that the ratings significantly increased with ASEL [$F(2,38)=153$, $p<0.000001$] and were significantly affected by impulse type [$F(4,76)=29.5$, $p<0.000001$]. In addition, there was a significant interaction effect between impulse type and sound level [$F(8,152)=4.9$, $p<0.0001$]. The second analysis yielded similar results.

TABLE IV. Annoyance ratings, averaged across subjects and replications, for the 11 impulse types and the outdoor measured ASELs (dB) in the three listening conditions with the windows closed.

Impulse type no.	ASEL:	Windows closed (median isolation)					Windows closed (high isolation)			Windows closed (very high isolation)			
		47	54	61	68	75	61	68	75	54	61	68	75
1		1.6	2.2	3.5	1.9
2		1.6	2.4	3.5	2.1
3		1.9	2.7	4.1	...	1.8	2.4
4		2.0	3.1	4.1	...	1.7	2.7
5		...	1.3	2.2	3.2	4.7	...	2.0	2.8
6		...	1.3	2.1	3.0	4.3	1.1	1.8	2.5
7		...	1.2	2.2	3.4	4.7	...	2.0	3.0
8		...	1.6	2.6	3.8	5.3	1.2	2.6	3.6	...	1.5	2.1	3.2
9		...	1.7	2.8	4.2	5.6	1.7	2.6	4.0	...	1.7	2.5	3.7
10		1.4	2.0	3.4	4.6	6.5	2.2	3.3	4.8	1.2	1.9	2.9	4.4
11		...	1.8	3.0	4.5	6.2	2.0	2.6	4.1	...	1.8	3.0	4.0

The 25 mean annoyance ratings (y) from Table IV were subjected to the regression analysis with the same potential predictors³ used in Sec. III A 3. ASEL was selected first, with $r^2=40.2\%$. The product $(L_{CE}-L_{AE})(L_{AE})$ was selected as the second predictor, with (multiple) $r^2=94.9\%$ (Table II). The increase of 54.7 percent points in the explained variance was highly significant. No third predictor was selected for a further improvement of r^2 .

5. Very high isolation with windows closed

Figure 4(c) shows the mean annoyance ratings in the condition in which a very high isolation with the windows closed was simulated. Again, the bangs from the large firearms were more annoying than those of the medium-large firearms. The growth in the annoyance with increasing ASEL tended to be slightly greater for the bangs from the large firearms than it was for the bangs from the medium-large firearms.

The mean annoyance ratings are given in columns 10–13 of Table IV. Only 13 conditions were included. The differences between the high and the very high degrees of façade attenuation were restricted to the very low frequencies only. Since the bangs from impulse types 1–7 did not contain significant degrees of energy in these low-frequency bands, inclusion of these bangs would have resulted in the same ratings obtained in the conditions described in the previous section. For impulse types 8–11, the bangs with outdoor levels of 47 dB, and most of the bangs with outdoor levels of 54 dB were excluded because, again, these impulses were inaudible or only faintly audible.

To test the significance of the effects described above, an analysis of variance was performed for three versions of impulse types 8–11, with ASELs of 61, 68, or 75 dB. The analysis showed that the ratings significantly increased with ASEL [$F(2,38)=104$, $p<0.000\,001$] and were significantly affected by impulse type [$F(3,57)=13.5$, $p<0.000\,01$]. In addition, there was a small but significant interaction effect between impulse type and sound level [$F(6,114)=2.4$, $p<0.05$].

The 13 mean annoyance ratings (y) from Table IV were subjected to an analysis with the same potential predictors used in Sec. III A 1. ASEL was selected as the first predictor,

with $r^2=86.4\%$. The product $(L_{CE}-L_{AE})(L_{AE})$ as the second predictor yielded a (multiple) r^2 equal to 96.7% (see Table II). The increase of 10.3 percent points in the explained variance was highly significant. As an alternative second predictor, $L_{CE}-L_{AE}$ would have yielded a similar level of predictability. No third predictor allowed a further significant improvement of r^2 .

6. A comparison of the effects of the various façade attenuation types

In Secs. III A 1–5, the annoyance ratings were presented for each façade attenuation type separately. Here, it is shown to which extent the ratings were affected by the degree of façade attenuation.

For obtaining an overall view of this effect, the data from Figs. 3 and 4 are reproduced in Fig. 5. The various panels of Fig. 5 show the mean annoyance ratings caused by the bangs from either the small, the medium-large, or the large firearms as a function of outdoor ASEL for each separate façade attenuation type.

First, it must be concluded from Fig. 5 that the effect of façade attenuation type was large and consistent. Second, the differences among the various façade conditions were slightly larger for the bangs from the small firearms than for the bangs from the medium-large and large firearms. Third, Fig. 5 shows that for all three weapon caliber categories, the effect of façade attenuation slightly increased with increasing ASEL. Fourth, for the bangs from the large firearms it is shown in Fig. 5(c) that in the condition with a high isolation the ratings were almost equal to those obtained in the condition with a very high isolation.

For the first three effects discussed above, the significance was tested in an analysis of variance [20 (subjects) \times 3 (façade attenuation; windows wide open, windows slightly open, or median isolation with windows closed) \times 11 (impulse type) \times 3 (outdoor ASEL of 61, 68, or 75 dB) \times 2 (replication), all repeated measures]. As expected, the differences among the three façade attenuation conditions were highly significant [$F(2,38)=437$, $p<0.000\,001$]. The effect of façade attenuation was dependent on impulse type [$F(20,380)=4.17$, $p<0.000\,002$], which confirms the previ-

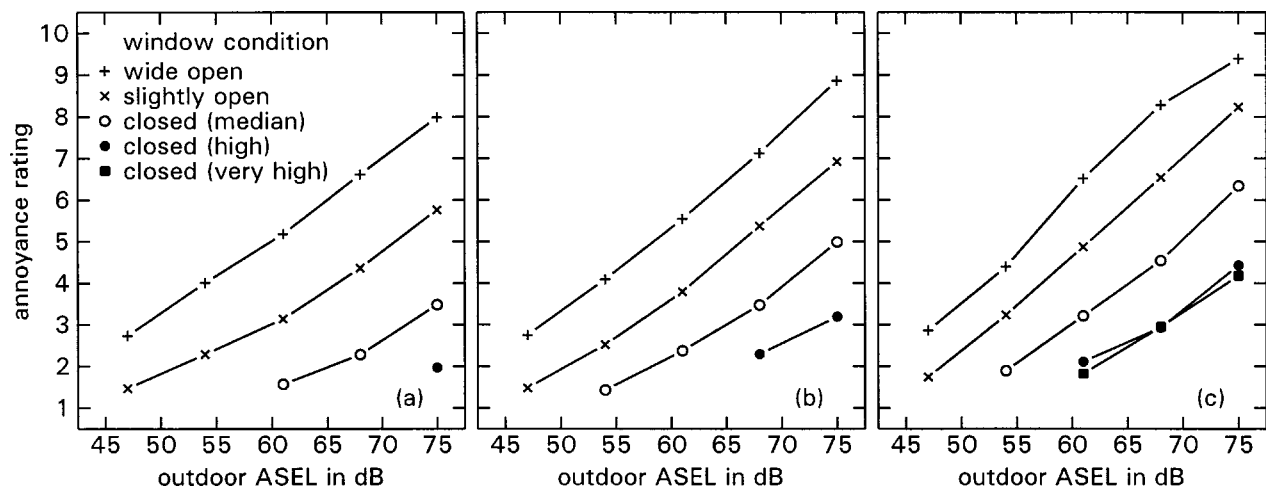


FIG. 5. Mean annoyance ratings as a function of outdoor ASEL, for various façade attenuation types and for bangs produced by (a) small; (b) medium-large; and (c) large firearms.

ous observation that the effect of façade attenuation type was larger for the bangs from the small firearms than for those of the medium-large and large firearms. The observation that the effect of façade condition was slightly larger for the higher than for the lower sound levels was confirmed also [$F(4,76) = 4.74, p < 0.005$].

For the prediction of the indoor annoyance ratings determined for the whole set of 189 conditions, it is necessary to include a predictor that represents the degree of façade attenuation. As potential predictors, the reduction in sound level in each of the nine octave bands between 16 and 4000 Hz were selected.

For each façade attenuation type, these values are given in Table V. A multiple linear regression analysis, with the (189) mean annoyance ratings as criterion, and ASEL, CSEL, $L_{CE} - L_{AE}$, $(L_{CE} - L_{AE})(L_{AE})$, and the sound reduction in the nine octave bands as predictors, showed that for an accurate prediction of the annoyance, only three independent variables are needed.

The sound reduction in the 1000-Hz octave band (R_{1000}) was selected as the first predictor⁴ [$y = 5.9 - 0.095R_{1000}$, $r^2 = 0.31$]. ASEL was selected as the second predictor [$y = -4.8 + 0.18L_{AE} - 0.137R_{1000}$, (multiple) $r^2 = 0.90$]. As a result, by adding ASEL, the explained variance was increased by 59 percent points. A further increase of 7 percent points in the explained variance was obtained by the selection of $(L_{CE} - L_{AE})(L_{AE})$ as the third predictor [$y = -5.9 + 0.19L_{AE} + 0.0011(L_{CE} - L_{AE})(L_{AE}) - 0.147R_{1000}$, (multiple) $r^2 = 0.97$].

Additional regression analyses showed that with alternative representatives of the degree of façade attenuation, such as the reduction in sound level in the 63- or 125-Hz octave bands, the total explained variance was lower by only 0.7 and 0.1 percent point, respectively, than by using the reduction in the 1000-Hz octave band. By using the level reduction in the 16- or 31.5-Hz octave bands as predictors, however, the total explained variance would have been significantly lower by 5.8 and 3.7 percent points, respectively.

B. Indoor ratings as a function of indoor levels

1. Windows wide open

In the condition with the windows wide open, the indoor ASELs of the bangs were 5–6 dB lower than the outdoor ASELs. For indoor levels, the differences $L_{CE} - L_{AE}$ were close to the differences listed in Table III for the outdoor levels.

As in Sec. III A 1, the 55 mean annoyance ratings (y) from Table I were subjected to a forward stepwise multiple linear regression analysis, but now with *indoor* ASEL, CSEL, $L_{CE} - L_{AE}$, and $(L_{CE} - L_{AE})(L_{AE})$ as the potential predictors. ASEL was selected as the first predictor ($y = -6.2 + 0.21L_{AE}$; $r^2 = 95.9\%$). The product $(L_{CE} - L_{AE})(L_{AE})$ was selected as the second predictor [$y = -6.6 + 0.21L_{AE} + 0.0068(L_{CE} - L_{AE})(L_{AE})$, (multiple) $r^2 = 97.9\%$]. The increase of 2 percent points in the explained variance was highly significant ($p < 0.000001$).

TABLE V. Sound-level reduction (dB) in nine octave bands for the various façade attenuation conditions. Values are arithmetic means of the levels in the corresponding $\frac{1}{3}$ -octave bands shown in Fig. 1.

Window condition	Center frequency of the octave bands (Hz)								
	16	31.5	63	125	250	500	1000	2000	4000
Wide open	5.0	5.0	5.0	5.0	5.0	5.0	5.1	6.0	7.0
Slightly open	8.0	8.3	9.9	11.5	13.1	14.9	16.5	17.9	19.0
Closed (median isolation)	12.0	12.5	15.0	18.0	21.1	25.0	28.6	31.5	33.6
Closed (high isolation)	15.0	16.5	20.2	24.5	29.2	34.2	38.7	43.2	46.8
Closed (very high isolation)	20.0	20.3	21.8	24.6	29.2	34.2	38.7	43.2	46.8

2. Windows slightly open

In the condition with the windows slightly open, the indoor ASELs of the bangs from the small firearms were 17–18 dB lower than the outdoor ASELs. For the large firearms, the differences between the outdoor and indoor ASELs were equal to 10–14 dB. Especially for the low-level bangs from the small firearms and the high-level bangs from the large firearms, the indoor level differences $L_{CE} - L_{AE}$ were 2–5 dB larger than the differences for the outdoor levels (Table III).

As in Sec. III A 2, the 55 mean annoyance ratings (y) from Table I were subjected to a regression analysis, but now with the same potential predictors used in Sec. III B 1. ASEL was selected as the first predictor ($y = -5.3 + 0.20L_{AE}$; $r^2 = 94.2\%$). The product $(L_{CE} - L_{AE})(L_{AE})$ was selected as the second predictor [$y = -5.4 + 0.20L_{AE} + 0.00045(L_{CE} - L_{AE})(L_{AE})$, (multiple) $r^2 = 95.1\%$]. The increase of almost 1 percent point in the explained variance was statistically significant ($p < 0.005$). The regression weight of the second predictor increased by a factor of 10 after addition of $L_{CE} - L_{AE}$ as the third predictor [$y = -3.1 + 0.15L_{AE} + 0.004(L_{CE} - L_{AE})(L_{AE}) - 0.17(L_{CE} - L_{AE})$, (multiple) $r^2 = 97.4\%$]. The latter increase in r^2 was highly significant ($p < 0.000001$).

3. Median isolation with windows closed

In the condition which simulated a median degree of isolation, the indoor ASELs of the bangs from the small firearms were about 30 dB lower than the outdoor ASELs. For the large firearms, the differences between the outdoor and indoor ASELs were equal to 15–23 dB. Especially for the high-level bangs from the large firearms, the differences $L_{CE} - L_{AE}$ were 4–9 dB larger than the differences for the outdoor levels (Table III).

In the multiple linear regression analysis performed on the 41 mean ratings from Table IV, only indoor ASEL was selected as a significant predictor ($y = -5.1 + 0.20L_{AE}$; $r^2 = 94.2\%$).

4. High isolation with windows closed

In the condition which simulated a high degree of isolation, the indoor ASELs of the bangs from the small firearms were about 40 dB lower than the outdoor ASELs. For the large firearms, the differences between the outdoor and indoor ASELs were equal to 22–30 dB. Indoors, the differences $L_{CE} - L_{AE}$ were larger than the outdoor differences by 4–6 dB for the bangs from the small firearms, and by 6–12 dB for the bangs from the large firearms.

In the multiple linear regression analysis performed on the 25 mean ratings from Table IV, only indoor ASEL was selected as a significant predictor ($y = -3.9 + 0.17L_{AE}$; $r^2 = 91.0\%$).

5. Very high isolation with windows closed

In the condition which simulated a very high degree of isolation, the indoor ASELs of the bangs produced by the

large firearms were only 1–2 dB lower than the ASELs of the corresponding bangs presented in the high-isolation condition.

In the multiple linear regression analysis performed on the 13 mean ratings from Table IV, only indoor ASEL was selected as a significant predictor ($y = -4.5 + 0.18L_{AE}$; $r^2 = 91.4\%$).

6. A comparison of the effects of the various façade attenuation types

In Secs. III B 1–5, the annoyance ratings were related to the indoor acoustic predictors for each façade attenuation type separately. For an overall description of the annoyance for all conditions together, it might in addition to the pertinent indoor acoustic variables be relevant to include one or more predictors that somehow represent features of the façade attenuation.

A multiple linear regression analysis, with the (189) mean annoyance ratings as a criterion, and indoor ASEL, $L_{CE} - L_{AE}$, $(L_{CE} - L_{AE})(L_{AE})$, and the sound reduction in the nine octave bands (see Table V) as the potential predictors, showed that for an accurate prediction of the annoyance, only two independent variables are needed.

Indoor ASEL was selected as the first predictor ($y = -5.1 + 0.20L_{AE}$; $r^2 = 96.0\%$). The product $(L_{CE} - L_{AE})(L_{AE})$ was selected as the second predictor [$y = -5.3 + 0.19L_{AE} + 0.0004(L_{CE} - L_{AE})(L_{AE})$, (multiple) $r^2 = 96.6\%$]. The small increase of 0.6 percent points in the explained variance was statistically significant ($p < 0.00001$). Finally, the sound reduction in the 1000-Hz octave band was selected as the third predictor. However, the increase in the total explained variance was less than 0.1 percent points and no longer statistically significant ($p > 0.08$).

Consequently, indoor ASEL is a very powerful single predictor. For the total set of 189 conditions, this is shown in Fig. 6(a). The significance of the product $(L_{CE} - L_{AE})(L_{AE})$ was confirmed in the regression analysis also. This is illustrated in Fig. 6(b), where the mean annoyance ratings from the 28 bangs produced by the small firearms (impulse types 1 and 2) and the 42 bangs produced by the large firearms (impulse types 10 and 11) are plotted as a function of indoor ASEL.

The regression functions are inserted to facilitate the appreciation of the level-dependent effect of firearm caliber. The data from Fig. 6(b) show that for indoor ASELs higher than about 40 dB, the bangs from the large firearms (relatively high $L_{CE} - L_{AE}$ -values) were more annoying than the bangs from the small firearms (low or very low $L_{CE} - L_{AE}$ -values), and that this difference increases with the indoor ASEL of the bangs.

For indoor ASELs lower than about 40 dB, the bangs from the large firearms tended to be less annoying than those from the small firearms. The annoyance ratings for the bangs produced by the medium-large firearms are situated in between those for the bangs from the small and large firearms [cf. Figs. 6(a) and (b)].

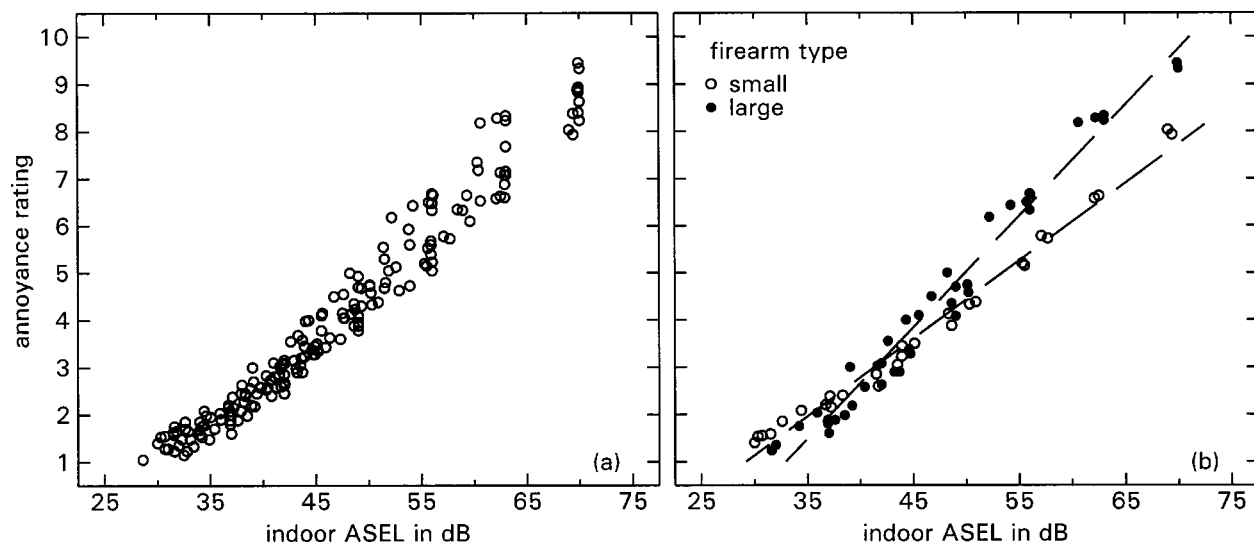


FIG. 6. Mean annoyance ratings obtained in the various façade attenuation conditions as a function of indoor ASEL. (a) for the total set of 189 bangs; (b) for the bangs produced by the small and large firearms only. Inserted broken lines are regression functions.

IV. DISCUSSION

A. The benefit of $(L_{CE} - L_{AE})(L_{AE})$ as a second predictor of the annoyance

In all conditions described in Secs. III A 1–5, an optimal prediction of the indoor rated annoyance was obtained with *outdoor* ASEL as the first, and *outdoor* $(L_{CE} - L_{AE})(L_{AE})$ as the second predictor. The benefit of the second predictor, expressed as the increase in the explained variance, ranged from 2.5% to 55%, and strongly increased with the degree of façade attenuation. The relatively small increase in the explained variance of 10 percent points found in the façade condition with a very high sound isolation is explained by the homogeneity of the stimuli included: here, only a few sounds produced by medium-large and large firearms were investigated.

In the five façade attenuation types investigated, the regression weights α and β in $y = \gamma + \alpha L_{AE} + \beta (L_{CE} - L_{AE})(L_{AE})$ ranged between 0.14–0.21 and between 0.0007–0.0015, respectively (see Table II). For the whole set of 189 conditions, and with the sound reduction in the 1000-Hz octave band as an additional predictor, the optimal values for α and β were equal to 0.19 and 0.0011, respectively.

For each separate façade attenuation type, it was determined to what extent the explained variance in the mean annoyance ratings decreased if the regression weights were fixed at $\alpha = 0.19$ and $\beta = 0.0011$. In the condition in which a high isolation with the windows closed was simulated, r^2 decreased from 94.9% to 87.3%. For the other four façade attenuation types, however, the decrease in r^2 was very low, ranging between 0.1% and 2.5%. Independent of the façade attenuation, it might therefore, as a rule of thumb, be justified to weight the contribution of ASEL with a factor of 0.19, and the contribution of $(L_{CE} - L_{AE})(L_{AE})$ with a factor of about 0.001. In validation studies, in which the effects of the present procedure will be compared to field data, it has to be determined to what extent these weights have to be adjusted.

B. Features of a rating procedure for shooting sounds with indoor levels as a criterion

1. The additional adjustment for heavy bangs

The rating sound level for the great variety of shooting sounds is expressed as the level of equally annoying vehicle passby sounds. For obtaining ASEL of equally annoying vehicle sounds, ASEL for impulse sounds produced by small firearms ($L_{CE} - L_{AE} \sim 0$ dB) has to be increased by an adjustment of 12 dB (Vos, 1995b). Since at the relevant receiver points, the differences between the spectra for the sounds from small firearms and the spectra for (local) road-traffic sounds are relatively small, the 12-dB adjustment holds for all window conditions investigated (Schomer *et al.*, 1994; Schomer and Wagner, 1995; Vos, 1995b).

A small but statistically significant increase in the predictability of the indoor annoyance ratings was obtained by adding indoor $(L_{CE} - L_{AE})(L_{AE})$ as a second variable (see Sec. III B 6). Consequently, for rating shooting sounds in general, in addition to the 12-dB adjustment, a second level-dependent adjustment is required. This latter adjustment will now be quantified on the basis of the results of the present experiment.

The maximum size of the second adjustment was already shown in Fig. 6(b), where the indoor ratings are plotted as a function of indoor ASEL for the bangs from the two heavier firearms, with the ratings for the bangs from the small firearms as a reference. With respect to the difference between indoor CSEL and indoor ASEL, the bangs produced by these heavier firearms were clearly distinct from the other bangs: For $L_{AE} \sim 35$ dB, $L_{CE} - L_{AE}$ was equal to 28–30 dB, and for L_{AE} between about 65 and 70 dB, $L_{CE} - L_{AE}$ ranged between 18 and 23 dB.

In addition to the relatively high values of $L_{CE} - L_{AE}$, the bangs from these heavier firearms also yielded about the same indoor annoyance ratings (y) at comparable ASELs: the regression line fitted to the data ($y = -6.8 + 0.236L_{AE}$) explained 97.3% of the variance in the mean ratings. Relative

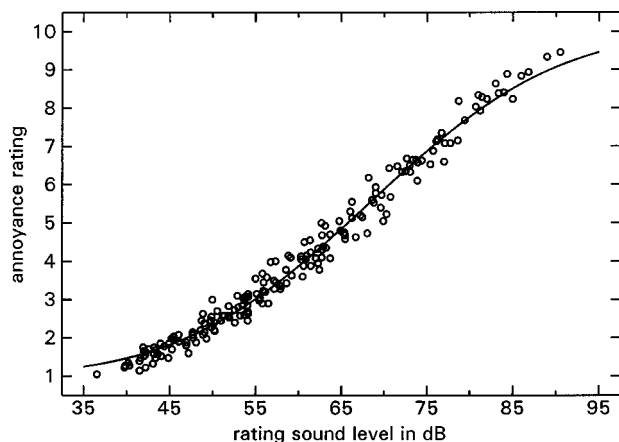


FIG. 7. Mean annoyance ratings obtained for the total set of 189 bangs, as a function of the indoor rating sound level. The inserted regression line explains 98% of the variance in the mean annoyance scores.

to the dose-response relation for the bangs from the small firearms ($y = -3.8 + 0.165L_{AE}$; $r^2 = 98.6\%$), the additional adjustment for the heavier bangs increased from 5 dB at an indoor ASEL of 50 dB to 10 dB at an indoor ASEL of 65 dB. The general equation for the additional adjustment, P_a in decibel, follows from the slopes and intercepts of the two functions, and is given by $P_a = -17.9 + 0.43L_{AE}$, or $P_a = 0.43(L_{AE} - 41.6)$ dB.

2. Determination of the rating sound level for single events

In Sec. IV B 1, it was shown that for the bangs from the large firearms, the additional adjustment was equal to $P_a = 0.43(L_{AE} - 41.6)$ dB. For these bangs, $L_{CE} - L_{AE}$ was 30 dB at the maximum. For bangs with lower values of $L_{CE} - L_{AE}$, the additional adjustment must be smaller. Lower adjustments might be obtained by introducing the term $(L_{CE} - L_{AE})/\max(L_{CE} - L_{AE})$. With maximum $L_{CE} - L_{AE}$ set to 30 dB, the equation reduces to $P_a = 0.014(L_{CE} - L_{AE})(L_{AE} - 41.6)$ dB.

With indoor levels as a criterion, the rating sound level for any single impulsive event is given by

$$L_r = L_{AE} + 12 \text{ dB} + \beta(L_{CE} - L_{AE})(L_{AE} - \alpha) \text{ dB}, \quad (1)$$

in which $\alpha = 41.6$ dB and $\beta = 0.014 \text{ dB}^{-1}$.

Figure 7 shows the indoor annoyance ratings as a function of the proposed rating sound level for all 189 impulses. As expected, the statistical association between the rating sound level and the annoyance score was very high, with a (Pearson) correlation coefficient equal to 0.986 ($r^2 = 97.3\%$).

For obtaining an even better association, the function $y = 1 + 9 \cdot \Phi[(L_r - \mu)/\sigma]$ was fitted to the data; $\Phi(z)$ denotes the cumulative normal (Gaussian) distribution. A least-squares fit of this function to the mean annoyance ratings yielded $\mu = 68.2$ dB and $\sigma = 17.4$ dB. The regression function is inserted in Fig. 7 and explained 98.3% of the variance in the annoyance ratings.

V. GENERAL CONCLUSIONS

- (1) The effect of façade attenuation on the indoor rated annoyance of shootings sounds was large and consistent.
- (2) For the bangs produced by small firearms, the effects were slightly larger than for the bangs produced by the medium-large and large firearms. This can be understood from the spectral content of the bangs and the frequency-dependent façade attenuation characteristics investigated.
- (3) The relevance of *outdoor* ASEL as the primary predictor, and the product $(L_{CE} - L_{AE})(L_{AE})$ as the secondary predictor in the determination of the annoyance rated indoors, as found in a previous study, was convincingly demonstrated for a variety of façade attenuation types. The benefit of the second predictor, expressed as the increase in the explained variance, ranged from 2.5 to 55 percent points, and strongly increased with the degree of façade attenuation.
- (4) By and large, a satisfactory prediction of the indoor annoyance for each separate façade attenuation type was obtained by weighting the contribution of (outdoor) ASEL with a factor of 0.19, and the contribution of $(L_{CE} - L_{AE})(L_{AE})$ with a factor of about 0.001. These proposed weightings must be validated in field studies.
- (5) For the whole set of impulses included, an almost perfect prediction of the indoor annoyance ratings was obtained on the basis of the weighted sum of the façade attenuation for the 1000-Hz octave band and the two predictors described in the previous conclusion.
- (6) Again for the whole set of impulses included, the annoyance could also be predicted very well by the weighted sum of *indoor* ASEL and the product $(L_{CE} - L_{AE})(L_{AE})$.
- (7) With the noise dose expressed as *indoor* levels, the rating sound level, L_r , is given by $L_r = L_{AE} + 12 \text{ dB} + \beta(L_{CE} - L_{AE})(L_{AE} - \alpha)$, with $\alpha = 42$ dB and $\beta = 0.014 \text{ dB}^{-1}$. In validation studies it has to be determined to what extent the constants α and β have to be adjusted.

ACKNOWLEDGMENTS

This research was financed by the Netherlands Ministry of Defense in close cooperation with Pieter I. J. van der Weele. The preparation of the present paper was further supported by Grant No. D99-101 from TNO Human Factors.

¹The analysis of variance performed on the ratings obtained in the condition with the windows slightly open showed that there was a small but statistically significant interaction effect of replication and impulse type ($p < 0.01$): in the second measurements, the annoyance ratings for the bangs from the small firearms were slightly higher (by about 0.2 scale units), and those for the bangs from the large firearms were slightly lower (by 0.25 scale units) than those in the first measurements.

²With CSEL included, CSEL is selected as the first predictor (r^2 is 0.7 percent points higher than that obtained with ASEL) and ASEL is selected as the second predictor (multiple r^2 is equal to 0.959). Since with CSEL and ASEL, the explained variance is clearly lower than that obtained with ASEL and $(L_{CE} - L_{AE})(L_{AE})$, it was decided to exclude CSEL from the final regression analysis.

³With CSEL included, CSEL is selected as the first predictor (r^2 is 34 percent points higher than that obtained with ASEL) and ASEL is selected as the second predictor (multiple r^2 is equal to 0.93). Since with CSEL and

ASEL, the explained variance is clearly lower than that obtained with ASEL and $(L_{CE} - L_{AE})/L_{AE}$, it was decided to exclude CSEL from the final regression analysis.

⁴The variance explained by the sound reduction in the 1000-Hz octave band was slightly higher than that explained by ASEL ($r^2 = 0.3098$ vs $r^2 = 0.3088$).

- Buchta, E. (1990). "A field survey on annoyance caused by sounds from small firearms," J. Acoust. Soc. Am. **88**, 1459–1467.
- Buchta, E. (1996). "Annoyance caused by shooting noise—determination of the penalty for various weapon calibers," in *Proceedings Internoise 1996* (Institute of Acoustics, St. Albans, U.K.), Book 5, pp. 2495–2500.
- Bullen, R. B., Hede, A. J., and Job, R. F. S. (1991). "Community reaction to noise from an artillery range," Noise Control Eng. J. **37**, 115–128.
- Fields, J. M. (1993). "Effect of personal and situational variables on noise annoyance in residential areas," J. Acoust. Soc. Am. **93**, 2753–2763.
- Gerretsen, E. (1996). Personal communication.
- ISO (1978). ISO 3891. *Acoustics—Procedure for Describing Aircraft Noise Heard on the Ground* (International Organization for Standardization, Switzerland).
- Kerry, G., Ford, R. D., and James, D. (1996). "Bandwidth limitation effects on low-frequency impulse noise prediction and assessment." Appl. Acoust. **47**(4), 331–344.
- Meloni, T., and Rosenheck, A. (1995). "Choice of frequency weighting for the evaluation of weapon noise," J. Acoust. Soc. Am. **97**, 3636–3641.
- Schomer, P. D. (1977). "Evaluation of C-weighted L_{dn} for assessment of impulse noise," J. Acoust. Soc. Am. **62**, 396–399.
- Schomer, P. D., and Sias, J. W. (1998). "On spectral weightings to assess human response, indoors, to blast noise and sonic booms," Noise Control Eng. J. **46**, 57–71.
- Schomer, P. D., and Wagner, L. R. (1995). "Human and community response to military sounds. II. Results from field-laboratory tests of sounds of small arms, 25-mm cannons, helicopters, and blasts," Noise Control Eng. J. **43**, 1–13.
- Schomer, P. D., Wagner, L. R., Benson, L. J., Buchta, E., Hirsch, K.-W., and Krahé, D. (1994). "Human and community response to military sounds: Results from field-laboratory tests of small-arms, tracked-vehicle, and blast sounds," Noise Control Eng. J. **42**, 71–84.
- Vos, J. (1990). "On the level-dependent penalty for impulse sound," J. Acoust. Soc. Am. **88**, 883–893.
- Vos, J. (1995a). "Technical Note: On the comparability of community responses to noise from artillery and rifle ranges, as determined in two Australian studies," Noise Control Eng. J. **43**, 39–41.
- Vos, J. (1995b). "A review of research on the annoyance caused by impulse sounds produced by small firearms," in *Proceedings Internoise 1995* (Newport Beach, CA), Vol. 2, pp. 875–878.
- Vos, J. (2001). "On the annoyance caused by impulse sounds produced by small, medium-large, and large firearms," J. Acoust. Soc. Am. **109**, 244–253.
- Vos, J., and Geurtsen, F. W. M. (1987). " L_{eq} as a measure of annoyance caused by gunfire consisting of impulses with various proportions of higher and lower sound levels," J. Acoust. Soc. Am. **82**, 1201–1206.
- Winer, B. J. (1970). *Statistical Principles in Experimental Design* (McGraw-Hill, London).

Investigation of phase coupling phenomena in sustained portion of musical instruments sound

Shlomo Dubnov^{a)}

Ben Gurion University, Beer-Sheva 84105, Israel

Xavier Rodet^{b)}

Analysis/Synthesis Team, IRCAM, Paris 75004, France

(Received 5 February 2002; revised 9 August 2002; accepted 16 August 2002)

This work investigates aperiodicities that occur in the sustained portion of a sound of musical instrument played by a human player, due to synchronous versus asynchronous deviations of the partial phases. By using an additive sinusoidal analysis, phases of individual partials are precisely extracted and their correlation statistics and coupling effects are analyzed. It is shown that various musical instruments exhibit different phase coupling characteristics. The effect of phase coupling is compared to analysis by means of higher order statistics and it is shown that both methods are closely mathematically related. Following a detailed analysis of phase coupling for various musical instruments it is suggested that phase coupling is an important characteristic of a sustained portion of sound of individual musical instruments, and possibly even of instrumental families. Interesting differences in phase deviations were found for the flute, trumpet and cello. For the cello, the effect of vibrato is examined by comparing the analysis of a closed string sound played with a natural vibrato to analysis of an open string sound that contains no vibrato. Following, a possible model for phase deviations in the cello is presented and a simulation of phase fluctuations for this model is performed. © 2003 Acoustical Society of America. [DOI: 10.1121/1.1518981]

PACS numbers: 43.60.Cg, 43.75.De, 43.75.Ef [NHF]

I. INTRODUCTION

Acoustical musical instruments, which are considered to produce a well-defined pitch, emit waveforms that are never exactly periodic. These aperiodicities, which occur in the sustained portion of musical instrument, supposedly originate in some not-well-known fundamental mechanism of their sound production that depends both on the manner of playing the instrument and the instrument specific physical properties.

Among the many mechanisms of possible deviations from periodicity (Beauchamp, 1974; McIntyre *et al.*, 1981; Schumacher, 1992; Rodet, 1993, 1995; Vettori, 1995; Weinreich, 1997; Vergez and Rodet, 2000), we analyze two contrasting conditions which appear to be important for sustained portion of sound in musical instruments: synchronous phase deviations of proportional magnitude¹ that preserve the relative phase relations between the partials and thus do not change the shape of the waveform except for compressing or stretching in time, versus independent or phase asynchronous deviations that change the shape of the signal due to the changing phase relations between the different frequency components. By using a sinusoidal analysis, phases of individual partials are precisely extracted and their correlation statistics and coupling effects are analyzed. It is shown that various musical instruments exhibit different phase coupling characteristics.

One must note that in this work we analyze sounds as played by a human player, with all the attendant vibrato and

pitch and amplitude variability. The dependence on the playing method is analyzed in detail for the cello, where naturally played sound on a closed string with vibrato is compared to a naturally played open string cello sound that has no vibrato.

In earlier works (Dubnov *et al.*, 1998, 1997, 1995), we have shown that the particular aspect of phase synchronous versus asynchronous phase fluctuations is strongly related to nonlinear properties of the time series model of the signal. These properties are measured by higher order statistics (HOS) or polyspectra (Mendel, 1991; Nikias and Mendel, 1993) and were shown to be important for characterization of musical instruments in the sustained portion of the sound.

It should be noted that statistical properties of a signal due to phase variations can not be easily revealed by standard spectral analysis methods due to the fact that second-order statistics and the power spectrum are “phase blind,” i.e., they are not sensitive to phase variations. In the current work we employ sinusoidal analysis in order to estimate precisely the phase behavior of each partial in sustained portion of musical instruments. We analyze the relative phase fluctuations among different partials using a measure called quadratic phase coupling (QPC). The precise definition of QPC will be given in the next section.² The QPC analysis is compared and mathematically related to higher order statistical analysis that is applied directly to the signal.

In the paper we first consider the problem of detection of QPC and define a detector function that receives values in the range [0, 1], with value one indicating perfect phase coupling and value zero indicating that partials have completely uncoupled phases. We show that phase coupling is a major property of musical instruments with a clearly distinct be-

^{a)}Electronic mail: dubnov@bgumail.bgu.ac.il

^{b)}Electronic mail: rod@ircam.fr

havior for the case of brass versus string instruments. Specifically, we extend the earlier HOS research (Dubnov *et al.*, 1997) by introducing a discrete bispectral measure that is shown to be equivalent to the phase coupling detector under some mild shift invariance assumptions.

Finally, a detailed analysis of cello instrument is given, comparing the QPC for naturally played sound on a closed string that includes vibrato with a sound of an open string with no vibrato. For the case of the cello, and possibly string instruments in general, we suggest a source-filter model that can generate some phase fluctuations. Simulations with this model create a signal with uncoherent phase deviations that look like the fluctuations that were observed in the original signal.

II. PHASE SYNCHRONOUS VERSUS ASYNCHRONOUS APERIODICITIES

The additive sinusoidal model (Rodet, 1997; Serra and Smith, 1989) of an almost perfectly periodic signal is mathematically expressed by

$$x(t) = \sum_{l=-L, l \neq 0}^L A_l(t) e^{i\theta_l(t)}, \quad (1)$$

with the phase $\theta_l(t)$ defined as

$$\theta_l(t) = l \cdot \omega_0 \cdot t + \phi_l(t), \quad (2)$$

where ω_0 is the fundamental frequency and A_l , ϕ_l are the amplitudes and phases of the l th sinusoidal component (partial).

Among the many possible mechanisms of deviations from periodicity that may occur in the sustained portion of a pitched sound, we analyze two extreme cases:

- (1) application of a synchronous and proportional random modulation to the phases of each partial, such as $\phi_l(t) = l \cdot \phi_1(t)$, and
- (2) application of random and asynchronous phase modulations to each partial.

A. Synthetic example

In order to demonstrate the effect of synchronous versus asynchronous deviations we constructed a synthetic signal consisting of a sum of eight equal-amplitude cosine functions at harmonic frequencies, with fundamental frequency of 220 Hz. The signal was generated at 8000-Hz sampling rate.

For the purpose of generating the phase noise, an initial random vector was created using a random Gaussian noise generator, producing a signal at a sampling rate of 160 Hz. Then a phase noise signal at the signal sampling rate was generated by resampling of the original random vector at a rate that is 50 times higher than the original random vector, thus creating a random phase noise signal at 8000-Hz sampling rate.

Next, two sets of phase noise signals were created, for the synchronous and asynchronous cases, respectively. In the first case, a single-phase noise signal $\phi_1(n)$ was used to

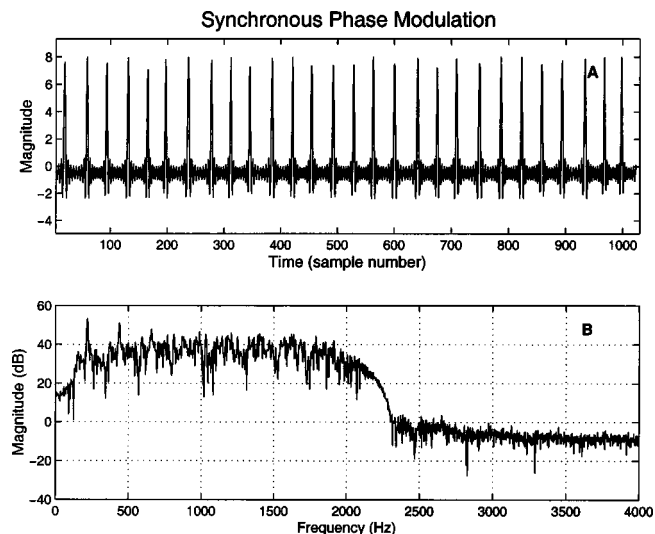


FIG. 1. Synthetic signal that was produced by applying synchronous modulation to phases of the harmonic partials. This type of modulation preserves the shape of the waveform, except for period to period time stretching or shortening, i.e., the period between successive peaks is modulated. In frequency this amounts to spread in bandwidth of the partials.

create the separate phase noise signals of the eight harmonics, with phase noise at harmonic $k = [1, \dots, 8]$, being $\phi_k(n) = k \phi_1(n)$. In the asynchronous case, eight independent noises were created for the eight partials. In order to match the noise variance in the synchronous and asynchronous cases, the standard deviation of the noise in the asynchronous case at partial k was set to be k times the standard deviation of the noise at partial 1. One additional free parameter is the standard deviation of the phase noise in the first partial. In the simulation presented below (Figs. 1 and 2) we used the value of 0.6 for standard deviation of the first partial.

Figures 1 and 2 demonstrate the signal waveform and magnitude spectra in the case of synchronous and asynchronous phase deviations, respectively. The top figure (a) shows

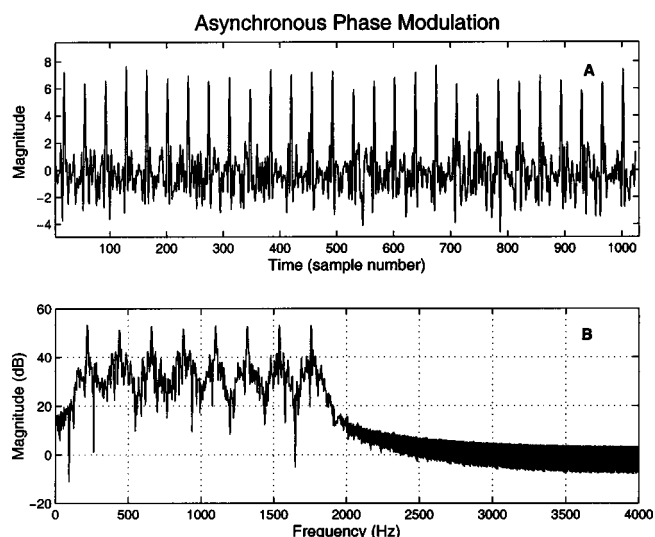


FIG. 2. Synthetic signal that was produced by applying asynchronous modulation to phases of the harmonic partials. This type of modulation does not preserve the shape of the waveform. In frequency this causes a relatively smaller spread in bandwidth of the partials.

the time domain signal and the bottom figure (b) represents the Fourier analysis of a segment of 1024 samples of the signal, with a rectangular analysis window. In the synchronous case, the small variation of the signal period, although not altering the basic waveform, significantly spread the spectral peaks of the higher partials, effectively turning partials higher than 3 or 4 into noise. For the asynchronous case we observe that the original, pulselike shape of the waveform is significantly distorted, giving a visual impression of pulses submerged in a high level of noise. This noise effect can be seen also in the signal's spectrum. One should note that the spectral peaks for the asynchronous case remain significantly pronounced above noise level.

B. Additive sinusoidal analysis procedure

The additive sinusoidal model represents the audio signal as a sum of sinusoids (partials) with time-varying amplitudes and frequencies. Mathematical expression of this model was given earlier in Eqs. (1) and (2) in Sec. II. For review of sinusoidal modeling for musical signals see Rodet (1997). The signal parameters are estimated in the following manner:

- (1) Window audio signal segment. The windowed segment will be termed in the following "analysis frame," or simply a frame.
- (2) Estimate instantaneous pitch (this can be done using a variety of methods). Since a precise pitch is crucial for quality modeling, an extra pitch refinement step is performed.
- (3) Searching for peaks of the local periodogram, i.e., peaks in amplitudes of the short-time Fourier transform (STFT).
- (4) Amplitudes and the instantaneous frequencies are estimated at the precise frequency of the spectral peaks. In our analysis we use a quadratic interpolation of three points around each spectral extrema in order to determine the precise peak location.
- (5) Advance the signal segment to the following frame and repeat previous analysis steps. It is referred in the following as the "analysis time step."
- (6) Finally, a nearest-neighbor matching in time is performed, in order to relate different partials in succession of analysis frames.

The analysis in the paper was performed using a 20-ms analysis window with analysis time step of 4 ms. For the purpose of phase correlation and phase-coupling analysis, only the sustained portion of the analysis was retained. There were some cases where "death" or "birth" of harmonics was observed. In such a case, the instances with almost zero partial amplitudes were removed from the analysis since the phase in such a case was meaningless.

C. Statistical analysis of a sinusoidal model

Taking the phases of a signal derived from sinusoidal analysis we look at the instantaneous harmonicity among different groups of partials. For a triplet of harmonically related partials j , k , and $l=j+k$, a "synchronous" phase be-

havior means that the respective phases ϕ_j , ϕ_k , ϕ_l obey the following relation $\phi_j + \phi_k - \phi_l = 0$, i.e., that any deviations that occurs for ϕ_j and ϕ_k sum up to occur identically in ϕ_l , up to a constant additive factor of the initial phase of each partial. In the case when phase coupling does not occur, a difference in phase deviations occurs between the phases. This phase coupling difference signal can be either bounded (and possibly periodic), or increase by accumulating over time, so that it eventually passes through all values in $[0, 2\pi]$ range.

We introduce a measure $d_3(j, k)$ that evaluates the effect of stochastic phase deviations that occur between partials j and k ,

$$d_3(j, k) \stackrel{\text{def}}{=} \frac{1}{N_F} \sum_{n=1}^{N_F} e^{i(\phi_j(n) + \phi_k(n) - \phi_l(n))}, \quad (3)$$

where N_F is the number of frames available from sinusoidal analysis. The integral of the exponent of the phase coupling difference has the following property: in the case of a perfect coupling, the argument in the exponent is identically 0 and $d_3(j, k)$ equals 1. In the case when the phase coupling difference oscillates in a limited range, the resulting $d_3(j, k)$ will converge to some value between 1 and 0. If the error "spreads" over the whole $[0, 2\pi]$ range, the value of d_3 approaches 0.

D. Phase correlation and phase-coupling analysis

In this section two statistical measures of phase deviations among partials of a sinusoidal model are considered—correlation and coupling. In order to be able to calculate correlation between phases, a careful unwrapping of the phases must be done. One should note that unwrapping is **not** necessary for phase coupling analysis, since the phase differences that appear in the exponent are not sensitive to jumps of 2π . The unwrapping is performed in the following manner:

- (i) Phase derivative of the k th partial's phase is calculated and divided by 2π . The resulting signal is an estimate of an instantaneous frequency of the k th partial.
- (ii) A difference signal between the measured instantaneous frequency and theoretical instantaneous frequency (estimated as a k times multiplication of the fundamental frequency) is calculated.
- (iii) Points of 2π jumps are detected by rounding the difference signal to a nearest integer. The piecewise constant signal is then integrated and multiplied by 2π to create a "phase correction" signal.
- (iv) The "phase correction" signal is added to the original phase to create the unwrapped phase.

This procedure results in unwrapped phase values that represent phase fluctuations around an ideal theoretical value that is derived from the fundamental frequency. This step also eliminates phase deviations due to effects such as vibrato or slight pitch changes. This unwrapped phase is used to calculate the phase correlation. The QPC measure is calculated according to Eq. (3).

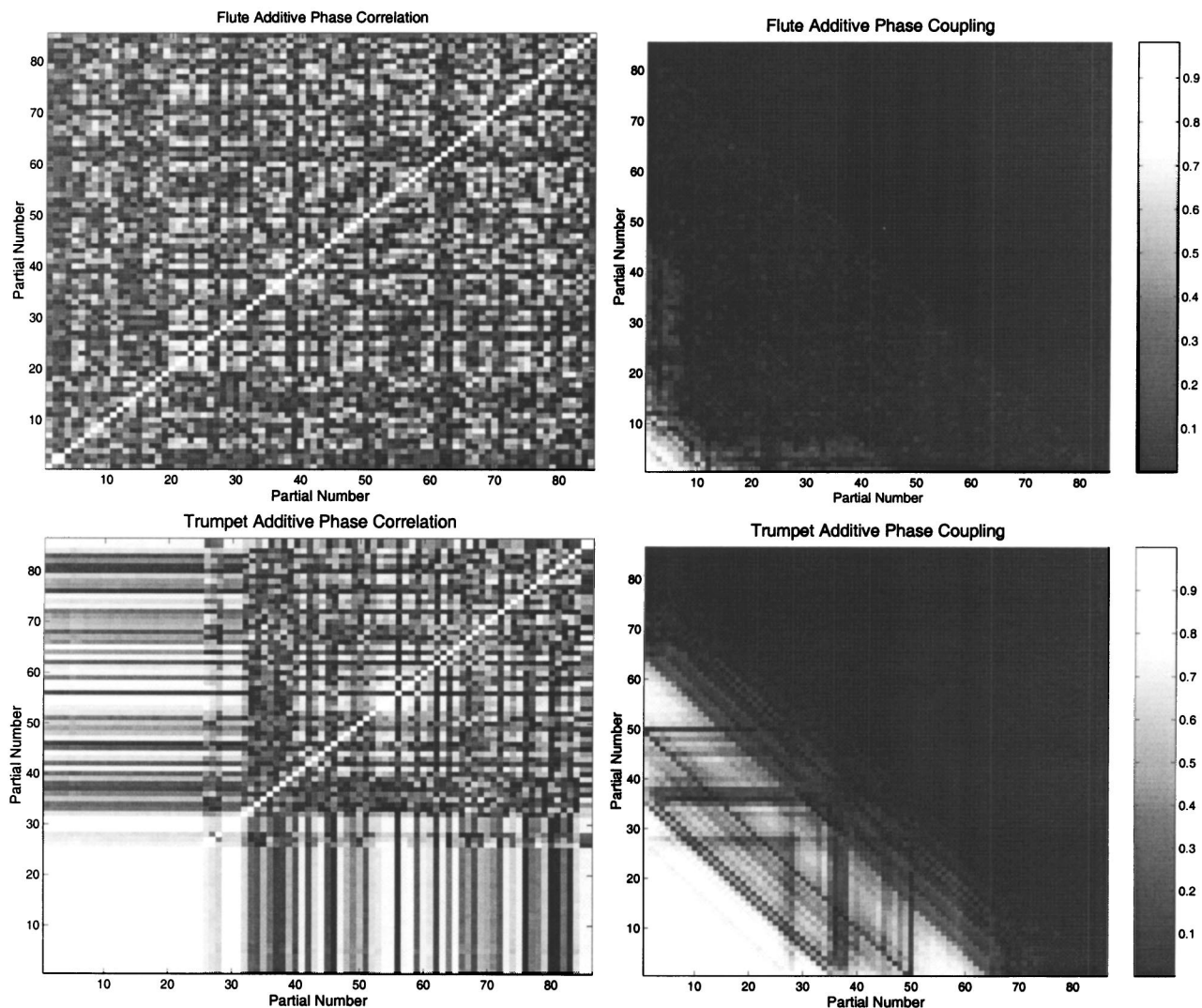


FIG. 3. Flute (top) and trumpet (bottom) correlation and QPC analysis. Phase correlation is plotted on the left side, QPC on the right side. The axes correspond to partial numbers, each point on the graph representing the value of correlation or QPC analysis between the two partials. The color scale is white corresponding to 1, which represents high correlation/coupling, and black corresponding to 0, no correlation or coupling. One should note also that QPC analysis is meaningful only at the lower left triangular part of the figure, since there exists no partial beyond Nyquist frequency. The right top part should be ignored (it is colored black).

In order to examine the difference between phase correlation and coupling, we calculated the matrix of pairwise correlations among the phases and compared them to the two-dimensional matrix of quadratic phase coupling (QPC). Figure 3 presents the phase correlation and QPC for flute and trumpet sounds. As can be readily seen from Fig. 3, the two instruments exhibit a very different correlation and QPC behavior. In the trumpet signal we observe a common behavior of the phase correlation and phase-coupling measure. The flute exhibits a very little QPC but still a rather significant correlation. This figure demonstrates the difference between the two analysis methods: QPC requires a precise instantaneous canceling of the relative phase deviations among triplets of partials, while the correlation coefficient depends on normalized inner product between phase functions.

The differences between correlation and QPC behavior of the two instruments can be further understood by considering the behavior of QPC estimates as a function of time. In the trumpet signal, the phase deviations among the different

partials occur in an almost exact instantaneous correspondence with each other,³ as demonstrated in Fig. 4. This causes the QPC in the trumpet to remain high. In the flute signal pairwise correlations occur to a large extent, but the phase deviations are mostly uncoupled. This lack of instantaneous phase coupling in the flute signal causes the QPC estimate to converge to zero. The behavior of the QPC estimate as function of time for the trumpet and the flute signals are shown in Fig. 5.

III. RELATION TO HIGHER ORDER STATISTICAL ANALYSIS

Higher order statistical (HOS) analysis investigates the behavior of higher order cumulants of stochastic signals. For third-order analysis we consider triple correlations of the signal, which equals the third-order cumulant assuming a zero mean signal,

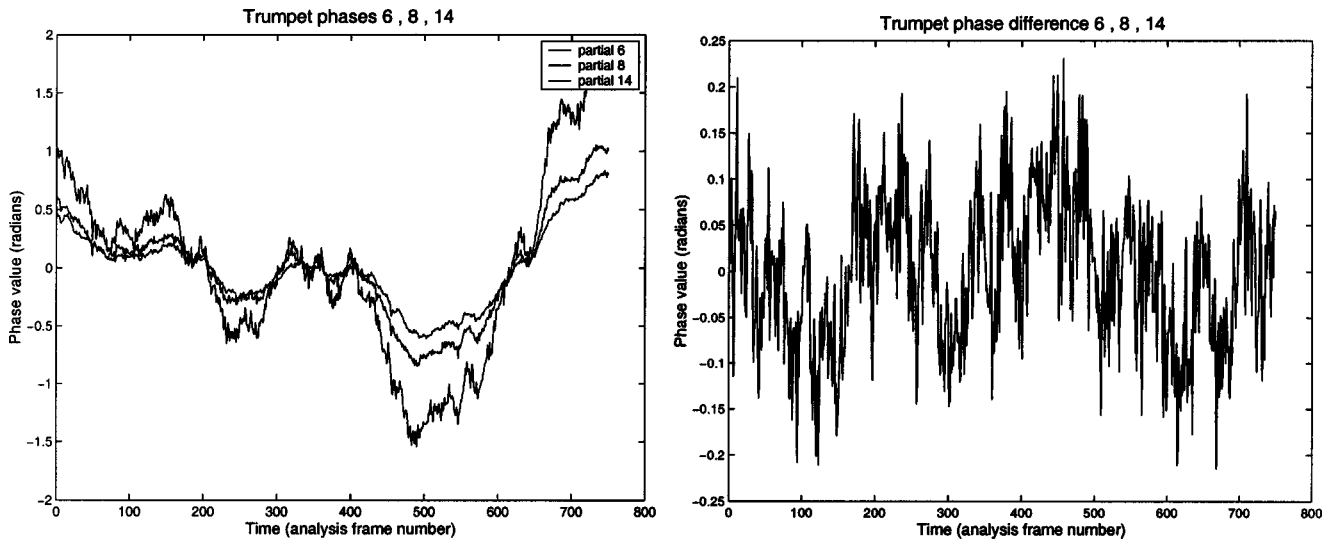


FIG. 4. Phase behavior of partials 6,8,14 of the trumpet. Phases of the partials appear on the left, phase triplet difference appears on the right (see text).

$$c_3(n,m) \stackrel{\text{def}}{=} \langle x(t)x(t+n)x(t+m) \rangle, \quad (4)$$

where $\langle \rangle$ means an ensemble average or time average for ergodic signals. Transforming the third-order cumulant into frequency domain gives the bispectrum

$$B_x(\omega_1, \omega_2) \stackrel{\text{def}}{=} \sum_{n=-\infty}^{\infty} \sum_{m=-\infty}^{\infty} c_3(n,m) e^{-i(\omega_1 n + \omega_2 m)}. \quad (5)$$

Note that bispectrum is calculated by applying a 2D Fourier transform to the third-order cumulant function. It can be shown, moreover, that B_x is equivalently expressed as an average over the Fourier transform $X(\omega)$ of $x(t)$. (This result is known as the 2D version of the Parseval theorem.)

$$B_x(\omega_1, \omega_2) = \langle X(\omega_1)X(\omega_2)X^*(\omega_1 + \omega_2) \rangle. \quad (6)$$

Let us consider now a sinusoidal signal \hat{x} that has equal amplitudes for all partials. We shall term this signal “white.”

We can express this signal as a sum of complex exponentials with unit amplitude

$$\hat{x}(t) = \frac{1}{2} \sum_{l=-L, l \neq 0}^L e^{i\theta_l}$$

with $\theta_l = -\theta_{-l}$, where θ_l is defined in Eq. (2).

In the Appendix we prove that, under not too severe assumptions, a discrete version of $B_{\hat{x}}(\omega_1, \omega_2)$ can be defined, which approximately equals to $d(j,k)$. Assuming that the frequency resolution of the Fourier analysis is M , we get the following lemma:

Lemma: For pseudo-periodic signal $\hat{x}(t) = \frac{1}{2} \sum_{l=-L, l \neq 0}^L e^{i\theta_l(t)}$ with $\theta_l(t) = l\omega_0 t + \phi_l(t)$, the discrete bispectrum obeys

$$B_{\hat{x}}\left(\frac{2\pi}{L}j, \frac{2\pi}{L}k\right) = d_3(j,k) \quad (7)$$

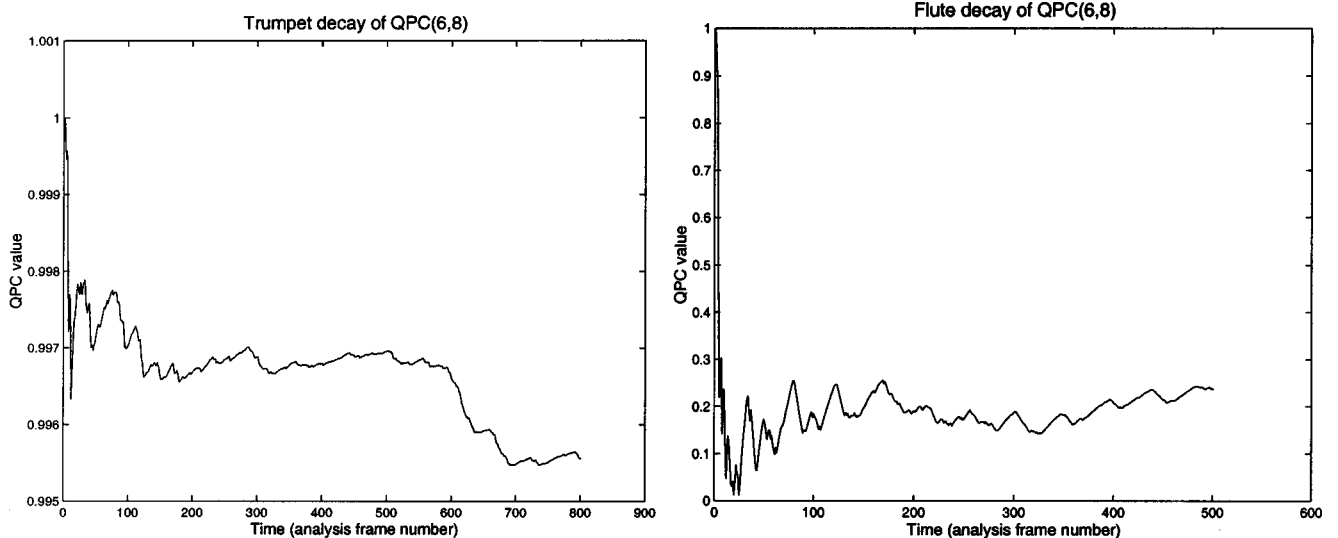


FIG. 5. QPC of the trumpet (left) and flute (right) partials for triplet (6,8,14). The graphs show the decay of QPC as a function of time (analysis frame number).

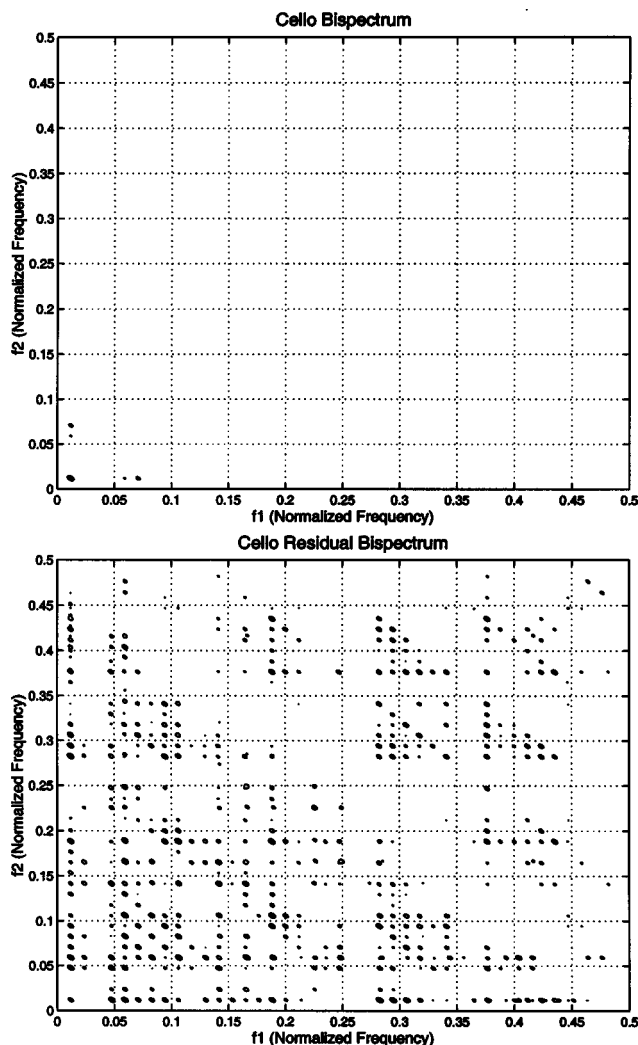


FIG. 6. Bispectrum of a cello original signal (top) and the bispectrum of the residual Cello sound (bottom). See text for more details.

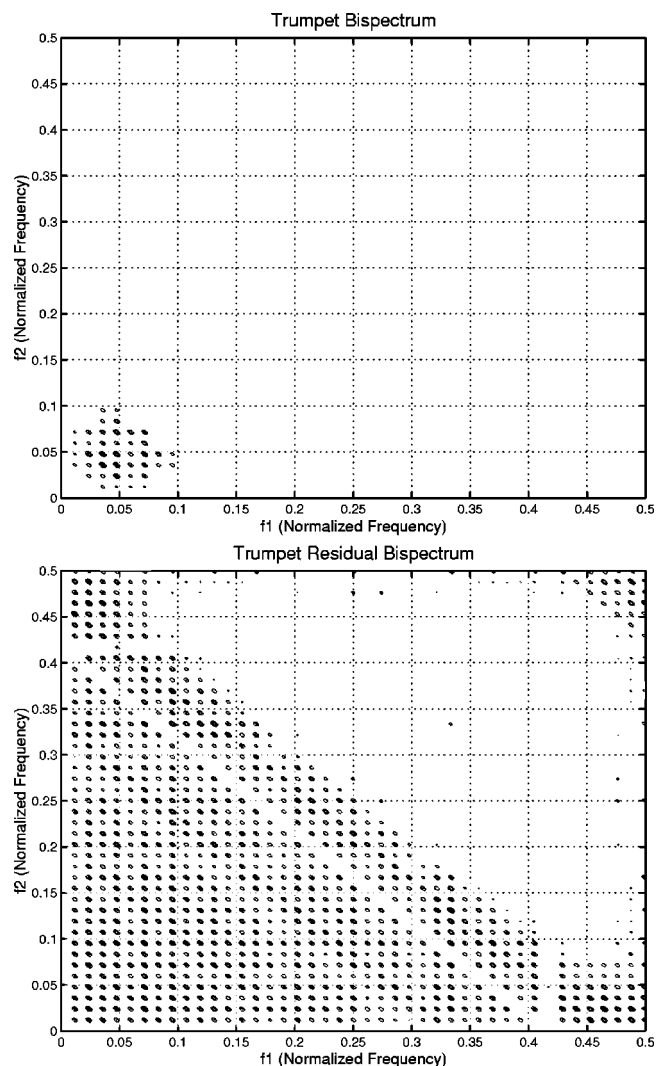


FIG. 7. Bispectrum of a trumpet original signal (top) and the bispectrum of the trumpet residual sound (bottom). See text for more details.

for phase deviation $\phi_l(t)$ being a white random process.

Proof: See the Appendix.

A. Comparison to bispectral analysis

In order to compare the sinusoidal phase coupling analysis to bispectral methods of detection of QPC, all amplitudes of the partials must be made approximately equal. This is required in order to remove the effect of the spectral envelope, which contains information about the amplitudes of harmonics, on the bispectrum. The estimation of the spectral envelope was done using linear prediction analysis (LPC) analysis (Markel and Gray, 1976), using filter of order 16. The process of equalizing the partial amplitudes was done by passing the original signal through an inverse LPC filter. Having performed the equalization step, we remove an initial segment of the signal that contains the transient behavior of the filter and look at the HOS properties of the remaining inversely filtered result, or the so-called *residual* or “white” signal. We chose to do a LPC equalization due to its simplicity, and also due to the fact that other methods such as the bicoherence estimator, which divide FFT bins by their absolute values for eliminating the amplitude dependence, often

suffer from numerical problems, due to nearly zero amplitudes of the FFT bins that do not fall on the partials.

The bispectral analysis of the cello and trumpet residual signals are given in Figs. 6 and 7, respectively. The strong presence of the high harmonics in the residual significantly affects the bispectral analysis. Notice that cello residual has only a few peaks. The analysis is performed on a 2000-sample-long signal segment, sampled at frequency of 22 050 Hz, i.e., a 90 ms segment. The method of analysis employed is a so-called “direct” Bispectrum estimation method that uses the FFT (this is in contrast to “indirect” method that uses third order cumulant matrix). In the direct method, the original frame of analysis is subdivided into eight segments with 50% overlap. Analysis resolution is 1024 (FFT size). In Figs. 6 and 7 the axes correspond to normalized frequency, with $f=1$ corresponding to sampling frequency of 22 050 Hz. When comparing bispectral analysis to additive phase coupling analysis, one should note the following differences in the analysis plots.

- (i) While phase coupling analysis is performed on a full CD-bandwidth signal, i.e., signal with sampling frequency of 44 100 Hz, the bispectral analysis is per-

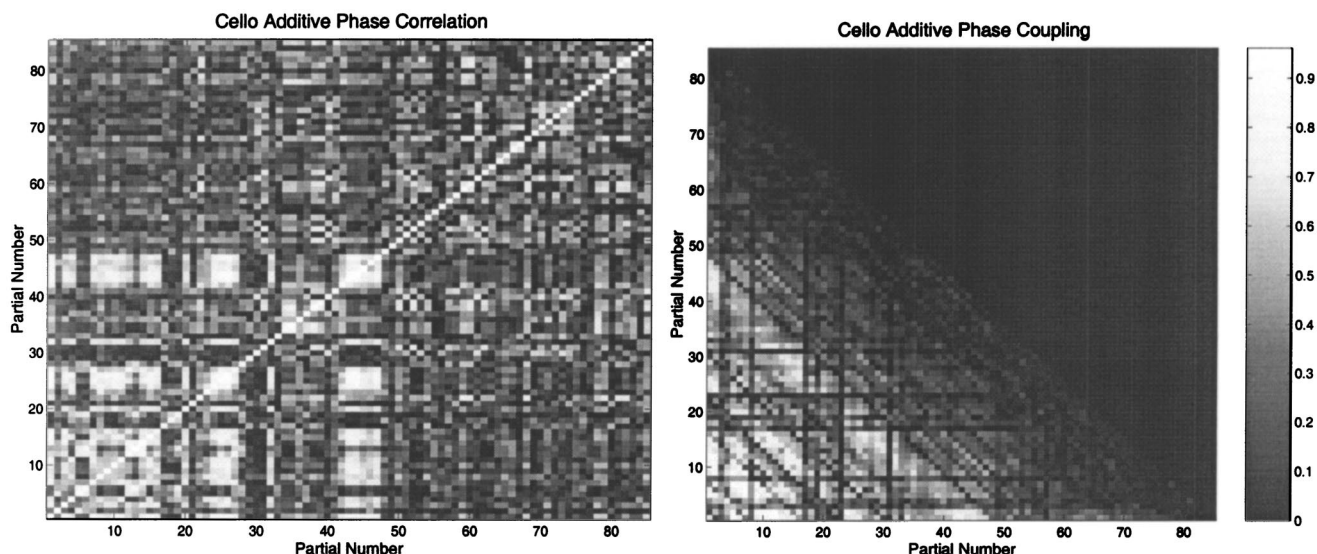


FIG. 8. Cello phase correlation and QPC analysis.

formed on a subsampled signal at 22 050 Hz. The reason for using a lower bandwidth in the bispectral analysis stems from practical considerations of memory and time requirements of the bispectral estimation algorithm. Moreover, since most of higher order statistical information appears at lower frequencies, there is no need to consider the high frequencies.

- (ii) Bispectral analysis is done on a shorter segment compared to additive phase coupling analysis. In the additive analysis the QPC estimate is averaged over a large segment that contains several hundred analysis frames, with frame step of 4 ms. This amounts to an analysis segment of an order of magnitude of few seconds. In order to compare this to the shorter averaging times of the bispectral analysis, one can evaluate the decay of the QPC as function of time in the appropriate graphs in the previous sections (90 ms in bispectral analysis corresponds to 22.5 analysis frames in QPC).
- (iii) The resolution of bispectral analysis is approximately 43 Hz. This resolution allows one to clearly see the separate peaks that correspond to the harmonics. This is in contrast to the phase-coupling graph where the values of the axes correspond to partial numbers. Thus, the partial numbers correspond, in frequency, to sampling of the bi-frequency plane at a resolution that correspond to fundamental frequency.

It is interesting and important to note the similarity between the bispectral analysis and the QPC analysis of Fig. 3. Apparently, although the QPC method and the bispectral method are different, they discover similar phenomena.

IV. THE MYSTERY OF THE CELLO: MODELING OF ASYNCHRONOUS PERIODIC PHASE DEVIATIONS

Cello produces its sound through a nonlinear bow-excitation process that excites a complex resonance body with many closely spaced resonances. Since our analysis is

applied to the final sound, we cannot separate the bow-excitation properties from the effect of the body resonances. Moreover, we would like to examine the difference between natural vibrato sound and open-string sound that has no vibrato. Accordingly, we analyzed two different cello sounds: a closed-string C4 pitch sound that contained natural vibrato and an open-string A3 sound that had no vibrato.

Applying phase analysis to string instruments reveals a particularly interesting phenomenon. Repeating the same analysis as done previously for the flute and trumpet, one finds out (see Fig. 8) that cello played with vibrato exhibits very little phase coupling among higher partials.

Considering the phase behavior of the various partials of the cello, it seems that the phase deviations have a random behavior. A closer look at specific triplets of partials reveals actually quite a smooth phase behavior, at least for the lower partials. The phase deviations are periodic, with a period corresponding approximately to the vibrato rate. This lack of coupling is different from the random phase deviations of the flute and possibly is caused by a different acoustical mechanism. In Fig. 9 the phases, phase differences, and phase coupling analysis for two triplets of cello partials are shown.

Comparing these results to analysis of an open-string cello sound (Fig. 10) reveals another interesting phenomenon. An open-string sound has a significantly higher QPC, showing strongly coupled harmonics up to partial number 60. Moreover, looking at the phase behavior (Fig. 11), one sees that the deviations of the phases among the different partials have similar trajectories, giving high phase correlations as well. These results suggest that the phase coupling and phase correlation in the cello are closely linked to the vibrato.

In order to understand the origin of the very asynchronous behavior of the phases in string instruments (Weinreich, 1997; Schumacher, 1992; McIntyre *et al.*, 1981; Beauchamp, 1974; Rodet, 1993, 1995) we have tried to model the periodic temporal variations of the phases of the cello using a source-filter model. The bow-excitation and the resonance

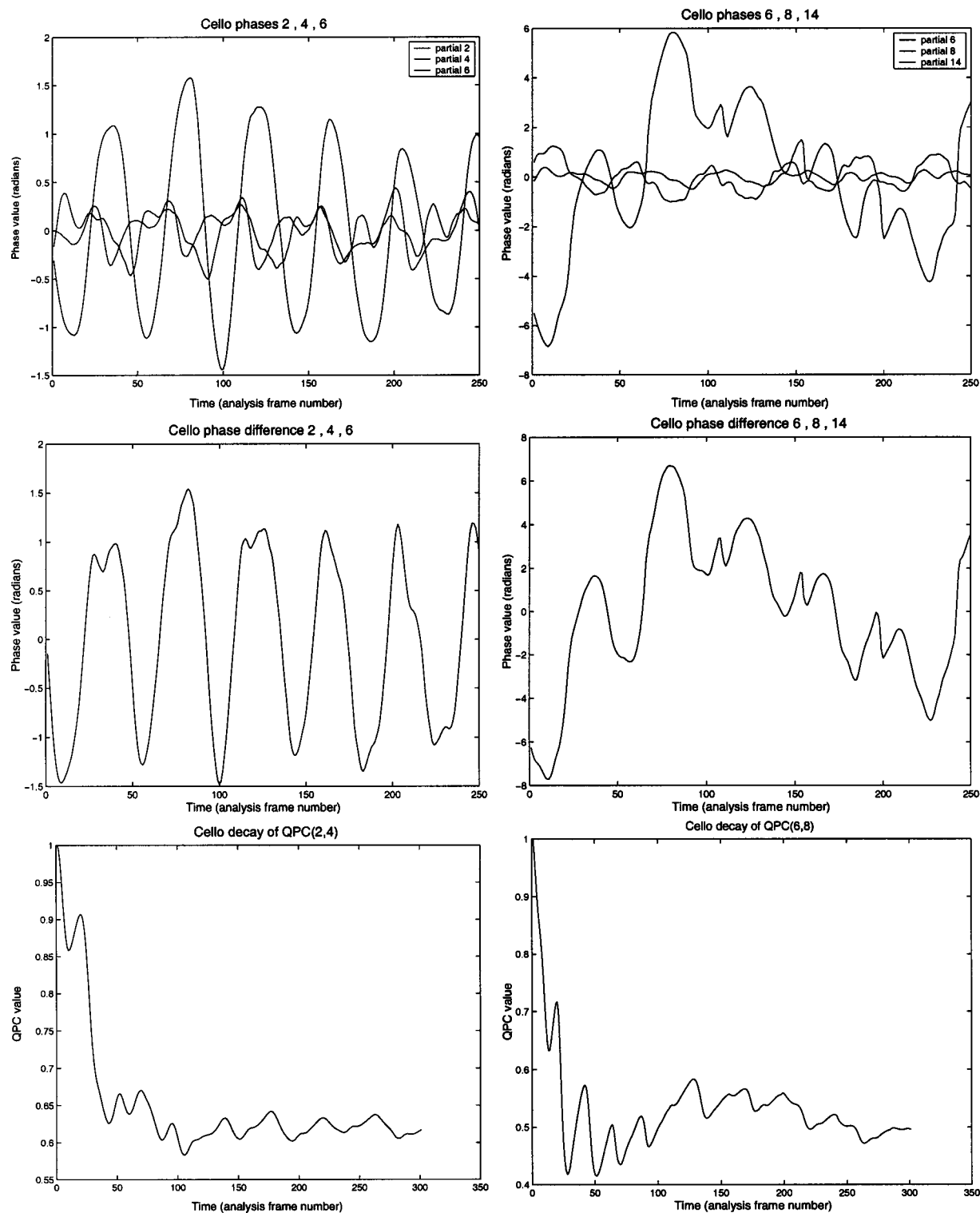


FIG. 9. Cello phases, phase differences, and QPC for two triplets of partials, numbers 2,4,6 and 6,8,14. The graphs in the left column correspond to analysis of partials 2,4,6. Right column graphs show analysis of partials 6,8,14. The different rows correspond to phases (top), phase difference (middle), and QPC analysis (bottom).

body effect are approximately modeled by a harmonic excitation that passes through a bank of closely spaced resonators. In this model the origin of the uncoupled phase behavior could be created as a result of an interaction between a time-varying excitation signal and the resonator body. Accordingly, we model it by a slowly varying frequency excitation signal, i.e., a harmonic signal with time-varying fun-

damental frequency $f_0(t)$ that simulates a vibrato, consequently filtering it by a linear filter that represents an instrument body resonance. If the instruments' body resonances, at the frequencies of the partials, are comprised of very close and narrow peaks, two situations might occur:

- (1) Relative phase shifts, up to π , could exist between dif-

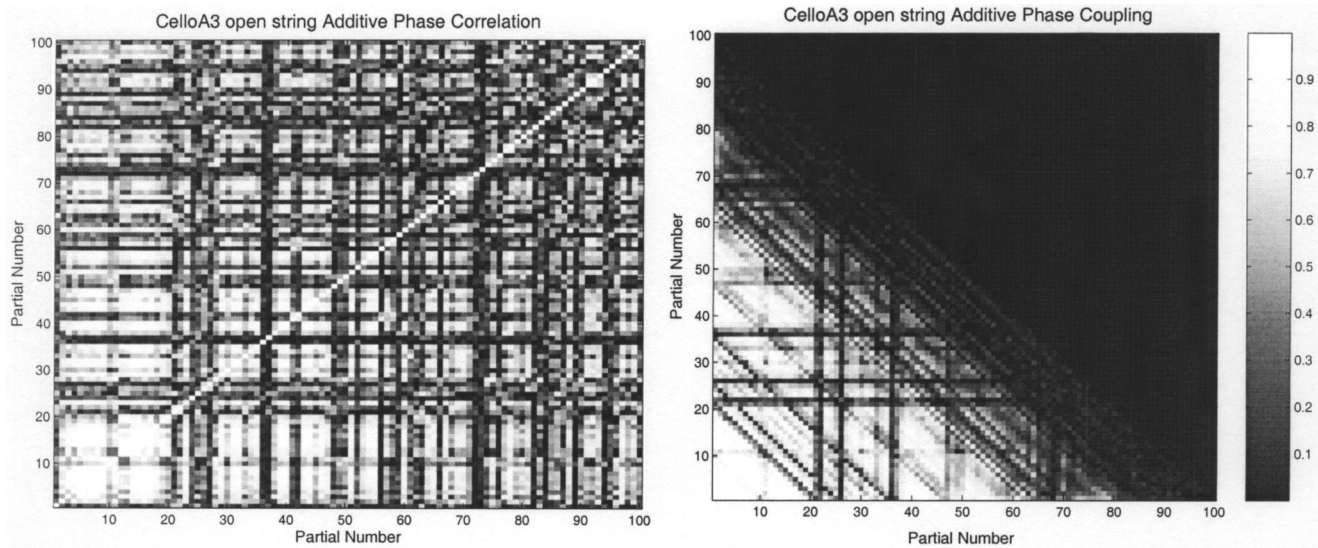


FIG. 10. Cello A3 open string phase correlation and QPC analysis.

ferent partials, due to differences in phase response of the body resonance at their corresponding frequencies.

- (2) A large phase deviation would occur for a single partial with a varying frequency, when it passes through a narrow peak of a body filter resonance.

The first case could be simulated by having harmonically related, time-varying partials, that move on the opposite slopes of very narrow resonators (McAdams and Rodet, 1988). For the second case, a single time-varying sinusoid might excite almost simultaneously a pair of very closely spaced and narrow filters. This causes two peaks in the spectrum to be present for a single partial (!) when the excitation occurs between the two resonances. In terms of phase, a jump would occur again in the middle region, i.e., when moving away from one and approaching the other resonance, it reaches a point where a phase difference is nearly 2π .

We expected, at least for the second case, that this effect would be visible in the spectrum as well. Figure 12 presents a high resolution analysis of a cello sound around its fifth partial. The sound was recorded with a close microphone to eliminate room effects (Studio Online, IRCAM). Surprisingly enough, we find that instead of having one peak, we have two very close peaks with their average frequency lying at the expected harmonic. The additive analysis in such a case would capture this as a single partial with a widely varying phase.

A. Modeling of the phase deviation

Simulation of this phenomena was done using a perfectly harmonic excitation, whose fundamental frequency variation was obtained from analysis of the fundamental frequency of an original cello signal. The body resonances were simulated using a bank of closely spaced (30 Hz) and narrow-band (BW=10 Hz) filters. A single resonator filter can be designed as a filter having two poles in conjugate location in the Z plane, located at radius R and angle θ , with corresponding transfer function

$$H(z) = \frac{1}{1 - 2R \cos(\theta)z^{-1} + R^2 z^{-2}}, \quad (8)$$

so that θ corresponds to the center frequency of the resonator and R is determined according to the desired bandwidth⁴ B , with the relation between bandwidth and R being $R \approx 1 - B/2$. Inspecting the phase response of a resonator shows an abrupt phase change when going through the center peak frequency.

When a time-varying harmonic sinusoidal excitation (harmonic excitation with simulated vibrato) passes through a bank of such filters, nonsynchronous phase deviations occur between the different sinusoidal components as each component passes through a different set of filters (one must note also that the rate of frequency sweep in every partial is different and proportional to the partial number, i.e., higher frequencies move faster and “pass” on their way through more resonator filters). Figure 13 demonstrates the phases and the QPC of the simulated signal for partials pair (2,4) obtained by sinusoidal analysis. As can be seen from the figure, this behavior is very much reminiscent of the real cello behavior. Although the simulation does not constitute a “proof” that the actual cello resonance behaves in this manner, both the analysis and listening impression seem to support this assumption.

B. Discussion

In our analysis we were dealing with sounds of instruments that were played by a human player (McGill University Master Samples), thus containing vibrato and pitch variations that are typical to human playing, even when playing a single note. In the flute there was a significant vibrato, while in the trumpet there was almost no vibrato. The two instruments were analyzed at the same pitch (C4). For cello we have investigated two cases, a natural playing closed-string note (C4) that contained a vibrato and an open-string note (A3) that contained no vibrato. Our findings in all cases

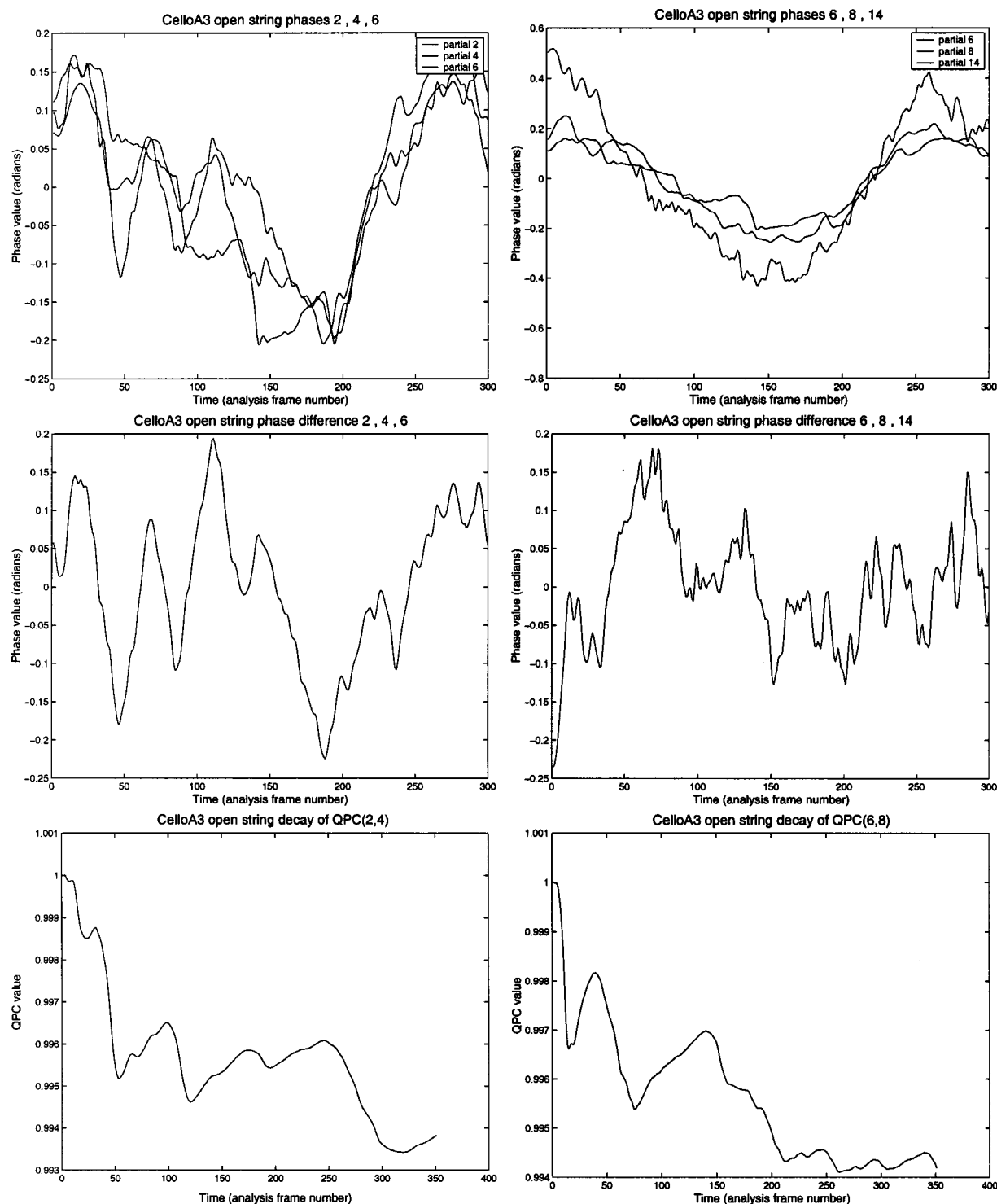


FIG. 11. Cello A3 open string: the phases, phases differences, and QPC for two triplets of partials numbers 2,4,6 and 8,6,14. The graphs in the left column correspond to analysis of the phases for partials 2,4,6. Right column graphs show analysis of partials 6,8,14. The different rows correspond to phases (top), phase difference (middle), and QPC analysis (bottom).

are consistent with what might be expected from physical considerations. In the flute vibrato is produced by variations in blowing pressure. The production of harmonics is influenced partly by jet-propagation and largely by variations in the exact intersection plane of the embouchure edge and the jet (Fletcher and Rossing, 1995). In the trumpet, blowing pressure is nearly steady and the primary excitation is caused by motion of the lips at a frequency dependent on the natural

resonance frequency. This generates higher partials by non-linear variation of lip opening and the flow velocity. In the cello, vibrato is produced by varying the length of the string, which interacts also with the nonlinear bow-excitation process. Our findings for the flute and the trumpet seem to be consistent with these physical interpretations. Moreover, for the cello we see a clear distinction between open-string and close-string with vibrato sounds. The lower QPC in the vi-

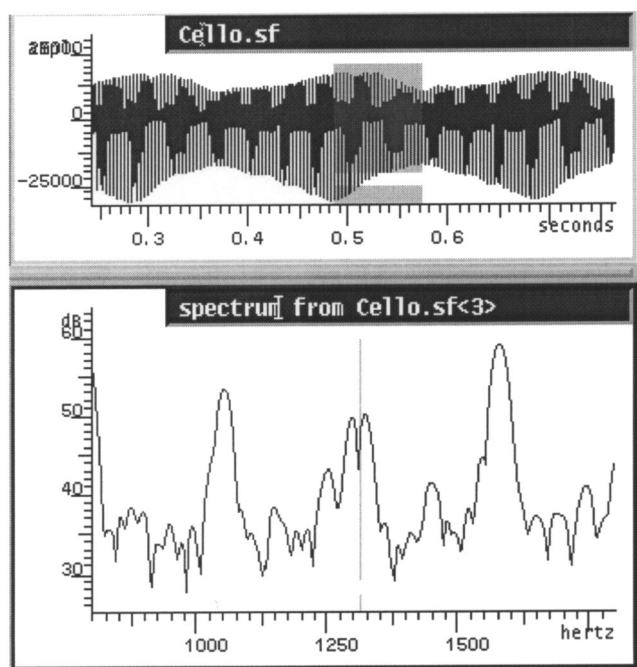


FIG. 12. The occurrence of double spectral peaks instead of a single partial in a cello signal recorded with a close microphone to eliminate room effects. The top graph shows the signal and the segment analyzed. Bottom graph shows the window Fourier transform of the corresponding signal segment (0.49–0.58 s).

brato sound could be related to the phase asynchronous effect due the closely spaced resonances of the cello body, occurring in a signal with varying fundamental frequency, as our simulation experiment suggests.

V. CONCLUSION

In this paper we have investigated the nature of a periodicities that occur in the sustained portion of harmonic instrumental sounds. Specifically, we focused on phenomena of phase deviations that occur in different partials of the sound.

Comparative study of the phase fluctuations was performed for several instruments. The results suggest that phase coupling, which is basically a nonlinear phenomenon, is a significant feature that distinctly characterizes for instance cello and flute versus trumpet sound.

Finally, a model for the mechanism that might cause the phase uncoupling effect in vibrato sounds of string instruments was suggested. A simulation of this phenomena was presented and the findings are shown to be in support of this model.

ACKNOWLEDGMENTS

We would like to thank Neville Fletcher for pointing out the relation between our analysis and the physics of musical instruments. We also thank the reviewers for the many most useful and important comments.

APPENDIX: PROOF OF THE RELATIONS BETWEEN ADDITIVE PHASE COUPLING AND HIGHER ORDER STATISTICS

We want now to establish the relationship between $B(\nu_1, \nu_2)$ and $d_3(i, k)$ in general, which is formulated also in terms of $c_3(n, m)$ for n and $m \neq 0$.

The definition of $B(\nu_1, \nu_2)$ is

$$B(\nu_1, \nu_2) \stackrel{\text{def}}{=} \sum_{n=-\infty}^{\infty} \sum_{m=-\infty}^{\infty} c_3(n, m) e^{-j(\nu_1 n + \nu_2 m)},$$

and $c_3(n, m)$ is defined as

$$c_3(n, m) \stackrel{\text{def}}{=} \langle x(t)x(t+n)x(t+m) \rangle$$

for zero mean x and independent of t due to third-order stationarity. We take $t=0$ for simplicity of the derivations

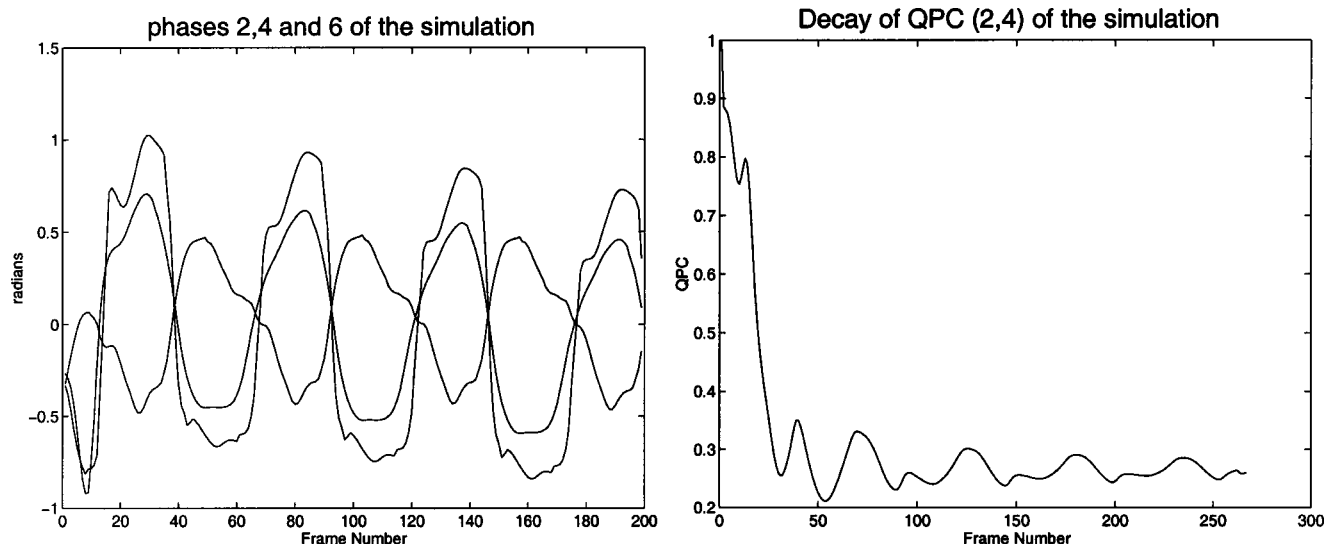


FIG. 13. Phases 2,4,6 and QPC decay of the simulation signal.

$$c_3(n, m) = \left\langle \sum_{i=-N, i \neq 0}^N e^{j(\omega_0 i \tau + \phi_i(0))} \sum_{k=-N, k \neq 0}^N e^{j(\omega_0 k(n+\tau) + \phi_k(n))} \sum_{l=-N, l \neq 0}^N e^{j(\omega_0 l(m+\tau) + \phi_l(m))} \right\rangle$$

$$= \sum_{i, k, l} \langle e^{j\omega_0(i+k+l)\tau} \rangle e^{j\omega_0(kn+lm)} \langle e^{j(\phi_i(0) + \phi_k(n) + \phi_l(m))} \rangle = \sum_{k, l} e^{j\omega_0(kn+lm)} \langle e^{j(\phi_k(n) + \phi_l(m) - \phi_{k+l}(0))} \rangle.$$

The right-hand term is called now a “lagged” d_3 , which contains the lag arguments

$$d_3(k, l; n, m) \stackrel{\text{def}}{=} \langle e^{j(\phi_k(n) + \phi_l(m) - \phi_{k+l}(0))} \rangle.$$

In such a case, we have $c_3(n, m)$ as a function of d_3 ,

$$c_3(n, m) = \sum_{k, l=-N, \neq 0}^N e^{j\omega_0(kn+lm)} d_3(k, l; n, m).$$

Let us now consider the discretization of the bispectral expression $B(\nu_1, \nu_2)$. Assuming that $c_3(n, m)$ is of finite support of size M , let us define a discrete frequency bispectrum

$$B_D(p, q) \stackrel{\text{def}}{=} \frac{1}{M^2} \sum_{m, n=-M/2+1}^{M/2} c_3(n, m) e^{-j((2\pi/M)pn + (2\pi/M)qm)}.$$

The relations between B_D and d_3 are

$$B_D(p, q) = \frac{1}{M^2} \sum_{m, n=-M/2+1}^{M/2} \left(\sum_{k, l=-N, \neq 0}^N e^{j\omega_0(kn+lm)} \right. \\ \left. \times d_3(k, l; n, m) \right) e^{-j((2\pi/M)pn + (2\pi/M)qm)}.$$

From physical considerations we assume that d_3 is independent of m, n , i.e., $d_3(k, l; n, m) = d_3(k, l)$. Rewriting the above expression,

$$B_D(p, q) = \frac{1}{M^2} \sum_{k, l=-N, \neq 0}^N \sum_{m, n=-M/2+1}^{M/2} e^{j(\omega_0 k - p 2\pi/M)n} \\ \times e^{j(\omega_0 l - q 2\pi/M)m} d_3(k, l),$$

and in the case that ω_0 falls into one of the FT bins, i.e., $\omega_0 = r 2\pi/M$ for some r , we get

$$B_D(p, q) = \frac{1}{M^2} \sum_{k, l=-N, \neq 0}^N M^2 \delta(rk, p) \delta(rl, q) d_3(k, l) \\ = d_3(p/r, q/r).$$

¹The proportion in magnitude of deviations among different partials corresponds to their partial number, i.e., k th partial will have k times the magnitude of the deviation of the fundamental. The reason for this proportion will become clear in later sections.

²The term “quadratic” comes from the fact that partials that are created by nonlinear interaction, such as multiplication, between lower partials have phase deviations that are a sum of phase deviations of their constituent lower partials. Since we consider statistical deviations among triplets of harmonically related partials, the corresponding measure is called quadratic phase coupling (QPC).

³One must note that correlation analysis is sensitive to the phase unwrapping. There are situations where a sound may exhibit high coupling with almost no correlation. This occurs when a signal has very few phase deviations,

resulting in small and uncorrelated phase difference signal.

⁴Bandwidth is determined as the width of magnitude response at half-power points relative to the peak value.

- Beauchamp, J. W. (1974). “Time-variant spectra of violin tones,” *J. Acoust. Soc. Am.* **56**.
- Dubnov, S., and Tishby, N. (1998). “Testing for Gaussianity and Non Linearity in the Sustained Portion of Musical Sounds,” *Recherches et Applications en Informatique Musicale*, edited by M. Chemillier and F. Pachet, Editions HERMES, pp. 212–224.
- Dubnov, S., Tishby, N., and Cohen, D. (1995). “Hearing Beyond The Spectrum,” *J. New Music Res.* **24**(4), 342–368.
- Dubnov, S., Tishby, N., and Cohen, D. (1997). “Polyspectra as Measures of Sound Texture and Timbre,” *J. New Music Res.* **26**(4), 277–314.
- Fletcher, N. H., and Rossing, T. D. (1995). *The Physics of Musical Instruments*, 3rd ed. (Springer Verlag, New York).
- Hinich, M. J. (1982). “Testing for Gaussainity and Linearity of a Stationary Time Series,” *J. Time Series Anal.* **3**(3), 169–176.
- McAdams, S., and Rodet, X. (1988). “The role of FM-induced AM in dynamic spectral profile analysis,” in *Basic Issues in Hearing*, edited by H. Duifhuis, J. Horst, and H. Wit (Academic, London), pp. 359–369.
- McGill University Master Samples. Faculty of Music, McGill University, 555 Sherbrooke St. West, Montreal, Quebec.
- McIntyre, M. E., Schumacher, R. T., and Woodhouse, J. (1981). “Aperiodicity in bowed string motion,” *Acustica* **49**, 13–32.
- Markel, J. D., and Gray, Jr., A. H. (1976). *Linear Prediction of Speech* (Springer-Verlag, Berlin).
- Mendel, J. M. (1991). “Tutorial on Higher-Order Statistics (Spectra) in Signal Processing and System Theory,” *Proc. IEEE* **79**(3), 278–305.
- Nikias, C. L., and Mendel, J. M. (1993). “Signal Processing with Higher-Order Spectra,” *IEEE Signal Process. Mag.* July.
- Priestley, M. B. (1989). *Non-Linear and Non-Stationary Time Series Analysis* (Academic, New York).
- Rodet, X. (1993). *Nonlinear Oscillations in Sustained Musical Instruments: Models and Control* (Euromech, Hamburg).
- Rodet, X. (1995). “Oscillations, Chaos and Control of Nonlinear Dynamical Models,” NOLTA, Las Vegas.
- Rodet, X. (1997). “Musical Sound Signals Analysis/Synthesis: Sinusoidal + Residual and Elementary Waveform Models,” in *Proc. of the IEEE Time-Frequency and Time-Scale Workshop (TFTS’97)*, Coventy, UK.
- Schumacher, R. T. (1992). “Analysis of aperiodicities in nearly periodic waveforms,” *J. Acoust. Soc. Am.* **91**, 438–451.
- Serra, X., and Smith, J. O. (1989). “Spectral Modeling Synthesis: A sound analysis/synthesis system based on deterministic plus stochastic decomposition,” *Comput. Music J.* **14**(4), 12–24.
- Studio Online. IRCAM, Paris, <http://sol.ircam.fr>
- Vergez, C., and Rodet, X. (2000). “Dynamical Systems and Physical Models of Trumpet-like Instruments: Analytical Study and Asymptotical Properties,” *Acustica-acta acustica* **86**, 147–162.
- Vettori, P. (1995). “Fractional ARIMA Modeling of Microvariations in Additive Synthesis,” *Proceedings of the XI Colloquium on Musical Informatics*, Bologna.
- Weinreich, G. (1997). “Directional tone color,” *J. Acoust. Soc. Am.* **101**, 2389–2406.

Compensation for source nonstationarity in multireference, scan-based near-field acoustical holography

Hyu-Sang Kwon^{a)}

Acoustics and Vibration Research Group, Korea Research Institute of Standards and Science, P.O. Box 102, Yusong, Taejeon 305-600, Korea

Yong-Joe Kim^{b)} and J. Stuart Bolton

1077 Ray W. Herrick Laboratories, School of Mechanical Engineering, Purdue University, West Lafayette, Indiana 47907-1077

(Received 23 May 2002; revised 18 October 2002; accepted 28 October 2002)

Multireference, scan-based near-field acoustical holography is a useful measurement tool that can be applied when an insufficient number of microphones is available to make measurements on a complete hologram surface simultaneously. The scan-based procedure can be used to construct a complete hologram by joining together subholograms captured using a relatively small, roving scan array and a fixed reference array. For the procedure to be successful, the source levels must remain stationary for the time taken to record the complete hologram; that is unlikely to be the case in practice, however. Usually, the reference signal levels measured during each scan differ from each other with the result that spatial noise is added to the hologram. A procedure to suppress the effects of source level, and hence reference level, variations is proposed here. The procedure is based on a formulation that explicitly features the acoustical transfer functions between the sources and both the reference and scanning, field microphones. When it is assumed that source level changes do not affect the sources' directivity, a nonstationarity compensation procedure can be derived that is based on measured transfer functions between the reference and field microphones. It has been verified both experimentally and in numerical simulations that the proposed procedure can help suppress spatially distributed noise caused by the type of source level nonstationarity that is characteristic of realistic sources. © 2003 Acoustical Society of America. [DOI: 10.1121/1.1529669]

PACS numbers: 43.60.Sx [EGW]

I. INTRODUCTION

Near-field acoustical holography (NAH) is a useful tool for identifying noise sources and reconstructing sound fields in a three-dimensional space.¹ The holographic projection and reconstruction process is based on a phase-coherent, spatial wave-field transformation that in turn requires the sound field on the hologram aperture to be fully coherent. However, in many practical cases, the sound field is created by a combination of incoherent or partially coherent sources with the result that the sound field at the hologram aperture is only partially spatially correlated.

When the sound field represents the superposition of fields radiated by incoherent or partially coherent sources, the total measured field must be decomposed into a set of spatially coherent partial fields (which are themselves mutually incoherent) before application of the holographic process to each of the partial fields in turn.² The projected partial fields are then added quadratically on the reconstruction surface to give the quadratic properties of the total field (e.g., sound power passing through the hologram aperture). When performing a partial field decomposition, reference signals that are linearly related to source signals must be used instead of the "source" signals themselves, since in the case of most mechanical and flow noise sources, those signals can-

not be directly measured. The number of fixed-location reference transducers must be equal to or greater than the number of incoherent sources to effect the partial field decomposition and to ensure that the quadratic sum of the partial fields accurately represents the quadratic properties of the total field.

Multireference, scan-based NAH as described above was introduced by Hald;³ that procedure is referred to as spatial transformation of sound fields (STSF). The latter procedure is based on the use of spectral matrix relations linking

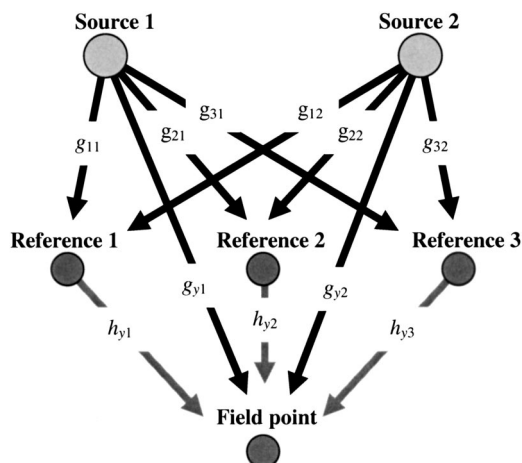


FIG. 1. The geometrical relations between sources, references, and field points and the associated transfer functions.

^{a)}Electronic mail: hyusang@kriss.re.kr

^{b)}Electronic mail: kimyl1@purdue.edu

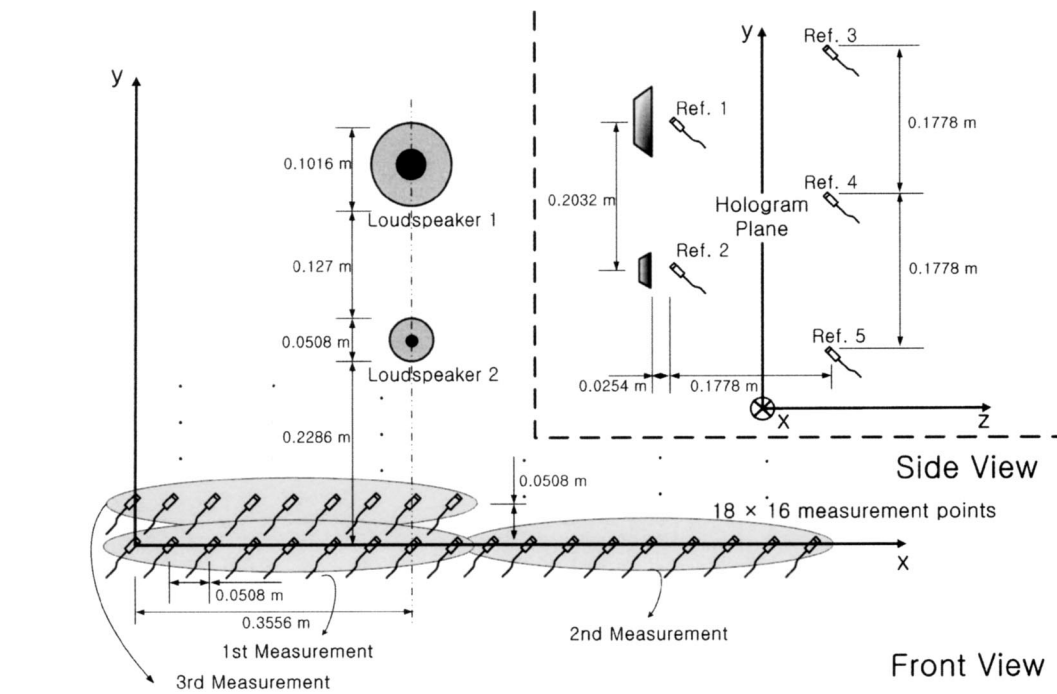


FIG. 2. Sketch of experimental setup.

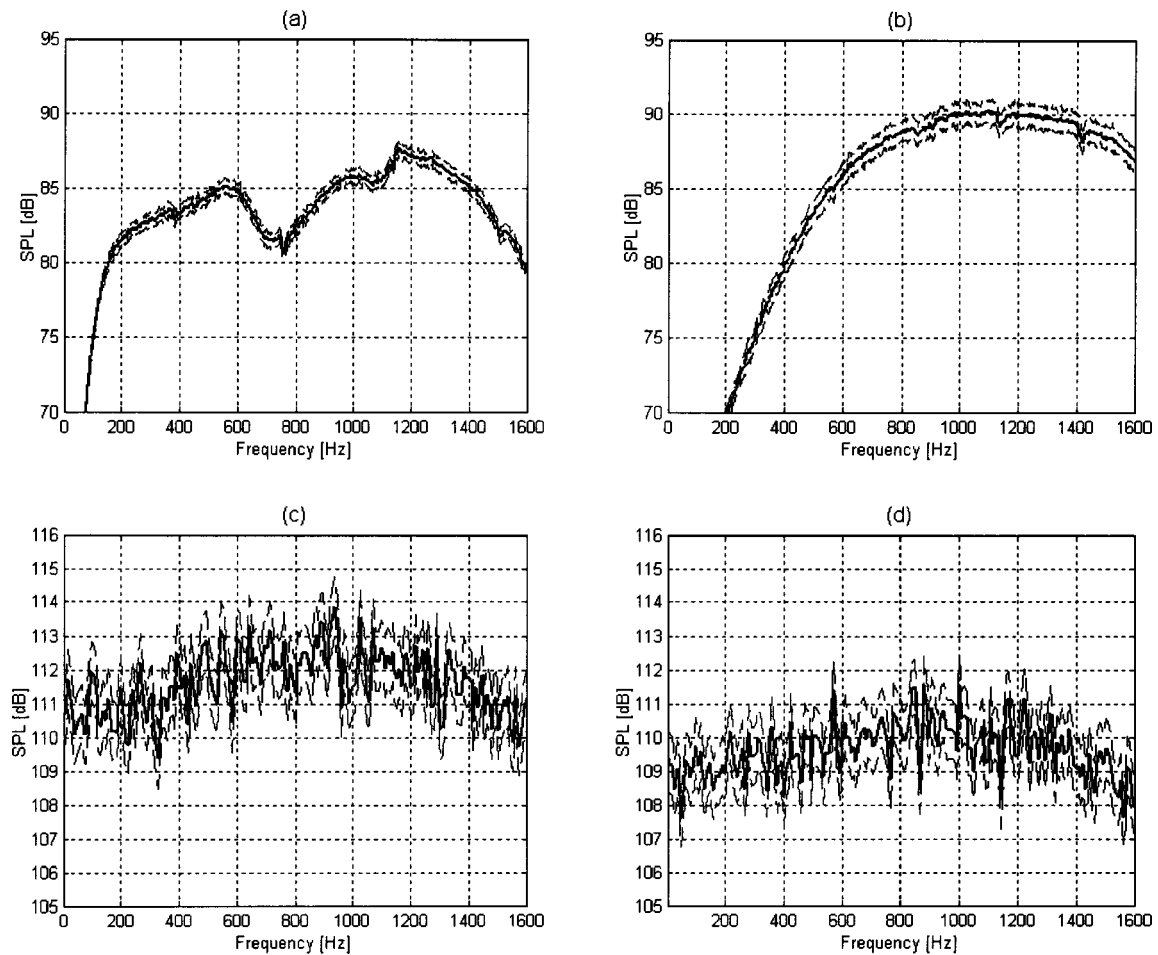


FIG. 3. Mean reference spectra (solid line) and \pm one standard deviation (dashed lines) for the 9 by 1 microphone array case: (a) reference 1 (experiment); (b) reference 2 (experiment); (c) reference 1 (simulation); and (d) reference 2 (simulation).

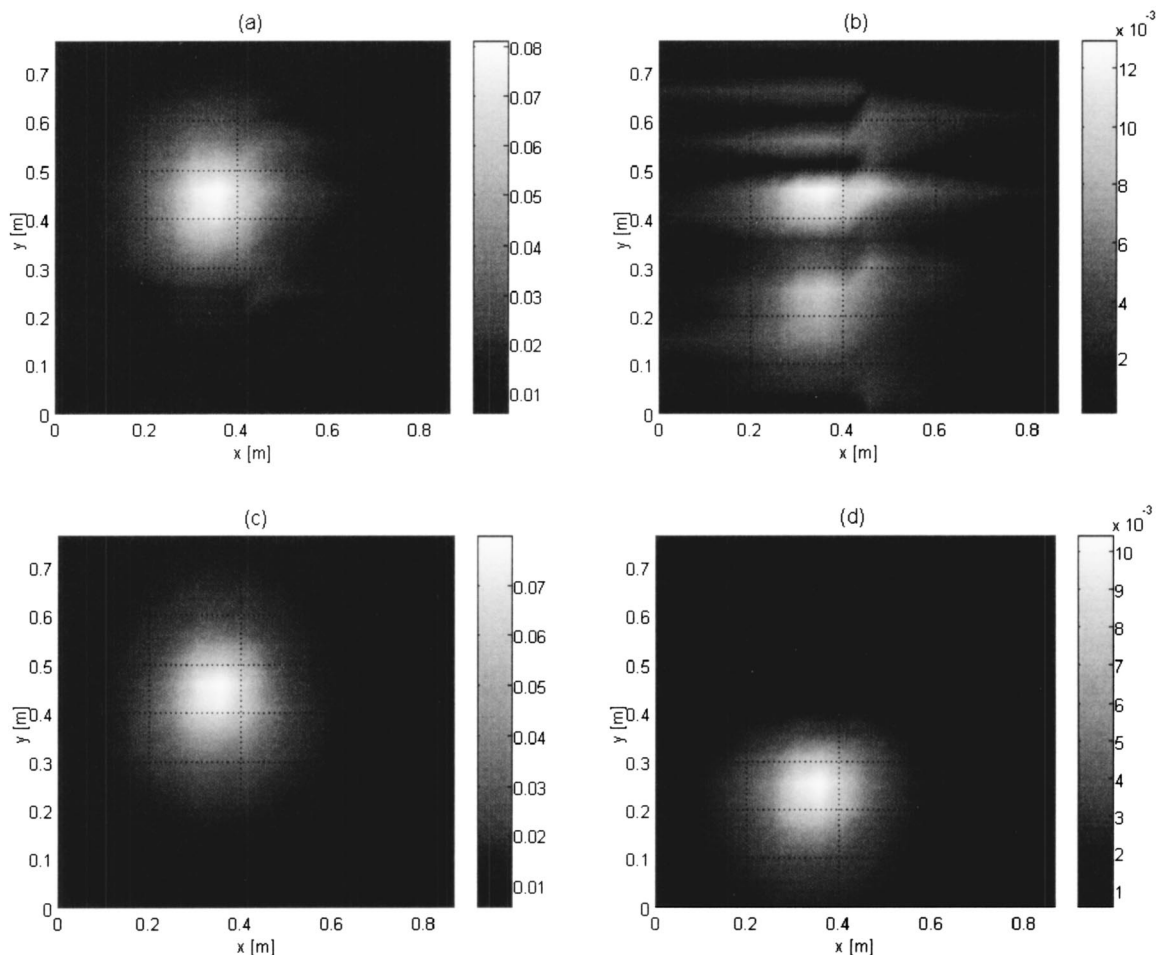


FIG. 4. Partial pressure fields at 200 Hz (experiment with 9 by 1 microphone array): (a) first field without compensation; (b) second field without compensation; (c) first field with compensation; and (d) second field with compensation.

the reference and field signals and makes use of pseudoreferences identified using singular value decomposition (SVD). The STSF procedure can be used to construct a complete hologram by joining together subholograms measured on each scan sector by using a relatively small scan array, provided only that the sound sources are stationary during the complete measurement: i.e., the measured reference spectra should be consistent from scan to scan. However, in practice, source levels vary during a measurement.

The effect of field-level variation from scan to scan is to add spatially distributed noise to the hologram. That spatial noise can be reduced to some extent by using long averaging times, and by the application of low-pass wave-number filtering to eliminate high spatial frequencies resulting from discontinuities at the edges of the subholograms. However, the latter procedure cannot effectively eliminate spurious low wave-number components that are generated when the scan array is relatively large in at least one dimension.

To develop a procedure for suppressing source nonstationarity effects, a detailed consideration of the signal and system relations between source, reference, and field data is required.² Based on such an investigation, a method to compensate for source nonstationarity is introduced here. The procedure is based on identifying the acoustical transfer functions that should be calculated on a scan-by-scan basis

and the cross-spectral matrices that should be averaged across all the scans. It is shown through experiment and simulation that the proposed procedure yields significant benefits in situations when the sources are nonstationary.

II. THEORY

A. General approach to multireference NAH

The theory of NAH is based on the use of the Kirchhoff–Helmholtz integral equation to describe the sound field in a volume that encloses the sound sources.¹ The holographic projection and reconstruction procedure can be expressed in matrix form as³

$$\mathbf{y}' = \mathbf{T}\mathbf{y}, \quad (1)$$

where \mathbf{y} and \mathbf{y}' represent the temporally Fourier transformed acoustic fields, e.g., pressure or velocity, on the hologram and reconstruction surfaces, respectively. The matrix \mathbf{T} represents the NAH projection procedure relating the sound field on the hologram surface to that on the reconstruction surface. Equation (1) can be applied when all the hologram data are captured simultaneously. However, when data are measured over portions of the hologram aperture in sequence, it is necessary to use reference transducers to provide phase references. In the latter case, it is convenient to

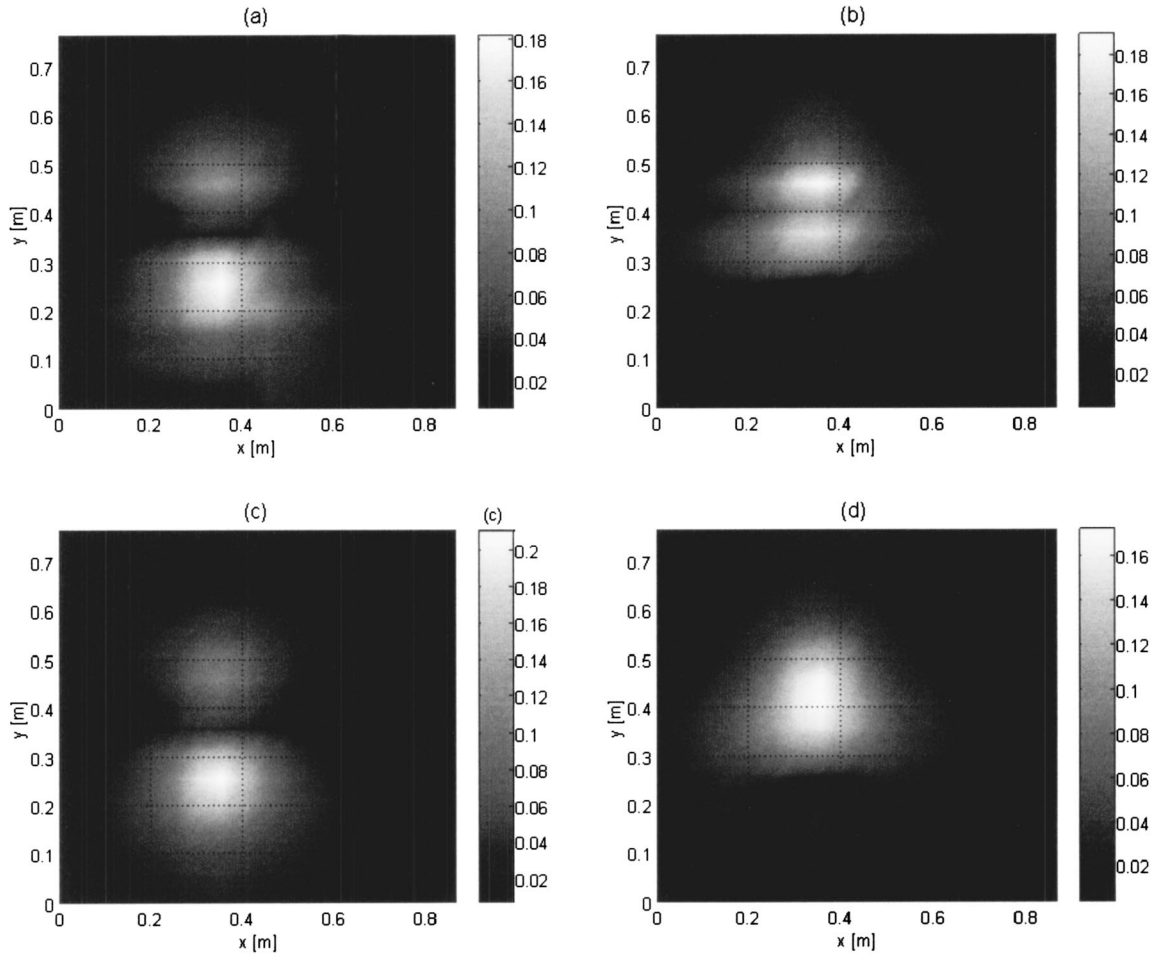


FIG. 5. Partial pressure fields at 1200 Hz (experiment with 9 by 1 microphone array): (a) first field without compensation; (b) second field without compensation; (c) first field with compensation; and (d) second field with compensation.

begin from a statistical description of the sound field, in which case the holographic procedure can be expressed as³

$$\mathbf{S}_{\mathbf{y}'\mathbf{y}'} = E\{\mathbf{y}'\mathbf{y}'^H\} = \mathbf{T}E\{\mathbf{y}\mathbf{y}^H\}\mathbf{T}^H = \mathbf{T}\mathbf{S}_{\mathbf{y}\mathbf{y}}\mathbf{T}^H, \quad (2)$$

where E denotes the expectation operator, the superscript H denotes the Hermitian transpose, and $\mathbf{S}_{\mathbf{y}\mathbf{y}}$ and $\mathbf{S}_{\mathbf{y}'\mathbf{y}'}$ are the cross-spectral matrices on the hologram and reconstruction surfaces, respectively. The reconstructed fields, in the magnitude sense, are then the diagonal terms of the cross-spectral matrix on the reconstruction surface.

Since the cross-spectral matrices in Eq. (2) comprise the auto- and cross spectra formed among the complete set of field signals on the hologram or reconstruction surfaces, the measurement and calculation of the cross-spectral matrices can be very time consuming given that a measurement may involve hundreds or thousands of field points. To simplify the hologram measurement and attendant calculation of the spectral matrices, a multireference method was developed.^{3,4}

When the sound field is generated by a finite number of sources, the field signals can be expressed as a linear combination of a set of reference signals when the number of reference signals is equal to or larger than the number of sources and when the reference signals span the complete source signal space. In that case, the hologram cross-spectral matrix can be calculated indirectly when both the cross-

spectral matrix of a suitable set of reference signals and the cross spectra between the reference and field signals are known.³ Once the complete hologram cross-spectral matrix is estimated using a multireference method, the hologram cross-spectral matrix must be decomposed into a set of coherent but mutually incoherent partial fields before the holographic projections can be performed: either SVD or partial coherence procedure may be used for that purpose.^{2,4} Note that the partial fields are not unique and that their natures depend on both the decomposition procedure and the reference microphone locations with respect to the sources. In general, the decomposed partial fields do not coincide with the physical partial fields radiated by the independent noise sources: the identified partial fields can themselves, however, be expressed as linear combinations of the physical partial fields.

As well as reducing the time taken to measure and compute the cross-spectral matrices, the multireference method has the advantage that it makes it possible to use a reduced set of scan microphones to measure the sound field on sectors of the hologram surface in sequence when the field can be assumed stationary. That is, the field signals are gathered step-by-step using a scanning microphone array that is smaller than the hologram aperture. During such a measure-

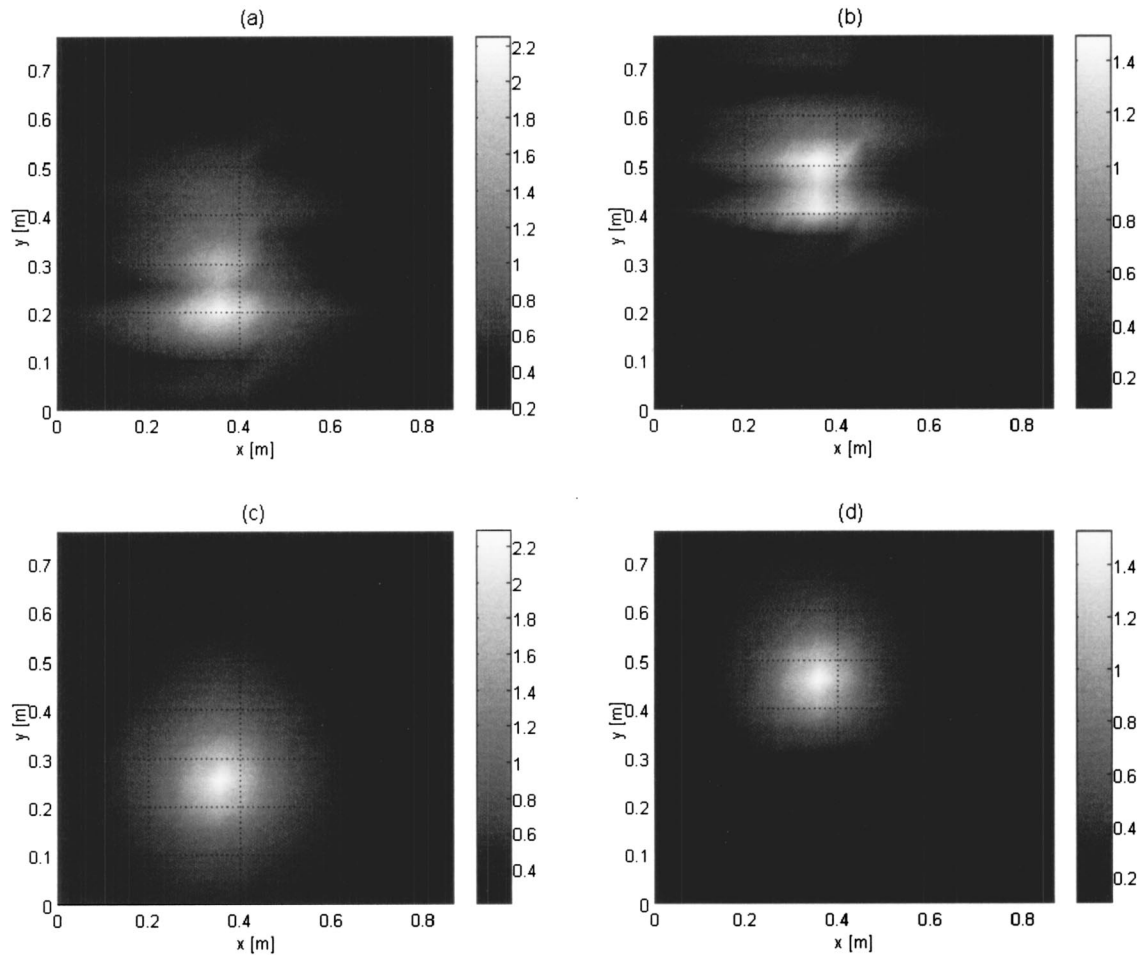


FIG. 6. Partial pressure fields at 200 Hz (numerical simulation with 9 by 1 microphone array): (a) first field without compensation; (b) second field without compensation; (c) first field with compensation; and (d) second field with compensation.

ment, the location of the reference transducers must be fixed in space with respect to the various sources.

B. Source and signal relations

Here, the “source” signals are considered to be mutually uncorrelated signals that represent distinct physical source mechanisms. Next, assume that the total sound field generated by the collection of physical sound sources is completely sensed by a set of reference transducers: i.e., it is assumed that the number of references is equal to or larger than the number of sound sources and that one or more of the reference transducers measures a signal linearly related to each of the component sources. The reference and sound field signals can then be expressed as a linear combination of the source signals multiplied by appropriate acoustical transfer functions.

As an example, the sound field radiated by two independent sources operating simultaneously can be represented by the system model illustrated in Fig. 1.² In Fig. 1, g_{ij} represents the transfer function between source j and reference i , g_{yj} denotes the transfer function between source j and a field point, and h_{yi} denotes the transfer function between reference i and the field point. Note that when representing the system in terms of source signals and transfer functions, the transfer functions, g_{ij} and g_{yj} , depend both on the geometry

of the source and field point arrangement, and on the radiation characteristics of the sources: e.g., their directivity. Here, it is assumed that the physical sources’ radiation characteristics are not affected by source-level fluctuations, and therefore remain constant through an entire holographic measurement: i.e., the transfer functions g_{ij} and g_{yj} are assumed to be the same during each scan.

For the general case of N incoherent sources and M references where $M \geq N$, the reference signals can be expressed in vector-matrix form as²

$$\mathbf{r} = \mathbf{G}_{\mathbf{rs}} \mathbf{s}, \quad (3)$$

where \mathbf{r} and \mathbf{s} are the M by 1 reference signal vector and the N by 1 source signal vector, respectively, and $\mathbf{G}_{\mathbf{rs}}$ is the M by N transfer function matrix that relates the source and reference signals. The field signals on the hologram surface can also be represented as the product of a transfer function matrix and the source signal vector: i.e.,

$$\mathbf{y} = \mathbf{G}_{\mathbf{ys}} \mathbf{s}, \quad (4)$$

where \mathbf{y} is the field signal vector on the hologram surface and $\mathbf{G}_{\mathbf{ys}}$ is the transfer function matrix relating the source and field signals. From Eqs. (3) and (4), the cross-spectral matrix relating the reference and field signals can be expressed as

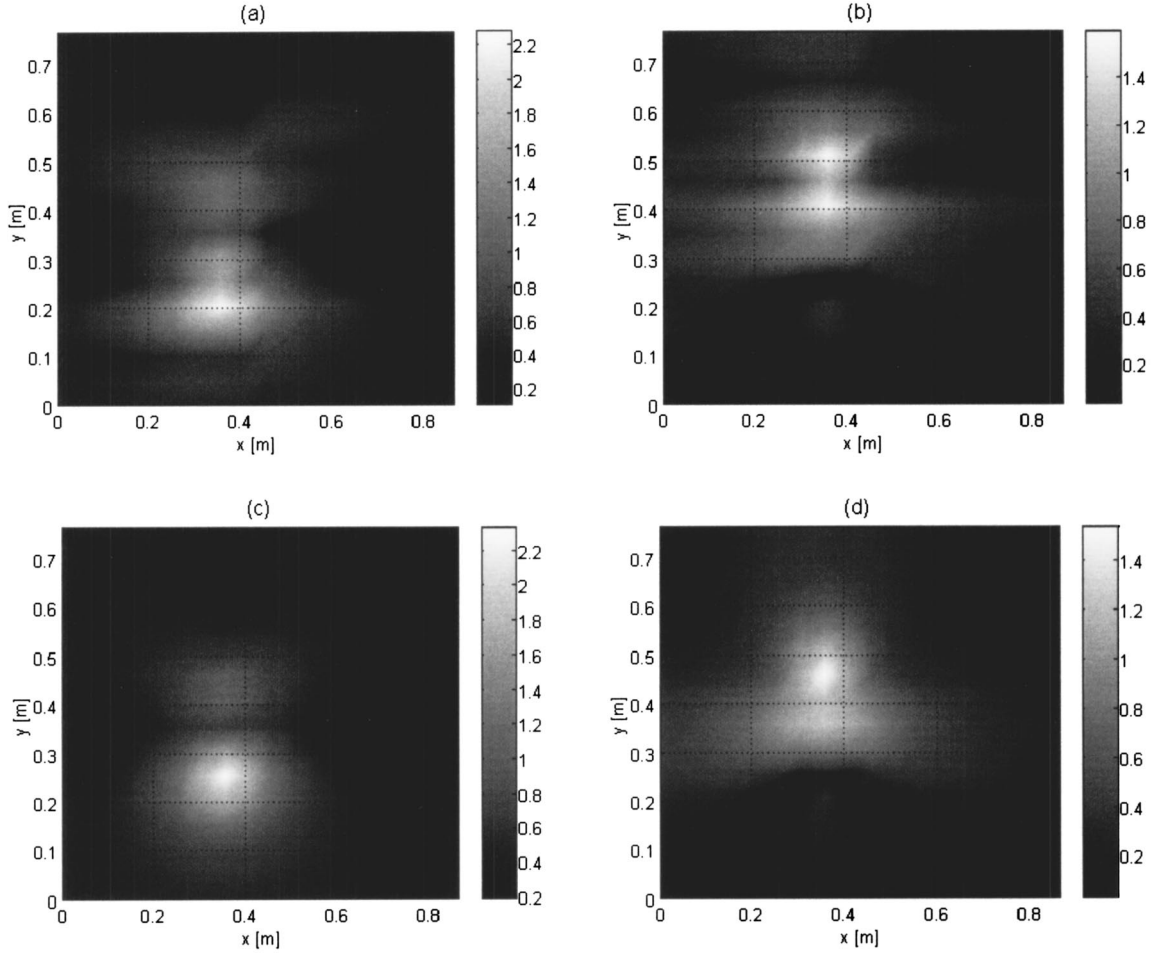


FIG. 7. Partial pressure fields at 1200 Hz (numerical simulation with 9 by 1 microphone array): (a) first field without compensation; (b) second field without compensation; (c) first field with compensation; and (d) second field with compensation.

$$\mathbf{S}_{\mathbf{r}\mathbf{y}} = \mathbf{E}\{\mathbf{r}\mathbf{y}^H\} = \mathbf{G}_{\mathbf{r}\mathbf{s}}\mathbf{S}_{\mathbf{s}\mathbf{s}}\mathbf{G}_{\mathbf{y}\mathbf{s}}^H, \quad (5)$$

where $\mathbf{S}_{\mathbf{r}\mathbf{y}}$ is the cross-spectral matrix between the reference and field signals and $\mathbf{S}_{\mathbf{s}\mathbf{s}}$ is the source signal cross-spectral matrix which, under the conditions prescribed above, is diagonal (the diagonal components being the auto spectra of the source signals). By using Eq. (3), the reference spectral matrix can be also written as

$$\mathbf{S}_{\mathbf{r}\mathbf{r}} = \mathbf{E}\{\mathbf{r}\mathbf{r}^H\} = \mathbf{G}_{\mathbf{r}\mathbf{s}}\mathbf{S}_{\mathbf{s}\mathbf{s}}\mathbf{G}_{\mathbf{r}\mathbf{s}}^H, \quad (6)$$

where $\mathbf{S}_{\mathbf{r}\mathbf{r}}$ is the reference cross-spectral matrix. Note that any source-level variation appearing in the source auto spectra on the right-hand side of Eq. (6) translates directly into variation of the reference cross-spectral matrix through the transfer function matrix, $\mathbf{G}_{\mathbf{r}\mathbf{s}}$.

C. Description of multireference NAH

The field signals on the hologram surface can be expressed as a linear combination of the reference signals multiplied by appropriate transfer functions: i.e.,

$$\mathbf{y} = \mathbf{H}_{\mathbf{y}\mathbf{r}}\mathbf{r}, \quad (7)$$

where \mathbf{r} is the reference signal vector, and $\mathbf{H}_{\mathbf{y}\mathbf{r}}$ is the transfer matrix that relates the reference and field signals on the hologram surface. By multiplying each side by Eq. (7) by \mathbf{r}^H

and then finding the expectation of the result, an equation for the latter transfer function matrix can be obtained: i.e.,

$$\mathbf{H}_{\mathbf{y}\mathbf{r}} = \mathbf{S}_{\mathbf{r}\mathbf{y}}\mathbf{S}_{\mathbf{r}\mathbf{r}}^{-1}, \quad (8)$$

where the inverse of the reference cross-spectral matrix represents a generalized inverse to accommodate situations in which the reference cross-spectral matrix is rank deficient. Similarly, the cross-spectral matrix on the hologram surface can be expressed as

$$\mathbf{S}_{\mathbf{y}\mathbf{y}} = \mathbf{H}_{\mathbf{y}\mathbf{r}}\mathbf{S}_{\mathbf{r}\mathbf{y}}. \quad (9)$$

By substituting Eq. (8) into Eq. (9), the hologram cross-spectral matrix can be estimated by using the reference cross-spectral matrix in combination with the cross-spectral matrix relating the reference and field signals on the hologram surface: i.e.,

$$\mathbf{S}_{\mathbf{y}\mathbf{y}} = \mathbf{S}_{\mathbf{r}\mathbf{y}}\mathbf{S}_{\mathbf{r}\mathbf{r}}^{-1}\mathbf{S}_{\mathbf{r}\mathbf{y}}. \quad (10)$$

Note that the cross-spectral matrix can be decomposed into any set of incoherent partial fields subject only to the condition that $\mathbf{S}_{\mathbf{y}\mathbf{y}} = \mathbf{a}\mathbf{a}^H$, where \mathbf{a} represents a partial field vector. From Eqs. (8) and (10), the partial field matrix, \mathbf{a} , can be then represented as²

$$\mathbf{a} = \mathbf{S}_{\mathbf{r}\mathbf{y}}\mathbf{S}_{\mathbf{r}\mathbf{r}}^{-1/2} = \mathbf{H}_{\mathbf{y}\mathbf{r}}\mathbf{S}_{\mathbf{r}\mathbf{r}}^{1/2}. \quad (11)$$

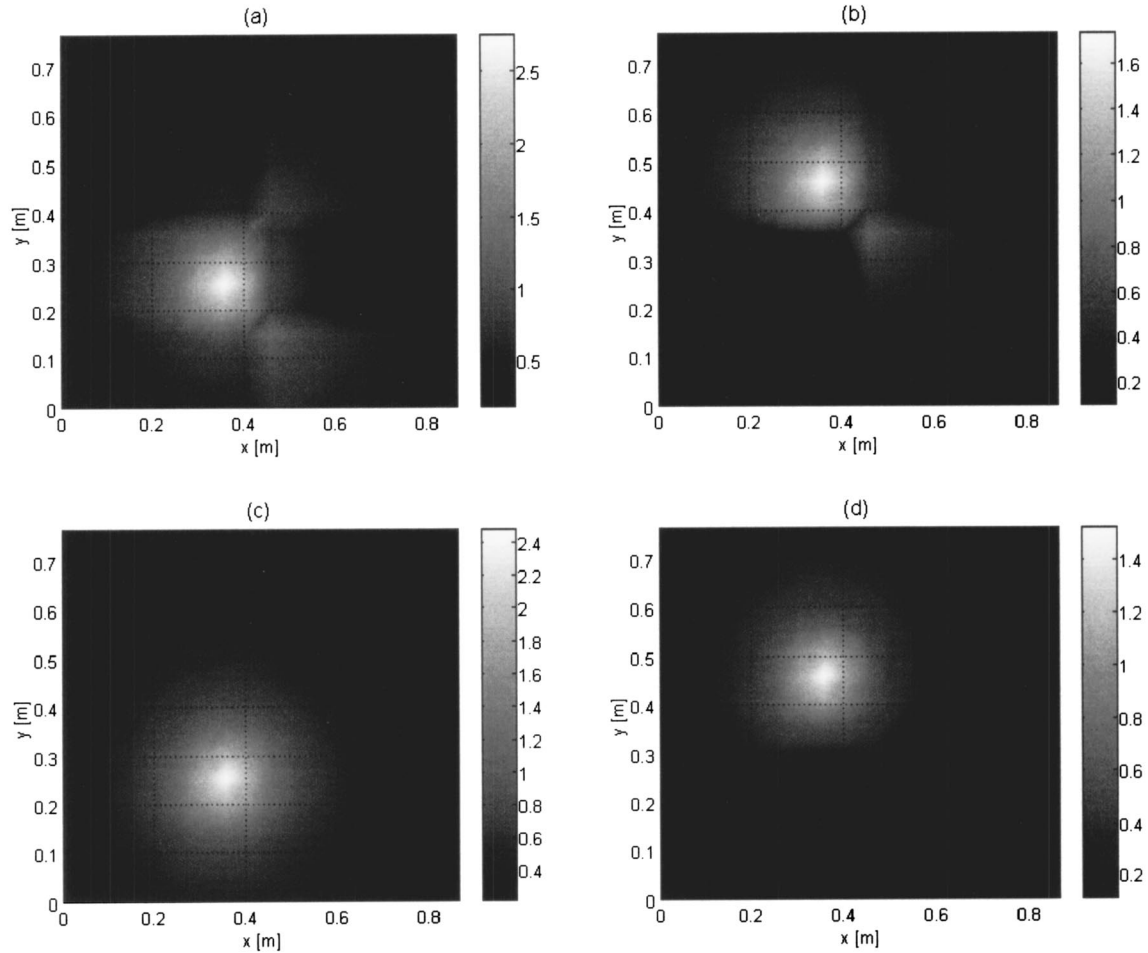


FIG. 8. Partial pressure fields at 200 Hz (numerical simulation with 9 by 4 microphone array): (a) first field without compensation; (b) second field without compensation; (c) first field with compensation; and (d) second field with compensation.

The SVD and partial coherence methods have been widely used for calculation of the partial field decomposition given in Eq. (11). In the SVD method, the reference cross-spectral matrix is decomposed by using SVD, and thus the partial fields can be represented as

$$\mathbf{a} = \mathbf{S}_{\text{ry}}^H \mathbf{V} \mathbf{\Lambda}^{-1/2} = \mathbf{H}_{\text{yr}} \mathbf{V} \mathbf{\Lambda}^{1/2}, \quad (12)$$

where \mathbf{V} is the unitary matrix and $\mathbf{\Lambda}$ is the diagonal matrix of singular values. The partial coherence method is based on the use of Cholesky decomposition⁵ to separate the reference cross-spectral matrix into two parts, and in that case the partial fields are written as

$$\mathbf{a} = \mathbf{S}_{\text{ry}}^H \mathbf{L}^{-1} \mathbf{D}^{-1/2} = \mathbf{H}_{\text{yr}} \mathbf{L} \mathbf{D}^{1/2}, \quad (13)$$

where \mathbf{L} is the lower triangular matrix and \mathbf{D} is the diagonal matrix with pivots. The SVD procedure has been used in the experiments and simulations presented in this article.

D. Nonstationarity compensation for scan-based NAH

By substituting Eqs. (5) and (6) into Eq. (8), the transfer function matrix relating the reference and field signals can be expressed in terms of the source matrix and the associated transfer matrix: i.e.,

$$\mathbf{H}_{\text{yr}} = \mathbf{S}_{\text{ry}}^H \mathbf{S}_{\text{rr}}^{-1} = \mathbf{G}_{\text{ys}} \mathbf{S}_{\text{ss}} \mathbf{G}_{\text{rs}}^H (\mathbf{G}_{\text{rs}} \mathbf{S}_{\text{ss}} \mathbf{G}_{\text{rs}}^H)^{-1} = \mathbf{G}_{\text{ys}} \mathbf{G}_{\text{rs}}^{-1}. \quad (14)$$

Note that the source cross-spectral matrix cancels out in this calculation and thus the transfer matrix between the reference and field signals is independent of source-level variation since the transfer matrices between the source and reference and field signals are themselves assumed to be independent of source level. Under these conditions, the reference cross-spectral matrix varies in direct proportion to the source level nonstationarity, as shown in Eq. (6), from one scan sector to the next, but the transfer function matrix appropriate for each scan is consistent even when the source levels vary.

Based on the above considerations, the partial field matrix, Eq. (11), can finally be written in modified form as

$$\mathbf{a} = \mathbf{H}_{\text{yr},(\text{step})} \mathbf{S}_{\text{rr},(\text{avg})}^{1/2} = \mathbf{S}_{\text{ry},(\text{step})}^H \mathbf{S}_{\text{rr},(\text{step})}^{-1} \mathbf{S}_{\text{rr},(\text{avg})}^{1/2}, \quad (15)$$

where the subscripts (step) and (avg) denote spectral matrix estimates calculated during each scan or averaged over all the scans, respectively. The partial field decomposition represented by Eq. (15) thus combines transfer functions estimated during each scan with reference information averaged over the complete measurement set to create a consistent set of partial fields. Given the above assumptions, nonstationary effects are suppressed in partial fields calculated using Eq. (15). For the purpose of comparison, the conventional partial

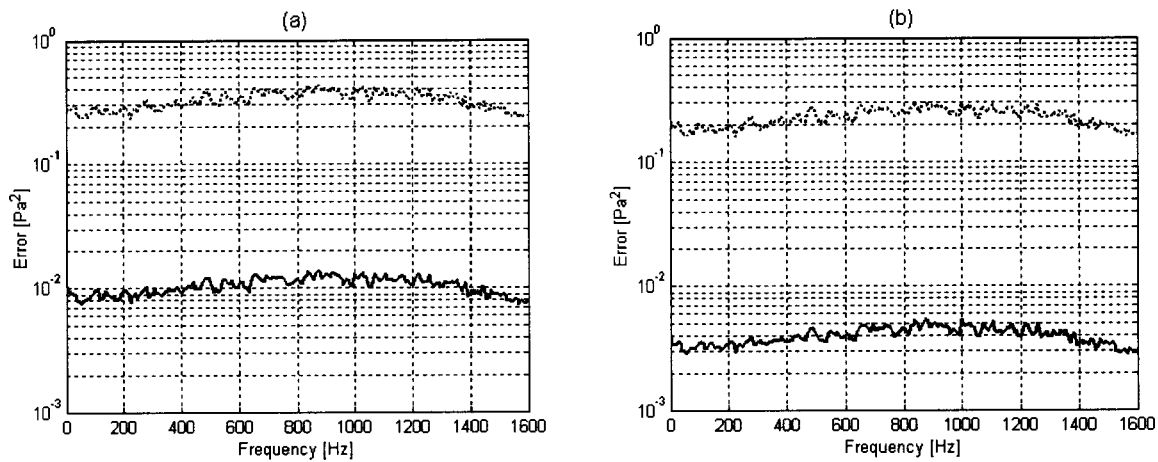


FIG. 9. Spatially averaged absolute difference between total power, resulting from squared summation of two partial pressure fields, of stationary simulation and total power of nonstationary simulation (solid line—with compensation and dashed line—without compensation): (a) 9 by 1 microphone array and (b) 9 by 4 microphone array.

field matrix without nonstationarity compensation is expressed here in terms of the estimates shown in Eq. (15): i.e.,

$$\mathbf{a} = \mathbf{S}_{\text{ry, (step)}}^H \mathbf{S}_{\text{rr, (avg)}}^{-1/2}. \quad (16)$$

III. EXPERIMENT AND NUMERICAL SIMULATION

An experiment was performed in an anechoic chamber to verify the compensation procedure described above. Two loudspeakers having different frequency characteristics were driven by independent white-noise sources (see Fig. 2). A horizontal line array of nine microphones with a spacing of 0.0508 m was used to scan the hologram following the procedure indicated in Fig. 2. The aperture thus comprised 32 subholograms and a total 18 by 16 field points. During the scanning, five reference microphones were fixed in front of the loudspeakers as shown in Fig. 2. During each scan, the data record length was 512 points at a sampling rate of 4096 Hz and 20 linear averages were performed when estimating the various spectra; during the latter operations a 256-point overlap was used and a Hanning window was applied to each record. Note that the use of a relatively small number of averages in the spectral estimation, as here, may exaggerate the effects of nonstationarity and make the partial field separation less accurate.

A numerical simulation of the experiment was also performed: in this case, two monopole sources were located at the loudspeaker locations on the source plane. Two independent random signals were generated having almost identical levels. These signals were used as source signals during each scan after being scaled by randomly chosen source weights: i.e., the source strength was varied slightly from scan to scan to simulate source nonstationarity. For the purpose of qualitative simulation of the experiment described above, these 32 pairs of weights were randomly chosen so that the mean and standard deviation of the weights was approximately 0 and 1 dB, respectively. The equivalent stationary case was reproduced by setting all the source weights to be 0 dB. In addition to the simulation of the 9 by 1 microphone array, the

case of a 9 by 4 microphone array was also simulated. The data obtained from both simulations were then processed as in the experimental case.

IV. RESULTS

To illustrate the spectral variance due to source level nonstationary, the mean and standard deviation of 32 reference auto spectra (i.e., one per scan) are plotted in Fig. 3 for the experimental and matching simulated results for the 9 by 1 microphone array case. Note that the standard deviation of the spectra was approximately 1 dB in both the experiment and the simulation. That is, the nonstationarity was relatively small, as in a well-controlled experiment. Figures 4–7 show partial pressure fields, calculated by using SVD, on the hologram surface for the 9 by 1 microphone array case: the partial fields labeled (a) and (b) were obtained without applying the nonstationarity compensation, while the compensation was applied to the partial fields labeled (c) and (d). It can be seen that the experimental results (Figs. 4 and 5) are consistent with the simulation results (Figs. 6 and 7): i.e., a spatial distortion in the shape of the line-field array is visible in the uncompensated results in all cases. Note that particularly in the 200-Hz case each partial field approximates the sound field radiated by one of the sources owing to the positioning of references directly in front of each source. However, there is still some leakage from the other source in each case: the leakage is particularly evident in the 1200-Hz case. By comparing Figs. 4(a) and (c) for the first partial field at 200 Hz [or Figs. 4(b) and (d) for the second partial field], it can be seen that the spatial noise resulting from source nonstationarity that is visible in Fig. 4(a) [or Fig. 4(b)] is essentially eliminated in Fig. 4(c) [or Fig. 4(d)] by application of the compensation. The same is also true for the experimental results at 1200 Hz (Fig. 5) and for the simulation results at 200 Hz (Fig. 6) and at 1200 Hz (Fig. 7). The simulation results for the 9 by 4 microphone array (Fig. 8) also clearly show a spatial noise pattern in the shape of the measurement array: that effect is again suppressed by the compensation procedure.

Finally, the total power difference between the stationary and nonstationary simulations is shown in Fig. 9. Here, the power difference (error) is written as

$$E_p(f) = \frac{1}{(18)(16)} \times \sum_{n=1}^{18} \sum_{m=1}^{16} \left| \sum_{i=1}^2 \frac{p_i^2(f, x_n, y_m) - \bar{p}_i^2(f, x_n, y_m)}{2} \right|, \quad (17)$$

where f is the frequency, $p_i(x_n, y_m)$ is the i th partial pressure at (x_n, y_m) , and the overbar denotes the stationary case. It can be seen that the source-level compensation reduces the spatial noise resulting from source nonstationarity by more than an order of magnitude at all frequencies.

V. CONCLUSIONS

Multireference, scan-based NAH has been formulated here by using a mathematical description that explicitly features the acoustic transfer functions between the references and the field points. It was thus possible to separate spectral matrices that should be calculated during individual scans from those that can safely be averaged over all scans. Based upon the present description, a procedure to compensate for source nonstationarity was proposed. It was shown through both an experiment and a numerical simulation that the proposed procedure reduces the spatial noise resulting from source nonstationarity even when the standard deviation of the source levels was approximately 1 dB.

ACKNOWLEDGMENTS

The authors gratefully acknowledge partial financial support for this work from Isuzu Motors Ltd. (contract monitor: Hiroshi Takata). We would also like to thank Jørgen Hald of Brüel & Kjaer for a number of helpful conversations. The third author would like to thank the Korea Research Foundation for providing financial support during his sabbatical at the Korea Advanced Institute of Science and Technology (KAIST) in Taejeon, Korea, where work on this article was begun; and his thanks also go to Professor Yang-Hann Kim and Professor Jeong-Guon Ih, both of the Center for Noise and Vibration Control (NOVIC), Department of Mechanical Engineering, KAIST, for their hospitality and for making the arrangements that made that visit possible.

- ¹J. D. Maynard, E. G. Williams, and Y. Lee, "Near field Acoustics Holography I. Theory of Generalized Holography and the Development of NAH," *J. Acoust. Soc. Am.* **78**, 1395–1413 (1985).
- ²H.-S. Kwon and J. S. Bolton, "Partial Field Decomposition in Near-field Acoustical Holography by the Use of Singular Value Decomposition and Partial Coherence Procedures," *Proc. NOISE-CON 98*, 649–654 (1998).
- ³J. Hald, "STSF—A Unique Technique for Scan-Based Near-Field Acoustical Holography Without Restriction on Coherence," B&K Technical Review No. 1 (1988).
- ⁴D. L. Hallman and J. S. Bolton, "A Comparison of MultiReference Near-field Acoustical Holography Procedures," *Proc. NOISE-CON 94*, 929–934 (1994).
- ⁵G. Strang, *Linear Algebra and Its Applications*, 3rd ed. (Harcourt, New York, 1988).

An auditory-periphery model of the effects of acoustic trauma on auditory nerve responses

Ian C. Bruce,^{a)} Murray B. Sachs, and Eric D. Young

Center for Hearing Sciences and Department of Biomedical Engineering, Johns Hopkins University
School of Medicine, Baltimore, Maryland 21205

(Received 20 June 2002; revised 12 September 2002; accepted 16 September 2002)

Acoustic trauma degrades the auditory nerve's tonotopic representation of acoustic stimuli. Recent physiological studies have quantified the degradation in responses to the vowel /ε/ and have investigated amplification schemes designed to restore a more correct tonotopic representation than is achieved with conventional hearing aids. However, it is difficult from the data to quantify how much different aspects of the cochlear pathology contribute to the impaired responses. Furthermore, extensive experimental testing of potential hearing aids is infeasible. Here, both of these concerns are addressed by developing models of the normal and impaired auditory peripheries that are tested against a wide range of physiological data. The effects of both outer and inner hair cell status on model predictions of the vowel data were investigated. The modeling results indicate that impairment of both outer and inner hair cells contribute to degradation in the tonotopic representation of the formant frequencies in the auditory nerve. Additionally, the model is able to predict the effects of frequency-shaping amplification on auditory nerve responses, indicating the model's potential suitability for more rapid development and testing of hearing aid schemes.

© 2003 Acoustical Society of America. [DOI: 10.1121/1.1519544]

PACS numbers: 43.64.Bt, 43.64.Pg, 43.64.Sj, 43.66.Ts [BLM]

I. INTRODUCTION

Recent physiological studies (Miller *et al.*, 1997; Schilling *et al.*, 1998; Wong *et al.*, 1998; Miller *et al.*, 1999a, b) have shown that acoustic trauma causes substantial changes in the auditory nerve (AN) representation of a speechlike stimulus, in this case the synthesized vowel /ε/ as in "met." The responses of a normal AN fiber to the vowel presented at stimulus levels appropriate for conversational speech are dominated by the formant frequency nearest the fiber's best frequency (BF), a phenomenon known as synchrony capture (Young and Sachs, 1979; Deng and Geisler, 1987b; Deng *et al.*, 1987; Miller *et al.*, 1997). In contrast, fibers in an ear impaired by acoustic trauma respond to a broad range of frequency components in the vowel, particularly to formants at frequencies below the fibers' BFs. As a result, the normal tonotopic representation of the vowel is degraded; most important, responses to the first formant (*F*₁) spread away from their tonotopically appropriate location towards higher BFs. The upward spread of *F*₁ responses means that cochlear locations at which responses to *F*₂ and *F*₃ are normally seen now respond primarily to *F*₁. This spread of *F*₁ response reduces the quality of the representation of *F*₂ and *F*₃; for example, the discriminability, based on AN responses, of vowels with different *F*₂s is substantially reduced (Miller *et al.*, 1999b). In this paper, we describe a computational model of the auditory periphery that is able to describe this degradation of AN representation of speech stimuli.

Anatomical investigations of acoustically traumatized

cochleae show damage to both the outer (OHC) and inner (IHC) hair cells (Liberman and Dodds, 1984a). OHC impairment produces broadened and elevated AN fiber threshold tuning curves (e.g., Kiang *et al.*, 1976; Robertson, 1982; Liberman and Dodds, 1984a). Also observed are reductions in nonlinearities in AN responses, such as two-tone rate suppression (Schmiedt *et al.*, 1980, 1990; Salvi *et al.*, 1982; Miller *et al.*, 1997) and the compressive nature of basilar-membrane (BM) responses (Robles and Ruggero, 2001). The latter are seen, for example, in the growth of discharge rate of AN fibers with sound level (Harrison, 1981). IHC damage causes elevation of AN fiber threshold tuning curves without broadening their tuning (Liberman and Dodds, 1984a).

Because the cochlea is nonlinear, it is difficult to attribute changes in AN responses to speech following acoustic trauma to particular aspects of the damage, such as IHC versus OHC or tuning versus compression. A model is helpful in that process. The effects of broadened tuning on responses to speech have been studied using computational models (Geisler, 1989; Sachs *et al.*, 2002), but these models do not include two-tone rate suppression (the former also lacks BM compression), and IHC impairment was not investigated. Our methodology in this paper is to modify the OHC and IHC sections of an auditory periphery model (Zhang *et al.*, 2001) to produce the desired impairment of model AN fiber tuning curves, both threshold and bandwidth, and observe the effects of these changes on model responses to the vowel. The physiological accuracy of the model's predictions is assessed by comparison with published data. This sort of model should be useful as a means of quickly and efficiently testing potential hearing-aid amplification schemes and will provide a kind of test not commonly used, which is to evaluate the ability of amplification to restore normal patterns of auditory nerve activity in response to speech. Such informa-

^{a)} Author to whom correspondence should be addressed. Department of Electrical and Computer Engineering, Room CRL-229, McMaster University, 1280 Main Street West, Hamilton, Ontario L8S 4K1, Canada. Electronic mail: ibruce@ieee.org

tion should be a useful adjunct to psychophysical testing.

We have selected the model of Zhang *et al.* (2001) because it has a number of features that make it suitable to the task. First, the model input can be any arbitrary sound-pressure waveform and its output consists of simulated AN fiber spike times, so the same types of data analyses can be performed on the model as on the physiological data. Second, the model has been designed particularly to describe the synchrony (or phase locking) behavior of low-frequency AN fibers. Synchronized response are important to this effort because synchrony shows directly to which frequency components of a complex stimulus a fiber is responding. Synchrony is particularly revealing when used to analyze the effects of impairment on responses to speech. Third, the model contains sections that separately represent the IHCs and OHCs, making it possible to simulate effects of damage to particular aspects of cochlear function. Fourth, the model parameters have been adjusted for the cat auditory periphery and the model has been extensively validated by comparison with data from cat, the same species in which the comparison vowel data were collected.

There exist a number of alternative models of the auditory periphery, which we decided were less suitable to the task at hand. The model of Zhang *et al.* (2001) is based on an earlier model by Carney (1993). The latter model accounts for variation of frequency tuning with stimulus level and BM compression but does not produce two-tone rate suppression, which has been shown to be important in AN responses to speech (Young and Sachs, 1979; Sachs and Young, 1979; Miller *et al.*, 1997; Wong *et al.*, 1998). Models by Deng and Geisler (1987a), Payton (1988), Jenison *et al.* (1991), and Giguère and Woodland (1994) also do not include two-tone rate suppression and have not been as extensively validated against physiological data. The models of Kates (1995) and Robert and Eriksson (1999) do include two-tone rate suppression, but this is achieved via feedback control from neighboring BM filters. Such lateral feedback does not have an obvious correlate in cochlear physiology and could lead to unpredictable effects when one section is impaired but adjacent sections are normal. Several studies have modeled the nonlinear properties of the BM, including level-dependent tuning, compression, and two-tone rate suppression (Pfeiffer, 1970; Duifhuis, 1976; Goldstein, 1990, 1995; Meddis *et al.*, 2001; Irino and Patterson, 2001; Lopez-Poveda and Meddis, 2001). The more recent of these models produce some features not seen in the Zhang *et al.* (2001) model, such as a shift in BF with intensity (as reported by Anderson *et al.*, 1971; Johnstone *et al.*, 1986; Zhang and Zwislocki, 1996; Robles and Ruggero, 2001) and abrupt phase changes in AN responses at very high stimulus levels (the component 1/component 2 transition, Liberman and Kiang, 1984). However, these BM models do not include IHCs, synapses, and AN fibers and therefore are not suitable for comparison with AN data (Meddis *et al.*, 2001).

Although the Zhang *et al.* (2001) model is accurate in predicting a large range of physiological data for pure-tone and two-tone stimuli, it has not been tested previously with speechlike stimuli. In this paper, we show that some changes to the OHC control of BM tuning are required to improve the

model's predictions of normal AN responses to the vowel stimulus. A simple modification of OHC function in our improved model allows the effects of acoustic trauma to be modeled, including various degrees of elevation and broadening of tuning curves and a proportional loss of compression and suppression. An analogous modification to the IHC section of the model leads primarily to elevation of the tuning curve without substantially changing the bandwidth as measured by Q_{10} values. These different effects of OHC and IHC impairment are consistent with the physiological data (e.g., Liberman and Dodds, 1984a). Here we show that both IHC and OHC impairment can cause model fibers with BFs near the second and third formants to lose synchrony to those formants and become more synchronized to other components of the vowel spectrum, as observed in the physiological data. The model also predicts that the amplification scheme previously suggested by Miller *et al.* (1999a) restores synchrony capture by the second formant for model fibers with BFs in the second formant region.

II. MODELING THE NORMAL AUDITORY PERIPHERY

The auditory-periphery model, modified from Zhang *et al.* (2001), comprises several sections, each providing a phenomenological description of a different part of cochlea function. The model is illustrated in the schematic diagram of Fig. 1(a). The details of the normal model can be found in Zhang *et al.* (2001). In this paper we only describe modifications made to the Zhang *et al.* model to improve its accuracy in predicting responses to speech sounds and the changes that are needed to model OHC and IHC impairment. The model code is available on request. All the changes to the normal AN-periphery model from that of Zhang *et al.* (2001) are summarized in Table I.

The first section models the filtering properties of the middle ear (ME), described in detail in Appendix A. Filtering by the outer ear is not included, because we are using the model to predict physiological data for acoustic stimuli that were delivered directly to the tympanic membrane via ear-bars (e.g., Miller *et al.*, 1997). Outer-ear filtering would need to be considered for free-field acoustic stimulation.

The second section describes the “control path,” which includes a wideband, nonlinear, time-varying, band-pass filter followed by an OHC nonlinearity (NL) and low-pass (LP) filter. The purpose of this section is to control the time-varying, nonlinear behavior of the narrow-band signal-path BM filter, which it does by adjusting the bandwidth and gain of that filter through its time constant τ_{sp} . The control-path filter must be wider than the signal-path filter to account for wideband nonlinear phenomena such as two-tone rate suppression (e.g., Sachs and Kiang, 1968; Costalupes *et al.*, 1987; Javel *et al.*, 1978, 1983; Delgutte, 1990; Temchin *et al.*, 1997).

The third section of the model is the “signal path” describing the filter properties and traveling wave delay of the BM (time-varying, narrow-band filter); the nonlinear transduction and low-pass filtering of the IHC (IHC NL and LP); spontaneous and driven activity and adaptation in synaptic transmission (synapse model); and spike generation and refractoriness in the AN (spike generator). The center fre-

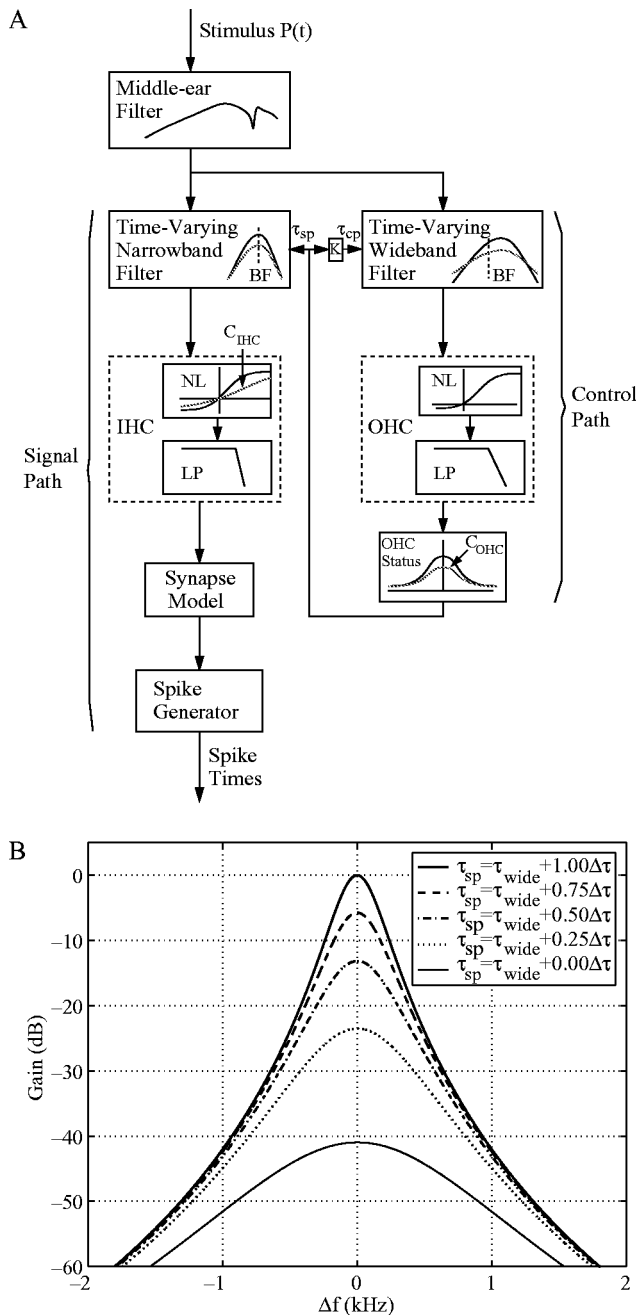


FIG. 1. (a) The auditory-periphery model modified from Zhang *et al.* (2001) (cf. Fig. 1 of that paper). Abbreviations: outer hair cell (OHC); low-pass (LP) filter; static nonlinearity (NL); inner hair cell (IHC); best frequency (BF). C_{IHC} and C_{OHC} are scaling constants that control IHC and OHC status, respectively. (b) Gain functions of linear versions of the time-varying narrow-band filter in the signal path, plotted as gain versus frequency deviation Δf from BF. The filter is fourth-order and is plotted for five different values of τ_{sp} between τ_{narrow} and τ_{wide} ; $\Delta\tau = \tau_{narrow} - \tau_{wide}$. τ_{narrow} was chosen to produce a 10-dB bandwidth of ~ 450 Hz, and τ_{wide} was chosen to produce a maximum gain change at BF of ~ 41 dB. This plot can be interpreted as showing the nominal tuning of the filter with normal OHC function at five different sound pressure levels or alternatively as the nominal tuning of the filter for five different degrees of OHC impairment.

quency of the signal-path BM filter is the primary determinant of the model fiber's BF. The bandwidth and gain of both the signal-path, narrow-band filter and the control-path, wideband filter are varied continuously as a function of the control path output. The low-pass filtering of the IHC de-

TABLE I. Summary of differences between the normal auditory periphery models of Zhang *et al.* (2001) and of this paper.

Zhang <i>et al.</i> (2001)	This paper
No middle-ear filtering	Middle-ear filtering as described in Appendix A
Synapse gain compensates for IHC filtering	Synapse gain compensates for IHC and ME filtering [see Eq. (1)]
Symmetric nonlinearity between wideband filter and OHC Boltzmann nonlinearity	Linear scaling of 4×10^3 after wideband filter to compensate for removal of symmetric nonlinearity
Wideband-filter gain normalized to unity at BF	Wideband-filter gain normalized to match narrow-band-filter gain at BF (see Appendix B)
OHC LP filter cutoff = 800 Hz	OHC LP filter cutoff = 600 Hz
BM gain versus BF based on other species	BM gain versus BF estimated from cat AN data [see Eq. (B3)]

scribes the fall-off in pure-tone synchrony with increasing BF above 1 kHz. The preceding IHC nonlinearity produces a dc component in the IHCs of high-BF model fibers, providing nonsynchronized synaptic drive to such fibers. The spontaneous rate (in this paper, 50 spikes/second before the effects of refractoriness), adaptation properties, and rate-level behavior (including threshold and saturation) of a model fiber are determined by the synapse model. Only high spontaneous rate fibers are modeled. The spiking and refractory behavior are set to model the statistics of spike timing in AN fibers.

A. Middle-ear filter

A ME filter was not included in the Zhang *et al.* (2001) model but is important in modeling responses to wideband stimuli such as vowels, because the ME filter changes the relative levels of stimulus components. We have added a ME section to the model by combining the ME-cavities model of Peake *et al.* (1992) with the ME (with cavities open) model of Matthews (1983). A digital-filter representation of this model is described in Appendix A. The ME model has a maximum gain of 32 dB [Fig. 19(b)]. Because the parameters of the Zhang *et al.* (2001) model are set for no ME model, we scale the gain of the ME filter to a maximum gain of 0 dB. This allows us to avoid adjusting other level-dependent parameters of the auditory periphery model. The principal effect of the ME filter is on model thresholds, which are shown by the black dashed line in Fig. 2(a) and are compared to experimental data (Miller *et al.*, 1997).

There are three differences between model and data. First, the model thresholds are consistently higher than experimental ones, which requires an increase in the synapse gain (see below) relative to that of Zhang *et al.* (2001). Second, the model does not accurately reproduce the slope of the best threshold curve below 1 kHz [BTC; thin dashed line in Fig. 2(a)]. Low-frequency thresholds in cat preparations vary from animal to animal (e.g., Liberman, 1978) and are affected by the status of the middle ear bulla cavity (open or

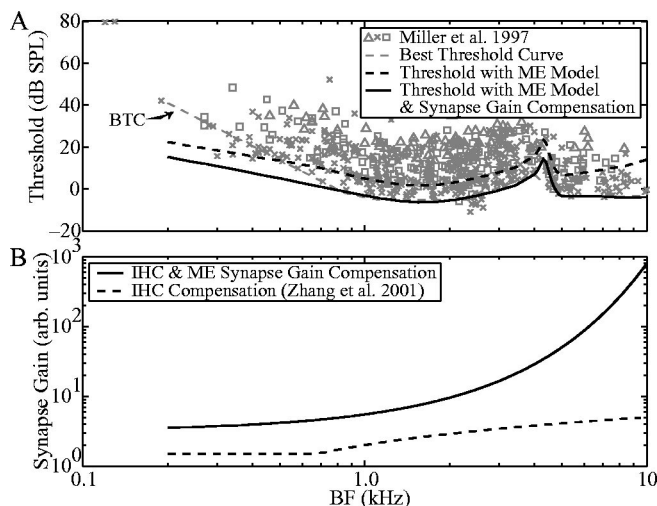


FIG. 2. (a) Thresholds versus BF. The gray symbols are single-fiber thresholds and the thin dashed line is the best threshold curve (BTC) for these data (Miller *et al.*, 1997). The black dashed line shows the model threshold with the ME included. The black solid line shows the model threshold with the ME included plus frequency compensation in the synapse gain for the low-pass filtering of the ME (at ~ 4.5 kHz), as described below. (b) Synapse gain [parameter K_{CF} in Eq. (A17) of Zhang *et al.*, 2001] as a function of BF. The dashed line shows the function used in Zhang *et al.* (2001), which compensates for the low-pass filtering of the IHC to create constant thresholds as a function of BF without ME filtering. The solid line shows the new function described by Eq. (1) that also compensates for the low-pass filtering of the ME to create constant thresholds above ~ 1 kHz, except for the notch just above 4 kHz [see panel (a)].

closed; Guinan and Peake, 1967). The model gives thresholds near the lower end of the published range and the particular data shown are near the upper end. In order to better fit the thresholds at low frequencies, the ME gain function or the synapse gain could be changed. Neither has been done here, because of the uncertainty in the data. Third, the low-pass filtering of the ME produces elevated thresholds for BFs above 4.5 kHz relative to thresholds in the BF region around 1.5 kHz. In contrast, thresholds in the experimental data are similar in these two regions. In Zhang *et al.* (2001) the synapse gain (i.e., the function relating the IHC potential to the synaptic release rate) varied as a function of BF to compensate for the low-pass filtering of the IHC, thus maintaining a constant AN-fiber threshold as a function of BF. We propose that the synapse gain also compensates for the low-pass filtering of the ME above 4.5 kHz. This can be achieved in the model by using a new function for the synapse gain [parameter K_{CF} in Eq. (A17) of Zhang *et al.*, 2001]:

$$K_{CF} = 10^{0.24BF + 0.5}, \quad (1)$$

where BF has the units of kHz. This new function also includes an increase in the absolute gain so that model thresholds better match the BTC. Plotted in Fig. 2(b) are the old (dashed line) and new (solid line) functions.

B. OHC control of BM tuning

The signal-path BM filters are fourth-order, nonlinear, infinite impulse response (IIR) gamma-tone filters (Patterson *et al.*, 1988). Each filter is realized by cascading three nonlinear and one linear first-order, low-pass filters (Zhang *et al.*, 2001). The stimulus waveform is first down-shifted in

frequency by the desired center frequency of the filter, then filtered, and finally up-shifted to its original frequencies. Each of the three nonlinear low-pass filters may be described by the difference equation [modified from Eq. (A4) of Carney (1993)]:

$$y[n] = c1_{LP}[n]y[n-1] + c2_{LP}[n](x[n] + x[n-1]), \quad (2)$$

where x is the filter input, y is the filter output, n is the sample number, and the filter coefficients $c1_{LP}[n]$ and $c2_{LP}[n]$ are determined by the time constant for the signal-path filter $\tau_{sp}[n]$ [see Fig. 1(a)] according to the bilinear transform (Oppenheim and Schaffer, 1989):

$$c1_{LP}[n] = (\tau_{sp}[n]2F_s - 1) / (\tau_{sp}[n]2F_s + 1) \quad (3)$$

and

$$c2_{LP}[n] = 1 / (\tau_{sp}[n]2F_s + 1), \quad (4)$$

where the sampling frequency F_s is set at 500 kHz (Zhang *et al.*, 2001). The time constant $\tau_{sp}[n]$ determines both the gain and the bandwidth of the filter and varies between the values τ_{narrow} and τ_{wide} according to the output signal of the control path. Note that the control path is modified somewhat from that of Zhang *et al.* (2001) to improve the filter dynamics—see Appendix B for details. The single linear LP filter that follows the three nonlinear LP filters in the signal-path BM filters is identical to the nonlinear filters except that its time constant is always τ_{wide} and its dc gain (i.e., the gain at BF) is always unity. Figure 1(b) shows the gain of the signal-path filter for values of τ_{sp} over its whole range; decreasing τ_{sp} from τ_{narrow} to τ_{wide} increases both the bandwidth and the attenuation.

We will consider the behavior of the nonlinear signal-path filter over three different ranges of stimulus intensity. First, at low stimulus intensities the control path signal is negligible and therefore $\tau_{sp}[n] \approx \tau_{narrow}$. Consequently, the bandwidth is narrow, gain is high, and the filter is effectively linear. Second, at moderate stimulus intensities the control path signal becomes significant, such that $\tau_{sp}[n]$ dynamically varies between τ_{narrow} and τ_{wide} , creating effectively broadened tuning, a compressive nonlinearity for stimuli with frequency components near BF, and two-tone suppression for wideband stimuli. The time constant of the control-path filter $\tau_{cp}[n]$ is set to a constant fraction K of $\tau_{sp}[n]$, to create an area of suppression that is appropriately wider than the excitation tuning curve (Zhang *et al.*, 2001). Two-tone rate suppression is created in the model when a suppressor tone produces negligible energy at the output of the signal-path filter but has enough energy at the output of the broader control-path filter to reduce $\tau_{sp}[n]$ via the control path and consequently reduce the gain of the signal-path filter. Third, for very large signals, the control path saturates and $\tau_{sp}[n]$ has an essentially constant value near τ_{wide} . Thus, at high intensities the filter has a broad bandwidth and low gain and is once more linear. These properties simulate the BM tuning and nonlinearities that are caused by the activity of healthy OHCs (e.g., Johnstone *et al.*, 1986; Robles and Ruggero, 2001).

The value of the time constant τ_{narrow} determines the bandwidth of model threshold tuning curves. The bandwidth

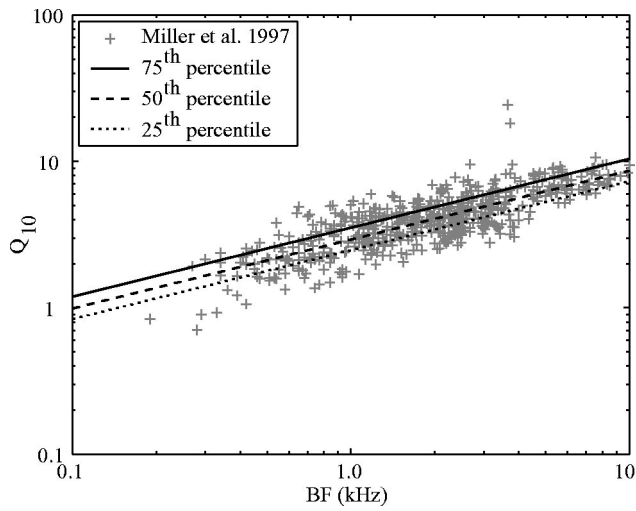


FIG. 3. Normal-cat Q_{10} values as a function of BF from Miller *et al.* (1997). The gray symbols indicate values for individual fibers and lines indicate the 75th (solid line), 50th (dashed line), and 25th (dotted line) percentiles of Q_{10} values after normalization by a linear fit of $\log(Q_{10})$ versus $\log(\text{BF})$.

of a tuning curve is usually quantified according to its Q_{10} value, which is equal to BF divided by the bandwidth of the tuning curve 10 dB above threshold at BF. The desired Q_{10} value can be produced in the model by setting $\tau_{\text{nar}} = 2Q_{10}/(2\pi\text{BF})$ [Eq. (4) of Zhang *et al.*, 2001]. In Secs. IV A, IV B, and IV D, where data from individual AN fibers are presented, we match model Q_{10} values to the example fibers. In Sec. IV C, where data from populations of AN fibers are presented, we use functional relationships to describe trends in Q_{10} versus BF observed in the population data. In Fig. 3, Q_{10} values from the normal-cat data of Miller *et al.* (1997) are plotted as gray symbols as a function of BF on a log-log scale. Zhang *et al.* (2001) used a linear fit of $\log(Q_{10})$ values from these data versus $\log(\text{BF})$ to set model Q_{10} values. However, at any particular BF there is a range of Q_{10} values observed in the data. AN fibers with different Q_{10} values are likely to have somewhat different responses to wideband stimuli such as vowels. Therefore, in this paper we use the three different functions for Q_{10} versus BF shown in Fig. 3, which correspond to the 75th, 50th, and 25th percentiles of Q_{10} values after normalization by the linear fit of $\log(Q_{10})$ versus $\log(\text{BF})$. The equations for the these functions are, respectively,

$$\log_{10} Q_{10}^{75\text{th}} = 0.4708 \log_{10}(\text{BF}) + 0.5469, \quad (5)$$

$$\log_{10} Q_{10}^{50\text{th}} = 0.4708 \log_{10}(\text{BF}) + 0.4664, \quad (6)$$

$$\log_{10} Q_{10}^{25\text{th}} = 0.4708 \log_{10}(\text{BF}) + 0.3934, \quad (7)$$

where BF has the units of kHz.

The value of the time constant τ_{wide} determines the maximum bandwidth and the minimum gain of the signal-path narrow-band filter, as illustrated in Fig. 1(b). Zhang *et al.* (2001) refer to the difference in filter gain between τ_{nar} and τ_{wide} as the cochlear amplifier (CA) gain. Based on the third-order nonlinear filter, $\tau_{\text{wide}} = \tau_{\text{nar}} 10^{-\text{gain}_{\text{CA}}(\text{BF})/60}$, where $\text{gain}_{\text{CA}}(\text{BF})$ is determined by

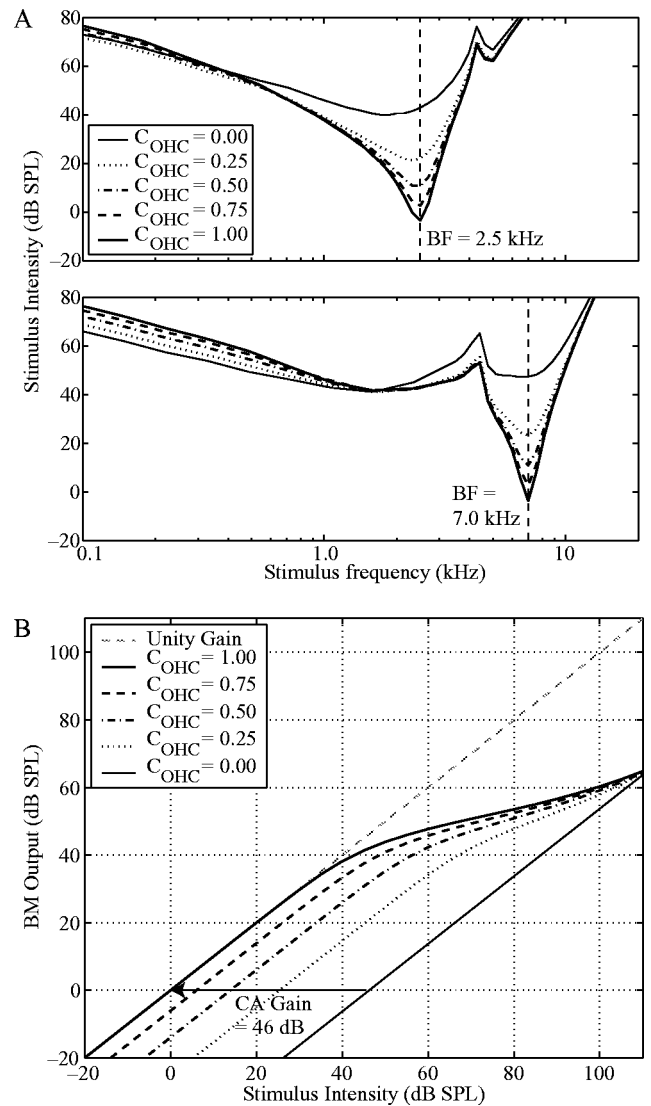


FIG. 4. (a) Model tuning curves as a function of OHC impairment: no impairment $\Rightarrow C_{\text{OHC}} = 1.00$; complete impairment $\Rightarrow C_{\text{OHC}} = 0.00$. Top panel: BF = 2.5 kHz; Bottom panel: BF = 7.0 kHz. (b) The effects of C_{OHC} on BM compression for a fiber with BF = 2.5 kHz. The thin dashed line shows a linear input/output function (no compression), shallower slopes indicate compression. The arrow indicates that normal OHC function produces a difference in the filter gain of 46 dB between low-intensity stimuli and high-intensity stimuli at a BF of 2.5 kHz. At moderate intensities the filter is normally compressive, i.e., slope < 1. This cochlear amplifier (CA) gain and associated compression are progressively lost with increasing OHC impairment, i.e., decreasing C_{OHC} .

Eq. (B3) for a given BF. The CA gain also determines the strength of BM compression [see Fig. 4(b)] and two-tone rate suppression (Zhang *et al.*, 2001).

III. MODELING THE IMPAIRED AUDITORY PERIPHERY

A. Modeling OHC impairment

In order to model the effects of OHC status on the non-linear BM filter, we introduce a scaling constant C_{OHC} to the output of the control path, such that

$$\tau_{\text{sp_impaired}}[n] = C_{\text{OHC}}(\tau_{\text{sp}}[n] - \tau_{\text{wide}}) + \tau_{\text{wide}}, \quad (8)$$

where $0 \leq C_{\text{OHC}} \leq 1$. The effects of C_{OHC} on the tuning of the signal-path filter at its narrowest bandwidth and largest gain ($\tau_{\text{sp}} = \tau_{\text{nar}}$) are shown in Fig. 1(b).¹

The effects of C_{OHC} on tuning curves are illustrated in Fig. 4(a) for model fibers at two different BFs. To model normal OHC function, C_{OHC} is set to 1 and consequently the filter behavior is normal: tuning curves are narrow and thresholds are low. The upward “notches” in the tuning curves just above 4 kHz are due to the notch in the ME filter [see Fig. 19(b)]. The effects of C_{OHC} on compression are shown in Fig. 4(b) for one model fiber. With $C_{\text{OHC}}=1$ the BM filter exhibits compression for a BF tone from ~ 30 dB SPL to >100 dB SPL. Not shown here, the model also exhibits two-tone suppression due to the behavior of the wideband non-linear filter (Zhang *et al.*, 2001), which is also apparent in responses to vowel stimuli (see Sec. IV).

To model impaired OHC function, C_{OHC} is set to some value between 1 and 0; the lower the value, the greater the impairment. Reducing C_{OHC} causes two changes in the filter behavior.

First, the effect when the control path signal is small (i.e., at low sound levels) is to increase the tuning curve bandwidth and elevate thresholds around BF. Thresholds in the low-frequency “tail” of the tuning curve decrease slightly with increasing impairment. This behavior is qualitatively consistent with physiological reports of hypersensitive tails in tuning curves with OHC impairment (Liberman and Dodds, 1984a). In addition, a small downward shift in BF is observed in Fig. 4(a) for the model fiber with an unimpaired BF of 2.5 kHz; we refer to this shifted-BF following impairment as the “impaired BF.” The shift is due to the effects of the ME filter and IHC LP filter on the tuning curve shape, not a change in the BM filter’s center frequency, and only occurs in the steep transition bands of the ME and IHC filters. Upward shifts of less than 0.15 oct occur for unimpaired BFs less than 0.5 kHz (i.e., in the high-pass transition band of the ME filter) and between ~ 4.2 and 5.0 kHz (i.e., in the upper edge of the ME notch); downward shifts of less than 0.35 oct occur for unimpaired BFs between ~ 1.3 and 4.2 kHz (i.e., in the lower edge of the ME notch and the low-pass transition band of the IHC filter). Physiological data show shifts in the BM filter’s center frequency at high intensities or with impairment (e.g., Robles and Ruggero, 2001) that are larger than those seen in this model.

Second, when the control path signal is significant (i.e., at moderate to high stimulus intensities), compression and suppression are reduced because of the scaling down of the time-varying component of $\tau_{\text{sp}}[n]$ [Fig. 4(b)]. The extreme case of $C_{\text{OHC}}=0$ describes complete loss of OHC function: tuning curves are at their highest and broadest and compression and suppression are completely lost. Figure 4(b) shows that for a BF of 2.5 kHz the normal model produces a cochlear-amplifier gain of ~ 46 dB SPL, as prescribed by Eq. (B3).

B. OHC impairment as a function of BF

In order to predict data from populations of AN fibers, we must have estimates of the levels of OHC and IHC impairment as a function of BF. As described by Liberman and Dodds (1984a) and modeled in Fig. 4, damage to the OHCs causes both an increase in thresholds and a broadening in tuning. However, damage to the IHCs also leads to elevated

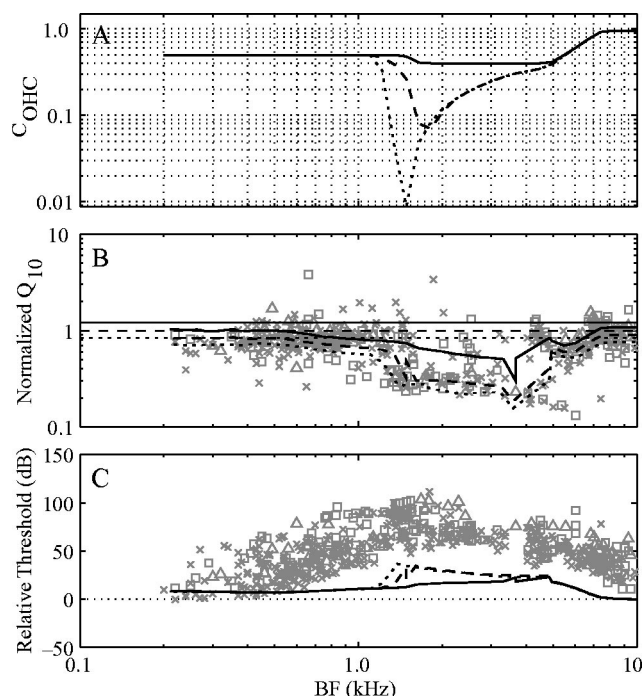


FIG. 5. Determination of model OHC impairment to fit impaired Q_{10} values as a function of BF. (a) Three different functions for C_{OHC} versus unimpaired BF to produce mild (solid line), moderate (dashed line), and severe (dotted line) OHC impairment as shown by the corresponding lines in (b). Definitions of these three cases are given in the text. (b) Impaired Q_{10} versus impaired BF, with Q_{10} values normalized by a linear fit to the normal-cat data plotted in Fig. 3. Gray symbols indicate data from individual fibers and thick lines indicate model predictions given the three functions for C_{OHC} shown in (a). Thin lines show the 75th, 50th, and 25th percentile of the normal data when normalized by the linear fit. (c) Impaired threshold versus impaired BF, where threshold values are given relative to the respective normal best threshold curves for the data and model. Gray symbols indicate data from individual fibers and lines indicate the model predictions given the functions for C_{OHC} shown in (a).

thresholds (Liberman and Dodds, 1984a), and therefore the increase in thresholds is not an uncontaminated indicator of the degree of OHC impairment. In contrast, Q_{10} values are not thought to be affected greatly by IHC impairment (Liberman and Dodds, 1984a). The following method is used in Secs. IV A, IV B, and IV D to model data from single impaired AN fibers. First, we set the value of τ_{narrow} in the model using the Q_{10} value of an example *normal* fiber with approximately matching BF. Second, we find a value for C_{OHC} that explains the estimated Q_{10} value of the example *impaired* fiber. Third, we apply enough IHC impairment (see Sec. III C) to explain the remaining threshold shift not accounted for by the OHC impairment.

In Sec. IV C, functional relationships between C_{OHC} and BF are derived to allow modeling of data from populations of AN fibers. Three functions are used, which are designed to follow the 75th, 50th, and 25th percentiles of the Q_{10} data from Miller *et al.* (1997). Figure 5(b) shows the Q_{10} data from impaired animals normalized by the best fit log-log line from normal animals (Fig. 3). The three horizontal lines show the 75th, 50th, and 25th percentiles of the normal data. The decrease in Q_{10} data points below the lines are a result of acoustic trauma. Figure 5(a) shows three empirical C_{OHC} functions designed to fit the 75th, 50th, and 25th percentiles of the impaired data. In doing these fits, the normal model fit

to the 75th percentile line of the normal data was adjusted to fit the 75th percentile of the impaired data by varying C_{OHC} , and similarly for the 50th and 25th percentiles. The three lines that follow the data points in Fig. 5(b) show the resulting Q_{10} 's for model tuning curves. The irregularities in the model Q_{10} values between 3 and 5 kHz result from the ME notch.

The threshold shifts resulting from the model OHC impairment are shown in Fig. 5(c). Even severe OHC impairment, as derived from the Q_{10} data, can at best account for around two-thirds of the threshold shift seen in the impaired-cat data; we postulate that the remainder should be attributed to IHC damage. Miller *et al.* (1997) found that fibers with BFs near the exposure frequency were under-represented in the impaired cats, relative to the normal cats, and argued for substantial IHC damage, followed by silencing and perhaps degeneration of some AN fibers. Fibers with less severe IHC damage should still be responsive to acoustic stimuli but with elevated thresholds. Modeling of such IHC impairment is described next.

C. Modeling IHC impairment

Elevated threshold tuning curves due to IHC impairment can be modeled by decreasing the slope of the function that relates BM vibration to IHC potential [the block IHC NL in Fig. 1(a)]. At the same time, the saturation potential must remain the same to retain maximum discharge rates close to those of normal fibers (e.g., Liberman and Kiang, 1984; Miller *et al.*, 1999a). Both of these effects can be achieved together in the model by decreasing the slope of the IHC NL block, or equivalently by scaling down the output of the narrow-band BM filter at the input of the IHC nonlinearity using a scaling constant C_{IHC} , where $0 \leq C_{\text{IHC}} \leq 1$. A value of one produces normal IHC function and a value of zero gives total IHC disfunction. To model individual example fibers, a value for C_{IHC} is chosen that accounts for the threshold shift not explained by OHC impairment.

Figure 6(a) shows the values of C_{IHC} that are needed to explain the minimum threshold shift in the AN population data not accounted for by the OHC impairment of Fig. 5(a). Figure 6(b) shows the threshold shifts as a function of impaired BF resulting from the IHC impairment in panel (a) in combination with the three cases of OHC impairment from Fig. 5 (heavy lines). The combined threshold shifts match the minimum threshold shifts in the data reasonably well. Minimum rather than average thresholds are fit because we assume that the distribution of thresholds at any given BF reflects variation in synapse gain, i.e., the difference between low and high spontaneous rate AN fibers (Geisler, 1981; Heinz *et al.*, 2001). Consistent with the data of Liberman and Dodds (1984a), Q_{10} values are relatively unaffected by IHC impairment in the model, although tuning at levels 20 dB or greater above threshold is broadened due to the broadened filtering of the normal BM at higher stimulus levels.

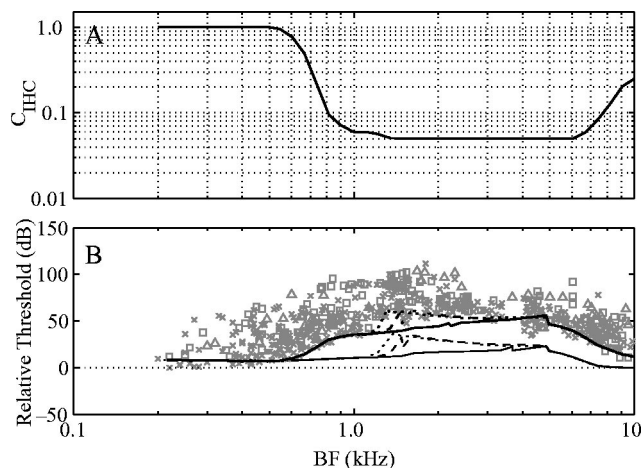


FIG. 6. Determination of model IHC impairment to fit minimum threshold shifts as a function of BF. (a) Function for C_{IHC} versus unimpaired BF to produce the threshold shifts as shown in panel (b). (b) Impaired thresholds relative to the respective normal best threshold curves for the data and model versus impaired BF. Gray symbols show data from individual fibers and thin lines show threshold shifts for OHC impairment alone (replotted from Fig. 5). The thick lines show the model threshold shifts with IHC impairment as described in panel (a) in combination with the three cases of OHC impairment: mild (solid line), moderate (dashed line), and severe (dotted line).

IV. SYNCHRONIZED RESPONSE TO THE VOWEL /ε/

A. Single-fiber data and predictions

Miller *et al.* (1997) recorded AN single-fiber responses to the synthesized vowel /ε/ with the spectrum shown in Fig. 7. This synthesized vowel is periodic with a fundamental frequency (F_0) of 100 Hz and formant frequencies (F_1 - F_5) of 0.5, 1.7, 2.5, 3.3, and 3.7 kHz. Note that the stimulus has been filtered by the head related transfer function (HRTF) of a human head (Wiener and Ross, 1946).

The synchronized responses of AN fibers to an ~80 ms vowel stimulus were evaluated by taking the Fourier transform of the poststimulus time histogram (PSTH) normalized to units of spikes/second (Miller *et al.*, 1997). Synchronized rates for two fibers with BFs near F_2 are plotted in Fig. 8. At the lowest presentation level [panel (c)], the normal fiber responds to a number of frequency components of the vowel

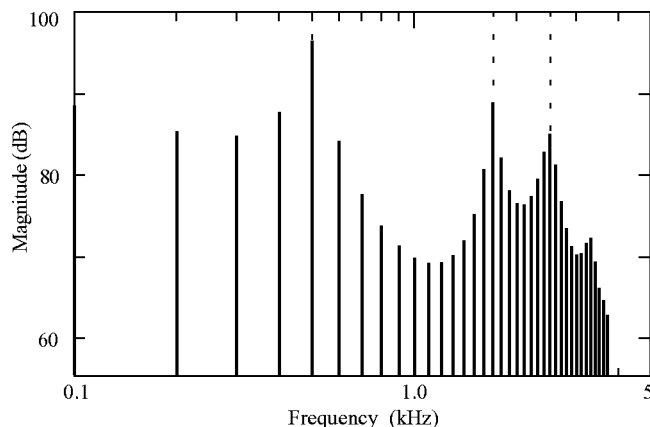


FIG. 7. Power spectrum of the vowel /ε/ used in the physiological experiments. Modified from Fig. 1 of Miller *et al.* (1997) with permission from the Acoustical Society of America® (1997).

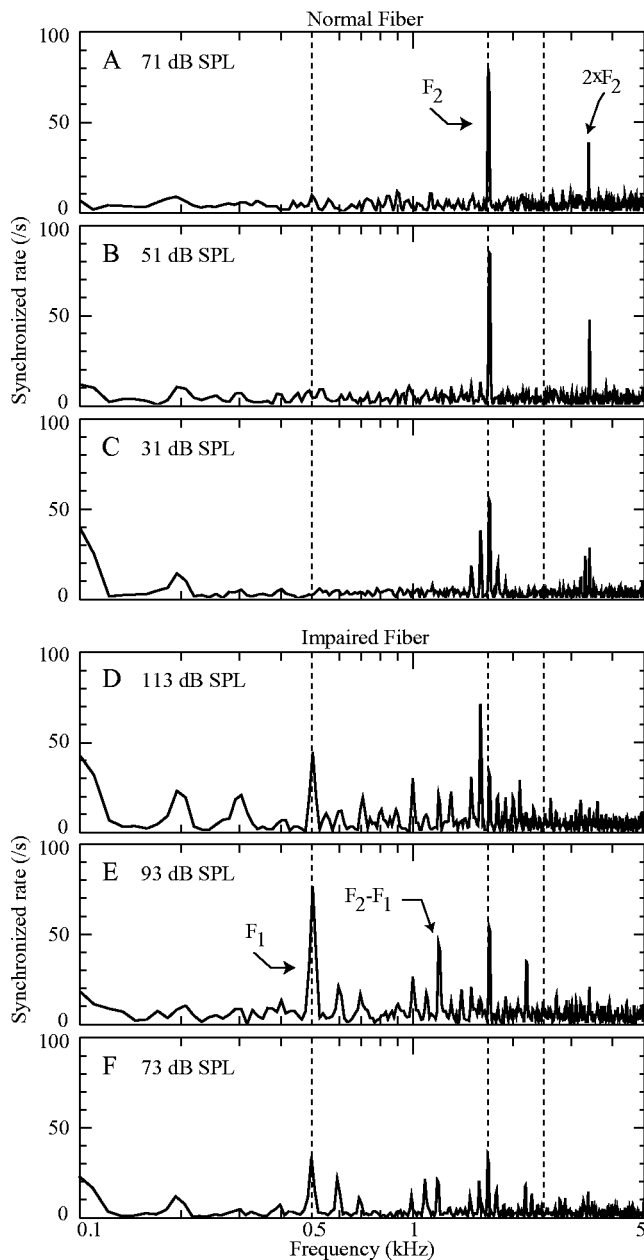


FIG. 8. Synchronized response of a normal [(a)–(c)] and an impaired [(d)–(f)] fiber, both with BFs around F_2 , to the vowel /ε/. Synchronized rate is the magnitude of the Fourier transform of a PSTH (binwidth $20 \mu\text{s}$), with units of spikes/s. The normal fiber had a BF of 1.7 kHz and a Q_{10} of 4.4, and the impaired fiber had a BF of 1.6 kHz, a threshold shift of ~ 60 dB, and a Q_{10} of 3.8. Reprinted from Fig. 9 of Miller *et al.* (1997) with permission from the Acoustical Society of America © (1997).

in the spectral peak around F_2 . This fiber exhibits synchrony capture at the two higher stimulus levels [panels (a) and (b)]: as the stimulus level increases above the fiber threshold, the responses becomes synchronized almost exclusively to the vowel component at F_2 . In contrast, the impaired fiber [(d)–(f)] shows a much more broadband response, particularly to the higher-intensity first formant. Note the higher presentation levels used to compensate for the elevated threshold of this impaired fiber.

Shown in Fig. 9(a) are synchronized responses of a model fiber with normal OHC and IHC function ($C_{\text{OHC}} = C_{\text{IHC}} = 1$); the BF, threshold, and Q_{10} approximately

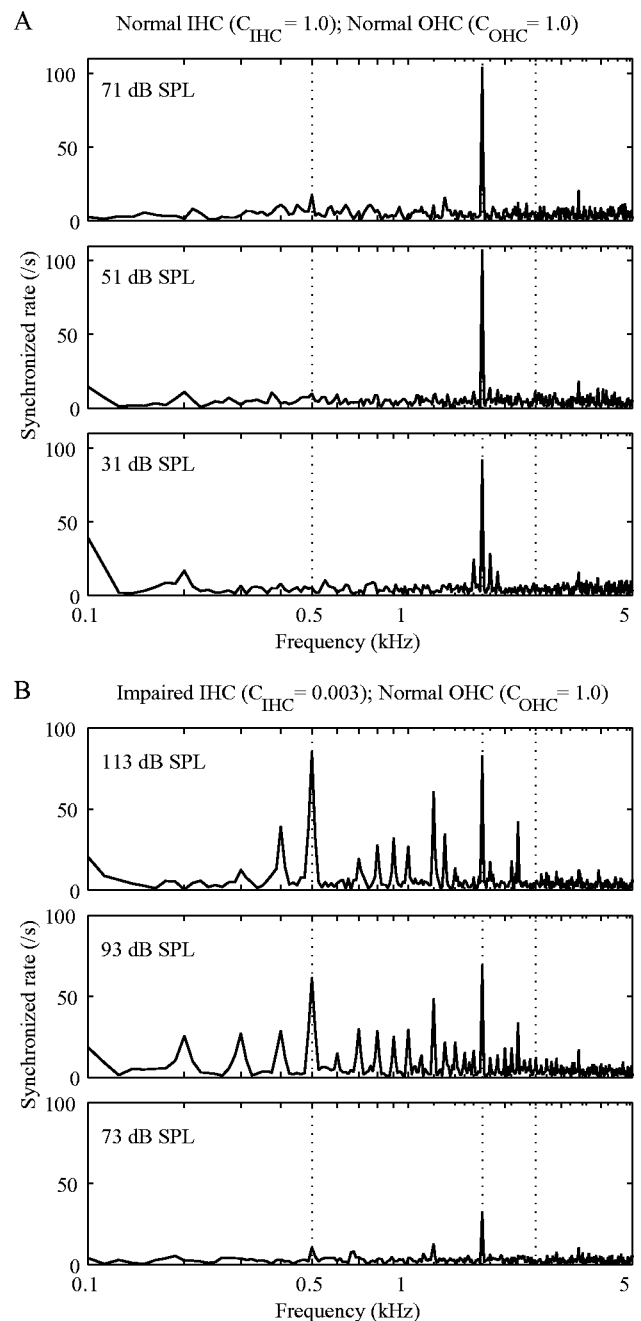


FIG. 9. Model predictions of a low-frequency (BF $\approx F_2$) AN fiber's synchronized response to the vowel /ε/. (a) Normal OHC and IHC ($C_{\text{OHC}} = C_{\text{IHC}} = 1$); BF = 1.7 kHz. (b) Severely impaired IHC ($C_{\text{IHC}} = 0.003$) and normal OHC ($C_{\text{OHC}} = 1$); unimpaired BF = 1.7 kHz, impaired BF ≈ 1.6 kHz, threshold shift ≈ 60 dB, and impaired $Q_{10} \approx 3.8$.

match those of the normal fiber from Fig. 8. Like the normal fiber of Fig. 8, the model fiber synchronizes to a number of vowel components around the F_2 spectral peak at the lowest stimulus intensity (31 dB SPL) and almost exclusively to the F_2 component at the higher intensities. Also observed is a synchronized response to the second harmonic of F_2 , although it is somewhat smaller than that of the example normal fiber. The major cause of the synchrony capture by F_2 at the higher intensities is the compressive/suppressive nonlinearity of the signal-path, narrow-band BM filter. At the 31 dB SPL presentation level, around 82% of the signal power at the output of the narrow-band BM filter is at the F_2 fre-

quency; the narrow-band filter is effectively linear at this presentation level [Fig. 4(b)]. At 51 and 71 dB SPL, the narrow-band filter is operating in its nonlinear range, causing the percentage of the signal power at F_2 to increase to 89% and 92%, respectively. These percentage values are relatively unaffected by further processing of the signal by the IHC, synapse, and spike generator sections of the model.

The example impaired fiber of Figs. 8(d)–(f) presents an interesting case: it has relatively normal pure-tone tuning as measured by Q_{10} values but has a broadband synchronized response to the vowel (Miller *et al.*, 1997). How could this come about? Shown in Fig. 9(b) are synchronized responses of a model fiber with severely impaired IHC function ($C_{\text{IHC}}=0.003$) and normal OHC function ($C_{\text{OHC}}=1$); the impaired BF, threshold shift, and Q_{10} approximately match those of the impaired fiber from Fig. 8. The model predictions are consistent with the data plotted in Figs. 8(d)–(f), showing synchrony to many frequency components of the vowel (i.e., loss of synchrony capture), including a particularly large response to F_1 . Examination of the output of each stage of the model's signal path shows how synchrony capture is lost without impairment to the BM filter. As stated above, around 92% of the signal power at the output of the narrow-band BM filter is at the F_2 frequency for a presentation level of 71 dB SPL. This percentage value drops to only 59% if the presentation level is increased to 93 dB SPL, because at this level the narrow-band BM filter tuning is very broad [see Fig. 1(b)] and its gain is fairly linear again [see Fig. 4(b)]. However, with normal IHC function the signal at the output of the narrow-band BM filter is so large that it falls within the nonlinear (saturating) ranges of the IHC nonlinearity and the synapse model. Saturation of the signal suppresses the smaller frequency components such that the percentage of the signal power at F_2 increases to 80% at the output of the IHC and 91% at the output of synapse model. That is, synchrony capture is lost at the narrow-band BM filter at high presentation level but is regained through the nonlinear processing of the normal IHC and synapse. When the IHC is impaired, the signal no longer saturates the IHC nonlinearity and synapse model, and the percentage of the signal power at F_2 drops to 38% at the output of the IHC and 27% at the output of the synapse model, producing the broadband synchrony observed in Fig. 9(b). These results show that loss of synchrony capture at high stimulus levels can be produced solely by IHC impairment, with no impairment of BM tuning necessary.

OHC impairment alone can also give rise to broadband synchrony at some stimulus levels. Results are shown in Fig. 10(a) for a model fiber with BF matching the example impaired fiber of Fig. 8, but with normal IHC function ($C_{\text{IHC}}=1$) and total OHC impairment ($C_{\text{OHC}}=0$). At the lower two presentation levels the impaired BM response is broad enough to create broad synchrony in the model AN fiber. In these cases, the BM response is broader and more linear than for the normal BM, and the reduced gain of the BM means that the signal falls more within the linear regions of the IHC nonlinearity and the synapse model, as was the case for IHC impairment. At the highest level the signal is large enough for the IHC and synapse to produce synchrony capture to F_2

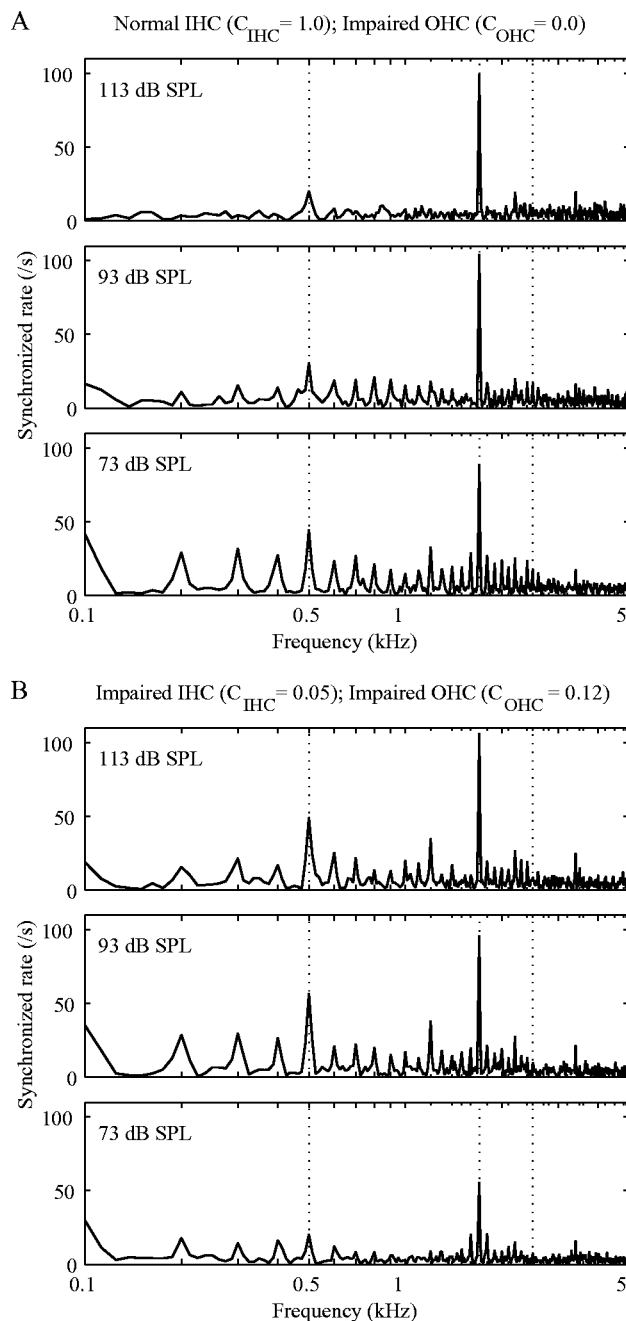


FIG. 10. Model predictions of a low-frequency ($\text{BF} \approx F_2$) AN fiber's synchronized response to the vowel / ϵ /. (a) Totally impaired OHC ($C_{\text{IHC}}=0$) and normal IHC ($C_{\text{IHC}}=1$). (b) Moderately impaired OHC ($C_{\text{OHC}}=0.12$) and impaired IHC ($C_{\text{OHC}}=0.05$).

once again. This illustrates how in some cases synchrony capture can occur without suppression at the level of the BM. A more typical situation is combined IHC and OHC impairment like that discussed in Fig. 6. Moderate OHC impairment ($C_{\text{OHC}}=0.12$) combined with IHC impairment ($C_{\text{OHC}}=0.05$) produces broadband synchrony at all presentation levels [Fig. 10(b)].

The effects of combined IHC and OHC impairment can also be observed for fibers with BFs in the F_3 region. Synchronized rates for two fibers from Miller *et al.* (1997), one normal and one impaired, with BFs near F_3 are plotted in Fig. 11. Limited synchrony capture is observed in this nor-

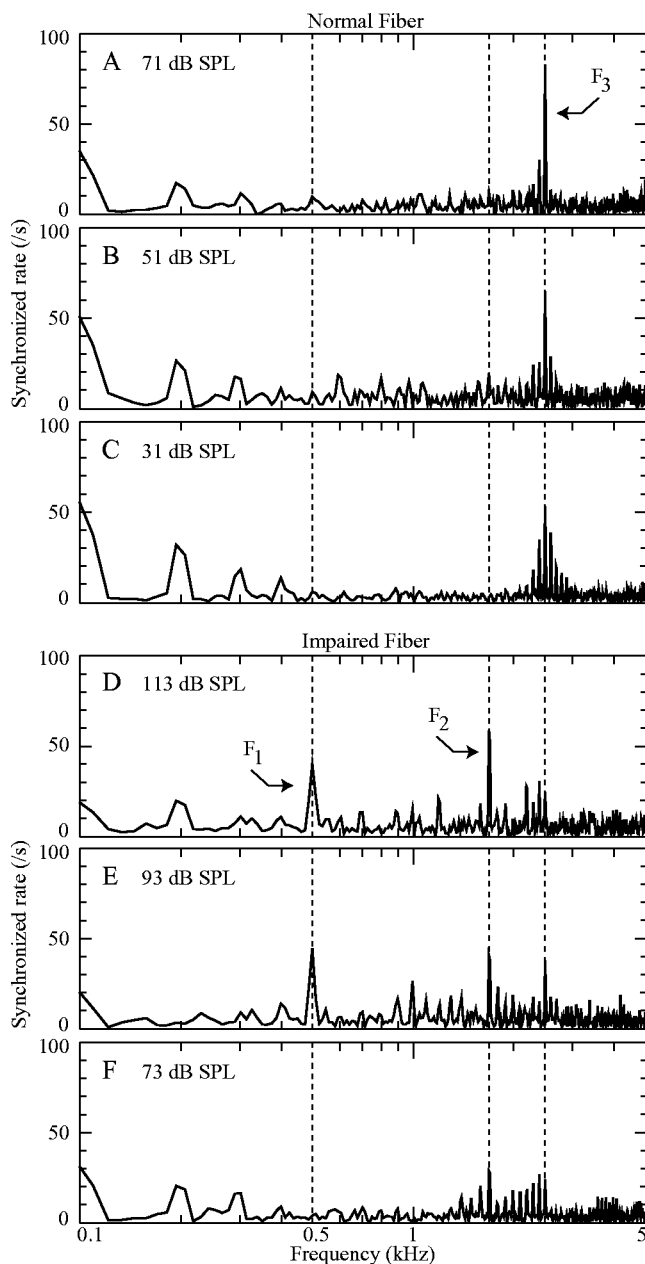


FIG. 11. Synchronized response of a normal [(a)–(c)] and an impaired [(d)–(f)] fiber, both with BFs around F_3 , to the vowel /ε/. The normal fiber had a BF of 2.5 kHz and a Q_{10} of 4.3, and the impaired fiber had a BF of 2.6 kHz, a threshold shift of ~ 60 dB, and a Q_{10} of 1.4. Reprinted from Fig. 10 of Miller *et al.* (1997) with permission from the Acoustical Society of America © (1997).

mal fiber [(a)–(c)]; synchrony capture is not observed in most normal fibers with BFs near F_3 , although they do exhibit a strong response to F_3 . The impaired fiber [(d)–(f)] again shows much broader tuning, synchronizing particularly to F_1 and F_2 , with little response to F_3 .

Shown in Fig. 12(a) are synchronized responses of a model fiber with normal OHC and IHC function ($C_{\text{OHC}} = C_{\text{IHC}} = 1$); the BF, threshold and Q_{10} approximately match those of the normal fiber from Figs. 11(a)–(c). The model fiber synchronizes predominantly to frequency components around its BF, consistent with the example normal fiber, although it does not show the same degree of synchrony capture at the highest presentation level. Results are shown in

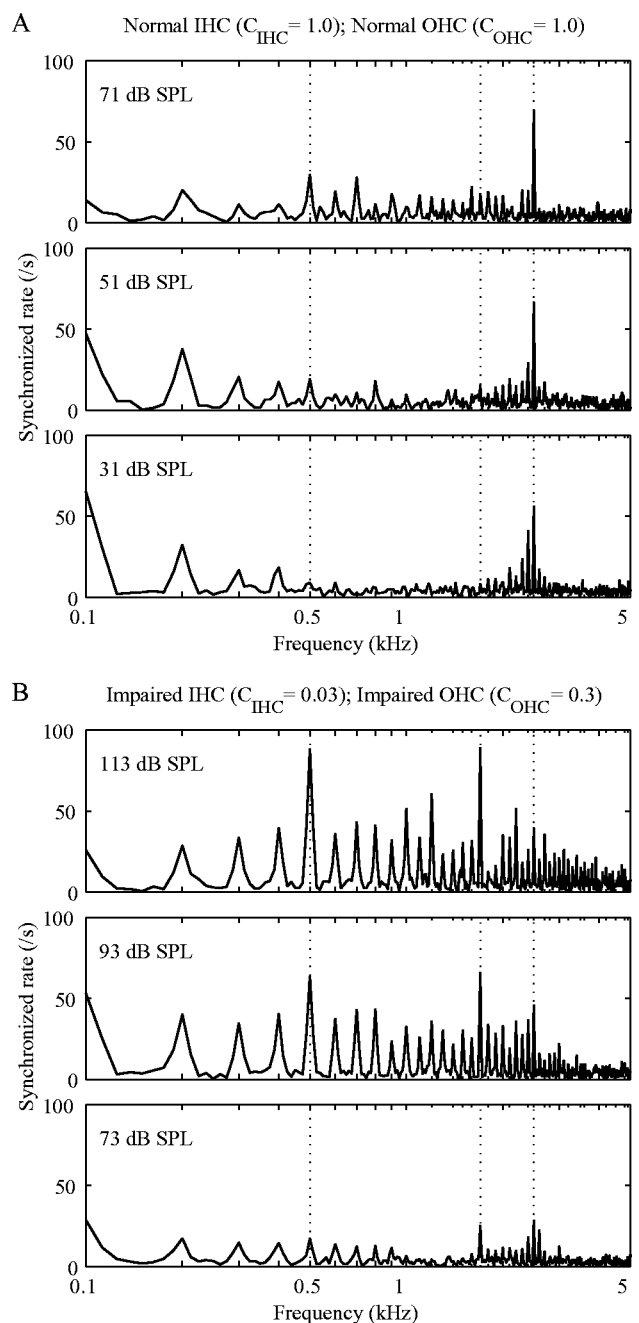


FIG. 12. Model predictions of a moderate-frequency (BF $\approx F_3$) AN fiber's synchronized response to the vowel /ε/. (a) Normal IHC and OHC ($C_{\text{IHC}} = C_{\text{OHC}} = 1$). (b) Impaired IHC ($C_{\text{IHC}} = 0.03$) and impaired OHC ($C_{\text{OHC}} = 0.3$); unimpaired BF = 2.93 kHz, impaired BF ≈ 2.6 kHz, threshold shift ≈ 60 dB, and impaired $Q_{10} \approx 1.4$.

Fig. 12(b) for a model fiber with impaired IHC ($C_{\text{IHC}} = 0.03$) and OHC ($C_{\text{OHC}} = 0.3$) function; the impaired BF, threshold shift, and Q_{10} approximately match those of the impaired fiber from Figs. 11(d)–(f). Like the example fiber, the impaired model fiber exhibits broadband synchrony to the vowel, particularly to the lower-frequency formants F_1 and F_2 , although the synchrony to nonformant harmonics is larger in the model fiber.

B. Quantitative assessment of synchrony capture

Wong *et al.* (1998) quantified synchrony capture using power ratios (PRs), which subdivide the response into com-

ponents related to the formants and other components. Total power is the sum of the squares of the synchronized rates $R(kf_0)$ over the first 20 harmonics of the stimulus. The $F2$ PR is the fraction of the total power that is phase-locked to the second formant (the 17th harmonic). $F1$ & $F2$ -related power is the sum of the squares of the synchronized rates at the harmonics related to $F1$ and $F2$, which include the 5th ($F1$), 7th ($F2 - 2 \times F1$), 10th ($2 \times F1$), 12th ($F2 - F1$), 15th ($3 \times F1$), 17th ($F2$), and 20th ($4 \times F1$); the distortion products are included in the $F1$ & $F2$ response because they most likely result from rectifier distortion in the IHC-AN synapse (Young and Sachs, 1979). The $F1$ & $F2$ -related PR is the fraction of the total power contained in the $F1$ & $F2$ -related harmonics.

Wong *et al.* (1998) measured power-ratios in AN fibers in response to a 400-ms synthetic vowel with a spectrum identical to that of the / ϵ / vowel stimulus shown in Fig. 7, except that the sampling rate was adjusted so that $F2$ always fell at the BF of the fiber. Example power-ratio data from Wong *et al.* (1998) are shown in the left column of Fig. 13 for four normal fibers with different BFs as labeled. These data reveal a breakdown in synchrony capture by $F2$ at very high sound levels, where significant response to $F1$ occurs at the expense of response to $F2$. In the left column of Fig. 13, fiber A exhibits synchrony capture by $F2$ (dashed line) at all stimulus levels. Fiber B exhibits synchrony capture by $F2$ at moderate stimulus levels, which is lost at very high levels (≥ 80 dB SPL). When the $F2$ PR drops, the $F1$ & $F2$ PR (solid line) stay the same, showing that the $F2$ response is replaced by a response to $F1$. Fibers C and D have progressively lower intensities at which the transition from $F2$ to $F1$ synchrony begins. This tendency occurs consistently as BF increases (Wong *et al.*, 1998). The lower and upper bounds of the shaded regions in the left column of Fig. 13 represent, respectively, the sound levels at which synchrony capture by $F2$ is lost, meaning the vector strength $VS(F2) = |R(F2)|/R(0) < 0.5$, and the component-2 (C2) threshold for $F1$ (Liberman and Kiang, 1984). The C2 threshold is the stimulus level at which a substantial phase change occurs in the synchronized response (see Fig. 1 of Wong *et al.*, 1998) and is thought to correspond to a change in the mode of stimulation of the fiber. Modeling the component-1 (C1) to C2 transition for pure-tone stimuli has been accomplished using a dual-path BM filter (e.g., Goldstein, 1990; Schoonhoven *et al.*, 1994; Meddis *et al.*, 2001), not included in this model.

Predictions have been obtained for model fibers with BFs roughly covering the range of BFs in the Wong *et al.* (1998) data. Consistent with the physiological data, the model predictions for normal IHC and OHC function ($C_{IHC} = C_{OHC} = 1$) shown in the right column of Fig. 13 exhibit synchrony capture by $F2$ at moderate sound levels (< 70 dB SPL in all cases). One factor that is crucial in producing synchrony capture by $F2$ at moderate sound levels is the high-pass filtering of the ME below 1 kHz; without ME filtering, $F1$ [< 1 kHz for all the Wong *et al.* (1998) stimuli] also produces a strong response at moderate intensities.

Also seen in the model predictions in the right column of Fig. 13 is the transition in synchrony from $F2$ to $F1$ at

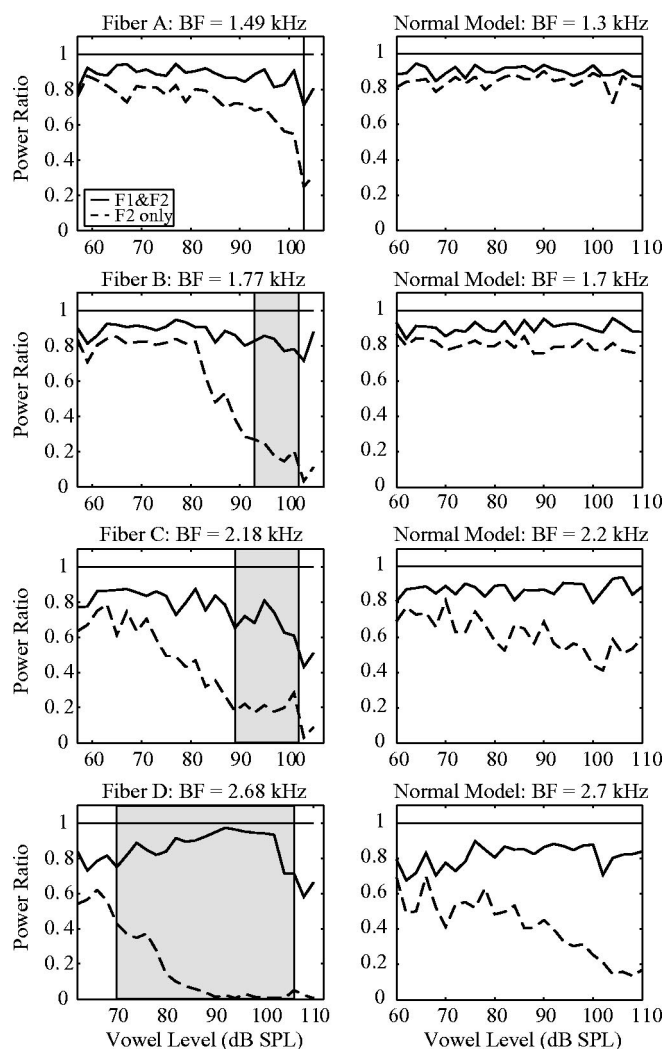


FIG. 13. Normal power ratio data at high sound levels. Left column: four normal fibers with BFs as labeled, redrawn from Fig. 4 of Wong *et al.* (1998) with permission from Elsevier Science[©] (1998). The solid and dashed lines, respectively, show the fraction of total power in the fiber's response that is synchronized to $F1$ and $F2$ combined ($F1$ & $F2$) or to $F2$ alone. The lower and upper bounds of the shaded regions represent, respectively, the sound levels at which a loss of synchrony capture by $F2$ occurs and the component 2 threshold for $F1$. Right column: four normal model fibers with BFs as labeled.

higher intensities, although the effect is weaker than in the data and the stimulus intensity at which the switch occurs does not appear to decrease with increasing BF. Wong *et al.* (1998) argued that the lower-level switch from $F2$ to $F1$ synchrony with increasing BF is likely due to the increasing strength of two-tone suppression with increasing BF. This effect is partly represented in the model by the increase in cochlear-amplifier gain with BF (Fig. 20). Reducing the gain for a model fiber with BF = 2.7 kHz to the gain prescribed for a model fiber with BF = 1.3 kHz greatly reduces the switch in synchrony at high intensities (results not shown). In addition, there is a small secondary factor not considered by Wong *et al.* (1998), which is that with increasing BF, the frequency-scaled vowel has an increasing ratio of power at the $F1$ frequency relative to power at the $F2$ frequency, because $F1$ is attenuated less by the ME filter. This effect

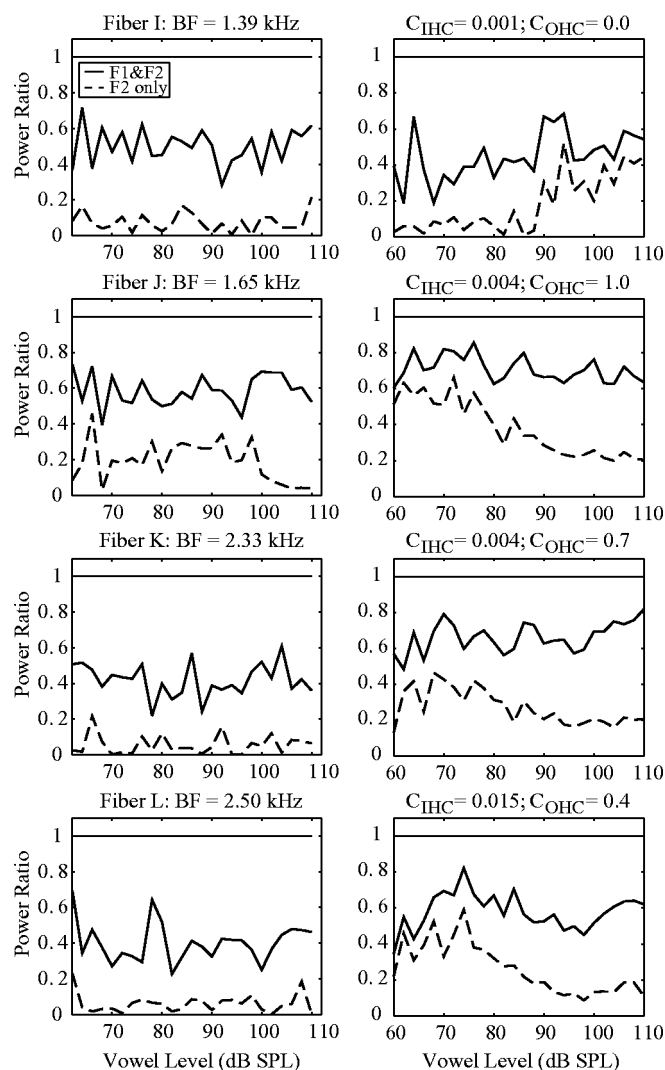


FIG. 14. Power ratio data for impaired fibers at high sound levels. Left column: four fibers exhibiting threshold shifts, with BF's as labeled, redrawn from Fig. 6 of Wong *et al.* (1998) with permission from Elsevier Science[®] (1998). Right column: four impaired model fibers (IHC and OHC impairment for each as labeled) with BF's of 1.3, 1.7, 2.2, and 2.7 kHz, respectively.

produces a slightly weaker response to F_2 at the highest intensities.

During the course of Wong *et al.*'s experiments, the high presentation levels caused threshold shifts in a number of fibers. The left column of Fig. 14 shows that in four fibers exhibiting threshold shifts, with different BF's as labeled, the synchrony to F_2 is low at all levels ($PR \approx 0.1$ – 0.2) and is only partly shifted to F_1 ; around 40%–50% of the synchrony is lost to other components of the vowel, as was observed in Figs. 8(d)–(f) and 11(d)–(f).

While the threshold shifts in the Wong *et al.* (1998) experiments may be temporary and therefore different in mechanism from permanent acoustic trauma (Liberman and Mulroy, 1982; Gao *et al.*, 1992; Nordmann *et al.*, 2000), it is of interest to see how IHC and OHC impairment as modeled in this paper predict the synchrony data in the left column of Fig. 14. Plotted in the right column of Fig. 14 are results from the four model fibers of Fig. 13 with individual IHC and OHC impairment as indicated in the figure. These im-

pairments give rise to thresholds and Q_{10} values approximately matching those of the four example fibers in the left column of Fig. 14. The model predicts the broadband synchrony (loss of synchrony to F_1 & F_2) seen in the data. The loss of synchrony to F_2 alone is fairly well described for some vowel presentation levels but not for others. Example fiber I (top-left panel in Fig. 14) has an extremely broad and elevated tuning curve (threshold ≈ 90 dB SPL; see Fig. 6 of Wong *et al.*, 1998), suggesting that only a C2 response remains in this impaired fiber. The model fiber with similar BF (top-right panel in Fig. 14) has a sharper tuning curve than the example fiber, even with C_{OHC} set to zero, because the model can only describe C1 responses. Consequently, the model exhibits some synchrony to F_2 at high presentation levels, which is not seen in the experimental data. The other three model fibers with BF's of 1.7, 2.2, and 2.7 kHz (right column in Fig. 14) are set to have relatively normal OHC function because of the fairly sharp tuning curve tips of example fibers J, K, and L (left column in Fig. 14). The model BM nonlinearity (compression and suppression) produces higher synchrony to F_2 at moderate presentation levels than is observed in the example fibers, suggesting that the example fibers may be subject to less compression and suppression than the model predicts from the tuning curves. These inaccuracies in the model predictions show the limitations in setting model OHC and IHC impairment to match individual experimental tuning curves.

C. Synchrony capture versus BF

Miller *et al.* (1997) measured F_1 , F_2 , and F_3 PRs in a population of fibers across a range of BF's. Model predictions of PRs for F_1 , F_2 , and F_3 are plotted as a function of BF in Fig. 15 for normal fibers and in Fig. 16 for impaired fibers. Following Miller *et al.* (1997), PRs here include the phase-locked response to the first, second, and third harmonics of the formant frequency, as long as the frequency of the harmonic is less than or equal to 5 kHz. Lines show model predictions and gray hatched areas indicate the range of values observed in the physiological data of Miller *et al.* (1997).

The model predictions for normal fibers (Fig. 15) fall predominantly within the range of values seen in the physiological data at both presentation levels (69 and 49 dB SPL). Normal fibers synchronize almost exclusively to the formant frequency closest to their BF's. The small peak in the F_1 PR of the model predictions at 1 kHz ($2 \times F_1$) is due to harmonic distortion in the nonlinear BM filter. Such harmonic distortion of F_1 is also observed in the physiological data at 69 dB SPL but is not apparent in the data at 49 dB SPL.

With impaired IHC and OHC function (Fig. 16), model predictions of PRs fall within the range of single-fiber values for F_1 and F_3 , but not for F_2 . At both levels (112 and 92 dB SPL), synchrony to F_2 is overestimated in the BF region around F_2 —possible causes are examined in Sec. V. A second discrepancy is observed at the higher presentation level (112 dB SPL): an upward shift in the peak of F_1 synchrony is observed in the data when compared to the lower presentation level (92 dB SPL). This shift is seen in the model predictions but is less pronounced.

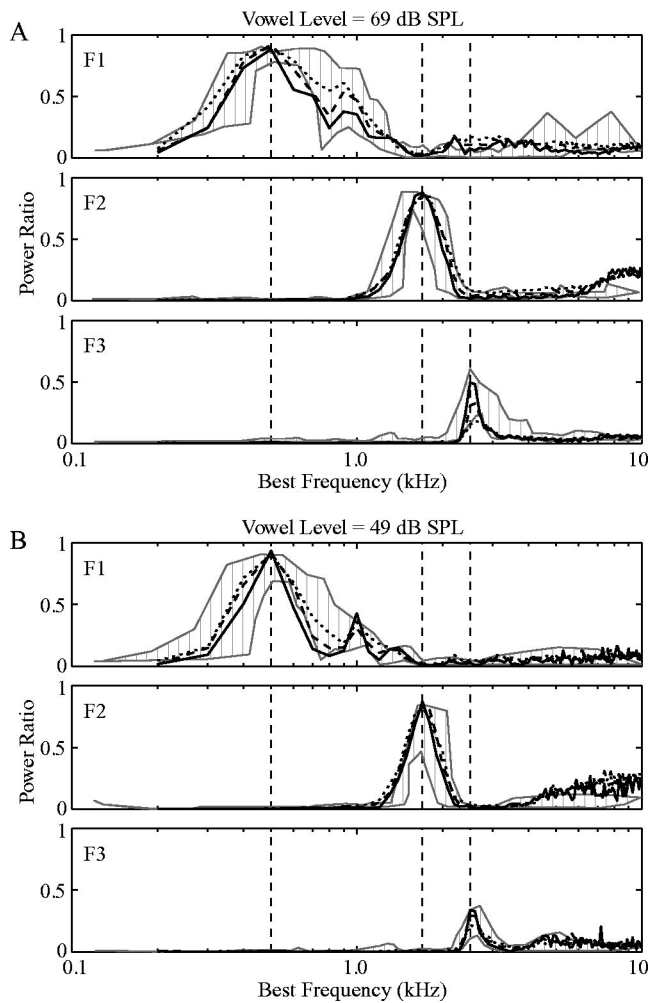


FIG. 15. Model predictions of normal power ratios for $F1$, $F2$, and $F3$ as a function of BF for stimulus intensities of 69 dB SPL (a) and 49 dB SPL (b). Thick lines show model predictions and gray hatched areas indicate the range of values observed in the normal physiological data of Miller *et al.* (1997). Vertical dashed lines show the formant frequencies. Predictions are shown for model Q_{10} values that are at the 75th (solid lines), 50th (dashed lines), and 25th (dotted lines) percentiles of Q_{10} values for the physiological data.

D. Signal processing to restore synchrony capture

In Schilling *et al.* (1998) and Miller *et al.* (1999a), two different amplification schemes were investigated for their potential to restore normal BF-dependent pattern of synchrony capture for the vowel / ϵ / in acoustically traumatized cats. Schilling *et al.* (1998) tested a common hearing-aid processing scheme, where the amplification has a frequency-shaped gain function in which the gain is larger in regions of greater threshold shift. They found that this amplification scheme did indeed restrict the upward spread of synchrony to $F1$ when compared to flat amplification. However, it could not prevent the upward spread of synchrony to $F2$ and $F3$. Perhaps more importantly, there was a strong and inappropriate synchrony of fibers with BFs in the trough region (~ 1 kHz) between $F1$ and $F2$ to energy at their BFs. This response was presumably created by the low-frequency edge of the amplification gain function and, in a hearing impaired individual, could produce an anomalous perception of a for-

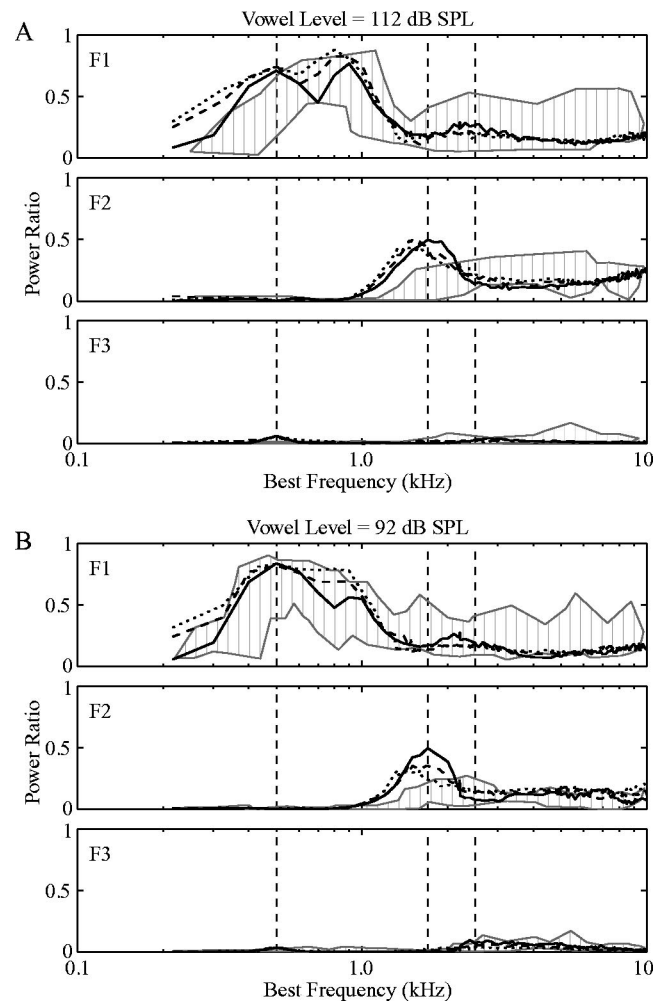


FIG. 16. Model predictions of impaired power ratios for $F1$, $F2$, and $F3$ as a function of impaired BF for stimulus intensities of 112 dB SPL (a) and 92 dB SPL (b). Thick lines show model predictions and gray hatched areas indicate the range of values observed in the impaired physiological data of Miller *et al.* (1997). Vertical dashed lines show the formant frequencies. Predictions are shown for model Q_{10} values that are at the 75th (solid lines), 50th (dashed lines), and 25th (dotted lines) percentiles of Q_{10} values for the impaired physiological data, i.e., for the three functions of C_{OHC} given in Fig. 5(a), and with IHC impairment as shown in Fig. 6(a).

mant, confounding the identification or discrimination of actual vowel formants.

To overcome this problem, Miller *et al.* (1999a) developed an alternative frequency-shaping scheme, contrast-enhancing frequency shaping (CEFS), where the edge of the gain profile is placed not at the frequency where thresholds begin to increase but rather just below the $F2$ frequency, creating a stronger contrast between $F2$ and the lower-frequency components such as $F1$ and the trough. The spectra of the standard and CEFS vowels are shown in Fig. 17. A 30 dB of gain has been applied to the frequencies above $F2$, to compensate for threshold shifts of around 60 dB in that region (see Lybarger, 1978, for an explanation of the “half gain rule”). The formant frequencies are identical to the previously described / ϵ / stimulus. In contrast to the previous stimulus, no HRTF filtering has been applied to the vowels in Fig. 17, so the $F3$ intensity is lower relative to $F2$, and both formant intensities are lower relative to $F1$.

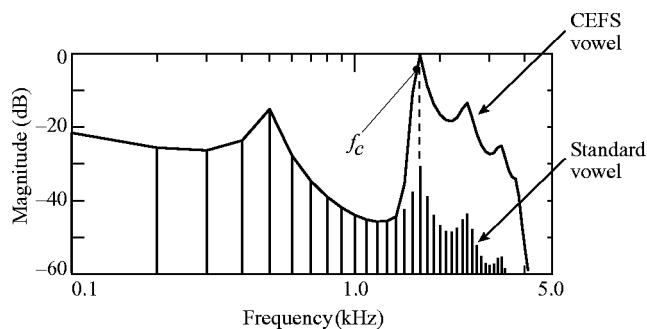


FIG. 17. Power spectra of the standard and CEFS versions of the vowel / ϵ /. The line spectrum shows the unprocessed vowel's spectral shape and the solid line shows the CEFS-modified spectral envelope. The CEFS vowel was obtained by high-pass filtering the standard vowel with a cutoff frequency f_c , which is 50 Hz below the second formant frequency (indicated by the vertical dashed line). Modified from Fig. 1(b) of Miller *et al.* (1999a) with permission from the Acoustical Society of America[®] (1999).

Shown in Fig. 18 are predictions for the CEFS vowel with the same impaired model fibers as in Figs. 9(b) and 12(b). The presentation levels for the CEFS vowel are 8 dB lower than those used in Figs. 9 and 12 so that the F_2 intensities are matched to those of the standard vowels. For a model fiber with parameters the same as for Fig. 9(b) (impaired IHC, normal OHC, and impaired BF=1.6 kHz $\approx F_2$), synchrony capture to F_2 is mostly regained with the CEFS vowel [Fig. 18(a); cf. normal data in Fig. 8(a)]. A model fiber with parameters the same as for Fig. 12(b) (impaired IHC, impaired OHC, and impaired BF=2.6 kHz $\approx F_3$) exhibits synchrony capture to the *second* formant of the modified vowel, instead of to F_3 [Fig. 18(b); cf. normal data in Fig. 11(a)]. The same undesirable effect is seen in the AN fiber data with CEFS amplification (see Figs. 10 and 11 of Miller *et al.*, 1999a).

V. DISCUSSION

A. Sources of changes in synchrony in acoustically traumatized cats

The model predictions presented in this paper suggest that both OHC and IHC impairment contribute to the degradation of the tonotopic representation of formant frequencies (i.e., BF-appropriate synchrony) in AN fibers damaged by acoustic trauma. OHC impairment broadens and linearizes BM tuning, thereby causing AN fibers to synchronize to many vowel components. This is consistent with the results of Geisler (1989), who used an AN model with a linear BM filter and found that broadened tuning led to an upward spread of synchrony to F_1 in a few example model fibers. Similar results were found by Sachs *et al.* (2002) with a model including a nonlinear BM filter. Geisler (1989) argued that IHC impairment was not necessary to explain physiological data from sound-damaged cochleae, in spite of histological data showing that the degree and extent (i.e., BF region) of damage to IHC stereocilia is typically equal to or greater than damage to OHC stereocilia (Liberman, 1984; Liberman and Dodds, 1984a, b) for a sound-exposure paradigm similar to that of Miller *et al.* (1997). Geisler (1989) modeled OHC impairment by directly fitting filter functions to impaired tuning curves, i.e., by independently varying the

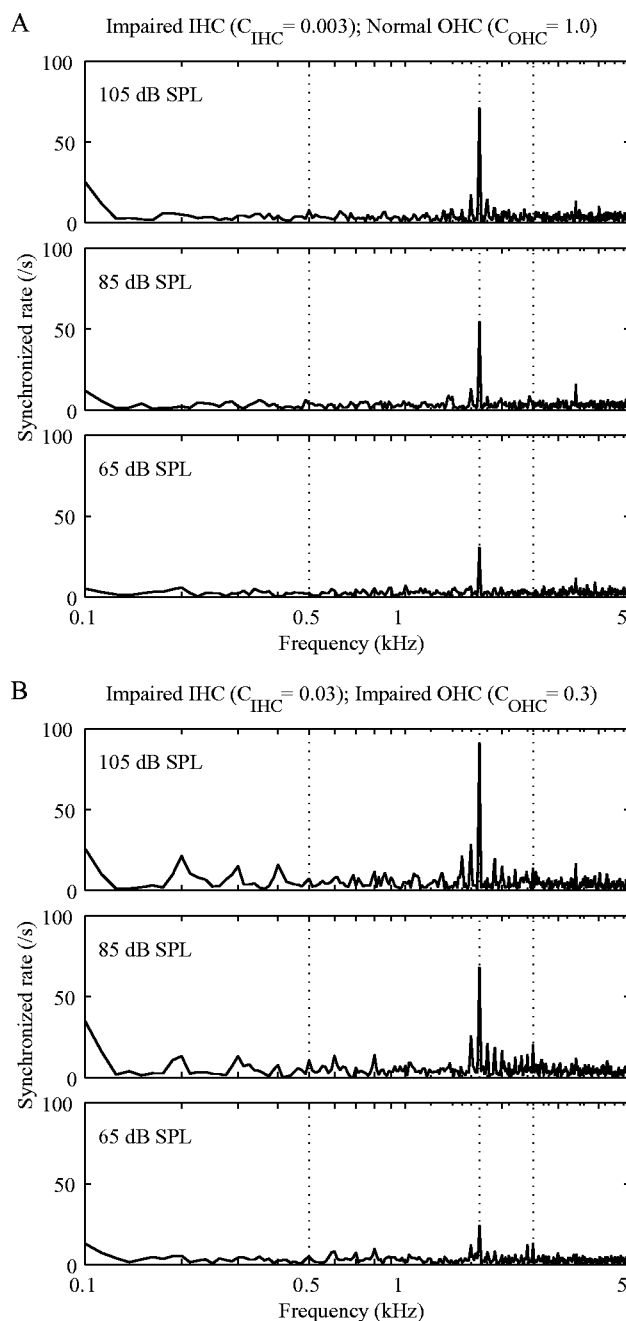


FIG. 18. Model predictions of responses to the CEFS vowel by impaired AN fibers. The presentation levels are reduced by 8 dB from those used for the standard vowel so that the levels of the F_2 components are matched for the CEFS vowel and the standard vowel. (a) Model fiber with parameters the same as for Fig. 9(b): impaired IHC ($C_{\text{IHC}}=0.003$) and normal OHC ($C_{\text{OHC}}=1$); impaired BF=1.6 kHz. (b) Model fiber with parameters the same as for Fig. 12(b): impaired IHC ($C_{\text{IHC}}=0.03$) and impaired OHC ($C_{\text{OHC}}=0.3$); impaired BF=2.6 kHz.

filter gain and bandwidth. However, our results suggest that some of the reduced gain in the Geisler (1989) filters may be better attributed to IHC impairment.

Our results show that IHC impairment *alone* can produce significant changes in the synchronized response to a vowel [see Fig. 9(b)]. The BM tuning is normally quite broad for high-intensity stimuli [see Fig. 1(b)], but normal IHC function leads to synchrony suppression of smaller vowel components. Synchrony capture caused by the IHC and the

IHC-AN synapse has also been illustrated in previous modeling studies (Schroeder and Hall, 1974; Geisler, 1985; Payton, 1988). The results of this paper add to these previous studies by suggesting over what range of stimulus intensities this occurs. As discussed in Sec. IV A, our model predicts that BM nonlinearity (compression and suppression) are the primary cause of synchrony capture for stimulus intensities between approximately 40 and 80 dB SPL, whereas IHC and synaptic nonlinearity (saturation) are the major cause of synchrony capture above 80 dB SPL. In the case of IHC impairment as modeled in Sec. III C, high-intensity signals fall within the linear region of the expanded IHC dynamic range and synchrony suppression is substantially reduced. In a similar fashion, the reduced BM gain in the case of OHC impairment causes the signal to fall within the linear region of the normal IHC dynamic range, leading to a reduction in synchrony suppression in the IHC, in addition to the already broader BM response. Note that the results described above are obtained only with a model including two-tone suppression. In the model of Carney (1993), which does not include any wideband nonlinearities in the BM filter, BM tuning remains relatively narrow even at high intensities and therefore IHC impairment has little effect. Without two-tone suppression, only broadening of BM tuning by OHC impairment causes any substantial change in the AN's synchrony to the vowel (Bruce *et al.*, 1999).

B. IHC impairment in acoustically traumatized cats

Geisler (1989) argued against the significance of IHC impairment for AN responses partly because a number of studies found relatively normal rate-level dynamic ranges for impaired fibers (e.g., Salvi *et al.*, 1983; Liberman and Kiang, 1984). The reasoning was that IHC impairment of the type we have modeled should decrease the slopes of rate-level functions, increasing their dynamic ranges (here slope is measured in a plot of rate versus log sound pressure, as dB). This is true in the model, in that the decrease in IHC gain increases the thresholds of AN fibers, which moves their dynamic ranges into the compression region of the BM input/output function [Fig. 4(b)], thus decreasing their slopes. The effect would, of course, be smaller for low spontaneous rate (high threshold) fibers, whose dynamic ranges normally incorporate more of the compression region (Sachs and Abbas, 1974; Yates, 1990). Computation of rate-level slopes for model fibers shows that, when level is expressed on a dB scale, the effect of IHC impairment with no OHC damage translates mainly into a threshold shift and the slopes with severe IHC impairment are approximately as shallow as normal low-spontaneous rate (high threshold) fibers (results not shown). OHC damage, of course has the opposite effect, either increasing or making no change in rate-level slopes, because OHC damage reduces the compression in the BM input/output function [Fig. 4(b)]. Increases in slope consistent with this expectation have been shown in AN fibers following OHC poisoning with kanamycin (Harrison, 1981) and similar changes are inferred from psychophysical masking experiments in hearing-impaired subjects (Oxenham and Plack, 1997). The opposite effects of IHC and OHC damage on rate-level slopes mean that, with the mixed losses in the

physiological data of Miller *et al.*, the effect on the slope of an individual AN fiber is difficult to predict and could be any of the three possibilities: increased, unchanged, or decreased. Measurements of rate-level slopes using a preparation similar to that of Miller *et al.* are consistent with this expectation (M. G. Heinz, personal communication). Thus Geisler's argument, while correct, does not apply to mixed losses of the type considered here.

Our method of separately determining OHC and IHC damage (see Secs. III B and III C) is consistent with the conclusion that both were present in the impaired cats of Miller *et al.* (1997), although histological analysis was not performed on these cochleae. Furthermore, the extent (i.e., BF region) of IHC impairment [Fig. 6(a)] is greater than the extent of OHC impairment [Fig. 5(a)], in agreement with the histological data described previously (Liberman, 1984; Liberman and Dodds, 1984a, b). IHC impairment was achieved in the model by decreasing the slope of the IHC nonlinearity. However, it is not clear what could be the physiological correlate of this manipulation. Permanently closed transduction channels (e.g., Pickels *et al.*, 1987) could lead to a reduced saturation potential and reduced maximum AN discharge rate, not seen in the data (Miller *et al.*, 1997). Permanently open transduction channels (Meyer *et al.*, 1998) would likely result in a large increase in the resting IHC potential and perhaps also in the spontaneous discharge rate of AN fibers, also not seen in the physiological data (Liberman and Dodds, 1984b; Miller *et al.*, 1997). More consistent with the AN data would be disarray of the stereociliar bundle (Liberman and Dodds, 1984a), such that greater pressure is required to reach both threshold and IHC saturation.

C. Future model improvements

The results of this study show good qualitative prediction of the effects of acoustic trauma on synchrony to a vowel, but the quantitative accuracy could benefit from improvements to the model. One possibility is that our methods of creating OHC and IHC impairment are too simple to capture the complex biophysical consequences of the mechanical trauma and subsequent cellular damage. A second possibility is that the inaccuracy of the *normal* model at high presentation levels, as seen in Sec. IV B, may produce similar inaccuracies in predicting the impaired data. Two physiological phenomena that are not included in the normal model and which may help explain its inaccuracy at high presentation levels are frequency glides and multi-modal excitation.

Frequency glides are modulations or sweeps in the instantaneous frequency of the impulse response of BM filters, also reflected in the impulse response of AN fibers (Carney *et al.*, 1999). Carney *et al.* (1999) found that the impulse response has an upward frequency glide for fibers with BFs greater than 1500 Hz, almost no glide for BFs between 750 and 1500 Hz, and a downward glide for BFs less than 750 Hz. They also found that glides are independent of stimulus intensity, but pointed out that the interaction of the glide with the nonlinear envelope of the impulse response could lead to shifts in BF with level. Broad filters have short time constants and, consequently, their response will be dominated

more by the starting frequency of the glide; narrow filters have long time constants and will therefore be dominated more by the final frequency of the glide. This level-dependent behavior may at least partially explain the BF shifts in BM tuning observed in the impaired cochlea and at high intensities in the normal cochlea (e.g., Robles and Ruggero, 2001). The lack of a BF shift may contribute to the model's inaccuracy in predicting the Wong *et al.* (1998) data (see Fig. 13); a larger downward BF shift at high intensities could reduce synchrony to $F2$ and increase synchrony to $F1$. This is consistent with the growth of low-side two-tone rate suppression in the model, which is also weaker than is observed in physiological data (Zhang *et al.*, 2001).

Multi-modal excitation is the presence of more than one vibrational mode in the BM response because of the complex micromechanics of the organ of Corti (e.g., Robles and Ruggero, 2001). Such multi-modal excitation, also observed in AN responses (Lin and Guinan, 2000), cannot be explained by a single-path BM filter as used in our model; parallel paths are required to model each mode of vibration (Goldstein, 1990; Schoonhoven *et al.*, 1994; Meddis *et al.*, 2001). In multi-path models, the center frequencies of each of the parallel filters are typically different, which along with the frequency glide in individual filters could contribute to shifts in BF with OHC impairment or at high presentation levels (Goldstein, 1990; Schoonhoven *et al.*, 1994; Meddis *et al.*, 2001). The interactions of the different paths might also explain the C1/C2 transition (Lieberman and Kiang, 1984; Wong *et al.*, 1998).

One feature not considered in any of these models is the stapedial reflex, which has been shown to reduce the upward spread of masking (i.e., low-side suppression) in AN fibers (Pang and Guinan, 1997). The physiological data examined in this paper (Miller *et al.*, 1997; Wong *et al.*, 1998; Miller *et al.*, 1999a) were from anesthetized cats in which the reflex is not present, and therefore modeling of the reflex is not necessary to describe the data. However, if the data and modeling results are to be applicable to hearing-aid design, then the stapedial reflex could be a significant factor in determining the AN response to vowels in hearing-impaired individuals. The ME section of our model could be adapted to describe the effects of the stapedial reflex. This would create another time-varying, nonlinear filter, and the control signal for the reflex could likely be obtained from a large population of model fibers.

Additionally, it is known that fibers with different spontaneous rates (and corresponding thresholds) provide different representations of speech stimuli across stimulus intensities (Sachs and Young, 1979). In particular, low and medium spontaneous rate fibers provide a better representation of vowels in their average discharge rates at high intensities. It would therefore be useful to extend the synapse model to be able to produce an arbitrary spontaneous rate and the associated change in the rate-level function (Sachs and Abbas, 1974; Yates, 1990).

The major deviation between the model and data is the difference in response to $F2$ in the impaired case (Fig. 16). This difference is apparently related to the weak suppression of $F2$ by $F1$ shown in Fig. 13. While the main cause is

probably the fact that the Zhang *et al.* (2001) model produces insufficient two-tone suppression for suppressors below BF, other factors may contribute. We have already argued that the lack of frequency glides in the model's filters could contribute to this difference. Another possibility, related to the modeling of low and medium spontaneous rate (higher threshold) fibers, is the fact that the model incorporates only the minimal threshold shift [Fig. 6(b)]. Additional threshold shift to model the average thresholds in the data would require a decrease in the IHC/synapse gain. As discussed above, decreases in IHC synapse gain have the effect of reducing large-signal suppression in the IHC and synapse and result in more broadband responses. Thus if the full range of thresholds were modeled, then the model data in Fig. 16 would scatter in the direction of lower synchrony to $F2$, which would decrease the difference between model and data.

D. Applicability of the model to hearing-aid design

The model presented in this paper appears accurate enough to be useful in testing the effects of potential hearing-aid processing schemes on the neural representation of speech. Such testing would provide information about hearing aids to supplement that provided by psychophysics and perceptual testing. Because the primary lesion in hearing impairment is usually in the cochlea, it seems clear that a useful goal for hearing-aid design should be producing auditory nerve responses that are as normal as possible. The value of the model in this regard is that it is much simpler, more flexible, and cheaper than physiological experiments. As a validation of the model's usefulness in this regard, it predicts both the benefits and the limitations of the CEFS amplification scheme (Sec. IVD), as they were observed in physiological experiments. There are two limitations on the usefulness of the model for such testing: first, there is the uncertainty about the quantitative relationship of cat and human auditory nerve responses. Recio *et al.* (2002) have argued that suppressive interactions among the formants and upward spread of $F1$ may be a smaller issue in the human cochlea, because of its longer length relative to the range of frequencies represented. Thus the model will have to be modified and validated for the human auditory periphery (Heinz *et al.*, 2001). Second, there is no direct way, at present, of estimating the specific degree of IHC and OHC impairment in individual human subjects. Methods of diagnosing IHC and OHC impairment are beginning to be developed (Moore *et al.*, 1999, 2000; Plack and Oxenham, 2000), but these methods do not yet provide a practical method of diagnosing individuals' degrees of hair cell damage. Nevertheless, the model can still provide valuable information by evaluating the effectiveness of signal processing for various commonly encountered lesions.

ACKNOWLEDGMENTS

The authors would like to thank Xuedong (Frank) Zhang, Michael Heinz, and Laurel Carney for providing source code for the Zhang *et al.* (2001) auditory-periphery model and for discussions on improving the normal model;

Bill Peake for invaluable assistance with the middle-ear model; Roger Miller for supplying physiological data; and Brad May, Kevin Davis, Michael Heinz, Laurel Carney, Ray Meddis, and three anonymous reviewers for helpful comments on earlier versions of the manuscript. This research was supported by NIDCD Grant Nos. DC00109 and DC00023.

APPENDIX A: MIDDLE-EAR MODEL

The ME section of the auditory-periphery model was created by combining the ME cavities model of Peake *et al.* (1992) with the ME model of Matthews (1983). Both of these are based on data from cats and are therefore suitable for use in this model. An electrical-circuit representation of the composite model is shown in Fig. 19(a); circuit-element values are given in Table II. The circuit was simplified by omitting the round-window compliance C_{rw} , which does not produce any significant change in the transfer function.

A transfer-function representation $G(s)$ of the circuit (i.e., the transfer of pressure outside the eardrum to pressure across the cochlear partition) was determined using the computer program SAPWIN (Liberatore *et al.*, 1995), giving

$$G(s) = \frac{\text{NUM}(s)}{\text{DEN}(s)}, \quad (\text{A1})$$

where

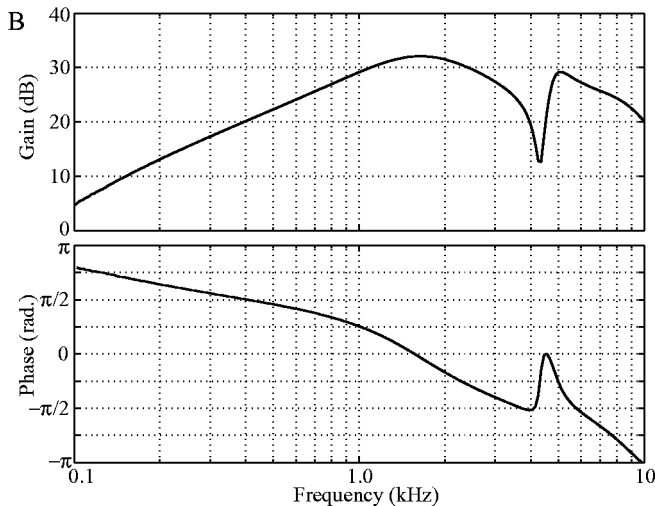
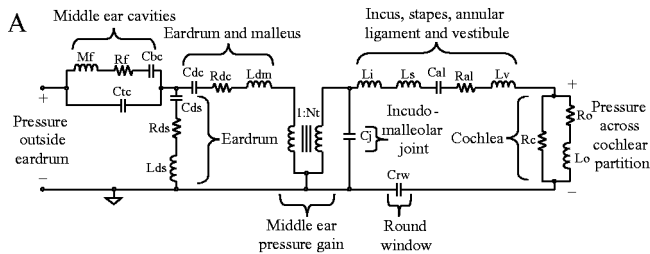


FIG. 19. (a) Electrical-circuit representation of middle-ear model. Circuit-element values are given in Table II. (b) Gain (top panel) and phase (bottom panel) of the frequency response of the middle-ear model shown in (a).

TABLE II. Circuit-element values for the middle-ear model. Values for M_f , R_f , C_{bc} , and C_{tc} are taken from the caption of Fig. 4 in Peake *et al.* (1992) and converted into cgs-units for compatibility with the units used by Matthews (1983) for all the other values: [pressure] = dyne/cm² = [voltage] = volt; [volume velocity] = cm³/s = [current] = ampere; [acoustic compliance] = cm⁵/dyne = [capacitance] = farad; [acoustic mass] = g/cm⁴ = [inductance] = henry; [acoustic damping] = dyne · s/cm⁵ = [resistance] = ohm; [acoustic impedance] = dyne · s/cm⁵ = [impedance] = ohm.

$M_f = 0.0101$	$C_j = 1.2 \times 10^{-11}$
$R_f = 13.7$	$L_i = 1.6$
$C_{bc} = 5.55 \times 10^{-7}$	$L_s = 3.3$
$C_{tc} = 1.75 \times 10^{-7}$	$L_v = 22$
$C_{ds} = 8 \times 10^{-8}$	$Cal = 3.7 \times 10^{-10}$
$R_{ds} = 1300$	$Ral = 2 \times 10^5$
$L_{ds} = 0.054$	$Rc = 1.2 \times 10^6$
$C_{dc} = 3.5 \times 10^{-7}$	$Ro = 2.8 \times 10^5$
$R_{dc} = 55.2$	$Lo = 2250$
$L_{dm} = 0.04$	$Crw = 1 \times 10^{-8}$
$Nt = 55$	

$$\begin{aligned} \text{NUM}(s) = & 4.07874 \times 10^{-55} s^8 + 1.04232 \times 10^{-50} s^7 \\ & + 4.1255 \times 10^{-46} s^6 + 7.48636 \times 10^{-42} s^5 \\ & + 7.1186 \times 10^{-38} s^4 + 8.74363 \times 10^{-36} s^3, \end{aligned} \quad (\text{A2})$$

and

$$\begin{aligned} \text{DEN}(s) = & 2.41138 \times 10^{-70} s^{11} + 1.91739 \times 10^{-65} s^{10} \\ & + 1.60971 \times 10^{-60} s^9 + 5.76989 \times 10^{-56} s^8 \\ & + 1.90447 \times 10^{-51} s^7 + 3.87288 \times 10^{-47} s^6 \\ & + 5.37782 \times 10^{-43} s^5 + 4.18754 \times 10^{-39} s^4 \\ & + 1.99923 \times 10^{-35} s^3 + 1.20211 \times 10^{-32} s^2 \\ & + 2.61157 \times 10^{-44} s, \end{aligned} \quad (\text{A3})$$

and s is in units of rad/s. From this continuous-time transfer function, a tenth-order, IIR digital filter was created using the `invfreqz` function in MATLAB (The MathWorks, Natick, MA) with a sampling frequency of 100 kHz.² The gain and phase of the frequency response of the digital filter are shown in Fig. 19(b).

APPENDIX B: IMPROVED DYNAMICS FOR OHC CONTROL OF THE BM FILTER

The dynamics of BM compression and suppression (Robles *et al.*, 1976; Ruggero and Rich, 1991) are determined in the model by the combination of the control-path OHC nonlinearity (a Boltzmann function) and the OHC LP filter [see Fig. 1(a)]. The wideband filter of Zhang *et al.* (2001) has a varying bandwidth, but the gain at BF is normalized to unity at each time step. With the prescribed asymmetry for the Boltzmann function, the control path produces compression in the signal path only over a restricted dynamic range (<30 dB), so Zhang *et al.* added a symmetrical, compressive nonlinearity between the wideband filter and the Boltzmann function to extend this dynamic range (see Fig. 1 of Zhang *et al.*, 2001). However, we have found that this

nonlinearity introduces distortion products into τ_{sp} and τ_{cp} for multi-tone or vowel stimuli, which induce the same undesired distortion products into the output of the signal-path, narrow-band filter. These distortion products can be avoided if compression in the control path is produced not by a static nonlinearity but rather by dynamic compression in the wide-band filter, as it is for the narrow-band filter. This is achieved by normalizing the gain at BF not to unity but rather to the gain of the narrow-band (signal path) filter, such that both filters have roughly the same output for a BF tone.³

The gain normalization is achieved by first setting the gain of each control-path low-pass filter to unity at BF. The filter coefficients are calculated for the present value of $\tau_{cp}[n]$ {using Eqs. (3) and (4) with $\tau_{cp}[n] = K\tau_{sp}[n]$ instead of $\tau_{sp}[n]$ }. The center frequency of the control-path wide band filter is not at BF but rather shifted to a frequency corresponding to a point on the basilar membrane 1.2 mm basal to the fiber BF, i.e., higher in frequency than BF (Zhang *et al.*, 2001). Consequently, the gain ($\text{gain}_{cp}[n]$) and the group delay ($\text{grd}_{cp}[n]$) at BF can be calculated for the control-path filter according to the equations [see pp. 213–230 of Oppenheim and Schaffer (1989)]:

$$\text{gain}_{cp}[n] = \sqrt{\frac{1 + c1_{LP}[n]^2 - 2c1_{LP}[n]\cos((\omega_{cp} - \omega_{BF})/F_s)}{2c2_{LP}[n]^2(1 - \cos((\omega_{cp} - \omega_{BF})/F_s))}} \quad (\text{B1})$$

and

$$\text{grd}_{cp}[n] = 0.5 - \frac{c1_{LP}[n]^2 - c1_{LP}[n]\cos((\omega_{cp} - \omega_{BF})/F_s)}{1 + c1_{LP}[n]^2 - 2c1_{LP}[n]\cos((\omega_{cp} - \omega_{BF})/F_s)}, \quad (\text{B2})$$

where ω_{BF} is the radian frequency ($2\pi \times \text{BF}$) corresponding to the fiber's BF and ω_{cp} is the center radian frequency of the wideband filter. The gain normalization is applied to the filter by multiplying $c2_{LP}[n]$ by $\text{gain}_{cp}[n]$ as given by Eq. (B1) after the number of samples given by the group delay has elapsed. That is, the gain normalization value is delayed to match the group delay. The gain might not be set for every sample because of the fluctuating group delay, in which case the most recent value for the gain normalization is used. After the gain at BF for each of the low-pass filters has been set to unity, the output of the entire wideband filter is multiplied by $(\tau_{sp}[n]/\tau_{narrow})^3$ to make its gain track that of the narrow-band filter.

This method of normalizing the gain does not correct for the phase changes with $\tau_{cp}[n]$. The phase changes could be compensated for by a time-varying all-pass filter, but we have not found this necessary in our simulations if we (i) reduce the cutoff frequency of the LP filter following the OHC nonlinearity [see Fig. 1(a)] from 800 to 600 Hz and (ii) ensure that the magnitude of the cochlear-amplifier gain for BFs less than 3 kHz is not too large.

Note that in our version of the model, the output of the wideband filter is also multiplied by a scaling factor of 4×10^3 at the input to the Boltzmann function to compensate

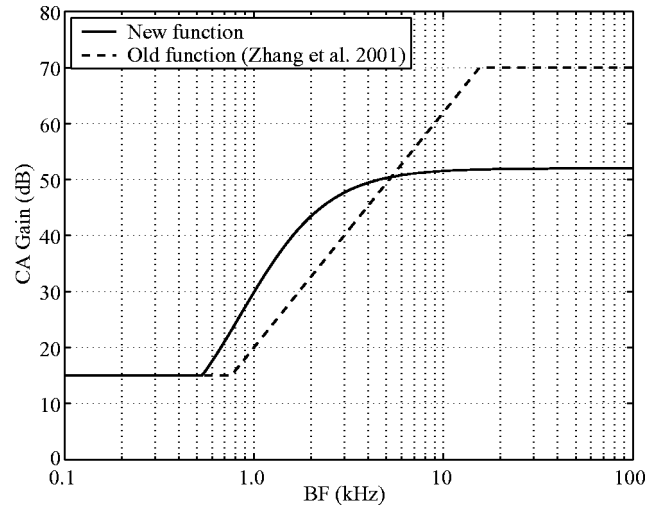


FIG. 20. Cochlear amplifier gain versus BF. The dashed line shows the function used in Zhang *et al.* (2001), and the solid line shows the new function described by Eq. (B3).

for the removal of the symmetrical nonlinearity, that is, so that the published parameters for the Boltzmann function are still appropriate.

We have also found it necessary to modify how much CA gain [see Fig. 4(b)] is applied at each BF to explain (i) the change in Q_{10} values for impaired AN fibers (see Sec. III B) and (ii) AN vowel responses at high stimulus intensities (see Sec. IV B). Equation (7) of Zhang *et al.* (2001) has been modified to

$$\text{gain}_{CA}(\text{BF}) = \max\{15, 52(\tanh(2.2 \log_{10}(\text{BF}) + 0.15) + 1)/2\}, \quad (\text{B3})$$

where BF is in the units of kHz. Plotted in Fig. 20 are the old (dashed line) and new (solid line) functions for CA gain. The old function was quite arbitrary and was roughly based on BM data from guinea pigs and chinchillas; such BM data do not exist for cats. While the new function is still arbitrary and was obtained indirectly by looking at the degradation of tuning in impaired fibers and at responses to vowel stimuli, it may provide a more accurate estimate of cochlear amplifier gain for cats. One indication of this is that the maximum gain is now 52 dB instead of 70 dB: high-BF, low-spontaneous-rate model fibers with 70 dB of gain have “straight” rate-level functions (Heinz *et al.*, 2001) which are observed in guinea pigs and chinchillas but not in cats (Sachs and Abbas, 1974); reducing the gain to 52 dB for high-BF fibers produces “sloping-saturation” rate-level functions, as observed in cats (results not shown).

¹ Scaling τ_{sp} in this fashion produces a linear change in the filter's Q_{10} as a function of C_{OHC} . For example, if $C_{OHC} = 0.5$, then the filter's Q_{10} will be halfway between the filter's Q_{10} value for normal OHC function ($C_{OHC} = 1$) and its Q_{10} value for complete OHC impairment ($C_{OHC} = 0$). We have chosen this method of scaling τ_{sp} because in Sec. III B we use Q_{10} values from physiological data to set the level of OHC impairment as a function of BF. The filter gain at BF is $(\tau_{sp_impaired}[n]/\tau_{narrow})^3$, and consequently the impaired gain (either linear or in dB) does not change linearly with C_{OHC} [see Fig. 1(b)]. It is possible to apply an alternative scaling method

$$\tau_{sp_impaired}[n] = \tau_{sp}[n](\tau_{wide}/\tau_{sp}[n])^{1-C'_{OHC}},$$

so that the gain in dB changes linearly with an alternative scaling factor C'_{OHC} .

²This sampling frequency is sufficient to produce an accurate and stable filter over the important frequency range (0.1–10 kHz). Even so, care must be taken to ensure stability when implementing the filter with fixed-precision algorithms—please contact the authors for further advice on this issue.

³The outputs of the narrow- and wideband filters will not be identical for a BF tone because (i) the center-frequency of the wideband filter is above BF and consequently the phase at BF fluctuates with $\tau_{\text{cp}}[n]$ and (ii) the wideband filter, in contrast to the narrow-band filter, is not followed by a linear band-pass filter.

Anderson, D. J., Rose, J. E., Hind, J. E., and Brugge, J. F. (1971). "Temporal position of discharges in single auditory nerve fibers within the cycle of a sine-wave stimulus: Frequency and intensity effects," *J. Acoust. Soc. Am.* **49**, 1131–1139.

Bruce, I. C., Young, E. D., and Sachs, M. B. (1999). "Modification of an auditory-periphery model to describe the effects of acoustic trauma on auditory nerve response," in *Abstracts of the 22nd ARO Midwinter Meeting*.

Carney, L. H. (1993). "A model for the responses of low-frequency auditory-nerve fibers in cat," *J. Acoust. Soc. Am.* **93**, 401–417.

Carney, L. H., McDuffy, M. J., and Shekhter, I. (1999). "Frequency glides in the impulse responses of auditory-nerve fibers," *J. Acoust. Soc. Am.* **105**, 2384–2391.

Costalupes, J. A., Rich, N. C., and Ruggero, M. A. (1987). "Effects of excitatory and non-excitatory suppressor tones on two-tone rate suppression in auditory nerve fibers," *Hear. Res.* **26**, 155–164.

Delgutte, B. (1990). "Two-tone rate suppression in auditory-nerve fibers: Dependence on suppressor frequency and level," *Hear. Res.* **49**, 225–246.

Deng, L., and Geisler, C. D. (1987a). "A composite auditory model for processing speech sounds," *J. Acoust. Soc. Am.* **82**, 2001–2012.

Deng, L., and Geisler, C. D. (1987b). "Responses of auditory-nerve fibers to nasal consonant-vowel syllables," *J. Acoust. Soc. Am.* **82**, 1977–1988.

Deng, L., Geisler, C. D., and Greenberg, S. (1987). "Responses of auditory-nerve fibers to multiple-tone complexes," *J. Acoust. Soc. Am.* **82**, 1989–2000.

Duifhuis, H. (1976). "Cochlear nonlinearity and second filter: Possible mechanism and implications," *J. Acoust. Soc. Am.* **59**, 408–423.

Gao, W. Y., Ding, D. L., Zheng, X. Y., Ruan, F. M., and Liu, Y. J. (1992). "A comparison of changes in the stereocilia between temporary and permanent hearing losses in acoustic trauma," *Hear. Res.* **62**, 27–41.

Geisler, C. D. (1981). "A model for discharge patterns of primary auditory-nerve fibers," *Brain Res.* **212**, 198–201.

Geisler, C. D. (1985). "Effects of a compressive nonlinearity in a cochlear model," *J. Acoust. Soc. Am.* **78**, 257–260.

Geisler, C. D. (1989). "The responses of models of 'high-spontaneous' auditory-nerve fibers in a damaged cochlea to speech syllables in noise," *J. Acoust. Soc. Am.* **86**, 2192–2205.

Giguère, C., and Woodland, P. C. (1994). "A computational model of the auditory periphery for speech and hearing research. II. Descending paths," *J. Acoust. Soc. Am.* **95**, 343–349.

Goldstein, J. L. (1990). "Modeling rapid waveform compression on the basilar membrane as multiple-bandpass-nonlinearity filtering," *Hear. Res.* **49**, 39–60.

Goldstein, J. L. (1995). "Relations among compression, suppression, and combination tones in mechanical responses of the basilar membrane: Data and MBPNL model," *Hear. Res.* **89**, 52–68.

Guinan, Jr., J. J., and Peake, W. T. (1967). "Middle-ear characteristics of anesthetized cats," *J. Acoust. Soc. Am.* **41**, 1237–1261.

Harrison, R. V. (1981). "Rate-versus-intensity functions and related AP responses in normal and pathological guinea pig and human cochleas," *J. Acoust. Soc. Am.* **70**, 1036–1044.

Heinz, M. G., Zhang, X., Bruce, I. C., and Carney, L. H. (2001). "Auditory nerve model for predicting performance limits of normal and impaired listeners," *ARLO* **2**, 91–96.

Irino, T., and Patterson, R. D. (2001). "A compressive gammachirp auditory filter for both physiological and psychophysical data," *J. Acoust. Soc. Am.* **109**, 2008–2022.

Javel, E., Geisler, C. D., and Ravindran, A. (1978). "Two-tone suppression in auditory nerve of the cat: Rate-intensity and temporal analyses," *J. Acoust. Soc. Am.* **63**, 1093–1104.

Javel, E., McGee, J., Walsh, E. J., Farley, G. R., and Gorga, M. P. (1983).

"Suppression of auditory nerve responses. II. Suppression threshold and growth, iso-suppression contours," *J. Acoust. Soc. Am.* **74**, 801–813.

Jenison, R. L., Greenberg, S., Kluender, K. R., and Rhode, W. S. (1991). "A composite model of the auditory periphery for the processing of speech based on the filter response functions of single auditory-nerve fibers," *J. Acoust. Soc. Am.* **89**, 773–786.

Johnstone, B. M., Patuzzi, R., and Yates, G. K. (1986). "Basilar membrane measurements and the travelling wave," *Hear. Res.* **22**, 147–153.

Kates, J. M. (1995). "Two-tone suppression in a cochlear model," *IEEE Trans. Speech Audio Process.* **3**, 396–406.

Kiang, N. Y., Liberman, M. C., and Levine, R. A. (1976). "Auditory-nerve activity in cats exposed to ototoxic drugs and high-intensity sounds," *Ann. Otol. Rhinol. Laryngol.* **85**, 752–768.

Liberatore, A., Luchetta, A., Manetti, S., and Piccirilli, M. C. (1995). "A new symbolic program package for the interactive design of analog circuits," in *ISCAS'95, IEEE International Symposium on Circuits and Systems, 1995, Vol. 3* (IEEE, Piscataway, NJ), pp. 2209–2212.

Liberman, M. C. (1978). "Auditory nerve response from cats raised in a low noise chamber," *J. Acoust. Soc. Am.* **63**, 442–455.

Liberman, M. C. (1984). "Single-neuron labeling and chronic cochlear pathology. I. Threshold shift and characteristic-frequency shift," *Hear. Res.* **16**, 33–41.

Liberman, M. C., and Dodds, L. W. (1984a). "Single-neuron labeling and chronic cochlear pathology. III. Stereocilia damage and alterations of threshold tuning curves," *Hear. Res.* **16**, 55–74.

Liberman, M. C., and Dodds, L. W. (1984b). "Single-neuron labeling and chronic cochlear pathology. II. Stereocilia damage and alterations of spontaneous discharge rates," *Hear. Res.* **16**, 43–53.

Liberman, M. C., and Kiang, N. Y.-S. (1984). "Single-neuron labeling and chronic cochlear pathology. IV. Stereocilia damage and alterations in rate- and phase-level functions," *Hear. Res.* **16**, 75–90.

Liberman, M. C., and Mulroy, M. J. (1982). "Acute and chronic effects of acoustic trauma: Cochlear pathology and auditory nerve pathophysiology," in *New Perspectives on Noise-Induced Hearing Loss*, edited by R. P. Hamernik, D. Henderson, and R. Salvi (Raven, New York), pp. 105–135.

Lin, T., and Guinan, Jr., J. J. (2000). "Auditory-nerve-fiber responses to high-level clicks: Interference patterns indicate that excitation is due to the combination of multiple drives," *J. Acoust. Soc. Am.* **107**, 2615–2630.

Lopez-Poveda, E. A., and Meddis, R. (2001). "A human nonlinear cochlear filterbank," *J. Acoust. Soc. Am.* **110**, 3107–3118.

Lybarger, S. F. (1978). "Selective amplification—a review and evaluation," *J. Am. Audiol. Soc.* **3**, 258–266.

Matthews, J. W. (1983). "Modeling reverse middle ear transmission of acoustic distortion signals," in *Mechanics of Hearing: Proceedings of the IUTAM/ICA Symposium*, edited by E. de Boer and M. A. Viergever (Delft U. P., Delft), pp. 11–18.

Meddis, R., O'Mard, L. P., and Lopez-Poveda, E. A. (2001). "A computational algorithm for computing nonlinear auditory frequency selectivity," *J. Acoust. Soc. Am.* **109**, 2852–2861.

Meyer, J., Furness, D. N., Zenner, H.-P., Hackney, C. M., and Gummer, A. W. (1998). "Evidence for opening of hair-cell transducer channels after tip-link loss," *J. Neurosci.* **18**, 6748–6756.

Miller, R. L., Calhoun, B. M., and Young, E. D. (1999a). "Contrast enhancement improves the representation of /ε/-like vowels in the hearing-impaired auditory nerve," *J. Acoust. Soc. Am.* **106**, 2693–2708.

Miller, R. L., Calhoun, B. M., and Young, E. D. (1999b). "Discriminability of vowel representations in cat auditory-nerve fibers after acoustic trauma," *J. Acoust. Soc. Am.* **105**, 311–325.

Miller, R. L., Schilling, J. R., Franck, K. R., and Young, E. D. (1997). "Effects of acoustic trauma on the representation of the vowel /ε/ in cat auditory nerve fibers," *J. Acoust. Soc. Am.* **101**, 3602–3616.

Moore, B. C., Glasberg, B. R., and Vickers, D. A. (1999). "Further evaluation of a model of loudness perception applied to cochlear hearing loss," *J. Acoust. Soc. Am.* **106**, 898–907.

Moore, B. C., Huss, M., Vickers, D. A., Glasberg, B. R., and Alcantara, J. I. (2000). "A test for the diagnosis of dead regions in the cochlea," *Br. J. Audiol.* **34**, 205–224.

Nordmann, A. S., Böhne, B. A., and Harding, G. W. (2000). "Histopathological differences between temporary and permanent threshold shift," *Hear. Res.* **139**, 13–30.

Oppenheim, A. V., and Schaffer, R. W. (1989). *Discrete-Time Signal Processing* (Prentice-Hall, Englewood Cliffs, NJ).

Oxenham, A. J., and Plack, C. J. (1997). "A behavioral measure of basilar-

- membrane nonlinearity in listeners with normal and impaired hearing," *J. Acoust. Soc. Am.* **101**, 3666–3675.
- Pang, X. D., and Guinan, Jr., J. J. (1997). "Effects of stapedius-muscle contractions on the masking of auditory-nerve responses," *J. Acoust. Soc. Am.* **102**, 3576–3586.
- Patterson, R., Nimmo-Smith, I., Holdsworth, J., and Rice, P. (1988). "Implementing a gammatone filter bank," SVOS Final Report: The Auditory Filter Bank.
- Payton, K. L. (1988). "Vowel processing by a model of the auditory periphery: A comparison to eighth-nerve responses," *J. Acoust. Soc. Am.* **83**, 145–162.
- Peake, W. T., Rosowski, J. J., and Lynch, III, T. J. (1992). "Middle-ear transmission: Acoustic versus ossicular coupling in cat and human," *Hear. Res.* **57**, 245–268.
- Pfeiffer, R. R. (1970). "A model for two-tone inhibition of single cochlear-nerve fibers," *J. Acoust. Soc. Am.* **48**, 1373–1378.
- Pickles, J. O., Osborne, M. P., and Comis, S. D. (1987). "Vulnerability of tip links between stereocilia to acoustic trauma in the guinea pig," *Hear. Res.* **25**, 173–183.
- Plack, C. J., and Oxenham, A. J. (2000). "Basilar-membrane nonlinearity estimated by pulsation threshold," *J. Acoust. Soc. Am.* **107**, 501–507.
- Rocio, A., Rhode, W. S., Kieffe, M., and Kluender, K. R. (2002). "Responses to cochlear normalized speech stimuli in the auditory nerve of cat," *J. Acoust. Soc. Am.* **111**, 2213–2218.
- Robert, A., and Eriksson, J. L. (1999). "A composite model of the auditory periphery for simulating responses to complex sounds," *J. Acoust. Soc. Am.* **106**, 1852–1864.
- Robertson, D. (1982). "Effects of acoustic trauma on stereocilia structure and spiral ganglion cell tuning properties in the guinea pig cochlea," *Hear. Res.* **7**, 55–74.
- Robles, L., and Ruggero, M. A. (2001). "Mechanics of the mammalian cochlea," *Physiol. Rev.* **81**, 1305–1352.
- Robles, L., Rhode, W. S., and Geisler, C. D. (1976). "Transient response of the basilar membrane measured in squirrel monkeys using the Mossbauer effect," *J. Acoust. Soc. Am.* **59**, 926–939.
- Ruggero, M. A., and Rich, N. C. (1991). "Application of a commercially-manufactured Doppler-shift laser velocimeter to the measurement of basilar-membrane vibration," *Hear. Res.* **51**, 215–230.
- Sachs, M. B., and Abbas, P. J. (1974). "Rate versus level functions for auditory-nerve fibers in cats: Tone-burst stimuli," *J. Acoust. Soc. Am.* **56**, 1835–1847.
- Sachs, M. B., and Kiang, N. Y. (1968). "Two-tone inhibition in auditory-nerve fibers," *J. Acoust. Soc. Am.* **43**, 1120–1128.
- Sachs, M. B., and Young, E. D. (1979). "Encoding of steady-state vowels in the auditory nerve: Representation in terms of discharge rate," *J. Acoust. Soc. Am.* **66**, 470–479.
- Sachs, M. B., Bruce, I. C., Miller, R. L., and Young, E. D. (2002). "Biological basis of hearing-aid design," *Ann. Biomed. Eng.* **30**, 157–168.
- Salvi, R., Henderson, D., and Hamernik, R. (1983). "Physiological bases of sensorineural hearing loss," in *Hearing Research and Theory*, edited by J. V. Tobias and E. D. Schubert (Academic, New York), pp. 173–231.
- Salvi, R., Perry, J., Hamernik, R. P., and Henderson, D. (1982). "Relationships between cochlear pathologies and auditory nerve and behavioral responses following acoustic trauma," in *New Perspectives on Noise-Induced Hearing Loss*, edited by R. P. Hamernik, D. Henderson, and R. Salvi (Raven, New York), pp. 165–188.
- Schilling, J. R., Miller, R. L., Sachs, M. B., and Young, E. D. (1998). "Frequency-shaped amplification changes the neural representation of speech with noise-induced hearing loss," *Hear. Res.* **117**, 57–70.
- Schmiedt, R. A., Mills, J. H., and Adams, J. C. (1990). "Tuning and suppression in auditory nerve fibers of aged gerbils raised in quiet or noise," *Hear. Res.* **45**, 221–236.
- Schmiedt, R. A., Zwislocki, J. J., and Hamernik, R. P. (1980). "Effects of hair cell lesions on responses of cochlear nerve fibers. I. Lesions, tuning curves, two-tone inhibition, and responses to trapezoidal-wave patterns," *J. Neurophysiol.* **43**, 1367–1389.
- Schoonhoven, R., Keijzer, J., Versnel, H., and Prijs, V. F. (1994). "A dual filter model describing single-fiber responses to clicks in the normal and noise-damaged cochlea," *J. Acoust. Soc. Am.* **95**, 2104–2121.
- Schroeder, M. R., and Hall, J. L. (1974). "Model for mechanical to neural transduction in the auditory receptor," *J. Acoust. Soc. Am.* **55**, 1055–1060.
- Temchin, A. N., Rich, N. C., and Ruggero, M. A. (1997). "Low-frequency suppression of auditory nerve responses to characteristic frequency tones," *Hear. Res.* **113**, 29–56.
- Wiener, F. M., and Ross, D. A. (1946). "The pressure distribution in the auditory canal in a progressive sound field," *J. Acoust. Soc. Am.* **18**, 401–408.
- Wong, J. C., Miller, R. L., Calhoun, B. M., Sachs, M. B., and Young, E. D. (1998). "Effects of high sound levels on responses to the vowel/eh/in cat auditory nerve," *Hear. Res.* **123**, 61–77.
- Yates, G. K. (1990). "Basilar membrane nonlinearity and its influence on auditory nerve rate-intensity functions," *Hear. Res.* **50**, 145–162.
- Young, E. D., and Sachs, M. B. (1979). "Representation of steady-state vowels in the temporal aspects of the discharge patterns of populations of auditory nerve fibers," *J. Acoust. Soc. Am.* **66**, 1381–1403.
- Zhang, M., and Zwislocki, J. J. (1996). "Intensity-dependent peak shift in cochlear transfer functions at the cellular level, its elimination by sound exposure, and its possible underlying mechanisms," *Hear. Res.* **96**, 46–58.
- Zhang, X., Heinz, M. G., Bruce, I. C., and Carney, L. H. (2001). "A phenomenological model for the responses of auditory-nerve fibers: I. Nonlinear tuning with compression and suppression," *J. Acoust. Soc. Am.* **109**, 648–670.

Ear-canal acoustic admittance and reflectance effects in human neonates. I. Predictions of otoacoustic emission and auditory brainstem responses

Douglas H. Keefe,^{a)} Fei Zhao,^{b)} Stephen T. Neely, and Michael P. Gorga
Boys Town National Research Hospital, 555 North 30th Street, Omaha, Nebraska 68131

Betty R. Vohr
Women's and Infant's Hospital, Providence, Rhode Island

(Received 28 April 2002; revised 26 September 2002; accepted 30 September 2002)

This report describes the extent to which ear-canal acoustic admittance and energy reflectance (YR) in human neonates (1) predict otoacoustic emission (OAE) levels and auditory brainstem response (ABR) latencies, and (2) classify OAE and ABR responses as present or absent. Analyses are reported on a subset of ears in which hearing screening measurements were obtained previously [Norton *et al.*, *Ear. Hear.* **21**, 348–356 (2000a)]. Tests on 1405 ears included YR, distortion-product OAEs, transient-evoked OAEs, and ABR. Principal components analysis reduced the 33 YR variables to 5–7 factors. OAE levels decreased and ABR latencies increased with increasing high-frequency energy reflectance. Up to 28% of the variance in OAE levels and 12% of the variance in ABR wave-V latencies were explained by these factors. Thus, the YR response indirectly encodes information on inter-ear variations in forward and reverse middle-ear transmission. The YR factors classify OAEs with an area under the relative operating characteristic (ROC) curve as high as 0.79, suggesting that middle-ear dysfunction is partly responsible for the inability to record OAEs in some ears. The YR factors classified ABR responses less well, with ROC areas of 0.64 for predicting wave-V latency and 0.56 for predicting *Fsp*. © 2003 Acoustical Society of America. [DOI: 10.1121/1.1523387]

PACS numbers: 43.64.Ha, 43.64.Jb, 43.64.Nf [BLM]

I. INTRODUCTION

The effect in human neonates of sound transmission from the ear canal to the middle ear, and into the cochlea is poorly understood. This acoustical functioning influences the patterns of evoked otoacoustic emissions (EOAE), which are ear-canal acoustical signals generated within the cochlea, and auditory brainstem responses (ABR), which are evoked electrical signals generated by multiple sources within the auditory neural pathway. Current neonatal hearing screening (NHS) programs are based on the use of EOAE and/or (air-conducted) ABR responses that are each elicited by an acoustic stimulus in the ear canal. Both EOAEs and ABRs are objective in the sense that they do not rely on a voluntary response from the patient. This feature is particularly useful in NHS because it is not possible to behaviorally assess hearing status in neonates. A significant issue in such programs, however, is the problem of “false positives,” which refers to ears with normal hearing that do not have sufficiently strong EOAE and/or ABR responses at the time of the newborn screening test. A widely held view is that middle-ear dysfunction, most often transient in nature during the neonatal and perinatal periods, is responsible for such false-positive outcomes. The facts that the neonate's middle-ear cavities contain mesenchyme and other material, and are not fully

pneumatized at birth are thought to be contributing factors to this transient middle-ear dysfunction (Stuart *et al.*, 1994). Improved understanding of the interaction between middle-ear and cochlear functioning may have relevance for clinical NHS programs designed to identify hearing loss in infants.

The first step towards such an understanding is to examine the extent to which variations in a population of ears in a test of middle-ear functioning are able to predict variations in EOAE and ABR tests. This is a basic research question to better understand how the external ear and middle ear influence measures of cochlear functioning such as EOAE and ABR tests. If such a middle-ear test were to lack the ability to predict EOAE and ABR tests, then it is reasonable to assume that it would also lack the ability to predict false positives in neonatal hearing screening programs. On the other hand, if a middle-ear test had the ability to predict EOAE and ABR tests, then a second step relevant to clinical utility would be to evaluate its application in an NHS program.

The test of ear-canal and middle-ear functioning that is examined in this report is the acoustical admittance and reflectance (YR) response. This report describes analyses based on a database of YR, EOAE, and ABR test responses, with the purpose of better understanding the influence of the middle ear on cochlear and neural responses in neonatal ears. As such, its scope concerns the first step in understanding the extent to which inter-ear variations in the YR test are able to predict inter-ear variations in EOAE and ABR tests. Anticipating the finding that the YR test is predictive of EOAE and

^{a)}Electronic mail: keefe@boystown.org

^{b)}Current affiliation: School of Health Science, University of Wales Swansea, Singleton Park, Swansea SA2 8PP, U.K.

ABR tests, a second report (Keefe *et al.*, 2003) evaluates the application of YR test responses in the context of an NHS program for the purpose of measuring middle-ear status.

The YR test is an input frequency response test based on noninvasive stimulus and response measurements in the ear canal. This is contrasted with a transfer function response measured between an input location of the middle ear (e.g., including the ear canal), and an output location (such as pressure in the cochlear vestibule or stapes footplate velocity). The input frequency response is, at best, an indirect measurement of forward and reverse middle-ear transmission because it lacks direct measurement of the output signal. Middle-ear transmission functions have been reported for adult human temporal bones with middle-ear cavities open for forward transmission (Puria *et al.*, 1997; Hudde and Engel, 1998; Voss *et al.*, 2000), and reverse transmission (Puria and Rosowski, 1996; Hudde and Engel, 1998). Corresponding measurements in neonatal human temporal bones have not been reported. Such transfer functions provide direct measurements of forward and reverse middle-ear transmission, but they are invasive measurements that cannot be used under *in vivo* conditions in humans. In measurements on acoustic impedance and stapes velocity in adult human temporal bones, Voss *et al.* (2000) concluded that inter-ear variations of acoustic impedance (middle-ear input) were not strong predictors of inter-ear variations of stapes velocity (middle-ear output) using temporal bones without apparent otologic disease that appeared normal under an otologic-operating microscope. This would appear problematical for developing noninvasive tests of middle-ear functioning based on acoustic responses measured in the ear canal, but it has also been reported that YR responses in a population of normal-hearing ears and a population of ears at risk for otitis media with effusion predict the presence of conductive hearing loss in clinical populations (Piskorski *et al.*, 1999). Thus, there is insufficient evidence to reject the use of noninvasive acoustical tests of middle-ear function (Keefe, 2001). Voss *et al.* (2001) described the possibility that the inter-ear variations reported by Voss *et al.* (2000) were dependent on different physical processes than those in the normal and abnormal ears tested by Piskorski *et al.* (1999).

Currently, little is known concerning the use of input acoustic frequency response functions in the ear canal to predict middle-ear transmission in clinical populations, and particularly so in hearing screening studies of neonatal ears. Tympanometry is effective in screening for middle-ear dysfunction in older children, but its use in infants younger than 6 months remains controversial (Rhodes *et al.*, 1999), and especially for infants younger than 3 months. The approach of Piskorski *et al.* used the presence or absence of a conductive hearing loss as a “gold standard” [this terminology is used in a generic sense as in clinical research studies, e.g., Norton *et al.* (2000b)] against which to test the predictive efficacy of the YR response. Conductive hearing loss was defined in terms of a threshold value of the gap between air-conduction and bone-conduction behavioral thresholds. An alternative means to define a conductive hearing loss is in terms of the air-bone gap in ABR thresholds (Hooks and Weber, 1984; Foxe and Stapells, 1993; Stuart *et al.*, 1994).

However, such definitions of conductive hearing loss are unavailable in neonatal hearing screening program tests because: (1) a behavioral audiogram cannot be measured on a neonate; (2) bone-conduction ABR measurements are not typically part of neonatal hearing screening protocols for several reasons (such as issues associated with calibration and the difficulty of maintaining a calibrated force on a neonatal head). Thus, a neonatal gold standard for conductive hearing loss currently does not exist or, at the very least, is unavailable from typical clinical measurements during the neonatal period. Some researchers recommend neonatal hearing screening using an air-conduction ABR, and those infants failing such a screening test are further tested using diagnostic ABR with both air-conduction and bone-conduction stimuli (Chen *et al.*, 1996; Stevens, 2001). Stevens considers three ways to measure a conductive component of a hearing loss in a neonate. He concludes that the latency of the air-conduction ABR wave-V response varies too much with age, tympanometry does not predict conductive hearing loss, while bone-conduction ABR is a viable choice.

Thus, the problem remains of assessing middle-ear functioning in the context of a neonatal screening program. One possible alternative to the direct measurement of conductive hearing loss in neonates is to base a clinical decision for middle-ear dysfunction on those physiological tests that are used in neonatal hearing screening programs, and which indirectly encode information on forward and reverse middle-ear transmission. Given such an alternative, the question can be asked of the extent to which the YR test, or some other test of middle-ear functioning, is able to correctly classify ears as having middle-ear dysfunction. Such a question is addressed in Keefe *et al.* (2003) based on the research in the present report.

The ABR test is sensitive to forward middle-ear transmission, and the EOAE test is sensitive to both forward and reverse middle-ear transmission. If the YR response should predict some of the structure of ABR and EOAE responses, then this would be evidence that the direct measurement of middle-ear input encodes information, albeit indirectly, on forward and reverse transmission through the middle ear. The YR response is sensitive to sound transmission in the ear canal and to the acoustical termination at the middle ear at the position of the tympanic membrane, i.e., the YR response is a measure of ear-canal and middle-ear functioning. For simplicity, it is often termed a middle-ear response in this report, but the potential influence of ear-canal acoustics is always implied. This has particular relevance in neonatal ear canals, in which there are observed interactions between ear-canal wall motion and ear-canal acoustical responses (Holte *et al.*, 1990). It is also relevant to the hypothesis that the presence of ear-canal wall motions can account for the presence of an additional shunt resonance in the acoustical admittance, which has been observed in the ears of infants up to age 12 months at frequencies from 0.125–1.5 kHz (Keefe *et al.*, 1993).

A. Overview of the INHI project

The data for the analyses to follow were collected as part of the Identification of Neonatal Hearing Impairment (INHI) project (Norton, 2000a), of which the principal goal was to test the effectiveness of physiological tests in identifying hearing loss in neonates. Hearing status in the INHI project was assessed using transient-evoked otoacoustic emissions (TEOAE), distortion-product otoacoustic emissions (DPOAE), and air-conduction ABRs. These three responses were obtained whenever possible for both ears of each subject. INHI results have been described for TEOAEs (Norton *et al.*, 2000c), DPOAEs (Gorga *et al.*, 2000), and ABRs (Sininger *et al.*, 2000). A secondary goal of the INHI project was to examine whether a YR test of middle-ear functioning would provide data on middle-ear functioning in neonates relevant to the outcomes on the primary screening measures. YR responses were acquired at four of the six INHI centers, preliminary analyses of which suggested that the data may be useful in interpreting neonatal tests of hearing screening (Keefe *et al.*, 2000). The study found that a contributor to the false-alarm rate of TEOAEs was a leaky probe fit that can be detected by examination of the low-frequency YR response (from 0.25–1.0 kHz); 13% of the responses had a leaky probe fit. The only analysis in the INHI project of the combined middle-ear and cochlear responses examined the influence of probe fit on TEOAEs, in which the YR test provided the data to evaluate the quality of the fit (leaky or adequate fit). The false-positive rate associated with TEOAE testing decreased from 12.4% in the population with a leaky probe fit to 5.8% in the population without a leaky probe fit, with the assessment of probe fit coming from the YR test rather than the TEOAE test. Thus, the YR response accounted for some of the false positives in TEOAE testing.

This report uses the INHI data acquired at the Boys Town National Research Hospital, and Women and Infants Hospital, which were combined into a database for new analyses. These two sites had collected both primary screening data (TEOAE, DPOAE, ABR) and most of the middle-ear data (YR) on subjects tested in the INHI project.

B. Response variables

The variables used in the present analyses are described below.

1. TEOAEs

The stimuli were unfiltered clicks of 80- μ s duration, delivered at an approximate ear-canal level of 80 dB pSPL. Responses to a minimum of 60 stimulus sweeps were averaged. Signal and noise SPLs were evaluated in five half-octave frequency bands centered at 1.0, 1.5, 2.0, 3.0, and 4.0 kHz, or 10 TEOAE variables in total (Norton *et al.*, 2000c).

2. DPOAEs

The DPOAE stimuli were pairs of sinusoidal tones (f_1 and f_2) with a fixed frequency ratio ($f_2/f_1 = 1.22$). DPOAE signal and noise SPLs were measured in response to tones with f_2 set at 1.0, 1.5, 2.0, 3.0, and 4.0 kHz. Although two

primary-tone levels were used during the original study, the present analyses used data collected at stimulus levels of $L_1 = 65$ dB and $L_2 = 50$ dB SPL. There are 10 DPOAE variables in total (Gorga *et al.*, 2000).

3. ABR

ABRs were recorded for click stimuli of 30 and 70 dB nHL. In the original study, these data were recorded simultaneously from the vertex to the nape of the neck, and from vertex to the ipsilateral mastoid. The present analyses used only the data recorded from the vertex to the mastoid. At 30 dB nHL, only wave V latency [$L_V(30)$] was measured. At 70-dB nHL, wave I latency [$L_I(70)$], wave V [$L_V(70)$], and the wave V–I latency [$L_{V-I}(70)$] were measured. The ABR variable used to predict hearing loss in the INHI project is the F_{sp} value measured at 30 dB (nHL), which is a measure of the relative level of signal to noise. These and other details regarding the ABR results are described by Sininger *et al.* (2000).

4. YR

The YR variables were based on the acoustic admittance (Y) and energy reflectance (R) at the probe tip. The trio of YR variables at each of 11 test frequencies f consisted of acoustic conductance G (real part of admittance), equivalent volume V (calculated in terms of the imaginary part of the admittance), and energy reflectance. The 11 test frequencies were at half-octaves from 0.25 up to 8.0 kHz, so that each YR response contained a set of 33 variables (Keefe *et al.*, 2000).

C. Research issues

The aim in this study is to better understand the relationship of EOA and ABR responses in ears for which the YR response is also known. Because of the high prevalence of measurements in normal-hearing ears in the sample population (because hearing loss is a rare event among neonates), the relationships obtained are characteristic of a population mainly dominated by normal-hearing ears. Research issues are listed below.

1. Can middle-ear functioning be described by a small number of YR variables?

Many of the 33 variables in the YR response are highly correlated with one another so that it may be possible to define a set of new variables that is fewer in number that adequately describe the original YR data set. It would be useful to describe middle-ear functioning using fewer variables, because the subsequent analyses would be simpler and any significant results would more likely generalize to a new sample population. A principal component analysis (PCA) examines the extent to which the information contained in the YR response may be represented by fewer variables, or factors. Previous work using PCA showed that a set of YR measurements on 433 adult human subjects could be represented using factor analysis in terms of five variables, each having significant loadings across approximately one octave in frequency (Levi *et al.*, 1998).

2. Should responses with poor probe fits be excluded?

Previous research showed this variable to be significant in the structure of the YR responses. If the presence of a leak adds measurement noise, then the statistical relationships between YR response and EOAE or ABR responses may be more evident in the subset of responses with a good probe fit.

3. Does knowledge of the middle-ear functioning help explain EOAE and ABR responses?

This question asks whether the YR response accounts for a significant fraction of the variance of the EOAE and ABR responses. If so, then middle-ear functioning, as assessed in the YR response, is intertwined in the interpretation of EOAE or ABR responses. Examining the similarities and dissimilarities between these test types may provide valuable data on the overall functioning of the auditory periphery.

4. Can knowledge of middle-ear functioning account for false-positives in EOAE or ABR testing, i.e., for those ears that have small or absent EOAEs or ABRs in subjects with normal hearing?

This question perhaps has the most clinical, practical relevance for NHS programs. The majority of neonates who fail EOAE hearing screening programs based on absent (or low-level) EOAEs does not have sensorineural hearing loss, meaning they are false positives. It is often assumed that such neonates have a transient middle-ear condition that interferes with the forward transmission of stimulus energy and/or the reverse transmission of the EOAE, if generated, thus leading to an inability to record a detectable EOAE. If the YR test is a measure of middle-ear functioning, it may be possible to classify ears as having present or absent EOAEs on the basis of YR data. The ability of the YR test to classify EOAEs or ABRs as present or absent is well defined even in the absence of the determination of hearing status, and relates to how middle-ear functioning influences these signals.

5. How well do the statistical relationships existing between responses in one sample population generalize to a new sample population?

If the YR test is a robust test of middle-ear functioning, the results should generalize to a new sample population of similar subject characteristics.

II. METHODS

A. Subjects

The data used in the present study consist of measurements in 2766 ears for which all neonatal hearing screening tests (i.e., DPOAE, TEOAE, and ABR tests) as well as middle-ear (YR) tests were completed.

B. Test protocol

The standard neonatal screening protocol for the INHI project has been described (Harrison *et al.*, 2000), as has been the augmentation of the standard protocol to include the YR test (Keefe *et al.*, 2000). In particular, the order of

TEOAE, DPOAE, and ABR tests was randomized, but the YR test always preceded the TEOAE test. The same probe (Otodynamics ILO92) was used to deliver stimuli for all tests, and record EOAE and YR responses. More details on TEOAE, DPOAE, ABR, and YR measurements are described elsewhere (Norton *et al.*, 2000c; Gorga *et al.*, 2000; Sininger *et al.*, 2000; Keefe *et al.*, 2000).

C. Statistical analyses

The data from the two INHI sites were merged and transferred into STATA for Windows software for statistical analyses. The merged set was separated into a training set ($N=1405$) and evaluation set ($N=1361$). The training set was used in the initial analyses to construct various predictors, and the evaluation set was used to test the generalization of these predictors. Subjects in whom data were acquired in only one ear were assigned to the training set. For the remainder of subjects in whom data were acquired in both ears ($N=1361$), individual test results were randomly assigned to one of these sets under the constraint that each set was balanced across ear (left or right) and gender. This was to control for the variability in YR results in neonates due to ear and gender (Keefe, 2000).

III. RESULTS

Section A describes a principal component analysis (PCA) on the training set to reduce the number of variables in the YR response. Each variable in this reduced set of new variables is called a factor. Separate analyses were performed on the full training data set as well as on that portion of the training data set with leaky probe fits excluded, termed the partial training set. Section B describes correlations on the training set between the YR factors and each of the DPOAE and TEOAE levels, and the ABR latencies. These correlations test whether individual YR factors are related to inter-ear differences in cochlear and neural response variables. Section C describes results on the training set using multiple linear regression analysis to test whether the factors describing middle-ear functioning are able to predict the linear patterns of DPOAE, TEOAE, and ABR responses. These regression analyses differ from the simpler correlation analyses insofar as all the YR factors enter as independent variables rather than single factors. Section D describes results on the training set using multivariate logistic regression analyses to test whether the set of YR factors is able to predict the presence or absence of a DPOAE and TEOAE classified on the basis of a threshold signal-to-noise level, and of an ABR response classified by F_{sp} .

Section E describes analyses of how well the test results on the training set, including linear and logistic regression models, generalize to a validation set. It should be noted that intersubject correlations were present between the training and validation sets because the sets contained opposite-ear data from many of the same subjects. The decision to include one ear per subject in the training set allowed the largest possible number of independent measurements in the main data set used for analyses. Nevertheless, separate analyses of the training and validation sets provided information on gen-

eralization that would otherwise have been unavailable, and, in particular, provided a test of whether the results generalize to a new data set composed of opposite-ear data.

Section F describes differences in the results using full and partial data sets, which differ on whether those ears with leaky probe fits are included in the sample. While it is expected that the YR test might be refined in future studies to give real-time feedback on the quality of the probe seal, it is worthwhile to understand how such a leak may influence the ability of the YR response to predict EOAE and ABR responses. Such analyses on the full training set and full validation set summarize the relationships observed between YR, EOAE, and ABR tests without artificially discarding any of the data. The analyses on the partial training set and partial validation sets, which exclude ears with leaky probe fits, summarize the relationships between test variables in a manner appropriate for future applications that might provide real-time control of probe seal.

A. Principal component analyses on the training set

In PCA, each of the 33 YR variables is normalized to have a mean of zero and a standard deviation of 1, and the correlation matrix between these normalized YR variables is calculated. This correlation matrix has a well-defined eigenvector decomposition with a corresponding spectrum of eigenvalues. A common rule in PCA is that factors with eigenvalues greater than 1 are retained, and the remaining factors discarded (Kleinbaum *et al.*, 1988). Adopting this rule gives the desired reduction in the number of factors in the reduced set of variables, which ranged from 5 to 7 for the various YR data sets. The eigenvector coefficients are the factor-loading coefficients of the original YR variables onto the factors: each factor is calculated as the sum across all YR variables of the product of a factor-loading coefficient, which is a number between -1 and 1 , and the normalized YR variable. The factors are orthogonal and thus well suited for subsequent regression analyses. They are sorted by the decreasing variance accounted for in the original YR data set, so that the first factor accounts for the most variance in the YR data, followed by the second factor, etc. This advantage of a reduction in the number of factors is balanced by the disadvantage that there is not necessarily a simple relationship between each factor and the original YR variables. To retain such a simple relationship, a new set of factors is calculated using a varimax rotation of the eigenvectors, which preserves the eigenvalues and orthonormality of the (new) factors, but increases the similarity of individual factors to a relatively small number of the original YR variables. This allows an interpretation of the rotated factors in terms of the YR variables as described below. Before and after rotation, the cumulative variance in the YR variables accounted for by a given set of factors (with eigenvalues exceeding 1) is the same, even though the individual YR variance accounted for by each factor differs following the rotation.

Based on the PCA (with rotation of eigenvectors) of the full training set (including ears with leaky probe fits), there are five significant factors that account for 88% of the variance in the original YR data set. In the partial data set (excluding ears with leaky probe fits), there are seven factors

that account for 84% of the variance. Hence, 5–7 new variables describe most of the variance in the original 33 YR variables.

For the partial training set, the (rotated) factor loadings are visualized by plotting those factor loadings exceeding 0.5 in absolute value as a function of frequency for each of the YR variables, energy reflectance (R), equivalent volume (V), and acoustic conductance (G) (see Fig. 1). The factor loading is represented by the height of each stem, and each stem is labeled by the factor number (1–7). This plot represents the mapping of the largest-magnitude factor loadings onto the YR variables, and preserves the sign of the factor loading. The corresponding variance accounted for by each (rotated) factor is listed in Table I. All factor loadings for the partial training set are listed in Table II, from which the loadings in Fig. 1 are plotted.

Table I summarizes the interpretation of the factors in terms of the YR variables and frequencies, and presents more meaningful names for the variables. For example, the factor $F2$, which plays a key role in the regressions to be described, is named $FRHI$ (and sometimes denoted as $FRHI-2$ with the factor number) to indicate that it is the factor with high loadings on energy reflectance at high frequencies. The factor number was assigned by the statistics software in order of declining variance accounted for in the PCA before rotation, in contrast to the factor names, which give the variables and frequencies over which the factor loadings are largest in magnitude.

This set of names is useful for comparing PCA's on various data sets— $F2$ in a given pair of data sets may have quite different interpretations in terms of factor loadings on the YR variables, but if a factor exists with high loadings on reflectance at high frequencies, then $FRHI$ is said to exist in each data set.

Factor 1 ($FYLO$), which accounts for the largest variance (23%), has large positive loadings on V at frequencies from 0.25–1 kHz and large negative loadings on G from 0.25–0.71 kHz. This means that: (1) an ear with a large V at low frequencies tends to have a large $F1$; (2) an ear with a small G at low frequencies tends to have a large $F1$; (3) $V(f)$ is highly correlated across the lower frequencies; (4) $G(f)$ is highly correlated across the lower frequencies; and (5) $V(f)$ and $G(f)$ are highly inverse correlated at low frequencies (see Table I).

Factor 2 ($FRHI$), which accounts for the next most variance (14%), has large positive loadings on R at frequencies from 2–8 kHz. This means that energy reflectance is highly correlated across the frequencies at and above 2 kHz. It also means that high-frequency reflectance tends to be uncorrelated with low-frequency equivalent volume or conductance, because all factors from a PCA are orthogonal. The evidence underlying such statements is expressed in the YR correlation matrix that is used in the PCA to calculate the loadings.

For the full training set (including ears with leaky probe fits), there are five factors retained, with factor loadings listed in Table III. The factor loadings are plotted for those with magnitudes exceeding 0.5 in Fig. 2. The complete set of factor loadings for the full training set is listed in Table IV, from which the loadings in Fig. 2 are plotted. Ranking each

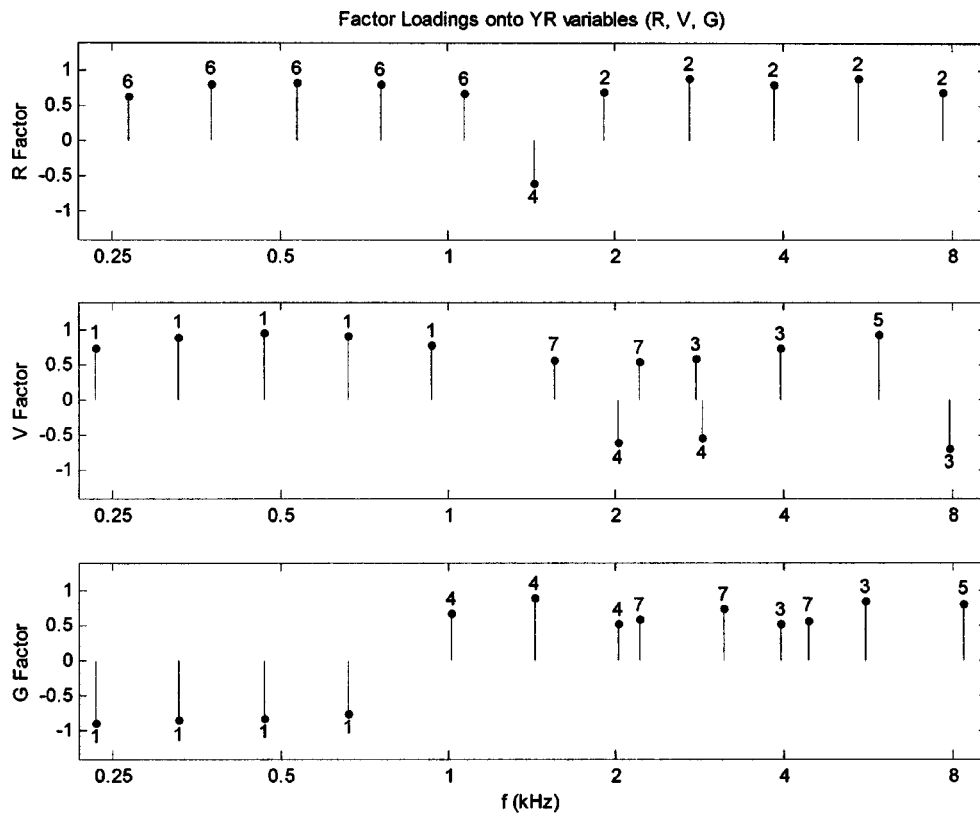


FIG. 1. Those factor-loading coefficients with magnitudes exceeding 0.5 are plotted as a function of YR variable type (R, V, G) and half-octave frequency for the PCA of the training set with leaky ears excluded. The stem height encodes the factor loading. The number above or below each stem indicates the factor number.

factor according to the percentage of variance in the YR data set that it explains, there are similarities and differences in the partial versus full training sets. The factor *FYLO* accounts for approximately the same variance in both sets (23% in Table I, and 25% in Table III), as is the case for

FRHI (14% in Table I, and 11% in Table III), *FYRMI*, and *FRLO*. However, factor *FYHI* accounts for much less variance in the training set with leaky ears excluded (9% in Table I, versus 33% in Table III). The two factors *FY7k-5* and *FYMI-7* in Table I, which do not occur by name in Table III, also account for the least variance in the YR responses in Table I.

TABLE I. PCA results for training set excluding leaky ears.

Factor	% of YR variance	Factor name ^a	Description
1	23%	<i>FYLO</i>	Low-frequency admittance (0.25–1 kHz)
2	14%	<i>FRHI</i>	High-frequency reflectance (2–8 kHz)
3	9%	<i>FYHI</i>	High-frequency admittance (3–8 kHz)
4	11%	<i>FYRMI</i>	Mid-frequency YR (1–2 kHz)
5	7%	<i>FY7k</i>	Admittance near 6–8 kHz
6	13%	<i>FRLO</i>	Low-frequency reflectance (0.25–1 kHz)
7	8%	<i>FYMI</i>	Midfrequency admittance (1.4–4 kHz)
Total	84%		

^aThe first character of each name is *F* for factor; the next character(s) identify the variable that predominates—*Y* for admittance (factors 1, 3, 5, 7), *R* for reflectance (factors 2, 6), or YR for both admittance and reflectance (factor 4); the last two characters identify the frequency range that predominates—*LO* for low frequencies, *MI* for middle frequencies, *HI* for high frequencies, or *7k* for frequencies near 7 kHz. Note that the complex admittance *Y* includes both the acoustic conductance *G*, which is the in-phase component of *Y*, and the equivalent volume *V*, which is proportional to the ratio of the out-of-phase component of *Y* and the frequency. The factor loadings of *G* and *V* are plotted in Fig. 1, and serve to define the *Y*-related factors.

B. Correlations on the training set

Correlation analysis is well suited for the study of the relationships between EOA levels and each of the factors (Kleinbaum *et al.*, 1988). Using the partial training set, those correlation coefficients that differ significantly from zero are illustrated in Fig. 3. The correlation for each factor is plotted versus the f_2 frequency of the DPOAE or the center frequency of the TEOAE half-octave-averaged responses.

The factor *FRHI* has the largest magnitude, but a negative correlation with both DPOAE and TEOAE levels at 2, 3, and 4 kHz. The correlation is more negative with increasing frequency, with a minimum of -0.47 for the TEOAE level at 4 kHz. Therefore, the EOA level decreases as high-frequency energy reflectance increases. These correlations are defined between EOA variables in the 2–4-kHz range and a factor highly correlated to reflectance in the same 2–4-kHz range.

For EOAs below 2 kHz, there are a number of factors with weaker correlations. At 1.5 kHz, the DPOAE level has a correlation of -0.20 with *FRHI* but a larger-magnitude correlation of 0.24 with *FYRMI*. The TEOAE level has a corre-

TABLE II. Factor loadings for partial training set.

	Frequency (kHz)	<i>FYLO-1</i>	<i>FRHI-2</i>	<i>FYHI-3</i>	<i>FYRMI-4</i>	<i>FY7k-5</i>	<i>FRLO-6</i>	<i>FYMI-7</i>
Reflectance	0.25	0.302	0.299	0.222	-0.109	0.009	0.620	0.182
	0.35	0.322	0.188	0.172	-0.061	0.040	0.810	0.091
	0.50	0.364	0.063	0.189	-0.079	0.114	0.830	0.023
	0.71	0.377	0.052	0.220	-0.156	0.106	0.805	0.109
	1.00	0.282	0.079	0.014	-0.388	0.031	0.664	0.258
	1.40	0.034	0.338	0.084	-0.604	-0.135	0.411	0.310
	2.00	-0.073	0.698	0.080	-0.452	-0.204	0.128	0.040
	2.83	-0.002	0.887	0.026	-0.107	-0.039	0.058	-0.216
	4.00	0.098	0.801	0.004	-0.055	0.332	0.086	-0.199
	5.66	-0.032	0.891	-0.016	-0.138	0.136	0.087	-0.017
Equiv. volume	8.00	-0.037	0.697	0.160	-0.046	-0.285	0.225	-0.079
	0.25	0.745	0.103	0.223	-0.085	0.079	0.001	0.250
	0.35	0.901	0.102	0.177	-0.015	0.034	0.070	0.219
	0.50	0.948	0.001	0.075	0.078	0.052	0.143	0.099
	0.71	0.908	-0.094	0.062	0.221	0.071	0.163	0.062
	1.00	0.773	-0.211	0.079	0.402	0.058	0.224	0.163
	1.40	0.393	-0.320	0.030	-0.021	0.118	0.447	0.572
	2.00	0.093	-0.059	0.306	-0.618	0.164	0.274	0.545
	2.83	0.132	0.388	0.584	-0.550	0.066	0.004	0.109
	4.00	0.092	0.365	0.744	-0.070	0.267	0.121	0.082
Conductance	5.66	0.127	0.126	-0.010	-0.079	0.923	0.056	-0.112
	8.00	0.068	0.298	-0.695	-0.109	0.223	-0.318	0.103
	0.25	-0.885	-0.106	0.108	0.289	0.000	-0.194	0.163
	0.35	-0.854	-0.047	0.181	0.275	-0.011	-0.225	0.246
	0.50	-0.830	0.002	0.200	0.300	-0.035	-0.235	0.302
	0.71	-0.760	0.012	0.196	0.404	-0.038	-0.280	0.275
	1.00	-0.441	-0.006	0.251	0.668	-0.061	-0.353	0.039
	1.40	-0.042	-0.240	0.040	0.896	-0.071	-0.088	0.085
	2.00	-0.085	-0.466	-0.056	0.514	0.014	0.232	0.584
	2.83	-0.202	-0.422	0.195	-0.087	-0.045	0.183	0.729
	4.00	-0.121	-0.031	0.521	-0.036	-0.415	0.065	0.572
	5.66	-0.074	-0.013	0.848	0.076	0.151	0.298	0.196
	8.00	0.017	-0.079	0.247	0.000	0.812	0.174	0.158

lation with *FRHI* of -0.18 , which is approximately twice as large in magnitude as any other correlation at this frequency. Results are difficult to interpret at 1 kHz, a condition in which the EOAEs were dominated by noise. In the 2–4-kHz range, the other factors have weak correlations with EOA level, while *FRHI* remains the most important factor.

For ABR responses, correlations with the factors were calculated for $L_V(30)$, $L_V(70)$, $L_I(70)$, and $L_{V-I}(70)$. While significant correlations were obtained for some ABR variables with all factors except *FRLO*, the largest correlations are 0.30 between *FRHI* and $L_V(30)$, and 0.28 between *FRHI* and $L_I(70)$. This means that ABR latencies increase as high-frequency reflectance increases.

TABLE III. PCA results for full training set.

Factor	% of YR variance	Factor name	Description
1	33%	<i>FYHI</i>	High-frequency admittance (2–8 kHz)
2	25%	<i>FYLO</i>	Low-frequency admittance (0.25–1 kHz)
3	13%	<i>FRLO</i>	Low-frequency reflectance (0.25–1 kHz)
4	11%	<i>FRHI</i>	High-frequency reflectance (2–8 kHz)
5	6%	<i>FYRMI</i>	Midfrequency YR (1–2 kHz)
Total	88%		

C. Linear regressions on the training set

Multiple linear regressions (Kleinbaum *et al.*, 1988) were performed on the training set to test the extent to which the set of YR factors predicts the patterns of DPOAEs, TEOAEs, and ABRs by calculating the total variance accounted for R^2 (this R^2 should not be confused with energy reflectance R). If R^2 differs significantly from zero, this is evidence that inter-ear variations in the EOA level and ABR are explained, at least in part, by inter-ear variations in middle-ear functioning. The set of factors for the partial or full training set were inputs to each regression, with DPOAE SPL, TEOAE SPL, and ABR latencies selected as dependent variables in separate regressions. The R^2 is plotted in Fig. 4 for the partial and full training sets for EOA levels (solid line plots in top two rows) as a function of frequency, and for ABR latencies (filled bar graphs in bottom row).

For EOA levels, R^2 increases with increasing frequency and is similar for DPOAEs and TEOAEs. The significant linear regression coefficients for the partial training set are listed in Table V. These provide information on the parts of the YR response that individually account for inter-ear variations of EOA level and ABR tests. The structures of the coefficients are similar for DPOAE and TEOAE responses. As with the correlations, more variance in the EOA levels is explained as frequency increases, with as much as 28% of the variance explained at 4 kHz for EOA levels in the partial training

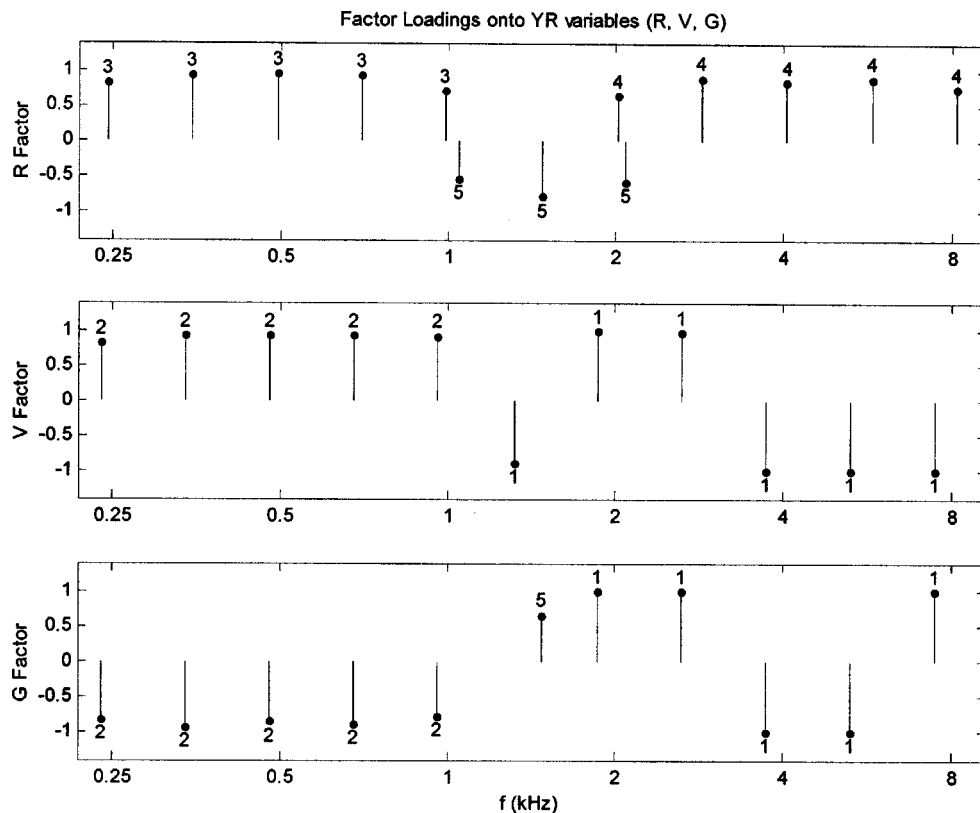


FIG. 2. Those factor-loading coefficients with magnitudes exceeding 0.5 are plotted as a function of YR variable type (R, V, G) and half-octave frequency for the PCA of the full training set (including leaky ears and ears with good probe fits). The stem height encodes the factor loading. The number above or below each stem indicates the factor number.

set. Also in common with the correlations, the factor *FRHI* accounts for most of the variance, but other factors play a role. The comparative role of *FRHI* is summarized by considering the correlation value -0.47 between TEOAE level and *FRHI* at 4 kHz (Fig. 3), for which its squared correlation $R^2 = (-0.47)^2 = 0.22$. The corresponding $R^2 = 0.28$ for the multiple regression on TEOAE level in the partial training set (Fig. 4), so that *FRHI* in this example accounts for 22% of the variance, leaving the other factors to account for the remaining 6%. These are additive because the factors are orthogonal.

Table V shows that for the TEOAE response at 4 kHz, *FRHI*, *FYRMI*, *FRLO*, and *FYMI* are significant, and the steepest slope is that for *FRHI*. The relative steepness of slope (-4.22) is due to the large magnitude of the corresponding correlation (-0.47). For the other factors in Table V for both EOA types, no factor is significant at the 0.05 level in both EOA types at 1 kHz, while the factors *FRHI* and *FYRMI* are the most important at frequencies at and above 1.5 kHz, except for the stronger effect of *FYMI* than *FYRMI* at 3 and 4 kHz. The factors *FYLO*, *FYHI*, *FY7k*, and *FRLO* sometimes differ significantly from 0, but their slope coefficients never exceed 1.05. While *FRHI* for high-frequency reflectance is the most important regression variable at and above 1.5 kHz, the other factors encoding admittance and reflectance make significant contributions.

Before performing the regressions on the ABR latencies, ears for which latency data were absent for $L_V(30)$, $L_V(70)$, or $L_I(70)$ were eliminated. Analyses on ears with valid la-

tency measurements included 1295 ears in the full training set, and 1158 ears in the partial training set. Overall, the results for the ABR dependent variables show less variance accounted for by the YR factors than for EOA-dependent variables (Fig. 4). In the full training set, the highest $R^2 = 0.11$ occurs for $L_I(70)$. $L_V(30)$ accounts for the next-highest amount of variance ($R^2 = 0.09$). The corresponding R^2 is larger in the partial training set than that for the full training set for each latency, approximately 0.13–0.15 for wave I and wave V latencies. The R^2 for $L_{V-I}(70)$ is always smaller than that for any of the wave V and wave I latencies, which means that the YR response predicts less of the variance of the latency difference than either of the absolute latencies.

The corresponding ABR slope coefficients are more than an order of magnitude smaller than those for DPOAE and TEOAE responses above 1 kHz (Table V), consistent with the fact that the YR response predicts less of the overall variance of the ABR latencies. The three most important factors for predicting ABR latencies are *FRHI*, *FYHI*, and *FYMI*. These are all factors encoding the mid- to high-frequency portions of the YR response. The slope coefficients for predicting wave V and wave I latencies have similar signs, but the sign of *FRHI* changes polarity for predicting $L_{V-I}(70)$. Increasing high-frequency reflectance increases wave I and wave V latencies, but slightly decreases $L_{V-I}(70)$, meaning that wave I latency increases more than wave V latency. The admittance factors *FYHI* and *FYMI* are of comparable or greater importance than the reflectance fac-

TABLE IV. Factor loadings for full training set.

	Frequency (kHz)	<i>FYHI-1</i>	<i>FYLO-2</i>	<i>FRLO-3</i>	<i>FRHI-4</i>	<i>FYRMI-5</i>
Reflectance	0.25	0.055	-0.137	0.817	0.207	-0.035
	0.35	0.051	-0.133	0.928	0.138	-0.018
	0.50	0.068	-0.075	0.948	0.059	-0.037
	0.71	0.075	-0.030	0.935	0.036	-0.155
	1.00	0.053	0.062	0.709	0.001	-0.542
	1.40	0.053	-0.070	0.404	0.258	-0.791
	2.00	0.033	-0.121	0.111	0.654	-0.585
	2.83	0.028	-0.061	0.047	0.901	-0.159
	4.00	0.021	0.086	0.127	0.842	-0.010
	5.66	0.076	-0.067	0.104	0.900	-0.105
	8.00	0.049	-0.068	0.176	0.750	-0.002
Equiv. volume	0.25	0.137	0.824	-0.196	0.014	0.031
	0.35	-0.001	0.935	-0.169	-0.042	0.071
	0.50	-0.118	0.935	-0.141	-0.040	0.051
	0.71	-0.136	0.929	-0.113	-0.062	0.101
	1.00	-0.060	0.918	-0.057	-0.114	0.154
	1.40	-0.887	0.393	0.007	-0.118	0.019
	2.00	0.991	0.071	0.049	0.012	-0.059
	2.83	0.974	0.112	0.043	0.083	-0.076
	4.00	-0.998	0.037	-0.028	-0.019	0.014
	5.66	-0.998	0.032	-0.030	-0.024	0.014
	8.00	-0.998	0.030	-0.033	-0.024	0.013
Conductance	0.25	-0.108	-0.822	0.025	0.009	0.079
	0.35	0.085	-0.936	0.006	-0.014	0.071
	0.50	0.362	-0.854	-0.037	-0.008	0.127
	0.71	-0.212	-0.894	-0.093	-0.025	0.170
	1.00	0.100	-0.774	-0.168	-0.014	0.455
	1.40	-0.198	-0.408	-0.039	-0.268	0.658
	2.00	0.989	-0.067	0.052	-0.042	0.031
	2.83	0.990	-0.078	0.059	-0.035	-0.026
	4.00	-0.991	-0.015	-0.007	-0.040	0.007
	5.66	-0.998	0.028	-0.026	-0.025	0.015
	8.00	0.998	-0.028	0.038	0.023	-0.011

tor; at frequencies at and above 1.5 kHz, decreasing equivalent volume and decreasing acoustic conductance increases each latency and the V-I latency difference.

D. Using YR factors to classify DPOAE, TEOAE, and ABR results

This section describes the extent to which the YR responses were able to classify EOAEs and ABRs as present or

absent. This test, which is based on a logistic regression, is relevant to classifying ears in hearing screening tests that are false positives on EOAE or ABR tests. The EOAE responses were measured across frequency, and their corresponding signal-to-noise ratios (SNR expressed as a level in dB) at each frequency were used as dependent variables to be classified as present or absent by the YR factors. The INHI study used the minimum EOAE SNR at 2, 3, and 4 kHz to predict

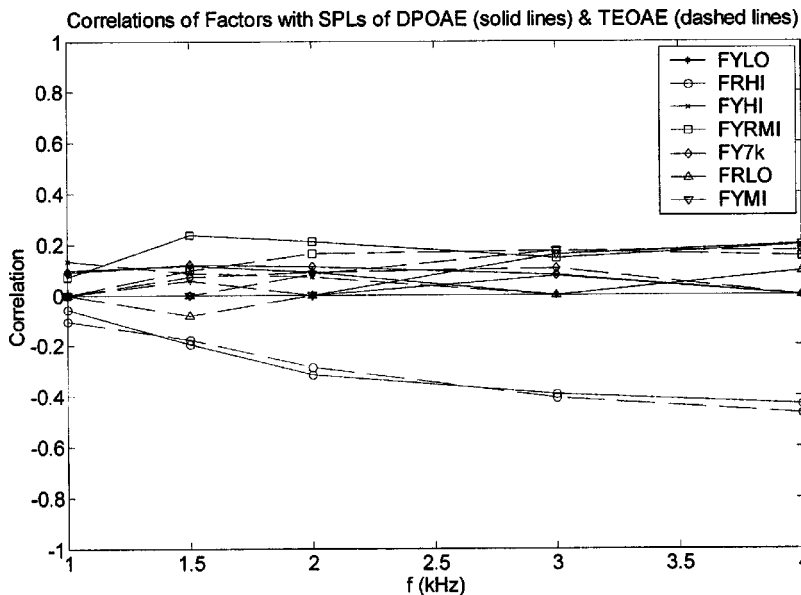


FIG. 3. Correlations of factor scores and DPOAE SPL, and of factor scores and TEOAE SPL for each of the seven factors in the partial training set. Only correlations significantly different than zero are plotted. The largest magnitude correlations occur for factor *FRHI* (open circles) for both DPOAEs and TEOAEs. The legend shows the marker type associated with each factor, while the line style represents correlations with DPOAE (solid lines) or with TEOAE (dashed lines).

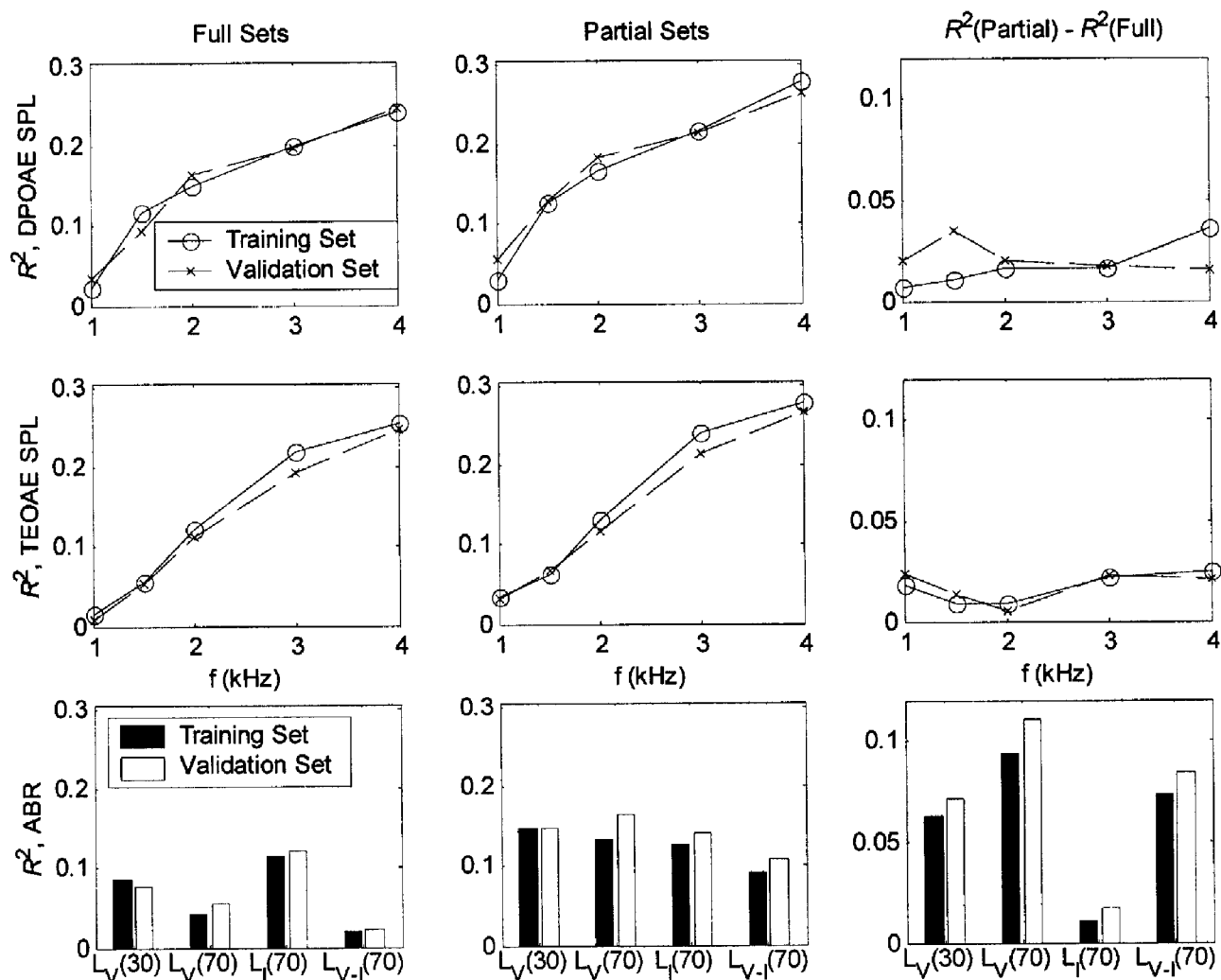


FIG. 4. The total variance accounted for (R^2) by the multiple regression analyses on the factors is plotted for the full training and validation sets (left column), and the partial training and validation sets (middle column). The difference in the total variances accounted for between the partial and full training sets, and the difference between the partial and full validation sets are plotted (right column). The solid lines denote training set analyses, and the dashed lines denote validation set analyses. The top row shows R^2 for DPOAE SPL as the dependent regression variable, and the middle row shows R^2 for TEOAE SPL as the dependent regression variable, both functions across frequency for the dependent variables. The bottom row shows R^2 for the ABR latencies as dependent regression variables as defined on the bar graphs by the ordinate labels for the training and validation sets.

auditory status as defined by the pure-tone audiograms at 2 and 4 kHz (Norton *et al.*, 2000b). To address the clinical issue of whether middle-ear functioning influences EOA responses in NHS programs, this broadband EOA SNR variable was also selected as a dependent EOA variable.

Using the training set, the YR factors were used to predict whether DPOAE and TEOAE responses were present or absent based on a threshold SNR criterion. Each SNR was defined in accordance with the methodology of the INHI Study. Specifically, the mean noise level was used for TEOAE measurements, whereas the noise plus 2 standard deviations was used to calculate DPOAE SNR. To control for EOA type and test frequency, the threshold of each EOA SNR was selected to achieve 80% specificity, i.e., the threshold was selected for which 80% of responses equaled or exceeded the threshold, and 20% of responses did not. This criterion was not practical for the EOA responses at 1 kHz, because the SNR was zero for too many cases—in the partial training set, 515 of 1274 ears had SNR=0 for DPOAEs, and 543 of 1274 ears had SNR=0 for TEOAEs.

Thus, the criterion for the EOA responses at 1 kHz was SNR=0 for absent EOAs, and SNR>0 for present EOAs. Except for 1 kHz, the constraint of fixing the specificity at 80% allowed a consistent comparison across frequency and EOA type.

Using the training set, the YR factors were used to predict whether an ABR response was present based on a threshold F_{sp} value selected so that 80% of responses were classified as present, and the remaining responses as absent. This facilitated comparisons between YR classifiers of EOAs and ABRs. This same criterion of 80% specificity in the DPOAE, TEOAE, and ABR tests was used in the INHI project to compare their predictions of auditory status (Fig. 10 of Norton *et al.*, 2000b), although for a larger set of ears. This is in spite of the fact that a 80% specificity is too low for practical hearing screening program.

The independent variables in each logistic regression were the YR factors in the full and partial training sets. A logistic regression was used to predict each SNR or F_{sp} as present or absent based on a logit function defined as a linear

TABLE V. Linear regression coefficients for partial training set that are significantly different from 0. Coefficients with $p < 0.01$ are in bold or with $p < 0.05$ are in normal font.

	<i>FYLO-1</i>	<i>FRHI-2</i>	<i>FYHI-3</i>	<i>FYRMI-4</i>	<i>FY7k-5</i>	<i>FRLO-6</i>	<i>FYMI-7</i>
DPOAE							
f (kHz)							
1.0	0.85	-0.51		0.64	0.82		
1.5	1.02	-1.72		2.06	1.05	-0.47	
2.0	0.81	-2.87		1.92	1.01		
3.0	0.51	-3.82	0.74	1.41	0.78		1.57
4.0		-4.76	0.53	2.17		1.05	2.18
TEOAE							
f (kHz)							
1.0		-0.64	0.82				
1.5	0.41	-1.32	0.64	0.72	0.55	-0.61	
2.0		-2.23	0.54	1.25	0.70		0.64
3.0		-3.36		1.45	0.86		1.45
4.0		-4.22		1.38		0.45	1.57
ABR							
Type							
$L_V(30)$	-0.03	0.12	-0.12		-0.03		-0.12
$L_V(70)$	-0.03	0.04	-0.12				-0.10
$L_I(70)$		0.07	-0.02	-0.02			-0.03
$L_{V-I}(70)$		-0.03	-0.10				-0.07

combination of YR factors. The classification of the logit predictor was assessed by calculating the nonparametric area under the relative operating characteristic (ROC) curve, which is sometimes denoted for brevity as the “ROC area.” Nonparametric tests of significance were based on the standard error of the area under the ROC curve (Cleves, 2000; DeLong *et al.*, 1988).

The results of two approaches were compared to assess classification of the broadband EOAE responses. The *multifrequency logit* used the YR factors as independent variables to classify the broadband SNR variable described above (minimum EOAE SNR at 2, 3, and 4 kHz). A logistic regression was performed on this dependent variable. The second approach defined a *minimum logit* as the minimum of the three single-frequency logit functions that were calculated at

2, 3, and 4 kHz, and used this minimum logit to predict the broadband EOAE SNR. In this approach, no additional logistic regression was performed. The expectation was that the multifrequency logit would outperform the minimum logit as a classifier, because it used an explicit logistic regression over the broadband dependent variable. Use of the minimum logit tested the extent to which single-frequency logits can be combined to form a broadband predictor.

For classifying DPOAE and TEOAE responses, the ROC areas increase with increasing frequency from values near 0.62–0.66 at 1 kHz to 0.74–0.78 at 4 kHz (Fig. 5). The ROC areas for DPOAE and TEOAE responses are generally similar. The broadband ROC areas of the multifrequency and minimum logits vary slightly by EOAE type; e.g., they range in the partial sets from 0.77–0.79 for DPOAEs and 0.73–

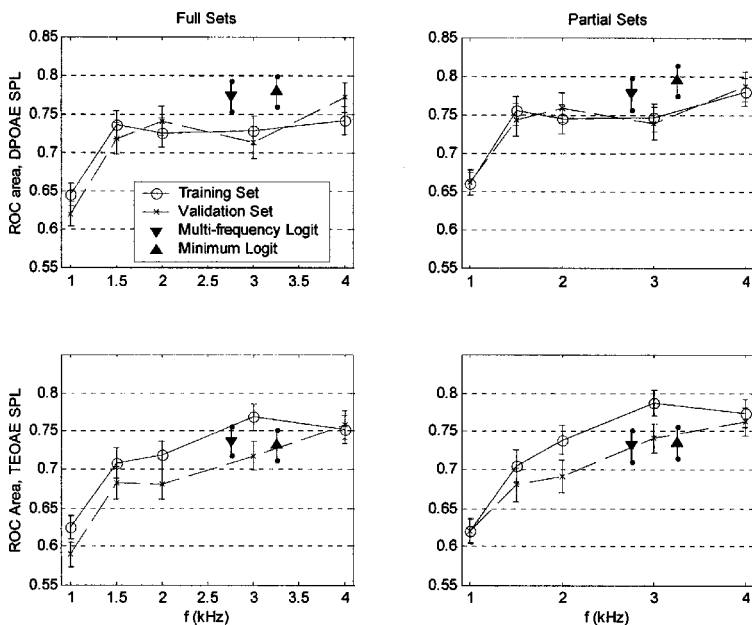


FIG. 5. The areas under the ROC curve, which are based on the logit functions predicting the DPOAE (top row) and TEOAE (bottom row) responses from the YR factors, are plotted for the full training and validation sets (left column solid line and dashed line curves, unfilled markers), and the partial training and validation sets (right column solid line and dashed line curves, unfilled markers). The filled markers show the area under the ROC curve (and standard error as error bar) for the multifrequency logit and minimum logit functions to predict DPOAE (top row) and TEOAE (bottom row) responses in the 2–4-kHz bandwidth. The standard error of the area under the ROC curve is shown as an error bar (\pm standard error) on the training and validation set curves.

0.74 for TEOAEs (note that Fig. 5 shows only the broadband ROC areas for the validation set, which are slightly less than those for the training set). The standard errors range from 0.015 to 0.023 across all EOAE responses in the training set. There is no significant difference between the areas of the multifrequency and minimum logits for any condition. Thus, both predictors have similar classification ability. The broadband ROC areas exceed the single-frequency ROC areas at 2, 3, and 4 kHz for DPOAEs, but tend to be less than the single-frequency ROC areas for TEOAEs.

The relation of the logit function to the underlying factors is summarized in Table VI for the case of the multifrequency logit functions used to classify the broadband EOAE responses. The slope coefficient b in the logistic regression logit function is shown in the table for each factor, and the corresponding odds ratio is calculated as $\exp(b)$. While all seven factors were used in the logit function to calculate ROC areas, only those slope coefficients with a Wald p value <0.05 are shown. The odds ratio is defined as the ratio of the odds of predicting an absent EOAE for a unit change in its factor to the odds of predicting an absent EOAE in the control condition without the unit change (Hosmer and Lemeshow, 2000). A unit change in each factor corresponds to a change of 1 standard deviation in that factor since each factor score is normalized. Such a unit change amounts to a substantial step change in terms of the full distribution of responses. Thus, for positive slope coefficients, a factor with an odds ratio much larger than 1 is an important predictor of an absent EOAE, and a factor with an odds ratio much smaller than 1 is an important predictor of a present EOAE. The relation is inverted for negative slope coefficients. Factors with odds ratios close to 1 are minor contributors to the predictor. To simplify interpretation, Table VI also lists the inverse odds ratio (1/odds ratio). For DPOAEs, the most important factor is *FRHI* (odds ratio of 2.44). The 95% ranges of the remaining factors overlap, but in rank order the next two most important variables are *FYRMI* (inverse odds ratio of 1.84) and *FYLO* (inverse odds ratio of 1.40). The results

for TEOAEs are similar with respect to the slope coefficients and odds ratios.

For classifying ABRs as present or absent, the corresponding areas under the ROC curve are only 0.58 for both partial and full sets, with standard errors of 0.020. These areas demonstrate relative poor performance in using YR responses to classify the ABR response. The significant factors in the ABR predictor are *FRHI* (odds ratio 1.33) and *FYRMI* (inverse odds ratio 1.27).

The poor classification performance of the YR factors on ABR *Fsp* appears to contrast with the results described earlier in which the YR factors accounted for significant fractions of the variance in the ABR latencies. This issue was investigated further for the partial set by assessing the classification performance of the YR factors on ABR $L_V(70)$. This latency was selected because it is the least influenced by noise. Middle-ear dysfunction increases the latency of wave-V, mainly by attenuating the forward transmission of stimulus energy through the middle ear. If there is middle-ear dysfunction and if the YR factors are sensitive to middle-ear functioning, then the YR factors should predict whether $L_V(70)$ is larger than some threshold latency, which is defined as the criterion for dysfunction.

A confounding effect is that $L_V(70)$ decreases with increasing conceptional age (CA) (Gorga *et al.*, 1987). This confound was addressed by including the variation in threshold latency with CA. The responses were sorted by CA, and grouped into nine categories with equal numbers (140) of responses. The 80th percentile of $L_V(70)$ was calculated within each category and used as the threshold duration. For a given CA, if $L_V(70)$ exceeded its 80th percentile, then the ABR was classified as “absent,” otherwise the response was “present.” If it was impossible to estimate a latency, the response was discarded from the analysis. The observed variation in the mean $L_V(70)$ across CA is in accord with the results of Gorga *et al.* (1987), obtained at click stimulus levels of 60 and 80 dB HL. The mean $L_V(70)$ is 7.64 ms at a mean CA of 34 weeks (CA range 31.7–35.1 weeks), and

TABLE VI. Significant logistic regression coefficients and odds ratios for partial training set. Wald coefficients $p < 0.01$ are in bold or with $p < 0.05$ are in normal font.

	<i>FYLO-1</i>	<i>FRHI-2</i>	<i>FYHI-3</i>	<i>FYRMI-4</i>	<i>FY7k-5</i>	<i>FRLO-6</i>	<i>FYMI-7</i>
DPOAE: Multifrequency logit							
f (kHz)							
Slope coefficient	-0.34	0.89	0.19	-0.61	-0.23		
Odds ratio	0.71	2.44	1.21	0.54	0.80		
Inverse odds ratio	1.40	0.41	0.83	1.84	1.26		
95% range of odds ratio	0.61–0.83	2.09–2.86	1.04–1.42	0.46–0.64	0.68–0.93		
TEOAE: Multifrequency logit							
f (kHz)							
Slope coefficient	-0.30	0.90		-0.49	-0.16	-0.21	-0.34
Odds ratio	0.74	2.47		0.61	0.85	0.81	0.71
Inverse odds ratio	1.35	0.41		1.64	1.17	1.24	1.41
95% range of odds ratio	0.64–0.88	2.12–2.87		0.52–0.72	0.73–0.99	0.69–0.95	0.60–0.84
ABR: Logit							
Slope coefficient		0.29		-0.24			
Odds ratio		1.33		0.79			
Inverse odds ratio		0.75		1.27			
95% range of odds ratio		1.18–1.51		0.69–0.90			

decreases to 6.84 ms at mean CA of 48 weeks (CA range 44.3–53.3 weeks). The 80th percentile of $L_V(70)$, which is the threshold latency for dysfunction, is 7.99 ms at 34 weeks, and decreases to 7.09 ms at 48 weeks. It should be noted that the presence of age effects was examined in other analyses of YR, EOAE, and ABR responses, but was not found to be an important variable beyond the ones discussed in this report.

The latency $L_V(70)$ was classified on the partial training set using a logit function with *FYLO-1*, *FRHI-2*, and *FYMI-7* as significant factors. The corresponding ROC area is 0.64, which is larger than that for classifying the *Fsp* as present or absent.

E. Test of generalization

Generalization was assessed on both the linear and logistic regression analyses between the training and validation sets. Summarizing the analysis steps thus far, the PCA of the YR responses was performed on the training set and the factors obtained were used as independent variables in multiple linear regressions to predict dependent variables drawn from the DPOAEs, TEOAEs, and ABRs. These regressions were performed on the same training set for which the factors were defined. Each PCA provided factor loadings defining each factor as a linear combination of YR variables. Each regression analysis provided regression coefficients defining each predictor variable as a linear combination of the factors.

To test how these linear regression analyses generalize to the validation data set, a twofold process is necessary to calculate both the new factors and the new predictor variables. The factor loadings derived from the PCA on the training set (as illustrated in Figs. 1 and 2 for the most important loadings, and listed in Tables II and IV for all loadings) were used to calculate the factors on the validation set. No PCAs were performed on the validation set. The regression coefficients derived from the multiple regression analyses on the training set (for which the significant coefficients are listed in Table V for the partial training set) were used to calculate the predictor variables of DPOAEs, TEOAEs, and ABRs on the validation set. No multiple linear regressions were performed on the validation set. Both the factor loadings and the regression coefficients must generalize to the new data set in order for the predictor to be considered robust. The relative variance accounted for R^2 in the *validation* set is calculated based on the sum of squares of errors between the predictor variable, as calculated above, and the observed data. The extent to which the predictors from the training set generalize to the validation set is assessed by the extent to which R^2 is in agreement for the two data sets.

The results in Fig. 4 show excellent generalization for both full and partial sets in predicting DPOAE and TEOAE levels, and excellent generalization for predicting ABR latencies. In most cases, the R^2 values are similar between the validation and training sets, while, in some cases, the R^2 for the validation set exceeds that for the training set. This means that the factor loadings defined on the YR training set are equally applicable to the YR validation set, and that the relationships between YR responses and EOAE/ABR results generalize to novel data.

To test how the logistic regression analyses generalize to the validation data set, a similar twofold process is used. The factor loadings are calculated for the validation set as described above. The logit regression coefficients derived from the logistic regression analyses on the training set are used to calculate the logits of DPOAEs, TEOAEs, and ABRs on the validation set (some of these coefficients are listed in Table VI for the multifrequency logit of the EOAE partial training sets, and the ABR partial training set). Thus, no logistic regressions were performed on the validation set. The performance of the logit functions on the validation set is calculated in terms of the area under the ROC curve and compared to performance on the original training set for both full and partial subsets of responses.

For classifying DPOAE and TEOAE responses in the validation set, the ROC areas tend to increase with increasing frequency from values near 0.59–0.66 at 1 kHz to 0.74–0.78 at 4 kHz (Fig. 5). The ROC areas for the validation and training sets are similar from 1–1.5 kHz, but the ROC areas for the TEOAE validation sets may be smaller than those for the TEOAE training sets at 3 kHz. The broadband ROC areas of the multifrequency and minimum logits may be larger for DPOAEs than TEOAEs; e.g., they range from 0.77–0.79 for DPOAEs and 0.73–0.74 for TEOAEs (Fig. 5). The broadband ROC areas are slightly larger than the single-frequency ROC areas for DPOAEs, but the broadband and single-frequency ROC areas are similar for TEOAEs (based on comparisons on the validation sets). EOAEs are classified by the YR response at least as well across a bandwidth of frequencies as compared to single frequencies.

The dependent variables used in classifying ABR responses were the *Fsp* value and $L_V(70)$. Both variables were used because *Fsp* was the primary ABR variable in the INHI study for determining whether a response was present or absent, and $L_V(70)$ was chosen because the YR factors performed relatively well in linear regressions predicting this latency as described earlier. The areas under the ROC curve for classifying *Fsp* are only 0.54 for the partial validation set and 0.56 for the full validation set, with standard errors close to 0.020. These areas demonstrate performance not much larger than chance levels in using YR responses to classify whether an ABR *Fsp* response is present or absent. The areas under the ROC curve for classifying $L_V(70)$ are 0.64 for the partial validation set, the same area as for the training set. The YR response weakly classifies ABR latencies in a manner that generalizes to a new data sample.

In summary, the ability of YR responses to classify EOAE responses generalized well in both linear and logistic analyses. The ability of YR responses to classify ABR responses generalized in a meaningful way only for latency responses, and not for *Fsp* responses.

F. Comparison of full and partial sets

Analyses were performed on both full and partial data sets, with the latter defined in order to examine the influence of excluding those ears with leaky probe fits. Independent PCAs were described for both full and partial data sets, with seven factors obtained for the partial set (Tables I and II) and

five factors obtained for the full set (Tables III and IV). The results from the linear and logistic regressions show differential effects in the full and partial sets.

The R^2 was calculated in the linear regressions for the full and partial sets of EOAEs, and the difference in variance $\Delta R^2 = R^2(\text{partial}) - R^2(\text{full})$ is plotted in Fig. 4 (top and middle rows, right column). While the trends with frequency are similar in both the full and partial training sets, ΔR^2 is always positive, meaning that more variance is accounted for in the partial training set. This observation is consistent with additional noise being present in those ears with leaky probe fits that were included in the full training set. The effect is robust in generalizing to a new sample population for both DPOAEs and TEOAEs.

The ΔR^2 is positive for all ABR latencies (Fig. 4, bottom right plot), which is interpreted in regard to the confounding effect of leaky probe fits in the same manner as for EOAEs. However, the relative change in the explained variance of $L_V(70)$ is 0.11, which is a larger change than that for other EOAE or ABR variables.

The logistic regressions to test the performance of the YR factors in classifying EOAE and ABR responses were also performed for both full and partial sets. The ROC areas for the full and partial sets are similar for EOAE responses (Fig. 5).

In summary, the YR factors are better predictors of the EOAE levels in the partial set than the full set. The classification performance is similar for classifying EOAEs in the partial and full sets.

IV. DISCUSSION

The YR response is an input frequency response measurement at a probe location in the ear canal. As described in the Introduction, inter-ear variations in this response indicate inter-ear variations in how the middle ear and ear canal receive, absorb, and transmit sound energy. The structure of the YR response, viewed as an overall response pattern, provides indirect information on middle-ear transmission to the extent that it is able to predict inter-ear variations in EOAE levels and ABR latencies.

A. Principal component analyses

It is important to determine the number of independent variables comprising the original YR response, because a reduced number of variables simplifies subsequent analyses. The PCA determines that 5–7 factors, or orthogonal variables, are sufficient to capture most of the variance in the 33 variables of the YR response—84% of the variance in the partial training set and 88% in the full training set (Tables I and III). The raw data in the INHI project were spectral measurements of the YR response at frequency bins more narrowly spaced than a half-octave. In the INHI project, averaging within each half octave was judged sufficiently narrow in frequency to capture the essential features of the YR response, minimize the overall data storage requirements in the project database, and limit the number of variables that might be used in subsequent analyses. The usefulness of the half-octave spacing is confirmed by the observation that most factors have a bandwidth composed of a number of

contiguous half-octaves over which the factor loadings are large (Figs. 1 and 2). The sufficiency of half-octave spacing has also been confirmed by the PCA results of Levi *et al.* (1998) in adult normal-hearing ears, in which the inputs to the PCA were 1/12th-octave YR responses. It might be preferable to calculate the factors with PCA using such a finer suboctave spacing; the resulting retained factors would be expected to be approximately the same in number, but their factor loadings would be calculated with improved accuracy.

The factors for the full training set contain a factor encoding information about probe fit. Given that a large negative V at low frequencies (0.25–1 kHz) can be used as a criterion for excluding leaky ears (Keefe *et al.*, 2000), the factor *FYLO* should classify leaky ears equally well. This hypothesis is supported in the full training set in the correlations between *FYLO* and V at low frequencies (0.25–1 kHz), which range from 0.88 to 0.92 with a mean of 0.90. No other correlation coefficient magnitude exceeds 0.18 between any other factor and V at frequencies up to 1 kHz. This is not surprising because the factor loadings of *FYLO* for V (Fig. 2) take the form of a low-pass filter up to 1 kHz, and the probe-fit criterion is based on the average V up to 1 kHz. Results show that *FYLO* correctly classifies the ears with respect to probe fit with an area under the ROC curve of 0.995.

This suggests that *FYLO* in the full training set may be dominated by the quality of the probe fit; there remain four other factors to assess middle-ear functioning, but these factors may also be influenced by probe fit. In contrast, with the exclusion of the ears with leaky probe fits, all seven factors in the partial training set describe variations in ear canal and middle-ear functioning. In this sense, they may provide a better representation of middle-ear functioning than the corresponding factors calculated on the full training set.

Some factors are similar in both full and partial training sets. The three factors that are relatively consistent in terms of the YR variance accounted for in the partial and full training sets (see Tables I and III) are strongly loaded on low-frequency admittance (*FYLO*), low-frequency reflectance (*FRLO*), and high-frequency reflectance (*FRHI*). *FYLO* in the partial training set assesses ear-canal and middle-ear functioning, and *FYLO* does so in the full set in those ears with an adequate probe fit. It is expected that tympanometric responses measured clinically at frequencies from 0.226–1 kHz should be closely related to *FYLO*, because both are low-frequency admittance responses. That *FYLO* and *FRHI* are independent in the training sets, and nearly so in the validation sets, means that a measurement of energy reflectance in the frequency range 2–8 kHz, which overlaps the most clinically useful frequency range of EOAE measurements, gives an assessment of middle-ear functioning that is qualitatively different from a measurement of a low-frequency admittance response. Information on middle-ear functioning contained in *FRHI* may not be duplicated in tympanometric measurements. The importance of *FRHI* in the linear and logistic regressions is evidence that the YR test provides useful information on middle-ear functioning in neonates. Because ear-canal effects in neonates are probably localized to lower frequencies (Keefe, 1993) in a testing bandwidth up to 8 kHz, it may be appropriate to interpret

FRHI as a measure of middle-ear transmission.

The fact that high-frequency admittance scores quantified by *FYHI* are much more variable in the full than the partial training set is probably due to added noise, in the sense that the variability encodes information about quality of probe fit rather than about middle-ear functioning.

B. Correlation analyses

The correlation analyses on the training set at frequencies in the range 2–4 kHz show a relationship between EOA levels and reflectance (*FRHI*) that is stronger than the correlations with other YR factors and consistent across middle and high frequencies. This supports the hypothesis that forward transmission of energy from the ear canal to the cochlea is reduced by increased energy reflectance in this frequency range (Keefe *et al.*, 1993). It also supports the hypothesis that reverse transmission from the ear canal to the cochlea is reduced by increased reflectance. These correlations are similar for DPOAEs and TEOAEs. High-frequency reflectance (*FRHI*), and mid- and high-frequency admittance (*FYMI*, *FYHI*), are the most important factors in the correlations with ABR latencies, with the general trend that ABR latencies increase with increasing reflectance and decreasing admittance magnitude (Table V and Fig. 1). This observation may be consistent with the view that click-evoked ABRs correlate with audiometric thresholds at 2–4 kHz, and that click-evoked ABR latencies are dominated by responses coming from the high-frequency region of the cochlea (Jerger and Mauldin, 1978; Gorga *et al.*, 1985a; Gorga *et al.*, 1985b; van der Drift *et al.*, 1987). Increased latencies suggest that less energy is reaching the cochlea, consistent with the increased energy reflectance at high frequencies.

A scatter plot of TEOAE level versus *FRHI* (Fig. 6), along with the regression line of TEOAE level on *FRHI*, shows the inverse relationship of high-frequency reflectance and TEOAE level expressed by their negative correlation (see Fig. 3). The distribution of TEOAE level for many ears with low reflectance (negative *FRHI*) is probably indicative of ears with normal middle-ear functioning. The remaining distribution of TEOAE levels around the regression line is due to variables unrelated to ear-canal and middle-ear status, at least as can be explained by *FRHI*. Similar remarks apply to the relationship between DPOAE level and *FRHI*.

C. Linear regression analyses

The multiple linear regression analyses were complementary to the correlation analyses, and were used to assess the role of all the YR factors in accounting for the variability in EOA and ABR results across subjects. The multiple linear regressions calculated the R^2 in the EOA levels and ABR latencies by the YR factors. The EOA results show that (ear-canal and) middle-ear functioning account for as much as a quarter of the variation in observed EOA levels in neonatal ears. Therefore, three quarters, or more, of the variation in observed EOA levels in neonatal ears is due to effects other than those aspects of ear-canal and middle-ear functioning encoded by the YR response. Analogous results have been obtained, but are not described in detail, for re-

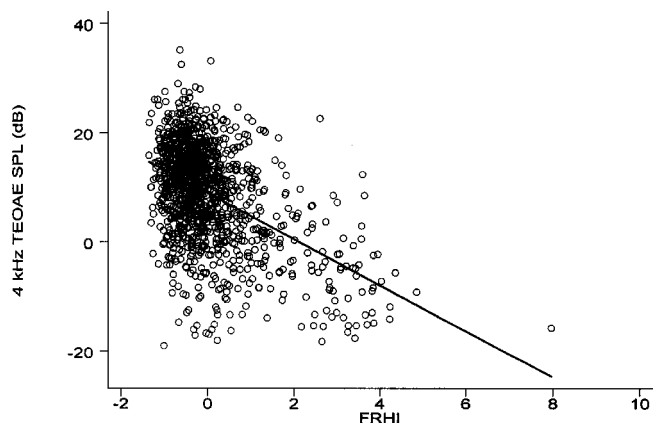


FIG. 6. The scatter plot of TEOAE SPL (dB) and *FRHI* (dimensionless) for each ear in the training set. The linear regression of TEOAE SPL on *FRHI* is also shown.

gressions on EOA SNR. The R^2 plots are similar between DPOAE and TEOAE levels at each frequency, suggesting that the role of the middle ear on both EOA types is similar. The tendency for increasing R^2 with increasing frequency is due not only to the decreased influence of noise on the EOA levels at higher frequencies, but also includes an increased predictive component in the YR response on forward and reverse middle-ear transmission.

The reason for including ABR latencies $L_I(70)$, $L_V(70)$, and $L_{V-I}(30)$ in the linear regressions is that the absolute latencies may include a peripheral ear-canal and middle-ear component, whereas the I–V latency difference $L_{V-I}(70)$ may not. Thus, the YR factors may account for part of the variance in the absolute latencies, but may account for very little of the I–V latency difference. The present results are consistent with this hypothesis insofar as the R^2 for $L_{V-I}(70)$ is slightly smaller than the R^2 for $L_I(70)$ and $L_V(70)$ (Fig. 4). The results are not consistent with this hypothesis in that the R^2 for $L_{V-I}(70)$ is approximately 0.10 (e.g., for the partial validation set) rather than zero. Concerning the stimulus level effect, R^2 for $L_V(70)$ and $L_V(30)$ in both the partial and full training sets are similar. Obviously, reverse transmission from the cochlea to the external ear plays no role in ABR latencies. Thus, these results support the theory that the YR factors encode information on forward transmission from the ear canal to cochlea. The regression coefficients in Table V show that wave V and wave I latencies increase with increasing high-frequency reflectance, and decreasing mid- and high-frequency equivalent volume and conductance. The latency difference $L_{V-I}(70)$ increases with decreasing high-frequency reflectance and decreasing mid- and high-frequency equivalent volume and conductance, with these admittance variables as the more important contributors. To refine this hypothesis, even though the middle ear is common to both wave I and wave V latencies, their latency difference [$L_{V-I}(70)$] may be sensitive to middle-ear functioning if the rate of change of absolute latencies with input cochlear level differs between wave I and wave V. This view is consistent with the present results, but the detailed relationships between forward transmission, which controls the input co-

chlear level, and each of the factors *FRHI*, *FYHI*, and *FYMI*, are unknown.

Differences in the YR regression coefficients (in Table V) in predicting EOAE and ABR results provide information on those factors important for both forward and reverse middle-ear transmission (EOAE) as compared to those for forward transmission alone (ABR). *FYMI* and *FYHI* are more important than *FRHI* in predicting ABR latencies [especially $L_V(70)$] as compared to their relative role in predicting EOAE levels. This is consistent with a more important role for mid- and high-frequency admittance in predicting forward middle-ear transmission than in predicting reverse middle-ear transmission. As previously described, *FRHI* is the dominant factor in predictions of EOAE levels (at and above 2 kHz), which suggests that *FRHI* is a predictor of reverse middle-ear transmission. *FRHI* is present in the predictors of forward middle-ear transmission (i.e., ABR latencies), but it accounts for less variance, on average, than the admittance factors (*FYHI*, *FYMI*). Because the ear canals are so small relative to the scale of acoustic wavelengths, ear-canal standing wave effects on YR responses are minimal in neonates in the frequency range of these measurements. This would not be the case in corresponding YR measurements in adult ears over the same frequency range.

D. Classification of EOAEs and ABRs

In the analyses classifying the EOAE responses as present or absent at a single frequency (above 1 kHz), the areas under the ROC curve range from 0.71–0.79 for the training sets, and from 0.68–0.79 for the validation sets (Fig. 5). This demonstrates the extent to which a test of ear-canal and middle-ear response predicts whether a frequency-specific EOAE response is present or absent. The most important factor in the predictor is *FRHI*, which heavily weights the reflectance at frequencies in the same range as the EOAEs (Table VI). The corresponding odds ratios of *FRHI* are 2.44 for classifying DPOAEs, and 2.47 for classifying TEOAEs. An odds ratio of 2.47 means that if the *FRHI* increases by 1 standard deviation with respect to its underlying distribution of responses, the probability (i.e., odds) that a TEOAE response will be absent increases by 2.47. Both the mean and standard deviation of energy reflectance in the range 2–4 kHz are approximately equal to 0.2, so that an energy reflectance close to 0.4 would more than double the odds that an EOAE response is absent. It was shown in the INHI study that infants with cleft lip or palate had higher energy reflectance (Keefe *et al.*, 2000). This pathology is associated with increased risk of middle-ear dysfunction, which is consistent with the present results. This also provides data relative to the problem of false positives in EOAE testing. The high odds ratio on *FRHI* implies that an ear with high reflectance in the 2–4-kHz range is more likely to have middle-ear dysfunction. While this odds ratio does not take into account the actual hearing status of the ear, i.e., whether or not there exists a hearing loss, the prevalence of hearing loss in the test population was low (approximately 1.6%). This prevalence in the test sample exceeds the prevalence in the general population due to the effort to recruit impaired

ears into the INHI study. With so few ears with hearing loss, absent EOAEs might be interpreted as false positives.

In the partial-set analyses classifying the single-frequency EOAE responses in the frequency range 2–4 kHz, the ROC areas lie between 0.69 and 0.79, and for multifrequency predictors across the same frequency range, the ROC areas lie between 0.73 and 0.79. These results suggest that it may be possible to construct a test of ear-canal and middle-ear functioning for use in hearing screening programs. If one were to observe abnormal YR results and absent EOAEs—i.e., an ear for which the YR response correctly predicts an absent EOAE—then one might consider the cause of the failure to be related to middle-ear energy transmission, either forward or reverse, or both. Thus, one might gain insight into the causes for referral rates in typical screening populations that are more than an order of magnitude greater than the incidence of hearing loss. While this information would be useful from a counseling perspective, it would still be necessary to retest the infant in order to determine whether sensorineural hearing loss exists. These ideas are further developed in a companion paper (Keefe *et al.*, 2003).

The multifrequency predictors (multifrequency and minimum logits) showed similar performance. This demonstrates that single-frequency predictors over a range of frequencies can be combined into a multifrequency predictor.

Based on the *Fsp* at 30 dB (nHL), the YR factors are poor classifiers of ABRs in the training set. Based on the latency $L_V(70)$, the YR factors have some ability to classify responses as having latencies in the normal range. These observations suggest that the ABR latencies contain more information relevant to middle-ear status than do ABR *Fsp* responses.

E. Generalization

The performance of the YR factors as predictors of EOAEs and ABRs, and as classifiers of responses as present or absent, generalized well. The R^2 in the multiple linear regressions predicting EOAE level is similar for the training set, on which the factors are calculated, and the validation set, on which generalization was assessed (Fig. 4). In particular, the importance of high-frequency reflectance in predicting EOAE responses, and ABRs to a lesser extent, generalized to a new sample population of neonatal ears. In comparing DPOAE and TEOAE classification performance across frequency in the validation set (by comparing top and bottom rows of plots in Fig. 5), the YR factors classify DPOAE responses about equally well across frequency, while they classify TEOAE responses better at 3 and 4 kHz. The DPOAE predictors generalized better than the TEOAE predictors in the sense that there tended to be larger reductions in the TEOAE validation set compared to the TEOAE training set than for the corresponding DPOAE sets.

The performance of the YR factors in predicting and classifying ABR responses was similar in the training and validation sets. This suggests that the relatively small R^2 values in predicting ABR latencies, and small ROC areas in classifying ABR latencies, are nonetheless evidence for relationships between ABRs and differences in middle-ear forward transmission.

It should be noted that this test of generalization is not as strong as one might wish, insofar as the two sample populations were largely composed of opposite-ear data from the same population of subjects. A stronger case would have been made if the data came from independent samples of subjects. Nevertheless, any failure of test generalization would have suggested that the observed relationships between YR and other variables might have been a statistical artifact. No such failure of generalization was observed, lending confidence in the validity of the observed relationships.

F. Effect of probe seal

The INHI study demonstrated that slightly more than 10% of YR responses showed evidence of poor probe fit. Leaks were observable in the YR response even in ears that passed the probe-fit test associated with TEOAE measurements (Keefe *et al.*, 2000). It is unknown whether a leaky probe fit in the YR test on a given ear was always associated with a leaky probe fit in the EOAE and ABR tests, because probe fit may not have remained constant throughout the various tests. Nevertheless, it is reasonable to assume that a leaky probe fit in the YR test made it more likely that the corresponding EOAE and ABR tests also had leaky probe fits. The relationships between a test of ear-canal and middle-ear status, and a test of cochlear or neural status, might be more apparent in a sample population that excluded those ears that were likely to have probe-fit problems. This was the rationale for present analyses using the partial data set, and for the analyses on the corresponding subset of ears in Keefe *et al.* (2000). The YR test of probe fit was based on the low-frequency YR response, because the high-frequency YR responses shifted by smaller amounts than low-frequency responses in the presence of leaks that were systematically introduced. This trend is evident in Fig. 1 of Keefe *et al.* (2000), in which the effect of a large leak is illustrated, in that some of the structure of the YR response above 4 kHz is preserved. It may be that relationships involving high-frequency YR factors are less sensitive than low-frequency factors to probe leaks for the present dependent variables (EOAEs and ABRs). This may explain the performance of *FRHI* in predicting EOAEs in both full and partial sets.

For predicting EOAE level, the R^2 was larger for the partial sets than the corresponding full sets in both the training and validation sets (Fig. 4, right column), demonstrating that the relationships between ear-canal and middle-ear functioning and EOAE responses are stronger in the sample for which all ears had an adequate probe fit. This confirms expectations because the partial sets have YR factors that assess ear-canal and middle-ear functioning, uncontaminated by probe-fit issues including increased noise. The factor *FYLO* in the full training set classifies ears as having a leaky probe fit with an ROC area of 0.995. For the subset of ears with an adequate probe fit, i.e., ~90% of ears in the full set and ~100% in the partial set, *FYLO* measures the low-frequency admittance of the ear. In classifying EOAE SNR, the ROC curves are similar across all frequencies in the full and partial sets (Fig. 5). This means that, regardless of probe fit, the YR response is able to classify an EOAE response.

This may be related to the observation that high-frequency reflectance is more insensitive to probe fit than the YR response at lower frequencies.

The YR predictors of ABR $L_V(70)$ responses have larger R^2 in the partial versus the full training sets, and in the partial versus the full validation sets (Fig. 4). Thus, the YR responses are better predictors for ears with adequate probe fit. For the partial sets in predicting $L_V(70)$, the significant factors, listed in order of decreasing magnitude of regression slope coefficient, are: *FYHI* (−0.117), *FYMI* (−0.101), *FRHI* (0.041), and *FYLO* (−0.028). Thus, $L_V(70)$ increases with decreasing equivalent volume and conductance at both high and middle frequencies, and increasing reflectance at high frequencies. Because the dependence on *FYLO* is weak, this suggests the hypothesis that tympanometry below 1.4 kHz, which also is a low-frequency admittance measurement, would be a weak predictor of ABR $L_V(70)$. This is consistent with the preceding discussion of the importance of high-frequency stimulus energy to the interpretation of ABR latencies.

V. CONCLUSIONS

The YR responses measured in a large sample of neonates contain approximately 5–7 independent degrees of freedom, or factors. Among these factors, one based on the energy reflectance at high frequencies is inversely correlated to EOAE signal levels (including DPOAEs and TEOAEs). The YR factors can account for more than a quarter of the total variance of EOAE levels. The remaining three-quarters of the total variance of EOAE levels is due to variability in cochlear generation of EOAEs and/or variability in forward and reverse middle-ear transmission that is not described by the YR factors. The latter variability may arise because the YR response does not directly assess forward and reverse transmission. The YR factors classify EOAE responses as present or absent with areas under the ROC curve on the order of 0.69–0.79. The YR factors perform less well at classifying ABR wave-V latencies (ROC area of 0.64), and they classify ABR *Fsp* poorly (ROC area of 0.56). These results quantify the extent to which YR measurements of middle-ear functioning account for the structure of EOAE and ABR responses. The ability of the YR response to predict and classify EOAEs and ABRs is evidence that the YR response is sensitive to forward and reverse transmission through the ear canal and middle ear.

ACKNOWLEDGMENTS

We appreciate the assistance of Susan J. Norton, Kelley Mascher, and Kristin Fletcher in transferring of research data from the INHI Project. The INHI Project data were collected and analyzed with the support of the NIDCD (DC01958). The work in this report was partially supported by the NIDCD (DC03784).

Chen, S.-J., Yang, E. Y., Kwan, M.-L., Chang, P., Shiao, A.-S., and Lien, C.-F. (1996). "Infant hearing screening with an automated auditory brainstem response screener and the auditory brainstem response," *Acta Paediatr.* **85**, 14–18.

- Cleves, M. (2000). "Receiver operating characteristic (ROC) analysis," in *Stata Technical Bulletin Reprints*, Vol. 9, 212–229.
- DeLong, E. R., DeLong, D. M., and Clarke-Pearson, D. L. (1988). "Comparing the areas under two or more correlated receiver operating curves: A nonparametric approach," *Biometrics* **44**, 837–845.
- Foxe, J. J., and Stapells, D. R. (1993). "Normal infant and adult auditory brainstem responses to bone-conducted tones," *Audiology* **32**, 95–109.
- Gorga, M. P., Reiland, J. K., Beauchaine, K. A., Worthington, D. W., and Jesteadt, W. (1987). "Auditory brainstem responses from graduates of an intensive care nursery: Normal patterns of response," *J. Speech Hear. Res.* **30**, 311–318.
- Gorga, M. P., Norton, S. J., Sininger, Y. S., Cone-Wesson, B., Folsom, R. C., Vohr, B. R., and Widen, J. E. (2000). "Identification of neonatal hearing impairment: Distortion product otoacoustic emissions during the perinatal period," *Ear Hear.* **21**, 400–424.
- Gorga, M. P., Reiland, J. K., and Beauchaine, K. A. (1985a). "Auditory brainstem responses in a case of high-frequency conductive hearing loss," *J. Speech Hear. Disord.* **50**, 346–350.
- Gorga, M. P., Worthington, D. W., Reiland, J. K., Beauchaine, K. A., and Goldgar, D. E. (1985b). "Some comparisons between auditory brainstem response thresholds, latencies, and the pure-tone audiogram," *Ear Hear.* **6**, 105–112.
- Harrison, W. A., Dunnell, J. J., Mascher, K., Fletcher, K., Vohr, B. R., Gorga, M. P., Widen, J. E., Cone-Wesson, B., Folsom, R. C., Sininger, Y. S., and Norton, S. J. (2000). "Identification of neonatal hearing impairment: Experimental protocol and database management," *Ear Hear.* **21**, 357–372.
- Hooks, R. G., and Weber, B. A. (1984). "Auditory brain stem responses of premature infants to bone-conducted stimuli: A feasibility study," *Ear Hear.* **5**, 42–46.
- Holte, L. A., Cavanagh, R. M., and Margolis, R. H. (1990). "Ear canal wall mobility and tympanometric change in young infants," *J. Pediatr.* **117**, 77–80.
- Hosmer, D. W., and Lemeshow, S. (2000). *Applied Logistic Regression*, 2nd ed. (Wiley, New York).
- Hudde, H., and Engel, A. (1998). "Measuring and modeling basic properties of the human middle ear and ear canal. III. Eardrum impedances, transfer functions, and model calculations," *Acta Acust. (Beijing)* **73**, 242–247.
- Jerger, J., and Mauldin, L. (1978). "Predictions of sensorineural hearing level from the brainstem evoked response," *Arch. Otolaryngol.* **104**, 456–461.
- Keefe, D. H. (2001). "Inter-ear variations in the eardrum impedance and stapes velocity in the human middle ear," *Hear. Res.* **159**, 150–152.
- Keefe, D. H., Bulen, J. C., Arehart, K. H., and Burns, E. M. (1993). "Ear-canal impedance and reflection coefficient in human infants and adults," *J. Acoust. Soc. Am.* **94**, 2617–2638.
- Keefe, D. H., Folsom, R. C., Gorga, M. P., Vohr, B. R., Bulen, J. C., and Norton, S. J. (2000). "Identification of neonatal hearing impairment: Ear-canal measurements of acoustic admittance and reflectance in neonates," *Ear Hear.* **21**, 443–461.
- Keefe, D. H., Gorga, M. P., Neely, S. T., Zhao, F., and Vohr, B. R. (2003). "Ear-canal acoustic admittance and reflectance measurements in human neonates. II. Predictions of middle-ear dysfunction and sensorineural hearing loss," *J. Acoust. Soc. Am.* **113**, 407–422.
- Kleinbaum, D. H., Kupper, L. L., and Muller, K. E. (1988). *Applied Regression Analysis and Other Multivariable Methods* (PWS-Kent, Boston).
- Levi, E., Werner, L. A., and Keefe, D. H. (1998). "Toward using ear-canal impedance and reflectance measurements to screen middle-ear function in infants and young adults," *Assoc. Res. Otolaryngol. Abs.* **21**, 106.
- Norton, S. J., Gorga, M. P., Widen, J. E., Folsom, R. C., Sininger, Y. S., Cone-Wesson, B., Vohr, B. R., and Fletcher, K. (2000a). "Identification of neonatal hearing impairment: A multicenter investigation," *Ear Hear.* **21**, 348–356.
- Norton, S. J., Gorga, M. P., Widen, J. E., Folsom, R. C., Sininger, Y. S., Cone-Wesson, B., Vohr, B. R., Mascher, K., and Fletcher, K. (2000b). "Identification of neonatal hearing impairment: Evaluation of transient evoked otoacoustic emission, distortion product otoacoustic emission, and auditory brain stem evoked response test performance," *Ear Hear.* **21**, 508–528.
- Norton, S. J., Gorga, M. P., Widen, J. E., Vohr, B. R., Folsom, R. C., Sininger, Y. S., Cone-Wesson, B., and Fletcher, K. (2000c). "Identification of neonatal hearing impairment: Transient evoked otoacoustic emissions during the perinatal period," *Ear Hear.* **21**, 425–442.
- Piskorski, P., Keefe, D. H., Simmons, J. L., and Gorga, M. P. (1999). "Prediction of conductive hearing loss based on acoustic ear-canal response using a multivariate clinical decision theory," *J. Acoust. Soc. Am.* **105**, 1749–1764.
- Puria, S., Peake, W. T., and Rosowski, J. J. (1997). "Sound-pressure measurements in the cochlear vestibule of human-cadaver ears," *J. Acoust. Soc. Am.* **101**, 2754–2770.
- Puria, S., and Rosowski, J. J. (1996). "Measurement of reverse transmission in the human middle ear: Preliminary results," in *Diversity in Auditory Mechanics*, edited by E. Lewis, G. Long, R. Lyon, P. Narins, and C. Steele (World Scientific, Singapore).
- Rhodes, M. C., Margolis, R. H., Hirsch, J. E., and Napp, A. P. (1999). "Hearing screening in the newborn intensive care nursery: Comparison of methods," *Otolaryngol.-Head Neck Surg.* **120**, 799–808.
- Sininger, Y. S., Cone-Wesson, B., Folsom, R. C., Gorga, M. P., Vohr, B. R., Widen, J. E., Ekelid, M., and Norton, S. J. (2000). "Identification of neonatal hearing impairment: Auditory brain stem responses in the perinatal period," *Ear Hear.* **21**, 400–424.
- Stevens, J. (2001). "State of the art neonatal hearing screening with auditory brainstem response," *Scand. Audiol.* **30**, Suppl 52, 10–12.
- Stuart, A., Yang, E. Y., and Green, W. B. (1994). "Neonatal auditory brainstem response thresholds to air- and bone-conducted clicks: 0 to 96 hours postpartum," *J. Am. Acad. Audiol.* **5**, 163–172.
- van der Drift, J. F. C., Brocaar, M. P., and van Zanten, G. A. (1987). "The relation between pure-tone audiogram and the click auditory brainstem response threshold in cochlear hearing loss," *Audiology* **26**, 1–10.
- Voss, S. E., Rosowski, J. J., Merchant, S. M., and Peake, W. T. (2000). "Acoustic responses of the human middle ear," *Hear. Res.* **150**, 43–69.
- Voss, S. E., Rosowski, J. J., Merchant, S. M., and Peake, W. T. (2001). "Correlation of impedance at the TM with stapes velocity? Reply to the letter of D. H. Keefe," *Hear. Res.* **159**, 153–154.

Ear-canal acoustic admittance and reflectance measurements in human neonates. II. Predictions of middle-ear dysfunction and sensorineural hearing loss

Douglas H. Keefe,^{a)} Michael P. Gorga, Stephen T. Neely, and Fei Zhao^{b)}
Boys Town National Research Hospital, 555 North 30th Street, Omaha, Nebraska 68131

Betty R. Vohr
Women and Infants Hospital, Providence, Rhode Island

(Received 28 April 2002; revised 26 September 2002; accepted 30 September 2002)

This report describes relationships between middle-ear measurements of acoustic admittance and energy reflectance (YR) and measurements of hearing status using visual reinforcement audiometry in a neonatal hearing-screening population. Analyses were performed on 2638 ears in which combined measurements were obtained [Norton *et al.*, *Ear Hear.* **21**, 348–356 (2000)]. The measurements included distortion-product otoacoustic emissions (DPOAE), transient evoked otoacoustic emissions (TEOAE), and auditory brainstem responses (ABR). Models to predict hearing status using DPOAEs, TEOAEs, or ABRs were each improved by the addition of the YR factors as interactions, in which factors were calculated using factor loadings from Keefe *et al.* [*J. Acoust. Soc. Am.* **113**, 389–406 (2003)]. This result suggests that information on middle-ear status improves the ability to predict hearing status. The YR factors were used to construct a middle-ear dysfunction test on 1027 normal-hearing ears in which DPOAE and TEOAE responses were either both present or both absent, the latter condition being viewed as indicative of middle-ear dysfunction. The middle-ear dysfunction test classified these ears with a nonparametric area (A) under the relative operating characteristic curve of $A = 0.86$, and classified normal-hearing ears that failed two-stage hearing-screening tests with areas $A = 0.84$ for DPOAE/ABR, and $A = 0.81$ for TEOAE/ABR tests. The middle-ear dysfunction test adequately generalized to a new sample population ($A = 0.82$). © 2003 Acoustical Society of America. [DOI: 10.1121/1.1523388]

PACS numbers: 43.64.Ha, 43.64.Jb, 43.64.Nf [BLM]

I. INTRODUCTION

An important problem in neonatal hearing screening (NHS) programs is to interpret the effect of middle-ear status on the results obtained using physiological tests of hearing status. NHS tests are frequently performed by personnel without special training in audiology in the hospital or birthing unit just prior to discharge. NHS is currently based on the use of evoked otoacoustic emissions (EOAE), including distortion product otoacoustic emissions (DPOAE) and click-evoked otoacoustic emissions (TEOAE), and/or a screening auditory brain stem response (ABR) using an air-conducted stimulus. If an infant is screened as lacking normal responses to these screening OAE and ABR tests, subsequent diagnostic tests are used to diagnose the extent and type of hearing loss. Such diagnostic tests must differentiate, in part, between conductive hearing losses produced by middle-ear pathology and sensorineural hearing loss. One problem in NHS programs is that many infants eventually shown to have normal sensorineural function do not produce “normal” responses to the OAE and ABR tests. Unfortunately, there currently is no neonatal middle-ear test in common use to evaluate at the time of screening whether the absence of these responses may be due to middle-ear dysfunction. The

goal of this report is the description of the role of middle-ear functioning on the interpretation of results from an NHS study aimed at the early identification of sensorineural hearing loss. As such, the evaluation of the tests in a NHS program is distinct from the evaluation of follow-up diagnostic testing of infants, in which tests of middle-ear functioning on a much smaller number of infants are performed by pediatric audiologists. Whereas greater technical sophistication can be brought to bear during diagnostic evaluations, practical and financial factors make it impossible to perform the same diagnostic tests as part of a mass NHS program.

A hearing-screening measurement of middle-ear functioning was assessed by measuring the acoustical admittance and energy reflectance (YR) in the ear canal. The data were obtained in the Identification of Neonatal Hearing Impairment (INHI) study (Norton *et al.*, 2000a), which evaluated the ability of DPOAE (Gorga *et al.*, 2000), TEOAE (Norton *et al.*, 2000d), and ABR (Sininger *et al.*, 2000) tests to predict sensorineural hearing loss, the YR test to assess middle-ear functioning (Keefe *et al.*, 2000), and a follow-up behavioral audiogram and related tests to measure the hearing loss at age 8–12 months (Widen *et al.*, 2000). The behavioral hearing test served as the gold standard against which the performance of the DPOAE, TEOAE, and ABR tests was evaluated.

This report describes the incorporation of YR measure-

^{a)}Electronic mail: keefe@boystown.org

^{b)}Current affiliation: School of Health Science, University of Wales Swansea, Singleton Park, Swansea SA2 8PP, U.K.

ments into a test battery to predict sensorineural hearing loss, and the design and evaluation of a screening test to detect middle-ear dysfunction based on the YR response. Relationships between the YR response and EOAEs and ABRs are described elsewhere (Keefe *et al.*, 2003). Middle-ear functioning influences EOAE test outcomes inasmuch as the relative success of infant hearing screening programs is thought to depend on the ability to minimize false-positive screening outcomes that are caused by transient external and middle-ear conditions (Margolis, 2001). The present study describes issues relating middle-ear status to the outcomes of typical NHS tests.

Infants who are identified in the screening as potentially having hearing loss are referred for rescreening or more specialized diagnostic testing. A significant practical problem in hearing screening evaluations is the problem of “false positives,” which refers to those infants that do not pass their NHS test, but who are later found in follow-up testing not to have a sensorineural hearing loss. It is widely thought that false-positive NHS results in neonates are due to transient middle-ear dysfunction, i.e., a dysfunction that is present at the time of neonatal screening and subsequently resolved. As reviewed by Stuart *et al.* (1994), the neonate’s middle ear may contain embryonic connective tissue, mesenchyme, and other materials, and the ear canal may contain vernix. Current screening tests do not characterize the origin of the likely hearing loss as sensorineural, conductive, or mixed (i.e., a combination of sensorineural and conductive losses), although more specialized diagnostic tests may allow such differential assessments of type of loss. Stuart *et al.* (1994) showed that air-conducted ABR thresholds were elevated by more than 10 dB in the initial 48 hours after birth compared to 49–96 hours after birth, while bone-conducted ABR thresholds changed by less than 1 dB. This physiologic conductive deficit is consistent with the resolution of fluids and residuals in the middle ear and ear canal. However, a 10-dB threshold shift does not necessarily account for the absence of an air-conducted ABR response, which remains unaccounted for by the composite air/bone results.

Depending on the age of the child, the subsequent diagnostic tests may include behavioral audiograms (Widen *et al.*, 2000) and/or diagnostic ABR testing (Stevens, 2001). Both test types may be used with a combination of air-conduction and bone-conduction stimuli, which allows one to categorize the ear as having a sensorineural, conductive, or mixed hearing loss, or else as having normal hearing (indicative of a false-positive screening outcome). Diagnostic testing may also be performed using only air-conduction stimuli, for which the aim is to characterize the amount of hearing loss without categorizing as to type of hearing loss. The feasibility of including bone-conduction stimuli in pediatric ABRs has been demonstrated (Yang *et al.*, 1987; Stuart *et al.*, 1994; Chen *et al.*, 1996; Cone-Wesson and Ramirez, 1997). While bone-conduction ABR is recommended for infants who are referred after failing a hearing screening test in order to detect conductive loss (Stevens *et al.*, 2001), bone-conduction ABR has apparently not been used in hearing screening applications. Among its limitations from the standpoint of screening are problems associated with the place-

ment of the vibrator and uncertainties related to force that is applied during the testing.

The absence of a hearing screening test of middle-ear functioning was the primary factor motivating the research described in this report. The fact that the YR test was able to predict whether or not an EOAE response was present or absent in a screening sample of neonatal ears (Keefe *et al.*, 2003) suggested the hypothesis that the YR test may be sensitive to middle-ear dysfunction in such a population. The research in the present report examines this hypothesis from two viewpoints: (1) whether a combination of EOAE and YR tests, or ABR and YR tests, improves the prediction of hearing loss in a screening sample of neonates compared to the EOAE or ABR test alone, and (2) whether a YR test of middle-ear dysfunction can be constructed and evaluated based on measurements in a screening sample.

II. THEORETICAL APPROACH

The main physiological variables used in the present analyses include the minimum signal to noise ratio (SNR, expressed as a level in dB) of DPOAE and TEOAE responses at frequencies of 2, 3, and 4 kHz, the ABR *Fsp* for a click at 30 dB (nHL), and the YR response. These variables are described in more detail in Keefe *et al.* (2003). These responses were measured as part of the INHI project (Norton, 2000b), of which the principal goal was to test the effectiveness of physiological tests in identifying sensorineural hearing loss in newborns. The physiological responses were measured at a time just before the infant was discharged from the birthing hospital. These tests were performed over a range of corrected ages of 1 day up to 3 months, which varied according to the health status of each infant.

Visual reinforcement audiometry (VRA) was performed at 8 to 12 months corrected age (Widen *et al.*, 2000) to behaviorally assess hearing status, and served as the gold standard for classifying infants into normal-hearing or hearing-loss groups. This classification was based on pure-tone responses at 1, 2, and 4 kHz. Normal hearing was defined as VRA thresholds (i.e., minimum response levels) of 20-dB hearing level (HL, ANSI, 1996) for at least two of the three test frequencies. Sensorineural hearing loss was defined for VRA responses exceeding this limit.

Test performance to predict hearing status in the INHI study, which was assessed by comparing the areas under the relative operating characteristic (ROC) curve, was similar for TEOAEs, DPOAEs, and ABRs, except that the ABR performed slightly better in predicting hearing status at 1 kHz (Norton *et al.*, 2000b). For brevity in the present report, the area under the ROC curve for any predictor is sometimes denoted as the “ROC area.”

A. Theory underlying the prediction of sensorineural hearing loss

While the INHI project assessed the accuracy of EOAEs and ABR in predicting auditory status in infants, one goal of the present study is to test the accuracy of these predictors when augmented by the YR response, which describes ear-canal and middle-ear functioning. Based on a binary depen-

dent variable (impaired or normal hearing), a logistic regression approach was adopted, which was performed using maximum likelihood estimation. The main question is whether a logit function including both EOAE and YR variables is a better predictive model than a logit function using only EOAE variables (and similarly for ABR and YR variables). This question has two aspects—does the model's goodness of fit improve when YR variables are included, and does the model classification performance improve when YR variables are included? The dependent variable for hearing status is denoted as presence ($LOSS=1$) or absence ($LOSS=0$) of sensorineural hearing loss. The smaller univariate model is denoted as $LOSS=o(SNR)$, in which it is understood that the right-hand side includes a logistic function o of the logit function L to predict the binary variable $LOSS$, i.e., a function of the form $LOSS=o(L)=e^L/(1+e^L)$, with $L=SNR$ in this smaller model.

The VRA sample population is a subset of that used in the earlier analyses of YR, EOAE, and ABR data (Keefe, *et al.* 2003), because only a subset of the INHI sample population was tested using VRA for hearing status. Among subjects with bilateral normal hearing (defined by VRA), only one ear per subject was included in the VRA sample population. If a subject had sensorineural hearing loss in one ear and normal hearing in the other, then the ear with sensorineural hearing loss was included in the impaired-ear database while the results were discarded for the opposite ear. If a subject had sensorineural hearing loss in both ears, then both ears were included in the VRA sample population in order to maximize the number of impaired ears. The number of impaired ears was 16 for DPOAE, 16 for TEOAE, 19 for ABR analyses, and 15 for ears in which all tests were completed. These numbers differ because not all subjects with sensorineural hearing loss completed all neonatal tests, although all completed the VRA and YR tests.

The minimum SNR at 2, 3, and 4 kHz was used in the INHI project to predict hearing status (Norton *et al.*, 2000c). The DPOAE SNR was set to zero for tests in which the noise level plus 2 standard deviations exceeded the signal level (Harrison *et al.*, 2000; Gorga *et al.*, 2000). The independent variable in the ABR predictor was the F_{sp} value at a click level of 30 dB nHL. The YR responses measured in the INHI project were influenced by probe fit (Keefe *et al.*, 2000, 2003). A probe-fit test was described in these references that would allow a YR measurement to verify the quality of probe fit during data acquisition. Therefore, it is sufficient in the present study to include only those YR responses from the INHI project that were judged to have an adequate probe fit. This was termed the partial data set of YR responses in Keefe *et al.* (2003).

These YR responses are expressed in terms of a set of factors calculated using principal components analysis. For each ear, the factors are defined in terms of factor loadings tabulated in Keefe *et al.* (2003) and the YR response specific to that ear. These factor loadings were calculated on a larger population of ears for which the VRA tests were not necessarily available. These factors are listed in Table I in terms of the frequencies and variables in the YR response on which they have the greatest loadings [these factors have the load-

TABLE I. Factor names

Factor	Factor name	Description
1	<i>FYLO</i>	Low-frequency admittance (0.25–1 kHz)
2	<i>FRHI</i>	High-frequency reflectance (2–8 kHz)
3	<i>FYHI</i>	High-frequency admittance (3–8 kHz)
4	<i>FYRMI</i>	Mid-frequency YR (1–2 kHz)
5	<i>FY7k</i>	Admittance near 6–8 kHz
6	<i>FRLO</i>	Low-frequency reflectance (0.25–1 kHz)
7	<i>FYMI</i>	Mid-frequency admittance (1.4–4 kHz)

ings reported in Keefe *et al.* (2003) for the partial training set].

Many NHS programs are based upon the findings that EOAE SNR and ABR F_{sp} predict hearing status. A related hypothesis is that the YR variables predict the status of external and middle ears, for example, the YR response predicts the presence of conductive hearing loss in a population of older children at risk for otitis media with effusion (Piskorski *et al.*, 1999). Thus, it is hypothesized that the YR response may predict middle-ear dysfunction (which is taken to include ear-canal dysfunction) in neonatal ears, which may be associated with a conductive hearing loss, even though the risk characteristics for a neonatal population differ from those for a population of older children at risk for otitis media with effusion. To test the hypothesis, a middle-ear factor would enter the predictor as a main variable. For the case of EOAEs with a single factor F , the predictor would take the form $LOSS=o(SNR+F)$. This abbreviated notation $LOSS=o(L)$ has as its argument a logit function L of the form, $L=c_1*SNR+c_2*F$, with constant coefficients c_1 and c_2 to be determined.

To the extent that an ear classified as impaired has a pure sensorineural loss, then one would not expect a middle-ear factor to predict hearing status, and such a factor would not enter the predictor as a main variable. If a middle-ear factor enters as a main effect, this would be evidence that the population of impaired ears contains ears with a pure conductive or mixed loss, even though there was no gold standard in the INHI study to classify pure conductive and mixed losses.

If no middle-ear factor enters as a main effect, it remains possible that the presence of middle-ear or ear-canal dysfunction may influence both forward transmission of EOAE and ABR stimuli, and reverse transmission of cochlear-generated signals. Hence, the EOAE and ABR responses in an ear with middle-ear or ear-canal dysfunction may differ from those in an ear with normal middle-ear functioning. Thus, the variables used to predict hearing status would be influenced by middle-ear status. To test such a possibility, a class of models is considered in which the YR variables enter the predictor as an interaction with the main variable (EOAE SNR or ABR F_{sp}). Defining F_m as the m th factor, these models in the case of EOAEs are denoted as $LOSS=o(SNR+SNR \times F_m)$, in which $SNR+SNR \times F_m$ denotes a logit function that is linear in SNR, and linear in $SNR \times F_m$. For the principal components analysis of the set with $M=7$ factors (see Table I), there are seven possible interactions $SNR \times F_1, SNR \times F_2, \dots, SNR \times F_7$. If a mixed loss exists, the model might also include factors as main effects, and

take the form $LOSS = o(SNR + F_m + SNR \times F_m)$.

The analyses of EOAEs proceed in the following steps, which follow the recommendations of Hosmer and Lemeshow (2000) except for the present emphasis on adding interactions with main variables.

- (1) For M factors, perform $2M$ univariate logistic regressions using SNR and $SNR \times F_m$, and SNR and F_m .
- (2) Retain those factors and interactions which have some association based on the Wald statistic ($p < 0.25$) and discard remaining variables.
- (3) Perform all multivariate logistic regressions using SNR and all retained factors and interactions, and all logistic regressions on all smaller models (using subsets of the above-listed independent variables).
- (4) Choose the final model to be the smallest model for which the likelihood is not significantly smaller than any larger model based on a chi-squares test.
- (5) Likelihood analyses are performed with a chi-squares test using $p = 0.05$ and $p = 0.10$, the latter to control for a type-II error that may result from the small number of impaired ears. If the likelihood of the final model is significantly larger than the likelihood of the univariate model $LOSS = o(SNR)$, then the influence of middle-ear variables improves the prediction of auditory status; if not, there is no effect on predicting auditory status by measuring the YR response.
- (6) Compare the classification performance of the final and univariate models based on the calculated area under the ROC curve.
- (7) Assess the shape of the ROC curves to compare the final and univariate models based on pairs of sensitivity and specificity values.

The analysis of ABRs takes the same form with F_{sp} replacing SNR . The advantage of using univariate analyses in step 1, rather than a single multivariate analysis including all the factors and interactions, is that relatively small models are used with no more than two independent variables in each logistic regression. This is beneficial because the number of ears with sensorineural hearing loss is small (16–19 ears), and so the number of independent variables should be small.

B. Theory underlying the test of middle-ear dysfunction

The presence or absence of EOAE responses was predicted by the YR response, but the presence or absence of ABR signals was only weakly predicted (Keefe *et al.*, 2003). For example, the ROC area was 0.77–0.79 for classifying the minimum DPOAE SNR between 2–4 kHz as present or absent, and 0.73–0.73 for classifying the minimum TEOAE SNR between 2–4 kHz as present or absent. The ROC area was only 0.58 for classifying the ABR FSP as present or absent. Because an absent response may be due to middle-ear dysfunction, such a classification task, which is based on responses in normal-hearing subjects, can be used to construct a predictive test of middle-ear dysfunction. This has particular relevance to the neonatal population for which no gold standard of middle-ear dysfunction is available. In con-

trast to the previous results including ears with sensorineural hearing loss, it is unnecessary to include such ears in constructing a test of middle-ear dysfunction. This simplifies the analyses because the problem of the small number of impaired ears is circumvented.

One approach to construct a test of middle-ear dysfunction is to calculate normative percentiles of test responses in normal-hearing ears, and classify an ear with dysfunction if its response falls outside some normal range, e.g., the 5th and 95th percentiles of responses. Such percentiles have been presented based on all ears tested in the INHI project, excluding those with leaky probe fits (Fig. 5 in Keefe *et al.*, 2000). This approach is advantageous when the response is based on one variable, but the YR response has 33 variables that are partially correlated across frequency and response type (a YR response includes energy reflectance, equivalent volume, and acoustic conductance responses at each of 11 half-octave frequencies from 0.25–8.0 kHz (Keefe *et al.*, 2000). With 33 variables, random variability may increase a response outside the percentile boundaries for one variable, while it may not indicate an unusual YR response overall.

Use of the YR factors in place of all variables in the YR response reduces the set of variables to seven, which are separated in frequency and response type. Thus, it would be preferable to construct percentiles based on these factors rather than the original YR response. One could identify middle-ear dysfunction in terms of whether a particular response has any factor score outside some normal baseline range. However, the results described in Keefe *et al.* (2003) suggest that some factors are important predictors of middle-ear status, while others are not. Thus, a definition of middle-ear dysfunction that gives equal weight to the factors is not in accord with the differential predictive strength of the factors.

The approach adopted is to develop tests of middle-ear dysfunction using a linear combination of the factors, but with coefficients chosen according to a gold standard that isolates middle-ear status to the extent possible.

Because middle-ear dysfunction is distinct from sensorineural hearing loss, and because the number of ears with sensorineural hearing loss is so small, a test of middle-ear dysfunction should not be dependent on responses in ears with sensorineural hearing loss. The analyses that classified DPOAEs, TEOAEs, and ABRs as present or absent (Keefe *et al.*, 2003) represent possible choices for constructing a test of middle-ear dysfunction, but some aspects of the analyses are problematical. The ABR predictor of F_{sp} achieved ROC areas only modestly larger than 0.5 (i.e., performance near chance levels), while the ABR predictor of wave-V latency was more effective (Keefe *et al.*, 2003). Thus, ABR latency appears to be a better choice than F_{sp} value on which to design a YR test of middle-ear dysfunction. Some ears failed one of the EOAE tests and passed the other. These ears, which were classified inconsistently by the EOAE tests, may not form the best sample population on which to define a test of middle-ear dysfunction. Finally, the analyses were performed on ears with unknown hearing status, while it is preferable to construct a test of middle-ear dysfunction on

normal-hearing ears for which the possibility of sensorineural hearing loss has been excluded.

A first gold standard is defined in the present study by categorizing normal-hearing ears that pass both the DPOAE and TEOAE tests as having normal middle-ear functioning, and those that fail both tests as having middle-ear dysfunction. This is termed the DT gold standard. A second, more stringent gold standard is defined by categorizing normal-hearing ears that pass all the DPOAE, TEOAE, and ABR tests as having normal middle-ear functioning, and those that fail all three tests as having middle-ear dysfunction. This is termed the DTA gold standard. Consistent with the above discussion, the ABR component of the DTA gold standard is based on $L_V(70)$.

The criteria for a pass are based on the 80% specificity calculated for normal-hearing ears in the VRA sample—3.1 dB for the minimum DPOAE SNR at 2, 3, and 4 kHz, 6.1 dB for the minimum TEOAE SNR at 2, 3, and 4 kHz, and the critical value of ABR $L_V(70)$ in seven age-dependent subgroups. The latter controls for the monotonic decrease of $L_V(70)$ with increasing conceptional age in the subgroups. This critical value of $L_V(70)$ at 80% specificity ranges from 7.99 ms at mean conceptional age 35.1 weeks down to 7.24 ms at mean age 53 weeks.

III. METHODS

The data used in the present study were obtained from the INHI project data collected at Boys Town National Research Hospital in Omaha, NE, and Women's and Infant's Hospital in Providence, RI. The INHI sample population included high-risk infants who had been treated in a neonatal intensive care unit (NICU), well babies with no risk factors, and well babies with one or more risk factors for sensorineural hearing loss (Vohr *et al.*, 2000). This INHI sample population overweighed infants in the NICU, who were more likely to have sensorineural hearing loss, in an effort to increase their number in the study. The INHI test protocol is summarized elsewhere for the standard protocol (Harrison *et al.*, 2000) and the protocol including the YR test (Keefe *et al.*, 2000).

The calculation of the YR factor loadings in the present study is based on a subset of the INHI database ($N=2425$) including ears for which there are neonatal screening data (the YR test, and one or more of the DPOAE, TEOAE, and ABR tests), an adequate YR probe-fit test (Keefe *et al.*, 2000; Keefe *et al.*, 2003), but not necessarily VRA data. This screening sample includes ears for which the hearing status is unknown. The screening sample is identical to the "partial data set" used by Keefe *et al.* (2003). It was split into a training set ($N=1278$ ears) and a validation set ($N=1147$ ears).

The predictions of hearing status in the present study are analyzed on a VRA sample population ($N=1094$) with inclusion criteria of completed YR measurements with adequate probe fit, one or more of the NHS tests (i.e., DPOAE, TEOAE, and ABR tests), and VRA tests. The VRA sample population is the subset of the screening sample population for which VRA tests results were available. Because there were so few impaired ears in the VRA sample population

($N=19$), it was not feasible to divide the VRA sample into training and validation samples; as a consequence, it was not possible to test generalization of the predictors of hearing status. A similar constraint was present in the INHI study, although more impaired ears were available in the complete INHI data base (Norton *et al.*, 2000b).

The YR tests for middle-ear dysfunction are developed on a sample of "normal-hearing" ears with adequate YR probe fits. "Normal hearing" is taken to mean a demonstrated absence of sensorineural hearing loss during the VRA test performed at ages 8–12 months. The gold standards of the hearing screening tests are based on criterion values of EOAE SNR and ABR latencies that achieve 80% specificity; hence, the need to restrict the sample to normal-hearing ears. Because a test of middle-ear dysfunction might be useful for a sample population in which hearing status is unknown, i.e., a typical hearing-screening population including normal and impaired ears, the YR tests for middle-ear dysfunction are subsequently evaluated to assess test generalization on such a sample. Finally, the YR tests of middle-ear dysfunction are used on the VRA screening population to separately assess results on normal and impaired ears.

IV. RESULTS

A. Predictions of sensorineural hearing loss

The factor loadings are those listed in Table II of Keefe *et al.* (2003). Using these loadings, the factors on the VRA sample are calculated and represented using the factor names in Table I. On completing steps 1–5 of the procedures described in Sec. II A, the final models to predict sensorineural hearing loss on the VRA sample are

$$\begin{aligned} \text{DPOAE:} \quad \text{LOSS} &= o(\text{SNR} + \text{SNR} * \text{FYLO} + \text{SNR} * \text{FYHI} \\ &\quad + \text{SNR} * \text{FRLO}), \\ \text{TEOAE:} \quad \text{LOSS} &= o(\text{SNR} + \text{SNR} * \text{FYLO}), \\ \text{ABR:} \quad \text{LOSS} &= o(\text{Fsp} + \text{Fsp} * \text{FRLO}). \end{aligned}$$

As expected, none of the factors is present as a main variable in any of these models, meaning that YR factors are not main effects in predicting sensorineural hearing loss. Some factors are present as interactions. None of these models includes *FRHI*, the factor that is predominant in most of the linear regressions predicting EOAE level and in the logistic regressions classifying EOAE responses as present or absent (Keefe *et al.*, 2003). The factors *FYLO-1*, *FYHI-3*, and *FRLO-6*, which are present in the above predictor models, are factors that were usually absent in the corresponding linear regressions described by Keefe *et al.*, especially for EOAE-dependent variables for frequencies at and above 2 kHz. The low-frequency YR response is always present as an interaction with a main variable: low-frequency admittance *FYLO* is present in the DPOAE and TEOAE predictors, and low-frequency reflectance *FRLO* is present in the ABR and DPOAE predictors. The only high-frequency factor present is *FYHI* in the DPOAE predictor.

The final models for the DPOAE and ABR predictors have a significantly higher likelihood than that of the corresponding univariate model at the $p=0.05$ level (Table II).

TABLE II. Significant logistic regression coefficients and odds ratios to predict hearing status.

Var	Coef.	Odds ratio	1/(Odds ratio)	Wald p	[95% Conf. interval of odds ratio]	
DPOAE:						
Log likelihood ration compared to SNR-only model exceeds 0 with $p=0.0019$						
SNR	-1.192	0.30	3.29	0.002	0.15	0.64
SNR \times FYLO	0.624	1.87	0.54	0.007	1.18	2.94
SNR \times FYHI	-0.469	0.63	1.60	0.032	0.41	0.96
SNR \times FRLO	-0.278	0.76	1.32	0.035	0.58	0.98
Constant	-2.436			0.000		
TEOAE:						
Log likelihood ratio compared to SNR-only model exceeds 0 with $p=0.0729$						
SNR	-0.389	0.68	1.48	0.000	0.55	0.83
SNR \times FYLO	0.190	1.21	0.83	0.096	0.97	1.51
Constant	-2.365			0.000		
ABR:						
Log likelihood ratio compared to SNR-only model exceeds 0 with $p=0.0179$						
Fsp	-2.100	0.12	8.17	0.000	0.07	0.23
Fsp \times FRLO	-0.390	0.68	1.48	0.036	0.47	0.98
Constant	1.269			0.015		

The final model for the TEOAE predictor is significant only at the $p=0.10$ level. Therefore, inclusion of the YR measurement of middle-ear functioning improves the model to predict sensorineural hearing loss in DPOAE and ABR measurements, and possibly so in TEOAE measurements.

For the DPOAE model, each of the independent variables can be interpreted as influencing the odds ratio because the range of the 95th percentile does not include the odds ratio of 1 (Table II). Equivalently, the Wald p -value for each interaction is less than 0.05. The SNR has an inverse odds ratio of 3.29, while the strongest interaction SNR \times FYLO has an odds ratio of 1.87. An explanation of the odds ratio and the inverse odds ratio is given elsewhere (Keefe *et al.*, 2003). For the TEOAE model, the SNR has an inverse odds ratio of 1.48, but the interaction SNR \times FYLO is not significant because its 95th percentile range includes the odds ratio of 1 (its Wald p -value is significant at the 0.10 level). For the ABR model, each of the independent variables influences the odds ratio. The Fsp has an inverse odds ratio of 8.17, while the interaction SNR \times FRLO has an inverse odds ratio of 1.48.

The classification performance of each model is assessed using the areas under the ROC curves in Fig. 1. For all DPOAE, TEOAE, and ABR models, the ROC curve of the multivariate model has sensitivities that are greater than or equal to the sensitivities on the corresponding ROC curve of the univariate model across all specificities. For the ROC curves based on EOAE data, the curves ascend linearly to a sensitivity value in the range of 0.80–0.85. This point corresponds to a SNR of 0 dB and includes most of the impaired ears (e.g., 13 of 16 impaired ears in the DPOAE measurement have 0 dB SNR). The multivariate and univariate curves overlay at this sensitivity (and specificity) value. All differences in the ROC curves occur at SNRs exceeding 0 dB for which the interaction terms in the model (SNR \times F_m) exert influence. Thus, the models differ in their predictions only at high sensitivities. The ABR curves using Fsp are similar to the EOAE curves. The areas under the ROC curves in Fig. 1 are listed on each curve for the multivariate and

univariate models. The area is always larger for the multivariate model than the corresponding univariate model. None of the area differences is significant at the 0.05 level, although the TEOAE and ABR model differences are significant at the 0.10 level for the full VRA sample. The small number of impaired ears limits the ability to interpret this test of significance.

Figure 2 plots the specificity versus sensitivity over the range of sensitivities exceeding 0.79, which includes the sensitivities for which the multivariate and univariate tests differ. This is the range in which EOAE SNR exceeds 0 dB. The difference in specificity between equal-sensitivity pairs of data is the reduction in the false-positive rate provided by using the information on middle-ear status. The reduction in false-positive rate can be large: for the set at the highest test sensitivity (upper panel), the DPOAE specificity increases from 13% in the univariate model to 69% in the multivariate model.

The low number of ears with sensorineural hearing loss in the VRA sample should be considered when evaluating these outcomes. For example, there were only 16 ears with sensorineural hearing loss in the EOAE-related outcomes. Of these, 13 failed to produce a SNR exceeding 0 dB. Thus, the sensitivity values for those parts of the ROC curves where the two models differed represent data from three ears. While confidence is greater in terms of test specificity because the number of ears with normal hearing is much larger, the limited number of hearing-impaired ears on the interesting parts of the ROC curves must be considered. Having offered this caveat, in every case, the multivariate model represented an improvement over the univariate model.

B. Predictions of middle-ear dysfunction

After pruning those YR factors that have negligible effect on the likelihood ratio (at the $p=0.05$ level of significance), the predictors for the DT and DTA gold standards take the forms listed in Table III. Each predictor uses the same factors with the same sign. The most important factor is FRHI, with an odds ratio of 3.58 in the DT and 4.19 in the

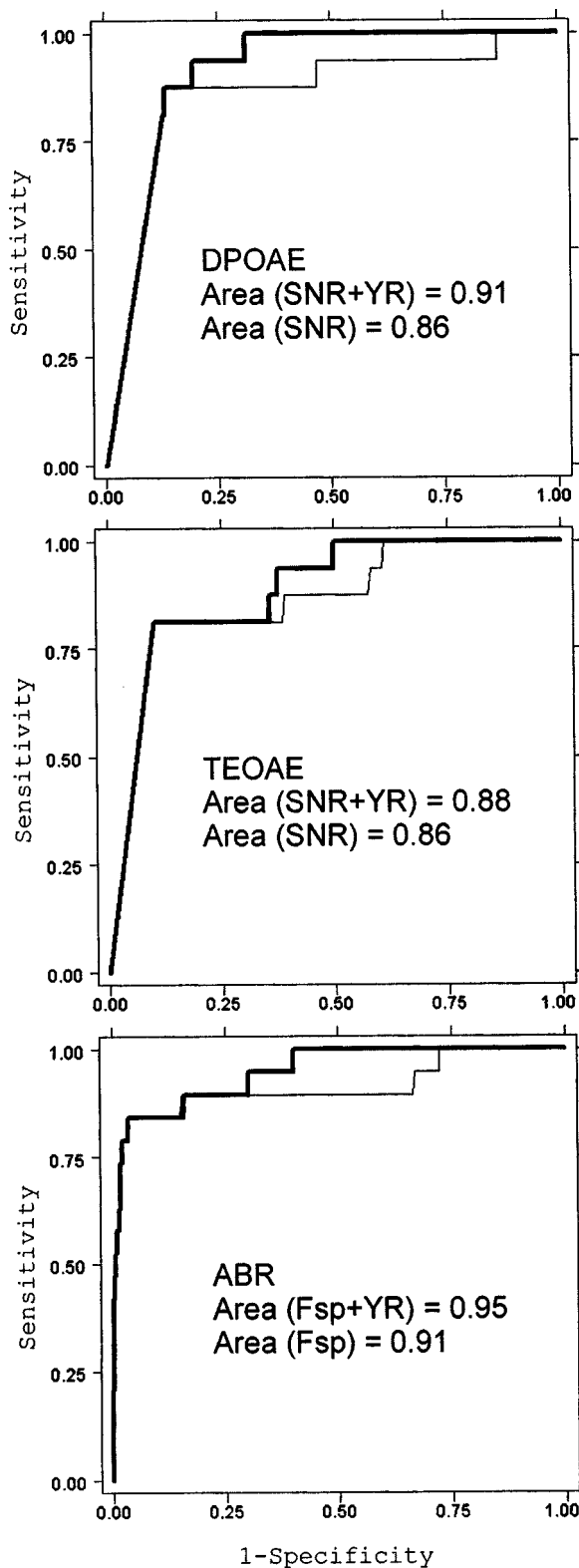


FIG. 1. The ROC curve is plotted for the VRA sample. Results are shown for DPOAE models (top row), TEOAE models (middle row), and ABR models (bottom row). The thick line plots the ROC curve for the multivariate model (including YR factors), and the thin line plots the ROC curve for the univariate model (SNR for EOAE models or *Esp* for ABR models). The corresponding areas under the ROC curve are listed for the multivariate and univariate models.

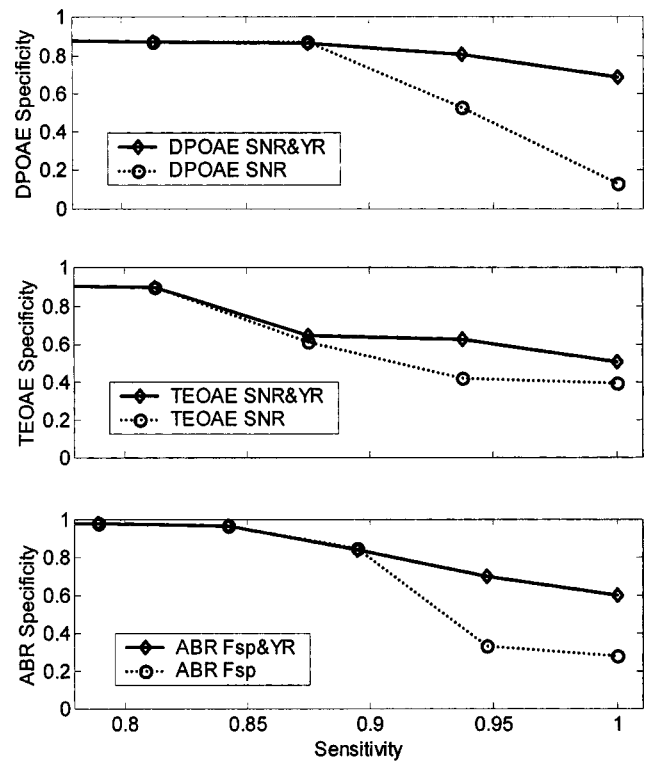


FIG. 2. The specificity versus sensitivity is plotted for the VRA sample for those data with sensitivities exceeding 0.79. Results are shown for DPOAE models (top row), TEOAE models (middle row), and ABR models (bottom row). In each panel, the solid line with diamonds as symbols is the curve for the multivariate model, and the dashed line with circles as symbols is the curve for the univariate model. The difference in specificity between equal-sensitivity pairs of data in each panel is the reduction in the false-positive rate by the multivariate model.

DTA predictor. The only other factor with an odds ratio or inverse odds ratio larger than 2 is *FYRMI* for DT and DTA.

The ROC curve for the DT predictor is plotted in Fig. 3. The area under the ROC curve is 0.86 for the DT predictor and is 0.91 for the DTA predictor (its ROC curve is not shown). These ROC areas are not directly comparable be

TABLE III. Significant logistic regression coefficients and odds ratios for DT and DTA gold standards.

Factor	Coefficient	Odds ratio	1/(Odds ratio)	Wald <i>p</i>
DT predictor based on DP0AE and TEOAE responses				
<i>FYLO-1</i>	-0.208	0.81	1.23	0.079
<i>FRHI-2</i>	1.277	3.58	0.28	0.000
<i>FYRMI-4</i>	-0.915	0.40	2.50	0.000
<i>FY7k-5</i>	-0.274	0.76	1.32	0.020
<i>FYMI-7</i>	-0.520	0.59	1.68	0.000
Constant	-2.430			0.000
DTA predictor based on DPOAE, TEOAE, and ABR responses				
<i>FYLO-1</i>	-0.514	0.60	1.67	0.001
<i>FRHI-2</i>	1.432	4.19	0.24	0.000
<i>FYRMI-4</i>	-0.815	0.44	2.26	0.000
<i>FY7k-5</i>	-0.529	0.59	1.70	0.005
Constant	-3.531			0.000

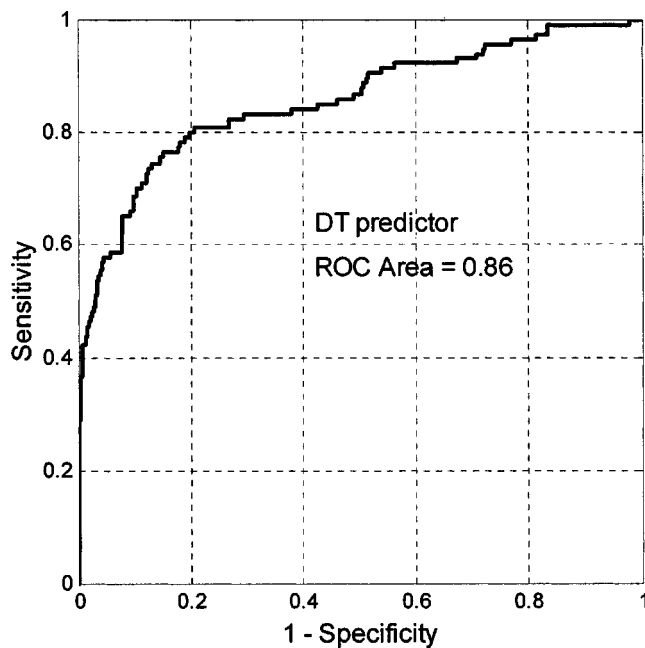


FIG. 3. The ROC curve is plotted for the DT predictor of middle-ear dysfunction in the population on which the DT predictor is defined. The gold standard includes those ears as having normal middle-ear functioning in which both DPOAE and TEOAE responses are present, and as having middle-ear dysfunction in which both DPOAE and TEOAE responses are absent. The EOAE pass/fail criteria are based on 80% specificity.

cause the numbers of test subjects differ depending on the differing definitions of gold standard—876 normal-hearing ears in the DT analysis (762 pass and 114 fail), and 716 normal-hearing ears in the DTA analysis (669 pass and 47 fail).

The purpose of constructing a test of middle-ear dysfunction is to identify those false positives in hearing screening tests likely to have middle-ear dysfunction. The comparisons are performed for EOAE and ABR test criteria of 80% specificity, as described in Keefe *et al.* (2003). The ABR test criterion of hearing status at 80% specificity is a pass if the F_{sp} is at or above 3.25. This ABR criterion using F_{sp} is in contrast with the absence of ABR variables in the DT gold standard, and the presence of ABR $L_V(70)$ in the DTA gold standard, but it is in accord with the use of ABR F_{sp} in the INHI study.

The areas under the ROC curve are compared for the DT and DTA predictors for the normal-hearing group in order to focus on false positives (FP). For each diagnostic test of hearing status, its group is called the VRA-FP. Because each test performs differentially in predicting sensorineural hearing loss, the composition of the VRA-FP group varies for

each test. Using the DPOAE test as an example, the task for the DT and DTA predictors is to classify each infant as having passed or failed the DPOAE test due to middle-ear dysfunction, i.e., to discriminate on the DPOAE test between the false positives and the true negatives. The ability of each predictor in this classification task is assessed by its area under the ROC curve. There are no free parameters in this comparison.

The false-positive/true-negative groups are

- (1) ABR test
- (2) DPOAE test
- (3) TEOAE test
- (4) Two-stage test, DPOAE/ABR
- (5) Two-stage test, TEOAE/ABR.

Groups 1–3 compare middle-ear dysfunction test performance on the VRA-FP populations from the separate DPOAE, TEOAE, and ABR tests. Groups 4–5 compare middle-ear dysfunction test performance on the two-stage paradigm recommended by the NIH (1993) in its Consensus Conference Report, and evaluated in the INHI study (Norton *et al.*, 2000c). This recommendation is to use EOAE screening followed by an ABR only on those infants failing the OAE screening, an approach that results in the fewest referrals and the lowest cost (Gorga *et al.*, 2001). For those infants failing the initial OAE test in such a paradigm, it is generally thought that middle-ear dysfunction plays a role in those infants who subsequently pass the ABR test.

The results shown in Table IV show better performance for the DT test than the DTA test across the five VRA-FP test groups. The ROC area of the DT test is significantly larger than that of the DTA test for the two-stage DPOAE/ABR test group at the $p=0.05$ level, and for the TEOAE and two-stage TEOAE/ABR test groups at the $p=0.10$ level. The ROC areas are larger for the DT than the DTA test for the DPOAE and ABR test groups, but the differences are not significant. Still, the DTA test does not outperform the DT test on any test group. Thus, the DT test is selected in subsequent analyses as the preferred test of middle-ear dysfunction.

The DT test performs poorly at identifying ABR false positives (ROC area of 0.58). The DT test identifies false positives in DPOAE screening with an ROC area of 0.78 and in TEOAE screening with an area of 0.74. For the two-stage hearing screening tests recommended by the NIH (1993), the DT test identifies false positives in DPOAE/ABR screening with an ROC area of 0.84 and in TEOAE/ABR screening with an ROC area of 0.81. The ROC curves, on which these

TABLE IV. ROC areas for DT and DTA tests on VRA-FP populations with p -values for area differences.

VRA-FP Test ID	VRA-FP Diagnostic test	N total	N pass	N fail	ROC areas		
					DT test	DTA test	p
1	DPOAE	1027	842	185	0.784	0.778	0.632
2	TEOAE	1027	833	194	0.735	0.715	0.069
3	ABR	1027	829	198	0.578	0.571	0.565
4	DPOAE/ABR	1027	976	51	0.841	0.813	0.043
5	TEOAE/ABR	1027	977	50	0.812	0.784	0.052

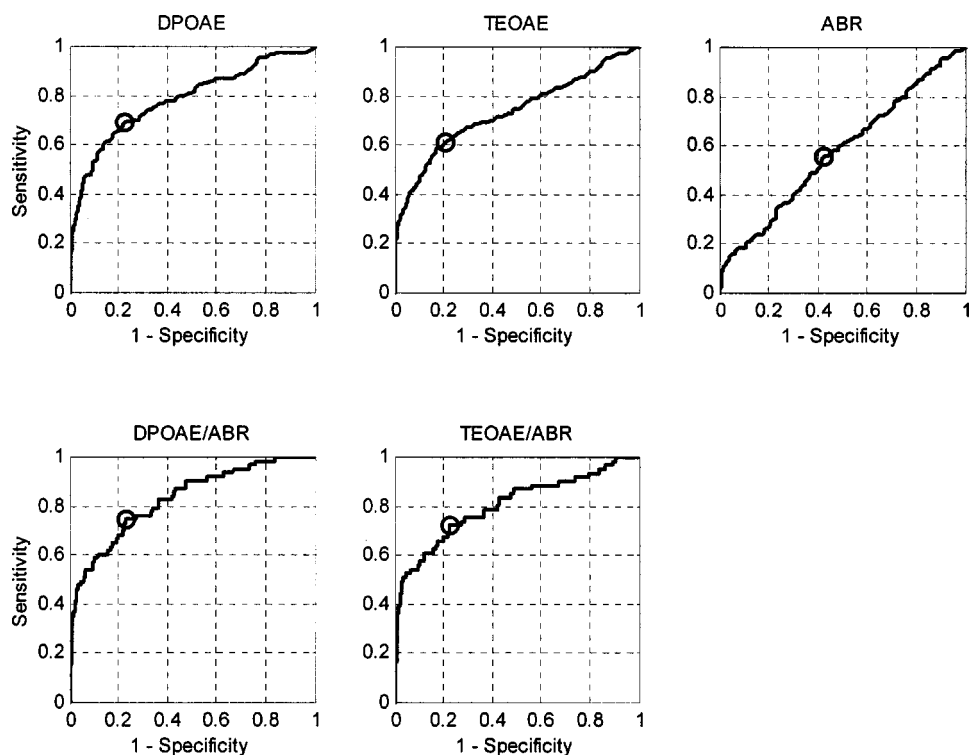


FIG. 4. The ROC curves are plotted for the DT predictor of middle-ear dysfunction in a population of normal-hearing ears using DPOAE, TEOAE, ABR, two-stage DPOAE/ABR, and TEOAE/ABR screening tests as labeled on each panel. The DT predictor classifies ears as passing or failing the screening test, with a fail interpreted as evidence of middle-ear dysfunction. The optimal choice of DT screening criterion is shown for each test by the circle.

ROC areas are calculated, are plotted in Fig. 4 for the DT test on each of the five VRA-FP groups. Like the ROC curve on the population on which the DT predictor was constructed (Fig. 3), the ROC curves for the two-stage tests have steep slopes at low sensitivities (lower-left corner of each ROC curve), which means that moderate sensitivities may be achieved at specificities close to 100%. For example, at fixed specificities of 98% and 95%, the corresponding sensitivities are 37% and 49% for the DPOAE/ABR, and 39% and 52% for the TEOAE/ABR test group. This trend is present, but in a weaker form, for the DPOAE and TEOAE test groups. The ROC curves depart from symmetry about the diagonal that connects the points at which the sensitivity and specificity both equal 100% (upper-left corner of ROC curve) and both equal 0% (lower right corner). This means that it is more difficult to achieve moderate specificities at sensitivities close to 100% than it is to achieve moderate sensitivities at specificities close to 100%.

The generalization performance of the DT test is analyzed by examining its test performance on a group of ears not included in the VRA sample. Because of the unavailability of VRA responses, it is impossible to categorize ears by hearing status in the DT generalization sample, but this generalization sample is statistically independent from the VRA sample on which the DT test was constructed. The accuracy of the DT test to predict middle-ear dysfunction is assessed in ears according to the DT gold standard, and according to the inclusion criteria in each of the five VRA-FP test groups. The prevalence of sensorineural hearing loss in the VRA sample is 1.4%–1.6%, which varies depending on exclusions of impaired ears that lack at least one of the EOAE or ABR test responses. This prevalence is expected to be higher than that in the DT generalization sample, because there was an effort in the INHI study to recruit a higher ratio of impaired

ears at the time of VRA testing than in the original neonatal screening. Thus, the preponderance of ears failing one or more of the VRA-FP tests are normal hearing. In the first test of generalization, the area under the ROC curve for the DT test on ears categorized according to the DT gold standard is 0.82, compared to 0.86 for the DT test on normal-hearing ears in the VRA sample as described above. This level of performance demonstrates that the DT test of middle-ear dysfunction generalizes to a new population with acceptable accuracy.

To test generalization of the test of middle-ear dysfunction on each of the VRA-FP test groups, the criterion that a response (DPOAE, TEOAE, or ABR) is absent in the DT generalization sample is based on the SNR or F_{sp} score that provides 80% specificity in the single-test VRA-FP sample groups in Table IV. The fail rates and corresponding ROC areas for the DT test are 14% fails and an area of 0.82 for predicting both DPOAE and TEOAE status, 22% fails and an area of 0.57 for predicting ABR status, and 5% fails and an area of 0.85 for predicting test status in the DPOAE/ABR and TEOAE/ABR tests. The prevalence of fails for the EOAE tests (14%) is less than the 20% fail rate that would be expected (at 80% specificity) in a population of normal-hearing ears of similar characteristics to the VRA sample. This is mainly due to a difference in sampling inasmuch as the DT generalization sample includes fewer ears with EOAE SNRs of 0 dB than the VRA sample, and, hence, has reduced fail rates. The prevalence of fails for the two-stage tests (5%) is nearly the same as the false-positive rate for the two-stage tests in Table IV, i.e., 50–51 fails in 1027 normal-hearing ears is a false-positive rate of 5%.

By coincidence, the independently selected pass/fail criteria for the DPOAE and TEOAE tests categorized the DT generalization sample into identical subgroups that passed or

failed each test. This explains their identical fail rates and ROC test performance, and, similarly, the identical fail rates and ROC test performance between the two-stage tests. Comparing results on the DT generalization sample and those listed in Table IV, the ROC areas for the DT generalization sample are larger for predicting DPOAE and TEOAE test status (0.82 versus 0.78 and 0.74 in Table IV), similarly poor for predicting ABR status (0.57 versus 0.58), and similar for the two-stage tests (0.85 versus 0.84 and 0.81). These ROC analyses suggest that the DT test has adequate generalization properties on a different population at risk for middle-ear dysfunction, even with the added confound of the unknown hearing status in the DT generalization sample.

V. DISCUSSION

The YR response measures the input frequency response at a probe location in the ear canal a small distance from the tympanic membrane. Inter-ear variations in this response indicate inter-ear variations in how the middle ear and ear canal receive, absorb, and transmit sound energy. The YR response is not a direct measurement of forward or reverse sound transmission between the middle ear and cochlea. Nevertheless, inter-ear variations in this input YR response in neonatal ears are influenced by differences in forward and reverse transmission, as evidenced by the influence of inter-ear variations of YR responses on inter-ear variations of EOAEs and ABRs (Keefe *et al.*, 2003). The structure of the YR response, viewed as an overall response pattern, provides indirect information on middle-ear transmission and may assist in NHS applications.

Results using the YR response have been obtained on classifying sensorineural hearing status and in predicting middle-ear dysfunctions. To classify hearing status, the YR response is included with the main hearing screening variables (EOAE, ABR) to predict the results of the behavioral VRA test. The YR factors enter the predictor as interactions with the main screening variables rather than as main variables, because an assessment of middle-ear functioning does not directly provide information on sensorineural hearing loss but rather provides information on the relative weighting of the main screening variables as influenced by the effects of middle-ear functioning. These results are discussed below in Sec. V A. To predict middle-ear dysfunction, the YR factors are main variables in predicting those normal-hearing ears in which the EOAEs and ABRs are outside the normal range of responses. In this task, the YR factors are predicting a physiological outcome (i.e., absent or anomalous EOAEs and ABRs) rather than a behavioral outcome as in the predictor of hearing status. These results are discussed below in Sec. V B.

A. Classification of hearing status

The present results indicate that knowledge of ear-canal and middle-ear status improves the prediction of hearing status. The criterion for improvement is based on the likelihood ratio test of the larger logistic regression model including the YR factor(s) as interactions and the smaller model including only the EOAE SNR or ABR *Fsp*. The DPOAE and ABR models are improved by inclusion of selected factors with a

p value of 0.05, and the TEOAE models are improved with a *p*-value of 0.10 (Table II). This latter *p* value is accepted because the paucity of subjects with sensorineural hearing loss in the sample increases the likelihood that an effect may be present, but difficult to observe from the background experimental noise.

The particular factors entering each solution are also tabulated, showing that *FRHI* is not included in any predictor. At face value, this might appear to contrast with the analyses in Keefe *et al.* (2003), which showed that *FRHI* was highly correlated with EOAE levels and some ABR latencies, and *FRHI* was the most important factor in classifying EOAE responses. However, this apparent contrast arises because *FRHI* has a strong negative correlation with EOAE level as well as EOAE SNR. Because the EOAE SNR is present as an independent variable in the model, then *FRHI* becomes redundant. Those factors that are less well correlated to the EOAE SNR are the ones that add new information when included in a model to predict sensorineural hearing loss. The case of *FRHI* and the ABR is similar. The multivariate models include the low-frequency portions of the YR response, which provide information on ear-canal and middle-ear functioning that is largely independent of the information in the YR response at high frequencies. This is because the factors were constructed to be uncorrelated (Keefe *et al.*, 2003).

An important structural property of the model is that the YR factors enter as *interactions* with EOAE or ABR variables rather than as main effects. It would be appropriate to use YR factors as main effects if there were a conductive component to the hearing loss, but such models with factors as main effects do not improve the prediction of sensorineural hearing loss. The best models of sensorineural hearing loss are constructed using interactions of YR factors with EOAE or ABR variables. Examples of how the individual YR factors influence the predictions of sensorineural hearing loss are described in detail in Appendix A, and summarized as follows. In the context of EOAE or ABR screening, the likelihood of middle-ear dysfunction is increased by: (1) large reflectance at low frequencies (large *FRLO*); (2) small equivalent volume or large acoustic conductance at low frequencies (small *FYLO*); and (3) large equivalent volume and acoustic conductance at 3–6 kHz, and small equivalent volume at 8 kHz (large *FYHI*). An important clinical problem limiting the efficacy of NHS programs is the high false-positive rate. It is advantageous in a screening program to have high sensitivity to accomplish its main goal of identifying infants with sensorineural hearing loss, and high specificity to control unnecessary referrals of infants with normal hearing. The present results show that including YR factors in the predictive model of sensorineural hearing loss can reduce the false-positive rate, when comparisons are made with univariate predictive models at fixed sensitivities (Fig. 2). The YR factors exert influence in the models over the range of EOAE SNR and ABR *Fsp* values that are intermediate between very low values, predictive of sensorineural hearing loss, and high values, predictive of normal hearing. Because the factors enter the EOAE-based predictors as interactions

with SNR, they have no effect on the predictions in approximately 15% of ears in the sample in which SNR=0.

These results suggest that the false-positive rates of NHS programs using EOAE and ABR tests may be better controlled by including a YR test. The YR test, which takes only seconds to perform (Keefe *et al.*, 2000), might be completed before the EOAE or ABR test, because the YR test includes a more accurate test of probe fit. Thus, the operator could adjust probe fit before concluding the YR test and proceeding to the EOAE or ABR test. Any improvement in probe fit would likely be beneficial for the subsequent EOAE or ABR test. The steps in constructing the predictor of hearing based on measurements of EOAE or ABR responses, and a YR response, are described in Appendix B.

The areas under the ROC curves for the models with and without the YR factors do not differ significantly at the $p = 0.05$ level, although the TEOAE and ABR areas in the full set are different at the $p = 0.10$ level. These area estimates are probably more inaccurate than the estimates of the likelihood ratio because the area under the ROC curve is highly sensitive to the small number of impaired ears. For example, each ROC curve in Fig. 1 is based on less than 20 observations in impaired ears, evidenced as discrete steps along the sensitivity axis, compared to approximately a thousand observations in normal-hearing ears, evidenced as discrete steps along the specificity axis. This reflects the low prevalence of sensorineural hearing loss in the sample population. The likelihood ratio test is an overall test of model fit, and not overly dependent on the distribution of responses in ears with sensorineural hearing loss. The present emphasis on reduction in false-positive rates is based on observed shifts of tens or hundreds of responses along the specificity axis, and it appears reasonable given the large number of ears with normal hearing. Nevertheless, there is the potential for error due to the small number of observations in impaired ears. These limitations notwithstanding, models that included measures of middle-ear functioning (YR responses) resulted in slightly higher ROC areas in every case. Additional studies are needed on sample populations with more neonates with sensorineural hearing loss.

A different interpretation of these results is that the observed improvement in predicting hearing status in models including EOAE SNR and YR factors may be due to simply having provided more information concerning the auditory system in adding the YR factors, which may have been equally resident in other EOAE variables. In studies on predicting sensorineural hearing loss in older children using TEOAEs (Hussain *et al.*, 1998) and in patients of all ages using DPOAEs (Dorn *et al.*, 1999), the inclusion of multiple EOAE response variables into a multivariate predictor had better test performance than a model using a single EOAE level or SNR variable. In the results described above, the independent EOAE variable in the predictor was the minimum SNR at 2, 3, or 4 kHz. A reasonable choice of inputs for a multivariate EOAE predictor are the corresponding signal and noise variables at 2, 3, and 4 kHz, or six inputs in all, as these represent the conditions in which reliable data were obtained most often in the INHI study (Norton *et al.*, 2000b). Their use also parallels multivariate analyses used in previ-

TABLE V. The effect of adding YR factors to multivariate EOAE models.

Model	p	ROC area
DPOAE		0.90
DPOAE+ Interactions	0.034	0.94
TEOAE		0.87
TEOAE+ Interactions	0.095	0.90

ous research. These allow the predictor to separately weight the EOAE and noise levels at different frequencies. Such a model becomes the new baseline model against which to test whether the addition of YR factors to this baseline model improves test performance.

To examine this possibility, the YR factors are added as interactions in a larger model, such that the particular factors added are those listed for DPOAE and TEOAE models in Table II. As described earlier, there is a need to keep the number of independent variables small, and the new baseline model already has six variables whereas the older baseline model used one variable. Constructing each interaction between each of the EOAE levels at three frequencies, and up to three factors per model, would lead to as many as nine interactions, or 15 independent variables in total, a number that is excessive in relation to the small number of ears with sensorineural hearing loss. For this reason, interactions are calculated between the broadband EOAE SNR variable used in the earlier results and each factor. For the case of three factors, there are only three interactions for a total of nine variables.

The results of this comparison show that the larger model including YR factors is better for both DPOAE and TEOAE predictors. The p values associated with the likelihood ratio test are significant at the 0.05 level for DPOAEs, and at the 0.10 level for TEOAEs (Table V). This pattern of p values duplicates the results described earlier for models using a single EOAE variable, which showed a stronger effect for interactions with ear-canal and middle-ear status using DPOAE variables than TEOAE variables. The predictive information in the YR response is retained despite the added information in the multivariate EOAE response. The corresponding ROC areas are always larger when the YR factors are included, e.g., equal to 0.94 for the DPOAE-based predictor. These results confirm and extend the previous analyses that demonstrate that knowledge of ear-canal and middle-ear status improves test performance for predicting sensorineural hearing loss. The YR response contains information concerning the response of the ear that is not duplicated in the multivariate EOAE response.

B. Tests of middle-ear dysfunction to interpret false-positive screening results

Based on the observations that middle-ear dysfunction reduced EOAE levels and increased ABR latency, a test of middle-ear dysfunction (DT test) was devised based on the presence or absence of DPOAEs and TEOAEs in normal-hearing ears using threshold values of DPOAE and TEOAE SNR. An alternative test of middle-ear dysfunction (DTA) was devised based on the presence or absence of DPOAEs,

TEOAEs, and ABRs using threshold values of DPOAE and TEOAE SNR, and ABR $L_V(70)$. The DT and DTA tests were constructed on a sample population of normal-hearing ears, and compared with respect to their ability to correctly classify ears as having middle-ear dysfunction. The criterion for middle-ear dysfunction was a fail on the predictive test of hearing status during the neonatal period, followed in the original INHI data collection by VRA results (8 or more months later) indicating that hearing was normal. Several hearing-status screening tests or test combinations were evaluated, including DPOAE, TEOAE, ABR, two-stage DPOAE/ABR, and two-stage TEOAE/ABR tests. For each hearing-status test, the ROC area for the DT test exceeded that for the DTA test; this area difference was significant at the $p=0.05$ level for the DPOAE/ABR test and at the $p=0.10$ level for the TEOAE and TEOAE/ABR tests. This suggests that the DT test is, overall, a better predictor of middle-ear dysfunction than the DTA test. In addition, the DT test is favored over the DTA test because it is expected to be a more robust test. This is based on the larger number of false-positives in the DT training set (114 ears) than the DTA training set (47 ears). For classifying false positives in the two-stage EAOE and ABR tests using the DT predictor, the areas under the ROC curve are in the range 0.81–0.84 (Table IV).

The DT and DTA logit coefficients are similar (Table III), with both strongly weighting the high-frequency reflectance factor *FRHI* that is important in accounting for the structure of EAOE responses and ABRs (Keefe *et al.*, 2003). The weighting strength is assayed in terms of the large *FRHI* odds ratio of 3.58 in the DT predictor. The other factors entering the DT predictor, sorted in order of decreasing odds ratio or inverse odds ratio (using whichever of the pair exceeds unity), are *FYRMI* (2.50), *FYMI* (1.68), *FY7k* (1.32), and *FYLO* (1.23). The factors that do not enter the DT predictor are *FYHI* and *FRLO*. It is interesting that *FYHI* and *FRLO* enter one or more of the predictors of hearing status (Table II), but not the predictors for middle-ear dysfunction, and vice versa for *FRHI*, *FYRMI*, *FY7k*, and *FYMI*. The only factor entering both types of predictors is *FYLO*. *FYLO* is hypothesized to be the most highly correlated YR factor with tympanometry at frequencies up to 1 kHz, because both are measures of acoustic admittance in this frequency range. This inclusion asymmetry in the factors entering the hearing-loss and middle-ear dysfunction predictors was described earlier for *FRHI*, and arises because EAOE SNR and ABR *Fsp* are main variables in the predictors of hearing status. When these main variables are present in the predictor, the factors that account for their presence or absence become redundant and are therefore not included in the predictor.

A practical example is presented of the performance of the DT test of middle-ear dysfunction in hearing screening based on DPOAE, TEOAE, ABR, two-stage DPOAE/ABR, and two-stage TEOAE/ABR tests in the VRA-FP populations. These VRA-FP tests use the same 80% specificity criterion for pass/fail thresholds that was used in the INHI study (Fig. 10 in Norton *et al.*, 2000b). The test criterion for the DT test is at the “optimal” choice of specificity and sensitivity, which is defined as the point on each ROC curve

at which the product of specificity and sensitivity is a maximum. This might be a reasonable pass/fail criterion in a test of middle-ear dysfunction, as a compromise between the twin, and usually opposing, requirements of high specificity and high sensitivity, because the optimal point tends to have nearly equal specificity and sensitivity. These are opposing requirements when there is overlap between the pair of distributions defined by the gold standard, as is the case here. The optimal point on each ROC curve in Fig. 4 is represented by a circle. Table VI lists for each test at its optimal point the corresponding specificity (“true negative” and middle-ear dysfunction “absent”) and sensitivity (“false positive” and middle-ear dysfunction “present”).

Table VI provides an opportunity to review the implications of the choice of a hearing screening test specificity of 80%. The DPOAE test specificity is $842/1027=0.82$, which corresponds to that choice of SNR threshold producing a specificity closest to 80%, and the corresponding DPOAE test sensitivity is $13/15=0.87$. The two-stage DPOAE/ABR test specificity is $976/1027=0.95$ and its test sensitivity is $12/15=0.80$. In this instance, the addition of the ABR test (with a test specificity of $829/1027=0.81$) improves the two-stage DPOAE/ABR test specificity at the cost of diminished sensitivity (one less impaired ear was correctly classified). This illustrates a problem analogous to that which arises in evaluating the addition of a test of middle-ear dysfunction to NHS programs, insofar as an improvement in DPOAE test specificity (by adding ABR) is obtained at the cost of a reduction in DPOAE test sensitivity. Appendix A describes trade-offs between specificity and sensitivity when YR factors are added as interactions with EAOE or ABR variables to predict hearing status. This example shows the trade-offs are not unique to the addition of the YR tests, but are present in the two-stage DPOAE/ABR tests as well (the same trade-off occurs in the two-stage TEOAE/ABR tests). One approach to ameliorate this problem might be to modify the test criteria for the DPOAE and ABR tests to maintain the same sensitivity as for the DPOAE test alone, but the ability to effectively assess the modification is limited by the small number of impaired ears.

Returning to the issue of predicting middle-ear dysfunction and the DT test performance listed in Table VI, for the results of DPOAE testing on normal-hearing ears, the optimal DT criterion provides a true-negative rate (or middle-ear specificity) of $654/842=0.78$, and a false-positive rate (or middle-ear sensitivity) of $128/185=0.69$. The DT test for the results of TEOAE testing on normal-hearing ears also has a higher true-negative rate (0.80) than false-positive rate (0.61), but the results on the ABR and two-stage tests have true-negative (0.58) and false-positive (0.56) rates that are nearly equal. For predicting two-stage EAOE/ABR test performance on normal-hearing ears, the DT test has true-negative and false-positive rates within 1% of 77%.

Selecting the two-stage DPOAE/ABR test results for further study (similar results are obtained for the two-stage TEOAE/ABR test), 78% of the false positives are classified as having failed due to middle-ear dysfunction. Of the 51 of 1027 ears (5.0%) failing the two-stage screening, 40 ears have middle-ear dysfunction and 11 ears do not. From this

TABLE VI. Performance table of DT test of middle-ear dysfunction for DPOAE, TEOAE, ABR, DPOAE/ABR, and TEOAE/ABR hearing tests in which each hearing test is set at 80% specificity and each DT test set at the optimal criterion at which the product of DT specificity and sensitivity is a maximum. In each boxed row containing two lines, the top number is the number of ears and the bottom number is the corresponding proportion. For example, in the DPOAE test type for the true negative test outcome, 654 ears had absent middle-ear dysfunction corresponding to a proportion of 0.78 of the total number of ears.

Test type	Normal-hearing ears				Sensorineural hearing-loss ears			
	Test outcome	Middle-ear dysfunction			Test outcome	Middle-ear dysfunction		
		Absent	Present	Total		Absent	Present	Total
DPOAE	True negative	654	188	842	False negative	2	0	2
		0.78	0.22			1.00	0.00	
	False positive	57	128	185	True positive	5	8	13
		0.31	0.69				0.38	0.62
		Total normal	711	316	1027	Total impaired	7	8
TEOAE	True negative	663	170	833	False negative	2	1	3
		0.80	0.20			0.67	0.33	
	False positive	75	119	194	True positive	5	7	12
		0.39	0.61			0.42	0.04	
		Total normal	738	289	1027	Total impaired	7	8
ABR	True negative	482	347	829	False negative	1	1	2
		0.58	0.42			0.50	0.50	
	False positive	88	110	198	True positive	3	10	13
		0.44	0.56			0.23	0.77	
		Total normal	570	457	1027	Total impaired	4	11
Two-Stage DPOAE/ABR	True negative	750	226	976	False negative	2	1	3
		0.77	0.23			0.67	0.33	
	False positive	11	40	51	True positive	5	7	12
		0.22	0.78			0.42	0.58	
		Total normal	761	266	1027	Total impaired	7	8
Two-Stage TEOAE/ABR	True negative	758	219	977	False negative	2	2	4
		0.78	0.22			0.50	0.50	
	False positive	12	38	50	True positive	5	6	11
		0.24	0.76			0.45	0.55	
		Total normal	770	257	1027	Total impaired	7	8
		0.75	0.25			0.47	0.53	

perspective, the unexplained fail rate is reduced from 5.0% to $11/1027 = 1.1\%$.

However, the results on the 15 ears with sensorineural hearing loss must also be considered, corresponding to a prevalence of sensorineural hearing loss of $15/(1027 + 15) = 1.4\%$. This prevalence is approximately an order of magnitude larger than that for a general screening population because of the effort in the INHI study to preferentially recruit subjects with risk factors for sensorineural hearing loss. The DPOAE/ABR test correctly classifies 12 of 15 ears with sensorineural hearing loss (the total true positives in Table VI). Of these 12 true positives, 7 ears are judged to have middle-ear dysfunction and 5 ears are not. The 5 ears with normal middle-ear functioning are unambiguously identified as having sensorineural hearing loss, but there is ambiguity between the results on the 7 ears failing the DPOAE/ABR test and failing the middle-ear test. These test results may be explained by identifying the ears as having sensorineural hearing loss and middle-ear dysfunction. The DPOAE/ABR test incorrectly classifies 3 of 15 ears with sensorineural hearing loss (the total false negatives in Table VI). Of these 3 false negatives, 1 ear is judged to have middle-ear dysfunction

and 2 ears are not. The middle-ear test does not help explain why these ears passed the two-stage DPOAE/ABR test but nonetheless had sensorineural hearing loss at the time of VRA testing, and particularly so for the 1 ear that was judged to have middle-ear dysfunction (unless middle-ear pathology was related to subsequent development of sensorineural hearing loss).

These results illustrate the fact that ears with middle-ear dysfunction may or may not have sensorineural hearing loss. Just because an ear fails a hearing-screening test due to middle-ear dysfunction does not mean that the ear does not have a sensorineural hearing loss. There can be ears with pure sensorineural hearing loss, pure conductive loss, or a mixed loss with both sensorineural and conductive components. The test of middle-ear dysfunction provides an outcome measure that may be useful for diagnosing the sensorineural hearing loss. It is probably more robust than the multivariate tests that include YR variables in the predictor of sensorineural hearing loss due to the much larger number of impaired ears in its accompanying gold standard—15 ears for the predictors in Table II versus 114 ears for the DT predictor in Table III. The test of generalization using the DT

test confirms that the predictor is robust. If a subject fails a hearing-screening test, the subject is retested later. By tracking the test results for predicting both hearing status and middle-ear dysfunction, it may be possible to improve the identification of the type of sensorineural hearing loss. The inclusion of air-conduction and bone-conduction ABR and/or behavioral testing, the latter at an age for which reliable results can be obtained, might be used to judge the relative effectiveness of the YR test in predicting a conductive hearing loss.

In summary, a test of middle-ear status would help to refine the overall diagnosis of sensorineural hearing loss, and in interpreting measurements of YR responses in conjunction with EOAE (and ABR) results. The DT test was constructed on normal-hearing ears in which both DPOAE and TEOAE responses were either present or absent. This redundancy in EOAE testing assisted in categorizing those ears with both EOAEs present as having normal middle-ear functioning, and those ears with both EOAEs absent as having middle-ear dysfunction. The latter interpretation was supported by the constraint on subject inclusion that all ears had normal VRA results. After constructing the DT predictor, it was used to explain single-stage and two-stage test results using EOAE and ABR measurements on two populations, one on which hearing status was known and another on which hearing status was unknown (the generalization test). Knowing that a middle-ear dysfunction exists during the perinatal period may have the benefit of providing greater information on the condition of the ear, even though a subsequent hearing test still will be needed in order to establish whether a sensorineural hearing loss exists. These results suggest that the YR response may provide such a screening test of middle-ear dysfunction.

VI. CONCLUSIONS

In screening tests to predict sensorineural hearing loss in neonates using DPOAEs, TEOAEs, and ABRs, the inclusion of the YR response improves the performance of tests based on DPOAEs and ABRs, and perhaps improves the performance of tests based on TEOAEs. This suggests that the YR test of middle-ear and ear-canal functioning may improve the overall accuracy of NHS programs based on EOAE and ABR testing. A YR test to predict middle-ear dysfunction has been constructed that classifies EOAE responses in normal-hearing ears as present or absent. The false-positive outcomes in the two-stage screening tests in normal-hearing neonates are classified as having middle-ear dysfunction with areas under the ROC curve of 0.84 for DPOAE/ABR and 0.81 for TEOAE/ABR. The addition of a YR test to a NHS program may have benefits for the subsequent diagnosis of sensorineural hearing loss, because the YR response improves the models of test performance of EOAE and ABR screening tests, and predicts the presence of middle-ear dysfunction as evidenced in the inability to record EOAEs in normal-hearing ears.

The use of YR testing in hearing screening does not duplicate or replace the use of bone-conduction ABR and bone-conduction audiometry in follow-up testing to diagnose the specific type of hearing loss. Assuming that the bone-

conduction and air-conduction tests were suitably cross calibrated on populations of normal-hearing neonatal ears across a range of ages, an assumption for which objective criteria are not presently available, the comparison of bone-conduction and air-conduction ABRs and audiograms would give a direct measure of a possible conductive component to the hearing loss. Even if such objective criteria were available, this still leaves open the problem in early newborn hearing screening programs of classifying ears as having probable middle-ear dysfunction, for which the present results provide objective test performance.

ACKNOWLEDGMENTS

We appreciate the assistance of Susan J. Norton, Kelley Mascher, and Kristin Fletcher in transferring of research data from the INHI project. The INHI project data were collected and analyzed with the support of the NIDCD (DC01958). This research was partially supported by the NIDCD (DC03784).

APPENDIX A: INTERPRETATION OF MULTIVARIABLE PREDICTOR COEFFICIENTS PREDICTING HEARING STATUS

One example using the ABR response is considered in detail to understand how the ear-canal and middle-ear factors influence the prediction of sensorineural hearing loss. The logit L for this predictor is taken from the results in Table II to be

$$L = c_1 * Fsp + c_2 * Fsp * FRLO + c_0,$$

in terms of the regression coefficients $c_1 = -2.10$, $c_2 = -0.39$, and $c_0 = 1.27$. An increase in the logit function increases the probability p_L of sensorineural hearing loss, because $p_L = o(L)$. The coefficient $c_1 < 0$ in this example, signifies that increasing Fsp is associated with decreasing probability of sensorineural hearing loss, because Fsp is always positive (as the SNR of the EOAEs is always non-negative). It is revealing to rewrite the logit as

$$L = (c_1 + c_2 * FRLO) * Fsp + c_0,$$

which shows that the more negative is the term $(c_1 + c_2 * FRLO)$, the lower is the probability of sensorineural hearing loss. Because $c_2 < 0$, a positive value of $FRLO$, which is normalized like all factors to have a mean of zero and standard deviation (s.d.) of 1, decreases L and thus decreases the probability of classifying the ear as having sensorineural hearing loss. In an ear with normal hearing, this reduces the false-positive rate. Therefore, large values of $FRLO$ are associated in this model with probable middle-ear dysfunction. In the corresponding univariate predictor based solely on ABR Fsp , there is no possibility for a reduction in L due to the large $FRLO$ value; its calculated probability of sensorineural hearing loss is higher, which increases the likelihood of a false-positive test result. Figure 1 and Table II of Keefe *et al.* (2003) show that the largest magnitude factor loadings of $FRLO-6$ are on the energy reflectance in the range 0.25–1 kHz, so that large values of $FRLO$ are produced by large energy reflectance at these frequencies. A

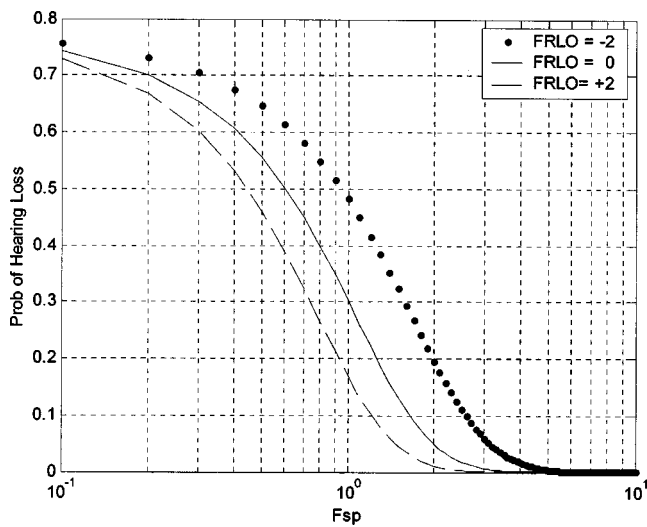


FIG. 5. The predicted probability of hearing loss is plotted versus ABR F_{sp} for the VRA sample for values of factor $FRLO$ of -2 , 0 , and 2 .

small (i.e., negative) value of $FRLO$ would be evidence that the ear-canal and middle-ear status is not responsible for a predicted sensorineural hearing loss in an ear. This, too, may be useful information in a neonatal hearing screening program.

The predicted probability for sensorineural hearing loss is plotted in Fig. 5 for the cases that $FRLO = -2$, 0 , and $+2$. The nonzero values correspond to shifts in the reflectance factor by two standard deviations below and above the mean $FRLO = 0$. High values of $FRLO$ show the reduction in the predicted probability of sensorineural hearing loss, which acts to reduce the false-positive rate.

The same trend occurs for false-negative ears, which are those ears with sensorineural hearing loss and strong ABR responses, but the consequences are opposite. A large $FRLO$ value associated with probable middle-ear dysfunction reduces the probability of sensorineural hearing loss, which increases the false-negative rate and decreases the sensitivity. This is an unavoidable consequence of adding a test of ear-canal and middle-ear status to a hearing screening program. Identification of middle-ear dysfunction reduces the false-positive rate and increases the false-negative rate, because an ear with sensorineural hearing loss may also have middle-ear dysfunction. There are trade-offs between the high prevalence of false positives and low prevalence of false negatives, versus the societal costs of missing an ear with sensorineural hearing loss. The problem of a middle-ear test increasing the false negative rate may be lessened if the ear identified as having middle-ear dysfunction receives a follow-up clinical evaluation, including a hearing test. Thus, a reliable outcome on a test of hearing is needed at some point early in life.

Because the predictor models based on EOAE SNR and ABR F_{sp} in Table II have a main effect with $c_1 < 0$, the interpretation of the YR interaction variables is the same as in this example. For those interaction coefficients (such as c_2 in this example) that are negative, a large factor score is associated with an increased likelihood of middle-ear dysfunction. This acts to decrease the false-positive rate, and

increase the false-negative rate. For those interaction coefficients c_2 that are positive, a small (i.e., negative) factor score is associated with increased likelihood of middle-ear dysfunction, a decrease in false-positive rate, and an increase in false-negative rate.

An example of the latter is the TEOAE predictor, for which the coefficient associated with the interaction $SNR \times FYLO$ is $c_2 = 0.19$ (Table II). A small value of $FYLO$ is produced by small equivalent volume and large acoustic conductance in the frequency range 0.25 – 1 kHz [see Fig. 1 in Keefe *et al.* (2003)]. Small, but positive, equivalent volumes at these frequencies are associated with a stiffened tympanic membrane, while smaller, and negative, equivalent volumes are associated with an additional shunt resonance that may be related to a resonant motion of the ear-canal wall (Keefe *et al.*, 1993). This type of shunt-resonance response in neonates and young infants complicates the interpretation of low-frequency tympanometry. These same issues may help explain the high false-positive rate in EOAE testing. Large acoustic conductances are associated with large amounts of power absorbed in the ear canal and middle ear, and are observed in conjunction with this same shunt resonance. This interaction involving $FYLO$ with positive coefficient is present for both TEOAEs and DPOAEs.

TABLE VII. Mean and standard deviation (s.d.) of YR variables.

	f (kHz)	Mean	s.d.
Reflectance	0.25	0.216	0.210
	0.35	0.229	0.179
	0.50	0.249	0.169
	0.71	0.258	0.165
	1.00	0.290	0.209
	1.40	0.191	0.187
	2.00	0.177	0.204
	2.83	0.230	0.209
	4.00	0.315	0.234
	5.66	0.199	0.168
Equiv. volume (cm ³)	8.00	0.302	0.209
	0.25	0.115	0.518
	0.35	0.028	0.359
	0.50	0.073	0.267
	0.71	0.139	0.209
	1.00	0.189	0.174
	1.40	0.121	0.160
	2.00	−0.003	0.133
	2.83	−0.022	0.085
	4.00	0.040	0.080
Conductance (mmho)	5.66	0.020	0.070
	8.00	−0.038	0.073
	0.25	0.934	0.772
	0.35	0.832	0.713
	0.50	0.753	0.599
	0.71	0.730	0.481
	1.00	0.837	0.536
	1.40	1.421	0.748
	2.00	1.525	0.892
	2.83	1.025	0.771
	4.00	0.912	0.910
	5.66	2.113	1.658
	8.00	1.958	1.653

APPENDIX B: CALCULATING THE MULTIVARIABLE PREDICTOR OF SENSORINEURAL HEARING LOSS FOR AN INDIVIDUAL EAR

Using test results in a single ear, the steps in calculating the predicted sensorineural hearing loss are as follows:

- (1) Convert the YR response to a normalized YR response using the population norms. Each YR variable is characterized by a population sample mean μ and standard deviation (s.d.) σ , with subscripts R for energy reflectance, V for equivalent volume, or G for acoustic conductance to denote the variable type. The normalized YR variables R_N , V_N , and G_N are calculated at each frequency by

$$R_N = (R - \mu_R) / \sigma_R,$$

$$V_N = (V - \mu_V) / \sigma_V,$$

$$G_N = (G - \mu_G) / \sigma_G.$$

The mean and s.d. of each YR variable are listed in Table VII.

- (2) Calculate each YR factor as a sum over products of each factor loading [Tables II and IV in Keefe *et al.* (2003)], and each normalized YR variable.
- (3) Calculate the logit function and probability of sensorineural hearing loss using the logistic regression coefficients (Table II), the YR factors, and the individual scores for EOAE SNR and ABR F_{sp} .

The tabulated mean and s.d. are similar to the percentiles of the YR responses with leaky ears excluded in the INHI study [Fig. 5 of Keefe *et al.* (2000)]. In a computer implementation of the tests, these YR means and s.d.'s, factor loadings, and logistic regression coefficients may be stored and accessed by software to calculate a prediction of hearing status based on YR and EOAE test results, or YR and ABR test results.

- ANSI (1996). ANSI S3.6, "Specifications for Audiometers" (American National Standards Institute, New York).
- Chen, S.-J., Yang, E. Y., Kwan, M.-L., Chang, P., Ahiao, A.-S., and Lien, C.-F. (1996). "Infant hearing screening with an automated auditory brainstem response screener and the auditory brainstem response," *Acta Paediatr.* **85**, 14–18.
- Cone-Wesson, B., and Ramirez, G. M. (1997). "Hearing sensitivity in newborns estimated from ABRs to bone-conducted sounds," *J. Am. Acad. Audiol.* **8**, 288–307.
- Dorn, P. A., Piskorski, P., Gorga, M. P., Neely, S. T., and Keefe, D. H. (1999). "Predicting audiometric status from distortion product emissions using multivariate analyses," *Ear Hear.* **20**, 149–163.
- Gorga, M. P., Norton, S. J., Sininger, Y. S., Cone-Wesson, B., Folsom, R. C., Vohr, B. R., and Widen, J. E. (2000). "Identification of neonatal hearing impairment: Distortion product otoacoustic emissions during the perinatal period," *Ear Hear.* **21**, 400–424.
- Gorga, M. P., Preissler, K., Simmons, J., Walker, L., and Hoover, B. (2001). "Some issues relevant to establishing a universal newborn hearing screening program," *J. Am. Acad. Audiol.* **10**, 101–112.
- Harrison, W. A., Dunnell, J. J., Mascher, K., Fletcher, K., Vohr, B. R., Gorga, M. P., Widen, J. E., Cone-Wesson, B., Folsom, R. C., Sininger, Y. S., and Norton, S. J. (2000). "Identification of neonatal hearing impairment: Experimental protocol and database management," *Ear Hear.* **21**, 357–372.

- Hosmer, D. W., and Lemeshow, S. (2000). *Applied Logistic Regression*, 2nd ed. (Wiley, New York).
- Hussain, D. M., Gorga, M. P., Neely, S. T., Keefe, D. H., and Peters, J. (1998). "Transient evoked otoacoustic emissions in patients with normal hearing and in patients with hearing loss," *Ear Hear.* **19**, 434–449.
- Keefe, D. H., Bulen, J. C., Arehart, K. H., and Burns, E. M. (1993). "Ear-canal impedance and reflection coefficient in human infants and adults," *J. Acoust. Soc. Am.* **94**, 2617–2638.
- Keefe, D. H., Folsom, R. C., Gorga, M. P., Vohr, B. R., Bulen, J. C., and Norton, S. J. (2000). "Identification of neonatal hearing impairment: Ear-canal measurements of acoustic admittance and reflectance in neonates," *Ear Hear.* **21**, 443–461.
- Keefe, D. H., Zhao, F., Neely, S. T., Gorga, M. P., and Vohr, B. R. (2003). "Ear-canal acoustic admittance and reflectance measurements in human neonates. I. Effects on otoacoustic emission and auditory brainstem responses," *J. Acoust. Soc. Am.* **113**, 389–406.
- Margolis, R. H. (2001). "Influence of middle ear disease on otoacoustic emissions," in *Otoacoustic Emissions Clinical Applications*, 2nd ed., edited by M. S. Robinette and T. J. Glatke (Thieme, New York), pp. 190–212.
- National Institutes of Health (1993). "Early identification of hearing impairment in infants and young children," NIH Consens. Statement **11**, 1–24.
- Norton, S. J., Gorga, M. P., Widen, J. E., Folsom, R. C., Sininger, Y. S., Cone-Wesson, B., Vohr, B. R., and Fletcher, K. (2000a). "Identification of neonatal hearing impairment: A multicenter investigation," *Ear Hear.* **21**, 348–356.
- Norton, S. J., Gorga, M. P., Widen, J. E., Folsom, R. C., Sininger, Y. S., Cone-Wesson, B., Vohr, B. R., Mascher, K., and Fletcher, K. (2000b). "Identification of neonatal hearing impairment: Evaluation of transient evoked otoacoustic emission, distortion product otoacoustic emission, and auditory brain stem evoked response test performance," *Ear Hear.* **21**, 508–528.
- Norton, S. J., Gorga, M. P., Widen, J. E., Folsom, R. C., Sininger, Y. S., Cone-Wesson, B., Vohr, B. R., and Fletcher, K. (2000c). "Identification of neonatal hearing impairment: Summary and recommendations," *Ear Hear.* **21**, 529–535.
- Norton, S. J., Gorga, M. P., Widen, J. E., Vohr, B. R., Folsom, R. C., Sininger, Y. S., Cone-Wesson, B., and Fletcher, K. (2000d). "Identification of neonatal hearing impairment: Transient evoked otoacoustic emissions during the perinatal period," *Ear Hear.* **21**, 425–442.
- Piskorski, P., Keefe, D. H., Simmons, J. L., and Gorga, M. P. (1999). "Prediction of conductive hearing loss based on acoustic ear-canal response using a multivariate clinical decision theory," *J. Acoust. Soc. Am.* **105**, 1749–1764.
- Sininger, Y. S., Cone-Wesson, B., Folsom, R. C., Gorga, M. P., Vohr, B. R., Widen, J. E., Ekelid, M., and Norton, S. J. (2000). "Identification of neonatal hearing impairment: Auditory brain stem responses in the perinatal period," *Ear Hear.* **21**, 400–424.
- Stevens, J. (2001). "State of the art neonatal hearing screening with auditory brainstem response," *Scand. Audiol.* **30**, Suppl. 52, 10–12.
- Stuart, A., Yang, E. Y., and Green, W. B. (1994). "Neonatal auditory brainstem response thresholds to air- and bone-conducted clicks: 0 to 96 hours postpartum," *J. Am. Acad. Audiol.* **5**, 163–172.
- Vohr, B. R., Widen, J. E., Cone-Wesson, B., Sininger, Y. S., Gorga, M. P., Folsom, R. C., and Norton, S. J. (2000). "Identification of neonatal hearing impairment: Characteristics of infants in the neonatal intensive care unit and well-baby nursery," *Ear Hear.* **21**, 373–382.
- Widen, J. E., Folsom, R. C., Cone-Wesson, B., Carty, L., Dunnell, J. J., Koebse, K., Levi, A., Mancl, L., Ohlrich, B., Trouba, S., Gorga, M. P., Sininger, Y. S., Vohr, B. R., and Norton, S. J. (2000). "Identification of neonatal hearing impairment: Hearing status at 8 to 12 months corrected age using a visual reinforcement audiometry protocol," *Ear Hear.* **21**, 471–487.
- Yang, E. Y., Rupert, A. L., and Moushegian, G. (1987). "A developmental study of bone conduction auditory brain stem response in infants," *Ear Hear.* **8**, 244–251.

Objective estimates of cochlear tuning by otoacoustic emission analysis

Arturo Moleti^{a)}

Dipartimento di Fisica, Università di Roma "Tor Vergata," Via della Ricerca Scientifica, 1, 00133 Roma, Italy

Renata Sisto^{b)}

Dipartimento Igiene del Lavoro, ISPESL, Via Fontana Candida, 1, 00040 Monte Porzio Catone (Roma), Italy

(Received 6 June 2002; revised 26 September 2002; accepted 30 September 2002)

A new method is presented for estimating cochlear tuning starting from measurements of either the transient evoked otoacoustic emission latency or the spontaneous otoacoustic emission minimal spacing. This method could be useful in obtaining indirect information about the tuning curve, particularly for subjects that, like neonates, cannot be studied with psycho-acoustical techniques. Theoretical models of the acoustic transmission along the cochlea based on the transmission line formalism predict a relation between the otoacoustic emission latency and the frequency. This relation depends on the tuning curve, i.e., the frequency dependence of the quality factor of the cochlear resonances. On the other hand, models for the generation of spontaneous emissions based on the concept of coherent scattering from cochlear random inhomogeneities imply an independent relation between the tuning curve and the minimal frequency spacing between spontaneous emissions. In this study, experimental measurements of the otoacoustic emission latency and of the minimal spacing between spontaneous emissions are presented. Theoretical relations are derived, which connect these two measured quantities and the tuning curve. The typically longer latency of neonates implies a higher degree of tuning at high levels of stimulation. © 2003 Acoustical Society of America. [DOI: 10.1121/1.1523389]

PACS numbers: 43.64.Jb [BLM]

I. INTRODUCTION

Otoacoustic emissions (OAEs) provide many different experimental techniques for studying the cochlear physiology (Probst *et al.*, 1991). The possibility of getting noninvasive cochlear tuning estimates by analyzing either the transiently evoked OAEs (TEOAEs) latency or the spontaneous OAE (SOAE) spectrum is analyzed in this study. Distortion product OAEs (DPOAEs) suppression tuning curves (STCs) have been used to estimate the cochlear tuning in adults (Brown and Kemp, 1984; Harris *et al.*, 1992; Kummer *et al.*, 1995) and neonates, finding narrower STCs in preterm neonates (Abdala, 2001, 1998).

A different approach can provide information about cochlear tuning from measurements of the cochlear latency. The theoretical link between tuning and latency is provided by cochlear models based on the transmission line formalism. This formalism is based on the analogy between the cochlear membrane and an equivalent electrical transmission line. The cochlear analog of the line voltage is the pressure difference between the two sides of the membrane, while the equivalent of the electric current is the time derivative of the membrane transverse displacement. To account for the tonotopic properties of the cochlea, the transverse electrical impedance of the line is assumed to be locally resonant at the frequency given by the Greenwood map (Greenwood, 1990).

In this theoretical framework, the relation between cochlear latency and tuning may be computed. As it will be shown in some detail in the Model section, the basic idea is that the OAE spectral latency is the delay due to the round-trip acoustic transmission to the OAE generation place and back to the detector. This delay is dominated by the cochlear contribution, which can be computed for each frequency as the integral over the cochlear path of the inverse group velocity. The group velocity is computed from the relation between the wave vector k and the angular frequency ω . The details of this relation are dependent on the assumed cochlear model. However, in any reasonable model the relation between k and ω has a resonance at the tonotopic place. The traveling wave velocity decreases when approaching the tonotopic place proportionally to the sharpness of the resonance. Thus, the total delay is dependent on the sharpness of the resonance, expressed by the quality factor Q , which is defined as the ratio between the frequency ω and the bandwidth Γ of the resonance itself. Symmetry considerations can be used to get general results, which are not dependent on the details of the assumed model. For example, the scale-invariance hypothesis, which is approximately, but not exactly, verified in a real cochlea, leads to a prediction of inverse proportionality between latency and frequency (Talmadge *et al.*, 1998).

Recently, it has been suggested that group-delay data obtained from stimulus-frequency OAE (SFOAE) phase measurements be used to get information about the tuning curve (Shera *et al.*, 2002). The slope of the relation between SFOAE phase and frequency gives an estimate of this delay,

^{a)}Electronic mail: arturo.moleti@roma2.infn.it

^{b)}Electronic mail: sisto@dil.ispesl.it

whose relation with tuning can be predicted using various cochlear models. Accurate knowledge of the functional relation between group delay and tuning is needed to get reliable tuning estimates.

For the same purpose, the use of measurements of the $2f_1-f_2$ distortion product OAE (DPOAE) group delay (Moulin and Kemp, 1996a; Prijs *et al.*, 2000; Schoonoven *et al.*, 2001) has already been proposed (Moulin and Kemp, 1996b; Bowman *et al.*, 1998). The physical quantity that is measured is, in this case, the DPOAE phase-gradient delay, which is a characteristic time associated with the slope of the functional relation between the DPOAE phase and the DPOAE frequency $f_{DP}=2f_1-f_2$.

The DPOAE phase-gradient delay is actually measured by sweeping f_{DP} within a narrow range around a set of suitably chosen frequencies (typically spaced by one third of an octave). This measure can be performed by sweeping either f_2 (fixed- f_1 paradigm, yielding the characteristic delay τ_1) or f_1 (fixed- f_2 paradigm, yielding a conceptually different delay, τ_2).

Schoonoven *et al.* (2001) measured the frequency dependence of both τ_1 and τ_2 , finding $\tau_1=9.31f_2^{-0.64}$ and $\tau_2=6.48f_2^{-0.74}$, with a typical value of 1.55 ± 0.23 , and a weak frequency dependence, for the ratio τ_1/τ_2 . They also compared their findings with simultaneous measurements of the derived acoustic brainstem response (ABR) and compound action potential (CAP) latencies. They found that their electrophysiological estimates of the forward cochlear delay were in very good agreement with $\tau_2/2$.

The DPOAE group delays are related to the round-trip delay introduced by the forward transmission along the cochlear membrane of the primary tones from the source to the DPOAE generation place and the backward transmission of the DPOAE to the detector. The DPOAE generation place is assumed to be near the cochlear place that is resonant at f_2 , at least for the $2f_1-f_2$ DPOAE. The so-called “wave-fixed model” actually assumes that the generation place coincide exactly with the f_2 place, while in the “place-fixed model” it is associated with some cochlear irregularity at a fixed place near the f_2 place (e.g., Moulin and Kemp, 1996b; Prijs *et al.*, 2000). In the wave-fixed model, sweeping f_2 implies sweeping the DPOAE generation place, while in the place-fixed model it does not. In both models, sweeping f_1 does not change the generation place. An intermediate hypothesis has also been considered by Moulin and Kemp (1996b), in which the generation place is actually fixed only for small f_2 changes. On the basis of these simple models, it has been suggested that the contribution of the filter build-up time, which is dependent on the sharpness of the cochlear resonance, plays an important role, and affects τ_1 and τ_2 differently. Hence, the idea of estimating the cochlear filter properties from DPOAE phase-gradient measurements, in particular, from the difference (or the ratio) between τ_1 and τ_2 (Moulin and Kemp, 1996b; Bowman *et al.*, 1998).

Moulin and Kemp (1996b) found a ratio τ_1/τ_2 varying between 1.2 and 1.6, increasing with increasing frequency up to 4 kHz, and decreasing again above 4 kHz, and suggested that this behavior could be related to that of the auditory frequency selectivity.

Bowman *et al.* (1998) measured the difference between τ_1 and τ_2 as a function of the stimulus frequency and intensity. Their results show that this difference is more sensitive to stimulus amplitude the higher the frequency. If, as they assume, this difference is related to the filter build-up time, this means that cochlear tuning is significantly sharper at high frequencies. Assuming that a linear gamma-tone filter impulse response approximate that of the real cochlear filter, they also provided quantitative estimates of the cochlear tuning.

Doubts were cast by Shera *et al.* (2000) on the correctness of the above-described arguments, because the relation between the measured quantities and cochlear latency and tuning is not straightforward and model independent. The theoretically predicted relations are dependent on many rather uncertain physical assumptions: the number and spatial location of the DPOAE generation sources, their point-like or distributed nature, the traveling wave transmission, and the contribution of the filter build-up time. In particular, it is difficult to disentangle the “filter build-up” time from the “wave-travel” time, and even to correctly define those two terms, which actually refer to two contributions to the overall latency that are both included in the general formalism of the resonant transmission line. It was also observed that the experimental values of the ratio τ_1/τ_2 are in fair agreement with model-independent theoretical predictions based only on dimensional analysis arguments in the scale-invariant limit. This observation suggests that the ratio τ_1/τ_2 is not very sensitive to cochlear physiological parameters such as the tuning curve (Shera *et al.*, 2000; Prijs *et al.*, 2000).

In addition to the above-described methods, which give indirect estimates of the cochlear characteristic time delays from the slope of the OAE phase-frequency function, other methods have been proposed, based on the direct measure of the OAE response delay relative to the stimulus onset. One of these methods is based on the analysis of the DPOAE waveform in the time domain, using an averaging technique that, by suitably varying the phase of the primary tones, permits effectively the cancellation of the primaries and all other DPOAEs in the average waveform (Whitehead *et al.*, 1996). The authors, comparing the latency data obtained with this technique with phase-gradient delays measured on the same subjects, found a reasonable agreement with regard to the dependence on frequency and on stimulus amplitude. The interpretation of all the DPOAE latency data, in terms of cochlear latency and traveling wave velocity, is complicated by the fact that the stimulus (inward) and the DPOAE (outward) traveling times are not expected to be the same, due to the frequency difference.

Another method has been proposed which provides estimates of the OAE latency from the time-frequency analysis of the TEOAE waveform (Tognola *et al.*, 1997; Sisto and Moleti, 2002). In general, time-frequency analysis techniques provide information on the time evolution of each frequency component of the TEOAE cochlear response, with a rather coarse resolution both in the time and in the frequency domain. Nevertheless, this coarse information is often very useful to study the cochlear transmission mecha-

nisms. Both the relationship between the wave vector and the frequency, which determines the traveling wave velocity (TWV) function, and the spatial distribution of the cochlear resonant places (Greenwood, 1990) are reflected in the frequency dependence of the OAE latency. The details of the experimental latency–frequency relationship provide information that is useful for investigating the transmission properties of the cochlear membrane and for testing theoretical cochlear models (Sisto and Moleti, 2002).

In the case of TEOAEs, the traveling wave frequency is the same for the forward and backward contributions to the latency. Thus, it could be reasonable, at first approximation, to assume the measured time delay to be twice the cochlear traveling time in each direction.

A recent analysis of the transiently evoked OAE (TEOAE) spectral latency generation mechanisms (Sisto and Moleti, 2002) has shown that, for a simple cochlear transmission model, the TEOAE spectral latency is dependent on the quality factor of the resonance in a rather simple way, without making a full scale-invariance hypothesis. Indeed, in the Model section, it will be shown that it is possible to split the total cochlear latency into two contributions, only one of which is dependent on the tuning (Sisto and Moleti, 2002). Thus, it is possible to apply to the TEOAE data a variant of the method proposed by Shera *et al.* (2002) for SFOAEs, and, if the model is accurate enough, the measure of the transiently evoked OAE (TEOAE) latency could result in a powerful tool for estimating cochlear tuning.

From a completely different point of view, it is interesting to note that cochlear models based on the transmission line formalism and on the concept of coherent reflection by random inhomogeneities (Zweig and Shera, 1995; Talmadge *et al.*, 1998) can also be used to predict an independent relation between the tuning curve and the minimal frequency spacing between SOAEs. In fact, as it will be shown in the Model section, the Bragg condition for coherent backscattering of the traveling wave, which is assumed in these models to determine the possible SOAE frequencies, is fulfilled only for a set of frequency values that are equally spaced on a logarithmic scale (quasiperiodicity). The minimal spacing between SOAEs is related to some cochlear length scale, which in scale-invariant models is assumed to be a constant. If tuning is not constant along the cochlea, scale invariance is broken, and the expected minimal spacing between SOAEs becomes a function of frequency, whose slope is directly related to that of the tuning curve. Therefore, another independent evaluation of the average tuning curve may be obtained starting from measurements of the minimal SOAE spacings in a homogeneous population of subjects.

All the above-described methods provide information about the tuning curve from a micromechanical point of view, because they are sensitive to the local value of the bandwidth of the cochlear filters. The relation between such objective measurements and the psychoacoustical determinations of the frequency discrimination capability is beyond the scope of the present work.

The estimation of cochlear tuning by OAE measurements could be particularly important in the case of neonates, because, for them, no psycho-acoustical technique is

available. Thus, OAE techniques could represent a precious tool for providing important information about this fundamental parameter of cochlear activity in the first days of life.

II. METHOD

In this study, TEOAE and synchronized SOAE (SSOAE) waveforms recorded using the ILO96 V.5 system (Otodynamics Ltd.), from 116 normally hearing ears, 94 from young adults (age=18–25 years) and 22 from full-term neonates, have been analyzed. The neonate data were taken within the first 3 days of life. The same adult data had been previously analyzed in other studies (Sisto *et al.*, 2001; Sisto and Moleti, 2002; Lucertini *et al.*, 2002).

Normal hearing was assessed for the adults using standard audiometry. The ear was defined as normal if the hearing loss was lower than 20 dB at all test frequencies (0.25, 0.5, 1, 2, 3, 4, 6, 8 kHz). However, none of the adult subjects had HL higher than 10 dB at any frequency. For the neonates, normal hearing was hypothesized on the basis of their high TEOAE reproducibility (>70%), measured on the global waveform, and, separately, in the 2-, 3-, 4-, and 5-kHz bands. The average global and band reproducibilities were all higher than 90%.

The data sampling frequency was 25 kHz. TEOAEs were recorded in the “nonlinear” mode of acquisition to minimize contamination by linear ringing. In this acquisition mode, the system records the average response to a train of click stimuli consisting of repeated (≈ 250) sequences of three stimuli of a given polarity followed by a stimulus of triple amplitude and opposite polarity. In principle, the linear component of the response is canceled with this technique, at the price of reducing the achievable signal-to-noise ratio (SNR), for a given total integration time.

The reproducibility of the TEOAE response (i.e., the SNR) is evaluated by the ILO system by separately recording two averages, named A and B, of the otoacoustic responses to identical alternated trains of stimuli. The difference waveform A–B provides a rough estimate of the instrumental noise. The default spacing between successive stimuli is 20 ms, which is also the duration of the acquired digitized waveform.

High-amplitude click stimuli (80 ± 2 dB) and the default ILO window, which is a trapezoidal function starting from zero at 2.5 ms and reaching the flat top linearly 5 ms after the click, were used for all subjects.

The 20-ms TEOAE waveforms were time–frequency analyzed by iterative application of filter banks. Spline biorthogonal wavelets were obtained by perfect reconstruction FIR filter banks. The procedure yields a set of wavelet coefficients, which are functions of time, whose frequency bandwidth is proportional to frequency, while their time step is inversely proportional to frequency. Each wavelet coefficient describes the time evolution of the evoked signal in a given octave band.

Two different analysis techniques, described in Sisto and Moleti (2002), can be used to get an estimate of the cochlear latency from these data. In the first one, an average of the wavelet coefficients $W(f_i, t)$ is performed over the ears

$$\langle W(f_i, t) \rangle = \frac{1}{N_{\text{ears}}} \sum_{k=1}^{N_{\text{ears}}} W_k(f_i, t), \quad (1)$$

and for each average coefficient the time of the maximum $t_{\text{max}}(f_i)$ is found. This time is an estimate of the average spectral latency $\langle \tau(f_i) \rangle$ of the i th frequency band.

The second technique is based upon the identification, within the wavelet coefficient of a given octave band, of the response peak associated to a given OAE of known frequency, observed in the TEOAE spectrum of the same ear. This second technique can be applied only to a subset of ears for which the structure of the OAE spectrum permits the unambiguous identification of spectral lines in the wavelet coefficient waveforms.

The first technique is suitable for the automatic analysis of large amounts of data, and it has been successfully used to show significant differences between the latencies of normal-hearing and impaired ears (Sisto and Moleti, 2002), and also between those of normal-hearing ears of subjects exposed to impulsive firearm noise and of nonexposed subjects (Lucertini *et al.*, 2002). Unfortunately, due to its poor frequency resolution and to the shape of the typical TEOAE spectrum, this technique systematically underestimates the slope of the latency–frequency relation (Sisto and Moleti, 2002). This systematic effect suggests that this technique be used only for clinical purposes, to detect statistical differences between populations, because the absolute evaluation of the above-mentioned slope is not very important in this case. In this study, which makes use of theoretical model predictions dependent on the details of the functional relationship relating latency to frequency, only the data taken with the second technique were used.

SSOAEs were recorded in the “linear” mode of acquisition. In this acquisition mode, the system records the average response to a train of stimuli consisting of repeated (≈ 250) identical click stimuli of the same polarity. The spacing between successive stimuli is 80 ms, which is also the duration of the acquired waveform. The resulting Fourier spectrum has a frequency resolution of 12 Hz. Despite the fact that the cochlear response is, also in this case, evoked by a wideband stimulus, the spectrum of the whole 80-ms waveform shows only the lines corresponding to very long-lasting cochlear resonances. These lines correspond almost exactly to the properly named SOAEs, which should be measured in the absence of stimulation, by simply integrating the output of a microphone placed in the ear canal. The SSOAE technique takes advantage of the synchronization of the response to the click stimuli, to increase the SNR by summing coherently only the signal.

The SSOAE spectra were searched for spontaneous emissions, defined here as the spectral lines whose amplitude exceeded the local noise level by at least 10 dB.

III. MODEL

The measured latency is made up of a cochlear contribution, τ_c , due to the round-trip delay associated with the transmission of the acoustic signal along the cochlear membrane, and of a much smaller contribution from the outer and middle ear, τ_{nc} . Here, it will be assumed to be on the order

of 0.5 ms, according to Sisto and Moleti (2002). Thus, the OAE latency is essentially due to the travel time of the acoustic signal along the basilar membrane from the oval window to the tonotopic place and back. In the cochlea, which is the dispersive element of the auditory system, the temporal dispersion of the different frequency components of the input signal takes place. This dispersion yields a precise functional relation between latency and frequency of the OAEs. The Greenwood map (Greenwood, 1990), which describes the tonotopic relation between cochlear position and resonance frequency, implies that the high-frequency components of a complex signal travel a shorter path along the cochlea than low-frequency components. Thus, it is expected that the latency is a decreasing function of frequency. To make quantitative predictions, a full model of the resonant transmission along the cochlear membrane is needed. An important class of models, developed with some differences by many authors (Furst *et al.*, 1988; Talmadge *et al.*, 1998), is based on the electric transmission line formalism. Here, a simple model of this class is used (Sisto and Moleti, 2002), in which a relation is obtained between the wave vector and the frequency.

A. Cochlear latency and tuning

Due to the tonotopic resonant nature of the line, the relation between the wave vector and the frequency is a function of the cochlear position x

$$k(\omega, x) = \frac{\omega k_0}{\sqrt{\omega^2(x) - \omega^2 + i\omega\Gamma(x)}}, \quad (2)$$

where $\omega = 2\pi f$ is the angular frequency of the wave. It is possible to compute, as a function of x , the TWV for a wave packet of angular frequency ω , as the group velocity associated with Eq. (2)

$$v_g^{-1}(\omega, x) = \frac{\partial k(\omega, x)}{\partial \omega}. \quad (3)$$

Here, and in the following, the real part of complex quantities is considered. Integration over the round-trip cochlear path yields an estimate of the cochlear latency

$$\tau_c(\omega) = 2 \int_0^{x(\omega)} dx v_g^{-1} = 2 \int_0^{x(\omega)} dx \frac{\partial k}{\partial \omega}. \quad (4)$$

Near the resonant place, the group velocity drops rapidly, increasingly with larger quality factors Q , over a spatial extension that is, in turn, inversely proportional to Q . It is possible to compute separately the contribution to the latency given by the resonant part of the path, within a constant fraction of the resonance width, and that coming from the remaining path, outside the resonance width. It turns out that the contribution to the latency of the resonance [arbitrarily assumed to start at $x(\omega) - \Delta x$, with $\Delta x = 2\Gamma/\omega k_\omega$] is quite independent of Q , and shows an ω^{-1} dependence

$$\tau_{\text{res}}(\omega) = 2 \int_{x(\omega) - \Delta x}^{x(\omega)} dx \frac{\partial k}{\partial \omega} \cong \sqrt{2} \frac{k_0}{\omega k_\omega}. \quad (5)$$

The other contribution [up to $x(\omega) - 2\Gamma/\omega k_\omega$] can be analytically computed, applying to Eq. (2) a scale-invariance

hypothesis, which is approximately valid far from the resonance, even if Q is not constant

$$\begin{aligned}\tau_{\text{far}}(\omega) &\cong 2 \int_0^{x(\omega)-\Delta x} dx \frac{\partial k}{\partial x} \frac{\partial x}{\partial \omega} \\ &= \frac{2(k(x(\omega)-\Delta x)-k(0))}{\omega k_\omega} \\ &= \frac{k_0}{\omega k_\omega} \frac{\sqrt{Q}}{4 \sqrt{\frac{17}{16} + \frac{2}{Q} + \frac{1}{Q^2}}} - \frac{2k_0}{\omega_{\text{max}} k_\omega} \\ &= \alpha(Q) \frac{k_0}{\omega k_\omega} \sqrt{Q} - \beta,\end{aligned}\quad (6)$$

where

$$\alpha(Q) \cong \left(1 - \frac{1}{64}\right) \left(1 - \frac{8}{17Q}\right). \quad (7)$$

The factor $\alpha(Q)$ is very close to unity (0.98) for very high Q s, and its value is between 0.85 and 0.95 for values of Q between 3 and 15, while the small constant, $\beta \sim 0.3$ ms, can be neglected, as a first approximation.

It should be noted here that the scale-invariance hypothesis is not verified in the low-frequency range (below 1 kHz), due to the presence of a scale-invariance breaking term in the Greenwood law, whose effect should be taken into account to get more accurate predictions at low frequencies.

Using Eqs. (5) and (6), it is possible to get information about the tuning curve $Q(\omega)$, starting from experimental measurements of the OAE latency $\tau_{\text{exp}}(\omega)$. Assuming a constant $\alpha=0.9$, and neglecting β , the following approximate relation is obtained:

$$\begin{aligned}Q(\omega) &= \left(\frac{\omega k_\omega}{\alpha k_0} \tau_{\text{far}}(\omega) \right)^2 \\ &= \left(\frac{\omega k_\omega}{\alpha k_0} (\tau_{\text{exp}}(\omega) - \tau_{nc} - \tau_{\text{res}}(\omega)) \right)^2.\end{aligned}\quad (8)$$

B. SOAE minimal spacing and tuning

On the other hand, cochlear models of SOAE generation based on the coherent scattering from cochlear inhomogeneities near the resonance place (Zweig and Shera, 1995; Talmadge *et al.*, 1998), predict that the minimal spatial separation between the SOAE source places be given by the condition

$$\hat{k} \Delta \hat{x} \approx \pi, \quad (9)$$

where \hat{k} is the maximum value of the real part of the wave vector, which is reached near the resonance place. Generalizing the model to a frequency-dependent tuning

$$\hat{k} = \gamma k_0 \sqrt{Q}. \quad (10)$$

In the present model, the constant γ is quite independent of Q and approximately equal to 0.8. Using the Greenwood

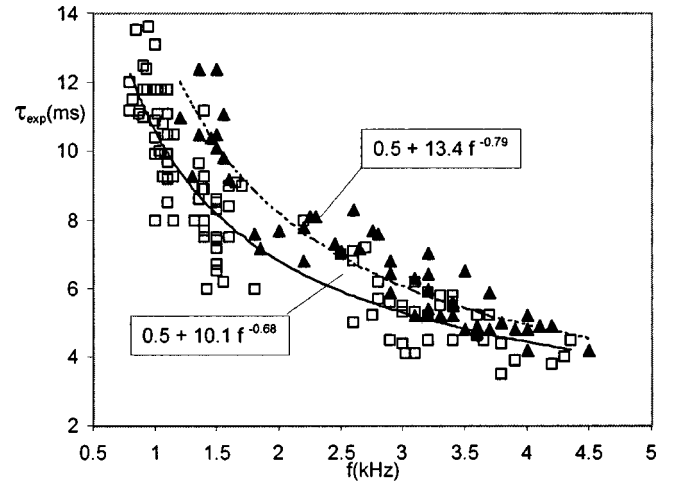


FIG. 1. OAE spectral latency obtained by individual spectral lines identification in the time–frequency analyzed signal, for adults (squares) and neonates (triangles). The lines are power law fit functions of the form of Eq. (14).

map, Eq. (9) yields a condition for the minimal frequency spacing between contiguous SOAEs

$$\frac{f_{\text{SOAE}}}{\Delta f_{\text{SOAE}}} \approx \frac{\gamma k_0}{\pi k_\omega} \sqrt{Q}, \quad (11)$$

where f_{SOAE} is the geometric mean of the two SOAE frequencies. Equation (11) permits an independent evaluation of the tuning curve, starting, in this case, from experimental measurements of the minimal SOAE spacing

$$Q(\omega) = \left(\frac{\pi k_\omega}{\gamma k_0} \frac{f_{\text{SOAE}}}{\Delta f_{\text{SOAE}}} \right)^2. \quad (12)$$

Equation (12) is independent of Eq. (8), and together they imply a relation between latency and minimal SOAE spacing, which must be verified if the model is internally coherent

$$\frac{f_{\text{SOAE}}}{\Delta f_{\text{SOAE}}} \approx \frac{2\gamma}{\alpha} f \tau_{\text{far}}. \quad (13)$$

IV. RESULTS

The line identification analysis method was applied to the data collected in this experiment. In the adult subjects, the latency of 105 spectral lines was measured, in the frequency range of 0.8–4.4 kHz, while for neonates it was possible to identify 52 OAEs in the range of 1.2–4.5 kHz. In Fig. 1 the spectral latency data obtained with this method are shown for adults and neonates.

The data were best fitted to a power law of the form

$$\tau = \tau_{nc} + D f^b, \quad (14)$$

with f in kHz and $\tau_{nc}=0.5$ ms, obtaining $D_n=13.4 \pm 0.6$ ms and $b_n=-0.79 \pm 0.04$ for neonates and $D_a=10.1 \pm 0.2$ ms and $b_a=-0.68 \pm 0.03$ for adults.

The adult fit parameters are in this case very similar to those obtained for the DPOAE group delay by Schoonhoven *et al.* (2001), using the fixed- f_1 (also defined as f_2 -sweep) paradigm. Quoted errors represent one standard deviation of

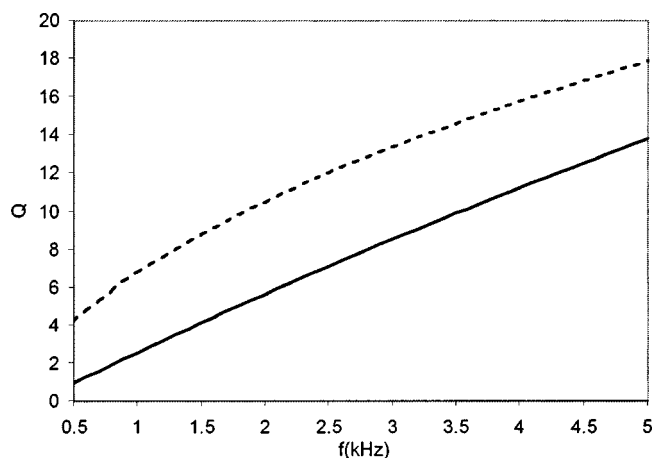


FIG. 2. Tuning curves $Q(f)$ for adults (solid line) and neonates (dotted line), obtained by applying Eq. (8) to the latency fit functions of Fig. 1.

the best-fit parameters D and b , which were estimated using a standard least-square fit. The systematic difference between adults and neonates is clearly visible in Fig. 1. To be more quantitative, there is a statistically significant difference between the fit parameters of neonates and adults: we found $\Delta D = D_n - D_a = 5.2\sigma_{\Delta D}$ and $\Delta b = 2.3\sigma_{\Delta b}$, where $\sigma_{\Delta D}$ and $\sigma_{\Delta b}$ are the standard deviations of the differences between the corresponding fit parameters.

In Fig. 2 the tuning curves $Q(f)$, obtained by applying Eq. (8) to the adult and neonate latency fit functions Eq. (14), are shown. According to Eq. (8), the observed difference between the latencies implies a larger relative difference between the tuning curves. The dependence on the frequency of the estimated tuning curves is rather steep. This observation, if confirmed, would imply a significant scale-invariance violation near the resonance, which would modify the cochlear transmission properties predicted by scale-invariant models. The comparison with other OAE estimates of the cochlear tuning curve is rather difficult, due to the dependence on the stimulus intensity of the cochlear filters tuning. In fact, as the filter bandwidth is assumed to be dependent on the amount of acoustic power instantaneously delivered within a small cochlear portion near the resonance, it is not easy to compare the effect of a broadband click stimulation (TEOAEs) to that of a continuous stimulation by one (SFOAEs) or two tones (DPOAEs) of given amplitude. Much information could be obtained by repeating the experiment described in this study for different levels of stimulation.

In Fig. 3 the experimental SOAE inverse relative spacing, $f/\Delta f$, is shown as a function of frequency, for neonates. For each ear, all frequency spacings between pairs of contiguous SOAEs are shown. As the detection of a SOAE is possible only if its equilibrium amplitude is significantly higher than the experimental noise floor, it is expected that only a few of these pairs be separated by the minimal frequency spacing predicted by the theory. Thus, the data shown in Fig. 3 should be limited by the theoretical upper limit curve of Eq. (11), which is expected to be a function of frequency if Q is not constant. The data tend to cluster along an upper limit curve, which is a slowly increasing function of frequency, as expected from Eq. (11), because Q is an in-

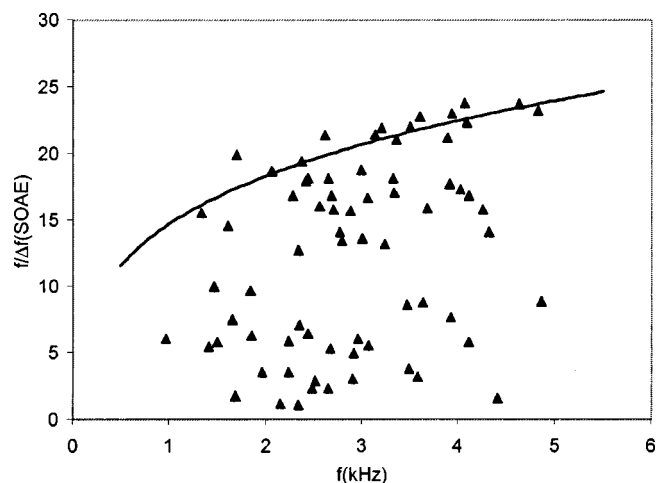


FIG. 3. Experimental SOAE spacing as a function of frequency for neonates. For each subject, all spacings between contiguous SOAEs have been plotted. The solid line is the theoretical prediction for minimal spacing, obtained by applying Eq. (13) to the experimental latency data.

creasing function of frequency. The solid line is not a fit to the data; it is just the minimal SOAE spacing predicted by Eq. (13), using the experimental latency measurements. It should be stressed that the SOAE spacing data and the latency data are independent from each other and come from separate TEOAE and SSOAE recordings of the same subjects. The number of closely spaced SOAEs in the adult spectra was not sufficient to show a similar trend of the minimal inverse spacing.

Summarizing, the results of this study show that: (1) the proposed methods provide reasonable estimates of the cochlear tuning curves; (2) TEOAE latencies in adults and neonates are significantly different; (3) the transmission line cochlear model described here is not contradicted by independent observations on the SOAE spacing, if one interprets them according to the SOAE generation models based on the concept of coherent reflection by random inhomogeneities.

V. DISCUSSION

The experimental data show that OAE latencies are systematically longer in neonates than in adults. If this result is confirmed, and if the model is accurate enough, this observation implies a higher degree of tuning for neonates, at least in the high-stimulus amplitude range explored in this study. The good agreement, shown in Fig. 3, between the experimental minimal spacing data and that predicted by the model using the experimental latency data may surely be considered a positive indication about the internal coherence of the theory, even if it is not a proof of its correctness. The agreement shown in Fig. 3 also means that almost exactly the same tuning curves of Fig. 2 could have been estimated starting from a fit to the minimal SOAE spacing data, independently from any latency estimate and from any time-frequency analysis of TEOAE data. In the case of neonates, the large number of high-amplitude SOAEs extending up to high frequencies could make this alternative method very useful and straightforward.

The evidence for a higher degree of tuning in neonates with respect to adults could be important also for safety purposes. In fact, there is currently some concern about the exposure to noise of neonates in hospital environment. As only high levels of stimulation are considered here, no information can be obtained about the threshold sensitivity, which is dependent on the degree of tuning at very low levels of stimulation. A higher tuning in neonates for high stimulus levels could be instead an indication of a less effective protection by the nonlinear saturation mechanism driven by the efferent system (Abdala *et al.*, 2001), resulting also in a higher cochlear gain for intense stimulation. In fact, according to theoretical OAE models, saturation of the TEOAE stimulus-response curve at high stimulus levels is due to nonlinear damping, which reduces both the response gain and the resonance quality factor, or tuning (Sisto *et al.*, 2001). In fact, in any transmission line cochlear model, the amplitude of the local cochlear transverse displacement, which is associated with the detection of sound of a given frequency, is an increasing function of the tuning of the associated cochlear filter.

VI. CONCLUSIONS

OAE latency and minimal SOAE spacing data of adults and neonates are presented, and discussed using a cochlear model based on the transmission line formalism and on the condition for coherent reflection. Theoretical expressions are derived, which are used to estimate the cochlear tuning curves, either from latency TEOAE data or from minimal SOAE spacing measurements, and to test the internal coherence of the theory, which is not contradicted by the results of this study.

As usual, the information provided by this study travels in opposite directions: a reasonably good theoretical model permits to get indirect measurements of a quantity (cochlear tuning) that cannot be directly measured; on the other hand, the coherence with independent model predictions of a set of independent measurements enhances the confidence about the correctness of the model itself.

The predicted dependence of tuning on the measured quantities is quadratic, which is both an experimental advantage and a theoretical problem. In fact, this means that the method is sensitive to the true variations of the measured quantity, but also that its results are also significantly affected by any wrong theoretical assumption. For example, even if Eq. (2) represents a rather general form for the resonance line shape in transmission line models, even small variations of the cochlear parameters k_0 and k_ω would significantly alter the values of Q estimated using either Eq. (8) or Eq. (12). With this warning, it seems that TEOAE and SOAE data could be effectively used to measure cochlear tuning using the proposed methods.

The experimental results of this work extend to full-term neonates previous DPOAE STC results (Abdala, 2001) indicating that preterm neonates have a higher degree of tuning than adults. As tuning and gain of the cochlear amplifier are expected to be strictly related in a resonant transmission line cochlear model, this would suggest a higher neonate cochlear

gain for intense stimuli, i.e., a less efficient protection against intense noise. This conclusion, if confirmed, would suggest reducing the noise levels in neonatal hospital areas.

ACKNOWLEDGMENTS

We wish to thank M. Lucertini and D. Tufarelli for experimental data and helpful discussions.

- Abdala, C. (2001). "DPOAE suppression tuning: Cochlear immaturity in premature neonates or auditory aging in normal-hearing adults?," *J. Acoust. Soc. Am.* **110**, 3155–3162.
- Abdala, C. (1998). "A developmental study of distortion product otoacoustic emission ($2f_1-f_2$) suppression in humans," *Hear. Res.* **121**, 125–138.
- Bowman, D. M., Eggermont, J. J., Brown, D. K., and Kimberley, B. P. (1998). "Estimating cochlear filter response properties from distortion product otoacoustic emission (DPOAE) phase delay measurements in normal hearing human adults," *Hear. Res.* **119**, 14–26.
- Brown, A. M., and Kemp, D. T. (1984). "Suppressibility of the $2f_1-f_2$ stimulated acoustic emissions in gerbil and man," *Hear. Res.* **13**, 29–37.
- Furst, M., and Lapid, M. (1988). "A cochlear model for acoustic emissions," *J. Acoust. Soc. Am.* **84**, 222–229.
- Greenwood, D. D. (1990). "A cochlear frequency position function for several species—29 years later," *J. Acoust. Soc. Am.* **87**, 2592–2605.
- Harris, F. P., Probst, R., and Xu, L. (1992). "Suppression of the $2f_1-f_2$ otoacoustic emission in humans," *Hear. Res.* **64**, 133–141.
- Kummer, P., Janssen, T., and Arnold, W. (1995). "Suppression tuning characteristics of the $2f_1-f_2$ distortion-product otoacoustic emission in humans," *J. Acoust. Soc. Am.* **98**, 197–210.
- Lucertini, M., Moleti, A., and Sisto, R. (2002). "On the detection of early cochlear damage by otoacoustic emission analysis," *J. Acoust. Soc. Am.* **111**, 972–978.
- Moulin, A., and Kemp, D. T. (1996a). "Multicomponent acoustic distortion product otoacoustic emission phase in humans. I. General characteristics," *J. Acoust. Soc. Am.* **100**, 1617–1639.
- Moulin, A., and Kemp, D. T. (1996b). "Multicomponent acoustic distortion product otoacoustic emission phase in humans. II. Implications for distortion product otoacoustic emissions generation," *J. Acoust. Soc. Am.* **100**, 1640–1662.
- Prijs, V. F., Schneider, S., and Schoonhoven, R. (2000). "Group delays of distortion product otoacoustic emissions: Relating delays measured with f_1 - and f_2 - sweep paradigms," *J. Acoust. Soc. Am.* **107**, 3298–3307.
- Probst, R., Lonsbury-Martin, B. L., and Martin, G. K. (1991). "A review of otoacoustic emissions," *J. Acoust. Soc. Am.* **89**, 2027–2067.
- Schoonhoven, R., Prijs, V. F., and Schneider, S. (2001). "DPOAE group delays versus electrophysiological measures of cochlear delay in normal human ears," *J. Acoust. Soc. Am.* **109**, 1503–1512.
- Shera, C. A., Talmadge, C. L., and Tubis, A. (2000). "Interrelations among distortion-product phase-gradient delays: Their connection to scaling symmetry and its breaking," *J. Acoust. Soc. Am.* **108**, 2933–2948.
- Shera, C. A., Guinan, Jr., J. J., and Oxenham, A. J. (2002). "Revised estimates of human cochlear tuning from otoacoustic and behavioral measurements," *Proc. Natl. Acad. Sci. U.S.A.* **99**(5), 3318–3323.
- Sisto, R., Moleti, A., and Lucertini, M. (2001). "Spontaneous otoacoustic emissions and relaxation dynamics of long decay time OAEs in audiometrically normal and impaired subjects," *J. Acoust. Soc. Am.* **109**, 638–647.
- Sisto, R., and Moleti, A. (2002). "On the frequency dependence of the otoacoustic emission latency in hypoacoustic and normal ears," *J. Acoust. Soc. Am.* **111**, 297–308.
- Talmadge, C. L., Tubis, A., Long, G. R., and Piskorski, P. (1998). "Modeling otoacoustic emission and hearing threshold fine structures," *J. Acoust. Soc. Am.* **104**, 1517–1543.
- Tognola, G., Ravazzani, P., and Grandori, F. (1997). "Time-frequency distributions of click-evoked otoacoustic emissions," *Hear. Res.* **106**, 112–122.
- Whitehead, M. L., Stanger, B. B., Martin, G. K., and Lonsbury-Martin, B. L. (1996). "Visualization of the onset of distortion-product otoacoustic emissions, and measurement of their latency," *J. Acoust. Soc. Am.* **100**, 1663–1679.
- Zweig, G., and Shera, C. A. (1995). "The origin of periodicity in the spectrum of otoacoustic emissions," *J. Acoust. Soc. Am.* **98**, 2018–2047.

Physiopathological significance of distortion-product otoacoustic emissions at $2f_1-f_2$ produced by high- versus low-level stimuli

Paul Avan,^{a)} Pierre Bonfils,^{b)} Laurent Gilain, and Thierry Mom

Laboratory of Sensory Biophysics (EA 2667), School of Medicine, Clermont-Ferrand, France

(Received 7 March 2002; revised 4 October 2002; accepted 7 October 2002)

Distortion product otoacoustic emissions emitted by the cochlea at $2f_1-f_2$ in response to pairs of pure tones at f_1 and f_2 (DPOAE) form a class of otoacoustic emissions and as such, are viewed as a reliable tool for screening outer hair cell (OHC) dysfunctions on a pass/fail basis. However, the persistence of residual DPOAEs from impaired cochleae at high stimulus levels has suggested that above 60–70 dB SPL, instead of reflecting “active” cochlear motion, DPOAEs might represent another “passive” modality: they would thus become unsuitable for analyzing cochlear function. The present work reports the consequences on high- vs low-level DPOAEs of three types of cochlear impairments involving OHCs: progressive OHC degeneration of genetic origin in CD1 mice, complete cochlear ischemia in gerbils, and furosemide injection vs ischemia–reperfusion in gerbils. An alternative to the “active–passive” model was used wherein regardless of stimulus level, cubic DPOAEs are produced by N (probably OHC-borne) nonlinear elements driven by input I and modulated by a function F_3 of their operating point o ; thus, $\text{DPOAE} \propto NI^3 F_3(o)$. When OHCs degenerated, thereby implying a decrease of N , DPOAE levels also decreased regardless of the stimulus level up to 80 dB SPL, in line with the previous formula but at variance with the prediction of the active–passive concept. Instead of affecting N , the other two experiments impaired the efficiency of the cochlear feedback loop as a result of its electrical drive being decreased by strial dysfunction. As it is well accepted that the impaired basilar-membrane motion, although greatly reduced at low levels, tends to catch up with a normal one at higher levels, it was assumed the same was true with I so that DPOAE levels had to be, and indeed were little affected at high levels while plummeting at low levels, without any need for invoking two modalities for DPOAE generation. Finally, comparisons of furosemide vs ischemia effects revealed additional influences on DPOAEs, possibly accounted for by function $F_3(o)$. These results lead to the proposal that although high-level DPOAEs are expected to be poor audiometric indicators, they seem well adapted to assessing the functional integrity of nonlinear elements in OHCs, i.e., presumably their mechano-electrical transduction channels. © 2003 Acoustical Society of America.

[DOI: 10.1121/1.1525285]

PACS numbers: 43.64.Jb, 43.64.Kc [BLM]

I. INTRODUCTION

Since Kemp (1978) discovered otoacoustic emissions (OAE), the idea that OAEs reliably probe the function of cochlear outer hair cells (OHC) has first been supported by circumstantial evidence. Tight links between OHC status or mechanical performance of the cochlea on the one hand, and presence or absence of OAEs on the other hand, have been reported in relation to noise-induced damage (Zurek *et al.*, 1982; Schmiedt, 1986; Lonsbury-Martin *et al.*, 1987; Martin *et al.*, 1987; review in Avan *et al.*, 1996) and other types of OHC dysfunctions, e.g., due to genetic (Horner *et al.*, 1985) or ototoxic causes (gentamicin: Brown *et al.*, 1989; ethacrynic acid: Lonsbury-Martin *et al.*, 1993; cisplatin:

Probst *et al.*, 1993). Current views of cochlear physiology explain why OAEs must somehow reflect the quality of cochlear mechanisms (Brownell, 1990). The motile OHCs (Brownell *et al.*, 1985) are the core of a regenerative system (Gold, 1948) made of a series of coupled stages organized in a loop that feeds vibratory energy back to the cochlear partition (Patuzzi *et al.*, 1989b). When it works properly, the cochlear loop enhances the basilar-membrane (BM) response to low- and intermediate-level sound in a sharply tuned manner (Khanna and Leonard, 1982; review in Ruggero, 1992). Through partly unknown coupling mechanisms, some of the fed-back energy propagates backward as OAEs. Intermodulation OAEs (the DPOAE at $2f_1-f_2$ being the most frequently recorded in response to a pair of tones at f_1 and f_2) exemplify the ability of the cochlea to emit sound while being essentially nonlinear (Eguiluz *et al.*, 2000).

It is thought that DPOAEs and more generally OAEs disappear when OHCs stop enhancing the BM motion so that it loses its tuning and sensitivity. It provides the rationale for a hearing-screening test that would pass when DPOAEs are

^{a)} Author to whom correspondence should be addressed: Paul Avan, Laboratory of Sensory Biophysics, P.O. Box 38, School of Medicine, 63001 Clermont-Ferrand, France, electronic mail: paul.avan@u-clermont1.fr

^{b)} Present address: Laboratoire de Recherche sur l'Audition, Formation Associée Claude-Bernard and Unité CNRS UPRESA 7060, Hôpital Européen Georges-Pompidou, Paris, France.

present and fail when they are absent. The clinical effectiveness of such tests has been confirmed, for instance, by Martin *et al.* (1990), Avan and Bonfils (1993), and Gorga *et al.* (1993), with an optimal screening limit lying between 30 and 60 dB HL depending on the recording protocol. However, many reports have raised an important concern by observing that DPOAE screening tests tend to perform more poorly, with too many false negatives, when the level of primary DPOAE-generating stimuli is set too high (typically, above 60 dB SPL). Ideal screening levels as low as 55 dB SPL for f_1 and 30 dB SPL for f_2 have been proposed (Sutton *et al.*, 1994) along this line of reasoning. The most noticeable problem with high-level stimuli and DPOAEs occurs in experimental models of ischemia, hypoxia, and furosemide action: high-level DPOAEs turn out to be very robust for minutes despite an immediate impairment of cochlear function.

Elaborating on the observations of Norton and Rubel (1990) and Whitehead *et al.* (1990, 1992), the two-component model of Mills (1997) was an elegant attempt toward explaining this paradoxical level-dependent sensitivity to impairment: it assumes that DPOAEs are the vector sum of an “active” and a “passive” contribution. The passive component is normally negligible except at high levels, i.e., from around 60–70 dB SPL on up, and would be uncovered thanks to its robustness and the impairment of the active one. According to Mills (1997), the physiological origin of hypothetical passive DPOAEs may well be the same as that of active DPOAEs, i.e., some intracochlear nonlinearity: only the position and extent of their source along the BM would differ from the active ones. However, other theories can be brought forward where passive DPOAEs, being produced by IHCs, BM, or some other macromechanical process, would only reflect primarily passive cochlear motion. It would then be highly unreliable to design screening tests such that the detected DPOAEs might be spurious ones with no relation whatsoever to OHC function, and negative results might well be false ones in an unpredictable percentage of cases. It would be even more troublesome with regard to the default setups of many commercial DPOAE instruments, namely 60 and even 70 dB SPL (Kemp, 1992). On the other hand, Mom *et al.* (2001) have recently called into question the notion of passive DPOAEs in the case of ischemia by showing that residual, ischemic DPOAEs elicited by high-level stimuli did not exist when mild auditory fatigue had been applied prior to ischemia: they were thus likely produced by the same elements that suffered from auditory fatigue, i.e., presumably the OHC stereocilia bundles (see Patuzzi, 1998), and there was no grounds for invoking a passive origin to those highly vulnerable DPOAEs.

The goal of the present work was to contribute to identifying the significance of high-level DPOAEs. Three experiments were designed in order to examine how specific cochlear impairments influence the residual high-level DPOAEs. The first one exploited a well-documented model of genetic OHC impairment in CD1 mice (Shone *et al.*, 1991; Le Calvez *et al.*, 1998a, b) and explored correlations among DPOAE levels, thresholds of auditory brainstem-evoked responses, and cytochrome c oxidase at various stages of OHC degeneration. The second one revisited the ischemia

model of Mom *et al.* (1997) in gerbils and compared the outcomes of systematic perispheric monitoring of DPOAEs with 60- to 80-dB SPL stimuli. The last experiment compared the changes of DPOAE levels to those of cochlear microphonic potential (CM, so as to gain indirect access to endocochlear potential as explained in Mom *et al.*, 2001) following either transient ischemia or furosemide injection, as both manipulations are known to sharply decrease the endocochlear potential, thereby impairing the whole cochlear feedback loop and performance without necessarily damaging the OHCs.

As an alternative to an active/passive framework, we hypothesized that DPOAEs always come from the same nonlinear elements in the cochlea regardless of the stimulus level and regardless of the presence or absence of cochlear “gain.” A nonlinear element can be fully characterized by its transfer function and operating point o : every distortion term of order p is described by a coefficient $F_p(o)$ arising from the Taylor-series expansion of the transfer function around o (Wever and Lawrence, 1954; Frank and Koessl, 1996; Cheng, 1999). The amount of distortion at the output of the nonlinear element will then depend on $F_p(o)$ times the input level I to the power p (with $p=2$ for quadratic distortion at f_2-f_1 , 3 for cubic at $2f_1-f_2$ and $2f_2-f_1$, etc.). Finally, the overall distortion should be the sum of all contributions from the excited nonlinear elements; thus, it is expected to be roughly proportional to their number (N). The resulting approximation for DPOAE pressure (in linear units) is as follows:

$$\text{DPOAE} \propto NI^3 F_3(o). \quad (1)$$

The predictions of (1) are not straightforward because the input I to the alleged nonlinear elements is not the sound level in the ear canal. Instead, I relates to the BM displacement, and, assuming the cochlea functions as a loop, the input to the loop is also the output from the loop. What became of the BM displacement for different stimulus levels in the ear canal was not ascertained in our three experiments, but the effects under investigation were classical enough that BM behavior was guessed from the literature (e.g., Ruggero, 1992). All three experiments were meant to affect the cochlear loop and make it ineffective; thus, they probably sharply reduced I at low levels. Conversely, it has been shown that pathological BM growth functions catch up with normal ones at high levels (Patuzzi *et al.*, 1984; Ruggero, 1992); thus, pathological changes suffered by I should gradually decrease with increasing level. The genetic impairment in CD1 mice was expected to primarily affect N , thereby inducing a drop in DPOAE level regardless of stimulus level. Transient ischemia was thought to induce no change to N and little change to I at high levels, thus leaving high-level DPOAEs unaffected. Furosemide was thought to have possibly modified o and $F_p(o)$ in a different manner to ischemia so that at low- and moderate stimulus levels, different DPOAE level changes were expected. The model was deliberately left in the unfinished form of formula (1), as its goal was restricted to affording a general framework for the features of pathological DPOAEs to be discussed. Previous models of DPOAE generation such as Patuzzi *et al.*'s (1989b) used more accurate descriptions of cochlear func-

tion; however, their adaptation to describing the particulars of ischemia, reperfusion, OHC degeneration, or auditory fatigue was beyond our scope as it would have required guessing at several scantily documented parameters.

Comparative interpretations of the experimental outcomes were made along the lines of the active/passive vs $DPOAE \propto NI^3 F_3(o)$ frameworks. A survey was also made of the reports of DPOAE response to cochlear pathologies, from noise-induced hearing loss to genetic cochlear diseases to ischemia, ototoxic drugs, and furosemide injections, in an attempt to categorize what experimental pathologies are more prone to being associated with persistent high-level DPOAEs and what significance could be attributed to them.

II. MATERIAL AND METHODS

Of the three experiments designed here, the first one (genetic deafness) used mice owing to the availability of strains with appropriate cochlear status, and the other two (selective cochlear ischemia and furosemide administration), gerbils as the larger size of this species allowed controlled selective cochlear ischemia and IV injections of furosemide to be done. The procedures for DPOAE recordings were common to all experiments.

A. Animals

In experiment 1, 32 mice from the genetically impaired strain CD1 (Swiss albino from the local Charles River laboratories, males and females aged from 5 to 24 weeks—Shone *et al.*, 1991; Le Calvez *et al.*, 1998a) were tested against 12 normally hearing CBA/CaJ adult mice (Jackson Laboratories) serving as controls (Henry and McGinn, 1992). Thirty-six Mongolian gerbils (*Meriones unguiculatus*, males, 3 months, 45–65 g) used for experiments 2 and 3 came from a local breeding colony.

The animals were deeply anesthetized by an i.p. injection of chloral hydrate (480 mg/kg, renewed as needed), accompanied (in mice) or preceded (in gerbils) by premedication (atropin sulfate 0.1 mg; levomepromazin chlorhydrate 1 mg; i.p.). The core temperature was kept at 38 °C in gerbils (39 °C in mice) by a heating blanket regulated by a rectal probe. A punctured myringotomy was performed under microscopic control in order to ensure long-term middle-ear pressure stability without altering cochlear responses by more than 1 dB over the whole frequency range. The tapered tip of an acoustic probe containing a sensitive microphone (ER10B, Etymotic Research) and two plastic sound tubes connected to the outputs of two earphones (ER2, Etymotic Research) was sealed in the external auditory canal of the right ear with cyanoacrylate glue. Ongoing measurements of cochlear responses were performed in a sound-insulated booth.

B. DPOAE monitoring

A computer-controlled Cub^eDis system collected the DPOAEs (Allen, 1990; software CUBDISP v2.43, Mimosa Acoustics). After automatic in-the-ear calibration, two primary tones at frequencies f_1 and f_2 ($f_2/f_1 = 1.20$) were emitted with the same levels $L_1 = L_2$ or L in the right ear

canal by the two earphones. Although a slightly larger f_2/f_1 and some level asymmetry usually allow slightly larger DPOAE levels to be recorded (Kummer *et al.*, 1998), this is thought to be the result of optimal stimulus interaction on the BM, whereas the basic mechanisms at the origin of DPOAEs are likely unaffected. We chose not to optimize the stimulus parameters for three reasons; the first one was that DPOAE changes, rather than absolute levels, were relevant to the present work; the second was that $f_2/f_1 = 1.20$ is more commonly used in clinical routine; last, as level asymmetry ensuring the “best” DPOAE is level dependent (Kummer *et al.*, 1998) while different stimulus levels had to be tested here, using different level asymmetries would have been impractical while affording little benefit.

The processor board of the Cub^eDis system recorded the sound pressure measured in the ear canal by the microphone. The spectral component at frequency $2f_1 - f_2$ was extracted. An estimation of the noise floor was derived from the average level of a few components close to $2f_1 - f_2$. For a DPOAE frequency profile (called DPgram henceforth) to be obtained, f_2 was swept from 17 to 2 kHz (10 steps/octave, 1 s/step). Experiments always involved collecting a series of control DPgrams with $L = 40$ dB SPL then increasing from 45 to 80 dB SPL in 5-dB steps. Input/output plots of DPOAE level vs L were readily derived at each f_2 from the data obtained in the form of DPgrams. For ischemia experiments in gerbils, DPOAEs were monitored throughout an experiment at fixed f_2 (4, 6, or 8 kHz) and L (60, 70, 75, or 80 dB SPL) and plotted at a rate of one data point every 10 s, owing to the comparatively slow changes observed.

C. Experiment 1 with CD1 mice

1. Functional assessment

In mice, frequency-specific auditory brainstem response (ABR) thresholds were evaluated first, before fixing the DPOAE-recording system. Trapezoidal tone pips (3–40 kHz, rise and decay time 1 ms, plateau duration 4 ms, fixed phase of sine waves relative to envelope onset) were generated by an arbitrary waveform synthesizer (Wavetek 70) at a repetition rate of 50/s. They were sent to a high-voltage amplifier with built-in equalizer driving a $\frac{1}{2}$ -in. condenser microphone (Bruel & Kjaer 4134) serving as emitter. This emitter was terminated by a tapered tip tightly sealed in the right ear canal. Stimulus levels varied from 0 to 120 dB SPL in 5-dB steps. Acoustic calibration was performed in the ear canal by means of a thin probe microphone (Bruel & Kjaer 4182), ensuring reliable measurements up to 40 kHz. Stimulus frequencies were 3, 5, 10, 15, 20, 30, and 40 kHz, and around the transition from normal to elevated ABR thresholds, finer 0.5- to 1-kHz steps were used in order to improve the definition of the normal-to-impaired boundary. The spectrum of the acoustic signal detected in the ear canal was checked by a real-time frequency analyzer (Ono Sokki CF4220): the width of the central lobe, as measured at 20 dB below its maximum, was <0.7 kHz regardless of the tone frequency, and secondary lobes were at least 30 dB below the maximum.

ABR responses were recorded between subcutaneous stainless-steel electrodes at the vertex and ipsilateral mastoid, with the lower back serving as ground. The signal passed through a Grass preamplifier (Grass P511, $\times 200\,000$, band-pass 0.3–3 kHz) and was averaged by a CED 1401+ intelligent interface driven by SIGAVG software (v.6.04, Cambridge Electronic Design). At suprathreshold stimulus levels, ABRs consisted of four regularly spaced waves, whereas only the wave with the longest latency was clearly distinguished from the noise background at lower, near-threshold levels. The stimulus level was initially set at 100 dB SPL, then was decreased in 20-, 10-, then 5-dB steps while the ABR waves gradually disappeared (or increased to 120 dB SPL if no ABR wave was present at 100 dB). The ABR threshold at every frequency was defined as the smallest stimulus level needed for producing at least one repeatable wave $>0.15\ \mu\text{V}$.

The 12 adult CBA/CaJ mice were submitted to the same audiological protocol running on the same equipment. Their average ABR thresholds served as references (0 dB nHL) for CD1 mice.

2. Surface preparations and cell counts

After decapitation, CD1 cochleae ($n=8$) were removed from the temporal bones and processed for soft-surface preparations. The apical portion of the bony cochlea was gently opened in 4% paraformaldehyde in phosphate-buffered saline ($\text{pH}=7.4$) to let the fixative bathe the cochlear tissues. The cochlea remained in the fixative solution for 3 h, then after rinsing it was decalcified in 10% EDTA (Fluka, $\text{pH}\ 7.4$), widely opened, and the organ of Corti was dissected and incubated in fluorescent labeled phalloidin (TRITC; 0.3%; Sigma). The preparation was examined with a fluorescence light microscope (Nikon Optiphot). The stereocilia bundles and cuticular plates of inner hair cells (IHC) were visible from apex to base. For every 200- μm -long section, containing about 15 IHCs, three rows of OHCs (or of scars replacing missing cells) were easily identified (four rows near the apex) and OHCs were counted in every row.

D. Experiment 2: Selective cochlear ischemia in gerbils

The right auditory bulla was opened dorsally in order to place the tip of a thin flexible optic fiber probe (Perimed PF 418, B500-0, 0.5-mm diameter) in front of the stria vascularis and a silver-wire electrode against the round-window membrane. Once the optic fiber and electrode were secured, the bulla was closed with dental cement. The eighth-nerve complex was then exposed at the porus acusticus through a posterior transcranial approach, so that the labyrinthine artery running along the eighth-nerve bundle could be compressed by means of a fire-shaped glass pipette blocked in the porus (Mom *et al.*, 1997, 2001). Cochlear blood flow (CBF) was continuously monitored with a laser Doppler velocimeter (LDV, Perimed PF 4000) connected to the optic fiber (sampling period of LDV output 0.2 s).

When the pressure exerted by the pipette at the porus acusticus was sufficient to counteract the arterial blood pres-

sure, a sharp decrease in CBF signal from the LDV was observed. For the experiment to be valid, complete ischemia had to be achieved within seconds and the ensuing LDV signal had to remain stable until after the whole eighth-nerve bundle including the labyrinthine artery had been severed after the end of an experiment.

The DPOAEs were continuously monitored at $f_2=8\ \text{kHz}$ in 20 gerbils, 6 kHz in 6 gerbils, and 4 kHz in 10 gerbils. As no significant influence of f_2 on DPOAE levels was eventually observed, the results at all f_2 s were later merged. Perischemic monitoring was done with a primary level $L=80\ \text{dB SPL}$ in 14 ears, $L=75\ \text{dB SPL}$ in 5 ears, $L=70\ \text{dB SPL}$ in 6 ears, and $L=60\ \text{dB SPL}$ in 11 ears.

E. Experiment 3: Intravenous injection of furosemide versus reversible ischemia

In the first subset of animals ($n=6$), a bolus injection of furosemide (10 to 75 mg/kg) was introduced into a femoral vein. In the second subset ($n=6$), CBF was blocked for 3 min and once the pipette pressure was released, CBF returned to its initial level within 10% in $<15\ \text{s}$. Monitoring started 1 min before injection or ischemia onset with a primary level of 60 dB SPL at $f_2=8\ \text{kHz}$ and $f_1=6.67\ \text{kHz}$, and was carried out for 1 h. A moderate primary level was chosen as, contrary to what was done in the previous experiments, terms I and N in (1) did not need to be controlled in such strict a manner. A 60-dB SPL level was meant to enhance the possible small differences between DPOAE responses to ischemia vs furosemide.

Throughout an experiment, the CM was recorded from the round-window electrode along with DPOAE data collection. The electrode output was preamplified (Grass P511, filter bandwidth 0.3–10 kHz, gain $\times 5000$) and sent to a lock-in amplifier (EG&G 5201, 0.3-s averaging time) whose reference input received a copy of the f_1 electric stimulus (adjusted to 1 V rms through a voltage amplifier). The lock-in output thus represented CM at 6.67 kHz; it was sampled every 10 s and plotted with the DPOAE. For the basal cochlea, from where most of the CM collected by the round-window electrode comes (Patuzzi *et al.*, 1989a), f_1 was far enough from the best frequency that CM could be assumed proportional to the endocochlear potential, regardless of whether the cochlear gain was normal or impaired (as in Mom *et al.*, 2001).

F. Statistical analysis

Relationships between DPgram and ABR data from experiment 1, and between furosemide doses and CM decrease in experiment 3, were investigated by means of Pearson linear regression analysis, assuming the variables of interest were normally distributed. Condition $p<0.05$ was required for significance to be reached.

III. RESULTS

A. CD1 mice, genetic cochlear impairment

In keeping with Shone *et al.* (1991) and Le Calvez *et al.* (1998a), the hearing loss of CD1 mice increased from low to

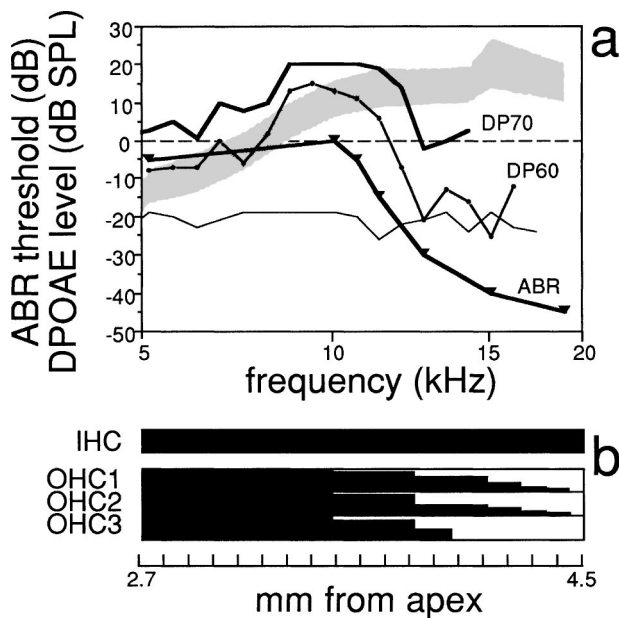


FIG. 1. (a) Example of DPOAE level and ABR threshold changes in one 7-week-old CD1 mouse, against frequency, with DPOAEs being referred to f_2 and ABR thresholds to the center frequency of the tone pip. Shaded area: normative data in CBA/J mice, that is average levels ± 1.96 s.d. for 60-dB SPL equilevel stimuli; continuous line with closed circles: 60-dB SPL induced DPOAEs (labeled DP60); bold line: 70-dB SPL induced DPOAEs (labeled DP70); thin continuous line: average background noise; bold lines, closed inverted triangles: ABR thresholds in this ear. DPOAE levels are plotted in dB SPL and ABR thresholds in dB relative to normal thresholds as observed in CBA/J mice. (b) Cytocochleogram determined from the phalloidin-stained surface preparation. Its horizontal scale in mm from apex was adjusted to the frequency scale of the top diagram according to (Greenwood, 1990).

high frequencies. Their age and the corresponding stage of cochlear impairment were such that the border between normal and impaired ABR thresholds fell between 7 and 25 kHz. The analysis was therefore focused on the DPOAEs from this frequency range, as it afforded a larger range for the variables of interest. Surface preparations of the organ of Corti confirmed that OHCs from all rows gradually disappeared from apical to basal areas, as shown in Fig. 1, depicting an example of DPgram, ABR thresholds [panel (a)], and cytocochleogram (b). Meanwhile, no IHC damage was visible. Figure 1(a) also shows that while the DPgram at 60 dB SPL paralleled the plot of ABR thresholds against frequency, the DPgram at 70 dB SPL did not perform well as an audiometric “pass or fail” test, as DPOAEs were still present above 12 kHz in spite of the hearing loss. Thus, the interest of DPOAEs at 70 dB SPL and higher was seemingly called into question.

In order to address this issue, correlations between DPOAE levels and ABR thresholds at f_2 were investigated at primary levels as high as possible, as shown in Fig. 2 (open circles: $f_2 = 12$ kHz, $L = 75$ dB SPL; crosses: $f_2 = 15$ kHz, $L = 80$ dB SPL). The instrumental distortion measured in a dummy ear (0.25-cm³ cavity) or postmortem (3 h after the mouse had been euthanized) was < -15 dB SPL at $L = 80$ dB SPL on average over the frequency range of interest; thus, all data points above the dashed line in Fig. 2 were likely genuine ones. The two Pearson regressions were

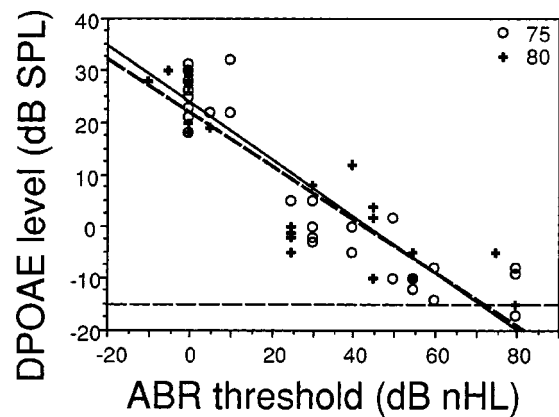


FIG. 2. DPOAE levels against ABR thresholds of CD1 ears (in dB nHL referring to the average ABR thresholds in control CBA/J mice). Open circles, continuous regression line: 75-dB SPL equilevel stimuli, $f_2 = 12$ kHz; crosses, dashed regression line: 80-dB SPL stimuli, $f_2 = 15$ kHz. Horizontal dashed line: DPOAE floor in an artificial ear, i.e., limit of instrumental distortion with 80-dB SPL stimuli.

highly significant ($p < 0.0001$), with large r^2 determination coefficients explaining more than 77% of data variance, and a slope of -0.51 to -0.55 . Owing to the bimodal rather than normal distribution of ABR thresholds in Fig. 2, linear regressions were also computed for the subsets of data with ABR thresholds > 20 dB nHL; they remained significant ($p < 0.01$) with shallower slopes around -0.27 ; thus, the cluster of points around 0 dB nHL did not induce too large a bias in the analysis. Overall, these statistical findings indicate that DPOAE levels decreased with ABR thresholds, approximately linearly by half a dB per dB increase in threshold. Instrumental distortion was reached (thus, true DPOAEs had vanished) when ABR threshold elevation exceeded about 70 dB nHL.

Cell counts from surface preparations confirmed that ABR thresholds were elevated in frequency areas with OHC losses (Ryan and Dallos, 1975). Figure 1 depicts a typical case illustrating the good correspondence between functional and morphological damage [panel (a) vs (b)]. Although the first and second rows of OHCs in this cochlea tended to present less damage than the third one, OHC losses in all three rows exceeded 20% beyond 3.8 mm from apex, corresponding to about 12 kHz on Greenwood’s (1990) map of the mouse cochlea. Besides, ABR threshold shifts exceeded 20 dB beyond 11 kHz and DPOAEs elicited at 60 dB SPL fell out of the normative range of CBA mice [shaded area in Fig. 1(a)] beyond the same 11-kHz boundary. DPOAEs at 70 dB SPL followed the same pattern. These higher-level DPOAEs remained present (albeit about 20 dB below their normal level) between 13 and 15 kHz while about 50% of the remaining OHCs were counted in the corresponding area. Data from the area where 100% OHCs were missing (> 19 kHz) are not conclusive as the probe earphones would have required too high a voltage drive to emit levels > 50 dB SPL.

Input–output DPOAE curves were derived from the DPgrams at $f_2 = 15$ kHz, as the largest possible range of cell losses and threshold elevations was encountered at this frequency. They are plotted in Fig. 3, where percentages of remaining OHCs, all rows included, and ABR thresholds in

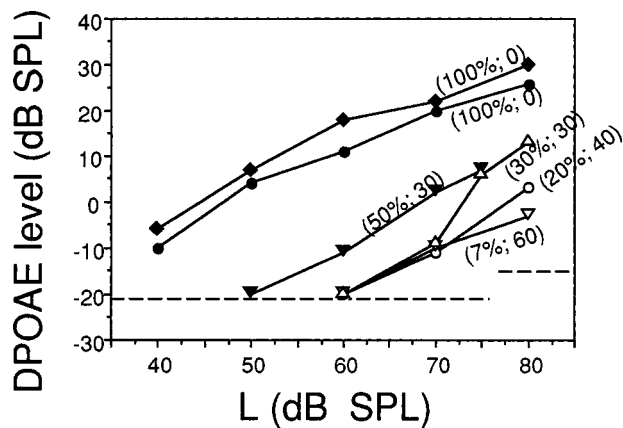


FIG. 3. DPOAE levels versus level L of equilevel stimuli in six CD1 ears tested at $f_2 = 15$ kHz. In parentheses: 1st figure=percentage of residual OHCs at the place tuned to f_2 ; 2nd figure=ABR threshold in dB nHL in response to tone pips of center frequency $f = 15$ kHz. Dashed horizontal lines: limits of background noise (below 75 dB SPL) or instrumental distortion (at 80 dB SPL). The three data points near the background noise limit may be overestimations of true DPOAE levels.

dB nHL are printed between brackets along with every curve. Most curves presented a rather shallow slope, near 1 dB/dB [in keeping, for example, with Parham *et al.* (1999) in CBA/J mice], over the whole range of levels except the one labeled (30%; 30). The two top curves of Fig. 3 correspond to intact OHCs in two cochleae with normal ABR thresholds at 15 kHz, and DPOAEs were still present at 40 dB SPL. Conversely, the two bottom curves show DPOAEs above noise floor only above 70 dB SPL. DPOAE levels hardly reached 3 dB SPL at 80 dB SPL. The corresponding percentages of extant OHCs were the lowest in this series, namely 7% and 20%. Not surprisingly, ABR thresholds were the most elevated ones, 40 and 60 dB nHL. The remaining plots lay between these two extremes: 30% and 50% remaining OHCs, and 30-dB ABR threshold elevations.

Seventeen of the tested CD1 mice presented steep “ski-sloped” audiograms with a roll-off frequency between 7 and 25 kHz: ABR thresholds increased by more than 30 dB within <5 kHz (see Fig. 1). The roll-off frequency was arbitrarily defined as the first frequency in an ABR threshold vs frequency chart (0.5-kHz resolution), with ABR threshold >20 dB nHL whereas ABR thresholds were normal at lower frequencies. Corresponding DPOAE roll-off frequencies were defined on a DPgram as the first frequency with a DPOAE level more than 10 dB below the lower limit of the normative range of CBA/J mice, whereas DPOAE levels were within normal at lower frequencies. Figure 4 depicts the effect of increasing stimulus levels on a series of DPgrams collected in one ear exhibiting a clear-cut transition from normal to impaired function around 10 kHz. The lack of influence of stimulus level on DPOAE roll-offs can be derived from the fact that all DPOAE levels decrease sharply between 9 and 11 kHz, by more than 10 dB/kHz except at 50 dB SPL owing to insufficient signal-to-noise ratio. Figure 5 represents the relationships between ABR and DPOAE roll-offs for primary levels of 50, 60, 70, and 75 dB SPL. The voltage required for delivering 80 dB SPL in the ear canal would have damaged the earphones in too many ears. It is

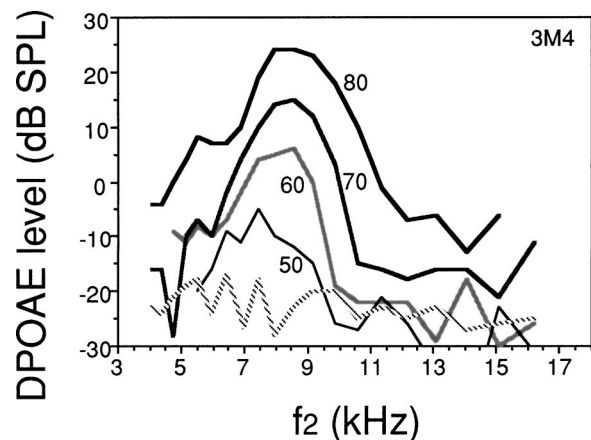


FIG. 4. Example of a series of DPgrams collected with equilevel stimuli (80 to 50 dB SPL as indicated by labels on each DPgram) from the right ear of mouse 3M4 (7 weeks of age). Hatched line: average background noise.

for the same reason that data from several ears are missing at 75 dB SPL. Figure 5 shows that the DPOAE roll-off linearly followed the ABR-threshold one, with a slope of about 0.57 and an intercept of about 3–4 kHz regardless of the monitoring level. Data at 75 dB SPL were too scarce for a meaningful regression to be computed; nevertheless, the available points lined up with those obtained at lower levels. In other words, DPgrams allowed the fine structure of ABR thresholds vs frequency to be accurately tracked regardless of the stimulus level. DPOAEs tended to “anticipate” the evolution of ABR threshold elevations at lower frequencies and OHC degeneration toward the apex, since DPOAE levels could already be decreased in a frequency range where ABR thresholds remained near normal.

B. Gerbils and selective cochlear ischemia

In all gerbils, the signal from the laser Doppler velocimeter decreased within a few seconds to the same floor value as that observed after the acousticofacial bundle had been finally cut, thereby showing that CBF was completely interrupted immediately after the pipette was pushed into the porus acusticus. The DPOAE level changes with time exhib-

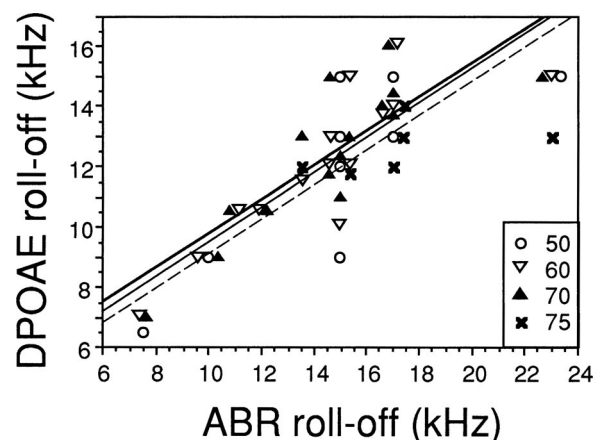


FIG. 5. Scatterplots and correlations among DPOAE vs ABR roll-off frequencies in CD1 mice with sharp transitions between normal and impaired areas. Right-hand insert: symbols for every stimulus level. Linear regressions: bold line, 50 dB SPL; thin line: 60 dB SPL; dashed line: 70 dB SPL.

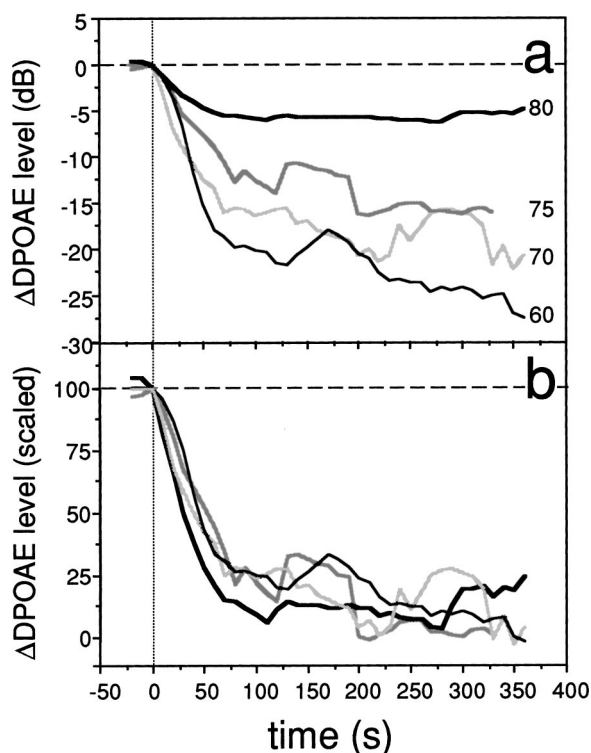


FIG. 6. (a) Changes in DPOAE levels with time relative to preischemic levels when 80- to 60-dB SPL equilevel stimuli were used for monitoring purposes (labels). (b) Same plots after applying a scaling factor such that plateau levels are made to coincide, representing reference 0% while 100% refers to the initial levels. The steepest and earliest decrease after ischemia onset is the one observed with 80-dB SPL stimulus levels.

ited several common features independent of stimulus level. Figure 6(a) shows the average decreases in DPOAE levels. They were monotonic over the first minute of ischemia, then a plateau was reached either directly or, in more than half individual ears and below 80 dB SPL, after a level notch followed by a rebound had occurred: once averaged across ears, notches got smoothed out while rebounds appeared as humps visible at 60, 70, and 75 dB SPL (between 150 and 200 s, and around 300 s) in Fig. 6(a). The plateau lasted until at least 6 min after ischemia onset, after which the pipette pressure was released and the monitoring interrupted.

The plateau level drops relative to preischemic levels decreased in size with increasing level: on average across time and ears, -25 dB at 60 dB SPL after about 6 min, -20 dB at 70 dB SPL, -16 dB at 75 dB SPL, and -5 dB at 80 dB SPL. In dB SPL, the plateau levels are represented in Fig. 7. These curves resemble reconstructed average DPOAE "growth functions," only differing from regular ones in that measurements at different levels were performed in different ears. The average preischemic DPOAE growth function was similar to already-published data in the same frequency range (e.g., Sie *et al.*, 1999), with a tendency to plateau around 70–75 dB SPL. Figure 7 shows that the ischemic growth function became steeper and monotonic even though DPOAE growth kept slowing down around 70 dB SPL. The overall ischemic slope was about 1.8 dB/dB between 60 and 80 dB SPL and approached 3 dB/dB between 75 and 80 dB SPL.

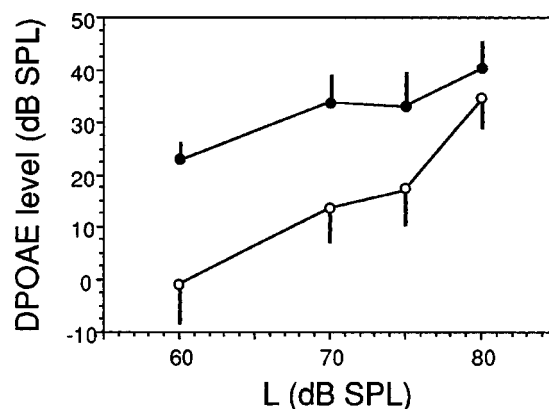


FIG. 7. Average DPOAE levels in dB SPL reached after 5 min following ischemia onset against stimulus level (open circles) versus average preischemic DPOAE levels as observed in the same ears (closed circles). Bars: one s.d.

The average plots of DPOAE level decrease vs time were scaled in order to offset the differences in plateau levels relative to preischemic levels and replotted in Fig. 6(b). They exhibited very similar profiles of decrease from ischemia onset to plateau. The results of monitoring at 80 dB SPL actually reacted slightly faster to the cochlear impairment, whereas those at 60 dB SPL were slowest to drop, with about a 10-s lag.

C. Gerbils, furosemide versus cochlear ischemia

1. Furosemide

The effects of furosemide injection on DPOAEs and CM were dose dependent. The effect of 10 mg/kg was by far the smallest one, with a maximum decrease after 5–10 min of 7 dB for DPOAE level and 2.5 dB for CM. Thus, the same animal was administered a second, 30 mg/kg shot an hour after having fully recovered. The other five animals received a single bolus of 20, 25, 30, 35, and 60 mg/kg, respectively. An attempt at injecting 75 mg/kg was discarded because CM and DPOAE never fully recovered after more than 1-h monitoring.

The time courses of CM and DPOAE were similar, as shown in the example of Fig. 8(a) (CM: open circles; DPOAE: continuous line), and this held regardless of the injected dose, with a rapid monotonic decay to a minimum reached after 2–5 min. The maximum CM decrease ranged from 2.5 to 14 dB with an approximately linear dose dependence ($\text{CM drop in dB} = 0.18 \times \text{dose in mg/kg} + 2.5$; $r^2 = 0.50$; $p < 0.05$), whereas the maximum DPOAE decrease varied from 7.3 to 32 dB. After about 1 min of stability, both CM and DPOAE slowly and monotonically recovered to within 2 dB of their initial values. The two recoveries were approximately linear [in dB; Fig. 8(a)] and took 17 to 20 min regardless of the injected amount. The ratio of DPOAE to CM decrease, in dB per dB, was stable throughout the decay and recovery periods: it ranged from 1.7 to 3.2 with no evident dose dependence [2.7 in the example of Fig. 8(b)]. In keeping with Mills and Rubel (1994) and Mills (1997), the DPOAE phase [Fig. 8(c)] underwent a sudden shift of about

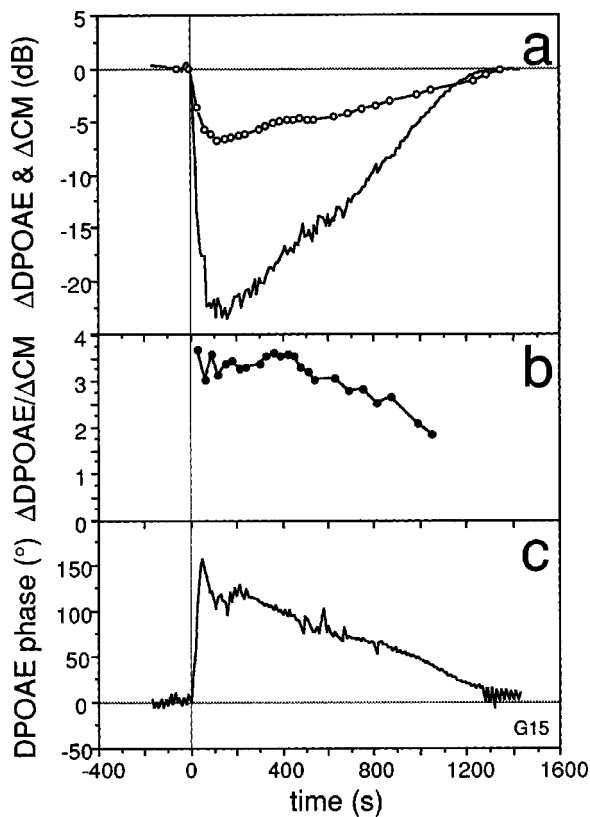


FIG. 8. (a) Time course of DPOAEs ($f_2=8$ kHz; $f_1=6.6$ kHz, 60-dB SPL equilevel stimuli; continuous line) vs CM at f_1 (open circles) (both in dB relative to preischemic levels), following a single i.v. injection of furosemide at $t=0$ (G15, 25 mg/kg). (b) Time course of the ratio of DPOAE to CM changes in dB. (c) DPOAE phase changes.

180° when the DPOAE level initially dropped to its plateau, then its recovery followed the same time course as the level one.

2. Ischemia

Ears exposed to complete selective cochlear ischemia behaved, for the 3 min following ischemia onset, as already explained in the previous section. Figure 9 depicts an example presenting a sharp and relatively regular DPOAE level drop [continuous line, panel (a)] starting after 10–20 s. A minimum was reached after 60 s, next the DPOAE level immediately bounced back to a higher plateau [10 to 12 dB below initial level in Fig. 9(a)]. After ischemia onset, the CM (inverted triangles) exhibited an almost immediate and fast decrease; in a majority of ears, it was monotonic and an asymptote was reached after less than 2 min. Compared with the furosemide experiment, the maximum CM reduction was larger (average—19.6 dB; s.d.=6.3, vs a furosemide average —8.0 dB; s.d.=4.4). Conversely, the maximum DPOAE level decrease tended to be less with ischemia (–15.0 dB; s.d.=4.2) than furosemide (–17.4 dB; s.d.=9.7).

3. Reperfusion

In this experiment, CBF was allowed to return to normal after about 3 min. The DPOAE level immediately started increasing sharply so that it almost reached its initial value in about 50 s. This stage is marked by the vertical line on the

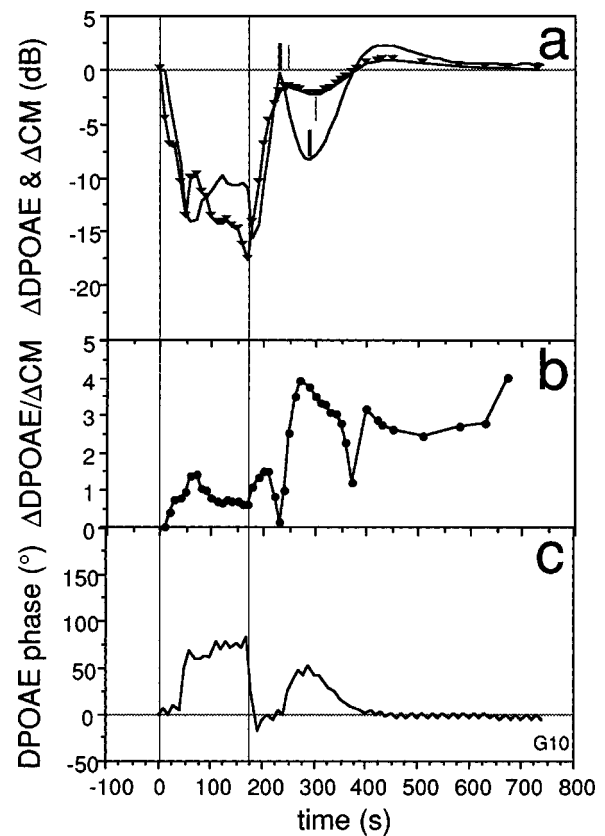


FIG. 9. (a) Time course of DPOAEs ($f_2=8$ kHz; $f_1=6.6$ kHz, 60-dB SPL equilevel stimuli; continuous line) vs CM at f_1 (closed triangles) (both in dB relative to preischemic levels), following onset of complete ischemia at $t=0$. Bold (respectively, thin) short vertical labels locate the first maximum and minimum for DPOAE level (respectively, CM) following reperfusion; bold and thin labels do not coincide, showing that DPOAE and CM courses are not perfectly synchronous. (b) Time course of the ratio of DPOAE to CM changes in dB. (c) DPOAE phase changes. Thin vertical lines extending through all panels: onset of ischemia ($t=0$) and reperfusion ($t=180$ s).

example of Fig. 9(a) (first bold vertical mark). Next, a large secondary decrease of DPOAE [Fig. 9(a) second bold mark] often followed by an overshoot was always observed. CM showed a similar course, with a fast, almost complete recovery [Fig. 9(a), first thin vertical mark], a secondary decrease [Fig. 9(a), second thin mark], and a final overshoot. Compared to the DPOAEs, the amplitudes of secondary decrease and overshoot were much smaller, barely exceeding 2 dB. Furthermore, CM decrease and overshoot always lagged the DPOAE ones by >20 s [Fig. 9(a)].

In sharp contrast to the furosemide experiment, the ratios of DPOAE to CM decreases, in dB/dB, greatly differed in the ischemia versus reperfusion periods [Fig. 9(b)]. The ischemic DPOAE/CM varied little with time and ranged from 0.4 to 1.2. During reperfusion, DPOAE/CM ratios were always much larger than ischemic ones and varied much, especially around the times when transitions were observed from initial recovery to secondary decrease, and from secondary increase to overshoot: then they exhibited sharp drops. Most of the time, DPOAE/CM ranged between 1.8 and 15. DPOAE phase changes were also markedly different from those induced by furosemide injection [Fig. 9(c) vs 8(c)] in that they never exceeded a quarter cycle.

IV. DISCUSSION

Owing to the small volume of the external ear canals of the two species tested here, high-level stimuli could be used (75–80 dB SPL) without generating any annoying instrumental distortion: it was <-15 dB SPL, thus hardly above acoustic noise floor. At a few frequencies around 10–12 kHz, it could exceed this limit with stimulus levels >75 dB SPL and the corresponding data were discarded. This shortcoming is not critical to discussing which of formula (1) or the “active/passive” theory better matches experimental data, as the limit between active and passive regimes is supposed to be around 60–70 dB SPL in rodents (e.g., Mills, 1997; Whitehead, 1997). Indeed, functions considered to be particularly relevant to the active/passive issue present a shallow low-level segment below 60 dB SPL, a plateau and even a notch between 60 and 70 dB SPL, then the slope may increase again, thus enabling a high-level segment to be delineated. Actually, in the present work, although visible in gerbils (Fig. 7), the plateau separating the low- from the high-level segment was not observed in mice. Whitehead (1997) pointed out that the plateau configuration requires some particular combination of stimulus parameters, and for instance, in the active/passive framework, the notch in the DPOAE growth function appears only when active and passive components become equal and almost out of phase. Accordingly, instead of requiring a particular shape of growth function, the present work called “low-level” the DPOAEs produced at and below 60 dB SPL, and high-level those produced at 70, 75, and if possible 80 dB SPL, and scrutinized their respective responses to pathologies.

In the mouse strain CD1, Le Calvez *et al.* (1998a, b) reported significant linear regressions between DPOAE levels at 60 dB SPL on the one hand, and frequency-specific ABR thresholds or number of residual OHCs on the other hand. The present data extend the range of measurements in the same strain by showing that similar results held when DPOAEs were elicited by stimuli up to 80 dB SPL. Notably, there was no high-level DPOAE above instrumental distortion levels when ABR thresholds exceeded 70 dB nHL (Fig. 2) and, when OHCs remained, the residual 80-dB DPOAE levels matched the percentage of residual OHCs (Fig. 3). No finer quantitative analysis could be made of the parameter N occurring in (1). One could have assumed for instance that the nonlinear elements were the mechano-electrical channels in the stereocilia of OHCs and tried to evaluate the number of intact ones, but surface preparations are too coarse a method for the stereocilia status to be evaluated. Even scanning electron micrographs would not necessarily have told how functional the stereocilia bundles of extant OHCs were (Le Calvez *et al.*, 1998b). Nonetheless, high-level DPOAEs varied in keeping with (1) provided N was replaced by the number of residual OHCs, given that at high SPL in the ear canal, I was expected to be unchanged even though the cochlear loop was impaired (Patuzzi *et al.*, 1984; Ruggero and Rich, 1991; Ruggero, 1992). The assumption that $F_3(o)$ underwent little change when OHCs were present seems tenable.

For practical screening purposes, higher-level DPOAEs even allowed clear-cut audiometric notches to be tracked as

accurately as with lower-level DPOAEs or reference tests such as ABR and cytochrome cograms. The main caveat with high-level DPOAEs is that, due to their starting from higher levels when the cochlea is normal, they may need more hearing loss to vanish than low-level ones; thus, the DPOAE criterion of presence vs absence must be associated with a higher screening limit—i.e., the amount of hearing loss beyond which DPOAEs are absent, about 60 dB HL here (see Bonfils *et al.*, 1997, in humans). In contrast with (1), the active vs passive picture is of no help unless it is accepted that the passive modality reflects OHC presence. The seemingly monotonic decrease of the overall DPOAE with the percentage of residual OHCs provides no evidence for any transition from a dominant active to a residual passive component, and the persistent accuracy of audiometric-notch tracking by high-level DPOAEs precludes any sudden shift of the DPOAE source from an active to a different passive place.

When OHC function is disrupted, the low-level segment reportedly shifts downward while the high-level one (i.e., at and above 70 dB SPL) can be little affected. Its persistence was reported by Brown *et al.* (1989) two days after onset of gentamicin treatment in guinea pigs, Norton *et al.* (1991) post mortem in gerbils, Fitzgerald *et al.* (1993) after intracochlear perfusion of salicylate in guinea pigs, Mills and Rubel (1994) after furosemide injection in gerbils, and Mom *et al.* (1997) after complete selective cochlear ischemia in gerbil. This seemingly low vulnerability of the high-level segment is at the origin of the active/passive model (Norton *et al.*, 1991; Mills, 1997). Actually, markedly different incidences of other pathologies on high-level DPOAEs have been commonly reported. Absence of high-level DPOAEs was observed by Horner *et al.* (1985) in genetically defective ears up to 90 dB SPL, Le Calvez *et al.* (1998a) in mutant mice or Frolenkov *et al.* (1998) after round-window administration of an inhibitor of OHC electromotility. Lonsbury-Martin *et al.* (1993) pointed out that although sometimes more robust than the low-level segment, the high-level segment of the DPOAE input–output curve could be eliminated by combined factors known for destroying OHCs, such as ethacrynic acid plus gentamicin.

In the literature, results from noise-exposed ears are quite homogeneous in that most authors report little or no influence of stimulus level on DPOAE level shifts. Zurek *et al.* (1982) found that DPOAEs were sensitive indicators of noise-induced hearing loss regardless of the stimulus level between 30 and 90 dB SPL, and Schmiedt (1986) confirmed this finding with 70- and 80-dB SPL stimuli. Most examples of DPOAE growth functions in Hamernik *et al.* (1996) depicted similar DPOAE level changes at all stimulus levels from 30 to 75 dB SPL. Clock Eddins *et al.* (1999) reported that low-level portions of DPOAE growth functions dropped down to noise floor after noise exposure, and that although high-level portions were retained, their decrease was systematic and almost as large for 80-dB SPL primary levels as for 60-dB SPL ones. Drawing a distinction between different categories of experimental damage, as suggested by Eq. (1), can largely solve the apparent lack of consistency of the

effects of pathology on high-level DPOAEs. The first category involves a loss of cochlear activity due to either drugs that primarily affect the endocochlear potential (e.g., furosemide at low doses; early stages of ischemia according to Mom *et al.*, 1997, 2001) or mild damage to OHCs (e.g., first installments of gentamicin)—thereby affecting I .

The second category includes complete losses of OHC structure or function (i.e., N and I decrease), and hardly raises the issue of “passive” high-level DPOAEs: there are none. This striking positive correlation between fatal damage to OHCs and absence of high-level DPOAEs makes it tempting to identify healthy OHCs as the sources of high-level DPOAEs. This analysis lines up with the statement by Lonsbury-Martin *et al.* (1993) that the high-level DPOAEs require the structural integrity of OHCs instead of being produced at a macromechanical level such as the BM. Mom *et al.* (2001) elaborated on this idea by showing that ischemia following mild auditory fatigue no longer produced high-level DPOAEs: they proposed that these DPOAEs were produced by the same elements that suffered from auditory fatigue, i.e., the OHC stereocilia bundles (Patuzzi, 1998). Indeed, hair cell bundles present a conspicuous nonlinearity (Flock and Strelioff, 1984; Patuzzi *et al.*, 1989b; Kros *et al.*, 1992; Jaramillo *et al.*, 1993). As already hypothesized, N in (1) would amount to counting how many functional channels persist in OHC stereocilia.

The present results of the ischemia experiment in gerbils contradict none of the tested models. The detailed active/passive interpretation as expounded in Mills (1997) can be tentatively applied here since ischemia and furosemide effect share common points. As for Eq. (1)’s prediction, it is likely that ischemia affects I as the drop in endocochlear potential due to stria anoxia prevents the cochlear loop from effectively feeding back enough energy into the cochlear partition, thereby diminishing its gain. In the meantime, N has no reason to be affected immediately as reperfusion rapidly restores DPOAEs (Mom *et al.*, 1997). From (1), in the absence of significant gain, the DPOAE level should decrease three times faster (in dB) than I when the sound level in the ear canal is decreased. Again, BM movements being scarcely affected by pathology above 80 dB SPL, (1) predicts an almost unchanged DPOAE level (−6 dB here). Hence, it is not necessary to hypothesize a differential vulnerability of the DPOAE generators: once their input reaches near-normal, they are expected to produce near-normal DPOAEs by normal mechanisms. At lower levels, while the slope of I is normally as small as 0.20 dB per dB decrease in the ear canal according to Cooper and Rhode (1997, basal turn of guinea pig), it should gradually reach 1 dB/dB along with the impairment of the cochlear gain: accordingly, the DPOAE level should tend to decrease by 3 dB/dB decrease of the stimulus level. Here, its slope was about 1.8 dB/dB (Fig. 7). Its being <3 dB/dB may be attributed to residual activity or adaptation (Mills, 1997). Nevertheless, monitoring the cochlea with high levels did not prevent the onset of ischemia from being detected, and it happened even a little earlier than with 60-dB SPL stimuli. Again, of course, the criterion for detecting a reliable change would have to be adapted to the monitoring level.

The interest of considering $F_p(o)$ as possible modulating factors of distortion responses has already been emphasized by the experiments of Frank and Koessl (1996, 1997), who showed how a controlled displacement of o could differentially influence quadratic and cubic distortion. Likewise, the models of Bian and Chertoff (1998, 2001) and Lukashkin and Russell (1999) explicitly refer to o . The interest of $F_p(o)$ in pathologies is suggested by the results of the third experiment. Individual experiments produced somewhat dissimilar CM decreases that were balanced by computing DPOAE-to-CM decrease ratios. Round-window CM was extracted at f_1 : being much lower than the characteristic frequency at the recording place, CM could be safely assumed to reflect the electrochemical gradient at the apex of OHCs (Patuzzi *et al.*, 1989a; Mom *et al.*, 2001); therefore, if V_{OHC} represents the voltage inside OHCs and EP the endocochlear potential

$$\text{CM(during)}/\text{CM(before)} = (V_{\text{OHC}} - \text{EP})(\text{during}) / (V_{\text{OHC}} - \text{EP})(\text{before}).$$

Furosemide at reasonable doses as well as short-term ischemia reversibly act on the stria vascularis and decrease EP while leaving OHCs intact (Ruggero and Rich, 1991). This results in an impairment of the cochlear feedback loop [I in (1)] without altering N (1). As the concurrent DPOAEs decreased much less with ischemia than furosemide (0.4 to 1.2 instead of 1.7 to 3.2, in dB per dB), one expects that the decrease of I in (1) was partly offset, for example by an adaptive change of $F_3(o)$ in (1). Reperfusion-induced changes were even more complex, as the ratio $\Delta\text{DPOAE}/\Delta\text{CM}$ not only differed from the furosemide one, but varied with time. The nonmonotonic CM recovery matched the nonmonotonic recovery of EP mentioned by Rebillard and Lavigne-Rebillard (1992) and discussed by Mills *et al.* (1993) in relation to adaptation. Nevertheless, although also nonmonotonic, DPOAE recovery was clearly different and not synchronous. The most spectacular behavior was seen when DPOAEs systematically plummeted after initially recovering while CM was near normal. Such findings can be explained, for example, by a transient displacement of the operating point o toward a less asymmetric position along the input–output characteristics of the nonlinear element (Frank and Koessl, 1997; Bian and Chertoff, 1998, 2001).

V. CONCLUSION

In summary, the present results suggest that, provided of course the recording equipment is reliably distortion-free, the persistence of high-level DPOAEs reveals the persistence of functional nonlinear elements in the cochlea, and specifically those showing the ability to transform sine waves into richer harmonic complexes, thereby generating intermodulation. In the meantime, the compressive nonlinearity exhibited by the BM growth function may well have disappeared but this is not paradoxical: intermodulation and compression are of a completely different physical nature, the latter as a consequence of the enhancement of BM motion by OHCs being level dependent. Although it is well acknowledged that in the normal cochlea, these two nonlinearities happen to come

with one another, it must be kept in mind that they are independent in many systems (e.g., hearing aids).

That high-level DPOAEs can persist despite cochlear pathology is of genuine physiological significance if it were confirmed that the nonlinear elements are the mechano-electrical transduction channels of OHCs. This is already suggested by a variety of experiments (Patuzzi *et al.*, 1989b; Kros *et al.*, 1992; Jaramillo *et al.*, 1993; Lukashkin and Russell, 1999; Mom *et al.*, 2001). Without referring to any active or passive mode of cochlear functioning, the proposed model (1) (despite its oversimplifications: for example, the spatial distribution of DPOAE sources over the normal or pathological BM was overlooked) rightly predicts that regardless of the OHC pathology, low-level DPOAEs systematically vanish whenever the resulting hearing loss is large enough. As it is already well acknowledged, their detection thus provides the experimenter with a simple screening test. On the other hand, the model also explains that because high levels move the BM regardless of whether the cochlear loop acts or not, high-level DPOAEs allow two categories of pathologies to be differentiated: the first one damages the very origin of distortion and/or interrupts the loop, and the second one impairs any other stage(s) of the cochlear feedback loop while at the same time respecting the nonlinear elements (and presumably the coupling mechanisms allowing DPOAEs to reach the oval window). Recorded alone, high-level DPOAEs would be unsuitable for screening purposes; however, in the course of a more complex protocol comparing the outcomes of several stimulus levels, their diagnostic value could be high (Kemp, 1992; Brass and Kemp, 1994) instead of being frequently called into question as nonconservative. However, the case of human ears deserves further studies along this line, first because in the larger volume of external ear canals, DPOAE recording systems may exhibit troublesome instrumental distortion at lower stimulus levels than in smaller rodent ears, and second because the splitting of DPOAE growth function in low- and high-level segments in humans may differ from that in rodents (Whitehead, 1997).

In addition, the existence of adaptive-like phenomena that modulate what relates DPOAE level to hearing loss probably makes it deceptive to expect a universal DPOAE loss-to-hearing loss relationship to be available. This adds to the previously mentioned shortcomings of too simple of a DPOAE screening strategy. Therefore, instead of focusing on probably hopeless attempts at achieving some kind of objective audiometry, diagnostic procedures using DPOAEs might benefit from exploiting the insights into the amount of remaining functional OHCs as indicated by high-level measurements.

ACKNOWLEDGMENTS

The contribution of Azel Zine to preparing the mouse cochleae for microscopy is gratefully acknowledged, as well as that of Sophie Monceau and Christine Puchol for animal care. The care and use of all animals was approved according to the rules promulgated by the French Department of Agriculture (Grant No. EA2667-2000).

- Allen, J. B. (1990). User manual for the CUBDIS distortion product measurement system. AT&T Bell Labs.
- Avan, P., and Bonfils, P. (1993). "Frequency specificity of human distortion product otoacoustic emissions," *Audiology* **32**, 12–26.
- Avan, P., Bonfils, P., and Loth, D. (1996). "Effects of acoustic overstimulation on distortion-product and transient-evoked otoacoustic emissions," in *Scientific Basis of Noise-induced Hearing Loss*, edited by A. Axelsson, H. Borchgrevink, R. P. Hamernik, P. A. Hellstrom, D. Henderson, and R. J. Salvi (Thieme, New York), pp. 65–81.
- Bian, L., and Chertoff, M. E. (1998). "Differentiation of cochlear pathophysiology in ears damaged by salicylate or a pure tone using a nonlinear systems identification technique," *J. Acoust. Soc. Am.* **104**, 2261–2271.
- Bian, L., and Chertoff, M. E. (2001). "Distinguishing cochlear pathophysiology in 4-aminopyridine and furosemide treated ears using a nonlinear systems identification technique," *J. Acoust. Soc. Am.* **109**, 671–685.
- Bonfils, P., Avan, P., Landais, P., Erminy, M., and Biacabe, B. (1997). "Statistical evaluation of hearing screening by distortion product otoacoustic emissions," *Ann. Otol. Rhinol. Laryngol.* **106**, 1052–1062.
- Brass, D., and Kemp, D. T. (1994). "Quantitative assessment of methods for the detection of otoacoustic emissions," *Ear Hear.* **15**, 378–389.
- Brown, A. M., McDowell, B., and Forge, A. (1989). "Acoustic distortion products can be used to monitor the effects of chronic gentamicin treatment," *Hear. Res.* **42**, 143–156.
- Brownell, W. E. (1990). "Outer hair cell electromotility and otoacoustic emissions," *Ear Hear.* **11**, 82–92.
- Brownell, W. E., Bader, C. R., Bertrand, D., and de Ribaupierre, Y. (1985). "Evoked mechanical responses of isolated cochlear outer hair cells," *Science* **227**, 194–196.
- Cheng, J. (1999). "Estimation of active cochlear nonlinearity by multicomponent distortion-product otoacoustic emissions," *Acta Acustica (Germany) united with Acustica* **85**, 721–727.
- Clock Eddins, A., Zuskov, M., and Salvi, R. J. (1999). "Changes in distortion product otoacoustic emissions during prolonged noise exposure," *Hear. Res.* **127**, 119–128.
- Cooper, N. P., and Rhode, W. S. (1997). "Mechanical responses to two-tone distortion products in the apical and basal turns of the mammalian cochlea," *J. Neurophysiol.* **78**, 261–270.
- Eguiluz, V. M., Ospeck, M., Choe, Y., Hudspeth, A. J., and Magnasco, M. O. (2000). "Essential nonlinearities in hearing," *Phys. Rev. Lett.* **84**, 5232–5235.
- Fitzgerald, J. J., Robertson, D., and Johnstone, B. M. (1993). "Effects of intracochlear perfusion of salicylates on cochlear microphonic and other auditory responses in the guinea pig," *Hear. Res.* **67**, 147–156.
- Flock, A., and Strelhoff, D. (1984). "Graded and nonlinear mechanical properties of sensory hairs in the mammalian hearing organ," *Nature (London)* **310**, 597–599.
- Frank, G., and Koessl, M. (1996). "The acoustic two-tone distortions $2f_1-f_2$ and f_2-f_1 and their possible relations to changes in the operating point of the cochlear amplifier," *Hear. Res.* **98**, 104–115.
- Frank, G., and Koessl, M. (1997). "Acoustic and electrical biasing of the cochlear partition, effects on the acoustic two-tone distortions $2f_1-f_2$ and f_2-f_1 ," *Hear. Res.* **113**, 57–68.
- Frolenkov, G. I., Belyantseva, I. A., Kurc, M., Mastroianni, M. A., and Kachar, B. (1998). "Cochlear outer hair cell electromotility can provide force for both low and high level distortion product otoacoustic emissions," *Hear. Res.* **126**, 67–74.
- Gold, T. (1948). "Hearing II. The physical basis for the action of the cochlea," *Proc. R. Soc. (London) Ser. B* **135**, 492–498.
- Gorga, M. P., Neely, S. T., Bergman, B., Beauchaine, K. L., Kaminski, J. R., Peters, J., and Jesteadt, W. (1993). "Otoacoustic emissions from normal-hearing and hearing-impaired subjects: Distortion product responses," *J. Acoust. Soc. Am.* **93**, 2050–2060.
- Greenwood, D. D. (1990). "A cochlear frequency-position function for several species—29 years later," *J. Acoust. Soc. Am.* **87**, 2592–2605.
- Hamernik, R. P., Ahroon, W. A., and Lei, S. F. (1996). "The cubic distortion product otoacoustic emissions from the normal and noise-damaged chinchilla cochlea," *J. Acoust. Soc. Am.* **100**, 1003–1012.
- Henry, K. R., and McGinn, M. D. (1992). "The mouse as a model for human audition (a review of the literature)," *Audiology* **31**, 181–189.
- Horner, K. C., Lenoir, M., and Bock, G. R. (1985). "Distortion product otoacoustic emissions in hearing-impaired mutant mice," *J. Acoust. Soc. Am.* **78**, 1603–1611.
- Jaramillo, F., Markin, V. S., and Hudspeth, A. J. (1993). "Auditory illusions and the single hair cell," *Nature (London)* **364**, 527–529.

- Kemp, D. T. (1978). "Stimulated acoustic emissions from within the human auditory system," *J. Acoust. Soc. Am.* **64**, 1386–1391.
- Kemp, D. T. (1992). User manual for the IL092 Otodynamics equipment, Otodynamics.
- Khanna, S. M., and Leonard, D. G. (1982). "Basilar membrane tuning in the cat cochlea," *Science* **215**, 305–306.
- Kros, C. J., Rusch, A., and Richardson, G. P. (1992). "Mechano-electrical transducer currents in hair cells of the cultured neonatal mouse cochlea," *Proc. R. Soc. London, Ser. B* **249**, 185–193.
- Kummer, P., Janssen, T., and Arnold, W. (1998). "The level and growth behavior of the $2f_1-f_2$ distortion product otoacoustic emission and its relationship to auditory sensitivity in normal hearing and cochlear hearing loss," *J. Acoust. Soc. Am.* **103**, 3431–3444.
- Le Calvez, S., Avan, P., Gilain, L., and Romand, R. (1998a). "CD1 hearing-impaired mice. I. Distortion product otoacoustic emission levels, cochlear function, and morphology," *Hear. Res.* **120**, 37–50.
- Le Calvez, S., Guilhaume, A., Romand, R., Aran, J. M., and Avan, P. (1998b). "CD1 hearing-impaired mice. II. Group latencies and optimal f_2/f_1 ratios of distortion product otoacoustic emissions, and scanning electron microscopy," *Hear. Res.* **120**, 51–61.
- Lonsbury-Martin, B. L., Whitehead, M. L., and Martin, G. K. (1993). "Distortion-product otoacoustic emissions in normal and impaired ears: Insight into generation processes," *Prog. Brain Res.* **97**, 77–90.
- Lonsbury-Martin, B. L., Martin, G. K., Probst, R., and Coats, A. C. (1987). "Acoustic distortion products in rabbit ear canal. I. Basic features and physiological vulnerability," *Hear. Res.* **28**, 173–189.
- Lukashkin, A. N., and Russell, I. J. (1999). "Analysis of the f_2-f_1 and $2f_1-f_2$ distortion components generated by the hair cell mechanoelectrical transducer: Dependence on the amplitudes of the primaries and feedback gain," *J. Acoust. Soc. Am.* **106**, 2661–2668.
- Martin, G. K., Lonsbury-Martin, B. L., Probst, R., Scheinin, S. A., and Coats, A. C. (1987). "Acoustic distortion products in rabbit ear canal. II. Sites of origin revealed by suppression contours and pure-tone exposures," *Hear. Res.* **28**, 191–208.
- Martin, G. K., Ohlms, L. A., Franklin, D. J., Harris, F. P., and Lonsbury-Martin, B. L. (1990). "Distortion product emissions in humans. III. Influence of sensorineural hearing loss," *Ann. Otol. Rhinol. Laryngol.* **99**, 30–42.
- Mills, D. M. (1997). "Interpretation of distortion product otoacoustic emissions measurements. I. Two stimulus tones," *J. Acoust. Soc. Am.* **102**, 413–429.
- Mills, D. M., and Rubel, E. W. (1994). "Variation of distortion product otoacoustic emissions with furosemide injection," *Hear. Res.* **77**, 183–199.
- Mills, D. M., Norton, S. J., and Rubel, E. W. (1993). "Vulnerability and adaptation of distortion product otoacoustic emissions to endocochlear potential variation," *J. Acoust. Soc. Am.* **94**, 2108–2122.
- Mom, T., Avan, P., Romand, R., and Gilain, L. (1997). "Monitoring of functional changes after transient ischemia in gerbil cochlea," *Brain Res.* **751**, 20–30.
- Mom, T., Bonfils, P., Gilain, L., and Avan, P. (2001). "Origin of cubic difference tones generated by high-level stimuli: Effect of ischemia and auditory fatigue on the gerbil cochlea," *J. Acoust. Soc. Am.* **110**, 1477–1488.
- Norton, S. J., and Rubel, E. W. (1990). "Active and passive ADP components in mammalian and avian ears," in *Mechanics and Biophysics of Hearing*, edited by P. Dallos, C. D. Geisler, J. W. Matthews, M. A. Ruggero, and C. R. Steele (Springer, New York), pp. 219–226.
- Norton, S. J., Bargones, J. Y., and Rubel, E. W. (1991). "Development of otoacoustic emissions in gerbil: Evidence for micromechanical changes underlying development of the place code," *Hear. Res.* **51**, 73–91.
- Parham, K., Sun, X. M., and Kim, D. O. (1999). "Distortion product otoacoustic emissions in the CBA/J mouse model of presbycusis," *Hear. Res.* **134**, 29–38.
- Patuzzi, R. B. (1998). "A four state kinetic model of the temporary threshold shift after loud sound based on inactivation of hair cell transduction channels," *Hear. Res.* **125**, 39–70.
- Patuzzi, R. B., Johnstone, B. M., and Sellick, P. M. (1984). "The alteration of the vibration of the basilar membrane produced by loud sound," *Hear. Res.* **13**, 99–100.
- Patuzzi, R. B., Yates, G. K., and Johnstone, B. M. (1989a). "The origin of the low-frequency microphonic in the first cochlear turn of guinea pig," *Hear. Res.* **39**, 177–188.
- Patuzzi, R. B., Yates, G. K., and Johnstone, B. M. (1989b). "Outer hair cell receptor and sensorineural hearing loss," *Hear. Res.* **42**, 47–72.
- Probst, R., Harris, F. P., and Hauser, R. (1993). "Clinical monitoring using otoacoustic emissions," *Br. J. Audiol.* **27**, 85–90.
- Rebillard, G., and Lavigne-Rebillard, M. (1992). "Effect of reversible hypoxia on the compared time courses of endocochlear potential and $2f_1-f_2$ distortion products," *Hear. Res.* **62**, 142–148.
- Ruggero, M. A. (1992). "Responses to sound of the basilar membrane of the mammalian cochlea," *Curr. Opin. Neurobiol.* **2**, 449–456.
- Ruggero, M. A., and Rich, N. C. (1991). "Furosemide alters organ of Corti mechanics: Evidence for feedback of outer hair cells upon the basilar membrane," *J. Neurosci.* **11**, 1057–1067.
- Ryan, A., and Dallos, P. (1975). "Effect of absence of cochlear outer hair cells on behavioral auditory thresholds," *Nature (London)* **253**, 44–46.
- Schmiedt, R. A. (1986). "Acoustic distortion in the ear canal. I. Cubic difference tones: Effects of acute noise injury," *J. Acoust. Soc. Am.* **79**, 1481–1490.
- Shone, G., Raphael, Y., and Miller, J. M. (1991). "Hereditary deafness occurring in cd/1 mice," *Hear. Res.* **57**, 153–156.
- Sie, K. C. Y., deSerres, L. M., and Norton, S. J. (1999). "Age-related sensitivity to cisplatin ototoxicity in gerbils," *Hear. Res.* **134**, 39–47.
- Sutton, L. A., Lonsbury-Martin, B. L., Martin, G. K., and Whitehead, M. L. (1994). "Sensitivity of distortion-product otoacoustic emissions in humans to tonal over-exposure: Time course of recovery and effects of lowering L_2 ," *Hear. Res.* **75**, 161–174.
- Wever, E. G., and Lawrence, M. (1954). *Physiological Acoustics* (Princeton University Press, Princeton, NJ), Chap. 8, pp. 117–144.
- Whitehead, M. L. (1997). "Species differences of distortion-product otoacoustic emissions: Comment on Interpretation of distortion product otoacoustic emissions measurements: I. Two stimulus tones, [J. Acoust. Soc. Am. **102**, 413–429]," *J. Acoust. Soc. Am.* **103**, 2740–2742.
- Whitehead, M. L., Lonsbury-Martin, B. L., and Martin, G. K. (1990). "Actively and passively generated acoustic distortion at $2f_1-f_2$ in rabbits," in *Mechanics and Biophysics of Hearing*, edited by P. Dallos, C. D. Geisler, J. W. Matthews, M. A. Ruggero, and C. R. Steele (Springer, New York), pp. 243–250.
- Whitehead, M. L., Lonsbury-Martin, B. L., and Martin, G. K. (1992). "Evidence for two discrete sources of $2f_1-f_2$ distortion-product otoacoustic emission in rabbit. II. Differential physiological vulnerability," *J. Acoust. Soc. Am.* **92**, 2662–2682.
- Zurek, P. M., Clark, W. W., and Kim, D. O. (1982). "The behavior of acoustic distortion products in the ear canals of chinchillas with normal or damaged ears," *J. Acoust. Soc. Am.* **72**, 774–780.

Effect of current stimulus on *in vivo* cochlear mechanics

Anand A. Parthasarathi^{a)}

Department of Biomedical Engineering, 3304 G. G. Brown, University of Michigan, Ann Arbor, Michigan 48109

Karl Grosh^{b)}

Department of Mechanical Engineering, 2350 Hayward Avenue, University of Michigan, Ann Arbor, Michigan 48109

Jiefu Zheng^{c)}

Oregon Health and Science University, 3181 SW Sam Jackson Park Road, Portland, Oregon 97201

Alfred L. Nuttall

Oregon Health and Science University, 3181 SW Sam Jackson Park Road, Portland, Oregon 97201 and Kresge Hearing Research Institute, 1301 East Ann Street, Ann Arbor, Michigan 48109

(Received 29 March 2002; revised 13 September 2002; accepted 16 September 2002)

In this paper, the influence of direct current stimulation on the acoustic impulse response of the basilar membrane (BM) is studied. A positive current applied in the scala vestibuli relative to a ground electrode in the scala tympani is found to enhance gain and increase the best frequency at a given location on the BM. An opposite effect is found for a negative current. Also, the amplitude of low-frequency cochlear microphonic at high sound levels is found to change with the concurrent application of direct current stimulus. BM vibrations in response to pure tone acoustic excitation are found to possess harmonics whose levels relative to the fundamental increase with the application of positive current and decrease with the application of negative current. A model for outer hair cell activity that couples changes in length and stiffness to transmembrane potential is used to interpret the results of these experiments and others in the literature. The importance of the *in vivo* mechanical and electrical loading is emphasized. Simulation results show the somewhat paradoxical finding that for outer hair cells under tension, hyperpolarization causes shortening of the cell length due to the dominance of voltage dependent stiffness changes. © 2003 Acoustical Society of America. [DOI: 10.1121/1.1519546]

PACS numbers: 43.64.Kc, 43.64.Me, 43.64.Nf [LHC]

I. INTRODUCTION

Outer hair cells (OHCs) have been postulated to play an important role in the nonlinear properties of the cochlea (Dallos, 1992). To this end, experiments over the past several years have focused on obtaining the mechanical and electrical properties of isolated OHCs. *In vitro* experiments have shown that the OHC length (Santos-Sacchi, 1992) and the stiffness (He and Dallos, 1999) depend on the transmembrane potential. These results suggest that the force generated by the OHC due to a change in transmembrane potential contains voltage-dependent active and reactive components and that the contributions of the OHC should be studied under its loaded *in vivo* state.

The experiments reported in this paper were performed to determine the change in basilar membrane (BM) response to combined electrical and acoustical stimuli. The current stimulus can cause a “steady” change of the OHC transmembrane potential and provides a means to study *in vivo* OHC behavior. In particular, these measurements are used to

infer the relationship between current polarities and the state of polarization in the OHCs and to interrogate the dependence of harmonics in the BM velocity response to applied electric and acoustic stimulation. Using a nonlinear transducer model for force generation by the OHC, the conditions under which the experimental results can be simulated are studied. An important prediction is that, *in vivo*, the OHC stiffness variations arising from a change in the transmembrane potential change could play a more important role compared to changes in its length (electromotility). The model also provides a framework for the design of experimental protocols for further electro-acoustic studies and to formulate and test nonlinear micromechanical constitutive laws that may be included into a global cochlear dynamics predictive code, such as that described in Parthasarathi *et al.* (1999).

II. METHODS

A. Surgical preparation

Healthy young pigmented guinea pigs (250–400 g) were used in this study. The animals were housed in an American Association for Accreditation of Laboratory Animal Care approved facility and experimental protocols approved by the Committee on Use and Care of Animals at the Oregon Health Sciences University. A combination of ketamine (40

^{a)}Current address: at Bose Corporation, Framingham, MA.

^{b)}Author to whom correspondence should be addressed. Electronic mail: grosh@engin.umich.edu

^{c)}Current address: DoD Spatial Orientation Center, Department of Otolaryngology, Naval Medical Center, San Diego, 34800 Bob Wilson Dr. Suite 200, San Diego, CA 92134

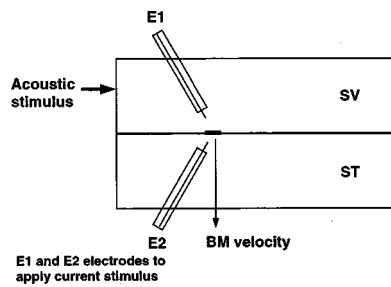


FIG. 1. Schematic of the electro-acoustic experimental setup. The acoustic stimulus is a pseudo-random noise applied through a speculum coupled to the ear canal. Two electrodes of size 1T, one each in *scala vestibuli* (SV) and *scala tympani* (ST), are used to simultaneously apply a current stimulus. The electrodes are placed as deep into the scala as possible to minimize the current spread.

mg/kg i.m.) and xylazine (10 mg/kg i.m.) was used to anesthetize the animal. Supplementary doses of ketamine and xylazine were given every 60 min. A tracheotomy was performed and a ventilating tube was inserted into the trachea to ensure free breathing. Then the animal's head was fixed to a headholder. After the bulla was opened to expose the cochlea, a silver (200–300 μm diameter) electrode was placed on the round window. The compound action potential (CAP) measured from the round window electrode, with reference to an Ag–AgCl ground electrode in the soft tissues of the neck, was used to obtain information on the N_1 detection threshold (10 μV at the round window) of the CAP at a given acoustic frequency. The threshold was used as an indicator of the cochlear “sensitivity.” Figure 1 is a schematic of the experimental setup.

A total of three openings [two in the *scala tympani* (ST) and one in the *scala vestibuli* (SV)] were made. One opening, approximately 300 μm wide, was made on the ST side

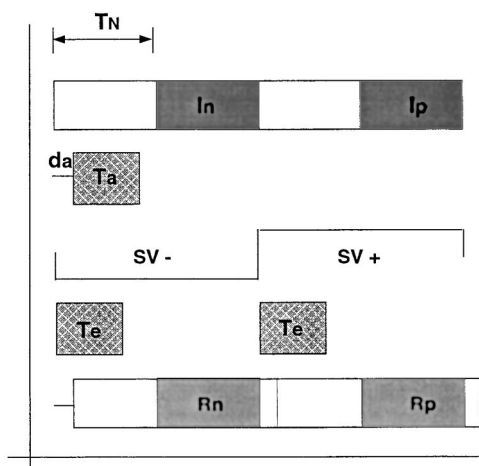


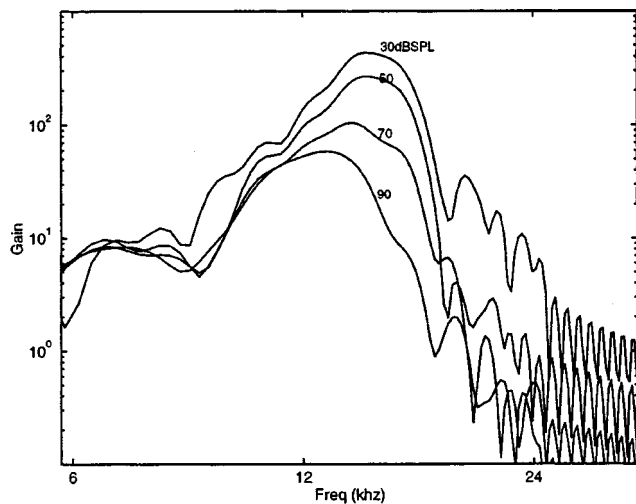
FIG. 2. Schematic of the protocol for tuning curve measurement using pseudo-random noise. In a single epoch, the random process is presented four times. T_N is the duration of each epoch corresponding to the N points in the random sequence sent to the D/A converter. A simultaneous bipolar current stimulus is also applied. d_a is the acoustic time delay from the D/A converter to the stapes. The onset acoustic transient response duration is T_a , and the onset and offset electric transient response durations are T_e . It can be seen that R_n and R_p are just the shifted responses to inputs I_n and I_p , respectively, and are not corrupted by the transients. The tuning curve is obtained through cross correlation between I_n and R_n for the “negative” current effect and between I_p and R_p for the “positive” current effect.

of the cochlear basal turn for measurement of BM velocity. BM velocity was measured using a laser Doppler velocimeter (Polytec OFV-1101), after placing gold-coated glass beads (20 μm diameter) on the ST side of the BM to improve the BM reflectivity (Nuttall *et al.*, 1991). Two electrodes of size 1T (Teflon-insulated platinum-iridium wire of 25 μm diameter, exclusive of insulation) were inserted into the two other openings, one in the ST and the other in the SV, at the basal turn for bipolar current stimulation across the cochlear partition (CP). An opto-isolated current source was used to drive the two electrodes. When used to deliver current across the cochlear partition, a positive current is defined as that flowing from a positively polarized SV electrode relative to a negatively polarized ST electrode. Acoustic stimuli were delivered through a $\frac{1}{2}$ -in. B&K condenser microphone coupled to the external ear through a speculum.

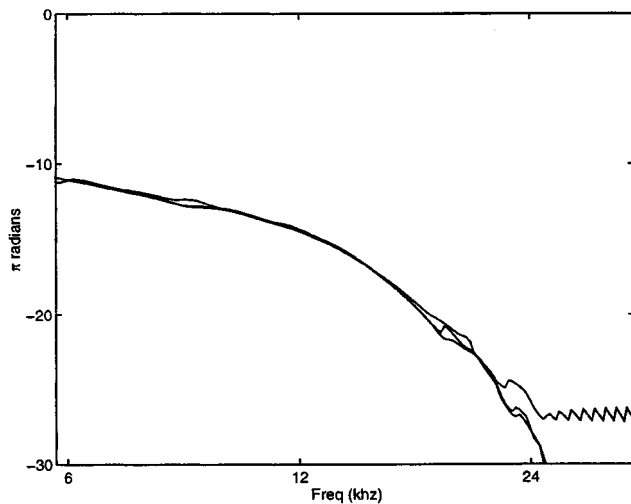
It should be noted here that the N_1 detection thresholds of CAP for the preparations used in this study were usually increased by up to 20–25 dB after the surgery. The loss in sensitivity was a consequence of the damage caused by the surgery needed to make three holes in the cochlear wall. Cochleas with CAP losses greater than 30 dB were termed “insensitive” and were not considered for further analysis of the type reported in this study.

B. Tuning curve measurement

In Fig. 2 a schematic of the protocol used for tuning curve measurements is shown. Pseudo-random noise was used to estimate the tuning curve through cross-correlation between the input process and the response. An N -point band-limited random sequence with a normal probability distribution and whose power spectrum is limited to two octaves, centered at 12 kHz, was sent to the digital-to-analog converter. The normal distribution is a sufficient condition for the convolution to exist (Papoulis, 1991). Under ideal low-pass conditions, as predicted by the stochastic version of the sampling theorem, the resulting random process would preserve the power spectral distribution. However, for practical purposes the generated random process could be assumed to have the desired power spectrum in the ergodic sense. Onset transients and acoustic delays from the sound delivery system were eliminated, by presenting the signal twice and sampling only from the second N -point sequence. The corresponding BM velocity response was first passed through a 40-kHz antialiasing filter and then sampled at 250 kHz. Of the $2N$ velocity points acquired, the latter N points would contain the response to the random sequence, only circular shifted modulo N , and was used for spectral estimation. Ideally N should be high, however the duration of the direct current pulse is restricted in order to avoid gassing at the electrode surface for any particular electrode surface area. In the experiments, the current pulse was limited to 2 ms ($N=512$ at 250 kHz) and was used in the estimation of tuning curves. (This duration is sufficient to avoid transients during the current onset and offset, since a typical BM impulse response lasts less than 2 ms.) The polarity of the electrode in the SV was negative for the first $2N$ points followed by a positive polarity for $2N$ points. As mentioned above, current due to the former will be denoted as “negative” cur-



(a)



(b)

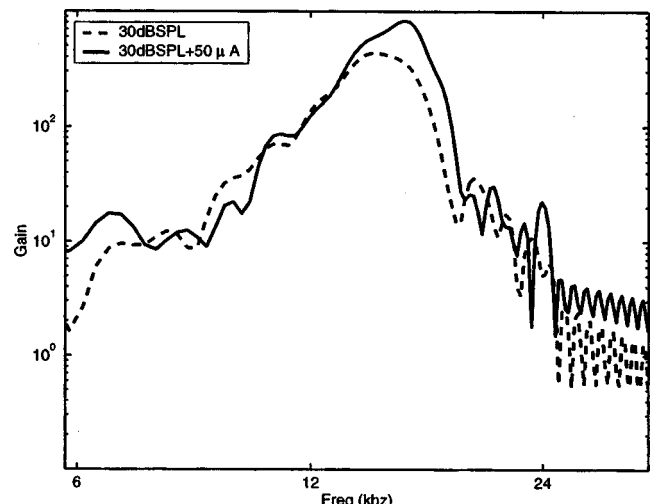
FIG. 3. Basilar membrane velocity tuning curve responses to an acoustic stimulus (GP217).

rent and the latter as “positive” current. A stimulus level matrix consisting of acoustic input levels 30, 50, 70, and 90 dB SPL and current levels 0, 50, and 75 microamperes (μA) rms with a 5-ms pulse phase were typically used. The tuning curves were estimated after normalizing with the corresponding stapes response resulting in the cochlear “gain” functions.

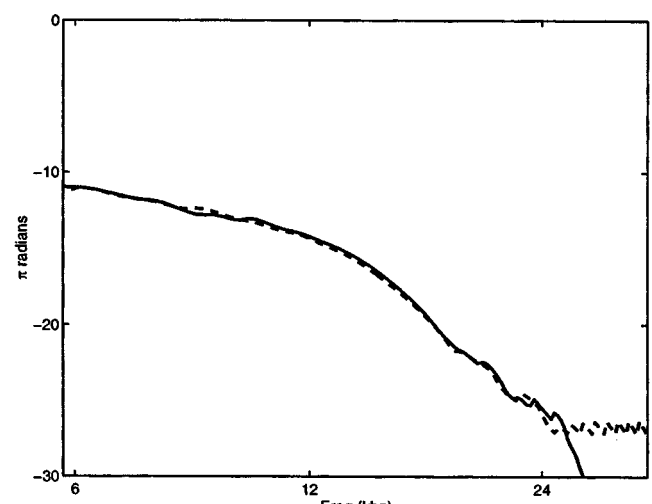
In each experiment, BM velocity response to a series of pure tones was also measured. The frequencies were stepped through 1-kHz steps from 11 to 20 kHz for the same stimulus level matrix as for the noise. Intensity functions were constructed from these measurements. Also, the BM velocity data were windowed and used for Fourier analysis to obtain the harmonic distortion.

III. TUNING CURVES

As a point of reference, the stapes normalized BM velocity tuning curves for acoustic inputs at different levels are shown in Fig. 3 for no current stimulation. The gain and characteristic frequency (CF) change as a function of the



(a)



(b)

FIG. 4. Influence of 50 μA positive current on BM tuning curve for 30 dB SPL acoustic input (GP217). The CF is shifted upwards from 15.3 to 16.3 kHz. The BM gain at the new CF is about 6 dB higher than without the current stimulus. No detectable changes were seen in the phase response. Experiments with pure tones, and hence better signal-to-noise ratio, showed that gain can be achieved at all frequencies, though it decreases at frequencies above and below the new CF.

input acoustic level, similar to results available in the literature (e.g., Nuttall and Dolan, 1996; de Boer and Nuttall, 1997; Ruggero *et al.*, 1997). In Fig. 4, the tuning curve at 30 dB SPL with and without a positive current stimulus of 50 μA is shown. As a second example, the influence of a positive and negative 75 μA direct current in conjunction with a 50 dB SPL acoustic input on the tuning curve is shown in Fig. 5.

Application of a positive current causes two important effects on the BM velocity tuning curve: (1) an enhanced gain for the BM velocity and (2) an upward shift in the CF. In Fig. 4, an increase in the maximum gain of about 6 dB is achieved close to the new CF, shifted up from 15.3 to 16.3 kHz. Conversely, a negative current causes velocity reduction, and decreases the CF (see Fig. 5). These results were observed in all the three animals used in this study.

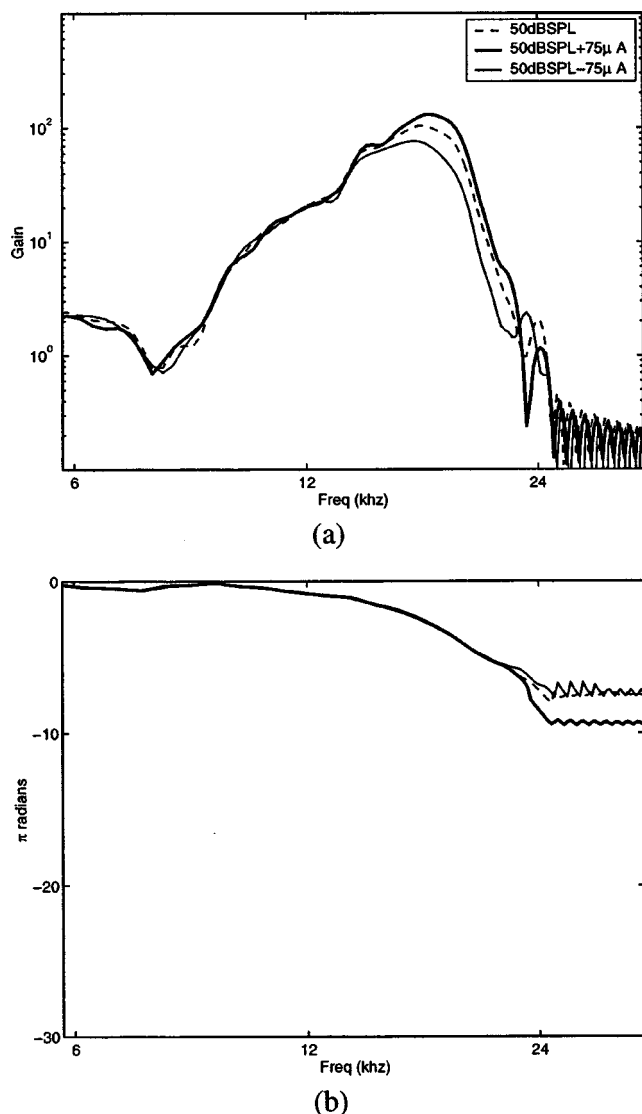


FIG. 5. Electro-acoustic response at 50 dB SPL (GP252). The CFs with the negative and positive currents are 16.6 and 17.3 kHz, respectively. Again, no detectable changes were seen in the phase response.

The response enhancement/reduction occurs at all tested current levels and were monotonic in their correlation to positive or negative current injection. These effects are increased with the current level in this study (i.e., a larger negative currents give rise to greater response reduction and larger positive currents gives rise to greater response enhancement). The shifts associated with electrical stimulation are decreased with increasing input acoustic levels. The intensity function is also modified as seen in Fig. 6, where the influence of current stimulus on the BM velocity intensity function is shown. The dynamic range of the intensity function is decreased during a positive current stimulus and increased during the negative current stimulus.

At very high acoustic stimulus levels (90 dB SPL), it was still possible to produce changes in the tuning curves, but only at current levels above 300 μ A. At such current levels the sensitivity of the cochlea was often lost subsequent to gassing at the electrode tip due to electrochemical reactions and hence was not consistently studied. [Higher current levels, up to 500 μ A, have been reported in Nuttall's labo-

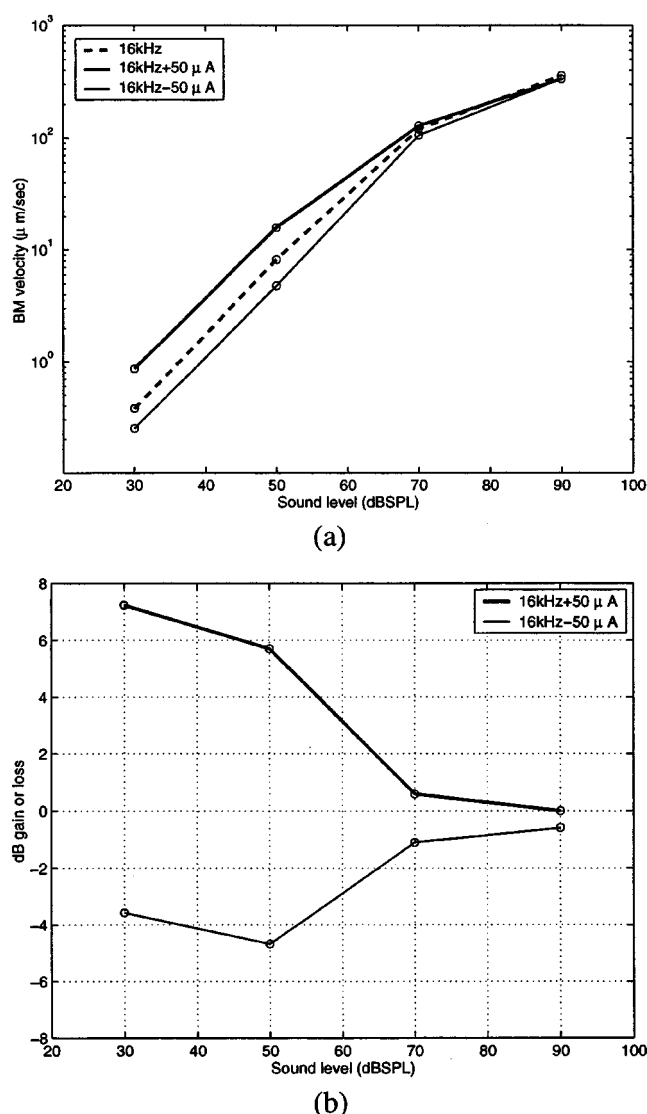


FIG. 6. (a) Influence of 50 μ A current stimulus on the intensity function at 16 kHz (GP217). (b) The BM velocity gain or loss due to the current stimulus. The gain/loss drops with increasing acoustic level.

ratory (Nuttall *et al.*, 1999) using 3T size platinum wires which have a larger surface area compared to the 1T size wires used in this study.] Also, the response reduction or enhancement was influenced by the sensitivity of the cochlea. In insensitive preparations, with a CAP threshold loss of more than 30 dB during the course of the surgery, velocity modulation could not be detected at the current levels used. Also, in an additional experiment, measurements were performed on a kanamycin-treated guinea pig with no observable enhancement or suppression of the acoustic response. Since kanamycin selectively eliminates OHC, as assessed by electrically evoked emissions (Nuttall and Ren, 1995), it was concluded that intact OHCs were requisite to evoke changes in BM motion by electric stimulation.

The impulse response and instantaneous frequency estimated from the tuning curves is shown in Fig. 7. The impulse response was obtained through inverse Fourier transform and the instantaneous frequency through a derivative of the phase of the corresponding analytical signal. It should be noted that the impulse response is not accurate as it is not

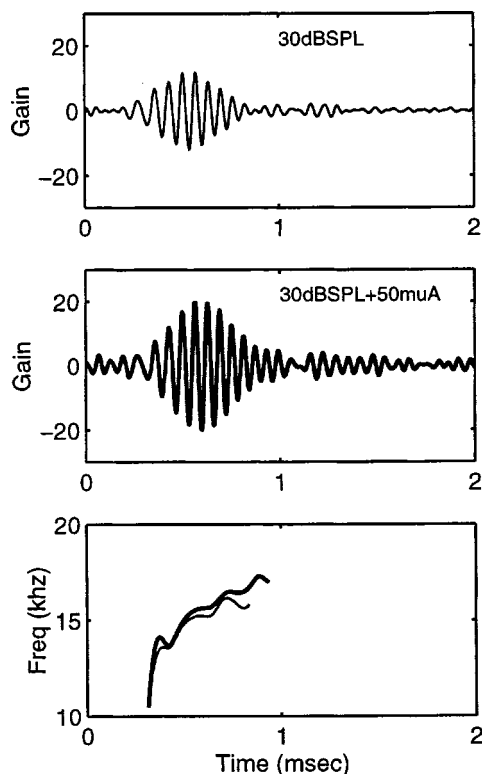


FIG. 7. The positive current stimulus increases the amplitude of the impulse response, indicative of the increased gain. Application of the positive current stimulus causes the instantaneous frequency to go up to a higher value.

derived from the complete spectrum, since only a 2-octave-wide input was used. However, within the context of determining the influence of the current stimulus, it is an acceptable representation since current stimulus has most of its influence only close to CF. The positive current stimulus increases the amplitude of the impulse response, indicative of the increased gain, and also causes the instantaneous frequency to “glide” to a higher value.

IV. QUASI-STATIC BASILAR MEMBRANE RESPONSE

The experimentally observed changes in the CF during a direct current stimulus are indicative of a change in the properties of the OHC. However, it is not known, for example, if the positive current stimulus causes a depolarization or hyperpolarization of the OHC transmembrane potential. Using a *scala media* (SM) voltage stimulus, Xue *et al.* (1995) concluded that a positive voltage in the *scala media* causes OHC shortening, and hence depolarization. More recently, Nuttall *et al.* (1999), using the same preparation techniques as used in the current work, measured a shortening of the OHC due to positive current pulse in the *scala vestibuli*; results reproduced in Fig. 8. The *in situ* measurements of Mammano and Ashmore (Mammano and Ashmore, 1993) attempt to do the same. By measuring the voltage inside the OHC and the displacement of the BM and reticular lamina, they show that OHCs hyperpolarize and also lengthen in response to a positive current pulse at the apical side of the hair cells. Their observations were however made in the apical turn (where the resting potential is about -16 mV) while Xue *et al.* and Nuttall *et al.* performed their experiments on the basal turn

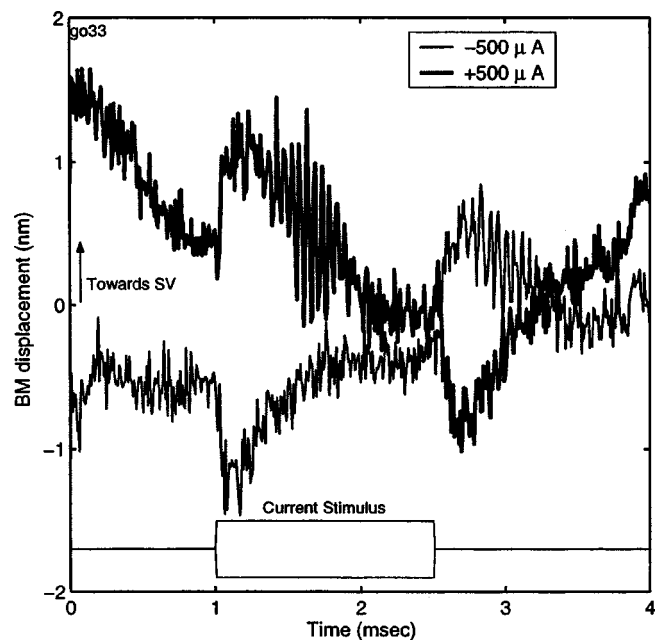


FIG. 8. BM displacement measurements (GP033) due to a current pulse measured by Nuttall and co-workers (Nuttall *et al.*, 1999). Measurement location is near the first row of OHCs. A positive voltage causes the BM to move towards *scala vestibuli* indicating OHC contraction. The stimulus current level was $500 \mu\text{A}$.

(where the resting potential is about -70 mV). In the following analysis, we attempt to reconcile these apparently conflicting results using a local quasi-static analysis.

A. Nonlinear OHC transducer model

We consider the length changes of the OHC due to forces applied to the basal and apical ends and changes in the transmembrane potential. The OHC is assumed to be internally pressurized and variations about the resting pressurization of the cell are considered. We assume an effective OHC constitutive law of the form (He and Dallos, 1999):

$$F_{\text{OHC}} = K_{\text{OHC}}(V)(L_{\text{OHC}} - L_{\text{OHC}}^f(0)) - g(V), \quad (1)$$

where $K_{\text{OHC}}(V)$ is OHC stiffness under voltage clamp conditions, L_{OHC} is the length of the OHC at a given voltage and force level, the force on the OHC is F_{OHC} , $g(V)$ is the active force which is taken to be a function of the transmembrane potential (and not displacement), and $L_{\text{OHC}}^f(0)$ is the free (zero force) length of the OHC at zero transmembrane potential difference. In this model, the OHC stiffness has a nonlinear dependence on the applied voltage (possibly attributable to a voltage dependent conformational change in a transmembrane constituent). While a voltage-dependent nonlinearity is assumed to exist *in vivo*, we assume that deformations are sufficiently small so that geometric stiffening does not occur, thereby making the forces linear in displacement. Validation of such a model warrants further consideration of the micromechanics of the lateral cortex of the OHC (note that the static transmembrane pressure difference will also set the resting position of the OHC, although it is not explicitly written in the equations). However, for the purposes of this study, we need only consider the effective properties, properties that have been measured in isolated hair

cells. Finally, note that Eq. (1) is the first of two equations necessary to define the state of the OHC. The second equation is a constitutive law that relates the total transmembrane current to the displacement and voltage. Our goal in presenting a model for the OHC force response is to explain observed *in vivo* behavior of the OHC—and only Eq. (1) is needed for this purpose. In summary, the model underlying Eq. (1) contains two important assumptions, related to those presented in He and Dallos (1999): (1) the OHC stiffness depends on voltage but not displacement and (2) the active component depends only on voltage. The total force therefore consists of reactive and active components dependent on the voltage, displacement, and boundary conditions.

Most measurements of OHC properties have been under voltage clamp conditions with zero external force applied to the OHC (i.e., $F_{\text{OHC}}=0$); this experiment gives rise to the free length of the OHC as a function of voltage as computed from Eq. (1),

$$g(V)/K_{\text{OHC}}(V) = (L_{\text{OHC}}^f(V) - L_{\text{OHC}}^f(0)), \quad (2)$$

where the special free boundary condition is denoted by the superscript *f*. Experimentally, $g(V)/K_{\text{OHC}}(V)$ is a function that increases with hyperpolarization of the cell (Santos-Sacchi, 1991) and $g(0)=0$. The free length change of isolated OHCs as a function of voltage has been measured (e.g., Santos-Sacchi, 1991).

B. Quasi-static response *in situ*

Next a simplified static model of a radial section of the CP is considered. The CP stiffness is assumed to be most influenced by three series stiffnesses: K_t (tectorial membrane); K_b (basilar membrane), and $K_{\text{OHC}}(V)$. $K_{\text{OHC}}(V)$ is the stiffness of the isolated OHC measured under voltage clamp conditions (He and Dallos, 1999). For simplicity, the stereocilia and Deiters' cells are neglected but can be lumped within K_t and K_b , respectively. Likewise, the radial dependence of the interaction of the three different OHCs in each radial segment and the BM stiffness can also be considered. The model here includes one OHC and utilizes the point stiffness for the BM and TM found in the literature; hence it is assumed that the average effect is roughly the same for the three OHCs as for a single OHC.

The OHC is inserted between the BM and TM (see Fig. 9 and an additional length scale must be included at this point), the length of the OHC that gives rise to zero deflection in the springs associated with the TM and BM. This distance is denoted as l and can be thought of (loosely) as the distance between the Deiters' cells and TM in the absence of an OHC. A static analysis of the forces acting on the OHC, BM, and TM yields the following relation,

$$F_{\text{OHC}} = \gamma \delta, \quad (3)$$

where $\gamma = K_b K_t / (K_b + K_t)$ is the series combination of TM and BM stiffness and $\delta = X_2 - X_1$, where X_1 and X_2 represent the displacement of the springs associated with the BM and TM, respectively, away from their unstretched positions (i.e., their positions in the absence of the OHC) as shown in Fig. 9. In this simplified model, the motion of the basal end of the OHC is the same as the BM and the apical end of the

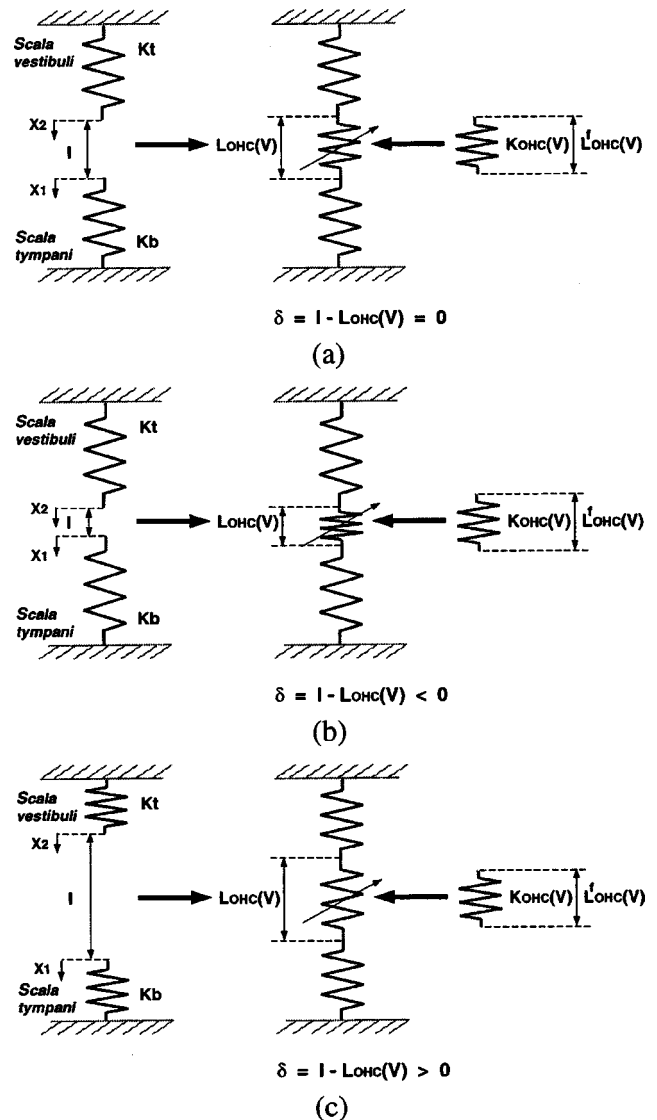


FIG. 9. Three possible configurations for the OHC to exist *in vivo* at the resting potential. l is the separation between the TM and the BM, in the absence of the OHC. $L_{\text{OHC}}^f(V)$ is the length of the OHC at a voltage V in the unloaded condition. (a) OHC is neither in tension nor compression. (b) OHC is in compression. (c) OHC is in tension.

OHC moves in concert with the TM. Note that l is the separation of the attachment points for the OHC in a stress-free condition and that δ measures the deformation away from that position.

Using the relation $L_{\text{OHC}} = l - \delta$ and combining Eqs. (3) and (1) yields

$$K_{\text{OHC}}(V)(l - \delta - L_{\text{OHC}}^f(0)) - g(V) = \gamma \delta. \quad (4)$$

Solving for δ ,

$$\delta = \frac{l - L_{\text{OHC}}^f(V)}{1 + \gamma/K_{\text{OHC}}(V)}, \quad (5)$$

where $g(V)/K_{\text{OHC}}(V) = (L_{\text{OHC}}^f(V) - L_{\text{OHC}}^f(0))$, Eq. (2), has been used to rewrite δ in terms of the most readily available experimentally measured quantities. Experimental values for the length of OHC *in vivo* or the separation between TM and BM in the absence of OHCs are not available. Therefore,

depending on the actual value of l , δ could be positive, negative, or zero.

Figure 9 is a schematic of the nonlinear transducer model showing the three possible cases. The motion of the OHC predicted by the model in response to a quasi-static voltage excitation is next considered using these three different stress conditions as the resting or initial state. Since physiological deformations are likely on the order of nanometers, only small deformations of the loaded OHC in equilibrium about the resting transmembrane potential difference, V^R , are considered. The resting potential is denoted as V^R while the equilibrium deformation at V^R is denoted as δ^R . Predictions of the deformation, δ , due to a hyperpolarizing voltage $V < V^R$ (assuming that the resting transmembrane potential is negative, as usual), will be studied along with the concomitant changes in the OHC length.

1. Case 1: Initially stress free $l = L_{\text{OHC}}^f(V^R)$

Increasing hyperpolarization will result in an increasing value of $L_{\text{OHC}}^f(V)$, thereby increasing the magnitude of the negative number δ [see Eq. (5)]. Since $L_{\text{OHC}} = l - \delta$, hyperpolarization will cause the OHC to lengthen and the BM moves towards the *scala tympani*. For this case, quasi-static hyperpolarization always gives rise to an increase in OHC length and depolarization will result in shortening. The restraining stiffness of the supporting cells (embodied in the term γ/K_{OHC}) reduce the amount of deformation compared to the unloaded case.

2. Case 2: Initial compression $l < L_{\text{OHC}}^f(V^R)$ and $\delta^R < 0$

The ratio of δ at voltage V to δ^R at the resting potential, V^R is

$$\frac{\delta}{\delta^R} = \underbrace{\left[\frac{l - L_{\text{OHC}}^f(V)}{l - L_{\text{OHC}}^f(V^R)} \right]}_{\beta} \underbrace{\left[\frac{1 + \gamma/K_{\text{OHC}}(V^R)}{1 + \gamma/K_{\text{OHC}}(V)} \right]}_{\eta}. \quad (6)$$

For a hyperpolarizing voltage ($V < V^R$) magnitudes of both the terms in the brackets are greater than unity and increasing. Hence, $\delta/\delta^R > 1$. Since $\delta^R < 0$ and $\delta < 0$ for hyperpolarization, this implies that the OHC expands with hyperpolarization and the BM again moves towards the *scala tympani*. Once again, hyperpolarization gives rise to an increase in the *in situ* length of the OHC just as in the free condition. Depolarization of a compressed cell will necessarily result in shortening until the OHC goes into tension [i.e., $l - L_{\text{OHC}}^f(V) > 0$]. After that, incremental changes in voltage are governed by the analysis below. The factors β and η will be utilized in the next section.

3. Case 3: Initial tension $l > L_{\text{OHC}}^f(V^R)$ and $\delta^R > 0$

Equation (6) is also valid for this case. However, β is less than unity, decreasing with greater hyperpolarization while η is greater than unity (as in the compression case). Hence the OHC will expand or contract depending on the relative dominance of the two effects. In order to facilitate analysis, Eq. (6) is simplified further. It is known that the

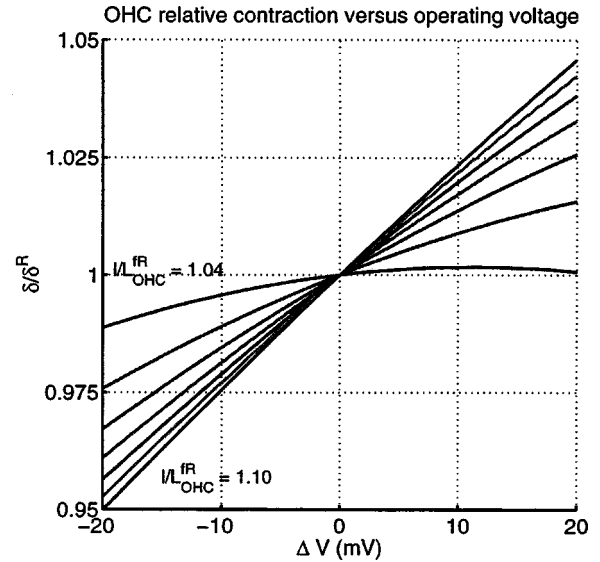


FIG. 10. The predicted *in vivo* relative deformation of the OHC δ compared to its deformation at the resting potential, V^R , for different values of $l/L_{\text{OHC}}^f(V^R)$. The assumed value for $L_{\text{OHC}}^f(V^R)$ is $70 \mu\text{m}$. In the x axis a positive value indicates depolarization and a negative value indicates hyperpolarization. In the y axis a value greater than one indicates extension and less than one indicates contraction. It is seen that hyperpolarization causes the OHC to contract and depolarization causes it to expand from its resting state. Also, δ has a nonlinear dependence on ΔV that would give rise to harmonic distortion.

axial stiffness of the OHC is much less than that of the TM and the BM. As an example of the order of magnitude that is expected, $K_b = 9 \text{ N/m}$ for gerbils (Olson and Mountain, 1991), $K_t = 0.125 \text{ N/m}$ for gerbils (Zwislocki and Cefaratti, 1989); and $K_{\text{OHC}} = 4.8 \text{ mN/m}$ for guinea pigs (He and Dallos, 1999). Hence it is reasonable to expect that $K_{\text{TM}} \gg K_{\text{OHC}}$. Therefore $\eta \approx K_{\text{OHC}}(V)/K_{\text{OHC}}(V^R)$ since $\gamma/K_{\text{OHC}} \gg 1$ and

$$\frac{\delta}{\delta^R} = \left[\frac{l - L_{\text{OHC}}^f(V)}{l - L_{\text{OHC}}^f(V^R)} \right] \left[\frac{K_{\text{OHC}}(V)}{K_{\text{OHC}}(V^R)} \right]. \quad (7)$$

The sensitivity of the isolated OHC length and stiffness changes to a change in the transmembrane potential at the resting potential (-70 mV) is given below:

- (1) Isolated OHC length increases with hyperpolarization. The sensitivity of the isolated guinea pig OHC is about 10 nm/mV (Santos-Sacchi, 1992), thus quantifying $L_{\text{OHC}}^f(V)/L_{\text{OHC}}^f(V^R)$.
- (2) Isolated OHC stiffness increases with hyperpolarization. The slope of the percentage change in the stiffness is about $0.38\%/mV$ for isolated guinea pig hair cells (He and Dallos, 1999) thus quantifying $K_{\text{OHC}}(V)/K_{\text{OHC}}(V^R)$.

Using these values and assuming an OHC length of $L_{\text{OHC}}^f(V^R) = 70 \mu\text{m}$ at the resting potential,

$$\frac{\delta}{\delta^R} = \left[\frac{l/L_{\text{OHC}}^f(V^R) - (1 + 1.4 \times 10^{-4} \Delta V)}{l/L_{\text{OHC}}^f(V^R) - 1} \right] \times [1 + 38 \times 10^{-4} \Delta V]. \quad (8)$$

Equation (8) predicts that the effect of the stiffness change is about 30 times greater than that of the length change. Figure

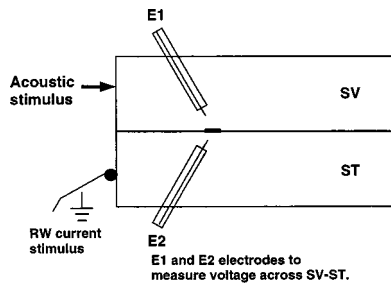


FIG. 11. Schematic of CM measurement setup. A ST/SV bipolar electrode influences a narrow region of OHCs and hence its effect on the CM measured at the round window may not be detectable. Instead current stimulus was applied at the round window (which affects a wider region of OHCs) and the CM measured across the SV/ST. CM was measured for an 0.8-kHz sound at 90 dB SPL, delivered in conjunction with the current stimulus pulse. A positive current applied to the RW is similar to a negative current from a SV to ST bipolar electrode pair and a negative current at the RW is similar to a positive current from a SV to ST bipolar electrode pair (see text for discussion).

10 is a plot of δ/δ^R for hyperpolarization and depolarization at different values of $l/L_{\text{OHC}}^R(V^R)$.

Therefore, under the restrictions set out for the ratio of the BM, TM, and OHC stiffness and the voltage sensitivities of the active and reactive length changes, a hyperpolarization can give rise to a contraction of the OHC. This effect is also seen in the following simple analogy. Consider a spring under tension. If the spring stiffness is somehow increased while the force remains the same, the spring will contract. In this model of the OHC under tensile load *in vivo*, OHC hyperpolarization contraction due to stiffness increase dominates electromotile expansion during hyperpolarization. These predictions are valid for transmembrane potential changes of up to ± 20 mV about the resting potential. The main result of this prediction is the dependence of *in vivo* OHC motility on the loading of the OHC. This dependence makes the interpretation of the results from experiments more difficult, since contraction of the OHC does not necessarily mean depolarization of the cell.

V. COCHLEAR MICROPHONIC

Low-frequency cochlear microphonic at high sound levels measured near the round window is an indicator of the OHC receptor potential near the basal region. An increase or decrease in the CM, during the application of a concurrent direct current stimulus can be construed as a corresponding change in the receptor potential.

A SV/ST bipolar stimulation electrode likely influences a narrow region of OHCs and hence its effect on the CM measured at the round window may not be detectable. Therefore, an alternative approach was taken where a current stimulus was applied at the round window (which affects a wider region of OHCs) using a monopolar platinum wire of size 2T (ground wire in the neck muscle) and the differential CM measured across the SV/ST near the 16–18 kHz CF location (Fig. 11) with the electrode in the SV wired to the negative input of the differential amplifier while the ST electrode was wired to the positive input.

The current level used was 50 μA which was applied for 5 ms. The CM was measured for an 0.8-kHz sound at 90 dB

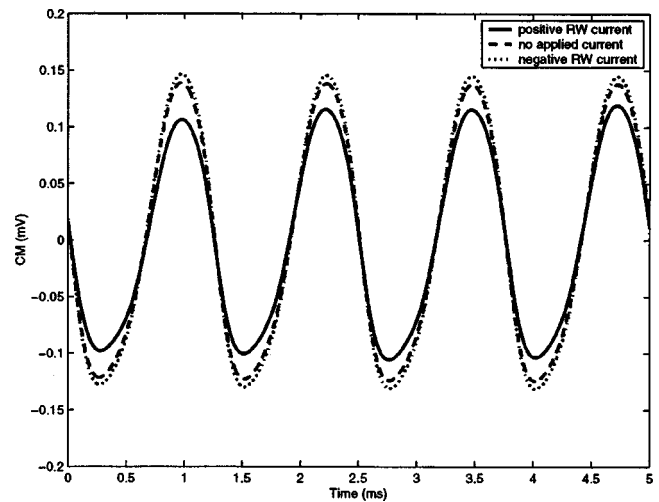


FIG. 12. Influence of 50 μA current stimulus on the cochlear microphonic response (GP451).

SPL, delivered in conjunction with the current stimulus. The voltage presented in Fig. 12 is computed as follows. The voltage measured from the electrical stimulation alone is subtracted from that measured under combined acoustic and electrical loading. In this way, the effect of the acoustic stimulus on the CM is made more evident while the electric “only” effect is extracted. Since the vibration levels at the 16–18-kHz CF place due to 0.8-kHz acoustic stimulation are quite small, the slight asymmetry seen in the CM is most likely a manifestation of this subtraction processing and not from the nonlinear conductance stereocilia motion transfer function. The transducer channels are not saturated at this location (as the bipolar electrodes are hypothesized to sense localized voltage fluctuations) so the local voltage fluctuations should be, and are, roughly symmetric about the resting potential.

A negative RW current increases the CM while a positive RW current decreases the CM relative to the CM with no current applied. From an equivalent circuit approximation of the cochlear fluids (e.g., Geisler, 1998; Evans and Dallos, 1993) a negative current applied to the RW relative to a distant ground corresponds to a positive current applied from the SV electrode to the ground electrode in the ST. This is because adding a negative current to the ST at the round window can be thought of as adding a current sink to that duct, thus making the SV relatively more positive (as a current source). This prediction was verified by microelectrode insertion into the cochlear fluids during current stimulation. A glass pipet microelectrode was inserted into the ST during round window (RW) excitation and separately during SV/ST current injection. The voltage measured using RW excitation was found to be of the opposite polarity to that measured using the SV/ST stimulation protocol. Note also that microelectrode pipet investigations determined that a positive current applied to the SV increases the endocochlear potential (EP) by increasing the voltage in both the scala media and SV while reducing the voltage in the ST (a negative current has the opposite effect).

An increased CM due to a negative RW current (corresponding to a positive SV/ST current) is indicative of an

increase in the receptor potential arising from the increased transduction current produced by the total driving potential (i.e., the effective endocochlear potential is increased) and/or an increase in the stereocilia motion due to a decrease in the stiffness of the OHC or the stereocilia.

In conjunction with the measurements of the electrical response, the basilar membrane velocity in response to the combined acoustic and electric loading described in this section (the protocol associated with Fig. 11) was measured. This was done in order to characterize the mechanical response of one end of the OHC (through the Dieters' cell connection to the BM). It was noted that the basilar membrane velocity in response to low-frequency steady-state acoustic excitation (0.8-kHz vibrations measured at the 18-kHz place) is relatively insensitive to alterations in the injection of current at the RW. Measurements were taken on several animals and no measurable change in the velocity was found under the current modification. Using the noise protocol rather than the steady-state measurements, the low-frequency vibrations (see the 6-kHz response in Figs. 4 and 5) show in one case no change in the response (Fig. 5) and in the other an increase with positive current (Fig. 4). Since signal processing associated with the noise was more focused to a band of frequencies around the CF, the steady-state measurements of low-frequency vibration are taken as more reliable at this time. More study on this is needed to determine if SV/ST current stimulation gives rise to low-frequency changes in the velocity (thereby indicating a change in the stiffness). Measurement of the apical end of OHC is not yet possible in this preparation, a measurement that would clarify this discussion greatly.

VI. HARMONIC DISTORTION

Equation (8) predicts quadratic distortion in the displacement (and hence velocity) response of the BM to a time harmonic input. Also the mechano-electric (stereocilia) and electro-mechanic (OHC) transducer functions, which exhibit a saturating nonlinearity, could introduce distortion in the BM vibrations. Harmonic distortion has been reported in the mechanical responses of isolated OHC preparations (Santos-Sacchi, 1993), intracellular receptor potentials (Dallos and Cheatham, 1989), and in cochlear models using the nonlinear function describing the OHC voltage-dependent mechanical activity (Nobili and Mammano, 1996). Cooper has reported harmonic distortion in BM displacement response in the guinea-pig cochlea (Cooper, 1998). BM velocity responses to acoustic stimulus in guinea pigs have also been shown previously to contain harmonics, by Parthasarathi *et al.* (1998). Both even (second) and odd (third) harmonics were present in response to a purely acoustic stimulus, though the latter could not be quantified in this study due to the 40-kHz anti-aliasing filter cutoff before A/D conversion. The second harmonic distortion was usually at 30 dB below the fundamental, though at low stimulus levels it was below the noise floor. In general, the relative second harmonic distortion decreased with increasing input acoustic levels. Changing the OHC polarization could influence the harmonics. In Fig. 13,

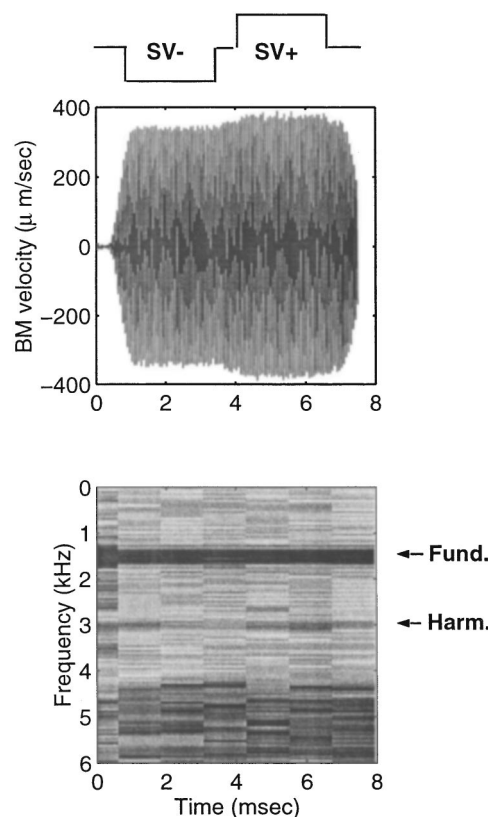


FIG. 13. Spectrogram of BM velocity response during response enhancement using positive current of 50 μ A (GP252). The amplitudes are plot relative to the response magnitude at 15 kHz. The current stimulus protocol used in this measurement is shown at the top. A negative current is applied from 1.0 to 3.5 ms. A positive current is applied from 4.0 to 6.5 ms.

BM velocity response to a 15-kHz tone burst (CF at the stimulus level 70 dB SPL) and a bipolar current pulse at 50 μ A is shown.

Also shown is the spectrogram of the total response normalized to the magnitude at the fundamental. The spectrogram shows the fundamental response at 15 kHz and also a weaker response at the second harmonic at 30 kHz. The level of the harmonic is lower when SV is negative than during SV positive. The relative harmonic level during the negative current stimulus is -34 dB and -31 dB during the positive current. In the absence of any current stimulus it is -33 dB. Hence, the relative second harmonic distortion decreases during a negative current and increases with a positive current. This behavior was consistently observed across animals. Also to be noted here is that while the relative second harmonic distortion changes by about 3 dB between negative and positive current, the amplitude of the fundamental change by less than 1 dB. The 15-kHz tone was chosen to be slightly lower in frequency than the CF of the location where velocity is measured. Analysis of some of our earlier data on enhancement/reduction (Parthasarathi *et al.*, 1998) also revealed a corresponding increase/decrease in relative second harmonic distortion (Fig. 14).

VII. DISCUSSION

The main experimental findings of this paper relate the effects of SV/ST bipolar current stimulation to the mechani-

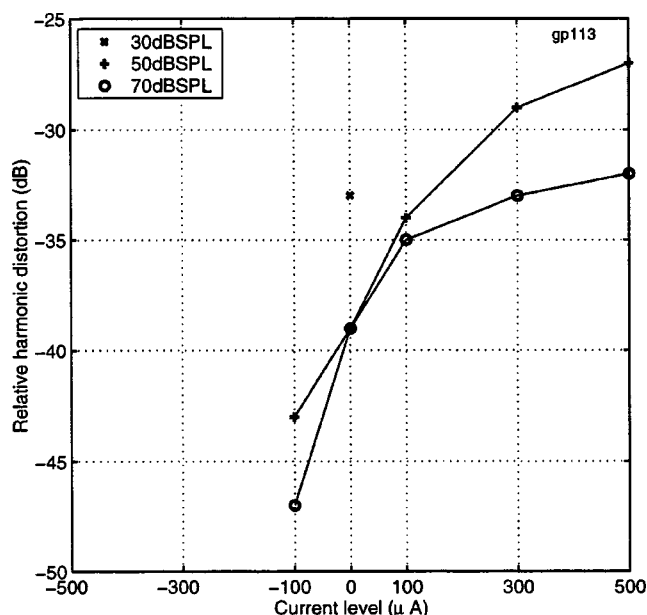


FIG. 14. Influence of positive and negative current on BM velocity relative harmonic distortion (GP113). The amplitudes are plotted relative to the response magnitude at 18 kHz (CF of measurement location). Note also that at 30 dB SPL (\times), the relative second harmonic content is -32 dB which falls to -39 dB when the input level is increased to 70 dB SPL (\circ), similar to predictions by Cooper (Cooper, 1998).

cal measurement of the velocity of the basilar membrane. The influence of electric stimulus on OHC polarization is still not clearly known—its future resolution is important in that it forms the basis of elucidating the *in vivo* role of OHCs through these electro-acoustic experiments. This discussion focuses on the interpretation of these electrophysiological experiments in view of the current literature on OHC micro-mechanics.

Xue *et al.* (1995) concluded that a positive voltage in the *scala media* causes OHC shortening, and hence depolarization. More recently, Nuttall *et al.* (1999) predicted that a positive current pulse in the *scala vestibuli* causes OHC depolarization. These conclusions were arrived at through extrapolating the direction of motion (motility) of an isolated OHC to a change in its transmembrane potential. Hence they may not be valid for an OHC under load (as is the interpretation given in Sec. V of this paper). The *in situ* measurements of Mammano and Ashmore (1993) of the intracellular voltage of the OHC and the displacement of the BM and reticular lamina show that OHCs hyperpolarize and also lengthen in response to a positive current pulse at the apical side of the hair cells. Our theoretical results show that knowledge of the OHC response to voltage alone is not sufficient to determine the polarization of the OHC; either the initial mechanical load or the intracellular voltage is also needed to completely characterize the loaded response. The effect of the OHC initial mechanical and electrical configuration is likely important for *in vivo* effects other than that studied in this paper, such as olivocochlear efferent stimulation, given the coupled dependence of the cochlear transducer on the electrical and mechanical setpoint.

The current study brings to the fore the issue of voltage-induced change of OHC stiffness and length for the *in vivo*

situation. Results and analysis indicate that stiffness changes should be included in predictions of the motion of the cochlear partition as well as OHC length changes. The current material property data indicate that stiffness has a higher sensitivity to voltage than length changes around the OHC operating point. Two interesting implications arise from the quasi-static analysis. First, under a specific set of boundary conditions and loadings, the seemingly paradoxical prediction that OHC hyperpolarization can give rise to contraction of the cell *in vivo*. Second, for cycle-by-cycle force generation via OHC mediated activity, OHC stiffness changes may dominate length changes in their contribution to the load applied to the BM and organ of Corti.

This second result does not imply, however, that the load applied through the stiffness change will be completely phasic with displacement. The stiffness change is dependent on the transmembrane potential (V). The dynamic “stiffness change” generated force applied to the BM and organ of Corti at the excitation frequency is proportional to the dynamic, voltage-induced stiffness change times the static deflection of the OHC. Therefore, the associated forces can be in phase with the basilar membrane velocity or displacement depending on the details of the mechanical to electrical transducer function (i.e., the electrical circuit of the OHC and cochlear fluids). This circuitry is not yet completely understood nor are the precise details of the manner in which the OHC stereocilia are mechanically sheared in order to open the transduction channels. Two forces are certainly present: (1) tectorial membrane shear force and (2) fluid-flow-induced shear forces. The relative dominance of these forces has not yet been determined. More electro-fluidic modeling (both local to the OHC and global to the cochlea) and experimentation are needed to elucidate the phase of the *in vivo* active loading and relative voltage contributions. The present study emphasizes the importance of determining the current paths and impedances in order to understand the macroscopic behavior of the cochlea.

This question of whether positive bipolar current stimulation applied to the SV/ST in the first turn gives rise to hyperpolarization or depolarization of the OHC is still open. The increase in the CF (and increased frequency to which the glide asymptotes) is indicative of an increase in stiffness (consistent with hyperpolarization). However, a cautionary remark about the relative size of the OHC-mediated stiffness changes is warranted at this point. While the quasi-static deformations can be attributed to OHC stiffness changes alone, the shifts in best frequency seen in the data presented here are far too large to be attributable to only a shift in the OHC stiffness, using currently available material property data. The OHC stiffness constitutes only a small portion of the overall cochlear partition stiffness. A change in the amount of damping in a mechanical system can also give rise to a shift in the frequency of peak response of the system. If the system is nominally highly damped, then a decrease in damping will increase both the amplitude of the maximum displacement response and the frequency where this maximum occurs. The change in the glide (or instantaneous frequency) could be due to a reduction in the apparent damping due to an appropriately phased active control from the OHC.

The interpretation of the instantaneous frequency result is ambiguous at this point. Positive current yields a glide to higher frequencies than when negative current or no current is applied. This larger glide could be due to a stiffening of the system or simply that the response has not been damped out before the higher frequency is seen (see Fig. 7) because the damping is lower. Hence, the level-dependent shift in CF seen in Fig. 3, which is very similar to the electrical modification seen in Fig. 5, may be due to the cochlear amplifier counteracting the viscous losses in the system, an increase in the cellular stiffness or a combination of these effects. Shera (2001) presents results for a model that produces variable glide and amplitude shifts with very little (or no) change in the stiffness of the global system. The glide can be accounted for through the dispersive nature of wave propagation in the cochlea.

The increase in the relative second harmonic distortion during a positive SV/ST current suggests that the electro-mechanical transducer function may be biased towards its saturation point (indicating OHC hyperpolarization and a shift away from the linear part of the length to voltage transducer function), giving rise to higher levels of nonlinearity. Increased motion of the apical end of the OHC would also give rise to higher harmonic levels, through increased motion of the stereocilia. The latter effect is consistent with depolarization of the OHC and attendant decrease in the stiffness. The increased motion of the BM during positive current would yield higher level of nonlinearity through saturation of the stereocilia gating resistance. The enhancement of the CM seen with negative RW current (which causes an increase in the EP just as positive SV/ST current does) is consistent with (1) an increased EP and (2) decreased OHC stiffness and increased OHC motion. The correlation of higher relative harmonic level with decreased applied acoustic load (see Fig. 14) points out the interesting effect that the nonlinearities are relatively more important at low levels.

The increased endocochlear potential (EP) induced by a positive SV/ST applied current explains much of the enhancement and increase in harmonic levels. With the combined effects of OHC stiffness changes and elongation, indirect determination of the OHC polarization is somewhat problematic in the current preparation. Comprehensive microelectrode studies, probing the electrical response of the OHC and the surrounding cells in response to electrical stimulation, hold the hope of directly measuring the electrical potentials in the cells (with the challenging proposition of actually measuring the intracellular voltage of an OHC *in vivo*). Another possibility is optical measurement of OHC receptor potentials via the use of voltage sensitive dyes. Determining the effect of current stimulation on the OHC potential will assist in interpreting the results of these experiments which will lead to important determinations as to the resting mechanical (i.e., the *in situ* OHC loading) and electrical configurations.

ACKNOWLEDGMENTS

This work was supported in part by Research Grant Nos. RO1 DC00141, PO1 00078, and RO1 DC04084-01 from the National Institute of Deafness and Other Communication Disorders, National Institutes of Health.

- Cooper, N. P. (1998). "Harmonic distortion on the basilar membrane in the basal turn of the guinea-pig cochlea," *J. Physiol. (London)* **509**, 277–288.
- Dallos, P. (1992). "The active cochlea," *Neuroscience* **12**, 4575–4585.
- Dallos, P., and Cheatham, M. (1989). "Nonlinearities in cochlear receptor potentials and their origins," *J. Acoust. Soc. Am.* **86**, 1790–1796.
- de Boer, E., and Nuttall, A. (1997). "The mechanical waveform of the basilar membrane. I. frequency modulations (glides) in impulse responses and cross-correlation functions," *J. Acoust. Soc. Am.* **101**, 3583–3592.
- Evans, B., and Dallos, P. (1993). "Stereocilia displacement induced somatic motility of cochlear outer hair cells," *Proc. Natl. Acad. Sci. Neurobiology* **90**, 8347–8351.
- Geisler, C. (1998). *From Sound to Synapse* (Oxford U.P., New York).
- He, D., and Dallos, P. (1999). "Somatic stiffness of cochlear outer hair cell is voltage-dependent," *Proc. Natl. Acad. Sci., Neurobiology* **96**, 8223–8228.
- Mammano, F., and Ashmore, J. (1993). "Reverse transduction measured in the isolated cochlea by laser michelson interferometry," *Lett. Nature* **365**, 838–841.
- Nobili, R., and Mammano, F. (1996). "Biophysics of the cochlea ii: Stationary nonlinear phenomenology," *J. Acoust. Soc. Am.* **99**, 2244–2255.
- Nuttall, A., and Dolan, D. (1996). "Steady-state sinusoidal velocity responses of the basilar membrane in guinea pig," *J. Acoust. Soc. Am.* **99**, 1556–1565.
- Nuttall, A., and Ren, T. (1995). "Electromotile hearing: evidence from basilar membrane motion and otoacoustic emissions," *Hear. Res.* **92**, 170–177.
- Nuttall, A., Dolan, D., and Avinash, G. (1991). "Laser Doppler velocimetry of basilar membrane vibration," *Hear. Res.* **51**, 203–213.
- Nuttall, A., Guo, M., and Ren, T. (1999). "The radial pattern of basilar membrane motion evoked by electric stimulation of the cochlea," *Hear. Res.* **131**, 39–46.
- Olson, E., and Mountain, D. (1991). "In vivo measurement of basilar membrane stiffness," *J. Acoust. Soc. Am.* **89**, 1262–1275.
- Papoulis, A. (1991). *Probability, Random Variables, and Stochastic Processes* (McGraw-Hill, New York).
- Parthasarathi, A., Grosh, K., and Nuttall, A. (1999). "Three-dimensional numerical modeling for global cochlear dynamics," *J. Acoust. Soc. Am.* **106**, 474–485.
- Parthasarathi, A., Guo, M., Grosh, K., and Nuttall, A. (1998). "Analysis of frequency glides and harmonics in basilar membrane velocity response to acoustic and electric stimulation," in *Abstracts of the 21st Midwinter Research Meeting, Association for Research in Otolaryngology*.
- Ruggero, M., Rich, N., Narayan, S., and Robles, L. (1997). "Basilar-membrane responses to tones at the base of the chinchilla cochlea," *J. Acoust. Soc. Am.* **101**, 2151–2163.
- Santos-Sacchi, J. (1991). "Reversible inhibition of voltage-dependent outer hair cell motility and capacitance," *J. Neurosci.* **11**, 3096–3110.
- Santos-Sacchi, J. (1992). "On the frequency limit and phase of outer hair cell motility: Effect of the membrane filter," *J. Neurosci.* **12**, 1906–1916.
- Santos-Sacchi, J. (1993). "Harmonics of outer hair cell motility," *Biophys. J.* **65**, 2217–2227.
- Shera, C. (2001). "Intensity-invariance of fine time structure in basilar-membrane click responses: Implications for cochlear mechanics," *J. Acoust. Soc. Am.* **110**, 332–348.
- Xue, S., Mountain, D., and Hubbard, A. (1995). "Electrically evoked basilar membrane motion," *J. Acoust. Soc. Am.* **97**, 3030–3041.
- Zwislocki, J., and Cefaratti, L. (1989). "Tectorial membrane ii: Stiffness measurement *in vivo*," *Hear. Res.* **42**, 211–228.

Effect of outer hair cell piezoelectricity on high-frequency receptor potentials

Alexander A. Spector^{a)}

Department of Biomedical Engineering and Center for Computational Medicine and Biology,
Johns Hopkins University, Baltimore, Maryland 21205

William E. Brownell

Bobby R. Alford Department of Otorhinolaryngology and Communicative Sciences,
Baylor College of Medicine, Houston, Texas 77030

Aleksander S. Popel

Department of Biomedical Engineering and Center for Computational Medicine and Biology,
Johns Hopkins University, Baltimore, Maryland 21205

(Received 4 April 2002; revised 30 August 2002; accepted 2 October 2002)

The low-pass voltage response of outer hair cells predicted by conventional equivalent circuit analysis would preclude the active force production at high frequencies. We have found that the band pass characteristics can be improved by introducing the piezoelectric properties of the cell wall. In contrast to the conventional analysis, the receptor potential does not tend to zero and at any frequency is greater than a limiting value. In addition, the phase shift between the transduction current and receptor potential tends to zero. The piezoelectric properties cause an additional, strain-dependent, displacement current in the cell wall. The wall strain is estimated on the basis of a model of the cell deformation in the organ of Corti. The limiting value of the receptor potential depends on the ratio of a parameter determined by the piezoelectric coefficients and the strain to the membrane capacitance. In short cells, we have found that for the low-frequency value of about 2–3 mV and the strain level of 0.1% the receptor potential can reach 0.4 mV throughout the whole frequency range. In long cells, we have found that the effect of the piezoelectric properties is much weaker. These results are consistent with major features of the cochlear amplifier. © 2003 Acoustical Society of America. [DOI: 10.1121/1.1526493]

PACS numbers: 43.64.Ld, 43.64.Nf, 43.64.Bt [LHC]

I. INTRODUCTION

An understanding of the frequency response and selectivity has always been a central problem of cochlear mechanics and hearing science (Zwislocki, 1953; Zweig *et al.*, 1976). It is thought now that outer hair cell electromotility (Brownell *et al.*, 1985, 2001)—changes in the cell length caused by changes in the cell membrane's electric potential—is a key contributor to the sharp frequency selectivity and active amplification (cochlear amplifier) in the mammalian ear (Geisler, 1998; Dallos, 1996; Ruggero, 1992). Passive vibration of the basilar membrane and tectorial membrane in the cochlea is amplified by the active force and energy produced by the electromotile outer hair cells. Such amplification is observed under high-frequency stimulation in the basal turn of the cochlea where outer hair cells are short (Rhode, 1971; Cooper and Rhode, 1992). The active amplification disappears in the deeper areas of the cochlea where outer hair cells are long (Zinn *et al.*, 2000; Hemmert *et al.*, 2000; Cooper and Rhode, 1995). Direct measurements of the active force produced by outer hair cells *in vivo* under high-frequency conditions are unavailable

at this time. The activation of isolated outer hair cells in the microchamber has shown the production of electromotile length changes and an active force at a constant level throughout the whole acoustic range of frequencies (Frank *et al.*, 1999). Simulation of the high-frequency electromotile response of isolated outer hair cells has confirmed the production of significant length changes beyond 20 kHz (Tolomeo and Steele, 1998). These results indicate that if the outer hair cell is provided with sufficient changes in its membrane potential, then the cell is capable of producing the active force necessary for the cochlear amplifier in a broad range of frequencies. The conventional view of the changes in the outer hair cell membrane potential (receptor potential) relates them to the transduction current coming to the cell as ionic channels open in response to an inclination of the stereocilia (Geisler, 1998; Pickles, 1988). This view leads to a paradox: the analysis of the basic circuit, including the stereocilia and the cell membrane with their electrical properties, shows a severe attenuation of the receptor potential at higher frequencies that would preclude the outer hair cells from producing the active force (Santos-Sacchi, 1988 and 1992; Housley and Ashmore, 1992). Mathematically, this attenuation is manifested in the receptor potential tending to zero with increasing frequencies (Housley and Ashmore, 1992). In addition, the phase shift (delay) between the trans-

^{a)}Author to whom correspondence should be addressed. Department of Biomedical Engineering, Johns Hopkins University, 720 Rutland Ave., Traylor 411, Baltimore, MD 21205. Electronic mail: aspector@bme.jhu.edu

duction current and receptor potential increases with frequency tending to the angle equal to -90 degrees. An alternative view of the electric potential that drives outer hair cell electromotility under physiological conditions was developed by Dallos and Evans (1995) who assumed that outer hair cell motility is driven by the prescribed electric gradient between the cell core and the extracellular environment. The corresponding analysis showed a significant resulting potential of the cell membrane.

The major features of the outer cell mechanics and electromotility fit well the piezoelectric model because dimensional changes in the cell are observed in response to the application of an electric field (Brownell *et al.*, 1985), and, conversely, an electric current is observed in response to the mechanical deformation of the cell (Gale and Ashmore, 1994). Although the outer hair cell is structurally far from piezoelectric crystals, the cell exhibits similar electromechanical coupling. The molecular mechanism of the piezoelectric-type behavior of the outer hair cell is related to motor protein Prestin (Zheng, 2000), voltage sensor (ions of chloride), and an interaction between the two (Oliver, 2001). The motor protein can be presented as fluctuating between two states with a probability depending on elementary electrical and mechanical energies (Dallos *et al.*, 1993; Iwasa, 1994). The direct piezoeffect is associated with a perturbation of the electrical energy that enters the probability of the motor's fluctuation. The motor's fluctuation results in an effective mechanical response: cell's length and radius changes. The converse piezoeffect underlying the phenomena considered in the present paper is associated with a perturbation of the mechanical energy that also enters the probability of the motor's fluctuation. This fluctuation results in an effective electrical response and produces a displacement current.

Mountain and Hubbard (1994) discussed a piezoelectric model of the outer hair cell function and estimated a number of characteristics on the basis of electromechanical coupling in the cell. Steele *et al.* (1993) and Tolomeo and Steele (1995) have proposed linear piezoelectric constitutive relationships for the outer hair cell wall. These relationships are reciprocal in terms of the mechanical and electrical components. Dong *et al.* (2002) have confirmed the reciprocity by showing that the experimentally determined off-diagonal coefficients in linear piezoelectric relationships for the cell as a whole are close to each other. Spector (2001) has proposed a thermodynamically consistent mechanically linear and electrically nonlinear model of the cell wall. Spector (2000) has also analyzed the effect of the piezoelectric properties on the cell membrane potential under current-clamp conditions. Weitzel *et al.* (2002) have recently modeled the outer hair cell as a length-thickness extension piezoelectric resonator.

In the present paper, we have shown that much larger values of the receptor potential than those given by the conventional resistance–capacitance (RC) analysis can be predicted in the same traditional paradigm (stereocilia inclination–transduction current–receptor potential) if the piezoelectric properties of the cell wall are taken into account. These effective properties are attributed to the whole composite cell wall that includes the outermost lipid bilayer

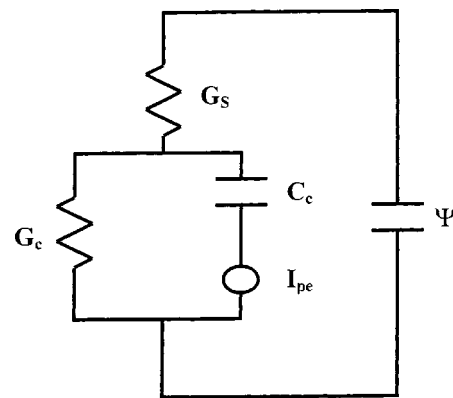


FIG. 1. Modified electric circuit, including the stereocilia and cell electrical properties, with an additional element I_{pe} that represents a displacement current caused by the piezoelectric properties of the outer hair cell wall; c refers to the cell and s refers to the stereocilia; G_c and G_s are, respectively, the conductances of the cell and stereocilia, C_c is cell membrane capacitance, and Ψ is the endocochlear potential with respect to the outer hair cell core.

with motor-proteins, the intermediate cytoskeleton, and the innermost subsurface cisternae. In contrast to results of RC analysis, the receptor potential in our analysis does not tend to zero but is greater than a certain value throughout the whole frequency range. The limiting (asymptotic) value of the receptor potential depends on the ratio of a parameter that includes the piezoelectric coefficients of the wall and typical wall strain to cell capacitance. This ratio reaches 0.4 mV in short cells, and is small (probably, physiologically negligible) in long cells. This finding is consistent with the outer hair cells' performance in the cochlear amplifier. The major result of the paper means that the intrinsic properties of an individual outer hair cell contribute to the high-frequency receptor potential. This contribution along with those from electrical coupling among the cochlear elements is, probably, sufficient for the active force needed for the cochlear amplifier.

The major results of the present paper were announced in Spector *et al.* (2002).

II. MODEL

A. Equivalent circuit and equation in terms of the receptor potential

The equivalent electric circuit, including the stereocilia and the cell wall, is shown in Fig. 1. As in conventional RC analysis (Santos-Sacchi, 1992; Housley and Ashmore, 1992), the components of the circuit are characterized by their electrical properties (conductances and capacitances), and the sum of their electric potentials is equal to the prescribed value of the endocochlear potential with respect to the cell core Ψ . The new component of the circuit is the element responsible for an additional displacement current, a manifestation of the piezoelectric properties of the cell wall.

The linear version of the piezoelectric relationships in the cell wall has the form (Tolomeo and Steele, 1995; Spector, 2000)

$$N_x = C_{11}\epsilon_x + C_{12}\epsilon_\theta + e_x\Delta\Psi_c, \quad (1)$$

$$N_\theta = C_{12}\varepsilon_x + C_{22}\varepsilon_\theta + e_\theta\Delta\Psi_c, \quad (2)$$

$$\frac{dD}{dS} = -e_x\varepsilon_x - e_\theta\varepsilon_\theta + c\Delta\Psi_c, \quad (3)$$

where N_x and N_θ are the longitudinal and circumferential components of the resultant, ε_x and ε_θ are the components of the strain, C_{11} , C_{12} , and C_{22} are the orthotropic elastic moduli, e_x and e_θ are the components of the active force per unit membrane potential change, $\Delta\Psi_c$ is the change in the membrane potential (receptor potential), D is electrical displacement, S is the surface area of the cell wall, and c is the specific capacitance of the cell.

The balance of the currents in the circuit (Fig. 1) can be written as

$$G_c\Delta\Psi_c + \frac{dD}{dt} = G_s\Delta\Psi_s, \quad (4)$$

where G_c and G_s are, respectively, the membrane and stereocilia conductances, and $\Delta\Psi_s$ is the potential change associated with the stereocilia. Conductance G_s is a nonlinear function of the inclination of the stereocilia (Kros, 1996). We consider small inclinations of the stereocilia and use a linear approximation for G_s . We assume that the cell is deformed by two vibrating complexes where one is associated with the basilar membrane and the Deiter's cell and the other is associated with the reticular lamina and tectorial membrane (more detailed analysis of the cell deformation is given below). We also assume that the stereocilia are firmly attached to the tectorial membrane. These assumptions result in the equations

$$\varepsilon_x = \varepsilon_x^o \sin \omega t, \quad \varepsilon_\theta = \varepsilon_\theta^o \sin \omega t, \quad G_s = G_s^o + G_s^1 \sin \omega t. \quad (5)$$

Considering ε_x and ε_θ in Eq. (3) as effective (uniform) strains, taking into account that the sum of $\Delta\Psi_c$ and $\Delta\Psi_s$ is equal to Ψ , and substituting Eqs. (3) and (5) into Eq. (4) we obtain

$$C_c \frac{d\Delta\Psi_c}{dt} + (G + G_s^1 \sin \omega t) \Delta\Psi_c = G_s^1 \Psi \sin \omega t - \beta \omega \cos \omega t, \quad (6)$$

where C_c is whole-cell capacitance and

$$G = G_c + G_s^o, \quad (7)$$

$$\beta = -S(\varepsilon_x^o e_x + \varepsilon_\theta^o e_\theta). \quad (8)$$

In Eq. (6), the terms resulting in the constant component of the membrane potential are omitted.

B. Model of the cell deformation in the organ of Corti

In our model of the deformation of an outer hair cell in the organ of Corti, the cell is deformed by two planes moving with respect to each other [Fig. 2(a)]. The lower plane represents the basilar membrane and Deiter's cell complex, and the upper plane represents the reticular lamina and tectorial membrane complex. The anatomy of the organ of Corti is such that outer hair cells are inclined in two directions (Geisler, 1998): along the cochlea toward the base [Fig. 2(b)]

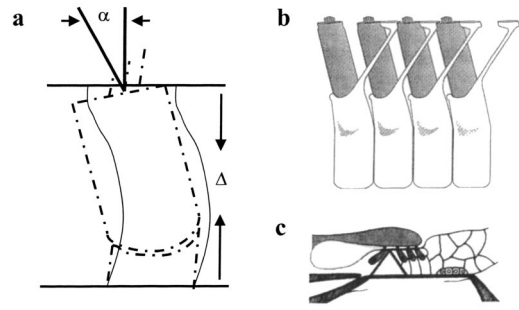


FIG. 2. Model of the outer hair cell deformation in the organ of Corti: (a) deformation of an individual outer hair cell as a result of the relative displacement Δ of two planes to which the cell is attached. The upper plane represents the reticular lamina and tectorial membrane complex, and the lower plane represents the basilar membrane and Deiter's cell complex. The dashed-dotted line shows the cell in the undeformed state, and the solid line shows a cylindrical beam that represents the cell in its deformed state. Angle α characterizes the overall cell's inclination with respect to the basilar membrane and reticular lamina, (b) sketch showing cell inclination along the cochlea toward its base, and (c) sketch showing cell inclination across the cochlea toward the inner hair cell.

and across the cochlea toward the inner hair cell [Fig. 2(c)]. Thus, angle α of the cell's inclination with respect to the two planes in our model is a combination of two angles observed in the organ of Corti. To find the strain in the cell, we represent the cell by a hollow beam with an incompressible core inside. The deformation of the beam results from the relative displacement of its ends. This displacement is equal to the relative displacement Δ of the upper and lower planes. Therefore, the cell (beam) is deformed by two components of the relative displacement of its ends: one is along the beam axes ($\Delta \cos \alpha$) and the other is normal to the beam axes ($\Delta \sin \alpha$). The first component causes a uniform axial strain of the cell accompanied by a circumferential strain that is two times smaller in magnitude and has the opposite sign. Such circumferential strain preserves the volume inside the cylindrical beam. The second, normal to the cell axes, component of the relative displacement causes bending of the beam. We now obtain the bending-related component of the axial strain in the beam. Since the upper end of the cell is embedded in the reticular lamina, we assume the fixed-end boundary condition for the upper end of the beam. The boundary condition for the lower end of the beam is determined by the mechanics of contact between the basal end of the outer hair cell and the supporting Deiter's cell. Experimental information on this interaction is unavailable at this time. For that reason, we will estimate the cell deformation in two extreme cases of the contact between the outer hair and Deiter's cell: no-slip contact (the fixed-end condition) and no-friction contact (the hinge-type condition). In both cases, the corresponding axial strain is skew-symmetric with respect to the beam axes, and it does not change the internal volume. Therefore the bending mode is not accompanied by an additional circumferential strain.

At the upper end of the beam, the displacement equal to $\Delta \sin \alpha$ and the angle of inclination equal to zero are prescribed. At the lower end of the beam, the displacement equal to zero and either the angle of inclination or the bending moment equal to zero are prescribed. Equations (9) and

(10) below (e.g., Popov, 1990) give, respectively, the axial strain (ε_x^b) in the bent beam that correspond to the first and second boundary condition at the lower end,

$$\varepsilon_x^b = -y \frac{12\Delta \sin \alpha (0.5L - x)}{L^3}, \quad (9)$$

$$\varepsilon_x^b = -y \frac{3\Delta \sin \alpha (L - x)}{L^3}, \quad (10)$$

where L is the length of the cell (beam), and coordinates x and y specify the plane of bending of the cell (beam) with the x -axis directed along the cell. Thus, the total axial strain (ε_x) in the cell (beam) is given (depending on the boundary condition) by one of the following equations:

$$\varepsilon_x = \frac{\Delta}{L} \left[\cos \alpha - y \frac{12(0.5L - x)}{L^2} \sin \alpha \right], \quad (11)$$

$$\varepsilon_x = \frac{\Delta}{L} \left[\cos \alpha - y \frac{3(L - x)}{L^2} \sin \alpha \right]. \quad (12)$$

In both cases, the circumferential component of the strain is given by the equation

$$\varepsilon_\theta = -0.5 \frac{\Delta}{L} \cos \alpha. \quad (13)$$

III. RESULTS

A. Analytical consideration

In terms of the receptor potential, Eq. (6) can be solved analytically by using separation of variables; the solution, however, is expressed in terms of complicated integrals. To implement this solution, an isolation of the limiting periodic solution and the following numerical integration are required. In the next sections, we use the direct numerical integration of Eq. (6). Here we treat analytically the case of short cells by neglecting the term $G_s^1 \sin \omega t$ compared to the term G in Eq. (6). For a 20- μm cell, the ratio G_s^1/G is about 0.02–0.05 (see Sec. III B). The harmonic solution of the simplified Eq. (6) takes the form

$$\Delta\Psi_c = \frac{\sqrt{[f_1(\omega)]^2 + [f_2(\omega)]^2}}{f_3(\omega)}, \quad (14)$$

where

$$f_1(\omega) = G_s^1 G \Psi - \beta \omega^2 C_c, \quad (15)$$

$$f_2(\omega) = \omega (C_c G_s^1 \Psi + \beta G), \quad (16)$$

and

$$f_3(\omega) = \omega^2 C_c^2 + G^2. \quad (17)$$

The phase shift between the transduction current and the resulting receptor potential is given by the equation

$$\Theta = -\frac{180^\circ}{\pi} \arctan \frac{f_2(\omega)}{f_1(\omega)}. \quad (18)$$

The asymptotic analysis of Eqs. (14)–(18) gives

$$\Delta\Psi_c \rightarrow \frac{\beta}{C_c} \quad \text{if } \omega \rightarrow \infty \quad (19)$$

and

$$\Theta \rightarrow 0 \quad \text{if } \omega \rightarrow \infty. \quad (20)$$

If $\beta = 0$, Eq. (6) reduces to the equation describing the traditional RC circuit. In contrast to Eqs. (19) and (20), the traditional RC consideration results in the equations

$$\Delta\Psi_c \rightarrow 0 \quad \text{if } \omega \rightarrow \infty \quad (21)$$

and

$$\Theta \rightarrow -90^\circ \quad \text{if } \omega \rightarrow \infty. \quad (22)$$

B. Parameters used

We consider the effect of the piezoelectric properties on the receptor potential in long and short cells. We chose the lengths 20 and 60 μm , respectively, to represent these two types of outer hair cells. Housley and Ashmore (1992) measured the cell membrane capacitance and conductance and determined the dependence of these characteristics on the cell length. On the basis of those data, we use the values $C_c = 20$ pF and $G_c = 40$ nS for 20- μm cells and the values $C_c = 36$ pF and $G_c = 15$ nS for 60- μm cells. A similar value of long-cell (55.5 μm) capacitance was obtained by Kakehata and Santos-Sacchi (1995). For the endocochlear potential, we use the range $\Psi = 120$ –150 mV (Housley and Ashmore, 1992).

The conductance of the stereocilia can be estimated on the basis of its nonlinear dependence on the stereocilia displacement (Kros, 1996) by using a linear approximation. An alternative way to estimate conductance of the stereocilia is via a range of the low-frequency receptor potential. By using Eqs. (14)–(17), the following equation in terms of conductance of the stereocilia can be obtained:

$$\frac{G_s^1}{G_s^1 + G_c} = \frac{\Delta\Psi_c^0}{\Psi}. \quad (23)$$

The parameter $\Delta\Psi_c^0 = \Delta\Psi_c(\omega = 0)$ can be interpreted as a low-frequency receptor potential that has been measured by several groups. Dallos (1996) estimated the low-frequency receptor potential corresponding to a low-level acoustic signal, 40 dB, to be close to 5 mV. Mammano and Ashmore (1993) obtained comprehensive experimental data on mechanical and electrical parameters inside the organ of Corti. The low-frequency receptor potential estimated on the basis of the known value of the injected current was found to be about 2.5 mV. Taking into account these estimates of $\Delta\Psi_c^0$, the range of the endocochlear potential Ψ , and the value of the conductance of the cell membrane G_c , we estimate conductance of the stereocilia as 1–2 nS.

We now discuss the characteristics that enter the equation for parameter β [Eq. (8)]. On the basis of measurements of the reticular lamina and the basilar membrane amplitudes

(Mammano and Ashmore, 1993), the corresponding relative displacement can be estimated to be close to 20 nm. We use this value as an estimate of the parameter Δ that characterizes the relative displacement of two planes and the strain in the outer hair cell in our model. At this time, experimental estimates of the outer hair cell's deformation under high-frequency conditions are unavailable. However, it has been shown that for high frequencies, particularly in the area of the active amplification, displacements of the cochlear partition become much greater. Therefore, we could expect an increase in the strain of outer hair cells situated in a confined space between the partitions. There is also independent evidence that the active component of the strain does not decrease significantly up to high frequencies. Frank *et al.* (1999) have shown that the active force that can be considered approximately proportional to the active strain stays almost constant within a broad range of frequencies. Thus, our value of the strain obtained on the basis of Mammano and Ashmore's (1993) measurements can be considered a conservative estimate.

Spector *et al.* (1999) and Spector (2001) obtained the piezoelectric coefficients e_x and e_θ in the form of functions of the cell stiffness parameter. Differences in the stiffness of the cell were the major source of the variability (see data from several groups below) of the estimates of the active force per unit transmembrane potential. By having the dependence of the piezoelectric coefficients e_x and e_θ on the cell stiffness, we were able to compare more accurately our estimates with those from other groups.

The stiffness parameter introduced by Spector *et al.* (1999) is inversely proportional to the length of the cell. We use the dependence of the piezoelectric coefficients on the cell stiffness parameter to estimate these coefficients for cells of different lengths. The coefficient e_x does not change significantly between the length 20 and 60 μm . Thus we use the value $e_x = 5 \times 10^{-3} \text{ NV}^{-1} \text{ m}^{-1}$ in both cases. This value falls within a range of the data obtained by several groups. The estimates of the parameter e_x made by Xue *et al.* (1993), Iwasa and Adachi (1997), Hallworth (1997), and Tolomeo and Steele (1998) are, respectively, 6.4×10^{-3} , 4×10^{-3} , 2×10^{-3} , and $1.6 \times 10^{-3} \text{ NV}^{-1} \text{ m}^{-1}$. The piezoelectric coefficients also enter the parameter β via combination $e_x - 0.5e_\theta$ that appears as a result of the substitution of the circumferential strain [Eq. (13)] into parameter β . This combination changes very significantly between the lengths 20 and 60 μm . By using the data of Spector *et al.* (1999) we estimate the discussed combinations of the piezoelectric coefficients as 4×10^{-3} and $0.3 \times 10^{-3} \text{ NV}^{-1} \text{ m}^{-1}$, respectively, in the cases of 20 and 60 μm lengths of the cell. The angle of the cell's inclination α affects the strain in the cell membrane. As we mentioned before, this angle is a combination of two angles of inclination of the outer hair cell, along and across the cochlea. The first angle is about the same for short and long cells (Geisler, 1998). The second angle changes strongly along the cochlea decreasing toward short cells (Geisler, 1998). We use the values 25 and 45 degrees of angle α , respectively, in our consideration of short and long cells.

C. Numerical results

Below we present the data on the amplitude and phase shift of the outer hair cell's membrane receptor potential for short (20 μm) and long (60 μm) cells. In the analytical solution above, we neglected the time-dependent term in front of $\Delta\Psi_c$ in Eq. (6). For longer cells, this term becomes more significant (the ratios G_s^1/G are equal, respectively, to 0.05, 0.13, and 7.1 for cells of 20-, 60-, and 85- μm lengths) and here we use the direct integration of Eq. (6). For any initial conditions the transient part of the numerical solution was oscillatory with the amplitude changing with time. After a certain number of cycles (oscillations) the solutions stabilized and reached a limiting periodic solution. In the case of 20- μm cells, the numerical limiting periodic solution did not differ more than 6%–7% from the purely sinusoidal solution predicted by the analytical treatment above. In the case of longer cells (especially, 80- μm cells) the limiting periodic solutions looked like distorted sinusoidal functions asymmetric with respect to the time axis because of a dc shift. The numerical results presented below are based on the limiting periodic components of the solutions of Eq. (6). This equation was integrated by using software Mathematica, and in all cases the initial condition was $\Delta\Psi_c^0 = 0$. We discuss first the results for short, 20- μm cells. To demonstrate the effect of the piezoelectric properties more explicitly, we represent the frequency dependence in two ranges of frequency: from 1 to 4 kHz and from 10 to 40 kHz. We discussed above the parameters G_s^1 and Ψ that determine the initial value of the receptor potential $\Delta\Psi_c^0$. To reflect the variation of these two parameters, we present two sets of curves corresponding to combinations of G_s^1 and Ψ that result in the values $\Delta\Psi_c^0 = 2.5 \text{ mV}$ and $\Delta\Psi_c^0 = 5.6 \text{ mV}$. Taking into account the ranges of the relative displacement of two planes in our model of the cell deformation, the strain in the cell wall, the angle of the cell's inclination, and the piezoelectric coefficients, we present the curves for three values of the parameter β : 4×10^{-15} , 5×10^{-15} , and $7 \times 10^{-15} \text{ NmV}^{-1}$. For comparison, we also include the curves for $\beta = 0$, the case that corresponds to the conventional RC analysis.

Figures 3(a) and (b) show the variation of the amplitude of the receptor potential for the frequencies within ranges 1–4 and 10–40 kHz, respectively. Figure 3(c) shows the amplitudes of the receptor potential throughout the whole frequency range in the log/log scale. The initial value of the receptor potential is 2.5 mV in all three cases. Four curves in each figure correspond to the values of the parameter β equal to 0, 4×10^{-15} , 5×10^{-15} , and $7 \times 10^{-15} \text{ NmV}^{-1}$. Figures 4(a) and (b) show similar sets of graphs in the case of $\Delta\Psi_c^0 = 5.6 \text{ mV}$. In Figs. 5(a) and (b), the phase shift between the receptor potential and the transduction current is plotted. The sets of curves in Figs. 5(a) and (b) correspond to the cases $\Delta\Psi_c^0 = 2.5 \text{ mV}$ and $\Delta\Psi_c^0 = 5.6 \text{ mV}$, respectively.

We also present the results for longer, 60- μm , cells. Figures 6(a) and (b) show the variation of the receptor potential in the frequency range 10–40 kHz for the cases $\Delta\Psi_c^0 = 2.5 \text{ mV}$ and $\Delta\Psi_c^0 = 5.6 \text{ mV}$, respectively. If we assume the same relative displacement of two planes and take into ac-

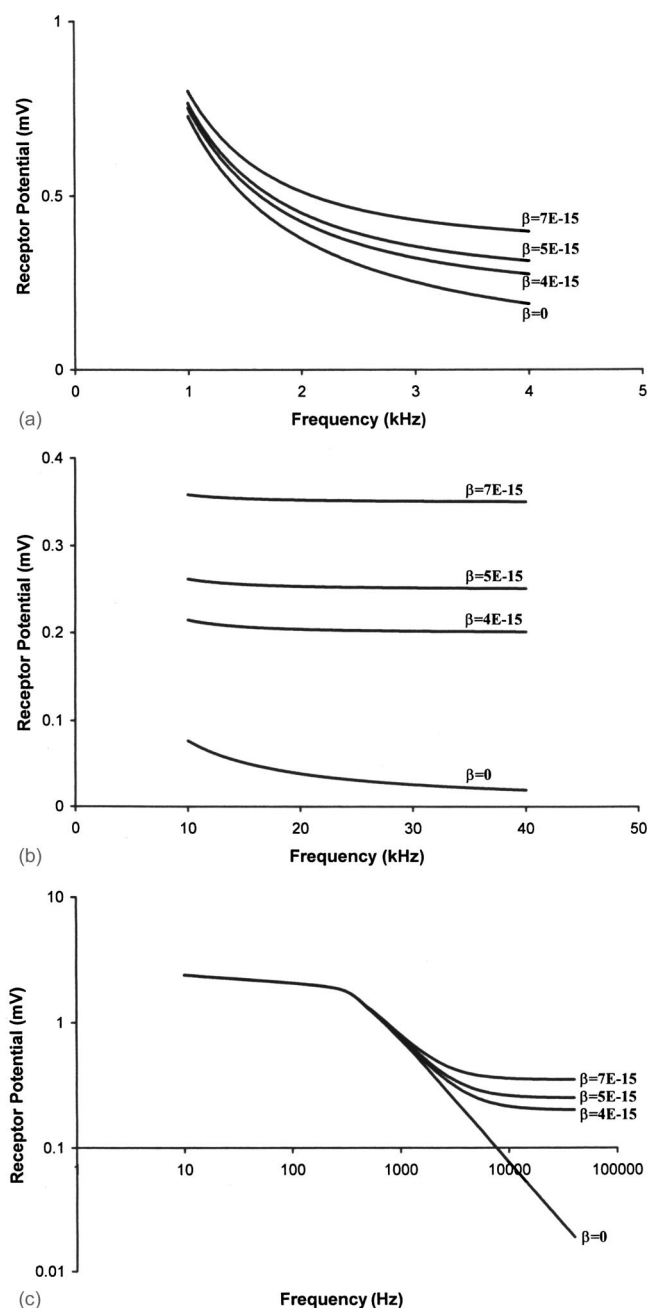


FIG. 3. The amplitude of the receptor potential in short ($20\ \mu\text{m}$) cells versus frequency in (a) low-frequency range 1–4 kHz, (b) high-frequency range 10–40 kHz, and (c) whole-frequency range presented in the log/log scale. Three upper curves in each figure correspond to different values of the parameter β (NmV^{-1}) that specifies the piezoelectric properties of the cell membrane. The lower curve for $\beta=0$ corresponds to the conventional RC analysis. The low-frequency value of the receptor potential $\Delta\Psi_c^0$ is 2.5 mV.

count the corresponding piezoelectric coefficients, then the values of the parameter β used above in the case of short cells reduce, respectively, to 0.7×10^{-15} , 0.8×10^{-15} , and $1.1 \times 10^{-15}\ \text{NmV}^{-1}$ in the case of long cells. In Figs. 6(a) and (b), the curves for this set of β are presented. The curves that correspond to $\beta=0$ are also included.

IV. DISCUSSION

The main result of the present study is that the outer hair cells in the basal part of the cochlea are under the action of a

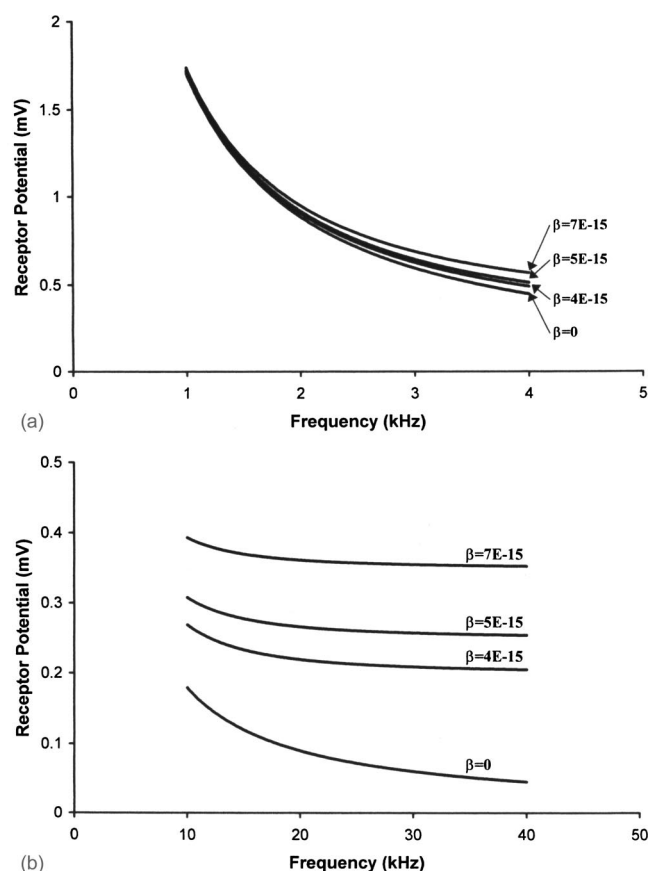


FIG. 4. The amplitude of the receptor potential in short ($20\ \mu\text{m}$) cells versus frequency in (a) low-frequency range 1–4 kHz and (b) high-frequency range 10–40 kHz. Three upper curves correspond to different values of the parameter β (NmV^{-1}) that specifies the piezoelectric properties of the cell membrane. The lower curve for $\beta=0$ corresponds to the conventional RC analysis. The low-frequency value of the receptor potential $\Delta\Psi_c^0$ is 5.6 mV.

much greater electromotility-driving receptor potential than it was previously thought on the basis of the RC-type analysis. This new estimate of the receptor potential is obtained by taking into account intrinsic piezoelectric properties of the cell under the traditional paradigm in which inclination of the stereocilia causes the transduction current and this current results in a receptor potential. The piezoelectric properties result in an additional displacement current that balances the severe attenuation of the high-frequency receptor potential caused by the capacitive properties of the cell wall.

The found values of the receptor potential in short cells are six to ten times greater (depending on the parameter β) than those obtained without consideration of the piezoelectric properties for frequencies above 30 kHz [Figs. 3(b) and 4(b)]. Such potential coincides with the result of the RC analysis. The piezoelectric wall has a qualitatively new behavior under high-frequency conditions: the receptor potential is greater than a certain value throughout the whole frequency range. This value is equal to the ratio of the composite piezoelectric parameter β [Eq. (8)] to the capacitance of the cell. The asymptotic value of the receptor potential is independent of its low-frequency value $\Delta\Psi_c^0$. Because of this property the ratios of the newly estimated receptor potential to that obtained from the RC analysis in the cases in Figs. 3(b) and 4(b) are close to each other.

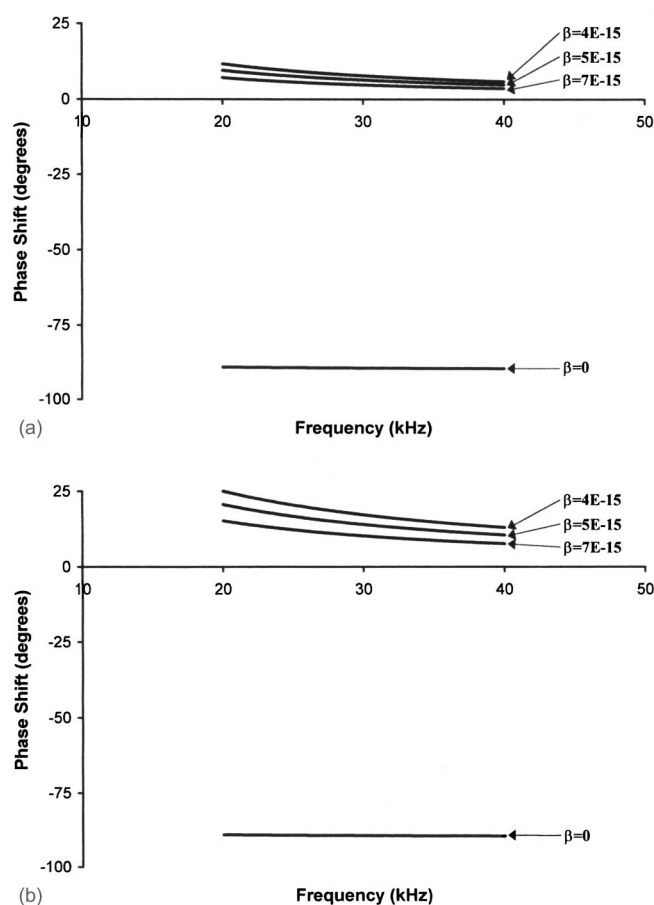


FIG. 5. The phase shift between the receptor potential and transduction current in short ($20\ \mu\text{m}$) cells versus frequency in a high-frequency range 20–40 kHz. The low-frequency values of the receptor potential $\Delta\Psi_c^0$ are (a) 2.5 mV and (b) 5.6 mV. Three upper curves in each figure correspond to different values of the parameter β (NmV^{-1}) that specifies the piezoelectric properties of the cell wall. The lower curve for $\beta=0$ corresponds to the conventional RC analysis.

Our analysis shows that high-frequency receptor potentials are determined by two displacement currents: capacitive and piezoelectric-type. The transduction current proportional to the endocochlear potential plays a smaller role in the establishing of the high-frequency receptor potential. However, the importance of the endocochlear potential becomes clear if we consider the machinery of electromotility as a whole. One argument for that is related to the balance of chloride ions. Oliver *et al.* (2001) have recently shown that the moving charges that trigger the motor's response are chloride ions. The balance of these ions is maintained via chloride channels located along the lateral wall (Rybalchenko and Santos-Sacchi, 2002). The endocochlear potential provides a potential gradient necessary for transport of chloride ions. The balance of ions of potassium is also important. Although in our model parameter β is mostly associated with chloride ions, the resulting changes in the endocochlear potential open voltage-gated potassium channels at the bottom of the cell (Housley and Ashmore, 1992; Mammano and Ashmore, 1996). The balance of potassium ions is provided by transduction channels located in the stereocilia bundle, and those channels are governed by the endocochlear potential. Thus, our model is consistent with the endocochlear potential being

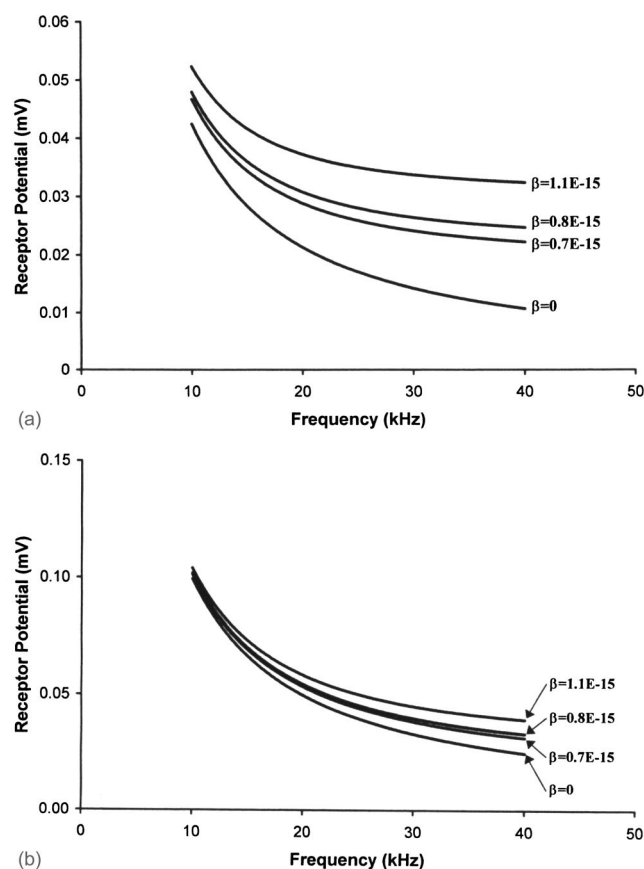


FIG. 6. The amplitude of the receptor potential in long ($60\ \mu\text{m}$) cells versus frequency in the high-frequency range 10–40 kHz. The low-frequency values of the receptor potential $\Delta\Psi_c^0$ are (a) 2.5 mV and (b) 5.6 mV. Three upper curves in each figure correspond to different values of the parameter β (NmV^{-1}) that specifies the piezoelectric properties of the cell wall. The values of the parameter β were calculated by using the piezoelectric coefficients that correspond to long cells; the rest of the parameters were the same as in Figs. 3–5. The lower curve for $\beta=0$ corresponds to the conventional RC analysis.

a necessary component of ionic balance (transport) and a contributor to the active force and energy produced by electromotile outer hair cells.

When the frequencies are low, the effect of the piezoelectric properties is small [Figs. 3(a) and 4(a)]. In the case of Fig. 4(a) ($\Delta\Psi_c^0=5.6\ \text{mV}$), the difference between the present analysis and the RC consideration is below 25% throughout the whole range of frequencies 1–4 kHz. In the case of Fig. 3(a) ($\Delta\Psi_c^0=2.5\ \text{mV}$), the difference is more visible and reaches 1.4–2 times depending on the value of β . Nevertheless, in both cases the effect of the piezoelectric properties on the receptor potential is much smaller than that in the case of high frequencies.

The frequency response in the proposed model still exhibits a roll-off, as in the RC analysis. The high-frequency asymptotic value of the receptor potential is 7–10 and 9–16 times smaller than its initial value in the cases $\Delta\Psi_c^0=2.5\ \text{mV}$ and $\Delta\Psi_c^0=5.6\ \text{mV}$, respectively. Because the piezoelectric properties do not produce a significant effect below several kilohertz, the corner frequencies in our model are close to those determined by the RC analysis both in short and long cells. However, the roll-off in our model of the outer hair cell membrane is much less severe than that pre-

TABLE I. The effect of the piezoelectric properties of the cell wall on outer hair cells in the cochlea for different frequency ranges of the acoustic signal

	High frequencies	Low frequencies
Short cells	strong	weak
Long cells	weak	weak

dicted by the RC analysis: the estimated ratios of the high-frequency potential to its low-frequency value is about an order of magnitude greater than the result of the RC analysis.

According to the mathematical analysis of the problem presented above, the phase shift between the transduction current and receptor potential tends to zero when the frequency tends to infinity. Figures 5(a) and (b) show the phase shift in short cells within a realistic high frequency range, 20–40 kHz. This phase shift indicates a small lead of the receptor potential: the corresponding angle is between 6 and 10 degrees in the case of Fig. 5(a) and it is between 15 and 25 degrees in the case of Fig. 5(b). This differs completely from the case $\beta=0$ where the piezoelectric properties are disregarded and the phase shift is practically constant and equal to -90 degrees. The phase shift between the input transduction current and the output active force produced by outer hair cells is a characteristic of the effectiveness of the machinery of electromotility. This phase shift is an important parameter of models of the whole cochlea. For example, Chadwick (1996) and Geisler and Sang (1995) assume this phase shift (phase shift between the deflection of the stereocilia and the active force) to be equal to zero, but Fukuzawa (1997) uses the value -90 degrees referring to the effect of the cell's membrane capacitance predicted by the RC analysis. The phase shift between the transduction current and the active force can be represented by the sum of two components. The first is the phase shift between the transduction current and the receptor potential, and the second is the phase shift between the receptor potential and the active force. Experimental information on either of these components under high-frequency *in vivo* conditions is unavailable at this time. Frank *et al.* (1999) have demonstrated *in vitro* that the second of these angles is small up to high frequencies [in Frank *et al.*'s (1999) notations, that angle is close to 180 degrees]. Thus, in combination with Frank *et al.*'s (1999) data, our result on the phase shift between the transduction current and the receptor potential supports the models of the cochlea with zero phase shifts between the deflection of the stereocilia and the produced active force.

The results for long, 60- μm , cells are presented in Figs. 6(a) and (b). Qualitatively, the behavior of the receptor potential is similar to that in the case of short cells: the potential has a lower limit when frequencies increase. Because of the length dependence of the piezoelectric properties, the high-frequency values of the receptor potential are about six to seven times smaller than those for short cells under the conditions of the same relative displacements of two cochlear complexes. The high-frequency values of the receptor potential in long cells are about 0.05 mV and are, probably, physiologically insignificant. The main results presented in Figs. 3–5 are briefly summarized in Table I. The table indicates that the effect of the piezoelectric properties of the

membrane is strong when short cells are under high-frequency stimulation. This effect is weak in short cells stimulated by a low-frequency signal as well as in long cells throughout the whole frequency range. This finding is consistent with observations of the cochlear amplifier in the basal and apical parts of the cochlea stimulated by high- and low-frequency signals.

We use the inhomogeneous axial strain (11) and (12) for an estimate of the constant receptor potential of the outer hair cell wall. The piezoelectric model of the present paper describes the electromechanical coupling in an element of the cell wall. Thus, a more accurate analysis of the 3-D distribution of the strain in the cell wall can be used for estimates of electrical gradients along and around the cell. This might be important for a better understanding of transport (diffusion) of ions involved in the mechanism of electromotility.

The model and findings of the present paper are supported by a number of experimental observations. First, the piezoelectric model reflects electromechanical coupling in the cell wall where active strains (dimensional changes) are generated in response to the application of an electric field and, conversely, an electric current is generated in response to the application of a strain (strain rate) to the cell. There is also a molecular-level interpretation of these properties that is based on the identified molecular motor and its voltage sensor. Second, the piezoelectric parameter β , the key characteristic that in our model determines the high-frequency receptor potentials, is a combination of the derivatives of the active force with respect to the receptor potential and the strain in the cell wall. Despite some differences in measurements of the active force production per unit transmembrane potential there is a reasonable range for this characteristic that we used in this study. Also, the strain level was estimated on the basis of the displacements of the basilar membrane and tectorial membrane measured *in situ*. Third, the electrical properties of the stereocilia and the cell wall entering the major circuit equation were experimentally determined for cells of different lengths.

The supporting experimental facts mentioned above do not provide a more direct test of the main prediction of the paper that the piezoelectric properties of the cell wall increase the receptor potential driving outer hair cell electromotility. Thus, it is important to suggest a doable experiment that could confirm our prediction. Such an experiment could be an analysis of the high-frequency performance of outer hair cells under different level of strain (He, 2002). The level of strain can be regulated by loading (unloading) the cell. The strain variation cause changes in the piezoelectric parameter β that, in turn, changes the high-frequency receptor potential. The level of loading should leave the strain small enough to correspond to a low (moderate) level of the acoustic signal.

The model proposed in the paper shows that an individual outer hair cell is capable of producing a significant receptor potential through the traditionally viewed mechanism that includes inclination of the stereocilia, transduction current, and receptor potential. The piezoelectricity-related contribution of an individual outer hair cell, along with those

related to the cochlear electrical environment, could result in high-frequency receptor potentials sufficient for the production of the active force driving the cochlear amplifier.

ACKNOWLEDGMENTS

The authors thank Dr. George Zweig and Dr. David He for valuable discussions of experimental testing of the results of the paper. This work was supported by research grants DC02775 and DC00354 from the National Institute of Deafness and other Communication Disorders (NIH).

- Brownell, W. E., Bader, C. R., Bertrand, D., and de Ribaupierre, Y. (1985). "Evoked mechanical responses of isolated cochlear outer hair cell," *Science* **227**, 194–196.
- Brownell, W. E., Spector, A. A., Raphael, R. M., and Popel, A. S. (2001). "Micro- and Nanomechanics of the Cochlear Outer Hair Cell," *Annu. Rev. Biomed. Eng.* **3**, 169–194.
- Chadwick, R. S. (1996). "Compression, gain, and nonlinear distortion in an active cochlear model with subpartitions," *Proc. Natl. Acad. Sci. U.S.A.* **95**, 14594–14599.
- Cooper, N. P., and Rhode, W. S. (1992). "Basilar membrane mechanics in the hook region of cat and guinea-pig cochleae: Sharp tuning and nonlinearity in the absence of baseline position shifts," *Hear. Res.* **63**, 163–190.
- Cooper, N. P., and Rhode, W. S. (1995). "Nonlinear mechanics at the apex of the guinea-pig cochlea," *Hear. Res.* **82**, 225–243.
- Dallos, P. (1996). "Overview: Cochlear Neurobiology," in *The Cochlea*, edited by P. Dallos, A. N. Popper, and R. R. Fay (Springer, New York), pp. 1–43.
- Dallos, P., and Evans, B. N. (1995). "High-frequency motility of outer hair cells and the cochlear amplifier," *Science* **267**, 2006–2009.
- Dallos, P., Hallworth, R., and Evans, B. N. (1993). "Theory of electrically driven shape changes of cochlear outer hair cells," *J. Neurophysiol.* **70**, 299–323.
- Dong, X.-x., Ospeck, M., and Iwasa, K. H. (2002). "Piezoelectric reciprocal relationships of the membrane motor in the cochlear outer hair cell," *Biophys. J.* **82**, 1254–1259.
- Frank, G., Hemmer, W., and Gummer, A. W. (1999). "Limiting dynamics of high-frequency electromechanical transduction of outer hair cells," *Proc. Natl. Acad. Sci. U.S.A.* **96**, 4420–4425.
- Fuzukawa, T. (1997). "A model of cochlear micromechanics," *Hear. Res.* **113**, 182–190.
- Gale, J. E., and Ashmore, J. F. (1994). "Charge displacement induced by rapid stretch in the basolateral membrane of the guinea-pig outer hair cell," *Proc. R. Soc. London, Ser. B* **255**, 243–249.
- Geisler, C. D. (1998). *From Sound to Synapse* (Oxford U. P., New York).
- Geisler, C. D., and Sang, C. (1995). "A cochlear model using feed-forward outer-hair-cell forces," *Hear. Res.* **86**, 132–146.
- Hallworth, R. (1997). "Modulation of OHC force generation and stiffness by agents known to affect hearing," in *Diversity in Auditory Mechanics*, edited by E. R. Lewis, G. R. Long, R. F. Lyon, P. M. Narins, C. R. Steele, and E. Hecht-Poinar (World Scientific, Singapore), pp. 524–530.
- He, D. Z.-Z. (2002). Personal communication.
- Hemmert, W., Zenner, H.-P., and Gummer, A. W. (2000). "Characteristics of the traveling wave in the low-frequency region of a temporal-bone preparation of the guinea-pig cochlea," *Hear. Res.* **142**, 184–202.
- Housley, G. D., and Ashmore, J. F. (1992). "Ionic currents of outer hair cells isolated from guinea-pig cochlea," *J. Physiol. (London)* **448**, 73–98.
- Iwasa, K. H. (1994). "A membrane motor model for the fast motility of the outer hair cell," *J. Acoust. Soc. Am.* **96**, 2216–2224.
- Iwasa, K. H., and Adachi, M. (1997). "Force generation in the outer hair cell in the cochlea," *Biophys. J.* **73**, 546–555.
- Kakehata, S., and Santos-Sacchi, J. (1995). "Membrane tension directly shifts voltage dependence of outer hair cell motility and associated gating charge," *Biophys. J.* **68**, 2190–2197.
- Kros, C. J. (1996). "Physiology of Mammalian Cochlear Hair Cells," in *The Cochlea*, edited by P. Dallos, A. N. Popper, and R. R. Fay (Springer, New York), pp. 318–385.
- Mammano, F., and Ashmore, J. F. (1993). "Reverse transduction measured in the isolated cochlea by laser Michelson interferometry," *Nature (London)* **365**, 838–841.
- Mammano, F., and Ashmore, J. F. (1996). "Differential expression of outer hair cell potassium currents in the isolated cochlea of the guinea-pig," *J. Physiol. (London)* **496**, 639–646.
- Mountain, D. C., and Hubbard, A. E. (1994). "A piezoelectric model of outer hair cell function," *J. Acoust. Soc. Am.* **95**, 350–354.
- Oliver, D., He, D. Z.-Z., Klocker, N., Ludwig, J., Schulte, U., Waldegger, S., Ruppersberg, J. P., Dallos, P., and Fakler, B. (2001). "Intracellular anions as the voltage-sensor of Prestin, the outer hair cell motor protein," *Science* **292**, 2340–2343.
- Pickles, J. O. (1988). *An Introduction to the Physiology of Hearing*, 2nd ed. (Academic, London).
- Popov, E. P. (1990). *Engineering Mechanics of Solids* (Prentice-Hall, Englewood Cliffs, NJ).
- Rhode, W. S. (1971). "Observations of the vibration of the basilar membrane in the squirrel monkey using the Mössbauer technique," *J. Acoust. Soc. Am.* **49**, 1218–1231.
- Ruggero, M. A. (1992). "Responses to sound of the basilar membrane of the mammalian cochlea," *Curr. Opin. Neurobiol.* **2**, 449–456.
- Rybalchenko, V., and Santos-Sacchi, J. (2002). "An unusual Cl^- conductance in isolated guinea-pig outer hair cells," in *Abstracts of the 29th Meeting of ARO*, January, 2002, St. Petersburg Beach, FL, p. 165.
- Santos-Sacchi, T. (1988). "Cochlear Physiology," in *Physiology of the Ear*, edited by A. F. Jahn and J. Santos-Sacchi (Raven Press, New York), pp. 271–293.
- Santos-Sacchi, J. (1992). "On the frequency limit and phase of outer hair cell motility: effects of the membrane filter," *J. Neurosci.* **12**, 1906–1916.
- Spector, A. A. (2000). "On the mechano-electrical coupling in the cochlear outer hair cell," *J. Acoust. Soc. Am.* **107**, 1435–1441.
- Spector, A. A. (2001). "A nonlinear electroelastic model of the auditory outer hair cell," *Int. J. Solids Struct.* **38**, 2115–2129.
- Spector, A. A., Brownell, W. E., and Popel, A. S. (1999). "Nonlinear active force generation by cochlear outer hair cell," *J. Acoust. Soc. Am.* **105**, 2414–2420.
- Spector, A. A., Brownell, W. E., and Popel, A. S. (2002). "Effect of the membrane piezoelectric properties on the outer hair cell receptor potential under high-frequency conditions," in *Abstracts of the 29th Meeting of ARO*, January, 2002, St. Petersburg Beach, FL, p. 255.
- Steele, C. R., Baker, G., Tolomeo, J. A., and Zetes, D. (1993). "Electromechanical models of outer hair cell," in *Biophysics of Hair Cell Sensory Systems*, edited by H. Duifhuis, J. W. Horst, P. van Dijk, and S. M. van Netten (World Scientific, Singapore), pp. 207–214.
- Tolomeo, J. A., and Steele, C. R. (1995). "Orthotropic piezoelectric properties of cochlear outer hair cell wall," *J. Acoust. Soc. Am.* **97**, 3006–3011.
- Tolomeo, J. A., and Steele, C. D. (1998). "A dynamic model of outer hair cell motility including intracellular and extracellular viscosity," *J. Acoust. Soc. Am.* **103**, 524–534.
- Xue, S., Mountain, D. C., and Hubbard, A. E. (1993). "Direct measurements of electrically-evoked basilar membrane motion," in *Biophysics of Hair Cell Sensory Systems*, edited by H. Duifhuis, J. W. Horst, P. van Dijk, and S. M. van Netten (World Scientific, Singapore), pp. 361–368.
- Weitzel, E. K., Tasker, R., and Brownell, W. E. (2002). "Influence of reciprocal electromechanical transduction on outer hair cell admittance," (submitted).
- Zinn, C., Maier, H., Zenner, H.-P., and Gummer, A. W. (2000). "Evidence for active, nonlinear, negative feedback in the vibration response of the apical region of the *in-vivo* guinea-pig cochlea," *Hear. Res.* **142**, 159–183.
- Zheng, J., Shen, W., He, D. Z.-Z., Long, K. B., Madison, L. D., and Dallos, P. (2000). "Prestin is the motor protein of cochlear outer hair cell," *Nature (London)* **405**, 149–155.
- Zweig, G., Lipes, R., and Pierce, J. R. (1976). "The cochlear compromise," *J. Acoust. Soc. Am.* **59**, 975–982.
- Zwislocki, J. J. (1953). "Review of recent mechanical theories of cochlear dynamics," *J. Acoust. Soc. Am.* **25**, 743–751.

Effect of amplitude modulation coherence for masked speech signals filtered into narrow bands

Emily Buss,^{a)} Joseph W. Wall III, and John H. Grose

Department of Otolaryngology/Head and Neck Surgery, University of North Carolina School of Medicine,
Chapel Hill, North Carolina 27599

(Received 18 September 2001; revised 14 March 2002; accepted 21 October 2002)

Introduction of masker amplitude modulation (AM) can improve signal detection in a number of paradigms. In some cases this advantage depends on the coherence of modulation across a relatively wide frequency range. In the experiments described below, observers were asked to identify masked spondee words produced by a single male talker. The target spondees and masking noise were filtered into nine narrow bands, and the coherence of AM of either the speech signal or noise masker was manipulated. Inherent modulation of the masker bands was manipulated via assignment of real and imaginary values to the associated components of each band in the frequency domain, and AM of speech bands was achieved via multiplication with envelopes extracted from these maskers. Responses were based on two alternatives, four alternatives, or open response sets. The effect of masker AM coherence was highly dependent upon the size of the response set: coherent AM was associated with better thresholds in a two-alternative response set, but poorer thresholds in an open response set. Results with AM speech did not depend critically upon the across-frequency temporal synchrony of AM imposed on the speech material. © 2003 Acoustical Society of America. [DOI: 10.1121/1.1528927]

PACS numbers: 43.66.Dc, 43.66.Mk, 43.72.Dv [MRL]

I. INTRODUCTION

At high signal-to-noise ratios there are multiple redundant cues present across frequency that indicate the identity of a speech sample. One example of this is demonstrated by Shannon *et al.* (1995). In that study, speech was filtered into bands, and the envelope of each band was extracted. Bands of Gaussian noise in the same frequency regions as the original speech bands were then multiplied by these envelopes, a manipulation that reduces spectral resolution as well as eliminating temporal fine-structure cues present in the speech signal. Speech recognition under these conditions can be quite good for as few as four or five bands. Another example of the resiliency of the speech signal uses time reversal of brief segments of the speech signal (Saber and Perrott, 1999). Further, under some listening conditions, such as near-threshold speech in the presence of multiple background talkers, the multiple redundant cues to the identity of the speech sample may not all be audible for any given epoch. These observations are often interpreted as demonstrating that minimal cues are sufficient for processing a degraded speech signal.

One example of the resiliency of speech processing is the improvement in masked speech identification threshold when the masker is amplitude modulated (AM). This improvement has been argued to be based on the introduction of brief epochs of improved signal-to-noise ratio, coinciding with masker modulation minima, during which time advantageous speech cues are present (Miller and Licklider, 1950; Gustafsson and Arlinger, 1994). Despite the fact that these epochs of minimally masked speech segments are distributed

over time, providing only sporadic cues, the auditory system is quite good at piecing together these cues into an interpretable speech sample. It is not clear, however, what role temporal coincidence of these “glimpses” across frequency plays in this result.

Some aspects of the improved intelligibility of a speech signal associated with masker AM resemble comodulation masking release (CMR), a paradigm in which the detection threshold of a pure tone is lower in the presence of a coherently rather than randomly modulating masker (e.g., Hall *et al.*, 1984). If these phenomena are based on the same underlying processing, then the coherence of masker AM would be a necessary precondition of improved performance for speech identification with masker AM. In other words, the coincidence of “glimpses” would be of great importance. On the other hand, if the detection advantage conferred by AM in a masked speech paradigm is driven solely by the epochs of improved signal-to-noise ratio in the redundant speech signal, then coincidence of “glimpses” might not be necessary to support that detection advantage. From a purely informational perspective it is plausible that asynchronous “glimpses” might provide information absent in the case of coherent masker AM. For example, speech sounds that are redundant across frequency, as in the case of /t/, could be efficiently detected based on “glimpses” in a small number of channels, with additional glimpses in other channels providing no new information. In that case, a distribution of “glimpses” across different frequency regions over time would provide information about an ongoing speech stream, and clustering of “glimpses” would only serve to provide redundant information at particular epochs.

Howard-Jones and Rosen (1993) report some data relevant to the role of masker modulation coherence and dis-

^{a)}Electronic mail: ebuss@med.unc.edu

cuss their results in terms of coincidence of “glimpses” of speech during masker modulation minima. Their data provide some evidence that noncoincident “glimpses” can be integrated across frequency under some circumstances. In that paradigm maskers were filtered into contiguous bands and amplitude modulated via multiplication with a 50% duty cycle raised square wave, with neighboring bands modulated either in phase or 180 degrees out of phase. Results of a consonant identification task in the out-of-phase condition with two or more bands was interpreted as reflecting integration if sensitivity exceeded that associated either subset of coherently modulated bands. Integration was observed only when masker bandwidth was relatively wide; that is, with a small number of bands. Howard-Jones and Rosen’s results could have been influenced by several factors other than the ability to integrate speech cues across frequency and across asynchronous “glimpses,” such as upward spread of masking across abutting bands of masking noise. However, these results do suggest that the auditory system has at least a limited ability to perform this type of integration.

The experiment described below was carried out to further explore whether coincidence of “glimpses” of speech information across frequency is a necessary prerequisite for obtaining the AM advantage in speech identification, or whether subsets of noncoincident cues at different frequencies can also provide this advantage. Thresholds were obtained in conditions with the AM of either the masker or the speech signal manipulated to be either coherent or random across frequency. While the methods used here roughly parallel those used in the CMR paradigm, there are several factors that would lead to an expectation of a smaller effect than that typically observed in CMR. Most CMR experiments, for example, have utilized spectrally narrow signals, and while a CMR effect has been demonstrated with spectrally complex signals, it is smaller than that obtained with narrow stimuli (e.g., Hall *et al.*, 1988). Several studies have shown that CMR is larger for simple detection than for discrimination. Using simple psychophysical stimuli, CMR has been shown to be larger for detection of a pure tone than for discrimination of a change in the amplitude (Hall and Grose, 1995) or frequency (Hall *et al.*, 1997) of that pure tone. Similar patterns have been observed with speech stimuli. Grose and Hall (1992) argued that the advantage conferred by AM coherence is evident at the low signal-to-noise ratios required for simple speech detection, but that CMR is either greatly reduced or absent at the higher signal levels necessary to support recognition. Similarly, Kwon and Turner (2001) reported that there was an advantage associated with masker AM coherence for masked consonant identification, but that this advantage was reduced or lost when the target consonants were spectrally degraded; this effect was interpreted as reflecting a greater masking release under conditions of redundant signal information.

These results have been interpreted as demonstrating that the coherence advantage is larger for tasks that rely on very minimal information about the signal than for tasks that rely on more detailed information about the signal. In the present study, data were collected with several different response sets, including two-alternative, four-alternative, and

open response set, to see whether there are similar effects of cue complexity for the masker AM coherence advantage with speech identification. The rationale was that a correct response in a spondee identification task given a very small response set might require a very small number of cues (sufficient to identify a single phoneme), while correct identification from an open set would require more cue complexity (sufficient to identify the majority of phonemes). If the advantage conferred by AM coherence is based on some of the same processing as underlies CMR, then this effect should diminish with increases in response set size.

II. METHODS

A. Observers

Observers were 45 adults, 36 females and 9 males, ranging in age from 19 to 55. All had pure-tone thresholds 15 dB HL or better at octave frequencies between 250 and 8000 Hz. None of these observers had previously participated in any experiments utilizing speech stimuli, though some had experience in nonspeech psychoacoustic tasks. Each observer was randomly assigned to complete either the two-alternative, four-alternative, or open response set conditions.

B. Stimuli

Target stimuli were spondees filtered into nine narrow bands. In the masker AM conditions the masker was comprised of nine bands of Gaussian noise at these same frequencies. In the signal AM conditions the masker was a single band of Gaussian noise low-pass filtered at 5 kHz. Stimulus generation for nine-band stimuli, both signal and masker, was performed prior to the experiment using MATLAB, and the resulting files were saved to disk. Filtering was achieved by convolution with a 512-tap array, with a single point in the frequency domain defining each band. The center frequencies of the bands used in this experiment were selected based on simulated excitation patterns generated following the procedures described in Glasberg and Moore (1990). This method, described below, was adopted in order to ensure that the cues present at each frequency were primarily driven by stimulus energy at that frequency (i.e., “within channel”). The lowest frequency band was 159 Hz, and the excitation pattern for a band at this center frequency was calculated. Excitation patterns were then estimated for increasing masker band center frequencies, assuming a flat spectrum input noise. This continued in the smallest steps allowed by the filtering method (12.5 kHz/512 taps, or 24.4 Hz) until an excitation pattern was obtained such that the signal-to-noise ratio in the presence of other (lower frequency) masker bands was 30 dB or greater at the center frequency of that additional band. Based on this technique, center frequencies of 159, 305, 500, 745, 1062, 1477, 2014, 2722, and 3674 Hz were chosen. Results of a FFT of the summed impulse response of all bandpass filters can be seen in Fig. 1.

For the speech AM conditions the masker was a low-pass Gaussian noise. For the masker AM conditions, however, maskers were bandpass filtered. Maskers submitted to

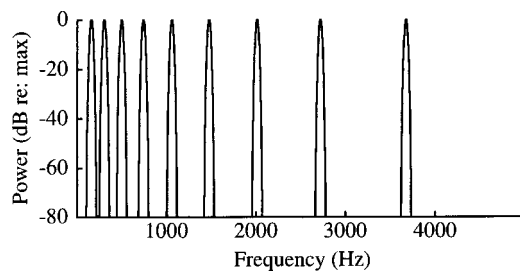


FIG. 1. A FFT was performed on the summed impulse response associated with each of the filters used to generate the nine narrow bands of Gaussian noise and speech. The result is plotted here in dB (*re*: max) as a function of frequency.

this filtering were Gaussian noise samples generated individually in the frequency domain. A set of nine coherently AM bands was generated as follows: an array of 2^{13} real and imaginary values were drawn from a Gaussian distribution, and this array served as the basis for band 1. The array was then duplicated, and the sample values were shifted up in frequency by the number of points separating bands 1 and 2. Arrays for bands 3–9 were generated in the same way. An inverse FFT performed on each of the arrays yielded a set of nine Gaussian noise samples for which, when filtered via the 512 tap convolution, all bands had identical envelopes and different center frequencies. All masker bands were of equal amplitude and so did not have the same relative long-term power spectra as that of the speech. A set of 40 such maskers was generated and saved to disk. The Hilbert envelope of each set of maskers was computed and saved to disk at this point as well. For the coherent AM conditions, all bands were taken from a single randomly selected set of coherently AM bands. For the random AM conditions, each band was randomly selected from the pool of 40. Figure 2 shows a typical time waveform of a single masker band. Figure 3 shows the average magnitude power spectrum of all 40 masker envelopes, with the shaded region indicating \pm one standard deviation from the mean. As indicated in this figure, most of the envelope energy was at or below 40 Hz.

Speech stimuli were 62 spondees,¹ resampled at 12.5 kHz from CD recordings of the adult and child spondee lists (CD101R2, Auditek). Ten spondees were eliminated from the original pool of 72 based on pilot data from naive observers, indicating that these spondees were particularly difficult to identify after filtering into nine bands. While all words were equal rms initially, this was not the case after filtering. The nominal signal level was computed as the mean dB SPL across the set of 62 words, and results are reported in dB SPL. In the masker AM conditions, speech bands were presented without further modification. In the speech AM conditions, coherent speech AM was achieved by multiplication of each speech band with a single randomly selected masker band envelope, and random AM was achieved by multiplying each speech band by a different randomly selected masker band envelope.

In the AM masker conditions, both masker and speech bands were loaded and summed, and the signal and masker streams were played out of two channels of a DAC (PD1; TDT) at 12.5 kHz. In the case of AM speech, speech and Hilbert envelope files were loaded and multiplied, and

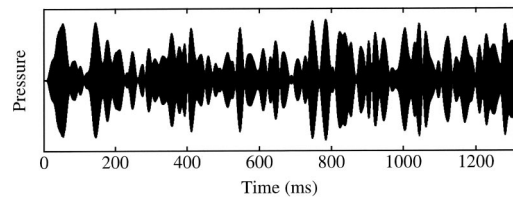


FIG. 2. A typical masker band is plotted as a function of time (ms).

played out of a single channel of the DAC. The masker was generated by a Gaussian noise generator (WG1, TDT). Other stages of processing were the same for the masker AM and the signal AM conditions: that is, the signal and masker channels were attenuated (PA4; TDT), anti-alias filtered at 5 kHz (Kemo VBF 8), added (SM2; TDT), passed through a switch (SW2; TDT), and routed to the left ear of Sony MDRV6 headphones via a headphone buffer (HB6; TDT). The masker for both the masker AM and the signal AM conditions was 55 dB SPL and 1350 ms in duration, with masker onset preceding the speech sample by 155 ms. All stimuli were ramped on and off with the shaping provided by convolution used to improve the bandpass filtering, which was approximately 26 ms.

C. Procedures

All of the data presented below were collected according to a two-down, one-up adaptive procedure (Levitt, 1971), resulting in an estimate of the signal level associated with 71% correct. A track was comprised of six reversals; the signal level was adjusted in steps of 8 dB until the first reversal, reduced to 4 dB until the second reversal, and 2 dB thereafter. A threshold estimate was calculated as the mean signal level at the last four track reversals. All threshold estimates reported below were the mean of three threshold estimates in each condition. The size of the response set was varied across observer, with either two-alternative, four-alternative, or open response set. In the case of two- and four-alternative response sets, the alternatives were randomly selected without replacement from the list of 62 and presented visually; the observer entered a response via a keyboard, and no feedback was provided other than that which could be inferred from subsequent presentation level. In the case of the open response set an experimenter sat in the booth with the observer and typed in the observer's verbal

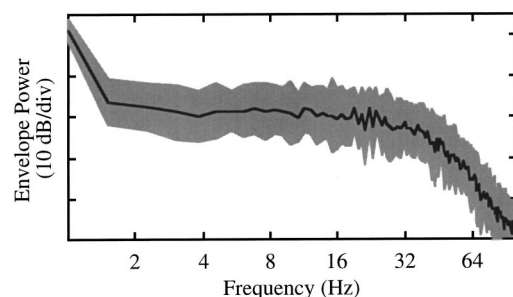


FIG. 3. The Hilbert envelope of one band from each of the 40 masker sets was submitted to a FFT. The mean (dB) is plotted with the dark line as a function of frequency, and the shaded area indicates ± 1 standard deviation from that mean.

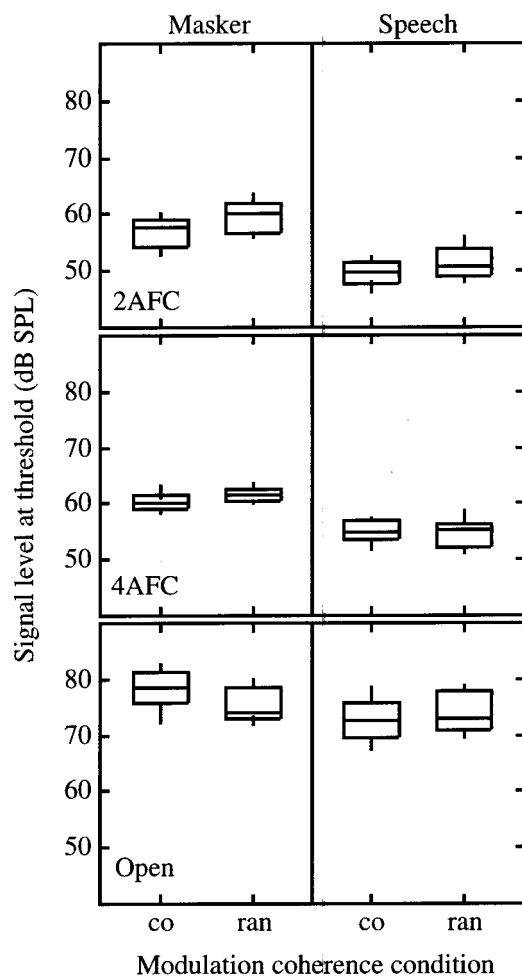


FIG. 4. Box plots indicate the distribution of thresholds in dB SPL for each condition ($n=15$). Boxes span the 25th–75th percentiles, with the center bar indicating the median and vertical bars indicating the 10th and 90th percentiles. The two columns contain data for the masker AM (left) and speech AM (right), and the three rows contain data from the open (top), four-alternative (middle), and two-alternative (bottom) response sets. Data for the two AM coherence conditions are shown separately in each panel.

response. Any discrepancy between the observer's report and the target spondee presented was scored as an incorrect response. As in the closed set conditions, no explicit feedback was provided to the observer. Three threshold estimates were obtained in each of four conditions (2 AM patterns \times 2 stimuli carrying that AM). If thresholds varied by 15 dB or more, an additional threshold was obtained and the outlier estimate discarded.

Each listening session lasted for approximately 45 min and included all conditions for one of the three response set paradigms, both coherent and random conditions for masker AM and speech AM. In order to prevent practice effects or stimulus familiarity from biasing the results, thresholds were obtained in random order. Observers participated in a single listening session.

III. RESULTS

Figure 4 shows the box plots of thresholds comprising each condition. Boxes span the 25th–75th percentiles, with the center bar indicating the median. Vertical bars mark the 10th and 90th percentile values. As one would expect, signal

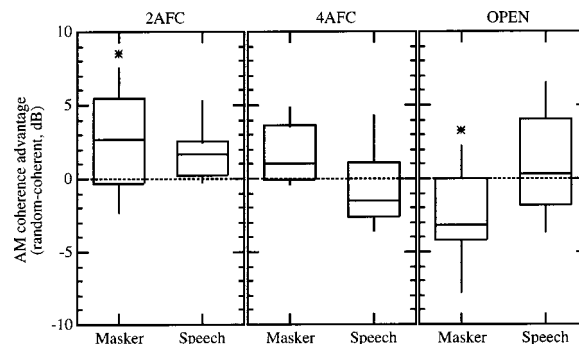


FIG. 5. The average effect of AM coherence within observer is plotted separately for the masker AM and the speech AM conditions. Data from the three response sets are plotted separately in the three panels. Stars indicate the two conditions for which the AM coherence effect was significantly different from zero ($p<0.05$).

level at threshold was considerably higher for the open set than for the two- and four-alternative sets. The effect of AM coherence for the masker AM and speech AM conditions is illustrated in Fig. 5 as the difference in threshold for the random and coherent conditions computed for each observer. As in Fig. 4, boxes span the 25th–75th percentiles, and vertical bars indicate the 10th and 90th percentiles. These results suggested an advantage for coherent AM in some but not all conditions.

An ANOVA was performed including stimulus (masker AM versus speech AM) and AM pattern (coherent versus random) as within-subject factors, and response set size (two-alternative, four-alternative, and open) as a between-subject factor. There was a main effect of stimulus ($F_{1,42}=192.77$, $p<0.0001$) and of set size ($F_{2,42}=319.44$, $p<0.0001$), but no main effect of AM pattern ($F_{1,42}=2.97$, $p=0.09$). There was a two-way interaction for stimulus versus set size ($F_{2,42}=10.33$, $p<0.0005$) and for AM pattern versus set size ($F_{2,42}=4.48$, $p<0.05$), but not for stimulus versus AM pattern ($F_{1,42}=0.15$, $p=0.70$). The three-way interaction was significant ($F_{2,42}=5.88$, $p<0.01$).

Because the three-way interaction was significant, main effects must be interpreted with care. The nature of this interaction was examined by a test of simple-simple effects, as derived from the ANOVA (Kirk, 1982). Six tests of simple-simple main effects were performed to assess the effects of AM coherence. The difference in thresholds for the random and coherent AM was significantly different from zero for two conditions at the 0.05 level (Sidak adjustment for multiple test; Kirk, 1982), as indicated by stars in Fig. 5. For the two-alternative masker AM condition, thresholds were lower for the coherent than the random AM ($F_{1,42}=8.56$, $p<0.05$). The opposite result was observed for the open set masker AM conditions; that is, thresholds were higher for the coherent than the random AM ($F_{1,42}=8.49$, $p<0.05$). There was no significant difference for the four-alternative masker AM condition or for any of the speech AM conditions.

IV. DISCUSSION

In this data set, AM coherence was found to have an effect on spondee identification in the masker AM but not the speech AM conditions. The effect of masker AM coherence

was not consistent across conditions. Thresholds were better (lower) with the coherent AM in the two-alternative response set and poorer (higher) with the open response set. Whereas CMR can often be of high magnitude in paradigms measuring pure-tone detection, CMR is usually relatively small in paradigms requiring the discrimination of a fine frequency (Hall *et al.*, 1997) or amplitude (Hall and Grose, 1995) characteristic of a suprathreshold signal. This has been interpreted as indicating that information available at the output of the CMR process is in some sense relatively coarse. Based upon this interpretation, one might expect a larger advantage of coherent AM for a small response set than a large response set, to the extent that the correct identification can be made based on simpler features of the stimuli in the context of a smaller response set. For example, if the cues received by an observer on a particular listening interval indicate the presence of a /t/ in the stimulus and the alternatives presented are “armchair” and “football,” those cues would support a correct response. However, the same cues to the presence of a /t/ would be quite unlikely to produce a correct response under open response set conditions.

Finding an interaction between this CMR-like effect and response set size is not surprising. Finding a reversal of the AM coherence advantage in the open response set conditions (i.e., poorer performance with coherent AM), however, is somewhat unexpected. One interpretation of this result pertains to the disparate levels of the speech signals between the open and two-alternative response set conditions. The speech signal at threshold was approximately 15 dB higher in the open than in the two-alternative response set condition. Thus, in the open set condition, even the speech signal energy coincident with masker peaks may have been at a sufficiently high signal-to-noise ratio to be detected. Whereas speech energy in masker peaks would be of potential benefit in the random noise conditions, it may have been of less benefit in the comodulated noise due to the relatively low weighting given to signal information coinciding with modulation maxima of comodulated noise (Buus, 1985). Results from the four-alternative response set are consistent with this hypothesis in that speech levels at threshold were only marginally higher than those in the two-alternative data set, and the AM coherence effect, while nonsignificant, was in the same direction as that demonstrated for the two-alternative response set.

Processing advantages of AM coherence under some conditions and advantages for random AM under other conditions raises the question of whether there is an AM coherence advantage under naturalistic listening circumstances. There were many features of the current experiment that make direct comparisons to natural listening situations difficult. First, the speech materials themselves were highly selective, being comprised of two single-syllable words and each receiving equal stress. While the observers in the open response set conditions were not told about these stimulus characteristics *a priori*, the most salient features of the stimuli quickly became apparent over the course of the experiment as an increasing number of suprathreshold stimuli were presented. Second, the response set conditions were extreme compared to those encountered under natural listen-

ing conditions. For example, there are few listening contexts in which a listener knows without doubt that a particular input is one of two words, but on the other hand it is unusual for a listener to have no expectations regarding the semantic content of a speech stimulus. While the paradigm used here was highly artificial, it seems quite likely that the effect of masker AM coherence is dependent on listening context and the expectations of the listener, as well as the distribution of acoustic cues relative to the masker maxima and minima across frequency.

The lack of a coherence effect in the speech AM data suggests that the auditory system is relatively adept at piecing together asynchronous components of speech information that are presented in different frequency regions. The fact that synchrony was controlled relatively grossly here (i.e., coherent or random speech AM) prevents a fine-grained analysis, but results are generally consistent with an interpretation that the temporal coincidence of “glimpses” across frequency is not of great importance. This result is broadly consistent with those reported by Greenberg and Arai (1998), where it was found that speech understanding is relatively robust with respect to time delays between different spectral regions. The present results also invite comparison to the results of Howard-Jones and Rosen (1993). Both of these investigations are consistent with an interpretation that speech can be synthesized from asynchronous spectral information. However, whereas the present results support this interpretation for nine speech bands, Howard-Jones and Rosen found evidence of this type of synthesis only when the number of speech bands was small. We are currently conducting further research to obtain a better understanding of this apparent discrepancy.

It is of interest to compare the present results with those of Carrell and Opie (1992). In that study the target speech was sentence material consisting of time-varying sinusoid speech. Amplitude modulation at 100 Hz was found to improve intelligibility of those sentences but only when the component tones were coherently modulated, as compared to random phase AM across the tones. The mechanism suggested to explain these results was that the common AM encouraged the grouping of tones into a single stream, serving a similar function as the fundamental frequency of the voice in natural speech. While coherent speech AM could theoretically have filled the same function in the stimuli used in the current experiment, there are several differences between that study and the experiment reported here that bear on this interpretation. First, the speech used here was much more naturalistic than that used by Carrell and Opie, including nine bands spread across a wide range of frequencies, one of which being a very low frequency band (159-Hz center frequency). This configuration of bands would provide grouping cues not present in sine-wave speech. Unlike sine-wave speech, these stimuli “sounded like speech” to subjects on the very first presentation and did not require training trials. This suggests that the speech stream was interpreted as a single stream even without the introduction of coherent AM. Second, the modulation rate imposed in the coherent AM condition was relatively low frequency, with the majority of energy at or below 40 Hz. The work of Drullman and

colleagues (Drullman *et al.*, 1994a, b) shows that the AM in this frequency range is characteristic of natural speech and can play a role in speech processing. Therefore, superpositioning of masker AM onto the speech signal could have introduced contradictory cues to the identity of the speech signal. If this were the case, then AM would have been detrimental to target identification in both the coherent and random AM conditions.

V. CONCLUSIONS

The present work supports two conclusions:

- (1) The modulated noise results suggest that the effect of AM coherence on speech recognition is highly dependent upon the size of the response set. Coherent AM was associated with better thresholds in a two-alternative response set, but was actually associated with poorer thresholds in an open response set.
- (2) The modulated speech results suggest that speech understanding does not depend critically upon the across-frequency temporal synchrony of AM imposed on the speech material.

The extent to which these conclusions are generalized beyond the spondee material used here remains to be seen.

ACKNOWLEDGMENTS

This work was supported by NIH NIDCD Grant No. 5 RO1 DC00418. Initial data from this experiment were presented at the 139th Meeting of the Acoustical Society of America [J. W. Hall III, E. Buss, and J. H. Grose, "Detection advantage with coherent amplitude modulation for speech filtered into narrow bands," *J. Acoust. Soc. Am.* **107**, 2914 (2000)]. This manuscript was greatly improved by suggestions from M. Leek, A. Faulkner, and one anonymous reviewer.

¹Spondees are two-syllable words with equal stress on both syllables. Typically each syllable is itself a word, such as "armchair."

- Buss, S. (1985). "Release from masking caused by envelope fluctuations," *J. Acoust. Soc. Am.* **78**, 1958–1965.
- Carrell, T. D., and Opie, J. M. (1992). "The effect of amplitude comodulation on auditory object formation in sentence perception," *Percept. Psychophys.* **52**, 437–445.
- Drullman, R., Festen, J. M., and Plomp, R. (1994a). "Effect of reducing slow temporal modulations on speech reception," *J. Acoust. Soc. Am.* **95**, 2670–2680.
- Drullman, R., Festen, J. M., and Plomp, R. (1994b). "Effect of temporal envelope smearing on speech reception," *J. Acoust. Soc. Am.* **95**, 1053–1064.
- Glasberg, B. R., and Moore, B. C. J. (1990). "Derivation of auditory filter shapes from notched-noise data," *Hear. Res.* **47**, 103–138.
- Greenberg, S., and Arai, T. (1998). "Speech intelligibility is highly tolerant of cross-channel spectral asynchrony," in *Proceedings of the Joint Meeting of the Acoustical Society of America and the International Congress on Acoustics*, Seattle, pp. 2677–2678.
- Grose, J. H., and Hall III, J. W. (1992). "Comodulation masking release for speech stimuli," *J. Acoust. Soc. Am.* **91**, 1042–1050.
- Gustafsson, H. A., and Arlinger, S. D. (1994). "Masking of speech by amplitude-modulated noise," *J. Acoust. Soc. Am.* **95**, 518–529.
- Hall III, J. W., and Grose, J. H. (1995). "Amplitude discrimination in masking release paradigms," *J. Acoust. Soc. Am.* **98**, 847–852.
- Hall III, J. W., Grose, J. H., and Dev, M. B. (1997). "Signal detection and pitch ranking in conditions of masking release," *J. Acoust. Soc. Am.* **83**, 677–686.
- Hall III, J. W., Grose, J. H., and Haggard, M. P. (1988). "Comodulation masking release for multicomponent signals," *J. Acoust. Soc. Am.* **83**, 677–686.
- Hall III, J. W., Haggard, M. P., and Fernandez, M. A. (1984). "Detection in noise by spectrotemporal pattern analysis," *J. Acoust. Soc. Am.* **76**, 50–56.
- Howard-Jones, P. A., and Rosen, S. (1993). "Uncomodulated glimpsing in 'checkerboard' noise," *J. Acoust. Soc. Am.* **93**, 2915–2922.
- Kirk, R. E. (1982). *Experimental Design: Procedures for the Behavioral Sciences* (Brooks/Cole, Pacific Grove, CA).
- Kwon, B. J., and Turner, C. W. (2001). "Consonant identification under maskers with sinusoidal modulation: Masking release or modulation interference?" *J. Acoust. Soc. Am.* **110**, 1130–1140.
- Levitt, H. (1971). "Transformed up-down methods in psychoacoustics," *J. Acoust. Soc. Am.* **49**, 467–477.
- Miller, G. A., and Licklider, J. C. R. (1950). "The intelligibility of interrupted speech," *J. Acoust. Soc. Am.* **22**, 167–173.
- Saberi, K., and Perrott, D. R. (1999). "Cognitive restoration of reversed speech," *Nature (London)* **398**, 760.
- Shannon, R. V., Zeng, F. G., Kamath, V., Wygonski, J., and Ekelid, M. (1995). "Speech recognition with primarily temporal cues," *Science* **270**, 303–304.

Detection and direction-discrimination of diotic and dichotic ramp modulations in amplitude and phase

Caroline Witton^{a)}

*Neurosciences Research Institute (Behavioural and Cognitive Sciences Research Group), Aston University,
Aston Triangle, Birmingham B4 7ET, United Kingdom*

Michael I. G. Simpson

*Department of Physiological Sciences, The Medical School, University of Newcastle upon Tyne,
Framlington Place, Newcastle upon Tyne NE2 4HH, United Kingdom*

G. Bruce Henning

*SRU, Department of Experimental Psychology, University of Oxford, South Parks Road, Oxford OX1 3UD,
United Kingdom*

Adrian Rees and G. G. R. Green

*Department of Physiological Sciences, The Medical School, University of Newcastle upon Tyne,
Framlington Place, Newcastle upon Tyne NE2 4HH, United Kingdom*

(Received 11 July 2001; revised 3 October 2002; accepted 4 October 2002)

When the source of a tone moves with respect to a listener's ears, dichotic (or interaural) phase and amplitude modulations (PM and AM) are produced. Two experiments investigated the psychophysical characteristics of dichotic linear ramp modulations in phase and amplitude, and compared them with the psychophysics of diotic PM and AM. In experiment 1, subjects were substantially more sensitive to dichotic PM than diotic PM, but AM sensitivity was equivalent in the dichotic and diotic conditions. Thresholds for discriminating modulation direction were smaller than detection thresholds for dichotic AM, and both diotic AM and PM. Dichotic PM discrimination thresholds were similar to detection thresholds. In experiment 2, the effects of ramp duration were examined. Sensitivity to dichotic AM and PM, and diotic AM increased as duration was increased from 20 ms to 200 ms. The functions relating sensitivity to ramp duration differed across the stimuli; sensitivity to dichotic PM increased more rapidly than sensitivity to dichotic or diotic AM. This was also reflected in shorter time-constants and minimum integration times for dichotic PM detection. These findings support the hypothesis that the analysis of dichotic PM and AM rely on separate mechanisms. © 2003 Acoustical Society of America. [DOI: 10.1121/1.1525286]

PACS numbers: 43.66.Pn [LRB]

I. INTRODUCTION

Interaural differences in phase and amplitude permit a listener to determine the horizontal bearing of the source of a tone (Rayleigh, 1907). Moreover, when the source of a continuous tone moves in the horizontal plane with respect to a listener (or the listener's ears move with respect to the tone's source, as when the head is turned), dichotic modulations in the phase and amplitude of the sound are produced. In this paper, we report studies of dichotic phase and amplitude modulation (PM and AM) as cues to motion.

Sinusoidal modulations of dichotic phase can be produced by presenting sinusoidally frequency-modulated (FM) signals to each ear and introducing a phase-delay between the modulations at each ear. Despite the physical similarity between FM and dichotic PM, detection thresholds for sinusoidal dichotic PM are an order of magnitude smaller than monaural or diotic thresholds for sinusoidal FM, when the modulation rate is 1 Hz (Green *et al.*, 1976; Henning and Zwicker, 1984; Zwicker and Henning, 1985; Witton *et al.*, 2000). This dichotic advantage persists (with decreasing

magnitude) up to modulation rates of 40–60 Hz (Green *et al.*, 1976; Witton *et al.*, 2000), and is not affected by several tens of decibels of fixed interaural level difference (Witton *et al.*, 2000). In other words, at low modulation rates, subjects can make use of the interaural phase-delay present in the dichotic PM stimulus, enabling detection to occur at smaller modulation depths than the detection of monaural or diotic FM. Henning and Zwicker (1984) noted the absence of such an advantage for detecting dichotic over diotic AM.

It has been suggested that the responses of human listeners to moving tone stimuli cued by dichotic PM are sluggish or slow. This suggestion is based principally on observations that thresholds for discriminating modulation of interaural temporal differences (ITD) from FM of a low-pass noise deteriorate rapidly with increasing modulation rate (Grantham and Wightman, 1978). Further evidence for sluggishness was provided by measurements of minimum audible movement angle (MAMA)—the azimuth through which a sound source is required to move for a listener to determine that it is moving or to discriminate the moving source from a stationary sound. Perrott and Musicant (1977) showed that the MAMA for a free-field moving sound increases with increasing sound-source velocity. This finding

^{a)}Electronic mail: c.witton@aston.ac.uk

was later confirmed for simulated sound movement (generated by varying the output levels of two loudspeakers), where MAMA increased sharply as stimulus duration was decreased below 100–150 ms (Grantham, 1986), indicating a long time constant or, equivalently, a sluggish system. Chandler and Grantham (1992) again showed that MAMA increased with increasing velocity and calculated a minimum integration time of 336 ms for dynamic spatial resolution of a 500-Hz tone.

A common problem in sound movement research is that attempts to identify the contributions of velocity, distance, and duration of movement are confounded by their interrelation and it can be difficult to determine which is the controlling variable in an experiment. However, taken with the finding that velocity discrimination thresholds deteriorate with increasing reference velocity, Grantham's data have been interpreted to mean that subjects are relatively insensitive to changes in the *velocity* of sound movement, and, further, that movement sensitivity is specifically impaired at high movement velocities. Recently, Carlile and Best (2002), using broadband stimuli presented in virtual auditory space, have suggested that the auditory system actually can discern movement velocity, but that velocity discrimination performance is greatly improved by the use of displacement cues in addition to velocity cues.

Grantham (1982, 1984) provided evidence that dynamic ITDs are processed differently from dynamic interaural intensity differences (IIDs), when he showed that thresholds for detecting fluctuating IIDs increase less than thresholds for detecting fluctuating ITDs as the rate of fluctuation is increased. There is, therefore, evidence for some difference between the temporal aspects of the mechanisms by which dichotic phase and amplitude cues are processed. It is possible that such differences could have affected the results of previous studies of sound movement perception that have used stimuli composed of different cues.

In this study, we sought to extend the findings of Witton *et al.* (2000) by examining the psychophysics of dichotic linear ramp modulations similar to those which occur during the movements used in previous studies (e.g., Perrott and Musicant, 1977; Grantham, 1986; Chandler and Grantham, 1992). These ramp modulation stimuli give a percept of smooth unidirectional horizontal movement. We first determined detection thresholds for linear dichotic PM ramps, and for linear diotic PM ramps where no interaural delay was present. Then, to investigate sensitivity to direction (rather than the simple presence of a modulation) we measured thresholds for discriminating between leftwards and rightwards movement. Analogous measurements were also made for dichotic and diotic amplitude modulations, allowing us to test Henning and Zwicker's finding that no dichotic advantage occurs for AM stimuli (Henning and Zwicker, 1984). In a second experiment, we investigated how sensitivity to linear ramps in dichotic PM and AM was affected by restricting the duration of modulation (and hence the extent and duration of any perceived motion). This experiment was designed to allow the comparison of thresholds for isolated dichotic PM and dichotic AM with the data from Grantham (1986) and Chandler and Grantham (1992), and to allow us, like

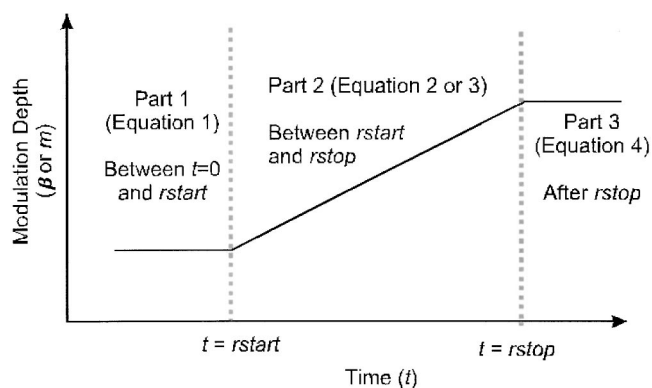


FIG. 1. Sketch of the ramp modulation as a function of time. The stimulus is divided into three parts; the modulation itself begins at time $rstart$ and ends at time $rstop$. See text for details.

Grantham, to calculate time constants for detection of these modulations.

II. EXPERIMENT 1. DETECTION AND DISCRIMINATION THRESHOLDS FOR 1-s RAMP MODULATION STIMULI

A. Methods

1. Subjects

Five trained subjects took part in experiments to measure detection and direction-discrimination thresholds for dichotic ramp modulations of phase and then of amplitude. Three of the subjects also took part in threshold measurements for diotic phase and amplitude ramps. The subjects were aged between 20 and 45 years of age, one was female, and none had any known hearing loss or neurological disorder. All of the subjects underwent a period of at least 5 h training before data collection.

2. Stimuli

The signals were generated using Tucker-Davis Technology equipment (TDT System II). The required waveforms were created digitally and scaled to fill the dynamic range of two independent 16-bit digital-to-analog converters. The sampling rate was 40 kHz and the signals for each ear were low-pass filtered at 12 kHz, separately attenuated, and used to drive calibrated Sennheiser HD40 earphones working in phase.

The modulations were linear ramps in phase or amplitude, imposed on a 500-Hz pure tone and presented at 55 dB SL. The stimuli had a total duration of 1000 ms and are best described by subdividing them into three parts, each of which can be defined by a single equation. This subdivision is illustrated in Fig. 1. For the first part of the signal, $s(t)$, a pure unmodulated tone of frequency f (equal to 500 Hz in the present study), of amplitude A , occurs for 20 ms and is given by

$$s(t) = A \sin(2\pi ft) \quad (0 \leq t \leq 0.02). \quad (1)$$

During this 20-ms unmodulated portion of the stimulus, the tone is gated on with a half-Gaussian envelope. The second, modulated portion of the stimulus (duration 960 ms) can be an increase (as illustrated in Fig. 1) or a decrease in phase or

amplitude, and is defined differently according to the parameter being modulated. The signal associated with a linear phase modulation (PM) is described as

$$s(t) = A \sin\left(2\pi ft + \frac{\beta(t - rstart)}{rstop - rstart}\right) \quad (rstart \leq t \leq rstop), \quad (2)$$

where the modulation index (i.e., the maximum excursion of the ramp, equivalent to modulation depth expressed in radians, but conventionally reported without units) is denoted β , and the terms $rstart$ and $rstop$ denote the times at which the ramp modulation begins and ends; see Fig. 1 for details. As the phase of the signal changes linearly, there is an accompanying frequency change, in the form of a square pulse. The magnitude of this frequency change is determined by the *rate* at which the phase is modulated.

When linear AM is applied, the signal can be described as follows:

$$s(t) = A \left(1 + \frac{m(t - rstart)}{rstop - rstart}\right) \sin(2\pi ft) \quad (rstart \leq t \leq rstop), \quad (3)$$

where the symbol m denotes the modulation index (for AM, this is equivalent to the modulation depth as a proportion of the total amplitude of the signal).

The third and final portion of the stimulus, after termination of the modulation, is described by Eq. (4) if PM was applied to the signal, or by Eq. (5) if AM was applied:

$$s(t) = A \sin(2\pi ft + \beta) \quad (rstop \leq t \leq rstop + 0.02), \quad (4)$$

$$s(t) = A(1 + m) \sin(2\pi ft) \quad (rstop \leq t \leq rstop + 0.02). \quad (5)$$

The duration of the third part of the stimulus was 20 ms during which the sound was gated off with a half-Gaussian envelope.

The modulation depths in the second and third parts of the stimulus [Eqs. (2)–(5)], β and m , were positive for an increasing ramp (as in Fig. 1), and negative for a decreasing ramp. Note that for a sinusoidal modulation, the modulation index would normally describe the amount by which the signal is modulated above and below its average. For these stimuli, it represents a *unidirectional* increase or decrease in the parameter being modulated.

If dichotic modulation was required, the ramps were applied to the subjects' ears with an interaural phase difference such that an increase in the modulated parameter in one ear was matched with a decrease of equal depth in the other ear. If diotic modulation was required, identical signals were presented at the ears. For a positive (upwards) diotic phase or amplitude modulation of a given depth, D , the modulation depth of the ramp in each ear was D . For a positive (rightwards) dichotic modulation of the same depth, the modulation depth was $+D$ in the right ear and $-D$ in the left ear. Therefore, in this example, the modulation depth, considered at each ear independently ("monaural" depth), was always D . When the degree of *interaural* modulation is considered, however, the diotic and dichotic stimuli differ. For a diotic modulation, the ramps in both ears are identical and there is an *interaural* phase or amplitude modulation of 0. Conversely, when ramps are presented in opposite directions (as

in the dichotic condition), there is an *interaural* modulation of $2D$, i.e., twice the depth of "monaural" modulation. In this paper, all thresholds are presented in terms of the "monaural" depth of modulation at criterion; however, dichotic phase or amplitude thresholds can be converted to threshold depth of *interaural* phase or amplitude modulation by multiplying by a factor of 2.¹

When identical PM is applied to both ears with no interaural phase difference, as in our diotic PM ramps, the resulting stimulus is equivalent to a diotic frequency change. Because frequency change is the derivative of phase change, the frequency modulation associated with the linear phase-ramp takes the form of a square pulse, not a linear frequency ramp. The magnitude of this square frequency pulse is determined by the slope of the phase ramp, and the pulse is of the same duration as the phase ramp. If the duration of a phase ramp of a given depth is increased, its slope—and hence the magnitude of the frequency pulse—decreases. Phase ramp detection thresholds can thus be converted to thresholds for discrimination of frequency pulses in Hz (Δf) as follows:

$$\Delta f = \frac{\beta}{2\pi(rstop - rstart)}, \quad (6)$$

where β is the phase ramp depth in modulation index and $(rstop - rstart)$ is the ramp duration in seconds (see Fig. 1 for details). Therefore, where appropriate, PM detection thresholds are numerically expressed as frequency changes as well as phase changes.

3. Psychophysics

In the *detection* paradigm, the target interval contained a modulated tone and the other interval contained a pure tone of the same duration. When the modulation was dichotic, the waveforms were presented in such a way that an increase in amplitude or phase occurred at the right ear, and a decrease at the left ear. This resulted in the percept of sound movement towards the right. When the modulation was diotic, increases in phase or amplitude were presented to both ears, in phase, resulting in perception of an increase in intensity, or in a higher pitch. Subjects were simply required to report in which interval, first or second, the modulation had occurred.

In the *discrimination* paradigm, the target interval was identical to that in the detection paradigm but both intervals contained a modulation. Thus, for dichotic modulations in the target interval, an increase in phase or amplitude was presented to the right ear and a decrease to the left (resulting in a percept of movement to the right). The other interval contained modulations in the opposite direction, i.e., a decrease in phase or amplitude in the right ear, and an increase in the left ear. Thus, in one interval the movement of the intracranial image was to the right, and in the other interval this movement was to the left. Subjects were required to report in which interval they perceived movement to the right. For the diotic condition, in the target interval, an increase in amplitude or phase was presented to both ears and in the other interval, a decrease. Subjects were required to report which interval contained an increase in amplitude or the higher pitch.

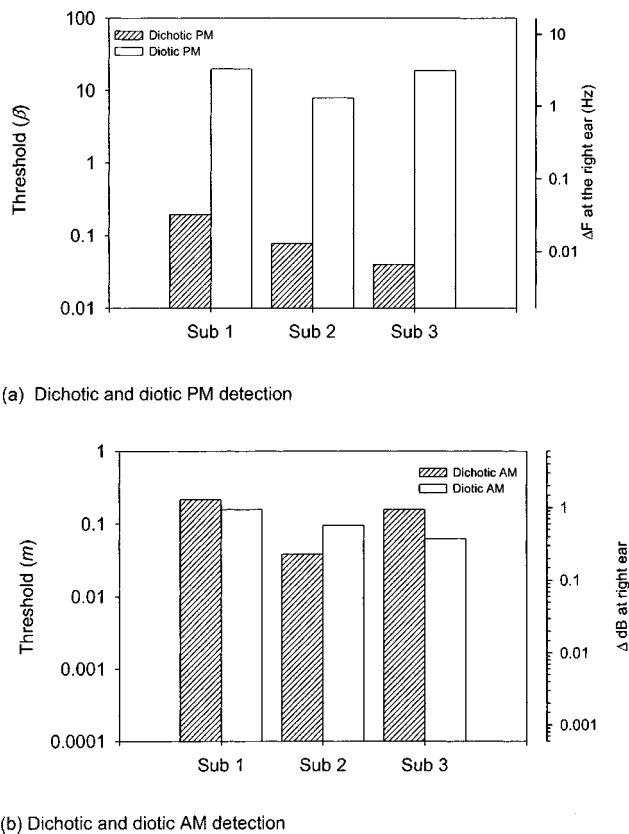


FIG. 2. (a) Thresholds for detecting diotic and dichotic PM and (b) thresholds for detecting diotic and dichotic AM. Each pair of bars represents data from a single subject. Note the logarithmic scale on the ordinate.

The discrimination paradigm contained two opposite modulations, whereas the detection paradigm compared a modulation with a pure tone. Thus the extent of modulation, when considered across both intervals, was twice as far in the discrimination paradigm as it was in the detection paradigm. This was true for both diotic and dichotic modulations.

Subjects responded using a set of push buttons, and feedback was provided by lights, which indicated the correct response after the subject had made his or her choice. For each experiment, at least 100 trials were performed at each of 6 stimulus depths, to create a psychometric function. The data were then fitted with a Weibull function (Wichmann and Hill, 2001a, b), allowing the estimation of threshold, which was defined as the stimulus depth corresponding to 75% correct. All data were collected in an IAC soundproofed room.

B. Results and discussion of experiment 1

When presented with dichotic ramps in phase or amplitude, all five subjects reported perceiving smooth linear movement of the intracranial image. Subjects reported that the increasing diotic amplitude ramps were perceived as a smooth increase in loudness, and the increasing diotic phase ramps were perceived as having a higher pitch and *vice-versa* for decreasing ramps. For the subject, the diotic PM detection and discrimination tasks were indistinguishable from a standard frequency difference limens task.

1. Ramp detection

Figure 2 shows thresholds for detection of dichotic and diotic PM [Fig. 2(a)], and dichotic and diotic AM [Fig. 2(b)] for the three subjects who took part in all conditions. The dichotic performance of the other two subjects was similar to that for the three presented here (see the following section).

The ordinate is shown on a logarithmic axis; depth of phase change is expressed on the left ordinate. Diotic PM detection thresholds (clear columns) are of a similar order of magnitude for all three subjects (mean = 15.5 [SD = 6.7]). We can compare diotic PM thresholds in this study with those from Witton *et al.* (2000) by converting into Hz [Eq. (6); see Sec. II A for details]. This yields threshold values of 3.3 for subject 1, 1.3 for subject 2, and 3.1 for subject 3. Units of monaural frequency change are indicated on the right ordinate of Fig. 2. These values are approximately equivalent to thresholds for detecting 1-Hz FM in our previous study (about 1.5–4 Hz) and are in accordance with other estimates of frequency discrimination threshold for long tone durations (e.g., Henning 1970).

There is some intersubject variability for dichotic PM detection (shaded columns; mean = 0.1 [s.d. = 0.08]), but sensitivity to dichotic PM is greater than to diotic PM for all three subjects [Fig. 2(a)]. Thus, the dichotic advantage for detecting PM, previously described for sinusoidal stimuli (Green *et al.*, 1976; Henning and Zwicker, 1984; Zwicker and Henning, 1985; Witton *et al.*, 2000), was also observed in the data described here. In those previous studies, the amount of interaural phase modulation was identical to the amount of monaural phase modulation, so dichotic advantage could be expressed by simply taking the ratio of the thresholds in each condition. Here, however, the interaural phase modulation in the dichotic condition is twice the phase modulation in each ear. If subjects detect dichotic PM on the basis of the monaural phase modulation, we could simply compare diotic and dichotic PM thresholds, which give 100-fold advantages for subjects 1 and 2, and a 470-fold advantage for subject 3. On the other hand, if the auditory system makes use of the *interaural* phase modulation, then the measured dichotic PM thresholds, which represent only the phase change at one ear, should be doubled to account for the overall interaural phase modulation in the stimulus. This yields 50-fold advantages for subjects 1 and 2, and a factor of about 236 for subject 3. Whichever way the advantage is calculated, subjects are clearly substantially more sensitive to PM in the dichotic than the diotic condition as can be seen from the plots in Fig. 2. In addition, the values from this study are larger than those reported by Witton *et al.*, for 1-Hz modulations where advantages of 10–20-fold were obtained. This difference may be because the ramp modulations used here contain much slower modulations than the 1-Hz sinusoidal modulations used by Witton *et al.* (2000). Green *et al.* (1976) used modulation rates as low as 0.2 Hz and also found larger dichotic advantages.

When thresholds for detecting dichotic amplitude ramps are compared with thresholds for diotic amplitude ramps [Fig. 2(b)], a different pattern is observed. Diotic (clear columns) and dichotic (shaded columns) amplitude ramp detection thresholds are similar for all three subjects (diotic AM:

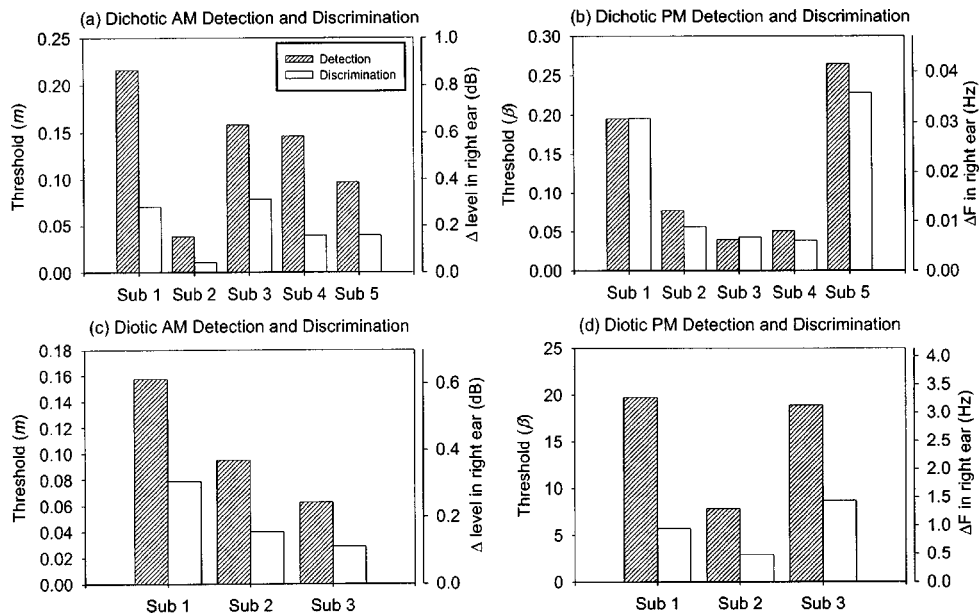


FIG. 3. Detection and direction-discrimination thresholds for (a) dichotic AM, (b) dichotic PM, (c) diotic AM, and (d) diotic PM ramps. Each pair of bars on each chart represents data from a single subject; shaded bars denote detection thresholds and unfilled bars denote discrimination thresholds.

mean=0.11 [s.d.=0.05]; dichotic AM: mean=0.14 [s.d.=0.09]). Subjects 1 and 3 have a smaller threshold in the diotic condition, whereas subject 2 has the opposite pattern for thresholds. When a simple ratio of thresholds is taken, the advantages are factors of 0.7 and 0.4 for subjects 1 and 3, respectively, and 2.5 for subject 2, where a number less than unity denotes a “negative advantage,” or a disadvantage. When dichotic AM thresholds are multiplied by 2, to account for the overall interaural amplitude modulation present in the stimulus, the advantages become 0.35 and 0.2 for subjects 1 and 3, and 1.2 for subject 2. Therefore, although some degree of dichotic advantage was observed for amplitude ramps, it is not consistent across all subjects and the effect is negligible compared to that observed for detection of dichotic and diotic phase ramps.

2. Ramp discrimination

Figures 3(a)–(d) show both the modulation detection (shaded columns) and discrimination (clear columns) thresholds for each subject, for dichotic and diotic PM, and dichotic and diotic AM, all on linear axes. Table I shows discrimination thresholds, for each subject, expressed as a percentage of the detection threshold for each modulation type.

TABLE I. Ramp discrimination thresholds, expressed as a percentage of detection threshold for the same ramp modulation, for each subject and each stimulus. The bottom row shows the mean and standard deviation of percentages for each stimulus, across all subjects who collected data in each condition.

Subject no.	Dichotic AM	Dichotic PM	Diotic AM	Diotic PM
1	33%	100%	50%	29%
2	28%	76%	42%	37%
3	49%	110%	46%	46%
4	27%	76%
5	41%	86%
Mean (sd)	36% (9.3%)	90% (15%)	46% (4%)	37% (8.5%)

In the discrimination paradigm, the maximum extent of modulation across both intervals was twice that in the detection paradigm, since the discrimination intervals contained modulations in opposite directions and of equal depths. If subjects base psychophysical decisions on the overall extent of modulation, rather than on the simple percept of modulation direction, discrimination thresholds could be as little as 50% of detection thresholds.

Discrimination thresholds for dichotic AM [Fig. 3(a)] are between 27% and 49% of those obtained in the detection condition (Table I), suggesting that subjects are at least able to make use of extent-of-modulation information in performing this task. There is also large variability in absolute threshold magnitude, clearly seen in Fig. 3(a). This is in accordance with previous observations of wide intersubject variability in studies of perception of moving sounds (e.g., Grantham, 1986). The fact that some subjects obtained discrimination thresholds substantially lower than 50% of detection thresholds (e.g., 27%) is difficult to interpret. Our fitting procedure (Wichmann and Hill, 2001a, b) provides estimates of the standard deviation of the thresholds; obtaining a detection-discrimination ratio as small as 0.27 when the true ratio is 0.5 is somewhat unlikely and may well merit further exploration.

Data for the detection and discrimination of dichotic phase ramps are shown in Fig. 3(b) and in Table I. As for the dichotic AM tasks, the overall extent of modulation in the discrimination paradigm was twice that in the detection paradigm. However, for dichotic PM, subjects’ discrimination thresholds were a minimum of 76% of their detection thresholds, indicating that the information about overall extent of modulation in the discrimination trials did not contribute to thresholds. This observation suggests that there is a major difference between the ways in which subjects detect or discriminate dichotic PM and dichotic AM. As observed for dichotic AM detection and discrimination thresholds, there is a degree of intersubject variability in the absolute magnitude of the dichotic PM detection and discrimination thresholds.

Data for three subjects' detection and discrimination of diotic ramps in amplitude and phase can be found in Figs. 3(c) and (d), respectively, and in Table I. For amplitude ramps, the ratio of thresholds varies between 42% and 50%, indicating that, like for dichotic AM, subjects are able to make use of information about the difference between the endpoints of the amplitude modulation in the discrimination paradigm.

In the diotic phase ramp condition, subjects were essentially performing a frequency difference limens task in both the detection and discrimination paradigms (i.e., discriminating between two tones of different pitch). In the discrimination paradigm, the tones were simply twice as far apart in frequency as in the detection paradigm. Discrimination thresholds would therefore still be expected to be approximately 50% of detection thresholds for diotic phase, even if subjects could not make use of information about the difference between the endpoints of the phase-modulation. Diotic PM discrimination thresholds were indeed found to be 50%, or less than 50%, of detection thresholds, for all three subjects who participated.

In summary, for dichotic AM, and diotic AM and PM, discrimination thresholds are 50% or less than 50% of detection thresholds, indicating that subjects are able to make use of information about the overall extent of modulation when discriminating between two opposite modulations. The lack of even a 50% threshold-decrease in the discrimination paradigm for dichotic PM indicates that subjects are unable to use extent-of-modulation information to perform this task.

C. Discussion of experiment 1

Although dichotic ramps in amplitude and phase are perceived similarly (all the subjects reported hearing a smooth, linear movement of the apparent source of the sound from the midline towards the right ear), it is evident from the data described here that there are some significant differences between the detection-discrimination differences for these two dichotic stimuli. The psychophysics of dichotic and diotic AM are similar, but there are clear differences between the psychophysically determined characteristics of dichotic and diotic PM.

1. The dichotic advantage

As reported previously (Witton *et al.*, 2000; Henning and Zwicker, 1984; Zwicker and Henning, 1985), it was found that subjects are more sensitive to PM in the dichotic than the diotic condition. This dichotic advantage was greater than previously observed for 1-Hz sinusoidal modulations, perhaps because the modulations in our ramp stimuli were slower and modulated in only one direction over the 1-s stimulus interval. Dichotic PM detection is, thus, not determined simply by the detection of diotic or single-ear modulation.

The lack of a large dichotic advantage for detection of dichotic over diotic AM is in accordance with previous findings (Henning and Zwicker, 1984; Zwicker and Henning, 1985). Subjects do not appear to gain any advantage in detecting dichotic AM from the binaural cues available in the interaural modulation, and threshold appears to be limited by

diotic sensitivity to amplitude change rather than by any other measurable factor.

Our diotic PM detection task was essentially a frequency-difference limens task, and this is supported by the similarity of our thresholds with those reported by Henning (1970) and others for frequency discrimination. Dichotic PM detection could (at low modulation rates) be based on the percept of motion, or on some other qualitative perceptual difference, as the modulation depth at threshold is below that at which pitch cues could be used.

The lack of a clear dichotic advantage for AM could suggest that dichotic and diotic AM are processed in the same way; for example, dichotic AM could be detected simply by listening "monaurally" to the AM which occurs at either ear. However, the fact that the perception of the signal is fundamentally different for dichotic and diotic AM suggests that they are indeed sensitive to the interaural changes that occur in the dichotic AM stimulus. This implies that the auditory system does possess a mechanism that can specifically detect dichotic AM, although this may be limited by diotic sensitivity to AM. Our data simply show that subjects are approximately equally sensitive to diotic and dichotic AM.

2. Detection versus discrimination thresholds

Dichotic and diotic AM discrimination thresholds were less than 50% of detection thresholds for the same stimuli. This observation implies that our subjects were making use of information about the difference between the endpoints of the modulations (i.e., overall extent of modulation). This was also the case for the diotic PM tasks, but as noted above subjects were probably basing their decisions on pitch differences rather than modulation.

For the dichotic PM thresholds, discrimination thresholds were on average 90% of detection thresholds. The data indicate that subjects are not basing their psychophysical judgments on the overall extent of interaural phase modulation across the two intervals, even though they are sensitive to the direction of the modulations, as evidenced by the fact that they are capable of performing the discrimination. The small magnitude of the threshold differences between the detection and discrimination thresholds (especially for subjects 1 and 3) implies that they might be making use of the same qualitative information when performing the detection task as well.

III. EXPERIMENT 2: THE EFFECT OF RAMP DURATION ON DETECTION THRESHOLDS

Chandler and Grantham (1992) showed that sensitivity to free-field sounds moving linearly in the horizontal plane decreased sharply when the duration of the movement was restricted below 200 ms, indicating a sluggish system. The results of experiment 1 have suggested that there are some significant differences between the psychophysically defined characteristics of dichotic PM and AM sensitivity. Therefore, in experiment 2, we compared the effects of restricting the duration of the ramp modulation on sensitivity to dichotic PM and dichotic AM.

A. Methods

1. Subjects

The subjects were subjects 1 and 3 from experiment 1, and one additional subject ("subject 6"), and they were all aged between 20 and 45 years. All underwent a training period of at least 5 h before beginning to collect data.

2. Stimuli

Stimuli were dichotic ramp modulations in phase or in amplitude, and diotic phase and amplitude ramps. They were designed exactly as described in Sec. II A, except that the duration of the ramp portion of the stimulus (part 2 in Fig. 1) was varied so that thresholds could be measured for different ramp durations. The duration of the pure tone in the other interval was always the same as the total duration of the modulated tone in the other interval. For example, a 20-ms ramp with 20-ms rise and fall times (a total of 60 ms) was always accompanied by a 60-ms pure tone (including 20-ms rise and fall times) in the nontarget interval. The carrier frequency was 500 Hz and the interstimulus interval was 500 ms.

3. Psychophysics

Detection thresholds for each modulation were measured using the same psychophysical procedure as for experiment 1. Thresholds were obtained for dichotic and diotic PM and AM at ramp durations between 20 (a 60-ms stimulus when rise and fall portions are added in; see Fig. 1) and 960 ms (a total sound duration of 1 s.).

B. Results of experiment 2

Data for all three subjects' detection of dichotic and diotic AM and PM at ramp durations between 20 and 960 ms are shown in Fig. 4.

1. Effects of ramp duration on detection threshold

Figure 4(a) shows detection thresholds for dichotic PM and AM as a function of ramp duration for all three subjects. Comparison of the two duration-dependency curves reveals that for both dichotic AM and PM sensitivity is greatest at the longest ramp durations. When considered in terms of modulation index, thresholds for both dichotic PM and dichotic AM are comparable at these longer ramp durations. Thresholds are highest for the shortest ramp duration (20 ms) and for both modulations they decrease sharply and appear to asymptote with increasing ramp duration. However, the rate of decrease in threshold with ramp duration differs for each modulation type. Dichotic PM detection thresholds decrease more sharply, approaching their minimum value at a duration of about 100 ms whereas dichotic AM detection thresholds do not approach this plateau until durations are at least 200 ms. This pattern is the same for all three subjects, although the threshold of subject 6 at 20 ms is comparatively less elevated than for subjects 1 and 3, so the increase in sensitivity with increasing duration is not as pronounced for this listener.

Figures 4(b) and (c) show thresholds for detecting diotic AM and PM, respectively. In Fig. 4(b), dichotic AM detection thresholds from Fig. 4(a) are replotted, and, similarly, in Fig. 4(c) dichotic PM thresholds from Fig. 4(a) are replotted, for the purposes of comparison of thresholds for detecting diotic and dichotic modulations.

In Fig. 4(b), it can be seen that detection thresholds for diotic AM decrease as durations are increased up to about 200 ms, in the same way as for dichotic AM thresholds. Dichotic and diotic AM thresholds have approximately the same duration-dependency, although this similarity is less pronounced for subject 1 between durations of about 50 and 200 ms. Subject 6 has an approximately twofold dichotic advantage at the shortest ramp duration (20 ms) but this decreases in an irregular way with increasing duration and is reversed at durations above 200 ms. No such dichotic advantage is consistently observed for subjects 1 or 3, which confirms the lack of advantage observed in experiment 1.

In Fig. 4(c), it can be seen that detection thresholds for diotic PM, plotted in terms of phase modulation index, increase with increasing ramp duration. This increase is sharpest at the shortest ramp durations, between 20 and 160 ms. The shape of the curves confirms that the *slope* of the phase change, instead of just the extent, may be important in determining threshold. Phase modulation thresholds can be converted into equivalent Δf , following Eq. (6) (see also Sec. II A). Figure 5 shows the diotic PM detection threshold data plotted as a function of the frequency change calculated using this method. Plotted in this way the thresholds decrease with increasing duration, like the curves relating thresholds for the other ramp modulations to ramp duration. This pattern of duration dependency is very similar to the many previous accounts of the effects of tone duration on frequency difference limens (e.g., Turnbull, 1944; König, 1957; Henning, 1970; Moore, 1972), illustrating that subjects are effectively performing a frequency discrimination task when detecting diotic phase ramps.

2. Time constants

The curves relating thresholds for dichotic PM, frequency pulse detection, and dichotic and diotic AM to duration were fitted with exponential functions, to enable comparison of time constants for the decay of sensitivity. The only exponential function that fit the data to give a significant correlation coefficient (r) was a single exponential with three parameters,

$$y = y_0 + ae^{-t/T}, \quad (7)$$

where t and y are the duration and threshold values respectively, y_0 is the asymptotic threshold value, a is a scalar and T is the time constant. All of the r -values from these fits were greater than 0.900 ($p < 0.001$), except for the dichotic PM data of subject 6, which could not be significantly fit with a single exponential. Table II shows the time constants calculated using this method for all three subjects, for dichotic PM, dichotic and diotic AM, and frequency pulses.

Time constants for dichotic PM and frequency pulses are

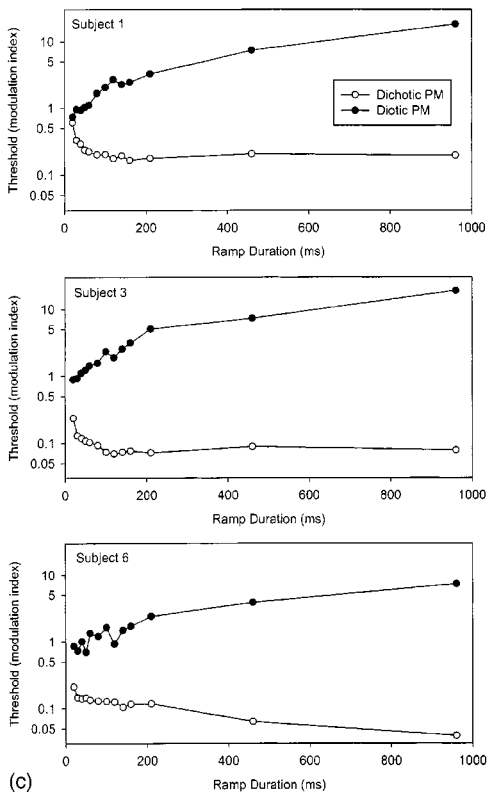
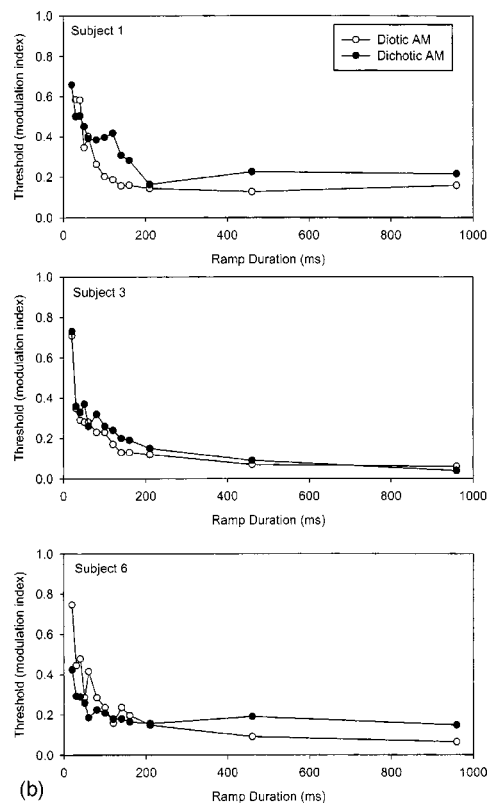
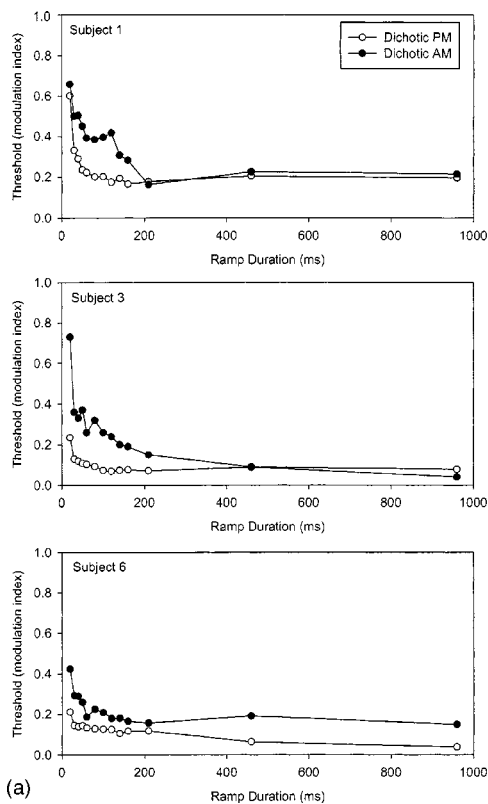


FIG. 4. Detection thresholds as a function of ramp duration: (a) thresholds for dichotic PM and AM; (b) thresholds for dichotic and diotic AM; and (c) thresholds for dichotic and diotic PM. Each graph in each figure shows data from a single subject. Note that the data in (c) are plotted on a logarithmic scale, in order to show the data more clearly.

of the same order of magnitude (for the two subjects whose dichotic PM data could be fit with the curve), indicating that the effects of reducing ramp duration on sensitivity are comparable for each stimulus. Due to the presence of a dichotic advantage, subjects are making use of more than just diotic information when detecting dichotic PM at threshold. However, the dynamics of the mechanisms responsible for detect-

ing dichotic PM and frequency pulses are approximately equally resistant to reductions in ramp duration. This observation might reflect the similar roles of temporal interval measurements, based on phase-locked neural impulses, which may underlie both frequency discrimination (Henning, 1970; Moore, 1972) and dichotic PM detection (Palmer *et al.*, 1998).

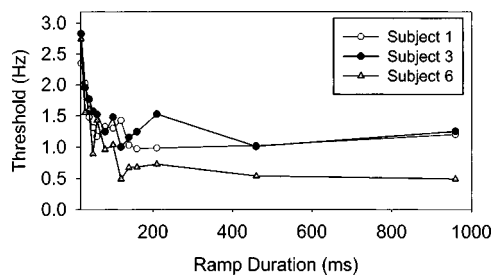


FIG. 5. Detection thresholds for diotic PM as a function of ramp duration, with thresholds converted to a measure of frequency pulse magnitude (Hz) rather than phase (see text for details).

Time constants for dichotic and diotic AM are greater than those for dichotic PM and frequency pulse detection. There seems to be no simple pattern of relations between time constants for dichotic and diotic AM across subjects and there is quite a range of variability among them. Henning (1970) reported amplitude discrimination thresholds as a function of tone duration, and showed that sensitivity decreased with decreasing duration. However, the time-course of this decay in threshold was slightly faster than the equivalent decay for frequency discrimination thresholds, at least for low carrier frequencies. This observation is not in accordance with ours, that dichotic and diotic AM detection thresholds have a longer time constant than dichotic PM and frequency pulse thresholds. This difference may arise from differences between the effects of duration on amplitude discrimination and amplitude modulation detection: in the latter stimulus, the amplitude is only at its maximum for a brief time instead of for the whole duration of the tone. Grantham (1982, 1984) found that sensitivity to dynamic ITDs was more robust to temporal constraints than sensitivity to dynamic ITDs, a finding with which our data are also inconsistent. Grantham used broadband sounds and interaural differences were modulated in a sinusoidal manner, which could be the cause of the differences between our respective findings. With sinusoidal modulations, the number of times that the modulation depth reaches its maximum is increased as modulation rate increases, whereas our method of decreasing ramp duration does not have such an effect.

C. Discussion of experiment 2

1. Comparisons with data from other studies

The shape of the threshold-duration functions for our dichotic PM and AM stimuli is similar to that obtained by

TABLE II. Time constants in ms for dichotic PM and AM, diotic AM, and frequency pulses for three subjects, calculated using the method described in the text. No data are available for the dichotic PM data of subject 6 (see text for details).

	Dichotic PM	Dichotic AM	Diotic AM	Frequency pulse
Subject 1	11.7	82.4	38.8	18.8
Subject 3	13.4	29.3	89.0	17.9
Subject 6	...	86.6	81.0	24.7
Mean (sd)	12.6 (1.2)	66.1 (31.9)	69.6 (27.0)	20.5 (3.7)

TABLE III. Minimum integration times for detecting dichotic PM and AM, diotic AM and frequency pulses for three subjects, calculated using the method of Chandler and Grantham (1992). See text for details.

	Dichotic PM	Dichotic AM	Diotic AM	Frequency pulse
Subject 1	44.8	183.5	131.9	48.2
Subject 3	46.8	92.0	292.7	48.6
Subject 6	-	159.4	266.0	80.0

Grantham (1986) for movement simulated by stereophonic balancing of the sound in two speakers separated by 30° (producing changing ITDs as well as changing ILDs). The time-course of the decay in sensitivity with decreasing duration appears to be slower in Grantham's data, since thresholds become elevated at durations longer than 200 ms, although there are clear intersubject differences. One difference between the experimental paradigm employed by Grantham (1986) and the one employed here is that Grantham jittered the spatial position of stimulus onset, in an attempt to stop subjects from basing their decisions on the location of the onset or offset positions of either interval. This did appear to have a slight detrimental effect on the performance of some subjects and could account for some or all of the differences between our data. However, in a previous experiment where there was no jittering, thresholds still appeared to asymptote somewhere between 150 and 300 ms (Grantham, 1986).

The shape of the threshold-duration function for dichotic PM and dichotic AM (i.e., an exponential decay) is also similar to that calculated by Chandler and Grantham (1992) from their MAMAs at different velocities. However, the time-course of this decay is faster in the present paper, both for dichotic PM and for dichotic AM. Chandler and Grantham (1992) used a free-field moving source with a carrier frequency of 500 Hz. When detecting movement, subjects are therefore likely to have been making use of dichotic PM, rather than dichotic AM (as well as some spectral cues generated by the pinna and head), as a cue. This methodological difference could account for the differences between our findings.

Similarly, Chandler and Grantham's (1992) minimum integration times—about 300 ms for a 500-Hz tone—are longer than the time constants reported here for either dichotic PM or dichotic AM. This difference probably results, in part, from differences in the method of calculating the integration time as well as differences in the data. Chandler and Grantham (1992) plotted MAMA against movement duration (similar to our plots in Fig. 4) and calculated integration time as the duration corresponding to a MAMA 25% above the asymptote. For our data, we chose a different method to quantify time constants, by fitting similar curves with an exponential function. However, it is possible to calculate minimum integration times for our data in the same way as Chandler and Grantham (1992), based on our exponential fits: the value of x [from Eq. (7)] when y is 25% above the asymptote y_0 .

Table III shows the minimum integration time for the

data of subjects 1, 3, and 6, calculated using Chandler and Grantham's method. Although larger in value, the minimum integration times reflect a similar pattern of results to our time constants. Integration times are smallest for dichotic PM, around 44 ms for the two subjects whose data could be fit. They increase at least twofold for dichotic and diotic AM thresholds, but there is no observable pattern across these two stimuli. The minimum integration times reported here are clearly shorter than those reported by Chandler and Grantham (1992), probably as a result of methodological difference. However, the dissociation between integration times obtained for the different interaural modulations supports our hypothesis that there are significant differences between the processing of interaural phase and amplitude modulations.

2. Sluggishness

Recently, Bernstein *et al.* (2001) have used measurements of sensitivity to brief changes in ITD or IIDs under different conditions to model the temporal characteristics of sensitivity to these stimuli. They reported that sensitivity to both dynamic ITDs and IIDs is constrained by a single, symmetric, double-exponential, temporal window, characterized by a short (0.09 ms) and a longer (13.8 ms) time constant. The shortness of these time constants indicates that the binaural system may not be intrinsically sluggish. Nevertheless, the frequency response of this window had an initial low-pass segment, and it was found to reliably predict Grantham and Wightman's (1978) data for discrimination of dynamic ITDs.

In this study, it was found that thresholds for detecting dichotic PM are influenced by the duration of the modulation, and this is illustrated by their sharp increase when duration is reduced below about 150 ms. However, the observation that duration has an even stronger limiting effect on thresholds for detecting dichotic and diotic AM, where sensitivity to dynamic interaural phase differences is not required for detection, suggests that dichotic PM detection, for tonal stimuli, might not be more sluggish than detection of other types of modulation. Other studies (e.g., Grantham, 1986; Chandler and Grantham, 1992) have found longer integration times for sound movement detection than were found for dichotic PM and AM detection in this study. It is therefore possible that although sound movement perception *per se* may be sluggish, perception of dichotic PM or AM of a 500-Hz tone is not sluggish.

IV. SUMMARY AND CONCLUSIONS

In summary, the findings presented in this paper suggest that there are significant differences between the psychophysically determined characteristics of dichotic PM and dichotic AM. These differences are reflected in comparisons of dichotic and diotic detection thresholds (dichotic advantage), in direction discrimination performance, and in the temporal limitations on detection.

ACKNOWLEDGMENTS

C.W. was supported by a studentship from the Medical Research Council.

¹The reader might find it helpful to note that in our previous study (Witton *et al.*, 2000), the degree of interaural phase modulation in the dichotic condition was always numerically identical to the degree of "monaural" phase modulation.

- Bernstein, L. R., Trahiotis, C., Akeroyd, M. A., Hartung, K. (2001). "Sensitivity to brief changes of interaural time and interaural intensity," *J. Acoust. Soc. Am.* **109**, 1604–1615.
- Carlile, S., and Best, V. (2002). "Discrimination of sound source velocity in human listeners," *J. Acoust. Soc. Am.* **111**, 1026–1035.
- Chandler, D. W., and Grantham, D. W. (1992). "Minimum audible movement angle in the horizontal plane as a function of stimulus frequency and bandwidth, source azimuth, and velocity," *J. Acoust. Soc. Am.* **91**, 1624–1636.
- Grantham, D. W. (1982). "Detectability of time-varying interaural correlation in narrow-band noise stimuli," *J. Acoust. Soc. Am.* **72**, 1178–1184.
- Grantham, D. W. (1984). "Discrimination of dynamic interaural intensity differences," *J. Acoust. Soc. Am.* **76**, 71–76.
- Grantham, D. W. (1986). "Detection and discrimination of simulated motion of auditory targets in the horizontal plane," *J. Acoust. Soc. Am.* **79**, 1939–1949.
- Grantham, D. W., and Wightman, F. L. (1978). "Detectability of varying interaural temporal differences," *J. Acoust. Soc. Am.* **63**, 511–523.
- Green, G. G. R., Heffer, J. S., and Ross, D. A. (1976). "The detectability of apparent source movement effected by interaural phase modulation," *J. Physiol. (London)* **260**, 49P.
- Henning, G. B. (1970). "A comparison of the effects of signal duration on frequency and amplitude discrimination," in *Frequency Analysis and Periodicity Detection in Hearing*, edited by R. Plomp and G. F. Smoorenberg (Sijthoff, Leiden).
- Henning, G. B., and Zwicker, E. (1984). "Binaural masking level differences with tonal maskers," *Hear. Res.* **16**, 279–290.
- König, E. (1957). "Effect of time on pitch discrimination thresholds under several psychophysical procedures; comparison with intensity discrimination thresholds," *J. Acoust. Soc. Am.* **29**, 606–612.
- Moore, B. C. J. (1972). "Frequency difference limens for short-duration tones," *J. Acoust. Soc. Am.* **54**, 610–619.
- Palmer, A. R., Jiang, D., and McAlpine, D. (1998). "Responses to sound motion: interaural amplitude and phase modulation in the inferior colliculus" in *Psychophysical and Physiological Advances in Hearing, Proceedings of the 11th International Symposium on Hearing*, edited by A. R. Plamer, A. Rees, A. Q. Summerfield, and R. Meedis (Whurr Publishers, London), pp. 368–375.
- Perrott, D. R., and Musicant, A. D. (1977). "Minimum auditory movement angle: Binaural localization of moving sound sources," *J. Acoust. Soc. Am.* **62**, 1463–1466.
- Rayleigh, L. (1907). "On our perception of sound direction," *Philos. Mag.* **13**, 214–232.
- Turnbull, W. (1944). "Pitch discrimination as a function of tonal duration," *J. Exp. Psychol.* **34**, 302–316.
- Wichmann, F. A., and Hill, N. J. (2001a). "The psychometric function I: Fitting, sampling and goodness-of-fit," *Percept. Psychophys.* **63**, 1293–1313.
- Wichmann, F. A., and Hill, N. J. (2001b). "The psychometric function II: Bootstrap based confidence intervals and sampling," *Percept. Psychophys.* **63**, 1314–1329.
- Witton, C., Green, G. G. R., Rees, A., and Henning, G. B. (2000). "Monaural and binaural detection of sinusoidal phase-modulation of a 500-Hz tone," *J. Acoust. Soc. Am.* **108**, 1826–1833.
- Zwicker, E. (1952). "Die Grenzen der Hörbarkeit der Amplitudenmodulation und der Frequenzmodulation eines Tones" ("The limits of just perceptible amplitude modulation and frequency modulation of a tone"), *Acustica* **2**, 125–133.
- Zwicker, E., and Henning, G. B. (1985). "The four factors leading to binaural masking level differences," *Hear. Res.* **19**, 29–47.

Analysis of the three-dimensional tongue shape using a three-index factor analysis model

Yanli Zheng and Mark Hasegawa-Johnson

Department of Electrical and Computer Engineering, University of Illinois at Urbana-Champaign, Urbana, Illinois 61801

Shamala Pizze

University of California at Los Angeles, Los Angeles, California 90095

(Received 11 June 2001; revised 19 August 2002; accepted 17 September 2002)

Three-dimensional tongue shape during vowel production is analyzed using the three-mode PARAFAC (parallel factors) model. Three-dimensional MRI images of five speakers (9 vowels) are analyzed. Sixty-five virtual fleshpoints (13 segments along the rostral–caudal dimension and 5 segments along the right–left direction) are chosen based on the interpolated tongue shape images. Methods used to adjust the alignment of MRI images, to set up the fleshpoints, and to measure the position of the fleshpoints are presented. PARAFAC analysis of this 3D coordinate data results in a stable two-factor solution that explains about 70% of the variance. © 2003 Acoustical Society of America. [DOI: 10.1121/1.1520538]

PACS numbers: 43.70.Aj, 43.70.Bk [AL]

I. INTRODUCTION

Harshman *et al.* (1977) demonstrated that a vector of midline-orthogonal vocal-tract widths, measured from lateral x-ray cineradiograph tracings, can be represented using a specific three-index factor analysis model called PARAFAC (parallel factors). In their analysis, every tongue shape was represented as a 13-dimensional vector of vocal-tract width measurements, arranged in order from the region of the epiglottis to the region of the tongue tip. PARAFAC is similar to standard two-index factor analysis in that it models every vocal-tract width measurement as the product of two independent terms: a term that depends on the vocal-tract position (commonly called the “factor shape”), and a term that depends only on the vowel identity and speaker identity (commonly called the “factor weight”). PARAFAC differs from standard two-index factor analysis in that the factor weight, in turn, is represented as the product of a vowel-independent speaker weight and a speaker-independent vowel weight. The highly constrained form of the PARAFAC model is both the reason that it is useful, and the reason that it is rarely used in practice. In practice, PARAFAC is rarely used because there are few datasets in nature that satisfy the PARAFAC constraints. When the PARAFAC constraints are satisfied, however, the constrained form of the analysis results in an intuitively appealing simplification of the data. In particular, the vowel weights define a phonemic vowel space that is speaker independent in the strong sense of that word: if the weights on a particular factor of the vowels /i/ and /u/ are related by a ratio of 2:1 for one speaker, then they are related by a ratio of 2:1 for every speaker.

In practice, PARAFAC has been found to apply to very few types of natural data. Specifically, the literature indicates that the success of PARAFAC analysis depends strongly on the methods used to acquire data, the choice of index variables, and the methods used for statistical preprocessing. Among the many possible measurements of speech articulation, successful PARAFAC analysis has only been reported

for radial tongue heights from lateral cineradiograph tracings (Harshman *et al.*, 1977), pseudo-fleshpoint coordinates extracted from lateral cineradiography tracings (Nix *et al.*, 1996), and electromagnetic midsagittal articulometry (EMA; Hoole, 1999). Among the many possible index variables of interest in speech production, PARAFAC has only been reported to explain the interaction among rostral–caudal vocal-tract position, speaker identity, and the phonological features of tongue height and tongue fronting. Hoole (1999) found that PARAFAC was unable to model consonant context, and Geng and Mooshammer (2000) found that PARAFAC was unable to model lexical stress. Finally, Harshman and Lundy (1984) report that the success of a PARAFAC analysis depends on the use of adequate statistical preprocessing. The preprocessing methods of Harshman *et al.* (1977) include implicit vocal-tract length normalization, and explicit subtraction of each speaker’s mean tongue shape. Hoole (1999), Nix *et al.* (1996), and Geng and Mooshammer (2000) also report subtracting each speaker’s mean tongue shape, but apparently none of these studies found it necessary to perform any type of vocal-tract length normalization.

The purpose of this paper is to demonstrate that PARAFAC successfully represents the three-dimensional shape of the tongue surface extracted from coronal magnetic resonance (MR) image stacks. Two types of measurement vectors are analyzed: a vector of 3D pseudo-fleshpoint coordinates extracted uniformly from the length and width of the tongue surface, and a vector of 2D pseudo-fleshpoint coordinates extracted from a curve along the tongue surface close to the midsagittal plane. The 2D pseudo-fleshpoint coordinates are structurally similar to the type of data analyzed by Nix *et al.* (1996). Measurement data are indexed by speaker identity, phonemic vowel identity, and two-dimensional measurement position. A variety of data preprocessing strategies were attempted; the method that yields the best results is similar but not identical to the preprocessing methods of Nix *et al.* (1996).

II. BACKGROUND: THREE-WAY FACTOR ANALYSIS MODELS

The model used in three-way factor analysis (PARAFAC; Harshman *et al.*, 1977) is represented as follows:

$$d_{ijk} = \sum_{w=1}^F c_{iw} \nu_{jw} s_{kw} + e_{ijk}, \quad (1)$$

$$i = 1, 2, \dots, n_c, \quad j = 1, 2, \dots, n_v, \quad k = 1, 2, \dots, n_s, \quad (2)$$

where d_{ijk} is the displacement of the i th measurement during utterance of the j th vowel by the k th speaker, c_{iw} is the relative effect of factor w on the displacement of the i th measurement, ν_{jw} is the relative contribution of factor w on the j th vowel, s_{kw} is the relative contribution of factor w on the k th speaker, F is the number of factors, n_c is product of the number of fleshpoints (throughout this paper, $n_{fp} = 13$ for midsagittal analysis, and $n_{fp} = 65$ for three-dimension analysis) times the number of dimensions of the analyzed images, e.g., for midsagittal images, $n_c = n_{fp} \times 2 = 26$; and for 3D images, $n_c = n_{fp} \times 3 = 195$, n_v is the number of vowels, and n_s is the number of speakers.

PARAFAC analysis is capable of finding only those factors that are used in the same way by all speakers. The PARAFAC model assumes that, for example, if a speaker uses 20% more than the average amount of factor 1 in production of /a/, then he must also use 20% more than the average amount of factor 1 in production of all vowels. The PARAFAC model is too restrictive to accurately represent stress distinctions (Geng and Mooshammer, 2000) or consonant context (Hoole, 1999), but the results of Harshman *et al.* (1977) indicate that vowel height and fronting may be modeled using PARAFAC.

A more flexible alternative to PARAFAC analysis is provided by the Tucker3 model, represented as follows: (Bro, 1998)

$$d_{ijk} = \sum_{w_1=1}^{F_1} \sum_{w_2=1}^{F_2} \sum_{w_3=1}^{F_3} c_{iw_1} \nu_{jw_2} s_{kw_3} g_{w_1 w_2 w_3} + e_{ijk} \quad (3)$$

$$i = 1, 2, \dots, n_c, \quad j = 1, 2, \dots, n_v, \quad k = 1, 2, \dots, n_s. \quad (4)$$

The definitions of d_{ijk} , c_{iw_1} , ν_{jw_2} , s_{kw_3} , n_c , n_v , n_s are the same as those in the PARAFAC model, except that a core matrix $G (F_1 \times F_2 \times F_3)$ is introduced, where $g_{w_1 w_2 w_3}$ is the element of G . The flexibility of the Tucker3 model allows it to represent regularities that cannot be represented using PARAFAC, but because of this flexibility, it can be difficult to determine when the correct number of factors has been chosen.

Kiers (1991) shows that PARAFAC can be considered a constrained version of the Tucker3 model. Although Tucker3 will always fit better than PARAFAC, Tucker3 tends to use excess parameters when the PARAFAC model is adequate (which is easy to observe from the mathematical model of PARAFAC and Tucker3). Another obvious merit of PARAFAC is its structural uniqueness, whereas the Tucker3 model has rotational freedom and thus gives an ambiguous result.

Based on the considerations above, and based on the result of Harshman *et al.* (1977), the PARAFAC model was chosen for the analyses reported in this article. Comparison between PARAFAC and Tucker3 analysis results will provide a method for verifying the statistical significance of any given PARAFAC analysis order.

III. METHODS

In this study, magnetic resonance images of five speakers of American English were collected during production of nine English vowels (/a, æ, ε, o, e, u, i, ɪ, ɪ/). The shape of the tongue was manually transcribed on all coronal images. Reconstructed tongue shapes were analyzed using the PARAFAC three-way factor analysis algorithm.

A. Data acquisition

The vowel tongue shapes of five speakers (three male: m1, m2 and m3, two female: f1 and f2) were imaged using a fast gradient echo magnetic resonance imaging protocol (GE 1.5T SIGNA scanner, $T_e = 1.9$ ms, $T_r = 150$ – 300 ms, depending on subject). Four speakers were natives of Southern California, while one speaker (m2) was a native of northern New York State.

Subjects produced the English vowels /a, æ, ε, o, e, u, i, ɪ, ɪ/. Subjects were told to imagine the words “father, bat, bet, boat, bait, put, boot, bit, beat,” respectively, as a guide to pronunciation. Subject training was conducted prior to imaging. During training, subjects lay on a couch in a sound-treated recording room, in a supine position similar to subject position in the MRI scanner. Subjects were then asked to sustain for 12–15 seconds. Pronunciation errors were corrected by the experimenter. When subjects were comfortable with the vowel list, each subject recorded each vowel three times, again sustaining each vowel for 12–15 s per repetition (speaker m1 recorded only one sustained example of each vowel). Acoustic recordings were analyzed using the Entropic formant tracker (Talkin, 1987). Vowels produced by subject m3 were too breathy for accurate format frequency analysis, but were judged to be perceptually valid exemplars of the desired vowels. Formant frequency trajectories of the vowels of every other speaker were measured approximately 1/3, 1/2, and 2/3 of the way through the vowel. All format frequency measurements were compared to the values reported in (Peterson and Barney 1952), and were found to be within the range of variation predicted by that paper.

Coronal and axial image stacks were collected for each vowel, but only coronal images are analyzed in this article. Images are 256×256 pixels, covering a 24-cm field of view, with a 3-mm interslice interval. Each image stack was collected in two breath holds of 15–20 s in duration: odd-numbered images were collected in the first breath hold, and even-numbered images were collected in the second breath hold. Subjects m1 and f1 were instructed to phonate during imaging, but the resulting images suffer from substantial vibration artifact, especially in the region of the vocal folds, ventricular folds, and aryepiglottic ligament. Subjects m2, f2, and m3 were instructed to hold their breath during imaging while maintaining a posture appropriate to the requested vowel.

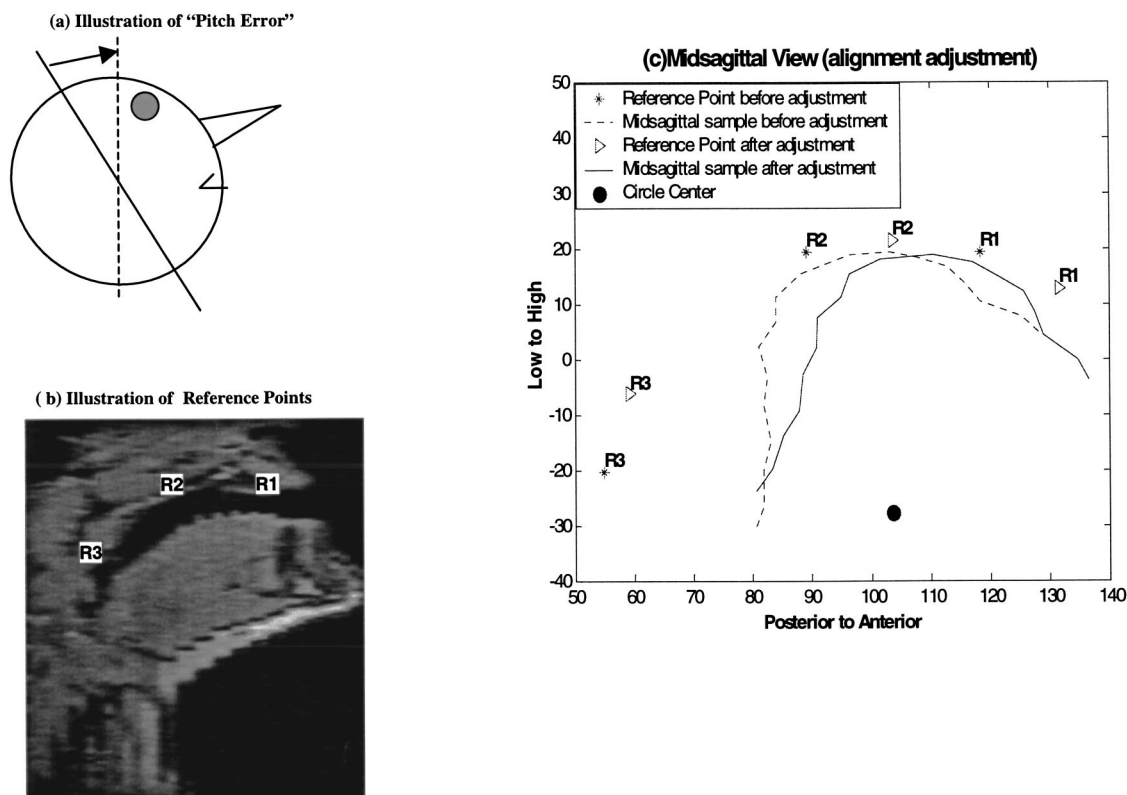


FIG. 1. Image alignment methods. (a) Illustration of the “pitch error.” (b) Illustration of the positions of reference points R1, R2, and R3. (c) Midsagittal view of tongue surface before and after alignment adjustment. Dotted line represents the tongue surface before the rotation adjustment, solid line represents the tongue surface after the rotation adjustment, star points represent the reference landmarks before the adjustment, left triangles represent the reference landmarks after the adjustment, and solid circle represents the center of the reference circle.

Images were segmented by hand using custom MRI display and segmentation software (Hasegawa-Johnson *et al.*, 1999a, 1999b). On each coronal image, the location of the entire tongue was outlined, including the dorsal surface of the tongue and all lateral surfaces in contact with the cheek or interdental airway. The remainder of the vocal tract (borders of the palate, teeth, cheek, lips, and pharynx) was outlined in a different color, and the positions of the peak of the palatal dome and of the four gingival margins were marked.

All images and segmentation files are available from the second author, or over the Internet at <http://www.ifp.uiuc.edu/speech/mri>

B. Image alignment

Preliminary analysis of our data revealed that different subjects were positioned at different angles within the scanner, and that despite the head restraint, some subjects changed position between one vowel and the next. Before the statistical analysis, it is necessary to correct the misalignment error across the collected data and to measure the 3D shape in a systematic way. The subject head front/back declination [pitch; shown schematically in Fig. 1(a)] was quite obvious in our dataset. Image alignment is very important before the fleshpoints measurements. Tiede (2000) pointed out that measurements according to the tract midline [i.e., the method used by Harshman *et al.* (1977)] are difficult to begin with and sensitive to asymmetrical articulation. In his report, a modified “shape-based” semipolar method was

used, which takes into consideration the shape of the hard palate. In our study, we adopted the idea in Tiede’s report for our image alignment.

The steps that were taken to align tongue shape data are as follows.

- (1) Generating pseudosagittal images. Since only coronal images were used in our analysis, pseudosagittal images were constructed only for the purpose of placing reference points. Pseudosagittal images were generated by resampling a sagittal slice through the coronal image stack. Figure 1(b) shows a pseudosagittal image with reference points marked.
- (2) Marking reference points in the midsagittal plane. As illustrated in Fig. 1(b), three reference points (R1, R2, and R3) were used, where R1 is the maxillary incisor, R2 is the highest visible point of the palatal vault, and R3 is the point on the rear pharyngeal wall adjoining the anterior apex of the second cervical vertebra.
- (3) Adjusting the pitch error. R1, R2, and R3 determine a circle, and C is the center of the circle. The sagittal images were rotated by an angle θ , where θ is the angle between the vertical axis and the C–R2 line segment. Figure 1(c) shows the midsagittal view before and after the rotation, respectively.

C. Measurement vector composition

Harshman *et al.* (1977) measured the vocal-tract width along dorsoventral gridlines. Nix *et al.* (1996) point out that

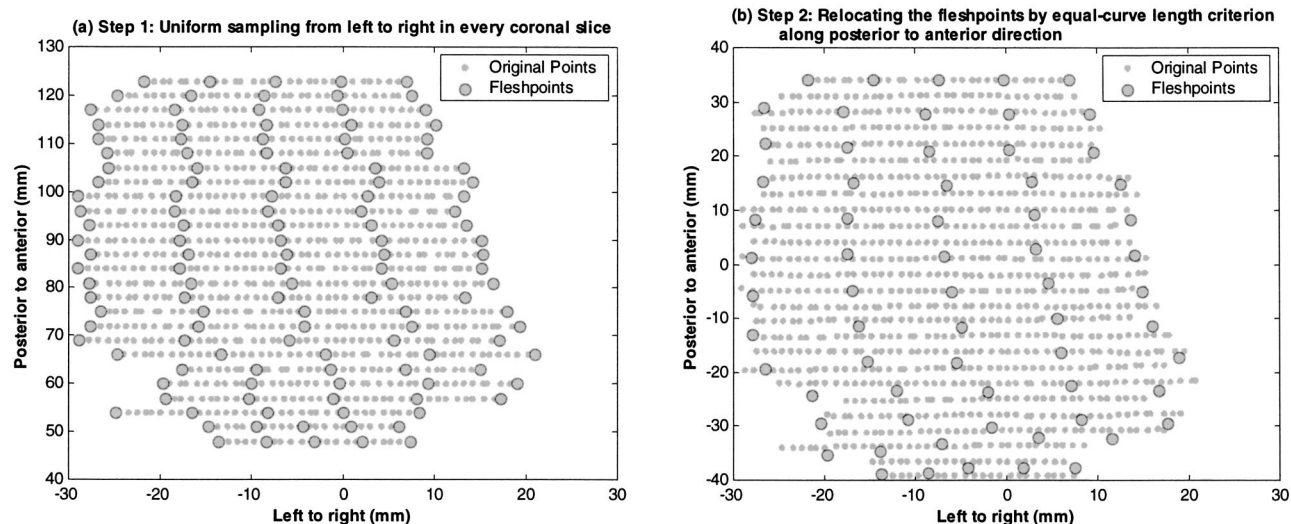


FIG. 2. Two steps for placing the fleshpoints in the X - Y plane. (a) Step 1, the fleshpoints are uniformly spaced from left to right in every coronal slice. (b) Step 2, the fleshpoints are repositioned according to an “equal-curve length” criterion along each of the five rostral-caudal tongue surface curves.

this method reduces the ability of the model to represent important interdimensional correlations; instead, they propose the analysis of “virtual fleshpoints” located by segmenting the arc length of the tongue. In our study, spatially unconstrained factors were analyzed with PARAFAC using the (X, Y, Z) coordinates of 65 fleshpoints, with 13 points in the posterior–anterior direction, i.e., Y direction, and 5 points in the left–right direction i.e., X direction.

From the coronal tongue outlines, the 3D tongue shape was reconstructed using piecewise-linear interpolation. In order to determine the location of virtual fleshpoints, the raw data was projected onto the X - Y plane. Projection into the X - Y plane results in many-to-one projection near the lateral margins, where the tongue bulges into the interdental airway. In order to simplify analysis, first, all points inferior to the bulge were discarded, so that tongue height is a single-valued function of X and Y ; second, because of the noise at the edge of the X direction in the extracted tongue surface, one-twelfth is cut from both edges in the X direction. Then, the fleshpoints are placed based on the extracted tongue surface, using the following procedure. First, uniform sampling along the X direction in every coronal slice generates five fleshpoints in each coronal plane. Second, points are connected to form five rostral-caudal piecewise linear “curves” along the tongue surface. Thirteen fleshpoints are placed on each curve using an equal curve length criterion. Figure 2 shows the two steps for placing the fleshpoints in the X - Y plane. The Z values (i.e., low/high positions) of the fleshpoints are obtained by piecewise linear interpolation between coronal planes. “Equal-curve length” is defined as equal length along each of the five rostral-caudal curves. The main purpose of this step is to distribute the fleshpoints as uniformly as possible over the surface of interest.

Two types of measurement vectors were constructed for subsequent preprocessing and PARAFAC analysis. One of the measurement vectors contained 3D coordinate data from the 65 reconstructed fleshpoints described above. The 3D measurement vectors contained the Cartesian (X, Y, Z) coordinates of each fleshpoint, as previously defined. Each 3D

measurement vector contained a total of $65 \times 3 = 195$ measurements. In addition to the 3D measurement vectors, 2D measurement vectors were also constructed. Each 2D measurement vector contained a 2D representation of every fleshpoint on the median curve in Fig. 2(b). The 2D Cartesian-coordinate vector contained (Y, Z) measurements of each of these points. Each 2D measurement vector contained a total of $13 \times 2 = 26$ measurements.

The 2D measurement vectors are of interest for two reasons. First, the 2D measurement vectors are similar to the measurement vectors used by Nix *et al.* (1996). By comparing the 2D measurement results in this paper to the results of Nix *et al.*, it is possible to qualitatively evaluate some of the structural measurement differences that result from the differences in our measurement methodologies (the comparison is not perfect, because of differences in the subject pool; see the Discussion section). Second, the 2D measurement vectors are interesting because each 2D measurement dataset is a strict subset of one of the 3D datasets: the data in the 2D Cartesian coordinate vector are a strict subset of the data in the 3D Cartesian coordinate vector. Harshman and Lundy (1984) proposed the use of split-half analysis in order to determine the validity of a PARAFAC solution. In split-half analysis, the dataset is split into two or more subsets along one of the index variables; if factor weights along the two nonsplit index variables are unaffected by the split, Harshman and Lundy argue that the PARAFAC analysis should be considered valid. In our case, similarity between the vowel weights and talker weights of 2D and 3D analysis may be considered evidence that the PARAFAC model of the 3D dataset is valid.

D. Data preprocessing

To make the data compatible with the PARAFAC model, preprocessing is required. In this research, two preprocessing equations were used in order to improve the effectiveness of PARAFAC analysis: removing the mean across the vowels in some dimensions as defined in Eq. (5), and scaling the inter-

speaker variation in some dimensions as defined in Eq. (6). In these equations $n=1,2,3$, is the index of the coordinates (e.g., 1 is the X, 2 is the Y, and 3 is the Z coordinate), and n_s , n_{fp} , n_v are defined as in Eq. (1). The matrix for PARAFAC analysis, d_{ijk} in Eq. (1), is defined by putting $d_{ijk}^{(1)}$, $d_{ijk}^{(2)}$, and $d_{ijk}^{(3)}$ in the same matrix sequentially along the dimension i

$$d_{ijk}^{(n)} = d_{ijk}^{(n)} - \mu_{ik}^{(n)}, \quad \mu_{ik}^{(n)} = \frac{\sum_{j=1}^{n_v} d_{ijk}^{(n)}}{n_v}, \quad (5)$$

$$d_{ijk}^{(n)} = \frac{d_{ijk}^{(n)}}{s_k^{(n)}}, \quad s_k^{(n)} = \sqrt{\sum_{i=1}^{n_{fp}} \sum_{j=1}^{n_v} (d_{ijk}^{(n)})^2}. \quad (6)$$

Bro (1998) specifies two criteria for the selection of PARAFAC preprocessing algorithms. He demonstrates, both theoretically and empirically, that violation of either criterion may change the statistical structure of the data. For example, data that are properly explained by a two-factor PARAFAC solution may seem to support a three-factor solution if the data are improperly preprocessed. The two criteria are, first, that mean subtraction must be within a single mode of the data matrix, and second, that all scaling operations must follow any mean subtraction operations.

The single-mode mean subtraction rule means that the sum in Eq. (5) must be a sum over only one index variable. The subtraction before scaling rule means that equations like Eq. (6) must follow equations like Eq. (5). In Eq. (5), the mode variable is j , the vowel mode. Equation (5) is thus identical to the statistical preprocessing applied by Harshman *et al.* (1977) and Nix *et al.* (1996).

In addition to these two essential criteria, Bro (1998) suggests two additional criteria without proving their effect on the statistical results. First, he suggests that scaling should be done “within” a mode, i.e., the sum in an equation like Eq. (6) should be a sum over two of the mode variables [in Eq. (6), the sum is over mode variables i and j , the fleshpoint and vowel modes]. Second, he suggests that one of the modes in the summation in Eq. (6) should always be the mode that was subjected to mean subtraction in Eq. (5).

Provided that all four criteria are satisfied, Bro (1998) demonstrates that scaling does not change the number of factors in the PARAFAC solution. Instead, scaling as in Eq. (6) is equivalent to the use of a weighted least-squared-error metric in the PARAFAC model fitting process. The effect of Eq. (6), in particular, is to normalize each talker’s data to unit sum-squared variation, so that talkers with greater variability and/or larger vocal tracts do not dominate the PARAFAC fitting process.

Subject to Bro’s ordering constraints, experiments were performed to determine the combination of mean subtraction and scaling operations with the highest percentage of variance explained by both 2D and 3D PARAFAC models. Operations similar to Eq. (5) were applied to the intertalker mean, the intervowel mean, or the interfleshpoint mean (three possibilities). The resulting data were either scaled or not scaled; if scaled, all possible combinations of index variables were considered. Similar operations were repeated for all possible combinations of X, Y, and Z coordinate data, and the resulting processed data were in each case fitted using a

PARAFAC model. The highest percentage of variance explained by PARAFAC modeling of any candidate dataset was 70.6% for 3D analysis, 76.2% for 2D analysis. The optimum preprocessing strategy was not unique: more than a dozen different candidate preprocessing strategies resulted in the same percentage of variance explained. Among the set of optimum preprocessing strategies, the strategy with the simplest algorithm is as follows.

- (1) Remove the mean across the vowels using Eq. (5) in all the three coordinates that are used in the analysis; and
- (2) Correct for interspeaker scale differences in the low-high and left-right coordinates (X and Z coordinates) using Eq. (6).

E. Choosing the number of factors

The core consistency diagnostic (Bro, 1998) is a new approach for determining the appropriate number of components for a PARAFAC model. By observing the mathematical models of PARAFAC and Tucker3, one discovers that PARAFAC is a restricted Tucker3 model in which the core matrix G is defined to equal the superdiagonal matrix I . The definition of a super-diagonal matrix I is as follows:

$$i_{w_1, w_2, w_3} = \begin{cases} 1, & \text{where } w_1 = w_2 = w_3 \\ 0, & \text{otherwise} \end{cases}. \quad (7)$$

The “goodness of fit” of a PARAFAC model can be verified by first computing t_{iw} , v_{jw} , and s_{kw} using PARAFAC, and then calculating the least-squares Tucker3 core G given t_{iw} , v_{jw} , and s_{kw} . If the PARAFAC model is valid, the core matrix G should be superdiagonal. By simply monitoring the distribution of superdiagonal and off-superdiagonal elements, one can assess whether the model structure is reasonable or not. There are two simple criteria: (1) the superdiagonal elements should be all close to 1, and (2) off-superdiagonal elements should be close to zero. If these criteria are met, the model is not over fitting. If these criteria are not met, then either too many components have been extracted, the model is mis-specified, or gross outliers disturb the model. It is possible to calculate the superidentity of G to obtain a single parameter for the model quality. The superidentity or core consistency is defined here as

Core consistency

$$= 100 \times \left(\frac{1 - \sum_{w_1=1}^F \sum_{w_2=1}^F \sum_{w_3=1}^F (g_{w_1 w_2 w_3} - i_{w_1 w_2 w_3})^2}{\sum_{w_1=1}^F \sum_{w_2=1}^F \sum_{w_3=1}^F (i_{w_1 w_2 w_3})^2} \right), \quad (8)$$

where $g_{w_1 w_2 w_3}$ are elements of the core matrix G . The probability distribution of core consistency has not been analyzed, but Bro and Kiers (2002) suggest that a core consistency of at least 90% is a good indicator of a valid model.

F. Checking the reliability of the solutions

Generally there are two steps to check the reliability of the solutions (Bro, 1998). First, one should check for the convergence of the solution, i.e., the algorithm should reach

TABLE I. Variance explained and congruence coefficients by two-factor PARAFAC models.

Variance explained			Congruence coefficients
Our analysis	2D	76.2%	0.08
	3D	70.7%	0.06
Harshman <i>et al.</i> (1977)		92%	0.07
Nix <i>et al.</i> (1996)		88%	N/A

the same solution when initiated from several different random start points. Second, one should check for the signs of a degenerate solution. A typical sign of degeneracy is that two of the components become almost identical, but with opposite contributions to the model.

In the PARAFAC model, each rank-one component Z_w can be expressed as the vectorized rank-one array obtained as follows, where \otimes denotes the Kronecker tensor:

$$Z_w = C_w \otimes V_w \otimes S_w, \quad w = 1, 2, \dots, F, \quad (9)$$

$$C_w = [c_{1w}, c_{2w}, \dots, c_{n_c w}]', \quad (10)$$

$$V_w = [v_{1w}, v_{2w}, \dots, v_{n_v w}]', \quad S_w = [s_{1w}, s_{2w}, \dots, s_{n_s w}]'.$$

For the degenerate model, the loading vectors in component f and component g will be almost equal in shape, but negatively correlated. The similarity between component f and component g can be measured using the congruence coefficient $\cos(Z_f, Z_g)$ (Tucker, 1951), defined as

$$\cos(Z_f, Z_g) = \cos(C_f, C_g) \cos(V_f, V_g) \cos(S_f, S_g). \quad (11)$$

Bro (1998) suggests that a degenerate model is indicated whenever the congruence coefficient between any components f and g is less than or equal to -0.85 .

IV. RESULTS

The percentage of variance explained for 2D midsagittal analysis and 3D analysis is shown in Table I. For purposes of

comparison, Table I also shows the results reported by Harshman *et al.* (1977) and Nix *et al.* (1996). Section IV A describes the results of core consistency tests and congruence coefficient tests conducted in order to verify that a two-factor PARAFAC analysis is appropriate for these data. Factor shapes, vowel loadings, and speaker loadings of PARAFAC analysis from both 2D and 3D analysis are described in Secs. IV B and C.

A. Core consistency diagnostic and congruence coefficients

As mentioned in the last section, the *core consistency diagnostic* is used to decide how many factors underlie variations in the data. Figure 3 shows core consistency results for one, two, three, and four-factor PARAFAC models. The tests of both 2D and 3D Cartesian models are shown in Fig. 3. The two-factor PARAFAC model has a core consistency of nearly 100%. The three-factor model has a core consistency of about 65% (2D) to 82% (3D). Core consistency measurements in this range are described as “problematic” by Bro and Kiers (2002); they report on some valid solutions with core consistency measurements in this range, but they do not claim that core consistency measurements in this range always indicate a valid model. In order to ensure that the results are meaningful, the rest of this paper will assume a two-factor PARAFAC model.

Congruence coefficients for two-factor PARAFAC models are listed in Table I. Table I, supporting the conclusions of Fig. 3, shows that two-factor PARAFAC is appropriate for these data.

B. Analysis of semi-midsagittal data

Results of the PARAFAC analyses of the semi-midsagittal data using Cartesian coordinates are shown in Fig. 4. The semi-midsagittal data consist of the (Y, Z) coordinates of the 13 fleshpoints located on the middle “curve” in Fig. 2(b).

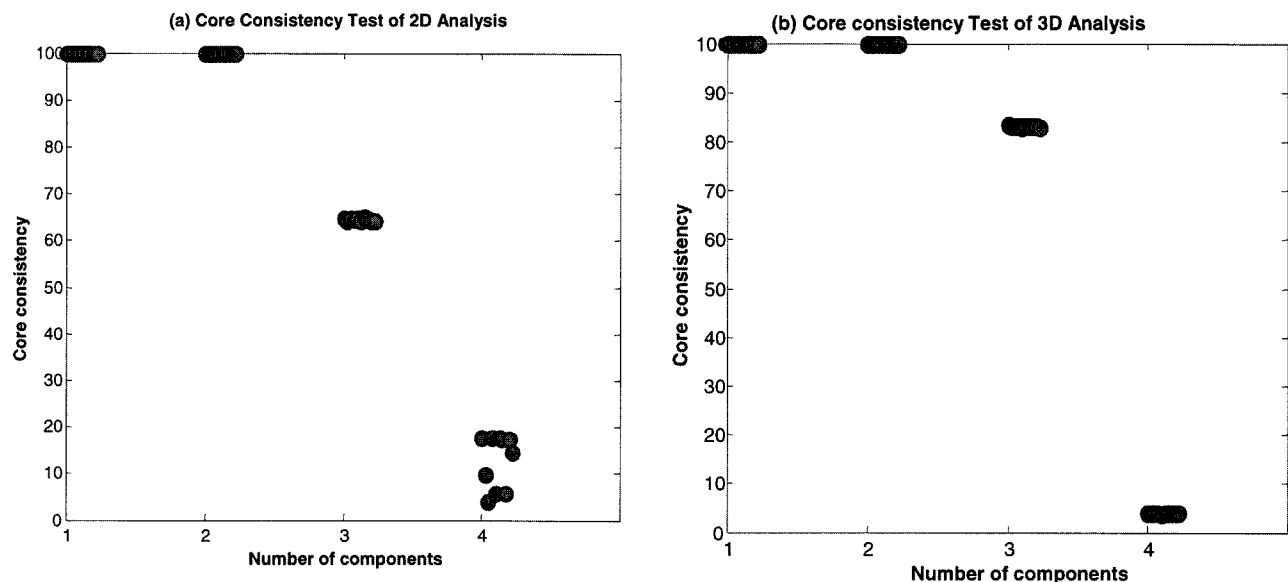


FIG. 3. Core consistency diagnostic. (a) Test results of 2D analysis. (b) Test results of 3D analysis. (Different circles represent the results of PARAFAC analysis beginning with different start points.)

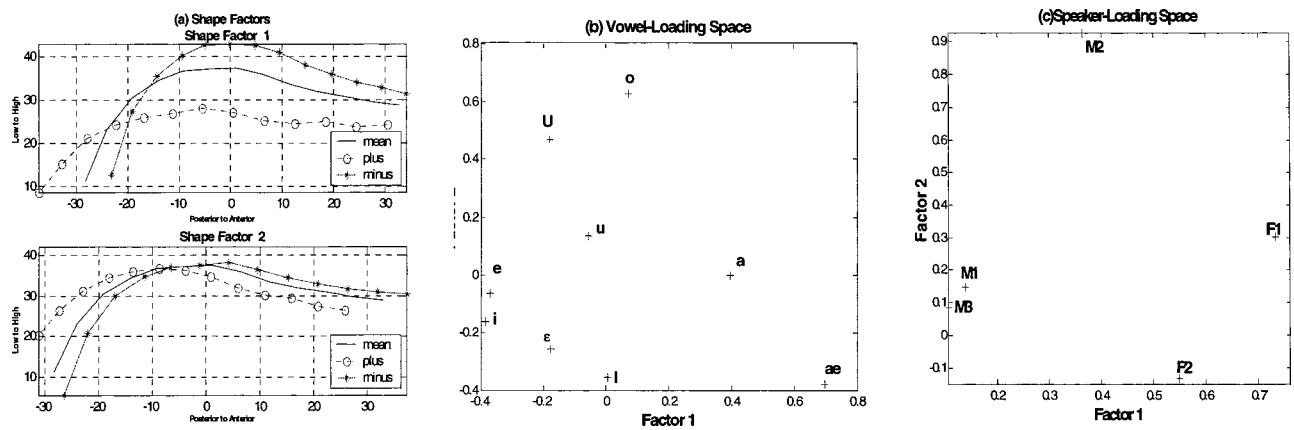


FIG. 4. Factors of 2D Analysis. (a) Shape factors. (b) Vowel loading space. (c) Speaker loading space.

Figure 4 shows the shape factors, vowel weights, and speaker weights resulting from the results of analyzing Cartesian coordinate data. In these figures, the “mean shape” c_{i0} is defined as the average shape across all the speakers and all the vowels, c_{iw}^* is the c_{iw} after the scaling adjustment (meaning that the factors corresponding to the X coordinates in the c_{iw} are back-scaled using $s^{(1)}$, and the factors corresponding to the Z coordinates in the c_{iw} are back-scaled using $s^{(3)}$), while the “plus shape” c_{iw+} , “minus shape” c_{iw-} , and $s(n)$ are defined as

$$c_{iw+} = c_{i0} + c_{iw}^* \times \max_j(\nu_{jw}) \times \text{mean}_k(s_{kw}), \quad (12)$$

$$c_{iw-} = c_{i0} + c_{iw}^* \times \min_j(\nu_{jw}) \times \text{mean}_k(s_{kw}), \quad (13)$$

$$s^{(n)} = \frac{1}{n_s} \sum_{k=1}^{n_s} s_k^{(n)}. \quad (14)$$

In the figure, shape factor 1 [upper plot in Fig. 4(a)] appears to represent raising or lowering of the entire tongue. The raised tongue has a peak about 2/5 of the way from the back, while the lowered tongue is flat over the anterior 2/3. Shape factor 2 [lower plot in Fig. 4(a)] appears to represent anterior–posterior movement of the entire tongue.

Vowel weights are shown in Fig. 4(b). In the analysis by Harshman *et al.* (1977), the vowel space formed a rough quadrilateral, with vowels arranged around the quadrilateral in the order /i, e, ɪ, ε, æ, α, o, u, u/. The arrangement of vowels in Fig. 4(b) is similar, except that /o/ has a higher factor 2 weighting than /u, ʊ/.

In the results of Harshman *et al.* (1977), the vowel quadrilateral was tilted approximately 30 deg relative to the factor axes; Harshman *et al.* described their factors as a “front raising” factor and a “back raising factor.” Factor 2 seems to represent the distinction between back and front vowels. Factor 1 could be said to represent the distinction between high and low vowels. The vowels /ε, e, i, ʊ, u/ are produced with negative factor 1 weights, apparently indicating raising of the whole tongue. The vowels /α, æ/ have positive factor 1 weights, apparently indicating lowering of the whole tongue. The vowels /ʊ, o, u/ are produced with positive factor 2 weights, apparently indicating posterior tongue raising. The

vowels /ε, e, i, ʊ, æ/ have negative factor 2 weights, apparently indicating lowering of the posterior tongue.

Speaker loadings are shown in Fig. 4(c). Speaker f2 and f1 weights factor 1 most heavily, and speaker m3 weights factor 1 least heavily. Factor 2 is most heavily utilized by speaker m2. Speaker f2 has a negative factor 2 weight, meaning that the tongue shape measurements acquired from MRI of this subject may be troublesome.

C. Analysis of 3D data

Results of the PARAFAC analyses of 3D Cartesian coordinate data are shown in Fig. 5 and Fig. 6. The “plus,” “minus,” and “mean” shapes are defined same as in the analysis of semi-midsagittal data.

Midsagittal views of the shape factor are similar to the 2D case. The correlation coefficient between the 2D factors and the corresponding 26 dimensions of the 3D factor is 0.99. And vowel and speaker loadings are almost the same as the 2D case with correlation coefficients 0.98 and 0.99, respectively. This is an interesting result because the results of the 2D analysis is exactly split half analysis [Harshman *et al.* (1984)] of the 3D analysis. The result also confirms that two-factor PARAFAC is suitable for our data.

V. DISCUSSION AND CONCLUSION

The two-factor PARAFAC model is capable of extracting linguistically meaningful and statistically valid 2D and 3D factors from our MRI-derived tongue data. The 2D analysis works as the split-half analysis of the 3D analysis. Splitting the measurement vector into a pseudo-midsagittal part and a non-midsagittal part does not change analysis results in the nonsplit modes (i.e., vowel and speaker modes).

The 2D MRI measurement vector analyzed in this paper is similar in form to the x-ray measurement vector analyzed by Nix *et al.* (1996), but the results of PARAFAC analysis are not identical. The percentage of variance explained using MRI data is lower than the percentage of variance explained using x-ray data (Table I), and the vowel space is somewhat distorted. In order to better understand the difference in results between PARAFAC of x-ray and PARAFAC of MRI, it is worth considering the similarities and differences between our methodology and the methodology of Nix *et al.*

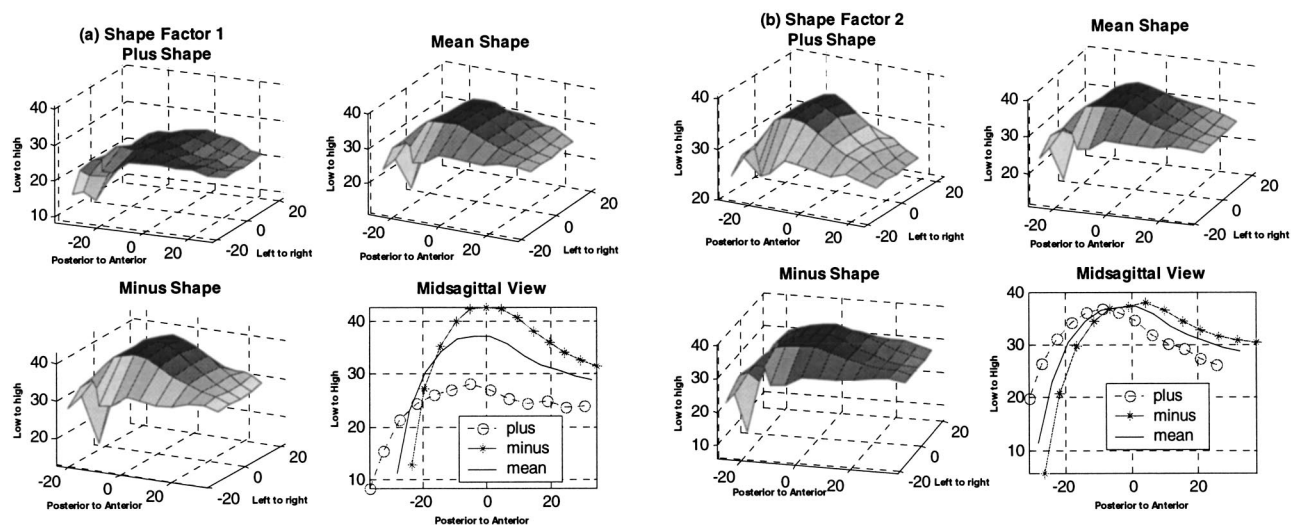


FIG. 5. Shape factors of 3D Analysis. (a) Shape factor 1. (b) Shape factor 2.

First, like the x-ray measurement vector of Nix *et al.*, the 2D MRI measurement vector consists of the Y and Z coordinates of 13 fleshpoints uniformly distributed between the tongue tip and the base of the tongue. Nix *et al.* spaced their fleshpoints uniformly in a sagittal (Y - Z) projection, while ours were spaced uniformly in an axial (X - Y) projection; as a result, our data cover the dorsum of the tongue more densely and the tongue root less densely than the data of Nix *et al.* We have compared pseudosagittal and coronal segmentations of the same data, and the comparison indicates that coronal segmentation is an accurate representation of tongue position as far back as the tip of the epiglottis. Position of the tongue root between the tip of the epiglottis and the base of the epiglottis was part of Nix *et al.*'s measurement vector, but not ours, and this difference may explain some of the differences in the resulting vowel spaces.

Second, Nix *et al.* preprocessed their data by removing the intervowel average value of each measurement. Our preprocessing methods included the same intervowel mean subtraction, as well as intertalker scaling of the X and Z coordinates. Scaling after mean subtraction is guaranteed not to

change the statistical structure of the data (Bro, 1998), but will change the relative weight assigned by the PARAFAC algorithm to fitting errors incurred by different talkers. We found that scaling using Eq. (6) improved the percentage of variance explained by the model, but did not change the resulting vowel space. Other types of preprocessing sometimes changed the vowel space substantially, and are therefore not reported in this paper.

Third, the difference between tongue surface measurements acquired using MRI and those acquired using x ray may be substantial, for several reasons. In an x-ray projection, there is no way to tell whether the observed tongue surface is midsagittal, right of midsagittal, or left of midsagittal. MRI produces true 3D images, so there is no lateral-midsagittal ambiguity. X ray also has important advantages over MRI. First, bony anatomical landmarks such as the tip of the incisor and the second cervical vertebra are visible in x ray, but are invisible or ambiguous in MRI. Intertalker differences in head position can be easily corrected when bony fixed landmarks are visible. In MRI, intertalker differences in head position must be corrected using less precise

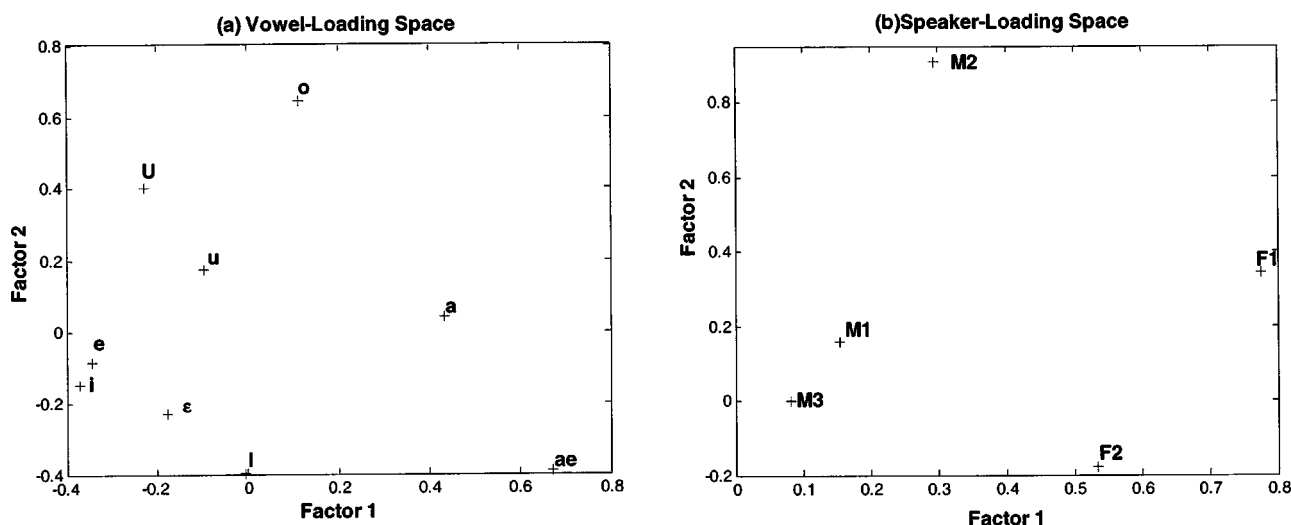


FIG. 6. Vowel and speaker loading spaces of 3D Analysis. (a) Vowel loading space. (b) Speaker loading space.

soft tissue landmarks, such as the pharynx wall and the peak of the palate. It is possible that ambiguity in the position of soft tissue landmarks may result in some imprecision in the measurement data analyzed using PARAFAC. The second important difference between x ray and MRI is in the type of speech being performed by subjects. The MRI data acquired in this paper were acquired during sustained production of the target vowels, while the x-ray data used by Nix *et al.* were frames selected from a cineradiograph of continuous fluent speech. Engwall (2000) compared the static vowel positions observed during MRI to the dynamic vowel extrema observed using electropalatography and electromagnetic articulometry. His data suggest that the vowels observed in MRI experiments are hyperarticulated, hypercanonical productions, related but not identical to the productions observed during fluent speech. Engwall's results suggest that the vowel space derived from an MRI study should be slightly more extreme than the vowel space derived from an x-ray study. It also seems reasonable to speculate that sustained phonation is more difficult for subjects than fluent articulation, and that the increased difficulty of the task may cause extra measurement variability that cannot be explained using a two-factor PARAFAC model.

Fourth, the five talkers analyzed by Nix *et al.* (1996) were imaged prior to 1977 (Harshman *et al.*, 1977). All five of the talkers that we imaged were born after 1977. It is possible that dialect changes since 1977 may have changed the tongue positions used to produce the vowels of English. All five talkers analyzed by Nix *et al.* (1996) were male; in our study, three talkers were male, and two were female. Male–female differences in vocal-tract size may have caused extra variability in our data that was not well explained using a two-factor PARAFAC model.

VI. CONCLUSION

In summary, the interaction between speaker identity and vowel identity in MRI-derived tongue surface shape measurements can be modeled using a two-factor PARAFAC statistical model. The two-factor model is statistically valid and the resulting vowel space represents most of the information in the traditional tongue height and tongue fronting relationships.

ACKNOWLEDGMENTS

The work reported in this paper was supported by NIH Fellowship F32 DC 00323-01, and by a grant from the University of Illinois Research Board.

- Bro, R. (1998). "Multi-way analysis in the Food Industry, Models, Algorithms, and Application," Ph.D. thesis, Royal Veterinary and Agriculture University, Denmark.
- Bro, R., and Kiers, H. (2002). "A new efficient methods for determining the number of components in PARAFAC models," J. Chemom. (in press).
- Engwall, O. (2000). "Are static MRI data representative of dynamic speech? Results from a comparative study using MRI, EPG and EMA," in Proceedings of ICSLP 2000, 1:17–20.
- Geng, C., and Mooshammer, C. (2000). "Modeling the German stress distinction," in Proceedings of the 5th Speech Production Seminar, Kloster Seon, Germany.
- Harshman, R., Ladefoged, P., and Goldstein, L. (1977). "Factor analysis of tongue shapes," J. Acoust. Soc. Am. **62**, 693–707.
- Harshman, R. A., and Lundy, M. E. (1984). "The PARAFAC model for three-way factor analysis and multidimensional scaling," in *Research Methods of Multimode Data Analysis*, edited by H. G. Law, C. W. Snyder, J. A. Hattie, and R. P. MacDonald (Praeger, New York), pp. 122–215.
- Hasegawa-Johnson, M. A., Cha, J. S., Pizza, S., and Haker, K. (1999a). "MRCAT: A Case Study in Human-Computer Interface Design," in Proceedings of the International Conference on Public Participation and Information Technology, Lisbon.
- Hasegawa-Johnson, M. A., Cha, J. S., and Haker, K. (1999b). "CTMRedit: A MATLAB-based Tool for Viewing, Editing, and 3D Reconstruction of MR and CT Images," in Proceedings of Meeting BMES/EMBS, Atlanta, p. 1170.
- Hoole, P. (1999). "On the lingual organization of the German vowel system," J. Acoust. Soc. Am. **106**, 1020–1032.
- Kiers, H. A. L. (1991). "An efficient algorithm for PARAFAC of three-way data with large numbers of observation units," Psychometrika **56**, 147.
- Nix, D. A., Papcun, G., Hogden, J., and Zlokarnik, I. (1996). "Two cross-linguistic factors underlying tongue shapes for vowels," J. Acoust. Soc. Am. **99**, 3707–3717.
- Peterson, G., and Barney, H. (1952). "Control methods used in a study of the vowels," J. Acoust. Soc. Am. **24**(2), 175–184.
- Talkin, D. (1987). "Speech formant trajectory estimation using dynamic programming with modulated transition costs," J. Acoust. Soc. Am. Suppl. **1** **82**, S55.
- Tiede, M. K. (2000). "An MRI-based morphological approach to vocal tract area function estimation," ATR Technical Report TR-H-XXX.
- Tucker, L. R. (1951). "A method for synthesis of factor analysis studies," Personal Research Section Report No. 984, Dept. of the Army, Washington, D.C.

Flow visualization and pressure distributions in a model of the glottis with a symmetric and oblique divergent angle of 10 degrees

Daoud Shinwari and Ronald C. Scherer^{a)}

Department of Communication Disorders, Bowling Green State University, 200 Health Center,
Bowling Green, Ohio 43402

Kenneth J. DeWitt

Department of Communication Disorders, Bowling Green State University, 200 Health Center,
Bowling Green, Ohio 43402 and Chemical Engineering, The University of Toledo, 3060 Nitschke Hall,
Toledo, Ohio 43606-3390

Abdollah A. Afjeh

Mechanical, Industrial and Manufacturing Engineering, The University of Toledo, 4006D Nitschke Hall,
Toledo, Ohio 43606-3390

(Received 28 May 2001; revised 20 September 2002; accepted 8 October 2002)

Modeling the human larynx can provide insights into the nature of the flow and pressures within the glottis. In this study, the intraglottal pressures and glottal jet flow were studied for a divergent glottis that was symmetric for one case and oblique for another. A Plexiglas model of the larynx (7.5 times life size) with interchangeable vocal folds was used. Each vocal fold had at least 11 pressure taps. The minimal glottal diameter was held constant at 0.04 cm. The glottis had an included divergent angle of 10 degrees. In one case the glottis was symmetric. In the other case, the glottis had an obliquity of 15 degrees. For each geometry, transglottal pressure drops of 3, 5, 10, and 15 cm H₂O were used. Pressure distribution results, suggesting significantly different cross-channel pressures at glottal entry for the oblique case, replicate the data in another study by Scherer *et al.* [J. Acoust. Soc. Am. **109**, 1616–1630 (2001b)]. Flow visualization using a LASER sheet and seeded airflow indicated separated flow inside the glottis. Separation points did not appear to change with flow for the symmetric glottis, but for the oblique glottis moved upstream on the divergent glottal wall as flow rate increased. The outgoing glottal jet was skewed off-axis for both the symmetric and oblique cases. The laser sheet showed asymmetric circulating regions in the downstream region. The length of the laminar core of the glottal jet was less than approximately 0.6 cm, and decreased in length as flow increased. The results suggest that the glottal obliquity studied here creates significantly different driving forces on the two sides of the glottis (especially at the entrance to the glottis), and that the skewed glottal jet characteristics need to be taken into consideration for modeling and aeroacoustic purposes. © 2003 Acoustical Society of America. [DOI: 10.1121/1.1526468]

PACS numbers: 43.70.Aj, 43.70.Bk [AL]

I. INTRODUCTION

During normal vocal fold vibration, the shape of the glottis typically changes from convergent during glottal opening to divergent during glottal closure (Hirano, 1981). Movement of the vocal fold surfaces depends on the tissue properties of the vocal folds and the intraglottal pressures (Ishizaka and Flanagan, 1972). The intraglottal pressures differ depending upon geometric and dynamic factors, including the transglottal pressure and glottal adduction (van den Berg *et al.*, 1957; Ishizaka and Matsudaira, 1972), the angle of the glottis (Gauffin *et al.*, 1983; Scherer and Titze, 1983), the radius of the glottal exit (Scherer *et al.*, 2001a), the slant (obliquity) of the glottis (Scherer *et al.*, 2001b; Hofmans, 1998), and the longitudinal location on the medial surfaces (Alipour and Scherer, 2000).

One purpose of this study was to measure wall pressures on both sides of the glottis for a symmetric and an oblique divergent glottis. The pressures may differ enough on either side to aid out-of-phase motion of the two vocal folds, a speculation needing study. The model chosen was a replication of the one used in Scherer *et al.* (2001b). A replication was important in order to (a) check those results, (b) test the methods of obtaining those pressures, and (c) test pushing versus pulling the airflow through such models. Another purpose of the study was to use flow visualization to determine flow separation locations and characteristics of the exit glottal jet. This information may add greater insight into the cause of the surface pressure distributions and the potential acoustic consequences of glottal jet flow.

For a symmetric diffuser with constant volume flow, the air (or fluid) may separate in the diffuser before arriving at the exit, and move closer to one of the two walls (Kline *et al.*, 1959; Reneau *et al.*, 1967). When flow separation occurs in a symmetric diffuser having straight walls, the pres-

^{a)} Author to whom correspondence should be addressed. Electronic mail: ronalds@bgnet.bgsu.edu

sures on the two walls may differ due to flow instability (Ashjaee and Johnston, 1980; Carlson *et al.*, 1967), resulting in a skewed flow in the duct. Also, flow from a centrally located slit into a larger rectangular duct is known to move toward one side of the downstream duct [Durst *et al.*, 1974; Cherdron *et al.*, 1978; Tsui and Wang, 1995; Yang and Hou, 1999; this phenomenon is also mentioned in Shadle *et al.* (1991) for an eccentric glottal orifice].

Alipour *et al.* (1996b) studied velocity distributions within three models of the human larynx: steady flow through a divergent glottis in both a rigid Plexiglas model and a computational model, and an excised canine larynx with vibrating vocal folds. Results from all three models indicated asymmetric velocity profiles downstream of the glottal constriction. The downstream velocity was observed to be less asymmetrical in studies of *in vivo* larynges (Berke *et al.*, 1989; Bielamowicz *et al.*, 1999). Alipour *et al.* (1996a) found flow more prominent on one side of the glottis using a numerical model with oscillating (forced) glottal walls and tracheal flow, results which also included the effects of the motion of the glottal walls.

Pelorsen *et al.* (1994) offered a description of the air-flow through the glottis in which the separation point was allowed to move. The results were studied using steady and unsteady flow measurements combined with flow visualization. The results suggested that their theoretical model was more accurate than earlier theoretical models. Pelorsen *et al.* (1995) and Hofmans (1998) emphasized that during accelerated flow through divergent glottis models, the flow is symmetric through the glottal duct, with the flow moving toward one dominant side (the Coanda effect) only when steady flow was attained.

Asymmetric ducts have asymmetric pressures on their side walls, with higher pressures on the outer wall and lower pressures on the inner wall (Ward Smith, 1971). This cross-channel difference was found in our earlier glottal obliquity study (Scherer *et al.*, 2001b).

This background suggests that the divergent glottis cases studied here with steady flow will exhibit (1) different pressures on one side of the glottis compared to the other side, (2) flow within and downstream of the glottis that tends to favor one side of the duct, and (3) complex asymmetric flow patterns in the duct downstream of the glottis.

II. METHODS

A. Model TM5

The model used in this experiment was larger than a human-sized male larynx. The enlargement provided greater accuracy in creation of the vocal folds and in placing relatively smaller pressure taps into the vocal fold surfaces than could be reasonably attained with a human-size model. This enlargement required scaling the flows and pressures actually obtained to those that would pertain in the human. The lengths and volume flows in the model were greater than human size by a factor of 7.5, and the pressures in the model were smaller than human size by a factor of $(7.5)^{-2}$. This scaling comes from a straightforward dimensional analysis (Munson *et al.*, 1998).

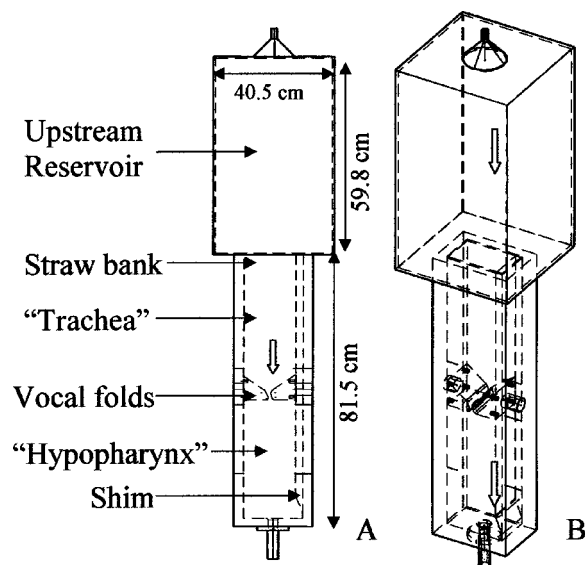


FIG. 1. Model TM5. (a) Top view. (b) Isometric view. The flow entered from the top into the stagnation tank (upstream reservoir), then into the test section that housed the two vocal folds. Distances are for the model, which are 7.5 times human size.

The model of the larynx was built with interchangeable vocal fold pieces. The vocal fold pieces were precisely manufactured using a digital milling machine at the mechanical engineering workshop at the University of Toledo. This laryngeal model is referred to as model TM5 (Fig. 1). The design of model TM5 was based on the previous model M5 (Scherer and Guo, 1990, 1991; Scherer *et al.*, 2001b). The vocal fold design equations and parameters were reported in Scherer *et al.* (2001b).

The test sections of both models M5 and TM5 consisted of a rectangular cross section with inside dimensions of 15.0 cm by 9.0 cm by 81.5 cm. The distance from the exit of the glottis to the end of the downstream "hypopharynx" was 36.5 cm. Model TM5 had a stagnation tank upstream of the test section with dimensions of 40.5 cm by 40.5 cm by 59.8 cm (Fig. 1). The purpose of this tank was to ensure that the incoming air had dissipated most of its kinetic energy and swirl before entering the test section, preserving the two-dimensional character of the desired flow. Additionally, model TM5 had a bank of smooth drinking straws (not shown in Fig. 1) placed at the entrance of the test section just downstream of the stagnation tank in order to straighten the fluid particle paths and remove velocity fluctuations from the flow upstream of the vocal folds.

The minimal diameter between the two vocal fold pieces was controlled using a shim placed on one side of the tunnel, as shown in Fig. 1. The actual minimal diameter was measured using feeler gages (accuracy of measurement was 0.01 mm). For this experiment, the case of $D = 0.0400$ cm (human size; 0.30 cm in the model) was used. The vocal fold pieces of model TM5 were equipped with 13 pressure taps (i.d. of 0.0044 cm human size) on each piece. A few taps became clogged during the experiment. Additional pressure taps were placed at 0.16 cm (human size) upstream of the start of the vocal fold piece (the reference subglottal pressure tap), and 0.15 cm (human size, tap 15) and 3.1 cm (human size,

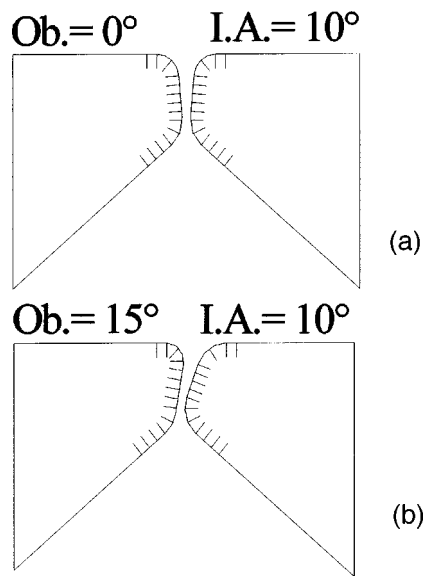


FIG. 2. Cases studied. (a) Symmetric glottis. (b) Oblique glottis slanted at 15 degrees. For both cases, the included glottal angle is 10 degrees divergent (narrower at glottal entrance, wider at glottal exit). The location of the pressure taps are also shown. Note the oblique case (b) has one divergent side (seen on the right) and one convergent side (left).

tap 16) downstream of the exit plane of the vocal folds. All pressures were measured as a pressure drop with respect to the subglottal pressure tap.

Figure 2 shows the two cases of divergent glottal ducts that were studied. Case (a) was a symmetric glottal duct with an included divergent angle (between the two sides of the glottis) of 10 degrees. Case (b) had a 15-degree oblique (slanted) glottal duct with the same included angle of 10 degrees. Both cases were subjected to transglottal pressures of 3, 5, 10, and 15 cm of H_2O (human values).

B. Pressure and flow measurements

This experiment had two main parts. The first part was to determine the pressure distributions on the vocal folds for the two glottal geometries as a replication of an earlier study. The second part was to visualize and describe the flow for those cases.

Pressures on the vocal fold walls were obtained using a micromanometer (Dwyer Microtector; resolution of 0.0006 cm H_2O). Flow through the model was measured using a mass flowmeter (model HFM 201, Teledyne Hastings) that was calibrated to measure volumetric flow rates. A pressure scanner (Scanivalve Corp. model WS5 with 48 pressure ports) was placed in the line between the model and the micromanometer. This arrangement is shown in Fig. 3.

The air passed through an atomizer (model 9306, TSI, Inc.; see below) before reaching the upstream air stilling box. Before pressure values could be measured, the atomizer was cleaned and emptied of all particles. The main gate valve and the valve on the atomizer were used to control the flow until the desired transglottal pressure drop was attained. Using the scanner, pressure drop values were sequentially read on both vocal fold pieces. The value of the flow rate (voltage on the multimeter) was monitored during the runs to guarantee negligible change in the flow rate. In the present study, the flow

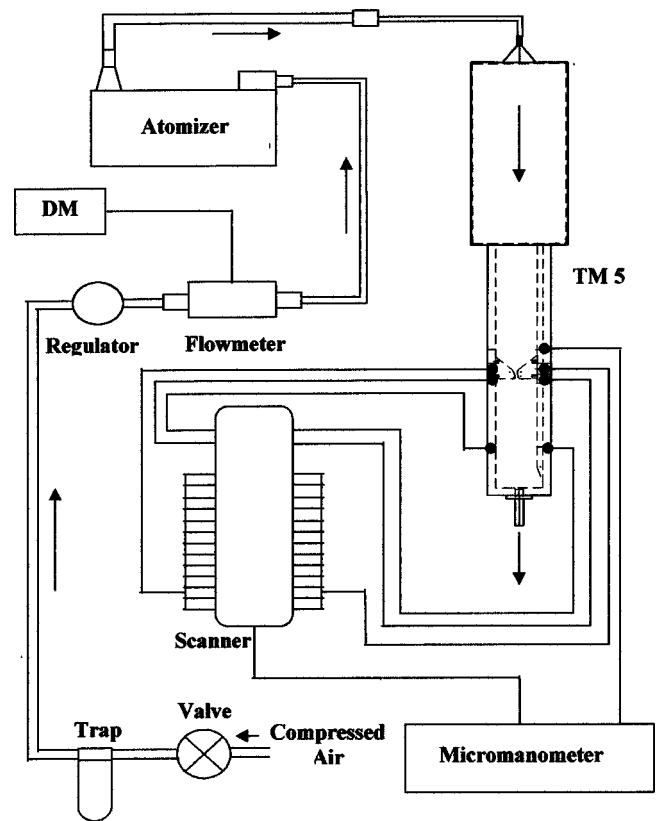


FIG. 3. Schematic for the pressure measuring setup (TM5). See text for details.

was pushed by a compressed air supply, whereas the air was pulled by a vacuum in the earlier model M5 work.

C. Flow visualization

Figure 4 shows the setup that was used to visualize the flow through model TM5. Seeding the flow was achieved by using the atomizer, which added a mixture of wetted hollow spherical glass particles to the flow. The spheres (TSI Inc., Hampton, VA) had diameters ranging from 8 to 12 μm . The test section received the flow from the stagnation tank. After passing through the model, the particles went into a floor drainpipe using tubing attached to the exit pipe of the wind tunnel.

The beam from an argon-ion LASER (model 95 Ar Ion LASER, TSI Inc.) was transformed into a "sheet" via a cylindrical lens. The two lines emanating from the lens shown in Fig. 4 depict the plane of the LASER sheet. The LASER plane was guided into the glottis from the downstream direction. The reflecting mirror had a circular shape with a diameter of 2.5 cm. The mirror was located far downstream in the reservoir and had no apparent effect on the flow close to the glottis exit. The Reynolds numbers¹ were relatively low, between 1000 and 2000, and thus the velocities in the vicinity of the mirror were relatively low. The surface area of the circular mirror was about 3.6% of the reservoir cross-sectional area.

In order to avoid clogging the pressure taps on the vocal folds during the flow visualization procedure, the taps were taped over using regular transparent scotch tape (thickness of

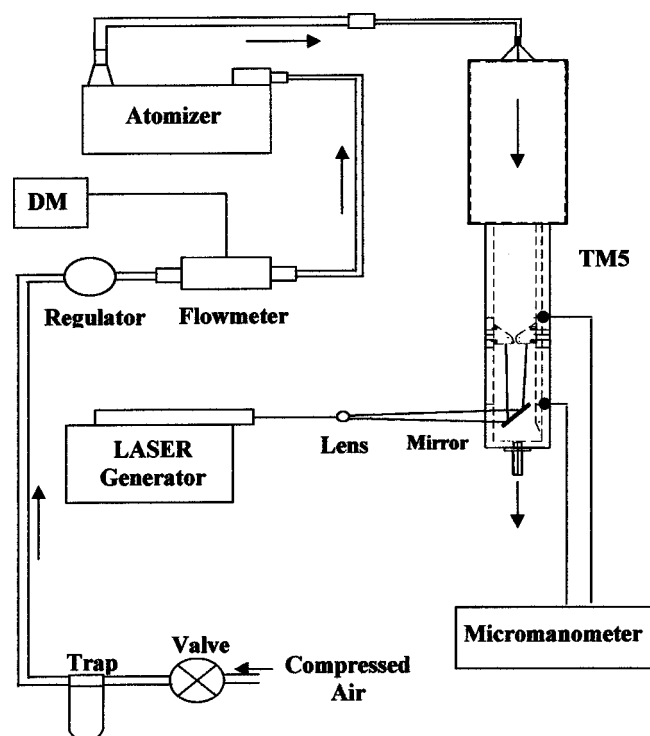


FIG. 4. Schematic for the flow visualization setup (TM5). See text for details.

approximately 0.00543 cm, or 0.000724 cm human size). The minimal glottal diameter was established using a proper size shim combined with feeler gauges for fine adjustment (measured after the tape was placed over the pressure taps). The combination of the main gate valve and the fine-tune valve on the atomizer was used to establish the desired transglottal pressure drop.

A digital camera and a video camera were used to record the flow behavior. Distance measurements and landmark locations (e.g., the locations of the flow separation points) on the resulting photographs were obtained by consensus of three collaborators who examined the photographs together. The traverse table on which the LASER generator was mounted was moved along the length of the vocal folds (on the axis out of the page of Fig. 4) to scan for any apparent or visible 3D effect. No such effects were observed.

III. RESULTS

A. Symmetric glottis results

1. Pressure distributions

Figure 5 shows the pressure distributions for both walls for the symmetric case. The minimum glottal diameter was at pressure tap 6 (indicated by "T6" in the figure), the entrance to the glottis. Upstream of the glottal entrance (in the region of the subglottal vocal fold walls) the cross-sectional area decreased toward the glottis. This decrease in area caused the flow to accelerate and the pressure drop along the walls to increase. The minimum pressure (largest pressure drop) was recorded at the minimum diameter section. Pressure recovery (that is, pressure increase) is evident past tap 6 as the glottal cross-sectional area increased. A complete pressure recovery

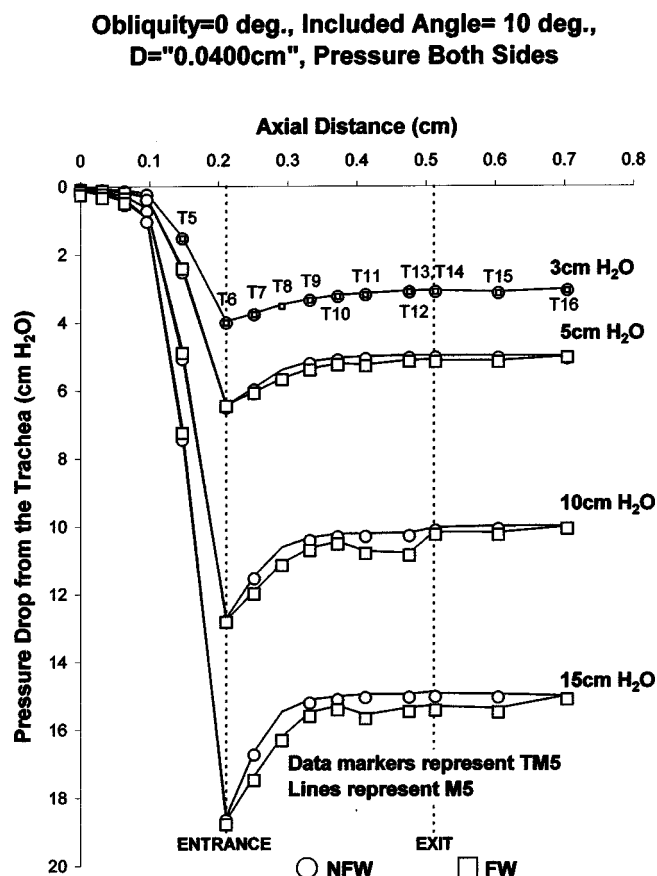


FIG. 5. Pressure distributions for symmetric cases (both sides of the glottis) obtained using TM5. Pressures are scaled to human values. The straight line segments connect corresponding data from Scherer *et al.* (2001b) and the circle and square symbols refer to data from this study. The zero of the horizontal axis refers to the axial location of the first pressure tap on the vocal fold surface (the first pressure tap downstream of the subglottal pressure tap). The pressure tap numbers are indicated and correspond to the taps shown in Fig. 2(a). Tap 16 was downstream of tap 15 by 2.93 cm human size (22 cm in TM5), a distance further than indicated in the figure. "NFW" means nonflow wall, and "FW" means flow wall (see text).

(back to the subglottal pressure) was not possible due to the losses that occurred within the glottis because of friction and form drag.

It is known from previous studies that diffusers with a half-angle of 5 degrees or larger may cause the flow to separate from the diffuser walls (Kline *et al.*, 1959). If the separation points on both surfaces are not at the same location due to flow instability, unequal pressure distributions between the two surfaces can result. It can be seen in Fig. 5 that

TABLE I. Flow values (human size) for cases (a) (symmetric glottis) and (b) (oblique glottis). The "computational" flow rates are those reported in Scherer *et al.* (2001b) using the FLUENT computational software.

Transglottal pressure cm H ₂ O	Flow for symmetric cases (cm ³ /s)			Flow for oblique cases (cm ³ /s)		
	M5	TM5	Computational	M5	TM5	Computational
3	97	95	108	95	93	104
5	126	125	141	125	123	137
10	185	182	202	180	177	188
15	230	223	248	225	217	232

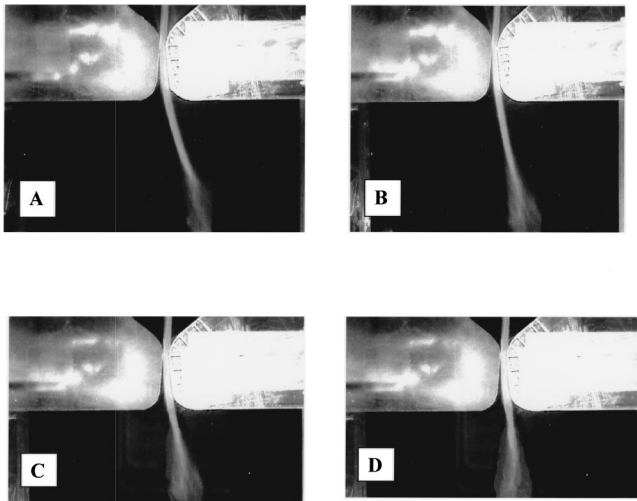


FIG. 6. (a) Flow visualization image for the symmetric case, 3 cm H₂O (TM5). The lower portion of the figure is downstream of the glottis. The “flow wall” side is on the right (the flow “clings” to that side in the glottis), and the “nonflow wall” side is on the left (where flow separation is seen upstream in the glottis). The pressure taps in the vocal fold on the left are present but not obvious due to the manner in which the laser was used. (b) 5 cm H₂O. (c) 10 cm H₂O. (d) 15 cm H₂O.

the pressure distributions for this symmetric divergent glottis were asymmetric, with different pressures on the two glottal walls at the same cross section (except for the 3 cm H₂O condition, for which the pressures were the same). The largest difference was 5.9% of the transglottal pressure (0.59 cm H₂O) at tap 12 for a transglottal pressure drop of 10 cm H₂O. The asymmetry of pressures indicates higher pressures on the nonflow wall (NFW) (circles), and lower wall pressures on the flow wall (FW) (squares; the NFW and FW designations correspond to the flow visualization results discussed below, where FW refers to the side of the glottis on which the flow remained, and NFW where the flow separated from the wall within the glottis region). Each of the empirical pressure values inside the glottis shown in Fig. 5 match those of the earlier study of the same case (Scherer *et al.*, 2001b) within 1.7%. The straight-line segments in Fig. 5 connect the pressure values from the *earlier* study. Also, Table I shows that the flow values for the M5 and TM5 experiments agree within 3.6%.

2. Flow visualization

Figures 6(a)–(d) are photographs of the flow visualization experiments for the symmetric glottis for the 3, 5, 10, and 15 cm H₂O conditions, respectively. These figures illustrate that the flow was skewed both in the glottis and in the downstream region for all inlet pressures. Flow separated upstream in the glottis from the vocal fold shown on the left (NFW) just past the minimum glottal cross section. The flow remained attached to the glottal wall of the other vocal fold (FW) until reaching the glottal exit expansion.

For the 3 cm H₂O case, Fig. 6(a) illustrates that the flow skewed. However, Fig. 5 did not reveal any significant difference in the wall pressures for the two surfaces. For this low inertia case, these results are consistent with the earlier work by Scherer *et al.* (2001b) which illustrated (using the computational software FLUENT) that only a very slight difference in wall pressures in the downstream region (less than 2 Pa) was required to skew the flow at low Reynolds numbers.

Table II gives the location of the flow separation points. They did not appear to change on the nonflow wall side as the flow increased, remaining at approximately 0.02 cm from the glottal minimum diameter location. The separation points on the flow wall side were more downstream and appeared to move further downstream by only 0.01 cm for the higher transglottal pressures.

Once the flow separates in a diffuser, the main flow is susceptible to instabilities originating from small unsteady perturbations in the shear layers. These instabilities can be amplified to form wavy flow patterns. Sato (1959) showed that the velocity fluctuates in the vicinity of the shear layers near a nozzle exit in two-dimensional jet flow. Figure 7 shows the schematized flow patterns adapted from photographs of the glottis and the downstream duct. The exiting jet oscillated slowly (easily seen by eye) along the direction of A-A, consistent with Sato (1959). This oscillation was small, however, not more than ± 0.05 cm (human size) for any condition.

Upstream of the glottis there were two standing, slowly circulating regions of flow in the lateral regions where the subglottal contraction began (Fig. 7). Downstream of the glottis, the flow was transitional. Four flow circulation regions (C1, C2, C3, C4) and two reverse flow regions (R1, R2) were formed as shown in Fig. 7. The circulation region

TABLE II. Separation point locations and 90% pressure recovery locations (human size) for case (a) (TM5), the symmetric glottis with a divergent angle of 10 degrees. The tabled values are distances measured downstream from the minimal cross-section (tap 6). The values in the right-most column were obtained by using FLUENT, a computational package (see Scherer *et al.*, 2001b). The glottal axial length was 0.30 cm (human size).

Transglottal pressure drop (cm H ₂ O)	Separation location nonflow wall (cm)	90% Pressure recovery location on nonflow wall (cm)	Separation location on flow wall (cm)	90% Pressure recovery location on flow wall (cm)	Separation location for symmetric computation (cm)
3	0.02	0.23	0.23	0.23	0.131
5	0.02	0.12	0.23	0.26	0.099
10	0.02	0.15	0.24	0.29	0.096
15	0.02	0.09	0.24	0.26	0.094

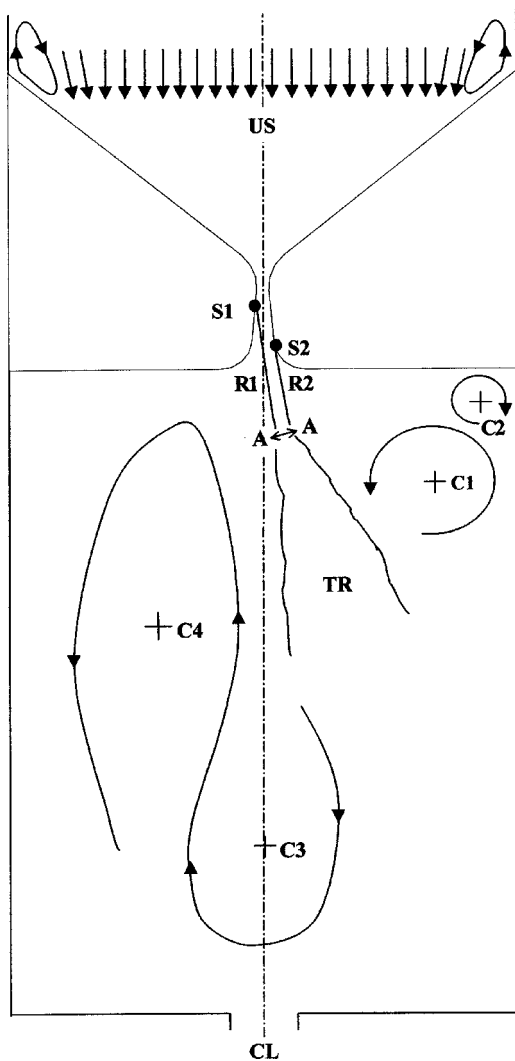


FIG. 7. Schematic of the flow details for (a) (symmetric glottis). US =upstream; S1, S2=the two separation point locations in the glottis; R1, R2=regions of reverse flow back into the glottis; the A-A line is to suggest that the jet moves somewhat back and forth while exiting the glottis; TR =transition region from the laminar core (upstream of A-A) to turbulent flow; C1, C2, C3, C4=circulation regions; CL=center line.

centered at C1 appeared to have the highest velocities. For the lower inertia flow corresponding to a transglottal pressure drop of 3 cm H₂O, the circulating point at C2 was not visible and point C1 moved toward C2. The circulating regions with centers at points C3 and C4 were steady and slowly moving. In the regions R1 and R2, air flowed in the reverse direction (toward the glottis).

It was possible to make crude measurements of the laminar core length of the glottal jet, skew angle, and width from the photographs (see Table III). As the flow rate and transglottal pressure increased, skewing of the jet leaving the glottis shifted toward the centerline (71 to 81 degrees, where 90 degrees would be on the center line). Greater volume flow “straightened” the jet flow more toward the glottal centerline presumably due to the greater momentum of the flow. The width of the jet measured at the glottal exit plane decreased only slightly (0.05 to 0.04 cm) as flow and pressure increased. The greatest change was seen in the length of the laminar core of the jet from the glottal exit plane to the

TABLE III. Glottal jet characteristics (human size) for case (a) (TM5), the symmetric glottis with a divergence angle of 10 degrees. A skew angle of 90 degrees would be along the center line of the glottis.

Transglottal pressure drop (cm H ₂ O)	Skew angle (degrees)	Jet width (cm)	Jet length (cm)
3	71	0.05	0.41
5	77	0.05	0.35
10	78	0.05	0.10
15	81	0.04	0.09

location at which transitional widening appeared to begin (see Fig. 7 near the A-A line). The length of the core decreased by 0.32 cm from 0.41 to 0.09 cm, shortening with higher flows and pressures.

3. Pressure recovery relative to separation point locations

The pressure rose within the glottis past the minimum glottal diameter. The total pressure recovery was defined here to be the difference in pressure between tap 6 (at the minimum diameter) and tap 16 (the downstream pressure away from the glottis). The location within the glottis where this pressure rose to 90% of its final value is given in Table II for both the flow wall and nonflow wall sides. For example, for a transglottal pressure of 3 cm H₂O, the separation point on the nonflow wall was at approximately 0.02 cm away from the minimum diameter location, but the 90% pressure recovery location was located much further along the glottis, approximately at 0.23 cm from the minimum diameter. As transglottal pressure increased, the location of the 90% pressure recovery moved upstream dramatically on the nonflow wall (despite negligible change in the location of the separation point), and slightly downstream on the flow wall side from an already downstream location in the glottis.

B. Oblique glottis results

1. Pressure distributions

Figure 8 shows the empirical pressure distributions for the oblique case. In the glottal entrance region (T6), the pressures on the convergent wall (squares) were 27% higher than the pressures on the divergent wall (circles). This inequality of the pressures in the entry region may promote asymmetric motion patterns of the vocal folds. Inside the glottis (T6 to T12), the wall pressure values agreed within 1.9% with the data in Scherer *et al.* (2001b) (as in Fig. 5, the lines connect data values from the *earlier* study). From T11 to T13, the pressure between the two sides of the glottis again differed, with higher pressure on the convergent side (except for the 3 cm H₂O case where they were essentially the same). This difference continued into the downstream reservoir region. Table I again shows good agreement (within 3.6%) for the flow rates between the TM5 and the M5 studies.

2. Flow visualization

Figures 9(a)–(d) are photographs of the flow visualization experiments for the oblique case for the 3, 5, 10, and 15 cm H₂O conditions, respectively. The pictures show that the

**Obliquity=15 deg., Included Angle= 10 deg.,
D="0.0400cm", Pressure Both Sides**

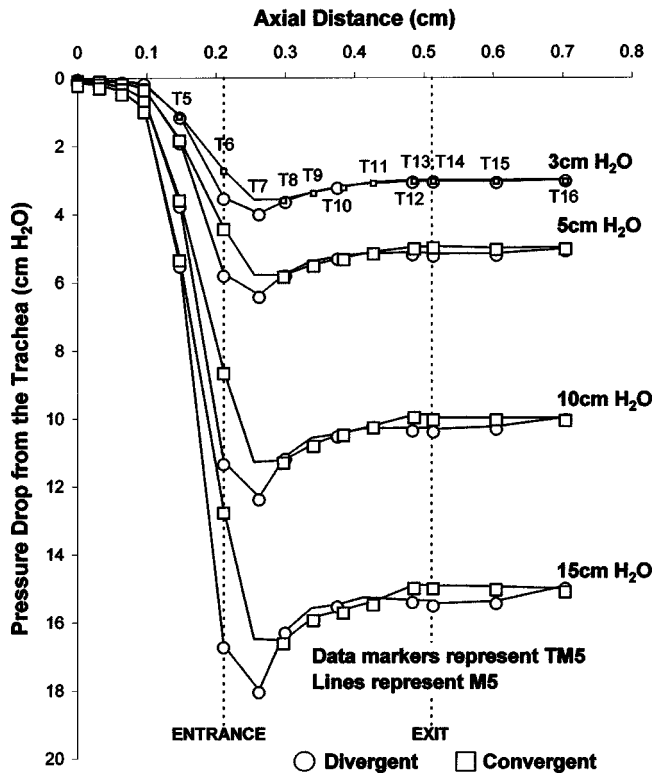


FIG. 8. Pressure distributions for oblique cases (both sides of the glottis) obtained using TM5. Pressures are scaled to human values. The pressure tap numbers are indicated and correspond to the taps shown in Fig. 2(b). See Fig. 5 caption for further explanatory details.

flow in the glottis remained more on the convergent side as the flow and pressure increased. At low flow and inlet pressure values, the viscous effects caused the flow to fill the glottis and the separation point to occur downstream on the

divergent side near the beginning of exit rounding. As the flow rate increased, the separation point moved upstream from a position of 0.20 cm (3 cm H₂O) to 0.02 cm (15 cm H₂O) from the minimal glottal diameter (see Table IV). This change in the separation point location on the divergent wall corresponded to a change in the exiting flow direction as the flow rate increased. The separation point on the convergent wall remained at approximately 0.22 cm.

The flow in the region downstream of the glottis for the oblique condition is shown schematized in Fig. 10. The flow is structurally similar to that observed for the symmetric glottis. The circulation region C1 again appeared to be the fastest of the four observed circulations. For low flows, region C2 was not visible and point C1 moved toward the C2 corner. The circulation regions for C3 and C4 were relatively steady and slow. The flow near R1 and R2 was toward the glottis and again small oscillation was seen along A-A.

The jet direction increased from 69 degrees (relative to the glottal exit plane) for the 3 cm H₂O condition to 80 degrees for the 15 cm H₂O condition, as shown in Fig. 9. This behavior is consistent with the change in the separation point location on the divergent wall (more upstream with higher transglottal pressure). Table V lists the jet skew angle, width, and length for different transglottal pressures. As the transglottal pressure increased, the jet width at the glottal exit plane decreased from 0.08 to 0.04 cm, and the laminar core length decreased from 0.60 to 0.13 cm. The fractional change of the jet core length from 3 to 15 cm H₂O was approximately the same for both the oblique and symmetric cases.

3. Pressure recovery relative to separation point locations

Although the oblique (15 degrees) glottis had a convergent and a divergent side, the glottal angle was still divergent (10 degrees), and the question of pressure recovery within the glottis in relation to the separation point locations is pertinent. Table IV gives the locations of the 90% pressure recovery for the oblique glottis. Those locations were near the separation points for the convergent side, for which the separation point is located near the initiation of the glottal exit expansion. For the divergent wall, although the separation point location moved upstream with increased transglottal pressure, the 90% pressure recovery remained near the glottal exit rounding or further downstream past the glottal exit. This finding was due to the pressures remaining relatively reduced through the glottal exit (Fig. 8).

IV. DISCUSSION

A. Pressures

The pressure distributions and flow visualization results for the symmetric glottis appear mutually consistent. The pressures on the two sides of the glottis were essentially the same at the minimal glottal diameter (tap 6). Pelorson *et al.* (1995) and Hofmans (1998) also used a physical model of a glottis with a 10-degree divergence and a rounded entrance and exit. The pressure results between that model and TM5 here are consistent in that they both found that the pressure at

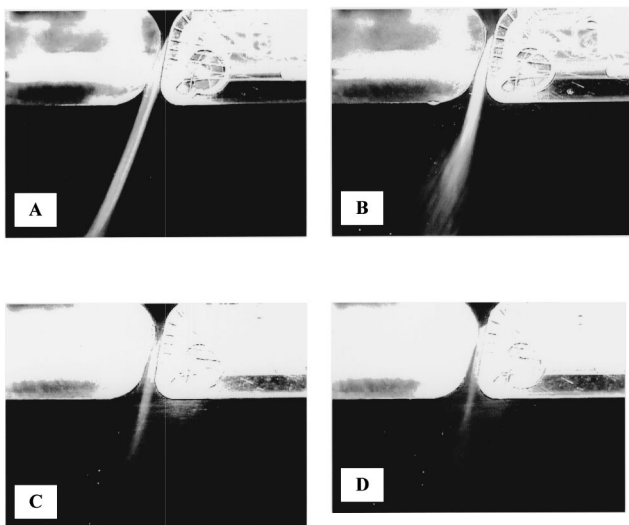


FIG. 9. (a) Flow visualization image for the oblique case, 3 cm H₂O (TM5). The lower portion of the figure is downstream of the glottis. The vocal fold on the right creates a convergent glottal side, and on the left a divergent glottal side. (b) 5 cm H₂O. (c) 10 cm H₂O. (d) 15 cm H₂O.

TABLE IV. Separation point locations and 90% pressure recovery locations for case (b), the oblique glottis with a divergence angle of 10 degrees. The “computational” separation point locations are those reported in Scherer *et al.* (2001b) using the FLUENT computational software.

Transglottal pressure drop (cm H ₂ O)	Separation on convergent wall (cm)		Convergence: 90% pressure recovery location	Separation on divergent wall (cm)		Divergence: 90% pressure recovery location
	TM5	Computational		TM5	Computational	
3	0.22	0.16	0.21	0.20	0.11	0.22
5	0.22	0.15	0.23	0.15	0.09	0.22
10	0.22	0.23	0.22	0.07	0.07	^a
15	0.22	0.23	0.24	0.02	0.07	^a

^aPressures rose to 90% pressure recovery downstream of the glottal exit.

the minimal diameter location was the same on the two sides of the glottis. The results here, however, show different cross-channel pressures downstream of that location (the other model was not used to obtain those pressures). The

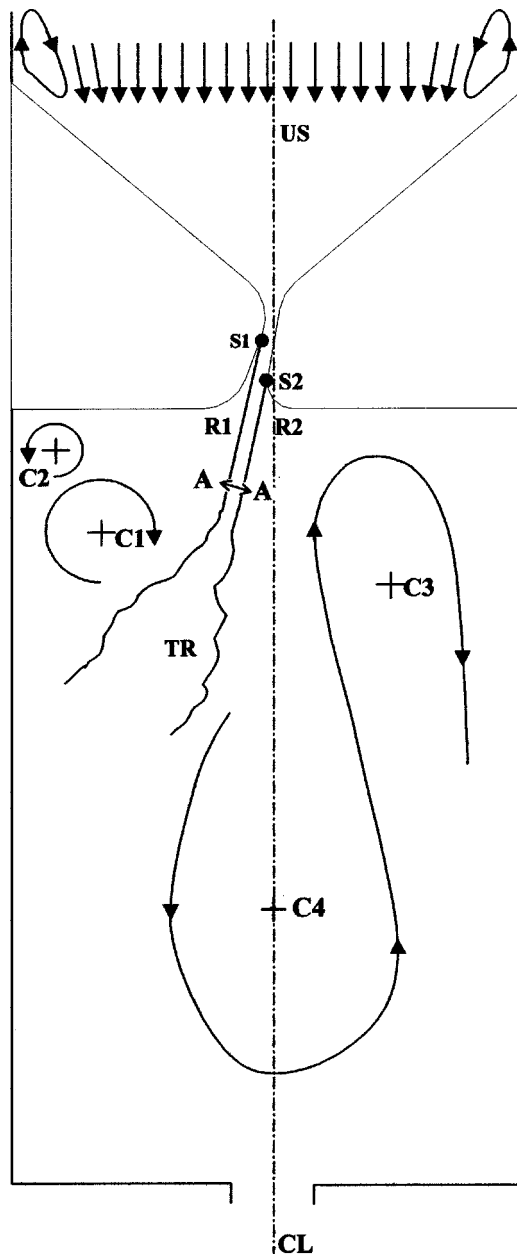


FIG. 10. Schematic of the flow details for case (b) (asymmetric glottis). See caption for Fig. 7 for details.

flow separated approximately 0.02 cm past the minimal diameter location (tap 6) (Table II), which is upstream of tap 7 (located 0.0402 cm from tap 6). At the location of tap 7 the cross-channel pressures were seen to be different, being lower on the wall where the flow was still attached (Fig. 5). The lower pressure on the flow wall was maintained throughout the glottis and just downstream of the glottal exit for the transglottal pressures of 5, 10, and 15 cm H₂O (the pressures on the two sides were the same for the 3 cm H₂O condition, even though the flow in the glottis was skewed).

It is noted that the false vocal folds were excluded in this study. If they were present and if the gap between the two false folds were narrow enough, the glottal flow may straighten instead of skew (“guided” by the false fold gap), and the intraglottal pressures may become more similar on the two vocal folds.

The results for the oblique case were highly affected by the slant of the glottal duct. Unlike the symmetric case, the oblique glottis *lacked* flow separation near the entrance except for the highest flow and pressure condition. The large cross-channel pressure difference at glottal entry (Fig. 8) was therefore due to the obliquity itself, with higher pressures on the convergent side. Also unlike the symmetric case, the pressures from taps 8–11 were almost identical except for the largest transglottal pressure of 15 cm H₂O, where the separation was upstream of tap 8; flow separated from the divergent wall, and pressures on the divergent side were slightly higher than on the convergent wall.

Hofmans (1998) studied an oblique glottis for which pressure differences at glottal entry were also found. The divergent angle was 15 degrees and the obliquity was 7.5 degrees, with both sides being divergent (5 and 10 degrees, respectively). The glottis diameters were 0.105 and 0.343 cm (which scale to about 0.042 and 0.137 cm in human values using a scaling factor of 2.5). He used a flow pulse lasting approximately 30 ms. During the mid-pulse portion, the

TABLE V. Glottal jet characteristics (human size) for case (b) (TM5), the oblique glottis with a divergence angle of 10 degrees.

Transglottal pressure drop (cm H ₂ O)	Skew angle (degrees)	Jet width (cm)	Jet length (cm)
3	69	0.08	0.60
5	75	0.07	0.26
10	78	0.05	0.22
15	80	0.04	0.13

pressures on the two sides at the minimum diameter were slightly different, also suggesting that the asymmetric geometry (and perhaps a Coanda effect) helped determine the pressure differences.

The cross-channel pressure differences on the glottal exit expansion (tap 12), on the top of the vocal fold (tap 14), and in the side wall just downstream of the glottal exit plane (tap 15) were opposite between the two cases. For the symmetric case, the pressures at those locations were always less on the flow-attachment side. For the oblique case, however, the pressures from taps 12–15 were *greater* on the flow-attachment (impingement) side of the glottis, which was the convergent side. These results were consistent with the computational fluid dynamics results in the Scherer *et al.* (2001b) study.

B. Separation points and pressure recovery

Lucero (1999), noting the work of Pelorson *et al.* (1994) for symmetric glottal flow, suggested that the flow in the symmetric glottis would remain symmetric and separation would take place from both sides of the glottis at a location where the area was approximately 1.3 times the minimal glottal area. This area ratio to determine flow separation location need not be constant. If (a) the flow were symmetric in the glottis, (b) the pressure in the glottis at the point of separation equaled the pressure further downstream, (c) the lossless steady flow Bernoulli equation were used, and (d) the downstream pressure were assumed to be atmospheric, it is straightforward to show that

$$d_s/d_m = (1 - P_6/P_t)^{0.5}, \quad (1)$$

where d_s/d_m is the ratio of the glottal diameter at the separation point to the minimum glottal diameter, P_6 is the pressure at the minimum diameter (tap 6), and P_t is the transglottal pressure. This equation allows an estimate of the axial location of the separation points for a diffuser. Using the pressure data of this study, the range of estimated d_s/d_m would be approximately 1.11 to 1.17, yielding an axial distance of 0.025 to 0.039 cm from the minimum diameter location, being shorter for higher transglottal pressures. The low end of these estimations is fairly representative for the separation on the nonflow wall only (0.02 cm, Table II). Using laminar assumptions in the computational software FLUENT (Fluent, Inc., Lebanon, NH) for symmetric flow in the glottis, the separation point moved upstream as transglottal pressure increased (0.131 to 0.094 cm, for 3 to 15 cm H₂O; see Table II). This computational result suggests that if the flow were symmetric in the glottis, higher transglottal pressures would move the separation point toward the entrance in the divergent glottis, but not as far upstream in the glottis as suggested by Eq. (1). On the other hand, applying Eq. (1) to his data for a 10-degree diffuser glottis, Hofmans (1998) showed that the separation point moved *downstream* in the glottis as flow increased, rather than upstream. This finding is most likely due to the use of higher transglottal pressures and the tendency toward turbulent flow compared to the flow in the present study.

The use of Eq. (1) to estimate the separation point assumes that the pressure in the glottis at the location of separation

is the same as downstream of the glottis. This is highly questionable, however. Flow separation would be expected somewhere between taps 6 and 8 in our model, but the pressures are rising within and past this range. [Hofmans (1998) also pointed out the incorrect assumption that the pressure at the separation location is equal to the downstream pressure.] Assuming P_s , the pressure at the separation location, was not the same as downstream, P_6/P_t in Eq. (1) would be replaced by $(P_6 - P_s)/(P_t - P_s)$ in the expression given above. This new expression would result in separation points occurring even more upstream in this study (and less than 0.006 cm from T6). Indeed, the results for model TM5, for both the symmetric and oblique glottis, suggest that the location of separation points is not sufficient to predict intraglottal pressures for glottal flows that are not symmetric (see Tables II and IV). One needs to examine the pressures themselves in the attempt to develop rules for intraglottal pressures.

The measured separation point locations for the oblique glottis are compared to those obtained using FLUENT in Table IV. The separation point locations on both glottal walls were similar for the 10 cm H₂O transglottal pressure. The general trend for the divergent wall was similar for both approaches in that the separation points were more upstream for higher transglottal pressures. For the convergent wall and 3 and 5 cm H₂O, the empirical separation points were more downstream. It is noted that the downstream pressure boundary condition used with FLUENT was specified as a uniform pressure distribution, whereas the complex flow patterns shown in Fig. 10 would suggest otherwise, apparently enhancing the inaccuracy of the predicted separation point locations at lower, less inertial, flows.

C. Glottal jet

The width of the jet at the glottal exit plane changed only slightly for the symmetric case (from 0.05 cm at the lower three transglottal pressures to 0.04 cm at 15 cm H₂O, Table III). This width is consistent with the size of the minimal diameter (0.04 cm) with slight expansion of the jet for the lower transglottal pressures. The width of the jet was considerably greater for the oblique case, however, being 0.08 cm for the 3 cm H₂O condition, decreasing gradually to 0.04 for the 15 cm H₂O condition (Table V). A wider jet should have lower average velocity but a greater chance to interact with the edges of the false vocal folds. A recent study on false vocal fold geometry (Agarwal *et al.*, in press) suggests that for the 3 cm H₂O condition and average dimensions for the false vocal fold region, the jet would impinge on the medial edge of the false vocal fold. Interaction of flow jets and the false vocal folds may create sound sources (Zhang *et al.*, 2002). The results here suggest that higher transglottal pressures would move the jet more medially, away from the false fold edges.

The length of the laminar core of the glottal jet up to the jet expansion suggesting turbulence extended into the supraglottal duct between 0.09 and 0.60 cm, taking data across both cases (Tables III and V). The distance decreased as the flow increased [Hofmans (1998) showed hot wire measures within and downstream of a glottis demonstrating the change

from nonfluctuating to highly fluctuating velocities as the hot-wire was moved outside the glottis]. Assuming the jet length characteristics were to obtain when the false folds are present, the transition to the turbulent regime would take place essentially at or upstream of the ventricular folds. The average distance from the glottal exit to the minimum diameter between the ventricular folds for male nonsingers is approximately 0.5 cm (s.d. 0.11 cm) (Agarwal *et al.*, in press; see also Wilson, 1972). Therefore, the acoustic effect of the ventricles may come into play relative to the near-field acoustics of the turbulence of the glottal jet. The length of the core of the glottal jet of this study is also consistent with hot-wire measures of glottal flow approximately 1 cm above the exit of the glottis for vibrating tissue models; modulated turbulence has been reported at this location (Berke *et al.*, 1989; Alipour and Scherer, 1995; Bielamowicz *et al.*, 1999).

D. Coanda effect

The works by Pelorson *et al.* (1995) and Hofmans (1998) have added significant empirical information on dynamic flows and pressures in static glottal models. A primary conclusion pertinent to this study is that the Coanda effect (flow skewing to one side within divergent ducts) takes too long to develop and therefore should not exist in the divergent glottis (also see Hirschberg *et al.*, 1996), suggesting that nearly symmetric flows only should exist. The conclusion comes from studies using rapidly increasing volume flows through divergent glottal models. However, during phonation the glottis begins to take on a divergent shape only near the peak of the glottal flow. It may be at this point in the cycle when the Coanda effect may have the best chance to form. It is noted that Figs. 11 and 14 in Hofmans (1998), showing transglottal and intraglottal (minimum diameter) pressures for a 20-degree divergent glottis, suggest that once the volume flow acceleration decreases sufficiently, the Coanda effect takes place very quickly (within 1–2 ms). Furthermore, Iijima *et al.* (1992), using computational and electrical analog models, determined that for an instantaneous pressure change, the asymptotic pressure was reached typically within 1 ms, being faster for higher transglottal pressures and smaller minimum diameters. Their results suggest that the establishment of the aerodynamics within the glottis is rapid, and dependent upon the glottal inductance. This may include the presence of the separated flow (about which they did not report). In general, then, it is still open as to the presence and influence of the Coanda effect in phonation.

V. CONCLUSIONS

Using a Plexiglas, nonmoving model of the larynx (enlarged by a factor of 7.5), this study examined the steady flow glottal wall pressures and air movement for a symmetric and an oblique glottis having an included divergent angle of 10 degrees, a minimal glottal diameter of 0.04 cm (human size), rounded entrance and exit, and an axial length of 0.30 cm (human size). The model was made with 13 pressure taps on both vocal folds. Flow visualization was made possible

by use of seeded airflow and a LASER sheet pointed toward the glottis from downstream of the glottis. Results indicated the following:

- (1) The glottal wall pressures for both the symmetric and oblique glottis for the 3, 5, 10, and 15 cm H₂O transglottal pressure drop cases were well within 2% of those studied in an earlier experiment, for which this study was therefore a strong replication. The method of obtaining the pressures on both sides of the glottis by manually changing the airflow path in the earlier study was validated. Airflow was pushed in this study and pulled in the earlier study, also validating either method of creating pressure drops in laryngeal models.
- (2) The cross-channel wall pressure differences were not the same for the symmetric and oblique glottal cases. For the symmetric glottis, pressures were higher on the nonflow wall of the symmetric glottis (except for the condition of 3 cm H₂O transglottal pressure, for which pressure differences could not be detected), and were lowest at the minimal glottal diameter. For the oblique glottis, pressures were higher by 27% of the transglottal pressure in the glottal entrance region on the convergent side. Therefore, obliquity created a change in the pressure patterns and values especially in the glottal entrance region.
- (3) Flow from the symmetric glottis discharged into the downstream rectangular duct asymmetrically; the direction of the flow jet moved more toward the geometric axis of the glottis as flow rate increased. The direction of the glottal jet from the oblique glottis also varied with flow rate, moving across the geometric axis of the glottis with flow increase. Small jet oscillation was present at the glottal exit for both the symmetric and oblique cases.
- (4) Flow separated consistently from one side of the symmetric divergent glottis with essentially negligible movement of the separation points. Glottal obliquity, however, created a strongly contrastive separation phenomenon. Flow separated from the divergent side at a point that progressively moved upstream as flow rate increased. The glottal wall pressure at the location of flow separation was always less than the pressure at the glottal exit (or further downstream).
- (5) The length of the laminar core of the glottal jet decreased as transglottal pressure increased. The length of the core for pressures above 3 cm H₂O was less than the expected distance from the glottis to the minimal width location between the false vocal folds, suggesting that the turbulent noise from the glottal jet may excite the expansion chamber formed by the bilateral ventricles between the true and false vocal folds.

The results suggest that the aerodynamic and aeroacoustic study of phonation should take into consideration the effects of oblique glottal shapes that may occur during phonation. The current report suggests that the driving forces on the two vocal folds may be different for symmetric glottal shapes compared to oblique glottal shapes having the same angle and minimal diameter, and that acoustic glottal jet effects may depend upon glottal obliquity and flow rate.

ACKNOWLEDGMENTS

This research was supported by NIH Grant No. 1 R01 DC03577 from the National Institute on Deafness and Other Communication Disorders. We would like to thank Professor Terry Ng for his suggestions concerning flow visualization, Larry Cousino for help in the machine shop, Bogdan Kucinski for his assistance, and the reviewers for their helpful suggestions.

¹The Reynolds number was defined as $Re = D_h^* V / \nu = 4 * U / (P * \nu)$, where D_h is the hydraulic diameter (four times the cross-sectional area divided by the perimeter), V is the mean velocity at the location of the minimal glottal diameter, ν is the kinematic viscosity, U is the volume flow, and P is the perimeter of the glottis at the minimal diameter.

- Agarwal, M., Scherer, R. C., and Hollien, H. (in press). "The false vocal folds: shape and size in the coronal view during phonation," *J. Voice*.
- Alipour, F., and Scherer, R. C. (2000). "Dynamic glottal pressures in an excised hemilarynx model," *J. Voice* **14**, 443–454.
- Alipour, F., and Scherer, R. C. (1995). "Pulsatile airflow during phonation: An excised larynx model," *J. Acoust. Soc. Am.* **97**, 1241–1248.
- Alipour, F., Fan, C., and Scherer, R. C. (1996b). "A numerical simulation of laryngeal flow in a forced-oscillation glottal model," *Comput. Speech Lang.* **10**, 75–93.
- Alipour, F., Scherer, R. C., and Knowles, J. (1996a). "Velocity distribution in glottal models," *J. Voice* **10**, 50–58.
- Ashjaee, J., and Johnston, J. P. (1980). "Straight-walled, two-dimensional diffusers—transitory stall and peak pressure recovery," *J. Fluids Eng.* **102**, 275–282.
- Berg, Jw. van den, Zantema, J. T., and Doornenbal, P. (1957). "On the air resistance and the Bernoulli effect of the human larynx," *J. Acoust. Soc. Am.* **29**, 626–631.
- Berke, G. S., Moore, D. M., Monkewitz, P. A., Hanson, D. G., and Gerratt, B. R. (1989). "A preliminary study of particle velocity during phonation in an in vivo canine model," *J. Voice* **3**, 306–313.
- Bielamowicz, S., Berke, G. S., Kreiman, J., and Gerratt, B. R. (1999). "Exit jet particle velocity in the in vivo canine laryngeal model with variable nerve stimulation," *J. Voice* **13**, 153–160.
- Carlson, J. J., Johnston, J. P., and Sagi, C. J. (1967). "Effects of wall shape on flow regimes and performance in straight, two-dimensional diffusers," *J. Basic Eng.* **89**, 151–160.
- Cherdron, W., Durst, F., and Whitelaw, J. H. (1978). "Asymmetric flows and instabilities in symmetric ducts with sudden expansions," *J. Fluid Mech.* **84**, 13–31.
- Durst, F., Melling, A., and Whitelaw, J. H. (1974). "Low Reynolds number flow over a plane symmetric sudden expansion," *J. Fluid Mech.* **64**, part 1, 111–128.
- Gauffin, J., Binh, N., Ananthapadmanabha, T. V., and Fant, G. (1983). "Glottal geometry and volume velocity waveform," in *Vocal Fold Physiology: Contemporary Research and Clinical Issues*, edited by D. M. Bless and J. H. Abbs (College-Hill, San Diego), pp. 194–201.
- Hirano, M. (1981). *Clinical Examination of Voice* (Springer-Verlag, New York).
- Hirschberg, A., Pelorson, X., Hofmans, G. C. J., van Hassel, R. R., and Wijnands, P. J. (1996). "Starting transient of the flow through an in-vitro model of the vocal folds," in *Vocal Fold Physiology, Controlling Complexity and Chaos*, edited by P. J. Davis and N. H. Fletcher (Singular, San Diego), pp. 31–46.
- Hofmans, G. C. J. (1998). *Vortex Sound in Confined Flows* (Technische Universiteit Eindhoven, Eindhoven).
- Iijima, H., Miki, N., and Nagai, N. (1992). "Glottal impedance based on a finite element analysis of two-dimensional unsteady viscous flow in a static glottis," *IEEE Trans. Signal Process.* **40**, 2125–2135.
- Ishizaka, K., and Flanagan, J. L. (1972). "Synthesis of voiced sounds from a two-mass model of the vocal cords," *Bell Syst. Tech. J.* **51**, 1233–1267.
- Ishizaka, K., and Matsudaira, M. (1972). *Fluid Mechanical Considerations of Vocal Cord Vibration*, SCRL Monograph No. 8 (Speech Communications Research Laboratory, Santa Barbara).
- Kline, S. J., Abbott, D. E., and Fox, R. W. (1959). "Optimum design of straight-walled diffusers," *J. Basic Eng.* **81**, Series D, No. 3, 321–331.
- Lucero, J. C. (1999). "A theoretical study of the hysteresis phenomenon at vocal fold oscillation onset-offset," *J. Acoust. Soc. Am.* **105**, 423–431.
- Munson, B. R., Young, D. F., and Okiishi, T. H. (1998). *Fundamentals of Fluid Mechanics*, 3rd ed. (Wiley, New York).
- Pelorson, X., Hirschberg, A., van Hassel, R. R., and Wijnands, A. P. J. (1994). "Theoretical and experimental study of quasisteady flow separation within the glottis during phonation. Application to a modified two-mass model," *J. Acoust. Soc. Am.* **96**, 3416–3431.
- Pelorson, X., Hirschberg, A., Wijnands, A. P. J., and Bailliet, H. (1995). "Description of the flow through in-vitro models of the glottis during phonation," *Acta Acustica* **3**, 191–202.
- Reneau, L. R., Johnston, J. P., and Kline, S. J. (1967). "Performance and design of straight two-dimensional diffusers," *J. Basic Eng.* **89**, 141–150.
- Sato, H. (1959). "The stability and transition of a two-dimensional jet," *J. Fluid Mech.* **7**, 53–80.
- Scherer, R. C., and Guo, C. G. (1990). "Laryngeal modeling: translaryngeal pressure for a model with many glottal shapes," in *ICSLP Proceedings, 1990 International Conference on Spoken Language Proceedings*, Vol. 1 (Acoustical Society of Japan, Japan), pp. 3.1.1–3.1.4.
- Scherer, R. C., and Guo, C. G. (1991). "Generalized translaryngeal pressure coefficient for a wide range of laryngeal configurations," in *Vocal Fold Physiology: Acoustics, Perceptual and Physiological Aspects of Voice Mechanisms*, edited by J. Gauffin and B. Hammarberg (Singular, San Diego), pp. 83–90.
- Scherer, R. C., De Witt, K., and Kucinski, B. R. (2001a). "The effect of exit radii on intraglottal pressure distributions in the convergent glottis," *J. Acoust. Soc. Am.* **110**, 2267–2269.
- Scherer, R. C., and Titze, I. R. (1983). "Pressure-flow relationships in a models of the laryngeal airway with diverging glottis," in *Vocal Fold Physiology: Contemporary Research and Clinical Issues*, edited by D. M. Bless and J. H. Abbs (College-Hill, San Diego), pp. 179–193.
- Scherer, R. C., Shinwari, D., DeWitt, K., Zhang, C., Kucinski, B., and Afjeh, A. (2001b). "Intraglottal pressure profiles for a symmetric and oblique glottis with a divergence angle of 10 degrees," *J. Acoust. Soc. Am.* **109**, 1616–1630.
- Shadle, C. H., Barney, A. M., and Thomas, D. W. (1991). "An investigation into the acoustics and aerodynamics of the larynx," in *Vocal Fold Physiology: Acoustics, Perceptual and Physiological Aspects of Voice Mechanisms*, edited by J. Gauffin and B. Hammarberg (Singular, San Diego), pp. 73–82.
- Tsui, Y. Y., and Wang, C. K. (1995). "Calculation of laminar separated flow in symmetric two-dimensional diffusers," *J. Fluids Eng.* **117**, 612–616.
- Ward Smith, A. J. (1971). *Pressure Losses in Ducted Flows* (Davey, Harford, England).
- Wilson, J. E. (1972). "A Study of the Conformation of the Laryngo-Pharynx in Singers during Alteration of Intensity, Frequency, and Vowel," doctoral thesis, Indiana University, Bloomington.
- Yang, Y. T., and Hou, C. F. (1999). "Numerical calculation of turbulent flow in symmetric two-dimensional diffusers," *Acta Mech.* **137**, 43–54.
- Zhang, C., Zhao, W., Frankel, S. H., and Mongeau, L. (2002). "Computational aeroacoustics of phonation, Part II: Effects of subglottal pressure, glottal oscillation frequency, and ventricular folds," *J. Acoust. Soc. Am.* **112**, 2147–2154.

The synergy between speech production and perception

Powen Ru,^{a)} Taishih Chi, and Shihab Shamma

Center for Auditory and Acoustics Research, Institute for Systems Research, Electrical and Computer Engineering Department, University of Maryland, College Park, Maryland 20742

(Received 1 August 2000; accepted for publication 1 October 2002)

Speech intelligibility is known to be relatively unaffected by certain deformations of the acoustic spectrum. These include translations, stretching or contracting dilations, and shearing of the spectrum (represented along the logarithmic frequency axis). It is argued here that such robustness reflects a synergy between vocal production and auditory perception. Thus, on the one hand, it is shown that these spectral distortions are produced by common and unavoidable variations among different speakers pertaining to the length, cross-sectional profile, and losses of their vocal tracts. On the other hand, it is argued that these spectral changes leave the auditory cortical representation of the spectrum largely unchanged except for translations along one of its representational axes. These assertions are supported by analyses of production and perception models. On the production side, a simplified sinusoidal model of the vocal tract is developed which analytically relates a few “articulatory” parameters, such as the extent and location of the vocal tract constriction, to the spectral peaks of the acoustic spectra synthesized from it. The model is evaluated by comparing the identification of synthesized sustained vowels to labeled natural vowels extracted from the TIMIT corpus. On the perception side a “multiscale” model of sound processing is utilized to elucidate the effects of the deformations on the representation of the acoustic spectrum in the primary auditory cortex. Finally, the implications of these results for the perception of generally identifiable classes of sound sources beyond the specific case of speech and the vocal tract are discussed. © 2003 Acoustical Society of America. [DOI: 10.1121/1.1525288]

PACS numbers: 43.70.Bk [KRK]

I. INTRODUCTION

A remarkable aspect of speech is the robustness of its intelligibility despite the enormous variability of the acoustic features associated with the signal. In our normal everyday experience, a common utterance can be produced by speakers with a broad range of vocal tract shapes, dimensions, and dynamics, yet it is likely to be perceived as different voices, rather than as different words. This robustness can be attributed to many different factors, including the categorical perception of speech segments, contextual effects (Ladefoged and Broadbent, 1957), the role of inference from linguistic context.

However, a separate factor contributing to robustness is the innate *tolerance* of the auditory perception of certain systematic deformations of the acoustic signal. For instance, male and female speakers differ considerably in the length of their vocal tracts, leading to a systematic divergence of acoustic features between genders, such as a general upward shift of female formant frequencies. This trend rarely affects speech intelligibility, yet it is devastating to automatic speech recognition systems unless specific measures are employed such as the use of speaker-adaptation techniques with delta or double-delta cepstral features (Lee *et al.*, 1992). The robustness of auditory perception to changes in vocal-tract length may stem in large part from the way which affects the acoustic spectrum as represented along the *tonotopic* axis of the cochlea. Specifically, the *tonotopic* axis is approximately

logarithmic in frequency (Greenwood, 1961; Moore and Glasberg, 1983). Consequently, linear dilations of the acoustic spectrum such as those caused by vocal-tract-length changes (Fant, 1960), appear as simple translations which do not alter the shape of the acoustic spectral pattern along the *tonotopic* axis.

In this spirit, one may ask whether there are other spectral deformations that are perceptually tolerable because of the way they are represented in the auditory system. If so, what sources of variability do they reflect in the vocal tract? And finally, how might this relate to the functional organization of the auditory system and to the broader issue of synergy that potentially exists between the vocal tract that generates the message and the auditory system that decodes it?

Recent investigations into the functional organization of the primary auditory cortex (AI) have suggested the existence of at least three axes related to the representation of the monaural acoustic spectrum: (1) *The tonotopic axis*: This is the best known and studied, and has its origins in the cochlear analysis of acoustic frequency (Merzenich, Knight, and Roth, 1975). (2) *A bandwidth axis*: At each frequency, the sharpness of tuning (or equivalently, the bandwidth of the frequency analysis) varies systematically and topographically from sharp tuning near the center of the AI to broad tuning towards the edges (Schreiner and Mendelson, 1990). (3) *An asymmetry axis*: At each frequency and bandwidth the *edges* of tuning curves exhibit a range of relative asymmetry, ranging from (a) steep, high-frequency slopes, to (b) sym-

^{a)}Present address: Cybernetics InfoTech, Inc., 15245 Shady Grove Road, Suite 190, Rockville, Maryland 20850.

metric to (c) steep, low-frequency slopes in different cell populations (Shamma *et al.*, 1993).

Acoustic spectra elicit response patterns in AI along all three dimensions. Therefore, we postulate (by analogy to the tonotopic axis translations associated with changes in vocal tract length) that there are other specific spectral distortions that result only in translations along either the bandwidth or asymmetry axes, and which do not otherwise cause a significant change in excitation pattern. We further hypothesize that auditory perception of these distortions, *and by extension of the vocal-tract-parameter variations from which they arise*, is relatively invariant (or robust). We elucidate in this paper the production mechanisms that give rise to these kinds of spectral changes. We then proceed to relate them to the robust perception of speech, specifically to the identification of relatively static American English vowels. We focus here on *static* spectra because we have excluded from consideration of dynamic spectral representations in the cortex, such as those encoding spectral FM and AM rates (Schreiner and Calhoun, 1994; Shamma, Versnel, and Kowalski, 1995).

This paper is organized as follows. We shall first describe a model of the vocal tract that is sufficiently detailed to capture the rich variety of vocal-tract shapes observed, yet is simple enough to have closed-form solutions and an intuitively interpretable structure. In Sec. III, we illustrate the relationship between the model parameters, their spectral outputs, and the perception of natural American English vowels. We then use the model to synthesize the vowels and test identification of these signals in relation to variations in the model parameters. In Sec. IV, we relate model parameters to three common spectral distortions that are shown in Sec. V to correspond to translations along each of the three representational axes of an auditory cortical model. Section VI summarizes the main thesis of the paper, that perceptual robustness to certain spectral distortions reflects a synergy between vocal production and perception.

II. A SINUSOIDAL MODEL OF THE VOCAL TRACT

There has long been considerable interest in modeling speech in terms of vocal-tract articulatory parameters, as well as the inverse problem, that of determining the shape of the vocal tract from the utterance dynamics (Atal *et al.*, 1978; Ladefoged *et al.*, 1978; Wakita, 1973; Gopinath and Sondhi, 1970; Schroeder, 1967). In most production models the vocal tract is viewed as an acoustic filter which modifies the spectrum of the signal produced by vibration of the vocal folds. Some models characterize the vocal tract as a segmented tube in order to capture fundamental properties of the vocal-tract transfer function (Fant, 1960; Stevens, 1989; Bardin *et al.*, 1990). Others describe the articulatory structures more explicitly as in Lindblom and Sundberg, 1971; Rubin, Baer, and Mermelstein, 1981; Maeda, 1990.

Our point of departure is a model proposed by Ladefoged and colleagues (Ladefoged *et al.*, 1978; Harshman, Ladefoged, and Goldstein, 1977) designed to calculate the tongue-shape deviation from a neutral shape by tracing x rays recorded during the pronunciation of ten American English vowels. The vowels were [i], [ɪ], [eɪ], [ɛ], [æ], [a], [ɔ],

[o], [u], [u] as in “heed, hid, hayed, head, had, hod, hawed, hoed, hood, who’d,” and were recorded within sentences of the form “Say h(vowel)d again.” A single frame of recordings was chosen (either from the most steady-state part of the second formant or approximately 30 ms after the first consonant) for analysis. The model divides the vocal tract into 18 approximately equal-length sections, as shown in Fig. 1(a). A distance, $\mathbf{d}(i)$, is defined from the palatal surface (upper surface of the vocal tract) to the tongue for each i th section (except for $i=17$ and 18) as

$$\mathbf{d}(i) = \boldsymbol{\delta}(i) + \mathbf{d}_{\text{neu}}(i), \quad (1)$$

where $\mathbf{d}_{\text{neu}}(i)$ is the neutral position [mean position of the tongue, Fig. 1(b)], and $\boldsymbol{\delta}(i)$ is the deviation from the neutral position [Fig. 1(a)]. Ladefoged’s group conducted a three-way principal-component and factor analysis (PARAFAC) of tongue positions for different vowels, and concluded that the tongue shape can be well described by two separate factors, \mathbf{t}_1 and \mathbf{t}_2 (especially for $i=4, \dots, 16$) as shown in Fig. 1(c). The total distance can then be expressed as

$$\mathbf{d}(i) = w_1 \mathbf{t}_1(i) + w_2 \mathbf{t}_2(i) + \mathbf{d}_{\text{neu}}(i), \quad (2)$$

where w_1 and w_2 are the two weights (computed for each vowel based on the formants associated with the model).

The two functions, $\mathbf{t}_1(i)$ and $\mathbf{t}_2(i)$, resemble two single-cycle sinusoids with a sine and cosine spatial phases (but both forced towards zero as i goes to 1 at the glottal end). The neutral position $\mathbf{d}_{\text{neu}}(i)$ is of relatively smaller amplitude and resembles a three-cycle sinusoid. Since any weighted sum of the single-cycle sinusoids still resembles a sinusoid, then the total distance \mathbf{d} is approximately a single-cycle sinusoid added to a smaller three-cycle sinusoid. This three-cycle sinusoid, however, affects mostly the locations of the third and the fourth formants (see Ehrenfest’s theorem in Appendix A). Therefore, ignoring the variations due to this \mathbf{d}_{neu} leads to a simplified vocal tract model with a single sinusoidal (log) cross-sectional area $A(x)$, along with an arbitrary amplitude (a) and phase (θ)

$$A(x) = A_0 e^{a \cos(2\pi \nu x/l + \theta)}, \quad (3)$$

where ν is the normalized spatial frequency of the sinusoid, and A_0 is the reference area of the uniform vocal tract. Note that the normalized spatial frequency specifies the number of cycles in the region $0 \leq x \leq l$. Furthermore, we include an exponentially decaying term to account for the constraint at the glottis where the perturbation must always stay at zero.

The overall area function of the vocal tract model is therefore given by

$$A(x) = A_0 e^{a(\cos(2\pi x/l + \theta) - \cos \theta e^{-b(x/l)^s})}, \quad (4)$$

with the added perturbation

$$\delta A(x)/A_0 = -a \cos \theta e^{-b(x/l)^s}, \quad (5)$$

where the decay rate $b > 0$ and the scaling power $s \geq 1$.

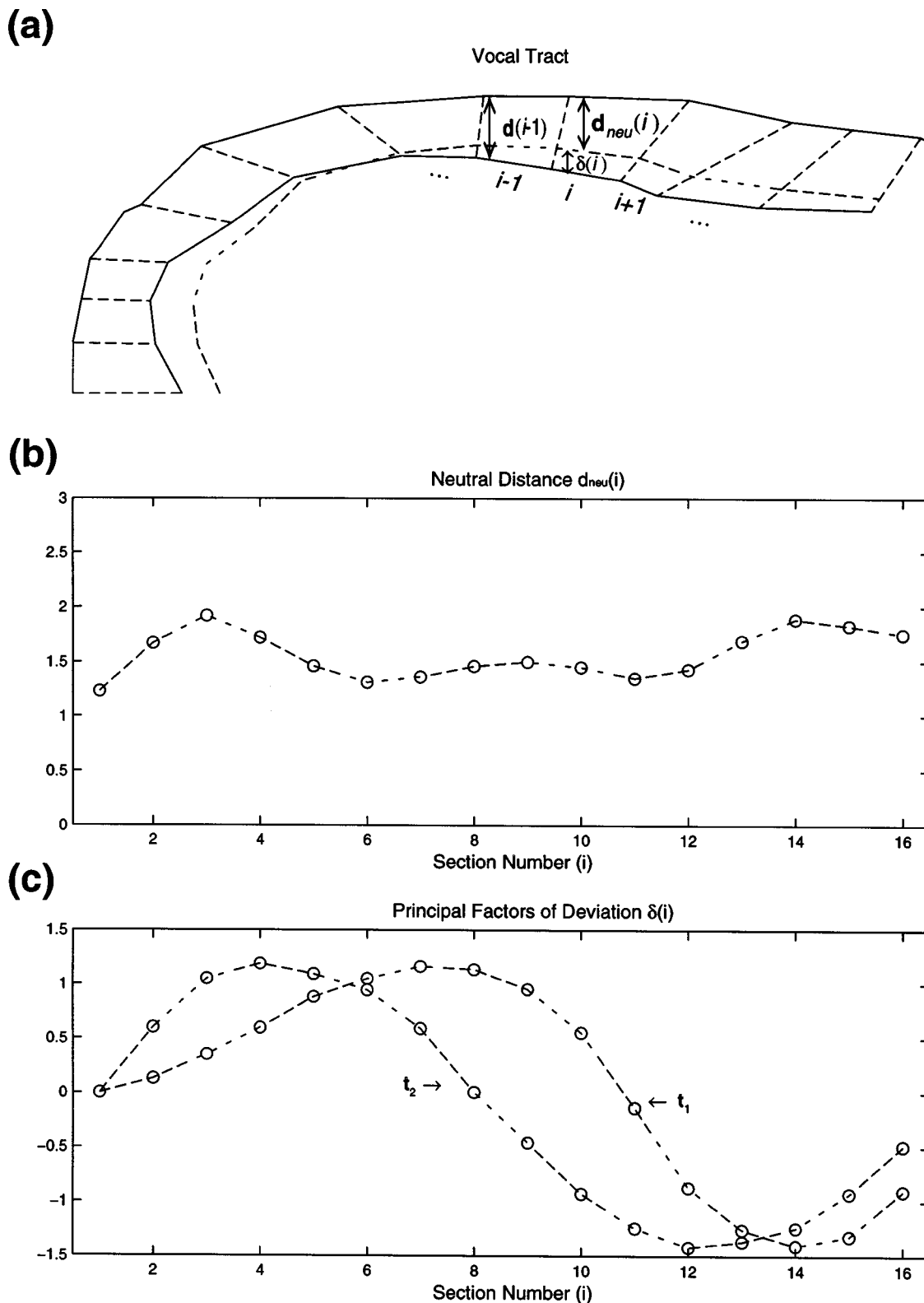


FIG. 1. The Ladefoged model of the vocal tract. (a) A schematic of a simplified vocal tract with several sections (indexed by i , and cross-sectional areas parametrized by a tongue-to-palate distance d , a neutral distance d_{neu} , and a deviation between the two δ). (b) The distance, d , of a neutral vocal tract as a function of section index, i . (c) The deviation, δ , as a function of section index, i , for the first and second factors that emerge from PARAFAC analysis of all vowels (see the text for details). The two functions resemble sine and cosine waves with a forced-zero deviation (boundary condition) at the glottis ($i = 1$).

Results of simulations with the full model are shown in the nomograms of Fig. 2(a) (solid lines), where the spatial phase, θ , is varied over its full range, while $A_0 = 5 \text{ cm}^2$, $b = 16$ and $s = 2$.¹ The simulations assumed a 17.5-cm-long

lossless tube divided into 18 uniform sections. Acoustic inertance (L_a), and compliance (C_a) per unit length are computed for each section (Flanagan, 1972). The transfer function of the vocal tract $V(f)$ (and hence the formant tracks) is

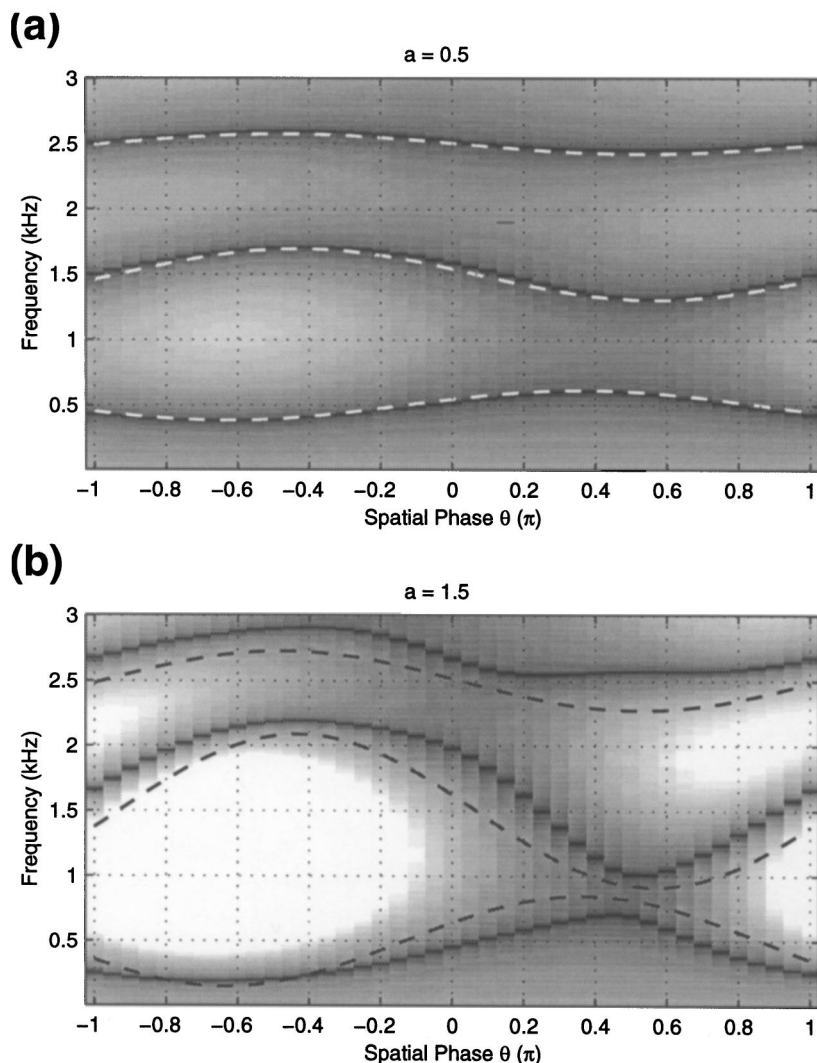


FIG. 2. The spectra generated by the sinusoidal vocal tract model. (a) The spectra produced by the model as a function of the phase of the sinusoid θ , which corresponds to the location of the constriction along the tract. The amplitude of the sinusoidal cross section is controlled by the parameter a which is set to a moderate value in this plot ($a = 0.5$). The dashed lines depict the estimated formant locations using Ehrenfest's theorem approximation. The correspondence between the estimated and computed peak frequencies is excellent. (b) The correspondence between estimated and calculated spectral peak frequencies deteriorates with increasing a values ($a = 1.5$).

then calculated based on the equivalent electrical circuit.

A useful approximation of the model computations can be derived based on Ehrenfest's theorem as described in detail in Appendix A. In this simplified formulation, changes in the formant locations can be directly related to the parameters of the model, especially the articulatory parameter a . Specifically, Appendix A equations (plotted as dashed lines in Fig. 2) reveal that for small perturbations ($a < 1$) the approximation is quite accurate, but it gradually deteriorates for larger perturbations ($a > 1$) as shown in Fig. 2(b).

Another important property of the model is illustrated by the nomograms of Fig. 3. Each nomogram is for $0 < a < 1.5$ at a fixed θ . The rate and direction of formant dilation (inward or outward) depends on the θ value, and is approximately linear with parameter a as shown in the figures. Since higher formants remain fixed (a consequence of the single sinusoidal simplified model), these shifts can be described as a *local* dilation (compression for $\theta = \pi/2$ and expansion for $\theta = -\pi/2$) of the spectrum. These results are explicitly derived from Eq. (A5), where the deviation ratio is proportional to the perturbation amplitude and the following approximation $\delta \log F_i \approx \delta F_i / F_i$ is valid for moderate degrees of perturbation. As we shall discuss in detail in Sec. IV, this type of

spectral dilation is a special case of distortion that is considered perceptually tolerable.

A. Relating the sinusoidal model to Ladefoged's model

The sinusoidal model can be explicitly related to bases functions (t_1 and t_2) by rewriting the normalized perturbation in Eq. (4) as

$$\delta A(x)/A_0 = v_1 t_1(x) + v_2 t_2(x), \quad (6)$$

where

$$\begin{aligned} v_1 &= a \cos \theta \Rightarrow -w_1, \\ v_2 &= a \sin \theta \Rightarrow -w_2, \\ t_1(x) &= \cos(2\pi x/l) - e^{-b(x/l)^s} \Rightarrow -\mathbf{t}_1, \\ t_2(x) &= -\sin(2\pi x/l) \Rightarrow -\mathbf{t}_2. \end{aligned} \quad (7)$$

The variables, v_1 and v_2 , control the modified cosine part and the negative sine part, respectively, of the logarithmic area function. Compared to Ladefoged's model [see Eq. (2)

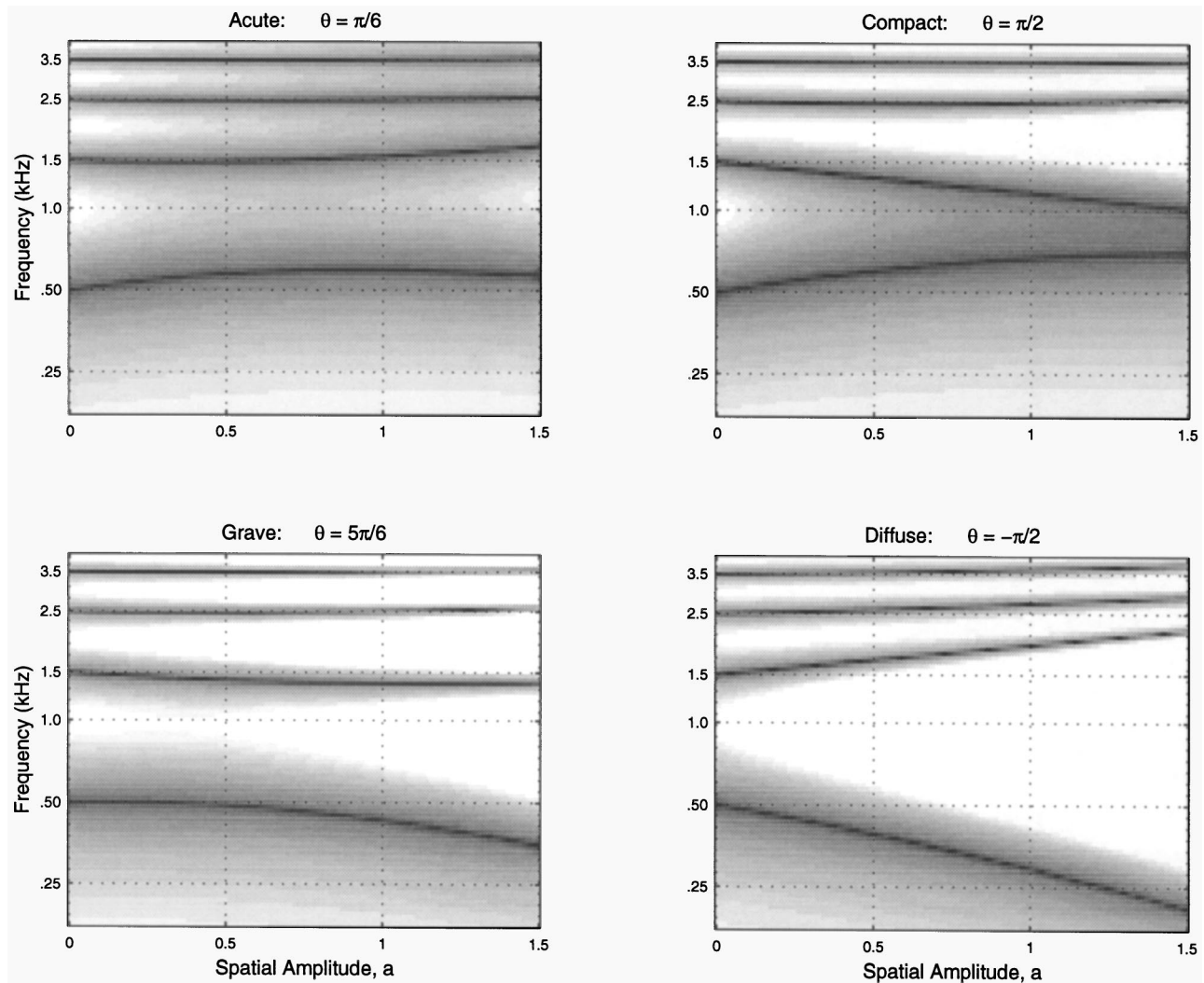


FIG. 3. The vowel spectra generated by the sinusoidal vocal-tract model as a function of a and θ . Within each of the four different classes of vowels [acute, compact, grave, and diffuse]² a range of spectra is possible, depending on the degree of vocal-tract constriction (or value of a). Vowels exhibit the largest distinctions for large values of a . Vowels converge to the neutral tube position as a decreases.

and Fig. 1], v_1 is analogous to $-w_1$ and v_2 to $-w_2$. Therefore, v_1 can be viewed as a *back-raising factor* whereas v_2 can be viewed as a *front-lowering factor*. In addition, the constriction area, A_c , and the constriction location, X_c , can be written in terms of a and θ , respectively, as

$$A_c = e^{-a} A_0, \quad (8)$$

$$X_c = \left(\frac{1}{2} + \frac{\theta}{2\pi} \right) l. \quad (9)$$

In the following section, we relate these vocal-tract parameters directly to spectral features important in the characterization of speech, especially vowels.

III. REPRESENTATION AND IDENTIFICATION OF NATURAL AND SYNTHESIZED VOWELS

To relate the vocal-tract model to speech, it is important to characterize it in terms of the spectral resonance patterns it generates. In the sinusoidal model the formants are determined both by the perturbation amplitude, a , and the angle, θ , as depicted in Figs. 2 and 3. These parameters also imply

a relationship between $v_1 - v_2$ and the formants as displayed in Fig. 4. The first formant ranges between 0.2 and 0.75 kHz, while the second formant ranges from 1 to 2.4 kHz. This formant range approximately matches that observed for the human vocal tract as shown in Table I.

Using such data, we can assign different vowels to different ranges of a and θ . The results of such an assignment derived from thousands of vowels from the TIMIT corpus are illustrated in Fig. 5. The large vowel symbols are placed at the center of each vowel's distribution. It is evident that the vowels subdivide only a portion of the full range of possible vocalic categories within the circle. It is also clear that each vowel occupies a *range* of parameter values, and not simply one specific value, i.e., there are certain spectral variations (or distortions) that are deemed inconsequential for the identity of a vowel. We hypothesize that these spectral distortions are perceptually tolerable³ partly because (i) they reflect vocal-tract parameter variations that are natural, common and difficult to control, and (ii) because their auditory representations are invariant in the sense described earlier in the introductory section. We shall address in Sec. IV

Formant Contours, F_1 (solid) and F_2 (dashed), in kHz

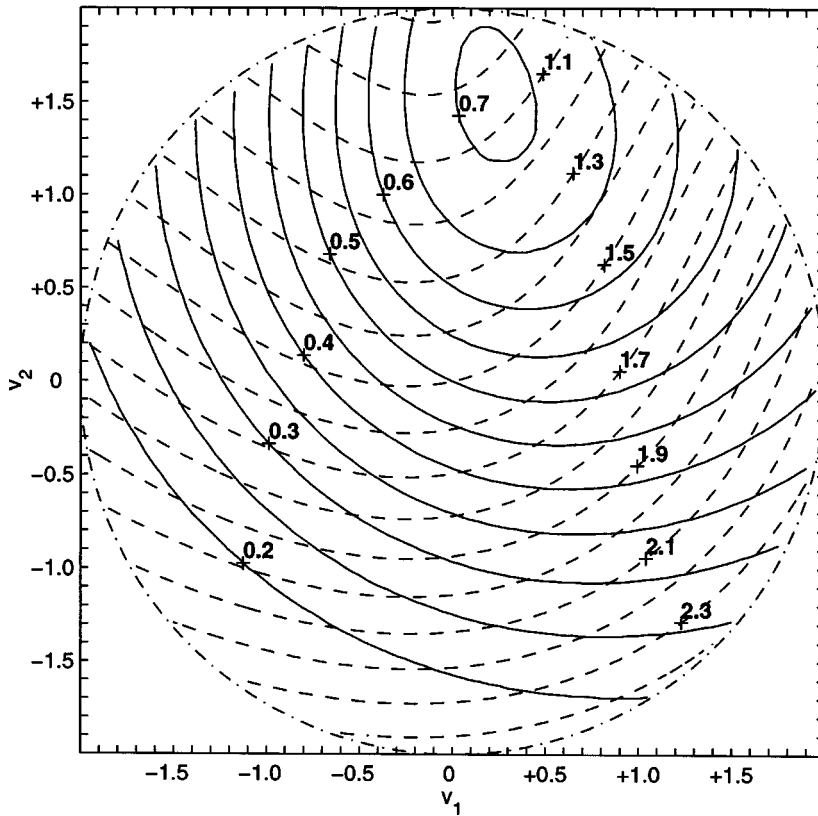


FIG. 4. Formant peaks (F_1 —solid lines, F_2 —dashed lines in kHz) generated by the sinusoidal vocal-tract model as a function of the Euclidean parameters, v_1 and v_2 , corresponding to the polar parameters $a = \sqrt{v_1^2 + v_2^2}$ and $\theta = \tan^{-1}(v_2/v_1)$.

the articulatory relationship, and touch upon the auditory aspects later in Sec. V. But, first we discuss in further detail the perceptual tolerance of these vowels using tokens synthesized with the vocal-tract model directly.

A. Identification of synthesized vowels

To explore the organization of the entire perceptual space afforded by the vocal-tract model, we carried out the following psychoacoustic experiment to partition the (v_1, v_2) [or equivalently the (a, θ)] space into different *synthesized* vowels. The experiment consisted of using the

TABLE I. Formant frequencies for the vowels in the TIMIT corpus (male speakers). The first and second formants, F_1 , F_2 , are determined from a smoothed magnitude spectrum of each vowel as in the spectral cross section at a scale=0.5 cyc/oct in Fig. 10. Each static spectrum is obtained by averaging over a 24-ms central segment of the spectrogram of the vowel. Such a choice reduces coarticulation effects from surrounding consonantal segments. The mean and standard deviation of the formant frequencies shown in the table are calculated from all vowels (>62.5 ms) in all dialect regions of the training set of the TIMIT corpus.

IPA symbol	Typical word	F_1	F_2
a	(hot)	637 ± 112	1150 ± 188
æ	(bat)	600 ± 57	1660 ± 177
ʌ	(but)	560 ± 63	1231 ± 208
ɔ	(bought)	589 ± 112	861 ± 146
ɛ	(bet)	531 ± 56	1578 ± 195
ə	(ago)	459 ± 57	1361 ± 155
ɪ	(bit)	439 ± 71	1765 ± 298
i	(beet)	354 ± 67	2139 ± 234
u	(foot)	435 ± 37	1200 ± 245
u	(boot)	380 ± 47	1086 ± 138

model to generate sounds with all possible formant combinations and then asking subjects to identify the sounds as one of eleven vowels, as described in detail below.

1. Stimuli and methods

For each stimulus, the area function of the vocal tract $A(x)$ is generated by Eq. (4) ($A_0 = 5 \text{ cm}^2$) for a randomly chosen $0 < a < 2$ and $0 \leq \theta < 2\pi$. The 17.5-cm-long lossy tube is then divided into 18 uniform sections. Acoustic inductance (L_a), resistance (R_a), compliance (C_a), and conductance (G_a) per unit length are computed for each section, and the radiation load at the lips is approximated by a parallel connection of a radiation resistance (R_r) and inductance (L_r).⁴ The transfer function of the vocal tract $V(f)$ is calculated based on the equivalent electrical circuit. The excitation signal, with a fundamental frequency of 120 Hz, is generated according to Rosenberg's model (1971), and then filtered by the transfer function $V(f)$. Signals are computed and sampled at 16 kHz, then are gated by a 250-ms window including a 20-ms rise/decay function, and delivered to the subjects via a loudspeaker inside an acoustic chamber.

Eleven vowels were selected for the test (see Table I), viz., [a], [æ], [ʌ], [ɔ], [ɛ], [ə], [ɪ], [i], [u], [ʊ], and [ü]. After presenting the stimulus, a subject is asked to identify it as one of the 11 vowels above or as "none-of-the-above." Up to three replays are allowed. Following a decision, the next stimulus is presented 3 s later. A complete session consisted of 100 trials and took approximately 15 min to complete. Three subjects completed 600 valid trials. Two of the subjects were native speakers of American English.

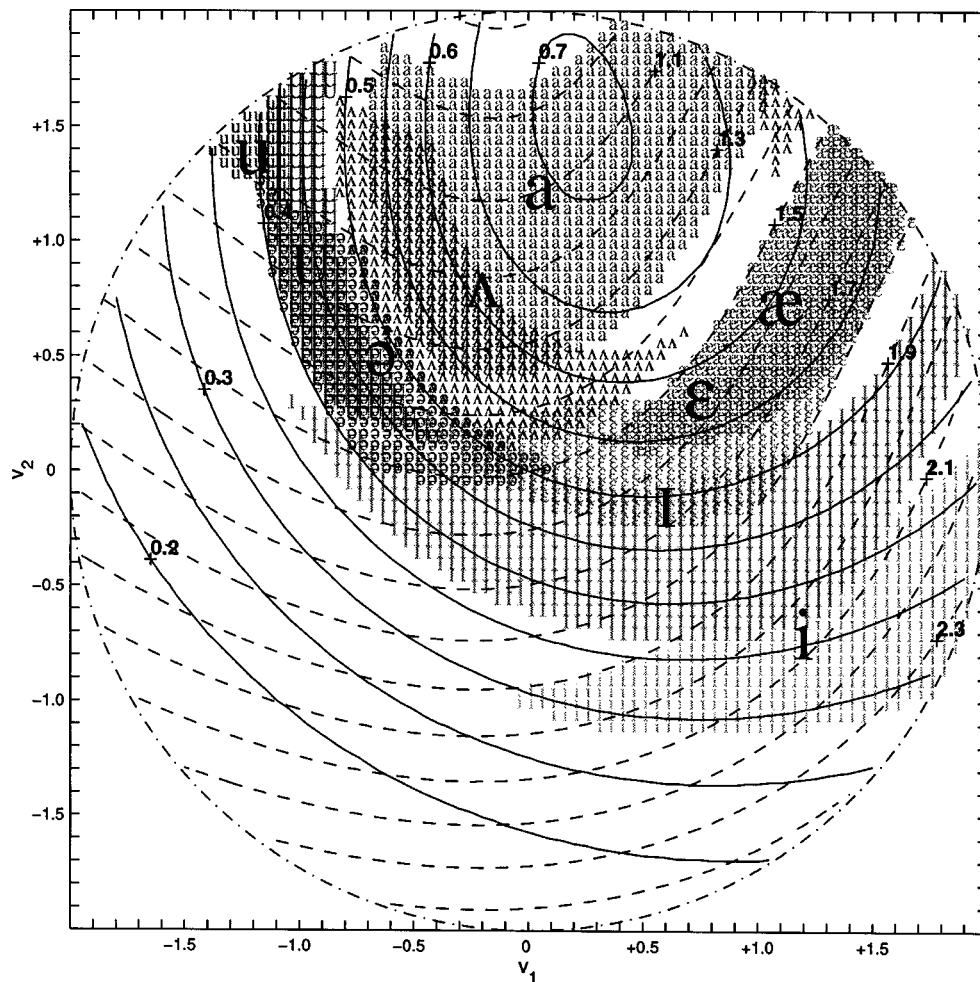


FIG. 5. The distribution of ten American English vowels (extracted from the TIMIT corpus, male speakers) as determined from the formant frequencies ($F1$ and $F2$) and hence indirectly as a function of model parameters v_1 and v_2 . The labels are situated at the center of each vowel's distribution as described in the text.

2. Results

The raw trial outcomes and the “smoothed” overall distribution of identified vowels from all three subjects are shown in Fig. 6, along with background contours [Fig. 6(b)] duplicated from Fig. 4 and superimposed upon the vowel clusters. The cumulative results in Fig. 6(a) are typical of each of the three subjects. In each panel, the distribution of a vowel is shown together with its mean location (marked by the appropriate vowel symbol). Also indicated for comparison is the mean location of the TIMIT-corpus vowels from Fig. 5 (center of the distribution is indicated by an “x” symbol).

The overall smoothed distribution in Fig. 6(b) is obtained by selecting at each point in the circle the phonetic symbol associated with the majority of responses within a radial area of 0.1. The large vowel symbols are placed at the center of each vowel's distribution. This summary plot displays similar overall patterns for each vowel as those seen in the raw data. Three important observations can be made about the results in Fig. 6.

- (1) Vowel clusters are contiguous.
- (2) Vowel clusters tend to “radiate” out from the center towards the perimeter of the circle.

- (3) Going clockwise around the circle ($\theta=0 \rightarrow 2\pi$) at a radius $a>0.5$, one encounters the vowel series $[\epsilon]$, $[\æ]$, $[a]$, $[\ɔ]$, $[u]$, $[\ʊ]$, $[i]$, and $[ɪ]$. Towards the center, the vowels begin to blend into the more neutral vowels $[\partial]$ and $[\Lambda]$.

3. Discussion

The synthesized vowel map of Fig. 6 roughly matches that of the natural vowels in Fig. 5 earlier. Specifically, the center of each vowel's distribution are at approximately similar locations on the two maps. Furthermore, as with the natural vowels, there is a broad range of parameter values perceived as the same vowel, particularly (though not exclusively) along the radial axis. There is one prominent difference between the two maps: natural vowels are more crowded towards the top of the circle, leaving the bottom half of the vowel circle empty. This is because the natural vowel set had no vowels with such formant combinations. By contrast, the synthesized vowel set does contain these “novel” combinations, and listeners either extended the $[i]$, $[u]$ labels to fill up part of the lower half-circle, or identified these vowels as $[\ʊ]$, which was not in the natural set (for American English).

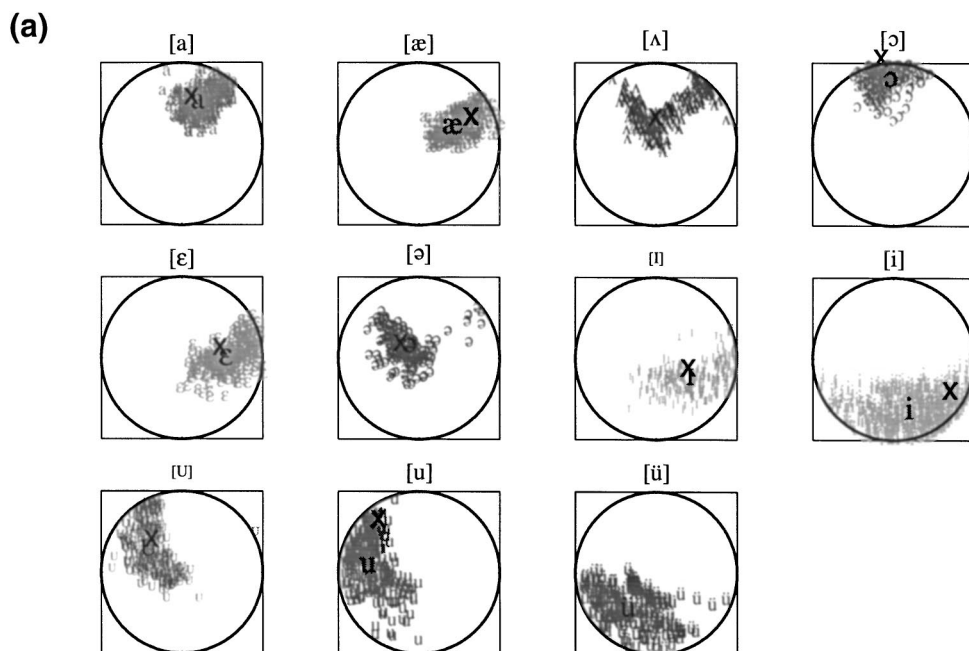
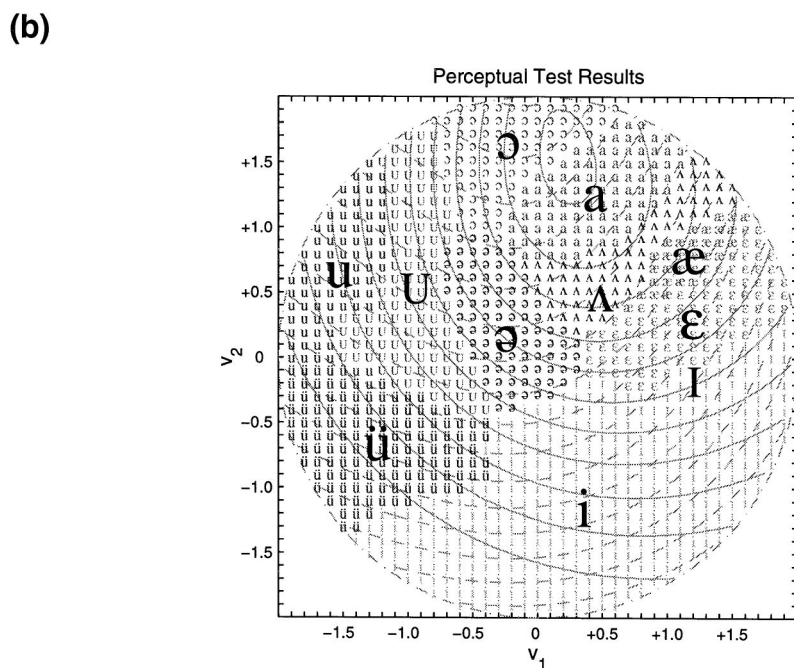


FIG. 6. The distribution of 11 identified vowels generated by the sinusoidal vocal tract model for $0 < a < 2$ and $0 \leq \theta < 2\pi$ (or the equivalent values of v_1 and v_2). (a) The cumulative distribution of v_1 and v_2 associated with each vowel label as reported by three subjects. The labels are situated at the center of each vowel's distribution as described in the text. The "x" symbols mark the location of the TIMIT corpus vowels distributions (Fig. 5) for comparison. (b) A summary smoothed distribution of the total results reported by the three subjects. Vowels towards the periphery (larger a values) are more distinctive, and span most vowel labels as a function of θ . Towards the center $a=0$, the reported labels are associated with neutral vowels.



IV. TOLERABLE AND COMMON SPECTRAL DISTORTIONS

We have hypothesized that there are certain common spectral distortions that are perceptually tolerable in that they do not change the identity of the vowels. We suggested that these distortions may correspond, on the one hand, to specific commonly varying (or perhaps difficult to control) parameters of the vocal tract, and on the other hand, to an invariant aspect in their auditory representation. Figure 7 illustrates three types of such tolerable spectral distortions that are readily related to the vocal-tract model. In the next section we shall relate these three types of distortions to translations along the representational axes of the auditory cortex.

A. Relating articulation to common spectral distortions

The first spectral distortion we address pertains to translations along the logarithmic frequency axis (or equivalently, dilations in the linear frequency axis) as illustrated in Fig. 7(a). These are related to changes in the length of the vocal tract, l , which shifts the resonance of the vocal tract (Fant, 1960; Rabinder and Shafer, 1978). This parameter changes with age (e.g., through childhood), and is fairly variable among individuals and is largely dependent on gender. Speech intelligibility is nevertheless robust to this form of spectral distortion. For instance, recent vowel recognition experiments (Fu and Shannon, 1999) reveal that identification is hardly affected by up to 2/3-octave shift of the spectrum

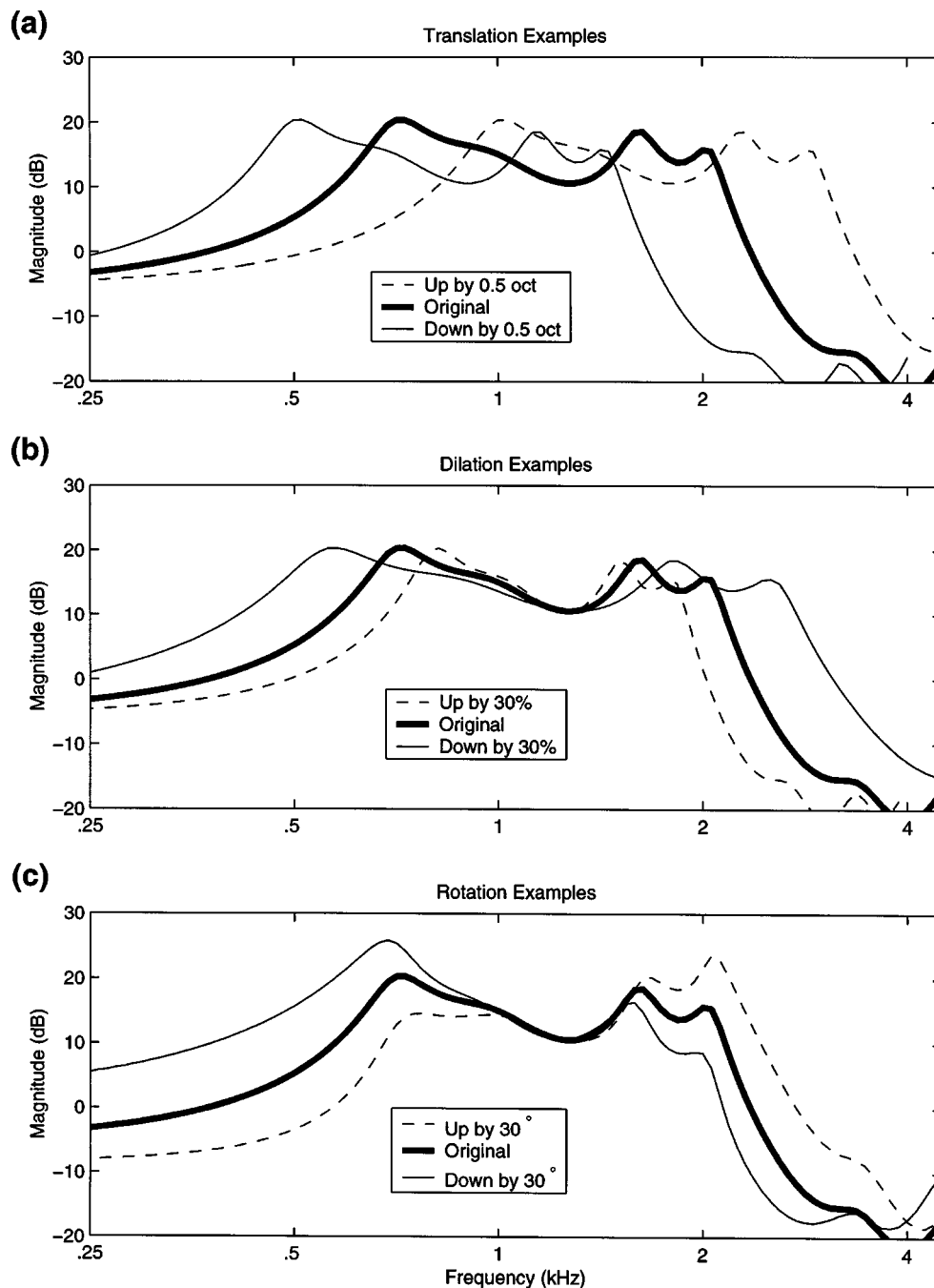


FIG. 7. Three spectral distortions attributable to common vocal-tract variations. (a) Translation of a spectrum along the logarithmic frequency axis (or dilation along the linear frequency axis) associated with vocal-tract length variations. (b) Dilation of the spectrum along the logarithmic frequency axis due to variations in the overall constriction of the vocal tract. (c) Shearing (or tilting) of the spectrum along the logarithmic frequency axis associated with vocal-tract losses, lip radiation, and microphone distortions.

despite the fact that formant locations are significantly altered.

The second spectral deformation is an exponential dilation or compression of the spectrum with respect to frequency, or equivalently a linear dilation with respect to *logarithmic frequency* as illustrated in Fig. 7(b). Informal listening to such distorted speech indicates that its main effect is a dramatic change in voice quality, but with relatively little loss of intelligibility. Baskent and Shannon recently tested the identification of such spectral distortions (Baskent and Shannon, 2001), reporting a maximum of 20% loss of recognition (and less than that for consonant and vowel con-

fusions) with a spectral compression factor of $2/3$.⁵

What kind of vocal-tract parameter variations might generate such a linear spectral dilation along the *logarithmic* frequency axis? Figure 3 demonstrates that such “local” dilations occur in the transfer function of the sinusoidal model as a function of a (while holding θ fixed). The term “local” refers to the fact that in the panels for $\theta = \pi/2$ ($\theta = -\pi/2$) the spectra contract (and expand) around 800 Hz with a increasing only locally, i.e., without too much effect on the third and fourth formants. Normally, a might be relatively constant for a given speaker, a factor that reflects the extent to which the speaker articulates his/her speech (see below).

This “factor” is likely to be different across speakers depending on acquired habits (e.g., dialect or speaking style), or innate causes such as overall size of the vocal tract.

It is also possible to produce a “global” dilation of the entire spectrum by a geometric deformation of the vocal tract. For example, if the uniform tube is replaced by an exponential (or power law) tube reflecting some individual’s unique vocal tract shape

$$A(x) = A_0 e^{\alpha x}, \quad \text{for } 0 \leq x \leq l, \quad (10)$$

where α is a real number which determines the openness of the tube. It can be shown that such a tube has resonance peaks that are dilated (or compressed) relative to a uniform tube as elaborated in Appendix C (Ru, 2000). By combining this deformation with a change in length, it is possible to have the spectral dilation centered about any arbitrarily chosen frequency.⁶ In general, the speech of such a compressed spectrum is perceived as that emanating from a vocal tract that is held at an exaggeratedly open and elongated position during production [as in $A(l) = 4A_0$ in Fig. 11(a) of Appendix C]. The expanded spectrum has the opposite character. It is as if produced by a vocal tract that is held in a “narrow” posture during production [$A(l) = A_0/4$ in Fig. 11(a)]. Note that in this dilation both the overall location of the formants and the extent of their frequency modulations are either compressed or expanded.

Finally, the third spectral deformation is a “tilt” or “shearing” of the spectral pattern as depicted in Fig. 7(c). In the vocal tract such a spectral tilt may result from such factors as (a) acoustic radiation at the lips; (b) friction; and (c) thermal losses of the vocal tract, all of which lower the resonant frequencies and reduce the peak amplitude with increasing frequency. Opposing this trend are the yielding walls of the vocal tract, which tend to raise the resonant frequencies and increase the peak amplitude as a function of increasing frequency. Spectral tilt can also be the result of voices with different spectral slopes associated with the glottal source (an average value of -12 dB/octave for the roll-off), and is also common in engineering systems, either added intentionally as in pre-emphasis, or unintentionally because of the variable characteristics of different microphones and communication channels. Clearly, such moderate degrees of spectral tilt rarely have a significant effect on speech intelligibility.

In summary, we hypothesize that perceptual robustness to certain spectral deformations reflects their unique origin as attributable to common unintentional natural variations in the length, cross-sectional profile, and overall tract losses among different speakers. The perceptual robustness may also be due to the fact that these specific distortions have limited consequences upon the auditory representation of the spectrum, and are therefore not perceptually disruptive, as is discussed in Sec. V.

B. Relating robust vowel perception and vocal tract variability

The results of the vowel identification experiments demonstrate that vowels can be represented and synthesized by the sinusoidal model in a manner that is consistent with previously known relationships (Fig. 5 vs Fig. 6). They also

point to two fundamental insights into the relation between production and perception that is discussed next.

The key observation concerns the relationship between the vowels’ distribution [Fig. 6(a)] and the pair of articulatory parameters (a, θ) of the sinusoidal model. As noted earlier, an interesting feature of the vowel distributions in Fig. 6(a) is that, except for the neutral vowels, they tend to radiate out from the central region of the circle. This implies that vowel perception is relatively insensitive to variations in the parameter a . This may be explained in articulatory terms as follows. In the vocal-tract model, the parameter a is proportional to the maximum amplitude of the sinusoidal constriction. Intuitively, parameter a reflects the “degree of expression” or the “clarity” of the articulatory movements. For example, fixing a at a large value (> 1) is intuitively equivalent to speaking with an exaggerated motion of the tongue and jaw, or causing the cross-sectional area at any location to traverse large amplitudes from the open to close positions. Consequently, the spectrogram of an utterance synthesized with such a vocal tract will have exaggerated formant frequency excursions as illustrated in Fig. 8. The opposite occurs when a is small, where the vocal tract has a more constrained jaw and tongue. The resulting spectrogram exhibits much smaller formant excursions. With this intuitive interpretation in mind, it is understandable why varying a affects the quality of the speech but not so much its intelligibility. These ideas share a similar outlook to what Lindblom calls hyper- and hypoarticulation in the context of clear speech (Lindblom, 1990). Specifically, changing parameter a during conversation is one of many possible ways for speakers to adapt their acoustic output according to communicative and situational demands. Therefore, the parameter a can be one of many possible quantitative measures for the intraspeaker phonetic variation addressed by the hyper- and hypoarticulation theory.

V. CORTICAL PHYSIOLOGY AND PERCEPTUALLY ROBUST SPECTRAL DISTORTIONS

It is possible that perceptual robustness to the spectral deformations illustrated in Fig. 7 is partially attributable to the nature of spectral representation in the primary auditory cortex (Shamma *et al.*, 1993; Wang and Shamma, 1995). Specifically, it may be that applying these deformations on a spectral pattern only causes simple translations of its auditory representation, and hence does not affect its perception in a fundamental way. To elaborate on this hypothesis, we first briefly review a model of sound representation in the auditory cortex (AI), and then examine how it is affected by the spectral deformations alluded to above (Fig. 7).

Responses of cells in AI can generally be ordered according to one of three common parameters depicted by the *response area* shown in Fig. 9(a). This plot illustrates the response threshold (or the minimum signal intensity required) at each frequency to excite or suppress (i.e., inhibit) the neuron. The first important parameter is the *best frequency (BF)*—the signal frequency to which the neuron is most sensitive. Cells in AI (and all along the primary auditory pathway) are topographically ordered with respect to their BF, forming the well-known tonotopic axis. A key fea-

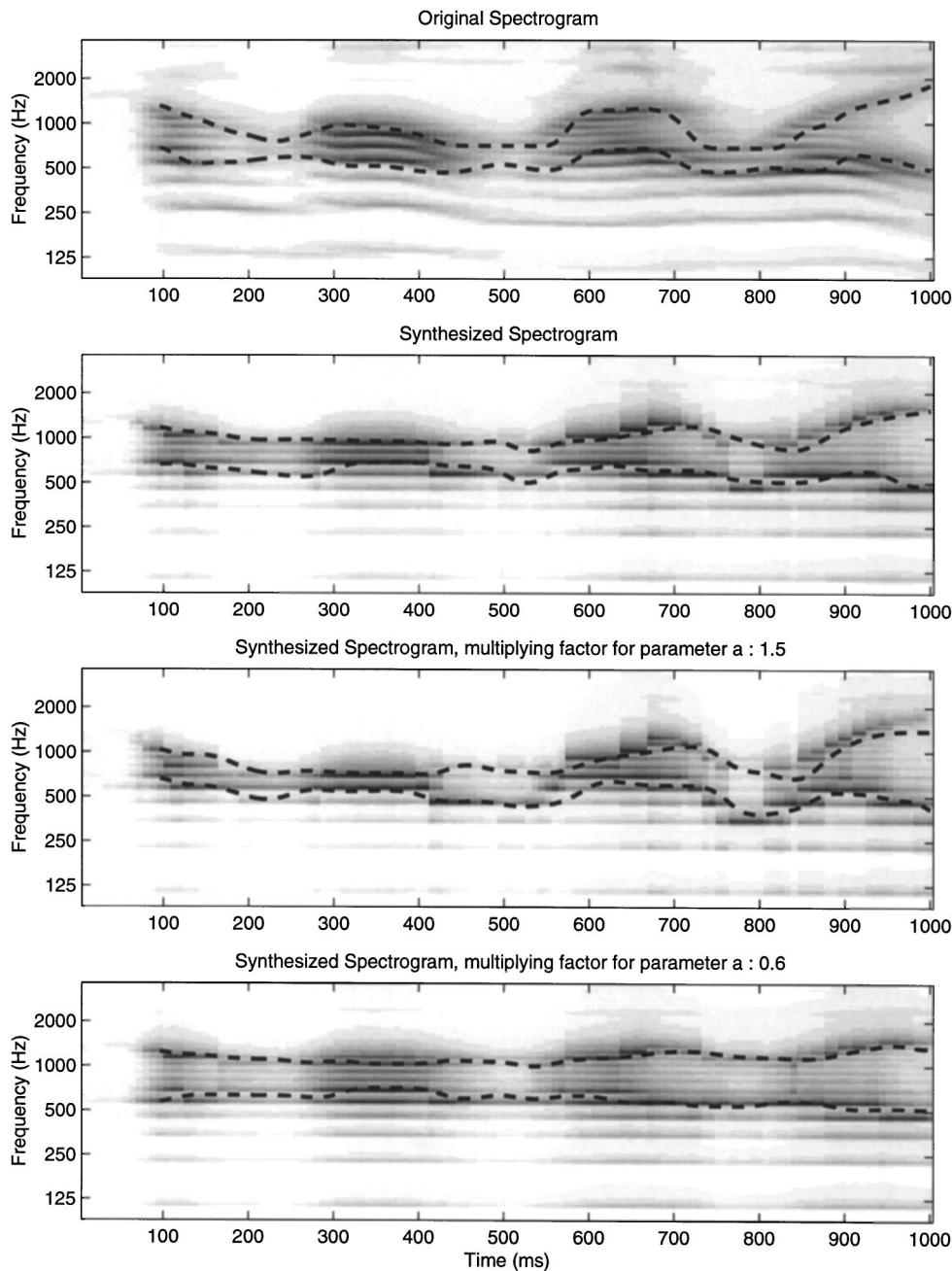


FIG. 8. Spectrograms of natural and synthesized speech with different model parameter values. The top spectrogram is of the natural utterance “Come home right away” by a male speaker. The second spectrogram is synthesized, frame-by-frame with parameters (a_i, θ_i) , which minimize the Euclidean distance between natural and synthesized spectra of frame i . The next two synthesized spectrograms are generated by modifying the parameter a . The first two formants are traced (dashed lines) in each spectrogram. Acoustic waves are available at <http://www.isr.umd.edu/CAAR/pubs.html>

ture of the tonotopic axis is its (approximately) logarithmic representation of frequency as shown in Fig. 9(b).

The second important parameter is width (or bandwidth) of the overall response area (or just of its excitatory portion). The representative neuron in Fig. 9(a), displays an excitatory area (central white region) surrounded by “inhibitory sidebands” (shaded regions). AI neurons tend to be organized topographically along a “bandwidth” (or *scale*) axis where they gradually change their tuning from narrow to broad (in terms of bandwidth), and hence the scale of resolution (or coarseness) of the spectrum they represent (Schreiner and Mendelson, 1990).

The third qualitative response area parameter is the degree of asymmetry associated with the extent and strength of the inhibitory sidebands. AI units are found with a wide range of asymmetries, from balanced to highly one-sided,

with stronger inhibition above or below BF (Shamma *et al.*, 1993).

These three parameters of the response area (BF, bandwidth, and asymmetry) are also captured by the *response field* (RF) of the neuron shown in the right panel of Fig. 9(a). The RF represents approximately how a neuron is driven by an iso-intensity signal at different frequencies. Figure 9(c) depicts the RF of neurons organized along each of these three dimensions. If we take the centrally depicted RF as the *canonical RF* [denoted by $\mathcal{RF}(x; x_c, \Omega_c, \phi_c)$], where x denotes the tonotopic frequency in octaves, x_c is the center of the RF (which roughly corresponds to the BF), Ω_c is a parameter related to the bandwidth of the RF, and ϕ_c determines the asymmetry of the RF. Details of the mathematical formulation of this model are available in Appendix B. The

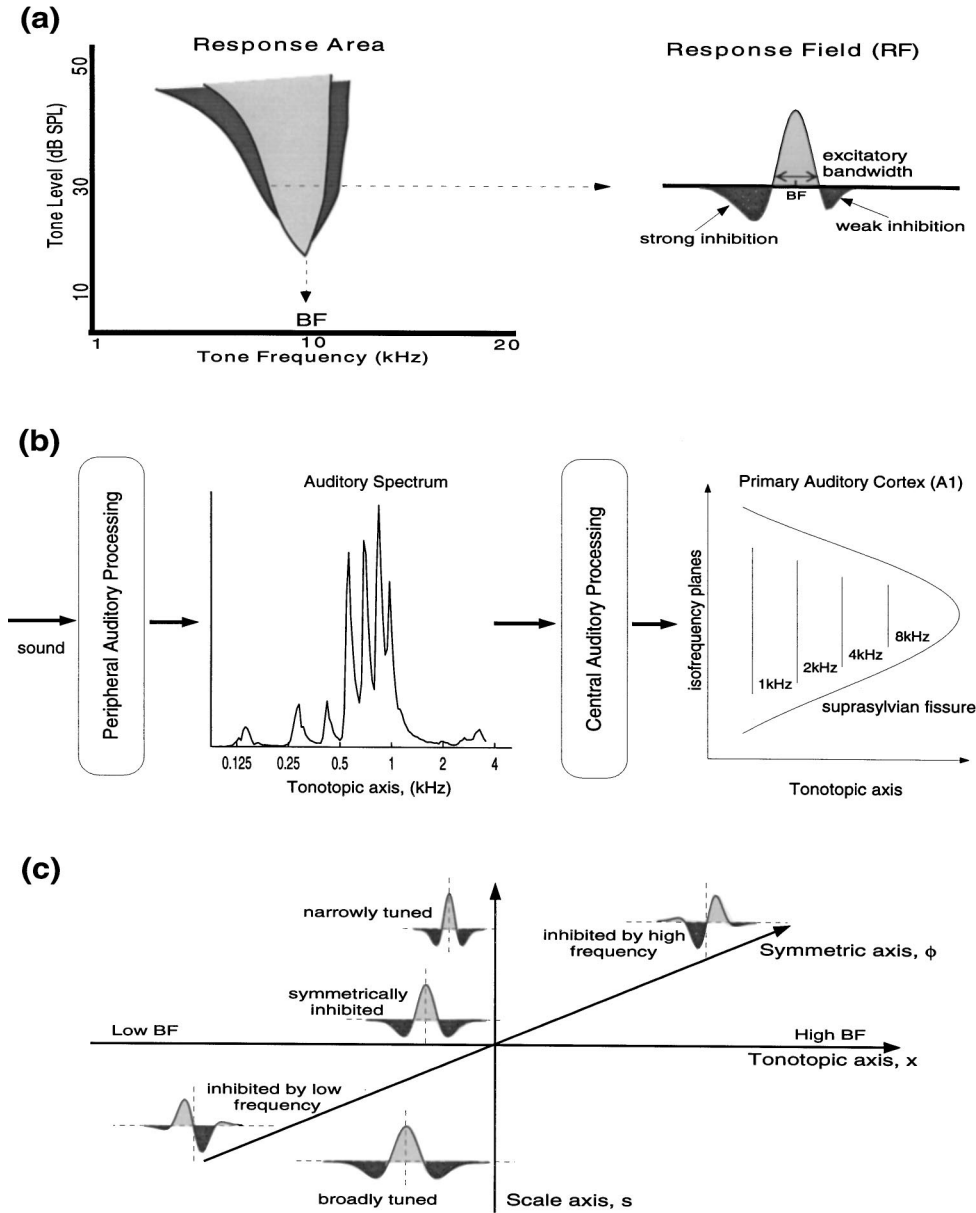


FIG. 9. The physiology of the primary auditory cortex (AI). (a) The response area of a typical neuron in ferret AI. The plot depicts the tone amplitudes and frequencies needed to evoke an excitatory (the light-shaded region) or an inhibitory (the dark-shaded region) neural response. In most cases, the central response region is excitatory, with surrounding inhibitory sidebands. The response field (RF) roughly captures the strength of the excitatory and inhibitory responses to an iso-intensity sinusoid as a function of frequency. Three important response properties are indicated: The best frequency (BF), the excitatory bandwidth, and the asymmetry of the inhibitory sidebands. (b) The representation of the auditory spectrum and the tonotopic axis. The sound spectrum is extracted early in the auditory pathway, and is represented by responses of neurons with tonotopically ordered BFs forming the tonotopic axis. The tonotopic axis in the auditory cortex becomes two-dimensional as depicted in the figure. Presumably other sound features are represented along the iso-frequency axis. (c) The organization of the RFs along three cortical axes. Cortical cells exhibit a wide variety of RFs. Variations with respect to three specific parameters form the three axes of the cortical representation of the spectrum. These are: (1) The BF along the tonotopic axis (from low to high); (2) The excitatory bandwidth along the scale axis (from narrowly tuned, to broadly tuned); (3) The asymmetry of the inhibitory sidebands along the phase axis ϕ (from $\phi_0 = 0$ to 2π ; shown are RFs from $-\pi/2$ to $\pi/2$).

RF transformations can be mathematically described as follows:

- (1) The RFs *translate* by x_0 along the tonotopic axis:
 $\mathcal{RF}(x; x_c - x_0, \Omega_c, \phi_c)$;
- (2) The RFs *dilate* by Ω_0 along the scale axis:
 $\mathcal{RF}(x; x_c, \Omega_c - \Omega_0, \phi_c)$; and
- (3) The RFs *rotate* with angle ϕ_0 in Hilbert space along the asymmetry axis: $\mathcal{RF}(x; x_c, \Omega_c, \phi_c - \phi_0)$.

It is unclear precisely what function is served by this variety of RFs. One hypothesis is that arrays of neurons with such variable RFs effectively compute a *multiresolution* (or multiscale) representation. To see intuitively how this representation arises, consider the spectrum of the vowel [a] (as in “father”) shown at the bottom of Fig. 10. We assume this spectral pattern is extracted early in the auditory pathway and is then projected to the primary auditory cortex. Cortical cells tuned to different bandwidths will respond well only to

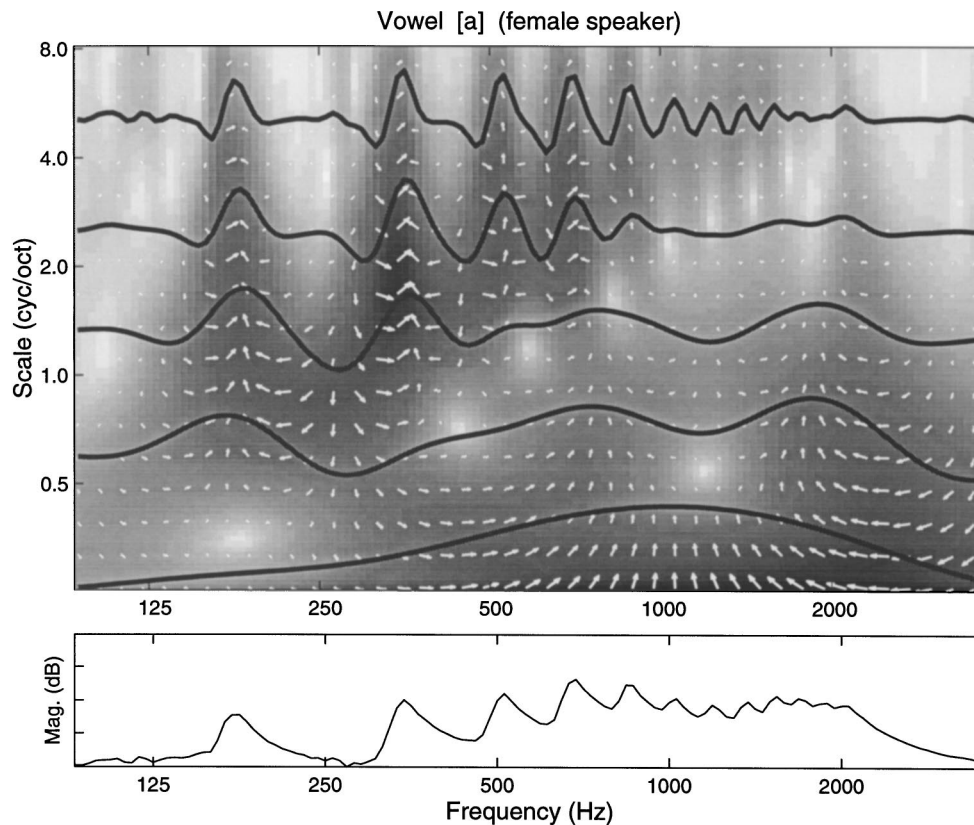


FIG. 10. A multiscale representation of the vowel [a] (female speaker). The log magnitude spectrum is depicted at the bottom. The cortical multiscale response is displayed above it against three axes. The abscissa is the tonotopic axis. The ordinate is the scale axis. The phase axis is represented by the direction of the white arrows (“→” to “←” counterclockwise depict responses of cells with $\phi_c = -\pi/2$ to $\pi/2$, respectively). The strength of the response is represented by the gray scale (black is strongest) and also by the direction and size of the phase arrow. In addition, several cross-sectional profiles of the response are shown at different scales ($\Omega_c = 0.25, 0.5, 1.0, 2.0$, and 4.0 cyc/oct). Note that the spectral profile becomes progressively more coarsely represented at lower scales. This figure can also be thought of as depicting the magnitude and phase of an affine wavelet transform of the vowel spectrum using the central RF in Fig. 9(c) as the mother wavelet.

spectral features commensurate with their bandwidth. Such a response pattern is depicted in Fig. 10, where cortical RFs are organized along three axes: according to their BF (abscissa), their bandwidth (ordinate), and their asymmetry (indicated by the arrows). Broadly tuned RFs would represent by their responses only the gross features of the spectral profile. For instance, the strength of the responses of the widest RFs (at the lowest scale of $\Omega_c = 0.25$) capture only the outline of the spectrum. Cells with progressively narrower bandwidths capture finer features (peaks and valleys). Consequently, the cortical model simultaneously represents the vowel spectral pattern at various degrees of resolution. The same explanation applies to the representation along the asymmetry axis depicted by the arrows in Fig. 10. Mathematically, such a multiscale representation is also known as an “affine wavelet transform” of the auditory spectral pattern, with the central RF in Fig. 9(c) being the canonical basis function (or “mother wavelet”) (Wang and Shamma, 1995).

Assuming such a cortical representation of the spectrum, it is possible to show analytically (Appendix B) that the three types of spectral deformations (shown in Fig. 7) are unique in that they cause a translation of the cortical model response along each of its axes. Thus, a linear dilation of the spectrum with respect to frequency [Fig. 7(a)] causes a simple trans-

lation of the cortical response along the tonotopic (logarithmic) frequency axis as discussed earlier. This property is of course inherited by the cortex from the (roughly) constant-Q filtering of the cochlea, and hence is not strictly a cortical representational feature. The other two invariant translations are a product of cortical-specific processing. That is, a linear dilation with respect to the *tonotopic axis* as in Fig. 7(b) results in a translation of the cortical representation along the scale axis, but with no change along the asymmetry axis. The opposite occurs in the third spectral deformation [Fig. 7(c)].

In summary, we hypothesize that perceptual robustness to certain spectral deformations partly reflects their unique impact on the cortical multiscale representation. Specifically, they cause translations along one of these axes without altering the overall response pattern.

VI. SUMMARY AND CONCLUSIONS

This paper has examined some potential bases of perceptual robustness of speech signals. Specifically, we explored the synergy between properties of the source (vocal tract) and receiver (auditory system). For the source we formulated a simplified sinusoidal model of the vocal tract based on detailed cross-sectional x-ray images and PARAFAC analysis performed by Ladefoged and colleagues.

The model utilizes a few essential parameters to synthesize vowel sounds. We then related parameters of this model to the perception of natural and synthesized vowels. The results demonstrated that vowel perception tends to be robust with respect to length and overall constriction of the vocal tract, two parameters that significantly vary across different speakers.

On the receiver end, a physiologically inspired model of primary auditory cortical responses is described to analyze and represent the received sound. The representation is effectively a multiscale wavelet transform with three axes: (a) a tonotopic (frequency) axis, and (b) the bandwidth and (c) phase of an affine wavelet transform (scale and phase axes).

The synergy between source and receiver models can be summarized as follows. *Relatively large variations in vocal-tract parameters can be perceptually stable if they result in spectral changes that are manifested in the cortical model as translations along one of its three axes.* Translations are considered “harmless” because they do not change the representational *pattern*, but simply its location relative to the representational axes. The specific correspondence between source parameters and receiver representation is: (1) Changes in vocal-tract length cause translations along the tonotopic axis; (2) Total effective area of constriction (or parameter a in the sinusoidal model) controls the (local or global) dilation of the spectrum, or equivalently causes translations along the scale axis; (3) Lip radiation and vocal-tract wall losses cause translations along the phase axis.

This perceptual robustness is also relevant to more general sound sources. For instance, animal vocal tracts exhibit the same kind of constraints and variations as those of humans. In fact, most natural and manmade resonators exhibit similar parameter variations within any particular class. Of course, whether these variations are considered perceptually significant by human listeners depends partly on contextual (semantic) factors. For example, violins of different sizes (or lengths) and made of different wood materials (hence, different damping losses and radiation) are perceived to be “violins” because their spectral envelope and its dynamics (and hence the timbre) remains otherwise roughly unaltered. Clearly, if the size of a violin increases significantly, its timbre is reclassified by listeners as that of a viola or a cello.

It is interesting to note that the multiscale auditory cortical representation is formally equivalent to the multiscale representation of two-dimensional images thought to exist in the visual cortex (DeValois and DeValois, 1990). Thus, the three cortical axes in audition—tonotopic, scale, and phase—have corresponding analogs in vision—space, size, and phase. Perceptual tolerance to translations along these visual axes is intuitively easier to imagine here; they correspond to an image varying in its position, size, and shear.

Finally, another important dimension in the cortical representation of the auditory spectrum is “time.” The dynamics of the auditory spectrum reflects the energy modulations due to the movement of the articulators. These are evident in the speech signal in the syllabic rates which are roughly in the range of 2–20 Hz. This range exactly matches the rate of signal energy modulations that is most effective in evoking responses in primary auditory cortex (Kowalski, Depireux,

and Shamma, 1996). A detailed analysis of the representation of these temporal modulations in speech and in the cortex, and its utility for assessing the “intelligibility” of noisy and reverberant signals can be found in (Chi *et al.*, 1999).

APPENDIX A: EHRENFEST’S APPROXIMATION THEOREM FOR THE GENERAL AREA FUNCTION

For the general area function, $A(x)$, only approximate solutions of resonances of the vocal tract are possible. One approach entails the application of Ehrenfest’s theorem where we express $A(x)$ as a small perturbation ($\delta A(x)$) on a uniform tube A_0

$$\delta A(x) = A_0 \sum_{m=1}^{\infty} a_m \cos(\pi m x / l). \quad (\text{A1})$$

The approximate formant deviation, associated with the departure from a uniform tube, is given by

$$\delta F_i / F_i = -a_{2i-1} / 2, \quad (\text{A2})$$

for $a_m \ll 1$ (Schroeder, 1967). In other words, the formant location is controlled by the odd cosine terms of the perturbation function. Since the first three formants are the perceptually most important in speech perception, only a few coefficients are sufficient to compose a perturbation that produces a variety of different vocalic signals. A generalized formula for the formant-deviation ratio can be written as

$$\frac{\delta F_i}{F_i} = - \int_0^l \cos\left((2i-1)\pi \frac{x}{l}\right) \frac{\delta A(x)}{A_0} \frac{dx}{l}. \quad (\text{A3})$$

Moreover, Mermelstein (1967) found empirically that this approximation, given the area function

$$A(x) = A_0 e^{\delta A(x)/A_0}, \quad (\text{A4})$$

is surprisingly good even for large perturbations.

1. The sinusoidal model

As stated in Sec. II, the vocal tract (log) area function can be approximated by a single spatial sinusoid,

$$A(x) = A_0 e^{a \cos(2\pi \nu x / l + \theta)}.$$

According to Eq. (A4), the relative perturbation $\delta A(x)/A_0$ is exactly the exponent in the above equation. The formant deviation can thus be derived from Eq. (A3)

$$\frac{\delta F_i}{F_i} = - \int_0^l \cos\left((2i-1)\pi \frac{x}{l}\right) a \cos\left(2\pi \nu \frac{x}{l} + \theta\right) d\frac{x}{l} \quad (\text{A5})$$

$$= \begin{cases} -\frac{a \cos \theta}{2}, & \text{if } \nu = i - \frac{1}{2} \\ -\frac{4a \nu \sin(\pi \nu + \theta) \cos(\pi \nu)}{\pi((2i-1)^2 - 4\nu^2)}, & \text{otherwise.} \end{cases} \quad (\text{A6})$$

Experimental observations of vocal-tract area functions in Fant (1960) (see also Fig. 1) suggest that for most vowels a one-period-sinusoid approximation (with different phases) is adequate. Therefore, combined with the formants of the uniform tube, $F_i = [c(2i-1)]/4l$, where c is the sound velocity (Portnoff, 1973; Rabiner and Schafer, 1978), the de-

viation of the i -th formant can be obtained by setting $\nu=1$.

$$\delta F_i = -\frac{c}{l} \frac{a}{\pi} \frac{2i-1}{(2i-1)^2-4} \sin \theta. \quad (\text{A7})$$

In addition, the formant change due to the added perturbation

$$\delta A(x)/A_0 = -a \cos \theta e^{-b(x/l)^s},$$

which accounts for the glottal constraint is given by

$$\frac{(\delta F_i)_{\text{exp}}}{F_i} = a \cos \theta \int_0^l \cos \left((2i-1) \pi \frac{x}{l} \right) e^{-b(x/l)^s} \frac{dx}{l}. \quad (\text{A8})$$

For $s=1$, a closed-form solution can be derived as:⁷

$$\left. \frac{(\delta F_i)_{\text{exp}}}{F_i} \right|_{s=1} = \frac{b(1+e^{-b})}{(2i-1)^2 \pi^2 + b^2} a \cos \theta. \quad (\text{A9})$$

An approximate solution is possible for $s=2$ and large b .^{8,9}

$$\left. \frac{(\delta F_i)_{\text{exp}}}{F_i} \right|_{s=2} \simeq \sqrt{\frac{\pi}{4b}} e^{-(2i-1)^2 \pi^2 / 4b} a \cos \theta. \quad (\text{A10})$$

Therefore, the total amount of formant deviations is given by the sum of the terms in Eq. (A5) and Eq. (A8) above.

APPENDIX B: CORTICAL MODEL RESPONSES ASSOCIATED WITH SPECTRAL DEFORMATIONS

From a mathematical point of view, the auditory cortex can be modeled as a wavelet analysis of the spectral profile (Wang and Shamma, 1995). Each RF can be described as

$$\begin{aligned} \mathcal{RF}(x; x_c, \Omega_c, \phi_c) &= h(x - x_c; \Omega_c) \cos \phi_c \\ &\quad - \hat{h}(x - x_c; \Omega_c) \sin \phi_c \\ h(x; \Omega_c) &= h(c^{\Omega_c} x), \end{aligned}$$

where x denotes the tonotopic frequency in octaves, the seed function $h(x; \Omega_c)$ is a real even function with peak spatial frequency response at Ω_c (in cycle/octave), x_c is the center frequency, ϕ_c is the characteristic phase (in radians) which determines the asymmetry of the receptive field, and \hat{h} denotes the Hilbert transform of the function h . The exact shape of this even function is not important as long as it can manifest the lateral-inhibition structure, i.e., a central excitatory band symmetrically flanked by inhibitory side bands. The response of the cell tuned to (x_c, Ω_c, ϕ_c) for an input auditory spectrum $y(x)$ is

$$r(x_c, \Omega_c, \phi_c) = \langle \mathcal{RF}(x; x_c, \Omega_c, \phi_c), y(x) \rangle,$$

where $\langle \cdot, \cdot \rangle$ denotes the inner product. The inner product process is equivalent to a filtering process with the spatial impulse response

$$h_{\mathcal{RF}}(x; \Omega_c, \phi_c) = h(x; \Omega_c) \cos \phi_c + \hat{h}(x; \Omega_c) \sin \phi_c.$$

Thus, the response can be efficiently computed by the following convolution:

$$\begin{aligned} r(x_c, \Omega_c, \phi_c) &= y(x) * h_{\mathcal{RF}}(x; \Omega_c, \phi_c) \big|_{x=x_c} \\ &= \int_{\tau} y(\tau) h(x_c - \tau; \Omega_c) \cos \phi_c \, d\tau \\ &\quad + \int_{\tau} y(\tau) \hat{h}(x_c - \tau; \Omega_c) \sin \phi_c \, d\tau. \end{aligned}$$

If the input spectrum $y(x)$ dilates with respect to frequency [translation along the tonotopic (log) frequency axis], the cortical response simply translates along the tonotopic axis as shown below:

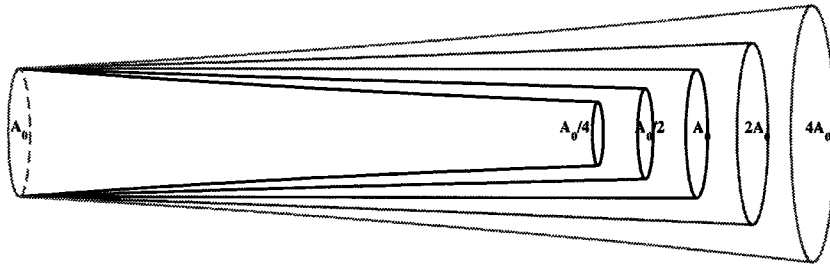
$$\begin{aligned} y(x - x_0) * h_{\mathcal{RF}}(x; \Omega_c, \phi_c) \big|_{x=x_c} \\ &= \int_{\tau} y(\tau - x_0) h(x_c - \tau; \Omega_c) \cos \phi_c \, d\tau \\ &\quad + \int_{\tau} y(\tau - x_0) \hat{h}(x_c - \tau; \Omega_c) \sin \phi_c \, d\tau \\ &= \int_{\tau'} y(\tau') h(x_c - x_0 - \tau; \Omega_c) \cos \phi_c \, d\tau' \\ &\quad + \int_{\tau'} y(\tau') \hat{h}(x_c - x_0 - \tau; \Omega_c) \sin \phi_c \, d\tau' \\ &= r(x_c - x_0, \Omega_c, \phi_c). \end{aligned}$$

If the input spectrum dilates with respect to tonotopic frequency $y(x) \rightarrow y(c^{\Omega_0} x)$, the cortical response can be shown to translate along the scale axis

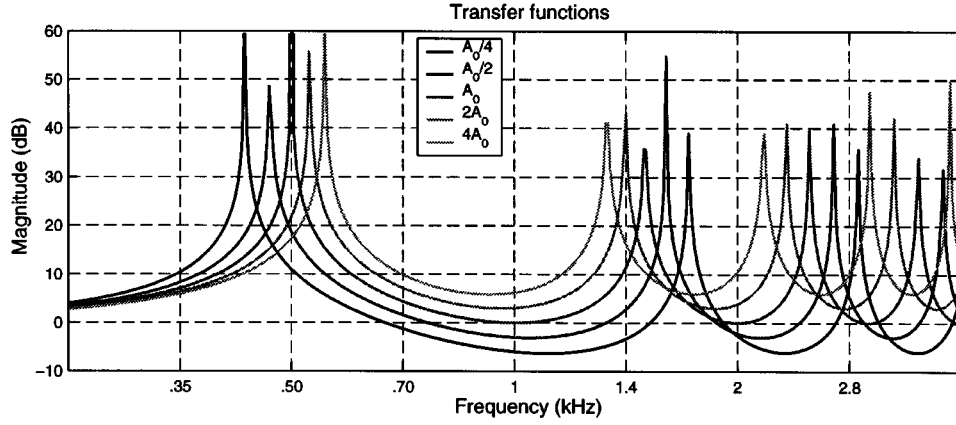
$$\begin{aligned} y(c^{\Omega_0} x) * h_{\mathcal{RF}}(x; \Omega_c, \phi_c) \big|_{x=x_c} \\ &= \int_{\tau} y(c^{\Omega_0} \tau) h(x_c - \tau; \Omega_c) \cos \phi_c \, d\tau \\ &\quad + \int_{\tau} y(c^{\Omega_0} \tau) \hat{h}(x_c - \tau; \Omega_c) \sin \phi_c \, d\tau \\ &= \frac{1}{c^{\Omega_0}} \left[\int_{\tau'} y(\tau') h\left(x_c - \frac{\tau'}{c^{\Omega_0}}; \Omega_c\right) \cos \phi_c \, d\tau' \right. \\ &\quad \left. + \int_{\tau'} y(\tau') \hat{h}\left(x_c - \frac{\tau'}{c^{\Omega_0}}; \Omega_c\right) \sin \phi_c \, d\tau' \right] \\ &= \frac{1}{c^{\Omega_0}} \left[\int_{\tau'} y(\tau') h(c^{\Omega_0} x_c - \tau'; \Omega_c - \Omega_0) \cos \phi_c \, d\tau' \right. \\ &\quad \left. + \int_{\tau'} y(\tau') \hat{h}(c^{\Omega_0} x_c - \tau'; \Omega_c - \Omega_0) \sin \phi_c \, d\tau' \right] \\ &= \frac{1}{c^{\Omega_0}} \cdot r(c^{\Omega_0} x_c, \Omega_c - \Omega_0, \phi_c). \end{aligned}$$

The asymmetry deformation is a shearing (or tilt) in the peaks of the spectrum which can be approximated by the following model: $y(x) \rightarrow y(x) \cos \phi_0 + \hat{y}(x) \sin \phi_0$, where ϕ refers as before to the phase of the Fourier transform of the pattern $y(x)$, and ϕ_0 is a constant phase added to the phase of the Fourier transform of $y(x)$. We can combine the facts

(a)



(b)



(c)

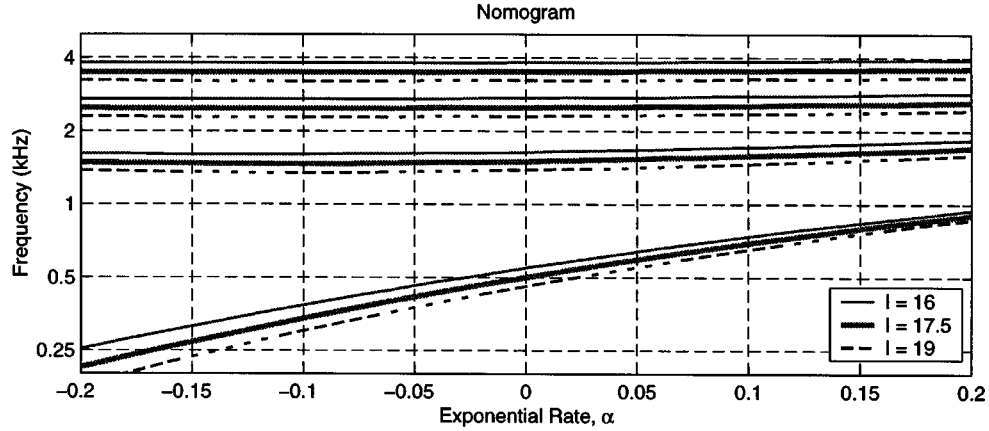


FIG. 11. Frequency responses of exponential tubes with different parameters l and α . (a) Exponential tubes for different parameters. (b) Corresponding transfer functions for tubes shown in (a). Local dilation (around 866 Hz) can be obtained by adjusting length l and rate α simultaneously. (c) The nomograms for length l (16, 17.5, and 19 cm) with varying exponential rate α .

that

$$y(x) * \hat{h}(x) = \hat{y}(x) * h(x), \quad \hat{\hat{h}}(x) = -h(x),$$

$$\widehat{\cos}(\Omega x + \phi) = \sin(\Omega x + \phi),$$

and show the cortical response will translate along the cortical asymmetry axis.

$$[y(x) \cos \phi_0 + \hat{y}(x) \sin \phi_0] * h_{\mathcal{RF}}(x; \Omega_c, \phi_c) \big|_{x=x_c}$$

$$= [y(x) * h(x; \Omega_c) \cos \phi_c \cos \phi_0$$

$$+ y(x) * \hat{h}(x; \Omega_c) \cos \phi_c \sin \phi_0$$

$$+ y(x) * \hat{h}(x; \Omega_c) \sin \phi_c \cos \phi_0$$

$$- y(x) * h(x; \Omega_c) \sin \phi_c \sin \phi_0] \big|_{x=x_c}$$

$$= [y(x) * h(x; \Omega_c) \cos(\phi_c + \phi_0)$$

$$+ y(x) * \hat{h}(x; \Omega_c) \sin(\phi_c + \phi_0)] \big|_{x=x_c}$$

$$= r(x_c, \Omega_c, \phi_c + \phi_0).$$

APPENDIX C: THE EXPONENTIAL TUBE

The area function of an exponential tube is formulated as

$$A(x) = A_0 e^{\alpha x}, \quad \text{for } 0 \leq x \leq l, \quad (\text{C1})$$

where α is a real number which determines the openness of the tube. Obviously, an exponential tube degenerates into a uniform tube when $\alpha = 0$. A tube with a positive α is often called a *horn*, while one with a negative α is called an *inverse horn*. Its frequency response can be derived from the algebra in Temkin, 1981.

$$V(f) = \begin{cases} \frac{e^{\alpha l/2}}{\cosh \beta l + (\alpha/2\beta) \sinh \beta l}, & \text{if } f \neq \frac{|\alpha|c}{4\pi} \\ \frac{e^{\alpha l/2}}{1 + \alpha l/2}, & \text{if } f = \frac{|\alpha|c}{4\pi}, \end{cases} \quad (\text{C2})$$

where $\beta = \sqrt{(\alpha/2)^2 - (2\pi f/c)^2}$. The frequency response at $f = (|\alpha|c)/4\pi$ is actually a limiting edition of the general solution.¹⁰

Equation (C2) clearly demonstrates the formant values change as a function of different model parameters l and α . The nomogram in Fig. 11(c) shows that the formants shift toward high frequency as α increases with fixed length $l = 17.5$ cm. The outcome looks like a *global dilation* of the spectrum. To get a *local dilation* around a specific chosen frequency, both the length (l) and (α) need to vary. Fig. 11(b) shows that the first two formants merge around a dilation center about $\sqrt{500 \cdot 1500} \approx 866$ Hz. The area-length relation is roughly formulated as

$$A_1/A_0 = (l_1/l_0)^{8.8}. \quad (\text{C3})$$

When $A_1 = A_0$, i.e., a uniform tube, the spacing between first and second formants is $\log_2(1500/500) \approx 1.5849$ octaves. The spacings are 1.9507 and 1.2192 octaves when $A_1/A_0 = 0.25$ and 4, respectively. This spacing can be approximated by

$$\Delta x(A_1) \approx 1.5849 - 0.1829 \log_2 \frac{A_1}{A_0}. \quad (\text{C4})$$

Therefore, the dilation rule can be formulated by

$$\frac{\Omega_0}{\Omega_1} \approx 1 - 0.1154 \log_2 \frac{A_1}{A_0}, \quad (\text{C5})$$

where $\Omega_i = (\Delta x(A_i))^{-1}$.

¹The selection of b and s is somewhat flexible as long as the resulting shape is roughly similar to the shape of the Ladefoged's vocal-tract model. For the exponent s , values $s=1$ and $s=2$ are preferred because they yield mathematically tractable solutions. The parameter b controls the perturbation decays and should be such that it affects a moderate number of sections (A value of $b=16$, as well as $s=2$, is used in the simulations). Even though these values do not yield a closed-form solution, an approximation can be found as b is large enough (see Appendix A).

²"Acute" speech sounds are characterized by the relative predominance of the high-frequency portion of the spectrum as opposed to "grave" segments in which the low frequency of the spectrum predominates. Compact segments are characterized by the relative predominance of a single centrally located spectral peak. Diffuse segments are those in which one or more noncentral formants predominate. A detailed description can be found in Jakobson, Fant, and Halle (1963).

³For our purposes, we define spectral deformations here as perceptually tolerable when they affect primarily the acoustic quality, rather than the

identity of the signal. For instance, in nontonal languages such as English, scaling up the amplitude of the spectrum of a speech signal or the frequency of its harmonics while keeping the spectral envelope intact only increases its loudness and pitch, respectively, but does not normally change the meaning of the utterance. The analogous situation in vision is the set of deformations of a portrait that leave its identity unchanged, such as shifting the location of an image, enlarging it, or slightly rotating or shearing it within reasonable limits.

⁴The inertance (L_a) which opposes acceleration is exhibited because of the mass of the air in the tube. The compliance (C_a) is exhibited because of the compressibility of the air. Viscous losses, which are proportional to the square of the particle velocity, are represented by the acoustic resistance (R_a). Heat conduction losses, which are proportional to the square of the sound pressure, are represented by the conductance (G_a). The detailed equations to compute L_a , R_a , C_a , and G_a can be found in (Flanagan, 1972). In this work, $R_r (= 128/9\pi^2)$ and $L_r (= 8r/3\pi c)$, where r is the radius of the opening and c is the sound velocity, provide a good approximation to the infinite plane baffle.

⁵Baskent and Shannon (2001) report bigger intelligibility losses with dilations (or expansions) of a factor of 2/3. However, interpreting these results is complicated by the fact they chose to keep constant the overall width of the spectrum within a specific value despite the expansion, effectively removing increasing amounts of the spectrum falling outside of this bandwidth.

⁶We have simulated all of the aforementioned manipulations to demonstrate the persistence of intelligibility despite large shifts in formant frequencies. These demonstrations are accessible at <http://www.isr.umd.edu/CAAR/pubs.html>

⁷ $\int_0^1 \cos(\alpha y) e^{-\beta y^2} dy = [\beta(1+e^{-\beta})] [\alpha^2 + \beta^2]$.

⁸ $\int_0^\infty \cos(\alpha y) e^{-\beta y^2} dy = \sqrt{\pi/4\beta} e^{-\alpha^2/4\beta}$.

⁹ $\int_1^\infty \cos(\alpha y) e^{-\beta y^2} dy < \int_1^\infty e^{-\beta y^2} dy = \sqrt{\pi/\beta} (1 - \Phi(\sqrt{2\beta}))$, where $\Phi(\cdot)$ is the cumulative distribution function (cdf) of normal distribution $\mathcal{N}(0,1)$.

¹⁰ $\lim_{f \rightarrow |\alpha|c/4\pi} \beta = 0$, $\cosh \beta l \rightarrow 1$, and $\sinh \beta l \rightarrow 0$.

Atal, B. S., Chang, J. J., Mathews, M. V., and Tukey, J. W. (1978). "Inversion of articulatory-to-acoustic transformation in the vocal tract by a computer-sorting technique," J. Acoust. Soc. Am. **63**, 1535–1555.

Badin, P., Perrier, P., Boe, L.-J., and Abry, C. (1990). "Vocalic nomograms: Acoustic and articulatory considerations upon formant convergences," J. Acoust. Soc. Am. **87**, 1290–1300.

Baskent, D., and Shannon, R. V. (2001). "Speech recognition under conditions of frequency-place compression and expansion," J. Acoust. Soc. Am. (submitted).

Chi, T., Gao, Y., Guyton, C. G., Ru, P., and Shamma, S. (1999). "Spectro-temporal modulation transfer functions and speech intelligibility," J. Acoust. Soc. Am. **106**, 2719–2732.

DeValois, R., and DeValois, K. (1990). *Spatial Vision* (Oxford, New York).

Fant, G. (1960). *Acoustic Theory of Speech Production* (Mouton, The Hague).

Flanagan, J. L. (1972). *Speech Analysis, Synthesis and Perception*, 2nd ed. (Springer, New York).

Fu, Q.-J., and Shannon, R. V. (1999). "Recognition of spectrally degraded and frequency-shifted vowels in acoustic and electric hearing," J. Acoust. Soc. Am. **105**, 1889–1900.

Gopinath, B., and Sondhi, M. M. (1970). "Determination of the shape of the human vocal tract from acoustical measurements," Bell Syst. Tech. J. **49**, 1195–1214.

Greenwood, D. D. (1961). "Critical bandwidth and the frequency coordinates of the basilar membrane," J. Acoust. Soc. Am. **33**, 1344–1356.

Harshman, R., Ladefoged, P., and Goldstein, L. (1977). "Factor analysis of tongue shapes," J. Acoust. Soc. Am. **62**, 693–707.

Jakobson, R., Fant, G., and Halle, M. (1963). *Preliminaries to Speech Analysis: The Distinctive Features and Their Correlates* (MIT Press, Cambridge, MA).

Kowalski, N., Depireux, D., and Shamma, S. A. (1996). "Analysis of dynamic spectra in ferret primary auditory cortex. II. Prediction of single unit responses to arbitrary dynamic spectra," J. Neurophysiol. **76**, 3524–3534.

Ladefoged, P., and Broadbent, D. E. (1957). "Information conveyed by vowels," J. Acoust. Soc. Am. **29**, 98–104.

Ladefoged, P., Harshman, R., Goldstein, L., and Rice, L. (1978). "Generating vocal tract shapes from formant frequencies," J. Acoust. Soc. Am. **64**, 1027–1035.

- Lee, C., Giachin, E., Rabiner, L., Pieraccini, R., and Rosenberg, A. (1992). "Improved acoustic modeling for large vocabulary continuous speech recognition," *Comput. Speech Lang.* **6**, 103–127.
- Lindblom, B. (1990). "Explaining phonetic variation: A sketch of the h&h theory," in *Speech Production and Speech Modelling*, edited by W. J. Hardcastle and A. Marchal (Kluwer Academic, Boston), pp. 403–439.
- Lindblom, B. E. F., and Sundberg, J. E. F. (1971). "Acoustic consequences of lip, tongue, jaw, and larynx movement," *J. Acoust. Soc. Am.* **50**, 1166–1179.
- Maeda, S. (1990). "Compensatory articulation during speech: Evidence from the analysis and synthesis of vocal-tract shapes using an articulatory model," in *Speech Production and Speech Modelling*, edited by W. J. Hardcastle and A. Marchal (Kluwer Academic, Boston), pp. 131–149.
- Mermelstein, P. (1967). "Determination of the vocal-tract shape from measured formant frequencies," *J. Acoust. Soc. Am.* **41**, 1283–1294.
- Merzenich, M., Knight, P., and Roth, G. (1975). "Representation of cochlea within primary auditory cortex in the cat," *J. Neurophysiol.* **38**, 231–249.
- Moore, B. C. J., and Glasberg, B. R. (1983). "Suggested formula for calculating auditory-filter bandwidth and excitation patterns," *J. Acoust. Soc. Am.* **74**, 750–753.
- Portnoff, M. R. (1973). "A quasi-one-dimensional digital simulation for the time-varying vocal tract," Master's thesis, MIT.
- Rabiner, L. R., and Schafer, R. W. (1978). *Digital Processing of Speech Signals* (Prentice-Hall, Englewood Cliffs, NJ).
- Rosenberg, A. E. (1971). "Effect of glottal pulse shape on the quality of natural vowels," *J. Acoust. Soc. Am.* **49**, 583–590.
- Ru, P. (2000). "Perception-based multiresolution auditory processing of acoustic signal," Ph.D. thesis, University of Maryland, College Park, MD.
- Rubin, P., Baer, T., and Mermelstein, P. (1981). "An articulatory synthesizer for perceptual research," *J. Acoust. Soc. Am.* **70**, 321–328.
- Schreiner, C. E., and Calhoun, B. M. (1994). "Spectral envelope coding in cat primary auditory cortex. Properties of ripple transfer functions," *J. Aud. Neurosci.* **1**, 39–61.
- Schreiner, C. E., and Mendelson, J. R. (1990). "Functional topography of cat primary auditory cortex: Distribution of integrated excitation," *J. Neurophysiol.* **64**, 1442–1459.
- Schroeder, M. R. (1967). "Determination of the geometry of the human vocal tract by acoustic measurements," *J. Acoust. Soc. Am.* **41**, 1002–1010.
- Shamma, S. A., Fleschman, J. W., Wiser, P. R., and Versnel, H. (1993). "Organization of the response areas in ferret primary auditory cortex," *J. Neurophysiol.* **69**, 367–383.
- Shamma, S. A., Versnel, H., and Kowalski, N. (1995). "Ripple analysis in the ferret auditory cortex. I. Response characteristics of single units to sinusoidally rippled spectra," *J. Auditory Neuroscience* **1**, 233–254.
- Stevens, K. N. (1989). "On the quantal nature of speech," *J. Phonetics* **17**, 3–45.
- Temkin, S. (1981). *Elements of Acoustics* (Wiley, New York).
- Wakita, H. (1973). "Direct estimation of the vocal tract shape by inverse filtering of acoustic speech waveforms," *IEEE Trans. Audio Electroacoust.* **73**, 417–427.
- Wang, K., and Shamma, S. A. (1995). "Representation of spectral profiles in primary auditory cortex," *IEEE Trans. Speech Audio Process.* **3**, 382–395.

Effects of prosodic boundary on /aC/ sequences: Acoustic results

Marija Tabain^{a)}

Institut de la Communication Parlée, Institut National Polytechnique de Grenoble, 46, avenue Félix Viallet, 38031 Grenoble, France

(Received 1 February 2002; accepted for publication 30 September 2002)

This study presents various acoustic measures used to examine the sequence /a # C/, where “#” represents different prosodic boundaries in French. The 6 consonants studied are /b d g f s ʃ/ (3 stops and 3 fricatives). The prosodic units investigated are the utterance, the intonational phrase, the accentual phrase, and the word. It is found that vowel target values, formant transitions into the stop consonant, and the rate of change in spectral tilt into the fricative, are affected by the strength of the prosodic boundary. *F*₁ becomes higher for /a/ the stronger the prosodic boundary, with the exception of one speaker’s utterance data, which show the effects of articulatory declension at the utterance level. Various effects of the stop consonant context are observed, the most notable being a tendency for the vowel /a/ to be displaced in the direction of the *F*₂ consonant “locus” for /d/ (the *F*₂ consonant values for which remain relatively stable across prosodic boundaries) and for /g/ (the *F*₂ consonant values for which are displaced in the direction of the velar locus in weaker prosodic boundaries, together with those of the vowel). Velocity of formant transition may be affected by prosodic boundary (with greater velocity at weaker boundaries), though results are not consistent across speakers. There is also a tendency for the rate of change in spectral tilt moving from the vowel to the fricative to be affected by the presence of a prosodic boundary, with a greater rate of change at the weaker prosodic boundaries. It is suggested that spectral cues, in addition to duration, amplitude, and *F*₀ cues, may alert listeners to the presence of a prosodic boundary. © 2003 Acoustical Society of America. [DOI: 10.1121/1.1523390]

PACS numbers: 43.70.Fq [AL]

I. INTRODUCTION

In recent years, it has been shown (Fougeron and Keating, 1997; Fougeron, 2001; Cho and Keating, 2001; Byrd and Saltzman, 1998; Byrd, 2000; Byrd *et al.*, 2000; Keating *et al.*, in press) that there are systematic strategies used by speakers at the supralaryngeal level to delineate prosodic boundaries. In brief, segments are believed to be “strengthened” (or hyperarticulated) at stronger prosodic boundaries such as the utterance or the intonational phrase, and “weakened” at weaker prosodic boundaries such as the word or the syllable.¹ For instance, the nasal /n/ has greater contact between the tongue and the palate at a stronger prosodic boundary, and lesser contact at a weaker prosodic boundary (Fougeron and Keating, 1997); and the vowel /a/ is lower at a stronger prosodic boundary than at a weaker prosodic boundary (Tabain [submitted]). The study of such strategies is termed “articulatory prosody,” and indeed most work within this framework has been based on articulatory data. It is therefore the purpose of the current paper to explore possible acoustic effects of such articulatory strengthening strategies. This is done in the belief that if a linguistic structure, in this case the prosodic structure, is encoded in the supralaryngeal articulation, there must be acoustic consequences which are discernible to the listener [cf. Lindblom’s Hyper and Hypo Theory of Speech (Lindblom, 1990), which fo-

cuses on the communicative function of speech]. In particular, the focus is on possible spectral effects of supralaryngeal strategies to encode prosody, since these are somewhat less well understood than duration effects (see the literature review below). It is envisioned that the results presented in the current paper will provide an initial guide for studies of the perceptual importance of any such spectral effects of the prosodic structure.

We consider now the various acoustic effects which have thus far been observed at prosodic boundaries. The reader is referred to Tabain (submitted) and the references cited above for a more detailed description of the articulatory strategies used to delineate prosodic boundaries.

As already mentioned, only a small number of studies have looked at acoustic data in relation to the prosodic structure of the utterance. In perhaps the most systematic acoustic study within the articulatory prosody framework, Cho and Keating (2001) showed that for Korean, VOT of stop consonants was greater at the higher prosodic boundaries, and that acoustic nasal energy was *lesser* for nasal consonants at higher prosodic boundaries (the nasal consonant therefore becomes more “consonant-like” at these higher boundaries, rather than more vowel-like, as would be implied by increased nasality). Dilley, Shattuck-Hufnagel, and Ostendorf (1996) showed that, for English, a vowel is more likely to be glottalized when it is initial in a higher prosodic phrase than when it is initial in a lower prosodic phrase.

By far the vast majority of studies on acoustic effects of prosodic structure has looked at duration. In terms of articulatory prosody, it has been shown (Fougeron and Keating,

^{a)}Electronic mail: mtabain@maccs.mq.edu.au. Current address: Speech, Hearing and Language Research Center & Macquarie Centre for Cognitive Science, Division of Linguistics and Psychology, Macquarie University, Sydney NSW 2109, Australia.

1997) that the duration of individual segments at the edges of prosodic boundaries increases with increasing strength of the boundary (so that, for instance, a segment at an utterance boundary is longer than a segment at a word boundary). However, in terms of duration effects of prosodic and linguistic structure in general, research in this area has a relatively long tradition, meriting a literature review as early as the mid-1970s (Klatt, 1976). Much early work by Lehiste (e.g., Lehiste, 1972) examined what has come to be known as phrase-final lengthening, whereby syllables are lengthened at the end of a prosodic phrase (see also Fletcher, 1991, for data on French, which is the language under study in the present paper). In terms of articulatory prosody, such phrase-final lengthening correlates with the longer durations seen at stronger prosodic boundaries, such as the utterance or the intonational phrase. Other work by Lehiste showed effects of polysyllabic shortening, whereby individual syllables in the word are shortened to a greater extent the greater the total number of syllables in that word (Lehiste, 1974—this result will be mentioned again below). Lehiste's other early work on accentual lengthening, whereby syllables are lengthened if they carry stress or accent, has been further refined in more recent work by Turk and colleagues (e.g., Turk and White, 1999). Looking at syllables which are lengthened due to the presence of stress/accent, Turk and colleagues have tried to specify the extent of such accentual lengthening rightwards or leftwards of the syllable which carries the pitch accent. Their work has focused in particular on what type of boundary blocks spreading of accentual lengthening: the syllable, the foot, or the prosodic word (the spreading is also dependent on whether the words concerned are content words or function words, but unfortunately, such issues are beyond the scope of the present discussion). Turk and colleagues' work may then correspond to the lower/weaker levels of the prosodic hierarchy, such as the word or syllable boundary.

From this brief outline of the area, it can be seen that the study of prosodic effects on segment and syllable durations is multifaceted (see Turk and Shattuck-Hufnagel, 2000 for an evaluation of the various duration adjustment mechanisms discussed here, and of others). The fact that pitch accent affects segment durations is of relevance to the present study, since placement of the pitch accent and the structure of the prosodic hierarchy interact in French. This interaction will be briefly discussed below when the prosodic structure of French is described.

So far, the effects of the prosodic hierarchy on duration, vowel glottalization, VOT, and nasal energy have been outlined. However, there are apparently no studies which have looked at effects of prosodic boundaries on formants. Given that formants are known to be affected by duration (Lindblom, 1963), it could be hypothesized that formants would be affected by prosodic factors as well. The issue of changes in spectral characteristics according to prosodic structure is discussed in the next section.

A. Rate of change in relation to the prosodic boundary

Certain results in the acoustic literature suggest that the change in a particular spectral parameter over time may be

affected by the prosodic structure of the utterance. Various studies which have looked at prosodic effects on spectral characteristics will now be discussed.

Early work by Lindblom showed that the extent of formant movement is affected by the duration of the syllable (Lindblom, 1963). It has already been made clear above that syllable and segment durations are affected by the prosodic structure of the utterance. Moon and Lindblom (1994) extended these early prosodic and formant results by examining the effects on formant transitions of the total number of syllables in the word (polysyllabic shortening). They showed that not only are the duration and target values of the formant transition affected by the suprasegmental properties of a given syllable, but also the velocity of the transition. Their data consisted of the series "will, willing, willingham," where the stressed /t/ in the initial syllable becomes progressively shorter due to the increasing number of syllables in the word. They elicited both typical citation form speech, and (hyper) clear speech. Moon and Lindblom found that vowel formant patterns were displaced in the direction of the frequencies of the consonants, and that the extent of the displacement depended on vowel duration. Moreover, the context- and duration-dependent effects were more pronounced for citation form speech than for (hyper) clear speech. The smaller formant shifts (compared to vowel target in isolation) in the clear speech were achieved by an increased rate of formant change. It is therefore clear that duration, the extent of formant movement, and the velocity of formant movement all interact according to prosodic structure.

A more recent study by Wouton and Macon (2002a) has looked at the effects of various other prosodic factors on formant rate of change. Wouton and Macon examined stressed vs unstressed; pitch-accented vs not pitch-accented; utterance medial position vs final position; and clear, fast, and relaxed speaking styles. They found that these prosodic factors did indeed have an effect on the rate of change of the $F1$, $F2$, and $F3$ movement, with greater rate of change correlated with greater linguistic prominence (e.g., stressed syllables had a greater rate of change than unstressed syllables). Interestingly, Wouton and Macon found an asymmetrical behavior for CV vs VC formant movements, with greater rate of change in linguistically prominent syllables encoded in the CV rather than the VC transitions. Based on Kozhevnikov and Chistovich's (1965) view that syllable onset movements constitute elementary planning units for speech articulation, Wouton and Macon speculate that the duration and articulation effort of a CV movement determines the extent of the formant movement, and that the dynamics of the VC movement depend on the time available between the end of the preceding CV movement and the start of the next CV movement. These results are relevant to the present study, since it is /V # C/ movements (where # denotes some prosodic boundary) which are examined here.

Since formant movement has been shown to be affected by such various prosodic factors as stress/accent, utterance position, and speaking rate, there is reason to believe that it is also affected by the strength of the prosodic boundary.

Thus, formant movements will be examined in the current study.

Although formant transitions are useful in classifying fricative consonants, in particular the nonsibilants, it is the fricative spectrum which is of greater importance to sibilants, and which serves to distinguish sibilants from nonsibilants (Harris, 1958; Mann and Repp, 1980). In a study evaluating the various acoustic cues to prevocalic stop consonants (based largely on Lahiri, Gewirth, and Blumstein, 1984), Smits, ten Bosch, and Collier (1996) found that the spectral tilt at the onset of the burst, and the change in spectral tilt over a fixed period of time, were useful cues to place of articulation for certain stops in certain vowel contexts. Comparably, Jongman, Wayland, and Wong (2000) showed that spectral moment data vary from the beginning to the middle to the end of the fricative, and Munson (2001), using a non-linear regression on first spectral moment values generated at the boundaries of /s/ and adjacent /t/ or /p/, has also shown that spectral properties of the fricative change during the acoustic duration of the fricative. Taken together, these results suggest that there are gross spectral properties whose changes over time are perceptually important. In light of Moon and Lindblom's and Wouton and Macon's studies, showing that similar dynamic properties (i.e., formant movement) are affected by the suprasegmental structure of the utterance, it is reasonable to assume that a spectral property such as spectral tilt or moment may likewise be affected by suprasegmental characteristics of the utterance. For this reason, spectral tilt is studied in relation to the strength of the prosodic boundary, as are formant movements. Further details are provided below.

We turn now to a brief description of the prosodic structure of French, the language under study here.

B. Prosodic accent in French

In French, words do not carry lexical stress, but they can attract prosodic accent at the sentence level. Following Fougeron and Jun (1998), the prosodic structure of French is based on the accentual phrase (AP), which is dominated by the intonational phrase (IP). The IP is in turn dominated by the utterance.²

What Fougeron and Jun call the AP has been described by different authors as the "rhythmic group," "intonation group," "prosodic word," or "intonème mineur," and what Fougeron and Jun call the IP has been variously called the "intonème majeur" or "unité intonative" (see di Cristo, 1998 for a review and references on French intonation).

According to Fougeron and Jun, the AP has the underlying tonal representation /L Hi L H*/, with a more common phonetic realization being [L H*] (their approach is based on Pierrehumbert, 1980 and Beckman and Pierrehumbert, 1986). The initial high tone, Hi, has been described as the peak of the "accent secondaire," and its appearance or non-appearance is conditioned by several linguistic and extralinguistic factors. The final high tone, H*, has been described as the peak of the "accent primaire," and is realized on the phrase-final full syllable. In neutral utterances, the Hi, when it appears, is usually shorter and has a lower *F0* value than the following H*. In these cases it is not considered to have

a pitch accent. However, in producing a focused word, the Hi is often promoted to pitch accent status. As regards the L tone, it is realized on the syllable preceding the H tone syllable. The reader is referred to Jun and Fougeron for further discussion of the status of Hi and H*, respectively, as well as other issues of debate in the study of French prosody.

The IP is marked by a major continuation rise (H%) or fall (L%) and also by a significant final lengthening (see also Fletcher, 1991), often followed by a pause.

It was mentioned in the Introduction section that effects of the prosodic hierarchy occur precisely at the edges of adjacent prosodic constituents at the same level—i.e., at the segments immediately adjacent to the boundary. It was also mentioned that the placement of the pitch accent and the prosodic hierarchy interact in French. It can now be seen that since the H* in the AP is placed on the final syllable of the phrase, an AP and any higher level is defined as having a pitch accent on the final syllable of the prosodic constituent.

For the purposes of this study, an utterance dominates an intonational-phrase level, which dominates an accentual-phrase level, which in turn dominates a word level. The focus in particular is on /V # C/ sequences (as opposed to CV sequences), where a given prosodic boundary separates the vowel from the consonant. The following will be examined.

- (1) Duration—Given the literature review above, duration is clearly an important parameter in any prosodic study. It is expected that duration will be greater at stronger prosodic boundaries than at weaker prosodic boundaries.
- (2) Vowel formant values—Given the premise of articulatory prosody that segments become more hyperarticulated at stronger prosodic boundaries, it is expected that *F1* will be higher at stronger prosodic boundaries, reflecting a lower tongue and jaw position. *F2* will also be examined to see if there are any effects. It should also be noted that Tabain (submitted) presents articulatory data showing that /a/ becomes lower at stronger prosodic boundaries (this is the study from which the present acoustic data were taken).
- (3) Formant transition—It is clear from the discussion above that duration has a profound effect on formant transitions, and for this reason the effects of prosodic structure on *F1* and *F2* movement will be examined. These analyses of formant movement duration, distance, and velocity will only be carried out for the stop consonants /b d g/, and not for the fricative consonants, since formant transitions for fricatives are partly obscured by the fricative noise. The reader is reminded that only VC transitions are concerned.
- (4) Rate of change in spectral tilt—Again, given the discussion above, the rate of change in spectral tilt moving from the vowel into the fricative will be examined. More precisely, what is of interest is the rate of change going from the negative tilt of the vowel spectrum to the positive tilt of the fricative spectrum (more details are provided in the Method section).³

II. METHOD

A. Speakers, stimuli, and recordings

Three native speakers of metropolitan French (two male—CV and GR—and one female—AV) were recorded in a sound-treated room at ICP, Grenoble. Articulatory (EMA—electromagnetic articulography) and acoustic data were recorded simultaneously and time synchronized. The acoustic data were recorded directly onto a DAT recorder at a sampling rate of 44.1 kHz, and transferred onto PC. Data were subsequently down sampled to 20 kHz. Details on collection of the EMA data are given in Tabain (submitted).

Stimuli consisted of 4 sentences (based on Fougeron, 2001), each containing a prosodic boundary of interest between the fourth and fifth syllables. These sentences were (with the type of prosodic boundary listed in parentheses)

- (1) Paul aime Tata. **B**aba les protège en secret.
(utterance)
- (2) La pau^v Tata, **B**aba et Paul arriveront demain.
(intonational phrase)
- (3) Tonton, Tata, **B**aba et Paul arriveront demain.
(accentual phrase)
- (4) Paul et Tata **B**aba arriveront demain.
(word)

The consonant in bold was varied to be one of /b d g f s ʃ/, and the vowel following this consonant was varied to be one of /a i u y ø/ (where “ø” is the vowel found in the word “feu”). There was thus a total of 120 sentences (4 prosodic contexts × 6 consonants × 5 vowels). Two of the speakers (AV [female] and GR [male]) produced 4 repetitions of the corpus, giving a total of approximately 480 utterances. The second male speaker, CV, produced 2 repetitions of the corpus, giving a total of approximately 240 utterances.

For the purposes of the current study, speakers were encouraged to produce a final intonation contour followed by a pause for the utterance boundary, and a continuation contour while avoiding a pause for the intonational boundary. Speakers tended to read the stimuli for the accentual boundary as a list.

The current paper focuses on the relationship between the /a/ at the end of “Tata” and the three stop and three fricative consonants following. Although the vowel following the consonant was varied, with the aim of examining vowel-to-vowel coarticulation, these results will not be presented here due to the small number of tokens that would exist for each following vowel context (either two or four tokens per following vowel). For this reason, data are collapsed across following vowel context.

B. Labeling and analysis environment

Acoustic data were segmented and labeled according to standard acoustic criteria (cf. Harrington and Cassidy, 1999, Chap. 4), using the EMU hierarchical speech labeling tool (Cassidy and Harrington, 2001). The noise following the release of the /t/ in /ta/ was labeled separately and included as part of the /a/ duration. (This was done so that the acoustic and articulatory data were more comparable, since the articu-

latory vowel onset was labeled at /t/ release).⁴ Formants were automatically tracked in EMU using LPC with a sample rate of 200 Hz, and hand corrected during the labeling process. In addition, an *F1* target event for the /a/ preceding the consonant of interest was labeled at the *F1* peak moving *backwards* in time from the /a/-consonant boundary. Where *F1* attained a steady state after an initial rise, the first pitch period of the steady state moving backwards from the boundary was marked as the *F1* target. Figure 1 shows an example of these labeling criteria using the EMU speech tool. It shows the stop closure for the /t/ followed by the vowel /a/, which in this case is followed by the stop /d/. This token is from an accentual phrase boundary as spoken by speaker AV (female). It can be seen that the *F1* vowel target (the vertical white line in the middle of the /a/) is marked at about 9.03 seconds: it is marked in relation to the /d/ which follows. Had the *F1* target been marked in relation to the /t/ which precedes, the target would have been placed at about 9.01 s (a difference of about 20 ms).

Regarding the utterance boundary, it should be noted that the pause between the two utterances in sentence 1 (utterance boundary) was labeled separately, and not included as part of the total syllable duration of /aC/. Since the /a/ at the end of “Tata” is in this sentence followed by a pause, there is no /aC/ transition such as is found in the other sentences. Instead, an attempt was made to mark the onset of an *F1* steady state moving leftwards from the end of the vowel. However, a short period of voicelessness at the end of the vowel meant that measurement of the vowel endpoint and *F1* target was less reliable than for the other sentences. This must be kept in mind when interpreting the velocity results, which will be presented below. It must also be kept in mind that due to the presence of a pause at the utterance boundary, the measurement of acoustic stop consonant duration was not reliable. It should be remembered that the stops examined here are /b d g/—i.e., all voiced. Stop consonant duration following the utterance boundary was therefore measured from the onset of voicing for the consonant, which is of course not an accurate measure of stop closure. This must be kept in mind when examining duration results. There was of course no problem in locating the onset of frication for the voiceless fricatives examined here, /f s ʃ/.

All formant values were automatically extracted using EMU. *F1* and *F2* for the “static” vowel target were taken at the acoustic midpoint of the vowel. However, for examining the formant transitions, *F1* and *F2* were treated differently: for *F2*, the vowel formant value was taken at the midpoint; and for *F1*, the vowel formant value was taken at the hand-marked *F1* target. For both *F1* and *F2*, the consonant value was taken at the VC boundary. The distance of the transition was calculated as the difference between the formant value extracted at the VC boundary, and the formant value extracted from the hand-marked target (in the case of *F1*) or the acoustic midpoint of the vowel (in the case of *F2*). The duration of the transition was calculated as the difference in time between the consonant and the vowel values. For *F1*, this was the difference in time between the hand-marked target and the VC boundary, and for *F2*, this was effectively half the total vowel duration (since the vowel target value

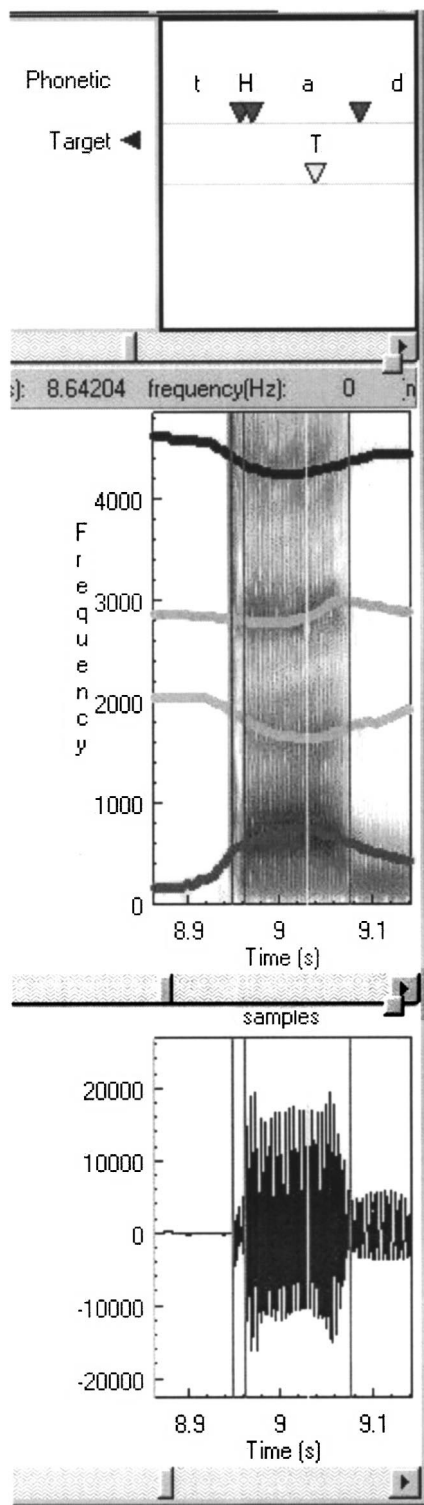


FIG. 1. Example of the hand-marked F_1 target using the EMU labeler. The speaker is AV (female), and the / t # d / sequence occurs at an accentual phrase boundary (the “H” in the phonetic transcription in the top panel marks the noise portion following release of the / t /). The F_1 target (the white vertical line in the vowel, marked with a “T” on the Target line in the top panel) is marked in relation to the / d / which follows the vowel, rather than the / t / which precedes it.

was taken at the vowel midpoint). Peak velocity was calculated as the maximum value of the first differential of the formant transition for F_1 and F_2 separately.

All analyses of the data as described above were carried

out using the EMU database speech analysis system (Harrington *et al.*, 1993), interfaced with the R statistical package (Ihaka and Gentleman, 1996). The analysis of spectral tilt for the fricatives, described below, was carried out using PRAAT (www.praat.org).

C. Spectral tilt analysis of fricatives

Analysis of spectral tilt was based on Smits *et al.* (1996). Overlapping FFTs were carried out across a portion of the token, using a 12-ms Hanning window and a frame shift of 5 ms. The token duration over which the successive FFTs were calculated was determined as follows: for each VC token, 15% of the vowel duration was calculated, and 15% of the fricative duration was calculated, based on the hand-marked segment boundaries. The left boundary of the analysis was placed at 15% of the vowel duration leftwards from the vowel–fricative boundary, and the right boundary was placed at 15% of the fricative duration rightwards of the vowel–fricative boundary. A typical value for the duration of the analysis token was 40–50 ms (cf. Tables I and II, which will be presented below)—this compares well with the 50 ms used uniformly by Smits *et al.* The first FFT was centered at the leftward boundary of the token.

In order to obtain the spectral tilt values for each FFT, a regression was carried out on the returned FFT values between 1000 and 5000 Hz for each spectrum using an equivalent rectangular bandwidth (ERB) and dB scales. The choice of this range of values for both the male and female speakers was motivated by the following considerations: (1) By excluding values below 1000 Hz, spectral energy due to voicing is for the most part excluded (the first 3–4 harmonics are excluded for the female speaker, and the first 5–8 harmonics are excluded for the male speakers). Hence, the presence of voicing in the early part of the fricative does not affect the measurement of the fricative tilt (cf. Tabain, 2001, where data below 1 kHz were similarly excluded in a spectral moment analysis). Although part of F_1 for the vowel was excluded, a visual inspection of the data showed that the tilt value for the vowel was still highly negative (rather than flat or positive, such as fricative slope values may be). (2) By excluding returned values above 5000 Hz, it was felt that the spectral characteristics of fricative consonants as a class were best captured. The spectral peak for / j / for all three speakers, and of / s / for the male speakers, was included in the measure (the female speaker’s spectral peak for / s / occurred at about 6–7 kHz, although a visual inspection of the spectra suggested that there should be little difference between a low-pass filter at 5 kHz and one at 6 or 7 kHz for this speaker). Visual inspection of spectra for / f / showed a diffuse peak in the 5–6-kHz range, though of lesser intensity than for the sibilants. By high-pass filtering at 5 kHz (rather than at 9–10 kHz), a greater spectral tilt would be calculated for / f /, and hence the difference between the vowel tilt and the fricative tilt would be enhanced.

Following calculation of the tilt values for each FFT spectrum, a second regression was carried out on the tilt values calculated across each VC token, with the tilt value as the dependent variable, and the FFT frame number as the independent variable. The slope value from this analysis

gives the rate of change in tilt value. This second regression was not forced to include any particular point, since no one calculated FFT was deemed to be more important than the others (contrary to Smits *et al.*, for whom the tilt calculated at the stop burst was of crucial importance).

The above description of how the duration of each token was calculated applies only for the intonational-, accentual-, and word-boundary data. Since the utterance-boundary fricative data are preceded by a pause, no change from vowel tilt values can be obtained for this context. However, in order to have a value for fricative data which, in theory, should not change greatly in spectral tilt over time, tilt values were calculated from a point at 0.2 of the fricative duration to a point at 0.5 of the fricative duration. This then gives spectral tilt values for 30% of the fricative duration at the utterance boundary, in comparison to 30% of the syllable duration of the vowel–fricative syllable for the other boundaries. Although an examination of Tables I and II (presented below) suggests that 30% of the fricative in utterance context should be both relatively and absolutely greater than 30% of the VC syllable for the other contexts, it will become evident that more data are necessary when the fricative spectrum is relatively steady, than when the spectrum is changing from vowel to fricative. The points 0.2 and 0.5 of token duration were chosen as containing data that had both reached sufficient fricative amplitude⁵ (it will be recalled that the fricative is preceded by a pause in the utterance context) and that as yet contained little influence from the following vowel.

Figure 2 shows an FFT spectrum generated by the spectral tilt analysis. The top graph shows the last FFT calculated for a VC token at a word boundary. The fricative is /s/, as spoken by male speaker GR. The vertical lines on the graph mark 1000 and 5000 Hz. The tilt is calculated based on the FFT values contained within these boundaries. The regression line is marked on the graph. The *x* axis marks the intervals at each 500 Hz along the ERB scale (the tilt is calculated using the ERB scale). The bottom graph shows the regression on the tilt values generated for this particular VC token. It can be seen that eight FFTs were calculated for this token (since there are eight points on the graph), and that the token duration was 36.5 ms. It can also be seen that the tilt values for the vowel are negative (the first few points on the bottom graph), and those for the fricative positive (the last few points on the bottom graph).

Results are tested using an analysis of variance (ANOVA) followed by least significant difference *post hoc* tests, and a Levene test for homogeneity of variances (Levene, 1960), which tests for differences in the variability regardless of the mean. Alpha is set at 0.05. All *post hoc* tests are adjusted according to the Bonferroni method, with alpha set at 0.017.

Eta-squared results are also presented at the end of the paper—these determine to what extent a given factor (in this case prosodic boundary) accounts for the total variability in the data.

Duration measurements will be presented first, followed by vowel formant measurements. This will be followed by the more “dynamic” data: formant movement, and the rate of change in spectral tilt. Where appropriate, data are col-

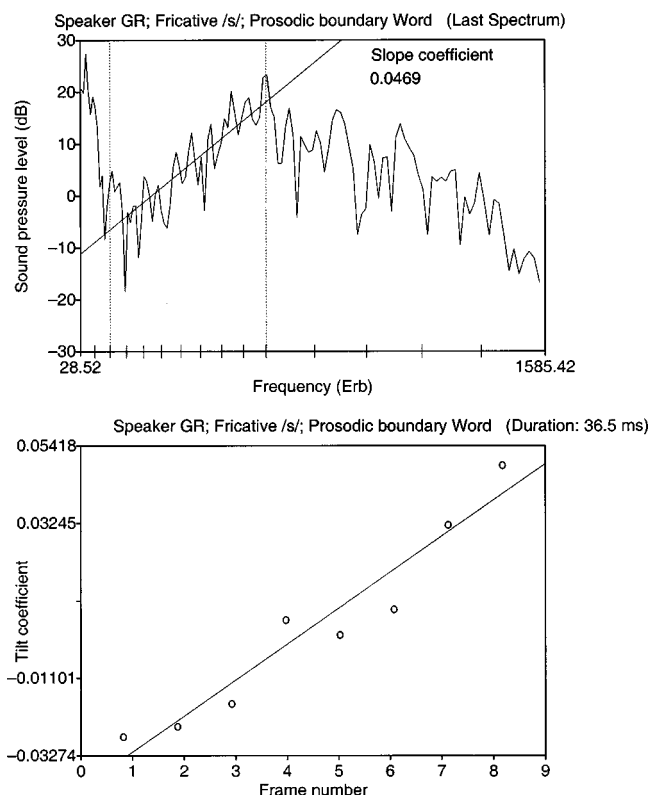


FIG. 2. Example of an FFT spectrum with calculated tilt (top) from the end of the token, and secondary regression based on the entire token (below). The spectrum is for the fricative /s/, as spoken by male speaker GR in a word-boundary context. The vertical lines on the top graph mark 1000 and 5000 Hz. The regression line, giving the tilt, is shown on the graph. The *x* axis marks the intervals at each 500 Hz according to the ERB scale. The bottom graph shows the regression on the tilt values generated for this particular VC token. The slope value calculated from the top graph (0.0469) corresponds to the value for frame #8 in the bottom graph. The slope, intercept, and correlation values for the regression shown in the bottom graph are 0.0101, -0.0418, and 0.9626, respectively.

lapsed across following vowel context (i.e., for vowel duration and vowel target values). However, where appropriate, data will be treated separately for the different consonants (i.e., for consonant duration and for formant transitions). Results from the spectral tilt analysis of the fricatives will be collapsed across fricatives, since the measure was not designed to capture differences between the different fricative places of articulation.

III. RESULTS

A. Duration and formant measures

Table I(a) shows mean and standard deviations for vowel duration, consonant duration, and for the percentage of the syllable taken up by the vowel. Table I(b) presents significance results for these data. For each speaker, results are listed separately for each of the prosodic contexts (U = Utterance boundary, I = Intonational phrase boundary, A = Accentual phrase boundary, W = Word boundary). It can be seen that for speakers AV and GR, there is a significant decrease in vowel duration the weaker the prosodic boundary, whereas speaker CV groups the three higher boundaries together, with the word boundary having a significantly shorter vowel duration. For the consonant durations (stop

TABLE I. (a) Acoustic durational data for 3 speakers of metropolitan French. Results are listed separately for each prosodic boundary context (U=Utterance boundary, I=Intonational-phrase boundary; A=Accental-phrase boundary; W=Word boundary). (b) Significance results for data presented in (a). For each speaker, results from a one-way ANOVA are presented in the first column, and *post hoc* pairwise comparisons are presented for adjacent pairs in the prosodic hierarchy in the second column (with alpha adjusted to 0.017 following the Bonferroni method). The direction of the difference is marked by either “<” or “>,” or “=” in the case where the result is not significant.

		Vowel duration (ms)		Consonant duration (ms)		Percentage duration: Vowel/syllable		
(a)		Mean	s.d.	Mean	s.d.	Mean	s.d.	N
AV	U	216.9	21.50	140.2	62.95	62.68	11.78	126
	I	163.6	20.74	136.2	41.42	55.49	6.88	127
	A	139.2	17.67	133.4	42.59	52.11	8.16	128
	W	105.0	11.11	116.1	41.73	49.12	9.20	127
CV	U	167.5	15.37	122.4	42.99	59.11	11.04	62
	I	169.7	12.94	109.9	40.89	61.94	9.07	63
	A	165.2	14.00	110.8	42.70	61.20	9.76	63
	W	98.6	7.92	99.0	40.05	51.93	11.11	63
GR	U	196.2	17.51	126.9	27.93	61.10	5.71	126
	I	179.0	24.47	133.7	28.04	57.53	5.19	126
	A	169.8	24.18	127.1	28.76	57.55	5.62	126
	W	109.8	10.27	106.0	34.80	52.24	8.86	127
		AV d.f. = 3504		CV d.f. = 3247		GR d.f. = 3501		
Vowel		$F = 845.40$	U>I>A>W	$F = 453.23$	U=I=A>W	$F = 448.89$	U>I>A>W	
duration		$p < 0.001$		$p = 0.00$		$p = 0.00$		
Consonant		$F = 6.21$	U=I=A>W	$F = 3.30$	U=I=A= W	$F = 20.45$	U=I=A>W	
duration		$p = 0.00$		$p < 0.05$		$p = 0.00$		
% Duration		$F = 51.13$	U>I>A>W	$F = 12.46$	U=I=A>W	$F = 39.72$	U>I=A>W	
vowel/syll.		$p = 0.00$		$p = 0.00$		$p = 0.00$		

and fricative contexts are combined here), there is less of an effect according to the prosodic boundary, although speakers AV and GR distinguish the word boundary from the higher level boundaries. In terms of the percentage of the syllable duration taken up by the vowel, it is clear that the stronger the prosodic boundary, the greater the percentage duration of the vowel. Speaker AV distinguishes all four boundaries, whereas speaker CV distinguishes the word boundary from the higher boundaries, and speaker GR distinguishes the word and accentual boundaries from the utterance and intonational boundaries. It can therefore be seen that in acoustic terms, the vowel is temporally reduced the weaker the prosodic boundary, whereas the duration of the consonant is relatively invariant.

Table II gives the same data as listed in Table I, but with the durational data listed according to the consonant context, rather than the prosodic context. Of note here is the significantly greater duration of the fricative consonants as opposed to the stop consonants, but accompanied by *less* variability, for speakers CV and GR. These results are significant according to a one-way ANOVA and a Levene test for homogeneity of variances (with the three fricatives collapsed and the three stops collapsed to form two groups—**CV**: ANOVA: $F(1,249) = 909.68$, $p = 0.00^6$ Levene: $F(1,249) = 4.95$, $p < 0.05$; **GR**: ANOVA $F(1,503) = 487.77$, $p = 0.00$ Levene $F(1,503) = 48.67$, $p = 0.00$). For speaker AV, the longer fricatives [**AV**: ANOVA: $F(1,506) = 1346.83$, $p = 0.00$] are not accompanied by less variability, although her percentage durational data (percentage of the syllable containing the

vowel) do show significantly less variability for the fricatives [**AV**: Levene: $F(1,506) = 32.84$, $p = 0.00$]. In all, these results suggest much more stable timing across prosodic boundaries for the fricatives than for the stops.

Figure 3 presents ellipse plots of mean $F1$ and $F2$ values for the vowel /a/ according to prosodic context. Table III presents significance results for these data. The ellipses represent 2.45 standard deviations from the mean. The formant values were sampled at the temporal midpoint of the vowel. There is a pattern of increasing $F1$ values the stronger the prosodic boundary (the only exception is speaker GR's utterance value). There is also a pattern of decreasing $F2$ values the stronger the prosodic boundary. These results suggest that, in articulatory terms, the stronger the prosodic boundary, the lower and more back the /a/ vowel becomes. It can be seen that for all three speakers, /a/ in the word boundary context is higher and more forward in the acoustic space. For speakers AV and CV, the vowel in the utterance boundary context is lower and more back. The vowel in the intonational- and accentual-phrase boundaries is between the other two boundaries. For speaker GR, however, the utterance context /a/ is contained within a very small region in the center of the plot. This unexpected result will be discussed below.

B. Formant movement

We now turn to an examination of the more “dynamic” aspects of the acoustic signal. Figure 4 presents formant tran-

TABLE II. Acoustic durational data for three speakers. Results are listed separately for each consonant context.

		Vowel duration (ms)		Consonant duration (ms)		Percentage duration: Vowel/syllable		<i>N</i>
		Mean	s.d.	Mean	s.d.	Mean	s.d.	
AV	b	148.5	46.06	85.17	18.55	62.45	9.15	84
	d	154.5	44.53	91.31	21.78	62.26	7.31	81
	g	150.9	49.22	92.26	31.11	61.64	10.31	87
	f	160.5	42.53	161.4	27.22	49.35	6.33	80
	s	162.0	41.73	175.1	25.90	47.51	5.34	84
	ʃ	159.7	42.58	180.2	22.62	46.35	5.28	92
CV	b	147.3	30.35	65.75	18.01	68.91	7.38	40
	d	150.0	35.35	74.32	27.50	66.85	8.63	39
	g	152.1	29.18	73.40	21.03	67.59	5.40	40
	f	146.0	33.60	140.6	17.13	50.37	6.38	44
	s	154.2	33.02	150.2	13.93	50.12	5.47	48
	ʃ	151.0	34.77	146.8	17.20	50.14	5.88	40
GR	b	155.6	33.79	105.6	22.97	59.41	4.57	84
	d	159.1	35.55	107.8	26.56	59.67	4.17	88
	g	155.8	38.27	92.5	29.08	62.94	8.73	89
	f	165.3	40.08	143.0	16.49	52.96	6.53	84
	s	175.6	39.81	146.3	16.52	53.98	5.30	80
	ʃ	171.6	38.04	150.0	15.81	52.79	6.01	80

sitions for $F1$ and $F2$ according to stop consonant context for the three speakers. Only the intonational, accentual, and word data are shown on each plot, since the utterance context was followed by a pause rather than a consonant. Data are time normalized, and extend from the temporal midpoint of the vowel /a/ to the VC boundary.

Table IV(a) presents numerical distance, duration, and peak velocity data for the $F1$ transition (moving backwards in time) from the VC boundary to the manually-labeled $F1$ target (described above in the Method section). Table IV(b) presents the corresponding significance results. Utterance

data are included in the table for completeness, but will not be discussed due to the presence of the pause at the boundary. It should be noted that data presented in Table IV are based on the hand-marked $F1$ target, whereas the data plotted in Fig. 4(a) extend from the temporal midpoint of the vowel to the endpoint.

It can be seen in Fig. 4(a) that $F1$ at the VC boundary remains relatively constant. The minimal difference in $F1$ value at the VC boundary across prosodic contexts is most likely a reflection of the fact that consonant closure is achieved, since $F1$ is effectively zero at stop closure. Typical

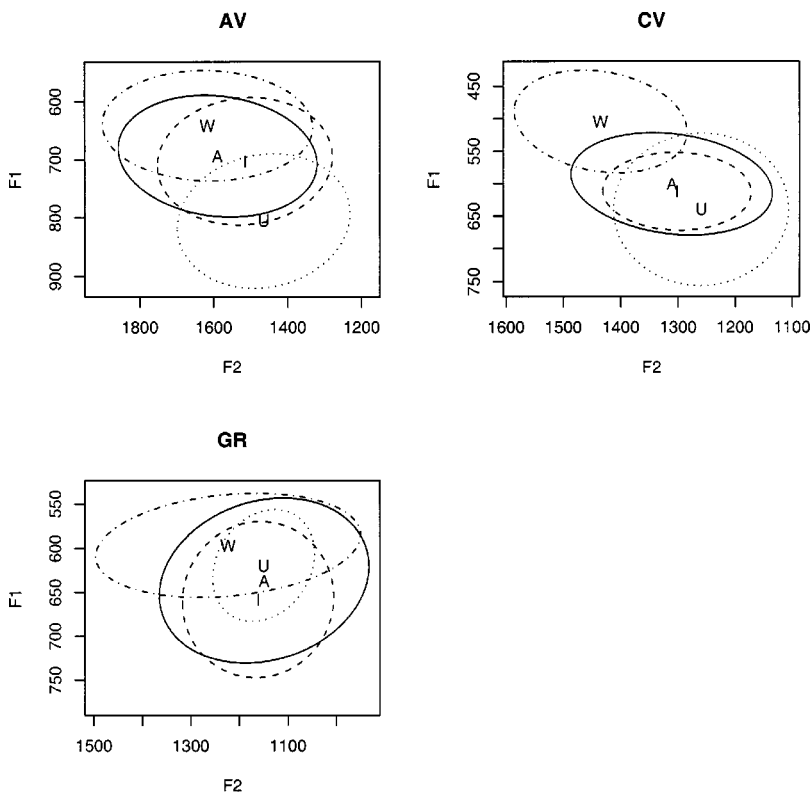


FIG. 3. Ellipse plots of $F1$ – $F2$ data for /a/, for three speakers of metropolitan French (AV=female; CV and GR=male). Only the mean values for each prosodic context are shown, with ellipses representing 2.45 standard deviations from the mean. Data were sampled at the acoustic midpoint of the vowel. U=Utterance boundary, I=Intonational-phrase boundary; A=Accentual-phrase boundary; W=Word boundary.

TABLE III. Significance results for *F1* and *F2* vowel data presented in Fig. 3. For each speaker, results from a one-way ANOVA are presented in the first column, and *post hoc* pairwise comparisons are presented for adjacent pairs in the prosodic hierarchy in the second column (with alpha adjusted to 0.017 following the Bonferroni method). The direction of the difference is marked by either “<” or “>,” or “=” in the case where the result is not significant.

	AV d.f.=3504		CV d.f.=3247		GR d.f.=3501	
<i>F1</i> Vowel	$F=312.11$ $p=0.00$	U>I=A>W	$F=175.00$ $p=0.00$	U>I=A>W	$F=85.92$ $p=0.00$	U<I>A>W
<i>F2</i> Vowel	$F=55.53$ $p=0.00$	U<I<A=W	$F=91.56$ $p=0.00$	U<I=A<W	$F=24.00$ $p=0.00$	U=I=A<W

coarticulatory effects, such as the higher *F1* in the /b/ context (cf. Recasens, 1999), can also be discerned on the plot.

It can be seen in Table IV that distance of the *F1* transition increases with the stronger prosodic boundaries (speaker AV, however, shows very little difference in distance values). Examination of Fig. 4(a) shows that this is primarily due to the vowel target changing, since *F1* at the VC boundary was relatively invariant. Duration values also generally increase with the stronger prosodic boundaries. As regards the velocity data, it is only speaker AV who seems to show an effect of peak velocity in *F1* across prosodic contexts, with velocity being greater in the word context than in the intonational or accentual contexts. This is perhaps due to the fact that her *F1* distance remains relatively constant, while duration decreases.

A different scenario applies for *F2* compared to *F1*.⁷ Here, two sets of observations can be made: the first regards the consonant values at the VC boundary, and the second regards the vowel target values in relation to the consonant values. Regarding the consonant values, it can be seen in Fig. 4(b) that for /g/, the *F2* values at the VC boundary are displaced towards the *F2*–*F3* velar “pinch” for this consonant in the *weaker* prosodic boundaries. Although the trend is apparent, results are only significant for speaker AV [**AV**: ANOVA: $F(2,63)=8.44$, $p<0.001$] with Bonferroni-adjusted *post hoc* tests showing: intonational (mean = 1858 Hz) < accentual (1978 Hz) = word (2058 Hz).

By contrast, for /d/, there is no significant difference in *F2* values at the boundary. This said, for speakers AV and CV there is a significant difference in the distance between the *F2* boundary and the *F2* target for /d/, but not for either of the other consonants [/d/: **AV**: ANOVA: $F(2,58)=4.08$, $p<0.05$; **CV**: ANOVA: $F(2,27)=8.06$, $p<0.01$]. Bonferroni-adjusted *post hoc* tests for both speakers showed that intonational=accentual>word. As can be seen in Fig. 4(b) speakers AV and CV’s word context data for /d/ show effectively a straight-line transition. This shows that the vowel target values preceding /d/ accommodate to the consonant more in the weaker prosodic boundaries. It can further be seen in Fig. 4(b) that the vowel target values for /g/ are likewise displaced in the direction of the consonant. Thus, there is evidence that for both /d/ and /g/, the *F2* vowel data are displaced in the direction of the consonant, and that for /g/, there is greater variability in the consonant *F2* than for /d/. These observations on variability are confirmed by the statistics: there is a significant effect on variability in *F2* at the consonant boundary for all three speakers [**AV**: Levene:

$F(2,187)=9.98$, $p<0.0001$; **CV**: Levene: $F(2,87)=6.57$, $p<0.01$; **GR**: Levene: $F(2,193)=5.03$, $p<0.01$], with *post hoc* tests showing that /d/ has less variability than /b/ and /g/ for speakers AV and CV, and /b/ has more variability than /d/ and /g/ for speaker GR. Clearly, there is very little variability in *F2* for /d/.

An examination of peak velocity data (calculated as the maximum value of the first differential of the transition) for *F2* showed few differences between the intonational, accentual, and word contexts. Of course, peak velocity was significantly less in the utterance context since the vowel was always followed by a pause (peak velocity in this case was near zero). However, speaker GR did show a significant effect of prosodic boundary on peak velocity for his /g/ data only [**GR**: ANOVA: $F(2,64)=3.56$, $p<0.05$], but Bonferroni-adjusted *post hoc* tests did not show any significant differences. Nevertheless, both speaker GR’s and AV’s /g/ data showed a slight increase in peak velocity in the weaker prosodic boundaries (speaker GR’s /b/ data also gave significant results, but examination of the mean values showed that the word data patterned with the intonational data rather than the accentual data). The *F2* peak velocity data are presented in Fig. 5. There is a significant effect of consonant for two of the speakers [**AV**: ANOVA: $F(2,187)=37.43$, $p=0.00$; **CV**: ANOVA: $F(2,87)=30.71$, $p=0.00$], with *post hoc* tests showing that /g/ has a greater peak velocity for both speakers, with /d/ also having a lesser peak velocity for speaker AV. There are also some effects on variability in peak velocity [**AV**: Levene: $F(2,187)=3.77$, $p<0.05$; **CV**: Levene: $F(2,87)=3.87$, $p<0.05$], with *post hoc* tests showing that speaker AV has greater variability for /b/ than /d/, and speaker CV has greater variability for /g/ than /d/. The plots in Fig. 5 indicate that /d/ has slightly less variability in peak velocity. This further supports the hypothesis that for this consonant, the vowel target is displaced in the direction of the consonant (since distance is reduced together with duration, thereby making changes in velocity superfluous).

In sum, there is evidence to suggest that *F2* at the VC boundary for /d/ remains relatively stable, with the vowel target value moving towards the *F2* consonant value the weaker the prosodic boundary. The greatest effect of prosodic context on *F2* at VC boundary was for /g/, with *F2* moving closer to the velar consonant value in the weaker prosodic boundaries. The vowel target for /g/ was also displaced in the same direction. Such effects of the vowel being

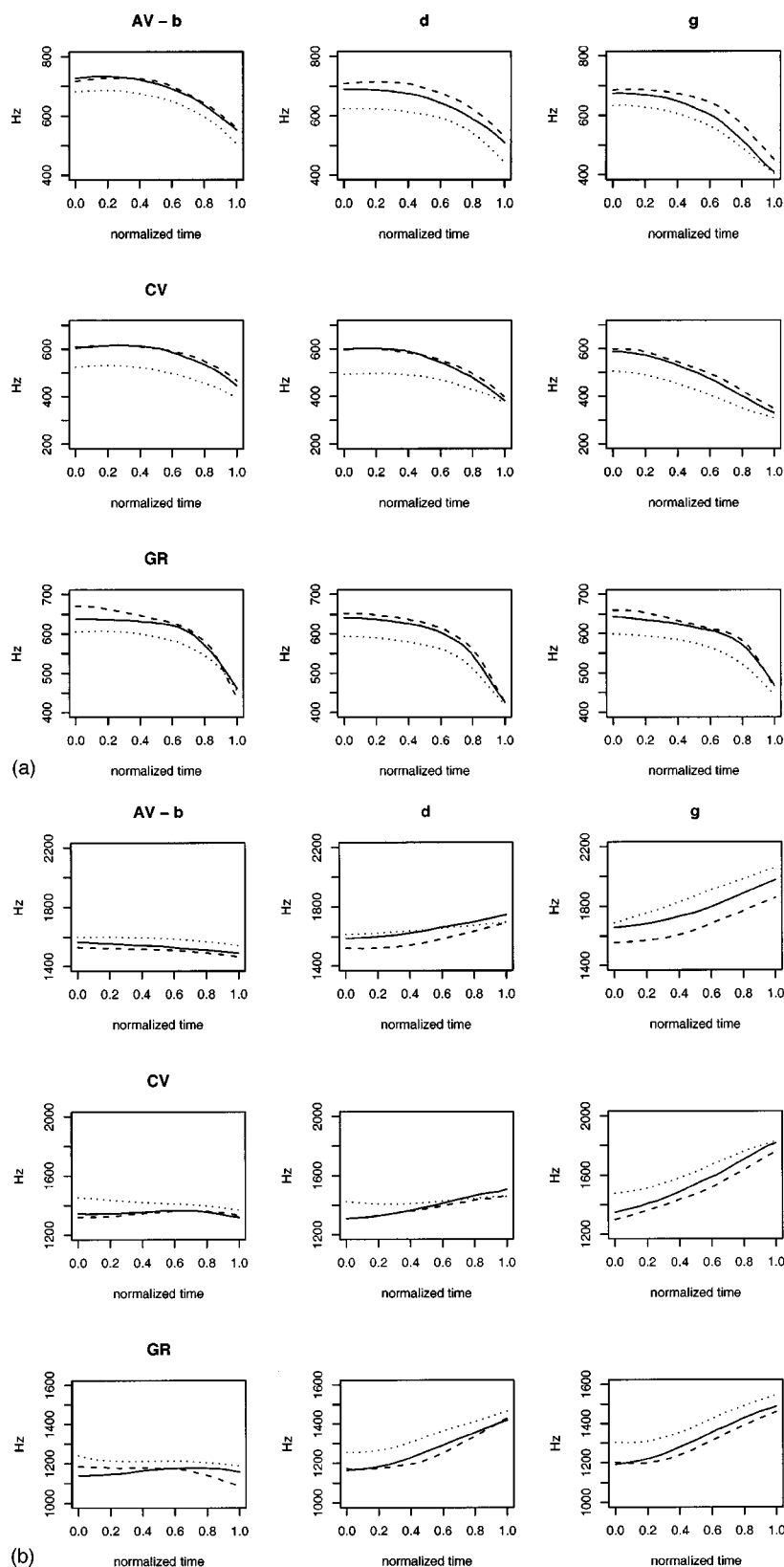


FIG. 4. Plots showing formant transitions for (a) $F1$ and (b) $F2$. Each plot shows data separately for each consonant context for each speaker. Tracks are time normalized. Each track presents data from the temporal midpoint to the temporal endpoint of the /a/ vowel. Dotted lines present data for the word boundary; solid lines present data for the accentual-phrase boundary; and dashed lines present data for the intonational-phrase boundary.

displaced in the direction of the consonant in weaker prosodic boundaries recall the results of Moon and Lindblom (1994), who showed that the vowel /i/ was displaced in the direction of the consonant as the number of syllables in the word increased. However, with the exception of AV's $F1$ data, velocity did not seem to play an important role in signaling prosodic boundaries in the present study: it may be

that velocity only comes into play when the distance between the consonant and the vowel must be increased for reasons of clarity, without a concomitant increase in duration.

C. Rate of change in fricative spectral tilt

Table V(a) presents spectral tilt data according to prosodic context for each speaker. Data presented are the num-

TABLE IV. (a) Transition distance, duration, and peak velocity data for three speakers. Data are calculated based on the hand-labeled *F1* target. Results are listed separately for each prosodic boundary. Only stop consonant contexts are included. (b) Significance results for data presented in (a). For each speaker, results from a one-way ANOVA are presented in the first column, and *post hoc* pairwise comparisons are presented for adjacent pairs in the prosodic hierarchy in the second column (with alpha adjusted to 0.017 following the Bonferroni method). The direction of the difference is marked by either “<” or “>,” or “=” in the case where the result is not significant.

		<i>F1</i> transition distance (Hz)		<i>F1</i> transition duration (ms)		<i>F1</i> transition velocity (Hz/ms)		
(a)		Mean	s.d.	Mean	s.d.	Mean	s.d.	<i>N</i>
AV	U	−3.22	117.86	73.64	21.39	0.774	2.028	62
	I	198.64	77.41	54.46	13.06	7.301	3.500	63
	A	211.61	89.26	56.89	16.08	7.395	3.625	64
	W	195.63	67.36	44.80	8.37	10.230	4.593	63
CV	U	−54.48	67.17	39.42	16.44	0.414	1.240	29
	I	199.89	58.21	71.39	15.36	5.849	2.426	30
	A	212.02	57.56	68.51	15.42	5.651	1.837	30
	W	149.33	47.70	44.52	11.05	5.064	1.659	30
GR	U	59.64	126.21	61.88	22.69	3.292	4.517	65
	I	220.94	56.17	73.25	15.57	9.769	3.913	65
	A	191.29	57.58	65.63	21.68	8.433	3.128	65
	W	156.67	48.96	48.64	8.12	9.905	3.331	66
		AV d.f. = 3248		CV d.f. = 3115		GR d.f. = 3257		
(b)		<i>F1</i> transition distance $F = 81.68$ $p = 0.00$		<i>F1</i> transition duration $F = 37.61$ $p = 0.00$		<i>F1</i> transition velocity $F = 78.83$ $p = 0.00$		
		U<I=A=W		U<I=A>W		U<I=A>W		
		U>I=A>W		U<I=A>W		U<I>A>W		
		U<I=A<W		U<I=A=W		U<I=A=W		

ber of frames for each class (this allows an approximate calculation of the duration in each analysis context, given the frame shift of 5 ms); the mean correlation (r) of the secondary regression (the tilt values plotted as a dependent variable of the frame number); and the mean slope of the secondary regression. It is this slope value which measures the rate of

change in spectral tilt across the VC boundary. Table V(b) presents significance results based on the slope value in Table V(a).

Although data are not tabled, tilt values for the vowel /a/ had consistently negative tilt values, whereas the maximum fricative tilt values in each token were consistently positive.⁸

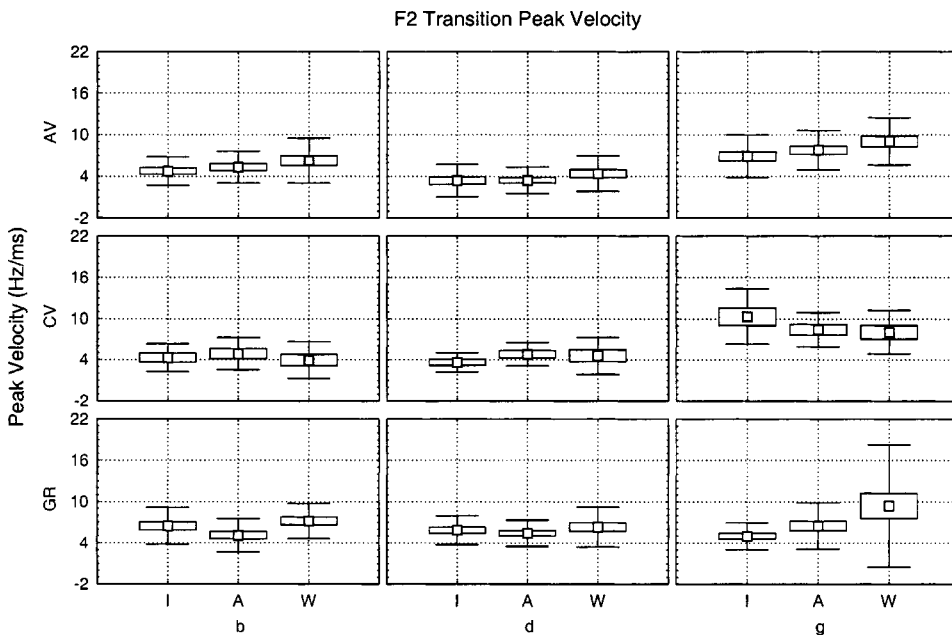


FIG. 5. Boxplots of *F2* peak velocity data for three speakers. Data are plotted according to consonant context and prosodic context.

TABLE V. (a) Spectral tilt data for fricatives in four prosodic context. “No. of Frames” gives the number of FFTs carried out across the vowel–fricative token, with spectral tilt being calculated for each FFT. The r value is based on a Pearson product-moment correlation of the spectral tilt values for each FFT plotted against its frame number in the token. The slope value is calculated based on a regression of these tilt values plotted against the frame number, and gives the rate of change in tilt. (b) Significance results for data presented in (a). For each speaker, results from a one-way ANOVA are presented in the first column, and *post hoc* pairwise comparisons are presented for adjacent pairs in the prosodic hierarchy in the second column (with alpha adjusted to 0.017 following the Bonferroni method). The direction of the difference is marked by either “<” or “>,” or “=” in the case where the result is not significant.

		No. of frames		r		Slope		N
(a)		Mean	s.d.	Mean	s.d.	Mean e^{-3}	s.d. e^{-3}	
AV	U	14.59	2.17	0.17	0.37	0.33	0.71	64
	I	10.84	0.89	0.93	0.04	6.96	1.87	64
	A	10.00	0.82	0.92	0.05	7.35	2.01	64
	W	8.39	0.68	0.90	0.08	7.67	2.48	64
CV	U	11.36	1.29	0.06	0.45	0.18	1.14	33
	I	10.00	0.83	0.92	0.04	9.41	2.72	33
	A	9.94	0.75	0.91	0.05	9.31	2.67	33
	W	7.51	0.62	0.93	0.05	12.42	2.98	33
GR	U	10.61	1.49	0.18	0.45	0.50	1.17	61
	I	10.90	0.89	0.87	0.10	6.19	2.10	61
	A	10.28	1.03	0.88	0.10	7.01	2.31	61
	W	7.97	0.63	0.94	0.04	10.23	2.64	61
		AV		CV		GR		
(b)		d.f. = 3252		d.f. = 3128		d.f. = 3240		
Spectral tilt		$F = 222.04$ $p = 0.00$	U < I = A = W	$F = 150.06$ $p = 0.00$	U < I = A < W	$F = 220.76$ $p = 0.00$	U < I = A < W	

The difference between the minimum tilt and maximum tilt for each token was, as expected, far greater for the intonational, accentual, and word contexts than for the utterance context, since only the fricative portion was examined in the latter context.

It can be seen in Table V that the r values for the intonational-, accentual-, and word-boundaries are extremely high, typically above 0.9. This shows that the spectral tilt values cluster tightly around the line of best fit. The lower r values for the utterance context are to be expected, since a relatively unchanging signal is being measured, thereby magnifying any measurement errors. These values (generally around 0.1) suggest, nevertheless, that the utterance data are reasonably reliable.

It can also be seen in Table V that there is a clear increase in slope values the weaker the prosodic boundary. This is true for all three speakers (with the exception of speaker CV's intonational boundary). Table V also shows that the slope values in the utterance context are close to zero, suggesting no change in the tilt values during the portion which was measured. It can be seen that the utterance data are clearly separated from the other data. Although the other three prosodic contexts are not reliably differentiated by speaker AV, it can be seen that speakers GR and CV collapse the intonational- and accentual-boundary data into one class, with the word-boundary data clearly forming a class of its own. The higher slope values for the word class suggest that the change from the vowel spectrum to the fricative spectrum occurs much more rapidly in the word context than in the intonational or accentual contexts.

The fact that speaker AV does not seem to differentiate

the accentual, intonational, and word contexts does not immediately seem to be due to measurement error, since increasing the analysis duration from 15% of the syllable to 25% of the syllable made no difference to her results. However, since Table V shows a pattern of increasing spectral tilt values the weaker the prosodic boundary for this speaker, it may be the case that the relatively small number of tokens (around 20 for each prosodic boundary for each fricative) leads to less statistically reliable results for this particular speaker.

D. Summary of prosodic data

Table VI presents eta-squared values for the all of the data presented above. Eta-squared measures the proportion of the total observed variance that is accounted for by the independent variable (in this case, prosodic boundary), and is presented as a value between zero and 1. Since the presence of a pause at the utterance boundary presented a problem for some of the measures used in this paper, it has been excluded in the eta-squared analysis for some of the measures (namely, the fricative spectral tilt measures and the $F1$ stop transition measures). Although the presence of the pause at the utterance boundary made measurement of stop consonant duration less reliable, no consistent differences across speakers were found when the utterance data were excluded from the eta-squared analysis of consonant duration. For this reason, utterance data are included in the eta-squared values for consonant duration. Furthermore, since there were no problems measuring vowel duration at the utterance boundary, the ut-

TABLE VI. Eta-squared results for various measures examined in this study. The eta-squared value gives the proportion of total variance accounted for by the independent variable of prosodic boundary. Note that utterance boundary data were excluded for the measures marked with an asterisk (*), since the presence of a pause at the utterance boundary was problematic for these measures (see the Method section for more details).

	AV	CV	GR
Vowel duration	0.834	0.846	0.729
Consonant duration	0.036	0.039	0.109
% vowel	0.233	0.131	0.192
<i>F1</i> vowel	0.650	0.680	0.340
<i>F2</i> vowel	0.248	0.527	0.126
<i>F1</i> transition distance*	0.008	0.203	0.192
<i>F1</i> transition duration*	0.142	0.430	0.294
<i>F1</i> transition velocity*	0.108	0.028	0.036
Spectral tilt*	0.018	0.216	0.357

terance data were included in the eta-squared analysis of percentage vowel duration (percentage of the syllable comprised of the vowel).

It can be seen that prosodic boundary has an extremely large effect on vowel duration (explaining around 80% of the total variance), and an almost negligible effect on consonant duration. Presumably, consonant identity has a large effect on consonant duration; nevertheless, previous observations have suggested that the effect of prosodic boundary is greater for the vowel than for the consonant duration, so that these eta-squared results are consistent with data that have already been presented. By extension, prosodic boundary also has an important effect on syllable duration, and to a lesser extent on percentage vowel duration.

An interesting result is that prosodic boundary has a greater effect on *F1* vowel than on *F2* vowel, with the results being particularly strong for speakers AV and CV (around 65% for *F1* vowel). This is presumably related to differences in tongue body and jaw height (see Tabain [submitted], where strong prosodic effects were found for tongue body height, but not so for backness).

Turning to the more dynamic measures, for which the utterance boundary data have been excluded: the effect of prosodic boundary on *F1* distance and duration is reasonably strong for speakers CV and GR, and less so for speaker AV (the effect on *F1* distance is almost negligible for this speaker). The effect on *F1* velocity is reasonably strong for speaker AV and less so for speakers CV and GR. The effect of prosodic boundary on rate of change in spectral tilt is reasonably strong for speakers CV and GR, and negligible for speaker AV.

In sum, the effects of prosodic boundary are extremely strong on vowel duration and on *F1* vowel.

IV. SUMMARY AND DISCUSSION

The current results have shown that there is an interaction between acoustic segment durations and the prosodic hierarchy, with consonants relatively unaffected by the pro-

sodic boundary and vowels highly affected by the prosodic boundary. In addition, the stability of the fricative consonants is much greater than that of the stop consonants in terms of duration. Vowel formant values suggest a lower and more back articulation for the /a/ the stronger the prosodic boundary.

For one speaker, GR, the vowel data for the three lower prosodic boundaries showed the effects of the prosodic hierarchy, whereas the data for the utterance context showed a more centralized vowel in this context. This acoustic patterning is similar to that seen in Johnson and Martin (2001): namely, a centralization of the vowel data at the end of the utterance compared to the start of the utterance. Such effects are believed to be due to articulatory declension (greater hyperarticulation at the beginnings of utterances than at the ends of utterances—Vayra and Fowler, 1992; Krakow, Bell-Berti, and Wang, 1994). Articulatory declension (as the name suggests) is believed to have an articulatory/biological basis, and indeed, the results from speaker GR's jaw movement data presented in Tabain (submitted) show that the utterance boundary data pattern between the accentual-phrase and the word data with their higher jaw position, rather than lower jaw position. It is interesting that speaker GR's tongue data, however, do not show the same pattern (i.e., in the utterance context, the tongue data show the expected effects of the prosodic hierarchy). It is not clear just why the tongue has no apparent effect on the acoustic output as shown here, and why the jaw seems to have “won out” in terms of acoustic effects. It may be noted that Harrington, Beckman, and Fletcher (2000) present similar results where the lower jaw position for a stressed /i/ leads to a greater rms energy despite a higher and more fronted tongue position. For further discussion of the competing constraints of articulatory declension and the prosodic hierarchy, the reader is referred to Tabain (submitted).

Regarding the dynamic data, *F2* at the VC boundary was more affected by the prosodic context for /g/ than for the other consonants. *F2* boundary remained relatively invariant for /d/. There was evidence to suggest that the vowel target for /a/ was displaced in the direction of the consonant for both /d/ and /g/. It was less clear what was happening with the /b/ data. In terms of variability in *F2* for the consonant, /b/ seemed to behave like /g/, although there was no clear pattern of *F2* consonant moving either in the direction of the consonant or towards the vowel.

For one speaker, *F1* peak velocity increased in the weaker prosodic boundaries for the stop consonants (accompanied by no difference in distance, but reduced duration), and *F2* peak velocity seemed to increase in the weaker prosodic boundaries for /g/ only, for another speaker. For two speakers, rate of change in spectral tilt increased in the weaker prosodic boundaries for the fricative consonants. These results suggest that velocity plays a role in the marking of prosodic boundaries.

Taken together, the above results suggest the presence of acoustic, and hence possibly perceptual, cues to the various prosodic boundaries examined. However, the study of articulatory prosody is relatively new, and perceptual studies based on the few acoustic findings to date have not really begun.

Although many studies have focused on duration as cues to prosodic boundaries (e.g., Turk and Sawusch, 1996), perceptual studies of spectral and dynamic cues to prosodic organization are rare. However, if the cues to prosodic boundary include spectral cues as well as duration, intensity, and F_0 cues, we will have further evidence that the speech signal shows a good deal of redundancy in order to facilitate the task for the listener.

One type of redundancy which may exist involves the interaction of duration and velocity cues. For instance, it may be suggested that the increase in velocity at the weaker prosodic boundaries observed for the fricative tilt data could be predicted by durational measures. However, this would not explain the results for speaker AV, for example, who did not show significant results in the spectral tilt data, but who (like the other speakers) did show significant results in the duration data. It was also observed that there was an interaction between distance, duration, and velocity for the F_1 transition, with one speaker using velocity to effect an unchanging distance as duration decreased according to prosodic boundary, whereas the other two speakers had no velocity effects due to both distance and duration decreasing together. How would listeners reconcile the different temporal strategies used by the different speakers, assuming listeners use such temporal information as cues? Such interactions between duration and velocity need to be better understood.

A further point of interest also regards velocity. It was mentioned in the Introduction that Wouton and Macon (2002a) found that $F_1-F_2-F_3$ transition slopes (=velocity) were greater in more linguistically prominent positions such as stressed syllables or pitch-accented syllables. However, the opposite effect was observed here: velocity tended to be greater in less linguistically salient positions, such as the word boundary, rather than more prominent positions, such as the utterance or intonational phrase boundary. This is most probably due to the fact that VC transitions were examined in the present study, since Wouton and Macon noted that the effects they described were true for CV transitions, and that the case was not so clear for VC transitions. The possible reasons for these differences were outlined in the Introduction section with reference to Kozhevnikov and Chistovich's theories of articulatory planning. It should be noted that articulatory results presented in Tabain (submitted) show that there is a tendency for velocity to *increase* going from /t/ to /a/ the stronger the prosodic boundary, and to *decrease* going from /a/ to another consonant the stronger the prosodic boundary. The /ta #/ transition was not examined in the present acoustic study; however, it is expected that such a CV transition would show the opposite effect to the VC transitions examined here (namely, an increase in peak velocity the stronger the prosodic boundary).

Several differences were observed in the present study according to consonant class. Perhaps one of the more interesting results was for the F_2 transitions, which showed that the consonant formant value for /d/ was much more stable across prosodic contexts than that for /g/—these are precisely the sorts of results which occur in studies of CV coarticulation for these consonants (Ohman, 1966; Butcher and Weiher, 1976; Krull, 1987). It was also interesting to note

that the F_2 for the vowel appeared to be displaced in the direction of the consonant in the weaker prosodic boundaries, similarly to Moon and Lindblom's (1994) results according to number of syllables in the word. All these results are in addition to the clear acoustic effects observed on vowel target formant values, with a lower and more back /a/ vowel in the stronger prosodic boundaries.

In sum, this study has shown that the effects of the prosodic hierarchy on the speech signal are not restricted to durational effects—there are spectral effects which the present paper has only begun to elucidate. One can only assume that these spectral effects have perceptual consequences, for, as recent work by Wouton and Macon (2002b) has shown, a good description of such effects can lead to a significant improvement in the quality of synthetic speech. It is hoped that the acoustic results presented in the current paper will motivate perceptual studies of the relative importance of spectral effects (in addition to amplitude, duration, and F_0 cues) in alerting listeners to the presence of a prosodic boundary.

ACKNOWLEDGMENTS

This work was supported by the French Ministère de l'Éducation Nationale, de la Recherche et de la Technologie (MENRT), and by the Fondation Fyssen. I would like to thank Pierre Badin for discussion; Guillaume Rolland for programming help; Anders Lofqvist for his editorial support; two anonymous reviewers for their enthusiasm; and my speakers for their time. I would particularly like to thank Pascal Perrier for all of his support and help throughout this project. An earlier version of this work was presented at Eurospeech 2001, in Aalborg, Denmark (Tabain, Rolland, and Savariaux, 2001).

¹Since prosodic structure as described here is treated as hierarchical, "stronger" prosodic boundaries such as the utterance or intonational phrase may also be referred to as "higher" prosodic boundaries in the hierarchy. Likewise, a "weaker" prosodic boundary such as the word or syllable may be referred to as "lower" in the hierarchy.

²It should be noted that Jun and Fougeron (2000) have proposed an additional level, namely the intermediate phrase (ip), between the AP and the IP. However, they note that further research is needed to support this level of the ip, and for this reason, the hypothesized ip is ignored in the present study.

³One reviewer asked why the spectral tilt analysis was carried out only for the fricative data, and not for the stop data, given that Smits *et al.*'s (1996) results were for stops. The initial reasoning for this approach to the current study was that Smits *et al.*'s results were for CV transitions, which by definition include a stop burst, whereas in the present study, the VC transitions studied precluded the existence of a stop burst. Since a stop burst, like a fricative spectrum, has a concentration of energy in the higher frequencies, whereas a vowel has a concentration of energy in the lower frequencies, the change in spectral tilt will not be as great if only a vowel-like portion is analyzed, as opposed to a sequence of vowel-like and burst-like spectra. Given that the purpose of the current study was to explore possible spectral effects of the prosodic structure, it was felt that the analysis of formant movement into the stop consonant was sufficient in this case. However, it is true that there is no reason why an analysis of spectral rate of change moving from the vowel into the stop consonant should not be attempted, so long as the fact that there is no stop burst present is taken into consideration.

⁴A reviewer asked whether the fact that the burst following release of the /t/ was included as part of the vowel duration would in any way make comparison with results from other studies on articulatory prosody problematic, since the burst is not usually included as part of vowel duration in these

studies. In answer to this questions, it is expected that the inclusion of the burst would have a minimal effect on comparison across studies, since voiceless stops in French are not aspirated, and since the duration of the burst is small compared to the duration of the vocalic portion proper.

⁵Badin (1989) has shown that the spectral tilt of fricatives is strongly affected by the intensity of the articulation, with greater dB intensity resulting in a greater enhancement of the higher frequencies, and hence a greater tilt value. It is therefore important not to include the initial few milliseconds of fricative duration, where rms energy has not yet reached its peak. It should also be mentioned here that rms energy in the fricatives was examined according to prosodic context, and that no pattern was found to these data. One can therefore be confident that the tilt values presented here are not affected by different intensities of articulation according to prosodic context. (Note that since the acoustic recordings were carried out together with EMA data recordings, the microphone was fixed to the headset worn by the subject for the articulographic measurements; hence, distance between the speech output and the microphone remained constant throughout the recording).

⁶In the text and in tables, " $p=0.00$ " means that " p " is equivalent to zero since in the statistics program used for this study (STATISTICA), the value returned for " p " was 0 to 6 decimal places.

⁷Due to the importance of $F2$ to consonant place of articulation, the results for the three different stops are treated separately here. For this reason, each consonant is discussed separately and data are not presented in a table collapsed across consonants.

⁸Interestingly, the tilt values for the fricative /f/ were consistently lower than those for the nonsibilants, which is consistent with a lower-intensity spectral peak for the nonsibilant fricative.

Badin, P. (1989). "Acoustics of voiceless fricatives: Production theory and data," *Speech Transmission Laboratory—Quarterly Progress Status Report* 3/1989 33–55.

Beckman, M., and Pierrehumbert, J. (1986). "Intonational structure in English and Japanese," *Phonology* 3, 255–310.

Butcher, A., and Weiher, E. (1976). "An electropalatographic investigation of coarticulation in VCV sequences," *J. Phonetics* 4, 59–74.

Byrd, D. (2000). "Articulatory vowel lengthening and coordination at phrasal junctures," *Phonetica* 57, 3–16.

Byrd, D., Kaun, A., Narayanan, S., and Saltzman, E. (2000). "Phrasal signatures in articulation," in *Papers in Laboratory Phonology V: Acquisition and the Lexicon*, edited by M. Broe and J. Pierrehumbert (Cambridge University Press, Cambridge), pp. 70–87.

Byrd, D., and Saltzman, E. (1998). "Intragestural dynamics of multiple prosodic boundaries," *J. Phonetics* 26, 173–199.

Cassidy, S., and Harrington, J. (2001). "Multilevel annotation in the EMU speech database management system," *Speech Commun.* 33, 61–77.

Cho, T., and Keating, P. (2001). "Articulatory and acoustic studies on domain-initial strengthening in Korean," *J. Phonetics* 29, 155–190.

di Cristo, A. (1998). "Intonation in French," in *Intonation Systems: A Survey of Twenty Languages*, edited by D. Hirst and A. di Cristo (Cambridge University Press, Cambridge), pp. 195–212.

Dilley, L., Shattuck-Hufnagel, S., and Ostendorf, M. (1996). "Glottalization of word-initial vowels as a function of prosodic structure," *J. Phonetics* 24, 423–444.

Fletcher, J. (1991). "Rhythm and final lengthening in French," *J. Phonetics* 19, 193–212.

Fougeron, C. (2001). "Articulatory properties of initial segments in several prosodic constituents in French," *J. Phonetics* 29, 109–135.

Fougeron, C., and Jun, S.-A. (1998). "Rate effects on French intonation: Prosodic organization and phonetic realization," *J. Phonetics* 26, 45–69.

Fougeron, C., and Keating, P. (1997). "Articulatory strengthening at edges of prosodic domains," *J. Acoust. Soc. Am.* 101, 3728–3740.

Harrington, J., Beckman, M., and Fletcher, J. (2000). "Manner and place conflicts in the articulation of accent in Australian English," in *Papers in Laboratory Phonology V: Acquisition and the Lexicon*, edited by M. Broe and J. Pierrehumbert (Cambridge University Press, Cambridge), pp. 40–51.

Harrington, J., and Cassidy, S. (1999). *Techniques in Speech Acoustics* (Kluwer, Dordrecht).

Harrington, J., Cassidy, S., Fletcher, J., and McVeigh, A. (1993). "The MU⁺ system for corpus based speech research," *Comput. Speech Lang.* 7, 305–331.

Harris, K. (1958). "Cues for the discrimination of American English fricatives in spoken syllables," *Lang Speech* 1, 1–7.

Ihaka, R., and Gentleman, R. (1996). "R: A language for data analysis and graphics," *J. Comput. Graph. Stat.* 5, 299–314.

Johnson, K., and Martin, J. (2001). "Acoustic vowel reduction in Greek: Effects of distinctive length and position in the word," *Phonetica* 58, 81–102.

Jongman, A., Wayland, R., and Wong, S. (2000). "Acoustic characteristics of English fricatives," *J. Acoust. Soc. Am.* 108, 1252–1263.

Jun, S.-A., and Fougeron, C. (2000). "A phonological model of French intonation," in *Intonation: Analysis, Modelling and Technology*, edited by A. Botinis (Kluwer, Dordrecht), pp. 209–242.

Keating, P., Cho, T., Fougeron, C., and Hsu, C.-S. (in press). "Domain-initial articulatory strengthening in four languages," in *Papers in Laboratory Phonology VI*, edited by J. Local, R. Ogden, and R. Temple (Cambridge University Press, Cambridge).

Klatt, D. (1976). "Linguistic uses of segmental duration in English: Acoustic and perceptual evidence," *J. Acoust. Soc. Am.* 59, 1208–1221.

Kozhevnikov, V., and Chistovich, L. (1965) *Speech: Articulation and Perception* (Joint Publication Research Service, Washington, D.C.).

Krakow, R., Bell-Berti, F., and Wang, Q. (1994). "Supralaryngeal declination: Evidence from the velum," in *Producing Speech: A Festschrift for Katherine Safford Harris*, edited by F. Bell-Berti and L. Raphael (AIP, Woodbury, NY), pp. 333–353.

Krull, D. (1987). "Second-formant locus patterns as a measure of consonant–vowel coarticulation," *Phonetic Experimental Research at the Institute of Linguistics: University of Stockholm (PERILUS)* 5, 43–61.

Lahiri, A., Gwirth, L., and Blumstein, S. (1984). "A reconsideration of acoustic invariance for place of articulation in diffuse stop consonants: Evidence from a cross-language study," *J. Acoust. Soc. Am.* 76, 391–404.

Lehiste, I. (1972). "The timing of utterances and linguistic boundaries," *J. Acoust. Soc. Am.* 51, 2018–2024.

Lehiste, I. (1974). "Duration of syllable nuclei as a function of word length and stress pattern," *Proceedings of the 8th International Congress on Acoustics London*, 300.

Levene, H. (1960). "Robust test for equality of variance," in *Contributions to Probability and Statistics*, edited by I. Olkin, S. Ghurye, W. Hoeffding, W. Madow, and H. Mann (Stanford University Press, Stanford), pp. 278–292.

Lindblom, B. (1963). "Spectrographic study of vowel reduction," *J. Acoust. Soc. Am.* 35, 1773–1781.

Lindblom, B. (1990). "Explaining phonetic variation: A sketch of the H and H theory," in *Speech Production and Speech Modelling*, edited by W. Hardcastle and A. Marchal (Kluwer, Dordrecht), pp. 403–439.

Mann, V., and Repp, B. (1980). "Influence of vocalic context on perception of the [j]–[s] distinction," *Percept. Psychophys.* 28, 213–228.

Moon, S.-J., and Lindblom, B. (1994). "Interaction between duration, context and speaking style in English stressed vowels," *J. Acoust. Soc. Am.* 96, 40–55.

Munson, B. (2001). "A method for studying variability in fricatives using time-dependent changes in spectral moments," *J. Acoust. Soc. Am.* 110, 1203–1206.

Ohman, S. (1966). "Coarticulation in VCV utterances: Spectrographic measurements," *J. Acoust. Soc. Am.* 39, 151–168.

Pierrehumbert, J. (1980). "The Phonology and Phonetics of English Intonation," Ph.D. thesis, MIT.

Recasens, D. (1999). "Lingual coarticulation," in *Coarticulation: Theory, Data and Techniques*, edited by W. Hardcastle and N. Hewlett (Cambridge University Press, Cambridge), pp. 80–104.

Smits, R., ten Bosch, L., and Collier, R. (1996). "Evaluation of various sets of acoustic cues for the perception of prevocalic stop consonants. I. Perception experiment," *J. Acoust. Soc. Am.* 100, 3852–3864.

Tabain, M. (2001). "Variability in fricative production and spectra: Implications for the Hyper- and Hypo- and Quantal theories of speech production," *Lang. Speech* 44, 58–93.

Tabain, M. (submitted). "Effects of prosodic boundary on /aC/ sequences: Articulatory results."

Tabain, M., Rolland, G., and Savariaux, C. (2001). "Coarticulatory effects at prosodic boundaries: Some acoustic results," *Proceedings of Eurospeech 2001* (Aalborg, Denmark), pp. 963–966.

Turk, A., and Sawusch, J. (1996). "The processing of duration and intensity cues to prominence," *J. Acoust. Soc. Am.* 99, 3782–3790.

Turk, A., and Shattuck-Hufnagel, S. (2000). "Word-boundary-related duration patterns in English," *J. Phonetics* 28, 397–440.

- Turk, A., and White, L. (1999). "Structural influences on accentual lengthening in English," *J. Phonetics* **27**, 171–206.
- Vayra, M., and Fowler, C. (1992). "Declination of supralaryngeal gestures in spoken Italian," *Phonetica* **49**, 48–60.
- Wouton, J., and Macon, M. (2002a). "Effects of prosodic factors on spectral dynamics. I. Analysis," *J. Acoust. Soc. Am.* **111**, 417–427.
- Wouton, J., and Macon, M. (2002b). "Effects of prosodic factors on spectral dynamics. II. Synthesis," *J. Acoust. Soc. Am.* **111**, 428–438.

Learning to produce speech with an altered vocal tract: The role of auditory feedback

Jeffery A. Jones^{a)}

ATR International—Human Information Science Laboratories, Communication Dynamics Project,
2-2-2 Hikaridai, Seika-cho, Soraku-gun, Kyoto 619-0288, Japan

K. G. Munhall

Department of Psychology, Department of Otolaryngology, Queen's University, Kingston, Ontario K7L 3N6,
Canada

(Received 21 February 2002; revised 28 October 2002; accepted 28 October 2002)

Modifying the vocal tract alters a speaker's previously learned acoustic–articulatory relationship. This study investigated the contribution of auditory feedback to the process of adapting to vocal-tract modifications. Subjects said the word /tas/ while wearing a dental prosthesis that extended the length of their maxillary incisor teeth. The prosthesis affected /s/ productions and the subjects were asked to learn to produce “normal” /s/'s. They alternately received normal auditory feedback and noise that masked their natural feedback during productions. Acoustic analysis of the speakers' /s/ productions showed that the distribution of energy across the spectra moved toward that of normal, unperturbed production with increased experience with the prosthesis. However, the acoustic analysis did not show any significant differences in learning dependent on auditory feedback. By contrast, when naive listeners were asked to rate the quality of the speakers' utterances, productions made when auditory feedback was available were evaluated to be closer to the subjects' normal productions than when feedback was masked. The perceptual analysis showed that speakers were able to use auditory information to partially compensate for the vocal-tract modification. Furthermore, utterances produced during the masked conditions also improved over a session, demonstrating that the compensatory articulations were learned and available after auditory feedback was removed. © 2003 Acoustical Society of America. [DOI: 10.1121/1.1529670]

PACS numbers: 43.70.Fq, 43.70.Aj, 43.70.Dn [AL]

I. INTRODUCTION

In order to learn to produce speech, children must learn the unique configuration of their vocal tracts. Even after speech acquisition, children's speech motor control systems must adapt to gradual changes in the shape and size of their vocal tract due to growth. By comparison, changes to the vocal tract are relatively minor after puberty (Benjamin, 1997). However, adults may still be confronted with severe vocal-tract modifications if they lose teeth, acquire dentures, or wear other types of dental appliances. These vocal-tract alterations often mean that previously learned articulations do not produce speech sounds of the same quality. To adjust to the new articulatory–acoustic relationship resulting from vocal-tract modifications, speakers must modify their previously learned articulations in order to produce perceptually adequate speech sounds.

A number of studies have demonstrated that adult speakers can compensate to some degree for structural changes to the oral cavity. Laboratory manipulations have involved subjects wearing dental prostheses. For instance, Hamlet and her colleagues conducted a series of studies in which subjects had to learn to speak while wearing an “artificial palate” that covered the alveolar ridge region of the mouth (Hamlet, 1973; Hamlet, Cullison, and Stone, 1979; Hamlet and Stone, 1976, 1978; Hamlet, Stone, and McCarty, 1978). Observa-

tions of sibilant articulations using techniques such as electropalatography, ultrasound, and magnetic resonance imaging have shown that accurate sibilant production relies on the exact placement of the tongue relative to the palate in order to form a medial groove (Fletcher and Newman, 1991; Narayanan, Alwan, and Haker, 1995; Stone *et al.*, 1992). The presence of the artificial palate caused the tongue to contact the alveolar ridge sooner than it would normally and to release contact later than it should, lengthening frication and altering the width of the groove of the tongue (Hamlet *et al.*, 1979). These deleterious effects tend to be greater when the thickness of the palate is increased.

Subjects eventually do improve the quality of their speech in the presence of the artificial palate (Hamlet, 1973; Hamlet and Stone, 1976, 1978; Hamlet *et al.*, 1978, 1979). Small improvements are apparent after a relatively small number of practice trials that occur within an hour-long experimental session (McFarland, Baum, and Chabot, 1996). However, several days to weeks are often needed to achieve normal sounding productions (Hamlet and Stone, 1976; Hamlet *et al.*, 1978). Once adaptation has occurred, it takes only a few minutes of practice to readapt to the artificial palate even if months have elapsed since a subject's previous exposure to the altered oral environment (Hamlet *et al.*, 1978).

The contribution of auditory feedback to learning to produce normal speech in the presence of these novel vocal-tract manipulations is not known. It is widely believed that the

^{a)}Electronic mail: jones@atr.co.jp

availability of auditory feedback regarding speech performance is particularly important for the development of normal speech in children (Borden, 1979; Oller and Eilers, 1988; Osberger and McGarr, 1982; Smith, 1975). However, longitudinal studies of postlingually deafened individuals suggest that auditory feedback is also a factor in the long-term maintenance of accurate speech in adults. Abnormalities in the control of pitch, loudness, and the rate of speech appear quite soon after hearing is lost. Longer periods of deafness lead to increased variability in consonant and vowel production (Binnie, Daniloff, and Buckingham, 1982; Cowie and Douglas-Cowie, 1992; Lane and Webster, 1991; Waldstein, 1990).

Evidence from the experimental manipulation of the auditory feedback received by normal-hearing individuals confirms these clinical data. For example, masking the auditory feedback of hearing individuals affects aspects of speech such as pitch (e.g., Rivers and Rastatter, 1985; Ternström, Sundberg, and Collden, 1988). Modifications of the spectra of feedback often lead to immediate changes in speech that are dependent on the frequencies filtered (Garber and Moller, 1979). If subjects' feedback regarding their F_0 is artificially raised or lowered, they tend to compensate by shifting their vocal pitch in the opposite direction of the perturbation (Burnett *et al.*, 1998; Donath, Natke, and Kalveram, 2002; Eiman, 1981; Jones and Munhall, 2000, 2002; Kawahara, 1995a, 1995b).

Longer-term effects have also been induced. For example, Houde and Jordan (1998) asked subjects to whisper one-syllable words while they received altered auditory feedback regarding their vowel productions. Subjects heard feedback in which the formants of the vowels they were producing were gradually shifted enough over time to change the vowels' phonetic identity. Subjects compensated for the formant transformations. These compensations persisted even during trials in which feedback was masked by noise. Subjects either modified their existing mapping between their vocal-tract productions and their acoustic feedback or developed a new mapping. Analogous results were obtained when Jones and Munhall (2000, 2002) gave subjects altered auditory feedback regarding their fundamental frequency productions.

These data suggest that auditory feedback is used both to make online corrections and for the longer-term calibration of the mapping between speech gestures and the resulting acoustic feedback. Feedback may become even more crucial under circumstances where the characteristics of the vocal tract or motor system are altered.

There is little previous work on the specific importance of auditory feedback in adapting to the novel acoustic-motor mapping brought about by altering the vocal tract. However, a number of clinical observations indicate that recovery without auditory feedback is very difficult. For example, Perkell *et al.* (1995, 2000a) described a subject who became deaf as a result of surgery to remove bilateral acoustic neuromas. During the surgery, the subject received an auditory brainstem implant that provided her with information regarding the auditory envelope but did not provide information regarding spectral cues. Despite her situation, the subject still

maintained a good /s/ versus /ʃ/ contrast. However, when a subsequent operation caused her to suffer a slight weakness on the left side of her tongue due to denervation of the tongue muscles, she lost the /s/ and /ʃ/ contrast and could not regain accuracy. Perkell and his colleagues concluded that the loss of the important auditory information did not allow her to correct for the altered acoustic-motor relationship.

Experimental data have so far not supported these clinical findings. For example, Garber *et al.* (1980b) conducted one of the few investigations on the effect that noise has on adapting to an artificial palate. They found that masking noise did not differentially affect productions with the appliance in the mouth compared to productions made without it. More recently, Honda and Kaburagi (2000) examined the effect masking noise had on compensations to rapid changes in palatal thickness. Immediate but incomplete compensations of tongue position were found when the thickness of an artificial palate was suddenly changed during production of fricatives. Although only a small number of subjects participated in a perceptual experiment assessing the quality of the speakers' productions, the authors concluded that auditory information did not play a significant role in compensations and that tactile information regarding tongue-palate contact or intraoral pressure is likely essential for the process.

Indeed, the importance of tactile information for compensations to vocal-tract perturbations has been shown for other types of manipulations. For example, a number of influential studies have shown that when subjects are asked to produce vowels with a "bite block" inserted between their teeth, they compensate for the bite block's presence with very little or no practice (Fowler and Turvey, 1980; Gay, Lindblom, and Lubker, 1981; Kelso and Tuller, 1983; Lindblom and Sundberg, 1971), even from the first glottal pulse (Lindblom, Lubker, and Gay, 1979; cf. Flege *et al.*, 1988; McFarland and Baum, 1995). In order for the perceptual identity of a phoneme to be maintained with a bite block in a speaker's mouth, an unnatural articulator configuration must be used. Somatosensory and proprioceptive information is available regarding the position of the articulators and the nature of the bite block restricting movement before speakers speak. This information helps the speech motor control system reorganize speech even prior to movement initiation.

The results from bite block studies highlight the importance of somatosensory information in adjusting to novel speech conditions. They also illustrate a potential confound that exists in many of the studies that have experimentally altered vocal tracts in ways that reduce or affect tactile feedback. In particular, studies that have involved artificial palates as a tool to explore adaptation have all been confounded by a reduction of tactile information. Covering the palate with an acrylic shield results in a loss of sensory information and may affect the strategies that subjects use during adaptation. Therefore, discerning the precise contributions of auditory and tactile feedback to the adaptation process is very difficult using these kinds of manipulations.

The goal of the present investigation was to examine the contribution of auditory feedback to learning a novel acoustic-motor relationship by modifying the vocal tract in a way that did not hinder movement or reduce somatosensory

information. To that end, speakers wore a dental prosthesis that extended the length of their teeth by a few millimeters. The prosthesis did not affect the speakers' bite. In addition, it was only in contact with the teeth and did not cover any oral tissues so that tactile information normally available was still present with the prosthesis inserted.

Because the prosthesis extended the teeth, production of sibilants was altered. To produce an /s/, speakers must position their tongue against the dento-alveolar ridge and force air through a short midsagittal groove along the anterior of their tongue blade. Sound is generated when the airstream hits the lower or upper incisors (Shadle, 1985). The presence of the teeth causes an increase in the amplitude of the noise and generates an antiresonance in lower frequencies (Shadle, 1991). The lengthened teeth provided an abnormal obstruction to the airflow normally required for sibilant production and modified the turbulence. The small cavity in front of the constriction would therefore be increased, causing the resonance frequencies to be lower. Speakers would have to find a way to increase the power of higher frequencies and would likely do this by moving their tongue blade to a more anterior position.

In the first experiment, subjects were asked to produce normal sounding /s/'s while wearing the dental prosthesis. This task required subjects to modify their normal /s/ tongue position in order to produce a good-sounding sibilant. The quality of the /s/'s was measured by having subjects say the monosyllable /tas/. Incorporating the /s/ into the word /tas/ prevented subjects from simply maintaining a static tongue position for the entire experiment; in order to say the word /tas/, the tongue must move from the position necessary to produce the open vowel /a/, up to the dento-alveolar ridge to produce the /s/. Thus, the /s/ production had to be coordinated for each trial.

During the experiment, subjects were allowed to practice with the dental appliance while hearing their speech and then were tested in the presence of masking noise in order to track their adaptation to the device. Acoustic analyses were used to parametrize the changes in the power spectrum of the /s/ over time (see Stoica and Moses, 1997, for discussion of the computation of power spectral density). In a second experiment, the perceptual judgments of naive listeners were used to evaluate the quality of the /s/'s speakers produced over the course of the experimental session.

Our design allowed us to tease apart the contribution of auditory feedback from that of other sources of feedback. If auditory feedback is the primary vehicle for learning, then we should observe that greater improvement occurs during blocks when utterances are produced with feedback available in comparison to blocks in which utterances are produced with feedback unavailable. Thus, the learning we observe over a session should occur in a stepwise fashion, with incremental improvements only occurring during blocks when feedback is available. On the other hand, if auditory feedback is not crucial for learning the compensations necessary in the presence of the prosthesis, then any improvements observed should be equivalent for the feedback and masked conditions.

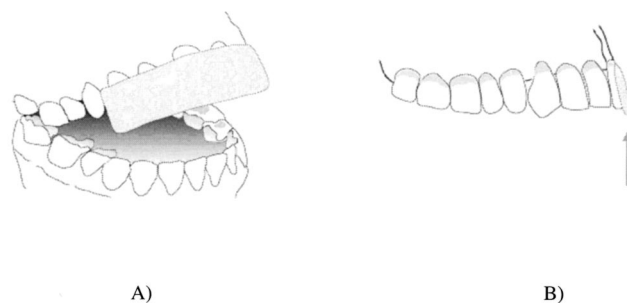


FIG. 1. (A) Depiction of the dental prosthesis in the subject's mouth. (B) A sagittal view of the maxillary teeth with the prosthesis in position (prosthesis indicated by the gray arrow). Note that the prosthesis did not affect the subject's bite when the mouth was closed.

II. EXPERIMENT 1

In the first experiment, speakers were asked to learn to produce adequate /s/ sounds in the context of the word /tas/ over the course of training trials.

A. Method

1. Vocal tract modification

a. Subjects. Six females between 22 and 36 years of age (mean age=27 years) participated. All subjects were graduate students at Queen's University in Canada and were native speakers of Canadian English. They reported having no history of hearing, speech, or language difficulties or disorders. Five of the subjects had received orthodontic treatment for an average of 2.4 years during their teenage years. All the subjects had a Class I occlusion ("normal bite") and thus their maxillary incisors were situated anterior to the mandibular incisors when their mouth was closed.

b. Dental prosthesis. Dental impressions were made of each subject's maxillary and mandibular teeth. Using the impressions, an acrylic prosthesis was constructed. The prosthesis lengthened the teeth between 5 and 6 millimeters but did not affect the subjects' bite. The prosthesis fit onto the buccal and occlusal surfaces of the maxillary incisor teeth and did not require an adhesive or wire clasps to remain fixed in place. Figure 1 is a depiction of the prosthesis on a subject's teeth.

c. Recording equipment. Sessions took place in a double-walled soundproof booth (Industrial Acoustics Corporation, model 1204). The sessions were recorded on digital audiotape so that analysis of the signals could later be carried out using algorithms incorporated into the PRAAT software program (Boersma, 1993). Subjects' speech sounds were transduced with a headset microphone (Shure WH20) positioned a fixed distance from their mouth (approximately 5 cm). The speech signals were amplified (Tucker-Davis MA2 microphone amplifier) and filtered (Tucker-Davis FT6-2) with a 9 kHz cutoff. The signals were then routed to a mixer (Rolls RA62) where they were mixed with white noise (Grason-Stadler 901B). The combined noise and signal were together sent to a Yorkville reference amplifier (model SR 300) that transmitted the sound through Etymotic (ER-2) earphones foam inserts placed in the subjects' ear canals. The masking noise was approximately 75 dB SPL. Our pilot work showed that this level effectively masked voiceless

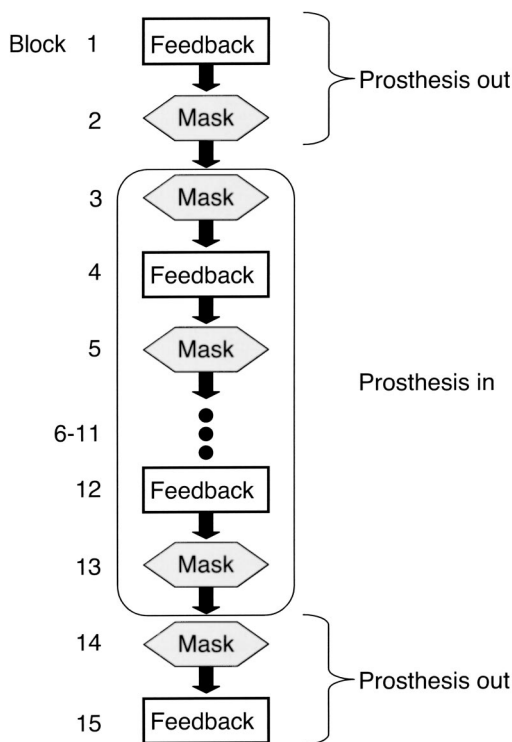


FIG. 2. Flow diagram depicting the order of conditions subjects encountered in each of the two sessions in the experiment.

sounds. The white noise was absent during trials in which the subjects were to receive auditory feedback regarding their utterances. Subjects monitored a vertical array of light-emitting diodes located in front of them. The array indicated the sound level of their productions and was used to keep their speech at similar levels across the different auditory conditions.

d. Procedure. The design of the experiment is schematically depicted in Fig. 2. Each experimental session consisted of two sessions. After the first session, subjects were given the opportunity to rest and drink water. However, both sessions occurred in a single stint that lasted less than an hour. Within each block, subjects made 10 productions of /tas/ in each of the following 15 blocks.

- (1) The first block was a baseline condition in which subjects were recorded producing /tas/ without the prosthesis inserted into their mouth, and without any masking noise present. These initial utterances represented the normal /s/ productions for each subject and were later compared to other blocks to evaluate the progress of learning and the effects noise and the prosthesis had on production.
- (2) The second block involved subjects producing utterances without the prosthesis in their mouth but in the presence of the white noise. This block controlled for the influence of masking noise on subjects' utterances in the absence of the vocal tract perturbation. It was used to establish the subjects' baseline productions in the absence of auditory feedback.
- (3) In the next block, subjects produced utterances while wearing the prosthesis. Their auditory feedback was masked by noise and these utterances demonstrated the

subjects' ability to compensate for the modification of the oral environment without the aid of auditory feedback.

- (4) During the fourth block, subjects were given their first opportunity to practice saying /tas/ while wearing the prosthesis and receiving auditory feedback regarding the accuracy of their productions. Any differences observed between this block and the one previous can be attributed to the availability of the acoustic feedback (interacting with potential practice effects).
- (5) Subjects were again asked to produce utterances in the presence of masking noise while wearing the prosthesis. These utterances were later compared to those made in the block previous to this one in order to test learning that may have occurred while receiving auditory feedback.
- (6)–(13) These blocks were merely alternations of the availability of auditory feedback (block 4) and speaking in the presence of masking noise (block 5) to give speakers practice over a number of trials.
- (14) During the second to last block, the subjects removed the prosthesis from their mouth and produced ten utterances in the presence of masking noise. These utterances were compared to those they made before the appliance was first placed in their mouth to determine if there was any evidence of carry-over effects that resulted from learning the new articulatory behavior.
- (15) Subjects produced /tas/ in the absence of noise and without the prosthesis in their mouth.

2. Acoustic analyses

Although a number of techniques for parametrizing fricatives have been proposed, finding a good numerical method for characterization and classification of fricatives is still a problem. We determined the centroid (first moment) of the long-term average spectrum of each /s/ production using functions implemented in PRAAT (Boersma, 1993). The first moment or "centroid" is an index of the "center of gravity" of the spectrum for each fricative. Centroids have been found to correlate with the perceptual categorization of some fricatives and may therefore represent a perceptually salient features that speakers modify to alter the quality of their fricative productions (Forrest *et al.*, 1988). For example, /s/ sounds typically have higher centroid frequencies than /ʃ/ sounds produced by the same speaker (Nitttrouer, Studdert-Kennedy, and McGowan, 1989).

During the production of an /s/, speakers modify their air pressure as well as their tongue blade and tip position in order to direct a jet of air at the teeth. This jet of air is directed to the surface of the teeth. The presence of unexpectedly long teeth would cause the normally small cavity in front of the constriction to be larger and make the resonance frequencies lower. This change would make speakers' initial productions more /ʃ/-like. Centroid values were therefore expected to be lower than normal until speakers learned to compensate.

In addition to the computation of the central moment, we also applied a technique first implemented by Evers, Reetz, and Lahiri (1998) to distinguish the acoustics of an /s/

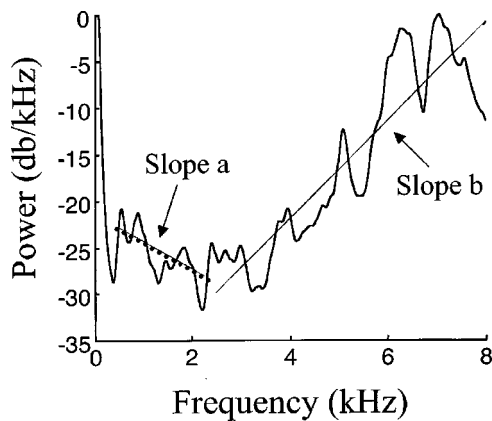


FIG. 3. The power spectrum of an unperturbed /s/ produced by a speaker in experiment 1. The linear regression lines between 0.5 and 2.5 kHz and 2.5 and 8 kHz are present for slope a and b, respectively.

from /ʃ/. Evers *et al.* (1998) compared the distribution of intensity over frequency of the spectra for /s/ and /ʃ/ in different languages. They noted that based on the slope of the spectral envelope below 2.5 kHz, and the slope between 2.5 and 8 kHz, one could visually distinguish between the two fricatives. The authors developed a reliable metric they called the “steepness difference” in which intensity values were regressed onto corresponding frequency values in these two frequency regions and subtracted. That is, the difference between the slope of a linear regression line (slope a) between 0 and 2.5 kHz and the slope of a linear regression line (slope b) between 2.5 and 8 kHz was used to reliably separate /s/ and /ʃ/. Figure 3 shows the power spectrum and the two regression lines for an /s/ produced by one of the speakers in this study. Evers *et al.* (1998) found that the spectral slope for frequencies up to 2.5 kHz quickly rises then above this frequency, abruptly levels off or declines for /ʃ/’s. For /s/’s, the slope is initially near zero or negative and then there is a slow rise through to the 8-kHz range. This distinction is reflected in a smaller difference in the rate of increase between the lower and higher frequencies for /s/ as compared to an /ʃ/.

Since the prosthesis speakers encountered created a slightly larger cavity within which the fricative noise would resonate, initial productions were expected to have more power in lower frequencies than productions without the prosthesis. Thus, the steepness difference may reflect changes in production as well or better than the centroid of the frequency distribution. We calculated the index in the same way as Evers *et al.* (1998) with two exceptions. First, Evers and his colleagues computed their slopes based on a 40-ms window placed in the middle of the fricative. We chose to calculate the power spectrum over the entire /s/ produced using Welch’s method (Welch, 1967). In addition, our linear regression lines were calculated over the 0.5 to 2.5-kHz (slope a) and 2.5 to 8-kHz (slope b) frequency ranges. We expected the steepness difference to be initially larger for productions made with the prosthesis in the mouth. After a period of learning, this value was expected to decrease towards previously observed unperturbed values.

Apart from our spectral parametrizations, we were also interested in the relative intensity of the utterances. The pres-

ence of noise in a speaker’s environment often causes them to produce utterances with higher amplitudes than environments without noise (Lane and Tranel, 1971). Amplitude does not affect the classification of sibilants (Behrens and Blumstein, 1988). However, to avoid any complication, we provided our speakers with a visual aid to help them make each production with the same amplitude. Nevertheless, the noise that was intended to mask the fricative sounds did not entirely mask the voiced portions of their utterances. Therefore, it is possible that speakers may have used the vowel portions to maintain their speaking level while fricative sounds remained affected by the masking noise. In order to test this notion we calculated the root mean squared (rms) for each /s/ production and evaluated the relative sound levels.

B. Results and discussion

The analysis of the relative intensity of the utterances showed that speakers’ productions had a higher amplitude when the masking noise was present (61 dB) in comparison to when it was not (55.6 dB) [$F(1,5)=124.4$, $p<0.05$]. However, this difference was stable across the blocks [$F(1,5)=1.16$, $p>0.05$] and across the two sessions [$F(1,5)=2.35$, $p>0.05$], so any patterns observed across the sessions can be attributed to increased experience with the prosthesis and not the presence of the masking noise.

The centroid analysis showed that the presence of the tooth prosthesis affected the center of gravity of the distribution of energy over the spectrum of each subject’s initial /s/ productions. The average centroid frequency values changed markedly after the prosthesis was inserted [$F(1,5)=56.71$, $p<0.01$]. The mean centroid frequency before the prosthesis was inserted into the subjects’ mouths was 6171.8 Hz. After the prosthesis was inserted the mean centroid frequency dropped to 4482.0 Hz.

Apart from this initial difference, no other significant difference was observed in the centroid values between the auditory and masked conditions or across the sessions. There are at least two possible reasons for the null effects in the acoustic analyses. The most obvious explanation is that speakers were unable to learn to compensate for the dental prosthesis. Perhaps if speakers were given more extensive training, improvements in their productions might have been detectable with these statistical analyses. Notwithstanding the null finding in the acoustic analyses, the experimenters’ subjective experience while listening to each subject was that the speakers’ productions changed, if not improved, over the two experimental sessions. Thus, a second, alternative explanation for the null results is that the centroid was not an adequate measure for the evaluation of changes in the quality of the fricative in this particular context. It is clear from the literature that finding robust summary statistics that adequately characterize and distinguish between fricatives has been a difficult endeavor. Indeed, the reliability of such statistical measures seems to be dependent on the corpus used in a study (Evers *et al.*, 1998; Jesus and Shadle, 2002). Small, nonsignificant changes in the spectral distribution may be associated with significant changes in the perception of the /s/.

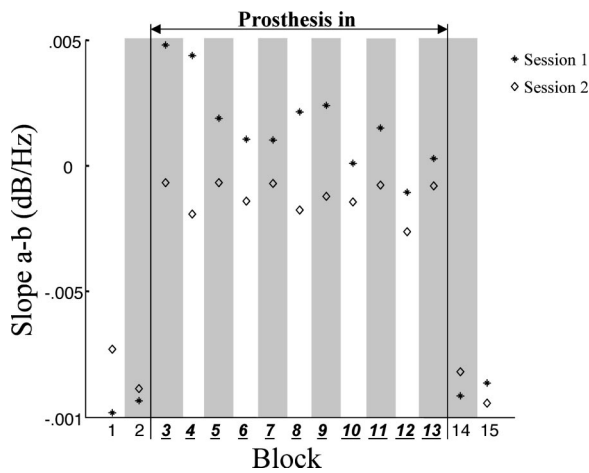


FIG. 4. The mean steepness difference (slope a–slope b) for the 15 blocks in sessions 1 and 2. Block numbers that are underlined indicate that the prosthesis was in the speakers' mouth during these blocks. The gray shading indicates that auditory feedback was masked during these blocks. The underlining of the block numbers between the two black vertical lines indicates that speakers had the prosthesis in their mouth for these productions.

Figure 4 shows the values for the steepness difference, the difference between slope a and b, over the course of the 15 blocks in each of the two sessions. A clear pattern is observable in that the values for the second session are closer to values measured before exposure to the prosthesis. The steepness difference values not only reflect a clear improvement between the two sessions, but also a linear trend toward normal values over the course of training in session 1. Both the difference between sessions 1 and 2 [$F(1,5)=11.25$, $p<0.05$] and the interaction between session and block [$F(1,5)=3.5$, $p<0.05$] are statistically significant. However, there was no statistically verifiable difference between the auditory and masked conditions.

In addition to our interest in the learning across blocks and sessions, we were also interested in differences in the learning within a block. Figure 5 shows the steepness difference for the first and last production within each of the 15 blocks across session 1 [see Fig. 5(a)] and session 2 [see Fig. 5(b)]. Even within these selected trials a significant improvement across the two sessions [$F(1,5)=8.23$, $p<0.05$] and across the blocks [$F(1,5)=2.88$, $p<0.05$] was observed. Again, no significant difference existed between the auditory and masked feedback conditions. Moreover, despite the pattern visible in the data from session 1 [Fig. 5(a)] there were no significant differences observed between the first and last trials within a block.

To summarize, the presence of the prosthesis caused centroid values to drop significantly. However, evidence that speakers were improving their productions over the experimental sessions was only observed in the spectral slope measure. Although normal production was never completely restored, the steepness difference values approached normal values gradually over blocks in session 1. This learning appears to have leveled off so that the improvement observed in session 1 is maintained during session 2.

III. EXPERIMENT 2

The acoustic analyses of speaker productions indicated that speakers were altering the acoustics of their productions

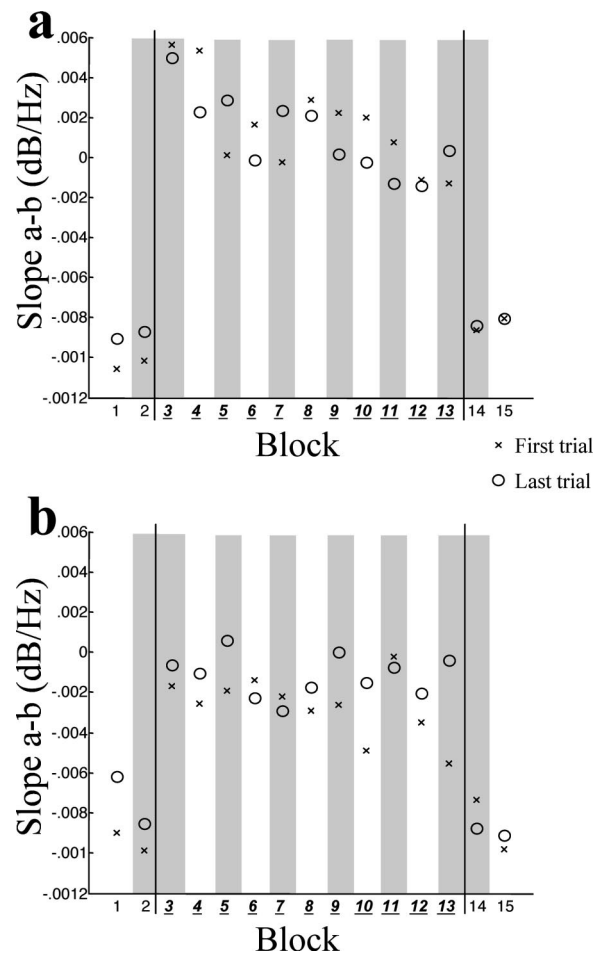


FIG. 5. The mean steepness difference (slope a–slope b) for the first and last utterances produced in the 15 blocks in sessions 1 (panel a) and 2 (panel b). Block numbers that are underlined indicate that the prosthesis was in the speakers' mouth during these blocks. The gray shading indicates that auditory feedback was masked during these blocks. The underlining of the block numbers between the two black vertical lines indicates that speakers had the prosthesis in their mouth for these productions.

as a function of experience wearing the prosthesis. However, there were no statistically verifiable differences between productions produced at the beginning as opposed to the end of a particular block. Neither was a difference between the two auditory conditions observed. As previously mentioned, steepness difference has been shown valuable for separating /j/ from /s/ sounds (Evers *et al.*, 1998). However, the index is a simple and relatively crude representation of the power spectrum of a fricative. Listeners, and therefore speakers, are likely sensitive to smaller changes in the shape of the power spectrum. We therefore obtained listener judgments to see if the results we found in the acoustic analysis were comparable to the perceived quality of the /s/ productions.

As a result of the experimental design, a large quantity of data was collected. For the perceptual experiment, we therefore focused on a subset of these data. Only productions from the first and last trials of key blocks were presented to listeners. Specifically, listeners heard the first and last trials of blocks 3 and 4 which were the first masked and auditory feedback blocks after the prosthesis was inserted into the subjects' mouth (see Fig. 2). We presented the first and last trials of blocks 12 and 13, the last masked and auditory feed-

back blocks prior to the removal of the prosthesis. Finally, the subjects rated the first and last trials of blocks 14 and 15, which were the masked and auditory feedback blocks immediately after the prosthesis was removed from the subjects' mouth. The /s/ productions from both sessions for the blocks and trials above were rated by listeners.

A. Method

1. Subjects

Sixteen listeners (13 women and 3 men) between 20 and 25 years of age (mean age 21.4 years) made judgments regarding a subset of the /s/ productions made by the speakers. The listeners were native speakers of Canadian English and reported having no history of hearing, speech, or language difficulties or disorders.

2. Stimuli

The stimuli consisted of the subset of the segmented /s/ productions analyzed using the acoustical analyses described in experiment 1. The fifth utterance produced during the baseline blocks 1 and 2 (without the prosthesis present, with or without noise) of the first session were selected as comparison exemplars of each speaker's normal /s/ production. The fifth or middle production of these blocks was chosen because subjects were most likely to be acclimated to the speaking condition by this trial. Productions made with and without the presence of the masking noise were chosen to control for any differences that may have been solely caused by the presence of the masker.

The test utterances were the first and last utterances produced during blocks 3, 4, 12, and 13. Blocks 3 and 4 were the first masked and auditory conditions during which speakers wore the prosthesis; blocks 12 and 13 were the last auditory and masked conditions during which speakers wore the prosthesis. Each comparison exemplar was paired with all the test conditions. This design meant that exemplars that were produced during the masking condition and exemplars produced during the feedback condition were both paired with test stimuli that were produced with and without feedback. This procedure allowed us to test for any differences that could be attributed to the presence of noise, and not merely the result of the presence or absence of feedback. Only the first and last productions from these blocks were presented in order to reduce the number of trials listeners had to judge. Testing these trials also allowed us to track the effects of learning within the blocks.

The exemplars were also paired with the first and last productions of blocks 14 and 15 in each session. These blocks occurred after the removal of the prosthesis and, respectively, with and without the presence of the masking noise. Asking listeners to judge utterances from these blocks allowed us to evaluate the effects noise had on normal production. In all, each listener made 192 judgments.

3. Procedure

Perceptual judgment sessions took place in the sound-proof booth previously used to record the speakers. The digitized auditory stimuli were equally amplified relative to the

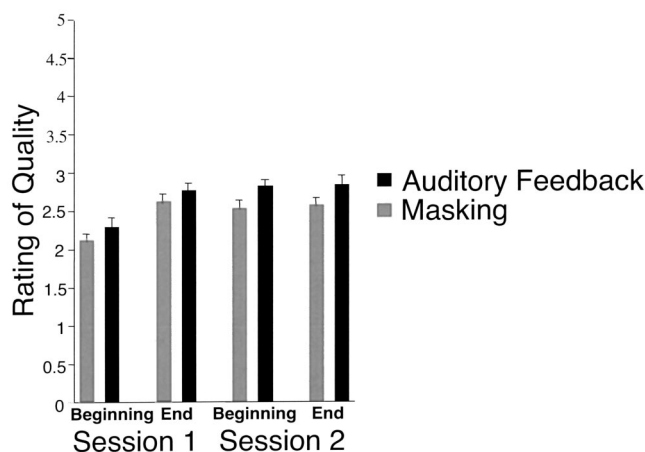


FIG. 6. The mean and standard errors of listeners' ratings of the quality of /s/ productions during the auditory and masked feedback conditions at the beginning and end of session 1 and 2.

original, recorded level (NAD Electronics, model 3020I) and presented over headphones (Sennheiser, HD 265 Linear). Each speaker's tokens were presented within a single block with the order of the six different speakers randomized across listeners. The presentation of the tokens within each of the six-speaker blocks was also randomized. On each trial, subjects first heard an exemplar (a baseline /s/ from blocks 1 and 2 that was produced with or without the presence of noise) and then an /s/ production that had been produced in the presence or absence of masking noise while the speaker wore the dental prosthesis.¹ Subjects were asked to consider the first stimulus to be a normal /s/ production for that speaker. They then rated the quality of the second /s/ production on a scale of 1 through 5, with 5 representing a perfect /s/ production and 1 representing a very poor quality production. Subjects made responses by pressing appropriately labeled keys on a keyboard.

B. Results

The results of our perceptual study showed that utterances produced while speakers could hear their own feedback were rated by listeners to be higher quality /s/'s than the productions that occurred while speakers' feedback was masked by noise. The study also showed that speakers' utterances improved with increased practice. In addition to evaluating the perceptions of listeners, we also wished to acoustically quantify the differences between the utterances produced during the two auditory conditions across the two sessions.

Figure 6 shows the mean and standard errors of listeners' perceptual ratings of the auditory stimuli speakers produced during the four blocks from the first and second sessions. A 5-way ANOVA [session \times position in session (beginning versus end of each of the two sessions) \times auditory feedback (feedback versus masked) \times exemplar (tokens produced in the presences of feedback versus those in masking noise) \times trial (first versus last trial within a block)] was used to analyze the subjects' responses. The ANOVA revealed an overall main effect for session [$F(1,15) = 24.98$, $p < 0.01$]. As can be seen in Fig. 6, productions made during the second

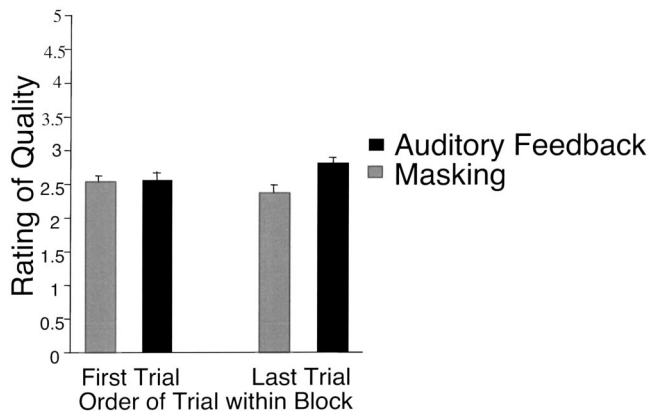


FIG. 7. The mean and standard error of listener ratings for the first and last utterances produced in the auditory feedback and masked conditions averaged across the first and second session.

session were judged to be better /s/'s than those produced during the first session. In addition, there was no interaction between session and auditory condition. Thus, speakers learned to produce better /s/'s in both the auditory feedback and masked conditions.

A similar main effect of practice was observed within each session. Utterances produced at the beginning of each session were rated poorer in quality than those produced at the end of each session across both the auditory feedback and masked conditions [$F(1,15)=49.5$, $p<0.01$]. As can be seen in Fig. 6, the amount of improvement observed in the ratings from the beginning of a session to the end was greatest in the first session for both the auditory feedback and masked conditions. This difference in improvement generated a significant interaction between session and the order of conditions [$F(1,15)=39.72$, $p<0.01$].

The availability of auditory feedback during production had a significant effect on the listener's ratings of the speakers' utterances. When auditory feedback was available during productions, utterances were judged to be of significantly higher quality than those produced in the presence of the masking noise [$F(1,15)=13.93$, $p<0.01$]. The difference in ratings between the auditory conditions was greatest during the second session, but the interaction effect did not quite reach statistical significance [$F(1,15)=2.39$, $p>0.05$] (see Fig. 6).

In addition to the main effect for auditory condition, there was also a significant interaction between auditory condition and trial [$F(1,15)=25.4$, $p<0.01$]. Figure 7 shows the mean ratings for the first and last of the ten utterances produced in the auditory feedback and masked conditions averaged across the first and second session. In only this comparison were the results complicated by the use of exemplars from different auditory feedback conditions. When test stimuli produced in the presence of auditory feedback were paired with exemplars produced in either feedback condition, last utterances were rated more "/s/-like" than first utterances [exemplar produced with feedback; $F(1,15)=8.92$, $p<0.01$; exemplar produced in noise, $F(1,15)=11.31$, $p<0.01$]. However, the opposite pattern of results was observed when test stimuli produced in noise were paired with exemplars that were also produced in noise; the

first utterances were rated more /s/-like than the last utterances. On the other hand, the first and final utterances of test stimuli produced in noise received equivalent ratings when paired with exemplars that speakers produced in the presence of auditory feedback [$F(1,15)=0.13$, $p>0.05$]. In either case, however, there was no improvement in /s/ quality over each block of ten trials when there was no auditory feedback.

Finally, we examined the ratings assigned to blocks 14 and 15 of each session. These blocks occurred immediately after the dental prosthesis had been removed from the subjects' mouths. A separate ANOVA did not reveal a significant difference between utterances produced in the presence or absence of noise during these blocks [$F(1,15)=0.84$, $p>0.05$]. However, there was a significant difference between these trials and the training trials at the end of the two sessions [Tukey honest significance test, $p<0.01$; mean rating for the final two blocks of unperturbed trials was 3.6; mean rating for the final two blocks of training trials was 2.7].

In summary, the results of the perceptual study confirm and extend the acoustic analyses of the speakers' /s/ productions. Listeners judged productions made at the end of the first session to be better than those produced at the beginning. This improvement was maintained throughout the second session. Listeners also rated productions made while auditory feedback was available to be of higher quality than those produced while the feedback was masked with noise. In addition to the learning that occurred with increased experience across the blocks of session 1, utterances produced at the end of individual blocks were more highly rated than those produced first in a block. However, this pattern was only observed for utterances produced in the auditory feedback condition.

IV. GENERAL DISCUSSION

Subjects were asked to learn to say the word /tAs/ wearing a prosthesis that elongated their maxillary incisor teeth while receiving intermittent auditory feedback. When speakers produce the word in the auditory feedback condition, a naive group of listeners judged their final utterance to be of higher quality than their initial utterances in the condition. The opposite trend was observed when speakers' feedback was masked; their initial utterances were judged to be higher in quality than their final utterances. This difference suggests that speakers were able to use auditory information to adjust their articulations and compensate online and the lack of auditory feedback led to degraded performance over trials.

In addition to the immediate effects caused by the presence of auditory feedback, speakers also gradually improved their productions with increased exposure to the novel vocal-tract configuration. The learning curve resembled patterns from other skill acquisitions studies (e.g., Rosenbaum, Carlson, and Gilmore, 2001). Large gains are made initially and performance slowly asymptotes, producing an exponential learning curve (Heathcote, Brown, and Mewhort, 2000). Within and across each session, productions were judged to be higher in quality with increasing amounts of practice. This effect was also observed for tokens produced in the presence of the masking noise. These observations suggest that the

learning that occurred while feedback was available to the speakers transferred to utterances produced in the absence of feedback.

The multidimensional nature of speech perception means that identifying acoustic correlates is often difficult. The learning effects we observed were partially supported by acoustical analysis of the data. The size of the steepness difference moved toward unperturbed values as speakers gained more experience during the first session. This improvement plateaued but was maintained through session 2. However, in contrast to listener judgments, no statistically significant difference was found between the auditory and masked conditions. Additionally, no differences were observed between the first and the last trials within a block. We believe that the null effects in the acoustic analysis reflect a lack of sensitivity rather than the absence of effects. The steepness difference reflected the larger differences that occurred over the course of the experiment, but we must rely on listener perceptions for evaluation of smaller changes in the spectra of the speakers' productions.

Speakers were asked to make productions of similar amplitude. Nevertheless, an analysis of the intensity of the utterances showed that productions made in the masked feedback condition were higher in amplitude than those made when feedback was available. Although undesirable, the difference in intensity between the feedback conditions does not complicate interpretation of the learning effects we observed because this difference was constant within and across the sessions. The effect of the masking noise was equivalent across the entire experiment and not confounded with learning. In any case, the amplitude of fricative production does not affect classification (Behrens and Blumstein, 1988).

Our finding that the overall quality of the speech sound improved with increased practice with our novel vocal-tract arrangement is not surprising and replicates the observations of a number of other researchers. For example, Baum and McFarland (1997) found comparable results when they asked subjects to speak with an artificial palate in their mouth. Subjects read /s/-laden passages in order to promote adaptation. Every 15 min over the course of an hour, subjects produced the consonant-vowel /sa/ a number of times. The results showed that subjects gradually improved their /s/ productions with increased exposure to the altered vocal tract. Thus, even short periods of exposure can lead to significant improvements in speech.

However, others have found that it can take speakers from several hours to weeks of practice with an artificial palate before a speaker regains the high quality of their original speech categories (Hamlet and Stone, 1976; Hamlet *et al.*, 1978). Although our speakers improved over the course of the experimental session, they did not fully compensate for their artificially elongated teeth. Listeners on average judged the speakers' productions at the end of the session to be much lower in quality than utterances produced after the prosthesis was removed.

Even within this short experiment there is evidence that longer-term learning took place. Subjects' performance in the second session of training showed benefits from experience

in the previous session. Similar benefits have been reported in other speech and motor learning studies. In one study, subjects quickly readapted to the presence of an artificial palate even though the original training with the palate had occurred months earlier (Hamlet *et al.*, 1978). This facility for rapid adaptation during subsequent exposure to an artificial palate suggests that new speech motor programs can be learned and then later recalled for the appropriate context (McFarland *et al.*, 1996). These findings are strikingly similar to observations that subjects reaching for visual targets adapt to visual perturbations (e.g., McGonigle and Flook, 1978) and dynamic perturbations (Brashers-Krug, Shadmehr, and Bizzi, 1996) faster if they have previously experienced the unusual sensorimotor conditions.

The improvements that we observed resulted from the opportunity for speakers to practice in the presence of auditory feedback. This finding that auditory feedback provides information used to compensate for altered vocal tracts is contrary to prior observations in adults (Garber *et al.*, 1980b; Honda and Kaburagi, 2000) and even young children (Garber, Speidel, and Siegel, 1980a). The null effects observed in these other studies, however, could be related to measurement sensitivity or the task that subjects were asked to perform. For example, Honda and Kaburagi (2000) tracked compensations made to dynamical structural perturbations of the palate shape while we imposed a static perturbation. Recovery from other static perturbations such as the restriction of articulator movement with a bite block is enhanced by the presence of auditory feedback (e.g., Hoole, 1987; Flege *et al.*, 1988; McFarland and Baum, 1995; Baum, McFarland, and Diab, 1996; McFarland *et al.*, 1996).

Even in the absence of vocal-tract modifications, auditory feedback has been shown to increase the precision with which speech categories are produced. For instance, studies of cochlear implant patients for whom feedback can be directly manipulated by turning the implanted device on and off have shown rapid modifications in speaking level, F_0 , and vowel formants (Svirsky and Tobey, 1991). Small differences have also been observed in fricatives (Perkell *et al.*, 2000b).

Furthermore, larger effects tend to occur when the implant is turned on compared to when it is suddenly turned off (Perkell *et al.*, 2000a). That is, the improvements observed when deaf speakers receive auditory feedback after a period of time without it are larger than the degradations that appear immediately after feedback is removed. These observations indicate that the speakers maintained the parameters necessary for normal speech production for a period of time after the feedback was removed. This result parallels our own observations that utterances produced while speakers' auditory feedback was masked, improved as a function of their previous practice while feedback was available. In essence, we "turned off" the feedback received by subjects and found that the new articulations they learned while feedback was present persisted to some extent when feedback was removed. Thus, the improvements we observed were not strictly due to feedback control but were also a function of learning: The auditory feedback was used by the speech mo-

tor control system to modify an underlying representation mapping vocal gestures to their acoustic consequences.

Although the quality of /s/ productions improved during the masked condition, the new articulatory movements that were learned during the auditory feedback conditions did not completely transfer to production in the absence of feedback. Utterances produced in the presence of feedback consistently received higher quality ratings from listeners. There are a number of possible reasons for this effect. First, it is possible that auditory feedback provides information that the speech motor system can use to adjust ongoing articulation, and over time, these compensatory modifications are learned so that the new speech gestures can be reproduced in the absence of feedback. There is evidence that auditory feedback is used for both online compensation and long-term adaptation. For instance, Houde (1997) asked speakers to whisper one-syllable words while hearing altered auditory feedback. His speakers heard the formants of their vowel productions gradually shifted enough over successive utterances to eventually change the vowels' phonetic identity. Speakers spontaneously compensated for the formant transformations. Houde intermittently tested the speakers' productions in noise and found that speakers slowly adjusted their speech in the same direction as their compensation, suggesting that a modification of the mapping between their vocal-tract productions and their acoustic feedback occurred.

A second possibility is that somatosensory feedback was solely responsible for the improvements in production observed with practice during the masked conditions. There is a large amount of information available to the speech motor control system from proprioceptive and cutaneous receptors in the vocal tract (Gracco, 1995; Kent, Martin, and Sufit, 1990). Vocal-tract manipulations such as the insertion of artificial palates reduce tactile cues regarding, for example, tongue contact against the palate. However, in our study, the prosthesis that extended the subjects' teeth did not reduce sensation in any way. Information regarding tongue–palate contact and cues indicating airflow were unaffected. One might therefore assume that the improvement we observed in the masking condition was due to the fact that the motor system used somatosensory feedback to modify productions in the noise conditions, and not evidence that learning was dependent on auditory information acquired during the feedback conditions. However, our observation that final utterances were judged to be lower in quality than initial productions does not support this conclusion. Nevertheless, the superior quality of production observed when auditory feedback was available to speakers could have been the result of the use of tactile and auditory feedback in combination. Only careful manipulation of both the presence and the absence of auditory feedback in conjunction with manipulations of tactile feedback can satisfactorily resolve the particular contributions of the two modalities (see Hoole, 1987; Gammon *et al.*, 1971; Ringel and Steer, 1963; Scott and Ringel, 1971).

Finally, it should be noted that our data represent the average across speakers. Individual differences in the magnitude of the perturbation and subsequent learning were observed; these differences can have a number of origins. For example, people differ in their response or strategy to vocal-

tract perturbations. In addition, although the lengthening of the teeth was relatively equivalent (6 mm), the effective perturbation differed depending on the shape of a speaker's alveolar ridge, the position of their teeth, or how they normally produce an /s/.

V. CONCLUSIONS

The nature of the learning that takes place when adults encounter modified vocal tracts is still a matter of debate. The merit of the unique vocal-tract modification is that all normal tactile information remains intact, allowing a more direct evaluation of the role feedback plays. The results of our investigation show that the availability of auditory feedback can help speakers compensate for structural modifications of their vocal tract. Indeed, the learning we observed only occurred when speakers could hear their speech. In addition, our data also suggest that auditory feedback provides information necessary for long-term modification of a subject's productions.

ACKNOWLEDGMENTS

This work was funded by NIH Grant No. DC-00594 from the National Institute of Deafness and other Communications Disorders, NSERC and CRL Keihanna Human Information Communication Research Center. We wish to thank Dr. Craig Morison, who made the dental prostheses, and Amanda Rothwell for her help with the collection and preparation of the data in the perceptual study. Thanks also to Christine Shadle for helpful discussions regarding the acoustic analysis of fricatives. Finally, thanks to Yoh'ichi Tohkura for originally suggesting the study.

¹Because the speakers were exposed to noise through headphones, the utterances they produced both in presence and absence of the masking noise were recorded under the same noise-free conditions. Therefore, listeners were not aware of the acoustic conditions under which the talkers spoke.

- Baum, S. R., and McFarland, D. H. (1997). "The development of speech adaptation to an artificial palate," *J. Acoust. Soc. Am.* **102**, 2353–2359.
- Baum, S. R., McFarland, D. H., and Diab, M. (1996). "Compensation to articulatory perturbation: Perceptual data," *J. Acoust. Soc. Am.* **99**, 3791–3794.
- Behrens, S. J., and Blumstein, S. E. (1988). "Acoustic characteristics of English voiceless fricatives," *J. Phonetics* **16**, 295–298.
- Benjamin, B. J. (1997). "Speech production of normally aging adults," *Semin Speech Lang* **18**, 135–141.
- Binnie, C. A., Daniloff, R. G., and Buckingham, H. W. (1982). "Phonetic disintegration in a five-year-old following sudden hearing loss," *J. Speech Hear Disord.* **47**, 181–189.
- Boersma, P. and Weenink, D. (1996). Praat, a System for doing Phonetics by Computer, version 3.4. Institute of Phonetic Sciences of the University of Amsterdam, Report 132.
- Borden, G. (1979). "An interpretation of research on feedback interruption during speech," *Brain Lang* **7**, 302–319.
- Brashers-Krug, T., Shadmehr, R., and Bizzi, E. (1996). "Consolidation in human motor memory," *Nature (London)* **382**, 252–255.
- Burnett, T. A., Freedland, M. B., Larson, C. R., and Hain, T. C. (1998). "Voice F_0 responses to manipulations in pitch feedback," *J. Acoust. Soc. Am.* **103**, 3153–3161.
- Cowie, R., and Douglas-Cowie, E. (1992). "Postlingually acquired deafness," in *Trends in Linguistics, Studies and Monographs*, 62 (Mouton de Gruyter, New York).

- Donath, T. M., Natke, U., and Kalveram, K. T. (2002). "Effects of frequency-shifted auditory feedback on voice F_0 contours in syllables," *J. Acoust. Soc. Am.* **111**, 357–366.
- Elman, J. L. (1981). "Effects of frequency-shifted feedback on the pitch of vocal productions," *J. Acoust. Soc. Am.* **70**, 45–50.
- Evers, H., Reetz, H., and Lahiri, A. (1998). "Cross-linguistic acoustic categorization of sibilants independent of phonological status," *J. Phonetics* **26**, 345–370.
- Flège, J. E., Fletcher, S. G., and Homiedan, A. (1988). "Compensating for a bite block in /s/ and /t/ production: Palatographic, acoustic, and perceptual data," *J. Acoust. Soc. Am.* **83**, 212–228.
- Fletcher, S. G., and Newman, D. G. (1991). "[s] and [j] as a function of linguopalatal contact place and sibilant groove width," *J. Acoust. Soc. Am.* **89**, 850–858.
- Forrest, K., Weismer, G., Milenkovic, P., and Dougall, R. N. (1988). "Statistical analysis of word-initial voiceless obstruents: Preliminary data," *J. Acoust. Soc. Am.* **84**, 115–123.
- Fowler, C. A., and Turvey, M. T. (1980). "Immediate compensation in bite-block speech," *Phonetica* **37**, 306–326.
- Gammon, S. A., Smith, P. J., Daniloff, R. G., and Kim, C. W. (1971). "Articulation and stress/juncture production under oral anesthetization and masking," *J. Speech Hear. Res.* **14**, 271–282.
- Garber, S. R., and Moller, K. T. (1979). "The effects of feedback filtering on nasalization in normal and hypernasal speakers," *J. Speech Hear. Res.* **22**, 321–333.
- Garber, S. R., Speidel, T. M., and Siegel, G. M. (1980a). "The effects of noise and palatal appliances on the speech of five-year-old children," *J. Speech Hear. Res.* **23**, 853–862.
- Garber, S. R., Speidel, T. M., Siegel, G. M., Miller, E., and Glass, L. (1980b). "The effects of presentation of noise and dental appliances on speech," *J. Speech Hear. Res.* **23**, 838–852.
- Gay, T., Lindblom, B. E. F., and Lubker, J. (1981). "Productions of bite-block vowels: Acoustical equivalence by selective compensation," *J. Acoust. Soc. Am.* **69**, 802–810.
- Gracco, V. L. (1995). "Central and peripheral components in the control of speech movements," in *Producing Speech: Contemporary Issues*, edited by F. Bell-Berti and L. J. Raphael (American Institute of Physics, New York).
- Hamlet, S. L. (1973). "Speech adaptation to dental appliances: Theoretical considerations," *J. Baltimore Coll. Dent. Surg.* **28**, 51–63.
- Hamlet, S. L., Cullison, B. L., and Stone, M. L. (1979). "Physiological control of sibilant duration: Insights afforded by speech compensation to dental prostheses," *J. Acoust. Soc. Am.* **65**, 1276–1285.
- Hamlet, S., and Stone, M. (1976). "Compensatory vowel characteristics resulting from the presence of different types of experimental dental prostheses," *J. Phonetics* **4**, 199–218.
- Hamlet, S., and Stone, M. (1978). "Compensatory alveolar consonant production induced by wearing a dental prosthesis," *J. Phonetics* **6**, 227–248.
- Hamlet, S., Stone, M., and McCarty, T. (1978). "Conditioning dentures viewed from the standpoint of speech adaptation," *J. Prosthet. Dent.* **40**, 60–66.
- Heathcote, A., Brown, S., and Mewhort, D. J. K. (2000). "The Power law repealed: The case for an exponential law of practice," *Psych. Bull. Rev.* **7**, 185–207.
- Honda, M., and Kaburagi, T. (2000). "Speech compensation to dynamical structural perturbation of the palate shape," in *Proceedings of the 5th Seminar on Speech Production: Models and Data*, 21–24.
- Hoole, P. (1987). "Bite-block speech in the absence of oral sensibility," in *Proceedings of the XIth International Congress of Phonetic Sciences*, **4**, 16–19.
- Houde, J. F. (1997). "Sensorimotor adaptation in speech production," unpublished doctoral dissertation, Massachusetts Institute of Technology, Cambridge, MA.
- Houde, J. F., and Jordan, M. I. (1998). "Sensorimotor adaptation in speech production," *Science* **279**, 1213–1216.
- Jesus, L. M. T., and Shadle, C. H. (2002). "A parametric study of the spectral characteristics of European Portuguese fricatives," *J. Phonetics* **30**, 437–464.
- Jones, J. A., and Munhall, K. G. (2002). "The role of auditory feedback during phonation: Studies of Mandarin tone production," *J. Phonetics* **30**, 303–320.
- Jones, J. A., and Munhall, K. G. (2000). "Perceptual calibration of F_0 production: Evidence from feedback perturbation," *J. Acoust. Soc. Am.* **108**, 1246–1251.
- Kawahara, H. (1995a). "Transformed auditory feedback: The collection of data from 1993.1 to 1994.12 by a new set of analysis procedures," ATR Technical Report, TR-H-120.
- Kawahara, H. (1995b). "Hearing voice: Transformed auditory feedback effects on voice pitch control," in *Proceedings of the International Joint Conference on Artificial Intelligence Workshop on Computational Auditory Scene Analysis*, pp. 143–148.
- Kelso, J. A. S., and Tuller, B. (1983). "Compensatory articulation under conditions of reduced afferent information: A dynamic formulation," *J. Speech Hear. Res.* **26**, 217–224.
- Kent, R. D., Martin, R. E., and Sufit, R. L. (1990). "Oral sensation: A review and clinical perspective," in *Human Communication and its Disorders*, edited by H. Winitz (Ablex, Norwood, NJ).
- Lane, H., and Tranel, B. (1971). "The Lombard sign and the role of hearing in speech," *J. Speech Hear. Res.* **14**, 677–709.
- Lane, H., and Webster, J. W. (1991). "Speech deterioration in postlingually deafened adults," *J. Acoust. Soc. Am.* **89**, 859–866.
- Lindblom, B., Lubker, J., and Gay, T. (1979). "Formant frequencies of some fixed-mandible vowels and a model of speech motor programming by predictive simulation," *J. Phonetics* **7**, 147–161.
- Lindblom, B. E. F., and Sundberg, J. (1971). "Acoustical consequences of lip, tongue, jaw, and larynx movement," *J. Acoust. Soc. Am.* **50**, 1166–1179.
- McFarland, D. H., and Baum, S. R. (1995). "Incomplete compensation to articulatory perturbation," *J. Acoust. Soc. Am.* **97**, 1865–1873.
- McFarland, D. H., Baum, S. R., and Chabot, C. (1996). "Speech compensation to structural modifications of the oral cavity," *J. Acoust. Soc. Am.* **100**, 1093–104.
- McGonigle, B. O., and Flook, J. P. (1978). "Long-term retention of single and multistate prismatic adaptation by humans," *Nature (London)* **272**, 364–366.
- Narayanan, S. S., Alwan, A. A., and Haker, K. (1995). "An articulatory study of fricative consonants using magnetic resonance imaging," *J. Acoust. Soc. Am.* **98**, 1325–1347.
- Nittrouer, S., Studdert-Kennedy, M., and McGowan, R. S. (1989). "The emergence of phonetic segments: Evidence from the spectral structure of fricative-vowel syllables spoken by children and adults," *J. Speech Hear. Res.* **32**, 120–132.
- Oller, D., and Eilers, R. (1988). "The role of audition in infant babbling," *Child Dev.* **59**, 441–449.
- Osberger, M. J., and McGarr, N. S. (1982). "Speech production characteristics of the hearing impaired," in *Speech and Language: Advances in Basic Research and Practice*, edited by N. J. Lass (Academic, New York).
- Perkell, J. S., Manzella, J., Wozniak, J., Matthies, M. L., Lane, H., Svirsky, M. A., Guidi, P., Delhorne, L., Short, P., MacCollin, M., and Mitchell, C. (1995). "Changes in speech production following hearing loss due to bilateral acoustic neuromas," in *Proceedings of the XIIIth International Congress of Phonetic Sciences*, **3**, 194–197.
- Perkell, J. S., Guenther, F. H., Lane, H., Matthies, M. L., Perrier, P., Vick, J., Wilhelms-Tricarico, R., and Zandipour, M. (2000a). "A theory of speech motor control and supporting data from speakers with normal hearing and with profound hearing loss," *J. Phonetics* **28**, 233–272.
- Perkell, J. S., Zandipour, M., Vick, J., Matthies, M. L., Lane, H., Guenther, F. H., and Gould, J. (2000b). "Rapid changes in speech production parameters in response to a change in hearing," in *Proceeding of the 5th Seminar on Speech Production: Models and Data*, 245–248.
- Ringel, R. L., and Steer, M. (1963). "Some effects of tactile and auditory alterations on speech output," *J. Speech Hear. Res.* **6**, 369–378.
- Rivers, C., and Rastatter, M. P. (1985). "The effects of multitalker and masker noise on fundamental frequency variability during spontaneous speech for children and adults," *J. Aud. Res.* **25**, 37–45.
- Rosenbaum, D., Carlson, R., and Gilmore, R. (2001). "Acquisition of intellectual and perceptual-motor skills," *Annu. Rev. Psychol.* **52**, 453–470.
- Scott, C. M., and Ringel, R. L. (1971). "Articulation without oral sensory control," *J. Speech Hear. Res.* **14**, 804–818.
- Shadle, C. (1985). "The acoustics of fricative consonants," in *Research Laboratory of Electronics, Technical Report 506* (Massachusetts Institute of Technology, Cambridge, MA).
- Shadle, C. H. (1991). "The effect of geometry on source mechanisms of fricative consonants," *J. Phonetics* **19**, 409–424.
- Smith, C. (1975). "Residual hearing and speech production in deaf children," *J. Speech Hear. Res.* **18**, 795–811.
- Stoica, P., and Moses, R. (1997). *Introduction to Spectral Analysis* (Prentice Hall, Upper Saddle River, NJ).

- Stone, M., Faber, A., Raphael, L. J., and Shawker, T. H. (1992). "Cross-sectional tongue shapes and linguopalatal contact patterns in [s], [ʃ], and [l]," J. Phonetics **20**, 253–270.
- Svirsky, M., and Tobey, E. (1991). "Effect of different types of auditory stimulation on vowel formant frequencies in multichannel cochlear implant users," J. Acoust. Soc. Am. **89**, 2895–2904.
- Ternström, S., Sundberg, J., and Collden, A. (1988). "Articulatory F_0 perturbations and auditory feedback," J. Speech Hear. Res. **31**, 187–192.
- Waldstein, R. (1990). "Effects of postlingual deafness on speech production: Implications for the role of auditory feedback," J. Acoust. Soc. Am. **88**, 2099–2114.
- Welch, P. D. (1967). "The use of fast Fourier transform for the estimation of power spectra: A method based on time averaging over short, modified periodograms," IEEE Trans. Audio Electroacoust. **AU-15**, 70–73.

Individual talker differences in voice-onset-time^{a)}

J. Sean Allen, Joanne L. Miller,^{b)} and David DeSteno

Department of Psychology, Northeastern University, Boston, Massachusetts 02115

(Received 21 February 2002; accepted for publication 21 October 2002)

Individual talkers differ in the acoustic properties of their speech, and at least some of these differences are in acoustic properties relevant for phonetic perception. Recent findings from studies of speech perception have shown that listeners can exploit such differences to facilitate both the recognition of talkers' voices and the recognition of words spoken by familiar talkers. These findings motivate the current study, whose aim is to examine individual talker variation in a particular phonetically-relevant acoustic property, voice-onset-time (VOT). VOT is a temporal property that robustly specifies voicing in stop consonants. From the broad literature involving VOT, it appears that individual talkers differ from one another in their VOT productions. The current study confirmed this finding for eight talkers producing monosyllabic words beginning with voiceless stop consonants. Moreover, when differences in VOT due to variability in speaking rate across the talkers were factored out using hierarchical linear modeling, individual talkers still differed from one another in VOT, though these differences were attenuated. These findings provide evidence that VOT varies systematically from talker to talker and may therefore be one phonetically-relevant acoustic property underlying listeners' capacity to benefit from talker-specific experience. © 2003 Acoustical Society of America. [DOI: 10.1121/1.1528172]

PACS numbers: 43.70.Fq, 43.70.Gr, 43.71.Es [AL]

I. INTRODUCTION

It is well known that individual talkers differ in the acoustic properties of their speech. These differences arise from many factors, including dialect (Byrd, 1992), idiosyncratic articulatory habits (Klatt, 1986), vocal tract size and shape (Peterson and Barney, 1952), and glottal characteristics (Klatt and Klatt, 1990). Some of the resulting acoustic differences are known to give rise to perceived differences in vocal timbre or voice quality; these acoustic properties are traditionally called indexical properties. Indexical properties, it has generally been assumed, are distinct from the acoustic properties involved in phonetic perception (Abercrombie, 1967). However, talkers' voices also differ in some phonetically-relevant acoustic properties as well as in indexical properties. For example, the voices of individual talkers of the same gender and dialect have been shown to differ in formant frequencies specifying vowels (Peterson and Barney, 1952; see also Hillenbrand *et al.*, 1995) and in frication centroid frequencies and skewness specifying fricative consonants (Newman *et al.*, 2001). The present investigation focuses on another phonetically-relevant acoustic property, important for the perception of voicing in stop consonants, that of voice-onset-time (VOT).

Individual talker differences in phonetically-relevant acoustic properties like VOT are of theoretical interest because recent findings in speech perception have suggested that listeners can exploit such differences to facilitate both the recognition of talkers (e.g., Remez *et al.*, 1997) and the recognition of spoken words (e.g., Nygaard *et al.*, 1994). In the domain of talker recognition, the results of Remez *et al.*

(1997; see also Fellowes *et al.*, 1997) have suggested that individual talker differences in phonetically-relevant acoustic properties are sufficient for listeners to recognize a talker's voice. Remez *et al.* created sinewave replicas of sentences spoken by ten talkers. This method of speech synthesis yields a drastically impoverished speech signal that eliminates acoustic properties traditionally considered indexical properties while preserving many phonetically-relevant acoustic properties (Remez *et al.*, 1981). The result is highly unnatural-sounding speech that is nonetheless intelligible for most listeners. Surprisingly, even under such conditions, listeners could successfully recognize most of the talkers by matching the sinewave replicas to natural samples of the talkers' voices. Other listeners who were highly familiar with the voices of the ten talkers from everyday interactions were able to recognize most of the talkers even without reference to a natural sample, that is, by relying solely on long-term memory of talker-specific voice information. Because listeners were able to recognize talkers in the absence of any known indexical acoustic properties, Remez *et al.* (1997; see also Fellowes *et al.*, 1997) argue that listeners relied on phonetically-relevant acoustic properties to recognize the talkers. This represents a considerable departure from traditional accounts, in which talker recognition is thought to be mediated by indexical properties (Bricker and Pruzansky, 1976).

In the domain of spoken word recognition, recent studies have indicated that listeners are sensitive to individual talker differences in phonetically-relevant acoustic properties during processing. The main finding from these studies is that previous experience with a particular talker's voice allows listeners to better recognize words spoken by that talker (Bradlow and Pisoni, 1999; Goldinger, 1996; Nygaard *et al.*, 1994; Nygaard and Pisoni, 1998). For example, Nygaard *et al.* (1994) trained listeners over a period of nine days to

^{a)}Portions of this work were presented at the 140th meeting of the Acoustical Society of America, Newport Beach, CA, December 2000.

^{b)}Author to whom correspondence should be addressed. Electronic mail: j.miller@neu.edu

recognize the voices of ten different talkers. During the tenth day listeners were administered a word recognition task, in which they were asked to identify new words in noise. Half of the listeners heard words spoken by the ten talkers with whom they had been familiarized; the other half heard words spoken by ten different talkers. The listeners who heard the familiar talkers were more accurate at identifying the words in noise than were those who heard unfamiliar talkers. This finding suggests that listeners can learn a given talker's characteristic implementation of phonetically-relevant acoustic properties and can later use that information to facilitate processing of the talker's speech. These results challenge the traditional view that any talker differences in phonetically-relevant acoustic properties are neutralized during the course of phonetic processing, and suggest instead that phonetically-relevant details are retained in a talker-specific manner (and see Palmeri *et al.*, 1993).

It appears then that individual talker differences in phonetically-relevant acoustic properties are perceptually significant, both for the recognition of talkers and for the recognition of spoken words. Although relatively little work has focused on documenting the existence or nature of individual talker variability in phonetically-relevant acoustic properties, there are studies, as mentioned above, that have shown that talkers differ from one another in spectral properties used to specify particular vowels and consonants. For example, in a classic study Peterson and Barney (1952; see also Hillenbrand *et al.*, 1995) measured vowel formant frequencies of many different vowels produced by many different talkers, and found substantial individual differences in formant frequencies. And more recently, Newman *et al.* (2001) measured centroid frequencies and skewness of /s/ and /ʃ/ produced by many different talkers, and found substantial individual talker differences in these properties.

The goal of the current work is to examine talker variability in another kind of phonetically-relevant acoustic property, one that is manifested not in the spectral domain but in the temporal domain. Specifically, we focus on VOT, a temporal acoustic property that specifies voicing in stop consonants. VOT is defined as the time from the initial release burst of a stop consonant to the onset of high-amplitude periodic energy. Voiced stop consonants (/b d g/) are associated with relatively short VOT values whereas voiceless stop consonants (/p t k/) are associated with relatively long VOT values (Lisker and Abramson, 1964). Following the previous studies showing talker variability described above (Hillenbrand *et al.*, 1995; Newman *et al.*, 2001; Peterson and Barney, 1952), this property was measured in isolated monosyllabic words produced by multiple talkers. The question of interest was whether systematic differences among the talkers in VOT would emerge.

A complicating factor in the case of VOT is that VOT varies strongly as a function of speaking rate. As a talker speaks more slowly and produces words that are longer in duration, he or she produces longer VOT values as well, especially for voiceless stop consonants (Kessinger and Blumstein, 1998; Miller *et al.*, 1986; Volaitis and Miller, 1992). Moreover, individual talkers can differ from one another in their speaking rates (Miller *et al.*, 1984). Given this,

an observed difference between two talkers in absolute VOT may be due solely to a difference in speaking rate; if the same two talkers were to adjust their speaking rates such that they spoke at comparable rates, they might then produce nondiffering VOT values. As a result, the question of whether individual talkers' voices differ in VOT cannot be adequately addressed without consideration of the factor of speaking rate.

In addition, the factor of speaking rate is especially relevant because evidence from experiments in phonetic perception has shown that VOT is processed by listeners in a rate-dependent manner. That is, the mapping of VOT onto perceptual phonetic categories varies as a function of speaking rate. For example, the perceived boundary between a voiced and a voiceless stop consonant shifts toward longer VOT values as speaking rate slows down (Summerfield, 1981). Moreover, studies examining the internal structure of perceptual phonetic categories have shown that not only does the boundary between voicing categories vary as a function of a speaking rate, but also that the entire structure of the category itself shifts as a function of a speaking rate. In particular, the best-rated, or most prototypical, exemplars of a voiceless stop consonant have longer VOT values as speaking rate slows down (e.g., Miller and Volaitis, 1989). This suggests that a change in speaking rate has the effect of fundamentally altering the perceptual mapping from VOT value to phonetic category. Further, this rate-dependent processing appears to be the result of an obligatory mechanism of the phonetic processing system, such that information about speaking rate cannot be ignored during phonetic processing (Miller, 1987). We take these findings to indicate that the phonetic processing system does not operate on absolute VOT values but rather on VOT relative to the speaking rate.

For these reasons, the present research asks not only whether individual talkers' voices differ in absolute VOT values, but also whether they differ in VOT *after controlling for differences among the talkers in speaking rate*. In the broad literature involving analyses of VOT in normal adult speakers of English, individual talker data are sometimes reported and substantial differences in absolute VOT across talkers are apparent in those data (e.g., Bailey and Haggard, 1973; Koenig, 2000; Newman, 1997) and, further, there is some evidence that a given talker's VOT productions are consistent over time (e.g., Itoh *et al.*, 1982; Schiavetti *et al.*, 1999). However, it remains unclear whether individual talkers' voices differ in VOT when differences in speaking rate are controlled. Suggestive evidence can be found in studies reporting individual talker data on both VOT and speaking rate (e.g., Koenig, 2000) as well as in our own recent speech production studies that have measured VOT and speaking rate (e.g., Allen and Miller, 1999, 2001). In these data one can find cases in which talkers appear to be well-matched on some measure of speaking rate but differ in VOT. The present study sought to expand on these previous data in the context of an experiment specifically designed for the purpose of assessing individual talker differences in VOT. Our approach was to attempt to minimize differences among talkers in speaking rate by requiring them to produce words in isolation prompted at regular intervals by computer presen-

TABLE I. Words used in the experiment.

/p/-initial words	/t/-initial words	/k/-initial words
pace	tale	cash
pause	tease	cause
pen	time	cave
pill	ton	comb
pose	tool	come
push	town	kiss

tation of visual word tokens. It was expected that talkers would nonetheless differ to some extent in speaking rate. The effect of these differences among talkers in speaking rate was factored out using statistical methods, as described below, permitting us to effectively control for differences in speaking rate. The main question was whether talkers differed in VOT after correcting for these differences.

II. METHOD

A. Talkers

Eight talkers participated in the experiment. Four of the talkers were female, designated as talkers F1 through F4, and four of the talkers were male, designated as talkers M1 through M4. All were native speakers of English with general American accents, between 18 and 45 years of age, with no reported speech or hearing disorders. Talkers were paid for their participation.

B. Materials

Eighteen highly familiar, monosyllabic consonant-vowel-consonant (CVC) words were selected, each of which began with a voiceless stop consonant. Six of the eighteen words began with /p/, six began with /t/, and six began with /k/. Words beginning with voiced stop consonants (/b/, /d/, /g/) were not used, because previous work has indicated that VOT values associated with voiced stops are subject to less variability than are VOT values associated with voiceless stops (e.g., Kessinger and Blumstein, 1997; Miller *et al.*, 1986); we therefore chose to concentrate on voiceless stop consonants, where we expected that any individual differences in VOT would appear more clearly. Words were selected so that a variety of different vowels were represented, and the final consonants consisted of a nasal, fricative, or liquid consonant (final stop consonants were not used to avoid variability associated with some talkers' tendency to not release final stops). The 18 words selected for use in this study are shown in Table I.

The 18 words were pooled into a single stimulus block, which was repeated 30 times with a different within-block randomization each time. This yielded a list of 540 items that was presented to talkers.

C. Procedure

Each talker was recorded individually in a sound-treated booth. The words to be produced were presented to the talker

visually on a computer screen, one at a time. Each visual stimulus was displayed for 1500 ms, followed by a pause of 2500 ms before the next word was displayed. Talkers were instructed to say each word as it appeared on the screen, in a clear but natural manner. Their speech was recorded via a microphone (AKG C460B) onto digital audiotape (Aiwa HHB 1 PRO DAT recorder). Talkers were given a short break midway through the session.

D. Acoustic analysis

The recording of each word was transferred to a Pentium PC at a sampling rate of 20 kHz using the CSL system (Kay Elemetrics Corp.). For each word token, two measurements were determined using the CSL waveform and spectrogram displays, VOT and word duration. VOT was measured as the interval from the onset of the initial release burst to the onset of periodicity. Word duration was measured as the interval from the onset of the initial release burst to the offset of energy associated with the final consonant. For final nasal and liquid consonants, consonant offset was defined as the offset of periodicity. For final fricative consonants, consonant offset was defined as the offset of frication. For two of the talkers (talkers M2 and M4), the offset of the final /v/ in the word *cave* was too low in amplitude to be measured reliably. Consequently, we discarded the data from the word *cave* from all analyses. Thus, all reported analyses are based on data from 17 of the 18 words listed in Table I. We also discarded data from items incorrectly produced (e.g., disfluencies or substituted phonemes); these items accounted for less than 1% of the data.

Word duration served as the primary measure of the speaking rate at which the word was produced. This operationalized definition of speaking rate, following that used in previous studies (e.g., Miller *et al.*, 1986; Volaitis and Miller, 1992), corresponds to the classical definition of speaking rate as the number of words (or syllables) uttered per unit time in running speech, translated into the time per word (or syllable) spoken in isolation. A secondary measure of speaking rate was also employed in certain analyses reported below. This was the duration of the vowel and final consonant (i.e., the VC portion of the word), defined as word duration minus VOT. This secondary measure was used to ensure that the VOT measure and the measure of speaking rate were independent of one another in these analyses; this issue is discussed in detail in Sec. III.

All acoustic measurements were carried out by a pool of three trained experimenters including the first author. To assess cross-experimenter reliability, a random subset of 10% of the tokens of each word for each talker was selected to be measured by all three experimenters. Across the eight talkers, mean absolute differences among measurements from any given pair of experimenters never exceeded 2 ms for VOT or 11 ms for word duration. For each talker, correlations (Pearson's *r*) between pairs of experimenters' measurements were always 0.96 or higher for both VOT and word duration measurements, except for the word duration measurements for talker M2, which were 0.85 or higher.

TABLE II. Mean word duration and VOT, in milliseconds, for the eight talkers, collapsed across words. Standard errors of the mean are shown in parentheses.

Talker	Word duration	VOT
F1	523 (22)	72 (2.0)
F2	536 (18)	96 (2.8)
F3	668 (25)	119 (2.6)
F4	614 (19)	105 (2.7)
M1	614 (17)	111 (2.3)
M2	437 (10)	69 (1.5)
M3	374 (20)	71 (2.4)
M4	505 (14)	86 (2.2)

III. RESULTS AND DISCUSSION

For each of the 17 different words (after eliminating the word *cave*; see Sec. IID) mean word duration and mean VOT for each talker were calculated across the 30 tokens of a given word, less discarded data due to errors in production. The resulting values are provided in the Appendix. Table II summarizes these data, showing overall means for word duration and VOT for the eight talkers averaged across the 17 words.

Consider first the VOT data. Mean VOT varied substantially across the talkers in this sample, ranging from 69 to 119 ms. These large individual talker differences in absolute VOT values replicate previous reports (e.g., Bailey and Haggard, 1973; Koenig, 2000; Newman, 1997). Additional analyses were conducted to further explore these individual differences in VOT. As noted above, each of the talker means was based on the VOTs of 17 words. An examination of each talker's VOT distribution for the 17 words showed that the distributions were roughly the same shape across the talkers. First, the standard deviations of the distributions were comparable (within a factor of 2 of one another, ranging from 6.2 to 11.4 ms across talkers) and, second, for none of the distributions was there significant skew (i.e., the skew estimate for each talker's distribution did not differ significantly from 0 based on evaluation of 95% confidence intervals surrounding each subject's skew estimate).

Moreover, the ordering of the 17 words within a given talker's VOT distribution was largely consistent across talkers. This can be seen in Table III, which shows the rank order for the 17 words spoken by each of the eight talkers. The rank orders were obtained separately for each talker by ordering their 17 words from shortest to longest VOT and assigning them ranks with 1 corresponding to the shortest VOT and 17 corresponding to the longest VOT. In the table, the words are ordered from top to bottom by median VOT across talkers. Examination of the table reveals that talkers were relatively consistent with one another, so that ranks for a given word tended to be similar across talkers, with the result that words near the top of the table generally received low ranks and words near the bottom of the table generally received high ranks. Statistical analysis confirmed that the rank orderings of the words were consistent across talkers ($R = 0.86$, using the Spearman–Brown formula of internal consistency). Thus, the intratalker distributions of VOT were stable across individuals. This indicates that the observed

TABLE III. Rank ordering of words by mean VOT for each talker. Words are ordered in the table by their median ranks across talkers.

Word	Talker								Median
	F1	F2	F3	F4	M1	M2	M3	M4	
pace	4.0	2.0	1.0	2.0	6.0	2.5	2.0	1.0	2.00
pose	2.5	5.5	2.0	4.0	2.0	2.5	4.0	2.0	2.50
push	1.0	1.0	8.0	3.0	10.0	5.5	1.0	6.5	4.25
pill	2.5	9.5	3.0	10.5	4.0	1.0	7.0	8.0	5.50
pen	5.0	14.0	6.5	1.0	9.0	8.0	4.0	5.0	5.75
pause	6.5	11.0	6.5	7.5	1.0	4.0	13.0	9.0	7.00
kiss	6.5	3.0	11.0	6.0	13.0	7.0	9.0	13.5	8.00
comb	12.0	7.0	4.5	7.5	5.0	10.0	14.0	13.5	8.75
come	10.0	8.0	9.5	5.0	11.5	5.5	11.0	13.5	9.75
tale	11.0	9.5	14.0	13.0	7.5	13.5	6.0	4.0	10.25
town	9.0	15.0	13.0	9.0	16.0	11.5	8.0	3.0	10.25
cash	14.5	12.5	9.5	13.0	15.0	9.0	12.0	6.5	12.25
ton	8.0	16.0	16.5	10.5	17.0	13.5	4.0	11.0	12.25
time	13.0	17.0	16.5	16.0	14.0	11.5	10.0	10.0	13.50
tease	14.5	4.0	12.0	13.0	7.5	17.0	16.0	16.0	13.75
cause	17.0	12.5	4.5	15.0	3.0	15.5	17.0	13.5	14.25
tool	16.0	5.5	15.0	17.0	11.5	15.5	15.0	17.0	15.25

mean VOT differences among talkers (seen in Table II) were largely systematic across words, with VOT for any given word shifting toward shorter or longer VOTs as a function of the identity of the talker.

Next consider word duration, which provides a measure of speaking rate. The observed mean differences in VOT across talkers, described above, may be attributable at least in part to differences among the talkers in speaking rate. As can be seen in Table II, there is substantial individual variation in mean word duration in this sample, ranging from 374 to 668 ms across the eight talkers. Because VOT is highly correlated with word duration (indeed, $r = 0.91$ for the data shown in Table II), it is necessary to somehow control for these differences in order to determine whether individual talker differences in VOT exist when speaking rate is held constant.

One analytic approach to address the question of whether talkers differ in VOT at a particular speaking rate is to compare VOT values among talkers only in cases in which talkers do not differ from one another in mean word duration. More specifically, talkers can be matched based on their distributions of word durations across the 30 tokens of a particular word (e.g., *pace*), and the distributions of VOT values across the 30 tokens of that word can then be compared for the talkers so matched. Applying that approach to the present data set, one can find cases in which pairs of talkers are matched in word duration for a particular word but have significantly different distributions of VOT values for that word. An example is provided in Fig. 1, which shows a comparison of talkers F1 and F2 producing the word *pace*. The left side of the figure shows the distribution of word durations across the 30 repetitions of the word *pace* for the two talkers. The means of these two distributions do not differ significantly from one another [$t(58) = 1.5$; $p > 0.10$]. The right side of the figure shows the distribution of VOT values for the same talkers. Talker F2's distribution of VOT values is clearly displaced toward longer values relative to that of talker F1, and the means of the distributions are sig-

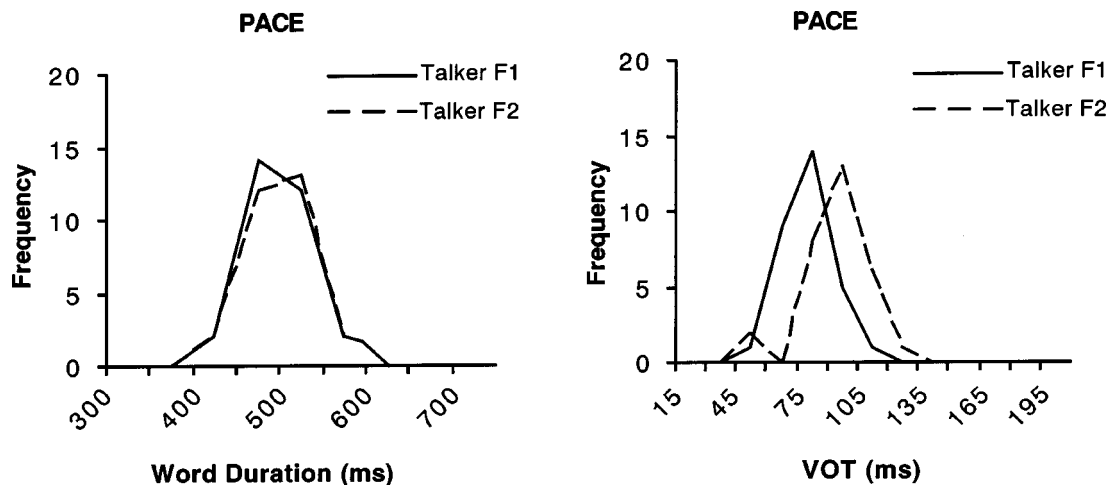


FIG. 1. Distributions of word durations (shown on the left) and VOT values (shown on the right) for the word *pace* spoken by talkers F1 and F2. (Frequency data are grouped in bins of 50 ms for word duration and 15 ms for VOT.)

nificantly different [$t(58)=3.6$, $p<0.001$]. This pattern is representative of the comparisons of other words spoken by these two talkers; of the eight words for which these two talkers did not differ significantly in word duration ($p>0.10$ in each case), all eight comparisons showed that talker F2 produced significantly longer VOT values than talker F1 ($p<0.001$ in each case). Comparisons between other pairs of talkers matched on word duration in some cases revealed similar significant differences in VOT. Evidence such as this can be taken to indicate that there are cases in which talkers differ in VOT even when speaking rate is held constant.

However, this analytic approach is limited because only in a minority of cases did pairs of talkers match on word duration for particular words; more typically, talkers differed. All together, of the possible 476 cases (28 possible talker pairings \times 17 different words), only in 49 cases (or 10%) did talkers not differ significantly from one another in word duration (with a conservative criterion of $\alpha=0.10$). Thus this approach did not consider 90% of the data, giving rise to the concern that the selected portion of the data was unrepresentative of the whole. A more sophisticated analysis would involve controlling for differences in speaking rate statistically through regression techniques rather than discarding data when precise matches in speaking rate are not found. To that end, a hierarchical linear modeling analysis (HLM; see Bryk and Raudenbush, 1992) was applied to the data. The HLM analysis makes fewer assumptions in comparison to ANOVA models and, critically, permits the separation of variance associated with individual talker identity from variance associated with other factors and from true error variance.¹ The specific goal of the HLM analysis was to determine whether differences among talkers accounted for any portion of the remaining variability in VOT after differences in speaking rate were factored out.

The structure of the HLM was as follows. Each of the 17 different words (level 1) was nested hierarchically within each of the eight talkers (level 2). The VOT of a given word (i) spoken by a particular talker (j) was defined as

Level 1 model:

$$\text{VOT}_{ij} = \beta_{0j} + \beta_{1j} (\text{intrinsic word duration}) + r_{ij}$$

Thus, VOT for a particular word and talker was a linear function specified by an intercept (β_{0j}) for each talker, a slope (β_{1j}) for each talker representing the influence of intrinsic word duration, and an error term (r_{ij}) for each talker and word. In this analysis, the intercept terms are defined as the intercept at the grand mean word duration for each talker rather than at 0. The intrinsic word duration factor was the mean word duration of a given word spoken by a given talker, averaged across the 30 tokens of the word (less discarded data due to errors in production); the outcome variable of VOT was likewise averaged across word repetitions.² At this level of the model (level 1, the word level), the intrinsic word duration factor captured differences across the 17 different words in their intrinsic durations; each talker's coefficient represented the relation between these durations and his or her respective VOT values. This factor was included in the HLM for completeness, but did not directly bear on the main question concerning differences across talkers. For that, it is necessary to examine the second level of the model (level 2, the talker level), which entered the above equation via the slope and intercept terms specific to each talker (β_{0j} and β_{1j} , respectively):

$$\text{Level 2 model: } \beta_{0j} = \gamma_{00} + \gamma_{01} (\text{overall rate}) + u_{0j}$$

$$\beta_{1j} = \gamma_{10} + \gamma_{11} (\text{overall rate}) + u_{1j}$$

Thus, these terms were themselves linear functions specified by an intercept, a slope, and an error term. The intercept terms represent the mean VOT (γ_{00}) and effect of intrinsic word duration (γ_{10}) across talkers; these are then adjusted for each talker by the overall rate factor and by a talker-specific error term. The overall rate factor was determined for each talker by averaging word duration values across all 17 words in the study. This factor thus served to capture differences among talkers in their average speaking rates

across the experiment. Of particular interest were the talker-specific error terms (u_{0j} and u_{1j}); these terms specified the remaining variance in VOT after differences across talkers in speaking rate were factored out. Thus the HLM, once applied to the data, allowed us to parcel out variability in VOT attributable to individual talker differences, above and beyond that attributable to speaking rate and random error.

The data were fitted to the model using a maximum likelihood estimation technique (Bryk and Raudenbush, 1992). The results of the analysis indicated that the effect of the level 1 factor of intrinsic word duration was negligible [$t(6) < 1$ for both slope and intercept]. That is, although some words were intrinsically longer than others due to the durational characteristics of their constituent phonemes (e.g., *cash* is longer in duration than *kiss*), such intrinsic differences in word duration were not predictive of VOT. (Of course, differences in duration associated with changes in speaking rate, rather than those associated with different phonemes, were expected to be highly predictive of VOT, as discussed below.) Because the intrinsic word duration factor was found to be negligible, a simplified version of the HLM was run, excluding this factor. Other than the absence of the intrinsic word duration factor, the results of this simpler HLM were not qualitatively different from those of the previous HLM; the results reported below are therefore based on the simpler model. The structure of the simpler HLM was as follows:

Level 1 model: $VOT_{ij} = \beta_{0j} + r_{ij}$

Level 2 model: $\beta_{0j} = \gamma_{00} + \gamma_{01} (\text{overall rate}) + u_{0j}$

The results of the analysis based on this model showed that, as expected, the effect of the overall rate factor was highly significant [$t(6) = 29.7$, $p < 0.001$]. That is, talkers who spoke slowly tended to produce longer VOT values than those who spoke quickly. By far, most of the variability in VOT in this sample, 82% of the total variability, was attributable to differences among talkers in overall rate.³ Clearly, then, speaking rate was the strongest single predictor of VOT. The critical question addressed by the HLM was whether any portion of the remaining 18% of the variability in VOT (after factoring out speaking rate) was explained by individual talker differences. The results revealed that differences among talkers indeed accounted for a significant portion of the variability [$\chi^2(6) = 83$, $p < 0.001$]; after factoring out variability due to speaking rate, 43% of the remaining variability in VOT (or 8% of the total variability) was explained by individual talker identity, leaving 57% unexplained (i.e., true error). Thus, individual differences in VOT were present, even after controlling for differences associated with changes in speaking rate.

In order to compare VOT values across talkers after controlling for speaking rate, we compared each talker's intercept value (β_{0j}) at the grand mean of overall rate. These values reflect each talker's predicted VOT value if they had all produced words of the same mean duration (534 ms). These rate-corrected VOT values are shown in Table IV. It is clear from the data in the table that one talker in the sample, talker F1, had particularly short VOT values compared to the

TABLE IV. Corrected word duration and VOT, in milliseconds, for the eight talkers, collapsed across words, as given by the hierarchical linear model (see main text).

Talker	Corrected word duration	Corrected VOT
F1	534	74
F2	534	95
F3	534	95
F4	534	96
M1	534	87
M2	534	100
M3	534	92
M4	534	90

other talkers. This raised the concern that this single talker might be responsible for the statistically significant individual differences in VOT detected by the HLM above. We therefore excluded this talker from the HLM and ran the model again based on seven talkers. The results revealed that individual talkers still differed significantly from one another [$\chi^2(5) = 18.9$, $p < 0.01$] though these differences accounted for a much smaller portion of the variability in VOT after speaking rate was factored out (14% as compared to 43%). The presence of this outlier talker (talker F1) in our sample suggests that some talkers deviate considerably from others in VOT, though most talkers appear to cluster relatively closer to one another in their VOT productions. However, given the small sample size in this study, it is not possible to draw any strong conclusions about this sample's representativeness of the population at large or about the true extent of variability in VOT in the population at large. Rather, the present results should be taken only as evidence that talkers do differ from one another in their VOT productions, even when differences in speaking rate are controlled.⁴

In the analyses above, mean word duration was used as the measure of each talker's speaking rate. However, as mentioned in Sec. IID, operationalizing speaking rate as word duration raises a possible concern in the present analysis: Because word duration subsumes the VOT interval of the word, this measure of speaking rate is not independent from VOT. In particular, it may be that at least part of the observed covariation between VOT and word duration arises from word duration changing as a direct result of changes in VOT rather than as a result of changes in speaking rate *per se*. This would have the effect of exaggerating the relationship between VOT and speaking rate, such that the true percentage of variability in VOT accounted for by speaking rate should be lower than that described by the HLM above (82%). It follows that the portion of variability incorrectly allotted to differences in speaking rate would then be added to the variability accounted for by individual talker differences or by random error or by both. Therefore, for purposes of assessing individual talker differences, the use of word duration as a measure of speaking rate is a conservative measure, in that it may have underestimated the amount of variability in VOT explained by individual talker differences. In order to test this possibility, we ran another HLM using the secondary measure of speaking rate described in Sec. IID, which did not include the VOT interval. Specifically, this

measure of speaking rate was defined as word duration minus the VOT interval, that is, as the duration of the VC portion of the word. The results of this analysis showed that the effect of overall rate was still highly significant [$t(6) = 28.1, p < 0.001$] and differences among talkers still accounted for a significant portion of the variability in VOT [$\chi^2(6) = 123, p < 0.001$]. But compared to the previous analysis, overall rate now accounted for a smaller portion of the overall variability in VOT, 72% as compared to 82%. Of the remaining variability in VOT, individual talker differences accounted for 54% (or 15% of the total variability in VOT), as compared to 43% (or 8% of the total variability in VOT). Thus, using VC duration rather than word duration as an estimate of speaking rate confirmed the presence of individual talker differences in VOT and in fact revealed that the main analysis above may have underestimated their prevalence.

IV. CONCLUSION

The current study asked whether individual talkers differ from one another in their VOT productions. The results showed that, in line with previous results (e.g., Bailey and Haggard, 1973; Koenig, 2000; Newman, 1997), individual talkers’ voices do differ in their absolute VOT values. The single strongest predictor of VOT, however, was a given talker’s speaking rate. When these differences across talkers in speaking rate were controlled using a hierarchical linear model (HLM), individual talker differences in VOT were attenuated but differences among talkers remained. Thus, the main conclusion from this study is that individual talkers do differ from one another in their VOT productions even when differences in speaking rate are controlled. As a secondary procedural point, given the strong influence of speaking rate on VOT, the results also underscore the importance of controlling for differences in speaking rate in some manner when attempting to compare VOT productions across individuals, groups, or experimental conditions. In particular, it is important to consider the role of speaking rate in studies attempting to demonstrate a difference in VOT between two populations (e.g., clinical populations, age, or gender groups) when those two populations may well differ in characteristic speaking rates.

Traditionally, the existence of individual talker differences in a phonetically-relevant property such as VOT has been considered problematic “noise” that the phonetic perception system must filter out in order to recover the linguistic message from the signal. However, if listeners are capable of tracking these individual talker differences, then they could benefit from such information in at least two ways, as reviewed in the Introduction. First, listeners could use such information to facilitate recognition of a talker (Remez *et al.*, 1997)—that is, listeners could compare VOT information in the speech signal with stored VOT information about a particular talker’s voice in order to better recognize individual voices. Second, listeners could use talker-specific VOT information to facilitate recognition of spoken words (Nygaard *et al.*, 1994)—that is, they could use stored VOT information about a particular talker’s voice to customize for each talker the mapping from VOT information in the speech signal to perceptual phonetic categories in order to better recognize words spoken by that talker. That VOT differs from talker to talker, even when speaking rate is controlled, indicates that VOT may indeed be one phonetically-relevant acoustic property used by listeners in these ways. If so, then we would expect that listeners would exhibit a sensitivity to talker-specific differences in VOT; future research is aimed at addressing this question.

ACKNOWLEDGMENTS

This research was conducted as part of a doctoral dissertation at Northeastern University by the first author under the direction of the second author, and was supported by NIH Grant No. DC00130 from the National Institute on Deafness and Other Communication Disorders. We thank Michèle Mondini for her helpful comments on an earlier version of the manuscript, and Jennifer Turco and Sharon Clayman for assistance in the acoustic measurements.

APPENDIX

Each talker’s mean VOT and word duration values, in milliseconds, for each of the 17 different words are provided below. These values are averaged across the 30 repetitions of each of the words (less discarded data due to errors in production). Standard errors of the mean are shown in parentheses.

	Talker F1		Talker F2		Talker F3		Talker F4	
	Word duration	VOT	Word duration	VOT	Word duration	VOT	Word duration	VOT
pace	565 (6.6)	66 (2.4)	580 (8.1)	79 (2.8)	683 (9.4)	106 (2.9)	591 (7.0)	89 (2.8)
pause	625 (6.7)	70 (3.0)	613 (8.5)	99 (3.8)	845 (12.1)	112 (2.7)	729 (6.1)	103 (2.4)
pen	425 (9.0)	69 (3.1)	452 (8.5)	103 (4.0)	554 (10.5)	112 (2.6)	521 (6.3)	87 (3.1)
pill	376 (6.1)	58 (2.7)	425 (6.5)	98 (3.4)	537 (8.7)	110 (2.2)	489 (8.4)	107 (2.8)
pose	631 (7.5)	58 (2.6)	627 (9.6)	92 (3.8)	772 (10.2)	109 (2.3)	717 (9.1)	96 (2.1)
push	534 (6.9)	57 (2.2)	542 (9.0)	74 (3.2)	629 (8.9)	114 (2.3)	580 (8.1)	90 (1.9)
tale	471 (4.5)	75 (2.0)	487 (7.2)	98 (3.2)	621 (8.4)	129 (2.7)	590 (8.0)	111 (2.7)
tease	611 (7.2)	79 (2.0)	584 (7.7)	88 (2.5)	784 (11.9)	126 (2.6)	728 (8.8)	111 (3.1)
time	529 (7.1)	77 (2.3)	555 (6.0)	116 (4.4)	677 (10.2)	138 (2.8)	663 (8.5)	123 (2.4)
ton	412 (5.3)	72 (2.2)	472 (7.1)	115 (4.3)	566 (9.6)	138 (3.3)	554 (7.0)	107 (2.7)
tool	458 (5.9)	82 (3.0)	432 (6.4)	92 (3.1)	582 (6.5)	134 (2.0)	573 (7.4)	129 (2.6)
town	527 (6.2)	73 (3.1)	542 (8.3)	105 (4.3)	676 (10.8)	127 (3.3)	641 (8.6)	104 (3.3)

	Talker F1		Talker F2		Talker F3		Talker F4	
	Word duration	VOT	Word duration	VOT	Word duration	VOT	Word duration	VOT
cash	665 (8.8)	79 (1.9)	654 (7.6)	100 (3.8)	780 (11.0)	115 (2.7)	645 (5.4)	111 (3.0)
cause	646 (6.4)	83 (2.4)	636 (7.9)	100 (3.3)	835 (10.0)	111 (2.4)	736 (7.4)	113 (4.2)
comb	491 (7.0)	76 (2.3)	503 (6.4)	93 (3.0)	642 (9.5)	111 (2.2)	614 (9.6)	103 (3.1)
come	420 (6.5)	74 (2.8)	451 (6.3)	94 (3.8)	553 (10.4)	115 (2.0)	517 (8.1)	100 (2.8)
kiss	498 (6.0)	70 (2.4)	551 (5.9)	80 (3.4)	623 (9.8)	124 (2.8)	557 (6.5)	102 (2.6)

	Talker M1		Talker M2		Talker M3		Talker M4	
	Word duration	VOT	Word duration	VOT	Word duration	VOT	Word duration	VOT
pace	605 (9.5)	109 (5.1)	431 (4.4)	61 (2.0)	425 (6.4)	59 (2.8)	523 (7.2)	70 (2.5)
pause	686 (11.2)	93 (3.8)	482 (5.4)	64 (2.1)	479 (5.6)	79 (2.4)	573 (6.4)	86 (2.4)
pen	544 (10.8)	111 (5.8)	392 (4.6)	69 (1.8)	290 (4.8)	61 (2.2)	430 (5.7)	81 (2.5)
pill	507 (9.8)	105 (4.5)	362 (3.8)	60 (1.9)	257 (6.4)	67 (2.7)	418 (6.9)	84 (2.1)
pose	671 (14.4)	95 (4.6)	486 (6.4)	61 (1.5)	449 (6.7)	61 (2.6)	565 (4.7)	75 (2.1)
push	609 (13.0)	112 (8.4)	415 (5.6)	65 (2.1)	404 (4.5)	52 (1.9)	515 (5.0)	82 (2.5)
tale	552 (11.9)	110 (4.1)	416 (4.0)	74 (1.5)	299 (5.2)	66 (1.9)	480 (6.0)	80 (2.2)
tease	697 (14.1)	110 (2.9)	459 (4.6)	79 (1.4)	455 (5.2)	84 (2.1)	565 (4.0)	94 (3.3)
time	633 (11.0)	118 (4.6)	448 (5.6)	72 (1.8)	341 (6.2)	73 (2.5)	519 (6.5)	88 (3.0)
ton	546 (9.2)	128 (5.4)	399 (4.6)	74 (1.7)	284 (4.9)	61 (2.4)	440 (7.3)	90 (3.6)
tool	557 (11.4)	113 (4.4)	445 (7.8)	78 (1.9)	312 (7.6)	83 (2.7)	459 (5.6)	109 (3.0)
town	670 (14.1)	124 (6.7)	463 (7.9)	72 (1.5)	336 (7.0)	68 (2.5)	526 (5.7)	78 (2.2)
cash	756 (14.1)	121 (3.6)	504 (4.7)	70 (1.9)	508 (4.9)	76 (2.5)	589 (7.5)	82 (2.2)
cause	693 (13.8)	100 (3.5)	488 (5.4)	78 (2.7)	490 (6.1)	86 (2.5)	568 (10.1)	92 (1.8)
comb	604 (13.2)	106 (4.0)	445 (5.7)	71 (2.0)	338 (6.7)	80 (2.4)	496 (6.0)	92 (2.6)
come	536 (11.0)	113 (4.1)	393 (3.7)	65 (1.6)	299 (4.6)	75 (2.0)	433 (6.0)	92 (2.8)
kiss	568 (9.0)	116 (4.4)	393 (4.3)	68 (1.6)	383 (4.3)	69 (1.9)	486 (6.4)	92 (2.4)

¹The model does assume a linear relationship between predictor and outcome variables, in this case between speaking rate (as measured by word duration) and VOT. Although the true relationship between speaking rate and VOT may well be nonlinear, their relationship in the present data set approximated a linear function; therefore the HLM was deemed appropriate.

²The data were averaged across the 30 repetitions of each word spoken by each talker to serve as an estimate of VOT and intrinsic word duration for a given word spoken by a given talker. Note that with the inclusion of an additional level to the model, the HLM could accommodate the level of specificity of individual word repetitions, but this was not deemed necessary for purposes of the current investigation.

³We calculated this proportion of variability explained by overall rate by running another version of the HLM, identical to the main HLM but excluding the factor of overall rate. By comparing variance components with and without the factor in the model we used a simple proportion to determine how much of the variability was explained by the factor.

⁴A further point of interest concerns gender differences in VOT. Some claims have been advanced in the literature that females tend to have longer VOT values for voiceless stop consonants than do males (Ryalls *et al.*, 1997; Swartz, 1992; Whiteside and Irving, 1998). This claim appears to be supported by the absolute VOT data shown in Table II, where an average across the four female talkers yields an absolute VOT of 98 ms whereas an average across the four male talkers yields an absolute VOT of 84 ms. However, this gender difference is not evident when differences among the talkers in speaking rate are controlled; in Table IV the mean rate-corrected VOT for females is 90 ms and for the males it is 92 ms.

Abercrombie, D. (1967). *Elements of General Phonetics* (Aldine, Chicago, IL).

Allen, J. S., and Miller, J. L. (1999). "Effects of syllable-initial voicing and speaking rate on the temporal characteristics of monosyllabic words," *J. Acoust. Soc. Am.* **106**, 2031–2039.

Allen, J. S., and Miller, J. L. (2001). "Contextual influences on the internal structure of phonetic categories: A distinction between lexical status and speaking rate," *Percept. Psychophys.* **63**, 798–810.

Bailey, P. J., and Haggard, M. P. (1973). "Perception and production: Some correlations on voicing of an initial stop," *Lang. Speech* **16**, 189–195.

Bradlow, A. R., and Pisoni, D. B. (1999). "Recognition of spoken words by native and non-native listeners: Talker-, listener-, and item-related factors," *J. Acoust. Soc. Am.* **106**, 2074–2085.

Bricker, P. D., and Pruzansky, S. (1976). "Speaker recognition," in *Contemporary Issues in Experimental Phonetics*, edited by N. J. Lass (Academic, New York), pp. 295–326.

Bryk, A. S., and Raudenbush, S. W. (1992). *Hierarchical Linear Models: Applications and Data Analysis Methods* (Sage, Newbury Park, CA).

Byrd, D. (1992). "Preliminary results on speaker-dependent variation in the TIMIT database," *J. Acoust. Soc. Am.* **92**, 593–596.

Fellowes, J. M., Remez, R. E., and Rubin, P. E. (1997). "Perceiving the sex and identity of a talker without natural vocal timbre," *Percept. Psychophys.* **59**, 839–849.

Goldinger, S. D. (1996). "Words and voices: Episodic traces in spoken word identification and recognition memory," *J. Exp. Psychol. Learn. Mem. Cogn.* **22**, 1166–1183.

Hillenbrand, J., Getty, L. A., Clark, M. J., and Wheeler, K. (1995). "Acoustic characteristics of American English vowels," *J. Acoust. Soc. Am.* **97**, 3099–3111.

Itoh, M., Sasanuma, S., Tatsumi, I. F., Murakami, S., Fukusako, Y., and Suzuki, T. (1982). "Voice onset time characteristics in apraxia of speech," *Brain Lang.* **17**, 193–210.

Kessinger, R. H., and Blumstein, S. E. (1997). "Effects of speaking rate on voice-onset time in Thai, French, and English," *J. Phonetics* **25**, 143–168.

Kessinger, R. H., and Blumstein, S. E. (1998). "Effects of speaking rate on voice-onset time and vowel production: Some implications for perception studies," *J. Phonetics* **26**, 117–128.

Klatt, D. H. (1986). "The problem of variability in speech recognition and in models of speech perception," in *Invariance and Variability in Speech Processes*, edited by J. S. Perkell and D. H. Klatt (Erlbaum, Hillsdale, NJ), pp. 300–319.

Klatt, D. H., and Klatt, L. C. (1990). "Analysis, synthesis, and perception of voice quality variations among female and male talkers," *J. Acoust. Soc. Am.* **87**, 820–857.

- Koenig, L. L. (2000). "Laryngeal factors in voiceless consonant production in men, women, and 5-year-olds," *J. Speech Hear. Res.* **43**, 1211–1228.
- Lisker, L., and Abramson, A. S. (1964). "A cross-language study of voicing in initial stops: Acoustical measurements," *Word* **20**, 384–422.
- Miller, J. L. (1987). "Rate-dependent processing in speech perception," in *Progress in the Psychology of Language*, edited by A. W. Ellis (Erlbaum, Hillsdale, NJ), pp. 119–156.
- Miller, J. L., and Volaitis, L. E. (1989). "Effect of speaking rate on the perceptual structure of a phonetic category," *Percept. Psychophys.* **46**, 505–512.
- Miller, J. L., Green, K. P., and Reeves, A. (1986). "Speaking rate and segments: A look at the relation between speech production and speech perception for the voicing contrast," *Phonetica* **43**, 106–115.
- Miller, J. L., Grosjean, F., and Lomanto, C. (1984). "Articulation rate and its variability in spontaneous speech: A reanalysis and some implications," *Phonetica* **41**, 215–225.
- Newman, R. S. (1997). "Individual differences and the link between speech perception and speech production," doctoral dissertation, University of New York at Buffalo.
- Newman, R. S., Clouse, S. A., and Burnham, J. L. (2001). "The perceptual consequences of within-talker variability in fricative production," *J. Acoust. Soc. Am.* **109**, 1181–1196.
- Nygaard, L. C., and Pisoni, D. B. (1998). "Talker-specific learning in speech perception," *Percept. Psychophys.* **60**, 355–376.
- Nygaard, L. C., Sommers, M. S., and Pisoni, D. B. (1994). "Speech perception as a talker-contingent process," *Psychol. Sci.* **5**, 42–46.
- Palmeri, T. J., Goldinger, S. D., and Pisoni, D. B. (1993). "Episodic encoding of voice attributes and recognition memory for spoken words," *J. Exp. Psychol. Learn. Mem. Cogn.* **19**, 309–328.
- Peterson, G. E., and Barney, H. L. (1952). "Control methods used in a study of vowels," *J. Acoust. Soc. Am.* **24**, 175–184.
- Remez, R. E., Fellowes, J. M., and Rubin, P. E. (1997). "Talker identification based on phonetic information," *J. Exp. Psychol. Hum. Percept. Perform.* **23**, 651–666.
- Remez, R. E., Rubin, P. E., Pisoni, D. B., and Carrell, T. D. (1981). "Speech perception without traditional speech cues," *Science* **212**, 947–950.
- Ryalls, J., Zipprer, A., and Baldauff, P. (1997). "A preliminary investigation of the effects of gender and race on voice onset time," *J. Speech Lang. Hear. Res.* **40**, 642–645.
- Schiavetti, N., Whitehead, R. L., Metz, D. E., and Moore, N. (1999). "Voice onset time in speech produced by inexperienced signers during simultaneous communication," *J. Commun. Disord.* **32**, 37–49.
- Summerfield, Q. (1981). "Articulatory rate and perceptual constancy in phonetic perception," *J. Exp. Psychol. Hum. Percept. Perform.* **7**, 1074–1095.
- Swartz, B. L. (1992). "Gender difference in voice onset time," *Percept. Mot. Skills* **75**, 983–992.
- Volaitis, L. E., and Miller, J. L. (1992). "Phonetic prototypes: Influence of place of articulation and speaking rate on the internal structure of voicing categories," *J. Acoust. Soc. Am.* **92**, 723–735.
- Whiteside, S. P., and Irving, C. J. (1998). "Speakers' sex differences in voice onset time: A study of isolated word production," *Percept. Mot. Skills* **86**, 651–654.

Spectral models of additive and modulation noise in speech and phonatory excitation signals

Jean Schoentgen^{a)}

*Laboratory of Experimental Phonetics, Université Libre de Bruxelles, 50 Av. F.-D. Roosevelt,
B-1050 Brussels, Belgium*

(Received 10 June 2002; revised 7 September 2002; accepted 19 September 2002)

The article presents spectral models of additive and modulation noise in speech. The purpose is to learn about the causes of noise in the spectra of normal and disordered voices and to gauge whether the spectral properties of the perturbations of the phonatory excitation signal can be inferred from the spectral properties of the speech signal. The approach to modeling consists of deducing the Fourier series of the perturbed speech, assuming that the Fourier series of the noise and of the clean monocyte-periodic excitation are known. The models explain published data, take into account the effects of supraglottal tremor, demonstrate the modulation distortion owing to vocal tract filtering, establish conditions under which noise cues of different speech signals may be compared, and predict the impossibility of inferring the spectral properties of the frequency modulating noise from the spectral properties of the frequency modulation noise (e.g., phonatory jitter and frequency tremor). The general conclusion is that only phonatory frequency modulation noise is spectrally relevant. Other types of noise in speech are either epiphenomenal, or their spectral effects are masked by the spectral effects of frequency modulation noise. © 2003 Acoustical Society of America. [DOI: 10.1121/1.1523384]

PACS numbers: 43.70.Gr, 43.70.Bk [AL]

I. INTRODUCTION

The objective of the article is to model the spectral effects of additive noise owing to turbulent airflow, as well as of modulation noise owing to perturbations of the vocal cycle amplitudes and lengths. The purpose of the modeling is to learn about the causes of noise in the spectra of normal and disordered voices and to gauge whether the spectral properties of the perturbations of the phonatory excitation signal can be inferred from the spectral properties of the speech signal.

Modulation noise and additive noise are acoustic features of the phonatory timbre. Generally speaking, acoustic primitives of the phonatory timbre may be classified as follows.

First, the acoustic source formed by the glottal vibration and pulsatile airflow must be distinguished from the acoustic source due to turbulent airflow. Glottal vibrations and pulsatile airflow generate the phonatory excitation signal and turbulent airflow generates acoustic noise (Stevens, 1998).

Second, acoustic primitives that are the outcome of noisy or voluntary perturbations of the parameters of the acoustic excitation signal are, in decreasing order of size and time scale, intonation, accentuation, declination, vibrato, tremolo, phonatory frequency and amplitude tremor, phonatory jitter and shimmy (also known as shimmer) (Schoentgen, 2001).

Third, acoustic primitives that are related to the dynamics of the vocal folds and glottis are the so-called voice types that distinguish between signals that are monocyte periodic,

multicycle periodic, quasiperiodic, or random (Behrman *et al.*, 1998).

Fourth, acoustic primitives that describe the spectral contour of the phonatory excitation are the spectral balance or spectral slope. They enable the distinction between pressed and breathy voices to be made (Van Son and Van Santen, 1997; Stevens, 1998). The spectral contour is the shape of the phonatory magnitude spectrum, disregarding harmonicity, phonatory frequency range, and overall amplitude.

The spectral models that are developed in this article are focused on noisy perturbations of clean periodic monocyclic excitation signals. The term “noise” designates an undesired or extraneous signal. Frequently, extraneous vocal noise involves a stochastic component. The model, however, enables deterministically as well as stochastically patterned perturbations to be considered.

Klingholz and Martin (1985) have been among the first to mimic vocal jitter and shimmy by a sinusoidal modulation of the instantaneous length and amplitude of a sinusoid. They have also synthesized single-formant speech cycles whose amplitudes and lengths are perturbed independently and they have estimated the spectral signal-to-noise ratio. The perturbations are Gaussian white noise. The authors have concluded that in the case of jitter, the spectral signal-to-noise ratio depends on the amplitude and frequency of the modulation. Jitter creates higher noise levels than shimmy, which has only a small effect on the noise content of speech spectra. Since shimmy is correlated with jitter, it is expected to be a redundant vocal feature. The observation that vocal jitter and shimmy are correlated is based on natural speech data, however.

Hillenbrand (1987) has published spectra of synthetic

^{a)}Electronic mail: jschoent@ulb.ac.be

speech perturbed by additive noise, amplitude-modulation noise, and frequency-modulation noise. The additive noise has been generated by the default noise source of a speech synthesizer, and the modulation noise by inserting scaled speech cycle lengths and amplitudes that have been obtained from the speech of a male speaker. The frequency and amplitude perturbations of the synthetic excitation have been larger than normal, and their spectral properties are not genuine. The spectra display the conventional signatures of modulation and additive noise, i.e., noise partials at all frequencies for the additive noise, weak sidebands for the amplitude-modulation noise, and strong sidebands and decreasing partials at the harmonic frequencies for the frequency-modulation noise. The author has concluded that strong measurement interactions exist among the three categories of synthetic noise.

Muta *et al.* (1988) have published spectra of synthetic speech that has been perturbed by additive noise, amplitude-modulation noise, and frequency-modulation noise. The synthetic speech signals have been sinusoidally amplitude- and frequency modulated at 8 Hz independently from the synthetic phonatory jitter and shimmy. The size of the modulation noise and additive noise has been larger than normal. An analysis window four speech cycles in length has been used. The authors have concluded that glottal source perturbations distort the harmonic structure and thus affect both noise measures and harmonic strength measures. Also, the harmonic structure of a voice signal shows greater distortion in higher harmonics than in lower harmonics. The modulation effects of the source perturbations increase in proportion to the order of the harmonics.

Murphy (2000) has presented a spectral description of jitter, shimmy, and additive noise in synthetically generated voice signals. The article contains a heuristic mathematical development based on a Fourier series of two cycles of a model of the glottal airflow rate, which provides a qualitative insight into the appearance of sidebands and noise partials as well as the decrease of the harmonics in the case of jittered signals. These qualitative predictions have been tested with synthetic signals that involve modulation noise and additive noise. The synthetic modulation and additive noise has been Gaussian white noise or square waves. The synthetic perturbations have been larger than normal. Synthetic noisy speech spectra have been presented but the modulation distortion owing to the vocal tract transfer function has not been discussed. The following predictions have been made. For shimmied signals the amplitudes of the harmonics are unchanged and the interharmonic partials increase with the variance of the amplitude-modulating noise. For jittered signals the amplitudes of the harmonics are reduced and the interharmonic partials increased. Additive noise does not change the average amplitudes of the harmonics of the clean signal, as long as the amplitudes of the noise partials at the same frequency are small. The interharmonic partials owing to jitter and shimmy depend on the spectral properties of the clean signal that is perturbed.

Hereafter, a model is presented in the framework of which the spectral properties of noisy phonatory and speech signals are derived analytically. The empirical results that

have been discussed above are explained. Other reasons for developing spectral models of perturbed excitation and speech signals are the following.

First, algebraic or trigonometric models have the advantages over numerical simulations of making explicit all parameters that are involved and implicitly considering all possible values of these parameters. Examples of relevant parameters are the amplitude, shape, and cyclicity of the signals and noise, the vocal tract transfer function, as well as the length of the analysis window and the analysis bandwidth.

Second, spectral cues that involve the harmonics and interharmonics are often used to describe disordered voices in a clinical framework. Disordered voices may be characterized by increasing amounts of modulation and additive noise, as well as by phonation types that are not monocyte periodic. The synthetic data that have been reviewed above suggest, however, that different acoustic primitives do not contribute equally to the spectral properties of disordered speech. Therefore, spectral modeling enables predictions to be made regarding the spectral prominence of different kinds of perturbations and, consequently, the relevance of spectral cues for the description of disordered voices.

Third, spectral cues that involve the ratio of the amplitudes of the first and second harmonic or the ratio of the amplitude of the first harmonic and the amplitude of the first formant have been used to infer the abduction quotient or the spectral tilt of the phonatory excitation (Ladefoged, Maddieson, and Jackson, 1988; Hanson, 1997). It is therefore important to understand how the amplitudes of the harmonics depend on the frequency-modulation noise of the speech signal.

Fourth, a problem that has frequently been omitted from previous studies is the modulation distortion that takes place inside the vocal tract and which creates extraneous phase and amplitude modulations of the speech signal via the amplitude and frequency modulations of the phonatory excitation signal. Modulation distortion designates a change in the modulation of the phonatory excitation signal during the transmission through the vocal tract (Panther, 1965).

Generally speaking, the frequency modulation of the phonatory excitation causes a frequency modulation and amplitude modulation of the speech signal. This means that the amplitude modulation of the excitation signal cannot be inferred from the amplitude modulation of the speech signal, which is epiphenomenal.

Similarly, the amplitude modulation of the phonatory excitation causes an amplitude modulation and phase modulation of the speech signal. However, the consequences of the phase modulation are considered to be harmless (Michaelis *et al.*, 1998). One purpose of the modeling in this article is therefore to explain the asymmetry between amplitude-modulation and frequency-modulation distortion.

Modulation distortion is studied within the framework of spectral models because sinusoids are eigenfunctions of linear filters. But, the effects of the modulation distortion concern both the spectral and temporal properties of the speech signal.

Fifth, modulation distortion by the vocal tract is but a single facet of a more general question, which is whether the spectral properties of additive or modulating noise can be

inferred from the spectral properties of a noisy excitation, and the latter from the spectral properties of noisy speech.

Sixth, physiological tremor of the articulators is common (Freund, 1987). It is therefore likely that articulatory tremor causes tremor of the vocal tract shape and, consequently, tremor of the frequencies and bandwidths of the formants and antiformants. Spectral modeling enables the tremor of the formant frequencies to be related to the tremor of the amplitude of the speech cycles.

The article is organized as follows. In Sec. II, the model is developed mathematically. The modeling approach is the following. The spectral properties of the clean excitation as well as of the perturbations are assumed to be known. The perturbations are inserted into the parameters of the clean excitation. The resulting expressions are mathematically transformed to obtain expressions that are sums of sines and cosines, i.e., the spectra of the perturbed signals. In Sec. III, the relevant properties of the perturbed excitation and speech signals are summarized. Section IV, finally, considers the consequences of what has been learned by modeling for the analysis of disordered or nonmodal voices in a clinical or laboratory framework.

Data regarding the properties of the clean and noisy excitation or speech are referred to in order to interpret modeling results. Gauffin and Sundberg (1989) have discussed the spectral properties of the clean excitation. Isshiki *et al.* (1978) and Hillman, Oesterle, and Feth (1983) have studied additive noise that is generated at the glottis. Schoentgen (2001) gives an overview of the properties of the perturbations of the phonatory frequency, and Schoentgen, Bensaid, and Bucella (2000) have reviewed acoustic cues for spectral noise.

As far as we know, few data are available concerning phonatory shimmy or phonatory amplitude tremor. Phonatory amplitude perturbations must indeed be distinguished from speech amplitude perturbations and vocal fold contact area perturbations. Data published by Horii (1982) suggest that phonatory shimmy is of the order of 0.1% of the cycle amplitude, which is ten times less than speech shimmy.

Similarly, no data are available about the shape perturbations of the phonatory cycles, as far as we know. Shape perturbations are therefore not modeled in the framework of this article. Shape perturbations are due to a nonhomogeneous amplitude modulation of the harmonics of the clean excitation, and their modeling would require a model of the relation between excitation spectrum and amplitude.

Finally, as far as we know, no data are available regarding speech tremor that is caused by physiological supraglottal tremor. However, one simulation study has been published about artificial tremor of the chest, throat, and vocal tract. This study concludes that the long-term amplitude modulation of the acoustic signal is greatest when the source of tremor is located at the chest (subglottal level) and the least when the perturbation source is at the cheek (Jiang *et al.*, 2000).

II. MODELS

A. Fourier sums of the noise and clean excitation

The purpose of the models is the explanation of the spectral properties of phonatory excitation signals and speech signals that are perturbed by modulation noise or additive noise. The spectral properties of the clean excitation and of the noise are assumed to be known. These can therefore be written in terms of their Fourier sums. In the framework of this article, Fourier sums are generic, that is, no numeric values are assigned to the Fourier coefficients.

One assumes that the clean excitation is monocycle periodic and that it can be represented by its Fourier sum on an analysis interval of finite length T that comprises an integer number M of periods. The fundamental frequency f_0 of the clean excitation is therefore equal to the following:

$$f_0 = \frac{M}{T}. \quad (1)$$

Reasons for considering finite analysis intervals are the following. First, speech data are always obtained on analysis intervals of finite length. A model parameter that represents the analysis window length is therefore useful. Second, aperiodic signals can be described by means of a Fourier sum over an analysis interval of finite length. Noise and clean signal can therefore be represented by means of a common formalism.

Generally speaking, the conditions under which finite-length bandlimited signals can be represented by their Fourier sums are mild (Duffy, 1998). When the signals are bandlimited, which they always are in practice, the number of Fourier partials is finite. The clean periodic excitation $E(t)$ and noise $e(t)$ can therefore be represented as follows. Variable t is the time coordinate, integers N and L are the number of partials that are involved in the Fourier sums of the clean excitation and noise, respectively, symbols Φ_n and φ_j are the initial phases, and symbols C_n and c_j are the Fourier amplitudes

$$E(t) = \sum_{n=1}^N C_n \sin\left(n \frac{2\pi M}{T} t + \Phi_n\right), \quad (2)$$

$$e(t) = \sum_{j=1}^L c_j \sin\left(j \frac{2\pi}{T} t + \varphi_j\right). \quad (3)$$

Expression (2) applies at all times and expression (3) only over the finite analysis interval, because the clean excitation is periodic and the noise aperiodic. For modeling purposes, Fourier sum (3) is consecutively assigned to the additive noise, amplitude-modulating noise, and frequency-modulating noise. The term “modulating noise” designates the external perturbations and the term “modulation noise” designates the spectral effects of the modulating noise in the perturbed signal.

B. Trigonometric identity

In this article, a trigonometric identity is used that concerns the sum of two cosines of unequal amplitudes A and B and unequal phases α and β (Black, 1953)

$$A \cos(\alpha) + B \cos(\beta) = A \sqrt{1 + 2x \cos(\delta) + x^2} \\ \times \cos(\alpha - \theta),$$

$$x = \frac{B}{A}, \quad \delta = \alpha - \beta, \quad (4)$$

$$\theta = \arctan \frac{x \sin(\delta)}{1 + x \cos(\delta)},$$

$$\theta = \frac{\delta}{2}, \quad \text{when } x = 1.$$

C. Additive noise

When clean excitation (2) and noise (3) are generated by two distinct acoustic sources, then noisy signal (5) is the sum of the clean signal and the noise because in the case of two weak acoustic signals superposition holds. This sum is also the Fourier sum of the noisy signal, because it involves only sums of sinusoids

$$S(t) = \sum_{n=1}^N C_n \sin\left(n \frac{2\pi M}{T} t + \phi_n\right) + \sum_{j=1}^L c_j \sin\left(j \frac{2\pi}{T} t + \varphi_j\right). \quad (5)$$

When index $j \neq nM$, the partials of the noisy excitation are identical with the partials of the noise. On the contrary, when index $j = nM$ the j th Fourier amplitude of the noisy signal lies between the sum and difference of the Fourier amplitudes of the noise and clean excitation, depending as expected on the initial phases of the Fourier partials. Fourier amplitude (6) is obtained via trigonometric identity (4).

$$\sqrt{C_j^2 + 2C_j c_j \cos(\phi_j - \varphi_j) + c_j^2}. \quad (6)$$

Expression (6) applies whenever two partials share the same Fourier frequency, whatever their cause.

D. Amplitude modulation

Instances of noisy amplitude modulation are phonatory shimmy and phonatory amplitude tremor, about which almost nothing is known. The most parsimonious assumption, therefore, is that the overall gain of the clean excitation is modulated by noise. This means that the clean excitation is multiplied by the following expression:

$$1 + \sum_{j=1}^L c_j \sin\left(j \frac{2\pi}{T} t + \varphi_j\right). \quad (7)$$

The leftmost addend is the unperturbed (unitary) gain and the rightmost addend is the noisy amplitude modulation. The multiplication of the clean excitation (2) with the noisy gain (7) yields the noisily amplitude-modulated excitation (8)

$$S(t) = \sum_{n=1}^N \left[C_n \sin\left(n \frac{2\pi M}{T} t + \phi_n\right) + \sum_{j=1}^L C_n c_j \sin\left(j \frac{2\pi}{T} t + \varphi_j\right) \sin\left(n \frac{2\pi M}{T} t + \phi_n\right) \right]. \quad (8)$$

The amplitude-modulated excitation (8) is transformed by means of elementary trigonometric identities into its spectral representation (9) involving only sums of sinusoids. The pairs of cosines whose Fourier frequencies are symmetrically positioned below and above the harmonic frequencies nM/T are known as sidebands

$$S(t) = \sum_{n=1}^N \left\{ C_n \sin\left(n \frac{2\pi M}{T} t + \phi_n\right) + \sum_{j=1}^L \frac{C_n c_j}{2} \left[\cos\left((nM - j) \frac{2\pi}{T} t + \phi_n - \varphi_j\right) - \cos\left((nM + j) \frac{2\pi}{T} t + \phi_n + \varphi_j\right) \right] \right\}. \quad (9)$$

Excitation (9) shows that when the hemiperiod number $M/2$ is larger than the noise partial number L , the sidebands of adjacent harmonics do not overlap. When, on the contrary, $M/2 < L$, the sidebands of adjacent harmonics overlap, and when $M < L$, the harmonics overlap with the sidebands of the harmonics to their left or right. In the case of overlap, the Fourier amplitudes are added according to relation (6). Otherwise, the harmonics of the noisy signal are identical to the harmonics of the clean signal.

E. Frequency modulation

Instances of noisy frequency modulation of the phonatory excitation signal are phonatory jitter and phonatory frequency tremor. The most parsimonious assumption, which agrees with the data, is that the fundamental frequency of the clean excitation is perturbed. Consequently, the frequency modulation of a harmonic is proportional to the harmonic number n . By definition, the instantaneous frequency of a harmonic is equal to the derivative with respect to time of the phase of the harmonic. For notational reasons, the modulation noise of the instantaneous frequency is written in terms of a sum of cosines. The noisily modulated instantaneous frequency of a harmonic is then equal to the following:

$$\dot{\theta} = n \left[\frac{2\pi M}{T} + 2\pi \sum_{j=1}^L c_j \cos\left(j \frac{2\pi}{T} t + \varphi_j\right) \right]. \quad (10)$$

The phase is obtained by integrating the instantaneous frequency (10) before it is inserted into the phase of the harmonics of the clean signal to obtain the frequency-modulated signal (11)

$$S(t) = \sum_{n=1}^N C_n \sin \left[n \frac{2\pi M}{T} t + \phi_n + n \sum_{j=1}^L c_j \frac{T}{j} \times \sin\left(j \frac{2\pi}{T} t + \varphi_j\right) \right]. \quad (11)$$

The frequency-modulated excitation (11) is rewritten by assigning the modulation index I and phase γ to the following expressions (12). The product of the modulation index with the derivative with respect to time of the matching phase is used at a later stage

$$I_{j,n} = nc_j \frac{T}{j},$$

$$\gamma_j = j \frac{2\pi}{T} t + \varphi_j, \quad (12)$$

$$I_{j,n} \dot{\gamma}_j = 2\pi n c_j.$$

The perturbed excitation is then compactly rewritten as follows:

$$S(t) = \sum_{n=1}^N C_n \sin \left[n \frac{2\pi M}{T} t + \phi_n + \sum_{j=1}^L I_{j,n} \sin(\gamma_j) \right]. \quad (13)$$

The Fourier series of a sinusoid that is frequency modulated by a nonsinusoidal modulating signal has been discovered more than once (Black, 1953). Fourier sum (14) is obtained by inserting Black's result into the frequency-modulated excitation (13)

$$S(t) = \sum_{n=1}^N C_n \sum_{k_1=-\infty}^{\infty} \cdots \sum_{k_L=-\infty}^{\infty} J_{k_1}(I_{1,n}) \cdots J_{k_L}(I_{L,n}) \times \sin \left(n \frac{2\pi M}{T} t + \phi_n + k_1 \gamma_1 + \cdots + k_L \gamma_L \right). \quad (14)$$

Symbols $J(\cdot)$ are Bessel functions of the first kind whose relevant properties are the following.

First, the zero-order Bessel function has a shape that is similar to a dampened cosinusoid; $J_0(0)=1$ and the first zero crossing occurs when the modulation index is approximately equal to 12/5.

Second, Bessel functions whose orders are strictly positive evolve similarly to dampened sinusoids: the higher the order of the Bessel function the slower the initial increase and the lower the first maximum.

Third, a Bessel function whose integer order is strictly negative is equal to the corresponding Bessel function whose order is positive, multiplied by -1 when the order is odd.

F. Filtered clean excitation

Generally speaking, the spectrum of the acoustic excitation signal cannot be observed directly. The spectra that are observed are those of the speech signal that is obtained by filtering the acoustic excitation by the vocal tract transfer function (Stevens, 1998).

Sine and cosine functions are the eigenfunctions of linear transfer functions. That is, when a sinusoid is used as the input of a linear filter H , a sinusoid is output that has the same frequency, but whose amplitude and initial phase are different. Consequently, the filtered clean excitation (2) is equal to the following. Symbol α is the phase shift owing to the filtering and H the transfer function amplitude

$$S_f = \sum_{n=1}^N C_n H(nf_0) \sin[2\pi n f_0 t + \phi_n + \alpha(nf_0)]. \quad (15)$$

G. Filtered added-noise excitation

The filtered excitation S_p perturbed by additive noise is obtained by applying filter H to the added-noise excitation (5)

$$S_p = S_f + \sum_{j=1}^L c_j H \left(j \frac{2\pi}{T} \right) \sin \left[j \frac{2\pi}{T} t + \varphi_j + \alpha \left(j \frac{2\pi}{T} \right) \right]. \quad (16)$$

As expected, the filtered added-noise excitation is the sum of the filtered clean excitation and the filtered additive noise.

H. Filtered amplitude-modulated excitation

Generally speaking, a vocal tract transfer function is a smooth curve that connects resonance peaks and antiresonance troughs, which are few. This means that in the vicinity of most of the harmonics the transfer function evolves linearly. Therefore, when the modulating noise causes sidebands that tightly cluster around the modulated harmonics, the effects of the filtering can be understood by expanding the vocal tract transfer function in the vicinity of the harmonics. Symbol n is the harmonic number, ω the angular frequency, and f the frequency variable

$$H(\omega) \approx H_n + \left[\frac{dH}{d\omega} \right]_n (2\pi f - 2\pi n f_0) = H_n + h_n (2\pi f - 2\pi n f_0). \quad (17)$$

The filtered amplitude-modulated excitation S_p is obtained by applying filter (17) to the amplitude-modulated excitation (9)

$$S_p(t) = S_f + \sum_{n=1}^N \sum_{j=1}^L \frac{C_n c_j}{2} \left[\left(H_n - h_n j \frac{2\pi}{T} \right) \cos \left((nM - j) \times \frac{2\pi}{T} t + \phi_n - \varphi_j + \alpha_{n,-j} \right) - \left(H_n + h_n j \frac{2\pi}{T} \right) \times \cos \left((nM + j) \frac{2\pi}{T} t + \phi_n + \varphi_j + \alpha_{n,j} \right) \right]. \quad (18)$$

As expected, filtering causes a change in the sizes of the sidebands and harmonics. In particular, the amplitudes of matching sidebands that are equal before filtering are unequal after filtering. The changes are proportional to the Fourier frequencies of the modulating noise. This is expected because high-frequency partials of the noise cause sidebands that are further removed from the harmonics.

The effects of filtering can be qualitatively understood by applying trigonometric identity (4) to the filtered output (18)

$$S(t) = S_f + \sum_{n=1}^N \sum_{j=1}^L \frac{C_n c_j}{2} \left\{ \left(H_n + h_n j \frac{2\pi}{T} \right) \times \sqrt{1 + x \cos(\delta) + x^2} \cos \left[(nM + j) \frac{2\pi}{T} t + \phi_n + \varphi_j + \alpha_{n,j} - \theta \right] \right\},$$

$$x = - \frac{H_n - h_n j \frac{2\pi}{T}}{H_n + h_n j \frac{2\pi}{T}}, \quad (19)$$

$$\delta = j \frac{4\pi}{T} t + 2\varphi_j + \alpha_{n,j} - \alpha_{n,-j},$$

$$\theta = \arctan \frac{x \sin(\delta)}{1 + x \cos(\delta)}.$$

The previous relations show that the filtered amplitude-modulated excitation is a signal that is amplitude modulated via the term $\cos(\delta)$ in the argument of the square root, and phase modulated via the angle θ in the argument of the cosine. Phase-shift θ is a phase modulation when its derivative with respect to time is not a constant. The Taylor expansion of the derivative with reference to time of the phase shift and its primitive (20) establishes that the derivative is not a constant when ratio x is different from unity, i.e., when the vocal tract transfer function is not flat

$$\begin{aligned} \dot{\theta} &= \frac{xj \frac{4\pi}{T}}{(1+x^2) + (1-x^2)\cos(\delta)} \\ &\approx j \frac{2\pi}{T} + j \frac{2\pi}{T} \cos(\delta)(x-1), \\ \theta &\approx j \frac{2\pi}{T} t + \frac{1}{2}(x-1)\sin(\delta). \end{aligned} \quad (20)$$

However, as long as ratio x is nearly equal to 1, the phase modulation is spectrally similar to an amplitude modulation (Oppenheim, Willsky, and Young, 1983). Indeed, the following expression is obtained by inserting phase (20) into the filtered signal (19) and taking into account conventional trigonometric identities, assuming that $\sin(z) \approx z$ and $\cos(z) \approx 1$ when z is small:

$$\begin{aligned} S_p(t) &= S_f + \sum_{n=1}^N \sum_{j=1}^L \frac{C_n c_j}{2} \left(H_n + h_n j \frac{2\pi}{T} \right) \\ &\quad \times \sqrt{1 + x \cos(\delta) + x^2} \left[\cos \left(nM \frac{2\pi}{T} t \right. \right. \\ &\quad \left. \left. + \phi_n + \varphi_j + \alpha_{n,j} \right) + \frac{1}{2}(x-1)\sin(\delta) \right. \\ &\quad \left. \times \sin \left(nM \frac{2\pi}{T} t + \phi_n + \varphi_j + \alpha_{n,j} \right) \right]. \end{aligned} \quad (21)$$

In relation (21) the weak phase modulation has been turned into an amplitude modulation of the sidebands.

I. Filtered frequency-modulated excitation

The filtered frequency-modulated excitation S_p is obtained by applying filter (17) to the frequency-modulated excitation (14). The frequency variable f in filter (17) takes on the value of the instantaneous frequency of the frequency-modulated sinusoid

$$\begin{aligned} S_p(t) &= \sum_{n=1}^N C_n \sum_{k_1=-\infty}^{\infty} \sum_{k_2=-\infty}^{\infty} \cdots \sum_{k_L=-\infty}^{\infty} J_{k_1}(I_{1,n}) \\ &\quad \times J_{k_2}(I_{2,n}) \cdots J_{k_L}(I_{L,n}) [H_n + h_n(k_1 \dot{\gamma}_1 + \cdots + k_L \dot{\gamma}_L)] \\ &\quad \times \sin \left(n \frac{2\pi M}{T} t + \phi_n + k_1 \gamma_1 + \cdots + k_L \gamma_L + \alpha_{n,k_1 \cdots k_L} \right). \end{aligned} \quad (22)$$

Fourier sum (22) suggests that filtering causes modulation distortion by changing the amplitudes of matching sidebands unequally. The relevant term is the weighted sum of the instantaneous frequencies of the noise partials. This sum is different for matching sidebands, because the weights k of the instantaneous frequencies to the left and right of each harmonic are negative and positive respectively.

Fourier sum (22) provides little intuitive insight into the effects of filtering. A qualitative understanding can be obtained, of the creation of extraneous amplitude-modulation noise by means of frequency-modulation noise, by combining the frequency-modulated excitation (13) with the filter (17). Relation (23) so obtained is an approximation only because the functions in the Fourier sum are not pure sine functions but frequency-modulated sine functions, which are not eigenfunctions of linear filters. Still, one may assume that the approximation is valid when the modulation is slow. This means that the typical modulating period must be much longer than the effective length of the impulse response of the vocal tract filter. Inspecting vowels shows that the effective length of the impulse response is two glottal cycles at most, whereas the typical tremor period for normophonic speakers is 1/3 s (Schoentgen, 2002)

$$\begin{aligned} S_p(t) &\approx \sum_{n=1}^N C_n \left[H_n + h_n \sum_{j=1}^L I_{j,n} \dot{\gamma}_j \cos(\gamma_j) \right] \sin \left[2\pi n f_0 t \right. \\ &\quad \left. + \phi_n + \sum_{j=1}^L I_{j,n} \sin(\gamma_j) + \alpha_{n,j} \right]. \end{aligned} \quad (23)$$

Relation (23) suggests that filtering turns a frequency-modulated input into a frequency-modulated and amplitude-modulated output.

J. Tremor of the vocal tract area function

Tremor of the vocal tract walls causes small changes of the shape of the vocal tract area function. If the rhythm of these changes is slow compared to the phonatory frequency, the area function tremor can be modeled as a modulation of the vocal tract transfer function (Jospa, 1983). This postulate is satisfied by typical tremor frequencies that are contained in an interval from 1 to 15 Hz (Titze, 1995).

A resonance filter whose frequency is time variable can be expanded by means of its Taylor series when the perturbation $\Delta\omega_0$ of the resonance frequency is weak

$$\begin{aligned} H(\omega, \omega_0) &\approx H_{n,\omega_0} + h_{n,\omega_0}(\omega - 2\pi n f_0) + g_{n,\omega_0} \Delta\omega_0, \\ \alpha(\omega, \omega_0) &\approx \alpha_{\omega_0}(\omega) + c_{\omega_0} \Delta\omega_0. \end{aligned} \quad (24)$$

It is easy to check by means of the amplitude and phase characteristics (25) of a resonance filter that constants h , g , and c are bounded when the bandwidth of the filter is finite (Tempelaars, 1996). Symbol $\omega = 2\pi f$ is the angular frequency variable, ω_0 the resonance frequency of the undamped filter, ν the damping constant, and G the filter gain

$$H(\omega, \omega_0) = \frac{C}{\sqrt{\nu^2 \omega^2 + (\omega_0^2 - \omega^2)^2}},$$

$$\alpha(\omega, \omega_0) = -\arctan \frac{\nu \omega}{\omega_0^2 - \omega^2}. \quad (25)$$

Relations (24) show that a resonance filter with frequency tremor $\Delta\omega_0$ causes an amplitude modulation and a phase modulation of the filtered excitation. But, because the phase modulation is weak, it is spectrally similar to an amplitude modulation. Indeed, the following relations are obtained by filtering the clean excitation (2) by the time-variable filter (24), taking into account elementary trigonometric identities, and omitting all terms that are products of quantities that are assumed to be small

$$S_p(t) = \sum_{n=1}^N C_n(H_{n,\omega_0} + h_{n,\omega_0} c_{\omega_0} \Delta\omega_0 + g_{n,\omega_0} \Delta\omega_0) \times \sin(2\pi n f_0 t + \phi_n + \alpha_{\omega_0} + c_{\omega_0} \Delta\omega_0),$$

$$S_p(t) \approx \sum_{n=1}^N C_n(H_{n,\omega_0} + h_{n,\omega_0} c_{\omega_0} \Delta\omega_0 + g_{n,\omega_0} \Delta\omega_0) \times \sin(2\pi n f_0 t + \phi_n + \alpha_{\omega_0})$$

$$+ \sum_{n=1}^N C_n(H_{n,\omega_0} c_{\omega_0} \Delta\omega_0) \times \cos(2\pi n f_0 t + \phi_n + \alpha_{\omega_0}). \quad (26)$$

The previous relations show that the resonance frequency perturbation and its rate modulate the amplitude of the output signal. None of the terms involves a product with the harmonic number.

III. RESULTS

A. Additive noise

When the additive noise (3) is feeble compared to the clean excitation (2), the spectrum of the noisy excitation (5) is formed by the harmonics of the clean signal between which the weak partials of the noise are inserted. The result is a spectrum in which the relative contributions of the noise and the excitation are preserved.

B. Amplitude-modulation noise

Each partial of the modulating noise gives rise to a pair of matching side partials that are positioned symmetrically to the left and right of each harmonic. This means that the total number of partials is twice the number of noise partials multiplied by the number of harmonics. This number is reduced when some sidebands and harmonics share the same Fourier

frequency. Relation (6) shows that the overlap between harmonics and sidebands has negligible consequences for the harmonics as long as the amplitudes of the noise partials are small.

The amplitudes of the sidebands are proportional to the amplitudes of the partials and harmonics. The spectrum (19) of an amplitude-modulated excitation is therefore formed by the harmonics of the clean excitation and by the sidebands whose amplitudes are feeble as long as phonatory shimmy and amplitude tremor are weak.

C. Frequency modulation noise

When the excitation is frequency modulated, a distinction must be made between partials that are positioned at the harmonic frequencies of the clean excitation and sidebands that are positioned in between. The Fourier sum (14) shows that the amplitude of a partial that is positioned at a harmonic frequency involves the product of several zero-order Bessel functions, one for each partial of the frequency-modulating noise.

The value of a zero-order Bessel function decreases with the modulation index. The modulation index (12) increases with the harmonic number and the amplitude of the noise partial, and decreases with the frequency of the noise partial. This means that even small frequency perturbations have large spectral effects owing to the dependence of the modulation index on the harmonic number. That is, for a given modulating noise, the amplitudes of the “harmonic” partials of the modulated signal decrease with the harmonic number. The harmonic partials therefore become masked by their own sidebands when the harmonic number is large.

Fourier sum (14) also shows that the size of each sideband is a function of the product of several non-zero-order Bessel functions, one for each partial of the frequency-modulating noise. The orders of the Bessel functions are not bounded and the values of the Bessel functions depend on the modulation index.

For an isolated noise partial, a rule of thumb gives the effective bandwidth of the sidebands around each harmonic as twice the value of the product (12) of the modulation index and modulating frequency (Oppenheim, Willsky, and Young, 1983). This means that the bandwidth of the sidebands broadens with the number of the harmonic and the size of the modulating noise. High-frequency interharmonic intervals are therefore progressively filled in with increasingly spread sidebands.

To sum up, the increase of the modulation index with the harmonic number explains the increasing size and spread of the sidebands and the decreasing size of the harmonic partials. This is a property of the frequency modulation, which boosts the noise via the harmonic number. It is not a property of the modulating noise *per se*. Modulation index (12) indeed predicts that high-frequency partials of the modulating noise contribute less to the sidebands of the modulated harmonics than low-frequency partials. Examples of perturbations that are characterized by low-frequency partials are nonflat intonation, declination, and tremor.

D. Filtered added-noise excitation

Filtering by the vocal tract transfer function is a linear operation. Therefore, the spectrum of the filtered output (16) is equal to the sum of the spectra of the filtered noise and filtered clean excitation (15).

E. Filtered amplitude-modulation noise

Predictably, the effect of the filtering is to change the size of the sidebands and harmonics. A distinction must be made, however, between equal and unequal changes of matching sidebands that are symmetrically positioned to the left and right of the modulated harmonics. Hereafter, the resultant creation of a phase modulation is examined.

Modulation distortion is the result of the unequal filtering of matching sidebands. In filtered signal (19) the effects of the filtering are evidenced by the ratio of the amplitudes of matching filtered sidebands and by the phase shift of the sidebands. The sidebands are phase modulated when the rate of the phase shift varies in time. Relations (20) show that this happens when the amplitudes of the filtered matching sidebands are unequal.

The phase modulation remains weak, however, as long as the filtered matching sideband amplitudes are not too different. This is the case when the sidebands cluster tightly around the harmonics or when the slope of the vocal tract transfer function is shallow. Then, the phase modulation is spectrally similar to an amplitude modulation.

Even if the phase modulation was not small, the spectral effects of the phase modulation would still be expected to be small because the phase modulation involves the sidebands only, which are small and because the modulation does not involve the harmonic number.

F. Filtered frequency-modulated excitation

Predictably, filtering changes the sizes of the sidebands and harmonics. Again, a distinction must be made between equal and unequal changes of matching sidebands. Filter output (22) shows that the vocal tract transfer function changes the amplitudes of matching sidebands unequally.

The frequency modulation therefore causes amplitude modulation. The modulation distortion may be intuitively understood in the framework of approximate expression (23). This expression suggests that the amplitude modulation owing to filtering is proportional to the steepness of the slope of the vocal tract transfer function, the amplitudes of the modulating noise partials, and the harmonic number.

G. Amplitude modulation noise owing to supraglottal tremor

When a vocal tract filter that is modulated owing to tremor filters the clean excitation, the filter output (26) is amplitude modulated. The conditions are that the modulation depth of the formant frequencies is weak and the modulating rate small compared to the phonatory frequency.

The amplitude modulation owing to supraglottal tremor is proportional to the size of the harmonics, the size and rate

of the tremor, as well as the vocal tract transfer function and the steepness of its slope, but does not involve the harmonic number.

IV. DISCUSSION

A. Former studies

Additive noise model (5), amplitude-modulation noise model (9), and frequency-modulation noise model (14) explain the simulation data that have been published by Klingholz and Martin (1985), Hillenbrand (1987), Muta *et al.* (1988), and Murphy (2000). Hereafter, the model-predicted consequences are discussed for the analysis of disordered or nonmodal voices, taking into account that perturbations owing to several noise sources coexist in natural data and that the perturbations of speech and excitation signals are qualitatively different.

B. Analysis bandwidth

Fourier sum (14) shows that the prominence of the sidebands owing to frequency modulation depends on the bandwidth of the clean signal via the harmonic number, which is contained in the modulation index. The cue values for spectral noise therefore depend on the bandwidths of the analyzed speech signals, because noise cues are based on the relative prominence of the sidebands. Consequently, noise cues can only be compared meaningfully for different speech signals when the analysis bandwidths are the same.

C. Analysis window length

The values of cues for spectral noise are also expected to depend on the analysis window length. The explanation for the link between modulation noise and window length is the dependency of the modulation index on the frequencies of the noise partials.

Indeed, nonflat intonation, phonatory frequency declination or drift are common in naive normophonic and dysphonic speakers who sustain vowels. For increasing window lengths any slow variation of the phonatory frequency is expected to create increasingly larger low-frequency partials in the spectrum of the modulating noise. Modulation index (12) shows that low-frequency partials contribute more than high-frequency partials. This means that the modulation index increases with the analysis window length, owing to the inability of speakers to sustain speech sounds whose phonatory frequency contours are flat. But, for reasons that are explained later, modulation noise due to nonflat intonation cannot be distinguished from modulation noise due to genuine jitter and tremor. This suggests that data concerning spectral noise cues can only be compared meaningfully for different speech signals when the cues are obtained on analysis intervals of the same length.

D. Frequency modulation

In the case of frequency modulation, the prominence of the sidebands and the deemphasis of the harmonics depend on the modulation index. The modulation index evolves proportionally to the harmonic number, which therefore ampli-

fies the effects of the modulating noise. This amplification is typical of frequency-modulation noise and is not a property of amplitude-modulation, phase-modulation, or additive noise. This means that when different types of noise coexist that are of the same order, the spectral effects of frequency-modulating noise exceed the spectral effects of the other types of noise beyond a critical harmonic number. This prediction agrees with what can be observed in any speech spectrum or spectrogram whenever the spectral analysis window is longer than a few speech cycles.

Also, the cutback of the amplitudes of the harmonics due to frequency modulation biases the ratios of the harmonic amplitudes, which have been used as cues of the spectral tilt of the phonatory excitation and of the abduction quotient of the vocal folds. The rule is: the greater the distance between the harmonics the greater the bias.

E. Modulation distortion

It is unlikely that the amplitude perturbation of the phonatory excitation signal can be inferred from the amplitude perturbation of the speech signal. The reasons are the following, in increasing order of importance.

First, amplitude modulation of the phonatory excitation is converted by vocal tract filtering into amplitude modulation of the speech signal and phase modulation of the sidebands of the speech signal. Because the phase modulation is weak, it is spectrally similar to an extraneous speech cycle amplitude modulation.

Second, physiological tremor of the articulators causes tremor of the vocal tract area function and therefore a frequency modulation of the resonance frequencies and bandwidths. Transfer function (24) and filter output (26) suggest that resonance frequency tremor causes speech cycle amplitude and phase tremor. When the physiological tremor depth and rate are weak, the phase modulation is spectrally similar to an extraneous speech cycle amplitude tremor.

Third, approximate relation (24) suggests that frequency modulation of the phonatory excitation causes amplitude modulation of the speech signal, owing to modulation distortion via the vocal tract transfer function. The size of the extraneous amplitude modulation depends on the amplitude of the harmonics, the amplitude of the noise partials, the steepness of the slope of the vocal tract transfer function, and the harmonic number.

The second and third mechanisms cause speech cycle amplitude perturbations that are extraneous. In speech spectra, the effects owing to modulation distortion are expected to exceed the effects of other extrinsic or intrinsic amplitude modulation mechanisms. The reason is the amplification via the harmonic number of the filtering-induced amplitude-modulation noise. The conclusions are that perturbations of the speech cycle amplitude are epiphenomenal and that they are caused by the frequency perturbation of the phonatory excitation. Michaelis *et al.* (1998) have confirmed these conclusions by simulations. The conclusions also agree with the observations that phonatory shimmy is roughly ten times smaller than speech shimmy (Horii, 1982), and that speech cycle amplitude modulation owing to artificial tremor of the

chest and neck exceed the speech cycle amplitude modulation owing to artificial tremor of the cheek (Jiang *et al.*, 2000).

The conclusions are different concerning perturbations of the speech cycle lengths. Generally speaking, perturbations of the speech cycle lengths agree with the perturbations of the phonatory cycle lengths (Michaelis *et al.*, 1998). The explanation appears to be the lack of an extraneous frequency modulation and the weakness of the extraneous phase modulations due to the vocal tract. The relevant mechanisms are those that are labeled first and second in the paragraphs above.

Modeling results therefore appear to confirm the co-gency of the common practice that identifies the speech cycle lengths with the excitation cycle lengths. The results also agree with what has been found by simulation, as well as by experiments in which cycle lengths obtained via the speech signal have been compared to cycle lengths obtained via the electroglottogram (De Guchteneere, 1996; Michaelis *et al.*, 1998).

F. Invertibility

The question whether the perturbations of the phonatory cycle amplitudes can be inferred from the perturbations of the speech cycle amplitudes has been answered negatively. The same question regarding the perturbations of the cycle lengths has been answered positively. The question whether the spectral properties of the perturbations *per se* can be inferred from the spectral properties of the phonatory excitation is examined next. The discussion concentrates on frequency modulation noise, disregarding amplitude-modulation noise, additive noise, and filtering.

Frequency-modulated signal (14) shows that the magnitudes of its sidebands depend on the modulation index via a product of Bessel functions. Each modulation index involves the harmonic number, as well as the amplitude and frequency of a partial. Each noise partial theoretically involves infinitely many side partials that overlap. Because of the overlap and the product of Bessel functions, the mathematical relation between the noise partials and the sidebands cannot be inverted, and the spectral properties of the modulating noise cannot be inferred from the spectral properties of the modulation noise.

G. Vocal fold dynamics

The assumptions underlying the models that have been developed are that the clean excitation is monocyte periodic. The modulating and additive noise are therefore understood as external perturbations of the cycle amplitude, cycle shape, cycle phase, or cycle length of the phonatory excitation.

Other dynamic regimes are possible, however. That is, the phonatory excitation signal may be multicycle periodic, quasiperiodic, or random. These qualitatively different excitation signals are due to qualitatively different vibratory regimes of the vocal folds, and they are therefore not the consequence of external perturbations. Mathematically speaking, some forms of multicycle periodicity or randomness of the

phonatory excitation signal can, however, be mimicked by macroperturbations of the constant frequency of a clean monocyclic phonatory signal. Consequently, the spectral effects of some phonatory regimes that are not monocycle periodic may be qualitatively similar to the spectral effects that have been discussed above. However, because the mimicked perturbations are large, the corresponding spectral effects are also large compared to the spectral effects of genuine external microperturbations. Some of the approximations that have been made above and which are based on the assumption that microperturbations are small, may therefore not be valid for clean excitation signals that are not monocycle periodic.

V. CONCLUSION

The general conclusion is that only noise arising from the modulation of the phonatory frequency seems to be spectrally relevant. Other types of noise in speech, e.g., amplitude modulation noise, phase modulation noise, and additive noise, appear to be either masked by the spectral effects of the frequency modulation noise, or epiphenomenal. The models explain real and simulated data and predict the following spectral or temporal properties for additive and modulation noise in speech.

- (a) The spectral noise of the speech signal is dominated by the modulation noise due to perturbations of the phonatory frequency.
- (b) The spectral properties of the frequency-modulating noise cannot be inferred from the spectral properties of the frequency-modulation noise.
- (c) Tremor of the articulators causes frequency modulation of the formant frequencies and bandwidths, which causes an amplitude modulation of the speech signal.
- (d) The intrinsic amplitude perturbations of the phonatory excitation are masked by amplitude perturbations due to modulation distortion and supraglottal tremor.
- (e) The phonatory cycle-length perturbations agree with the speech cycle-length perturbations.
- (f) Values for spectral noise cues may only be compared for speech signals that have the same bandwidth and that are analyzed over analysis intervals that have the same length.

ACKNOWLEDGMENTS

This work has been supported by the National Fund for Scientific Research, Belgium, and has been carried out in the framework of an *Action de Recherche Concertée* (98-02; 226), *Communauté Française de Belgique*.

Behrman, A., Agresti, C., Blumstein, E., and Lee, N. (1998). "Microphone and electroglottographic data from dysphonic patients: type 1, 2 and 3 signals," *J. Voice* **12**, 249–260.

- Black, H. S. (1953). *Modulation Theory* (Van Nostrand, New York), pp. 181–204.
- De Guchteneere, R. (1996). "Mesure et analyse chronologique des fluctuations de la durée des cycles glottiques," ("Measurement and time series analysis of the fluctuations of the glottal cycle lengths"), unpublished Doctoral thesis, Université Libre de Bruxelles, Brussels, Belgium.
- Duffy, D. G. (1998). *Advanced Engineering Mathematics* (CRC Press, Boca Raton), pp. 51–111.
- Freund, H.-J. (1987). "Central rhythmicities in motor control and its perturbances," in *Temporal Disorder in Human Oscillatory Systems*, edited by L. Rensing, U. an der Heiden, and M. C. Mackey (Springer, Berlin), pp. 79–82.
- Gauffin, J., and Sundberg, J. (1989). "Spectral correlates of glottal voice source waveform characteristics," *J. Speech Hear. Res.* **32**, 556–565.
- Hanson, H. H. (1997). "Glottal characteristics of female speakers: Acoustic correlates," *J. Acoust. Soc. Am.* **101**, 466–481.
- Hillenbrand, J. (1987). "A methodological study of perturbation and additive noise in synthetically generated voice signals," *J. Speech Hear. Res.* **30**, 448–461.
- Hillman, R., Oesterle, E., and Feth, L. (1983). "Characteristics of the glottal turbulent noise source," *J. Acoust. Soc. Am.* **74**, 691–694.
- Horii, Y. (1982). "Jitter and shimmer differences among sustained vowel phonations," *J. Speech Hear. Res.* **25**, 12–14.
- Isshiki, N., Kitajima, K., Kojima, H., and Harita, Y. (1978). "Turbulent noise in dysphonia," *Folia Phoniatr.* **30**, 214–224.
- Jiang, J., Lin, E., Wu, J., Gener, C., and Hanson, D. (2000). "Effects of simulated source of tremor on acoustic and airflow voice measures," *J. Voice* **14**, 47–57.
- Jospa, P. (1983). "Theory of evolving normal modes and the vocal tract," *Acustica* **52**, 86–94.
- Klingholtz, F., and Martin, F. (1985). "Quantitative spectral evaluation of shimmer and jitter," *J. Speech Hear. Res.* **28**, 169–174.
- Ladefoged, P., Maddieson, I., and Jackson, M. (1988). "Investigating phonation types in different languages," in *Vocal Physiology: Voice Production, Mechanisms and Functions*, edited by O. Fujimura (Raven, New York), pp. 297–317.
- Michaelis, D., Fröhlich, M., Strube, H. W., Kruse, E., Story, B., and Titze, I. (1998). "Some simulations concerning jitter and shimmer measurement," in *Proceedings of the 3rd International Workshop Advances in Quantitative Laryngoscopy, Voice and Speech Research* (Aachen), pp. 71–80.
- Murphy, P. (2000). "Spectral characterization of jitter, shimmer, and additive noise in synthetically generated voice signals," *J. Acoust. Soc. Am.* **107**, 978–988.
- Muta, H., Baer, T., Wagatsuma, K., Muraoka, T., and Fukuda, H. (1988). "A pitch-synchronous analysis of hoarseness in running speech," *J. Acoust. Soc. Am.* **84**, 1292–1301.
- Oppenheim, A. V., Willsky, A. S., and Young, I. T. (1983). *Signals and Systems* (Prentice Hall, London), pp. 481–485.
- Panther, Ph. F. (1965). *Modulation, Noise, and Spectral Analysis* (McGraw-Hill, New York), pp. 273–300.
- Schoentgen, J. (2002). "Modulation frequency and modulation level owing to vocal microtremor," *J. Acoust. Soc. Am.* **112**, 690–700.
- Schoentgen, J. (2001). "Stochastic models of jitter," *J. Acoust. Soc. Am.* **109**, 1631–1650.
- Schoentgen, J., Bensaid, M., and Bucella, F. (2000). "Multivariate statistical analysis of flat vowel spectra with a view to characterizing dysphonic voices," *J. Speech Lang. Hear. Res.* **43**, 1493–1508.
- Stevens, K. N. (1998). *Acoustic Phonetics* (MIT Press, Cambridge).
- Tempelaars, S. (1996). *Signal Processing, Speech and Music* (Swets & Zeitlinger, Lisse), pp. 61–96.
- Titze, I. R. (1995). "Definitions and nomenclature related to voice quality," in *Vocal Fold Physiology*, edited by O. Fujimura and M. Hirano (Singular, San Diego), pp. 335–342.
- Van Son, R., and Van Santen, J. (1997). "Word-level prosodical marking of consonant duration and spectral balance," *Proc. Inst. Phon. Sci., Univ. Amsterdam* **21**, pp. 21–36.

Unfolding of phonetic information over time: A database of Dutch diphone perception

Roel Smits^{a)}

Max Planck Institute for Psycholinguistics, Postbus 310, 6500 AH Nijmegen, The Netherlands

Natasha Warner

Max Planck Institute for Psycholinguistics, Nijmegen, The Netherlands and Department of Linguistics, University of Arizona, Tucson, Arizona

James M. McQueen and Anne Cutler

Max Planck Institute for Psycholinguistics, Nijmegen, The Netherlands

(Received 19 December 2001; accepted for publication 3 October 2002)

We present the results of a large-scale study on speech perception, assessing the number and type of perceptual hypotheses which listeners entertain about possible phoneme sequences in their language. Dutch listeners were asked to identify gated fragments of all 1179 diphones of Dutch, providing a total of 488 520 phoneme categorizations. The results manifest orderly uptake of acoustic information in the signal. Differences across phonemes in the rate at which fully correct recognition was achieved arose as a result of whether or not potential confusions could occur with other phonemes of the language (long with short vowels, affricates with their initial components, etc.). These data can be used to improve models of how acoustic-phonetic information is mapped onto the mental lexicon during speech comprehension. © 2003 Acoustical Society of America. [DOI: 10.1121/1.1525287]

PACS numbers: 43.71.Es [KRK]

I. INTRODUCTION

We describe a database of phonetic perception in Dutch, in which 18 listeners judged the first and the second phoneme in gated fragments of all possible Dutch diphones, providing 27 140 identification responses per listener. This database constitutes the largest source of data that is currently available on phonetic perception in Dutch or any other language.

We undertook the project with the aim of motivating a more realistic and fine-grained representation of speech input in computational models of human spoken-language processing such as TRACE (McClelland and Elman, 1986) and Shortlist (Norris, 1994). To this end we wished to determine the accuracy with which human listeners can evaluate acoustic information as speech input unfolds over time, and to compile this information for the entire phoneme inventory of a language, in all potential left and right phonetic contexts. Although phoneme confusion matrices have in the past been obtained from speech in noise (e.g., Miller and Nicely, 1955) as well as from gated signals (e.g., Smits, 2000), we chose the latter method for two reasons. First, we were primarily concerned to examine the detailed temporal resolution of speech perception, and gating easily permits any desired temporal resolution. Second, our interest is in speech perception under general listening conditions. Adding noise to a speech signal creates difficult listening conditions, and moreover differentially affects speech sound categories such as consonants versus vowels.

Our choice of gating does not imply any claim that this task directly reflects online activation of phonemes in speech perception. It is clear that to perform the task, listeners engage a decision process which presumably has no part in normal speech perception (Grosjean, 1996). This decision mechanism will use additional processing time and may incorporate additional information (e.g., phoneme transition statistics) not present in the acoustic stimulus. We believe, however, that gating offers the currently best available window into listeners' resolution of ambiguity as speech signals unfold.

Our materials consisted of a total of 2294 sequences (1179 diphone sequences, of which most were recorded in multiple stress conditions to enable us also to assess effects of stress on acoustic information in phoneme realizations). Each listener heard six gates of each sequence, based on six gating points, three in each sound of the diphone. The shortest gate included only the first third of the first sound; each subsequent gate included another sixth of the entire diphone. The entire stimulus set (all gates from all diphone sequences) was presented to each listener in a different pseudo-random order.

II. METHOD

A. Materials

1. Choice of diphones

We first compiled a list of all possible diphones of the Dutch language. For this purpose, we considered the phonemic inventory of Dutch to be as in Tables I and II.

^{a)}Electronic mail: roel.smits@mpi.nl

TABLE I. The 16 Dutch vowels used in the experiment.^a

	Front unrounded			Front rounded			Central	Back		
	Diphthong	Long	Short	Diphthong	Long	Short		Diphthong	Long	Short
High		i			y				u	
Mid		e	ɪ, ɛ		œ	ʏ	ə		o	ɔ
Low									a	ɑ
	ɛi			œy				au		

^aCompared to Booij (1995), we have simplified the vowel system slightly by combining upper and lower mid vowels into a single height.

Decisions as to what constitutes a single phoneme versus a sequence of two phonemes were based on CELEX, an electronic database containing lexical data for English, Dutch, and German (Baayen *et al.*, 1993). We did not, however, include all phonemes and diphones in CELEX (see Appendix A for explanation of exceptions). We constructed a list of diphones consisting of all possible combinations of any two of these phonemes. Appendix B lists the selection rules we applied. Appendix C lists the 2294 diphones included in the experiment, and reasons for exclusion of missing diphones.

2. Recording

Each diphone in Appendix C was placed in a nonsense environment which, with the diphone, formed a phonotactically legal sequence in Dutch. CV and VC diphones were recorded with both stressed and unstressed vowels; VV diphones were recorded with all four possible stress combinations. Table III lists the environments in which the various diphones were recorded.

The nonsense environment always included at least one phoneme after the target diphone, so that the diphone would not be final to the item. This prevented excessive lengthening within the diphone, as would for example apply to the vowel in a CV diphone recorded in isolation. Stressed CV diphones were always followed by the unstressed syllable /kə/, whereas unstressed CV diphones were always followed by stressed /ke/. VCs always straddled a syllable boundary, with one of the syllables stressed and the other unstressed. If unstressed, the final syllable was Cə, if stressed it was Ce. If CC was a legal onset, it formed the onset of the syllable CCa. Otherwise it straddled a syllable boundary, with the first syllable aC stressed and the second Cə unstressed. VV

diphones always straddled a syllable boundary. Depending on the stress pattern, the contexts /b/ or /ab/ were prefixed, and the contexts /k/, /kə/, or /ke/ were suffixed, to make the sequences easier to produce with correct stress.

All items (diphones in their environments) were transcribed phonemically, with stress and syllable boundaries marked. A phonetically trained female native speaker of Dutch, whose pronunciation exhibits no strong regional accent, read all of the items from this transcription. The recording was made on DAT in a sound-treated recording booth using high-quality equipment. Any items which were initially mispronounced were rerecorded. The recording was low-pass filtered at 7.5 kHz and resampled at 16 kHz.

3. Stimuli for the perception experiment

Past gating studies have employed two methods for dividing the signal. First, gates can be positioned at fixed time intervals [e.g., 20 ms, as in Smits (2000)], leading to a variable number of gates per diphone. Alternatively, gates can be positioned “proportionally,” i.e., using a constant number of gates per phoneme (e.g., Cutler and Otake, 1999), leading to a variable gate duration. We chose proportional gating for two reasons. First, the number of stimuli for our experiment would become unrealistically large if we were to use fixed intervals while at the same time making several gates available for even the shortest diphone. Second, as described above, the ultimate aim of the study was to provide data on which to base computational modeling of the arrival of phonetic information over time; proportional gating provides data which is relatively straightforward to use in this way.

Beginnings and ends of all phonemes were identified manually using the criteria in Appendix D. Each item was

TABLE II. The 22 Dutch consonants used in the experiment.

	Labial/ Labiodental		Alveolar		Postalveolar/ Palatal		Velar/ Uvular		Glottal	
	Voiceless	Voiced	Voiceless	Voiced	Voiceless	Voiced	Voiceless	Voiced	Voiceless	Voiced
Stops	p	b	t	d			k	g		
Nasals		m		n				ŋ		
Fricatives	f	v	s	z	ʃ	ʒ	x ^a			h
Affricate						dʒ				
Liquids				l				r ^b		
Glides		w ^c				j				

^aThis fricative is /x/, but for ease of transcription we will use /x/.

^bThis liquid is /ʀ/, but for ease of transcription we will use /r/.

^cThis glide is /v/, but for ease of transcription, we will use /w/.

TABLE III. Environments in which diphones were recorded (in phonemic transcription). Syllable boundaries are marked by hyphens.

Diphone class	Environment	Proportion with each environment
CV (stressed)	'CV-kə	2/3
	a-'CV-kə ^a	1/3
CV (unstressed)	CV-'ke	2/3
	'a-CV-ke	1/3
VC (vowel stressed)	'V-Cə	1/2
	'bV-Cə	1/2
VC (vowel unstressed)	V-'Ce	1/2
	bV-'Ce	1/2
CC	'CCa	if CC is a legal onset
	'aC-Cə	otherwise
VV (stressed–unstressed)	'bV-Vk	all
VV (unstressed–stressed)	bV-'Vk	all
VV (stressed–stressed)	'bV-'V-kə	all
VV (unstressed–unstressed)	'a-bV-V-'ke	all

^aFor all diphones beginning with /ŋ/, /a/ was used as the preceding vowel instead of /a/ because /ŋ/ cannot follow long vowels.

final-gated at six points during the target diphone, three in each of the target phonemes (with exceptions for initial stops and affricates, see below), to create stimuli consisting of the entire item up to the gating point, including any preceding context.

For phonemes which lack abrupt acoustic changes during the segment, such as nasals, fricatives, and vowels in most environments, gate end points were placed automatically at one-third and two-thirds through the duration of the segment as well as at the end of the segment. For segments with abrupt acoustic changes within the segment, such as stops and affricates, gate end points were determined relative to those abrupt changes. Any preceding environment was always included in the stimuli, but following environment was never included.

With gating it is most important to avoid introducing extraneous acoustic cues in the gated segments. Pols and Schouten (1978), among others, showed that careless truncation of speech signals may bias listeners towards labial and or plosive responses. They also showed, however, that such biases can be minimized by applying smoothing windows and replacing the missing speech by another signal such as noise. At gate end points, items were therefore ramped down to zero using a linear 5-ms ramp. In order to further avoid noise-introduced fricative biases, we used as a replacement signal a 500-Hz square wave, which is not misperceived as a speech sound (Warner, 1998). The square wave had a duration of 300 ms, with the same 5-ms ramp applied at onset and offset, and was overlap-added to the end of the item such that the start of the item's falling ramp coincided with the start of the square wave's rising ramp. The amplitude of the square wave was fixed across stimuli. The rms amplitude of a 50-ms portion of the square wave was 22 dB lower than the rms amplitude of the loudest 50-ms portion across all stimuli.

Mean phoneme duration across all utterances was 138 ms, with a standard deviation of 64 ms. Mean duration of a signal portion between two consecutive gate points was 48

ms, with a standard deviation of 23 ms. The total number of stimuli was 13 570.

B. Subjects and procedures

Twenty-two listeners participated in the experiment, and 19 completed it. All were native speakers of Dutch who had grown up in the Netherlands, and had no known hearing impairment; most were students at the University of Nijmegen. Subjects were paid for each hour of participation, with a bonus on finishing the experiment. Data from the three subjects who did not finish the entire experiment were excluded.

The task involved identifying the two phonemes of the target diphone. Subjects were tested individually in a sound-treated booth. Stimuli were presented over closed headphones. As each stimulus was played, a response screen appeared on a computer screen visible through the booth window. The response screen showed two panels, each containing buttons for each phoneme used in the experiment. Subjects used a computer mouse to click on one button of the left-hand panel for the first sound of the diphone, and one of the right-hand panel for the second sound. If the stimulus included preceding context (/a/, /ə/, /b/, or /ab/), the letters "aa," "a," "b," or "aab," respectively, appeared on the screen to the left of the left-hand response panel to inform subjects that those sounds were not the ones to which they should respond. The response buttons for these phonemes were also crossed out in the left response panel to remind subjects not to respond to the preceding environment.

Before beginning the experiment, subjects were trained on the set of symbols to use for responses. Since Dutch orthography is straightforward, most phonemes could be represented orthographically (with double vowels used for long vowels and single vowels used for short vowels); special symbols were necessary only for /ə/ ("@"") and /g/ ("G"). Examples of each phoneme were provided, and special attention was called to phonemes which appear only in loan words. Subjects were told that they would hear the beginning of a nonsense word followed by a beep, and that they should identify the two sounds of the nonsense word using the mouse. They were informed about possible additional initial sounds which they were not to respond to, and warned that they would sometimes hear very little of the nonsense word, making it difficult to identify the two sounds. A native Dutch speaker instructed each subject and checked subjects' understanding of the mapping of response symbols to sounds.

Subjects then completed a practice session, comprising 185 stimuli drawn from the actual experiment. Diphones containing potentially problematic phonemes, such as /ə, ŋ/ and phonemes occurring only in loan words, were well represented in the practice session. The experimenter evaluated subjects' performance on stimuli which included these sounds or a vowel in their entirety to ensure that subjects could perform the task. No subjects were excluded at this stage, since none had difficulty with the task.

Subsequently, subjects completed a series of one-hour experimental sessions, with a break during each session. Subjects returned for as many sessions as needed to respond to all 13 570 stimuli, an average of 27.9 sessions. The total

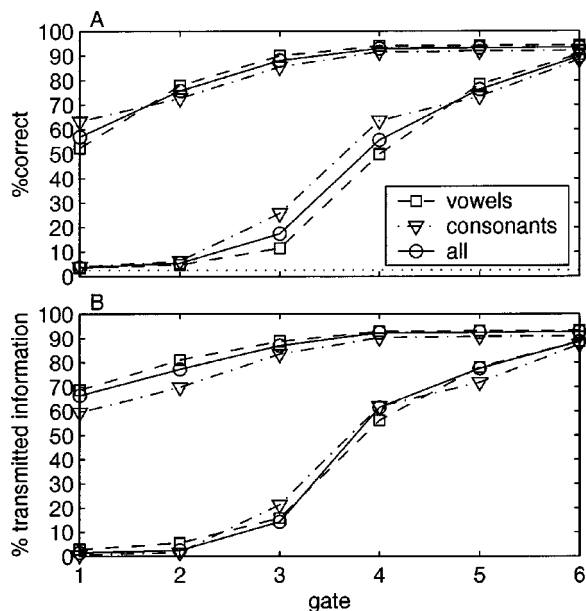


FIG. 1. Correct phoneme recognition rates (a) and percentages transmitted information (b) as a function of gate, averaged across listeners. Results for vowels only, consonants only, and all phonemes are given by separate lines. The upper and lower lines are associated with the first and second phoneme in the diphone, respectively. The dotted line in (a) indicates chance level (2.63%).

set of stimuli was divided into four blocks. For each subject a different pseudo-random order of stimuli within blocks was generated and different subjects received the blocks in a different order. Two gates of the same diphone were separated by at least six stimuli, stimuli from diphones beginning with the same phoneme were separated by at least four stimuli, and no stimuli which appeared in the practice session or other gates of those diphones occurred within the first 1200 experimental stimuli. In total 488 520 phoneme categorizations were collected.

III. RESULTS

A. Summary results

One subject performed much worse than the others in correctly recognizing the first phoneme at gates 1–3. For these gates this subject's recognition rates were more than four standard deviations below the mean recognition rates for all other subjects. The data of this subject were therefore excluded. Figure 1 shows average phoneme recognition rates (panel a) and percentages transmitted information (TI, panel b) as a function of gate, pooled across the remaining 18 subjects, for consonants, vowels, and all phonemes. TI is a measure of the covariance between input and output when both have a categorical nature (e.g., Miller and Nicely, 1955; Smits, 2000).

At gate 1, that is, one-third into the first phoneme of the diphone, the first phoneme (top line) was recognized at almost 60% correct, while TI reaches almost 70%. With increasing gates, levels rose smoothly to about 90% at gate 4 and hardly changed thereafter. The recognition rate for the second phoneme (bottom line) started close to chance level (2.6% correct, or 0% TI) at gate 1 and rose smoothly to almost 90% at gate 6. One-tailed *t*-tests showed that at all gates average recognition rates for both phonemes were significantly above chance level as well as below perfect performance (all p 's < 0.0005). In these as well as all subsequent tests, subject was the random variable, and the Bonferroni criterion was applied in calculating the significance levels (above, 24 comparisons were made, so the significance level was $\alpha = 0.002$).

Recognition rates for gates 4–6 of the second phoneme were quite similar to those for gates 1–3 of the first phoneme. The longer preceding context for the second phoneme therefore did not affect recognition much compared to the first phoneme. The recognition curves for vowels and consonants are very similar. In first position, TI is somewhat lower for consonants than for vowels (about 10% for gates 1 and

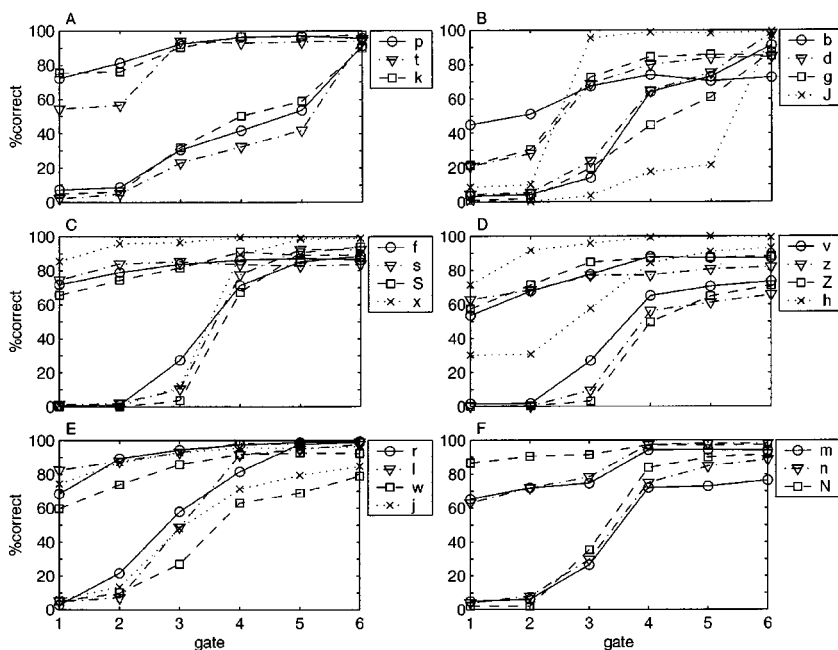


FIG. 2. Correct consonant recognition rates plotted separately for each of the 22 consonants. Phoneme symbols are in accordance with IPA, except for J, S, Z, and N, indicating /dʒ ʃ ʒ ŋ/, respectively. The upper and lower lines are associated with the first and second phoneme in the diphone, respectively.

TABLE IV. Confusion matrix for consonants. Responses were summed across subjects, contexts, and stress conditions. For each stimulus, the first row gives responses to gate 1 for consonants in initial position in the diphone, whereas the second row gives responses to gate 4 for consonants in second position. The last column gives the number of vowel responses to each of the consonants.

Stimulus	Response																						
	p	t	k	b	d	g	dʒ	f	s	ʃ	x	v	z	ʒ	h	r	l	w	j	m	n	ŋ	Vowel
p	325	6	3	62	0	0	0	0	0	0	0	0	0	0	22	0	0	4	0	9	0	0	19
	331	8	34	187	13	16	0	11	0	0	0	11	0	0	58	2	10	43	15	15	13	5	20
t	33	235	4	13	81	1	0	3	0	0	0	5	0	0	25	1	3	15	2	0	0	0	11
	28	258	7	12	340	2	9	2	1	1	1	10	0	0	35	3	5	11	13	6	26	3	19
k	0	0	340	0	0	66	0	0	0	0	3	0	1	0	23	0	1	2	3	0	1	1	9
	26	18	399	11	7	120	1	8	1	0	2	6	0	0	77	6	9	28	13	3	5	5	47
b	77	0	2	275	9	1	0	3	0	0	0	11	1	0	95	2	0	25	1	76	20	0	14
	18	2	0	566	32	18	0	2	0	0	0	10	2	0	11	2	3	98	4	92	10	4	8
d	11	29	0	89	116	2	9	6	1	0	0	11	0	0	99	1	9	67	8	48	37	5	10
	6	5	3	45	571	2	1	1	0	0	3	3	0	0	25	0	40	61	8	6	71	3	28
g	5	0	60	99	19	123	0	1	0	0	6	10	0	0	92	2	4	39	2	58	36	11	9
	6	1	75	82	33	394	4	4	0	1	22	9	1	1	30	4	8	88	22	8	16	11	62
dʒ	8	46	1	95	35	2	49	5	0	0	0	16	0	0	113	2	2	49	21	70	51	6	5
	9	12	1	10	457	2	148	0	0	0	0	2	4	2	17	3	8	8	94	1	47	3	18
f	4	0	0	0	1	0	0	646	1	0	9	172	0	0	43	3	0	6	0	2	0	0	13
	3	0	1	0	1	0	0	565	0	0	12	179	0	0	9	0	1	17	3	0	0	0	1
s	6	2	0	0	0	1	0	1	670	46	0	0	141	3	27	2	0	0	0	1	0	0	0
	3	6	0	1	1	0	0	0	601	26	0	0	107	14	2	2	1	2	1	4	1	0	2
ʃ	4	0	0	0	0	3	2	1	91	590	1	0	17	139	18	0	0	0	26	1	0	0	7
	2	5	1	1	0	1	19	2	112	522	2	2	15	66	5	0	0	2	10	2	1	0	4
x	2	1	2	1	0	0	0	6	0	0	784	1	1	0	52	54	0	1	1	2	0	0	10
	0	0	1	0	0	1	0	3	0	1	709	2	0	0	47	19	0	1	1	0	1	0	6
v	3	2	0	1	1	0	0	126	0	0	0	385	0	0	66	3	0	114	2	4	0	0	13
	1	0	0	0	1	0	0	116	1	0	3	445	2	0	8	4	1	84	9	0	2	0	7
z	5	2	0	2	2	0	5	0	67	23	0	0	452	96	32	3	16	0	7	1	0	0	7
	2	2	0	1	5	0	7	1	106	20	0	1	394	90	12	0	7	5	16	5	1	0	27
ʒ	3	2	0	0	5	4	9	0	17	86	0	0	44	330	31	2	3	0	28	1	2	0	9
	0	3	0	0	3	2	32	0	27	115	1	1	136	428	6	1	1	1	57	2	2	0	46
h	10	1	1	9	1	0	0	25	1	1	16	20	0	0	386	2	6	29	16	5	6	0	5
	2	0	1	2	1	0	0	10	0	1	6	2	0	0	683	3	7	21	12	0	2	0	57
r	1	0	9	1	1	3	0	1	2	0	5	4	0	0	174	628	12	18	5	10	10	3	31
	0	1	0	0	0	0	0	0	1	1	0	4	0	0	16	691	5	6	1	0	1	0	119
l	5	1	4	2	0	0	0	1	0	0	1	1	0	0	67	0	758	10	21	5	3	0	39
	0	0	0	0	1	0	0	0	0	0	1	3	0	0	5	6	759	11	5	1	5	2	29
w	17	0	1	32	3	1	0	0	1	0	0	17	0	0	107	5	20	549	3	101	31	1	29
	2	5	1	3	6	1	0	10	3	0	1	65	1	0	46	22	19	534	15	6	6	2	98
j	0	1	1	3	1	0	0	1	4	0	1	3	5	0	84	0	12	4	683	5	4	3	103
	4	2	2	4	0	0	0	0	3	0	0	0	0	0	20	3	8	15	591	1	3	0	172
m	5	0	0	3	0	0	0	0	0	0	0	2	0	0	120	1	11	30	11	599	113	2	21
	0	0	0	1	0	0	0	1	0	0	0	4	0	0	13	2	11	67	1	609	103	20	14
n	4	0	2	3	2	0	0	0	0	0	0	5	0	0	108	2	9	17	15	140	579	11	21
	1	0	0	2	3	0	0	2	1	0	1	3	4	0	10	1	25	41	4	88	648	7	23
ŋ	0	1	2	0	0	1	0	0	0	0	1	1	0	0	18	6	3	2	5	0	28	810	58
	0	0	1	0	0	0	0	0	0	0	0	0	0	0	8	1	1	2	1	1	13	166	4

2), but in second position this difference disappears.

Figure 2 shows correct recognition rates by gate separately for the 22 consonants, grouped by manner and voicing, while Fig. 3 presents those for the 16 vowels, grouped partly according to vowel features and partly according to similarities of the individual curves. Tables IV and V present confusion matrices for consonants and vowels, respectively, summed across listeners, contexts, and stress conditions, in responses to gate 1 for the first phoneme and to gate 4 for the second phoneme.

B. Consonants

(1) *Voiceless stops* /p t k/ [Fig. 2(a)]: As shown in Table III, some diphones were recorded with preceding context and some without. For those without preceding context, gates 1 and 2 were not presented because they contained only silence. Gates 1 and 2 in Fig. 2(a) therefore represent only responses to gated diphones with preceding context—that is, the vowel /a/ with formant transitions plus respectively half or all of the following stop closure. Subjects could recognize

TABLE V. Confusion matrix for vowels. Responses were summed across subjects, contexts, and stress conditions. For each stimulus, the first row gives responses to gate 1 for vowels in initial position in the diphone, whereas the second row gives responses to gate 4 for vowels in second position. The last column gives the number of consonant responses to each of the vowels.

Stimulus	Response																
	ɑ	ɛ	ɪ	ɔ	ʏ	ə	i	u	y	e	o	œ	a	ɛi	œy	au	Consonant
ɑ	640	0	0	4	1	9	0	0	0	0	0	0	26	0	1	11	28
	1275	5	1	27	7	13	0	1	0	0	1	0	131	3	29	45	10
ɛ	0	642	3	0	0	22	0	0	0	1	0	0	0	29	0	0	23
	42	1165	64	2	5	21	2	0	3	15	0	4	37	159	4	0	25
ɪ	2	1	611	0	1	6	32	0	0	30	0	0	0	0	0	0	37
	5	81	1125	2	25	18	90	1	17	127	0	6	4	4	0	0	43
ɔ	3	0	0	634	2	5	0	2	0	0	28	0	0	0	0	0	46
	92	1	2	1291	6	14	1	5	3	0	81	4	1	0	0	1	46
ʏ	0	1	6	1	450	144	0	0	20	1	0	59	0	0	0	0	38
	18	9	5	59	793	404	1	3	36	3	10	119	3	0	9	1	75
ə	10	5	20	8	439	259	4	5	51	4	0	46	12	1	4	0	86
	7	4	21	23	367	205	0	3	21	1	2	53	3	0	1	2	43
i	0	0	34	0	0	13	1671	0	5	2	0	0	2	0	0	0	145
	0	0	163	2	7	13	1260	1	12	3	0	5	1	1	0	0	80
u	0	0	1	18	4	29	0	1732	2	0	2	1	0	0	1	0	82
	0	1	3	47	21	21	1	1307	32	0	4	2	0	0	1	2	106
y	0	0	0	1	59	56	4	4	1588	0	0	4	0	0	0	0	156
	0	0	11	8	104	60	29	115	1048	0	1	8	0	0	4	2	158
e	0	30	1301	0	6	32	6	0	0	411	0	0	1	2	0	0	83
	1	179	989	2	7	11	30	2	0	289	1	2	0	3	1	0	31
o	4	2	0	1189	8	47	0	30	1	0	474	0	1	0	0	0	116
	23	1	0	1136	14	19	0	7	1	0	289	4	1	0	0	7	46
œ	0	9	9	2	1052	400	0	0	5	20	1	290	0	1	2	2	79
	13	4	10	18	814	373	8	5	28	7	4	191	0	0	0	1	72
a	426	23	2	0	0	66	1	1	1	0	0	0	1211	45	10	1	85
	431	90	2	0	8	7	3	0	1	0	1	1	841	76	51	1	35
ɛi	55	828	0	1	0	84	2	1	0	2	0	0	43	815	2	0	39
	149	602	4	0	5	19	3	0	1	3	0	2	248	457	18	3	34
œy	412	78	1	0	12	120	0	0	0	0	0	3	417	135	614	4	76
	602	48	3	2	24	33	1	0	1	1	0	3	452	34	306	12	26
au	1484	1	2	9	3	52	1	0	0	1	0	0	54	0	6	168	91
	1307	3	2	33	2	6	0	0	0	0	1	1	59	0	12	105	17

the stops well from these portions, with recognition rates between 50% and 80%. Note that Dutch voiceless stops are produced without aspiration, while voiced stops are usually produced with negative VOT (voice bar). Recognition of /t/ was somewhat poorer than of /p/ and /k/. This is supported by *t*-tests (all comparisons between /t/ and /p/ or /t/ and /k/ at gates 1 and 2 reached significance, $\alpha=0.01$). The difference was mainly caused by more place and voicing errors for /t/ than for /p/ and /k/ (see Table IV). Gate 3 included the release burst, which strongly improved recognition.

Recognition of voiceless stops in second position in the diphone at gates 4 and 5 was considerably worse than recognition of the first phoneme at gates 1 and 2 ($p<0.005$ for all six comparisons, $\alpha=0.008$). The raw data show that, on average, /a/ as preceding context led to better recognition of the following stop than other preceding contexts. This agrees with reports of Dorman *et al.* (1977) and Smits *et al.* (1996) that formant transitions in /a/ are more informative about place of articulation of an adjacent consonant than transitions in other vowels. At gate 6, when the stop burst is audible, recognition levels exceeded 90%.

(2) *Voiced stops /b d g/ and the voiced affricate /dʒ/* [Fig. 2(b)]: Gates 1 and 2 included half or all of the voice bar, while the third gate included the release burst. In first position, recognition of voiced stops was poorer than for voiceless stops (only 1 out of 18 comparisons did not reach significance, $\alpha=0.0025$). /b/ fared better than /d/ and /g/ for gates 1 and 2 ($p<0.001$ for all four comparisons, $\alpha=0.01$), reconfirming the findings of, among others, Pols and Schouten (1978) and Smits (2000) that an isolated voice bar sounds more like a /b/ than a /d/ or /g/. For later gates, place and voicing confusions were the main source of errors (see Table IV). Voiced stops were more often confused with their voiceless counterparts than vice versa. Especially /b/ was classified relatively frequently as /p/ up to gate 6. The voiced affricate /dʒ/ was not recognized reliably until its final gate, when burst and frication become audible. At earlier gates /dʒ/ was mainly confused with /j/ and /d/.

(3) *Voiceless fricatives /f s ʃ x/* [Fig. 2(c)]: For all fricatives, the three gates comprise one-third, two-thirds and all of the frication noise, respectively. At gate 1 of the first phoneme recognition was already good, with levels between

60% and 90%. Recognition gradually improved with increasing amounts of frication and subsequent context. Remaining confusions of /f s ʃ/ were with their voiced counterparts. In addition, there was some confusion between /s/ and /ʃ/ (see Table IV). The voiceless velar fricative /x/ was recognized very well at all gates. Note that /x/ has no voiced counterpart in most regional variants of Dutch, including that of our speaker. Recognition levels for gates 4–6 of the second phoneme resembled those for gates 1–3 for the first. Note the marked jump in recognition between gates 3 and 4, that is, when some frication noise became audible.

(4) *Voiced fricatives* /v z ʒ h/ [Fig. 2(d)]: In initial position, voiced fricatives were generally recognized as well as their voiceless counterparts (only 1 out of 18 comparisons reaches significance, $\alpha=0.0025$). In second position, however, voiced fricatives were recognized less well than their voiceless counterparts at gates 4–6 ($p<0.0005$, $\alpha=0.0025$). Although the pattern is thus less clear than for the stop consonants, it has the same cause, namely asymmetric confusions of the voicing feature. Voiced fricatives were categorized as their voiceless counterparts more often than the reverse (see Table IV). This pattern may be related to the fact that for many regional variants of Dutch, including the one spoken in Nijmegen (but not the native variant spoken by the talker), the voicing distinction in fricatives is weak, with voiced fricatives being pronounced as their voiceless counterparts.

The glottal fricative /h/ was recognized better than the other fricatives (in initial position 11 out of 18 comparisons reach significance, $\alpha=0.0025$; in second position 17 out of 18 comparisons reach significance, $\alpha=0.0025$). In first position recognition already exceeded 90% at gate 2. Note that /h/ has no voiceless counterpart, so if manner and place of articulation are recognized, there is no room for voicing errors. In second position /h/ was recognized well even at gate 1. This is an artifact of the gating method: some subjects used a default /h/ response for the second phoneme when they had no information about that phoneme. As the second phoneme sometimes actually was /h/, this response bias increased recognition rates for the early gates of /h/ in this position.

(5) *Liquids* /r l/ and *glides* /w j/ [Fig. 2(e)]: Positioning of begin and end points for these phonemes varied greatly depending on context, but the three gate points always divided the phoneme into equal thirds (see Appendix D). Recognition in first position was already good at gate 1, with recognition rates between 60% and 85%. At later gates recognition further increased to very high levels. In second position, recognition of the labiodental glide /w/ was significantly poorer than of the liquids for gates 3–6 ($\alpha=0.001$); confusions occurred with the voiced labiodental fricative /v/ and the vowels /ʏ/ and /ə/ (N.B. /w/ was hardly ever confused with the vowel /u/). Recognition of liquids and glides in second position gradually increased across all six gates. From gate 4 onwards, however, recognition of the glides was substantially lower than that of the liquids ($\alpha=0.002$ is reached for all 12 comparisons), and asymptoted at levels close to 80%. /w/ was again mainly confused with /v/ and /j/ was mainly confused with /i/, while the main confusions for

/r/ were with /h/ and /a/. The confusions for /l/ were rather scattered and include consonants /d j h r w/ and vowels /i ɪ ə/.

(6) *Nasals* /m n ŋ/ [Fig. 2(f)]: The three gate points divided the nasal murmur into equal thirds. For nasals in first position it is striking that /ŋ/ was recognized much better than /m n/ at gates 1 to 3 (all six comparisons reach significance, $\alpha=0.008$). This is again an artifact: Because /ŋ/ cannot occur in syllable-initial position, recognition levels of /ŋ/ in initial position were based on tokens with preceding context /a/, which therefore includes formant transitions into the nasal. In contrast, /m/ and /n/ occurred in initial position in two-thirds of the tokens, without informative preceding transitions. For nasals in second position a marked increase in correct recognition can be seen at gates 3 and 4, which include the speech signal up to oral closure and one-third into the murmur, respectively. Table IV shows that at gate 1 in first position and at gate 4 in second, confusions were mainly across place, while at later gates the remaining confusions were across manner and place was recognized reasonably well. At gates 5 and 6, recognition of /m/ was some 15% lower than that of /n/ and /ŋ/. The raw data show that /m/ was often confused with /n/ at these gates.

C. Vowels

(1) *Short vowels* /a ɛ ɪ ʊ/ [Fig. 3(a)]: At gate 1, recognition of these vowels in first position was already very good, with levels close to 90% correct. In second position, recognition jumped to levels between 70% and 85% at gate 4 and rose further at subsequent gates. When listeners heard one-third or more of the target vowel, the remaining confusions were as follows. /a/ was mainly confused with /ɑ/, /ɛ/ with /ɛi/ and /i/, /ɪ/ with /e/ and /i/, /ʊ/ with /a/ and /o/ (see Table V). That is, short vowels were confused with any nearby long counterpart.

(2) *Long vowels* /i u y/ [Fig. 3(b)]: These, like the short vowels, were recognized well in first position at gate 1. Note that these vowels do not have short counterparts (Booij, 1995). When a third or more of the vowels was audible, the remaining confusions tended to be with similar short vowels: /i/ was confused with /ɪ/, /u/ with /ʊ ɐ w/, and /y/ with /ə ʏ u/ (see Table V).

(3) *Short vowels* /ʏ/ and /ə/ [Fig. 3(c)]: Recognition of /ə/ was poor, showing little improvement over the six gates and never exceeding 40% correct. /ʏ/ was recognized better, but still much worse than the short vowels in Fig. 3(a). As shown in Table V, /ʏ/ and /ə/ more or less form a single category: responses to both stimuli were very similar, and listeners seem to have selected at random between the two responses, with a bias against /ə/ (such a bias has also been encountered by others, Van Son, personal communication). We therefore grouped stimuli and responses for these two vowels together and calculated recognition rates for the compound vowel class. The resulting recognition curves are displayed in Fig. 3(c) with the label “Y/@.” In first and second position, recognition for the new class was significantly better than that of /ə/ at all gates ($\alpha=0.002$). Compared to /ʏ/,

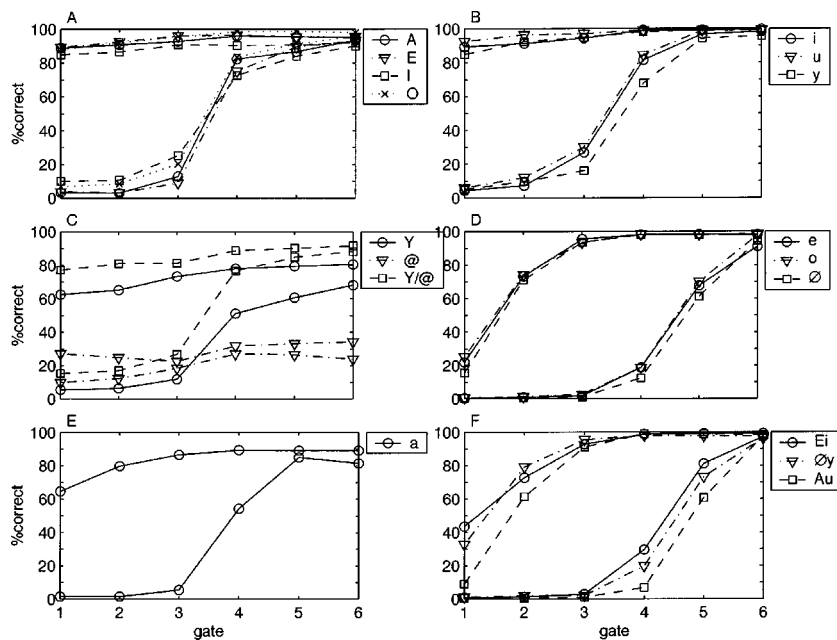


FIG. 3. Correct vowel recognition rates plotted separately for each of the 16 vowels. Phoneme symbols are in accordance with IPA, except for A, E, I, O, @, and \emptyset , indicating /a ϵ i ɔ æ /, respectively. The upper and lower lines are associated with the first and second phoneme in the diphthong, respectively.

the new class was better for gates 1, 4, 5, and 6 in second position only ($\alpha=0.002$). This shows that at gates where at least a third of the vowel is audible, the majority of confusions were indeed between /y/ and /ə/. The remaining confusions were mainly with /œ/ (see Table V).

(4) *Long vowels* /e o œ/ [Fig. 3(d)]: In most regional variants of Dutch, including that of our speaker, these vowels are slightly diphthongized, ending in articulatory positions corresponding to /i u y/, respectively (Booij, 1995). In first position, these phonemes were initially not well recognized. At gate 1, recognition levels were between 15% and 25%, which is much lower than for other vowels discussed so far. At gate 1, /e/ and /o/ were mainly confused with /t/ and /ɔ/, respectively, while /œ/ was mainly confused with /y/ and /ə/ (see Table V). This is partly supported by Booij's (1995) position that the short counterparts of /e/ and /œ/ are indeed /t/ and /y/ (with /y/ and /ə/ being highly confusable, as discussed earlier), while /o/ and /ɔ/ do not form a long-short pair because /o/ is higher than /ɔ/. Our data suggest, however, that, perceptually, the relation between /ɔ/ and /o/ is very similar to that between /t/ and /e/. At gate 2, recognition levels were just above 70%, and the full three gates were necessary for recognition to exceed 90%. The recognition results for /e o œ/ in second position are very similar to those for the first position, shifted by three gates.

(5) *Vowel* /a/ [Fig. 3(e)]: This vowel is depicted separately because it shows a pattern between that of /i u y/, which have no short counterpart, and that of /e o œ/, which do. This finding tallies with the description of /a/ as "almost" a long-short pair, with the qualification that both vowels are back, but /a/ is somewhat fronted compared to /ɑ/ (Booij, 1995). Another aspect which sets /a/ apart from the other long vowels is that its recognition asymptoted just below 90%, whereas the others were eventually recognized at levels close to 100%.

The raw data show that at all gates /a/ was recognized better when stressed than unstressed. When it was unstressed

/a/ was mainly confused with /ɑ/ and to a lesser extent with /ə/ and /ɛi/. The pattern is, however, more subtle. When /a/ was part of a VV diphthong (which always has a syllable boundary in the middle), and the stress pattern of this diphthong was either weak-strong or strong-weak, the confusion with /ɑ/ was much less than when it was part of an unstressed CV or VC diphthong, or a VV diphthong with a weak-weak stress pattern. We hypothesize that when /a/ is stressed or it is possible to hear that /a/ is unstressed (by contrast to the adjacent syllable), listeners are more likely to choose the (correct) /a/ response. The data show that the same general pattern applies to /e/ and /œ/, but the effect is much weaker, possibly due to their slight diphthongization, which makes confusions with their short counterparts less likely.

(6) *Diphthongs* /ɛi œy au/ [Fig. 3(f)]: The general picture is similar to that for the diphthongized long vowels [Fig. 3(d)], but there is more variability. When only part of the diphthong was audible, /au/ was recognized worse than the other two diphthongs (in first position both comparisons reached significance at gate 1 while only /œy/ versus /au/ did so at gate 2; in second position all comparisons involving /au/ reached significance for gates 4 and 5, $\alpha=0.001$). Not surprisingly, /au/ was predominantly classified as /ɑ/ for these gates (see Table V). /œy/ was mainly confused with /ɑ/, /a/, and /ə/ at early gates, while /ɛi/ was mainly confused with /ɛ/ (see Table V). When the diphthongs were fully audible, recognition levels were close to 100%.

IV. SUMMARY AND CONCLUSIONS

We have presented the method and results of a large-scale study of the perception of gated versions of all possible Dutch diphthongs. For the consonants we found the following six confusion patterns. First, inclusion of bursts considerably improved recognition of both voiced and voiceless stops. This finding agrees with past studies on stop recognition

(e.g., Schouten and Pols, 1983; Smits *et al.*, 1996). Second, voiceless stops were recognized better than voiced stops. This difference was caused by asymmetrical voicing confusions: voiced stops were classified as voiceless more often than the reverse. This pattern has not been reported earlier. Third, fricatives were recognized well from only a third of their frication noise. This had already been established for English (Jongman, 1989; Smits, 2000), but not for Dutch. Fourth, the same asymmetrical pattern of voicing confusions that we found for stops applied to the fricatives. This pattern has been documented for American English by Jongman (1989). Fifth, perceptually relevant information was temporally more spread out for liquids and glides than for other consonants. A similar pattern was reported by Klaassen-Don (1983). Sixth and finally, in accordance with Kurowski and Blumstein (1984) and Smits (2000), our results show that transitions into the nasal murmur, together with the first few pulses of the murmur, contain important information for nasal recognition.

The confusion patterns for vowels were dominated by the long–short distinction. This corresponds well with previous studies employing gated vowels (e.g., Strange *et al.*, 1976; van Bergem, 1993). Short vowels were recognized well as soon as a third of their duration became available. However, /ɪ/ and /ə/ formed an exception to this rule, mainly because they were mutually confused. Long vowels that do not have short counterparts were also recognized well from a third of their duration. For long vowels with short counterparts, on the other hand, as well as for diphthongs, the entire vowel was needed for correct recognition. The pattern for the long vowel /a/, which forms an approximate long–short pair with /a/, fell between the two extreme patterns.

The database of Dutch diphone perception described here is available at <http://www.mpi.nl/world/dcsdpdiphones>. It was collected with the aim of improving existing models of spoken word recognition. In particular, we plan to replace the input representation of the Shortlist model (Norris, 1994), which currently consists of a string of phoneme labels, by phoneme activation patterns that are graded and temporally more fine-grained. These activation patterns will be derived from the present database. The planned improvements will enable a start to be made on modeling the match between the speech signal and competing word candidates in a more realistic manner.

ACKNOWLEDGMENTS

We are grateful to Dennis Norris for discussion of this material. We further thank Mattijn Morren, Keren Shatzman, Petra van Alphen, Niels Janssen, Tau van Dijck, Anne Pier Salverda, and Aoju Chen for their great efforts in preparing and running the experiment, and Saskia Bayerl for assistance with preparing the database for the Internet. Finally, we thank James Hillenbrand, Rob van Son, and an anonymous reviewer for very helpful comments on an earlier version of this paper.

APPENDIX A: PHONEME SELECTION CRITERIA

Reasons for selection or exclusion of certain phonemes are as follows:

- (1) Besides the voiceless velar fricative /x/, CELEX and Booij (1995) recognize the voiced velar fricative /ɣ/. We excluded /ɣ/ because many Dutch speakers—including the speaker for the experiment—neutralize the distinction, maintaining only /x/ (Gussenhoven, 1992).
- (2) The vowels /i:, y:, u:, ɔ:, œ:, ε:/ occur only in a few unassimilated loan words (e.g., *analyse*, *centrifuge*, *cruise*, *zone*, *oeuvre*, *serre*, respectively), and contrast with native phonemes only in length. We excluded these non-native vowels as Gussenhoven (1992) and Booij (1995) both hold them to be marginal.
- (3) We did include some consonants which occur in Dutch only in unassimilated loan words: the voiced velar stop /g/, the fricative /ʒ/, and the affricate /dʒ/. These appear in a relatively large number of loans, many quite frequent (e.g., *goal*; *jam*, /ʒɛm/; and *jazz*).
- (4) There are inconsistencies in the CELEX inventory, e.g., the fact that [tʃ] is treated as a sequence of a stop and a fricative, /tʃ/, while [dʒ] is treated as a single affricate segment /dʒ/. In these cases we observed the CELEX standard.

APPENDIX B: DIPHONE SELECTION CRITERIA

The following criteria were applied in selection of the diphones:

- (1) For each sequence of two phonemes containing a vowel other than /ə/ (which is never stressed), one diphone was included with the vowel stressed, and another with it unstressed. For vowel–vowel diphones, all four stress combinations (stressed–stressed, unstressed–unstressed, stressed–unstressed, unstressed–stressed) were included.
- (2) We included diphones which can only occur across word or morpheme boundaries in Dutch (e.g., /ɣp/), but we excluded sequences which, because of phonotactic constraints, could never occur even across word boundaries.
- (3) In cases where phonotactic constraints were violated by large numbers of loan words, we included the diphones. Thus Booij's (1995) claim that short vowels cannot be followed by a glide within the syllable might be considered to be violated by *timing*, *tranquilizer*, and *boiler*.
- (4) We excluded certain diphones which are possible (at least across morpheme boundaries) according to a phonemic transcription, but unlikely ever to be produced as a sequence of the two sounds, e.g., /sʃ, ʃs, tɔ̃ʒ/.
- (5) We excluded all sequences of identical consonants ($C_1 = C_2$), since Dutch phonology requires that these be degeminated within the prosodic word (Booij, 1995), and they are likely to be reduced to a single consonant even across word boundaries unless produced with a pause.
- (6) A few diphones which probably never occur in Dutch, e.g., /a, ε, ɪ/ followed by /ʒ/, were included simply because no known phonotactic constraint excludes them.

APPENDIX C: DIPHONE TEST SET

TABLE VI. Diphones included in the experiment, and reasons for exclusions. Each row represents diphones X_1X_2 , where X_1 is each of the phonemes in the X_1 column and X_2 is each of the phonemes in the X_2 column.

Class	X_1	X_2
CV diphones		
C=stop, affricate, nasal, liquid, or glide	p, t, k, b, d, g, dʒ, m, n, ŋ, r, l, j, w	all full vowels stressed, all vowels unstressed
C=fricative	f, v, s, z, ʃ, ʒ, x, h	all full vowels stressed
	f, v, s, z, ʃ, ʒ, x	all vowels unstressed
	h	all full vowels unstressed
	Exclusion: */hə/ within the syllable, and /h/ cannot be syllable-final ^a	
VC diphones		
C=stop, affricate, liquid, or glide	all full vowels stressed, all vowels unstressed	p, t, k, b, d, g, dʒ, r, l, j, w
C=fricative	all full vowels stressed, all vowels unstressed	f, s, ʃ, ʒ, x, h
	all long vowels and diphthongs stressed; all long vowels, diphthongs, and /ə/ unstressed	v, z
	Exclusion: short vowels before /v z/ not possible within the syllable, and short vowels cannot be syllable-final ^b	
	C=nasal	all full vowels stressed, all vowels unstressed
	all full short vowels stressed; all short vowels unstressed	ŋ
	Exclusion: /ŋ/ cannot follow long vowels within the syllable ^c and cannot be syllable-initial	
VV diphones		
stressed–unstressed	all long vowels and diphthongs	all vowels
unstressed–stressed	all long vowels, diphthongs, and /ə/	all full vowels
unstressed–unstressed	all long vowels, diphthongs, and /ə/	all vowels
stressed–stressed	all long vowels and diphthongs	all full vowels
stressed	Exclusion for all VV categories: short vowels cannot be V_1 because they cannot be syllable-final	
CC diphones		
C ₁ =voiceless stop, nasal, liquid, or glide	p, t, k, m, n, ŋ, l, r, j, w	all consonants except C ₁ =C ₂ and /ŋ/
C ₁ =voiced stop	Exclusion: /ŋ/ cannot follow a stop or another sonorant within the syllable or be an onset	
	b	d, g, dʒ, v, z, ʒ, n, l, r
	d	b, g, v, z, ʒ, m, n, r, j, w
	Exclusions for /b d/: */bw bj bm dl/ in syllable onset, and voiced stops must devoice if not in onset unless followed by a voiced obstruent; ^d cannot be followed by /ŋ/ because /ŋ/ cannot be an onset	
	g	b, d, v, z
	Exclusions: syllable-final /g/ without devoicing is only followed by these consonants, and /g/ is never word-final ^e	
	f	all consonants except f, v, ŋ
	Exclusion: /fv/ too difficult for speaker to produce without assimilation	
	s, ʃ	all consonants except s, ʃ, ŋ
	Exclusions; /sʃ/ and /ʃs/ are unlikely, unless assimilated	
	x	all consonants except x, ŋ
	v	b, d, g, z, ʒ, dʒ, n, l, r
	Exclusions: */vʃ vw vm/ as onsets and /v/ must devoice if not in onset	
	z	b, d, g, v, dʒ, m, n, j, w
	Exclusions: */zl zr/ as onsets and /z/ must devoice if not in onset; /zʒ/ is likely to assimilate	
	Exclusion for /v z/: cannot be followed by a voiceless fricative within the syllable, and will devoice in coda position unless followed by a voiced obstruent	

Table VI. (Continued.)

Class	X_1	X_2
C_1 =affricate	3	w
	Exclusions: /ʒ/ never occurs syllable-finally and in onset occurs only before vowels or /w/ (e.g., in <i>bourgeois</i>)	
	Exclusion for all fricatives: /ŋ/ cannot follow a fricative within the syllable and cannot be an onset	
	dʒ	m
	Exclusions: /dʒ/ never occurs word-finally, occurs syllable-finally only in the word <i>management</i> , and cannot be followed by any other consonant within an onset	
	Exclusion for all CC diphones: no geminates	

^aCELEX does list three forms with /hə/, all based on the word *coherent*.

^bShort vowel-/h/ diphones should be impossible, and thus should have been excluded, since short vowels cannot be syllable-final and /h/ cannot be in a coda. Also, although Booij (1995) states the prohibition of short vowels followed by /v z/ within the syllable as a phonotactic constraint, another rule in the phonology voices underlying /f s/ before a voiced stop (Booij, 1995). Thus, a short vowel can be followed by [v z] if a voiced stop follows, as in *zesde* [zɛzdə], sixth; *afdeling* [ɑvdɛlɪŋ], department; etc. These diphones should have been included.

^cAlthough Booij (1995) states this phonotactic constraint, CELEX includes many words with long vowels followed by [ŋ]. However, the [ŋ] is always derived from underlying /n/ by assimilation to a following velar, e.g., *aangelegenheid*, affair; *woonkamer*, living room. Place assimilation in these cases tends to be optional.

^dBooij (1995) states that coda voiced stops only remain voiced if followed by another voiced stop, not a voiced fricative or a sonorant. Since /bv dz/, etc. are unlikely onsets, these diphones, as well as /bn dm/ etc., may also be impossible. We included them since Booij mentions that some stop-fricative and stop-nasal onsets do occur in a few words. CELEX lists words with the excluded diphones /bw/ (*clubwedstrijd*, club contest), /bj/ (*objectief*, objective), /bm/ (*schrabmes*, scraping knife), and /dl/ (*woordloos*, wordless), but in all these cases the voiced stop is in coda position and should be devoiced.

^e/gr, gl/ do occur as onsets in some loan words (e.g., *groupie*, *glamour*) and should have been included.

APPENDIX D: GATE POSITIONING CRITERIA

The following criteria were applied in establishing phoneme beginnings (B) and ends (E).

- (1) Nasal: Sudden change in spectral distribution of energy (B, E).
- (2) Fricative, after or before consonant: onset (B) or cessation (E) of frication.
- (3) Voiceless fricative, after or before vowel: cessation (B) or onset (E) of voicing.
- (4) Voiced fricative, after or before vowel: cessation (B) or onset (E) of vowel's first formant.
- (5) Voiceless stop, after or before consonant: beginning of stop closure (B) or end of release burst (E).
- (6) Voiceless stop, after or before vowel: cessation (B) or onset (E) of voicing.
- (7) Voiced stop: beginning of prevoicing (B) or end of burst (E).
- (8) Affricate /dʒ/: beginning of prevoicing (B) or end of frication (E).
- (9) Trilled /r/: amplitude minimum just before first tap of trill (B), or after last tap, sometimes realized as slight burst (E).
- (10) Approximant or fricative /r/: changes in formant frequencies or frication (B, E).
- (11) Onset (light) /l/: sudden change in the spectral distribution of energy (B, E).
- (12) Coda (dark)/l/: moment of maximum decline of energy in the first and second formants of the preceding vowel (B).
- (13) Glide or /l/, after or before consonant: use criteria for the other consonant (B, E).

- (14) Glide, after or before other glide or vowel: point halfway through the duration of the F2 transition (B, E).
- (15) Vowel, after or before consonant: use criteria for the consonant (B, E).
- (16) Vowel to vowel: vowels were always separated by creaky voicing, the silence of a glottal stop, or both. Boundary was set at onset of creaky voicing or silence (B, E).

As a default, gate end points were positioned at one-third, two-thirds, and the end of a phoneme. For certain phonemes in certain environments, however, the following special gate end points were used:

- (1) Vowel to vowel: First gate end point for second vowel at the end of creaky voicing or silence. Third gate end point at the end of second vowel. Second gate end point halfway between the other two.
- (2) Stops: First gate end point halfway through the silence or prevoicing. Second gate end point just before the beginning of the stop burst.
- (3) Initial voiceless stops: only the final gate end point was used, because earlier gate end points, during the stop closure, would produce stimuli containing only silence. Therefore, diphones with a voiceless stop as the first phoneme, if recorded without preceding environment, had only four gates instead of the usual six.
- (4) Voiced stops without prevoicing: In Dutch, /b d g/ are often produced without prevoicing (van Alphen, 2000). If no prevoicing was visible in the waveform at all in initial position, gate end points were placed as for a voiceless stop, producing four gates for the diphone.

- Baayen, H., Piepenbrock, R., and Rijn, H. van (1993). *The CELEX Lexical Database (CD-ROM)* (Linguistic Data Consortium, Univ. of Pennsylvania, Philadelphia).
- Booij, G. (1995). *The Phonology of Dutch* (Clarendon, Oxford).
- Cutler, A., and Otake, T. (1999). "Pitch accent in spoken-word recognition in Japanese," *J. Acoust. Soc. Am.* **105**, 1877–1888.
- Dorman, M. F., Studdert-Kennedy, M., and Raphael, L. J. (1977). "Stop-consonant recognition: Release bursts and formant transitions as functionally equivalent, context-dependent cues," *Percept. Psychophys.* **22**, 109–122.
- Grosjean, F. (1996). "Gating," *Language and Cognitive Processes* **11**, 597–604.
- Gussenhoven, C. (1992). "Illustrations of the IPA: Dutch," *J. Intern. Phonet. Assoc.* **22**, 45–47.
- Jongman, A. (1989). "Duration of frication noise required for identification of English fricatives," *J. Acoust. Soc. Am.* **85**, 1718–1725.
- Klaassen-Don, L. E. O. (1983). "The influence of vowels on the perception of consonants," unpublished doctoral dissertation, Leiden University.
- Kurowski, K., and Blumstein, S. E. (1984). "Perceptual integration of the murmur and formant transitions for place of articulation in nasal consonants," *J. Acoust. Soc. Am.* **76**, 383–390.
- McClelland, J. L., and Elman, J. L. (1986). "The TRACE model of speech perception," *Cognit. Psychol.* **18**, 1–86.
- Miller, G. A., and Nicely, P. E. (1955). "An analysis of perceptual confusions among some English consonants," *J. Acoust. Soc. Am.* **27**, 338–352.
- Norris, D. (1994). "Shortlist: a connectionist model of continuous speech recognition," *Cognition* **52**, 189–234.
- Pols, L. C. W., and Schouten, M. E. H. (1978). "Identification of deleted consonants," *J. Acoust. Soc. Am.* **64**, 1333–1337.
- Schouten, M. E. H., and Pols, L. C. W. (1983). "Perception of plosive consonants—The relative contributions of bursts and vocalic transitions," in *Sound Structures: Studies for Antonie Cohen*, edited by M. P. R. van den Broecke, V. J. J. P. van Heuven, and W. Zonneveld (Foris, Dordrecht), pp. 227–243.
- Smits, R. (2000). "Temporal distribution of information for human consonant recognition in VCV utterances," *J. Phonetics* **27**, 111–135.
- Smits, R., Ten Bosch, L., and Collier, R. (1996). "Evaluation of various sets of acoustical cues for the perception of prevocalic stop consonants: I. Perception experiment," *J. Acoust. Soc. Am.* **100**, 3852–3864.
- Strange, W., Verbrugge, R. R., Shankweiler, D. P., and Edman, T. R. (1976). "Consonant environment specifies vowel identity," *J. Acoust. Soc. Am.* **60**, 213–224.
- van Alphen, P. (2000). "Does subcategorical variation influence lexical access?" in *Proceedings of the Workshop on Spoken Word Access Processes*, edited by A. Cutler, J. M. McQueen, and R. Zondervan (MPI for Psycholinguistics, Nijmegen), pp. 55–58.
- van Bergem, D. R. (1993). "Acoustic vowel reduction as a function of sentence accent, word stress, and word class," *Speech Commun.* **12**, 1–23.
- Warner, N. (1998). "The Role of Dynamic Cues in Speech Perception, Spoken Word Recognition, and Phonological Universals," unpublished doctoral dissertation, Univ. of California, Berkeley.

Discrete-time modeling of woodwind instrument bores using wave variables

Maarten van Walstijn and Murray Campbell

School of Physics, University of Edinburgh, Mayfield Road, Edinburgh EH9 3JZ, United Kingdom

(Received 30 January 2002; revised 24 August 2002; accepted 26 August 2002)

A method for simulation of acoustical bores, useful in the context of sound synthesis by physical modeling of woodwind instruments, is presented. As with previously developed methods, such as digital waveguide modeling (DWM) [Smith, *Comput. Music J.* **16**, 74–91 (1992)] and the multi convolution algorithm (MCA) [Martínez *et al.*, *J. Acoust. Soc. Am.* **84**, 1620–1627 (1988)], the approach is based on a one-dimensional model of wave propagation in the bore. Both the DWM method and the MCA explicitly compute the transmission and reflection of wave variables that represent actual traveling pressure waves. The method presented in this report, the wave digital modeling (WDM) method, avoids the typical limitations associated with these methods by using a more general definition of the wave variables. An efficient and spatially modular discrete-time model is constructed from the digital representations of elemental bore units such as cylindrical sections, conical sections, and toneholes. Frequency-dependent phenomena, such as boundary losses, are approximated with digital filters. The stability of a simulation of a complete acoustic bore is investigated empirically. Results of the simulation of a full clarinet show that a very good concordance with classic transmission-line theory is obtained. © 2003 Acoustical Society of America. [DOI: 10.1121/1.1515776]

PACS numbers: 43.75.Ef, 43.75.Pq [NHF]

I. INTRODUCTION

The objective of this paper is to present a method for time-domain simulation of woodwind instrument bores that can be used for musical sound synthesis purposes. The advantages of the time-domain approach over the frequency-domain approach have been discussed by Schumacher;¹ time-domain methods are inherently more suited to the prediction of perceptually important transient phenomena. The bore, assumed to behave linearly, is usually represented by its impulse response, and the interaction between the bore and the driver is modeled by a set of differential equations in combination with a convolution of the impulse response with the out-going pressure wave. A general framework for modeling of sustained musical tones on this basis was developed by McIntyre *et al.*²

However, musical use of a physical model of a woodwind instrument requires a spatially modular description of the bore. That is, the bore has to be modeled in such a way that the acoustic variables are defined at various specific points along the air column axis. This is because in order to vary the pitch, the player manipulates the acoustical response of the bore via opening and closing toneholes. A spatially modular description is also advantageous for the inclusion of nonlinear effects in the bore; a recent experimental study on woodwind toneholes³ has indicated that such nonlinear effects are substantial at large amplitudes.

Two main techniques for obtaining a spatial description appear in the literature, namely digital waveguide modeling (DWM)^{4–6} and the multiconvolution algorithm (MCA).⁷ The latter has recently been adapted by Barjau *et al.*⁸ for simulation of acoustical bores of arbitrary length. These techniques are remarkably similar in the sense that they are both based on a one-dimensional model of wave propagation in the

bore, in which discontinuities in the bore are modeled through reflection and transmission of propagating waves; they differ mainly in the details of the numerical formulation. The main advantage of the DWM approach is that it allows the adjustment of the balance between accuracy and efficiency. Frequency-dependent phenomena (such as boundary or radiation losses) are modeled using a digital approximation of a continuous-domain formulation, where both the continuous formulation and the digital approximation technique may be chosen freely. In this respect the MCA approach is more limited, since it relies on the possibility of performing analytic inverse Fourier transforms of continuous-domain formulations. The possibility of adjusting the trade-off between accuracy and efficiency is particularly important with respect to musical sound synthesis; while efficiency is always an important criterion in this context,⁹ a synthesis method should anticipate and exploit the steady increasing in computational power of commonly available computing resources.

However, the feasibility of the DWM approach for modeling a variety of wind instrument bores has yet to be demonstrated. This is partly due to numerical instability problems that can occur in simulations of conical sections.⁶ Another obstacle is that the DWM approach does not provide methods for modeling of toneholes in a conical bore. This shortcoming stems directly from the fact that DWM techniques are specifically defined to simulate distributed systems; as a consequence, uncomputable loops are created when a conical section is directly connected to an acoustic unit with a nonzero instantaneous reflection (such as a tonehole).

This report presents a time-domain method, the wave digital modeling (WDM) method, that overcomes the majority of these problems. The method makes strong use of the classical analogy between electrical and acoustical systems, and combines DWM techniques with wave digital filter (WDF) techniques. The latter, which were originally designed for simulation of analog networks, are suited to modeling small acoustic units that may be considered as lumped elements, and are therefore conveniently complementary to DWM techniques. The main purpose of the present work is to formulate a unified description that encompasses both techniques, and that can be used as a general modeling framework for digital simulation of woodwind instrument bores.

The paper is organized as follows: the basic modeling principles are outlined in Sec. II. Piecewise conical bore modeling has proved to be a useful concept in many previous studies on wind instrument modeling; how to apply WDM techniques for the simulation of such systems is discussed in Sec. III, where accuracy is assessed via direct comparison with a transmission-line model, and stability properties are investigated empirically. In Sec. IV a tonehole model is presented that can simulate holes of a wide variety of musically and physically feasible dimensions, and can be controlled dynamically. The main results are presented in Sec. V, where the method is applied to the simulation of a full clarinet bore. Accuracy is again assessed via direct comparison with a transmission-line description. Finally the perspectives of this work are discussed in the conclusions.

II. GENERAL DESCRIPTION OF THE METHOD

WDF techniques are used for discretization of analog networks.¹⁰ The resulting digital networks are called *wave digital filters* (WDFs). The classical analogy between electric and acoustic systems raises the possibility of employing WDF techniques for the discretization of lumped elements in a model of an acoustic system. WDF techniques are similar to DWM techniques in the sense that they both digitize continuous-time models using *wave variables*. As already suggested by Smith¹¹ and recently elaborated by Bilbao,¹² a combined approach is possible. The latter work addresses the more general problem of numerically solving partial differential equations by means of methods that use wave variables. The methods presented in the present study are limited to cases in which lumped elements are modeled using WDF techniques and distributed elements are modeled using DWM techniques, and can be considered as a specific subclass of the “wave” or “scattering” methods described by Bilbao. A rare musical acoustics application of such an approach is the digital simulation of the force interaction between string and hammer in a piano, developed by Duyne and Smith.¹³ The resulting piano hammer model is referred to as the *wave digital hammer*; an appropriate general term for the combined approach is *wave digital modeling*.

A. Modeling principles

The wave digital models presented in this work are derived from a transmission-line description of a woodwind bore. The approach thus requires that a transmission-line de-

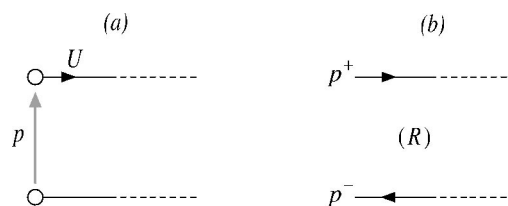


FIG. 1. (a) A port and its associated acoustic variables. (b) The corresponding signal flow diagram after decomposition of the acoustic variables into wave variables.

scription or “equivalent network” is found for each individual bore component. In principle these networks may have any number of ports and may contain any type of linear element; the only restriction is that the complete network that represents the entire bore is stable.

The procedure for the derivation of the wave digital model of an individual bore component is similar to the derivation of a wave digital filter, and consists of three steps:

- (1) decomposition of the acoustic variables into wave variables,
- (2) discretization of frequency-dependent elements,
- (3) satisfaction of the computability condition.

Step (1) is accomplished by using the following relationships:

$$p_i = p_i^+ + p_i^- \quad \text{and} \quad U_i = \frac{p_i^+ - p_i^-}{R_i}, \quad (1)$$

where for port i , p_i is the pressure and U_i is the volume velocity, while p_i^+ and p_i^- are the wave variables. The quantity R_i has the dimension resistance and, following WDF theory, is referred to as the *port-resistance*. In the case of a distributed acoustic element, the wave variables represent pressure-waves traveling through a certain medium. The port-resistance then equals the reference impedance that characterizes the medium; in the case of a wave traveling through an air-filled pipe, this is the characteristic impedance $Z_0 = \rho c / S$, where S is the cross-sectional pipe area, ρ is the mean air density, and c is the wave velocity. In the case of a lumped acoustic element, the wave variables do not represent waves that actually travel any distance; the decomposition is in this case merely a matter of mathematical description, and from an acoustical point of view the port-resistance may then be considered arbitrary. As in the derivation of WDFs, this freedom of choice is exploited to avoid delay-free loops in the final modeling structure. The decomposition of acoustic variables has to be carried out at each port of the system. Figure 1 depicts a single port and its corresponding signal flow after decomposition.

Step (2) concerns the approximation in the digital domain of linear, frequency-dependent, continuous domain phenomena, which is realized in the present study by means of digital filters. A wave digital model contains various computational loops, in which these filters are placed. In order for the model to be stable, the gain of these loops must not exceed unity, and therefore the digital filters that are used here are designed such that their magnitude response is equal to or less than unity at all frequencies. Three different types

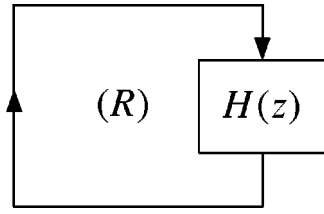


FIG. 2. A computational loop with transfer function $H(z)$ and port-resistance R .

of filter design techniques are employed, each of them for a specific category of frequency-dependent elements. The first category comprises lumped circuit elements, such as inertances and compliances, which are mathematically described by a rational polynomial transfer function of the Laplace variable $s = j\omega$. As is customary in WDF theory, such elements are discretized via the bilinear transform (BT):

$$s = \beta \left(\frac{1 - z^{-1}}{1 + z^{-1}} \right), \quad (2)$$

where z^{-1} is the frequency-domain representation of a single delay of $T = 1/f_s$ seconds, $\beta = 2f_s$ is the bilinear operator, and f_s is the sample rate. Frequency-dependent phenomena which cannot be described with a rational polynomial transfer function fall into the second category. Digital approximation of such elements is predominantly carried out by means of infinite impulse response (IIR) filters. For the current purposes, the output-error minimization technique,¹⁴ which uses iterative gradient descent search methods to minimize a weighted least-square approximation error, is a particularly suitable method of IIR filter design, since it allows emphasis on accuracy at lower frequencies. Given that in wind instrument modeling, the frequencies below cutoff are of greater importance than the frequencies above cutoff, such “navigation” of the approximation error is helpful in improving the balance between accuracy and efficiency. The details of such IIR filter approximation can be found in previous work.^{6,15} The third category concerns the approximation of a fractional delay. As is explained in Sec. II C, fractional delay filters are required to simulate wave propagation in tubes of arbitrary length. In the present study, Lagrange FIR interpolation filters⁵ are employed. The FIR and IIR filters used in the present study are typically of the order 3 to 5.

Step (3) is concerned with the computability of the resulting digital structure. Like a digital filter, a wave digital model is described mathematically by a system of difference equations. Such a system is called *computable* if the arithmetic operations prescribed by these equations can be ordered sequentially at each discrete-time instant.¹⁰ In practice this condition is satisfied if the system contains no delay-free loops. In a wave digital model, such delay-free loops may arise in the discretization of a lumped element. One possible way to solve this problem is to insert a fictitious delay into the loop. However, such an approach leads to significant errors, unless a very high sample rate is used. Following WDF theory, these loops can be ensured to have at least one delay by choosing the appropriate port-resistance of that loop. For example, consider the loop in Fig. 2, in which $H(z)$ repre-

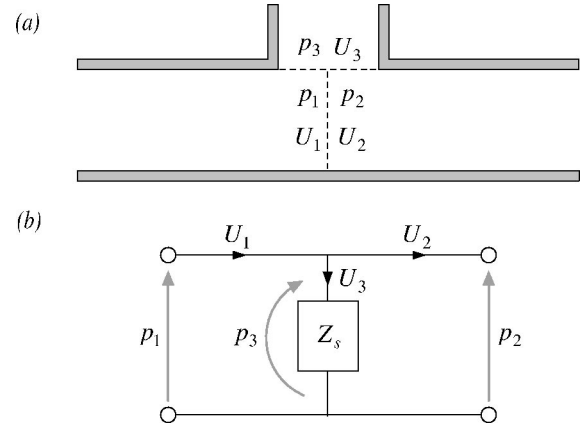


FIG. 3. (a) A side branch in a cylindrical pipe. (b) The equivalent network.

sents the digital transfer function of the loop. In a wave digital model, this transfer function can always be written in the form:

$$H(z) = \frac{b_0 + b_1 z^{-1} + \dots + b_N z^{-N}}{1 + a_1 z^{-1} + \dots + a_N z^{-N}}, \quad (3)$$

where the coefficients b_k, a_k depend on the port-resistance of the loop. The coefficient b_0 represents the factor by which the wave is multiplied before it is passed on *without delay*. Hence in order for this loop to be computable, this factor must be zero. If $H(z)$ represents a lumped element, the port-resistance may be chosen such that $b_0 = 0$.

B. Lumped elements

An acoustical device may be treated as a lumped acoustic element if the wavelength is considerably greater than its dimensions. An example of such a device is a short side branch in a cylindrical pipe [see Fig. 3(a)]. In the low-frequency limit, the wavelength is long compared to the complicated flow patterns near the junction, and the acoustic behavior of the side branch is characterized by a simple shunt impedance network [see Fig. 3(b)]. This is a three-port network to which Kirchhoff's laws apply, i.e.,

$$p_1 = p_2 = p_3 \quad \text{and} \quad U_1 = U_2 + U_3. \quad (4)$$

The shunt impedance defines the relation between the acoustical pressure and volume velocity in the side branch:

$$p_3 = Z_s(\omega) U_3. \quad (5)$$

If inner length corrections are neglected, the side branch approximately acts as an inertance for an open branch [superscript (o)] and as a compliance for a closed branch [superscript (c)], i.e.,

$$Z_s^{(o)}(\omega) = j\omega M \quad \text{and} \quad Z_s^{(c)}(\omega) = \frac{1}{j\omega C}, \quad (6)$$

where $M = (\rho t_e^{(o)})/S_h$ is the open-branch inertance, $C = S_h t_e^{(c)}/(\rho c^2)$ is the closed-branch compliance, S_h is the branch cross-section, and $t_e^{(o)}$ and $t_e^{(c)}$ are the (real-valued) open-branch and closed-branch effective lengths, respectively.

A wave digital simulation of the open or closed branch is derived by carrying out the steps described in Sec. II A. Decomposition of the acoustic variables in Eqs. (4) yields the three-port junction scattering equations

$$p_1^- = p_2^- + W, \quad (7)$$

$$p_2^+ = p_1^+ + W, \quad (8)$$

$$p_3^+ = p_1^+ + p_2^- - p_3^- + W, \quad (9)$$

where

$$W = k_1[p_1^+ - p_3^-] + k_2[p_2^- - p_3^-], \quad (10)$$

with the coefficients

$$k_1 = \frac{R_2 R_3 - R_1 R_3 - R_1 R_2}{R_2 R_3 + R_1 R_3 + R_1 R_2}, \quad (11)$$

$$k_2 = \frac{R_1 R_3 - R_2 R_3 - R_1 R_2}{R_2 R_3 + R_1 R_3 + R_1 R_2}. \quad (12)$$

Decomposition of the acoustic variables in Eq. (5) gives

$$p_3^- = R_s(\omega) p_3^+, \quad (13)$$

where $R_s(\omega)$ is a frequency-dependent wave reflectance:

$$R_s(\omega) = \frac{Z_s(\omega) - R_3}{Z_s(\omega) + R_3}. \quad (14)$$

Note that this reflectance is not equivalent to what is usually referred to as a “plane wave reflectance,” since the wave variables p_3^+ and p_3^- do not represent actual traveling waves; from an acoustical point of view, their port-resistance value (R_3) may be chosen arbitrarily. Equation (14) is discretized using the BT, which yields the digitized wave reflectance or “wave digital reflectance.” In contrast to some other methods for discretizing analogue filters (such as the impulse invariance method), the use of the BT guarantees that there exists an R_3 for which the resulting digital filter has a zero impulse response at $t=0$. In the case of an open side branch, one obtains the wave digital reflectance

$$R_s^{(o)}(z) = \frac{\alpha - z^{-1}}{1 - \alpha z^{-1}} \quad \text{with} \quad \alpha = \frac{\beta M - R_3}{\beta M + R_3}. \quad (15)$$

For a closed side branch, the discretization gives

$$R_s^{(c)}(z) = \frac{\alpha + z^{-1}}{1 + \alpha z^{-1}} \quad \text{with} \quad \alpha = \frac{1 - \beta C R_3}{1 + \beta C R_3}. \quad (16)$$

Figure 4 depicts the signal flow diagram of the obtained equations.

The next step is to ensure computability of this structure. A possible delay-free loop exists in that p_3^+ depends on p_3^- according to (9), but p_3^- also depends on p_3^+ via (13). In order to avoid an uncomputable loop, the port-resistance R_3 must be chosen such that there is no instantaneous reflection from p_3^+ into p_3^- . In other words, the coefficient α in Eqs. (15) and (16) must equal zero. For the open branch, this is achieved by setting $R_3 = \beta M$, whereas for the closed branch the port-resistance must be set to $R_3 = 1/(\beta C)$. Substitution of these values into Eqs. (15) and (16) yields

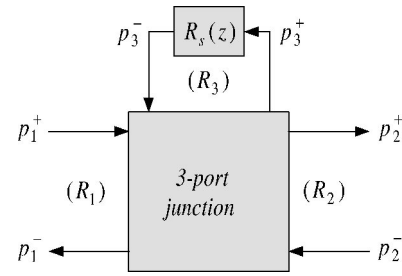


FIG. 4. The signal flow diagram of a wave digital model of a shunt network. The 3-port junction block implements wave scattering. The wave digital reflectance $R_s(z)$ implements the shunt element.

$$R_s^{(o)}(z) = -z^{-1} \quad \text{and} \quad R_s^{(c)}(z) = z^{-1}. \quad (17)$$

Thus the side branch is modeled with nothing more than a delay that is interfaced to the main bore with a three-port junction, where an extra sign-inversion is required when the branch is open.

C. Distributed elements

In the analogy between electrical circuits and tubular acoustic systems, distributed acoustic elements are modeled as transmission lines. The simplest system of this type is one in which plane waves propagate through a cylindrical pipe. This system is mathematically described by a 2×2 matrix equation:¹⁶

$$\begin{bmatrix} p_1 \\ U_1 \end{bmatrix} = \begin{bmatrix} \cosh(\Gamma L) & Z_0 \sinh(\Gamma L) \\ Z_0^{-1} \sinh(\Gamma L) & \cosh(\Gamma L) \end{bmatrix} \begin{bmatrix} p_2 \\ U_2 \end{bmatrix}, \quad (18)$$

where p_1, U_1 , and p_2, U_2 , respectively denote the pressure and volume velocity at the input- and the output-end of the pipe, L is the pipe length, Γ is the complex propagation constant and Z_0 is the characteristic impedance. As with lumped acoustic elements, this description is only valid at low frequencies, this time because it takes into account only the principal mode of propagation. Again, the wave digital model is derived by carrying out the steps described in Sec. II A; in this case the procedure is in fact equivalent to applying DWM techniques. Since a pipe is a distributed system, the port-resistances on both sides of the system have to equal the characteristic impedance of the pipe, i.e., $R_1 = R_2 = Z_0$. The decomposition of the acoustic variables into wave variables then yields the relationships:

$$p_2^+ = [e^{-\Gamma L}] p_1^+, \quad p_1^- = [e^{-\Gamma L}] p_2^-. \quad (19)$$

If viscothermal losses are ignored, one may substitute $\Gamma = j\omega/c$, and the term $e^{-\Gamma L}$ is the frequency-domain description of a pure time delay L/c . As is customary in digital waveguide modeling, such a delay can be realized in discrete time with a digital delay line in cascade with a fractional delay filter.⁵ The latter performs a numerical operation that is equivalent to time interpolation, which allows modeling of wave propagation in a pipe of arbitrary length.

Viscothermal losses can be taken into account in the transmission-line description by using a lossy, frequency-dependent formulation of Γ , such as that described by Keefe,¹⁷ and can be assimilated into the wave digital model

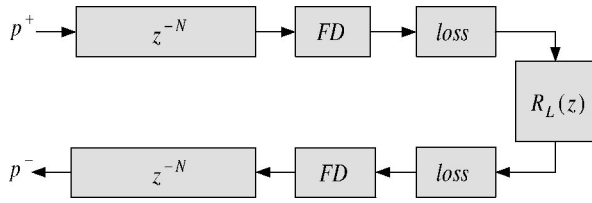


FIG. 5. Signal flow diagram of a wave digital model of an open-ended pipe. Each z^{-N} unit indicates a delay-line. A *loss* unit represents a digital filter that approximates viscothermal losses, and an *FD* unit indicates a fractional delay filter. The open end is modeled with the reflectance filter $R_L(z)$.

by cascading another digital filter with each delay line. This filter is designed to approximate the continuous-domain expression

$$H_{\text{loss}}(\omega) = e^{-(\Gamma - j\omega/c)L}. \quad (20)$$

The output-error method mentioned in Sec. II A can be used for this purpose. Frequency-dependent termination losses, such as occur at an open end of a pipe, are also approximated with a digital filter. This filter is designed to approximate the termination reflectance

$$R_L(\omega) = \frac{Z_L(\omega) - Z_0}{Z_L(\omega) + Z_0}, \quad (21)$$

where $Z_L(\omega)$ is the termination load. For most wind instruments, the radiation impedance of unflanged open ends as formulated by Levine and Schwinger¹⁸ gives a suitable formulation of the termination load. Scavone⁶ gives a convenient approximation to these formulas, that can be applied directly in the present context. After arranging the individual units in the appropriate way, the signal flow diagram of the wave digital model is obtained (see Fig. 5).

III. PIECEWISE CONICAL BORES

A woodwind bore may be considered as a succession of conical and cylindrical bore sections with a set of open or closed holes in their sides.⁷ This section presents methods for simulation of piecewise conical bores with the WDM method.

A. Benade's equivalent network

A conical bore section is similar to a cylindrical bore section in the sense that both are pure waveguides. That is, plane waves propagate without back-scattering in a cylindrical section, while spherical waves propagate in the same way in a conical section. This similarity is highlighted in the work of Benade,¹⁹ in which a conical section is represented as an *equivalent circuit consisting of a pair of inertances, a transformer, and a nontapered duct that has the same length and small-end radius as the cone to be represented*. This equivalent network is depicted in Fig. 6. The values of the inertances are

$$M_0 = \rho r_0 / S_0 \quad \text{and} \quad M_e = \rho r_e / S_e, \quad (22)$$

where r_0 and r_e are the distances from the cone apex and S_0 and S_e the wavefront areas at the left-hand and right-hand side of the cone, respectively. The distance from the cone

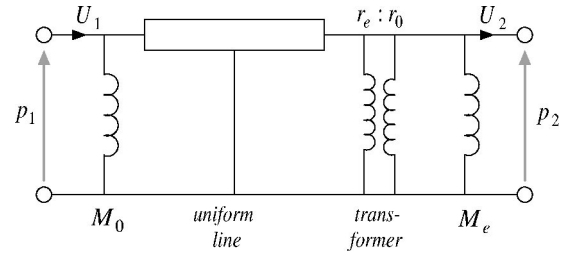


FIG. 6. Equivalent circuit of a conical waveguide constructed of a uniform line, two shunt inertances, and transformer [after Benade (Ref. 19)].

apex is defined as negative if the apex is positioned on the right-hand side of the cone.

The methods presented in Sec. II can be used to derive a wave digital simulation of the equivalent circuit; a shunt inertance is modeled as a three-port junction with a single delay attached to one of its ports, and a bi-directional delay-line simulates the uniform line, with added filters for time interpolation and inclusion of viscothermal losses. The transformer represents the decrease in pressure with increasing wavefront area, and can be modeled by adding a scaling factor to each delay line. However, these scaling factors may be removed from the system without changing the overall reflectance at the input-end of the model. In such a scenario, one must apply them “extrinsically” when calculating the actual pressure at any point in the cone.¹⁵

B. A junction of two conical sections

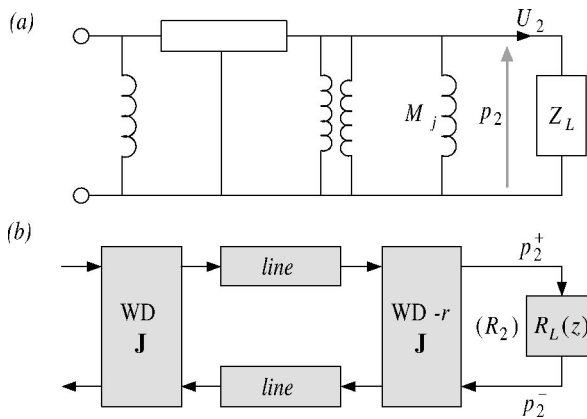
An equivalent network of two successive conical sections can be constructed by attaching two networks of the kind depicted in Fig. 6. A junction of two conical sections is thus described with a network which has the right-hand inertance $M_1 = -(\rho r_1)/S_1$ of the first cone in parallel with the left-hand inertance $M_2 = (\rho r_2)/S_2$ of the second cone. As pointed out in Ref. 19, this arrangement of the junction network is equivalent to a single shunt inertance

$$M_j = \frac{M_1 M_2}{M_1 + M_2} = \frac{\rho r_1 r_2}{r_1 S_2 - r_2 S_1}. \quad (23)$$

It follows that the *wave digital junction* is derived in the same way as the wave digital structure of the open side branch discussed in Sec. II B. The signal flow of the wave digital junction is thus as depicted in Fig. 4. For certain junctions, the value of M_j is negative. The problems related to discrete-time modeling of such a negative inertance are discussed in Sec. III E.

C. A junction of a conical section and a lumped element

Consider the network in Fig. 7(a). This network is the electrical equivalent of a conical section that is terminated by a load $Z_L(\omega)$. This load could for example represent the open-end radiation impedance. The value of the shunt inertance at the termination is $M_j = -(\rho r)/S$, where r is the distance from the cone apex to the end of the cone, and S is the wave area at the cone end. Figure 7(b) shows the wave digital model of this system. The term $R_L(z)$ indicates a digital filter approximation of the wave reflectance



$$R_L(\omega) = \frac{Z_L(\omega) - R_2}{Z_L(\omega) + R_2}, \quad (24)$$

where R_2 is the port-resistance as defined for the wave variables p_2^+ and p_2^- . If the taper junction modeled in discrete-time without taking special care concerning the wave reflectances (i.e., if R_2 is set equal to the local characteristic impedance), then the system would exhibit a delay-free loop, because in that scenario both the junction and the lumped element have a nonzero instantaneous reflection. In order to avoid such a delay-free loop, the junction near the lumped element is designed in such a way that has no immediate reflection of the wave incident from the right. It will therefore be referred to as a "WD-r junction," where the letter r indicates that the junction has a zero instantaneous reflection in right-going direction. The first few steps in the derivation of the WD-r junction are the same as in the case of the normal wave digital junction. That is, the basic structure is again a three-port junction (see Fig. 4), with an inductance wave reflectance

$$R_s(\omega) = \frac{j\omega M_j - R_3}{j\omega M_j + R_3} \quad (25)$$

attached to one of its ports. The port-admittance R_3 relates in the same way to the inductance as for the normal wave digital junction, i.e., $R_3 = \beta M_j$, and the wave digital reflectance again reduces to a negative delay. As explained in Sec. II B, Eqs. (7), (8), and (9) describe the scattering of wave variables at the three-port junction. In this case the port-resistance R_2 on the right-hand side may be chosen arbitrary because it connects directly to a lumped element. In order to derive a realizable structure, the instantaneous reflection of the incident wave p_2^- should be zero, which is true only if

$$R_2 = \frac{R_1 R_3}{R_1 + R_3}. \quad (26)$$

Substitution of Eq. (26) into Eqs. (11) and (12), yields the normal three-port equations [i.e., Eqs. (7), (8), and (9)], but with Eq. (10) replaced by

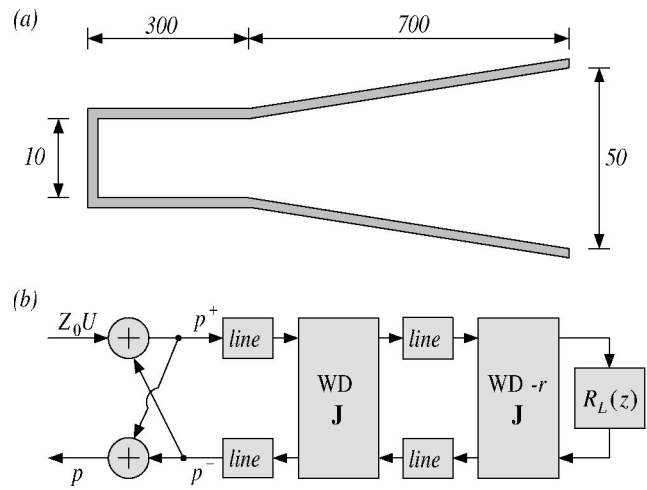


FIG. 8. (a) Bore dimensions (in millimeter). (b) Signal flow diagram of the wave digital model.

$$W = -\left(\frac{R_1}{R_1 + R_3}\right) [p_1^+ - p_3^-]. \quad (27)$$

In the case of modeling a lumped element attached to the left-hand side of the cone, a "WD-l junction" (that has a zero instantaneous reflection in the left-going direction) is required, and the derivation is again similar to that of the normal wave digital junction. In this case, the port-resistance R_1 has to be set to

$$R_1 = \frac{R_2 R_3}{R_2 + R_3}. \quad (28)$$

Substitution into Eqs. (11) and (12) again yields the normal three-port equations, but this time with Eq. (10) replaced by

$$W = -\left(\frac{R_2}{R_2 + R_3}\right) [p_1^+ - p_3^-]. \quad (29)$$

D. Example application

In this section the wave digital modeling approach is demonstrated for the bore configuration depicted in Fig. 8(a). This configuration has been used in two previous studies^{7,8} on time-domain modeling. In this case, an interface that converts to the acoustic variables p and $Z_0 U$ is added to the input-end of the wave digital model [see Fig. 8(b)], so that the impulse response of the system is equivalent to the inverse Fourier transform of the input impedance (normalized by the characteristic impedance Z_0 of the cylindrical section). Third-order Lagrange interpolation filters were used for modeling fractional delay lengths and fourth-order IIR filters to approximate the viscothermal losses of each bore section. The wave digital reflectance $R_L(\omega)$ was approximated with a third-order IIR filter.

For comparison, the impulse response was also computed by taking the inverse Fourier transform of a frequency-domain computation using transmission-line matrices, as described by Keefe.¹⁶ Figure 9 shows that the two resulting impulse responses are effectively identical.

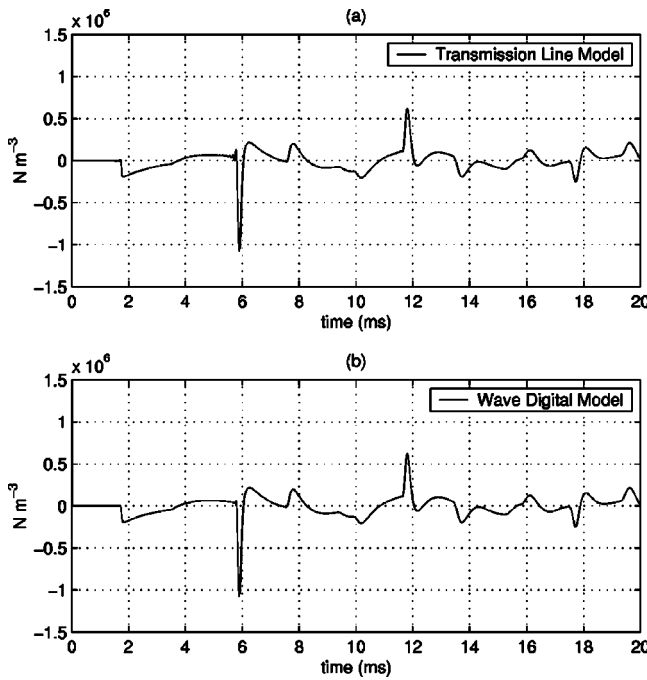


FIG. 9. (a) Impulse response of the bore configuration depicted in Fig. 8(a), computed as the inverse Fourier transform of the input impedance that was calculated with transmission-line matrices. (b) The same impulse response, computed with the wave digital model. These results may also be compared to those given in Ref. 7 (Fig. 8) and Ref. 8 [Fig. 6(c)].

E. Stability properties

For a normal wave digital junction [inertance given by Eq. (23)], the inertance remains positive for $S_2/r_2 > S_1/r_1$. Hence for certain, physically feasible junction configurations, the junction inertance M_j is negative. This amounts to using a negative port-resistance, which normally leads to an unstable filter structure.¹⁰ Berners²⁰ has recently shown that the unstable junction filter is ultimately due to the presence of a trapped mode, such that traveling wave components due not constitute a complete basis set in the region surrounding the junction. However, this does not have to imply that the numerical formulation of a complete conical bore model is unstable, because such trapped modes do not exist for passively terminated systems.²⁰

In order to empirically test whether wave digital models of piecewise conical bore systems are stable, the bore configuration depicted in Fig. 10 was simulated. The simulation was run for a very long time (up to 250 seconds), using a variety of different input signals, and the resulting impulse response was analyzed; if the system is stable, then this signal must not exhibit amplitudal growth after the initial deflections. The simulation was run with various different ter-

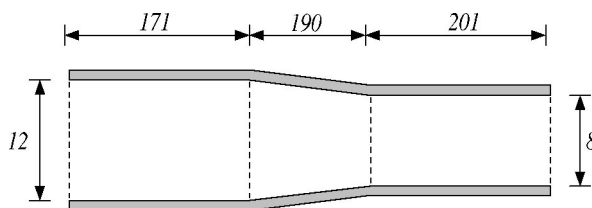


FIG. 10. Bore configuration used in the stability tests. Dimensions are given in millimeter.

minations (i.e., anechoic, open, closed). The results show that the system remains unconditionally stable when visco-thermal losses are not included. However when such losses are included, the system is in all cases unstable. When anechoic terminations are avoided, the signal starts to grow significantly only after a very long simulation time (typically 200 seconds); for such cases, the impulse response of the system, which typically has effectively decayed within less than one second for musical instrument bores, can be computed without any significant error due to instability problems. It must be noted that these findings are subject to the precision of the floating points used in the computations; all results presented here are computed using 64-bit precision.

The fact that the inclusion of losses has a strong influence on the stability may be explained by the inconsistency in the formulation of the propagation constant. That is, the junctions are formulated using a *lossless* Γ , whereas wave propagation in the bore sections is formulated with a *lossy* Γ . Gilbert *et al.*²¹ have proved that a continuous-domain formulation of a piecewise conical bore system is stable; this proof was carried out for a lossless as well as for a lossy version of the propagation constant. No such proof exists however for a continuous-domain formulation in which the propagation constant is inconsistent. It is worthwhile pointing out that not only the WDM method but also the MCA and the DWM approaches are based on such an “inconsistent” continuous-domain formulation.

IV. TONEHOLES

Physical modeling of woodwind instruments with application to sound synthesis requires a tonehole model that characterizes all tonehole states from open to closed. Scavone and Cook²² developed a model that meets this requirement, but their “three-port tonehole model” has the limitation that the tonehole length is restricted to a minimum of $t = c/(2f_s)$. Hence an alternative method is required for simulation of shorter toneholes.

A. Lumped model

Following Dubos *et al.*²³ and Dalmont *et al.*,³ the shunt impedance of a tonehole is written

$$Z_s(\omega) = Z_h(\omega) + j\omega M_s, \quad (30)$$

where Z_h is the planar mode input impedance of the hole, and $M_s = t_s \rho / S_h$ is an inertance due to the higher order symmetrical modes at the intersection between the hole and the main bore, with

$$t_s = b \left(\frac{8}{3\pi} - 0.193\delta - 1.09\delta^2 + 1.27\delta^3 - 0.71\delta^4 \right), \quad (31)$$

where $\delta = b/a$, b is the tonehole radius, and a is the main bore radius. At low frequencies, the open- and the closed-hole formulas for Z_h as given by Dubos *et al.* may be approximated with the lumped model formulas for Z_s in Eqs. (6), using the same effective length formulations as given in Ref. 23:

$$t_e^{(0)} = t_w + t_m + t_r, \quad t_e^{(c)} = t_w + t_m, \quad (32)$$

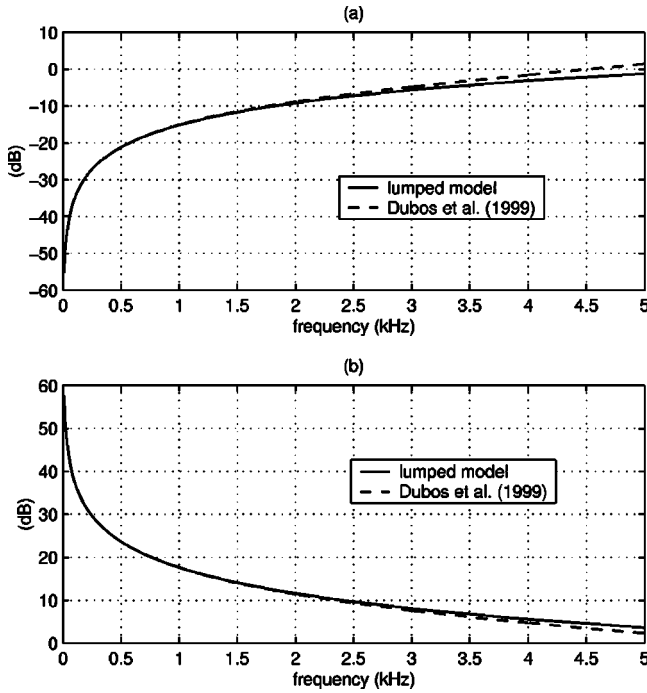


FIG. 11. Magnitude of the (normalized) planar mode impedance $Z_h \cdot S_h / (\rho c)$ of a sidehole of dimensions (in mm) $a=7.5$, $b=3.1$, $t_w=7.0$, $R=5.1$, $h=2.4$. (a) Open hole. (b) Closed hole.

where t_w is the sum of the shortest geometrically tonehole length and t_m is the extra length due to the matching volume between the hole and the main bore:

$$t_m = \frac{b\delta}{8} (1 + 0.207\delta^3). \quad (33)$$

The term t_r in Eqs. (32) represents the length correction due to radiation, for which Nederveen²⁴ gives the empirical formula:

$$t_r = b[0.821 - 0.135(b/R_c) - 0.073(b/R_c)^4] + t_d, \quad (34)$$

where R_c is the outer radius of the hole, and t_d is the extra length correction for cases where a key of radius R_{pad} hanging a distance h above the hole ($t_d=0$ for holes without key):

$$t_d = 0.613 b [(R_{pad}/b)^{0.18} (R_{pad}/h)^{0.39} - 1]. \quad (35)$$

Figure 11 compares the lumped model formulations of Z_h with the formulas by Dubos *et al.*, for typical clarinet tonehole dimensions. In the lower frequency range, the approximation is extremely close.

An additional effect of inserting a hole in a woodwind bore is that the effective acoustic length of the bore is slightly reduced on both sides of the hole. In the present study, the total length correction for an open or closed tonehole is formulated:

$$t_a = -b\delta^2 [2.72 + 0.540\delta + 0.285\delta^2]^{-1}. \quad (36)$$

Thus if the lengths of the main bore sections on each side of the tonehole are l_1 and l_2 , they should be corrected to $l_1 + t_a/2$ and $l_2 + t_a/2$, respectively. This length-correction formulation approximates the series inertance formulation in Ref. 23.

B. Partially open holes

As discussed in Sec. II B, the planar mode impedance Z_h of a sidehole is approximately that of a pure inertance or compliance depending on whether the hole is open or closed, respectively. For intermediate tonehole states (i.e., partially open holes), the tonehole volume can be divided into an “open part” that behaves as an inertance, and a “closed part” that behaves as a compliance. These volumes operate in parallel, thus Eq. (30) becomes

$$Z_s(\omega) = \frac{j\omega M}{1 - \omega^2 MC} + j\omega M_s, \quad (37)$$

where the compliance and inertance of the partially open hole are formulated

$$C = (1 - g) \frac{S_h t_e^{(c)}}{\rho c^2} \quad \text{and} \quad M = \frac{\rho t_e^{(o)}}{g S_h}. \quad (38)$$

The parameter g expresses the tonehole state, defined as the ratio between *open* and *total* tonehole volume.

C. Discretization

The first step in the derivation of the wave digital tonehole model (i.e., the decomposition into wave variables) is analogous to the corresponding step discussed in Sec. II B. The signal flow diagram is thus as depicted in Fig. 4. In this case, the wave digital reflectance is found after substitution of Eq. (37) into Eq. (14), and applying the BT, which yields

$$R_s(z) = -\frac{\alpha_1 + \alpha_2 z^{-1} + \alpha_3 z^{-2} + z^{-3}}{1 + \alpha_3 z^{-1} + \alpha_2 z^{-2} + \alpha_1 z^{-3}}. \quad (39)$$

This is a digital all-pass filter with coefficients

$$\alpha_1 = \frac{-\beta^3 M_s MC - \beta(M + M_s) + R_3(1 + \beta^2 MC)}{\beta^3 M_s MC + \beta(M + M_s) + R_3(1 + \beta^2 MC)}, \quad (40)$$

$$\alpha_2 = \frac{3\beta^3 M_s MC - \beta(M + M_s) + R_3(3 - \beta^2 MC)}{\beta^3 M_s MC + \beta(M + M_s) + R_3(1 + \beta^2 MC)}, \quad (41)$$

$$\alpha_3 = \frac{-3\beta^3 M_s MC + \beta(M + M_s) + R_3(3 - \beta^2 MC)}{\beta^3 M_s MC + \beta(M + M_s) + R_3(1 + \beta^2 MC)}. \quad (42)$$

In order to avoid a delay-free loop, R_3 must be chosen such that the wave p_3^+ entering $R_s(z)$ is not immediately reflected back towards the three-port scattering junction via p_3^- . This requires setting the filter coefficient $\alpha_1=0$, which means that the port-resistance must be set to

$$R_3 = \frac{\beta^3 M_s C + \beta(1 + M_s G)}{G + \beta^2 C}, \quad (43)$$

where the term $G = M^{-1}$ is introduced in order to allow the tonehole state parameter g in Eqs. (38) to go to zero, which corresponds to fully closing the tonehole. Substitution into Eq. (39) gives the final wave digital reflectance:

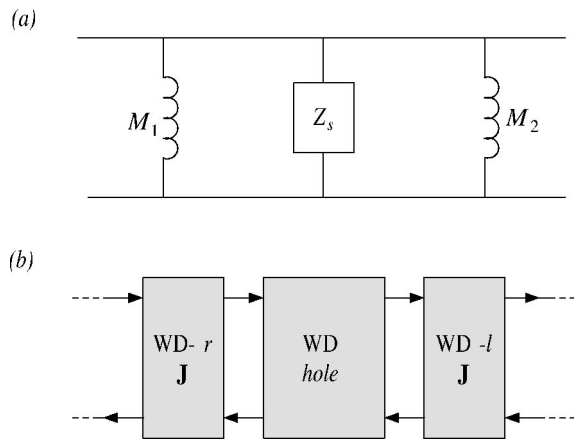


FIG. 12. (a) Equivalent network of a partially open tonehole in a piecewise conical bore. (b): The wave digital model structure for digital simulation of this network. The “WD hole” unit indicates the wave digital tonehole model. The inertances associated with the conical sections on either side of the hole are modeled with a WD-*r* and a WD-*l* junction, such that no delay-free loops arise.

$$R_s(z) = -z^{-1} \left(\frac{\alpha_2 + \alpha_3 z^{-1} + z^{-2}}{1 + \alpha_3 z^{-1} + \alpha_2 z^{-2}} \right), \quad (44)$$

with

$$\alpha_2 = \frac{\beta^4 M_s C^2 + \beta^2 C(2M_s G - 1) + G(1 + M_s G)}{\beta^4 M_s C^2 + \beta^2 C(2M_s G + 1) + G(1 + M_s G)}, \quad (45)$$

$$\alpha_3 = \frac{-2\beta^4 M_s C^2 + 2G(1 + M_s G)}{\beta^4 M_s C^2 + \beta^2 C(2M_s G + 1) + G(1 + M_s G)}. \quad (46)$$

D. A tonehole in a piecewise conical bore

As discussed in Sec. III A, a conical section may be modeled as a cylindrical waveguide in combination with two shunt inertances and an ideal transformer. A tonehole in a conical section may be considered as a system of two conical sections separated by a tonehole. The equivalent network of the hole and its connections to the two conical sections is depicted in Fig. 12(a). This formulation does not require that the conical taper on the left-hand side of the hole equals the taper on the right-hand side. The wave digital model takes the form as depicted in Fig. 12(b). In order to avoid delay-free loops, the cone inertances on the left and the right of the hole have to be modeled with a WD-*r* and a WD-*l* junction, respectively.

V. RESULTS WITH A FULL CLARINET BORE

The bore of a clarinet can be divided into three parts: the mouthpiece, the main bore with toneholes, and the bell. The mouthpiece usually consists of a small entry section plus a slightly tapered section that connects to the main bore. In most mouthpieces, there is a small cross-sectional step at the boundary between these two sections. In the low-frequency limit, the entry section may be modeled with a cylindrical section of equivalent volume. The tapered section can then be modeled as a perfect conical section, where the radius of the cylindrical section is chosen such that the cross-sectional step is the same as that in the real mouthpiece. Figure 13

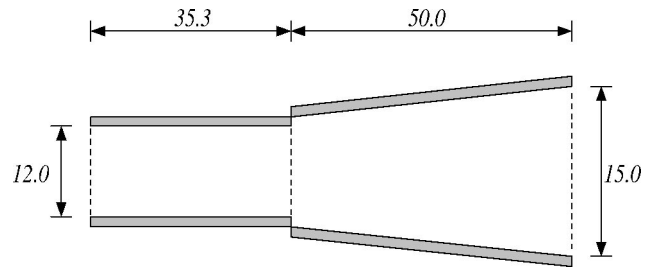


FIG. 13. Cylinder-cone model of a Bundy mouthpiece. The conical section represents the tapered part of the mouthpiece that connects directly to the main bore, and the cylindrical section models the entry section closest to the reed channel. Dimensions are given in millimeter.

depicts such a “cylinder-cone model” of a *Bundy* mouthpiece.

The dimensions of the main bore and the toneholes of a Selmer clarinet (No. 1400) were measured. The geometrical data of the toneholes is given in Table I. Each interhole section is modeled as cylindrical section of mean radius; because the main bore taper is extremely small, this simplification does not introduce any significant error. The remaining part of the bore (that is, the part starting directly after hole No. 1) is considered as the bell. The bell is typically mildly flared, and may therefore be approximated with a small number of piecewise conical sections.

The choice of the sample rate of the wave digital model of the clarinet depends on the shortest interhole bore distance. In order to avoid the use of a very high sample rate, hole No. 13 was omitted from the model. The sample rate was then set to the smallest multiple of 44.1 kHz that is sufficiently high for digital simulation of the shortest remaining inter-hole section, which is $f_s = 176.4$ kHz. This sample

TABLE I. Dimensions of the Selmer clarinet. All dimensions are given in millimeters. *x* indicates the distance along the bore axis between the mouthpiece and the center of the hole.

Hole no.	<i>x</i>	2 <i>a</i>	2 <i>b</i>	<i>t_w</i>	2 <i>R_{pad}</i>	<i>h</i>
24	68.4	15.0	2.1	12.7	10.4	3.1
23	78.7	15.0	4.0	7.3	10.4	3.3
22	104.3	15.0	5.5	7.0	10.2	2.6
21	114.0	15.0	5.5	7.0	10.3	3.4
20	127.9	15.0	5.7	7.0	10.4	3.4
19	142.6	15.0	4.0	6.5	9.8	3.1
18	153.2	15.0	7.6	10.3		
17	157.2	15.0	5.0	7.0	10.1	2.3
16	165.6	15.0	5.0	8.3		
15	185.2	15.0	5.0	7.0	10.3	2.4
14	198.3	15.0	6.4	8.3		
13	202.9	15.0	6.1	7.0	10.2	3.0
12	203.7	15.0	6.3	7.0	10.2	3.1
11	221.8	15.0	8.2	7.5		
10	232.6	15.0	5.0	7.0	10.3	3.7
9	296.6	15.0	7.2	6.0	12.0	2.4
8	312.6	15.0	8.6	7.8		
7	314.6	15.0	6.3	6.5	17.1	2.5
6	339.0	15.0	8.5	7.8		
5	362.0	15.0	9.3	7.8		
4	391.6	15.0	10.3	5.0	17.1	2.5
3	420.2	15.0	12.6	5.0	17.1	3.3
2	453.6	17.3	11.3	4.5	17.2	3.5
1	486.8	21.0	10.1	4.5	17.2	3.8

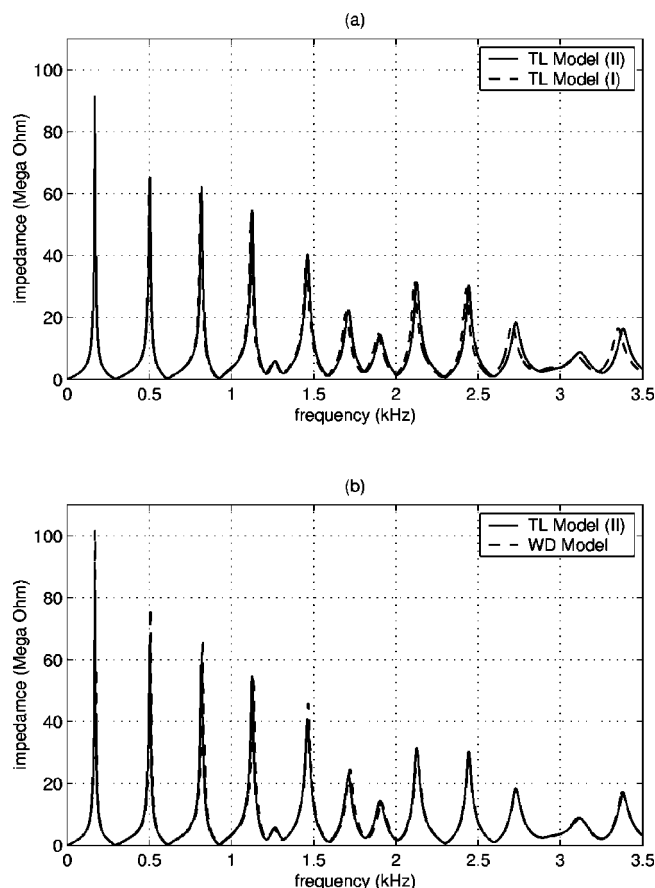


FIG. 14. Input impedance of the Selmer clarinet. Plot (a) compares the two transmission-line models: TL model (I) is computed using the tonehole formulations by Dubos *et al.*, and TL model (II) is computed with the lumped model approximation to these formulations used in the present study. Plot (b) compares TL model (II) to the wave digital model. The computations were done with the fingering for note F_3 (all holes closed except no. 1 and no. 3).

rate choice allows for a simple conversion to a conventional audio rate, so that direct audio playback of output signals on standard audio equipment is possible.

In the wave digital model, fourth-order IIR filters were used for digital approximation of the boundary losses, and a fifth-order IIR filter was used to model the wave reflectance at the open-end. In order to avoid instability problems, viscothermal losses were not modeled in any of the conical sections.

Figure 14(a) shows the input impedance of the complete clarinet bore as computed with two different transmission-line (TL) models. TL model (I) was formulated using the tonehole formulations of Dubos *et al.*, while the lumped model described in Sec. IV A was used in TL model (II). At the higher frequencies, the curves exhibit a slight difference in the position of the impedance peaks, which is mainly due to the different way in which the negative length-corrections associated with the toneholes are modeled. Figure 14(b) compares TL model (II) with the wave digital model. As can be seen, the effects due to discretization are very small. The main discrepancy is the higher amplitude of the first few resonance peaks, which is due to not taking into account viscothermal losses in any of the conical sections.

VI. CONCLUSIONS

Woodwind instrument bores can be accurately simulated in discrete time with the WDM method. Using a transmission-line description of the bore, a spatially modular bore model is constructed from which a traveling-wave based simulation is derived through decomposition into wave variables and discretization of the frequency-dependent elements. Toneholes are modeled in such a way that each possible state (from open to closed) can be simulated and controlled dynamically. The possibility of such parameterization is essential in the context of generating musically meaningful output with the model. Another key feature of the WDM method is the flexibility concerning the formulation and digital approximation of frequency-dependent phenomena, which allows adjustment of the trade-off between accuracy and efficiency. As such, wave digital modeling is well suited to synthesis-orientated simulation of wind instruments.

Although the present study is limited to calculation of vibrations inside the bore of a woodwind instrument, the WDM method can be adapted to predict the sound radiated from the instrument, and also to simulate other wind instruments, such as brass instruments and flutes.

The results presented in Secs. III D and V show that a wave digital model closely approximates the transmission-line description of an acoustic bore. The main discrepancies were found to be due to the following limitations: (1) the accuracy is sensitive to the way in which the length-corrections associated with the toneholes are taken into account, and (2) the simulation of a piecewise conical bore system is stable only if viscothermal losses are not taken into account in any of the conical sections. Limitation (2) has no significant consequences for simulation of bores which are predominantly cylindrical, such as the clarinet. However, for simulation of conical bore instrument, such as the saxophone, further research is required. In particular, stable simulation of lossy conical bores would require a discrete-time junction model that is formulated using a lossy version of the propagation constant. The effects of limitation (1) are very small at low frequencies. Effects due to discretization aspects and further simplifications are usually extremely small; the results show that if the transmission-line model of a full clarinet bore is adapted such that the effects of limitation (1) are removed from the comparisons, the models no longer show any significant discrepancy in the important frequency range. Possibly limitation (1) can be removed in future work, by modeling the length corrections with wave digital modules that simulate negative series inductances.

A further useful improvement could be include some form of resistance in the wave digital tonehole model. Nederveen²⁴ includes a nonlinear resistive term in the tonehole shunt impedance. Such a resistive term could explain particular phenomena observed with very small holes, and may need to be included for accurate simulation of register holes.

ACKNOWLEDGMENTS

We gratefully acknowledge Gary Scavone for helpful suggestions on the subject of modeling of woodwind toneholes.

- ¹R. T. Schumacher, "Ab initio calculations of the oscillations of a clarinet," *Acustica* **48**, 71–85 (1981).
- ²M. E. McIntyre, R. T. Schumacher, and J. Woodhouse, "On the oscillations of musical instruments," *J. Acoust. Soc. Am.* **74**, 1325–1345 (1983).
- ³J.-P. Dalmont, C. J. Nederveen, S. Dubos, S. Ollivier, V. Meserette, and E. te Sligte, "Experimental determination of the equivalent circuit of a side hole: linear and non-linear behaviour," *Acust. Acta Acust.* **88**, 567–575 (2002).
- ⁴J. O. Smith, "Physical modeling using digital waveguides," *Comput. Music J.* **16**, 74–91 (1992), special issue: Physical Modeling of Musical Instruments, Part I.
- ⁵V. Välimäki, "Discrete-time modeling of acoustic tubes using fractional delay filters," Ph.D. thesis, Helsinki University of Technology, Faculty of Electrical Engineering, Laboratory of Acoustic and Audio Signal Processing, Espoo, Finland, Report No. 37, 1995.
- ⁶G. P. Scavone, "An acoustic analysis of single-reed woodwind instruments with an emphasis on design and performance issues and digital waveguide modeling techniques," Ph.D. thesis, Music Dept., Stanford University, 1997.
- ⁷J. Martínez, J. Agulló, and S. Cardona, "Conical bores. Part II: Multiconvolution," *J. Acoust. Soc. Am.* **84**, 1620–1627 (1988).
- ⁸A. Barjau, D. H. Keefe, and S. Cardona, "Time-domain simulation of acoustical waveguides with arbitrarily spaced discontinuities," *J. Acoust. Soc. Am.* **105**, 1951–1964 (1999).
- ⁹D. A. Jaffe, "Ten criteria for evaluating synthesis techniques," *Comput. Music J.* **19**, 76–87 (1995).
- ¹⁰A. Fettweis, "Wave digital filters: theory and practice," in *Proceedings of the IEEE*, 1986, pp. 270–327.
- ¹¹J. O. Smith, "Discrete-time modeling of acoustic systems with applications to sound synthesis of musical instruments," in *Proceedings of the Nordic Acoustical Meeting, Helsinki*, 1996, pp. 21–32 plenary paper.
- ¹²D. Bilbao, "Wave scattering methods for the numerical integration of partial differential equations," Ph.D. thesis, Elec. Eng. Dept., Stanford University, 2001.
- ¹³S. Van Duyne and J. O. Smith, "The wave digital hammer: A traveling wave model of the piano hammer and the felt mallet," in *Proceedings of the 1994 International Computer Music Conference* (Computer Music Association, Århus, Denmark, 1994), pp. 411–418.
- ¹⁴J. O. Smith, "Techniques for digital filter design and system identification with application to the violin," Ph.D. thesis, Elec. Eng. Dept., Stanford University, 1983.
- ¹⁵M. O. van Walstijn, "Discrete-time modelling of brass and reed woodwind instruments with application to musical sound synthesis," Ph.D. thesis, Department of Physics and Astronomy, University of Edinburgh, 2002.
- ¹⁶D. H. Keefe, "Woodwind air column models," *J. Acoust. Soc. Am.* **88**, 35–51 (1990).
- ¹⁷D. H. Keefe, "Acoustical wave propagation in cylindrical ducts: Transmission line parameter approximations for isothermal and nonisothermal boundary conditions," *J. Acoust. Soc. Am.* **75**, 58–62 (1984).
- ¹⁸H. Levine and J. Schwinger, "On the radiation of sound from an unflanged circular pipe," *Phys. Rev.* **73**, 383–406 (1948).
- ¹⁹A. H. Benade, "Equivalent circuits for conical waveguides," *J. Acoust. Soc. Am.* **83**, 1764–1769 (1988).
- ²⁰D. Berners, "Acoustics and signal processing techniques for physical modelling of brass instruments," Ph.D. thesis, Elec. Eng. Dept., Stanford University, 1999.
- ²¹J. Gilbert, J. Kergomard, and J. D. Polack, "On the reflection functions associated with discontinuities in conical bores," *J. Acoust. Soc. Am.* **87**, 1773–1780 (1990).
- ²²G. P. Scavone and P. R. Cook, "Real-time computer modeling of woodwind instruments," in *Proceedings of the 1998 International Symposium on Musical Acoustics* (The Acoustical Society of America, Leavenworth, Washington, 1998), pp. 197–202.
- ²³V. Dubos, J. Kergomard, A. Khettabi, J.-P. Dalmont, D. H. Keefe, and C. J. Nederveen, "Theory of sound propagation in a duct with a branched Ttbe using modal decomposition," *Acust. Acta Acust.* **85**, 153–169 (1999).
- ²⁴C. J. Nederveen, *Acoustical Aspects of Woodwind Instruments* (Northern Illinois University Press, DeKalb, Illinois, 1998).

Suppression of large intraluminal bubble expansion in shock wave lithotripsy without compromising stone comminution: Refinement of reflector geometry

Yufeng Zhou and Pei Zhong^{a)}

Department of Mechanical Engineering and Materials Science, Duke University, Durham, North Carolina 27708

(Received 15 June 2002; revised 12 October 2002; accepted 21 October 2002)

Using the Hamilton model [Hamilton, J. Acoust. Soc. Am. **93**, 1256–1266 (1993)], the effects of reflector geometry on the pulse profile and sequence of the shock waves produced by the original and upgraded reflector of an HM-3 lithotripter were evaluated qualitatively. Guided by this analysis, we have refined the geometry of the upgraded reflector to enhance its suppressive effect on intraluminal bubble expansion without compromising stone comminution in shock wave lithotripsy. Using the original HM-3 reflector at 20 kV, rupture of a standard vessel phantom made of cellulose hollow fiber (i.d.=0.2 mm), in which degassed water seeded with ultrasound contrast agents was circulated, was produced at the lithotripter focus after about 30 shocks. In contrast, using the upgraded reflector at 24 kV no rupture of the vessel phantom could be produced within a 20-mm diameter around the lithotripter focus even after 200 shocks. On the other hand, stone comminution was comparable between the two reflector configurations, although slightly larger fragments were produced by the upgraded reflector. After 2000 shocks, stone comminution efficiency produced by the original HM-3 reflector at 20 kV is $97.15 \pm 1.92\%$ (mean \pm SD), compared to $90.35 \pm 1.96\%$ produced by the upgraded reflector at 24 kV ($p < 0.02$). All together, it was found that the upgraded reflector could significantly reduce the propensity for vessel rupture in shock wave lithotripsy while maintaining satisfactory stone comminution. © 2003 Acoustical Society of America. [DOI: 10.1121/1.1528174]

PACS numbers: 43.80.Ev, 43.80.Gx, 43.25.Yw [FD]

I. INTRODUCTION

Reducing vascular injury in shock wave lithotripsy (SWL) is becoming an increasing clinical concern and a primary challenge for basic research,¹ especially with the much higher pressure output of the third-generation lithotripters.² Following SWL, although most young adult patients recover well, a subgroup of patients, such as pediatric and elderly patients, and patients with preexisting renal function impairment, are at much higher risk for SWL-induced chronic injury.^{1,3,4} Therefore, it is highly desirable to improve lithotripsy technology to ameliorate renal injury while maintaining successful stone comminution.

Previous studies using *in vitro* phantom systems and *in vivo* animal models have demonstrated that cavitation, the formation and subsequent expansion and collapse of gas/vapor bubbles in an acoustic field, is an important mechanism for vascular injury in SWL.^{5–7} Theoretical analyses have shown that in free field the tensile pressure of a lithotripter shock wave (LSW) can cause preexisting cavitation nuclei in the range of 10 nm–10 μ m to expand rapidly in about one hundred microseconds to bubbles of 1–2 mm in diameter, which then collapse violently.^{8,9} It has been postulated that SWL-induced rupture of capillaries and small blood vessels, in which bubble oscillation is severely constrained, is caused by the rapid, large dilation of the vessel wall from expanding intraluminal bubbles,^{5,9} whereas dam-

age in large blood vessels may be caused by high-speed microjets or secondary shock waves produced by the violent collapse of cavitation bubbles, either with or without the aid of an impinging LSW.^{10,11} Based on the results of these previous studies, various strategies have been proposed to reduce tissue injury in SWL. Overall, these strategies can be categorized into two groups. The objective for the first group of strategies is to minimize or eliminate cavitation nuclei in the medium so that bubbles will not be induced by LSW. This includes the use of overpressure,^{12,13} low pulse repetition rate,^{14–16} and staged SWL treatment combining low- and high-amplitude shock wave exposures.¹⁷ In contrast, the second group of approach relies on the modification of the profile of LSW to actively suppress cavitation, and thus to reduce its damage potential to surrounding tissues. This later approach includes inversion of the lithotripter pressure waveform by the use of a pressure-release reflector¹⁸ or by inverting the polarity of input excitation voltage to piezoceramic transducers¹⁹ and various pulse superposition techniques.^{20–23} Among these approaches, the *in situ* pulse superposition technique that we developed recently²³ has the advantage of reducing tissue injury without compromising stone comminution or increasing treatment time.

The basic principle of the *in situ* pulse superposition technique is to use a relatively weak compressive wave to superimpose onto the trailing tensile component of a LSW to suppress the expansion of cavitation bubbles induced in a lithotripter field.²³ To implement this technique in an HM-3 lithotripter, a thin shell ellipsoidal reflector insert with its

^{a)}Electronic mail: pzhong@duke.edu

inner surface sharing the same first focus (F_1) with the original HM-3 reflector, but its second focus shifted 5 mm proximal to the shock wave generator was designed and fabricated as previously described.²³ The reflector insert, with its lower edge extending to the focal plane across F_1 and perpendicular to the lithotripter axis, covers a large portion of the original HM-3 reflector. Therefore, the reflector insert becomes the primary reflecting surface to form a leading LSW after each spark discharge, whereas a second weakly focused shock wave, delayed by about 4 μ s, is produced by wave reflection from the uncovered bottom surface of the original HM-3 reflector.²³ *In vitro* phantom tests have shown that stone comminution produced by the upgraded reflector at 24 kV is comparable to that produced by the original HM-3 reflector at 20 kV. However, the upgraded reflector significantly reduces the potential for vascular injury. At corresponding output voltages, rupture of a standard hollow fiber vessel phantom (perfused with degassed water seeded with ultrasound contrast agents) around the lithotripter beam focus was produced after about 30 shocks using the original HM-3 reflector, yet no rupture could be produced by the upgraded reflector even after 200 shocks. The only exception is at the geometric focus of the reflector insert where the tensile pressure of the LSW reaches its maximum and rupture of the vessel phantom could be produced after about 130 shocks.²³ Apparently, refinement of the upgraded reflector is needed to further suppress intraluminal bubble expansion and to reduce the potential of vascular injury in SWL without compromising stone comminution.

In this work, we analyzed qualitatively the effect of reflector geometry on the profile of LSW produced by the upgraded reflector, using a linear wave propagation model developed by Hamilton.²⁴ Guided by this analysis, we have refined the geometry of the reflector insert and characterized the resultant acoustic field and bubble dynamics using a fiber optic probe hydrophone and high-speed imaging technique. The performance of the refined upgraded reflector *in vitro* was evaluated using established stone and vessel phantom systems; and the dynamics of cavitation bubbles induced by the original and upgraded HM-3 lithotripter were analyzed using the Gilmore model. All together, it was found that with refinement in geometry the upgraded reflector can further reduce the potential of vascular injury in SWL while maintaining satisfactory stone comminution.

II. THE EFFECT OF REFLECTOR GEOMETRY ON WAVEFORM PROFILE ALONG LITHOTRIPTER AXIS

To increase the strength of the second shock wave, the original reflector insert²³ needs to be further truncated to increase the area for the uncovered bottom surface of the original HM-3 reflector. However, truncation of the reflector insert also reduces the reflecting surface area for the leading LSW. Therefore, a balance needs to be reached between reducing vascular injury and maintaining successful stone comminution using the upgraded reflector. For this purpose, it would be helpful to understand the relationship between the geometry of the upgraded reflector and the pressure field produced at the lithotripter beam focus. In this work, we used a linear wave propagation model that was developed by

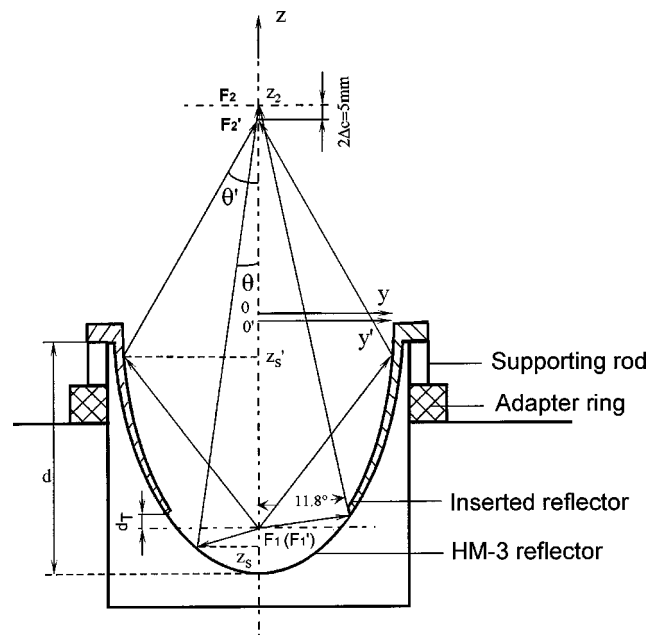


FIG. 1. A schematic diagram of the geometry of a reflector insert, in relation to the original HM-3 reflector. Note that the reflector insert shares the same first focus with the original HM-3 reflector ($F_1 = F_1'$), but its second focus (F_2') is 5 mm proximal to the shock wave source relative to that of the original HM-3 reflector (F_2).

Hamilton to describe small-amplitude wave reflection, focusing, and diffraction from an ellipsoidal reflector.²⁴ A unique feature of the Hamilton model is that it describes the contribution and evolution of different wave components to the pressure waveform produced along a lithotripter axis. Therefore, the Hamilton model was used to provide a qualitative assessment of the effect of reflector insert geometry on the pressure amplitude at the reflector focus, and to facilitate the interpretation of the pressure waveforms measured experimentally. It should be noted that optimization of the reflector insert design would require a quantitative prediction of the pressure waveform in a lithotripter field based on nonlinear shock wave propagation models in an electrohydraulic lithotripter,^{25–27} which is beyond the scope of this work.

A. The Hamilton model

Let's consider the situation where an outgoing omnidirectional spherical pressure wave, centered at the first focus (F_1), is reflected and refocused towards the second focus (F_2) of an ellipsoidal reflector (see Fig. 1). Based on a geometrical acoustics approximation, the reflected pressure field p_{2g} can be expressed by²⁴

$$\frac{p_{2g}}{p_0} = D(z_s) \left(\frac{1+\varepsilon}{1-\varepsilon} \right) \frac{r_0}{r_2} f \left(t + \frac{r_2 - 2a}{c_0} \right), \quad (1)$$

where p_0 is the pressure amplitude at a fixed but arbitrary distance r_0 from F_1 , $D(z_s)$ is the directivity function with z_s denoting the coordinate on the surface of the ellipsoidal reflector, ε the eccentricity of the ellipsoidal reflector, r_2 the distance from F_2 , $f(t)$ a dimensionless function of time representing the source waveform, and c_0 sound speed in water. The directivity function, corresponding to the density of rays

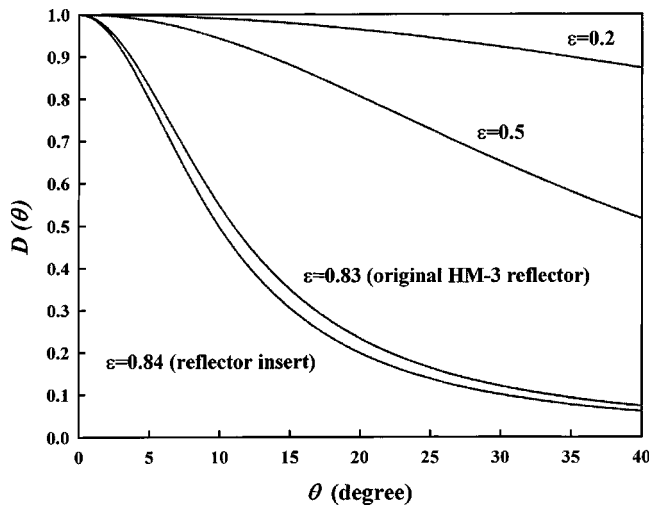


FIG. 2. Angular dependence of the directivity function $D(\theta)$ in the reflected pressure field predicted by geometrical acoustics with four different eccentricity values ($\varepsilon = 0.2, 0.5, 0.83$, and 0.84).

reflected from different regions of the ellipsoidal reflector, is given by

$$D(\vartheta) = \left[1 + \frac{4\varepsilon \sin^2(\vartheta/2)}{(1-\varepsilon)^2} \right]^{-1}, \quad (2)$$

in which, ε is defined by

$$\varepsilon = \sqrt{1 - (b/a)^2} = c/a \quad (0 \leq \varepsilon < 1), \quad (3)$$

where a , b , c are the semimajor axis, semiminor axis, and half-focal length of the ellipsoidal reflector, respectively, and θ is an angle between the ray normal to the reflected wavefront and the lithotripter axis, which is defined as the z -axis in Fig. 1.

The directivity function determines the amplitude shading of the pressure field across the aperture of the lithotripter reflector. As shown in Fig. 2, the directivity decreases monotonically with θ and it also depends on the eccentricity of the reflector. When $\varepsilon \rightarrow 0$ (i.e., for a spherical reflector), the reflected wave becomes spherically converging, whereas as $\varepsilon \rightarrow 1$, the reflected field becomes increasingly localized along the z -axis. For the original and upgraded HM-3 reflectors ($\varepsilon = 0.826$ and 0.842 , respectively), their directivity functions are similar and the amplitude of the pressure reflected from the edge of the reflector aperture is about 10% of that reflected from the bottom along the reflector axis (see Fig. 2).

Using the Kirchhoff integral, the reflected pressure along the z -axis can be determined.²⁴ The solution, accounting for the effect of wave diffraction at the aperture of the ellipsoidal reflector, can be expressed by two closed form expressions, representing the center wave and the edge wave, respectively, and a convolution integral over time representing the wake:

$$\begin{aligned} \frac{p_2}{p_0} = & H_c(z)f(\tau_c) + H_e(z)f(\tau_e) + \frac{c_0}{a} \int_{t_1}^{t_2} H_w(z, t') \\ & \times f(t - t') dt', \end{aligned} \quad (4)$$

where H_c , H_e , and H_w are the impulse strengths for the center wave, the edge wave, and the wake, respectively, and τ_c , τ_e , t_1 , and t_2 are the retarded times for the corresponding waves. Detailed expressions of these parameters can be found in the original reference.²⁴

Moreover, it has been shown that at beam focus of the ellipsoidal reflector the pressure can be expressed by

$$\frac{p_2}{p_0} = F \frac{r_0}{c_0} \frac{d}{dt} f\left(t - \frac{2a}{c_0}\right), \quad z = z_2, \quad (5)$$

where F is the focusing factor defined by

$$F = \left(\frac{1 - \varepsilon^2}{2\varepsilon} \right) \ln \left(\frac{a + \varepsilon d / (1 - \varepsilon)}{a - \varepsilon d / (1 + \varepsilon)} \right), \quad (6)$$

in which d is the depth of the ellipsoidal reflector (see Fig. 1).

The Hamilton model describes linear wave propagation in a truncated ellipsoidal reflector such as in the HM3 lithotripter. To determine the pressure waveform produced by the upgraded reflector, the Hamilton model was used to calculate pressure waveforms (PW) produced by three different truncated ellipsoidal reflectors, namely, (1) PW_1 from the reflector insert that is assumed to be not truncated at the bottom (thus covering completely the original HM-3 reflector), (2) PW_2 from the truncated bottom of the reflector insert, and (3) PW_3 from the uncovered bottom surface of the original HM-3 reflector. Because of the linear wave propagation described by the Hamilton model, the pressure waveform produced by the upgraded reflector can be calculated by $(PW_1 - PW_2) + PW_3$.

B. The effect of reflector geometry on focusing factor

It can be seen from Eq. (6) that, for a given ε , F is only a function of the depth of the reflector. Therefore, for small amplitude waves, F represents the influence of reflector geometry on the pressure produced at F_2 . On a first order approximation, F may be used to evaluate qualitatively the influence of the reflector insert geometry on the leading LSW and the second shock wave produced by the upgraded reflector.

Figure 3 shows the relative change in F associated with the reflecting surfaces for the leading LSW and the second shock wave, respectively, when the truncation depth of the reflector insert (d_T , see Fig. 1) increases from 0 to 10 mm. Here, the results were normalized with respect to the corresponding values for the prototype upgraded reflector,²³ in which the lower edge of the reflector insert was extended to the focal plane across F_1 . It can be seen that, as the truncation depth increases (i.e., the lower edge of the reflector insert retracts toward the reflector aperture), the focusing factor for the leading LSW will decrease and the corresponding value for the second shock wave will increase. The magnitude of the relative change in F for the second shock wave is about twice that for the leading LSW. Considering that the leading LSW is much stronger than the second shock wave, this result suggests that a small truncation of the reflector

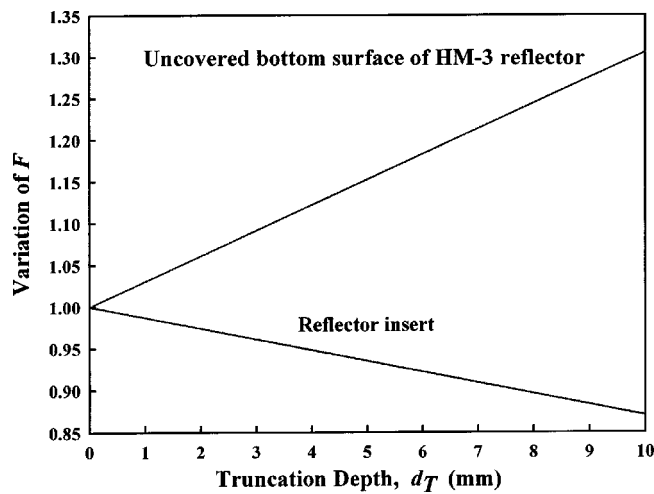


FIG. 3. Normalized value of the focusing factor (F) associated with the reflector insert and uncovered bottom surface of the original HM-3 reflector in relation to the truncation depth (d_T) of the lower rim of the reflector insert. The focusing factor is normalized by the corresponding value when the lower rim of the reflector insert is extended to the focal plane across the first focus of the original HM-3 reflector.

insert will significantly increase the pressure amplitude of the second shock wave without affecting greatly the leading LSW.

C. The effect of reflector geometry on waveform profile

Using the Hamilton model, we calculated the pressure waveforms along the lithotripter axis produced by the original HM-3 and the upgraded reflectors. The incident wave from the spark discharge at F_1 is assumed to be a triangle pulse of $4 \mu\text{s}$ duration and $0.75 \mu\text{s}$ rise time, similar to the

values used in previous studies.^{24–26} To facilitate comparison, the pressure waveform was normalized by the maximal pulse amplitude at each location and the retarded time for the wave propagation was used. A cross-sectional view of the original and upgraded reflector is shown in Fig. 1. The geometric parameters of the reflectors are described in the next section.

Figure 4 shows the evolutions of three main components of the waveform along the z -axis in the original HM-3 lithotripter. Hereinafter, Δz_2 is used to denote the distance between the location where the waveform is calculated and the beam focus on the z -axis, z_2 . At $\Delta z_2 = -43.8 \text{ mm}$, the center wave and edge wave (produced by wave diffraction at the reflector aperture) are clearly separated, and the wake contributes to the tensile pressure immediately following the center wave. As the waveform propagates towards the focus the edge wave catches up with the wake, generating a large tensile pressure before F_2 (see $\Delta z_2 = -27.3 \text{ mm}$). Subsequently, the edge wave and wake overlap with the center wave near F_2 , and eventually, they overtake the center wave far beyond F_2 (see $\Delta z_2 = 65.7 \text{ mm}$). As shown by Hamilton, the polarity of the wake is the same as that of the edge wave, but opposite to the center wave.²⁴ That is, in the pre-focal region, the center wave is compressive, yet the wake and edge wave are tensile. However, in the post-focal region the polarities of all the wave components are reversed.

Using the upgraded reflector, two waves that travel in tandem are predicted (Fig. 5). Because the reflector insert has both an upper and a lower rim, two edge waves associated with the leading LSW are produced at different time instants. At $\Delta z_2 = -63.3 \text{ mm}$, the edge wave produced by the lower rim of the reflector insert (which is close to the spark discharge at F_1) has already merged with the wake of the LSW.

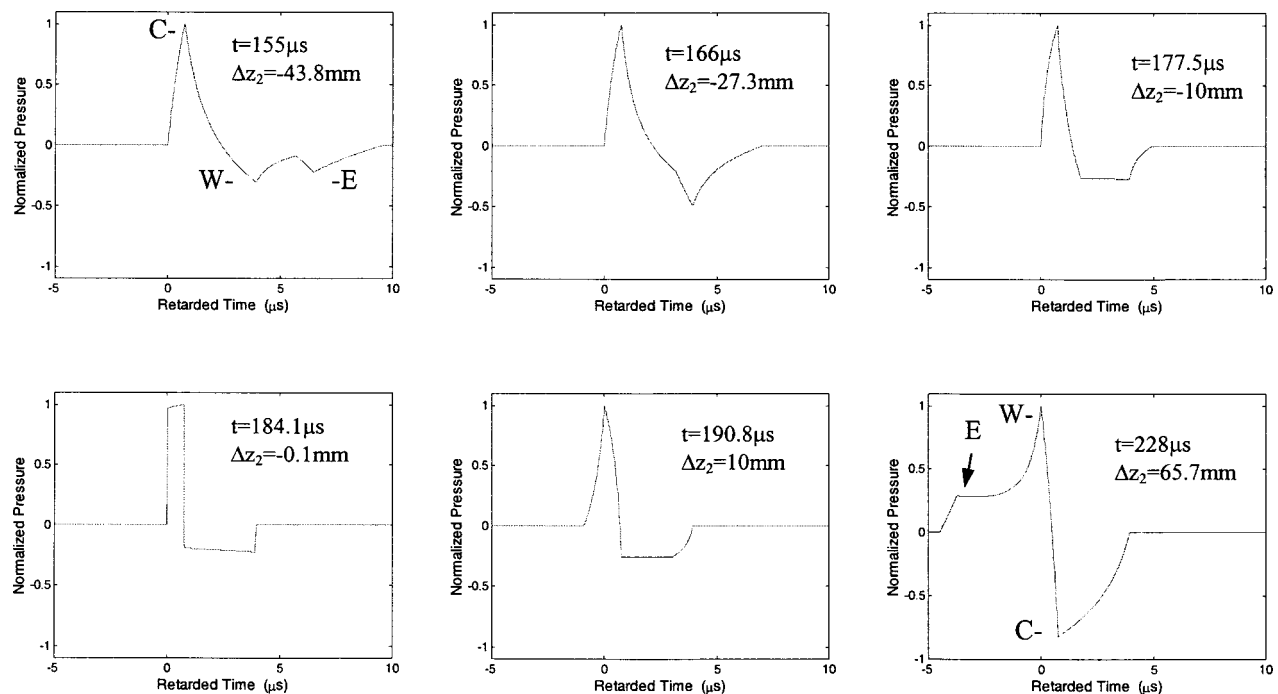


FIG. 4. Theoretical prediction of the pressure waveforms along the lithotripter axis using the original HM-3 reflector. Here, t denotes the propagation time of a reflected sound pulse originated from the first focus of the lithotripter reflector, and Δz_2 is the distance from the second focus of the original HM-3 reflector on the z -axis (z_2). C: center wave, W: wake, and E: edge wave.

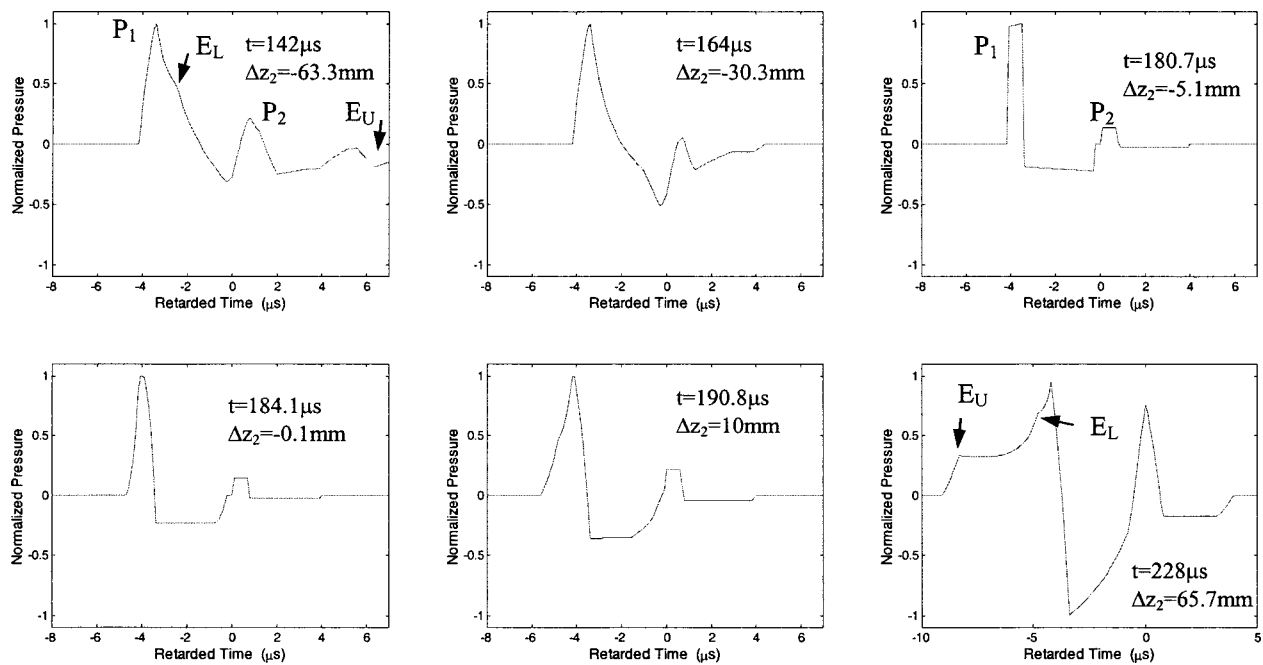


FIG. 5. Theoretical prediction of the pressure waveforms along the lithotripter axis using the upgraded reflector. Here, t denotes the propagation time of a reflected sound pulse originated from the first focus of the lithotripter reflector, and Δz_2 is the distance from the second focus of the original HM-3 reflector on the z -axis (z_2). Arrows indicate the edge waves, originated from the lower (L) and upper (U) rim of the reflector insert.

In comparison, the edge wave produced by the upper rim of the reflector insert (which is distal from the spark discharge at F_1) arrives later; however, it converges to the center wave faster than the edge wave from the lower rim. Beyond F_2 both edge waves and the wake overtakes the center wave, with the edge wave from the upper rim diverging away from the center wave faster than its counterpart from the lower rim (see $\Delta z_2 = 65.7$ mm in Fig. 5).

Because of the shallow depth of the uncovered bottom surface of the HM-3 reflector, the second shock wave is weakly focused with a resultant long beam size along the lithotripter axis. Consequently, the center wave and the edge wave of the second shock wave overlap with each other most of the time when propagating along the lithotripter axis. For the same reason, the rate at which the edge wave diverges away from the wake and center wave beyond the focus is much faster for the first shock wave than for the second shock wave. In comparison, it is interesting to note that around the beam focus, the waveform profiles of the leading LSWs produced by the original HM-3 reflector and the upgraded reflector (whose geometrical foci are separated by 5 mm) are quite similar.

III. EXPERIMENTAL MATERIALS AND METHOD

A. Lithotripter

The experiments were carried out in a Dornier HM-3 lithotripter with a 80 nF capacitor and a truncated brass ellipsoidal reflector with semimajor axis $a = 138$ mm, semiminor axis $b = 77.5$ mm, and half-focal length $c = 114$ mm. In our previous study, to produce *in situ* pulse superposition we fabricated a thin shell ellipsoidal reflector insert that had an outer surface matching with the original HM-3 reflector and an inner surface with $a' = 132.5$ mm, $b' = 71.5$ mm, and c'

$= 111.5$ mm.²³ The lower edge of the reflector insert was extended to the focal plane across F_1 where the tips of the spark electrode are centered. In this study, the lower edge of the original reflector insert²³ was truncated by 4 mm in order to increase the pressure amplitude of the second shock wave without weakening significantly the LSW (see Fig. 3). In addition, to reduce the effect of wave diffraction the lower edge of the reflector insert was trimmed into a conical shape of 11.8° angle with respect to the lithotripter axis, extending to the focus of the original HM-3 reflector (see Fig. 1).

B. Pressure waveform measurements

The pressure waveforms produced by the HM-3 lithotripter using either the original or upgraded reflector were measured using a fiber optic probe hydrophone (FOPH 300, Universität Stuttgart, Germany) that can accurately record both the compressive and tensile components of the LSW.²⁸ The sensing probe of the FOPH 300, a 100- μ m optical fiber, was placed inside a holder and attached to a three-axis translation stage titled at 14° so that the probe could be aligned parallel to the lithotripter axis. Accurate alignment of the probe tip with F_2 was aided by a mechanical pointer that coincides with the beam focus of the HM-3 lithotripter. The probe tip of the hydrophone was scanned along the lithotripter axis in 5-mm steps (-15 mm $< \Delta z_2 < 15$ mm) around the beam focus. At each location, at least four pressure waveforms were recorded using a digital oscilloscope (LeCroy 9314M, Chestnut Ridge, NY) operated at 100 MHz sampling rate.

C. High-speed shadowgraph imaging

Based on the design principle used in our previous studies,^{5,29} a high-speed shadowgraph imaging system was

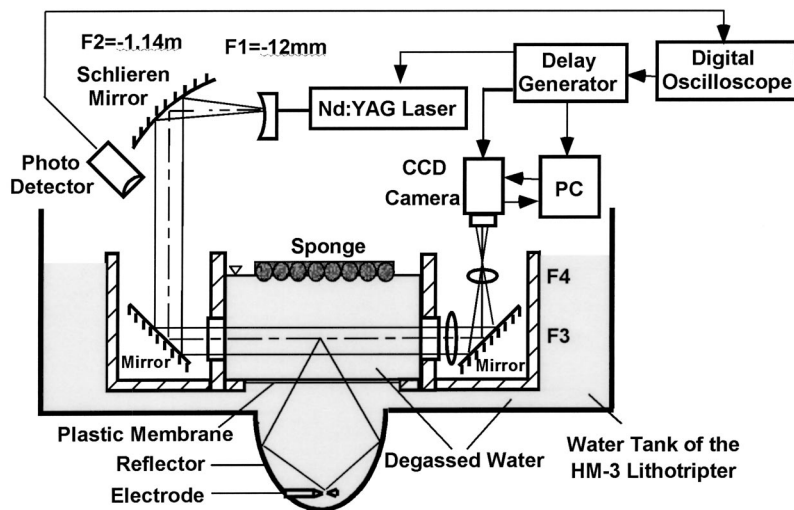


FIG. 6. Experimental setup for high-speed shadow-graph imaging in an HM-3 lithotripter. See text for details.

set up to capture the dynamics of cavitation bubbles produced in the HM-3 lithotripter field (Fig. 6). A Lucite chamber ($73.7 \times 29.2 \times 15.2$ – 21.6 cm, $L \times W \times H$), consisting of a wet test chamber at the center and two dry chambers on the lateral side to accommodate various imaging components, was constructed and fixed firmly inside the water tub of the HM-3 lithotripter. An illumination pulse, produced by a Nd:YAG laser (MiniLaseI, New Wave Research, Sunnyvale, CA, $\lambda = 512$ nm and $t_p = 6$ ns), was collimated using a combination of a concave lens and a Schlieren mirror that were mounted on an optical breadboard placed on top of the HM-3 tub. Using a steering mirror, the collimated laser beam was passed through the test chamber, and the image was projected through a combination of lenses and mirror onto a CCD camera. By adjusting the trigger delay to the camera and the Nd:YAG laser with respect to the spark discharge of the lithotripter, a series of images of shock wave propagation and bubble dynamics could be captured. In addition, a sponge was placed at the water surface inside the test chamber to reduce wave reflection and its influence on bubble dynamics at the lithotripter focus.

D. Stone comminution

For stone comminution tests, spherical stone phantoms ($D = 10$ mm) made of BegoStone (BEGO USA, Smithfield, RI) were used. The acoustic properties of BegoStone have been characterized and found to be similar to those of calcium oxalate monohydrate stone,³⁰ which is the most frequently observed kidney stone in patients.³¹ Following our established protocol, the fragmentation test was carried out by using a phantom system that mimics stone comminution in the renal pelvis.¹⁷ However, in contrast to our previous study in which stone comminution was compared after 100 shocks, we evaluated the progression of stone comminution produced by the original HM-3 and upgraded reflector within the typical clinical dose of 2000 shocks at a pulse repetition rate of 1 Hz. Moreover, after each 100 shocks the position of the stone fragments with respect to F_2 was checked using the bi-planar fluoroscopic imaging system of the HM-3 lithotripter. If necessary, re-positioning was carried out to ensure that the largest fragment was aligned with F_2 . After 1000

shocks, most of the original stone phantom was reduced to small fragments that accumulated around several large residual pieces, which were difficult to discern from each other in fluoroscopic images. Therefore, after 1000 shocks, the lithotripter focus was scanned every 100 shocks throughout the fragments to ensure sufficient shock wave exposure to all the residual large fragments. At the end of each experiment, all the fragments were carefully removed from the holder, spread out on paper, and dried in air for 24 hours. The dry fragments were then filtered through a series of ASTM standard sieves (No. 5, No. 10, No. 18, No. 35, W. S. Tyler, Mentor, OH) with 4, 2, 1, and 0.5 mm grids, respectively. Stone comminution efficiency was determined by the percentage of fragments less than 2 mm, which can be discharged spontaneously in urine following clinical SWL.³² Six samples were used under each test configuration.

E. Vessel phantom rupture

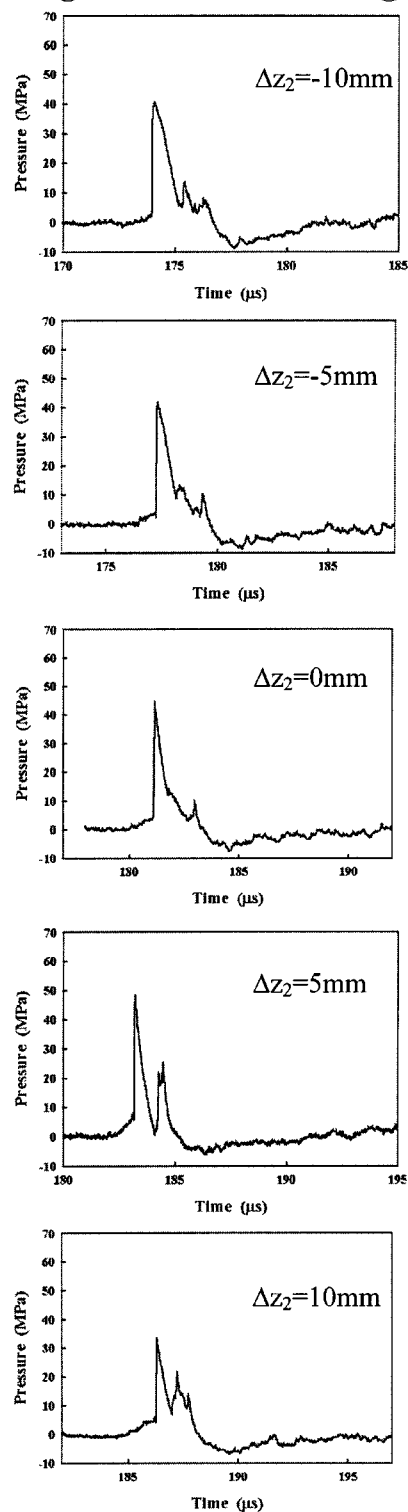
The potential for vascular injury produced by the upgraded reflector was evaluated using a vessel phantom made of a single regenerated cellulose hollow fiber (i.d. = 0.2 mm) following our established protocol.^{5,23} Briefly, the hollow fiber was immersed in the test chamber filled with highly viscous fresh castor oil and placed on the lithotripter axis around F_2 . Degassed water seeded with 0.1% ultrasound contrast agent Optison was circulated inside the hollow fiber to ensure that intraluminal cavitation could be produced consistently by each shock wave. A slow pulse repetition rate of ~ 0.1 Hz was used so that before the next shock any visible bubbles outside the hollow fiber could be carefully removed. The experiment was stopped either when a rupture was produced or when the total number of shocks delivered to the hollow fiber reached 200.

IV. RESULTS

A. Pressure waveforms

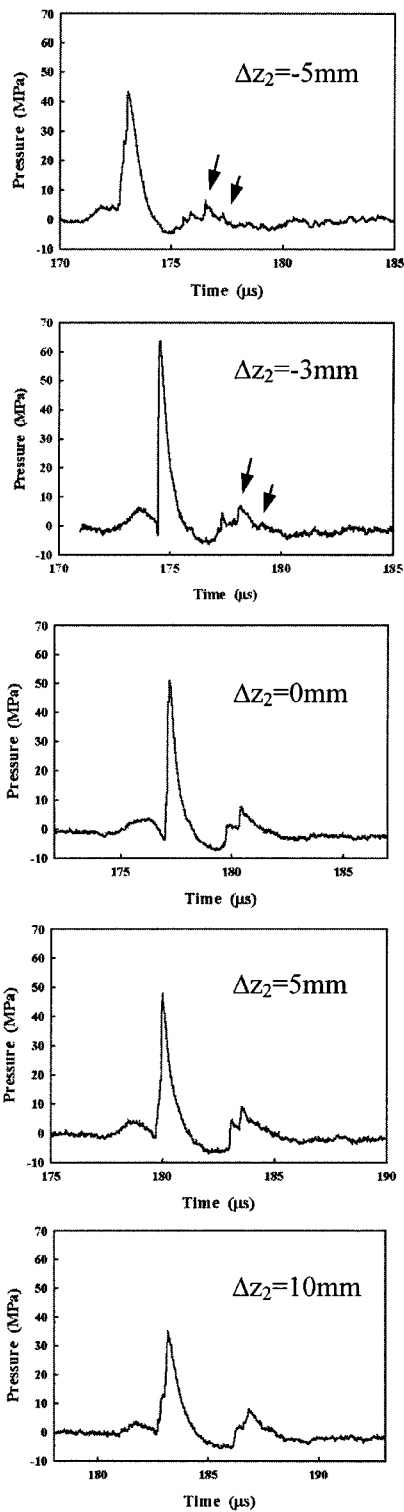
Figure 7 shows representative pressure waveforms produced along the lithotripter axis. Using the original HM-3 reflector, a typical shock wave consisting of a leading compressive wave followed immediately by a tensile wave was

Original HM-3 Reflector @ 20 kV



(a)

Upgraded Reflector @ 24 kV



(b)

FIG. 7. Representative pressure waveforms measured along the lithotripter axis by using a fiber optic probe hydrophone, FOPH 300. (a) Original HM-3 reflector at 20 kV and (b) upgraded reflector at 24 kV. Here, Δz_2 denotes the distance from the second focus of the original HM-3 reflector on the z -axis (z_2). Arrows indicate the double-peak structure in the second shock wave.

produced. In addition to the leading shock front, a second positive pressure peak was also observed in the compressive wave. This double-peak structure is most obvious and consistently observed in an HM-3 lithotripter,^{33–35} whose ellipsoidal reflector is truncated on the lateral sides to accommodate the bi-planar fluoroscopic imaging system for stone localization. In contrast, pressure waveforms produced by other experimental electrohydraulic lithotripters with similar

reflector geometry yet without truncation on the lateral sides reveal less distinct second peak in the compressive wave.^{18,35} This second positive pressure peak, much smaller in amplitude than the leading shock front, may be related to the superposition of the edge wave originated from wave diffraction at the aperture of the reflector and the center wave, which are opposite to each other in phase polarity. Truncation of the lateral sides of the HM-3 reflector strengthens the

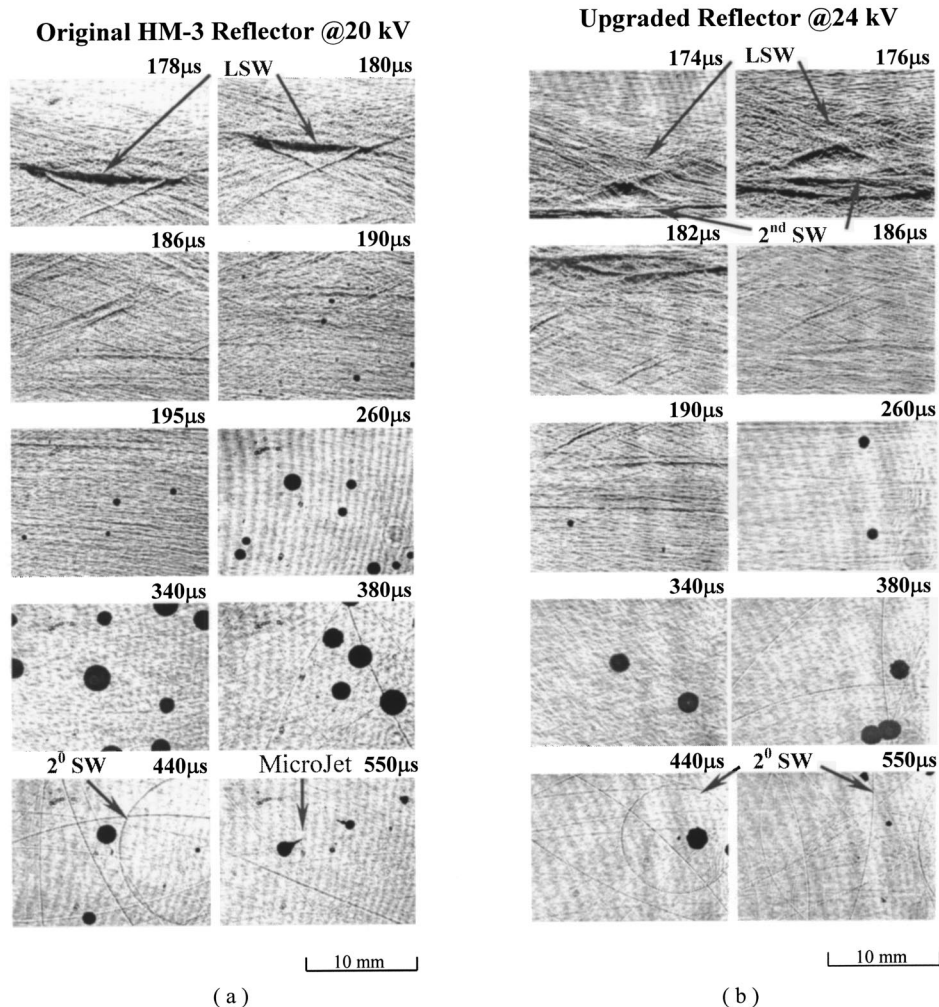


FIG. 8. Representative high-speed shadowgraph images of shock wave propagation and bubble dynamics produced in water around the lithotripter focus (center of each frame). (a) Original HM-3 reflector at 20 kV and (b) upgraded reflector at 24 kV. The number above each image frame indicates the time delay from the spark discharge of the lithotripter electrode. LSW: lithotripter shock wave, 2nd SW: second shock wave generated from the uncovered bottom surface of the original HM-3 reflector, 2⁰ SW: secondary shock wave produced by the collapse of cavitation bubbles.

edge wave when portions of the reflector become shallower.²⁴ The strong edge wave causes a significant ditch on the compressive wave following the shock front, leading to the appearance of the second positive peak.

In comparison, the pressure waveform produced by the upgraded reflector has a leading compressive wave following by a modified trailing tensile component. An edge wave preceding the lithotripter shock front is apparent when the pressure waveforms were measured at locations beyond the geometrical focus of the reflector insert. More importantly, a second shock wave produced by wave reflection from the uncovered bottom surface of the original HM-3 reflector is observed, which superimposes on the trailing tensile component of the LSW. The amplitude of the second shock wave at F_2 is estimated to be 15.6 MPa, compared to 10.4 MPa produced by our prototype upgraded reflector.²³ The higher amplitude of the second shock wave produced by the refined upgraded reflector is consistent with the increased reflecting surface area for the second shock wave. Interestingly, a double-peak structure (indicated by arrows in Fig. 7) was also observed for the second shock wave before its geometric focus, F_2 , which may relate to the strong edge wave produced by the shallow, uncovered bottom surface of the HM-3 reflector. Beyond F_2 , the edge wave overtakes the center wave (Fig. 7).

B. High-speed shadowgraph imaging

Figure 8 shows two representative sequences of bubble dynamics produced in water (O_2 concentration: <2.0 mg/L) by the original HM-3 reflector at 20 kV and the upgraded reflector at 24 kV, respectively. With the original reflector, the leading focused shock front, and, following immediately behind it, the convex edge waves propagating laterally and crossing each other on the lithotripter axis can be clearly observed [$t=178\ \mu\text{s}$ and $t=180\ \mu\text{s}$ in Fig. 8(a)]. Subsequently, cavitation bubbles were induced in the wake of the shock front by the trailing tensile component of the LSW. The initial bubble expansion was quite large. With only $10\ \mu\text{s}$ after the passage of the shock front, some bubbles have grown to a size of about $0.8\ \text{mm}$ [$t=190\ \mu\text{s}$ in Fig. 8(a)]. Although initially individual bubbles appeared to expand spherically, bubble aggregation might occur later on near the lithotripter axis [$t=330\ \mu\text{s}$ in Fig. 8(a)]. Following the maximum expansion, most bubbles collapsed violently, generating secondary shock waves [$440\ \mu\text{s}$ in Fig. 8(a)]. The collapse of rebound bubbles appeared to be affected by the secondary shock wave, leading to microjet formation along the propagation direction of the secondary shock wave [$t=550\ \mu\text{s}$ in Fig. 8(a)].

Using the upgraded reflector, a leading focused shock

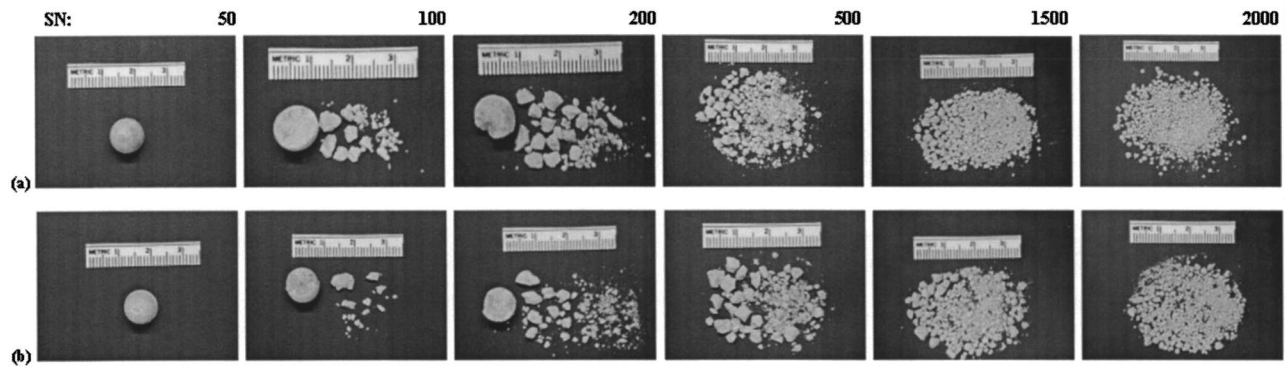


FIG. 9. Photographs of BegoStone fragments after exposure to 50–2000 shocks produced by (a) the original HM-3 reflector at 20 kV and (b) the upgraded reflector at 24 kV.

front with the accompanying edge waves were observed, and their arrival time at F_2 is about $4 \mu\text{s}$ earlier than the LSW produced by the original HM-3 reflector [Fig. 8(b)]. In addition, a second shock wave produced by wave reflection from the uncovered bottom surface of the original HM-3 reflector was observed [$t=176 \mu\text{s}$ in Fig. 8(b)]. Interestingly, the edge wave, separated from the leading shock front by about $1 \mu\text{s}$, could be identified from the shadowgraph imaging, which correlates well with the double-peak structure of the second shock wave measured by the FOPH 300 hydrophone (Fig. 7). In comparison to the bubble dynamics produced by the original HM-3 reflector, three major differences were identified. First, the second shock wave significantly suppressed the initial bubble expansion produced by the leading LSW. Smaller bubbles were observed at $10 \mu\text{s}$ after the passage of the leading LSW front [$t=186 \mu\text{s}$ in Fig. 8(b)]. Second, the perturbation of the second shock wave on the initial bubble expansion largely disrupted the spherical geometry of the bubbles, which appeared uneven at the boundary [$t=190 \mu\text{s}$ and $t=260 \mu\text{s}$ in Fig. 8(b)]. Third, although these disrupted bubbles could continue to expand to a maximal size, their subsequent collapse appeared to be very weak with few microjets produced as a result of the secondary shock wave-bubble interaction [$t=550 \mu\text{s}$ in Fig. 8(b)].

C. Stone comminution

Figure 9 shows the dose-dependent stone comminution produced by the original HM-3 reflector at 20 kV and the upgraded reflector at 24 kV, respectively. In both cases, a progressive fragmentation of the BegoStone phantom was produced as the number of shocks delivered increased. It is noted that although only about 500 shocks were needed to disintegrate each stone phantom into a distribution of fragments of various sizes, a much higher number of shocks (up to 1500 additional pulses) was required to reduce the fragments to small and passable sizes. In comparison, the upgraded reflector was found to produce a slightly higher number of large fragments than the original HM-3 reflector (Fig. 9). This observation is expected because the upgraded reflector suppresses cavitation, which, in addition to its role in vascular injury, is also critical for producing small and passable fragments in SWL.³⁶ Quantitatively, no statistically significant difference in stone comminution was observed be-

tween the two reflector configurations when the exposure was less than 500 shocks ($p>0.05$, Fig. 10). From 500 to 1500 shocks, the original HM-3 reflector was found to produce better stone fragmentation than the upgraded reflector. Yet, towards the end, after a typical clinical dose of 2000 shocks, stone comminution produced by the two reflector configurations were again close to each other, i.e., $97.15 \pm 1.92\%$ (mean \pm SD) for the original HM-3 reflector at 20 kV and $90.35 \pm 1.96\%$ for the upgraded reflector at 24 kV, although the difference is statistically significant ($p<0.02$).

D. Rupture of vessel phantoms

Using the upgraded reflector with refined geometry, no rupture of the hollow fiber vessel phantom could be produced around the lithotripter beam focus ($-10 \text{ mm} < \Delta z_2 < 10 \text{ mm}$) even after 200 shocks at 24 kV [Fig. 11(a)]. In comparison, consistent and spatial position-dependent rupture of the vessel phantom was produced by the original HM-3 reflector at both 20 and 24 kV.¹⁷ Previously, rupture of the vessel phantom was produced using our prototype up-

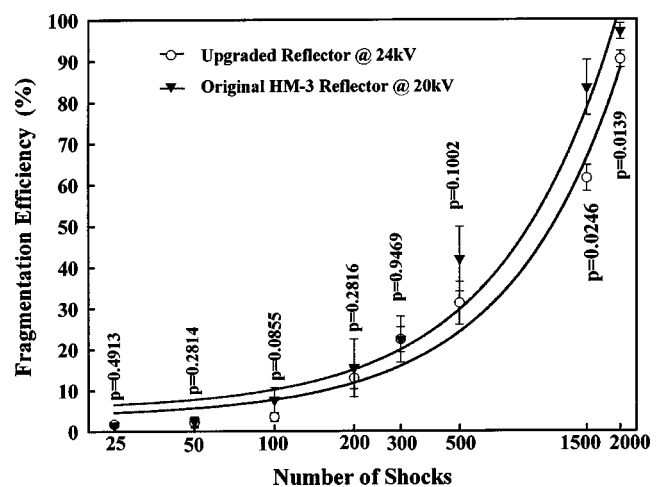


FIG. 10. Dose-dependent fragmentation efficiency produced by the original HM-3 and upgraded reflector. The fragmentation efficiency was determined by the weight percentage of fragments less than 2 mm in size following shock wave treatment. A Student's t -test was performed to determine statistically significant differences ($p<0.05$) between the results produced by the original HM-3 reflector at 20 kV and that from the upgraded reflector at 24 kV. The significance levels (p values) are shown in the figure.

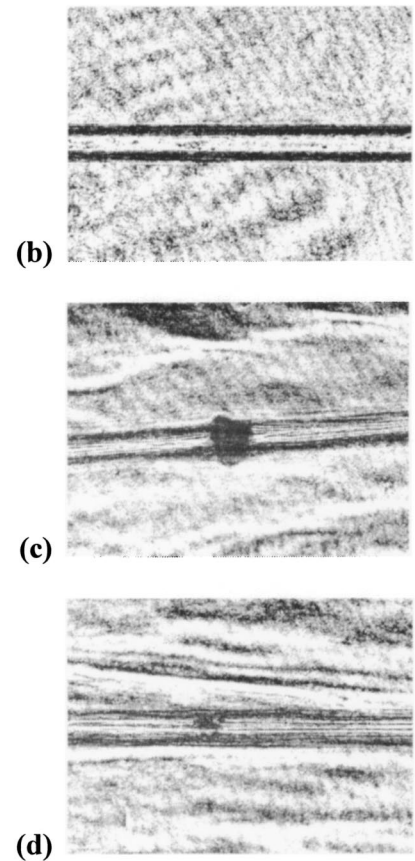
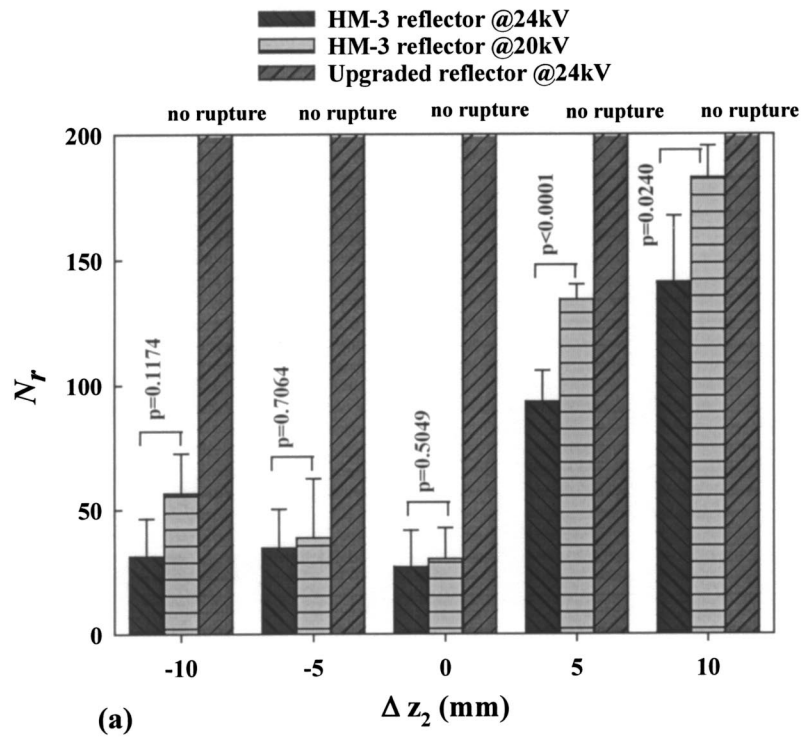


FIG. 11. (a) Relationship between the number of shocks to cause a rupture of a cellulose hollow fiber (N_r) and the axial position of the fiber in the lithotripter field ($n=6$). Here, Δz_2 denotes the distance from the second focus of the original HM-3 reflector on the z axis (z_2). A Student's t -test was performed for each location between the results of 20 kV and 24 kV using the original HM-3 reflector. The significance levels (p -values) are shown in the figure, (b) a cellulose hollow fiber (i.d.=0.2 mm) at lithotripter focus before shock wave exposure, and (c) and (d) maximum intraluminal bubble expansion produced by the original HM-3 reflector at 20 kV and the upgraded reflector at 24 kV, respectively.

graded reflector at $\Delta z_2 = -5$ mm where the highest tensile pressure was induced.¹⁷ Therefore, refinement of the reflector geometry has resulted in further suppression of the large intraluminal bubble expansion around the lithotripter focus, and concomitantly, a further reduction of the potential for vascular injury in SWL.

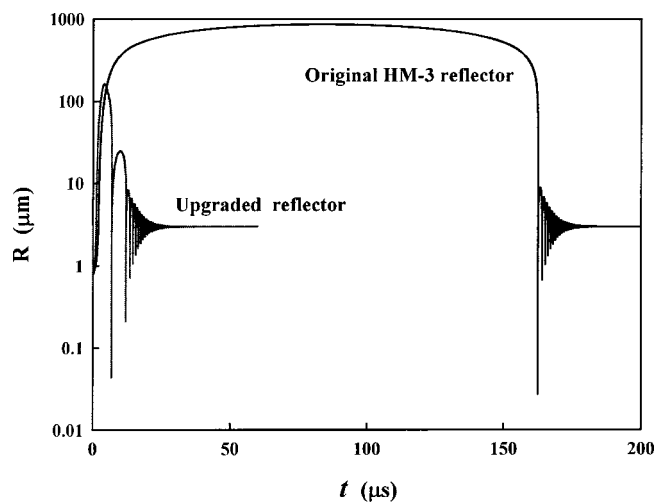
The maximum bubble expansion produced inside a hollow fiber vessel phantom by the original HM-3 and upgraded reflector was captured using the high-speed shadowgraph imaging system shown in Fig. 6. While substantial circumferential dilation of the vessel wall was observed using the original HM-3 reflector, minimal dilation was produced by the upgraded reflector [Figs. 11(c) and (d)]. This observation is consistent with the significantly reduced potential for vessel phantom rupture by the upgraded reflector [Fig. 11(a)]. All together, these results suggest that compared to the original HM-3 reflector, the upgraded reflector can produce satisfactory stone comminution with greatly reduced potential for vascular injury.

E. Bubble dynamics predicted by the Gilmore model

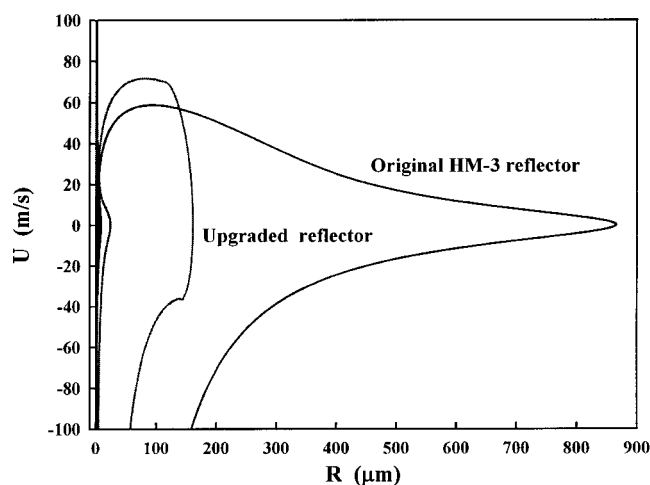
To confirm theoretically that the upgraded reflector can suppress cavitation, bubble dynamics in response to the pressure waveforms measured by the FOPH 300 at F_2 were calculated using the Gilmore model.⁸ No gas diffusion was con-

sidered in the model calculation because we were mainly interested in the expansion phase of the bubble oscillation.¹⁷ The results, shown in Fig. 12(a), revealed a dramatic reduction in the maximum bubble expansion. For the original HM-3 reflector at 20 kV, a maximum bubble radius (R_{\max}) of 866 μm with an associated collapse time (t_c) of 163 μs was predicted. In comparison, corresponding values of $R_{\max} = 161 \mu\text{m}$ and $t_c = 12 \mu\text{s}$ were predicted for the upgraded reflector at 24 kV. Although the model prediction is comparable to the experimental results (see Fig. 8) for the original HM-3 reflector, there is an apparent discrepancy for the upgraded reflector. This discrepancy may be caused in part by the fact that a bubble induced in the acoustic field of the upgraded HM-3 lithotripter tends to expand non-spherically as a result of *in situ* pulse superposition. In addition, the variation in pressure waveform profile off-axis and away from F_2 may also contribute to the differences between the theoretical prediction and experimental results. Nevertheless, on a qualitative basis, both the theoretical prediction and the experimental results strongly suggest that the upgraded reflector can significantly suppress bubble expansion and, therefore, greatly reduce the propensity for vessel rupture in SWL.²³

From the phase diagram shown in Fig. 12(b), it is noted that the bubble expansion produced by both the original



(a)



(b)

FIG. 12. Computed bubble dynamics of a cavitation nucleus ($R_0 = 3 \mu\text{m}$) in response to the pressure waveforms measured at the lithotripter focus using a fiber optic probe hydrophone (see Fig. 7). (a) Bubble radius (R) vs time and (b) phase plot of bubble wall velocity (U) vs R .

HM-3 and the upgraded reflector reaches a maximal outward speed at a bubble radius of about $80 \mu\text{m}$. Therefore, capillaries that have a typical inner diameter on the order of $10 \mu\text{m}$ are still at high risk for rupture due to intraluminal bubble expansion even when the upgraded reflector is used. However, the propensity for the rupture of small blood vessels should be greatly reduced by the upgraded reflector.

V. DISCUSSION

By refining the geometry of the reflector insert, we have strengthened the second shock wave and, consequently, further suppressed the intraluminal expansion of cavitation bubbles induced by LSW. Comparing to our prototype design, the refined reflector insert prevents the rupture of the hollow fiber vessel phantom throughout a large area around F_2 ($-10 \text{ mm} < \Delta z_2 < 10 \text{ mm}$) while maintaining satisfactory stone comminution. In addition, we have demonstrated via high-speed shadowgraph imaging that the second shock

wave significantly suppresses the initial bubble expansion and reduces the dilation of the vessel wall by the intraluminal bubbles. Based on the pressure waveforms measured by using an optical fiber probe hydrophone, numerical simulation of bubble dynamics also predicts a substantial reduction in maximum bubble expansion due to *in situ* pulse superposition. All together, these findings corroborate the experimental observation that the upgraded reflector can greatly reduce the propensity for vessel rupture. Furthermore, preliminary results from animal studies have also demonstrated a significant reduction in gross and microscopic renal injury using the upgraded reflector.³⁷ After a typical clinical dose of 2000 shocks, histology evaluation revealed more than threefold reduction in tissue injury in the kidney treated by the upgraded reflector at 24 kV, compared to that produced by the original HM-3 reflector at 20 kV. Microscopically, although extensive hemorrhages were produced throughout the thickness of the kidney using the original HM-3 reflector, only discrete microbleeding spots were generated by the upgraded reflector.³⁷

Although the overall profile and sequence of the pressure waveforms along the lithotripter axis can be evaluated qualitatively by the Hamilton model, an accurate prediction of the peak pressure at the beam focus will require the use of nonlinear wave propagation models that also accounts for thermoviscous absorption and dispersion in tissue.^{25–27} However, an accurate description of the initial pressure distribution around the spark discharge at F_1 needs to be determined before one can use these nonlinear models to guide the optimization of the HM-3 reflector geometry to achieve the most desirable bubble activity in SWL.²⁷

Finally, it is interesting to note that the upgraded reflector produces slightly larger fragments than the original HM-3 reflector (see Figs. 9 and 10). This finding is consistent with the results of our recent study, which suggests that although stress waves play an important role in the initial disintegration of kidney stones, cavitation is necessary to produce small and passable fragments, which is most critical for the success of clinical SWL.³⁶ Because the upgraded reflector suppresses cavitation, it has the tendency to produce larger residual fragments and therefore reduce slightly ($\sim 7\%$) the concomitant fragmentation efficiency after a clinical dose of 2000 shocks. Such a small loss in fragmentation efficiency, however, may be compensated by selectively enhancing the collapse of cavitation bubbles near the stone surface produced by the upgraded HM-3 lithotripter using an auxiliary shock wave source, such as a piezoelectric annular array shock wave generator.³⁸

ACKNOWLEDGMENTS

This work was supported in part by NIH through Grants Nos. RO1-DK52985 and RO1-DK58266. The authors are grateful to Thomas Dreyer and Marko Liebler from Universität Karlsruhe, Germany for their help in pressure waveform measurements using a fiber optic probe hydrophone (FOPH 300). The authors are also grateful to Dr. Songlin Zhu, who designed and fabricated the test chamber and set up the high-speed imaging system in the HM-3 lithotripter.

- ¹A. P. Evan, L. R. Willis, J. E. Lingeman, and J. A. McAteer, "Renal trauma and the risk of long-term complications in shock wave lithotripsy," *Nephron* **78**, 1–8 (1998).
- ²J. E. Lingeman, "Extracorporeal shock wave lithotripsy—Development, instrumentation, and current status," *Urol. Clin. North Am.* **24**, 185–211 (1997).
- ³D. A. Lifshitz, J. E. Lingeman, F. S. Zafar, D. W. Hollensbe, A. W. Nyhuis, and A. P. Evan, "Alterations in predicted growth rates of pediatric kidneys treated with extracorporeal shockwave lithotripsy," *J. Endourol.* **12**, 469–475 (1998).
- ⁴G. Janetschek, F. Frauscher, R. Knapp, G. Hofle, R. Peschel, and G. Bartsch, "New onset hypertension after extracorporeal shock wave lithotripsy: age related incidence and prediction by intrarenal resistive index," *J. Urol. (Baltimore)* **158**, 346–351 (1997).
- ⁵P. Zhong, Y. F. Zhou, and S. L. Zhu, "Dynamics of bubble oscillation in constrained media and mechanisms of vessel rupture in SWL," *Ultrasound Med. Biol.* **27**, 119–134 (2001).
- ⁶A. P. Evan, L. R. Willis, B. A. Connors, J. A. McAteer, J. E. Lingeman, R. O. Cleveland, M. R. Bailey, and L. A. Crum, "Can SWL-induced cavitation and renal injury be separated from SWL-induced impairment of renal hemodynamics?" *J. Acoust. Soc. Am.* **103**, 3037 (1998).
- ⁷G. Delacretaz, J. T. Walsh, Jr., and T. Aasshauer, "Dynamic polariscopic imaging of laser-induced strain in a tissue phantom," *Appl. Phys. Lett.* **70**, 3510–3512 (1997).
- ⁸C. C. Church, "A theoretical study of cavitation generated by an extracorporeal shock wave lithotripter," *J. Acoust. Soc. Am.* **86**, 215–227 (1989).
- ⁹P. Zhong, I. Cioanta, S. L. Zhu, F. H. Cocks, and G. M. Preminger, "Effects of tissue constraint on shock wave-induced bubble expansion *in vivo*," *J. Acoust. Soc. Am.* **104**, 3126–3129 (1998).
- ¹⁰A. Philipp, M. Delius, C. Scheffczyk, A. Vogel, and W. Lauterborn, "Interaction of lithotripter-generated shock waves in air bubbles," *J. Acoust. Soc. Am.* **93**, 2496–2509 (1993).
- ¹¹A. Philipp and W. Lauterborn, "Cavitation erosion by single laser-produced bubbles," *J. Fluid Mech.* **361**, 75–116 (1998).
- ¹²M. Delius, "Minimal static excess pressure minimises the effect of extracorporeal shock waves on cells and reduces it on gallstones," *Ultrasound Med. Biol.* **23**, 611–617 (1997).
- ¹³J. A. McAteer, M. A. Stonehill, K. Colmenares, J. C. Williams, A. P. Evan, R. O. Cleveland, M. R. Bailey, and L. A. Crum, "SWL cavitation damage *in vitro*: Pressurization unmasks a differential response of foil targets and isolated cells," *Proceedings of the 16th International Congress on Acoustics and 135th Meeting of the Acoustical Society of America*, 1998, Vol. 3, pp. 2497–2498.
- ¹⁴M. Delius, M. Jordan, H. G. Liebich, and W. Brendel, "Biological effects of shock waves: effect of shock waves on the liver and gallbladder wall of dogs—administration rate dependence," *Ultrasound Med. Biol.* **16**, 459–466 (1990).
- ¹⁵R. F. Paterson, D. A. Lifshitz, J. E. Lingeman, J. C. Williams, Jr., D. L. Rietjens, A. P. Evan, B. B. Connors, M. R. Bailey, L. A. Crum, R. O. Cleveland, Y. A. Pishchalnikov, I. V. Pishchalnikova, and J. A. McAteer, "Slowing the pulse repetition frequency in shock wave lithotripsy (SWL) improves stone fragmentation *in vivo*," *Proceedings of 17th International Congress on Acoustics*, Rome, Italy, 2001.
- ¹⁶P. Huber, J. Debus, K. Jochle, I. Simiantonakia, J. Jenne, R. Rasert, J. Spoo, W. J. Lorenz, and M. Wannenmacher, "Control of cavitation by different shockwave pulsing regimes," *Phys. Med. Biol.* **44**, 1427–1437 (1999).
- ¹⁷A. P. Evan and J. E. Lingeman, "Shockwave lithotripsy induces structural and functional changes in the kidney," *ROCK Society Meeting*, San Antonio, Texas, February, 2002.
- ¹⁸M. R. Bailey, D. T. Blackstock, R. O. Cleveland, and L. A. Crum, "Comparison of electrohydraulic lithotripters with rigid and pressure-release ellipsoidal reflectors. I. Acoustic fields," *J. Acoust. Soc. Am.* **104**, 2517–2524 (1998).
- ¹⁹D. Cathignol, J. Tavakkoli, A. Birer, and A. Arefiev, "Comparison between the effects of cavitation induced by two different pressure-time shock waveform pulses," *IEEE Trans. Ultrason. Ferroelectr. Freq. Control* **45**, 788–799 (1998).
- ²⁰M. R. Bailey, "Control of acoustic cavitation with application to lithotripsy," *Technical Report ARL-TR-97-1*, Applied Research Laboratories, The University of Texas at Austin, pp. 1–210, 1997.
- ²¹F. E. Prieto and A. M. Loske, "Bifocal reflector for electrohydraulic lithotripters," *J. Endourol.* **13**, 65–75 (1999).
- ²²D. L. Sokolov, M. R. Bailey, and L. A. Crum, "Effect of dual-reflector lithotripter on stone fragmentation and cell damage," *J. Acoust. Soc. Am.* **108**, 2518 (2000).
- ²³P. Zhong and Y. F. Zhou, "Suppression of large intraluminal bubble expansion in shock wave lithotripsy without compromising stone comminution: Methodology and *in vitro* experiments," *J. Acoust. Soc. Am.* **110**, 3283–3291 (2001).
- ²⁴M. F. Hamilton, "Transient axial solution for the reflection of a spherical wave from a concave ellipsoidal mirror," *J. Acoust. Soc. Am.* **93**, 1256–1266 (1993).
- ²⁵T. Christopher, "Modeling the Dornier HM-3 lithotripter," *J. Acoust. Soc. Am.* **96**, 3088–3095 (1994).
- ²⁶M. A. Averkiou, and R. O. Cleveland, "Modeling of an electrohydraulic lithotripter with the KZK equation," *J. Acoust. Soc. Am.* **106**, 102–112 (1999).
- ²⁷M. Tanguay and T. Colonius, "Numerical simulation of bubbly cavitating flow in shock wave lithotripsy," *CAV2001: session B6.004*, Pasadena, California, 2001.
- ²⁸J. Staudenraus and W. Eisenmenger, "Fiberoptic probe hydrophone for ultrasonic and shock-wave measurements in water," *Ultrasonics* **31**, 267–273 (1993).
- ²⁹P. Zhong, H. F. Lin, X. F. Xi, S. L. Zhu, and E. S. Bhogte, "Shock wave-inertial microbubble interaction: Methodology, physical characterization, and bioeffect study," *J. Acoust. Soc. Am.* **105**, 1997–2009 (1999).
- ³⁰Y. Liu and P. Zhong, "BegoStone—A new stone phantom for shock wave lithotripsy research," *J. Acoust. Soc. Am.* **112**, 1265–1268 (2002).
- ³¹G. Mandel and N. Mandel, "Crystal-crystal interactions," in *Kidney Stones: Medical and Surgical Management*, edited by F. L. Coe *et al.* (Lippincott-Raven, Philadelphia, 1996), pp. 115–127.
- ³²*Extracorporeal Shock Wave Lithotripsy: New Aspects in the Treatment of Kidney Stone Disease*, edited by C. Chaussy (S. Karger, Basel, 1982).
- ³³A. J. Coleman, J. E. Saunders, R. C. Preston, and D. R. Bacon, "Pressure waveforms generated by a Dornier extracorporeal shock-wave lithotripter," *Ultrasound Med. Biol.* **13**, 651–657 (1987).
- ³⁴R. O. Cleveland, D. A. Lifshitz, B. A. Connors, A. P. Evan, L. R. Willis, and L. A. Crum, "*In vivo* pressure measurements of lithotripsy shock waves in pigs," *Ultrasound Med. Biol.* **24**, 293–306 (1998).
- ³⁵R. O. Cleveland, M. R. Bailey, N. Fineberg, B. Hartenbaum, M. Lokhandwalla, J. A. McAteer, and B. Sturtevant, "Design and characterization of a research electrohydraulic lithotripter patterned after the Dornier HM3," *Rev. Sci. Instrum.* **71**, 2514–2525 (2000).
- ³⁶S. L. Zhu, F. H. Cocks, G. M. Preminger, and P. Zhong, "The role of stress waves and cavitation in stone comminution in shock wave lithotripsy," *Ultrasound Med. Biol.* **28**, 661–671 (2002).
- ³⁷B. Auge, P. Zhong, Y. F. Zhou, C. Lallas, and G. M. Preminger, "Suppression of large intraluminal bubble expansion during SWL," *J. Endourol.* **15**, A18 (2001).
- ³⁸X. F. Xi and P. Zhong, "Improvement of stone fragmentation during shock wave lithotripsy using a combined EH/PEAA shock wave generator—*In vitro* experiments," *Ultrasound Med. Biol.* **26**, 457–467 (2000).

Echolocation signals of wild Atlantic spotted dolphin (*Stenella frontalis*)

Whitlow W. L. Au^{a)}

Marine Mammal Research Program, Hawaii Institute of Marine Biology, University of Hawaii,
P.O. Box 1109, Kailua, Hawaii 96734

Denise L. Herzing^{b)}

Department of Biological Sciences, Florida Atlantic University, 777 Glades Road, Boca Raton,
Florida 33431

(Received 27 April 2002; accepted for publication 9 September 2002)

An array of four hydrophones arranged in a symmetrical star configuration was used to measure the echolocation signals of the Atlantic spotted dolphin (*Stenella frontalis*) in the Bahamas. The spacing between the center hydrophone and the other hydrophones was 45.7 cm. A video camera was attached to the array and a video tape recorder was time synchronized with the computer used to digitize the acoustic signals. The echolocation signals had bi-modal frequency spectra with a low-frequency peak between 40 and 50 kHz and a high-frequency peak between 110 and 130 kHz. The low-frequency peak was dominant when the signal the source level was low and the high-frequency peak dominated when the source level was high. Peak-to-peak source levels as high as 210 dB *re* 1 μ Pa were measured. The source level varied in amplitude approximately as a function of the one-way transmission loss for signals traveling from the animals to the array. The characteristics of the signals were similar to those of captive *Tursiops truncatus*, *Delphinapterus leucas* and *Pseudorca crassidens* measured in open waters under controlled conditions. © 2003 Acoustical Society of America. [DOI: 10.1121/1.1518980]

PACS numbers: 43.80.Ev, 43.80.Ka, 43.80.Jz [FD]

I. INTRODUCTION

The Bahama Islands are an archipelago in the tropical West Atlantic east of Florida that are surrounded by deep water while the Bahamas banks are relatively shallow (<15 m). The banks are thick, submerged platforms of calcareous rock providing diverse habitats, including fringe and patch reefs, atolls, grassy flats, and ledges. Since 1985, a resident community of approximately 200 spotted and 200 bottlenose dolphins have been identified, sexed, and observed in a variety of behavioral contexts in this area (see Fig. 1). Basic life history and age class categories for the Atlantic spotted dolphin, *S. frontalis*, have been described (Herzing, 1997). Underwater behavior and correlated sound (narrow-band frequency <20 kHz) have also been described including sounds correlated with (1) contact/reunion (whistles), (2) excitement/distress (whistle-squawks), (3) pursuit/herding (buzzes), (4) aggression (burst-pulses), (5) group synchrony (synch pulses), (6) interspecific interactions (barks, screams, squawks), (7) nonvocal sounds (tail-slaps), and (8) foraging/feeding (echolocation clicks) (Herzing, 1996, 2000). Previous studies on the behavior and sound production of *S. frontalis* in captivity also exist (Wood, 1953; Caldwell and Caldwell, 1966, 1971; Caldwell *et al.*, 1973).

The echolocation signals used by *S. frontalis* in the Bahama banks, measured on a broadband basis, will be considered in this paper. The echolocation characteristics of delphinid species have been studied primarily in captivity (Au,

1993). Measurements from stationary dolphins in captivity have shown that echolocation clicks are emitted in a directional beam and signals measured off-axis are distorted with respect to the signals measured along the major axis of the beam. Therefore, it is very difficult to obtain accurate measurements of free-ranging, fast moving dolphins in the wild. Another complicating factor is associated with the broadband nature of echolocation signals and the possibility that the center frequency of echolocation clicks tends to vary with the intensity of the emitted clicks. Au *et al.* (1985) found that higher intensity clicks emitted by a beluga whale (*Delphinapterus leucas*) in Hawaii had higher frequencies than the lower intensity clicks used by the same animal in San Diego Bay. Au *et al.* (1995) also found a nearly linear relationship between the center frequency and source level of a false killer whale (*Pseudorca crassidens*), i.e., the higher the source level, the higher the center frequency of the emitted clicks. Therefore, any measurements of the spectra of echolocation clicks should be accompanied by an estimate of the source levels.

II. PROCEDURE

A. Measurement system

A four-hydrophone array with the hydrophones arranged as a symmetrical star was used to measure the echolocation signals of *S. frontalis*. Such a sensor geometry was used successfully by Aubauer (1995) in tracking echolocating bats in the field. The array structure resembled the letter “Y,” with each arm being 45.7 cm in length and separated by an angle of 120 degrees as shown in Fig. 2. The arms of the

^{a)}Electronic mail: wau@hawaii.edu

^{b)}Electronic mail: wilddolphin@igc.org

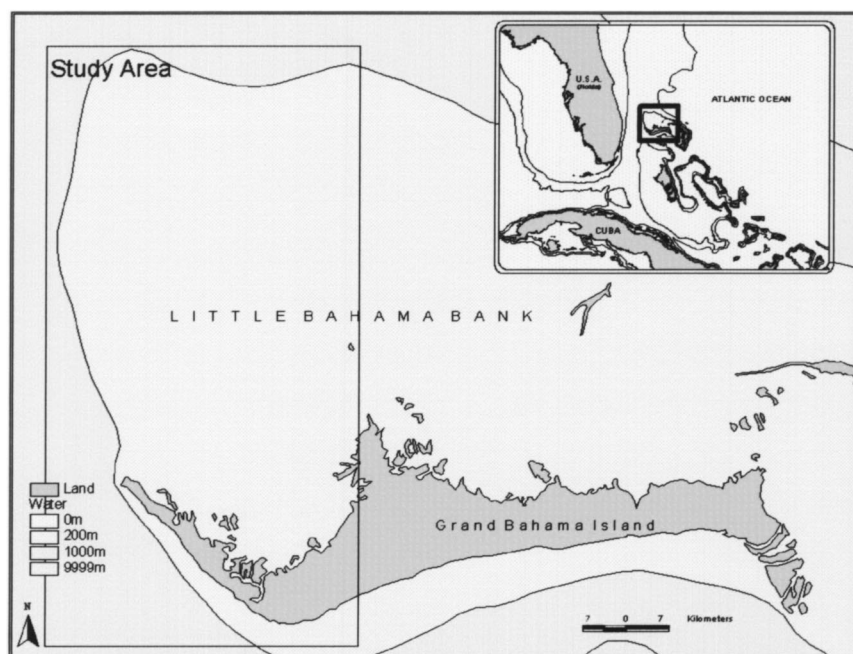


FIG. 1. Map of the study site in the banks area of the Bahama Island.

array were constructed out of 1.27-cm o.d. PVC pipe with a spherical hydrophone connected to the end of each pipe and the cable running through the center of the pipe. Another hydrophone was connected at the geometric center of the “Y.” The PVC pipes fit into holes drilled into a 2.54-cm-thick delrin plate. The range of a sound source can be determined by measuring the time of arrival differences between the signal at the center and the three other hydrophones. If the arrival time difference between the center and the other hydrophones is denoted as τ_{0i} , where $i = 1, 2$, and 3 , then the range, R , of the source can be expressed as (see Appendix)

$$R = \frac{c^2(\tau_{01}^2 + \tau_{02}^2 + \tau_{03}^2) - 3a^2}{2c(\tau_{01} + \tau_{02} + \tau_{03})}, \quad (1)$$

where c is the speed of sound, and a is the distance between the center and the other hydrophones.

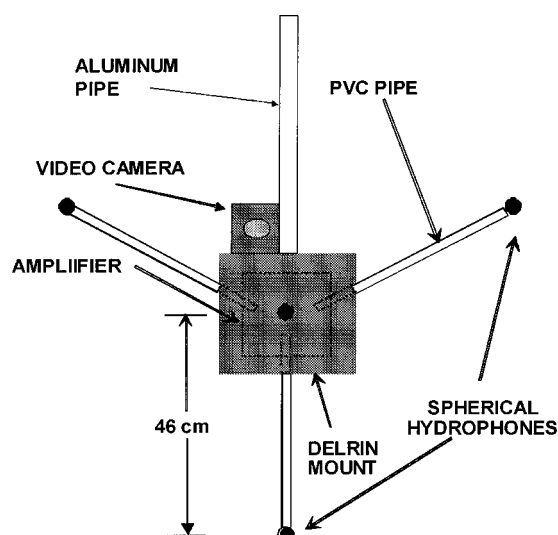


FIG. 2. Schematic diagram of the four-hydrophone symmetrical star array along with a video camera on a pole.

An underwater housing connected to the back of the hydrophone mounting plate contained an amplifier and line-driver for each of the hydrophones. A CCD video camera in an underwater housing was mounted next to the center hydrophone. A multi-conductor cable, 77 m in length, consisting of five coaxial lines and two d.c. power lines, connected the array to an adjustable amplifier-filter box containing a power supply.

Echolocation signals were digitized with two Gage-1210, 12 bit dual simultaneous sampling data acquisition boards that were connected to a “lunch box” computer via two EISA slots. The data acquisition system operated at a sample rate of 500 kHz with a pretrigger capability. When the computer signaled the Gage-1210 to collect data, four channels of acoustic signals were simultaneously and continuously digitized with the results going into separate circular memories on each Gage-1210 board. When an echolocation signal was detected by the center hydrophone, it triggered the data acquisition board. Two hundred pretriggered points and two hundred posttrigger points were collected for each channel and downloaded into the computer. A total of 80 clicks could be downloaded for each episode before the data had to be stored on the hard drive. A specially constructed ISA board was also used to measure the time interval between the clicks being acquired and to cause a light-emitting diode to flash, indicating that clicks were being captured. The interclick interval data was also downloaded and stored on the hard drive. The time of capture (to the closest 18-ms interval of the computer timing system) of each click was also saved and stored on the hard drive. The clock on a portable VCR was synchronized to the computer’s clock so that the video images could be synchronized with the acoustic data.

B. Acoustic measurements

Measurement of echolocation signals was conducted from the Wild Dolphin Project’s 60-ft power catamaran,

Stenella. A map of the field site showing the Bahama bank where the study was conducted is shown in Fig. 1. All the electronics including the lunch-box computer and video tape recorder were housed on the deck of the catamaran. The field work was performed in the summers of 1996 and 1997.

The four-hydrophone array was deployed by two methods. In the first method, the array was connected to a 1-m long, 2.54-cm o.d. aluminum pipe with a handle grip at one end of the pipe. Dolphins were first located by patrolling the sandbank, an area of approximately 644 km². When the animals were located, the speed of the catamaran was reduced, and the dolphins were encouraged to bow ride for a short period while swimmers prepared to enter the water. The engine of the catamaran was then placed into idle and swimmers entered the water equipped with swim fins and snorkels. The array was then handed over to one of the swimmers who then swam towards the dolphins. At the same time, an operator controlled the data acquisition sequence by arming the computer to start the data acquisition process and by starting the video tape recorder.

The second method involved positioning the catamaran at night along the edge of the drop-off from the sandbank to deeper waters. A spotlight was directed into the water next to the catamaran, attracting various small fishes and squid to the surface. Spotted dolphins were also attracted by either the spotlight or the congregation of micronekton. The array was attached to a 3-m-long aluminum pole and placed in the water along side the boat close to where the spotlight intersected the water's surface. The center of the array was lowered to a depth of 1 to 1.5 m below the surface. Spotted dolphins often milled about 20–30 m from the boat foraging on prey, and also made “runs” into the lit area towards the array, continuously echolocating as they did so.

III. RESULTS

A total of 43 files of echolocation clicks were collected on three field trips. The quantity of data collected was limited by periods of equipment malfunction requiring repair. There were also occasions when a dolphin approached the array only a few degrees from the plane of the array so that one of the hydrophones would not detect the click because of the direction of the animal's beam. The number of clicks collected per file varied considerably from as low as 3 to a high of 80, the maximum number of clicks that the system could handle. Only echolocation events in which the amplitude of the signals received by the center hydrophone was either the highest or within 3 dB of the highest were accepted for analysis. This criterion was chosen to ensure that a dolphin beam was directed at the array. The beam patterns measured for three different odontocete species (Au, 1993; Au *et al.*, 1995) indicate that when the major axis of the beam is directed to within ± 5 degrees of the center hydrophone, the signal received by the center hydrophone will either have the highest or will be within 3 dB of the highest amplitude. A total of 1277 clicks met the appropriate criterion.

Three typical types of clicks are shown in Fig. 3 with the signal waveforms on the right and the frequency spectra on the left. These clicks are very brief, generally less than 70 μ s in duration, with broad frequency spectra. Clicks with bimo-

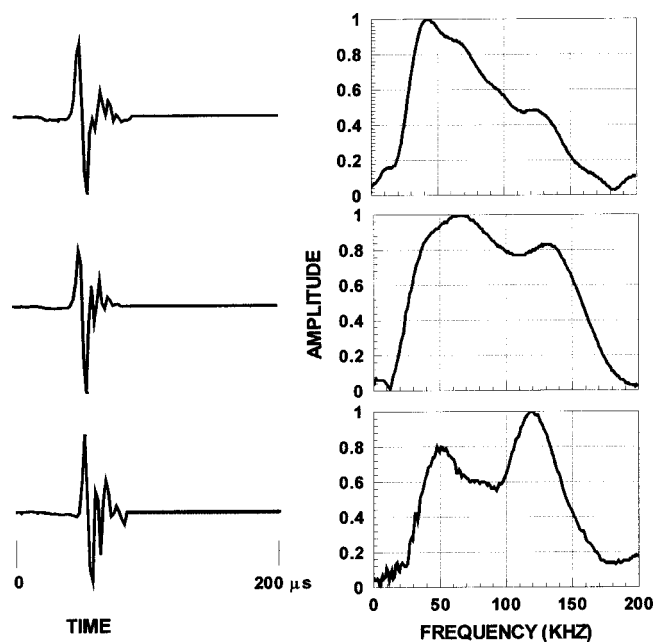


FIG. 3. Examples of the some representative waveforms and frequency spectra emitted by *Stenella frontalis* in the Bahamas banks.

dal spectra are obvious in the spectra plots. Some of the bimodal spectra have relatively high peak frequencies (> 80 kHz) whereas some have low peak frequencies (< 40 kHz). The majority ($\sim 80\%$) of the clicks examined had bimodal spectra. The click waveforms resemble those used by other odontocetes such as *Tursiops truncatus*, *Delphinapterus leucas* (Au, 1993), *Pseudorca crassidens* (Au *et al.*, 1995), and *Lagorhynchus albirostris* (Rasmussen *et al.*, 2002).

The peak-to-peak source level as a function of range between an echolocating dolphin and the array is shown in Fig. 4. As the dolphin's range to the array decreased, the source level also decreased. The solid curve in Fig. 4 is a regression curve represented by the equation

$$SL = 185.3 + 20 \log(R) \quad (2)$$

and has an r^2 value of 0.52, where SL is the source level in dB re 1 μ Pa and R is the range in meters. The decrease in

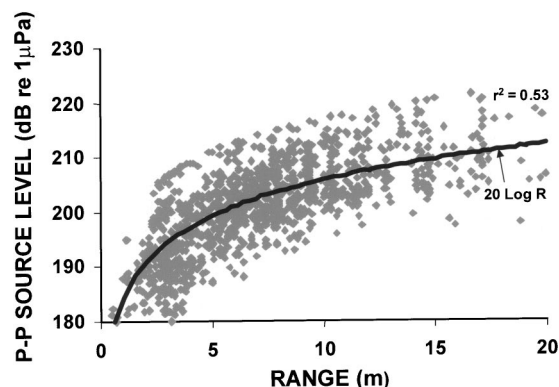


FIG. 4. Scatter plot of source level as a function of the range between an echolocating dolphin and the hydrophone array. The solid curve represents the one-way spherical spreading curve-fitted to the data in a least-square fashion with $r^2 = 0.56$.

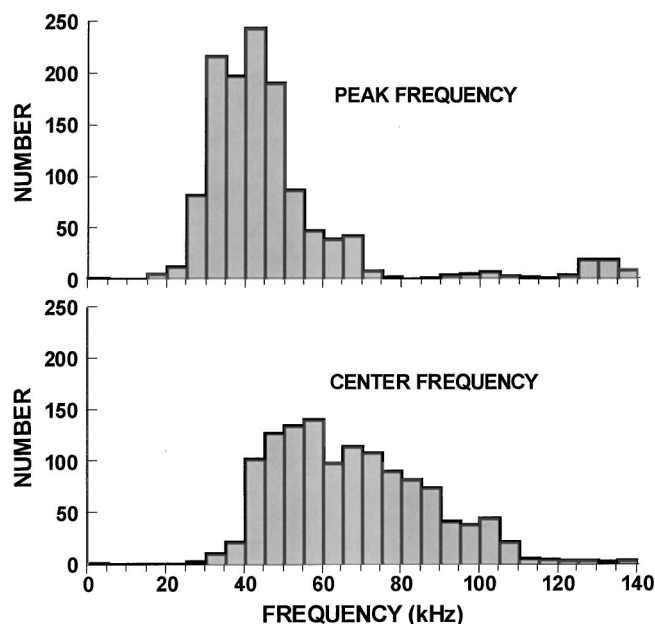


FIG. 5. Histograms of peak and center frequencies of echolocation signals.

SL corresponded to the decrease in the one-way spherical spreading loss. Therefore, the amplitude of the echoes returning to the dolphins increased in magnitude as the range decreased, suggesting that the dolphins prefer to receive echoes that have increasing signal-to-noise. The results also suggest that the dolphins were echolocating on the hydrophone array and not on some other objects since the source level decreased as the range to the array decreased. Also, the inter-click intervals were always greater than the two-way travel time from the animals to the array and back, which is consistent with the notion that the dolphins were echolocating on the array. The fitted curve was constrained to vary as $20 \log R$, however, the “best-fit” logarithm’s curve would be very similar to the $20 \log R$ fit and the difference in r^2 would be in the third decimal place.

The distributions of peak and center frequencies of the echolocation signals are shown in Fig. 5. Peak frequency is defined as the frequency at which the frequency spectrum of a signal has its maximum amplitude. Center frequency is defined as that frequency which divides the energy in a frequency spectrum into two equal parts; it is defined mathematically as

$$f_o = \frac{\int_0^\infty f |S(f)|^2 df}{\int_0^\infty |S(f)|^2 df}, \quad (3)$$

where $S(f)$ is the Fourier transform of the echolocation signal and f is the instantaneous frequency. Seventy-six percent of the signals had center frequencies greater than 50 kHz and 23% had center frequencies greater than 80 kHz. The center frequency extends to much higher frequencies than the peak frequency and this property is indicative of signals with bimodal spectra. Eighty percent of the echolocation clicks had bimodal spectra in which the amplitudes of the secondary peaks were within 50% of the amplitude of the primary peak. Therefore, center frequency is a more representative measure of signals with bimodal spectra (Au *et al.*, 1995).

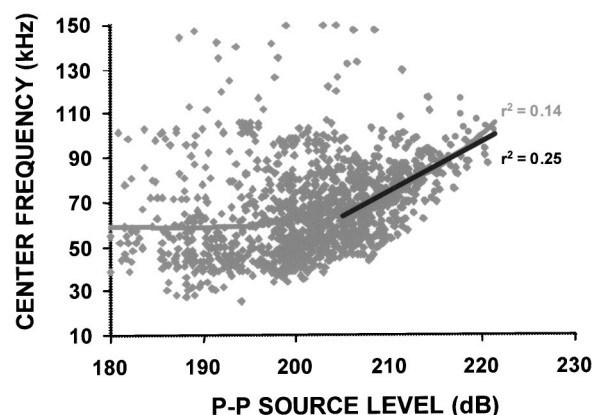


FIG. 6. Scatter plot of center frequency versus source level. A third-order polynomial is fitted for all data and has an r^2 value of 0.14 while a linear regression curve is shown for source levels greater than and equal to 205 dB with $r^2 = 0.25$.

The variation of the center frequency as a function of the source level is shown in Fig. 6. A third order polynomial regression with an r^2 value of 0.14 is also shown in the figure. The regression line suggests that the center frequency is independent of the source level for levels lower than 200 dB *re* 1 μ Pa. However, as the source level increases beyond 205 dB, the center frequency also increases. If only signals with source levels equal to or greater than 205 dB are considered, the dependence of center frequency on source level becomes stronger with an r^2 value of 0.25. The dependence of the center frequency on source level is weaker than for *Pseudorca crassidens* (Au *et al.*, 1995) where a linear regression line has an r^2 value of 0.44.

Histograms of the 3-dB bandwidth and the rms bandwidth are shown in Fig. 7. The 3-dB bandwidth is the width of the frequency band between the two points that are 3-dB lower than the maximum amplitude of a spectrum. The 3-dB points are also referred to as the half-power points. The rms bandwidth is a measure of the frequency width about the

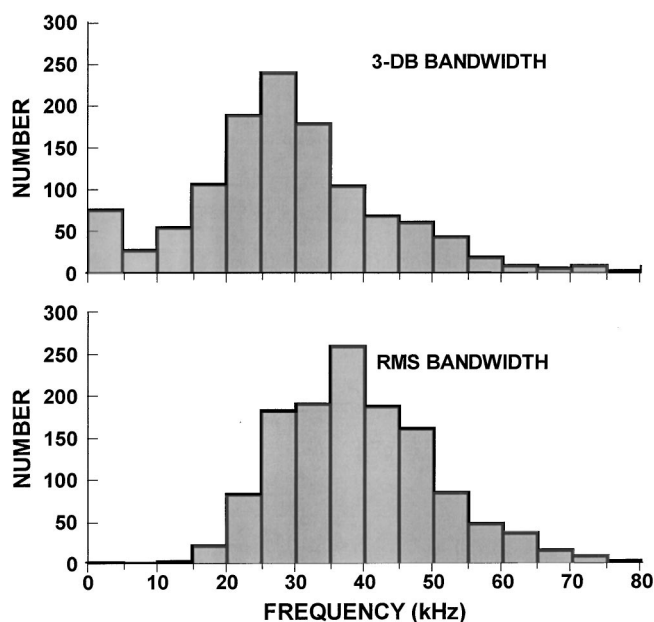


FIG. 7. Histograms of 3-dB and rms bandwidth of echolocation signals.

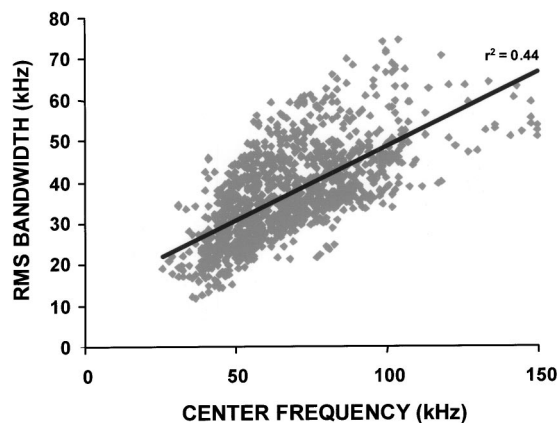


FIG. 8. Scatter plot of rms bandwidth versus center frequency. The linear regression line has an r^2 of 0.44.

center frequency. It is defined as (Rihaczek, 1969)

$$\beta = \frac{\int_0^\infty (f - f_o)^2 |S(f)|^2 df}{\int_0^\infty |S(f)|^2 df}, \quad (4)$$

where f_o is the center frequency given in Eq. (3). The 3-dB bandwidth for bimodal spectra can often provide a misrepresentation of the width of the signal since the bandwidth might cover only the frequency range about the peak frequency. The rms bandwidth is probably a better measure of the width of signals with bimodal spectra. The histograms clearly show higher values for the rms bandwidth than the 3-dB bandwidth.

A scatter plot of rms bandwidth as a function of center frequency along with a linear regression line is shown in Fig. 8. The linear regression has a relatively high r^2 value of 0.44, indicating a strong relationship between rms bandwidth and center frequency. As the frequency increased, the bandwidth also increased almost linearly. The range or temporal resolution of a signal is related to the inverse of the bandwidth so that the wider the bandwidth, the smaller the temporal resolution capability of the signal (Burdic, 1969).

IV. DISCUSSION AND CONCLUSIONS

Atlantic spotted dolphin (*Stenella frontalis*) project broadband, short duration echolocation signals similar to those of other odontocetes. Most of the signals have a bimodal frequency distribution, which also contributes to the broadband nature of the signals. The broad bandwidth of the echolocation signal provides a good range resolution capability (Au, 1993) that should enable *Stenella frontalis* to be able to perform fine target discrimination in a shallow water environment where bottom reverberation can be troublesome. Spotted dolphin also project relatively high-amplitude signals with maximum source level measured about 223 dB *re* 1 μ Pa, although most of the source levels were between 200 and 210 dB *re* 1 μ Pa.

The peak-to-peak source levels measured for *Stenella frontalis* are comparable to those measured for *Tursiops truncatus* in open-water captive echolocation experiments (Au, 1980, 1993), for comparable target ranges. For target ranges between 6 and 20 m, *Tursiops* source levels varied from about 204 to 216 dB *re* 1 μ Pa, which are similar to that of

Stenella frontalis. However, there is a large difference between the target strengths of targets used in the echolocation experiments for *Tursiops* and the target strength of the array assembly used to measure signals in the field. Although the target strength of the array was not measured, the theoretical target strength of an aluminum pipe, connected to a flat plexiglass container mounted on a flat delrin plate along with a camera holder, should be approximately 15–20 dB greater than the small cylinders and spheres used in the *Tursiops* experiments (Au, 1980, 1993). This comparison suggests the importance of range on the source levels utilized by dolphins. Despite the higher target strength of the array, the spotted dolphins emitted similar levels of echolocation signals as *Tursiops* echolocating on much weaker targets at similar ranges.

The variation of source level as a function of the one-way transmission loss is similar to that of the white beaked dolphin, *Lagenorhynchus albirostris* (Rasmussen *et al.*, 2002) and killer whales, *Orcinus orca* (Au *et al.*, 2001). This type of variation in source levels is also similar to variations found with captive dolphins. If the data shown in Fig. 7.14 of Au (1993) are rearranged into a plot of source level versus range, the variation with range will also be a function of the one-way transmission loss.

Our results suggest that several basic signal parameters are interrelated in a complex relationship. Source level is dependent on target range, center frequency is dependent on source level (at least for source levels greater than 205 dB), and rms bandwidth is dependent on center frequency. However, it seems that the most basic parameter in this interrelationship is target range. Therefore, it is important to be able to ascertain the range of echolocating dolphins when measuring echolocation signals, even for on-axis signals.

The results of this study also clearly demonstrate the utility of using a multi-hydrophone array to measure echolocation signals of dolphins in the wild. The symmetrical star array used in this study is relatively compact and easy to handle, and can provide information on whether a specific received echolocation signal originated in the vicinity of the major axis of the animal's transmission beam. Time of arrival differences between hydrophones were easily ascertained because of the rapid onset of the echolocation signals. Our results suggest that it is very difficult to obtain reliable data on echolocation signals without the use of some kind of array.

ACKNOWLEDGMENTS

Grateful thanks are given to the crew and staff of the Wild Dolphin Project. Special thanks to Lisa Harrod, Alice and Ed Crawford, Randy and Michelle Wells, Will Engleby, and Tim Barrett. The senior author thanks Dr. Roland Aubauer for his suggestion of using a symmetrical star geometry and for various discussions associated with his research on detection flying bats. The assistance of Michiel Schotten in testing and calibrating the array is also appreciated. This work was conducted under Bahamas Department of Fisheries Research Permit No. MAF/FIS 12 and funded by the Office of Naval Research, Dr. Robert Gisiner, program manager. This is HIMB Contribution No. 1136.

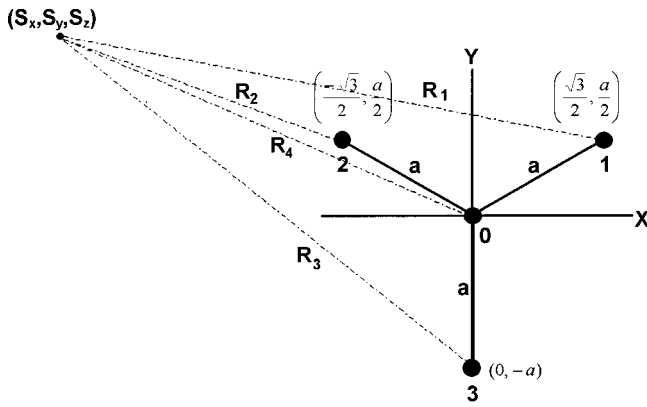


FIG. 9. Geometry for determining the location of a sound source from time of arrival difference information with a symmetrical star array.

APPENDIX

Let us consider the four hydrophone array with on the x - y plane and a sound source located at coordinates (S_x, S_y, S_z) as shown in Fig. 9. Let R_i be the range from the source to the i th hydrophone, where $i = 1, 2, 3$. Then the range to each hydrophone can be expressed by the equation

$$\begin{aligned} S_x^2 + S_y^2 + S_z^2 &= R^2 = c^2 t_0^2, \\ (S_x - la)^2 + (S_y - a/2)^2 + S_z^2 &= R_1^2 = c^2 (t_0 - \tau_{01})^2, \\ (S_x + la)^2 + (S_y - a/2)^2 + S_z^2 &= R_2^2 = c^2 (t_0 - \tau_{02})^2, \\ S_x^2 + (S_y + a)^2 + S_z^2 &= R_3^2 = c^2 (t_0 - \tau_{03})^2, \end{aligned} \quad (\text{A1})$$

where c is the speed of sound in water, τ_{0i} is the time of arrival difference between the center hydrophone and the i th hydrophone, and $l = \sqrt{3}/2 = \cos 30^\circ$. Using the technique of Watkins and Schevill (1972), the top equation of the system of equations in (A1) is subtracted from the other equations to give (after some rearranging)

$$\begin{aligned} -2laS_x - aS_y + 2c^2\tau_{01}t_0 &= c^2 t_0^2 - a^2, \\ 2laS_x - aS_y + 2c^2\tau_{02}t_0 &= c^2 t_0^2 - a^2, \\ 2aS_y + 2c^2\tau_{03}t_0 &= c^2 t_0^2 - a^2. \end{aligned} \quad (\text{A2})$$

This is a system of three equations with three unknowns. There are a variety of methods to solve for the unknowns S_x , S_y , and t_0 . The equations of (A2) can be expressed in a matrix format as

$$\begin{pmatrix} -2la & -a & 2c^2\tau_{01} \\ 2la & -a & 2c^2\tau_{02} \\ 0 & 2a & 2c^2\tau_{03} \end{pmatrix} \begin{pmatrix} S_x \\ S_y \\ t_0 \end{pmatrix} = \begin{pmatrix} c^2 t_0^2 - a^2 \\ c^2 t_0^2 - a^2 \\ c^2 t_0^2 - a^2 \end{pmatrix}. \quad (\text{A3})$$

Using Cramer's rule (Kreyszig, 1983) we can solve for t_0 by solving the determinant equation

$$t_0 = \frac{\begin{vmatrix} -2la & -a & c^2\tau_{01}^2 - a^2 \\ 2la & -a & c^2\tau_{02}^2 - a^2 \\ 0 & 2a & c^2\tau_{03}^2 - a^2 \end{vmatrix}}{\Delta}, \quad (\text{A4})$$

where Δ is the characteristic determinant defined by

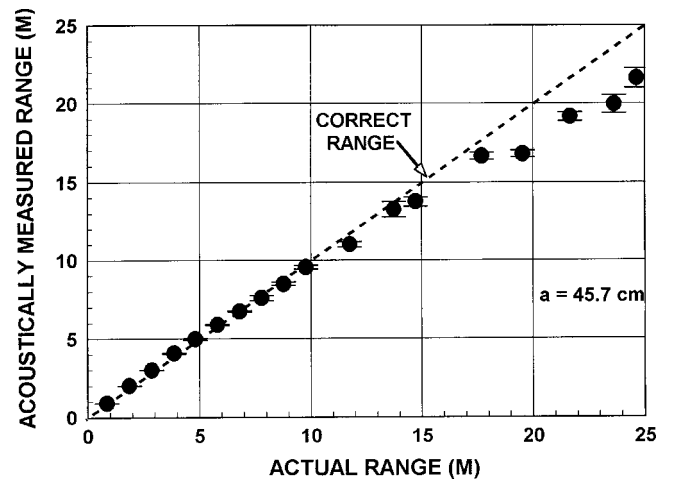


FIG. 10. Calibration measurement for the symmetrical star array used in this study. The mean and standard deviation of the estimated range from ten measures are plotted against the actual range.

$$\Delta = \begin{vmatrix} -2la & -a & 2c^2\tau_{01} \\ 2la & -a & 2c^2\tau_{02} \\ 0 & 2a & 2c^2\tau_{03} \end{vmatrix} = 8la^2c^2[\tau_{01} + \tau_{02} + \tau_{03}]. \quad (\text{A5})$$

Solving the determinant in Eq. (A4) for t_0 using the relationship of $R = t_0 c$, we obtain the equation for the range from the source to the center hydrophone in the array as

$$R = \frac{c^2[\tau_{01}^2 + \tau_{02}^2 + \tau_{03}^2] - 3a^2}{2c[\tau_{01} + \tau_{02} + \tau_{03}]}. \quad (\text{A6})$$

For a given set of delay times, solutions for S_z will have a \pm ambiguity, indicating that the source can be either above or below the X - Y plane of Fig. 9.

The accuracy of using the symmetrical star array to determine the range of a sound source was measured by projecting a simulated dolphin echolocation signal at different ranges from the array and using Eq. (A6) to estimate the range. The results of the measurements shown in Fig. 10 suggest that this technique can give very accurate results out to about 17.5 m. Ten pings were measured at each range. If the purpose of estimating R is to obtain the transmission loss due to spherical spreading, then the difference in the estimated and actual ranges will result in only a 1.2-dB error for an actual range of 25 m.

- Au, W. W. L. (1980). "Echolocation signals of the Atlantic bottlenose dolphin (*Tursiops truncatus*) in open waters," in *Animal Sonar Systems*, edited by R. G. Busnel and J. F. Fish, (Plenum, New York), pp. 251–282.
- Au, W. W. L. (1993). *The Sonar of Dolphins* (Springer-Verlag, New York).
- Au, W. W. L., Ford, J., and Allman, K. (2001). "Echolocation signal of killer whales (*Orcinus orca*) in Johnstone Strait, Canada," in Proc. 14th Biennial Conf. on the Biology of Marine Mammals, Vancouver, BC, Canada, pp. 11–12 (A).
- Au, W. W. L., Carder, D. A., Penner, R. H., and Scronce, B. L. (1985). "Demonstration of adaptation in Beluga whale echolocation signals," *J. Acoust. Soc. Am.* **77**, 726–730.
- Au, W. W. L., Pawloski, J., Nachtigall, P. E., Blonz, M., and Gisner, R. (1995). "Echolocation signal and transmission beam pattern of a false killer whale (*Pseudorca crassidens*)," *J. Acoust. Soc. Am.* **98**, 51–59.
- Aubauer, R. (1995). "Korrelationsverfahren zur Flugbahnverfolgung echoortender Fledermäuse," Fortschr.-Ber. VDI Reihe 17 Nr. 132 Dusseldorf: VDI-Verlag.

- Burdic, W. S. (1969). *Radar Signal Analysis* (Prentice-Hall, Englewood Cliffs, NJ).
- Caldwell, D. K., and Caldwell, M. C. (1966). "Observations on the distribution, coloration, behavior and audible sound production of the spotted dolphin, *Stenella plagiodon*," *Contrib. Sci.* **104**, 1–28.
- Caldwell, D. K., and Caldwell, M. C. (1971). "Underwater pulsed sounds produced by captive spotted dolphins, *Stenella plagiodon*," *Cetol.* **1**, 1–7.
- Caldwell, M. C., Caldwell, D. K., and Miller, J. F. (1973). "Statistical evidence for individual signature whistles in the spotted dolphin, *Stenella plagiodon*," *Cetol.* **16**, 1–21.
- Herzing, D. L. (1996). "Underwater behavioral observations and associated vocalizations of free-ranging Atlantic spotted dolphins, *Stenella frontalis*, and bottlenose dolphin, *Tursiops truncatus*," *Aq. Mamm.* **22**, 61–79.
- Herzing, D. L. (1997). "The natural history of free-ranging Atlantic spotted dolphins, (*Stenella frontalis*): Age classes, color phases and female reproduction," *Marine Mammal Sci.* **13**, 40–59.
- Herzing, D. L. (2000). "Acoustics and Social Behavior of wild dolphins: implications for a sound society," in *Hearing by Whales and Dolphins*, edited by W. W. L. Au, A. N. Popper, and R. R. Fay (Springer, New York).
- Kreyszig, E. (1983). *Advanced Engineering Mathematics*, 5th ed. (Wiley, New York).
- Rasmussen, M. H., Miller, L. A., and Au, W. W. L. (2002). "Source levels of clicks from free-ranging white-beaked dolphins (*Lagenorhynchus albirostris*, Gray, 1846) recorded in Icelandic waters," *J. Acoust. Soc. Am.* **111**, 1122–1126.
- Rihaczek, A. W. (1969). *Principles of High-Resolution Radar* (McGraw-Hill, New York).
- Watkins, W. A., and Schevill, W. E. (1972). "Sound source location by arrival-times on a non-rigid three-dimensional hydrophone array," *Deep-Sea Res. Oceanogr. Abstr.* **19**, 691–705.
- Wood, Jr., F. G. (1953). "Underwater sound production and concurrent behavior of captive porpoise, *Tursiops truncatus* and *Stenella plagiodon*," *Bull. Mar. Sci. Gulf Carib.* **3**, 120–133.

Echolocation in the Risso's dolphin, *Grampus griseus*

Jennifer D. Philips,^{a)} Paul E. Nachtigall, Whitlow W. L. Au, Jeffrey L. Pawloski, and Herbert L. Roitblat

Marine Mammal Research Program, Hawaii Institute of Marine Biology, P.O. Box 1106, Kailua, Hawaii 96734

(Received 27 June 2001; accepted for publication 11 October 2002)

The Risso's dolphin (*Grampus griseus*) is an exclusively cephalopod-consuming delphinid with a distinctive vertical indentation along its forehead. To investigate whether or not the species echolocates, a female Risso's dolphin was trained to discriminate an aluminum cylinder from a nylon sphere (experiment 1) or an aluminum sphere (experiment 2) while wearing eyecups and free swimming in an open-water pen in Kaneohe Bay, Hawaii. The dolphin completed the task with little difficulty despite being blindfolded. Clicks emitted by the dolphin were acquired at average amplitudes of 192.6 dB *re* 1 μ Pa, with estimated sources levels up to 216 dB *re* 1 μ Pa-1 m. Clicks were acquired with peak frequencies as high as 104.7 kHz ($M_{fp} = 47.9$ kHz), center frequencies as high as 85.7 kHz ($M_{f0} = 56.5$ kHz), 3-dB bandwidths up to 94.1 kHz ($M_{BW} = 39.7$ kHz), and root-mean-square bandwidths up to 32.8 kHz ($M_{RMS} = 23.3$ kHz). Click durations were between 40 and 70 μ s. The data establish that the Risso's dolphin echolocates, and that, aside from slightly lower amplitudes and frequencies, the clicks emitted by the dolphin were similar to those emitted by other echolocating odontocetes. The particular acoustic and behavioral findings in the study are discussed with respect to the possible direction of the sonar transmission beam of the species. © 2003 Acoustical Society of America. [DOI: 10.1121/1.1527964]

PACS numbers: 43.80.Ka, 43.80.Jz [FD]

I. INTRODUCTION

The Risso's dolphin (*Grampus griseus*) is a relatively little-known member of the delphinid family that occurs gregariously in predominantly temperate and tropical deep waters near continental shelf-edges and submarine canyons (Baumgartner, 1997; Leatherwood *et al.*, 1980). The species has an appearance very unlike that of other delphinids (Fig. 1). It is relatively large (to 4 m in length), with a robust body form compared to other delphinids, and has a squared head with few teeth and no beak (Fig. 1). It also has a unique vertical indentation along its forehead, extending from the top of the anterior surface of the forehead down to the tip of the upper jaw (Leatherwood *et al.*, 1983). This indented forehead is markedly different from the smoothly rounded foreheads of other odontocete species. Because the smooth curvature and rounded shape of the typical odontocete forehead and melon are thought to be acoustically important for the directional propagation of an outgoing sonar pulse (Litchfield *et al.*, 1979; Norris, 1968), an indentation in the Risso's dolphin's forehead could be functionally important for the sonar of the species.

The acoustic repertoire of the Risso's dolphin has been only briefly described. Caldwell *et al.* (1969) recorded whistles from a captive subadult male Risso's dolphin, and whistles and pulsed sounds have often been recorded in the presence of Risso's dolphins in captivity and in the wild (e.g., Corkeron and Van Parijs, 2001). Au (1993) reported an analysis of the frequency and amplitude characteristics of the sonarlike pulsed sounds (clicks) emitted by a captive Risso's

dolphin during training sessions. The clicks had peak frequencies of 65 kHz, 3-dB bandwidths of 72 kHz, and durations of 40–100 μ s, generally consistent with the echolocation clicks emitted by other delphinid species. Although these data suggest that the Risso's dolphin produces echolocation signals, no controlled experiment was completed to demonstrate that the species actually uses these clicks as part of a biological sonar system.

Philips *et al.* (in press) analyzed the clicks emitted by a captive Risso's dolphin and found additional putative evidence of echolocation ability in the species. In that study, we trained a blindfolded dolphin to swim to and touch an underwater object and used a four-hydrophone array to record the clicks emitted by the dolphin during its approach. The clicks had peak frequencies up to 50 kHz, 3-dB bandwidths up to 35 kHz, durations of 35–75 μ s, and source levels up to 208 dB *re* 1 μ Pa. However, although the animal was able to complete the basic task, the study was a preliminary investigation and therefore did not use the psychophysical methodology necessary to ensure that the animal's performance was not due to behavioral response bias or potential nonsonar response cues. Therefore, we were unable to conclude that the species possesses a sonar system.

Other evidence suggests that Risso's dolphins echolocate. The species has the same asymmetrical sound production anatomy (i.e., phonic lips/dorsal bursae complex; Cranford, 1988; Cranford *et al.*, 1996) found in other echolocating odontocete species, suggesting that it has the capability of producing the high-frequency clicks used for echolocation. The pulsed sounds recorded by Au (1993) and Philips *et al.* (in press) corroborate that suggestion. It also appears that the Risso's dolphin is capable of hearing high

^{a)}Electronic mail: jphilips@hawaii.edu

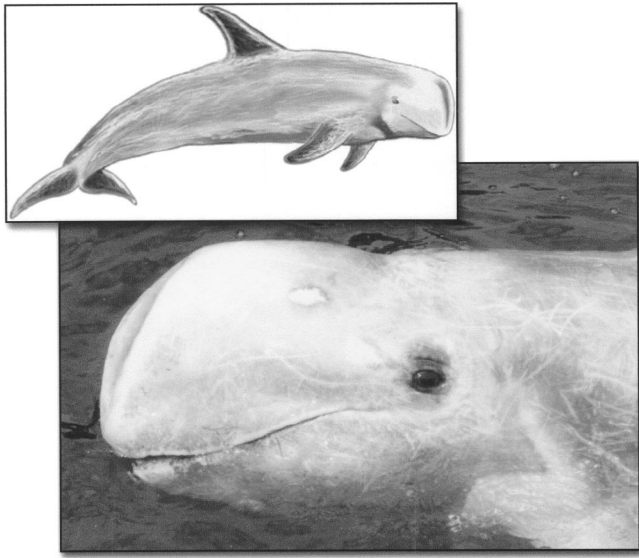


FIG. 1. The Risso's dolphin (*Grampus griseus*), showing the species' unique physical appearance, characteristic squared head, and indented forehead.

frequencies to 80 kHz, as are other odontocetes (Nachtigall *et al.*, 1995); a high-frequency hearing system likely evolved along with an active high-frequency echolocation system in dolphins (Nachtigall *et al.*, 2000).

Risso's dolphins in the wild feed nearly exclusively on cephalopods (including squid, octopus, and cuttlefish; Clarke and Pascoe, 1985; Clarke and Young, 1998; Cockcroft *et al.*, 1993; Wurtz *et al.*, 1992). Unlike most fish species preyed upon by other echolocating dolphins, cephalopods do not contain gas-filled swimbladders, the feature in many fish species believed to be responsible for the majority of the energy returned in a reflected sonar signal (Foote, 1980). As a result, the acoustic target strength of a squid is considerably lower (from 18 to 25 dB lower) than that of swimbladder possessing fish (Jefferts *et al.*, 1987; MacLennan and Simmonds, 1992; Penrose and Kaye, 1979). The cephalopod is probably, therefore, a more difficult sonar target for the echolocating dolphin than is a fish with an gas-filled swim bladder. Although cephalopods make up a portion of the diets of many species of odontocetes, only 13 species of odontocetes (7 Ziphiidae, 2 Physteridae, 1 Phocoenidae, 1 Globicephalidae, and 2 Delphinidae) consume cephalopods exclusively (Clark, 1986). Of these species, none has been investigated in the laboratory for the ability to echolocate, and only two, the Dall's porpoise (Hatekeyama and Soide, 1990) and the short-finned pilot whale (Wood and Evans, 1980), have been observed in relatively uncontrolled situations to produce clicklike sounds while performing tasks that appeared to require a biosonar sensory system. The unique problems faced by any exclusively cephalopod-consuming odontocete using echolocation to locate its prey may have led to specializations in its sonar system relative to that of fish-eating dolphins.

The present study was undertaken to (1) determine experimentally if the Risso's dolphin echolocates and (2) describe the sonar clicks emitted by the species.

II. METHODS

A. Subject

The subject of the study was an older, female Risso's dolphin named Hana, housed at the Marine Mammal Research Program (MMRP) facilities at the Hawaii Institute of Marine Biology (HIMB) in Kaneohe Bay, Oahu, Hawaii. Her age was unknown, though numerous markings, white-overall coloration and the worn-down appearance of her teeth suggested that she was mature and perhaps already relatively old at the time of her 1989 capture. At the time of the study (conducted July to September 1999), the dolphin weighed 295 kg and measured 2.82 m in length. The dolphin suddenly died following the conclusion of the study (September 1999); the dolphin's sudden death prevented the continuation of a second phase of the study, and there are no other Risso's dolphins known to be in captivity at any research facility.

The dolphin in this study was the subject of a previous psychometric hearing experiment, in which her hearing sensitivity for frequencies to 80 kHz was found to be similar to that of other delphinid species at those frequencies, with no apparent hearing loss (Nachtigall *et al.*, 1995). The dolphin was also the subject of a preliminary, training-phase echolocation study (Philips *et al.*, in press) which measured the sonar clicks she emitted while blind-folded and swimming toward a submerged training target.

B. Experimental apparatus and procedure

The dolphin was trained to perform a target-discrimination task while free-swimming in a $9 \times 12\text{-m}^2$ open-water pen. The choice was made to use a free-swimming methodology, rather than the more conventional methodology in which the dolphin is trained to position itself in or on an underwater stationary apparatus (such as a hoop or bite plate), after difficulties were encountered during the training phase of the study. Although standard training methods for psychophysical experiments were used to introduce the dolphin to the novel echolocation task involved in the study, the dolphin had unusual difficulty learning the hoop-based task. To investigate the possibility that the confined physical setup of the stationary hoop apparatus during training was somehow negatively affecting her performance, the choice was made to allow the dolphin to swim freely in the pen for this phase of study; analysis of echolocation signals from free-swimming odontocetes has been done in a variety of recent studies (e.g., Verfuss *et al.*, 1998; Rasmussen *et al.*, 2002).

The dolphin's task was to discriminate a hollow aluminum cylinder ["standard" target—12.7-cm length, 3.7-cm outer diameter, and 0.6-cm wall thickness, target strength (TS) $\cong -21$ dB¹] from a solid nylon (experiment 1) or aluminum (experiment 2) sphere ("comparison" targets—both 7.6 cm in diameter, TS $\cong -34$ dB), and indicate her choice by swimming to the target and touching it directly with her rostrum/melon. The standard and comparison targets for each experiment were suspended on monofilament line from opposite ends of a 1-m PVC pole, and were placed into the water at 1-m depth during each trial. The standard target was presented in each trial to the left or right of the comparison

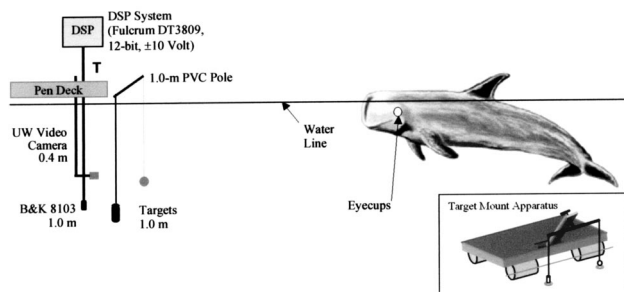


FIG. 2. Experimental apparatus. Targets were suspended from the ends of a 1-m PVC pole, which was either held in the hands of the trainer (T) in experiment 1, or mounted onto a stationary rack in experiment 2 (inset; the rack was attached to the deck where the trainer had been positioned in experiment 1). The dolphin wore eyecups and was allowed to swim freely in the open-water pen during sessions. She typically swam a general loop-shaped pattern, swimming away from the “target area” at the start of a trial, looping around at about 2- to 5-m range and returning toward the targets to locate the standard cylinder.

sphere, with the center point of the targets at a fixed position, following a blocked-Gellermann sequence (Gellermann, 1933), with ten sessions of 50 trials (five blocks of ten trials each) conducted in each experiment. The dolphin was trained to voluntarily accept eyecups placed over her eyes, ensuring that she could not use vision to perform the target discrimination. The first ten trials (one block) of each session were performed without eyecups covering the dolphin’s eyes to ensure that she was motivated to participate before placing the eyecups. After trial 10, the eyecups were placed over her eyes and remained in place until the end of the session.

Experimental sessions began with the dolphin stationed in the water directly below the trainer (T; Fig. 2). On a command from the trainer, the dolphin (wearing eyecups) then left the starting station and swam away from the trainer, marking the start of the experimental portion of the session. As the dolphin swam away, the trainer placed the targets into the water below him (the “target area”) with the standard target (aluminum cylinder) on the dolphin’s left or right. In experiment 1 (aluminum cylinder standard versus nylon sphere comparison), the trainer held the targets in place at 1-m depth by holding the center of the PVC pole. In experiment 2 (aluminum cylinder standard versus aluminum sphere comparison), the trainer lowered the targets into the water to 1-m depth by tilting the arm of a deck-mounted target presentation rack to its down position (Fig. 2, inset). The dolphin swam to a variable distance away from the trainer (approximately 2- to 5-m range), looped around, and swam back toward the target area. As she approached the targets, she located the position of the standard target, swam toward it, and touched it directly with her rostrum/melon. A successful response to the standard cylinder was rewarded with a squid (*Loligo opalescens*). Incorrect responses were not rewarded. The targets were then completely removed from the water (either by the trainer pulling the target apparatus completely out of the water, or by tilting the arm of the target mount apparatus up). Pulling the targets out of the water signaled the dolphin to begin the next trial by again swimming away from the target area. The targets were then reinserted into the water, marking the start of the next trial. The dolphin was

trained to continue uninterrupted through the entire session (50 trials), leaving the target area as soon as the targets had been removed from the water after the previous trial.

An underwater video camera was used to record the dolphin’s behavior as she approached the targets. The camera was positioned to view directly out from the target area toward the approaching dolphin and was centered between the two targets at a depth of 0.4 m. Time to the nearest second was stamped on the video and was used to roughly synchronize the video recordings of the dolphin’s approach with the click-data acquisition. Clicks acquired early or late in her approach could therefore be roughly correlated with her behavior at that approximate time. The video recordings were useful during data analysis for observing the dolphin’s behavior as she performed the target discrimination task.

C. Experimental control methods

Numerous measures were taken during all experimental sessions to ensure that the dolphin’s performance was not influenced by unknown behavioral bias or external cues. For example, eyecups to occlude the dolphin’s use of vision were used in all experimental trials, and standard psychophysical methods were used (e.g., blocked-Gellermann presentation of the standard target, two-alternative forced-choice procedure for target presentation). In addition to these measures, two specially designed control sessions were conducted (controls 1 and 2) in which additional efforts were made to ensure that the dolphin’s performance was not externally influenced. First, the deck-mounted target rack was introduced in control 1 and was used throughout experiment 2, and ensured that the targets were not moved once they were placed at 1-m depth during trials. The introduction of the target rack midway through sessions (during control 1 at the start of experiment 2) was useful for determining if such movement cues were assisting the dolphin during previous sessions in which the trainer held the target apparatus. Second, during both controls 1 and 2, the trainer normally presenting the targets was replaced by a different person. Using a novel target presenter helped ensure that the dolphin had not been receiving cueing information from the usual presenter’s habitual body patterns during trials (e.g., arm movements that might have pointed toward the standard target). Third, the novel target presenter was rendered “blind” during the second of these sessions (control 2); she wore opaque goggles, was not told the trial condition, and was therefore unable to cue the dolphin. Any decline in the dolphin’s behavioral performance when these control measures were used would have indicated that she might have been using external cues unrelated to her active sonar to assist her during normal sessions.

D. Electronic apparatus

Sonar clicks emitted by the dolphin during her approach toward the targets were acquired using a Brüel and Kjaer 8103 hydrophone placed 0.5 m behind the center point between the two targets, at 1-m depth. The hydrophone was placed between the two targets, and not directly behind the standard target, because the dolphin was observed to move

her head considerably during preliminary trials—she scanned her head back and forth between the targets often multiple times during each approach. Because her sonar beam was not focused toward either target during her approach, the click acquisition hydrophone was placed between the two targets to optimize the acquisition of the clicks she emitted during her discrimination of the two targets. (Additionally, placing the hydrophone consistently behind the standard would have cued the dolphin to the standard target's location.) The hydrophone had a flat frequency response (± 2 dB) up to 150 kHz, with a free-field sensitivity of -211 dB re 1 V/ μ Pa at 100 kHz. Signals received at the hydrophone were amplified by a 15-dB in-line preamplifier, filtered with high- and low-pass filters (200 kHz low pass and 500 Hz high pass), and amplified by a custom-built preamplifier set to 18-dB input gain. When the amplitude of an input signal exceeded a user-set threshold (trigger point), the signal was passed to a digital signal processor (DSP) (Fulcrum DT3809, 12-bit, ± 10 V A/D board) and digitized at a sample rate of 1 MHz. Forty-eight pretrigger and 80 posttrigger sample points of each click (128-points per click) were digitized and saved sequentially to a memory buffer on the acquisition board. Time intervals between clicks (i.e., interclick intervals) were measured and saved to the memory buffer between each pair of clicks. At the end of each trial, the memory buffer was saved to a unique file for each trial. Data acquisition by the DSP system was controlled both by on-board software running under the SPOX operating system and through a custom-written user-interface operating in the MS-DOS environment on a host personal computer.

E. Click analysis

Because the dolphin was allowed to swim freely while performing the task, the clicks collected during her approach were very likely acquired from both directly on and off the axis of her sonar transmission beam. Echolocation clicks acquired from off the beam propagation axis are distorted relative to the source click, with lower peak frequencies and lower amplitude levels than clicks acquired from directly along the propagation axis (Au, 1980). Although a large portion of the dolphin's clicks were likely acquired from off-axis, our desire was to describe only the clicks that had the greatest likelihood of having been acquired from as close to the beam axis as possible. Following the principle (Au, 1980) that dolphin echolocation clicks acquired from along the beam axis are higher in amplitude and peak frequency than when they are acquired from off the beam axis, the choice was made to analyze and report signal characteristics for only the two clicks per trial acquired at the highest amplitude and highest peak frequency. If in a trial the same click had both the maximum amplitude and the maximum peak frequency, only that click was analyzed further for that trial. The resulting click data set is reported here as the presumably most representative description of the on-axis sonar clicks emitted by this dolphin. Additionally, only trials in which the dolphin wore eyecups were analyzed.

Analysis of the selected clicks was performed using custom written MATLAB v.5.3 signal-analysis routines. Amplitude, time, and frequency characteristics of the signals were

described. Amplitude was defined as the peak-to-peak sound pressure level (SPL, dB referenced to 1 μ Pa) acquired at the hydrophone, and was calculated in the absence of absolute source level measurements for the purpose of describing the level at which a click was emitted, at minimum (i.e., clicks acquired at a received amplitude of 200 dB could be assumed to have been emitted by the animal at least at that level). Source levels (SL, dB referenced to 1 μ Pa at 1 m) were very roughly approximated for a small set of clicks by estimating the range to the dolphin using the video recordings; range was estimated as 3 to 5 m for clicks acquired early in a trial and confirmed (from the video record) to have been acquired when the dolphin was relatively far from the hydrophone. (Of course, a goal of the longer term experiment was to integrate apparatus design changes that would facilitate accurate source level measurements, and we would have liked to have reported those numbers here, however such design changes were not integrated into the study before the death of the dolphin.)

Signal duration (τ , μ s) was determined from the relative signal energy [expressed as $E_N = 10 \log \int_0^T s^2(t) dt$, where $s(t)$ is the instantaneous pressure of the signal as a function of time, (Au, 1993)]; onset of the signal was established as the time at which the relative energy reached a minimum value of 0.3% of the maximum signal energy, and termination of the signal was established as the time at which the relative energy came within 0.3% of the maximum signal energy. Frequency characteristics for the clicks were determined from 1024-point fast Fourier Transform (FFT) results. Peak frequency (f_p , kHz) was defined as the highest amplitude point on the spectrum. Center frequency (f_0 , kHz) was defined as the point in the linear frequency spectrum that divided the total energy in the spectrum equally in half, expressed as (Au, 1993),

$$f_0 = \frac{\int_{-\infty}^{\infty} f \cdot |S(f)|^2 df}{\int_{-\infty}^{\infty} |S(f)|^2 df},$$

where $S(f)$ is the Fourier transform of the signal.

Bandwidth of the clicks was defined both in terms of the 3-dB bandwidth (3-dB BW, kHz, the range of frequencies bounded by the high and low half-power points on the spectrum) and the root mean square bandwidth (RMS BW, kHz), expressed as (Au, 1993)

$$\text{RMS BW} = \sqrt{\frac{\int_{-\infty}^{\infty} (f - f_0)^2 \cdot |S(f)|^2 df}{\int_{-\infty}^{\infty} |S(f)|^2 df}}.$$

III. RESULTS

A. Behavioral performance

The dolphin's choice accuracy for trials in which eyecups were on for experiments 1 and 2 are shown in Fig. 3. Choice accuracy for all experimental sessions was 95% or above ($M_{\text{Exp1}} = 98.3$, $sd = 2.4\%$ and $M_{\text{Exp2}} = 99.5$, $sd = 0.8\%$). Overall, the dolphin was able to perform both discrimination tasks with little difficulty despite being blindfolded. The dolphin's choice accuracy for both control sessions (Controls 1 and 2; 50 trials each, conducted at the start of experiment 2)

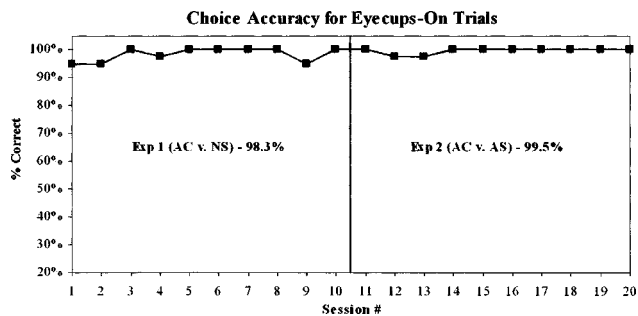


FIG. 3. The dolphin's choice accuracy for experiments 1 and 2 for trials in which she wore eyecups.

was 100%. Her behavior did not appear to be at all affected by the changes in experimental procedure or apparatus.

Interestingly, the dolphin remained at the surface of the water, with the upper portion of her forehead/melon out of the water, during the majority of trials. After swimming away at the start of the trial and looping back, she swam toward the targets, moving her head laterally and vertically as she apparently examined them to locate the standard. She remained at the surface during more than 95% of trials, with at times more than 50% of her forehead above the water's surface during her entire approach. She then submerged to touch the standard target only when she was very close to the target area (less than 1–2 m). Time synchronized video and acoustic data collected during her approach show that she emitted sonar clicks, and they were received by the acquisition hydrophone, even when she was at the surface.

B. Click analysis

Clicks were acquired during 17 of the 20 sessions, comprising a total of 38,182 clicks (acoustic data were not acquired in three noncontrol sessions due to equipment difficulties). An example of the full series of clicks acquired during one trial (from the time the dolphin left the target area until she touched the standard target) is shown in Fig. 4(a). Vertical pulses along the x -axis represent sonar clicks, and spaces between vertical pulses represent time intervals between clicks (ICI, compressed 100 times relative to the time scale of the clicks). Clusters of clicks along the time axis represent groupings of click acquisitions related partly to the head movements of the free-swimming dolphin. The same series of clicks with interclick intervals removed is shown in Fig. 4(b), and plots of amplitudes and peak frequencies for the full-trial click series are shown in Fig. 4(c) (amplitude and frequency values were computed in an initial raw data analysis, and are provided to present an example of the raw data set acquired during sessions; from this raw data, two clicks, indicated, were analyzed in detail). Evident in the example depicted in Fig. 4 are the predominately low (<50 kHz) peak frequencies of this dolphin's clicks when all clicks acquired were examined together. Overall, peak frequencies in the raw data were below 50 kHz for the majority (>95%) of the clicks acquired.

Of the over 38 000 clicks acquired, a total of 1030 clicks were selected for detailed analysis (representing the at-most two clicks acquired at the highest amplitude and the highest peak frequency from each trial in each session), examples of

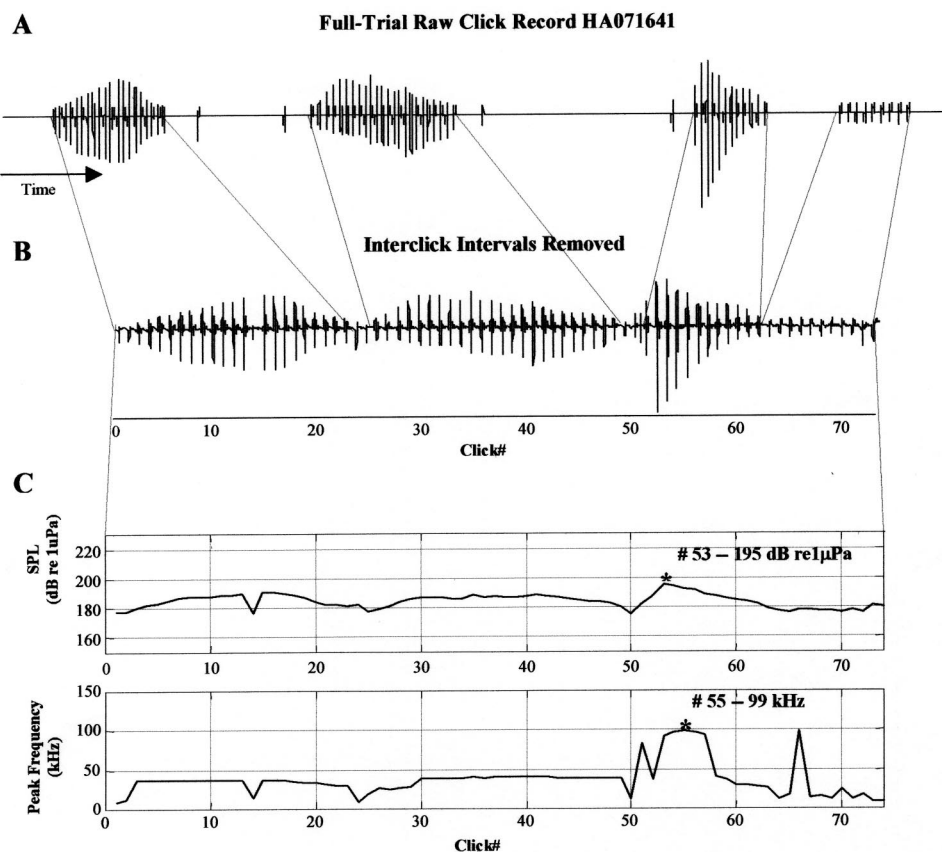


FIG. 4. Analysis of the clicks acquired during one full trial, from the point the dolphin left the target area to the point she touched the standard cylinder. (a) Full-trial click series for trial HA071641, showing clicks and interclick intervals. (b) Full-trial click series with interclick intervals removed. (c) The amplitudes and peak frequencies of the clicks.

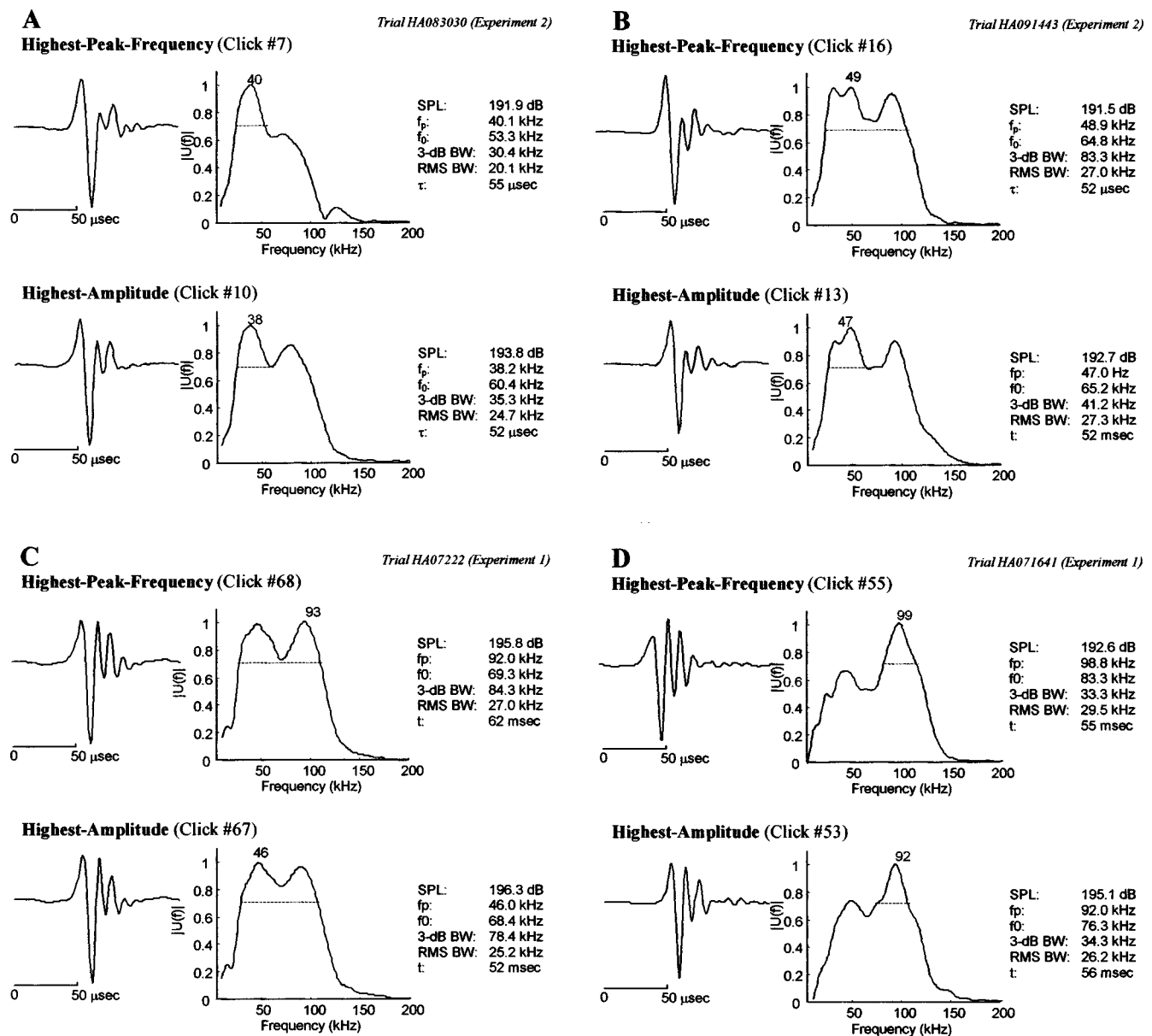


FIG. 5. Examples of clicks acquired from the dolphin during the study. Each example shows the highest amplitude and the highest peak frequency clicks acquired during that trial, selected for further detailed analysis, with signal waveforms (left), frequency spectra (center), and quantitative characteristics (right). Examples are representative of the types of signals emitted by the dolphin. SPL=sound pressure level, f_p =peak frequency, f_0 =center frequency, 3-dB BW=3-dB bandwidth, RMS BW=rms bandwidth, τ =duration.

which are given in Fig. 5. The figure is representative of the types of clicks acquired from the dolphin. As was evident in the raw click data, clicks predominantly had peak frequencies below 50 kHz, as shown in Figs. 5(a) and (b), but were broadband and had strong higher frequency components (i.e., clicks were often bimodal, with two prominent energy peaks in the frequency spectra). Very high peak frequency clicks (>80 kHz), as in Fig. 5(d), were acquired, though much more rarely.

The frequency spectra of the clicks acquired from the dolphin during this study were typically bimodal, as is illustrated by the examples in Fig. 5. Clicks very often had two very prominent peaks in the frequency spectra, so that the total energy represented by the peak frequency [e.g., 93 kHz for click 68 in Fig. 5(c)] was only slightly more than the total energy represented by the secondary peak. To quantify the

occurrence of this bimodality, peak frequency histograms were plotted (Fig. 6). Evident here, again, is the bimodality of the spectra; peak frequencies tended to be either around 30 to 50 kHz (LF) or around 80 to 100 kHz (HF), and much more rarely were below 30 kHz, between 50 and 80 kHz, or above 100 kHz.

Also noticeable in the peak frequency histograms in Fig. 6 is that more clicks were acquired at the higher peak frequencies (i.e., >80 kHz) during experiment 2 than during experiment 1 ($\chi^2_{(1,N=1030)}=66.13$, $p<0.0001$). The majority of the clicks acquired in both experiments, however, had peak frequencies below 50 kHz (93% in experiment 1 and 73% in experiment 2).

A summary of the signal characteristics for the clicks selected from each trial is given in Fig. 7 ($N=1030$). Clicks

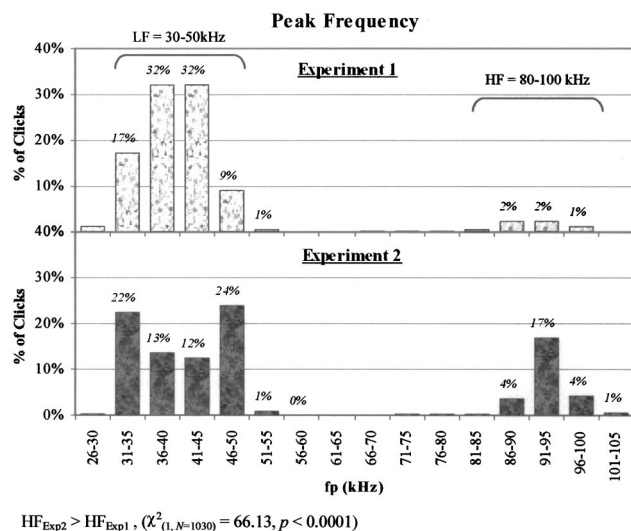


FIG. 6. Distributions of peak frequencies for all clicks analyzed for experiments 1 and 2. Two prominent peaks in the frequency spectra of the dolphin's clicks are evident—30–50 kHz (LF) and 80–100 kHz (HF). More clicks of very high peak frequency (HF) were acquired during experiment 2 than during experiment 1 ($\chi^2_{(1, N=1030)} = 66.13, p < 0.0001$).

were acquired at amplitudes (SPL) ranging from 183.9 to 201.6 dB *re* 1 μ Pa, with an overall mean of 192.6 dB *re* 1 μ Pa (sd=3.4 dB). Mean amplitude was slightly, yet significantly, greater for the clicks acquired during experiment 2 than during experiment 1 ($M_{\text{Exp1}} = 191.6$, sd=3.1 dB, and $M_{\text{Exp2}} = 193.8$, sd=3.1 dB; Student's $t = -10.97$, $p < 0.0001$).

Peak frequency ranged from 27.4 to 104.7 kHz, with an overall mean of 47.9 kHz (sd=20.1 kHz). Mean peak frequency was significantly higher in experiment 2 than in experiment 1 ($M_{\text{Exp1}} = 42.6$, sd=13.9 kHz, and $M_{\text{Exp2}} = 53.8$, sd=23.9 kHz; Mann-Whitney $U = 166585$, $p < 0.0001$). Center frequency ranged from 24.1 to 85.7 kHz, with an overall mean of 56.5 kHz (sd=10.4 kHz). As with peak frequencies, mean center frequency was significantly higher in experiment 2 than in experiment 1 ($M_{\text{Exp1}} = 52.7$, sd=9.2 kHz and $M_{\text{Exp2}} = 60.7$, sd=10.0 kHz; $t = -13.54$, $p < 0.0001$).

The 3-dB bandwidth varied considerably from one click to the next, ranging from a minimum of 15.7 kHz to a maximum of 94.1 kHz, and averaging 39.7 kHz (sd=18.5 kHz) overall. Mean 3-dB bandwidths were significantly greater in experiment 2 than in experiment 1 ($M_{\text{Exp1}} = 36.9$, sd=16.5 kHz and $M_{\text{Exp2}} = 42.7$, sd=20.1 kHz; $U = 162091$, $p < 0.0001$). The acuteness of a click's frequency bimodality had a substantial effect on 3-dB bandwidth values. Higher levels of energy at both the low- and high-frequency modes was associated with decreased energy levels at frequencies between the modes, thus creating a "barrier" to the 3-dB bandwidth measure [i.e., the measure of high and low half-power points, as determined from the peak frequency, measures the width across only one of the two peaks in the bimodal spectrum; see Fig. 5(b), for example]. The root mean square bandwidth (RMS BW) accounts for energy levels about the center, or centroid, frequency, and is perhaps more appropriate for the types of bimodal clicks acquired here.

RMS bandwidths for the clicks emitted by the dolphin ranged from 11.8 to 32.7 kHz and averaged 23.3 kHz (sd=3.6 kHz) overall. Mean RMS bandwidth was higher for the clicks acquired during experiment 2 than during experiment 1 ($M_{\text{Exp1}} = 21.8$, sd=3.4 kHz and $M_{\text{Exp2}} = 24.9$, sd=3.1 kHz; $t = -15.01$, $p < 0.0001$).

Click duration ranged from 32 to 96 μ s, with an overall mean of 61.0 μ s (sd=11.8 μ s), and 82% of clicks having durations between 40 and 70 μ s. Click durations were significantly longer in experiment 1 than in experiment 2 ($M_{\text{Exp1}} = 64.5$, sd=12.2 kHz and $M_{\text{Exp2}} = 57.4$, sd=10.2 kHz; $t = 12.12$, $p < 0.0001$).

Clicks were acquired at interclick intervals of 11.6 to 47.6 ms, averaging 25.2 ms (sd=5.8 ms) overall. Interclick interval was not significantly different between the two experiments ($p > 0.05$).

Click source levels for this study could only be approximated based upon analysis of the roughly time-synchronized video recordings with accompanying acoustic data. The approach taken was to estimate the maximum possible source level ranges for the clicks acquired early in a trial, where video recordings could verify that the dolphin began the trial at a relatively large range from the target area, or approximately 3 to 5 m given the known dimensions of the test pen. For example, a click of 193-dB measured amplitude acquired early in a trial [such as click 13 in Fig. 5(b)] would have an estimated maximum possible source level of 207 dB *re* 1 μ Pa [given an estimated maximum range (R) of approximately 5 m, equivalent to $20 \cdot \log(R) = 14$ dB in signal transmission loss]. The highest amplitude click acquired in this study was collected early in a trial at 201.6 dB *re* 1 μ Pa. A review of the video record confirmed that she began that trial relatively far from the targets, estimated at 3- to 5-m range. Given this range, the source level for this click was estimated to be between 211 and 216 dB *re* 1 μ Pa.

IV. DISCUSSION

A. Clicks

The behavioral and acoustic results acquired in this study provide evidence of echolocation use in the Risso's dolphin. The dolphin was able to discriminate an aluminum cylinder from two different comparison spheres with little difficulty, despite being blindfolded. Her performance was 95% correct or greater during all test sessions. Her performance was 100% correct during special control sessions, despite measures taken during those sessions to ensure she was not being inadvertently assisted by other cues. She moved her head laterally and vertically as she approached the targets, and emitted sonar clicks during all trials. These findings are consistent with the existence of a sonar sensory system in this species of dolphin.

The acquisition of significantly higher click amplitudes (SPL) and frequencies (peak, center, and 3-dB and RMS BW's) and significantly lower click durations in experiment 2 than in experiment 1 could have a number of possible explanations. Of course, due to the free-swimming methodology employed in this study, the different clicks acquired in experiment 2 could merely have been the result of possible

Amplitude (p-p SPL, dB re1 μ Pa)		
	Mean (sd)	Overall Mean (sd)
Experiment 1	191.6 (3.1)	192.6 (3.4) Exp 2 > Exp 1 $t = -10.97, p < .0001^*$
Experiment 2	193.8 (3.1)	
Peak Frequency (f_p , kHz)		
	Mean (sd)	Overall Mean (sd)
Experiment 1	42.6 (13.9)	47.9 (20.1) Exp 2 > Exp 1 $U = 166585, p < .0001^\dagger$
Experiment 2	53.8 (23.9)	
Center Frequency (f_0 , kHz)		
	Mean (sd)	Overall Mean (sd)
Experiment 1	52.7 (9.2)	56.5 (10.4) Exp 2 > Exp 1 $t = -13.54, p < .0001^*$
Experiment 2	60.7 (10.0)	
3-dB Bandwidth (3-dB BW, kHz)		
	Mean (sd)	Overall Mean (sd)
Experiment 1	36.9 (16.5)	39.7 (18.5) Exp 2 > Exp 1 $U = 162091, p < .0001^\dagger$
Experiment 2	42.7 (20.1)	
RMS Bandwidth (RMS BW, kHz)		
	Mean (sd)	Overall Mean (sd)
Experiment 1	21.8 (3.4)	23.3 (3.6) Exp 2 > Exp 1 $t = -15.01, p < .0001^*$
Experiment 2	24.9 (3.1)	
Duration (τ , μ sec)		
	Mean (sd)	Overall Mean (sd)
Experiment 1	64.5 (12.2)	61.0 (11.8) Exp 1 > Exp 2 $t = 12.12, p < .0001^*$
Experiment 2	57.4 (10.2)	

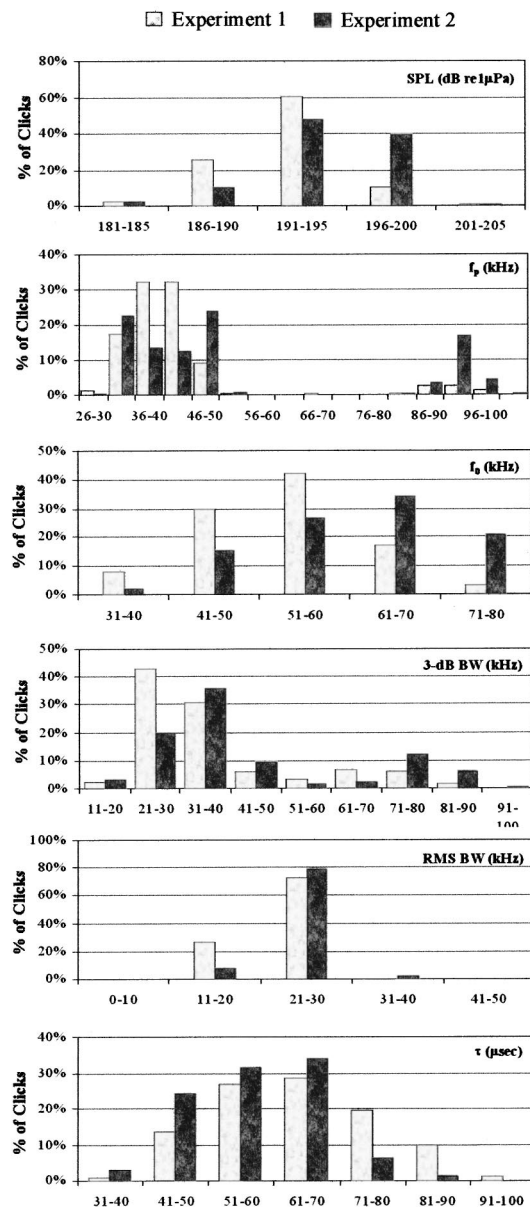


FIG. 7. Summary of signal characteristics for the highest peak frequency and highest amplitude clicks selected from each trial of Experiments 1 and 2 ($N = 1030$). Note: Difference between the means of Experiments 1 and 2 tested for significance using the Student's t -test (*), or using the Mann-Whitney U -test (\dagger , nonparametric test for non-normally distributed data).

acquisition artifacts. That is, higher amplitudes may have been collected in experiment 2 merely because more clicks were acquired from directly along the dolphin's sonar propagation axis in that experiment, due at least in part to variations in the dolphin's movements. This explanation is certainly possible, although because only the two clicks of the highest amplitude and the highest peak frequency were analyzed for each trial, there is a better likelihood that all analyzed clicks were acquired along or close to the propagation axis for both experiments. Session video records also show that the dolphins's swim behavior was not noticeably different between the two experiments.

If acquisition artifacts were indeed not a significant factor, it is a possibility that higher amplitude, higher frequency, and shorter duration clicks were acquired in experiment 2 because the dolphin actually emitted such clicks, perhaps as

a response to a more difficult discrimination in experiment 2 relative to experiment 1. The dolphin may have needed to use higher amplitude/higher frequency clicks during experiment 2 (where the standard and comparison targets were made of the same material but differed in shape), than she needed in experiment 1 (where the targets differed both in material and in shape). Of course, given that the standard cylinder had a theoretical target strength of 13 dB higher than the comparison spheres, it should be more likely that the most salient cue for the dolphin in both experiments was this large difference in target strength. The dolphin's task should, in theory, have been one of object detection—because the echo of the cylinder was so much louder than that of the sphere, she might simply have “looked for” that strong echo. A change from targets of different materials to targets of the same material should not, theoretically, have effected a

change in the acoustic behavior of the dolphin. Despite this, the data do indicate that the dolphin emitted clicks of higher amplitude and higher frequency in experiment 2. Possibly, the strategy employed by the dolphin in performing the discrimination in both experiments was not simply that of target strength comparison, as would have been theoretically predicted, but included some aspect of the particular physical characteristics of the targets. When the comparison target was changed from a nylon sphere in experiment 1 to an aluminum sphere in experiment 2, the dolphin might have compensated for a more difficult discrimination by emitting clicks of higher amplitude, and as a result higher frequency and shorter duration, making use of their higher capacity for feature resolution (see Au *et al.*, 1974, Au *et al.*, 1985, for a discussion of the hypothesized dependence of click frequency on amplitude).

B. Behavior

The dolphin's ability to emit sonar clicks into the water when much of her forehead was above the surface is unique in comparison to the echolocation behavior of other echolocating odontocetes (*T. truncatus*, bottlenose dolphin; *P. crassidens*, false killer whale; *D. leucas*, beluga; *P. phocoena*, harbor porpoise). In these species, the sonar beam emerges from near the center, front surface of the forehead and, as a result, these species must submerge their foreheads in order to emit sonar clicks into the water. The dolphin in this study, however, emitted clicks with at times only the lower portion of her forehead submerged. Additionally, although the dolphin echolocated from the surface, clicks of very high amplitude and peak frequency were acquired by the 1-m-deep acquisition hydrophone, suggesting that they were acquired from along or very near the propagation axis of the sonar beam even when the dolphin was at the water's surface.

While the possibility of off-axis detection could be proposed to explain the dolphin's ability to echolocate from the surface of the water (i.e., the dolphin could have used echoes of the off-axis portion of her clicks to perform the discrimination from the surface), the acquisition of high-frequency/high-amplitude clicks at the 1-m-deep hydrophone makes this explanation less likely. At a range of 5 m, the angle between the dolphin's horizontal line of approach and the submerged targets would have been approximately 11 degrees, and at 3 m, that angle would have been nearly 20 degrees. Clicks acquired from a propagating sonar beam from 11 to 20 degrees off-axis would have exhibited significantly distorted waveforms, with low peak frequencies and amplitudes. This was not found in the data. Additionally, while strong surface (i.e., air/water interface) reflections would certainly be expected when a dolphin echolocates from so close to the surface of the water, we did not find evidence of the presence of surface reflected energy in the acquired signal data. Clicks had clean and typical waveforms, in comparison to the clicks of previously studied dolphin species, with no obvious distortions due to surface reflections.

Overall, observations of the dolphin's surface-based swim pattern, along with acoustic and video data, suggest the

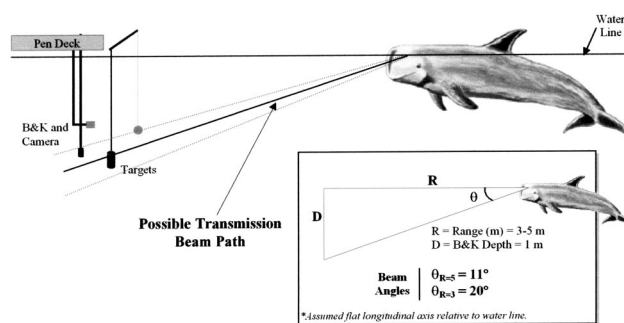


FIG. 8. Possible vertical sonar transmission beam path of the Risso's dolphin, based upon observations of the dolphin's surface-based swim pattern during target scans and accompanying acoustic data. Estimated beam angles are presented, relative to an assumed horizontal body longitudinal axis.

possibility that the vertical sonar transmission beam of the Risso's dolphin may project downward from the lower portion of the forehead by more than 10 or 20 degrees, referenced to the longitudinal axis of the dolphin's body (Fig. 8). This downward angled beam may correspond with the downward angle of the mouth line in this species. In other species for which the vertical signal transmission beam has been measured (*T. truncatus*, *D. leucas*, *P. crassidens*, and *P. phocoena*), the angle of the vertical beam has typically been stated in reference to the line along the jaw formed at the mouth, which in these species is essentially horizontal (± 5 degrees), and the projection angle of the vertical sonar beam appears to correspond closely (again, ± 5 degrees) with the mouth line in these species (Au *et al.*, 1986, 1987, 1995, 1999). In the Risso's dolphin, the line formed by the mouth is tilted downward anteriorly by about 30 to 40 degrees. The projection of the vertical sonar beam in this species might closely correspond to the line of the mouth as it does in other species.

The possibility of a downward angled sonar beam in this species could help to explain the unusual difficulty encountered during the training-phase of the study, in which the dolphin was unable to learn a basic target detection task from an underwater hoop. In that phase of training, the dolphin's task was to swim to a 1-m-deep, stationary hoop and report the presence or absence of a 5-in. aluminum water-filled sphere presented 3 m in front of her at the same depth (1 m). After considerable efforts to train the dolphin to perform the task, the dolphin's performance remained at chance levels. Although the dolphin emitted clicks from the hoop, which were acquired by a 1-m-deep B&K 8103 hydrophone positioned 1 m in front of the tip of her rostrum, the clicks were very low in amplitude and frequency and were considerably distorted compared to the clicks of other echolocating species. Overall, they exhibited the characteristics of off-axis echolocation clicks acquired from other dolphin species. If the Risso's dolphin sonar beam is angled downward by more than 10 or 20 degrees, a target positioned 3 m in front of her and at her same depth might not have been acoustically "visible" to her. The clicks she would have emitted from her position in the hoop would have angled downward, with the majority of their acoustic energy passing below both the hydrophone and the target. Of course, detailed future measurements of the signal transmission beam pattern of the Risso's

TABLE I. Summary of the acoustic characteristics of the Risso's dolphin's echolocation clicks, along with those of previously studied nonphocoenid odontocete species housed in open-water pens in Kaneohe Bay, Hawaii. Values listed represent the range of averages (with the maximum value in parentheses) reported in the literature for that parameter, except RMS bandwidth and duration (τ), for which the ranges of typical values are listed. 1—Au (1993); 2—Au (1980); 3—Au *et al.* (1985); 4—Thomas and Turl (1990); 5—Au *et al.* (1995); 6—Brill *et al.* (1992).

	f_p (kHz)	f_0 (kHz)	-3 dB BW (kHz)	RMS BW (kHz)	SL (dB re 1 μ Pa 1 m)	τ (μ s)	Source
<i>G. griseus</i>	48 (105)	57 (86)	40 (94)	20–30	(~216)	40–70	...
<i>T. truncatus</i>	115–120 (130)	93–120 (125)	38–46 (60)	30–45	205–225 (230)	50–80	2,1
<i>P. crassidens</i>	40–110 (~125)	44–81 (81)	20–54 (78)	...	202–223 (225)	50–70	4,5,6
<i>D. leucas</i>	104–109 (120)	...	20–50 (65)	...	207 (225)	50–80	3,1

dolphin will be necessary to test the possibility of a downward angled sonar transmission beam in this species.

C. Comparison of Risso's dolphin clicks with the clicks of other species

Table I summarizes the acoustic characteristics of the Risso's dolphin's clicks, along with those of the three species of echolocating nonphocoenid odontocetes whose clicks have been experimentally described, *T. truncatus*, *D. leucas*, and *P. crassidens*. All comparisons concern data collected during experiments conducted in Kaneohe Bay, Hawaii (snapping shrimp in Kaneohe Bay generate high levels of masking noise, causing the echolocating dolphins housed there to emit higher amplitude and higher frequency clicks than those emitted by dolphins in tanks or less noisy open waters; e.g., Au *et al.*, 1974, 1985). Generally, the characteristics of the Risso's dolphin's clicks were similar to those of the other nonphocoenid odontocetes, with a few notable exceptions.

First, the highest estimated source levels of the Risso's dolphin's clicks were lower (by as much as 14 dB) than the source levels reported for the other species. It appears, however, that dolphins adjust the output amplitudes of their clicks depending on specific aspects of the task and environment, such as signal-to-noise ratio, target strength, target range, and the specific echolocation task (Au *et al.*, 1985; Brill *et al.*, 1992). In this case, differences in target range between the studies probably account for differences in click amplitudes observed. The high-amplitude clicks reported for the three species in Table I were acquired when each of the animals was detecting or discriminating targets from far greater ranges (20–100 m) than the maximum 6 m from which the Risso's dolphin in this study was working. Au (1980) reported the source levels of five echolocating *T. truncatus* discriminating targets in Kaneohe Bay at ranges of 6 to 77.7 m. The dolphins echolocating from 6-m range emitted clicks with source levels around 210 dB and did not increase their emitted source levels until the targets were moved to ranges greater than 20 m. These lower source levels emitted by *T. truncatus* at shorter ranges are very close to the estimated click source levels of the Risso's dolphin working from similar ranges in this study.

Second, the frequency characteristics of the Risso's dolphin's clicks compared to those of other nonphocoenid odontocetes are also noteworthy. Although the highest peak fre-

quencies of the clicks acquired from the Risso's dolphin were extremely high, they did not range as high as the peak frequencies of the clicks acquired from the other odontocetes (105 kHz for Risso's compared to 130 kHz for *T. truncatus*, 125 kHz for *P. crassidens*, and 120 kHz for *D. leucas*). Furthermore, high peak frequency clicks (>80 kHz) were much less common for the Risso's dolphin than they typically are for a *T. truncatus* performing a basic object detection or discrimination task in Kaneohe Bay (see Au, 1993). Maximum center frequencies were also considerably lower for the Risso's dolphin than for *T. truncatus* (up to 86 kHz for Risso's compared to 125 kHz for *T. truncatus*), but were similar to the center frequencies reported for *P. crassidens* (up to 81 kHz). The highest 3-dB bandwidths found for the Risso's dolphin were above those reported for *T. truncatus* (up to 94 kHz for the Risso's dolphin compared to 60 kHz reported for *T. truncatus*), although analysis of the clicks acquired from a *T. truncatus* echolocating from an approximately 6-m target range in Kaneohe Bay reveals many instances of 3-dB bandwidths ranging higher than 90 kHz (personal observation, from unpublished data). RMS bandwidth for Risso's dolphin clicks was consistently lower than that reported for *T. truncatus* (20–30 kHz for more than 80% of the analyzed Risso's clicks, compared to 30–45 kHz for *T. truncatus*).

Aside from these specific frequency differences, the overall frequency structure of the Risso's dolphin's clicks was similar to that of the other nonphocoenid species; that is, their spectra ranged across a similar frequency band (from as low as 30 kHz to over 100 kHz) with considerable energy being represented by a broad range of frequency bins. The overall shape of the frequency spectra of the Risso's dolphin's clicks was bimodal, with two prominent energy peaks at opposite ends of the spectrum. Similar bimodality has been observed in clicks emitted by the other species (e.g., Au *et al.*, 1995; Moore and Pawloski, 1990), and appears to be a characteristic of the short-duration, broadband, pulse-type signals emitted by these animals. The consistently lower findings for peak frequency, center frequency, 3-dB bandwidth, and RMS bandwidth for the Risso's dolphin's clicks could merely have been a result of the specific task the dolphin was performing. If she had been echolocating on targets at greater ranges, and thus emitting clicks of higher amplitude (e.g., Au, 1980), it is possible that the frequency characteristics of her clicks would have been consistently higher and more in line with the frequency findings for the other species.

Alternatively, however, the lower frequency characteristics for the clicks emitted by the Risso's dolphin are consistent with the audiometric data reported for this species by Nachtigall *et al.* (1995). According to Nachtigall *et al.*, the Risso's dolphin can hear very well to frequencies as high as 80 kHz. Above 80 kHz, however, its sensitivity drops off dramatically. The auditory sensitivity of the Risso's dolphin differs from the that of *T. truncatus* and *D. leucas*, for example; *T. truncatus* can hear very well to 110 kHz (upper limit of the 10-dB down hearing range; Johnson, 1967), and *D. leucas* is very sensitive to 105 kHz (White *et al.*, 1978). These species are reported to emit clicks of very high peak frequency (>80 kHz) apparently more often than did the Risso's dolphin in this study, and given reported hearing sensitivities for these species, they can apparently hear such frequencies quite readily. The Risso's dolphin, by contrast, seems to more often emit clicks of lower peak and center frequency (<80 kHz), the reflected echoes of which might more closely match the sensitivity of its auditory system. However, although the auditory sensitivities measured for *P. crassidens* closely match that of the Risso's dolphin [with a best sensitivity cutoff of 64 kHz (Thomas *et al.*, 1988)], the echolocation clicks emitted by *P. Crassidens* in Kaneohe Bay have been measured to be often of very high peak frequencies [>80 kHz (Thomas and Turl, 1990)].

The time-domain characteristics (i.e., waveform, duration, and interclick interval) of the echolocation clicks emitted by the Risso's dolphin in this study were very similar to those of the clicks emitted by other echolocating nonphocoenid odontocetes. Overall, the duration of the clicks emitted by the Risso's dolphin was about the same as the reported click durations for *T. truncatus*, *D. leucas*, and *P. crassidens* ($\tau=40\text{--}70\ \mu\text{s}$ for the Risso's dolphin, $50\text{--}80\ \mu\text{s}$ for *T. truncatus* and *D. leucas*, and $50\text{--}70\ \mu\text{s}$ for *P. crassidens*).

The similarity of the physical properties of the clicks emitted by this dolphin to the clicks emitted by the other odontocetes is perhaps a bit surprising considering the biological peculiarities of this species. The Risso's dolphin is the first exclusive cephalopod consumer demonstrated to echolocate and is the only species to possess such a radically indented forehead. Lacking gaseous (i.e., highly acoustically reflective) swimbladders, cephalopods probably present a much more difficult sonar target than do fish with swimbladders, and a vertical groove in the forehead could affect an outgoing sonar pulse. Nevertheless, the examination of the clicks does not suggest that any obvious specialization exists which might be related to these features. Less obvious are the apparently lower frequency characteristics of the Risso's dolphin's clicks. If the lower frequencies were indeed not merely a result of the lower amplitudes emitted by the dolphin for the shorter-ranged task in this study, and were in fact an accurate sample of the sonar clicks of this species even at greater ranges, then the lower frequencies could represent an adaptive specialization in this species' sonar system.

V. CONCLUSIONS

The data show that this species of odontocete has the ability to use sonar signals for the detection of objects underwater. The sonar clicks it generates are similar to the

clicks generated by other members of its delphinid family, yet the specific context in which it is assumed to apply its sonar system in a natural setting is unique—unlike all other odontocete species previously studied for the faculty of echolocation, this species feeds entirely upon animals that are comparatively difficult targets for a sonar system to detect and which live very deep in the water column. This species also has a very dramatic vertical groove along its forehead, something no other species of dolphin possesses, and the function of which remains unknown. Most interestingly, this individual was able to echolocate downward into the water from a position at the surface, with a large portion of its grooved forehead out of the water. It is proposed here that this ability points toward the possibility of a uniquely angled sonar beam in this species.

A more complete knowledge of sonar use in dolphins can be gained by studying echolocation in species, such as the Risso's dolphin, which are biologically and behaviorally different from the species typically studied, such as *T. truncatus*. Further study into echolocation use of the Risso's dolphin will be needed to better characterize the functional roles of its biological and behavioral specializations. In light of these particular specializations, data gathered from echolocation studies with Risso's dolphins could likely provide a more complete picture of the use of sonar in dolphins.

ACKNOWLEDGMENTS

The authors express their appreciation to Dr. Roland Aubauer for his work on the DSP system, and Dr. David Lemonds and Caroline Delong for assisting at many stages throughout this study. This manuscript is Hawaii Institute of Marine Biology Contribution No. 1109. This work was funded under ONR Grant No. N00014-99-1-800 to Paul E. Nachtigall with the support of Harold Hawkins, ONR code 342. Illustration: Jason Caselli.

¹Acoustic target strengths of the experimental targets were theoretically computed, based upon the linear dimensions of the targets. For the cylinder, target strength is expressed as $TS_{\text{cyl}} = 10 \log(aL^2/2\lambda)$, where a is the radius, L is the length, and λ is the wavelength of the signal, or 75 kHz (Urick, 1983). For the spheres, target strength is expressed as $TS_{\text{sph}} = 20 \log(a/2)$, where a is the radius (Urick, 1983), and is regardless of material composition. The cylinder, therefore, had an echo amplitude approximately 13 dB higher than did the spheres.

- Au, W. W. L. (1980). "Echolocation signals of the Atlantic bottlenose dolphin (*Tursiops truncatus*) in open waters," in *Animal Sonar Systems*, edited by R. G. Bushnel and J. F. Fish (Plenum, New York), pp. 251–282.
- Au, W. W. L. (1993). *The Sonar of Dolphins* (Springer-Verlag, New York).
- Au, W. W. L., Carder, D. A., Penner, R. H., and Scronce, B. L. (1985). "Demonstration of adaptation in beluga whale echolocation signals," *J. Acoust. Soc. Am.* **77**, 726–730.
- Au, W. W. L., Moore, P. W. B., and Pawloski, D. (1986). "Echolocation transmitting beam of the Atlantic bottlenose dolphin," *J. Acoust. Soc. Am.* **80**, 688–691.
- Au, W. W. L., Penner, R. H., and Turl, C. W. (1987). "Propagation of beluga echolocation signals," *J. Acoust. Soc. Am.* **82**, 807–813.
- Au, W. W. L., Floyd, R. W., Penner, R. H., and Murchison, A. E. (1974). "Measurement of echolocation signals of the Atlantic bottlenose dolphin, *Tursiops truncatus* Montagu, in open waters," *J. Acoust. Soc. Am.* **56**, 1280–1290.
- Au, W. W. L., Kasteleini, R. A., Rippe, T., and Schooneman, N. M. (1999). "Transmission beam pattern and echolocation signals of a harbor porpoise (*Phocoena phocoena*)," *J. Acoust. Soc. Am.* **106**, 3699–3705.

- Au, W. W. L., Pawloski, J. L., Nachtigall, P. E., Blonz, M., and Gisner, R. C. (1995). "Echolocation signals and transmission beam pattern of a false killer whale (*Pseudorca crassidens*)," J. Acoust. Soc. Am. **98**, 51–59.
- Baumgartner, M. F. (1997). "The distribution of Risso's dolphin (*Grampus griseus*) with respect to the physiography of the Northern Gulf of Mexico," Marine Mammal Sci. **13**, 614–638.
- Brill, R. L., Pawloski, J. L., Helweg, D. A., Au, W. W., and Moore, P. W. B. (1992). "Target detection, shape discrimination, and signal characteristics of an echolocating false killer whale (*Pseudorca crassidens*)," J. Acoust. Soc. Am. **92**, 1324–1330.
- Caldwell, D. K., Caldwell, M. C., and Miller, J. F. (1969). "Three brief narrow-band sound emissions by a captive male Risso's dolphin, *Grampus griseus*," Bull. So. Calif. Acad. Sci. **68**, 252–256.
- Clarke, M. R. (1986). "Cephalopods in the diet of odontocetes," in *Research on Dolphins*, edited by M. M. Bryden and R. Harrison (Clarendon, Oxford), pp. 281–321.
- Clarke, M. R., and Pascoe, P. L. (1985). "The stomach contents of Risso's dolphin (*Grampus griseus*) stranded at Thurlstone, South Devon," J. Mar. Biol. Assoc. U.K. **65**, 663–665.
- Clarke, M., and Young, R. (1998). "Description and analysis of cephalopod beaks from the stomachs of six species of odontocete cetaceans stranded on Hawaiian shores," J. Mar. Biol. Assoc. U.K. **78**, 623–641.
- Cockcroft, V. G., Haschick, S. L., and Klages, N. T. W. (1993). "The diet of Risso's dolphin, *Grampus griseus* (Cuvier, 1812), from the east coast of South Africa," Z. Säugetierkunde **58**, 286–293.
- Corkeron, P. J., and Van Parijs, S. M. (2001). "Vocalizations of eastern Australian Risso's dolphins, *Grampus griseus*," Can. J. Zool. **79**, 160–164.
- Cranford, T. (1988). "The anatomy of acoustic structures in the spinner dolphin forehead as shown by X-ray computed tomography and computer graphics," in *Animal Sonar: Processes and Performance*, edited by P. E. Nachtigall and P. W. B. Moore (Plenum, New York), pp. 67–77.
- Cranford, T. W., Amundin, M., and Norris, K. S. (1996). "Functional morphology and homology in the odontocete nasal complex: Implications for sound generation," J. Morphol. **228**, 223–285.
- Foote, K. G. (1980). "Importance of the swimbladder in acoustic scattering by fish: A comparison of gadoid and mackerel target strengths," J. Acoust. Soc. Am. **67**, 2084–2089.
- Gellermann, L. W. (1933). "Chance orders of alternating stimuli in visual discrimination experiments," J. Gen. Psychol. **42**, 206–208.
- Hatakeyama, Y., and Soeda, H. (1990). "Studies on echolocation of porpoises taken in salmon gillnet fisheries," in *Sensory Abilities of Cetaceans: Laboratory and Field Evidence*, edited by J. A. Thomas and R. A. Kastelein (Plenum, New York), pp. 269–281.
- Jefferts, K., Burczynski, J. J., and Percy, W. G. (1987). "Acoustical assessment of squid *Loligo opalescens* off the Central Oregon coast," Can. J. Fish. Aquat. Sci. **44**, 1261–1267.
- Johnson, C. S. (1967). "Sound detection thresholds in marine mammals," in *Marine BioAcoustics*, edited by W. Tavolga (Pergamon, New York), pp. 240–260.
- Leatherwood, S., Reeves, R. R., and Foster, L. (1983). *The Sierra Club Handbook of Whales and Dolphins* (Tien Wah, Singapore).
- Leatherwood, S., Perrin, W. F., Kirby, V. L., Hubbs, C. L., and Dahleim, M. (1980). "Distribution and movements of Risso's dolphin, *Grampus griseus*, in the Eastern North Pacific," Fish. Bull. **77**, 951–963.
- Litchfield, C., Karol, R., Mullen, M. E., Dilger, J. P., and Lüthi, B. (1979). "Physical factors influencing refraction of the echolocative sound beam in delphinid cetaceans," Mar. Biol. **52**, 285–290.
- MacLennan, D. N., and Simmonds, E. J. (1992). *Fisheries Acoustics* (Chapman and Hall, London), Chap. 6.
- Moore, P. W. B., and Pawloski, D. A. (1990). "Investigations on the control of echolocation pulses in the dolphin (*Tursiops truncatus*)," in *Sensory Abilities of Cetaceans: Laboratory and Field Evidence*, edited by J. Thomas and R. Kastelein (Plenum, New York), pp. 305–316.
- Nachtigall, P. E., Au, W. W. L., Pawloski, J. L., and Moore, P. W. B. (1995). "Risso's dolphin (*Grampus griseus*) hearing thresholds in Kaneohe Bay, Hawaii," in *Sensory Systems of Aquatic Mammals*, edited by R. A. Kastelein, J. A. Thomas, and P. E. Nachtigall (De Spil, The Netherlands), pp. 49–53.
- Nachtigall, P. E., Lemonds, D. W., and Roitblat, H. L. (2000). "Psychoacoustic studies of dolphin and whale hearing," in *Hearing by Whales*, edited by W. W. L. Au, A. N. Popper, and R. J. Fay (Springer-Verlag, New York), pp. 330–363.
- Norris, K. S. (1968). "The evolution of acoustic mechanisms in odontocete cetaceans," in *Evolution and Environment*, edited by E. T. Drake (Yale Univ., New Haven), pp. 297–324.
- Penrose, J. D., and Kaye, G. T. (1979). "Acoustic target strengths of marine organisms," J. Acoust. Soc. Am. **65**, 374–380.
- Philips, J. D., Au, W. W. L., Nachtigall, P. E., Pawloski, J. L., and Roitblat, H. L. (in press). "Echolocation in the Risso's dolphin, *Grampus griseus*: A preliminary report," in *Echolocation in Bats and Dolphins*, edited by J. Thomas, C. Moss, and M. Vater (Univ. of Chicago, Chicago).
- Rasmussen, M. H., Miller, L. A., and Au, W. W. L. (2002). "Source levels of clicks from free-ranging white-beaked dolphins (*Lagenorhynchus albirostris*, Gray, 1846) recorded in Icelandic waters," J. Acoust. Soc. Am. **111**, 1122–1125.
- Thomas, J. A., and Turl, C. W. (1990). "Echolocation characteristics and range detection by a false killer whale (*Pseudorca crassidens*)," in *Sensory Abilities of Cetaceans: Laboratory and Field Evidence*, edited by J. A. Thomas and R. A. Kastelein (Plenum, New York), pp. 321–334.
- Thomas, J., Chun, M., Au, W., and Pugh, K. (1988). "Underwater audiogram of a false killer whale (*Pseudorca crassidens*)," J. Acoust. Soc. Am. **84**, 936–940.
- Urick, R. J. (1983). *Principles of Underwater Sound* (McGraw-Hill, New York).
- Verfuss, U. K., Garcia-Hartmann, M., and Schnitzler, H.-U. (1998). "Hunting and echolocation behavior of a captive Amazon river dolphin (*Inia geoffrensis*)," Biological Sonar Conference, 27 May to 2 June 1998, Carvoeiro, Portugal, p. 45 (abstract).
- White, M. J., Jr., Norris, J., Ljungblad, D., Baron, K., and di Sciara, G. (1978). "Auditory thresholds of two beluga whales (*Delphinapterus leucas*)," HSWRI Technical Report No. 78-109, Hubbs Marine Research Institute, San Diego, CA.
- Wood, F. G., and Evans, W. E. (1980). "Adaptiveness and ecology of echolocation in toothed whales," in *Animal Sonar Systems*, edited by R. G. Busnel and J. F. Fish (Plenum, New York), pp. 381–425.
- Wurtz, M., Poggi, R., and Clarke, M. R. (1992). "Cephalopods from the stomachs of a Risso's dolphin (*Grampus griseus*) from the Mediterranean," J. Mar. Biol. Assoc. U.K. **72**, 861–867.

The influence of flight speed on the ranging performance of bats using frequency modulated echolocation pulses

Arjan M. Boonman,^{a)} Stuart Parsons, and Gareth Jones

School of Biological Sciences, University of Bristol, Woodland Road, Bristol BS8 1UG, United Kingdom

(Received 24 November 2001; revised 14 October 2002; accepted 21 October 2002)

Many species of bat use ultrasonic frequency modulated (FM) pulses to measure the distance to objects by timing the emission and reception of each pulse. Echolocation is mainly used in flight. Since the flight speed of bats often exceeds 1% of the speed of sound, Doppler effects will lead to compression of the time between emission and reception as well as an elevation of the echo frequencies, resulting in a distortion of the perceived range. This paper describes the consequences of these Doppler effects on the ranging performance of bats using different pulse designs. The consequences of Doppler effects on ranging performance described in this paper assume bats to have a very accurate ranging resolution, which is feasible with a filterbank receiver. By modeling two receiver types, it was first established that the effects of Doppler compression are virtually independent of the receiver type. Then, used a cross-correlation model was used to investigate the effect of flight speed on Doppler tolerance and range–Doppler coupling separately. This paper further shows how pulse duration, bandwidth, function type, and harmonics influence Doppler tolerance and range–Doppler coupling. The influence of each signal parameter is illustrated using calls of several bat species. It is argued that range–Doppler coupling is a significant source of error in bat echolocation, and various strategies bats could employ to deal with this problem, including the use of range rate information are discussed. © 2003 Acoustical Society of America.

[DOI: 10.1121/1.1528175]

PACS numbers: 43.80.Ka, 43.80.Lb, 43.60.Gk [WWA]

I. INTRODUCTION

Bats often use frequency modulated (FM) calls in their echolocation to measure distance (Simmons, 1973). Since bats regularly fly at speeds between 3–8 m/s, their echoes are likely to be Doppler shifted by 1.8%–4.8% [Eq. (2)]. Under natural conditions, FM bats are not known to compensate their emitted pulses for Doppler shifts, as Doppler-compensating CF bats do (Schnitzler, 1968; Schuller *et al.*, 1974), and also lack the cochlear and neural adaptations thought to subserve the detection of Doppler shifts. These cochlear and neural adaptations have been described only for Doppler compensating CF bats such as *Rhinolophus* and *Pteronotus parnellii* (Grinnell, 1995).

When trained, the FM bat *Eptesicus fuscus* is able to detect Doppler shifts in replayed echoes only if this shift represents a flight speed of at least 6 m/s, or even 16 m/s in some individuals (Wadsworth and Moss, 2000). The high thresholds for detecting a difference in virtual flight speeds found in this study corroborate the view that, under natural circumstances, FM bats only measure distance and not flight speed with a single pulse.

Since the earliest investigations on bat echolocation, it has been speculated that FM bats may have evolved a pulse design suited to minimize errors in measuring distance caused by Doppler shifts (Strother, 1961; Cahlander *et al.*, 1964; McCue, 1966; Cahlander, 1967; Altes and Titlebaum, 1970; Simmons and Stein, 1980). The pulse design that

would make a bat least sensitive to Doppler effects was found to have a period that increases linearly over time, called linear period modulation, LPM, or hyperbolic frequency modulation (Kroszczyński, 1969). Five pulses emitted by the bat *Myotis lucifugus* in the laboratory appeared to be hyperbolic and therefore proved to be Doppler tolerant (Cahlander, 1967). However, calls of a number of species have been analyzed that were not perfectly Doppler tolerant (Escudé, 1988; Lin, 1988; Zbinden, 1988; Masters *et al.*, 1991; Parsons *et al.*, 1997). Only for *Eptesicus fuscus* echolocating in a laboratory do systematic data exist on all pulse parameters including sweep function (Masters *et al.*, 1991; Masters and Raver, 2000) from which Doppler errors can be calculated.

The aim of this paper is to show how pulse design affects the measurement of delay at different flight speeds. We used cross correlation as a method to investigate ranging acuity with the calls of different bat species. The underlying assumption is that a filterbank model which is the most likely candidate for the bat's receiver system will give results similar to a cross correlator (Altes, 1980). To test this assumption, we first compared the performance of a filterbank model with cross correlation.

Our way of displaying the errors induced by Doppler effects is more specific compared to most other papers since we investigate Doppler tolerance (acuity) and range–Doppler coupling (bias, offset) (Altes and Titlebaum, 1970; Menne, 1988) separately. Since Altes and Titlebaum (1970) discovered that range–Doppler coupling can be reduced to zero by relating the echo reception to an instant in the past (reference time, time to zero period; Pye, 1986), pulses well

^{a)}Present address: University of Tübingen, Animal Physiology, Auf der Morgenstelle 28, 72076 Tübingen, Germany. Electronic mail: arjan.boonman@uni-tuebingen.de

designed to minimize Doppler errors have been assumed to be hyperbolic by many authors (e.g., Masters *et al.*, 1991; Hartley, 1992). However, in this paper we argue that bats are unlikely to use a reference time in the past. Although there are various strategies a bat could use to reduce range–Doppler coupling, no information about this is yet available. This prompted us to treat range–Doppler coupling as a possible source of error that is not necessarily minimized by using a hyperbolic pulse design.

By varying different pulse parameters systematically, we show how each of them affects the two Doppler errors. Curvature was used as one of the parameters that was varied since curvature determines the degree to which a pulse is hyperbolic.

These data are then used to explain the different error trends in bat calls. This information can be used in further investigations in target-directed or flight-speed-dependent echolocation.

II. METHODS

A. Cross-correlation receiver

We used cross correlation to measure Doppler tolerance and range–Doppler coupling. In this paper, the target is always assumed to be a stationary point target (reflecting the entire spectrum), while the bat is assumed to be moving towards the target on axis. In this context, a relevant cross-correlation model can be given by

$$C_u(\tau) = s^{1/2} \int_{-\infty}^{\infty} u(t) u^*[s(t+\tau)] dt, \quad (1)$$

in which $u(t)$ is the waveform function over time t , τ is the expected time of arrival of the echo, $*$ denotes complex conjugation, and s is the Doppler factor given by

$$s = \frac{1 + V_{\text{bat}}/c}{1 - V_{\text{bat}}/c}, \quad (2)$$

in which V_{bat} is the flight speed of the bat (m/s), in which c is the speed of sound in air, for which we used 343 m/s. When $s > 1$ (the bat is flying towards the target) the echo is compressed in time. In this case the pulse $u(t)$ becomes $u(ts)$. In compressing waveforms, we corrected for sampling errors arising from this compression. The simulated flight speed of the bat was varied from 0–8 m/s, in increments of 0.5 m/s.

Range–Doppler coupling was defined as the increase in offset with flight speed of the bat [$\mu\text{s}/(\text{m/s})$]. Offset in range was derived from the cross-correlation function defined as the difference in time at which the maximum value of the function occurred between a flight speed of 0 m/s and any higher flight speed toward the target, up to 8 m/s.

Doppler (in)tolerance was calculated as the half-power width of the analytical envelope (Altes, 1980) of the cross-correlation function. We defined the Doppler intolerance as the increase of the half-power width of the envelope of the cross-correlation function with flight speed.

With Eq. (1), only the signal-dependent range–Doppler coupling can be calculated. However, compression of traveling time also leads to a range–Doppler coupling error that is

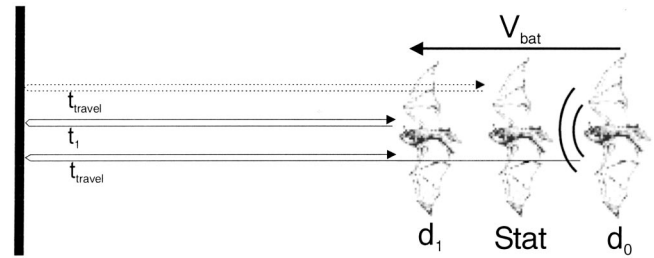


FIG. 1. A bat in flight emits a signal at distance d_0 relative to a target. At the time the signal has reflected back from the target to the bat, the bat has arrived at distance d_1 relative to the target. The traveling time of the signal is t_{travel} . If the bat emitted a pulse while being stationary at d_1 , the traveling time of the signal would be t_1 instead of t_{travel} . Therefore, the position of the bat at echo reception does not correspond with the delay (t_{travel}) received by the bat. The stationary position of the bat that would correspond to the received delay is the point exactly halfway between d_0 and d_1 , disregarding the Doppler compression of the signal.

independent of the signal used by the bat. The time between pulse emission and reception of the echo (t_{travel}) depends on the speed of sound c , the flight speed of the bat V_{bat} and the initial distance d_0 from bat to target (Fig. 1)

$$t_{\text{travel}} = \frac{2d_0}{V_{\text{bat}} + c}. \quad (3)$$

This means that the distance bat-to-target (d_1) at echo reception is given by

$$d_1 = d_0 - t_{\text{travel}} V_{\text{bat}} = d_0 \frac{1 - 2V_{\text{bat}}}{V_{\text{bat}} + c} = d_0 \frac{c - V_{\text{bat}}}{c + V_{\text{bat}}}. \quad (4)$$

The delay t_1 a stationary bat would measure at d_1 (the point of echo reception) is given by

$$t_1 = \frac{2d_1}{c} = \frac{2d_0}{c} \frac{c - V_{\text{bat}}}{c + V_{\text{bat}}} = t_{\text{travel}} \frac{c - V_{\text{bat}}}{c}. \quad (5)$$

Therefore, the delay perceived by the moving bat is t_{travel} , which is longer than the delay that belongs to the distance of echo reception t_1 . At the position of echo reception (d_1) the bat therefore overestimates delay by a factor $(c - V_{\text{bat}})/c$ (Fig. 1). This flight-speed-dependent offset in delay is an additional range–Doppler coupling to the range–Doppler coupling caused by the signal. Range–Doppler coupling can be eliminated by using a reference time (T_{ref}) (Altes and Titlebaum, 1970). The concept of reference time is discussed by Pye (1986) and Masters *et al.* (1991) and can be best understood by first examining Doppler errors that arise independently of the signal being used, as will be done below.

Using T_{ref} means that the bat does not interpret the received delay to belong to the position of reception (d_1), but a point where it was T_{ref} time ago. This point will therefore be at a distance $T_{\text{ref}} \times V_{\text{bat}}$ closer to d_0 , in other words: $d_1 = d_0 - (t_{\text{travel}} + T_{\text{ref}}) V_{\text{bat}}$. As a consequence Eq. (5) becomes

$$t_1 = \frac{2d_0}{c} - (t_{\text{travel}} + T_{\text{ref}}) \frac{2V_{\text{bat}}}{c}. \quad (6)$$

The Doppler error, ignoring any errors arising from the Doppler compression of the pulse, is therefore

$$t_{\text{travel}} - t_1 = \frac{2d_0}{V_{\text{bat}} + c} - \frac{2d_0}{c} + (t_{\text{travel}} + T_{\text{ref}}) \frac{2V_{\text{bat}}}{c}.$$

For one specific time T_{ref} before echo reception the signal-independent Doppler error will be zero. If we rearrange the equation and set it to zero

$$\begin{aligned} \frac{2d_0}{V_{\text{bat}} + c} - \frac{2d_0}{c} + \frac{2d_0}{V_{\text{bat}} + c} \frac{2V_{\text{bat}}}{c} + T_{\text{ref}} \frac{2V_{\text{bat}}}{c} &= 0, \\ T_{\text{ref}} &= -\frac{d_0}{V_{\text{bat}} + c}. \end{aligned} \quad (7)$$

Therefore, T_{ref} equals $-0.5 \times t_{\text{travel}}$. The two equations above are mainly useful for flight speeds between 1 and 10 m/s. Over this range the bias can be clearly minimized by one specific T_{ref} , while V_{bat} does not significantly affect the value of T_{ref} .

In other words, $T_{\text{ref}} = -0.5 \times t_{\text{travel}}$ means that if the bat was stationary halfway between d_1 and d_0 the delay it would receive is equal to the delay the bat did receive in flight, having flown from d_0 to d_1 (Fig. 1). T_{ref} therefore denotes a moment before echo reception at which the received delay would have been correct. If a bat used T_{ref} to eliminate Doppler errors, it therefore needs to project itself back in time. Note that, in principle, T_{ref} could also be defined in units of distance before echo reception, instead of units of time, as in this paper. If T_{ref} is defined in time it refers to a range of distances (depending on V_{bat}) where the bat could have been, and if T_{ref} is defined in distance it refers to a range of moments (depending on V_{bat}) before echo reception at which the bat could have been.

The range-Doppler coupling and its cancellation by applying T_{ref} , described above, only concerned the signal-independent Doppler errors, and not the signal-dependent Doppler errors. We will define the absolute signal-dependent range-Doppler error as $S \times V_{\text{bat}}$. If we add this error to $t_{\text{travel}} - t_1$ in Eq. (7), the T_{ref} needed to cancel the total error equals: $-0.5 \times t_{\text{travel}} - 0.5 \times S \times c$.

B. Pulse design and distance of focus (DOF)

Animals do not steer themselves by entering numbers into an absolute coordinate system over absolute time, but are more likely to use guidance systems relative to objects in distance or time (Trullier *et al.*, 1997). Therefore, if a bat used T_{ref} , and projected itself back to a specific moment before echo reception, this moment may be unambiguously defined on a video recording of this bat, but the bat itself is unlikely to possess such a precise memory of its absolute position in space at all possible moments. To know how far it has flown between T_{ref} and echo reception, the bat needs some clear event to which it can relate the absolute moment of T_{ref} . Since perception of the environment does not take place until the reception of the echo, the event has to be a behavioral event, such as beating the wing or sending the motor command to execute a behavioral action. The problem that arises here with the biological implementation of T_{ref} is that the time scale of action patterns in the bat is much cruder than the accuracy with which T_{ref} needs to be defined to cancel the error. In defining the correct value of T_{ref} ,

differences of 1 millisecond are relevant, whereas locomotive patterns in bats, such as wing beats, show that these patterns last for several tens of milliseconds (Valentine and Moss, 1998). We therefore think that bats are unlikely to use a system to eliminate range-Doppler coupling based on T_{ref} .

However, a way to accurately mark the onset of T_{ref} would be to make it coincide with an instant during pulse emission. In this way the moment of T_{ref} is clearly defined by a behavioral or neurophysiological event, for example by neurons in the cochlea firing upon the reception of the pulse during emission.

If the point of emission is used as point of perception $T_{\text{ref}} = -t_{\text{travel}}$ (or $d_1 = d_0$). This means that the signal-independent range-Doppler coupling becomes negative, since

$$t_{\text{travel}} - t_1 = \frac{2d_0}{V_{\text{bat}} + c} - \frac{2d_0}{c}.$$

At any speed V_{bat} , $S \times V_{\text{bat}}$ should cancel $t_{\text{travel}} - t_1$. Therefore

$$S V_{\text{bat}} = -\frac{2d_0}{V_{\text{bat}} + c} + \frac{2d_0}{c} = \frac{2d_0 V_{\text{bat}}}{c(V_{\text{bat}} + c)}. \quad (8)$$

If the time of emission is used as a reference point of perception, the range-Doppler coupling of the emitted pulse needed to cancel the entire range-Doppler coupling is the partial derivative of Eq. (8) with respect to flight speed V_{bat} :

$$S = \frac{\partial S V_{\text{bat}}}{\partial V_{\text{bat}}} = \frac{2d_0}{(V_{\text{bat}} + c)^2}. \quad (9)$$

A pulse with a specific range-Doppler coupling S will therefore give an unbiased estimate of an ensonified distance d_0 at any flight speed if the reference point (T_{ref}) is set at a point during pulse emission. In this paper we call this distance d_0 the distance of focus (DOF). According to our theory, a bat will have some idea how far a target of interest is and will emit a pulse with characteristics such that its range-Doppler coupling S equals $2d_0 / (V_{\text{bat}} + c)^2$. In doing this the bat can ignore its flight speed V_{bat} , since its influence on the outcome is negligible between 0 and 10 m/s. If the bat can project the received delay to its position during pulse emission, its perceived distance to the target is without offset. The disadvantage of the DOF strategy is that prediction of distance is needed to measure distance. In the results we describe how the accuracy of prediction affects the accuracy of the eventual measurement.

In this paper we used the start of the pulse as a time marker from which range is measured. This choice is arbitrary. The position of the time marker affects the result since the Doppler compression of the pulse is stronger than the compression of the traveling time of the pulse.

All models and calculations referred to in this paper were written in MATLAB (Mathworks, Natick, MA), version 5.3.0 with signal processing and statistics toolboxes.

C. The filterbank model

We compared the measurements of Doppler tolerance and range-Doppler coupling using cross correlation with the

results obtained with the SCAT-filterbank model (Saillant *et al.*, 1993), by using a script written by Peremans and Hallam (1998). SCAT is an echo processing model based on neurophysiological findings (Suga, 1990), which achieves a similar ranging accuracy as found in behavioral experiments on bats (Saillant *et al.*, 1993). In our study we used the cochlear and spectrogram correlation blocks, leaving out the spectrogram transformation block. For a further discussion of the SCAT model, see Masters and Raver (2000). The output of the SCAT model mimics neural activity over a range axis, with each neuron representing a different delay (delay-tuned neurons). In our study, the filterbank of the cochlear block was adjusted to the emission by ordering the frequency lines according to the sweep function that was used in the pulse. Echoes were Doppler shifted as in the cross-correlation model. This causes a mismatch between echo and filterbank, resulting in a change in delay (offset) and in Doppler tolerance.

For the alignment of pulse and echo in the “correlation process,” the same conventions were used as in the cross-correlation model with the delay measured between the starting points of pulse and echo and $T_{\text{ref}} = 0$.

In the case of the filterbank model, delay was measured as the delay belonging to the most strongly stimulated neuron of the delay-tuned neurons. Offset at each speed was measured by subtracting the delay at $V_{\text{bat}} = 0$ from the delay at that particular speed. Doppler tolerance was measured as the number of delay-tuned neurons activated at greater than half the level of the maximum value, while ignoring the delay-tuned neurons activated at this maximum value. In this way Doppler tolerance was effectively measured as “surround peak activity,” representing neural activity around the actual delay perceived by the bat. We only used artificial calls to compare the performance of the SCAT filterbank with cross correlation.

D. Echolocation calls

Artificial echolocation calls of bats were generated using a sampling rate of 1 MHz. To simulate a natural amplitude envelope, the waveform of each call was amplitude weighted using a tanh window over the first and last third of the call. The frequency–time course of each bat call was modeled using seven functions whose equations can be found in Parsons and Jones (2000). All of these functions allow the curvature of the frequency–time course to be adjusted, except the exponential1, linear, and hyperbolic function. The artificial calls were also varied in duration and frequency range.

Curvature, in this paper, is defined as the time span relative to half the pulse duration between the instant the center frequency is reached and the instant half the duration is reached (Fig. 5). When a pulse is linear, the instant when the center frequency is reached is equal to the instant where half the duration is reached, causing a time span of zero, and therefore a curvature of 0%. Convex pulses would cause a negative curvature.

The cross correlation was also executed on real bat calls, recorded in the field (for details see Parsons and Jones, 2000). As with the artificial calls, the real calls were correlated with Doppler-shifted versions of them, thus simulating

different flight speeds. Calls were Doppler shifted by compressing them in the time domain, and corrected for sampling errors arising from this compression. To generate an “average” artificial call for each bat species, real bat calls were ascribed a certain sweep function by reconstructing the frequency–time course of the dominant harmonic, following the methods described in detail by Parsons and Jones (2000). Pulses of the long-eared bat *Plecotus auritus* contained strong harmonics and were therefore individually submitted to a cross-correlation analysis. The same was done for *Pipistrellus pipistrellus* and *Pipistrellus pygmaeus*, since their calls were expected to exhibit a different response in a cross-correlation analysis than in a filterbank analysis (see Sec. III). The FM component of each *Pipistrellus* call was extracted from the entire pulse with its endpoint defined as the time where it first reaches the frequency 4% above the peak frequency of the entire call. This peak frequency was calculated with an FFT. The last 25% duration of the extracted FM component was first tapered with a Hann window before subjecting it to a cross-correlation analysis.

III. RESULTS

A. Filterbank model and cross correlation: Doppler intolerance

The acuity with which a target is defined in space decreases with increasing flight speed. This Doppler intolerance is displayed in Fig. 2 for a pulse sweeping down from 65 to 25 kHz in 5 ms and 75 to 25 kHz in 2 ms, respectively. The extent of Doppler intolerance, i.e., how quickly acuity degrades with flight speed, depends on curvature. The coupling between acuity and flight speed is nearly zero for curvatures close to a hyperbolic sweep in both receiver types. The near-hyperbolic curvature that is used in Fig. 2 is 44% for the pulse from 65 to 25 kHz and 50% for the pulse sweeping down from 75 to 25 kHz. Both the cross-correlation and the filterbank model show decreased Doppler tolerance with decreasing curvature. According to both models, acuity decreases dramatically at moderate and high flight speeds if linear or convex curvatures are used. For example, using a linear sweep from 75 to 25 kHz in 2 ms, the Doppler intolerance is 12.4 $\mu\text{s}/(\text{m/s})$. A linear sweep from 65–25 in 5 ms results in a Doppler intolerance of 39.1 $\mu\text{s}/(\text{m/s})$. These latter two figures are a measure of the widening of the envelope of the cross-correlation function due to flight speed.

The cross correlation and SCAT receiver agree less well at strong curvatures. In the cross-correlation receiver, the length of the constant frequency component (more prominent at strong curvatures) will effectively define the width of the envelope of the cross-correlation function. If the length of the CF component is relatively short compared to the bandwidth of the FM component, Doppler tolerance will be defined by the FM component. However, as flight speed increases, the peak in the cross-correlation function caused by the FM component will gradually merge with the wide zone of correlation caused by the CF component, causing Doppler tolerance to decrease. The SCAT model is more robust to the presence of a CF component at strong curvatures, as this affects only a very limited proportion of all frequency chan-

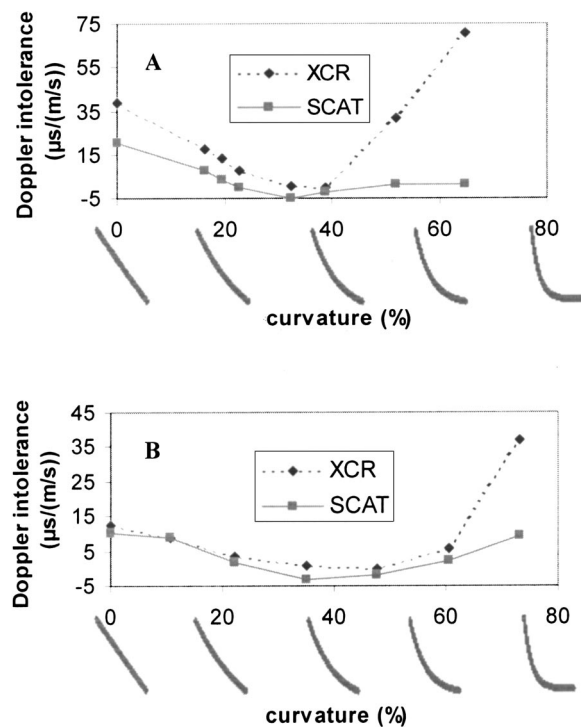


FIG. 2. Comparison between the performance of the cross-correlation and the SCAT model, using pulses of different curvatures (x axis). The top panel (A) shows the Doppler intolerance incurring with a pulse sweeping down from 65–25 kHz in 5 ms. The lower panel (B) shows the same for a pulse sweeping down from 75–25 kHz in 2 ms. The units along the x axis range from zero curvature (linear) to moderately strong curvature (QCF portion starting to level out). An exponential 2 function was used to model the pulses. Strong curvatures result in different results for the two receiver models due to the QCF component being processed differently (see Secs. III A and III B).

nels. Therefore, as long as the signal contains a wideband FM component Doppler tolerance will not decrease dramatically at strong curvatures in the filterbank receiver.

B. Filterbank model and cross correlation: Range–Doppler coupling

For linear to moderately strong curvatures the cross-correlation technique and the SCAT model result in similar range–Doppler couplings (Fig. 3). Curvatures close to hyperbolic in particular give rise to virtually identical range–Doppler couplings. The general trend exhibited by both receiver types is a decreasing range–Doppler coupling with decreasing curvature. The same differences between the receiver types that cause Doppler tolerance to be different at strong curvatures also cause range–Doppler coupling to differ at strong curvatures. The peak of the cross-correlation function is “drowned” in the noise as the CF component becomes dominant, resulting in a stronger range–Doppler coupling at increasing curvature. As explained above, the SCAT model is less affected by a CF component. Since an increasing curvature means an increased sweep rate for the FM component, the SCAT model effectively processes the same bandwidth within a shorter duration, leading to a decrease in range–Doppler coupling. This explains the difference between the two receiver types at strong curvatures. Linear pulses lead to a low range–Doppler coupling. Convex

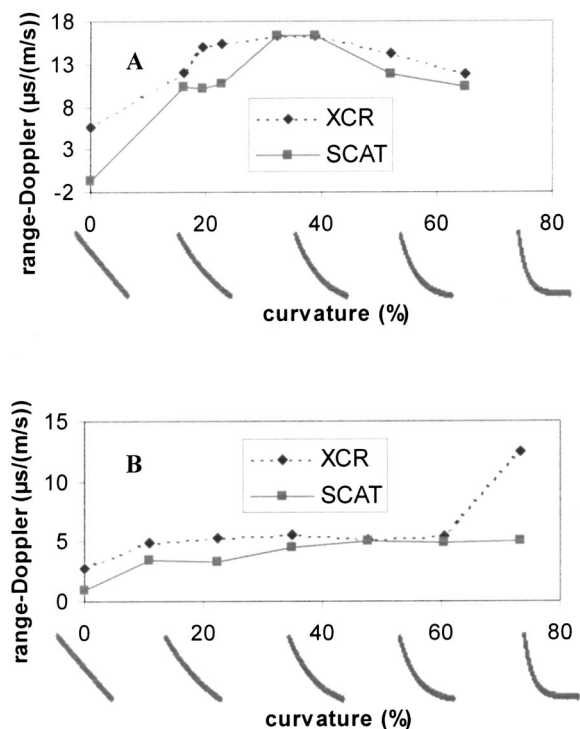


FIG. 3. Comparison between the performance of the cross-correlation and the SCAT model, using pulses of different curvatures (x axis). The top panel (A) shows the range–Doppler coupling incurring with a pulse sweeping down from 65–25 kHz in 5 ms. The lower panel (B) shows the same for a pulse sweeping down from 75–25 kHz in 2 ms. The units along the x axis range from zero curvature (linear) to moderately strong curvature (QCF portion starting to level out). An exponential 2 function was used to model the pulses.

pulses, however, can reduce range–Doppler coupling even further in the SCAT receiver, whereas Doppler intolerance caused by the convex curvature increases range–Doppler coupling in the cross-correlation receiver. The influence of all pulse parameters described below are based on the cross-correlation receiver.

C. Pulse duration

Short pulses (<1 ms) over a broad bandwidth result in a good Doppler tolerance for flight speeds up to 8 m/s, even for linear and strong curvatures [Figs. 4(a) and (c)]. The curvatures used in Figs. 4(a) and (c) are 16% and 49%, respectively. For a pulse sweeping down from 75–25 kHz, pulse durations longer than 1 ms already cause a strong coupling between acuity and flight speed. Both curvatures show a fairly similar pattern of decreasing Doppler tolerance with increasing pulse duration. Complete Doppler tolerance would be achieved only at all pulse durations if the curvature is close to hyperbolic. The effect of optimizing Doppler tolerance by making the pulse hyperbolic is most dramatic at long pulse durations. The same is also true for range–Doppler coupling; the longer pulse duration, the bigger the difference in range–Doppler coupling between linear and strongly curved sweeps [Figs. 4(b) and (d)]. At short pulse durations the effect of curvature on range–Doppler coupling is least profound. Short pulses therefore result in low offsets

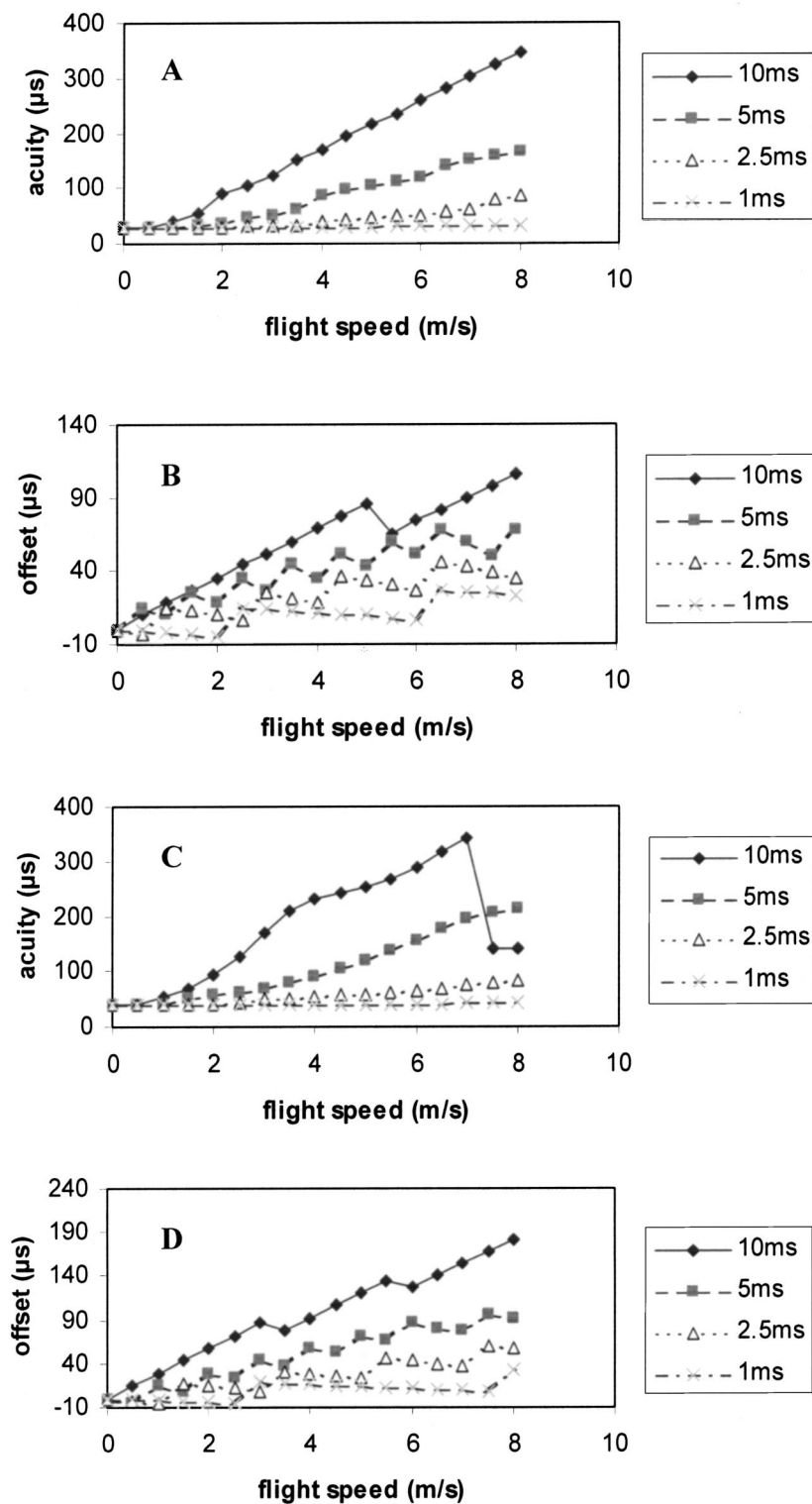


FIG. 4. The influence of pulse duration on Doppler intolerance (A,C) and range-Doppler coupling (B,D) for a pulse sweeping down from 75–25 kHz. Figures 4(A) and (B) represent a curvature of 16%, while Figs. 4(C) and (D) represent a curvature of 49%. These curvatures are too low to cause Doppler tolerance in any of the pulses of long duration (>2.5 ms).

at all speeds, whereas long pulses give rise to increased offsets at high speeds, especially at strong curvatures.

D. Bandwidth

When varying bandwidth, the rate of change in frequency over time was kept inversely proportional to bandwidth; in other words, curvature was kept constant. The influence of bandwidth on Doppler tolerance and range-Doppler coupling was measured at curvatures of 20% and

50%. The Doppler tolerance of the call with 20% curvature (4 ms) starting at 75 kHz was maximized at a bandwidth of 30 kHz, whereas the Doppler tolerance of the call with 50% curvature was maximized at a bandwidth of 50 kHz. From our calculations it becomes clear that a decreasing bandwidth leads to less Doppler tolerance. This intolerance can be minimized by reducing curvature. Therefore, it can be said that bandwidth offsets optimum curvature negatively. In other words, a narrow bandwidth pulse has to be more linear than a broad bandwidth pulse to result in the same Doppler errors.

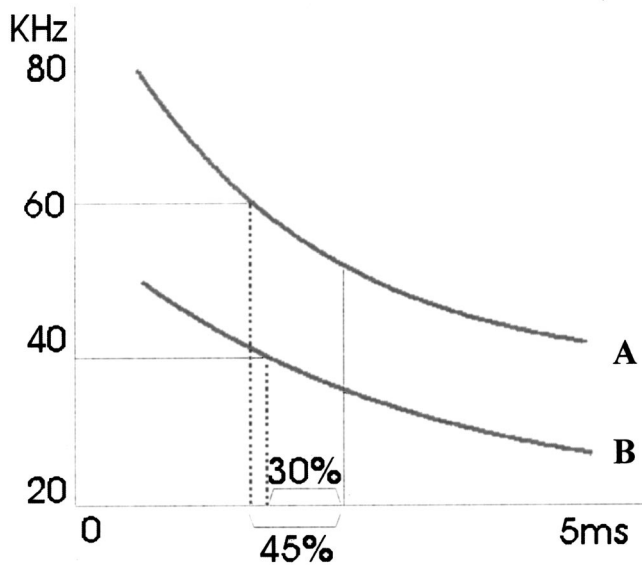


FIG. 5. Two hyperbolic pulses A and B sweeping down from 80 to 40 kHz and 50 to 25 kHz in 4 ms, respectively. Since the bandwidths of the two pulses are different, their curvatures differ to make both pulses hyperbolic. Curvature is defined as the time span from the center frequency to half the pulse duration, divided by half the pulse duration. Since call A has an Hf/Lf ratio identical to call B, range–Doppler coupling is equal between the two pulses. Both pulses also show Doppler tolerance, the absolute values of acuity being lower than for pulse A than for pulse B, due to its broader bandwidth.

This is also shown in Fig. 5, in which pulse b is more linear than pulse a, while both are Doppler tolerant (hyperbolic). Since the curvature of a hyperbolic function decreases with decreasing bandwidth it always maximizes Doppler tolerance, independent of bandwidth. If the bandwidth of a call covers less than one octave (Hf/Lf ratio <2 , see “absolute frequency”), lowering bandwidth leads to decreased Doppler tolerance. Range–Doppler coupling decreases with increasing bandwidth, regardless of curvature. The range–Doppler coupling we found with various hyperbolic pulses corresponds with an equation published by Glaser (1974)

$$r\text{-D coupling} = 2V_{\text{bat}}/cT_{\text{pulse}}f_2/(f_1-f_2), \quad (10)$$

in which T_{pulse} denotes the duration of the pulse, f_1 is the highest frequency, and f_2 is the lowest frequency of the pulse.

E. Absolute frequency

Absolute frequency affects the ratio between the upper and lower frequency (Hf/Lf ratio). A ratio of 2 or higher leads to Doppler tolerance if curvature is hyperbolic. If the ratio is increased from 2 by lowering the lower frequency, Doppler tolerance is maintained. Range–Doppler coupling, however, will continue to decrease when the Hf/Lf ratio is increased beyond 2. Figure 5 shows two pulses (a and b) having a different bandwidth, but the same range–Doppler coupling because of identical Hf/Lf ratios Eq. (10). Since the pulses are hyperbolic, both are Doppler tolerant ($Hf/Lf=2$), but the acuity is higher for pulse b than for pulse a, as a has a broader bandwidth.

F. Harmonics

The influence of harmonics on the two types of Doppler errors was investigated for an artificial signal similar to those used by *Eptesicus*, sweeping from 60–25 kHz in 4 ms, with a curvature of 61% (hyperbolic=44% with this pulse). Doppler tolerance is achieved only if the second harmonic is stronger than -6 dB and the third -12 dB relative to the fundamental. When using an optimal (hyperbolic) curvature, adding strong harmonics will improve acuity while Doppler tolerance is maintained. Harmonics hardly affects offset, regardless of their relative strength.

G. Different functions

Doppler tolerance can also be achieved with functions other than hyperbolic, providing that their curvature can be adjusted to approximate a hyperbolic call [Fig. 6(a)]. Although the curvature of a parabolic call can be adjusted, increasing the curvature beyond a certain level causes an upward sweep after the downward sweep, a phenomenon rarely observed in real bat calls. The maximum level of curvature causing only a downward sweep is insufficient to decouple acuity and flight speed to the same extent as with the other adjustable functions. Figure 6 therefore displays only curvature values of a parabolic function causing a downward sweep. The power and logarithmic functions are also limited in the amount of curvature that can be applied to them. Forcing a strong curvature in these functions results in the start of the call decreasing in frequency almost instantaneously with the rest of the sweep remaining virtually linear.

The low curvature values of, for example, the power function are therefore not perfectly comparable to the same low curvature values of the exponential 2 function, which levels out in a constant frequency. This explains why the decrease in Doppler tolerance is more dramatic for the exponential 2 function at decreasing curvature than it is for the other functions.

The logarithmic, exponential1, exponential2, and hyperbolic function agree fairly well in the amount of range–Doppler coupling they cause [Fig. 6(b)]. The power function fits the pattern less well, probably because changes in curvature mainly affect the upper frequency region of the pulse, rather than the lower region. The optimum curvature to cause Doppler tolerance for each function does not appear to have any particular effect on the range–Doppler coupling. When four of the functions displayed in Fig. 6 are set to approximate a hyperbolic function, they result in the following range–Doppler couplings (required T_{ref} values for a target at 1 m in brackets): hyperbolic: 18.2 (-6.0 ms), logarithmic: 19 (-6.1 ms), power: 23.8 (-7.0 ms), and exponential2: 16.3 (-5.7 ms) $\mu\text{s}/(\text{m/s})$ for a pulse sweeping down from 65 to 25 kHz in 5 ms. The values for T_{ref} were calculated using Eq. (7).

H. Real bat calls

The two *Myotis* species whose calls were analyzed are examples of bats that use short duration pulses with a high ratio between highest and lowest frequency (Hf/Lf ratio) caused by the broad bandwidth of their pulses. Since both

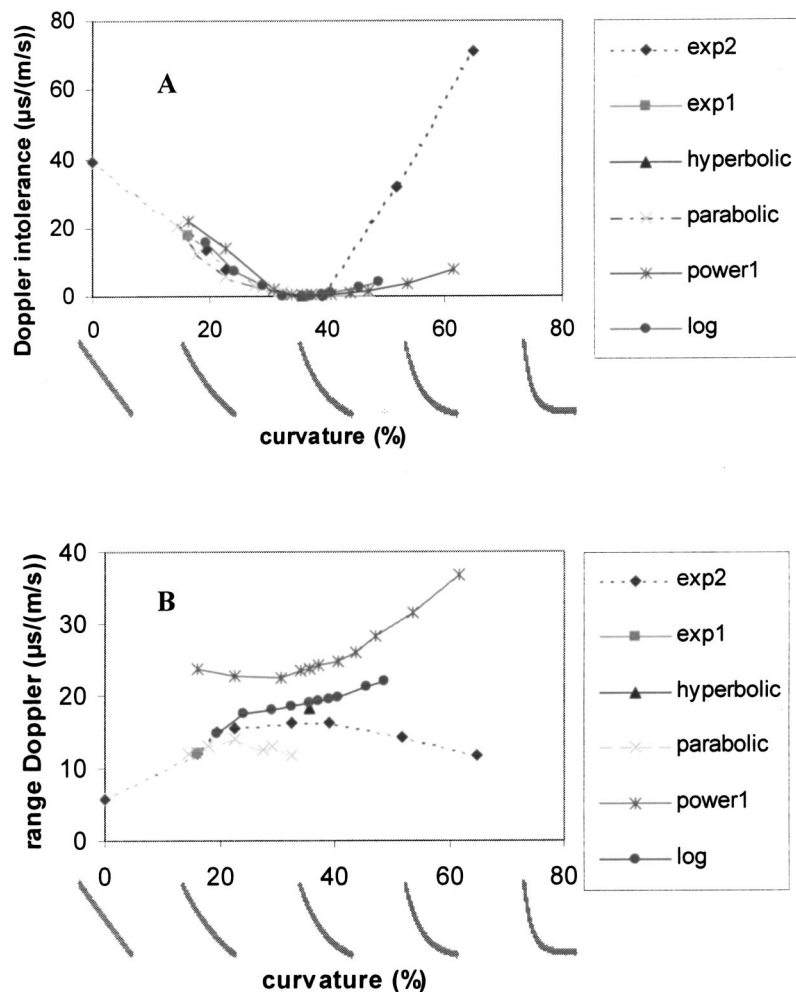


FIG. 6. The influence of the function used to model bat echolocation calls. The exponential 2 function causes a stronger Doppler intolerance at strong curvatures than other functions, due to its property of leveling out in a constant frequency at the end of the pulse (see Secs. III A and III B). The power function causes a stronger range–Doppler coupling at strong curvatures than most other functions since its low-frequency portion remains linear when a strong curvature is applied.

species generally emit calls longer than 1 ms, Doppler tolerance depends on the curvature of the pulse (see Sec. III C). Recordings of both *Myotis* species were made outdoors of individuals that were released from the hand and hence flew slowly in a relatively cluttered environment. The one real pulse of *Myotis daubentonii* that was analyzed happened to be Doppler tolerant [$0.1 \mu\text{s}/(\text{m/s})$], but most calls emitted by this species are not Doppler tolerant. This is shown by the fit to the average pulse function of this species (second row for each species in Table I). Since *Myotis nattereri* emits calls with a higher Hf/Lf ratio, range–Doppler coupling in *Myotis nattereri* is lower than in *Myotis daubentonii*, in this case even negative. *Myotis nattereri* often (at least in clutter) emits calls that are nearly linearly frequency modulated and are therefore Doppler intolerant (Table I). Both *Myotis* species seem to use pulses to reduce range–Doppler coupling, rather than to optimize Doppler tolerance, at least during slow flight in a cluttered environment.

The echolocation calls of *Eptesicus* and *Nyctalus* were recorded while they were flying in open or partly open environments. The calls of these bats consist of an FM component, and a component which is more constant in frequency (quasiconstant frequency; QCF, Kalko and Schnitzler, 1993). In a cross-correlation analysis, a QCF component can be longer than a CF component before it “drowns” the peak in

the cross-correlation function caused by the FM component (see Secs. III A and III B). Calls with a long duration and a narrow bandwidth in *Eptesicus* and *Nyctalus* often have such a long duration that the cross-correlation values of the FM component are drowned, despite the QCF character of the pulses. This effect is shown in Table I by the values of Doppler tolerance and range–Doppler coupling for the average *Nyctalus noctula* and *Nyctalus leisleri* call. The real calls from *Eptesicus serotinus* and *Nyctalus leisleri* that were selected for analysis had a moderate curvature, which leads to similar results using either a filterbank or a cross-correlation analysis. As expected for calls with a relatively low Hf/Lf ratio (narrow-band) and a long duration, the range–Doppler coupling is high while Doppler tolerance is low. Doppler tolerance is better for the single call of *Nyctalus leisleri* than for *Eptesicus serotinus*, but most calls emitted by these species, especially in open areas, seem to be too curved to achieve a high Doppler tolerance.

Calls emitted by most European Pipistrelle bats consist of a clear FM and QCF component, with little variation in the duration of the FM component (Kalko and Schnitzler, 1993). Because the QCF component of calls emitted by Pipistrelle bats is very constant in frequency, even a short-duration QCF component will drown the peak in the cross-correlation function associated with the FM component of

TABLE I. Range–Doppler coupling, distance of focus (DOF), Doppler tolerance, the number of real calls used, and the number of averaged call parameters to describe the average function for eight species of bat. Upper data in each cell denote a real pulse, lower data denote the average pulse, modeled by the best fitting function. The data of both *Pipistrellus* refer to the FM component of the real pulses only. The data of *Plecotus auritus* refer to real pulses only. The additional range–Doppler coupling $t_{\text{travel}} - t_1$ is not taken into account.

Species	Function type	# Real calls # Model. calls	Range– Doppler $\mu\text{s}/(\text{m}/\text{s})$	Distance of focus (cm)	Doppler intolerance $\mu\text{s}/(\text{m}/\text{s})$
<i>Myotis daubentonii</i>	no function	1	12.8	78.0	0.1
	power 1	24	10.4	63.4	11.8
<i>Myotis nattereri</i>	no function	1	–2.6	–15.8	12.2
	power 1	39	–2.4	–14.6	21.8
<i>Eptesicus serotinus</i>	no function	1	30.5	185.0	18.7
	exponential 2	14	19.8	120.7	53.9
<i>Nyctalus noctula</i>	no function	1	132	804.0	98.9
	exponential 2	13	297	1801.0	392.0
<i>Nyctalus leisleri</i>	no function	1	18.9	115.0	6.6
	exponential 2	16	24.0	146.3	78.5
<i>Pipistrellus pipistrellus</i>	no function	22	24.2	147.5	4.4
<i>Pipistrellus pygmaeus</i>	n.a.	n.a.	n.a.	n.a.	n.a.
	no function	76	27.1	165.1	12.3
	n.a.	n.a.	n.a.	n.a.	n.a.
<i>Plecotus auritus</i>	no function	22	12.8	78.0	2.0
	n.a.	n.a.	n.a.	n.a.	n.a.

the call. From the analyses with the SCAT filterbank model it was revealed that a pure QCF component hardly affects a filterbank receiver as very few neurons are triggered by this component (see Sec. III B). For this reason we chose to analyze only the FM component of each call. To extract the FM component we followed the procedure described in Sec. II.

Our analysis revealed that the pulse design in both *Pipistrellus* bats is less flexible than in the other bats we describe here. The average duration of the FM component in *Pipistrellus pipistrellus* is 1.5 ms (s.d.=0.4 ms; $n=22$). In *Pipistrellus pygmaeus* the average duration of the FM component is 1.8 ms (s.d.=0.3 ms; $n=76$). The curvature of the FM component in *Pipistrellus pipistrellus* is always close to hyperbolic, resulting in a Doppler tolerance of $4.44 \mu\text{s}/(\text{m}/\text{s})$ ($n=22$). *Pipistrellus pygmaeus* is less Doppler tolerant with $12.3 \mu\text{s}/(\text{m}/\text{s})$ ($n=76$). This difference in Doppler tolerance between the two species is likely to be caused by *Pipistrellus pygmaeus* using pulses that are less hyperbolic than in *Pipistrellus pipistrellus*, since both species show the same Hf/Lf ratio (1.6–1.7) (Vaughan *et al.*, 1997; Parsons and Jones, 2000). The values of the range–Doppler coupling are $27.1 \mu\text{s}/(\text{m}/\text{s})$ and $24.2 \mu\text{s}/(\text{m}/\text{s})$, respectively. The inflexible pulse design in the two *Pipistrellus* species means that range–Doppler coupling can only be controlled by varying the Hf/Lf ratio of the pulse.

The calls emitted by *Plecotus* recorded in a relatively cluttered environment showed good Doppler tolerance (see Table I), which is achieved by the harmonic composition of its pulses (see Sec. III F) and the relatively short pulse duration of 1.4 ms for the 22 calls that were analyzed. The average range–Doppler coupling of these 22 calls is $12.8 \mu\text{s}/(\text{m}/\text{s})$. This is the same value as found for a pulse of *Myotis daubentonii*, despite this species having a much broader bandwidth. However, since the first harmonic of *Plecotus auritus* sweeps over relatively low frequencies, the Hf/Lf ratio is reduced little, despite the limited bandwidth. An ad-

ditional reduction of range–Doppler coupling is achieved in this species by using a short pulse duration.

The calls emitted by *Plecotus* in an open environment showed good Doppler tolerance (see Table I), which is achieved by the harmonic composition of its pulses (see Sec. III F).

I. The influence of prediction accuracy on accuracy of the measurement

In Sec. II B, we described an alternative way of using a reference time in the past (T_{ref}) by emitting a pulse whose range–Doppler coupling is equal to the negative range–Doppler coupling that results from relating the measured delay to a moment during pulse emission. Since the bat has to adjust the frequency–time structure of the pulse to the distance of the target, we call this strategy a distance of focus (DOF) strategy. Equation (9) shows what range–Doppler coupling is required to focus on the distance d_0 to obtain the correct estimate of distance.

The apparent disadvantage of the DOF strategy is that a bat has to predict distance in order to measure it correctly. However, the following calculation will show that this estimation can be very rough while the bat will still get accurate information on the actual distance. If the actual distance from bat to target is 80 cm, but the bat predicts it to be 1 m, according to Eq. (9), the emitted pulse will have a range–Doppler coupling of $16.5 \mu\text{s}/(\text{m}/\text{s})$, instead of $13.2 \mu\text{s}/(\text{m}/\text{s})$. At a flight speed of 5 m/s, this means the target will appear $(16.5 - 13.2) \times 5 \times 343 / 2000 = 2.8$ mm further than its real distance. This means that the error in prediction (200 mm) was reduced 70 times in the eventual perception. Rather than errors in prediction, errors in pulse design under the right prediction should be regarded as the main source of error, if bats used a DOF strategy. From Eq. (10) it can be derived that slight shifts in start- or end frequency will affect the range–

Doppler coupling of a hyperbolic pulse. This effect will be less dramatic when pulses with a broad bandwidth are used.

We calculated the distance on which the typical echolocation calls of the eight investigated bat species are focused (Table I, third column). The calculated distances seem to correspond with the maximum prey detection distance of each bat species. The only exceptions are *Myotis nattereri* and *Nyctalus noctula*. In the former species the DOF was calculated to lie behind it, whereas it lies too far ahead in the latter species.

IV. DISCUSSION

In this paper, pulse design in FM bats has been explained in terms of minimizing ranging errors. It may well be that many other factors, such as optimizing detection, as in the case of the signals used by *Nyctalus noctula* flying in open air (Table I), play a more important role in governing the signal design used by FM bats. The further away a bat is from a target, the less precise its estimate of target distance needs to be. The relevance to bats of different signal designs with respect to Doppler effects as we describe in this paper can therefore be questioned. Another reason for caution is that the bat's echo processing system may differ from the models used in this study. However, several independent studies show that bats must possess a very accurate echo processing mechanism (Moss and Schnitzler, 1995). The echo processing mechanism of bats is therefore likely to exhibit some similarities in the responses to Doppler shifts to the models used in this study. Although it is still unclear if bats reduce range–Doppler coupling through pulse design, our results show that this source of error is significant to bats. Moss and Schnitzler (1995) summarize the ranging accuracy in six species of bats, stating it to vary between 8 and 15 mm (46–87 μ s). Recent experiments on distance discrimination in the big brown bat *Eptesicus fuscus* using acoustic playbacks (phantom targets) of the emitted call show a lower limit of 6 mm (35 μ s) for discriminating between two different echo arrival times (Masters and Raver, 1996; Masters *et al.*, 1997; Masters and Raver, 2000). The actual ability of the bat to measure distance to a target could even be better than this figure as a result of the uncertainty in triggering the phantom echo in these experiments (Masters *et al.*, 1997). For our average *Eptesicus serotinus* pulse (nearly identical in pulse design to *Eptesicus fuscus*) we found a range–Doppler coupling of 19.8 μ s/(m/s). This means that the target would be seen displaced at a flight speed higher than 1.8 m/s, which is nearly always the case in *Eptesicus*. This range–Doppler coupling is without the distance-dependent range–Doppler coupling $t_{\text{travel}} - t_1$. If the bat tries to estimate its distance to a target at 2-m distance, this would cause an additional range–Doppler coupling of 33 μ s/(m/s). The total range–Doppler coupling would therefore be 52.8 μ s/(m/s) at 2-m distance from a target. Table I shows that range–Doppler coupling, especially with the additional error $t_{\text{travel}} - t_1$, must be of relevance to bats, since the resulting error would be clearly noticeable by the bat. This fact has not been pointed out before. Bats can remedy this problem in a number of ways, by signal design, special timing strategies, or both, as described in the methods of this paper and dis-

cussed below. Masters and Raver (2000) hypothesize that *Eptesicus* has a linear error correction system (LEC) that will make the bat tolerant to Doppler shifts, even with a not optimally Doppler-tolerant pulse design. LEC works by correcting for linear trends in range estimates across frequency channels. In this way, errors due to Doppler shifts (and other echo manipulations) are eliminated and accuracy remains unaffected (Masters and Raver, 2000). A possible reason for bats to reduce Doppler intolerance is to minimize Doppler-induced “smearing” of targets, which would make it harder to resolve target structure from echoes (Simmons and Chen, 1989).

The pulse design employed by the two *Myotis* species investigated in this paper seems to be suited more to reduce range–Doppler coupling than to Doppler tolerance, at least during slow flight in a cluttered environment. This is especially pronounced in *Myotis nattereri*, which will often use convex pulses (Siemers and Schnitzler, 2000), but other *Myotis* species also use near-linear frequency-modulated pulses while flying in a cluttered environment (Siemers, 2000). It may be that the low flight speed of these bats when using linear FM pulses may not necessitate the use of a Doppler-tolerant pulse design. The question remains, however, if *Myotis* bats sometimes use hyperbolic pulses (*Myotis daubentonii*, Table I), what is the advantage of switching to a linear pulse design in clutter?

The echolocation used by *Eptesicus* and *Nyctalus* in open environments seems to be designed primarily to improve detection and not range resolution. However, *Eptesicus serotinus* is known to chase insects into vegetation and will need a good ranging resolution in such circumstances. During ranging experiments, where optimum pulse design with regard to ranging is expected, *Eptesicus fuscus*, a species very similar to *Eptesicus serotinus*, uses a pulse design that is more curved than hyperbolic (Masters *et al.*, 1991). In situations close to a target, the second harmonic may be strong enough to reduce Doppler intolerance. Judging from field recordings of *Eptesicus serotinus* made by Jensen and Miller (1999), it seems unlikely that the harmonics produced by *Eptesicus serotinus* will substantially improve Doppler tolerance when ensonifying targets at 2 m or further, since the second harmonic is already –8 dB, and the third –22 dB relative to the first harmonic at 4 m (2 m back and forth) distance. Since the second harmonic used by *Plecotus* is often as strong as the first harmonic, as in other bat species using multiple harmonic FM calls (*Phyllostomidae*, *Megadermatidae*), it will affect the Doppler tolerance gained with the signal. Since range–Doppler coupling is not affected by harmonics, the two errors can be manipulated independently by using a specific curvature and harmonic composition. Simmons and Stein (1980) did find an influence of a harmonic on range–Doppler coupling of a pulse sweeping down from 50 to 20 kHz for a simulated flight speed between 0 and 2 m/s. It is possible that the influence does not persist when range–Doppler coupling is plotted on a rougher scale between 0 and 8 m/s.

In the Methods section we argued why a reference time in the past (T_{ref}) would be hard to implement by bats, and instead proposed an alternative strategy, fairly similar to

T_{ref} . We referred to this alternative strategy in the results as distance of focus, or DOF.

There are other solutions to the range–Doppler coupling problem. One of these solutions is the use of rate range information (Wenstrup and Suthers, 1984; Tanaka and Wong, 1993). This means that a bat measures its flight speed by comparing consecutive measurements of delay. Each of these measurements is offset due to the flight speed of the bat and the range–Doppler coupling of each pulse, but these would cancel if both factors remained constant. Masters *et al.* (1991) investigated the effect of Doppler tolerance on ranging acuity, and showed that increasing the length of the pulse interval decreases velocity uncertainty. This is because acuity then becomes less significant relative to the interval over which velocity is measured. However, since each indication of speed is the average in between the two emissions it also becomes less accurate in reducing the ranging error with increasing pulse interval. To reduce range–Doppler coupling the optimum pulse interval would be zero, but this is not true if acuity is taken into account as explained above.

V. CONCLUSIONS

This paper describes the errors in measuring the distance of objects bats will encounter in flight, argues that some of these errors are noticeable by bats, and describes how pulse design and delay timing strategies could help in reducing these errors. First, we argue why we think our cross-correlation analyses on bat pulses are applicable to a bat-like (filterbank) receiver by showing the similarity in performance between the filterbank receiver and cross-correlation analysis of linear to moderately curved pulses (Figs. 2 and 3). We also argue that the curvature of the signal, rather than the function used to model it, is of importance with respect to error reduction in range estimation in bats in flight (Fig. 6). In separating the ranging errors due to “Doppler intolerance” and “range–Doppler coupling,” we confirmed that hyperbolic pulses lead to Doppler tolerance if their H_f/L_f ratio is 2 or higher, but found a strong range–Doppler coupling for these signals if we assume the target is perceived when it is received ($T_{\text{ref}}=0$). Linear pulses with a high H_f/L_f ratio reduce range–Doppler coupling, but such pulses are Doppler intolerant. This means that if linear pulses are used at high speed the target will appear at the correct location, but its spatial location will be poorly defined.

Signals of different curvatures can be found in the group of *Myotis* bats, but in cluttered conditions linear FM sweeps (low range–Doppler coupling, but Doppler intolerant) are used most frequently. Since the implementation of T_{ref} to reduce Doppler errors does not seem biologically feasible, we propose DOF as an alternative strategy for eliminating Doppler errors with a single pulse, or else range rate information over at least two pulse–echo pairs. Our calculations and examples show that more research is needed to establish if the pulse structure used by different bat species is an adaptation to Doppler errors, to a fixed sensitivity of the filterbank, or to both.

ACKNOWLEDGMENTS

We would like to thank the following people for technical assistance and/or commenting on earlier drafts of the paper: Kristian Beedholm, René Breeuwer, Cathy Gasson, Mitch Masters, Dieter Menne, Herbert Peremans, Jeremy Rayner, Snježana Rendulić, Björn Siemers, Peter Stiltz, and William Thorpe. This work was funded by a scholarship from the University of Bristol to A.M.B.

- Altes, R. A. (1980). “Detection, estimation, and classification with spectrograms,” *J. Acoust. Soc. Am.* **67**, 1232–1246.
- Altes, R. A., and Titlebaum, E. L. (1970). “Bat signals as optimally Doppler tolerant waveforms,” *J. Acoust. Soc. Am.* **48**, 1014–1020.
- Cahlander, D. A. (1967). “Theories of sonar systems and their application to biological organisms: Discussion,” in *Animal Sonar Systems: Biology and Bionics*, edited by R. G. Busnel (Laboratoire de Physiologie Acoustique, Jouy-en-Josas, France), Vol. 2, pp. 1052–1081.
- Cahlander, D. A., McCue, J. J. G., and Webster, F. A. (1964). “The determination of distance by echolocating bats,” *Nature (London)* **201**, 544–546.
- Escudé, B. (1988). “Take off signals emitted by *Myotis mystacinus*: Theory of receivers and modelling,” in *Animal Sonar: Processes and Performance*, edited by P. E. Nachtigall and P. W. B. Moore (Plenum, New York), pp. 785–790.
- Glaser, W. (1974). “Zur Hypothese des Optimalempfangs bei der Fledermausortung,” (“On the hypothesis of coherent reception in bat echolocation”), *J. Comp. Physiol.* **94**, 227–248.
- Grinnell, A. D. (1995). “Hearing in bats: An overview,” in *Hearing by Bats*, edited by A. N. Popper and R. R. Fay (Springer, New York), pp. 1–36.
- Hartley, D. J. (1992). “Stabilization of perceived echo amplitudes in echolocating bats. II. The acoustic behavior of the big brown bat, *Eptesicus fuscus*, when tracking moving prey,” *J. Acoust. Soc. Am.* **91**, 1133–1149.
- Jensen, M. E., and Miller, L. A. (1999). “Echolocation signals of the bat *Eptesicus serotinus* recorded using a vertical microphone array: Effect of flight altitude on searching signals,” *Behav. Ecol. Sociobiol.* **47**, 60–69.
- Kalko, E. K. V., and Schnitzler, H.-U. (1993). “Plasticity in echolocation signals of European pipistrelle bats in search flight: Implications for habitat use and prey detection,” *Behav. Ecol. Sociobiol.* **33**, 415–428.
- Kroszczynski, J. J. (1969). “Pulse compression by means of linear period modulation,” *Proc. IEEE* **57**, 1260–1266.
- Lin, Z.-b. (1988). “Wideband ambiguity function of broadband signals,” *J. Acoust. Soc. Am.* **83**, 2108–2116.
- Masters, W. M., Jacobs, S. C., and Simmons, J. A. (1991). “The structure of echolocation sounds used by the big brown bat *Eptesicus fuscus*: Some consequences for echo processing,” *J. Acoust. Soc. Am.* **89**, 1402–1413.
- Masters, W. M., and Raver, K. A. S. (1996). “The degradation of distance discrimination in big brown bats *Eptesicus fuscus* caused by different interference signals,” *J. Comp. Physiol., A* **179**, 703–713.
- Masters, W. M., Raver, K. A. S., Kornacker, K., and Burnett, S. C. (1997). “Detection of jitter in intertarget spacing by the big brown bat *Eptesicus fuscus*,” *J. Comp. Physiol., A* **181**, 279–290.
- Masters, W. M., and Raver, K. A. S. (2000). “Range discrimination by big brown bats *Eptesicus fuscus* using altered model echoes: Implications for signal processing,” *J. Acoust. Soc. Am.* **107**, 625–637.
- McCue, J. J. G. (1966). “Aural pulse compression by bats and humans,” *J. Acoust. Soc. Am.* **40**, 545–548.
- Menne, D. (1988). “Designing critical experiments on detection and estimation in echolocating bats,” in *Animal Sonar: Processes and Performance*, edited by P. E. Nachtigall and P. W. B. Moore (Plenum, New York), pp. 387–411.
- Moss, C. F., and Schnitzler, H.-U. (1995). “Behavioral studies of hearing in bats,” in *Hearing by Bats*, edited by A. N. Popper and R. R. Fay (Springer, New York), pp. 87–145.
- Parsons, S., Thorpe, C. W., and Dawson, S. M. (1997). “Echolocation calls of the long-tailed bat: a quantitative analysis of types of calls,” *J. Mammal.* **78**, 964–976.
- Parsons, S., and Jones, G. (2000). “Acoustic identification of 12 species of echolocating bat by discriminant function analysis and artificial neural networks,” *J. Exp. Biol.* **203**, 2641–2656.
- Peremans, H., and Hallam, J. (1998). “The spectrogram correlation and transformation receiver, revisited,” *J. Acoust. Soc. Am.* **104**, 1101–1110.

- Pye, J. D. (1986). "Sonar signals as clues to system performance," *Acustica* **61**, 166–175.
- Saillant, P. A., Simmons, J. A., Dear, S. P., and McMullen, T. A. (1993). "A computational model of echo processing and acoustic imaging in frequency-modulated echolocating bats: The spectrogram correlation and transformation receiver," *J. Acoust. Soc. Am.* **94**, 2691–2712.
- Schnitzler, H.-U. (1968). "Die Ultraschall-Ortungslaute der Hufeisen-Fledermäuse (*Chiroptera-Rhinolophidae*) in verschiedenen Orientierungssituationen," ("The ultrasonic echolocation calls of horseshoe bats (*Chiroptera-Rhinolophidae*) in different orientation situations"), *Z. Vgl. Physiol.* **57**, 376–408.
- Schuller, G., Beuter, K., and Schnitzler, H.-U. (1974). "Response to frequency-shifted artificial echoes in the bat, *Rhinolophus ferrumequinum*," *J. Comp. Physiol.* **89**, 275–286.
- Siemers, B. M. (2000). "Prey perception by echolocation in *Myotis* bats," Ph.D. dissertation, University of Tuebingen, Faculty of Biology, Germany.
- Siemers, B. M., and Schnitzler, H.-U. (2000). "Natterer's bat (*Myotis nattereri*, Kuhl, 1818) hawks for prey close to vegetation using echolocation signals of very broad bandwidth," *Behav. Ecol. Sociobiol.* **47**, 400–412.
- Simmons, J. A. (1973). "The resolution of target range by echolocating bats," *J. Acoust. Soc. Am.* **54**, 157–173.
- Simmons, J. A., and Stein, R. A. (1980). "Acoustic imaging in bat sonar: Echolocation signals and the evolution of echolocation," *J. Comp. Physiol.* **135**, 61–84.
- Simmons, J. A., and Chen, L. (1989). "The acoustic basis for target discrimination by FM echolocating bats," *J. Acoust. Soc. Am.* **86**, 1333–1350.
- Strother, G. K. (1961). "Note on the possible use of ultrasonic pulse compression by bats," *J. Acoust. Soc. Am.* **33**, 696–697.
- Suga, N. (1990). "Cortical computational maps for auditory imaging," *Neural Networks* **3**, 3–21.
- Tanaka, H., and Wong, D. (1993). "The influence of temporal pattern of stimulation on delay tuning of neurons in the auditory cortex of the FM bat, *Myotis lucifugus*," *Hear. Res.* **66**, 58–66.
- Trullier, O., Wiener, S. I., Berthoz, A., and Meyer, J. A. (1997). "Biologically based artificial navigation systems: Review and prospects," *Prog. Neurobiol.* **51**, 483–544.
- Valentine, D. E., and Moss, C. F. (1998). "Sensorimotor integration in bat sonar," in *Bat Biology and Conservation*, edited by T. Kunz and P. A. Racey (Smithsonian Institution Press, Washington, D.C.), pp. 220–230.
- Vaughan, N., Jones, G., and Harris, S. (1997). "Identification of British bat species by multivariate analysis of echolocation call parameters," *Bioacoustics* **7**, 189–207.
- Wadsworth, J., and Moss, C. F. (2000). "Vocal control of acoustic information for sonar discriminations by the echolocating bat, *Eptesicus fuscus*," *J. Acoust. Soc. Am.* **107**, 2265–2271.
- Wenstrup, J. J., and Suthers, R. A. (1984). "Echolocation of moving targets by the fish-catching bat, *Noctilio leporinus*," *J. Comp. Physiol., A* **155**, 75–89.
- Zbinden, K. (1988). "Harmonic structure of bat echolocation signals," in *Animal Sonar: Processes and Performance*, edited by P. E. Nachtigall and P. W. B. Moore (Plenum, New York), pp. 581–587.

Measuring hearing in the harbor seal (*Phoca vitulina*): Comparison of behavioral and auditory brainstem response techniques

Lawrence F. Wolski,^{a)} Rindy C. Anderson,^{b)} Ann E. Bowles, and Pamela K. Yochem
Hubbs-Sea World Research Institute, 2595 Ingraham Drive, San Diego, California 92109

(Received 8 January 2001; revised 30 September 2002; accepted 10 October 2002)

Auditory brainstem response (ABR) and standard behavioral methods were compared by measuring in-air audiograms for an adult female harbor seal (*Phoca vitulina*). Behavioral audiograms were obtained using two techniques: the method of constant stimuli and the staircase method. Sensitivity was tested from 0.250 to 30 kHz. The seal showed good sensitivity from 6 to 12 kHz [best sensitivity 8.1 dB (*re* 20 $\mu\text{Pa}^2 \cdot \text{s}$) RMS at 8 kHz]. The staircase method yielded thresholds that were lower by 10 dB on average than the method of constant stimuli. ABRs were recorded at 2, 4, 8, 16, and 22 kHz and showed a similar best range (8–16 kHz). ABR thresholds averaged 5.7 dB higher than behavioral thresholds at 2, 4, and 8 kHz. ABRs were at least 7 dB lower at 16 kHz, and approximately 3 dB higher at 22 kHz. The better sensitivity of ABRs at higher frequencies could have reflected differences in the seal's behavior during ABR testing and/or bandwidth characteristics of test stimuli. These results agree with comparisons of ABR and behavioral methods performed in other recent studies and indicate that ABR methods represent a good alternative for estimating hearing range and sensitivity in pinnipeds, particularly when time is a critical factor and animals are untrained. © 2003 Acoustical Society of America. [DOI: 10.1121/1.1527961]

PACS numbers: 43.80.Lb, 43.80.Nd [WA]

I. INTRODUCTION

Audiometric testing of pinnipeds usually has been conducted using standard psychoacoustic methods such as the method of constant stimuli or the staircase method (Gelfand, 1998). These methods have been used to determine hearing sensitivities in the California sea lion (Schusterman *et al.*, 1972; Schusterman, 1974), harbor seal (Mohl, 1968; Turnbull and Terhune, 1990; Terhune, 1991; Kastak and Schusterman, 1998), elephant seal (Kastak and Schusterman, 1998), harp seal (Terhune and Ronald, 1971, 1972), northern fur seal (Moore and Schusterman, 1987; Babushina *et al.*, 1991), and ringed seal (Terhune and Ronald, 1975). To date, however, only a few individuals of each species have been tested. The paucity of audiograms for most pinniped species makes it difficult to establish normative hearing capabilities and intra- and interspecies variation. Such information is needed to interpret measures of hearing loss and to estimate risk factors for populations of animals. To accomplish this, hearing measurement techniques that are conducive to testing multiple untrained animals must be refined.

The auditory brainstem response (ABR) method may be used as an alternative for determining hearing sensitivity across a range of frequencies. The ABR directly measures whole-brain evoked potentials produced by neurophysiological activity as it travels from the auditory nerve to the brain. The ABR has been used to examine hearing sensitivities in a variety of species, including harbor seals and California sea

lions (Bullock *et al.*, 1971), bottlenose dolphins (Supin *et al.*, 1993; Ridgway *et al.*, 1981), and killer whales (Symanski *et al.*, 1999).

While both behavioral and ABR methods are useful for determining hearing ranges and sensitivities, each has limitations. Behavioral methods are preferred because they produce the most sensitive threshold measurements (Fay, 1988). Unfortunately, the animal training required prohibits testing of free-ranging animals or large numbers of individuals. For example, only four harbor seals have been tested since work began on this species in 1968. The ABR presents an attractive alternative method to behavioral testing because it requires less time to complete and no animal training. However, it usually yields higher thresholds (Katz, 1994) and is less reliable at the extremes of an animal's hearing range, particularly at low frequencies (Erhet, 1983). ABRs are generally thought to be 10–15 dB less sensitive than behavioral methods (Gorga *et al.*, 1988), but careful work with humans has shown that an experienced investigator can obtain agreement within 5–10 dB (Sininger, 1993).

A comparison of behavioral and ABR measurements is most useful when the two methods are performed on the same individual, thus controlling for individual differences in hearing sensitivity. One recent study measured audiograms of two individual killer whales (Symanski *et al.*, 1999) using both methods and found good agreement (± 5 dB), suggesting that the ABR can provide a good suprathreshold estimate of hearing range and sensitivity in toothed whales (Ridgway *et al.*, 1981; Popov and Supin, 1990; Dolphin, 1995; Symanski *et al.*, 1995).

The present study arose from a project investigating the effects of low-frequency impulse noise on hearing sensitivity in pinnipeds (Bowles *et al.*, 1998). The objective was to as-

^{a)}Current address: Department of Biological Sciences, Florida International University, University Park, Miami, FL 33199. Electronic mail: larrywolski@yahoo.com

^{b)}Current address: Department of Biological Sciences, University of Miami, Miami, FL 33146.

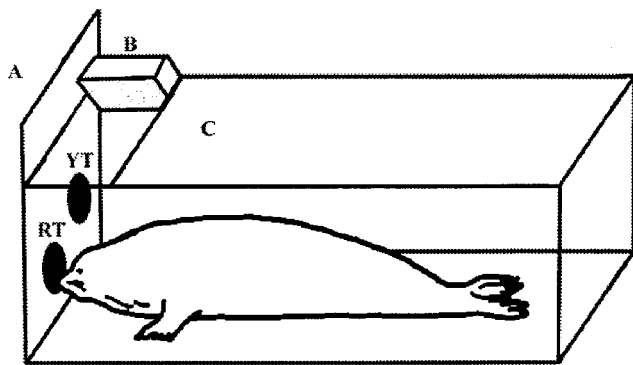


FIG. 1. Sound isolation box illustrating targeting stations and locations of speakers. A—Location of trainer during trials, B—speaker, C—location of speaker mounted to the roof of the box, RT—ready target, and YT—yes target.

sess the potential for temporary threshold shifts (TTS) as a result of exposure to simulated sonic booms in rehabilitated pinnipeds of three species [California sea lions (*Zalophus californianus*), harbor seals (*Phoca vitulina*), and elephant seals (*Mirounga angustirostris*)]. Because behavioral methods are considered the “gold standard” for audiometric testing (Fay, 1988), it was necessary first to establish that ABR and behavioral methods yielded comparable results.

II. MATERIAL AND METHODS

A. Subject

The subject was an adult female harbor seal (NMFS No. SWCPV9614B). She was a beached, rehabilitated animal residing at the Wild Arctic facility at SeaWorld, San Diego. The seal was 4 years old at the time of testing and was naïve to testing procedures when the study began.

B. Behavioral methods

1. Experimental conditions

Behavioral testing was conducted between August 1998 and September 1999, following six months of behavioral training to the experimental procedures. All testing was completed in an acoustic attenuation box that reduced ambient noise by 10–20 dB from 200 Hz to 30 kHz, increasing in attenuation with increasing frequency. The attenuation box measured $1.78 \times 0.76 \times 0.76$ m³ and was constructed from 1.3-cm-thick plywood and 5.25-cm-thick Sonex acoustic foam (Fig. 1). Two Polk M4 speakers were used in parallel to generate sound stimuli. One speaker was mounted above and to the side of the seal’s head during testing. The speaker was approximately 1 m away and at a 45-degree angle to the animal’s ear. A second speaker was mounted on the roof of the box 1.2 m behind the seal’s head to reduce reflections, thereby increasing the area around the head with an acceptable variance of signal strength ($< \pm 2$ dB).

Sound levels at each test frequency were calibrated before and after each trial block using ACO 7012 and ACO 7013 microphones and a Spectral Dynamics 780 Signal Analyzer. The microphones themselves were calibrated daily with a Bruel & Kjaer 4228 pistonphone as well as a Bruel & Kjaer 4230 acoustic calibrator. The calibration before each

test block was done with a “dummy” seal head in place at the appropriate location, and a microphone at the approximate location of the seal’s meatus.

The seal was tested using a go/no-go procedure. Two targeting stations were placed at one end of the testing box (Fig. 1). The seal was trained to enter the box on command and station on the “ready” target (RT). Each trial began with the trainer giving an auditory command (“target!”) that cued the seal to position herself at the RT. The seal nearly always remained motionless with eyes closed while at the RT. Closure of the eyes was a convenient idiosyncratic behavior for this animal—it reduced the chance that she could detect visual cues from the trainer. Latencies to tone onset after the seal had positioned herself on the RT were varied from 3 to 8 s. When the subject heard a tone she touched the “yes” target (YT), then returned to the RT. The seal had to move to the YT within 2 s after the tone was played in order to receive a positive response score (hit). A false alarm was scored if the seal moved from the RT to the YT at any other time during a trial session. If the seal touched the YT more than 2 s after the tone, or not at all, the response was scored as a negative response (miss) and the trainer gave an auditory cue to signal the end of the individual trial. A false response was scored if the seal touched the YT during a catch trial—a trial performed with no stimulus to determine the rate of spontaneous reactions.

Two to five testing blocks were conducted per day. Each testing block consisted of 26 trials, with tones presented 70% of the time, and catch trials 30%. Following each testing block, the subject was allowed access to a holding pool. The seal appeared strongly motivated to perform the experiments, spontaneously entering the test box whenever the opportunity was presented. If either the false response rate, false alarm rate, or any combination of the two rose above 10% in any given testing block, that testing block was terminated and the animal was given a rest period before testing resumed.

2. Method of constant stimuli (MCS)

Thirty percent of all behavioral trials (1111 of 3699 trials) were conducted using the method of constant stimuli. Frequencies tested were 0.25, 0.50, 1.0, 2.0, 4.0, 6.0, 8.0, 10.0, 12.0, and 14.0 kHz. Tones (500-ms duration, 0.5-ms rise-time, Blackman-filtered) were delivered using a laptop computer and the Wave SE (Turtle Beach) software program. Stimulus amplitudes were calibrated before each testing session. A testing block consisted of one stimulus frequency presented 18 times at various amplitudes interspersed with blanks (30% catch trial rate). The presentation order of stimuli was randomized by performing three iterations of the MATLAB (The MathWorks, Inc.) “randomize” function. The minimum difference between any two stimulus amplitudes was set at 5 dB to control for variability in signal strength. Each stimulus frequency was tested in at least four testing blocks for a total of approximately 80 trials per frequency. The seal was reinforced verbally and with a food reward for responding correctly to both tones (moving to the YT) and catch trials (remaining on the RT). False responses were not reinforced.

3. Staircase method (SM)

Seventy percent of all behavioral trials (2588 of 3699 trials) were completed using an adaptive up-down procedure (Levitt, 1970) carried through at least five reversals, referred to herein as the staircase method. Tone amplitudes were decreased in 5-dB increments until the seal's response was scored as a miss. Following a miss, the next tone was increased by 10 dB. If the seal scored a hit on this tone, the intensity was lowered in 5-dB increments until another miss was scored. Each series of descending intensities was termed a "descent." Five descents were performed in each trial block, resulting in five threshold measurements per block. This approach was used to minimize the number of trials needed to measure the seal's thresholds and to ensure that the relatively inexperienced seal was exposed to as few inaudible stimuli as possible.

Frequencies tested were 0.25, 0.50, 1.0, 1.5, 2.0, 3.0, 4.0, 6.0, 8.0, 10.0, 12.0, 14.0, 16.0, 18.0, 20.0, 22.0, 25.0, and 30.0 kHz. Tones were delivered using a Pragmatic 2411A Arbitrary Waveform Generator (ARB) and a Yamaha P1150C amplifier. Each testing block consisted of 18 tone presentations at a fixed frequency and eight randomly placed catch trials (30% catch trial rate). The seal was reinforced only after correctly responding to tone trials. This change in reinforcement schedule from the MCS method was desirable because it reduced the number of trial blocks that had to be eliminated due to a high false response rate (see Sec. IV).

C. Determination of behavioral thresholds

For the MCS trials, the percentage of positive responses was calculated for each decibel level presented during that day's trial session. The lowest level at which the animal responded positively 70% of the time was determined to be the threshold. This percentage approximated the location on the psychometric function that would be produced by the staircase method (Gelfand, 1998; Nachtigall *et al.*, 2000). Trial blocks in which the false response rate, false alarm rate, or both rose above 10% were excluded from the determination of thresholds.

During SM trials, thresholds were determined by noting the lowest intensity in each descent that scored a hit. The midpoint between this intensity and the intensity at which the animal scored a miss during that descent was considered the threshold. This method yielded a threshold criterion of approximately 71% (Nachtigall *et al.*, 2000). Five thresholds per trial block were generated, and the mean of these measurements was taken as the threshold for the block.

For both methods, the sensitivity (d') of the testing paradigms was calculated using methods given in Elliott (1964), Swets (1964), and Gelfand (1998). Sensitivity was used as a measure of the separation between the seal's criterion level for false responses to noise alone and correct responses to the noise-signal combination. It was calculated as the difference in mean response level to the noise-signal

combination versus noise over the standard deviation of all levels.

D. ABR experimental conditions

Evoked potential measurements were completed at the Wild Arctic facility on 30 August 1999. During testing the seal was placed on a restraint board fitted with 2-in nylon straps and a neck board in order to minimize movements and the range of head motion, and was sedated with diazepam (0.15 mg/kg) to reduce muscle activity. This dosage is not believed to affect ABR morphology or amplitude (Doring and Daub, 1980). Several other physiological parameters were measured in addition to ABRs. Electrocardiogram (ECG) electrodes were placed on opposite sides of the spine, just posterior to the flippers, electrooculogram (EOG) and electromyogram (EMG) electrodes were placed into the muscle just above the eye, and a respiration band was fitted around the rib cage.

E. ABR measurement

ABRs were measured using a Bio-Logic Traveler SE computer running the Evoked Potential (EP) program. This is a turnkey measurement system that can generate stimulus waveforms and simultaneously acquire evoked responses. Three platinum-iridium electrodes were inserted subdermally on the seal's head. The reference electrode was placed between the right auditory meatus and mastoid, the active electrode was placed at the vertex of the head along the plane of the reference electrode, and a ground was placed in the nape of the neck. Impedances of electrodes were kept under 10 k Ω and the differences between any two electrodes were kept at 3 k Ω or less.

F. ABR stimuli and presentation

Wideband stimuli (clicks) as well as tone bursts (2, 4, 8, 16, and 22 kHz) were presented. Stimuli were generated using the ARB. The Bio-Logic system collected all ABR responses. Each stimulus was five cycles in length, with two cycles each for the rise and decay, and one cycle at the plateau (Hall, 1992). The rise and decay were Blackman-filtered. Clicks and tone pips were delivered at a rate of 29.3/s. This rate did not affect ABR waveform morphology or amplitude, and allowed rapid testing at each stimulus amplitude. All waveforms in this experiment were presented through a Polk M-4 Studio Tweeter. Levels were calibrated with two ACO 7013 microphones, one of which was placed at the approximate location of the seal's meatus and oriented towards the speaker as the meatus would be during trials ("ear microphone"). The other microphone was placed approximately 30 cm from the tweeter and 70 cm from the animal's head, and was used to verify stimulus levels during trials ("reference microphone"). Sound levels presented during the experiment were calibrated for the ear microphone position and the corresponding reference microphone sound level was noted. At the conclusion of the experiment, spectra were recorded for all waveforms presented, both at high amplitudes and at near-threshold levels.

TABLE I. Mean hearing thresholds using method of constant stimuli.

Frequency (kHz)	Threshold (dB <i>re</i> 20 $\mu\text{Pa}^2\cdot\text{s}$) RMS	Standard deviation (dB <i>re</i> 20 $\mu\text{Pa}^2\cdot\text{s}$) RMS	Threshold (dB SPL <i>re</i> 20 μPa)	Total no. of trials
0.25	61.0	4.2	64.0	97
0.50	51.8	4.5	54.8	67
1.0	45.8	4.8	48.8	69
2.0	42.0	7.4	45.0	107
4.0	31.5	5.0	34.5	207
6.0	23.1	4.9	26.1	150
8.0	22.9	7.4	25.9	126
10.0	20.8	6.3	23.8	162
12.0	14.7	4.0	17.7	51
14.0	20.2	5.4	23.2	75

G. Determination of ABR thresholds

Latency and amplitude of the most prominent ABR waveform peaks were used to quantify responses. Response waveforms were considered valid only if their electrical variability was within a pre-set range ($1.2\ \mu\text{V}$). Signals with excessive myogenic noise or otherwise outside of the pre-set range were discarded. Approximately 1000 valid response waveforms were collected and averaged at each stimulus level. For each frequency, stimulus level was dropped in 10-dB increments until the most prominent peak was reduced in amplitude. At this point the stimulus level was decreased in 5-dB increments until the peak could no longer be detected. Two to five replicates were collected at each stimulus level for each frequency. Thresholds were determined *post-hoc* by noting the lowest stimulus level where the most prominent peak was detectable, repeatable in replicates, and above the background noise of zero-amplitude ABR responses ($\pm 0.3\ \mu\text{V}$).

H. Comparison of stimulus levels

In order to directly compare audiograms using auditory stimuli of different durations, a normalizing procedure was followed to equate stimulus duration. Time waveforms for each stimulus were recorded and the RMS (root-mean squared) sound pressure (RMS SPL in Pascals) for each stimulus intensity was calculated. Sound pressure was converted to decibels (*re* 20 μPa). The duration of the stimulus was then used to calculate energy level in dB *re* 20 $\mu\text{Pa}^2\cdot\text{s}$. In the following sections, the unit dB will always be referenced to 20 $\mu\text{Pa}^2\cdot\text{s}$.

III. RESULTS

A. Behavioral data

1. Method of constant stimuli (MCS)

Hearing threshold estimates for tones between 0.25 and 14 kHz were generated using the method of constant stimuli (Table I). The seal displayed best sensitivity at 12 kHz (14.7 dB), with the best range (± 10 dB) between 6 and 14 kHz. Thirteen of 79 testing blocks (16%) had false alarm rates above 10% and were therefore not included in the analysis. False response rates were $< 9\%$ during catch trials.

2. Staircase method (SM)

The best sensitivity measured using the staircase method was 8.1 dB at 8 kHz, and best range was 6–12 kHz (Table II). The seal displayed a notch in sensitivity centered at 2 kHz (231 trials, 52 reversals); thresholds at 1 and 3 kHz were approximately 12 dB lower. Interestingly, a similar increase in threshold near the same frequency (1.6 kHz) was observed in an earlier study with a harbor seal (Kastak and Schusterman, 1998).

The seal performed more consistently during SM trials. False response rates were $< 6\%$ during catch trials. Fewer

TABLE II. Mean hearing thresholds using descending staircase method.

Frequency (kHz)	Threshold (dB <i>re</i> 20 $\mu\text{Pa}^2\cdot\text{s}$) RMS	Standard deviation (dB <i>re</i> 20 $\mu\text{Pa}^2\cdot\text{s}$) RMS	Threshold (dB SPL <i>re</i> 20 μPa)	No. of reversals	Total no. of trials
0.25	44.5	3.3	47.5	23	137
0.50	34.5	2.6	37.5	28	130
1.0	27.8	2.7	30.8	24	132
1.50	35.3	1.0	38.3	32	133
2.0	39.6	4.9	42.6	52	231
3.0	26.1	2.2	29.1	25	133
4.0	26.8	2.9	29.8	24	139
6.0	10.9	2.3	13.9	28	142
8.0	8.1	2.4	11.1	32	162
10.0	12.8	3.0	15.8	27	139
12.0	10.1	1.2	13.1	25	137
14.0	23.1	2.4	26.1	33	157
16.0	24.3	2.4	27.3	30	134
18.0	27.7	3.6	30.6	28	137
20.0	25.0	3.6	28.0	29	141
22.0	25.6	3.7	28.6	28	135
25.0	29.3	2.0	32.3	28	137
30.0	39.9	2.9	42.9	27	132

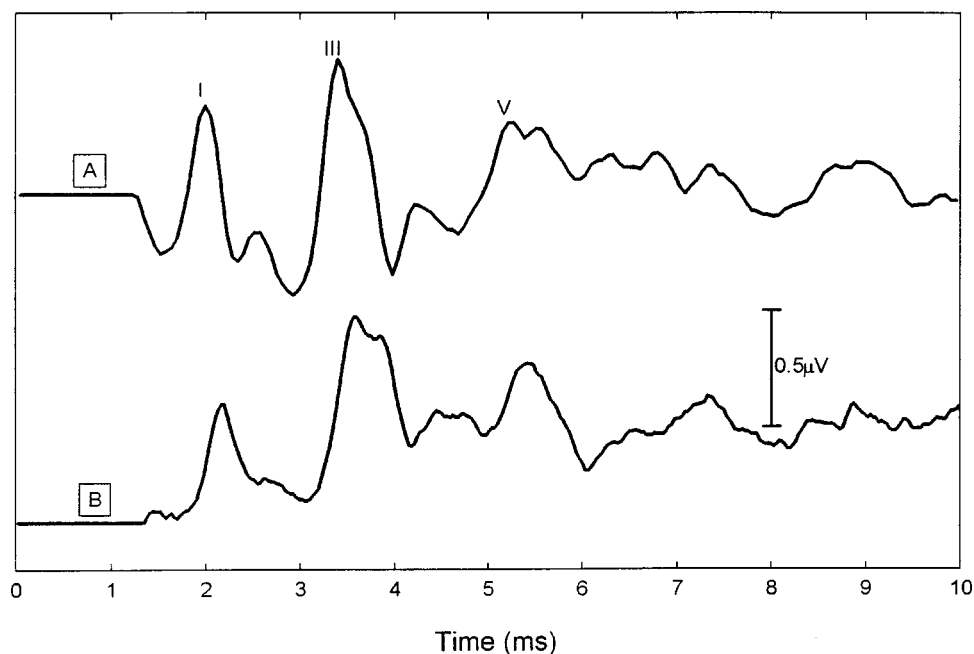


FIG. 2. ABR waveforms generated with (a) clicks and (b) tone-bursts.

testing blocks were discarded due to high false alarm rates as well (only 4 of 100). Standard deviations for the SM method were consistently smaller compared to the MCS method (± 2.7 dB vs ± 5.4 dB).

B. ABR data

ABRs stimulated by both clicks and tone bursts had similar waveforms, with three large peaks (PI, PIII, PV) and two smaller peaks (PII, PIV; Fig. 2). At high intensities, the ABR PI latency was 2 ms and PV latency was 5 ms. The largest waveform peak, PIII, had a maximum amplitude of $0.98 \mu\text{V}$, and occurred approximately 4 ms after the tone onset at high intensities. Latencies of the ABR peaks increased with decreasing amplitude, as expected (Hall, 1992).

Thresholds could not be obtained at 8 and 16 kHz due to high ambient noise levels at the time these frequencies were tested (14 dB at 8 kHz, 12 dB at 16 kHz). Thus, points on the ABR audiogram at 8 and 16 kHz are best viewed as the lowest response intensities that could be measured before test stimuli were masked by ambient noise.

C. Comparison of ABR and SM audiograms

The more thoroughly tested behavioral hearing curve (SM) was compared to the ABR curve (Fig. 3). At 2 and 4 kHz, ABR thresholds were 5.3 and 5.1 dB less sensitive than behavioral thresholds, respectively. At 22 kHz, the ABR threshold was less sensitive than the behavioral threshold, although the difference was small, 3.0 dB. ABR thresholds

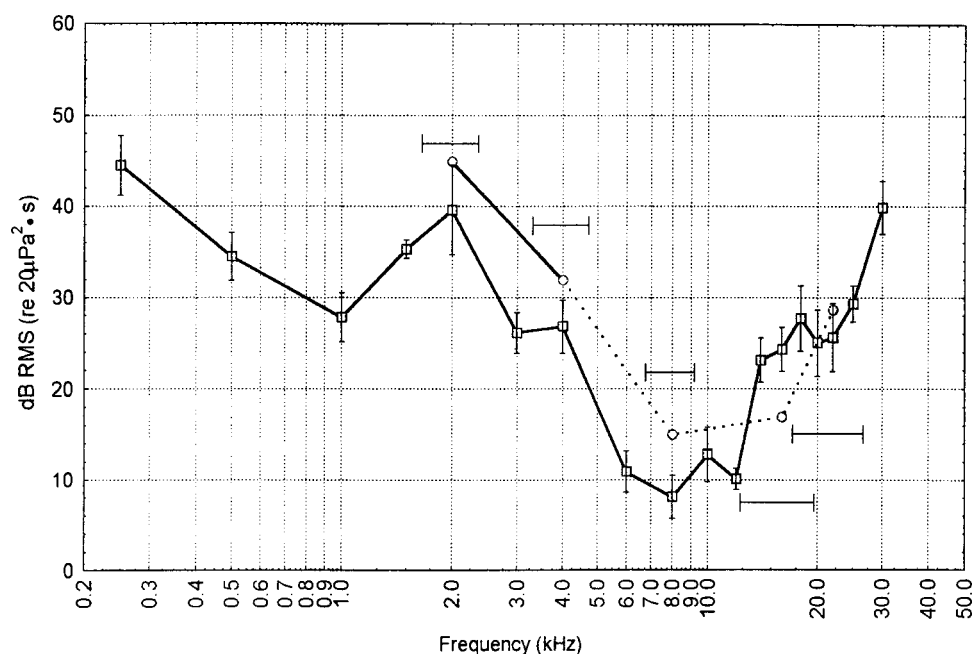


FIG. 3. Comparison of audiograms generated by the DS method (squares) and ABR method (circles). Horizontal range bars indicate the frequency bandwidth of ABR stimuli at threshold. The points on the ABR curve at 8 and 16 kHz are not threshold values; they are the lowest intensities in which a positive ABR was generated before the test stimuli dropped into the noise floor.

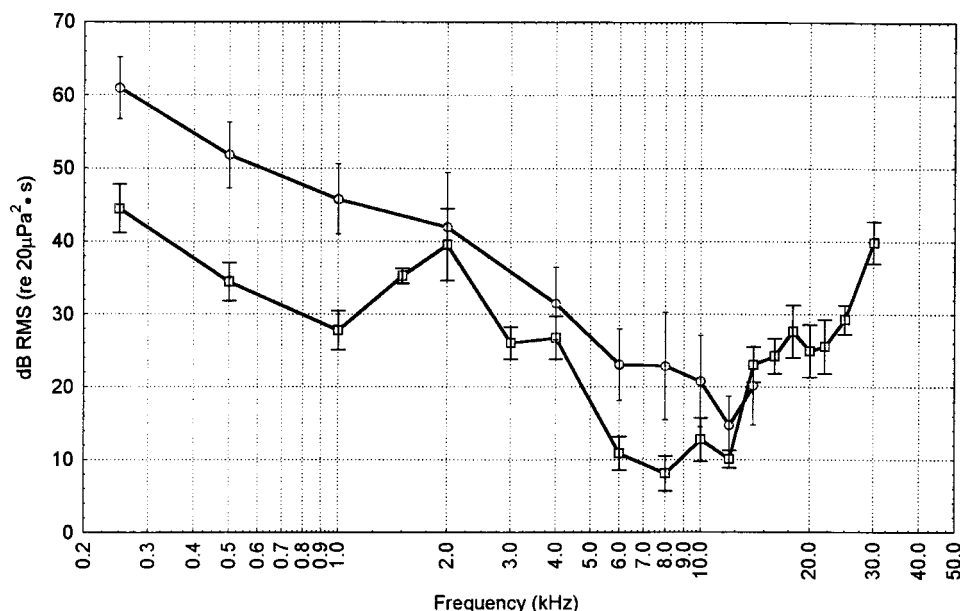


FIG. 4. Comparison of audiograms generated by the DS method (squares) and MCS method (circles).

were not obtained at 8 and 16 kHz. PIII was detectable at the lowest amplitudes tested, 14.9 and 16.9 dB, respectively; at 16 kHz, the lowest amplitude at which PIII was detectable was at least 7.4 dB lower than the behavioral threshold (24.3 dB).

IV. DISCUSSION

A. Comparison of behavioral audiograms

Both behavioral methods employed in this study yielded audiograms of similar form, with best sensitivities ranging between 6 and 12 kHz (Fig. 4). Across the range of frequencies tested, the SM method yielded lower threshold estimates and smaller standard errors. In addition, the SM method yielded a higher measure of sensitivity (d' : 2.318 versus 2.201 for the MCS). Minimum differences between the two methods ranged from 1 to 4 dB and the largest differences ranged from 15 to 20 dB.

Several factors may explain the higher sensitivity of the SM method. First, audiometric testing that employs an adaptive up-down procedure yields lower threshold estimates than simple up-down methods or random stimulus presentation (Levitt, 1970). It has been suggested that patterned stimulus presentation increases the attention and concentration of the test subject, resulting in the detection of stimuli at lower amplitudes. The subject in these experiments appeared to be most attentive and motivated when the number of consecutive negative responses (no-go) was minimized, introducing an increase in probability of correct responses relative to the MCS trials. Note that this bias was not a result of an increase in false positive responses, which were kept low in both sets of experiments by terminating trial blocks with too many incorrect catch trial responses.

Second, it may be that subjects can process a predictable stimulus more easily than an unpredictable one, particularly if given feedback during trials (Zwislocki *et al.*, 1958). To reduce false positive responses, we reduced predictability by varying latency to tone presentation, varying initial stimulus levels, and introducing catch trials unpredictably. However,

the seal could still be sure that (1) the first tone actually presented in a trial block would be audible, and (2) that a reversal would occur within a few trials. There may have been a greater motivation to perform in SM versus MCS trials if the seal perceived a task with a greater proportion of detectable tones as “easier” or more rewarding.

A third factor could have been the change in reinforcement schedule between paradigms. During the MCS experiment, the seal was reinforced both for responding correctly to the presentation of a tone (moving to the YT) and for remaining on the RT during catch trials. The average false response rate using this reinforcement schedule was 8.7% (97 of 1111 trials). During SM testing, the seal was reinforced only for responding correctly to a tone (moving to the YT). This pay-off schedule change was expected to result in a lower false response rate, as the animal adopted a stricter criterion for making only correct responses. After this change in protocol, the average false response rate dropped (5.6%, 145 in 2588 trials) and there was a decrease in the number of trial blocks with a false response rate above 10% (16% during MCS trials versus 4% during SM trials). During SM trials the seal often remained motionless on the RT for long periods (20–40 s), only moving off the target when a tone was given or when the trainer signaled the end of the trial block, as expected given the change in reinforcement schedule and subsequent change in response bias. In contrast, during MCS trials the seal moved frequently during intertrial intervals and did not remain on the RT for extended periods.

The behavioral audiograms obtained during this study were consistent with those of Mohl (1968), Terhune and Turnbull (1995), and Kastak and Schusterman (1998). The thresholds between 6 and 12 kHz, to our knowledge, are the lowest reported to date for a harbor seal. The audiograms show a high frequency roll-off similar to that reported by Mohl (16–22 kHz), but at higher frequencies (22–30 kHz). Both observations suggest that the subject of these experiments had better hearing than other harbor seals that have been tested.

An alternate explanation for the low threshold measure-

ments between 6 and 12 kHz is that the seal might have taken advantage of standing wave patterns in the test chamber by positioning herself in an area where signal strength was maximized by reflections. This seems doubtful, as the seal's head was positioned in an area that was precisely mapped prior to testing. The seal did not exhibit any behaviors consistent with a search for a "sweet spot." The multiple-speaker setup reduced reflections of test signals, thereby reducing the strength of any standing waves. Test stimuli in the immediate area around the head had a signal strength variance of $<\pm 2$ dB, meaning that any standing waves increased signal amplitude by no more than 2 dB, within the error of the threshold measurements.

B. Stimulus and procedural issues

The behavioral and ABR audiograms had similar shapes. However, the SM method produced lower thresholds than ABRs at mid-range frequencies (3–8 kHz) while the ABR method produced a lower threshold than the SM method at 16 kHz. The SM method was more sensitive at 22 kHz, although by a smaller margin than at lower frequencies. These differences in measured sensitivity between the methods may be the result of stimulus characteristics, as well as the testing environment and activity of the subject during testing.

1. Stimulus characteristics

Stimulus characteristics affect the results of physiological and behavioral testing. In mammals, behavioral thresholds are often higher for tones with durations shorter than the integration time of the ear (Watson and Gengel, 1969), consistent with the extensive knowledge of how integration time affects sound perception (Yost, 1994). This is why behavioral studies are typically performed with stimuli lasting between 250 and 500 ms. These longer stimuli also have relatively narrow bandwidths, less than 50 Hz for 500-ms tones.

In contrast, ABR stimuli must be brief to elicit good response waveforms, usually less than 5 ms. Hall (1992) recommends using five-cycle stimuli in a 2–1–2 pattern (rise–plateau–fall) for ABR testing. The resulting time waveforms have wider bandwidth than tone pips used in behavioral studies. A five-cycle ABR waveform centered at 8 kHz is 0.6 ms in duration and has a bandwidth of 2 kHz at or near threshold level. Thus, in the current study, behavioral responses were stimulated using narrow-band stimuli and ABR responses were stimulated using wideband stimuli simply as a result of differences between the two techniques. The frequency bandwidths of ABR stimuli near observed thresholds are shown in Table III. This difference may account for some of the observed differences in threshold estimates between the two methods. Generally, broader-band ABR stimuli correlate with more robust responses because larger portions of the cochlea are excited by wideband stimuli (Hall, 1992).

As an example, in our study the ABR threshold at 16 kHz was estimated to be at least 16.9 dB and the SM behavioral threshold was 24.3 dB. The bandwidth of the ABR stimulus at threshold was approximately 7.4 kHz centered at 16 kHz, while the bandwidth of the behavioral stimulus at 16 kHz was less than 25 Hz (Fig. 5). Thus, the 16 kHz ABR test

TABLE III. Frequency bandwidth of ABR stimuli at threshold.

Center frequency (kHz)	ABR threshold (dB <i>re</i> 20 $\mu\text{Pa}^2\cdot\text{s}$) RMS	Frequency bandwidth at threshold (kHz)
2	44.9	0.7
4	31.9	1.4
8	~ 15.0	2.4
16	~ 16.9	7.4
22	28.6	9.4

signal would have stimulated the cochlea with frequencies as low as 13 kHz. The contribution of neurons tuned to this frequency could easily explain the greater sensitivity of the ABR response observed at 16 kHz.

2. Testing environment and subject activity

Myogenic noise resulting from muscle activity interferes with ABR test sensitivity, which is recognized as a major contributor to the lower sensitivity of ABR measurements (Hall, 1992). Human infants commonly fall asleep during ABR testing, resulting in better signal-to-noise ratio and thus clearer and more sensitive ABR measurements (Sininger, 1993). During this study, ABR stimuli were presented in order of ascending frequency. The seal was alert during the first half of the ABR testing period, but approximately halfway through testing (near the completion of data collection at 8 kHz) she became deeply relaxed and remained relatively motionless. The relaxed state was evidenced by lower heart rate and muscle activity observable from EEG and EMG traces, and a reduction in stimulus artifacts reported by the BioLogics system. The decrease in myogenic noise while testing at 16 and 22 kHz appears correlated with estimated thresholds lower than those yielded by SM measurements at 16 and 22 kHz. Thus, the seal's reduced activity during high-frequency testing may have contributed to lower threshold estimates at these frequencies. This relationship has been observed during audiometric testing of elephant seals and sea lions (Bowles, unpublished data); ABRs had better morphology and amplitude when test animals were quiescent, making thresholds easier to measure.

C. Summary

In summary, the two audiograms resulting from behavioral and ABR testing of an individual harbor seal agreed well, indicating that ABR measurements, which can be collected in a single day from an untrained animal, can produce results comparable to six months of behavioral testing. The results must be interpreted with caution because the frequency bandwidths of ABR stimuli can affect sensitivity and threshold estimates. In future studies of this kind, ABR stimulus characteristics should be varied systematically to obtain a more refined test signal, one that yields a clear ABR but has the minimum possible bandwidth.

For absolute threshold determination at discrete frequencies, behavioral methods remain the most accurate method. However, with careful selection of ABR stimuli and control of the testing environment, hearing sensitivities can be measured for a much larger number of individuals than is usually

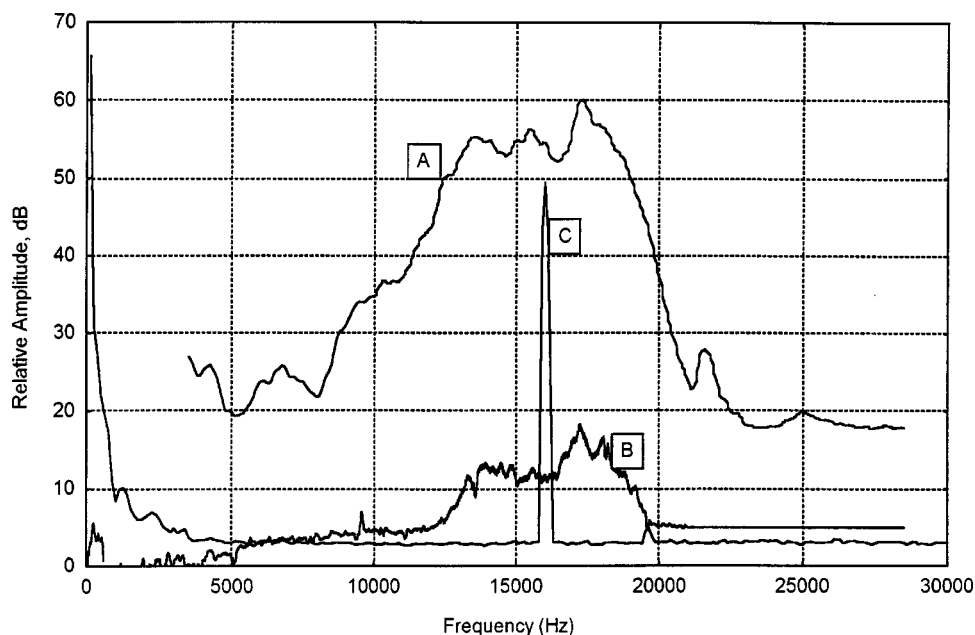


FIG. 5. Comparison of ABR and behavioral stimuli at 16 kHz. (a) 16-kHz ABR stimuli at high amplitudes. (b) ABR stimuli near recorded threshold; note the bandwidth at this point is approximately 6 kHz, ranging from 13 to 16 kHz. (c) 16-kHz behavioral stimuli at high amplitude. Bandwidth did not change appreciably as amplitude was lowered. Horizontal range bars indicate the frequency bandwidth of ABR stimuli at threshold.

possible using behavioral testing methods. Given the difference in sensitivity between our test subject and other subjects in previous experiments, it is likely that significant variation in hearing ability will be found across individuals in pinniped populations, just as in humans and laboratory animals. Once perfected, ABR measurements could be used to obtain much needed data on population-level characteristics of pinniped hearing.

ACKNOWLEDGMENTS

Thanks to the Wild Arctic Animal Care Team of Sea-World San Diego. Erik Berg made important contributions such as designing the sound isolation box and performing acoustic calibrations. Carolyn Schlundt at SPAWAR in San Diego and Yvonne Sininger at the House Ear Institute provided technical insight and helpful discussions. Two anonymous reviewers offered valuable comments on drafts of the manuscript. Special thanks to Kevin Shepard at NASA/Langley for his staunch support and patience throughout this study. Funding was provided by a NASA Research Grant No. NAS1-20101 and a generous grant from the Joan Irvine Smith and Athalie R. Clarke Foundation. The work was permitted by the National Marine Fisheries Service (No. 872-1397).

Babushina, Y. S., Zaslavskii, G. L., and Yurkevich, L. I. (1991). "Air and underwater hearing characteristics of the northern fur seal: Audiograms, frequency and differential thresholds," *Biophysics (Engl. Transl.)* **36**, 909–913.

Bowles, A. E., Wolski, L., and Berg, E. (1998). "Effects of simulated N-waves on the auditory brainstem response of three species of pinnipeds," *J. Acoust. Soc. Am.* **104**, 1861(A).

Bullock, T. H., Ridgway, S. H., and Suga, N. (1971). "Acoustically evoked potentials in midbrain auditory structures in sea lions (Pinnipedia)," *Z. Vergl. Physiologie* **74**, 372–387.

Dolphin, W. (1995). "Steady-state auditory evoked potentials in three cetacean species elicited using amplitude-modulated stimuli," in *Sensory Systems of Aquatic Mammals*, edited by R. A. Kastelein, J. A. Thomas, and P. E. Nachtigall (De Spil, The Netherlands), pp. 25–47.

Doring, W. H., and Daub, D. (1980). "Acoustically evoked responses under sedation with Diazepam," *Arch. Oto-Rhino-Laryngol.* **227**(3-4), 522–525.

Elliot, P. B. (1964). "Tables of d'," in *Signal Detection and Recognition by Human Observers*, edited by J. A. Swets (Wiley, New York), pp. 651–684.

Erhet, G. (1983). "Psychoacoustics," in *The Auditory Psychobiology of the Mouse*, edited by J. F. Williot (Thomas, Springfield, IL), Chap. 2, p. 24, Fig. 2-2.

Fay, R. R. (1988). *Hearing in Vertebrates: A Psychophysics Databook* (Hill-Fay, Winnetka, IL).

Gelfand, S. A. (1998). *Hearing: An Introduction to Psychological and Physiological Acoustics* (Marcel Dekker, New York).

Gorga, M. P., Kaminski, J. R., Beauchaine, K. A., and Jesteadt, W. (1988). "Auditory brainstem responses to tone bursts in normally hearing subjects," *J. Speech Hear. Res.* **31**, 87–97.

Hall, J. W. (1992). *Handbook of Auditory Evoked Responses* (Allyn and Bacon, Boston).

Kastak, D., and Schusterman, R. J. (1998). "Low-frequency amphibious hearing in pinnipeds: Methods, measurements, noise & ecology," *J. Acoust. Soc. Am.* **103**, 2216–2228.

Katz, J. (1994). *Handbook of Clinical Audiology* (William and Williams, Baltimore, MD).

Levitt, H. (1970). "Transformed up-down procedures in psychoacoustics," *J. Acoust. Soc. Am.* **49**, 467–477.

Mohl, B. (1968). "Auditory sensitivity of the common seal in air and water," *J. Aud. Res.* **8**, 27–38.

Moore, P. W., and Schusterman, R. J. (1987). "Audiometric assessment of northern fur seals *Callorhinus ursinus*," *Marine Mammal Sci.* **3**, 31–53.

Nachtigall, P. E., Lemonds, D. W., and Roitblat, H. L. (2000). "Psychoacoustic studies of dolphin and whale hearing," in *Hearing by Whales and Dolphins*, edited by W. Au, A. Popper, and R. Fay (Springer-Verlag, New York), pp. 330–362.

Popov, V. V., and Supin, A. Y. (1990). "Electrophysiological studies of hearing in some cetaceans and a manatee," in *Sensory Abilities of Cetaceans*, edited by J. A. Thomas and R. A. Kastelein (Plenum, New York), pp. 405–415.

Ridgway, S. H., Bullock, T. H., Carder, D. A., Seeley, R. L., Woods, D., and Galambos, R. (1981). "Auditory brainstem response in dolphins," *Proc. Natl. Acad. Sci. U.S.A.* **78**, 1943–1947.

Schusterman, R. J. (1974). "Auditory sensitivity of a California sea lion to airborne sound," *J. Acoust. Soc. Am.* **56**, 1248–1251.

Schusterman, R. J., Balliet, R. F., and Nixon, J. (1972). "Underwater audiogram of the California sea lion by the conditioned vocalization technique," *J. Exp. Anal. Behav.* **17**, 339–350.

Sininger, Y. (1993). "Auditory brainstem response for objective measures of hearing," *Ear Hear.* **14**, 23–30.

Supin, A. Y., Popov, V. V., and Klishin, V. O. (1993). "ABR frequency tuning curves in dolphins," *J. Comp. Physiol., A* **173**, 699–656.

Swets, J. A. (1964). *Signal Detection and Recognition by Human Observers* (Wiley, New York).

- Symanski, M. D., Bain, D. E., and Henry, K. R. (1995). "Auditory evoked potentials of a killer whale (*Orcinus orca*)," in *Sensory Systems of Aquatic Mammals*, edited by R. A. Kastelein, J. A. Thomas, and P. E. Nachtigall (De Spil, The Netherlands), pp. 1–10.
- Symanski, M. D., Bain, D. E., Kiehl, K., Pennington, S., Wong, S., and Henry, K. R. (1999). "Killer whale (*Orcinus orca*) hearing: Auditory brainstem response and behavioral audiograms," *J. Acoust. Soc. Am.* **106**, 1134–1141.
- Terhune, J. M. (1991). "Masked and unmasked pure tone thresholds of a harbor seal listening in air," *Can. J. Zool.* **51**, 319–321.
- Terhune, J. M., and Ronald, K. (1971). "The harp seal, *Pagophilus groenlandicus* (Erxleben, 1777). X. The air audiogram," *Can. J. Zool.* **49**, 285–290.
- Terhune, J. M., and Ronald, K. (1972). "The harp seal, *Pagophilus groenlandicus* (Erxleben, 1777). III. The underwater audiogram," *Can. J. Zool.* **50**, 565–569.
- Terhune, J. M., and Ronald, K. (1975). "Underwater hearing sensitivity of two ring seals (*Pusa hispida*)," *Can. J. Zool.* **53**, 227–231.
- Terhune, J., and Turnbull, S. (1995). "Variation in the psychometric functions and hearing thresholds of a harbor seal," in *Sensory Systems of Aquatic Mammals*, edited by R. A. Kastelein, J. A. Thomas, and P. E. Nachtigall (De Spil, The Netherlands), pp. 81–93.
- Turnbull, S. D., and Terhune, J. M. (1990). "White noise and pure tone masking of pure tone thresholds of a harbor seal listening in air and underwater," *Can. J. Zool.* **68**, 2090–2097.
- Watson, C. S., and Gengel, R. W. (1969). "Signal duration and signal frequency in relation to auditory sensitivity," *J. Acoust. Soc. Am.* **46**, 989–997.
- Yost, W. A. (1994). *Fundamentals of Hearing: An Introduction*, 3rd ed. (Academic, San Diego).
- Zwislocki, J., Maire, F., Feldman, A. F., and Rubin, H. (1958). "On the effect of practice and motivation on the threshold of audibility," *J. Acoust. Soc. Am.* **30**, 254–262.

High intensity anthropogenic sound damages fish ears

Robert D. McCauley^{a)}

Centre for Marine Science and Technology, Curtin University, GPO Box U 1987, Perth 6845, Western Australia

Jane Fewtrell^{b)}

Aquatic Science Research Unit, Curtin University, GPO Box U 1987, Perth 6845, Western Australia

Arthur N. Popper^{c)}

Department of Biology and Neuroscience and Cognitive Science Program, University of Maryland, College Park, Maryland 20742

(Received 13 June 2002; revised 5 October 2002; accepted 10 October 2002)

Marine petroleum exploration involves the repetitive use of high-energy noise sources, air-guns, that produce a short, sharp, low-frequency sound. Despite reports of behavioral responses of fishes and marine mammals to such noise, it is not known whether exposure to air-guns has the potential to damage the ears of aquatic vertebrates. It is shown here that the ears of fish exposed to an operating air-gun sustained extensive damage to their sensory epithelia that was apparent as ablated hair cells. The damage was regionally severe, with no evidence of repair or replacement of damaged sensory cells up to 58 days after air-gun exposure. © 2003 Acoustical Society of America.
[DOI: 10.1121/1.1527962]

PACS numbers: 43.80.Nd, 43.64.Wn [WWA]

I. INTRODUCTION

There is a growing concern that intense human-generated (=anthropogenic) sounds in the marine environment may potentially have a substantial impact on marine organisms (e.g., NRC, 1994, 2000; Richardson *et al.*, 1995). Depending upon the magnitude of the signal, there may be no impact on animals or the impact may involve disruption of behavior or even physical or physiological damage to the animals (e.g., McCauley, 1994; Richardson *et al.*, 1995; NRC, 2000).

Much of the interest in the effects of anthropogenic sounds arises from concern for the well-being of marine mammals (e.g., NRC, 2000). However, the marine ecosystem includes a wide range of organisms that detect and use sound for their survival, and their survival is of equal importance to that of marine mammals.

Research on the impact of anthropogenic sounds on non-mammalian species, and particularly fishes, has been extremely limited. The two most relevant studies showed that very high intensity pure tones (e.g., over 180 dB *re* 1 μ Pa) presented for several hours may cause damage to the sensory hair cells of the ears of several fish species (Enger, 1981; Hastings *et al.*, 1996), while other studies suggested that some sounds will alter the behavior of marine fishes (Engås *et al.*, 1996). Though these investigations hint at potential impacts on fish by anthropogenic sounds, the Engås *et al.* (1996) study is one of the very few that has dealt with anthropogenic sounds that are encountered by wild fishes.

One of the major sources of anthropogenic sounds in the marine environment involves the repetitive use of high-

energy noise sources in the water column for marine seismic petroleum exploration. In such investigations, impulsive signals are directed downward and then reflected upwards again by density discontinuities within sub-sea rock strata. The travel times of reflected signals allow geological profiles to be determined. A typical seismic survey may involve many hundred thousand signals spread over several weeks. The most commonly used noise sources are arrays of air-guns that vent high-pressure gas to produce a short, sharp, low-frequency sound (Parks and Hatton, 1986). Although there are references reporting behavioral responses of fishes and marine mammals to seismic survey noise (Pearson *et al.*, 1992; Richardson *et al.*, 1995; Engås *et al.*, 1996), no investigation has been carried out on the potential for damage to the ears of aquatic vertebrates from air-gun exposure.

Here we show that the ears of fish exposed to an operating air-gun that was moved toward and away from the animals sustained extensive damage to their sensory epithelia that was apparent as ablated hair cells. The damage was regionally severe and there was no evidence of repair or replacement of damaged sensory cells up to 58 days after exposure.

II. METHODS

To investigate possible effects of air-gun noise on the hearing system of fishes, we carried out trials where pink snapper (*Pagrus auratus*) held in cages were exposed to signals from an air-gun towed toward and away from the cages, mimicking the stimulus from a passing seismic vessel. Control fish (group I) were kept in the same cages used for experimental animals but were removed from cages and sacrificed just before air-gun stimulation. Group II fish were sacrificed 18 h after air-gun stimulation, and group III fish were sacrificed 58 days later. Air-gun stimulation involved

^{a)}Electronic mail: r.mccauley@cmst.curtin.edu.au

^{b)}Electronic mail: j.fewtrell@cc.curtin.edu.au

^{c)}Author to whom correspondence should be addressed. Electronic mail: apopper@umd.edu

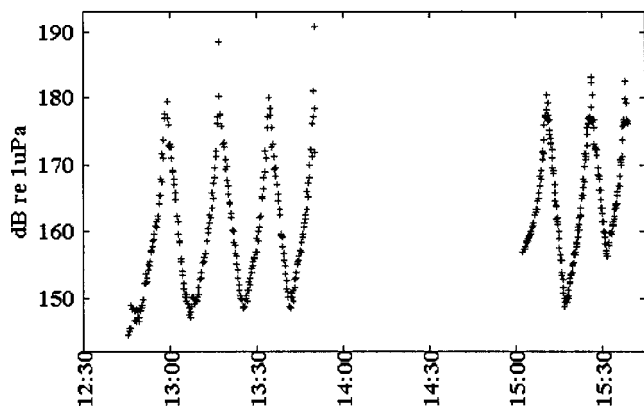


FIG. 1. Received air-gun signal levels with time (lower axis). Units are mean squared pressure over the portion of the signal which encompassed 95% of its energy, as measured from the cage bottom. The signal source was moved toward and then away from the cage as described in the text.

four approaches towards the cage over 1:05 h, a break of 1:12 h, and then three further approaches over 0:36 h, as shown in Fig. 1. Group III fish held after exposure continued to grow and showed no signs of disease.

Trials were carried out in Jervoise Bay, Western Australia. The average depth of the bay is 9 m. Captive fish were held in a 10-m-long by 6-m-wide by 3-m-deep cage or in 1-m³ cages. A 0.33 L (20 cubic inch) Bolt PAR 600B air-gun deployed at 5-m depth and operating at a gas pressure of 10 MPa and a 10-s repetition period (6 pulses per minute) was towed from start up at 400–800 m away to 5–15 m at closest approach to the cage. This air-gun has a source level at 1 m of 222.6 dB re 1 μ Pa peak to peak, or 203.6 dB re 1 μ Pa mean squared pressure. Example power spectra of the air-gun signal received at the cage from 50 and 100 m are shown in Fig. 2. The frequency spectra of the air-gun signal had highest energy over 20–100 Hz (the bubble pulse energy) and significant energy over the 100–1000 Hz range. The air-gun signal at 100-m range was more than 25 dB above the background level in the bay, over 100–1000 Hz. Most fish are known to have their best sensitivity to sound energy in the frequency range 100–1000 Hz (Fay, 1988), although many fish also display high sensitivity at lower frequencies (Sand and Karlsen, 1986).

Hydrophones deployed on the long axis of the cage, facing the closest air-gun passage and at depths of 0.2 and 3 m,

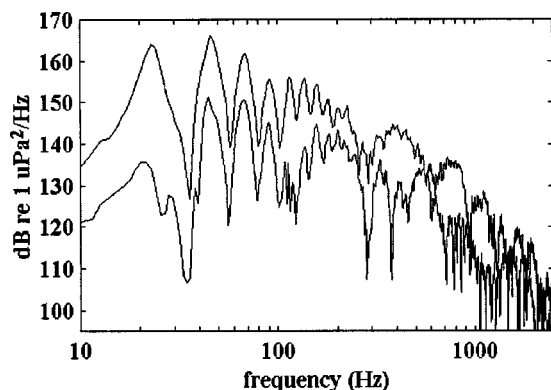


FIG. 2. Power spectra of air-gun signals received at the cage, at 50 m (top curve) and 100 m (bottom curve) range (1.27-Hz frequency resolution).

were used to record air-gun signals. Two underwater video cameras placed in corners of the cage were used to monitor fish behavior. Pink snapper were obtained from an aquaculture farm and acclimated for 24 days at the trial site. Mean fish lengths the day of exposure were 230 ± 24 mm and 58 days later 250 ± 8 mm.

At appropriate times, fish were sacrificed with an overdose of 2-phenoxyethanol. The cranium was quickly opened, and the ears were exposed and fixed in 4% glutaraldehyde buffered with filtered seawater. Ears were dissected out, dehydrated, and progressively graded through 50%, 60%, 70%, 90%, 95%, and 100% acetone, critically point dried, mounted on stubs and sputter coated with gold (2 min).

Tissue was viewed with a Philips XL 30 SEM. To quantify damage, three vertical transects of digital images (each 532×712 pixels) were made along the horizontally aligned epithelium—near the caudal, midsection, and rostral ends [Fig. 3(a)]. Vertically adjacent images ($800 \times$ magnification) were taken down each transect. For each correctly scaled image, overlain with 25- μ m gridlines, the number of missing hair cells in $24 \times 625 \mu\text{m}^2$ squares were counted. Missing hair cells were obvious as a “rounded hole” in the epithelia in an expected hair cell position. “Expected” hair cell locations were based on the local matrix of hair cells. Any $24 \times 625 \mu\text{m}^2$ square which had an artifact of some sort or which did not encompass a full field of hair cells was not included in counts and $625 \mu\text{m}^2$ were subtracted from the total area searched per image. Artifacts included preparation tears, overexposed regions of image or regions covered in “gunk” which obscured hair cells and epithelia. Only sections of epithelia populated with hair cells were included in calculations (i.e., edges were not included). Counts were conservative. Thus, any holes of which we were not certain were not included. Experiments were carried out under Curtin University Animal Experimentation Ethics permits.

III. RESULTS

The sensory hair cells of fish ears are similar to those of other vertebrates (Popper and Fay, 1999). The fish ear acts as an accelerometer, with hair cell deflection driven by differential motion between a dense calcareous otolith and a sensory epithelium (deVries, 1950; Popper and Fay, 1999). Using scanning electron microscopy, we analyzed hair cells on the sensory epithelium of the saccule [Fig. 3(a)], the otolithic end organ primarily involved in hearing in most fish species (Popper and Fay, 1999). The epithelia of group I (control) snapper had an appearance similar to that reported for other species of fishes (Popper and Fay, 1999), with fields of ciliary bundles distributed across the epithelia [Figs. 3(b) and (c)]. A small number of holes, correlating with the expected locations of hair cells, were found in the group I epithelia.

Group II fish (sacrificed 18 h after exposure) were observed to have localized dense patches of holes and “blebbing” or “blistering” on the surface of the epithelia coincident with the location of hair cells [Fig. 4(c)]. However, when the number of holes/10 000 μm^2 along three transects across the epithelium was compared with the group I fish (controls) [Table I, Fig. 3(a)], group II fish did not have

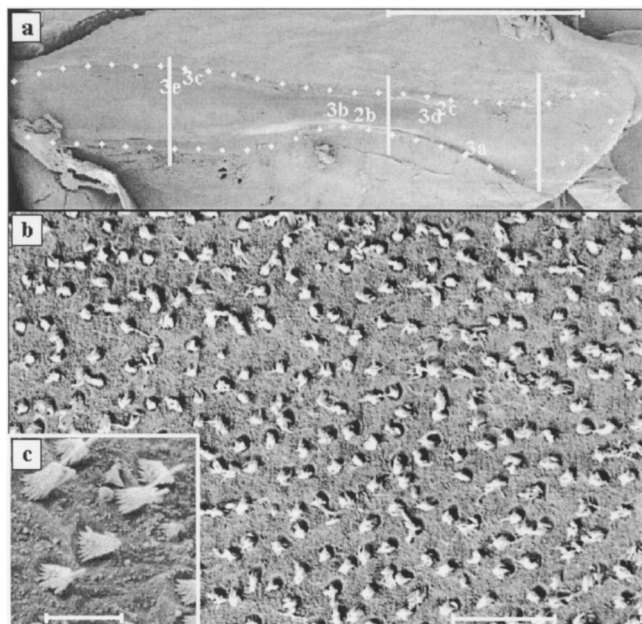


FIG. 3. (a) Horizontally aligned, sensory epithelium from a right pink snapper ear (anterior to the left, dorsal to the top). The area containing sensory hair cells is shown bounded by white dots. The locations of the three transects taken on each epithelium are shown by the white vertical lines. The locations of the various images used in this figure and in Fig. 4 are indicated with the figure number. (b, c) Undamaged hair cells from group I fish. (b) A field of normal ciliary bundles on the sensory hair cells. (c) Higher magnification of several ciliary bundles. Scale bars: (a) 2 mm; (b) 20 μm ; (c) 2 μm .

significantly greater numbers of holes/10 000 μm^2 than group I fish ($p > 0.1$, two tailed t -test).

In contrast, group III specimens [sacrificed 58 days after exposure, Figs. 4(d) and (e)] showed significantly greater numbers of holes/10 000 μm^2 than group I or II fish ($p \leq 0.001$, two tailed t -test), and greater areas of “blebbing.” The nature of the holes suggest that hair cells had been “ripped” from the epithelia (immediate mechanical damage) or, alternatively, had “exploded” after exposure (physiologi-

TABLE I. Number of holes in the epithelia of sample groups.

Group ^a	N (E) ^b	N (I) ^c	Holes ^d	Area (10 000 μm^2) ^e	Holes/10 000 μm^2 ^f
I	6	84	58	119.19	0.53 ± 0.227
II	3	38	39	54.75	0.75 ± 0.455
III	5	56	665	76.69	8.48 ± 2.636

^aExposure regimen.

^bNumber of epithelia examined.

^cNumber of images analyzed per group.

^dTotal number of holes per group.

^eTotal area perused per group.

^fThe mean $\pm 95\%$ confidence limits of the ratio of holes per area, using all images per group (not the same as total holes divided by total area per group).

cal damage associated with cell death, group III fish). “Blebbing” was consistent with expansions of the hair cell ciliary bundle surface, with eventual rupture leading to a hole [Fig. 4(e)]. The finding of significantly more damage in group III fish compared to group I or II is consistent with previous findings that have shown damage to hair cells is not visible until one or more days after the exposure to intense noise (Corwin and Cotanche, 1988; Hastings *et al.*, 1996).

To give an indication of the relative level of damage as indicated by the presence of missing hair cells, we compared the number of holes with hair cell densities. To obtain an estimate of hair cell density was the total number of hair cells counted in 97 625- μm^2 grids across five images from three epithelia, one a control group I fish and two from group II fish. The mean density of hair cells across the three epithelia was 317 ± 8.9 hair cells/10 000 μm^2 ($n = 97 \times 625 \mu\text{m}^2$ squares, $\pm 95\%$ confidence limits). The tight confidence limits about the mean value implied that hair cell densities were consistent across epithelia. Thus, using this value as a general estimate of hair cell density across the epithelia, localized damage reached 15% (hair cells missing) at the caudal end of the saccular epithelium of group III fishes. Although when averaged across the three transects,

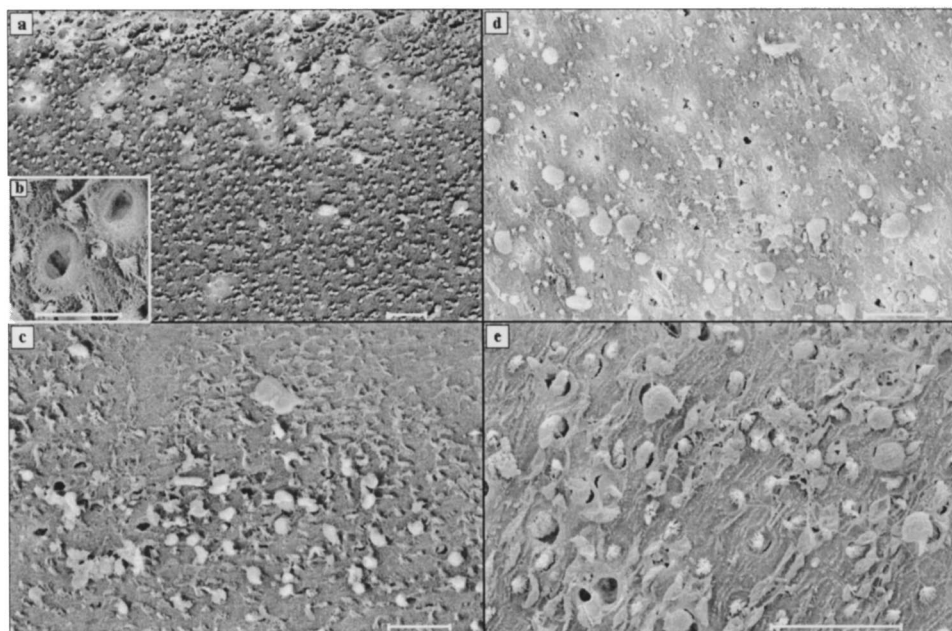


FIG. 4. (a, b, c) Epithelia from group II fish (18 h after exposure to the air-gun). The photographs show numerous holes and “blebbing.” (d, e) Photographs from saccular epithelia of group III fish (58 days after exposure) tissue showing extensive damage. Scale bars: (a) 20 μm ; (b) 2 μm ; (c, d, e) 20 μm .

the number of missing cells/10 000 μm^2 for the group III fishes was relatively low (2.7%), it should be noted that the counts were of gross damage only as evidenced by hair cells ejected from the epithelia. Damage severe enough to create the holes must have had wider implications for remaining hair cells, particularly for tip link function (Pickles, 1993). Without neurophysiological experimentation, it was not possible to determine if hair cells remaining intact on the epithelia after air-gun exposure were still fully functional.

IV. DISCUSSION AND CONCLUSIONS

It is known that a number of species of teleost fish continue to produce sensory hair cells for much of their lives (Popper and Hoxter, 1994; Lombarte and Popper, 1994) and that sensory hair cells are regenerated after insult with ototoxic drugs in at least one species, and probably all (Lombarte *et al.*, 1993). It is also known that some avian species will regenerate sensory cells after intense sonic insult (Corwin and Cotanche, 1988). However, the damage in the ears of the pink snapper suggests that regeneration, even if it occurred over 58 days, did not counteract the loss of cells resulting from sonic insult. Either damage continued to accrue well after insult, regeneration was slowed or ceased, or significant regeneration did not occur until beyond the 58-day sample period.

There are a number of caveats that must be pointed out in considering the implications of our results. First, the fish studied were caged and could not swim away from the sound source. Video monitoring of behavior suggested that the fish would have fled the sound source if possible. It is also likely that many, but perhaps not all, species hearing an approaching air-gun would swim away, as has been observed on a large scale by Engås *et al.* (1996). Second, we only examined a single species. While the snapper ear is typical of the majority of commercially important species (e.g., salmon, tuna, cod, haddock) (Dale, 1976; Popper, 1977; Lombarte and Popper, 1994), it is possible that pink snapper are more or less sensitive to intense stimulation than other species. Third, the impact of exposure on ultimate survival of the fish is not clear. Behavioral studies have observed that some fish exposed to air-gun signals display aberrant and disoriented swimming behavior, suggesting that damage to the ears may also have vestibular impact (authors, personal observation). Fishes with impaired hearing would have reduced fitness, potentially leaving them vulnerable to predators, possibly unable to locate prey, sense their acoustic environment, or, in the case of vocal fishes, unable to communicate acoustically. Fourth, although the full exposure regimen was accurately quantified, the approach-departure nature of trials meant a precise air-gun exposure required to produce the damage observed was not obtained. Was it the few high level signals or the accumulation of many moderate to high level signals? The sound exposure (intensity and time) required to produce damage has important ramifications in the range from a full scale seismic source at which such impacts may be expected. As a comparison, air-gun signals of level ≥ 180 dB *re* $1\mu\text{Pa}$ (mean squared pressure, see Fig. 1 for levels experienced by

fish in these trials) could be expected at ranges <500 m from a large seismic array (44 L, R.M. data).

This study demonstrates that exposure to seismic air-guns can cause significant damage to the ears of fishes. While additional studies are needed to better understand the mechanical and physiological process leading to damage, the repair process, impact on behavior and fitness, and the exposure regimen required to produce a specified amount of damage, our results suggest caution in the application of very intense sounds in environments inhabited by fish. Furthermore, given that hair cells form the ultimate end organs of the hearings system of all vertebrates, the results presented here may have important implications for other marine vertebrates.

ACKNOWLEDGMENTS

This work was supported by the Australian Petroleum Production and Exploration Association. Analysis of the data was supported by the U.S. Minerals Management Service. Julia Shand critically reviewed this manuscript.

- Corwin, J. T., and Cotanche, D. A. (1988). "Regeneration of sensory hair cells after acoustic trauma," *Science* **240**, 1772–1774.
- Dale, T. (1976). "The labyrinthine mechanoreceptor organs of the cod *Gadus morhua* L. (Teleostei, Gadidae)," *Norw. J. Zool.* **24**, 85–128.
- de Vries, H. L. (1950). "The mechanics of the labyrinth otoliths," *Acta Oto-Laryngol.* **38**, 262–273.
- Engås, A., Løkkeborg, S., Ona, E., and Soldal, A. V. (1996). "Effects of seismic shooting on local abundance and catch rates of cod (*Gadus Morhua*) and haddock (*Melanogrammus aeglefinus*)," *Can. J. Fish. Aquat. Sci.* **53**, 2238–2249.
- Enger, P. S. (1981). "Frequency discrimination in teleosts—central or peripheral?" in *Hearing and Sound Communication in Fishes*, edited by W. N. Tavolga, A. N. Popper, and R. R. Fay (Springer-Verlag, New York), pp. 243–255.
- Fay, R. R. (1988). *Hearing in Vertebrates: A Psychophysics Databook* (Hill-Fay, Winnetka, IL).
- Hastings, M. C., Popper, A. N., Finneran, J. J., and Lanford, P. J. (1996). "Effect of low frequency underwater sound on hair cells of the inner ear and lateral line of the teleost fish *Astronotus ocellatus*," *J. Acoust. Soc. Am.* **99**, 1759–1766.
- Lombarte, A., and Popper, A. N. (1994). "Quantitative analyses of postembryonic hair cell addition in the otolithic endorgans of the inner ear of the European hake, *Merluccius merluccius* (Gadiformes, Teleostei)," *J. Comp. Neurol.* **345**, 419–428.
- Lombarte, A., Yan, H. Y., Popper, A. N., Chang, J. C., and Platt, C. (1993). "Damage and regeneration of hair cell ciliary bundles in a fish ear following treatment with gentamicin," *Hear. Res.* **66**, 166–174.
- McCauley, R. D. (1994). "Seismic surveys," in *Environmental Implications of Offshore Oil and Gas Development in Australia—The Findings of an Independent Scientific Review*, edited by J. M. Swan, J. M. Neff, and P. C. Young (Australian Petroleum Exploration Association, Sydney), pp. 19–122.
- NRC (National Research Council) (1994). *Low-Frequency Sound and Marine Mammals: Current Knowledge and Research Needs* (National Academy, Washington, DC).
- NRC (National Research Council) (2000). *Marine Mammals and Low Frequency Sound: Progress Since 1994* (National Academy, Washington, DC).
- Parkes, G., and Hatton, L. (1986). *The Marine Seismic Source* (Reidel, Dordrecht).
- Pearson, W. H., Skalski, J. R., and Malme, C. I. (1992). "Effects of sounds from a geophysical survey device on behavior of captive rockfish (*Sebastes* spp.)," *Can. J. Fish. Aquat. Sci.* **49**, 1343–1356.
- Pickles, J. O. (1993). "Hair cells—mechanosensors and motors," *Acoust. Aust.* **21**, 82–85.

- Popper, A. N. (1977). "A scanning electron microscopic study of the sacculus and lagena in the ears of fifteen species of teleost fishes," *J. Morphol.* **153**, 397–418.
- Popper, A. N., and Fay, R. R. (1999). "The auditory periphery in fishes," in *Comparative Hearing: Fish and Amphibians*, edited by R. R. Fay and A. N. Popper (Springer-Verlag, New York), pp. 43–100.
- Popper, A. N., and Hoxter, B. (1994). "Growth of a fish ear: 1. Quantitative analysis of sensory hair cell and ganglion cell proliferation," *Hear. Res.* **15**, 133–142.
- Richardson, W. J., Greene, Jr., C. R., Malme, C. L., and Thomson, D. H. (1995). *Marine Mammals and Noise* (Academic, New York).
- Sand, O., and Karlsen, H. E. (1986). "Detection of infrasound by the Atlantic cod," *J. Exp. Biol.* **125**, 197–204.

A comparison of the fragmentation thresholds and inertial cavitation doses of different ultrasound contrast agents

Wen-Shiang Chen,^{a)} Thomas J. Matula, Andrew A. Brayman, and Lawrence A. Crum
Center for Industrial and Medical Ultrasound, Applied Physics Laboratory, University of Washington, Seattle, Washington 98105

(Received 18 June 2002; revised 18 October 2002; accepted 28 October 2002)

Contrast bubble destruction is important in several new diagnostic and therapeutic applications. The pressure threshold of destruction is determined by the shell material, while the propensity for the bubbles to undergo inertial cavitation (IC) depends both on the gas and shell properties of the ultrasound contrast agent (UCA). The ultrasonic fragmentation thresholds of three specific UCAs (Optison, Sonazoid, and biSpheres), each with different shell and gas properties, were determined under various acoustic conditions. The acoustic emissions generated by the agents, or their derivatives, characteristic of IC after fragmentation, was also compared, using cumulated broadband-noise emissions (IC “dose”). Albumin-shelled Optison and surfactant-shelled Sonazoid had low fragmentation thresholds (mean = 0.13 and 0.15 MPa at 1.1 MHz, 0.48 and 0.58 MPa at 3.5 MHz, respectively), while polymer-shelled biSpheres had a significant higher threshold (mean = 0.19 and 0.23 MPa at 1.1 MHz, 0.73 and 0.96 MPa for thin- and thick-shell biSpheres at 3.5 MHz, respectively, $p < 0.01$). At comparable initial concentrations, surfactant-shelled Sonazoid produced a much larger IC dose after shell destruction than did either biSpheres or Optison ($p < 0.01$). Thick-shelled biSpheres had the highest fragmentation threshold and produced the lowest IC dose. More than two and five acoustic cycles, respectively, were necessary for the thin- and thick-shell biSpheres to reach a steady-state fragmentation threshold. © 2003 Acoustical Society of America. [DOI: 10.1121/1.1529667]

PACS numbers: 43.80.Qf, 43.25.Yw [FD]

I. INTRODUCTION

The destruction of ultrasound contrast agent (UCA) and the associated acoustic emissions have been used recently in several novel imaging methods, including flash echo, destruction–reperfusion, and stimulated acoustic emission imaging. Broadband noise emissions and a bidirectional shift of frequency spectra before the complete destruction of UCA bubbles (stimulated acoustic emission)¹ have been demonstrated with a pulsed-wave Doppler system. Poorly contrasted, or isoechoic lesions, such as metastatic tumors in liver, can be clearly delineated by infusing UCA.^{2,3} Subtraction of the B-mode images acquired before and after the high-intensity pulses (flash echo) increases the sensitivity of detection and eliminates the effect of tissue motion.^{4,5} In addition, destructive pulses followed by low-amplitude ones allow the assessment of the perfusion status of the myocardium and other tissues by estimating the replenishment rate of contrast microbubbles (destruction–reperfusion imaging).^{6,7}

Ultrasound-mediated UCA destruction has also been proposed as an essential part in certain therapeutic applications, such as localized gene transfer and drug delivery. Protein expression in target tissue, such as myocardium or coronary arteries, is enhanced by the transfection of specific

DNA-loaded microbubbles.^{8,9} The destruction of paclitaxel-carrying lipospheres by applied ultrasound shows the potential of this technique to achieve localized drug delivery.¹⁰ However, the requirements for backscattering, fragility, and cavitation characteristics of UCA differ for different imaging methods and therapeutic applications. The shell material and gas content of a UCA determine the microbubbles’ acoustic response, and thus their optimal use. For example, thin-shelled microbubbles that are active at low acoustic pressures but can be destroyed at modest pressures may be most useful for destruction–reperfusion imaging of the myocardium. Conversely, thick-shelled microbubbles that are sufficiently robust to carry their contents to a specific site and disrupt only at high acoustic pressures may be better suited for localized drug delivery. Moreover, some applications of UCA (e.g., ultrasound-enhanced thrombolysis) may be improved by use of targeted UCA that can then be driven to vigorous inertial cavitation at the target site. Therefore, understanding the relationship between the acoustic properties, especially those related to microsphere fragmentation and inertial cavitation IC, and the physical structure of UCA is important in the selection or design of effective UCA for specific applications.

In our previous studies with Alburnex, transient acoustic emissions characterized as broadband noise at the Alburnex destruction pressure threshold.¹¹ In a study of the ultrasonic destruction of a UCA that used a fast camera, Chomas *et al.*¹² described two different, pressure-dependent mechanisms of bubble destruction under ultrasound exposure: (1) acoustically-driven diffusion at low-pressure levels, and (2)

^{a)}Author to whom correspondence should be addressed. Current address: Department of Mechanical Engineering and Material Science, Duke University, Box 90300, Pratt School of Engineering, Durham, NC 27708. Telephone: (919)660-5176; fax: (919)660-8963; electronic mail: wschen@duke.edu

TABLE I. Physical properties of UCAs in use.

Type of UCA	Gas	Shell	Mean shell thickness	Mean diameter	Size distribution (diameter)	Concentration (bubbles mL)
Optison	C ₃ F ₈	Albumin	15 nm ^a (Ref. 30)	2–4.5 μ m	93% <10 μ m	5–8 $\times 10^8$ (6.5 $\times 10^8$) 5 $\times 10^8$
biSpheres 0.2X	N ₂	Inner: lactide polymer; outer: protein	Inner: 64.8 nm, outer: 350 nm ^b	4 μ m ^b	0% (0–1 μ m), 6% (1–2 μ m), 54.5% (2–4.2 μ m), 31% (4.2–6.6 μ m), 7.3% (6.6–9 μ m), 1.2% (9–12.2 μ m) ^b	5 $\times 10^8$
biSpheres 0.3X	N ₂	Inner: lactide polymer; outer: protein	Inner: 97.2 nm, outer: 350 nm ^b			
biSpheres 0.7X	N ₂	Inner: lactide polymer; outer: protein	Inner: 226.8 nm, outer: 350 nm ^b			5 $\times 10^8$
Sonazoid	C ₄ F ₁₀	Surfactant (lipid) ^c	4 nm (Ref. 30)	2.17 μ m ^c	88.4% (1–3 μ m), 11.3% (3–5 μ m), 0.3% (5–7 μ m) ^c	1.3 $\times 10^9$ ^c

^aAlbunex's shell thickness. Assume that it is the same for Optison.

^bProvided by Point Biomedical, San Carlos, CA. The inner polymer layer is for structure stability while the outer layer is for biocompatibility.

^cProvided by Amersham Health, London, UK.

fragmentation at high-pressure levels. For a UCA with a fragile shell (e.g., Optison), fragmentation might be the major mechanism for bubble destruction. For acoustic pressures at or above the fragmentation threshold, large-amplitude expansion and contraction of the UCA microbubbles damages the protective shells and induces instability. The bubbles thus break into small pieces by inertial collapse (fragmentation), and emit broadband noise in the process. In the current study, this emission property is used as an indicator to determine the acoustic pressure threshold for the fragmentation of UCAs having different compositions.

The current study was performed to test the following hypotheses: (1) thin-shelled UCAs (Optison, Sonazoid, and 0.2X biSpheres) have lower fragmentation (IC) thresholds than do thick-shelled ones (0.7X biSpheres); (2) UCAs containing less soluble gas produce more IC activity than those with more soluble gas (e.g., perfluorocarbon vs air, C₄F₁₀ vs C₃F₈), and (3) longer pulse lengths are necessary for the thick-shelled UCA (0.7X biSpheres) than the thin-shelled ones (Optison, Sonazoid, and 0.3X biSpheres) to induce fragmentation. In this study, we will show readers the results of (1) the fragmentation threshold and IC “dose” determinations for UCAs with different shell materials and gas contents; (2) the pulse length dependence of microbubble fragmentation for different UCAs.

Our long-term objective in this study is to further the understanding of the fundamental physical and acoustical properties of commercial UCAs, in order to (1) permit the improvement of ultrasonic imaging methods that depend on UCA destruction, (2) provide a basis for the development of drug-carrying microbubbles that are “programmable” for fragility, and (3) evaluate the potential of these agents to facilitate cavitation-related mechanical bioeffects.

II. MATERIALS AND METHODS

A. Ultrasound apparatus

All experiments were performed in an acrylic tank (16.5 cm L \times 12.5 cm W \times 12.5 cm H) containing 1.2 l of

deionized water. A high-intensity focused ultrasound (HIFU) transducer (either 1.1 or 3.5 MHz) and a 5 MHz hydrophone (Sonic Concepts, Woodinville, WA) were mounted in quadrature on two adjacent sidewalls. Reflections were minimized by placing a silicone rubber acoustic absorber on the end wall of the tank opposite the HIFU transducer. Preselected pulse length, pulse repetition frequency (PRF), and the amplitude of sinusoidal waveforms were supplied by a function generator (33120A, Hewlett Packard, Loveland, CO) and attenuated 34 dB by an attenuator (Kay Elemetrics Corp., Lincoln Park, NJ). The output signal was amplified by a power amplifier (B400, ENI, Rochester, NY) at a fixed gain of 50 dB before being routed to either the 1.1 MHz ($f = 1.0$) or 3.5 MHz ($f = 1.6$) HIFU transducer. The 1.1 MHz transducer's -6 dB profile (full width half-maximal intensity) is approximately 1.8 mm wide by 13 mm long, while that of the 3.5 MHz transducer is 1 by 11.5 mm. Further details of the experimental system are described elsewhere.¹³

The scattering and emission signals from the bubbles in the focal volume were collected by the 5 MHz hydrophone (1.2 cm diameter, 4.6 cm focal length) and amplified 20 dB by a pulser/receiver (5072, Panametrics, Waltham, MA) before being digitized by an oscilloscope (LC334AM, LeCroy, Chestnut Ridge, NY). A LabView program (v.6.1, National Instruments, Austin, TX) was used to control the trigger signal and pulse parameters of the function generator.

B. Contrast agents

The physical properties of the contrast agents used in this study are listed in Table I. The outer shells of biSpheres provide no structure support, and thus are not considered as the limiting factor of fragmentation and IC. UCAs with shells thinner than 100 nm were considered as thin shelled, including Optison, Sonazoid, 0.2X, and 0.3X biSpheres. 0.7X biSpheres is the only thick UCA we have studied. Sonazoid and biSpheres were stored at room temperature and reconstituted before use according to the manufacturer's recommended protocol. Optison was stored at 5 $^{\circ}$ C until use. In each experiment, an approximately equivalent number of mi-

crobbles for each UCA was withdrawn and added directly to the water in the exposure tank. A magnetic stir bar in the tank was driven at a rate of 60 rpm to ensure that a uniform distribution of bubbles was maintained.

The focal volume (-6 dB) of the 1.1 MHz HIFU transducer is about 43.6 mm^3 . The added bubble concentration was about 2 bubbles/ mm^3 for each UCA. The initial number of bubbles present within the focal volume was therefore ~ 90 . Somewhat fewer bubbles were present in the focal volume of the 3.5 MHz transducer because of its smaller focal -6 dB boundary.

C. Experimental series

For short pulses, the fragmentation threshold is a function of both pressure amplitude and pulse length. That is, the threshold is higher for short pulses, and decreases as the pulse length increases. For longer pulses, the threshold should only depend on the pressure amplitude. We call this latter regime the “steady-state” fragmentation threshold, because the threshold will not change with increasing pulse length. To determine these thresholds, and to measure the resulting IC, we performed the following series of experiments.

1. Fragmentation thresholds

Fragmentation thresholds for each UCA were determined by increasing the output voltage of the function generator in 20 mV increments every 10 s from a preselected initial voltage over a 4 min period. The passively collected waveforms by the 5 MHz hydrophone were sent to the oscilloscope and processed. Briefly, the maximal peak-to-peak amplitude of each waveform was calculated and downloaded using a LabView program to a nearby PC via a GPIB interface. The program collected ten peak-to-peak amplitudes and averaged them. Approximately seven averaged values were obtained per second. Three replicate measurements were performed for each UCA and each frequency (1.1 or 3.5 MHz). The pulse length was 10 cycles and the PRF was 100 Hz for both frequencies. The stored data were analyzed off-line by Matlab programs.

2. Steady-state threshold

The pulse length dependence on the fragmentation threshold for the UCAs was determined using four selected cycles, 2, 4 (or 5), 10, or 20. We substituted 0.3X biSpheres for the thin-shelled 0.2X biSphere in the pulse length experiments because our supply of the latter was exhausted. For different pulse lengths, the total “on” time was kept constant by adjusting the PRF (from 500–50 Hz for pulse lengths of 2–20 cycles, respectively). The pressure levels were increased gradually and stepwise as described for Series 1. Only the 1.1 MHz transducer was used for this series. The total treatment time was fixed at 4 min. Three replicate measurements were performed for each UCA and pulse length. Signal recording and processing were as described earlier.

3. Inertial cavitation dose

The acoustic emissions from fragmented UCA were quantified at a selected pressure level (0.31 MPa), which was above the fragmentation thresholds of all four UCAs (determined by Series 1 and Series 2 experiments). The total treatment time, the pulse length, and PRF were fixed at 10 min, 10 cycles, and 100 Hz, respectively, for each UCA. The method by which IC “dose” (ICD) was quantified will be described in detail in a later section. The UCAs in use for Series 1 and 3 were Optison, 0.7X biSpheres, 0.2X biSpheres, and Sonazoid. The same pulse length and PRF were used as in the Series 1 experiments. Three to four replicate measurements were performed for each UCA.

D. Determination of threshold parameters

In order to determine the IC threshold, frequency spectra of the emission signals were first recorded and averaged (500 waveforms) at each pressure level. The pressure threshold of IC was defined as the pressure level at which a sudden increase of the frequency spectra between each pair of harmonics (broadband noise) was found. For example, by his definition, the IC threshold of Sonazoid was 0.14 MPa (see Fig. 1).

However, determining the fragmentation threshold using frequency spectra was difficult; the typical broadband noise of IC overlapped with the harmonics. Moreover, established methods of an IC “dose” measurement have been based on the integration of the amplitude–time traces in the time domain.¹³ To be consistent, we used the method based on time domain recordings to determine the pressure threshold of the various UCAs at different acoustic pressure levels and pulse lengths. We did, however, use the frequency domain spectra to differentiate between scattering from UCA and acoustic emission by UCA, as described below.

For each sample (e.g., Sonazoid with a 20-cycle tone burst), the pressure levels were increased from an initial level (e.g., 0.07 MPa at 1.1 MHz) with fixed voltage steps from the function generator (viz., 10 mV) every 10 s over 4 min. The signals from the focal area were collected and processed, as described in Series 1 experiments.

For each of the four UCAs studied, the values of the averaged maximal peak-to-peak amplitudes from IC [presented as “spikes” above the baseline in the recorded trace (Fig. 2, inset)] increased in both amplitude and “density” (i.e., frequency of occurrence) with increasing acoustic pressure (Fig. 2). The recorded spikes included both the scattering of the UCA bubbles drifting across the focus (below the IC threshold) and the emissions during inertial collapsing (above the IC threshold), and needed to be separated. To do so, we assumed that the pressure threshold determined by the frequency spectra method should be the same as the threshold determined by the pressure-step method. Therefore, at the threshold pressure as determined by the spectral method, we analyzed the amplitudes and the density of the spikes and obtained two parameters; viz., the threshold voltage (in mV) and the percentage of spikes exceeding the threshold voltage

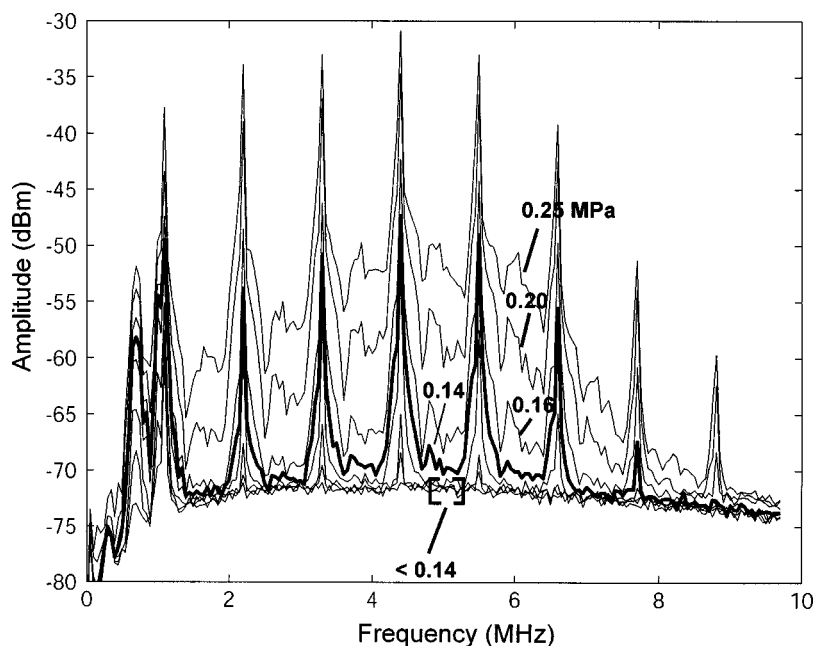


FIG. 1. Method for the determination of the IC threshold. In this example, averaged frequency spectra for Sonazoid UCA (1.1 MHz, 20 cycles) were plotted at different pressure levels. The first four curves overlay between harmonics (background). The first signal trace above this background (0.14 MPa) is shown as a dark line. At this pressure (IC threshold), UCA bubbles began to break and undergo IC.

(spike density). For example, in Fig. 2, the threshold parameters used for determining the IC threshold of Sonazoid in the “pressure-step” experiment was that at least 5% of the recorded “spikes” were higher than 20 mV in amplitude. Also, the UCA bubbles added was in a certain size distribution, and a bubble of different size has a different IC threshold. By setting the 5% limit, we ignored the sporadic emission from a few bubbles (<5%) with a lower fragmentation threshold, and focused on the threshold of the majority, i.e., bubbles with sizes near the distribution mean. For peak voltage value less than 20 mV, the signal is usually from the scattering of an intact UCA bubble, instead of a bubble undergoing inertial cavitation.

By applying the same method described above, we found that same threshold parameters (5% of spikes >20 mV) could also be applied to other UCAs in this study.

We therefore used the same parameters for both series of threshold experiments.

E. Determination of IC dose

To study the IC doses of various agents, a suprathreshold pressure level (0.31 MPa, higher than all four fragmentation thresholds obtained in a previous section of experiments) was selected. The IC signals were collected for a period of 10 min for each UCA. We defined the integral of the signal amplitude over time, corrected by controls (i.e., background noise obtained from samples without UCA) as the IC dose.¹³ It needs to be stressed here that IC dose is a relative value that depends highly on the experimental setup,

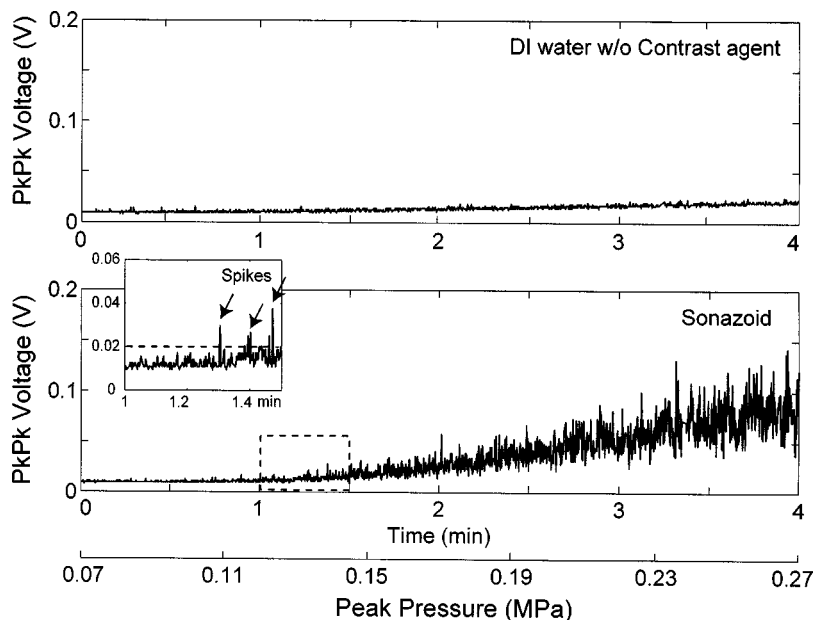


FIG. 2. Passively detected signals for samples with or without UCA. The source frequency was 1.1 MHz. The upper trace is the recorded signal of the control experiment without the addition of UCA. The baseline amplitude (noise from the source beam side lobe as well as reflection waves from the tank wall) increases as the pressure increases from 0.07 to 0.27 MPa. The lower trace is a recording of an experiment with 5 μ L of Sonazoid dispersed in the 1.2 L tank volume at the same increasing pressure levels. An insert plot is the blow-up of the dashed square area in the lower trace. A dashed line in the insert represents the threshold voltage, while solid arrows in the insert show the spikes above the threshold voltage.

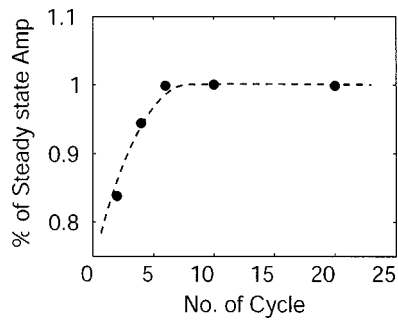


FIG. 3. Pulse length necessary for transducer (1.1 MHz) to achieve steady-state output ($n=3$ and standard deviation=0.0%).

and especially on the sensitivity of the receiving hydrophone. Results can be compared quantitatively only for experiments using exactly the same equipment setup.

F. Special consideration for short pulse lengths

For the pulse length experiments, the pulse length and PRF were changed simultaneously in order to keep the same total “on” time for each treatment. In experiments involving short pulses (viz., two or four cycles), the amplitude of the output waveform at the focus was smaller than the value specified by the transducer calibration curves, which had been obtained using 20-cycle pulses, since it took a few cycles for the HIFU transducer to “ring up” to the steady state. The peak amplitudes of the actual waveforms for different pulse lengths are plotted in Fig. 3. The amplitude values of each pulse length were obtained by recording the signal outputs from the HIFU transducer after reflection by an aluminum reflector 45° to both the HIFU and 5 MHz receiving hydrophone in water without UCA. The same values were obtained every time and thus show a minimal standard deviation. From our results, we found that more than five cycles were necessary for the output waveform to reach the steady-state amplitude. On average, the peak amplitude of a 4-cycle waveform was 94.5% of the steady state (10 or 20 cycles), and was 83.9% for a 2-cycle pulse. It was thus necessary to compensate the pressure thresholds for 2- and 4-cycle pulses to avoid overestimating the pressure threshold. The compensation was performed as the equation below:

$$\text{Corrected IC threshold} = (\text{uncorrected threshold value}) \times (\% \text{ of steady-state amplitude}). \quad (1)$$

G. Statistics

Data are presented as means ± 1 standard deviation of three or four replicates. The F test for an overall comparison of group means of one-way ANOVAs were used to determine if there were differences in the pressure thresholds for samples with different UCAs and exposure pulse lengths. The least significant difference (LSD) procedure (t test) for the comparison of pairs of groups in one-way ANOVAs (single-tailed) were performed to compare the pressure thresholds and IC doses of UCAs in pairs, and test our hypotheses, i.e., if thin shell UCAs have a lower fragmentation

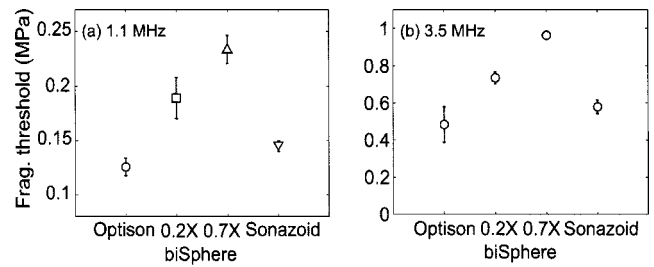


FIG. 4. Fragmentation threshold of four different UCAs at (1) 1.1 MHz or (2) 3.5 MHz. The pulse length was 10 cycles, and the PRF was 100 Hz. Three replicate experiments were performed for each UCA.

threshold, and if less soluble gases generated more IC dose. Furthermore, the mean fragmentation thresholds of each UCA at different exposure pulse lengths were compared in pairs (e.g., 20 vs 10 cycles, 10 vs 4 cycles, and 4 vs 2 cycles for Sonazoid at 1.1 MHz) to determine their steady-state threshold values (a single-tailed LSD procedure of one-way ANOVA). Equal variance was assumed and a $p \leq 0.05$ was considered significant. All statistical calculations were performed using SPSS software (v. 10.0, SPSS, Inc., Chicago, IL).

III. RESULTS

A. IC threshold for different UCAs

Figure 4 shows the fragmentation thresholds of four different UCAs when exposed to either 1.1 or 3.5 MHz ultrasound. At 1.1 MHz, the albumin-shelled Optison was the most fragile UCA of the group, and could be destroyed at a pressure level as low as 0.13 MPa. The thick-shelled biSpheres (0.7X) did not show significant breakage until 0.23 MPa of acoustic pressure was experienced. Sonazoid and thin-shelled biSpheres (0.2X) had mean thresholds intermediate between those of Optison and thick-shelled biSpheres.

The data in Fig. 4 also demonstrate the frequency dependence of the fragmentation threshold. For each UCA, the fragmentation threshold pressure was nominally greater at 3.5 MHz than at 1.1 MHz. As at the 1.1 MHz frequency, at 3.5 MHz the thick-shelled biSphere (0.7X) again had the highest fragmentation threshold (mean=0.96 MPa), while Optison again had the lowest (mean=0.48 MPa).

TABLE II. Statistic results of fragmentation threshold and IC doses of four different UCAs at 1.1 and 3.5 MHz.

UCA	Significance (single-tailed)		
	Fragmentation threshold exp.		IC dose exp.
	1.1 MHz	3.5 MHz	1.1 MHz
Overall F test	b	b	b
Optison vs 0.7X biSpheres	b	b	N/S (0.432)
Optison vs Sonazoid	(0.047) ^a	(0.031) ^a	b
Optison vs 0.2X biSpheres	b	b	b
0.7X biSpheres vs Sonazoid	b	b	b
0.7X biSpheres vs 0.2X biSpheres	b	b	b
Sonazoid vs 0.2X biSpheres	b	b	b

^a0.01 < p < 0.05.

^b p < 0.01; N/S not significant.

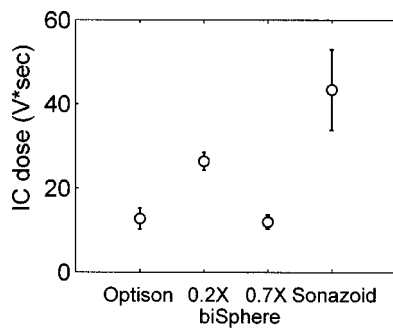


FIG. 5. A comparison of IC doses for four UCAs at 1.1 MHz, with the acoustic pressure fixed at 0.31 MPa for 10 min. The pulse length and PRF were 10 cycles and 100 Hz, respectively.

Table II shows the statistical comparisons of the fragmentation thresholds of four UCAs. The p values for the overall F test of one-way ANOVA were smaller than 0.001 for both frequencies, which indicated that the fragmentation thresholds of four UCAs were not all the same. Thin-shelled UCAs, i.e., Optison, Sonazoid, and 0.2X biSpheres, all had thresholds significantly lower than that of the thick-shell biSpheres (0.7X) (p values ≤ 0.001 at both frequencies).

B. IC dose for different UCAs

The ability of these UCAs to generate IC at a fixed pressure was not all the same (Fig. 5 and Table II). Sonazoid produced the highest level of IC dose, while 0.2X biSpheres was the second, but much less. Thick-shelled biSpheres produced the lowest mean IC dose value. The IC dose generated by Optison was not higher than that of the 0.7X ($p > 0.4$), though Optison microbubbles contained a less dissolvable gas and a more fragile shell (lower fragmentation threshold, $p < 0.05$ for both frequencies). Furthermore, Sonazoid produced a much larger IC dose than did Optison ($p < 0.001$) at 0.31 MPa. Examples of signal traces recorded from four different UCAs are shown in Fig. 6.

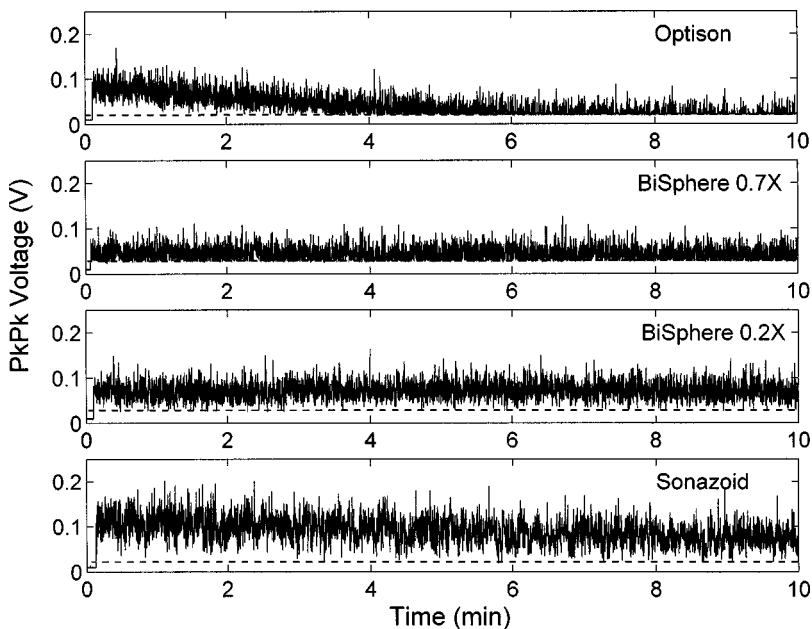


FIG. 6. Examples of the signal traces recorded using the 5 MHz hydrophone for 4 UCAs at a fixed pressure of 0.31 MPa, which is higher than the fragmentation threshold pressure for any of UCAs studied here (PRF = 100 Hz, pulse length = 10 cycles, 10 min total time). These traces represent the ability of the 4 UCAs to generate IC activity above the fragmentation threshold. Dashed lines represent baseline signals.

C. Pulse length effect for different UCAs

Results of the fragmentation threshold determinations made at different pulse lengths are shown in Fig. 7. There was no difference of the fragmentation thresholds between 20 and 10 cycles for all UCAs. Significantly lower thresholds were found for ten cycles than four (or five) cycles for Optison, Sonazoid, and 0.7X biSpheres, but not for the 0.3X biSpheres (Table III). That is, at least five cycles were necessary for Optison, Sonazoid, and 0.7X biSphere to achieve their steady-state fragmentation thresholds; while only three or four cycles are necessary for thin-shelled biSpheres.

IV. DISCUSSIONS

Nonlinear bubble oscillation of intact UCA or free gas bubbles emit frequency components other than harmonics (f_0 , $2f_0$, $3f_0$, etc., f_0 is the transmitting frequency), such as subharmonic ($f_0/2$, $f_0/3$, etc.) and ultraharmonic ($3f_0/2$, $5f_0/2$, etc.) spectra.^{14–16} These bubble-specific frequency components provide an excellent separation between the echoes from contrast agents and the surrounding tissue, and can be used as new ultrasound imaging methods.^{17–19} Quantitative measurement of the subharmonic spectra were also used to correlate with the membrane permeabilization of red blood cells.²⁰ At higher ultrasound pressure, bubbles show rapid growth and collapse, a phenomenon referred to as IC (or transient cavitation).^{14–16} The shock waves emitted by the collapsing bubbles and the resulting broadband noise are specific for destroying UCA bubbles, or free gas bubbles from UCA fragments undergoing IC. Quantitative measurements of the IC were used in the study of certain IC-related bioeffects, such as hemolysis and thrombolysis.^{13,21–23} In the current study, we recorded the threshold of the broadband noise emission and used it as an indicator for the presence of IC activity and UCA destruction. We also quantified the amount of IC activity of four different UCA at a specific supra-IC threshold pressure level to compare their ability of generating IC.

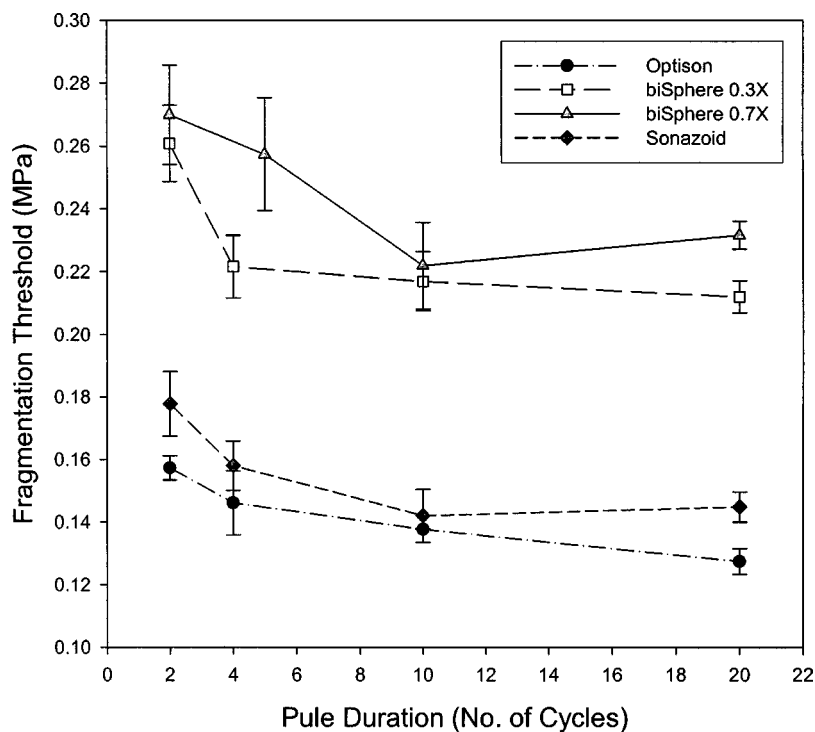


FIG. 7. Fragmentation thresholds of four different UCAs at different pulse lengths (1.1 MHz). Steady state is reached after four cycles for Optison, Sonazoid and 0.2X biSpheres, but after ten cycles for 0.7X biSpheres.

The fragmentation threshold pressures for the various UCAs used here varied with the agent. Optison, Sonazoid, and 0.2X biSpheres had low fragmentation thresholds, while thick-shelled biSpheres had the highest. Our results thus support the hypothesis that thin-shelled UCAs have lower fragmentation thresholds. The differences in acoustic stability of the different UCAs may be important for different potential therapeutic applications. For example, 0.7X biSpheres are relatively resistant to disruption by applied acoustic pressures as high as ~ 1 MPa at the clinically relevant frequency of 3.5 MHz, but can be destroyed at higher pressure levels. Agents of this or similar design might therefore prove useful for localized, ultrasound-mediated drug delivery, wherein diagnostic ultrasound would be used to trace the location of drug-loaded UCA bubbles in the body, with a subsequent local release of the drug achieved *via* fragmentation of the bubbles using a few strong pulses of targeted high-pressure ultrasound. For example, intravenous administration of

biSphere-encapsulated drugs followed by ultrasound-triggered release in the heart is intended to effectively treat certain cardiac conditions, and reduce the necessity of using cardiac catheters.²⁴

The frequency dependence of the fragmentation thresholds can be explained by the frequency dependence of IC thresholds. For a free gas bubble, the IC threshold is lower at a lower frequency.²⁵ It is reasonable to assume that a UCA bubble behaves like a free bubble after shell fragmentation. However, the quantitative comparison of the fragmentation thresholds for the various agents across ultrasound frequencies is not possible in our experiments, because the 5 MHz listening transducer used in this study had different sensitivities to 1.1 and 3.5 MHz ultrasound. Nonetheless, at a particular ultrasound frequency, the data provide useful *relative* information.

The type of gas used in the manufacture of various microbubble-based UCAs undoubtedly influences the

TABLE III. Statistical comparisons of the fragmentation thresholds for four different UCAs at various pulse lengths (frequency=1.1 MHz, peak-negative pressure=0.31 MPa).

UCA	Pulse length (cycles)	Significance (<i>p</i> value)	UCA	Pulse length (cycles)	Significance (<i>p</i> value)
Optison	Overall	^b	biSpheres 0.7X	Overall	^a
	20 vs 10	N/S (0.081)		20 vs 10	N/S (0.211)
	10 vs 4	^a		10 vs 5	^a
	4 vs 2	^a		5 vs 2	N/S (0.153)
Sonazoid	Overall	^b	biSpheres 0.3X	Overall	^b
	20 vs 10	N/S (0.347)		20 vs 10	N/S (0.240)
	10 vs 4	^a		10 vs 4	N/S (0.250)
	4 vs 2	^a		4 vs 2	^b

^a0.01 $\leq p < 0.05$.

^b $p < 0.01$; N/S: not significant.

“amount” of IC activity produced after agent fragmentation. In the study of Miller *et al.*,²³ passive cavitation detection demonstrated that Optison (octafluoropropane content) produced higher rms values for noise emissions and longer periods of IC activity, than did Albunex (air content). For comparable concentrations of microbubbles, the perfluorocarbon-based agents lead to greater values of ultrasonically induced hemolysis and petechial hemorrhage in mouse intestine.^{26,27} In our experiments, Sonazoid exhibited persistent and strong IC activity for at least 10 min, and produced the highest level of IC dose. The solubility of the C_4F_{10} in Sonazoid is about 1/8 the solubility of the C_3F_8 in Optison,²⁸ and is only 1/30 of nitrogen,²⁹ which could explain the difference in the IC activity of these agents.

However, Optison failed to show more IC dose than the air-containing 0.7X biSpheres ($p=0.43$), and even showed significantly less IC activity than the 0.2X biSpheres ($p<0.01$, reversed direction). The low IC dose for Optison appeared to be due to the early termination of IC activity, or a short period of continuous IC activity, in the 10 min of treatment. This is illustrated by Fig. 6, in which the continuous IC activity (signal above the baseline) for Optison started at a high level, but sustained for only about 3.5 min. Thereafter, IC activity became increasingly less frequent over time. Sonazoid started at a similar level, but stayed constant. Although 0.7X biSpheres did not exhibit strong initial IC activity, their relatively weak activity was sustained at approximately constant amplitude and density over the entire 10 min treatment period.

Shell permeability might be used to explain the early termination of IC activity of Optison. In a preliminary study aiming at determining the life expectancy of highly diluted UCA bubbles in air-saturated water (no perfluorocarbon), Optison microbubbles were found to lose their scattering ability in 5 min by subthreshold (fragmentation threshold) 5 MHz pulse echoes (results not shown). On the other hand, the scattering signals of both biSpheres and Sonazoid lasted for more than 10 min. The shells of biSpheres and Sonazoid seemed to be much less gas permeable.

Both thin- and thick-shelled biSpheres contain air, and have similar size distributions. Thus, free bubbles generated upon shell disruption might be expected to dissolve at similar rates. In turn, this might suggest that both thin- and thick-shelled biSpheres would produce a similar IC dose when exposed to acoustic pressures above the fragmentation threshold. However, this was not the case; thick-shelled biSpheres produced the lowest IC dose over the course of 10 min exposures to suprathreshold acoustic pressures. A possible explanation for this is the *amount* of gas contained in the different biSphere types. For biSpheres of the same diameter, the volume of air in one 0.7X biSphere is ~70% that in a 0.2X biSphere by calculation. One might therefore expect that upon fragmentation, free “daughter bubbles” produced by 0.7X biSpheres would be less in number, and thus generate less IC activity than do 0.2X biSpheres.

Composed of the same material (polymer), the thick-shelled biSphere (0.7X) microbubbles required longer ultrasound pulses to fragment compared to the thin-shelled biSpheres (0.3X). We might speculate that a thicker and thus

stronger protective structure could tolerate more repetitive stretches before material fatigue and failure. However, thin-shelled Optison and Sonazoid did not show the steady-state pulse length until five to nine cycles were achieved. This result suggests that factors such as material stiffness might be more important in determining the fragmentation threshold.

It is important to note here that all our experiments were performed in deionized water, not in blood. The high concentration of red blood cells, various kinds of proteins, lipids, and ions in blood may affect the response of contrast agents. We are performing further studies to elucidate the behavior of UCAs in blood.

V. CONCLUSIONS

Different UCAs with various gas contents and stabilizing shell materials had different fragmentation pressure thresholds and produced different “amounts” of IC activity of suprathreshold acoustic pressures. Optison had the lowest fragmentation threshold while thick polymer-shelled biSpheres had the highest. Sonazoid exhibited the maximal IC dose after fragmentation. The fragmentation threshold for shorter pulses, which is typical in clinical diagnostic ultrasound situations, was higher. Three or more cycles were necessary for thin-shell biSpheres to reach the steady-state fragmentation threshold. More cycles were required for the thick-shell biSpheres. Our results may provide useful guidance for a wiser selection of UCA bubbles based on their destruction properties and IC response.

ACKNOWLEDGMENTS

The authors wish to thank Glenn Tickner and Lars Hoff for numerous discussions. This study was supported in part by NIH Grants No. 8RO1 EB00350-2 and No. 1 R41 RR14886-01.

- ¹ K. Tiemann, C. Pohl, T. Schlosser, J. Goenechea, M. Bruce, C. Veltmann, S. Kuntz, M. Bangard, and H. Becher, “Stimulated acoustic emission: pseudo-Doppler shifts seen during the destruction of nonmoving microbubbles,” *Ultrasound Med. Biol.* **26**, 1161–1167 (2000).
- ² M. J. Blomley, T. Albrecht, D. O. Cosgrove, N. Patel, V. Jayaram, J. Butler-Barnes, R. J. Eckersley, A. Bauer, and R. Schliel, “Improved imaging of liver metastases with stimulated acoustic emission in the late phase of enhancement with the US contrast agent SHU 508A: early experience,” *Radiology* **210**, 409–416 (1999).
- ³ M. Blomley, T. Albrecht, D. Cosgrove, V. Jayaram, J. Butler-Barnes, and R. Eckersley, “Stimulated acoustic emission in liver parenchyma with Levovist,” *Lancet* **351**, 568–568 (1998).
- ⁴ P. J. A. Frinking, E. I. Cespedes, J. Kirkhorn, H. G. Torp, and N. de Jong, “A new ultrasound contrast imaging approach based on the combination of multiple imaging pulses and a separate release burst,” *IEEE Trans. Ultrason. Ferroelectr. Freq. Control* **48**, 643–651 (2001).
- ⁵ R. A. Pelberg, K. Wei, N. Kamiyama, J. Sklenar, J. Bin, and S. Kaul, “Potential advantage of flash echocardiography for digital subtraction of B-mode images acquired during myocardial contrast echocardiography,” *J. Am. Soc. Echocardiogr* **12**, 85–93 (1999).
- ⁶ K. Wei, A. R. Jayaweera, S. Firoozan, A. Linka, D. M. Skyba, and S. Kaul, “Quantification of myocardial blood flow with ultrasound-induced destruction of microbubbles administered as a constant venous infusion,” *Circulation* **97**, 473–483 (1998).
- ⁷ T. Schlosser, C. Pohl, C. Veltmann, S. Lohmaier, J. Goenechea, A. Ehlgren, J. Koster, D. Bimmel, S. Kuntz-Hehner, H. Becher, and K. Tiemann, “Feasibility of the flash-replenishment concept in renal tissue: which pa-

- rameters affect the assessment of the contrast replenishment?," *Ultrasound Med. Biol.* **27**, 937–944 (2001).
- ⁸R. V. Shohet, S. Chen, Y. T. Zhou, Z. Wang, R. S. Meidell, R. H. Unger, and P. A. Grayburn, "Echocardiographic destruction of albumin microbubbles directs gene delivery to the myocardium," *Circulation* **101**, 2554–2556 (2000).
 - ⁹C. Teupe, S. Richter, B. Fisslthaler, V. Randriamboavonjy, C. Ihling, I. Fleming, R. Busse, A. M. Zeiher, and S. Dimmeler, "Vascular gene transfer of phosphomimetic endothelial nitric oxide synthase (S1177D) using ultrasound-enhanced destruction of plasmid-loaded microbubbles improves vasoreactivity," *Circulation* **105**, 1104–1109 (2002).
 - ¹⁰E. C. Unger, T. P. McCreery, R. H. Sweitzer, V. E. Caldwell, and Y. Wu, "Acoustically active lipospheres containing paclitaxel: a new therapeutic ultrasound contrast agent," *Invest. Radiol.* **33**, 886–892 (1998).
 - ¹¹P. P. Chang, W. S. Chen, P. D. Mourad, S. L. Poliachik, and L. A. Crum, "Thresholds for inertial cavitation in Albunex suspensions under pulsed ultrasound conditions," *IEEE Trans. Ultrason. Ferroelectr. Freq. Control* **48**, 161–170 (2001).
 - ¹²J. E. Chomas, P. Dayton, J. Allen, K. Morgan, and K. W. Ferrara, "Mechanisms of contrast agent destruction," *IEEE Trans. Ultrason. Ferroelectr. Freq. Control* **48**, 232–248 (2001).
 - ¹³S. L. Poliachik, W. L. Chandler, P. D. Mourad, M. R. Bailey, S. Bloch, R. O. Cleveland, P. Kaczkowski, G. Keilman, T. Porter, and L. A. Crum, "Effect of high-intensity focused ultrasound on whole blood with and without microbubble contrast agent," *Ultrasound Med. Biol.* **25**, 991–998 (1999).
 - ¹⁴E. Cramer and W. Lauterborn, "Acoustic cavitation noise spectra," *Appl. Sci. Res.* **38**, 209–214 (1982).
 - ¹⁵W. Lauterborn and E. Cramer, "On the dynamics of acoustic cavitation noise spectra," *Acustica* **49**, 280–287 (1981).
 - ¹⁶E. A. Nappiras, "Subharmonic and other low-frequency emission from bubbles in sound-irradiated field," *J. Acoust. Soc. Am.* **46**, 587–601 (1968).
 - ¹⁷F. Forsberg, W. T. Shi, and B. B. Goldberg, "Subharmonic imaging of contrast agents," *Ultrasonics* **38**, 93–98 (2000).
 - ¹⁸P. M. Shankar, P. D. Krishna, and V. L. Newhouse, "Subharmonic back-scattering from ultrasound contrast agents," *J. Acoust. Soc. Am.* **106**, 2104–2110 (1999).
 - ¹⁹R. Basude and M. A. Wheatley, "Generation of ultraharmonics in surfactant based ultrasound contrast agents: use and advantages," *Ultrasonics* **39**, 437–444 (2001).
 - ²⁰J. Liu, T. N. Lewis, and M. R. Prausnitz, "Non-invasive assessment and control of ultrasound-mediated membrane permeabilization," *Pharm. Res.* **15**, 918–924 (1998).
 - ²¹E. C. Everbach, I. R. Makin, M. Azadniv, and R. S. Meltzer, "Correlation of ultrasound-induced hemolysis with cavitation detector output in vitro," *Ultrasound Med. Biol.* **23**, 619–624 (1997).
 - ²²E. C. Everbach and C. W. Francis, "Cavitation mechanisms in ultrasound-accelerated thrombolysis at 1 MHz," *Ultrasound Med. Biol.* **26**, 1153–1160 (2000).
 - ²³M. W. Miller, E. C. Everbach, C. Cox, R. R. Knapp, A. A. Brayman, and T. A. Sherman, "A comparison of the hemolytic potential of Optison and Albunex in whole human blood in vitro: acoustic pressure, ultrasound frequency, donor and passive cavitation detection considerations," *Ultrasound Med. Biol.* **27**, 709–721 (2001).
 - ²⁴Point Biomedical, *Microsphere Drug Delivery* (Point Biomedical, 887L Industrial Road, San Carlos, CA 94070). This is available online at (<http://www.pointbio.com/drugdelivery.htm>)
 - ²⁵R. E. Apfel and C. K. Holland, "Gauging the likelihood of cavitation from short-pulse, low-duty cycle diagnostic ultrasound," *Ultrasound Med. Biol.* **17**, 179–185 (1991).
 - ²⁶D. L. Miller and R. A. Gies, "Enhancement of ultrasonically-induced hemolysis by perfluorocarbon-based compared to air-based echo-contrast agents," *Ultrasound Med. Biol.* **24**, 285–292 (1998).
 - ²⁷D. L. Miller and R. A. Gies, "The influence of ultrasound frequency and gas-body composition on the contrast agent-mediated enhancement of vascular bioeffects in mouse intestine," *Ultrasound Med. Biol.* **26**, 307–313 (2000).
 - ²⁸A. Kabalnov, K. N. Makarov, and O. V. Shcherbakova, "Solubility of fluorocarbons in water as a key parameter determining fluorocarbon emulsion stability," *J. Fluorine Chem.* **50**, 271–284 (1990).
 - ²⁹D. R. Lide, *The CRC Handbook of Chemistry and Physics* (CRC Press, Boca Raton, FL, 2000).
 - ³⁰L. Hoff, "A comparison between three different contrast agents," in *Acoustic Characterization of Contrast Agents for Medical Ultrasound Imaging* (Kluwer Academic, Dordrecht, The Netherlands, 2001), pp. 121–128.

Microparticle column geometry in acoustic stationary fields

Andrew Hancock, Michael F. Insana,^{a)} and John S. Allen

Department of Biomedical Engineering, University of California, One Shields Avenue, Davis, California 95616-5294

(Received 21 February 2002; revised 5 October 2002; accepted 22 October 2002)

Particles suspended in a fluid will experience forces from stationary acoustic fields. The magnitude of the force depends on the time-averaged energy density of the field and the material properties of the particles and fluid. Forces acting on known particles smaller than 20 μm were studied. Within a 500 kHz acoustic beam generated by a plane-piston circular source, observations were made of the geometry of the particle column that is formed. Varying the acoustic energy altered the column width in a manner predicted by equations for the primary acoustic radiation force from scattering of particles in the long-wavelength limit. The minimum pressures required to trap gas, solid, and liquid particles in a water medium at room temperature were also estimated to within 12%. These results highlight the ability of stationary acoustic fields from a plane-piston radiator to impose nano-Newton-scale forces onto fluid particles with properties similar to biological cells, and suggest that it is possible to accurately quantify these forces. © 2003 Acoustical Society of America. [DOI: 10.1121/1.1528171]

PACS numbers: 43.80.Vj, 43.20.Rz, 43.25.Uv, 43.25.Qp [MFH]

I. INTRODUCTION

Acoustic energy has been used extensively to trap, concentrate, and sort many types of particles suspended in fluids. Our long-term goal is to evaluate the potential for using a stationary acoustic pressure field of known topography to probe and measure mechanical forces on biological cells. Applications may include the study of cellular mechanotransduction¹ and the mechanics of cell adhesion.^{2,3} Forces on liquid particles captured in standing waves were explored by Söllner and Bondy⁴ and Crum.⁵ These works provide a basis for studying forces on cell suspensions in fluids. More recently, investigators have studied columns of inorganic and organic particles formed from acoustic forces,^{6–9} and they report that details of the column geometry depend on the physical properties of the particles and the fluid as well as the acoustic energy field. Based on the physics of particle column formation, flow chambers were developed to sort, concentrate, and fractionate dilute particle suspensions.^{8,10–12} Similar experimental techniques have been applied at reduced scales using standing surface waves in microsystems.¹³

One experimental goal has been to control the position of individual or groups of particles in static or streaming fluids with a radiation force. For example, time-independent radiation forces from plane standing waves will trap particles in planes separated by half-wavelength intervals if the radiation force exceeds the sum of other forces acting on the particles (predominantly gravitational for fluid particles). Three aspects of the experiment must be known to accurately control particle position and measure the radiation force distribution: the time-averaged energy density of the stationary pressure field, the material properties of the suspended par-

ticles and the fluid, and the relationship between the acoustic energy density and the radiation force.

A few investigators^{9,14} have used the geometry of levitated particle columns to validate force predictions. Standing wave beams concentrate acoustic energy along an axis, so the margin of the particle column occurs where the primary acoustic radiation force equals the gravitational force. Consequently, the radiation force distribution can be calibrated using particles of known properties suspended in water. Once calibrated, the method can be used to study important unknown properties of particles.

Our purpose in this report is to verify that acoustic radiation force theory¹⁵ for weakly interacting particles with dimensions smaller than the acoustic wavelength can quantitatively predict the width of columns formed in beams of acoustic energy. For these experiments, we use a 500 kHz beam of standing waves in a water chamber with suspended gas, solid, or liquid particles. Our chamber is similar to a chamber used by Asaki.^{16,17} This chamber design, unlike other experiments, is not intended to resonate with the source.⁸ Therefore standard techniques for predicting pressure fields from an unfocused circular source apply.

II. METHODS

In the following section we describe components of the acoustic force model assembled from the literature specifically for our experimental conditions.

A. Stationary field from unfocused source

A planar standing pressure wave p_s is generated when a continuous compressional wave $p_t(z, t) = P \cos(\omega_0(t - z/c))$ traveling in lossless media along the z axis at speed c , with radial frequency ω_0 and amplitude P , is reflected by a surface in the x, y plane. If the reflector has reflection co-

^{a)} Author to whom correspondence should be addressed. Electronic mail: mfinnsana@ucdavis.edu

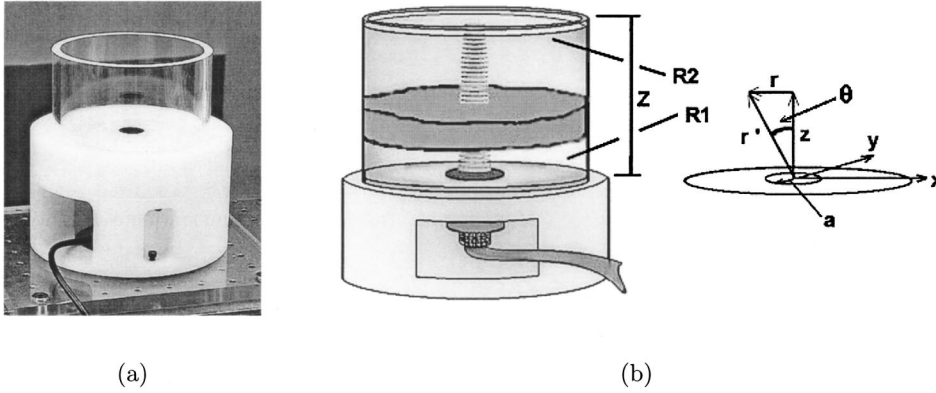


FIG. 1. (a) A photograph of the acoustic levitation chamber. (b) The standing wave beam is illustrated and the measurement geometry is defined. The transducer radius is a , and the reflection coefficients at the base and water–air surfaces are R_1 and R_2 , respectively. A low-attenuation agar phantom (dark disk) with acoustic impedance matched to the water medium is inserted near the center of the chamber.

efficient $R = -1$ and is placed a distance $z = Z$ from the source plane at a spatial pressure node, such that $Z = m\lambda/2$ for integer m and wavelength λ , then

$$p_s(z, t) = \text{Re}\{P e^{i\omega_0(t-z/c)} - P e^{i\omega_0(t+z/c)}\} \\ = 2P \sin(kz) \sin(\omega_0 t), \quad (1)$$

where $k = \omega_0/c$ is the wave number and Re is the real part of the complex quantity.

Radiation force theory is well established for plane waves, but these pressure fields are difficult to generate experimentally. However, acoustic beams are readily available. Like plane waves, acoustic beams form standing waves when a planar air–water reflecting surface is parallel to the source plane at $z = Z$. The amplitude is increased when the source plane is also a plane reflector; e.g., Plexiglas has $R = 0.389$. To minimize chamber resonances, the diameter of the cylindrical water chamber is much larger than the beam width and the radiator is mechanically uncoupled from the chamber as much as possible (Fig. 1). We now examine the farfield pressure of a traveling wave in water from an unbaffled, circular piston, flush-mounted to the base of a cylindrical water chamber.¹⁸ Beyond the last axial maximum, the stationary pressure field, p_s , is the sum of reflected traveling waves:

$$p_s(z, r, t) = \text{Re}\left\{i \frac{P_0 k a^2}{4} e^{i\omega_0 t} \sum_{n=0}^{\infty} \left[R_1^n R_2^n \left(\frac{2J_1(\Omega_r)}{\Omega_r} \right) \frac{e^{-ikr'_n}}{r'_n} \right. \right. \\ \left. \left. + R_1^n R_2^{n+1} \left(\frac{2J_1(\Omega_s)}{\Omega_s} \right) \frac{e^{iks'_n}}{s'_n} \right] \right\}. \quad (2)$$

J_1 is the first-order Bessel function of the first kind, $r'_n{}^2 = (2nZ + z)^2 + r^2$ and $s'_n{}^2 = (2(n+1)Z - z)^2 + r^2$ are radial positions relative to the source center, a is the source radius, $\Omega_r = kar/r'_n$, $\Omega_s = kar/s'_n$, $-1 \leq R_1, R_2 \leq 1$, and n is an integer denoting reflection number. The sum in Eq. (2) converges because of losses from beam divergence and imperfect reflections. R_2 for the upper water–air reflecting surface is approximately -1 , but R_1 of the lower water–Plexiglas surface is just 0.389 at 20°C (Plexiglas:¹⁹ 2700 m s^{-1} , 1.150 g cm^{-3} ; water:^{20,21} 1483 m s^{-1} , 0.998 g cm^{-3}). Wave propagation is essentially lossless in degassed water^{21,22} at 0.5 MHz because $\alpha_w = (3.733\mu\omega_0^2)/(2\rho c^3)$, $\mu = 0.010 \text{ g cm}^{-1} \text{ s}^{-1}$, and therefore $\alpha_w = 1.96 \times 10^{-3} \text{ dB cm}^{-1} \text{ MHz}^{-2}$.

Nodes and antinodes occur in the farfield main lobe of the beam at surfaces separated by $\lambda/2$. The nodal surfaces are predicted by Eq. (2) by setting $n=0$, integrating over time, and locating contours of relatively constant phase. Our criterion for defining a “relatively constant phase” is determined experimentally, as described in Sec. IV.

We also examined the behavior of numerically simulated stationary fields throughout the chamber. Field II²³ was used to predict the relative traveling-wave pressure field at ω_0 for an axial length $> 20Z$. To use Eq. (2) or numerical field simulators for comparison with experiments, the system must be calibrated to relate the rms transducer drive voltage V to the pressure amplitude P_0 . A relationship between P_0 and V provided by Gonnard²⁴ for traveling waves satisfies this requirement:

$$P_0 = \frac{\sqrt{2}}{t_c} \frac{d_{33}}{S_{33}} V, \quad (3)$$

where t_c is the transducer crystal thickness, d_{33} is the piezoelectric coefficient, and S_{33} is the elastic compliance of the element. These parameters can be measured or obtained from the manufacturer. Based on this equation, the axial pressure amplitude for the unbaffled, circular plane piston¹⁸ is

$$P(z) = P_0 \left| \sin \left[\frac{kz}{2} (\sqrt{1 + (a/z)^2} - 1) \right] \right|, \quad (4)$$

and gives $P(a^2/\lambda) \approx P_0$. After calibration, we numerically “folded” the pressure field to simulate reflection, weighting values according to the reflection coefficients, and summed via Eq. (2) to obtain an absolute numerical estimate of the stationary pressure field throughout the chamber. We computed the magnitude and phase of this stationary field along the radial axis r near $z = a^2/\lambda$ and plotted the result in Fig. 2. From the geometry of Fig. 1(b), it is straightforward to show that the phase varies quadratically with r in the paraxial region where $Z \gg r$, i.e., $\Delta\varphi \approx r^2/2Z$. So the lateral phase plot in Fig. 2(b) is expected for our stationary field.

B. Primary radiation force

Particles suspended in a stationary field experience forces depending on their position. This primary radiation force was predicted for traveling waves from a finite-size radiator²⁵ using the approach introduced by Yosioka and

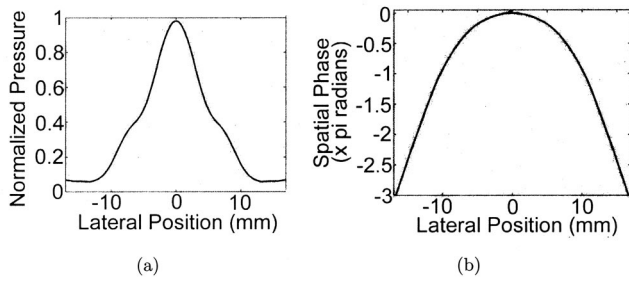


FIG. 2. The (a) normalized magnitude and (b) spatial phase of the stationary pressure field as a function of the lateral position at an antinode in the transducer farfield, $z = 33.6$ mm.

Kawasima.²⁶ Such methods are not easily applied to acoustic beams because of the complexity of the equations that account for spherical divergence and multiple reflections. We seek a solution valid for regions of a relatively planar phase. Here we show in the long-wavelength limit the equivalence of Gor'kov's solution of the primary radiation force to that obtained from the scattering solution of plane stationary waves.

Gor'kov¹⁵ took a more general approach to predicting radiation force that holds for spherical particles in the long-wavelength limit for an otherwise arbitrary pressure field. He defined the primary radiation force vector as the gradient of a field potential \mathcal{U} :

$$\mathbf{F}_p = -\nabla \mathcal{U}, \quad (5)$$

where

$$\mathcal{U} = V_0 [\langle \text{PE} \rangle f_1 - \frac{3}{2} \langle \text{KE} \rangle f_2]. \quad (6)$$

∇ is the gradient operator, $V_0 = \frac{4}{3}\pi R_0^3$ is the spherical particle volume, and $\langle \text{KE} \rangle$ and $\langle \text{PE} \rangle$ are the time-averaged kinetic and potential energy densities.^{22,27} The monopole and dipole scattering contributions are $f_1 = 1 - \rho c^2 / \rho_0 c_0^2$ and $f_2 = 2(\rho_0 - \rho) / (2\rho_0 + \rho)$ with ρ_0 and c_0 the particle density and sound speed.

Yosioka and Kawasima and others have used a velocity potential approach to show that the primary radiation force for plane standing waves^{26,28,29} described by Eq. (1) is

$$\mathbf{F}_p = -\pi R_0^3 \frac{4P^2}{\rho c^2} X k \sin(2kz) \hat{\mathbf{e}}_z, \quad (7)$$

where $\hat{\mathbf{e}}_z$ is the unit vector oriented along the z axis and X is a force factor that depends on properties of the particle and medium. In the long-wavelength limit defined in terms of the particle radius R_0 and wave number k_0 as $k_0 R_0 \ll 1$ and $k R_0 \ll 1$, it has been shown that²⁶

$$X = - \left[\frac{(c/c_0)^2 (3\rho_0/\rho - (k_0 R_0)^2)}{(c_0/c)^2 (k_0 R_0)^6 + (3\rho_0/\rho - (k_0 R_0)^2)^2} \right] \quad (8)$$

for gas spheres in fluid and

$$X = \left[\frac{\rho_0/\rho + \frac{2}{3}(\rho_0/\rho - 1)}{1 + 2\rho_0/\rho} \right] - \left[\frac{1}{3(\rho_0/\rho)(c_0/c)^2} \right], \quad (9)$$

for solid or liquid spheres suspended in fluid. Equations (7)–(9) describe the primary radiation force if ρ/ρ_0 is of order

one for solid or liquid particles, and of order $(kR_0)^2$ for gas-phase particles. Ishimaru³⁰ approximates the threshold for long wavelength to be $R_0 = 0.05\lambda$. For our studies, $\omega_0/2\pi = 500$ kHz. The wavelength is $440 \mu\text{m}$ in isobutane microbubbles and 5 mm in polystyrene microspheres, requiring diameters less than $22 \mu\text{m}$ for gases and less than $250 \mu\text{m}$ for solids (Table II later).

If we limit radiation force predictions to regions in the stationary field with relatively planar phase, Eq. (5) may be compared directly with Eq. (7) to relate the force factor X defined by Yosioka and Kawasima with the particle monopole and dipole contributions f_1 and f_2 . Using the pressure field of a plane standing wave, Eq. (1), and setting Eq. (5) equal to Eq. (7), we find that $X = f_1/3 + f_2/2$ (see the Appendix). For gas-phase particles, $f_1 \gg f_2$, so that $X = f_1/3$. A comparison of $f_1 = 1 - \rho c^2 / \rho_0 c_0^2$ and Eq. (8) shows this is valid under the assumptions of $f_1 \gg 1$ and $k_0 R_0 \ll 1$. Hence, for gas-phase particles, Eq. (6) reduces to

$$\mathcal{U} = 3V_0 \langle \text{PE} \rangle X. \quad (10)$$

The above radiation force equations presume that thermal and viscous effects may be ignored. At 500 kHz, the particle viscous boundary layer $\delta_v = \sqrt{2\mu/\omega_0\rho}$ is $0.799 \mu\text{m}$ at 20°C , so we consider viscous damping effects negligible since $R_0 > 10\delta_v$.^{22,31,32} The thermal layer thickness $\delta_t = \sqrt{2\chi/\omega_0}$ is typically $0.100 \mu\text{m}$, where χ is the thermal diffusivity constant,³³ so for $R_0 > \delta_t$, losses due to thermal damping are also negligible.

C. Column formation

In addition to the primary radiation force, particles experience forces from gravity, secondary radiation,³⁴ acoustic streaming,³⁵ thermal convection, viscous drag,³⁶ Oseen forces arising from pressure field distortions, Brownian diffusion, and those from hydrostatic pressure gradients. Thus, particle column formation may be affected by any of these forces. We evaluated all forces for our experiment to determine their relative contributions. Only the primary and secondary radiation forces and gravitational forces were significant. For a Mach number of 1 and field intensity of 2 W cm^{-2} , the maximum traveling-wave peak pressure is 240 kPa . Finite-amplitude wave distortion will not occur until the pressure wave has traveled more than 100 cm from the transducer,³⁷ so Oseen forces can be neglected. The magnitude of acoustic streaming is dependent on the mean free pathlength,³⁵ which was reduced through insertion of a solid phase medium that had acoustic properties closely matched to water.

An equation for the secondary radiation force between two particles of similar properties in a standing wave was developed by Weiser and Apfel:^{22,34}

$$\mathbf{F}_s = 4\pi R_0^6 \left[\frac{(\rho_0 - \rho)^2 (3 \cos^2 \varphi - 1)}{6\rho d^4} \langle v^2(z, r, t) \rangle - \frac{\omega^2 \rho (1/\rho_0 c_0^2 - 1/\rho c^2)^2}{9d^2} \langle p^2(z, r, t) \rangle \right] \hat{\mathbf{e}}_\varphi. \quad (11)$$

φ is the angle between the centerline of the two particles and the direction of acoustic wave propagation, d is the interparticle distance, and $\hat{\mathbf{e}}_\varphi$ is a unit vector from particle 1 to particle 2, where particle 1 is the radiator and particle 2 experiences the secondary radiation force. Negative values of \mathbf{F}_s represent an attractive force on particle 2 and positive values represent a repulsive force. Evaluating this equation in regions of column formation where particles are in close proximity ($<5 \mu\text{m}$), solid particles experience secondary radiation forces 10^{-5} smaller than the primary radiation force. However gas-phase particles experience attractive secondary radiation forces of significant magnitude, resulting in small average interparticle spacing that acts to narrow the width of columns that form.

The gravitational force is

$$\mathbf{F}_g = \frac{4}{3} \pi R_0^3 (\rho - \rho_0) \mathbf{g}, \quad (12)$$

where the gravitational acceleration \mathbf{g} is directed along the $-z$ axis. Particles are at equilibrium in the pressure field when the net force acting on them is zero. The minimum pressure amplitude required to trap particles, P_{mtp} , is found for plane standing waves by equating (5) and (12) at axial positions $z = (2m + 1)\lambda/8$. There we find

$$P_{\text{mtp}} = 2P|_{\text{equil.}} = \left| \left(\frac{4g\rho(\rho - \rho_0)c^3}{(f_1 + 3f_2/2)\omega_0} \right)^{1/2} \right| = \left| \left(\frac{4g\rho(\rho - \rho_0)c^3}{3X\omega_0} \right)^{1/2} \right|. \quad (13)$$

The minimum trap pressure amplitude for nonplanar stationary fields will remain the same although locations where the particles are trapped will vary. Increasing the transmission power level from zero, the first particles trapped are on the beam axis. Increasing power widens the column. Gas particles ($X < 0$) are trapped at the pressure antinodes while solid and liquid particles ($X > 0$) are trapped at the pressure nodes. In theory, surrounding each pressure node (antinode) there are two locations where the net force is zero, and particles may gather at either location. In practice, however, most particles are present at only one of these two force nodes depending on the direction of the gravitational force. There will be a curvature to the particle columns up or down because the radiation force in the main lobe of the beam varies [see Fig. 3(b)]. The beam profile limits the column width; particle columns form only within the region of the main lobe, where the phase front is approximately planar and parallel to the reflectors. An important result for this study will be to establish experimentally the extent of this region.

III. EXPERIMENTAL DESIGN

A. Chamber design

A narrow-band, plane circular PZT-4 source (Table I) was mounted flush with the base surface of a cylindrical Plexiglas water tank (Fig. 1). The power rating and electro-mechanical coupling factor of the transducer were selected to levitate all particles examined in this study.

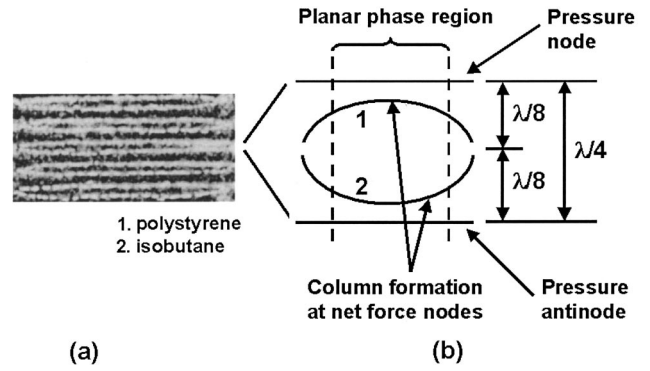


FIG. 3. (a) Photograph of double column formation for a mixture of gaseous (isobutane, $\rho_0 < \rho$ and $X < 0$) and solid (polystyrene, $\rho_0 > \rho$ and $X > 0$) particles. (b) Geometry of particles trapped near pressure nodes and antinodes.

The chamber was designed to minimize resonances other than those from the PZT source. External vibrations were minimized by placing the chamber on a vibration damping table. A silicon rubber O ring surrounded the transducer housing as a water seal and for mechanical isolation. However, isolation was not perfect and Plexiglas is an inefficient reflector. Energy was transmitted into the base by leakage through the O ring, and from energy reflected from the top surface. Measurable axial chamber resonances were produced that were detected by examining the magnitude of the Fourier transform of the time-averaged signal envelope obtained from a hydrophone at discrete spatial locations along the beam axis. We found spectral peaks at frequencies much lower than the transducer resonant frequency and at amplitudes 15–20 dB below the transducer fundamental.³⁸ At these strengths, the results presented herein were not adversely affected. Three axial chamber resonance peaks were found at the frequencies $\ell c/\lambda_c = \ell \times 13.6 \text{ kHz}$, where $\ell = 1, 2, 3$ and $Z = \lambda_c/2$. The fundamental wavelength for axial chamber resonance λ_c was determined by the water height set at $Z = 54.73 \text{ mm}$.

A chamber radius of 57 mm was used to minimize sidewall reflections of the beam energy. At this radius sidewall pressures were $< -30 \text{ dB}$ relative to the axial peak pressure, and lateral chamber resonances were not detected, i.e., the lateral margins could be considered a pressure relief boundary. The beam was found to be axisymmetric by hydrophone

TABLE I. Transducer design specifications.

Manufacturer/Model	Etalon/LIHP-40-0.5019-SCB1
Type	Immersion
Crystal material	PZT-4
d_{33}^a	$330 \times 10^{-12} \text{ m V}^{-1}$
S_{33}^b	$15.5 \times 10^{-12} \text{ m}^2 \text{ N}^{-1}$
Crystal sound speed	3831 m s^{-1}
Crystal diam. $2a/\text{Thick. } t_c$	19.0/3.5 mm
Resonant frequency	544 kHz
Focusing	None
Power rating	60 W
Maximum achievable intensity ^c	8 W cm^{-2}
Maximum achievable pressure ^c	490 kPa peak

^aDisplacement coefficient.

^bElastic compliance coefficient.

^cReported for traveling wave pressure field at $z = a^2/\lambda$.

measurements of pressure contours in planes at several farfield axial positions.³⁸ Forty half-wavelengths were generated over Z at 22 °C and $\omega_0/2\pi = 544$ kHz. It was discovered that placing the water surface exactly at a pressure null is not critical since radiation pressure appears to move the water surface to a node. The sound beam was oriented normal to the water–air surface using a tripod built into the chamber base.

The transducer was driven near resonance by a continuous wave (CW) sinusoidal voltage or with CW bursts by the output of a rf linear power amplifier (ENI 3100LA, Rochester, NY) responding to an arbitrary waveform generator signal (LeCroy LW420B Wavestation, Chestnut Ridge, NY). Standing waves formed if the duty factor was ≥ 0.4 .

B. Pressure and force models

Equation (2) provides intuition about the stationary farfield topography. However, a Matlab version of the Field II program²³ provided numerical simulations that accurately described the field throughout the chamber. CW pressure fields were computed for our experimental conditions with an axial resolution of 50 μm and lateral resolution of 250 μm . The model was rescaled to establish predictions of absolute pressure in two ways: from Eqs. (3) and (4) and from calibrated hydrophone measurements. The stationary field was generated as described in Sec. II A by multiply reflecting the calibrated traveling wave pressures between the two reflecting planes, assuming coefficients $R_1 = -0.999$ for the water–air surface and $R_2 = 0.389$ for the water–Plexiglas surface, and time averaging over several periods.

Using Eqs. (5) and (12), we computed the net force acting on spherical gas-phase, solid particles and liquids throughout the volume. We assumed the liquid particles consisted of a uniform suspension of 20 μm microspheres, such that forces predicted are for that particle diameter. Nevertheless, predictions of the factor X , minimum trap pressure, and column widths are valid regardless of the true diameter because the functional dependence of the gravitational and radiation forces on R_0 is the same.

C. Pressure field measurement

The stationary pressure field was mapped using a 0.4 mm diam PVDF needle hydrophone (Specialty Engineering Associates PVDFZ44-0400, Soquel, CA). The hydrophone response was amplified (Specialty Engineering A101), low-pass filtered (1.9 MHz corner frequency), recorded with a digital oscilloscope (LeCroy Wavepro 940) at 20 MSamples/s and 8 bits, and transferred using Labview to a PC for an analysis. The hydrophone position was indexed under Labview PC control in the y, z plane at a spatial resolution of 50 μm axially and 0.5 mm laterally, using a Parker Daedel XYZ positioner (Rohnert Park, CA) and a Galil motion controller (Rocklin, CA). The size of the needle hydrophone limited the lateral resolution. The temporal waveform, which was sinusoidal, was recorded for 20 periods at each spatial position. The amplitude of the stationary field was found by squaring the waveform, averaging the result over time, and taking the square root.

TABLE II. Particle properties.

Particle	Type	Diameter $2R_0$ (μm)	Density ρ_0 (g cm^{-3})	Sound speed c_0 (m s^{-1})
Isobutane ^b	encap.gas	9.0	0.036 ^f	220 ^f
Polystyrene ^c	solid	19.0	1.045 ^g	2350 ^g
Glycerine ^d	liquid	20.0 ^e	1.260 ^g	1920 ^g

^aAll values reported for 20 °C and 0.1 MPa atmospheric pressure.

^bExpancel 551-DU-20 microbubbles, dry-packaged.

^cBangs Laboratories Dynospheres PS07N, wet packaged.

^dFisher Scientific Chemical G33-4, 99.7% pure glycerine, contrasted with a few drops of McCormick blue and red food coloring dye.

^eAssumed value.

^fFor encapsulated gases, density and sound speed are based on the shell–gas composite. Values for pure isobutane (i.e., no shell) (Ref. 45) are $2.485 \times 10^{-3} \text{ g cm}^{-3}$ and 209.4 m s^{-1} .

^gValues from Kaye and Laby (Ref. 21).

The hydrophone frequency response was relatively flat below 10 MHz, and was cross-calibrated to calibrated needle (Specialty Engineering Associates PVDFZ44-0200, 0.2 mm diam³⁹) and membrane (Marconi Y-34-3578, MRQ-IP033) hydrophones using a substitution method.^{40–42} Calibration uncertainty is estimated at $\leq \pm 1.5$ dB ($-247.31 \text{ dB re } 1 \text{ V}/\mu\text{Pa}$).

D. Particle levitation

Gas, liquid, and solid-phase particles listed in Table II were examined. Cavitation in water was minimized by a degassing procedure and by limiting the chamber peak pressures to 400 kPa. Acoustic streaming was minimized by replacing water near the source with a congealed agar cylinder whose specific acoustic impedance was similar to water (agar: 25 mm thick, 1486 m s^{-1} , 1.015 g cm^{-3}). Measured using a through-transmission technique,⁴³ the scatter-free agar had a low attenuation coefficient ($0.087 \text{ dB cm}^{-1} \pm 10\%$ at 2.5 MHz), which is approximately six times that of water.

The fluid was illuminated for photography with a high-intensity fiberoptic illuminator (Dolan Jenner Industries Fiber Lite 181, Lawrence, MA) or a mercury arc lamp (Opti-Quip 1200, Highland Mills, NY). To reduce thermal gradients, extended hot mirrors (Edmund Industrial Optics, Barrington, NJ) with 425–675 nm transmission/750–1150 nm reflection were placed between the optical source and chamber to remove infrared energy. A digital zoom camera (Olympus Camedia C3030, Melville, NY) photographically recorded the particle columns.

The stationary field was mapped after the particle levitation experiments using particulate-free agar–water media. Particles were attracted to the hydrophone tip due to secondary radiation forces, thus reducing the signal amplitude. Consequently, P_{mtp} was estimated from measurements made in

TABLE III. Force magnitude (nN) and P_{mtp} (kPa peak).

Particle	F_{pz} ^a	F_{pr} ^a	F_{gz}	X	P_{mtp} ^b	Location
Isobutane	16.750	5.169	0.0036	−443	5.9(5.2)	antinode
Polystyrene	0.079	0.024	0.0017	0.221	52.9(52.0)	node
Glycerine	0.104	0.032	0.0108	0.249	119.5(115.1)	node

^aPrimary radiation force F_p is calculated at the peak pressure 374.2 kPa.

^bMeasured (predicted) values.

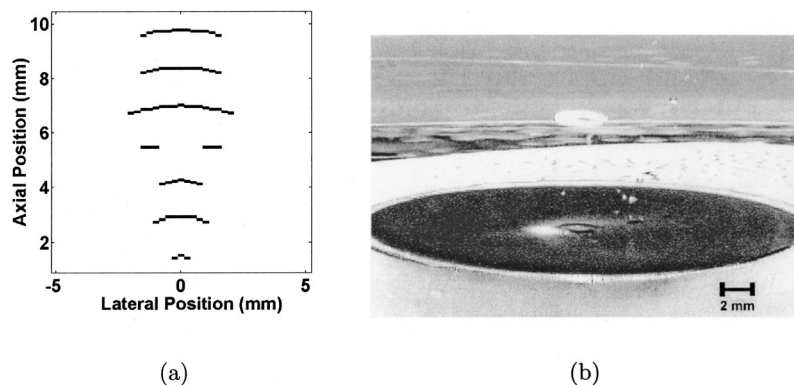


FIG. 4. A ring of 19.0 μm diam polystyrene microspheres predicted by the force model (a) is shown in the near field of the source (b). The ring is 5.5 mm above the transducer surface. The ring dimensions are 3.2 mm O.D. and 2.2 mm I.D. The predicted peak pressure at the location of the ring is 113.1 kPa. A shadow of the ring is visible on the transducer surface.

pure water under otherwise identical experimental conditions to the particle column experiments. The minimum trap pressures reported are based on the average of results from five independent experiments for each particle type.

IV. RESULTS

Pressure field simulations calibrated using properties of the transducer were verified by a comparison with hydrophone measurements at the region of peak pressure in the chamber. Measurement uncertainty was approximately 2% of the mean. Force magnitudes in the range of 10^{-12} – 10^{-9} N (pN–nN) were estimated by combining the simulation results, Eq. (5), and physical properties of the particles (Table II) and medium. Results of these calculations are shown in Table III along with measured and predicted minimum trap pressures and the location of particle trapping. For the calculations in the tables, the drive voltage was arbitrarily chosen to be 31.6 V peak, corresponding to electrical power dissipation of 10 W. This value is within the power rating of the source and therefore is achievable experimentally. Measurements of the particle minimum trap pressures confirmed the force model predictions.

We were able to levitate all three particle types within a few seconds of applying the drive voltage to the transducer. In all cases, the geometry of the column was in accordance with predictions from the force model. Column formation in a mixed particulate suspension of 19.0 μm polystyrene microspheres and 9.0 μm isobutane encapsulated microbubbles was examined to show how gas-filled particles are levitated at pressure antinodes and solids at pressure nodes, as previously described by Söllner and Bondy.⁴ The maximum pressure was 72.7 kPa peak in the region of column formation. See Fig. 3(b).

We also demonstrated that solid particles can be trapped in the pressure near-field, where the stationary field topography is more complex. We found that when a dense concentration of 19.0 μm diam polystyrene microspheres was injected 5.5 mm from the source, the microspheres were seen to cluster in a 3 mm diam ring. See Fig. 4. The axial position and inner diameter of the ring corresponded to those predicted by the model. However, the observed outer diameter of the ring was smaller than predicted, most likely because of the influence of secondary radiation forces. This ring formation demonstrates that particle trapping, even in the near field, is possible and predictable.

Although columns were formed with all three types of particles,³⁸ our greatest interest lies with fluid and solid particles because their properties can be similar to biological cells. We were able to levitate liquid glycerine in the farfield of the source (a few drops of food coloring dye were added to provide optical contrast). Glycerine is miscible in water and will eventually dissipate. However, its viscosity allowed stable column formation for 30–60 s—sufficient for photographic recording. The measured widths of glycerine columns seen in Fig. 5 are compared with predictions in Fig. 6. The comparison is based on a criterion that defines the planar phase region as the area where the phase varies from the axial value less than $\pi/4$ (or $\lambda/8$). This phase limit is an experimentally determined parameter that was adjusted until we found the closest agreement between measured and predicted values plotted in Fig. 6. The cause of the abrupt increase in measured column width at an intermediate source voltage is unknown, but is likely due to transducer beam effects that were not predicted by the model. Error bars on the predicted column widths indicate the range possible arising from a pressure uncertainty caused by a hydrophone error of ± 1.5 dB. Error bars on the measured column widths indicate one standard deviation of the mean width from several photographs of a single experiment.

V. CONCLUSIONS AND DISCUSSION

The manipulation of cells by acoustic standing waves has been the subject of previous research efforts, notably

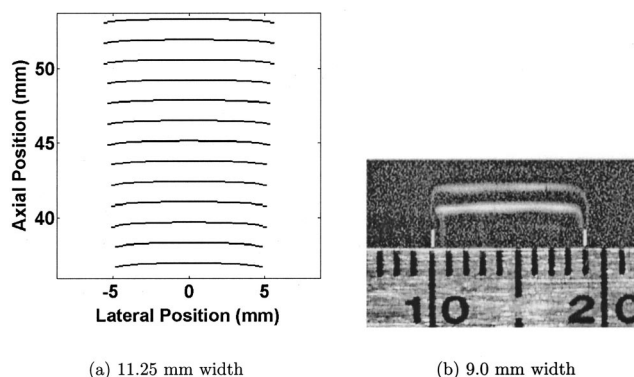


FIG. 5. (a) Predicted column formation of glycerine located 50 mm from the transducer surface. The pressure at the location of column formation is 277.1 kPa peak. (b) Photograph of the measured column width.

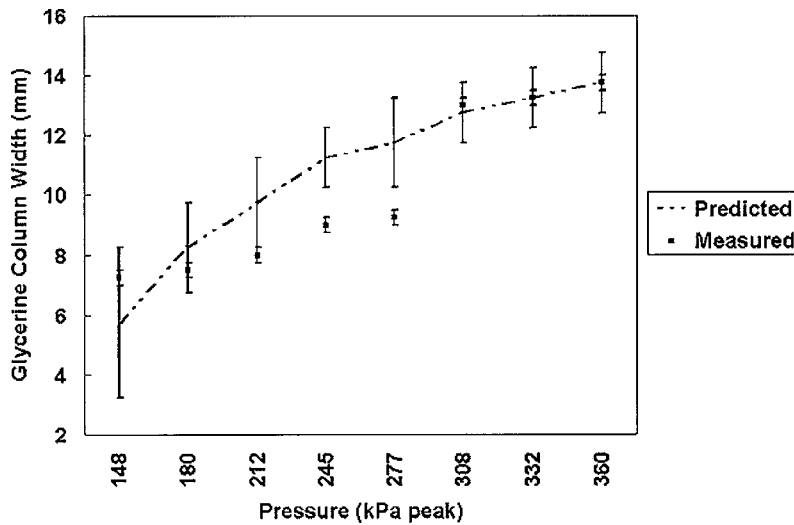


FIG. 6. Plot of glycerine column widths versus pressure. Points on the dashed line are predicted columns widths. The squares are the experimentally measured column widths.

Weiser and Apfel in red cell manipulation³⁴ and Tilley in cell adhesion.³ Previous experimental work simplified the analysis by utilizing standing waves based on efficient chamber designs, such as acoustic resonant chambers or narrow-walled chambers. Our contribution to the field is the rigorous characterization of levitation by an acoustic beam via the determination of the radiation force values and particle column geometries. We used wide-walled chambers so that the maximum width of column formation was minimally influenced by the chamber walls and mainly dependent on the beam geometry.

Characterization of levitation is achieved by utilizing a plane-wave scattering model that describes the force from a stationary pressure field on particles suspended in liquid and can predict measurements in acoustic beams from a circular piston radiator in specific regions of the field. It is the plane-wave analysis that limits force predictions to regions in the pressure field, where the phase front varies less than $\pi/4$ from the axial phase value. Under these conditions, the gravitational and primary radiation forces predict the size and curvature of columns formed in water. The extent of allowable deviation from a true planar phase front was determined empirically by fitting measurements to predicted values over a range of output power. The radiation forces are on the order of pN (for solid particles and liquids) to nN (for gas-phase particles), covering the range of most cellular adhesion forces.

As long as waves propagate linearly, the results developed in this study can be scaled down in size and wavelength using microsystems technology so that individual particles or small particle groups can be observed under a light microscope. Such microsystems are necessary to directly study secondary radiation forces arising from particle-particle interactions and individual cellular adhesion forces.

ACKNOWLEDGMENTS

We gratefully acknowledge the contributions of Christian Kargel, Jerome J. Mai, Dustin E. Kruse, and Paul A. Dayton. The research was supported in part by a grant from the National Institute of Health, Grant No. R01 CA82497.

APPENDIX: $X(f_1, f_2)$ FOR PLANE STANDING WAVES WHERE $kR_0 \ll 1$

The integral form of the linear Euler's equation⁴⁴ relates fluid particle velocity \mathbf{v} to pressure via Newton's second law,

$$\mathbf{v}(r', t, t_0) = -\frac{1}{\rho} \int_{t_0}^t \nabla p_s(r', t') dt'. \quad (\text{A1})$$

For the plane standing waves and $t_0 = 0$,

$$\mathbf{v}(z, t) = 2 \frac{P}{\rho c} \cos(kz) \cos(\omega t) \hat{\mathbf{e}}_z. \quad (\text{A2})$$

The time-averaged kinetic and potential energy densities of plane standing waves are^{22,27}

$$\langle \text{KE} \rangle = \frac{\rho \langle v^2(z, r, t) \rangle}{2} = \frac{P^2}{\rho c^2} \cos^2 kz \quad (\text{A3})$$

and

$$\langle \text{PE} \rangle = \frac{\langle p_s^2(z, r, t) \rangle}{2\rho c^2} = \frac{P^2}{\rho c^2} \sin^2 kz. \quad (\text{A4})$$

Setting Eqs. (5) and (6) equal to Eq. (7) for spherical particles, $V_0 = \frac{4}{3}\pi R_0^3$, we have

$$\frac{1}{3} \left[f_1 \nabla \langle \text{PE} \rangle - \frac{3}{2} f_2 \nabla \langle \text{KE} \rangle \right] = \frac{P^2}{\rho c^2} X k \sin(2kz). \quad (\text{A5})$$

Combining Eqs. (A3)–(A5), we obtain

$$\frac{1}{3} \frac{P^2}{\rho c^2} \left[f_1 + \frac{3}{2} f_2 \right] k \sin(2kz) = \frac{P^2}{\rho c^2} X k \sin(2kz). \quad (\text{A6})$$

Consequently, the relationship between the force factor X and particles properties f_1 and f_2 is $X = f_1/3 + f_2/2$ for stationary plane waves.

¹J. D. Humphrey, J. Biomech. Eng. **123**, 638 (2001).

²H. L. Goldsmith and S. I. Simon, Ann. Biomed. Eng. **30**, 1 (2002).

³T. Tilley *et al.*, J. Eur. Biophys. **14**, 499 (1987).

⁴K. Sollner and C. Bondy, Trans. Faraday Soc. **32**, 616 (1936).

⁵L. A. Crum, J. Acoust. Soc. Am. **50**, 157 (1971).

- ⁶W. T. Coakley, G. Whitworth, M. A. Grundy, R. K. Gould, and R. Allman, *Bioseparation* **4**, 73 (1994).
- ⁷K. Higashitani, M. Fukushima, and Y. Matsuno, *Chem. Eng. Sci.* **36**, 1877 (1981).
- ⁸T. L. Tolt and D. L. Feke, *Chem. Eng. Sci.* **48**, 527 (1993).
- ⁹S. M. Woodside, J. M. Piret, M. Gröschl, E. Benes, and B. D. Bowen, *AIChE J.* **44**, 1976 (1998).
- ¹⁰S. Gupta and D. L. Feke, *Chem. Eng. Sci.* **50**, 3275 (1998).
- ¹¹K. Yasuda *et al.*, *J. Acoust. Soc. Am.* **102**, 642 (1997).
- ¹²M. Gröschl, *Acustica* **84**, 632 (1998).
- ¹³A. W. Wang, R. Kiwan, R. M. White, and R. L. Ceriani, *Sens. Actuators B* **49**, 13 (1998).
- ¹⁴G. Whitworth and W. T. Coakley, *J. Acoust. Soc. Am.* **91**, 79 (1992).
- ¹⁵L. P. Gor'kov, *Sov. Phys. Dokl.* **6**, 773 (1962) (English translation).
- ¹⁶T. J. Asaki, P. L. Marston, and E. H. Trinh, *J. Acoust. Soc. Am.* **93**, 706 (1993).
- ¹⁷T. J. Asaki and P. L. Marston, *J. Acoust. Soc. Am.* **96**, 3096 (1994).
- ¹⁸L. E. Kinsler, A. R. Frey, A. B. Coppens, and J. V. Sanders, *Fundamentals of Acoustics*, 4th ed. (Wiley, New York, 2000), Chap. 7, pp. 175–189.
- ¹⁹L. Pederson and A. R. Selfridge, "Tables of material properties," Specialty Engineering Associates Website, 2000.
- ²⁰M. Greenspan and C. E. Tschiegg, *J. Acoust. Soc. Am.* **31**, 75 (1959).
- ²¹G. W. C. Kaye and T. H. Laby, *Tables of Physical and Chemical Constants* (Longman, New York, 1986).
- ²²M. Gröschl, *Acustica* **84**, 432 (1998).
- ²³J. A. Jensen and N. B. Svendsen, *IEEE Trans. Ultrason. Ferroelectr. Freq. Control* **39**, 262 (1992).
- ²⁴P. Gonnard, P. Champ, and L. Eyraud, "Characterization of piezoelectric ceramics for high power transducers," in *Power Sonics and Ultrasonic Transducer Design*, 1988, pp. 25–40.
- ²⁵T. Hasegawa, T. Kido, S. Takeda, N. Inoue, and K. Matsuzawa, *J. Acoust. Soc. Am.* **88**, 1578 (1990).
- ²⁶K. Yosioka and Y. Kawasima, *Acustica* **5**, 167 (1955).
- ²⁷S. M. Woodside, B. D. Bowen, and J. M. Piret, *AIChE J.* **43**, 1727 (1997).
- ²⁸J. Wu and G. Du, *J. Acoust. Soc. Am.* **87**, 997 (1990).
- ²⁹C. P. Lee and T. G. Wang, *J. Acoust. Soc. Am.* **93**, 1637 (1993).
- ³⁰A. Ishimaru, *Wave Propagation and Scattering in Random Media* (Academic, New York, 1978).
- ³¹A. A. Doinikov, *J. Acoust. Soc. Am.* **96**, 3100 (1994).
- ³²A. A. Doinikov, *Wave Motion* **24**, 275 (1996).
- ³³T. L. Tolt, "Agglomeration and collection of fine secondary phases in flowing suspensions utilizing resonant ultrasonic fields," Ph.D. thesis, Case Western Reserve University, 1990.
- ³⁴M. A. H. Weiser and R. E. Apfel, *Acustica* **56**, 114 (1984).
- ³⁵J. Spengler and M. Jekel, *Ultrasonics* **38**, 624 (2000).
- ³⁶G. Ter Haar and S. J. Wyard, *Ultrasound Med. Biol.* **4**, 111 (1978).
- ³⁷A. R. Williams, *Ultrasonic Biological Effects and Potential Hazards* (Academic, New York, 1983).
- ³⁸A. Hancock, "Observation of forces on microparticles in acoustic standing waves," Master's thesis, University of California, Davis, 2001.
- ³⁹A. Selfridge and P. A. Lewin, *IEEE Trans. Ultrason. Ferroelectr. Freq. Control* **47**, 1372 (2000).
- ⁴⁰P. M. Gammell and G. R. Harris, *ARLO* **106**, L41 (1999).
- ⁴¹G. Ludwig and K. Brendel, *IEEE Trans. Ultrason. Ferroelectr. Freq. Control* **35**, 168 (1988).
- ⁴²P. A. Lewin, G. Lypacewicz, R. Bautista, and V. Devaraju, *Ultrasonics* **38**, 135 (2000).
- ⁴³E. L. Madsen, J. A. Zagzebski, R. A. Banjavic, and R. Jutila, *Med. Phys.* **5**, 391 (1978).
- ⁴⁴L. E. Kinsler, A. R. Frey, A. B. Coppens, and J. V. Sanders, in Ref. 18.
- ⁴⁵E. W. Lemmon, M. O. McLinden, and D. G. Friend, "Thermophysical properties of fluid systems," NIST Chemistry WebBook, NIST Standard Reference Database Number 69, National Institute of Standards and Technology, Gaithersburg, MD, 2001.

Erratum: “Analysis of the time-reversal operator for scatterers of finite size” [J. Acoust. Soc. Am. 112, 411–419 (2002)]

David Chambers

Lawrence Livermore National Laboratory, P.O. Box 808, L-154, Livermore, California 94551

(Received 14 October 2002; accepted for publication 14 October 2002)

[DOI: 10.1121/1.1527930]

PACS numbers: 43.20.Fn, 43.60.Pt, 43.10.Vx

Figure 5 and the corrected caption are shown below:

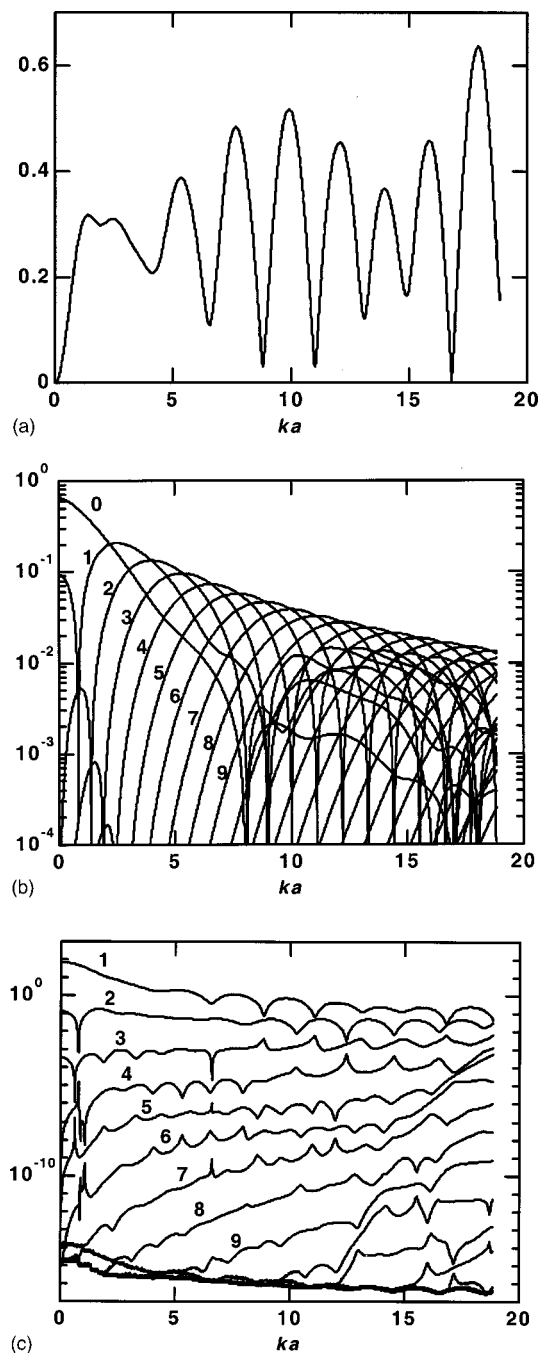


FIG. 5. Analysis of time reversal with a 96-element linear array and a rubber sphere for a range of ka . (a) Backscatter form factor. (b) Magnitude of coefficients, $|B_n|$, in the expansion for the scattered field (labels indicate values of n). (c) Spectrum of the first 20 singular values μ_n (labels are shown for the first nine).